A Celebration of a Great Partnership: Teledyne Webb and RU COOL

2010-2025

“Work Hard, Have Fun, and Change the World”
Quoting Doug Webb in Baiona, Spain, 2009
At the Celebration for the First Underwater Glider to Cross an Ocean Basin

Progress in ocean science, while tightly connected to innovating new technologies, is only possible through partnership of like-minded dedicated people working together for a vision of what could be. This partnership with the leaders-engineers-scientists at Teledyne Webb has been a shining example of what great partnerships can be. This partnership took a vision first articulated in Henry Stommel’s 1989 science fiction hope in *Oceanography,* to then, in 1999, successfully demonstrate for the first time a glider working in the coastal waters offshore New Jersey. From that initial flight, gliders have been widely adopted by the ocean community to build a globally distributed network spanning our planet.

Autonomous gliders are now a transformative technology serving diverse stakeholders that use and live with the ocean. Gliders were first included in the World Ocean Database (WOD) 2018 holdings (WOD18) and by the 2023 WOD23 glider collected data accounted for 15.9% of all ocean data holdings, second only to the historical Ocean Station Data (OSD) at 17.5%, which goes back to 1974. Gliders will likely surpass that dataset in the next WOD update and will represent the largest source of data to the WOD. Taking a moment to reflect on another aspect of this partnership, this collection of science literature published over the last decade illustrates the impact of gliders on a wide range of research questions and technical achievements. But even while taking this moment to look back, most of our energy is focused on the great adventures to come.

In celebration of Doug Webb’s contributions to humanity, we are so excited and honored with the start of the Sentinel mission in 2025 where our partnership will together navigate a glider around the world’s ocean. This book documents our science enabled by Teledyne Marine gliders. We look forward to our continued partnership and the discoveries to come. Looking forward, let’s go and “Smell the sea and feel the sky. Let your soul and spirit fly.” (*Van Morrison)*

Your friends and partners at RU COOL

Scott Glenn, Oscar Schofield, Josh Kohut, Grace Saba, Daphne Munroe, Travis Miles, Alexander Lopez, Thomas Grothues, and Joe Gradone

Teledyne Webb has helped educate a new generation of scientists through generous contributions of graduate fellowships. Their funding has supported a wide range of science spanning the physics of extreme storms to the seasonal migration of the Antarctic krill. Here is the current list of the 11 Ph.D. theses supported by Teledyne Webb.

Teledyne Marine and Doug Webb Graduate Fellowship at Rutgers			
Ph.D. Grad Student	**Graduation Year**	**Thesis Title or Topic**	**Post-Graduation Position**
Travis Miles	2014	Observations and Modeling of the Coastal Ocean Beneath Tropical and Extra-Tropical Cyclones	Tenured Rutgers Associate Professor
Filipa Carvalho	2017	Coupled Physical and Phytoplankton Dynamics in Antarctica's Coastal Seas	National Ocean Centre (NOC)
Nicole Couto	2017	Circulation and hear Transport on the West Antarctic Peninsula Continental Shelf	Scripps Institute of Oceanography (SIO)
Clifford Watkins	2021	Mixed Layer Dynamics: Exploring the Impact of Storms in the Mid Atlantic Bight	Naval Research Lab – Monterey
Schuyler Nardelli	2022	Seasonal Dynamics of Plankton Ecology in Coastal Antarctica	US Geological Survey (USGS)
Michael Chen	2024	Spatial and Seasonal Controls on Eddy Subduction in the Southern Ocean	Oceana Inc.
Lauren Cook	Expected June 2025	Exploring fish carbon cycling off the coast of New Jersey	Faculty @ St. Mary's College, MD
Teemer Barry	Expected July 2025	Deoxygenation in coastal New Jersey bottom water	Applied for Knauss Fellow
Leah Hopson	Ph.D. Candidate	Upper ocean mixing in hurricanes	
Jacob Kuenzil	Grad Student	Distribution and habitat use of sharks in the Mid Atlantic	
Becca Horwitz	Grad Student	Marine heat waves and cold spells in the coastal ocean	

Working together Rutgers and Teledyne Webb have trained a new generation of glider operators. The people who have taken the training have spanned from the Navy, Universities, Federal Laboratories, and students. Over the last 20 years over 165 have been trained between February 2005 and June 2024. The demographics of the training is provided below.

Participant Category	Number	Percentage
Undergraduate	46	28%
Graduate Students	48	29%
Government (Navy, NOAA, etc)	45	27%
Other Researchers	26	16%
Total	**165**	**100%**

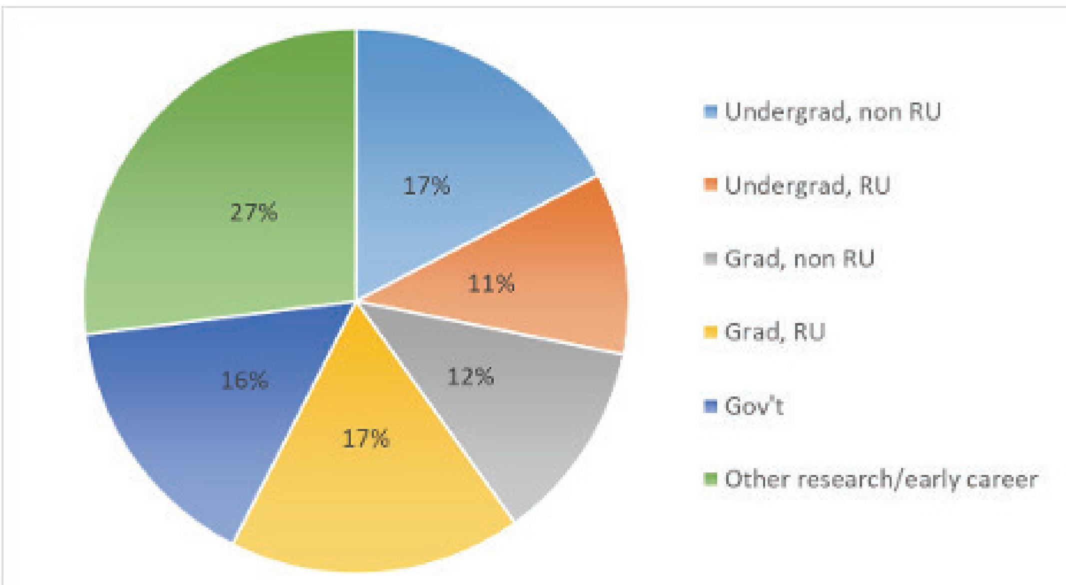

Given the adoption of glider technology across the marine communities, increasing the pool of technical expertise for the community is critical. Rutgers established in 2020, a Masters of Operational Oceanography program. Since its establishment 35 students have taken the program of which 11 of the students' projects were focused on various aspects of glider technology.

MS of Operational Oceanography degree program, Rutgers University (34 Students total)			
Graduation Year	**Grad Student**	**Thesis Title**	**Post-Graduation Career**
2025 (Current)	Matt Learn	Comparative Analysis of Global Ocean Currents for Slocum Glider Path Planning: Evaluating Uncertainty and Time-Optimal Routing	Glider Technician, Stony Brook University
	Jessica Leonard	Using Slocum gliders with nontraditional flight behaviors to accommodate advancements in sensor development	Glider Technician, Rutgers University
2024	Jesse Hope Noble	A dive into theoretical heat flux of diffuse flow hydrothermal vent plumes and applications to extraterrestrial oceans	APEX Applications Engineer Teledyne Webb Research
	Nick Occhiogrosso	Glider-observed seasonal and spatial distributions of zooplankton in the Mid-Atlantic Bight	
	Salvatore Fricano	The glider guidance system (GGS): a model-guided path-planning program for advancing glider operations through depth-averaged ocean currents	Slocum Glider Field Application Engineer Teledyne Webb Research
	Sophie Scopazzi	Sensor and behavior frameworks for implementing backseat driver on a slocum glider	Third Mate Alaskan Tanker Company
2023	Leslie Birch	Dodging Cargo Ships: Can Gliders Use Hydrophones for Ship Detection	Technician Aqua Survey
2022	Casey Jones	Above and below the waves: analysis of coordinated surface and subsurface autonomous vehicle data	Oceanographer IBSS
	Malarie O'Brien	Action Argo: adapting the Argo network to collect actionable data and advance intensity forecasts of storms	Physical Scientist Naval Oceanographic Office
2021	Ailey Sheehan	Developing an open-source analysis pipeline for a glider-based acoustic zooplankton fish profiler (AZFP)	Laboratory Technician Rutgers University
	Theodore Thompson	Best practices for Sea-bird scientific deep ISFET-based pH sensor integrated into a Slocum Webb glider	Physical Scientist/Data Scientist U.S. Geological Survey
2020	Joseph Anarumo	An Open-Source Software Application for Drifter Trajectory Prediction in the Mid-Atlantic Bight	Environmental Science Analyst Sage Services

Peer-reviewed glider manuscripts since the establishment of the Teledyne Webb student Fellowship program

Automated Sensor Networks to Advance Ocean Science

Oceanography is evolving from a ship-based expeditionary science to a distributed, observatory-based approach in which scientists continuously interact with instruments in the field. These new capabilities will facilitate the collection of long-term time series while also providing an interactive capability to conduct experiments using data streaming in real time.

The U.S. National Science Foundation has funded the Ocean Observatories Initiative (OOI), which over the next 5 years will deploy infrastructure to expand scientists' ability to remotely study the ocean. The OOI is deploying infrastructure that spans global, regional, and coastal scales. A global component will address planetary-scale problems using a new network of moored buoys linked to shore via satellite telecommunications. A regional cabled observatory will "wire" a single region in the northeastern Pacific Ocean with a high-speed optical and power grid. The coastal component will expand existing coastal observing assets in order to study the importance of high-frequency forcing on the coastal environments.

These components will be linked by a robust cyberinfrastructure (CI) that will integrate marine observatories into a coherent system-of-systems. This CI infrastructure will also provide a Web-based social network enabled by real-time visualization and access to numerical model information, to provide the foundation for adaptive sampling science. Thus, oceanographers will have access to automated machine-to-machine sensor networks that can be scalable to increase in size and incorporate new technology for decades to come. A case study of this CI in action shows how a community of ocean scientists and engineers located throughout the United States at 12 different institutions used the automated ocean observatory to address daily adaptive science priorities in real time.

Connectivity Between Observations and Models

During its 5-year construction period, the OOI is committed to engaging the ocean sciences community. To fulfill this goal, researchers are developing a useful CI by using a "spiral design strategy" so that the oceanography community can provide input throughout the construction phase.

An example of this strategy was conducted in fall 2009 when the OOI CI development team used an existing ocean-observing network in the Mid-Atlantic Bight waters (MAB, spanning offshore regions from Massachusetts to North Carolina) to test OOI CI software. The objectives of this CI test were to aggregate data from ships, autonomous underwater vehicles (AUVs), shore-based radars, and satellites and then make the aggregated information available in real time to five different data-assimilating ocean forecast models. Scientists use these multimodel forecasts to automate future underwater glider missions so that they can study quickly developing and fast changing characteristics of nearshore marine environments. Scientific interests spanned from the formation of the winter phytoplankton bloom to the role of storms that induce sediment resuspension from the seafloor. The test demonstrated the feasibility of two-way interactivity between the sensor web and predictive models.

Specifically, this effort tested the CI planning and prosecution software, which enables operators to monitor and control individual components within an ocean-observing network. The CI software coordinates and prioritizes the shared resources, allows for the semiautomated reconfiguration of asset tasking, and thus facilitates an autonomous execution of observation plans for both fixed and mobile observation platforms. For this effort, numerical model ocean forecasts, made interoperable by standard Web services, allowed scientists to simulate potential robot trajectories. This was used to guide scientists' decisions about whether desired target areas could be reached by autonomous vehicles.

For example, the software allows a scientist to determine if any available underwater glider could be redirected to map a surface plume of turbid water that had been identified in an ocean color image within a 24-hour period. The software then could determine the optimal path to map the turbid plume. Such efforts were coordinated through a Web portal that provided an access point for the observational data and model forecasts. Researchers could use the CI software in tandem with the Web data portal to assess the performance of individual numerical model results, or multimodel ensembles, through real-time comparisons with satellite, shore-based radar, and in situ robotic measurements.

Testing CI Outputs

To try out the CI's capabilities, scientists investigated the program's ability to remotely coordinate the mission of an array of AUVs that were acoustically networked. Scientists on shore in New Jersey used satellite data to define an operations area, which was forwarded to planners at the NASA/California Institute of Technology's Jet Propulsion Laboratory (Pasadena), who in turn e-mailed hourly AUV deployment instructions back to

Ocean Science cont. on page 346

cont. from page 345

at-sea teams on boats off New Jersey. Each AUV was equipped with an acoustic modem that enabled underwater communications with other AUVs. A gateway buoy allowed real-time communication with science personnel on a ship. This system enabled AUV reports of status information such as position, speed, heading, and scientific sensor readings to be published on Google Earth™ and distributed to scientists around the United States in real time. These AUVs were outfitted with software that enabled them to access the available onboard data to autonomously adapt to the environmental features measured by scientific sensors.

Another test of the CI was to try to coordinate sampling between underwater gliders and the space-based Hyperion imager flying on the Earth Observing-1 (EO-1) (http://eo1.gsfc.nasa.gov) spacecraft. Hyperion images have a footprint of 7.5 × 100 kilometers, with a spatial resolution of 30 meters. This small spatial footprint makes it difficult to ensure that instruments closer to the ground are present for in situ verification measurements. The Hyperion swath can be adjusted to survey different regions, and therefore there is a possibility to mobilize in situ assets and simultaneously adjust the satellite sampling region to be coincident. During the field experiment, observational data and multimodel forecasts were analyzed to determine an optimal redirection for the satellite. These new coordinates were used by the EO-1 Web-based capability to change the spacecraft's surveying patterns (http://ase.jpl.nasa.gov). A 48-hour model forecast was then used by the CI software to colocate any gliders and plan their paths within the new EO-1 Hyperion swath. Two gliders were successfully moved to the swath; other gliders, which were not capable of reaching the swath, were diverted to accomplish other science missions.

Improving the Ease of Science

OOI's CI represents a major technology breakthrough in simultaneously coordinating satellite and underwater assets guided by multimodel forecasts. It provides a machine-to-machine interactive loop driven by a geographically distributed group of scientists.

As the number of ocean observatories increases globally, a sophisticated and scalable CI will be required. The OOI CI will provide functionality, allowing scientists to manage the complex networks while optimizing the science data being collected. The CI will also provide pathways to link other ocean networks, allowing more distributed groups to interact. The resulting global sensor net will be a new means to explore and study the world's oceans by providing scientists with real-time data that can be accessed via any wireless network.

—Oscar Schofield and Scott Glenn, Institute of Marine and Coastal Sciences, Rutgers University, New Brunswick, N. J.; E-mail: oscar@marine.rutgers.edu; John Orcutt, Matthew Arrott, and Michael Meisinger, Scripps Institution of Oceanography and California Institute for Telecommunications and Information Technology, University of California, San Diego, La Jolla; Avijit Gangopadhyay and Wendell Brown, School for Marine Science and Technology, University of Massachusetts Dartmouth, New Bedford; Rich Signell, Coastal and Marine Geology Program, U.S. Geological Survey, Woods Hole, Mass.; Mark Moline, Center for Coastal Marine Sciences, California Polytechnic State University, San Luis Obispo; Yi Chao, Steve Chien, and David Thompson, Jet Propulsion Laboratory, NASA/California Institute of Technology, Pasadena; Arjuna Balasuriya and Pierre Lermusiaux, Applied Ocean Science and Engineering, Massachusetts Institute of Technology, Cambridge; and Matthew Oliver, School of Marine Science and Policy, College of Earth, Ocean, and Environment, University of Delaware, Lewes

BY SCOTT GLENN AND OSCAR SCHOFIELD

Growing a Distributed Ocean Observatory: Our View From the COOL Room

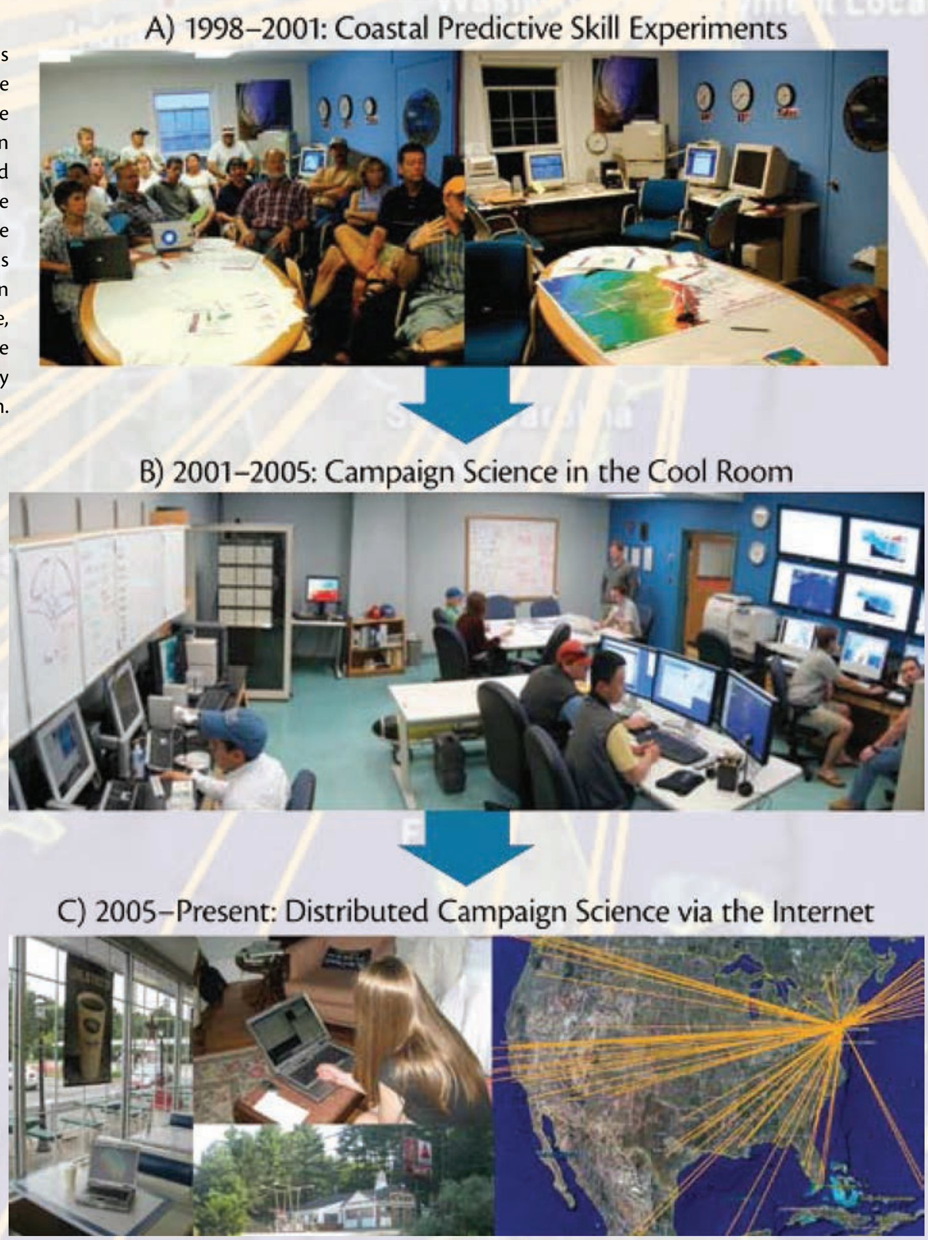

Figure 1. The evolution of the COOL operations center. (A) In the early years, science campaigns were conducted at remote field sites, such as the marine labs in Tuckerton, New Jersey. The remote location limited the duration of the experiments that could be conducted. (B) Improvements in the World Wide Web, combined with wireless technologies, allowed the operations center to be moved to the main campus of Rutgers University. (C) The most recent evolution allows experiments to be sustained remotely anywhere, anytime. Many large field deployments can now be supported from restaurants, from home, or from any location with a decent wireless connection.

ABSTRACT. The Rutgers University (RU) Coastal Ocean Observation Lab (COOL) is an enduring product of the National Oceanographic Partnership Program (NOPP). The key to its longevity is the academic, industry, and government partnerships that were formed through the NOPP process. These partnerships were galvanized by time at sea and then sustained through peer-reviewed proposals. The lab operates an advanced ocean observatory that has maintained a continuous presence on the New Jersey continental shelf since 1992. Key technologies for sustained spatial observations include locally acquired satellite infrared and ocean color imagery, a multistatic high-frequency radar array, and a fleet of autonomous underwater gliders. COOL provides a regional perspective that supports interdisciplinary process studies; provides a test bed, allowing rapid spiral development of sensors and platforms; and has anchored new "campaign" science programs where hundreds of scientists come together for intensive multi-institutional experiments. RU COOL is now a core component of the National Oceanic and Atmospheric Administration Mid-Atlantic Regional Ocean Observing System that, in 2007, began providing data for the full shelf from Cape Cod to Cape Hatteras. Looking to the future, in collaboration with partners from around the globe, the International Consortium of Ocean Observing Labs was formed to focus on improving global ocean observing. The NOPP approach was new and unique when introduced. Its philosophy of partnership among diverse groups was fundamental to the success of COOL and, we believe, will sustain international collaborations into the future.

INTRODUCTION

The Rutgers University Coastal Ocean Observation Lab (COOL) has sustained a continuous observational presence in New Jersey's coastal ocean for 16 years. Over this time, technology improvements have expanded its spatial observing capabilities. The system now provides: (a) a well-sampled region for process studies that range in size from the purview of individual principal investigators to multi-institutional science campaigns, (b) real-time and historical data sets and numerical forecasts supporting a wide variety of scientific and applied users, (c) a local test bed for new technologies, and (d) a focal point for a range of educational activities spanning K–12, undergraduate, graduate, and informal audiences, as well as in-service training. A broad portfolio of competitive grants awarded by US federal and state agencies, industry partners, private foundations, and foreign countries supports these varied activities. The diversified funding portfolio grows directly from our participation in the National Oceanographic Partnership Program (NOPP), which transformed our predominantly academic endeavors of the early 1990s into sustained academic-industry-government partnerships. NOPP provided the seed money to initiate and demonstrate the effectiveness of these approaches, and it continues to attract new partners from different disciplines.

In *Oceanography* and other publications, we have reviewed the evolution of our coastal ocean observatory and the international ocean observatory movement (Glenn et al., 2000a,b, 2004; Schofield et al., 2002, 2003, 2007; Glenn and Schofield, 2003; Schofield and Glenn, 2004). Here, we trace our progress, emphasizing developments since 2003 when our observatory operations center moved from a remote coastal location to the main campus of our research university, which is located two hours from shore (Figure 1A). The transition made the observatory an integral part of everyday campus life year round. This change also increased student involvement, most significantly at the undergraduate level. Since then, improvements in wireless technologies now allow the observatory to be controlled from any global location that has access to the World Wide Web.

THE NOPP DECADE

COOL has participated in six NOPP projects to date (Table 1). Beginning with the first round of NOPP awards, Rutgers-led projects focused on demonstrating the capabilities of an integrated ocean observing and forecast system to maintain a well-sampled 30 km x 30 km portion of the coastal ocean. The need for personnel to be moved to the coastal site to conduct these experiments, and the broad spatial coverage of these experiments, meant that they could only be sustained for about one month (Figure 1A). New sampling technologies and communications systems were required to expand the footprint in space and time. More importantly, initial partnerships formed through the NOPP process grew into a self-sustaining technology development and scientific study team. The team conducted process studies supported by the Office of Naval Research (ONR) and the National Science Foundation (NSF), and enabled

Table 1. The decade of NOPP grants in which COOL participated

TITLE	PARTICIPANTS		INSTITUTIONS	YEARS
Multi-scale model-driven sampling with autonomous systems at a national littoral laboratory	J.F. Grassle S.M. Glenn D.B. Haidvogel C.J. von Alt	E.R. Levine D.E. Barrick B. Lipa J.W. Young	Rutgers University Woods Hole Oceanographic Institution National Undersea Warfare Center CODAR Ocean Sensors Ltd.	1997–1999
Demonstration of a relocatable regional ocean atmosphere modeling system with coastal autonomous sampling networks	S.M. Glenn D.B. Haidvogel R. Avissar J.F. Grassle O. Schofield C.J. von Alt	E.R. Levine D.C. Webb D.E. Barrick B. Lipa J.W. Young R.P. Signell	Rutgers University Woods Hole Oceanographic Institution National Undersea Warfare Center Webb Research Corporation CODAR Ocean Sensors Ltd. Teledyne RD Instruments United States Geological Survey	1998–2000
Bringing the ocean into the precollege classroom through field investigations at a national underwater laboratory	M.P. DeLuca C.J. von Alt J.F. Grassle J. McDonnell	K.A. Able S.M. Glenn O. Schofield	Rutgers University Woods Hole Oceanographic Institution	1997–1998
An integrated wireless coastal communication network	R. Nichols J. Burbank W. Kasch D.L. Porter	S. Glenn O. Schofield C. Jones	The Johns Hopkins University Rutgers University Webb Research Corporation	2004–2006
Novel acoustic techniques to measure schooling in pelagic fish in the context of an operational coastal ocean observation	K. Benoit-Bird C. Jones O. Schofield	S. Glenn J. Quinlan J. Condiotty	Oregon State University University of Washington Rutgers University Simrad	2005–2008
Development of fluorescent induction and relaxation systems for the measurement of biomass	O. Schofield S. Glenn P. Falkowski	M. Gorbunov C. Jones S. McLean	Rutgers University Webb Research Corporation Satlantic Inc.	2005–2009

technology-development projects supported by ONR, the Department of Homeland Security (DHS), and the National Aeronautics and Space Administration (NASA).

NOPP also invested funds to develop key technologies and grow a diverse observatory community. Some NOPP efforts focused on improving communication networks for coastal observatories by enabling virtual collocation, ultimately freeing scientists from the constraints of having to move all operations to the shore lab for one-month time periods (Figure 1B, C). NOPP also supported the development of new sensors that were rapidly transitioned into the observatory for prototyping and feedback to developers. Additionally, NOPP focused on building linkages to K–12 and the education research community. We explored the concepts of using real-time ocean data in the classroom, a highly successful effort leading to the establishment of two NSF Centers for Ocean Science Education Excellence (COSEE) at Rutgers. The key lessons of our NOPP experiences are that equal partnership, rapid spiral development[1], and leveraging of resources lead to successful programs.

Scott Glenn *(glenn@marine.rutgers.edu) is Professor of Physical Oceanography, Institute of Marine and Coastal Sciences, Rutgers University, New Brunswick, NJ, USA.* **Oscar Schofield** *(oscar@marine.rutgers.edu) is Professor of Biological Oceanography, Institute of Marine and Coastal Sciences, Rutgers University, New Brunswick, NJ, USA.*

[1] Spiral development was introduced in the mid 1980s by Barry Boehm of TRW Inc. as a way to reduce risk on large software projects after finding that these programs were too often designed and built with little input from end users, resulting in failure to meet objectives. Boehm's cyclical approach included early customer evaluation and identification of potential trouble spots by in-house engineers at an early stage. This approach has since been applied more generally to large projects.

Partnerships

NOPP proposals required partnerships among academic, industry, and government laboratories. Our strategy was to assemble a distributed collaborative team regardless of each partner's academic status, proximity, or congressional district. The net result was a virtual institution fueled by a shared vision. The diversity of the partners contributed new perspectives, which were assessed through the peer-review process. The participants, whether they were data providers or data users, were always considered equal partners in the project's execution. This goal-driven mode of construction was in contrast to early efforts by others who built systems based on input from external users.

Spiral Development

The NOPP process recognized that many of the sampling, communication, and modeling technologies required to provide a self-sustaining ocean observatory had not yet been developed. The fixed duration of the NOPP funding promoted a rapid spiral development cycle, which encouraged engineers to work alongside scientists in the field. Early NOPP projects focused on developing novel sampling technologies such as high-frequency [HF] radar and autonomous underwater gliders; later projects were devoted to sensor development. With no guarantee of sustained support, survival of the partnerships was contingent on producing results that would support the next round of peer review or survive the commercial marketplace. This process accelerated the pace of development.

Leveraging of Resources

NOPP was founded, in part, to allow all relevant federal agencies to address ocean observation, modeling, and data management needs jointly. As NOPP challenged scientists and engineers to cross departmental and academic-industry-government lines, the research community was challenging the federal agencies to fund efforts that often overlapped the different agencies' missions. This arrangement resulted in the development of ocean test beds that could simultaneously serve multiple needs. The cyclical support from individual agencies was merged to provide a more continuous funding stream. As the technologies matured, the test beds became more cost efficient, so that keeping an ocean observatory running 24/7/365 was not much more expensive then the cost of repeated mobilization and demobilization cycles. Addressing the scientific research problems of multiple agencies resulted in diverse scientific programs that constantly pushed the limits of available technology and improved the observatory over time.

DEVELOPMENT OF THE COOL ROOM

Our initial NOPP efforts focused on the three-dimensional topographic steering of coastal upwelling and its role in driving bottom water hypoxia/anoxia along the New Jersey coast (Glenn and Schofield, 2003; Glenn et al., 2004b; Schofield et al., 2004; Figure 2A). To study the dynamics of upwelling events, we deployed a month-long coastal observatory during July 1998–2001. The network consisted of real-time remote-sensing data from multiple satellites, aircraft, and shore-based HF radars; a cross-shelf mooring array; and numerous research vessels, autonomous underwater vehicles (AUVs), and numerical forecast models. Nearly 200 researchers from over 30 institutions participated (Schofield et al., 2002, 2004; Glenn and Schofield, 2003) as part of NOPP-supported efforts and ONR programs. Overall, the scientific results: (1) provided a physical understanding of recurrent upwelling zones, (2) defined the biological dynamics within the upwelling eddies, (3) indicated significant loading of anthropogenic materials by small, nearshore, coastal jets not resolved using traditional sampling strategies, (4) quantified the annual importance of the summer upwelling events, and (5) linked biological dynamics to bottom-water hypoxia. While successful, the need for all operations and personnel to be moved to the shore-based center was a fundamental factor limiting the experiment's duration. Thus, future efforts focused on developing an operational command location on the main Rutgers campus.

The new COOL room was established on the Rutgers campus in 2001 (Figure 1B). It was designed to operate throughout the year and integrate students into the field efforts during the academic year. The first major effort to use the campus COOL room was the NSF 2003–2005 Lagrangian Transport and Transformation Experiment (LaTTE; Figure 2B). LaTTE focused on understanding how mixing and transport in the Hudson River plume regulates biological and chemical transformations within the coastal zone. The observatory guided the multi-ship field effort to track the buoyant plume, which was highly sensitive to local wind

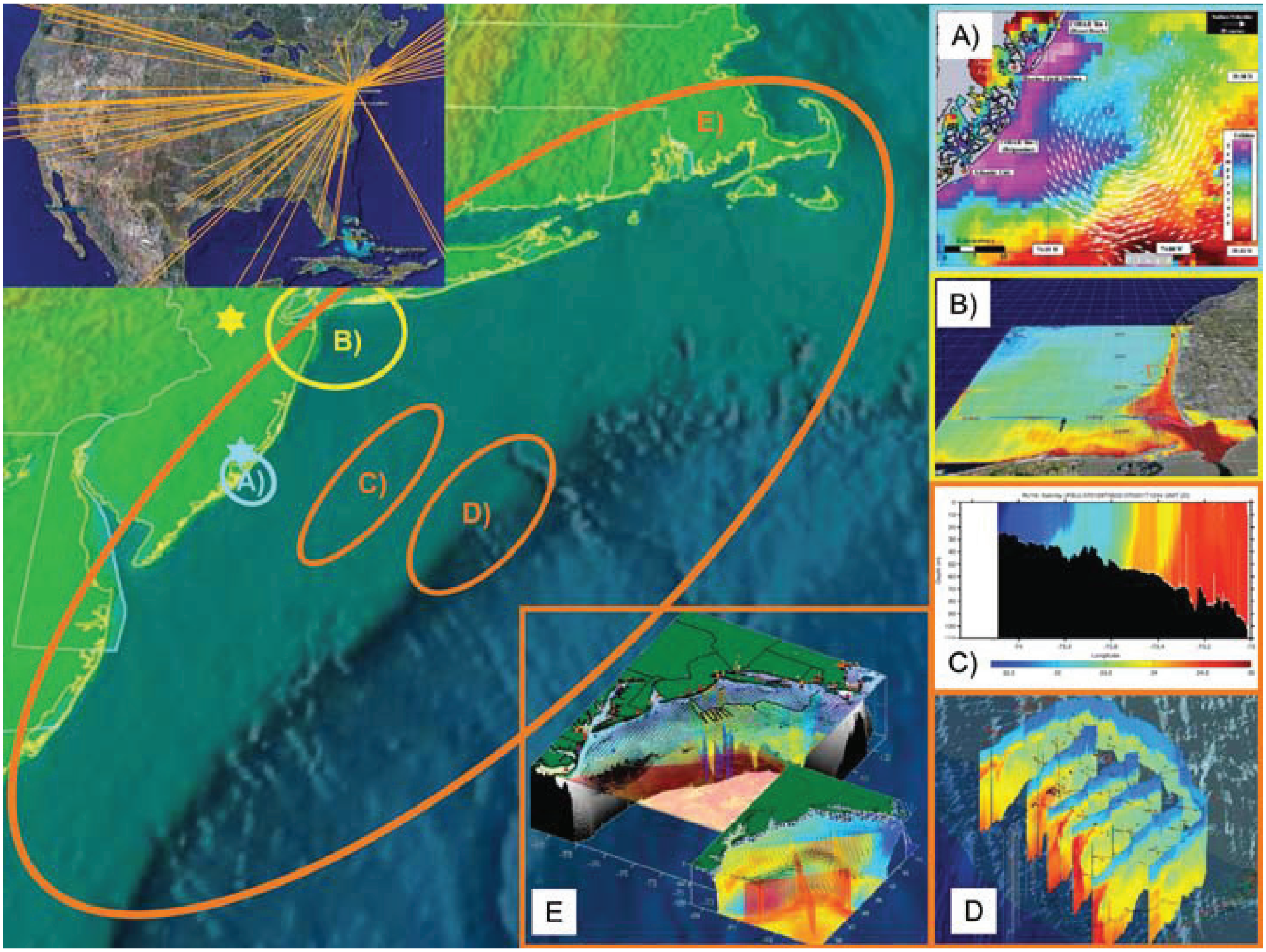

Figure 2. The experimental domains of the major COOL experiments supported by the observatory on the Mid-Atlantic Bight. Circles indicate the spatial range of the different experiments. (A) The first focus was on recurrent upwelling along the New Jersey coast and its role in driving local hypoxia/anoxia. (B) LaTTE focused on the transport and transformation of chemical and biological constituents present in the Hudson River buoyant plume. (C) Glider surveys were a critical component in efforts to resolve the physics driving front formation in Mid-Atlantic Bight waters. (D) The ONR Shallow Water 2006 joint experiment used fleets of gliders to support large mooring deployments focused on understanding the role of internal waves and the corresponding impact on acoustic uncertainty. (E) Recent work involves developing large, regional-scale observing networks to support data assimilative forecast models.

forcing. Scientists, graduate students, and undergraduates maintained the observatory with 24-hour shift rotations. Data from the Coastal Ocean Dynamics Applications Radar (CODAR) and satellites were combined with numerical forecast models to direct ship and glider operations using the wireless network available in this location (Schofield et al., 2007). The observatory-driven sampling effort provided data showing that the Hudson River recirculated in a near-shore eddy before being dispersed in an unexpected cross-shelf pathway, which represented two-thirds of the buoyant plume water being delivered to the shelf (Castelao et al., 2008; Chant et al., 2008). This unexpected cross-shore transport pathway provided a direct conduit between the urbanized watershed and the continental slope. Within the buoyant plume, phytoplankton assimilated nutrients, resulting in high rates of productivity associated with large chain-forming diatoms. The size structure of the phytoplankton mediated the accumulation of anthropogenic nutrients and contaminants in the higher trophic levels of the food web (Moline et al., 2008).

The success of the campus-based

efforts resulted in year-round offshore operations for sustained time periods (Schofield et al., 2008). For example, since late 2003, the lab's glider efforts have supported over 2300 glider days at sea spanning over 50,000 km under water (Figure 2C). Global glider efforts resulted in optimization of Iridium satellite communications, allowing a global footprint to be supported locally. The ONR Shallow Water 2006 joint experiment conducted on the outer shelf of the Mid-Atlantic Bight drove the next stage of observatory evolution (Figure 2D; Tang et al., 2007). The multi-ship and 60-mooring deployment was complemented with a fleet of Webb gliders. The efforts were supported with a daily environmental report that was delivered to the ships offshore via High Seas Net. This daily report summarized all the data for all the distributed parties. Additionally, the report provided the semblance of a social network for the large science campaign involving several hundred scientists. The daily report was coordinated through the COOL room over the three-month experiment duration; however, the lead Rutgers investigator was required to travel during the experiment for other obligations. This absence required the development of a suite of mission planning tools and Web-based products that would allow the daily report to be produced in any location with access to the Internet.

Scientific results from the glider fleet revealed four types of slope water salinity intrusions—surface, pycnocline, subpycnocline, and bottom—each appearing to be forced by different mechanisms. The extensive pycnocline intrusions were affected by stronger than usual shelf stratification due to remnants of low-density Hudson River water associated with a heavy rainfall. The new transport pathway discovered during LaTTE was observed in the CODAR surface current fields and verified with Coast Guard drifters (Castelao et al., 2008). Tropical Storm Ernesto went through an extratropical transition (the process by which a hurricane can change from a tropical cyclone to a mid-latitude depression) while transiting the region, with the transition and path well matched by an ensemble of high-resolution atmospheric forecast models that included the latest boundary-layer physics. Ernesto was observed by the gliders to resuspend significant amounts of sediment below the thermocline, which could not mix across it, motivating additional research on storms (Glenn et al., 2008).

With the success of distributed control for remote assets coordinated through COOL, the "footprint" of the observing efforts has increased significantly. Currently, ONR and NOAA are combining ocean observations and modeling dynamics to extend the limits of biological predictability using a technique called "data assimilation" (Figure 2E). Using this method requires observations at ecologically relevant scales spanning large marine ecosystems. The multiplatform observing networks provide the needed three-dimensional snapshots of water mass properties in near real time. These data are then assimilated into different models. Model uncertainties are estimated by comparing the different three-dimensional models with actual measurements. Ultimately, these models will be used to characterize regional three-dimensional water mass patterns to enable adaptive sampling.

SCIENTIFICALLY MOTIVATED TECHNOLOGY DEVELOPMENT

The expanding set of scientific problems that could be tackled by continuous data collection by our observatory resulted in an atmosphere conducive to technology development, which focused on enabling scientists to collect spatial time series. The major relevant technologies have included satellites, HF radars, gliders, and communications.

Satellites

A number of improvements have been made to observatory satellite data collection over the last five years (Figure 3). First, we set out to minimize the temporal gaps between satellite images by incorporating data from the international constellation of satellites, including Chinese and Indian ocean-color systems (Figure 3B, E). The international satellites' multiple passes per day at varying spatial and spectral resolutions provide numerous scientific and applied users with desired real-time imagery (Figure 3G). We developed customized views with input from thousands of satellite-imagery users. For example, a user could request enhanced imagery for a specific location at a specific time, allowing retrieval of the information needed without downloading a large file; this method is particularly useful for people who are working at sea with limited communication bandwidth. These real-time satellite images are complemented with a range of products developed in collaboration with the Naval Research Laboratory at Stennis Space Center, the University of Delaware, and Saint Andrews University. These collaborative efforts focused on deriving inherent optical properties from

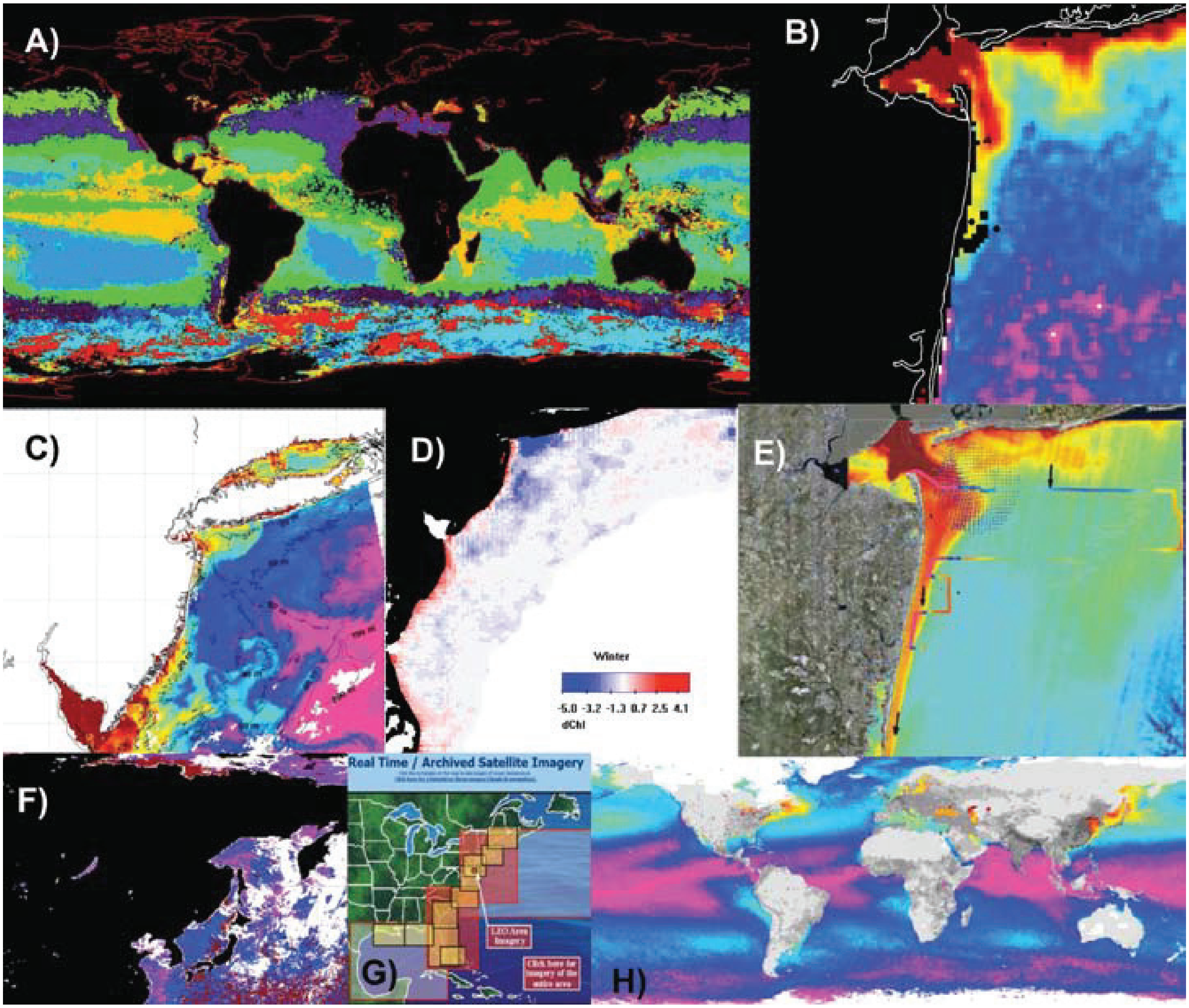

Figure 3. The major efforts in developing the capabilities of ocean remote sensing over the last decade. (A) A map of the major water masses delineated using objective bio-informatic approaches applied to satellite imagery. (B) The Hudson River plume visualized with the Chinese Fung Yen-1D polar-orbiting ocean color satellite. (C) A satellite image of the inherent optical properties (here, phytoplankton absorption) measured using ocean color satellite imagery. (D) The decadal change in the winter-season chlorophyll estimated by comparing imagery measured with the Coastal Zone Color Scanner and the SeaWIFs systems. (E) An ocean color image of the Hudson River plume visualized using the Ocean Colour Monitor on the Indian Remote Sensing Satellite. (F) Water mass classification approaches for delineating the presence of river plumes. (G) Customized satellite maps developed at the request of users who constantly access the COOL Web site. (H) The maximum annual temperature change in sea surface temperature.

space and validating the satellite estimates in the coastal ocean.

Another goal was to develop water mass classification procedures using satellite imagery. Computer algorithms were developed to identify on the satellite images the spatial extent of waters containing highly colored, dissolved organic matter associated with river inputs (Figure 3F). Because these initial algorithms were locally tuned, our recent efforts focused on developing methods that might have wider utility to the community. Instead of using subjective expert decisions (Longhurst, 1998; Devred, 2007), we used objective classification techniques that combine multiple satellite data sources to generate regional maps (Oliver et al., 2004). These objective mapping tools have been validated over a range of spatial and temporal scales and permit quick identification of water masses with particular characteristics. We also explored decadal changes in winter-season chlorophyll by comparing imagery from the Coastal Zone Color Scanner (operational from the late 1970s to the mid 1980s) with current SeaWIFs imagery. (Schofield et al., 2008; Figure 3D). Finally, there has been improvement in estimates of inherent optical properties (IOPs) from ocean color imagery (Figure 3C). IOPs are optical parameters that provide information on all materials that have color (phytoplankton, detritus, colored dissolved organic matter) and scattered light (organic and inorganic particles), and that are easier to interpret than traditional radiometry measurements. This attribute makes these optical parameters ideal for enhancing biological models. For example, photosynthetic rates are a function of total light absorption of the phytoplankton and the efficiency with which the absorbed radiation is converted into organic carbon.

HF Radar

The Rutgers CODAR HF radar network was reconfigured for LaTTE into a nested, multifrequency current mapping system that covered the New Jersey continental shelf and then focused in at higher resolution on New York Harbor and the Hudson River plume (Figure 4A). A 5-MHz network (Figure 4B) covers the shelf at 6-km resolution, a 13-MHz system covers the approaches to New York Harbor at 3-km resolution, and a 25-MHz inner nest covers the harbor entrance and the inside of the harbor at 1.5-km resolution (Figure 4 C,D). Similar nested networks were set up by other universities to cover the major bays to our south and the sounds to our east. NOAA-owned transportable HF radars designed for quick deployments from trailers were used temporarily to locally enhance coverage and for rapid response tests of simulated oil spills in remote locations (Figure 4E). Radial current data from each group participating in what came to be known as the Mid-Atlantic HF Radar Consortium (MAHFRC) was aggregated as part of the NOAA-sponsored HF radar national network server demonstration. The resulting regional array (Figure 4A) runs along ~ 1000 km of coastline, extending from Cape Hatteras to Cape Cod, though coverage at any given time remained subject to the research grant support available to each radar's host institution. The Coast Guard has conducted field tests using surface drifters to quantify improvements to search and rescue planning enabled by real-time CODAR surface currents. Similarly, NOAA was interested in validating the CODAR HF radar nearshore wave and current parameters to support rip current forecasting for lifeguards. These results were used to develop a three-phase plan to transition the current mapping network to sustained operations.

Beyond the development and demonstration of a regional current mapping capability, research on new CODAR hardware, processing algorithms, and products continued. The most significant hardware improvement was CODAR's addition of GPS timing to each radar. GPS timing enables multiple radars in close proximity to share the same frequency without interference, thus minimizing the network's footprint on the broadcast frequency spectrum. GPS timing also enables coordinated, multistatic operation of radars that are within range of one another. Standard monostatic radars, whose transmitters and receivers are collocated, operate in backscatter mode only. In multistatic operations, each receiver can acquire scattered signals from any radar transmitter within range. The result is that N monostatic radars are transformed into a multistatic network with N^2 look angles. Beyond construction of the land-based multistatic network, new bistatic transmitters were developed for stand-alone operation as either land-based systems (Figure 4B–D) or for offshore deployments on fixed platforms (Figure 4I) and buoys (Figure 4J). The network of fixed shore-based receivers acquires scattered signals from the bistatic transmitters.

Tests of the multistatic HF radar network capability were first funded by ONR for vessel-tracking experiments. The research question asked whether an HF radar network could detect and track surface ships. The positive outcome resulted in efforts to increase the range of over-the-horizon vessel detection without increasing the broadcast power of the radars. These efforts focused on improving the methodologies for enhancing signals acquired by land-based receivers, including test deployments of a super-directive multistatic receiver antenna (Figure 4F). Complementary strategies were undertaken to increase the offshore range by placing bistatic HF radar transmitters on offshore buoys, thus decreasing the distance from transmitter to target. The two approaches, both tested in the

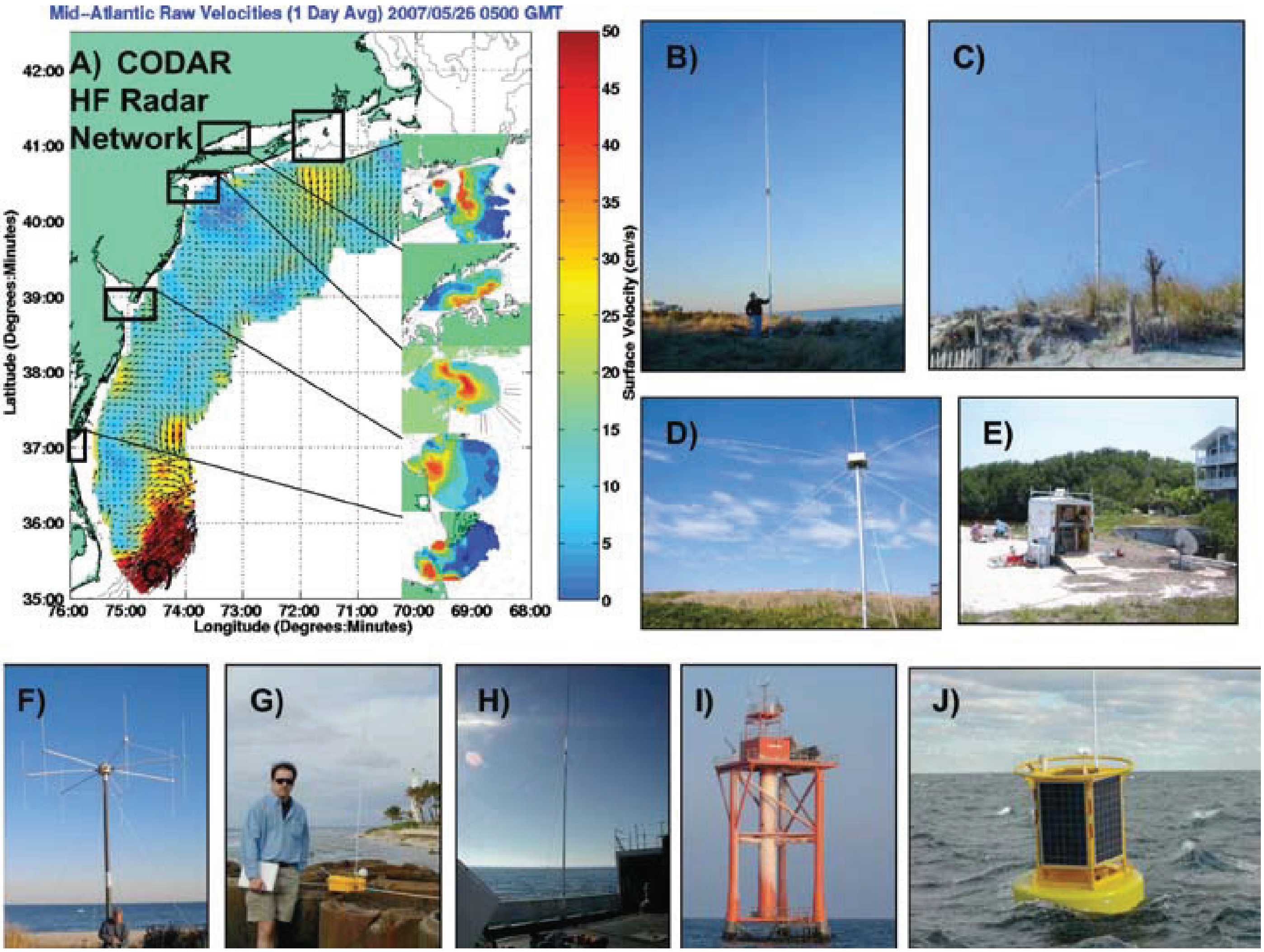

Figure 4. (A) The nested Mid-Atlantic HF radar network as currently supported by US IOOS through NOAA. Components include (B) transmitters for long-range systems (5 MHz), (C) transmitters for medium (13 MHz) and short (25 MHz) systems, (D) common receivers for all three, (E) NOAA mobile CODARs for temporary deployments and fast response, (F) superdirective receivers to increase the signal-to-noise ratio, and a series of bistatic transmitters that include (G) shore-based portable systems, (H) long-range systems deployed on ships, (I), short-range systems deployed on offshore platforms, and (J) medium-range systems deployed on buoys.

Mid-Atlantic HF radar test bed, led to improvements to the Coast Guard mapping capabilities.

Gliders

Mobile platforms are developing quickly and are transitioning into observational tools (Rudnick and Perry, 2003). One autonomous platform that is rapidly becoming indispensable is the underwater glider (Figure 5). Publicized in 1989 by Henry Stommel's view of a futuristic smart fleet of mobile, long-duration sensor platforms (Stommel, 1989), gliders are steadily earning their reputation for efficiency and endurance. A number of different gliders have been developed (Davis et al., 2003) but our group uses the Slocum glider developed by Webb Research Corporation (now Teledyne Webb Research). Gliders are a robust technology capable of anchoring large field campaigns and providing a sustained presence in the ocean (Schofield et al., 2007). Our efforts have focused on enhancing glider capabilities as part of a long-term NOPP-style partnership with Teledyne Webb Research by improving glider hardware, software, and increasing the sensors carried onboard these platforms (Figure 5).

Steady improvements in hardware and software over the last five years have

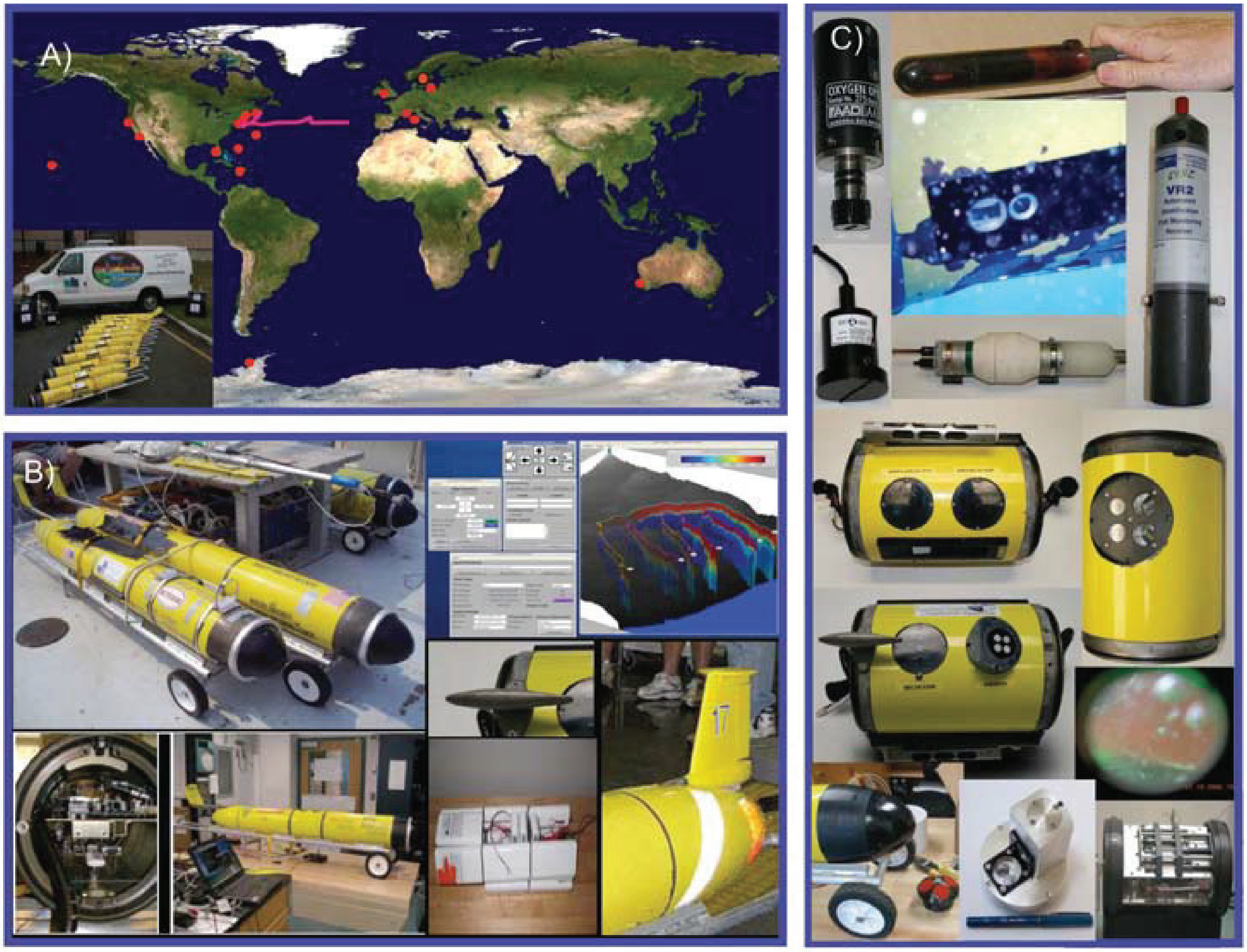

Figure 5. The success of Webb gliders deployed by Rutgers since late autumn 2003. (A) The global deployment map of the Rutgers Webb Glider fleet. (B) Hardware improvements developed under a Teledyne Webb Research/Rutgers partnership include extended glider payload bays, command/control and visualization software, pick points on the gliders, new more powerful computers inserted into the glider science bay, lithium battery packs to increase glider duration, and the new robust digi-fin. (C) Many instruments have been carried on Rutgers gliders over the last five years, including (starting at the top left panel) oxygen sensors, passive acoustic sensors, attenuation sensors, chlorophyll/colored dissolved organic flourometers, turbulence sensors, fish bioacoustic sensors, scattering and backscattering sensor packages, spectral backscatter sensors, radiometer sensors, video imaging components, acoustic Doppler current meters, fast-repetition-rate flourometers, and hyperspectral absorption sensors.

included simple features such as pick-up points to enable glider deployment/recovery from large ships, extended body forms for carrying larger sensors or extra battery packs, robust tail fins, command/control and visualization software, and improved onboard science computers (Figure 5B). The hardware improvements have extended glider duration and performance. Additionally, a wide range of new sensors has been incorporated into the gliders. Measurements presently being made by gliders include physical (temperature, salinity, turbulence), acoustic (active and passive), optical (spectral radiometry, backscatter, attenuation scattering, absorption, video imagery), fluorescence (chlorophyll *a*, colored dissolved organic fluorescence, fast repetition rate fluorometry), and dissolved gas (oxygen) (Figure 5C).

Communication Networks

During the 1998–2001 Coastal Predictive Skill Experiments, lack of communication capabilities necessitated removal of the entire shore-based team from the Rutgers main campus to a coastal site. The camaraderie stimulated by collocating personnel at one shore-based control center was similar to that of going to sea, but the multiple ships and shore crews involved in the experiment still required a means to communicate. During this time period, virtual collocation was enabled with radio modems that connected ships and aircraft to the shore-based science crew. This mode of communication was complemented by shore-based Web broadcasts of live video and radio chatter in an effort to involve the outside community. For these communication efforts, the physical range was limited to line of sight (~ 30 km). In 2003, the range changed with our participation in the Ocean.US Iridium Pioneers program. The ability to communicate globally using Iridium SIM cards was transformational.

During LaTTE programs from 2003–2005, we worked with a commercial vendor to expand communication regionally using higher-bandwidth cell phone modems. During the ONR Shallow Water 2006 experiments, which required coordination for three months and a virtual presence for COOL, all data sets were available via the World Wide Web. These changes in the mode by which the field teams communicated allowed science planning to be conducted from another research lab, from restaurants, or even from our living rooms via wireless Internet connections (Figure 1C). Global access to the observatory through WiFi hotspots remains in constant use today. Observatory assets can be accessed, systems checked, data visualized, and adaptive sampling plans adjusted on a sustained basis from any location in the world as part of normal life activities. Daily achievements are documented on public blog sites, enabling anyone—from collaborating scientists to the general public—to follow along on missions of discovery.

DEVELOPMENT OF A SUSTAINED REGIONAL TEST BED

The first long-range 5-MHz CODAR HF radar was deployed on the East Coast in the summer of 2000 during the third ONR/NOPP Coastal Predictive Skill Experiment. The 200+ km range of the radial current field covered the full cross-shelf distance to the shelf break. It solidified plans for developing a regional observatory spanning the Large Marine Ecosystem (#7) of the Northeast US Continental Shelf (see http://www.lme.noaa.gov/ for more information on the 64 Large Marine Ecosystems designated worldwide). The regional network would be anchored by a nested, multistatic HF radar network. Initial attempts focused on combining our existing subregional ocean-observing assets into a loose federation that we called the North East Observing System (NEOS). Building on the strength of the NOPP partnership approach, NEOS consisted of academic observatories, government backbone observatories, and industry networks collaborating with instrument developers. At that time, NEOS partners believed the observatory should be based on the best science available to improve coupled forecast models.

The NOAA regional network developed in the Mid-Atlantic Bight (MAB) is the foundation of the developing NEOS network (Figure 6). In 2007, NOAA funded the Mid Atlantic Regional Coastal Ocean Observing System (MARCOOS), which revolved around two regional themes. Theme 1, Maritime Safety, would provide maps of nowcasts and forecasts of regional surface currents to improve search and rescue and hazardous material spill response, as well as nearshore products to improve rip current forecasting. Theme 2, Ecosystem Decision Support, would provide regional three-dimensional temperature and circulation data, nowcasts, and forecasts of the ocean, extending from Cape Cod to Cape Hatteras, for the recreational, commercial, and fishery management communities. To generate the nowcasts and forecasts, an extensive array of existing observational data, data management, and modeling assets required coordination (Figure 6).

This NOAA investment will be augmented by other agencies. Currently, NSF proposes to build the Ocean Observatories Initiative (OOI), which calls for a robotic array to be placed on the MAB shelf south of Cape Cod near the shelf break. Research funded by ONR, while designed to support the Navy in forward deployed areas, often uses the same region as a test bed for instrument development and scientific process studies. Although there is no substitute for actually going to sea in specific regions of interest, the cost of foreign deployments exceeds the cost of local deployments by an order of magnitude. Local surrogate test beds for regions of interest are cost effective for development and training of operational Navy personnel. DHS is interested in the over-the-horizon capabilities of HF radar for maritime domain awareness. Leveraging the existing network was one cornerstone for a recently formed DHS Center of Excellence for

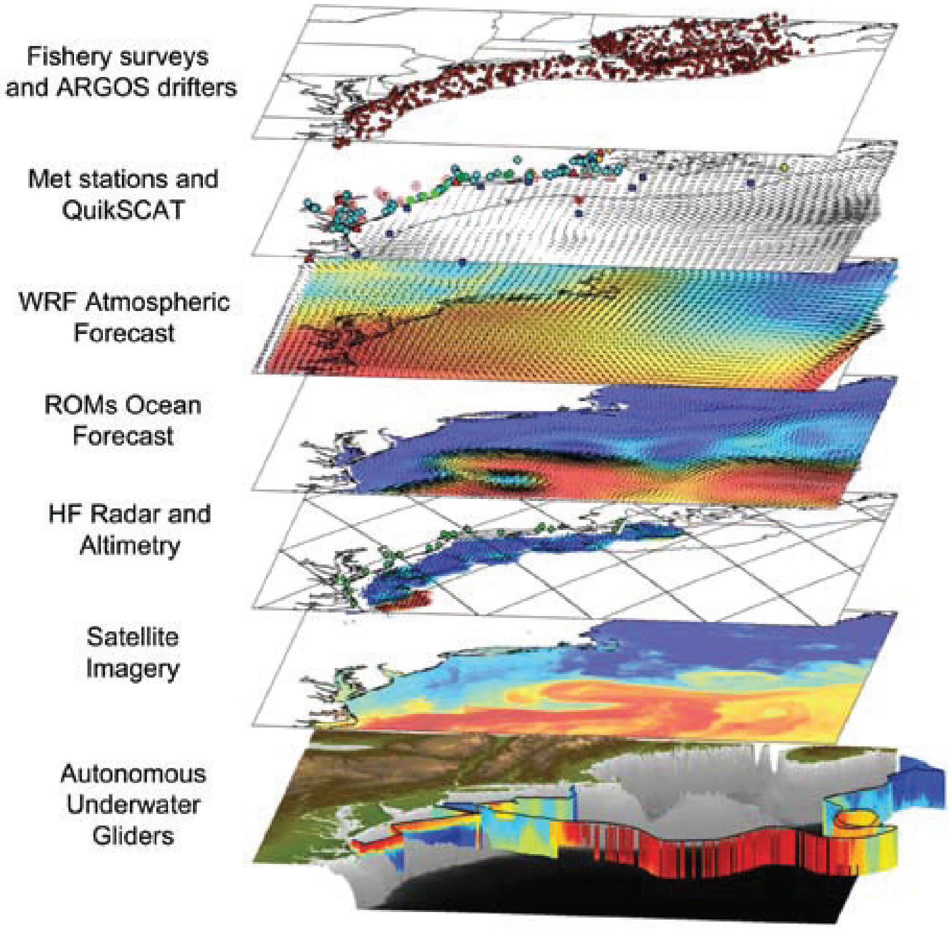

Figure 6. The current status of the North East Observing System (NEOS) showing the numerous data streams being compiled by the distributed academic-federal-commercial team.

Port Security. Additionally, there is rapidly expanding interest from the energy industry. Public Service Electric & Gas (PSE&G) funded high-resolution weather forecasts to pre-position service trucks during storms to reduce response time to power outages. Offshore wind energy companies provide support to enhance the observing network in the vicinity of proposed offshore wind farms. Offshore wave power companies are investing money to enhance offshore platforms in the region, using it as a test bed for energy harvesting systems.

Funding for the observatory emphasized commonalities. Development of new enabling technologies was central to all observatory users. All benefited from investments of others and all required access to real-time data and forecasts for operational decisions, ranging from adaptive scientific sampling with autonomous vehicles to adaptive response to storms by repair vehicles. All desired access to historical data to study specific events of interest in order to improve future responses. All required a sustained data stream to identify long-term trends that could affect their event-based responses. The result is a wide variety of observatory users that also happen to be observatory funders, spanning eight federal agencies and industry.

Collaboration and leveraging is evident throughout. Glider operations run by several universities in the region are supported by ONR, NOAA, and NSF. Satellite ground stations at Rutgers, University of Maine, and The Johns Hopkins University Applied Physics Laboratory each acquire the real-time direct broadcast data and provide a back-up data source in case one station goes down. Academic institutions mostly own the HF radars, with support now provided by NOAA for the US Integrated Ocean Observing System (IOOS). As with the gliders, ONR, NOAA, and NSF support the regional ocean models typically run by multiple academic institutions, while the Navy and NOAA operate the basin-scale models. Local NOAA Weather Service Offices, academics, and industrial partners run the ensemble of atmospheric models. NOAA operates the main regional fisheries cruises on agency vessels, while academics cover the supplemental surveys with fishing industry vessels.

DEVELOPMENT OF AN INTERNATIONAL COLLABORATORY

IOOS is the US contribution to the Global Ocean Observing System (GOOS), which, in turn, is the international oceanographic community's contribution to the Global Earth Observing System of Systems (GEOSS). The structure provides an international forum for governments to collaborate on the critical need for observing the world ocean in an era of human-induced climate change and population growth. Still, it is unclear how the practicing scientist contributes to the global expansion of the already difficult task of making observations in an often hostile ocean environment.

The 2005 Oceanography Society meeting in Paris was one turning point in the promotion of international collaborations in the spirit of NOPP. Discussion focused on how best to collaborate, share data, and begin to form a coherent network. This coalescing collaboration was reminiscent of the atmospheric observing community in the early 1900s when the telegraph first connected individual weather forecasters from different countries independent of official government organizations. It became clear there was much to be gained by sharing expertise and limited observational assets. Although enabling technologies continue to be demonstrated locally or even regionally in many places around the world, we remain capacity limited if we try to address the challenges of globalization.

Seeing the collaborative spirit at the Paris meeting as a way forward for the working scientist, at a Paris sidewalk café, John Cullen from Dalhousie University initiated the International Consortium of Ocean Observing Labs (I-COOL). Plans for the first collaborative I-COOL deployment followed the next morning with John Howarth from the Liverpool Bay Observatory proposing a glider mission coordinated with his ongoing shipboard cruises. Collaborations continue today, fueled by the need to sample the ocean with new satellite, HF radar, glider, and AUV-based technologies. Our objective is to distribute the technologies developed locally in the Northeast regional test bed to the global marketplace.

Currently, I-COOL has three main themes. One is to provide platforms and expertise that enable local scientists to demonstrate success and hence fuel local funding for programs that contribute to the larger I-COOL effort. There have already been many successful collaborations with European, Australian, and Caribbean scientists. For example, CODAR HF radars are being deployed in Norway, with gliders and AUVs to follow with support from the Norwegian government, which is interested in the environmental impacts of climate change.

The second I-COOL theme uses these novel technologies to explore extreme environments. Targeted environments include the poles, severe storms, urbanized ports, and developed coastlines, all of which are often avoided by scientists because of hazardous operating conditions. Now, gliders are being deployed along the West Antarctic Peninsula for climate change research as part of NSF's Palmer Station Long-term Ecological Research study in collaboration with British scientists. Because observing networks are robust, they are allowing scientists to safely study severe storm processes in real time without having to curtail operations, for example, glider operations on the New Jersey shelf that continued unperturbed and yielded to insights into shelf-water processes during a very stormy period in fall 2003 (Glenn et al., 2008). The natural and anthropogenic forcing at work in urbanized ports often result in extremely dynamic environments whose turbulence and spatial complexity are difficult to sample using traditional technologies; observing networks will help overcome the difficulties of conducting research in these heavily used environments.

The third I-COOL theme is to extend the limits of long-duration underwater glider flights by developing new power and control systems. The long-duration studies are powerful magnets that get undergraduates interested in science (see Box 1) and have the potential to increase the visibility of ocean exploration to the general public. Currently, efforts are underway to re-occupy the many legs of the 1872–1876 HMS *Challenger* voyage using a global fleet of long-duration gliders and to compare modern and historical physical and biological characteristics. This effort will require a global collaboration of scientists and students over the Internet. We hope to include developing nations in this project, but must overcome the lack of infrastructure in these countries, which have the fastest growing human coastal populations and thus a great need for ocean observing applications such as for fisheries management.

LESSONS LEARNED

Glenn and Schofield (2003) outlined concerns, lessons learned, and conclusions based on initial construction of the New Jersey shelf-wide observatory. Some of those lessons still apply, including the necessity of coalescing scientific and societal goals, the importance of iterative development supported by peer-reviewed grants, and the need to train a new workforce that currently does not exist. Other concerns have evolved, in particular those surrounding sustained funding. In 2003, entrance into the IOOS family of observatories was best obtained through congressional earmarking. The change to a scientific peer-review system in 2007 made it particularly painful for those systems that had not diversified their funding base through spiral development.

Observatories Inspire Young Scientists

In the 1990s, senior-level scientists warned us that our work on ocean observatories would negatively impact our scientific careers. We may have heeded that advice if not for the tenure system and the nine months of university salary support we received for teaching, research, and service activities. Thus, while NOPP enabled new partnerships, institutional support was critical in allowing those partnerships to mature. In 2003, we also warned young, untenured faculty that building and operating an ocean observatory was not a prudent choice at that early stage of their careers. This view was based on our experience with the excessive grant and management pressures required to sustain an observatory outside of the scientific mainstream. Our concern was that the required work would come at the expense of manuscript preparation, which is, and will remain, the central currency for earning tenure. We were not alone in sounding this alarm. In 2003, with the primary investment in observatories coming through congressional earmarks, faculty who did participate were required to focus on demonstrating accountability through political visibility rather than professional development. The end result was a missing generation of young, hard-working scientists supporting the ocean observatory movement.

In the last five years, we have seen dramatic changes. Observatories exist, they will continue to evolve, and in some form or another, they are here to stay. Young faculty members who access the observatories find they have a platform that provides them a competitive advantage. The existing infrastructure allows them to propose ambitious experiments that take advantage of the 24/7/365 spatial view of the ocean. Rather than having to raise all the money for expensive infrastructure themselves, young faculty can use existing observatory capabilities to meet many of their sampling needs, paying only for the incremental costs of pursuing their specific research problems. Two recent examples of multi-institutional research programs designed and led by untenured Rutgers COOL faculty are the NSF-supported LaTTE (Robert Chant) and Mid-Shelf Front Experiment (Josh Kohut) programs. Additionally, universities find that an environmental observation network serves the needs of multiple departments. The on-campus COOL control center provides an academic nexus that has enhanced collaborations spanning marine science, geological science, environmental science, microbiology, computer science, engineering, education, and economics. New joint faculty appointments among the Marine Science Department and the School of Engineering, the Graduate School of Education, and the Agricultural Experiment Station are growing the number of faculty interested in using or improving ocean observatories. These collaborations provide a means to unite diverse faculty interests while simultaneously accessing a wider range of sponsors. Our own Rutgers University Vice President for Research and Graduate and Professional Education, in a 2008 speech to incoming tenure-track faculty, warned that single-author papers are not enough anymore, and that collaborations, especially interdisciplinary, are highly valued by tenure reviewers. Observatories are an effective means for young faculty to conduct interdisciplinary research.

> "THE LESSONS LEARNED THROUGH THE NOPP EXPERIENCE DEMONSTRATED THE VALUE OF PARTNERSHIPS, THE ROLE OF RAPID SPIRAL DEVELOPMENT, AND THE VALUE OF LEVERAGING THE SUPPORT OF MULTIPLE FEDERAL AGENCIES."

Partnerships That Result in Diversification

In 2003, when congressional earmarks for ocean observatories were on the upswing, observatory management was being pushed away from the already successful NOPP model of equal partnerships. In the user-driven model that the earmarks encouraged, the scientist's role was undervalued. Data providers were made subservient to data users, and management did not understand the difficulties of operating in a hostile ocean environment. Narrow definitions of the users that were expected to drive this system, and the refusal of management to

Box 1. Transforming Undergraduate Education through Ocean Observatories

BY SCOTT GLENN, DAKOTA GOLDINGER, ETHAN HANDEL, SHANNON HARRISON, DANIELLE HOLDEN, JOSH KOHUT, ANTHONY LUND, JANICE MCDONNELL, EVAN RANDALL-GOODWIN, EMILY ROGALSKY, JUSTIN SHAPIRO, ERIC VOWINKLE, AND OSCAR SCHOFIELD

The Coastal Ocean Observation Lab is developing new initiatives as part of a university-wide effort to transform undergraduate education at Rutgers. Enabled by an ocean observatory operations center purposely located on the main campus of a major research university, the lab has established a program featuring hands-on, team-based research projects that complement course work and are specifically designed to engage undergraduates in science. The program encourages students to become involved as early as the freshman year, remaining in contact with many of the same students and professors for their full four years at Rutgers. A series of Introduction to Oceanography courses with significant freshman participation, and a variety of small seminars for first-semester freshmen, serve as the feeder courses. Interested students join faculty in the lab during their second semester, either through one-credit research courses or work-study programs. The students are organized into a NOPP-style research team, and given a task reflecting the core NOPP values —collaboration between scientists and engineers from multiple disciplines, rapid spiral development cycles that work toward achieving a long-term goal, and leveraging the support of multiple groups from around the world. The initial task supported by the undergraduate team—to be the first to fly an autonomous underwater glider from Tuckerton, New Jersey, to Halifax, Nova Scotia—was accomplished during spring 2008 with RU15. Their second task, still ongoing, is to fly the first glider across the Atlantic from New Jersey to Spain.

These long-duration underwater robotic flights are made possible through the convergence of research, engineering, and educational projects from multiple agencies. Slocum gliders are now being delivered with the new DigiFin, an improved design that requires testing by ONR to meet Navy needs. NOAA initiated testing of lithium primary batteries for the new higher-powered sensors proposed for a NOPP instrument development project. NSF required testing of an extended payload bay to enable additional batteries to be carried for flights between the United States and British bases in Antarctica. Still, the main purpose of the long-duration flights remains educational. Rutgers alumni donated a glider for use as the primary platform to engage undergraduates in projects related to ocean observatories. NSF provided a summer intern from its Research Internships in Ocean Sciences (RIOS) program, in this case, an aeronautical engineer from the University of Maryland. Qualitas, a Spanish company installing and operating the national HF radar network for Spain, contributed an internship for a student with a dual major in marine science and Spanish. Glider training courses, developed and delivered for NOAA-sponsored IOOS projects and used extensively by the operational Navy, NATO, and the European Glider Association, were used to spin students up in every aspect of glider operations over the winter break.

Each student on the team was responsible for a specific aspect of the long-duration flights. Two freshmen worked alongside the three glider technicians to help with construction and testing of the actual glider, RU17. At the end of their spring semester, they returned to their high school, giving talks to their science teacher's class and the high school robotics team at Marine Academy of Technology and Environmental Science, in Manahawkin, New Jersey, on what they accomplished at Rutgers in their freshman year. Two juniors worked on the flight characteristics of RU17, optimizing the flight controls and providing feedback to the manufacturer. Two freshmen worked on the NOAA-sponsored IOOS Mid-Atlantic HF radar network as the launch zone for these two flights, while a junior worked on HF radar in Spain to help prepare

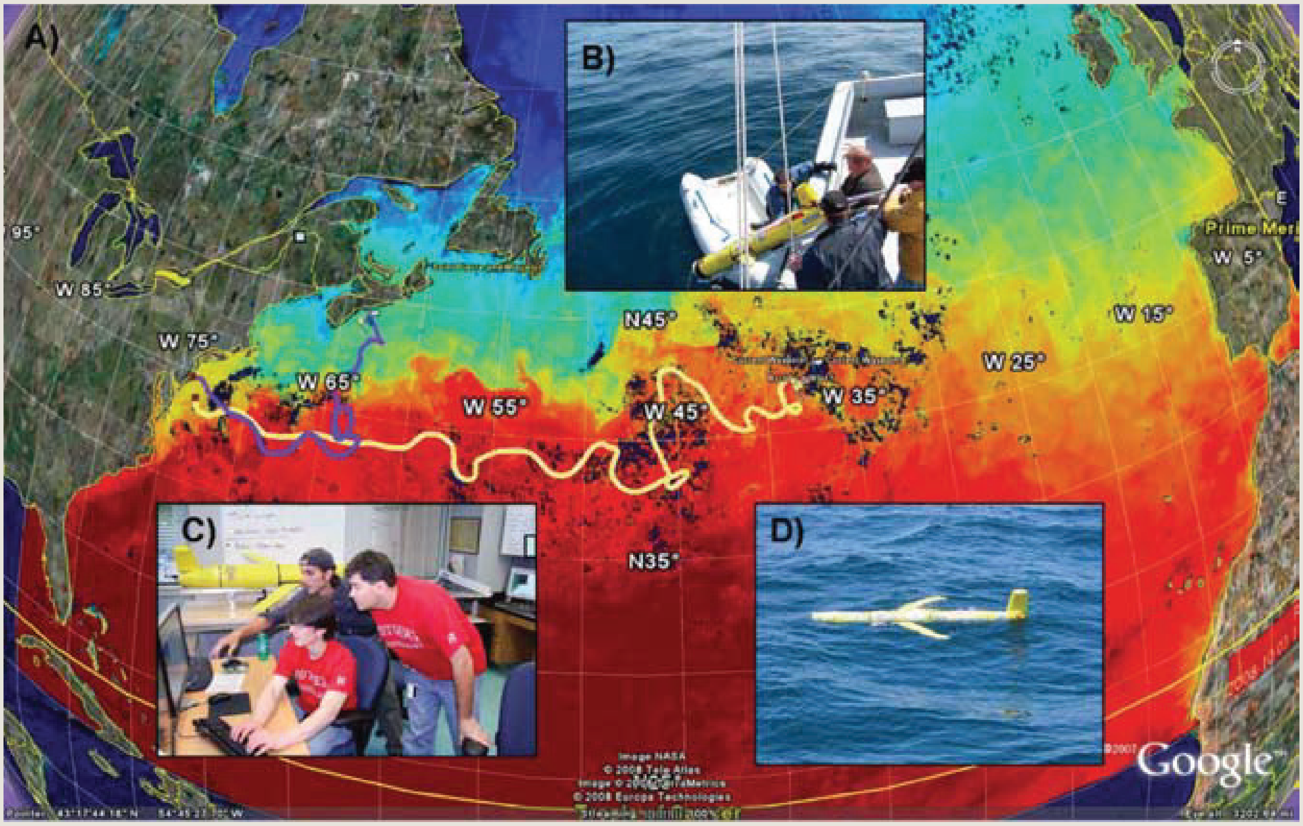

Figure B1. (A) Glider tracks overlain on a weekly composite satellite sea surface temperature image displayed in the Google Earth interface for the Halifax (RU15; blue) and Trans-Atlantic (RU17; yellow) missions. After setting the world record for distance traveled, communication with RU17 was lost just 220 miles shy of the Azores. Following our philosophy of rapid spiral development, lessons learned from the flight of RU17 are incorporated for the transatlantic mission of RU27, scheduled to begin its journey in April 2009. (B) Recovery of RU15 in Halifax, Nova Scotia, by NOPP partners at Satlantic Inc. (C) Undergraduates and a faculty member retasking RU17 to a new waypoint based on environmental data collected in the COOL room. (D) RU17 deployed off New Jersey prior to the start of its record-breaking journey.

the landing zone. Two seniors worked on path planning, Web site development, and the Google Earth interface that has been used in three Navy exercises, and is part of our Mid-Atlantic control center.

Our objective is to attract and retain students in lab activities for their full undergraduate careers. The on-campus operations center draws students from a variety of majors, and the excitement of the hands-on projects keeps them coming back semester after semester, and summer after summer. The students follow the cognitive apprenticeship learning model, which we reduce to the simple three-step teaching philosophy of "watch one, do one, teach one." They begin in freshman year with a lot of watching, often shadowing full-time research staff. By their sophomore and junior years, they know their way around the lab and are contributing key components to a variety of projects. By senior year, they are concluding their work, and passing their knowledge on to others by helping train the incoming freshmen. An NSF-sponsored education course, Communicating Ocean Sciences to Informal Audiences, is provided to the seniors so they can develop the teaching skills they will use in their last semester at Rutgers and beyond. The end result is a cluster of students that have demonstrated their ability to work together on a team for years, contributing to cutting-edge projects and building bonds they will remember as they pursue their careers.

upgrade technologies, limited the range of the data's applicability (Pettigrew et al., 2008). Ultimately, many of these observatories proved unsustainable due to overreliance on a single source of funding.

We have seen this increase in interest over the last five years as COOL continues to transition additional sampling and forecasting technologies from supporting discrete science experiments, government exercises, or industrial tests, to year-round operations. The transitions were coordinated with a growing number of academic, industry, and government partners that together sought federal, state, and foreign support as well as funding from industry and private foundations. We found that in many cases, the data users were also data providers regardless of their academic, industry, or government homes. We found that the NOPP concept of partnerships, focused on specific targeted and funded goals, moves observatories forward faster than general support for a wide range of observational parameters. Most users we ask will insist that they want the best science to support the decision-making process. In many cases, operational decisions are based on forecasts and their uncertainties rather than static historical data. Just as new technologies provide new data sets as a product of the observatory, new science that enables new forecast models is also a valued product.

Exploration and Discovery Enhances Education

The ocean is still a great unknown, far from being fully explored and understood. It is a difficult, exciting, and sometimes dangerous environment in which to work. These concepts are generally not taught in school. A common misconception is that everything is already understood. Daily difficulties that must be overcome to make progress typically go unshared, and dead ends encountered along the way go unreported. The public view is that science is conducted behind closed doors and that results are only shared when the scientist has already developed a complete story. This view contributes to a science culture that is risk adverse, where failure is viewed as a negative as opposed to a regular and common feature of scientific exploration and discovery. Additionally, the public does not see the ongoing process of science, and thus often has an incomplete perspective of how science is conducted and, therefore, how exhilarating the scientific process can be.

The committee appointed by the National Research Council identified the need to entrain the wider society to increase science and technical literacy of the United States by inspiring the next generation of scientists (National Academies, 2007). In oceanography, past discovery often involved unexpected events on the deck of a ship, far away and disconnected from the public we are trying to engage. Yet, the challenges of working in an extreme environment provide a great vehicle for capturing the public imagination. Observatories have developed the initial means to broadcast these adventures widely. Our experience indicates the audience that is excited to follow these adventures is much larger than our community might expect. Developing the means to broadcast our stories and thus entrain the wider community in our science requires effort prior to an experiment; the scientist must be prepared to be in public view through the full discovery process, including failures. Oceanography is fun, exciting, and suspenseful. It requires passion, blood, and sweat. Sometimes experiments don't work, but when they do, the excitement of discovery is indescribable. Therefore, we believe it is time to include wider society in the scientific "thrill of victory and the agony of defeat."

CONCLUSIONS

The lessons learned through the NOPP experience demonstrated the value of partnerships, the role of rapid spiral development, and the value of leveraging the support of multiple federal agencies. We have learned that partnerships are made by the hard work and dedication of the people involved based on the strengths of individuals and their belief in the synergies achievable through teamwork. New technologies born of the partnership model have enabled the evolution of our observatory with a diverse funding base in the Northeast United States at the scale of the Large Marine Ecosystem. Based on the same partnership model, we have expanded internationally, first with scientific partners around the world, followed by the exploration of extreme environments, and now the challenges of long-duration underwater flight. We have seen young faculty become involved and succeed through new science and new applications, and we have seen enabling technologies produce new data sets, and the science produce new forecast models. Public exploration of the ocean is attracting the next generation of scientists by involving undergraduates in the daily operation of an ocean observatory.

This is a unique time in the maturing of our field of oceanography. The world ocean is vastly under-sampled and presents a challenging work environment. Our generation of ocean scientists, originally trained only within our own core disciplines, is growing more collaborative as we tackle interdisciplinary problems. And federal funding agencies are growing more collaborative in their search for dual-use technologies, new science, local development test beds, and leveraging opportunities. People from academia, industry, and government are forming virtual communities for collaboration independent of their home institutions. The definition of an oceanographer continues to expand as we attract new people to the field and make it easier to spend time at sea. It is a great time to be an oceanographer.

ACKNOWLEDGEMENTS

The Rutgers University Coastal Ocean Observation Lab acknowledges the broad support of the oceanographic community. We are especially grateful for the friendships established with our long-term industry partners, including SeaSpace, CODAR Ocean Sensors, Teledyne Webb Research, Teledyne RD Instruments, Satlantic, WET Labs, Ocean Power Technologies, Deepwater Wind, and Public Service Electric & Gas. Our growing list of international colleagues, representing over ten different countries, is too long to list here. Finally, we acknowledge the daily support of COOL faculty, research staff, and students who work alongside us. The combined efforts of this diverse group are transforming ocean observing capabilities globally at a critical time for the unselfish benefit of generations to come. Thank you all for providing the inspiration that keeps us moving forward.

REFERENCES

Castelao, R., O. Schofield, S.M. Glenn, J. Kohut, and R. Chant. 2008. Cross-shelf transport of fresh water in New Jersey Shelf waters during spring and summer 2006. *Journal of Geophysical Research*, doi:10.1029/2007JC004241.

Chant, R.J., S.M. Glenn, E. Hunter, J. Kohut, R.F. Chen, R.H. Houghton, J. Bosch, and O. Schofield. 2008. Bulge formation of a buoyant river outflow. *Journal of Geophysical Research* 113, C01017, doi:10.1029/2007JC004100.

Davis, R.E., C.E. Eriksen, and C.P. Jones. 2003. Technology and applications of autonomous underwater vehicles. Pp. 37–58 in *Autonomous Buoyancy Driven Underwater Gliders*. G. Griffiths, ed., Taylor & Francis, London.

Devred, E., S. Sathyendranath, and T. Platt. 2007. Delineation of ecological provinces using ocean colour radiometry. *Marine Ecology Progress Series* 346:1–13.

Glenn, S.M., T.D. Dickey, B. Parker, and W. Boicourt. 2000a. Long-term real-time coastal ocean observation networks. *Oceanography* 13(1):24–34.

Glenn, S.M., W. Boicourt, B. Parker, and T.D. Dickey. 2000b. Operational observation networks for ports, a large estuary and an open shelf. *Oceanography* 13(1):12–23.

Glenn, S.M., and O. Schofield. 2003. Observing the oceans from the COOLroom: Our history, experience, and opinions. *Oceanography* 16(4):37–52.

Glenn, S.M., O. Schofield, T.D. Dickey, R. Chant, R., J.T. Kohut, H. Barrier, J. Bosch, L. Bowers, E. Creed, C. Haldeman, and others. 2004. The expanding role of ocean color and optics in the changing field of operational oceanography. *Oceanography*17(2):86–95.

Glenn, S.M., R. Arnone, T. Bergmann, W.P. Bissett, M. Crowley, J. Cullen, J. Gryzmski, D. Haidvogel. J. Kohut, M. Moline, and others. 2004. The biogeochemical impact of summertime coastal upwelling in the Mid-Atlantic Bight. *Journal of Geophysical Research* 109, C12S02, doi:10.1029/2003JC002265.

Glenn, S.M., C. Jones, M. Twardowski, L. Bowers, J. Kerfoot, D. Webb, and O. Schofield. 2008. Studying resuspension processes in the Mid-Atlantic Bight using Webb slocum gliders. *Limnology and Oceanography* 53(6):2,180–2,196.

Longhurst, A.R. 1998. *Ecological Geography of the Sea.* Academic Press, San Diego, CA, 398 pp.

Moline, M.A., T.K. Frazer, R. Chant, S. Glenn, C.A. Jacoby, J.R. Reinfelder, J. Yost, M. Zhou, and O. Schofield. 2008. Biological responses in a dynamic buoyant river plume. *Oceanography* 21(4):70–89.

National Academies. 2007. *Rising Above the Gathering Storm: Energizing and Employing America for a Brighter Economic Future.* Committee on Prospering in the Global Economy of the 21st Century: An Agenda for American Science and Technology, a joint effort of the National Academy of Sciences, National Academy of Engineering, and the Institute of Medicine. The National Academies Press, Washington, DC, 592 pages.

Oliver, M.J., J.T. Kohut, A.J. Irwin, S.M. Glenn, O. Schofield, M.A. Moline, and W.P. Bissett. 2004. Bioinformatic approaches for objective detection of water masses. *Journal of Geophysical Research* 109, C07S04, doi:10.1029/2003JC002072.

Pettigrew, N.R., H. Xue, J.D. Irish, W. Perrie, C.S. Roesler, A.C. Thomas, and D.W. Townsend, 2008. The Gulf of Maine Ocean Observing System: Generic lessons learned in the first seven years of operation (2001–2008). *Marine Technology Society Journal* 42(3):91–102.

Rudnick, D.L., and M.J. Perry, eds. 2003. *ALPS: Autonomous and Lagrangian Platforms and Sensors.* Workshop Report, 64 pp. Available online at: http://www.geo-prose.com/ALPS/report.html (accessed March 23, 2009).

Schofield, O., T. Bergmann, W.P. Bissett, F. Grassle, D. Haidvogel, J. Kohut, M. Moline, and S. Glenn. 2002. The Long-term Ecosystem Observatory: An integrated coastal observatory. *Journal of Oceanic Engineering* 27(2):146–154.

Schofield, O., W.P. Bissett, T.K. Frazer, D. Iglesias-Rodriguez, M.A. Moline, and S. Glenn. 2003. Development of regional coastal ocean observatories and the potential benefits to marine sanctuaries. *Marine Technology Society Journal* 37:54–67.

Schofield, O., and S.M. Glenn. 2004. The evolving coastal ocean observatories. *Journal of Geophysical Research* 109, C12S01, doi:10.1029/2004JC002577.

Schofield, O., J. Kohut, D. Aragon, L. Creed, J. Graver, C. Haldeman, J. Kerfoot, H. Roarty, C. Jones, D. Webb, and S.M. Glenn. 2007. Slocum gliders: Robust and ready. *Journal of Field Robotics* 24(6):1–14, doi:10:1009/rob.20200.

Schofield, O., R. Chant, B. Cahill, R. Castelao, D. Gong, J. Kohut, M. Montes-Hugo, R. Ramadurai, Y. Xu, and S.M. Glenn. 2008. The decadal view of the Mid-Atlantic Bight from the COOLroom: Is our coastal system changing? *Oceanography* 21(4):108–117.

Stommel, H. 1989. The Slocum mission. *Oceanography* 2(1):22–25.

Tang, D., J.A. Moum, J.F. Lynch, P. Abbott, R. Chapman, R. Capman, P.H. Dahl, T.F. Duda, G. Gawarkiewicz, S. Glenn, and others. 2007. Shallow Water '06: A joint acoustic propagation/nonlinear internal wave physics experiment. *Oceanography* 20(4):156–166.

PAPER

A Regional Slocum Glider Network in the Mid-Atlantic Bight Leverages Broad Community Engagement

AUTHORS

Oscar Schofield
Josh Kohut
Scott Glenn
Coastal Ocean Observation Laboratory, School of Environmental and Biological Sciences, Rutgers University

Julio Morell
Jorge Capella
Jorge Corredor
Department of Marine Sciences, University of Puerto Rico

John Orcutt
Mathew Arrott
Ingolf Krueger
Michael Meisinger
Cheryl Peach
Frank Vernon
Scripps Institution of Oceanography, University of California at San Diego

Alan Chave
Deep Submergence Laboratory, Department of Applied Ocean Physics and Engineering, Woods Hole Oceanographic Institution

Yi Chao
Steve Chien
David Thompson
Jet Propulsion Laboratory

Wendell Brown
School for Marine Science and Technology, University of Massachusetts at Dartmouth

Mathew Oliver
School of Marine Science and Policy, College of Earth, Ocean and Environment, University of Delaware

William Boicourt
Horn Point Laboratory, University of Maryland Center for Environmental Science

ABSTRACT

Autonomous underwater gliders have proven to be a cost-effective technology for measuring the 3-D ocean and now represent a critical component during the design and implementation of the Mid-Atlantic Regional Ocean Observing System (MARCOOS), a Region of the U.S. Integrated Ocean Observing System. The gliders have been conducting regional surveys of the Mid-Atlantic (MA) Bight, and during the 3 years of MARCOOS, the glider fleet has conducted 22 missions spanning 10,867 km and collecting 62,824 vertical profiles of data. In addition to collecting regional data, the gliders have facilitated collaboration for partners outside of MARCOOS. The existence of the MA glider observatory provided a unique test bed for cyber-infrastructure tools being developed as part of the National Science Foundation's Ocean Observatory Initiative. This effort allowed the Ocean Observatory Initiative software to integrate the MARCOOS assets and provided a successful demonstration of an ocean sensor net. The hands-on experience of the MA glider technicians supported training and provided assistance of collaborators within the Caribbean Regional Association, also a region of the U.S. Integrated Ocean Observing System, to assess the efficacy of gliders to resolve internal waves. Finally, the glider fleet has enabled sensor development and testing in a cost-effective manner. Generally, new sensors were tested within the MARCOOS domain before they were deployed in more extreme locations throughout the world's oceans. On the basis of this experience, the goal of the MARCOOS glider team will be to expand the MA network in coming years. The potential of how an expanded network of gliders might serve national needs was illustrated during the 2010 Macondo Gulf of Mexico oil spill, where gliders from many institutions collected subsurface mesoscale data to support regional models and oil response planning. The experience gained over the last 5 years suggests that it is time to develop a national glider network.

Keywords: Webb gliders, IOOS, Ocean observatories

Introduction

The Mid-Atlantic (MA) region, spanning from Massachusetts to Cape Hatteras, contains an extremely productive continental shelf supporting diverse and abundant fin and shellfish populations (Gates, 2009). The MA is characterized by a broad continental shelf that extends out for several hundred kilometers. The MA exhibits considerable seasonal and interannual variability in temperature and salinity (Mountain, 2003), which has a great influence on the abundance and distribution of its living resources. Seasonal hydrographic dynamics of the MA underlie many of the evolved life strategies of resident species that are evidenced by regional migrations and breeding dynamics. For example, the breeding success of many fish and shellfish are tied closely to overall hydrography off the MA (Weissberger and Grassle, 2003; Ma, 2004; Ma & Grassle, 2004; Lazzari & Able, 2006; Manderson, 2008). Therefore, understanding the dynamics of the MA ecosystem requires at minimum an understanding of the seasonal evolution of hydrographic features and preferably enough temporal/spatial information over the year to resolve the quantitative importance of episodic effects. Increasing our understanding of these processes is critical for the development of any ecosystem-based management strategy, which is extremely important as the MA hydrography (Mountain, 2003) and ecosystem (Schofield et al., 2008) appears to have changed over the last few decades.

Efforts to understand the seasonal dynamics of the MA has been a major research focus for decades (Walsh et al., 1988a,b; Biscaye et al., 1994). These research efforts have relied on ships (Walsh et al., 1988a,b; Mountain, 2003), moorings (Biscaye et al., 1994), satellites (Yoder et al., 2001, 2002; Ryan et al., 1999, 2001; Moline et al., 2004), and high-frequency (HF) radar (Gong et al., 2010). Satellites and HF radar provide a regional perspective and collect data continuously throughout the year; however, they only provide data on surface waters, which is problematic as the MA is characterized by a great deal of subsurface variability. In late spring and early summer, a strong thermocline develops across the entire continental shelf, isolating from the surface a continuous mid-shelf "cold pool" of water that extends from Nantucket to Cape Hatteras (Houghton et al., 1982). This stratification forms one of the most extreme coastal thermoclines on Earth with temperatures ranging from 30° at the surface to 8°C below the thermocline. The thermal gradient is very sharp with the majority of the change occurring within 5 m (Biscaye et al., 1994). Many of the biological features of interest reside at or below the thermocline, which is below the detection limits of satellites and HF radar. Ships can provide detailed 3-D data (through profiling and undulating instrument platforms); however, the expense of the ship operations limits the temporal coverage. Moorings can collect HF temporal data, although the maintenance and operations costs prohibit a sufficient number to be deployed that could resolve the spatial variability. Therefore, there is a critical need to deploy new technologies that can routinely provide a regional sustained presence at sea. Autonomous underwater gliders have proven to be a robust technology (Davis et al., 2003; Schofield et al., 2007; see Figure 1), which is why they were specifically chosen as a critical component during the design and implementation of the Mid-Atlantic Regional Ocean Observing System (MARCOOS), a region within the U.S. Integrated Ocean Observing System (IOOS®).

This manuscript will describe the glider efforts within MARCOOS. We will highlight the science motivations of the glider network and the current metrics (number of missions, costs) of the glider network. We will also provide three examples of how the gliders provide a unique capacity that has allowed MARCOOS to collaborate with science communities outside the MA. Finally, we look to future glider efforts as MARCOOS matures and argue that this and other regional glider programs will provide the foundation for a national glider network for United States.

FIGURE 1

The Webb glider tracks for deployments in the MA Bight since October 2003. Each color represents a different funding source. The turquoise lines represent joint deployments between ONR's ESPreSSO program and NOAA's MARCOOS program. The red lines represent the deployments associated with the Rutgers Endurance Line. The orange lines represent the glider deployments associated with the ONR's Shallow Water 2006 experiment. The green lines are associated with NSF's OOI Observing simulation experiment in November 2009. The light blue lines near New York Harbor represent deployments associated with the NSF Langragian Transport and Transformation Experiment. The dark blue lines are deployment funded by the State of New Jersey focused on conducting water quality surveys. (Color versions of figures available online at: http://www.ingentaconnect.com/content/mts/mtsj/2010/00000044/00000006.)

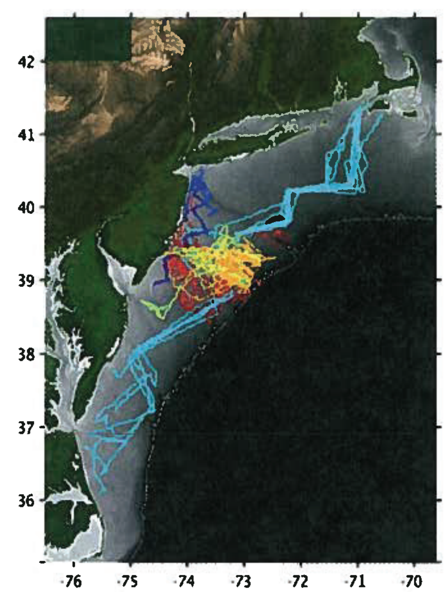

History and Motivations for the MARCOOS Glider Network

The regional glider efforts grew out of the Rutgers Endurance time series transect, which began in Fall 2003 (Glenn & Schofield, 2009). The endurance transect is a cross-shore survey from offshore Tuckerton, New Jersey, to the edge of the continental shelf and has been conducted as many times as possible as funds allowed over the last 7 years. To date, there have been 55 glider missions flown along the Endurance line since October 2003, collecting surveys more than 18,000 km from 826 glider-days at sea (Table 1). It has provided data allowing a full characterization of the seasonal dynamics offshore New Jersey (Castelao et al., 2008a,b, 2010a,b). It should be noted that this effort has been conducted with no formal funding award to maintain the time series. When MARCOOS was funded, the goal was to expand Endurance glider surveys to span the waters from Massachusetts to Cape Hatteras.

One scientific motivation for this effort was to provide a foundation to support ecosystem decision support. In the MARCOOS region, direct, indirect, and induced economic impacts of commercial and recreational fisheries are substantial, with the dockside value of commercial marine fish landings averaging approximately $1 billion/year and annual spending on recreational coastal and ocean fishing being estimated at $7.4 billion. The long-term economic value of fisheries would be increased if managers could prevent overfishing; however, uncertainty about the status of fish stocks and about how ocean conditions influence fish population dynamics and fishing success limit current management practices. Efforts are underway to develop "ecosystem-based fishery management" and "spatial marine planning." Both approaches rely on near synoptic ocean observations collected over ecologically relevant scales (spatial scales of meters to hundreds of kilometers, temporal scales of days to years) to better characterize the fishery dynamics. Defining habitat indicators for fishery resources is challenging because of the complex interactions between marine ecosystems and physical forcing; however, preliminary research efforts suggest that MARCOOS data can increase the explanatory power of habitat models (Palimera, personal communication). One of the most important subsurface physical features that structures fisheries on the MA is the cold pool water (CPW), which is spatially and temporally variable (Bignami & Hopkins, 2003). The CPW is the lowest temperature water and seasonally contains significant chlorophyll (Wood et al., 1996), and its location can affect the migration and spawning behavior of many fish (Sullivan et al., 2005).

Gliders provide a useful tool for collecting data on the CPW, which is not detectable by remote sensing techniques. They also provide data that can support numerical modeling via data assimilation. Past coastal predictive skill experiments have emphasized the importance of resolving the source waters (i.e., the upstream condition) to the model domain (Wilkin et al., 2005). This required that surveys span the entire MARCOOS domain, which require two separate glider missions to be conducted, because the standard glider batteries (alkaline) do not have sufficient energy to survey the entire MA; however, recently lithium batteries have been used and have sufficient

TABLE 1

The data collected by Webb Slocum gliders on the MA Bight. There were three major classes of missions. The first was the Rutgers Endurance line. The second was the surveys of the MA conducted by the IOOS and the Office of Naval Research's ESPreSSO program. The final class of MA glider missions was individual research projects. Some of the glider numbers collected by those individual research programs is also listed.

Mission	No. Missions	Glider-Days at Sea	Vertical Casts	Kilometers
Endurance line	55	826	159,011	18,028
MA surveys[a]	22	493	62,824	10,867
Research Projects	29	500	90,413	9,543
OOI[b]	4	74	23,332	1,673
SW06[c]	17	356	51,933	6,683
LATTE[d]	6	50	10,041	871
NJ DEP[e]	2	20	5,107	316
Total	106	1,819	312,248	38,438

[a]The glider surveys of MA Bight conducted by the Office of Naval Research's ESPreSSO and the IOOS MARCOOS programs.
[b]The glider surveys associated with the NSF's OOI.
[c]The glider surveys associated with the Office of Naval Research Shallow Water 2006 experiment.
[d]The glider surveys associated with the Lagrangian Advection Transport and Transformation Experiment.
[e]The glider surveys associated with the New Jersey Department of Environmental Protection coastal hypoxia surveys.

energy to survey the entire region. The drawback of the lithium batteries is the increased cost. For the alkaline surveys, one of the missions begins in southern Massachusetts and conducts a series of cross and along shore transects to central New Jersey. A second survey is typically conducted from central New Jersey to the mouth of Chesapeake Bay. Funding leveraged between the IOOS Program in the National Oceanic and Atmospheric Administration (NOAA) and the Office of Naval Research (ONR) Experimental Shelf Predictive Shelf-Slope Optics (ESPreSSO) program, allowed us to begin conducting MA surveys. To date, these programs have supported us to conduct 22 missions spanning 10,867 km while collecting 62,824 vertical profiles of data. The surveys were timed to coincide with the northeast National Marine Fishery Survey cruises.

The extensive glider experience in MA provides a basis for assessing the cost-effectiveness of these technologies. Cost estimates for glider missions are based on a full-time dedicated glider technician ($411 per day[1]), the coastal vessels for glider deployment and recovery,[2] and the expenses for batteries/Iridium/insurance/nominal maintenance and repair.[3] The estimated costs for MA operations assumes for each mission a dedicated technician for each day the glider is deployed as well as the deployment/recovery and ancillary expenses. Note, however, that a single technician can monitor many gliders when deployed, and the gliders represent cost-effective scalable technology. During past experiments, a single technician has monitored up to eight gliders. These estimates do not include support for the development of new hardware or software. On the basis of the MA deployment of gliders for 1,819 days, the costs are $1,815,534. This simplifies to $6 per vertical profile, $47 per kilometer traversed, and $998 per day. These costs compare favorably with research class vessels (nominal cost ~$25,000 per day) and a smaller coastal vessel ($1,500 per day) in which daily glider costs are 4% and 66% of comparable ship rates, respectively. Gliders cannot replace ships, which remain the most modular and flexible ocean sampling platform available to oceanography that far exceeds the current capabilities of existing sensors for gliders. Therefore, we recommended that gliders in near future take over the coastal monitoring needs, which would free up ships to conduct more sophisticated adaptive sampling without needing to dedicate time to ocean mapping.

[1]The costs include salary, fringe, and university indirect cost return.

[2]We have taken a high-end estimate of $4,000 per day for ships for deployment and recovery.

[3]We place the total upper end of costs for coastal waters at $10,000 per mission.

Collaboration Beyond the MARCOOS Domain

A major advantage of having a robust glider effort in the MA is that it has provided a means to galvanize collaborations from outside the MARCOOS community. MARCOOS (1) provides an existing open access observatory for users, (2) has a large pool of technical experience that can assist other groups in building observatories, and (3) provides a cost-effective test bed for new technologies. The benefits to MARCOOS are that this helps ensure that new technologies from external groups are integrated into the existing network and help develop a larger cohesive distributed ocean observatory community that provides a national resource (see below in future directions).

MARCOOS Provides an Existing Observatory

The MARCOOS glider network provides a test bed for partners external to the MA. One good example of this was demonstrated in November 2009 when the MARCOOS supported the U.S. National Science Foundation's (NSF) Ocean Observatory Initiative (OOI). A significant focus of the OOI is on developing a sophisticated cyber-infrastructure (CI) that links physical ocean observatories, computation, modeling, storage, and network infrastructure into a coherent system of systems. The software also provides a Web-based social network enabled by real-time visualization and access to model outputs allowing for adaptive sampling science. To ensure the development of a useful CI, a "spiral design strategy" is being used encouraging the oceanographic community to provide input during the construction phase. MARCOOS provided an existing test bed with a wide range of streaming data and an existing glider fleet that could be used to test the planning and prosecution software (Schofield et al., 2010).

The goal of the November experiment was to assess how well the CI software can aggregate data from ships, autonomous underwater vehicles, shore-based radars, and satellites and to make it available to ocean forecast models. Scientists used the model forecasts to guide future (next 24 h) glider missions, which then were used to coordinate satellite observing to demonstrate the feasibility of two-way interactivity between the sensor Web and predictive models. A distributed community of MARCOOS scientists provided the OOI CI team with daily adaptive guidance for a task-able satellite, using information from a fleet of four MARCOOS gliders.

The OOI software was being developed to enable operators to monitor and control individual components within an ocean observing network. The CI software coordinates and prioritizes the shared resources, allows for the semi-automated (Thompson et al., 2009, 2010) reconfiguration of asset tasking, and thus enables an autonomous execution of observation plans for the fixed and mobile observation platforms (Figure 2). For this effort, numerical model ocean forecasts allowed the simulation of future *in situ* robot trajectories, which could be used by a distributed group to optimize sampling on the basis of the science needs (Figure 3) and the practicability of moving gliders efficiently in the resolved current field (e.g., were targets actually "reachable"?) (Thompson et al., 2009, 2010). Thus, the CI software could deliver the community science needs back to the *in situ* observation network in a timely manner. The CI software coordinated sampling between underwater gliders and the space-based Hyperion imager flying on the Earth Observing One (EO-1) (http://eo1.gsfc.nasa.gov) spacecraft leveraging the Earth Observing Sensorweb (Chien et al., 2005, 2008) capability. The Hyperion images are typically 7.5 km (across track) by more than 100 km (along track) and resolve 220 spectral bands from 0.4 to 2.5 microns with a spatial resolution of 30 m. This small spatial footprint makes it difficult to ensure *in situ* assets are present for calibration. The Hyperion is a task-able platform and therefore an alternative approach would mobilize *in situ* assets and simultaneously adjust the satellite swath to be coincident. During the field experiment, observational data and multimodel forecasts were analyzed to determine the tasking location for the satellite. These coordinates were used by the EO-1 Web capability (http://sensorweb.jpl.nasa.gov) to retask the spacecraft. The 48-h model forecast was then used by the CI software to plan the optimal path to colocate any gliders within the tasked EO-1 Hyperion swath. Two MARCOOS gliders were successfully moved within the narrow Hyperion swath, which is only 7.5 km wide, whereas other gliders were diverted outside the swath to accomplish other science missions (Figure 4). This represents a major technology breakthrough in simultaneously coordinating satellite and underwater assets guided by multimodel forecasts. It provided a machine-to-machine interactive loop driven by a geographically distributed group of scientists.

FIGURE 2

The machine-to-machine data flow during the OOI's Observation Simulation Experiment. A fleet of gliders was informed by model-driven forecasts to optimize science sampling being conducted by a geographically distributed team of scientists. The observatory data were assimilated by an ensemble of numerical forecast models that were used to optimize the glider sampling. Optimized glider data were also used to adjust the data collected by the Hyperion EO-1 satellite.

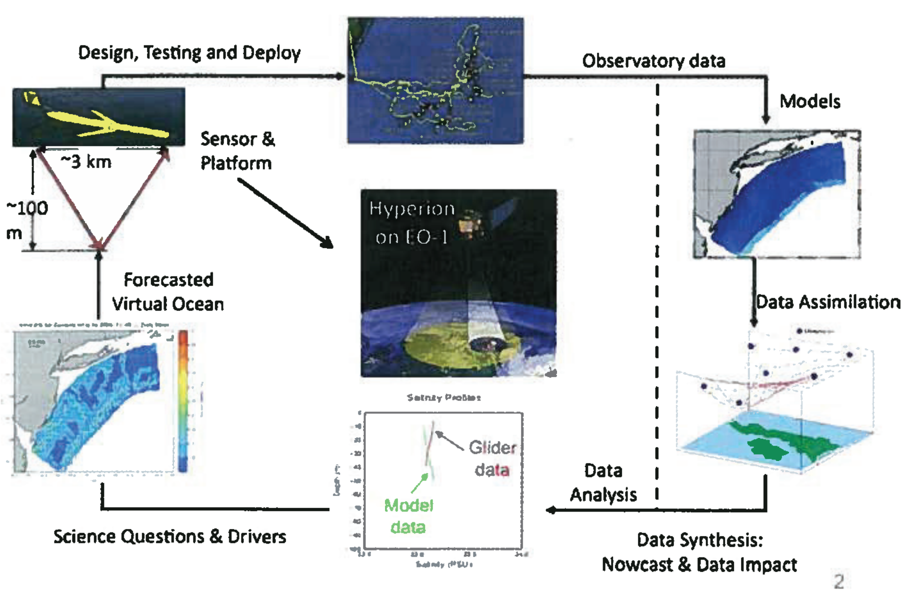

Partnership with Other IOOS Partners

The extensive pool of expertise within MARCOOS provides a resource to the wider IOOS community. This has been particularly true for glider operations where the community is small but rapidly growing. Through funding from the ONR Environmental Optics program, formal glider training sessions have been developed and have provided training to researchers from within the MARCOOS, international universities, NATO, and the Naval Research Laboratories. Here we highlight the partnership between MARCOOS and the IOOS CAribbean Regional Association (CARA). MARCOOS and CARA have partnered in sharing expertise in both the installation of HF radar and the deployment of Webb gliders.

The focus of the glider efforts in the Caribbean (Figure 5A) was on studying mixing processes in the coastal waters

FIGURE 3

The automated planning prosecution tools used by glider operators during the OOI CI test. The automated software involves a two-phase planning strategy. One component is a cartographic planner that allows glider operators to examine the "reachability envelopes" of a glider on the basis of the currents forecasted for the future ocean. This provides a tool for scientists to modify glider waypoints to assess if they can reach proposed goals in a specified amount of time. This is coupled to an automated state and resource planner. The state and resource planner allows the user to simulate different mission strategies to make wise strategic decisions, which are then uploaded to the glider as a series of waypoints. The state and resource planner not only keeps track of the physical state of the glider (remaining battery power) but also other features that need to be considered by the operator (commercial shipping lanes). The net result is that the scientist can optimize the science missions to collect the highest possible quality data.

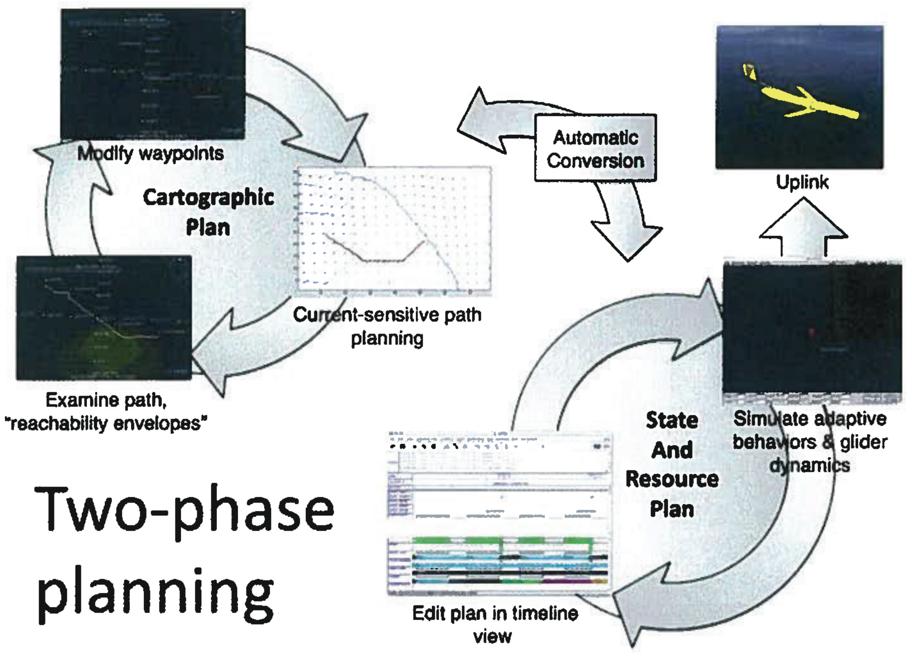

offshore Puerto Rico (Figure 5B). Internal tides, vertical oscillations of the pycnocline, can promote ocean mixing (St. Laurent & Garrett, 2002), modulate phytoplankton productivity (Evans et al., 2008), induce biological aggregations (Lennert-Cody & Franks, 1999; Moore & Lien, 2007), cause shelf break "scouring," modulate deep coral reef biology, and induce coastal seiching. Prior studies of internal tides in the Mona Passage between Puerto Rico and Hispaniola, initially driven by interest in billfish aggregations at the site, have shown that the Mona Passage and the shelf break along the SW coast of Puerto Rico are sites of internal wave generation. These phenomena have been partially characterized through the work of Bejarano (1997), who documented large-amplitude internal tides in the Mona Passage, by Teixeira (1999), who looked deeply into associated seiches and their excitation, and to Alfonso-Sosa (2001), who explored the local generation of internal tides through the action of tides impinging stratified waters on topographic slopes. In summary, these interfacial tides are approximately in phase with the astronomical tide, are of semidiurnal frequency, and exhibit amplitudes of up to 50 m (Teixeira & Capella, 2000).

Glider-based observations in the Mona Passage were used to characterize internal waves revealing the periodic generation of a wave train spanning the entire passage. Wave generation occurs in the region of "El Pichincho," a submerged ridge across the passage where tidal action induces hydraulic forcing of the wave (Figure 5B). Here, semidiurnal isopycnal displacement centered at depths around 100 m spans a vertical range of up to 50 m. Density sections along the glider transects to the south of the suspected generation site reveal a gradient of decreasing wave amplitude suggesting damping of the wave along its southward propagation axis toward the open Caribbean Sea (Figure 5C).

Chlorophyll sections for two transects (Figure 5D) show significant modulation of phytoplankton biomass within the subsurface chlorophyll maximum (SCM). We propose that this modulation is brought about by the spatial and temporal variation of the irradiance field, resulting from the vertical displacements of the SCM and the diurnal cycle. This hypothesis is supported by the correspondence between chlorophyll *a* concentration at the SCM and the depth of the pycnocline. These joint IOOS glider observations prompt us to propose that Caribbean passages may be the main source of internal tide energy prevalent throughout the Western North Atlantic.

MARCOOS Provides a Sensor Test Bed

The MA Webb gliders allow MARCOOS to act as a test bed for new sensors. The MA provides a location where the community has extensive experience as well as existing facilities that allow for field calibration of new sensors with ongoing operations. Sensors developed by funding from the ONR, the National Ocean Partnership

FIGURE 4

The IOOS observatory backbone that supported the OOI effort. The right-hand column shows the regional data provided by IOOS. The data included subsurface data from gliders, regional CODAR surface currents, ocean color and sea surface temperature remote sensing, and an ensemble of five numerical models. The data were coordinated and distributed over the world wide web via the Rutgers Coastal Ocean Observation (upper panel on left column) to the science/engineering teams distributed throughout the country. The bottom-left panel shows the Hyperion data swath that was collected after the ocean observatory directed the tilt of the satellite.

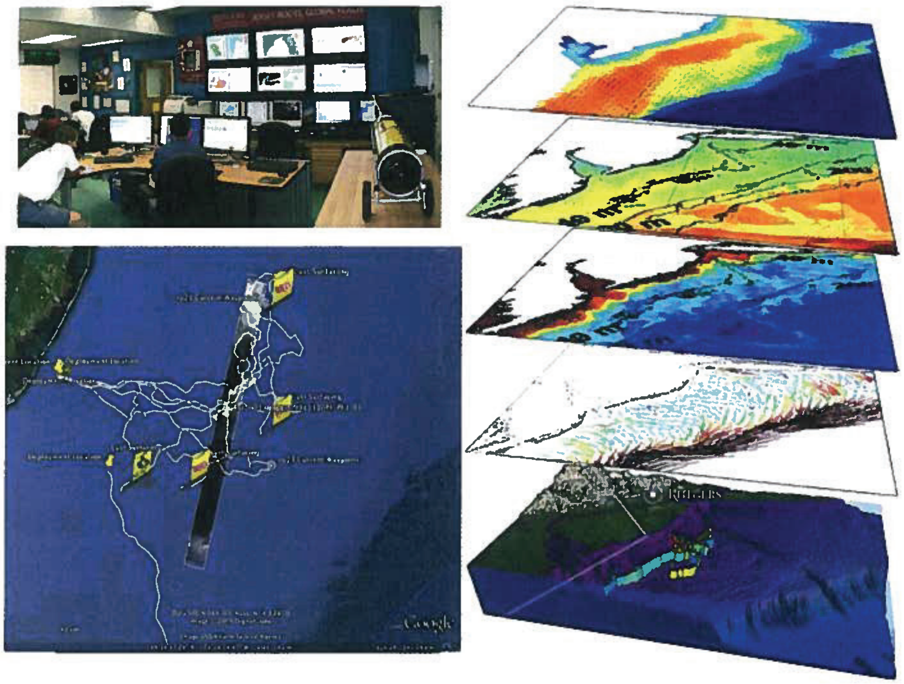

Program, the Environmental Protection Agency (EPA), the NSF, and the Gordon and Betty Moore Foundation have provided new sensor packages that were then first tested in the MA. These sensors are typically tested and refined in the MA before being deployed in more extreme locations that cannot provide the logistical support available within the MA. Initial testing and deployment of sensors aboard the gliders in the MA that have occurred over the last 5 years include development of physical sensors (acoustic Doppler current profilers, turbulence shear probes), optical instruments (backscatter sensors, multispectral radiometers, light attenuation sensors, light scattering sensors, hyperspectral spectrometers, cameras), fluorometers (chlorophyll, colored dissolved organic matter, fast repetition rate chlorophyll), oxygen sensors, and passive acoustic sensors (Glenn & Schofield, 2009). In addition, the glider test bed has supported the development of customized lithium batteries (Glenn et al., 2010), improved onboard computing (Woithe et al., 2010), new glider tail technologies (Glenn & Schofield, 2009), anti-fouling skin (Lobe et al., 2010), and extended payloads (Glenn & Schofield, 2009). Sensors that have been initially tested have then anchored missions along many of the North American coastlines (Chao et al., 2008; Glenn et al., 2008; Schofield et al., 2008), North Atlantic (Glenn et al., 2009), Pacific Northwest, Caribbean, Antarctica (Kahl et al., 2010), Baltic, Norwegian fjords, Sargasso Sea, and Alaska.

Future Directions

On the basis of the experience gained during the last 3 years of IOOS, the MARCOOS team has identified several key goals for the next 5-year effort. Within the MARCOOS domain, future strategies call for expanding the glider presence beyond a single seasonal survey each year. This need is based on one of the original goals of the MARCOOS gliders to assist in ecosystem-based management, which determined that defining the CPW was a critical need. Although the initial regional glider surveys could resolve the CPW, they could not resolve the formation, dynamics, and dissipation of the CPW; this calls for an aggressive expansion of the existing time series glider lines. This effort will require an expanded fleet of MARCOOS gliders (note MARCOOS currently owns one Webb glider) and increasing the surveys from a seasonal effort to a monthly time series. The high-resolution time series will enable numerical modeling of the CPW, which can resolve the dynamics in the MA.

IOOS represents the framework within which to establish a national backbone of ocean observation capabilities. This backbone is critical for overcoming the chronic undersampling of the coastal waters of the United States. The cost-effectiveness of gliders offers the potential to establish a cost-effective national backbone for subsurface spatial observations while HF radar and satellites complete the surface picture. The importance of developing a national capacity was clearly illustrated during the Deepwater Oil

FIGURE 5

The collaborative glider efforts between MARCOOS and CARA were crowned with joint deployments of the MARCOOS glider in Puerto Rican waters. (A) The CARA and the MARCOOS team members congratulating each other after the glider is deployed offshore (which can be seen in the white circle). (B) The glider transect into the Mona passage offshore Puerto Rico. (C) The glider measured density showing large internal waves. (D) The glider measured chlorophyll showing the phytoplankton concentrations being enhanced in the region of high internal wave activity.

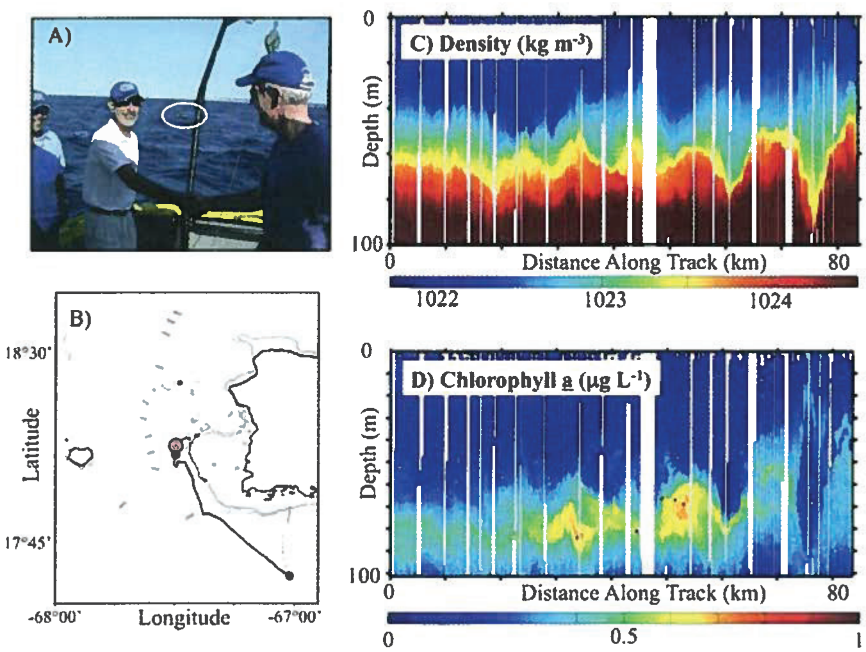

FIGURE 6

The positions of a community of gliders (yellow and gray circles) in the Gulf of Mexico on June 29, 2010. The glider fleet was assembled by community in response to the Deepwater oil spill. The community of partners included the U.S. Navy (sg135 and sg137), the Scripps/WHOI (spray-00-48), the iRobot/Applied Physics Lab (sg515), the University of South Florida (bass), the Rutgers University (ru23), the Mote Marine Laboratory (Waldo), and the University of Delaware (ud-134).

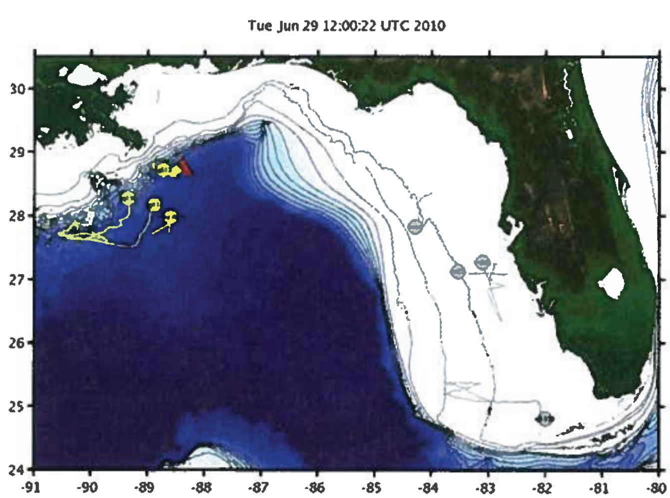

spill disaster (http://rucool.marine.rutgers.edu/deepwater/), when the paucity of subsurface measurements hindered response planning to the oil spill. This gap was addressed when a wide range of federal (U.S. Navy), commercial (iRobot, Teledyne Webb Research), and academic partners (Applied Physics Lab, Mote Marine Laboratory, Rutgers, Scripps Institution of Oceanography (under the IOOS Region–Southern California Coastal Ocean Observing System), University of Delaware, University of South Florida (under the IOOS Regions South Eastern Coastal Ocean Observing Regional Association and Gulf of Mexico Coastal Ocean Observing System), and Woods Hole Oceanographic Institution) joined forces and provided a fleet of gliders to make subsurface maps of the Gulf of Mexico (Figure 6). The gliders provided months of subsurface data, which would have been prohibitively expensive to collect using ships. Although the partners provided gliders, they came at the expense of their individual research efforts within their local waters; therefore, there is a critical need to develop the national capacity so the regional time series can be collected, the ocean modeled, and the assets tasked. There is a great need to develop a capacity to efficiently deal with events of national importance in the future. Additionally, strong partnerships with technology development initiatives, such as the OOI, are critical to ensure that despite the operational focus of IOOS, it is continuously infused with maturing technology that will provide expanded functionality to the growing network. Using these new technologies will make deploying a national glider fleet achievable and represents a cost-effective investment for IOOS.

Acknowledgments

The authors gratefully acknowledge support from the IOOS Program Office in NOAA, the Office of Naval Research, the NSF's OOI, the NASA New Investigator Program, and Delaware Sea Grant. This research was carried out, in part, by the Jet Propulsion Laboratory (JPL), California Institute of Technology, under contract with the National Aeronautics and Space Administration (NASA).

Lead Authors:

Oscar Schofield, Josh Kohut, and Scott Glenn
Coastal Ocean Observation Laboratory, School of Environmental and Biological Sciences, Rutgers University
New Brunswick, NJ
Emails: oscar@marine.rutgers.edu; kohut@marine.rutgers.edu; glenn@marine.rutgers.edu

References

Alfonso-Sosa, E. 2001. Variabilidad temporal de la producción primaria fitoplanctónica en la estación CATS (Caribbean Time Series Station): con énfasis en el impacto de la marea interna semidiurna sobre la producción. Ph.D. Thesis, University of Puerto Rico, Mayaguez, Puerto Rico.

Bejarano, L.F. 1997. Characterization of the internal tide north of Mona Passage. M.S. Thesis, University of Puerto rico, Mayaguez, Puerto Rico.

Bignami, F., Hopkins, T.S. 2003. Salt and heat trends in the shelf waters of the southern Middle-Atlantic Bight. Cont Shelf Res. 23:647-67. doi:10.1016/S0278-4343(03)00023-2.

Biscaye, P.E., Flagg, C.N., Falkowski, P. 1994. The Shelf Edge Exchange Processes experiment, SEEP-II: an introduction to hypotheses, results and conclusions. Deep Sea Res Part II 41:231-52. doi:10.1016/0967-0645(94)90022-1.

Castelao, R., Glenn, S., Schofield, O., Chant, R., Wilkin, J., Kohut, J. 2008a. Seasonal evolution of hydrographic fields in the central Middle Atlantic Bight from glider observations. Geophys Res Lett. 35:L03617. doi:10.1029/2007GL032335.

Castelao, R., Schofield, O., Glenn, S.M., Kohut, J., Chant, R. 2008b. Cross-shelf transport of fresh water in the New Jersey Shelf during spring and summer 2006. J Geophys Res. doi:10.1029/2007JC004241.

Castelao, R., Chant, R., Glenn, S.M., Schofield, O. 2010a. The effects of tides and oscillatory winds on the subtidal inner shelf cross-shelf circulation. J Phys Oceanogr. 40:775-88. doi:10.1175/2009JPO4273.1.

Castelao, R., Glenn, S.M., Schofield, O. 2010b. Temperature, salinity and density variability in the central Middle Atlantic Bight. J Geophys Res. 115(C10005):1-14. doi:10.1029/2009JC006082.

Chao, Y., Zhijin, L., Farrara, J.D., Moline, M.A., Schofield, O., Majumdar, S.J. 2008. Synergistic applications of autonomous underwater vehicles and regional ocean modeling system in coastal ocean forecasting. Limnol Oceanogr. 53:2251-63.

Chien, S., Cichy, B., Davies, A., Tran, D., Rabideau, G., Castano, R., Sherwood, R., Mandl, D., Frye, S., Shulman, S., Jones, J., Grosvenor, S. 2005. An autonomous Earth Observing Sensorweb. IEEE Intell Syst. 20:16-24. doi:10.1109/MIS.2005.40.

Chien, S., Tran, D., Johnston, M., Davies, A., Castano, R., Rabideau, G., Cichy, B., Doubleday, J., Pieri, D., Scharenbroich, L., Kedar, S., Mandl, D., Frye, S. 2008. Lights out operations of a multi-asset air, ground, space Sensorweb. International Symposium on Artificial Intelligence, Robotics, and Automation in Space (i-SAIRAS 2008). Universal City, CA.

Davis, R.E., Eriksen, C.E., Jones, C.P. 2003. Technology and applications of autonomous underwater vehicles. In: Autonomous Buoyancy Driven Underwater Gliders, ed. Griffiths, G., 37-58. London: Taylor & Francis.

Evans, M.A., MacIntyre, S., Kling, G.W. 2008. Internal wave effects on photosynthesis: experiments, theory, and modeling. Limnol Oceanogr. 53:339-53.

Gates, J.M. 2009. Investing in Our Future: The Economic Case for Rebuilding Mid-Atlantic Fish Populations. Washington, DC: Pew Environment Group. 21 pp.

Glenn et al. 2010. The Scarlett Knight's trans-Atlantic mission: lessons learned and opportunities for the future. Marine Technology Society. (this issue)

Glenn, S., Schofield, O. 2009. Growing a distributed ocean observatory: our view from the COOL room. Oceanography. 22:128-45.

Glenn, S.M., Goldinger, D., Handel, E., Harrison, S., Holden, D., Kohut, J., Lund, A., McDonnell, J., Randall-Goodwin, E., Rogalsky, E., Shapiro, J., Vowinkle, E., Schofield, O. 2009. Transforming undergraduate education through ocean observatories. Oceanography 22:142-3.

Glenn, S.M., Jones, C., Twardowski, M., Bowers, L., Kerfoot, J., Webb, D., Schofield, O. 2008. Studying resuspension processes in the Mid-Atlantic Bight using Webb Slocum gliders. Limnol Oceanogr. 53(6):2180-96.

Gong, D., Kohut, J.T., Glenn, S.M. 2010. Seasonal climatology of wind-driven circulation on the New Jersey Shelf. J Geophys Res. 115:C04006. doi:10.1029/2009JC005520.

Houghton, R.W., Schlitz, R., Beardsley, R.C., Butman, B., Chamberlin, J.L. 1982. The Mid-Atlantic bight cold pool: evolution of the temperature structure during summer 1979. J Phys Oceanogr. 12:1019-29. doi:10.1175/1520-0485(1982)012.

Kahl, A.L., Schofield, O., Fraser, W.R. 2010. Autonomous gliders reveal features of the water column associated with foraging by Adelie penguins. Integr Comp Biol. 1-10. doi:10.1093/icb/icq098.

Lazzari, M.A., Able, K.W. 2006. Northern pipefish, *Syngnathus fuscus*, occurrences over the Mid-Atlantic Bight continental shelf: evidence of seasonal migration. Environ Biol Fishes. 27:177-85. doi:10.1007/BF00001671.

Lennert-Cody, C.E., Franks, P.J.S. 1999. Plankton patchiness in high-frequency internal waves. Mar Ecol Prog Ser. 186:59-66. doi:10.3354/meps186059.

Lobe, H., Haldeman, C., Glenn, S.M. 2010. ClearSignal coating controls biofouling on Rutgers glider crossing. Sea Tech. 51:91-6.

Ma, H. 2004. Spatial and temporal variation in surfclam (*Spisula solidissima*) larval supply and settlement on the New Jersey inner shelf during summer upwelling and downwelling. Estuar Coast Shelf Sci. 62:837-65. doi:10.1357/0022240042880882.

Ma, H., Grassle, J.P. 2004. Invertebrate larval availability during summer upwelling and downwelling on the inner continental shelf off New Jersey. J Mar Res. 62:837-65.

Manderson, J.P. 2008. The spatial scale of phase synchrony in winter flounder (*Pseudopleuronectes americanus*) production increase among southern New England nurseries in the 1990s. Can J Fish Aquat Sci. 65:340-51. doi:10.1139/F07-169.

Moline, M.A., Blackwell, S., Chant, R., Oliver, M.J., Bergmann, T., Glenn, S., Schofield, O. 2004. Episodic physical forcing and the structure of phytoplankton communities in the coastal waters of New Jersey. J Geophys Res. 110:C12S05. doi:10.1029/2003JC001985.

Moore, S.E., Lien, R-L. 2007. Pilot whales follow internal solitary waves in the South China Sea. Mar Mamm Sci. 23:193-6. doi:10.1111/j.1748-7692.2006.00086.x.

Mountain, D.G. 2003. Variability in the properties of Shelf Water in the Middle Atlantic Bight, 1977-1999. J Geophys Res. 108(C1):3014. doi:10.1029/2001JC001044.

Ryan, J.P., Yoder, J.A., Cornillon, P.C. 1999. Enhanced chlorophyll at the shelfbreak of the Mid-Atlantic Bight and Georges Bank during the spring transition. Limnol Oceanogr. 44:1-11. doi:10.4319/lo.1999.44.1.0001.

Ryan, J.P., Yoder, J.A., Townsend, D.W. 2001. Influence of a Gulf Stream warm-core ring on water mass and chlorophyll distributions along the southern flank of Georges Bank. Deep Sea Res Part II. 48:159-78. doi:10.1016/S0967-0645(00)00117-X.

Schofield, O., Chant, R., Cahill, B., Castelao, R., Gong, D., Kahl, A., Kohut, J., Montes-Hugo, M., Ramadurai, R., Ramey, P., Xu, Y., Glenn, S.M. 2008. Seasonal forcing of primary productivity on broad continental shelves. Oceanography. 21:104-17.

Schofield, O., Glenn, S., Orcutt, J., Arrott, M., Brown, W., Signell, R., Moline, M.A., Chao, Y., Chien, S., Thompson, D., Balasuriya, A., Oliver, M. 2010. Automated sensor networks to advance ocean science. Trans Am Geophys Union. 91(39):345-6. doi:10.1029/2010EO390001.

Schofield, O., Kohut, J., Aragon, D., Creed, L., Graver, J., Haldeman, C., Kerfoot, J., Roarty, H., Jones, C., Webb, D., Glenn, S.M. 2007. Slocum gliders: robust and ready. J. Field Robot. 24:473-85. doi:10:1009/rob.20200.

St. Laurent, L., Garrett, C. 2002. The role of internal tides in mixing the deep ocean. J Phys Oceanogr. 32:2882-99. doi:10.1175/1520-0485(2002)032.

Sullivan, M.C., Cowen, R.K., Steves, B.P. 2005. Evidence for atmosphere-oceanforcing of yellowtail flounder (*Limanda ferruginea*) recruitment in the Mid-Atlnatic Bight. Fish Oceanogr. 14:386-99. doi:10.1111/j.1365-2419.2005.00343.x.

Teixeira, M. 1999. Characterization of coastal seiches along the Caribbean coast of the island of Puerto Rico. Ph.D. Thesis, University of Puerto Rico, Mayaguez, Puerto Rico.

Teixeira, M., Capella, J. 2000. A long-lead forecast model for the prediction of shelf water oscillations along the Caribbean coast of the island of Puerto Rico. In: Proceedings Oceans 2000 MTS/IEEE Conference, Providence, RI, September 12-14.

Thompson, D., Chien, S., Chao, Y., Li, P., Arrott, M., Meisinger, M., Balasuriya, A., Petillo, S., Schofield, O. 2009. Glider mission planning in a dynamic ocean Sensorweb. SPARK Workshop on Scheduling and Planning Applications. In: Intl Conference on Automated Planning and Scheduling, Thessaloniki, Greece, September 2009.

Thompson, D.R., Chien, S., Chao, Y., Li, P., Cahill, B., Levin, J., Schofield, O., Balasuriya, A., Petillo, S., Arrott, M., Meisinger, M. 2010. Path planning in strong, dynamic, uncertain currents. In: IEEE Conference on Robotics and Automation, Anchorage, AK, May 2010. doi:10.1109/ROBOT.2010.5509249.

Walsh, J.J., Biscaye, P.E., Csanady, G.T. 1988a. The 1983-1984 Shelf Edge Exchange Processes (SEEP)-I experiment: hypotheses and highlights. Cont Shelf Res. 8:435-56. doi:10.1016/0278-4343(88)90063-5.

Walsh, J.J., Wirick, C.D., Pietrafesa, L.J., Whitledge, T.E., Hoge, F.E., Swift, R.N. 1988b. High-frequency sampling of the 1984 spring bloom within the Mid-Atlantic Bight: synoptic shipboard, aircraft, and in situ perspectives of the SEEP-I experiment. Cont Shelf Res. 8:529-63. doi:10.1016/0278-4343(88)90067-2.

Weissberger, E.L., Grassle, J.P. 2003. Settlement, first-year growth, and mortality of surfclams, *Spisula solidissima*. Estuar Coast Shelf Sci. 56:669-84. doi:10.1016/S0272-7714(02)00218-4.

Wilkin, J.L., Arango, H.G., Haidvogel, D.B., Lichtenwalner, C.S., Glenn, S.M., Hedström, K.S. 2005. A regional ocean modeling system for the long-term ecosystem observatory. J Geophys Res. 110:C06S91. doi:10/1029/2003JC002218.

Woithe, H.C., Chigirev, I., Aragon, D., Iqbal, M., Shames, Y., Glenn, S.M., Schofield, O., Seskar, I., Kremer, U. 2010. Slocum glider energy measurement and simulation infrastructure. In: Our Ocean Conference. Sydney, Australia.

Wood, A.M., Sherry, N.D., Huyer, A. 1996. Mixing of chlorophyll from the Middle Atlantic Bight Cold Pool into the Gulf Stream at Cape Hatteras. J Geophys Res. 101(C9):20579-93. doi:10.1029/96JC01135.

Yoder, J.A., O'Reilly, J.E., Barnard, A.H., Moore, T.S., Ruhsam, C.M. 2001. Variability in coastal zone color scanner (CZCS) chlorophyll imagery of ocean margin waters off the US East Coast. Cont Shelf Res. 21:1191-218. doi:10.1016/S0278-4343(01)00009-7.

Yoder, J.A., Schollaert, S.E., O'Reilly, J.E. 2002. Climatological phytoplankton chlorophyll and sea surface temperature patterns in continental shelf and slope waters off the Northeast U.S. coast. Limnol Oceanogr. 3:672-82. doi:10.4319/lo.2002.47.3.0672.

Integrative and Comparative Biology Advance Access published August 2, 2010
Integrative and Comparative Biology, pp. 1–10
doi:10.1093/icb/icq098

SYMPOSIUM

Autonomous Gliders Reveal Features of the Water Column Associated with Foraging by Adélie Penguins

L. Alex Kahl,*[,1] Oscar Schofield* and William R. Fraser[†]

*Coastal Ocean Observation Lab, Institute of Marine and Coastal Sciences, School of Environmental and Biological Sciences, Rutgers University, New Brunswick, New Jersey 08901, USA; [†]Polar Oceans Research Group, Sheridan, Montana 59749, USA

From the symposium "Advances in Antarctic Marine Biology" presented at the annual meeting of the Society for Integrative and Comparative Biology, January 3–7, 2010, at Seattle, Washington.

[1]E-mail: alex@marine.rutgers.edu

Synopsis Despite their strong dependence on the pelagic environment, seabirds and other top predators in polar marine ecosystems are generally studied during their reproductive phases in terrestrial environments. As a result, a significant portion of their life history is understudied which in turn has led to limited understanding. Recent advances in autonomous underwater vehicle (AUV) technologies have allowed satellite-tagged Adélie penguins to guide AUV surveys of the marine environment at the Palmer Long-Term Ecological Research (LTER) site on the western Antarctic Peninsula. Near real-time data sent via Iridium satellites from the AUVs to a centralized control center thousands of miles away allowed scientists to adapt AUV sampling strategies to meet the changing conditions of the subsurface. Such AUV data revealed the water masses and fine-scale features associated with Adélie penguin foraging trips. During this study, the maximum concentration of chlorophyll was between 30 and 50 m deep. Encompassing this peak in the chlorophyll concentration, within the water-column, was a mixture of nutrient-laden Upper Circumpolar Deep (UCDW) and western Antarctic Peninsula winter water (WW). Together, data from the AUV survey and penguin dives reveal that 54% of foraging by Adélie penguins occurs immediately below the chlorophyll maximum. These data demonstrate how bringing together emerging technologies, such as AUVs, with established methods such as the radio-tagging of penguins can provide powerful tools for monitoring and hypothesis testing of previously inaccessible ecological processes. Ocean and atmosphere temperatures are expected to continue increasing along the western Antarctic Peninsula, which will undoubtedly affect regional marine ecosystems. New and emerging technologies such as unmanned underwater vehicles and individually mounted satellite tracking devices will provide the tools critical to documenting and understanding the widespread ecological change expected in polar regions.

Introduction

Climatic change is, and will continue, altering marine ecosystems. However, the complexity of marine food webs, combined with chronic under-sampling of the ocean, constrains efforts to predict the effects of future change. Furthermore, these limitations also restrict our capacity to suitably manage and protect marine resources. All of these problems are magnified in polar oceans because these environments are extremely difficult to observe and to study (Anisimov et al. 2007). The harsh conditions associated with low temperatures, restricted sunlight for much of the year, high wind, sea ice, and limited logistic support often curb the widespread application of new technologies that are increasingly being deployed in temperate and tropical oceans. Fortunately, these technologies are maturing and are ready to be deployed in polar oceans. This is vital as many polar seas are experiencing changes in atmospheric/oceanic circulation (Turner et al. 2006), ocean properties (Meredith and King 2005), sea ice cover (Stammerjohn et al. 2008), and ice sheets (Steig et al. 2009). These rapid climatic changes are triggering pronounced shifts and reorganizations in regional ecosystems and in biogeochemical cycles (Grebmeier et al. 2006). However, it remains difficult to link these changes in the ecosystem to shifts in the physical ocean–atmosphere system. Overcoming this missing link, to decipher the mechanisms of climate-driven variability in an ecosystem, is a critical step in establishing predictive skills capable of contributing to adaptation and risk reduction strategies related to climatic change.

Because of the planetary scale and localized effects of climatic change in polar regions (Kwok and Comiso 2002), sampling strategies linking the changing dynamics of ecosystems with underlying physical processes must span a wide range of temporal and spatial scales. To this end, the oceanographic community has been developing technologies and strategies intended to bridge these vast gaps in observational capacity. For example, multi-platform observatories have been able to deconstruct mechanisms of different scales to elucidate shifts in temperate coastal ecosystems (Schofield et al. 2008). Given that such interdisciplinary and multi-platform approaches have proven themselves in expedient locations, they are ready for application in remote and harsh environments. Essential to the successful application of this approach to high latitude marine ecology will be the integration of technologies that have already succeeded on their own in polar regions. To ensure efficient observing and sampling strategies of dynamic processes, key ecological indicators should be identified and utilized to adjust data collection in real-time.

Top predators, such as marine mammals and seabirds, are key components of Antarctic marine ecosystems. Life-history strategies and population dynamics of these generally long-lived predators can reflect variability occurring over large spatial and temporal scales in both the physical, and biological environment (Fraser et al. 1992). As beacons integrating the dynamics of their ecological niche over decadal time scales, these marine predators are often regarded as sensitive indicators of ecological change (Ainley 2002; Costa et al. 2010) and as important units for the conservation and management of marine resources (Turner et al. 2009). Unfortunately, much of our understanding of the ecology of Antarctic marine predators is derived from animals at terrestrial breeding areas during only a small portion of the annual cycle. Traditionally, researchers studying the ecology of Antarctic marine predators have tried to overcome this constraint by using ARGOS satellite-based tracking technologies. Yet, the scope of these satellite-based tracking technologies is limited by their size, duration of deployment, the breeding phase of the predator, and by the predator's strategies for acquisition of prey. For example, most satellite-based tags are applied to animals at their terrestrial breeding sites during their annual breeding phase. As such, the resultant data document behavior and strategies. associated only with the breeding phase of the tagged predators. Increasingly, technological advances are allowing these satellite-linked tracking tags to include meters capable of detecting environmental variables such as depth, temperature, and salinity (Charrassin et al. 2008). Despite ever more sophisticated instrumentation, the aforementioned limitations still confound researchers' ability to independently characterize the subsurface marine environment shaping the ecology of Antarctic marine top predators.

Background

Adélie penguins as integrators of Antarctic marine ecosystems

Of the world's 18 extant species of penguin (Spenisciformes: Spheniscidae) (Baker et al. 2006), the Adélie penguin (*Pygoscelis adeliae*) is one of only two (the other is the Emperor penguin, *Aptenodytes forsteri*) true Antarctic species (Williams 1995). Circumpolar and geographically distributed at high southern latitudes, the Adélie penguin is characterized by a life-history that has evolved in close association with sea-ice in the Southern Ocean (Ainley 2002). For example, the species generally winters at the edge of the pack ice where nutrient stores are maintained during the winter months. Along the ice's edge during the early spring, Adélie penguins accumulate critical nutrient reserves required to sustain several aspects of the early-summer breeding effort. These nutrient reserves are fueled by the presence of a reliable food source that itself depends on sea-ice as a critical habitat. The Adélie penguin's primary prey are krill (*Euphausia superba* and *E. crystallorophias*) and the Antarctic silverfish (*Pleuragramma antarcticum*). Specifically, the survival and cohort recruitment of juvenile krill depends on their ability to consistently forage upon sea-ice dependent algae (Daly 1990) while Antarctic silverfish forage on krill (Hubold 1985). Furthermore, by hauling out on the sea-ice, Adélie penguins reduce the demands of their maintenance metabolism. Diminished maintenance metabolism, in turn, allows individual Adélies to store more energy. By increasing their energy stores, individual penguins are better able to cope with demands such as the spring migration to terrestrial breeding colonies, egg production by females, and defense of nesting territories by males.

As oviparous marine vertebrates, the Adélie penguin is entirely dependent on the terrestrial habitat for incubating eggs and rearing chicks. Due to the energetic demands of reproduction, predictable and reliable foraging areas must be located in close proximity to so-called ‘‘biological hotspots’’. It has long been appreciated that marine ‘‘biological hotspots’’ are regions of high ecological significance (Steele 1976). In terrestrial and corral reef systems, the hotspots have often been defined in terms of biodiversity (Meyers 1997; Hughes et al. 2002) while in marine systems the hotspots have often been defined in terms of increased biomass in either phytoplankton (Valavanis et al. 2004) or higher organisms. Such hotspots of biological activity are driven by pelagic bio-physical interactions resulting in elevated new primary production (i.e., phytoplankton blooms driven by newly introduced rather than regenerated nutrients). These photosynthetically driven blooms result in a trophic cascade of new energy. As the physics and chemistry of the oceans varies rapidly in space and time (at the scale of minutes to days), plankton biology (and the subsequent introduction of energy into the marine food web) is extremely patchy and highly ephemeral (ranging from hours to days). In contrast, higher trophic levels (nekton, sea birds, and marine mammals) by virtue of their long life-times (years to decades) integrate over larger space and longer time scales. Consequently, mapping top-predators often identifies ‘‘biological hotspots’’—or regions where such energy flows readily through the ecosystem.

The subsequent transfer of this energy, from lower trophic levels upward, is essential to the nutritional condition and reproductive performance of top predators such as Adélie penguins. Inevitably, perturbations in climatic parameters of the ocean (e.g., extent and timing of occurrence of sea ice) and in climatic anomalies have a strong affect on the propagation of this energy, ultimately modifying the availability of food for top predators. In particular, such anomalies of oceanic climate have a significant influence on seabird life history such as the timing of nest initiation and egg size (Gaston et al. 2005). Due to the energetic demands of reproduction, predictable and reliable Adélie foraging areas must be located in close proximity to biological hotspots, which represent regions with consistently high and predictable food resources. These hotspots appear to related deep sea canyons. The Adélie penguins breed in locations where deep ocean canyons exist near the land margin; these canyons provide a possible conduit for the warm Upper Circumpolar Deep Water (UCDW) to extend to near the land margin (Klinck et al. 2004), keeping winter ice low and supporting high primary productivity rates (Prezelin et al. 2000). As a result, the life history of these seabirds, driven by sea-ice dynamics and associated food web dynamics, can spatially and temporally integrate variability in oceanic climate along the WAP. For these reasons, populations of the Adélie penguin are regarded as sensitive indicators of global climatic change (Ainley 2002).

Climatically, the WAP is among our planet’s fastest warming regions with an increase in average air temperature of 6°C during the winter months over the last half century (Ducklow et al. 2007). This rapid warming has resulted in a reduction in the extent and duration of annual sea-ice formation (Vaughan et al. 2003). Proximate causes of regional warming and sea-ice decline involve the impact of climatic phases such as El Niño-Southern Oscillation, and the Southern Annular Mode on the atmosphere–ocean systems (Kwok and Comiso 2002). The interactions within these atmosphere–ocean systems can result in an increase of the cross-shelf transport of relatively warm water derived from the Antarctic Circumpolar Current (ACC). Such cross-continental-shelf intrusions of the ACC are possible because the WAP is the only place where the ACC encounters the Antarctic continent. Furthermore, submarine canyons present on the WAP funnel the warmer ACC deep water across the continental shelf to the near-shore sea surface. In addition to being warmer than the locally formed Antarctic water masses, the ACC’s deepwater is nutrient-laden, and when brought to the sea surface may drive persistent upwelling that is localized at the head of each cross-shelf canyon (Ducklow et al. 2007).

As a result, the WAP is susceptible to the increase in oceanic heat transport across the continental shelf that appears to have intensified over the last 30 years (Martinson et al. 2008). In response, along the Palmer Archipelago near Anvers Island (64°46′S, 64°03′W, Fig. 1), *Pygoscelis* community composition has shifted over the last 30 years (see Forcada and Trathan 2009 for review). Most dramatically, the population of breeding adults has declined from ~15,000 in the mid-1970s to presently < 4000 (Ducklow et al. 2007). Concurrent community shifts are evident in rising populations and the expanding of the sea-ice intolerant chinstrap (*P. antarctica*) and gentoo (*P. papua*) penguins. Population growth and range expansion are occurring at chinstrap and gentoo nesting colonies, respectively established in 1976 and 1994, on islands in close proximity to the declining

Adélie colonies near Palmer Station (Ducklow et al. 2007, Fig. 2). Understanding why one species is declining while others are increasing remains an open question. The differences likely reflect distinct foraging strategies among the penguin species and the dependence of such strategies on the variability of sea ice along the WAP.

These broad shifts in top predator community structure point to significant and fundamental changes at the base of the WAP marine ecosystem (Schofield et al. 2010). Indeed, such shifts in the basic composition of the pelagic marine environment are manifest in variability in foraging strategies by top predators at the decadal-scale (Ainley et al. 2005). However, sampling of the pelagic marine environment at spatial and temporal scales contemporaneous to top predator foraging behavior will be required to develop an understanding of the mechanisms and processes underlying variability in the WAP marine ecosystem.

Diet sampling of seabirds, traditionally conducted from the terrestrial environment, provides an

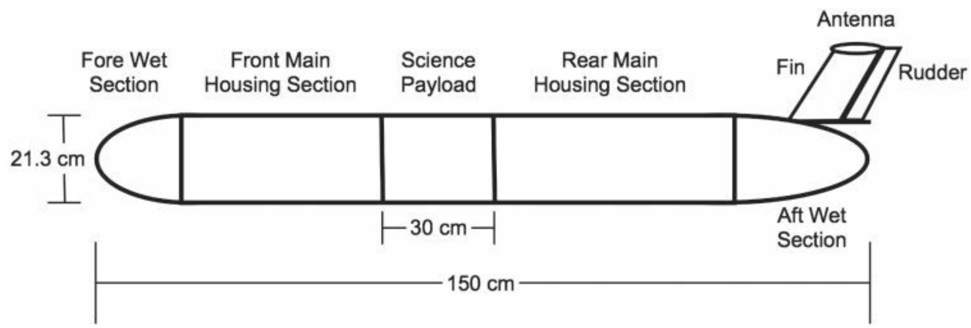

Fig. 1 Diagram of Teledyne-Webb Corporation's Slocum Glider (coastal model). The Front Main Housing Section glider's ballast, and consequently it's flight, is controlled by moving water into or out of the Fore Wet Section. The Front Main Section contains battery packs supplying power to both the ballast regulator and the Science Payload. The Science Payload can be modified to contain a wide variety of instrumentation including an externally mounted (port side) SBE CTD. The Rear Main Housing Section holds more battery packs and all of the glider's electronic hardware. While at the sea surface, a bladder is inflated in the Aft Wet Section to increase the fin-mounted antenna's clearance above the water. The rudder is controlled by the onboard computer (in the Rear Main Housing Section). Depending on the year of manufacture, the wings may be mounted on either the Science Payload or the Rear Main Housing Section.

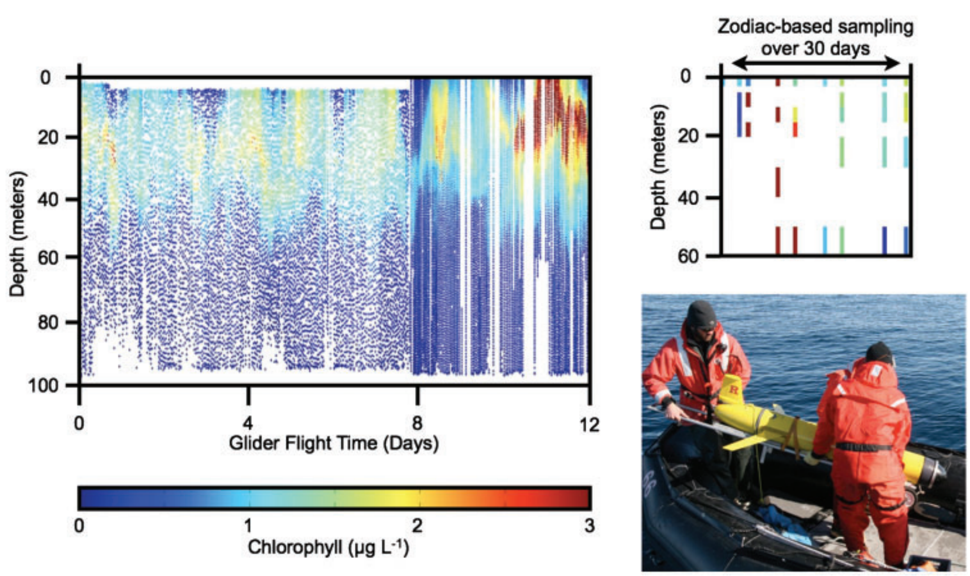

Fig. 2 Comparison of chlorophyll concentration at the Palmer LTER collected by the Slocum glider (12 days) and by hand via zodiac (30 days). The glider chlorophyll data also show the ability to change the sampling rate of the fluorometer (increased beginning on Day 8) without disrupting the glider flight. The image in the lower right depicts the deployment of the Slocum glider by hand over the side of a zodiac at the Palmer LTER.

integrated signal of the ecology of the foraging region. However, traditional diet sampling techniques do not provide insight into *in situ* foraging strategies and their constraining bio-physical factors. Indeed, some polar pelagic marine environments have been sampled (e.g., salinity and temperature with depth) with satellite-tracking tags on marine mammals (Boehme et al. 2008). However, the data derived from these tags are biased by the behavior of the tagged animal. Consequently, it has been difficult to illustrate a broad-scale picture of the hydrography driving the lower trophic levels in Antarctic marine ecosystems. Additionally, tagged marine animals only provide snapshots of the pelagic marine environment when conditions are ideal for the predator (e.g., during feeding or transit). Ideally, satellite-tagged animal data should be complimented by both contemporaneous and temporally extraneous high-resolution regional sampling of the oceanographic factors shaping these marine environments. For a robust definition of the factors, data focusing on both the biology and physics of these polar pelagic marine environments should be collected for sustained periods of time.

Integrating autonomous underwater vehicles into a long-term ecological study

Due to its remote location and harsh conditions, it is exceedingly difficult and expensive to observe polar marine ecosystems at the appropriate time and space scales. By necessity, observing and sampling of such systems must be highly efficient both in terms of logistics and costs. Inevitably highly efficient methods of observation in polar regions must be "scalable" to the process of interest (Rudnick and Perry 2003). Mobile platforms are undergoing exponential development and are transitioning into observational tools (Rudnick and Perry 2003). One autonomous platform that is rapidly becoming indispensable in temperate marine research is the buoyancy-driven underwater glider. Buoyancy-driven gliders, as currently configured, were first detailed in Doug Webb's lab book in February 1986 as a novel instrument approach. Gliders were widely publicized in 1989 by Henry Stommel's view of a futuristic smart fleet of instruments (Stommel 1989). During the time it has taken to bring these concepts to reality, gliders have earned their reputation as a high-endurance sensor platform. More importantly, this class of long-range and relatively low-cost autonomous underwater vehicle (AUV) is making affordable adaptive sampling networks a reality (Rudnick et al. 2004).

Slocum gliders

All of Rutgers University's Slocum gliders are controlled and monitored from a centralized control center located on Rutgers Campus in New Jersey (USA). The control center is called the Coastal Ocean Observation Lab (RU COOL) at the University's Institute of Marine and Coastal Sciences. For almost two decades RU COOL has posted freely available real-time data to the world-wide-web. RU COOL maintains control of a fleet of more than 24 gliders that are routinely deployed around the world. Taking advantage of rapidly expanding telecommunications technologies has allowed the centralized function of the COOL room to also be accessed remotely, continually increasing the flexibility of glider operations. However, glider operations in the Antarctic are unique from deployments and recoveries elsewhere because of the remoteness, unique hazards such as sea ice, and lack of reliable access to ships should a malfunction occur. High winds, heavy seas, or thick ice conditions also frequently hamper these deployments and recoveries.

The glider used for this study is the Webb Slocum Coastal Glider (Figs. 1 and 2). Coastal gliders such as the one deployed in this study have a hull diameter of 21.3 cm and an overall length of 1.5 m (Fig. 1). The 56 kg glider is rated to dive depths of 100 m and has a horizontal average speed of 0.4 m/s. The glider propels itself through the water column by changing its buoyancy. Consequently the glider's path of travel resembles a continuously advancing saw-tooth pattern between the surface and 100 m depth.

While at the surface, an internal air bladder thrusts the glider's tail above water allowing satellite communications. The glider can receive commands and send data via line-of-sight radio frequency modem, or satellite telephone link (i.e., Iridium Satellite phone). Each glider in our fleet uses its Iridium connection to call into the COOL room to upload scientific and engineering flight (each underwater Glider deployment is termed as an underwater flight) data. These data are generally archived for subsequent analysis and are also posted to the web in "real-time" to allow sampling strategies to be adapted in real-time based on the most recent information ("adaptive sampling"). Conversely, data transfer between the glider and the COOL room is bi-directional such that the Glider may also download new navigation or sampling command files from the COOL room. A glider can only transmit data or receive commands while at the surface of the ocean as all communications are transmitted via antennas located in the tail fin. Also contained within the tail is an ARGOS emergency beacon and a GPS. The glider uses the GPS to navigate between waypoints uploaded in a "mission" text file. Because the glider dead reckons between waypoints while underwater, upon surfacing any deviation from the intended path of travel is compensated for on the next dive by virtue of a rudder in the tail fin. During these "surfacings", flight parameters such as; duration until next surfacing, the list of upcoming GPS waypoints, and instrument sampling rate can be modified by the operator.

All Slocum gliders come with an external CTD and a modular science payload. The science payload module can be adapted to hold a wide variety of instruments. In this deployment, the glider had a fluorometer and two backscatter meters. Other scientific payloads include a photosynthetically available radiation sensor and a variable fluorescence detector. The factors limiting the type of scientific instrument onboard the glider are the size of the payload section (length = 30 cm, diameter = 21.3 cm, maximum weight = 4 kg) and power consumption of the scientific instrument. Depending on the science payload the duration of a glider deployment on one pack of batteries may last as long as one month. However, the duration of the deployment is subject to a wide variety of variables such as environmental temperature, scientific payload power requirements, and dive depth (i.e., shallower water requires more cycles of ballasting and unballasting seawater thus requiring more use of the pumps).

Glider personnel monitor the polar ocean deployments carefully because of the high risk of encountering objective hazards such as icebergs, sea ice, and uncharted seamounts. Conducting most glider flights during the peak of Austral summer has minimized risks associated with sea ice. Additionally, because objective ice hazards exist year-round but are primarily at or near the surface, keeping the glider away from the surface as much as possible further minimizes the risk of such encounters occurring. We also reduce the risk of colliding with various forms of ice in the marine environment by receiving annotated images from the National Oceanographic and Atmospheric Administration's National/Naval Ice Center. The combination of flying the gliders during the three months of annual ice minimum and using satellite ice images to avoid flying in ice-dense waters have both helped to increase the viability of operating gliders in polar regions.

Expanding the Palmer long-term ecological research

Spatial and scientific expansion at the Palmer long-term ecological research site

Since it's inception in the early 1990s, the bulk of the work at the Palmer long-term ecological research (LTER) site has been focused on collecting and maintaining time series data to study systemic shifts in polar environments due to climatic change. Historically, oceanographic measurements at the Palmer LTER have consisted of zodiac-based collection of *in situ* physical and optical parameters and acquisition of water samples for subsequent analysis. Such labor-intensive *in situ* measurements have been complimented by satellite remote sensing which opened the doors to quantifying ice-dependent ecosystem shifts along the WAP (Stammerjohn and Smith 1996). This sampling regime of combining *in situ* investigations with remotely sensed observations has been highly effective at capturing the seasonal variations and the decadal trends in primary production. However, the data required to resolve the dynamics linking primary production to top-predators have not been acquired because of spatial and temporal constraints associated with traditional Zodiac sampling techniques. Principally, the glider is able to survey the head of the adjacent submarine canyon, an area that has been outside the scope of operations of the traditional LTER sampling regime. This is especially crucial as the head of this canyon is increasingly being recognized as an area of elevated primary production responsible for supporting the large populations of breeding penguins (i.e., a "biological hotspot") nearby Palmer Station. In addition to expanding the spatial reach of the Palmer LTER scientists, underwater gliders are also increasing the temporal resolution of the data. While traditional sampling techniques may yield several hundred water column profiles of temperature, salinity, and other properties over the course of a summer season, the glider provides several hundred water column profiles in a matter of days (Fig. 2). By merging data from satellite-tagged penguins with data from an underwater glider, the monitoring and hypothesis testing capacity of the Palmer LTER site has been expanded.

As part of the Palmer LTER study, pelagic top-predators such as Adélie penguins have been used to integrate ecological shifts in the ecosystem. However it has been difficult to acquire environmental constraints that reside in the pelagic environment in which the Adélies forage. Indeed, relevant water-column characteristics such as salinity, temperature, chlorophyll-a, and mixed layer depth can now be measured using gliders. Adélie penguin diving behavior, which spans much of the euphotic zone, can be tracked using satellite-tagging techniques. Data from satellite-tagged penguins have shown that 90% of foraging by Adélies occurs over the region of deep water adjacent to the Palmer LTER site (Fraser WR, unpublished). Prior to incorporating gliders into the Palmer LTER, the water-column (i.e., vertical) characteristics of this "biological hotspot", have not been studied at relevant ecological time and spatial scales because this area is outside the safe boating limits of scientists working at the Palmer LTER site.

Results from penguin-driven adaptive sampling by gliders

Penguin tracking data from 2006 to 2008 were analyzed to determine the extent of the foraging region for the Adélie populations near Palmer Station. These historical data were then used to develop the flight plan for the Slocum underwater glider. The glider, RU05, was deployed and recovered from the Palmer LTER site in December 2008 and continuously surveyed the Palmer Basin "biological hotspot" during a 12 day deployment (Fig. 3). The glider was tasked with flying a box-like pattern around the penguin foraging zone and then conducting a series of cross-canyon transects within the same box. The data collected during the survey include; salinity, temperature, pressure, depth-averaged current, optical backscatter (470 nm, 532 nm, 660 nm), colored dissolved organic matter fluorescence, and chlorophyll fluorescence. RU05's flight path was adapted to cope with the currents and winds present during the mission by scientists in the COOL room at Rutgers University in New Jersey. This was enabled by the real-time data, which also allowed for adaptive sampling of changing conditions at the Palmer Basin "biological hotspot".

The Slocum glider transects of the Palmer Basin "biological hotspot" revealed a phytoplankton bloom, indicated by an elevated chlorophyll fluorescence signal, that lessened yet persisted over a six-day period (Fig. 4). The chlorophyll fluorescence signal of the phytoplankton bloom was more than an order of magnitude greater than the signal in the adjacent non-bloom waters. During the glider's survey of the "biological hotspot" the phytoplankton bloom predominated between 10 and 30 m below the sea surface. Accordingly, the temperature data show an intensification of nearly half a degree in the water being upwelled from below 100 m over the same period (Fig. 4). The intensification of the bloom likely comes from increased mixing of warmer, nutrient rich upper-circumpolar deep water (UCDW) and western Antarctic WW which are characterized by temperature and salinity (Martinson, Stammerjohn et al. 2008) relative to Antarctic Surface Water (AASW) (Fig. 5). While UCDW is nutrient-rich its relatively warm temperature often prevents mixing with significantly colder AASWs. However, if UCDW is mixed during

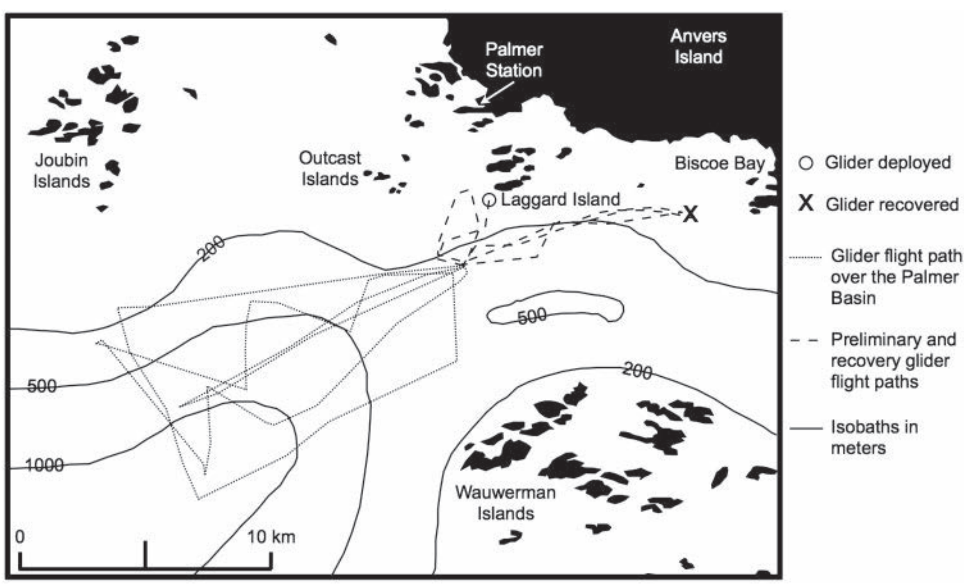

Fig. 3 Map of the Palmer Basin adjacent to Anvers Island on the western Antarctic Peninsula. Palmer Station is located at 64°46′S, 64°03′W. The Slocum glider was deployed for twelve days, six of which were spent over the Basin surveying the Adélie penguin foraging area.

cross-shelf transport and upwelling with WW, then the combined UCDW/WW water mass can more readily mix nutrients into locally formed AASW. The mixture of the nutrient-laden UCDW and WW with AASW provides an ideal environment for a phytoplankton bloom. Frequently, such phytoplankton blooms occur along the slope of the Palmer Basin closest to Anvers Island where the radio-tagged Adélie penguins preferentially forage.

The radio-tag information provides data on the location in the water column where the penguins forage. The radio-tagged data suggest that more than half (54%) of penguin foraging occurred at depths ranging from 30–50 m. Within the 90% foraging

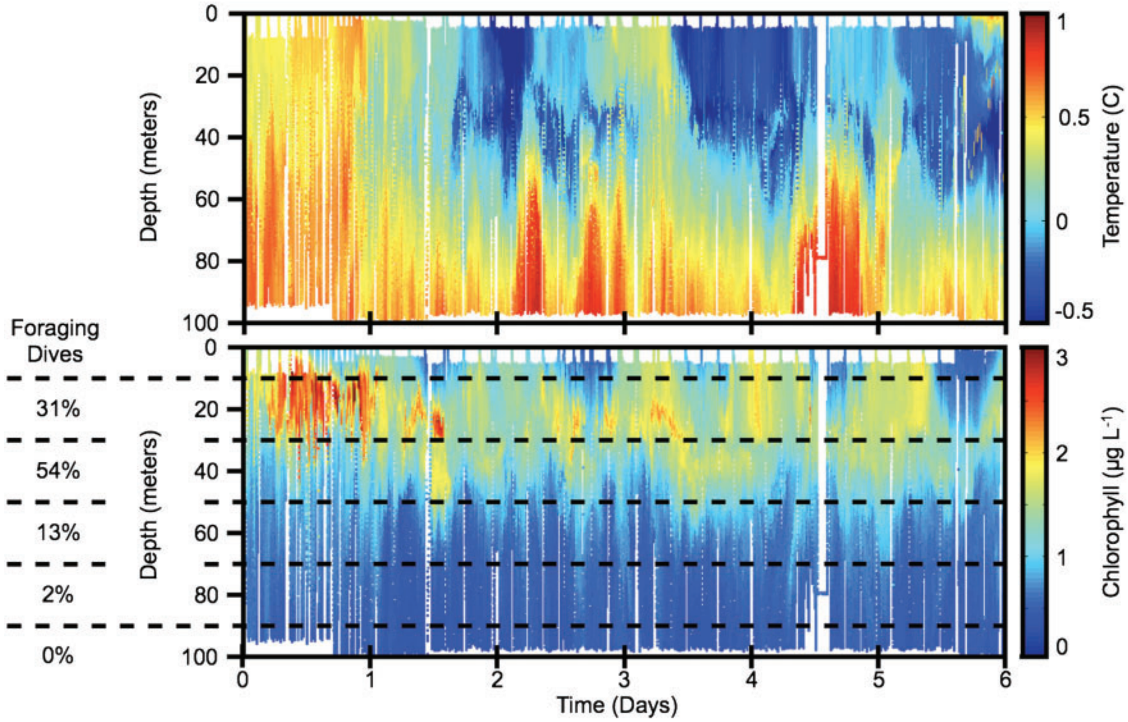

Fig. 4 Temperature (top) and chlorophyll concentration (bottom) measured by the Slocum glider within the Adélie penguin 90% foraging kernel over the Palmer Basin. Within the 90% foraging kernel, the percent of Adélie penguin foraging dives to five depth bins is aligned with the chlorophyll data.

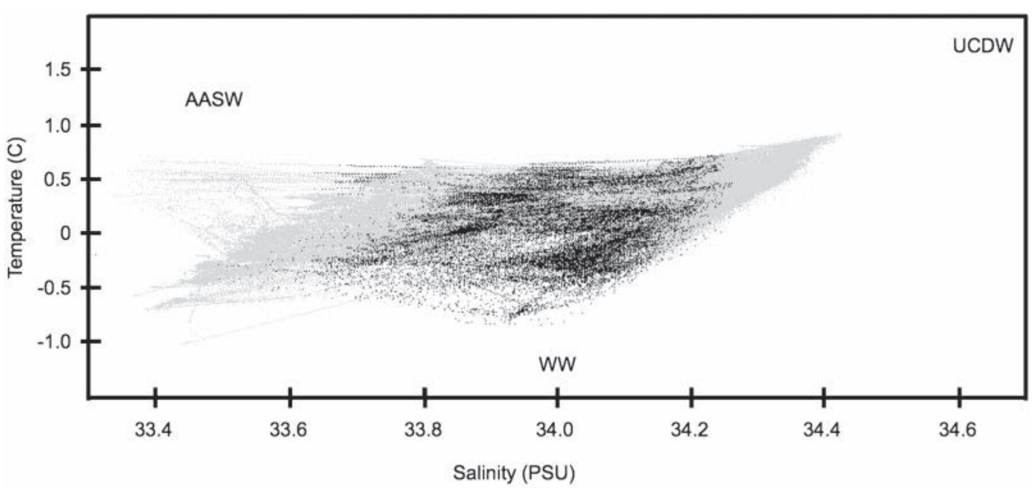

Fig. 5 Temperature versus salinity plot of water sampled by the Slocum glider. Black dots are samples collected from the primary foraging depth bin (30–50 m depth) of Adélie penguins in the Palmer Basin. The primary oceanic water masses, as defined by their temperature and salinity, in the region are; UCDW from the core of the Antarctic Circumpolar Current, western Antarctic Peninsula WW formed during the winter, and AASW formed during the summer along the coast of the western Antarctic Peninsula.

kernel, the maximum chlorophyll concentration was immediately above the 30–50 m penguin foraging dive depths. Comparatively, only 31% of foraging dives occurred at depths shallower than the depth of the chlorophyll concentration maximum. Because foraging dives originate at the surface, random feeding behavior would result in the highest number of dives occurring near the surface. However, in the Palmer Basin ‘‘biological hotspot’’, Adélie penguins appear to be targeting specific regions within the euphotic zone. In this study, the region being foraged was immediately below the most productive part of the water column. This foraging behavior suggests that the Adelies are preying on krill who are grazing on the phytoplankton cells at the base of the chlorophyll maximum. Krill undergo vertical migration (Morris et al. 1984; Godlewska and Klusek 1987) to graze in the high phytoplankton biomass regions in the surface waters at night, and have then been observed to migrate below the chlorophyll maximum during daylight hours (Morris et al. 1984) when Adelie penguin forage. Future studies will focus on this by deploying gliders outfitted with acoustic sensors to provide maps of the zooplankton biomass. These future efforts will combine swarms of gliders that measure the physical properties (temperature and salinity), phytoplankton biomass (chlorophyll fluorescence), and zooplankton (acoustic measurements). Further study is necessary to link krill at the bottom of the chlorophyll maximum to targeted Adélie foraging. Furthermore, because the depth of the mixed layer drives the location of the chlorophyll maximum in the water-column, variability of the mixed layer depth may have direct effects on the energetic balance for a foraging seabird. Bringing together satellite tagged birds and gliders to highlight linkages such as these will be critical towards expanding our knowledge of the role of environmental variability in Antarctic ‘‘biological hotspots’’.

Conclusion

While the traditional LTER needs to be maintained, modern ocean time series and ecosystem monitoring programs will increase the scientific questions that might be addressed (Ducklow et al. 2009). To this end, the subsurface-sustained- and high-resolution glider data will provide a critical tool. Not only do these low-cost emerging technologies expand scientific capabilities, they also have the potential to expand scientific collaboration. Indeed, these new technologies may provide a gateway for emerging earth science programs to enter polar research. For example, through collaborative purchasing of batteries or renting flight time on a glider, scientists working at institutions without a traditional capacity for polar research may be able to contribute to research that has traditionally been the province of well-established research entities. By focusing on innovative means of collaborating, low-cost, emerging technologies can lower the barrier of entry for many potential polar researchers. Increasing the capacity of scientists from around the world to help understand the climatically linked mechanisms already occurring in polar marine environments may have the added benefit of helping to prepare these same scientists to address similar responses to climatic change in marine ecosystems closer to home.

Acknowledgment

Kristen Gorman provided extensive help with the preparation of this article.

Funding

The National Science Foundation’s Office of Polar Programs; the Gordon and Betty Moore Foundation; and the National Aeronautics and Space Administration.

References

Ainley DG. 2002. The Adélie Penguin: Bellwether of Climate Change. New York: Columbia University Press.

Ainley DG, Clarke ED, Arrigo K, Fraser W, Kato A, Barton KJ, Wilson PR. 2005. Decadal-scale changes in the climate and biota of the Pacific sector of the Southern Ocean, 1950s to the 1990s. Antarctic Sci 17:171–82.

Anisimov OA, Vaughan DG, Callaghan TV, Furgal C, Marchant H, Prowse TD, Vilhjálmsson V, Walsh JE. 2007. Polar Regions (Arctic and Antarctic). Climate Change 2007: Impacts, Adaptation, and Vulnerability. In: Parry ML, Canziani OF, Palutikof JP, van der Linden PJ, Hanson CE, editors. Contribution of working group II to the fourth assessment report of the Integovernmental Panel on Climate Change. Cambridge: Cambridge University Press. p. 653–85.

Baker AJ, Pereira SL, Haddrath OP, Edge KA. 2006. Multiple gene evidence for expansion of extant penguins out of Antarctica due to global cooling. Proc R Soc Lond Ser B-Biol Sci 273:11–7.

Boehme L, Thorpe SE, Biuw M, Fedak M, Meredith MP. 2008. Monitoring Drake Passage with elephant seals: frontal structure and snapshots of transport. Limnol Oceanogr 53:2350–60.

Charrassin JB, et al. 2008. Southern Ocean frontal structure and sea-ice formation rates revealed by elephant seals. Prod Natl Acad Sci 105:11634–9.

Costa DP, Huckstadt LA, Crocker DE, McDonald BI, Goebel ME, Fedak MA. 2010. Approaches to studying climatic change and its role on the habitat selection of Antarctic pinnipeds. Integr Comp Biol, Advance Access publication June 3, 2010 (doi:10.1093/icb/icq054).

Daly KL. 1990. Overwintering development, growth, and feeding of larval Euphausia-superba in the Antarctic marginal ice-zone. Limnol Oceanogr 35:1564–76.

Ducklow HW, Baker K, Martinson DG, Quetin LB, Ross RM, Smith RC, Stammerjohn SE, Vernet M, Fraser W. 2007. Marine pelagic ecosystems: the West Antarctic Peninsula. Philos Trans R Soc Bio Sci 362:67–94.

Ducklow HW, Doney SC, Steinberg DK. 2009. Contributions of long-term research and time-series observations to marine ecology and biogeochemistry. Ann Rev Marine Sci 1:279–302.

Forcada J, Trathan PN. 2009. Penguin responses to climate change in the Southern Ocean. Glob Change Biol 15:1618–30.

Fraser WR, Trivelpiece WZ, Ainley DG, Trivelpiece SG. 1992. Increases in Antarctic penguin populations: reduced competition with whales or a loss of sea ice due to environmental warming. Polar Biol 11:525–31.

Gaston AJ, Gilchrist HG, Hipfner JM. 2005. Climate change, ice conditions and reproduction in an Arctic nesting marine bird: Brunnich's guillemot (Uria lomvia L.). J Anim Ecol 74:832–41.

Godlewska M, Klusek Z. 1987. Vertical distribution and diurnal migrations of krill — Euphausia superba Dana — from hydroacoustical observations, SIBEX, December 1983/January 1984. Polar Biol 8:17–22.

Grebmeier JM, et al. 2006. A major ecosystem shift in the northern Bering Sea. Science 311:1461–4.

Hubold G. 1985. Stomach contents of the Antarctic Silverfish Pleuragramma antarcticum from the southern and eastern Weddell Sea (Antarctica). Polar Biol 5:43–8.

Hughes TP, Bellwood DR, Connolly SR. 2002. Biodiversity hotspots, centres of endemicity, and the conservation of coral reefs. Ecol Lett 5:775–84.

Klinck JM, Hofmann EE, Beardsley RC, Salihoglu B, Howard S. 2004. Water-mass properties and circulation on the west Antarctic Peninsula Continental Shelf in Austral Fall and Winter 2001. Deep Sea Res Part II Top Stud Oceanogr 51:1925–46.

Kwok R, Comiso JC. 2002. Southern Ocean climate and sea ice anomalies associated with the Southern Oscillation. J Climate 15:487–501.

Martinson DG, Stammerjohn SE, Iannuzzi R, Smith RC, Vernet M. 2008. Western Antarctic Peninsula physical oceanography and spatio-temporal variability. Deep-Sea Res II 55:1964–87.

Meredith MP, King JC. 2005. Rapid climate change in the ocean west of the Antarctic Peninsula during the second half of the 20th century. Geophys Res Lett 32:L19604 (doi:10.1029/2005GL024042).

Meyers N. 1997. The rich diversity of biodiversity issues. In: Reaka-Kudla ML, Wilson DE, Wilson EO, editors. Biodiversity II. Washington DC: Joseph Henry Press. p. 125–38.

Morris DJ, Everson I, Ricketts C, Ward P. 1984. Feeding of krill around South Georgia. II. Relations between feeding activity, environment and vertical distribution. Mar Ecol Prog Ser 20:203–6.

Prezelin BB, Hofmann EE, Mengelt C, Klinck JM. 2000. The linkage between Upper Circumpolar Deep Water (UCDW) and phytoplankton assemblages on the west Antarctic Peninsula continental shelf. J Marine Res 58:165–202.

Rudnick DL, Perry MJ. 2003. ALPS: autonomous and Lagrangian platform and sensors. Workshop Report, La Jolla, CA.

Rudnick DL, Davis RE, Erikson CC, Fratantoni DM, Perry MJ. 2004. Underwater gliders for ocean research. Mar Technol Soc J 38:48–59.

Schofield O, et al. 2008. The decadal view of the mid-Atlantic bight from the COOLroom: is our coastal system changing? Oceanography 21:108–17.

Stammerjohn SE, Smith RC. 1996. Spatial and temporal variability of western Antarctic Peninsula sea ice coverage. In: Ross RM, Hofman EE, Quetin LB, editors. Foundations for ecological research west of the Antarctic Peninsula. Washington DC: American Geophysical Union. p. 81–104.

Stammerjohn SE, Martinson DG, Smith RC, Yuan X, Rind D. 2008. Trends in Antarctic annual sea ice retreat and advance and their relation to El Niño-Southern Oscillation and Southern Annular Mode variability. J Geophys Res 113:C03S90.

Steele JH. 1976. Patchiness. In: Cushing DH, Walsh JJ, editors. The Ecology of the Seas. Oxford: Blackwell Scientific Publications. p. 98–115.

Steig EJ, Schneider DP, Rutherford SD, Mann ME, Comiso JC, Shindell DT. 2009. Warming of the Antarctic ice-sheet surface since the 1957 International Geophysical Year. Nature 457:459–62.

Stommel H. 1989. The Slocum mission. Oceanography 2:22–5.

Turner J, Lachlan-Cope TA, Colwell S, Marshall G, Connolley WM. 2006. Significant warming of the Antarctic winter troposphere. Science 311:1914–7.

Turner J, Bindschadler R, Convey P, di Pricso G, Fahrbach E, Gutt J, Hodgson D, Mayewski P, Summerhayes C, editors. 2009. Antarctic Climate Change and the Environment. Cambridge, UK: Scientific Committee on Antarctic Research.

Valavanis V, Kapantagakis A, Katara I, Palialexis A. 2004. Critical regions: a GIS-based model of marine productivity hotspots. Aquatic Sciences - Research Across Boundaries 66:139–48.

Vaughan DG, Marshall GJ, Connolley WM, Parkinson C, Mulvaney R, Hodgson DA, King JC, Pudsey CJ, Turner J. 2003. Recent rapid regional climate warming on the Antarctic Peninsula. Clim Change 60:243–74.

Williams TD. 1995. The Penguins. Oxford: Oxford University Press.

Using Webb gliders to maintain a sustained ocean presence

O. Schofield, J. Kohut, S. Glenn
COOL, Institute of Marine and Coastal Sciences,
School of Environmental and Biological Sciences, Rutgers University
New Brunswick, NJ 08901 USA

Abstract- **Buoyancy driven Slocum gliders were a vision of Douglas Webb, which Henry Stommel championed in a vision published in 1989. Slocum gliders have transitioned from a concept to a technology serving research and environmental stewardship. The long duration and low costs of gliders allow them to anchor spatial time series. Large distances, over 600 km, can be covered using a set of alkaline batteries. Lithium batteries can anchor missions that are thousands of kilometers in length. Since the initial tests, a wide range of physical and optical sensors have been integrated into the glider allowing measurements of temperature, salinity, depth averaged currents, surface currents, fluorescence, apparent/inherent optical properties active and passive acoustics. A command/control center, entitled Dockserver, has been developed that allows users to fly fleets of gliders simultaneously in multiple places around the world via the Internet. Since October 2003, Rutgers gliders have conducted 157 missions, traversed >55,000 kilometers, logged >2600 days at sea, and logged ~350,000 vertical profiles. The capabilities of the glider make them an indispensable tool for the growing global effort to build integrated ocean observatories. For example, gliders are now a central tool within the National Science Foundation Ocean Observatory Initiative (OOI) and the National Oceanic and Atmospheric Administration's Integrated Ocean Observing System (IOOS). Gliders provide a new magnet in which to attract young people into the ocean science and engineering. For example Rutgers undergraduates now anchor long duration flights of gliders world-wide beginning their freshmen year. This is critical to training the next generation.**

I. INTRODUCTION

For centuries, oceanographers have relied on observations gathered from ships during cruises of limited duration. This expeditionary research approach has resulted in major advances in understanding the global ocean. These and many other successes have expanded our view of Earth and ocean processes, and have demonstrated a need for sampling strategies spanning temporal and spatial scales that are not effectively carried out using ships. To address this observational gap, the scientific community has consistently called for the development of the capability to maintain a continuous sampling and monitoring presence in the ocean [1].

Mobile platforms are undergoing exponential development and are transitioning into observational tools. One such autonomous platform that is rapidly becoming indispensable are gliders. Gliders, as currently configured, were first detailed in Doug Webb's lab book on 2/8/86 as a novel instrument approach and was subsequently publicized in 1989 by Henry Stommel's view of a futuristic smart fleet of instruments [3]. It has taken some time to bring these concepts to reality, yet gliders are steadily earning their reputation as a high-endurance sensor platform. More importantly, this class of long-range and relatively low-cost autonomous underwater vehicle (AUV) is making affordable adaptive sampling networks a reality.

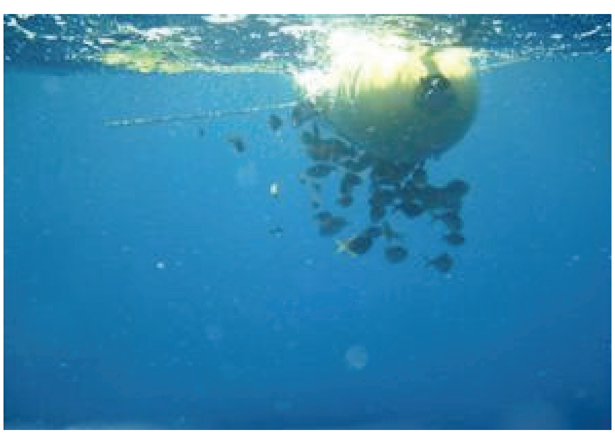

Fig. 1. A Webb glider at the surface offshore Hawaii attracting fish.

We will review our experience with Slocum gliders (Figure 1) and will demonstrate how they offer the potential improvement in our capability to observe the oceans. A number of different gliders have been developed and are being used by many organizations; however, for this paper we will only discuss the field efforts conducted by Rutgers University (RU) and Webb Research Corporation (WRC). We emphasize that the successes of this group are matched by other groups at other institutions. Our "take home" message is that Gliders are a robust technology capable of anchoring large field campaigns. Additionally, we will also highlight how Gliders will benefit many different users and serve as a magnet for the next generation of scientist and engineer.

II. OUR GLIDER EXPERIENCE AS OF WINTER 2009

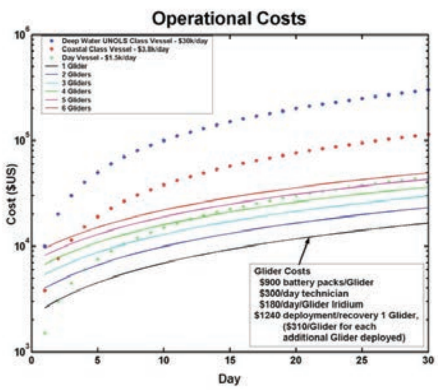

Figure 2. The costs in United States dollars for maintaining ships and gliders at sea. Ship costs represent the average daily charge that varies with ship class based on averages in the year 2005. The glider costs include the expenses of deploying, maintaining, and recovering a glider.

The Slocum glider is a 1.8 m long torpedo-shaped, winged AUV. It maneuvers through the ocean at a forward speed of 20–30 cm/s in a sawtooth-shaped gliding trajectory, deriving its forward propulsion by means of a buoyancy change and steering by means of a tail fin rudder. The altimeter and depth sensor enable preprogrammed sampling of the full water column. The primary vehicle navigation system uses an on-board GPS receiver coupled with an attitude sensor, depth sensor, and altimeter to provide dead-reckoned navigation, with backup positioning and communications provided by an Argos transmitter. Two-way communication with the vehicle is maintained by RF modem or the global satellite phone service Iridium. All antennas are carried within the tail fin that is raised out of the water when the vehicle is commanded to surface at some predetermined interval. Operational endurance, utilizing alkaline batteries, is 25 to 60 days, depending on sensor payload and sampling regimes. Horizontal distance traveled averages 24 km per day. The vehicle is operational in 5 to 200 m of water depth and can be optimized for 30, 100, 200 and 1000 m operation with select gearboxes.

The mission duration of a glider is largely a function of the number of sensors and the water depth. The largest power drain in the glider involves the operation of the pump and, therefore, the battery life is shortest in shallow seas. Despite the shortened battery life, deployments last over three weeks, providing the scientist usually several thousand vertical casts. The increase in data quickly justifies the costs of maintaining Gliders for sustained observations (Figure 2). The operational costs for Gliders include technician time, costs for deployment/recovery, batteries, and Iridium phone charges. Based on standard daily costs for a range of research vessels (deep water, medium, small coastal vessel), the operational costs of Gliders are economical (Figure 2). The typical costs of operating the deep-ocean and coastal class research vessels exceed the cost of operating single glider deployed for a full multi-week mission. The costs of smaller research vessels exceed a glider after three days. One technician can operate several gliders so the increased costs associated with operating multiple gliders reflect increased deployment/recovery costs, batteries, and Iridium charges. Given this the costs of medium research vessel will exceed operating a fleet of six gliders in about four days. Gliders will never replace ships, but populating the oceans with Gliders will allow ships to use their time wisely as they will

Figure 3. RU gliders ready for deployment.

know when and where to sample the ocean. This will allow the ship time to be used to spend its time at sea testing/deploying new instruments and conducting experiments.

Rutgers currently maintains a fleet of over 20 gliders (Figure 3). The glider built through competitive grants have to date conducted 157 missions, traversed >55,000 kilometers, logged >2600 days at sea, and logged ~350,000 vertical profiles. These gliders missions have been conducted world-wide and are coordinated at Rutgers main campus (Figure 4). The missions have spanned efforts from the polar to temperate and tropical seas. The data has been highly valuable and has been central to 13 peer reviewed manuscripts in 6 years with 9 more papers in press or in review. The manuscripts have a mean number of 7 authors and thus the gliders are central to interdisciplinary ocean science.

Operating a fleet of gliders necessitates an automated command and control (C2) system in order to optimize glider missions to resolve the temporal and spatial patterns of the process of interest. This requires the C2 to be flexible and adaptable as the environment is constantly evolving. We have been constructing a C2 system for a fleet of Webb Gliders; however, the system is scalable to allow the incorporation of a number of data inputs, allowing the fleet to make intelligent goal oriented decisions that feeds back into dynamic adaptive resource allocation. The software package allows information from a scientist, the glider itself, other sensing systems such as high frequency radar, satellites, or additional gliders, to optimize a particular glider's flight characteristics or waypoints. New mission directives are automatically uploaded to the glider during surfacing and the glider begins its new sampling regime or waypoint bearing. Optimization can be done for features like, but not limited to, currents, tides, thermoclines, and haloclines.

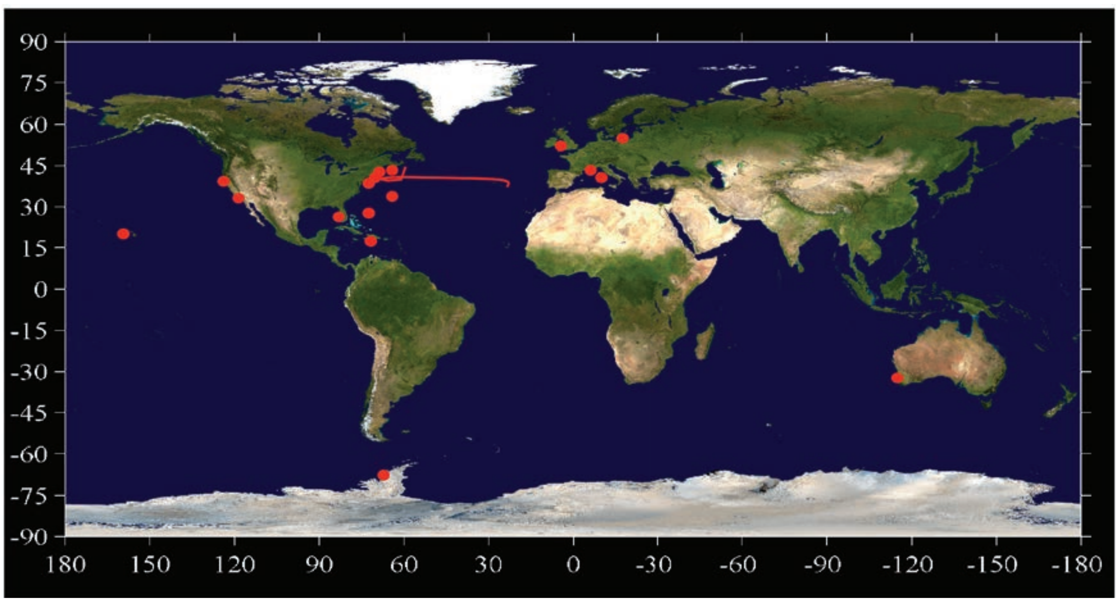

Figure 4. The global deployments for the RU gliders. The coming months in summer 2009 has missions planned for a second attempt to cross the Atlantic, along with science missions offshore Norway, Alaska, and Northeast seaboard of the United States.

Deployments can also allow ground-truthing of satellite imagery. Data are automatically pulled from the vehicle and made available for web based presentation.

III. GLIDER SENSORS

The value of the Glider surveys will increase as the sensors available for Webb Gliders expands (Figure 5). The main bottleneck for integrating sensors is minimizing their size and power consumption. In experience this has been a three-step process. The first is the efforts by the manufacturers to minimize the sensors for the gliders. Most often, the second phase involves mounting a self-recording sensor on a glider to collect data, which is often needed to secure funding from federal agencies for full sensor integration. The full integration and field demonstration is the final and third phase. Based on history working with WetLabs, Mote Marine Laboratory, Satlantic, and Webb Research this end-to-end process takes close to two to three years depending on the sensor complexity. This process has successfully integrated many diverse sensors into a Webb glider. Measurements presently being made by gliders include physical (temperature, salinity, turbulence), acoustic (active and passive), optical (spectral radiometry, backscatter, attenuation scattering, absorption, digital imagery), fluorescence (chlorophyll a, colored dissolved organic fluorescence, fast repetition rate fluorometry), and dissolved gas (oxygen)

Figure 5. The sensors that have been carried on Webb gliders. They include (starting at the top left panel) oxygen, passive acoustic, attenuation, chlorophyll/colored dissolved organic flourometers, turbulence, fish finders, scattering and backscattering packages, spectral backscatter, radiometer, digital cameras, acoustic doppler measurements, fast repetition rate flourometry, and absorption.

With so many sensors now available, the power required often outstrips the capabilities of a standard glider configuration. To address three strategies have been pursued. The first strategy is to increase the number of batteries that the glider can carry. This has resulted in the development of the "stretch" glider. The stretch glider's longer body allows for more battery packs and/or larger sensors. The second strategy has been to develop lithium battery packs for the Webb gliders. Working with Electrochem, a fully outfitted lithium glider was operated for several months and Coulomb meter measurements suggest glider lifetimes of 300-360 days is now available. The final strategy is to fly the gliders as swarms. The swarms represent packs of gliders carrying distributed sensors, allowing a full complement of data to be collected. These swarms we have termed "Darwin clusters" as the adaptive capabilities of gliders are operated as evolving network that allows data to be merged between the platforms while also providing a mesoscale network to map features in the ocean.

IV. Near Term Challenges

Gliders are key technologies to exploring extreme environments and episodic events, which are disproportionately important to many ocean processes. Targeted extreme environments include the poles, severe storms, urbanized ports and developed coastlines, which are often avoided by scientists because of the hazardous operating conditions.

Gliders are now a central technology that will anchor climate change research being conducted in the Antarctic and Arctic. One effort will use gliders along the West Antarctic Peninsula as part of the NSF's Long term Ecosystem Research program in collaboration with British scientists. Here the efforts will be to provide a sustained regional presence when the research vessel is not available. This requires scientists to utilize the Antarctic field stations as a staging facility. This strategy was demonstrated successfully in 2007 and 2009 (Figure 6). Additionally, gliders will help scientists to understand why deep canyons are associated with large penguin breeding colonies. Radio-tagged penguins will be used to adjust the sampling areas of a Darwin cluster of gliders capable of mapping the physics, chemistry, phytoplankton, currents and higher trophic levels, in order to understand if canyons are associated with sustained upwelling that provide a predictable food resource near the breeding colonies. The second polar effort will be conducted in the Arctic in collaboration with Norwegian researchers. Here the goal will be to develop a time series site between the Svalbard and Norway to understand regional circulation impacting ice flows and regional warming trends.

Science efforts are usually curtailed during severe storms; however observing networks are robust and allow scientists to safely study these processes in real-time. One nice example was from a storm event encountered in October of 2003 [2]. The gliders are equipped with a conductivity–temperature–depth sensor, and an ECO-sensor pucks. October is the transition between summer and winter seasons, which starts with surface cooling that preconditions the shelf for rapid mixing during fall storms. The mixing storm of October 2003 was a classic northeaster. Early in the storm when waves were high, sediment resuspension was limited to below the pycnocline. After the pycnocline eroded through growth of the bottom boundary layer, particles immediately filled the full water column. The spectral ratio of backscatter indicated that the particles were likely similar materials both before and after the stratification was eroded. The backscatter profiles in the bottom boundary layer decay with distance from the bed at rates consistent with theory but with variable slopes. The reduced slope of the backscatter profiles increased after stratification was lost, which is consistent with an increase in vertical transport or turbulent mixing. Wave bottom orbital velocities during this time were decreasing, and the glider vertical velocities showed no enhancement consistent with Langmuir cells. Enhanced mixing was related to the interaction of the surface and bottom boundary layers while the stratification was eroded, and the observed variability in the resuspension during the event was also due to the tide.

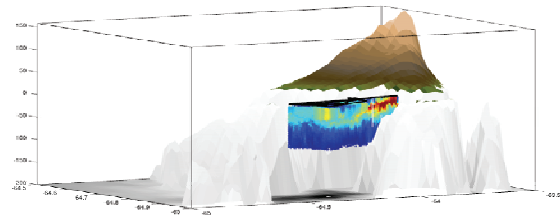

Figure 6. A 3-D section of chorophyll fluorescence measured offshore Palmer Station in December 2008. The high chlorophyll values are associated with upwelled water. The next phase of the research is to understand if this upwelled water is associated with the Antarctic Circumpolar Deep Water.

Urbanized ports are often process-rich environments with strong signals to study, but the difficulties of working in a heavily used environment often preclude scientific study. These areas are often regions of high current. Therefore it is critical to develop the new automated flight behaviors that allow the glider to sense its environment and make smart decisions to enact the best behavior to sample the local environment while avoiding contact with humans. This challenge is perhaps the most difficult to tackle.

A final theme is to extend the limits of long-duration underwater glider flights. These efforts have focused on developing new power and control systems. The long duration studies are powerful magnets to entrain undergraduate students. These flights have the potential to increase the visibility of ocean exploration to the general public. The Coastal Ocean Observation Lab is developing new undergraduate initiatives as part of a University-wide effort to transform undergraduate education at Rutgers. Enabled by an ocean observatory operations center purposely located on the main campus of a major research university, the lab has established a program featuring hands-on team-based research projects that compliment course-work and are specifically designed to entrain undergraduates. The program encourages students to become involved as early as their freshman year, remaining in contact with many of the same students and professors for their full 4 years at Rutgers. A series of Introduction to Oceanography courses with significant freshman participation, and a variety of small seminar courses given to first-semester freshman, serve as the feeder courses. Interested students join us in the lab in their second semester, either through 1-credit research courses or work-study programs.

These courses are focused on specific long duration glider missions to teach to students oceanography while simultaneously gaining hands-on experience. The initial task supported by the undergraduate student team - to be the first to fly an autonomous underwater glider from Tuckerton, New Jersey to Halifax, Nova Scotia - was accomplished in the spring of 2008. Their second task, still ongoing, is to be the first to fly a glider across the Atlantic from New Jersey to Spain. Rutgers alumni donated a glider for use as the primary platform to engage undergraduates in projects related to ocean observatories. The National Science Foundation provided a RIOS summer intern, in this case an aeronautical engineer from the University of Maryland. Qualitas, a Spanish company installing and operating the national HF Radar network for Spain, contributed an internship for a student with a dual major in Marine Science and Spanish. Glider training courses, developed and delivered for NOAA-sponsored IOOS projects, used extensively by the operational Navy, NATO and the European Glider Association were used to spin students up over the winter break in every aspect of glider operations. Each student on the team was responsible for a specific aspect of the long-duration flights. Two freshman worked alongside the three glider technicians to help with the construction and testing of the actual glider. At the end of their spring semester, they returned to their high school, giving talks to their science teacher's class and the high school robotics team on what they accomplished at Rutgers in their freshman year. Two juniors worked on the flight characteristics of RU17, optimizing the flight controls and providing feedback to the manufacturer. Two freshmen worked on the NOAA-sponsored IOOS Mid-Atlantic HF Radar network as the launch zone for these two flights, while a junior worked on HF Radar in Spain to help prepare the landing zone. Two seniors worked on path planning, website development, and the Google Earth interface that has been used in three Navy exercises, is part of our Middle Atlantic control center. The first attempt in 2008 failed, as the glider encountered problems close to 200 kilometers from the Azores. The students despite the set back set the world's record for distance covered by an AUV (Figure 7). A second attempt begins in Spring 2009.

V. SUMMARY

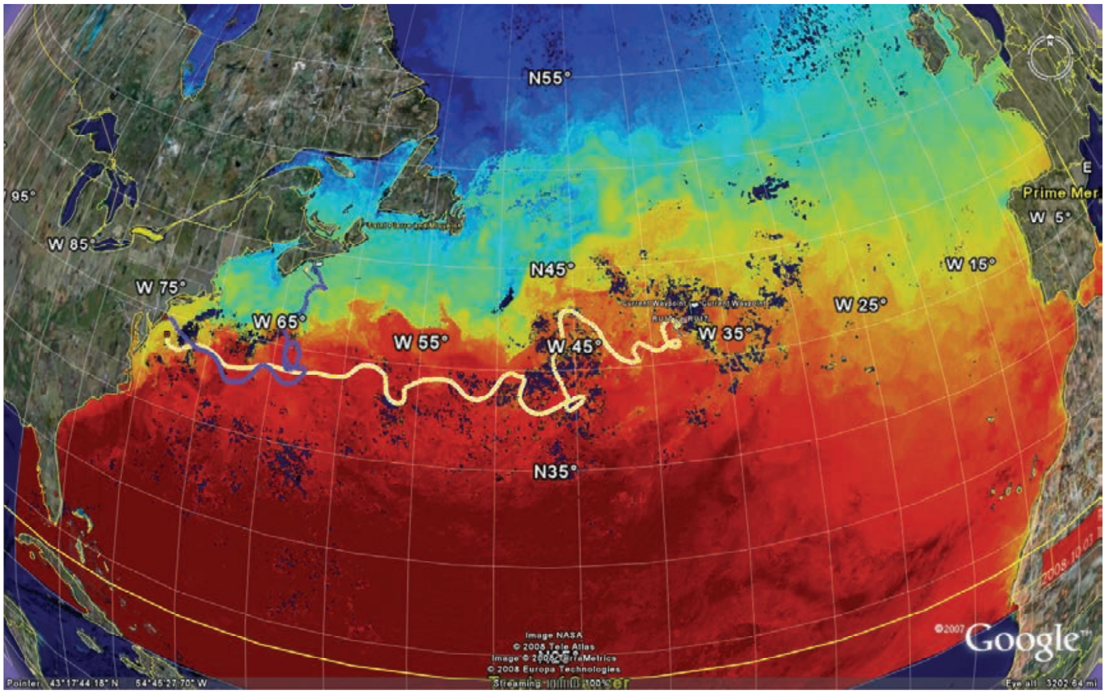

Figure 7. The path of undergraduate glider missions focused on long duration missions. The blue line shows the successful flight from New Jersey to Halifax. The yellow line shows the student's first attempt to cross the Atlantic.

Gliders are a robust technology that allows scientists to maintain a sustained presence in the ocean and this will enable oceanographic to tackle critical issues facing the community. The gliders will also provide a unique technology that will entrain the next generation ocean scientists and engineers. These two factors make it a very exciting time to be an oceanographer.

REFERENCES

[1] Ocean Observatories Initiative (OOI). Program website, http://www.oceanleadership.org/ocean_observing

[2] Glenn, S., C. Jones, M. Twardowski, L. Bowers, J. Kerfoot, J. K, D. Webb, O. Schofield, "Glider observations of sediment resuspension in a Middle Atlantic bight fall transition storm". Limnol. Oceanogr. 53, 2180-2196. (2009).

ClearSignal Coating Controls Biofouling On the Rutgers Glider Crossing

A Nonstick Coating Gives the Scarlet Knight Glider Permanent Biofouling Control on Trans-Atlantic Mission

By Hank Lobe
Principle
Severn Marine Technologies
Annapolis, Maryland
Chip Haldeman
Instrument Specialist
and
Dr. Scott M. Glenn
Professor
Institute of Marine & Coastal Sciences
Rutgers, The State University of New Jersey
New Brunswick, New Jersey

One of the most exciting new tools in present day oceanography is the glider, which can perform sustained collection of oceanographic data. Gliders are unique in that they provide the ability to conduct long-term oceanographic data collection missions on a mobile and directionally controllable platform.

The glider's performance is derived from its highly efficient buoyancy-derived propulsion system, enabling the platform and associated sensors to be deployed for many days or even months of sustained oceanographic sensing over navigationally controlled long distances.

The attributes of the glider—extended mission deployments and high-efficiency, low-power propulsion—are not without operational vulnerabilities. By virtue of their extended immersion times, long-deployment glider missions have an increased susceptibility to the settlement of biofouling organisms on all of the glider's exposed surfaces. Even a low to moderate degree of biofouling can impart enough hydrodynamic drag to significantly inhibit or prevent both forward movement and directional control of the glider.

Biofouling on Gliders

A glider's susceptibility to biofouling attachment depends on a number of environmental and operational factors. The most important of these are geographic location, water temperature, mission duration, operational depths and the seasonal variabilities of biofouling organisms. In general, seasonally warmer waters and shallower depths are more conducive to biofouling settlement. The gooseneck barnacle is the most common biofouling organism that gliders and other open-water platforms encounter.

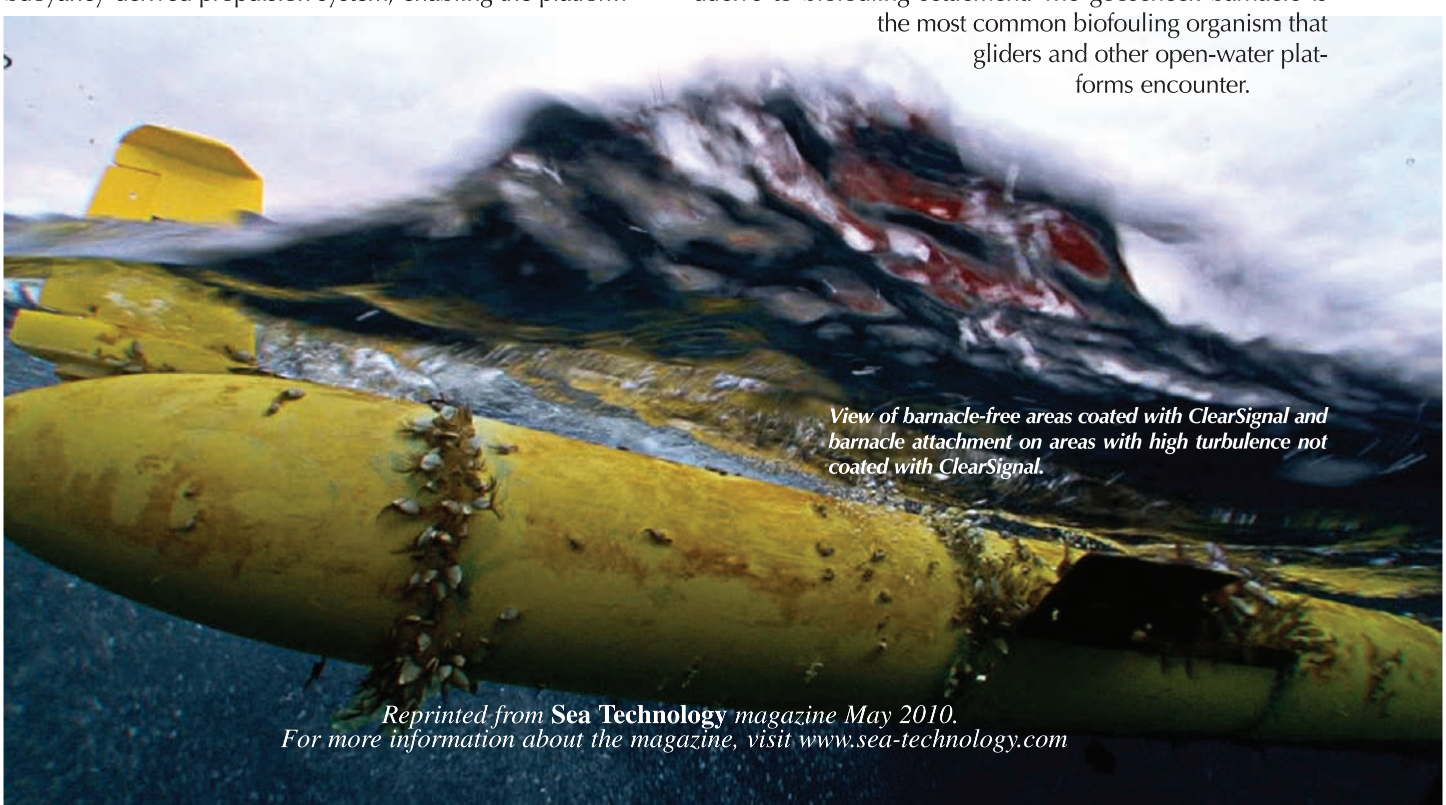

View of barnacle-free areas coated with ClearSignal and barnacle attachment on areas with high turbulence not coated with ClearSignal.

Reprinted from **Sea Technology** *magazine May 2010.*
For more information about the magazine, visit www.sea-technology.com

Glider prior to biofouling.

(Below) Recovery of the Scarlet Knight.

Scarlet Knight Atlantic Crossing

Rutgers hosts a glider team consisting of several professors/principle investigator scientists, an equal number of glider-dedicated engineers and technicians and a significant contribution from both undergraduate and graduate students. The overall goals of the team are to use and advance the capabilities of gliders for oceanographic data acquisition in support of advanced climate studies.

The team configures and operates several gliders manufactured by Teledyne Webb Research Corp. (East Falmouth, Massachusetts). The scientific data collected from glider missions is used to further develop and refine oceanographic prediction models that are a major component of climate and climate change studies.

One of these gliders, the Scarlet Knight, recently completed a trans-Atlantic crossing conceived so as to fulfill the following mission requirements: proving the ability of gliders to perform long-duration missions, collecting critical physical oceanographic data during the transit and providing a complex and science-based mission that could in large part be run by students.

The Scarlet Knight was launched on April 27, 2009, off the coast of New Jersey and recovered on December 4 off the coast of Northern Spain, having traveled a distance of just more than 4,600 miles.

Controlling Biofouling on Gliders

In the years leading up to the Scarlet Knight mission, as the Rutgers team worked on extending the mission durations of their glider fleet, it became increasingly evident that biofouling was becoming a major factor limiting shallow (less than 200 meters) glider mission durations and transit distances achieved.

In response to this concern, the Rutgers team initiated an investigation to determine if a suitable biofouling control technology existed for use on their Scarlet Knight glider. The first steps in the investigation were the development of a glider biofouling coating performance criteria and an analysis of available biofouling control solutions.

A somewhat unique requirement for gliders is that of a constant density anti-fouling coating. Gliders are ballasted and trimmed to within several grams of weight and must remain at this set condition for the entire mission. Durability, long-term effectiveness and safety in handling are obvious attributes that must be achieved by a biofouling control system. A final desired attribute is for the coating to be optically clear. This enables the glider as configured to retain its identity of color, logos and other identifying markings, including contact numbers and handling instructions for vessels it may encounter on its mission.

Traditional Biofouling Solutions

Historically, biofouling control has been achieved by exploiting the toxicity of metals, organometals and other similar marine invertebrate biocides and incorporating them in paint matrices to form anti-fouling coatings.

This class of coatings and associated methodology is unacceptable for gliders for a number of reasons.

The use of released organometals to achieve biofouling control is not acceptable for gliders because the density of the coating changes as the metal is released from the paint matrix. This is also true of most nonmetal biocides.

This problem is further exacerbated when using an ablative paint matrix, as is common in most traditional anti-fouling paints.

The traditional anti-fouling paints also often impose occupational hazards to those handling coated equipment. At Rutgers, many of the handlers are young students. Another consideration is that the long-term effectiveness of the paints is limited because the active biocide is eventually all released from the paint matrix over time. This would necessitate the annual removal and recoating of a paint system, which is time consuming and imposes additional occupational and hazardous material issues. Finally, the traditional anti-fouling paints are not transparent.

Other anti-fouling techniques that are sometimes used on oceanographic instrumentation, such as ablative greases containing various pepper extracts, were also evaluated, but they were judged to be unacceptable when evaluated against the performance requirements of long-term effectiveness, durability, occupational safety and constant density.

Biofouling Solutions for Gliders

A newer class of coating that is specifically formulated for undersea instruments (optical or acoustic, for example) and specialized platforms such as gliders has recently emerged and was identified by the Rutgers engineering group as a good candidate for the Scarlet Knight. This coating, ClearSignal™, is a clear, nontoxic, rubber-like coating that resists biofouling because of the nonstick properties of the material itself. The product is a permanent coating that is designed to last for the life of the platform or instrument it is protecting.

The ClearSignal biofouling control system is the product of a joint development effort by Severn Marine Technologies LLC (SMT) and Mercer Island, Washington-based Mid-Mountain Materials Inc. (MMM).

The companies originally developed ClearSignal to coat instruments used in the offshore seismic exploration industry. The product was recently reformulated to accommodate the larger oceanographic research community.

"ClearSignal is a clear, nontoxic, rubber-like coating that resists biofouling because of the nonstick properties of the material itself."

Coating Selection and Use

After a careful review and evaluation of a variety of biofouling solutions by the Rutgers marine lab, it was determined that the ClearSignal anti-fouling system was the best solution for meeting all of the performance requirements described. It was determined that for this initial implementation of ClearSignal, the yellow main body sections were to be coated. This comprised approximately 90 percent of the Scarlet Knight's surface area. The individual glider sections were sent by Teledyne Webb Research Corp. to the SMT-MMM coating facility in Arlington, Washington, for application of the coating. The coated sections were then sent to Rutgers so that the Scarlet Knight could be assembled and configured for the transatlantic crossing.

Coating Performance

The Rutgers research team documented the performance of the glider anti-fouling coating during its transit through diver inspection and photography in the Azores, as well as inspection upon recovery off the coast of Spain.

In early July, three months into the crossing, Rutgers observed that the glider was having trouble turning and holding its navigation course as instructed. This was the first indication that at least a moderate degree of biofouling was adversely affecting the glider. The control problems became more acute in mid-August, with the Scarlet Knight losing a significant portion of its steering and navigational ability as it headed toward the Azores.

With the journey three-quarters complete and the Scarlet Knight's forward propulsion and control now at a critical state, the Rutgers field service glider team intercepted the glider in late August at its location west of the Azores.

Observations and Actions Taken

An initial inspection of the Scarlet Knight revealed a significant settlement of gooseneck barnacles on specific areas of the glider. It was obvious from the outset that Scarlet Knight was being impeded by the observed barnacle settlement.

The ClearSignal-coated yellow main body sections of the Scarlet Knight were free of all but minor barnacle attachment. The biofouling that did occur was mostly sporadic and consisted of small individual barnacles. It was also noted that some of the sporadic biofouling that occurred on the ClearSignal-coated body were in areas where the biofouling had propagated from the heavily biofouled uncoated sections of the glider.

The glider sections that were not coated with ClearSignal, such as the front-nose-cone pump section aft of the nose cone, connecting seams and the conductivity, temperature, depth (CTD) sensor area had moderate to severe biofouling.

The areas that were most vulnerable and had the highest accumulation of barnacles were the seams between the glider sections, wing rails and the areas on and near the CTD sensor. It is important to note that these areas suffered from severe biofouling as a result of not being coated with ClearSignal and because of the turbulence generated by the glider surface discontinuities in these areas. It is a known phenomenon that barnacles accumulate in these types of low-pressure turbulent areas.

The biofouling noted was cleaned by the divers on site without removing the Scarlet Knight from the water. As reported by the divers, the small degree of biofouling removed from the ClearSignal-coated areas of the Scarlet Knight were removed with almost no effort. The significant barnacle accumulation removed from the areas not coated with ClearSignal required a moderate degree of effort.

After the Scarlet Knight was cleaned, it was given a check for operational soundness and sent back on its way to Spain.

Observations in Spain

The Scarlet Knight performed well on its final leg of the crossing, but did show impediments to its speed near the end of the journey in November and December. The recovery on December 4 provided a second opportunity to assess the glider's vulnerabilities to biofouling and the performance of the ClearSignal solution.

The biofouling settlement observed in Spain was the same species of gooseneck barnacle and was greater in degree and areas of settlement than observed in the Azores. Again, the most vulnerable areas were the body-connecting seam areas, wing rails and CTD areas, the portions of the glider unprotected by ClearSignal and subject to high turbulence. It was also observed that the wing sections were moderately biofouled. Overall, the ClearSignal-treated sections of the Scarlet Knight had little to no fouling settlement. There was, however, moderate biofouling on the ClearSignal-coated area where barnacle settlement had propagated from the vulnerable and uncoated highly biofouled areas of the glider.

"Overall, the ClearSignal-treated sections of the Scarlet Knight had little to no fouling settlement."

As with the cleaning in the Azores, the effort to remove the barnacles from the body-section seams, CTD areas and other nontreated areas of the glider was moderate. The effort required to clean the small degree of settlement on the ClearSignal-coated areas was minimal.

Conclusions

The implementation of the ClearSignal biofouling control coating was integral to the Scarlet Knight's successful and historic Atlantic crossing. The coating system achieved this performance while meeting the important criteria of providing an anti-fouling coating with constant density, constant efficacy over time, optical clarity and long-term durability.

"The coating system met the important criteria of providing an anti-fouling coating with constant density, constant efficacy over time, optical clarity and long-term durability."

The ClearSignal system worked extremely well, as there was little to no biofouling settlement on the majority of the surface area protected with ClearSignal. Where areas of moderate biofouling attachment to the ClearSignal were observed, it was due to the propagation of barnacle settlement from the most vulnerable areas noted.

Since the barnacle settlement occurring on the seams of the glider sections was due to the turbulence generated in these areas and the lack of a biofouling treatment, the prescribed approach for eliminating the biofouling associated with these areas is to tape off these seams to eliminate turbulence and then coat with ClearSignal.

The implementation of additional ClearSignal coating and the turbulence reduction methods noted will significantly reduce the settlement of biofouling in these areas and significantly reduce the propagation of barnacles.

This is especially important as oceanographers seek to extend the duration of glider missions focused on the upper ocean. ■

Visit our Web site at www.sea-technology.com and click on the title of this article in the Table of Contents to be linked to the respective company's Web site.

Hank Lobe is the co-developer of the ClearSignal biofouling control coating and also serves as a consultant in the marine industry for sensor and specialized platform applications.

Chip Haldeman served as the lead field technician for the Scarlet Knight Atlantic crossing. He is also a scientific research diver and, as such, was responsible for all underwater activities during the glider's deployment, intervention and recovery.

Dr. Scott M. Glenn is a professor of marine and coastal sciences at Rutgers, The State University of New Jersey, and the co-director of the Coastal Ocean Observation Lab. He co-teaches the undergraduate Atlantic Crossing class with professors Oscar Schofield and Josh Kohut.

Slocum Glider Energy Measurement and Simulation Infrastructure

Hans C. Woithe*, Ilya Chigirev†, David Aragon‡, Murium Iqbal†, Yuriy Shames†
Scott Glenn‡, Oscar Schofield‡, Ivan Seskar†, Ulrich Kremer*

*Department of Computer Science, †WINLAB, ‡Institute for Marine and Coastal Sciences,
Rutgers University

***Abstract*— Autonomous underwater vehicles (AUVs) are indispensable tools for marine scientists to study the world's oceans. Depending on their missions, AUVs are equipped with advanced sensors (sonar, cameras, acoustic communication, bio-sensors), have on-board computers for data analysis (image analysis, data compression), and are capable of on-board decision making (resource planning, swarming). Since AUVs operate solely on battery power, power and energy management is a crucial issue. Mission-critical tradeoff decisions have to be made between energy consumption and sensing, data processing, and communication activities. Mission planning has to consider these tradeoffs when provisioning resources for expected future events, or when dealing with changing environmental conditions such weather, water currents, and seafloor profiles. Effective power and energy management requires knowledge about the actual energy consumption of each active component within the AUV. Effective planning requires simulators that can predict energy consumptions based on expected future events and environmental conditions.**

In this paper, we discuss the design and implementation of a power measurement infrastructure for the Teledyne Webb research Slocum glider. This infrastructure can be used for online power/energy management or to better understand the time-dependent energy consumption profile of the active glider components during a particular mission. We also discuss the design of a new simulation environment for the Slocum glider which uses the power/energy data obtained by our measurement infrastructure, in addition to seafloor and coastal radar information. We illustrate the effectiveness of the new tools in the context of planning a glider flight across the continental shelf off the coast of New Jersey.

I. Introduction

The mission endurance of today's Autonomous Underwater Vehicles (AUVs) depends highly on the capacity and usage of the vehicle's batteries. Typically, missions for the Slocum Electric Glider last about 30 days [8]. Longer missions, such as the 221 day mission to cross the Atlantic by RU27 from Rutgers University [10] are possible through an increase in the number of batteries and through the careful planning of the usage of the vehicle's devices. Such planning is also crucial for shorter missions when gliders are equipped with advanced sensors such as an Acoustic Doppler Current Profiler (ADCP) or acoustic underwater communication.

With the recent integration of the coulomb meter into the glider, measuring the discharge of the battery has become more accurate. Knowing the rate at which energy is used and how much remains is vital to mission planning. However, the glider's coulomb meter only measures whole vehicle current. To perform more precise mission planning, being conscious of the energy consumption of individual components is necessary. We have developed a measurement infrastructure which captures the currents drawn from distinct components of the Slocum Glider. The infrastructure has been deployed in test missions off of the coast of New Jersey, and the data collected have been integrated into a Slocum Glider simulator. Our measurement board and simulation framework can be used to assist in the planning and decision making of missions and shows possible tradeoffs, for instance, between mission duration, speed, and energy consumption.

II. Measurement Infrastructure

We have created a measurement infrastructure to measure and record the electric current drawn by individual devices of the Slocum glider. The infrastructure consists of a measurement board and a data logger. The design philosophy in creating the infrastructure was to not compromise the safety of the vehicle, even if quality of the resulting measurements are affected. The

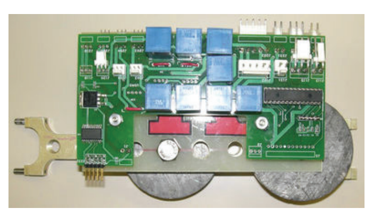

Fig. 1. Measurement board mounted on a weight bar used for ballasting the Slocum glider.

978-1-4244-5222-4/10/$26.00 ©2010 IEEE

glider components measured are: the main, external, and emergency power, the buoyancy pump and brake, and the pitch and fin servos.

The measurement board, shown in Fig 1, was intended to be housed above the glider's mainboard in the aft section of the vehicle. However, due to the different space constraints between different generations of gliders, the board was moved to the center payload bay. This allows the board to be quickly uninstalled and re-equipped onto another glider.

The board makes use of eight Hall Effect sensors which do not interfere with the vehicle's current flow. This ensures that in the event of sensor failure, the glider will continue to operate normally. Three 20A sensors are used for the main, external, and emergency power, while two 5A sensors are used for the buoyancy pump. Three 3A sensors are used for the buoyancy pump brake, pitch servo and fin servo. The sensors were over-provisioned for safety, but still allow the capture of large spikes in the current.

The microprocessor used in our design was the PIC16F767. The processor typically operates at less than 2mA at 8MHz. It contains eleven 10-bit analog-to-digital (A/D) channels of which eight are in use to measure the currents drawn by the glider using the Hall Effect sensors. The microprocessor has been programmed to use interrupts to generate constant samples at 32ms intervals. These samples are transmitted to the glider's science bay processor.

The measurement board communicates its samples via a 9,600 baud serial connection to the science bay processor. The stock 6.38 software version of the glider's science computer software has been retrofitted to record the samples produced and transmitted by our measurement board. The science processor, a CF1 from Persistor Instruments Inc. [6], is typically clocked to run at 3.68MHz using the stock software, but is usually run at higher clock speeds when collecting data as part of our infrastructure.

The power consumption of the science processor is shown in Table I. The CF1 as programmed during our previous deployments, was clocked at 14.72MHz which consumed approximately 520mW more power than the stock software release. We have since developed optimizations in the logging process to reduce energy consumption. These improvements allow the clock speed to be lowered down to 3.68MHz provided that the mission specifications allow for the trade off of four second, instead of two second, sampling from the conductivity, temperature and density (CTD) sensor. The CTD is a standard sensor on a Slocum glider.

The power consumption of the measurement board

TABLE I
CF1 POWER CONSUMPTION

Software	Clock Rate (kHz)	Power (Watts)
Stock 6.38	3680	0.19
Deployed 6.38	14720	0.71
Development 6.38	3680	0.35
Development 6.38	7360	0.49

TABLE II
MEASUREMENT BOARD POWER CONSUMPTION

Description	Channels	Power (Watts)
Deployed	8	0.76
Development	6	0.58

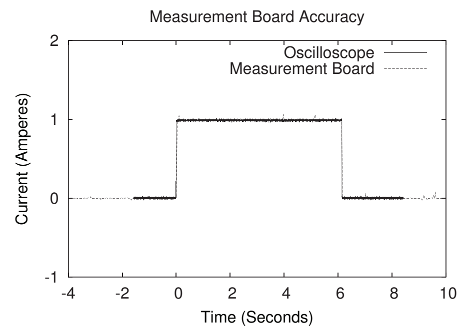

Fig. 2. Assessment of the measurement board's accuracy using a Tektronix MSO4034 oscilloscope.

itself is shown in Table II. After deploying gliders equipped with our infrastructure we have found little use in measuring the external and emergency current. The external power supply is only active on bench, so it is unnecessary for a board which will be deployed at sea. In the event of a emergency, the safe recovery of the vehicle is of higher priority than collecting good data. The presence of the emergency sensor could not be justified for the additional power it consumes. By removing the two Hall sensors, 180mW of power was saved. An additional benefit comes from the fact that the measurement board and the science processor now measure, transmit, and log less samples allowing for more data to be collected.

The measurement infrastructure has been extensively tested to ensure that recorded current samples are representative of the actual events. Fig 2 shows the results of a test where a current of 1A was applied to one of the sensors for approximately six seconds. The event was measured and logged by a Tektronix MS04034 oscilloscope as well as a PC connected to our measurement board. The results of these experiments indicate that the samples collected are within the expected error of the sampling rate, A/D conversion and the sensors

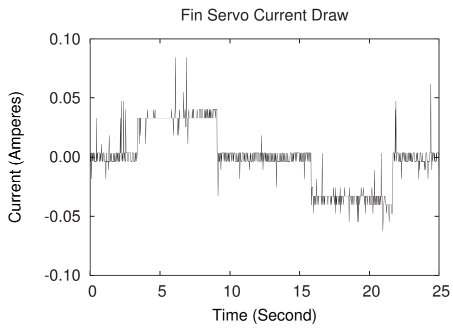

Fig. 3. Current draw of the fin servo during a "wiggle."

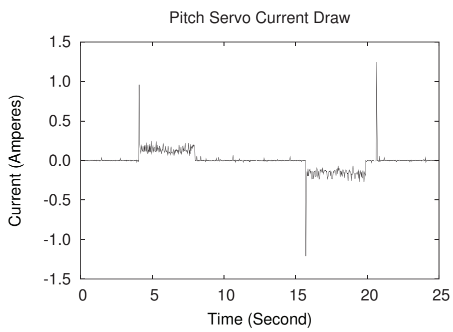

Fig. 4. Current draw of the pitch servo during a "wiggle."

themselves.

The infrastructure as installed on the gliders records all measured samples. Without compression, data can be recorded for mission lasting up to 26 days. However, multi-week missions using this revision of the board with alkaline batteries are not feasible due to the significant energy overhead. It may be possible if lithium batteries are used instead. In future work we hope to significantly reduce the power dissipation of the system so that full length deployments are possible.

III. Deployments And Measurements

The measurement infrastructure has been installed and deployed on two Slocum gliders. It has been used to collect current readings of the vehicles on the bench top as well as at sea. The sea trials took place off of the coast of New Jersey in September of 2009 and in February of 2010.

Before the measurement infrastructure was trusted to be deployed, it was installed in the glider and extensively tested on the bench top. To ensure the vehicle components still performed up to par in the presence of the measurement board, the vehicle's motors were subjected to "wiggle" tests. This entails moving its motors through their full range of motion. Sample results of such a wiggle of the fin and pitch servos are depicted in Fig. 3 and Fig. 4, respectively. The Hall Effect sensors used for these devices are bipolar so the reported currents show the current flow in both directions as the servos move the opposite direction. The fin is used to steer the vehicle, and the pitch motor is used to fine tune the vehicle to the commanded pitch by moving an internal battery pack. The power draw of these two motors is generally very low, and during a mission motor activities typically occur in brief bursts. Through wiggle, overnight, and weekend tests the system was deemed stable and reliable for sea tests.

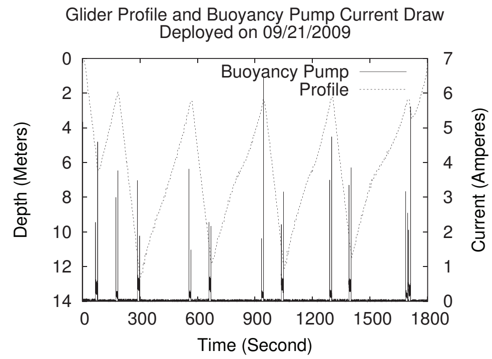

Fig. 5. Current drawn from the buoyancy engine during our deployment. The flight profile is shown together with the current draw of the buoyancy pump. It can clearly be seen that the buoyancy engine activities align with inflection points, and that the power consumption at depth is significantly higher than near the surface.

The first sea trial involved two short mission segments of approximately thirty minutes in length each. The glider was instructed to perform yos, sequences of dives and climbs, between 1 and 20 meters. The glider depth profile along with the current draw of the buoyancy pump of one mission segment are illustrated in Fig 5. The glider never reached a depth of 20 meters because the seafloor was not sufficiently deep enough at the deployment location. The experiences gained in the sea trial were used to prepare the infrastructure for a longer term mission.

The second deployment was a 6.5 day mission in early February of 2010. A map of the glider's path is shown in Fig 6. The mission's goal was to fly to the continental shelf to gather buoyancy engine readings at depths of up to 100 meters. The mission was cut short due the combination of inclement weather and the high power consumption of our measurement infrastructure. After heading east toward the shelf for two days, the vehicle was commanded to head north because a Nor'easter storm was expected to push the vehicle south. After being forced south for two days, it was again commanded to head east towards the shelf to gather readings at deeper

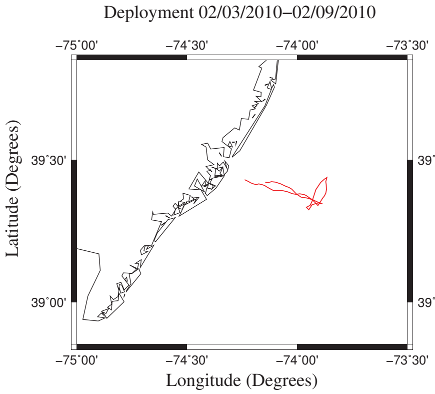

Fig. 6. Flight path of the mission deployed with the measurement infrastructure in February of 2010.

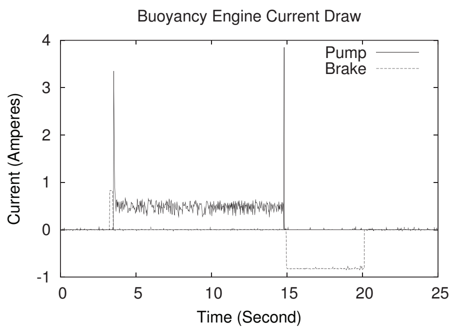

Fig. 7. Current draw of the buoyancy engine during an inflection at approximately 12 meters.

depths for a short time. Unfortunately, another Nor'easter was imminent so the mission was aborted and the glider spent the remaining time flying back to shore to be retrieved.

The buoyancy engine of the electric Slocum glider consists of a buoyancy pump and a brake mechanism. The pump moves a piston to change the vehicle's buoyancy by altering its displacement of water. The brake locks the pump's position in place which would otherwise be forced to retract due to water pressure. The current draw of the buoyancy engine is shown in Fig. 7. When commanded to inflect from a dive to a climb, or from a climb to a dive, the brake first unlocks the pump. The pump follows by moving the piston to the commanded position. When the position is reached, the brake again locks the pump's position in place.

The energy used by the buoyancy pump increases with depth because the pump must work harder to battle the additional pressure. This was confirmed by our first sea trials, Fig. 5, where inflections from a dive to a climb state used more energy when the inflections occurred at three, six and twelve meters. Fig. 8 depicts the measured

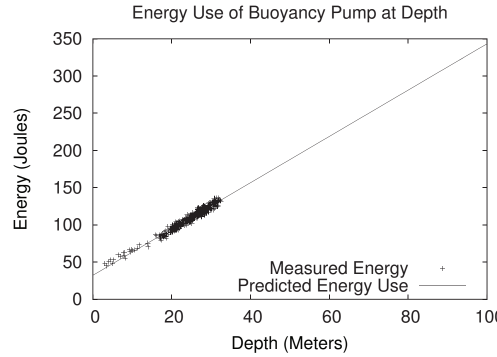

Fig. 8. Energy use of the buoyancy pump at depth.

energy used by the pump during the deployment in February of 2010. The energy used for similar depths in the two seal trials were comparable considering different gliders were used. In both missions, however, the energy necessary for the pump to perform inflections from a climb to a dive at shallow depths is at times less expensive than the cost associated with the brake. Having detailed knowledge of the cost of components is important when trying to optimize vehicle flights.

IV. Simulator

To assist in planning of future missions, we have created a simulator for the Slocum glider. The simulation environment incorporates energy, speed, seafloor and sea surface current models, and is used to predict the flight path, longevity and energy usage of a mission. The simulation environment has been validated against Teledyne Webb's Shoebox simulator and compared to a deployment to the continental shelf off of the coast of New Jersey.

A. Implementation

The longevity of missions performed by AUVs rely on the limited energy resources the vehicle carries on board in its batteries. This resource limit can effect the quality of missions. Missions which require the vehicle to maintain a constant presence at a location or require traveling to an area of interest are constrained in the amount of information they can collect. For the aforementioned reasons, we have developed and implemented new energy models in our simulation environment.

The energy models were formulated from the samples recorded by our infrastructure along with the voltages reported by the glider. Our simulator uses models for the buoyancy pump, brake and steady state load, where no motor and most devices are not in use. The average observed cost associated with the brake is applied at

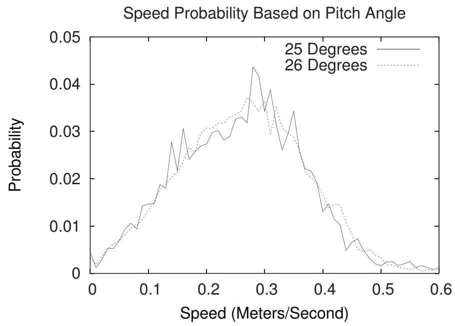

Fig. 9. Speed distribution derived from over four years of glider flights.

every inflection point. The expense of inflections near the surface where the vehicle state changes from a climb to a diving state is modeled as a constant. Inflection performed at depth from a diving to a climbing state use a linear cost function. The function has been fitted to the data points from the deployment in February 2010. The function is shown in Fig. 8 labeled "Predicted Energy Use." The energy used in simulated missions is dependent on the vehicle's pitch angle and speed. The pitch angle of the flight impacts the number of inflection points, and thus the use of the buoyancy engine. The speed determines the amount of time required to complete the mission.

The simulation environment makes use of two types of speed models. The first is a model similar to that of the Slocum glider's shoebox simulator. The Shoebox, named after its physical similarities to a shoe box, contains the essential glider electronics to perform simulations in real time. The software running in the Shoebox is the same software used during deployments but makes use of simulated device drivers. The speeds and missions generated by this model when used in our simulator should be similar to that of the commercial Shoebox. However, unlike the Shoebox, our framework is able to simulate missions significantly faster than real time.

The second speed model integrated into the simulator is based on speed distributions which were empirically derived from over four years worth of glider flight data. The flights took place off of the New Jersey coast between the years of 2003 and 2009. The resulting distributions are shown in Figure 9 and were constructed by measuring the distance covered in each dive segment and the time necessary to travel the segment. A dive segment starts when a glider submerges and ends when it resurfaces. The 25° distribution was comprised of 2,539 segments, covering 6,263km over 293 days, while the 26° distribution span 16,411 segments, 32,527km and 3.48 years. Sufficient data to build speed distributions were available only for 25° and 26°, which are the most common angles used by the Slocum Glider. These speeds are sampled by the simulation environment to produce realistic over-the-ground speeds. Although very similar, the 26° distribution is slightly faster than the 25° distribution. Along with the dive and climb pitch angles specified by the mission, the depth rate is calculated and used to position the glider in space. The depth rate and the seafloor determines the number of inflections that occur during flight.

The simulation environment also supports the use of a seafloor terrain. The seafloor model used may be artificial, come from prior deployments as measured by a glider, or can be interpolated from NOAA's National Geophysical Data Center's (NGDC) bathymetric data set [7]. The current data set (from the NGDC) used by the simulation environment is of the coast of New Jersey at a resolution of one arcminute. The addition of a seafloor model improves the quality of the vehicle's predicted energy usage especially in shallow waters. Simulated open ocean deployments, or deployments where it is known that the glider will never reach the seafloor will not benefit from a seafloor model, and could therefore be removed for such missions.

Time dependent sea currents can significantly impact the flight profile of a glider, and are therefore modeled within our simulation framework. The currents may be artificially and dynamically generated, or can be interpolated much like the seafloor. The use of Coastal Ocean Radar (CODAR) [5] data from Rutgers University has been integrated into the framework. This data describes the sea surface currents of the New Jersey area at a spatial resolution of six kilometers and a temporal resolution of one hour. The addition of sea currents add another degree of realism which should improve the prediction quality.

Our simulation framework can be used to analyze past glider flights, support active deployments, or help to plan future missions. CODAR information is valuable when simulating past flights and can be used in the decision making of active missions. For example, if recent sea surface current data is available, it can be used to predict the location of where the glider may resurface next. With the utilization of weather trend or prediction models, such as the Regional Oceanic Modeling System (ROMS) [9], the simulator could also forecast the general outlook of missions.

B. Validation

To validate our simulation infrastructure we have compared its predictions to that of Teledyne Webb's

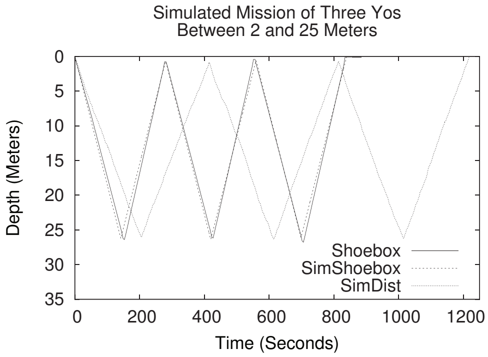

Fig. 10. Validation of the simulation environment with respect to the Shoebox simulator.

Shoebox simulator. The mission executed on both the Shoebox and our simulation framework entailed three yos (a sequence of climbs and dives) between 2 and 25 meters.

The depth profile of the simulations are shown in Fig. 10. The Shoebox profile describes the flight as performed by the Shoebox simulator. SimShoebox and SimDist are the flight profiles generated by our simulation environment. SimShoebox generates speeds similar to that of the Shoebox, while SimDist sampled speeds from the distribution in Fig. 9.

The time necessary to complete the missions for Shoebox and SimShoebox are very similar. Like the Shoebox, our simulated vehicle also slightly overshoots the commanded depth limits. On average, the SimShoebox is slightly slower, taking several seconds longer to complete the mission. The results produced are however a reasonable representation of what may be generated by the manufacturer's simulator. The advantage of our simulation framework lies in the runtime necessary to produce the simulated mission. The Shoebox took approximately 15 minutes to simulate the sample mission, while SimShoebox required only 0.35 seconds on a 2.2GHz dual core processor.

The flight simulation which applies the speed distribution model, SimDist, requires an additional 380 seconds longer in mission time than both the Shoebox and SimShoebox. The simulation took 0.5 seconds. This suggests that the vehicles speed is on average slower using this model than that of the Shoebox. We believe the speed model based on speed distributions is more accurate than the Shoebox model since it is derived from over fours years worth of vehicle flight time. The speed distribution model should then not be compared to that of the Shoebox simulator but against an actual deployment.

V. Deployment Simulations

To validate the simulator and its speed distribution model, a deployment from September 2009 is compared to similar flights in our simulation environment. The goal of the original mission was to fly to the continental shelf from the coast of New Jersey and back at 26°. The flight path of the mission is illustrated in Fig. 11(a). Due to strong currents for portions of the mission, the glider was pushed south preventing it from making steady forward progress towards the target waypoint. An operator interfered with the flight and changed the target waypoint due west back to shore before the vehicle reached the commanded waypoint near the continental shelf. Waypoints were changed further throughout the mission, causing the vehicle to reach none of the target waypoints except the last which was used to collect the vehicle. The total length of the deployment was 14.84 days. To validate the simulation framework a similar deployment length should be achieved.

A. Baseline

The baseline simulation assumes that no seafloor or currents exist in the environment. Consequently, the runtime needed to simulate the mission is small, but the predicted mission will also not be very accurate. The simulated mission flown in the remainder of this section will be that of Fig. 11(a) except that the vehicle will be commanded to keep flying until it has reached all its waypoints. It is difficult to reenact the intentions or reasoning behind the operator's actions so they are ignored.

The SimShoebox simulation of the mission predicts a mission length of 7.9 days, with the energy usage of 707kJ and a flight path as depicted in Fig. 11(b). A runtime of 20 seconds was needed to simulate the mission. SimShoebox, which has been shown in the previous section to be fairly representative of the Shoebox simulator, would suggest a real time simulation of 7.9 days. If the speed distribution is used instead in the simulation (SimDist), the mission length increases to 11.5 days, 785kJ and a runtime of 86 seconds. SimShoebox in this scenario has erroneously estimated the mission length by 6.94 days while SimDist by 3.34 days. Unlike the previous validation experiment, the speed distribution produces a better estimate when compared to a real deployment

B. Seafloor Model

To add a layer of realism, the simulation environment can use a seafloor as previously described. Instead of flying to the full commanded depth, the vehicle must inflect several meters above the seafloor to avoid impact.

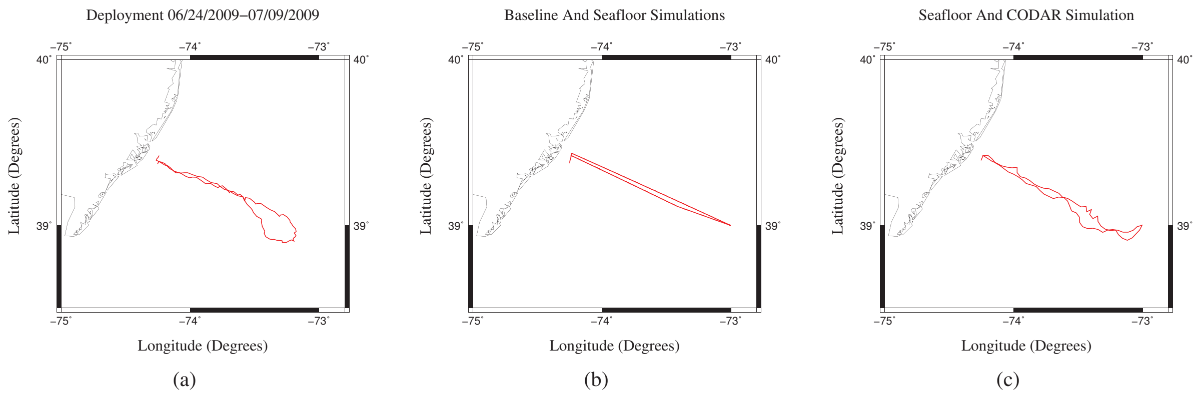

Fig. 11. (a) The flight path of the mission being simulated. (b) The flight path of the baseline and seafloor simulations. (c) The simulated mission using both seafloor and CODAR data.

TABLE III
SPEED DISTRIBUTION SIMULATION RESULTS

Mission	Seafloor	Currents	Time (days)	Energy (kJ)	Runtime (min)
Actual	N/A	N/A	14.84	N/A	N/A
Baseline	No	No	11.5	785	1.4
Seafloor	Yes	No	11.5	984	5.7
CODAR	Yes	Yes	14.89	1,235	20

This will increase the total number of inflections points in the mission which directly translates into more energy use because the buoyancy engine is activated at each inflection. The mission length and flight path for both SimShoebox and SimDist remain nearly identical to the baseline but the energy usage increase to 892kJ and 984kJ, respectively. The modeling of the seafloor is paramount so that missions may be more accurately predicted and planned for.

C. Seafloor And CODAR Models

The final model supported by our framework is that of the sea currents. The CODAR sea surface currents of the days surrounding the deployment of Fig. 11(a) were integrated and applied to the simulated mission. The flight map of SimDist is shown in Fig. 11(c). The SimDist mission flew for 14.89 days using 1,235kJ of energy and required 12 minutes to simulate. SimShoebox's mission flew for only 8.88 days, used 986kJ, and had a runtime of 5 minutes.

The presented simulation results indicate that the speed distribution model was more representative of the deployment in Fig. 11(a) than that of the speed model which is similar to the Shoebox. A summary of the simulations for SimDist is listed in Table III. The final SimDist mission using both the CODAR and seafloor resulted in a mission time slightly longer than that of the real deployment. This is however expected since the simulated mission flew a slightly different mission where the vehicle actually reached the waypoints and was not interrupted by an operator. Modeling the supervision as part of the mission is a difficult task because the intentions of the operator at the time are not known. Errors associated with the spatial and temporal resolution of the seafloor and CODAR data also add to the difficulty of recreating the original mission.

VI. RELATED WORK

The modeling of underwater gliders has been extensively studied in the previous work [1][2][3][4][11]. The primary focus lies in the formulation of hydrodynamic models that try to closely emulate the vehicle as it flies through the water. Our work differs in approach in that we use simpler mathematical models and make use of years of glider flight information. Our simulation environment also incorporates empirically derived energy costs of a subset of the vehicle's devices to assist in the planning and prediction of deployments.

VII. FUTURE WORK

We have begun the design of the second revision of the measurement infrastructure. Using the knowledge gathered from the deployments using the first revision, we are choosing more appropriate sensors for each measured component of the glider. Unlike the first revision, we plan to have the ability to customize the rate at which current readings are sampled and logged. This would also entail adding triggers so that only samples of interest are recorded, saving precious storage which would otherwise go to waste recording silent or noisy data. We will also add the ability to log data locally on the board while still maintaining the capability to send a subset of data to the science computer for transmission to shore via a satellite modem. Running the measurement board on a separate power source is also desirable so that longevity of the mission and the samples themselves are not influenced by the presence of the board. Finally, we would like to expand the number of glider components we monitor. Other devices such as the air pump (used to breach and keep the glider at the surface), and the iridium satellite modem use a great deal of energy over time due to the length and frequency that the vehicle surfaces. New sensor payloads such as an ADCP or an acoustic modem will require careful power and energy management as well.

In the future we will continue to improve the simulation environment by expanding and implementing more complex models. Integration of ROMS [9] may become an essential component to aid in the prediction and planning of future flights. Additionally, although energy models from the components we have measured have already been incorporated into the simulator, the focal point thus far has been the energy usage of the buoyancy pump. Refining the energy characteristics of the other devices in the simulator would lead to more accurate mission predictions. Once complete, we would like to simulate the deployment from February 2010 and compare the simulated energy usage against the actual energy usage measured by our measurement board.

During the development of the next revision of the measurement infrastructure we will continue to improve the current system to prepare it for additional deployments. Specifically, we are planning to fly to the edge of the continental shelf to gather more buoyancy pump samples at depths of up 100 meters, which is the operating depth of most of our gliders. The additional samples could help determining the accuracy of the buoyancy pump's energy cost function.

Finally, integration of the presented work with our previous work [12] is underway. The simulation framework will be used to execute and analyze missions specified in our programming language. The complete system will allow for the development and testing of complex missions. The Linux single board computers we have integrated into the Slocum glider allow for simulations to be run online and may assist in the steering of the vehicle so that dead reckoning error may be reduced.

VIII. Conclusion

We have described the implementation of a measurement and simulation infrastructure for the Slocum Glider. Energy cost models derived from two sea trials have been incorporated into the simulation environment. Using over four years of previous glider flight data we have constructed distributions to define the vehicle's speed over ground. Along with the use of a sea floor data set from NOAA, and sea surface current data from Rutgers University, we were able to simulate a vehicle's flight path, mission time, and energy usage. The framework has been evaluated against a simulator produced by the Slocum glider's manufacturer as well as a deployment off the coast of New Jersey. Simulation results indicate that the framework can produce sensible mission estimations with low computation costs.

Acknowledgement: This research has been partially funded by NSF awards CSR-CSI #0720836 and MRI #0821607.

References

[1] M. Arima, N. Ichihashi, and Y. Miwa. Modelling and motion simulation of an underwater glider with independently controllable main wings. pages 1–6, May 2009.
[2] A. Bender, D.M. Steinberg, A.L. Friedman, and Williams S.B. Analysis of an autonomous underwater glider. 2008.
[3] P. Bhatta and N.E. Leonard. Stabilization and coordination of underwater gliders. volume 2, pages 2081–2086 vol.2, Dec. 2002.
[4] Joshua G. Graver, Ralf Bachmayer, and Naomi Ehrich Leonard. Underwater glider model parameter identification. In *in Proc. 13th Int. Symposium on Unmanned Untethered Submersible Tech*, 2003.
[5] CODAR Corporate Headquarters. Codar. Mountain View, CA. http://www.codar.com.
[6] Persistor Instruments Inc. Cf1 computer system. Marstons Mills, MA. http://www.persistor.com.
[7] National Oceanic and Atmospheric Administration. National geophysical data center. http://www.ngdc.noaa.gov/.
[8] Teledyne Webb Research. Slocum glider. Falmouth, MA. http//www.webbresearch.com/slocum.htm.
[9] A.F. Shchepetkin and J.C. McWilliams. The regional oceanic modeling system (roms): a split-explicit, free-surface, topography-following-coordinate oceanic model. volume 9, pages 347–404, 2005.
[10] Rutgers University. The scarlet knight's trans-atlantic challenge. http://rucool.marine.rutgers.edu/atlantic/.
[11] C.D. Williams, R. Bachmayer, and B. deYoung. Progress in predicting the performance of ocean gliders from at-sea measurements. pages 1–8, Sept. 2008.
[12] H.C. Woithe and U. Kremer. A programming architecture for smart autonomous underwater vehicles. pages 4433–4438, Oct. 2009.

Vol. 438: 1–17, 2011
doi: 10.3354/meps09308

MARINE ECOLOGY PROGRESS SERIES
Mar Ecol Prog Ser

Published October 5

OPEN ACCESS

FEATURE ARTICLE

Ocean observatory data are useful for regional habitat modeling of species with different vertical habitat preferences

John Manderson[1,*], Laura Palamara[2], Josh Kohut[2], Matthew J. Oliver[3]

[1]Ecosystems Processes Division, NEFSC/NMFS/NOAA, James J. Howard Marine Highlands, New Jersey 07732, USA
[2]Institute of Marine and Coastal Science, Rutgers University, New Brunswick, New Jersey 08901, USA
[3]College of Earth, Ocean and Environment, University of Delaware, Lewes, Delaware 19958, USA

ABSTRACT: Ocean Observing Systems (OOS) now provide comprehensive descriptions of the physical forcing, circulation, primary productivity and water column properties that subsidize and structure habitats in the coastal ocean. We used generalized additive models (GAM) to evaluate the power of OOS remotely sensed ocean data along with *in situ* hydrographic and bottom data to explain distributions of 4 species important in the Mid-Atlantic Bight, USA, ecosystem that have different vertical habitat preferences. Our GAMs explained more abundance variation for pelagic species (longfin inshore squid and butterfish) than demersal species (spiny dogfish and summer flounder). Surface fronts and circulation patterns measured with OOS remote sensing as well as the rugosity and depth of the bottom were important for all species. *In situ* measurements of water column stability and structure were more useful for modeling pelagic species. Regardless of vertical habitat preference, the species were associated with vertical and horizontal current flows, and/or surface fronts, indicating that pelagic processes affecting movement costs, prey production and aggregation influenced distributions. Habitat-specific trends in abundance of 3 of the 4 species were well described by our OOS-informed GAMs based upon cross validation tests. Our analyses demonstrate that OOS are operationally useful for regional scale habitat modeling. Regional scale OOS-informed statistical habitat models could serve as bases for tactical ecosystem management and for the development of more sophisticated spatially explicit mechanistic models that couple ontogenic habitats and life history processes to simulate recruitment of organisms important to maintaining the resilience of coastal ecosystems.

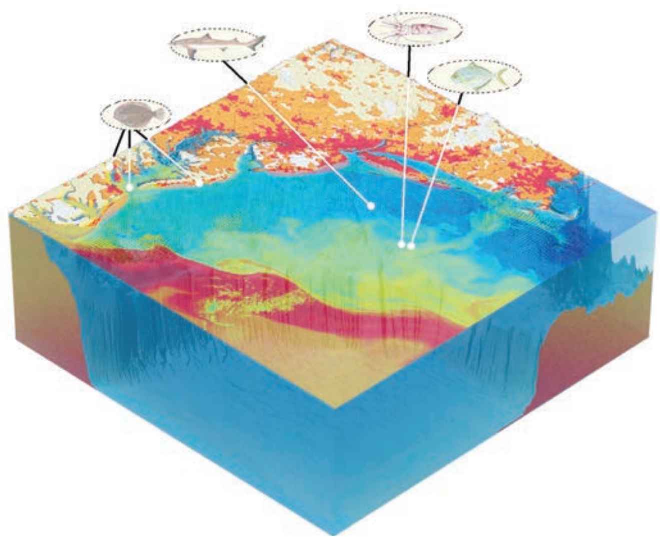

Data and models integrated in Ocean Observing Systems capture ocean dynamics at scales required for regional habitat modeling and management.

Image: Igor Heifetz

KEY WORDS: Ocean observing · Pelagic habitat · Remote sensing · Generalized Additive Modeling

INTRODUCTION

Species distributions reflect the habitat selection decisions individual animals make to maximize fitness under constraints imposed by their perceptual and movement capabilities. Variations in survival and reproduction are the consequences of con-

*Email: john.manderson@noaa.gov

strained habitat selection and the mechanistic underpinnings of spatial population dynamics. The diversity of habitats used by species, and effects of habitat variation on vital rates, including movements, determine the productivity, stability and resilience of regional populations (Secor et al. 2009, Tian et al. 2009, Kerr et al. 2010). Furthermore, the effects of habitat diversity and its loss on the resilience and stability of populations that serve as ecosystem keystones should be translated across a level of ecological organization to affect ecosystem productivity, resilience, and stability. Understanding the ways habitat effects on recruitment are translated into the emergent dynamics of regional populations important in maintaining the resilience of large marine ecosystems is crucial for the development of effective space-based ecosystem management, particularly in the face of rapid climate change (Mora et al. 2007, Hsieh et al. 2010). The development of statistical habitat models that are broad in scope and explicitly consider bottom features as well as the dynamic properties and processes of the water column (e.g. temperature, primary productivity, advection) known to regulate critical physiological, behavioral and demographic rates is a necessary first step toward this end.

Regional scale habitat models have been difficult to develop for coastal species, in part because data describing habitat variation at broad spatial but fine time scales have been unavailable. Ocean Observing Systems (OOS) now provide spatially and temporally comprehensive regional scale descriptions of pelagic features and processes required to understand the ways in which dynamic features of the ocean fluid affect the distribution and recruitment of fish living in it. Ocean Observing data include sea surface temperature and ocean color measured with satellite sensors, surface currents measured with networks of high-frequency (HF) radars deployed along the shore, and physical and optical properties measured by fleets of robots gliding beneath the ocean surface. The data describe the physical forcing, current flows, and sources and transport of detritus, primary and secondary productivity which structure, couple and fuel coastal ocean habitats and thus regulate the recruitment of animals using them. Remotely sensed data have been used to construct habitat models for open ocean pelagic predators, but are not commonly used for coastal species (Valavanis et al. 2008, Zainuddin et al. 2008, Becker et al. 2010, Mugo et al. 2010, Zydelis et al. 2011).

Presently, Ocean Observing data with the broadest spatial coverage are satellite measurements of ocean temperature and color, and HF radar measurements of surface currents. These data can be processed to describe upwelling and downwelling centers and the spatial dynamics of surface fronts where high primary productivity occurs or is concentrated. These products may therefore be most useful for identifying habitat associations of pelagic species. While surface data collected directly overhead of trawl samples may be less useful for describing habitats of demersal animals, particularly in deep water, the vital rates of demersal species are also regulated by surface processes, although effects may be downstream and delayed in time. Distributions of large demersal animals may be influenced to a greater degree by pelagic processes regulating movement costs and prey production, than by structural features of the bottom that may provide smaller and younger stages with predation refugia. Finally, surface features can serve as proxies for important subsurface properties and processes (Castelao et al. 2008).

We used generalized additive modeling to evaluate the power of Ocean Observing data, as well as *in situ* pelagic data and benthic data, to describe the distributions of 4 trophically important interacting species with different vertical habitat preferences in the Mid-Atlantic Bight US coastal ocean. We quantified the strength of species associations with mesoscale pelagic features described by OOS, as well as pelagic and benthic features measured with shipboard CTDs, acoustics and bottom grabs, emphasizing habitat characteristics likely to influence growth, dispersal, survival or reproduction. Finally, we discuss the potential value of current and future Ocean Observing assets and research for the development of regional scale habitat models that could serve as fundamental tools for understanding the role of marine habitat dynamics in ecosystem dynamics and the development of more effective space- and time-based ecosystem management strategies.

MATERIALS AND METHODS

Study area

Our study area was the Mid-Atlantic Bight (MAB), USA, where the dynamics of the coastal ocean are continuously monitored at broad spatial scales but fine time scales by the Mid-Atlantic Regional Association Coastal Ocean Observing System (MARACOOS: http://maracoos.org; Fig. 1). The oceanography of the MAB is described in detail elsewhere (Beardsley & Boicourt 1981, Epifanio & Garvine 2001, Lentz 2008). Briefly, the broad, gently sloping continental shelf in

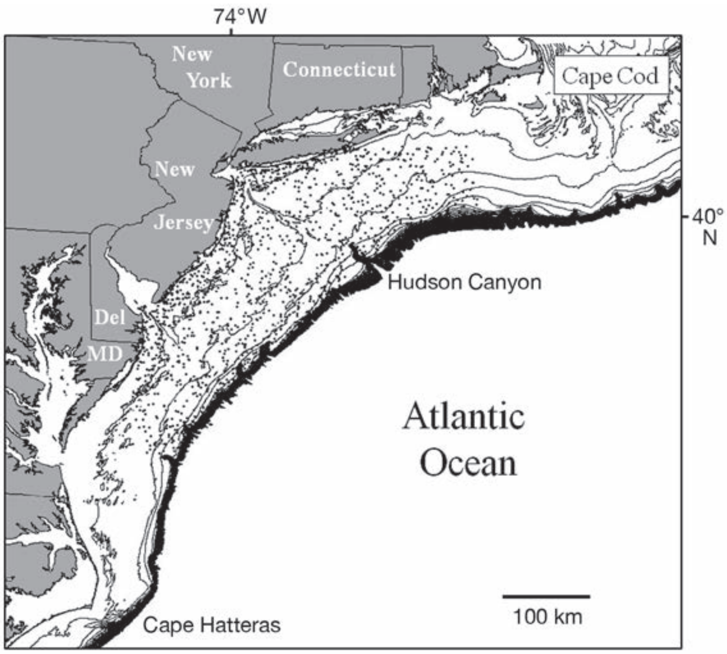

Fig. 1. Locations on the Mid-Atlantic Bight continental shelf, USA, of stations sampled during North East Fisheries Science Center fishery-independent bottom trawl surveys and considered in our analysis of longfin inshore squid, butterfish, spiny dogfish and summer flounder habitat

the MAB is incised by canyons and drowned river valleys that serve as important cross shelf transport pathways. Mean current flow is southwestward and driven by cold buoyant water derived from the northeast. Biological productivity is strongly seasonal. However, air and ocean temperatures, stratification, and wind and buoyancy forcing are extremely variable and superimpose complex, ecologically important variation on mean patterns. Mean southwestward current flows can be intensified by southward, downwelling favorable winds and estuarine discharge, or steered offshore by northward, upwelling favorable winds associated with approaching atmospheric fronts and summer sea breezes. Wind forcing results in sea surface set up and set down along the coast that produces cross-shelf, subsurface counter flows that are strongest along drowned river valleys. During the summer, areas of high primary productivity occur in estuaries and nearshore upwelling centers. During the spring, meanders in the shelf slope front produce upwelling of deep nutrient-rich oceanic waters that, with increasing solar radiation, promote an early bloom in the shelf slope sea (Marra et al. 1990, Ryan et al. 1999). Spring blooms fueled by nutrients supplied by winter water column overturning occur with the onset of stratification closer to shore, while blooms also occur on the shelf when stratification breaks down in the autumn. Organisms occupying the MAB exhibit complex seasonal cycles of reproduction and habitat use in response to the complex seasonal dynamics of ocean climate, circulation and primary productivity.

Species abundance data

We selected longfin inshore squid *Loligo pealeii*, butterfish *Peprilus triacanthus*, spiny dogfish *Squalus acanthias* and summer flounder *Paralichthys dentatus* for analysis because they exhibit differences in vertical habitat preference, are abundant in fishery-independent bottom trawl surveys and are trophically important interacting species in the MAB (Link et al. 2008). Butterfish and longfin squid are small pelagic species important in the transfer of energy from lower trophic levels to apex predators (Link et al. 2008). Both species reach maturity at a year or less of age and have very high reproductive rates (Hatfield & Cadrin 2002, Collette & Klein MacPhee 2002). Butterfish feed primarily upon zooplankton. Squid feed on small pelagic animals including butterfish.

Spiny dogfish and summer flounder feed upon squid and butterfish but generally spend more time deeper in the water column (Packer & Hoff 1999, Moustahfid et al. 2010, Staudinger 2006, Stehlik 2007). Spiny dogfish are not as surface oriented as squid and butterfish but still spend considerable amounts of time in the water column. They exert strong top down effects on the MAB food web. Summer flounder are subtropical flatfish more strongly associated with the seabed in the ocean and estuaries.

All 4 species migrate between lower latitude and/or offshore overwintering habitats to higher latitude, inshore habitats where they spend the summer. Longfin inshore squid, butterfish and summer flounder are abundant in the MAB throughout the year while spiny dogfish are more abundant in cooler waters to the northeast during the summer (Stehlik 2007).

We used collections of the 4 species made by National Marine Fisheries Service, Northeast Fisheries Science Center's (NMFS-NEFSC) autumn, winter, and spring fisheries independent bottom trawl survey (Fig. 1; www.nefsc.noaa.gov/epd/ocean/MainPage/ioos.html) in our statistical habitat modeling. Azarovitz (1981) described the design of the stratified random survey in detail. Winter surveys occurred in February, spring surveys from March to early May, and autumn surveys in September and October. Survey tows were made with a #36 Yankee trawl with a 10.4 m wide × 3.2 m high opening and rollers (12.7 cm stretched mesh [SM] opening, 11.4 cm SM cod end, 1.25 cm SM lining in the cod end and upper belly). The net was towed over the bottom at ~3.5 knots for 30 min. Distances the net was towed on the bottom averaged 3.5 km (95 % confidence limits 3.2 to 3.7 km). Tows were made throughout the 24 h day. Consecutive samples were collected approximately every 2 h (50th, 5th, and 95th quantiles: 2.07, 1.38, 3.53 h respectively) and 19 km apart (50th, 5th, and 95th quantiles: 19.02, 4.80, 41.88 km respectively) on each survey. Examination of available length and age frequencies confirmed that large age 1+ juveniles and adults dominated collections because the trawl mesh was relatively coarse and shallow coastal and estuarine nursery habitats were not sampled.

We selected the analysis domain for this study based upon the availability of remotely sensed data from the OOS. Bottom trawl samples collected from February 2003 through October 2007 between latitudes 37.14° and 40.85° N and longitudes 70.83° and 75.16° W fit within the domain (Fig. 1). An average of 101 stations was sampled during spring and autumn. An average of 70 stations was sampled during the winter.

Habitat data

For bottom data, we computed topographic characteristics of the bottom from the 3-arc-second NGDC Coastal Relief Model (www.ngdc.noaa.gov/mgg/coastal/coastal.html; cell size = 93 m; Table 1). We used circular moving window analysis in GRASS GIS to calculate median and standard deviations of bot-

Table 1. Data sources and potential ecological effects of environmental variables considered in generalized additive model (GAM) habitat models for longfin inshore squid, butterfish, spiny dogfish and summer flounder. Squid and butterfish were considered prey in auxiliary models for spiny dogfish and summer flounder predators. na = not applicable, ″: same data as given in the line above

Variables	Spatial grain	Possible ecological effect	Data source
Sun's elevation	na	Vertical migration/catchability	Calculated for trawl locations & times
Geographic coordinates	2 km	Unknown spatial process	NEFSC bottom trawl survey
Benthic data			
Depth (μ, SD)	1.95 km (93 m)	Structural/spatial refuge	NGDC 93 m grid[a]
Slope (μ, SD)[d]	″	″	″
Aspect (SD)[d]	″	″	″
Profile curvature (μ, SD)[d]	″	″	″
Sediment grain size (μ)	2 km	Structural/spatial refuge/enrichment	US seabed data base[b]
Pelagic data			
***In situ* CTD measurements**			
Bottom temperature	1 m	Metabolic rate	NEFSC bottom trawl survey
Bottom salinity[d]	″	Alias proximity to freshwater source	″
Mixed layer depth	″	Mixing/1° productivity	″
Stratification index[d]	″	″	″
Simpson's PE (30 m)	″	″	″
OOS remote sensing			
High–frequency radar			
Cross shelf velocity	10 km	Advection/movement cost/mixing	MARACOOS HF radar[c]
Along shelf velocity	″	″	″
Variance in velocity	″	Tidal mixing/episodic forcing	″
Divergence potential	″	Upwelling/downwelling & mixing	″
Vorticity potential[d]	″	Eddy development/retention	″
Satellites			
Sea surface temperature	10 km	Metabolic rate/other seasonal factors	MODIS through MARACOOS[c]
Chlorophyll *a*	″	Primary production/organic matter	″
Normalized water leaving radiances (412, 443, 488, 531, 551, 667 nm)[d]	″	Surface organic matter	″
Water mass class	″	Various	″
Frontal index (distance to & strength of gradient between water masses)	″	Concentration/enrichment	″
Prey abundance			
Squid	2 km	Prey	NEFSC bottom trawl survey
Butterfish	″	″	″

[a]www.ngdc.noaa.gov/mgg/coastal/coastal.html; [b]http://walrus.wr.usgs.gov/usseabed; [c]http://maracoos.org/data; [d]variables that were redundant or not ecologically meaningful and therefore excluded in the final analysis

tom depth, aspect, slope, and curvature from the relief model (e.g. see Fig. 3; Neteler & Mitasova 2008). The window diameter was 2 km. Profile and tangential curvature measured the concavity (negative values indicate valleys) and convexity of the bottom (positive values indicate ridges) parallel and tangential to major axes of the bottom slope. Sediment grain sizes were selected from a map interpolated from the usSEABED data base (Reid et al. 2005). The sediment map had a spatial resolution of 2 km and was constructed using sample bias correction, maximum *a posteriori* resampling, and a spline-in-tension algorithm (Goff et al. 2006, 2008).

For pelagic data, we used conductivity, temperature and depth (CTD) profiles collected during each NEFSC trawl survey to describe bottom temperature and salinity, water column structure and stability (Table 1; www.nefsc.noaa.gov/epd/ocean/MainPage/ioos.html). We considered the 'mixed layer' depth at which density was 0.125 kg m^{-3} higher than the surface (Levitus 1982), a stratification index calculated as the difference in seawater density between the surface and 50 m, and Simpson's potential energy anomaly (PE; Simpson 1981, Simpson & Bowers 1981). We calculated Simpson's PE within the upper 30 m of the water column because the stability index calculated for the entire water column was correlated with bottom depth.

A network of HF radar provided remotely sensed measurements of surface currents (Table 1; http://maracoos.org; frequency = 5 MHz; Barrick et. al. 1977). Radial current vectors from the network were combined to produce hourly surface current maps (resolution = 6 km). We de-tided the raw time series at each HF radar grid point using a least-squares fit of the 5 strongest principal body tide constituents (M2, S2, N2, K1, and O1). These data were then low pass filtered with a cutoff period of 30 h. We only used data for grid points with signal returns of >25% yr^{-1}. We calculated 8 d average cross-shore and along-shore velocity, variance in velocity, divergence (vertical velocity) and vorticity within 10 km of each trawl. Divergence and vorticity were calculated using finite difference. Divergence was calculated as the vertical current velocity in m d^{-1} at a depth of 1 m. Vorticity was normalized by the local Coriolis parameter. We also calculated indices describing seasonal trends in divergence and vorticity. Instantaneous divergence values were assigned a new value of –1 if values were <–0.1 m d^{-1}, 0, if between –0.1 and +0.1 m d^{-1}, or +1 if values were >+0.1 m d^{-1}. These new values were averaged for each grid point to produce a mapped index of upwelling and downwelling potential for each season and year (e.g. see Fig. 3). Seasonal trends in vorticity were calculated similarly using threshold values of ±0.02. Values for the trawl samples were extracted from the grids.

Satellite remote sensing provided surface temperature, chlorophyll *a* (chl *a*), raw light absorption and backscatter within 10 km of each trawl tow (Table 1). Moderate Resolution Imaging Spectrometer (http://oceancolor.gsfc.nasa.gov) data were binned to 1 km resolution using standard data quality flags. We considered measurements of sea surface temperature, chlorophyll (mg m^{-3}; e.g. see Fig. 3), and normalized water-leaving radiance (W m^{-2} st^{-1} μm^{-1}) at 412, 443, 488, 531, 551, and 667 nm in our analysis.

Ensemble clustering was applied to satellite sea surface temperature and normalized water-leaving radiance at 443 and 555 nm to classify water masses using the methods of Oliver et al. (2004) and Oliver & Irwin (2008). Clustering identified 27 water masses within the study domain. We made time series maps of the strengths of gradients along frontal boundaries between these water masses (e.g. see Fig. 3) and used them to compute distance (d_{km}) to, and gradient strength (G) of the nearest front for each trawl sample. We then calculated a frontal index (FI) for each station using the equation:

$$FI = \ln(G/d_{km} + 1) \quad (1)$$

Values for the frontal index were therefore higher for samples nearer to stronger fronts.

Many of 27 water masses identified with ensemble clustering contained 5 or fewer trawl samples. Thus, before final assignment of the samples to water masses, we used k–means clustering of the original satellite data to reduce the number of water masses from 27 to 8. Following this clustering, each of the 8 water masses contained at least 20 bottom trawl samples.

Analysis

GAMs

We developed our statistical habitat models for large juvenile and adult stage squid, butterfish, dogfish and summer flounder, using generalized additive models (GAM) implemented with the mgcv package in R software (Wood 2006). GAM is a nonparametric multiple regression technique that does not require shapes of abundance responses to habitat variables to be specified *a priori*. It has been used to statistically model ecological relationships, including habitat associations, and performs well in comparison with other methods (Pearce & Ferrier 2000, Ciannelli et al. 2007, Ficetola & Denoël 2009). Like all regressions, GAMs constructed with collinear independent variables perform poorly. We therefore eliminated intercorrelated variables prior to modeling, retaining those most likely to affect important physiological or behavioral processes (Table 1).

We standardized species abundances by trawl tow distances and found they were best modeled using an over-dispersed Poisson distribution. Using this distribution required that we round abundances to the nearest integer. Abundance in bottom trawls can vary with time of sampling if animals exhibit diel behavioral cycles, especially vertical migration (e.g. Brodziak & Hendrickson 1999). As a result, we considered solar elevation at trawl locations and times as a covariate in GAMs.

To construct GAMs we used a backward stepwise procedure to select habitat covariates that minimized the generalized cross validation statistic (GCV, Wood 2006). We set gamma to 1.4, which increased the penalty for models of greater complexity (higher degrees of freedom). We set the maximum basis dimension of smoothers (k) to 4, which limited the complexity of the response functions to the nonparametric equivalent of a 3rd degree polynomial, and thus a Gaussian-like response. These conservative settings reduced our chances of over fitting the models. We used smoothing splines to model single term covariates which we eliminated beginning with those with the highest p-values in approximate *F*-tests. We retained only those habitat covariates producing lower GCV and significant reduction in residual deviance at the $p < 0.05$ level in analysis of deviance of nested models, which were also likely to affect the animals through mechanisms we understood. We examined residual and convergence diagnostics throughout the modeling process.

Following the construction of single term models, we evaluated first order interactions among retained covariates using tensor product smooths (Wood 2006). We found that nearly all significant first order interactions included sea surface temperature (SST), which was seasonally discontinuous between the autumn (warm SST > 17°C) and the winter and spring (SST < 15°C) surveys. As a result, we constructed a factor for season based upon SSTs (warm [autumn] vs. cold [winter & spring]), and determined whether abundance responses to the habitat covariates were seasonally dependent. Seasonally dependent habitat responses were retained if they produced lower GCVs and residual deviance in analysis of nested models ($p < 0.05$). Once we formulated these final models we added spatial co-variates (latitude and longitude) to identify residual spatial variation in abundance that was not well described by retained habitat covariates. We also included log-transformed abundances of squid and butterfish as covariates in spiny dogfish and summer flounder GAMs to evaluate the effects of prey distributions on distributions of the predators.

We used deviance partitioning (~variance partitioning) to quantify the independent and joint effects on species distributions of habitat covariates included in the final models which we organized into 3 sets: mesoscale pelagic features described by OOS; pelagic features based on CTD casts and benthic features measured with acoustics or bottom grabs (Borcard & Legendre 1994, Cushman & McGarigal 2002). We used partial GAM regression and nested analysis of deviance to compute independent and intercorrelated effects of the 3 variable sets on abundance patterns.

Model evaluation

We evaluated our GAMs using a cross validation out-of-sample prediction procedure that bootstrapped Spearman correlations between standardized abundance and abundance predicted with habitat covariates in the final GAMs. In each of 1000 iterations, 10% of the observations were randomly selected using a uniform distribution and set aside as test data. The remaining training observations were used to fit abundance to the habitat covariates included in the final GAMs. At each iteration the trained GAM was used to predict the relationship between habitat covariates and abundance in the test data. Predicted abundances were then compared with measured abundances in the test data using Spearman's rho. We calculated 50th, 5th, and 95th quantiles to estimate median and 95% confidence intervals for the bootstrapped rhos.

Demonstration projection of a habitat model

We modified the final summer flounder habitat GAM to accept available raster data layers for the autumn of 2008, and qualitatively compared this model projection with animal collections made from September 3 through November 13 during the NEFSC bottom trawl survey. We selected autumn 2008 for the demonstration because it was nearest in time to surveys used to train the habitat model (2003 to 2007) and because 2008 was the first year the

MARACOOS HF radar network continuously monitored surface currents throughout the MAB coastal ocean from Cape Hatteras to Cape Cod. The October 1, 2008 model projection used 8 d averaged satellite data and a 32 d rolling 'seasonal' trend in divergence (see Fig. 3). In the demonstration, we eliminated subsurface measures of water column properties because estimates are not currently accessible in near real time using operational remote sensing assets or models.

RESULTS

The explanatory power of GAMs made for the 2 pelagic species, squid and butterfish, was higher than for models made for spiny dogfish and summer flounder (Table 2, Fig. 2). Our models accounted for 73% of abundance variation for pelagic species, and ~50% of the variation for the demersal species. Models for pelagic species incorporated more pelagic habitat covariates measured with *in situ* CTD sampling. Models for demersal species did not, however, accept more of the benthic habitat covariates measured at relatively coarse spatial grains. Benthic covariates did not have greater explanatory power in demersal species models. Responses of the animals to many of the habitat covariates were seasonally dependent, and habitat distributions were better described during the winter and early spring than during the autumn when surface waters were stratified and animals were migrating, or soon to migrate, to overwintering habitats.

Bottom depth and variations in bottom depth (SD depth) met selection criteria in GAMs for all 4 species, and associations with seabed characteristics were seasonally dependent in every case (Table 2; see the Supplement at www.int–res.com/articles/suppl/m438p001_supp.pdf). During winter and early spring when temperatures were cold, the animals were abundant in deeper, offshore waters. Squid, butterfish, and summer flounder were most abundant over bottoms with depths ranging from 50 to 150 m. Spiny dogfish were more abundant in shallower habitats (<75 m). Deep overwintering habitats for squid and summer flounder were topographically complex (high STD depth) and located in the outer Hudson shelf valley and along the edge of the continental shelf. During winter, dogfish were also abundant over complex bottoms. Butterfish were more common over smooth bottoms. During autumn, abundance varied with depth only for butterfish which were rare over bottoms deeper than 150 m. Butterfish preferred complex bottoms in the nearshore during the autumn.

Bottom water temperature met selection criteria in GAMs for all 4 species (Table 2, see Supplement). Temperature responses of longfin squid, butterfish, and summer flounder were not seasonally dependent. All 3 species were rare where bottom temperatures were <6.5°C. Summer flounder, butterfish and squid were also uncommon on the continental shelf where bottom temperatures were warmer than 12.5°C, 16°C, and 20°C, respectively. In contrast, the temperature response of spiny dogfish was seasonally dependent. The sharks overwintered where bottom water temperatures were warmer than 7°C. During the autumn, dogfish preferred cool temperatures measured in the northern part of the study area.

Water column stability measured *in situ* and indexed as Simpson's PE anomaly for the upper 30 m of the water column met model selection criteria for squid, butterfish and summer flounder, while the abundance of butterfish also varied with mixed layer depth (Table 2, see Supplement). Summer flounder were consistently more abundant where the water column was stable in the vicinity of estuarine plumes during the autumn and the outer continental shelf during the winter and spring. Both pelagic species were more abundant where the water column was unstable during the autumn. In the winter, butterfish were more abundant where the water column was stable and the mixed layer was deep near the shelf slope front (see below, this section). Water column stability and stratification measured *in situ* varied negatively with surface current velocities and positively with current variances measured with HF radar. This produced relatively high, intercorrelated habitat effects in GAMs for the pelagic species (Table 2, Fig. 2).

Pelagic habitat characteristics measured remotely with satellites and HF radar did not have consistently greater explanatory power in models for the pelagic species than the demersal species (Table 2, Fig. 2). At least one remotely sensed pelagic characteristic met selection criterion for each species and the independent effects of remotely sensed variables were actually slightly higher in the GAM for summer flounder than for the pelagic species (Table 2, Fig. 2, see Supplement).

Summer flounder, butterfish and squid were most abundant in areas where the index of surface current divergence, and thus upwelling potential, was high (Table 2, Fig. 3, see Supplement). This response was seasonally dependent for the 2 pelagic species, but not for summer flounder.

Table 2. Analysis of deviance from generalized additive habitat modeling of longfin inshore squid, butterfish, spiny dogfish and summer flounder abundances in the Mid-Atlantic Bight coastal ocean (see also Fig. 2). Partial deviance is the additional deviance 'explained' by each variable after effects of other variables were removed. Null model is an approximation of the total deviance (~ variance) in abundance data. % of Null expresses the deviance and partial deviance as a percentage of the Null Model for each species. The decrease in the generalized cross validation statistic (ΔGCV) is indicated in the last column. Only variables that resulted in an increase in GCV when they were removed in backward selection were included in the final models and reported here

Species	Habitat variable	Deviance	% of Null	Partial deviance	% of Null	ΔGCV
Longfin inshore squid	Bottom temperatures	260027.0	40.4	50878.0	7.9	150.7
	Cross shelf velocity[a]	24295.0	3.8	24173.0	3.8	62.2
	Watermass	135449.0	21.0	22388.0	3.5	59.6
	Bottom depth[a]	214195.0	33.2	17068.0	2.6	41.7
	STD bottom depth[a]	156599.0	24.3	14255.0	2.2	37.6
	Sun's elevation[a]	59145.0	9.2	13172.0	2.0	22.5
	Simpson's PE (30 m)[a]	77978.0	12.1	10939.0	1.7	21.1
	Divergence index[a]	24633.0	3.8	8038.2	1.2	15.4
	Frontal index[a]	5115.9	0.8	6971.1	1.1	6.3
	Cross shelf variance (vel.)	8614.1	1.3	4051.5	0.6	10.0
	Benthic habitat data			37586.0	5.8	
	Pelagic habitat data (*in situ*)			70533.0	10.9	
	Pelagic habitat data (remote)			80824.0	12.5	
	Final model	474644.5	73.7			
	Residual	169746.3	26.3			
	Null model	644390.8				
	Spatial coordinates	206838.0	32.1	66810.0	10.4	171.3
Butterfish	Bottom depth[a]	40207.0	23.6	8846.3	5.2	21.3
	Bottom temperature	27987.0	16.4	8152.1	4.8	23.7
	Cross shelf velocity[a]	6343.5	3.7	8090.8	4.7	22.5
	Sun's elevation	4759.3	2.8	7229.3	4.2	16.5
	STD bottom depth[a]	18282.0	10.7	6948.0	4.1	18.5
	Divergence index[a]	5482.3	3.2	6903.8	4.0	15.2
	Mixed layer depth[a]	873.4	0.5	5490.5	3.2	12.1
	Frontal index[a]	23422.0	13.7	4922.1	2.9	11.8
	Simpson's PE (30 m)[a]	11882.0	7.0	4288.6	2.5	9.6
	Cross shelf variance (vel.)	101.1	0.1	1335.1	0.8	3.2
	Benthic habitat data			21218.0	12.4	
	Pelagic habitat data (*in situ*)			23151.0	13.6	
	Pelagic habitat data (remote)			21269.0	12.5	
	Final model	124984.6	73.2			
	Residual	45673.4	26.8			
	Null model	170658.0				
	Spatial coordinates	63635.5	37.3	17360.0	10.2	44.6
Spiny dogfish	Bottom temperature [a]	42380.0	40.0	22554.0	21.3	35.7
	Along shelf variance (vel.)[a]	21770.0	20.6	3938.9	3.7	5.3
	Bottom depth[a]	7090.1	6.7	3409.8	3.2	4.5
	STD bottom depth[a]	4008.4	3.8	2414.9	2.3	3.1
	Sun's elevation	3628.1	3.4	844.0	0.8	0.8
	Benthic habitat data			5913.8	5.6	
	Pelagic habitat data (*in situ*)			22554.0	21.3	
	Pelagic habitat data (remote)			3938.9	3.7	
	Final model	53152.6	50.2			
	Residual	52670.0	49.8			
	Null model	105822.6				
	Prey [log(squid)]	29544.0	27.9	2434.2	2.3	3.1
	Spatial coordinates	40954.6	38.7	15075.0	14.2	20.1

Table 2 (continued)

Species	Habitat variable	Deviance	% of Null	Partial deviance	% of Null	ΔGCV
Summer flounder	Chlorophyll *a*[a]	2556.9				
	Bottom depth[a]	2955.5				
	Bottom temperature	1322.6				
	Frontal index[a]	290.3				
	STD bottom depth	214.4				
	Divergence index	161.9				
	Benthic habitat data			1288.8	12.9	
	Pelagic habitat data (*in situ*)			676.7	6.8	
	Pelagic habitat data (remote)			1302.3	13.1	
	Final model	5017.8	50.4			
	Residual	4934.5	49.6			
	Null model	9952.3				
	Spatial coordinates	2462.8	24.7	652.3	6.6	1.2
	Prey [log(squid)]	3379.7	34.0	1053.3	10.6	2.7
	Prey [log(butterfish)]	3561.7	35.8	795.7	8.0	2.0
	Both prey			1323.5	13.3	3.4

[a]Response to habitat variable was seasonally dependent and different during cruises conducted when water was warm (autumn) and cold (winter and early spring)

During autumn, summer flounder was associated with nearshore areas where chl *a* concentrations were relatively high (Fig. 3, see Supplement). These areas were in close proximity to estuarine plumes. The animals were rarely collected where surface chl *a* was highest during winter and spring.

Squid, butterfish and summer flounder abundance varied with proximity to, and the strength of, surface fronts identified with satellites (Table 2, Fig. 3, see Supplement). Associations with fronts were strong during cold seasons but weak or absent during the autumn when the water column was warm and stratified. The pelagic species were associated with fronts on the outer continental shelf during the winter and spring. Summer flounder were rarely collected close to these strong fronts.

Although proximity to fronts between water masses was important in 3 of 4 habitat models, water mass type only met model selection criterion for longfin squid (see Supplement). Squid were slightly more abundant in water masses of moderate temperature, salinity, and primary productivity that occurred over intermediate bottom depths.

Squid and butterfish appeared to respond to cross shelf surface current velocities (see Supplement). During autumn, the animals were common where strong surface currents were directed offshore. They were abundant during winter and spring where high surface current velocities were directed inshore. The pelagic species also preferred areas where surface current velocities were relatively consistent (low variance in velocity). The response of spiny dogfish to variance in velocity was similar.

During the winter and spring, summer flounder and spiny dogfish were associated with the pelagic species they prey upon on the outer continental shelf (Table 2, Fig. 2, see Supplement). Both predators were abundant where squid were abundant, while summer flounder were also associated with butterfish.

Maps of residual spatial variation made by adding spatial covariates indicated that abundances of squid and butterfish were lower in the nearshore off Long Island, New York, than predicted based upon the habitat covariates included in the final models (Table 2, see Supplement). Squid were more abundant during the winter offshore south of Hudson shelf valley, while butterfish abundance was higher than predicted in the autumn just southeast of the Sandy Hook peninsula where the Hudson-Raritan estuary discharges into the coastal ocean. Dogfish abundance was overestimated at the mouth of the Hudson-Raritan estuary and along the continental shelf break based upon retained habitat covariates. Finally, there was a cross shelf gradient in errors in the GAM for summer flounder, which were less abundant than predicted in the nearshore continental shelf, but more abundant offshore north of the Hudson Shelf Valley.

The out-of-sample prediction test indicated that habitat-specific trends in abundances of longfin inshore squid, spiny dogfish and summer flounder were well described by our GAMs (Fig. 4). Bootstrapped rank correlations between predicted and actual catches were >0.7 and confidence intervals were relatively narrow for squid and spiny dogfish. For the butterfish model, correlations between pre-

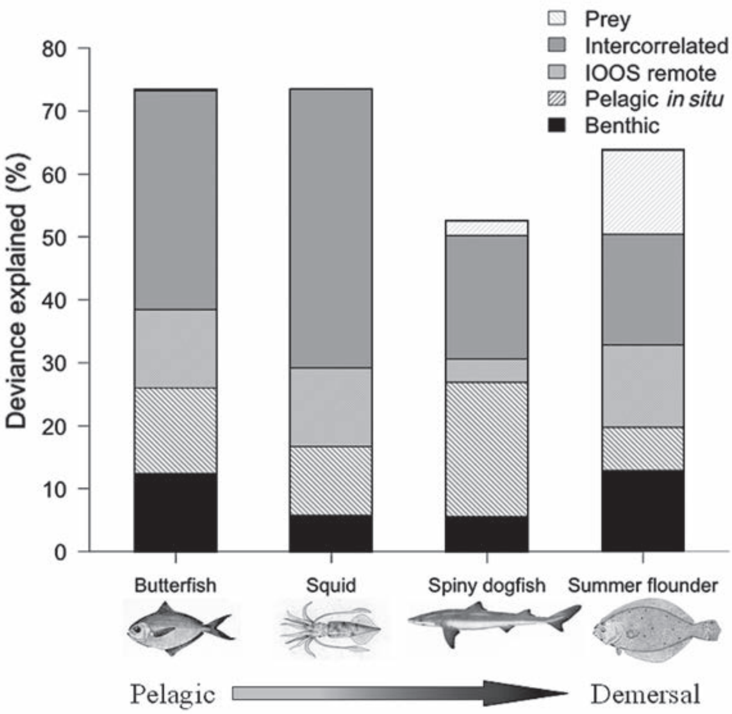

Fig. 2. Partial deviance (~variance) components calculated from generalized additive model (GAM) habitat modeling for 4 species with different vertical habitat preferences in the coastal ocean (see Table 2 and the Supplement available at www.int-res.com/articles/suppl/m438p001_supp.pdf). Less of the abundance variation was 'explained' for demersal than for pelagic species, whose distributions appeared to be more directly affected by water column stability and mixed layer depth measured *in situ*. These variables were correlated with HF radar surface current measurements. Percentages depicted for Prey, IOOS remote, Pelagic *in situ* and Benthic habitat feature groups are partial components after intercorrelated effects (also shown) were removed. Spatial covariates were not included in this analysis

dicted and actual abundances were weaker and confidence intervals were wide.

Actual catches of summer flounder during autumn 2008 generally matched the demonstration projection of the statistical habitat model we modified to accept OOS ocean data for October 1. Catches were relatively high offshore south of Martha's Vineyard, and in shallower water from the mouth of Long Island Sound west to the mouth of the Hudson-Raritan estuary to central New Jersey.

DISCUSSION

Broad scale dynamic habitat models for species contributing resilience to large marine ecosystems could be useful for space- and time-based ecosystem management. However, operational habitat models require sustained collection of high resolution data describing pelagic and benthic processes affecting the physiologies, behaviors and ecologies of important species at the scale of large marine ecosystems. These kinds of data are much too expensive and time consuming to collect using traditional shipboard techniques. OOS are designed to measure ocean variability at the space–time scales necessary to describe the fundamental physical and biological processes driving the spatial dynamics of coastal marine ecosystems (Schofield et al. 2008). It is therefore not surprising that OOS satellite and HF radar descriptions of mesoscale oceanographic features and processes were useful for modeling the habitats of several ecologically important species in the Mid-Atlantic Bight.

The availability of high resolution, spatially explicit time series data for the Mid-Atlantic Bight allowed us to build models of greater explanatory power than would have been possible using shipboard data alone. We built our GAMs conservatively, constraining the complexity of smoothers, increasing the penalty for model complexity, and considering only habitat features affecting ecological processes. Nevertheless, our models explained 50 to 70% of the variation in abundance of 4 species with diverse vertical habitat preferences. Furthermore, out-of-sample prediction capabilities of 3 of our 4 models were high. GAM models developed using just shipboard measurements of pelagic and benthic habitat heterogeneity typically explain between 10 to 50% of abundance variation and generally have poorer out-of-sample prediction capabilities than we measured (e.g. Stoner et al. 2001, 2007, Jensen et al. 2005). Becker et al (2010) also demonstrated that habitat models built with remotely sensed ocean data of the proper resolution have predictive capabilities as good or better than those made with analogous shipboard data alone.

As OOS are designed to sample at the space–time scales necessary to describe the physical and primary production dynamics of the coastal ocean, we were able to consider several fundamental processes controlling ecosystem productivity in our statistical habitat models. Measurements of vertical current velocities, and locations and strengths of fronts were the most valuable of these descriptors of processes known to regulate and structure coastal ocean food webs (Olson et al. 1994, Bakun 2010). Measurements of vertical current velocities allowed us to consider

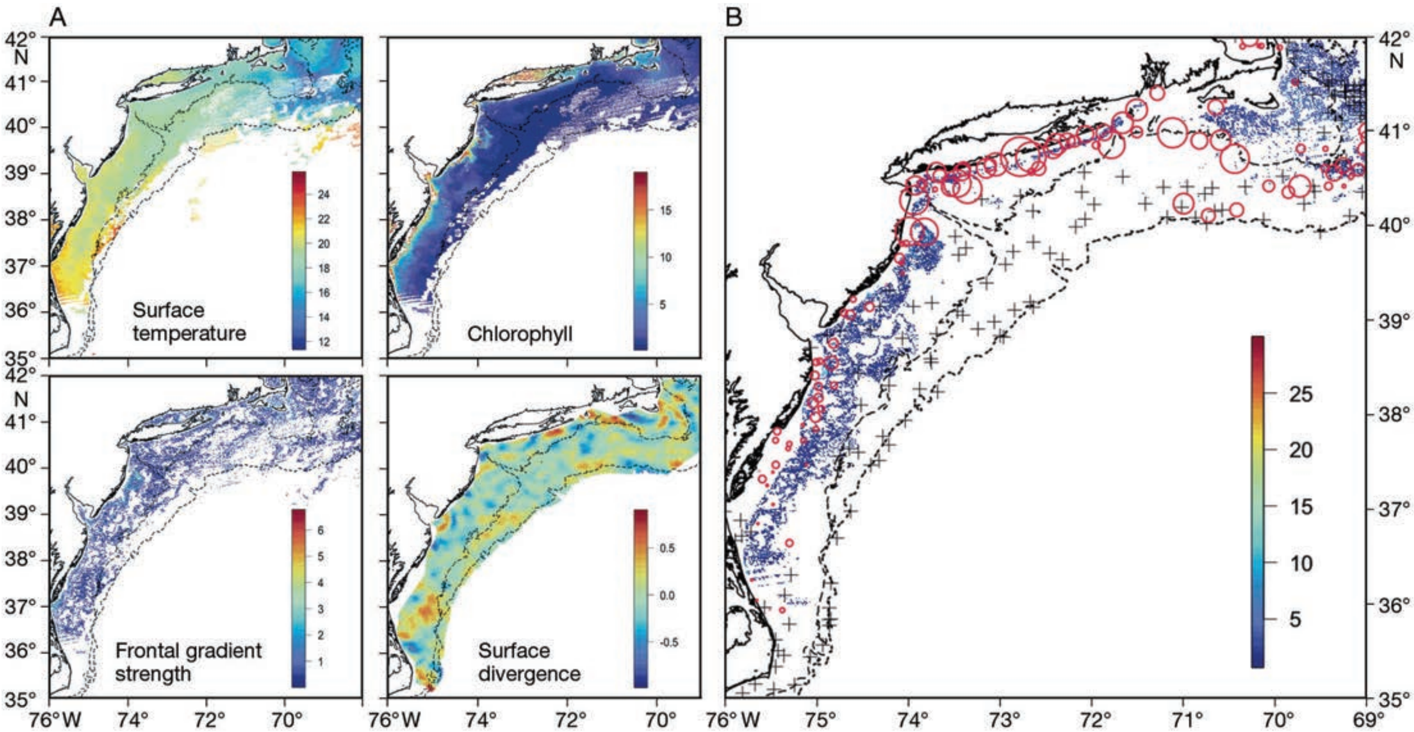

Fig. 3. Pelagic habitat gradients and predicted and realized summer flounder catches during autumn 2008. (A) Pelagic habitat variables (8 d average except for divergence which was 32 d) on October 1, 2008 that were used to project a modified generalized additive model (GAM) habitat model for summer flounder. The modified GAM did not include bottom temperature which was too sparsely measured during autumn 2008, and gradient index was replaced with gradient strength to make 'forecasting' tractable. The modified model included log transformed SD of bottom depth as well as the 4 gradients shown in panel A. (B) Summer flounder abundance projected for October 1, 2008 from the modified GAM habitat model in the color gradient. The open red symbols are scaled to the catch of summer flounder per unit effort (CPUE) in Northeast Fisheries Science Centre bottom trawl tows from September through mid-November 2008. + indicates tows in which fish were absent

spatial and temporal variation in upwelling and downwelling potential in our models. Summer flounder were consistently abundant in areas of the coastal ocean where the potential for upwelling was high, while butterfish and squid showed seasonally dependent associations with areas of upwelling. Strong gradients in temperature, salinity, and/or chl *a* are characteristic of ocean fronts where the interaction of circulation with the buoyancies and behaviors of organisms results in the concentration of food web constituents along them (Helfrich & Pineda 2003, Genin et al. 2005, Bakun 2010). Our frontal index, which integrated the strength of, and distance to, the nearest frontal gradient met the selection criterion in 3 of our 4 models. The pelagic species, longfin inshore squid and butterfish, were collected near strong surface fronts on the outer continental shelf during winter and early spring. During the same season, summer flounder were more abundant inshore of these strong fronts.

If indices of surface divergence and fronts between water masses referenced physical processes controlling the spatial structure and dynamics of coastal ocean food, we might have expected species responses to be similar and stronger, and satellite measurements of primary productivity to meet selection criterion in more than one of our GAMs. However, we modeled secondary and tertiary consumers with trophic positions ranging from 3.5 (butterfish) to 4.5 (summer flounder), using only surface habitat features measured directly overhead of trawl samples (Bowman et al. 2000, Hunsicker & Essington 2006, Smith & Link 2010). As these animals feed at high trophic levels, they may, under many circumstances, be distributed downstream and later in time than the physics and primary productivity that ultimately supports them (Yamamoto & Nishizawa 1986, Olson et al. 1994, Bakun 2010). These sorts of space-time lags are highly likely for demersal species like summer flounder and spiny dogfish in deep overwintering habitats that are linked by advection and prey behavior to primary production at the surface along the shelf slope front (Linder et al. 2004, Johnson et al. 2007). Demersal predators at high trophic levels

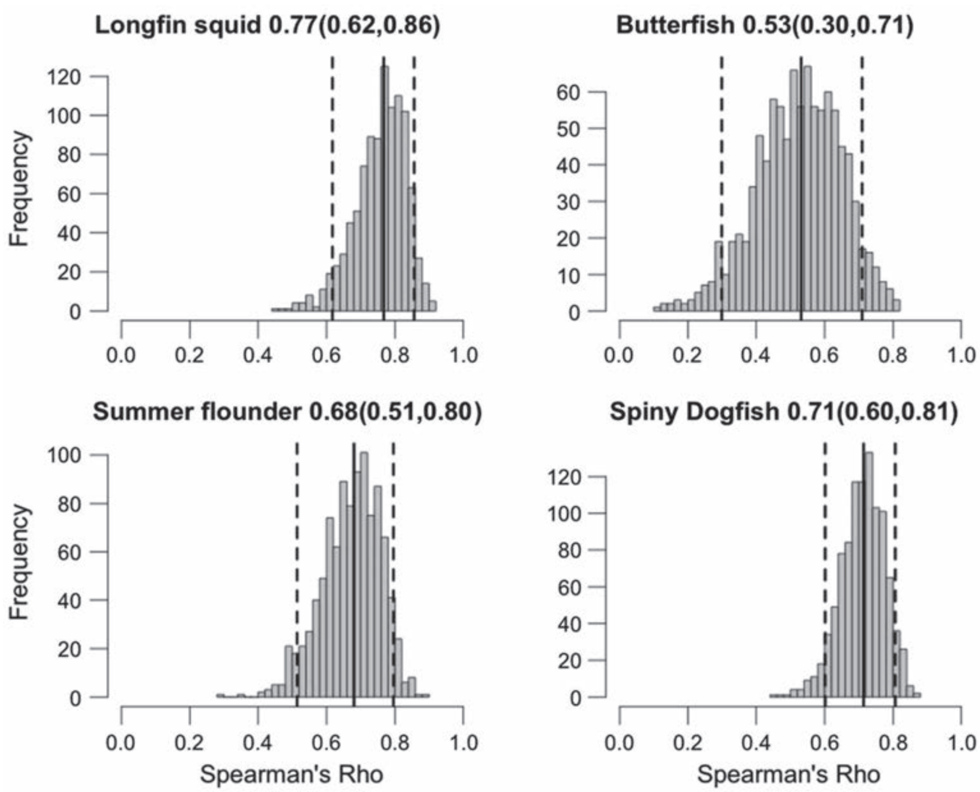

Fig. 4. Bootstrapped (1000 iterations) Spearman correlations (rho) between actual abundances and abundances predicted using habitat covariates in final generalized additive models (GAMs) for each of the 4 species generated with the cross validation out-of-sample prediction procedure (see 'Materials and methods'). Solid lines indicate median correlation while dashed lines are 5th and 95th quantiles for the bootstrapped rho values

should be more strongly associated in space and time with the prey they directly consume than with lower trophic levels. We found spiny dogfish and summer flounder to be strongly associated with the squid and butterfish they feed upon during the winter and spring (Torres et al. 2008, Moustahfid et al. 2009, Smith & Link 2010, Staudinger & Juanes 2010). In our analyses, the predators were not associated with these prey during autumn. However, during warmer months, including the autumn, spiny dogfish are more abundant north of our study domain, while estuaries are important nurseries and summer feeding habitats for summer flounder that are not sampled in the NEFSC fishery independent bottom trawl surveys (Packer et al. 1999, Stehlik 2009). Thus seasonal changes in the importance of prey in our statistical models for the demersal predators were probably related simultaneously to limitations of the data we analyzed and to seasonal changes in habitat overlap between the specific predators and prey.

Primary productivity as indexed by satellite estimates of chl *a* only met selection criteria in the model for summer flounder during the autumn migration and spawning period. (Fig. 3, see Supplement). Abundance of the flatfish increased with increases in chl *a* to a threshold, and the animals were associated with plumes of moderately high chl *a* occurring outside the mouths of several large MAB estuaries where upwelling potential was also high (Fig. 3). Areas of coastal ocean impacted by estuarine plumes are optically complex, but the high concentrations of colored dissolved organic matter and detritus that confound satellite-based estimates of phytoplankton production also contribute to high productivity (Moline et al. 2008, Pan et al. 2010). The association of summer flounder with estuarine plumes may be purely coincident with migratory pathways between shallow estuarine and coastal feeding habitats and overwintering habitats offshore. However, Berrien & Sibunka (1999) reported high densities of summer flounder eggs that have stage durations of 48 to 72 h in these same locations (Johns et al. 1981). We speculate that coastal ocean areas impacted by estuarine plumes where upwelling occurs and productivity is high could serve as high quality spawning grounds that place eggs in close proximity to optimal feeding habitats for larvae which are at a lower trophic level of ~3 (Grimes & Kingsford 1996). These same areas also have physical transport mechanisms likely to deliver larvae south and west to important estuarine nurseries (Epifanio & Garvine 2001, Lentz 2008, Tilburg et al. 2009, Zhang et al. 2009, Gong et al. 2010). Spawning habitat selection and suitability should be largely defined by conditions promoting the development, survival and successful transport of early life stages to juvenile nurseries rather than by the immediate requirements of adults.

Distributions of the 2 pelagic species were related to horizontal surface currents in our statistical habitat models. During autumn migration, squid and butterfish were more abundant in areas where higher velocity surface flows (and low variance) were directed offshore, while the species were associated with high velocity (low velocity variance) onshore surface flows during the spring. Most swimming and flying animals exploit complex 3-dimensional flows to conserve energy, particularly during long-distance migrations (Liao 2007, Mandel et al. 2008, Mansfield et al. 2009, Stehlik 2009). Associations of the pelagic species with specific surface flows in our models may have reflected the efficient use of cross shelf transport pathways during seasonal migrations. However, the animals were collected in trawls on the bottom where current flows can be different to seasonally complex surface flows (Lentz 2008, Gong et al. 2010). Furthermore, areas with higher velocity, low variance surface flows also tended to have weakly stratified water columns with shallow mixed layers. These are also characteristics of productive habitats (Mann & Lazier 2006, Bakun 2010). The inverse relationship between horizontal surface currents and water column stratification and stability was largely responsible for the inter-correlated habitat effects and the large amount of deviance explained in our models for pelagic species (Fig. 2). Mechanistic studies are therefore required to determine whether responses of the 2 pelagic species captured by our models reflected preferences for cross shelf transport pathways useful for energy efficient migration, physical conditions promoting high primary productivity, or for areas where both processes occur simultaneously.

The habitat associations of all 4 species, regardless of vertical preference, were better described by the pelagic than the benthic data available to us. Sediment grain sizes estimated at a spatial resolution of 2000 m did not meet selection criterion in any of our GAMs and species associations with bottom depths and seabed complexity measured at a grain of 93 m and resolution of 2 km were seasonally dependent in nearly every case. The interactions between bottom depth and season captured inshore–offshore migrations that were probably more directly related to the seasonal dynamics of temperature and the temperature preferences of the animals than to depth preferences. All of the species except spiny dogfish showed a seasonally independent response to bottom water temperature with a minimum threshold of ~6.5°C. The animals were concentrated in deep water near the edge of the continental shelf during the winter and early spring when water temperatures are generally warmer and less variable offshore than inshore. Abundance relationships with bottom habitat complexity could have reflected species associations with refuges from predation or current flow if our coarser grained index served as a proxy for bottom complexity at scales of tens of centimeters to tens of meters. However, responses to bottom habitat complexity were also seasonally dependent and complex for 3 of the 4 species, and therefore probably aliased other characteristics of overwintering habitats along submarine valleys and canyons on the outer continental shelf. Animals respond to centimeter to 100 m scale variability in bottom characteristics, and the data available to us were just too coarse to describe benthic habitat heterogeneity that might have directly affected the survival and energy budgets of the animals (Abookire et al. 2007, Liao 2007, Stoner et al. 2007, Gray & Elliott 2009). Centimeter to meter scale descriptions of the structural complexity of the seabed have been shown to increase the fit of habitat models (Abookire et al. 2007, Stoner et al. 2007) and the predictive capability of several of our models might have increased if data describing bottom habitat heterogeneity at finer, ecologically relevant scales had been available for our study domain (e.g. Harris & Stokesbury 2010). Higher resolution bottom data might have improved our model for longfin inshore squid, which deposit egg masses on hard structures located on sand and muddy substrata (Jacobson 2005). However, it is also true that bottom characteristics may be less important to large animals even when they are strongly demersal. Habitat associations of age 1+ summer flounder on the continental shelf are poorly described by fine scale characteristics of the seabed identified with side scan sonar or underwater video (Lathrop et al. 2006, Slacum et al. 2008). Our results are consistent with speculation that distributions of the flatfish on the continental shelf are determined primarily by mesoscale oceanographic features controlling patterns of productivity and prey distributions rather than by fine-scale seabed characteristics (Slacum et al. 2008).

CONCLUSIONS

Resource managers are turning increasingly to spatial management as a tool for conserving marine populations and ecosystems (Pérez-Ruzafa et al. 2008, Worm et al. 2009, Edwards & Plagányi 2011). Regional scale habitat modeling could serve as the foundation for tactical decisions as to where and when to site marine protected and closed areas designed to conserve species that provide essential ecosystem services. While much of the seabed remains unmapped, variability in the physical structure, dynamics and productivity of the water column is being measured and mapped at ecologically relevant space/time scales with remote sensing technology integrated into OOS. Furthermore, all OOS are actively developing ensembles of oceanographic models that assimilate data from sensors on satellite, HF radar, underwater robot, and fixed mooring platforms to make spatially and temporally explicit hindcasts and forecasts of the structure and dynamics of the coastal ocean including subsurface features (e.g. Zhang et al. 2010a,b,c). Many of the pelagic features and processes currently measured and modeled by OOS determine patterns of habitat suitability for species and their life stages and could be considered in spatial management (Game et al. 2009, Watson et al. 2011).

In our view, several avenues of research need to be pursued in order to develop habitat models useful for spatial management. These include investigation of the resolution and ranges of habitat variability measured with OOS resulting in biological responses, including the identification of space–time lags between variability in physical and primary production dynamics and responses of important upper level consumers, particularly those associated with the bottom. There is also a need for biological data, in addition to trawl net surveys, to be integrated into OOS (e.g. Kloser et al. 2009, Žydelis et al. 2011). Currently, the data available for broad scale habitat modeling are fisheries-independent surveys designed for stock assessment, not habitat assessment. These surveys are highly selective with respect to season and organism size and often do not sample habitats used during important periods in the life history of many species. Infrequent traditional net surveys cannot be used to distinguish dispersal corridors that many animals move through quickly from areas in which fewer individuals take up longer term residency because habitat resources meet the requirements of particular life history stages. Finally, habitat models based on abundance assume that organisms evaluate habitat quality accurately, without perceptual and movement constraints, and therefore reach abundances at equilibrium with habitat carrying capacity without time delays. This is probably rarely the case, particularly in regions like the Mid-Atlantic Bight where important habitat dimensions are highly dynamic in time and space and many animals are highly migratory. Integration of telemetry and fishery hydroacoustics data into regional OOS (e.g. Kloser et al. 2009, Zydelis et al. 2011) would be useful for addressing some of the sampling biases and assumptions inherent in habitat models based upon traditional fisheries survey data.

We view statistical habitat models informed by OOS, such as those we have developed here, as a first step toward the development of operational mechanistic habitat models: As hypothesis-generating tools that can be coupled with OOS products to perform mechanistic studies of the effects of pelagic, as well as benthic, habitat heterogeneity on the processes of growth, survival, dispersal and reproduction that underlie spatial population dynamics (Kritzer & Sale 2006, Buckley et al. 2010). This type of adaptive, iterative approach could be a cost-effective way to develop mechanistic models with scopes broad enough to meet the requirements of spatial resource management in the sea.

Acknowledgements. We thank S. Lucey, M. Taylor and J. Goff for generously providing us with the data used in our analysis, and S. Gray for his contributions to stimulating discussions about the role of the Integrated Ocean Observing System (IOOS) in fisheries science and management. B. Phelan also provided much needed support. We thank A. Stoner and 3 anonymous reviewers whose comments helped us to improve the manuscript. The NOAA Fisheries and the Environment Program (NA08NMF450626) provided primary support for this research. The authors also thank the following agencies for additional support during this project: NASA Biodiversity NNG06GH75G1/3, NASA New Investigator Program NNH07ZDA001N, NOAA IOOS Office (MARACOOS Grant NA01NOS4730014 and NA07NOS 4730221) and Delaware Sea Grant (NA10OAR4170084).

LITERATURE CITED

Abookire AA, Duffy-Anderson JT, Jump CM (2007) Habitat associations and diet of young-of-the-year Pacific cod (*Gadus macrocephalus*) near Kodiak, Alaska. Mar Biol 150:713–726

Azarovitz T (1981) A brief historical review of the Woods Hole Laboratory trawl survey time series. In: Doubleday WG, Rivard D (eds) Bottom trawl surveys. Can Spec Publ Fish Aquat Sci 58:62–67

Bakun A (2010) Linking climate to population variability in marine ecosystems characterized by non-simple dynamics: Conceptual templates and schematic constructs. J Mar Syst 79:361–373

Barrick DE, Evens MW, Weber BL (1977) Ocean surface currents mapped by radar. Science 198:138–144

Beardsley RC, Boicourt WC (1981) On estuarine and continental-shelf circulation in the Middle Atlantic Bight. In: Warren BA, Wunsch C (eds) Evolution of physical oceanography. MIT Press, Boston, p 198–235

Becker EA, Forney KA, Ferguson MC, Foley DG, Smith RC, Barlow J, Redfern JV (2010) Comparing California Current cetacean–habitat models developed using *in situ* and remotely sensed sea surface temperature data. Mar

Ecol Prog Ser 413:163–183
Berrien P, Sibunka J (1999) Distribution patterns of fish eggs in the U.S. Northeast Continent Shelf Ecosystem, 1977–1987. NOAA Tech Rep NMFS 145:310
Borcard D, Legendre P (1994) Environmental control and spatial structure in ecological communities: an example using oribatid mites (Acari, Orbiatei). Environ Ecol Stat 1:37–53
Bowman RE, Stillwell CE, Micheals WL, Grosslein MD (2000) Food of Northeast Atlantic fishes and two common species of squid. NOAA Tech Rep NMFS-F/ME-155
Brodziak JKT, Hendrickson LC (1999) An analysis of environmental effects on survey catches of squids, *Loligo pealeii* and *Illex illecebrosus* in the northwest Atlantic. Fish Bull 97:9–24
Buckley LB, Urban MC, Angilletta MJ, Crozier LG, Rissler LJ, Sears MW (2010) Can mechanism inform species' distribution models? Ecol Lett 13:1041–1054
Castelao R, Glenn S, Schofield O, Chant R, Wilkin J, Kohut J (2008) Seasonal evolution of hydrographic fields in the central Middle Atlantic Bight from glider observations. Geophys Res Lett 35; L03617 doi:10.1029/2007GL032335
Ciannelli L, Dingsør GE, Bogstad B, Ottersen G and others (2007) Spatial anatomy of species survival: effects of predation and climate driven environmental variability. Ecology 88:635–646
Collette BG, Klein-MacPhee G (2002) Bigelow and Schroeder's fishes of the Gulf of Maine, xxi. Smithsonian Institution Press, Washington, DC
Cushman SA, McGarigal K (2002) Hierarchical, multi-scale decomposition of species–environment relationships. Landsc Ecol 17:637–646
Edwards CTT, Plagányi ÉE (2011) Protecting old fish through spatial management: is there a benefit for sustainable exploitation? J Appl Ecol 48:853–863
Epifanio CE, Garvine RW (2001) Larval transport on the Atlantic continental shelf of North America: a review. Estuar Coast Shelf Sci 52:51–77
Ficetola GF, Denoël M (2009) Ecological thresholds: an assessment of methods to identify abrupt changes in species habitat relationships. Ecography 32:1075–1084
Game ET, Grantham HS, Hobday AJ, Pressey RL and others (2009) Pelagic protected areas: the missing dimension in ocean conservation. Trends Ecol Evol 24:360–369
Genin A, Jaffe JS, Reef R, Richter C, Franks PJS (2005) Swimming against the flow: a mechanism of zooplankton aggregation. Science 308:860–862
Goff JA, Jenkins C, Calder B (2006) Maximum a posteriori resampling of noisy, spatially correlated data. Geochem Geophys Geosys 7, Q08003 doi:10.1029/2006GC001297
Goff JA, Jenkins CJ, Williams SJ (2008) Seabed mapping and characterization of sediment variability using the usSEABED data base. Cont Shelf Res 28:614–633
Gong D, Kohut JT, Glenn SM (2010) Seasonal climatology of wind-driven circulation on the New Jersey Shelf. J Geophys Res 115:C04006 doi:10.1029/JC005520
Gray JS, Elliott M (2009) Ecology of marine sediments. Oxford University Press, Oxford
Grimes C, Kingsford M (1996) How do riverine plumes of different sizes influence fish larvae: Do they enhance recruitment? Mar Freshw Res 47:191–208
Harris BP, Stokesbury KDE (2010) The spatial structure of local surficial sediment characteristics on Georges Bank, USA. Cont Shelf Res 30:1840–1853
Hatfield EMC, Cadrin SX (2002) Geographic and temporal patterns in size and maturity of the longfin inshore squid (*Loligo pealeii*) off the northeastern United States. Fish Bull 100:200–213
Helfrich KR, Pineda J (2003) Accumulation of particles in propagating fronts. Limnol Oceanogr 48:1509–1520
Hsieh CH, Yamauchi A, Nakazawa T, Wang WF (2010) Fishing effects on age and spatial structures undermine population stability of fishes. Aquat Sci 72:165–178
Hunsicker ME, Essington TE (2006) Size-structured patterns of piscivory of the longfin inshore squid (*Loligo pealeii*) in the mid-Atlantic continental shelf ecosystem. Can J Fish Aquat Sci 63:754–765
Jacobson LD (2005) Essential fish habitat source document: Longfin inshore squid, *Loligo pealeii*, life history and habitat characteristics. NOAA Tech Memo NMFS-NE-193
Jensen OP, Seppelt R, Miller TJ, Bauer LJ (2005) Winter distribution of blue crab *Callinectes sapidus* in Chesapeake Bay: application and cross-validation of a two-stage generalized additive model. Mar Ecol Prog Ser 299:239–255
Johns DM, Howell WH, Klein-MacPhee G (1981) Yolk utilization and growth to yolk-sac absorption in summer flounder (*Paralichthys dentatus*) larvae at constant and cyclic temperatures. Mar Biol 63:301–308
Johnson NA, Campbell JW, Moore TS, Rex MA, Etter RJ, McClain CR, Dowell MD (2007) The relationship between the standing stock of deep-sea macrobenthos and surface production in the western North Atlantic. Deep-Sea Res I 54:1350–1360
Kerr LA, Cadrin SX, Secor DH (2010) The role of spatial dynamics in the stability, resilience, and productivity of an estuarine fish population. Ecol Appl 20:497–507
Kloser RJ, Ryan TE, Young JW, Lewis ME (2009) Acoustic observations of micronekton fish on the scale of an ocean basin: potential and challenges. ICES J Mar Sci 66: 998–1006
Kritzer JP, Sale PF (2006) Marine metapopulations. Academic Press, Amsterdam
Lathrop RG, Cole M, Senyk N, Butman B (2006) Seafloor habitat mapping of the New York Bight incorporating sidescan sonar data. Estuar Coast Shelf Sci 68:221–230
Lentz SJ (2008) Observations and a model of mean circulation over the Middle Atlantic Bight continental shelf. J Phys Oceanogr 38:1203–1220
Levitus S (1982) Climatological atlas of the world's oceans. NOAA Professional Paper 13:173
Liao JC (2007) A review of fish swimming mechanics and behaviour in altered flows. Philos Trans R Soc B 362: 1973–1993
Linder CA, Gawarkiewicz GG, Pickart RS (2004) Seasonal characteristics of bottom boundary layer detachment at the shelfbreak front in the Middle Atlantic Bight. J Geophys Res 109:C03049 doi:10.1029/U2003JC002032
Link J, Overholtz W, O'Reilly J, Green J and others (2008) The Northeast U.S. continental shelf Energy Modeling and Analysis exercise (EMAX): ecological network model development and basic ecosystem metrics. J Mar Syst 74:453–474
Mandel JT, Bildstein KL, Bohrer G, Winkler DW (2008) Movement ecology of migration in turkey vultures. Proc Natl Acad Sci USA 105:19102–19107
Mann K, Lazier J (2006) Dynamics of marine ecosystems: biological–physical interactions in the oceans, 3rd edn. Blackwell Publishing, Oxford
Mansfield K, Saba V, Keinath J, Musick J (2009) Satellite tracking reveals a dichotomy in migration strategies

among juvenile loggerhead turtles in the Northwest Atlantic. Mar Biol 156:2555–2570

Marra J, Houghton RW, Garside C (1990) Phytoplankton growth at the shelf-break front in the Middle Atlantic Bight. J Mar Res 48:851–868

Moline MA, Frazer TK, Chant R, Glenn S and others (2008) Biological responses in a dynamic buoyant river plume. Oceanography 21:70–89

Mora C, Metzger R, Rollo A, Myers RA (2007) Experimental simulations about the effects of overexploitation and habitat fragmentation on populations facing environmental warming. Proc R Soc B 274:1023–1028

Moustahfid H, Tyrrell MC, Link JS (2009) Accounting explicitly for predation mortality in surplus production models: an application to longfin inshore squid. North Am J Fish Manage 29:1555–1566

Moustahfid H, Tyrrell MC, Link JS, Nye JA, Smith BE, Gamble RJ (2010) Functional feeding responses of piscivorous fishes from the northeast US continental shelf. Oecologia. 163:1059–1067

Mugo R, Saitoh SI, Nihira A, Kuroyama T (2010) Habitat characteristics of skipjack tuna (*Katsuwonus pelamis*) in the western North Pacific: a remote sensing perspective. Fish Oceanogr 19:382–396

Neteler M, Mitasova H (2008) Open source GIS: A GRASS GIS approach. Springer, New York, NY

Oliver MJ, Irwin AJ (2008) Objective global ocean biogeographic provinces. Geophys Res Lett 35:L15601 doi: 10.1029/2008GL034238

Oliver MJ, Glenn SM, Kohut JT, Irwin AJ, Schofield OM, Moline MA, Bissett WP (2004) Bioinformatic approaches for objective detection of water masses on continental shelves. J Geophys Res 109:C07S04 doi:10.1029/2003JC002072

Olson DB, Hitchcock GL, Mariano AJ, Ashjian CJ, Peng G, Nero RW, Podestá GP (1994) Life on the edge: marine life and fronts. Oceanography 7:52–60

Packer DB, Hoff T (1999) Life history, habitat parameters, and essential habitat of Mid-Atlantic summer flounder. Am Fish Soc Symp 22:76–92

Packer DB, Griesbach S, Berrien PL, Zetlin C, Johnson DL, Morse WW (1999) Essential fish habitat source document: summer flounder, *Paralichthys dentatus*, life history and habitat characteristics. NOAA Tech Memo NMFS-NE-151

Pan X, Mannino A, Russ ME, Hooker SB, Harding LW Jr (2010) Remote sensing of phytoplankton pigment distribution in the United States northeast coast. Remote Sens Environ 114:2403–2416

Pérez-Ruzafa A, Martín E, Marcos C, Miguel Zamarro J and others (2008) Modeling spatial and temporal scales for spill-over and biomass exportation from MPAs and their potential for fisheries enhancement. J Nat Conserv 16: 234–255

Pearce J, Ferrier S (2000) An evaluation of alternative algorithms for fitting species distribution models using logistic regression. Ecol Model 128:127–147

Reid JM, Reid JA, Jenkins CJ, Hastings ME, Williams SJ, Poppe LJ (2005) usSEABED: Atlantic coast offshore surficial sediment data release: U.S. Geological Survey Data Series 118, version 1.0. Online at http://pubs.usgs.gov/ds/2005/118/

Ryan JP, Yoder JA, Cornillon PC (1999) Enhanced chlorophyll at the shelfbreak of the Mid-Atlantic Bight and Georges Bank during the spring transition. Limnol Oceanogr 44:1–11

Schofield O, Chant RB, Cahill RC, Gong D and others (2008) The decadal view of the Mid-Atlantic Bight from the COOLroom: Is our coastal system changing? Oceanography 21:108–117

Secor DH, Kerr LA, Cadrin SX (2009) Connectivity effects on productivity, stability, and persistence in a herring metapopulation model. ICES J Mar Sci 66:1726–1732

Simpson JH (1981) The shelf fronts: implications of their existence and behaviour. Philos Trans R Soc A 302: 531–546

Simpson JH, Bowers D (1981) Models of stratification and frontal movement in shelf seas. Deep-Sea Res A 28: 727–738

Slacum HW, Istad JH, Weber ED, Richkus WA, Diaz RJ, Tallent CO (2008) The value of applying commercial fishers experience to designed surveys for identifying characteristics of essential fish habitat for adult summer flounder. North Am J Fish Manage 28:710–721

Smith B, Link J (2010) The trophic dynamics of 50 finfish and 2 squid species on the Northeast US continental shelf. NOAA Tech Memo NMFS-NE-216

Staudinger MD (2006) Seasonal and size-based predation on two species of squid by four fish predators on the Northwest Atlantic continental shelf. Fish Bull 104: 605–615

Staudinger MD, Juanes F (2010) A size-based approach to quantifying predation on longfin inshore squid *Loligo pealeii* in the northwest Atlantic. Mar Ecol Prog Ser 399: 225–241

Stehlik LL (2007) Essential fish habitat source document: Spiny dogfish, *Squalus acanthias*, life history and habitat characteristics, 2nd edn. NOAA Tech Mem NMFS-NE-203

Stehlik LL (2009) Effects of seasonal change on activity rhythms and swimming behavior of age-0 bluefish (*Pomatomus saltatrix*) and a description of gliding behavior. Fish Bull 107:1–12

Stoner AW, Manderson JP, Pessutti J (2001) Spatially–explicit analysis of estuarine habitat for juvenile winter flounder (*Pseudopleuronectes americanus*): combining generalized additive models and geographic information systems. Mar Ecol Prog Ser 213:253–271

Stoner AW, Spencer ML, Ryer CH (2007) Flatfish–habitat associations in Alaska nursery grounds: use of continuous video records for multi-scale spatial analysis. J Sea Res 57:137–150

Tian RC, Chen C, Stokesbury KDE, Rothschild B and others (2009) Modeling the connectivity between sea scallop populations in the Middle Atlantic Bight and over Georges Bank. Mar Ecol Prog Ser 380:147–160

Tilburg CE, Dittel AI, Epifanio CE (2009) High concentrations of blue crab (*Callinectes sapidus*) larvae along the offshore edge of a coastal current: effects of convergent circulation. Fish Oceanogr 18:135–146

Torres LG, Read AJ, Halpin P (2008) Fine-scale habitat modeling of a top marine predator: Do prey data improve predictive capacity? Ecol Appl 18:1702–1717

Valavanis V, Pierce G, Zuur A, Palialexis A, Saveliev A, Katara I, Wang J (2008) Modeling of essential fish habitat based on remote sensing, spatial analysis and GIS. Hydrobiologia 612:5–20

Watson JR, Hays CG, Raimondi PT, Mitarai S and others (2011) Currents connecting communities: nearshore community similarity and ocean circulation. Ecology 92:

1193–1200

Wood S (2006) Generalized Additive Models: an introduction with R. Chapman & Hall, Boca Raton, FL

Worm B, Hilborn R, Baum JK, Branch TA and others (2009) Rebuilding global fisheries. Science 325:578–585

Yamamoto T, Nishizawa S (1986) Small-scale zooplankton aggregations at the front of a Kuroshio warm-core ring. Deep-Sea Res A 33:1729–1740

Zainuddin M, Katsuya S, Saitoh SI (2008) Albacore (*Thunnus alalunga*) fishing ground in relation to oceanographic conditions in the western North Pacific Ocean using remotely sensed satellite data. Fish Oceanogr 17: 61–73

Zhang W, Wilkin JL, Chant RJ (2009) Modeling the pathways and mean dynamics of river plume dispersal in the New York Bight. J Phys Oceanogr 39:1167–1183

Zhang WG, Wilkin JL, Arango HG (2010a) Towards an integrated observation and modeling system in the New York Bight using variational methods. Part I: 4DVAR data assimilation. Ocean Model 35:119–133

Zhang WG, Wilkin JL, Levin JC (2010b) Towards an integrated observation and modeling system in the New York Bight using variational methods. Part II: Repressenter-based observing strategy evaluation. Ocean Model 35:134–145

Zhang WG, Wilkin JL, Schofield OM (2010c) Simulation of water age and residence time in New York Bight. J Phys Oceanogr 40:965–982

Žydelis R, Lewison, RL, Shaffer SA, Moore JE and others (2011) Dynamic habitat models: using telemetry data to project fisheries bycatch. Proc R Soc B doi:10.1098/rspb.2011.0330

Editorial responsibility: Kenneth Sherman, Narragansett, Rhode Island, USA

Submitted: January 17, 2011; Accepted: July 19, 2011
Proofs received from author(s): September 15, 2011

Continental Shelf Research ▮ (▮▮▮▮) ▮▮▮–▮▮▮

Contents lists available at ScienceDirect

Continental Shelf Research

journal homepage: www.elsevier.com/locate/csr

Research Papers

Seasonal variability of chlorophyll a in the Mid-Atlantic Bight

Yi Xu [a], Robert Chant [a], Donglai Gong [a], Renato Castelao [b], Scott Glenn [a], Oscar Schofield [a,*]

[a] Coastal Ocean Observation Lab, Institute of Marine and Coastal Sciences, School of Environmental and Biological Sciences, Rutgers University, New Brunswick, NJ, 08901, USA
[b] Department of Marine Science, University of Georgia, Athens, GA, 30602, USA

ARTICLE INFO

Article history:
Received 9 June 2010
Received in revised form
13 May 2011
Accepted 31 May 2011

Keywords:
Ocean color
Phytoplankton
Mid-Atlantic Bight

ABSTRACT

For this manuscript we use a 9-year time series of Sea-viewing Wide Field of view Sensor (SeaWiFS), HF radar, and Webb Glider data to assess the physical forcing of the seasonal and inter-annual variability of the spatial distribution in phytoplankton. Using Empirical Orthogonal Function (EOF) analysis, based on 4-day average chlorophyll composites, we characterized the two major periods of enhanced chlorophyll biomass for the MAB in the fall–winter and the spring. Monthly averaged data showed a recurrent chlorophyll biomass in the fall–winter months, which represented 58% of the annual surface chlorophyll for the MAB. The first EOF mode explained $\sim$33% of the chlorophyll variance and was associated with the enhanced phytoplankton biomass in the fall–winter found between the 20 and 60 m isobaths. Variability in the magnitude of the enhanced chlorophyll in fall–winter was associated with buoyant plumes and the frequency of storms. The second EOF mode accounted for 8% of the variance and was associated with the spring time enhancements in chlorophyll at the shelf-break/slope (water depths greater than 80 m), which was influenced by factors determining the overall water column stability. Therefore the timing and the inter-annual magnitude of both events are regulated by factors influencing the stability of the water column, which determines the degree that phytoplankton are light-limited. Decadal changes observed in atmospheric forcing and ocean conditions on the MAB have the potential to influence these phytoplankton dynamics.

1. Introduction

The Mid-Atlantic Bight (MAB) is a biologically productive continental shelf that is characterized by consistently high chlorophyll biomass (>1 mg chlorophyll m^{-3}), which supports a diverse food web that includes abundant fin and shellfish populations (Yoder et al., 2001). The MAB's shelf extends out for several hundred kilometers and the associated water mass is bounded offshore by the shelf-break front. While the shelf-break front is often near the geological shelf-break, the surface outcrop of the front can extend beyond the continental slope (Wirick, 1994). In the nearshore regions there are numerous inputs from moderately sized, yet heavily urbanized, rivers (Hudson River and Delaware River), which are sources of fresh water, nutrients, and organic carbon to the MAB (O'Reilly and Busch, 1984). The waters on the MAB exhibit considerable seasonal and inter-annual variability in temperature and salinity (Mountain, 2003). In late spring and early summer, a strong thermocline (water temperatures can span from 30 to 8 °C in <5 m) develops at about the 20 m depth across the entire shelf, isolating a continuous mid-shelf "cold pool" (formed in winter months) that extends from Nantucket to Cape Hatteras (Houghton et al., 1982; Biscaye et al., 1994). The cold pool persists throughout the summer until fall when the water column overturns and mixes in the fall (Houghton et al., 1982), which presumably replenishes nutrients to the surface waters on the MAB shelf. Thermal stratification re-develops in spring as the frequency of winter storms decrease and surface heat flux increases (Lentz et al., 2003).

In temperate seas, seasonal phytoplankton variability has been related to stratification, destratification, and incident solar irradiance (Cushing, 1975; Longhurst, 1998; Dutkiewicz et al., 2001; Ueyama and Monger, 2005). During late winter and early spring, increasing solar illumination combined with decreasing wind result in shallower surface mixed layers, which allows for increased phytoplankton growth prior to the development of the thermal stratification (Stramska and Dickey, 1994; Townsend et al., 1994). As the physical regulation of water column turnover is spatially variable along the MAB, the temporal patterns in phytoplankton biomass are not always spatially coherent within the East Coast shelf/slope ecosystem (Yoder et al., 2001). While it has long been appreciated that seasonal phytoplankton blooms are important in shelf and slope waters of the MAB (Riley, 1946, 1947; Ryther and Yentsch, 1958), a 7.5-year (October 1978–July 1986) time series of the coastal zone color scanner (CZCS) imagery found that the maximum chlorophyll concentration appeared during

* Corresponding author. Tel.: +1 732 932 6555; fax: +1 732 932 8578.
E-mail address: oscar@marine.rutgers.edu (O. Schofield).

0278-4343/$ - see front matter © 2011 Elsevier Ltd. All rights reserved.
doi:10.1016/j.csr.2011.05.019

fall–winter on the continental shelf waters and that slope waters possessed a secondary spring peak in addition to the a fall–winter bloom (Yoder et al., 2001). Ryan et al. (1999) used CZCS imagery from 1979 to 1986 and found an annual enhancement of chlorophyll at the shelf-break of the MAB and Georges Bank during the spring transition from well-mixed to stratified conditions. The shelf-edge system was similar to inner shelf waters in terms of seasonal heating and cooling; however, meanders at the shelf slope were associated with iso-pycnal upwelling that supplied nutrients to the euphotic zone and enhanced chlorophyll biomass (Ryan et al., 1999). Despite past efforts, understanding what regulates the magnitude of these seasonal patterns remains an open question, which is especially important as the MAB has experienced significant changes in water properties over the last few decades (Mountain, 2003).

Many factors are known to regulate the upper mixed layer dynamics on the MAB. These features include wind driven mixing (Beardsley et al., 1985) as well as surface buoyant plumes that frequently extend over significant fractions of the MAB shelf (Castelao et al., 2008a; Chant et al., 2008a). These features are superimposed upon the seasonal warming that drives the stratification of the MAB. This seasonality of shelf stratification regulates the phasing and potential magnitude of the fall–winter and spring enhancements in chlorophyll concentration. For this manuscript we use a 9-year time series of Sea-viewing Wide Field of view Sensor (SeaWiFS), HF radar, and Webb Glider data to assess the physical forcing of the seasonal and inter-annual variability of the spatial distribution in phytoplankton.

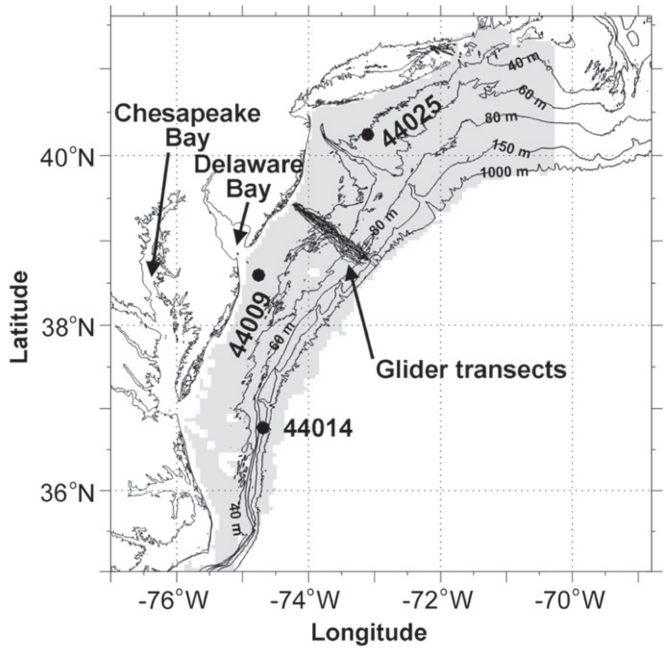

Fig. 1. Map showing study area, NDBC mooring stations, and glider tracks. Topographic contours shown are 40, 60, 80, 150, and 1000 m. Gray shaded area indicates region where SeaWiFS imagery was analyzed.

2. Methods

2.1. Ocean color remote sensing data

Time series of surface chlorophyll concentration in the MAB was studied using 4-day averaged composites of SeaWiFS satellite imagery collected from January 1998 to December 2006. We used 4-day average composites as they provided reasonable coverage for our study site and could resolve the dynamics of the chlorophyll over both seasonal and higher frequency scales (days to weeks) often observed in MAB. The 4-day average decreased the cloud contamination that heavily degraded the utility of the 1-day images. Many phytoplankton bloom events occur over time scales much shorter than a month in these waters. For example chlorophyll associated with buoyant plume events can last for the time scale of 4–5 days (Schofield et al., submitted for publication) and summer upwelling on average lasts for <7 days in the MAB (Glenn et al., 2004). Longer term averaging underemphasizes these shorter-lived phytoplankton bloom events that can explain up to 44% of the variability observed in daily satellite imagery (Yoder et al., 2001). The spatial resolution of the original images were 1.1 km, however, data were re-gridded to 5.5 km in order to identify the principal modes of variability in the data set by Empirical Orthogonal Function (EOF) analysis. Given the high spatial heterogeneity in the nearshore waters and the increasing error in satellite estimates of chlorophyll in shallow waters, we excluded regions with water depths shallower than 10 m for this analysis. We also excluded data for water depths deeper than 2000 m, as our focus was on the shelf and shelf-break region. Finally we excluded data from large inland Bays (Long Island Sound, Delaware Bay and Chesapeake Bay; Fig. 1). Monthly chlorophyll concentration was calculated by taking the geometric mean at each pixel. We chose to use the geometric rather than the arithmetic mean because the distribution of chlorophyll measurements in continental shelf and slope waters is approximated by a log–normal distribution (Campbell, 1995; Yoder et al., 2001).

Ocean color satellite remote sensing has limitations in coastal waters. Satellite coverage is limited by cloud cover especially in the winter months, which is characterized by frequent storms. Storms also can produce buoyant plumes that contain significant amounts of sediment and colored dissolved organic matter. The presence sediment and CDOM can influence the accuracy of the satellite-derived estimates of chlorophyll that can result in errors as large as 50–100% in the nearshore waters of the northeast United States (Harding et al., 2004). Finally, ocean color remote sensing does not provide information on subsurface phytoplankton peaks, below the detection limit of the satellite, which are often present in the MAB. While we acknowledge these shortcomings, satellite estimates of chlorophyll remains one of the only techniques that can provide decadal spatial time series over ecologically relevant scales.

We also calculated the monthly climatological sea surface temperature (SST) for each pixel based on 4-day averaged Advanced Very High-Resolution Radiometer (AVHRR) data sets from 1999 to 2006. The AVHRR data sets were collected by a satellite dish maintained by Rutgers University Coastal Ocean Observation Lab and processed using SeaSpace AVHRR processing software. Monthly SeaWiFS Level 3 photosynthetically available radiation (PAR) data from 1998 to 2006 were downloaded from http://oceancolor.gsfc.nasa.gov. The PAR data sets have the resolution of 9 km and the climatology of PAR was calculated based on the 9-year monthly data sets.

The mean satellite-derived chlorophyll fields were used as inputs to the Hydrolight 4.3 radiative transfer model (Mobley, 1994) to estimate the depth of the 1% light levels. For the Hydrolight simulations, we used default settings and assumed a constant backscatter to total scatter ratio of 0.05 based on data collected in this region (Moline et al., 2008). We assumed there was no inelastic scattering and kept wind speeds at zero. The surface flux of light was calculated using a semi-empirical sky model (Mobley, 1994) for the MAB at local noon on a cloudless day. We assumed that water column was infinitely deep. These Hydrolight simulations assumed no vertical structure in the phytoplankton biomass. We used this approach even though during the stratified season there can be subsurface chlorophyll layers however, satellite-derived chlorophyll estimates were used as the input to the Hydrolight simulation and these estimates are exponentially weighted to the surface waters (Mobley, 1994); therefore it is unlikely that satellite estimates included any significant proportion of the subsurface populations found at the base of the pycnocline in the late spring and summer months. Given this we did not impose a vertical structure for chlorophyll. For these simulations we treated the MAB as Case I waters (Johnson et al., 2003). This assumption is sometimes not the case when the Hudson River carries significant amounts of detritus and colored dissolved organic matter (CDOM) offshore onto the MAB (Johnson et al., 2003). Despite the optical complexity of these waters, SeaWiFS can accurately and reliably capture seasonal and inter-annual variability of chlorophyll a associated with variations of fresh water flow (Harding et al., 2004), which can increase chlorophyll biomass by an order of magnitude. To assess the impact of Case II conditions on our Hydrolight estimates of the 1% light depth, we used optical data collected as part of the LaTTE experiment (Chant et al., 2008b), which in part focused on characterizing the optical properties of the Hudson River waters being transported out onto the MAB (Moline et al., 2008). During the LaTTE experiment, data were collected from the Hudson River outflow over time with a WETLabs, Inc. absorption/attenuation meter using the methods outlined in Schofield et al. (2004). The waters were influenced by the Hudson River, which was characterized by significant contributions of chlorophyll and CDOM providing Case II waters. These measurements of the optical properties were inputted into the Hydrolight model to provide an estimate for light propagation in the Case II characteristics for MAB waters.

2.2. Winds and surface current observations

Wind data were obtained from moored buoys deployed by the National Data Buoy Center (NDBC) (http://www.ndbc.noaa.gov/maps/Northeast.shtml). We used data collected by mooring 44025 (Fig. 1) located at 40.25°N, 73.17°W with a water depth of 36 m and mooring 44014 (Fig. 1) located at 36.61°N, 74.84°W with a water depth of 48 m. The reason we chose these two moorings was because 44025 was located at the mid-shelf region while 44014 was located at shelf-break/slope region. We used the daily wind speed data to calculate the stormy frequency. The wind data used for calculating the correlation coefficient between the surface currents measured by CODAR and wind speed were based on the time series of the 6 years (2002–2007) wind measured at NDBC 44009 (Fig. 1) located at 38.46°N, 74.70°W with a water depth of 28 m. We used this mooring as it was central to a recently completed long-term analysis of the circulation on the MAB (Gong et al., 2010). The wind data for 44009 were decomposed into along-shelf and cross-shelf directions (30 degree rotation) and low-passed with a 33-hour filter. Shore-based High Frequency (HF) radar systems were used for surface current measurements. The radar network was a fully nested array of surface current mapping radars (Kohut and Glenn, 2003; Kohut et al., 2004). Hourly surface currents were measured with an array of CODAR HF Radar systems consisting of 6 long-range (5 MHz) and 2 high-resolution (25 MHz) backscatter systems from the start of 2002 to the end of 2007. For all systems measured beam patterns were used in surface current estimates (Kohut and Glenn, 2003). Details of HF radar development and theory can be found in Crombie (1955), Barrick (1972), Stewart and Joy (1974), Barrick et al. (1977). All CODAR surface currents were de-tided using the T_TIDE Matlab package (Pawlowicz et al., 2002) before further analysis is performed. The averaged seasonal surface current responses for the dominant winds were calculated for the well-mixed winter (December–March), the transitional seasons (April–May, October–November), and stratified summer (June–September; Gong et al., 2010).

2.3. River discharge and glider data

The monthly river discharge data were downloaded from http://nwis.waterdata.usgs.gov/nwis. The total river discharge into to the MAB was represented by the sum of the discharges from Mohawk River at Cohoes, NY (42.79°N, 73.71°W), Passaic River at Little Falls, NJ (40.89°N, 74.23°W), Raritan River below Calco Dam at Bound Brook, NJ (40.55°N, 74.55°W), Hudson River at Fort Edward, NY (43.27°N, 73.60°W), and Delaware River at Trenton, NJ (40.22°N, 74.78°W).

Webb Slocum gliders were used to obtain subsurface measurements over the shelf. The Webb gliders occupy a cross-shore transect across the MAB beginning in 2005 (Schofield et al., 2007); however, the coverage in each month is not always complete. The cross-shelf transects typically take on average 4–5 days and are appropriate for comparing to the 4-day averaged satellite imagery. The cross-shore transect typically spans the 15–100 m isobaths (Fig. 1). The gliders were outfitted with CTDs (Sea-Bird Electronics, Inc.) and occasionally with optical backscatter sensors (WETLabs, Inc.). For this effort we were able to utilize the data collected from 19 cross-shore transects; however, the coverage was not uniform over the year. There were 7 transects available during the fall and winter; however, many of the early transects consisted of a glider that was not outfitted with a fluorometer or a backscatter sensor. Only 2 of 7 transects in fall and winter had any optical sensors present on board. Unfortunately no fluorometry data is available for the winter season and only one transect had only partial data of optical backscatter. There were twelve transects that were available for both the spring and summer and all the gliders were outfitted with optical backscatter and chlorophyll fluorometers. We compared individual transects and to specific satellite imagery and also averaged the glider observations (Castelao et al., 2008b). While the glider data were sparser than the satellite and CODAR data, it represented the densest concurrent subsurface data available for the MAB.

2.4. EOF and cluster analysis

EOF analysis is the mapping of the multi-dimensional data sets onto a series of orthonormal functions and is useful in compressing the spatial and temporal variability of large data sets down to the most energetic and coherent statistical modes. EOF results can be quite informative; however, they do not necessarily demonstrate causality and should be interpreted with caution. This method was first applied by Lorenz (1956) to develop the technique for statistical weather prediction. These approaches have been extremely useful for analyzing ocean color images, which have long time series and significant spatial variability (Baldacci et al., 2001; Yoder et al., 2001; Brickley and Thomas, 2004; Navarro and Ruiz, 2006). As EOF requires data sets without spatial gaps, we only used images that had less than 20% of pixels removed because of clouds. Additionally, prior to performing EOF analysis, any gaps in the data, due to clouds, were replaced by the average of the surrounding 8 non-cloud pixels. Using the criteria of less than 20% cloud cover, our final data set resulted in total of 468 4-day composites images with sufficient temporal resolution to resolve short-lived chlorophyll events. The numbers of images in each month used in the EOF analysis are presented in Fig. 2. EOF analysis was performed after subtracting the temporal mean of each pixel over the entire time series.

Additionally, we analyzed the chlorophyll variability using a cluster analysis. This was used to access to what degree the different

Please cite this article as: Xu, Y., et al., Seasonal variability of chlorophyll a in the Mid-Atlantic Bight. Continental Shelf Research (2011), doi:10.1016/j.csr.2011.05.019

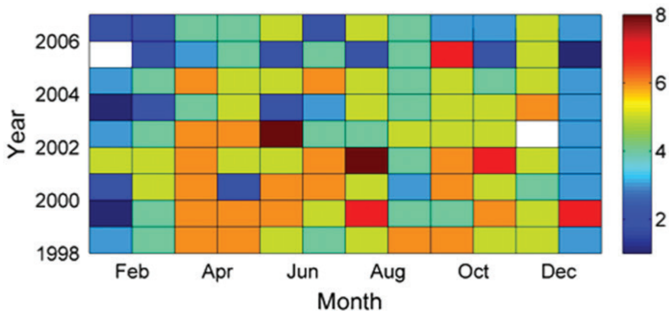

Fig. 2. Number of images used each month for the entire time series of 4-day chlorophyll composites.

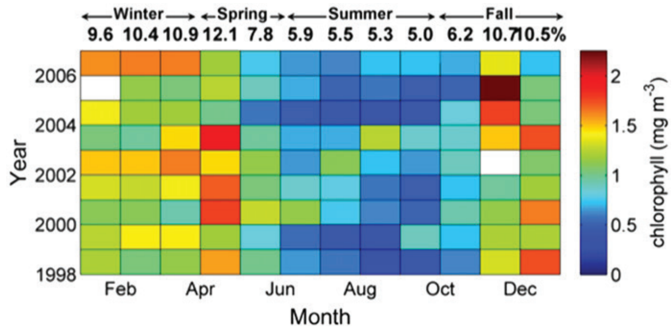

Fig. 3. Monthly mean chlorophyll (mg m^{-3}) from January 1998 to December 2006 for MAB (shaded gray area in Fig. 1). The numbers on the top indicate the relative percentage of annual mean chlorophyll associated for each month.

environmental conditions were associated with the chlorophyll concentrations over the 9-year data sets. Cluster analysis was carried out using Ward's method to minimize the sum of the squares of any two hypothetical clusters that can be formed at each step (Ward, 1963) in order to emphasize the homogeneous nature of each cluster. The cluster analysis was conducted using storm frequency, maximum chlorophyll concentration and mean river discharge during winter time (Dec.–Jan.) and carried out in SAS 9.1. The cluster analysis was complemented with regression analysis based on storm frequency, maximum chlorophyll concentration and mean river discharge.

3. Results

3.1. Seasonal cycle

For the MAB (shaded gray area in Fig. 1), the spatially averaged monthly chlorophyll concentration revealed an annual cycle characterized by high values during fall–winter months (October–March), which decreased until it reached lowest values during the highly stratified summer months (Fig. 3). The integrated chlorophyll from October to March represented 58% of the annual chlorophyll. The fall–winter peak in chlorophyll began in the late fall and it persisted throughout the winter into early spring of the next year. The enhanced phytoplankton biomass in the fall–winter was most obvious in 2005 when there were high chlorophyll concentrations in November, which remained high until March 2006. There was significant inter-annual variability in the magnitude of the fall–winter events, for example in 2002–2003 the fall–winter chlorophyll biomass was not as elevated as in the other years of this study.

The significance of the EOF modes for the spatial and temporal variability in chlorophyll was tested following methods described by North et al. (1982). The error produced in the EOF due to the finite number of images was $\delta\lambda \approx \lambda(2/n)^{1/2}$, where λ is the eigenvalue and n is the degree of freedom. Only the first two modes were found significant. Spatial coefficients are presented in Fig. 4A and C. The color of the coefficient is directly related to the amplitude of the spatial coefficient. Temporal amplitudes of the EOF modes are presented in Fig. 5A. Therefore, the combination of the spatial and temporal variability can be obtained multiplying the spatial coefficient by the temporal amplitude. In our case, the first mode (Fig. 4A) explained 33% of the total variance, and was related with the seasonal enhanced chlorophyll in the fall–winter. It explained most of the variance between the 20 and 60 m isobaths. All the spatial coefficients were positive with the maxima found nearshore and decreasing offshore. Consequently, when they were multiplied by positive temporal amplitudes the whole field increased with respect to the chlorophyll climatology. The temporal amplitude with a 4-day interval showed high values in the fall–winter almost every year. Sometimes, there was a small increase of temporal amplitude in summer when the overall chlorophyll concentration was low (<1 mg m^{-3} Chl) except for the nearshore waters (<30 m water depth) where summer upwelling is common (Glenn et al., 2004). The spatial and temporal coefficients suggested that in the middle and outer shelf the fall–winter enhanced chlorophyll was dominant.

The satellite-derived EOF Mode 1 was consistent with the available glider observations (Fig. 6). The average sections for salinity (Fig. 6A), temperature (Fig. 6B), and optical backscatter (Fig. 6C) for the winter season showed very little vertical structure, although there was a significant cross-shore gradient. Salinity increased with distance offshore with highest values beyond 60 km from shore (Fig. 6A). Associated with the inshore lower saline waters were optical backscatter values that were 4–5 fold higher than those found in the offshore waters. The cross-shore extent of high backscatter values corresponded to the boundaries of satellite EOF Mode 1 (near 60 m isobaths) along the glider transects; however it should be noted that the optical backscatter measurements are also sensitive to the presence of sediments and plankton; however the lack of vertical structure in the glider optical data suggests that the winter satellite chlorophyll estimates are not biased by the subsurface layering in the phytoplankton populations.

The second EOF mode (Fig. 4C) explained 8% of the normalized variance and the spatial variability in mode 2 identified two different zones. The first zone had negative spatial coefficients and was located in the coastal areas within the 60 m isobath. The second zone had positive spatial coefficients located between the 80 and 150 m isobaths and extended to the MAB shelf-break front (Linder and Gawarkiewicz, 1998). Given this, the second mode applied to depths greater than 80 m and explained up to 32% of the chlorophyll local variance at those locations (Fig. 4D). The amplitude time series of the second EOF mode (Fig. 5B) generally showed positive values during spring, so when multiplied by positive spatial coefficients (yellow and red region in Fig. 4C) the whole field indicated an increase in the chlorophyll concentration over the shelf-break/slope during spring. Vice versa, the negative amplitudes multiplied by negative spatial coefficients (dark blue region in Fig. 4C) indicated that chlorophyll concentration increased such as seen in New Jersey and Long Island coastal areas during the summer months in 2001 and 2002. The increases of chlorophyll concentration in the shallow coastal area during summer might be correlated with upwelling events. Our results confirm the conclusion by Glenn et al. (2004) that the coastal regions of New Jersey in the summer of 2001 had one of the most significant upwelling events over the 9-year records (1993–2001; Moline et al., 2004), which resulted in high phytoplankton biomass. Mode 2 also exhibited enhanced chlorophyll in the fall both on the shelf and over the continental slope. The spring glider observations did exhibit

Please cite this article as: Xu, Y., et al., Seasonal variability of chlorophyll a in the Mid-Atlantic Bight. Continental Shelf Research (2011), doi:10.1016/j.csr.2011.05.019

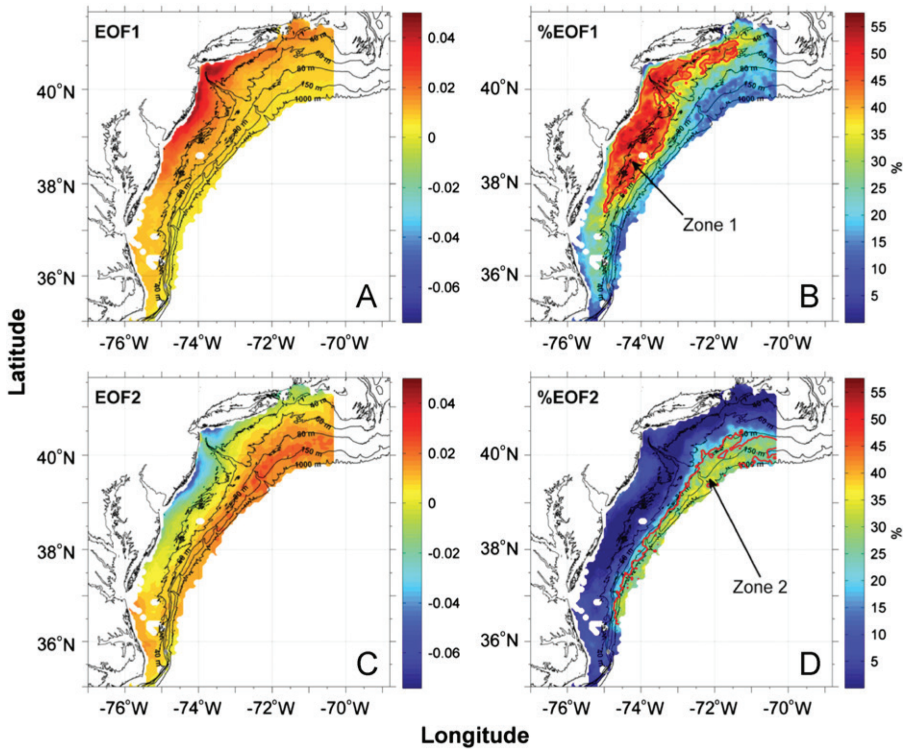

Fig. 4. The EOF modes for chlorophyll in MAB. Left panels are the first two EOF modes, right panels are percentage of the local variance explained by each mode.

enhanced particle concentrations (as detected by the optical backscatter data), both in nearshore (shallower than 30 m) and offshore (deeper than 80 m) waters (Fig. 6C, bottom panel). The enhanced particle concentrations in offshore waters were detectable during the spring, consistent with the EOF mode 2 measured by satellite. In contrast to the winter months, the spring optical data showed significant vertical heterogeneity, with the highest values found at depth. The enhanced backscatter values have been related to storm/wave/tidally driven resuspension processes (Glenn et al., 2008). The enhanced sea surface optical backscatter was associated with increased water column salinity. Low salinity water consistently had higher backscatter values in the surface (Fig. 6A, C, bottom panel).

The chlorophyll climatology in the MAB was analyzed for the two spatial zones delineated by the EOF analysis. The middle and outer shelf region (Zone 1 enclosed in Fig. 4B where the local variance were larger than 40%) identified by the first EOF mode showed mean chlorophyll concentration that ranged between 1.3 and 2.3 mg m^{-3} with highest values observed in fall–winter, and lowest values observed during summer (Fig. 7A, dotted thin line). The highest chlorophyll values were inversely related to the seasonal cycle of PAR and SST, which were highest in June and August respectively. There was a two-month phase lag between PAR and SST. The measured PAR values would lead to light limitation in phytoplankton photosynthesis based on the available photosynthesis-irradiance measurements.

Six years of surface HF radar current data showed that during winter the mean surface flow on the New Jersey shelf was generally offshore and down-shelf (Fig. 8A). Based on wind data from NDBC moored buoy 44009, winter was characterized by strong northwest winds, which we define as a mean velocity of 9.1 m s^{-1} and occur 39% of the time (Gong et al., 2010). Based on the extensive spatial and temporal analysis conducted by Gong et al. (2010), we analyzed the correlations between winds and surface transport during the winter. The cross-shelf wind and cross-shelf surface currents had strong correlations ($R^2 > 0.7$) during the late fall and winter (Fig. 7A, black bold line). Since winds were predominantly from the northwest in winter, cross-shelf flow was observed during this time (Fig. 8A, Gong et al., 2010). The strong northwest winds thus increased the transport of inner shelf fresh and nutrient rich water across the middle of the shelf (Gong et al., 2010). As this occurred when chlorophyll concentrations were high (Fig. 7A, thin line with dot), we hypothesize that the cross-shelf transport of fresh water induced intermittent surface stable layer, that promoted phytoplankton growth. Moreover, the cross-shelf transport may carry coastal phytoplankton populations from the nearshore (<20 m depths) out across the areal extent of EOF zone 1. Therefore, the highest phytoplankton concentrations occurred when the cross-shelf currents were correlated with cross-shelf wind in the late fall and winter. Simulations using passive particle tracers support this interpretation (Gong et al., 2010).

The second EOF mode explained more than 25% of the variance at the shelf-break/slope region (zone 2 enclosed in Fig. 4D). The spatially averaged chlorophyll concentration in zone 2 exhibited a maximum chlorophyll concentration in spring that fluctuated between 0.3 and 1.5 mg m^{-3} over the year. Chlorophyll concentrations began to increase as PAR began to increase. The chlorophyll concentration began to decline as SST began to increase late in spring. The second peak of chlorophyll concentration appeared in fall with a peak of 0.9 mg m^{-3} as climatological means of PAR and SST began to decrease.

The six-year climatology of seasonal flow on the shelf during spring was mostly down-shelf towards the southwest (Fig. 8B). Northeast (along-shelf) winds were more common in spring and fall. The response of surface flow under northeast winds was most energetic during the transition seasons (Gong et al., 2010). Therefore, the high correlation coefficient between along-shelf wind

Please cite this article as: Xu, Y., et al., Seasonal variability of chlorophyll a in the Mid-Atlantic Bight. Continental Shelf Research (2011), doi:10.1016/j.csr.2011.05.019

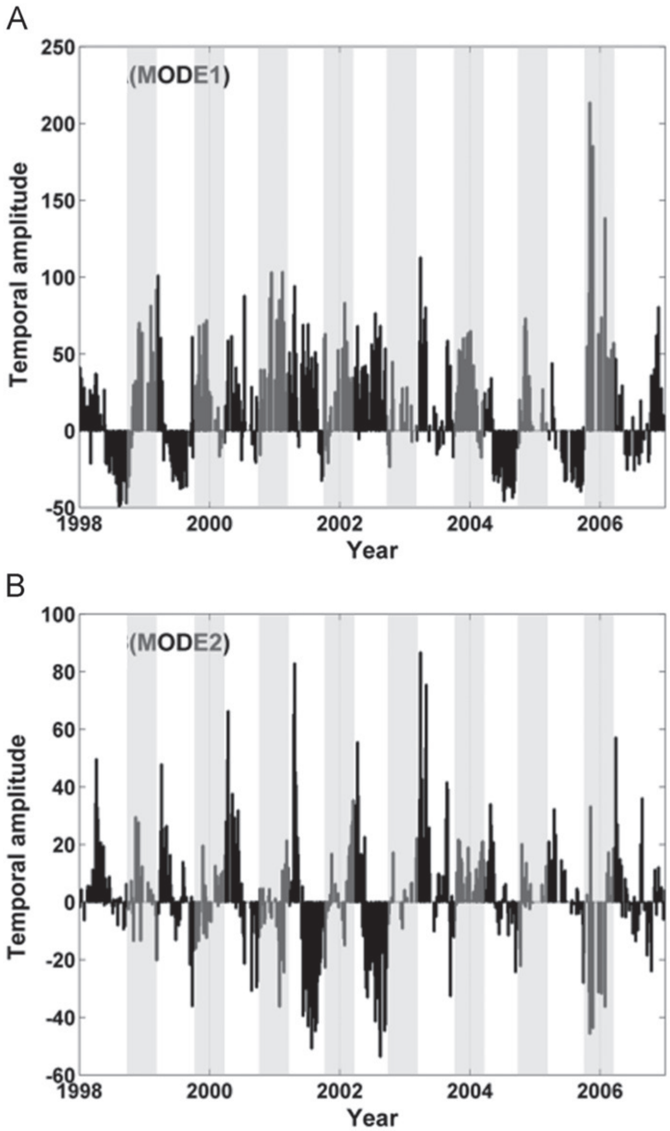

Fig. 5. Time series of the amplitude of the first two EOF modes. The gray transparent bars indicate the winter months.

and along-shelf current appeared during the transitional periods (April–May and October–November; Fig. 7B, black bold line), when the water column was stratifying in spring and as stratification was eroded in fall. The northerly winds potentially bring up shelf bottom boundary layer water through shelf-break upwelling, which is a source of nutrients and could contribute to enhanced chlorophyll in spring and fall (Siedlecki et al., 2008).

In EOF zone 2, there was another small peak of chlorophyll concentration during strongly stratified month of August. Phytoplankton growth earlier in the season would have depleted the nutrients in this region. Potentially onwelling along the slope, due to prevailing southerly wind, might have provided a source of nutrients (Siedlecki et al., 2008).

3.2. *Mechanisms underlying the inter-annual chlorophyll variability*

Over the 9-year time series, the magnitude of the enhanced chlorophyll in the fall–winter varied between 1.9 and 5.2 mg chl a m^{-3} (Fig. 9). One factor underlying the inter-annual variability was the presence of buoyant river plumes. In our data, the largest winter phytoplankton event occurred in 2006 and was associated with sustained high river discharge through the winter (Fig. 9). While precipitation that year was normal, it was a warm winter and runoff was high as ice and snow formation was low. The 2006 river discharge event was observed by a Webb glider as a mid-shelf low salinity plume (as indicated by declines of 2 salinity units) in the upper mixed layer (Fig. 10B). The January 2006 winter plume was also evident as enhanced chlorophyll biomass in the SeaWiFS chlorophyll 4-day composite image from January 25th to 28th (Fig. 10A). The river plume is often transported out onto and south across the MAB under northwest wind conditions (Chant et al., 2008b). The plume can promote phytoplankton growth by stabilizing the upper water column and by transporting chlorophyll rich water from the estuary out onto the outer shelf offshore (Malone et al., 1983; Cahill et al., 2008). Additionally the river transports CDOM and non-pigmented particulate matter that can also lead to a 50–100% overestimate of chlorophyll (Harding et al., 2004). This suggests that years of high river discharge have the most biased satellite imagery. In spite of the potential satellite bias, the large river plume in 2006 contributed to the winter bloom as the river also transports extremely high concentrations of phytoplankton (Moline et al., 2008). While 2006 was the most sustained winter river discharge event, there were significant fall–winter discharge events in 1998, 2004, and 2005, which were also associated with winter blooms (Fig. 9); however, there were two years (1999–2003) where no clear relationship between river discharge and winter bloom was found suggesting other factors are also important.

Another major factor influencing the inter-annual variability in the winter bloom magnitude was the frequency of storms. Storm-induced mixing lowers the irradiance available to the phytoplankton as cells are circulated deep in the water column. The role of the storms was difficult to study as storm periods are associated with heavy cloud cover. We measured storm frequency during the months of January and February using the NOAA moored buoy 44025 where a stormy day was defined as one when wind speeds exceeded 10 m s^{-1}. There was a significant inverse relationship between the percent of stormy days (storm) in the winter and maximum winter chlorophyll concentration (chl a; Fig. 11A): chl a$=4.34-0.05$ storm ($R^2=0.18$, $P=0.005$). In the winter, even small storms are able to induce significant mixing in the water column (Dickey and Williams., 2001; Glenn et al., 2008), which can increase overall light limitation of the phytoplankton populations. We hypothesize that the storm frequency and the river discharge are important to the winter phytoplankton as both impact the stability of the water column. Including winter river discharge in the estimation of the magnitude of the chlorophyll concentration improved the regression statistics (chl a$=4.04-0.05$ storm$+0.000309$ river ($R^2=0.21\%$, $P=0.02$)).

We performed a cluster analysis to explore the relationship between winter storm frequency, chlorophyll concentration and river discharge. Results from the ten years record clustered into two groups: one was 1998, 2000, 2003, 2004, and 2005; another was 1999, 2001, 2002, 2006, and 2007. As shown in Fig. 11A, these two clusters were separated at a winter storm frequency of 27%, which we hypothesize is the threshold where mixing is sustained to decrease overall seasonal winter phytoplankton concentrations.

The spring bloom occurred at the shelf-break/slope region. The spring bloom began in late March (mean start date was March 22nd) where we defined the start of the bloom as when the chlorophyll concentrations rise 5% above that year's annual median (Siegel et al., 2002). The initiation of the spring bloom was phased around 16 days after the onset of sea surface temperature warming on the MAB. This is consistent with the hypothesis that blooms begin as the water column stratifies and phytoplankton are maintained within the euphotic zone. Given this hypothesis, the

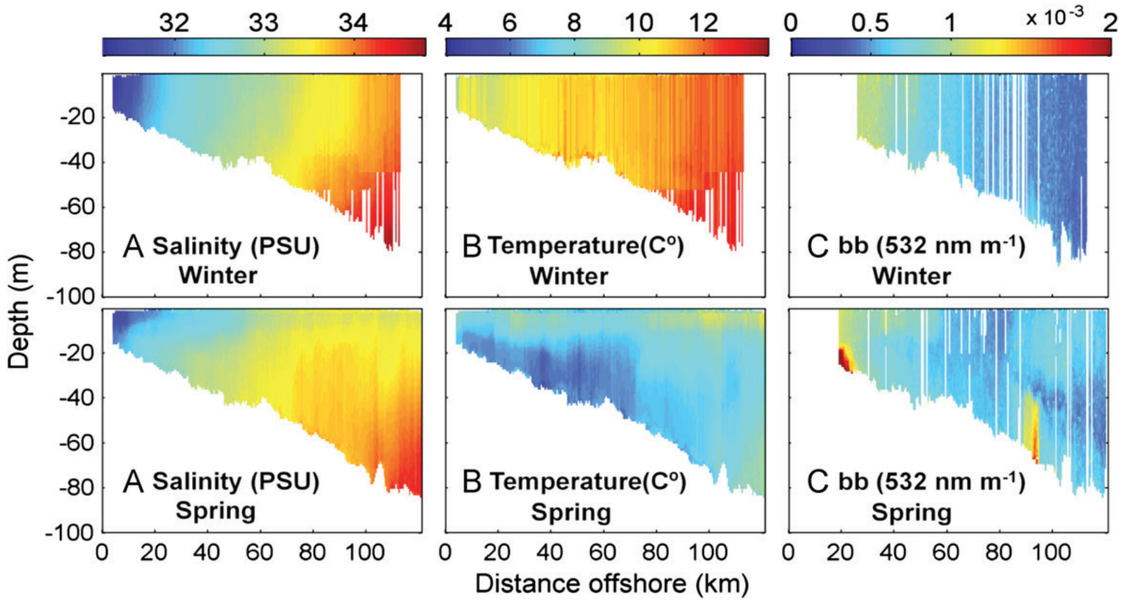

Fig. 6. Vertical sections of glider transect. Salinity (left), temperature (middle), and backscatter (right) collected along the Rutgers Glider Endurance line (see Fig. 1 for location; Schofield et al., 2007) during winter (top) and spring (bottom).

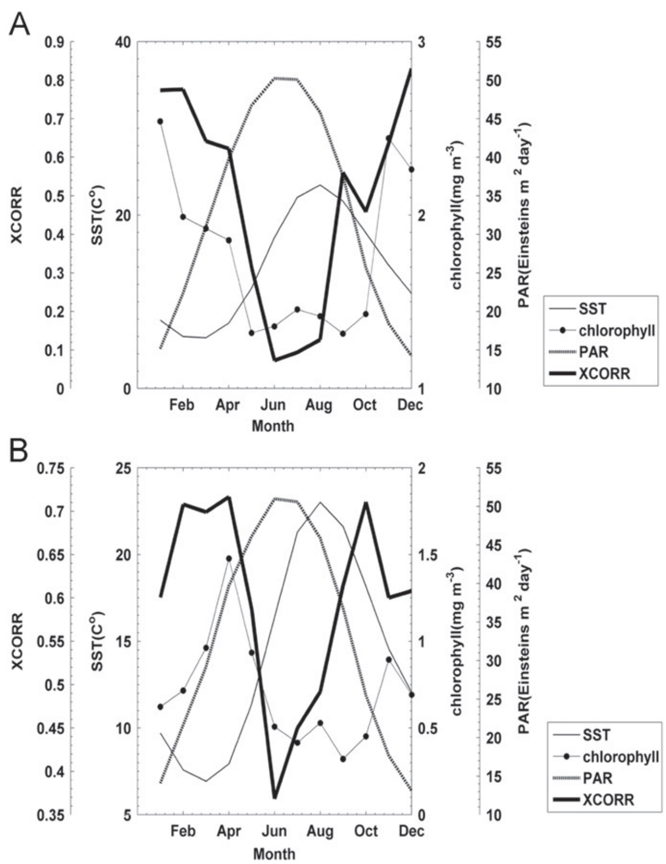

Fig. 7. Monthly climatology of SST (thin black line, °C), PAR (dash line, Einstein's m^{-2} day^{-1}) and chlorophyll (thin line with dot, mg m^{-3}) averaged over the two regions (zone 1 and zone 2 in Fig. 4) identified by the EOF analysis. Value averaged over zone 1 is shown on panel (A) together with correlation coefficient between cross-shelf wind and cross-shelf current (bold black line). Value averaged over zone 2 is shown on panel (B), together with correlation coefficient between along-shelf wind and along-shelf current. In both panels, correlation analysis used wind observations from NDBC 44009 station, and HF radar currents along the cross-shelf line, which is coincident with the glider endurance line (see Fig. 1 for location).

timing of the spring bloom should be sensitive to weather conditions in the early spring that can precondition the shelf's stratification rate. Additionally, the timing of bloom can be important to the magnitude of the spring bloom. If a bloom starts late, it may miss the 'window of opportunity' with optimum mixing and light conditions, resulting in a reduced bloom magnitude (Henson et al., 2006). Using all available data there was not a significant relationship between the magnitude of the spring bloom and number of stormy days in early spring (February–March); however, this was largely due to the spring 2003, which had a very high chlorophyll concentration despite moderate stormy conditions. Excluding 2003, there was a significant relationship (Chl a$=3.62-0.0745$ storm, $R^2=0.38$, $P=0.001$, Fig. 11B).

4. Discussion

Our 9-year of SeaWiFS chlorophyll data set showed two distinct zones for phytoplankton activity on the MAB. The middle and outer shelf region was associated with the recurrent winter phytoplankton blooms. The outer shelf-break/slope region was associated with the spring bloom. Although blooms in these two regions were separated in both space and time; however the magnitude of both blooms were both influenced by factors impacting water column stability.

Winter and spring phytoplankton blooms represent the major biological events in the MAB. The most recurrent and largest phytoplankton bloom occurs in winter (Ryan et al., 1999, 2001; Yoder et al., 1993, 2001, 2002), beginning in late fall and lasting through February. The winter bloom begins as the seasonal cooling erodes water column stratification, which results in the convective overturn of the water column. This process is accelerated by the passage of late fall storms (Glenn et al., 2008). The erosion of the stratification allows nutrient rich bottom waters to reach the surface alleviating nutrient limitation of phytoplankton within the euphotic zone. The spring bloom occurs on the outer shelf as seasonal warming begins to stabilize and stratify the water column. This is consistent with classical view advanced by Sverdrup (1953), and refined by Townsend et al. (1992) and

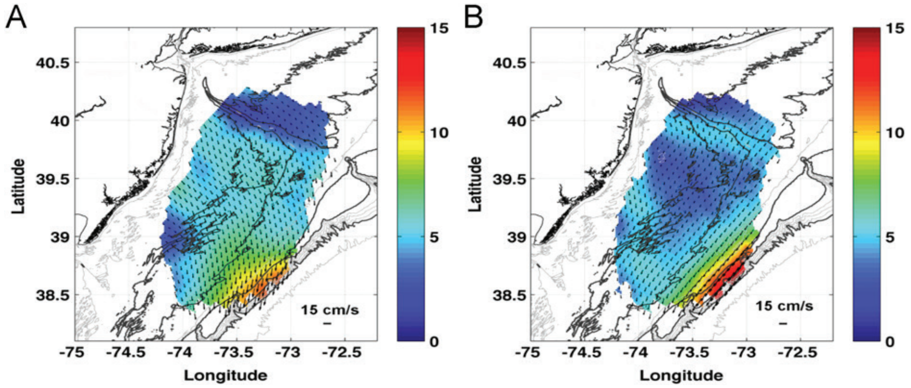

Fig. 8. Seasonal surface currents on the New Jersey Shelf (cm s^{-1}), vectors represent the current field and the color map is the magnitude of velocity: (A) Winter (December–February) (B) Spring (March–May).

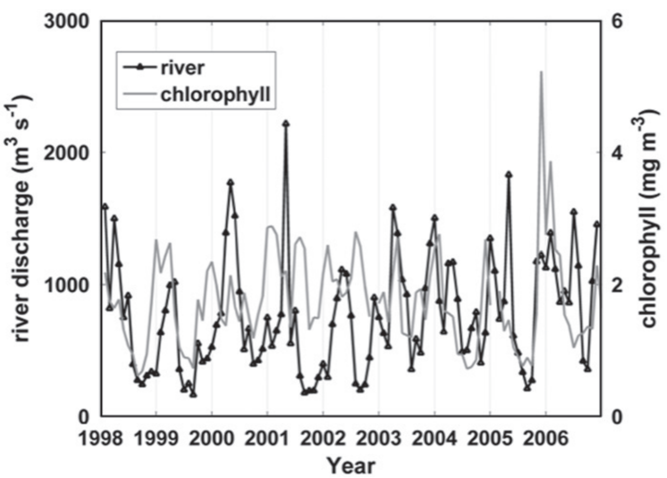

Fig. 9. Monthly and spatial averaged chlorophyll concentration (gray line) for area (zone 1 in Fig. 4(B)) depicted by the EOF mode 1 (mg m^{-3}). The triangle marked black line represents the monthly mean river discharge in $m^3\ s^{-1}$.

Huisman et al. (1999), that phytoplankton blooms are initiated in nutrient replete waters when vertical mixing rates are slow so that phytoplankton photosynthetic rates are sufficient to support significant phytoplankton growth. Thus light regulation is central to both the winter and spring phytoplankton blooms on the MAB.

The winter blooms over the middle and outer shelf spanned the 20–60 m isobath as delineated by EOF mode 1. We hypothesize that this depth range reflected the zone where a significant fraction of the water column had sufficient light to support phytoplankton growth. We used the satellite chlorophyll and the Hydrolight radiative transfer model to estimate the depth of the 1% light level for EOF mode 1 region. In the EOF mode 1 region, the mean water depth was 41 m and the calculated mean 1% light depth was close to 20 m; therefore 49% of the water column was above the 1% light levels (Table 1). This is significant as the winter blooms occur during the dimmest months of the year and incident light levels on the ocean surface are low. Even on the offshore side of the winter bloom at around 60 m a significant fraction of the water column resides above the 1% light level, which allows for significant photosynthesis (Falkowski and Raven, 2007). These calculations assume that the attenuation of light is only due to water and chlorophyll. In the MAB, especially when Hudson River water is present, there are other optical constituents (CDOM, detritus) that attenuate the light (Johnson et al., 2003). To assess the potential impact of the presence of Case II waters on the estimates of the 1% light depth, we combined the available optical measurements made in the Hudson River with Hydrolight. The turbidity of the Hudson River during the LaTTE experiment decreased as the water flowed offshore; therefore we calculated the impact for two scenarios. Scenario 1 was using data collected within the Hudson shelf valley where influence of Hudson River runoff was small. Scenario 2 was the offshore Hudson River, which represented turbid conditions within the Hudson River plume on the MAB. For these waters where river water was present, the depth 1% light level decreased to 10–20 m depending on the rivers turbidity; however despite the increase in turbidity 25–50% of the water column in EOF mode 1 would remain above the 1% light level (Table 1). Thus in winter, phytoplankton appears to have sufficient light to grow when storm activity remains below the critical threshold of mixing.

The spring bloom occurred further offshore than the winter bloom and extended inshore of the MAB into shelf-break/slope area. Climatological temperature and salinity observations generally placed the foot of the front at the 80 m isobaths (Wright, 1976); however, the front location can vary by as much as 20 km (Linder et al., 2004). Therefore, the shelf-break front can possibly affect the offshore extent of the winter bloom and generally coincides with offshore extent of the spring bloom. The shelf-break and slope area range from 200 to 681 m water depths and based upon the mean satellite measured chlorophyll the 1% light depth was 33 m. This euphotic zone represents 5–17% of water column. Therefore the phytoplankton blooms occur only after the solar radiation began to increase which increases the flux of light to the surface ocean and also helps stabilizing the water column by warming the surface water. This allows the cells to overcome chronic light limitation in a deeply mixing water column (Sverdrup, 1953).

The temporal amplitude of the EOF analysis (Fig. 5) demonstrates the seasonal timing of chlorophyll blooms was consistent between years; however, there was considerable inter-annual variability in the magnitude of the winter and spring blooms. The variability in the magnitude of the blooms was associated with factors that alter the water column stability. Winters with low storm activity were characterized by having large winter phytoplankton blooms. Additionally the middle and outer shelves can be significantly influenced by the Hudson River that can deliver large buoyant plumes (Castelao et al., 2008a). These buoyant plumes stabilize the water column and transports chlorophyll from estuaries onto the shelf (Moline et al., 2008). In contrast, the spring bloom requires the shelf-break/slope water to stratify before the bloom can occur. Once the system is stratified, the pycnocline on the MAB is extremely strong and is generally not disrupted until later autumn when wind mixing and surface cooling lead to convective overturn (Biscaye et al., 1994). Given this,

Please cite this article as: Xu, Y., et al., Seasonal variability of chlorophyll a in the Mid-Atlantic Bight. Continental Shelf Research (2011), doi:10.1016/j.csr.2011.05.019

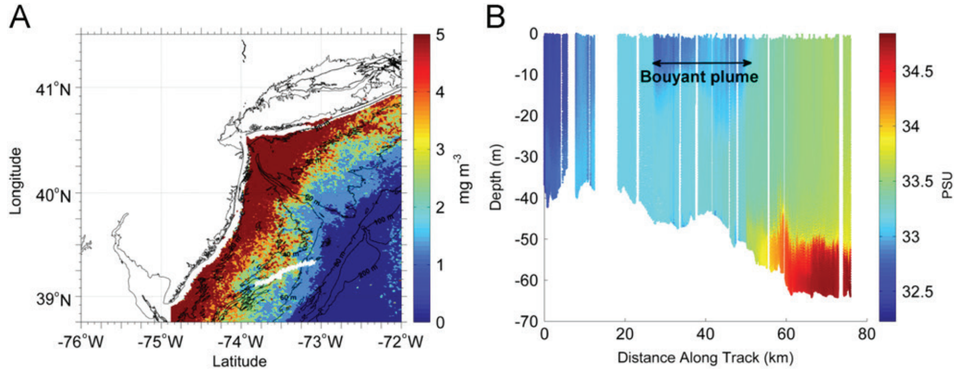

Fig. 10. (A) SeaWiFS chlorophyll 4-day composite image (January 25th–28th, 2006). The white line on this panel indicates the location of the glider transect. (B) Salinity cross-section measured with a glider along the transect shown in panel (A). The glider measurement is from 2006 January 18th to 23rd.

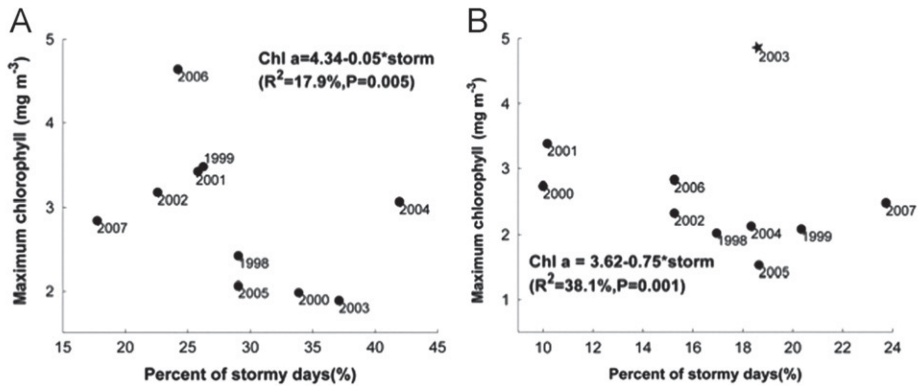

Fig. 11. (A) Percentage of stormy days against maximum SeaWiFS chlorophyll concentration (mg m^{-3}) in the area depicted by EOF mode 1, (B) Percentage of stormy days against maximum SeaWiFS chlorophyll concentration (mg m^{-3}) in area depicted by EOF mode 2. In panel (A), wind observations are from NDBC 44025 during Dec.–Jan., while in panel (B), winds are from NDBC 44014 during Feb.–Mar.; the star for 2003 marks it as an outlier.

Table 1
Chlorophyll (mg m^{-3}) and light environment for the two regions defined by the EOF analysis in the MAB. For the shelf waters the 1% light depth was calculated using Hydrolight combined with optical data collected during the LaTTE experiment (Chant et al., 2008b, Moline et al., 2008).

Parameter	Shelf (zone 1)	Shelf-break (zone 2)
Mean Chl a (mg m^{-3})	1.7	0.7
Maximum Chl a (mg m^{-3})	4.9	2.1
Minimum Chl a (mg m^{-3})	0.6	0.2
Mean 1% Light depth (m)	20	33
Maximum 1% Light depth (m)	12	27
Minimum 1% Light depth (m)	36	55
Mean Water Depth (m)	41	200–681[a]
Percent of water column above the 1% light (%)	49	5–17
Shelf valley ac-9 data 1% light depth (m)	20	
Offshore Hudson River ac-9 data 1% light depth (m)	10	

[a] Much of zone 2 occurs over the continental slope. Therefore we show the depths at the inner edge of the continental slope and the mean depth of zone 2.

the factors influencing the stratification rate are the key variables to predicting the shelf-break/slope phytoplankton bloom. In the work of Lentz et al. (2003), they suggest that the direction, magnitude, and timing of spring wind stress events play an important role in inter-annual variations in stratification. For the unique year 2003, precipitation, river runoff, sea surface temperature, and air temperature were not unusual and could not account for the high spring time chlorophyll concentration. The late winter 2003 were characterized by strong southwest winds; however, by early spring the winds shifted northeast. This resulted in predominately down-shelf and onshore transport. These northeast winds were not extremely strong in magnitude but they were sustained throughout the spring. Compared with other years, the 2003 spring had higher frequency of down-shore (53 days compared with the 11 year mean of 41 days) and towards-shore (48 days compared with the 11 year mean of 41 days) winds. Under such wind conditions, there was convergence in the bottom waters at the shelf/slope, which can result in upwelling conditions that promote phytoplankton blooms (Siedlecki et al., 2008). Therefore, while regional pre-spring wind does impact the magnitude of the spring bloom, this relationship is not particularly robust as it can be overcome by local winds. The correlation between storminess and bloom magnitude was consistent with open ocean sites (Henson et al., 2006) where storms delay the stratification of the upper ocean.

Since the MAB hydrography strongly influences the spatial and temporal patterns in satellite chlorophyll, understanding these processes is critical as the shelf water of MAB is experiencing significant changes in its temperature, salinity (Mountain, 2003). Since the 1990s, the shelf water, which is the primary water mass in the MAB, has become warmer, fresher, and more abundant than during 1977–1987. This has been correlated with transport of Scotian Shelf water and slope water and local atmospheric heat flux (Mountain, 2003). These changes are likely to influence the stratification dynamics on the MAB. The freshening of the ocean can enhance vertical stratification that has been shown to be critical to the timing and magnitude of phytoplankton blooms (Ji et al., 2007). Additionally winter wind stress has increased in the last decade on the MAB and these changes have been associated with decadal declines in chlorophyll biomass in the fall and winter (Schofield et al., 2008). Given this, future work should focus on determining the critical thresholds between water stability and phytoplankton growth. While maximum chlorophyll concentration was affected by storm frequency and river plume, other biological factors such as nutrient concentrations or grazing may also be important. This requires new data collected for sustained periods of time to complement satellite imagery. The use of gliders as observational platforms allowed for shelf waters to be sampled frequently over long periods of time. Therefore, we recommend gliders and satellite observations be focused during the transition season and provide the basis for evaluating the relationship between stratification/destratification and the blooms in the future.

Acknowledgments

We thank the members of the Rutgers University Coastal Ocean Observation Laboratory (RU COOL), who were responsible for the satellite, glider and CODAR operations, with particular gratitude to Jennifer Bosch and Lisa Ojanen, who helped with satellite data collection and processing. This work was supported by a grant from ONR MURI Espresso program (N000140610739) and NSF LaTTE program (OCE-0238957, OCE-0238745).

References

Baldacci, A., Corsini, G., Grasso, R., Manzella, G., Allen, T.J., Cipollini, P., Guymer, H.T., Snaith, M.H., 2001. A study of the Alboran sea mesoscale system by means of empirical orthogonal function decomposition of satellite data. J. Mar. Syst. 29, 293–311.
Barrick, D.E., 1972. First-order theory and analysis of mf/hf/vhf scatter from the sea. IEEE Trans. Antennas Propag 20, 2–10.
Barrick, D.E., Evens, M.W., Weber, B.L., 1977. Ocean surface currents mapped by radar. Science 198, 138–144.
Beardsley, R.C., Chapman, D.C., Brink, K.H., Ramp, S.R., Schlitz, R., 1985. The Nantucket Shoals flux experiment (NSFE79). Part I: a basic description of the current and temperature variability. J. Phys. Oceanogr. 15, 713–748.
Biscaye, P.E., Flagg, C.N., Falkowski, P., 1994. The Shelf Edge Exchange Processes experiment, SEEP-II: an introduction to hypotheses, results and conclusions. Deep-Sea Res. II 41, 231–252.
Brickley, J.P., Thomas, C.A., 2004. Satellite-measured seasonal and inter-annual chlorophyll variability in the Northeast Pacific and Coastal Gulf of Alaska. Deep-Sea Res. II 51, 229–245.
Cahill, B., Schofield, O., Chant, R., Wilkin, J., Hunter, E., Glenn, S., Bissett, P., 2008. Dynamics of turbid buoyant plumes and the feedbacks on near-shore biogeochemistry and physics. Geophys. Res. Lett. 35, L10605.
Campbell, J.W., 1995. The lognormal distribution as a model for bio-optical variability in the sea. J. Geophys. Res. 100, 13237–13254.
Castelao, R., Schofield, O., Glenn, S., Chant, R., Kohut, J., 2008a. Cross-shelf transport of freshwater on the New Jersey shelf. J. Geophys. Res. 113, C07017. doi:10.1029/2007JC004241.
Castelao, R., Glenn, S., Schofield, O., Chant, R., Wilkin, J., Kohut, J., 2008b. Seasonal evolution of hydrographic fields in the central Middle Atlantic Bight from glider observations. Geophys. Res. Lett. 35, L03617. doi:10.1029/2007GL032335.
Chant, R.J., Glenn, S.M., Hunter, E., Kohut, J., Chen, R.F., Houghton, R.W., Bosch, J., Schofield, O., 2008a. Bulge Formation of a Buoyant River Outflow. J. Geophys. Res. 113, C01017. doi:10.1029/2007JC004100.
Chant, R.J., Wilkin, J., Zhang, W., Choi, B.J., Hunter, E., Castelao, R., Glenn, S., Jurisa, J., Schofield, O., Houghton, R., Kohut, J., Frazer, T., Moline, M., 2008b. Dispersal of the Hudson River Plume on the New York Bight. Oceanography 24, 55–63.
Crombie, D.D., 1955. Doppler spectrum of sea echo at 13.56 Mc/s. Nature 175, 681–682.
Cushing, D.H., 1975. Marine Ecology and Fisheries. Cambridge Univ. Press, London 278 pp.
Dickey, T.D., Williams III, A.J., 2001. Interdisciplinary ocean process studies on the New England shelf. J. Geophys. Res. 106, 9427–9434.
Dutkiewicz, S., Follows, M., Marshall, J., Gregg, W.W., 2001. Interannual variability of phytoplankton abundances in the North Atlantic. Deep Sea Res. II 48, 2323–2344. doi:10.1016/S0967-0645(00)00178-8.
Falkowski, P., Raven, J., 2007. Aquatic Photosynthesis second ed. Princeton University Press, Princeton.
Glenn, S.M., et al., 2004. Biogeochemical impact of summertime coastal upwelling on the New Jersey Shelf. J. Geophys. Res. 109, C12S02. doi:10.1029/2003JC002265.
Glenn, S.M., Jones, C., Twardowski, M., Bowers, L., Kerfoot, J., Webb, D., Schofield, O., 2008. Glider observations of sediment resuspension in a Middle Atlantic Bight fall transition storm. Limnol. Oceanogr. 53, 2180–2196.
Gong, D., Kohut, J.T., Glenn, S.M., 2010. Wind driven circulation and seasonal climatology of surface current on the NJ Shelf (2002–2007). J. Geophys. Res. 115, C04006. doi:10.1029/2009JC005520.
Harding, W.L., Magnusona, A., Malloneea, M.E., 2004. SeaWiFS retrievals of chlorophyll in Chesapeake Bay and the mid-Atlantic bight. Estuarine Coastal Shelf Sci. 62, 75–94.
Henson, A.S., Robinson, I., Allen, J.T., Waniek, J.J., 2006. Effect of meteorological conditions on interannual variability in timing and magnitude of the spring bloom in the Irminger Basin, North Atlantic. Deep-Sea Res. I 53, 1601–1615.
Houghton, R., Schlitz, R., Beardsley, R., Butman, B., Chamberlin, J., 1982. The Middle Atlantic Bight cold pool: evolution of the temperature structure during Summer 1979. J. Geophys. Res. 12, 1019–1029.
Huisman, J., Van, O.P., Weissing, F.J., 1999. Critical depth and critical turbulence: two different mechanisms for the development of phytoplankton blooms. Limnol. Oceanogr. 44, 1781–1787.
Ji, R., Davis, C.S., Chen, C., Townsend, D.W., Mountain, D.G., Beardsley, R.C., 2007. Influence of ocean freshening on shelf phytoplankton dynamics. Geophys. Res. Lett. 34, L24607.
Johnson, D.M., Miller, J., Schofield, O., 2003. Dynamics and optics of the Hudson River outflow plume. J. Geophys. Res. 108, 1–9.
Kohut, J.T., Glenn, S.M., 2003. Calibration of HF radar surface current measurements using measured antenna beam patterns. J. Atmos. Oceanic Technol., 1303–1316.
Kohut, J.T., Glenn, S.M., Chant, R.J., 2004. Seasonal current variability on the New Jersey inner shelf. J. Geophys. Res. 109, C07S07. doi:10.1029/2003JC001963.
Lentz, S., Shearman, K., Anderson, S., Plueddemann, A., Edson, J., 2003. Evolution of stratification over the New England shelf during the Coastal Mixing and Optics study, August 1996–June 1997. J. Geophys. Res 108(C1), 3008. doi:10.1029/2001JC001121.
Linder, C.A., Gawarkiewicz, G., 1998. A climatology of the shelf-break front in theMiddle Atlantic Bight. J. Geophys. Res. 103, 18405–18423.
Linder, C.A., Gawarkiewicz, G., Pickart, R., 2004. Seasonal characteristics of bottom boundary layer detachment at the shelfbreak front in the Middle Atlantic Bight. J. Geophys. Res. 109, C03049. doi:10.1029/2003JC002032.
Longhurst, A.R., 1998. Ecological Geography of the Sea. Academic Press, San Diego 398 pp.
Lorenz, E.N., 1956. Empirical orthogonal functions and statistical weather prediction. Sci. Rep. 1, 49 Statist. Forecasting Proj., Department Meteor., MIT.
Malone, T.C., Hopkins, T.S., Falkowski, P.G., Whitledge, T.E., 1983. Production and transport of phytoplankton biomass over the continental shelf of the New York Bight. Cont. Shelf Res. 1, 305–337.
Mobley, C.D., 1994. Light and Water, Radiative Transfer in Natural Waters. Academic Press, California.
Moline, M.A., Blackwell, S., Chant, R., Oliver, M.J., Bergmann, T., Glenn, S., Schofield, O., 2004. Episodic physical forcing and the structure of phytoplankton communities in the coastal waters of New Jersey. J. Geophy. Res. 110, C12S05. doi:10.1029/2003JC001985.
Moline, M.A., Frazer, T.K., Chant, R., Glenn, S., Jacoby, C.A., Reinfelder, J.R., Yost, J., Zhou, M., Schofield, O., 2008. Biological responses in a dynamic, buoyant river plume. Oceanography 21, 71–89.
Mountain, D.G., 2003. Variability in the properties of Shelf Water in the Middle Atlantic Bight, 1977–1999. J. Geophys. Res. 108 (C1), 3014. doi:10.1029/2001JC001044.
Navarro, G., Ruiz, J., 2006. Spatial and temporal variability of phytoplankton in the Gulf of Ca´ diz through remote sensing images. Deep-Sea Res. II 53, 1241–1260.
North, G.R., Bell, T.L., Cahalan, R.F., Moeng, F.J., 1982. Sampling errors in the estimation of empirical orthogonal functions. Mon. Weather Rev. 110, 699–706.
O'Reilly, J., Busch, D., 1984. Phytoplankton primary production on the north-west Atlantic Shelf. Rapports et Proces-Verbaux des Reunions Conseil International pour l'Exploration de la Mer 183, 255–268.
Pawlowicz, R., Beardsley, R.C., Lentz, S.J., 2002. Classical tidal harmonic analysis including error estimates in MATLAB using T TIDE. Comput. Geosci. 28, 929–937.
Riley, G.A., 1946. Factors controlling phytoplankton populations on Georges Bank. J. Mar. Res. 6, 54–73.
Riley, G.A., 1947. Seasonal fluctuations of the phytoplankton population in New England coastal waters. J. Mar. Res. 6, 114–125.
Ryan, J.P., Yoder, J.A., Cornillon, P.C., 1999. Enhanced chlorophyll at the shelfbreak of the Mid-Atlantic Bight and Georges Bank during the Spring Transition. Limnol. Oceanogr. 44, 1–11.
Ryan, J.P., Yoder, J.A., Townsend, D.W., 2001. Influence of a Gulf Stream warm-core ring on water mass and chlorophyll distributions along the southern flank of Georges Bank. Deep-Sea Res. II 48, 159–178.
Ryther, J.H., Yentsch, C.S., 1958. Primary production of continental shelf waters off New York. Limnol. Oceanogr. 3, 327–335.
Schofield, O., Bergmann, T., Oliver, M., Irwin, A., Kirkpatrick, G., Bissett, W.P., Orrico, C., Moline, M.A., 2004. Inverting inherent optical signatures in the nearshore coastal waters at the Long Term Ecosystem Observatory. J. Geophys. Res. 109, C12S04. doi:10.1029/2003JC002071.
Schofield, O., et al., 2007. Slocum gliders: robust and ready. J. Field Robotics 24, 1–14. doi:10.1009/rob.20200.

Schofield, O., Chant, R., Cahill, B., Castelao, R., Gong, D., Kohut, J., Montes-Hugo, M., Ramanduri, R., Xu, Y., Glenn, S., 2008. Seasonal forcing of primary productivity on broad continental shelves. Oceanography 21, 108–117.

Schofield, O., Chant, R., Hunter, E., Moline M.A., Reinfelder, J., Glenn, S.M., Frazer, T. Optical transformations in a turbid buoyant plume on the Mid-Atlantic Bight. Continental Shelf Research, submitted for publication.

Siedlecki, S.A., Mahadevan, A., Archer, D., 2008. The Role of Shelf Break Upwelling Along the East Coast of the US in the Coastal Carbon Cycle: A Model's Tale. American Geophysical Union, Fall Meeting 2008, poster #OS53C-1322.

Siegel, D.A., Doney, S.C., Yoder, J.A., 2002. The North Atlantic spring phytoplankton bloom and Sverdrup's critical depth hypothesis. Science 296, 730–733.

Stewart, R.H., Joy, J.W., 1974. HF radio measurement of surface currents. Deep-Sea Res. 21, 1039–1049.

Stramska, M., Dickey, T., 1994. Modeling phytoplankton dynamics in the northeast Atlantic during the initiation of the spring bloom. J. Geophys. Res. 99, 10,241–10,253.

Sverdrup, H.U., 1953. On conditions for the vernal blooming of phytoplankton. J. Cons. Perm. Int. Explor. Mer. 18, 287–295.

Townsend, D.W., Keller, M.D., Sieracki, M.E., Ackleson, S.G., 1992. Spring phytoplankton blooms in the absence of vertical water column stratification. Nature 360, 59–62.

Townsend, D.W., Cammen, L.M., Holligan, P.M., Campbell, D.E., Pettigrew, N.R., 1994. Causes and consequences of variability in the timing of spring phytoplankton blooms. Deep-Sea Res. I 41, 747–765.

Ueyama, R., Monger, B.C., 2005. Wind-induced modulation of seasonal phytoplankton blooms in the North Atlantic derived from satellite observations. Limnol. Oceanogr. 50, 1820–1829.

Ward, J.H., 1963. Hierachical grouping to optimize an objective function. J. Am. Statist. Assoc. 58, 236–244.

Wright, W.R., 1976. The limits of shelf water south of Cape Cod, 1941–1972. J. Mar. Res. 34, 1–14.

Wirick, C.D., 1994. Exchange of phytoplankton across the continental shelf-slope boundary of the Middle Atlantic Bight during spring 1988. Deep-Sea Res. II 41, 391–410.

Yoder, J.A., McClain, C.R., Feldman, G.C., Esaias, W.E., 1993. Annual cycles of phytoplankton chlorophyll concentrations in the global ocean: a satellite view. Global Biogeochem. Cycles 7, 181–194.

Yoder, J.A., O'Reilly, J.E., Barnard, A.H., Moore, T.S., Ruhsam, C.M., 2001. Variability in coastal zone color scanner (CZCS) Chlorophyll imagery of ocean margin waters off the US East Coast. Cont. Shelf Res. 21, 1191–1218.

Yoder, J.A., Schollaert, S.E., O'Reilly, J.E., 2002. Climatological Phytoplankton Chlorophyll and Sea Surface Temperature Patterns in Continental Shelf and Slope Waters off the Northeast U.S. Coast. Limnol. Oceanogr. 3, 672–682.

Please cite this article as: Xu, Y., et al., Seasonal variability of chlorophyll a in the Mid-Atlantic Bight. Continental Shelf Research (2011), doi:10.1016/j.csr.2011.05.019

PAPER

The Trans-Atlantic Slocum Glider Expeditions: A Catalyst for Undergraduate Participation in Ocean Science and Technology

AUTHORS
Scott Glenn
Oscar Schofield
Josh Kohut
Janice McDonnell
Richard Ludescher
Dena Seidel
David Aragon
Tina Haskins
Ethan Handel
Clinton Haldeman
Igor Heifetz
John Kerfoot
Erick Lemus
Sage Lictenwalner
Lisa Ojanen
Hugh Roarty
Rutgers University

Atlantic Crossing Students, 2007-2010:
Frank Acevido, Samuel Aparicio, Nicolette Aquilino, Karan Arora, Justin Ash, Brian Bachrach, Katie Bianchini, Amanda Bullis, Katie Carson, Joyhee Cho, Megan Cimino, Kaycee Coleman, Alyssa Currie, Aissatou Diallo, Montana DiVita, Colin Evans, Nicholas Ewankov, Ana Filipa, Chris Filosa, Gina Francisco, Mario Garcia, Mike Garzio, Abe Gelb, Darcy Glenn, Dakota Goldinger, Melissa Grimm, Ethan Handel, Shannon Harrison, Danielle Holden, Erin Holswad, Holly Ibanez, Lisa Izzo, Dave Kaminsky, Marcus Kwasek, Anthony Lund, Joe Palmiery, Richa Patel, Emily Pirl, Andre Ramirez, Evan Randall, Dan Ravaioli, Kyle Richter, Leo Rishty, Emily Rogalsky, Steven Savard, Justin Shapiro, Jessica Silva, Mike Smith, Amelia Snow, Carisa Sousa, Nilsen Strandskov, Cael Sutherland, Eric Vowinkle, Jeff Wallace, Jason Werrel

ABSTRACT

Results of Office of Naval Research (ONR)- and National Science Foundation (NSF)-sponsored collaborative coastal science experiments using underwater gliders were reported at the E.U./U.S. Baltic Sea conference in 2006. The National Oceanic and Atmospheric Administration (NOAA) recognized the parallel educational potential and issued a trans-Atlantic challenge—modify one of the coastal gliders and fly it across the Atlantic, entraining and inspiring students along the way. Leveraging the experience of the NSF Centers for Ocean Sciences Education Excellence, a needs assessment process guided the development of a new undergraduate research program based on the cognitive apprenticeship model. The generalized model was applied to the specific opportunities provided by the trans-Atlantic challenge, involving students in every aspect of the missions. Students participated in the modifications and testing required to increase glider endurance and in the development of the mission planning tools. Scientist and student teams conducted three long-duration missions: (1) RU15's flight from New Jersey to Nova Scotia to test the lithium batteries and ruggedized fin technology in storms, (2) RU17's first attempt at the Atlantic crossing that provided the lessons learned, and (3) RU27's successful trans-Atlantic flight a year later. Post-flight activities included development of new intuitive glider data visualization software that enabled students to analyze the glider data and compare it with ocean forecast models, enabling students to create their own new knowledge. Lessons learned include the significant gains achieved by engaging students early, encouraging them to work as teams, giving them the tools to make their own discoveries, and developing a near-peer mentoring community for increasing retention and diversity. The success has inspired an even broader vision for international glider missions, that of a glider-enabled global classroom to repeat the track of the HMS *Challenger* and its first scientific circumnavigation of the globe.

European Exchange Students, 2009:
Filipa Carvalho
University of the Azores, Horta, Portugal

Alvaro Lopez
Adri Martin
Plataforma Oceanica de Canarias

Other Authors
Clayton Jones
Douglass Webb
Teledyne Webb Research Corporation

Jerry Miller
Office of Science and Technology Policy

Marlon Lewis
Scott McLean
Satlantic, Inc., Halifax, Nova Scotia, Canada

Ana Martins
University of the Azores, Horta, Portugal

Carlos Barrera
Plataforma Oceanica de Canarias

Antonio Ramos
Universidad de Las Palmas de Gran Canaria

Enrique Fanjul
Puertos del Estado, Madrid, Spain

Introduction

The field of oceanography is shaped by a rich history of expeditionary science. The inspiration provided by our short times at sea has spurred the imagination and creativity of ocean scientists for centuries, prompting us to imagine and implement new approaches for exploring, observing, understanding, and utilizing the world's oceans. One vision from 22 years ago (Stommel, 1989) was that of a global ocean patrolled by Slocum underwater gliders guided by satellite data and numerical model forecasts. In Hank Stommel's futuristic world, support for the network was galvanized by a 198-day trans-Atlantic flight of the glider *Sentinel 1* from Bermuda to northwest Africa. The mission was flown by researchers working from an attic control room in the Woods Hole Oceanographic Institution's Bigelow Building. At that time in Woods Hole's history, the attic of Bigelow was occupied by oceanography students.

Since that inspirational vision was published, ocean glider technology has matured and now routinely anchors scientific experiments, enabling scientists to conduct sustained and adaptively adjusted science missions (Davis et al., 2003; Schofield et al., 2007). The adaptive sampling capabilities of the gliders are enabled by their ability to navigate relative to the flow and the two-way communications provided by the global Iridium network, allowing glider data to be sent to control centers on shore and new sampling commands to be sent back to the gliders at sea. As ocean observatories continue to mature, coordinated fleets of gliders are growing contributors to the National Oceanic and Atmospheric Administration (NOAA)-led U.S. Integrated Ocean Observing System (IOOS®) (Schofield et al., 2010a), the National Science Foundation (NSF) Ocean Observing Initiative (OOI) (Schofield et al., 2010b), and the Navy's Littoral Battlespace Sensing-Glider (LBS-G) initiative. These initiatives and others are implementing what Walter Munk termed the 1 + 1 = 3 scenario for ocean sampling (Munk, 2000), where a new ocean omnipresence is enabled by satellites in space combined with vast in-water arrays of drifting profilers, gliders, and time series stations. The approach not only offers researchers new opportunities for ocean science but also provides a potential mechanism to share the real-time excitement of exploration and scientific discovery with students and the public.

The educational value of the gliders was recognized by NOAA leadership in May of 2006 at the E.U./U.S. sponsored conference promoting international collaborations in the Baltic Sea. NOAA responded to the growing number of glider presentations with a challenge to take one of the existing gliders, modify it, and fly it across the Atlantic, entraining and inspiring students along the way. It was presented as a response to the *Rising Above the Gathering Storm* (2007) report's observation that while the vitality of the U.S. economy depends on the scientific and technological innovations of a well-educated workforce, U.S. economic leadership was eroding partly because of the decreasing number of students choosing science, math, and engineering careers. The trans-Atlantic glider mission was viewed as an opportunity to re-spark interest in science and technology, invigorate student involvement, and influence their career path. It was considered high risk but, with the proper visibility, capable of producing high rewards.

Rutgers scientists attending the Baltic Sea conference viewed NOAA's trans-Atlantic challenge as an opportunity to develop a new educational program enabled by the gliders. Participation in high-risk ocean-scale glider expeditions would provide opportunities for students to directly experience the many difficulties of operating at sea, the value of perseverance and teamwork, and the feeling of accomplishment when successful. Students would experience the excitement of discovery through the analysis of data they helped collect from harsh environment, and they would gain a more global cultural perspective by communicating with scientists and students from around the world.

This led Rutgers, Teledyne Webb Research, and their international partners to conduct three long-duration glider missions in 2008–2009. The first extended-duration mission of the series, glider RU15's flight from Tuckerton, New Jersey to Halifax, Nova Scotia, crossed international borders and tested the new technologies that would be required on future trans-Atlantic missions. Glider RU17's first attempt at the Atlantic crossing started off the coast of New Jersey and ended in what may have been a biologically induced leak offshore the Azores and the always heartbreaking loss of a glider at sea. One year later, glider RU27, a second trans-Atlantic Slocum glider christened *Scarlet Knight* by U.S. IOOS, was launched off New Jersey. Visited by divers in the Azores for a visual inspection, it was freed of barnacles while still in the water and continued traveling its 7,400-km course. After spending 221 days at sea, it was recovered in Spanish waters by the Puertos del Estado buoy tender *Investigador,* making it the first underwater robot to cross an ocean basin. It now resides in the Smithsonian's National Museum of Natural History. What was unique about these three missions is that they were conducted with undergraduate students as part of their classroom experience, beginning in the construction phase, throughout the three ocean journeys, and into the post-mission data analysis phase, providing a unique opportunity for participatory science learning.

This manuscript provides an overview of the education programs developed, how they were applied to the trans-Atlantic missions, and the educational lessons learned. It concludes with a perspective on how this educational effort provides the foundation for an international partnership to explore the world ocean on a second NOAA challenge, a repeat of the 1870 Challenger Mission, the first scientific circumnavigation of the globe.

New Approaches to Undergraduate Education

Rising Above the Gathering Storm noted that while 30% of students entering U.S. colleges intend to major in science and engineering; less than half complete their bachelor's degrees in these subjects. Even qualified students grow discouraged before reaching the workforce. The report recommends providing undergraduate research experiences that extend beyond the classroom and across the summer as early as possible and emphasizes the need for near-peer mentorship to augment engaged faculty. Since the envisioned trans-Atlantic glider mission would require a workforce for construction, prelaunch testing, and post-launch path planning and data analysis with limited support for technician time, student participation was necessary. But how could the required long-term student involvement fit within an already busy undergraduate schedule, and how would it help the students in their future job searches?

Our approach was informed through a needs assessment process facilitated by the NSF Centers for Ocean Sciences Education Excellence-Networked Ocean World (COSEE-NOW). The needs assessment confirmed that oceanographic graduate education programs are still looking for Ph.D. students with strong basic science and math backgrounds, but it also revealed that federal agencies, companies, and even some university research laboratories are also looking for oceanographers with bachelor's and master's degrees. Other requirements include people to operate new observing technologies, to run and interpret forecast models, and to communicate scientific information. The assessment indicated that government agencies are willing to support undergraduate internships as a cost-effective way to both engage and evaluate students as potential new employees, with opportunities for earning of a master's degree once hired. Support for certification of oceanographic professionals was found to be greatest at the bachelor's degree level (Rosenfeld et al., 2009). Employers are looking for individuals with a cross-disciplinary education (oceanography plus a minor), a range of technical abilities that could adapt to different jobs, strong written and verbal communication skills, and hands-on real-world working-team experiences. An educational environment that developed the student's ability to work as part of a larger team was especially well received by companies. If a student receives a bad grade in a class, the bad grade can be hidden, since it only affects the individual. But workplace activities are often team efforts, where the failure of one team member publicly impacts the entire team. In addition, federal agencies emphasized that the desired workforce should be more diverse and more reflective of the U.S. general population. U.S. census bureau estimates for 2008 indicate that the 22-year-old resident population is 62% White, non-Hispanic. NSF graduation statistics for 2008 indicate that the existing undergraduate marine science pool is extremely small, with only 2,109 bachelor's degrees awarded nationally (Figure 1). In these marine academic disciplines, 82% of the bachelor's degrees were awarded to White, non-Hispanic students, and 59% were male.

In response to *Rising Above the Gathering Storm* and guided by the COSEE-NOW needs assessment, the NOAA trans-Atlantic glider challenge has become the catalyst for transforming our approach to undergraduate education in marine sciences. To move students beyond the marine science classroom into a team project environment and to increase diversity, an undergraduate education program was established based on the cognitive apprenticeship model restated more simply as "watch one, do one, teach one". (See education break-out box in Glenn and Schofield, 2009). The three phases start with the initial engagement, move on to team research, and culminate with veteran students in leadership roles mentoring the new students. Students from diverse disciplines across the campus are engaged as early as their freshman year, with opportunities to continue with the program through graduation. Initial engagement occurs by (a) recruiting from several traditional 100-level science-distribution Introduction to

FIGURE 1

Distribution of the 2,109 U.S. bachelor's degrees awarded in marine academic disciplines for 2008 by sex (A) and ethnicity (B). Source: *National Science Foundation*.

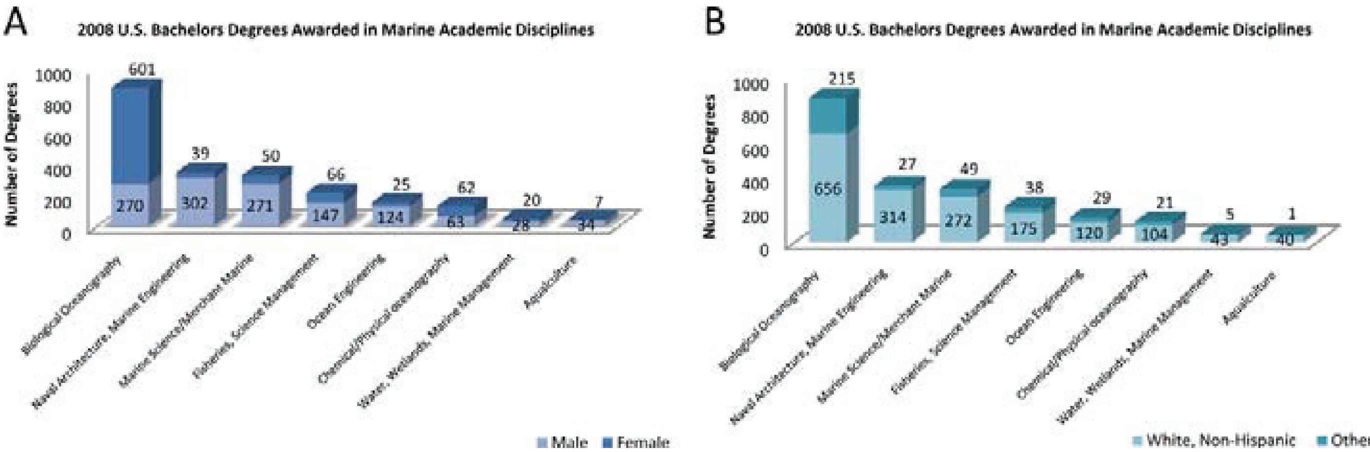

Oceanography lecture courses, to which we have added (b) faculty participation in a university-wide series of one-credit freshman seminars where small groups of 20 students are introduced to senior level faculty, (c) the establishment of the Oceanography House as an on-campus living-and-learning community for incoming freshmen with an interest in the ocean, and (d) through near-peer university-sponsored events and an active Oceanography Club where students already involved discuss their involvement with other Rutgers undergraduates or with students back at their high schools.

At the middle level, while students are completing their usual content courses for their major/minor, a new team research track that runs in parallel with their coursework was developed. Undergraduate marine science degrees, as do several other sciences at Rutgers, require at least six credits of research to graduate. To help students fulfill this requirement, the one-credit *Atlantic Crossing* research course was established. The team-taught course runs every semester, and as a research course, students can sign up for it multiple times, potentially taking it every semester of their undergraduate career. The class typically is divided into small working teams of two to three students. Team projects initially focused on the glider rebuilds for long duration, the testing of new systems, and the development of path planning tools to understand the uncertainty associated with the constantly evolving ocean currents used as a roadmap. The product at the end of each semester is a poster session by each working team similar to those conducted at science conferences.

Finally, three capstone opportunities are offered. First, as students become more experienced, they become team leaders, responsible for organizing and reporting their team's progress and acting as a mentor to younger students. Many students have found the long-term progression from a rookie to a veteran team member an achievable goal and a confidence-building experience. Second, the glider datasets provide senior thesis topics for those who want to expand their formal research skills through the preparation and defense of an honors thesis. Often senior theses begin through summer internships available after the student's junior year. Third, the NSF-sponsored nationally coordinated course *Communicating Ocean Sciences to Informal Audiences (COSIA)* is offered for those desiring an introduction to learning theory with participatory opportunities to develop their communication and teaching skills. In *COSIA*, the gliders are a proven magnet, providing a vehicle for engaging informal audiences outside the classroom in more interactive learning activities.

The above approach—needs assessment followed by implementation of a cognitive apprenticeship learning model—can be applied to develop a wide variety of undergraduate education opportunities. It does not require a fleet of gliders to implement.

Application to the Trans-Atlantic Glider Missions

Vehicle Construction. When the trans-Atlantic challenge was issued, Rutgers had completed 66 glider missions, ¾ being in shallow shelf waters and ¼ being in the surface layers of the deep ocean. Mission durations depend on the number of sensors on board, the water depth of operations (deeper water being more power efficient), and the amount of time spent communicating. The longest mission in May of 2006 was 27 days. Since then, many deeper missions were completed with standard alkaline battery packs and only Conductivity, Temperature and Depth (CTD) sensors in the 30- to 40-day range, with a theoretical value of 34 days. A trans-Atlantic mission would require an estimated 300 days, a factor of 10 increase in mission duration. This would not only require more power but also ruggedizing mechanical systems for surviving the longer durations at sea and protection from corrosion and biofouling that do not normally plague a mission of 1-month duration.

Students worked alongside Rutgers technicians in the laboratory to adapt gliders for long-duration missions. Some of these students were on work-study plans with their pay already supported as part of their financial aid package. Others worked for hourly pay or for course credit. This phase was especially well suited for entraining engineering undergraduates. The students learned to take gliders apart, reassemble them with new test parts, reballast, and prepare them for launch. Software changes were tested on simulators. When class schedules permitted, students would accompany technicians on the launch and recovery cruises. The required factor of 10 increase in power was achieved by switching from alkaline to lithium batteries that had four times the energy, building and test flying an extended payload bay that increased the number of batteries from 230 C-cells to 453 C-cells and by reducing the daily average power usage from 2 to 1.5 W by removing the altimeter, the payload bay computer, and lowering the amount of data transferred over Iridium. Corrosion protection was monitored and evaluated by students weighing all parts before and after each deployment. A variety of paints and coatings were tested as student projects to limit biofouling.

Mission Planning Tools. A flight across the Atlantic would require mission planning capabilities well beyond those available in May of 2006. Rutgers had coordinated several month-long Office of Naval Research (ONR) Coastal Predictive Skill Experiments from a collaboratory located at a remote field station (Glenn et al., 2000a, 2000b; Glenn and Schofield, 2003) and recently completed a series of NSF studies of the Hudson River plume with an on-campus collaboratory (Chant et al., 2008). But these studies were relatively short in duration compared with a trans-Atlantic mission that would require sustained operations for many months. Some of these capabilities were developed during the ONR Shallow Water 2006 Joint Experiment on the New Jersey outer shelf (Tang et al., 2007). In this experiment, a distributed team of collaborators was provided an online coordination portal where scientists posted environmental data updates that could be accessed over the Internet on shore or via HiSeasNet on board the fleet of ships. The portal provided a mission planning capability for a coordinated fleet of gliders and ships by sharing daily updates of the environmental conditions.

The trans-Atlantic glider missions required development of a similar collaborative workspace to coordinate the activities of a distributed team of scientists and students located on both sides of the Atlantic and living in different time zones. The international team would require (1) common access to the variety of datasets acquired and forecasts generated on both continents, (2) the ability to overlay the datasets and forecasts in a common operational environment to create new composite analyses for mission planning, and (3) the ability to share our analyses, results, and interpretations so flight decisions could be made. The collaborative portal also had to be constructed and operated with considerably fewer resources than were available to the Shallow Water 2006 Joint Experiment. To accomplish this, the expertise of COSEE-NOW was again tapped to establish an online learning community. The IOOS Mid-Atlantic region was chosen as our testbed, and our students became the beta testers.

To accomplish the first task above, a collaborative Web portal was designed that access points to all existing analyses products and programs could be posted and shared. Rather than build a dedicated set of software tools for overlaying the wide variety of available data and forecasts, Google Earth was chosen as our mission planning tool for the second task. Many of the required datasets (coastlines, bathymetry, weather) were already in Google Earth, and new datasets could be added relatively easily. The full capabilities provided by Google Earth were used to overlay and compare spatial maps, to zoom and pan, to pull off latitudes and longitudes, and to measure distances and bearings. Major data layers added to Google Earth include global ocean forecasts, satellite maps of sea surface height and the resulting geostrophic currents, satellite-derived sea surface temperature and ocean color maps, and the glider tracks with depth-averaged currents. Students

FIGURE 2

(A) Track for RU15 mission to Halifax, Nova Scotia, Canada. Significant wave height (C) and wave periods (D) from a nearby NOAA weather buoy during a late winter/early spring storm (B) event.

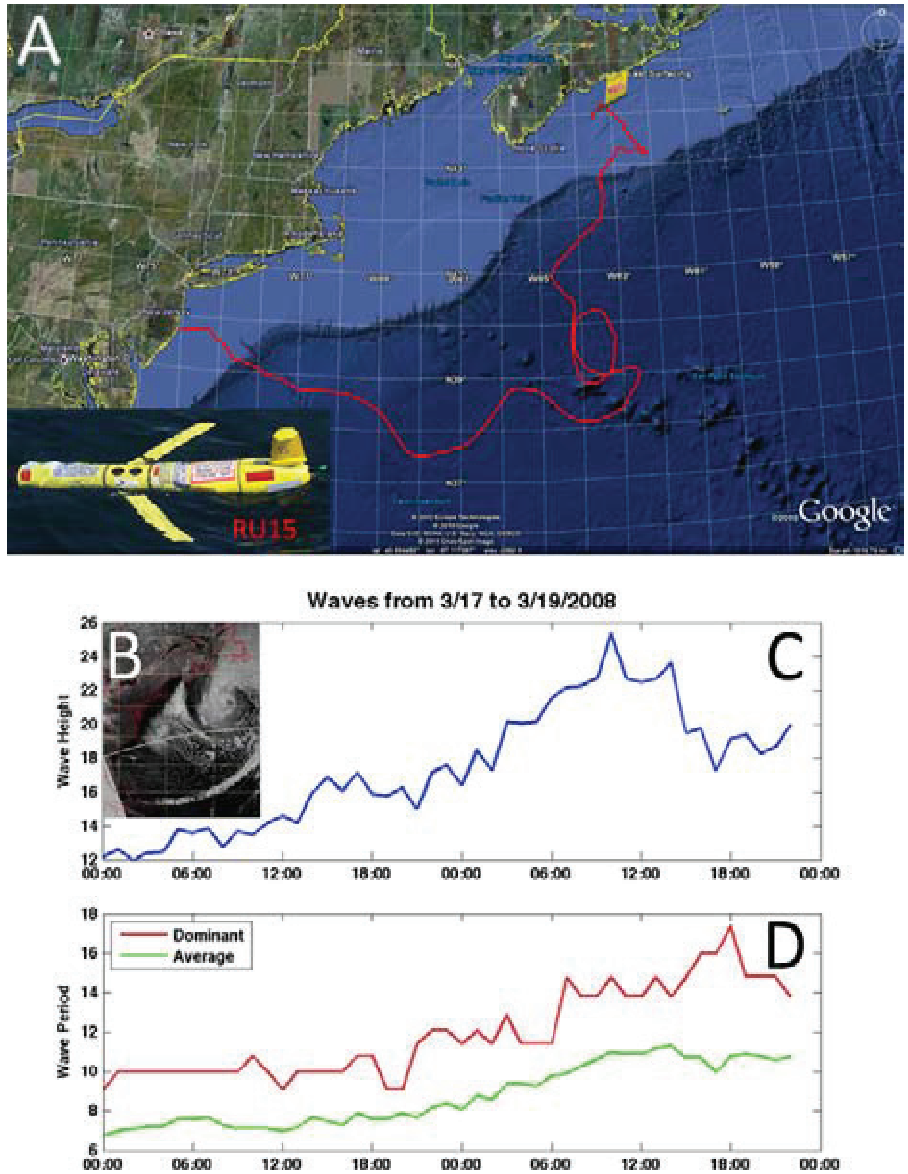

were quick to learn the many features of Google Earth and soon developed their ability to create their own analyses and interpretations. The third piece was the ability to post the new analyses products along with an explanation in an open forum. A blog space was established using open-source software. The blog was used not only as our own mission log but also as a means to share interpretations and comment on others. Students posted their weekly assignments to the blog and used the blog to discuss their results each week in class. The blog evolved into the students' textbook, written by the professors and students themselves, and quality controlled through weekly discussions of the postings.

RU15—New Jersey to Nova Scotia. Glider RU15's test flight to Halifax was our first long-duration test mission. It was run on a standard size glider, one of the first equipped with the new ruggedized tailfin designed for the Navy (Figure 2). ONR needed long-term tests of the new fin, especially to determine if the shorter tail would maintain communications during storms. NOAA needed a test of lithium batteries on the coastal gliders to see if they could provide the additional energy for power hungry biological sensors. RU15, modified by Rutgers glider technicians and students to fly off of lithium batteries, was deployed on the New Jersey coast in March of 2008 (Figure 2A). It flew for nearly 2 months on a track that took it out on the Tuckerton Endurance line (Castelao et al., 2008) across the shelf and slope and into the Gulf Stream. Weekly class activities included discussions of the best locations and methodologies for crossing the heavily fished shelf break. Students learned the commands for flying deep below the fishing nets and aiming for locations between the canyons that were focal points for fishing activity. Following the Gulf Stream downstream and exiting about 62.5 W, RU15 headed for a newly formed warm core ring for a boost of momentum to the north. In the process, students were introduced to the many satellite products for locating the meandering Gulf Stream, the ring formation, propagation and absorption process, and the history of ocean forecasting that developed from this region. Exiting the ring proved difficult, requiring a second lap around rather than a slow flight against the strong head current. Scientists and students learned the value of simple path planning tools to decide where to enter a ring and when to start leaving. After exiting the warm core ring on the second lap, RU15 flew from small eddy to small eddy across the Slope Sea, flying back up onto the continental shelf near 63 W and continuing east over the more wind-driven outer shelf until it reached the historic Halifax Line. From there, RU15 flew into shore where it was recovered by our collaborators at Satlantic, Inc., offshore Halifax Harbor. Along the way, RU15 encountered a large winter storm with significant wave heights exceeding 25 feet recorded by a nearby NOAA weather buoy (Figures 2B–2D). Even during the height of the storm, no Iridium satellite communication calls were missed by the antenna in RU15's shortened tail fin. But tests of the lithium batteries after recovery indicated that power was used faster than we expected. Our estimate of battery power available, the power draw of the vehicle, or both were in error.

RU17—New Jersey to the Azores (almost). With RU15's recovery on April 28, work on outfitting RU17 proceeded in earnest. There was little time to deal with the power uncertainty if we were to make the spring 2008 launch window. RU17 was launched on May 21 from an offshore location on the outer shelf to save power. RU17 would follow the same general path as RU15, crossing the shelf break between seafloor canyons to avoid the fishing activity. But getting into the Gulf Stream presented problems. There were no warm core rings to catch, and RU27 was on the western side of a Gulf Stream meander crest. It was shedding shingles of warm water that RU17 had to fly against, requiring a full month to get into the Gulf Stream. But the Gulf Stream was relatively straight that spring, and RU17 quickly flew down its length past the Grand Banks of Newfoundland (Figure 3A). The first third of the mission, New Jersey to the Grand Banks, was accomplished during the spring semester with a seasoned crew of students repeating what they had just learned from the RU15 test deployment.

The next task, passed from the *Atlantic Crossing* class onto our summer student interns in the NSF Research Internships in Ocean Sciences (RIOS) program, was to cover the middle third of the mission, flying RU17 from the Grand Banks to the Azores. After passing the Grand Banks, the Gulf Stream splits and filaments, taking several routes east. The region is characterized by an energetic mesoscale eddy field, with eddies that can speed the glider's progress east or totally halt it, sending it back west. This is precisely what occurred at 45 W where RU17 encountered a strong eddy that stopped eastward progress. Summer students running simulations with virtual gliders flying through the Navy's model forecast currents determined that our only alternative was to backtrack with the current to the west, then turn north to a zone of more favorable currents much farther north. The 5° of latitude excursion, with path decisions informed through model simulations, required a full month to complete. RU17 then turned east until about 38 W. During this segment of the flight, engineering students monitoring the flight parameters noted that the biological interactions intensified. Three types of interactions were discovered. One was a behavior that slowed down the glider's vertical motion during the night, and then let it speed up again during the day (Figure 3B). A second behavior included times that the glider's upward motion would nearly or completely stop (Figure 3C). Similar behaviors had been observed in the Gulf of Mexico when negatively buoyant Remora attach to a glider and hold the vehicle down until it triggers an emergency ascent. The third behavior student engineers discovered was the spinning of the glider caused by drag on one side. Hypothesizing that something may have been snagged by one of the wings, technicians and students developed a procedure to fly backwards that they tested on simulators. By deflating the tail floatation bag, pulling the pitch battery all the way back to lower the tail as if it is ascending and simultaneously pulling the pump in to reduce the volume, the glider sinks tail first, flying backwards. Repeated attempts could not clear whatever was causing the drag, and the spinning persisted. Over time, the engineers noted that the spinning was tied to the cycle of the moon. The spinning was worse during the new moon, when the biologists suspected that bioluminescence made the glider one of the brightest objects in the region. During the full moon, the spinning would cease, and the glider was able to fly a steady course again. Given this, our plan was to conserve power and use flight time during the new moon to reach the Azores so that an observation vessel could be launched for a visit.

That plan changed suddenly on October 26, when just before midnight GMT, RU17 scrambled to the surface to report a leak. Leak detection sensors are located in the nose and the tail of each glider. If even a drop of water crosses the leak sensor, a voltage drop is detected and the glider does an emergency ascent. We had seen leak detects with small voltage drops in gliders before, and upon recovery, a failure in an O-ring was detected by visual inspection. This leak detect was different, with an immediate and

FIGURE 3

(A) Track of RU17 on the flight towards the Azores. (B) Average duration of full excursion dives (bottom line) and climbs (top line) showing the day-night variation in climb performance. (C) Sample segment showing normal climbs (100–2 m) and numerous aborted climbs during the local night. (D) Time series of leak detect voltage (red) from the time of the last dive (black dots) on October 27 until the loss of communications on October 28, 2008. Yellow bars show the range of leak detect voltages in laboratory tests for water touching the leak detect sensor (top) to full immersion (bottom).

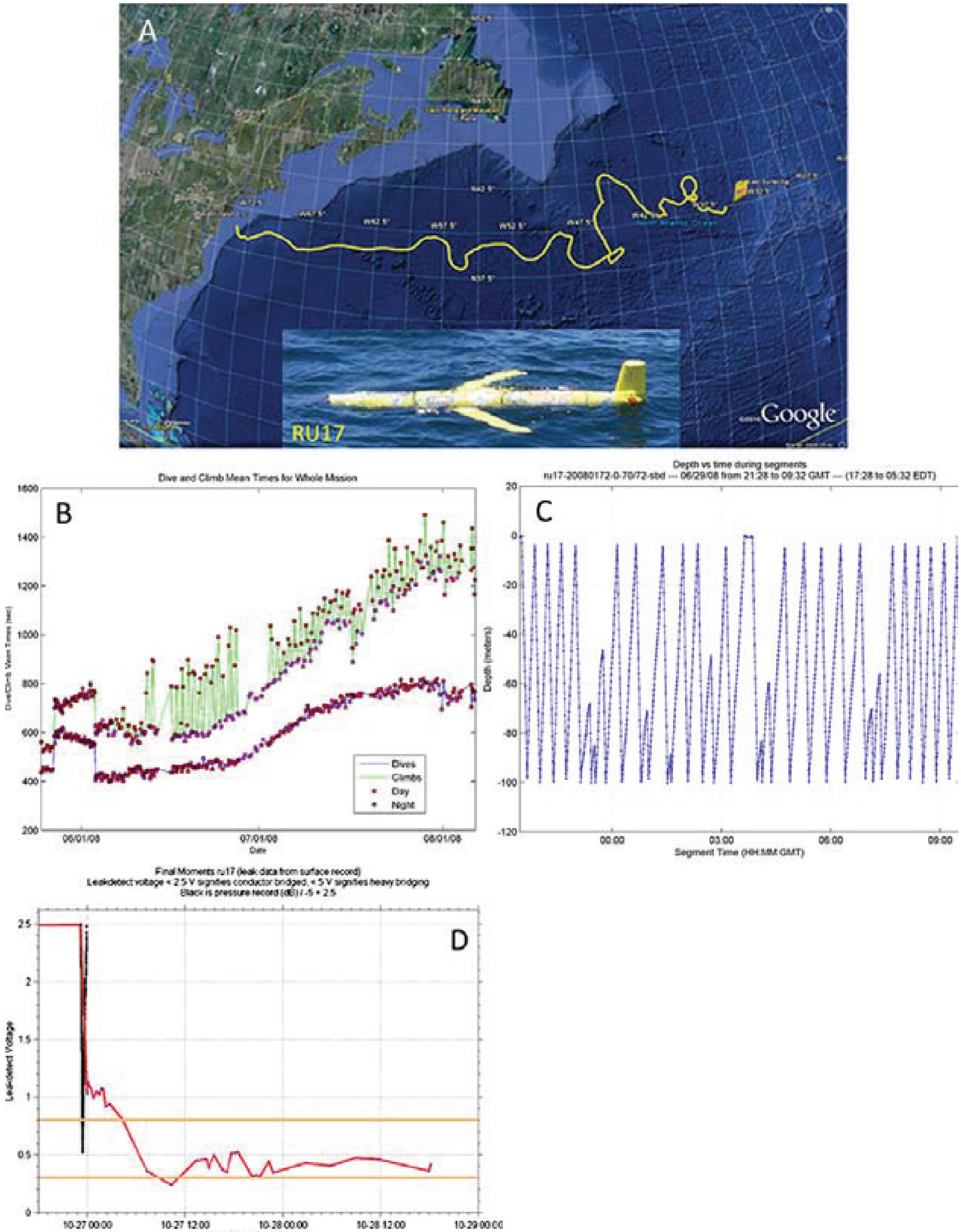

much larger voltage drop than we had ever seen. From the engineering data, the leak detect was triggered as RU17 was ascending toward the surface at a depth of about 50 m. The large voltage drop on the leak detect indicated that this was unlikely to be a similar O-ring failure. If it was corrosion, it is expected that the hole would break open on the way down as the pressure was increasing, not on the way up as pressure was decreasing. A leak in the air bladder would also result in a significant change in the vacuum inside the pressure hull. There was no change in vacuum, and an air bladder leak would be expected to occur at the surface when the bladder is being inflated, not at depth. Moving to the front, the seams on the movable piston on the buoyancy pump are a possibility, but the design cycles had not been exceeded, and a piston leak would be expected when it is moving at the top or bottom inflection points, not in the middle of a glide. We concluded that the most likely location for a leak of this size that could not be ruled out by the engineering data would be associated with the hull fittings of the CTD. In deployments off Hawaii, we have seen the CTDs damaged by big fish, including sharks, that can bend the sensor by bumping into it, presumably while they are chasing smaller preys that use the glider for cover.

RU17 remained at the surface for 2 days, transmitting its position and engineering data. While preparations were being made for recovery, the leak detect voltage continued to drop (Figure 3D). Students measured the reaction of the leak detect sensors to different amounts of seawater in the laboratory, discovering that the leak detect voltage was already suggesting that the sensors were fully submerged in seawater. Finally, on October 28, we received the last transmission from RU17. The flight of RU17 resulted in the loss glider and heartbreak but also the accumulation of significant knowledge on the long-duration flight requirements for shallow gliders. It reminded everyone of the risk.

RU27—New Jersey to Spain. Lessons learned from the flight of RU17 were used to inform the construction a second long-duration glider with an education mission. RU27 was constructed with an extended payload bay by Teledyne Webb Research as a new product, and as with RU17, the altimeter and payload bay computer were removed. The 100-m buoyancy pump used in RU17 was replaced with a 200-m pump based on the successful repeated deployments by Oregon State University. New pin supports strengthened the CTD. The 435 lithium C-cells on RU17 grew to 453 plus 15 reserve on RU27 by space-saving rearrangements of the internal electronics (Table 1). A Coulomb meter was developed and installed to measure how much energy was being drawn from the batteries. Hull sections and the tail cone were coated with the light rubberized ClearSignal (Lobe et al., 2010) to minimize the need for heavy ablative antifouling paints. Students were involved with all aspects of the build and conducted a test flight from February 18 to March 13, 2009, across the shelfbreak to deepwater to tune the steering and establish the power usage.

RU27 was christened the *Scarlet Knight* by IOOS on March 23, 2009. Placed inside the hull was a NOAA coin, a USB memory stick containing over 100 letters from school children to be printed in Spain and sent back upon arrival, and paper copies of the letters congratulating partners on both sides of the Atlantic, just in case the mission was successful. The *Scarlet Knight* was launched offshore Tuckerton, New Jersey, on April 27, 2009, 10 years after the first Slocum glider was flown at sea in the same location by Doug Webb and a Rutgers student and 20 years after the publication of *The Slocum Mission* (Stommel, 1989).

Continuous monitoring of the flight was coordinated by professors (S. Glenn, O. Schofield, and J. Kohut) working with teams of undergraduate students in the Rutgers *Atlantic Crossing* research course during the spring and fall semesters and with teams of undergraduate interns participating in the pilot for the Summer Research Institute sponsored by the DHS Center of Excellence for Port Security between semesters. Typically, 10 teams of two to three students were working in parallel on different aspects of the mission,

TABLE 1

Battery pack comparison for a standard alkaline-powered coastal glider and the RU27 lithium-powered trans-Atlantic glider (not including 15 batteries reserved for emergency power).

	Number of C-Cells	Energy per C-Cell	Daily Average Power Use	Theoretical Duration	Cost per C-Cell	Total Battery Cost
Alkaline Slocum	230	21.6 kJ	2 W	34 days	$5.22	$1,200
RU27	453	88.5 kJ	1.5 W	371 days	$50.60	$22,922
Factor	1.9	4.1	1.33	10.9	9.7	19.1

FIGURE 4

Trans-Atlantic track of RU27 marking the location of 16 significant events in the flight. Insets: (2) RU27 leaves the shallow water and fishing activity of the Mid-Atlantic Bight continental shelf; (3) RU27 navigates the meandering warm jet of the Gulf Stream flowing from Cape Hatteras to the Grand Banks; (6) RU27, after encountering a strong head-current, flies around the southern side of a large cyclonic cold-eddy; (8) RU27 approaches the Phantom Eddy in the HyCOM forecast, an artifact generated by the data assimilation scheme; (10) Hurricane Bill leaves the U.S. East Coast and turns east toward RU27; (16) RU27 is approached by the Spanish *R/V Investigador* for recovery (photo by diver Dan Crowell).

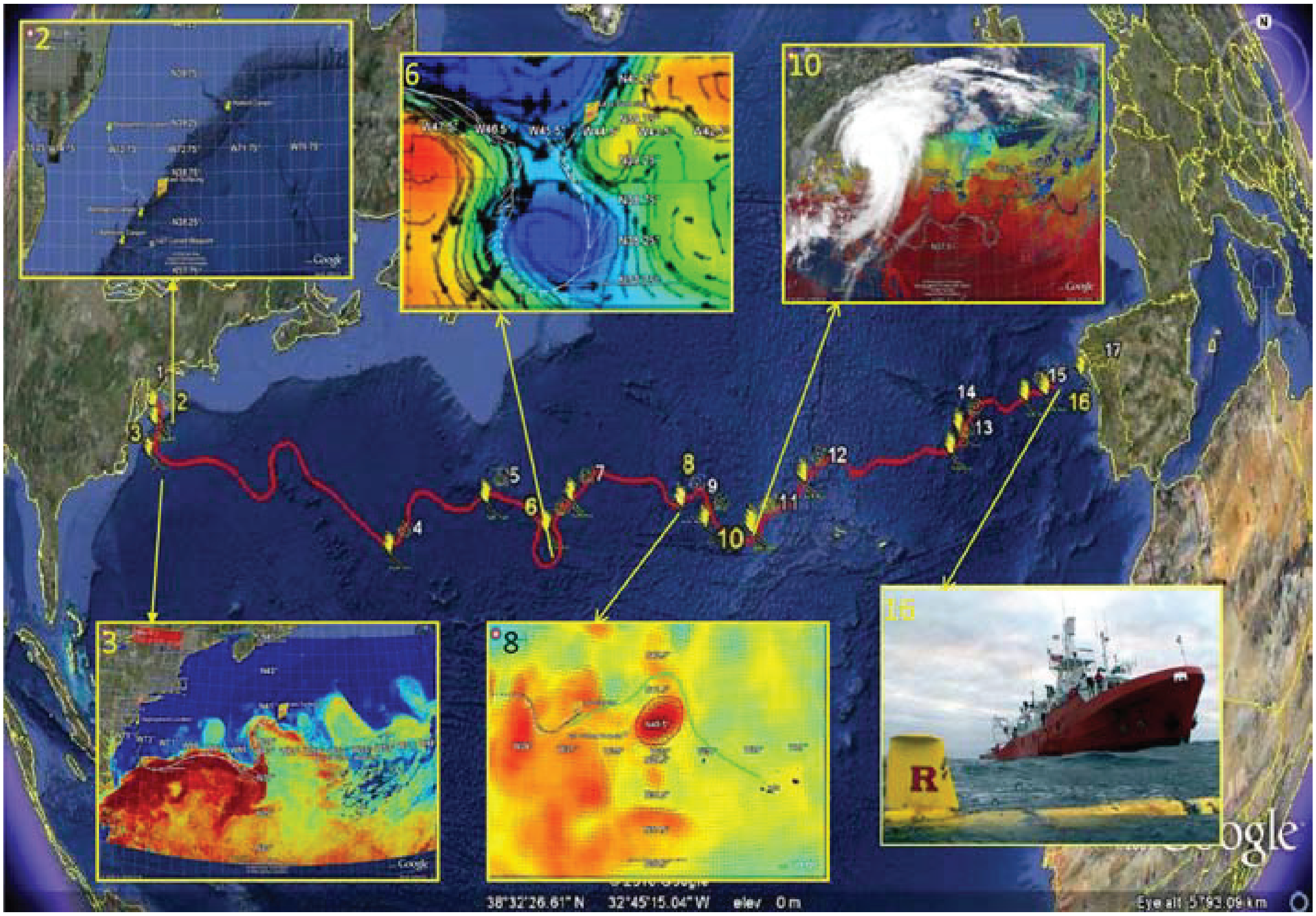

from watching the weather for winds and waves, validating the ocean current models, monitoring the glider flight performance and its ability to communicate, analyzing the glider data, definition of a safe landing zone, and logistics for recovery. The students blogged their results and met weekly as a group to discus new information and define strategies for the next week.

The flight track of RU27 across the Atlantic is shown in Figure 4, where the flight blog highlights labeled by number in the figure are described in Table 2. By May 2, RU27 had completed the dangerous trip across the continental shelf, where it encountered fishing fleets and shallow water without an altimeter. From there, the glider would be in deepwater, where it would remain for the rest of the mission. By May 7, RU27 had made it into the Gulf Stream. The strategy was different from before, with RU27 instead approaching an eastward propagating Gulf Stream meander from the downstream side. As the meander crest propagated forward, RU27 was entrained after only 10 days at sea and a full 10 days ahead of the projected schedule. With May being one of the historically best months for viewing satellite sea surface temperature (SST) images of the Gulf Stream, RU27 easily traversed the Gulf Stream's entire length in less than a month, with only a short delay caused by a quick encounter with a cold core ring near May 23. The first half of June was spent circling around the southern side of a large cyclonic eddy that

TABLE 2

RU27 Blog Highlights from 2009.

No.	Date	Event Description
1	Apr 27	Deployed from Tuckerton, NJ.
2	May 2	Leave the continental shelf and enter deepwater where it will remain for the entire deployment. Successfully made it through the fishing activity and did not collide with the bottom without an altimeter. First look at the deepwater power usage.
3	May 7	Into the Gulf Stream. Only 10 days at sea and already 10 days ahead of schedule.
4	May 23	Spun out of the southern side of the Gulf Stream and into a cold eddy. Turn north to fly back into the Stream.
5	Jun 5	Leave the Gulf Stream region, passing south of the Grand Banks of Newfoundland. Encounter a head current along the northern side of the largest cold eddy of the trip, requiring RU27 to loop around its southern side.
6	Jun 18	Finally pull out of the cold eddy on its eastern side, just before being swept around for a second loop.
7	Jun 29	Break through a countercurrent after a week-long struggle to fly just 125 km. This was RU27's first persistent countercurrent not associated with a strong eddy structure.
8	Jul 19	After navigating the eddy field with excellent ocean forecasts, RU27 encounters a forecast eddy that is clearly incorrect. RU27 focuses our attention on a series of sensitivity studies as to why this anticyclonic warm eddy incorrectly appears in the forecast.
9	Aug 2	Enter European waters for the first time. These are the Portuguese waters surrounding the Azores. The steering difficulties attributed to an unknown biological interaction begin.
10	Aug 25	Hurricane Bill passes to the north, generating large waves. The glider team prepares to depart the Azores on the sailboat *Nevertheless*.
11	Aug 28	Glider team completes its mission to document the biological activity on RU27, clean off the barnacles they found, and let it resume its mission without taking the glider out of the water.
12	Sep 8	RU27 breaks the along-track distance record of 5,700 km set by RU17 in 2008.
13	Oct 12	RU27 hits the half-power point on the theoretical power curve.
14	Oct 22	RU27 breaks free of the second persistent countercurrent. Like the first encounter, a full week of careful navigation was required.
15	Nov 14	RU27 crosses into European waters for the second time. This time it crosses into Spanish waters off of the Spanish mainland.
16	Dec 4	Recovery aboard the Spanish Research Vessel *Investigador*. RU27 exactly on target. Just north of the maritime border between Spain and Portugal and just west of the 12 W line, safe from the shipping traffic and fishing activity.
17	Dec 11	Landfall in Baiona, Spain

seemed to be parked just to the east of the Grand Banks. The rest of June and July was spent navigating the North Atlantic mesoscale eddy field, flying from eddy to eddy based on guidance from satellite altimeters and ocean forecast models. It was during July that RU27 focused attention on the largest forecast model error encountered on the trip, a mesoscale anticyclonic circulation that came to be known as the Phantom Eddy generated through the incorrect treatment of the combined drifter and satellite altimetry ingested by the data assimilation component of the forecast system.

In August, RU27 entered the European waters surrounding the Azores. This is where steering problems attributed to an unknown biological interaction began. At times, RU27 would fly straight, and at other times, it would spin in a tight circle, with no apparent day-night or moon phase cycling as observed for RU17. On August 25, Hurricane Bill passed to the north of RU27, leaving large waves in its wake. As Bill dissipated over the United Kingdom, a glider team left the Azores on the sailboat *Nevertheless* to document the cause of the steering problems. On August 27, the glider team rendezvoused with RU27, discovering that barnacles had attached themselves to the narrow uncoated seams between the five glider hull sections, forming four rings of barnacles that circled the glider. The barnacles could fan out or retract, creating significant and variable drag on RU27. The uneven growth resulted in uneven drag and steering offsets. The barnacles were photographically documented and then removed by hand by divers, while RU27 remained in the water.

Once cleaned and flight characteristics were verified, RU27 resumed its mission to fly east the next day on August 28. September and October continued the process of navigating the North Atlantic eddy field based on satellite altimetry and forecast model guidance. On November 14, RU27 crossed into European waters surrounding the coast of Spain and Portugal. Inspired by discussions with their student collaborators in the Azores and Canaries, the undergraduates chose Baiona, Spain, for RU27's potential landfall because of its historical significance. Baiona is the Spanish port where the caravel *Pinta,* the fastest of Columbus' three ships (the first to sight the New World and the first to return to Europe in 1493), made landfall. RU27 proceeded to the chosen pick-up point, a safe spot just north of the maritime Spanish-Portuguese border and just west of the high traffic north-south shipping lanes. It was recovered by Puertos del Estado using the *R/V Investigador* on December 4, 2009, the first underwater glider to be deployed on the western side of the Atlantic and recovered on the eastern side. The trans-Atlantic flight of RU27 required 221 days to cover the 7,400 km along-track distance, completing over 22,000 undulations and making over 1,000 satellite phone calls to report data and receive new commands. Total power used was 7,750 Wh, equivalent to a 100-W light bulb turned on for 77.5 h or just under 3.25 days.

On December 9, 2009, still aboard the recovery vessel *R/V Investigador,* RU27 made landfall in Baiona. It was here in Baiona that Spain's Minister of Development officially returned RU27 to the U.S. delegation, lead by representatives of the U.S. White House Office of Science and Technology Policy, NOAA, and Rutgers. A congratulatory video from the U.S. Secretary of Commerce was played, and the Mayor of Baiona unveiled a new RU27 plaque permanently placed on the seawall next to the plaque commemorating the voyage and crew of the *Pinta*.

Over 25 multiauthored student research posters were constructed from the flight and presented at research meetings, including one summary student poster representing the entire team that was presented at the 2010 Ocean Sciences meeting. The Dean of Undergraduate Education sponsored events for the students to tell their stories and inspire other undergraduates to get involved. Our class size doubled each semester, from 3 to 7, to 13, to 26 over the 2 years covering the flights of RU17 and RU27, leveled off near its present range of 50–60. The opportunity for undergraduate students to gain hands-on experience with the latest technology, to take risks with a robot at sea while remaining in a safe on-shore environment, and to experience the international collaborative teamwork required to successfully complete this mission are reasons cited by the students in their own recruiting video.

In addition to oceanography classes, the trans-Atlantic flight was used as the subject of a documentary filmed, edited, and produced by a collaborating English professor (D. Seidel) and her undergraduate students in a series of English courses, including *Documentary Filmmaking* and *Digital Storytelling*. The documentary *Atlantic Crossing: A Robot's Daring Journey* has now won eight film festival awards. English students in the class not only learned documentary film making but also learned about ocean science by working alongside oceanography undergraduates for 1.5 years. RU27 also was the inspirational centerpiece for the *Communicating Ocean Sciences* course (J. McDonnell) in the spring of 2009, using climate change as the science theme and gliders as the new enabling technology. Undergraduate designed and tested hands-on glider activities designed to demonstrate new technologies for monitoring climate change at informal education institutions are now in place at New Jersey's Liberty Science Center as a permanent docent-led activity and have also been demonstrated by students on the floor of the Smithsonian National Museum of Natural History.

RU27—Post-Flight Data Analysis. The datasets collected by RU27 were analyzed by a team of summer student interns in the 2010 NSF RIOS program. The three-person undergraduate team consisted of a physics major, a biology major, and an engineering major. The interdisciplinary team results on heat transport calculated from RU27 and compared with the Navy forecast model used in the crossing is shown in Figure 5. For RU27, temperature (Figure 5A) and the northward depth-averaged velocity (Figure 5B) were combined to provide a proxy for heat transport (Figure 5C). The same variables generated from an ocean numerical model (the Navy's Hybrid Coordinate Ocean Model, HyCOM) are plotted in Figures 5D–5F.

Starting on the Mid-Atlantic Bight shelf in late April and continuing into early May as RU27 crossed the Slope Sea, temperatures in the glider data and the model are cold, around 11°C. Currents are generally slow to the south for both glider and model. From May 7 through June 5, RU27 navigated the warm water of the Gulf Stream. The glider data indicates, as expected, that the warm water of the Gulf Stream is above 18°C in the

FIGURE 5

Comparison of measured (Glider RU27; A, B, C) and modeled (HyCOM; D, E, F) trans-Atlantic cross sections of temperature (A, D), north-south component of the current (B, E) and north-south component of the heat transport (C, F) along the track shown in Figure 4.

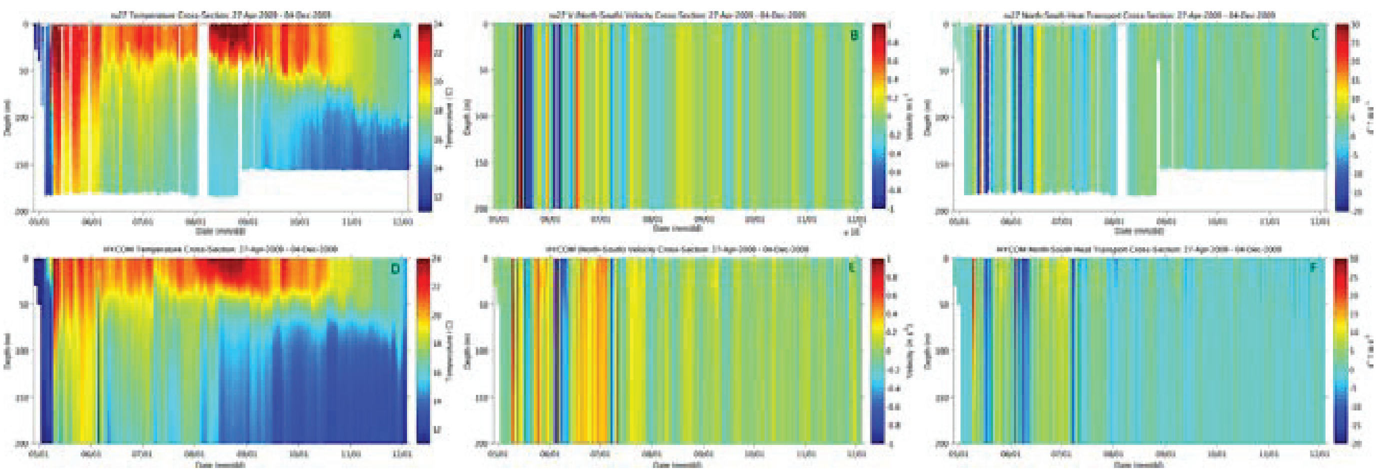

upper 200 m along the entire length of the Gulf Stream. Temperature differences between the model and data in this region, specifically the cold bands below 100 m, are due to imperfect forecasts of the Gulf Stream position. The banding in the north-south velocity time series is apparent in both the glider data and the model. Both have a strong band of northward velocity (red) as RU27 moves north with the Gulf Stream near 64 W, both exhibit southward velocity (blue) as RU27 travels the length of the Gulf Stream from 64 to 55 W, and both turn to positive northward velocities as RU27 turns north with the Gulf Stream on May 23 near 54 W. Small differences between the model and the data can be attributed to incorrect placement of the Gulf Stream in the model, but the general trends are reproduced. Most strikingly, the depth average current returned by RU27 is not that different in structure from the actual current profile in the model. This is important, since the resulting heat transport is dominated by the variability in the currents. In this region, the water is nearly uniformly warm in the upper 200 m, and the heat transport depends on the proper location of the Gulf Stream meander crests and troughs.

Leaving the Gulf Stream region on June 5, RU27 encounters a strong anti-cyclonic eddy on the southeast side of the Grand Banks. The warm water above 18°C is shallower than 50 m in both the glider data and the model. North-south currents in both abruptly switch from southward (blue) to northward (red) as the southern side of the cold eddy is crossed, remaining in place until mid-June when RU27 breaks free of this eddy and heads east. As in the Gulf Stream, the currents dominated heat transport in the eddy, and therefore, the location of this eddy in the forecast is critical. For the next month and a half, RU27 navigated the North Atlantic eddy field. On July 29, RU27 encounters the largest forecast error observed in the model. During this time, the warmest waters above 18°C are observed and forecast to be in the upper 40 m of the temperature field. Less variability is observed in the glider data than the model, which might indicate that the model may be overestimating the intensity of eddies and their impact on the surface layer temperature field. Currents in both the model and the data show alternating bands of ± 20 cm/s north-south currents, depending on the side of the eddy. Calculating the correct heat transport from model results becomes a challenge for placing the eddies in the proper locations. At the beginning of August, RU27 turns southeast towards Portuguese waters, and a warming trend is observed in the upper 30 m of the data and the model. This warming is abruptly halted by the passage of Hurricane Bill on August 25 and the resulting mixing in both the model and the data. Continuing east from the Azores, the process of flying eddy to eddy continues as the magnitude of the variability in the eddy currents remaining relatively constant, with only occasional currents exceeding 20 cm/s in the north or south direction. The surface layer of the ocean is observed to cool as winter approaches. Water less than 14°C rises above the 100 m depth. By December, the water column is nearly uniformly cool near 14°C. Heat transport is small compared with the western side of the basin earlier in the year.

Evolving the Undergraduate Education Experience—Lessons Learned

Traditional university marine science programs are often structured around a classical model of classroom learning in the first 2–3 years, after which a small minority of the students gain field experience by working in research laboratories and gaining prized access to research cruises. This has been an effective model for developing future Ph.D. students over the last 50 years. Given the challenges facing society today, there is a greater need for science education than only grooming future Ph.D. students. It is critical that the undergraduate experience expands ocean literacy across all of the sciences and humanities. This is especially important since the observed changes occurring throughout the world's ocean will have profound economic, cultural, and security consequences. Based on our experience, oceanography provides a level of adventure that is a vehicle to inspire students to begin and continue pursuing degrees in science and engineering. Given our positive experience of entraining undergraduates into the sciences via ocean exploration, we believe it provides a blueprint for redesigning the undergraduate education curriculum. In fact, it is now being reapplied at Rutgers with a larger and even more distributed group to engage students in environmental sciences issues associated with the Raritan River and Estuary. The Raritan Initiative utilizes Rutgers location on the banks of the Raritan River to involve students from across campuses in interdisciplinary studies that use the river and estuary as a natural laboratory. The natural environment provides motivation, and the co-location provides access. The course work includes freshman year seminars to entrain students, an interdisciplinary team taught sophomore year field course, and the support of senior thesis studies involving data from the Raritan.

The new approach has several characteristics that are important:

It is critical to engage students as early as their freshmen year in research. The Web-based nature of ocean observatories allows students to take part with ongoing experiments, which lets them live the excitement of doing research. They experience the uncertainty, adventure, and creativity required to conduct an experiment, which provides an effective counterbalance to classroom learning that often portrays science as a very linear process. Taking part in the ocean experiments, they experience the numerous stumbling blocks, such as the loss of RU17 after months of work. These hurdles, while emotionally draining, generally engage students to see the adventure through until the end. Many of the students who joined the Atlantic crossing effort of RU17 were freshmen and sophomores. The RU17 attempt, failure, engineering analysis, construction of RU27, and eventually successful Atlantic crossing was a 3-year process. For the students to experience the full adventure, they need to be engaged early in their academic career to realize the fruits of their labor. Designing strategies to entrain the students as they enter the university is critical.This realization led us to establish Oceanography House as a dedicated freshman dormitory for students interested in the oceans regardless of their major. The living and learning community is advertised during the university open house for incoming students and provides them with a direct link to marine science from their first day on campus. Undergraduates involved in the observatory work also visit their high schools to provide science talks and act as ambassadors. The students of Oceanography House meet weekly with professors and upper class students to focus ongoing scientific efforts.

Developing a near-peer community is important for expanding diversity. A critical component to the oceanography living learning community is that incoming students are provided guidance by upper class advanced oceanography students. These oceanography mentors provide assistance in transitioning the freshmen into the ocean exploration classes. This is critical as the students entering the classes as freshmen have a wide range of expertise, represent a wide range of disciplinary interests spanning from oceanography to English, and mirror the ethnic and cultural diversity of the Rutgers student body, one of the most diverse research universities in the U.S. For the upperclassmen, they are put in a position of mentorship that requires them to understand key concepts with sufficient detail to keep the new students on track, providing teaching experience. Many of the students who do not pursue graduate school often become science teachers. This is particularly important since there is a critical need to improve science education at the K-12 education level. To assist in this process, the students are provided the *COSIA* opportunity for developing the skills required to be an inspirational science teacher by providing a firm foundation in communication techniques and pedagogy.

Allow the students to work as teams. Given the goal of increasing the diversity of disciplines, the teacher is often confronted with a wide range of student skills/science knowledge. To help address these gaps and to facilitate the near-peer relationships, student are often given specific projects as a team of three to four students. The team consists of at least one advanced upperclassmen. Teams are coordinated in a systems engineering model, where initially individual projects are iterated over a period for a few months and then the individual parts are combined to provide an overall system to help coordinate glider activities. For example, during the RU27 journey, the undergraduate teams focused on a successful recovery off the coast of Spain. The teams documented the major shipping lanes, provided weather and wave forecasts, provided logistical planning for the ship crew, and researched the history of the Spanish port cities to help a develop a RU27 recovery plan.

Give students intuitive tools to analyze data and make their own discoveries. The analysis of the RU27 data and comparisons to ocean forecasts by undergraduate summer interns was enabled by a new toolkit of interactive glider software developed specifically for education. As students gain experience with program languages and complex file formats, they could do these same analyses on their own. But developing a working knowledge of these software skills is a barrier to many students. Simple intuitive interfaces, such as Google Earth, were used by students at any level to visualize and compare datasets, allowing them to draw their own conclusions. The glider data analysis interfaces developed here and tested by the undergraduates in the 2010 NSF RIOS program enabled the students to visualize and interpret vertical glider data as easily as they did with the horizontal data in Google Earth. The result of the software test was three research posters, one on the heat transport of RU27 discussed above, a second on the flight characteristics of a new Slocum Thermal Glider, and a third on optimizing the flight profiles for heat transport calculations along 26.5 N, a standard trans-Atlantic sampling line for monitoring the maximum in the north-south heat transport caused by the Meridional Overturning Circulation.

A Future Vision—The Challenger Mission and a Global Classroom

In Baiona, Spain, Rick Spinrad reflected on his initial 2006 challenge to modify one of our gliders and fly it across the Atlantic. With this challenge complete, Dr. Spinrad issued a second challenge, to send an internationally coordinated fleet of gliders on a circumnavigation that revisited the track of the HMS *Challenger*. The original *Challenger* mission (Cornfield, 2003) was the first dedicated scientific circumnavigation of the globe. It took 3.5 years, leaving England in December 1872, returning in May 1876, and traversing 111,000 km, exactly 15 times the distance covered by RU27.

As with the trans-Atlantic glider mission, a circumnavigation will require the development of new technologies, and it will require the development of new international teams. The range of technologies potentially includes not only the full suite of electric gliders available to the international community from both the U.S. and China but also the Slocum Thermal Glider, part of the original vision of Doug Webb and Hank Stommel. The fleet will likely include a mix of gliders or even hybrids of the thermal and lithium battery technology. Our own experience has shown that flexibility in glider design is again a desired trait. Thermal gliders work best when there is a large temperature difference between the surface and the bottom of the undulation, typically about 15°C. Winter and summer forecasts from the HyCOM model indicate that thermal gliders can be tuned to cover much of the subtropical ocean basins and the tropics. Our own student calculations have demonstrated that in some cases, for example, the calculation of heat transport in the subtropical ocean basins, that flying to the deepest allowable depth on every undulation may not be the optimal dive profile. Again, flexibility in the mix of dive profiles is going to be desired, with deep profiles interspersed with shallow.

As with the trans-Atlantic mission, the Challenger Mission will require new technologies, but it will also require people. We have found that many of those people already exist—they are already in our classrooms. Our students have already developed a prospectus and approach for the Challenger Mission, starting with an expansion from the North Atlantic to the South Atlantic, followed by a circling of the globe. Moving to the South Atlantic and eventually the globe will require a transformation from a Rutgers classroom to a globally distributed classroom, facilitated by on-line virtual learning communities, entraining an even more diverse range of partners and disciplines, and providing an even broader global perspective to the generation that must deal with climate change over their lifetimes. We hope that the perspectives gained through the local *Atlantic Crossing* course and the envisioned global *Challenger Mission* course will provide our students with the scientific perspective and the global cultural experience to meet the challenges of their generation.

Acknowledgments

Slocum gliders were developed through the vision and support of the Office of Naval Research, transitioning from an engineering demonstration on its first deployment at sea, to a research tool used by many federal agencies, to an operational Naval asset in less than a decade. NOAA provided the challenge for the first trans-Atlantic missions. Rutgers alumni, Teledyne Webb Research, NOAA, and U.S. IOOS provided support for the build and the launch. Educational support was provided by the National Science Foundation and the Department of Homeland Security. Our partners in Spain at Puertos del Estado and Universidad de Las Palmas de Gran Canaria provided support for the recovery. These and future missions would not be possible without the direct participation and continuing interest of the *Atlantic Crossing* students and their international collaborators.

Lead Author:

Scott Glenn
Coastal Ocean Observation Laboratory, Institute of Marine and Coastal Sciences, School of Environmental and Biological Sciences, Rutgers University
71 Dudley Road, New Brunswick, NJ 08901, USA
Email: glenn@marine.rutgers.edu

References

Castelao, R., Glenn, S., Schofield, O., Chant, R., Wilkin, J., & Kohut, J. 2008. Seasonal evolution of hydrographic fields in the central Middle Atlantic Bight from glider observations. Geophys Res Lett. 35, L03617, doi: 10.1029/2007GL032335.

Chant, R.J., Wilkin, J., Weifeng, Z., Choi, B., Hunter, E., Castelao, R., … Moline, M.A. 2008. Dispersal of the Hudson River Plume on the New York Bight. Oceanography. 21(4):149-162.

Committee on Prospering in the Global Economy of the 21st Century and Committee on Science, Engineering, and Public Policy. 2007. Rising above the Gathering Storm: Energizing and Employing America for a Brighter Economic Future. Washington, DC: National Academies Press. 592 pp.

Cornfield, R. 2003. The Silent Landscape: The Scientific Voyage of the HMS Challenger. Washington, DC: The Joseph Henry Press. 285pp.

Davis, R.E., Eriksen, C.E., & Jones, C.P. 2003. Technology and applications of autonomous underwater vehicles. In: Autonomous Buoyancy Driven Underwater Gliders, ed. Griffiths, G., 37-58. London: Taylor & Francis.

Glenn, S.M., Dickey, T.D., Parker, B., & Boicourt, W. 2000a. Long-term real-time coastal ocean observation networks. Oceanography. 13:24-34.

Glenn, S.M., Boicourt, W., Parker, B., & Dickey, T.D. 2000b. Operational observation networks for ports, a large estuary and an open shelf. Oceanography. 13:12-23.

Glenn, S.M., & Schofield, O. 2003. Observing the oceans from the COOL room: our history, experience, and opinions. Oceanography. 16(4):37-52.

Glenn, S., & Schofield, O. 2009. Growing a distributed ocean observatory: our view from the COOL room. Oceanogr Mag. 22(2):128-145.

Lobe, H., Haldeman, C., & Glenn, S. 2010. ClearSignal coating controls biofouling on Rutgers glider crossing. Sea Technol. 51:91-96.

Munk, W. 2000. Oceanography before, and after, the advent of satellites. Elsevier Oceanogr Ser. 63:1-4. doi: 10.1016/S0422-9894(00)80002-1.

Rosenfeld, L., Sullivan, D., & Murphree, T. 2009. Certification for oceanographic professionals: a needs assessment study. The MATE Center. 1-72 pp.

Schofield, O., Kohut, J., Aragon, D., Creed, L., Graver, J., Haldeman, C., … Glenn, S.M. 2007. Slocum gliders: robust and ready. J Field Robotics. 24(6):1-14. doi: 10:1009/rob.20200.

Schofield, O., Kohut, J., Glenn, S., Morell, J., Corredor, J., Orcutt, J., … Boicourt, W. 2010a. A regional Slocum glider network in the Mid-Atlantic bight leverages broad community engagement. Mar Technol Soc. 44(6): 185-195.

Schofield, O., Glenn, S., Orcutt, J., Arrott, M., Brown, W., Signell, R., … Oliver, M. 2010b. Automated sensor networks to advance ocean science. Trans Am Geophys Union. 91(39):345-346. doi: 10.1029/2010EO390001.

Stommel, H. 1989. The Slocum mission. Oceanography. 2(1):22-25.

Tang, D., Moum, J., Lynch, J.F., Abbott, P., Chapman, R., Dahl, P.H., … Newhall, A.E. 2007. Shallow Water ’06—A joint acoustic propagation/nonlinear internal wave physics experiment. Oceanography. 20(4):156-167.

Continental Shelf Research 63 (2013) S26–S35

Contents lists available at SciVerse ScienceDirect

Continental Shelf Research

journal homepage: www.elsevier.com/locate/csr

Research papers

Role of wind in regulating phytoplankton blooms on the Mid-Atlantic Bight

Y. Xu *, B. Cahill, J. Wilkin, O. Schofield

Coastal Ocean Observation Lab, Institute of Marine and Coastal Sciences, School of Environmental and Biological Sciences, Rutgers University, New Brunswick, NJ, 08901, US

ARTICLE INFO

Article history:
Received 13 April 2011
Received in revised form
11 September 2012
Accepted 17 September 2012
Available online 26 September 2012

Keywords:
Light
Nutrients
Mixed layer depth
Phytoplankton
Mid-Atlantic Bight

ABSTRACT

Mixing has long been recognized as having an important role in influencing underwater light and nutrient budgets and thus regulating phytoplankton bloom. Mixing related to stratification and de-stratification is a key parameter of the physical environment that can control the timing and magnitude of blooms. Here we use a high-resolution three-dimensional biogeochemical model in the Mid-Atlantic Bight (MAB) to study phytoplankton bloom dynamics for the years 2004–2007. We present a simulated fall-winter bloom in the shelf region and spring bloom in the shelf-break front region. The ratio of light over mixed layer depth (MLD) was used to determine the trade-off effects of mixing (increase mixing will increase nutrients availability but decrease light availability). We find that the critical light value ($I'_{chl\ \mathrm{mas}}$) is around 60 (W m^{-2}) for the shelf region and 150 (W m^{-2}) for the shelf-break front region. There is a predictable linear regression relationship between $I'_{chl\ \mathrm{mas}}$ and depth. A sensitivity run with no wind forcing was used to test the role of wind-induced mixing on the balance between light and nutrient terms and its influence on timing and magnitude of the bloom. The phytoplankton dynamics in the shelf-break front region are found to be more sensitive to the wind-induced mixing.

Published by Elsevier Ltd.

1. Introduction

Broad continental shelves are highly productive systems that are globally significant zones for the biogeochemical cycling of elements (Longhurst, 1998). This is especially true for the Mid-Atlantic Bight (MAB), which has an extremely productive ecosystem that is fueled by large seasonal phytoplankton blooms (O'Reilly and Busch, 1984; O'Reilly et al., 1987). This has motivated numerous observational studies on the physical forcing of phytoplankton blooms in the MAB. These studies have documented the spatial and temporal variability in phytoplankton biomass in the MAB and have hypothesized about the key physical processes that underlie the observed variability. The 12 yr (1977–1988) NOAA NMFS Marine Resource Monitoring and Prediction (MARMAP) survey of the Northeast of US continental shelf found the highest phytoplankton concentrations during the winter-spring (O'Reilly and Zetlin, 1998). This was consistent with previous results from the Coastal Zone Color Scanner (CZCS) and Sea-viewing Wide Field of view Sensor (SeaWiFS) imagery that showed a fall-winter maximum of chlorophyll concentration in the middle and outer shelf waters and a spring maximum in the shelf-break/slope waters (Ryan et al., 1999; Xu et al., 2011; Yoder et al., 2001). Despite these large data sets, the observational studies did not have the spatial and temporal data required to link the environmental factors that underlie the phytoplankton dynamics. This has prompted the development of coupled ecosystem models to test hypotheses about the physical regulation of the MAB phytoplankton communities (Fennel et al., 2006).

Models describing phytoplankton dynamics must reconcile a phytoplankton's need for light and nutrients, both of which are related to the overall mixing in the water column. The limitation of light to support phytoplankton growth builds on the (Sverdrup, 1953) "critical depth" model which predicts the initiation of phytoplankton blooms only after cells reside at a the critical depth where photosynthesis is larger than respiration allowing for the build-up of biomass. The maximum depth suitable for phytoplankton photosynthesis is most often defined as the depth where photosynthetic available radiation (PAR) is 1% of its surface value. While the absolute lower limit of light capable of supporting photosynthesis is still a subject of debate (Dubinsky and Schofield, 2010), estimates of the compensation depth irradiance based on Sverdrup's theory suggest it is relatively uniform throughout many regions of the ocean (Siegel et al., 2002). If light is present in sufficient quantities, the magnitude and duration of the bloom is then a complex function of mixing, nutrient availability (Tilman, 1982) and grazing pressure (Fasham et al., 1990; Gentleman et al., 2003; Martin, 1965; Turner and Tester, 1997). The flux of nutrients to the euphotic zone is determined by mixing across the nutricline, which can happen with mixed layer depth (MLD) increase if it is associated with

* Corresponding author.
E-mail address: xumeihao@gmail.com (Y. Xu).

0278-4343/$ - see front matter Published by Elsevier Ltd.
http://dx.doi.org/10.1016/j.csr.2012.09.011

entrainment. MLD thus has been demonstrated to be a key factor in determining phytoplankton abundance (Behrenfeld et al., 2002; Field et al., 1998); however while vertical mixing in the upper-ocean boundary layer can increase productivity in the surface waters through enhanced nutrient supply from deep waters it can also decrease productivity due to mixing phytoplankton below the critical depth and therefore introducing the possibility of light limitation (Dutkiewicz et al., 2001). To parameterize the relative roles of mixing and light availability the ratio of Z_{mld} (mixing layer depth) to Z_{eu} (euphotic depth) has been used to describe the regulating primary production (Huisman et al., 1999; Irigoien and Castel, 1997); however, this ratio only reflects the relationship between surface light condition and MLD. Therefore, the ratio of integral of light in the euphotic zone and MLD ($\int_{-Z_{\mathrm{eu}}}^{0} I(z)dz/z_{\mathrm{mld}}$) might be a preferred value to compare the balance between light limitation and nutrient limitation.

We use time series of satellite chlorophyll and 3-D biophysical model simulations to investigate the relative importance of mixing rates and light availability for phytoplankton populations in the MAB.

2. Methods

For this project we utilized data collected by the Mid-Atlantic Regional Coastal Ocean Observing System (MARCOOS) that is part of the United States Integrated Ocean Observing System (IOOS) (Schofield et al., 2010). MARCOOS provided an extensive data set to validate biological model simulations. In this effort we used surface data provided by ocean color satellite imagery and in situ data collected by Webb Slocum gliders (Schofield et al., 2007).

2.1. The biogeochemical model

In this study we used the Regional Ocean Modeling System (ROMS, http://www.myroms.org) (Haidvogel and Beckmann, 1999; Wilkin et al., 2005) which was configured to the continental shelf of the Middle Atlantic Bight (MAB) (the model domain is shown in Fig. 1). The model has a horizontal grid resolution of approximately 5 km, and uses 36 vertical layers in a terrain-following s-coordinate system. The biogeochemical model was developed and described in Fennel et al. (2006). The model here assumes nitrogen is the major limiting nutrient, which is a reasonable assumption as nutrient budgets indicate nitrogen limitation is frequently observed in the MAB (Ryther and Dunstan, 1971; Sharp and Church, 1981). Also nitrogen availability in the MAB is found the key nutrient to accurately simulating primary production (Fennel et al., 2006). The basic structure of this model follows a classical Fasham model (Fasham et al., 1990) and is constructed using seven state variables: phytoplankton, zooplankton, nitrate, ammonium, small and large detritus, and chlorophyll. The time rate change of phytoplankton is influenced by the growth rate of phytoplankton, grazing by zooplankton, mortality, aggregation of phytoplankton to small and large detritus, and vertical sinking of the aggregates. This model drives phytoplankton growth (μ) through variations in temperature (T) (Eppley, 1972), incident light intensity (I) (Evans and Parslow, 1985), and the availability of nutrients (Parker, 1993), following:

$$\mu = \mu_{\max} f(I)(L_{\mathrm{NO_3}} + L_{\mathrm{NH_4}}) \tag{1}$$

μ_{max} is the maximum growth rate which depends on temperature. I is the photosynthetically available radiation and decreases with water depth due to absorption by seawater (assumed constant) and the time and spatially varying chlorophyll computed by the model.

$$I = I(z) = I_0 par \exp\{-z(K_w + K_{chl} \int_z^0 Chl(\zeta)d\zeta)\} \tag{2}$$

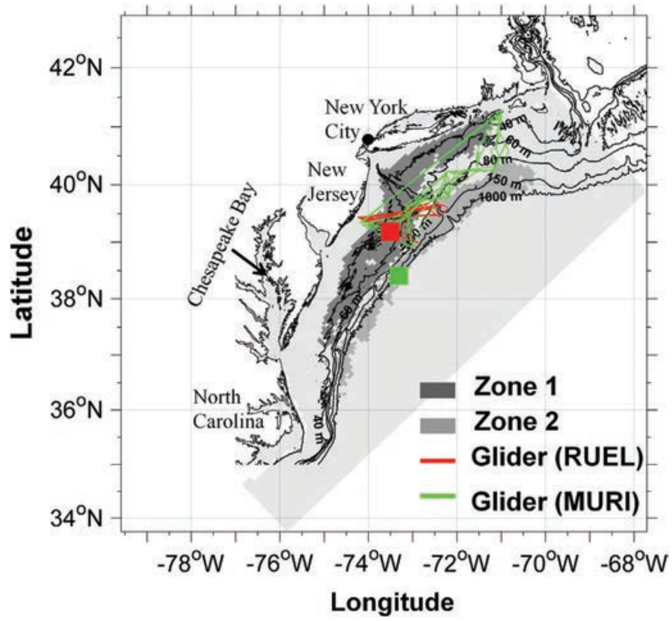

Fig. 1. Model domain (light gray). Dark gray and gray highlight the Zone 1 and Zone 2 region identified by Xu et al. (2011). Red and green lines show the glider transects. Red and green square symbols represent the grid point used for calculation in Zone 1 and Zone 2. The black lines with number show the bathymetry. (For interpretation of the references to color in this figure legend, the reader is referred to the web version of this article.)

where I_0 is the surface incoming light and is the shortwave radiation flux from NCEP reanalysis data, par is the fraction of light that is available for photosynthesis and equals 0.43. $K_w$and K_{chl} are the light attenuation coefficients for water and chlorophyll, and are set to 0.04 m^{-1} and 0.025 (mg Chl)$^{-1}$ m^{-2} respectively (Fennel et al., 2006). The$f(I)$ represents the photosynthesis-light (P–I) relationship. The parameter α is the initial slope of the P–I curve. The terms $L_{\mathrm{NO_3}}$and $L_{\mathrm{NH_4}}$ represents the nutrients limitation.

$$f(I) = \frac{\alpha I}{\sqrt{\mu_{\max}^2 + \alpha^2 I^2}}, \tag{3}$$

$$L_{\mathrm{NO_3}} = \frac{\mathrm{NO_3}}{K_{\mathrm{NO_3}} + \mathrm{NO_3}} \frac{1}{1 + \mathrm{NH_4}/K_{\mathrm{NH_4}}}, \tag{4}$$

$$L_{\mathrm{NH_4}} = \frac{\mathrm{NH_4}}{K_{\mathrm{NH_4}} + \mathrm{NH_4}} \tag{5}$$

The rate of grazing by zooplankton is represented by a Holling type s-shaped curve (Gentleman et al., 2003). The mortality loss term has linear relationship with phytoplankton. The aggregation rate is assumed to scale with the square of small particle abundance for more details see Fennel et al., 2006. The model was driven by atmospheric forcing provided by the North American R (NAM) forecast regional Reanalysis (NARR) from the National Centers for Environmental Prediction (NCEP). We used a 3-hourly re-analysis of surface air temperature, pressure, relative humidity, 10 m vector winds, precipitation, downward long-wave radiation, and net shortwave radiation to specify the surface fluxes of momentum and buoyancy using bulk formulae (Fairall et al., 2003). In the open boundary, we specified temperature, salinity, nitrate ($\mathrm{NO_3}$), total inorganic carbon (TIC), alkalinity, and oxygen. Because the focus of this study is the influence of wind forcing on phytoplankton dynamics, the open boundary inputs are specified by the climatology input based on the Fennel ROMS model simulation of the Northeast North American (NENA) shelf (Fennel et al., 2006). We included the inputs of seven rivers

(Hudson, Connecticut, Delaware, Susquehanna, Potomac, Choptank, and James River) on the boundary. River outflow was provided by the daily mean outflow from the United States Geological Survey (USGS) gauges (available online at http://waterdata.usgs.gov/nwis/). The riverine inputs of temperature, salinity, dissolved and particulate biological constituent concentrations were derived from the total nitrogen in the nitrate pool after Howarth et al., (1996). Here the inputs were multiplied by the freshwater transport to give discharge rates, which for our simulations was treated as time invariant. The model is initialized with model output in this domain described in Hofmann et al. (2011). The 4 yr (2004–2008) duration simulations were conducted with the first year used as a spin-up period; results presented here are from the analysis of the final three-years of simulation.

2.2. Satellite imagery

Seasonal cycles in MAB phytoplankton were characterized using four-day averaged nine-year time series of surface chlorophyll concentration derived from Sea-viewing Wide Field of view Sensor (SeaWiFS) ocean color imagery from January 1998 to December 2006. Images with more than 20% cloud coverage were excluded. Therefore we utilized the 4-day composite, which was the minimum time interval that minimized cloud contamination and provided a reasonable time series that could define seasonal phytoplankton dynamics on the shelf. Even using the 4-day average 43% of imagery was eliminated from the data set. The missing data was largest in the fall-winter in each year. The monthly SeaWiFS Level 3 photosynthetically available radiation (PAR) data from 1998 to 2006 were downloaded from http://oceancolor.gsfc.nasa.gov. We used the spatial mean for both chlorophyll-a and PAR for the shelf and shelf-break front regions (Zone 1 and Zone 2, as showed in Fig. 1 dark gray and gray area respectively) identified in Xu et al. (2011). The two zones were defined by a decadal Empirical Orthogonal Function analysis of ocean color imagery, which identified two major modes of variability. The first mode (Zone 1) was associated with the inner continental shelf of the MAB spanning the 20–60 m isobaths. Zone 1 was defined by the fall-winter bloom of phytoplankton (Xu et al., 2011). Zone 2 was located in the 80–150 m isobaths located at the edge of the MAB continental slope and was associated with the spring phytoplankton bloom.

2.3. Glider Observations

We utilized Webb Slocum gliders for this study (Schofield et al., 2007). The data was collected as part of local and regional glider time series in the MAB (Schofield et al., 2010, Fig. 1). The time series is not formally funded and thus is not a complete monthly time series; however the time series is a large data base providing vertical profiles of temperature and salinity. A smaller subset of chlorophyll data was available, however it should be noted that not every glider is equipped with a fluorometer. The data base used for this study spans from 2006 to 2008. During the periods, there are three missions (June 2006, July 2006, and July 2007) along Rutgers University Glider Endurance Line (RUEL) and three missions (March 2007, April 2007, and March 2008) along Multidisciplinary University Research Initiative Line (MURI). For the RUEL transect, it takes approximately 5–10 days to be completed, while for the MURI transect, it takes 12–25 days to be completed. The majority of the glider observations provide data for spring and summer time. These efforts provide over 8257 vertical profiles with temperature, salinity and chlorophyll data that were included in this study. All gliders are equipped with a Sea-Bird conductivity-temperature-depth (CTD) sensor. The MLDis based on the measurement of temperature and salinity and is defined using the criterion of a 0.125 kg m^{-3} density increase from the surface.

3. Results

3.1. Model simulation and observations of MAB phytoplankton

We have focused our analysis of the seasonal variability in phytoplankton in Zone 1 and Zone 2 as identified in Xu et al. (2011). Time series of the 4-day average spatial mean SeaWiFS

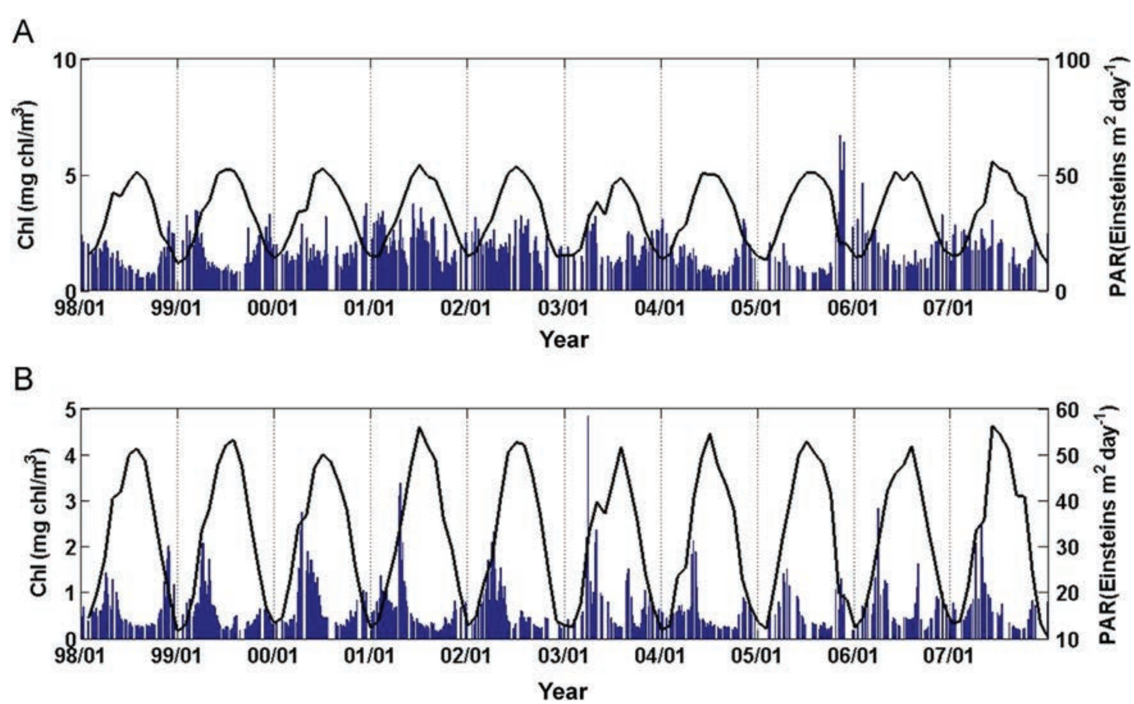

Fig. 2. The 9-year record of SeaWiFS chlorophyll (bar) compared to photosynthetically active radiation (PAR, black line) from the spatial mean in (A) Zone 1 and (B) Zone 2.

chlorophyll for both zones is shown in Fig. 2. Generally, the chlorophyll in Zone 1 showed a persistent phytoplankton bloom in the late fall and winter that typically lasted several weeks despite the solar illumination being lowest during this time of year. The timing of this bloom has been related to the seasonal destratification of the MAB, which replenishes nutrients to the surface waters. The magnitude of bloom has been related to the overall wind-induced mixing with the frequency of winter storms determining the overall seasonal light-limitation of the phytoplankton (Xu et al., 2011). In contrast, the phytoplankton blooms in Zone 2 occur in the spring and are associated with the onset of stratification in the deeper waters of the outer shelf (Fig. 2B). The spring bloom is shorter and has lower concentrations of chlorophyll than the fall-winter bloom. These seasonal cycles of chlorophyll are consistent with the *in situ* MARMAP data (Yoder et al., 2001, shown in Fig. 6), that show peak chlorophyll values occur during fall-winter in middle and outer shelf water and a distinct spring maximum in shelf-break slope waters (Yoder et al., 2001).

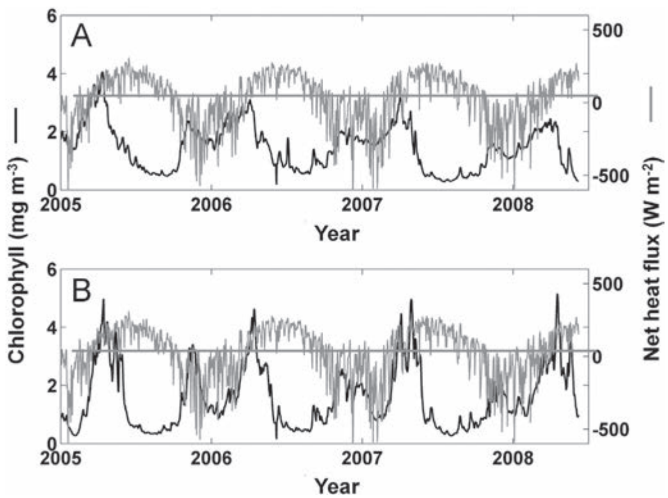

Fig. 3. Time series of surface chlorophyll concentration (black line) and net heat flux (gray line) of spatial mean in Zone 1 and Zone 2 calculated from model output.

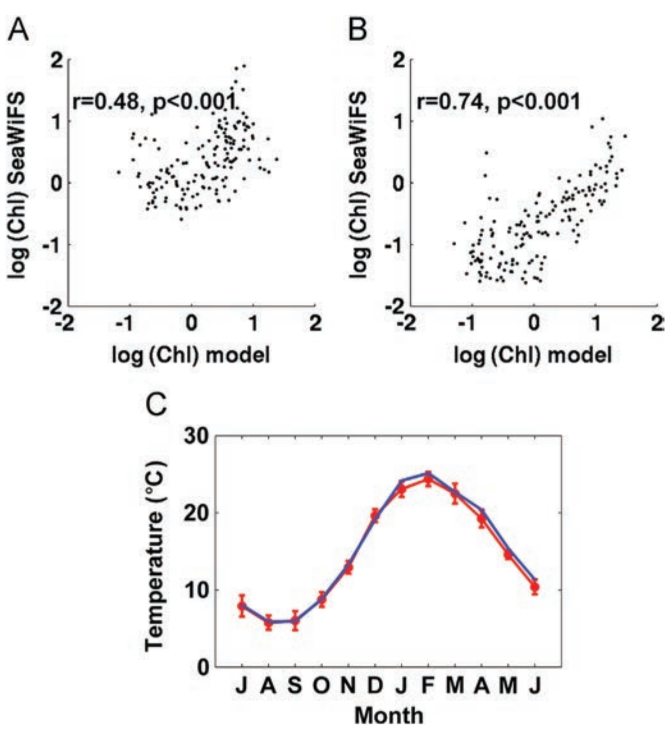

Fig. 4. Comparison between the log-transformed surface chlorophyll concentrations provide by SeaWiFS and mode output from spatial mean of Zone 1 and Zone 2. The linear correlation of the chlorophyll before log-transformed is 0.42 and 0.75 (P value < 0.001) for Zone 1 and Zone 2 respectively. The climatology of surface water temperature from the NDBC buoy 44009 (the red line with error bar) was used to compare with the simulated SST at the same location (blue line) in Fig. 4C. (For interpretation of the references to color in this figure legend, the reader is referred to the web version of this article.)

The satellite measured chlorophyll dynamics were successfully reproduced by the biological model (Fig. 3). The simulated sea surface temperature was also in the standard deviation range when compare with the climatology measurement from NDBC buoy 44009 (Fig. 4C). The simulated chlorophyll in Zone 1 increased in late fall and lasted through the winter. The correlation found between simulated chlorophyll and SeaWiFS chlorophyll was 0.48 ($p < 0.001$, Fig. 4A) which was mainly due to the winter bloom. The bloom showed a bimodal peak with lower concentrations found during the darkest periods of winter which was not readily evident in the satellite data that perhaps reflect the relatively low availability of ocean color images during the cloudy winter (Xu et al., 2011). The model also successfully simulated the timing and magnitude of spring bloom in Zone 2, which could explain ~74% of the log-transformed variance of the observed chlorophyll ($p < 0.001$, Fig. 4B).

The model overestimated observed chlorophyll and likely reflects the poor prediction of zooplankton grazing for the following reasons. During the SEEP II experiments in this area (Flagg et al., 1994), zooplankton concentrations ranged from 0.4–28.6 mmol N m^{-3}. Our modeled zooplankton concentrations varied from 0 to 2 mmol N m^{-3}, which is within the range observed during SEEP II (Flagg et al., 1994) but at the lower end the observations. If grazing pressures were too low, then major factor regulating the termination of the spring bloom in the model would be the depletion of nutrients. This would result in the modeled spring bloom lasting longer than the satellite observations if zooplankton is significant in driving bloom senescence. The spring bloom based on the 4-day average SeaWiFS data typically lasted 12–20 days over a 10-year data set (Fig. 2B). The spring bloom in the model simulations typically lasted for 30–40 days (Fig. 3B), which would be consistent with the model that underestimating grazing pressure.

3.2. Environmental regulation of phytoplankton

Accepting that the model describes the general variability observed for chlorophyll (Fig. 4), we used the model simulations to analyze the physical factors regulating phytoplankton biomass on the MAB. Time series of the modeled chlorophyll and key environmental variables (temperature, upper mixed layer, light, nutrients, and zooplankton) for both zones are shown in Figs. 5 and 6. In Zone 1(Fig. 5), water column cooling resulted in destratification, which was reflected as an increase in the upper mixed layer depth from 10 m at the beginning of October to 30 m deep at the end of February. The deepening of the upper mixed layer depth was associated with an increase of nitrate within the euphotic zone. Nitrate exhibited considerable variability within the upper 20 m showing that convective overturn and entrainment processes were effective increasing nutrients in surface waters. Nitrate within the mixed layer was consumed rapidly by phytoplankton from December to March. Phytoplankton growth was significant even during the dim winter months as >50% of the water column was above the 1% light level depth. Phytoplankton biomass remained high until the upper mixed layer depth began to shallow and nitrate was rapidly depleted and grazing pressure increased. After surface

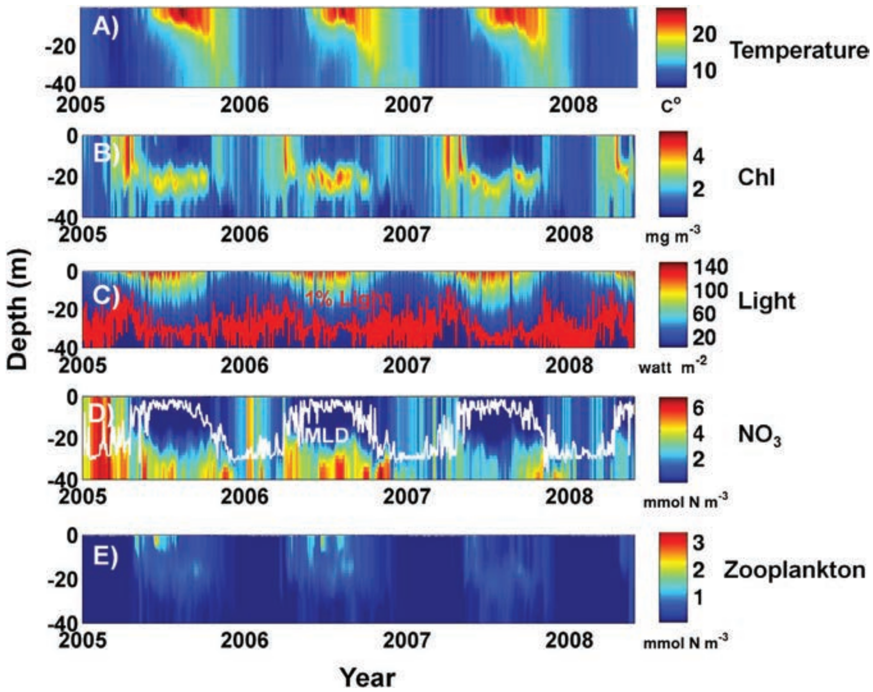

Fig. 5. Model simulated vertical distribution of temperature (A) chlorophyll concentration (B), light (C), NO_3 (D) and zooplankton (E) at a point located in Zone 1 (dot shown in Fig. 1). The 1% light level depth is plotted with light (in C, red line) and the MLD is plotted with NO_3 (in (D), white line). (For interpretation of the references to color in this figure legend, the reader is referred to the web version of this article.)

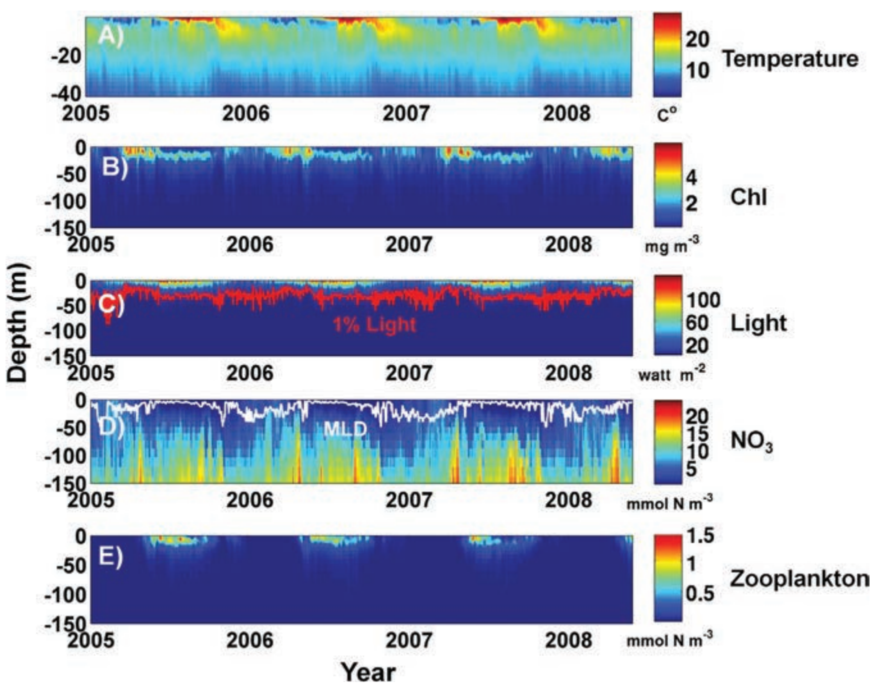

Fig. 6. Model simulated vertical distribution of temperature (A) chlorophyll concentration (B), light (C), NO_3 (D) and zooplankton (E) at a point located in Zone 2 (square shown in Fig. 1). The 1% light level depth is plotted with light (in C red line) and the MLD is plotted with NO_3 (in D, white line). (Here, we only show the upper 150 m of the water column). (For interpretation of the references to color in this figure legend, the reader is referred to the web version of this article.)

nitrate was depleted, a significant subsurface phytoplankton peak was maintained at the nutricline throughout the year.

In contrast, phytoplankton blooms in Zone 2 were found primarily in the spring with a smaller secondary bloom in the fall when stratification began to weaken (Fig. 6). No winter phytoplankton bloom was observed as the upper mixed layer was deep and the majority of the water column was below the 1% light level (Xu et al., 2011). The spring phytoplankton bloom formed in March every year during the simulation as the upper mixed layer depth decreased and nitrate concentrations were high. The nutrients were consumed in several weeks and nutrient depletion resulted in the termination of the bloom. As observed in Zone 1, a subsurface phytoplankton bloom formed, however the nutricline was deep and the subsurface concentrations of chlorophyll were less than half then observed on the inner continental shelf.

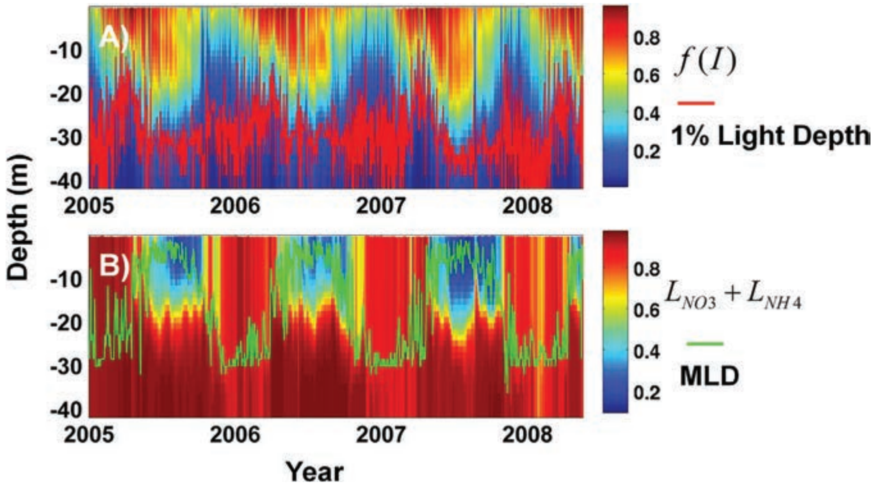

Fig. 7. Vertical distribution of limitation function of light (A) and nutrient (B) at a point located in Zone 1 (dot shown in Fig. 1). The 1% light level depth is plotted with function of light (in A, red line) and the MLD is plotted with nutrient limitation function (in (B), white line). (For interpretation of the references to color in this figure legend, the reader is referred to the web version of this article.)

The relative limitation of phytoplankton by light and nutrients is tightly coupled to the depth of the upper mixed layer as is illustrated in Fig. 7. The threshold for light limitation is described as Eq. (3). The threshold for nutrient limitation in the model is calculated as Eqs. (4) and (5). Value of 1 indicates no limitation. During winter months, when the upper mixed layer is deep, the majority of the phytoplankton in the water column are light limited (<0.8, Fig. 7A). During this period, nutrient limitation is low (>0.8, Fig. 7B). As solar illumination increases in spring, the mixed layer depth shallows and light limitation is decreased; however the entrainment of nutrients to surface waters is decreased and nitrate limitation begins to increase as the phytoplankton grow rapidly. In the euphotic zone, where there is sufficient light for photosynthesis, the reduction of CO_2 to organic carbon fuels the rate of cell doubling and population growth. Thus, the availability light drives the flux of carbon, and other elements, into cells and thereby determines the rate at which nutrients are utilized by photoautotroph for growth (Dubinsky and Schofield, 2010).

To test the role of mixing in regulating phytoplankton bloom dynamics we conducted a series of model simulations where we compared the models driven by measured wind (as above) to hypothetical simulations where no wind was applied to the ocean. Comparisons of the simulations for both Zone 1 and Zone 2 are shown in Fig. 8. In Zone 1, the "no wind" condition resulted in fall blooms later in the season, which reflects the importance of wind-induced mixing combined with seasonal cooling to drive the convective overturn on the MAB. The "no wind" condition does not show convective overturn and replenishment of nutrients to the surface waters until several weeks later in the season (Fig. 9D). The mid-winter depression in the winter bloom is not present in the "no wind" simulation. The magnitude and timing of the winter bloom is strongly tied to storms, which induce mixing during the dim winter months leading to increased light limitation of the phytoplankton (Xu et al., 2011); therefore the "no wind" condition diminishes mixing and light limitation and allows for larger winter blooms. The decline in the winter light limitation is also visible in the "no wind" plot (Fig. 10A, black line). Finally, as the spring transition begins and the water column begins to stratify due to increased radiant heating, the phytoplankton in the "no wind" experiment showed a more rapid biomass decrease reflecting an earlier onset of nutrient limitation (Fig. 10A). For Zone 2, the "no wind" condition resulted in an earlier spring bloom (Fig. 8B) reflecting the earlier onset of stratification of the offshore waters. This is consistent with satellite analyses that suggested pre-spring storms strongly influenced the timing and magnitude of the spring bloom in the MAB (Xu et al., 2011). The other major differences in Zone 2, is that the spring phytoplankton activities were higher under the normal windy conditions (Fig. 8B), which alleviated the early onset of nutrient limitation as the MLD became shallower (Fig. 10B). Finally the fall bloom observed in Zone 2 was not present (Fig. 8B), as the convective overturn on the MAB was delayed and cells were nutrient limited (Fig. 10B).

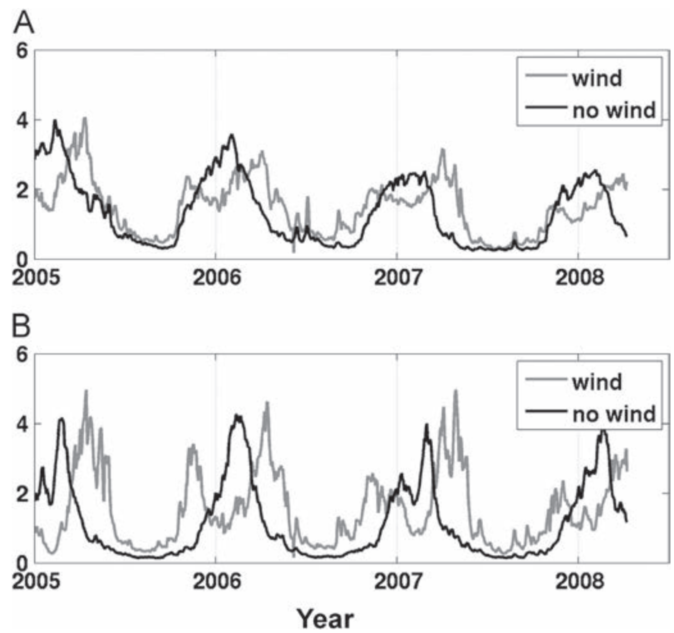

Fig. 8. Simulated time series of spatial mean surface chlorophyll concentration in Zone 1(A) and Zone 2(B). Black line represents the result under normal wind conditions; gray line represents the "no wind" forcing result.

3.3. Light, upper mixed layer depth, and chlorophyll

There is an inverse relationship between the MLD and the average light levels within the MLD (Fig. 11). Deeper mixed layers are associated with lower irradiance ($r=-0.84$, $p<0.001$; $r=0.72$, $p<0.001$ for Zone 1 and Zone 2 respectively). This relationship

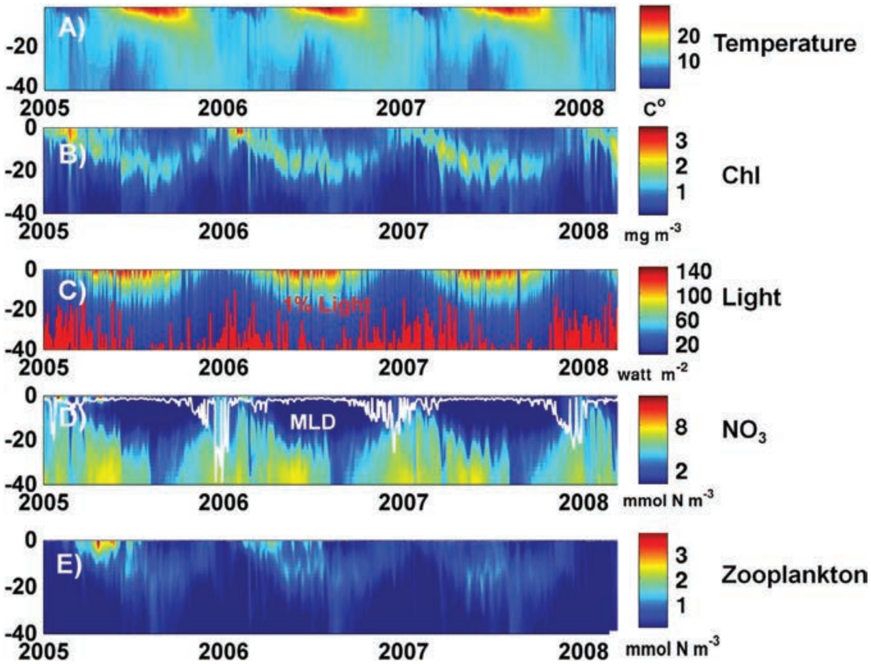

Fig. 9. Without wind forcing, the simulated vertical distribution of temperature (A) chlorophyll concentration (B), light (C), NO_3 (D) and zooplankton (E) in a dot located in Zone 1(dot shown in Fig. 1). The 1% light level depth is plotted with light (in C, red line) and the MLD is plotted with NO_3 (in (D), white line). (For interpretation of the references to color in this figure legend, the reader is referred to the web version of this article.)

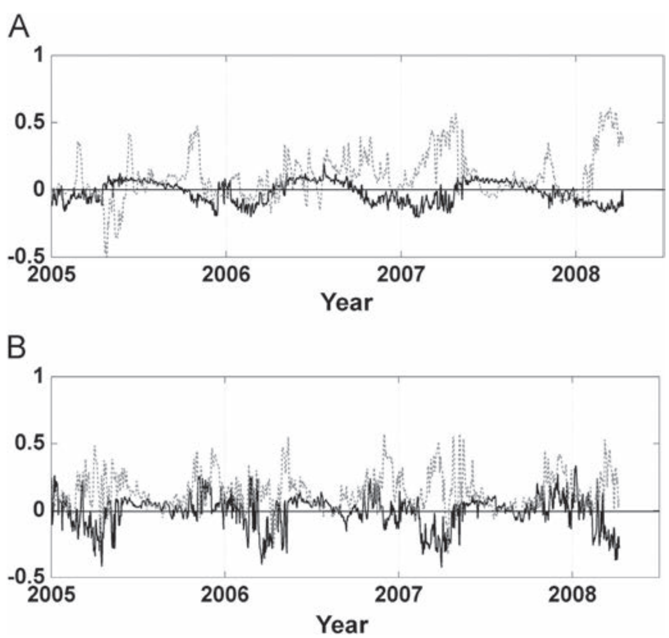

Fig. 10. Difference in light (black line) and nutrient (gray dashed line) limitation function between normal wind and no wind forcing condition in (A) Zone 1 and (B) Zone 2.

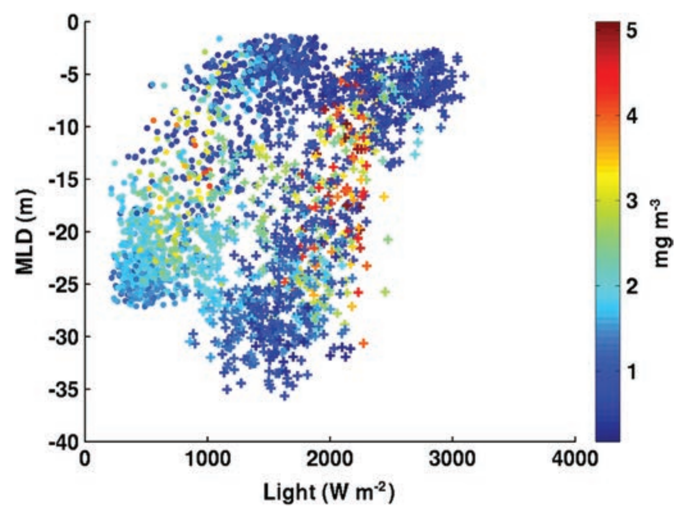

Fig. 11. Scatter plot of modeled mean light value in the mixed layer with MLD. The color represents the chlorophyll concentration in Zone 1 (dots) and Zone 2 (plus sign).

varies between Zone 1 and Zone 2, with offshore waters having a higher mean irradiance in the MLD. This reflects that the waters on the continental shelf are more turbid due to the enhanced attenuation of light by chlorophyll, colored dissolved organic matter and non-algal particles found in the shelf waters of the MAB (Schofield et al., 2004). While peak phytoplankton biomass ($> 4\ \mathrm{mg\ m^{-3}}$) is found over a 5-fold range of MLDs, there is a narrow range (50%) of mean irradiances associated with peak phytoplankton concentrations (Fig. 8). Peak chlorophyll values in Zone 1 were associated with lower mean light intensities compared to Zone 2. In order to parameterize both the MLD and light critical threshold of light to induce phytoplankton blooms we calculated mixing-light value (I') as the ratio of integral of light (I) in the euphotic zone (Z_{eu}) divided by the MLD (Z_{mld}) as

$$I' = \int_{-Z_{\mathrm{eu}}}^{0} I(z)dz / Z_{\mathrm{mld}} \tag{6}$$

The I' term incorporates both the incident light and the mixing environment through the depth of the MLD. The MLD also contains information on the probability of nutrient availability. We assessed if there is a critical I' value associated with both the observed and simulated chlorophyll maximum ($I'_{chl\mathrm{max}}$). The I' values derived from the model were integrated into $20\ \mathrm{W\ m^{-2}}$ bins for Zone 1 and Zone 2 (Fig. 12). There is an increase in chlorophyll with increasing I' up until 60 and $160\ \mathrm{W\ m^{-2}}$ ($I'_{chl\mathrm{max}}$) for Zones 1 and Zone 2 respectively. Under these conditions,

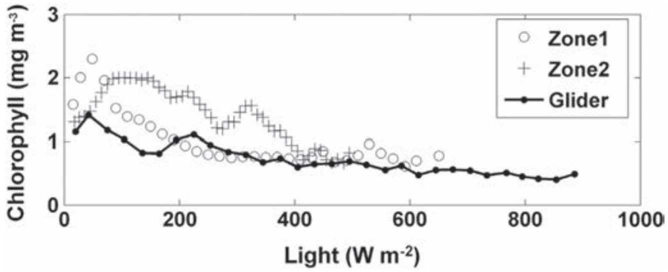

Fig. 12. Simulated mixed depth mean chlorophyll concentration and I' in every 20 W m^{-2}. I' value bins in Zone 1 (gray circle line) and Zone 2 (gray plus line), chlorophyll and I' based on glider observation are shown in black line with dots.

deeply mixed layers limited phytoplankton growth as overall light levels were low. For the waters of Zone 1 with shallow water depths, the mixed layer only need to decrease slightly to ensure that the majority of the water column is within the euphotic zone and phytoplankton have sufficient light to grow. In Zone 2, the deeper water depths require the MLD to decrease significantly in order to overcome light limitation. After this threshold has been reached, increasing I' is associated with declining chlorophyll. Here cells are maintained under high light but a shallow MLD does not allow for replenishment of the nutrients from depth. These chlorophyll and I' relationships were compared to chlorophyll data measured with Slocum gliders outfitted with fluorometers (Fig. 12, black line with dots). Despite that the glider data set is smaller and does not include many transects during the winter months, the relationship between I' and chlorophyll is similar showing an increase at low I' values to a value of 50 W m^{-2} and then decreasing values as I' increases. The glider chlorophyll values are lower than model estimates which is not surprising as the data set does not include many transects during the winter bloom. Calculations of I' for the "no wind" simulation show similar patterns except that it takes a high magnitude of I' to reach the peak chlorophyll values for Zone 2 (Fig. 15 plus line).

Is $I'_{chl\max}$ predictable? Spatial maps of $I'_{chl\max}$ associated with the chlorophyll maximum for the MAB are shown in Fig. 13. Generally, $I'_{chl\max}$ is low and relatively constant on the continental shelf and increases in magnitude out over the continental slope and deep sea. The one shallow water exception was associated with the Hudson River plume, which is extremely turbid and mixing rates in the buoyant plume water must be high enough to overcome chronic light limitation for phytoplankton bloom Schofield et al., submitted for publication. Excluding this river zone, the relationship between $I'_{chl\max}$ and bottom depth were robust (Fig. 14). Bottom depth could explain 70% of the variability in $I'_{chl\max}$ ($p < 0.001$).

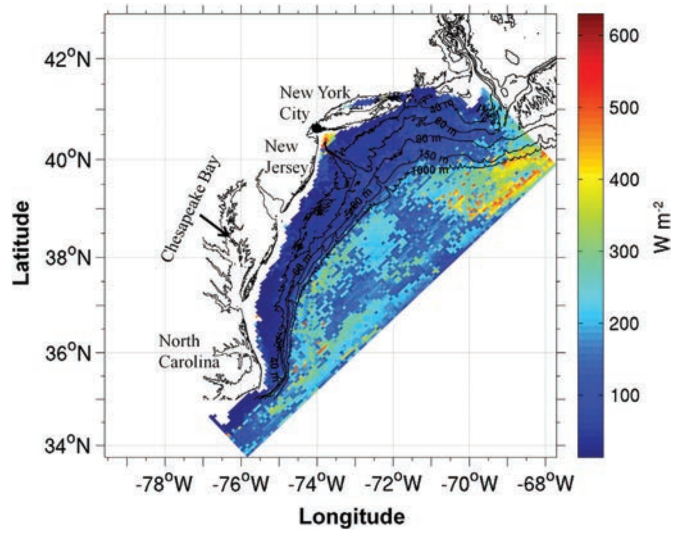

Fig. 13. The critical light value ($I'_{chl\max}$) in each grid of model domain.

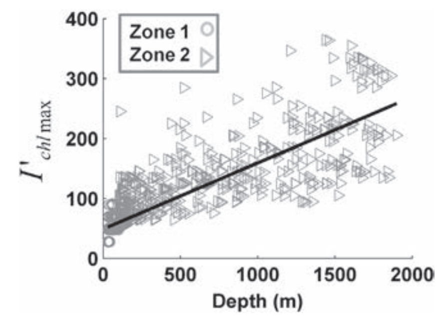

Fig. 14. Change of the critical light value with depth of all grids in Zone 1 (circle) and Zone 2 (triangle). Black line represents the linear regression of water depth and critical light value.

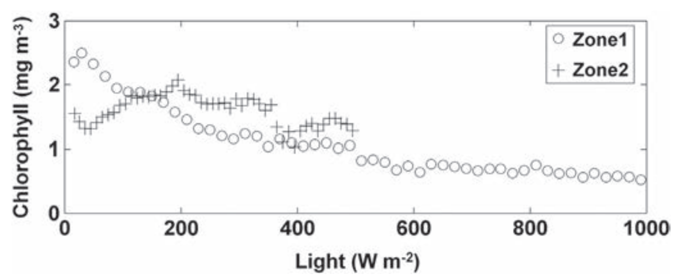

Fig. 15. Under no wind forcing, simulated mixed depth mean chlorophyll concentration and I' in every 20 W m^{-2} I' value bins in Zone 1 (red circle line) and Zone 2 (blue circle line), chlorophyll and I' based on glider observations are shown in black line with dots. (For interpretation of the references to color in this figure legend, the reader is referred to the web version of this article.)

4. Discussion

The late fall-winter bloom is the most recurrent and largest phytoplankton bloom in the MAB (Xu et al., 2011; Yoder et al., 2001). The fall-winter bloom is fueled by the replenishment of nutrients to the euphotic zone once the summer thermal stratification has been disrupted. This thermal stratification is dramatic (summer thermoclines on the MAB exhibit a temperature gradient of over 15 °C in only 5 m water depth, cf. Castelao et al., 2010) and this stratification deprives the surface phytoplankton of macro and micronutrients throughout the late spring, summer and early autumn. Observational studies have documented there is a great deal of inter-annual variability in the timing of the late fall-winter bloom (Yoder et al., 2001). The variability in the timing of the bloom has been related to the timing of destratification, which is driven by seasonal cooling of the surface waters and the passage of large storms that induce mixing (Beardsley et al., 1985; Glenn et al., 2008; Lentz et al., 2003). The magnitude of the fall-winter bloom is thought to be regulated by factors that stabilize the water column (Xu et al., 2011). In the MAB, these processes include the frequency of winter storms and the presence of low salinity buoyant plumes (Xu et al., 2011). While the observational data is compelling it has been insufficient to confirm the hypothesized forcing of the late fall-winter phytoplankton bloom.

To test the hypothesized physical forcing of the MAB phytoplankton we utilized the physical–biological ROMS model to conduct a series of simulations where we varied the physical forcing and analyzed the source and sinks of the phytoplankton.

The model which used realistic forcing was able to simulate the timing and spatial extent of the phytoplankton dynamics observed in SeaWiFS data. The model did a quantitatively good job of predicting the winter bloom; however the model had a more difficult time in reproducing the magnitude of the spring bloom. For the spring bloom region, there are large horizontal and vertical gradients in water properties and are associated with the shelf-break front, a feature susceptible to nonlinear instabilities and strong interactions with Gulf Stream warm-core rings (Gawarkiewicz et al., 2001, 2004). As a result, this region has complicated physical background that the mixing by wind cannot really be isolated. The discrepancy for the spring bloom likely reflected both by underestimated in chlorophyll by satellite-derived chlorophyll in this region (Fennel et al., 2006) and underestimated zooplankton grazing (Flagg et al., 1994). For the late fall-winter bloom, our numerical experiments explicitly demonstrated the role of wind-induced mixing in winter phytoplankton dynamics when all the other forcing factors were held constant. For the initiation of the late fall-winter bloom the no wind-induced mixing simulation demonstrated that wind was a secondary factor; therefore seasonal cooling and the corresponding convective overturn on the MAB is the dominant feature initiating the phytoplankton bloom. This is consistent with observations that tropical storms on the MAB can only induce water column turnover if the summer thermocline had been previously weakened by seasonal cooling (Glenn et al., 2008). After destratification, the frequency of high wind regulates the size of the phytoplankton bloom. Strong winds result in high mixing rates or less solar radiation because of cloudy weather, which results in the light limitation of the phytoplankton (Xu et al., 2011), which is confirmed by the model as an increased wind forcing resulted in smaller phytoplankton blooms.

Wind forcing also has a significant role on the timing and magnitude of the offshore spring bloom. Observational efforts have related the size and timing of the spring phytoplankton to the amount of wind-induced mixing present in the late winter (Xu et al., 2011). Wind-induced mixing in the late winter delays the thermal stratification of the MAB, which influences the spring bloom as cells require water column stabilization to overcome light limitation. During the no wind simulation, the spring bloom was dominated by a single event that occurred earlier in the season compared to normal wind conditions. This bloom was short lived as the cells rapidly consumed available nutrients. In contrast, the model simulation that used natural wind forcing resulted in a spring bloom that lasted longer throughout the season compared to the no wind condition as wind-induced mixing replenished the supply of nutrients and enhanced the overall amount of chlorophyll on the MAB. The SeaWiFS observed bloom in the shelf-break front region commenced in late March and lasted up to late April. In our simulated case with wind, the spring bloom in the shelf-break front region initiated in early March and lasted up to early April. It looks like that although the model simulated spring bloom start a little bit earlier under normal wind condition, it can better capture the both spring and fall bloom in this region compare with no wind forcing condition.

Is there a relatively predictable light condition that promotes a maximum chlorophyll concentration? Photosynthetic activity is confined to the euphotic zone, which is nominally defined as the depth where the light levels are 1% of the surface light intensity.

The depth of the euphotic zone is poor at predicting the initiation of phytoplankton blooms as any mixing to depth limits phytoplankton biomass accumulation in the upper mixed layer. This is due to the high respiratory costs to build cells (Falkowski and Raven, 2007). This discrepancy is accounted by Sverdrup's (1953) "critical depth" for bloom initiation (Obate et al., (1996); Smetacek and Passow, 1990). This framework has been highly effective for the open ocean where the compensation depth for phytoplankton growth appears to be relatively constant (Siegel et al., 2002). In MAB, the light regime is tied closely to mixing regime as light is rapidly attenuated by high phytoplankton biomass and significant inputs from buoyant turbid plumes (Cahill et al., 2008; Castelao et al., 2008). As mixing determines not only the light but also the nutrient availability, there is need to parameterize the relative impacts of both. To parameterize the relative tradeoffs of mixing and light availability the ratio of Z_{mld} to Z_{eu} has been used to describe the regulating primary production (Huisman et al., 1999; Irigoien and Castel, 1997); however, this ratio only reflects the relationship between surface light condition and MLD. We suggest that it is more appropriate to use I' which is the ratio of integral of light in the euphotic zone and MLD to compare the balance between light limitation and nutrient limitation. When I' is low, phytoplankton are light-limited due to low surface irradiance and deep mixed layer. The variability shows a single peak in both the offshore and nearshore conditions. At high values ofI', the mixed layer is shallow, coincident with the seasonal increase in solar illumination, which allowed the photosynthetic activity to consume the available nutrients. This in turn results in low biomass. We used the model to define this integral and then assess when it results in the maximum chlorophyll biomass ($I'_{chl\max}$). Model simulations suggest that on MAB, $I'_{chl\max}$ varied by a factor of three and were spatially variable. The spatial variability was positively correlated with water depth, suggesting that this term can be parameterized.

Our results based on numerical simulation and glider observations confirm the SeaWiFS observation of seasonal phytoplankton bloom in the MAB. The modified light values are used to describe the balance between light and nutrients limitation and so as the influence the timing and magnitude of bloom. Sensitivity study of no wind forcing simulation proves that the mixing plays a significant role in regulating the nutrient and light field and thus influences the phytoplankton dynamics.

Acknowledgments

We thank the members of the Rutgers University Coastal Ocean Observation Laboratory (RU COOL), who were responsible for the satellite, glider operations. This work was supported by a grant from ONR MURI Espresso program (N000140610739) and NSF LaTTE program (OCE-0238957 and OCE-0238745).

References

Beardsley, R.C., Chapman, D.C., Brink, K.H., Ramp, S.R., Schlitz, R., 1985. The Nantucket Shoals flux experiment (NSFE79). Part I: a basic description of the current and temperature variability. Journal of Physical Oceanography 15, 713–748.

Behrenfeld, M.J., Maranon, E., Siegel, D.A., Hooker, S.B., 2002. Photoacclimation and nutrient-based model of light-saturated photosynthesis for quantifying oceanic primary production. Marine Ecology Progress Series 228, 103–117, http://dx.doi.org/10.3354/meps228103.

Cahill, B., Schofield, O., Chant, R., Wilkin, J., Hunter, E., Glenn, S., Bissett, P., 2008. Dynamics of turbid buoyant plumes and the feedbacks on near-shore biogeochemistry and physics. Geophysical Research Letters 35, L10605, http://dx.doi.org/10.1029/2008GL033595.

Castelao, R., Schofield, O., Glenn, S., Chant, R., Kohut, J., 2008. Cross-shelf transport of freshwater on the New Jersey shelf. Journal of Geophysical Research 113, C07017, http://dx.doi.org/10.1029/2007JC004241.

Castelao, R., Glenn, S., Schofield, O., 2010. Temperature, salinity, and densty variability in the central Middle Atlantic Bight. Journal of Geophysical Research 115, C10005, http://dx.doi.org/10.1029/2009JC006082.

Dubinsky, Z., Schofield, O., 2010. From the light to the darkness: thriving at the light extremes in the oceans. Hydrobiologia 639, 153–171.

Dutkiewicz, S., Follows, M., Marshall, J., Gregg, W.W., 2001. Interannual variability of phytoplankton abundances in the North Atlantic. Deep Sea Research Part II:

Topical Studies in Oceanography 48, 2323–2344, http://dx.doi.org/10.1016/S0967-0645(00)00178-8.
Falkowski, P., Raven, J., 2007. Aquatic Photosynthesis, second ed.. Princeton University Press, Princeton.
Fairall, C.W., Bradley, E.F., Hare, J.E., Grachev, A.A., Edson, J.B., 2003. Bulk parameterization of air-sea fluxes: updates and verification for the coare algorithm. Journal of Climate 19 (4), 571–591.
Fasham, M.J.R., Ducklow, H.W., McKelvie, S.M., 1990. A nitrogen-based model of plankton dynamics in the oceanic mixed layer. Journal of Marine Research 48, 591–639.
Fennel, K., Wilkin, J., Levin, J., Moisan, J., O'Reilly, J., Haidvogel, D., 2006. Nitrogen cycling in the Middle Atlantic Bight: results from a three-dimensional model and implications for the North Atlantic nitrogen budget. Global Biogeochemical Cycles 20, GB3007, http://dx.doi.org/10.1029/2005GB002456.
Field, C.B., Behrenfeld, M.J., Randerson, J.T., Falkowski, P., 1998. Primary production of the biosphere: integrating terrestrial and oceanic components. Science 281 (5374), 237–240, http://dx.doi.org/10.1126/science.281.5374.237.
Flagg, C., Wirick, N., Smith, S. I., C.D., 1994. The interaction of phytoplankton, zooplankton and currents from 15 months of continuous data in the Mid-Atlantic Bight. Deep Sea Research Part II: Topical Studies in Oceanography 41, 411–435.
Gawarkiewicz, G., Bahr, F., Beardsley, R.C., Brink, K.H., 2001. Interaction of a slope eddy with the shelfbreak front in the Middle Atlantic Bight. Journal of Physical Oceanography 21, 2783–2796.
Gawarkiewicz, G., Brink, K.H., Bahr, F., Beardsley, R.C., Caruso, M., Lynch, J., Chiu, C.-S., 2004. A large-amplitude meander of the shelfbreak front in the Middle Atlantic Bight: observations from the Shelfbreak PRIMER experiment. Journal of geophysical research, 109, http://dx.doi.org/10.1029/2002JC001468.
Gentleman, W., Leising, A., Frost, B., Strom, S., Murray, J., 2003. Functional responses for zooplankton feeding on multiple resources: a review of assumption and biological dynamics. Deep Sea Research Part II: Topical Studies in Oceanography 50, 2847–2876.
Glenn, S.M., Jones, C., Twardowski, M., Bowers, L., Kerfoot, L., Webb, D., Schofield, O., 2008. Glider observations of sediment resuspension in a Middle Atlantic Bight fall transition storm. Limnology and Oceanography 53, 2180–2196.
Haidvogel, D.B., Beckmann, A., 1999. Numerical Ocean Circulation Modeling, Series on Environmental Science and Management, vol. 2. Imperial College Press, London 318 pp.
Hofmann, E.E., Cahill, B., Fennel, K., Friedrichs, M.A.M., Hyde, K., Lee, C., Mannino, A., Najjar, R.G., O'Reilly, J.E., Wilkin, J., Xue, J., 2011. Modeling the dynamics of continental shelf carbon. Annual Review of Marine Science 3, 93–122.
Howarth, et al., 1996. Regional nitrogen budgets and riverine N & P fluxes for the drainages to the North Atlantic Ocean: natural and human influences. Biogeochemistry 35, 181–226.
Huisman, J., Jonker, R.R., Zonneveld, C., Weissing, F.J., 1999a. Competition for light between phytoplankton species: experimental tests of mechanistic theory. Ecology 80, 211–222.
Irigoien, X., Castel, J., 1997. Light limitation and distribution of chlorophyll pigments in a highly turbid estuary: the Gironde (SW France). Estuarine, Coastal and Shelf Science 44, 507–517.
Lentz, S., Shearman, K., Anderson, S., Plueddemann, A., Edson, J., 2003. Evolution of stratification over the New England shelf during the coastal mixing and optics study, August 1996–June 1997. Journal of Geophysical Research 108 (C1), 3008, http://dx.doi.org/10.1029/2001JC001121.
Longhurst, A.R., 1998. Ecological Geography of the Sea. Academic Press, San Diego 398 pp.
Martin, H.J., 1965. Phytoplankton–zooplankton relationships in Narragansett Bay. Limnology and Oceanography 10, 185–191.
Obate, A., Ishizake, J., Endoh, M., 1996. Global verification of critical depth theory for phytoplankton bloom with climatological in situ temperature and satellite ocean color data. Journal of Geophysical Research 101, 20657–20667.
O'Reilly, J., Busch, D.A., 1984. Phytoplankton primary production on the north–west Atlantic Shelf. Rapports et Proces-Verbaux des Reunions Conseil International pour l'Exploration de la Mer. 183, pp. 255–268.
O'Reilly, J., Evans-Zetlin, E.C., Busch, D.A., 1987. Primary production. 220–233. In: Backus, R.H., Bourne, D.W. (Eds.), Georges Bank. MIT Press, Cambridge, MA.
O'Reilly, J., Zetlin, C., 1998. Seasonal, horizontal, and vertical distribution of phytoplankton chlorophyll a in the northeast US continental shelf ecosystem. NOAA Technical Report NMFS 139, US Department of Commerce.
Ryan, J.P., Yoder, J.A., Cornillon, P.C., 1999. Enhanced Chlorophyll at the Shelfbreak of the Mid-Atlantic Bight and Georges Bank during the Spring Transition. Limnology and Oceanography 44, 1–11.
Ryther, J.H., Dunstan, W.M., 1971. Nitrogen, phosphorus, and eutrophication in the coastal marine environment. Science 171, 1008–1112.
Schofield, O., Bergmann, T., Oliver, M., Irwin, A., Kirkpatrick, G., Bissett, W.P., Orrico, C., Moline, M.A., 2004. Inverting inherent optical signatures in the nearshore coastal waters at the long term ecosystem observatory. Journal of Geophysical Research 109, C12S04, http://dx.doi.org/10.1029/2003JC002071.
Schofield, O., et al., 2007. Slocum gliders: robust and ready. Journal of Field Robotics 24, 1–14, http://dx.doi.org/10.1009/rob.20200.
Schofield, O., et al., 2010. Automated sensor networks to advance ocean science. Transaction of the American Geophysical Union 91 (39), 345–346, http://dx.doi.org/10.1029/2010EO390001.
Schofield, O., Chant, R., Hunter, E., Moline, M.A., Reinfelder, J., Glenn, S.M., Frazer, T., Optical transformations in a turbid buoyant plume. Continental Shelf Research, submitted for publication.
Sharp, J.H., Church, T.M., 1981. Biochemical modeling in coastal waters of the Middle Atlantic States. Limnology and Oceanography 26 (5), 843–854.
Siegel, D.A., Doney, S.C., Yoder, J.A., 2002. The North Atlantic spring phytoplankton bloom and Sverdrup's critical depth hypothesis. Science 296, 730–733.
Smetacek, V., Passow, U., 1990. Spring bloom initiation and Sverdrup's critical depth model. Limnology and Oceanography 35 (1), 228–234.
Sverdrup, H.U., 1953. On conditions for the vernal blooming of phytoplankton. Journal du Conseil International pour l'Exploration de la Mer 18, 287–295.
Tilman, D., 1982. Resource competition and community structure. Princeton University Press, Princeton, NJ, USA.
Turner, J.T., Tester, P.A., 1997. Toxic marine phytoplankton, zooplankton grazers, and pelagic food webs. Limnology and Oceanography 42, 1203–1214.
Wilkin, J.L., Arango, H.G., Haidvogel, D.B., Lichtenwalner, C.S., Glenn, S.M., Hedstrom, K.S., 2005. A regional ocean modeling system for the Long-term ecosystem observatory. Journal of Geophysical Research 110, C06S91, http://dx.doi.org/10.1029/2003JC002218.
Xu, Y., Chant, R., Gong, D., Castelao, R., Glenn, S., Schofield, O., 2011. Seasonal variability of chlorophyll a in the Mid-Atlantic Bight. Continental Shelf Research 31, 1640.
Yoder, J.A., O'Reilly, J.E., Barnard, A.H., Moore, T.S., Ruhsam, C.M., 2001. Variability in coastal zone color scanner (CZCS) Chlorophyll imagery of ocean margin waters off the US East Coast. Continental Shelf Research 21, 1191–1218.

Continental Shelf Research 63 (2013) S159–S176

Contents lists available at SciVerse ScienceDirect

Continental Shelf Research

journal homepage: www.elsevier.com/locate/csr

Multiscale forecasting in the western North Atlantic: Sensitivity of model forecast skill to glider data assimilation

Avijit Gangopadhyay [a,*], Andre Schmidt [a], Laurie Agel [a], Oscar Schofield [b], Jenifer Clark [c]

[a] School of Marine Sciences, University of Massachusetts and School for Marine Science and Technology, University of Massachusetts, Dartmouth, 200 Mill Rd, Suite 325, Fairhaven, MA 02719, USA
[b] Coastal Ocean Observation Lab, Institute of Marine and Coastal Sciences, School of Environmental and Biological Sciences, Rutgers University, New Brunswick, NJ 08901, USA
[c] Jenifer Clark's Gulfstream, 3160 Lacrosse Court, Dunkirk, MD 20754, USA

ARTICLE INFO

Article history:
Received 29 April 2011
Received in revised form
15 September 2012
Accepted 26 September 2012
Available online 11 October 2012

Keywords:
Glider data assimilation
Multiscale real-time forecasting
Observing simulation experiment (OSE)
Western North Atlantic
Mid-Atlantic Bight

ABSTRACT

A recently implemented real-time ocean prediction system for the western North Atlantic based on the physical circulation model component of the Harvard Ocean Prediction System (HOPS) was used during an observation simulation experiment (OSE) in November 2009. The modeling system was built to capture the mesoscale dynamics of the Gulf Stream (GS), its meanders and rings, and its interaction with the shelf circulation. To accomplish this, the multiscale velocity-based feature models for the GS region are melded with the water-mass-based feature model for the Gulf of Maine and shelf climatology across the shelf/slope front for synoptic initialization. The feature-based initialization scheme was utilized for 4 short-term forecasts of varying lengths during the first two weeks of November 2009 in an ensemble mode with other forecasts to guide glider control.

A reanalysis was then carried out by sequentially assimilating the data from three gliders (RU05, RU21 and RU23) for the two-week period. This two-week-long reanalysis framework was used to (i) study model sensitivity to SST and glider data assimilation; and (ii) analyze the impact of assimilation in space and time with patchy glider data. The temporal decay of salinity assimilation is found to be different than that of temperature. The spatial footprint of assimilated temperature appears to be more defined than that of salinity. A strategy for assimilating temperature and salinity in an SST-glider phased manner is then offered. The reanalysis results point to a number of new research directions for future sensitivity and quantitative studies in modeling and data assimilation.

Published by Elsevier Ltd.

1. Introduction

Ocean observing has advanced in the last decade from a ship-based expeditionary science to a distributed and observatory-based approach. This transition, which has been occurring over last decade (Glenn and Schofield, 2003, 2009), reflects the maturation of a wide range of observation platforms, data assimilative numerical models, and improved global communications (Schofield et al., 2012). The expanding suite of observational assets include remote sensing (satellite: Halpern, 2000, aircraft: Lomax et al., 2005, HF Radar: Crombie, 1955; Barrick, 1972; Barrick et al., 1977), fixed location assets (moorings: Hayes et al., 1991, Weller et al., 2000, seafloor cables: Schofield et al., 2002, Kunze et al., 2006), and Lagrangian platforms (AUVs: Blackwell et al., 2008, gliders: Sherman et al., 2001, Eriksen et al., 2001, Webb et al., 2001, drifters: Niiler et al., 2003, floats: Davis et al., 1992, Gould et al., 2004). As the number of deployed platforms increases there is a growing need to aggregate the data and coordinate the sampling among the individual systems in order to create a system-of-systems. This will require the development of coherent software networks that allow a distributed group of sensors and/or scientists to operate as a group.

The integration of software systems is currently under development. For example, the U.S. National Science Foundation's Ocean Observatory Initiative (OOI, http://www.oceanleadership.org/programs-and-partnerships/ocean-observing/ooi/) has focused a significant effort on developing a sophisticated cyberinfrastructure (CI) that binds the physical observatory, computation, storage and network infrastructure into a coherent system-of-systems. This CI is also being designed to provide a web-based social network, enabled by real-time visualization and access to numerical models, to provide the foundation for adaptive sampling science. The OOI cyber-development has chosen to utilize a spiral design strategy, allowing the oceanographic community to provide input during the construction phase with the strategy of utilizing existing ocean observing networks. For this effort, the OOI utilized an existing

* Corresponding author. Tel.: +1 508 910 6330; fax: +1 508 910 6374.
E-mail address: avijit@umassd.edu (A. Gangopadhyay).

0278-4343/$ - see front matter Published by Elsevier Ltd.
http://dx.doi.org/10.1016/j.csr.2012.09.013

ocean observing network in the Mid-Atlantic Bight (MAB) as part of the National Oceanographic and Atmospheric Administration's (NOAA) Integrated Ocean Observing System (IOOS) in November 2009. The goal was to use this network to conduct an observation simulation experiment (OSE). The objective was to use the oceanographic testbed to support field operations of ships and mobile platforms aggregate data from fixed platforms, shore-based radars, and satellites; and offer these data streams to data-assimilative forecast models. Additional goals were to use multi-model forecasts to guide glider missions and coordinate satellite observing, and to demonstrate the ability to conduct two-way interactions between the sensor web and predictive models. While previous studies have focused on the phytoplankton dynamics during spring and/or spring transition (Ryan et al., 1999a, 1999b, 2001), this field effort was conducted to collect data on the status of the Mid-Atlantic shelf in early winter, when the winter phytoplankton bloom occurs (Schofield et al., 2010).

This paper uses data collected during the OSE to investigate the forecast sensitivity to glider data assimilation. One goal of this study is to understand and develop a protocol for future similar test experiments based on a careful reanalysis during the OSE period. An interesting new result from the assimilation analysis is the apparent difference of spatial and temporal scales of impact between temperature and salinity. These behavioral differences might lead to future areas of research in modeling and assimilation.

This paper is organized as follows. The methodology is presented in Section 2 and the analysis of the real-time forecasts made during the OSE period is presented in Section 3. A reanalysis based on systematic glider data assimilation is presented in Section 4, followed by a summary and discussion in Section 5.

2. Approach and methods

A distributed community of ocean scientists provided the CI team with regional surface datasets, a surface current mapping network, a constellation of fixed and taskable satellites, a fleet of autonomous Slocum gliders, a multi-vehicle network of autonomous underwater vehicles, and five different data-assimilative forecast ocean models that tested the OOI software. An overview of the OSE effort is described by Schofield et al. (2010). The OSE was a multi-institutional, multi-investigator effort. Various OSE groups coordinated satellites, multiple gliders, and an AUV during the OSE period of October 26 through November 17, 2009. A data and model portal was assembled (http://ourocean.jpl.nasa.gov/CI) (Wang et al., in this issue) for multi-model ensemble forecasting and glider guidance decision-making efforts.

2.1. Regional data streams

A large suite of satellites were used during this study. The satellites provided multiple passes of sea surface temperature and ocean color observations. The data was downloaded and processed at both the NASA Jet Propulsion Lab and the Rutgers Coastal Ocean Observation Lab. Data was processed in near real-time (hours) and posted to the data portal.

The surface currents on the MAB are measured by an extensive network of high frequency CODAR networks array. The CODAR network consists of twelve 5 MHz systems located along the northeast of the United States. The HF Radar uses the Doppler Shift of a radio signal backscattered off the ocean surface to measure the component of the flow in the direction of the antenna. The network provides surface current estimates to a depth of 2.4 m (Stewart and Joy, 1974).

2.2. Gliders

Slocum gliders are an autonomous underwater scientific platform (Webb et al., 2001) manufactured by the Teledyne-Webb Research Corporation. They are 1.8-m long, torpedo-shaped, buoyancy-driven vehicles with wings that enable them to maneuver through the ocean at a forward speed of 20–30 cm s^{-1} in a sawtooth-shaped gliding trajectory. Each Slocum glider has a payload bay that houses a SeaBird conductivity–temperature–depth sensor and includes space for a range of additional sensors. The glider acquires its global positioning system (GPS) location every time it surfaces, which is programmable and was set to call-in every 3 h for the purposes of this study. By dead reckoning along a compass bearing while flying underwater, estimates of depth averaged current can be calculated based on the difference between the glider's expected surfacing location and the actual new GPS position. Depth averaged current measurements obtained in this manner have been validated against stationary Acoustic Doppler Current Profiler data (Glenn and Schofield, 2003).

During this experiment, four Webb gliders were deployed by Rutgers University and the University of Delaware. The gliders were deployed prior to the start of the experiment on Nov 1 2009 and operated for two weeks. During that period the gliders traversed 1673 km underwater collecting 23,332 vertical profiles. The data collected were analyzed for various process studies including phytoplankton productivity (Schofield et al., 2012) and sediment re-suspension during fall storms (Miles et al., in this issue).

2.3. Numerical model

One of the five numerical models employed during the OSE is the SMAST-HOPS (School for Marine Science and Technology—Harvard Ocean Prediction System) real-time forecast system, which has been operational since March 9, 2009, providing a 7-day ocean forecast for the large-scale Gulf Stream region from Cape Hatteras to 55°W, including the Gulf of Maine and the Mid-Atlantic shelf region. The other four models were: (i) the New York Harbor Ocean Prediction System (NYHOPS) for MARACOOS (Bhushan et al., 2009; Georgas and Blumberg, 2009); (ii) the regional ocean modeling system for MARACOOS (Wilkin et al., 2005); (iii) the regional ocean modeling system from USGS (Warner et al., 2008); and (iv) the MIT multidisciplinary simulation, estimation and assimilation system (MSEAS) (Lam et al., 2009; Haley and Lermusiaux, 2010). The SMAST-HOPS operational system (described by Schmidt and Gangopadhyay, 2012, in this issue, SG12 henceforth; Brown et al., 2007a, b; Robinson et al., 2001) regularly assimilates satellite SST and, when available, MARACOOS glider-measured 4-D water properties to produce weekly 3-D nowcast and forecast MARACOOS regional temperature maps (see http://www.smast.umassd.edu/modeling/RTF/index.php). Four forecasts were provided during the OSE period, assimilating all available data from SST and the four gliders.

The horizontal structure of the SMAST-HOPS operational model domain consists of 131×83 grid points with 15 km resolution, extending from 30.5°N to 47.93°N in the meridional and from 80.54°W to 54.23°W in the zonal direction. The vertical structure of the model is resolved by 16 levels that are distributed according to a topography-following "double sigma" transformation described by Lozano et al. (1996) and Sloan (1996). The open boundary conditions for tracers and velocity are based on Orlanski (1976); and the horizontal subgridscale processes are parameterized using a set of scale-selective Shapiro filters: 4-1-1 (fourth order, one time, every time step) for velocity and tracers, a 2-2-1 for vorticity and 2-1-1 for streamfunction. The time step

Table 1
Objective analysis parameters for glider data initialization and assimilation with a 12-h time window.

	Initialization		Assimilation	
	Synoptic	Mean	Synoptic	Mean
Decay (km)	60	180	30	90
Zero crossing (km)	120	360	60	180
Time decay (day)	90	1000	10	80

used in all runs was 225 s. Some of the important numerical model parameters and their values are given in Table 1 of SG12. Note that this model system has yet to incorporate a real-time river runoff input.

The operational forecasting system is built on the feature-oriented initialization scheme developed by Gangopadhyay et al. (1997) for the Gulf stream meander and ring (GSMR) region and for the Gulf of Maine and Georges Bank (GOMGB) region (Gangopadhyay et al., 2003). The feature-oriented methodology is explained in detail for the GSMR–GOMGB region by SG12, and has now been developed for many other regions of the world ocean including the South Atlantic (Calado et al., 2008), the Trinidad North Brazil current (Schmidt et al., 2011) and the California current system (Gangopadhyay et al., 2011). Briefly, FORMS methodology (Gangopadhyay and Robinson, 2002) requires (i) the development of analytical–empirical formulation of the synoptic-dynamic characters of features such as fronts, eddies, gyres and currents etc. called 'feature models,' and then (ii) implementation of a multiscale melding using objective analysis of calibrated synoptic feature models (with available satellite and in-situ data) with background mean state to create the "most knowledgeable" nowcast. For the MARACOOS implementation, the deep-water feature model set for GSMR (Gulf Stream, Deep western boundary current, warm and cold core rings, southern and northern recirculation gyres; see Gangopadhyay et al. (1997) for details) is melded with the shallow-water feature model set in the GOMGB region (Maine coastal current, Georges Bank tidal front, Wilkinson–Jordan–Georges basin gyres, northeast channel inflow and great south channel outflow; see Gangopadhyay et al. (2003) for details), and further supplemented with the Levitus climatology as the background in a multiscale objective analysis framework. The initialization field is dynamically adjusted with wind forcing and used in an SST-assimilative forecast model using the methodology described by Brown et al. (2007b). The model is forced with atmospheric fields (surface momentum flux, surface heat flux, surface water flux and shortwave radiation) from the global forecast system (GFS) at 0.5-degree resolution for 7 days. Several products are used for assimilated SST, including 3-day composite products from the Johns Hopkins University/Applied Physics Laboratory, AVHRR passes processed by the MARACOOS group at the University of Delaware College of Marine and Earth Studies, and daily and multi-day blended products from remote sensing systems. See SG12 for full details of this implementation and the model skill validation using drifters and GS axis locations from satellite observation.

While the OSE period was a test of the development and implementation of the cyberinfrastructure, the data collected during this period provided a valuable opportunity to reanalyze and understand various aspects of underlying processes and methodologies, which depend on data, models and model-data synthesis exercises. One of them is the focus of this paper, in which we assess the impact of glider data assimilation on the SMAST-HOPS model simulation. Such an exercise would make possible the design of better and more effective schemes for real-time assimilation utilizing satellite, glider and other in-situ observations in future OSEs.

Assimilation of data in numerical ocean models has been in practice for over couple of decades now (Carter and Robinson, 1987; Robinson et al., 1989; Derber and Rosati, 1992; Ezer and Mellor, 1992; Fukumori and Malanotte-Rizzoli, 1995). A comprehensive set of studies on the different approaches to data assimilation in ocean modeling for the early nineties were compiled by Malanotte-Rizzoli (1996). More recent advances in data assimilation include, among many, the works with the regional ocean modeling system (3DVAR and 4DVAR) (Li et al., 2008a, 2008b; Chao et al., 2009; Broquet et al., 2009; Veneziani et al., 2009), with the navy's coastal ocean model (Barron et al., 2007; Shulman et al., 2007, 2009), and with the Harvard Ocean Prediction System (Lozano et al., 1996; Lermusiaux, 1999, 2002; SG12) and the MIT multidisciplinary simulation, estimation and assimilation aystem (MSEAS) (Lam et al., 2009; Haley and Lermusiaux, 2010). With increasing computing power, more mathematically elegant and computationally demanding methods such as extended Kalman Filters, ensemble Kalman Filters (EnKF) are being adapted to ocean and atmosphere modeling at a rapid pace (Kalnay, 2003; Ott et al., 2004; Hunt et al., 2004; Kalnay et al., 2007; Evensen, 2009). However, while the techniques are improving, the availability of data for assimilation in the ocean models still remains sparse and infrequent. This necessitates generating suitable initialization and assimilation fields from a set of irregularly occurring observations in both space and time. Specifically, a set of decay scales in space and time (based on data auto-correlations) is generally applied to construct the initialization and assimilation fields (Mooers, 1999). It is also expected, that the impact of such patchiness would result in an assimilated field where errors will dominate away from the center of assimilation. In this study, we attempt to understand this impact facilitated by the availability of the patchy glider data set in a selective region in the reanalysis mode.

3. Assimilation of glider data in model forecasts

The sensitivity of the model simulations to glider data assimilation is examined over the two-week period (Nov 2 through Nov 16). This section describes the Gulf Stream system during the OSE period, the glider data and the initialization and assimilation protocols. Section 4 then describes the numerical experiments and the results.

3.1. The gulf stream system during OOI–CI–OSE

The FORMS-based initialization for the SMAST-HOPS operational system requires an ocean analysis. This analysis for the western North Atlantic provides the surface characterizations of the locations, shapes and sizes of various features such the Gulf Stream, its rings, and the shelf-slope front. The specific product used for the SMAST-HOPS model is Jenifer Clark's Gulfstream (http://users.erols.com/gulfstrm/), which is a typical ocean analysis created primarily from the NOAA polar orbiting thermal infrared satellite imagery. The data are false-colored based on different sea surface temperatures. Other sources of data include altimetry, drifting and fixed buoys, model output, and sea surface isotherm analyses. The analyses extend from 80°W to 45°W and from 50°N to 30°N. The images are then subjectively analyzed by an oceanographic expert. They are generated once a week and have been analyzed since 1980. The analyses have improved over the years due to inputs and feedback from various stakeholders such as sailboat racers, coast guard search and rescue, fishermen,

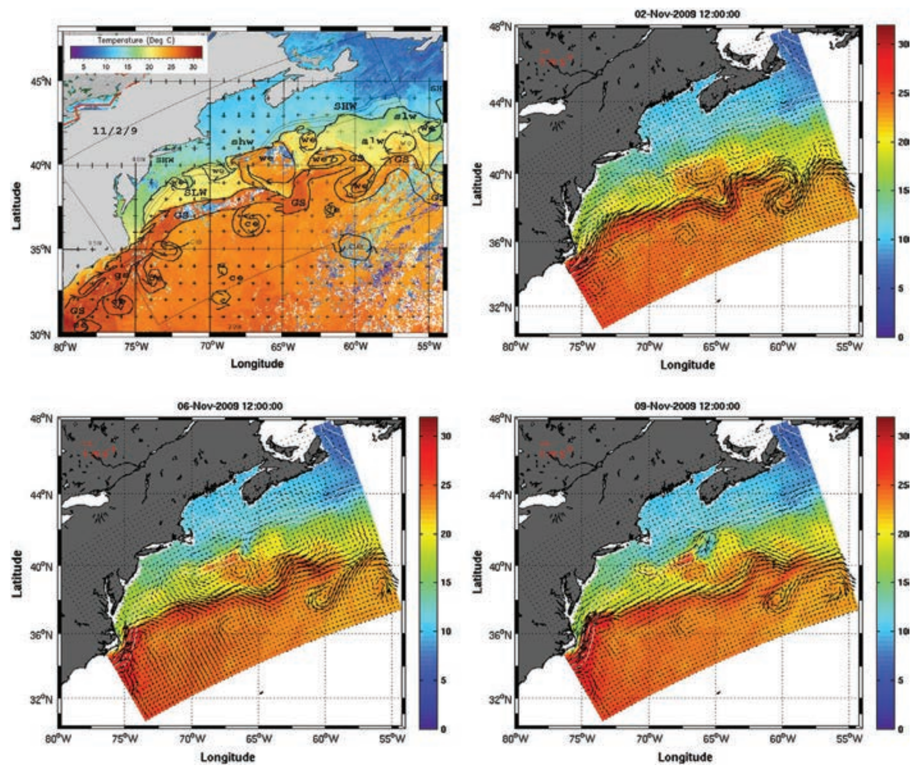

Fig. 1. Weekly Jenifer Clark analysis of Gulf Stream ring and eddy positions, with cold core rings and eddies noted as "ce" and warm core rings and eddies noted as "we" (top-left) for Nov 02, 2009.The SMAST-HOPS forecasts for Nov 2nd, Nov 6th and Nov 9th are shown in the other three panels.

scientists, forecast modelers, yacht deliveries, ocean rowers, swimmers, etc.

The week-long forecasts are issued generally by wednesday morning; monday 0-h is a typical model initialization state, with SST assimilation carried out on monday afternoon or on Tuesday morning. The forecast fields (temperature, salinity, currents) are available at www.smast.umassd.edu/modeling/RTF/MARCOOS for different levels at 6-hourly intervals for the full domain, and for zoom domains of the Mid-Atlantic shelf and the Gulf of Maine. To provide high-resolution, nested forecasts for the mission control of the AUV and glider fleets, the forecast data in netCDF format (CF-compliant) were made available from the OPeNDAP-enabled THREDDS server http://aqua.smast.umassd.edu:8080/thredds/catalog/models/catalog.html.

The configuration of the Gulf Stream system on November 02, 2009, as the study period begins, is shown in Fig. 1. The left panel shows the Jenifer Clark analysis, with outlines of the Gulf Stream and its filaments spreading out to the recirculation gyres and each independent ring. During the OOI–CI–OSE, the Gulf Stream system north of 32°N and west of 55°W includes 6–7 warm and 6–7 cold eddies, and a large meander from 65°W to 55°W. The meander shifts and changes shape over the 2-week period as it absorbs a large warm core ring and casts off a cold-core ring. The SMAST-HOPS forecasts for Nov 2, 6 and 9 are shown in Fig. 1 b–d. During these forecasts the SST and Glider data were assimilated in a strategic reanalysis to understand the behavior of assimilated fields after glider data assimilation.

3.2. Description of the glider sampling

The tracks of the gliders, showing the coverage area, are delineated in Fig. 2. The individual tracks for RU05, RU21, RU23 and UD134 are distinguished by color. The three Rutgers gliders

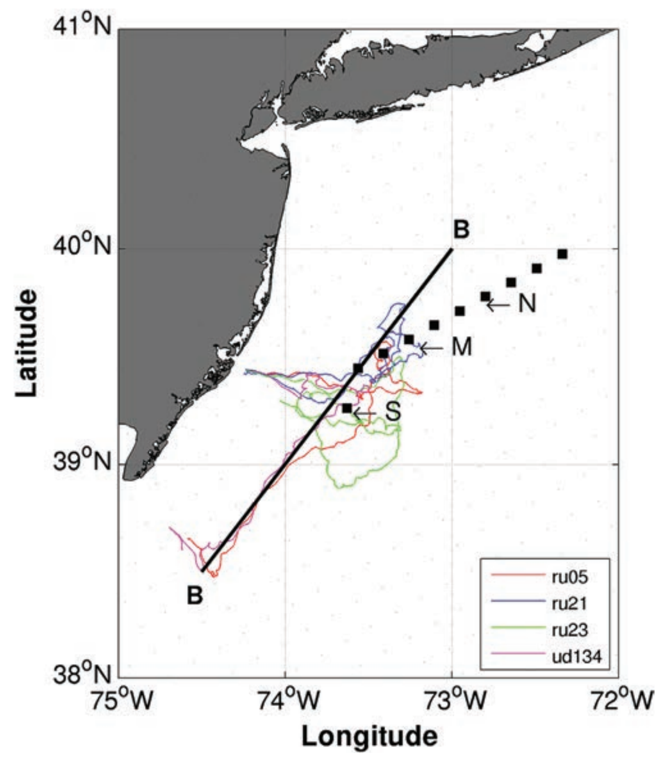

Fig. 2. Tracks of the three gliders (RU05, RU21 and RU23) used for initialization and assimilation of the 02 Nov 2009 SMAST-HOPS run. The tracks span from 30 Oct 2009 to 17 Nov 2009. Glider UD134, not used in the HOPS model, is also shown. The points marked by south (S), middle (M) and north (N), are where the spatio-temporal impact analysis of glider data assimilation is carried out. (For interpretation of the references to color in this figure legend, the reader is referred to the web version of this article.)

(RU05, RU21 and RU23) were deployed off the New Jersey coast on October 26, and moved across the shelf to near the 50-m isobath within the first 3–4 days. All of them were then used for CI–OSE control experiments (Schofield et al., 2010) and were guided in different directions before recovery. For example, after following the cross-shelf path, RU05 (red) was guided northward during Nov 6–9, then southward in the second week, and finally was recovered near Delaware Bay on Nov 17. RU23 (green) zigzagged during the OSE across the 50-m isobath and was recovered on Nov 17 near its original deployment site. RU21 (blue) started from the same location, moved in a northeastward direction and was engaged in sampling fine-scale features (Schofield et al., 2012, in this issue). UD134 (pink) was deployed later on Nov 6, followed a track similar to that of RU05 (red) for the latter part of the 2-week period, and was also recovered on Nov 17 2009. The sensitivity to assimilation was studied along the line of the black rectangles and is described later.

3.3. Initialization and assimilation methodologies with glider data

For the purpose of initialization, the temperature and salinity data from RU05, RU21 and RU23 between Oct 26 and Nov 2 were melded with the standard operational FORMS-derived initialization field (SG12). The melding was done by carrying out a multiscale objective analysis (OA) in which the synoptic glider data were statistically merged with the FORMS initialization following well-established procedure (Brown et al., 2007a; BG07 henceforth; SG12). The OA parameters, such as the correlation scale and decay scales of choice for the glider data, are summarized in Table 1. The total sampling coverage for Oct 26–Nov 1 is shown in Fig. 3a. This process of melding available glider observations over a week (or less) at initialization of the dynamical model run is also known as 'assimilation at initialization.'

The sequential assimilation protocol for SST is explained in detail by SG12 (see their Section 3.3 and equation 1 therein). Briefly, the OI assimilation is a data-fusion methodology, where the observation (SST or Glider T/S) is assimilated in the model using a time-varying weighting function within each assimilation cycle. Subsequent glider data were assimilated at regular intervals of 12 h. Examples of glider data locations used for assimilation for a selected set of days are shown in Fig. 3b–f for Nov 4, 6, 8, 10, and 12, respectively. Initial fields of salinity and associated error fields are presented in Fig. 4. The contrast between glider salinity and climatology-derived background is much more pronounced than that between the corresponding temperature fields (not shown). This is because the assimilation of glider temperature is smoothed by the SST-assimilation from satellite observations. The subsurface projection of the satellite-derived SST field also helps reduce such contrast between glider and background temperature.

The weighting assimilation scheme for SST is described by BG07 and SG12 in detail. The weights for assimilating the glider data are presented in Fig. 5. Specifically, to allow for the internal dynamical adjustment of the assimilative variable, our approach is to distribute the field over a temporal window with variable weights. The 12-h Glider data is thus slowly amplified from its 20% value (weight of 0.2) on the 6th hour (prior to the observation hour) to its 90% value (weight of 0.9) on the 12th hour and then decays for next 6 h. This ramp-up and decay-down strategy is cycled every 12 h allowing for continuous and sequential assimilation of glider data within the observation window.

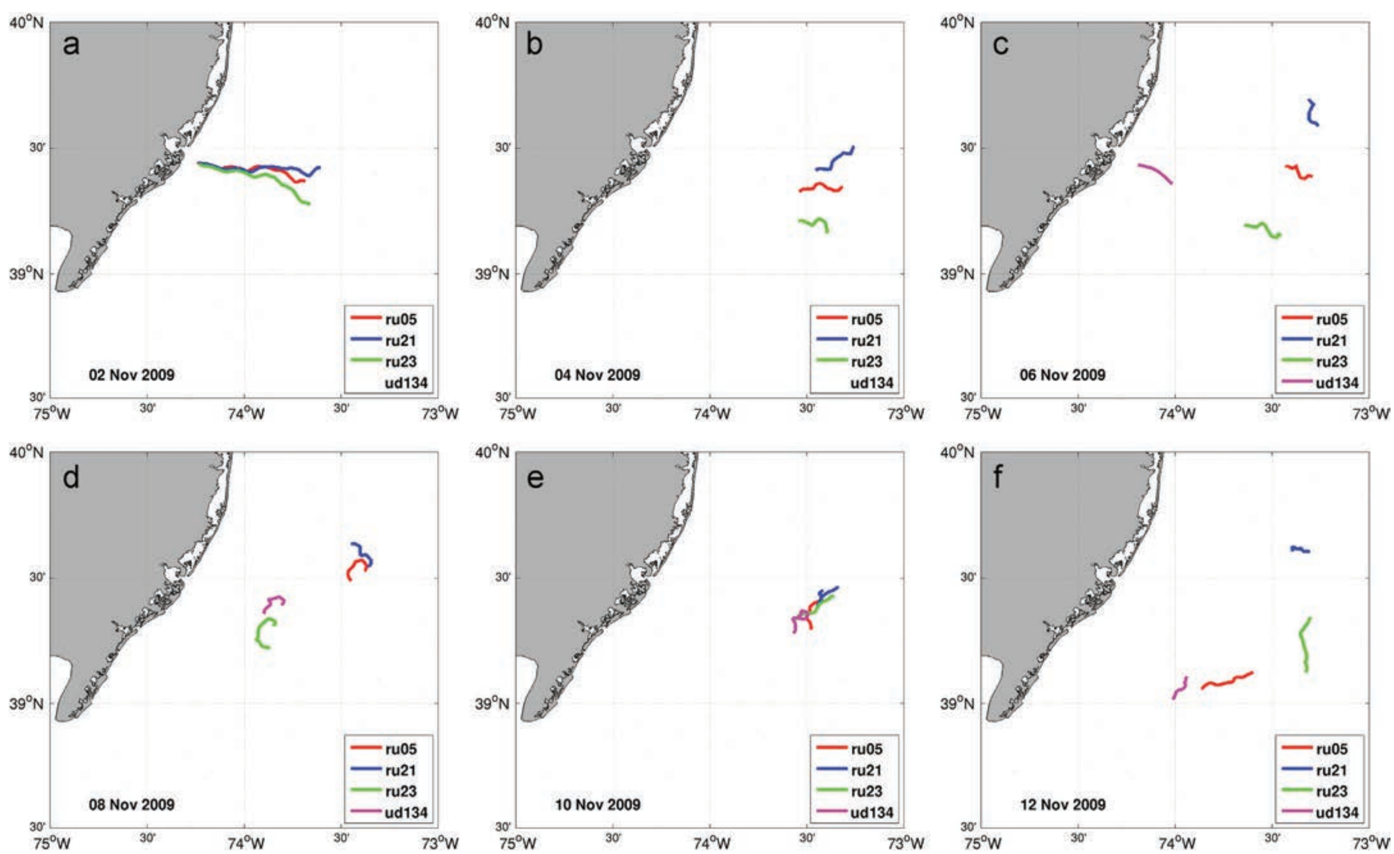

Fig. 3. Position of glider data used in the (a) initialization of the SMAST-HOPS 02 Nov 2009 run, and the assimilation of glider data for (b) 04 Nov 2009, (c) 06 Nov 2009, (d) 08 Nov 2009), (e) 10 Nov 2009, and (f) 12 Nov 2009. The initial field incorporates data collected from 30 Oct 2009 to 02 Nov 2009. The assimilation fields incorporate 12 h of glider data, centered on 0000 UTC.

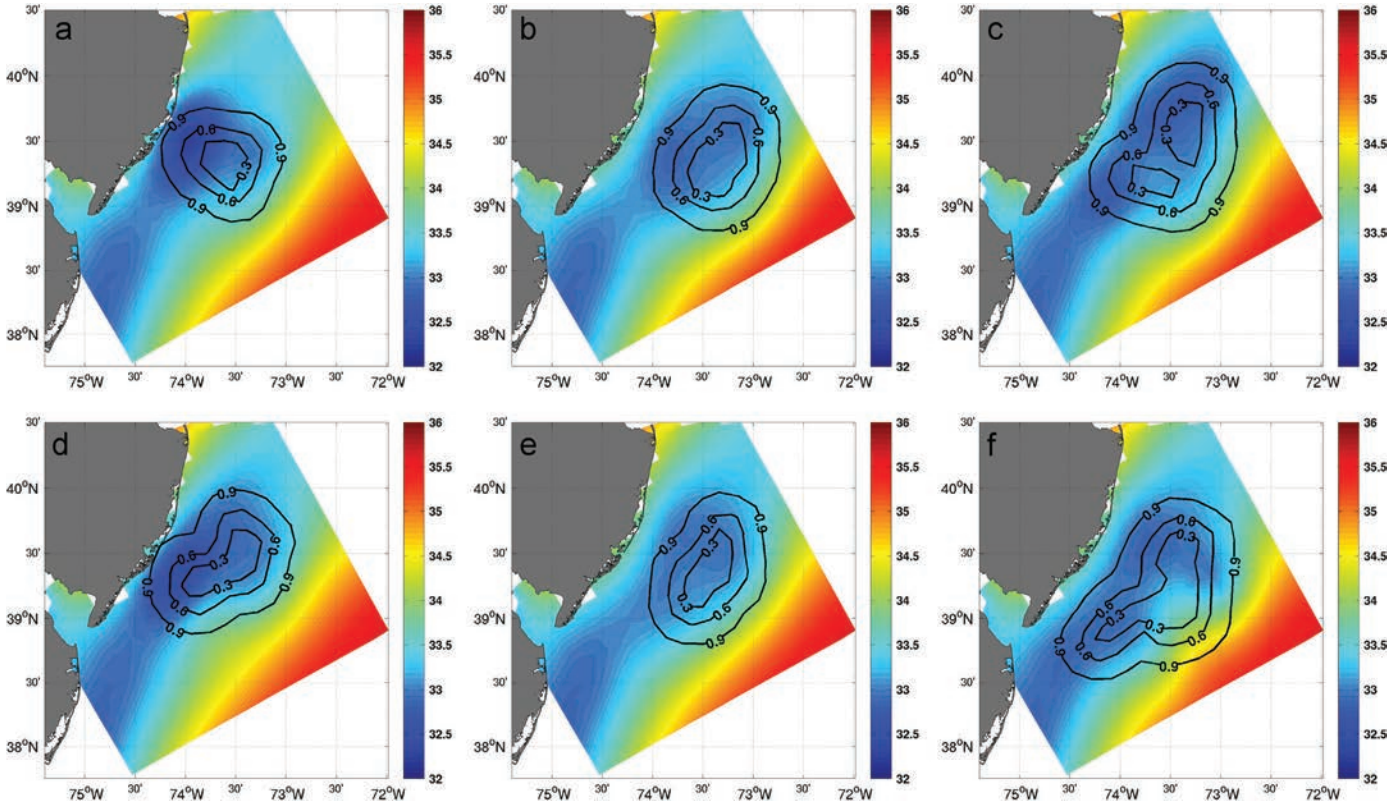

Fig. 4. OA salinity fields assimilated into SMAST-HOPS 02 Nov 2009 run for (a) 02 Nov 2009 (b) 04 Nov 2009 (c) 06 Nov 2009 (d) 08 Nov 2009 (e) 10 Nov 2009, and (f) 12 Nov 2009. Error is shown as contours.

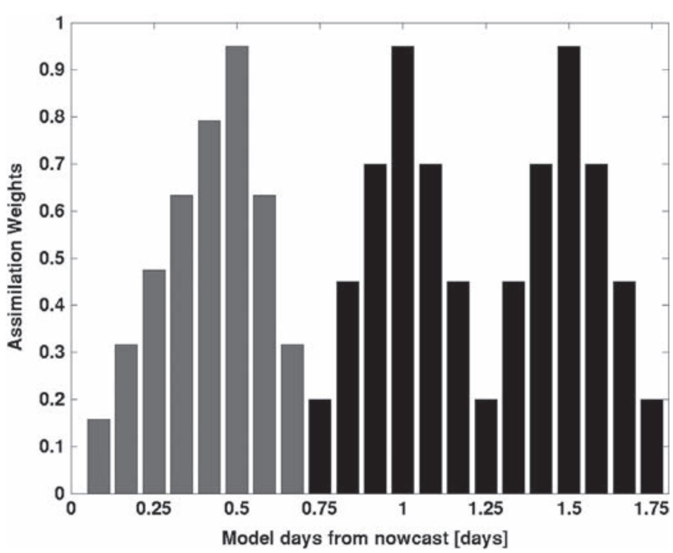

Fig. 5. Assimilation scheme used for SMAST-HOPS 02 Nov 2009 run, showing the weights used for SST (grey), and glider data (black) on the model days. Note that the glider assimilation is repeated with the same cycle as shown here after day 1.75.

It is instructive to analyze the differences between the glider profiles and the objectively analyzed profiles. Overall, the mean rms differences between the OA and glider data for temperature and salinity are comparable for all the gliders at all depths (Fig. 6). The depth-averaged rms difference between OA and the glider for temperature (salinity) at the glider locations for RU05 is 0.275 degree (0.15 psu), for RU21 is 0.22 degree (0.13 psu) and for RU23 is 0.225 degree (0.12 psu). Most of the gliders collected data within 25–30 m depth, while the maximum depth of a particular glider was 63 m.

4. Analysis of post-assimilation fields in forecast mode

This section describes the assimilative forecasts and their analyses in understanding the impact of assimilation from a spatial and temporal footprint perspective.

4.1. Description of assimilative forecasts

The effect of the glider data assimilation on the forecasts is presented next (Figs. 10 –18). In the SMAST-HOPS assimilation strategy, in which glider data is assimilated every 12 h, objectively analyzed fields with appropriate error fields are first computed. The multiscale OA uses the data in the observational window of ± 12 h, and uses the initial field of Nov 2 as the background. This choice of background avoids discontinuities between glider data and climatological background.

Two parallel runs were carried out. Both runs were initialized with the FORMS methodology (SG12). Furthermore, glider data for the initial period of October 26 through Nov 1 were objectively analyzed with the FORMS-derived temperature and salinity fields to produce the reanalysis initial field. The first run was then carried out with satellite-derived SST assimilation only during the first 12 h of simulation for Nov 2 and then continued without further assimilation of glider data (temperature and salinity). This run is designated as "Run1." This run can be described as a run with assimilation of the glider data at initialization.

Another run was done with successive assimilation of temperature and salinity data from gliders RU05, RU21 and RU23.

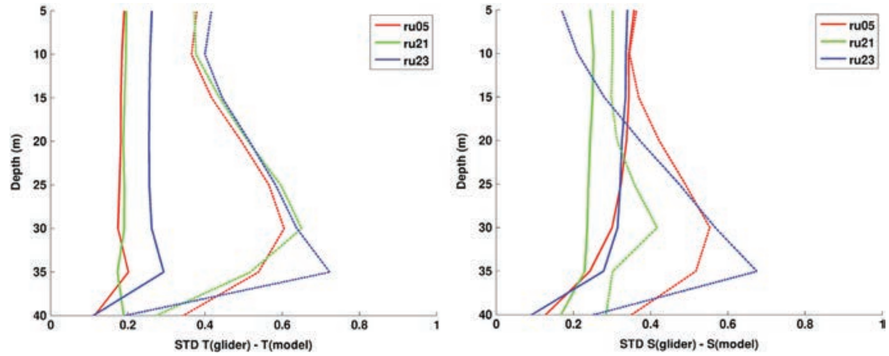

Fig. 6. Glider-OA error at various depths for (left) temperature and (right) salinity. The abscissa is the standard deviation of the difference between the glider data and the OA fields every 12 h.

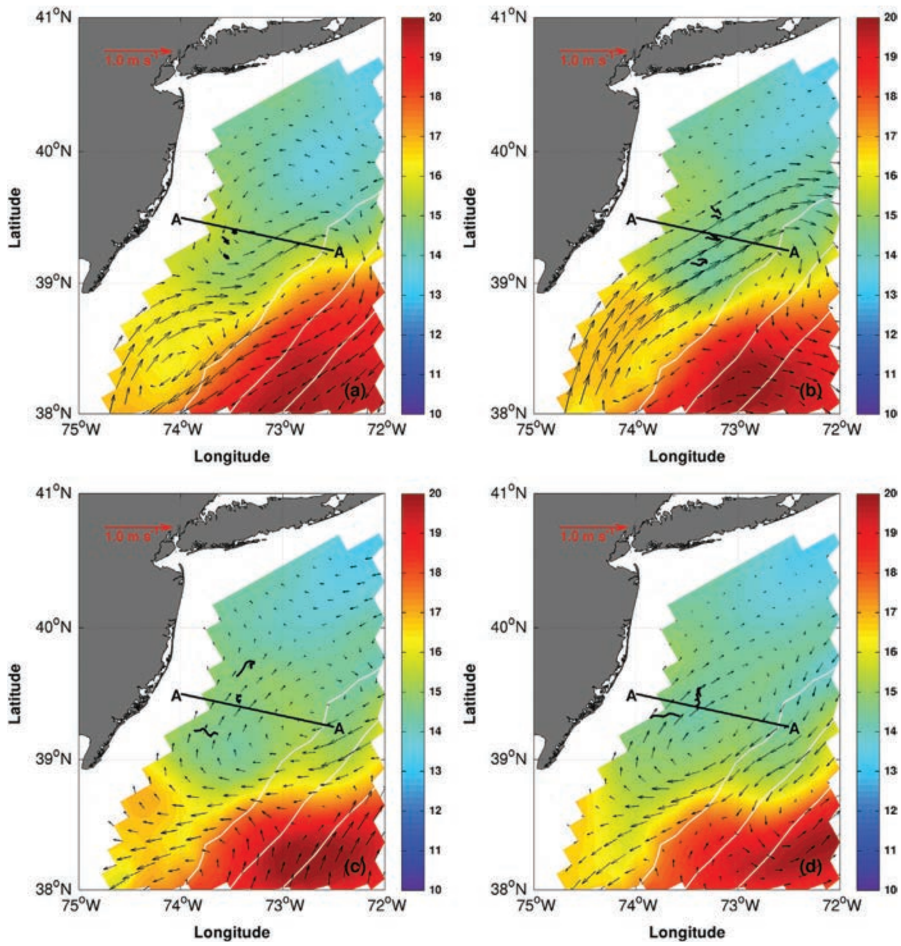

Fig. 7. Twenty-five metre temperature and velocity vectors from 02 Nov 2009 run for (a) 03 Nov 2009, (b) 05 Nov 2009, (c) 07 Nov 2009, and (d) 09 Nov 2009. Solid line A–A shows cross-section region and thick black squiggles show glider positions for data that is assimilated for each day. Temperature in °C.

The satellite-derived SST assimilation methodology is very similar to that described by SG12. Additionally, glider data was assimilated following the methodology described in Section 3. This run is designated as "Run2." Following SG12, the initial field was adjusted for SST assimilation on the first cycle (12 h), which also assimilated the temperature and salinity from the gliders between Oct 26 and Nov 2. The evolution of temperature at 25 m overlaid with velocity for the assimilation run (Run2) for the first week is presented in Fig. 7. The evolution of salinity at 25 m overlaid with velocity for the second week is shown in Fig. 8. The initially weak velocity field develops and adjusts to about 0.1 m s^{-1} of southwestward flow along the shelf between the 50- and 100-m isobaths, while an anticyclonic recirculation develops between 38°N and 39°N (not shown). The weak southward flow to the north of the glider confluence region (Fig. 7) dissipates by Nov 3–5, when a broad northwestward wind-induced flow occurs over the glider region (not shown). During Nov 5–7, the passage of a southwesterly storm was reported. The expansion of glider data assimilation is greatest (in terms of areal coverage) on Nov 7 (Fig. 7). The velocity field adjusts to an

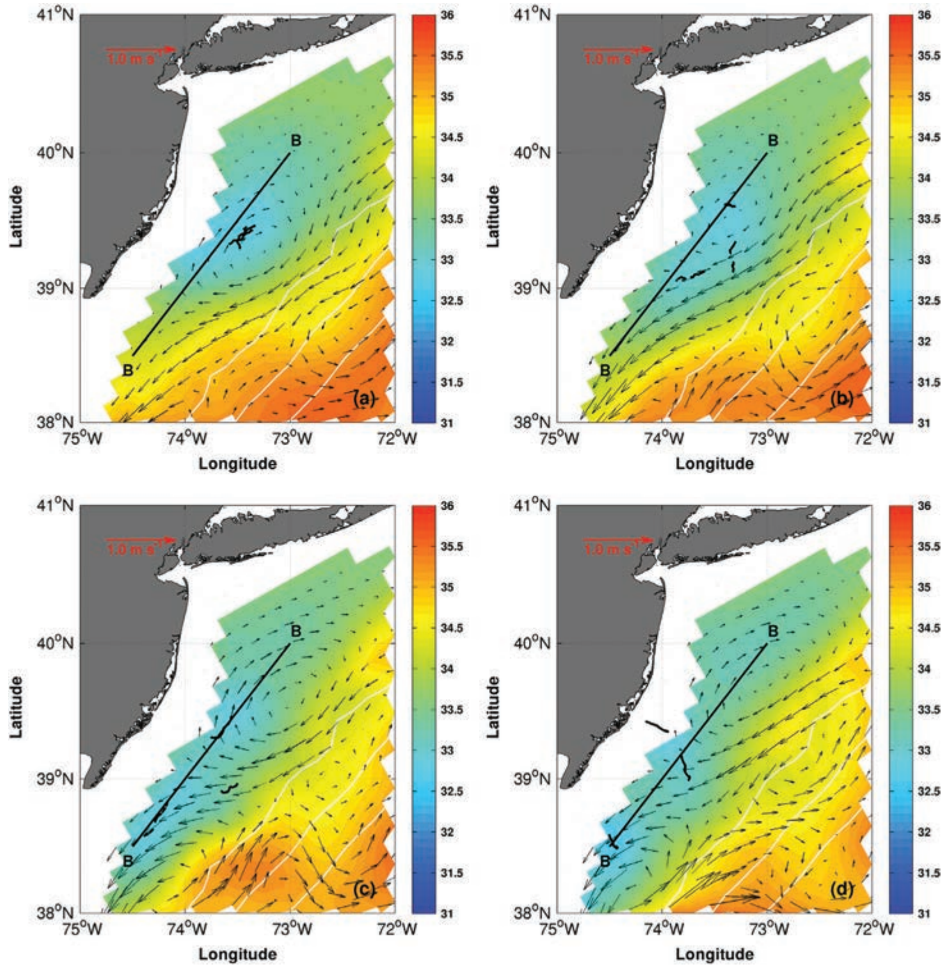

Fig. 8. Twenty-five metre salinity and velocity vectors from 02 Nov 2009 run for (top left) 10 Nov 2009, (top right) 12 Nov 2009, (bottom left) 14 Nov 2009, and (bottom right) 16 Nov 2009. Solid line B–B shows cross-section region, and thick black squiggles show glider positions for data that is assimilated for each day.

anticyclonic eddy-like shelf feature over the glider region (Fig. 7) by Nov 9 to the north of the steady southwestward along-shelf flow.

Fig. 9 shows a sectional view along line AA (Fig. 7) of the evolution of salinity during Nov 3–9. The initial shelf field is dominated by a shallow patch of relatively fresh water (S∼32–33 psu) (Fig. 9a). The contrast between this patch of fresh water and the higher-salinity water from climatological fields creates the salinity front (33–34 psu) between 60 km and 80 km offshore. Most of the glider data assimilated during Nov 3–5 has a uniform vertical profile. As assimilation progressively captures the low-salinity data, the frontal boundary between the near-coastal fresh water and offshore saline water moves gradually offshore and becomes tighter. The salinity front is visible between 80 km and 100 km offshore on Nov 5 and stabilizes at this location (Fig. 9b). The dynamical model shows further relative freshening of the offshore isohalines between 100 km and 150 km offshore during the latter part (Nov 7 through Nov 9) of the simulation (Fig. 9c and d). Note that the Jenifer Clark satellite analysis shows a possible intrusion around an anticyclonic shelf eddy near the glider assimilation region on Nov 6 (Fig. 10). However, in the dynamical model, the eddy was non-existence, as the model was initialized with the canonical shelf-slope front in this region. Thus the climatological signature of the shelf-slope front competes against the freshening and cooling induced by the assimilation of glider observations. Effectively, in the shallow inshore region, the dynamical model develops a weak signature of a fresher and cooler patch on the shelf. Had there been more observations around this area, one would then expect to capture dynamical events like "overrunning" (Kumar et al., 2006), which are deeper and closer to shelf-break.

The evolution of temperature during the week of Nov 2–9 is examined next (Fig. 11a–d) along the cross-shelf section indicated in Fig. 7. Since the SST from satellite images is also assimilated with a vertical projection algorithm, initial contrast between the cooler shelf and warmer offshore water decays rapidly. By day 3 of the assimilation, the temperature range on the shelf (<50 m) reduces to 14–15.3 °C (Fig. 14b and c) from the initial range of 14–16.5 °C (Fig. 11a). The signature of a significant front at about 150–200 km offshore (Fig. 11a) dissipates by day 3.

The weak signature of shelf water intrusion (evident in observation as shown in Fig. 10) across the shelf-break into the slope sea is visible in the temperature field by day 6 and also evident in the day-7 forecast at 60 km offshore (Fig. 11). The center of the simulated anomalous patch is cooler (14.1 °C) than its edges (14.7 °C) (Fig. 11d) at the surface. The patch is also fresher at the core, and the inshore salinity gradient is weaker than its offshore counterpart.

The impact of temperature and salinity assimilation of glider data during the first week is examined next (Figs. 12 and 13) along the north-south section (line *B* of Fig. 8). In the salinity section (Fig. 13a), the far-field impact of assimilation of the three drifters (RU05, RU21 and RU23) is evident in the fresh water signature near the middle of the section, bounded by the

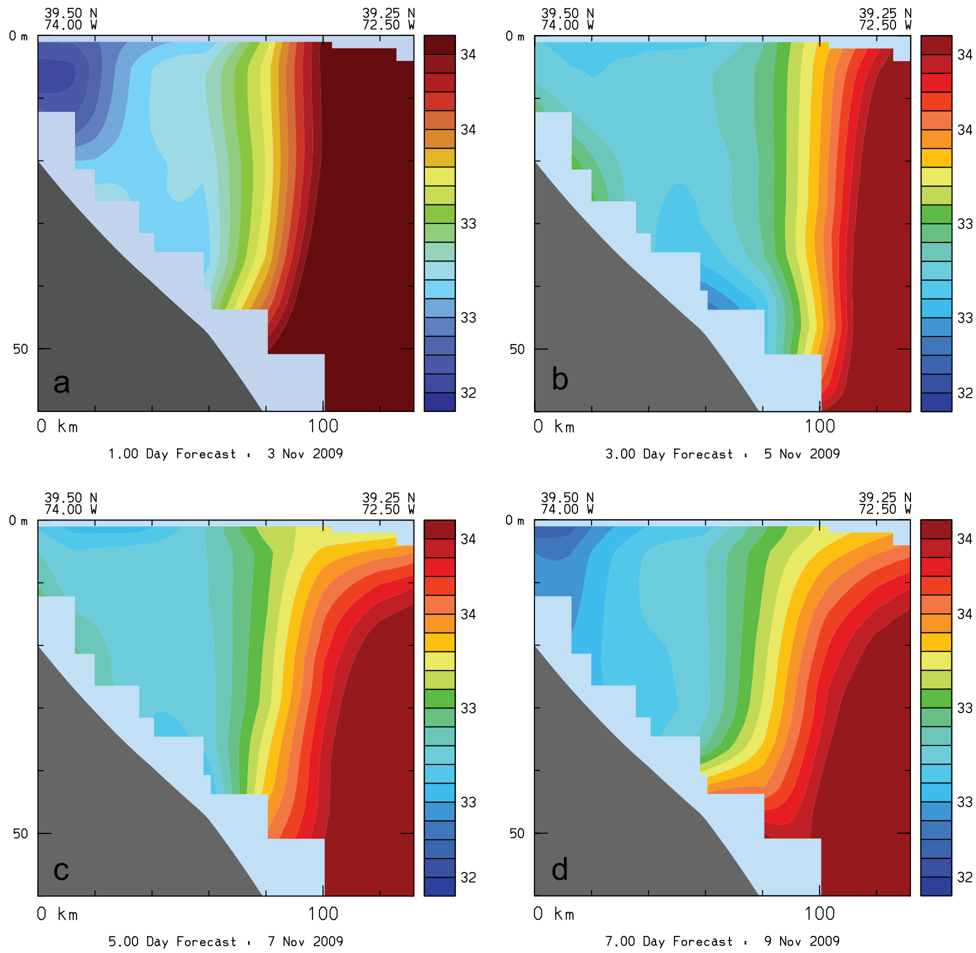

Fig. 9. Salinity cross sectional view of shelf along section line A–A, shown in Fig. 10 for 02 Nov 2009 SMAST-HOPS run with glider assimilation. Panels valid for (a) 03 Nov 2009, (b) 05 Nov 2009, (c) 07 Nov 2009, and (d) 09 Nov 2009.

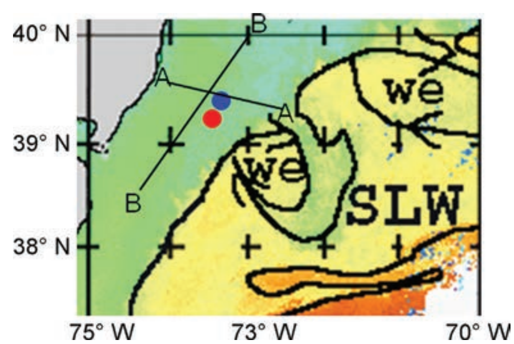

Fig. 10. Possible intrusion of shelf water into the slope during the OSE period. The image analysis is for Nov 6, 2009. Location of glider RU05 (RU23) is shown by the blue (red) dot in upper panel for Nov 6, 2009. The two sectional lines, A–A from Fig. 10, and B–B from Fig. 11, are also shown. (For interpretation of the references to color in this figure legend, the reader is referred to the web version of this article.)

climatological high-salinity patches. During the first week of the assimilation, the three gliders progressively sample the waters near and along this section, and the waters become fresher and colder due to assimilation. The vertical homogeneity of this assimilated water mass is strikingly different when compared to the unassimilated fields (not shown), which are generally more saline and warmer.

Further evolution of temperature and salinity along the north-south section (shown as B–B in Fig. 8) for the second week is shown in Figs. 14 and 15. This section follows the glider tracks of RU05 and UD134 during the second week of the OSE. Note that while the data from RU05 was assimilated into the model, the data from UD134 was used only for comparing the assimilated model results as an independent validation. The initial high-salinity patches are replaced by realistic fresher water on the shelf through subsequent glider data assimilation within the first week.

The weak signature of the shelf water intrusion across the shelf-break into the slope water, as discussed earlier, is also captured in the forecast fields of temperature (Fig. 14) and salinity (Fig. 15) of day 8 km, 100 km south of the northern end of the section. The subsurface saltier waters to the north and south are due to recirculation generated by the dynamical simulation.

4.2. Time-series comparison of Simulations against glider data

Fig. 16 shows a comparison of time-series of temperature and salinity of the assimilated reanalysis against the three gliders at 25 m. The simulated temperature and salinity profiles of the data-assimilative model are compared with the actual glider profiles at glider locations every half-hour. The assimilation evidently captures the inertial and sub-inertial variability reasonably well (Fig. 16). Difference in the initial 1–2 days between the assimilated simulation and glider data can be attributed to the possible mismatch between the satellite-derived SST (and its extrapolation

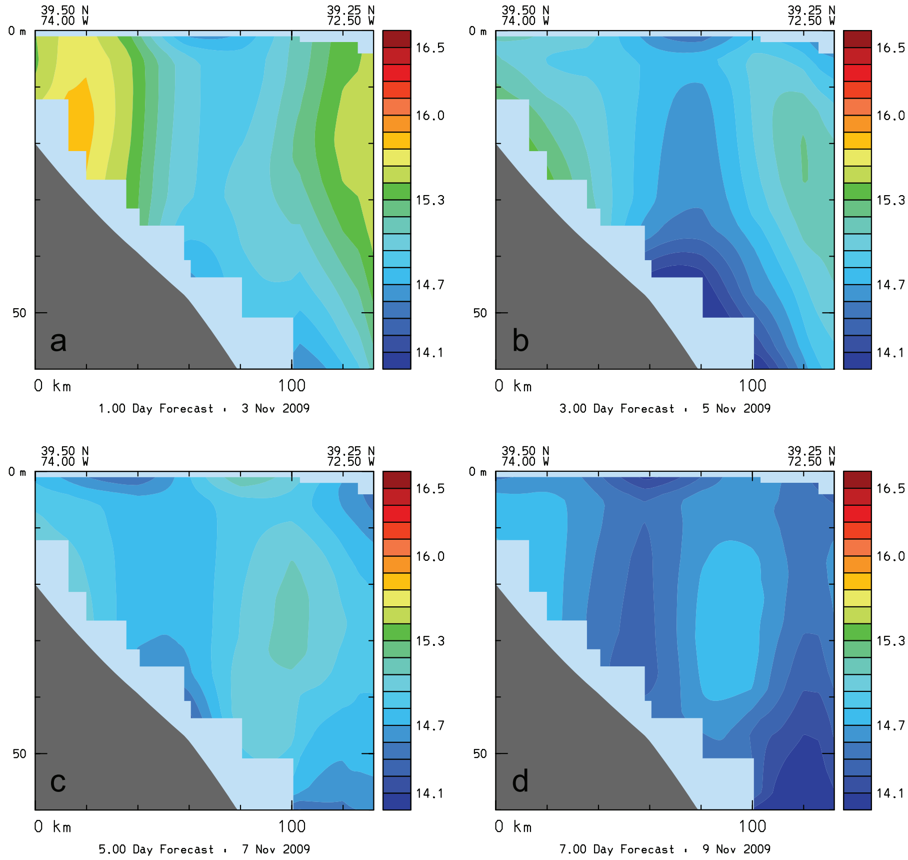

Fig. 11. Temperature cross sectional view of shelf along section line A–A, shown in Fig. 10 for 02 Nov 2009 SMAST-HOPS run with glider assimilation. Panels valid for (a) 03 Nov 2009, (b) 05 Nov 2009, (c) 07 Nov 2009, and (d) 09 Nov 2009.

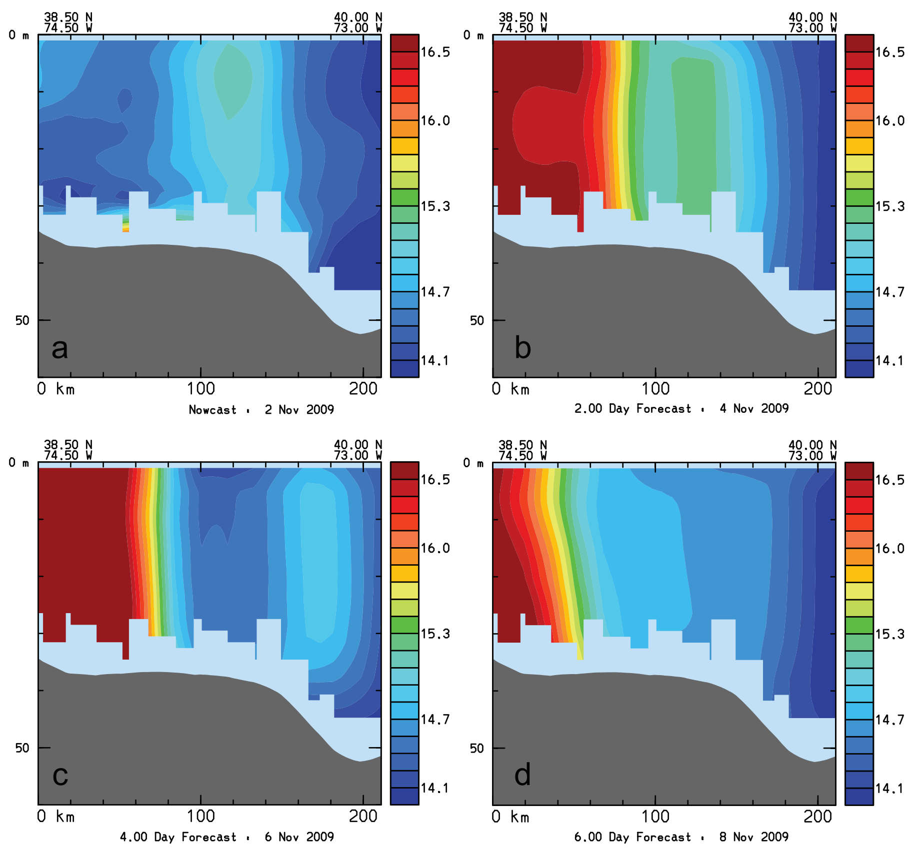

Fig. 12. Temperature cross sectional view of shelf along section line B–B, shown in Fig. 11 for 02 Nov 2009 SMAST-HOPS run with glider assimilation. Panels valid for (a) 02 Nov 2009, (b) 04 Nov 2009, (c) 06 Nov 2009, and (d) 09 Nov 2009.

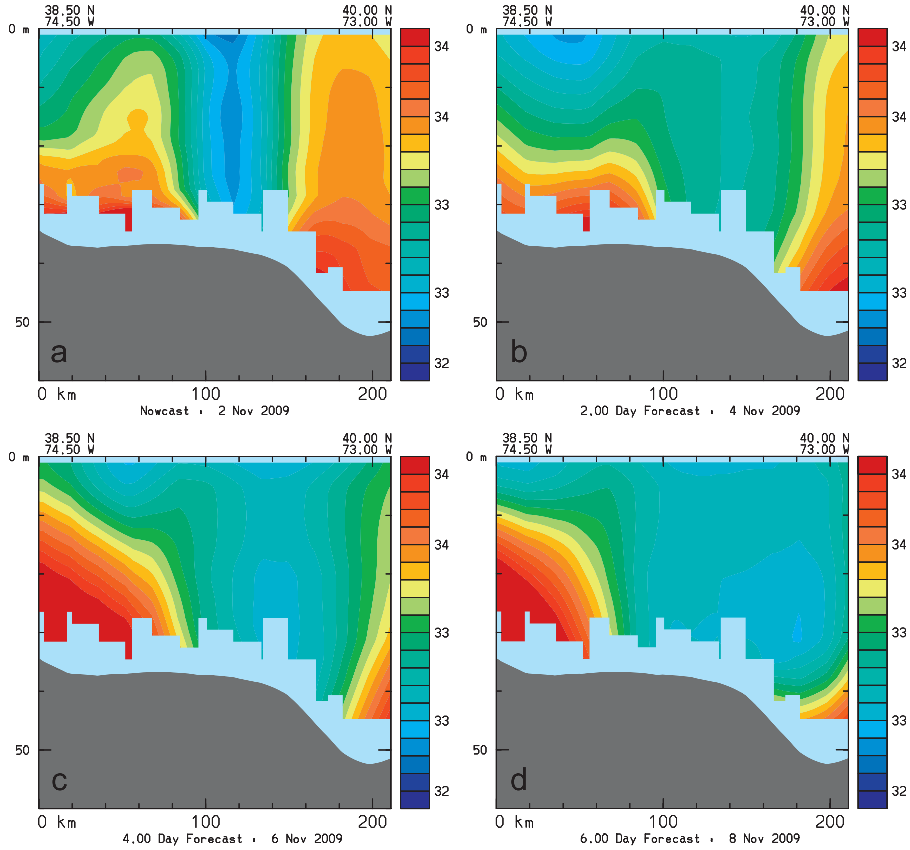

Fig. 13. Salinity cross sectional view of shelf along section line B–B, shown in Fig. 11 for 02 Nov 2009 SMAST-HOPS run with glider assimilation. Panels valid for (a) 02 Nov 2009, (b) 04 Nov 2009, (c) 06 Nov 2009, and (d) 09 Nov 2009.

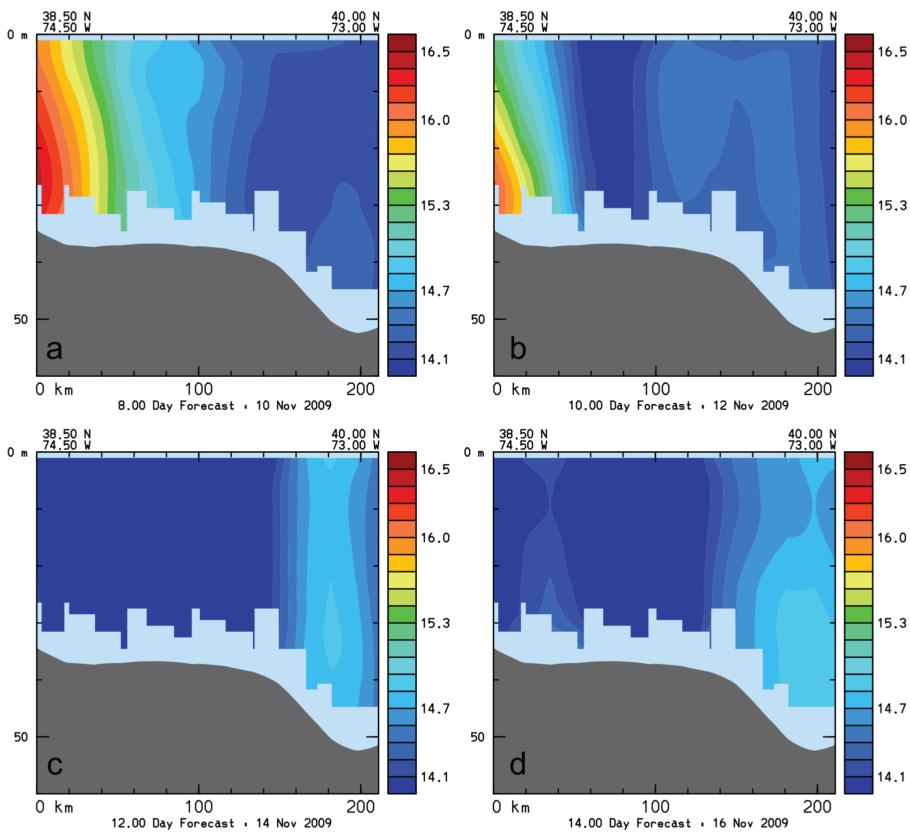

Fig. 14. Temperature cross sectional view of shelf along section line B–B, shown in Fig. 11 for 02 Nov 2009 SMAST-HOPS run with glider assimilation. Panels valid for (a) 10 Nov 2009, (b) 12 Nov 2009, (c) 14 Nov 2009, and (d) 16 Nov 2009.

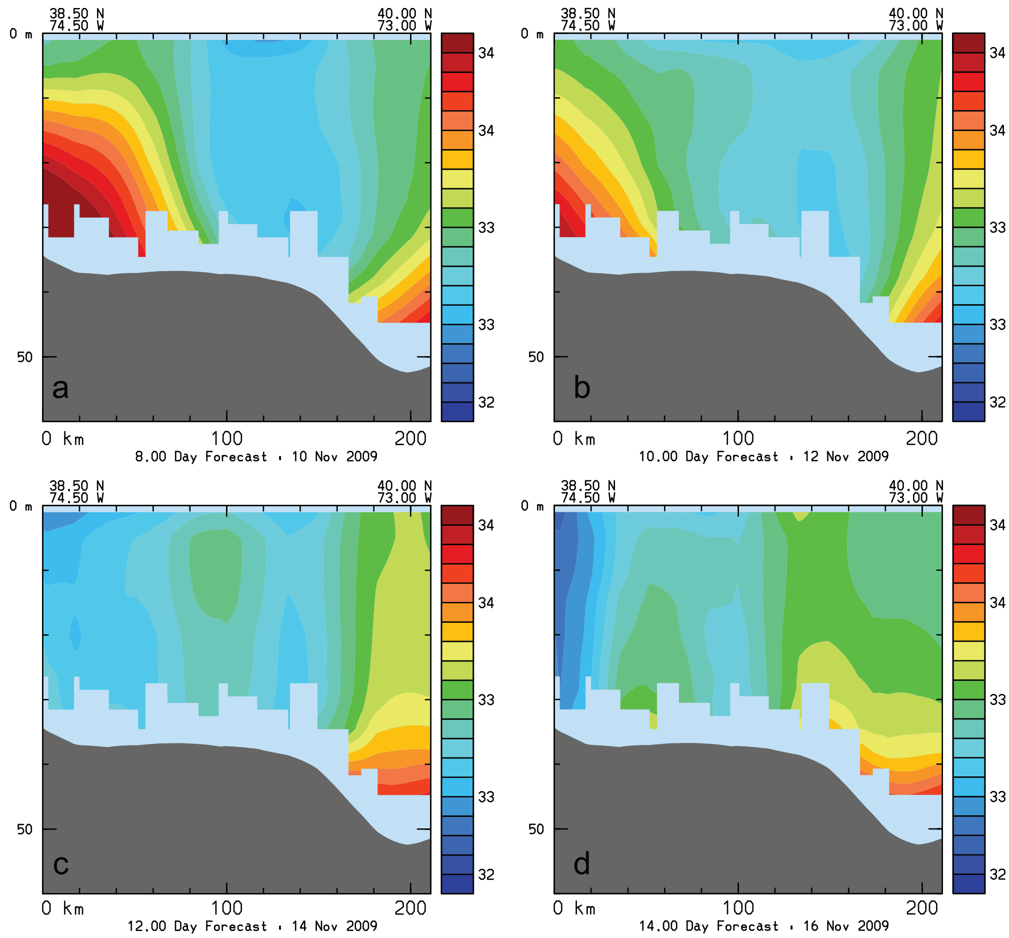

Fig. 15. Salinity cross sectional view of shelf along section line B–B, shown in Fig. 11 for 02 Nov 2009 SMAST-HOPS run with glider assimilation. Panels valid for (a) 10 Nov 2009, (b) 12 Nov 2009, (c) 14 Nov 2009, and (d) 16 Nov 2009.

to depth with a mixed-layer-dependent formulation) and glider temperature (and its vertical uniformity in shallow waters).

Differences between assimilated salinity and glider data can be attributed to the initial mismatch of climatological average salinity with glider data. In all cases, the assimilated temperature and salinity tends to match with glider observations after this initial 1- to 2-day period of internal adjustment (Fig. 16).

Fig. 17 shows a time-series comparison of UD134 data against assimilated forecast at available locations as an independent measure of model skill. The comparison is shown for forecast days 6 and 7. Note that the large biases of the non-assimilated temperature and salinity from the climatology-based shelf initialized run are on the order of 2 °C and 1 psu, respectively. This comparison points to the need for glider assimilation for monitoring the shelf circulation in the Mid-Atlantic Bight region.

The rms differences between the assimilated and non-assimilated runs and the glider data for various depths are shown in Fig. 18. It is apparent that the errors are depth-independent after assimilation. This is probably an artifact of most of the glider data being vertically uniform. However, the depth variation of the unassimilated differences indicates the possibility of assimilation having a bigger impact in the subsurface than at the surface due to glider data. This might be due to the lesser variability at depth than at surface, accentuating the impact of assimilation in the subsurface fields.

However, there are two other ways the glider data could show more impact on the subsurface than on the surface. The first is that SST is being assimilated prior to glider data assimilation, which should make the surface temperature in the model move closer to the glider observation at the surface, leaving the subsurface temperature un-corrected. Thus, the impact of temperature assimilation may seem larger after correction at subsurface (although, not so for salinity correction). Second, the observed Glider profiles for November 2009 depicts a well-mixed, almost-constant profile of temperature and salinity, while the claimtological profiles at these locations, which the model used for initialization had stratification, aka, more subsurface variability. So, after assimilation, the subsurface impact seems larger than that at the surface.

Furthermore, averaged over the two-day (Nov 8–10) time period, the salinity difference between assimilated and non-assimilated runs is about 0.5 psu (Fig. 17b), while the temperature deviation is about 2 °C (Fig. 17a). Since the salinity difference is comparable to the range of assimilation rms (Fig. 18b) of 0.4 ppt, while the SST difference of 2 °C is an order of magnitude higher than the temperature assimilation rms (0.2 °C, Fig. 18a), it is conceivable that salinity assimilation might affect the water column for a longer time period.

4.3. On the temporal and spatial decay of the assimilation footprint

The nature of the decay of the impact of temperature and salinity assimilation is examined next. To determine the temporal decay footprint, we chose two assimilation locations, one offshore (O) and another inshore (I). The OA contours of assimilation errors are presented in Fig. 19a and b, for Nov 6th and 10th, which show the coverage of assimilation for those respective dates. These two locations allowed for tracking the temperature and salinity decay

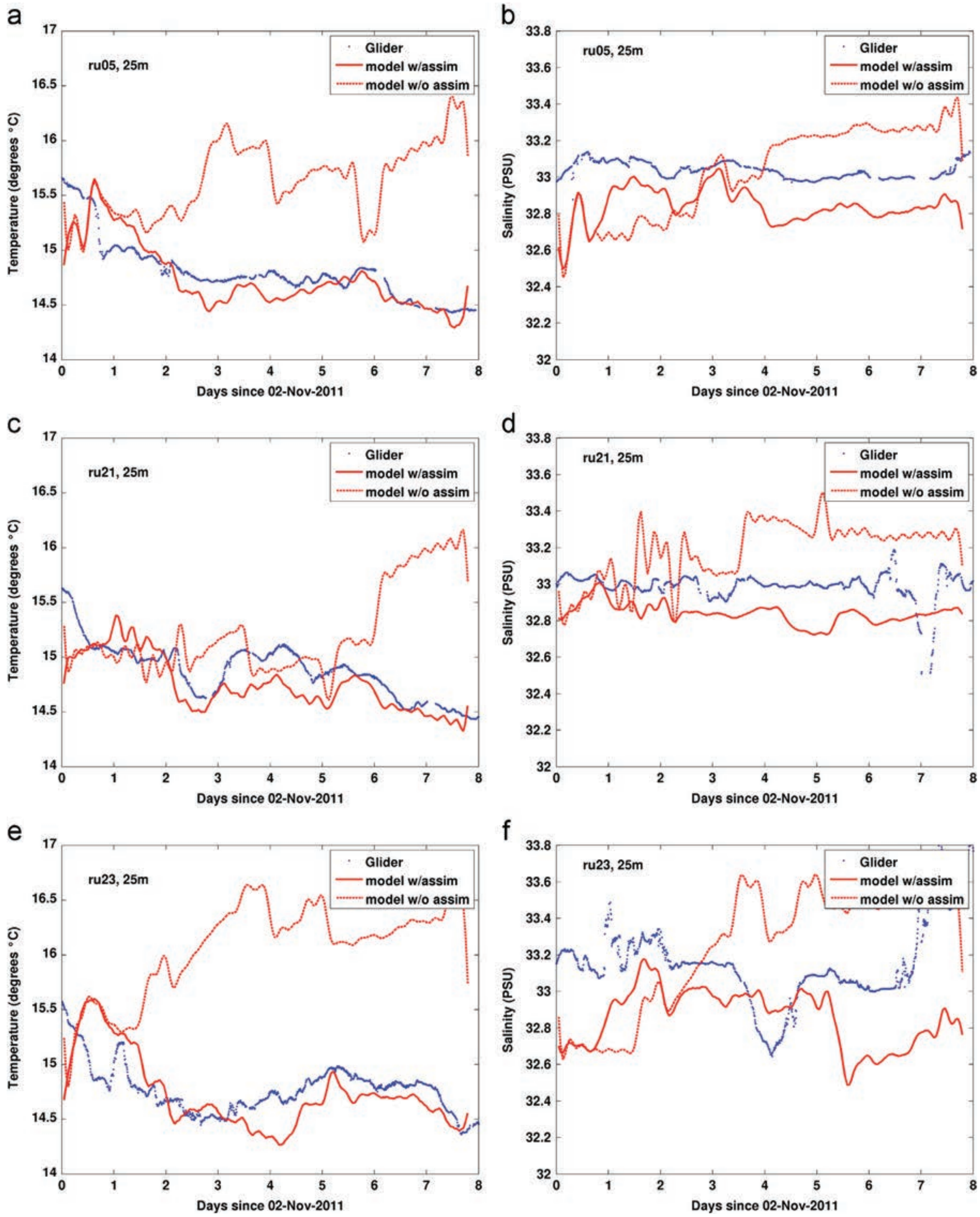

Fig. 16. Twenty-five metre time series of glider (left) temperature and (right) salinity for gliders ((a) and (b)) RU05, ((c) and (d)) RU21, and ((e) and (f)) RU23, compared to the SMAST-HOPS 02 Nov 2009 runs. Glider data are shown with blue dots, the model run with glider assimilation is shown with a solid line, and the model run with no glider assimilation is shown with a dashed line. Temperature in °C, salinity in psu.

scales after the peak of assimilation (marked by arrows in the figures on the error time-series) on Nov 8th for point I (Fig. 19c and e) and after Nov 6th for point O (Fig. 19d and f).

Effectively, there was a single assimilation window of about 2 days for I (Nov 6–8); while for point O, there were two assimilation windows: one for about two days (Nov 4–6) and another also for a different two days (Nov 12–14) at the end of the reanalysis period. The assimilation of satellite-derived SST during the first 12 h, and the ingestion of available glider data at initialization, induced similar impact up to about 0.75 day to both unassimilated and assimilated simulations (Fig. 19c–f). The assimilation during Nov 4–6 then corrects the developing forecast, while the unassimilated forecast behaves differently. After this initial phase, the assimilated temperature takes about

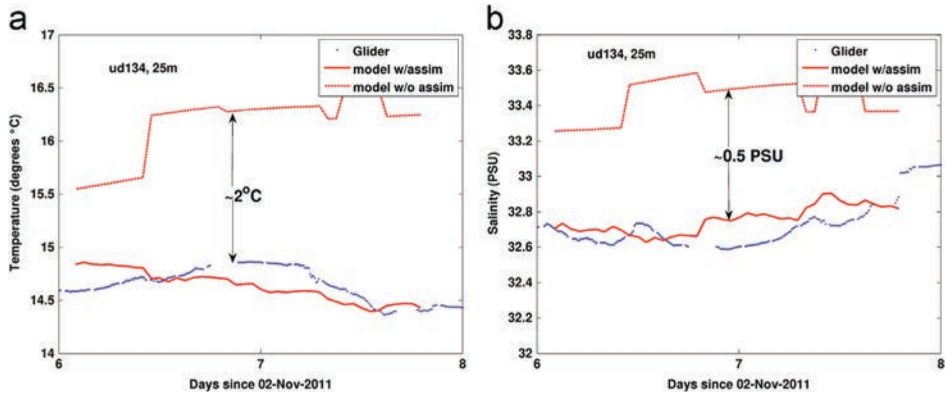

Fig. 17. Twenty-five metre time series of glider UD134 (a) temperature and (b) salinity, compared to the SMAST-HOPS 02 Nov 2009 runs. Glider data are shown with blue dots, the model run with glider assimilation is shown with a solid line, and the model run with no glider assimilation is shown with a dashed line. Temperature in °C, salinity in psu. Note the difference between assimilation and non-assimilation runs for temperature is about 2 °C; while that for salinity is about 0.5 psu.

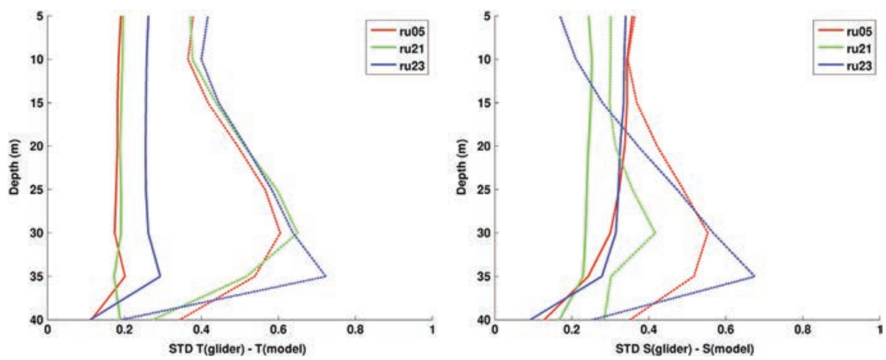

Fig. 18. Glider-model error at various depths for (left) temperature and (right) salinity. The abscissa is the standard deviation of the difference between the glider and the model. The solid lines represent differences between the gliders and the model run with glider assimilation; the dashed lines represent differences between the gliders and the model run with no assimilation. For both types of model runs, the gliders were used for the initial field.

1–2 days to degrade to the levels of non-assimilated run, while salinity takes 3–4 days for point I and about 2 days for point O. The temperature decay time-scales are similar to those (1–1.5 days) obtained for Monterey Bay by Shulman et al. (2009).

Two interesting results are clear from Fig. 19. First, after the assimilation is over, the salinity tends to approach back to the unassimilated value in time, while the temperature settles to a new threshold level and follows the behavior of the unassimilated temperature simulation. Second, the larger the difference between the unassimilated simulation and observation (at the beginning of the assimilation), the longer it takes for the tracer to approach the unassimilated behavior and/or the value itself. Note that we also found these two results to be depth-independent.

The spatial scales of decay for the impact of assimilation are investigated next. Three points (South—S; Middle—M; and North—N) were chosen along one transect through the glider array (Fig. 2) for the spatial decay experiment. The daily difference in temperature field between the runs with and without assimilation is presented in Fig. 20a. Greater difference at the time of assimilation indicates greater impact. Persistence of the initial difference over time beyond the point at which assimilation is discontinued would imply a prolonged impact of assimilation. It is clear from Fig. 20a that the temperature impact decays significantly within the first 2–4 days for all points (S, M, and N), and that the amplitude of the impact decreases with distance from the glider location (point of assimilation). The salinity impact does not show such drastic decay (Fig. 20c) at these locations. The spatial decay scale for the temperature is obtained from Fig. 20a, where the difference in temperature (assimilation vs. non-assimilation) is examined as a function of distance from the assimilation location for two consecutive days (days 3 and 4) after the assimilation is over on day 1.

The exponential nature of the spatial decay of temperature impact from the center of assimilation outward is evident for all days (other days not shown). The e-folding impact scale is determined to be about 100 km for the third day, and about 60 km for the fourth day. In contrast, the salinity signal does not show any preferential decay pattern (Fig. 20d). The salinity difference fluctuates within a narrow range around the initial difference for day 3, and stays almost same for day 4. No consistence spatial-decay pattern for salinity was found in these three locations.

The above differences in the temperature and salinity behavior beget the idea of using different decorrelation parameters for objective analysis of temperature and salt information for assimilation. For example, different decorrelation scales for temperature and salinity error covariance computation were used (Reinicker et al., 2011) by the Global Modeling and Assimilation Office (GMAO) at the NASA/Goddard Space Flight Center for ocean initialization for seasonal-to-interannual climate prediction efforts (http://gmao.gsfc.nasa.gov/research/ocean; Keppenne et al., 2005; Sun et al., 2007). Typically, temperature decorrelation scales (20° zonal, 8° meridional and 100 m in the vertical) are larger than those for salinity (8° zonal, 3° meridional and 40 m in the vertical). Our results indicate similar

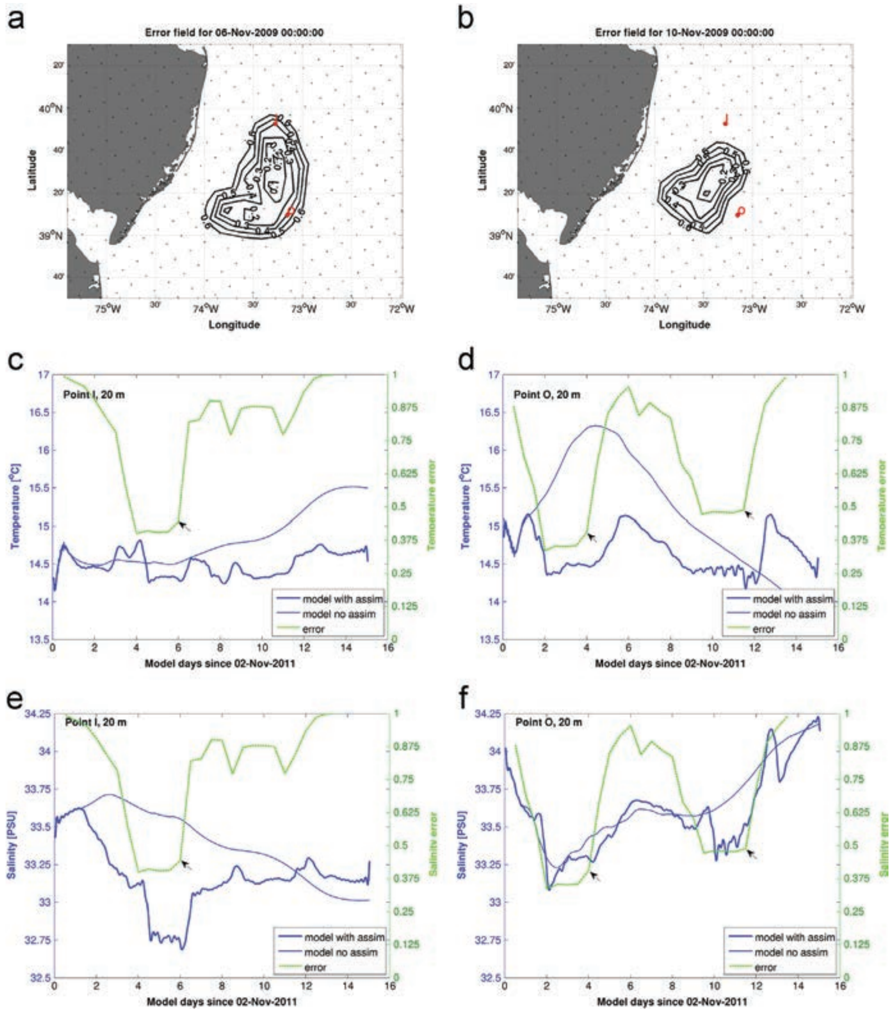

Fig. 19. Temporal behavior of temperature and salinity after assimilation. The error maps of OA fields (T, S) are shown for 4th Nov in (a) and for 10th Nov in (b). The simulation time-series with and without assimilation are shown for temperature at point I and point O are shown in the middle panels ((c) and (d)). Superimposed is the time-series of the error at these locations in dash-line. Similarly, the bottom panels show the salinity fields at these locations. The black arrow in the middle and bottom panels identifies the end of the assimilation period at each location.

qualitative differences in spatial impact of assimilation between temperature and salinity might also exist in the shelf region, albeit at a finer-scale (10s of kilometers for the shelf as opposed to 100s of kilometers for the global models).

5. Summary and discussion

This study presented an application of the SMAST-HOPS real-time forecast system developed for the western North Atlantic during the OOI–CI OSE period (Oct 26–Nov 17, 2009). The ring and front analysis from satellite imagery is used to feed into the feature modeling scheme for generating a three-dimensional initial field. The initialization field is dynamically adjusted with wind-forcing and used in an SST-glider-assimilative (temperature- and salinity-assimilative) forecast model. The model was forced by atmospheric fields from the global forecast system in real time. The forecast fields were made available via a THREDDS data server for easy and efficient extraction by scientists and application developers for glider planning, control and guidance.

The feature-based initialization scheme was utilized for 4 short-term forecasts of varying lengths during the first two weeks of November 2009 in an ensemble mode with other forecasts to guide glider control. A reanalysis was then carried out, assimilating the data from three gliders (RU05, RU21 and RU23) for the two-week period. Results are first compared against data from these three gliders, and then against the independent data from the other glider, UD134. Results from the assimilation are also analyzed to evaluate the impact of glider data and sensitivity of model forecasts to data assimilation. The assimilation of salinity improved the model performance in the area around the data and impacted the subsurface fields. An interesting result was that assimilating (or infusing) the available glider data at initialization enabled the model to smoothly absorb and adjust subsequent cycles of assimilation of patchy glider data.

The glider data assimilation led to a depth-averaged model-data difference of 2 °C for temperature and 0.5 psu for salinity for the upper 25 m of the Mid-Atlantic shelf. A sensitivity analysis was carried out to determine the short-term memory of the simulated ocean. The forecast fields retained assimilated temperature information for about 1–2 days. No coherent pattern for temporal decay of salinity was determined with its range varying from 1–4 days at different locations. However, significant differences in their patterns of behavior after assimilation were clearly observed.

It is interesting to note that the short-term retention period (of temperature and salinity impact) might be increased by

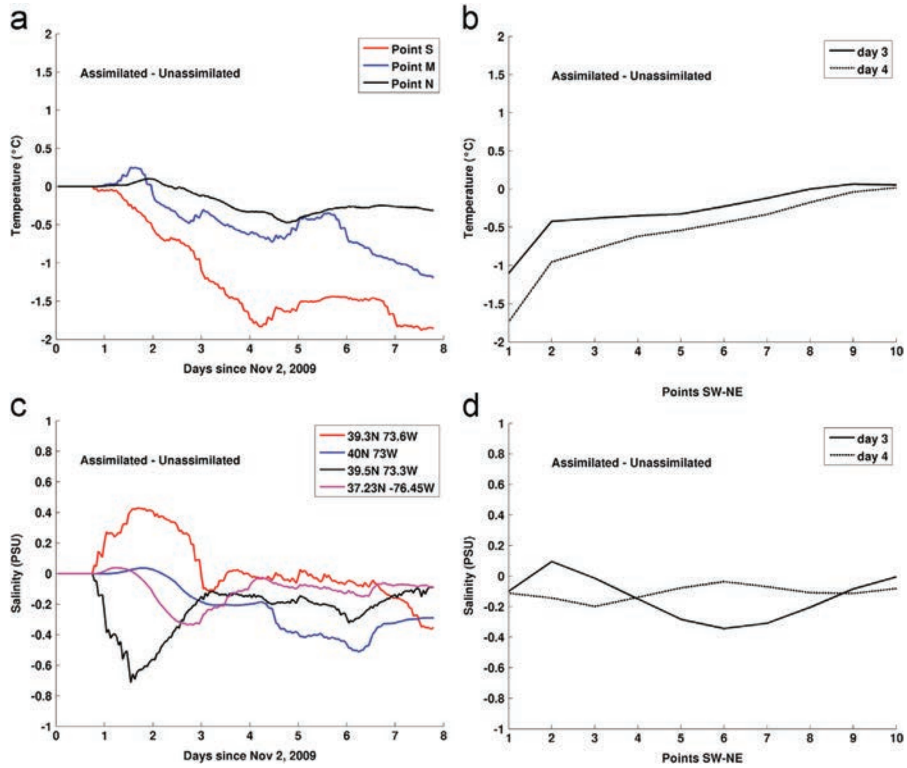

Fig. 20. (a) The temperature difference between the runs with and without assimilation at the three locations (S, M and N) as time progresses after assimilation on Nov 02, 2009 at point S; (b) the temperature difference for days 3 and 4 away from the assimilation point S as shown in Fig. 5; (c) similar to (a), but for salinity; (d) similar to (b), but for salinity.

increasing the model resolution in the horizontal and vertical. While increasing the resolution will result in resolving more features (effectively adding more wave numbers and reducing the de-correlation scales); the underlying OI assimilation scheme brings high-resolution assimilation (correction) fields, because the observations are mapped on the model grid prior to assimilation. Such sensitivity/competition studies would be carried out in future studies. Our results on temporal decay (1–3 days) of temperature after assimilation are consistent with those (1–1.5 days) found by Shulman et al. (2009) for the Monterey Bay region.

It is intriguing to also note that one would expect a sizeable difference in the decay scales of temperature and salinity linked to the underlying real (molecular) diffusivity of the variables. In reality, the short-term temporal memory of the ocean could be thought to be inversely proportional to the diffusivity of the tracer. For example, due to its slower diffusivity, the retention period of assimilated salinity signature may be longer than that of the temperature. Similarly, the spatial footprint of the impact could be directly proportional to the diffusivity. Consequently, the spatial decay scale for assimilated temperature would be larger than that of the assimilated salinity signal (consistent with Reinicker et al. 2010 for GMOA). However, most of the dynamical models (including the present one used here) employ the same numerical diffusivity for the prognostic runs, which might or might not be appropriate for both tracers. More sensitivity experiments would be necessary to further quantify and understand such differences between the temperature and salinity response after assimilation.

The impact analyses presented before clearly shows that there exists certain differences in the spatial and temporal influence windows (scales, footprints) after assimilation for the two tracers, temperature and salinity. These new results open up the possibility of developing new assimilation algorithms which might be similar to the new developments of the EnKF, where variables maintaining two different scales are assimilated in a combined scheme (Ballabrera-Poy et al., 2009). The ideas of scale-preserving assimilation (Lorenc, 2003; Kalnay et al., 2007) and of 'variable localization' for constructing covariance matrix in EnKF (Kang et al., 2011) seem worth investigating in this context of multiple tracers. Specifically, temperature and salinity could be the oceanic proxies for the temperature and carbon (and/or humidity) in the atmospheric models and these new assimilation techniques.

These differences in impact of assimilation of temperature and salinity data and their possible link to the real-ocean diffusion of heat and salt also points to another area of research. Typical large-scale models (Navy's coastal ocean model, hybrid co-ordinate ocean model, regional ocean modeling system, modular ocean model, etc.) use the same diffusivity for both tracers for most applications. Systematic studies with different diffusivities for different tracers in regional modeling exercises in coastal regions such as the Mid-Atlantic shelf might lead to better understanding of processes and better forecasting capabilities for the many operational observing systems.

Based on the sensitivity analysis, a phased-assimilation strategy to assimilate both satellite SST and glider data with different weighting functions for temperature and salinity can probably be developed. For example, while 2-day composite satellite-derived SST fields can be assimilated every two days, individual glider data could be assimilated every day with a 12-h weighting function. However, if salinity data can be retained by the simulated ocean for a longer period of time, independent salinity observations, or satellite-derived chlorophyll-inferred seas surface salinity can be assimilated with different weighting function (yet-to-be-determined) on a different assimilation cycle. Another example would be of designing a phased observation-assimilation scheme, in which XBT observations will be assimilated frequently to supplement SST fields to realize the subsurface thermal structure, while XCTD observations will be sampled and assimilated more sparsely to match and allow for larger retention period of salinity. In the near future, such a system of "phased assimilation" of satellite SST, sea surface color (SSC), glider data and other in-situ observations could be built for monitoring the changes of the water masses in the Mid-Atlantic more efficiently, economically, and knowledgeably.

Acknowledgements

This real-time forecast system has been made possible due to many years of research at Harvard University, UMass Dartmouth, MIT and other institutions by many researchers. We appreciate all of their past efforts and current support. Special thanks are due to our colleagues at MIT who are supporting our efforts with the software and analysis packages. Funding was made available from the Office of Naval Research (ONR) MURI program (N000140610739), the National Aeronautics and Space Administration (NASA), the National Oceanic and Atmospheric Administration (NOAA) and the National Science Foundation (NSF) at different times to different PIs at different institutions. We acknowledge all their efforts and support. Current funding from NOAA under IOOS for MARACOOS and the support of the MACOORA group are gratefully acknowledged. We appreciate the efforts of Applied Science Associates and the Rutgers group for making the glider data available in a format for easy analysis. Our special thanks to Dr. Wendell Brown for his insight in implementing an earlier version of the model system and many discussions in-house on the OSE–Glider-modeling exercises. We appreciate the help, support and guidance of Drs. Scott Glenn, Bill Boicort and the entire MARACOOS group during the OSE. Special thanks to John Kerfoot for his work in making the glider data available in real-time. We thank the other five modeling teams from Rutgers (John Wilkin and his group), Stevens (Alan Blumberg and his group), JPL (Yi Chao and his group), MIT (Pierre Lermusiaux and his group) and USGS (Rich Signell, John Warner and their group), with whom we participated in the OSE real-time ensemble exercises. We wish to acknowledge the invaluable experience gathered during the OOI–CI–OSE on the infrastructure issues of real-time forecasting from the interactions with the JPL, UCSD and the larger CI team. We are appreciative of the help provided by Mr. Frank Smith at SMAST with editing this manuscript.

Our sincere thanks to the reviewers and the editors of this special issue for their comments, patience and support during the revision of this manuscript, which helped clarify many details.

References

Ballabrera-Poy, J., Kalnay, E., Yang, S., 2009. Data assimilation in a system with two scales-combining two initialization techniques. Tellus 61A, 539–549.

Barrick, D.E., 1972. First-order theory and analysis of mf/hf/vhf scatter from the sea. IEEE Transactions on Antennas and Propagation AP-20, 2–10.

Barrick, D.E., Evens, M.W., Weber, B.L., 1977. Ocean surface currents mapped by radar. Science 198, 138–144.

Barron, C.N., Smedstad, L.F., Dastugue, J.M., Smedstad, O.M., 2007. Evaluation of ocean models using observed and simulated drifter trajectories: Impact of sea surface height on synthetic profiles for data assimilation. Journal of Geophysical Research 112, C07019, http://dx.doi.org/10.1029/2206JC003982.

Bhushan, S., Blumberg, A.F., Georgas, N., 2009. "Comparison of NYHOPS hydrodynamic model SST predictions with satellite observations in the Hudson River tidal, estuarine, and coastal plume region", Eleventh International Conference in Estuarine and Coastal Modeling. ECM11, 4–6 November 2009, Seattle, WA. American Society of Civil Engineers, pp. 11–26.

Blackwell, S.H., Moline, M.A., Schaffner, A., Garrison, T., Chang, G., 2008. Sub-kilometer length scales in coastal waters. Continental Shelf Research 28 (2), 215–226.

Broquet, G., Edwards, C.A., Moore, A.M., Powell, B.S., Veneziani, M., Doyle, J.D., 2009. Application of 4D-Variational data assimilation to the California current system, dynamics of atmos. Oceans, http://dx.doi.org/10.1016/j.dynatmoce.2009.03.001.

Brown, W.S., Gangopadhyay, A., Bub, F.L., Yu, Z., Strout, G., Robinson, A.R., 2007a. An operational circulation modeling system for the Gulf of Maine/Georges Bank region, Part 1: The basic elements. IEEE Journal of Oceanic Engineering 32 (4), 807–822.

Brown, W.S., Gangopadhyay, A., Yu, Z., 2007b. An operational circulation modeling system for the Gulf of Maine/Georges Bank region, Part 2: Applications. IEEE Journal of Oceanic Engineering 32 (4), 823–838.

Calado, L., Gangopadhyay, A., da Silveira, I.C.A., 2008. Feature-oriented regional modeling and simulations (FORMS) for the western South Atlantic, south-eastern Brazil region. Ocean Modeling 25, 48–64.

Carter, E.F., Robinson, A.R., 1987. Analysis models for the estimation of oceanic fields. Journal of Atmospheric and Oceanic Technology 4 (1), 49–74.

Chao, Y., Li, Z., Farrara, J., McWilliams, J.C., Bellingham, J., Capet, X., Chavez, F., Choi, J.-K., Davis, R., Doyle, J., Fratantoni, D., Li, P., Marchesiello, P., Moline, M.A., Paduan, J., Ramp, S., 2009. Development, implementation, evaluation of a data-assimilative ocean forecasting system off the central California coast. Deep-Sea Research II, http://dx.doi.org/10.1016/j.dsr2.2008.08.011.

Crombie, D.D., 1955. Doppler spectrum of sea echo at 13.56 Mc/s. Nature 175, 681–682.

Davis, R.E., Webb, D.C., Regier, L.A., Dufour, J., 1992. The autonomous Lagrangian circulation explorer (ALACE). Journal of Atmospheric and Oceanic Technology 9, 264–285.

Derber, J.C., Rosati, A., 1992. A global ocean data assimilation system. Journal of Physical Oceanography 19, 1333–1347.

Eriksen, C.C., Osse, T.J., Light, R.D., Wen, T., Lehman, T.W., Sabin, P.L., Ballard, J.W., Chiodi, A.M., 2001. Seaglider: a long-range autonomous underwater vehicle for oceanographic research. IEEE Journal of Oceanic Engineering 26, 424–436.

Evensen, G., 2009. Data Assimilation: The Ensemble Kalman Filter. Springer-Verlag.

Ezer, T., Mellor, G.L., 1992. A numerical study of the variability and the separation of the Gulf Stream induced by surface atmospheric forcing and lateral boundary flows. Journal of Physical Oceanography 22, 660–682.

Fukumori, I., Malanotte-Rizzoli, P., 1995. An Approximate Kalman Filter for ocean data assimilation: an example with an idealized Gulf Stream model. Journal of Geophysical Research 100, 6777–6793.

Gangopadhyay, A., Lermusiaux, P.F.J., Rosenfeld, L.K., Robinson, A.R., Calado, L., Kim, H.S., Leslie, W.G., Haley Jr., P.J., 2011. California current system: a multiscale overview and the development of a feature-oriented regional modeling system (FORMS). Dynamics of Atmopsheres and Oceans 52 (1–2), 131–169, http://dx.doi.org/10.1016/j.dynatmoce.2011.04.003, Sept 2011.

Gangopadhyay, A., Robinson, A.R., 2002. Feature oriented regional modeling of oceanic fronts. Dynamics of Atmosphere and Oceans 36 (1–3), 201–232.

Gangopadhyay, A., Robinson, A.R., Arango, H.G., 1997. Circulation and dynamics of the western North Atlantic, I: Multi-scale feature models. Journal of Atmospheric and Oceanic Technology 14 (6), 1314–1332.

Gangopadhyay, A., Robinson, A.R., Haley Jr., P.J., Leslie, W.G., Lozano, C.J., Bisagni, J.J., Yu, Z., 2003. Feature oriented regional modeling and simulations (FORMS) in the Gulf of Maine and Georges Bank. Continental Shelf Research. 23 (3–4), 317–353.

Georgas N., Blumberg, A.F., 2009. "Establishing confidence in marine forecast systems: the design and skill assessment of the New York Harbor observation and prediction system, version 3 (NYHOPS v3)", Eleventh International Conference in Estuarine and Coastal Modeling. ECM11, 4–6 November 2009, Seattle, WA. American Society of Civil Engineers, pp. 660–685.

Glenn, S.M., Schofield, O., 2003. Observing the oceans from the COOLroom: our history, experience, and opinions. Oceanography 16 (4), 37–52.

Glenn, S., Schofield, O., 2009. Growing a distributed ocean observatory: our view from the COOL room. Oceanography 22 (2), 78–92.

Gould, J., Roemmich, D., Wijffels, S.H., Freeland, H., Ignaszewsky, M., Jianping, X., Pouliquen, S., Desaubies, Y., Send, U., Radhakrishand, K., Takeuchi, K., Kim, K., Danchenkov, M., Sutton, P., King, B., Owens, B., Riser, S., 2004. Argo profiling floats bring new era of in situ ocean observations. EOS 85 (19), 1136843, OI: 10.1126/science.

Haley Jr., P.J., Lermusiaux, P.F.J., 2010. Multiscale two-way embedding schemes for free-surface primitive-equations in the multidisciplinary simulation, estimation and assimilation system. Ocean Dynamics 60, 1497–1537, http://dx.doi.org/10.1007/s10236-010-0349-4.

Halpern, D.A., 2000. Satellites, Oceanography and Society. Elsevier Sci., Amsterdam, 361 pp.

Hayes, S.P., Mangum, L.J., Picaut, J., Sumi, A., Takeuchi, K., 1991. TOGA–TAO: a moored array for real-time measurements in the tropical pacific ocean. Bulletin of the American Meteorological Society 72, 340–347.

Hunt, B.R., Kalnay, E., Kostelich, E.J., Ott, E., Patil, D.J., Sauer, T., Szunyogh, I., Yorke, J.A., Zimin, A.V., 2004. Four-dimensional ensemble Kalman Filtering. Tellus 56A, 273–277.

Kalnay, E., 2003. Atmospheric Modeling, Data Assimilation and Predictability. Cambridge University Press, Cambridge 364 pp.

Kalnay, E., Li, H., Miyoshi, T., Yang, S.-C., Ballabrera, J., 2007. 4-D-Var or Ensemble Kalman Filter? Tellus 59A, 758–773, http://dx.doi.org/10.1111/j.1600-0870.2007.00261.x.

Kang, J.-S., Kalnay, E., Liu, J., Fung, I., Miyoshi, T., Ide, K., 2011. Variable localization in an Ensemble Kalman Filter: application to the carbon cycle data assimilation. J. Geophys. Res. 116, http://dx.doi.org/10.1029/2010JD014673.

Keppenne, C.L., Rienecker, M.M., Kurkowski, N.P., Adamec, D.D., 2005. Ensemble Kalman filter assimilation of altimeter and temperature data with bias

correction and application to seasonal prediction. Nonlinear Processes in Geophysics 12, 491–503.
Kumar, A., Valle-Levinson, A., Atkinson, L.P., 2006. Overrunning of shelf water in the southern Mid-Atlantic Bight. Progress in Oceanography 70, 213–232.
Kunze, E., Dower, J.F., Beveridge, I., Dewey, R., Bartlett, K.P., 2006. Observations of biologically generated turbulence in a coastal inlet. Science 313, 1168–1170, http://dx.doi.org/10.1126/science.1129378.
Lam, F.P., Haley Jr., P.J., Janmaat, J., Lermusiaux, P.F.J., Leslie, W.G., Schouten, M.W., te Raa, L.A., Rixen, M., 2009. At-sea Real-time Coupled Four-dimensional Oceanographic and Acoustic Forecasts during Battlespace Preparation 2007. Special issue of the Journal of Marine Systems on "Coastal processes: Challenges for Monitoring and Prediction", Drs. J.W. Book, Prof. M. Orlic and Michel Rixen (Guest Eds.), 78, S306–S320, http://dx.doi.org/10.1016/j.jmarsys.2009.01.029.
Lermusiaux, P.F.J., 1999. Data assimilation via error subspace statistical estimation, Part II: Mid-Atlantic Bight shelfbreak front simulations and ESSE validation. Monthly Weather Review 127 (8), 1408–1432.
Lermusiaux, P.F.J., 2002. On the mapping of multivariate geophysical fields: sensitivity to size, scales and dynamics. Journal of Atmospheric and Oceanic Technology 19, 1602–1637.
Li, Z., Chao, Y., McWilliams, J.C., Ide, K., 2008a. A three-dimensional variational data assimilation scheme for the regional ocean modeling system. Journal of Atmospheric and Oceanic Technology 25, 2074–2090, http://dx.doi.org/10.1175/2008JTECHO594.1.
Li, Z., Chao, Y., McWilliams, J.C., Ide, K., 2008b. A three-dimensional variational data assimilation scheme for the regional ocean modeling system: implementation and basic experiments. Journal of Geophysical Research-Oceans 113, C05002, http://dx.doi.org/10.1029/2006JC004042.
Lomax, A.S., Corso, W., Etro, J.F. 2005. Employing unmanned aerial vehicles (UAVs) as an element of the Integrated Ocean Observing System. Ocean 2005, Proceedings of the MTS/IEEE. http://dx.doi.org///10.1109/OCEANS.2005.1639759.
Lorenc, A.C., 2003. The potential of the ensemble Kalman Filter for NWP—a comparison with 4D-Var. Quarterly Journal of the Royal Meteorological Society 129, 3183–3203.
Lozano, C.J., Robinson, A.R., Arango, H.G., Gangopadhyay, A., Sloan, N.Q., Haley, P.J., Anderson, L., Leslie, W.G., 1996. An interdisciplinary ocean prediction system: assimilation strategies and structured data models. In: Malanotte-Rizzoli, P. (Ed.), Modern Approaches to Data Assimilation on Ocean Modeling, 61. Elsevier Oceanography Series, Amsterdam, pp. 413–452.
Malanotte-Rizzoli, P. (Ed.), Modern Approaches to Data Assimilation in Ocean Modeling, 61. Elsevier Oceanography Series, Amsterdam, 455 pp.
Miles, T., Glenn, S.M., Schofield, O., Chao, Y., Spatial Variability in Fall Storm Induced Sediment Resuspension on the Mid-Atlantic Bight, Continental Shelf Research, http://dx.doi.org/10.1016/j.csr.2012.08.006, in this issue.
Mooers, C.N.K. (Ed.), 1999. Coastal and Estuarine Studies. AGU, Washington D.C..
Niiler, P.P., Maximenko, N.A., McWilliams, J.C., 2003. Dynamically balanced absolute sea level of the global ocean derived from near-surface velocity observations. Geophysical Research Letters 30 (22), http://dx.doi.org/10.1029/2003GL018628.
Orlanski, I., 1976. A simple boundary condition for unbounded hyperbolic flows. J. Comput. Phys. 21 (3), 251–269.
Ott, E., Hunt, B.R., Szunyogh, I., Zimin, A.V., Kostelich, E.J., Kostelich, M., Corazza, M., Sauer, T., Kalnay, E., Patil, D.J., Yorke, J.A., 2004. A local ensemble Kalman Filter for atmospheric data assimilation. Tellus 56A, 415–428.
Rienecker, M., Keppenne, C., Jacob, J., 2010. GMAO Global Ocean Data Assimilation System. 〈http://www.clivar.org/data/synthesis/projects/GMAO.pdf〉.
Robinson, A.R., Glenn, S.M., Spall, M.A., Walstad, L.J., Gardner, G.M., Leslie, W.G., 1989. Forecasting meanders and rings. EOS Oceanography Report 70 (45), 1464–1473.
Robinson, A.R., Rothschild, B.J., Leslie, W.J., Bisagni, J.J., Borges, M.F., Brown, W.S., Cai, D., Fortier, P., Gangopadhyay, A., Haley Jr., P.J., Kim, H.S., Lanerolle, L., Lermusiaux, P.F.J., Lozano, C.J., Miller, M.G., Strout, G., Sundermeyer, M.A., 2001. The Development and Demonstration of an Advanced Fisheries Management Information System (AFMIS). American Meteorological Society 186–190.
Ryan, J.P., Yoder, J.A., Barth, J.A., Cornillon, P.C., 1999a. Chlorophyll enhancement and mixing associated with meanders of the shelf break front in the Mid-Atlantic Bight. Journal of Geophysical Research 104, 23,479–23,493.
Ryan, J.P., Yoder, J.A., Cornillon, P.C., 1999b. Enhanced chlorophyll at the shelfbreak of the Mid-Atlantic Bight and Georges Bank during the spring transition. Limnology and Oceanography 44, 1–11.
Ryan, J.P., Yoder, J.A., Townsend, D., 2001. Influence of a Gulf Stream warm-core ring on water mass and chlorophyll distributions along the southern flank of Georges Bank. Deep-Sea Research, Part II 48, 159–178.
Schmidt, A.C.K., Brickley, P., Gangopadhyay, A., Cadwallader, M., Sharma, N., Nobre, C., Coholan, P., Feeney, J., 2011. A Feature oriented regional modeling system for the North Brazil current rings migration after retroflection, Proceedings of the Offshore Technology Conference, May 2011, Houston, TX, USA.
Schmidt, A.C.K., Gangopadhyay, A., 2012. An Operational Circulation Ocean Prediction System for the Northwest Atlantic: Validation During July-September of 2006. Continental Shelf Research, http://dx.doi.org/10.1016/j.csr.2012.08.017.
Schofield, O., Bergmann, T., Bissett, W.P., Grassle, F., Haidvogel, D., Kohut, J., Moline, M., Glenn, S., 2002. Linking regional coastal observatories to provide the foundation for a national ocean observation network. Journal of Oceanic Engineering 27 (2), 146–154.
Schofield, O., Glenn, S.M., Irwin, A., Oliver, M., Moline, M.A., Arrott, M., 2012. Earth system monitoring: ocean observatories and information. In: Meyers, R.A., Orcutt, J. (Eds.), Encyclopedia of Sustainability Science and Technology. Springer Science, New York.
Schofield, O., Glenn, S.M., Orcutt, J., Arrott, M., Meisinger, M., Gangopadhyay, A., Brown, W., Signell, R., Moline, M., Chao, Y., Chien, S., Thompson, D., Balasuriya, A., Lermusiaux, P., Oliver, M., 2010. Automated sensor networks to advance ocean science. EOS 91 (39) 28 Sept, 2010.
Schofield, O., Moline, M., Cahill, B., Frazer, T., Kahl, A., Oliver, M., Reinfelder, J., Glenn, S.M., Chant, R. The importance of mixing for phytoplankton productivity in turbid buoyant coastal plumes, Continental Shelf Research, in this issue.
Sherman, J., Davis, R.E., Owens, W.B., Valdes, J., 2001. The autonomous underwater glider "Spray". IEEE Journal of Oceanic Engineering 26, 437–446.
Shulman, I., Kindle, J., Martin, P., deRada, S., Doyle, J., Penta, B., Anderson, S., Chavez, F., Paduan, J., Ramp, S., 2007. Modeling of upwelling/relaxation events with the navy coastal ocean model. Journal of Geophysical Research 112, C06023, http://dx.doi.org/10.1029/2006JC003946.
Shulman, I., Rowley, C., Anderson, S., De Rada, S., Kindle, J., Martin, P., Doyle, J., Cummings, J., Ramp, S., Chavez, F., Fratantoni, D., Davis, R., 2009. Impact of glider data assimilation on the Monterey Bay model. Deep-Sea Research II 56 (2009), 188–198.
Sloan, N.Q.S., 1996. Dynamics of a shelf-slope front, process studies and data-driven simulations in the middle atlantic bight. Ph.D. Thesis, Harvard University, Cambridge, MA.
Stewart, R., Joy, J., 1974. HF Radio Measurements of Surface Currents, in Deep Sea Research and Oceanographic Abstracts, vol. 21. Elsevier, pp. 1039–1049.
Sun, C., Rienecker, M.M., Rosati, A., Harrison, M., Wittenberg, A., Keppenne, C.L., Jacob, J.P., Kovach, R.M., 2007. Comparison and sensitivity of ODASI ocean analyses in the Tropical Pacific. Monthly Weather Review 135, 2242–2264.
Veneziani, M., Edwards, C.A., Doyle, J.D., Foley, D., 2009. A central California coastal ocean modeling study: 1. Forward model and the influence of realistic versus climatological forcing. Journal of Geophysical Research 114, C04015, http://dx.doi.org/10.1029/2008JC004774.
Wang, X., Chao, Y., Thompson, D., Chien, S., Farrara, J., Li, P., Vu Q., Zhang, H., A Coastal Ocean Multi-model Ensemble Forecasting System for Eastern U.S., Continental Shelf Research, http://dx.doi.org/10.1016/j.csr.2012.07.006, in this issue.
Warner, J.C., Sherwood, C.R., Signell, R.P., Harris, C.K., Arango, H.G., 2008. Development of a three-dimensional, regional, coupled wave, current, and sediment-transport model. Computers & Geosciences 34, 1284–1306.
Webb, D.C., Simonetti, P.J., Jones, C.P., 2001. SLOCUM: an underwater glider propelled by environmental energy. IEEE Journal of Oceanic Engineering 26, 447–452.
Weller, R., Toole, J., McCartney, M., Hogg, N., 2000. Outposts in the ocean. Oceanus 42, 20–23.
Wilkin, J.L., Arango, H.G., Haidvogel, D.B., Lichtenwalner, C.S., Durski, S.M., Hedstrom, K.S., 2005. A regional Ocean Modeling System for the Long-term Ecosystem Observatory. Journal of Geophysical Research 110, C06S91, http://dx.doi.org/10.1029/2003JC002218.

Letting Penguins Lead: Dynamic Modeling of Penguin Locations Guides Autonomous Robotic Sampling

BY MATTHEW J. OLIVER, MARK A. MOLINE, IAN ROBBINS, WILLIAM FRASER, DONNA PATTERSON, AND OSCAR SCHOFIELD

The southwest coast of Anvers Island harbors one of five major populations of Adélie penguins in the West Antarctic Peninsula (WAP; Fraser and Trivelpiece, 1996). This "hotspot" is colocated with a submarine canyon that provides a conduit for warm, nutrient-rich Upper Circumpolar Deep Water to stimulate primary production and support a productive ecosystem (Prézelin et al., 2004). Paleoecological evidence shows Adélie penguins (*Pygoscelis adeliae*) have used this location for hundreds of years (Emslie et al., 1998). Since the mid- to late twentieth century, the Southern Ocean near the WAP has warmed significantly (Gille, 2002) and has lost significant sea ice (Stammerjohn et al., 2008). The maritime climate of the northern WAP has shifted poleward, replacing the cold continental Antarctic climate in the Anvers Island region. During this time period, there has been an 80% decrease in the sea ice dependent Adélie penguin populations and an introduction and increase of Gentoo penguins (*P. papua*; Ducklow et al., 2007). Sympatry of Adélie and Gentoo penguins during the breeding season is new to this coast, and it not known if these species will continue to coexist or if the Gentoos will supplant the Adélies. The stability of this new species interaction depends on how well each species is able to exploit the coastal ecosystem. It may be that while submarine canyons offer predictable prey populations, different foraging strategies may allow Gentoos better access to existing prey (krill and fish) populations relative to Adélies. This situation is difficult to assess because penguins are dynamic predators that rapidly forage for krill and fish across a heterogeneous and complex coastal ocean.

In January 2011, we implemented a nested and flexible sampling network to measure the physical and biological features of penguin foraging locations. We coupled 13 satellite-tagged Adélie and seven satellite-tagged Gentoo penguins with multiple deployments of a buoyancy-driven Slocum glider and a propeller-driven REMUS-100 (Figure 1A). When tags, autonomous underwater vehicles (AUVs), and global communications are combined, it is possible to sample the polar ocean as the penguins experience it. However, these robotic assets still require guidance for coordinated sampling strategies (Kahl et al., 2010). In a novel approach, we fused AUVs with satellite-tagged penguins, thus providing a means for seabird top predators to provide the ecological guidance needed to optimize sampling of robotic networks.

The core Adélie and Gentoo penguin foraging regions from Humble Island and Biscoe Point are near the submarine canyon (Figure 1a). We sampled historic penguin foraging locations according to AUV capabilities. The Slocum glider can maintain continued in-water presence for 30 days (Schofield et al., 2007). Therefore, we used the Slocum glider to map larger-scale oceanographic features over the canyon and to gather multiday time series of currents, temperature, salinity, oxygen, and optics. The REMUS-100 mimics the endurance (8–12 hrs), speed (~ 2.5 m s^{-1}), and depth range (0–75 m) of the foraging penguins, and was therefore used to sample temperature, salinity, optics, and acoustic krill densities in the shallow area of the core penguin foraging regions (Figure 1a).

The main feature of our sampling design is that it allowed us to react quickly to new penguin foraging locations. The new locations were relayed via the Argos satellite system to our team in Palmer Station. We then implemented a time-resolved utilization distribution kernel (Keating and Cherry, 2009) with bandwidths corresponding to the location errors of our Argos penguin positions to map likely foraging habitats at hourly resolution. The result was a multispecies dynamic probability map of penguin foraging locations that could be opportunistically targeted by both the Slocum glider and the REMUS-100 AUVs (Figure 1b). The dynamic foraging map enabled creation of a real-time adaptive sampling plan for the penguin foraging locations. Our team of seabird ecologists and oceanographers could change the mission of the AUVs to intersect the penguin foraging locations in order to sample them at high resolution. The fusion of seabird tracking and AUV guidance through the modeling of near-real-time distributions allows researchers to target critical sampling assets to understand the complex interactions between these species and to provide insight on how penguins access their environment in a changing climate.

ACKNOWLEDGEMENTS

These efforts were only possible with funding support provided by the NASA Biodiversity program (NNG06GH75G1/3 to M. Oliver), the NSF Office of Polar Programs (ANT-0823101 to PI Ducklow and Co-PI Schofield; ANT-1019839 to M. Moline), and the Gordon and Betty Moore Foundation. We thank the Palmer Station support staff for facilitating our data collection efforts. We also wish to thank Kaycee Coleman for AUV deployment support, Jennifer Blum, Marc Travers, and Kelsey Ducklow for penguin field support, and Dave Aragon and John Kerfoot for remote AUV control.

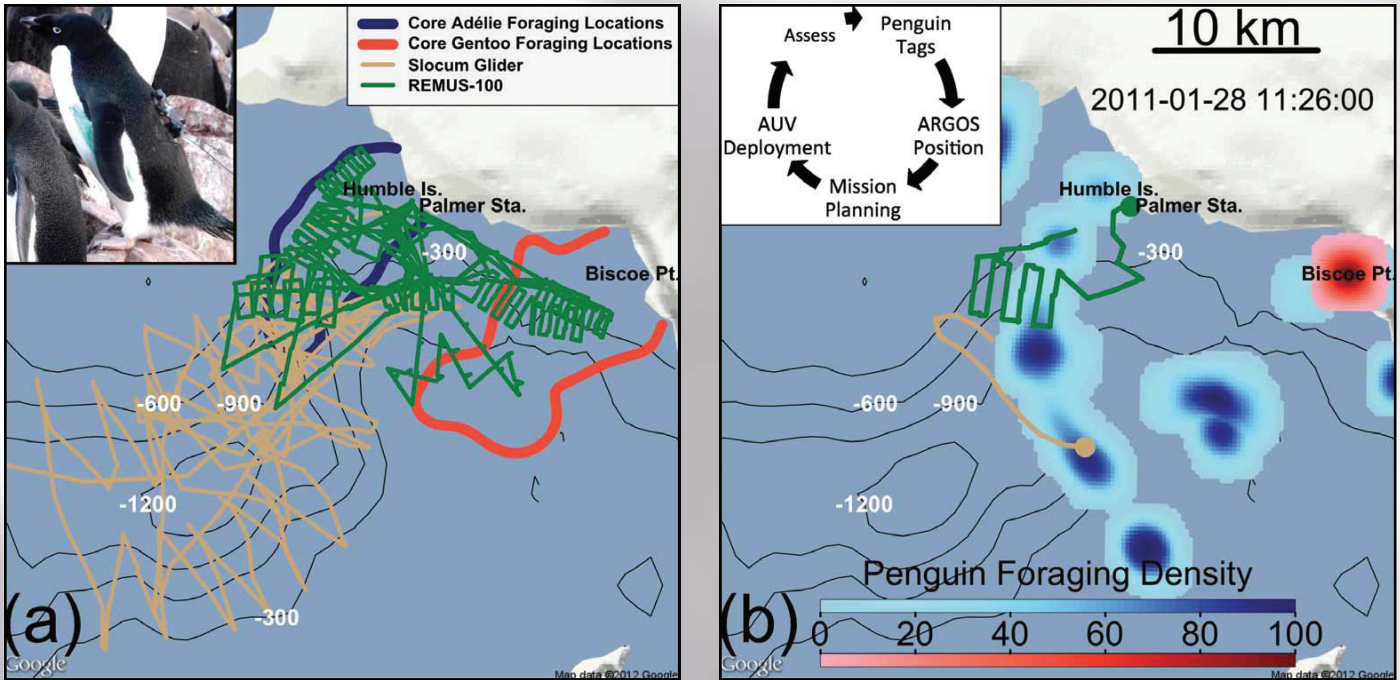

Figure 1. Adélie and Gentoo penguin colonies are located at Humble Island and Biscoe Point near Palmer Station on the south coast of Anvers Island. (a) The thick contours show the historic foraging locations of tagged Adélie (blue) and Gentoo (red) penguins. The inset is an Adélie penguin carrying a satellite tag. The regions around these contours were continually sampled by Slocum glider (tan) and REMUS-100 (green) autonomous underwater vehicles (AUVs). (b) During our experiment, real-time, species-specific foraging density maps based on penguin locations allowed us to intersect our AUVs with these foraging regions. On January 28 at 11:26:00 GMT, the Slocum glider and REMUS-100 intersected an Adélie penguin foraging location (blue). Tagged Gentoo penguins (red) are close to their colony on Biscoe Point at this time.

AUTHORS

Matthew J. Oliver *is Assistant Professor, School of Marine Science and Policy, University of Delaware, Lewes, DE, USA.* **Mark A. Moline** *is Director, School of Marine Science and Policy, University of Delaware, Lewes, DE, USA.* **Ian Robbins** *is Senior Research Scientist, Department of Biological Sciences, California Polytechnic State University, San Luis Obispo, CA, USA.* **William Fraser** *is President, Polar Oceans Research Group, Sheridan, MT, USA.* **Donna Patterson** *is a scientist with Polar Oceans Research Group, Sheridan, MT, USA.* **Oscar Schofield** *is Professor, Institute of Marine and Coastal Sciences, Rutgers University, New Brunswick, NJ, USA.*

REFERENCES

Ducklow, H.W., K. Baker, D.G. Martinson, L.B. Quetin, R.M. Ross, R.C. Smith, S.E. Stammerjohn, M. Vernet, and W. Fraser. 2007. Marine pelagic ecosystems: The West Antarctic Peninsula. *Philosophical Transactions of the Royal Society B* 362:67–94, http://dx.doi.org/10.1098/rstb.2006.1955.

Emslie, S.D., W. Fraser, R.C. Smith, and W. Walker. 1998. Abandoned penguin colonies and environmental change in the Palmer Station area, Anvers Island, Antarctic Peninsula. *Antarctic Science* 10:257–268, http://dx.doi.org/10.1017/S0954102098000352.

Fraser, W.R., and W.Z. Trivelpiece. 1996. Factors controlling the distribution of seabirds: Winter-summer heterogeneity in the distribution of Adélie penguin populations. Pp. 257–272 in *Foundations for Ecological Research West of the Antarctic Peninsula*. Antarctic Research Series, vol. 70, R.M. Ross, E.E. Hofmann, and L.B. Quetin, eds, American Geophysical Union, Washington, DC, http://dx.doi.org/10.1029/AR070p0257.

Gille, S.T. 2002. Warming of the Southern Ocean since the 1950s. *Science* 295:1,275–1,277, http://dx.doi.org/10.1126/science.1065863.

Kahl, L.A., O. Schofield, and W.R. Fraser. 2010. Autonomous gliders reveal features of the water column associated with foraging by Adélie penguins. *Integrative and Comparative Biology* 50:1,041–1,050, http://dx.doi.org/10.1093/icb/icq098.

Keating, K.A., and S. Cherry. 2009. Modeling utilization distributions in space and time. *Ecology* 90:1,971–1,980, http://dx.doi.org/10.1890/08-1131.1.

Prézelin, B.B., E.E. Hofmann, M. Moline, and J.M. Klinck. 2004. Physical forcing of phytoplankton community structure and primary production in continental shelf waters of the Western Antarctic Peninsula. *Journal of Marine Research* 62:419–460, http://dx.doi.org/10.1357/0022240041446173.

Schofield, O., J. Kohut, D. Aragon, L. Creed, J. Graver, C. Haldeman, J. Kerfoot, H. Roarty, C. Jones, D. Webb, and S.M. Glenn. 2007. Slocum gliders: Robust and ready. *Journal of Field Robotics* 24:473–485, http://dx.doi.org/10.1002/rob.20200.

Stammerjohn, S.E., D.G. Martinson, R.C. Smith, and R.A. Iannuzzi. 2008. Sea ice in the Western Antarctic Peninsula region: Spatio-temporal variability from ecological and climate change perspectives. *Deep Sea Research Part II* 55:2,041–2,058, http://dx.doi.org/10.1016/j.dsr2.2008.04.026.

Impact of Ocean Observations on Hurricane Forecasts in the Mid-Atlantic

Forecasting Lessons Learned from Hurricane Irene

Scott Glenn, Oscar Schofield, Josh Kohut, Louis Bowers, Michael Crowley, Rich Dunk, John Kerfoot, Travis Miles, Laura Palamara, Hugh Roarty, Greg Seroka and Yi Xu
Rutgers University
New Brunswick, NJ, USA
glenn@marine.rutgers.edu

Jay Titlow
Weatherflow, Inc
Poquoson, VA

Wendell Brown
University of Massachusetts
New Bedford, MA 02744

William Boicourt
University of Maryland
Cambridge, MD 21613

Larry Atkinson
Old Dominion University
Norfolk, VA 23529

Harvey Seim
University of North Carolina
Chappel Hill, NC 27599

Abstract—**Hurricane Irene followed a track that curved northward over the Bahamas and ran directly over the U.S. east coast from Cape Hatteras to New England in August of 2011, causing severe storm surges, intense inland flooding, loss of life and over $8 billon in storm damage. While the ensemble of atmospheric forecast models accurately predicted the hurricane timing and track, the hurricane intensity was consistently over-predicted. Data from the U.S. Integrated Ocean Observing System (IOOS) were used to better understand the potential impact of the Mid-Atlantic Bight's coastal ocean on the Hurricane Irene intensity forecast.**

***Index Terms*—Hurricane Forecasting, U.S. IOOS, Underwater Gliders, HF Radar, Air-Sea Interaction, Coastal Processes.**

I. Introduction

The Mid-Atlantic Regional Association Coastal Ocean Observing System (MARACOOS), one of eleven Regional Associations comprising the regional component of the U.S. Integrated Ocean Observing System (IOOS), operates a Regional-Scale Coastal Ocean Observatory that includes coastal weather mesonets, satellite data ground stations, a 1000 km long High Frequency (HF) Radar network (Roarty et al., 2010), and a distributed fleet of autonomous underwater gliders (Schofield et al., 2010). The Regional-Scale Coastal Ocean Observatory was fully operating when Hurricane Irene (Fig. 1) tracked along the U.S. East Coast over Labor Day weekend in 2011 (Glenn et al, 2011). Irene was the first hurricane to threaten New York City since Gloria in 1985. Intense rain from Irene broke flooding records on 26 rivers, causing at least 56 deaths and $8 billion in property damage. Power outages along the flood path lasted from days to weeks.

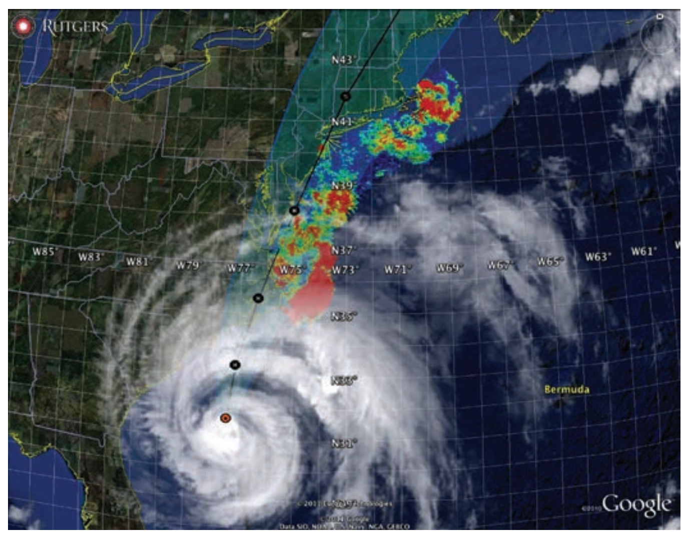

Fig. 1. Hurricane Irene in the South Atlantic Bight and forecast track as it approaches the Mid-Atlantic Regional HF Radar network.

Forecasts of Hurricane Irene's track (Fig. 1) derived by the National Hurricane Center (NHC) from the ensemble of forecast models were highly accurate. Surprisingly, much less damage than expected was caused by the hurricane winds, waves and storm surge along the beach. One reason for this was the consistent overestimate of Irene's intensity by the ensemble of atmospheric forecast models (Fig. 2). This led to numerous newspaper articles and television reports publicly reaffirming that "Intensity remains a big gap in storm science".

978-1-4673-0831-1/12/$31.00 ©2012 IEEE

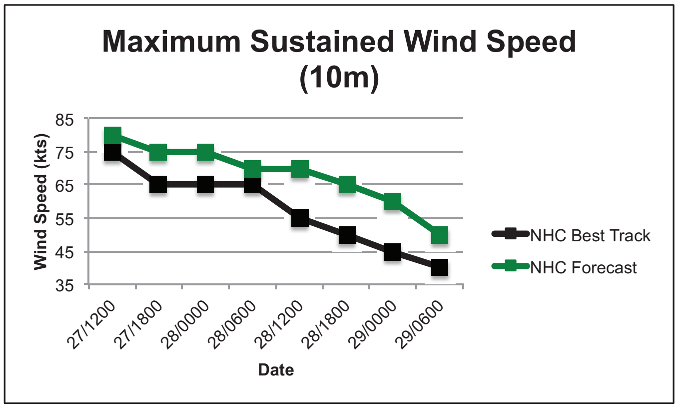

Fig. 2. Maximum sustained wind forecast (green) and best track reanalysis (black) showing the forecast overestimate of Irene's intensity.

In this paper, we discuss selected highlights of real-time ocean data acquired by the MARACOOS regional-scale network during Irene. Through a series of atmospheric model sensitivity studies, the potential impact of real-time ocean data on hurricane intensity forecasts in the Mid-Atlantic is demonstrated.

II. HF Radar Observations

The MARACOOS HF Radar network captured the shelf-wide surface current response to the intense hurricane forcing at the spatial scale of the storm. The direct wind forcing includes a rapid shift from intense onshore, to alongshore, and finally to offshore currents over the time scale of a day (Fig 3). As the eye of Hurricane Irene enters the Mid Atlantic Bight (MAB) on August 27 at 17:00 GMT, strong winds from offshore that precede the eye are forcing onshore currents and increasing the storm surge over much of the southern MAB (Fig 3a). Fifteen hours later on August 28 at 8:00 GMT, the eye of Hurricane Irene is offshore Delaware Bay, and the outer edge on the northeast side is reaching Cape Cod. Currents in the northern portion of the MAB are onshore, currents in the middle are alongshore, and currents in the southern portion have switched to offshore. By 14:00 GMT on August 28, the eye of Irene passes over New York City and the storm heads inland. Surface currents directly east of the eye are now onshore, and surface currents on the trailing side of the storm in the southern MAB are now diminishing and are beginning to turn in inertial circles.

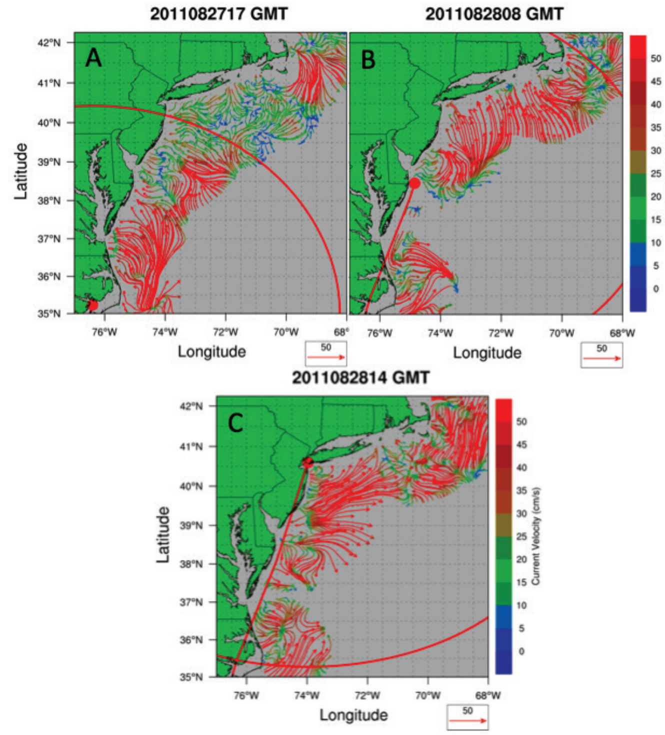

Fig. 3. Surface current response due to Hurricane Irene winds as (a) the eye enters the MAB near Cape Hatteras, (b) the eye crosses Delaware Bay, and (c) as the eye crosses over New York City and heads inland.

Observations of the lingering inertial current response to hurricanes are numerous in deepwater. Kohut et al. (200?) found the inertial response to Tropical Storm Floyd was quickly diminished in very shallow water as the stratification was eroded. The MAB HF Radar network provides the first look at the inertial tail of a hurricane over the full scale of the MAB shelf over a range of water depths and stratification. Starting with a single point at midshelf where an autonomous underwater glider was located (see Section III), a time series of the observed total currents along with the inertial component of the current derived from a least-squares fit to the current data is plotted for a 1 week period starting on August 26 before Hurricane Irene entered the MAB (Fig. 4). The peak in the direct wind forcing occurs on the scale of 1 day on August 28 (Fig. 4, top). The amplitude of the inertial component of the current (Fig. 4, bottom) increases until it peaks on August 29 as the back side of the storm crosses onto land in New England and New York. The inertial amplitude remains high for much of the day on August 29, then slowly decays at a linear rate over several days from August 29 through September 1.

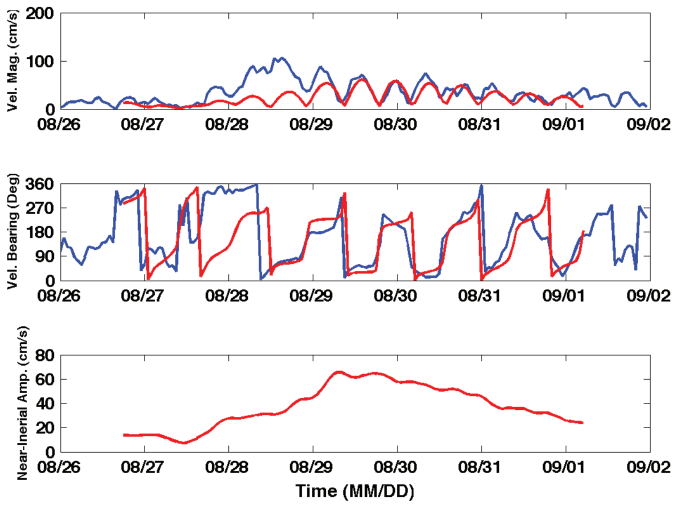

Fig. 4. Time series of total current (blue) and near-inertial current (red) calculated for a point on the outer shelf of NJ.

Spatial maps of the energy content in the diurnal and near-inertial frequency bands derived from a wavelet analysis of the surface currents are shown in Fig. 5. As the eye of Hurricane Irene moves into southern New England (Fig. 5a), the large amount of energy in both the diurnal and near-inertial frequency bands on the outer half of the shelf in the central MAB is visible. Two days later (Fig. 5b), the energy level in the diurnal band is reduced over the full MAB, while the energy in the near-inertial band persists.

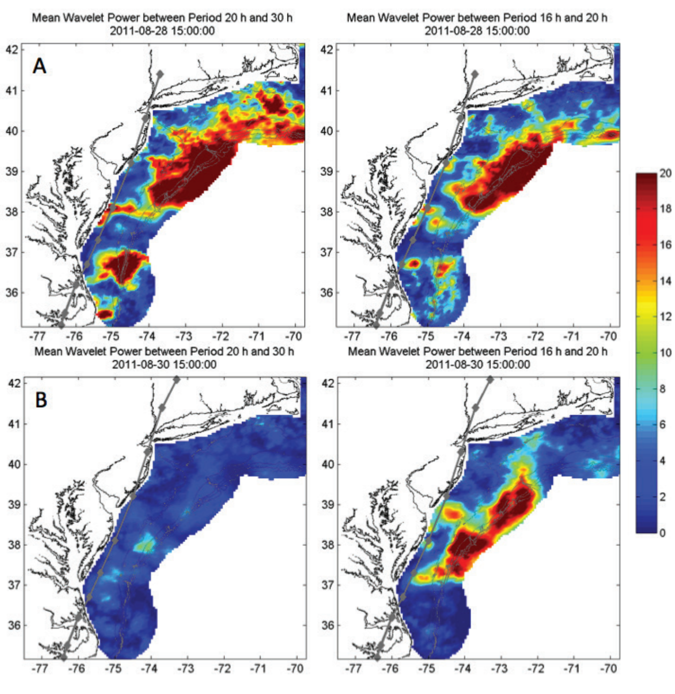

Fig. 5. Spatial maps of the diurnal (left) and near-inertial energy (right) as (a) the eye passes over NJ, and (b) 2 days later.

III. Glider Observations

Two autonomous underwater gliders were operating in the MAB when Hurricane Irene transited the region (Fig. 6). RU23 was deployed on a regional MARACOOS mission by UMass Dartmouth to map the subsurface temperature and salinity structure of the MAB during the decay phase of the Cold Pool to support ocean modeling activities for fisheries applications. RU23 was damaged early in the storm and was purposely kept at the surface through the storm to prevent its loss. Its track as a surface drifter illustrates the combination of the initial direct and persistent inertial forcing. RU23 was recovered after the storm by a sport-fishing vessel before it entered the shipping lanes as a drifter. RU16 was deployed on a New Jersey state mission to monitor dissolved oxygen concentrations for the Environmental Protection Agency. As Irene approached, RU16 was moved offshore to a mid-shelf point where it rode out the storm. This glider provides information on the magnitude and timing of the subsurface mixing that occurred during Irene.

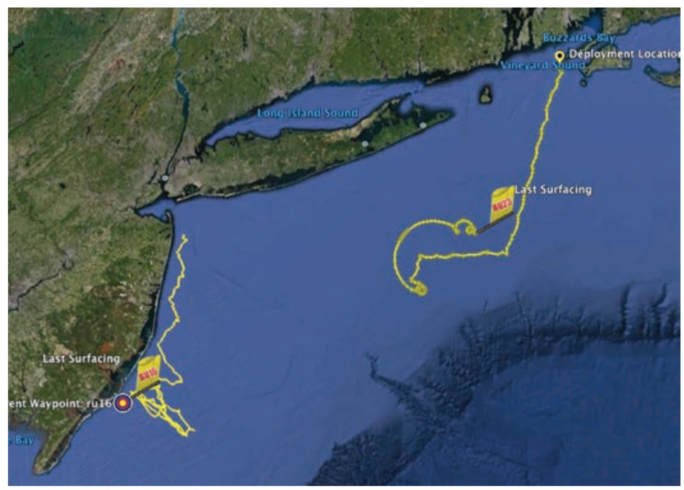

Fig. 6. Tracks for Gliders RU23 (deployed from Martha's Vineyard by UMass) and RU16 (deployed from New York Harbor by Rutgers).

The vertical sections of temperature, salinity and dissolved oxygen from the full RU16 EPA deployment are shown in Fig. 7. Initially in the deployment, as RU16 zig-zags along the New Jersey coast, the T,S and DO profiles illustrate the two distinct surface and bottom layers with the sharp interface typical of the New Jersey shelf in summertime. The surface layer is warmed by the sun, freshened by the riverine outflows from the MAB watersheds, and is oxygenated through its atmospheric interface. The bottom layer is known as the Cold Pool. It is what remains of the cold and salty winter water slowly flowing to the south along the shelf. Isolated from the surface waters by an intense pycnocline that inhibits mixing, dissolved oxygen values in the lower layer often plummet to values that can stress or even kill benthic organisms.

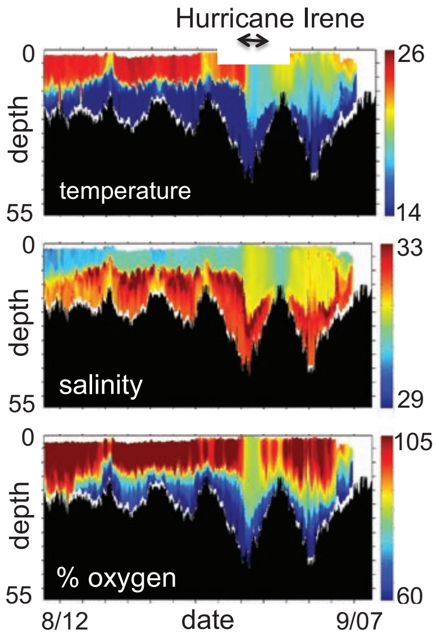

Fig. 7. Temperature, Salinity and Dissolved Oxygen sections from the full deployment of RU16.

Fig. 7 further illustrates the significant impact of Irene on the T, S and DO structure as it passes over the glider on August 28. The response is rapid. The interface between the two layers deepens and the surface layer gets cooler and saltier while the dissolved oxygen level decreases. Oxygen levels in the upper layer quickly recover after the storm, but the surface layer temperature never returns to its summertime pre-storm values. Zooming into the storm mixing period in the temperature section (Fig. 8), the transition from pre-storm to post-storm conditions occurs during the short time period between 00:00 GMT and 14:00 GMT as the eye of Irene passes the glider on August 28.

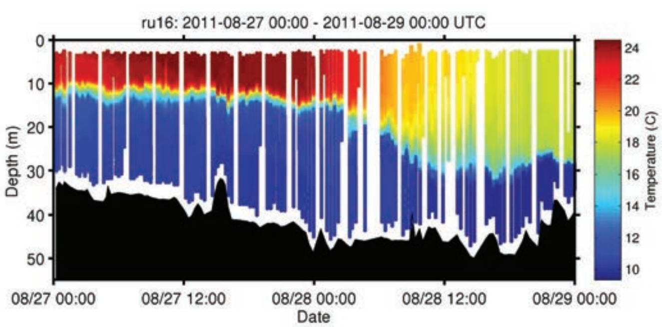

Fig. 8. Detailed plot of the temperature section showing the rapid mixing and cooling of the surface layer that occurred during Irene.

IV. Satellite Observations

V. Atmospheric forecasts over oceanic domains require a boundary condition for sea surface temperature. Numerous sea surface temperature products from a variety of sources are available for this purpose. The major difference between the products is how the cold pixels contaminated by clouds are removed and the resulting data gaps filled. Most commonly used methods include warmest pixel composites that combine multiple images in time, or by interpolating in space across pixels flagged as clouds.

VI. The existing product used to forecast Hurricane Irene's transit through the region is the Real-Time Global High Resolution Sea Surface Temperature product shown (Fig. 9a). For this product, the mixing that occurs during Hurricane Irene is not picked up by this product for several days after Irene left the region.

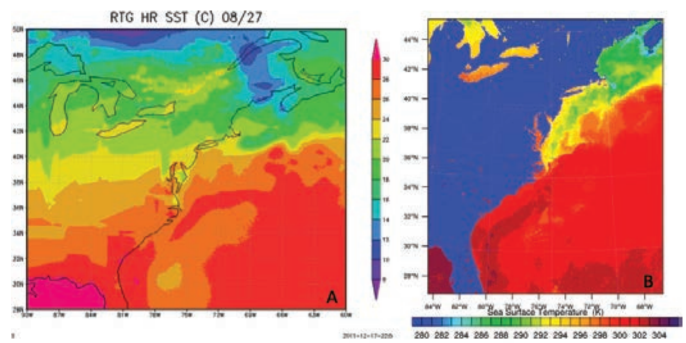

Fig. 9. Sea surface temperature maps (a) used in real time weather forecasts and (b) observed immediately after the clouds cleared from Irene.

To explore the impact of surface cooling during Irene, a new satellite SST product was produced that does not rely on warmest pixel compositing to remove clouds. Instead, daytime images of sea surface temperature where checked for their reflectivity in the visible part of the spectrum. High reflectivity pixels were flagged as clouds, and cooler pixels with low reflectivity were considered ocean pixels cooled by the storm. Retaining these cold but dark pixels observed after the storm produces the image in Fig. 9b. Significant cooling of order 5C-8C is observed on the MAB shelf, with the greatest cooling occurring in the middle of the shelf above the core of the Cold Pool.

VII. Atmospheric Forecast Sensitivities

The Rutgers University implementation of the Weather Research and Forecast (WRF) atmospheric model was used in a series of sensitivity studies to examine the impact of the cooler sea surface temperatures on the Hurricane Irene forecasts. Two endpoints of the sensitivity matrix are illustrated in Fig. 10 where the windfields are plotted at 18:00 GMT after the eye has propagated onto land. In all cases, the track of Hurricane Irene was reproduce, but the intensity of the forecast winds varied. The wind forecast on the left is the run with the standard sea surface temperature product that was available to the real-time forecast models (Fig. 9a). Maximum winds are located over the ocean and are in the 45-55 knot range. The wind forecast on the right is for the same time period but using the cooler sea surface temperature map of Fig. 9b assembled after the event. When this cooler sea surface temperature is used as a boundary condition, the forecast overwater winds are reduced to the 35-45 knot range.

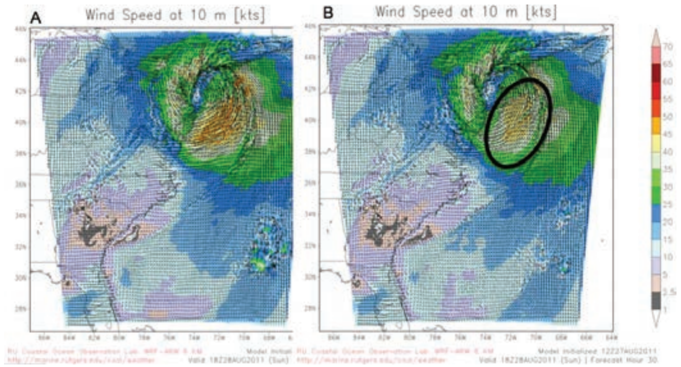

Fig. 10. Wind forecast from RU-WRF (a) using the warm sea surface temperature in figure 9a, and (b) applying the cold sea surface temperature in figure 9b at the time of the mixing observed by glider RU16.

The following table compares the Root Mean Square Error of the National Hurricane Center's best track estimates of Irene's intensity with their real time forecast, two runs of the RU-WRF model run with the warm SST from Fig. 9a, and one run of the RU-WRF model with the cold SST from Fig. 9b. The RSME of the RU-WRF model run using the warm sea surface temperature is similar to the RMSE of the real-time NHC forecast. The difference between the regular WRF model run and the "Hurricane WRF" with the attached Ocean Mixed Layer model is negligible. The WRF model run with the cold SST reduces the RMSE by a factor of 2-3.

TABLE I. MAXIMUM WIND SPEED FORECAST ERROR (KNOTS)

Date/Time (UTC)	*NHC Intensity Forecast*	*RU-WRF Warm SST (RTG) only*	*RU-WRF Warm SST (RTG) + OML Model*	*RU-WRF Cold SST (RTG+SPoRT+ AVHRR)*
27/1200	5	-17.22	-17.23	-6.17
27/1800	10	4.1	4.2	5.88
28/0000	10	1.39	-2.14	3.96
28/0600	5	-1.2	-1.04	-1.21
28/1200	15	2.39	4.79	0.5
28/1800	15	4.97	3.51	-2.67
29/0000	15	3.62	1.93	-0.89
29/0600	10	10.48	9.84	4.52
Sum of Squares	800	457	452	118
RMSE	9.43	7.13	7.09	3.61

VIII. CONCLUSIONS

Sensitivity studies of Hurricane Irene were conducted using the ensemble of MARACOOS atmospheric forecast models. The impact of a variety of Sea Surface Temperature (SST) boundary conditions were studied, ranging from persistence of the warm pre-storm SST to applying the cold post-storm SST at the time mixing was observed by the autonomous underwater gliders. The resulting timing and track are consistent with the real-time forecast ensemble. The composite SST developed using the observed variation in sea surface temperature was found to reduce the intensity of the storm, in some cases by 15 knots, bringing the hindcasts in line with offshore buoy and onshore mesonet observations.

The sensitivity matrix results indicate the potential importance of a coupled atmosphere-ocean model to hurricane intensity forecasting in the Mid Atlantic Bight. The coupled model will be required to produce realistic forecasts of sea surface temperature fields during intense mixing events before the clouds clear after the storm. This will require improved understanding of subsurface mixing processes during intense coastal storms, and sufficient subsurface data from autonomous gliders for assimilation into the ocean model to provide the proper initial state.

ACKNOWLEDGMENT

Support for this research was provided by the U.S. Integrated Ocean Observing System (IOOS) through the Mid-Atlantic Regional Association Coastal Ocean Observing System (MARACOOS). The deployment and operation of Glider RU16 was funded by the Environmental Protection Agency and the New Jersey Department of Environmental Protection.

REFERENCES

[1] S. Glenn, O. Schofield and J. Kohut, "Hurricane Irene 2011: Mid-Atlantic IOOS response to the hurricane", http://maracoos.org/sites/macoora/files/downloads/Hurricane_Irene_blog_2011.pdf, pp. 65, 2011.

[2] H. Roarty, S. Glenn, J. Kohut, D. Gong, E. Handel, E. Rivera, T. Garner, L. Atkinson, W. Brown, C. Jakubiak, M. Muglia, S. Haines, H. Seim, "Operation and Application of a Regional High-Frequency Radar Network in the Mid-Atlantic Bight" Marine Technology Society Journal, 44 (6), 2010.

[3] O. Schofield, J. Kohut, S. Glenn, J. Morell, J. Capella, J. Corredor, J. Orcutt, M. Arrott, I. Krueger, M. Meisinger, C. Peach, F. Vernon, A. Chave, Y. Chao, S. Chien, D. Thompson, W. Brown, M. Oliver, W. Boicourt, "A regional Slocum glider network in the Mid-Atlantic coastal waters leverages broad community engagement." Marine Technology Society 44(6): 64-74, 2010.

Continental Shelf Research ▪ (▪▪▪▪) ▪▪▪–▪▪▪

Contents lists available at SciVerse ScienceDirect

Continental Shelf Research

journal homepage: www.elsevier.com/locate/csr

Research papers

Temporal and spatial variability in fall storm induced sediment resuspension on the Mid-Atlantic Bight

Travis Miles *, Scott M. Glenn, Oscar Schofield

Coastal Ocean Observation Laboratory, Institute of Marine and Coastal Sciences, School of Environmental and Biological Sciences, Rutgers University, New Brunswick, NJ 08901, USA

ARTICLE INFO

Article history:
Received 15 February 2011
Received in revised form
20 July 2012
Accepted 3 August 2012

Keywords:
Sediment resuspension
Coastal oceanography
Turbulence
Autonomous underwater vehicles
Sediment transport
Ocean observing systems

ABSTRACT

Storm-driven sediment resuspension is an episodic process that is an important constraint on sediment transport on continental shelves; unfortunately, the spatial variability of the resuspension and transport processes are poorly quantified using traditional sampling techniques. Using two autonomous underwater gliders, long-range high frequency radar and buoy data, we quantified spatial variability of sediment resuspension and transport in a large fall storm in November of 2009. Wave, wind and current data in conjunction with glider profiles showed that waves and winds mixed the water column, waves initially mobilized the sediment and shear induced turbulence advected sediment throughout the water column. The separation of over 50 km between the two gliders (RU05 and RU21) is used to highlight the spatial variability of sediment resuspension. Both gliders were operating along the 40 m isobath with RU21 located 50 km north of RU05. Sediment resuspension on the New Jersey (NJ) shelf responded to synoptically forced turbulent motions. Currents transported this sediment toward the southwest in the along-shelf axis and onshore on the cross-shelf axis during the peak resuspension on November 13th through November 14th, with resuspension and transport on the southern NJ shelf measured by RU05 approximately twice that of RU21 on the northern MAB. Variability in resuspension profiles between the two gliders was largely a product of smaller mean grain sizes on the southern portion of the NJ shelf. These smaller grain sediment particles had a reduced fall velocity and were more easily retained throughout the water column by turbulent motions.

Published by Elsevier Ltd.

1. Introduction

Coastal storm-driven mixing events are episodic processes (Wiggert et al., 2000; Chang et al., 2001; Zedler et al., 2002) that are important for sediment transport. Despite numerous focused field campaigns on storm induced sediment resuspension (Traykovski et al., 1999; Styles and Glenn, 2002; Traykovski, 2007), the processes dominating the spatial variability of the storm response remains unresolved. The Mid-Atlantic Bight (MAB) is a region impacted by numerous physical forcing processes such as freshwater input from a complex network of rivers and estuaries, wave tidal and inertial fluctuations, variable topographic features such as the Hudson Shelf Valley and the ridge and swale topography (Beardsley and Boicourt, 1981; McBride and Moslow, 1991), the shelf-break jet (Chen and He, 2010) and Gulf Stream eddies near the shelf-break, seasonal wind variability (Gong et al., 2010), the summer cold pool (Lentz, 2008) and powerful winter storms (Beardsley and Boicourt, 1981).

Strong solar insolation drives the formation of the summer cold pool that results in large seasonal variations in the water column stratification between winter and summer seasons (Houghton et al., 1982; Lentz, 2003). This stratification is broken down by extra-tropical cyclones, commonly referred to as fall transition storms (Bigelow 1933, Beardsley and Boicourt, 1981). These storms result in a well-mixed water column in the winter until early spring (Lentz, 2003). The erosion of the stratification is important for the MAB ecosystem as it replenishes nutrients to the surface layer, which stimulates phytoplankton blooms (Xu et al., 2011). The winter phytoplankton bloom is the largest and most predictable biological event on the MAB (Xu et al., 2011). Resuspension of sandy sediments, which are dominant on the middle to outer-shelf of the MAB (Swift and Field, 1981; Amato, 1994; Reid et al., 2005; Goff et al., 2008), is commonly driven by fall transition storms through a combination of waves and currents (Glenn et al., 2008). For example, Styles and Glenn (2005) identified 25 sediment transport events over a 2-year period, with 63% of these events occurring in fall and winter on the MAB.

A combination of waves and currents are responsible for the resuspension and transport of sediment on the continental shelf. Though non-linear interactions between waves and currents

* Corresponding author. Tel.: +1 919 332 2705.
E-mail address: tnmiles@marine.rutgers.edu (T. Miles).

0278-4343/$ - see front matter Published by Elsevier Ltd.
http://dx.doi.org/10.1016/j.csr.2012.08.006

dominate sediment resuspension, seminal work by Grant and Madsen (1979; 1896) provides a qualitative explanation of the independent role each process plays. Wave bottom boundary shear stress can be an order of magnitude larger than current bottom boundary shear stress. From linear-wave theory wave-induced bottom orbital velocities have a similar magnitude to low-frequency currents but operate over a much smaller bottom boundary layer and thus result in an observed order of magnitude larger shear stress. Despite the high shear stress, wave velocities are orbital and therefore result in little net horizontal transport to first order. When sediment is suspended in the water column even relatively minor low-frequency currents are capable of horizontal sediment transport.

Keen and Glenn (1995) and Styles and Glenn (2005) show storm-induced sediment transport is generally aligned along-shelf toward the southwest through modeled and observed bottom currents during Nor'easter storms. Modeled cross-shelf sediment transport was offshore (Keen and Glenn, 1995); however the observed cross-shelf component of the transport was predominantly onshore in Styles and Glenn (2005). These observations are surprising as it might be expected that Nor'easters produce downwelling circulation with offshore bottom transport that is reinforced by the tides; therefore a more complex combination of processes must be important.

Several processes have been hypothesized to account for the onshore transport. Potential factors include topographic interactions that operate over the relatively small (a few kilometers) scale of the ubiquitous ridge and swale topography of the MAB inner shelf (McBride and Moslow, 1991), or over the larger (a few tens of kilometers) scale of the topographic highs associated with ancient river deltas (Glenn et al., 2004). Additionally, Gargett et al. (2004) identified full water column Langmuir cells as a significant driver of sediment resuspension events on the Mid-Atlantic Bight. Keen and Glenn (1995) also identified tides as critical to resuspension and transport modulation, as tidal currents can alternately enhance or reduce the more slowly varying storm driven currents. In their work, the tidal phase was important in determining onshore or offshore veering of the predominant along-shore bottom current. Styles and Glenn (2005) did not observe current veering with tidal phase and saw onshore transport near bottom, though their observations were limited to the 10 m water depth. Given this, the cross-shelf magnitude and direction of sediment transport are still unresolved.

Shipboard observations are likely biased to fair weather conditions as these sampling techniques are limited by the extreme conditions experienced in storms. Benthic tripods are ideally suited to resolve temporal variability effectively during extreme conditions but are expensive to deploy and are not designed to sample horizontal spatial variability. Recent work by Glenn et al. (2008) has demonstrated the potential of using autonomous Slocum gliders for sampling sediment transport events on the continental shelves. This work demonstrated that it is possible to average optical backscatter profiles of a single sensor and obtain results that are consistent with the theoretical understanding of coastal storm induced sediment resuspension. This manuscript builds on these results, using two simultaneously deployed gliders to examine the spatial and temporal variability during a fall transition storm on the MAB.

Hurricane Ida, was a low pressure system that developed into a category two hurricane over the Gulf of Mexico. Ida transitioned into an extratropical cyclone over the southeastern United States on November 10th, 2009. This system, commonly referred to as Nor'Ida, tracked northeastward along the eastern United States coast and into Canada causing extensive damage and coastal flooding. We present data from multiple gliders during Nor'Ida over large along- and cross-shelf spatial scales and incorporate shelf-wide HF radar surface currents (Roarty et al., 2010) measured with 6 km resolution for the duration of a fall transition storm. Both gliders started from the same location off Tuckerton, New Jersey (Fig. 1) and performed cross-shelf transects offshore. As in Glenn et al. (2008), deviation from flight paths and increases in glider depth-averaged currents indicate storm passage. Glider tracks and depth averaged currents for RU05 and RU21 can be seen in Figs. 2 and 3. RU05 took a brief northeastward turn followed by a long southwestward along-isobath track, which was enhanced by southwestward storm induced currents. RU21 finished its offshore cross-shelf transect and returned to complete an onshore cross-shelf transect, with deviations as a result of southwestward storm induced currents.

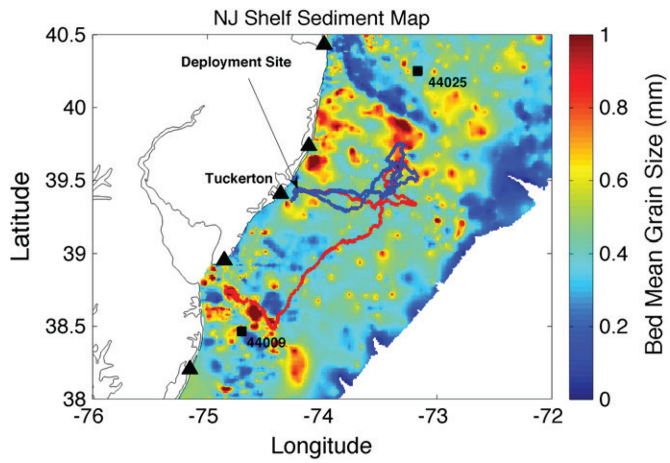

Fig. 1. The study location and 2 km resolution mean grain size map in mm with glider tracks from RU05(red), RU21 (blue), CODAR locations within the study region (black triangles) and Buoys 44009 and 44025 (black squares). Only CODAR stations in the immediate vicinity are shown, though others contributed to the data. The deployment site for both gliders is off Tuckerton, NJ. RU21 was recovered near the deployment site while RU05 was recovered in the south off of Delaware Bay, near buoy 44009. Details of sediment compilation from the usSEABED program are covered in Goff et al. (2008).

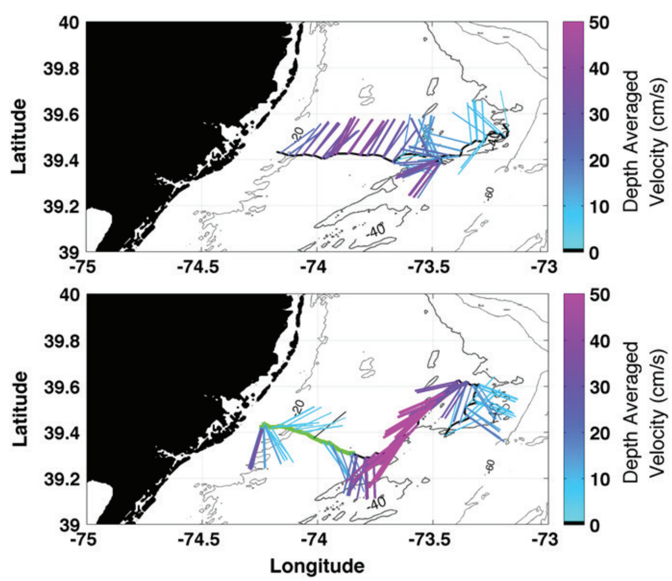

Fig. 2. RU21 depth averaged currents and offshore glider track from 10/31 to 11/05 (Top Panel) and onshore glider track from 11/10 to 11/18 (Bottom Panel). The green line indicates the portion of the transect from 11/15 to 11/18.

2. Materials and methods

This project relied on infrastructure operated by the Mid-Atlantic Regional Association Coastal Ocean Observing System (MARACOOS) that is part of the United States Integrated Ocean Observing System (U.S. IOOS) (Roarty et al., 2010; Schofield et al., 2010a). MARACOOS provides a suite of data collected by satellites, a high frequency CODAR network, and a fleet of Webb Slocum gliders (Glenn and Schofield, 2009). All of the above remote sensing techniques are coupled to a super ensemble of data assimilative numerical ocean models (see below).

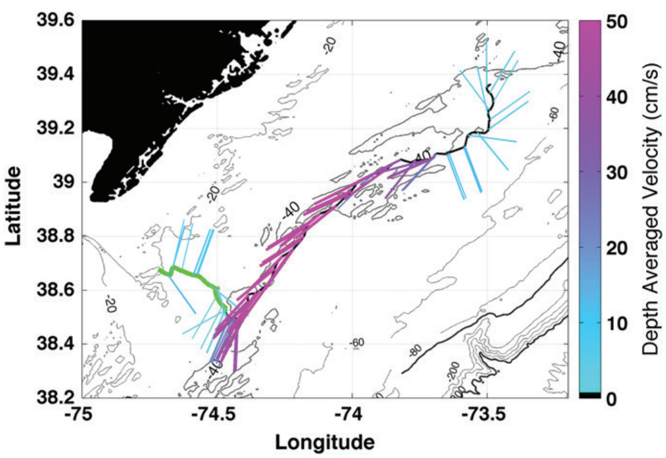

Fig. 3. RU05 glider track and depth-averaged currents between 11/10 and 11/18. The green line indicates the onshore glider track on 11/16 to 11/18.

2.1. Ocean observation dataset

A network of CODAR Ocean Sensors SeaSonde HF Radar systems measures surface currents on the MAB. The CODAR network consisted of 13 5-MHz HF Radar systems located along the northeast of the United States (Fig. 1). The HF Radar uses the Doppler Shift of a radio signal backscattered off the ocean surface to measure the component of the flow in the direction of the antenna (Barrick, 1971a, 1971b; Teague, 1971). Descriptions of the CODAR data and its shelf-wide applications are outlined in Dzwonkowski et al. (2009b) and Gong et al. (2010). The network provides surface current observations at the estimated equivalent depth of 2.4 m (Stewart and Joy, 1974). To minimize the geometric uncertainty in the radials we used the recommended threshold for the Geometric Dilution of Precision (GDOP) (Chapman and Graber, 1997) value of 1.5 or less to identify the vectors with acceptable GDOP (Dzwonkowski et al., 2009a). This value is chosen based on current comparison studies using CODAR and ship-mounted Acoustic Doppler Current Profilers (Kohut et al., 2006) and drifters (Ohlmann et al., 2007). The spatial resolution of the final total vector current maps is 6 km with a typical cross-shelf range of 150 km.

Sediment mean grain size is determined by taking a regional subsample of a 2 km resolution interpolated sediment map developed by Goff et al. (2008) from data compiled as part of the usSEABED project (http://walrus.wr.usgs.gov/usseabed/). We convert phi units into mm grain size as the sandy sediment only varies over two phi units (Fig. 1).

Oceanographic data from NOAA NDBC buoys 44009 and 44025 were used in this effort (Fig. 1). The moorings provided data on atmospheric pressure, wind speed/direction, wave-height, period and direction (Fig. 4).

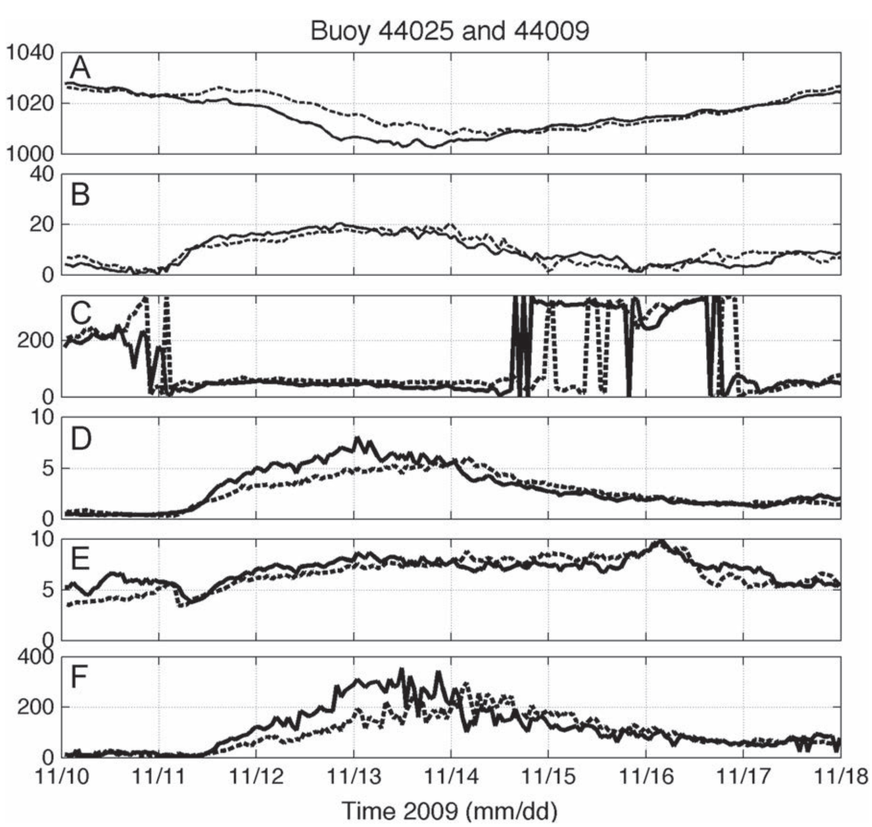

Fig. 4. Buoy 44009 (solid line) and 44025 (dashed line) (A) sea-level-pressure, (B) 5 m wind speed, (C) wind direction (D) wave height (E) wave period and (F) bottom orbital velocities for 11/10 to 11/18. Wave induced bottom orbital velocities were calculated from linear wave theory as in Glenn et al. (2008).

Please cite this article as: Miles, T., et al., Temporal and spatial variability in fall storm induced sediment resuspension on the Mid-Atlantic Bight. Continental Shelf Research (2012), http://dx.doi.org/10.1016/j.csr.2012.08.006

Slocum gliders are an autonomous underwater scientific platform (Davis et al. 2003; Schofield et al., 2007) manufactured by the Teledyne Webb Research Corporation. They are 1.8-m long, torpedo-shaped, buoyancy-driven vehicles with wings that enable them to maneuver through the ocean at a forward speed of 20–30 cm s^{-1} in a sawtooth-shaped gliding trajectory. A full description of our scientific operation of the Slocum gliders can be found in Schofield et al. (2007). Each Slocum glider has a payload bay that houses a SeaBird conductivity–temperature–depth sensor and includes space for a range of additional sensors. The glider acquires its global positioning system (GPS) location every time it surfaces, a programmable interval that was set to 3 h for the purposes of this study. By dead reckoning along a compass bearing while flying underwater, estimates of depth averaged current can be calculated based on the difference between the glider's expected surfacing location and the actual new GPS position. Depth averaged current measurements obtained in this manner have been validated against stationary Acoustic Doppler Current Profiler data (Davis et al. 2003). These physical measurements are complemented with several bio-optical sensors (Glenn and Schofield, 2009).

Two Webb Slocum gliders were deployed prior to November 1, 2009 and operated for two weeks. During that period the gliders traversed 1673 km underwater collecting 23,332 vertical profiles (Fig. 1). The gliders were outfitted with WetLabs Inc. EcoPucks, which provide measurements of optical backscatter, chlorophyll fluorescence and colored dissolved organic fluorescence. The EcoPucks measure optical backscatter at 440 (b_b470) and 660 (b_b660) nm. Optical backscatter, to first order, is used to measure the relative concentration of particulate matter (Roesler and Boss, 2008). A growing body of work indicates that optical backscatter is not only a function of particle concentration but also sediment characteristics such as refractive index, size, shape and particle composition (Twardowski et al., 2001; Boss et al., 2004). While we do not characterize sediment in great detail during the measured resuspension events, we use changes in backscatter ratios to indicate a change in character of suspended particles.

2.2. Adaptive sampling

To coordinate the numerous observed and forecast model data streams, we were able to utilize a novel cyberinfrastructure (CI) tool set being developed as part of the Ocean Observing Initiative (OOI). The software was used to coordinate sampling using multi-model forecasts to optimize glider missions (Schofield et al., 2010b). In brief, numerical model ocean forecasts allowed the simulation of future *in situ* glider trajectories. This guidance could be used by the team to optimize sampling based on the science needs. This provided scientists with a guide to determine whether desired target areas could be reached by Webb Slocum gliders in a predicted current field. Thus the CI software could deliver the community science needs back to the *in situ* observation network in a timely manner. Field operations were coordinated through a

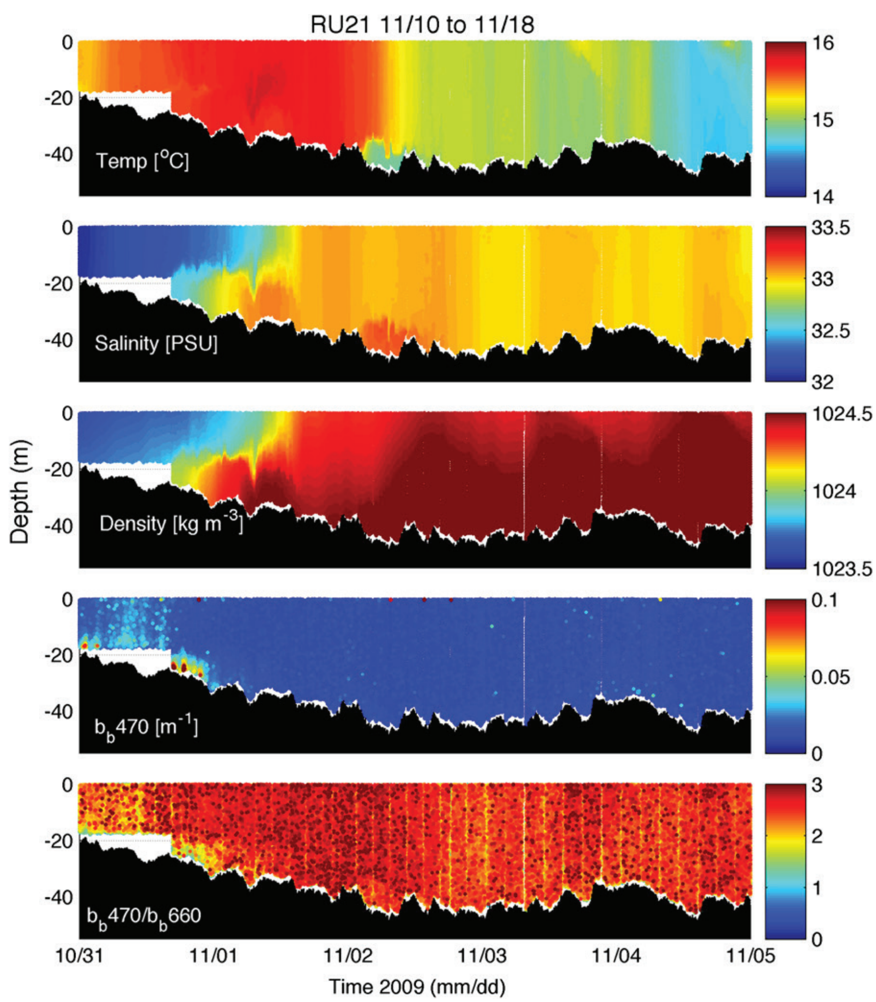

Fig. 5. RU21 Pre-storm cross sections of temperature, salinity, density, b_b470 and the ratio of b_b470/b_b660.

web portal (http://ourocean.jpl.nasa.gov/CI) that provided an access point for real-time observational data and model forecasts.

3. Results

3.1. Pre-storm hydrography

Pre-storm conditions were typical for fall on the MAB with predominantly vertical isotherms and a cross-shelf temperature gradient. RU21, on its offshore transect (Fig. 2) between October 31st and November 5th, showed a near-shore water mass that was approximately 1 kg m^{-3} lighter than offshore waters (Fig. 5). This lower density coastal water was largely due to the variability in salinity. Additionally, there was a warm core of water centered at 15 m depth, on the 35 m isobath, which contributed to the regional vertical and horizontal density gradients. This glider data shows that New Jersey shelf waters were generally colder, saltier and denser in the offshore direction. B_b470 was low (<0.005 m^{-1}) for the majority of the offshore pre-storm transect. There is a small region of elevated backscatter near-shore located below the pycnocline. RU21 was not programmed to dive below 20 m until after it reached the 25 m isobath so the optical backscatter at the bottom in the near-shore region was not completely sampled. Pre-storm water column b_b470 to b_b660 ratios were high ($\sim$3) relative to storm signatures (see below). There was a short period of elevated currents toward the north-east in the coastal region (Fig. 2). Prior to the storm both the gliders and CODAR (Figs. 2, 3, 6) showed variable currents between 5 and 40 cm s^{-1} along the coast of New Jersey, with daily averaged currents immediately prior to the storm event somewhat higher than the climatological mean of 5 cm s^{-1} (Beardsley and Boicourt, 1981).

3.2. Storm data

Buoy 44009, off of Delaware Bay, and 44025, off Long Island are separated by approximately 230 km with 44009 encountering Nor'Ida first (Fig. 4). As the storm entered the MAB region from the southwest, pressure fell from above 1020 mbar at both buoys to a minimum of 1002 mbar on November 13th at 2000 Greenwich Mean Time (GMT) at 44009 and a minimum of 1007 mbar on November 13th at 2350 GMT at 44025 (Fig. 4A). Winds at both locations began to increase at 0000 GMT on November 11th, but peak winds at 44025 lagged 44009 by 28 h with slightly lower magnitude until they reached a maximum of 20.5 ms^{-1} at 23:50 GMT on November 13th (Fig. 4B). Prior to November 11th wind direction was variable. Between November 11th and late on the 15th,wind direction at both buoys was from the northeast (Fig. 4C). Wave-heights began to build after a few hours of rising winds at both locations (Fig. 4D). Wave heights reached over 8 m at 0050 GMT on November 13th at 44009 and over 6 m at 0350 GMT on the 14th at 44025. Wave spectral periods were between 7 and 9 s for the duration of the storm at both locations and continued to increase after storm passage, eventually peaking at $\sim$10 s on the morning of November 16th (Fig. 4E). Maximum wave bottom orbital velocities were calculated from buoy data using linear wave theory as described by Glenn et al. (2008). Wave bottom orbital velocity estimates peaked at 2.4 m s^{-1} and 1.8 m s^{-1} at buoy 44009 and 44025 respectively (Fig. 4F), significantly higher than glider depth-averaged and CODAR surface currents (Figs. 2, 5, 8).

CODAR daily averaged currents (Fig. 6) were toward the south-west on November 11th and reached 30 cm s^{-1} on the central and southern MAB with values offshore nearing 50 cm s^{-1}. CODAR daily averaged surface currents peaked in excess of 50 cm s^{-1} shelf-wide on the central and southern MAB on the 13th. There was a low velocity region on the northwestern MAB near the Hudson River outflow. Over the two days following peak values, shelf-wide currents decreased back to near pre-storm values, below $\sim$15 cm s^{-1}.

3.3. RU21 northern glider storm variability

As Nor'Ida approached the New Jersey shelf, RU21 turned onshore and attempted to retrace the path of its offshore transect (Fig. 2). Initially it flew southwestward along the 40 m isobath until it turned onshore on the 15th. Cross-sections of glider measurements (Fig. 7) show that during its southwestward transect RU21 initially measured vertically uniform temperatures of 15 °C, salinity of 33 PSU, density near 1024.6 kg m^{-1}, optical backscatter at b_b470 nm was near 0 m^{-1} and the ratio of b_b470 to b_b660 was $\sim$3. Downcast vertical glider velocities were uniform at $\sim$0.3 m s^{-1}. Vertical glider velocities were calculated by the change in measured pressure over time and we used them to serve as a proxy for vertical water velocities. In uniform water masses with no external turbulent forcing and the glider on a new constant glide slope, vertical velocities should have also remained approximately constant except when the glider was inflecting near-bottom or near-surface.

As winds, waves and currents increased beginning on the 11th, there was a distinct water column response. First, glider vertical velocities began to undergo high-frequency variability of $\sim$0.1 to

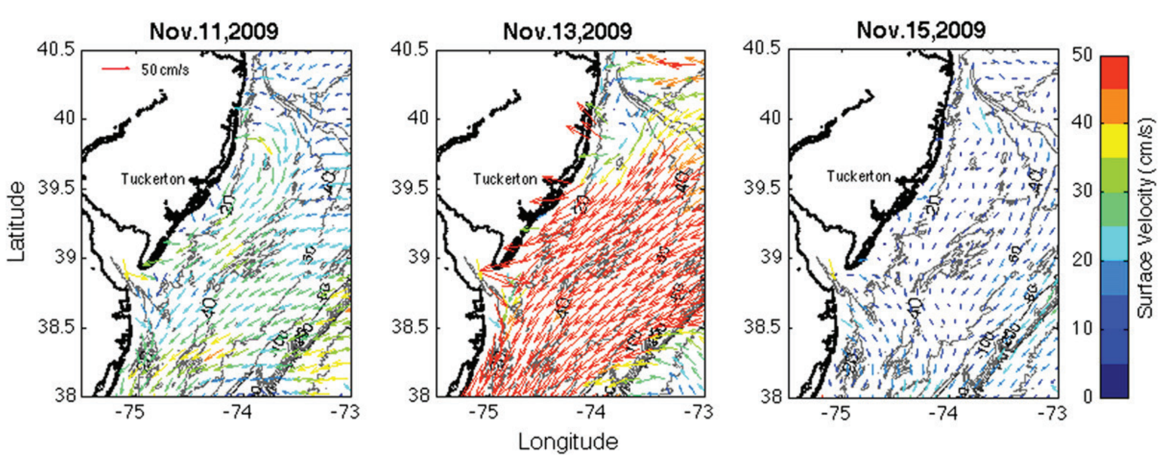

Fig. 6. Daily averaged CODAR surface currents for the New Jersey shelf for November 11th 13th and the 15th. Black contours represent bottom topography in units of meters.

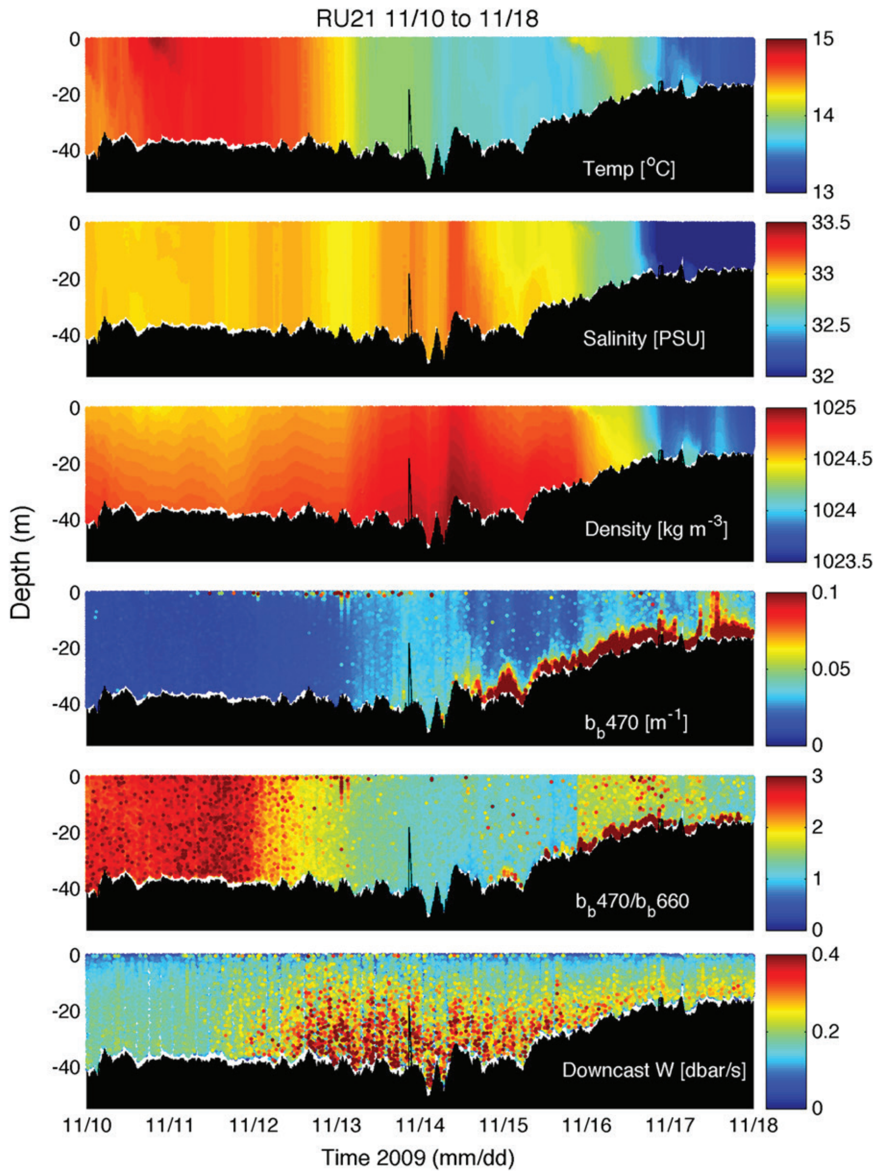

Fig. 7. RU21 during and post-storm cross-sections of temperature, salinity, density, b_b470, b_b470/b_b660 and downcast glider vertical velocities.

$0.2\ \mathrm{m\,s^{-1}}$ through the entire water column. These vertical velocity variations persisted through the 14th until they were restricted to a bottom layer and eventually relaxed after the 16th. As the magnitude of vertical velocities increased, temperatures cooled to 14 °C, salinity was elevated above 33 PSU and $1025\ \mathrm{kg\,m^{-1}}$ density water was raised to the surface. Values of b_b470 of $\sim 0.05\ \mathrm{m^{-1}}$ were evident throughout the water column on the 13th. The enhanced particle load remained suspended until the afternoon of the 14th. Optical backscatter spectral ratios changed from 3 to 1 as Nor'Ida impacted the region, reflecting a flattening of the backscatter spectra consistent with changes in either particle type and/or particle size in the water-column (Boss et al., 2004).

Previous studies have clearly defined the Rouse profile above the wave boundary layer (Glenn et al., 2008; Styles and Glenn, 2000; Glenn and Grant, 1987) as

$$C(z) = C(z_r)\left[\frac{z}{z_r}\right]^{[-\gamma w_f/\kappa u_*]} \quad (1)$$

where $C(z)$ is the concentration profile varying with depth z, $C(z_r)$ is the concentration at the reference height z_r, γ is a constant ratio of eddy diffusivities between momentum and mass, κ is von Karman's constant and u_* is friction velocity. Assuming constant γ (Glenn and Grant, 1987), the slope of $\ln(C(z)/C(z_r))$ to $\ln(z/z_r)$ is proportional to the ratio of the fall velocity, the tendency of sediment to fall out of the water column, to the friction velocity representing the turbulent shear that acts to keep sediment suspended in the water column, or w_f/u_*. In order to identify this ratio, we use optical backscatter as a proxy for sediment concentration similar to Glenn et al. (2008). Optical backscatter profiles were interpolated every 1 m in a reference frame measured from the bottom and averaged over three-hours. These three-hour profiles were then normalized using the backscatter observed at a 3.5 m reference height and plotted as the $\ln(z/z_r)$ *versus* $\ln(b_b(z)/b_b(z_r))$. The 3.5 m reference height ensures all profiles in each three-hour segment have data at this height and above. Normalized backscatter profiles from RU21 (Fig. 8) demonstrated Rouse-like character from the 14th at 04:24 GMT until the

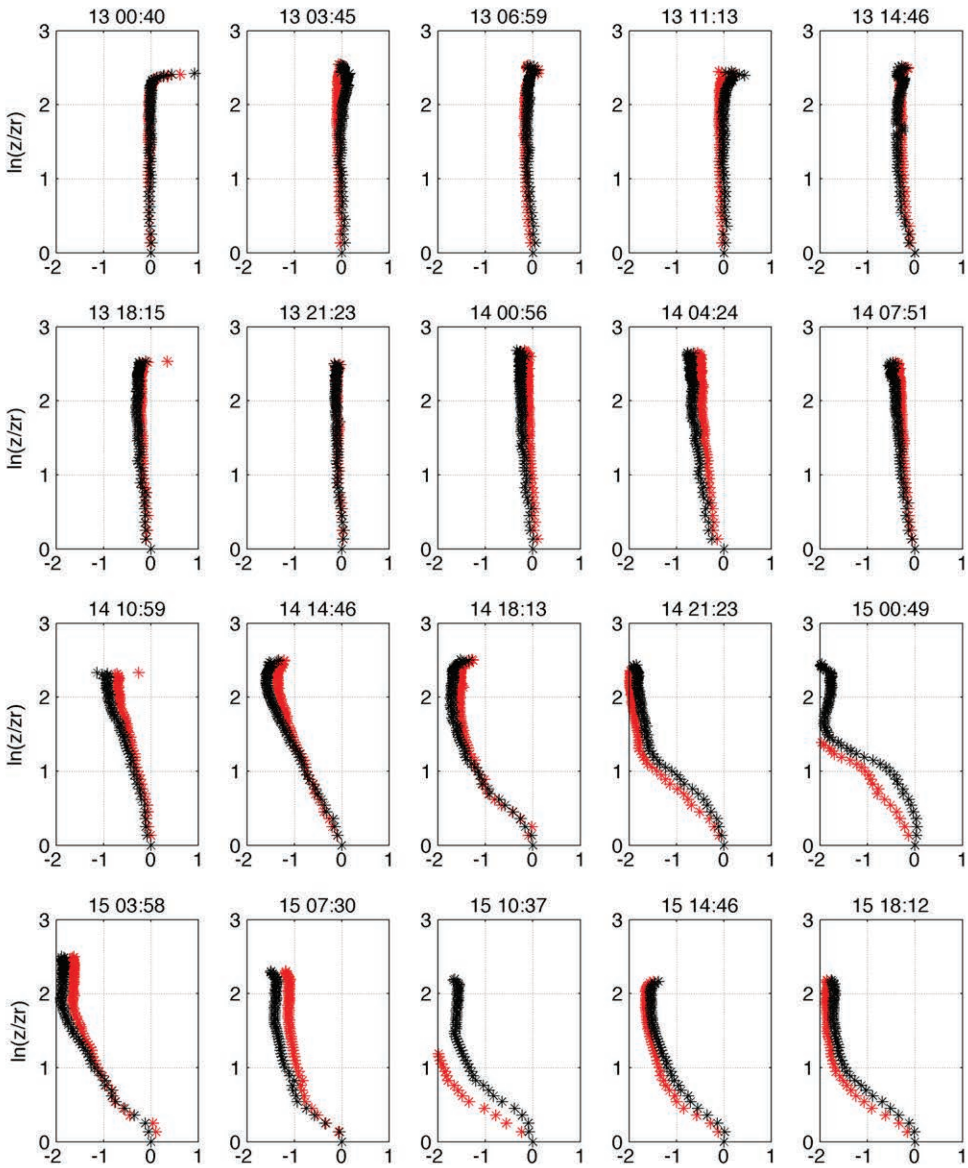

Fig. 8. RU21 log-normalized profiles of optical backscatter at b_b470 (red) and b_b660 (black). *Y*-axis is the natural logarithm of depth divided by z_r, a reference depth of 3.5 m. The *X*-axis is the natural logarithm of optical backscatter, b_b, divided by the optical backscatter at the reference depth b_r or $\ln(b/b_{zr})$. Titles are timestamps of November dd HH:MM.

14th at 21:23 GMT. High near-surface values in rough seas are likely due to bubbles being entrained by breaking waves. Terrill et al. (2001) has observed optical backscatter values of over 0.016 m^{-1} inside bubble clouds.

On November 15th, at approximately 06:00 GMT, RU21 turned onshore and left the 40 m isobath, indicated by the green section of Fig. 2b. As the glider entered the shallow coastal region, temperature, salinity and density remained well-mixed in the vertical while there were horizontal gradients of $\sim$1 °C, $\sim$1.5 PSU and $\sim$1.5 kg m^{-3} respectively (Fig. 7). On the 15th to the 18th a layer of high b_b470, over 0.1 m^{-1}, was apparent, elevated to 10–15 m off the bottom (Fig. 7). Profiles (Fig. 8) show a layer restricted below $\ln(z/z_r) = 1.5$, roughly equivalent to 15 m. The lower layer persists through the remainder of the deployment. Though winds and currents were reduced, wave-heights, wave-periods and bottom orbital velocities remained significantly elevated (Fig. 4). Glider measured vertical velocity variability remained elevated in the near-bottom layer through the 16th (Fig. 7).

3.4. RU05 southern glider storm variability

Between the 10th and 16th of November, RU05 was on a southwestward track along the 40 m isobath (Fig. 3). RU05 turned onshore toward the mouth of the Delaware River on the 16th through the 18th. RU05 cross-sections (Fig. 9) show that on November 10th the water column was initially stratified with relatively cool ($\sim$14 °C) and salty ($\sim$33.5 PSU) bottom water, likely a remnant of the summer cold pool. Cross-sections show that dense bottom water was advected through the lower half of the water column late on the 10th into the 11th. There were periodic bulges of weakly stratified water (0.6–0.2 kg m^{-3}), which grew progressively weaker until the water column was vertically well mixed on the 16th. Similar to RU21, b_b470 was low initially and spectral ratios of b_b470 to b_b660 were $\sim$3. Vertical velocities were initially constant at $\sim$0.3 m s^{-1} and variations of 0.1–0.2 m s^{-1} were apparent during elevated wind, waves and currents. A consistent background b_b470 value of 0.05 m^{-1} is apparent throughout the water column, and near-bottom values

Please cite this article as: Miles, T., et al., Temporal and spatial variability in fall storm induced sediment resuspension on the Mid-Atlantic Bight. Continental Shelf Research (2012), http://dx.doi.org/10.1016/j.csr.2012.08.006

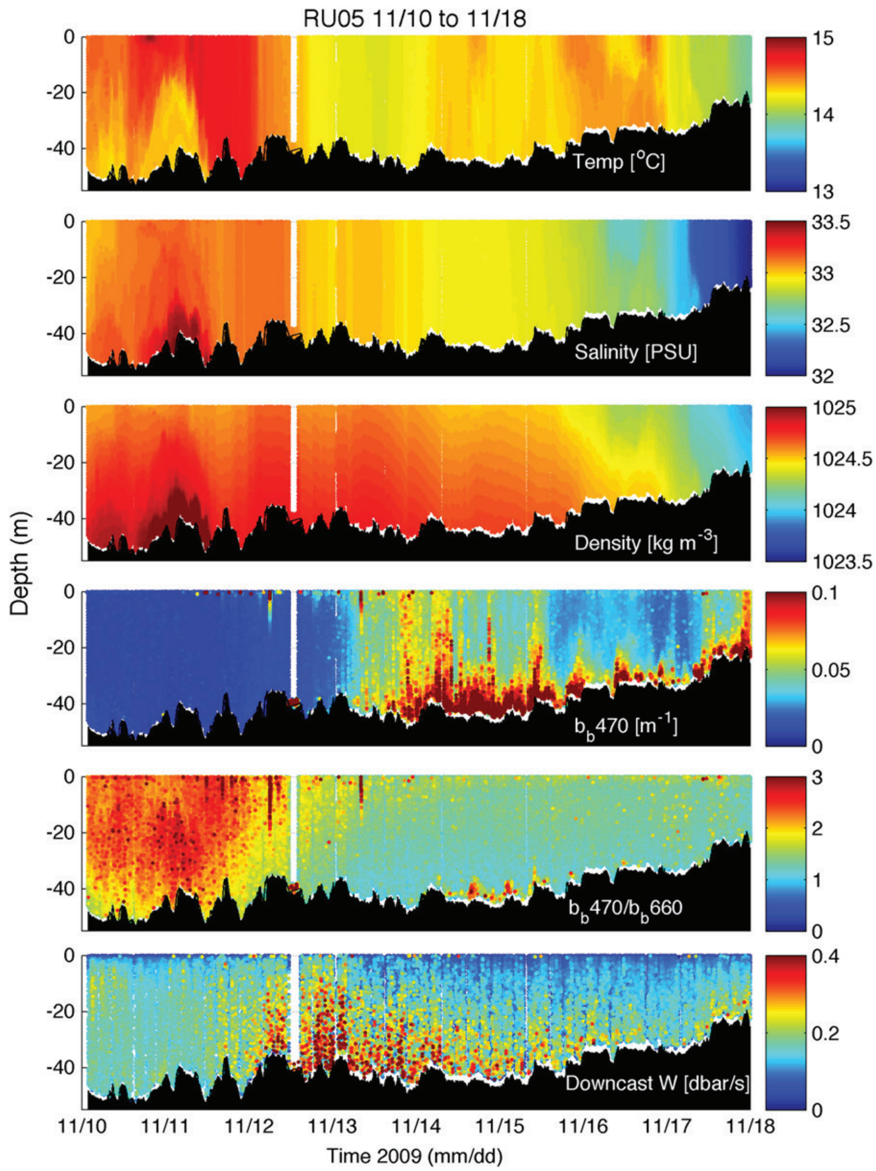

Fig. 9. RU05 cross-section of temperature, salinity, density, b_b470, b_b470/b_b660 and downcast glider vertical velocities.

are near 0.1 m^{-1} until RU05 turns onshore on the 16th. Unlike RU21, there were periodic full water column resuspension events with b_b470 of 0.1 m^{-1} that occur on time-scales less than a day. Similar to RU21, ratios of b_b470 to b_b660 dropped, which indicated changes in either particle type and/or particle size (Boss et al., 2004). Regardless of the periodicity seen in b_b470 cross-sections, the ratios are constant and $\sim$1 after the resuspension event was initiated.

RU05 profiles of optical backscatter (Fig. 10) were calculated in the same manner as for RU21 and for the same duration, from November 13th through the 15th. Reference depth normalized profiles were near 0 until 21:02 GMT on the 13th when the profiles became Rouse-like approximately eight hours earlier than the northern glider, RU21. RU05 then turned onshore toward the Delaware River mouth on the 16th to the 18th (indicated by green in Fig. 3), vertical velocities, winds and currents were reduced, while wave- height, period and orbital velocities remained elevated relative to pre-storm conditions.

3.5. Sediment transport

Three-hourly averaged CODAR surface velocities were compared with approximately three-hourly depth-averaged glider currents (Fig. 11). CODAR velocities are averaged in a 10 km radius of each glider surfacing latitude and longitude. There is a minor temporal and spatial mismatch between glider depth-averaged and CODAR currents as glider currents are averaged over a three-hour subsurface transit obtained by dead reckoning along a compass bearing and comparing the expected glider surfacing location with the actual surfacing location. Depth-averaged currents obtained in this manner have been validated against traditional current measurements from stationary ADCPs (Davis et al., 2003) While we could not obtain any subsurface current structure information directly, by comparing depth-averaged and surface currents, we can make some inferences about how subsurface currents change during the storm.

RU21 and RU05 depth-averaged along-shelf currents both showed similar results when compared with CODAR currents

Please cite this article as: Miles, T., et al., Temporal and spatial variability in fall storm induced sediment resuspension on the Mid-Atlantic Bight. Continental Shelf Research (2012), http://dx.doi.org/10.1016/j.csr.2012.08.006

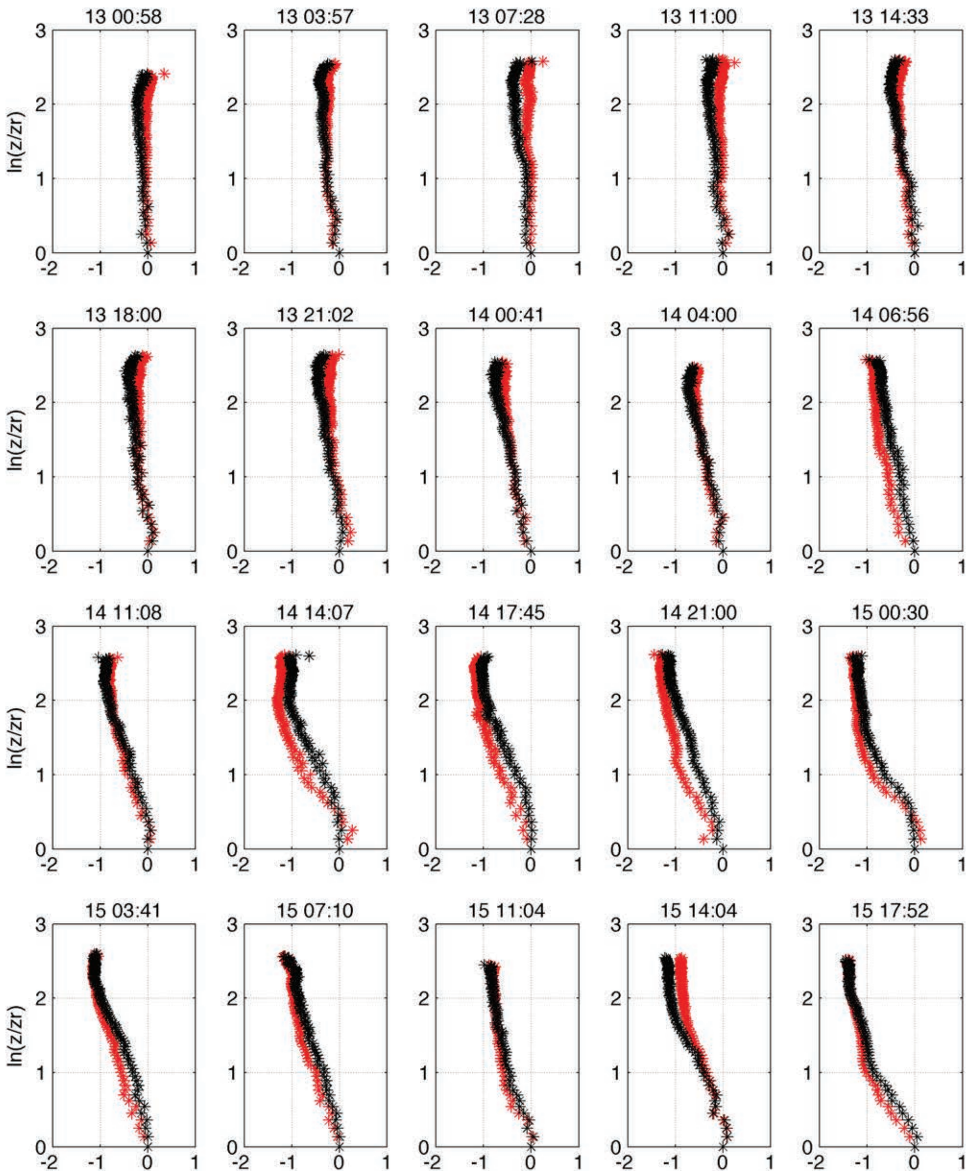

Fig. 10. RU05 log-normalized profiles of b_b470 (red) and b_b660 (black). *Y*-axis is the natural logarithm of depth divided by z_r, a reference depth of 3.5 m. The *X*-axis is the natural logarithm of optical backscatter, b_b, divided by the optical backscatter at the reference depth b_r or $\ln(b/b_{zr})$. Titles are timestamps of November dd HH:MM.

for the duration of each glider deployment. The storm event is easily identifiable in both gliders, which were approximately along the 40 m isobath, between the 10th and 15th, with onshore currents up to 40 cm s^{-1} and alongshore currents toward the southwest of up to 80 cm s^{-1}. Correlation coefficients calculated between glider and CODAR currents for the entire deployment showed a weak correlation in cross-shelf currents of 0.30 for RU05 and 0.33 for RU21. Correlation coefficients in the along-shelf direction were much greater, with values of 0.81 for RU05 and 0.77 for RU21. Correlation coefficients of CODAR and glider comparisons limited to during and after the storm, from the 10th to the 18th, showed that the cross-shelf components increased to 0.44 for RU05 and 0.5 for RU21 and the along-shelf components remained essentially the same at 0.81 for RU05 and 0.84 for RU21. The weak cross-shelf correlation coefficients suggest that deeper currents were initially weaker and not necessarily in the same direction as surface currents. Increased correlation during and after the storm suggest that subsurface currents in the cross-shelf direction either increased in magnitude or aligned more closely with surface currents.

In order to estimate sediment transport magnitude and direction, a time-series of integrated b_b470 was calculated by integrating over depth and segment b_b470 during the RU05 and RU21 deployments and then (Fig. 12). These depth and time integrated plots show elevated values of backscatter that initiated on the 13th and remained elevated through the duration of the storm until the 16th with the southern glider, RU05, showing much larger values during the storm. The northern glider, RU21, had a second peak after the storm, which was approximately double the size of the storm-induced values. Estimated transport was calculated by multiplying the integrated backscatter by the along- and cross-shelf depth-averaged currents reported by the gliders (Fig. 12). Prior to the storm, low sediment concentrations and low currents result in transport near 0 s^{-1}. During the resuspension event, sediment was transported toward the southwest in the along-shelf (Fig. 12) direction for both RU05 and RU21. RU05 showed approximately twice the along-shelf sediment transport as RU21 during the storm. RU05 and RU21 cross-shelf transport was approximately half of the along-shelf transport and in the onshore direction during the storm. Following the storm RU05

Please cite this article as: Miles, T., et al., Temporal and spatial variability in fall storm induced sediment resuspension on the Mid-Atlantic Bight. Continental Shelf Research (2012), http://dx.doi.org/10.1016/j.csr.2012.08.006

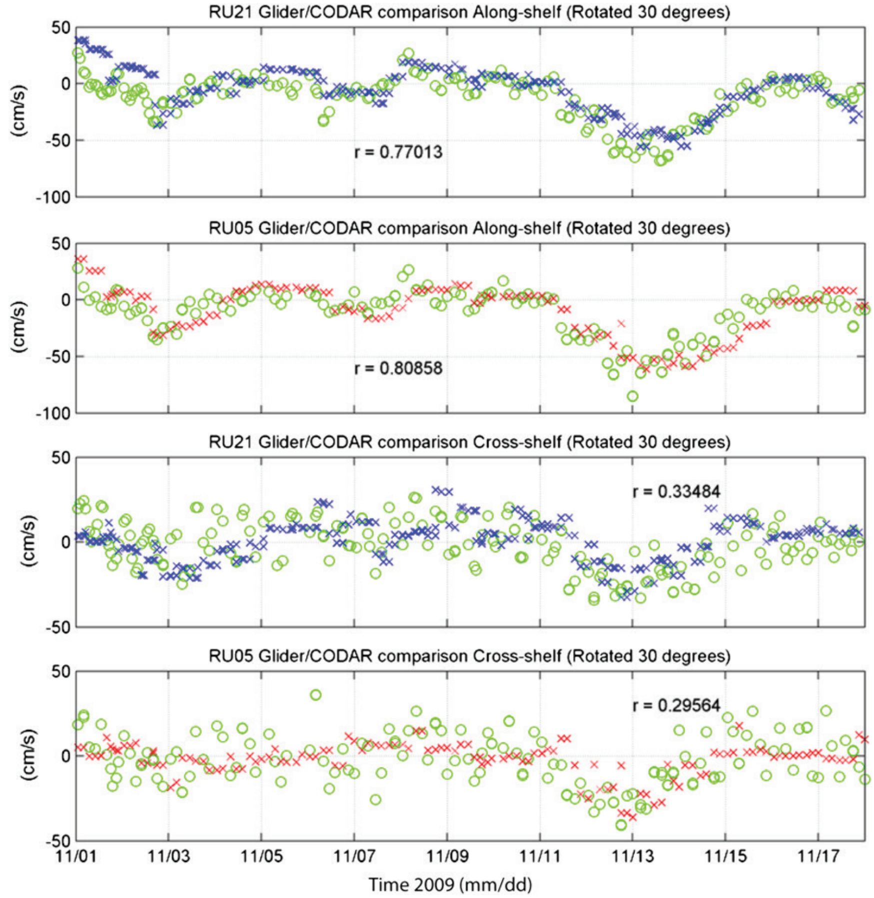

Fig. 11. Along-shelf currents for RU21 and RU05 (Top two panels) and cross-shelf currents for RU21 and RU05 (Bottom two panels) depth averaged glider currents(*x*'s) and along-track 3-hourly averaged CODAR surface currents (*o*'s) rotated clockwise 30 degrees to be in the cross- and along-shelf directions with positive along-shelf currents to the northeast and positive cross-shelf currents to the southeast. Correlation coefficients for the full time-period are displayed as *r*.

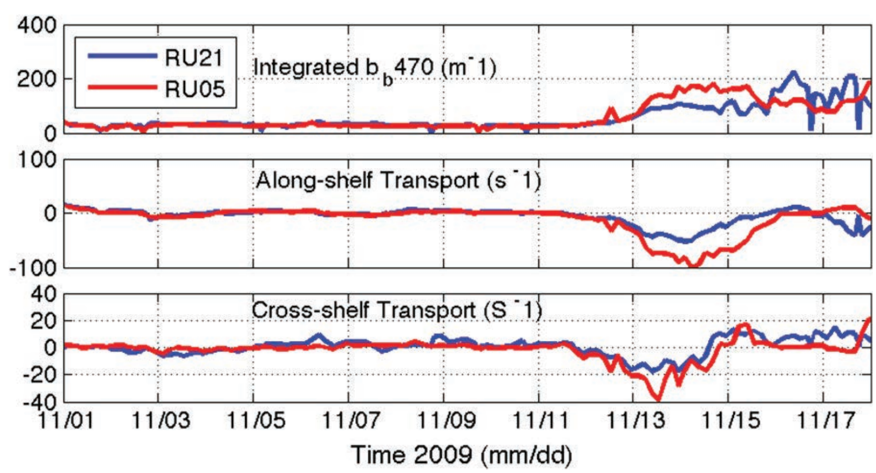

Fig. 12. Time-series of the (blue) RU21 and (red) RU05 (top) three-hour integrated b_b470 (m^{-1}) and estimated transport in the (middle) along- and (bottom) cross- shelf directions. Positive values indicate northeastward transport for along-shelf and southeastward transport for cross-shelf transport. Estimated transport is calculated by multiplying depth-averaged glider currents by integrated optical backscatter at b_b470.

transport was reduced to near $0\,s^{-1}$ when currents and integrated backscatter were both reduced (Fig. 12). RU21 transport shifted to the offshore direction as high b_b470 still remained in the water column (Fig. 12) and current velocities were reduced (Fig. 11) as it approached the coast.

4. Discussion

While many studies have focused on sediment resuspension at a single point on the MAB shelf (Traykovski et al., 1999; Agrawal and Pottsmith, 2000; Harris et al., 2003; Agrawal,

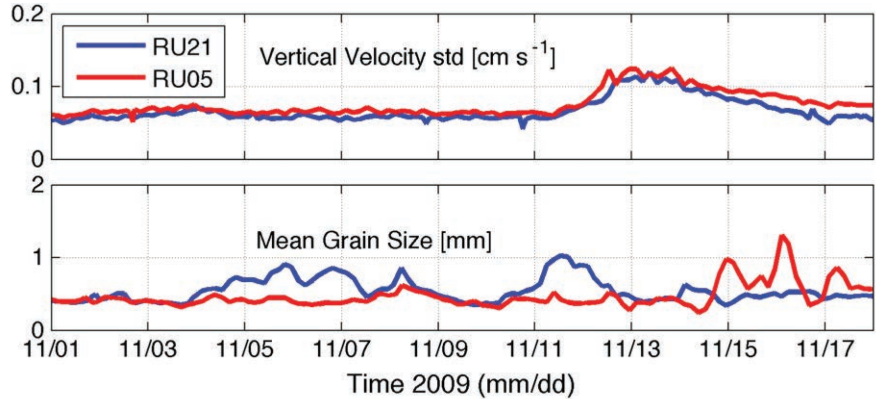

Fig. 13. Time-series of the (blue) RU21 and (red) RU05 (top) three-hour segment standard deviation of vertical velocity (cm s^{-1}) and (bottom) mean bed grain-size from Fig. 1 interpolated to the along-track glider positions.

2005; Traykovski, 2007; Cacchione et al., 2008) few observational studies have focused on the shelf-wide spatial variability of these processes. We were fortunate to have several gliders deployed to assess the spatial variability of sediment resuspension on the MAB during the Nor'Ida fall transition storm (Schofield et al., 2010b). The two gliders equipped with optical sensors, separated by ~50 km at the onset of storm conditions, documented the initiation of sediment resuspension through the increases in optical backscatter. Just like the two gliders, buoys 44009 and 44025 (separated by 230 km) showed similar characteristics, with a 1-day lag in peak values, through the initiation of elevated storm winds and waves. Despite the separation distances, along-shelf transport toward the southwest was a ubiquitous feature of both glider deployments with a lag in resuspension of approximately eight hours. With a separation distance of ~50 km this lag is on the same order as the lag seen in peak storm conditions at buoys 44025 and 44009. Peak sediment transport was associated with a combination of a maximum in suspended sediment concentration and high relative along-shelf southwestward currents. The nearly coincident maximum in sediment transport suggests that along-shelf transport is a common feature of the entire NJ shelf and MAB and is consistent with previous modeling studies (*e.g.* Keen and Glenn, 1995). The event duration is longer than the temporal lag between the southern and northern gliders so the large-scale storm effectively forces the shelf as a whole and there is little spatial variability in the timing of resuspension and transport as a result of storm passage.

While resuspension and transport occurred with an approximately eight hour lag, the strength of resuspension and transport varied by as much as a factor of two in the along-shelf direction, with higher transport associated with RU05 located on the southern NJ shelf. The major difference in sediment resuspension, and consequent transport, was related to the numerous discrete resuspension events that resulted in high sediment concentrations up into the water-column during the storm. The difference in the scale and frequency of resuspension events over spatial scales much smaller than the storm event points out the importance of local processes, which affect the magnitude of sediment resuspension and transport. Previous work by Styles and Glenn (2005); Keen and Glenn (1995); Gargett et al. (2004) have highlighted tidal forcing, topographic variations and Langmuir cells as potential processes affecting sediment resuspension and transport on time-periods shorter than a day. For both gliders, vertical velocity variability appeared random rather than spatially banded (Figs. 7 and 9), indicating that Langmuir cells were not likely the cause of the suspended sediment spatial heterogeneity. RU21 and RU05 were both flying approximately southwestward along the 40 m isobath during elevated winds, currents and waves therefore topography was essentially constant during the resuspension event (Figs. 7 and 9). RU21 did not experience fluctuations of sediment resuspension or transport on time-scales shorter than a day after the resuspension event was initiated, thus tidal forcing was not likely a dominant modulation process as in Keen and Glenn (1995). The scale of tidal forcing on the shelf is also much larger than the separation distance between the gliders; therefore variability seen in RU05 on shorter time-scales is likely not related to tidal fluctuations.

Glenn et al. (2008) suggested that in the absence of stratification, turbulence in the combined wind-driven surface layer and wave-enhanced bottom boundary layer is responsible for sediment resuspension upward through the water column, but observations were sparse. During the Nor'Ida storm there was a distinct change in vertical glider velocities, which serves as evidence of turbulence in the water column. The standard deviation of each three-hour glider segment for RU21 and RU05 vertical velocities show a distinct increase in vertical velocity variability beginning on the morning of the 12th and persisting through the 16th (Fig. 12). These fluctuations in the glider's vertical velocity serve as an estimate of the turbulent motions due to high storm-induced current-shear, similar to neutrally buoyant lagrangian floats used in Harcourt and D'Asaro (2010). Vertical velocity standard deviation values were approximately the same for RU05 and RU21. Uniform vertical velocity standard deviations suggest that the vertical component of turbulence was similar between the northern and southern portions of the NJ shelf, which is consistent with the scale of the storm and the uniform winds, waves and currents.

With little variability in turbulent vertical velocities between gliders, the differences in bed grain size likely play a major role in modulating the magnitude of resuspension by storm-induced turbulence. In order to assess the importance of local variability in grain size we interpolate mapped values (Goff et al., 2008; Reid et al., 2005) plotted in Fig. 1 to glider latitude and longitude. The resulting time-series (Fig. 13) shows mean grain size below the gliders throughout the deployment. The time-series shows mean grain sizes ranged from ~0.3 to ~1.4 mm with largest grain sizes seen by RU05 after storm passage, when it turned into the mouth of the Delaware. RU21 passed over a region of over 1 mm grain sizes between the 11th and 13th, after storm initiation but prior to peak conditions. The map in Fig. 1 shows a patch of coarse sediment along the northern portion of the NJ shelf where RU21 was flying and relatively smaller grain sizes in the along-shelf region where RU05 sampled, prior to turning in toward Delaware Bay. During the resuspension events on the 13th through the 15th, RU05 was located over a patch of sand with a mean grain size of 0.3 mm–0.4 mm (Fig. 13) before flying through a region

Please cite this article as: Miles, T., et al., Temporal and spatial variability in fall storm induced sediment resuspension on the Mid-Atlantic Bight. Continental Shelf Research (2012), http://dx.doi.org/10.1016/j.csr.2012.08.006

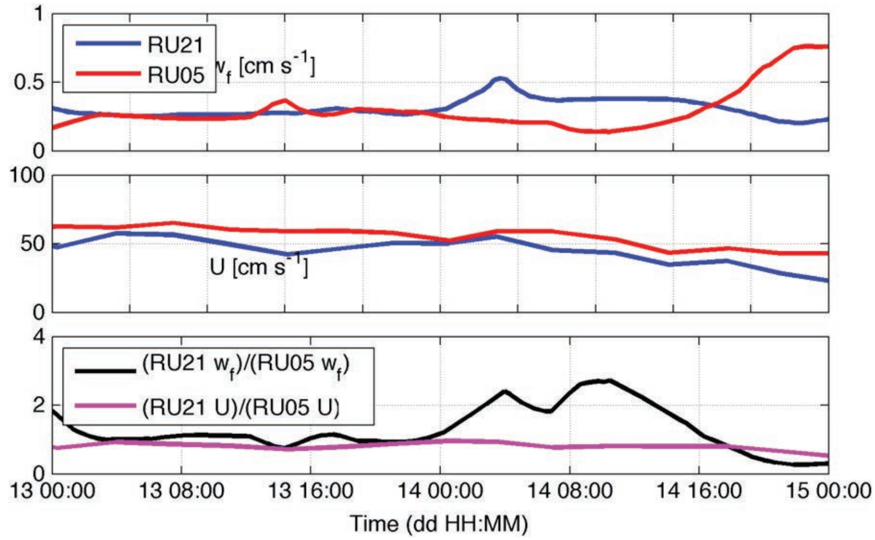

Fig. 14. Time-series of (top) estimated fall velocities for (blue) RU21 and (red) RU05, (middle) magnitude of depth-averaged currents for (blue) RU21 and (red) RU05, and (bottom) the ratio of (black) RU21 to RU05 fall velocities and (magenta) depth-averaged currents, all during the resuspension event.

with mean grain size of over 0.8 mm on the 15th. Conversely, RU21 was in a region with mean grain sizes from 0.4 mm to 0.6 mm on the 13th through 14th. On the 15th RU21 entered a region of reduced mean grain size of $\sim$0.3 m^{-1}.

A study by Agrawal and Pottsmith (2000) as part of the LEO-15 project, which took place within a few kilometers of the deployment location of RU05 and RU21, developed a local model for the fall velocity: $w_{f,n} = 0.45 \times 10^{-3} a_n^{1.2}$ where a_n is the radius in microns and w_f is the settling velocity in cm s^{-1}. As mentioned previously fall velocity is essentially the tendency of sediment to fall out of concentration and u_* is the tendency for particles to remain in suspension. Following the above equation we calculate fall velocities for the sediment grain sizes mapped below the glider during the resuspension event on the 13th through 15th (Fig. 14). Fall velocities are initially greater for RU21 at the peak of the storm, and initiation of the resuspension event at midnight on November 13th. As the gliders progress fall velocities are approximately equal for RU21 and RU05 until the 14th when RU21 fall velocities increase and RU05 fall velocities decrease. While we use the standard deviation of glider vertical velocities as a relative approximation of the timing of turbulent motions, these values are not sufficient to directly substitute for values of u_*. Lentz et al. (1999) uses depth-averaged velocities to estimate bottom stress τ_b. If we follow this model and subsequently calculate a depth-averaged representative friction velocity then we would see u_* values proportional to glider velocities. A time-series of depth-averaged velocities during the storm event are shown in Fig. 14. RU05 depth-averaged velocities are $\sim$5–10 cm/s greater than RU21 through the 13th and are approximately equal on the 14th. As our depth-averaged velocities are only proportional to friction velocity we cannot calculate a direct ratio of w_f/u_*.

For comparison, we calculated the ratio of RU21 to RU05 estimated fall velocities between the two gliders as well as the ratio of RU21 to RU05 depth-averaged glider velocities, which should be approximately equal to the ratio of friction velocities (Fig. 14). Fall velocity ratios were initially high, similar to RU21 fall velocities and grain-size. From 4:00 to 22:00 GMT on the 13th fall velocity ratios are near one. On the 14th the RU21 to RU05 fall velocity ratio increased by over a factor of two, until they drop again late on the 14th as the gliders began to turn onshore. The ratio of RU21 to RU05 depth-averaged glider velocities was just below one for the duration of the resuspension event on November 13th through the 14th. Calculated standard deviations of RU21 to RU05 fall velocities and depth-averaged glider velocities are 0.62 and 0.08 respectively. The much larger standard deviation in the estimated fall velocity ratio shows that differences in grain size and subsequently fall velocity plays a larger role than current variability in the resuspension and transport dynamics during this storm event. Comparison of our fall velocity ratio to slopes of optical backscatter profiles in Figs. 8 and 9 for RU21 and RU05 respectively, show that profiles were Rouse-like throughout the water column for the 13th and 14th for RU05. These profiles are indicative of full water column resuspension of relatively smaller particles, which remained in suspension for the duration of the event. Optical backscatter profiles from RU21 were much more vertical than RU05 until mid-day on the 14th when resuspension peaked throughout the water column. Later on the 14th and into the 15th profiles of RU21 optical backscatter demonstrated a near bottom layer, which along with fall velocities indicates that larger particles were falling out of suspension or unable to make it into the upper portion of the water column. The differences in grain size and resuspension characteristics from the northern glider, RU21 and southern glider RU05 show that even during the largest storms local variability in bed characteristics can play a major role in modulating sediment resuspension and subsequently transport on the continental shelf. Our study demonstrates that during storms on the continental shelf, variability in bottom character also drives local variability in the magnitude and direction of sediment transport. Through glider spatial surveys of sediment transport and resuspension, we have shown that detailed spatial surveys and continually updated spatial maps similar to those produced by Goff et al. (2008) may be necessary to fully understand water-column sediment transport. These spatial surveys will not only support further understanding of observational data over shelf-wide spatial scales, but can also be used to quantitatively enhance realistic regional sediment resuspension and transport models.

5. Conclusion

Here we have demonstrated the importance of utilizing novel ocean observation technology, such as gliders and CODAR to resolve shelf-scale resuspension and transport during storms. A fleet of autonomous gliders not only provided information on sediment transport and resuspension over large spatial areas, but

Please cite this article as: Miles, T., et al., Temporal and spatial variability in fall storm induced sediment resuspension on the Mid-Atlantic Bight. Continental Shelf Research (2012), http://dx.doi.org/10.1016/j.csr.2012.08.006

also emphasized the importance of local variability in grain-size on estimates of shelf-wide sediment resuspension and transport, even in the largest storms. With little observed influence from tides, Langmuir cells or topography, the simple balance between turbulent shear stress and fall velocity, which varies with grain-size, played a major role in observed differences in sediment resuspension and transport along the mid-shelf. Future inclusion of glider fleets and CODAR networks along with traditional tripod and buoy instrumentation will allow for a more holistic view of sediment transport and resuspension along continental shelves, during storm events in particular, when shipboard measurements are not possible. These data will also aid in developing more robust regional models by feeding real data into predictive models as storms occur. In order to further understand the dynamics of sediment resuspension and transport on shelf-wide scales, the inclusion of acoustic and holographic sensors in addition to optical sensors on glider platforms will be necessary. This will help to accurately identify the nature of suspended particles when sediment bed information is lacking and will also provide more *in situ* information regarding the magnitude and direction of current profiles and transport during storm events.

Acknowledgments

Data used in this study was acquired by the Rutgers University Coastal Ocean Observation Lab (R.U.COOL) and NOAA. R.U.COOL is supported by ONR, NOAA, IOOS, NSF, DHS, DoD, NASA, NOPP and the State of New Jersey. Glider data for this study came from a deployment for the NSF Ocean Observing Initiative as part of a Cyber Infrastructure Implementing Organization testbedding activity. We would also like to thank Teledyne-Webb Research for graduate student support and continued technical support. The Mid-Atlantic Bight High Frequency Radar network is funded by IOOS. This work was supported by ONR MURI grant number N000140610739, NOAA MARCOOS grant numbers NA07NOS4730221 and NA01NOS4730014 and NSF OOI NSF OCE 10307201 1/1.

References

Agrawal, Y.C., 2005. The optical volume scattering function: temporal and vertical variability in the water column off the New Jersey coast. Limnology and Oceanography 50, 1787–1794.

Agrawal, Y.C., Pottsmith, H.C., 2000. Instruments for particle size and settling velocity observations in sediment transport. Marine Geology 168, 89–114.

Amato, 1994. Sand and Gravel Maps of the Atlantic Continental Shelf. In: Service, M.M. (Ed.). OCS Monograph MMS, p. 35.

Barrick, D.E., 1971a. Theory of HF and VHF propagation across the rough sea, 1, the effective surface impedance for a slightly rough highly conducting medium at grazing incidence. Radio Science 6, 517–526.

Barrick, D.E., 1971b. Theory of HF and VHF propagation across the rough sea, 2, application to HF and VHF propagation above the sea. Radio Science 6, 527–533.

Beardsley, R.C., Boicourt, W.C., 1981. On estuarine and continental-shelf circulation in the middle Atlantic Bight. In: Warren, B.A., Wunsch, C. (Eds.), Evolution of Physical Oceanography. MIT Press, Cambridge, MA, pp. 198–241.

Bigelow, H.B., 1933. Studies of the waters on the continental shelf, Cape Cod to Chesapeake Bay. I. The cycle of temperature. Papers in Physical Oceanography and Meteorology 2, 1–135.

Boss, E., Pegau, W.S., Lee, M., Twardowski, M., Shybanov, E., Korotaev, G., Baratange, F., 2004. Particulate backscattering ratio at LEO 15 and its use to study particle composition and distribution. Journal of Geophysical Research 109, C01014.

Cacchione, D.A., Thorne, P.D., Agrawal, Y., Nidzieko, N.J, 2008. Time-averaged near-bed suspended sediment concentrations under waves and currents: comparison of measured and model estimates. Continental Shelf Research 28, 470–484.

Chang, G.C., Dickey, T.D., Williams III, A.J., 2001. Sediment resuspension over a continental shelf during Hurricanes Edouard and Hortense. Journal of Geophysical Research 106, 9517–9531.

Chapman, R.D., Graber, H.C., 1997. Validation of HF radar measurements. Oceanography 10, 76–79.

Chen, K., He, R., 2010. Numerical investigation of the Middle Atlantic Bight shelfbreak frontal circulation using a high-resolution ocean hindcast model. Journal of Physical Oceanography 40, 949–964.

Davis, R.E., Eriksen, C.E., Jones, C.P., 2003. Autonomous buoyancy driven underwater gliders. In: Griffiths, G. (Ed.), Technology and applications of autonomous underwater vehicles. Taylor & Francis, New York, pp. 37–58.

Dzwonkowski, B., Kohut, J.T., Yan, X.-H., 2009a. Seasonal differences in wind-driven across-shelf forcing and response relationships in the shelf surface layer of the central Mid-Atlantic Bight. Journal of Geophysical Research 114, C08018.

Dzwonkowski, B., Kohut, J.T., Yan, X.-H., 2009b. Sub-inertial characteristics of the surface flow field over the shelf of the central Mid-Atlantic Bight. Continental Shelf Research 29, 1873–1886.

Gargett, A., Wells, J., Tejada-Martinez, A.E., Grosch, C.E., 2004. Langmuir supercells: a mechanism for sediment resuspension and transport in shallow seas. Science 306, 1925–1928.

Glenn, S., Arnone, R., Bergmann, T., Bissett, W.P., Crowley, M., Cullen, J., Gryzmski, J., Haidvogel, D., Kohut, J., Moline, M., Oliver, M., Orrico, C., Sherrell, R., Song, T., Weidemann, A., Chant, R., Schofield, O., 2004. Biogeochemical impact of summertime coastal upwelling on the New Jersey shelf. Journal of Geophysical Research 109, C12S02.

Glenn, S., Clayton, J., Twardowski, M., Bowers, L., Kerfoot, J., Kohut, J., Webb, D., Schofield, O., 2008. Glider observations of sediment resuspension in a Middle Atlantic Bight Fall transition storm. Limnology and Oceanography 53, 2180–2196.

Glenn, S., Schofield, O., 2009. Growing a distributed ocean observatory: Our view from the COOLroom. Oceanography 22, 112–129.

Glenn, S.M., Grant, W.D., 1987. A suspended sediment stratification correction for combined wave and current flows. Journal of Geophysical Research 92, 8244–8264.

Goff, J.A., Jenkins, C.J., Jeffress Williams, S., 2008. Seabed mapping and characterization of sediment variability using the usSEABED data base. Continental Shelf Research 28, 614–633.

Gong, D., Kohut, J.T., Glenn, S.M., 2010. Seasonal climatology of wind-driven circulation on the New Jersey shelf. Journal of Geophysical Research 115, C04006.

Grant, W.D., Madsen, O.S., 1979. Combined wave and current interaction with a rough bottom. Journal of Geophysical Research 84, 1797–1808.

Grant, W.D., Madsen, O.S., 1986. The continental-shelf bottom boundary layer. Annual Review of Fluid Mechanics 18, 265–305.

Harcourt, R.R., D'Asaro, E.A., 2010. measurement of vertical kinetic energy and vertical velocity skewness in oceanic boundary layers by imperfectly Lagrangian floats. Journal of Atmospheric Oceanic Technology 27, 1918–1935 〈http://dx.doi.org/proxy.libraries.rutgers.edu/10.1175/2010JTECHO731.1〉.

Harris, C.K., Butman, B., Traykovski, P., 2003. Winter-time circulation and sediment transport in the Hudson Shelf Valley. Continental Shelf Research 23, 801–820.

Houghton, R.W., Schlitz, R., Beardsley, R.C., Butman, B., Chamberlin, J.L., 1982. The Middle Atlantic Bight cold pool: evolution of the temperature structure during summer 1979. Journal of Physical Oceanography 12, 1019–1029.

Keen, T.R., Glenn, S.M., 1995. A coupled hydrodynamic-bottom boundary layer model of storm and tidal flow in the Middle Atlantic Bight of North America. Journal of Physical Oceanography 25, 391–406.

Kohut, J.T., Roarty, H.J., Glenn, S.M., 2006. Characterizing observed environmental variability With HF Doppler Radar Surface Current Mappers and Acoustic Doppler Current Profilers: environmental variability in the coastal ocean. IEEE Journal of Oceanic Engineering 31, 876–884.

Lentz, S., Guza, R.T., Elgar, S., Feddersen, F., Herbers, T.H.C., 1999. Momentum balances on the North Carolina inner shelf. Journal of Geophysical Research 104, 18205–18226.

Lentz, S.J., 2003. A climatology of salty intrusions over the continental shelf from Georges Bank to Cape Hatteras. Journal of Geophysical Research 108, 3326.

Lentz, S.J., 2008. Seasonal variations in the circulation over the Middle Atlantic Bight continental shelf. Journal of Physical Oceanography 38, 1486–1500.

McBride, R.A., Moslow, T.F., 1991. Origin, evolution, and distribution of shoreface sand ridges, Atlantic inner shelf, U.S.A. Marine Geology 97, 57–85.

Ohlmann, C., White, P., Washburn, L., Terrill, E., Emery, B., Otero, M., 2007. Interpretation of coastal HF Radar-derived surface currents with high-resolution drifter data. Journal of Atmospheric & Oceanic Technology 24, 666–680.

Reid, J.M., Reid, J.A., Jenkins, C.J., Hastings, M.E., Williams, S.J., Poppe, L.J., 2005. usSEABED: Atlantic coast offshore surficial sediment data release. U.S. Geological Survey Data Series, 1st ed.

Roarty, H., Glenn, S., Kohut, J., 2010. Operation and application of a regional high-frequency radar network in the Mid-Atlantic Bight. Marine Technology Society Journal 44, 133–145.

Roesler, C.S., Boss, E., 2008. In situ measurement of the inherent optical properties (IOPs) and potential for harmful algal bloom (HAB) detection and coastal ecosystem observations, Chapter 5. In: Babin, M., Roesler, C.S., Cullen, J. (Eds.), Real-Time Coastal Observing Systems for Marine Ecosystem Dynamics and Harmful Algal Blooms: Theory, Instrumentation and Modeling; UNESCO, pp. 153–206.

Schofield, O., Glenn, S., Orcutt, J., Arrott, M., Meisinger, M., Gangopadhyay, A., Brown, W., Signell, R., Moline, M., Chao, Y., Chien, S., Thompson, D., Balasuriya, A., Lermusiaux, P., Oliver, M., 2010a. Automated sensor network to advance ocean science. Eos Transactions, American Geophysical Union 91 (39), 345–356.

Schofield, O., Kohut, J., Aragon, D., Creed, L., Graver, J., Haldeman, C., Kerfoot, J., Roarty, H., Jones, C., Webb, D., Glenn, S., 2007. Slocum gliders: robust and ready. Journal of Field Robotics 24, 473–485.

Schofield, O., Kohut, J., Glenn, S., Morell, J., Capella, J., Corredor, J., Orcutt, J., Arrott, M., Krueger, I., Meisinger, M., Peach, C., Vernon, F., Chave, A., Chao, Y., Chien, S., Thompson, D., Brown, W., Oliver, M., Boicourt, W., 2010b. A regional slocum glider network in the Mid-Atlantic Bight leverages broad community engagement. Marine Technology Society Journal 44, 185–195.

Stewart, R.H., Joy, J.W., 1974. HF radio measurements of surface currents. Deep Sea Research and Oceanographic Abstracts 21, 1039–1049.

Styles, R., Glenn, S.M., 2000. Modeling stratified wave-current bottom boundary layers for the continental shelf. Journal of Geophysical Research 105, 24119–24139.

Styles, R., Glenn, S.M., 2002. Modeling bottom roughness in the presence of wave-generated ripples. Journal of Geophysical Research 107, 3110.

Styles, R., Glenn, S.M., 2005. Long-term sediment mobilization at a sandy inner shelf site, LEO-15. Journal of Geophysical Research 110, C04S90.

Swift, D.J.P., Field, M.E., 1981. Evolution of a classic sand ridge field: Maryland sector, North American inner shelf. Sedimentology 28, 461–482.

Teague, C.C., 1971. High Frequency Resonant Scattering Techniques for the Observation of Directional Ocean-Wave Spectra, Calif. Stanford University, Palo Alto.

Terrill, E.J., Melville, W.K., Stramski, D., 2001. Bubble entrainment by breaking waves and their influence on optical scattering in the upper ocean. Journal of Geophysical Research 106, 16815–16823.

Traykovski, P., 2007. Observations of wave orbital scale ripples and a nonequilibrium time-dependent model. Journal of Geophysical Research 112, C06026.

Traykovski, P., Hay, A.E., Irish, J.D., Lynch, J.F., 1999. Geometry, migration, and evolution of wave orbital ripples at LEO-15. Journal of Geophysical Research 104, 1505–1524.

Twardowski, M.S., Boss, E., Macdonald, J.B., Pegau, W.S., Barnard, A.H., Zaneveld, J.R.V., 2001. A model for estimating bulk refractive index from the optical backscattering ratio and the implications for understanding particle composition in case I and case II waters. Journal of Geophysical Research 106, 14129–14142.

Wiggert, J.D., Jones, B.H., Dickey, T.D., Brink, K.H., Weller, R.A., Marra, J., Codispoti, L.A., 2000. The Northeast monsoon's impact on mixing, phytoplankton biomass and nutrient cycling in the Arabian Sea. Deep Sea Research Part II: Topical Studies in Oceanography 47, 1353–1385.

Xu, Y., Chant, R., Gong, D., Castelao, R., Glenn, S., Schofield, O., 2011. Seasonal variability of chlorophyll a in the Mid-Atlantic Bight. Continental Shelf Research 31, 1640–1650.

Zedler, S.E., Dickey, T.D., Doney, S.C., Price, J.F., Yu, X., Mellor, G.L., 2002. Analyses and simulations of the upper ocean's response to Hurricane Felix at the Bermuda Testbed Mooring site 13–23 August 1995. Journal of Geophysical Research 107, 3232.

Please cite this article as: Miles, T., et al., Temporal and spatial variability in fall storm induced sediment resuspension on the Mid-Atlantic Bight. Continental Shelf Research (2012), http://dx.doi.org/10.1016/j.csr.2012.08.006

Phytoplankton dynamics and bottom water oxygen during a large bloom in the summer of 2011

Oscar Schofield, Hugh Roarty, Grace Saba, Xu Yi, Josh Kohut, Scott Glenn
Coastal Ocean Observation Lab, Rutgers University, New Brunswick, NJ 08901
oscar@marine.rutgers.edu, roarty@marine.rutgers.edu, saba@marine.rutgers.edu, xuyi@marine.rutgers.edu, kohut@marine.rutgers.edu, glenn@marine.rutgers.edu

John Manderson
James J. Howard Marine Sciences Laboratory
Northeast Fisheries Science Center
74 Magruder Road, Sandy Hook, Highlands, NJ, 07732
John.Manderson@NOAA.gov

Matthew Oliver
School of Marine Science and Policy
College of Earth, Ocean and Environment,
University of Delaware,
700 Pilottown Rd. Lewes, DE, 19958
moliver@udel.edu

***Abstract*— During the summer of 2011 a large phytoplankton bloom occurred off the New Jersey coast, which was monitored using an existing ocean observatory. There was public concern about the root causes of the phytoplankton bloom and whether it reflected anthropogenic loading of nutrients from the Hudson River or whether it reflected coastal upwelling. We used the MARACOOS network to determine what were the likely drivers of the phytoplankton bloom. The bloom was studied using satellites, HF radar, a Hydroid REMUS and Webb Slocum gliders. Chlorophyll concentrations were over an order of magnitude larger than the decadal mean of ocean color data and the bloom was initiated by upwelling winds throughout the month of July that continued to dominate the wind patterns until the passage of Hurricane Irene. The high concentrations of phytoplankton resulted in the supersaturated oxygen values in the surface waters; however the flux of organic matter resulted in oxygen saturation values of <60% in the coastal bottom waters, which is sufficient to stress benthic communities in the MAB. Discrete samples identified the bloom was dominated by mixed assemblages of motile dinoflagellates. The passage of Hurricane Irene increased the oxygen saturation at depth by close to 20%, but was not sufficient to terminate the bloom. A re-analysis of the CODAR clearly indicated that the shelf wide bloom most likely originated from nearshore the New Jersey coast. Upwelling provided the source water that fueled the bloom. Alternating winds transported the bloom offshore and across the Mid-Atlantic Bight. This is consistent with past studies that observed regions of recurrent hypoxia on the New Jersey inner shelf are more related to coastal upwelling than riverine inputs.**

***Index Terms*—ocean observatories, hypoxia/anoxia, phytoplankton blooms**

I. Introduction

A widespread decline in bottom dissolved oxygen (DO) levels to hypoxic/anoxic conditions impacted nearly the entire New Jersey continental shelf in 1976, resulted in significant economic losses in shell-fishing and related industries [1, 2]. It was driven by a causal series of events that included large runoff during a warm winter resulting in early stratification of the shelf, followed by the development of a strong deep summer thermocline during an unusually hot summer, persistent southerly winds with fewer than usual storms, a large phytoplankton bloom with low grazing by zooplankton, and respiration and decomposition of the bloom below the seasonal thermocline. The source of the nutrients fueling the bloom was the major question. The initiation of coastal monitoring conducted in response to the 1976 event focused on the working hypothesis that the major source of nutrients was due to anthropogenic loading from urbanized riverine inputs [3]. An alternative hypothesis was posited by Glenn et al. [4], that regions of recurrent hypoxia on the New Jersey inner shelf were more related to coastal upwelling than riverine inputs of nutrients. The largest variations in ocean temperatures along the New Jersey coast, other than seasonal, are due to episodic summertime upwelling events driven by topographic variations associated with ancient river deltas that cause upwelled water to evolve into an alongshore line of recurrent upwelling centers [5]. These centers are co-located with historical regions of low dissolved oxygen [4].

In summer 2011, a series of visible images [Figure 1], indicated the presence of a large phytoplankton bloom off the coast of New Jersey. The dramatic imagery captured the

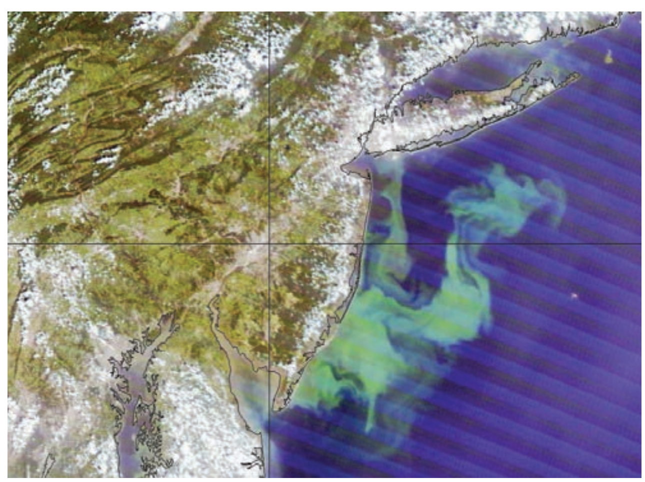

Figure 1. A visible image of a large phytoplankton bloom offshore the coast of New Jersey. The image resulted in a public debate about the causes.

978-1-4673-0831-1/12/$31.00 ©2012 IEEE

attention of the general public and the news media. The

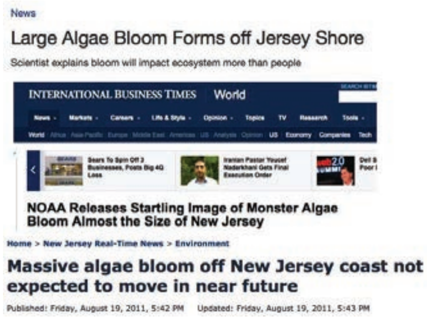
News

Large Algae Bloom Forms off Jersey Shore

Scientist explains bloom will impact ecosystem more than people

INTERNATIONAL BUSINESS TIMES World

NOAA Releases Startling Image of Monster Algae Bloom Almost the Size of New Jersey

Home > New Jersey Real-Time News > Environment

Massive algae bloom off New Jersey coast not expected to move in near future

Published: Friday, August 19, 2011, 5:42 PM Updated: Friday, August 19, 2011, 5:43 PM

Figure 2. Headlines in response the release of the satellite imagery of the phytoplankton off the New Jersey coast.

resulting discourse resulted in a series of debates of the cause ranging from the bloom being fueled from anthropogenic loading of nutrients from the Hudson River estuary or that it reflected the upwelling processes. Having access to an existing ocean observatory [6], we conducted an analysis of the factors to assess the likely causes of the algal bloom, its potential impact on the coastal water quality and the response to Hurricane Irene. The multiple assets present in the waters reflected a range of projects funded by a range of sponsors that included National Oceanic and Atmospheric Administration, Environmental Protection Agency, Office of Naval Research, and Department of Homeland Security.

Analysis of the Bloom. For this analysis we will focus on the mid-July through Hurricane Irene in late August. Throughout early July wind were largely from the Southwest, which is upwelling favorable followed by a week with generally weak downwelling winds [Figure 3]. An analysis of the satellite imagery shows the bloom in late July or early August. Prevailing cloud cover unfortunately resulted in relatively poor coverage during this time. The sea surface temperatures prior to the passage of Hurricane Irene show the Mid-Atlantic Bight (MAB) bounded by the Gulf Stream offshore and cooler waters to the north [Figure 4]. In mid-July along the coast of New Jersey and Delaware, there were small zones of cooler water, which is indicative of coastal upwelling. The amount and spatial extent of the cooler water was variable and reflected the variability in the winds; however overall the amount of upwelling appeared to decline into the month of August prior to the arrival of Hurricane Irene. The ocean imagery showed low phytoplankton in the middle of July however little of the coastlines were visible given the prevailing cloud cover [Figure 5]. There was a significant increases in biomass by the second week of August. By Mid-August chlorophyll concentrations were well above 10 mg m^{-3}, which is significantly greater than climatological summer mean of chlorophyll which is ~0.5 mg m^{-3} for the MAB shelf [7]. The high concentrations of chlorophyll was confirmed with *in situ* fluorometery measurements made with a Hydroid REMUS system that surveyed the inner half of the bloom offshore Tuckerton New Jersey. Discrete surface samples were collected and were analyzed on a microscope and the dominant alga present within the bloom appeared to be *Gymnodinium*

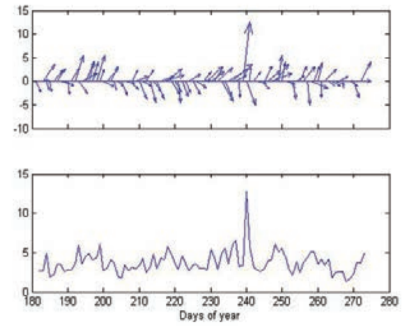

Figure 3. Prevailing wind speed for the month of July and August 2011 for the NODC buoy at Sandy Hook. The data stops upon the arrival of Hurricane Irene.

species. This is a motile dinoflagellate species, potentially allowing it access nutrients below the strong pyconcline and maintain themselves in the well lit euphotic zone.

The high concentration of phytoplankton had significant impacts on the biogeochemistry of the MAB which was documented by autonomous underwater vehicles. A Teledyne

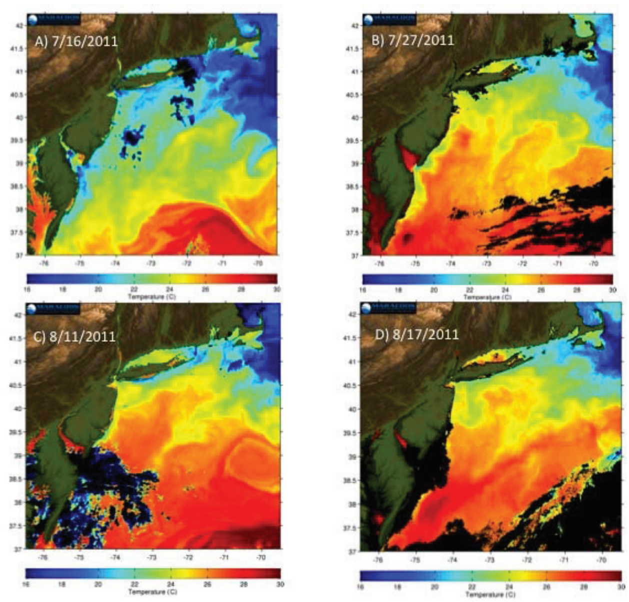

Figure 4. The sea surface temperatures for the Mid-Atlantic Bight (MAB) during the July and August in 2011. In mid-July there is evidence of upwelling new the New Jersey coast on July 16 through August 11th.

Webb glider had been deployed on the shelf and was outfitted with an Anderra Optode to provide measurements of oxygen concentrations for the New Jersey Department of Environmental Protection and the Environmental Protection Agency. The goal was to assess conduct a nearshore survey mapping if there were regions of low dissolved oxygen in bottom water offshore New Jersey. The glider conducted a southerly alongshore transect. The glider encountered super saturated oxygen concentrations in the upper mixed layer [Figure 6]. In contrast the bottom water show low dissolved oxygen concentrations with pre-Irene bottom water values heavily weighted to values lower then 5 mg L^{-1} [Figure 7]. These values were approaching values associated with potential animal mortality at 2.2 mg L^{-1} (indicated by the red arrow). The low values observed by the gliders prompted a series of adaptive surveys conducted by NOAA to confirm the presence of low bottom water oxygen levels. As part of those surveys, a Hydroid REMUS was utilized, outfitted with an Anderra Optode, and was deployed in low bottom water regions identified by the glider. The REMUS confirmed the low DO values during its high-resolution survey (inset in upper panel of Figure 7). The higher resolution surveys identified regions with low DO values close to the animal mortality concentrations. The passage of Hurricane and the associated mixing [Figure 6] significantly increased the oxygen concentration in the bottom water [Figure 7].

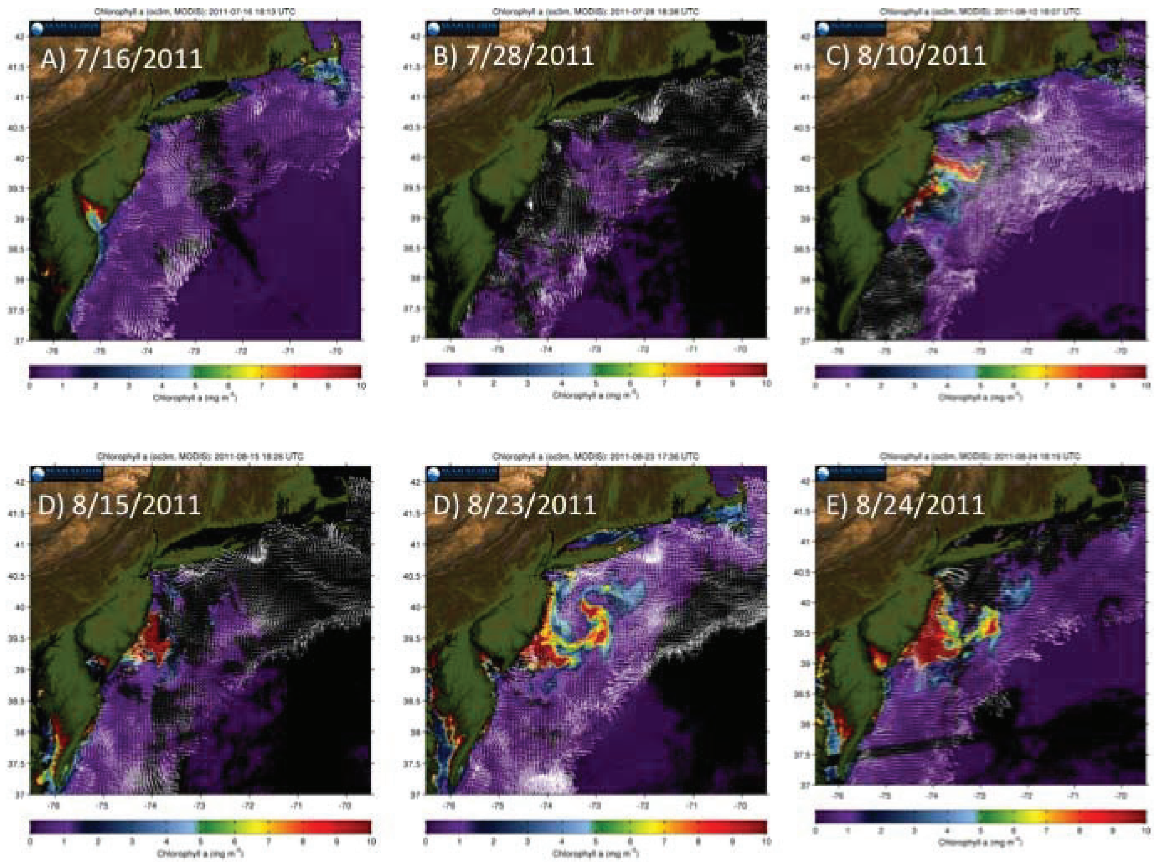

Figure 5. Ocean color estimates of chlorophyll a with the overlaid daily averaged surface currents measured by HF Radar.

The bloom was the result of nutrients provided by either riverine inputs, dominated by outflow from the Hudson river, and/or upwelling. So ultimately tracing the bloom back to its source waters is critical to understanding which processes fueled the bloom. At the start of the bloom and during the bloom, river outflow from the Hudson was low [Figure 8]. The impact of Irene is clearly visible, seen as a double peak in the river outflow [Figure 8], the first associated with the storm and the second to due the enhanced run-off associated with drainage of the water shed which received the majority of the rainfall associated with the storm. Therefore given the low river outflow, it is unlikely the bloom was caused by the Hudson river. This was in contrast to much of general media suggesting pollution run-off from the Hudson River estuary was to blame. To further assess the probable transport of the river and/or upwelled water we utilized the continuous record of data collected by the MARACOOS HF Radar array.

The HF radar surface currents maps were seeded with hypothetical passive particles, which were advected forward in time based on the measured currents. The trajectory of particles were tracked. Each day new particles were added, at three source locations [Figure 9]. The experiment was conducted for the month of July and up to the arrival of Hurricane Irene at the end of August. The final locations for all the drifters is shown in bottom panels in Figure 9. The left-handed panel is the trajectory of the particles released at the mouth of the Hudson river estuary. The majority of the particles are trapped at the mouth of the estuary, which reflects the bottom topographic

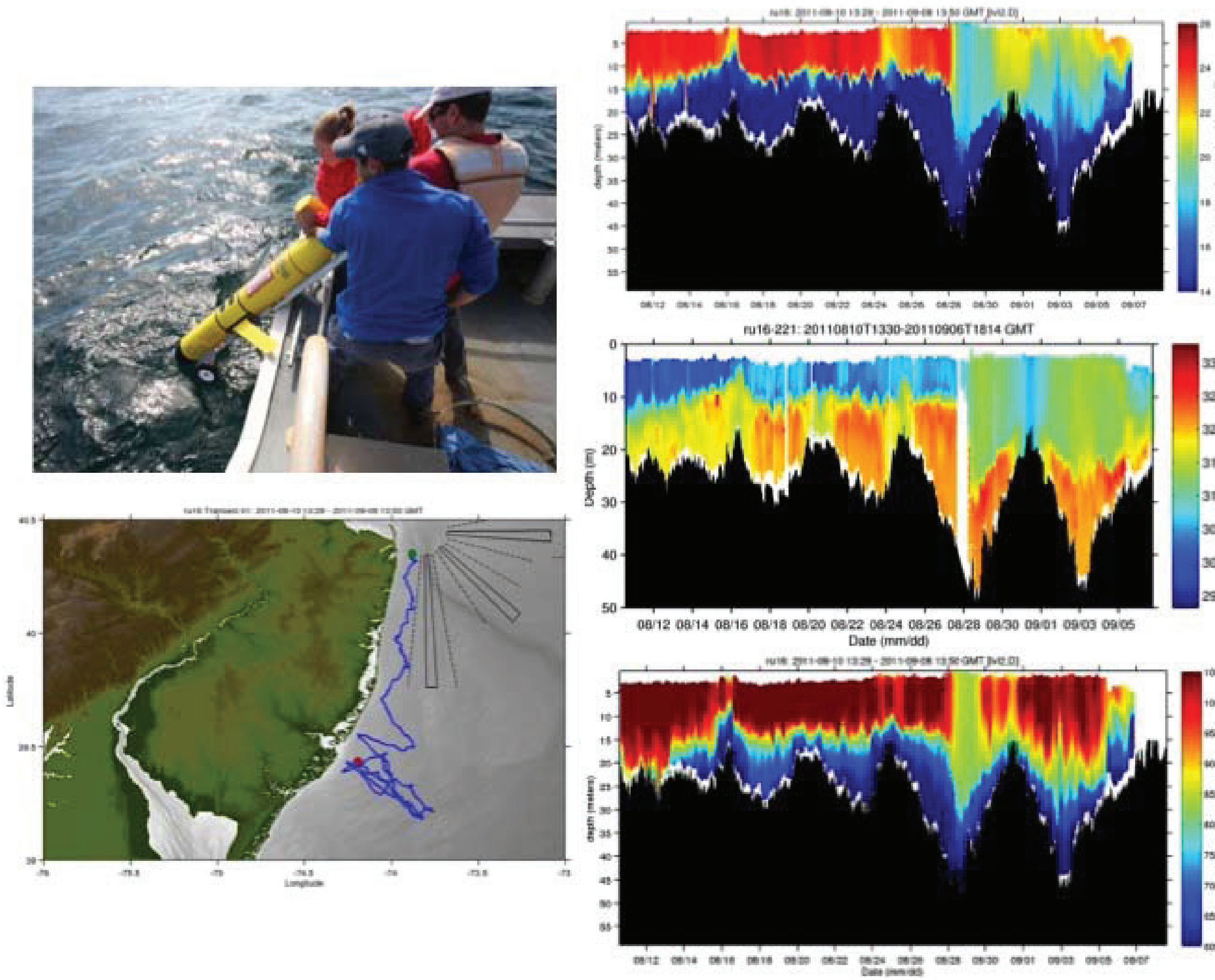

Figure 6. A Webb glider collected data offshore New Jersey in the summer of 2012. The glider, deployed by Rutgers collaborating with the New Jersey State of Environmental Protection (NJ DEP) and the EPA, was focused on measuring the water quality status in the New Jersey coastal waters. The mission consisted of a southerly transect "zig-zaging" inshore and offshore. Upon the approach of Hurricane Irene the glider was directed offshore and then was recovered after the conditions permitted boat operations. The right hand panels show glider data from the deployment. From top to bottom, the data is for temperature, salinity and the percent saturation of oxygen respectively. The passage of Hurricane Irene is clearly visible on August 28-29 as an immediate decline in surface water temperature. The mixing increased the salinity in the surface waters and increased the percent oxygen concentrations in the bottom water (see Figure 7).

affects on the river outflow circulation [8, 9]. The offshore boundary of the particles is associated with the edge of the Hudson Canyon. The majority of chlorophyll observed in the ocean color imagery is associated with the waters offshore and south of the river advection footprint. This combined with the overall low river outflow does not support hypothesis that the Hudson river is the source of chlorophyll (and/or nutrients promoting high growth) during the summer bloom in 2012. The right hand panel shows the advection footprint for the central New Jersey coast. The particles fan out over the broader shelf and high concentrations of advected particles are associated with the waters phytoplankton bloom. This is consistent with the hypothesis that the bloom is driven by upwelled water driven by the persistent Southwest winds found during the bloom. These maps represent a relatively

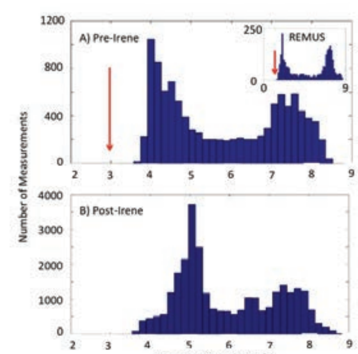

Figure 7. Dissolved oxygen measured pre and post Hurricane Irene. The inset is REMUS data flying in a similar location.

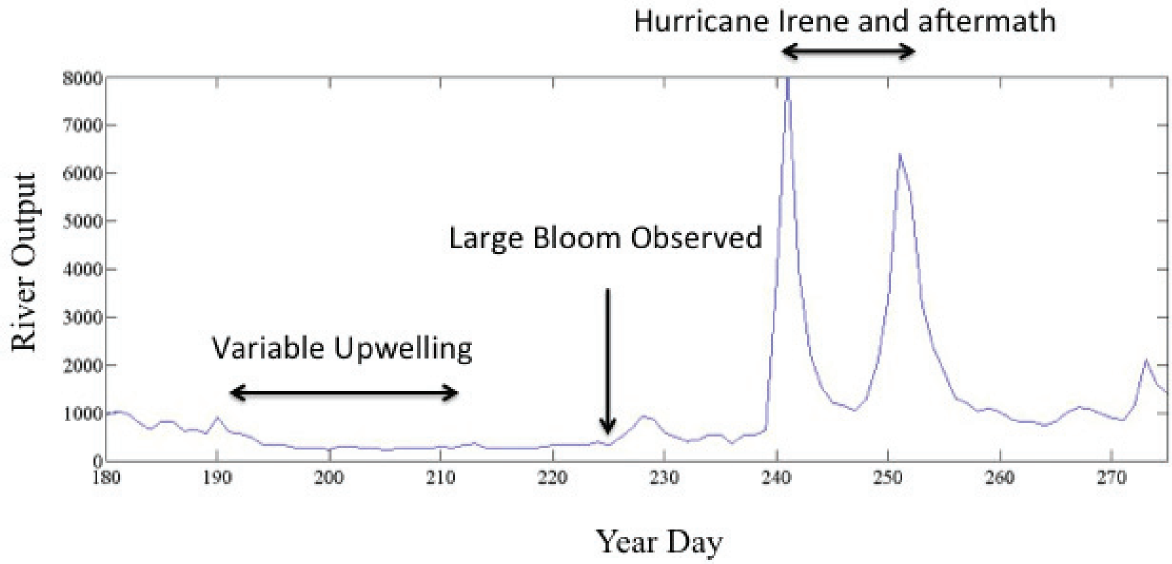

Figure 8. The outflow of the Hudson River during the summer bloom of 2012.

conservative estimate, as the phytoplankton biomass will be more dynamic given the variability in growth rates as well as the associated export to the sea floor.

CONCLUSIONS:

1) The phytoplankton bloom was most likely driven by upwelling, which induced the dinoflagellate bloom. The bloom was able to thrive given the ability of the cells to access nutrients in the subsurface waters.

2) The export of organic carbon associated with the bloom was likely the main culprit in driving the declines in the bottom water oxygen.

3) The availability of a existing ocean observatory allowed the bloom dynamics to be adaptively sampled in near real-time. This illustrates a unique tool for managing water quality of coastal waters.

ACKNOWLEDGMENT

This work represents the effort of the entire team of the Rutgers University Coastal Ocean Observation Lab (RU COOL). The work was supported by the IOOS MARACOOS program (NA11NOS0120038) and the ONR MURI program (N000140610739). Finally the support of Rutgers School of Environmental and Biological Sciences and the great state of New Jersey is acknowledged.

REFERENCES

[1] Figley, W., B. Pyle, and B. Halgren Oxygen depletion and associated benthic mortalities in New York Bight 1976. In Socioeconomic Imapcts, Swanson, R. L., and C. J. Sindermann, National Oceanic and Atmospheric Administration pp 315-335, 1979.

[2] Falkowski, P. G., T. S. Hopkin, and J. J. Walsh. An analysis of factors affecting oxygen depletion in the New York Bight, J. Mar. Res. 38, 479-506, 1980.

[3] Stoddard, A. J. E. O'Reilly, T. E. Whitledge, T. C. Malone and J. F. Malone. The application and development of a compatible historical data base for the analysis of water quality management issue in the New York Bight. IEEE Oceans, 18, 1030-1035, 1986.

[4] Glenn, S. M., R. Arnone, T. Bergmann, W. P. Bissett, M. Crowley, J. Cullen, J. Gryzmski, D. Haidvogel, J. Kohut, M. Moline, M. Oliver, C. Orrico, R. Sherrell, T. Song, A. Weidemann, R. Chant, and O. Schofield. The biogeochemical impact of summertime coastal upwelling on the New Jersey Shelf. J. Geophys. Res. Vol 109. C12S02, doi:10.1029/2003JC002265, 2004

[5] Song, T., D. B. Haidvogel, and S, M. Glenn. Effects of topography variability on the formation of upwelling centers off New Jersey: A theoretical model, Journal of Geophysical Research, Vol. 106, No. C5, pp. 9223-9240, 2001.

[6] Glenn, S. and O. Schofield. Growing a distributed ocean observatory: Our view from the COOL room. Oceanography 22(2): 78-92, 2009

[7] Xu, Y., R. C. Chant, R. Castaleo, D. Gong, S. M. Glenn, and O. Schofield,. Seasonal dynamics in the chlorophyll a in the Mid-Atlantic Bight. Cont. Sh. Res. 10.1016/j.csr.2011.05.019, 2011.

[8} Chant, R. J., S. M. Glenn, E. Hunter, J. Kohut, R. Chen, R. H. Houghton, J. Bosch, and O. Schofield. Bulge formation of a buoyant river outflow. J. Geophys Res. 113, C01017, DOI:10.1029/2007JC004100, 2008.

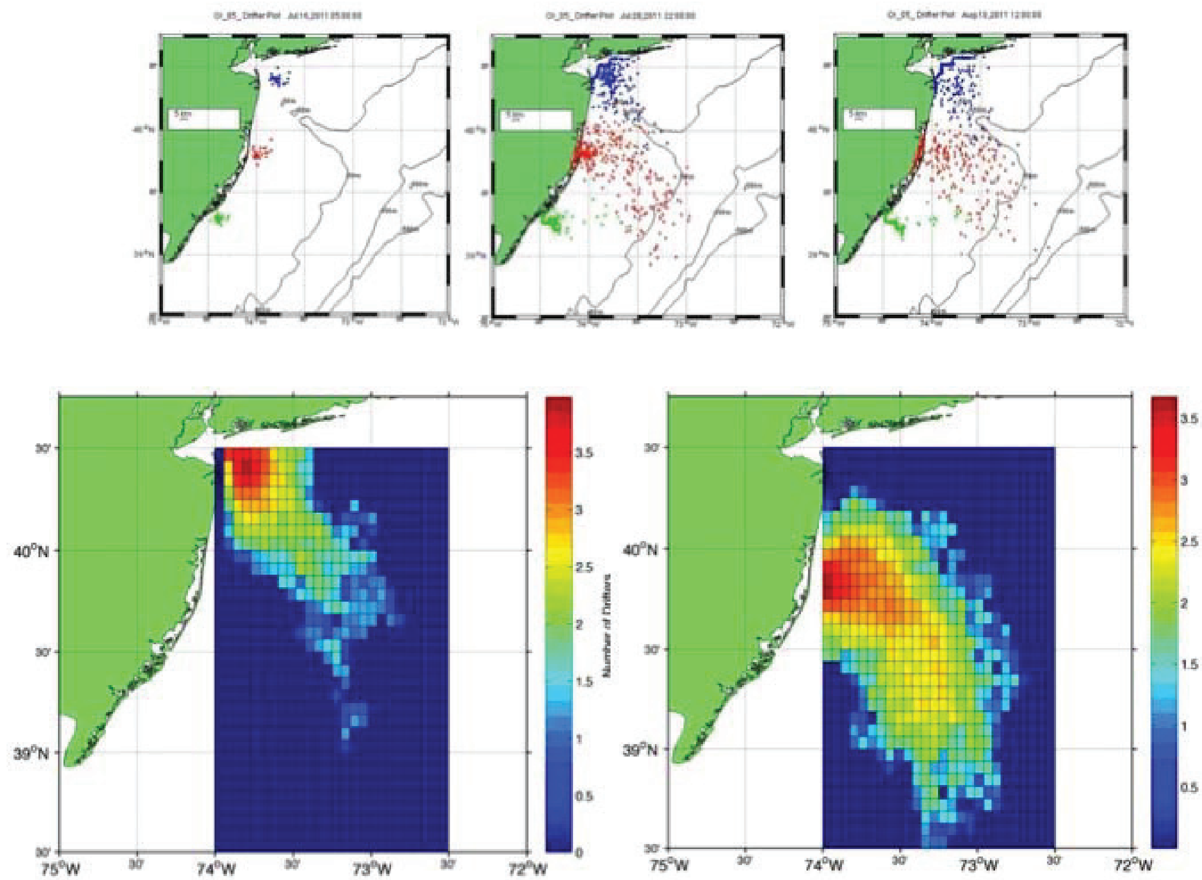

Figure 9. The utility of HF Radar in documenting surface particle transport for the month of July and August 2012. The upper three panels show three snapshots of particles being advected from three locations along the New Jersey coast. The upper left hand panel is the initial seeding location for particles on July 16th, and the subsequent transport for the particles on July 28th and August 10th are provided respectively. The lower two panels represent the final locations of all particles advected by the measured surface currents for the Hudson river estuary (left bottom panel) and from offshore the coast of New Jersey.

[9] Moline, M. A., T. K. Frazer, R. Chant, S. M. Glenn, C. A. Jacoby, J. R. Reinfelder, J. Yost, M. Zhou, and O. Schofield. Biological responses in a dynamic, buoyant river plume. Oceanography 21(4): 70-89, 2008.

.

Continental Shelf Research 63 (2013) S1

Contents lists available at SciVerse ScienceDirect

Continental Shelf Research

journal homepage: www.elsevier.com/locate/csr

Editorial

Accomplishments and future perspective of coastal ocean observing systems

Coastal oceans are the most densely urbanized regions on the planet with populations growing at rapid rate. In the near future close to 40% of the human population of Earth will live within 100 km of the shore. Many of the largest environmental changes are also found in coastal zones. The associated pressures will only increase as communities increasingly rely on the coastal ocean to provide additional sources of energy (wind, waves, oil and gas), demand that coastal fisheries remain a vital food source, and support enhanced maritime commerce and recreation. As coastal populations disproportionately drive national economies, the changes in coastal systems resulting from continued growth and resource use have the potential to influence national and international social and economic systems. Therefore management and policy need to be informed by science that can provide a quantitative understanding of coastal ecosystems.

Despite these pressing needs, our ability to map and forecast the coastal ocean remains low. While certain areas are difficult to sample, the turbulent nature of the coastal ocean makes it difficult to model. This has lead to repeated calls to develop and deploy coastal ocean observing systems throughout the world. Many of proposed networks will consist of distributed ocean observing/model networks that could provide a seamless 4D (3D in space plus time) view of the ocean with information being delivered to users through wireless networks allowing for two-way control of the network on demand. Ideally these networks map the future trajectory of the world's oceans allowing management/mitigation strategies to be explored based on quantitative understanding.

Advances in technology make these visions a reality in the near future. This special issue of Continental Shelf Research is focused on the coastal ocean observatories and highlights technical advancements that will form the foundation for distributed marine networks. This special issue draws on the results collected from the Alaska Ocean Observing System (AOOS) and the Mid-Atlantic Regional Coastal Ocean Observing System (MARCOOS). These two regional systems are part of the evolving Integrated Ocean Observing System (IOOS) in the United States [see Marine Technologies Society Journal volumes 44(No.6) and 45(No. 1)]. In this special issue we highlight key technologies that are central to coastal observatories spanning from satellites, data assimilative and forecast models, autonomous underwater vehicles (AUVs), and high frequency (HF) radars. As the AOOS and MARCOOS systems are rapidly maturing, they have collected valuable data. We therefore highlight how the observatory data is improving our understanding of coastal ecosystems. Examples provided in this special issue show how the observatories are improving our understanding of sediment resuspension and transport during storms, circulation in enclosed seas, atmosphere ocean coupling, role of mixing in structuring marine food webs, the dynamics and consequences of buoyant plumes into coastal waters, and atmosphere/ocean interactions.

This special issue will hopefully contribute to demonstrating how the expanding network observatories will improve our understanding of coastal ecosystems. This will in turn increase the number of tools available to us to better utilize, manage and sustain our coastal waters. This comes at a critical time, given the increasing human pressures being placed on our coastal waters.

Oscar Schofield
Coastal Ocean Observation Laboratory, Institute of Marine and Coastal Sciences, School of Environmental and Biological Sciences, Rutgers University, New Brunswick, NJ 08901, United States
E-mail address: oscar@marine.rutgers.edu

Yi Chao*
Remote Sensing Solutions, Inc., Pasadena, CA 91107, United States
E-mail address: ychao@remotesensingsolutions.com

Available online 9 April 2013

* Corresponding author. Also at: Joint Institute for Regional Earth System Science and Engineering, University of California at Los Angeles, Los Angeles, CA 90095, United States.

http://dx.doi.org/10.1016/j.csr.2013.04.001

Small-scale variability of the cross-shelf flow over the outer shelf of the Ross Sea

Josh Kohut,[1] Elias Hunter,[1] and Bruce Huber[2]

Received 31 May 2012; revised 11 December 2012; accepted 17 January 2013; published 10 April 2013.

[1] The importance of cross-shelf transport across the Ross Sea on local and remote processes has been well documented. In the Ross Sea, mid-water intrusions of Circumpolar Deep Water (CDW) are modified by shelf water near the shelf break to form Modified Circumpolar Deep Water (MCDW). In 2010–2011, we deployed multi-platform technologies focused on this MCDW intrusion in the vicinity of Mawson and Pennell Banks to better understand its role in ecosystem processes across the shelf. The high-resolution time and space sampling provided by an underwater glider, a short-term mooring, and a ship-based survey highlight the scales over which these critical cross-shelf transport processes occur. MCDW cores were observed as small-scale well-defined features over the western slopes of Pennell and Mawson Banks. The mean transport along Pennell Bank was estimated to be about 0.24 *Sv* but was highly variable in time (hours to days). The observations suggest that the core of MCDW is transported by a predominately barotropic flow that follows topography around the banks toward the south until the slope of the bank flattens and the warmer water moves up and over the bank. This pathway is shown to link the source MCDW with an area of high productivity over the shallows of Pennell Bank.

Citation: Kohut, J., E. Hunter, and B. Huber (2013), Small-scale variability of the cross-shelf flow over the outer shelf of the Ross Sea, *J. Geophys. Res. Oceans, 118*, 1863–1876, doi:10.1002/jgrc.20090.

1. Introduction

[2] The shelves of Antarctica's continental seas are critical centers for water mass transformation. The water masses that undergo these transformations have origins in the deep ocean and on the shelf itself [*Foster and Carmack*, 1976; *Killworth*, 1977; *Baines and Condie*, 1998]. The seasonal cycle of the high latitudes plays an important role in their formation, transformation, and exchange between the shallow shelves and the deep waters of the Southern Ocean [*Assmann et al*., 2003; *Assmann and Timmermann*, 2005]. In the winter, strong katabatic winds streaming off the Antarctic continent maintain open water polynas with nearly continuous ice formation [*Budillon and Spezie*, 2000; *Fusco et al*., 2009]. The newly formed dense water mixes completely to the bottom and eventually becomes Antarctic Bottom Water (AABW) [*Orsi et al*., 1999; *Gordon et al*., 2009b]. AABW is a key component of the global climate system, bringing cold, recently ventilated water to lower latitudes [*Orsi*, *et al*., 2002; *Jacobs*, 2004]. The austral summer brings warmer temperatures, weaker winds, and nearly continuous solar radiation. This leads to a more stratified water column with a cold fresher layer over the dense bottom water formed the winter seasons before. In the Ross Sea, relatively warm Circumpolar Deep Water (CDW) originating off the shelf preferentially intrudes onto the shelf at sites where the bottom topography changes direction relative to the coastal flow [*Klinck and Dinniman*, 2010]. The CDW then mixes with these shelf water masses at the shelf break to form Modified Circumpolar Deep Water (MCDW) [*Whitworth et al*., 1998]. With neutral densities between 28 and 28.27 [*Orsi and Wiederwohl*, 2009], these intrusions move onto the shelf as mid-water features sandwiched between the dense bottom and lighter surface water masses. This large mass of water injects onto the shelf as mid-water features at specific locations, bringing with it nutrients and heat [*Dinniman et al*., 2003; *Hiscock*, 2004; *Smith et al*., 2006]. The interaction, mixing, and exchange of these water masses helps to maintain deep ocean heat exchange, ventilation, and important ecosystems processes like seasonal blooms [*Arrigo et al*., 2008; *Budillon et al*., 2011; *Fragoso and Smith*, 2012]. While these coastal seas are typically small in area, the role that they play in the exchange of water masses between the shelf and open ocean has important implications to both the global circulation and the critical ecosystem it supports.

[3] Compared to other coastal seas surrounding Antarctica, the Ross Sea in the Pacific sector of the Southern Ocean is relatively well sampled (Figure 1). Following *Orsi and Wiederwohl* [2009], we characterize the water masses of the Ross Sea based on their neutral densities as follows: (1) dense bottom water (neutral densities greater than 28.27), (2) MCDW/CDW (neutral densities between 28.0 and 28.27),

[1] Institute of Marine and Coastal Sciences, Rutgers University, New Brunswick, New Jersey, USA.
[2] Lamont Doherty Earth Observatory, Columbia University, Palisades, New York, USA.

Corresponding author: J. Kohut, Institute of Marine and Coastal Sciences, Rutgers University, 71 Dudley Road, New Brunswick, NJ 08901, USA. (kohut@marine.rutgers.edu)

2169-9275/13/10.1002/jgrc.20090

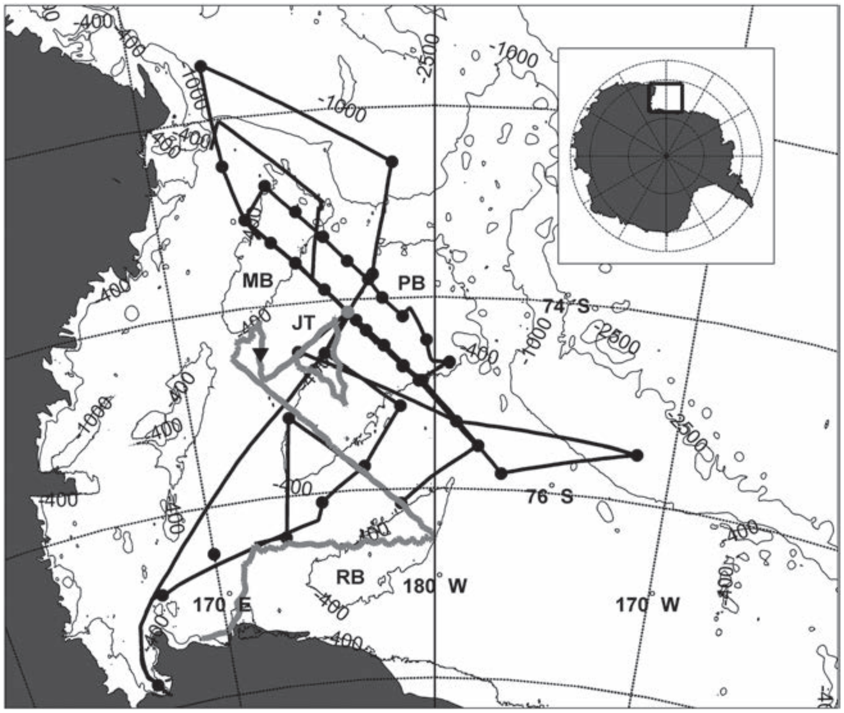

Figure 1. Map of the study site in the Western Ross Sea showing the ship track (black line), ship stations (black dots), glider track (gray line), and mooring location (gray dot). Isobaths highlight the relevant topographic features including Ross Bank (RB), Pennell Bank (PB), Joides Trough (JT), and Mawson Bank (MB). The black triangle indicates the glider's location at the start of the ship survey.

and (3) surface water with neutral densities less than 28.0 (Figure 2). The distribution of these water masses has been described in the context of available data primarily from ship surveys and moorings. In the western Ross Sea, dense High Salinity Shelf Water (HSSW) sinks to the seafloor and splits with a southward branch going under the Ross Ice Shelf and a northward branch heading toward the shelf break. The asymmetry of the deep water formation centers across the entire sea sets up an east/west density gradient with denser water under the formation centers to the west [*Jacobs and Giulivi*, 1998; *Rickard et al*., 2010]. The weaker winds and warmer temperatures of the Austral summer stratify the western Ross Sea with a layer of fresher water capping the HSSW formed the seasons before. As the small winter polyna grows to open the entire Ross Sea, blooms of phytoplankton form the base of the food web. It has been suggested that these blooms are maintained in part by the delivery of macro- and micro-nutrients from the deep water off the shelf [*Hiscock*, 2004; *Fragoso and Smith*, 2012]. In

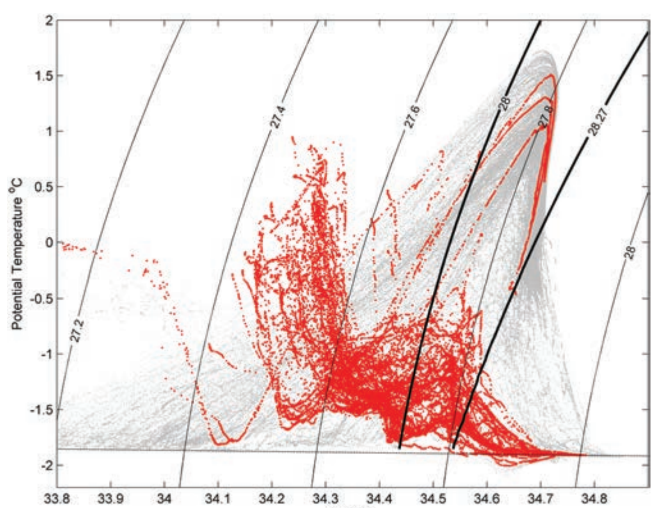

Figure 2. Potential temperature and salinity data for stations sampled by the *RVIB Nathaniel B. Palmer* from 2000 to 2005 (gray) and the SEAFAReRS cruise in 2011 (red). Isopycnals (thin black) and the neutral density bounds of 28.0 and 28.27 for MCDW (thick black) defined by *Orsi and Weiderwhol* [2009] are also shown.

addition to the nutrient supply, this warmer deep water is a source of heat that impacts the rate of sea ice formation and melt through the seasons and could impact the rate of basal melt below the ice shelf if it reaches far enough south.

[4] The Ross Sea shelf break is a critical region for both the exchange of bottom water that moves down the slope and eventually forms dense AABW [*Gordon et al*., 2009a] and the injection of warm CDW that comes from the mid-depths of the Southern Ocean. Both the deep water formed on the shelf and the mid-water of the deep ocean are modified as they move across the shelf break by local mixing processes [*Whitworth et al*., 1998; *Robertson et al*., 2003]. The most energetic process that likely contributes to this mixing is the tides. The tides of the Ross Sea are predominately diurnal with higher amplitudes over the shallow banks and along the shelf break [*Robertson*, 2005; *Whithworth and Orsi*, 2006; *Padman et al*., 2009]. The tides interact with the varying topography and the background flow along the shelf break toward the west to mix and modify the water masses before they move away from the shelf break [*Dinniman et al*., 2003; *Gordon et al*., 2009a]. The dominant advective feature along the shelf break is the mostly westward jet maintained by the density gradient across the shelf break. Instabilities and interactions of this jet with the underlying topography lead to preferential centers of CDW intrusions onto the shelf [*Klinck and Dinniman*, 2010].

[5] While this shelf break region is undersampled, both observations and numerical studies have identified its importance to the north/south exchange of water masses. These studies are based on observations collected during intensive surveys and mooring deployments [e.g., *Gordon et al*., 2009a] and numerical models verified by either the direct observations [e.g., *Dinniman et al*., 2003] or climatologies determined from the observations [e.g., *Klinck and Dinniman*, 2010]. In the early 2000s, a field program was conducted as part of the AnSlope project [*Gordon et al*., 2009a] with ship surveys and mooring deployments focused on the shelf break near Drygalski Trough in the northwest Ross Sea. These critical observations have shown the importance of the shelf break as the basis for the formation of the dense water that sink and form AABW [*Muench et al*., 2009; *Gordon et al*., 2009b]. These papers cite the importance of the tides in not only mixing the parent water masses of the Ross Sea but also modulating the position of the shelf break jet. The north south movement of this jet by the tides may facilitate the exchange of dense water off the shelf and into the deep sea along the seafloor. Similarly, the variability of this jet and its interaction with the underlying topography likely control the variability observed in the movement of CDW onto the shelf [*Dinniman et al*., 2003]. At specific locations along the shelf break, sharp changes in the orientation of the isobaths along the general path of the shelf break jet lead to preferential locations for intrusions of the jet onto the shelf. The models show that these regions of consistent upwelling of CDW coincide with sharp turns toward the north in front of the flow. One region of preferential upwelling is offshore of Joides Trough between Mawson and Pennell Banks (Figure 1). Virtual dye experiments within the modeled current fields identify Joides and Drygalski Troughs as regions of consistent MCDW intrusions. *Dinniman et al*. [2003] suggest that once this CDW is up on the shelf, it mixes with the surrounding shelf water and moves south along the eastern side of Joides trough toward the interior of the shelf.

[6] In this study, we use an extensive multi-platform observation array to characterize the southward flow of MCDW from the shelf break to the interior of the Ross Sea Shelf as part of the Slocum Enhanced Adaptive Fe Algal Research in the Ross Sea (SEAFAReRS) project. The sampling is focused on the western slope of Pennell Bank along the eastern edge of Joides Trough shoreward of the shelf break and the CDW mixing sites associated with the shelf break jet. Particular emphasis on the small time and space scales of the MCDW intrusion drove the sampling design. A ship survey, glider Autonomous Underwater Vehicle (AUV) mission, and a mooring deployed at a depth of 400 m are used to characterize the spatial and temporal variability of the southward flow of MCDW. Section 2 describes the platforms and available data, and section 3 presents the results. Implications and concluding remarks are discussed in sections 4 and 5, respectively.

2. Data

2.1. Glider AUV

[7] A deep Slocum electric glider manufactured by Teledyne Webb Research was deployed. The buoyancy-driven propulsion of the glider AUV affords high-efficiency and deployment endurance [*Schofield et al*., 2007]. Throughout the mission, the glider moved in a sawtooth pattern between 10 m below the surface and 10 m above the bottom determined from onboard pressure and altimeter data. This glider was equipped with a sensor suite that characterized the ecosystem's physical structure (conductivity, temperature, depth, and dissolved O_2), in situ phytoplankton fluorescence and optical backscatter. On 10 December 2010, the deep glider was deployed from the sea ice edge near Ross Island. The 52 day mission took the glider east along 76.5°S before turning toward the northwest over Ross Bank (Figure 1). The glider then completed a cross section of Pennell Bank, Joides Trough, and up the eastern slope of Mawson Bank before heading back east toward Pennell Bank. The glider began this section near Ross Bank on 28 December 2011 and completed the section 13 days later near Mawson Bank on 10 January 2011. Nine days before the ship left the dock, these data helped guide the initial ship sampling plan with a high-resolution section of temperature, salinity, density, and dissolved oxygen (Figure 3). Once the ship started its survey on 10 January 2011, the complimentary glider sampling provided high vertical and horizontal resolutions of the physical characteristics in the vicinity of the flow along western Pennell Bank and into Joides Trough. The glider was recovered on 4 February toward the end of the ship survey. The CTD resolution was 0.25 m in the vertical and approximately 2.2 times the water depth in the horizontal. The CTD data were verified against the ship's data during two calibration casts with the glider secured to the ship's rosette.

2.2. Ship Surveys

[8] A ship survey was completed aboard the *RVIB Nathaniel B. Palmer* (NBP). The ship left McMurdo Station on 20 January 2011 on a 26 day cruise across the Ross Sea.

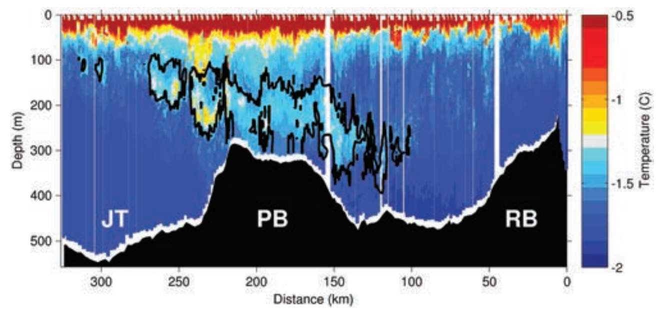

Figure 3. Glider cross section of potential temperature sampled between Ross Bank and Joides Trough. The black contour is the 5.1 ml/L dissolved oxygen isopleth showing the oxygen minimum coincident with the sub-surface temperature maximum associated with MCDW. The topographic features are labeled as in Figure 1.

The sampling focused on the banks and troughs of the outer shelf in the western Ross Sea (Figure 1). Throughout the cruise, underway measurements of temperature and salinity were taken every second with the NBP thermosalinograph at an intake depth of 6.7 m below the surface. These data were sub-sampled every 10 s along the ship's track. Vertical profiles of velocity were sampled by a ship mounted downward looking 150 KHz Acoustic Doppler Current Profiler (ADCP). These shipboard data were processed with the University of Hawaii Data Acquisition System (UHDAS) software. Five minute ensembles were collected with a vertical bin resolution of 8 m. Raw depth-averaged and depth-dependent data were de-tided using the predicted barotropic tide derived from Ross Sea sub-region of the Oregon Tidal Prediction System (Figure 4) [*Erofeeva et al*., 2005].

[9] In addition to the underway data, the ship survey completed 79 stations (Figure 1). At each station, at least one full water column profile of the ship's CTD rosette was completed. All stations were sampled at least once with more frequent repeat stations along the southern line crossing both Pennell and Mawson Banks. The Sea-Bird CTD mounted on the rosette was calibrated before and after the cruise. Our analysis will focus in on a single along-bank section from off the shelf to the southern end of Pennell Bank and eight repeat cross sections across Pennell Bank, Joides Trough, and Mawson Bank (Figure 1). The distribution of the potential temperature and salinity sampled over these stations is shown in Figure 2.

2.3. Mooring Deployment

[10] A surface-buoyed mooring was deployed on 27 January 2011 for 13 days on the western side of Pennell Bank (Figure 1). It was anchored to the bottom on 600 m of mooring wire in water 400 m deep. After recovery from a 3 year deployment as part of the Cape Adare Long-term Moorings (CALM) project earlier in the cruise, the sensors were quickly repurposed for this short redeployment focused on the MCDW intrusion. The

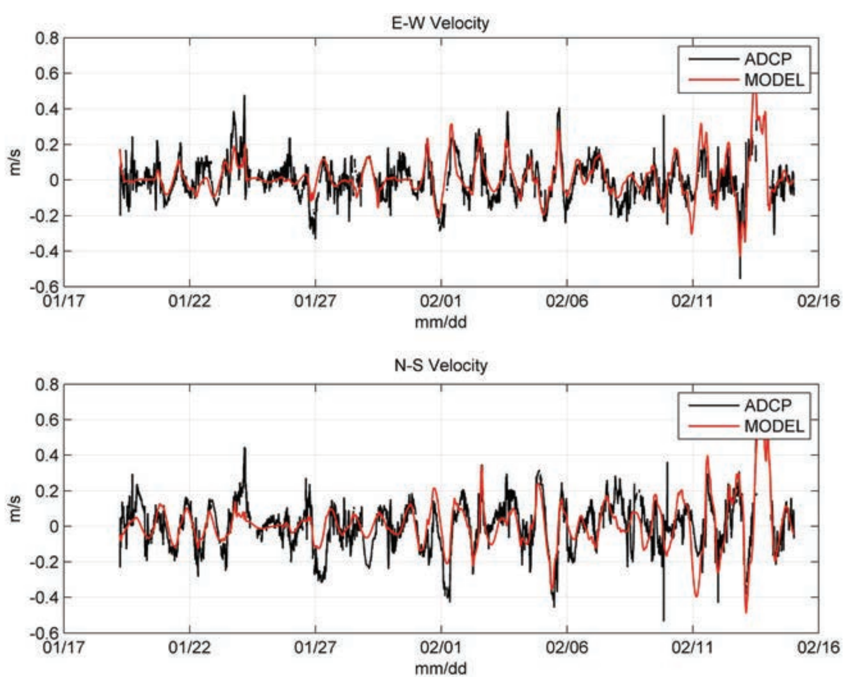

Figure 4. Time series of depth-averaged velocity in the east (top) and north (bottom) components from the NBP hull mounted ADCP (black) and matched tidal velocity estimated from the barotropic tide model Ross_TIM [*Erofeeva et al*., 2005] (red).

sensor distribution and mooring location were determined from by available ship and glider data to target the MCDW core flowing south along the western slope of Pennell Bank. Four depths were instrumented: 50 m (current meter with temperature and pressure), 225 m (current meter with temperature and pressure), 230 m (salinity, temperature and pressure), and 300 m (temperature and pressure). The two mid-water depths (225 m and 230 m) specifically targeted the MCDW water observed by the glider and ship survey. All instruments sampled every 5 min. Current meter magnetic compasses were corrected for the local magnetic declination of 112°.

3. Results

[11] A single glider section across the bank and trough topography of the Ross Sea shows the scale and possible dynamics driving the distribution of MCDW (Figure 3). The glider began the section on 28 December 2010 over Ross Bank and reached Joides Trough on 10 January 2011. The glider section identifies the relatively warmer potential temperature (greater than approximately -1.3°C) and minima in dissolved oxygen indicative of MCDW over the western slope of Pennell Bank and suggests that the core of MCDW mixes up and over the shallows of the bank (Figure 3). The location of the warmer water feature identified through the real-time data feeds from the glider guided the sampling strategy initiated on 19 January 2011 when the NBP left the pier at McMurdo Station. Unlike previous surveys conducted in the Ross Sea, the sampling design centered on this small feature seen on the glider section with repeat ship sections across the bank and subsequent mooring deployment in the core to resolve the relevant time and space scales.

[12] For this study, the observations are organized into along- and cross-bank sections. The along-bank direction was determined to be 20° clockwise from true north based on the largest bathymetric gradient over a scale of 0.5° in latitude (5.5 km) and longitude (1.7 km). In all of the figures, positive indicates flow toward the northeast (20°) and southeast (110°) for the along- and across-bank components, respectively.

3.1. Along-Bank Structure of the MCDW Intrusion

[13] The hydrographic data along the bank was taken over a series of five stations (Figure 5). The southernmost station (#2) was sampled early in the cruise based on initial guidance from the glider locating a core of MCDW along the western slope of Pennell Bank. Six days later, the along-bank section continued with a series of stations beginning off the shelf and moving south along Pennell Bank (stations 14–17, all sampled within 1.5 days of each other). For each station, we show the average profile of the upper 400 m (Figure 6). The gray-shaded region is the portion of the water column in which the neutral density fall within the range set for MCDW as defined in *Orsi and Wiederwohl* [2009]. The potential temperature-salinity plots below each profile are the data for that particular station in red plotted against all the data collected on the cruise in gray. At all the stations, there is a well-defined surface layer of warmer fresher water primarily associated with the melting of the seasonal sea ice and subsequent solar heating (Figure 6). Distinction between the stations is seen in the depth and strength of the thermal gradient between the surface layer and the cooler layer just below. Off the shelf break at the deep water station (14), the warmer CDW is seen at depths deeper than 300 m. Based on the Θ-S characteristics, this station has two clear water masses, a warmer fresh layer within the upper 70 m and the warmer saltier CDW layer below. On the inshore side of the shelf break at station 15, the deep water peak in potential temperature seen in station 14 cools and freshens as it mixes with shelf water, forming MCDW. Continuing south along the bank, the subsequent stations show that dilution of the pure CDW signal seen offshore (station 14) and a general increase in the potential temperature of the surface layer, likely driven by the earlier melt of the seasonal sea ice leading to longer exposure to solar heating. While the depth and vertical extent of the MCDW varies from station to station, this water lay within a broad range of depths between 200 m to 350 m deep.

[14] The velocity data identify how these water masses move across the shelf. Both the depth-averaged and depth-dependent velocity data show a significant rotation in the currents as the ship moved from the deep water off the shelf break southwest along the western slope of Pennell Bank (Figure 7). To the north, the depth-averaged flow of the shelf break jet peaks over the steep slope of the shelf break with a broad shoulder extending south over the shelf. Further to the south, the currents rotate counterclockwise to an approximate along-bank direction in the vicinity of the 400 m isobath west of Pennell Bank. The shelf break jet has a sub-surface velocity peak of about -0.3 m/s 100 m deep at about 73.25°S (Figure 7,

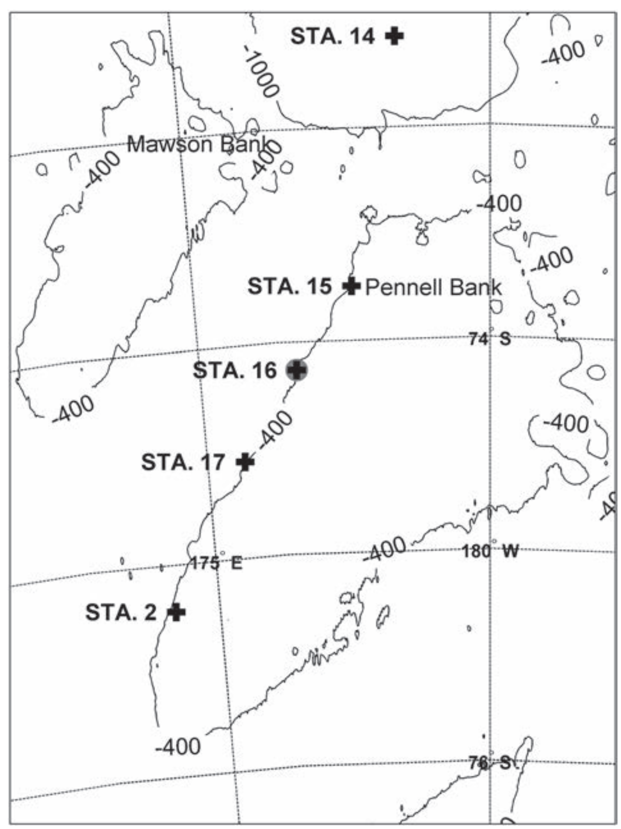

Figure 5. Map showing the ship stations (black cross) included in the along-bank section. The mooring location is shown as a small gray circle.

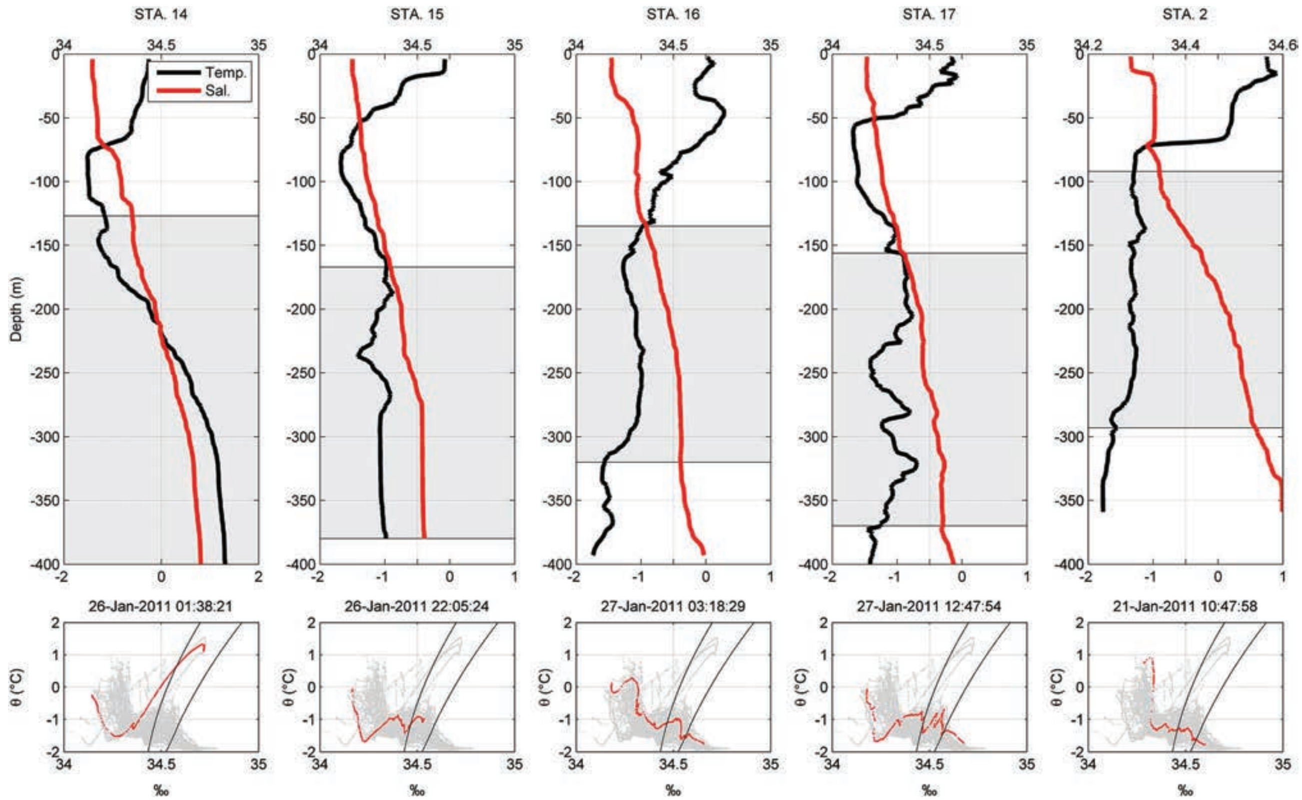

Figure 6. The average potential temperature (black) and salinity (red) for each station in the along-bank line. Vertical distributions of the neutral densities that define MCDW are shaded gray for each station. Below each section, the potential temperature-salinity plot is shown for all stations (gray) and that particular station (red). The neutral density bounds for MCDW are shown as thick black lines.

upper right). The along-bank flow further south is stronger with the strongest velocities exceeding 0.3 m/s in the upper 200 m of the water column.

3.2. Across-Bank Structure of the MCDW Intrusion

[15] Over the course of the cruise, the ship made eight repeat transects across Pennell Bank and Joides Trough (Figure 1). Along this cross section of the banks, we sampled nine stations, five over Pennell Bank, three over Mawson Bank, and one over Joides Trough (Figure 8). At each station, there were at least three CTD casts with a maximum of eight casts sampled at our mooring station over the 400 m isobath along the western slope of Pennell Bank. For each of these stations, we show the Θ-S diagrams for the casts taken at that station (red) relative to all stations sampled throughout the cruise (gray). The warmer fresher surface layer resulting from the sea ice melt earlier in the season and subsequent solar heating is seen across all stations with the warmest surface water over the shallows of the banks. The strongest MCDW signal is seen near Joides Trough and the western slope of Pennell and Mawson Banks, coincident with our mooring site over the 400 m isobath. The deep HSSW is only seen in stations at least 400 m deep.

[16] The mean cross section based on all the casts taken at each station shows the significant variation in water column properties across the complicated topography. There is a clear surface layer of warmer fresher water across the entire section with slightly fresher water over the western slopes of the banks (Figure 9). Below this roughly 80 m deep surface layer, there is significant variability in the distribution of the deeper water masses. At depth in Joides trough, there is a thick layer of dense shelf water reaching up from the bottom to a depth of about 250 m. At mid-depth, the most striking feature is the slug of warmer MCDW centered over the 400 m isobath above the western slope of Pennell Bank. The small region of MCDW is confined to a depth between 180 m and 250 m and is not seen in the neighboring stations. While there is evidence of a similar slug of MCDW over the western slope of Mawson Bank, its potential temperature and oxygen signal are more dilute and spread over a wider range of depths. The contrasting MCDW characteristics between the two banks are likely due to the more energetic tides over the narrower Mawson Bank. This section is consistent with the structure of the MCDW seen by the glider several weeks before with a core of MCDW over the 400 m isobath except that in this section, this warmer water does not extend east over the shallows of the bank (Figures 3 and 9). Unlike the glider section further south, this section completed closer to the shelf break clearly shows the presence of warmer deep water over the slope isolated from the shallows of the bank.

[17] The repeat sections of underway ADCP data describe the movement of these water masses across the shelf. The depth-averaged flow averaged over all eight cross sections shows a clear link to topography with the southward flow over the western slopes of Mawson and Penell Banks and the northward flow along the eastern slope of Mawson Bank (Figure 10, left). For both banks, the flow is about -0.3 m/s and centered just inside the

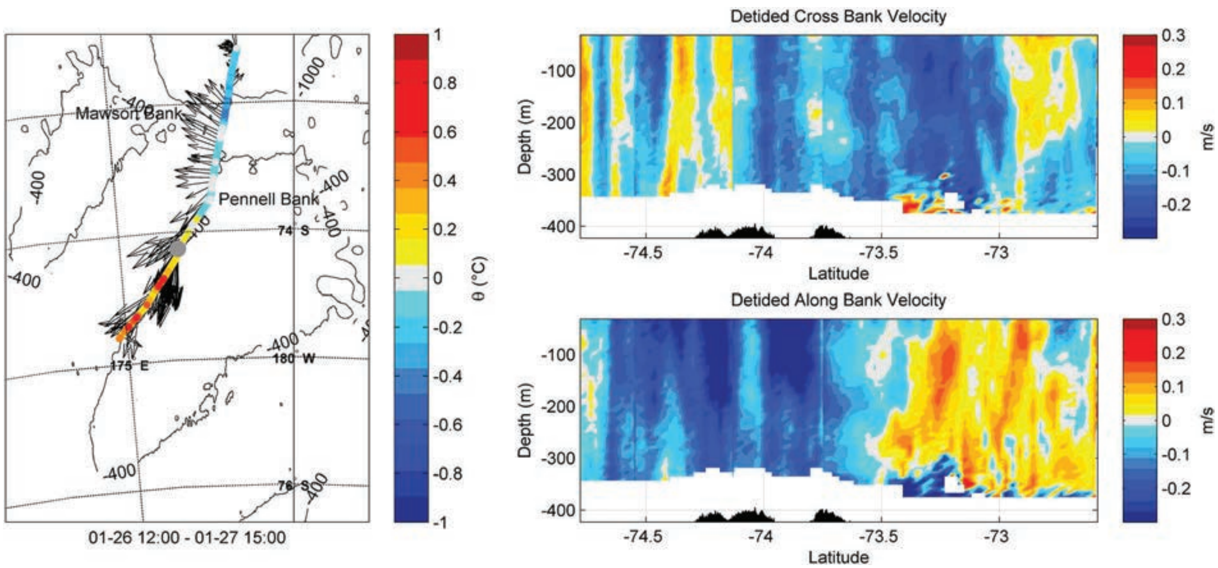

Figure 7. De-tided depth-averaged currents (m/s, black vectors) and surface temperature (colored track) over the along-bank section (left). The depth-dependent velocity sections for the cross-bank (above right) and along-bank (below right) velocity components. The mooring location is shown as a gray circle (left).

400 m isobaths. There is also a second region of southward flow centered over Joides Trough.

[18] The depth-dependent velocity data averaged across all eight cross sections of the banks show the largest vertical shear in the along-bank flows to the north and south over the eastern and western slopes of the banks, respectively. The southward flow along the banks is seen to vary with depth. This mean surface intensified flow of 0.3 m/s decays to about 0.1 m/s at 300 m but never reverses (Figure 10, right). Similarly along the western bank of Mawson, the stronger along-bank velocities are shallower and not as strong as those seen along Pennell. For both banks, this southward flow has a weak upslope component (<0.05 m/s). The upslope velocity is relatively uniform with depth except over Mawson Bank where there is a slight intensification at depth around 225 m deep.

[19] The depth-averaged flow of each individual pass across the banks shows regions of relatively constant and variable flow in time. For all eight sections, the flow over the shallows of the banks shows the most variation (Figure 11). This is particularly evident in the upper four sections sampled almost continuously between 8 February and 12 February. Over Pennell Bank, it transitions from relatively strong northward to periods of weak flow to the south. The most consistent feature across all the individual sections is the southward flow along the western slope of the banks. The depth-averaged flow over both slopes is consistently to the south. From section to section, the character of the flow changes from a relatively narrow jet to a broad feature spreading up toward the shallower depths of the banks.

3.3. Volume Transport Onto the Shelf

[20] Models and sparse observations have identified the importance of topography in steering the transport of MCDW south into the interior of the shelf [*Dinniman et al.*, 2003; *Klinck and Dinniman*, 2010]. Given the location, size, and velocity associated with the MCDW core identified over the western slope of Pennell Bank above, we characterize its transport and variability. Both the glider and ship CTD data identify a small core of MCDW centered over the 400 m isobath characterized by a sub-surface potential temperature maximum, dissolved oxygen minimum, and consistent with the neutral density definitions of *Orsi and Wiederwohl* [2009] (Figures 3 and 9). The depth of the sub-surface peak is about 250 m below the surface but is seen as shallow as 180 m and as deep as 280 m. The MCDW is characteristically warmer than the surrounding shelf water, with lower dissolved oxygen concentrations. These two traits are used in addition to the neutral density bounds defined by *Orsi and Weiderwhol* [2009] to tag water as MCDW.

[21] Using the ADCP and station data from the survey, we estimate a mean volume transport of the layer bounding MCDW (defined by neutral density surfaces as above) along the western slope of Pennell Bank. The height of the layer is estimated from the mean CTD profile taken at the 400 m isobath station. Based on this average profile, the MCDW is seen over 100 m of the water column between 180 m and 280 m deep (Figure 9). The width of the MCDW core was estimated from the ADCP sections. The mean velocity transect averaged across all eight cross sections of the bank shows a clearly defined flow moving south along the western slope of the bank. The width of this jet is approximately 20 km. Therefore, the approximate area of the MCDW layer along the western slope of Pennell bank is approximated as 20 km wide by 100 m high. Using the same ADCP data, we calculate the mean velocity in this sub-section of the average transect to be -0.12 m/s. Based on these data, the estimated transport of MCDW south along Pennell Bank is estimated at 2.4×10^6 m^3/s, or 0.24 *Sv*. Since the concentration of MCDW is not precisely known within the volume used in this estimate, this serves as an upper bound for MCDW transport onto the shelf given our available data.

3.4. Temporal and Spatial Variability of the MCDW Intrusion

[22] This estimate provides a scale for the input of MCDW onto the shelf along Pennell Bank. It does not however

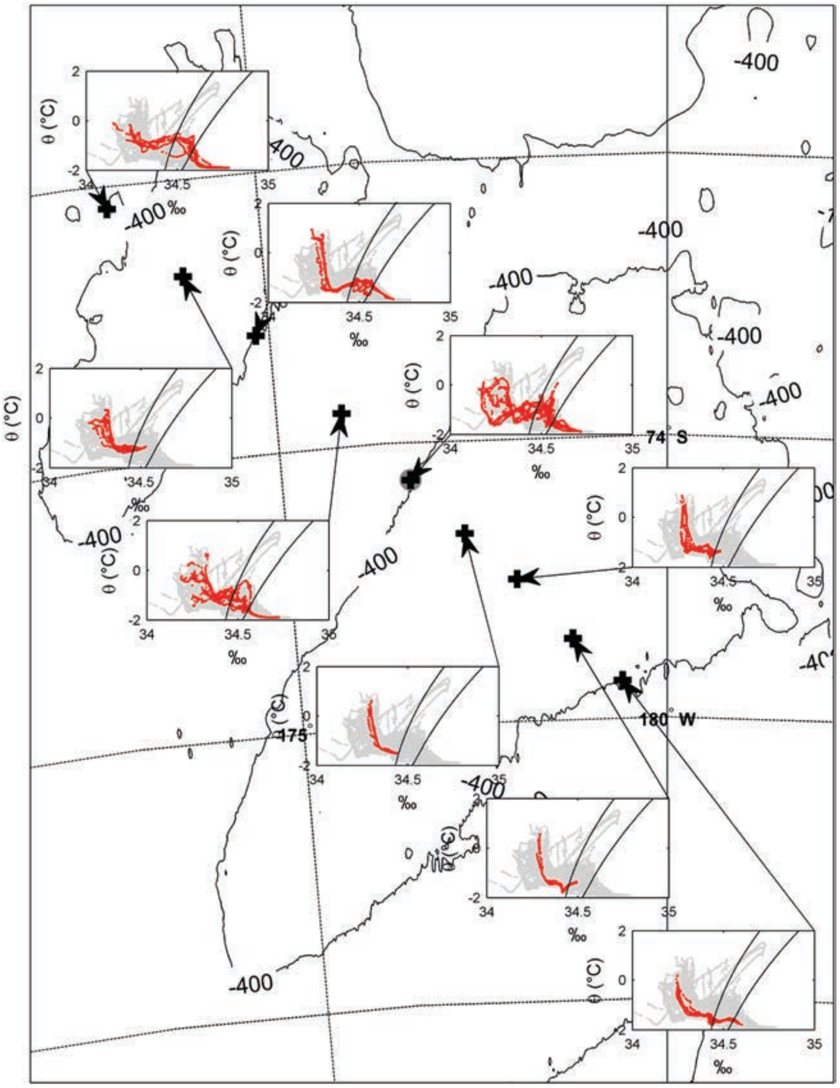

Figure 8. Potential temperature-salinity plots for the cross-bank stations for all stations (gray) and that particular station (red). The neutral density bounds for MCDW are shown as thick black lines. The mooring location (gray circle) is also shown.

adequately represent the significant time and space variability seen in the MCDW core along the banks. The velocity data used to estimate the transport was averaged over eight cross sections of the banks and eight CTD profiles over the 400 m isobath. Both the mooring and glider highlight the variability not captured in this mean estimate of transport. The mooring deployed directly over the 400 m isobath was instrumented at several depths including 225 m and 230 m within the approximate core of MCDW. The 13 day time series shows significant variation in velocity, potential temperature, and salinity. At least 85% of the variability in each velocity component is explained by the strong diurnal tide modulating the along-bank jet in both the along- and across-bank directions. The high-frequency velocity data at 225 m is dominated by the diurnal tide that transitioned from spring to neap over the duration of the deployment. Along-bank flow was consistently toward the southwest at 0.14 m/s, modulated by the tides. The cross-bank flow was upslope at 0.01 m/s, again modulated by the tides. Based on a 25 h running mean, the sub-tidal flow at 225 m depth is relatively steady along isobath throughout the deployment, slightly weakening toward the end of the deployment (Figure 12). The record mean of -0.14 m/s along isobath with a weak upslope component of 0.01 m/s is consistent with the MCDW area mean ADCP value of -0.12 m/s used in the transport calculations in section 3.3.

[23] In addition to the velocity, the potential temperature and salinity sampled at the 230 m depth within the MCDW core had significant variability (Figure 12). Like the velocity, the salinity had a large diurnal signal that ranged from 34.42 to 34.57 through the entire time series. The saltiest water is associated with a weak cross-shore velocity and strong southwestward along-bank velocity. The potential temperature data show a much different response with most of the variation occurring on scales of hours, much shorter than the diurnal signal seen in the velocity and salinity. This is strongest toward the end of 31 January when the potential temperature drops from $-0.4°$ to $-1.5°$ in a few hours. While the potential temperature data were much more variable over a large range of time scales, a diurnal signal was

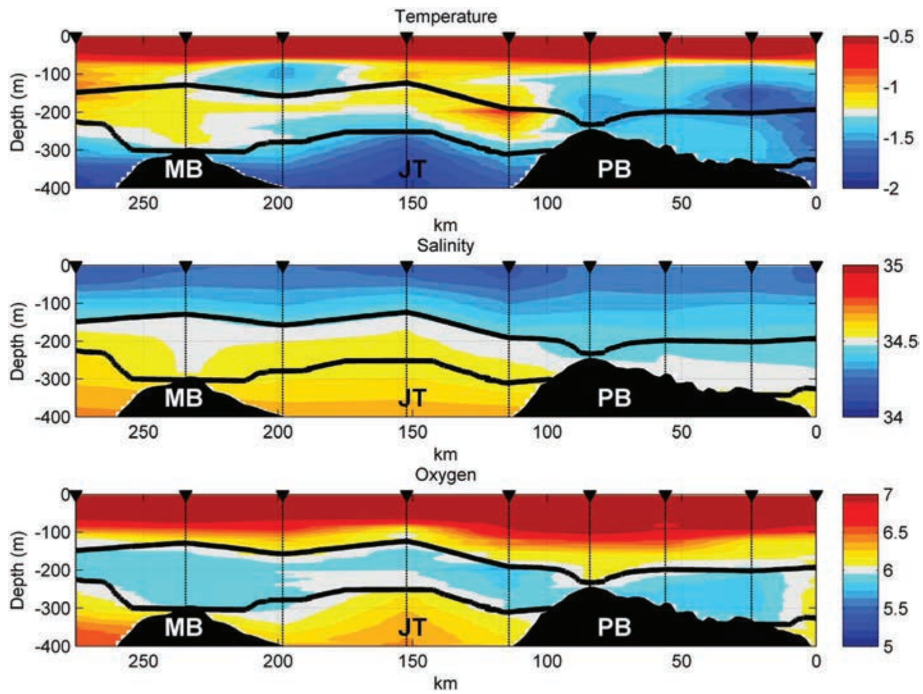

Figure 9. Average cross section of potential temperature (°C, top), salinity (psu, middle), and dissolved oxygen (ml/L, bottom). The stations sampled over the across-bank section are shown as vertical dashed lines. The neutral density bounds defining MCDW are shown in black, and the topographic features are labeled as in Figure 1.

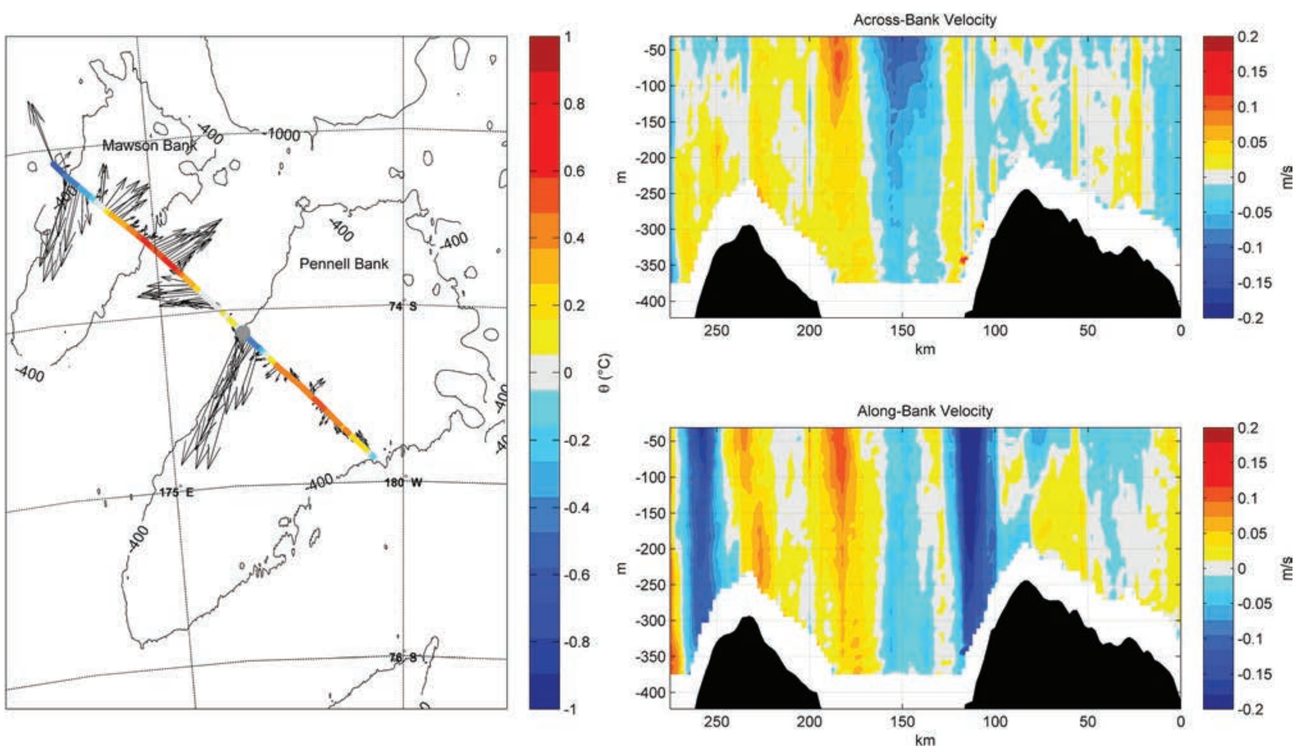

Figure 10. De-tided depth-averaged currents (black vectors) and surface temperature (colored track) over the across-bank section (left). The depth-dependent velocity sections (m/s) for the cross-bank (above right) and along-bank (below right) velocity components. These are the average of cross sections sampled between 22 January and 12 February 2011. The mooring location is shown as a gray circle (left).

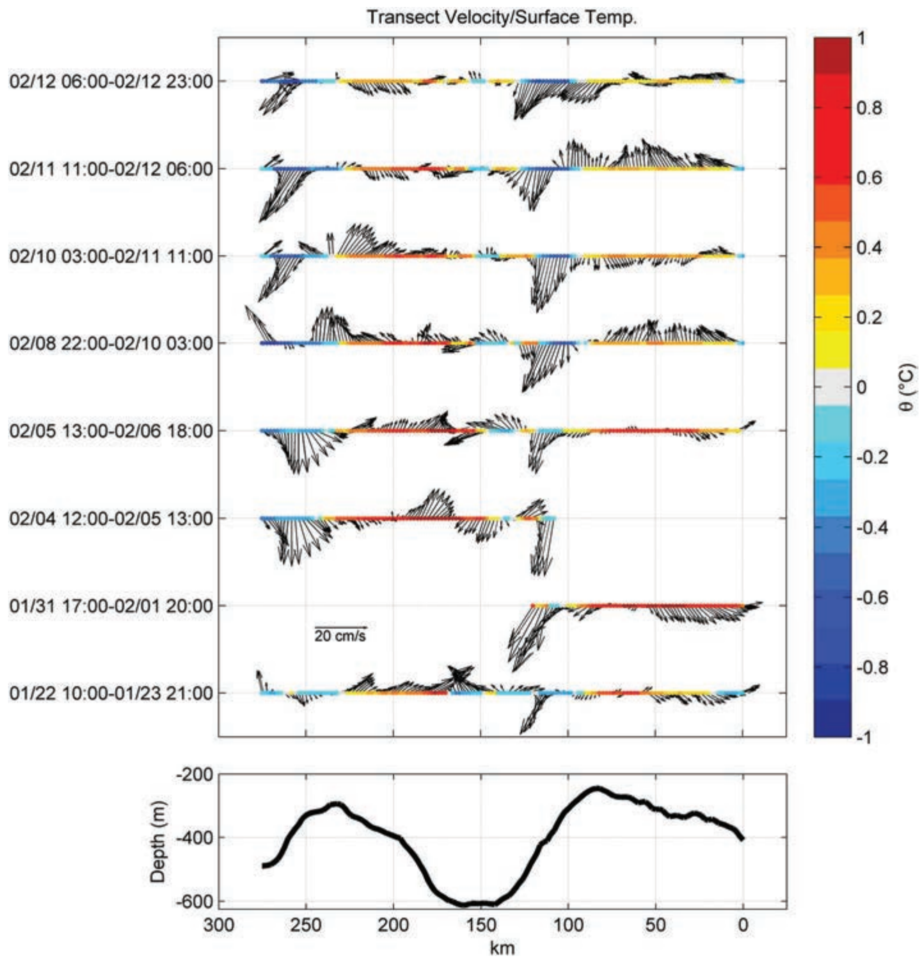

Figure 11. De-tided depth-averaged currents (black vectors) and surface temperature (colored track) for each of the across-bank sections. The topography identifying Pennell Bank (right) and Mawson Bank (left) is also shown (bottom).

present during the stronger spring tide. Throughout the record, there are also significant potential temperature shifts between -0.3°C and -1.6°C over periods much less than a day. The different response between the potential temperature and salinity time series at this depth is likely due to the difference in their vertical gradients and the relative influence each has on the density. At these salinity and temperature ranges, the ratio of beta to alpha is about 18 (beta ~ $d\rho/dS$, alpha ~ $d\rho/d\Theta$, where ρ is density, S is salinity, and Θ is potential temperature). Thus, fairly large excursions in potential temperature relative to salinity are to be expected. This is most evident at depth where there are large thermal gradients associated with MCDW. Here small vertical excursions lead to larger changes in potential temperature than salinity. The more gradual salinity changes with depth are seen only during the largest vertical excursions associated with the tides. The pressure data (not shown) indicate a fluctuation in the 225 m sensor depth of 10–30 m correlated with the tide. While significant, this sensor motion does not appear to account for all the variability in the diurnal band.

[24] The glider data collected in the vicinity of the mooring provides a spatial context for this temporal variability. A glider subsection of the transect that begins in the deeper water of Joides Trough moves up the slope of Pennell Bank toward the 280 m isobath (Figure 13). In the deeper water of the trough, the water column is seen to be relatively consistent with a layer of MCDW approximately 200 m deep. As the glider approaches the shallower water of the bank, this layer of MCDW deflects significantly in the vertical between 200 m and 350 m. The time scale of the depth variation of MCDW is consistent with the dominant diurnal tide that peaks over the shallows of the banks near the shelf break. The dashed black line approximates the location of the mooring. The apparent movement of the MCDW layer through the water column explains in part the variation in the potential temperature time series at 230 m from the mooring. This MCDW feature along the bank is highly variable over time scales of hours. This variation sampled by the glider is likely the result of tidal forcing on a spatially varying potential temperature field observed in the ship data.

4. Discussion

[25] Modified deep water intruding onto the shelf is a potential source of heat and micro-nutrients to the Ross Sea. Therefore, the magnitude and direction of MCDW transport are needed to quantify its impact on the heat and micronutrient budgets that influence Ross Sea processes. Throughout

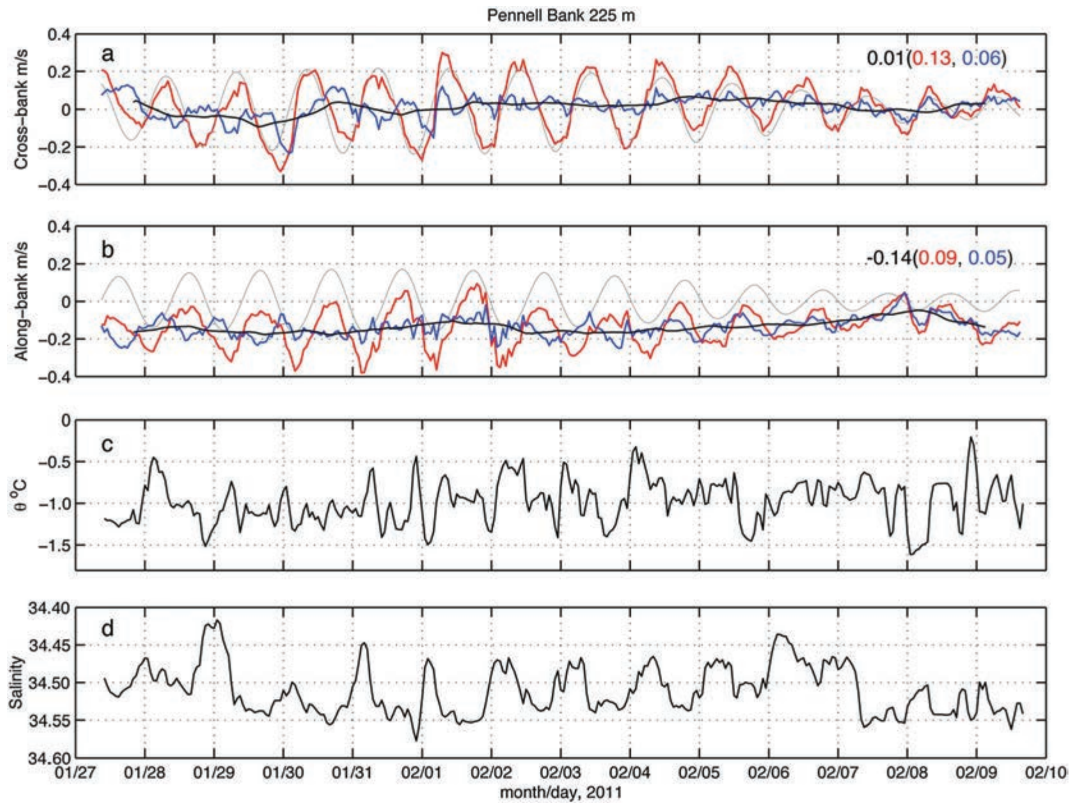

Figure 12. Moored hourly data including (a) cross-bank velocity (225 m), (b) along-bank velocity (225 m), (c) potential temperature (230 m), and (d) salinity (230 m). For Figures 12a and 12b, the red line is the hourly data, gray is velocity predicted by the barotropic tide model Ross_TIM [*Erofeeva, et al*., 2005], blue is de-tided data, and black is the 25 h running mean of the hourly data. Record-length mean of the hourly velocities is given in the upper-right corner, with the standard deviation of the hourly (red) and de-tided (blue) velocities in parentheses.

our survey, a large phytoplankton bloom was sustained over Pennell Bank (Figure 14). Both satellite remote sensing and ship board sampling identified this surface feature centered over the north east corner of Pennell Bank. Given the observed variation in MCDW transport and the apparent separation between it and the bloom, we can use our targeted dataset to identify two possible pathways that link the MCDW source waters to the bloom. The first is a direct transport eastward near the shelf break between the MCDW core observed at the mooring and the adjacent bloom over Pennell Bank. The large vertical excursion of the MCDW seen in the glider section could elevate that source above the minimum depth of the bank enabling cross-isobath transport onto the bank. During the cruise, we sampled stations between the troughs and the shallows of the bank along a line that bisected the mooring location. Along this line, there is no evidence of MCDW moving up slope over shallower water. A station 30 km east of the MCDW core in 280 m of water (80 km on the *x* axis of Figure 9) shows a water column predominately composed of a warm surface layer over a cooler, saltier bottom layer (Figure 9). The peak temperature and oxygen minimum characteristic of MCDW is not seen in any of the profiles sampled at this station. Based on these station data and the weak vertical shear in the ADCP velocities along this line, it is unlikely that the MCDW intrusion seen over the 400 m isobath is directly mixing up to the shallows of the adjacent bank, even with the significant vertical excursions of up to 100 m related to the dominant diurnal tide.

[26] An alternative pathway for the MCDW is to continue south along the bank, moving gradually upslope along the way. Once near the southern edge of the bank, the MCDW could turn north, continuing to follow the 400 m isobath back toward the shelf break. There is evidence of this isobath following flow pattern in model simulations [*Dinniman et al*., 2003]. This pathway is driven primarily by bathymetry given the mostly barotropic flow seen over the 400 m isobath. These model simulations are consistent with the mooring and ship-based ADCP data with a strong along isobath flow moving south over the 400 m isobath west of Pennell and Mawson Banks and a return flow back toward the shelf break on the eastern side of Mawson Bank. If we assume a barotropic flow following topography, we would expect the intrusion of MCDW over the 400 m isobath to be constrained by *f*/H, where *f* is the local Coriolis parameter and H is the water depth [*Marshall*, 1995]. Using the mooring site as an initial condition for the MCDW intrusion, we calculate the regions of the Ross Shelf that have consistent *f*/H values (Figure 15). If the MCDW is carried by a barotropic current south onto the shelf, then this flow would be limited to those areas shaded in tan. For Pennell Bank, we see the pathway continuing south and moving up onto the bank around the 74.5°S parallel where the steep slope of Pennell flattens. The shallower slope relaxes the dynamic constraint, allowing the MCDW to move up onto the bank. Once

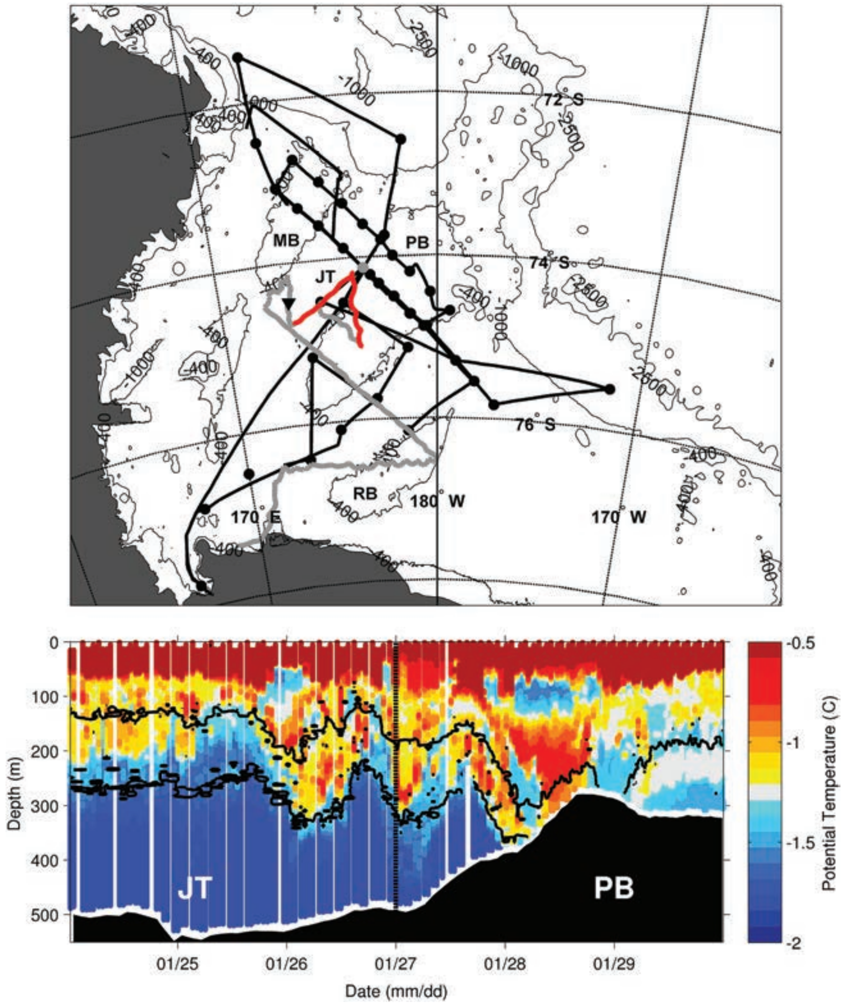

Figure 13. Subsection of the glider path that begins in Joides Trough and moves up the slope of Pennell Bank (red, above). Potential temperature along this section (below). The neutral density bounds defining MCDW are shown in black, and the topographic features are labeled as in Figure 1. The vertical dashed line (below) coincides with the sharp turn in the red transect (above).

over the bank, the MCDW is subject to the stronger diurnal tides and could be vertically mixed to the euphotic zone.

[27] The ADCP data identified a strong southward flow along the western edge of Pennell Bank coincident with the MCDW core. The depth-dependent data show that this flow is not truly barotropic. Given the observed shear, the *f*/H constraint may not apply to the MCDW intrusion along the bank. Recognizing that flow fields in the ocean are rarely fully barotropic, there is a modified denominator that considers the depth scale of the observed shear, f/F_o [*Krupitsky et al.*, 1996; *Gille*, 2003; *Gille et al.*, 2004], where

$$F_o = H_o(1 - \exp(-H/H_o)) \tag{1}$$

[28] H_o is the e-folding scale of the observed velocity shear:

$$v(z) = v(0)\ \exp(-z/H_o) \tag{2}$$

where $v(z)$ is the depth-dependent velocity, z is the depth of the measurement, and $v(0)$ is the magnitude of the surface velocity. Here we calculated H_o based on the average of the three velocity profiles within the MCDW core over the 400 m isobath (Figure 10). The exponential fit to this observed shear gives an e-folding depth scale of 380 m, approximately the depth of the water column. Since the shear is small, the modified constraint is not significantly different than the *f*/H constraint that assumes zero shear (not shown). With either definition, the flow transporting this MCDW from the shelf break onto the shelf likely follows the topography of both Pennell Bank and Mawson Bank toward the south. Unlike Pennell Bank, the water following Mawson is much less constrained to the slope and could quickly move over the shallows of the bank (Figure 15).

[29] Over Pennell Bank, there is a distinct separation between the MCDW core observed over the mooring site and the elevated chlorophyll concentrations over the shallower waters of the bank. The dynamic constraints shown in Figure 15 illustrate the isolation directly between them along ship sections sampled near the shelf break. Further south, however, the dynamic constraint relaxes and the glider section shows MCDW sliding up and over

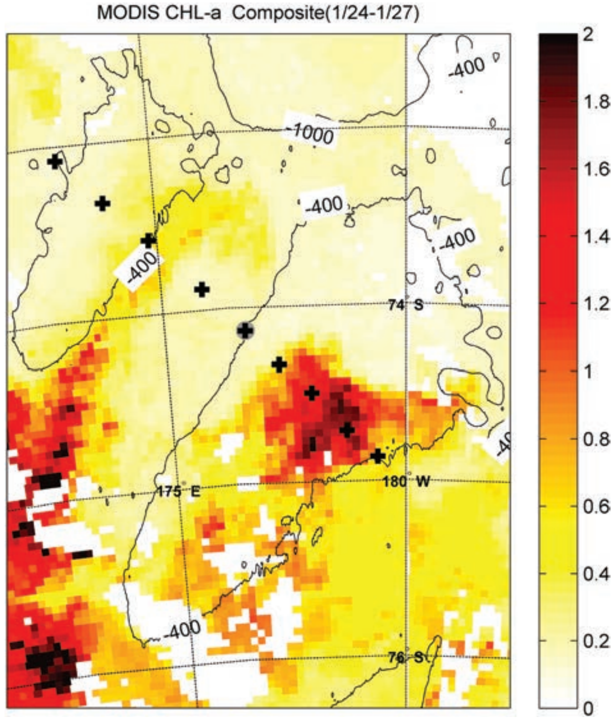

Figure 14. Surface map composite of satellite derived Chl-a concentration (mg/m^3). The cross-bank stations are shown as black crosses. The mooring location is also shown as a gray circle.

the bank (Figure 3). Once the MCDW reaches the shallows of the bank, it is subject to increased tides and could mix vertically toward the euphotic zone and the observed bloom. Through this pathway, the micronutrient supply of MCDW can reach the bloom and, if high enough concentration, help sustain its productivity.

5. Conclusion

[30] A multi-platform sampling strategy focused on the bank/trough topography near the outer shelf of the Ross Sea characterized the small scales that determine the transport of MCDW from preferred CDW intrusion sites at the shelf break south along the western slopes of both Pennell and Mawson Bank. For both banks, the MCDW signal is seen approximately over the 400 m isobath west of the banks. Using eight transects of ADCP sections across the bank/trough topography, we see a flow approximately barotropic moving southward along the bank. This flow is bringing with it cool fresher water on the surface and the warmer low oxygen water characteristic of MCDW at depth. The velocity and CTD sections averaged over eight cross sections were used to estimate a mean transport of MCDW over our survey of approximately 0.24 *Sv*. Both the glider and mooring data show that this mean transport is highly variable over scales of hours to days. The main variance, driven by the tides, appears to move this core of MCDW approximately 100 m in the water column every 12 h. At this point, we do not have the data coverage to determine the mechanism for this rapid movement of MCDW. However, we do conclude that this energetic tide is unlikely to drive the MCDW up and onto the Pennell Bank. Instead, given the small vertical shear in the flow, this intrusion of MCDW likely continues south along the bank until the slope flattens allowing the warmer mid-water to move over the bank. At that point, it is subject to the stronger tides of the bank and could be mixed up to the euphotic zone. The glider section across the southern edge of Pennell bank identifies the higher

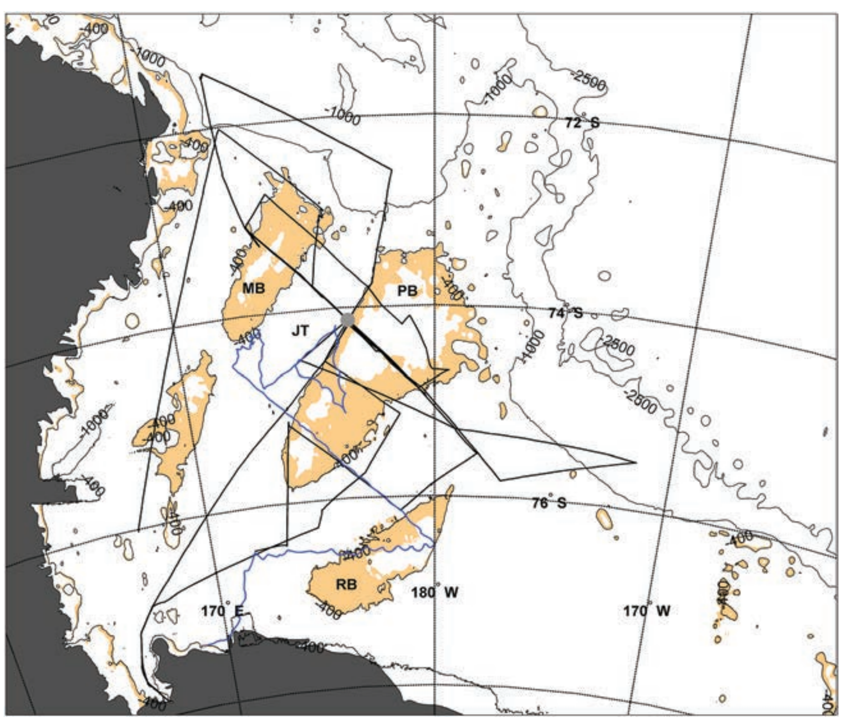

Figure 15. The regions of *f*/H (tan) consistent with the MCDW core identified in the vicinity of the mooring. The glider (blue) and ship track (black) are shown for reference. The mooring location is shown as a gray circle.

temperatures of the MCDW intrusion going up and over the bank. The scale of variability in time and space observed during this field study indicates a need for future study that incorporates longer time series, more detailed surveys, and eddy resolving models to fully describe the processes that govern the southward movement of MCDW into the Ross Sea.

[31] **Acknowledgments.** The NSF Office of Polar Programs (ANT-0839039) supported the Slocum Enhanced Adaptive Fe Algal Research in the Ross Sea (SEAFAReRS) project. The mooring was supported by the Cape Adare Long-term Moorings (CALM) project (ANT-0538148 and ANT-1141890). We want to specifically thank the project PIs for redeploying the mooring within days after recovery off Cape Adare. The successful deployment of the glider from the ice edge would not have been possible without the great effort of Chip Haldeman (Rutgers), Clayton Jones (Teledyne Webb Research), and Raytheon Polar Services. We would also like to thank the entire crew of the *RVIB Nathaniel B. Palmer* for their support throughout the cruise and John Kerfoot (Rutgers) for the glider processing before and after the deployment. This is Lamont-Doherty Earth Observatory contribution number 7662.

References

Arrigo, K. R., G. L. van Dijken, and S. Bushinsky (2008), Primary production in the Southern Ocean, 1997–2006, *J. Geophys. Res.*, *113*, C08004. doi:10.1029/2007JC004551.

Assmann, K., H. H. Hellmer, and A. Beckmann (2003), Seasonal variation in circulation and water mass distribution on the Ross Sea continental shelf, *Antarct. Sci.*, *15*(1), 3–11. doi:10.1017/S0954102003001007.

Assmann, K. M., and R. Timmermann (2005), Variability of dense water formation in the Ross Sea, *Ocean Dyn.*, *55*, 68–87.

Baines, P. G., and S. A. Condie (1998), Observations and modelling of Antarctic downslope flows: A review, *Antarct. Res. Ser.*, *75*, 29–49.

Budillon, G., and G. Spezie (2000), Thermohaline structure and variability in the Terra Nova Bay Polynya, Ross Sea, *Antarct. Sci.*, *12*, 493–508.

Budillon, G., P. Castagno, S. Aliani, G. Spezie, and L. Padman (2011), Thermohaline variability and Antarctic bottom water formation at the Ross Sea shelf break, *Deep Sea Res. I*, *58*, 1002–1018.

Dinniman, M. S., J. M. Klinck, and W. O. Smith (2003), Cross-shelf exchange in a model of the Ross Sea circulation and biogeochemistry, *Deep-Sea Res. II Top. Stud. Oceanogr.*, *50*(22–26), 3103–3120. doi:10.1016/j.dsr2.2003.07.011.

Erofeeva, S. Y., L. Padman, and G. Egbert (2005), Assimilation of ship-mounted ADCP data for barotropic tides: Application to the Ross Sea, *J. Atmos. Oceanic Technol.*, *22*(6), 721–734.

Foster, T. D., and E. C. Carmack (1976), Frontal zone mixing and Antarctic bottom water formation in the southern Weddell Sea, *Deep-Sea Res.*, *23*, 301–317.

Fragoso, G. M., and W. O. Smith (2012), Influence of hydrography on phytoplankton distribution in the Amundsen and Ross Seas, Antarctica, *J. Mar. Syst.*, *89*(1), 19–29. doi:10.1016/j.jmarsys.2011.07.008.

Fusco, G., G. Budillon, and G. Spezie (2009), Surface heat fluxes and thermohaline variability in the Ross Sea and in Terra Nova Bay polynyas, *Cont. Shelf Res.*, *29*, 1887–1895, doi:10.1016/j.csr.2009.07.006.

Gille, S. T. (2003), Float observations of the Southern Ocean: Part 1, Estimating mean fields, bottom velocities, and topographic steering, *J. Phys. Oceanogr.*, *33*, 1167–1181.

Gille, S. T., E. J. Metzger, and R. Tokmakian (2004), Sea floor topography and ocean circulation, *Oceanography*, *17*(1), 47–54.

Gordon, A. L., L. Padman, and A. Bergamasco (2009a), Southern Ocean shelf slope exchange, *Deep-Sea Res. II Top. Stud. Oceanogr.*, *56*(13–14), 775–777.

Gordon, A. L., A. H. Orsi, R. Muench, B. A. Huber, E. Zambianchi, and M. Visbeck (2009b), Western Ross Sea continental slope gravity currents, *Deep-Sea Res. II Top. Stud. Oceanogr.*, *56*(13–14), 796–817.

Hiscock, M. R. (2004), The regulation of primary productivity in the Southern Ocean. PhD Dissertation, Duke University, 150 pp.

Jacobs, S. S., and C. F. Giulivi (1998), Interannual ocean and sea ice variability in the Ross Sea. in Ocean, Ice, and atmosphere: Interactions at the Antarctic Continental Margin, edited by S. S. Jacobs, and R. F. Weiss, pp. 135–150, AGU.

Jacobs, S. (2004), Bottom water production and its links with the thermohaline circulation, *Antarct. Sci.*, *16*, 427–437.

Killworth, P. D. (1977), Mixing on the Weddell Sea continental slope, *Deep-Sea Res.*, *24*, 427–448.

Klinck, J. M., and M. S. Dinniman (2010), Exchange across the shelf break at high southern latitudes, *Ocean Sci.*, *6*(2), 513–524. doi:10.5194/os-6-513-2010.

Krupitsky, A., V. Kamenkovich, N. Naik, and M. A. Cane (1996), A linear equivalent barotropic model of the Antarctic Circumpolar Current with realistic coastlines and bottom topography, *J. Phys. Oceanogr.*, *26*, 1803–1824.

Marshall, D. (1995), Influence of topography on the large-scale ocean circulation, *J. Phys. Oceanogr.*, *25*, 1622–1635.

Muench, R., L. Padman, A. Gordon and A. Orsi (2009), A dense water outflow from the Ross Sea, Antarctica: Mixing and the contribution of tides, *J. Mar. Syst.*, *77*(4): 369–387.

Orsi, A. H., G. C. Johnson, and J. L. Bullister (1999), Circulation, mixing, and production of Antarctic Bottom Water, *Prog. Oceanogr.*, *43*(1), 55–109.

Orsi, A. H., W. M. Smethie, and J. L. Bullister (2002), On the total input of Antarctic waters to the deep ocean: A preliminary estimate from chlorofluorocarbon measurements, *J. Geophys. Res. Oceans*, *107*(3122), pp. 31-1–31-14.

Orsi, A. H., and C. L. Wiederwohl (2009), A recount of Ross Sea waters, *Deep-Sea Res. II Top. Stud. Oceanogr.*, *56*(13–14), 778–795.

Padman, L., S. Howard, A. Orsi, R. Muench (2009), Tides of the Northwestern Ross Sea and their impact on dense outflows of high salinity shelf water, in Deep-Sea Research AnSlope/Clima Topical Volume, edited by A. Gordon, L. Padman, A. Bergamasco, Southern Ocean Shelf Slope Exchange.

Rickard, G. J., M. J. Roberts, M. J. M. Williams, A. Dunn, and M. H. Smith (2010), Mean circulation and hydrography in the Ross Sea sector, Southern Ocean: Representation in numerical models, *Antarct. Sci.*, *22*(05), 533–558. doi:10.1017/s0954102010000246.

Robertson, R. (2005), Baroclinic and barotropic tides in the Ross Sea, *Antarct. Sci.*, *17*(1), 107–120. doi:10.1017/s0954102005002506.

Robertson, R., A. Beckmann, and H. Hellmer (2003), M2 tidal dynamics in the Ross Sea, *Antarct. Sci.*, *15*(1), 41–46. doi:10.1017/s0954102003001044.

Schofield, O., et al. (2007), Slocum Gliders: Robust and ready, *J. Field Rob.*, *24*(6), 1–14, doi:10:1009/rob.20200.

Smith, W. O., A. R. Shields, J. A. Peloquin, G. Catalano, S. Tozzi, M. S. Dinniman, and V. A. Asper (2006), Interannual variations in nutrients, net community production, and biogeochemical cycles in the Ross Sea, *Deep-Sea Res. II Top. Stud. Oceanogr.*, *53*(8–10), 815–833. doi:10.1016/j.dsr2.2006.02.014.

Whitworth, T., A. H. Orsi, S.-J. Kim, W. D. J. Nowlin, and R. A. Locarnini (1998), Water masses and mixing near the Antarctic Slope Front, *Ocean, Ice and Antarct. Res. Ser.*, *75*, 1–29.

Whitworth, T. III, and A. H. Orsi (2006), Antarctic Bottom Water production and export by tides in the Ross Sea, *Geophys. Res. Lett.*, *33*, L12609, doi:10.1029/2006GL026357.

The Robot Ocean Network

Automated underwater vehicles go where people cannot, filling in crucial details about weather, ecosystems, and Earth's changing climate.

Oscar Schofield, Scott Glenn, and Mark Moline

In the frigid waters off Antarctica, a team of our colleagues deploy a waterborne robot and conduct final wireless checks on the system's internal engines and onboard sensors, before sending the device on its way to explore the ocean conditions in an undersea canyon over a month-long expedition. The autonomous robot's mission will be monitored and adjusted on the fly by scientists and their students remotely located in the United States; the data it returns will become part of our overall picture of conditions in the Southern Ocean.

Ocean robots—more formally known as *autonomous underwater vehicles*, or *AUVs*—are improving our understanding of how the world's ocean works and expanding our ability to conduct science at sea even under the most hostile conditions. Such research is essential, now more than ever. The ocean drives the planet's climate and chemistry, supports ecosystems of unprecedented diversity, and harbors abundant natural resources. This richness has lead to centuries of exploration, yet despite a glorious history of discovery and adventure, the ocean remains relatively unknown. Many basic and fundamental questions remain: How biologically productive are the oceans? What processes dominate mixing between water layers? What is its total biodiversity? How does it influence the Earth's atmosphere? How is it changing and what are the consequences for human society?

The last question is particularly pressing, as many observations suggest that significant change is occurring right now. These shifts reflect both natural cycles and, increasingly, human activity, on a local and global scale. Local effects include alterations in circulation, increased introduction of nutrients and pollutants to the sea, the global transport of invasive species, and altered food web dynamics due to the overexploitation of commercially valuable fish species. Regional- and global-scale changes include altered physical (temperature, salinity, sea-level height), chemical (oxygen, pH, nutrients), and biological properties (fishing out of top predators).

Addressing the many unknowns about the ocean requires knowledge of its physics, geology, chemistry, and biology. On the most basic level, one has to be able to track the movement of water and its constituents over time to understand physical transport processes. But this fundamental first step remains a difficult problem given the three-dimensional structure of the ocean and the limited sampling capabilities of traditional oceanographic tools. About 71 percent of the world is covered by the ocean, with a volume of about 1.3 billion cubic kilometers. Only about 5 percent of that expanse has been explored. A further complication is the broad scale of ocean mixing—spatially, from centimeters to thousands of kilometers, and temporally, from minutes to decades. These processes are all modified by the interactions of currents with coastal boundaries and the seafloor.

If the problem of monitoring mixing can be solved, then focus can shift to the biological and chemical transformations that occur within the water. Factors that remain unknown include the amount of inorganic carbon being incorporated into organic carbon, and how quickly that organic matter is being transformed back into inorganic compounds—processes that are driven by marine food webs. Many of these transformation processes reflect the "history" of the water mass: where it has been and when it was last mixed away from the ocean surface. Because of the vast domain of the ocean, our ability to sample the relevant spatial and temporal scales has been limited.

Oceanographers usually collect data from ships during cruises that last days to a few months at most. The modern era of ship-based expeditionary research, launched just over a century ago, has resulted in major advances in our knowledge of the global ocean. But most ships do not travel much faster than a bicycle and they face harsh, often dangerous conditions. The high price of ships also limits how many are available for research. A moderately large modern research vessel may run about $50,000 a day even before the costs of the science. Ocean exploration requires transit to remote locations, a significant time investment. Once on site, wind and waves will influence when work can be safely conducted.

For example, one of us (Schofield) routinely works along the western Antarctic Peninsula. The travel time from New Jersey to the beginning of experimental work can take upward of a week: two days of air and land travel, one to two days of port operations, and four days of ship travel. During the writing of this article, Schofield was at sea offshore of Antarctica,

Oscar Schofield is a professor of oceanography and chair of the Department of Marine and Coastal Sciences at Rutgers University. Scott Glenn is a distinguished professor of oceanography at Rutgers. Their work has focused on developing ocean-observing networks. Mark Moline is the director of the School of Marine Science and Policy at the University of Delaware. His research centers on the diversity, interactions, and ecology of plankton. Email: oscar@marine.rutgers.edu.

In the icy waters off the Antarctic coast, researchers must be mindful of their physical safety. The aquatic robot they are deploying has no such needs and can operate in the forbidding conditions for weeks or months at a time. Legions of such autonomous underwater vehicles (AUVs) are now gathering data about the physical state of the world's ocean, collecting information that is inaccessible to ships or satellites. (Photograph courtesy of Jason Orfanon.)

where ship operations were halted for several days due to heavy winds, waves, and icy decks. All three of us have on multiple occasions experienced the "robust" work atmosphere—such as broken bones and lacerations—associated with working aboard ships. Despite these difficulties, ships are the central tool for oceanography, providing the best platform to put humans in the field to explore. But researchers realized decades ago that they needed to expand the ways they could collect data at sea.

Satellites provide a useful sampling tool to complement ships and can provide global estimates of surface temperature, salinity, sea surface height, and plant biomass. Their spatial resolution, however, is relatively low (kilometers to hundreds of kilometers), and they often cannot collect data in cloudy weather. Additionally, they are incapable of probing the ocean interior. Ocean moorings (a vertical array of instruments anchored to the seafloor) can provide a time series of measurements at single points, but their high cost (ranging from $200,000 to millions each) limits their numbers.

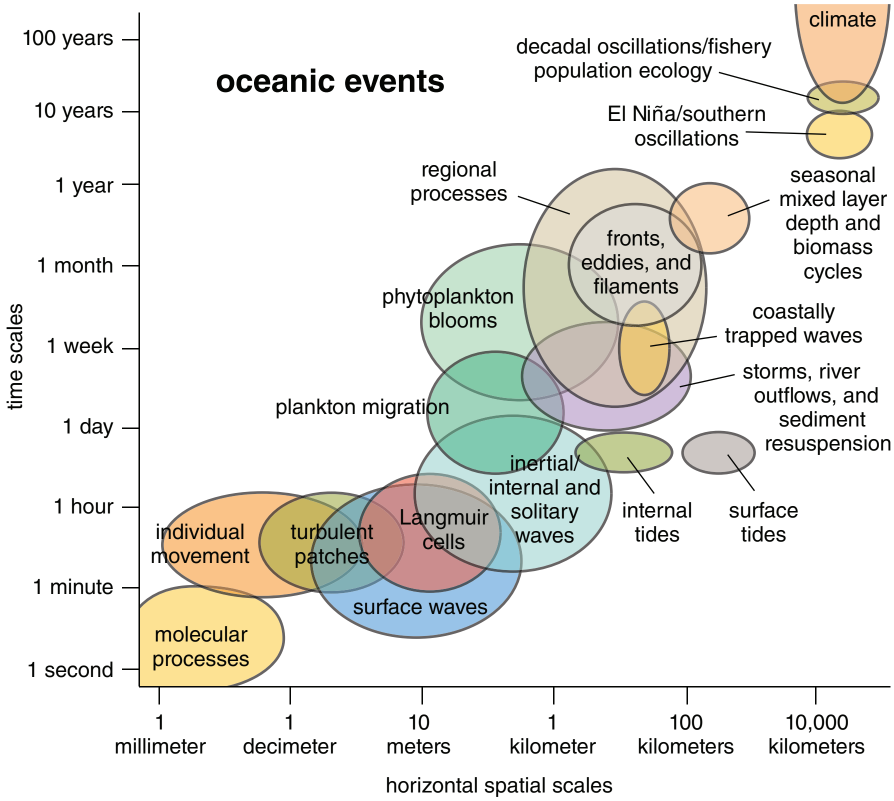

Processes in the ocean happen on a number of varying temporal and spatial scales, and these events often affect one other. But gathering data on these numerous scales has proven difficult using traditional research methods. AUVs may be able to bridge some of the gaps, given their long mission times and maneuverability in the ocean. (Adapted from an illustration by Tommy Dickey.)

Twenty-three years ago, those challenges inspired oceanographer Henry "Hank" Stommel to propose a globally distributed network of mobile sensors capable of giving a clearer look, on multiple time and space scales, at the processes going on in the world's ocean. His futuristic vision is finally becoming a reality. Thousands of robots are today moving through the world's ocean and communicating data back to shore. They provide crucial information on everything from basic processes—such as the ocean's temperature and salinity—to specific processes like storm dynamics and climate change.

Ocean Workhorses

The most vital component of the rapidly growing ocean sensor network is the AUV. These devices come in various types, carry a wide variety of sensors, and can operate for months at a time with little human guidance, even under harsh conditions.

Underwater robotics has made major advances over the past decade. Key technological gains include an affordable global telecommunication network that provides sufficient bandwidth to download data and remotely control AUVs from anywhere on the planet, the miniaturization of electronics and development of compact sensors, improved batteries, and the maturation of platforms capable of conducting a wide range of missions.

The AUVs being used in the ocean today generally come in three flavors: profiling floats, buoyancy-driven gliders, and propeller vehicles. In the first category, the international Argo program has deployed more than 3,500 relatively inexpensive profiling floats (costing about $15,000 each) throughout the ocean, creating the world's most extensive autonomous ocean network. These 1.3-meter-long platforms decrease their buoyancy by pumping in water, sinking themselves to a specified depth (often more than 1,000 meters), where they remain for about 10 days, drifting with the currents. The floats then increase their buoyancy by pumping out water, and rise to the surface. During the descent and ascent, onboard sensors collect vertical profiles of ocean properties (such as temperature, salinity, and a handful of ocean color and fluorescence measurements). New chemical sensors to measure pH and nutrients are also available. Data are transferred back to shore via a global satellite phone call. After transferring the data, the floats repeat the cycle.

Profiling floats are incapable of independent horizontal travel, leaving their movements at the mercy of the currents, but they are extremely efficient. A single battery pack can keep a float operating for four to six years. The combined data from large numbers of floats provides great scientific value, offering a comprehensive picture of conditions in the upper 1,000 meters of the ocean around the globe. When these data are combined with global satellite measurements of sea-surface height and temperature, they allow scientists to observe for the first time climate-related ocean variability in temperature, salinity, and circulation over global scales.

Cousin to the profiling floats are the buoyancy-driven gliders, which were highlighted in Stommel's original vision of a networked ocean. Several different types exist, but generally they are 1 to 2 meters long and maneuver up and down through the water column at a forward speed of 20 to 30 centimeters per second in a sawtooth-shaped gliding trajectory. They operate by means of a buoyancy change similar to that for floats, but wings redirect the vertical sinking motion due to gravity into forward movement. A tailfin rudder provides steering as the glider descends and ascends its way through the ocean, which makes these devices more controllable than the floats. They are more expensive, however, costing around $125,000. Therefore, they are often deployed for specific scientific missions.

A glider's navigation system includes an onboard GPS receiver coupled with an attitude sensor, a depth sensor, and an altimeter. The vehicle uses this equipment to perform dead reckoning navigation, where current position is calculated using a previously determined position, and that position is then updated based on known or estimated speeds over elapsed time and course. Scientists can also use a buoyancy-driven glider's altimeter and depth sensor to program the location of sampling in the water column. At predetermined intervals, the vehicle sits on the surface and raises

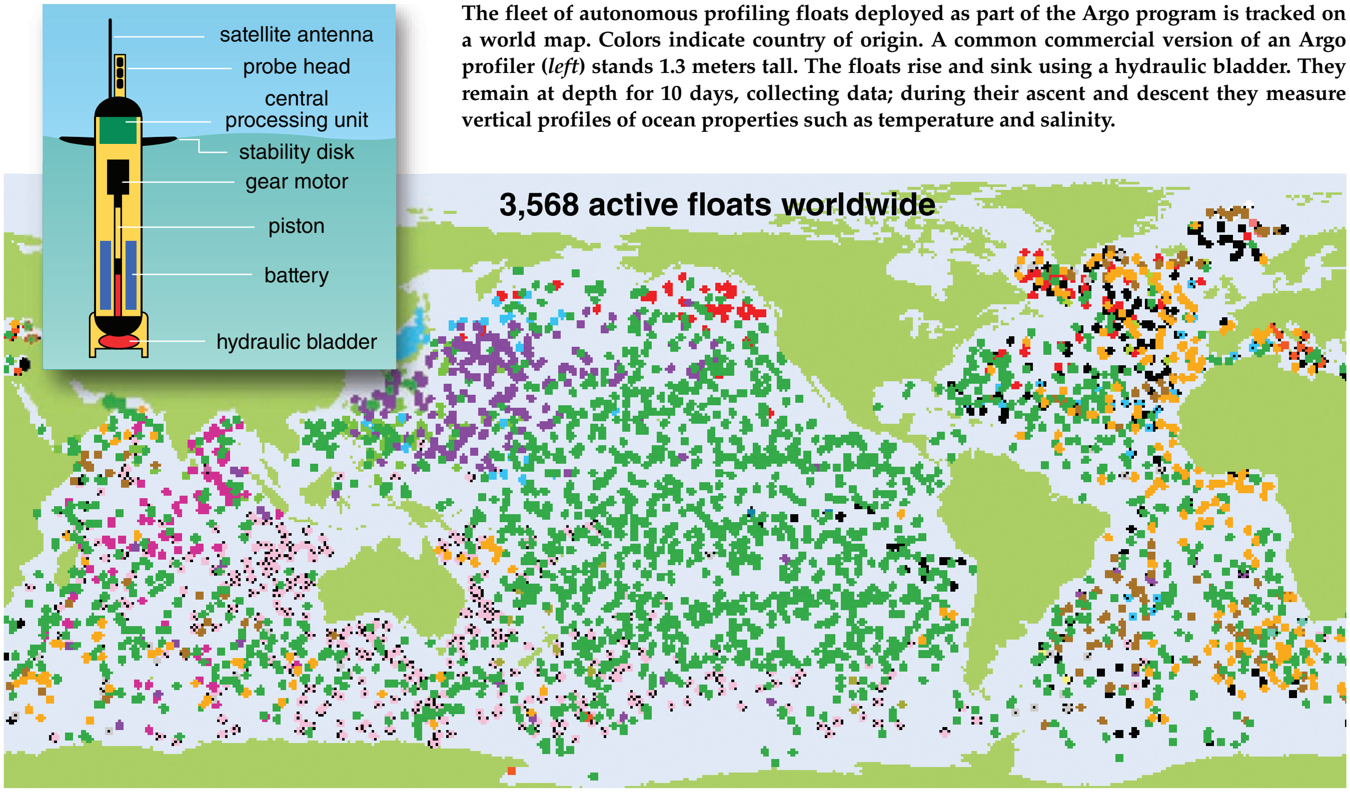

The fleet of autonomous profiling floats deployed as part of the Argo program is tracked on a world map. Colors indicate country of origin. A common commercial version of an Argo profiler (*left*) stands 1.3 meters tall. The floats rise and sink using a hydraulic bladder. They remain at depth for 10 days, collecting data; during their ascent and descent they measure vertical profiles of ocean properties such as temperature and salinity.

an antenna out of the water to retrieve its position via GPS, transmit data to shore, and check for any changes to the mission.

Because their motion is driven by buoyancy, the gliders' power consumption is low. They can coast for up to year on battery power. These robots are also modular: Researchers can attach sensors customized to one particular science mission, and then remotely reprogram what the sensors are searching for in near real time, based on collected data.

The most advanced, but also the most expensive, underwater robots are the propeller-driven AUVs. Costs can range from $50,000 to $5 million, depending on the size and depth rating of the AUV. They are powered by batteries or fuel cells, and can operate in water as deep as 6,000 meters. Like gliders on the surface, propeller AUVs receive a GPS fix and relay data and mission information to shore via satellite. While they are underwater, propeller AUVs navigate by various means. They can operate inside a network of acoustic beacons, by their position relative to a surface reference ship, or by an inertial navigation system, which measures the vehicle's acceleration with an accelerometer and orientation with a gyroscope. Travel speed is determined using Doppler velocity technology, which measures an acoustic shift in the sound waves that the vehicle bounces off the seafloor or other fixed objects. A pressure sensor measures vertical position.

Propeller-driven AUVs, unlike gliders, can move against most currents at 5 to 10 kilometers per hour, so they can systematically measure a particular line, area, or volume. This ability is particularly important for surveys of the ocean bottom and for operations near the coastline in areas with heavy traffic of ships and small crafts.

Most AUVs in use today are powered by rechargeable batteries (such as lithium ion ones similar to those in laptop computers). Their endurance depends on the size of the vehicle as well as its power consumption, but typically ranges from 6 to 75 hours of operation under a single charge, with

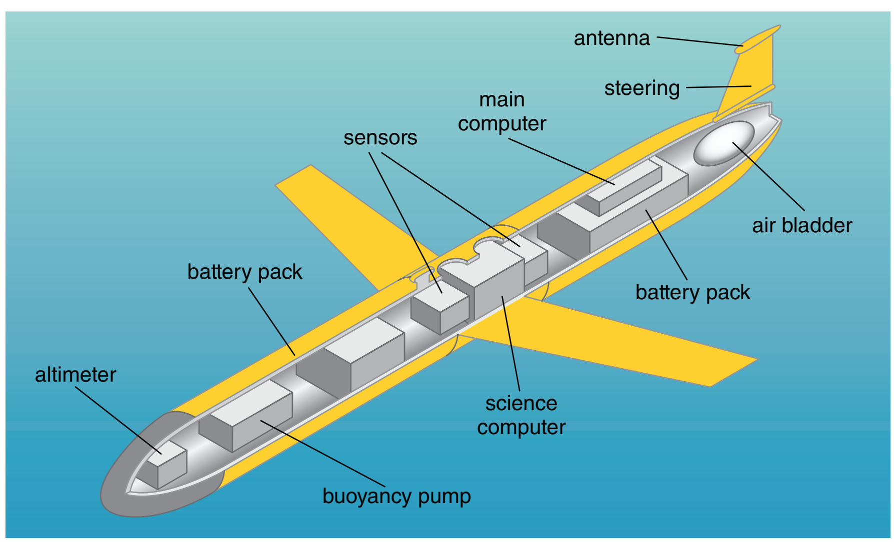

Anatomy of a typical buoyancy-driven AUV: A torpedo-shaped body minimizes drag. An altimeter is used to locate the seafloor. A buoyancy pump and air bladder regulate depth, and fins aid steering. Battery packs keep the robot powered for months. A main computer controls the AUV's actions; a science computer stores the data from the sensors. An antenna transmits the findings to shore.

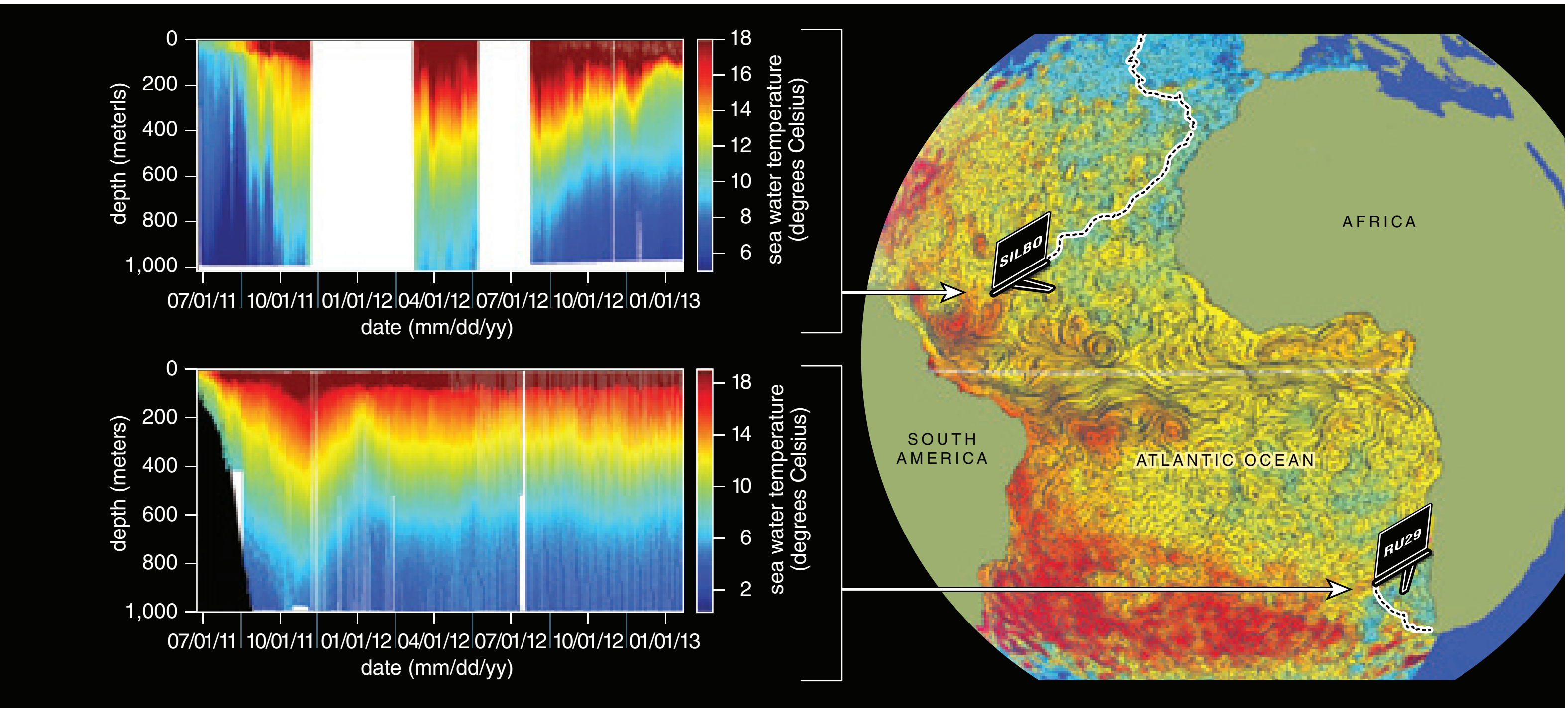

Global ocean circulation numerical models (*right*) were used by operators to guide two underwater gliders remotely. Currents are denoted by wavy lines; color indicates sea surface height. The positions of the gliders are denoted by their tailfins, with one heading toward Brazil and the other leaving the coast of South Africa. Temperature-profile data collected by the gliders are shown at left. (Unless otherwise indicated, images are courtesy of the authors.)

travel distances of 70 to 400 kilometers over that period. The sensor cargo they carry also depends on the size of the vehicle and its battery capacity.

Because of the additional power of propeller AUVs compared to gliders, they can run numerous sensor suites, and they remain the primary autonomous platform for sensor development. Hundreds of different propeller AUVs have been designed over the past 20 or so years, ranging in size from 0.5 to 7 meters in length and 0.15 to 1 meter in diameter. Most of these vehicles have been developed for military applications, with a few operated within the academic community. By the end of this decade, it is likely that propeller AUVs will be a standard tool used by most oceanographic laboratories and government agencies responsible for mapping and monitoring marine systems.

Riding a Hurricane

Together, the three types of ocean robots deployed throughout the world's ocean are bringing into scientific reach processes that are not accessible using ships or satellites. For example, these robots can study the ocean's response to, and feedback from, large storms such as hurricanes and typhoons. All three of us live in the mid-Atlantic region of the United States and have experienced Hurricanes Irene and Sandy,

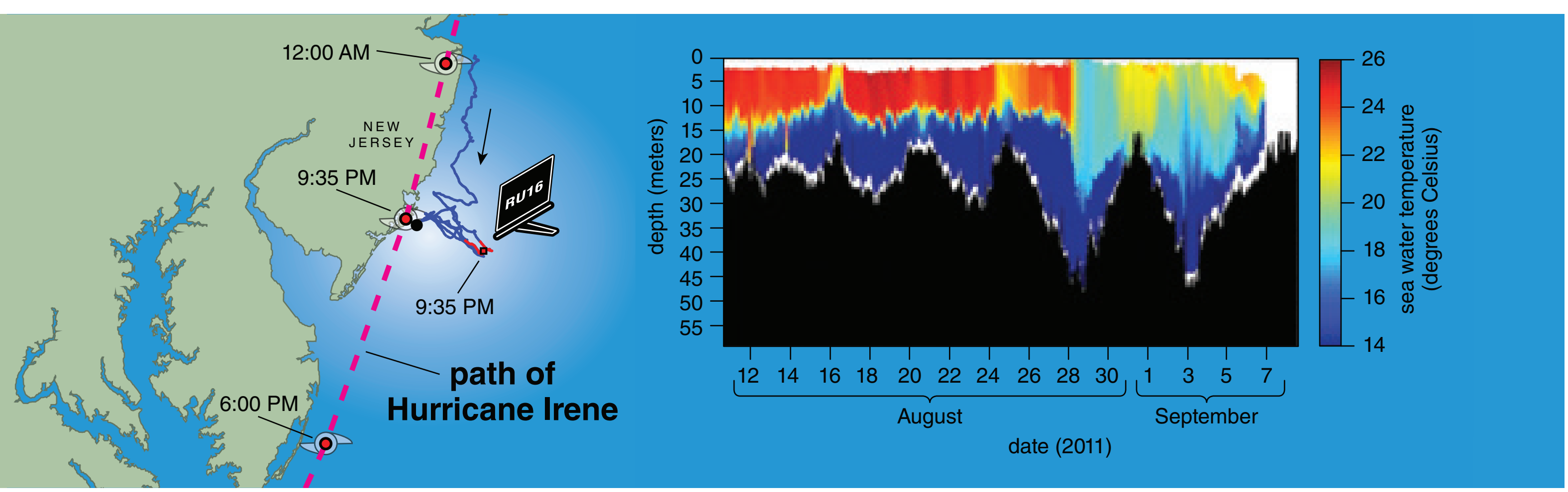

When Hurricane Irene grazed New Jersey (*left*) on August 28, 2011, a glider named RU16 was traveling nearby (*blue lines*). RU16 was originally deployed to map water quality for the state's Department of Environmental Protection; by luck it was in a perfect location (*red line*) to collect critical data on the storm. Readings from the glider (*right*) showed that the passage of the storm rapidly cooled the water column. Such data could lead to improved hurricane forecasts in the future.

so we are all too familiar with storm aftermath in our local communities.

Hurricane Irene, a category-1 storm offshore, moved rapidly northward along the U.S. East Coast in August 2011, resulting in torrential rains and significant flooding on inland waterways. Hurricane Sandy, a much larger category-2 storm offshore, made an uncharacteristic left turn and approached perpendicular to the coast in October 2012, causing significant damage to coastal communities. The U.S. National Hurricane Center ranks Sandy as the second-costliest hurricane ever in this country, producing over $60 billion of damage; Irene comes in eighth place, with at least $15 billion in damages.

Path forecasts by the U.S. National Hurricane Center for Irene and Sandy were extremely accurate even several days in advance, enabling evacuations that saved many lives. Hurricane intensity forecasts were less precise. The force of Irene was significantly overpredicted, and the rapid acceleration and strengthening of Sandy just before landfall was underpredicted. A more accurate forecast for Sandy would have triggered more effective preparations, which might have reduced the amount of damage.

The cause of the discrepancy between track forecasts and intensity forecasts remains an open research question. Global atmospheric model development over the past 20 years has successfully reduced forecast hurricane track errors by factors of two to three. The predictive skill of hurricane intensity forecasts has remained flat, however.

One possible reason is that more information is required about the interactions between the ocean and the atmosphere during storms, because the heat content of the upper ocean provides fuel for hurricanes. The expanding array of robotic ocean-observing technologies is providing a means for us to study storm interactions in the coastal ocean just before landfall, accessing information in ways not possible using traditional oceanographic sampling.

During the summer, the surface waters of the mid-Atlantic are divided into a thin, warm upper layer (10 to 20 meters deep and 24 to 26 degrees Celsius) overlying much colder bottom water (8 to 10 degrees). Gliders were navigating the ocean waters beneath both Hurricanes Irene and Sandy, collecting hydrographic profiles. Data taken during Irene suggest that as the leading edge of the storm approached the coast, the hurricane-induced increase in the flow of water onto the shore was compensated by an offshore flow below the thermocline (the region of maximum temperature change in the water column) in a downwelling flow created by high winds. This phenomenon minimized the potential storm surge. Simultaneously, storm-induced mixing of the water layers broadened the thermocline and cooled the ocean surface ahead of Irene by up to 8 degrees in a few hours, shortly before the eye of the storm passed over. This cold bottom water potentially weakened the storm as it came ashore. When data from a glider that measured the colder surface water were retrospectively input into the storm forecast models, that adjustment eliminated the overprediction of Irene's intensity.

In contrast to Irene, Hurricane Sandy arrived in the late fall, after seasonal cooling had already decreased the ocean surface temperatures by 8 degrees. As

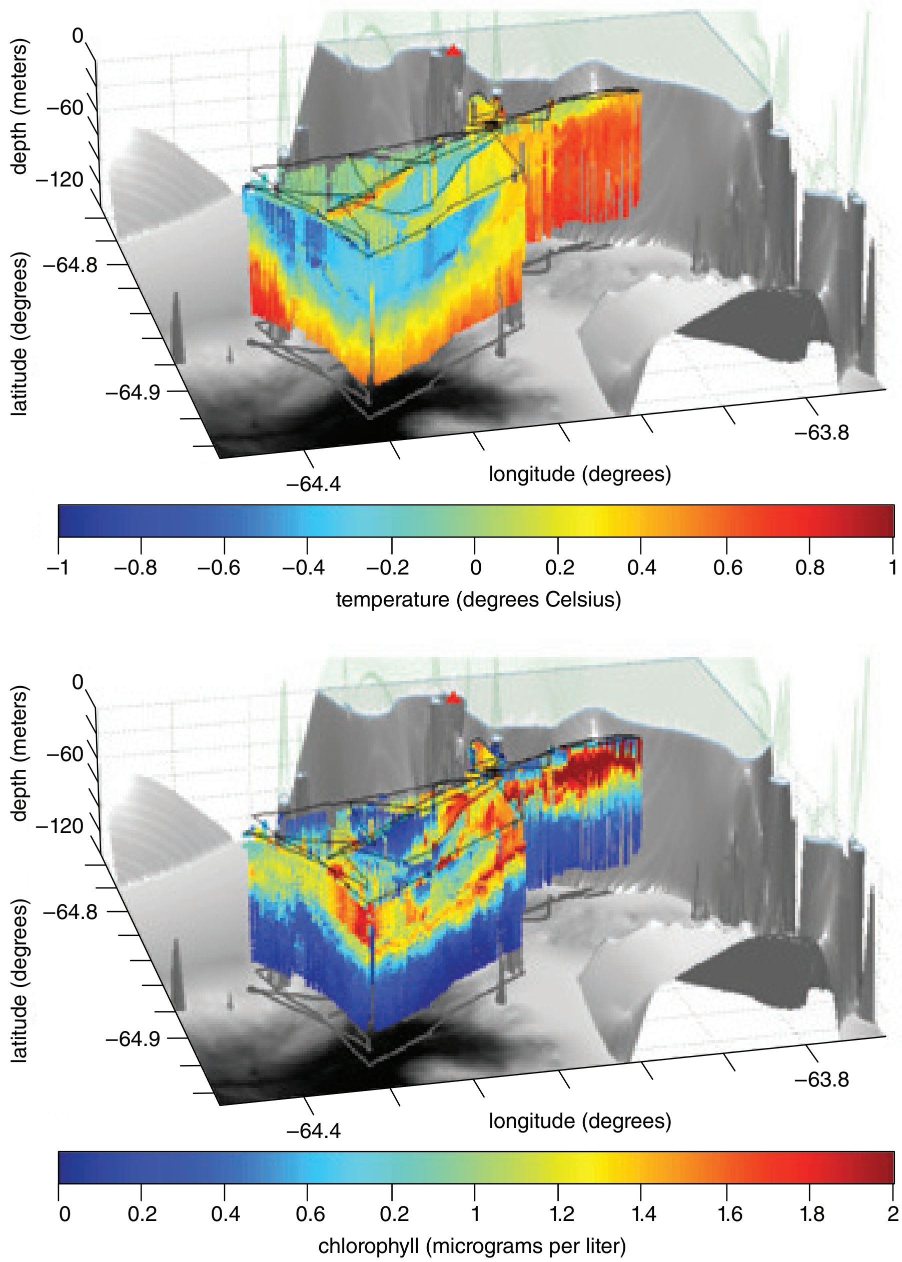

Glider data decode the complex dynamics of a deep-sea canyon in the western Antarctic Peninsula. Readings of water temperature (*top*) show an uplift of warm water, probably due to the coastward movement of the offshore circumpolar current. A chlorophyll map (*bottom*), from the same glider, indicates higher concentrations of phytoplankton where the warm water rises. This is the first hard evidence linking such upwelling with increased ocean productivity.

the storm came ashore, it induced mixing of cold water from the bottom to the surface—just as Hurricane Irene did—but because of the seasonal declines in temperature, the surface water temperature dropped by only around 1 degree. Such a small change did little to reduce the intensity of Hurricane Sandy as it approached the New Jersey and New York coastlines.

Robotic platforms have thus demonstrated their potential to sample storms and possibly aid future forecasts of hurricane intensity. The gliders operate effectively under rough ocean conditions that are not safe for people, and the mobility of gliders allows their positions to be adjusted as the storm moves. Their long deployment lifetime means these robots can be in place well before the storm's arrival until well after conditions calm down. Real-time data from the gliders should improve hurricane intensity forecast models and potentially help coastal communities proactively mitigate storm damage.

Heating Up Antarctica

As complex as hurricane forecasting may be, it pales in comparison to interpreting changes in ocean physics on a global scale, and then connecting those changes with local effects such as sea ice coverage or species decline.

Many questions oceanographers face are so complex that they require the combined data of several robotic platforms that span the range of spatial and temporal scales of marine ecosystems. Linking global changes to local effects has been difficult to impossible using conventional strategies.

One setting that illustrates the importance of bridging these scales is the western Antarctic Peninsula, which is undergoing one of the most dramatic climate-induced changes on Earth. This region has experienced a winter atmospheric warming trend during the past half-century that is about 5.4 times the global average (more than 6 degrees Celsius since 1951). The intensification of westerly winds and changing regional atmospheric circulation, some of which likely reflects the effect of human activity, has contributed to increasing transportation of warm offshore circumpolar deep water onto the continental shelf of the peninsula.

This water derives from the deep offshore waters of the Antarctic Circumpolar Current, the largest ocean current on Earth, and is the primary heat source in the peninsula. The altered positions of this current are implicated in amplifying atmospheric warming and accelerating glacier retreat in the region. Monitoring and tracking the dynamics of the warm offshore deep current require a sustained global presence in the sea, which is now being accomplished via the Argo network of autonomous floats. Data from Argo suggest that the Antarctic Circumpolar Current has exhibited warming trends for decades.

The increased presence and changing nature of the deep-water circulation has

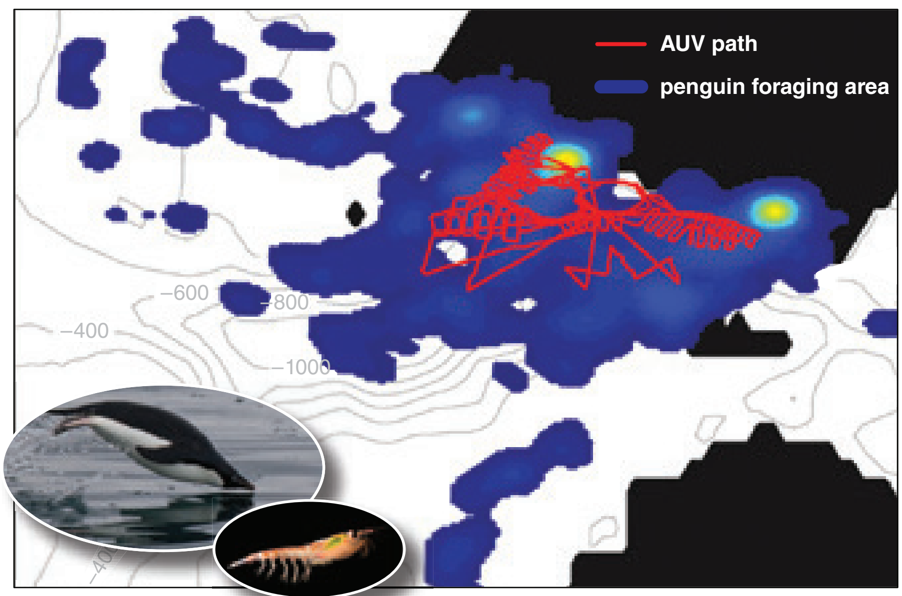

Penguin foraging locations (*left, blue areas*), identified by radio-tagged birds (*inset*), were used to guide a survey by a propeller AUV (*red lines*). The AUV was outfitted with an acoustic sensor that can detect Antarctic krill, the penguins' primary food source (*inset*). The resulting map of krill swarms (*below*), confirms the hypothesis that both krill and the penguins that feed on them congregate around canyons with warm-water upwelling.

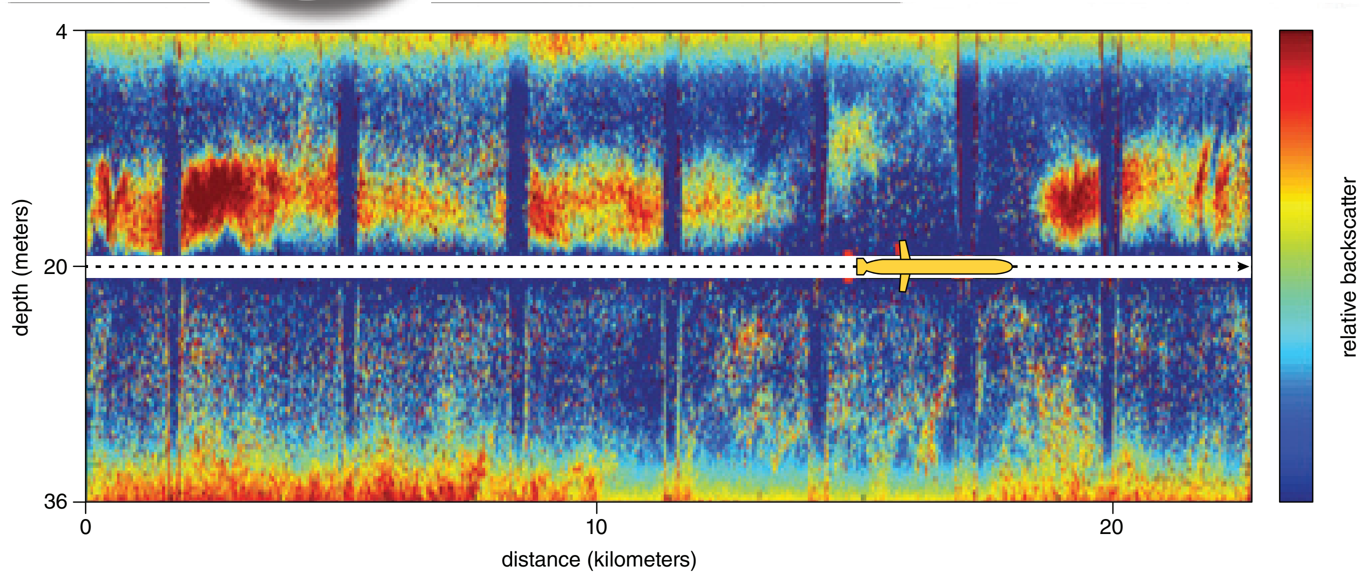

implications for the local food web. The Western Antarctic Peninsula is home to large breeding colonies of the Antarctic Adélie penguin (*Pygoscelis adeliae*), which live in large, localized colonies along the peninsula even though food resources are abundantly available along the entire inner continental shelf. This concentration of the population has raised a persistent question: What turns specific locations into penguin "hot spots?"

The locations of the Adélie colonies appear to be associated with deep seafloor submarine canyons, which are found throughout the continental shelf of the peninsula. This colocation has led to a hypothesis that unique physical and biological processes induced by these canyons produce regions of generally enhanced prey availability. The canyons were also hypothesized to provide recurrent locations for *polynyas* (areas of open water surrounded by sea ice), giving penguins year-round access to open water for foraging. But linking the regional physical and ecological dynamics to test the canyon hypothesis had been impossible, because brutal environmental conditions limited spatial and temporal sampling by ships.

Robotic AUVs now offer expanding capabilities for observing those conditions. As part of our research, for the past five years we have been using a combination of gliders and propeller AUVs to link the transport of the warm offshore circumpolar deep water to the ecology of the penguins in the colonies. Gliders surveying the larger scale of the continental shelf have documented intrusions of deep, warm water upwelling within the canyons near the breeding penguin colonies. These intrusions of warm water appear to be ephemeral features with an average lifetime of seven days, which is why earlier, infrequent ship-based studies did not effectively document them. Associated with this uplift of circumpolar deep water along the slope of the coastal canyon, the gliders found enhanced concentrations of phytoplankton, providing evidence of a productive food web hot spot capable of supporting the penguin colonies.

Satellite radio tagging is being used to characterize the foraging dynamics of the Adélie penguin, and has shown the majority of their foraging activity was centered at the slope of the canyon. These more localized foraging patterns were used to guide sampling of the physical and biological properties with a propeller AUV, because strong coastal currents hindered buoyancy-driven gliders. The propeller AUV data were used to generate high-resolution maps, which revealed that penguin foraging was associated with schools of Antarctic krill. The krill in turn were presumably grazing on the phytoplankton at the shelf-slope front.

It took the integration of all three classes of robotic systems (profilers, gliders, and propeller AUVs) to link the dynamics of the outer shelf to the coastal ecology of the penguins. But in the end, that combination of techniques turned out to be just what was needed to settle a long-standing mystery of penguin biogeography. Better understanding of these processes is critical to determining why these penguin populations are exhibiting dramatic declines in number—for example, the colonies located near Palmer Station in Antarctica have declined from about 16,000 to about 2,000 individuals over the past 30 years. Ongoing and future robotic deployment will help address how climate-induced local changes in these deep-sea canyons might underlie the observed declines in the penguin populations, which themselves are serving as a barometer for climate change.

Many questions are so complex that they require the combined data of several robotic platforms.

Diving In

The pace of innovation for ocean technology is accelerating, guaranteeing that the next-generation robotic systems and sensors will make current crusty oceanographers green with envy. Some of that future direction is evident in recent advances such as AUVs with onboard data analysis, so they can make smart decisions at sea by analyzing their own data. Improved sampling will also be achieved by developing methods to coordinate the efforts of multiple AUVs, either by communicating directly among themselves or by downloading commands sent from shore.

These technical advances will dramatically improve our ability to explore the ocean. But the largest effect of these systems is likely to be a cultural shift stemming from real-time, open-access data. Ocean science has historically been limited to a small number of individuals who have access to the ships that can carry them out to sea, but the realization of Hank Stommel's dream now allows anyone with interest to become involved. This outcome will democratize the ocean sciences and ultimately increase overall ocean literacy, relevant for 71 percent of this planet.

This cultural shift in oceanography comes at a critical time, given that observations suggest that climate change is altering ocean ecosystems. Examining past large-scale changes in the ocean has revealed global scale alterations in the biota of Earth, suggesting life is more intimately linked to the state of the world's ocean than we knew. The greater our awareness of these intricate connections, the better chance we have of coping with a changing ocean planet.

Bibliography

Davis, R. E., D. C. Webb, L. A. Regier, and J. Dufour. 1992. The Autonomous Lagrangian Circulation Explorer (ALACE). *Journal of Atmospheric and Oceanic Technology* 9:264–285.

Griffiths, G. 2003. *Technology and Applications of Autonomous Underwater Vehicles.* New York: Taylor and Francis.

Johnson, K. S., et al. 2009. Observing biogeochemical cycles at global scales with profiling floats and gliders: Prospects for a global array. *Oceanography* 22:216–225.

Moline, M. A., et al. 2005. Remote environmental monitoring units: An autonomous vehicle for characterizing coastal environments. *Journal of Atmospheric and Oceanic Technology* 22:1797–1808.

Roemmich, D., et al. 2009. Argo: The challenge of continuing 10 years of progress. *Oceanography* 22:46–55.

Rudnick, D. L., R. E. Davis, C. C. Eriksen, D. M. Fratantoni, and M. J. Perry. 2004. Underwater gliders for ocean research. *Marine Technology Society Journal* 38:73–84.

Schofield, O., et al. 2007. Slocum gliders: Robust and ready. *Journal of Field Robotics* 24:473–485.

Wilson, S. 2000. Launching the Argo armada. *Oceanus* 42:17–19.

For relevant Web links, consult this issue of *American Scientist Online:*

http://www.americanscientist.org/issues/id.105/past.aspx

The Challenger Glider Mission: A Global Ocean Predictive Skill Experiment

Collin Dobson, Jeffrey Mart, Nilsen Strandskov
Josh Kohut, Oscar Schofield, Scott Glenn
Coastal Ocean Observation Lab, Rutgers University
New Brunswick, USA

Clayton Jones*, Doug Webb*
Carlos Barrera**, Antonio Ramos***
*Teledyne Webb Research,
**Platforma Oceanic De Canaria
***Universidad de Las Palmas de Gran Canaria

***Abstract*— Ocean forecasting models are an extremely valuable tool for understanding Earth's oceans. Current ocean forecast models assimilate satellite sea surface height and temperature data as well as temperature/salinity profiles from the Argo network of over 3,000 drifters. Though assimilating datasets from these drifters is pertinent, it does provide some limitations. Observing System Simulation Experiments routinely indicate that additional profile data, especially profile data that crosses frontal features, are the most influential at reducing forecast uncertainty. Since Argos drifters cannot be controlled and are subject to the oceans currents, areas that would provide critical data to ocean forecasting models are often under sampled. A potential solution to this problem would be to implement datasets provided by Slocum Gliders into the ocean forecasting models. These Autonomous Underwater Gliders are not as limited by the conditions of the oceans as Argos drifters are. Through their ability to sample virtually anywhere in the ocean, they will be able to bridge the gap left by using Argos drifters. This project aims to show the validity of including glider data into forecasting projects by comparing temperature, salinity and surface current projections made by two different ocean models (RTOFS and MyOcean) to the in-situ datasets collected by two gliders: one in the North Atlantic (Silbo) and one in the South Atlantic (RU29). There was a larger variance found between the two models for temperature and salinity compared to Silbo at the 200 m level than the 800 m level. At 200 m there was also an interesting case of disagreement between the MyOcean model versus the RTOFS model and Silbo's observations. There was a considerable peak in values of salinity and temperature with the MyOcean that was not present with the other two sources of data. The results show that there is good reason for ocean forecasting models to incorporate glider data. As for the temperature comparison with RU29 at 200 m, the RTOFS model was typically 2°C too cold, while the MyOcean model was fairly accurate. For 800 m the RTOFS model was about 1°C too cold, while the MyOcean model was about 1°C too warm. The salinity projections made by both models at both depths were always consistently accurate with RU29. These results indicate that the models, while useful, are not free of error and can be improved by incorporating datasets from gliders. Improved ocean forecasting models will have many applications, most importantly the increased ability of predicting the paths of intense storms, especially hurricanes, which are heavily influenced by ocean conditions.**

Keywords — Ocean Forecasting; Autonomous Underwater Gliders; Challenger Glider Mission.

I. INTRODUCTION

Autonomous Underwater Gliders have a long and successful history of regional deployments serving scientific, societal, and security need. Application areas range from pole to pole and include the range of water depths from shallow coastal seas to the deep ocean. Glider deployments covering the basin scale are much fewer, with some well-known exceptions including the Woods Hole to Bermuda line that crosses the Gulf Stream and the Atlantic Crossing line that follows the Gulf Stream (Figure 1). New technologies for extending glider endurance are making year-long deployments and regular basin-scale missions a new reality (Figure 2). The new technologies include the capacity for more on-board lithium battery power, lower power sensors and energy harvesting to extend duration, and biofouling protection to maintain flight control and sensor calibrations.

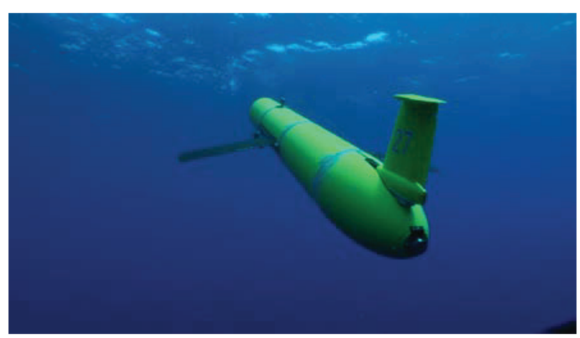

Figure 1: A photograph of RU27, an autonomous underwater glider that successfully crossed the Atlantic Ocean in 2009.

We have recently begun a globally coordinated underwater glider mission dedicated to research and education to demonstrate this new technological capability. The Challenger Glider Mission will include operation of a fleet of gliders on simultaneous basin-scale missions that revisit the historic track of the H.M.S. Challenger's first dedicated scientific circumnavigation. The scientific questions to be investigated focus on an assessment of the quality of the ensemble of available global-scale ocean models. The mission has already begun with one global-class G2 Slocum Electric glider deployed in the North Atlantic (Silbo) and a second deployed in the South Atlantic (RU29). These two gliders have already completed over 803 days at sea covering more than 15,000 km.

The goal is to match the 128,000 km distance covered by the H.M.S Challenger by 2016, the 140th anniversary of the research vessel's return to Great Britain. This goal can be achieved in 1 year with 16 gliders simultaneously flying 8,000 km legs following the gyre circulation around each of the 5 major ocean basins (Figure 3). Two additional Slocum Thermal gliders are scheduled to be deployed in the Pacific in 2013.

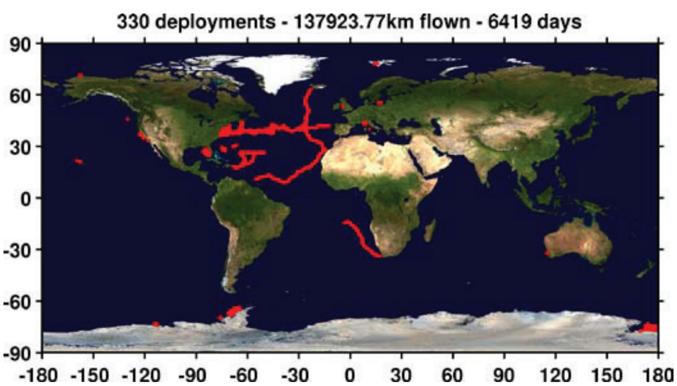

Figure 2: A map of the history of tracks covered by Rutgers Coastal Ocean Observation Lab's gliders. Basin scale missions, in collaboration with Teledyne Webb Research, Universidad de Las Palms de Gran Canaria.

The immediate scientific goals are to assess the current capabilities of the existing international suite of global ocean forecast models. The existing global ocean forecast models assimilate satellite sea surface height and temperature data as well as temperature/salinity profiles from the Argo network of over 3,000 drifters. Still, observing System Simulation Experiments routinely indicate that additional profile data, especially profile data that cross frontal features, are the most influential at reducing forecast uncertainty. Since the location of Argo drifters cannot be controlled after they are deployed, some regions are critically under sampled, and strong boundary currents are often unresolved.

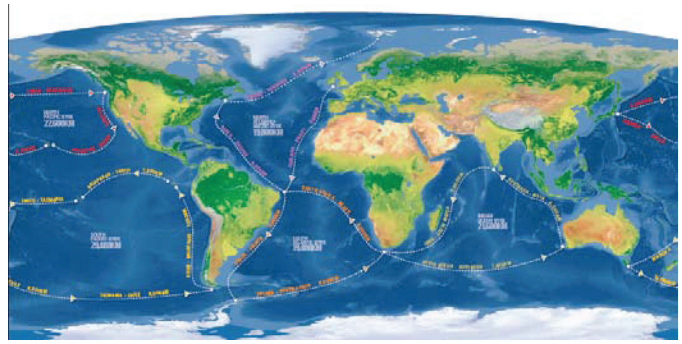

Figure 3: The projected paths of the Challenger Glider Mission.

This study will report the results of student investigations that compare the glider temperature and salinity profiles, along with depth-averaged currents, with the forecasts from the international ensemble of global ocean models. Preliminary student results indicate that the general structure of the model-generated temperature and salinity profiles agree well with the glider, but differ in the details. Much larger differences are found between the model and observed currents. Along the glider-tracks collected to date, the U.S. global model is found to compare more closely to the observations in the North Atlantic, while the European model is found to compare more closely in the South Atlantic. As an effort to improve the forecasting capabilities of ocean models, in-situ measurements of salinity, temperature, and currents, collected by gliders, were compared to conditions predicted by the models.

II. Methods

The first ocean forecasting model used in this comparison was the MyOcean model. This model is a product of Mercator and is a collaborative effort between European countries including the United Kingdom, France, Germany and Denmark. This model provides projected data for velocity, temperature, and salinity components of the water column in 5 m bins of depth, for the first 30m, and then in 10m bins for the next 70 m. The second ocean forecasting model used for comparison was the RTOFS (Real Time Ocean Forecast System) model. This model is a product of the National Center for Environmental Prediction (NCEP).

The primary oceanographic sensor on the G2 gliders is a SeaBird pumped Conductivity, Temperature and Depth (CTD) sensor. Temperature and salinity profiles are processed as described in Kerfoot et al. (2010), a process that includes correction for the thermal inertia of the conductivity sensor. RTOFS and MyOcean forecasts are harvested and archived each day in a 1000 km x 1000 km box surrounding the glider location. Glider data and model forecasts are compared every day to help determine new waypoints along paths with favorable currents, including new 3-D visualization tools developed at the Universidad de Las Palmas de Gran Canaria.

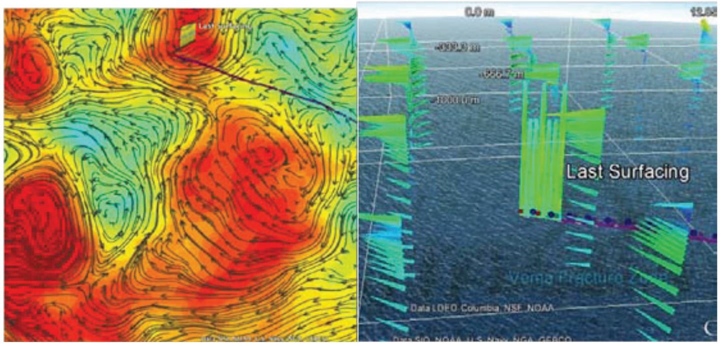

Figure 4: Example of the path planning tools that can be created using data from the ocean forecasting models RTOFS (left) and MyOcean (right).

The comparisons made between the glider data and the projected data formulated by the models were produced by analyzing estimates of temperature, salinity, and surface currents made by each. The data from the models was pulled the internet databases, while the glider data was collected by Silbo (Figure 5a) and RU29 (Figure 6a). The in-situ glider data was considered to be the ground truth conditions of the water column. The analysis was done by calculating the difference between conditions that the glider reported and the conditions that the models forecasted, as well as the differences between the two models. A series of MATLAB scripts allowed the data to be processed and various profiles to be made.

The plots for both Silbo and RU29 compare the 200 m and 800 m values of temperature and salinity as sampled from the gliders to the outputs from the RTOFS and MyOcean models. The 200 m level was chosen as a representation for the near surface layer of the ocean while the 800 m level was chosen to compare the deeper range of the gliders' approximately 1000 m maximum depth. There is a set of plots for each glider for each variable and depth level. To compare surface currents, the conditions reported by the glider were plotted against the conditions projected by the models, using Google Earth.

Figure 5a: The portion of Silbo's track that was used for comparison to the models, beginning at the green dot and ending at the red dot. This track represents an east to west section across the southern side of the North Atlantic Gyre.

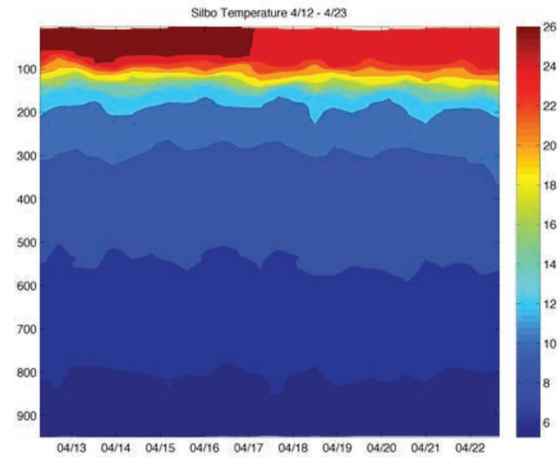

Figure 5b: The temperature dataset from Silbo, used for the case study of 4/12/13-4/23/13.

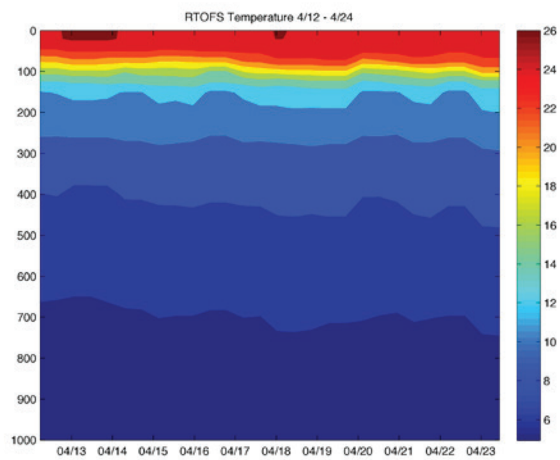

Figure 5c: The temperature dataset from the RTOFS model, used for the case study of 4/12/13-4/23/13.

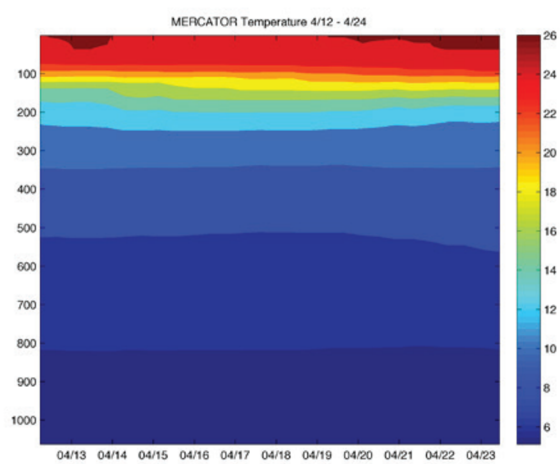

Figure 5d: The temperature dataset from the MyOcean model used for the Silbo case study of 4/12/13-4/23/13.

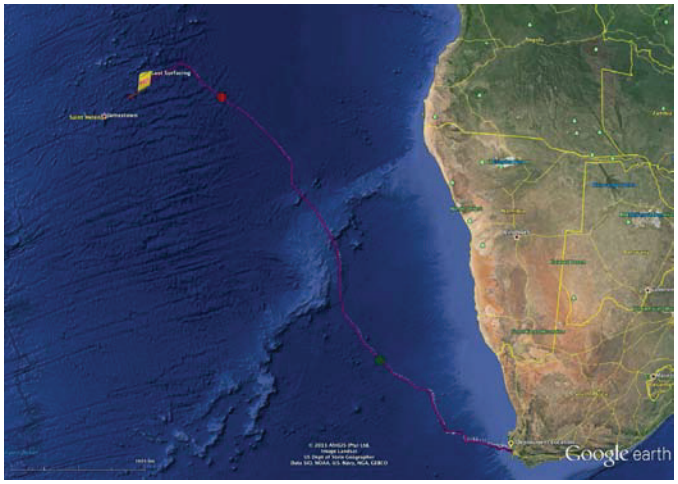

Figure 6a: The portion of RU29's track that was used for comparison to the models, beginning at the green dot and ending at the red dot. This track represents a south to north section along the eastern side of the South Atlantic Gyre.

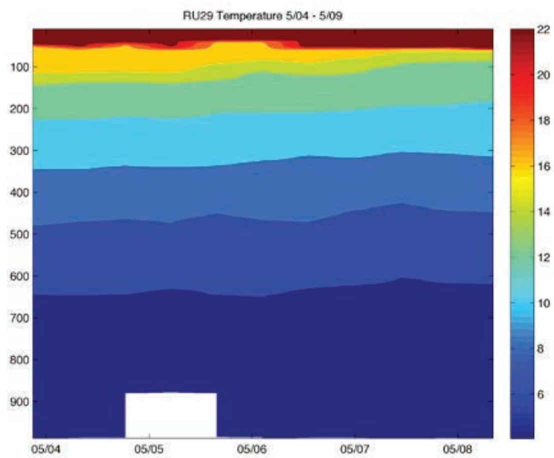

Figure 6b: The temperature dataset from RU29, used for the case study of 5/6/13.

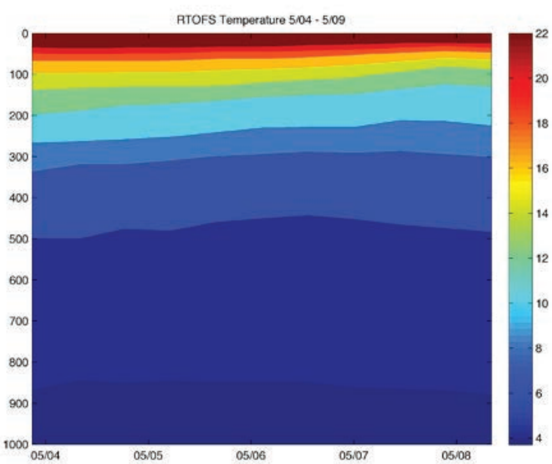

Figure 6c: The temperature dataset from RTOFS, used for the case study of 5/6/13.

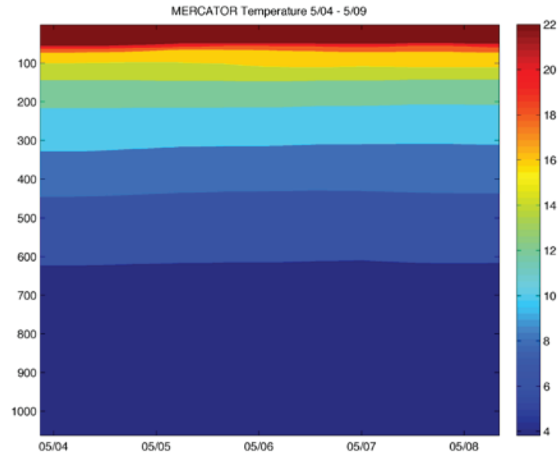

Figure 6d: Temperature dataset from the MyOcean model used for the RU29 case study on 5/06/13.

III. Results

A. Silbo

There is a 37 day period starting on April 9th, 2013 and ending on May 15th, 2013 that is plotted to compare the recorded values from Silbo to the two models on a daily basis (Figure 7). Beyond May 15th is when Silbo experienced its problems and was forced to abort so Silbo was no longer gliding and recording ocean profiles.

For the comparisons of salinity, at both 200 and 800 m the RTOFS model is more consistent with the data collected. At 200 m the salinity of the MyOcean model is seen to have a broad peak in which it diverges greatly from the observed temperatures from Silbo. By around the 24th of April the MyOcean model is shown to have recovered and then generally remains close in accuracy. The RTOFS model however is more accurate overall, especially with respect to the trends over the time period sampled. The fluctuations over time that Silbo recorded are also relatively well portrayed in the RTOFS salinity values at this level. The MyOcean model is off by about 0.6 PSU versus the Silbo observations and the RTOFS model during the MyOcean peak.

The consistency, accuracy and trends of the temperature plot for Silbo at 200 m are very similar to the 200 m plot for salinity. There is a jump or increase present in the MyOcean model approximately between the dates of April 10th and April 24nd where at the same time the RTOFS model shows one of its most accurate periods. The temperature between the MyOcean model and Silbo differ as much as 2-3°*C* between those dates. It is also evident from this plot that the RTOFS model is consistently cooler than the MyOcean model.

At 800 m the salinity differences of the models to the measurements from Silbo were considerably less than those found at 200 m. Both ocean models were found to be close in comparison to each other and any differences from either model rarely exceeded 0.1 PSU. The RTOFS is the better performer for the first half of the month time series but only by a small factor.

The temperatures at the 800 m level tell a different story than the 200 m level. Here the MyOcean model shows greater accuracy over the RTOFS model. Similarly to how the 800 and 200 m levels of salinity compared, the difference between the 800 m glider temperatures and the models did not have as great of a range as did the 200 m level. It is noticeable that the RTOFS model is about 0.5*°C* too cold at this 800 m level.

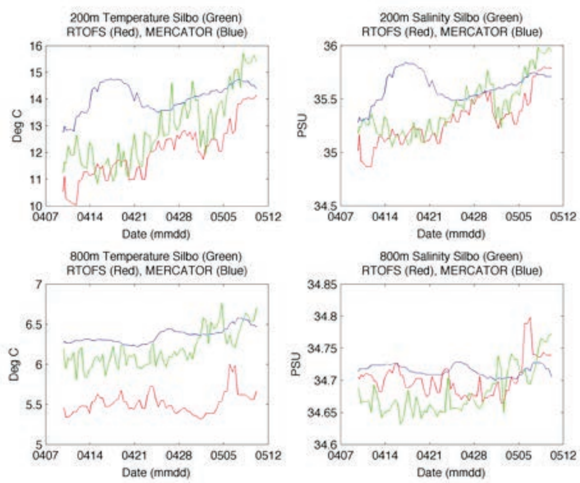

Figure 7: Comparisons of Silbo (green) with RTOFS (red) and MyOcean (blue) model data of temperature at 200m (top left), 800m (bottom left) and salinity at 200m (top right) and 800m (bottom right).

B. Silbo Case Study

Within Silbo's time series plots there is one feature that is most prevalent at the 200 m level which has been explored further here. As discussed earlier there is a period between 4/13/13 and 4/22/13 where there is a jump in the 200 m salinity and temperature as modeled by MyOcean. The RTOFS model however does not contain this feature and remains more accurate to the observations that Silbo recorded.

Figures 8a and 8b show two maps that display Silbo's path across a section of the Atlantic Ocean. There is a point labeled that represents the glider's surfacing location during the day of April 18th. This date was chosen because it falls near the MyOcean peak of temperature and salinity. The maps show the ocean temperatures and the ocean currents at 200 m with the upper being the RTOFS model run and the lower being the MyOcean model. Comparing the two vector fields alone on this same day show that there is a large amount of disagreement between the two and many of the eddy features are opposite in flow direction.

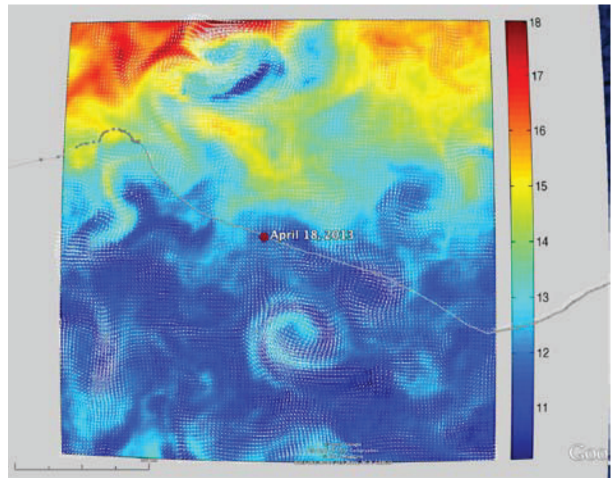

Figure 8a: RTOFS 200m temperature and currents on April 18th, 2013. The glider position is marked by the red dot.

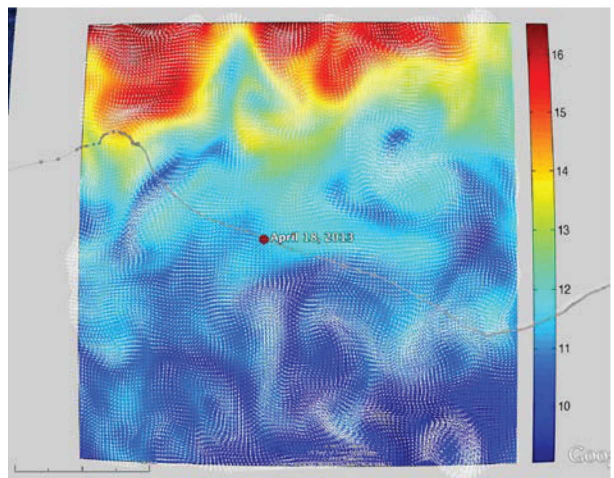

Figure 8b: MyOcean 200m temperature and currents on April 18th, 2013. The gliders position is marked by a red dot.

The RTOFS model displays currents at 200 m that are coming from the southeast at Silbo's location which would be providing cooler temperatures (Figure 8a). The MyOcean model however has currents at this level coming from the northeast towards Silbo and with them bringing comparatively warmer temperatures. The warmer area of water that MyOcean shows being pulled south is what it expected Silbo to fly through and would explain the broad peaked increase in temperatures (Figure 8b). At the surface, warmer water temperatures in the Northern Hemisphere would be to the south and closer to the equator. At 200 m, however, the warmer waters on the maps are shown to the north. This is the result of North Atlantic Gyre that creates a deeper layer of warm water which is visible at depth and is independent of what some of the surface solar-heated waters may be. In

Figure 9 two profiles, one for temperature and one for salinity show the entire depth range down to 1000 m. The warmer temperatures of the MyOcean model are visible here extending beyond the 200 m level (Figure 9).

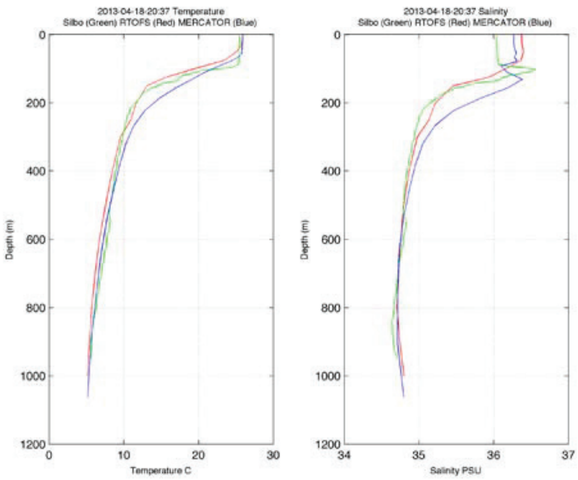

Figure 9: (Left) Profile of temperature comparison between Silbo (green), RTOFS (red) and MyOcean (blue) for 4/18/2013. (Right) Profile of salinity comparison between Silbo (green), RTOFS (red) and MyOcean(blue).

C. RU29

A time period consisting of 82 days, starting February 22nd, and ending May 15th was used for comparison with the two models (Figure 6a). These data sets were compared separately at 200m and 800m depths with respect to temperature and salinity. During this time period RU29 had begun to leave the coastal waters of South Africa and journey northeast towards the equator.

At 200m of depth, the RTOFS model was always about $2°C$ too cold, while the MyOcean model was quite accurate (Figure 10). As this time series progresses, the temperature reported by all three data sets show that the ocean is getting progressively colder. This corresponds to the transition of Summer to Winter in the Southern Hemisphere. Both models show an interesting spike in temperature around 3/25/13, but they are in different directions. The RTOFS model drops by about $1°C$ during this time, while the MyOcean increases by about $1.5°C$. The glider does show a slight decrease in temperature during this time, but not on the magnitude that the RTOFS model predicts.

At 800m depth, the RTOFS model was typically about $1°C$ too cold, while the MyOcean model was typically about $1°C$ too warm. As this time series progresses the three different datasets show a similar trend of a slight increase in temperature. This slight increase corresponds to the gliders approach to the equator. Neither model is ever off by more than $1°C$ during this time series.

At 200m depth, both models were very accurate in projecting salinity. The RTOFS model typically predicted low by about 0.2 PSU while the MyOcean model was pretty much spot on. Both models were also fairly accurate at projecting salinity at 800m depth. The RTOFS model typically over predicted but by only a very small margin. MyOcean again was pretty much spot on.

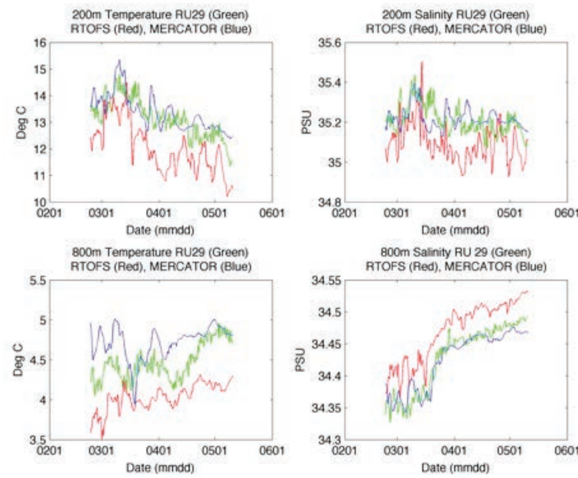

Figure 10: Comparisons of RU29 (green) with RTOFS (red) and MyOcean (blue) model data of temperature at 200m (top left), 800m (bottom left) and salinity at 200m (top right) and 800m (bottom right).

D. RU29 Case Study

Another day that provided results worth analyzing further was May 5th, 2013. On this day the MyOcean model depicted two different eddies, one north of RU29's location, and one south (Figure 11a). The eddy north of the glider was flowing in a counter-clockwise direction, and the eddy south of the glider was flowing in a clockwise direction. Since RU29 was located in the Southern Hemisphere, the southern eddy would be considered a warm eddy and the northern one a cold eddy. In order to verify that this phenomenon was actually occurring in the ocean, these projections were compared to both the RTOFS model and the glider data (Figure 11b).

RU29's location during this study is marked by yellow pins, and the currents it reported by red lines. The RTOFS model projections showed no sign of either eddy. The surface currents reported by the glider appear to be almost opposite of what the MyOcean model was predicting, and seem to agree more with the projections of the RTOFS model.

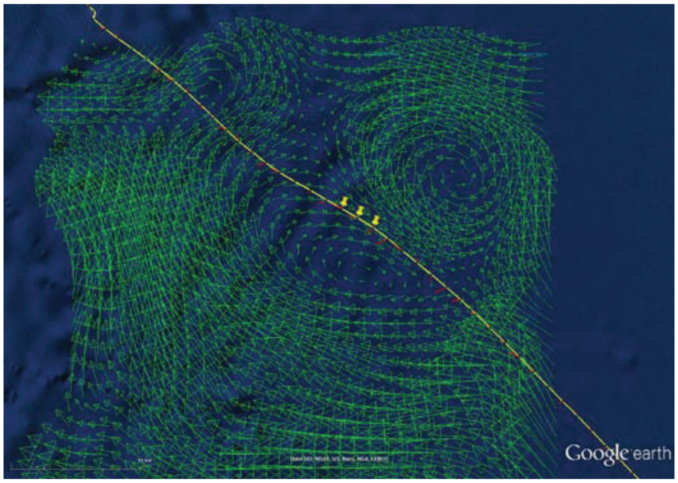

Figure 11a: MyOcean surface current projections and surface currents reported by RU29 for 5/06/2013.

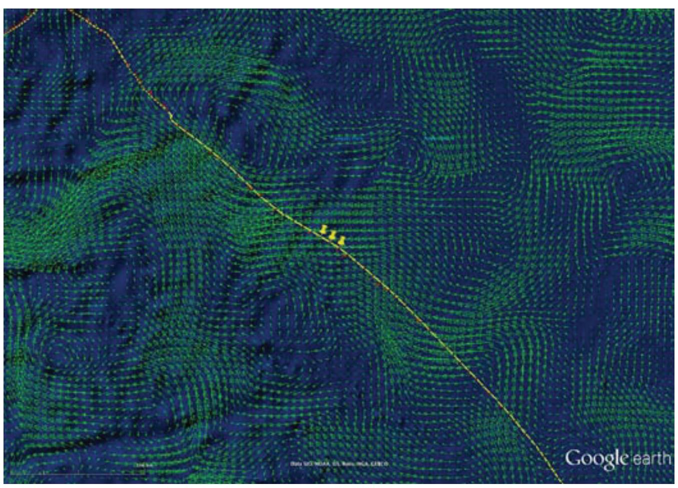

Figure 11b: RTOFS surface current projections and surface currents reported by RU29 for 5/06/2013.

In order to get a better understanding on whether the eddies were a valid feature or not, the salinity and temperature profiles of the models and RU29 were analyzed (Figure 12). According to these profiles, the data collected by RU29 agrees more with the MyOcean model for both temperature and salinity. So even though the surface currents experienced by RU29 were directly opposite of what the MyOcean model predicted, the MyOcean temperature and salinity projections were quite accurate.

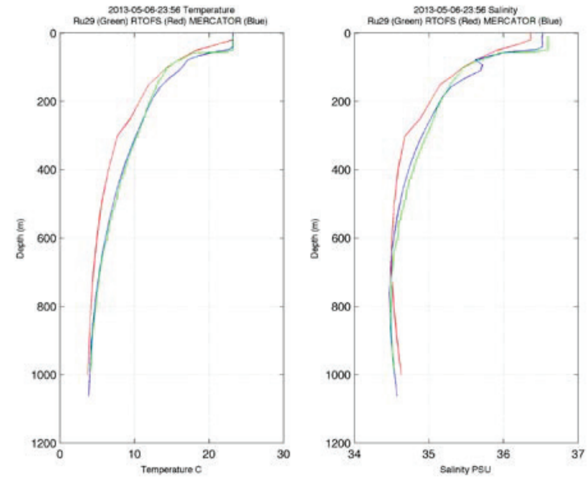

Figure 12: (Left) Profile of temperature comparison between RU29 (green), RTOFS (red) and MyOcean (blue) for 5/06/2013. (Right) Profile of salinity comparison between Silbo (green), RTOFS (red) and MyOcean(blue).

IV. DISCUSSION

The value of ocean forecast models has advanced well beyond scientific curiosity-driven research. The world's major forecast centers currently run operational global forecast models that are eddy-resolving, data assimilative, and are distributed free-of-charge to a wide variety of users. Global-scale ocean assimilation data include satellite-derived sea surface temperature and sea surface height, as well as the global array of Argo profiling floats and surface drifters. Forecast skill continues to improve, yet many offshore operators are faced with the same set of questions: (1) How good are the global ocean forecast models? (2) Can ocean forecasts for a specific area be improved through the use of nested regional-scale models? (3) Or can better improvements be obtained by locally enhancing the observations in either the global-scale or nested models?

Autonomous underwater gliders provide a means to test ocean models. Unlike drifters & floats, gliders also travel under their own power. They can be programmed to fly into areas with expected high forecast error and provide valuable assimilation data across fronts along the way. The model validation data includes not only the glider's subsurface temperature and salinity profiles, but also their depth averaged and surface drift velocity estimates. Depth averaged velocity profiles are a significant augmentation of the already invaluable Argo profile data. Model-derived temperature and salinity profiles often compare well to observed Argo and glider profiles, but as we see in the two case studies developed here, the model currents can be in opposite directions and the glider depth averaged velocity is required to discriminate.

At the surface, the two global ocean models compared here have very similar characteristics. This is not unexpected, since both are assimilating similar sea surface temperature and sea surface height products. Subsurface, the models look very different, especially at 200 m, near the seasonal thermocline. RTOFS contains many distinct and highly circular eddies at this level, while MyOcean exhibits many interconnected and meandering filaments wrapped around the same highs and lows. At times, the MyOcean filamental flow directions line up with the RTOFS eddy circulation, and at other times, they are in direct opposition. In the first case study presented here, the long filaments resulted in the advection of anomalous warm water from the southern edge of the North Atlantic gyre into the colder subsurface water to the south. The filament persisted for the full 10 days it took the glider to cross it, with no sign of the anomalously warm water in the glider data. In the second case study, surface currents from both models agreed well with the surface drift of the glider every time it surfaced to communicate. At 200 m depth, however, currents in the two models were exactly opposite, one generally in the direction of surface flow and one opposite. The glider depth averaged velocity indicates that one of the models did the better job of forecasting the observed temperature and salinity profiles, but that information was insufficient to decide which model produced the better velocity forecast. Neither model was in agreement with the observed currents at depth.

The two case studies highlight the need for a broader and more systematic validation study that could be conducted with a fleet of gliders with persistent coverage over a long period. In this paper we propose a global model skill assessment study focused on some of the more difficult to reproduce parts of the ocean, the edges of the major gyres. It is in these regions that glider observations may prove their greatest value in global model assimilation and validation by combining velocity profile observations with collocated standard CTD profiles. While surface parameters are important for many applications like Search and Rescue, vessel routing and floatable tracking, the fidelity of subsurface forecasts is required in other applications, in particular, understanding life cycles within pelagic ecosystems, subsurface pollutants, and upper ocean heat content for tropical storm intensity forecasting. Gliders provide the critical dataset to improve models below the surface, an area that is unseen from space, with a dataset that is not currently available from Argo CTD profilers or the global arrays of surface drifters.

V. Acknowledgements

The Challenger Glider Mission is growing global partnership of glider operators, scientists, educators and students coordinated by Rutgers University. The results presented in this paper were initiated in a Rutgers research course and completed by two undergraduate summer interns (Collin Dobson & Jeffrey Mart) supported by Teledyne Webb Research. Carlos Barrera teaches the companion course in the Canary Islands. Glider path planning and model/data comparison activities are led by Nilsen Standskov and Antonio Ramos. With cyber infrastructure support provided by John Kerfoot. Glider operators include Chip Haldeman, Dave Aragon, Tina Haskin (Rutgers) and Ben Alsup (TWR). Silbo was donated by Teledyne Webb Research and Challenger (RU29) by Rutgers. The RU29 deployment in South Africa was enabled by the University of Cape Town, The Nansen-Tutu Center, Sea Technologies, and the Department of Environmental Affairs. RU29 mission support is provided by U.S. IOOS. Support for the Pacific Basin Thermal Gliders is provided by ONR with path planning led by students in the U.S. Naval Academy.

VI. References

[1] Glenn, S., + 47 co-Authors, Process-driven improvement to hurricane intensity and storm surge forecasts in the Mid-Atlantic Bight: Lessons learned from Hurricanes Irene and Sandy. Oceans'13 MTS/IEEE Bergen.

[2] Glenn, S., Kohut, J., McDonnell, J., Seidel, D., Aragon, D., Haskins, T., Handel, E., Haldeman, C., Heifetz, I., Kerfoot, J., Lemus, E., Lictenwalder, S., Ojanen, L., Roarty, H., Atlantic Crossing Students, Jones, C., Webb, D., Schofield, O. 2011. The Trans-Atlantic Slocum glider expeditions: A catalyst for undergraduate participation in ocean science and technology. Marine Technology Society 45: 75-90.

[3] Kerfoot, J., S. Glenn, H. Arango, C. Haldeman, C. Jones and D. Pinkel, 2010. Correction and comparison of pumped and non-pumed CTS sensors on the Slocum Glider, EOS Transactions, AGU, 91(26), Ocean Sci. Meet. Suppl., Abstract IT35B-03.

[4] Schofield, O., Kohut, J., Glenn, S., Morell, J., Capella, J., Corredor, J., Orcutt, J., Arrott, M., Krueger, I., Meisinger, M., Peach, C., Vernon, F., Chave, A., Chao, Y., Chien, S., Thompson, D., Brown, W., Oliver, M., Boicourt, W. 2010. A regional Slocum glider network in the Mid-Atlantic coastal waters leverages broad community engagement. Marine Technology Society 44(6): 64-74.

Adélie Penguin Foraging Location Predicted by Tidal Regime Switching

Matthew J. Oliver[1]*, Andrew Irwin[2], Mark A. Moline[1], William Fraser[3], Donna Patterson[3], Oscar Schofield[4], Josh Kohut[4]

1 School of Marine Science and Policy, University of Delaware, Lewes, Delaware, United States of America, **2** Department of Mathematics and Computer Science, Mount Allison University, Sackville, New Brunswick, Canada, **3** Polar Oceans Research Group, Sheridan, Montana, United States of America, **4** Institute of Marine and Coastal Sciences, Rutgers University, New Brunswick, New Jersey, United States of America

Abstract

Penguin foraging and breeding success depend on broad-scale environmental and local-scale hydrographic features of their habitat. We investigated the effect of local tidal currents on a population of Adélie penguins on Humble Is., Antarctica. We used satellite-tagged penguins, an autonomous underwater vehicle, and historical tidal records to model of penguin foraging locations over ten seasons. The bearing of tidal currents did not oscillate daily, but rather between diurnal and semidiurnal tidal regimes. Adélie penguins foraging locations changed in response to tidal regime switching, and not to daily tidal patterns. The hydrography and foraging patterns of Adélie penguins during these switching tidal regimes suggest that they are responding to changing prey availability, as they are concentrated and dispersed in nearby Palmer Deep by variable tidal forcing on weekly timescales, providing a link between local currents and the ecology of this predator.

Citation: Oliver MJ, Irwin A, Moline MA, Fraser W, Patterson D, et al. (2013) Adélie Penguin Foraging Location Predicted by Tidal Regime Switching. PLoS ONE 8(1): e55163. doi:10.1371/journal.pone.0055163

Editor: David Hyrenbach, Hawaii Pacific University, United States of America

Received May 28, 2012; **Accepted** December 23, 2012; **Published** January 30, 2013

Funding: These efforts were only possible with funding support provided by the National Aeronautics and Space Administration Biodiversity program (NNG06GH75G1/3 to M. Oliver, http://www.nasa.gov/), the National Science Foundation Office of Polar Programs (ANT-0823101 to Co-PI O. Schofield; ANT-1019839 to M. Moline, http://www.nsf.gov/), and the Gordon and Betty Moore Foundation, http://www.moore.org/. The funders had no role in study design, data collection and analysis, decision to publish, or preparation of the manuscript.

Competing Interests: The authors have declared that no competing interests exist.

* E-mail: moliver@udel.edu

Introduction

The region surrounding Anvers Island, West Antarctic Peninsula (WAP) is a "hot-spot" for Adélie penguin activity. Adélie penguins (*Pygoscelis adeliae*) have been present in the Anvers Island region on millennial timescales [1,2]. The presence of a pronounced submarine canyon (Palmer Deep) near this area provides a conduit for warm Upper Circumpolar Deep Water (UCDW), locally increasing primary production, which supports a productive regional food web [3–5]. In addition, this region has warmed significantly [6,7] and has lost a significant amount of sea-ice [8,9]. The Adélie penguin population in this region has decreased dramatically since the 1970's [10], as climate conditions that support their chick rearing habitat have moved southward [11]. Understanding the interaction between the foraging behavior of the remaining Adélie penguins and physical dynamics in this historical "hot-spot" may provide insights into the future of this historic colony that has survived past warming and cooling events [12].

The effect of the tides on currents is most dramatic in coastal systems. Tidal forces interact with local geographic and bathymetric features that change sea level, cause water mass mixing, and create tidal fronts [13–16]. These features affect phytoplankton distribution [17–20], zooplankton aggregation [21–26], benthic grazers [27], fish behavior [28–30] and even marine mammal foraging activity [31–33]. Tidal fronts also influence seabird foraging timing and behavior by concentrating prey or providing favorable currents that regulate foraging trips. For example, short-tailed shearwaters (*Puffinus tenuirostris*) broaden their access to smaller euphausiids by foraging near recurrent tidal fronts in the Akutan Pass [34], while auklets coordinate their feeding behavior with peak tidal current velocities in the shallow passes in the Aleutian Islands [35]. In Vancouver Island, Canada, planktivorous diving birds prefer deep water with moderate to high tidal flow while benthic invertebrate feeders preferred shallow, tidally slack waters. Piscivorous diving birds feed in shallower water during moderate tidal flows and in a variety of water depths during slack water [36]. The impact of flood and ebb tidal forces has also influences the mode of transportation of Magellanic penguins (*Spheniscus magellanicus*), which avoid swimming against strong tidal currents by diving deeper or walking in San Julian Bay, Argentina [37]. Magellanic penguins also take advantage of tidal oscillations in the Beagle Channel, Argentina, to transport them to foraging locations maximize their foraging success [38]. The wide and varied exploitation of different tidal forces by sea birds show that tides produce regular and predictable concentrations of resources in an otherwise patchy coastal environment [39]. These local tidal concentrating mechanisms may become more ecologically important, as tides are not significantly affected by a changing climate.

In this study we test the hypothesis that tides are a significant predictor of Adélie penguin foraging locations in the Anvers Island region of the West Antarctic Peninsula (WAP). To do this, we used a combination of satellite-tagged Adélie penguins, historical tide records and currents derived from a Slocum glider autonomous underwater vehicle (AUV). We found a significant relationship between tidal regime and Adélie penguin foraging location during our field season and used an additional nine years of penguin location data to test the historical robustness of our results.

Methods

Penguin ARGOS Tags and Dive Recorders

From January 5–27, 2011, we tagged 11 Adélie penguins at the Humble Is. rookery near Palmer Station, Anvers Is., Antarctica (64° 46′ S, 64° 04′ W). This study area is characterized by large changes in bathymetry near shore, and narrow fjords characteristic of the WAP (Figure 1). Penguins selected for tagging were paired and had brood-stage nests containing two chicks. We use the brood stage as a "biological standard" to control for changes in parental foraging behavior that might be affected by chick age [40]. Tags were a custom mold based on SPOT and SPLASH tag configurations from Wildlife Computers (Redmond, WA, USA). Our tags had a sloped frontal area of 17×18 mm (306 mm^2), weighed 55 g and had an antenna length of 12 cm. Tag length was 86 mm. All tags in the 2011 season were equipped with pressure sensors to measure penguin dive depths (TDR, Lotek Wireless). Dive data was recorded at 1 Hz. Tags were fastened to anterior body feathers using double sided tape and small plastic cable ties. Tags were rotated to new penguins every 3–5 days depending on fair weather conditions allowing for access to the colony. The tag represents less than 2% of body mass of the lightest penguins that are typically tagged (range 3.2–4.7 kg). Some devices can affect foraging trip duration [41,42]; our study is focused on foraging location rather than trip duration. Furthermore, tags that have been shown to affect penguin foraging trip duration were in some cases up to three times heavier and had double the frontal area when compared with our custom tags [41,42]. Our tags are also among the lightest available and typically deployed for only 3–5 days before removal and rotation to other birds. We did not test explicitly for a "tag effect" on our penguins, but considering the size of the tag, we expect any effect to be small. Location-only data were collected from 103 Adélie penguins for ten breeding seasons (Dec–Feb) between 2002 and 2011 (Table 1) using similar tags and procedures.

Penguin Location Data Filtering

The quality of the location data depends on how many ARGOS satellites are in view while the tag is above the water. The porpoising and diving behavior of traveling penguins can result in poor quality location data. Location data qualities are classified as 3, 2, 1, 0, A, and B under the least-squares ARGOS algorithm. Class 3, 2, and 1 positions are accurate within 100 m, 250 m, 500 m−1500 m respectively. Class 0, A, and B positions are locations that have no error estimation [43]. We controlled the quality of our location data using three steps. First, we eliminated erroneous terrestrial positions using land masks from the National Snow and Ice Data Center, Atlas of the Cryosphere (http://nsidc.org/data/atlas/news/antarctic_coastlines.html). Second, we applied a sequential filter that considers location data quality flags and distance between successive locations based on maximum sustained swimming speed of the penguins [44] using the R argosfilter package [45]. Our threshold swimming speed was based on a maximum sustained swimming speed of 8 km hr^{-1} [40,46]. Finally, we visually inspected each track and manually removed

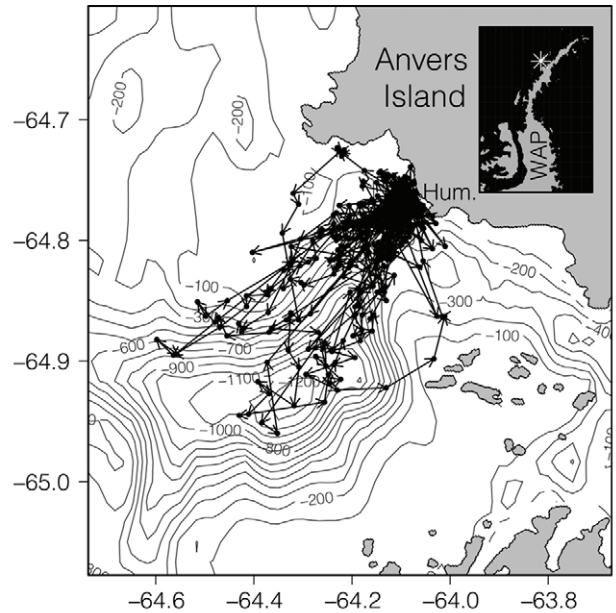

Figure 1. Filtered satellite tracks from Adélie penguins located at Humble Is. (Hum.), on the South coast of Anvers Island (white asterisk on inset) on the West Antarctic Peninsula (WAP) in January 2011. These birds also carried dive recorders. Arrows represent the path of foraging trips. Contours are bottom bathymetry (m) showing the location of Palmer Deep.
doi:10.1371/journal.pone.0055163.g001

any class B points that were unreasonable based on coastal geometry. For example, the distance filter considers only great circle distances and does not take into account geographic barriers such as islands, which would increase the travel time between points (Table 1).

Dive Records

Dive records from 2011 were zero-offset using the diveMove package in R [47]. Based on previous studies of penguin diving behavior, we considered dives deeper than 5 m to be foraging dives [48,49]. diveMove uses recursive filtering and a diving threshold to correct for drift in TDR depth sensors and identify diving behavior. This approach has been used to correct diving records of King penguins (*Aptenodytes patagonicus*) [50]. The dive records and penguin location data were then time merged. Location data within 150 seconds of a dive identified by the diveMove software were identified as foraging locations. Assuming a maximum swimming speed of 8 km hr^{-1} [40,46], diving must have occurred within one third of a kilometer of a location fix.

Tidal Measurements and Classification

A tide gauge mounted on the pier at Palmer Station, Anvers Island, Antarctica, recorded tidal amplitude during our experiment. The tide gauge is 1.7 km from Humble Is. We classified the tidal forcing regimes as diurnal or semidiurnal based on counting the number of high tides in a day. Time periods with one high tide per day were classified as a diurnal regime and all other tidal time periods were classified as a semidiurnal regime.

Depth Integrated Currents from a Slocum Glider

We deployed a Slocum electric glider AUV in two successive missions from January 10–14, 2011 for a 62 km mission and

Table 1. The deployment dates, number of ARGOS locations and mean range of the Adélie penguins tagged in each season.

Season	No. Birds	Dates Deployed	No. ARGOS locations (Post-filtering)	Mean range km (± s.d.)
2002	4	2002-01-19–2002-02-07	300 (256)	24.99 (±16.17)
2003	23	2002-12-28–2003 -02-11	2550 (1811)	11.29 (±7.56)
2004	22	2004-01-04–2004-02-08	2627 (1790)	7.72 (±5.12)
2005	19	2005-01-06–2005-02-07	1352 (991)	9.90 (±6.36)
2006	3	2006-01-18–2006-01-21	148 (119)	26.16 (±29.08)
2007	8	2007-01-11–2007-02-05	481 (340)	8.74 (±5.10)
2008	5	2008-01-19–2008-02-06	468 (367)	7.99 (±5.04)
2009	5	2009-01-06–2009-01-21	482 (445)	8.61 (±4.90)
2010	11	2010-01-12–2010-02-01	543 (478)	7.62 (±4.62)
2011	13	2011-01-05–2011-01-27	765 (690)	8.76 (±7.21)
2011*	11	2011-01-05–2011-01-27	729 (668)	11.31 (±7.86)

*Birds that recorded dive information in addition to ARGOS location.
doi:10.1371/journal.pone.0055163.t001

January 15–31, 2011 for a 178 km mission. These vehicles have previously been used to provide environmental context for penguin foraging behavior [51]. Gliders are buoyancy driven and travel in an underwater "saw-tooth" pattern [52] between 1 m and 100 m, with surface GPS fix every 2 hours or upon reaching a waypoint. While underwater, the glider used internal compass heading corrected for declination to navigate to its next waypoint. Integrated currents between glider surfacings were estimated by the difference between where the glider surfaced based on a GPS fix, and the estimated location of the glider based on internal navigation. This method produced a 100 m depth integrated current estimate every two hours of the glider mission. During this experiment, the glider estimated currents in the general area of the Palmer Deep, which is a historically important location for penguin activity [3]. Twice, during a diurnal and a semidiurnal tidal regime, the glider was programed to remain near a station ("station keep") at the northeast edge of the Palmer Deep to resolve the temporal changes in currents over a diurnal and semidiurnal tide cycle.

Analysis of Penguin Foraging Location

We tested the hypothesis that Adélie penguins forage at different locations different tidal regimes (diurnal vs. semi-diurnal) by using a linear mixed model [53] on locations merged with dive information in the 2011 season. Because successive locations and dives for each penguin are spatially auto-correlated, we divided the location records associated with diving behavior into trips. Trips were defined as a set of locations separated by return (within 0.5 km) to Humble Is. We then treated each trip as a random effect and tidal regime as a fixed effect in a linear mixed model. We also developed models that included tidal amplitude and Julian day as fixed effects to account for influences of short term (flood and ebb tide) and possible intra-seasonal dependencies on penguin location We repeated this analysis for location-only data (2002–2011), even though we could not distinguish diving locations from non-diving locations. We expect qualitative similarity to results from the 2011 season where diving locations can be separated from non-diving locations, however quantitative differences in estimated fixed effects are expected. To visualize differences in penguin location between tidal regimes, we used a two-dimensional kernel density filter with a grid cell of 725 m. The size of the Gaussian smoothing kernel was ~3 km.

Results

Penguin Locations and Dive Records

The ARGOS filtering technique removed 24% of the ARGOS locations for all years (Table 1). In 2011, we collected 738 hours of dive depth records from 11 Adélie penguins. We classified 201 locations as diving locations and 467 locations as non-diving locations. The 2011 record was separated into 30 trips, while the historic record was separated into 603 trips. The Adélie penguins from Humble Is. frequently forage over the northeast edge of Palmer Deep (Figure 1) and follow noticeably different trajectories during the diurnal and semidiurnal tidal regime are evident (Figure S1).

Palmer Tide Records

The tides at Palmer station are mixed, and switch between diurnal (one high and one low tide per day) and semidiurnal (two highs and two lows per day) (Figure 2). The principal tidal constituents are the diurnal K_1 and lunar O_1 and the semidiurnal K_2 and M_2 [54]. Mean tidal amplitudes during our study were 1.23 m and 0.93 m during diurnal and semidiurnal tidal regimes respectively. During the 2011 season, 32% of the penguin trips were during the diurnal tidal regime, while 68% were during the semidiurnal tidal regime. For all penguin trips from 2002–2011, 46% were during diurnal and 54% were during semidiurnal tide regimes.

Currents in Palmer Deep

In 2011, the AUV made 130 and 122 estimates of 100 m vertically integrated currents during diurnal and semidiurnal tides respectively. The mean current speed was 0.13 m s^{-1} with a range of 0–0.41 m s^{-1}. Currents directed toward the northeast, southeast, southwest and northwest quadrat were 59%, 19%, 11%, and 10% of all current observations, indicating a general flow towards the northeast edge of Palmer Deep (Figure 3). Mean current velocities during diurnal and semidiurnal regimes were 0.14 (s.d. ±0.09) and 0.11 (s.d. ±0.08) m s^{-1} respectively. A t-test showed that currents during diurnal tides were significantly stronger than currents during semidiurnal tides ($t = 3.10$, d.f. = 247.84, $p = 0.002$). During diurnal tides, current bearings

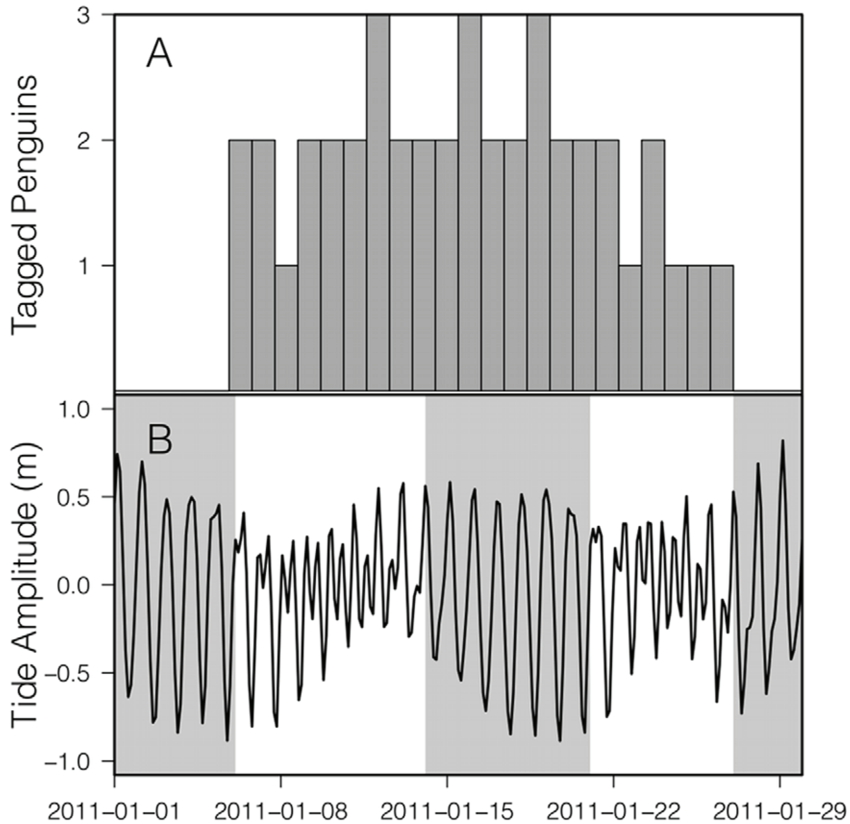

Figure 2. The number of tagged Adélie penguins deployed each day over the course of the 2011 experiment compared to the tidal record at Palmer Station. The number of penguins tagged was between 1 and 3 during the 2011 experiment (A). Mixed tide cycles at Palmer Station during the field season showing the shift from diurnal to semidiurnal tides. Diurnal tides are shaded in grey (B).
doi:10.1371/journal.pone.0055163.g002

were toward the northeast, southeast, southwest and northwest quadrats 68%, 16%, 7%, 9% as compared to 50%, 22%, 14%, 11% during semidiurnal tides indicating stronger flow toward the northeast edge of Palmer Deep, near Humble Is. more often during diurnal tides. The distribution of current bearings between the two tidal regimes was significantly different according to a Mardia-Watson-Wheeler test ($W = 13.988$, $p << 0.001$) [55]. The non-parametric Mardia-Watson-Wheeler test was necessary to test for differences in current bearing between the tidal regimes because the current bearing distribution did not follow a von-Mises (circular normal) distribution. During one diurnal tidal regime, and one semidiurnal tidal regime, the glider maintained its position ("station-kept") to measure currents over a tidal cycle at the northeast edge of Palmer Deep (Figure 4). During semidiurnal tides, the tidal currents are asymmetric over a tidal cycle with stronger currents directed up the canyon. However, during diurnal tides, there is no current to the southwest, indicating that the direction of flow is steady towards the northeast edge Palmer Deep and Humble Is. throughout the tidal cycle. The current bearings between the tidal regimes during the station-keeping missions were significantly different according to a Mardia-Watson-Wheeler test ($W = 21.009$, $p << 0.001$). Wind speeds at Palmer Station while station keeping were weak (mean 2.92 ± 1.45 m s^{-1} and 6.35 ± 2.41 m s^{-1} during the diurnal and semidiurnal tides respectively) and uncorrelated to the vertically integrated currents measured by the AUV during both the diurnal ($t = 1.0$, d.f. = 11, $p = 0.34$) and the semidiurnal ($t = -0.04$, d.f. = 15, $p = 0.96$) tidal regimes. This indicates that wind speed had little effect on the 100 m depth integrated currents during the station-keeping experiments of the AUV. The significant difference of tidal current bearing between the diurnal and semidiurnal regime provide justification for treating the two tidal regimes as factors in our statistical models.

Analysis of 2011 Penguin Diving Locations

We used a linear mixed effects model fit by maximum likelihood to estimate the relationship between tidal regime and the penguin locations relative to their rookery on Humble Is.:

$$DHI_{ijk} = tide\ regime_i \times \beta + tripID_j + \varepsilon_{ijk} \tag{1}$$

where DHI is the distance of the penguin location to Humble Is., tide regime ($i = 1, 2$) is a fixed effect factor that corresponds to the diurnal or semidiurnal regime, β is an estimated coefficient, tripID ($j = 1, 2, 3\ldots$) is a random effect and ε_{ijk} is the residual error, assumed to be normally distributed ($k = 1, 2, 3\ldots$). This model showed that locations associated with diving behavior were significantly farther from Humble Is. during the semidiurnal tide regime compared to a diurnal tide regime (Figure 5) in 2011. The mean ($\pm$ S.E.) distance to diving locations from Humble Is. was 5.4 ± 1.4 km during the diurnal tidal regime while the mean distance to diving locations from Humble Is. was 9.1 ± 1.5 km during the semidiurnal tidal regime ($AIC = 1284$, $t = 2.50$, $p = 0.015$). The residuals of this model satisfied the assumption of normality. Since non-diving locations are generally co-located with diving locations (Figure 5), we repeated the analysis on the

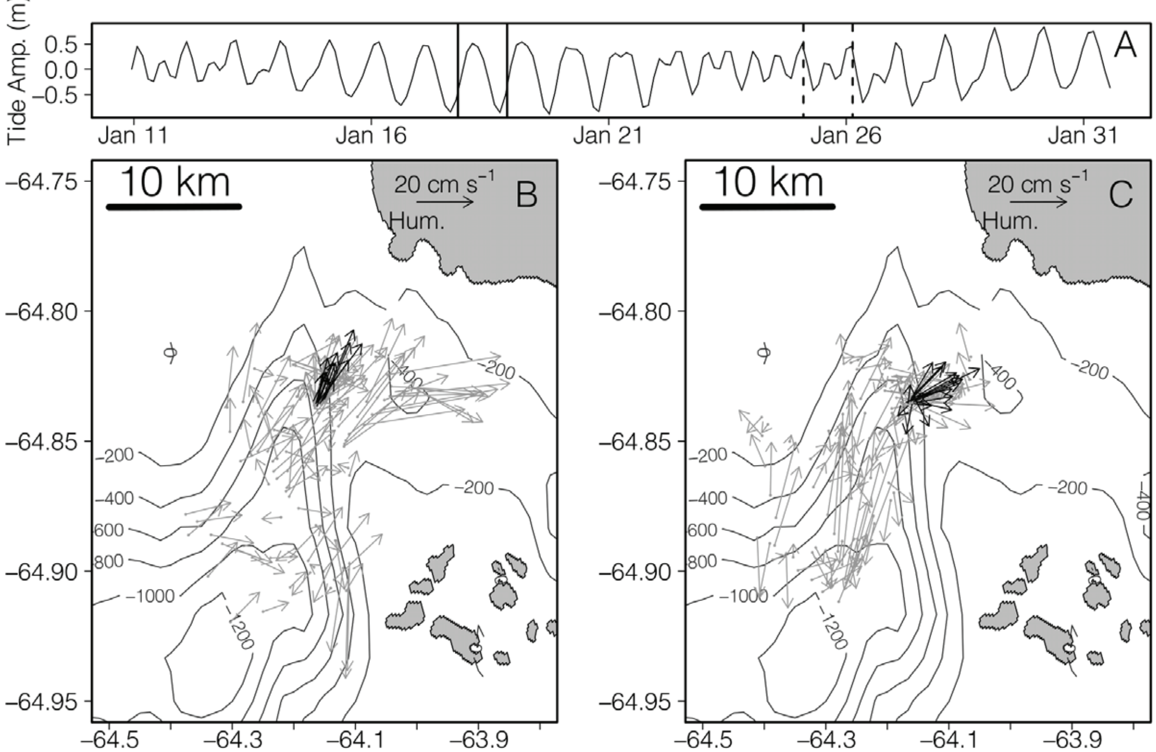

Figure 3. Depth integrated currents measured by a Slocum Glider AUV deployed for the month of January 2011 (arrows). Flow in both tidal regimes is complex, but onshore toward the northeast edge of Palmer Deep in both tide regimes throughout the glider mission. The two separate "station-keeping" periods during strong diurnal tides (station keeping between black lines) and semidiurnal tides (station keeping between dashed lines) are shown in panel A. Black arrows represent the currents measured while station keeping during diurnal and semidiurnal in panels B and C respectively. During the diurnal tides, flow was always toward the northeast edge of the canyon showing no reversals. During the semidiurnal tide, flow oscillated between shoreward and offshore flow, however the shoreward flow was much stronger.
doi:10.1371/journal.pone.0055163.g003

2011 data, for all diving and non-diving locations. The residuals of a linear mixed model that included all locations from 2011 indicated that the data were not normally distributed. Therefore, we $\log_{10}$ transformed DHI, after which model residuals were nearly normal. We found that penguin locations, irrespective of diving behavior, were significantly farther from Humble Is. during a semidiurnal tide compared to a diurnal tide (AIC = 345.3, t = 2.99, p = 0.004). The mean (±SE) distance to Humble Is. during a diurnal tide was 2.7±0.5 km and the mean distance to Humble Is. during a semidiurnal tide was 4.4±0.3 km. Mean distances are closer to Humble Is. when all locations are considered, compared to the diving-only locations. This is likely a consequence of not separating locations that are associated with diving behavior.

Changes in penguin foraging distance and location have been observed to vary with the season [56,57], and with daily flood and ebb tides [38]. To test for intra-seasonal changes or changes related to flood or ebb tides in the penguin location distance from Humble Is. we also included Julian day and tidal amplitude as additional fixed effects in the linear mixed effects models:

$$DHI_{ijk} = X_{ijk,l} \times \beta_l + tripID_j + \varepsilon_{ijk} \qquad (2)$$

where DHI is the distance of the penguin location to Humble Is., X is a three column (l = 1, 2, 3), fixed effects design matrix of the tide regime (i = 1, 2), tidal amplitude (m) and Julian Day (d) and β is a vector of three estimated coefficients of the fixed effects. tripID (j = 1, 2, 3…) is the random effect and ε_{ijk} is the residual error, assumed to be normally distributed (k = 1, 2, 3…).

Similar to Eq. (1), model fits of Eq. (2) showed that penguin diving locations (AIC = 1284, t = 2.68, p = 0.008) and all penguin locations in 2011 (AIC = 345, t = 2.75, p = 0.003) during the diurnal tide regime were significantly closer to Humble Is. compared with the semidiurnal tidal regime. Neither tidal amplitude nor Julian day were significant predictors of DHI for diving locations alone (tidal amplitude t = 1.19, p = 0.235; Julian Day t = −0.75, p = 0.941), nor all penguin locations (tidal amplitude t = 1.14, p = 0.254; Julian day t = −1.18, p = 0.237) in 2011. An AIC comparison of the model fits of Eq. (1) and (2) showed they were not significantly different for penguin diving locations (d.f. = 2, χ^2 = 1.41, p = 0.495), or for all penguin locations (d.f. = 2, χ^2 = 2.490, p = 0.288), indicating that there is not an effect of tidal amplitude or Julian day on penguin foraging location in 2011.

Analysis of 2002–2011 Penguin Locations

Location-only data from 2002–2011 also show a difference between penguin locations between tidal regimes. Contours containing 95% of observations showed that penguins used a smaller area to forage during diurnal tides (40.6 km^2), compared to semidiurnal tides (101.4 km^2) (Figure 6). A linear mixed effects model the same form as Eq. (1) on $\log_{10}$ transformed distance data showed that penguins were significantly farther from Humble Is. during semidiurnal tides, compared to diurnal tides (AIC = 13263, t = 2.054, p = 0.04). The mean distance (±SE) from Humble Is.

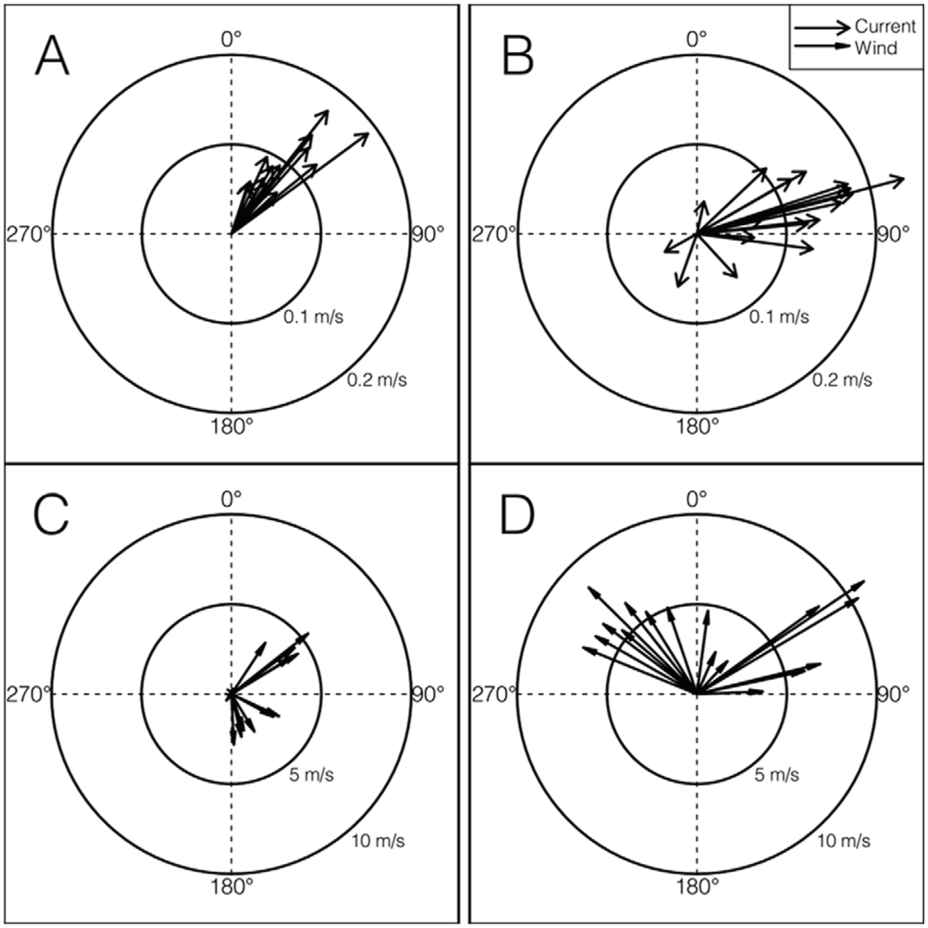

Figure 4. Depth integrated currents and surface winds during AUV station keeping. During diurnal (A) tidal regime, currents never reversed. Currents during a semidiurnal tidal regime reversed for part of the tidal cycle (B). Winds during the diurnal (C) and semidiurnal (D) tidal regimes were uncorrelated to current flow during while the AUV was station keeping.
doi:10.1371/journal.pone.0055163.g004

during diurnal tides was 2.02±0.11 km and 2.34±0.08 km for semidiurnal tides. Although significant differences in penguin distance from Humble Is. are observed (Figure 6), the inability to identify diving locations in seasons prior to 2011 likely occludes the true spatial separation of penguin diving behavior across tidal regimes.

We also tested the effect of tidal amplitude and Julian day on DHI for the 2002–2011 location data using Eq. (2) as the model. Neither tidal amplitude ($t = -0.524$, $p = 0.601$) nor Julian day ($t = -0.195$, $p = 0.845$) was a significant predictor of DHI. An AIC comparison of Eq. (1) and Eq. (2) using location-only data from 2002–2011 showed that the inclusion of tidal amplitude or Julian day as a predictor of DHI did not significantly change AIC (d.f. = 2, $\chi^2 = 0.303$, $p = 0.859$), indicating that tidal regime alone was the best predictor of penguin location.

Discussion

Our results show that weekly switching in tidal regimes, but not daily changes in tidal amplitude, is a significant predictor of Adélie penguin foraging locations near a historic penguin "hot-spot" that is characterized by deep submarine canyons and fjords. By comparison, the foraging location of Magellenic penguins that also inhabit the fjord rich environment of southern Chile, is best predicted by daily changes in tidal amplitude and current direction [38]. The contrast in response to tidal forces between these two penguin groups can only be understood in the light of the hydrography of their respective locations. An AUV consistently occupied the general foraging area of Adélie penguins, and showed that the bearing of the tidally driven flow patterns over Palmer Deep did not follow a daily oscillation, but rather oscillated between weekly tidal regimes (Figure 4). The link between both penguin diving and non-diving location and tidal regime switching is strongly supported statistically for both the 2011 field season (Figure 5), and for historical observations of Adélie penguin location (Figure 6) indicating that the weekly switching of tidal regime in our region plays a strong role in organizing the local coastal ecosystem near Palmer Deep.

The interaction of nutrient rich UCDW with switches in tidal regime has already been observed in primary producers near Palmer Deep. Phytoplankton concentrations are much higher near the Adélie penguin colonies during diurnal tides compared to semidiurnal tides [20], indicating that both the presence of the Palmer Deep and tidal regime switching impact the base of the food web. While we did not have direct krill observations during our 2011 field experiment, our observations of current magnitude and direction suggest that krill may also be differentially concentrated during different tidal regimes. During our experiment, the 100 m depth integrated flow measured by

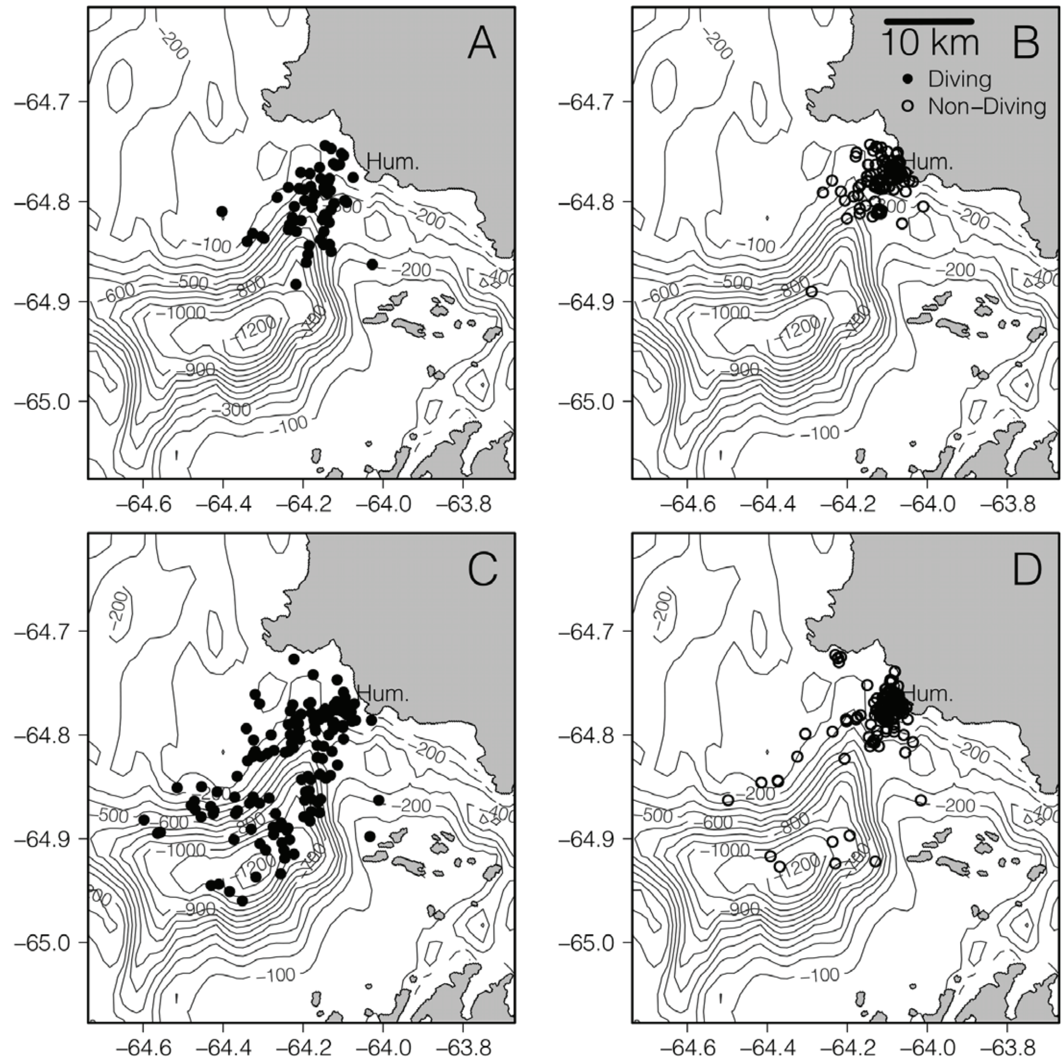

Figure 5. Penguin locations corresponding to diving and non-diving behavior during the 2011 season. Panels A and B are during the diurnal tidal regime and diving panels C and D are during the semidiurnal tidal regime.
doi:10.1371/journal.pone.0055163.g005

the AUV was predominantly northeast (59% of all depth integrated current measurements) toward the head of Palmer Deep suggesting water in our study area is continually being replaced by water from the continental shelf. The mean speed of depth integrated currents was 0.13 m s^{-1}, which is about half of the normal swimming velocity for krill [58], the predominant prey item in the region [59]. Also, in the summer season, krill are generally located in the upper 100 m of the water column [60]. Therefore the direction of the flow regime would influence the location of krill populations over Palmer Deep. During the diurnal tidal regime the flow towards the northeast edge of Palmer Deep never reversed, while there was only weak reversal during semidiurnal tides (Figure 4). Because tides in this region may stay in a diurnal or semidiurnal regime for up to a week, the diurnal tide regime would continually concentrate krill and other prey items at the northeast edge of Palmer Deep, near Humble Is. During the semidiurnal tide regime, the currents over Palmer Deep reverse for a portion of the tidal cycle, reducing this proposed concentration mechanism near the northeast edge of the canyon. We speculate that the reason Humble Is. Adélie penguins do not travel as far from Humble Is. during the diurnal tide compared to the semidiurnal tide is because krill are concentrated near Humble Is. by currents during the diurnal tidal regime.

It is difficult to tell from our data if the differences in Humble Is. Adélie penguin foraging locations are due to a physiological or behavioral constraint on the penguins, or if the penguins are following changing prey fields over Palmer Deep. Physiological and behavioral constraints seem unlikely, since the foraging distances of these particular Adélie penguins are short in comparison to other known breeding colonies that have foraging ranges of up to 100 km [40]. Also, the difference in mean current speeds between tidal regimes is only ~1% of the penguins' maximum sustained swimming speed indicating the direction of tidal currents are unlikely to have a large effect on the distance Adélie penguins forage from Humble Is.

Understanding the interaction between Palmer Deep and tidal regime switching as a potential prey concentrating mechanism has significant implications for understanding the future of Adélie penguins in this region. The climate driven southward translocation of Adélie penguin chick rearing habitats on the WAP [11] could be ameliorated by predictable, hydrographically concen-

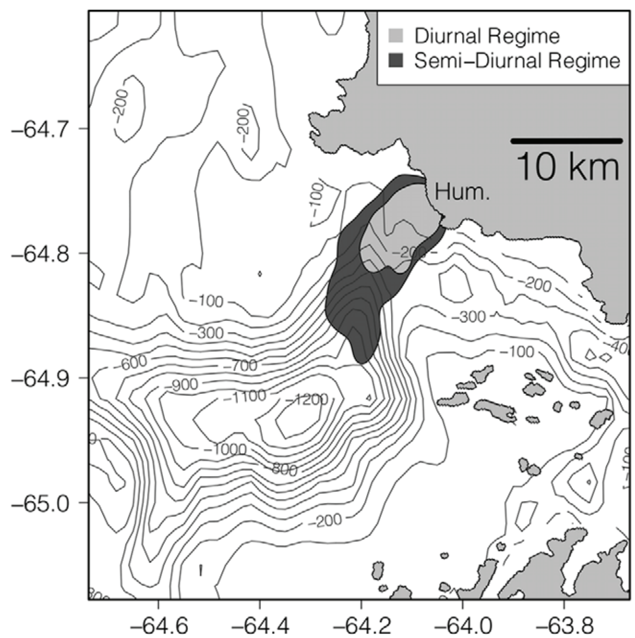

Figure 6. The locations of Adélie penguins during the diurnal and semidiurnal tidal regimes or ten seasons (2002–2011). Ninety five percent of Adélie penguin locations were within the light grey contour during diurnal tides and within the dark grey contour during semidiurnal tides indicating that Adélie penguins tended to be farther from Humble Is. during semidiurnal tides.
doi:10.1371/journal.pone.0055163.g006

trated food resources that allow Adélie penguins to persist in this region despite climactic change [12]. However, because the proposed concentrating oscillates with roughly weekly switches of tidal regime, and not daily scales of tidal amplitude, successive Adélie penguin breeding seasons do not have equal proportions of diurnal and semidiurnal tides. For example, in January 2003, 60% of the tides were during the diurnal regime, while in January 2008, 40% of the tides were during the diurnal regime. Uncovering the mechanics of this effect on krill will require more detailed surveys of local currents and krill densities to determine if the seasonal heterogeneity of tidal regime is a significant factor for Adélie penguin foraging in this region. Whether or not local hydrographic processes that concentrate prey items will provide local a refuge for Adélie penguins in a changing climate is unknown. A path forward could include the interaction between foraging and local hydrography in climate models, however downscaling these models to capture local dynamics present significant challenges [61,62].

Supporting Information

Figure S1 Filtered Adélie penguin satellite tracks from January 2011. Panels A and B are tracks during diurnal and semidiurnal tidal regimes.
(TIF)

Acknowledgments

We thank the Palmer Station support staff for facilitating our long-term data collection efforts. We also wish to thank Ian Robbins and Kaycee Coleman for AUV deployment support, Jennifer Blum, Marc Travers and Kelsey Ducklow for penguin field support, Dave Aragon and John Kerfoot for remote AUV control, and Megan Cimino and Danielle Haulsee for remote satellite support.

Author Contributions

Conceived and designed the experiments: MJO MAM WF DP OS. Performed the experiments: MJO MAM WF DP. Analyzed the data: MJO AI WF DP JK. Contributed reagents/materials/analysis tools: MJO MAM WF DP OS JK. Wrote the paper: MJO AI.

References

1. Emslie SD (2001) Radiocarbon dates from abandoned penguin colonies in the Antarctic Peninsula region. Antarctic Science 13: 289–295.
2. Emslie SD, Patterson WP (2007) Abrupt recent shift in δ13C and δ15N values in Adélie penguin eggshell in Antarctica. Proceedings of the National Academy of Sciences 104: 11666.
3. Schofield O, Ducklow HW, Martinson DG, Meredith MP, Moline MA et al. (2010) How do polar marine ecosystems respond to rapid climate change? Science 328: 1520.
4. Prézelin BB, Hofmann EE, Moline M, Klinck JM (2004) Physical forcing of phytoplankton community structure and primary production in continental shelf waters of the Western Antarctic Peninsula. Journal of Marine Research 62: 419–460.
5. Prézelin BB, Hofmann EE, Mengelt C, Klinck JM (2000) The linkage between Upper Circumpolar Deep Water (UCDW) and phytoplankton assemblages on the west Antarctic Peninsula continental shelf. Journal of Marine Research 58: 165–202.
6. Gille ST (2002) Warming of the Southern Ocean since the 1950s. Science 295: 1275.
7. Gille ST (2010) Decadal-scale temperature trends in the Southern Hemisphere Ocean. Journal of Climate 4749–4765.
8. Stammerjohn SE, Martinson DG, Smith RC, Iannuzzi RA (2008) Sea ice in the western Antarctic Peninsula region: spatio-temporal variability from ecological and climate change perspectives. Deep Sea Research Part II: Topical Studies in Oceanography 55: 2041–2058.
9. Martinson DG, Stammerjohn SE, Smith RC, Iannuzzi RA (2008) Palmer, Antarctica, Long-Term Ecological Research program first 12 years: physical oceanography, spatio-temporal variability. Deep Sea Research II 55: doi: 10.1016/j.dsr2.2008.04.038.
10. Ducklow HW, Baker K, Martinson DG, Quetin LB, Ross RM et al. (2007) Marine pelagic ecosystems: the west Antarctic Peninsula. Philosophical Transactions of the Royal Society B: Biological Sciences 362: 67.
11. Cimino MA, Fraser WR, Irwin AJ, Oliver MJ (2012) Satellite data identify decadal trends in the quality of *Pygoscelis* penguin chick-rearing habitat. Global Change Biology DOI: 10.1111/gcb.12016.
12. Emslie SD, Fraser W, Smith RC, Walker W (1998) Abandoned penguin colonies and environmental change in the Palmer Station area, Anvers Island, Antarctic Peninsula. Antarctic Science 10: 257–268.
13. Bowden KF (1963) The mixing processes in a tidal estuary. International Journal of Air and Water Pollution 7: 343–356.
14. Garrett CJR, Keeley JR, Greenberg DA (1978) Tidal mixing versus thermal stratification in the Bay of Fundy and Gulf of Maine. Atmosphere-Ocean 16: 403–423.
15. Munk W, Wunsch C (1998) Abyssal recipes II: energetics of tidal and wind mixing. Deep-Sea Research Part I 45: 1977–2010.
16. Pingree RD, Mardell GT, Maddock L (1985) Tidal mixing in the Channel Isles region derived from the results of remote sensing and measurements at sea. Estuarine, Coastal and Shelf Science 20: 1–18.
17. Bowman MJ, Esaias WE, Schnitzer MB (1981) Tidal stirring and the distribution of phytoplankton in Long Island and Block Island Sounds. Journal Of Marine Research 39: 587–603.
18. Cloern JE (1991) Tidal stirring and phytoplankton bloom dynamics in an estuary. Journal Of Marine Research 49: 203–221.
19. Loder JW, Platt T (1985) Physical controls on phytoplankton production at tidal fronts. In: Gibbs PE, editor. Proceedings of XIXth EMBS 1984. Cambridge: Cambridge University Press. 3–21.
20. Moline MA, Prézelin BB (1996) Long-term monitoring and analyses of physical factors regulating variability in coastal Antarctic phytoplankton biomass, in situ productivity and taxonomic composition over subseasonal, seasonal and interannual time scales. Marine Ecology Progress Series 145: 143–160.
21. Alldredge AL, Hamner WM (1980) Recurring aggregation of zooplankton by a tidal current. Estuarine and Coastal Marine Science 10: 31–37.
22. Barlow JP (1955) Physical and biological processes determining the distribution of zooplankton in a tidal estuary. The Biological Bulletin 109: 211.
23. Wooldridge T, Erasmus T (1980) Utilization of tidal currents by estuarine zooplankton. Estuarine and coastal marine science 11: 107–114.
24. Franks PJS, Chen C (1996) Plankton production in tidal fronts: a model of Georges Bank in summer. Journal of Marine Research 54: 631–651.

25. Epifanio CE (1987) The role of tidal fronts in maintaining patches of brachyuran zoeae in estuarine waters. Journal of Crustacean Biology 513–517.
26. Zamon JE (2002) Tidal changes in copepod abundance and maintenance of a summer *Coscinodiscus* bloom in the southern San Juan Channel, San Juan Islands, USA. Marine Ecology Progress Series 226: 193–210.
27. Jones PL, Shulman MJ (2008) Subtidal-intertidal trophic links: American lobsters [*Homarus americanus* (Milne-Edwards)] forage in the intertidal zone on nocturnal high tides. Journal of Experimental Marine Biology and Ecology 361: 98–103.
28. Ralston SL, Horn MH (1986) High tide movements of the temperate-zone herbivorous fish *Cebidichthys violaceus* (Girard) as determined by ultrasonic telemetry. Journal of experimental marine biology and ecology 98: 35–50.
29. Rowe PM, Epifanio CE (1994) Tidal stream transport of weakfish larvae in Delaware Bay, USA. Marine Ecology-Progress Series 110: 105–105.
30. Rowe PM, Epifanio CE (1994) Flux and transport of larval weakfish in Delaware Bay, USA. Marine Ecology Progress Series 110: 115–115.
31. Zamon JE (2001) Seal predation on salmon and forage fish schools as a function of tidal currents in the San Juan Islands, Washington, USA. Fisheries Oceanography 10: 353–366.
32. Cotté C, Simard Y (2005) Formation of dense krill patches under tidal forcing at whale feeding hot spots in the St. Lawrence Estuary. Marine Ecology Progress Series 288: 199–210.
33. Gregory PR, Rowden AA (2001) Behaviour patterns of bottlenose dolphins (*Tursiops truncatus*) relative to tidal state, time-of-day, and boat traffic in Cardigan Bay, West Wales. Aquatic Mammals 27: 105–113.
34. Vlietstra LS, Coyle KO, Kachel NB, Hunt Jr GL (2005) Tidal front affects the size of prey used by a top marine predator, the short-tailed shearwater (*Puffinus tenuirostris*). Fisheries Oceanography 14: 196–211.
35. Hunt Jr GL, Russell RW, Coyle KO, Weingartner T (1998) Comparative foraging ecology of planktivorous auklets in relation to ocean physics and prey availability. MEPS 167: 241–259.
36. Holm KJ, Burger AE (2002) Foraging behavior and resource partitioning by diving birds during winter in areas of strong tidal currents. Waterbirds 25: 312–325.
37. Wilson RP, Locca R, Alejandro Scolaro J, Laurenti S, Upton J et al. (2001) Magellanic Penguins Spheniscus magellanicus commuting through San Julian Bay; do current trends induce tidal tactics? Journal of avian biology 32: 83–89.
38. Raya Rey A, Bost CA, Schiavini A, Pütz K (2010) Foraging movements of Magellanic Penguins *Spheniscus magellanicus* in the Beagle Channel, Argentina, related to tide and tidal currents. Journal of Ornithology 151: 933–943.
39. Hunt GL (1997) Physics, zooplankton, and the distribution of least auklets in the Bering Sea–a review. ICES Journal of Marine Science: Journal du Conseil 54: 600.
40. Ainley DG (2002) The Adélie Penguin: Bellwether of Climate Change. New York: Cambridge University Press.
41. Croll DA, Osmek SD, Bengtson JL (1991) An effect of instrument attachment on foraging trip duration in chinstrap penguins. The Condor 93: 777–779.
42. Clarke J, Kerry K (1994) The effects of monitoring procedures on Adélie penguins. CCAMLR Science 1: 155–164.
43. Argo data management (2008) Argo User's Manual, Version 2.1.
44. Freitas C, Lydersen C, Fedak MA, Kovacs KM (2008) A simple new algorithm to filter marine mammal Argos locations. Marine Mammal Science 24: 315–325.
45. Freitas C (2010) argosfilter: Argos location filter. R package version 0.62.
46. Williams TD (1995) The penguins. Oxford University Press.
47. Luque SP (2007) Diving Behaviour Analysis in R. R News 7: 8–14.
48. Naito Y, Asaga T, Ohyama Y (1990) Diving behavior of Adélie penguins determined by time-depth recorder. The Condor 92: 582–586.
49. Bengtson JL, Croll DA, Goebel ME (1993) Diving behaviour of chinstrap penguins at Seal Island. Antarctic science 5: 9–15.
50. Luque SP, Fried R (2011) Recursive Filtering for Zero Offset Correction of Diving Depth Time Series with GNU R Package diveMove. PLoS ONE 6: e15850.
51. Kahl LA, Schofield O, Fraser WR (2010) Autonomous Gliders Reveal Features of the Water Column Associated with Foraging by Adélie Penguins. Integrative and Comparative Biology 50: 1041.
52. Schofield O, Kohut J, Aragon D, Creed L, Graver J, et al. (2007) Slocum Gliders: Robust and ready. Journal of Field Robotics 24: 473–485.
53. Bates DE, Maechler M, Bolker B (2011) lme4: Linear mixed-effects models using S4 classes. R package version 0.999375–42.
54. Amos AF (1993) RACER: the tides at Palmer Station. Antarctic Journal of the United States 28: 162–164.
55. Zar JH (1999) Biostatistical analysis. Prentice hall Upper Saddle River, NJ.
56. Kato A, Watanuki Y, Naito Y (2003) Annual and seasonal changes in foraging site and diving behavior in Adélie penguins. Polar Biology 26: 389–395.
57. Ainley DG, Ribic CA, Ballard G, Heath S, Gaffney I et al. (2004) Geographic Structure of Adélie Penguin Populations: Overlap in Colony-Specific Foraging Areas. Ecological Monographs 74: 159–178.
58. Kils U (1982) The swimming behavior, swimming performance and energy balance of Antarctic krill, *Euphausia superba*. SCAR and SCOR, Scott Polar Research Institute. 122 p.
59. Fraser WR, Hofmann EE (2003) A predator's perspective on causal links between climate change, physical forcing and ecosystem. Marine Ecology Progress Series 265: 1–15.
60. Lascara CM, Hofmann EE, Ross RM, Quetin LB (1999) Seasonal variability in the distribution of Antarctic krill, *Euphausia superba*, west of the Antarctic Peninsula. Deep-Sea Research(Part I, Oceanographic Research Papers) 46: 951–984.
61. Wood AW, Leung LR, Sridhar V, Lettenmaier DP (2004) Hydrologic implications of dynamical and statistical approaches to downscaling climate model outputs. Climatic Change 62: 189–216.
62. Fowler HJ, Blenkinsop S, Tebaldi C (2007) Linking climate change modelling to impacts studies: recent advances in downscaling techniques for hydrological modelling. International Journal of Climatology 27: 1547–1578.

Process-Driven Improvements to Hurricane Intensity and Storm Surge Forecasts in the Mid-Atlantic Bight:

Lessons Learned from Hurricanes Irene and Sandy

Scott Glenn, Dave Aragon, Louis Bowers, Michael Crowley, Rich Dunk, Colin Evans, Chip Haldeman, Ethan Handel, Tina Haskins, John Kerfoot, Josh Kohut, Julia Levin, Travis Miles, Laura Palamara, Hugh Roarty, Oscar Schofield, Greg Seroka, Mike Smith, Nilsen Strandskov, John Wilkin, Yi Xu & Javier Zavala-Garay
Rutgers University
New Brunswick, NJ 08901, USA
glenn@marine.rutgers.edu

Carolyn Thoroughgood, Gerhard Kuska, Bruce Lipphardt, Matt Oliver, Matt Shatley
University of Delaware
Newark, DE 19711

Wendell Brown, Avijit Gongopadhyay, Chris Jakubiak & Andre Schmidt
University of Massachusetts
New Bedford, MA 02744

Eoin Howlett
Applied Science Associates
Kingston, RI 02879

David Ullman
University of Rhode Island
Narragansett, RI 02882

Jim O'Donnell & Todd Fake
University of Connecticut
Groton, CT 06340

Nickitas Georgas, Alan Blumberg, Michael Bruno & Tom Herrington
Stevens Institute of Technology
Hoboken, NJ 07030

William Boicourt & Tom Wazniak
University of Maryland
Cambridge, MD 21613

Jay Titlow
Weatherflow, Inc
Poquoson, VA 23662

Ray Toll
Computer Sciences Corporation
VA

Larry Atkinson & Teresa Updyke
Old Dominion University
Norfolk, VA 23529

Nancy Verona
Center for Innovative Technology
Herndon, VA 20170

Harvey Seim & Mike Muglia
University of North Carolina
Chapel Hill, NC 27599

***Abstract*— The coastal northeast United States was heavily impacted by hurricanes Irene and Sandy. Track forecasts for both hurricanes were quite accurate days in advance. Intensity forecasts, however, were less accurate, with the intensity of Irene significantly over-predicted, and the rapid acceleration and intensification of Sandy just before landfall under-predicted. By operating a regional component of the Integrated Ocean Observing System (IOOS), we observed each hurricane's impact on the ocean in real-time, and we studied the impacted ocean's influence on each hurricane's intensity.**

Summertime conditions on the wide Mid-Atlantic continental shelf consist of a stratified water column with a thin (10m-20m) warm surface layer (24-26C) covering bottom Cold Pool water (8-10C). As the leading edge of Irene tracked along the coast, real-time temperature profiles from an underwater glider documented the mixing and broadening of the thermocline that rapidly cooled the surface by up to 8C, well before the eye passed over. Atmospheric forecast sensitivity studies indicate that the over prediction of intensity in Irene could be eliminated using the observed colder surface waters. In contrast, Hurricane Sandy arrived in the late Fall of 2012 after seasonal cooling had already deepened and decreased surface layer ocean temperatures by 8C. The thinner layer of cold bottom water still remaining before Sandy was

978-1-4799-0002-2/13/$31.00 ©2013 IEEE

forced offshore by downwelling favorable winds, resulting in little change in ocean surface temperature as Sandy crossed and mixed the shelf waters. Atmospheric sensitivity studies indicate that because there was little ocean cooling, there was little reduction in hurricane intensity as Sandy came ashore. Results from Irene and Sandy illustrate the important role of the U.S. IOOS in providing the best estimate of the rapidly evolving ocean conditions to atmospheric modelers forecasting the intensity of hurricanes. Data from IOOS may enable improved hurricane forecasting in the future.

***Index Terms*—Hurricane Forecasting, U.S. IOOS, Underwater Gliders, HF Radar, Ocean Modeling, Atmospheric Modeling.**

I. Introduction

Tropical storms are some of the most destructive and deadly weather phenomena on Earth, and have killed more people than any other natural catastrophe (Keim et al. 2006). For example, in the United States during the 20th-century, ten times as many deaths and >three times as much damage occurred from these extreme weather events as compared with earthquakes (Gray, 2003). The impacts are magnified given the human population density found along the coastlines that are prone to hurricanes. Despite the potential devastation, advances in technology, communication, and forecasting have resulted in significant declines in hurricane-related mortalities between 1900 and present day (Walker et al. 2006). Most recently these declines reflect the developments in global atmospheric models and an ensemble forecasting approach that have successfully reduced hurricane track forecast errors by factors of 2-3 over the last two decades, allowing communities sufficient time to proactively prepare for the storms and evacuate prior to their arrival. Despite the progress in predicting hurricane tracks, the predictive skill for hurricane intensity forecasts has remained “flat” over the last twenty years (Pasch & Blake, 2012).

This current state of the science was illustrated by the two recent hurricanes Irene and Sandy that devastated many communities along the Mid-Atlantic coastline spread over dozen states. Hurricanes Irene and Sandy struck dense population centers, and as a result, the National Hurricane Center’s list of costliest hurricanes in United States history ranks Sandy second with over $60 billion and Irene eighth with over $15 billion in damages. Despite the epic scale of devastation, the loss of life was greatly minimized due to accurate forecasts of the hurricane tracks days in advance. Unfortunately, forecasts of hurricane wind intensity were less accurate, impacting efforts to proactively mitigate the damage. For Irene, the wind intensity was significantly over predicted, and for Sandy, the rapid acceleration and wind intensification just before landfall were under predicted. The over prediction of Irene’s intensity in 2011 led to skepticism of the storm surge warnings for Sandy in 2012. To further complicate matters, the under predicted intensity of Sandy resulted in an under predicted storm surge that in some cases led to insufficient preparation.

The Mid-Atlantic Regional Association Coastal Ocean Observing System (MARACOOS), one of eleven Regional Associations comprising the regional component of the U.S. Integrated Ocean Observing System (IOOS), operates a Regional-Scale Coastal Ocean Observatory that includes coastal weather mesonets, satellite data ground stations, a 1000 km long High Frequency (HF) Radar network (Roarty et al., 2010), and a distributed fleet of autonomous underwater gliders (Schofield et al., 2010). Observatory data is assimilated into global and regional-scale ocean models, and an ensemble of regional atmospheric models beginning to use the ocean surface conditions as a boundary condition. The Regional-Scale Coastal Ocean Observatory was fully operating during both hurricanes. In this paper, we discuss selected highlights of real-time ocean data acquired by the MARACOOS regional-scale network during Irene and Sandy, and how the ocean forecasts faired. Through a series of atmospheric model sensitivity studies, the potential impact of accurate real-time ocean data and forecasts on hurricane intensity forecasts in the Mid-Atlantic is demonstrated.

II. Hurricanes Irene & Sandy

The Mid Atlantic Bight of North America was recently struck by two hurricane landfalls that devastated dense population centers and communities spread over a dozen neighboring states (Figure 1). Hurricane Irene, a category 1 storm offshore, tracked rapidly northward along the eastern seaboard in August of 2011, resulting in significant flooding on inland waterways due to torrential rains. Fourteen months later, Hurricane Sandy, a much larger category 2 storm offshore, made an uncharacteristic left turn and approached perpendicular to the coast in October of 2012, causing significant damage to coastal communities due to the extreme storm surge.

Fig. 1. National Weather Service tracks for hurricanes Irene (purple) and Sandy (orange).

Data from the Mid-Atlantic Regional Association Coastal Ocean Observing System (MARACOOS), one of eleven regional associations in the U.S. Integrated Ocean Observing System (IOOS), monitored the ocean response, and used that data to study the influence of the ocean on the intensity of both hurricanes.

Hurricane Irene approached the Mid Atlantic's regional ocean observatory from the south. The real-time observations of the evolving ocean are described in the MARACOOS blog (Glenn et al., 2011). Irene's size was similar to the 1,000 km length scale of the region's HF Radar network (Figure 2) Strong storm-related winds were experienced for only 1 day. Winds initially came from offshore, turned to an alongshore direction as the eye passed, and continued turning to come from the coast after the eye moved north into New England. Most atmospheric models in the ensemble converged on the track forecast days in advance, but unfortunately, the wind intensity was over-predicted by the ensemble. Because of the short duration of hurricane-forced winds, the relative timing between the high tide and the time of the most severe onshore currents for this rapidly moving storm were critical to determine the severity and location of the maximum storm surge. The severe damage from Irene instead occurred inland, where winds that picked up moisture over the warm ocean resulted in heavy rains and flood conditions along the Delaware, Hudson and Connecticut Rivers.

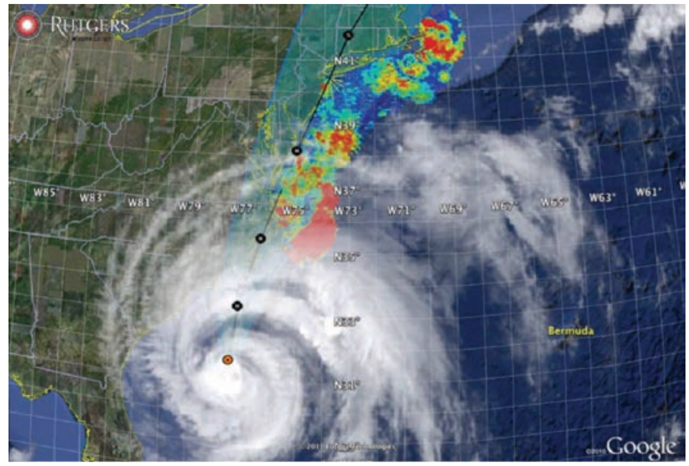

Fig. 2. Spatial extent of Hurricane Irene, August 27, 2011.

Hurricane Sandy approached the Mid-Atlantic's ocean observatory from offshore, perpendicular to the alongshore track of Irene. Real-time ocean observations were again described in the MARACOOS blog. The diameter of Sandy was twice as large as Irene, larger than the scale of the observatory (Figure 3). The approach direction had a significant impact on the areas with severe storm surge damage. North of the eye on the right hand side of the track, the counterclockwise circulation is in the same direction as the propagation. Here sustained winds from offshore that transported water towards the coast were experienced for multiple tidal cycles. South of the eye, winds blew from the coast and water was transported offshore. Compared to Irene, the relative timing between hurricane forcing and high tide was much less important for determining damage. More important for Sandy was your location north or south of the eye.

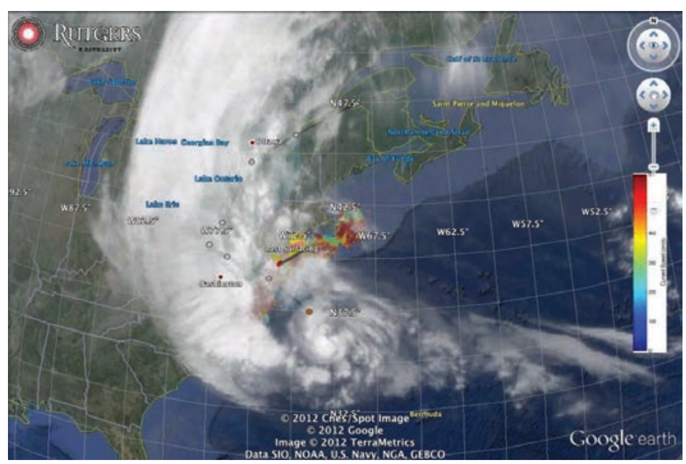

Fig. 3. Spatial extent of Hurricane Sandy, October 28, 2012.

III. Water Column Mixing in IRENE

The eye of Hurricane Irene made landfall in southern New Jersey near Atlantic City at 0900 UTC on August 28, 2011. Irene was moving rapidly northward, fully crossing the state of

New Jersey in about 6 hours. The rapidly evolving surface current response as Irene propagated along the New Jersey coast was observed (Figure 4) using the Mid-Atlantic's High Frequency (HF) Radar network (Roarty et al., 2010). At 0600 GMT, Irene's eye is still over water, with its location observed in the CODAR currents offshore southern New Jersey. Strong onshore currents over the entire width of the shelf are observed north of the eye. At 1200 GMT, the eye is over land in central New Jersey. The ocean currents have rotated to be along the coast to the northeast, and are reduced in speed. By 1800 GMT, the eye is over northern New Jersey. Currents behind the eye are again strong and offshore. The transition from strong onshore flow to strong offshore flow occurred over a short 6 hour period.

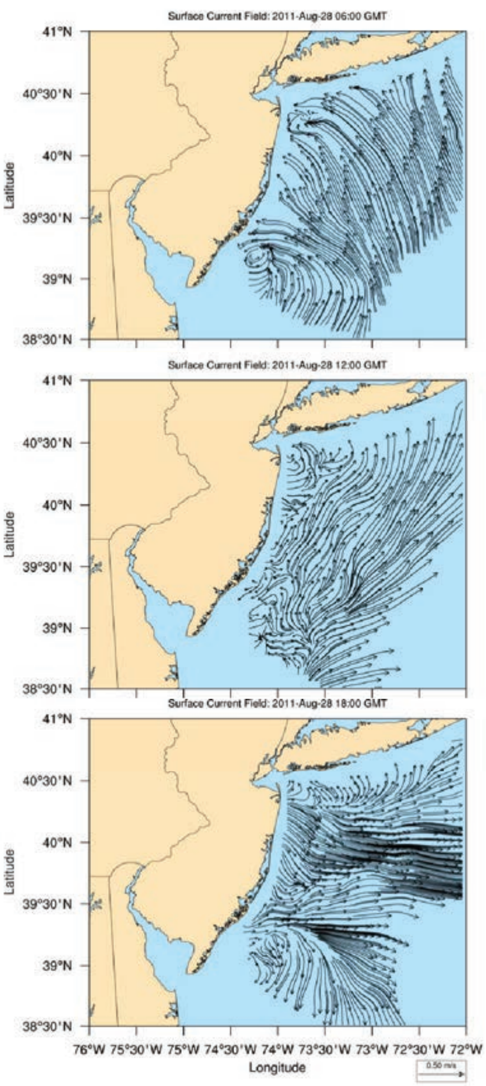

Fig. 4. CODAR-derived surface current spatial response as Irene tracks along the New Jersey coast.

Glider RU16 was deployed on the New Jersey shelf on a coastal survey mission well ahead of and independent of the hurricane. As Irene approached, the glider was purposely left at sea, but was moved offshore to the 40 m isobath to ride out the storm (Figure 5a) The 40 m isobath is an area of relatively uniform sandy sediment, and was considered far enough offshore that even strong hurricane currents faster than the glider's flight speed would not blow the glider onto the beach.

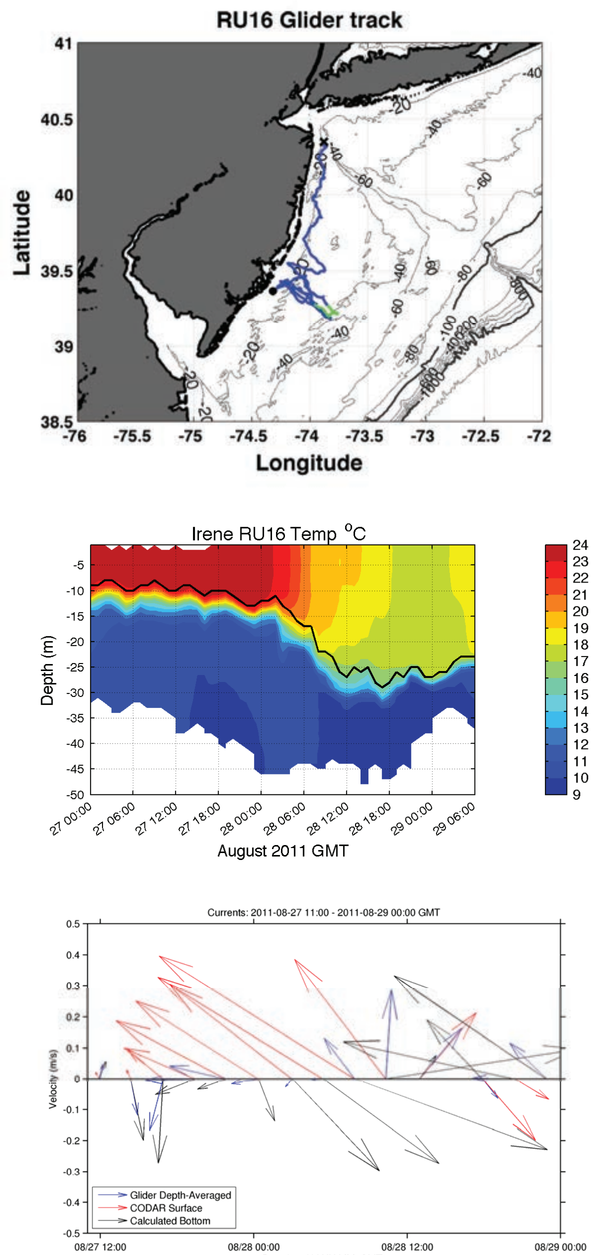

Fig. 5. (a) Glider track in Hurricane Irene. (b) Glider temperature section for the portion of the glider track marked in green. Black line is the depth of the surface mixed layer. (c) Glider depth averaged currents (blue), CODAR surface currents along the glider track (red), and inferred bottom layer currents (black).

The temperature section collected by the glider near the 40 m isobath during Irene (Figure 5b) indicates that on

August 27, the Mid Atlantic shelf was near its peak summer stratification, with a thin 10 m thick layer of warm surface water near 22-25C, and a thicker layer of bottom “Cold Pool” water near 8-10C. The summer thermocline was typically sharp, with the transition from warm surface waters to bottom Cold Pool waters occuring in a few meters. As Irene approached, mixing within each of the surface and bottom layers made each layer more uniform and tightened the thermocline. On August 28, between 0000 GMT and 1200 GMT, as the northern edge of Irene passed over the location of the glider, the thermocline broadened (from less than 5 m to over 15 m) and deepened (from 10 m to 28 m), and the surface layer cooled (from 24C to 18C). After 1200 GMT, as the backside of the hurricane passed over the glider, the deeper thermocline remained near 25 m. Both the surface and bottom layers continued to cool independent of each other as the thermocline reintensified.

Gliders report the depth averaged current over the previous segment with each surfacing. The depth averaged current is estimated by comparing the dead reckoned surface location with the actual surfacing location, and assuming the difference is due to advection of the glider by the depth averaged current. During the hurricane, depth averaged currents are initially southward at 20 cm/sec before the storm, drop to near zero during the approach of the storm, and transition to northward at 30 cm/sec on the backside of the storm (Figure 5c). The important observation is that the depth averaged current is near zero between 0000 GMT and 1200 GMT on August 28 when the thermocline deepening and surface layer cooling is observed. Plotting the CODAR surface currents at the location of the glider, shows how the surface layer is being forced directly onshore to the northwest by the hurricane winds starting on August 27 and peaking during the deepening event. After 1200 GMT on August 28, the CODAR surface currents rotate clockwise to alongshore and then to offshore as noted in the spatial maps (Figure 4). Using the observed CODAR surface current to represent the average current above the thermocline, the average current below the thermocline was estimated based on the requirement that the weighted average of the surface and bottom layers equal the observed glider depth averaged current. Based on the estimated bottom layer current, the onshore transport in the surface layer begins midday on August 27 and for the first 12 hours, there is little response in the bottom layer. During this time the storm surge is expected to grow. Between 0600 GMT and 1200 GMT, as the onshore currents in the surface peak, the offshore currents in the bottom layer accelerate, resulting in zero net transport towards the coast. This time interval when the greatest shear between the surface and bottom layers is expected is precisely the time when the thermocline is observed to deepen. The zero net transport also implies that the storm surge that would have resulted from the shoreward transport of surface water is compensated by the offshore transport of bottom water.

The Regional Ocean Modeling System (ROMS) was operated in forecast mode during the storm. The model was rerun here using the same forecast parameters for more in depth studies. The ROMS forecast/hindcast of the ocean response has several features consistent with these observations that enable further definition of the physical processes responsible for the surface layer cooling. But there are also several differences between the observations and the model. The initial state of the ocean in the ROMS model (Figure 6a) has a 10 m thick surface warm surface layer near 24 C, and bottom Cold Pool layer near 9C, but the initial thermocline is wider than observed, extending over 15 m thick instead of less than 5 m. So the initial condition has a less extreme thermocline that would be more easily mixed than observed. The model was driven by the North American Mesoscale (NAM) model winds. Despite the weaker thermocline, significant mixing does not begin in the model until 6 hours later than the observations. The initial response is an acceleration of the alongshore currents to over 60 cm/sec to the northwest at 0000 GMT on August 28 (Figure 6c). The cross-shore currents, in the onshore direction at the surface and the offshore direction in the bottom, spin up simultaneously and peak at 0600 GMT. At this peak in shear, the thermocline starts deepening and the surface water starts cooling. In the model, this process ends in 6 hours, with the surface water cooling 5C and the bottom water warming 1C. At 1200 GMT, the alongshore surface current reverses direction consistent with the CODAR observations, the bottom jet relaxes in the cross-shore current but remains present in the alongshore current. The glider observations indicate that the bottom jet should have remained in the cross-shore direction.

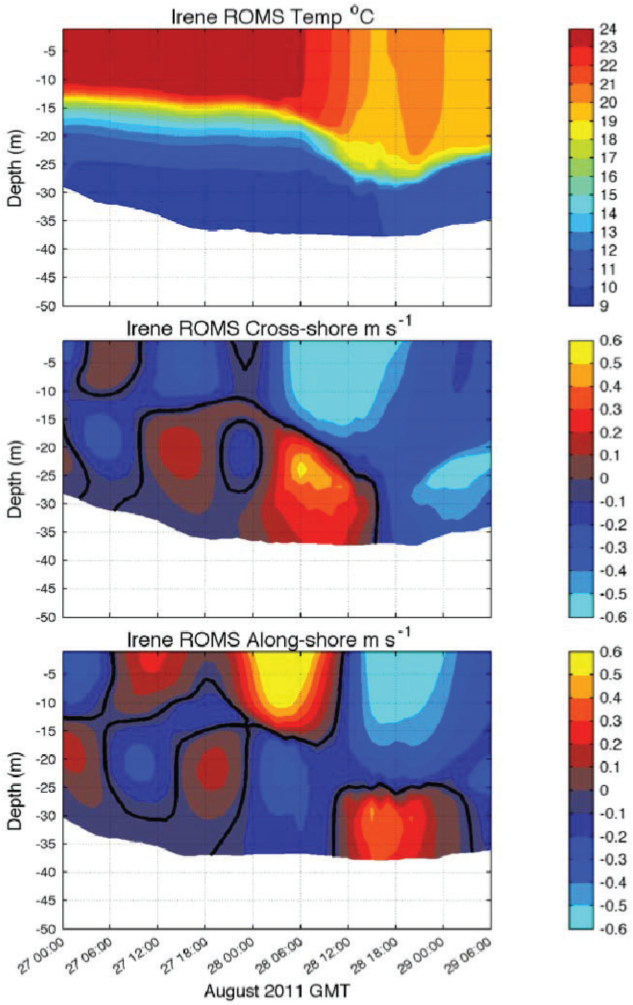

Fig. 6. Regional Ocean Modeling System (ROMS) hindcast of temperature, cross-shore (+offshore) and alongshore (+northeast) current sections along the green portion of the glider track in Figure 5a. Black lines indicate 0 cross and alongshore currents.

While the exact details of the deepening of the thermocline and the cooling of the surface layer do not exactly match those observered, model diagnostics indicate that the vertical diffusion in the surface layer dominate advective changes in the model. This points to improvements in the mixing parameterizations as a place to look to improve the model. Even with a weaker thermocline and stronger winds, the mixing is insufficient to cool the upper layer as much as observed.

Satellite-derived Sea Surface Temperature (SST) maps of the Mid-Atlantic Bight just after Irene indicate that the cooling was widespread (Figure 7). The locally generated SST product (Figure 7a) indicates that surface temperatures dropped to as low as 14C on the shelf, with the greatest cooling observed over the historical location of the Cold Pool and concentrated on the mid to outer shelf, shoreward of the shelfbreak. The cooling was so significant, even though skies were clear after the storm, the cloud detection algorithms rejected the data as being too cold, removing it from the Real Time Global (RTG) SST updates (Figure 7b). As a result, the RTG SST map is essentially unchanged before and after Irene. Since the RTG map is the SST used by several atmospheric forecast models as a bottom boundary condition, the ocean used in the Irene forecasts was too warm. The difference between the RTG and the actual sea surface temperatures after the storm is as large as 10C (Figure 7c).

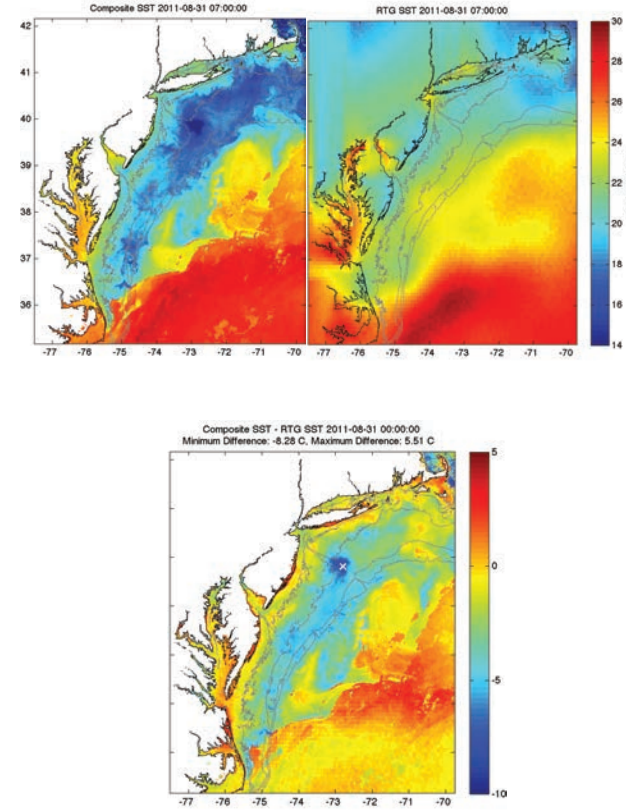

Fig. 7. Post-Hurricane Irene Satellite-derived Sea Surface Temperature (SST) products for August 31, 2011. (a) Locally composited SST showing the surface cooling. (b) Operational global SST product with the cool pixels incorrectly identified as clouds. (c) Difference.

The impact of the rapidly cooling SST on the Weather Research and Forecasting (WRF) model hindcast sensitivity studies of Hurricane Irene illustrates the significant impact of the cooler water. The glider data indicates that the cooling occurred ahead of the eye as the high winds of the outer wind bands approached. Thus the eye of the hurricane passed over cool water as it propagated northward. Since the RTG SST does not cool, it was used as the base case for comparison (Figure 8a). At the time of landfall, the hurricane intensity is over predicted. Since the ROMS model cools late and insufficiently, the locally composited SST product was used to simulate the change in SST as the storm passed. Starting with the warm pre-storm SST, the cold post-storm SST was applied everywhere at the time of peak mixing observed in the glider transect. The resulting WRF forecast is lower by 5-10 knots. (Figure 8b).

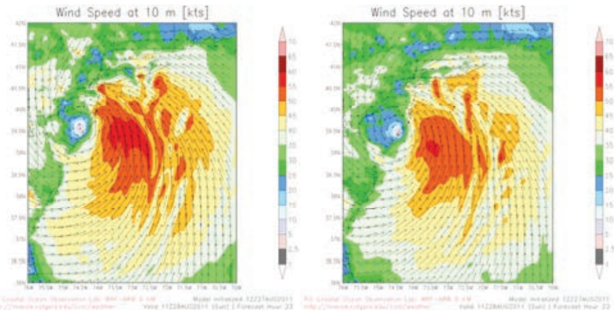

Fig. 8. Weather Research Forecast (WRF) atmospheric hindcasts of Hurricane Irene with different ocean boundary conditions. (a) Using the warm SST throughout the run. (b) Switching to the cold SST in Figure 7a when the cooling is observed in the glider data.

IV. Sandy

Hurricane Sandy followed Hurricane Irene by 14 months. Forecasts made by the European Center for Medium-range Weather Forecasting (ECMWF) alerted researchers to the possibility of a signficant storm hitting New Jersey a full week in advance. The importance of the glider observations in Irene prompted the deployment of glider RU23. Based on the lessons learned in Irene, the glider payload bay with its standard CTD was further equiped with optical sensors to look at the sediment concentrations as a tracer for mixing. A Nortek Aquadopp Acoustic Doppler Current Profiler (ADCP) was attached externally to examine the shear across the thermocline during the event. The glider was deployed nearshore with a small boat, and, as in Irene, was directed to fly to the 40 m isobath to ride out the storm (Figure 9).

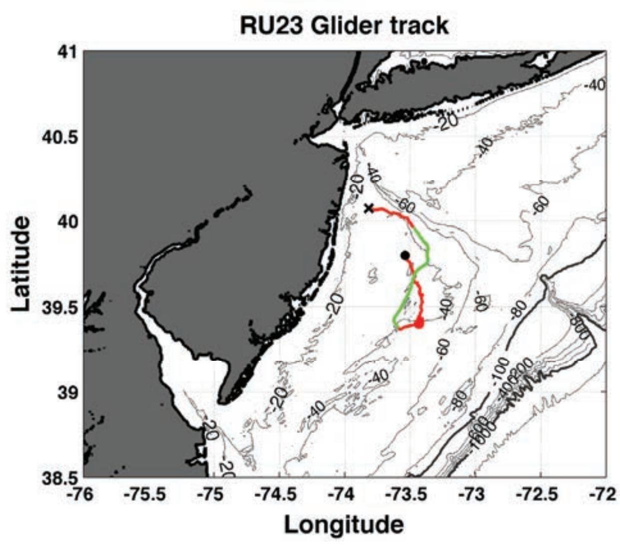

Fig. 9. Glider track during Hurricane Sandy.

Glider RU23 revealed that the initial ocean conditions for Hurricane Sandy were quite different than 14 months ago before Irene (Figure 10). The peak summer thermocline intensity observed in Irene was already 2 months into the fall transition. The two-layer structure was still present, but the surface layer had already cooled to 16C-17C, and thickened to a depth of 30 m. As usual, the bottom Cold Pool temperatures where observed to be around 9C-10C. Like Irene, the thermocline is again observed to be only a few meters thick. As Sandy approaches the coast, the increase in the thermocline depth is even more rapid than Irene, occuring within a few hours near 0600 GMT on October 29. After the deepening event, the water column is filled with a single surface layer, but the layer cooling is only 1 C from 16 C to 15 C. The glider data indicated that Sandy was going to make landfall propogating over SSTs that changed little from the pre-storm conditions. No ohterwise unobserved cooling to reduce intensity was expected.

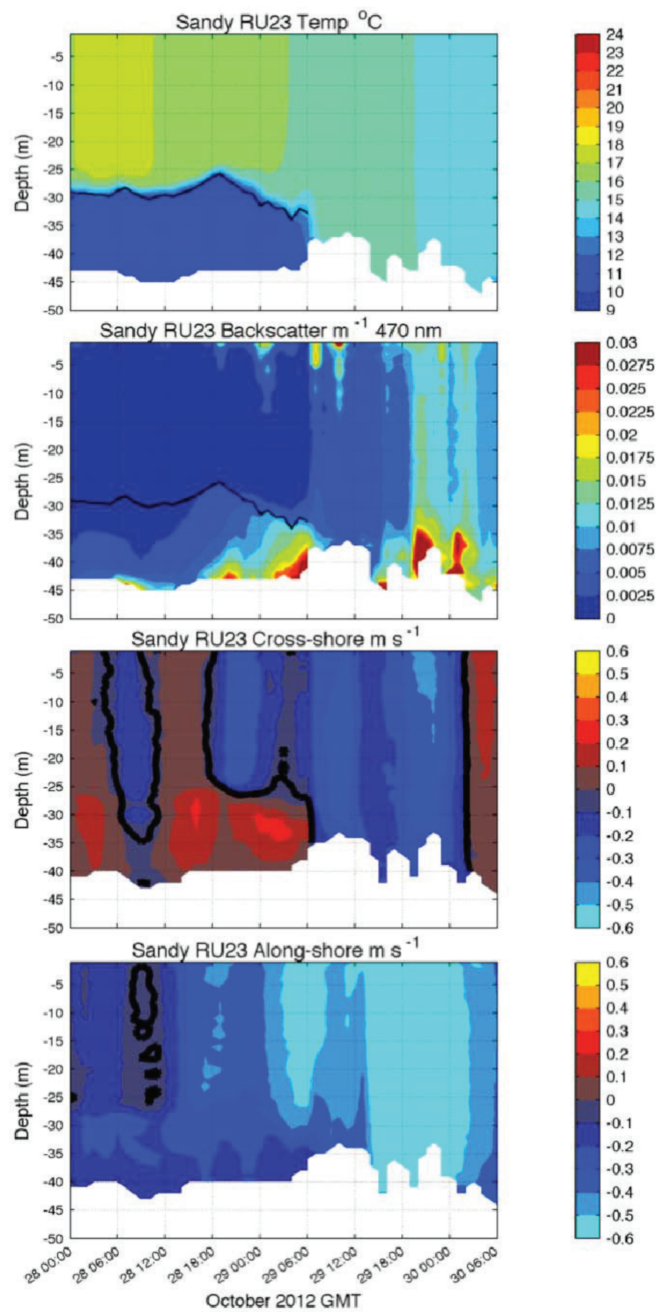

Fig. 10. Glider-derived temperature, backscatter, cross-shore (+offshore) and alongshore (+northeast currents for Hurricane Sandy.

The ocean model in Irene indicated the deepening and cooling of the surface layer, while inadequate, was dominated by a mixing processes. More extensive glider observations in Sandy indicate the layer deepening was likely dominated by an advective processes. Optical backscatter in Sandy indicates that before the transition to a fully mixed water column, sediment suspended from the bottom did not cross the thermocline. After the transition to one layer, optical sensors indicate that sediment resuspension filled the water column, with a single mixed layer going from surface to bottom. Currents measured by the glider-mounted ADCP indicate that before the transition, a two layer flow was observed, especially in the cross-shore direction. A strong offshore jet formed in the bottom layer and persisted for over 18 hours before the transition as the water in the bottom layer thinned and moved offshore. Once the transition was complete, the water column responded as a single layer. Most significantly, the cross-shore current was onshore throughout the water column and persisted for two tidal cycles as the alongshore current accelerated to the southwest.

The same two SST products used in Irene were also examined in Sandy for August 27 (Figure 11). There is little pre-storm difference between the two SSTs, both maps have shelf temperatures in the 16C-18C range before the storm. Because Sandy was so extensive, and it was followed several days later by a northeaster that dropped snow on the damaged area, new SST products were not available for 11 days after the storm.

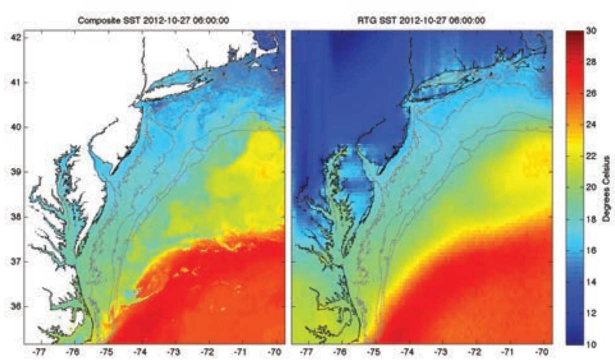

Fig. 11. Pre-Hurricane Sandy Satellite-derived Sea Surface Temperature (SST) products for October 27, 2012. (a) Locally composited SST. (b) Operational global SST product.

The Sandy observations indicated that there would be no significant cooling of the ocean surface layer as Sandy propagated shoreward. The WRF winds based on the conditions used in the real-time WRF forecasts, with atmospheric boundary conditions supplied by NCEP and ocean boundary conditions supplied by the locally composited SST are in Figure 12a. There is little sensitivity to the source of the SST, either the RTG or composite. Both result in an intensification of the storm as it makes landfall. The main sensitivity is the timing of landfall that is adjusted based on which NCEP atmospheric model is used for boundary conditions. WRF embedded within the North American Mesoscale (NAM) model captures the acceleration of Sandy during the last 6 hours before landfall better than WRF embedded in the Global Forecast System (GFS) model. The acceleration and intensification is significant, since the mean storm surge using operational products was under-predicted by 1 m in the hardest hit areas. Using the WRF model run in Figure 12a with the proper intensification and acceleration gains back the missing meter in the mean storm surge as predicted by the New York Harbor Ocean Prediction System (NYHOPS) run by Stevens Institute of Technology.

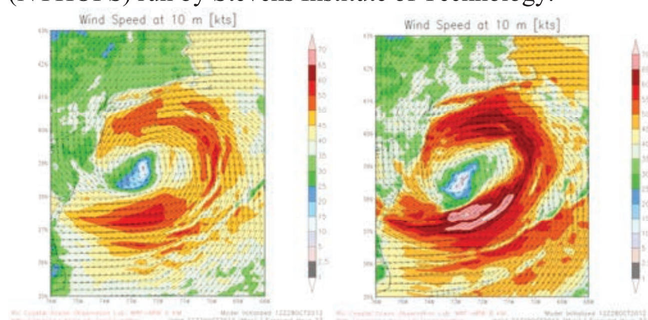

Fig. 12. Weather Research Forecast (WRF) atmospheric hindcasts of Hurricane Sandy with different ocean boundary conditions. (a) Using the cold SST from Figure 11a. (b) Using a warm SST characteristic of August conditions on the Mid-Atlantic continental shelf.

This series of model runs, while producing a hindcast that accurately recreates the observed storm surge, leaves unanswered the question of forecast sensitivity to SST in Sandy. If Sandy had hit earlier in the hurricane season during the peak summer stratification, would the forecast be sensitive to rapid changes in SST? As a test case, Sandy was rerun with typical August SSTs where, as in reality, it was assumed that no satellite updates to SST were available for over a week. The increase in forecast intensity at landfall is evident in Figure 12 b. Using these higher winds to force the NYHOPS storm surge model results in another meter increase in the predicted storm surge.

V. Conclusions

The back-to-back landfalls of hurricanes Irene and Sandy along the coast of New Jersey have hightened awareness of hurricanes and their potential impacts in the Mid-Atlantic. Irene’s alongshelf track was accurately forecast but the intensity was over-predicted. Ocean observations by U.S. IOOS provide guidance as to why. Operational SST products did not pick up the 8-10C cooling caused by Irene even several days after the weather had cleared. An autonomous underwater glider that flew through the storm indicated that the cooling occurred rapidly as the leading edge of the hurricane approached and well ahead of the eye. Even if the operational SST products were reconfigured to pick up the cooling after the storm, they could not be applied in time to impact Irene. A more useful SST mapping product that accurately captures the timing and spatial extent of the cooling can only be supplied by an ocean forecast model. The ocean observations indicate what processes the ocean model must capture. Specifically, the initial thermocline must be better represented as the starting point. Second, the model must be 3-D, with a coast and a bottom. An infinitely deep 1-D model, one potential option for coupled atmosphere-ocean modes, will not capture the processes observed here. These include the initial onshore transport in the surface layer towards the coast, and the delayed response of the bottom layer to produce an offshore transport that limits the net shoreward transport. When there are two layers, the water transported onshore has an escape route through the bottom layer that appears to limit the storm surge. It also appears that the bottom layer also should be sufficiently thin for the offshore transport to produce a large shear across the interface. It is when this large shear is present that the mixing and cooling occurs.

Sandy occurred later in the year than Irene, after the fall transition was well on its way. Real time ocean observations during Sandy provided different guidance on what to expect when Sandy came ashore. The surface layer was already much thicker and cooler, so significant additional cooling was not expected. Advection moved what remained of the bottom Cold Pool offshore, removing the midshelf source of cool water. The water column responded as a single layer as Sandy came ashore, with mixing from surface to bottom, no cooling to reduce the intensity, and no bottom layer for the water in the growing storm surge to escape offshore.

The U.S. IOOS observations of hurricanes Irene and Sandy as implemented by MARACOOS for the Mid-Atlantic provided unprecedented real-time views of the evolving coastal ocean as the hurricanes made landfall in New Jersey. The observations led to new process studies in the ocean using numerical ocean models to examine the role of shallow topography, stratification and mixing that ultimately will lead to better ocean forecasts in extreme forcing conditions. New atmospheric sensitifivity studies further indicate that the rapid evolution of the ocean's surface layer temperature can have a significant impact on hurricane intensity. These results provide further evidence that one step towards inrpoving hurricane intensity forecasting is to provide atmospheric modelers a better forecast of the rapidly changing coastal ocean beneath hurricanes.

ACKNOWLEDGMENT

Base support for this research was provided by the U.S. Integrated Ocean Observing System (IOOS) through the Mid-Atlantic Regional Association Coastal Ocean Observing System (MARACOOS). The Department of Homeland Security National Center for Secure and Resilient Maritime Commerce provided additional support for the HF Radar network. New Jersey Board of Public Utilities further augmented the satellite data products, the HF Radar network, and the atmospheric forecasting. The deployment and operation of Glider RU16 in Irene was funded by the Environmental Protection Agency and the New Jersey Department of Environmental Protection. The deployment and operation of Glider RU23 in Sandy was funded by graduate student grants from Teledyne Webb Research and Nortek.

REFERENCES

[1] S. Glenn, O. Schofield and J. Kohut, "Hurricane Irene 2011: Mid-Atlantic IOOS response to the hurricane", http://maracoos.org/sites/macoora/files/downloads/Hurricane_Irene_blog_2011.pdf, pp. 65, 2011.

[2] W. Gray, 2003. Twentieth century challenges and milestones. In: Hurricanes! Coping with Disaster, R. Simpson, ed., American Geophysical Union, Washington, DC. 10.1029/055SP02.

[3] B. Keim, R. Muller and G. Stone, Spatiotemporal patterns and return periods of tropical storm and hurricane strikes from Texas to Maine, Journal of Climate, 20, 3498-3509, 2007.

[4] H. Roarty, S. Glenn, J. Kohut, D. Gong, E. Handel, E. Rivera, T. Garner, L. Atkinson, W. Brown, C. Jakubiak, M. Muglia, S. Haines, H. Seim, "Operation and Application of a Regional High-Frequency Radar Network in the Mid-Atlantic Bight" Marine Technology Society Journal, 44 (6), 2010.

[5] Pasch, R. and E. Blake, 2012. 2012 Review of the NCEP Production Suite: Report from NHC, National Centers for Environmental Predictions, Maryland, December 4, 2012,

[6] O. Schofield, J. Kohut, S. Glenn, J. Morell, J. Capella, J. Corredor, J. Orcutt, M. Arrott, I. Krueger, M. Meisinger, C. Peach, F. Vernon, A. Chave, Y. Chao, S. Chien, D. Thompson, W. Brown, M. Oliver, W. Boicourt, "A regional Slocum glider network in the Mid-Atlantic coastal waters leverages broad community engagement." Marine Technology Society 44(6): 64-74, 2010.

[7] N. Walker, A. Haag, S. Balasubramanian, R. Leben, I. van Heerden, P. Kemp and H. Mashriqui, 2006. Hurricane prediction: A century of advances, Oceanography, 19(2), 24-36.

THE OFFICIAL MAGAZINE OF THE OCEANOGRAPHY SOCIETY

Oceanography

CITATION

Schofield, O., H. Ducklow, K. Bernard, S. Doney, D. Patterson-Fraser, K. Gorman, D. Martinson, M. Meredith, G. Saba, S. Stammerjohn, and others. 2013. Penguin biogeography along the West Antarctic Peninsula: Testing the Canyon Hypothesis with Palmer LTER observations. *Oceanography* 26(3):204–206, http://dx.doi.org/10.5670/oceanog.2013.63.

DOI

http://dx.doi.org/10.5670/oceanog.2013.63

Penguin Biogeography Along the West Antarctic Peninsula

Testing the Canyon Hypothesis with Palmer LTER Observations

BY OSCAR SCHOFIELD, HUGH DUCKLOW, KIM BERNARD, SCOTT DONEY, DONNA PATTERSON-FRASER, KRISTEN GORMAN, DOUG MARTINSON, MICHAEL MEREDITH, GRACE SABA, SHARON STAMMERJOHN, DEBORAH STEINBERG, AND WILLIAM FRASER

The West Antarctic Peninsula (WAP) is home to large breeding colonies of the ice-dependent Antarctic Adélie penguin (*Pygoscelis adeliae*). Although the entire inner continental shelf is highly productive, with abundant phytoplankton and krill populations, penguin colonies are distributed heterogeneously along the WAP (Ducklow et al., 2013, in this issue). This ecological conundrum targets a long-standing question of interest: what environmental factors structure the locations of Adélie penguin "hot spots" throughout the WAP?

Penguin colonies appear to be located in association with deep submarine canyons that are found all along the WAP continental shelf (Figure 1). These deep troughs extend from the shelf break to the land margin. Marine canyons are hypothesized to provide a cross-shelf conduit for warm (> 1°C), modified, Upper Circumpolar Deep Water to the coast. This water mass is the primary heat source within the WAP, and the observed warming of Upper Circumpolar Deep Water (Martinson et al., 2008) is driving regional atmospheric warming (Ducklow et al., 2012) and the observed declines in sea ice in this region (Stammerjohn et al., 2008). In the past, when annual and perennial sea ice dominated these coastal waters, canyons were hypothesized to drive the recurrent formation of polynyas (areas of open water surrounded by sea ice) that provided penguins year-round access to open-water foraging areas. Proximity of reliable foraging areas to breeding colonies is important given the energy costs for breeding parents needing to travel to forage and return to provision and protect chicks.

Close association of major WAP penguin colonies with marine canyons led to a long-standing hypothesis that unique physical and biological processes induced by these canyons produce regions of enhanced prey availability that are predictable over ecological time scales (decades to centuries). Linking the regional physical and ecological dynamics to test the "canyon" hypothesis has in the past been restricted by harsh environmental conditions that limit Zodiac and ship sampling. However, the Palmer Long Term Ecological Research (LTER) network recently expanded its observational efforts by incorporating autonomous underwater sampling and satellite tagging of penguins to increase sampling capabilities at two large Adélie penguin colonies along the WAP.

Anvers Island is a focal site of Palmer LTER efforts (Figure 1). Here, Palmer Deep is a cross-shelf canyon bathymetrically similar to others in the WAP that are also associated with large penguin populations. Satellite-tagged Adélie penguins breeding at Anvers Island appear to forage exclusively within Palmer Deep. A majority of Adélie foraging activity is centered over the canyon edge where the bathymetry rapidly shoals, and around which the spatial variability in foraging is strongly influenced by tides (Oliver et al., 2013). These foraging patterns were used to guide sampling of physical and biological properties using autonomous Webb Slocum gliders. Gliders revealed the uplift of

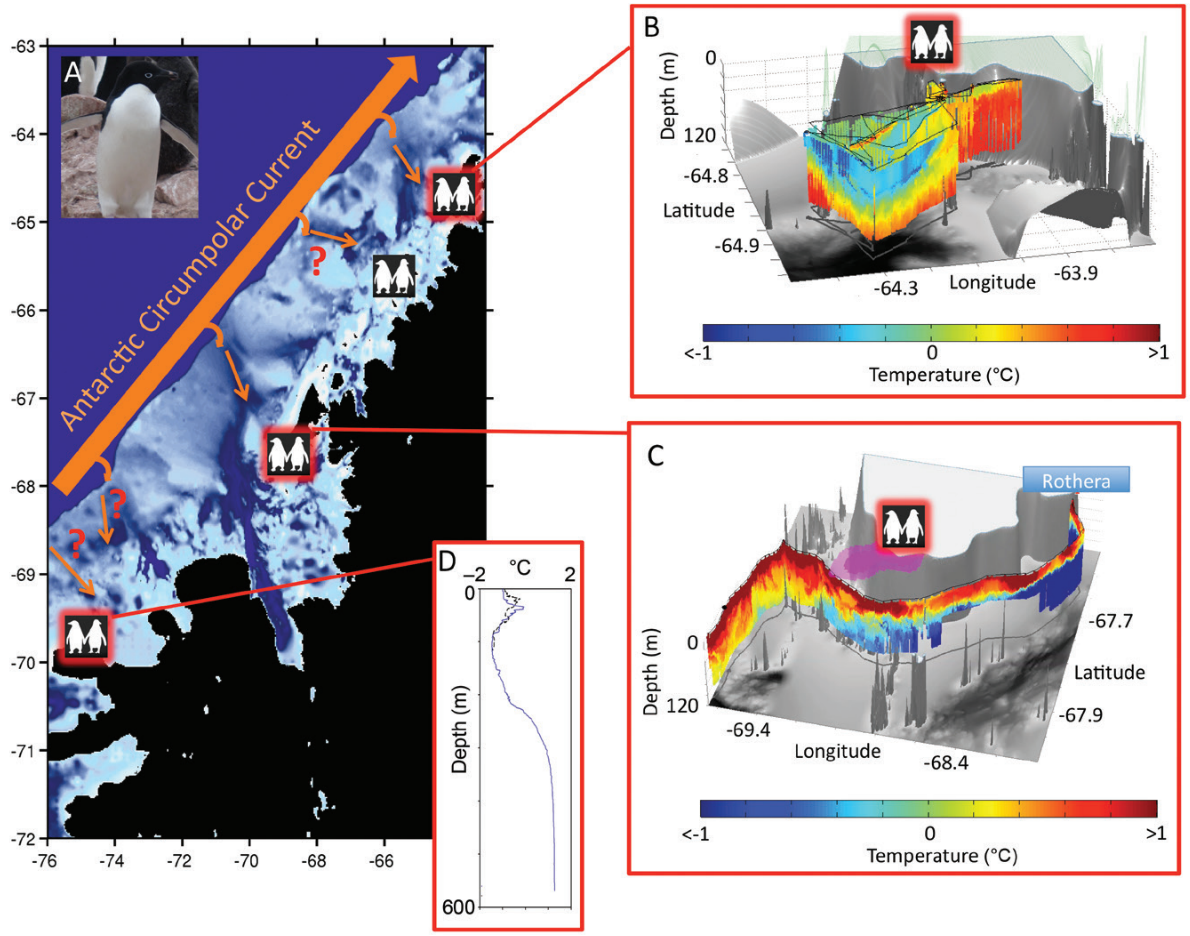

Figure 1. The 1,000 km sampling domain of the Palmer Long Term Ecological Research (LTER) program. (A) Bathymetry of the spatial sampling domain of the Palmer LTER. Orange arrows indicate the Antarctic Circumpolar Current and potential transport to coastal regions. Arrows with question marks indicate hypothesized routes requiring more data. Penguin breeding colonies are indicated by the paired-penguin symbols. For three of the penguin colonies (outlined in red), subsurface data have been collected with an effort to identify the presence of warmer deep waters of the modified Circumpolar Current near the penguin colonies. (B) Slocum glider temperature data collected offshore Palmer Station and its resident penguin colonies, showing the uplift of warm water along the canyon. (C) Glider temperature and penguin foraging data, collected by radio-tags at Avian Island near Rothera Station. The foraging locations are indicated by the surface purple shadow. It is associated with areas where warm water occurs at both surface and at depth. (D) Two temperature profiles measured by ship over the seafloor canyon adjacent to the penguin colony at Charcot Island, showing warm water at depth consistent with the presence of modified Upper Circumpolar Deep Water.

warm deep water along the slope of the canyon (Figure 1B), a hydrographic feature associated with enhanced concentrations of phytoplankton. Furthermore, glider-based measurements of phytoplankton health using a bio-optical measure, Fv/Fm, the quantum yield for photosystem II activity (Falkowski and Raven, 2007), indicated algal cells at the canyon edge were the healthiest in the region. Net tows and acoustic survey data indicate the presence of abundant krill near the canyon slope.

A second major Adélie breeding colony is located on Avian Island in Marguerite Bay (Figure 1), where chlorophyll and krill concentrations are high. Based on available satellite tag data, penguin foraging is concentrated on the southern flank of Avian Island (Figure 1C). This region is located near the seafloor canyon at the mouth of Marguerite Bay, where gliders revealed shoaling of warm bottom water. In contrast, on the inner reaches of Marguerite Bay by Rothera Base, gliders revealed high chlorophyll but no shoaling of warm bottom water. Penguin foraging does not appear to be significant at the inshore location, further suggesting the importance of warm deep water for foraging at Adélie colonies.

As the WAP warms, it might be expected that conditions surrounding breeding colonies in the south may become more favorable as sea ice and perennial land-fast ice continues to decline. This situation motivated the Palmer LTER program to expand its regional sampling grid to the south. Charcot Island, newly accessible following the collapse of the Wilkins Ice Shelf in 2008, borders the southern boundary of the new Palmer LTER regional grid. During our first exploration in 2009, the Palmer LTER team conducted only the third known landing on Charcot Island in the last century. We discovered the continued presence of a rarely documented breeding colony of Adélie penguins (Henderson, 1976). Consistent with our canyon hypothesis, a previously unmapped 800 m deep seafloor canyon was discovered adjacent to the penguin colony. Conductivity-temperature-depth (CTD) profiles within the canyon revealed warm (> 1.2°C) water at depth (> 200 m), consistent with the presence of modified Upper Circumpolar Deep Water (Figure 1D). The canyon was first located by the presence of a polynya, consistent with the hypothesis that canyons result in predictable access to open water for penguin foraging.

Shipboard measurements at the Charcot Island canyon revealed high concentrations of phytoplankton, bacteria, and krill. Satellite tags confirmed penguin foraging near the canyon. Subsequent visits also confirmed the sustained presence of the Charcot penguin colony; however, poor-quality bathymetric data requires future surveying to map the link between the nearshore seafloor canyon and the outer shelf. We discovered that navigational charts have Charcot Island misplaced by 5 km in this previously inaccessible region.

In conclusion, major WAP Adélie penguin colonies appear to be located in close proximity to the heads of seafloor canyons (although the presence of seafloor canyons does not assume an association with a penguin breeding colony). This connection may in part reflect that marine canyons can provide a conduit for warm Upper Circumpolar Deep Water near the coast. Taken together, these results emphasize the importance of geology in structuring the spatial heterogeneity of ecosystems.

Oscar Schofield *(oscar@marine.rutgers.edu) is Professor, Coastal Ocean Observation Laboratory, Institute of Marine and Coastal Sciences, School of Environmental and Biological Sciences, Rutgers University, New Brunswick, NJ, USA.* **Hugh Ducklow** *is Professor, Lamont-Doherty Earth Observatory of Columbia University, Palisades, NY, USA.* **Kim Bernard** *is Assistant Professor, College of Earth, Ocean, and Atmospheric Sciences, Oregon State University, Corvallis, OR, USA.* **Scott Doney** *is Senior Scientist, Marine Chemistry & Geochemistry Department, Woods Hole Oceanographic Institution, Woods Hole, MA, USA.* **Donna Patterson-Fraser** *is a seabird ecologist at the Polar Oceans Research Group, Sheridan, MT, USA.* **Kristen Gorman** *is a researcher with the Polar Oceans Research Group, Sheridan, MT, USA, and a PhD candidate in the Department of Biological Sciences, Simon Fraser University, Burnaby, BC, Canada.* **Doug Martinson** *is Doherty Senior Research Scientist, Lamont-Doherty Earth Observatory of Columbia University, Palisades, NY, USA.* **Michael Meredith** *is Science Leader, British Antarctic Survey, Cambridge, UK, and Honorary Professor, Scottish Association for Marine Science, Oban, UK.* **Grace Saba** *is Assistant Research Professor, Coastal Ocean Observation Laboratory, Institute of Marine and Coastal Sciences, School of Environmental and Biological Sciences, Rutgers University, New Brunswick, NJ, USA.* **Sharon Stammerjohn** *is Assistant Adjunct Professor of Ocean Science, Institute of Arctic and Alpine Research, University of Colorado, Boulder, CO, USA.* **Deborah Steinberg** *is Professor, Virginia Institute of Marine Science, College of William & Mary, Gloucester Pt., VA, USA.* **William Fraser** *is President and Lead Investigator, Polar Oceans Research Group, Sheridan, MT, USA.*

ACKNOWLEDGEMENTS

Palmer LTER is supported by NSF grant OPP-0823101 and the Gordon and Betty Moore Foundation (1859). Some of the data for this paper was drawn from the Rothera Time-Series (RaTS), a component of the Polar Oceans research program, funded by the British Antarctic Survey.

REFERENCES

Ducklow, H., A. Clarke, R. Dickhut, S.C. Doney, H. Geisz, K. Huang, D.G. Martinson, M.P. Meredith, H.V. Moeller, M. Montes-Hugo, and others. 2012. Marine pelagic ecosystems: The West Antarctic Peninsula. Pp 121–149 in *Antarctica: An Extreme Environment in a Changing World*. A.D. Rogers, ed., Wiley.

Ducklow, H.W., W.R. Fraser, M.P. Meredith, S.E. Stammerjohn, S.C. Doney, D.G. Martinson, S.F. Sailley, O.M. Schofield, D.K. Steinberg, H.J. Venables, and C.D. Amsler. 2013. West Antarctic Peninsula: An ice-dependent coastal marine ecosystem in transition. *Oceanography* 26(3):190–203, http://dx.doi.org/10.5670/oceanog.2013.62.

Falkowski, P.G., and J.A. Raven, 2007. *Aquatic Photosynthesis*. Blackwell Scientific Publishers, Oxford.

Henderson, I. 1976. Summer log of travel and work of sledge kilo in northern Alexander Island and Charcot Island, 1975/1976. British Antarctic Survey internal report ref. T/1975/K11.

Martinson, D.G., S.E. Stammerjohn, R.A. Iannuzzi, R.C. Smith, and M. Vernet. 2008. Western Antarctic Peninsula physical oceanography and spatio-temporal variability. *Deep Sea Research Part II* 55:1,964–1,987, http://dx.doi.org/10.1016/j.dsr2.2008.04.038.

Oliver, M.J., A. Irwin, M. Moline, W. Fraser, D. Patterson, O. Schofield, and J. Kohut. 2013. Adélie penguin foraging location correlated to local tides. *PLoS ONE* 8(1):e55163, http://dx.doi.org/10.1371/journal.pone.0055163.

Stammerjohn, S.E., D.G. Martinson, R.C. Smith, and R.A. Iannuzzi. 2008. Sea ice in the western Antarctic Peninsula region: Spatio-temporal variability from ecological and climate change perspectives. *Deep Sea Research Part II* 55:2,041–2,058, http://dx.doi.org/10.1016/j.dsr2.2008.04.026.

Encyclopedia of Natural Resources: Water

Publication details, including instructions for authors and subscription information:
http://www.tandfonline.com/doi/book/10.1081/E-ENRW

Oceans: Observation and Prediction

Oscar Schofield [a] , Josh Kohut [a] , Grace Saba [a] , Xu Yi [a] , John Wilkin [a] , Scott Glenn [a]

[a] Coastal Ocean Observation Laboratory, Institute of Marine and Coastal Sciences, School of Environmental and Biological Sciences , Rutgers University , New Brunswick , New Jersey , U.S.A.

Published online: 21 Oct 2014

To cite this entry: Oscar Schofield , Josh Kohut , Grace Saba , Xu Yi , John Wilkin , Scott Glenn . Oceans: Observation and Prediction. *In* Encyclopedia of Natural Resources: Water. Taylor and Francis: New York, Published online: 21 Oct 2014; 802-807.

To link to this chapter: http://dx.doi.org/10.1081/E-ENRW-120048087

Oceans: Observation and Prediction

Oscar Schofield
Josh Kohut
Grace Saba
Xu Yi
John Wilkin
Scott Glenn
Coastal Ocean Observation Laboratory, Institute of Marine and Coastal Sciences, School of Environmental and Biological Sciences, Rutgers University, New Brunswick, New Jersey, U.S.A.

Abstract
The ocean is a complex and difficult sample, and our understanding of how it operates and its future trajectory is poor. This has implications for humanity as increasing numbers are living in coastal zones. To better understand the ocean, it is necessary to adopt new sampling strategies that consist of coupling new observational technologies with numerical ocean models. New observational technologies are becoming available to oceanographers. Fixed assets include moorings, sea floor cables, and shore-based radars. These fixed assets are complemented with mobile platforms that provide spatial maps of subsurface data. The mobile platforms include profiling floats, gliders, and autonomous underwater vehicles. The observational data is complemented with numerical models. Many simulation models are becoming available to the community and the appropriate model is a function of the specific need of the user. Increasingly, observational data are used to constrain the models via data assimilation. The coupled observational and modeling networks will provide a critical tool to better understand the ocean.

INTRODUCTION

The oceans cover the majority of the Earth's surface and despite centuries of exploration they remain relatively unexplored. This gap of knowledge reflects the difficulty of collecting physical, chemical, and biological data in the ocean, as it is a harsh and unforgiving environment in which to operate. Despite centuries of ship-based exploration, the immense size and hazards associated with wind, waves, and storms limit the ability of humans to sustain a coherent global sampling network. Satellite and aircraft remote sensing approaches provide powerful tools to map global synoptic properties (Fig. 1); however, satellite systems largely provide information on the surface ocean. Fixed and mobile sensors deployed in the ocean can provide subsurface data, however, their numbers, while expanding, are limited and the technology still struggles with issues related to the onboard power availability and the number of available robust sensors. These sampling shortcomings have significant implications for human society especially as there is increasing evidence that the physics, chemistry, and biology of the ocean have changed over the last few decades. These changes reflect both natural cycles and the anthropogenic forcing from human activity.

Quantitatively understanding the relative importance of the natural and anthropogenic forcing in the ocean remains an open question, which needs to be resolved as the environmental impacts associated with human activity will increase, reflecting the growth of human populations.[1] The current projections suggest that human population growth at coastlines will be the most rapid and largest on the planet.[2] This will increase the importance of marine systems in national economies around the world making managing coastal systems critical. The close proximity of large populations will expose them to potential natural and man-made disasters associated with the oceans. These disasters include tsunamis, hurricanes, offshore industrial accidents, and human health issues such as outbreaks of waterborne disease. Our current capabilities to predict, respond to, manage, and mitigate these events is astonishingly poor. Improving our ability to observe and predict changes in the ocean will require technical improvements combined with an increased fundamental understanding of physical, chemical, and biological processes.

WHAT IS THE PATH FORWARD?

Improving our understanding and management of the ocean system will require an improved ability to map ocean properties in the present and improving our ability to forecast future ocean conditions. The ability to map ocean

Encyclopedia of Natural Resources DOI: 10.1081/E-ENRW-120048087

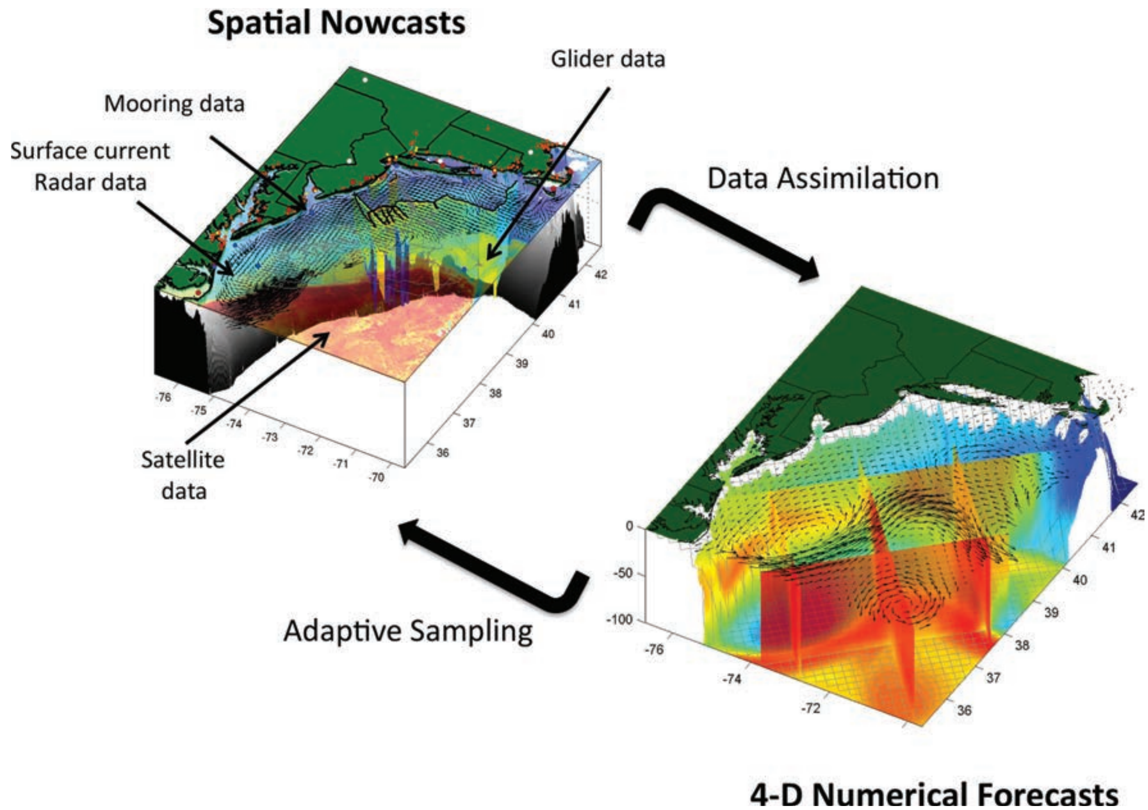

Fig. 1 An example of a coupled ocean observation and modelling network along the East coast of the United States. The spatial nowcast consists of observational data delivered in near real-time to shore. The nowcast consists of satellite data (sea surface temperature is shown), surface current radar (black arrows on the ocean), mooring data (black dots), subsurface data collected from gliders (water temperature shown here), and weather data collected by shore based stations (small white dots). The nowcast provides data to simulation models via data assimilation. The simulation model provides a 48-hour forecast, which is used to redistribute observational assets to provide an improved data set before the next forecast cycle.

properties will require a distributed portfolio of ocean infrastructure that will be linked together through an increasing number of ocean models.[3] The observation networks will collect quantitative data about the current status of the ocean. The forecasts are driven by numerical models that use current scientific understanding to project how the ocean will evolve. The combined observatory and numerical modelling capacity will improve our fundamental understanding and ability to respond to changes in the physics, chemistry, and biology of the marine systems.

The observations will assist the modelling efforts in several ways. Observations will provide data required to parameterize processes within the models. If the data are delivered in real-time they will be assimilated into the model to improve the predictive skill of the forecast. Finally, as new data are collected, they will be used to validate the predictive skill of the model. In turn the model forecasts will assist the observational efforts by providing forecasts that will allow scientists to adjust the spatial configuration and sampling rates of sensors to better sample future ocean conditions. These coupled systems are a rapidly maturing technology and builds off the more mature science of weather forecasting, which has its roots in the early 19th century. The fundamental approaches are based on the seminal work of Lewis Fry Richardson who is considered the father of numerical weather prediction in the 1920s. These approaches are computationally intensive and it was not until the advent of electronic computers that the science moved forward to become an indispensable tool for humanity. Modern computer models use data as inputs collected from automated weather stations and weather buoys at sea. These instruments, observing practices and timing are standardized through the World Meteorological Organization.

Oceanographic efforts are evolving in a similar fashion where observations inform operational models. The weather and ocean models, most often run by federal agencies, provide forecasts that are used by scientists, the maritime industry, state and local communities. Most often they are used to issue warnings of unsafe conditions due to storms and high waves. The motivation for global standardized ocean forecast systems can be traced back to the sinking of the Titanic in 1912, which prompted the international community to call for development of systems to improve safety at sea. Modern approaches and forecasting tools for the ocean did not mature until the 1980s and are rapidly evolving as the computing and ocean observation technologies are rapidly improving.

HOW ARE OBSERVATIONS MADE IN THE OCEANS?

Many platforms are available for making ocean measurements and, although the list below is not exhaustive, it provides a snapshot of the major platforms. The platforms carry sensors that can measure physical, chemical, and biological properties of the sea; however, most new novel sensors can only be carried on ships. A smaller number of sensors can be deployed on autonomous platforms and the discussion in this entry is focussed on those sensors that can be deployed on a variety of ocean platforms.

The most mature sensors are those that measure physical and geophysical variables, such as temperature, salinity, pressure, currents, waves, and seismic activity. Except for seismic variables, most of the physical sensors can be deployed on most of the platforms listed below. Many of the physical properties are the key variables in ocean numerical models. Currently, chemical sensors can measure dissolved gases (primarily oxygen) and dissolved organic material; however, recently the sensors capable of measuring nutrients (primarily nitrogen) are becoming commercially available. Biological sensors currently consist of optical and acoustic sensors. The optical sensors are used to provide information on the concentration, composition, and physiological state of the phytoplankton. Acoustic sensors can provide information on zooplankton to fish depending on the acoustic frequency band that is chosen.

Ships

The primary tool for oceanographers for centuries has been ships and will remain a central piece of infrastructure for the foreseeable future.[4] Ships are ideal as they are extremely flexible and allow teams to conduct experiments at sea. Ships are expensive to operate and must avoid hazardous conditions, such as storms, which limit the ability to make sustained measurements.

Satellites

Satellites are the most important oceanographic technology in modern times (beyond the ships).[5] Satellite observations have resulted in numerous advances in our fundamental understanding of the oceans[6] by resolving both global features associated with the mesoscale circulation of physical and biological properties. Satellite datum is fundamental to weather and ocean state prediction. Physical parameters available from space-based sensors include ocean surface temperature, wind speed and direction, sea surface height and topography, and sea ice distribution and thickness. Biological and chemical parameters can be derived from ocean colour radiometers.

High-Frequency Radar

High-frequency radar measures ocean surface current velocities over hundreds of square miles simultaneously. Each site measures the radial components of the ocean surface velocity directed towards or away from the site[7,8] and the estimated velocity components allow surface currents (upper meter of water column) to be estimated.[9] These systems are cost effective and have many applied uses.

Ocean Moorings

The modern ocean moorings grew out of the weather stations established in the 1940s. Since the 1960s, modern buoys have enabled a wide range of studies addressing the ocean's role in climate, weather, as well as providing insight into the biogeochemistry of the sea. Moorings provide the backbone to many of the global ocean networks studying ocean–atmosphere interactions and are the foundation for the global tsunami warning system network. They will continue to be a key element of ocean observing infrastructure for the foreseeable future.

Seafloor Cables

Scientists often require high bandwidth and power for sustained periods of time. Seafloor electro-optic cables provide a means for maintaining a sustained presence in the ocean. Cables have been deployed off the east and west coasts of the United States, Canada, Japan, and Europe. Many other countries are planning to deploy seafloor cables.

Drifters and Floats

Passive Lagrangian platforms are tools for creating surface and subsurface maps of ocean properties. These platforms are relatively inexpensive and thus allow thousands of these platforms to be deployed. Drifters have historically been a key tool for oceanography as evidenced by the important works by Benjamin Franklin[10] and Irving Langmuir.[11] The drifters can carry numerous sensors to create global maps of surface circulation. The first neutrally buoyant drifters were designed to observe subsurface currents.[12] The subsurface profiling drifters were enabled in the early 1990s with communication capabilities[13] and now anchor the international ARGO program, which has over 3000 floats deployed in the ocean.

Gliders are a type of autonomous underwater vehicle (Fig. 2) that use small changes in buoyancy in conjunction

Fig. 2 A Webb underwater glider being deployed in the Ross Sea Antarctica in February 2011.
Source: Photo credit Chris Linder.

with wings to convert vertical motion to horizontal motion, and thereby propel itself forward with very low-power consumption.[14] Gliders follow a saw-tooth path through the water, providing data on large temporal and spatial scales. They navigate with the help of periodic surfacing for Global Positioning System (GPS) fixes, pressure sensors, tilt sensors, and magnetic compasses. Using buoyancy-based propulsion, gliders have a significant range and duration, with missions lasting up to a year and covering over 3500 km of range.[15–17]

Propeller-driven autonomous underwater vehicles (AUVs) are powered by batteries or fuel cells and can operate in water as deep as 6000 m. Similar to gliders, AUVs relay data and mission information to shore via satellite. Between position fixes and for precise maneuvering, inertial navigation systems are often available onboard the AUV to measure the acceleration of the vehicle, and combined with Doppler velocity measurements, it is used to measure the rate of travel. A pressure sensor measures the vertical position. AUVs, unlike gliders, can move against most currents nominally at 3–5 knots, and can therefore systematically and synoptically survey a particular line, area, and/or volume.

WHAT NUMERICAL OCEAN MODELS ARE AVAILABLE?

Over the last 30 years, there have been significant developments in three-dimensional numerical models for the ocean.[18] Many models exist spanning from global ocean scales down to the scale of individual estuaries. Models vary in their coordinate system (linear, spherical, and others), resolution in space and time, complexity (i.e., number of state variables), and the parameterization of key processes within the model. There are several excellent texts that outline many of the details of numerical ocean modelling[19,20] and one key lesson is that the choice of particular modelling approach depends on its intended application and on the available computational resources. Although an exhaustive list of the ocean models is beyond the scope of this text, several classes are described in the following paragraphs.

Mechanistic models are simplified models used to study a specific process, and are used to provide insight into the underlying processes influencing the physics, chemistry, and biology of the ocean. These models are most often constructed as a learning tool in order to assess processes and feedbacks within marine systems.

Simulation models are complex and describe three-dimensional (3-D) ocean processes using the continuity and momentum equations. For this reason they are called the primitive equation models. These models can be used to simulate many processes, including ocean circulation, mixing, waves, and responses to external forces (such as storms). All these models are constructed using different assumptions. Additionally, the resolution of the models requires that the trade-offs of the computation burdens be measured against the processes that need to be simulated. For example, if the model must resolve mesoscale eddies, it will require the resolution of a few tenths of a degree of latitude and longitude. In contrast, most primitive equation climate models have much coarser horizontal resolution as they were designed to study large-scale hydrographic structure, climate dynamics, and water-mass formation over decadal time scales; however, for a specific question, there are climate models with sufficient resolution to resolve mesoscale eddies if one is willing to accept the computation cost. Simulations are also constructed for coastal systems and can resolve coastal currents, tides, and storm surges. Increasingly the biological and ocean chemistry models are being coupled into these 3-D simulation models. Although these biogeochemical models are rapidly improving, there is unfortunately no set of "primitive" equations yet capable for describing biological and chemical systems in the ocean; however, as these models evolve, they will be increasingly useful tools for managing living resources and water quality in the ocean.

Often models of varying resolutions are combined. Coarser-scale global or basin-scale models provide outer boundary inputs to higher resolution nested models, which allows a myriad of processes to be modelled with a lower computation burden but allow a range of processes to be simulated even if they require high resolution. This is often the case for coastal and continental shelf models. The advantage of this downscaling approach is that it allows basin scale models to resolve large-scale forcing that drives the regional to local-scale processes that are effectively modelled by a higher resolution model. The approach by which one links these models is a difficult problem and remains an area of active research.

Data assimilation is an approach by which model simulations are constrained by observations. For example, model calculations and observations of temperature and salinity can be compared, and then the model can be "adjusted" based on the mismatch. This is a difficult problem as 1) it represents an inverse problem (where a finite number of observations are used to estimate a continuous field), 2) many of the ocean processes of interest are non-linear, and 3) the observations and models both have unknown errors. Descriptions of data assimilation approaches for oceanography have been reviewed.[21,22] These approaches allow modellers to increase the forecast skill of their models by essentially keeping the models "on track" if the observations and data assimilation approaches can be provided in a timely fashion. Many in the ocean modelling community are focusing on using these approaches to increase model forecast skill as it determines how well these approaches will serve a wide range of science, commercial, and government needs.[23]

CONCLUSIONS

Ocean observation and modelling capabilities are rapidly diversifying and improving. These systems are increasingly linked by data assimilation approaches that when combined, provide a coupled observing and forecasting network. These approaches will increase the predictive skill of forecast models that in turn can serve a wide range of applications spanning from basic research to improving the efficiency of the maritime industry. The combined technologies will be critical to improving our understanding of the ocean today and the potential trajectory in the future.

ACKNOWLEDGMENTS

We acknowledge the support of the Office of Naval Research's Major University Research Program, the National Oceanic and Atmospheric Administration's Integrated Ocean Observing System, and the National Science Foundation's Ocean Observing Initiative.

REFERENCES

1. De Souza, R.; Williams, J.; Meyerson, F.A.B. Critical links: Population, health, and the environment. Popul. Bull. **2003**, *58* (3), 3–43.
2. Vitousek, P.M.; Mooney, H.A.; Lubchenco, J.; Melillo, J.M. Human domination of Earth's ecosystems. Science **1977**, *277*, 494–499, DOI: 10.1126/science.277.5325.494.
3. National Research Council. *Critical Infrastructure for Ocean Research and Societal Needs in 2030*; National Academy Press: Washington, D.C., 2011.
4. National Research Council. *Science at Sea: Meeting Future Oceanographic Goals with a Robust Academic Research Fleet;* National Academy Press: Washington, D.C., 2009.
5. Munk, W. Oceanography before, and after, the advent of satellites. In *Satellites, Oceanography and Society*, Halpern, D., Ed.; Elsevier Science: Amsterdam, 2000; 1–5.
6. Halpern, D., Ed. *Satellites, Oceanography and Society*; Elsevier Science: Amsterdam, 2000; 361 pp.
7. Crombie D.D. Doppler spectrum of sea echo at 13.56 Mc/s. Nature **1955**, *175*, 681–682.
8. Barrick, D.E.; Evens, M.W.; Weber, B.L. Ocean surface currents mapped by radar. Science **1977**, *198*, 138–144.
9. Stewart R.H.; Joy J.W. HF radio measurements of ocean surface currents. Deep Sea Res. **1974**, *21*, 1039–1049.
10. Franklin, B. Sundry marine observations. Trans. Am. Philos. Soc. **1785**, *1* (2), 294–329.
11. Langmuir, I. Surface motion of water induced by wind. Science **1938**, *87*, 119–123.
12. Swallow, J.C. A neutral-buoyancy float for measuring deep currents. Deep Sea Res. **1955**, *3*, 74–81.
13. Davis, R.E.; Webb, D.C.; Regier, L.A.; Dufour, J. The Autonomous Lagrangian Circulation Explorer (ALACE). J. Atmos. Ocean. Tech. **1992**, *9*, 264–285.
14. Rudnick, D.L.; Davis, R.E.; Eriksen, C.C.; Fratantoni, D.M.; Perry, M.J. Underwater gliders for ocean research. Mar. Technol. Soc. J. **2004**, *38*, 73–84.
15. Sherman, J.; Davis, R.E.; Owens, W.B.; Valdes, J. The autonomous underwater glider "Spray." IEEE J. Ocean. Eng. **2001**, *26*, 437–446.
16. Eriksen, C.C.; Osse, T.J.; Light, R.D.; Wen, T.; Lehman, T.W.; Sabin, P.L.; Ballard, J.W.; Chiodi, A.M. Seaglider: A long-range autonomous underwater vehicle for oceanographic research. IEEE J. Ocean. Eng. **2001**, *26*, 424–436.
17. Webb, D.C.; Simonetti, P.J.; Jones, C.P. SLOCUM: An underwater glider propelled by environmental energy. IEEE J. Ocean. Eng. **2001**, *26*, 447–452.
18. Bryan, K. A numerical method for the study of the circulation of the world ocean. J. Comput. Phys. **1969**, *4* (3), 347–376, DOI: 10.1016/0021-9991(69)90004-7.

19. Kantha, L.H.; Clayson, C.A. *Numerical Models of Oceans and Oceanic Processes*; International Geophysics Series, Elsevier: Amsterdam, 1995; 750 pp.
20. Haidvogel, D.; Beckmann, A. *Numerical Ocean Circulation Modeling*; Imperial College Press: London, 1999; 318 pp.
21. Wunsch, C. *The Ocean Circulation Inverse Problem*; Cambridge University Press: Cambridge, 1996; 442 pp.
22. Malanotte-Rizzoli P. *Modern Approaches to Data Assimilation in Ocean Modeling*; Elsevier Science: Amsterdam, Netherlands, 1996; 455 pp.
23. Pinardi, N.; Woods, J. *Ocean Forecasting: Conceptual Basis and Applications*; Springer Verlag: Berlin, Germany, 2002; 472 pp.

Gliderpalooza 2013 to Modelpalooza 2014: Joint U.S. & Canadian Ocean Glider Operations Supporting Multidisciplinary Scientific Research and Education

Michael Crowley, Oscar Schofield, Scott Glenn
Institute of Marine and Coastal Sciences
Rutgers University
New Brunswick, N.J. USA
crowley@rutgers.edu

Fred Whoriskey
Ocean Tracking Network
Dalhousie University
Halifax, N.S. Canada

Abstract— Gliderpalooza represented a grass-roots coordinated field demonstration of ocean observing technologies spanning the eastern seaboard of North America. The overarching goal was to coordinate disparate ocean research efforts, funded by disparate programs from a variety of agencies to demonstrate continental scale coordination of various ocean observing technologies to sample ecologically relevant scales.

The coordinated data from satellites, HF-Radar surface currents [1], moorings, drifters and models was focused on and around the distributed deployment of Slocum gliders. The seven science and technical goals were to:

1) provide a unique data set the modelers can use for years to come (real-time & hindcast),
2) provide a standardized dataset over ecological scales and information on fish/mammal migrations,
3) provide a 3-D snapshot of the MAB cold pool,
4) provide an extensive distributed instrumented network through the peak period of fall storms, demonstrating a community "surge" capacity,
5) provide one, of many demonstrations, of the potential U.S. national glider network,
6) proof of data flow throughput to the Global Telecommunications System (GTS) via DMAC and,
7) engage undergraduates in ocean observing efforts.

During the summer and fall of 2014, the Gliderpalooza team will once again work together, but with several additions to the group, the geographical scope will cover Texas to Newfoundland. There will be more than 30 glider deployments that will be assimilated by seven numerical ocean models. Acquisition of this massive data set of water column profiles will permit evaluation of the accuracy of the models, especially in the coastal zone. Additionally, new online educational tools developed through the NSF's Ocean Observatory Initiative (OOI) will be used to by students in the undergraduate classroom to analyze, compare and contrast the glider data in real-time during the fall 2014 semester.

Keywords — ocean glider, ocean modeling, data assimilation, physical oceanography, optics, mixing storm, cold pool, fish/mammal migrations, U.S. IOOS, MARACOOS.

I. Introduction

The research performed during Gliderpalooza grew out of the U.S. Integrated Ocean Observing System's (U.S. IOOS) Mid Atlantic Regional Association Coastal Ocean Observation System (MARACOOS) and Ocean Tracking Network's science priorities. Ten universities, one corporation and the US Navy worked together to perform 17 glider deployments along the eastern coast of the U.S. and Canada (Table 1 and Figure 1). Many of the deployment locations were determined by an ocean continuously well sampled by satellites, surface current data provided by the MARACOOS HF-Radar Regional Network [2] and drifters. Much of this data was assimilated into dynamical ocean models which were then used to direct the location of a handful of the deployments in the Mid-Atlantic bight. Upon completion of the project, full resolution data sets from almost all deployed gliders were shared amongst all researchers.

TABLE I. Gliderpalooza Glider Deployments

#	Group	Glider	Deployed
1	**Dalhousie**	OTN200 (2)	10-Sep, 2-Dec
2		OTN201	16-Sep
3	**U. Maine**	Penobscot (2)	10-Sep, 15-Oct
4	**WHOI**	Saul	10-Sep
5	**U. Mass**	Blue	6-Sep
6	**Rutgers**	RU28	12-Sep
7	**U. Maryland**	RU22	22-Sep
8	**Rutgers**	RU23 (2)	10-Sep, 10-Oct
9	**U. Delaware**	Otis	12-Sep
10	**VIMS**	Stewart	10-Oct
11	**NC State**	Salacia	17-Sep
12	**Skidaway**	Modena	10-Sep
13	**T. Webb**	Darwin	11-Sep
14	**U.S. Navy**	Navy1	10-Oct

978-1-4799-4918-2/14/$31.00 ©2014 IEEE

In late February of 2014, the Gliderpalooza team met in Honolulu during the Ocean Sciences meeting to plan research papers focusing on the seven program goals. This paper will summarize the seven science and logistical goals and elaborate on early results from initial data analysis performed during 2014. It will then discuss plans for Gliderpalooza 2 (aka Modelpalooza) which will occur during July-November 2015 but will now span from Texas north to Newfoundland and east to Bermuda.

Fig. 1. Gliderpalooza deployments in summer and fall 2013.

II. Gliderpalooza Goals & Early Results

A. Goal 1: Provide a Unique Dataset for Ocean Modelers

A shelf wide subsurface perspective for the North American east coast was collected through a coordinated range of regional combined with coastal surveys. All gilders provided an extensive survey for the hydrographic and optical data as well as acoustically tracked animal locations. The database spans from the upstream condition of Canadian waters through the South Atlantic Bight. The database is enabling studies to improve data assimilative forecast models.

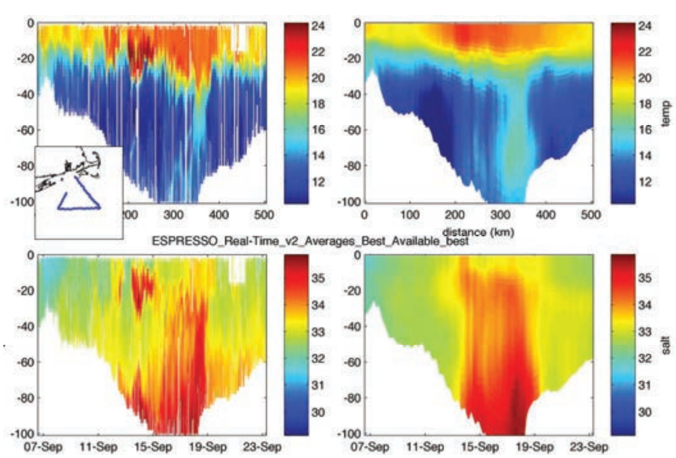

Fig. 2. Observed (left) and ROMS ESPRESSO model (right) temperature (top) and salinity (bottom) following glider BLUE. Inset shows the glider path south of Providence, RI (blue).

Moving forward, the goal is to support the improvement of the ensemble of ocean models through assimilation and validation. Figure 2 highlights a time series of temperature and salinity from a glider and compares it to the identical locations virtually sampled within the ROMS ESPRESSO model [3], [4].

B. Goal 2: Tracking Fish/Mammal Migrations

The glider survey was focused on collecting a broad environmental dataset to provide a map of the hydrography in which to interpret major migration patterns. The Ocean Tracking Network (OTN) is augmenting current capabilities to provide the foundation for a listening network. The collection of gliders provided a subsurface spatial snap shot of a Large Marine Ecosystem (LME) during the fall migration that was mined by scientists in both real-time and in hindcast mode as nine of the gliders were fitted with Vemco trackers. This effort is motivated as the region is home to some of the most migratory fish communities in the eastern United States and Canada. These data from multiple gliders are currently being combined by OTN. Species locations will be analyzed against the subsurface glider data as well as available satellite and CODAR assets and models of subsurface physical/biological parameters to provide a perspective of the northeast United States/Canada ecological domains.

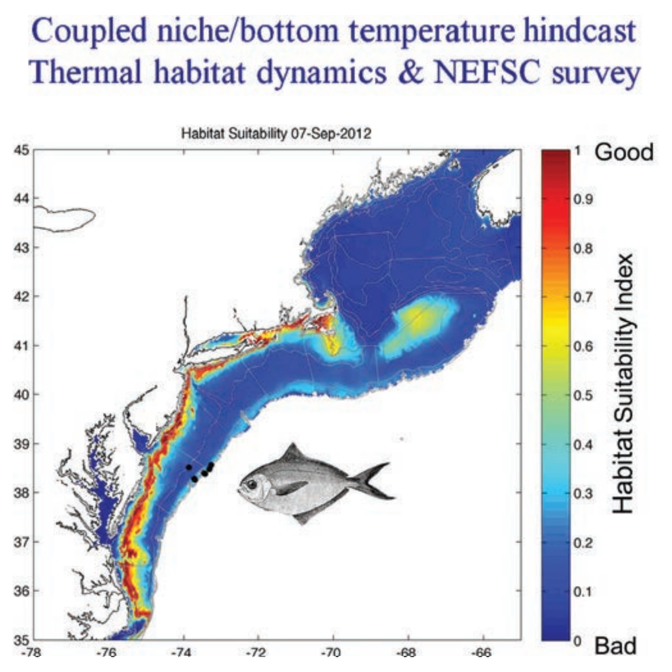

Fig. 3. A habitat sustainability model showing likelyhood of butterfish bycatch with likely areas shown in red. Block dots indicate in situ fishign surveys which tested the accuracy of this early model from 2012. Gliderpalooza data will help to improve these models in the future. Early funding for this work was from the NOAA NEFSC and Fisheries Habitat Program.

Sponsors of this work include NOAA's U.S. IOOS, Ocean Tracking Network Canada, N.J. Department of Environmental Protection, U.S. EPA, U. of Delaware, NASA, ONR, U. of Maine, College of William and Mary, U. of Georgia, Teledyne Webb, US NMFS, NSF Ocean Observatories Initiative and the U.S. Navy. Additional sponsors in 2014 will include Memorial University and Texas A&M U.

The data are also being used to improve fisheries bycatch models. Rutgers and NOAA's Northeast Fisheries Science Center (NEFSC) conducted in situ surveys in 2012 where forecast models were tested that predicted the butterfish bycatch amounts in the mid-Atlantic bight (Figure 2). Subsurface water column profile data, especially geographically distributed bottom temperatures, are key to these forecasting models, and the glider data sets will both aid in improving the models through assimilation and verifying the model's accuracy.

C. Goal 3: Mapping the Mid-Atlantic Cold Pool Water

During summer, a distinctive, bottom-trapped, cold water mass called the Cold Pool Water (CPW) resides as a swath over the mid to outer continental shelf throughout much of the Middle Atlantic Bight (MAB) [3]. This evolving CPW is important because it strongly influences the ecosystem, including several important fisheries. Thus there is a priority to better understand the relevant ocean processes and develop a CPW forecast capability.

Seven gliders crossed the area of Cold Pool during Gliderpalooza. The path of RU23 is show in red in figure 4 overlaid on a ROMS ESPRESSO modeled bottom temperature hindcast off of the New Jersey coast. Cold Pool water sits on the shelf between approximately 35m to 100m. Temperature and salinity glider transects are compared to a 2d version of this this model hindcast in figure 5.

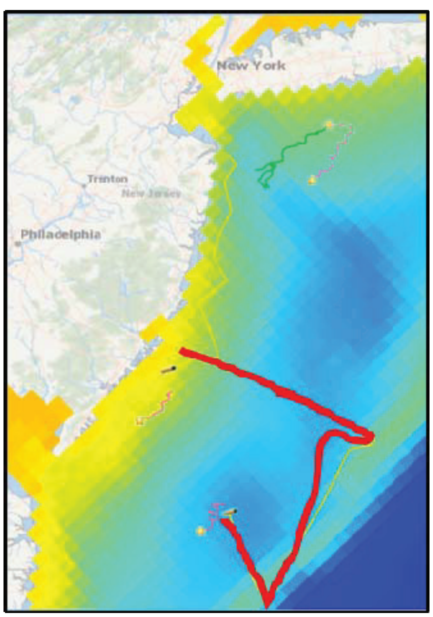

Fig. 4. A habitat sustainability model showing likelyhood of butterfish bycatch with likely areas shown in red. Black dots indicate in situ fishing surveys which tested the accuracy of this early model from 2012. Gliderpalooza data will help to better inform these models in the future through assimilation. Early funding for this work was from NOAA's Norteast Fisheries Science Center and Fisheries Habitat Programs.

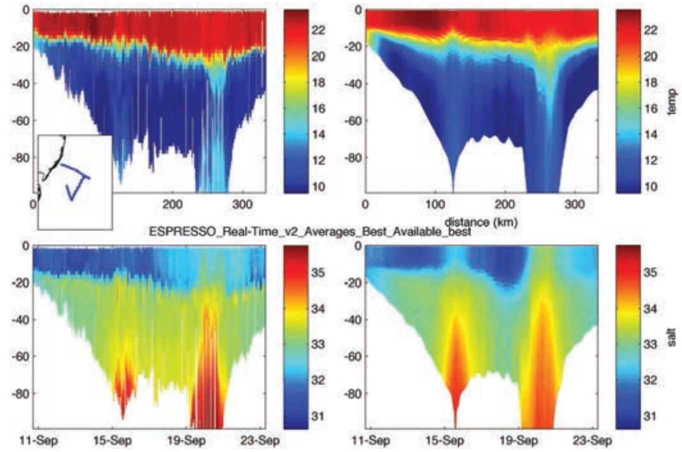

Fig. 5. RU23 glider temperature and salinity on the left are compared to modeled temperature and salinity on the right from ROMS ESPRESSO.

D. Goal 4: Analysis of Fall Mixing Storms

September is the peak month for tropical storm and hurricane landfall along the Eastern coast of North America. The regional array provided a comprehensive sampling of the continental shelves, which are the most undersampled with regards to subsurface temperatures. This subsurface temperature data is increasingly being viewed as valuable in potentially improving the ability to better predict hurricane intensity [6]. The 2013 Gliderpalooza dataset will serve as a baseline as it was a quiet tropical storm season. In 2014-2015, the Cooperative Institute for the North Atlantic Region (CINAR) is providing funding to support deployments of four storm gliders, rapid profile drifters and rapid deployable buoys into both tropical storms and winter Nor'easters. Storm gliders will be equipped with an acoustic Doppler current profiler, a full range of optical instruments, and accelerometers in addition to the standard CTD package. A preliminary in water test of these new storm gliders was performed during Hurricane Arthur in July, 2014 (figure 6).

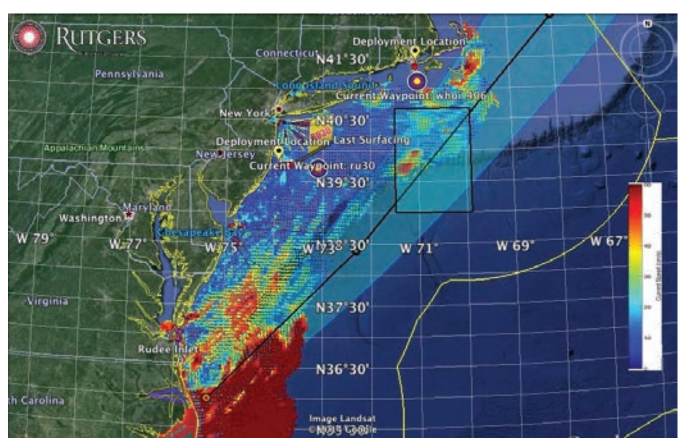

Fig. 6. Hurricane Arthur forecasted storm track from July 4, 2014. Locations of CINAR funded gliders RU30 and WHOI_406 are shown with target icons. HF-RADAR surface currents are shown, highlighting the counterclockwise circulation around the eye of Arthur just north of Cape Hatteras and the forecast track.

E. Goal 5: Demonstration of a National Glider Network

During the summer of 2012 a workshop funded by U.S. IOOS was held at Scripps Institute of Oceanography to discuss plans for a national glider network. As a result, multiple partners from federal agencies, IOOS Regional Associations (RAs) of coastal ocean observing systems, and universities were assembled to develop a National Glider Network Plan for a viable, sustainable, and reliable network that delivers timely monitoring and distribution of coastal subsurface glider data to federal, state, and local governments, as well as the general public. The plan is structured to develop an initial network that includes maintaining existing long term glider sampling lines, acquiring additional glider lines to fill high priority gaps, and improving data management, product development, and data/product delivery. The national plan was released in January 2014 and available at http://www.ioos.noaa.gov/glider/strategy/welcome.html.

Gliderpalooza enabled a first example of a multi-regional coherent effort to deploy, monitor and access glider data in real time through a central site at Rutgers University. The ultimate national goal is to attain funding for long term sustainability of deployments on all U.S. coasts (Figure 7).

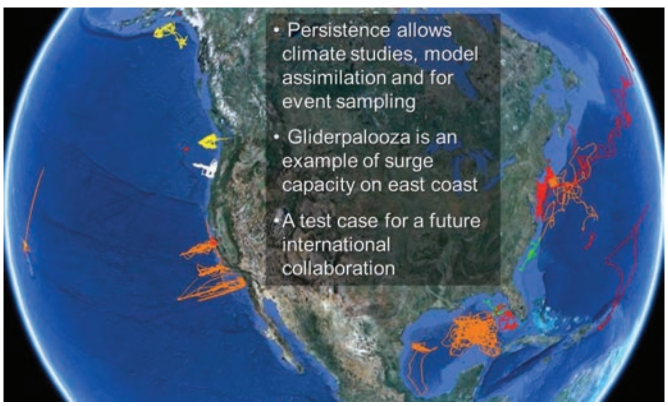

Fig. 7. U.S. glider deployments from 2000 through early 2013.

F. Goal 6: Data Throughput to the GTS

In 2013 IOOS secured funding to begin construction of a Data Management and Communications System (DMAC) specifically for glider data distribution. A successful goal of Gliderpalooza was to have real-time throughput of raw data from the gliders to Dockservers to the DMAC where it was converted to Climate and Forecast (CF) compliant NetCDF files and then sent to the National Data Buoy Center and finally to the Global Telecommunications System. This mission to make glider data available to modelers and forecasters worldwide will continue to expand outside the east coast region to the U.S. and eventually global throughput of glider data to NDBC and GTS.

Fig. 8. Schematic of glider data throughput from acquisition to the GTS.

G. Goal 7: Undergraduate Education

In addition to having undergraduate students assist with glider deployments and recoveries, the Gliderpalooza data were made available to undergraduate classrooms in real-time during the fall semester of 2013. During fall 2014, both real-time and archived glider data are going to be used by numerous Community and 4-Year college professors in the undergraduate classroom through cooperation with the NSF's Ocean Observatory Initiative's Education and Public Engagement team's (OOI EPE) newly developed online educational tools (Figure 9). This software can be used by undergraduate educators to build and share online lessons using ocean data from both the OOI and outside resources, including global glider deployments.

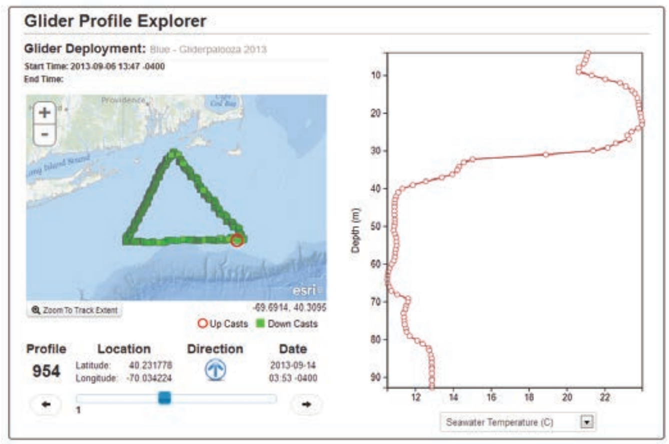

Fig. 9. Newly developed glider profile explorer tool that allows users to search and display glider profiles through the OOI EPE's website at: http://education.oceanobservatories.org/.

III. Next Steps: Gliderpalooza 2 – Modelpalooza!

The success of Gliderpalooza 2013 built on a collaborative community which was a great start, and one the team wishes to build on for the coming year. Gliderpalooza 2 will begin during the summer of 2014 but this time with a focus of using the real-time data for ocean model assimilation and validation in several models and, in turn, using model output to help drive sampling locations throughout the east coast, not just the mid-Atlantic bight. At least seven ocean models are going to be used for this effort (table 2). A new glider tool that will support comparison of the glider profiles to any of these ocean models is shown in figure 10.

The list of groups involved with glider deployments and models is expected to expand to include Memorial University of Newfoundland, Dalhousie University (Ocean Tracking Network), University of Maine, Woods Hole Oceanographic Institute, University of Massachusetts Dartmouth, Stevens Institute of Technology, Rutgers University, University of Delaware, University of Maryland, College of William and Mary, North Carolina State University, University of Georgia, Texas A&M University, the US Navy and the Bermuda Institute of Ocean Sciences.

TABLE II. MODELS TO BE USED FOR ASSIMILATION AND VALIDATION TESTING DURING GLIDERPALOOZA 2: MODELPALOOZA.

	Models	Affiliation
1	Regional Ocean Modeling System 1 (ROMS)	North Carolina State University
2	ROMS Experimental System for Predicting Shelf and Slope Optics (ROMS HOPS)	Rutgers University
3	Harvard Ocean Prediction System (HOPS)	University of Massachusetts Dartmouth
4	New York Harbor Ocean Prediction System (NYHOPS)	Stevens Institute of Technology
5	Real Time Ocean Forecast System (RTOFS)	NOAA National Centers for Environmental Prediction
6	MyOcean	European Union
7	Mercator Ocean	Europe (France)

In addition to the science and technical goals outlined in this paper, additional goals for Gliderpalooza 2 include; 1) Improved data flow of all gliders to the World Meteorological Organization's GTS, 2) Visualization of all data in the NOAA U.S. IOOS National Underwater Glider Network Map portal, 3) Data assimilation by four ocean models and validation testing of at least seven ocean models (hence the name Modelpalooza), 4) Using the ocean models to assist in planning glider sampling activities, 5) Building an active community blog, 5) Improving coordination between distributed teams, 6) Strengthening science working groups thereby accelerating the publishing of potential products/manuscripts/articles for the ocean science community and general public, and 7) Improving the existing web portal tools that link the community.

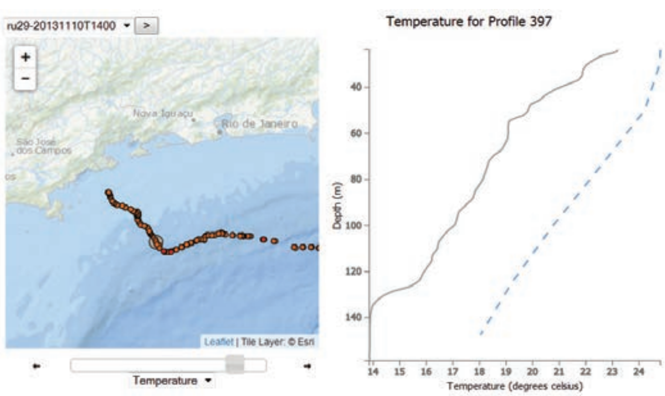

Fig. 10. Newly developed NSF OOI visualization tool that will enable researchers to compare glider profiles to model output. This example highlights a single profile from glider RU29 located just south of Rio de Janerio on the outer edge of the continental shelf (145 meters). The temperature data is compared to RTOFS and highlights that RTOFS is significantly warmer (~3C) throughout much of the water column. Development of this tool leveraged both NOAA US IOOS funds and NSF OOI funds.

ACKNOWLEDGMENTS

There were dozens of co-authors to this work from the numerous groups involved with the Gliderpalooza effort. They include J. Kerfoot, C. Haldeman, D. Aragon, A. Comeau, R. Davis, J. Pye, N. Beauchamp, K. Morton, S. Iverson, N. Fisher, M. Neary, N. Pettigrew, L. St. Laurent, J. Reilly, K. Decoteau, C. Jones, C. DeCollibus, C. Jacubiak, J. Kohut, T. Miles, T. Haskins, J. Wilkin, N. Strandskov, M. Breece, M. Oliver, D. Haulsee, G. Kuska, C. Thoroughgood, W. Boicourt, D. Gong, R. He, W. Woods, C. Edwards and the U.S. Navy Glider Team headed by C. Szczechowski

Funding for this work came from the National Oceanographic and Atmospheric Administration's U.S. Integrated Ocean Observing System (much of which came through the Mid Atlantic Regional Association Coastal Ocean Observation System Regional Association), Ocean Tracking Network, New Jersey Department of Environmental Protection, U.S. Environmental Protection Agency, U.S. Department of Environmental Protection, University of Delaware, National Aeronautics and Space Administration, U.S. Office of Naval Research, University of Maine, College of William and Mary, University of Georgia, Teledyne Webb Research Corporation, NOAA National Marine Fisheries Service, the National Science Foundation's Ocean Observatories Initiative and the U.S. Navy.

In addition to the funding agencies and partners listed here, the authors would like to thank Doug Webb for his futuristic vision, and, leading us one step at a time toward 'changing the world'.

"Have fun, work hard, change the world" – Doug Webb

REFERENCES

[1] D. Barrick, M. Evans, B. Weber, "Ocean surface currents mapped by radar," *Science* **198**, 138–44 (1977).

[2] H. Roarty *et al.*, Operation and Application of a Regional High-Frequency Radar Network in the Mid-Atlantic Bight, *Mar. Technol. Soc. J.* **44**, 133–145 (2010).

[3] D. B. Haidvogel *et al.*, Ocean forecasting in terrain-following coordinates: Formulation and skill assessment of the Regional Ocean Modeling System, *J. Comput. Phys.* **227**, 3595–3624 (2008).

[4] 20. J. L. Wilkin, E. J. Hunter, An assessment of the skill of real-time models of Mid-Atlantic Bight continental shelf circulation, *J. Geophys. Res. Ocean.* **118**, 2919–2933 (2013).

[5] W. Brown, W. Boicourt, C. Flagg, A Gangopadhyay, O. Schofield, S. Glenn, J. Kohut, "Maping the mid-Atlantic cold pool eveolution and variability with ocean gliders and numerical models," Oceans 2012 MTS/IEEE Hampton Roads Proceedings.

[6] S. Glenn, O. Schofield, T. Miles, G. Seroka, Y. Xu, H. Roarty, J. Kohut,"Ahead-of-eye Coastal ocean response and feedback on tropical cyclone activity," *Science*, in press.

Enabling Shallow Water Flight on Slocum Gliders

Clinton D. Haldeman III, David Aragon, Hugh Roarty, Joshua Kohut, Scott Glenn
Institute of Marine and Coastal Sciences
Rutgers University
New Brunswick, New Jersey 08901

Abstract— **Underwater gliders are a disruptive technology capable of transforming our understanding of the ocean. Efficient vehicle flight is critical for proper data collection, allowing successful completion of project goals. Slocum glider flights in less than 15 m of water have been only marginally successful, as use of deep water flight coefficients disables proper inflection at shallow depths. Groundings can damage sensors, degrade data, halt progress, and ultimately endanger the vehicle. To correct poor flight performance, sensor parameters responsible for inflection were individually analyzed and adjusted. Tests were conducted on repeated flights in the shallow state waters of New Jersey with glider RU28 while conducting dissolved oxygen surveys for the New Jersey Department of Environmental Protection (NJDEP) and the United States Environmental Protection Agency (USEPA); further verifications were conducted off the shoaling areas of Delaware with glider OTIS while searching for tagged sturgeon and sand tiger sharks. As a result of these tests, flight performance has been drastically improved, with efficient flight in 8 m of water, including several promising instances in water as shallow as 6 m. Prior to adjustments, gliders would make little forward progress and spend 50-100% of a flight segment grounded. With the new parameters loaded, groundings have been eliminated from coastal missions. Enabling shallow water flight for Slocum gliders allows vehicle operations in an area largely unexplored by this type of platform, opening up coastal areas to new project ideas and sampling schemes. Shallow water flight parameters can be shared with the community to increase sampling density in areas previously off limits to these vehicles**.

Keywords—Gliders; Slocum gliders; Shallow water; AUV operations; Glider flight parameters

I. INTRODUCTION

In 1989, Henry Stommel penned a science fiction article published in the journal Oceanography entitled "The Slocum Mission"[1]. In it, he elaborated on an idea conceived by Douglas C. Webb about a fleet of autonomous underwater vehicles driven by buoyancy changes, dubbed Slocums, that traversed the oceans while profiling in a sawtooth pattern, surfacing at regular intervals and sending data back to a control center via satellite. Today the Slocum glider is no longer a myth, but a reality with purposed missions, monitoring both deep ocean basins [2] and shallower coastal regions [3]. While the former presents its own suite of challenges, the latter has presented glider operators with a unique set of issues to overcome merely to enable continuous flight in a limited water column. Standard flight coefficient settings work well in depths of 15 meters or greater, but often fail in depths below that, causing the vehicle to strike the bottom. Several separate factors can lead to these groundings with differing severity. Short duration groundings are affectionately termed "bottom sampling" (Fig.1), while longer duration groundings are referred to as "dredging" (Fig. 2). Both are capable of degrading the data set, and can cause damage to the vehicle and payload sensors. As work in these regions expands, finding a solution becomes imperative.

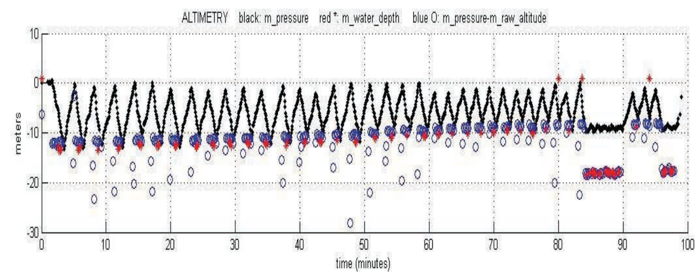

Fig. 1. *Pressure record from University of Delaware glider "OTIS". Towards the end of this segment, the otherwise uniform sawtooth pattern is interrupted by " bottom sampling"..*

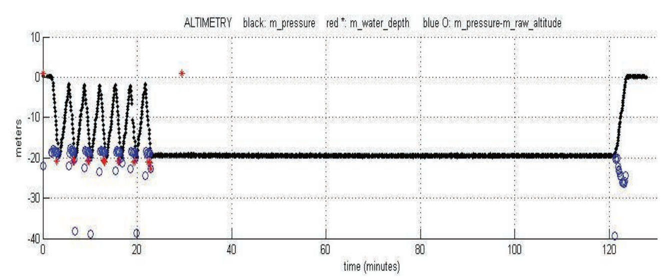

Fig. 2. *Pressure record from Rutgers University glider "RU28". In this example of "dredging", once the glider strikes the bottom, it is unable to recover and stays on the bottom for the remainder of the segment.*

II. Background

A. Glider Configuration

The Slocum glider, manufactured by Teledyne Webb Research Corporation (TWRC), is modular in design and available in several different configurations [4]. Aside from the payload bay that can be configured with a variety of different sensors, the primary differences lie in the depth rating of the buoyancy pump – currently 30 m, 100 m, 200 m, and 1000 m, with others well on the way. For very shallow coastal areas, the 30 m pump configuration is ideal, with a theoretical operational depth of between 4 m and 30 m of water. With the standard flight coefficients, the 30 m pump has not performed any better in shallower water than the deep rated 100 m pumps.

B. Applicaitons Requiring Efficent Shallow Water Flgiht

1) New Jersey Dissolved Oxygen Monitoring

With the arrival of the warm summer weather, the coastal waters of New Jersey often experience areas of low dissolved oxygen at depth. [3] These areas are of interest to and are occasionally monitored by the New Jersey Department of Environmental Protection (NJDEP) and the United States Environmental Protection Agency (USEPA), often leading to an "impaired" classification for the coastal waters of the region. Rutgers University has since partnered with these agencies to pilot a Slocum glider through the state's coastal waters, monitoring dissolved oxygen at a much higher spatial resolution than previous shipboard surveys. Data collected for the USEPA has a previously specified resolution and format, specified in a Quality Assurance Project Plan (QAPP), and state waters lie within three nautical miles from shore. The convergence of these constraints require reliable operation and data collection of a glider in very shallow water, in this case approaching as near to the seabed as possible without risking the glider.

2) University of Delaware Shark Tagging Project

The University of Delaware pioneered the integration of a Vemco VR2C hydrophone into a Slocum glider, effectively allowing the glider to receive information from sand tiger sharks, sturgeon, and other tagged species in the area while mapping out the physical properties of the associated preferred water masses [5]. Rutgers University partnered with the project team to pilot the glider, primarily in the shallow coastal region off Delaware, known for its shoaling. A glider in this area can often find itself operating in 6-8 m of water while winding its way through the navigable waters between shoals. Flight dynamics adjustments are necessary to successfully gather data in these regions.

III. Methods

Two gliders were flown for separate projects off the coasts of New Jersey and Delaware – RU28 to monitor areas of low dissolved oxygen off New Jersey, and OTIS in a search for tagged sharks and sturgeon off Delaware. While instances of bottom sampling and occasionally even dredging have been seen before, both became common occurrences during these flights. Glider pilots were not able to coerce the gliders to make headway, and the project data sets were in jeopardy. It was at this point that in-depth analyses of flight data were conducted in an attempt to pinpoint the root cause of the issues.

"Live" plots that update with the newest flight data after every surfacing were poured over time and time again, as were higher density datasets transferred directly from the glider representing suspect segments. Several plots began to point toward altimetry issues, both in the collection and processing of the sonar returns. The master file containing all sensors aboard the glider, masterdata was scoured for all sensors and settings related to the altimeter. Upon reasoning through the default settings, the root cause of bottom sampling had been found.

A rather specific set of criteria applies to altimeter returns to be considered "good", and thus be accepted by the glider. As the glider begins a dive in shallow water, a good altimeter return may be received and rejected, as the glider is still considered to be "on surface", or it may still be too soon after an inflection. As the glider continues its dive, it reaches a window where an altimeter return is recognized as "good", and that value is stored. The glider continues its dive, and receives another good return, but it may be rejected because the glider is too close to the bottom. The glider requires two valid altimeter returns to determine height above bottom and then inflect, but in very shallow water, it may only receive one, which is then ignored, and the glider strikes the bottom. (Fig. 3.) Fixing the bottom sampling issue requires taking multiple flight parameters into consideration at once, with an understanding of their interactions between each other and the glider. The initial step is to disable the filtered altimetry:

```
sensor:  u_alt_reqd_good_in_a_row(nodim)      1
sensor:  u_alt_filter_enabled(bool)           0
sensor:  u_alt_reduced_usage_mode(bool)       0
```

This step disables the built-in filter, turns off the standard reduced usage mode, and requires only one "good" return in a row to register as a valid altimeter return. Otherwise, valid returns are rejected. The second step requires changing parameters that effectively increases the size of the water column to the glider's altimeter.

```
sensor:  u_reqd_depth_at_surface(m)              2
sensor:  u_alt_min_post_inflection_time(sec)   4.0
sensor:  u_alt_min_depth(m)                    1.0
sensor:  u_min_altimeter(m)                    1.5
```

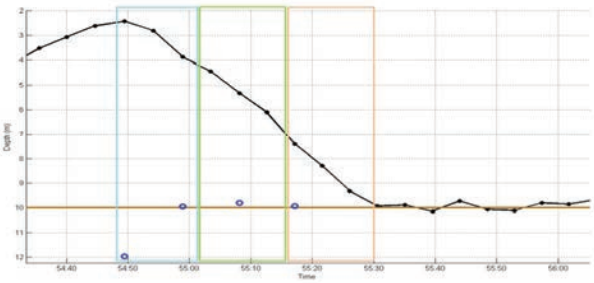

Fig. 3. Obtaining returns in very shallow water. The 2 initial returns are rejected, one valid return is accepted, and another later hit is rejected, causing the glider to ground.

The depth at which the glider considers itself on surface is reduced to 2 meters instead of 4, immediately increasing the depth in which valid returns can be obtained. The post-inflection time filter is reduced to 4 seconds, letting the glider take readings earlier after it inflects. The minimum depth the glider must obtain before taking altimeter readings is reduced to 1 meter, effectively keeping the altimeter on for the majority of the flight. The minimum reading the altimeter may return is then reduced to 1.5 meters, allowing the glider to reach as low as 1.5 meters above bottom prior to inflecting. Below this altimeter readings can be unstable, spiking up into unrealistic values. So the general summary of steps to avoid bottom sampling is to a) disable the filtering of valid altimeter returns and b) increase the depth of the water column in which the glider is able to receive returns. Should these fail, an additional safety can be added:

sensor: u_max_water_depth_lifetime(yos) 2

Setting this sensor allows the glider to use the measured altimetry from the last dive should it fail to obtain a valid measurement on the current dive. While not accurate, it can serve as a safety if the depth hasn't changed drastically.

Further refinements can be made to increase altimeter accuracy and nullify false hits:

sensor:	u_sound_speed(m/s)	1510.0
sensor:	u_max_bottom_slope(m/m)	3.0
sensor:	u_min_water_depth(m)	0
sensor:	u_max_water_depth(m)	2000

The speed of sound can be set to match as closely as possible the physical properties of the water mass in which the glider will be flying. Although the difference may not appear drastic, all attempts to increase altimeter accuracy had to be taken into consideration. The maximum slope of the seabed can be adjusted; this value is presented in vertical meters per horizontal meter. Strong caution is urged in reducing this value, as it may be acceptable where topography is generally flat, but can filter out valid returns in an environment with a more dynamic terrain, such as rocky coasts, reefs or wrecks. The final two sensors listed above are included as an altimeter fix for a very specific situation; their inclusion here will be clarified later in this section. Several glider flights have produced false altimetry hits, causing the glider to inflect up in the water column instead of down near the seabed. Although this has been seen occasionally off New Jersey in the shelf waters, it is primarily an issue in the colder waters of Antarctica. General speculation points towards masses of krill acting as a false bottom, giving the glider false returns. Setting the minimum water depth deeper than the false returns filters out any returns prior to the preset depth. Again caution must be used, especially if entering shallow water. This can inadvertently trigger a grounding. Setting the maximum water depth avoids null returns from the altimeter; i.e. generic placeholder values such as 9999. This is not an issue, as this is the default setting, and is included here only for completeness.

Preventing dredging, although related, is a separate issue. When bottom sampling, the groundings occur due to a lack of altimetry, but the glider can typically recover. When dredging occurs, the glider not only grounds, it remains on the bottom for extended periods of time, typically the remaining duration of the segment. On occasion, a trigger will cause the glider to recover, but the safeties in place often aren't enough to overcome the dredging. For example, the glider should attempt to surface if it has been at the same depth for a specified period of time, which seems plausible, as the glider is stuck on the bottom. However, in dynamic shallow water environments, the surge of the waves moving the glider around often creates enough of a pressure change that the glider's logic does not realize it is generally at the same depth. The underlying cause of dredging is yet another altimeter issue – surface reflections. When the glider is on the bottom, the ping of the altimeter reflects immediately off the seafloor, and again off the surface before returning to the glider. The glider registers these as valid returns, and continues trying to dive through the seafloor to reach the depth registered by the altimetry (Fig. 4). To circumvent this, one sensor is set:

sensor: u_max_altimeter(m) 6.0

The maximum value allowed to be returned by the altimeter is set to less than the actual water depth. This is considered to be a workaround rather than a final solution, as it prevents the glider from dredging, but also limits altimeter returns in deep water to the same value; e.g. if the glider is flying to 80 m in 100 m of water, no altimetry will be returned, as 20 > 6, even though the altimeter is easily capable of measurement at that depth.

Throughout the initial troubleshooting process, the above sensors were individually adjusted and tested to gain better understanding of how the glider's flight behaviors changed with each setting, and how the sensors interacted with one another. Once a best-practice set of parameters was decided upon, the sensors were collected and placed into a mission file that is now included in Rutgers' default software version. Using a simple "loadmission" command via short-range

Freewave communications or even through TWRC's dockserver over the Iridium network, shallow water flight parameters can quickly and easily be loaded on a glider at sea, preventing nearly all groundings.

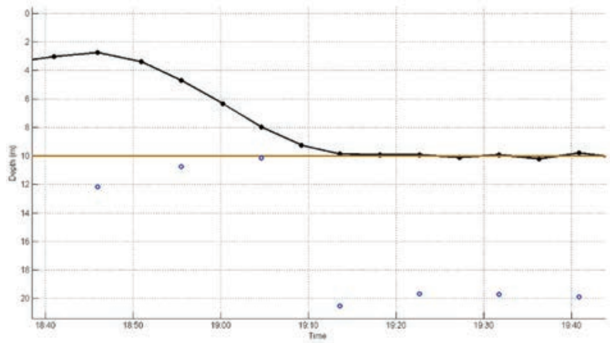

Fig. 4. Altimetry surface reflections during a grounding event. The glider remains grounded as it attempts to dive to the values returned by the altimetry.

IV. DISCUSSION

Slocum gliders are a powerful tool capable of sampling the marine environment with very high resolution, both vertically and horizontally. A standard suite of software included from the manufacturer generally enables glider flight across a range of pump configurations, providing the water depth is sufficient. This "one-size-fits-all" approach breaks down in shallow water, causing the glider to strike the bottom on multiple occasions, or strike the bottom and remain there for the duration of the segment. While adjusting sensors onboard the glider has lead to a software fix, not everything can be blamed on the software configuration.

A. Causes of grounding

Splitting the glider into two separate systems, denoting a hardware system and a software system, both have their faults that can result in groundings.

1) Hardware

Sonar altimeters, although used for decades and generally trustworthy, are not without their own idiosyncracies. As the physical properties of seawater (temperature, salt content) change, the speed of sound in that water mass changes, causing the altimeter's calibration to differ as well. Although this difference is typically small, it is still present.

In glider altimeters, as in many other lowered instrumentation packages, the altimeter will begin reporting erratic values when the altimeter reaches approximately one meter above bottom. Without filtering, the glider's logic would simply continue to send the glider on its dive, resulting in grounding.

Although less common, there have also been instances where the altimeter calibration has been incorrect, and an offset occurs. This calibration offset has been seen in both the positive and negative direction, causing one glider to ground while another could not seem to find the bottom.

While calibration issues can often be survived at sea and solved in the lab, some are intrinsic issues that cannot be resolved.

2) Software

The standard altimetry settings onboard the glider allow flight in sufficient water, but can cause grounding in water depths less than 15 meters. This is a direct result of the glider's cycle time and ability to obtain altimeter returns combined with its filtering logic ignoring valid returns. Unlike the hardware system, the user has control over the software system, and these settings can be adjusted to enable shallow water flight. By disabling the standard altimetry filters, more altimeter returns are considered for inflection determination. By decreasing the top and bottom boundaries for altimetry data, more of the water column becomes available to obtain valid altimeter returns. The culmination of these changes result in enough valid altimetry to inflect effectively and continue to collect data in very shallow water.

B. Detriments of groundings

1) Vehicle/platform risk

Groundings present a series of risks to gliders and the sensors they carry. Striking the seafloor - or any number of objects on the seafloor – has the potential to scratch, break, or otherwise damage attached sensors such as the external CTD (Conductivity, Temperature, Depth) sensor and the exposed faces of integrated fluorometers and backscatter meters. As the glider is pushed around by the surge, sediment can build up in the nosecone, resulting in a loss of buoyancy. With enough additional sediment, it is possible this could lead to the inability to surface, eventually resulting in the glider releasing its ejection weight. At that point, the glider's mission is over and a typical recovery becomes a rescue. On one occasion, University of Delaware's glider OTIS had gathered enough sand in the nosecone during a bottom sampling segment that small pieces of gravel became lodged between the buoyancy pump and the diaphragm. As the pump moved during inflection, the small pieces of gravel ground against the diaphragm, eventually ripping through and causing a leak. This put the vehicle in immediate risk of total loss.

2) Data quality risk

Aside from the obvious physical dangers presented by groundings, data quality can be affected as well, even jeopardizing projects. Deployments monitoring dissolved oxygen for the NJDEP and USEPA require a predetermined and preapproved glider path, horizontal, and vertical data resolution. Groundings halt forward progress, thereby wasting battery and possibly jeopardizing the path. Horizontal resolution is reduced, often drastically, as the glider cannot make expected progress. Vertical resolution is also affected, as the glider may still be sampling and taking high resolution data, but at a single point on the seafloor rather than monitoring the water column.

C. Summary/results

The software solution outlined above allows a quick, easy method for loading shallow water flight coefficients on a deployed Slocum glider. The end result is confident flight and data collection in 8 meters of water, with examples of successful flight in as little as 6 meters of water (Fig 5.).

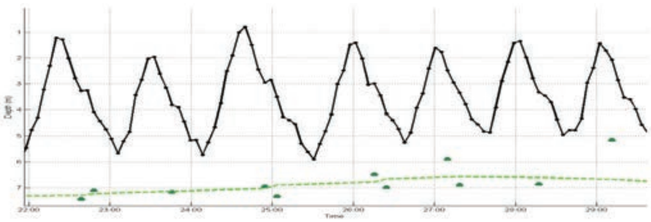

Fig. 5. Successful flight in 6-7 m of water after applying shallow water flight coefficients.

The ability to operate Slocum gliders in shallow water environments presents a new monitoring tool to the community. No longer are shallow coastal regions off limits to endurance sampling schemes. Future implications point towards the possible monitoring of harbors and bays, with the ability to transit to areas of interest, as opposed to single point moored arrays that require vessel intervention to reposition. Regions shallower than 6 meters currently pose flight mechanics issues, but shallower flight may be possible with further adjustments of flight characteristics such as pitch, pump flow rates, and stability. As the vertical speed of the platform is slowed, the ability to obtain altimeter returns is increased, possibly allowing full flight in the designed inflection range of 4 meters for the 30 m shallow pump configuration.

ACKNOWLEDGMENTS

New Jersey Department of Environmental Protection, United States Environmental Protection Agency, University of Delaware, Mid-Atlantic Regional Association Coastal Ocean Observation System,

REFERENCES

[1] Stommel, H. 1989. The Slocum Mission. Oceanography. 2(1): 22-25.

[2] Glenn, S., Kohut, J., McDonnell, J., Seidel, D., Aragon, D., Haskins, T., Handel, E., Haldeman, C., Heifetz, I., Kerfoot, J., Lemus, E., Lictenwalder, S., Ojanen, L., Roarty, H., Atlantic Crossing Students,Jones, C., Webb, D., Schofield, O. 2011. The Trans-Atlantic Slocum glider expeditions: A catalyst for undergraduate participation in ocean science and technology. Marine Technology Society 45: 75-90.

[3] Kohut, J., C. Haldeman, AND J. Kerfoot. Monitoring Dissolved Oxygen in New Jersey Coastal Waters Using Autonomous Gliders. U.S. Environmental Protection Agency, Washington, DC, EPA/600/R-13/180, 2014.

[4] Schofield, O., Kohut, J., Aragon, D., Creed, L., Graver, J., Haldeman, C., Kerfoot, J., Roarty, H., Jones, C., Webb, D., Glenn, S. M. 2007. Slocum Gliders: Robust and ready. Journal of Field Robotics. 24(6): 1-14. DOI: 10:1009/rob.20200

[5] Oliver, M. J., Breece, M. W., Fox, D. A., Haulsee, D., Kohut, J.T., Manderson, J., Savoy, T. 2013. Shrinking the Haystack: Using an AUV in an Integrated Ocean Observatory to Map Atlantic sturgeon in the Coastal Ocean. Fisheries, 10.1080/03632415.2013.782861.

Ocean Predictive Skill Assessments in the South Atlantic: Crowd-Sourcing of Student-Based Discovery

Rachael Sacatelli, Tobias Schofield, Katherine Todoroff, Angela Carandang*, Alyson Eng*, Ian Lowry*, Harrison Mather*, Antonio Ramos**, Sebastiaan Swart***, Marcelo Dottori****, Nilsen Strandskov, Josh Kohut, Oscar Schofield and Scott Glenn

Rutgers University
Coastal Ocean Observation Lab
New Brunswick, NJ, USA

*United States Naval Academy
Annapolis, MD, USA

**Universidad de Las Palmas de Gran Canaria
Las Palmas, Gran Canaria

***Southern Ocean Carbon & Climate Observatory, Council for Scientific and Industrial Research, Stellenbosch, South Africa
and
Department of Oceanography, Marine Research Institute, University of Cape Town, Rondebosch, South Africa

****University of São Paulo,
Oceanographic Institute
São Paulo, Brazil

Abstract— Autonomous Underwater Gliders have over a decade long history of successful regional deployments serving scientific, societal and security needs in application areas ranging from pole to pole and including the full range of water depths from shallow coastal seas to the deep ocean. Glider deployments covering the basin scale are much fewer, but are a growing capacity as demonstrated by the Woods Hole to Bermuda line that crosses the Gulf Stream, the Atlantic Crossing line that follows the Gulf Stream, and the basin circling flights now being conducted as part of the Challenger Glider Mission.

The next step in the evolution of the global Challenger mission is to enable an ensemble of modelers from different institutions and agencies to participate in a meaningful way. This process with be formalized in 2014 by leveraging the data management tools of the U.S. Integrated Ocean Observing System (IOOS) and the education tools of the U.S. National Science Foundation's (NSF) Ocean Observing Initiative (OOI). The Education Visualization (EV) tools developed by the OOI's Education and Public Engagement (EPE) Implementing Organization (IO) are currently being configured through the cyber OOI net to display real time OOI glider data with intuitive interactive browser-based tools, reducing the barriers for student participation in sea exploration and discovery. Through U.S. IOOS, forecast ocean data will be harvested from the ephemeral ocean snapshots produced by an ensemble of ocean models along the same glider tracks as Challenger. The parallel observed and forecast datasets, both evolving in real time, will be accessible through the same OOI EV tools, enabling student participation in a crowd-sourced ocean predictive skill experiment. The result will satisfy one of the important goals of the Challenger mission by enabling students to assess of the quality of the ensemble of available global scale ocean models.

Student research team projects that use the new model data comparison capabilities will be conducted during the summer of 2014. Students will compare an ensemble of the global ocean models along the high velocity transport pathways by gliders on basin-scale missions, such as one that traverses the northern side of the South Atlantic gyre along the Brazilian shelfbreak. The lasting impact of the Challenger mission will be a global fleet available to respond to events, an assessment of the ocean models along the fastest ocean transport pathways, and the establishment of a network of gliderports for global response.

Keywords — Ocean Forecasting; Autonomous Underwater Gliders; Challenger Glider Mission.

I. Introduction

Autonomous Underwater Gliders have been utilized by the scientific and defense communities for a multitude of different missions that cover all areas of the globe from the surface of the ocean to 1000 meters below. Recently, long scale endurance missions have started to become a focus. The Challenger Glider Mission is one such mission whose aim is to use gliders to explore five ocean basins covering 128,000 kilometers.

Figure 1: The projected paths of the Challenger Glider Mission.

Two of the gliders that are involved in this Challenger Glider Mission are Silbo and RU29. Silbo has not contributed significantly to the mission since the Dobson et al. [5] article where data from Silbo and RU29 were used to compare against the then current ocean models. As such, an extension on the analysis of the Silbo data is not needed. RU29, however, has stopped in the Ascension Islands and flown all the way to São Paulo, Brazil since the publication of the Dobson et al. [5] article.

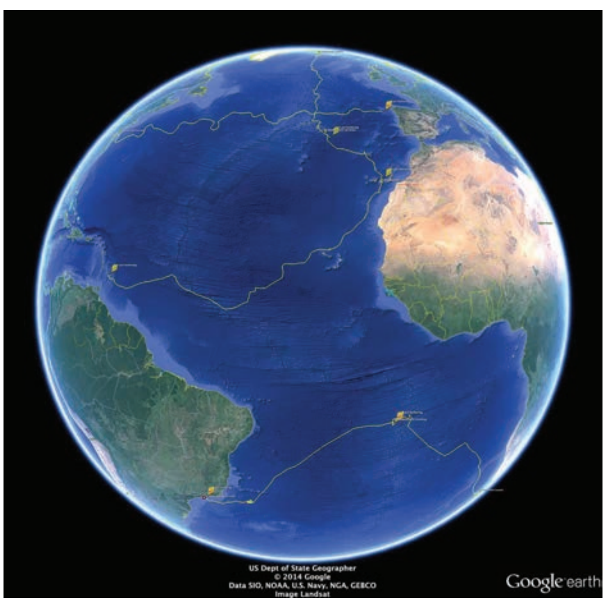

Figure 2: A map of the history of tracks covered by Rutgers Coastal Ocean Observation Lab's Challenger gliders. Basin scale missions, in collaboration with Teledyne Webb Research and Universidad de Las Palmas de Gran Canaria.

The data collected from the flight of RU29 from the Ascension Islands to São Paulo, Brazil can contribute significantly to our understanding of the accuracy of both the American RTOFS ocean model and the European MyOcean ocean model and expand upon the work done last year in the Dobson et al. [5] article. This flight completes the examination of the northern section of the South Atlantic gyre. While the ocean forecast models currently assimilate data from an Argo network of over 3000 drifters, assimilating glider data that crosses frontal features may be beneficial to increasing the forecast accuracy. Glider data can help to increase sampling resolution in areas not covered extensively by Argo drifters.

Figure 3: A photograph of RU29, an autonomous underwater glider that successfully crossed the Atlantic Ocean in 2014.Behind RU29, the Oceanographic Research Vessle Alpha Delphini, from the University of São Paulo

This study will report the results of student investigations comparing temperature, salinity, and depth-averaged currents between RU29 and the model forecasts. Preliminary student observations along RU29's flight indicate that the MyOcean model, while different from RU29 on a wider area, was closer to RU29 at points of discrepancy. The RTOFS model, however, had fewer areas of discrepancy, but the discrepancies that did exist were generally of a greater magnitude.

II. Methods

The two ocean forecasting models used in this paper are the MyOcean model and the RTOFS model. The MyOcean model is the result of collaboration between European countries such as the United Kingdom, France, Germany, and Denmark. The RTOFS model is created by the National Center for Environmental Prediction, a subgroup of the National Oceanic and Atmospheric Administration based in the United States.

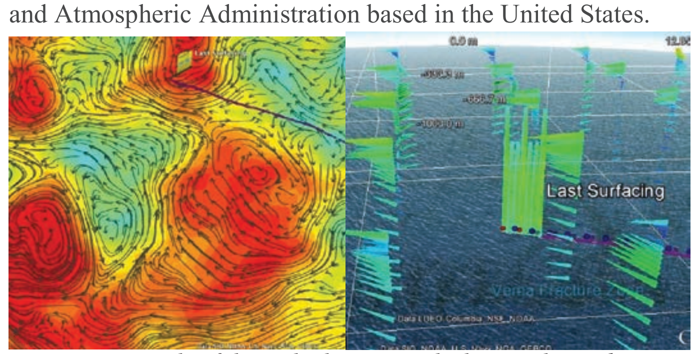

Figure 4: Example of the path planning tools that can be made using data from the ocean forecasting models RTOFS (left) and MyOcean (right) by Universidad de Las Palmas de Grab Canaria.

The sensor used by the G2 category of gliders is a SeaBird pumped Conductivity, Temperature and Depth (CTD) sensor. Temperature and Salinity data is recovered from the glider and thermal inertia from the conductivity sensor is corrected for using the process from Kerfoot et al. [3]. This data is compared to a section of the RTOFS model and the MyOcean model simulations along the path taken by the glider (Figure 5).

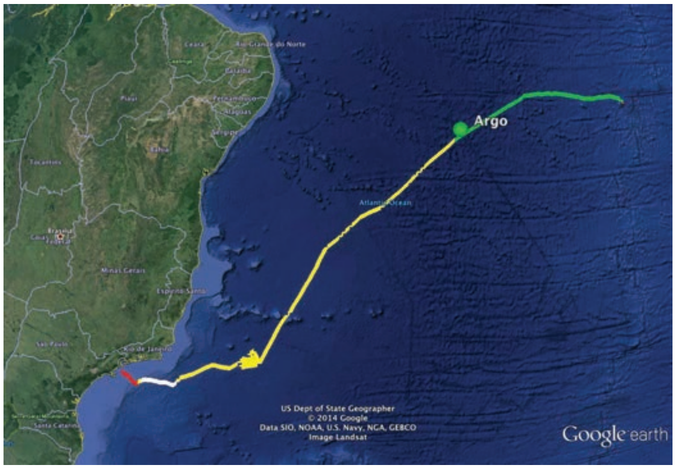

Figure 5: The portion of RU29's track that was used for comparison to the models, focusing on the green, white, and red sections. This track represents an east to west path along the northern side of the South Atlantic Gyre.

The comparisons made in this paper are a result of an analysis of temperature, salinity, and depth-averaged currents made by the models and RU29. MyOcean and RTOFS data was collected from respective Internet sources, while the glider data was collected by RU29 (Figure 3). A series of MATLAB scripts facilitated data processing and figure creation. By comparing the in-situ glider data to data obtained by the Argo Floats (Figures 7 & 9), we were able to confirm the quality of the glider temperature and salinity observations of the conditions of the water column. The most striking observation is of the temperature profiles, where the deep data from RU29, Argo, and RTOFS are similar, but MyOcean deep temperatures are about 1˚C higher.

The temperature and salinity data collected by RU29 was then compared to RTOFS and MyOcean (Figures 6 & 8). The figures were created by observing the difference between glider data and model predicted data. There was a general 1˚C difference between the MyOcean and RU29 temperature data (Figure 6b), whereas the discrepancies between the RTOFS and RU29 data were less widespread but more significant (Figure 6a). The most variation between the two models and RU29 exist within the first 300 meters of the water column, as shown in figures 6 and 8. Hence, the remainder of this paper will focus on analyses of depths above 300 meters.

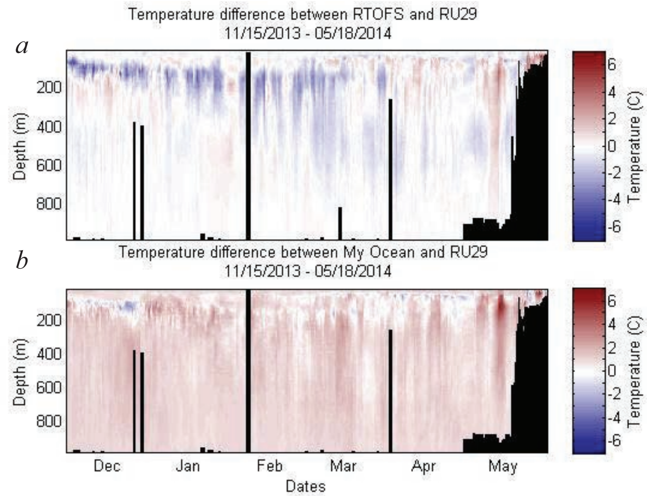

Figure 6: The difference in temperature between the RTOFS model with RU29 (a) and the MyOcean model with RU29 (b).

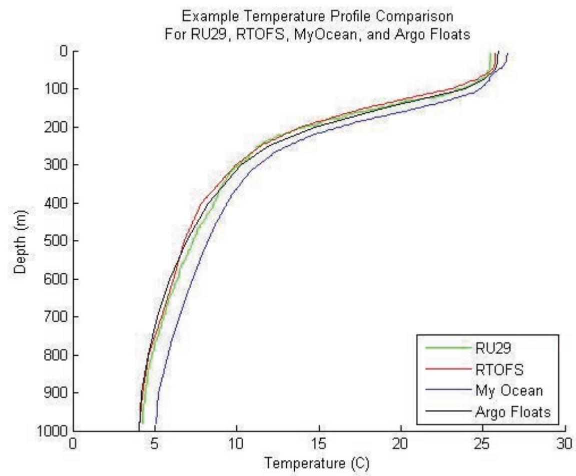

Figure 7: Temperature depth profile comparison between RU29, RTOFS, MyOcean, and Argo Float data at a sample point.

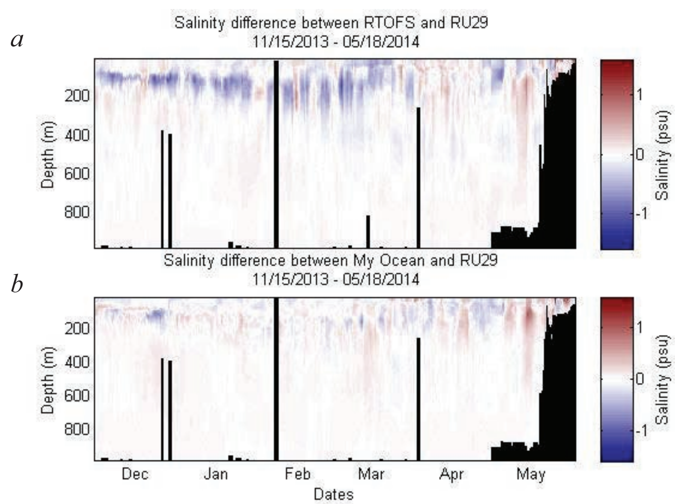

Figure 8: The difference in salinity between the RTOFS model with RU29 (a) and the MyOcean model with RU29 (b).

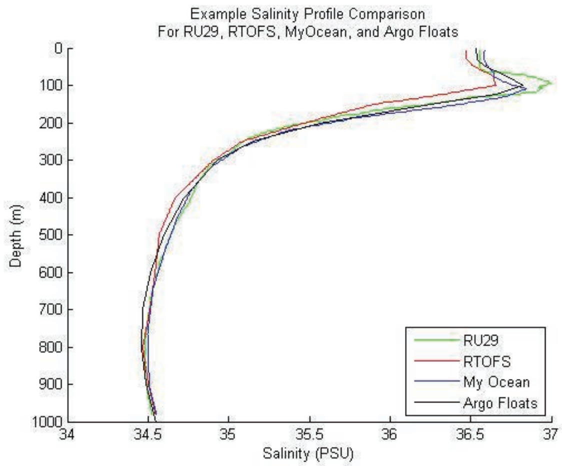

Figure 9: Salinity depth profile comparison between RU29, RTOFS, MyOcean, and Argo Float data at a sample point.

III. RESULTS

RU29's mission from Ascension Island to São Paulo, Brazil lasted from November 15, 2013 to May 18, 2014. It traveled 4,420 km crossing the Atlantic on the northern part of the South Atlantic gyre. An analysis of temperature, salinity and currents was conducted on three areas of interest: a 1,262 km leg off the coast of Ascension Island, a 265km leg off the coast of Brazil, and a 179km leg on the Brazilian continental shelf (Figure 5).

A. Turtle Tracks

The first area of interest occurred from November 15, 2013 to December 30, 2013. This section will be referred to as "Turtle Tracks" and is denoted by the green section of the track in Figure 5. It is worth noting because the migration path of Green Sea Turtles between Ascension Island and Brazil runs along this path.

An analysis of temperature and salinity was conducted. There was not much disparity in temperature between the two models and RU29 (Figure 10). However a difference between RU29 and MyOcean exists at the surface and between 250 and 300 meters (Figures 10b &10c). The salinities of RTOFS and RU29 have larger differences than the salinities of RU29 and MyOcean. Most noticeable is the consistent subsurface salinity peak near 100 m visible in RU29 and MyOcean, but missing from RTOFS. Neither model accurately depicts the depth averaged current vectors measured by RU29 along this area of the track.

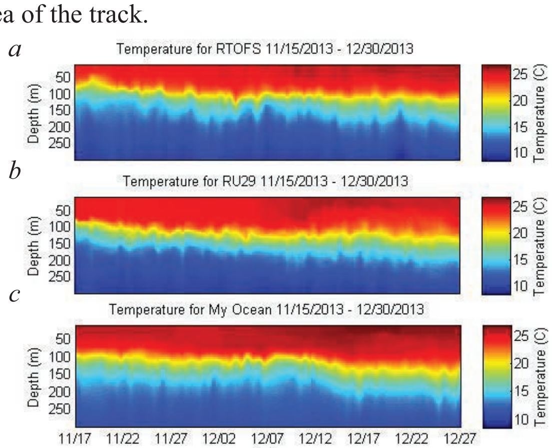

Figure 10: Temperature comparison between RTOFS (a), RU29 (b), and MyOcean (c) for the Turtle Tracks.

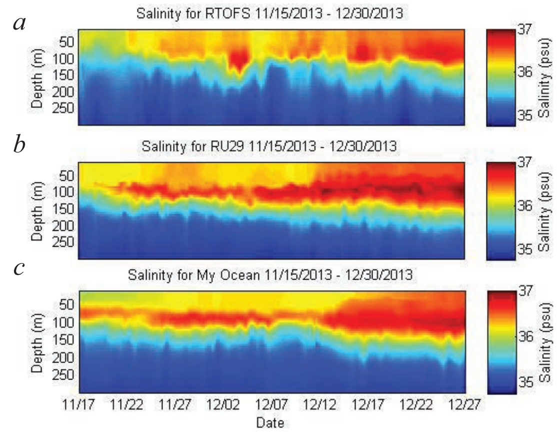

Figure 11: Temperature comparison between RTOFS (a), RU29 (b), and MyOcean (c) for the Turtle Tracks.

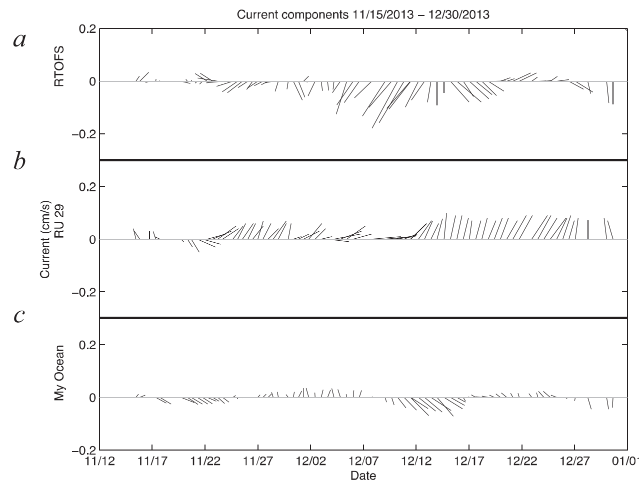

Figure 12: Current Vector comparison between RTOFS (a), RU29 (b), and MyOcean (c) for the Turtle Tracks.

B. Deep Eddy

The second area of interest occurred from April 26, 2014 to May 6, 2014. This section will be referred to as the "Deep Eddy" and is denoted by the white section of the track in Figure 5. It is worth noting because of the strong presence of an eddy. This is an area of strong meso-scale activity due to the Brazil Current[6] and the data collected with the glider can provide vertical and horizontal in-situ details that are not possible with other methods

There is evidence of a deep-water clockwise spinning eddy in the current plot of RU29 (Figure 15b), which is also seen in its temperature and salinity plots (Figure 13b & 14b). This eddy appears in the RTOFS current plot as well, with the same clockwise direction (Figure 15a). Although this eddy is present in the same spot as RU29 in both RTOFS' temperature and salinity plots, it manifests less gradually than the eddy shown in RU29's temperature and salinity plots (Figures 13a, 13b, 14a & 14b). MyOcean does not recognize the eddy structure at all (Figures 13c, 14c, & 15c).

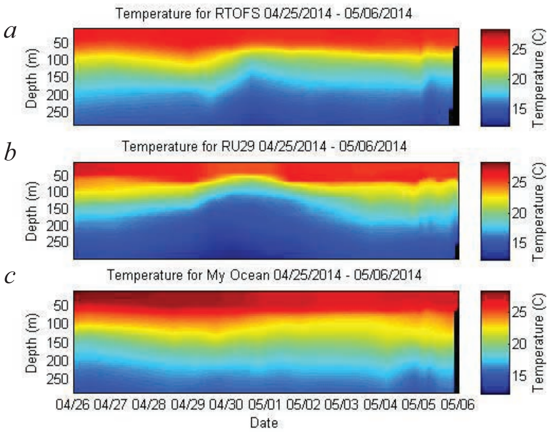

Figure 13: Temperature comparison between RTOFS (a), RU29 (b), and MyOcean (c) for the Deep Eddy.

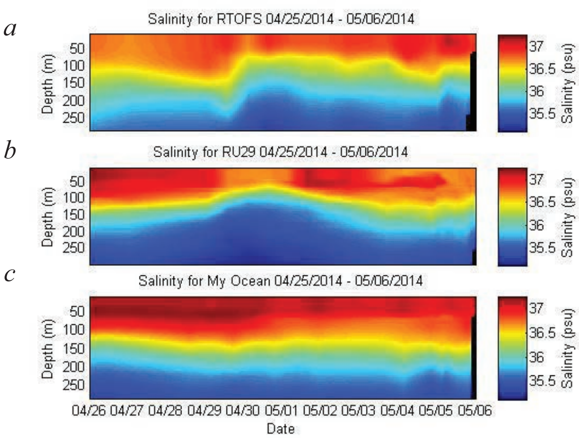

Figure 14: Salinity comparison between RTOFS (a), RU29 (b), and MyOcean (c) for the Deep Eddy.

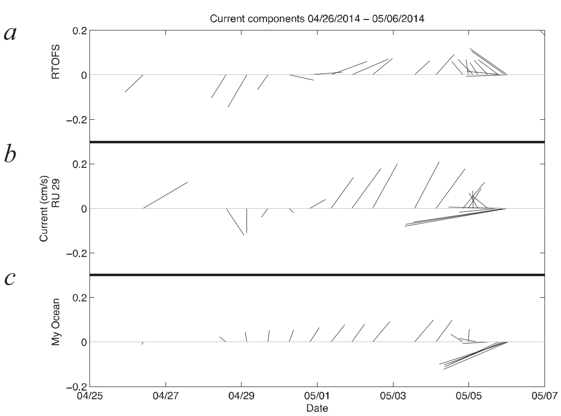

Figure 15: Current Vector comparison between RTOFS (a), RU29 (b), and MyOcean (c) for the Deep Eddy.

C. Continental Shelf and Cabo Frio Eddy

The third area of interest occurred from May 7, 2014 to May 18, 2014. This section will be referred to as "Continental Shelf and Cabo Frio Eddy" and is denoted by the red section of the track in Figure 5. It is worth noting because global models often have difficulty resolving features in shallow waters and the Cabo Frio Eddy is a well known eddy.

There is evidence of a shallow-water counter-clockwise spinning eddy in the current plot of RU29 (Figure 18b), which is also seen in its temperature and salinity plots (Figure 16b & 17b). This eddy appears in the MyOcean current plot as well, with the same counter-clockwise direction (Figure 18a). The eddy is present in the same spot as RU29 in the temperature and currents plots but the MyOcean model elongates the eddy (Figure 16b, 16c, 18b, & 18c). The MyOcean salinity plot also shows the eddy elongated, however, the eddy is shifted towards the coast. (Figure 17b &17c). RTOFS does not recognize the eddy structure at all (Figures 13c, 14c, & 15c).

On the continental shelf, possibly because MyOcean elongates the Cabo Frio eddy, the temperature and salinity it reports for the continental shelf are too warm and salty (Figures 16b, 16c, 17b, & 17c). While MyOcean is incorrect, it is not radically different from RU29, especially closest to the continent. RTOFS, however, reports noticeably warmer and saltier water in the very shallow waters (Figures 16a & 17a).

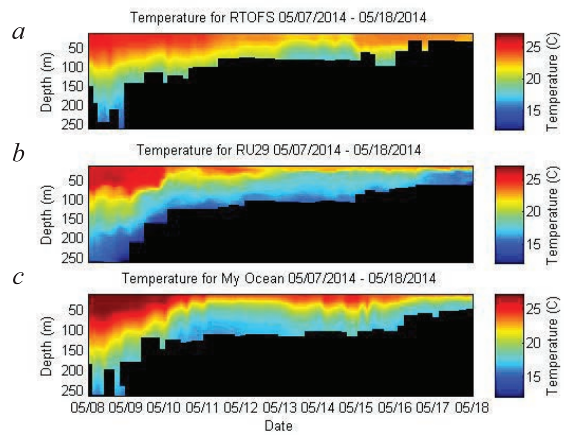

Figure 16: Temperature comparison between RTOFS (a), RU29 (b), and MyOcean (c) for the Continental Shelf and Cabo Frio Eddy.

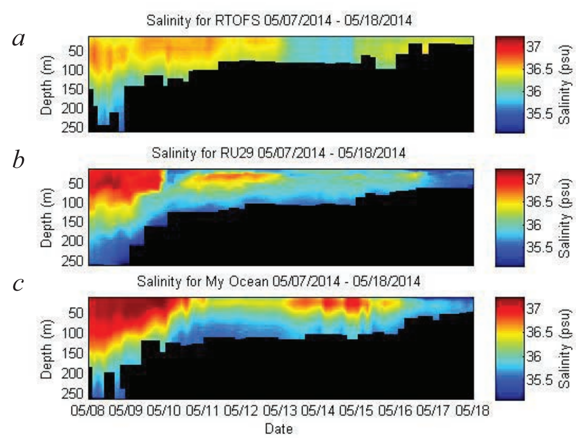

Figure 17: Salinity comparison between RTOFS (a), RU29 (b), and MyOcean (c) for the Continental Shelf and Cabo Frio Eddy.

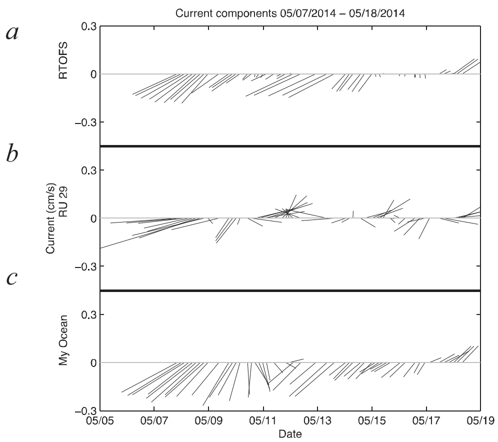

Figure 18: Current Vector comparison between RTOFS (a), RU29 (b), and MyOcean (c) for the Continental Shelf and Cabo Frio Eddy.

IV. Discussion

Two forecasting models, MyOcean and RTOFS have been studied in comparison to the glider RU29. The findings presented have lead to the conclusion that these two models have inconsistencies with in-situ glider data. Neither model can be considered superior as in certain areas, such as the “Deep Eddy”, the MyOcean model was lacking features in the ocean’s structure whereas the RTOFS model did not predict the existence of the Cabo Frio Eddy. Both the RTOFS model and the MyOcean model contain some important features that correspond with the glider data yet both also do not always reflect the structure apparent in the in-situ glider data.

Over the length of the RU29 Ascension Island to Brazil flight, the MyOcean model has a fairly consistent 1˚C to 2˚C difference in temperature from RU29, however there were not many places in either salinity or temperature that the MyOcean model differed notably from RU29. In comparison, the RTOFS model was fairly consistent with the RU29 data at lower depths but had very large discrepancies in magnitude at certain locations.

Ocean forecast models have become an indisputable tool for scientists and students, with the ability to resolve eddy structures and incorporate new data. They are easily accessible to researchers around the world. Such improvements to the models come from data taken from satellite and Argo floats that measure sea-surface temperature, sea surface height, and temperature/salinity profiles. In order to further improve the models, more data must be integrated from other sources. This will help advance forecast modeling in predicting features such as hurricane intensity.

Autonomous Underwater Gliders are able to contribute to the ocean forecast modeling because of their ability to traverse previously under-sampled regions of the ocean. It is crucial to the future of ocean modeling that glider-collected data be incorporated especially where areas of disagreement between the models occur.

V. Acknowledgements

The Challenger Glider Mission is growing global partnership of glider operators, scientists, educators and students coordinated by Rutgers University and endorsed by the Challenger Society. The results presented in this paper were initiated in a Rutgers research course and completed by three undergraduate summer interns (Rachael Sacatelli, Tobias Schofield, and Katherine Todoroff) supported by Teledyne Webb Research and four U.S. Naval Academy Interns (Angela Carandang, Alyson Eng, Ian Lowry, and Harrison Mather). Glider path planning and model/data comparison activities are led by Nilsen Strandskov (Rutgers) and Antonio Ramos (Universidad de Las Palma de Gran Canaria) with cyber infrastructure support provided by John Kerfoot (Rutgers). Glider operators include Chip Haldeman, Dave Aragon, Tina Haskin (Rutgers) and Ben Alsup (TWR). The RU29 deployment in South Africa was enabled by the University of Cape Town, The Nansen-Tutu Center, and the South African Marine Engineering & Robotics Centre at the Council for Scientific and Industrial Research (CSIR). The recovery and redeployment on Ascension Island was facilitated by the British Royal Navy, the U.S. Navy, and Ascension Island Fishing Charters (AIFC). The recovery and redeployment of RU29 in São Paulo, Brazil was enabled by University of São Paulo. RU29 mission support is provided by the U.S. Integrated Ocean Observing System, the U.S. Office of Naval Research – Global, and the G. Unger Vetlessen Foundation. Technology support provided by Teledyne Webb Research, Iridium and CLS America. Argo data was collected and made freely available by the International Argo Program and the national programs that contribute to it. (http://www.argo.ucsd.edu, http://argo.jcommops.org). The Argo Program is part of the Global Ocean Observing System.

VI. References

[1] Glenn, S., + 47 co-Authors, Process-driven improvement to hurricane intensity and storm surge forecasts in the Mid-Atlantic Bight: Lessons learned from Hurricanes Irene and Sandy. Oceans’13 MTS/IEEE Bergen.

[2] Glenn, S., Kohut, J., McDonnell, J., Seidel, D., Aragon, D., Haskins, T., Handel, E., Haldeman, C., Heifetz, I., Kerfoot, J., Lemus, E., Lictenwalder, S., Ojanen, L., Roarty, H., Atlantic Crossing Students, Jones, C., Webb, D., Schofield, O. 2011. The Trans-Atlantic Slocum glider expeditions: A catalyst for undergraduate participation in ocean science and technology. Marine Technology Society 45: 75-90.

[3] Kerfoot, J., S. Glenn, H. Arango, C. Haldeman, C. Jones and D. Pinkel, 2010. Correction and comparison of pumped and non-pumped CTS sensors on the Slocum Glider, EOS Transactions, AGU, 91(26), Ocean Sci. Meet. Suppl., Abstract IT35B-03.

[4] Schofield, O., Kohut, J., Glenn, S., Morell, J., Capella, J., Corredor, J., Orcutt, J., Arrott, M., Krueger, I., Meisinger, M., Peach, C., Vernon, F., Chave, A., Chao, Y., Chien, S., Thompson, D., Brown, W., Oliver, M., Boicourt, W. 2010. A regional Slocum glider network in the Mid-Atlantic coastal waters leverages broad community engagement. Marine Technology Society 44(6): 64-74.

[5] Dobson, C., Mart, J., Strandskov, N., Kohut, J., Schofield, O., Glenn, S., Jones, C., Webb, D., Barrera, C., Ramos, A. 2013. The challenger glider mission: a global ocean predictive skill experiment. Oceans’13 MTS/IEEE San Diego: 1-8.

[6] Calado, L., Gangopadhyay A., da Silveira I. C. A. 2006. A parametric model for the Brazil current meanders and eddies off southeastern Brazil, Geophysical research letters, *33*(12)

Gliderpalooza 2013 to Modelpalooza 2014: Joint U.S. & Canadian Ocean Glider Operations Supporting Multidisciplinary Scientific Research and Education

Michael Crowley, Oscar Schofield, Scott Glenn
Institute of Marine and Coastal Sciences
Rutgers University
New Brunswick, N.J. USA
crowley@rutgers.edu

Fred Whoriskey
Ocean Tracking Network
Dalhousie University
Halifax, N.S. Canada

Abstract— Gliderpalooza represented a grass-roots coordinated field demonstration of ocean observing technologies spanning the eastern seaboard of North America. The overarching goal was to coordinate disparate ocean research efforts, funded by disparate programs from a variety of agencies to demonstrate continental scale coordination of various ocean observing technologies to sample ecologically relevant scales.

The coordinated data from satellites, HF-Radar surface currents [1], moorings, drifters and models was focused on and around the distributed deployment of Slocum gliders. The seven science and technical goals were to:

1) provide a unique data set the modelers can use for years to come (real-time & hindcast),
2) provide a standardized dataset over ecological scales and information on fish/mammal migrations,
3) provide a 3-D snapshot of the MAB cold pool,
4) provide an extensive distributed instrumented network through the peak period of fall storms, demonstrating a community "surge" capacity,
5) provide one, of many demonstrations, of the potential U.S. national glider network,
6) proof of data flow throughput to the Global Telecommunications System (GTS) via DMAC and,
7) engage undergraduates in ocean observing efforts.

During the summer and fall of 2014, the Gliderpalooza team will once again work together, but with several additions to the group, the geographical scope will cover Texas to Newfoundland. There will be more than 30 glider deployments that will be assimilated by seven numerical ocean models. Acquisition of this massive data set of water column profiles will permit evaluation of the accuracy of the models, especially in the coastal zone. Additionally, new online educational tools developed through the NSF's Ocean Observatory Initiative (OOI) will be used to by students in the undergraduate classroom to analyze, compare and contrast the glider data in real-time during the fall 2014 semester.

Keywords — ocean glider, ocean modeling, data assimilation, physical oceanography, optics, mixing storm, cold pool, fish/mammal migrations, U.S. IOOS, MARACOOS.

I. Introduction

The research performed during Gliderpalooza grew out of the U.S. Integrated Ocean Observing System's (U.S. IOOS) Mid Atlantic Regional Association Coastal Ocean Observation System (MARACOOS) and Ocean Tracking Network's science priorities. Ten universities, one corporation and the US Navy worked together to perform 17 glider deployments along the eastern coast of the U.S. and Canada (Table 1 and Figure 1). Many of the deployment locations were determined by an ocean continuously well sampled by satellites, surface current data provided by the MARACOOS HF-Radar Regional Network [2] and drifters. Much of this data was assimilated into dynamical ocean models which were then used to direct the location of a handful of the deployments in the Mid-Atlantic bight. Upon completion of the project, full resolution data sets from almost all deployed gliders were shared amongst all researchers.

TABLE I. Gliderpalooza Glider Deployments

#	Group	Glider	Deployed
1	**Dalhousie**	OTN200 (2)	10-Sep, 2-Dec
2		OTN201	16-Sep
3	**U. Maine**	Penobscot (2)	10-Sep, 15-Oct
4	**WHOI**	Saul	10-Sep
5	**U. Mass**	Blue	6-Sep
6	**Rutgers**	RU28	12-Sep
7	**U. Maryland**	RU22	22-Sep
8	**Rutgers**	RU23 (2)	10-Sep, 10-Oct
9	**U. Delaware**	Otis	12-Sep
10	**VIMS**	Stewart	10-Oct
11	**NC State**	Salacia	17-Sep
12	**Skidaway**	Modena	10-Sep
13	**T. Webb**	Darwin	11-Sep
14	**U.S. Navy**	Navy1	10-Oct

In late February of 2014, the Gliderpalooza team met in Honolulu during the Ocean Sciences meeting to plan research papers focusing on the seven program goals. This paper will summarize the seven science and logistical goals and elaborate on early results from initial data analysis performed during 2014. It will then discuss plans for Gliderpalooza 2 (aka Modelpalooza) which will occur during July-November 2015 but will now span from Texas north to Newfoundland and east to Bermuda.

Fig. 1. Gliderpalooza deployments in summer and fall 2013.

II. GLIDERPALOOZA GOALS & EARLY RESULTS

A. Goal 1: Provide a Unique Dataset for Ocean Modelers

A shelf wide subsurface perspective for the North American east coast was collected through a coordinated range of regional combined with coastal surveys. All gilders provided an extensive survey for the hydrographic and optical data as well as acoustically tracked animal locations. The database spans from the upstream condition of Canadian waters through the South Atlantic Bight. The database is enabling studies to improve data assimilative forecast models.

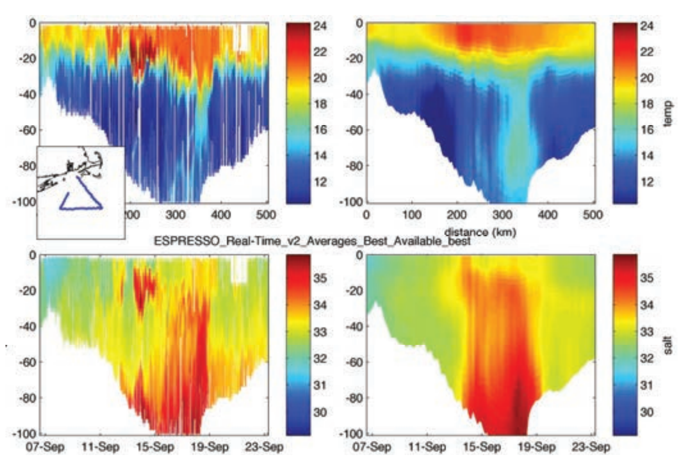

Fig. 2. Observed (left) and ROMS ESPRESSO model (right) temperature (top) and salinity (bottom) following glider BLUE. Inset shows the glider path south of Providence, RI (blue).

Moving forward, the goal is to support the improvement of the ensemble of ocean models through assimilation and validation. Figure 2 highlights a time series of temperature and salinity from a glider and compares it to the identical locations virtually sampled within the ROMS ESPRESSO model [3], [4].

B. Goal 2: Tracking Fish/Mammal Migrations

The glider survey was focused on collecting a broad environmental dataset to provide a map of the hydrography in which to interpret major migration patterns. The Ocean Tracking Network (OTN) is augmenting current capabilities to provide the foundation for a listening network. The collection of gliders provided a subsurface spatial snap shot of a Large Marine Ecosystem (LME) during the fall migration that was mined by scientists in both real-time and in hindcast mode as nine of the gliders were fitted with Vemco trackers. This effort is motivated as the region is home to some of the most migratory fish communities in the eastern United States and Canada. These data from multiple gliders are currently being combined by OTN. Species locations will be analyzed against the subsurface glider data as well as available satellite and CODAR assets and models of subsurface physical/biological parameters to provide a perspective of the northeast United States/Canada ecological domains.

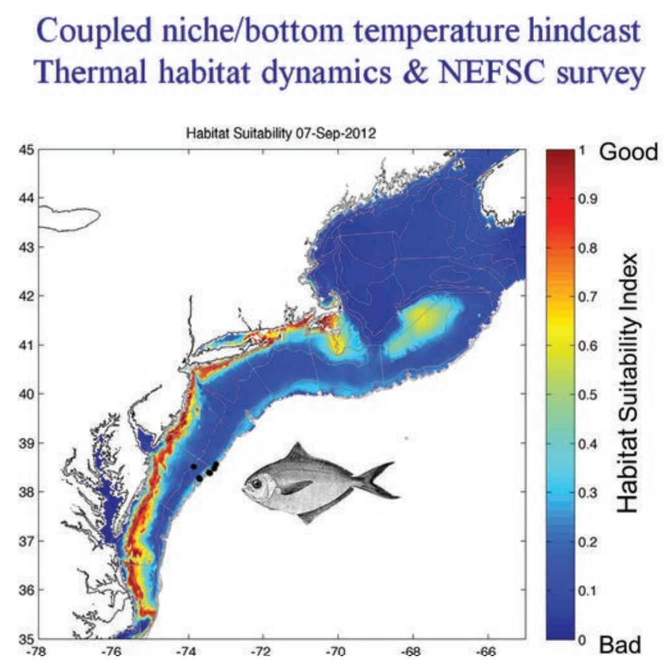

Fig. 3. A habitat sustainability model showing likelyhood of butterfish bycatch with likely areas shown in red. Block dots indicate in situ fishign surveys which tested the accuracy of this early model from 2012. Gliderpalooza data will help to improve these models in the future. Early funding for this work was from the NOAA NEFSC and Fisheries Habitat Program.

Sponsors of this work include NOAA's U.S. IOOS, Ocean Tracking Network Canada, N.J. Department of Environmental Protection, U.S. EPA, U. of Delaware, NASA, ONR, U. of Maine, College of William and Mary, U. of Georgia, Teledyne Webb, US NMFS, NSF Ocean Observatories Initiative and the U.S. Navy. Additional sponsors in 2014 will include Memorial University and Texas A&M U.

The data are also being used to improve fisheries bycatch models. Rutgers and NOAA's Northeast Fisheries Science Center (NEFSC) conducted in situ surveys in 2012 where forecast models were tested that predicted the butterfish bycatch amounts in the mid-Atlantic bight (Figure 2). Subsurface water column profile data, especially geographically distributed bottom temperatures, are key to these forecasting models, and the glider data sets will both aid in improving the models through assimilation and verifying the model's accuracy.

C. Goal 3: Mapping the Mid-Atlantic Cold Pool Water

During summer, a distinctive, bottom-trapped, cold water mass called the Cold Pool Water (CPW) resides as a swath over the mid to outer continental shelf throughout much of the Middle Atlantic Bight (MAB) [3]. This evolving CPW is important because it strongly influences the ecosystem, including several important fisheries. Thus there is a priority to better understand the relevant ocean processes and develop a CPW forecast capability.

Seven gliders crossed the area of Cold Pool during Gliderpalooza. The path of RU23 is show in red in figure 4 overlaid on a ROMS ESPRESSO modeled bottom temperature hindcast off of the New Jersey coast. Cold Pool water sits on the shelf between approximately 35m to 100m. Temperature and salinity glider transects are compared to a 2d version of this this model hindcast in figure 5.

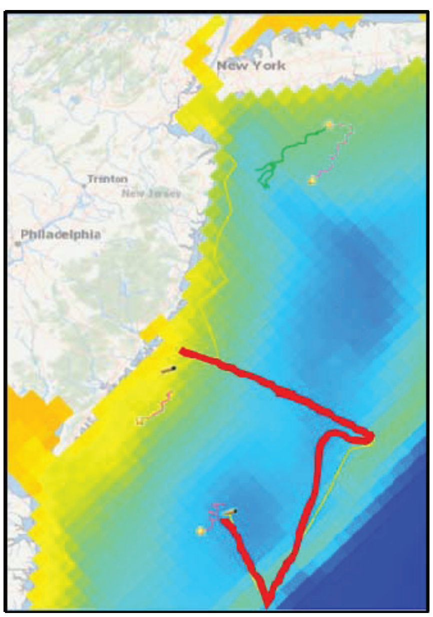

Fig. 4. A habitat sustainability model showing likelyhood of butterfish bycatch with likely areas shown in red. Black dots indicate in situ fishing surveys which tested the accuracy of this early model from 2012. Gliderpalooza data will help to better inform these models in the future through assimilation. Early funding for this work was from NOAA's Nortеast Fisheries Science Center and Fisheries Habitat Programs.

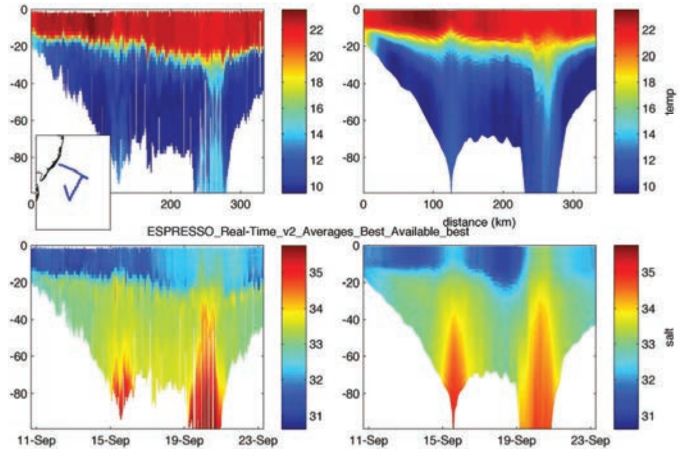

Fig. 5. RU23 glider temperature and salinity on the left are compared to modeled temperature and salinity on the right from ROMS ESPRESSO.

D. Goal 4: Analysis of Fall Mixing Storms

September is the peak month for tropical storm and hurricane landfall along the Eastern coast of North America. The regional array provided a comprehensive sampling of the continental shelves, which are the most undersampled with regards to subsurface temperatures. This subsurface temperature data is increasingly being viewed as valuable in potentially improving the ability to better predict hurricane intensity [6]. The 2013 Gliderpalooza dataset will serve as a baseline as it was a quiet tropical storm season. In 2014-2015, the Cooperative Institute for the North Atlantic Region (CINAR) is providing funding to support deployments of four storm gliders, rapid profile drifters and rapid deployable buoys into both tropical storms and winter Nor'easters. Storm gliders will be equipped with an acoustic Doppler current profiler, a full range of optical instruments, and accelerometers in addition to the standard CTD package. A preliminary in water test of these new storm gliders was performed during Hurricane Arthur in July, 2014 (figure 6).

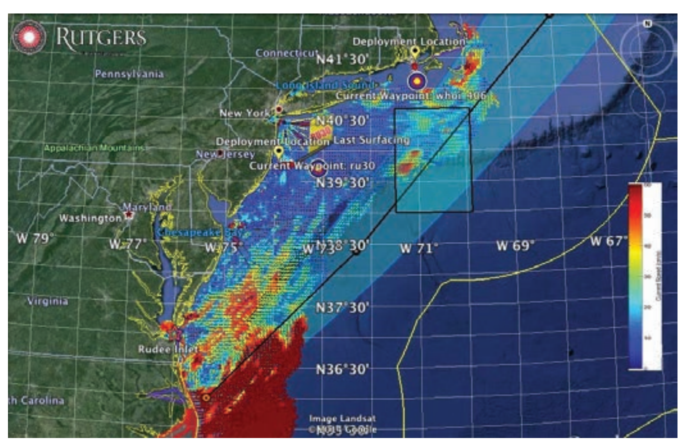

Fig. 6. Hurricane Arthur forecasted storm track from July 4, 2014. Locations of CINAR funded gliders RU30 and WHOI_406 are shown with target icons. HF-RADAR surface currents are shown, highlighting the counterclockwise circulation around the eye of Arthur just north of Cape Hatteras and the forecast track.

E. Goal 5: Demonstration of a National Glider Network

During the summer of 2012 a workshop funded by U.S. IOOS was held at Scripps Institute of Oceanography to discuss plans for a national glider network. As a result, multiple partners from federal agencies, IOOS Regional Associations (RAs) of coastal ocean observing systems, and universities were assembled to develop a National Glider Network Plan for a viable, sustainable, and reliable network that delivers timely monitoring and distribution of coastal subsurface glider data to federal, state, and local governments, as well as the general public. The plan is structured to develop an initial network that includes maintaining existing long term glider sampling lines, acquiring additional glider lines to fill high priority gaps, and improving data management, product development, and data/product delivery. The national plan was released in January 2014 and available at http://www.ioos.noaa.gov/glider/strategy/welcome.html.

Gliderpalooza enabled a first example of a multi-regional coherent effort to deploy, monitor and access glider data in real time through a central site at Rutgers University. The ultimate national goal is to attain funding for long term sustainability of deployments on all U.S. coasts (Figure 7).

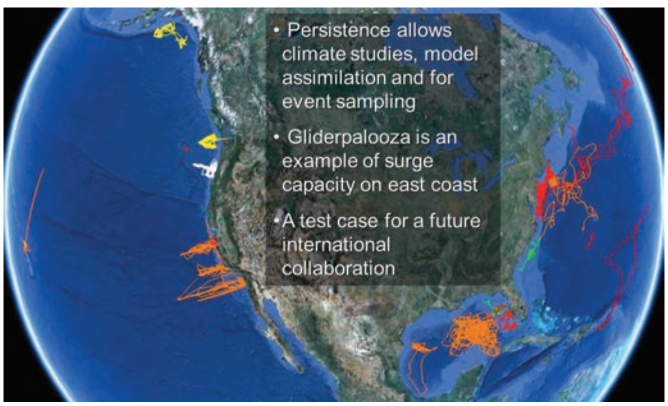

Fig. 7. U.S. glider deployments from 2000 through early 2013.

F. Goal 6: Data Throughput to the GTS

In 2013 IOOS secured funding to begin construction of a Data Management and Communications System (DMAC) specifically for glider data distribution. A successful goal of Gliderpalooza was to have real-time throughput of raw data from the gliders to Dockservers to the DMAC where it was converted to Climate and Forecast (CF) compliant NetCDF files and then sent to the National Data Buoy Center and finally to the Global Telecommunications System. This mission to make glider data available to modelers and forecasters worldwide will continue to expand outside the east coast region to the U.S. and eventually global throughput of glider data to NDBC and GTS.

Fig. 8. Schematic of glider data throughput from acquisition to the GTS.

G. Goal 7: Undergraduate Education

In addition to having undergraduate students assist with glider deployments and recoveries, the Gliderpalooza data were made available to undergraduate classrooms in real-time during the fall semester of 2013. During fall 2014, both real-time and archived glider data are going to be used by numerous Community and 4-Year college professors in the undergraduate classroom through cooperation with the NSF's Ocean Observatory Initiative's Education and Public Engagement team's (OOI EPE) newly developed online educational tools (Figure 9). This software can be used by undergraduate educators to build and share online lessons using ocean data from both the OOI and outside resources, including global glider deployments.

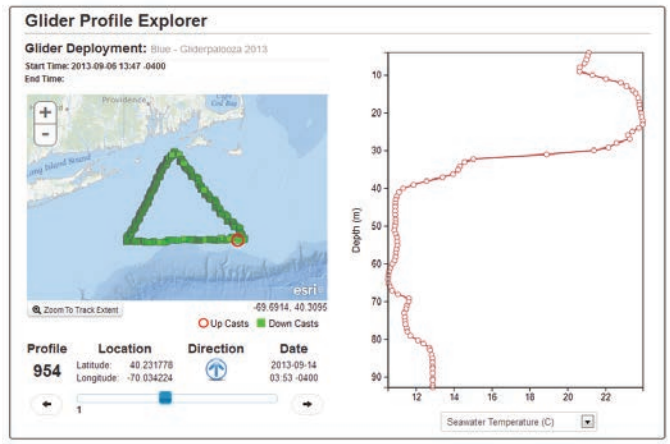

Fig. 9. Newly developed glider profile explorer tool that allows users to search and display glider profiles through the OOI EPE's website at: http://education.oceanobservatories.org/.

III. Next Steps: Gliderpalooza 2 – Modelpalooza!

The success of Gliderpalooza 2013 built on a collaborative community which was a great start, and one the team wishes to build on for the coming year. Gliderpalooza 2 will begin during the summer of 2014 but this time with a focus of using the real-time data for ocean model assimilation and validation in several models and, in turn, using model output to help drive sampling locations throughout the east coast, not just the mid-Atlantic bight. At least seven ocean models are going to be used for this effort (table 2). A new glider tool that will support comparison of the glider profiles to any of these ocean models is shown in figure 10.

The list of groups involved with glider deployments and models is expected to expand to include Memorial University of Newfoundland, Dalhousie University (Ocean Tracking Network), University of Maine, Woods Hole Oceanographic Institute, University of Massachusetts Dartmouth, Stevens Institute of Technology, Rutgers University, University of Delaware, University of Maryland, College of William and Mary, North Carolina State University, University of Georgia, Texas A&M University, the US Navy and the Bermuda Institute of Ocean Sciences.

TABLE II. MODELS TO BE USED FOR ASSIMILATION AND VALIDATION TESTING DURING GLIDERPALOOZA 2: MODELPALOOZA.

	Models	Affiliation
1	Regional Ocean Modeling System 1 (ROMS)	North Carolina State University
2	ROMS Experimental System for Predicting Shelf and Slope Optics (ROMS HOPS)	Rutgers University
3	Harvard Ocean Prediction System (HOPS)	University of Massachusetts Dartmouth
4	New York Harbor Ocean Prediction System (NYHOPS)	Stevens Institute of Technology
5	Real Time Ocean Forecast System (RTOFS)	NOAA National Centers for Environmental Prediction
6	MyOcean	European Union
7	Mercator Ocean	Europe (France)

In addition to the science and technical goals outlined in this paper, additional goals for Gliderpalooza 2 include; 1) Improved data flow of all gliders to the World Meteorological Organization's GTS, 2) Visualization of all data in the NOAA U.S. IOOS National Underwater Glider Network Map portal, 3) Data assimilation by four ocean models and validation testing of at least seven ocean models (hence the name Modelpalooza), 4) Using the ocean models to assist in planning glider sampling activities, 5) Building an active community blog, 5) Improving coordination between distributed teams, 6) Strengthening science working groups thereby accelerating the publishing of potential products/manuscripts/articles for the ocean science community and general public, and 7) Improving the existing web portal tools that link the community.

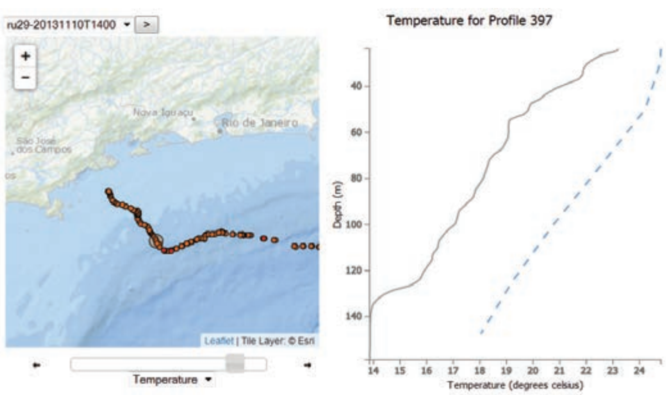

Fig. 10. Newly developed NSF OOI visualization tool that will enable researchers to compare glider profiles to model output. This example highlights a single profile from glider RU29 located just south of Rio de Janerio on the outer edge of the continental shelf (145 meters). The temperature data is compared to RTOFS and highlights that RTOFS is significantly warmer (~3C) throughout much of the water column. Development of this tool leveraged both NOAA US IOOS funds and NSF OOI funds.

ACKNOWLEDGMENTS

There were dozens of co-authors to this work from the numerous groups involved with the Gliderpalooza effort. They include J. Kerfoot, C. Haldeman, D. Aragon, A. Comeau, R. Davis, J. Pye, N. Beauchamp, K. Morton, S. Iverson, N. Fisher, M. Neary, N. Pettigrew, L. St. Laurent, J. Reilly, K. Decoteau, C. Jones, C. DeCollibus, C. Jacubiak, J. Kohut, T. Miles, T. Haskins, J. Wilkin, N. Strandskov, M. Breece, M. Oliver, D. Haulsee, G. Kuska, C. Thoroughgood, W. Boicourt, D. Gong, R. He, W. Woods, C. Edwards and the U.S. Navy Glider Team headed by C. Szczechowski

Funding for this work came from the National Oceanographic and Atmospheric Administration's U.S. Integrated Ocean Observing System (much of which came through the Mid Atlantic Regional Association Coastal Ocean Observation System Regional Association), Ocean Tracking Network, New Jersey Department of Environmental Protection, U.S. Environmental Protection Agency, U.S. Department of Environmental Protection, University of Delaware, National Aeronautics and Space Administration, U.S. Office of Naval Research, University of Maine, College of William and Mary, University of Georgia, Teledyne Webb Research Corporation, NOAA National Marine Fisheries Service, the National Science Foundation's Ocean Observatories Initiative and the U.S. Navy.

In addition to the funding agencies and partners listed here, the authors would like to thank Doug Webb for his futuristic vision, and, leading us one step at a time toward 'changing the world'.

"Have fun, work hard, change the world" – Doug Webb

REFERENCES

[1] D. Barrick, M. Evans, B. Weber, "Ocean surface currents mapped by radar," *Science* **198**, 138–44 (1977).

[2] H. Roarty *et al.*, Operation and Application of a Regional High-Frequency Radar Network in the Mid-Atlantic Bight, *Mar. Technol. Soc. J.* **44**, 133–145 (2010).

[3] D. B. Haidvogel *et al.*, Ocean forecasting in terrain-following coordinates: Formulation and skill assessment of the Regional Ocean Modeling System, *J. Comput. Phys.* **227**, 3595–3624 (2008).

[4] 20. J. L. Wilkin, E. J. Hunter, An assessment of the skill of real-time models of Mid-Atlantic Bight continental shelf circulation, *J. Geophys. Res. Ocean.* **118**, 2919–2933 (2013).

[5] W. Brown, W. Boicourt, C. Flagg, A Gangopadhyay, O. Schofield, S. Glenn, J. Kohut, "Maping the mid-Atlantic cold pool eveolution and variability with ocean gliders and numerical models," Oceans 2012 MTS/IEEE Hampton Roads Proceedings.

[6] S. Glenn, O. Schofield, T. Miles, G. Seroka, Y. Xu, H. Roarty, J. Kohut,"Ahead-of-eye Coastal ocean response and feedback on tropical cyclone activity," *Science*, in press.

Deep-Sea Research II 123 (2016) 16–29

Contents lists available at ScienceDirect

Deep-Sea Research II

journal homepage: www.elsevier.com/locate/dsr2

Glider observations of the Dotson Ice Shelf outflow

Travis Miles [a,*], Sang Hoon Lee [b], Anna Wåhlin [c], Ho Kyung Ha [b,d], Tae Wan Kim [b], Karen M. Assmann [c], Oscar Schofield [a]

[a] Department of Marine and Coastal Sciences, Rutgers University, New Brunswick, NJ 08901, USA
[b] Korea Polar Research Institute, Incheon 406-840, South Korea
[c] Department of Marine Sciences, University of Gothenburg, Gothenburg, Sweden
[d] Department of Ocean Sciences, Inha University, Incheon 402-751, South Korea

ARTICLE INFO

Available online 6 September 2015

Keywords:
Gliders
Circumpolar Deep Water
Dotson Ice Shelf
Amundsen Sea

ABSTRACT

The Amundsen Sea is one of the most productive polynyas in the Antarctic per unit area and is undergoing rapid changes including a reduction in sea ice duration, thinning ice sheets, retreat of glaciers and the potential collapse of the Thwaites Glacier in Pine Island Bay. A growing body of research has indicated that these changes are altering the water mass properties and associated biogeochemistry within the polynya. Unfortunately difficulties in accessing the remote location have greatly limited the amount of in situ data that has been collected. In this study data from a Teledyne-Webb Slocum glider was used to supplement ship-based sampling along the Dotson Ice Shelf (DIS). This autonomous underwater vehicle revealed a detailed view of a meltwater laden outflow from below the western flank of the DIS. Circumpolar Deep Water intruding onto the shelf drives glacial melt and the supply of macronutrients that, along with ample light, supports the large phytoplankton blooms in the Amundsen Sea Polynya. Less well understood is the source of micronutrients, such as iron, necessary to support this bloom to the central polynya where chlorophyll concentrations are highest. This outflow region showed decreasing optical backscatter with proximity to the bed indicating that particulate matter was sourced from the overlying glacier rather than resuspended sediment. This result suggests that particulate iron, and potentially phytoplankton primary productivity, is intrinsically linked to the magnitude and duration of sub-glacial melt from Circumpolar Deep Water intrusions onto the shelf.

1. Introduction

The collapse of the West Antarctic ice sheet appears to be irreversible (Joughin et al., 2014a; Mouginot et al., 2014; Rignot et al., 2014) due to changing winds, ocean warming, and changes in ocean circulation (Jenkins et al., 2010; Pritchard et al., 2012; Schmidtko et al., 2014). The largest changes are expressed in the Amundsen Sea, in the Southeast Pacific sector of the Antarctic. Climate changes in the Amundsen Sea, and its associated glaciers, include reductions in sea ice duration by 60 ± 9 days (Stammerjohn et al., 2012), thinning ice sheets (Rignot et al., 2014), and retreating glaciers (Rignot and Jacobs, 2002; Rignot et al., 2008, 2014). Recent studies (Joughin et al., 2014b; Sutterley et al., 2014) have indicated that the Thwaites Glacier in Pine Island Bay is losing mass at a rate of 83 ± 5 Gt yr^{-1} and has begun to undergo early-stage collapse, with the potential for causing over 1 mm yr^{-1} of global sea level rise. These changes are altering the water mass properties and associated biogeochemistry in the polynya. Unfortunately, difficulties in accessing the remote location have greatly limited the amount of *in situ* data that has been collected, which limits our understanding of the physical mechanisms that regulate the biological processes in this area (Lee et al., 2012).

The Amundsen Sea Polynya (ASP) has one of the highest satellite derived mean phytoplankton concentrations in the Antarctic with seasonally averaged chlorophyll concentrations (2.18 ± 3.01 mg m^{-3}) larger than the more frequently studied Ross Sea Polynya (1.51 ± 1.52 mg m^{-3}) (Arrigo and van Dijken, 2003). With high levels of unused macronutrients year-round, the availability of iron (Fe) or light, or both, is thought to limit primary productivity in the coastal Antarctic (Sunda and Huntsman, 1997; Boyd, 2002; Arrigo et al., 2012). Strong relationships exist between phytoplankton and the depth of the upper mixed layer suggesting the importance of light (Schofield et al., in press) while deck board incubations also confirm the importance of Fe (Alderkamp et al., 2015). Previous studies have observed high levels of dissolved (Alderkamp et al., 2012; Arrigo et al., 2012; Gerringa et al., 2012) and particulate (Planquette et al., 2013) Fe in proximity to the Pine Island Ice Shelf (PIIS) and the Crosson, Dotson, and Getz ice shelves

* Correspondence to: Department of Marine and Coastal Sciences, Rutgers University, Center for Ocean Observing Leadership ,71 Dudley Rd. New Brunswick, NJ. Tel.: 848 932 3293.
E-mail address: tnmiles@marine.rutgers.edu (T. Miles).

http://dx.doi.org/10.1016/j.dsr2.2015.08.008
0967-0645/© 2015 The Authors. Published by Elsevier Ltd. This is an open access article under the CC BY-NC-ND license (http://creativecommons.org/licenses/by-nc-nd/4.0/).

to the west. Likely sources of this Fe include basal melt from beneath ice shelves (Gerringa et al., 2012; Yager et al., 2012), and direct observations have been made of dissolved and particulate Fe in the meltwater-laden outflow from beneath the Dotson Ice Shelf (DIS) (Alderkamp et al., 2015).

The main driver of basal melt is believed to be the warm Circumpolar Deep Water (CDW) (up to 4 °C above the freezing point) intruding onto the Amundsen Sea continental shelf and below ice shelves (Jenkins et al., 2010; Jacobs et al., 2011; Dutrieux et al., 2014). Processes controlling the flow of warm CDW on the shelf are only broadly identified and there is a lack of sufficiently long (decadal or more) time series to enable linking of the oceanographic processes to climate variability. These processes include the establishment of an eastward undercurrent (Chavanne et al., 2010; Walker et al., 2013); bottom Ekman transport (Wåhlin et al., 2012); eddies (Thompson et al., 2014) and wind (Thoma et al., 2008). The cross shelf-break inflow to the DIS occurs through the same outer trough that channels CDW toward the Getz Ice Shelf, also known as the Dotson Trough. Closer to the ice shelves the trough branches out into three deep basins, leading into the sub-ice cavities below the Dotson and Getz ice shelves (Fig. 1). Observations of the circulation in these troughs (Walker et al., 2007; Wåhlin et al., 2010) show that CDW inflows are located on their eastern flanks and mooring data indicate the circulation patterns are persistent and steady (Arneborg et al., 2012; Assmann et al., 2013; Wåhlin et al., 2013). The outflows on their western flanks are colder and fresher due to the addition of meltwater (Ha et al., 2014; Wåhlin et al., 2015). As these water masses reach the glaciers and ice shelves the warm CDW melts ice and forms a modified CDW (mCDW) and meltwater mixture (Jenkins, 1999; Jenkins and Jacobs, 2008; Jenkins et al., 2010; Wåhlin et al., 2010; Jacobs et al., 2011; Randall-Goodwin et al., 2015). Few observations of the ocean circulation and water properties at ice shelf fronts exist. The paucity of data in this region is largely due to the remote location of the Amundsen Sea as well as limited resources to investigate the ~1200 km of coastline. A summary of three US-led cruises to the ice shelf fronts in the Amundsen Sea Embankment (ASE) can be found in Jacobs et al. (2013). A large number of these transects show a core of CDW leaning on the eastern flank of the entrance to the ice shelf cavity, i.e. associated with geostrophic flow into the cavity, and cooler, fresher, and more buoyant, water is commonly found on the western side higher up in the water column, associated with a geostrophic flow out of the cavity. Focused field campaigns (Jacobs et al., 1996, 2011) have observed this phenomenon along the Pine Island Glacier in 1994 and 2009.

The first observation of an outflow of meltwater-laden mCDW in the central Amundsen shelf area was done in 4 moorings placed in the Dotson Trough (Ha et al., 2014), where a steady outflow on the eastern flank of Dotson Trough was observed throughout 2011. Similar hydrographic properties at a nearby location were also recorded during 2012–2013 (Wåhlin et al., 2015). Due to challenging ice conditions cross-trough CTD transects extending sufficiently far west to cover the entire outflow do not exist, The estimates of volume flux derived from the single-point moorings are hence uncertain. Based on the most complete CTD transect, an outflow corresponding to about 1/3 of the inflow was obtained (Ha et al., 2014). It is not known which path the remainder of the outflow takes. Explanations that have been proposed include flow in a narrow coastal current; below a possible tunnel underneath the Getz Ice Shelf; or into the surface mixed layer (Ha et al., 2014). More recent work shows a similar circulation pattern, with outflow along the far western edge of the DIS with high meltwater concentrations (Randall-Goodwin et al., 2015). In this work we present observations from the front of the DIS collected by ship and a Teledyne-Webb Slocum glider. The glider permitted high vertical and horizontal resolution sampling in a relatively short time frame (days). The physical and bio-optical datasets collected provide a detailed snapshot of the location and water properties of the DIS outflow with optical backscatter profiles indicating ice melt as the primary source of particulate matter from the subglacial cavity to the near-surface ASP.

2. Methods

Data was collected in the Amundsen Sea during January of 2014 as part of the Korea Polar Research Institute (KOPRI) ANA04B cruise onboard the IBRV *Araon*. This cruise was designed with the goal of understanding regional circulation and how that circulation may impact the biogeochemistry of the ASP. A total of 35 hydrographic stations were sampled and two Teledyne-Webb Slocum gliders (one shallow class (< 100 m) and one deep class (< 1000 m)) were deployed and recovered during ANA04B. As this paper is focused on the transport of mCDW, only the glider capable of profiling to 1000 m was able to provide relevant data and was used in this paper.

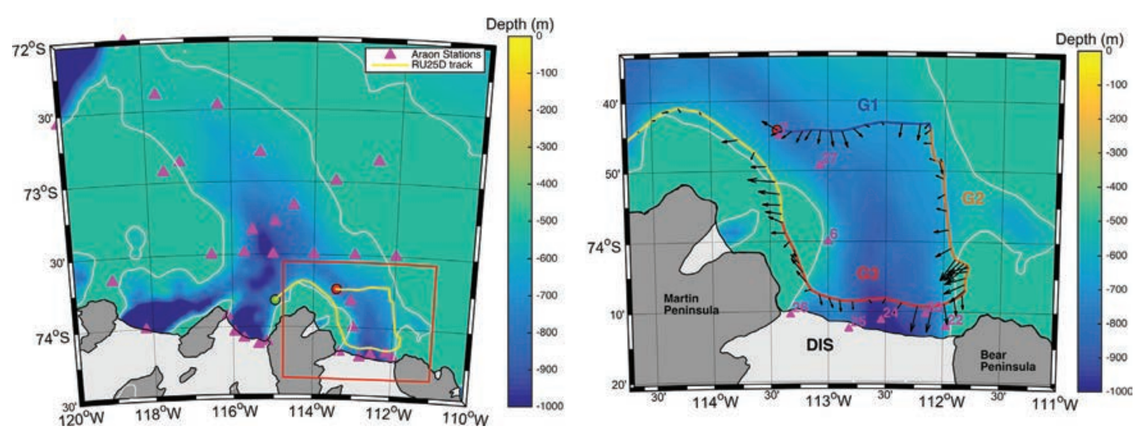

Fig. 1. (Left panel) Map of the KOPRI cruise ANA04B study area in the Amundsen Sea with hydrographic stations sampled by the IBRV Araon (magenta triangles) and the track of the glider RU25D (yellow line) with the deployment location (red circle) and the recovery location (green circle). The red box bounds the displayed area in the right panel. (Right panel) zoomed in view of the glider and ship sampling area directly in front of the Dotson Ice Shelf with the glider track separated into three distinct tracks including across trough (blue G1), along the eastern flank (orange G2), and along the Dotson Ice Shelf Face (red G3). Ship sampling locations are numbered and continue to be represented by magenta triangles. There are additional ship-based stations that were collected off the continental shelf not included in this map. Black vectors represent the depth- and time- averaged glider velocities.

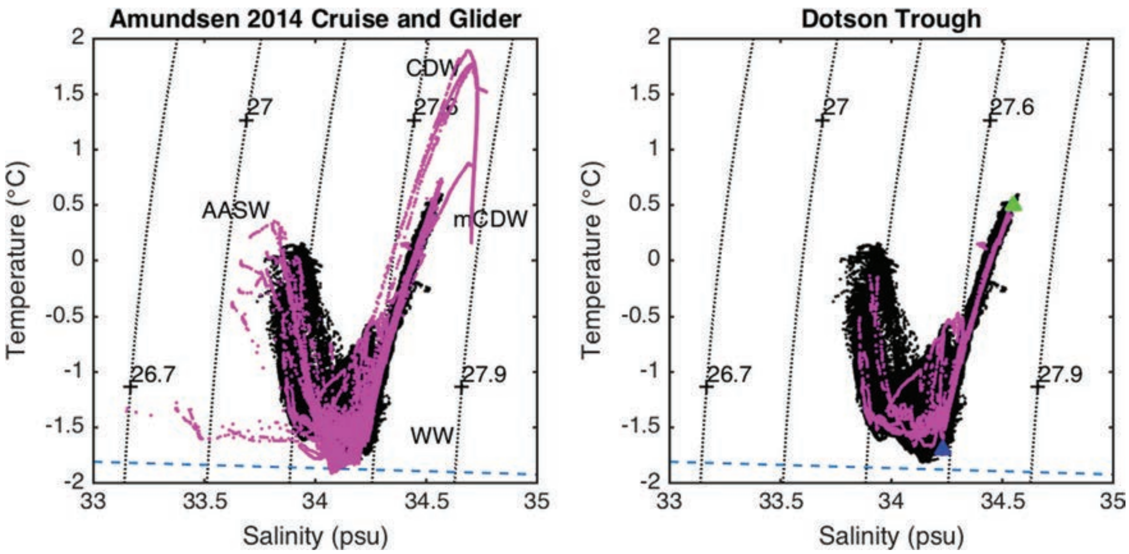

Fig. 2. (Left panel) A temperature and salinity diagram of all data collected by the IBRV Araon (magenta) and glider RU25D (black), with labels of the major water masses. (Right panel) A subset of the data collected directly in front of the Dotson Ice Shelf, corresponding to locations shown in the right panel of Fig. 1. Green and blue triangles represent the mCDW and WW end-members used for calculating meltwater fractions.

2.1. Ship sampling

Ship-based measurements were made from a rosette that included Niskin bottles for discrete water sampling, a Seabird SBE-911plus with dual conductivity temperature and depth (CTD) sensors, and velocity structure from a 300-kHz Teledyne-RDI lowered acoustic Doppler current profiler (LADCP). During upcast of the CTD, discrete water samples were collected and used to calibrate the temperature and conductivity probes following standard practices. The LADCP data was processed using Lamont Doherty Earth Observatory (LDEO) Matlab®-based software version IX (Thurnherr, 2010). Tidal signals were removed from the LADCP-measured velocity profiles using a 10-component barotropic tide model, CATS2008b (Padman et al., 2002).

2.2. Glider sampling

Teledyne-Webb Slocum gliders are buoyancy driven mobile sensor platforms with interchangeable and customizable science bays (Webb et al., 2001; Davis et al., 2003; Schofield et al., 2007). These 1.5 m torpedo shaped autonomous underwater vehicles profile the water column in a sawtooth pattern by shifting small amounts of ballast to dive and climb at $\sim$15–20 cm s^{-1}. Wings, vehicle shape, and the set nominal pitch angle of $\sim$26° result in horizontal speeds of $\sim$20–30 cm s^{-1}, or $\sim$20 km per day depending on ambient current conditions. Vehicle navigation is done using "dead-reckoning" to a set waypoint. When the glider surfaces an air-bladder in the aft section inflates, raising the tail section out of the water. An iridium satellite phone antenna within the tail section transmits data to shore and receives new mission characteristics depending on the sampling strategies designed by the operator. Oceanographic data is collected at two-second intervals resulting in high vertical resolutions. Gliders have been used in numerous difficult to sample environments including on continental shelves (Castelao et al., 2010; Adams et al., 2013; Pelland et al., 2013), long duration cross-basin missions (Glenn et al., 2011), within storms (Glenn et al., 2008; Miles et al., 2013; Mrvaljevic et al., 2013), and have had a significant presence in the Western Antarctic (Kahl et al., 2010; Schofield et al., 2013; Kohut et al., 2015).

The glider used in this study was a Deep glider (RU25D) rated to 1000 meters, near the maximum depth of the approach to the Dotson Trough. The glider was deployed on January 4th, 2014 at 113.4°W (Fig. 1) and 73.74°S and performed three distinct sections, with the first over 40 km west to east across the Dotson Trough at 74°S, the second was 46 km southward toward the DIS on the eastern flank of the Dotson Trough. The third transect was 54 km across the face of the DIS from east to west and was approximately 5 km from the ice edge and continued westward around the Martin Peninsula and toward the Getz Ice Shelf until recovery on January 13th. Throughout this deployment RU25D collected a total of 206 profiles and traveled 234 km in 9 days.

RU25D was equipped with a suite of oceanographic sensors including an un-pumped Seabird glider payload CTD (GPCTD), an Aanderaa Oxygen Optode (Model 3835), and a Wetlabs Environmental Characterization Optics puck (ECO-triplet). Glider temperature and conductivity measurements were compared with shipboard CTD casts on deployment and recovery to ensure data quality, as well as with a calibrated laboratory CTD prior to deployment. All measurements were binned into 2-m bins per segment (a segment is a collection of profiles between surfacing and acquisition by GPS) and assigned a mid-point latitude and longitude.

2.2.1. Oxygen measurements

The Aanderaa Oxygen Optode measures raw phase shifts across a calibrated foil. This instrument, in combination with temperature measurements from the CTD, provides the concentration and saturation percent of dissolved oxygen (DO). The manufacturer calibration and a two-point test (0% and 100% saturation) were performed in the laboratory prior to deployment (Kohut et al., 2014). During post-processing DO data was time shifted backward to account for a 25 s response rate of the foil.

2.2.2. Optical measurements

The Wetlabs ECO-triplet collected chlorophyll-a fluorescence, colored dissolved organic matter (CDOM), and the volume scattering function (VSF) of optical backscatter at a wavelength of 700 nm in the 117° back direction. The VSF measurements are then

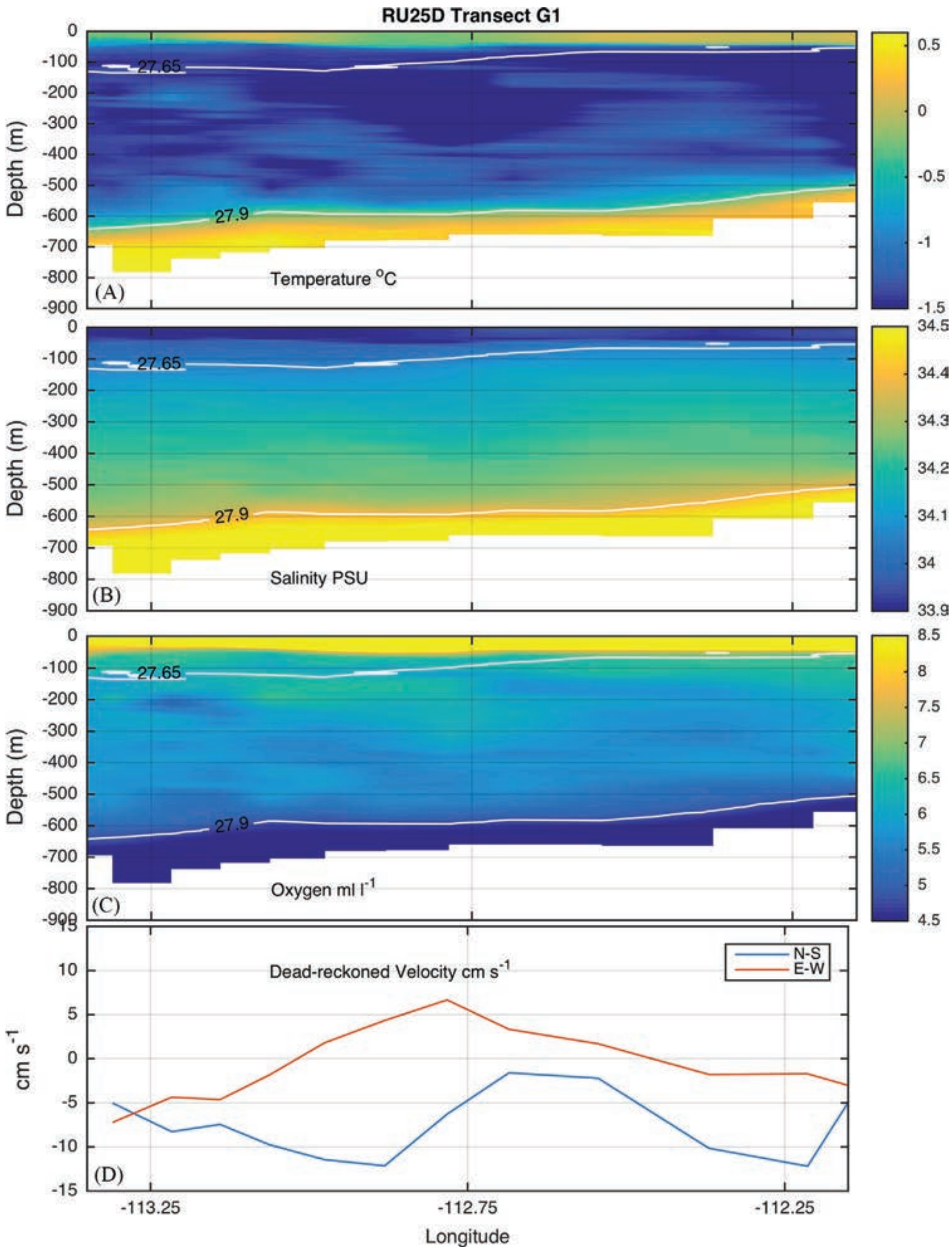

Fig. 3. Cross-sections of (A) temperature, (B) salinity, (C) oxygen, and depth averaged dead-reckoned glider currents along glider transect G1 with longitude along the *x*-axis. White contours are neutral densities of 27.65 and 27.9 (kg m^{-3}).

converted to backscatter coefficients following Boss and Pegau, (2001) with resultant units of m^{-1}. Optical backscatter responds linearly to suspended particle concentration, but is sensitive to particle size, shape, color, and composition (Boss and Pegau, 2001). Thus we used these values as a proxy for the relative changes in suspended particle concentration rather than absolute concentration.

2.2.3. Glider velocity calculations

Water velocities were calculated from the glider data using a dead-reckoning technique (Davis et al., 2003). Glider vertical speeds are derived from the pressure sensor and used in combination with a measured pitch angle to estimate the glider horizontal motion. The initial glider waypoint pre-dive and time integrated estimated horizontal speeds were used to estimate the gliders surfacing position. The difference between the expected and actual surfacing location divided by the total dive time results in a total depth and time-averaged velocity that we assign to the mid-point of the each pre- and post-dive latitude and longitude. RU25D did not surface frequently enough to resolve tidal currents, but as evidenced by the CATS2008b barotropic tidal model (Padman et al., 2002) the dominant M2 and S2 tidal currents were relatively small (<2 cm s^{-1}) for the duration of the deployment. Potential sources of error in dead-reckoned glider depth and time-averaged velocities have been discussed in detail previously (Todd et al., 2011) and include uncertainties in angle-of-attack, vertical water velocities, and accumulated errors from integrated measured heading, pitch, and glider vertical velocities. For RU25D heading dependent compass corrections were applied based on pre-deployment calibrations removing a major source of error. Uncertainties from other sources listed above have been found to be typically on the order of 1 cm s^{-1}.

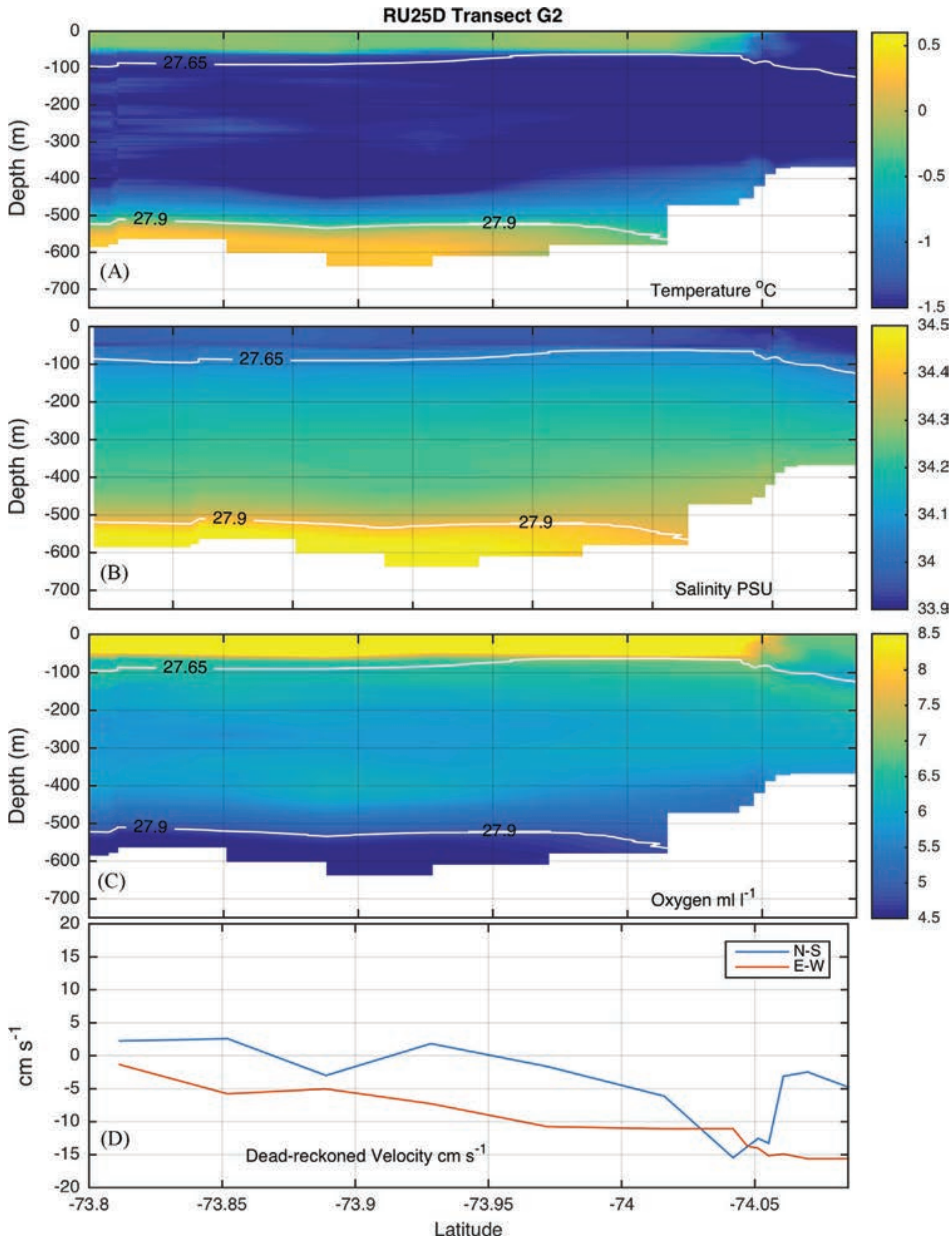

Fig. 4. Cross-sections of (A) temperature, (B) salinity, (C) oxygen, and depth averaged dead-reckoned glider currents along glider transect G2 with latitude along the *x*-axis. White contours are neutral densities of 27.65 and 27.9 (kg m^{-3}).

2.3. Meltwater concentrations

Meltwater fraction calculations are performed following Jenkins (1999) and Jenkins and Jacobs (2008). This method assumes that the ice-seawater system is closed and that in its simplest form, with only two uniform end-members including a single water mass and ice, the meltwater concentration of a single tracer can be represented as:

$$\frac{Q_i}{Q}=\frac{\chi_w-\chi}{\chi_w-\chi_i} \tag{1}$$

where Q_i is the mass of ice, Q is the total mass represented by $Q=Q_i+Q_w$, Q_w is the mass of seawater, χ is the measured tracer property, and χ_i and χ_w are the tracer properties of the ice and seawater, respectively. Mixtures of meltwater and seawater will have two conservative properties that plot as a straight line on a bivariate graph and the concentration of meltwater can be determined from where measurements fall on that mixing line. Temperature and salinity are two typical tracers used in this method (Gade, 1979). For our case, and many other realistic cases, there is a third water mass involved, namely Winter Water (WW) that mixes with the CDW-meltwater mixture and further complicates the analysis. In order to address this, a composite tracer approach (McDougall, 1990; Jenkins and Jacobs, 2008) has been developed, where $\psi^{2,1}$ is the composite of two tracers represented by

$$\psi^{2,1}=\left(\chi^2-\chi^2_{CDW}\right)-\left(\chi^1-\chi^1_{CDW}\right)\left(\frac{\chi^2_{WW}-\chi^2_{CDW}}{\chi^1_{WW}-\chi^1_{CDW}}\right), \tag{2}$$

which is the difference between the measured value of an additional tracer, such as oxygen, and the idealized two component mixture mentioned above. The resultant meltwater fraction is then the ratio of the mixture composite tracer $\psi^{2,1}_{mix}$, to the meltwater $\psi^{2,1}_{melt}$. The method is described in more detail in Jenkins (1999) and Jenkins and Jacobs (2008).

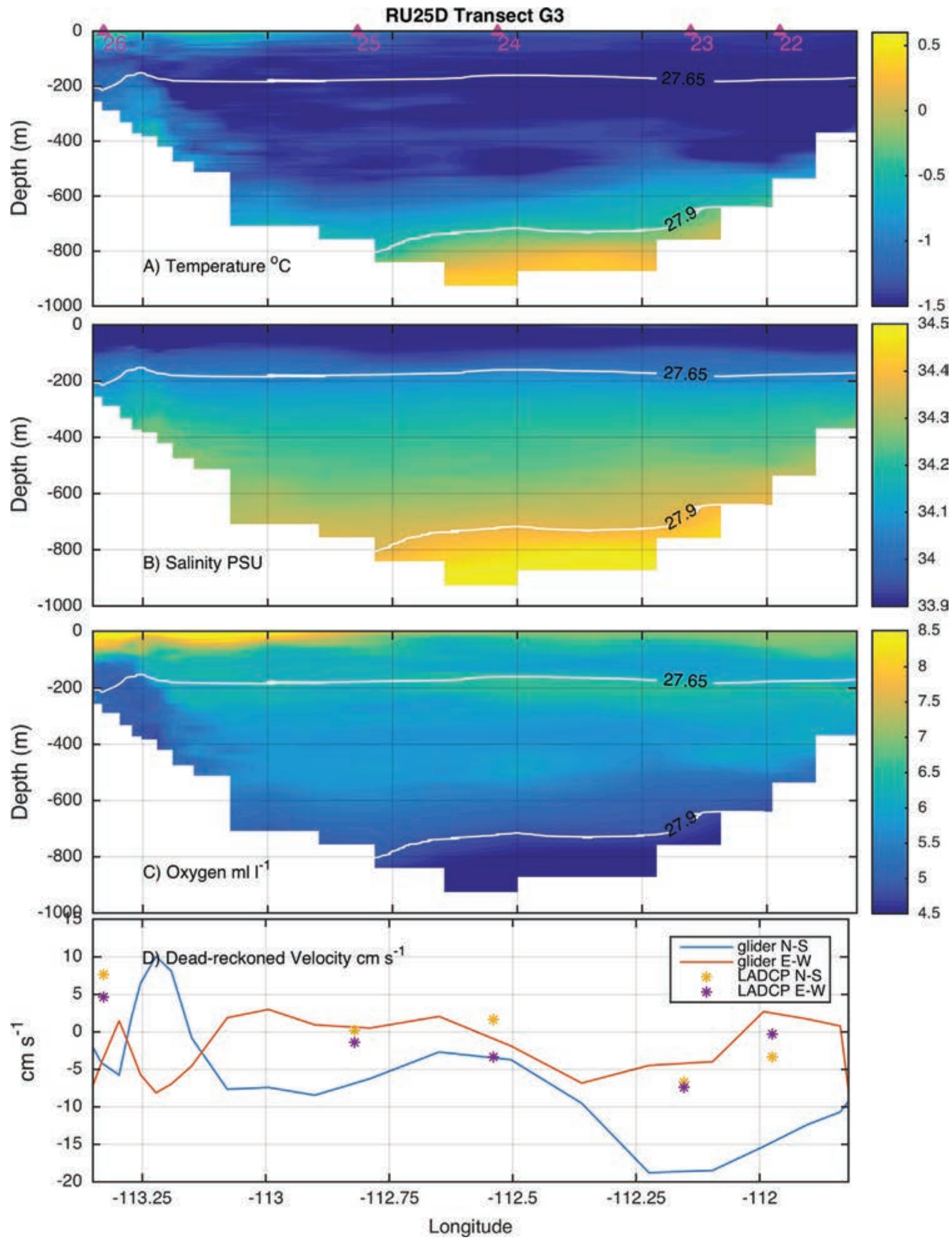

Fig. 5. Cross-sections of (A) temperature, (B) salinity, (C) oxygen, and (D) depth averaged dead-reckoned glider currents (lines) and depth averaged LADCP currents (stars) along glider transect G3 with longitude along the *x*-axis. Ship sampling locations are plotted along the top of Fig. 5A (magenta triangles) with numbers corresponding to the right panel of Fig. 1. White contours are neutral densities of 27.65 and 27.9 (kg m^{-3}).

The tracers used here are salinity, potential temperature, and dissolved oxygen. Outside of the surface layers where atmospheric properties influence these tracers there are distinct end members for WW, CDW, and glacial ice in the Amundsen Sea (Jenkins and Jacobs, 2008). Based on the ambient water masses observed on the Amundsen Sea continental shelf in 2014 we use an mCDW end-member derived from the maximum temperature and salinity measured by the glider in the Dotson Trough and its associated oxygen concentration with $T\sim0.5$ °C, $S\sim34.55$ PSU, and $O_2\sim4.2$ ml l^{-1}; WW derived from the minimum temperature on the shelf with properties ~-1.7 °C, $S\sim34.23$ PSU, and $O_2\sim6.15$ ml l^{-1} (Fig. 2b); and theoretical ice properties $T\sim-90.75$ °C, $S\sim0$ PSU, and $O_2\sim28.46$ ml l^{-1}. These ice values are derived from past studies in the Amundsen Sea (Hellmer et al., 1998; Jenkins, 1999; Jenkins and Jacobs, 2008), with temperature values representative of losses in the phase change from ice to liquid water. Oxygen values within the ice are drawn from oxygen concentrations within air pockets in the ice, which are forced entirely into solution when ice melts at the pressures beneath the ice sheet. Meltfractions are reported as the mean of the three independent meltfraction T–S, O_2–S, and O_2–T pairs. Standard deviations were calculated across all three pairs for each measured bin and values greater than one quarter of the theoretical upper bound of expected meltwater fractions were flagged and not included in the analysis. This occurred primarily in the upper mixed-layer where the calculations are unreliable due to the influence of air–sea exchanges on water properties.

In addition to calculating meltfractions using the above method, we also use the Gade line (Gade, 1979), a line of constant mixing between the ice and ocean water, to visualize meltwater in

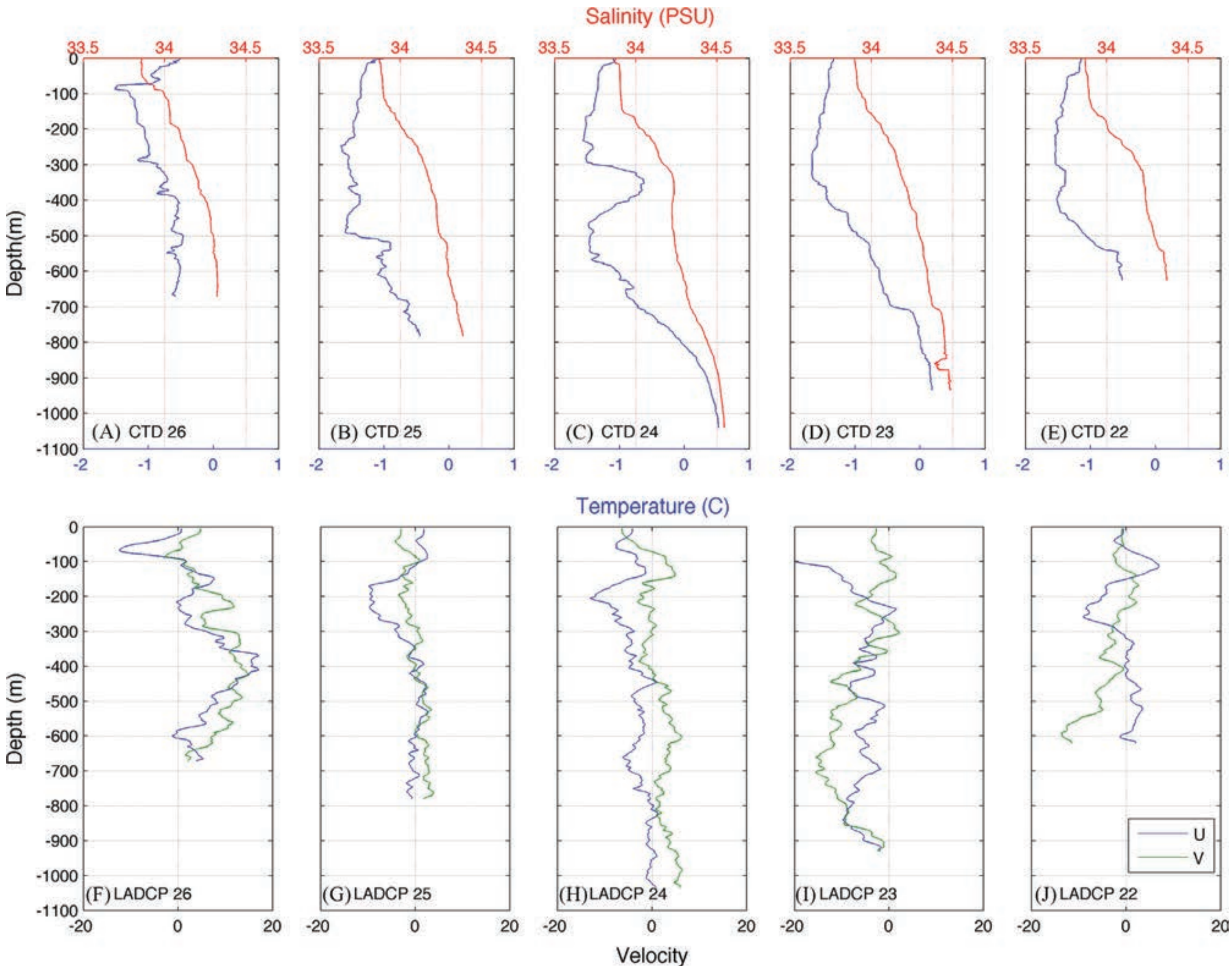

Fig. 6. Profiles of (A)–(E) IBRV *Araon* temperature (blue) and salinity (red) and (F)–(J) LADCP east-west (blue U) and north-south (green V) velocity at the locations indicated in Figs. 5A and 1B.

T–S space. The Gade line is represented by the equation:

$$T_p(S_p) = T_{ocean} + \frac{L_F}{C_p}\left(1 - \frac{S_{ocean}}{S_p}\right) \tag{3}$$

where T_{ocean} and S_{ocean} are the ocean end-members prior to melting, in this case mCDW end-members listed above. L_F is the latent heat of fusion for ice (334 kJ kg^{-1}); and C_P is the specific heat of water (3.97 kJ kg^{-1}) at salinity of 34.7 PSU, temperature of 1 °C, and pressure of 400 dbar.

3. Results

In January 2014 the Amundsen Sea continental shelf had three major water masses present (Fig. 2); i.e. Antarctic Surface Water (AASW) ($T > 0$ °C, $S < 34$ PSU), Winter Water (WW) ($T \sim -1.8$ °C, $S \sim 34.2$ PSU), and mCDW ($T \sim 0.5$ °C, $S \sim 34.55$ PSU). Pure CDW ($T > 1.5$ °C, $S > 34.5$ PSU) was observed in ship-borne CTD profiles off the shelf, and was not present in the Dotson Trough.

RU25 traveled across the Dotson Trough from east to west (transect G1) on January 4th 2014 (Fig. 1B). Along this transect warm (0.5 °C), salty (34.5 PSU) mCDW was observed leaning on the eastern flank of the trough (Fig. 3) consistent with along-isobath southward flow observed in previous studies (e.g. Wåhlin et al., 2010; Ha et al., 2014). Oxygen concentrations in the warm layer were below 5 ml l^{-1}, with minimum values of 4.2 ml l^{-1} near 800 m. dead-reckoned depth and time-averaged velocities are shown in Fig. 3D, with primarily southward velocities exceeding 5 cm s^{-1} for the majority of the transect, with minimum values near 0 cm s^{-1} at 112.75 °W. The velocity minimum in the center of the transect coincides with a region where the glider track runs parallel to curving bathymetry between 112.8 and 112.4 °W (Fig. 1B), so the current likely continued along-isobath although the direction changed.

RU25D was turned southward on January 6th, 2014 and traveled along the 600 m isobath toward the DIS (transect G2), along the ridge separating the Dotson from the Crosson basin. Temperature, salinity, and oxygen (Fig. 4) in the near bottom mCDW layer was uniformly distributed near bottom from north to south between between 73.8 and 74°S indicating limited interaction and mixing with overlying WW on the eastern side of the Dotson Trough. There was a persistent westward velocity increasing with proximity to DIS up to 10 cm s^{-1}, consistent with a coastal current that flowed along the DIS (Figs. 1B and 4D). RU25D was briefly piloted nearshore into shallower waters of ~400 m depth, just offshore of the Bear Peninsula. The velocity there showed a stronger westward current component, and the hydrography a significantly cooler (< -1.5 °C), fresher (< 33.9 PSU), and less oxygen rich (< 7 ml l^{-1}) surface water. No mCDW was present near the bottom in this region (Fig. 4), indicating that the mCDW remained at depth and continued along-isobath deeper than 400 meters.

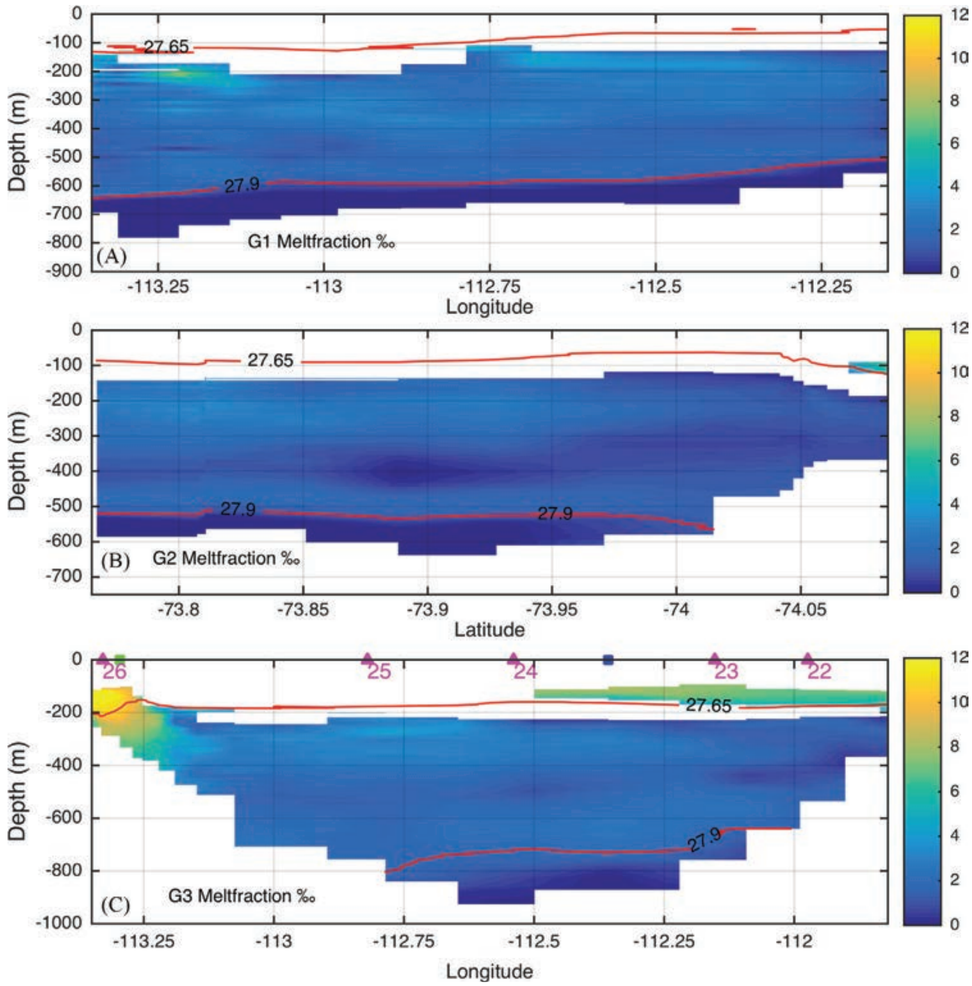

Fig. 7. Meltwater fraction cross-sections corresponding to 7A) transect G1, 7B) transect G2, and 7C) transect G3. Ship sampling locations are plotted along the top of 7C (magenta triangles) with numbers corresponding to the Fig. 1B and profiles in Fig. 6. Surface values where the three tracer pair meltwater fractions exceeded two standard deviations were removed as they are likely not valid due to atmospheric input. Red contours are neutral densities of 27.65 and 27.9 (kg m^{-3}).

3.1. *Dotson Ice Shelf inflow*

On January 8th, 2014 RU25D performed a cross-trough transect near the ice shelf front, G3 (Figs. 1B and 5), toward the west from the edge of the Bear Peninsula to within 8 km of the Martin Peninsula. The glider remained within 6 km of the DIS until ice conditions to the west forced RU25D to be piloted toward the northwest. Additionally, five CTD and LADCP stations (22 through 26) were performed by the IBRV *Araon* along the DIS within a few kilometers south of the glider track (Figs. 1B and 6). In similarity with the cross-trough glider section further north, the mCDW layer is spread on the eastern flank of the trough (Fig. 5). The shipboard profiles (Fig. 6) at stations 22 through 25 show similar characteristics as glider profiles with the warmest (> 0.5 °C) and saltiest waters at station 24 (> 34.55 PSU). However many of the fine-scale features are naturally lacking in the CTD transect, in particular the pronounced cold and fresh core seen at the bottom to the east of station 26. Oxygen concentrations in the central trough were less than 4.5 ml l^{-1} consistent with upstream values of mCDW along transects of G1 and G2. The 27.9 kg m^{-3} contour in all three transects (Figs. 3A, 4A, and 5A) shows that the near bottom layer is consistent throughout the trough and suggests that there was limited mixing of the core mCDW near the bottom with overlying WW prior to entering into the ice shelf cavity. A strong (up tp 20 cm/s) southward flow toward the ice shelf cavity can be seen over the eastern part of the transect (Fig. 5D) where weaker currents (near 5 cm s^{-1}) were present in the central portion of the trough. Ship-borne LADCP profiles at stations 22 and 23 show de-tided southward velocities below 200 m depth to the bottom with maximum values over 15 cm s^{-1} at 600 m in station 22 and at 700 m depth in station 23 (Fig. 6). At station 24 near the bottom within the mCDW layer velocities were near ~5 cm s^{-1} northward. Depth averaged LADCP velocities on the eastern flank of the Dotson Trough showed weaker (~7 cm s^{-1}) southward flow than glider measurements near the same location (Fig. 5D). If shipboard data is considered on its own, this would suggest that the waters flowing toward and beneath the DIS were limited to the slightly weaker mCDW signature at stations 22 and 23, though based on glider dead-reckoned currents and hydrographic observations there is still significant southward flow between stations 23 and 24 where mCDW presence remains high.

3.2. *Dotson Ice Shelf outflow*

On the western flank of the trough, west of 113.2°W there is a distinct water mass with elevated temperature and salinity and reduced oxygen relative to other water masses between 100 and 500 meters depth. Temperatures within this water mass ranged from −0.5 to −1.3 °C. Salinities were between 34 and 34.25 PSU. The signal is most clearly seen in the oxygen data; with oxygen

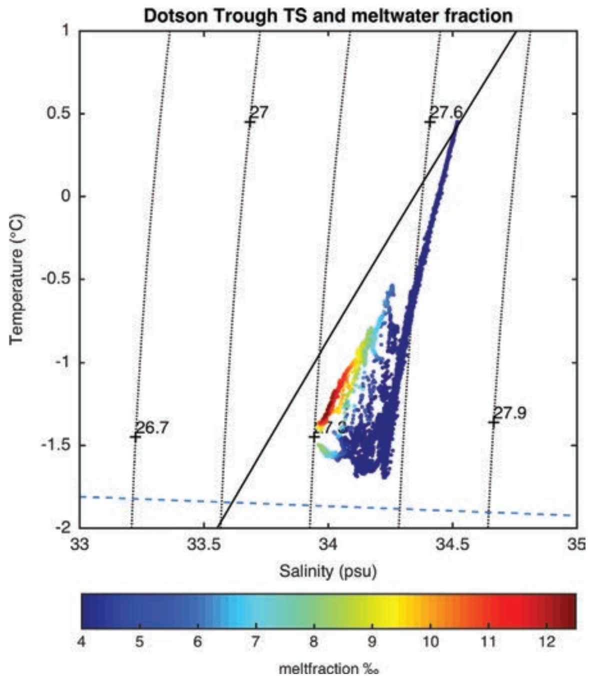

Fig. 8. Temperature and salinity diagram with meltwater fraction plotted in colors. The blue dashed line indicates the freezing point of seawater and the black solid line is the Gade Line (Gade, 1979) with end members of −0.5 °C and 34.55 PSU and for ice −90.75 °C and 0 PSU (Hellmer et al., 1998).

values between 5 and 5.5 ml l^{-1} standing in stark contrast to the oxygenated AASW and WW. Dead-reckoned glider velocities show northward flow of up to 10 cm s^{-1} coinciding with this water mass, indicating that this is a northward flowing jet focused on the steep bathymetry of the western flank of the DIS trough. While the CTD data at station 26 did not capture the main outflow clearly, the LADCP data does show northward velocities between 100 and 700 m, with peak vales of near 20 cm s^{-1} at 400 m, just below the core depth of the outflow region in the glider data. Depth-averaged LADCP velocities were northward at ~8 cm s^{-1} and compared well with glider velocities (Fig. 5D), though they were shifted westward as the glider sampled a more northerly location where bathymetry curved toward the east (Fig. 1B).

3.3. Meltwater fraction

Meltwater fractions for transects G1, G2, and G3 are all shown in Fig. 7, with the highest values of over 12 parts per thousand found on the western portion of G3. The lowest meltwater fractions are evident in the near bottom regions of G1, G2, and the inflow region of G3 between 112.75 and 112.20°W. The low values of G1, G2, and the inflow region of G3 indicate little mixing with the overlying WW along the trough. When plotted as a scatter plot in *T–S* space, along with the Gade Line (Gade, 1979), it can be seen that the meltwater falls bellow and parallel to the Gade Line with end members presented above (Fig. 8). This indicates that for the current time period WW is either further mixed with mCDW prior to inducing melt or mixed with outflowing meltwater before being sampled by the glider.

3.4. Optical properties

As mentioned above, optical backscatter serves as a proxy for suspended particle concentration in the water column. Values in the uppermost 50 m within the AASW layer on transects G1, G2, and G3 are elevated with values of consistently over 0.01 m^{-1} (Fig. 9). These surface values are highest further away from the glacial face along transect G1 and are most likely related to the high biomass associated with a large chlorophyll bloom away from the shelf. Chlorophyll values recorded by the glider were in excess of 25 mg m^{-3} along transect G1 and G2 and were much lower with proximity to the DIS in transect G3 (Fig. 10b). Winter water in all three transects has the lowest optical backscatter values, while near bottom values in the mCDW are approximately an order of magnitude greater than WW. Optical backscatter generally increases toward the bed indicating a possible sedimentary source of particles with near bottom maxima of ~0.001 m^{-1} for sections G1, G2, and the portion of G3 east of 112.8°W that is associated with the Dotson Trough inflow.

Meltfractions greater than 1 parts per thousand and optical backscatter have a linear relationship (Fig. 11A) with R^2 of 0.657, which suggests that suspended particulate matter is sourced from glacial melt water in the outflow region. Fig. 12 shows the lower 100 m of two optical and meltfraction profiles from the inflow and outflow regions. The western outflow region of G3 has near-bottom values of optical backscatter of about ~0.001 m^{-1}, nearly equal to the near-bottom values in the inflow but in contrast to the inflow region optical backscatter increases with distance from the bed, indicating an overlying particle source. There are two distinct regions where meltfractions increase and optical backscatter does not represented in blue and green in Fig. 11A. Both of these regions have neutral densities of less than 27.65 kg m^{-3} (Fig. 7). The first peak has an optical backscatter of ~0.0006 m^{-1} and meltwater fractions between 4 and 8 parts per thousand, while the second peak has an optical backscatter of ~0.00125 m^{-1} and meltfraction between 8 and 13 parts per thousand.

4. Discussion

Observations of the pathways of warm mCDW and glacial meltwater beneath ice shelf cavities are limited. Yet, the evolving circulation is critical to understanding how climate shifts will affect physical and biogeochemical processes in the highly productive polynya waters close to these cavities (Arrigo et al., 2012; Lee et al., 2012; Yager et al., 2012). Previous field campaigns have used a handful of individual ship-based profiles to identify inflow and outflow regions along Pine Island Glacier (Jenkins et al., 2010; Jacobs et al., 2011; Dutrieux et al., 2014), the DIS (Randall-Goodwin, 2012; Yager et al., 2012), and other systems (Jenkins and Jacobs, 2008). Traditional CTD transects would collect at best only a few profiles in outflow regions, and often miss them all together. For example, in the 2014 ANA04B cruise just one profile (station 26) was located on the western flank of the DIS, and it did not capture the core or the vertical and horizontal spatial extent of the main outflow.

As described by Ha et al. (2014), past studies have found the outflow on the western flank of the Dotson Trough to account for approximately 1/3 of the inflow. Using the width and height of the 27.9 kg m^{-3} neutral density contour from the bed and glider depth-averaged velocities we obtain an inflow estimate of ~0.39 Sv. This is slightly larger but on the same order of magnitudes as inflow estimates by Ha et al. (2014).

RU25 collected 15 profiles within the outflow region. At the time this outflow extended approximately 7 km from the 500 m isobaths to inshore of the 200 m isobaths. Using the glider sampled bathymetry, the 27.6 kg m^{-3} neutral density contour, the 7 km width of the outflow, and the depth and time-averaged velocities within the outflow we estimate a northward transport of ~0.06 Sv (1.9 × 10^{12} m^3 yr^{-1}). With an average metlwater fraction

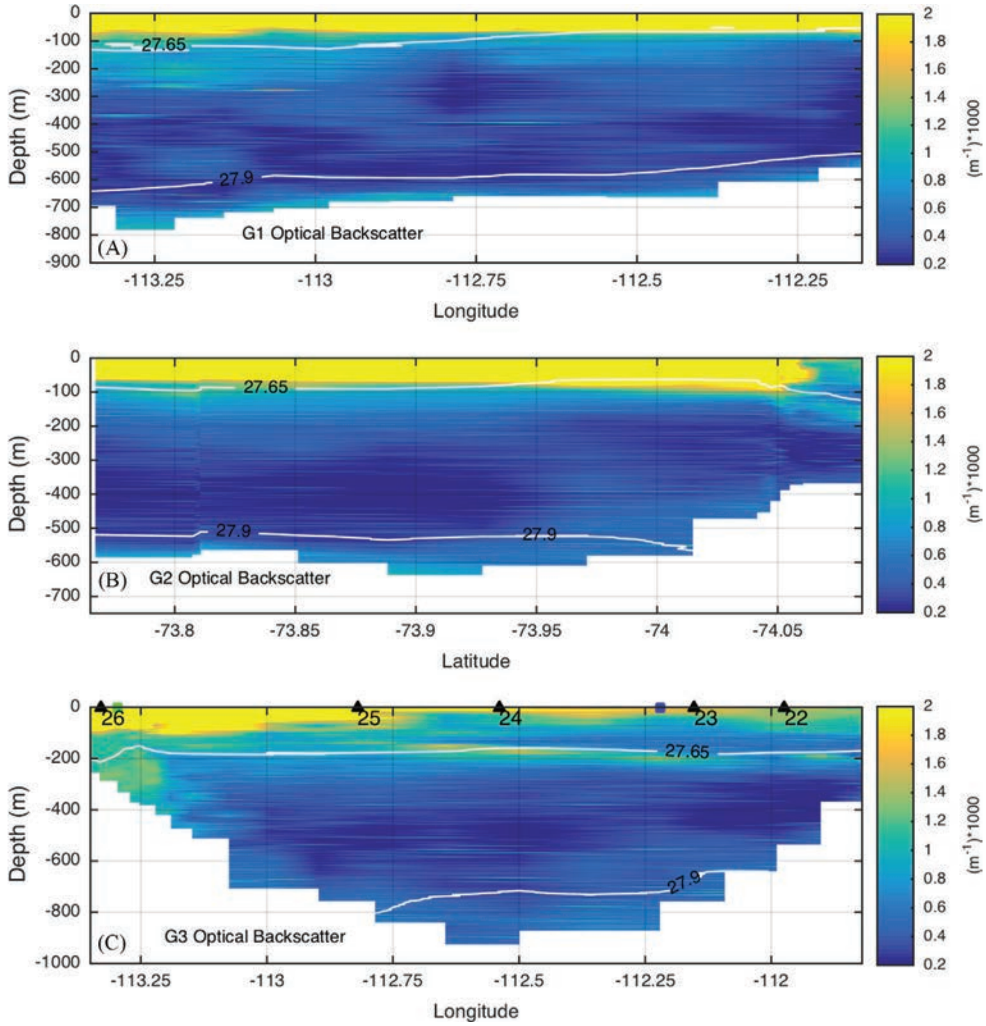

Fig. 9. Optical backscatter cross-sections corresponding to 9A) transect G1, 9B) transect G2, and 9C) transect G3. Ship sampling locations are plotted along the top of 9C (black triangles) with numbers corresponding to the right panel of Fig. 1 and profiles in Fig. 6. Blue and Green squares correspond to the glider profiles plotted in Fig. 12, with the Blue representing the inflow region and green representing the outflow region. White contours are neutral densities of 27.65 and 27.9 (kg m^{-3}).

of ~1% this equates to 1.9×10^{12} m^3 yr^{-1} of meltwater in the DIS outflow, or ~19 Gt yr^{-1}. This is less than instantaneous estimate of 81 Gt yr^{-1} from the 2011 ASPIRE cruise (Randall-Goodwin et al., 2015) and the 5-year average of 42 Gt yr^{-1} from Rignot et al. (2013), but likely reflects high seasonal and interannual variability in the region. While this value is uncertain due to the usage of glider depth and time-averaged velocities, a similar result using ship based methods would require extensive and focused LADCP profiling in this region, which is costly and not feasible due to the remote nature of the region. Furthermore, future modeling efforts will need to have resolutions that can capture the narrow width of the outflow in order to accurately represent the DIS outflow.

Among other environmental factors such as light availability, macronutrient supply, and upper mixed layer depth Fe has been identified as a necessary micronutrient to support large phytoplankton blooms in the ASP (Arrigo and van Dijken, 2003; Arrigo et al., 2008; Smith and Comiso, 2008). Recent studies have identified high levels of Fe in meltwater near the DIS (Alderkamp et al., 2015) and significant concentrations have been observed as far as 150 km from the Pine Island Glacier (Gerringa et al., 2012). Fe has been hypothesized to originate from a number of sources including basal melt of the sediment laden ice shelf or sub-glacial sediment resuspension from the bed.

While no direct observations of Fe are possible from the gliders, optical backscatter can serve as a proxy of suspended particulate matter. Not all particulate matter may contribute to Fe concentrations, but particulate Fe has been observed near the DIS and found to be important for the ASP. The glider based optical backscatter measurements increase logarithmically toward the bottom for the eastern (inflow) region. This is known as a Rousian sediment distribution and is typical of resuspended sediment on continental shelves (Grant and Madsen, 1986; Glenn and Grant, 1987; McLean, 1991; Madsen et al., 1993). In semi-log space, as in Fig. 12, Rousian profiles increase linearly toward the bed. The distribution is a result of the balance between the turbulence generated from the current shear within the bottom boundary layer that acts to keep sediment in suspension and gravitational forces, which cause sediment particles to fall out of suspension. A reduction in shear away from the bed leads to reduced turbulence and a smaller sediment concentration. Unlike the inflow region, the outflow region optical backscatter profile is non-Rousian (Fig. 12b). The fact that the optical backscatter increases with distance above the bottom in the glacial meltwater outflow indicates an external source of particles to the water column.

There are two regions where meltwater concentration increases but optical properties remain constant (Fig. 12) suggesting that some portion of the DIS is not sediment laden and contributes minimally

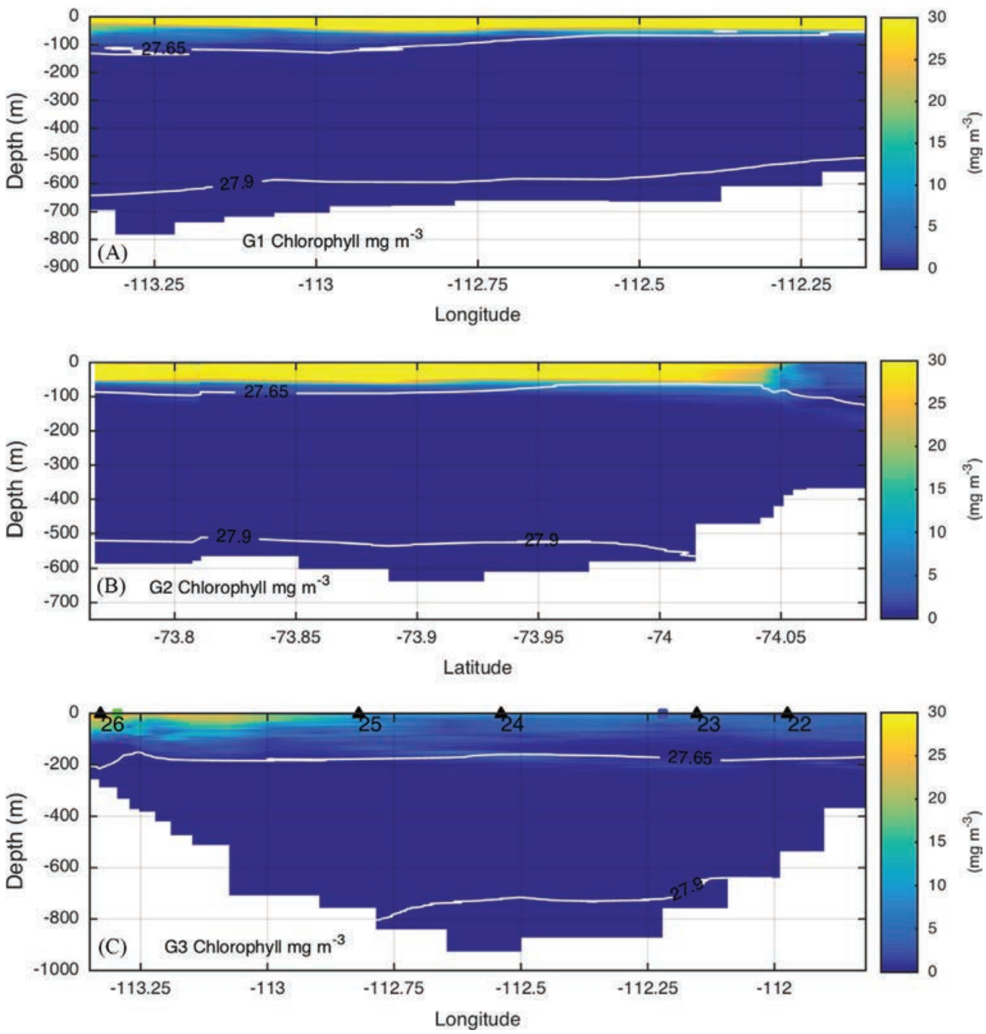

Fig. 10. Chlorophyll concentration cross-sections corresponding to 10A) transect G1, 10B) transect G2, and 10C) transect G3. Ship sampling locations are plotted along the top of 9C (black triangles) with numbers corresponding to the right panel of Fig. 1 and profiles in Fig. 6. Blue and Green squares correspond to the glider profiles plotted in Fig. 12, with the Blue representing the inflow region and green representing the outflow region. White contours are neutral densities of 27.65 and 27.9 (kg m^{-3}).

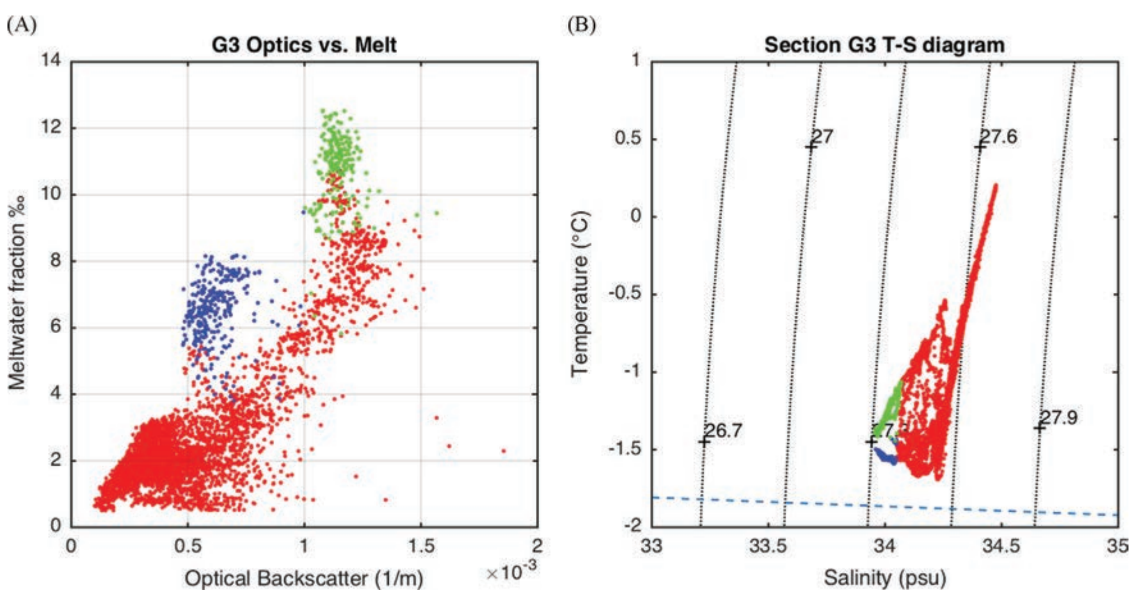

Fig. 11. (A) plot of meltwater fraction (*y*-axis) vs. optical backscatter (*x*-axis) and (B) *T–S* diagram of the data from panel A. Blue and green points represent regions where meltwater fractions increase independent of optical backscatter.

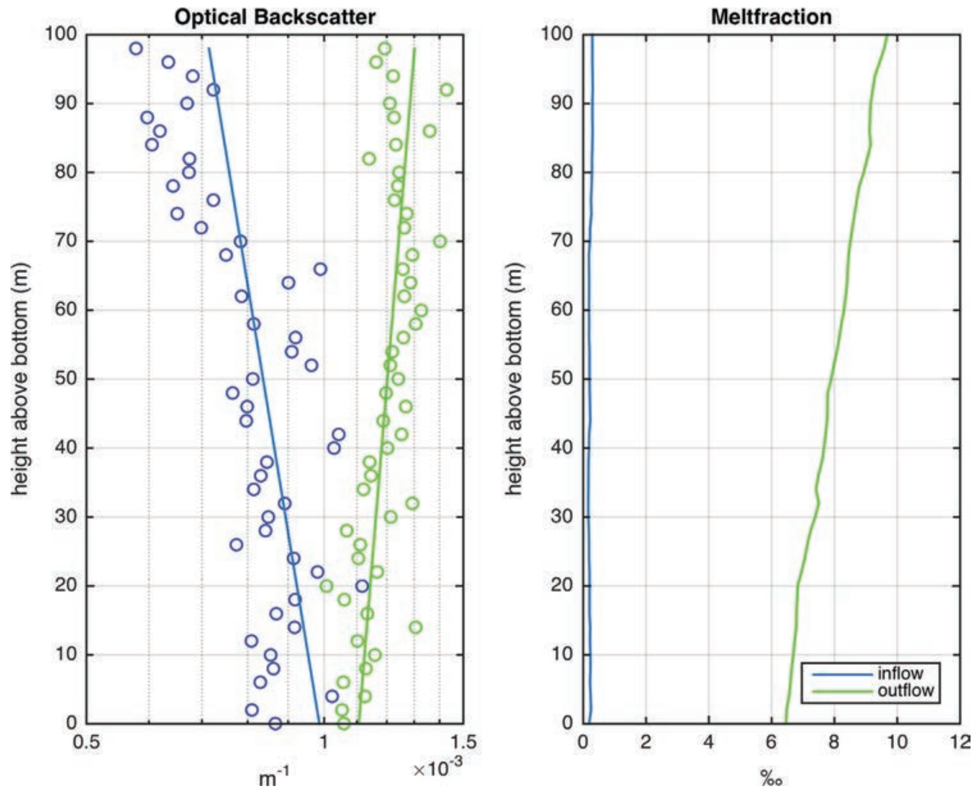

Fig. 12. (Left panel) Profiles of optical backscatter on a semi-logarithmic x scale and (right panel) meltwater fraction with the *y*-axis for both corresponding to height above bottom. Blue lines represent the inflow and green represent the outflow at locations denoted by the Blue and Green squares in Fig. 9C.

to the suspended particle concentration. In *T–S* space (Fig. 11B) the first peak (blue) with low optical backscatter is closely related to WW, indicating a region where WW reached the ice-shelf face near 150 meters depth (above the 27.65 kg m^{-3} contour in Fig. 7) on the eastern flank of the trough. Observations from the 2011 ASPIRE (Yager et al., 2012) cruise show the ice shelf draft on the eastern flank was at approximately 200 meters (Randall-Goodwin, 2012) depth, supporting this finding. The second peak (green) coincides with the region running parallel to the Gade line (Fig. 8) indicating that the same water mass that induced suspended particle laden melt also interacted with ice that made a limited particle contribution. One potential explanation for this is that buoyant meltwater rises up along the ice shelf base and induces further melt in the shallower part of the cavity close to the ice shelf edge where the ice may have lower sediment concentrations.

Aside from the two regions mentioned above, the nearly linear relationship between optical backscatter and meltwater fraction (Figs. 11 and 12b) points to glacial meltwater as the primary source of particles and the existence of a muddy ice shelf base inland of the grounding zone. This has implications for the flow speed of the grounded ice and also indicates that glaciers can serve as an important source of Fe to the water in this region. Detailed marine geological surveys and dating of the sediments (Smith et al., 2014) indicate that the ice sheet base has been sediment-laden for the last 20,000 years as it retreated across the ASE. Elevated optical and meltwater fraction signatures were also observed offshore near 113.25°W and 73.72°S in transect G1 at 200 m (Figs. 7 and 8). This is nearly 35 km north of the outflow and indicates that the particle heavy outflow waters continue northward toward the central ASP, and are not limited to the nearshore coastal zone consistent with glider observations of the phytoplankton blooms in the 2010–2011 field year (Schofield et al., in press). This is also consistent with the observations of meltwater-rich outflows near the outer shelf (Wåhlin et al., in press; Ha et al., 2014); i.e. observations that at least a third of the outflow makes it back to the outer shelf.

Past studies have indicated that the phytoplankton bloom in the ASP also has strong interannual variability (Arrigo and van Dijken, 2003). The intrusion of CDW into the Dotson Trough, while persistent (Arneborg et al., 2012) has significant interannual variability in the thickness and temperature (Assmann et al., 2013). The limited multi-year observations (Wåhlin et al., in press; Wåhlin et al., 2013; Ha et al., 2014) show a strong annual and interannual variability of CDW intrusion along the deep troughs, which presumably reflects on the circulation beneath the Dotson Ice Shelf, and subsequently to the supply of Fe to the ASP. This modulation of the Fe-supply could potentially account for variability in size and duration of the ASP summer and spring blooms.

5. Conclusions

In this study we used a Teledyne-Webb Slocum glider to obtain high spatial and temporal resolution oceanographic data along the front of DIS in the ASP. With the glider RU25D, a narrow ($\sim$7 km) outflow of glacial meltwater was identified on the western flank of the DIS, a feature nearly missed in the ship based profiles due to too large spacing between stations. The outflow was northward flowing, had high meltwater fractions, and elevated optical backscatter. The shape of the optical backscatter profiles and their high correlation with meltwater fraction indicate that particles in the outflow were primarily sourced from basal melt of the DIS, not resuspended sediments. This suggests that the DIS originates in a sediment-rich ice sheet base inland of the grounding zone, that particulate Fe previously found in the region is likely of glacial origin, and that its interannual variability could potentially be linked to the size and duration of CDW intrusions onto the shelf. In order to confirm this result future studies should target the DIS outflow, examination of the Kohler glacier base, and use a combination of ship-based profiles, moorings, and autonomous underwater vehicles to track the properties and fate of this outflow as it moves northward toward the central polynya. By leveraging glider systems to take over hydrographic survey responsibilities research vessels could be better focused on process-based studies in regions of interest and perform mooring recovery and deployment activities while increasing data density in these difficult to access, yet climate critical, regions of interest.

Acknowledgments

The authors acknowledge the Korea Polar Research Institute for its support and funding from Grant programs (PP14020 and PP15020), Teledyne-Webb graduate fellowship for graduate student funding, the Rutgers University Center for Ocean Observing Leadership for glider piloting and support, and the dedication and support of the crew and scientists of the IBRV Araon. Inha University research Grant (INHA-51416) supported Ho Kyung Ha. We would also like to thank Pierre Dutrieux for scientific codes and commentary on many of the draft figures. Additionally, we thank the two anonymous reviewers for the helpful and thoughtful comments that greatly improved this paper.

References

Adams, K.A, Barth, J.A, Chan, F., 2013. Temporal variability of near-bottom dissolved oxygen during upwelling off central Oregon. J. Geophys. Res. Ocean. 118 (10), 4839–4854. http://dx.doi.org/10.1002/jgrc.20361.
Alderkamp, A.-C., et al., 2012. Iron from melting glaciers fuels phytoplankton blooms in the Amundsen Sea (Southern Ocean): Phytoplankton characteristics and productivity. Deep Sea Res. Part II Top. Stud. Oceanogr. 71–76, 32–48. http://dx.doi.org/10.1016/j.dsr2.2012.03.005.
Alderkamp, A.-C., et al., 2015. Fe availability drives phytoplankton photosynthesis rates during spring bloom in the Amundsen Sea Polynya, Antarctica. Elem. Sci. Anthr. 3, 000043. http://dx.doi.org/10.12952/journal.elementa.000043.
Arneborg, L., Wåhlin, A.K., Björk, G., Liljebladh, B., Orsi, a H., 2012. Persistent inflow of warm water onto the central Amundsen shelf. Nat. Geosci. 5 (12), 876–880. http://dx.doi.org/10.1038/ngeo1644.
Arrigo, K.R., van Dijken, G.L., 2003. Phytoplankton dynamics within 37 Antarctic coastal polynya systems. J. Geophys. Res. 108 (C8), 3271. http://dx.doi.org/10.1029/2002JC001739.
Arrigo, K.R., van Dijken, G.L., Bushinsky, S., 2008. Primary production in the Southern Ocean, 1997–2006. J. Geophys. Res. 113 (C8), C08004. http://dx.doi.org/10.1029/2007JC004551.
Arrigo, K.R., Lowry, K.E., van Dijken, G.L., 2012. Annual changes in sea ice and phytoplankton in polynyas of the Amundsen Sea, Antarctica. Deep Sea Res. Part II Top. Stud. Oceanogr. 71–76, 5–15. http://dx.doi.org/10.1016/j.dsr2.2012.03.006.
Assmann, K.M., Jenkins, A., Shoosmith, D.R., Walker, D.P., Jacobs, S.S., Nicholls, K.W., 2013. Variability of Circumpolar Deep Water transport onto the Amundsen Sea continental shelf through a shelf break trough. J. Geophys. Res. Ocean. 118 (12), 6603–6620. http://dx.doi.org/10.1002/2013JC008871.
Boss, E., Pegau, W., 2001. Relationship of light scattering at an angle in the backward direction to the backscattering coefficient. Appl. Opt. 40 (30), 5503. http://dx.doi.org/10.1364/AO.40.005503.
Boyd, P.W., 2002. Modelling regional responses by marine pelagic ecosystems to global climate change. Geophys. Res. Lett. 29 (16), 1–4. http://dx.doi.org/10.1029/2001GL014130.
Castelao, R., Glenn, S., Schofield, O., 2010. Temperature, salinity, and density variability in the central Middle Atlantic Bight. J. Geophys. Res. 115 (C10), C10005. http://dx.doi.org/10.1029/2009JC006082.
Chavanne, C.P., Heywood, K.J., Nicholls, K.W., Fer, I., 2010. Observations of the Antarctic slope undercurrent in the Southeastern Weddell Sea. Geophys. Res. Lett. 37, 3–7. http://dx.doi.org/10.1029/2010GL043603.
Davis, R., Eriksen, C., Jones, C., 2003. Autonomous buoyancy-driven underwater gliders. In: Griffiths, G. (Ed.), Technology and Applications of Autonomous Underwater Vehicles. Taylor and Francis, p. 37.
Dutrieux, P., De Rydt, J., Jenkins, A., Holland, P.R., Ha, H.K., Lee, S.H., Steig, E.J., Ding, Q., Abrahamsen, E.P., Schröder, M., 2014. Strong sensitivity of Pine Island ice-shelf melting to climatic variability. Science 343 (6167), 174–178. http://dx.doi.org/10.1126/science.1244341.
Gade, H.G., 1979. Melting of ice in sea water: a primitive model with application to the antarctic ice shelf and icebergs. J. Phys. Oceanogr. . http://dx.doi.org/10.1175/1520-0485(1979)009 < 0189:MOIISW > 2.0.CO;2
Gerringa, L.J.A., Alderkamp, A.-C., Laan, P., Thuróczy, C.-E., De Baar, H.J.W., Mills, M. M., van Dijken, G.L., Van Haren, H., Arrigo, K.R., 2012. Iron from melting glaciers fuels the phytoplankton blooms in Amundsen Sea (Southern Ocean): Iron biogeochemistry. Deep Sea Res. Part II Top. Stud. Oceanogr. 71–76, 16–31. http://dx.doi.org/10.1016/j.dsr2.2012.03.007.
Glenn, S., Jones, C., Twardowski, M., Bowers, L., Kerfoot, J., Kohut, J., Webb, D., Schofield, O., 2008. Glider observations of sediment resuspension in a Middle Atlantic Bight fall transition storm. Limnol. Oceanogr. 53 (5 part 2), 2180–2196. http://dx.doi.org/10.4319/lo.2008.53.5_part_2.2180.
Glenn, S., et al., 2011. The trans-atlantic slocum glider expeditions: a catalyst for undergraduate participation in ocean science and technology. Mar. Technol. Soc. J. 45 (1), 52–67.
Glenn, S.M., Grant, W.D., 1987. A suspended sediment stratification correction for combined wave and current flows. J. Geophys. Res. 92 (C8), 8244. http://dx.doi.org/10.1029/JC092iC08p08244.
Grant, W.D., Madsen, O.S., 1986. The continental-shelf bottom boundary layer. Annu. Rev. Fluid Mech. 18 (1), 265–305. http://dx.doi.org/10.1146/annurev.fl.18.010186.001405.
Ha, H.K., Wåhlin, A.K., Kim, T.W., Lee, S.H., Lee, J.H., Lee, H.J., Hong, C.S., Arneborg, L., Björk, G., Kalén, O., 2014. Circulation and Modification of warm deep water on the Central Amundsen Shelf. J. Phys. Oceanogr. 44 (5), 1493–1501. http://dx.doi.org/10.1175/JPO-D-13-0240.1.
Hellmer, H., Jacobs, S., Jenkins, A., 1998. Ocean, Ice, and Atmosphere: Interactions at the Antarctic Continental Margin, Antarctic Research Series. In: Jacobs, S.S., Weiss, R.F. (Eds.), Ocean, Ice, and Atmosphere: Interactions at the Antarctic Continental Margin, Antarctic Research Series. American Geophysical Union, Washington, D. C.
Jacobs, S., Giulivi, C., Dutrieux, P., Rignot, E., Nitsche, F., Mouginot, J., 2013. Getz Ice Shelf melting response to changes in ocean forcing. J. Geophys. Res. Ocean. 118, 4152–4168. http://dx.doi.org/10.1002/jgrc.20298.
Jacobs, S.S., Hellmer, H.H., Jenkins, A., 1996. Antarctic Ice Sheet melting in the southeast Pacific. Geophys. Res. Lett. 23 (9), 957. http://dx.doi.org/10.1029/96GL00723.
Jacobs, S.S., Jenkins, A., Giulivi, C.F., Dutrieux, P., 2011. Stronger ocean circulation and increased melting under Pine Island Glacier ice shelf. Nat. Geosci. 4 (8), 519–523. http://dx.doi.org/10.1038/ngeo1188.
Jenkins, A., 1999. The impact of melting ice on ocean waters. J. Phys. Oceanogr. (3), 2370–2381.
Jenkins, A., Jacobs, S., 2008. Circulation and melting beneath George VI Ice Shelf, Antarctica. J. Geophys. Res. 113 (C4), C04013. http://dx.doi.org/10.1029/2007JC004449.
Jenkins, A., Dutrieux, P., Jacobs, S.S., McPhail, S.D., Perrett, J.R., Webb, A.T., White, D., 2010. Observations beneath Pine Island Glacier in West Antarctica and implications for its retreat. Nat. Geosci. 3 (7), 468–472. http://dx.doi.org/10.1038/ngeo890.
Joughin, I., Smith, B.E., Medley, B., 2014a. Marine ice sheet collapse potentially under way for the Thwaites Glacier Basin, West Antarctica. Science 344 (6185), 735–738. http://dx.doi.org/10.1126/science.1249055.
Joughin, I., Smith, B.E., Medley, B., 2014b. Marine ice sheet collapse potentially underway for the Thwaites Glacier Basin, West Antarctica. Science (80), 1. http://dx.doi.org/10.1038/ngeo1188.
Kahl, L.A., Schofield, O., Fraser, W.R., 2010. Autonomous gliders reveal features of the water column associated with foraging by adelie penguins. Integr. Comp. Biol. 50 (6), 1041–1050. http://dx.doi.org/10.1093/icb/icq098.
Kohut, J., Bernard, K., Fraser, W., Oliver, M.J., Statscewich, H., Winsor, P., Miles, T., 2015. Studying the impacts of local oceanographic processes on Adélie Penguin foraging ecology. Mar. Technol. Soc. J. 48 (5), 25–34. http://dx.doi.org/10.4031/MTSJ.48.5.10.
Kohut, J.T., Haldeman, C., Kerfoot, J., 2014. Monitoring dissolved oxygen in New Jersey Coastal waters using autonomous gliders., Washington, D.C.
Lee, S.H., Kim, B.K., Yun, M.S., Joo, H., Yang, E.J., Kim, Y.N., Shin, H.C., Lee, S., 2012. Spatial distribution of phytoplankton productivity in the Amundsen Sea, Antarctica. Polar Biol. 35 (11), 1721–1733. http://dx.doi.org/10.1007/s00300-012-1220-5.
Madsen, O.S., Wright, L.D., Boon, J.D., Chisholm, T.A., 1993. Wind stress, bed roughness and sediment suspension on the inner shelf during an extreme storm event. Cont. Shelf Res. 13, 1303–1324. http://dx.doi.org/10.1016/0278-4343(93)90054-2.
McDougall, T., 1990. Bulk properties of "hot smoker" plumes. Earth Planet. Sci. Lett. 99, 185–194.
McLean, S., 1991. Depth-integrated suspended-load calculations. J. Hydraul. Eng. 117 (11), 1440–1458.
Miles, T., Glenn, S., Schofield, O., 2013. Temporal and spatial variability in fall storm induced sediment resuspension on the mid-Atlantic bight. Cont. Shelf Res. 63.
Mouginot, J., Rignot, E., Scheuchl, B., 2014. Sustained increase in ice discharge from the Amundsen Sea Embayment, West Antarctica, from 1973 to 2013. Geophys. Res. Lett. 41, 1576–1584. http://dx.doi.org/10.1002/2013GL059069.
Mrvaljevic, R.K., et al., 2013. Observations of the cold wake of Typhoon Fanapi (2010). Geophys. Res. Lett. 40 (2), 316–321. http://dx.doi.org/10.1029/2012GL054282.
Padman, L., Fricker, H.A., Coleman, R., Howard, S., Erofeeva, L., 2002. A new tide model for the Antarctic ice shelves and seas. Ann. Glaciol. 34 (1), 247–254.

Pelland, N.A., Eriksen, C.C., Lee, C.M., 2013. Subthermocline eddies over the Washington Continental Slope as observed by seagliders, 2003–09. J. Phys. Oceanogr. 43 (10), 2025–2053. http://dx.doi.org/10.1175/JPO-D-12-086.1.
Planquette, H., Sherrell, R.M., Stammerjohn, S., Field, M.P., 2013. Particulate iron delivery to the water column of the Amundsen Sea, Antarctica. Mar. Chem. 153, 15–30. http://dx.doi.org/10.1016/j.marchem.2013.04.006.
Pritchard, H.D., Ligtenberg, S.R.M., Fricker, H.A., Vaughan, D.G., van den Broeke, M. R., Padman, L., 2012. Antarctic ice-sheet loss driven by basal melting of ice shelves. Nature 484 (7395), 502–505. http://dx.doi.org/10.1038/nature10968.
Randall-Goodwin, E., 2012. Detecting meltwater in the Amundsen Sea Polynya region, west Antarctica, University of California Santa Cruz.
Randall-Goodwin, E., et al., 2015. Freshwater distributions and water mass structure in the Amundsen Sea Polynya region, Antarctica. Elem. Sci. Anthr. 3:000065. http://dx.doi.org/10.12952/journal.elementa.000065.
Rignot, E., Jacobs, S.S., 2002. Rapid bottom melting widespread near Antarctic Ice Sheet grounding lines. Science 296 (5575), 2020–2023. http://dx.doi.org/10.1126/science.1070942.
Rignot, E., Bamber, J.L., van den Broeke, M.R., Davis, C., Li, Y., van de Berg, W.J., van Meijgaard, E., 2008. Recent Antarctic ice mass loss from radar interferometry and regional climate modelling. Nat. Geosci. 1 (2), 106–110. http://dx.doi.org/10.1038/ngeo102.
Rignot, E., Jacobs, S., Mouginot, J., Scheuchl, B., 2013. Ice-shelf melting around Antarctica. Science 341 (6143), 266–270. http://dx.doi.org/10.1126/science.1235798 (80-.).
Rignot, E., Mouginot, J., Morlighem, M., Seroussi, H., Scheuchl, B., 2014. Widespread, rapid grounding line retreat of Pine Island, Thwaites, Smith, and Kohler glaciers. West Antarctica, 3502–3509. http://dx.doi.org/10.1002/2014GL060140. Received.
Schmidtko, S., Heywood, K.J., Thompson, A.F., Aoki, S., 2014. Multidecadal warming of Antarctic waters. Science 346 (6214), 1227–1231. http://dx.doi.org/10.1126/science.1256117.
Schofield, O., et al., 2007. Slocum Gliders: Robust and ready. J. F. Robot. 24 (6), 473–485. http://dx.doi.org/10.1002/rob.20200.
Schofield, O., et al., 2013. Penguin biogeography along the west Antarctic peninsula: testing the canyon hypothesis with Palmer LTER Observations. Oceanography 26 (3), 204–206. http://dx.doi.org/10.5670/oceanog.2013.63.
Schofield, O.M., Miles, T.N., Alderkamp, A.-C., Lee, S., Haskins, C., Rogalsky, E., Sipler, Sherrell, R.M., Yager, P.L., 2015. In Situ phytoplankton distributions in the Amundsen Sea polynya measured by autonomous gliders., Elem. Sci. Anthr., 3, 2015 (in press).
Smith, J. a, Hillenbrand, C.-D., Kuhn, G., Klages, J.P., Graham, A.G.C., Larter, R.D., Ehrmann, W., Moreton, S.G., Wiers, S., Frederichs, T., 2014. New constraints on the timing of West Antarctic ice sheet retreat in the eastern Amundsen Sea since the Last Glacial Maximum. Glob. Planet. Change 122, 224–237. http://dx.doi.org/10.1016/j.gloplacha.2014.07.015.
Smith, W.O., Comiso, J.C., 2008. Influence of sea ice on primary production in the Southern Ocean: a satellite perspective. J. Geophys. Res. 113, 1–19. http://dx.doi.org/10.1029/2007JC004251.
Stammerjohn, S., Massom, R., Rind, D., Martinson, D., 2012. Regions of rapid sea ice change: an inter-hemispheric seasonal comparison. Geophys. Res. Lett. 39 (6). http://dx.doi.org/10.1029/2012GL050874, n/a–n/a.
Sunda, W.G., Huntsman, S.A., 1997. Interrelated influence of iron, light and cell size on marine phytoplankton growth. Nature 390 (1977), 389–392. http://dx.doi.org/10.1038/37093.
Sutterley, T.C., Velicogna, I., Rignot, E., Mouginot, J., Flament, T., van den Broeke, M. R., van Wessem, J.M., Reijmer, C.H., 2014. Mass loss of the Amundsen Sea embayment of west Antarctica from four independent techniques. Geophys. Res. Lett. . http://dx.doi.org/10.1002/2014GL061940
Thoma, M., Jenkins, A., Holland, D., Jacobs, S., 2008. Modelling Circumpolar Deep Water intrusions on the Amundsen Sea continental shelf, Antarctica. Geophys. Res. Lett. 35 (18), L18602. http://dx.doi.org/10.1029/2008GL034939.
Thompson, A.F., Heywood, K.J., Schmidtko, S., Stewart, A.L., 2014. Eddy transport as a key component of the Antarctic overturning circulation. Nat. Geosci. 7. http://dx.doi.org/10.1038/ngeo2289.
Thurnherr, A.M., 2010. A practical assessment of the errors associated with full-depth LADCP profiles obtained using teledyne RDI workhorse acoustic doppler current profilers. J. Atmos. Ocean. Technol. 27, 1215–1227. http://dx.doi.org/10.1175/2010JTECHO708.1.
Todd, R.E., Rudnick, D.L., Mazloff, M.R., Davis, R.E., Cornuelle, B.D., 2011. Poleward flows in the southern California current system: glider observations and numerical simulation. J. Geophys. Res. 116 (C2), C02026. http://dx.doi.org/10.1029/2010JC006536.
Wåhlin, A.K., Yuan, X., Björk, G., Nohr, C., 2010. Inflow of warm Circumpolar Deep Water in the Central Amundsen Shelf. J. Phys. Oceanogr. 40 (6), 1427–1434. http://dx.doi.org/10.1175/2010JPO4431.1.
Wåhlin, A.K., Kalén, O., Arneborg, L., Björk, G., Carvajal, G.K., Ha, H.K., Kim, T.W., Lee, S.H., Lee, J.H., Stranne, C., 2013. Variability of warm deep water inflow in a submarine trough on the Amundsen Sea shelf. J. Phys. Oceanogr. 43 (10), 2054–2070. http://dx.doi.org/10.1175/JPO-D-12-0157.1.
Wåhlin, A.K., Muench, R.D., Arneborg, L., Björk, G., Ha, H.K., Lee, S.H., Alsén, H., 2012. Some implications of ekman layer dynamics for cross-shelf exchange in the Amundsen Sea. J. Phys. Oceanogr. 42 (9), 1461–1474. http://dx.doi.org/10.1175/JPO-D-11-041.1.
Wåhlin, A.K., Kalén, O., Assmann, K.M., Darelius, H.K., Ha, Lee, S.H., 2015. Sub-inertial oscillations on the central Amundsen Shelf. J. Phys. Oceanogr. (in press)
Walker, D.P., Brandon, M.A., Jenkins, A., Allen, J.T., Dowdeswell, J.A., Evans, J., 2007. Oceanic heat transport onto the Amundsen Sea shelf through a submarine glacial trough. Geophys. Res. Lett. 34 (2), L02602. http://dx.doi.org/10.1029/2006GL028154.
Walker, D.P., Jenkins, A., Assmann, K.M., Shoosmith, D.R., Brandon, M.A., 2013. Oceanographic observations at the shelf break of the Amundsen Sea, Antarctica. J. Geophys. Res. Ocean. 118, 2906–2918. http://dx.doi.org/10.1002/jgrc.20212.
Webb, D.C., Simonetti, P.J., Jones, C.P., 2001. SLOCUM: an underwater glider propelled by environmental energy. IEEE J. Ocean. Eng. 26 (4), 447–452. http://dx.doi.org/10.1109/48.972077.
Yager, P.L., Sherrell, L.M., Stammerjohn, S.E., Alderkamp, A.-C., Schofield, O., Abrahamsen, E.P., Arrigo, K.R., Bertilsson, S., Garay, D., Guerrero, R., 2012. ASPIRE: the Amundsen Sea Polynya international research expedition. Oceanography 25 (3), 40–53.

Coastal Ocean Mixing and Advection During Hurricane Sandy and Arthur

Travis Miles, Greg Seroka, and Scott Glenn

Rutgers, The State University of New Jersey
Department of Marine and Coastal Sciences
Center for Ocean Observing Leadership
New Brunswick, New Jersey
tnmiles@marine.rutgers.edu

***Abstract*— The Mid Atlantic Bight continental shelf has one of the largest summer temperature gradients in the world, with near bottom temperatures below 8C and peak surface temperatures over 28C. This is largely due to the summer Cold Pool, remnant winter water that is generated on the northern MAB and transported southward along the continental shelf in spring and early summer. During tropical cyclones that impact the MAB continental shelf, such as Hurricane Irene in 2011, shear driven mixing of Cold Pool water across the thermocline has the potential to cool the oceans surface and reduce storm intensity. In this study we compare coastal ocean advection and mixing processes during Hurricane Sandy and Hurricane Arthur, an offshore tracking tropical cyclone in the summer of 2014, to demonstrate the range of potential storm impacts on the coastal ocean of the MAB. To perform this analysis we use data from advanced Slocum autonomous underwater glider deployments in each storm as well as the Regional Ocean Modeling System (ROMS).**

***Keywords*— Coastal storms, ocean observing systems, autonomous underwater vehicles, coastal ocean modeling.**

I. Introduction

The Mid Atlantic Bight continental shelf has one of the largest summer temperature gradients in the world, with near bottom temperatures below 8C and peak surface temperatures over 28C. This is largely due to the summer Cold Pool [1], remnant winter water that is generated on the northern MAB and transported southward along the continental shelf in spring and early summer. During tropical cyclones that impact the MAB continental shelf, such as Hurricane Irene in 2011, shear driven mixing of Cold Pool water across the thermocline has the potential to cool the oceans surface and reduce storm intensity [2]. While this process was observed in detail from a networked coastal ocean observatory in Hurricane Irene, a coupled ocean-atmosphere model study has shown the ocean to have a limited impact on Hurricane Sandy in 2012 [3].

In this study we compare coastal ocean advection and mixing processes during Hurricane Sandy and Hurricane Arthur, an offshore tracking tropical cyclone in the summer of 2014. Hurricane sandy was a late-season tropical cyclone that crossed the New Jersey shelf in late October, when stratification had already partially broken down for the season. Hurricane Arthur was one of the earliest tropical cyclones to make landfall in North Carolina in early July prior to crossing the southern portion of the Mid-Atlantic Bight, when stratification was at its highest. With vastly different trajectories and shelf stratification conditions they demonstrate the range of potential storm impacts on the coastal ocean of the MAB. To perform this analysis we use data from advanced Slocum autonomous underwater gliders deployed ahead ofeach storm as well as the Regional Ocean Modeling System (ROMS).

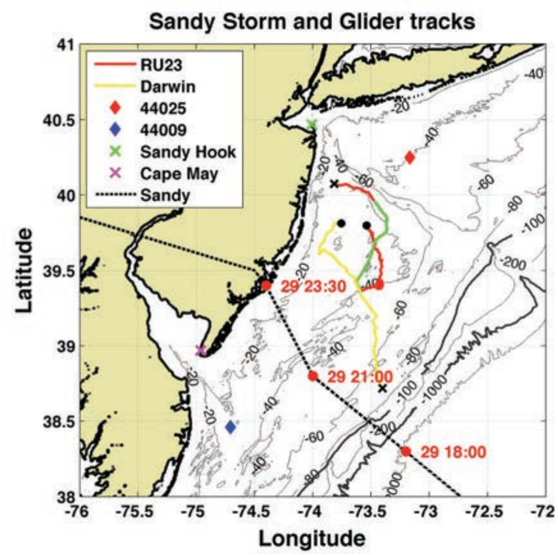

Figure 1 Map of the NJ Shelf with the dashed line representing Hurricane Sandy's onshore track (times in GMT). Glider RU23 (red) and it's storm sampling period represented in Figure 2 (green). A second glider, Darwin (yellow), is also plotted.

II. Methods

Teledyne-Webb Research Slocum gliders are buoyancy driven autonomous underwater vehicles that are mobile profiling sensor platforms, with interchangeable science bays [Schofield et al., 2007; Schofield et al., 2010]. Gliders have a proven history of sampling in extreme weather conditions, [4]–[7]. A Slocum G1 glider, RU23 was deployed

978-0-933957-43-5 ©2015 MTS

ahead of Hurricane Sandy in October 2012, while a specially designed G2 Storm glider RU30 was deployed ahead of Hurricane Arthur in July of 2014. RU23 and RU30 were equipped with Seabird Electronics (SBE) un-pumped and pumped conductivity temperature and depth (CTD) sensors, respectively. Both gliders were equipped with two Wetlabs Eco-triplets that measured chlorophyll fluorescence, colored dissolved organic matter (CDOM), and four channels of optical backscatter.

To measure water-column currents Nortek Aquadopp current profilers with custom glider heads were externally mounted in an upward looking position and logged data internally. The Aquadopps were configured to collect data in beam coordinates in one meter bins with a beam length of ten meters every two seconds. On downcasts with a glider pitch angle of 26.5 degrees the Aquadopps had a pitch angle of 0 degrees. We emply a shear-least squares method originally detailed for lowered current profilers [8] and adapted for use on autonomous platforms [9]. We calculate water column shear at one meter intervals on downcasts only and use a combination of pitch angle, heading and depth, known as dead-reckoning [10] to calculate the mean water-column velocity.

ROMS is a three-dimensional sigma coordinate numerical ocean model [11]–[13] that is commonly used for coastal and regional model applications. The Experimental System for Predicting Shelf and Slope Optics (ESPreSSO) setup [14]–[18] used here covers from Cape Hatteras to Cape Cod, and near shore to beyond the shelf-break. The system has an approximately 5 km horizontal resolution, 36 vertical levels and a 6-minute time step with model data output hourly. Boundary conditions are derived from the HYCOM-NCODA (http://hycom.org/) and tides derived from the ADCIRC tidal model (http://adcirc.org/). For the Sandy case the model is initialized from the original assimilative ESPreSSO 4-dimensional variational data assimilations (IS4DVAR) output on October 25th and run forward. Atmospheric forcing is from the Rutgers University Weather Research and Forecast model setup described in detail in [7]. The ESPreSSO model has been used extensively on the MAB for a range of applications including for sediment transport studies during Hurricane Sandy on the MAB[7].

III. Results

A. Hurricane Sandy

Hurricane Sandy developed as a late-season tropical wave off the coast of Africa on October 11th 2012. On October 24th the cyclone made landfall as a category 1 hurricane in Jamaica and continued to make landfall in Cuba as a category 3 on October 25th. The cyclone left the Caribbean the storm turned toward the northeast again as a category one hurricane. During this period, as the storm passed to the east of North Carolina, the radius of maximum winds covered approximately 180 kilometers. Early on October 29th Sandy took a sharp left turn toward the NY/NJ coastline. After a brief re-intensification period as the storm crossed the continental shelf it interacted with cooler waters and a cold air mass over the eastern United States, ultimately

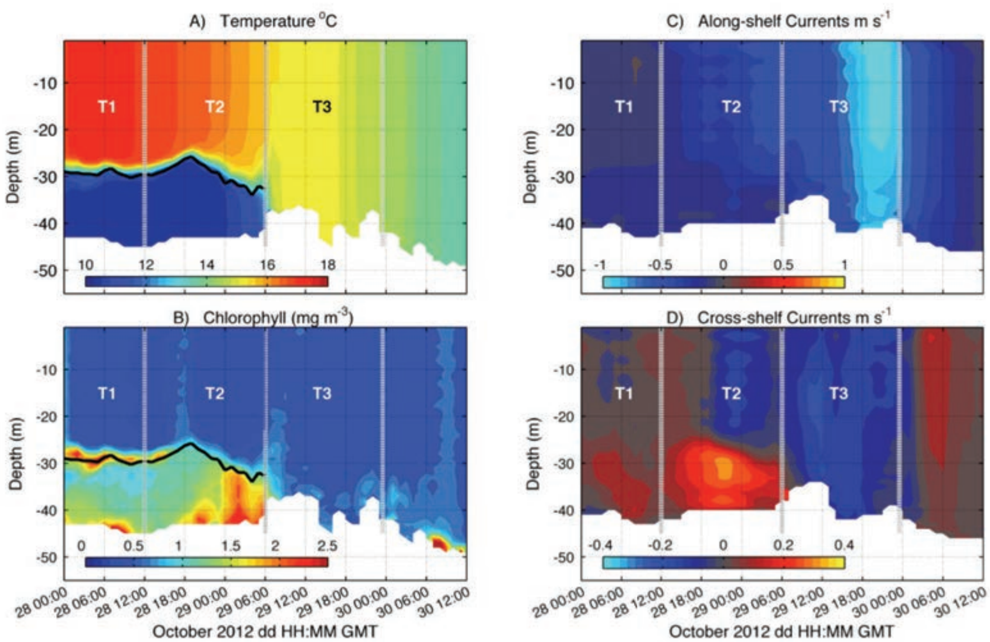

Figure 2 RU23 glider data during the storm forcing period on October 28th at 00:00 GMT to the 30th at 12:00 GMT (represented by the black line in Figure 1). A) Temperature and B) Chlorophyl (mg/m3) with a black contour representing the thermocline. C) Along-shelf and D) cross-shelf de-tided currents calculated from the Nortek Aquadopp current profiler. Positive is toward the southwest and offshore in the along- and cross- shelf directions respectively. Note the different colorbar between the along and cross- shelf currents.

transitioning to extra-tropical at 2100 GMT on October 29th just prior to landfall at 2330 GMT near Brigantine, New Jersey. This storm drove extensive storm surge along the NY/NJ coastlines and resulted in over $68 Billion in damages[19].

Glider RU23 was deployed 15 km southeast of Sandy Hook, NJ on October 25th, (Figure 1) as forecasts indicated Sandy would approach the MAB. The glider was piloted due east to the 40 meter isobath in order to sample the coastal ocean at a safe distance from the coastline. Cross-sections of RU23 temperature and currents (Figure 2) show three distinct time periods based on the evolution of the thermocline, which we refer to as T1, T2 and T3.The initial stratified period T1 was between 00:00 and 12:00 GMT on October 28th and showed warm surface temperatures of over 17°C consistent with pre-storm conditions sampled by Darwin and a sharp thermocline at 25 meters depth. Below the thermocline temperatures were 10°C and uniform to the bottom. During T1 de-tided along-shelf surface currents were weak and southwestward with flow below 0.1 m s^{-1}, while the lower layer showed bottom intensified flow over 0.2 m s^{-1}. There was slight onshore flow near the surface and offshore flow near the bottom of ~ 0.1 m s^{-1}. During T2 between 12:00 GMT on the 28th and 06:00 GMT on the 29th (Figure 2) the thermocline initially rose and then deepened dramatically, reaching the bottom in twelve hours. Along-shore currents increased to over 0.6 m s^{-1} in the surface layer and remained near 0.2 m s^{-1} in the bottom similar to the initial stratified phase. In the cross-shelf direction currents were onshore in the surface as along-shore surface winds, which had now persisted for over an inertial period (~18 hours), spun up the surface

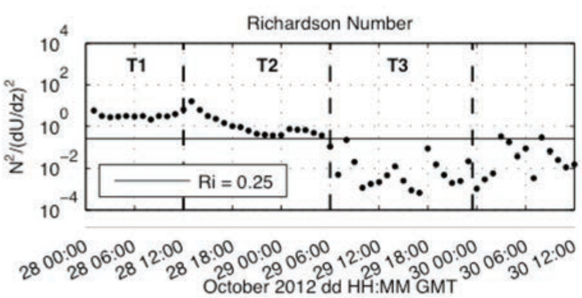

Figure 4 Bulk Richardson number calculated from equation 1 along the glider track. The horizontal black line represents Ri of 0.25.

Ekman layer. Cross-shelf flow in the lower layer was offshore and over 0.5 m s^{-1} at 20:00 GMT on the 28th. Surface temperatures dropped gradually, despite a sharp increase in bottom temperatures of 4°C in two hours as the thermocline deepened. In T3, between the 29th at 06:00 GMT and landfall on the 29th 23:30 GMT the watercolumn transitioned from a two- to one- layer system (Figure 2). Cross-shelf circulation shut down and currents rotated to be along-shelf and uniform throughout the watercolumn, with peak values over 1 m s^{-1} as the eye of Sandy crossed the shelf. Full watercolumn temperatures continued to gradually decrease until they dropped below 13C after eye passage

Two-layer cross-shelf flow during the deepening phase between 12:00 GMT on the 28th and 06:00 GMT on the 29th was consistent with the seaward side of a downwelling front, while single-layer flow was consistent with the shoreward side of a downwelling front similar to results discussed in [Lentz, 2001] and [Austin and Lentz, 2002]. Along-shelf displacement of the glider was over 50 km, but piloting to maintain cross-shelf position and two-layer flow limited cross-shelf displacement during T2 and T3, thus the glider likely sampled the shoreward and seaward sides of the downwelling front, in T2 and T3 respectively, as it was advected past the glider in the offshore direction. Bulk Richardson numbers from:

$$Ri = N2/(\partial u\ \partial z) \qquad (1)$$

where N^2 is the hourly averaged water-column buoyancy frequency across the thermocline, and $(\partial u\ \partial z)^2$ is the hourly averaged maximum shear across the thermocline calculated from the Aquadopp. Studies have shown [20], [21] that the water column is stable (unstable) when Richardson number is above (below) a critical number (Rc) of 0.25. Richardson numbers (Figure 3) were greater than 0.25 until the 29th at 06:00 after the thermocline had already deepened

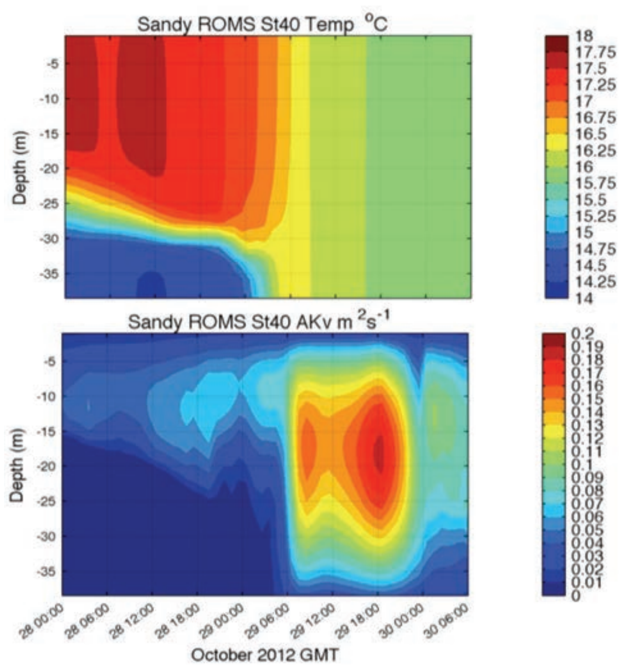

Figure 3 Cross sections of temperature (upper) and eddy diffusivity at the 40 meter isobaths in the ROMS model near the glider position.

approximately 5 meters.

A cross section of the storm time period from ROMS near the glider location on the 40 meter isobaths (Figure 4) shows similar stratification with a few differences. Bottom waters were approximately ~3°C warmer prior to the storm and the thermocline was deeper and slightly more diffuse. Similar deepening of the thermocline occurred ahead between

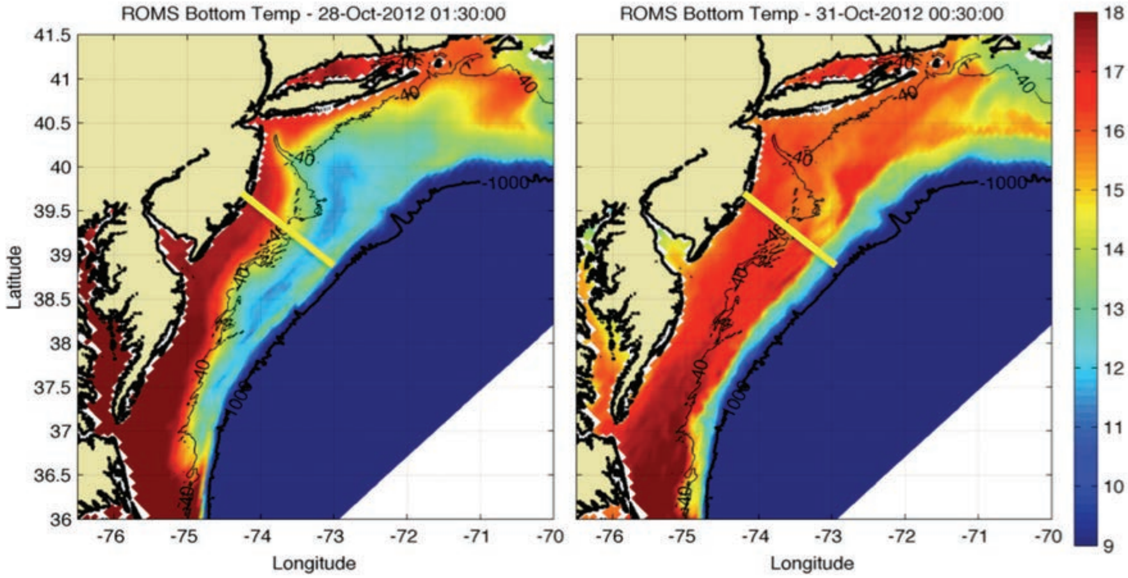

Figure 5 Bottom temperatures from the ESPreSSO ROMS model before (left panel) and after (right panel) eye passage.

the 28th at 00:00 GMT and the 29th at 06:00 GMT, followed by a transition from two-layers to one-layer (Figure 4). Eddy diffusivities were relatively low in prior to the 29th at 06:00 GMT with limited increases in the surface layer indicating limited mixing across the thermocline. Eddy diffusivities increase dramatically after the transition from a one- to two-layer system supporting the argument that advection was responsible for the transition rather than mixing (Figure 4). From a shelf-wide perspective bottom temperatures inshore of the 40 meter isobaths were near 18°C indicating a well-mixed nearshore region. Bottom temperatures offshore of the 40 meter isobaths pre-storm are near ~13°C across (Figure 5) the majority of the shelf. After the storm the warm bottom temperatures found inshore extend nearly to the shelf-break, with a total offshore advection of ~30 km.

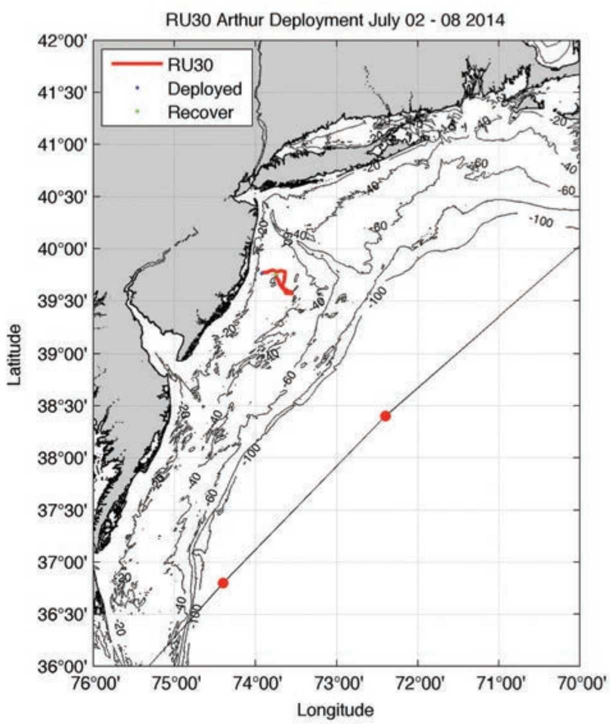

Figure 6 Map of the MAB with Hurricane Arthurs track (black with red dots), the glider track (red line).

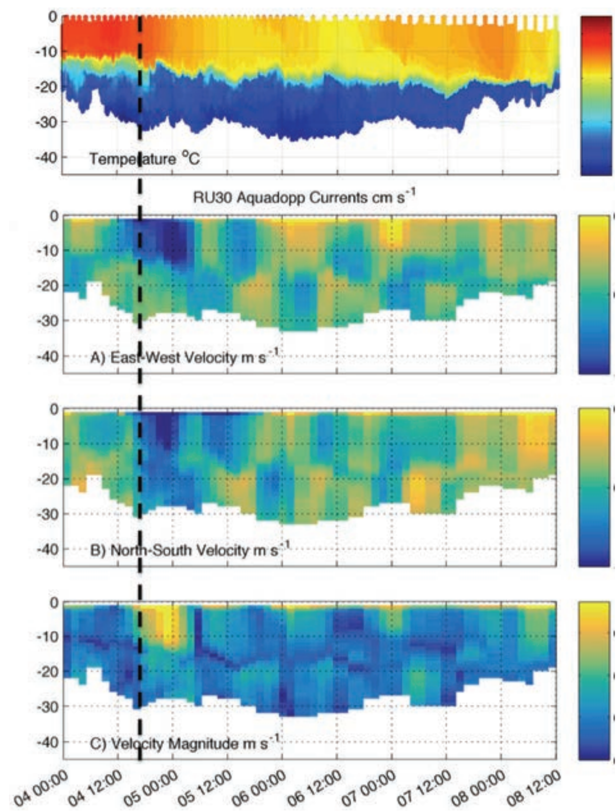

Figure 7 Cross-sections of glider RU30 temperature and velocity components and magnitude. Vertical black line denotes time of storm passage.

B. Hurricane Arthur

Hurricane Arthur developed east of Florida on July 1st when a depression that had crossed from the Gulf of Mexico into the South Atlantic bight interacted with a region of mid-level anticyclone over the Western Atlantic. This interaction caused Arthur to accelerate northward rapidly throughout July 2nd and 3rd. The hurricane strengthened as it passed east of Savannah Georgia and eventually reached peak intensity off the coast of Cape Fear, North Carolina. After crossing the Outer Banks, Arthur accelerated northeastward over the western Atlantic east of the Mid-Atlantic until it weakened into a tropical storm on July 5th east of Provincetown, Massachusetts.

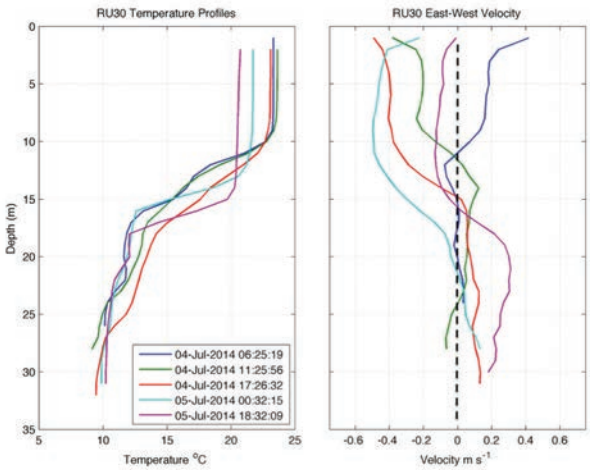

Figure 8 RU30 segment averaged profiles of temperature (left panel) and east-west velocity (right panel).

RU30 was deployed as part of a NOAA Cooperative Institute for the North Atlantic region (CINAR) Tempests project on July 3rd 2014 out of Tuckerton, NJ (Figure 6). The glider was piloted due east toward the 40 meter isobath similar to RU23 in Sandy. As Arthur was a fast moving storm the glider was only in the field for approximately 18 to 24 hours before experiencing outer edge winds from the storm. Initially on July 4th at 00:00 GMT the watercolumn (Figure 7) was highly stratified typical of summer conditions on the MAB. Surface temperatures were near 23 to 24^{o}C, bottom temperatures were near 10^{o}C and there was a shallow thermocline at 10 meters depth. Segment averaged profiles (mean profiles between each glider surfacing) between July 4th at 06:25 GMT and July 5th at 18:32 show limited cooling of only about 0.5^{o}C over the first 12 hours in the surface layer. Despite the limited surface cooling the thermocline deepened and grew less sharp by the end of July 4th at 17:26 GMT. After this first 12-hour period surface temperatures dropped over 3^{o}C and the thermocline lowered to 15 meters depth (Figure 8). Profiles of the east and west current velocities during this same period show maximum vertical shear starting on July 4th at 17:26 GMT with westward surface velocities and low near-bottom velocities.

After the eye passed the surface currents continue to rotate for a number of days after. Wavelet spectral analysis of the surface currents (Figure 9) shows the surface currents oscillating with a period of near 18 hours, near the local inertial period, that slowly lengthens with time. This suggests that any additional cooling is likely due to inertial surface currents driving intermittent shear driven mixing across the thermocline. Further analysis of glider data and ROMS modeling are underway in order to confirm this result.

IV. Discussion & Conclusion

RU23 and RU30 were deployed off the MAB continental shelves in response to Hurricanes Sandy and Arthur respectively. The storms had vastly different tracks, speeds, and struck at the far extremes of the Atlantic Hurricane season with different stratification regimes. Thus they represent two very different coastal ocean responses to summer storms on the MAB. Sandy struck during the late season fall transition period between summer and winter, thus temperatures were lower and the thermocline deeper than typically occurs on the shelf. The onshore track and large size of the storm drove large volumes of water above the thermocline onshore leading to a downwelling circulation that ultimately advected the bottom Cold Pool offshore nearly 30 kilometers. The limited mixing observed by the glider and model output support this finding. Previous studies have identified this type of circulation for persistent downwelling

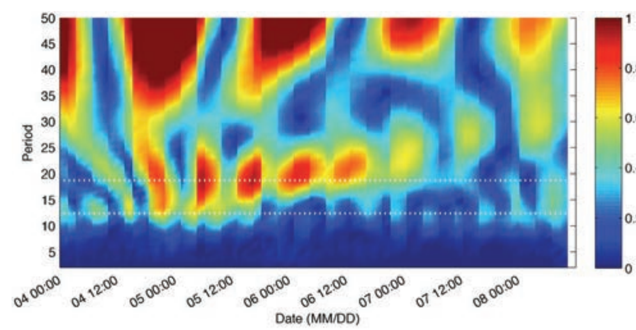

Figure 9 Wavelet spectrum of glider RU30 surface currents.

favorable winds, with deeper thermoclines resulting in more advection than shallower thermoclines [22], [23].

Hurricane Arthur, with its fast moving offshore track, and enhanced stratification did not setup advective downelling circulation on the MAB shelf. Rather the storm had limited direct mixing prior to eye-passage and enhanced mixing behind the eye during the post-storm inertial response. The shallower thermocline was more conducive to direct wind-forced mixing. Further analysis of these two storms, as well as Hurricane Irene are ongoing and provide a broad view of the three-dimensional processes that occur on the stratified MAB continental shelf during summer tropical cyclones.

The dynamic ocean response to these two storms indicates that fully coupled three-dimensional ocean and atmosphere models may be necessary to resolve changes to the surface ocean and further investigate the impact of the coastal ocean on atmospheric forecasts of hurricane intensity in the MAB. Further observational assets such as gliders and moorings should be included in data assimilation for these models to improve the accuracy the modeled ocean ahead of and during storm events. Future observational work will include downward looking current profilers to more accurately measure bottom stress, and accelerometers to resolve wave motions at glider locations.

V. Acknowledgements

Glider data used in this study is available through the MARACOOS assets page http://maracoos.org/data and http://marine.rutgers.edu/cool/auvs/index.php?did=369 with more detailed datasets available upon request to tnmiles@marine.rutgers.edu. Regional Ocean Modeling System and WRF model results are also available upon request to tnmiles@marine.rutgers.edu. Buoy data and WaveWatch III datasets are publicly available through http://www.ndbc.noaa.gov/ and http://polar.ncep.noaa.gov, respectively. We are grateful for the funding support provided by NOAA Grant NA11NOS0120038 as part of MARACOOS, the regional partner of U.S. IOOS and NOAA Grant NA13OAR4830233 as part of CINAR, the regional partner of the CIPO. We would also like to thank Teledyne-Webb Research for providing graduate student funding, NortekUSA for providing equipment through a student equipment grant.

VI. References

[1] R. W. Houghton, R. Schlitz, R. C. Beardsley, B. Butman, and J. L. Chamberlin, “The Middle Atlantic Bight Cold Pool: Evolution of the Temperature Structure During Summer 1979,” *J. Phys. Oceanogr.*, vol. 12, no. 10, pp. 1019–1029, Oct. 1982.

[2] S. Glenn, D. Aragon, L. Bowers, M. Crowley, R. Dunk, C. Evans, C. Haldeman, E. Handel, T. Haskins, J. Kerfoot, J. Kohut, J. Levin, T. Miles, L. Palamara, H. Roarty, O. Schofield, G. Seroka, M. Smith, N. Strandskov, J. Wilkin, Y. Xu, J. Zavala-Garay, C. Thoroughgood, G. Kuska, B. Lipphardt, M. Oliver, M. Shatley, W. Brown, A. Gongopadhyay, C. Jakubiak, A. Schmidt, E. Howlett, D. Ullman, J. O'Donnell, T. Fake, N. Georgas, A. Blumberg, M. Bruno, T. Herrington, W. Boicourt, T. Wazniak, J. Titlow, R. Toll, L. Atkinson, T. Updyke, N. Verona, H. Seim, and M. Muglia, “Process-driven improvements to hurricane intensity and storm surge forecasts in the mid-atlantic bight: Lessons learned from hurricanes irene and sandy,” in *OCEANS 2013 MTS/IEEE Bergen: The Challenges of the Northern Dimension*, 2013.

[3] J. B. Zambon, R. He, and J. C. Warner, “Tropical to extratropical: Marine environmental changes associated with SuperstormSandy prior to its landfall,” *Geophys. Res. Lett.*, vol. 41, pp. 8935–8943, 2014.

[4] S. Glenn, C. Jones, M. Twardowski, L. Bowers, J. Kerfoot, J. Kohut, D. Webb, and O. Schofield, “Glider observations of sediment resuspension in a Middle Atlantic Bight fall transition storm,” *Limnol. Oceanogr.*, vol. 53, no. 5 part 2, pp. 2180–2196, 2008.

[5] T. Miles, S. Glenn, and O. Schofield, “Temporal and spatial variability in fall storm induced sediment resuspension on the Mid-Atlantic Bight,” *Cont. Shelf Res.*, vol. 63, 2013.

[6] S. Ruiz, L. Renault, B. Garau, and J. Tintoré, “Underwater glider observations and modeling of an abrupt mixing event in the upper ocean,” *Geophys. Res. Lett.*, vol. 39, no. 1, p. n/a–n/a, Jan. 2012.

[7] T. Miles, G. Seroka, J. Kohut, O. Schofield, and S. Glenn, “Glider observations and modeling of sediment transport in Hurricane Sandy,” *J. Geophys. Res. Ocean.*, p. n/a–n/a, Feb. 2015.

[8] M. Visbeck, “Deep Velocity Profiling Useding Lowered Acoustic Doppler Current Profilers: Bottom Track and Inverse Solutions,” *J. Atmos. Ocean. Technol.*, 2002.

[9] R. E. Todd, D. L. Rudnick, M. R. Mazloff, R. E. Davis, and B. D. Cornuelle, “Poleward flows in the southern California Current System: Glider observations and numerical simulation,” *J. Geophys. Res.*, vol. 116, no. C2, p. C02026, Feb. 2011.

[10] R. Davis, C. Eriksen, and C. Jones, “Autonomous Buoyancy-driven Underwater Gliders,” in *Technology and Applications of Autonomous Underwater Vehicles*, G. Griffiths, Ed. Taylor & Francis, 2003, p. 37.

[11] A. F. Shchepetkin and J. C. McWilliams, “The regional oceanic modeling system (ROMS): a split-explicit, free-surface, topography-following-coordinate oceanic model,” *Ocean Model.*, vol. 9, no. 4, pp. 347–404, Jan. 2005.

[12] A. F. Shchepetkin and J. C. McWilliams, “Correction and commentary for ‘Ocean forecasting in terrain-following coordinates: Formulation and skill assessment of the regional ocean modeling system’ by Haidvogel et al., J. Comp. Phys. 227, pp. 3595–3624,” *J. Comput. Phys.*, vol. 228, no. 24, pp. 8985–9000, Dec. 2009.

[13] D. B. Haidvogel, H. Arango, W. P. Budgell, B. D. Cornuelle, E. Curchitser, E. Di Lorenzo, K. Fennel, W. R. Geyer, A. J. Hermann, L. Lanerolle, J. Levin, J.

C. McWilliams, A. J. Miller, A. M. Moore, T. M. Powell, A. F. Shchepetkin, C. R. Sherwood, R. P. Signell, J. C. Warner, and J. Wilkin, “Ocean forecasting in terrain-following coordinates: Formulation and skill assessment of the Regional Ocean Modeling System,” *J. Comput. Phys.*, vol. 227, no. 7, pp. 3595–3624, Mar. 2008.

[14] K. Fennel, J. Wilkin, J. Levin, J. Moisan, J. O’Reilly, and D. Haidvogel, “Nitrogen cycling in the Middle Atlantic Bight: Results from a three-dimensional model and implications for the North Atlantic nitrogen budget,” *Global Biogeochem. Cycles*, vol. 20, no. 3, p. n/a–n/a, Sep. 2006.

[15] B. Cahill, O. Schofield, R. Chant, J. Wilkin, E. Hunter, S. Glenn, and P. Bissett, “Dynamics of turbid buoyant plumes and the feedbacks on near-shore biogeochemistry and physics,” *Geophys. Res. Lett.*, vol. 35, no. 10, p. L10605, May 2008.

[16] W. G. Zhang, J. L. Wilkin, J. C. Levin, and H. G. Arango, “An Adjoint Sensitivity Study of Buoyancy- and Wind-Driven Circulation on the New Jersey Inner Shelf,” *J. Phys. Oceanogr.*, vol. 39, no. 7, pp. 1652–1668, Jul. 2009.

[17] W. G. Zhang, J. L. Wilkin, and R. J. Chant, “Modeling the Pathways and Mean Dynamics of River Plume Dispersal in the New York Bight,” *J. Phys. Oceanogr.*, vol. 39, no. 5, pp. 1167–1183, May 2009.

[18] J. L. Wilkin and E. J. Hunter, “An assessment of the skill of real-time models of Mid-Atlantic Bight continental shelf circulation,” *J. Geophys. Res. Ocean.*, vol. 118, no. 6, pp. 2919–2933, Jun. 2013.

[19] E. S. Blake, T. B. Kimberlain, R. J. Berg, P. C. John, and J. L. Beven II, “Tropical Cyclone Report: Hurricane Sandy,” *Natl. Hurric. Cent.*, vol. 12, 2013.

[20] R. J. Chant, W. R. Geyer, R. Houghton, E. Hunter, and J. Lerczak, “Estuarine Boundary Layer Mixing Processes: Insights from Dye Experiments*,” *J. Phys. Oceanogr.*, vol. 37, no. 7, pp. 1859–1877, Jul. 2007.

[21] J. H. Trowbridge, “A simple description of the deepening and structure of a stably stratified flow driven by a surface stress,” *J. Geophys. Res. Ocean.*, vol. 97, no. C10, pp. 15529–15543, Oct. 1992.

[22] J. Austin and S. Lentz, “The inner shelf response to wind-driven upwelling and downwelling.,” *J. Phys. Oceanogr.*, no. 1905, pp. 2171–2193, 2002.

[23] S. Lentz, “The Influence of Stratification on the Wind-Driven Cross-Shelf Circulation over the North Carolina Shelf*,” *J. Phys. Oceanogr.*, no. Lentz 1995, pp. 2749–2760, 2001.

ELEMENTA
Science of the Anthropocene

In situ phytoplankton distributions in the Amundsen Sea Polynya measured by autonomous gliders

Oscar Schofield[1*] • Travis Miles[1] • Anne-Carlijn Alderkamp[2] • SangHoon Lee[3] • Christina Haskins [1] • Emily Roaglsky[1] • Rachel Sipler[4] • Robert M. Sherrell [1,5] • Patricia L. Yager [6]

[1]Center for Ocean Observing Leadership, Department of Marine and Coastal Sciences, School of Environmental and Biological Sciences, Rutgers University, New Brunswick, New Jersey, United States
[2]Department of Environmental Earth System Science, Stanford University, Stanford, California, United States
[3]Korea Polar Research Institute, YonSu-Ku, Incheon, Korea
[4]Virginia Institute of Marine Science, College of William & Mary, Gloucester Point, Virginia, United States
[5]Department of Earth and Planetary Sciences, Rutgers University, Piscataway, New Jersey, United States
[6]Department of Marine Sciences, University of Georgia, Athens, Georgia, United States

*oscar@marine.rutgers.edu

Abstract

The Amundsen Sea Polynya is characterized by large phytoplankton blooms, which makes this region disproportionately important relative to its size for the biogeochemistry of the Southern Ocean. *In situ* data on phytoplankton are limited, which is problematic given recent reports of sustained change in the Amundsen Sea. During two field expeditions to the Amundsen Sea during austral summer 2010–2011 and 2014, we collected physical and bio-optical data from ships and autonomous underwater gliders. Gliders documented large phytoplankton blooms associated with Antarctic Surface Waters with low salinity surface water and shallow upper mixed layers (< 50 m). High biomass was not always associated with a specific water mass, suggesting the importance of upper mixed depth and light in influencing phytoplankton biomass. Spectral optical backscatter and ship pigment data suggested that the composition of phytoplankton was spatially heterogeneous, with the large blooms dominated by *Phaeocystis* and non-bloom waters dominated by diatoms. Phytoplankton growth rates estimated from field data ($\leq$ 0.10 day^{-1}) were at the lower end of the range measured during ship-based incubations, reflecting both *in situ* nutrient and light limitations. In the bloom waters, phytoplankton biomass was high throughout the 50-m thick upper mixed layer. Those biomass levels, along with the presence of colored dissolved organic matter and detritus, resulted in a euphotic zone that was often < 10 m deep. The net result was that the majority of phytoplankton were light-limited, suggesting that mixing rates within the upper mixed layer were critical to determining the overall productivity; however, regional productivity will ultimately be controlled by water column stability and the depth of the upper mixed layer, which may be enhanced with continued ice melt in the Amundsen Sea Polynya.

Domain Editor-in-Chief
Jody W. Deming, University of Washington

Associate Editor
Jean-Éric Tremblay, Université Laval

Knowledge Domain
Ocean Science

Article Type
Research Article

Part of an *Elementa* Special Feature
ASPIRE: The Amundsen Sea Polynya International Research Expedition

Received: September 17, 2014
Accepted: September 15, 2015
Published: September 22, 2015

Introduction

The Southern Ocean is disproportionately important to the global biogeochemical system, accounting for up to half of the annual oceanic uptake of anthropogenic carbon dioxide (CO_2) from the atmosphere (Arrigo et al., 2008; Gruber et al., 2009). Models suggest that the vertical mixing there supplies enough nutrients to fertilize three-quarters of the biological production in the global ocean north of 30°S (Sarmiento et al., 2004). Given the large-scale documented changes being observed in many sectors of the Southern Ocean gaining a better understanding of the biogeochemical dynamics is critical (Ducklow et al., 2007; Schofield et al., 2010).

One region showing dramatic change is the Amundsen Sea, which is influenced by some of the largest and most rapid glacier melt and ice sheet thinning in the Southern Ocean (Rignot, 2008). The Amundsen

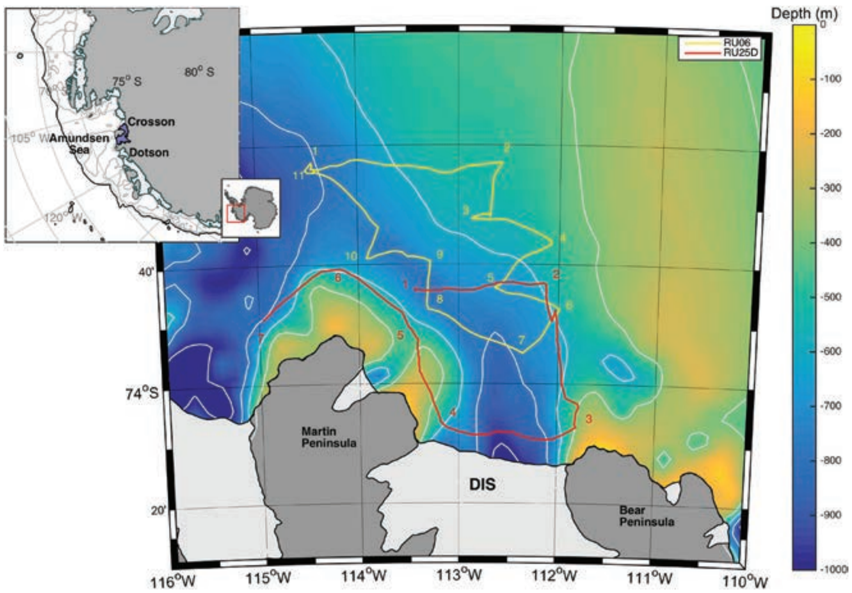

Figure 1

Map of the study area for the ASPIRE and KOPRI cruises.

The Amundsen Sea located near the Dotson and Crosson Ice shelves shown in blue on the inset map (adapted from Rignot et al., 2013). Colored lines indicate the glider missions: yellow for the glider mission during ASPIRE, red for the glider mission during the KOPRI cruise. Numbers on the lines are used to delineate different segments of a glider transect. Depths are indicated by the blue color scale and contour lines, the Antarctic continent is dark gray, and the ice shelves are light gray.

doi: 10.12952/journal.elementa.000073.f001

Sea (Figure 1) harbors two particularly productive polynyas, the Amundsen Sea Polynya (ASP) with an area of ~ 27,000 km^2 and the Pine Island Polynya at ~ 18,000 km^2 (Arrigo et al., 2012). The ASP is a perennially occurring latent heat polynya (Arrigo et al., 2012), though there are indications of a significant sensible component (Stammerjohn et al., 2015). A small portion appears to remain ice-free in winter, but in November it begins to expand, reaching a mean maximum opening in February, after which it rapidly closes in March. In the ASP, the length of the sea ice season has declined by 60 ± 9 days since 1979, a change largely due to the ASP opening earlier in the year by 52 ± 9 days (Arrigo et al., 2012). The shorter sea ice season facilitates increased solar ocean warming, leading to greater sea ice declines. The loss is hypothesized to reflect a poleward intensification of the prevailing storm tracks in the Amundsen-Bellingshausen Sea region (Marshall, 2007; Stammerjohn et al., 2012).

Changes in the Amundsen Sea have significant biological and chemical implications (Yager et al., 2012). The ASP is one of the most productive polynyas (per unit area) in the Antarctic (Arrigo and van Dijken, 2003). Satellite-derived seasonally averaged chlorophyll *a* levels (2.2 ± 3.0 mg m^{-3}) are 40% greater than the Ross Sea Polynya (RSP; 1.5 ± 1.5 mg m^{-3}). Primary productivity in Southern Ocean polynyas tends to be dominated by prymnesiophytes (*Phaeocystis antarctica*) or diatoms (Arrigo et al., 2008). The relative contributions of prymnesiophytes and diatoms reflect a complex interplay of physical circulation/mixing conditions, the light environment, and concentrations of macro- and micro-nutrients. A better understanding of the physical forcing of these communities is important because community composition has biogeochemical implications and this regional system is changing (Arrigo et al., 1999; Alderkamp et al., 2012; Fragoso and Smith, 2012). For example, *P. antarctica* takes up twice as much CO_2 per mole of phosphate removed as diatoms (Arrigo et al., 1999), it is not a preferred prey of microzooplankton (Caron et al., 2000), and its presence has been linked to dimethyl sulfide cycling between the ocean and atmosphere (Liss et al., 1994). The processes driving local productivity and community composition are affected by local weather, which results in high interannual variability in the phytoplankton concentrations (Smith et al., 2006). In the ASP, the interannual variability is higher (138%) than in the RSP (101%) (Arrigo and van Dijken, 2003), emphasizing the critical need to better understand the links between the physical environment of the Amundsen Sea region and the corresponding response in the phytoplankton communities.

Autonomous technologies, which have matured greatly over the last decade, provide means for sampling temporal and spatial domains that are difficult to resolve using traditional ship-based sampling (Davis et al., 2003; Schofield et al., 2007). Underwater Slocum gliders are effective at measuring a wide range of physical (temperature, salinity, currents; Schofield et al., 2007), chemical (oxygen) and bio-optical properties (spectral optical backscatter, chlorophyll fluorescence, colored dissolved organic fluorescence; Schofield et al., 2007; Glenn et al., 2008). Slocum gliders have proven to be effective at characterizing high-resolution horizontal scales, from tens of meters to thousands of kilometers with vertical resolutions < 1 m, and are important tools for studying physical/particle interactions in marine systems (Glenn et al., 2008; Rudnick and Cole, 2011; Miles et al., 2012; Xu et al., 2012; Schofield et al., 2013a).

Physical and bio-optical data were collected using both ship and gliders during two separate field expeditions to the Amundsen Sea. The combined data from both expeditions were used to assess commonalities in the phytoplankton distributions in the polynya. Both expeditions document that high phytoplankton biomass is associated with stratified, shallow, upper mixed layer depths, suggesting the critical role of light in promoting phytoplankton blooms.

Materials and methods

Data were collected during two expeditions to the Amundsen Sea in the South Pacific sector of the Southern Ocean in 2010 and 2013 (Figure 1). The majority of the data was collected during the 2010 field season of the Amundsen Sea Polynya International Research Expedition (ASPIRE; Yager et al., 2012). ASPIRE was conducted as part of the International Polar Year onboard the RVIB *Nathaniel B. Palmer* (NBP) chartered by the US National Science Foundation through its Antarctic Program. The primary objective of the ASPIRE program was to investigate the climate-sensitive processes driving the productivity and carbon sequestration of the ASP. The second data set was collected in January of 2014 as part of the ANA04B cruise of the Korean Polar Research Institute (KOPRI) onboard the IBRV Araon. This effort was conducted in the same area as ASPIRE, with a goal to understand regional circulation and corresponding impacts on Amundsen Sea biogeochemistry.

For both expeditions, discrete sampling was conducted with a CTD rosette outfitted with Niskin bottles allowing for water collection. In this paper we focus on the discrete data from the ASPIRE expedition. During ASPIRE, water was sampled with 12-L bottles from discrete depths in the upper 300 m of the water column at 19 stations (Sherrell et al., 2015). Continuous vertical profiles of temperature, salinity, irradiance, fluorescence, and beam attenuation were obtained from the water column using a SeaBird 911+ CTD, a Chelsea fluorometer, photosynthetically active radiation (PAR) sensor (Biospherical Instruments), and a 25-cm WetLabs transmissometer, mounted on a conventional rosette, deployed using a kevlar cable and winch. Discrete water samples were analyzed for chlorophyll *a* and phytoplankton accessory pigments. Chlorophyll *a* samples were filtered onto 25 mm Whatman GF/F filters, extracted overnight in 5 ml of 90% acetone, and analyzed on a Turner Model 10AU fluorometer before and after acidification (Holm-Hansen et al., 1965). High pressure liquid chromatography (HPLC) analyses were conducted on discrete samples to provide estimates of the chlorophylls and carotenoids. For the HPLC samples, 0.1–2 L were filtered onto 25 mm Whatman GF/F filters, flash-frozen in liquid nitrogen, and stored at –80°C until analysis on a Schimadzu system according to Wright et al. (1991). Chlorophyll *a* measurements on the discrete samples at the time of glider deployments (see below) were considered the "correct values" and used to adjust fluorometric estimates of chlorophyll *a*. Given the relatively short deployment times (just under two weeks) we assume that bio-fouling was negligible.

During both of these expeditions, Webb Slocum gliders (Schofield et al., 2007) were deployed to provide high-resolution surveys of the physical and bio-optical properties near the ice edge (Figure 1). Slocum gliders are autonomous buoyancy-driven vehicles. These 1.5 m long platforms maneuver up and down within the water column through the ocean at a forward speed of 20–30 cm s^{-1} in a sawtooth-shaped gliding trajectory by means of a buoyancy change, where wings translate the sinking motion, due to gravity, into the forward direction. A tail fin rudder provides the steering. The forward navigation system of the vehicle is based on an onboard GPS receiver coupled with an attitude sensor, depth sensor and altimeter. This configuration allows for "dead-reckoning" navigation to a designated waypoint based on the desired target location. Additionally the altimeter and depth sensor allow scientists to program the sampling in the water column. Global iridium phones embedded within the glider tails are periodically raised out of the water when the vehicle sits at the surface at predetermined intervals. Once at the surface, the glider retrieves its position, transmits data to shore, and checks for any programmed changes to the mission. For the gliders, sensor data are logged every 2 seconds on downcast and upcast as it travels with vertical speeds of 20 cm s^{-1}, resulting in high data density relative to traditional shipboard sampling. The gliders used in this study were G2 gliders equipped with a suite of oceanographic sensors. This suite included three science sensors: a Seabird unpumped conductivity temperature and depth (CTD) sensor, a Wetlabs triplet sensor, and an Aanderaa oxygen Optode. While a pumped CTD is preferred to minimize any thermal lag associated with the conductivity cell, none was available for these efforts; however, there was no evidence of salinity spiking, suggesting no bias in the derived salinity values resulting from thermal inertia. Prior to and after deployment, the glider CTD was compared to independent CTDs in a tank test, and the results indicated that the glider CTD did not exhibit any drift.

The pre- and post-dive latitude and longitude of the glider, along with glider pitch, heading, and vertical velocity, were combined to calculate dead-reckoned currents (Davis et al., 2003). The horizontal velocity of the glider was estimated using simple geometry by combining the systems-measured pitch angle and the vertical velocity calculated from the change in pressure with time, while the glider compass was used to determine heading. The instantaneous horizontal velocities were integrated in time for the duration of the glider dive time to obtain an estimated glider position independent of ambient currents. The difference between the estimated surfacing position and actual position divided by the duration of the dive results in a time- and depth-integrated, dead-reckoned water column velocity. The largest source of error in this method of current calculation is the calibration of the glider compass. Both RU06 and RU25D compasses were calibrated

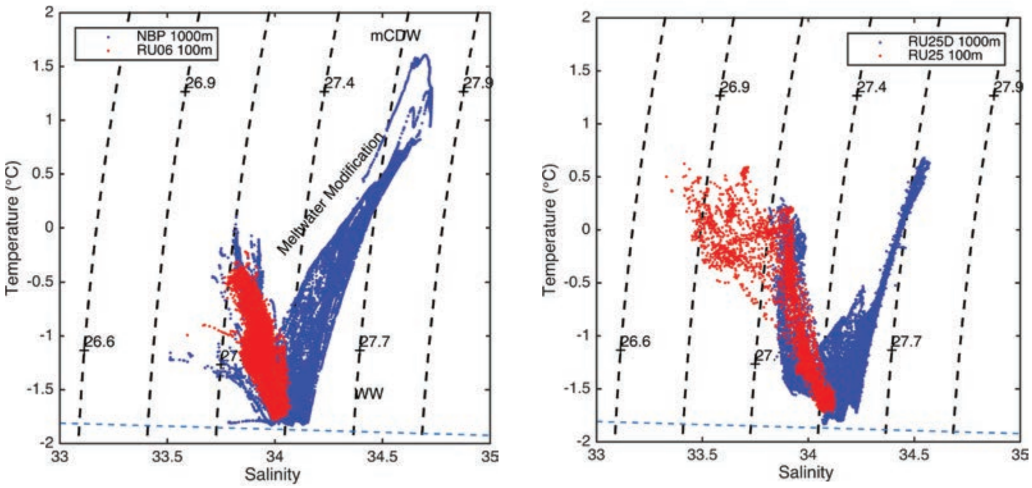

Figure 2

Temperature and salinity properties measured during the ASPIRE and KOPRI cruises.

Shown in (A) are the temperature and salinity properties measured during ASPIRE in austral summer of 2010–2011 using both the CTD from the ship (NBP) over the full 1000-m water column (blue) and the glider (RU06) which profiled only the upper 100 m (red). Glider data from the KOPRI cruise in austral summer of 2013–2014 are shown in (B) where blue indicates glider data for the full water column (RU25D) and red indicates glider data from the upper 100 m (RU25). Side by side casts of the ship CTDs and the gliders showed that both measured the same features in the water column, as shown for ASPIRE data in (A). Glider measurements for temperature were lower than the CTD by 0.05° C. Glider measurements for salinity were lower than the CTD by 0.01. We took the ship CTD data as correct and adjusted the glider measurements by those offsets.

doi: 10.12952/journal.elementa.000073.f002

following manufacturer specifications and checked using an 8-point heading test prior to deployment. This dead-reckoned current estimation method has been used extensively in a range of conditions (Glenn et al., 2008; Merckelbach et al., 2008; Miles et al., 2012, 2015a) and has been shown to perform well compared to moored acoustic Doppler current profilers (Davis et al., 2003).

In order to assess the influence of tidal velocities on glider currents for each deployment, we extracted all ten tidal constituents from the Circum-Antarctic Tidal Simulation Model (CATS2008b) (Padman et al., 2002) in the vicinity of the deployments (74° S and 112.5° W). CATS2008b represents the barotropic tidal velocities and has been used in previous studies in the Amundsen Sea Polynya (Wåhlin et al., 2010, 2012; Assmann et al., 2013; Ha et al., 2014).

ASPIRE took place between 25 November 2010 and 18 January 2011. Two glider deployments were conducted while in the ASP; the first mission (Dec 15–28) covered 300 km in 13 days. The glider was recovered and redeployed for a second shorter deployment (Jan 01–05) covering 75 km in 3.5 days. The glider for this mission (RU06) was outfitted with a 200-m buoyancy pump and a non-pumped SBE41cp Seabird Conductivity-Temperature sensor, though it only profiled in the upper 100 m of the water column. There was good agreement between the glider and ship rosette temperature and salinity data (Figure 2). The glider was also equipped with two WET Labs Environmental Characterization Optics (ECO) pucks. The ECO pucks measured chlorophyll *a* fluorescence, colored dissolved organic matter (CDOM) fluorescence and optical backscatter at 470, 532, and 660 nm. The CDOM fluorometer was outfitted with an excitation wavelength of 370 nm and emission wavelength of 460 nm, with the sensor having a sensitivity of 0.09 ppb. The ECO Pucks were factory-calibrated prior to deployments. The backscatter measurements were measured at 117 degrees, the angle determined as a minimum convergence point for variations in the volume-scattering function induced by suspended materials and water itself. We converted from the volume-scattering function to estimated backscatter coefficients following Boss and Pegau (2001). As a result, the signal measured was less determined by the type and size of the materials in the water and more directly correlated to the concentration of the materials.

For the KOPRI expedition (27 December 2013 – 18 January 2014), the RU25D glider was outfitted with a 1000-m pump, a non-pumped SBE41cp Seabird Conductivity-Temperature sensor, a single WET Labs puck configured to make measurements of optical backscatter at 470 and 532 nm, along with chlorophyll *a* and CDOM fluorescence and an Aandeara oxygen optode. This deep-water glider conducted a 234-km mission over 9 days (04–14 January 2014).

Ship-based ocean currents during ASPIRE were measured with a 'narrow beam' 150-kHz and 'Ocean Surveyor' 38-kHz hull mounted Acoustic Doppler Current Profilers (ADCP) from Teledyne RD Instruments, Inc. The ADCP data were calibrated and post-cruise corrected by the University of Hawaii. The Teledyne instrument provides accurate data to a depth of 400 m, while the Ocean Surveyor data cover a larger depth range but with coarser vertical resolution.

Ocean color imagery was obtained from the National Aeronautics and Space Administration (NASA) Moderate Resolution Imaging Spectroradiometer (MODIS) onboard the polar orbiting Aqua satellite. The products used here are the standard level-3 mapped 8-day composites for chlorophyll *a* (obtained from http://oceancolor.gsfc.nasa.gov/). Typically for these waters, satellite-derived chlorophyll concentrations tend to be under-estimated (Johnson et al., 2013); therefore, these maps should be considered lower limit estimates.

The mean satellite-derived chlorophyll fields, as well as the integrated water column chlorophyll data measured by the gliders, were used as inputs to the Hydrolight 4.3 radiative transfer model (Mobley, 1994) to estimate optical properties within the water. For the Hydrolight simulations, we used default settings and assumed a constant backscatter to total scatter ratio of 0.005. We assumed there was no inelastic scattering and kept wind speeds at zero. The surface flux of light was calculated using a semi-empirical sky model (Mobley, 1994) at local noon on a cloudless day. We assumed that the water column was infinitely deep. These Hydrolight simulations assumed no vertical structure in the phytoplankton biomass. For these simulations we treated these waters as Case I waters (Mobley et al., 1994).

Results

Water masses and flows along the ice sheet in the Amundsen Polynya

Ship and glider surveys encountered three major water masses in this region: Antarctic Surface Water (AASW), Winter Water (WW), and modified Circumpolar Deep Water (mCDW). AASW was observed by ships and gliders during both ASPIRE and KOPRI cruises (Figure 2). It ranged in thickness from ~ 5 to 80 m and was characterized by low salinity (< 34.1), presumably freshened by sea ice melt, and by a temperature range of −1.8 to > 0°C (Figures 3, 4). The glider encountered, at lower latitudes, low salinity surface water (salinity values reduced by ≥ 0.3) (Figure 3, 4). Cold (< −1.7°C) WW, with a well-defined salinity value (34.14) reflecting sea ice growth during the previous winter, was typically found extending either from the surface or from the AASW layer down to 300–400 m depth (Figure 4). The warmer (0.6 to 1.2°C) and saltier (34.5 to 34.7) mCDW was observed by RU25D, with warmest temperatures encountered below 600 m (Figure 4A, 5A). Regions with low surface salinity generally had homogeneous mixed layers with a stratified region at base over the WW. We defined the upper stratified layer by the depth of the highest water column buoyancy frequency (N^2). The upper mixed layer ranged from 20 to 80 m in depth (Figures 3D, 4D, 5D). Highest chlorophyll was associated with water columns when the N^2 was shallower than 50 m. During ASPIRE the shallow upper mixed layers and highest chlorophyll were associated with regions of lower surface salinity. During the KOPRI effort the shallow upper mixed layers and highest chlorophyll were associated with regions of warm surface waters (0.0–0.5° C). Possible reasons for these differences might reflect the general position of the glider missions, as the KOPRI glider surveyed directly adjacent the outflow at the ice edge while the ASPIRE glider surveyed further offshore in the polynya potentially allowing for radiant heating as the water flowed offshore (Figure 1).

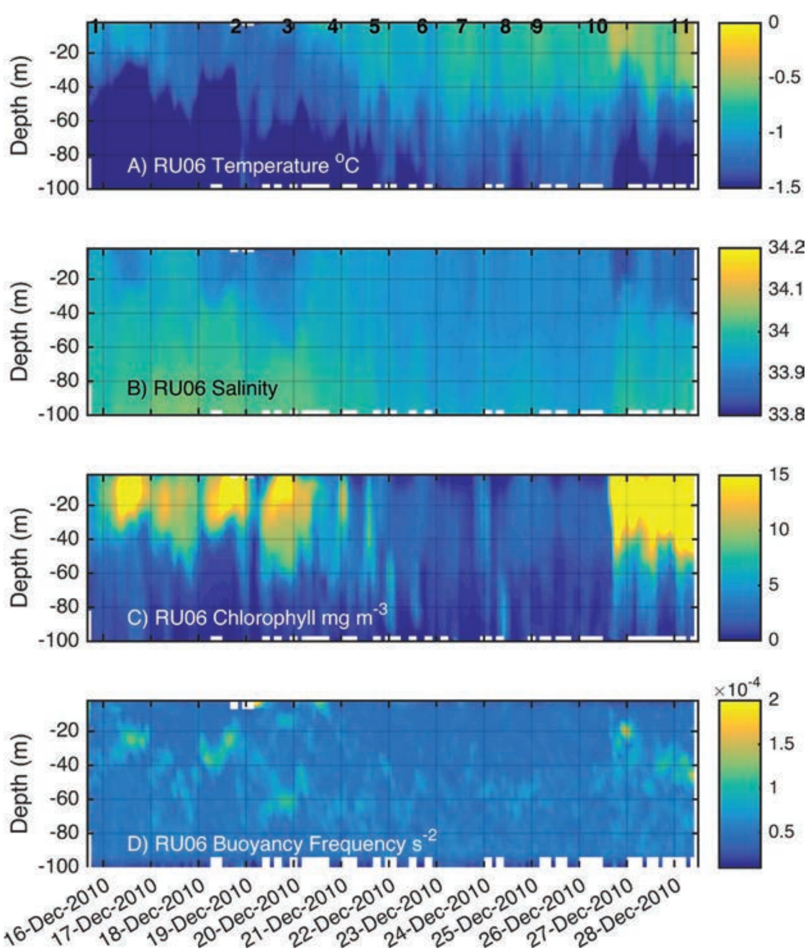

Figure 3

The water column data collected by the Webb Slocum glider during the ASPIRE cruise.

Temperature, salinity, chlorophyll fluorescence and buoyancy frequency are shown for the upper (100-m) water column, as measured by glider RU06. Temperature ranged from 0.0 to −1.5° C (A); salinity showed a range of 0.3 (B); chlorophyll fluorescence showed a range of 30 mg m^{-3} (C); and buoyancy frequency (s^{-2}) ranged in magnitude two-fold. The numbers along the top (A) are the markers of glider mission segments identified on the yellow line in Figure 1.

doi: 10.12952/journal.elementa.000073.f003

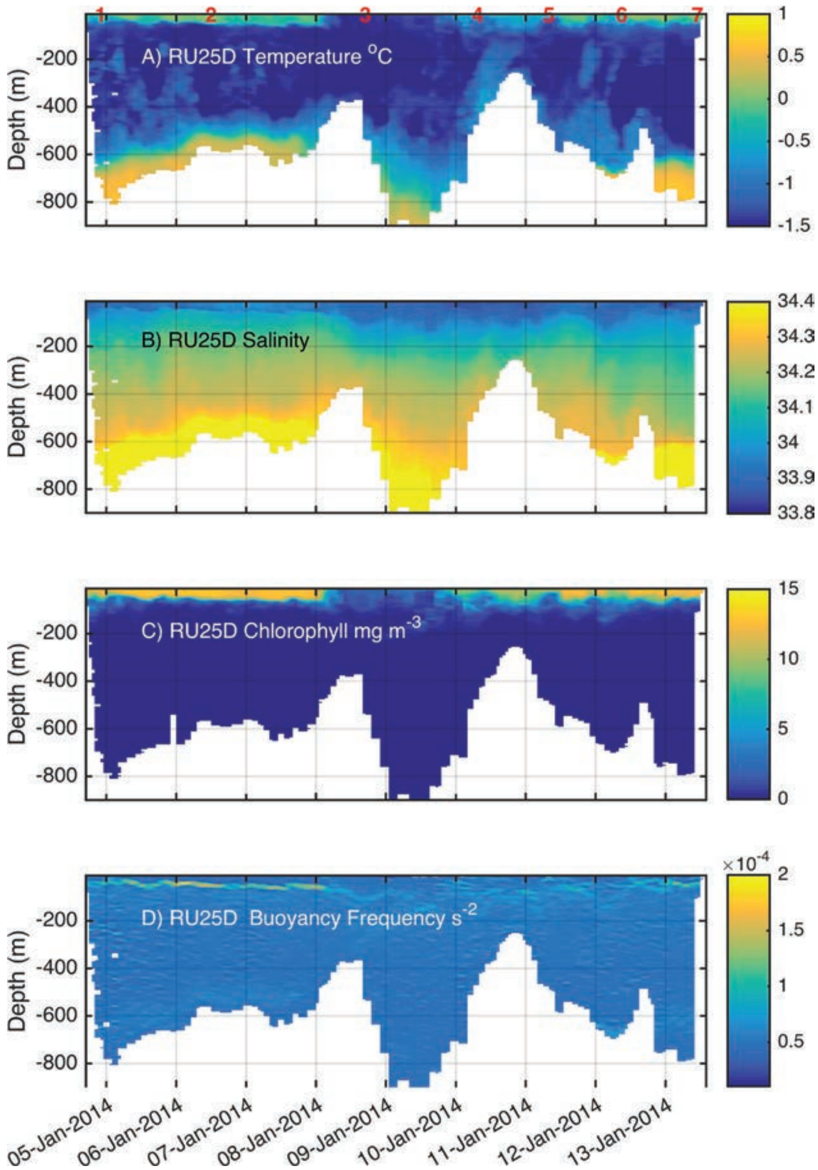

Figure 4

The full water column data collected by the deep-water glider during the KOPRI expedition.

Temperature, salinity, chlorophyll fluorescence and buoyancy frequency are shown throughout the water column, as measured by deep-water Webb glider RU25D. Temperature ranged from 1.0 to −1.5° C (A); salinity showed a range of 0.6 (B); chlorophyll fluorescence showed a range of 30 mg m^{-3} (C); and the buoyancy frequency (s^{-2}) calculated from the glider data ranged in magnitude greater than two-fold (D). The numbers along the top (A) are the markers of glider mission segments identified on the red line in Figure 1.

doi: 10.12952/journal.elementa.000073.f004

During ASPIRE, the ship and glider observed similar flow patterns. The depth-averaged currents from RU06 indicated the upper 100 m was characterized by low mean northward flow of 0.056 m s^{-1} and a mean east–west flow of –0.048 m s^{-1} (Figure 6, top panel) originating from the Dotson Ice Shelf. The shipboard along-shelf ADCP transect confirmed northward flow in the upper 100 m (Figure 7) with current speeds ranging from 0.15 to 0.05 m s^{-1}, similar in magnitude to the depth-averaged currents measured by the glider. The deeper current velocities measured by the ship showed depth dependence and spatial variability (Figure 7). At the eastern edge of the along-shelf transect, subsurface water (> 200 m) flowed south towards the ice sheet. On the western edge, bottom waters associated with a shallowing bathymetry showed subsurface waters (> 200 m) with a northward flow (> 0.25 m s^{-1}) associated with a topographic high. During most of the ASPIRE glider deployment, wind levels were consistent in direction and velocity; except during a few hours at the start of deployment, winds were consistently less than 10 m s^{-1}. Therefore, significant regional shifts in the upper ocean circulation were not likely driven by significant changes in weather forcing.

During the KOPRI cruise, RU25D encountered mean offshore flow relative to the Dotson Ice Shelf in the northwestern regions of the study area (Figure 8). Potential outflow of the deeper mCDW was observed on the western flank of the canyon during the KOPRI cruise. This outflow was seen as a filament of higher temperature water on the canyon edge (Figure 4, between segment 4 and 5 denoted at the top of panel A), located below 200-m water depth, and, like the ASPIRE ADCP sections, was associated with a shallowing of the seafloor. Generally, tidal currents were small relative to glider dead-reckoned velocities and thus were

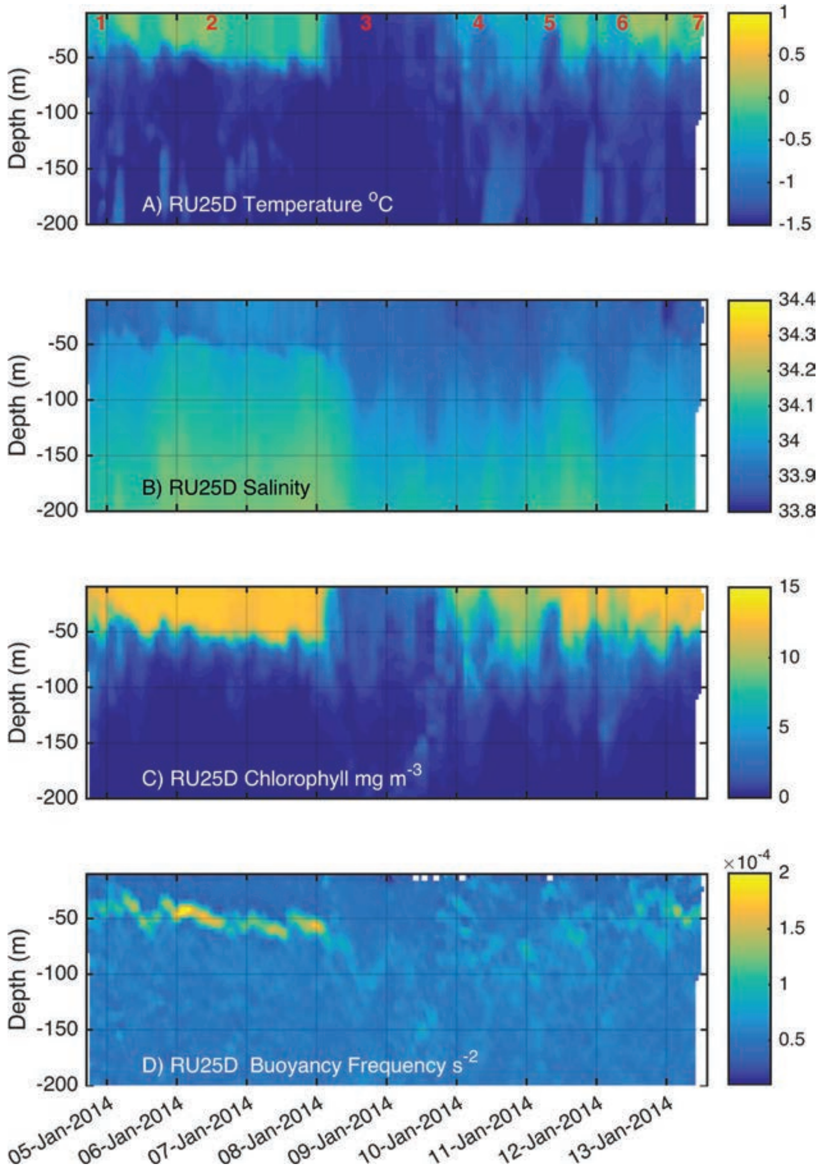

Figure 5

The upper 200-m water column data collected by the deep-water glider during the KOPRI expedition.

Temperature, salinity, chlorophyll fluorescence and buoyancy frequency are shown for the upper 200 m of the water column, as measured by deep-water Webb glider RU25D. Temperature ranged from of 0.0 to –1.5° C (A); salinity showed a range of 0.3 (B); chlorophyll fluorescence showed a range of 30 mg m^{-3} (C); and the buoyancy frequency (s^{-2}) calculated from the glider data ranged in magnitude just under two-fold (D). The numbers along the top (A) are the markers of glider mission segments identified on the red line in Figure 1.

doi: 10.12952/journal.elementa.000073.f005

not considered to greatly impact interpretation of mean flow patterns as derived from the glider and ship transects (Figures 6 and 8).

Bio-optical properties of the Amundsen Sea Polynya

Both the ASPIRE and KOPRI cruises coincided with the development of the phytoplankton spring/summer bloom (Figure 9). The timing of the peak phytoplankton concentrations in January was consistent with past studies (Arrigo et al., 2012). In both years, blooms were concentrated over deep water with lower phytoplankton biomass observed near the ice edge and on the shallower banks to the north (Figure 9). Satellite imagery indicated low biomass adjacent to the ice shelf consistent with ship and glider data; therefore, the land adjacency effects in the satellite imagery likely did not account for low values nearshore.

During ASPIRE, the RU06 mission was conducted when satellite-derived chlorophyll *a* concentrations (8-day average) ranged from < 1 to 10 mg m^{-2} (Figure 9). Highest phytoplankton biomass was found at the northern edge of the seafloor canyon, with lower levels on the northern polynya sea ice edge and bordering the Dotson and Getz ice shelves. By the end of the deployment, MODIS imagery showed that chlorophyll biomass had increased by ten-fold in the region (Figure 9). Glider chlorophyll estimates ranged from 1 to 15 mg chlorophyll *a* m^{-3}, which was similar to satellite estimates. During the KOPRI expedition, the blooms were spatially extensive with higher biomass observed throughout the same northern sector of the polynya

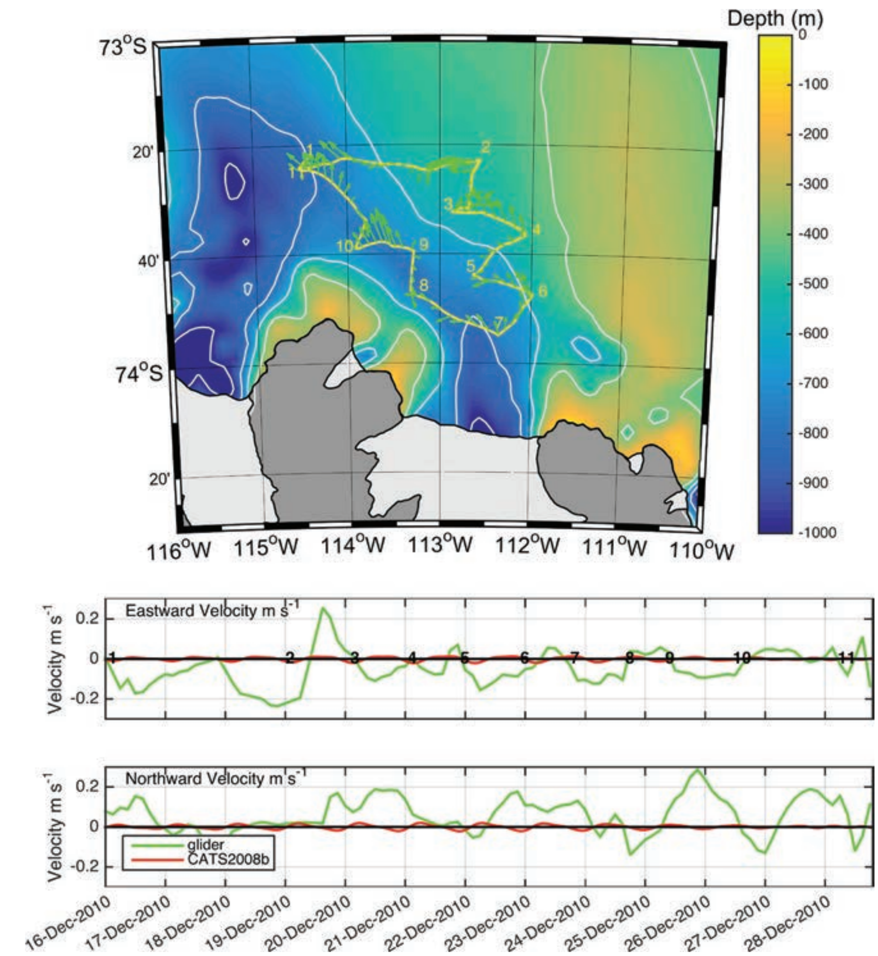

Figure 6

The depth-averaged current velocity and directional components estimated from the ASPIRE glider experiment.

The current velocity representing the average for the upper 100 m of the water column in austral summer 2010–2011 is shown for the study region, with the eastward and northward velocity components derived from the glider (green line) and modeled for the tides (red line). Numbers on the map and in the eastward velocity panel indicate segments of the glider mission presented in Figure 1.

doi: 10.12952/journal.elementa.000073.f006

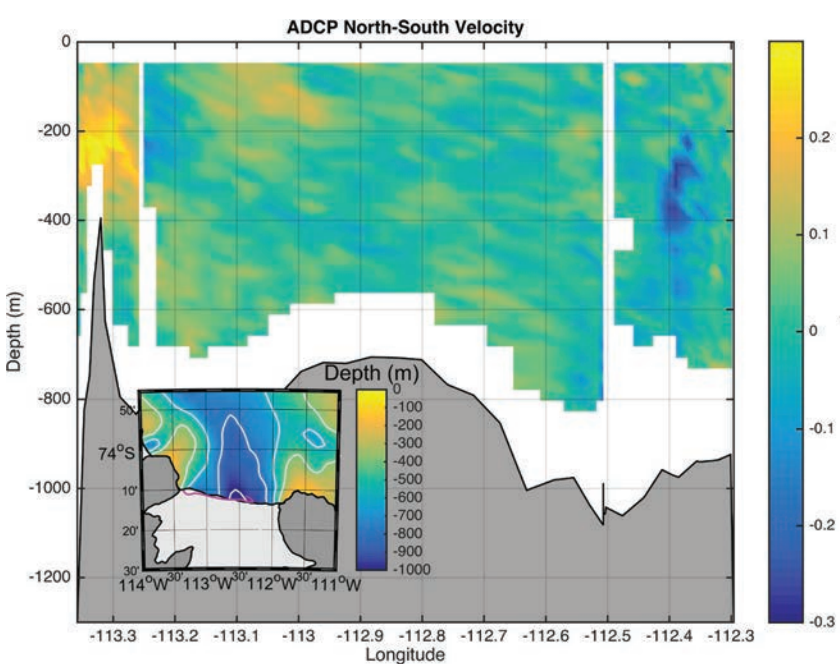

Figure 7

The water-column current velocities near Dotson Ice Shelf, measured from the ship-mounted ADCP.

Current velocities (color scale in m s^{-1}) are shown throughout the water column measured by the ship-mounted acoustic doppler current profiler (ADCP) during the ASPIRE cruise. The inset shows the location of the ship transect (purple line) along the ice shelf for the plotted ADCP data.

doi: 10.12952/journal.elementa.000073.f007

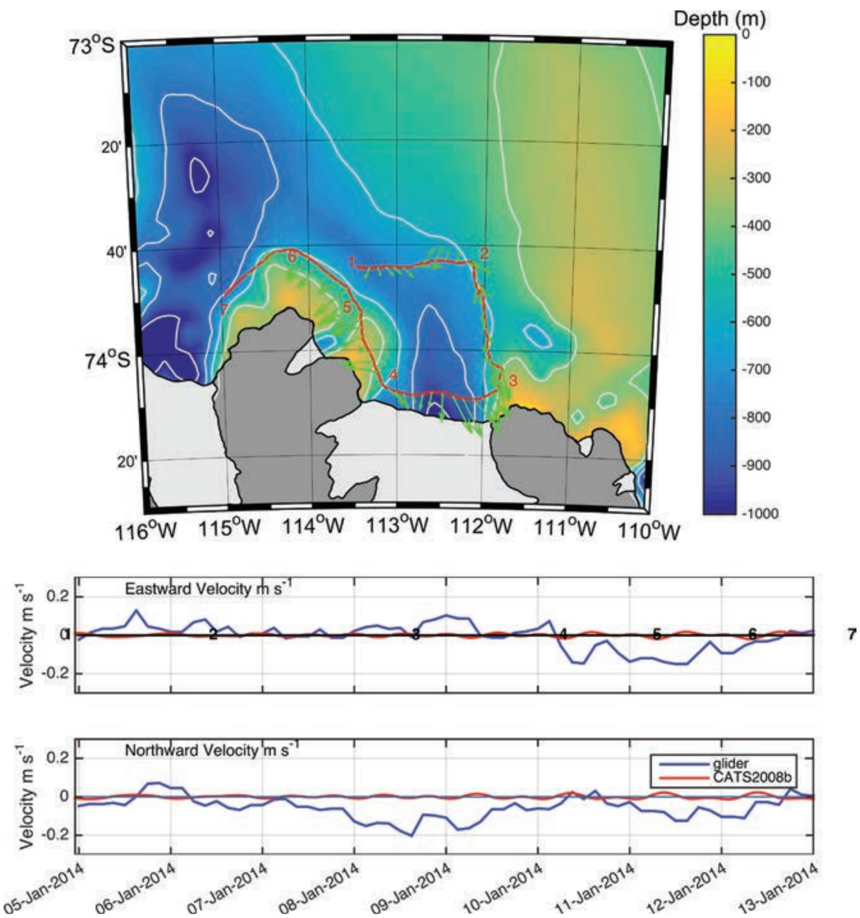

Figure 8

The depth-averaged current velocity and directional components estimated from the KOPRI glider experiment.

The current velocity representing the average for the upper 1000 m of water column in austral summer 2013–2014 is shown for the study region, with the eastward and northward velocity components derived from the glider (green line) and modeled for the tides (red line). Numbers on the map and in the eastward velocity panel indicate segments of the glider mission presented in Figure 1.

doi: 10.12952/journal.elementa.000073.f008

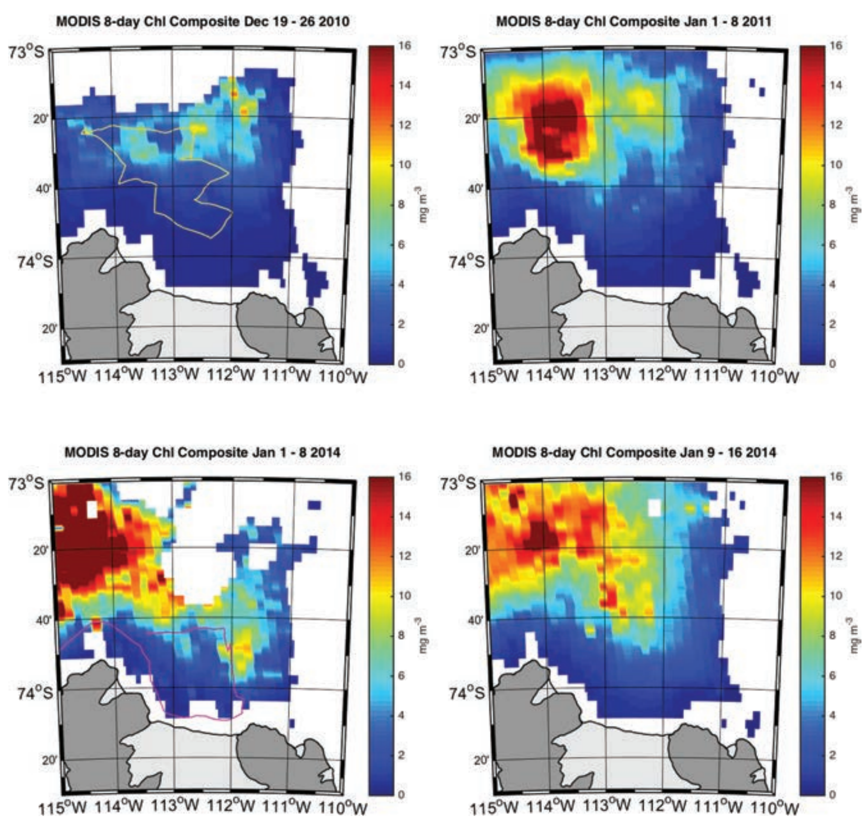

Figure 9

Satellite-derived chlorophyll estimates for the ASPIRE and KOPRI cruises.

Estimates of chlorophyll concentration (mg m^{-3}) based on MODIS-AQUA 8-day average ocean color images are shown for the study region. The yellow and red lines indicate the flight paths for the glider deployments.

doi: 10.12952/journal.elementa.000073.f009

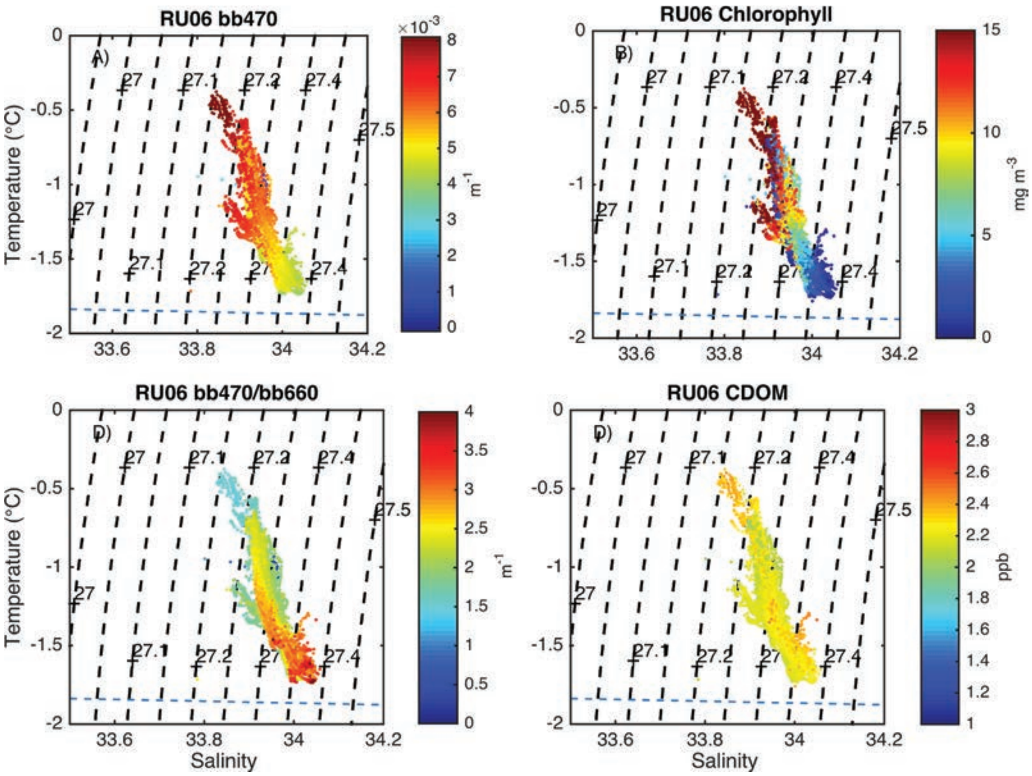

Figure 10

Bio-optical properties in temperature-salinity space measured by a 100-m glider experiment during the ASPIRE cruise.

Water column properties measured by Webb glider RU06 over a 100-m deployment are presented as a function of temperature and salinity: (A) optical backscatter at 470 nm (bb470 nm); (B) chlorophyll estimates (mg m^{-3}) from fluorescence; (C) the ratio of 470 to 880 nm optical backscatter (bb470/bb660); and (D) the fluorescence of colored dissolved organic matter (CDOM).

doi: 10.12952/journal.elementa.000073.f010

with the peak concentrations occurring in the first week of January (Figure 9B). The bloom appeared to have begun prior to the deployment of the glider with biomass remaining high by mid-January (Figure 9).

Glider surveys during ASPIRE indicated phytoplankton and particle concentrations were highest in warm (–1 to –0.5° C) lower salinity (< 34) AASW (Figures 10). In contrast, CDOM fluorescence indicated relatively uniform distributions across the temperature and salinity range encountered by the glider; therefore, the CDOM fluorescence did not have much power in discriminating water masses in this region. This finding was consistent with results from the Aaron expedition, when water masses were less well discriminated by CDOM compared to optical backscatter or oxygen data (Figure 11). Consistent with ASPIRE, during the Aaron cruise the highest values of optical backscatter were observed in the warm low saline waters (Figure 11). Fluorescence-based estimates of chlorophyll were > 10-fold higher in warmer and lower saline surface waters. Chlorophyll fluorescence measurements indicated concentrations > 15 mg m^{-3}. Chlorophyll fluorescence at ASPIRE glider recovery (same location after 13 d; Figure 12) showed a 5-fold increase relative to when the glider was deployed. This increase was consistent with the increasing chlorophyll concentrations observed in the satellite imagery (Figure 9). While chlorophyll increased dramatically, water temperature increased by < 0.5° C with a corresponding decrease of salinity by 0.1, suggesting a water mass with similar hydrographic features as when deployed. During the deployment there were steady, low wind speeds (10 m s^{-1}) which, combined with the depth-averaged flow measured by the glider, suggests flow from the low biomass waters near the ice sheet to the high biomass waters within the polynya. Given the minor shifts in water properties and transport, if we assume biomass accumulation represents the net growth rate of the phytoplankton, this observed increase translates to a net growth rate of ~ 0.10 d^{-1}. During the ASPIRE cruise deckboard incubations of natural phytoplankton populations over a range of modified light levels and micronutrient conditions exhibited growth rates that ranged from 0.07 to 0.28 d^{-1} (Alderkamp et al., 2015). Lowest growth rates were observed for low light (1% light incubation levels) and low iron (Fe) conditions consistent with the ambient conditions of the AASW (Alderkamp et al., 2015).

High phytoplankton biomass in the AASW resulted in extremely turbid surface waters. The depth of the 1% light level ranged from 5 to 40 m during ASPIRE, as measured with the CTD rosette and modeled based on chlorophyll inputs into the Hydrolight model. The high biomass layers ranged in thickness from 20 to 50 m, consistent with the depth of the upper mixed layer. The fluorescence estimates of chlorophyll showed little variability in the upper mixed layer. Thus, given the high biomass and depth of the upper mixed layer, the majority of the phytoplankton biomass resided well below the 1% light level at any given time. Photosynthesis-irradiance curves indicated the light saturation intensity for photosynthesis (E_k) ranged from 37 to 67 □mol photons m^{-2} s^{-1} (Alderkamp et al., 2015), which was consistent with low-light-acclimated phytoplankton populations when compared to average water column measurements of E_k in other pelagic

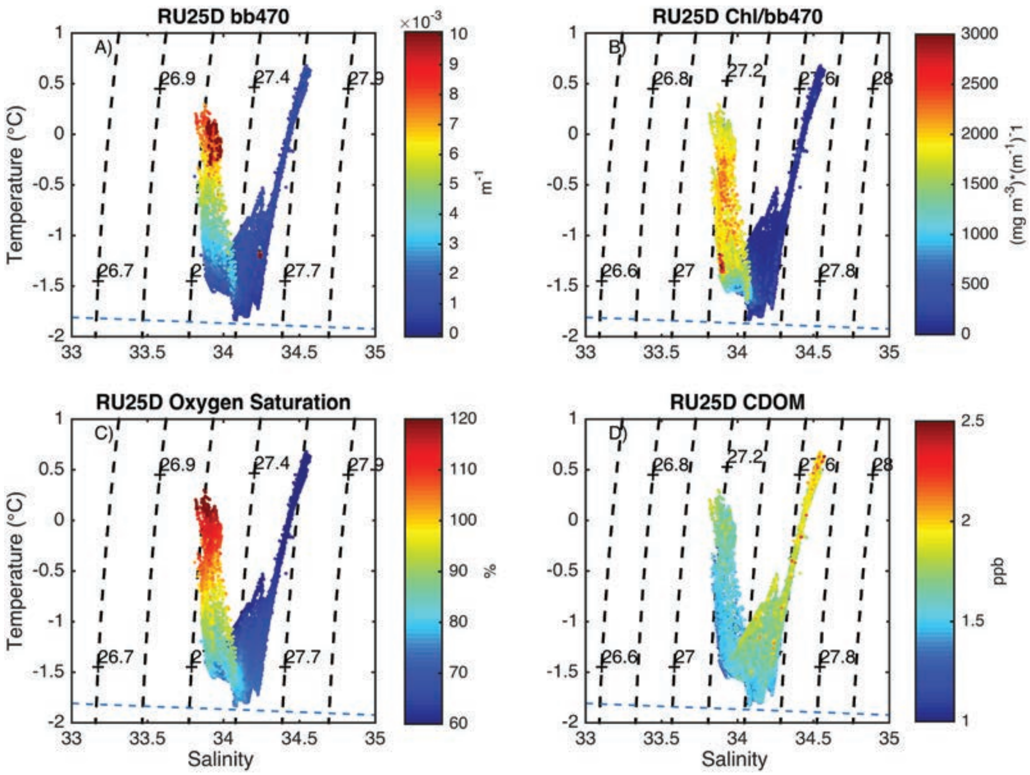

Figure 11

Bio-optical properties in temperature-salinity space measured by a 1000-m glider experiment during the KOPRI expedition.

Water column properties measured by Webb glider RU25D over a 1000-m deployment are presented as a function of temperature and salinity: (A) optical backscatter at 470 nm (bb470); (B) the ratio of chlorophyll from fluorescence to backscatter at 470 nm (mg m^{-3}/bb470); (C) the oxygen concentration (% saturation); and (D) the fluorescence of colored dissolved organic matter (CDOM).

doi: 10.12952/journal.elementa.000073.f011

and coastal locations in the Southern Ocean (Moline et al., 1998). While low salinity AASW was associated with regions of high phytoplankton biomass, it was not a guarantee of high phytoplankton biomass. During the KOPRI expedition high biomass was observed only when low salinity surface waters were confined to < 50 m. Near and along the ice edge, phytoplankton biomass was low within the upper 150 m despite the observed lower salinity (Figures 3, 5). Here, low water column stability confirmed the critical requirement of light in contributing to the phytoplankton blooms. There was a significant relationship with the depth of the upper mixed layer as defined by the maximum N^2 and the mean chlorophyll in the upper water column during both the ASPIRE and KOPRI expeditions (Figure 13; RU06 R^2 = 0.43 and p-value

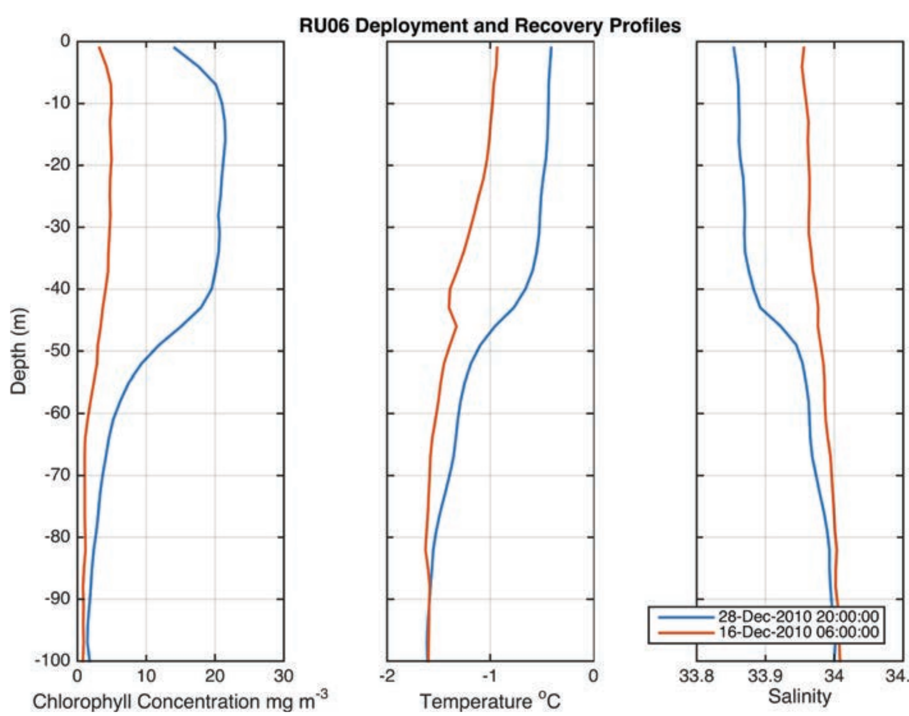

Figure 12

Depth profiles of chlorophyll fluorescence, temperature, and salinity at time of glider deployment and recovery.

The chlorophyll fluorescence (mg m^{-3}), temperature (°C), and salinity are shown as a function of depth for the deployment (green line) and recovery (blue line) of Webb Slocum glider RU06. The deployment and recovery locations were at the same geographic location (73 23 12°.15'S and 114 26° 04.91W).

doi: 10.12952/journal.elementa.000073.f012

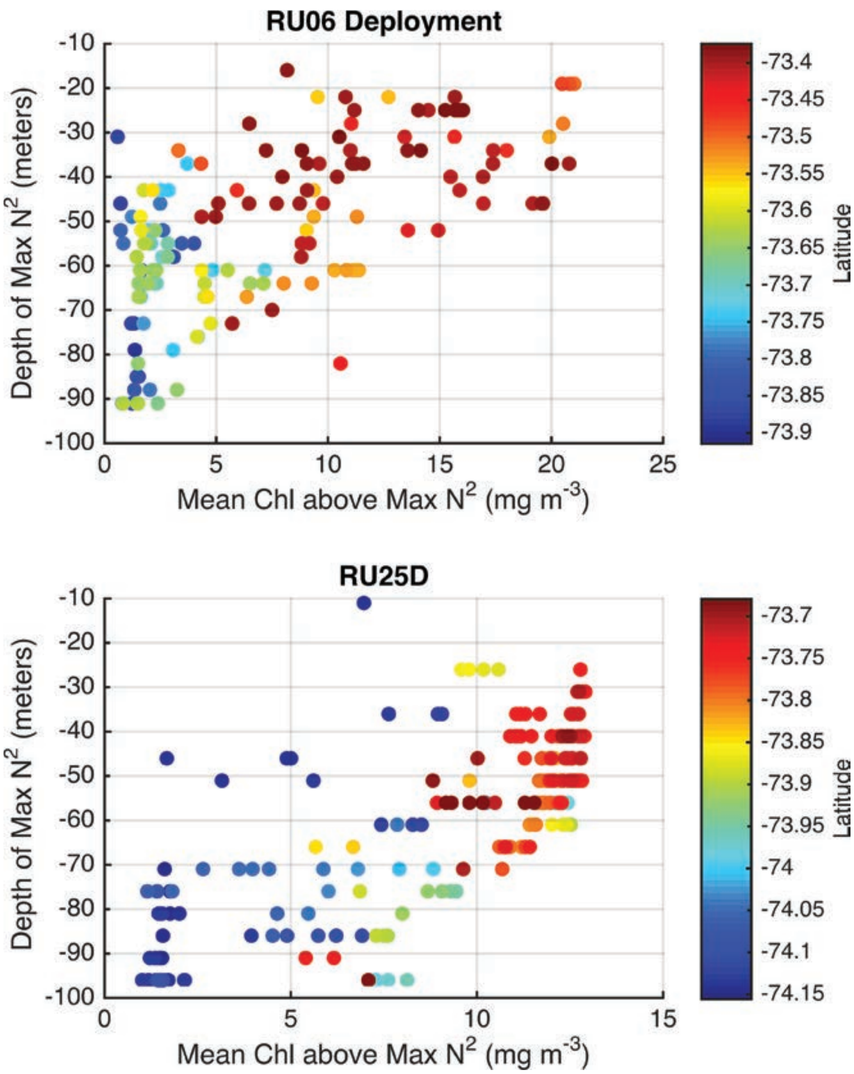

Figure 13

Relationship between depth of maximum water column buoyancy frequency (N^2) and mean chlorophyll concentration.

The relationship between the depth of maximum water column buoyancy frequency (N^2) and the mean chlorophyll *a* concentration (mg m^{-3}) is shown for the water column above the maximum N^2 depicted in Figures 4 and 5. The colors indicate the latitude of the water column measurements. Red colors generally indicate distance away from the ice shelf.

doi: 10.12952/journal.elementa.000073.f013

< 0.001, RU25D R^2 = 0.59 and p-value < 0.001). Higher chlorophyll was associated with lower latitudes (Figure 13) located offshore the ice edge (Figure 1B). The higher N^2 associated with the offshore waters was associated with increased solar warming of surface waters and the increased inputs of freshwater from sea ice melt (Alderkamp et al., 2015).

During ASPIRE, bio-optical data suggested that the nature of the particulate matter was unique in the lower salinity surface water compared to high salinity surface water. While fluorescence-based phytoplankton biomass estimates correlated with optical backscatter (for RU06 and RU25D, R^2 = 0.92 and 0.90, respectively, p-value < 0.001), there was variability in the chlorophyll/backscatter and spectral backscatter ratios (Figure 10, 11). The spectral optical backscatter ratio (470 nm/660 nm) was lower in the AASW. The portions of the water column associated with high values of optical backscatter at 470 nm had low spectral backscatter ratios (470 nm/660 nm; Figure 10). In the high backscatter regions, the 20–30% range in the spectral ratio reflected a flattening in the backscatter spectrum, indicating either a change in the particle size distribution or a change in the organic/inorganic make-up of the particles (Boss et al., 2004). Furthermore, the variability in backscatter spectra suggests that it would be difficult to convert the backscatter data to a particle concentration without information on the particle type and size distribution (Boss et al., 2004). Pigment analyses revealed that the high biomass waters were dominated by prymnesiophyte algae, as indicated by HPLC measurements of 19′-hexanoyfucoxanthin. Microscopic examination identified *Phaeocystis pouchetti* as the dominant species present. The low chlorophyll concentrations were characterized by diatom communities, as indicated by the presence of fucoxanthin. These shifts were consistent with the spatial variability in the optical backscatter ratio.

Discussion

Understanding the physical regulation of primary productivity and community structure along ice shelves and polynyas is critical to understanding the regional ecology and biogeochemistry. Polynyas in the Amundsen Sea region are characterized by large phytoplankton blooms (Arrigo et al., 2012; Lee et al., 2012) and are experiencing change due to climate forcing (Holland, 2014). Phytoplankton studies in key polynyas to date have focused on defining the relative importance of nutrient versus light regulation (Lee et al., 2012), with numerous efforts focusing on the importance of iron (Fe) in driving phytoplankton growth in polynyas (Buma et al., 1991; Sedwick and DiTullio, 1997; Sedwick et al., 2000; Tagliabue and Arrigo, 2005).

Deckboard incubations during ASPIRE confirmed the importance of Fe in promoting accelerated growth in phytoplankton (Alderkamp et al., 2015). There are several potential sources of Fe reflecting a range of ocean-ice sheet-seafloor interactions. The potential sources of Fe include basal melting of glaciers and beneath ice shelves, sediment resuspension within the sub-glacial cavity and at grounding lines, and direct input from calved icebergs (Gerringa Loes et al., 2012; Yager et al., 2012). While these sources are sufficiently large to support large phytoplankton blooms (Sherrell et al., 2015), deckboard incubations suggest increased input of Fe could increase primary productivity by a factor of 1.7 (Alderkamp et al., 2015).

The mCDW subsurface outflow from the ice sheet appears to be a major source of dissolved and particulate iron to the polynya (Gerringa Loes et al., 2012; Sherrell et al., 2015). Driven by Coriolis and pressure gradient forces, the relatively dense CDW travels along-isobath toward the ice shelves with the coastline to the left of the flow. This warm water mass affects the glaciers and ice shelves, melting ice and forming a modified CDW (mCDW) and meltwater mixture (Jenkins, 1999; Walker et al. 2007; Jenkins and Jacobs, 2008; Jenkins et al., 2010; Jacobs et al., 2011). Presumably the meltwater input increases buoyancy of the mCDW, causing upwelling, while the Coriolis force drives outflows on the southern and western sides of the ice shelves dependent on bathymetric orientation. The micronutrients associated with outflow can fuel productivity if mixing carries the deeper water into the euphotic zone. It has been hypothesized that transport of subsurface water to the surface is driven by horizontal diffusivity (Gerringa Loes et al., 2012), advective eddy transport (e.g., Årthun et al., 2013), mixing along the Dotson trough (St-Laurent et al., 2013), and wind- and iceberg-induced mixing (Randall-Goodwin et al., 2015). Given the slow, calculated *in situ* and deckboard growth rates of the phytoplankton and the observed high biomass, injection of nutrients through destratification of the full water column followed by stratification and subsequent regrowth is unlikely. The injection of micronutrients would thus likely be dominated by horizontal and vertical advection and diffusive mixing. Observations suggest that dissolved iron- and meltwater-rich deep water shoals from the basal ice shelf towards the central polynya and likely supports the bloom there (Sherrell et al., 2015). Recent results in the ice shelf outflow region, showing decreasing optical backscatter with proximity to the seafloor, suggest that particulate matter, which had a linear relationship with meltwater concentration, was sourced from the overlying glacier rather than resuspended sediment (Miles et al., 2015b).

The robust relationship between water column stability and chlorophyll concentration suggests the importance of the light environment in driving phytoplankton standing stock in the ASP. The high concentrations of phytoplankton encountered in this polynya indicate an extremely productive system. Productivity rates are similar to the high productivity rates found along the West Antarctic Peninsula (WAP; Ducklow et al., 2007), with the contrast that along the WAP the high productivity regions are associated with diatoms (Hart, 1942; Moline et al., 2004; Vernet et al., 2008; Montes-Hugo et al., 2009). The high productivity rates associated with *Phaeocystis* in the ASP are consistent with the Ross Sea (Smith et al., 1998, 2003). Additionally, the high concentrations of chlorophyll encountered during the ASPIRE and KOPRI cruises are consistent with past ship (Lee et al., 2012) and satellite studies (Arrigo et al., 2012). Given the high biomass in these waters, satellite estimates of chlorophyll would underestimate the overall biomass significantly, as the depth of the satellite section would span only the upper few meters of the water column, missing the majority of the phytoplankton biomass (Kirk, 2011).

The ASP with its high biomass conditions represents a unique environment in which the interplay between nutrient availability and light limitation is extremely complex (Dubinsky and Schofield, 2009). Phytoplankton populations are capable of photoacclimating to low light conditions and measured photosynthesis-irradiance curves during ASPIRE indicated the cells were low light-adapted (Alderkamp et al., 2015); however cells were still often chronically light-limited. This was especially true as the upper mixed layer was often deeper than the euphotic zone (defined as the 1% light level). The net result is that in the high biomass waters any small shift in the mean position of phytoplankton in the water column (meters) could shift a cell from being light-saturated to being light-limited; therefore, cell motility and/or mixing within the turbid upper mixed layer waters must play a predominant role in determining the overall water column productivity and corresponding growth of the phytoplankton (Kroon and Thoms, 2006; Dubinsky and Schofield, 2009; Schofield et al., 2013b).

Given that a relatively constant biomass of phytoplankton spanned the upper mixed layer (Figure 12) which was often over 10-fold deeper than the depth of the 1% light level, active movement of the phytoplankton in the upper mixed layer might be required to maintain growth rates in upper mixed layer. While many phytoplankton species exhibit significant movement through swimming (Blasco, 1978) and/or buoyancy regulation (Walsby et al., 1997), there is no evidence that *Phaeocystis* exhibits capabilities for significant vertical motility. The few available laboratory studies on *Phaeocystis* suggest that cells are either neutrally or slightly negatively buoyant under light-limiting conditions (Wang and Tang, 2010). Although these studies were not conducted on the Antarctic species encountered during the ASPIRE and KOPRI expeditions, it appears that the rate of mixing within the upper mixed layer and not cell motility is critical to supporting the observed accumulation of phytoplankton biomass.

Phytoplankton photosynthesis can be extremely efficient in turbid conditions if mixing promotes the "fluctuating light effect" (Phillips and Myers, 1954; Myers, 1994). The "fluctuating light effect" describes when phytoplankton exposed to dynamic light intensities can have photosynthesis rates and biomass yields that are higher than cells grown under a constant photon dose, due to differences in the slow kinetics of the xanthophyll cycle relative to the mixing rate (minutes-hours; Demmig et al., 1987; Demmig-Adams, 1990), thereby allowing cells to operate at maximal photosynthetic efficiencies. Past studies in turbid plumes have demonstrated that not accounting for mixing in the upper mixed layer could lead to large errors (as large as 40%) for traditional static biological measurements of phytoplankton productivity (Schofield et al., 2013b). Therefore, improved understanding of the phytoplankton ecology will require measurements of turbulent mixing rates to define the light environment for cells within the upper mixed layer.

Conclusions

Recent reports highlight that glacial melt in the Amundsen Sea will continue for the foreseeable future (Thoma et al., 2008; Holland, 2014). Continuing glacial melt will increase the delivery of low salinity water into the Amundsen Sea Polynya (Hellmer, 2004), which will have biogeochemical ramifications through potentially increasing the overall productivity of this polynya (Arrigo et al., 2012) if the physical integrity of the system is otherwise maintained. Glider results from two different expeditions support this interpretation, as low salinity plumes associated with pycnoclines shallower than 50 m corresponded to regions of highest phytoplankton biomass. Additionally, the overall regulation of the phytoplankton biomass must be strongly influenced by mixing within the upper mixed layer, as mixing determines the proportion of the community experiencing chronic light limitation. Therefore, there is a critical need to quantify mixing within the AASW to better understand the injection of iron into surface waters and to model the light environment in a turbid high-biomass environment.

References

Alderkamp AC, Mills MM, Van Dijken GL, Laan P, Thuyróczy C-E, et al. 2012. Iron from melting glaciers fuels phytoplankton blooms in the Amundsen Sea (Southern Ocean): Phytoplankton characteristics and productivity. *Deep-Sea Res Pt II* **71–76**: 32–48. doi: 10.1016/j.dsr2.2012.03.005.

Alderkamp A, van Dijken GL, Lowry KE, Connelly TL, Lagerstrom M, et al. 2015. Fe availability drives phytoplankton photosynthesis rates in the Amundsen Sea Polynya, Antarctica. *Elem Sci Anth* **3**. doi: 10.12952/journal.elementa.000043.

Arrigo KR, Robinson DH, Worthen DL, Dunbar RB, DiTullio GR, et al. 1999. Phytoplankton community structure and the drawdown of nutrients and CO_2 in the Southern Ocean. *Science* **285**(5400): 365–367. doi: 10.1126/science.283.5400.365.

Arrigo KR, van Dijken GL. 2003 Phytoplankton dynamics within 37 Antarctic coastal polynyas. *J Geophys Res* **108**(c8): 3271. doi: 10.1029/2002JC001739.

Arrigo KR, van Dijken GL, Long MC. 2008. The coastal Southern Ocean: A strong anthropogenic CO_2 sink. *Geophys Res Lett* **35**: 121602. doi: 10.1029/2008GL035624.

Arrigo KR, Lowry KE, van Dijken GL. 2012. Annual changes in sea ice and phytoplankton in polynyas of the Amundsen Sea, Antarctica. *Deep-Sea Res Pt II* **71**: 5–15. doi: 10.1016/j.dsr2.2012.03.006.

Årthun M, Holland PR, Nicholls KW, Feltham DL. 2013. Eddy-driven exchange between the open ocean and a sub-ice shelf cavity. *J Phys Oceanogr* **43**: 2372–2387.

Assmann KM, Jenkins A, Shoosmith DR, Walker DP, Jacobs SS, et al. 2013. Variability of Circumpolar Deep Water transport onto the Amundsen Sea continental shelf through a shelf break trough. *J Geophys Res-Oceans* **118**(12): 6603–6620. doi: 10.1002/2013JC008871.

Blasco D. 1978. Observations on the diel migration of marine dinoflagellate off the Baja California coast. *Mar Biol* **46**: 41–47.

Boss E, Pegau W. 2001. Relationship of light scattering at an angle in the 524 backward direction to the backscattering coefficient. *Appl Optics* **40**(30): 5503–5525. doi: 10.1364/AO.40.005503.

Boss E, Pegau SW, Lee M, Twardowski MS, Shybanov E, et al. 2004. The particulate backscattering ratio at LEO 15 and its use to study particle composition and distribution. *J Geophys Res* **109**: C01014. doi: 10.1029/2002JC001514.

Buma AGJ, De Baar HJW, Nolting RF, Van Bennekom AJ. 1991. Metal enrichment experiments in the Weddell-Scotia Seas - Effects of iron and manganese on various plankton communities. *Limnol Oceanogr* **36**: 1865–1878.

Caron DA, Dennett MR, Lonsdale DJ, Moran DM, Shalapyonok L. 2000. Microzooplankton herbivory in the Ross Sea, Antarctica. *Deep-Sea Res Pt II* **47**: 3249–3272.

Davis R, Eriksen C, Jones C. 2003. Autonomous buoyancy-driven underwater gliders, in Griffiths G, ed., *Technology and Applications of Autonomous Underwater Vehicles*. London: Taylor & Francis: pp. 37–58.

Demmig B, Winter K, Kruger A, Czygan FC. 1987. Photoinhibition and zeaxanthin formation in intact leaves: A possible role of the xanthophyll cycle in the dissipation of excess light energy. *Plant Physiol* **84**: 218–224.

Demmig-Adams B.1990. Carotenoids and photoprotection in plants: a role for the xanthophyll zeaxanthin. *Biochim Biophys Acta* **1020**: 1–24.

Dubinsky Z, Schofield O. 2009. From the light to the darkness: Thriving at the light extremes in the oceans. *Hydrobiologia* **639**(1): 153–171. doi: 10.1007/s10750-009-0026-0.

Ducklow HW, Baker KS, Martinson DG, Quetin LB, Ross RM, et al. 2007. Marine pelagic ecosystems: The West Antarctic Peninsula. *Philos Trans R Soc London* **362**: 67–94. doi: 10.1098/rstb.2006.1955.

Fragoso GM, Smith WO. 2012. Influence of hydrography on phytoplankton distribution in the Amundsen and Ross Seas, Antarctica. *J Marine Syst* **89**: 19–29. doi: 10.1016/j.jmarsys.2011.07.008.

Glenn SM, Jones C, Twardowski M, Bowers L, Kerfoot J, et al. 2008. Glider observations of sediment resuspension in a Mid-Atlantic Bight fall transition storm. *Limnol Oceanogr* **53**(5.2): 2180–2196.

Gerringa Loes JA, Alderkamp A, Lann O, Thuróczy CE, De Baar HJW, et al. 2012. Iron from melting glaciers fuels the phytoplankton blooms in Amundsen Sea (Southern Ocean): Iron biogeochemistry. *Deep-Sea Res Pt II* **71**: 16–31. doi: 10.1016/j.dsr2.2012.03.007.

Gruber N, Gloor M, Mikaloff-Fletcher SE, Dutkiewicz S, Follows M, et al. 2009. Oceanic sources and sinks for atmospheric CO_2. *Global Biogeochem Cy* **23**: GB1005. doi.org/10.1029/2008GB003349.

Ha HK, Wåhlin AV, Kim TW, Lee SH, Lee JH, et al. 2014. Circulation and modification of warm deep water on the central Amundsen Shelf. *J Phys Oceanogr* **44**(5): 1493–1501. doi: 10.1175/JPO-D-13-0240.1.

Hart TJ. 1942. Phytoplankton periodicity in Antarctic surface waters. *Discovery Rep* **21**: 261–356.

Hellmer HH. 2004. Impact of Antarctic ice shelf basal melting on sea ice and deep ocean properties. *Geophys Res Lett* **31**: L10307. doi: 10.1029/2004GL019506.

Holland PR. 2014. The seasonality of Antarctic sea ice trends. *Geophys Res Lett* **41**: 4230–4237. doi: 10.1002/2014GL060172.

Holm-Hansen O, Lorenzen C, Holmes RW, Strickland JDH. 1965. Fluorometric determination of chlorophyll in Chlorophyta, Chrysophyta, Phaeophyta, Pyrrophyta. *J Cons Perm Inter Explor Mer* **30**: 3–15.

Jacobs SS, Jenkins A, Giulivi CF, Dutrieux P. 2011. Stronger ocean circulation and increasing melting under Pine Island Glacier ice shelf. *Nat Geosci* **4**: 519–523.

Jenkins A. 1999. The impact of melting ice on ocean waters. *J Phys Oceanogr* **3**: 2370–2381.

Jenkins A, Jacobs S. 2008. Circulation and melting beneath George VI Ice Shelf, Antarctica. *J Geophys Res* **113**(C4): C04013. doi: 10.1029/2007JC004449.

Jenkins A, Dutrieux P, Jacobs S, McPhail SD, Perrett JR, et al. 2010. Observation beneth Pine Island Glacier in West Antarctica and implications for its retreat. *Nature Geosci* **3**(7): 468–472. doi: 10.1038/ngeo890.

Johnson R, Strutton PG, Wright SW, McMinn A, Meiners KM. 2013. Three improved satellite chlorophyll algorithms for the Southern Ocean. *J Geophys Res* **118**: 1–10. doi: 10.1002/jgrc.20270.

Kirk JTO. 2011. *Light and Photosynthesis in Aquatic Ecosystems*. New York: Cambridge University Press: 662 p.

Kroon BM, Thoms S. 2006. From electron to biomass: A mechanistic model to describe phytoplankton photosynthesis and steady-state growth rates. *J Phycol* **42**(3): 593–609.

Lee SH, Kim BK, Yun MA, Joo H, Yang EJ, et al. 2012. Spatial distribution of phytoplankton productivity in the Amundsen Sea, Antarctica. *Polar Biol* **35**(11): 1721–1733. doi: 10.1007/s00300-012-1220-5.

Liss PS, Malin G, Turner SM, Holigan PM. 1994. Dimethyl sulphide and *Phaeocystis*: A review. *J Marine Syst* **5**(1): 41–53.

Marshall GJ. 2007. Half-century seasonal relationships between the Southern Annular Mode and Antarctic temperatures. *Int J Climatol* **27**: 373–383. doi: 10.1002/joc.1407.

Merckelbach LM, Briggs RD, Smeed DA, Griffiths G. 2008. Current measurements from autonomous underwater gliders, in *Proceedings of the IEEE/OEC/CMTC Ninth Working Conference on Current Measurement Technology*: pp. 61–67.

Miles T, Glenn SM, Schofield O. 2012. Spatial variability in fall storm induced sediment resuspension on the Mid-Atlantic Bight. *Cont Shelf Res*. doi: 10.1016/j.csr.2012.08.006.

Miles T, Seroka G, Kohut J, Schofield O, Glenn SM. 2015a. Glider observations and modeling of sediment transport in Hurricane Sandy *J Geophys Res Oceans*. doi: 10.1002/2014JC010474.

Miles TN, Lee SH, Wåhlin A, Ha HK, Schofield O, Kim TW, Assmann K. 2015b. Observations of the Dotson Ice Shelf outflow: Implications for the iron fertilization of the Amundsen polynya. *Deep-Sea Res Pt II*. doi: 10.1016/j.dsr2.2015.08.008.

Mobley CD. 1994. *Light and Water: Radiative Transfer in Natural Waters*. New York: Academic Press: 592 p.

Moline MA, Claustre H, Frazer TK, Schofield O, Vernet M. 2004. Alteration of the food web along the Antarctic Peninsula in response to a regional warming trend. *Glob Change Biol* **10**: 1973–1980.

Moline MA, Schofield O, Boucher NB. 1998. Photosynthetic parameters and empirical modeling of primary production in the Southern ocean. *Antarct Sci* **10**: 45–54.

Montes-Hugo M, Doney SC, Ducklow HW, Fraser W, Martinson D, 2009. Recent changes in phytoplankton communities associated with rapid regional climate change along the Western Antarctic Peninsula. *Science* **323**: 1470–1473.

Myers J. 1994. The 1932 experiments. *Photosynth Res* **40**: 303–310.

Padman L, Fricker HA, Coleman R, Howard S, Erofeeva L. 2002. A new tide model for the Antarctic ice shelves and seas. *Ann Glaciol* **34**(1): 247–254.

Phillips JN, Myers J. 1954. Growth rate of *Chlorella* in flashing light. *Plant Physiol* **29**: 152–161.

Randall-Goodwin E, Meredith MP, Jenkins A, Yager PL, Sherrell RM, et al. 2015. Freshwater distributions and water mass structure in the Amundsen Sea Polynya region, Antarctica. *Elem Sci Anth* **3**: 000065. doi: 10.12952/journal.elementa.000065.

Rignot E. 2008. Changes in West Antarctic ice stream dynamics observed with ALOS PALSAR data. *Geophys Res Lett* **35**: L12505. doi: 10.1029/2008GL033365.

Rignot E, Jacobs S, Mouginot J, Scheuchi B. 2013. Ice-shelf melting around Antarctica. *Science* **341**(6143): 266–270. doi: 10.1126/science.1235798.

Rudnick DL, Cole ST. 2011. On sampling the ocean using underwater gliders. *J Geophy Res* **116**. doi: 10.1029/2010jc006849.

St-Laurent P, Klinck JM, Dinniman MS. 2013. On the role of the coastal troughs in the circulation of warm circumpolar deep water on Antarctic shelves. *J Phys Oceanogr* **43**: 51–64.

Sarmiento JL, Gruber N, Brzezinski MA, Dunne JP. 2004. High-latitude controls of thermocline nutrients and low latitude biological productivity. *Nature* **427**: 56–60. doi: 10.1038/nature02127.
Schofield O, Kohut J, Aragon D, Creed L, Graver J, et al. 2007. Slocum Gliders: Robust and ready. *J Field Robotics* **24**(6): 473–485. doi: 10:1009/rob.20200.
Schofield O, Ducklow HW, Martinson DG, Meredith MP, Moline MA, et al. 2010. How do polar marine ecosystems respond to rapid climate change? *Science* **328**: 1520. doi: 10.1126/science.1185779.
Schofield O, Ducklow H, Bernard K, Doney S, Fraser-Patterson D, et al. 2013a. Penguin biogeography along the West Antarctic Peninsula: Testing the canyon hypothesis with Palmer LTER observations. *Oceanography* **26**: 78–80.
Schofield O, Moline MA, Cahill B, Frazer T, Kahl A, et al. 2013b. Phytoplankton productivity in a turbid buoyant coastal plume. *Cont Shelf Res* **63**: S138–S148. doi: 10.1016/j.csr.2013.02.00.
Sedwick PN, DiTullio GR. 1997. Regulation of algal blooms in Antarctic shelf waters by the release of iron from melting sea ice. *Geophys Res Lett* **24**: 2515–2518.
Sedwick PN, DiTullio GR, Mackey DJ. 2000. Iron and manganese in the Ross Sea, Antarctica: Seasonal iron limitation in Antarctic shelf waters. *J Geophys Res* **105**: 11321–11336.
Sherrell RM, Lagerström M, Forsch K, Stammerjohn SE, Yager PL. 2015. Dynamics of dissolved iron and other bioactive trace metals (Mn, Ni, Cu, Zn) in the Amundsen Sea Polynya, Antarctica. *Elem Sci Anth*: in press for this Special Feature.
Smith WO Jr, Carlson CA, Ducklow HW, Hansell DA. 1998. Growth dynamics of *Phaeocystis antarctica*-dominated plankton assemblages from the Ross Sea. *Mar Ecol-Prog Ser* **168**: 229–244.
Smith WO Jr, Dennett MR, Mathot S, Caron DA. 2003. The temporal dynamics of the flagellated and colonial stages of *Phaeocystis antarctica* in the Ross Sea. *Deep-Sea Res Pt II* **50**: 605–618.
Smith WO Jr, Shields AR, Peloquin JA, Catalano G, Tozzi S, et al. 2006. Interannual variations in nutrients, net community production, and biogeochemical cycles in the Ross Sea. *Deep-Sea Res Pt II* **53**: 815–833. doi: 10.1016/j.dsr2.2006.02.014.
Stammerjohn S, Massom R, Rind D, Martinson D. 2012. Regions of rapid sea ice change: An inter-hemispheric seasonal comparison. *Geophys Res Lett* **39**: L06501. doi: 10.1029/2012GL050874.
Stammerjohn SE, Maksym T, Massom RA, Lowry KE, Arrigo KR, et al. 2015. Seasonal sea ice changes in the Amundsen Sea, Antarctica, over the period of 1979–2014. *Elem Sci Anth* **3**: 000055. doi: 10.12952/journal.elementa.000055.
Tagliabue A, Arrigo KR. 2005. Iron in the Ross Sea: 1. Impact on CO_2 fluxes via variation in phytoplankton functional group and non-Redfield stoichiometry. *J Geophys Res* **110**(C3): C03009. doi: 10.1029/2004JC002531.
Thoma M, Jenkins A, Holland D, Jacobs S. 2008. Modelling circumpolar deep water intrusions on the Amundsen Sea continental shelf, Antarctic. *Geophys Res Lett* **35**: L18602. doi: 10.1029/2008GL034939.
Vernet M, Martinson D, Iannuzzi R, Stammerjohn S, Kozlowski W, et al. 2008. Primary production within the sea-ice zone west of the Antarctic Peninsula: I—Sea ice, summer mixed layer, and irradiance. *Deep-Sea Res Pt II* **55**: 2068–2085.
Wåhlin AK, Yuan X, Björk G, Nohr C. 2010. Inflow of warm Circumpolar Deep Water in the central Amundsen Shelf. *J Phys Oceanogr* **40**: 1427–1434. doi: 10.1175/2010JPO4431.1.
Wåhlin AK, Muench RD, Arneborg L, Bjork G, Ha HK, et al. 2012. Some implications of Ekman layer dynamics for cross-shelf exchange in the Amundsen Sea. *J Phys Oceanogr* **42**(9): 1461–1474. doi: 10.1175/jpo-d-11-041.1.
Walker DP, Brandon MA, Jenkins A, Allen JT, Dowdeswell JA, et al. 2007. Oceanic heat transport onto the Amundsen Sea shelf through a submarine glacial trough. *Geophys Res Lett* **34**: L02602. doi: 10.1029/2006GL028154.
Walsby AE, Hayes PK, Boje R, Stal LJ. 1997. The selective advantage of buoyancy provided by gas vesicles for planktonic cyanobacteria in the Baltic Sea. *New Phytol* **136**: 407–417.
Wang X, Tang KW. 2010. Buoyancy regulation in *Phaeocystis globosa* Scherffel colonies. *Open Mar Biol J* **4**: 115–121.
Wright SW, Jeffrey SW, Mantoura RFC, Llewellyn CA, Bjornlan T, et al. 1991. Improved HPLC method for the analysis of chlorophylls and carotenoids from marine phytoplankton. *Mar Ecol-Prog Ser* **77**: 183–196.
Xu Y, Cahill B, Wilkin J, Schofield O. 2012. Role of wind in regulating phytoplankton blooms on the Mid-Atlantic Bight. *Cont Shelf Res* **63**: S26–S35. doi: 10.1016/J.CSR.2012.09.011.
Yager PL, Sherrell RM, Stammerjohn SE, Alderkamp AC, Schofield O, et al. 2012. ASPIRE: The Amundsen Sea Polynya International Research Expedition. *Oceanography* **25**(3): 40–53. doi: 10.5670/oceanog.2012.73.

Contributions

- Contributed to conception and design: OS, PY, RS, TM, SL
- Contributed to acquisition of data: TH, ER, RES
- Contributed to analysis and interpretation of data: OS, TM, ACA, PY, RS
- Contributed to draft and revised the article: OMS, TM, ACA, SLH, TH, ER, RES, RS, PY
- Approved and submitted version of publication: OS, PY

Acknowledgments

We thank the excellent support teams and ship crews of the RVIB Nathaniel B Palmer and the Aaron and the associated wider ASPIRE scientific teams. We also acknowledge the ongoing support from the great state of New Jersey.

Funding information

This project was funded by the National Science Foundation Office of Polar Programs, Antarctic Organisms and Ecosystems (ANT-0839069 to PY, ANT-0838995 to RS, ANT-0838975 to SS, ANT-0838995 to OS). Support was also provided by the Korea Polar Research Institute to OS.

Competing interests

The authors declare no competing interests

Data accessibility statement

Glider data can be accessed at a Thredds server: http://tds.marine.rutgers.edu:8080/thredds/catalog/cool/glider/all/catalog.html and at ERDDAP server at http://erddap.marine.rutgers.edu/erddap/info/index.html?page=1&itemsPerPage=1000

Glider Advancements in Efficiency: Enhancing Factors Necessary for Ocean-Wide Flights

Liam Ramsay, Andrenette Morrison, Josh Kohut,
Oscar Schofield, Travis Miles, Scott Glenn
Center for Ocean Observing Leadership
Rutgers University
New Brunswick, USA
Lar271@scarletmail.rutgers.edu

Caleb Lintz
US Naval Academy
Annapolis, USA

***Abstract*—The Slocum Glider is an instrument of efficiency and getting more out of less. When looking at getting the most distance out of a single battery, it is important to consider many different variables. Horizontal speed and flight path planning can both play a part in being able to achieve flight across ocean basins. With the ability to change a glider's velocity, a pilot could determine the quickest speed to fly the glider trans-ocean without depleting the battery. In other words, the pilot could choose the optimal pitch angle for a specific mission. Different pitch angles travel at different speeds while consuming battery power at different rates. One mission may carry great importance on speed rather than energy while another mission would rather go slow-and-steady in order to save as much power possible. Through enabling a pilot to change the speed of a glider through pitch angle, shorter missions can be done much more quickly while longer missions can conserve more energy while flying at a slower pace.**

Additionally, having a flight path that utilizes the currents in the ocean is a method used today to make gliders run efficiently. Making sure all instruments are reading properly is crucial to being able to navigate these currents. The key to this accurate navigation is a properly calibrated compass. Compass calibration can be complicated and frustrating but new methods of calibration have been able to remove a lot of the error that is associated with the compass. One comparison deals with a calibration of hanging a glider with ropes versus a calibration using a wooden tilt cart. Having the glider travel on the correct course between waypoints can cut miles off the overall trip that may add up and waste battery.

Keywords—Battery Consumption; Pitch Angle; Compass Calibration; Autonomous Underwater Gliders;

I. Introduction

Slocum gliders are autonomous under water vehicles that rely on bouyancy changes to slowly move through the ocean within the upper 1000m. Along the way, the gliders sample ocean parameters including temperature, salinity, and in some cases biological measures of phytoplankton occurance, abundance, and health. These gliders are designed in such a manner as to emphasize energy efficiency. By using simple changes in density, the glider is able to travel long distances with minimal power. Since the inception of Autonomous Underwater Vehicles (AUVs), multiple improvements have been made on the design and engineering of the instrument. In 2009, Rutgers University did what has never been done and sent a glider across the Atlantic, starting off the coast of New Jersey and ending at the coast of Spain. Since then, trans-ocean glider deployments have become a common goal in research. The current global glier flights are organized unde the umbrella of the Challenger Project. This project seeks to navigate along the path of the HMS challenger in the late 1800s on the first circumnavigation for science. Legs have been identified in each basin that together will track the path of this improtant science mission. In the South Atlantic, the glider 'Challenger' completed two legs from South Africa to Ascencsion Island and from Ascension Island to Brazil. In July of 2015 the glider was deployed on a mission that extends approximately 6500 kilometers from Ubatuba, Brazil back to Cape Town, South Africa. The current available battery power flying with default parameters will allow for only approximately 7000 kilometers of flight. There is potential to recover the glider, re-battery and deploy from Tristan da Cunha (37.1167° S, 12.2833° W) but this will require a boat trip of at least a month, which is cost and logistically prohibitive. Thus achieving optimum battery life and flight efficiency is critical to completing this mission. As the limits of glider travel are being pushed, designs need to be optimized in order to gain the most out of the increasingly important glider voyages.

A Slocum Glider is a very efficient machine as it currently stands however there is room for improvement. Battery consumption and currents all deal with the efficiency of a glider. Through glider engineering, we can manipulate these factors internally by improving pitch angle and compass precision. Data from previous glider missions along with our

978-0-933957-43-5 ©2015 MTS

own test models can provide the support necessary to prove what advancements will revolutionize the efficiency of the glider. Gliders have the potential to accomplish unimaginable feats without any need to physically change the vehicle.

II. PITCH ANGLE OPTIMIZATION

The glider consumes a variable amount of energy at different pitch angles and different pitch angles led to different horizontal speeds. It has been determined that the most optimal pitch angle to use for the Slocum Glider is about 26 degrees up and down. However, not all glider missions are the same. One glider could be collecting data for a few weeks in the Gulf of Mexico while another is traveling transatlantic for a whole year. Flexibility in speed would lead to getting the most use out of a fully charged glider. Adjusting the glider to a steeper pitch angle would lead to shorter long-distance voyages while maintaining enough energy onboard as a precaution. Here we present steps we have taken to optimze glider flight for the required enegy efficiency to cross an ocean basin.

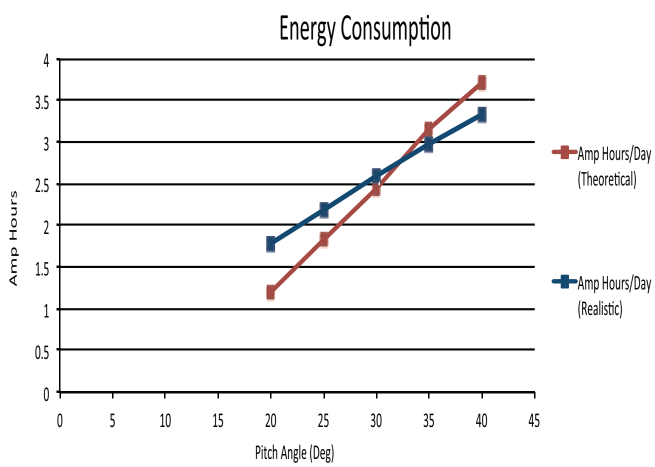

Fig. 1. The energy consumed by the Slocum Glider in Amp Hours at different pitch angles (degrees). The red line shows the theoretical Amp Hours/Day while the blue line shows the realistic Amp Hours/Day.

First, we focused on the rate of energy consumed at a range of pitch angles (Figure 1). Originally, we looked at energy consumption theoretically: using simple trigonometry and the comparison of the number of yos (consequtive upcast and downcast) to amp hours. After that, we computed a realistic trend showing the amp hours per day at different pitch angles using data gathered from the Slocum Glider. The realistic trend shows a smaller slope compared to the theoretical trend, illustrating that measured energy consumption is consistent with theory.

Taking the data retrieved from the Slocum Glider, another trend was calculated to estimate the number of spare days of battery life would be left if completing a 6000 kilometer voyage at different pitch angles (Figure 2). The linear trend indicates that a smaller pitch angle would lead to many more spare days compared to a steeper pitch angle.

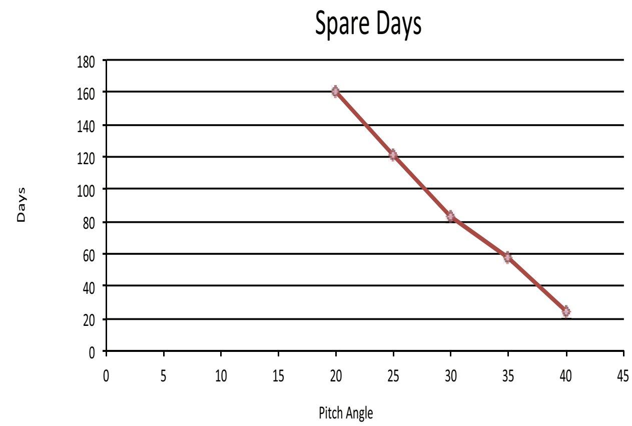

Fig. 2. The spare days of energy left at different pitch angles (degrees).

Next we looked at the horizontal velocities of the glider at different pitch angles. Figure 2 is based on information in Jeffery Sherman's paper, *The Autonomous Underwater Glider "Spray"*. The information describes where the maximum horizontal velocity and maximum range lie on the pitch angle scale. For ocean-wide deployments, the information concerning the horizontal velocity is most essential. According to the Sherman's equation, the maximum horizontal velocity occurs at a pitch angle of about 36 degrees, recommending to remain below it. The range maximized at around 19 degrees, recommending the glider remain above that angle. This window between 19 degrees and 36 degrees is the recommended range that a pilot should consider when flying a glider.

The equations designed by Sherman are derived from the following variables:

ρ	Fluid Density;
u	Horizontal Velocity;
E_0	Energy;
x	Range;
B	Buoyant Force;
C_D	Drag Coefficient;
A_D	Cross Sectional Area of Hull;
U_0	Characteristic Velocity;
X_0	Characteristic Range;

The following equations (1) (2) below describe how to calculate the characteristic velocity U_0 and the characteristic range X_0:

$$U_0 = (\frac{2B}{\rho A_D C_D})^{.5} \tag{1}$$

$$X_0 = \frac{E_0}{.5\rho A_D C_D u^2} \tag{2}$$

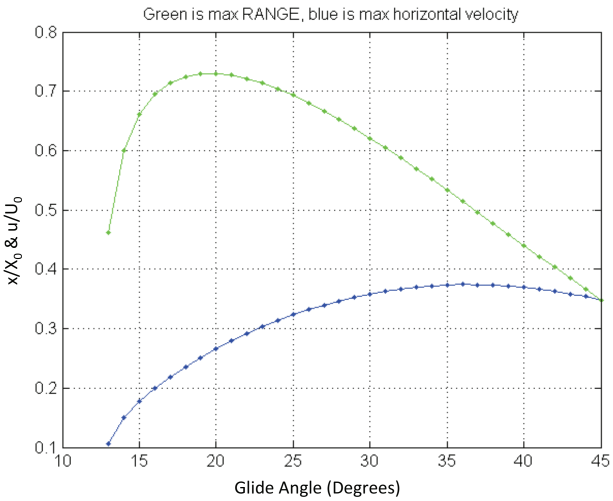

Fig. 3. The ratio between the range of the glider x and it characteristic range X_0 as well as the ratio between the horizontal velocities u and charateristic horizontal velocities are indicated at different pitch angles (degrees).

Comparing this with the information concerning energy consumption, our directive is to find the most optimal pitch angle that allows us to fly fast but safely. With so much spare energy stored in the glider, a pitch angle of 30 degrees may fair for a better transatlantic voyage for RU29.

III. COMPASS OPTIMIZATION

Finally we looked at energy saving opportunities within the glider hardware and software. Given the optimal flight parameters it is important that the glider logic efficiently navigate along its intended path. Deflections from its intended path could lead to energy loss in frequent rudder adjustments. Therefore, the distance traveled on a given day can be optimized with a more precise, properly calibrated compass. With a 6000-kilometer voyage, a simple 5% compass error could lead to a distance error of 300+ kilometer. In order to achieve a more precise compass, effective methods of calibration must be developed and implemented.

Rutgers University generally calibrates Slocum Gliders with a hanging apparatus (Figure 4). This method allows the glider to be rotated in 3D space while suspended, making the calibration process easy and generally effective.

Fig. 4. The hanging apparatus allows the glider to freely move in 3D space with ease. Object such as a tree is required to hang the apparatus.

However, in an environment with limited options to hang a glider (such as tree-less Antarctica), we developed a tilt cart that can be used in many more environments prior to deployment (Figure 5). While testing, the tilt cart prototype did have some issues in rolling the glider, which caused a few errors in our calibration trials. The tilt cart expressed much more error than the hanging method however I hypothesize that if a better method to roll the glider in the tilt cart or a more flexible calibration software was available, the tilt cart could prove to be a very effective method of calibration in the future.

Fig. 5. The tilt cart prototype designed to rotate the glider in 3D space without the necessity of an object to hang the glider from. Limitations in pitch angle exist at about 40 degrees and there is difficulty in rolling the glider in the wooden cradle.

Effective methods in calibration would not be as beneficial without an effective working compass. With both the True North Technologies Revolution Compass and the PNI Corperation TCM3 Compass models at our disposal, we put them to the test to see which model performed better in the hanging apparatus (Figure 6 & 7). Surprisingly, the results from our data show that the earlier TCM3 performed nearly 54% better than the newer Rev compass. More interesting was the errors calculated from the Rev compass as the trends resemble sine curves. We hypothesize that this error could be corrected with a more advanced calibration software however this software is not yet available to us to be tested.

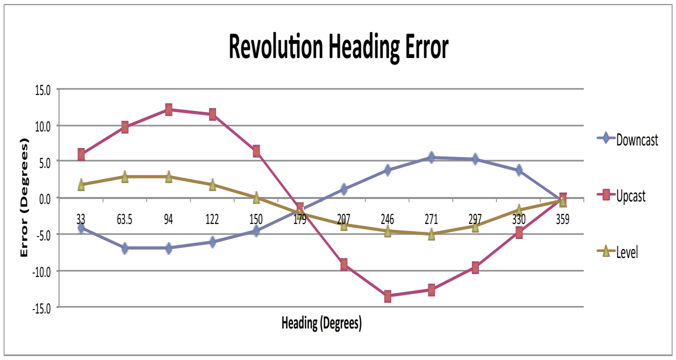

Fig. 6. The Revolution compass error (degrees) rotated around 360 degrees while pitched up 26 degrees, pitch at a level 0 degrees and pitched down at 26 degrees.

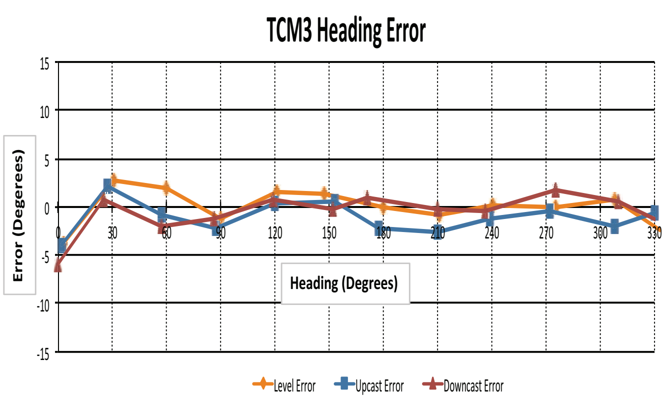

Fig. 7. The TCM3 compass was tested exactly like the Revolution compass by rotating the glider 360 degrees while being pitched up 26 degrees, down 26 degrees and kept level.

As a way to combine our different methods and compasses, we mixed-matched different calibration trials to present each comparison (Figure 8). The first comparison shows how the replacement Revolution compass performs better than the used, original Revolution compass with a 1.1 degree difference in error. The hanging apparatus was our control as our method of calibration. Next, the comparison between the tilt cart and the hanging apparatus provided some insight on how effective our prototype faired. With the replacement Revolution compass as our control, the tilt cart presented 1.3 degrees more error than the hanging method on average. This chart also includes the comparison between the TCM3 and Rev compass from previous.

Type of Compass/Calibration Method	Average Error
RU30 Original Rev Compass/ Hanging Method	4.9
RU30 Replacement Rev Compass/Hanging Method	2.8
RU30 Replacement Rev Compass/Tilt Cart	4.1
RU23 TCM3 Compass/Hanging Method	1.5

Fig. 8. The chart includes the amount of error present when testing a glider with different compasses (Original Rev Compass, Replacement Rev Compass and TCM3 Compass) with different calibration methods (Hanging Apparatus and Tilt Cart).

IV. Disscussion

The optimization of the Slocum Glider is within the ability to change the speed of the glider and pinpoint the best route available. These capabilities depend on the accuracy of the compass and pitch angle of the AUV.

Combining what we know about the horizontal speed of the glider and the rate of energy consumption used at a range of pitch angles allow the pilots to calculate the most efficient way of flight for the specific mission. A glider pilot should decide between the window of 26 and 36 degrees and compare it with the energy consumption at those angles. Any angle between 19 and 26 degrees would be an interesting range to test to see how the glider moves at such low angles. This window enacts as a possible speedometer for the pilot to use in order to operate the instrument for the mission at hand.

Once a pitch angle is agreed upon as the best choice for a mission, the most optimal route must be planned upon as well. A precise compass will allow a pilot to accurately direct the AUV into a favorable waters. For a voyage that is ocean-wide, the smallest compass error could lead to significant distance off course. As of now, the best mode of calibration is through the use of a hanging apparatus however a tilt cart could move in as a substitutable mechanism quite soon. The compass models themselves have shown that the TCM3 performed better than the Rev compass. The solution for the issues with the tilt cart and the Rev compass lies in an effective software. A forgiving calibration program would allow for the glider to halt, tilt and continue moving without presenting an error could allow for a significant drop in heading error. A program to correct the sine error generated from the Rev compass would allow it to compete well with the TCM3.

With more features available to the pilot, a glider could better adapt to the huge variety of environments in the ocean present in a deployment. Control in speed as well as pinpoint compass precision are necessary for anyone operating an AUV. The Slocum Glider has the potential to be so much more efficient with only simple changes in pitch angle and calibration.

V. Acknowledgement

The Challenger Gilder Mission is growing global partnership of gilder operators, scientists, educators and students coordinated by Rutgers University and endorsed by the Challenger Society. The results presented on this paper were initiated in a Rutgers research course and completed by two undergraduate summer interns (Andrenette Morrison and Liam Ramsay) supported by Teledyne Webb Research and six U.S. Naval Academy interns (Martin Arroyo, Kelsey Ashbrook, Olivia Czerewko, Stephanie Lee, Caleb Lintz and Erin Payne). Glider path planning and model/data comparison activites are led by Nilsen Strandskov (Rutgers) and Antonio Ramos (Universidad de Las Palma de Gran Canaria) with cyber infrastructure support provided by John Kerfoot (Rutgers). Glider operators include Chip Haldeman, Dave Aragon, Tina Haskin (Rutgers) and Ben Alsup (TWR).

VI. References

[1] Schofield, O., and Coauthors, 2007: Slocum Gliders: Robust and ready. *J. F. Robot.*, **24**, 473–485, doi:10.1002/rob.20200.

[2] *Challenger Glider Mission.* May 2014. <challenger.marine.rutgers.edu/mission/the-challenger-glider.mission.> (accessed June 8, 2015).

[3] Sherman, J., R. E. Davis, W. B. Owens, and J. Valdes, 2001: The autonomous underwater glider "Spray." *Ocean. Eng. IEEE J.*, **26**, 437–446.

Glider Performance During Hurricane Gonzalo

BIOS, Bermuda

David Aragon
Scott Glenn, Travis Miles
Rutgers University Department of Marine & Coastal Sciences
New Brunswick, NJ
dkaragon@marine.rutgers.edu

Ruth Curry
Bermuda Institute of Ocean Sciences
MAGIC Lab
St. George's, Bermuda
rcurry@whoi.edu

I. Introduction

Hurricane Gonzalo was 2nd in a series of sequential Atlantic tropical cyclones to hit the island of Bermuda during the 2014 season. Hurricane Fay landed as a Category 1 hurricane October 12 and the resulting efforts helped pre-condition the island for Gonzalo. Less than a week later on October 18, Hurricane Gonzalo made landfall as a Category 2 storm. It had peaked in intensity as a Category 4 storm less than 500 miles south of Bermuda [1].

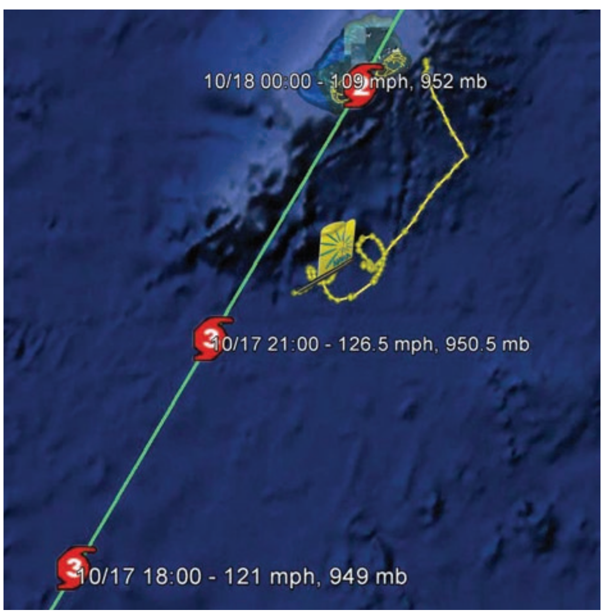

Fig. 1. Hurricane Gonzalo track with wind and pressure. Glider Anna path. (*Google Earth, NOAA*)

A Teledyne Webb Research Slocum G2 glider, owned by BIOS (Bermuda Institute of Ocean Sciences) was opportunistically deployed ahead of the storm, after being recovered before Hurricane Fay. The glider was equipped with CTD, optical backscatter and fluorescence, and a dissolved oxygen meter. The glider flew for a short time before and after the storm giving a snapshot of the post-Hurricane Fay ocean properties and Hurricane Gonzalo induced effects.

Noted during the flight of the glider under the hurricane, was strong turbulence as seen in attitude variables from the vehicle. The measurements were taken using the glider's onboard attitude sensor which measures pitch, roll, and magnetic heading. This turbulence was seen during peak storm intensity as the hurricane crossed over the glider and extending quite deep into the water field. The glider also experienced decreased communication reliability as well as damage to the tail from the storm or debris.

With gliders increasing presence and availability, unique events such as hurricanes will be sampled in ways never before seen. Sensors of greater complexity and quantity are being added to such vehicles and may be susceptible to extreme conditions such as seen during Hurricane Gonzalo.

II. Methods

Gliders have become robust tools for sampling the ocean during both normal and episodic events such as storms [2] [3]. Slocum gliders are capable of operating in shallow waters (5+ meters) to open ocean (up to 1000 m). By changing buoyancy they are able to descend or ascend vertically through the water column. Incorporating a pitch angle into their ascent or descent allows forward progress upwards of 35 cm/s. Steering mechanism and onboard attitude measurements allow navigation underwater for specified lengths of time.

Sensor payloads are added primarily to the center of the vehicle and data is collected during the ascent, descent, or surfacing phase of the glider's flight. Logged at a maximum rate of 1 Hz, gliders provide relatively high density sampling spatially and vertically. Low power allows operation across seasons and certainly during the durations of most storms or episodic events.

The glider deployed from Bermuda's BIOS MAGIC Lab (Mid-Atlantic Glider Initiative and Collaboration) was named Anna. This glider was a deep glider capable of descending to 1000 m. Science payload consisted of 3 oceanographic sensors. A Seabird pumped CTD unit for measuring temperature and salinity is a staple on all gliders. An optical Wetlabs ECO sensor, FLBBCD, measures proxies of phytoplankton abundance (chlorophyll fluorescence), total particle concentration (backscattering), and dissolved organic matter (CDOM fluorescence). An Aanderaa oxygen optode capable of measuring dissolved oxygen are installed at the rear of the vehicle.

Other observations from Bermuda include L.F. Wade airport, NOAA Station BEPB6 - 2695540 - Bermuda Esso Pier, as well as others mentioned in National Hurricane Center's Hurricane Gonzalo Report [1].

III. Results

A. The Ocean, the Storm, and the Robot

The storm approached Bermuda over the slightly cooled waters after Hurricane Fay had passed through. This likely weakened Gonzalo before making landfall, further giving Fay the credit of 'preparing' the island for another hurricane's landfall. Fay had also knocked most loose structures, limbs, and debris loose so that Gonzalo's impacts were limited on the island.

Gonzalo tracked over Bermuda, crossing the glider around 00 GMT October 18. The glider (Anna) was flown about 30 km from storm center. Anna continued to operate an additional 2 days after the storm departed before being recovered by R.V. Atlantic Explorer. At this point it was continuing to profile but was un-steerable due to damage from the- storm, thus recovery was a top priority. It would have been beneficial to continue flying beyond such date.

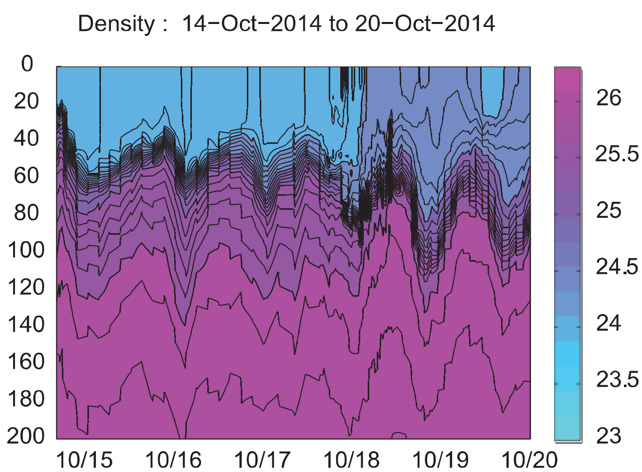

Fig. 2. Anna density, note: mix layer depth (credit: Ruth Curry, BIOS)

The passage of Hurricane Fay cooled the ocean 2-3 degrees C, likely weakening Gonzalo. A curiosity this brings is because both storms had similar tracks, how much effect of the cooling extended further south from the island along their paths. Finally, the mixing and turbulence layers as seen in temperature begin to show the picture of activity as deep as 80 m which affected the glider's attitude. Deeper scientific analysis of the glider data is ongoing and is outside the realm of this paper. This paper intends to focus on the performance of the G2 Slocum glider in an extreme event such as this.

B. Rudder: Lost at Sea

Underwater gliders steer using a variety of methods. Angling the glider about its roll axis (banking) allows gliders to steer during ascents and descents turning vertical motion into heading control. This is analogous to an airplane banking on a landing approach. Another method used is via a rudder or fin allowing the vehicle to turn by yawing. This changes heading much like a rudder in an airplane by rotating the glider about its heading axis. It is important to note vehicles that rely on yaw for heading control have no ability to roll or bank. Their only control methods are pitch and yaw. Roll can be induced by a rudder moment but is outside the scope of this discussion.

The rudder on the Slocum glider is an external moving part, essentially the only one besides an externally inflating and deflating buoyancy diaphragm. This urethane control surface can operate roughly +- 25 degrees for controlling heading. It is housed by a self-contained fin unit called the digifin. Also built into the fin are communication and GPS antennas.

To this date Rutgers University has had no major issues with the digifin system and rudder during its hundreds of individual deployments of gliders. Leading up to rudder loss were numerous reports from the glider that the fin was being pushed around by wind, water, and/or debris. It was expected the rudder would be able to continue to operate normally despite the warnings and conditions.

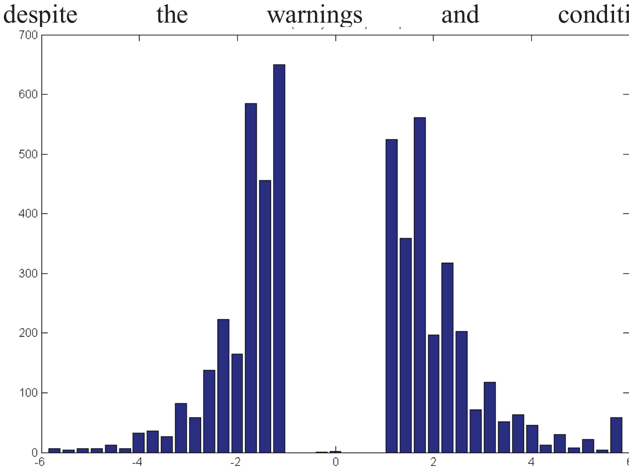

Fig.4. Rudder out of deadband histogram. Degrees rudder was found to be outside of +- 1 degree motor deadband

However, during the passage of Gonzalo over glider Anna the rudder system sustained complete loss minutes after surfacing. The loss occurred (10/17 18:30) several hours before the eye passed directly overhead. It is difficult to conclude the cause of rudder loss: options being biologic, wind driven debris or water. Given the path of the hurricane and wind direction during the loss, debris or flotsam density should be low. Biological loss is an option but would be highly coincidental given the timing and infrequency of rudder losses on previous glider missions.

C. Communications Reliability

Gliders rely on antennas in the top of the digifin (tail assembly) to maintain GPS and communication links. The tail of the glider is elevated out of the water by buoyancy provided from an external air bladder which inflates near the surface. This lifts the tail out of the water for antenna access to GPS and Iridium satellite constellations. The primary means of communication to a glider is via the Iridium system when out of range of radio communications.

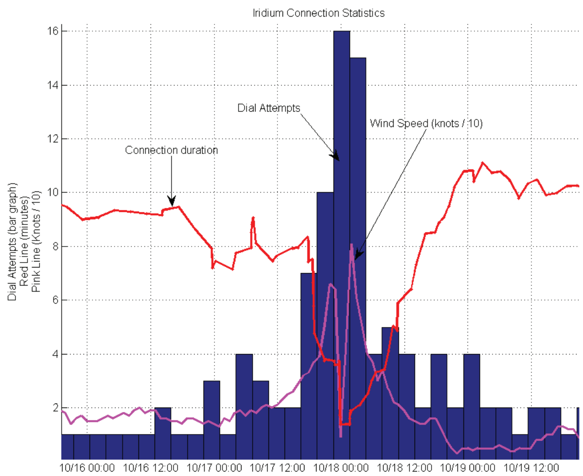

Fig 4. Iridium connection success rate

The mission plan had called for mixed sampling depths between 200 m and 500 m, alternating, during the storm. This was accomplished by changing mission parameters upon each surfacing via an automated scripting routine. Several hours prior to peak storm, communication success rate plummeted and thus dive depth cycling was halted for single 500 m yo's (a yo is a dive and a climb performed by glider) for the remainder of the mission.

Centered on 00 GMT 10/18 by about +- 3 hours, communications hit their low point with connections lasting less than 1-3 minutes. Such short connecting times made changing mission parameters difficult as well as transferring data. This also had an unintended effect of idle surface time perhaps better spent sampling rather than drifting in the dangerous winds.

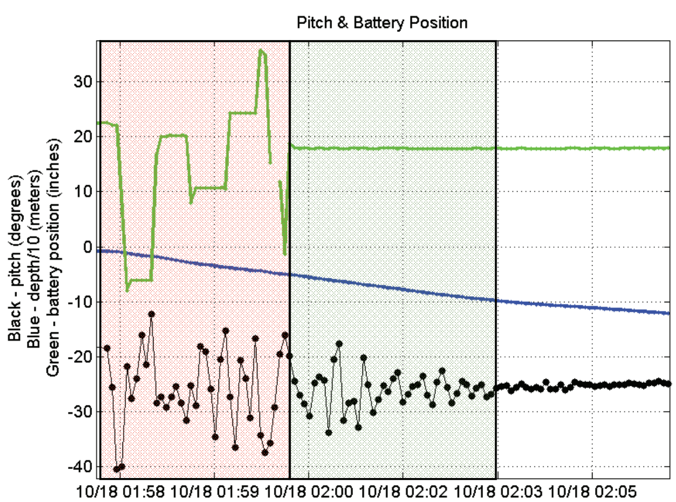

Fig 5. Glider pitch is in green, while depth is plotted in blue. Note even after pitch battery stops moving pitch oscillates down to 100 m

D. Rough Seas: Turbulence

The primary field for which we can look for turbulence in the glider flight is in the roll dimension of the attitude sensor. Roll is important to look at because it is the most independent of the glider's control surfaces. In other words the glider cannot directly control roll, thus most of the roll measurements are the result of the environment itself.

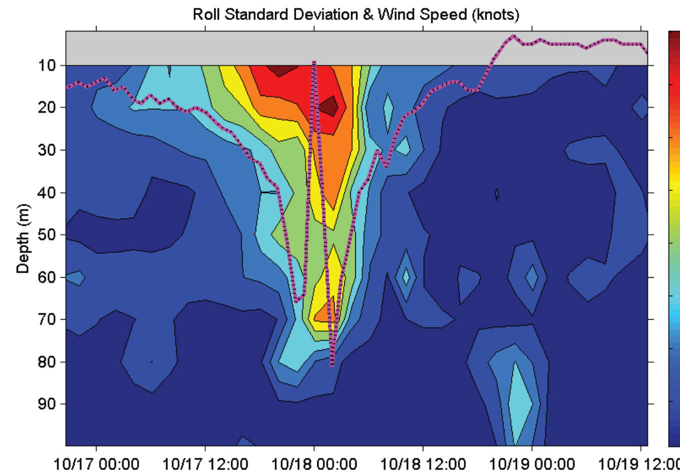

Fig 6. Vehicle roll (degrees) moving standard deviation

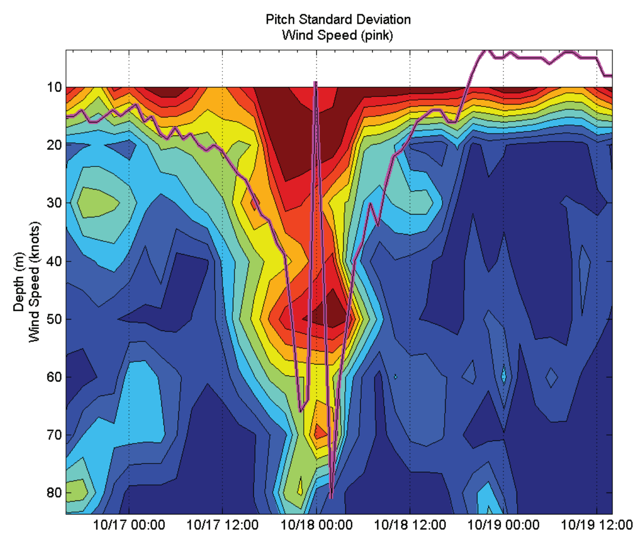

Fig 7. Vehicle pitch (degrees) moving standard deviation

The glider's ideally fly with 0 degrees of roll and outside of any influences should remain at 0 during all operating times. Of course turbulence, inflections, pitch changes, and rudder all create moments which roll the glider. Roll standard deviations of 5-10 degrees were seen during passage of the storm. Periods appeared to be 10-20 seconds in the roll data but further investigation needs to be done.

Pitch shows turbulence as well, but the glider is able to control this surface via a movable mass in the fore of the glider. This 9 kg mass is able to slide forward and aft to adjust the pitch angle. In Anna's case when the pitch error became too large (caused by turbulence) it began to move the pitch internal control surface (battery). Analysis should be done as independent of this as possible. Also worth noting is this may be an unintended consequence of the control system parameters as moving the battery may have contributed to higher pitch errors. A possible solution is flying with a fixed pitch battery or larger pitch deadband.

Pitch errors of +- 10 degrees were seen at depths as great as 80 m. This was centered on the storm and shallowed as the storm approached and departed. For a period of roughly 24 hours the glider showed turbulence in roll and pitch at depth, peaking just hours before the eye passed overhead.

IV. Conclusions

Operating remote platforms such as gliders in extreme events will continue to provide insightful measurements and observations. In parallel advancement, sensor development and integration will bring new sensors to AUV's that will help scientists answer questions they didn't have the means to observe prior.

New sensors often have increasing complexity as well since often scaling down is the largest technical challenge. Early gliders flew just a CTD sensor and that yielded some victories. However, multiple ADCP units by Nortek and Teledyne, as well as water quality sensors such as nitrate, and phytoplankton productivity (FIRE) sensors from Satlantic are all ready for glider use. Turbulence probes such as the Rockland Scientific Microrider can be mounted on top of gliders. Using these complex sensors in extreme events could have unintended effects and should be accounted for in operation. For example large roll and pitch movements could yield errors in ADCP measurements from gliders, especially in vertical water velocities [5]. Proper operation of the vehicle could alleviate some of the effects seen, especially in pitch fluctuations or at least allow predictive behavior. Onboard accelerometers may assist in understanding these effects and provide new insight. Additional understanding as to the response time and accuracy of the onboard attitude sensor will continue to be paramount. Open ocean current profiling gliders could perhaps benefit from upward looking instruments which would sense turbulent water while swimming in still water. This would only have benefits in situations where bottom track would always be impossible.

As the operational numbers of gliders increases so grows the percentage of risk of damage and unintended interactions. Gliders will hopefully continue to harden and become resilient amongst the many conditions they will face. Strong winds and similar incidents that lead to the rudder loss should be accounted for and tested against. Surface time should be limited to reduce risk to the glider.

It is important for scientists and operators of the gliders to understand the lessons from this paper. To summarize the conclusions for missions in the future:

1. Maintain maximum glider stability at all times. This will assist in mitigating external forces creating pitching, yawing, and rolling conditions to the vehicle and attached science sensors. Stability also plays a role in at surface communication success. The goal will be to minimize measurement errors and increase vehicle operability. Stabilizing surfaces are important as well, wings, canards, etc.

2. During episodes of extreme weather, less is more. Prepare to have your glider handle episodes of complete autonomy and make sure it continues to sample. Don't create an overly ambitious operating plan and be sure to sample more than what you need, in this case depths. When probing the unknown you can't predict what you will miss because you don't know what you will be measuring.

3. Limit surface times in the event it can't connect. Time at the surface is not only more dangerous, but it is also un-productive in that little useful data is being collected. Many Rutgers glider missions have had incidents happen at the surface yielding it is a dangerous place to be. Surface control scripts should have told Anna to immediately dive and forego data transfers until passage of the worst conditions.

4. Control algorithms for the glider optimized for normal flight may produce unintended consequences during storm flight. Simplifying or neutering such controls may be beneficial during instances of turbulence and high autonomy (not able to control vehicle). For example, increasing the pitch deadband, setting a fixed pitch battery position, or lowering the control gains could help the glider from trying to dampen turbulence caused pitch oscillations.

V. Future Work

Frequency analysis of the pitch and roll could be helpful to see if it somehow correlated with wave field experienced in the area. Work with a glider and an accelerometer would help augment the suite of useful data collected by the glider. Analyzing the pitch and heading controller during this time period to make a setup for the glider to operate more relaxed during a storm will prove useful.

Acknowledgment

Praise should go to the deployment crew from BIOS and R.V. Stommel who deployed Anna in less than ideal conditions prior to the storm. Also to the recovery team who were able to muster 2 days after the hurricane to rescue an un-steerable glider. This team consisted of the crew and scientists of R.V. Atlantic Explorer. Also special thanks for Ruth Curry and the MAGIC Lab for the opportunity to assist BIOS with their glider operations.

References

[1] Brown, Daniel, "National Hurricane Center Tropical Cyclone Report Hurricane Gonzalo", March 2015

[2] Glenn, S., C. Jones, M. Twardowski, L. Bowers, J. Kerfoot, J. Kohut, D. Webb, and O. Schofield (2008), Glider observations of sediment resuspension in a Middle Atlantic Bight fall transition storm, Limnol. Oceanogr. Methods, 53(5 part 2), 2180–2196, doi:10.4319/lo.2008.53.5_part_2.2180..

[3] Miles, T., G. Seroka, J. Kohut, O. Schofield, and S. Glenn (2015), Glider observations and modeling of sediment transport in Hurricane Sandy, J. Geophys. Res. Oceans, 120, doi:10.1002/2014JC010474.

[4] NASA World View, Terra and Modis Imagery

[5] Teledyne RD Instruments, "Acoustic Doppler Current Profiler Principles of Operation A Practical Prime

Gliders as maturing technology: Using gliderpalooza as means to develop an integrated glider community

Oscar Schofield, Josh Kohut, Ulrich Kremer, Travis Miles, Grace Saba, Scott Glenn
Center of Ocean Observing Leadership, Rutgers University
New Brunswick, NJ 08901
oscar@marine.rutgers.edu

Clayton Jones, Doug Webb
Teledyn-Webb Research
East Falmouth, Massachusetts 02536-4441

***Abstract*— Underwater autonomous gliders have transitioned from exotic experimental systems to becoming a standard platform capable of collecting data over a critical range of spatial and temporal scales in the ocean. The data are proving to be extremely valuable for addressing a wide range of basic and applied research questions. These communities are growing from distributed research and/or education groups. It is crucial as systems continue to evolve that there is an effort to "harmonize" data products while preserving the diversity of approaches/science/experimentation. As the gliders have matured and new battery solutions provide additional energy, there is an increased focus on the integration of a wider range of sensors to be incorporated into gliders. Many of these new classes of sensors will be particularly effective for characterizing biological processes in the coastal ocean. As biological sensors generally provide proxy estimates of a parameter, developing robust quality control and assurance procedures is critical. These new sensors will be more power intensive thus requiring the development of planning tools for increasing energy efficiency during missions. Given the significant growth in the highly distributed glider community, efforts are now focusing on the development mission planning tools to allow for efficient operation of glider fleets. To further collaboration and standardization of the growing number of glider operators we have initiated a series of community efforts called glider paloozas. We had an exceptional turnout last year, encompassing 18 U.S. and Canadian partners, 28 gliders, 36 glider deployments, and spatial coverage from coastal regions of Newfoundland to the Gulf of Mexico and offshore to Bermuda. The coordinated effort focused on several research themes including continental shelf circulation, fish migrations, and storm activity. The main goals of last year's effort were to produce a seamless flow of real-time glider data into the Global Telecommunications System (GTS) via DMAC and into the regional ocean models and demonstrate the potential of a U.S. national glider network. This is in line with the goal to increase glider data accessibility from Federal and Academic oceanographic modeling communities, the U.S. Integrated Ocean Observing System (IOOS), and other federal funding agencies (i.e., NSF). In order to demonstrate the value and necessity of the planned U.S. national glider network and build on last years successes, we hope to continue these efforts and require that all glider data produced by Gliderpalooza 2015 participants be uploaded by the individual operators to the DAC 2.0 and into GTS.**

Keywords—gliders, coastal oceanography, gliderpalooza, IOOS

I. Introduction

Many basic and applied oceanographic research questions facing humanity require a better understanding of the physical, chemical, and biological interactions in coastal waters. These coastal regions are difficult to sample given numerous turbulent boundary layers and high frequency atmospheric/land forcing. Additionally there are numerous pressures associated with a growing human population, the associated anthropogenic environmental impacts are significant and are only expected to increase as coastal populations continue to grow. Understanding of the ocean's physical, chemical, and biological responses, particularly in the context of anthropogenic forcing (climate change, resource extraction and utilization, waste production and nutrient pollution), remains a difficult problem that limits our ability to predict and manage coastal waters. The data most relevant to understanding/supporting critical coastal processes (ocean productivity, water quality, fisheries, weather, climate, shipping, recreation, and energy production) spans a range of temporal (days to years) and spatial (meters to 1000's of kilometers) scales. These scales cannot be affordably resolved using traditional (ships, moorings) oceanographic sampling approaches alone. There is a greater need to combine monitoring efforts with adaptive sampling in time and space as many of the critical processes of are ephemeral. Autonomous underwater gliders (Davis et al 2003) are mobile platforms that can be steered adaptively from shore and have proven to be a robust that is being taken up by the oceanographic community (Schofield et al. 2015).

Gliders, as currently configured, were first detailed in Doug Webb' s lab book on 2/8/86 (Webb 1986). The concept matured during many backyard discussions with Henry Stommel who, in 1989, publicized his science fiction vision of the future of a smart fleet of instruments being coordinated by

978-0-933957-43-5 ©2015 MTS

graduate students (Stommel 1989). These systems, a cousin to the Argo profiling float, were developed in parallel at several academic institutions and commercial companies through support from the Office of Naval Research in the United States. This progress has been mirrored in Europe, Asia, Australia and Africa They have now matured to the point that they are available for commercial purchase from several companies and there is a large growing community. Due to successes in the field, federal agencies in United States, Europe, Australia, and South Africa have begun to adopt gliders for a range of more applied and operational needs. The community is highly distributed and continues to grow. This evolution has stimulated the community to begin discussions about the potential for a national glider networks for several countries. One example is in the United States, glider community leaders working with NOAA's Integrated Ocean Observing System (IOOS) have been developing a draft national glider plan (http://www.ioos.noaa.gov/glider/strategy/glider_network_whitepaper_final.pdf).

While discussion about a potential national plan continues to evolve, there remains a need to continue to harmonize and accelerate collaboration among the growing glider community. As an example of this community-based coordination, a series of grass-roots regional ad-hoc experiments were conducted in 2013 and 2014. These efforts termed "gliderpalooza" represented coordinated individual experiments, funded by diverse federal and state sponsors, working together to provide regional data to modelers. The data supported their own local objectives while contributing to regional scale questions that could not be addressed by any one institution alone.

II. Path Forward

A. *Moving the glider technology forward*

Increasing the utility of glider technology will be based on increasing a range of activities that include increasing the number of available sensors, coordination of communities of gliders, improved energy efficiency and standardizing quality assurance/control.

An ocean research platform is only as useful as the sensors it can carry. Historically the type of sensor has been limited by the size and energy consumption of the sensor. Fortunately, there is a revolution occurring in instrument miniaturization. Additionally, the increased availability of high-density energy lithium batteries has increased the power availability over traditional alkaline-based batteries. This has opened the door for the potential to integrate a new suite of sensors into gliders in the coming decade. Currently a wide range of physical, chemical, optical and acoustic sensors are being integrated into gliders.

As the number of sensors available for these platforms. As the sensor suite expands, we expect community efforts to shift from mainly hardware/software development to tools that allow for more effective operation of individual or fleets of vehicles. Coordinated fleets will be more common and efficient as it is likely that lifetime costs of gliders will be dominated by the cost of operating them, rather than the cost of purchasing the vehicles.

As the number of gliders sensors increase in oceanography, establishing solid quality assurance and quality control procedures for sensors and data collected from observatory platforms, including gliders, is essential (Fredericks et al. 2009). This includes the production of Standard Operating Procedures (SOPs), quality assurance procedures such as a Quality Assurance Project Plan (QAPP) and QARTOD (Quality Assurance in Real Time Oceanographic Data), validating data, applying quality control in real-time, and developing a data analysis/data management system for future glider monitoring. A QAPP has been successfully implemented for the glider-integrated CTD and monitoring dissolved oxygen using a glider optode (nepis.epa.gov/Exe/ZyPURL.cgi?Dockey=P100IVXI.txt). However, there are still several gliders sensors that do not have established QA/QC protocols. Many teams are actively working to fill the gaps and establish standard operating procedures (SOPs) for quality assurance as well as quality control of real-time glider data. These SOPs should be publicly available. Formal groups such as the MTS or IEEE can and should play a critical role in the facilitating discussion in developing community agreement on the appropriate procedures and QA/QC protocols.

Incorporation of any sensor into a glider results in an immediate new "sink" of power, which limits the lifetime of a mission. Therefore increasing energy efficiency is absolutely critical. Tools that allow for increased efficiency and assist in mission planning are becoming critical as the newer instrument suites tend to have high power requirements. With improvements such as the recent integration of the coulomb meter into the Slocum glider, measuring the discharge of the battery has become more accurate and critical to long duration glider operations. Knowing the rate at which energy is used and how much remains is vital to mission planning. However, the glider's coulomb meter only measures whole vehicle current. To perform more precise mission planning, the energy consumption of individual components (especially power intensive sensors) is necessary. To that end, we have developed a measurement infrastructure, which captures the currents drawn from distinct components of the Slocum Glider. The infrastructure has been deployed in test missions off the coast of New Jersey, and the data collected have been integrated into a Slocum Glider simulator. This measurement board and simulation framework can be used to assist in the planning and decision making of missions and shows possible tradeoffs, for instance, between mission duration, speed, and energy consumption. The simulation environment incorporates energy, speed, seafloor and ocean current models, and is used to predict the flight path, longevity and energy usage of a mission. The simulation environment has been validated against Teledyne Webb's Shoebox simulator and compared to a deployment on the continental shelf off of the coast of New Jersey. Results between the three compared well (Woithe et al. 2010). Mission planning tools such as this will become increasingly important for glider operations in the coming years as more sensors are integrated into the glider.

In situations where the desired sensor activation profile of "everything, everywhere, all the time" is not feasible for the entire duration of a mission, mission planning tools will be particularly crucial. Mission planning tools can help oceanographers to assess the potential tradeoffs between different sensing activities in terms of overall energy consumption and peak power requirements. Sensor activity planning and path planning need to be done together while leaving enough energy reserves to ensure a safe recovery of the glider at the end of a mission. In some cases, the effectiveness of sensing activities can be improved by using lower power sensors to trigger high power sensors only in situations where acquiring expensive sensing data is important. Such trigger chains have been recently proposed with promising results for triggering backscatter sensors of a Slocum glider while flying through a thermocline (Woithe et al. 2015). Simulation results and results from two glider deployments off the coast of New Jersey show energy savings between 34% and 82% without significant loss of scientific relevant data. Mission planning tools have to consider all aspects of sensor activation including the desired spatiotemporal resolution, tradeoffs between sensing activities and their energy/power demands, and the applicability and effectiveness of sensor trigger chains.

B. Moving the community forward

Forming an integrated community will require glider operators share, leverage off the respective experince of individual operators, and optmize/ standardize approaches. It should follow the example of the successful efforts of the ARGO community. To this end, coordinating activities through the MARACOOS community, a regional association of the US IOOS network, there was a concept to conduct a coordinated, but dispartely funded, regional glider experiment. This was to accomplished through a community coordinated event of individual principal investigator efforts which was called a gliderpalooza. The goals were to enable the individual glider missions to meet their specific mission goals but also provide a larger regional glider dataset that could serve a wider range of science and operational needs.

The first gliderpalooza was conducted in 2013. The initial group consisted four of the MARACOOS glider groups (Rutgers, University of Delaware, University of Massachusetts, and University of Maryland). Informal communication and subsequent word of mouth grew the community to eleven institutions (list in Table 1). Listed in Table are the partners, their science funding sources and distances each gliders traveled. In total, the effort resulted in over 7000 kilometers being surveyed through the ad-hoc community effort. The effort faciltated sensor sharing with the Ocean Tracking Network providing Vemco fish recievers to all participants. The effort also helped mature data flow. The community effort

Table 1. The participants of the 2013 Gliderpalooza.

Gliderpalooza Gliders- 2013				
	Group	Glider	Funding	Dist (km)
1	Dalhousie	OTN200	OTN	707
2		OTN201	OTN	575
3		OTN201	OTN	240
4	UMaine	Penobscot	Maine	737
5	WHOI	Saul	ONR	362
6	UMass	Blue	IOOS	482
7	Rutgers	RU28	EPA	697
8		RU22	IOOS	331
9		RU23	IOOS	411
10		RU23	IOOS	443
11	UDelaware	Otis	Private	299
12	VIMS	Amelia	VIMS	455
13	NC State	Salacia	NASA	430
14	Skidaway	Modena	Skidaway/SECOORA	237
15	T. Webb	Darwin	Teledyne	351
16	Navy	Navy1	Navy	500
			TOTALS:	7257

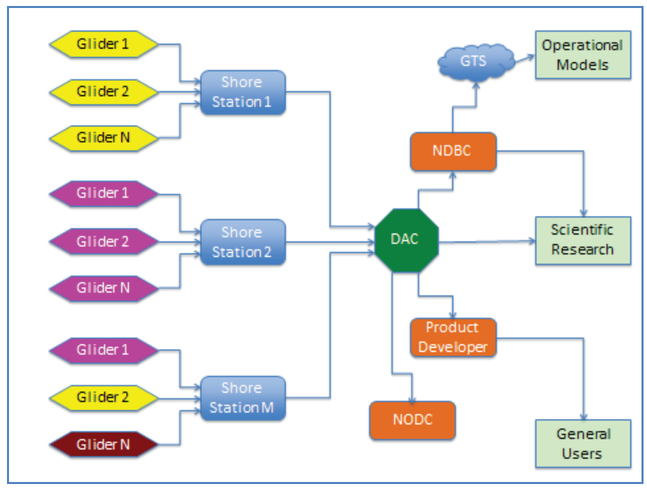

Figure 1. The data flow during the gliderpalooza efforts. During the first two years there was an effort of bringing larger proportions into the data systems illustrated above. The goal for the gliderpalooza in 2015 is to have all the members have their data flow through the NOAA DAC and onto the GTS.

was facilitated with data flow through the national Glider Data Assembly Center (DAC). The data flow through the DAC is illustrated in Figure 1. Efforts were coordinated through weekly telecons/web-ex, the near real-time data collected by the gliders, and regional satallite-HF radar-model datastreams coodinated through the MARACOOS asset map (http://assets.maracoos.org/).

We acknowledge the NOAA Integrated Ocean Observing System program and the Office of Naval Research.

The second gliderpalooza was conducted in 2014. This effort drew a much larger community response. The second

Figure 2. The yellow circles indicate the partners who partook in the 2014 gliderpalooza effort.

gliderpalooza drew communities spanning from the Gulf Mexico to the Bermuda Biological Station (Figure 2). The second effort expanded to 18 partners spanning federal agencies and academic partners. The partners and the number of gliders deployed are presented in Table 2. Glider missions were coordiated through NOAA glider portal which provided a larger framework larger the regional MARACOOS domain. The effort was conducted through the late summer into the Autumn season. As before the effort represented a range of individually funded efforts.

Table 2. The partners that were part of the 2014 gliderpalooza effort.

	Group	Gliders
1	Memorial University	3
2	Dalhousie (OTN)	2
3	Univ. of Maine	2
4	Woods Hole Inst.	5
5	Univ. of Mass. Dartmouth	1
6	Teledyne Webb	3
7	NSF OOI	3
8	Rutgers Univ.	4
9	Univ. of Delaware	1
10	Univ. of Maryland	1
11	VIMS	1
12	BIOS	1
13	Skidiaway Inst	1
14	Mote Marine Lab	1
15	Univ of S. Florida	1
16	US. Navy	2
17	Univ. of Southern Miss.	1
18	Texas A&M	3
	TOTAL:	36

The efforts have continued into 2015. There is a gliderpalooza planned for Fall in the Mid-Atlantic. It was however preceded by another complimentary community effort conducted in the Gulf of Mexico.

The Gulf of Mexico community coordinated a community event in the summer of 2015, which they called an AUV Jubilee. This effort was expanded beyond the gliderpalooza framework by expanding to a larger array of autonomous vehicles. The AUV Jubilee was an inaugural event to coordinate glider and other *in situ* ocean data operations in the Gulf of Mexico for the month of July 2015. The primary goal was to establish an open dialogue and collaboration with scientists across the Gulf, in order to acquire simultaneous ocean observations and leverage off of fellow participants to create a multifaceted and integrated data set. The AUV Jubilee was led by the University of Southern Mississippi's Ocean Weather Laboratory (http://www.usm.edu/marine/research-owx), which hosted a series of webinars to display real-time satellite ocean color and several ocean circulation models (HYCOM/NCOM), as well as maps of product uncertainty to allow the participating scientists to adaptively sample features of interest (e.g. eddies, river filaments, fronts, etc.). This data fusion tool enabled the display of up-to-date locations of various glider and ship/aerial operations while they were deployed, and facilitated near real-time data exchanges in order to further assist in decisions-making for adaptive sampling of ocean features. In addition to real-time operations, all participants were encouraged to submit data to the National Glider Data Assembly Center (NGDAC), so that the data

Table 3. The partners in the 2015 AUV Jubilee.

Institution	Platform
University of Southern Mississippi/CONCORDE	Ocean Weather Laboratory
Rutgers University/CONCORDE	Slocum
University of South Florida/MOTE Marine Lab	Slocum
Texas A&M	2 Slocums
Oregon State University/LADC-GEMM	Seaglider
Skidaway Institute of Oceanography/ University of Georgia/ECOGIG	Slocum
Gulf of Mexico Coastal Ocean Observing System (GCOOS)	GANDALF, data formatting, outreach
National Oceanic and Atmospheric Administration (NOAA)	Aerial LIDAR
Roffer's Ocean Fishing Forecasting Service, Inc.	Oceanographic Fishing Analysis
Florida Fish and Wildlife Research Institute	Vemco Mobile Tranceivers

could be available for assimilation into operational physical circulation models. The list of glider participants is shown in Table 3. The scope of the AUV Jubilee also included an educational outreach component, in which a competitively selected group of highly qualified teachers were brought in for an intensive one week program that included curriculum development, hands on oceanographic experience, and participation in real-time glider operations.

C. Conclusions

The glider community is rapidly growing as the technology has been demonstrated to be a transformative technology. As the platforms have matured, efforts are now focused on expanding the number of sensors, procedures to swarm fleets of gliders, improved/standardized data quality assurance/quality protocols, and extending duration of glider missions through improved energy efficiency. Just as important is the increasing number of open access community events that provide a means to collect valuable data and facilitate community exchange that will mature the community as a whole.

REFERENCES

[1] R. Davis, C. C. Eriksen, and C. P. Jones. "Autonomous buoyancy-driven underwater gliders" in Technology and Applications of Autonomous Underwater Vehicles. Taylor and Francis, London, pp. 37-58. 2003.

[2] O. Schofield, C. P. Jones, J. Kohut, U. Kremer, T. Miles, G. Saba, D. Webb, S. Glenn. "Building a coordinated community fleet of autonomous gliders for sampling coastal systems". Mar. Tech. Soc. 2015, 49(3), 9-16.

[3] H. tommel, H.." The Slocum mission" Oceanogr. 1989, *2*, 22-25.

[4]

[5] H. C. Woithe, C. C., Chigirev, D. Aragon, , M. Iqbal, Y. Shames, S. Glenn,, O. Schofield, I. Seskar, U. Kremer. "Slocum glider energy measurement and simulation infrastructure" OCEAN Conference, Sydney.

[6] H. C. Woithe, U. Kremer. "Feature based adaptive energy management of sensors on autonomous underwater vehicles" IEEE Ocean Engin. in press.

.

Implementation of Energy Harvesting System for Powering Thermal Gliders for Long Duration Ocean Research

Clinton D. Haldeman III, Oscar Schofield
Center for Ocean Observing Leadership
Rutgers, The State University of New Jersey
New Brunswick, NJ USA

Douglas C. Webb
Teledyne Webb Research Corporation
North Falmouth, MA USA

Thomas I. Valdez, Jack A. Jones
Jet Propulsion Laboratory
California Institute of Technology
Pasadena, CA USA

***Abstract*— The exploration of the Earth's oceans is aided by autonomous underwater vehicles (AUVs). AUVs in use today include floats and gliders; they can be deployed to profile salinity, temperature and pressure of the ocean at depths of up to 2 km. Both the floats and gliders typically control buoyancy by filling and deflating an external bladder with a hydraulic fluid delivered by an electrical pump. The operation time of an AUV is limited by energy storage. For floats, such as the Argo float, the operating duration is approximately 5 years with the capability to dive once every 10 days. For electric gliders, such as the deep G2 Slocum, the mission duration can be up to one year with lithium primary batteries. An energy storage system has been developed that can harvest energy from the temperature differences at various depths of the ocean. This system was demonstrated on an Argo style float and has been implemented in a thermal version of the Slocum glider. The energy harvesting system is based on a phase change material with a freeze thaw cycle that pressurizes hydraulic oil that is converted to electrical energy. The thermal Slocum glider does not use an electrical pump, but harvested thermal energy to control buoyancy. The goal for the thermal Slocum glider is for persistent ocean operation for a duration of up to 10 years. A thermal powered glider with an energy harvesting system as described can collect conductivity, temperature, and pressure data and deliver it to the National Data Buoy Center (NDBC) Glider Data Monitoring System and the World Meteorological Organization (WMO) Global Telecommunications System (GTS). Feeding into operational modeling centers such as the National Centers for Environmental Prediction (NCEP) and the U.S. Naval Observatory (NAVO), this data will enable advanced climate predictions over a timespan not currently achievable with present technology. Current testing of the thermal powered Slocum glider is to determine the durability of the technology and quantify the glider system design. Previous issues with this technology included energy storage system management and glider mechanical limitations. Our objective is to learn how to fly an energy harvesting thermal glider that interacts with the ocean environment efficiently. We would also like to establish the latitudinal range of operation. This thermal powered Slocum glider, dubbed Clark, after the famous explorer duo Lewis and Clark, has been deployed off of St. Thomas for flight dynamics and durability testing. The following paper will discuss the deployment and testing of the thermal powered Slocum glider. We will also discuss the advantages of ocean energy harvesting technology for oceanographic research.**

Keywords—glider, thermal glider, thermal recharging

I. INTRODUCTION (*HEADING 1*)

Stemming from a technology development cycle in the early days of the National Oceanographic Partnership Program (NOPP), Rutgers University has maintained a close working relationship with Teledyne Webb Research Corporation (TWRC), often serving as a testbed for new designs, improvements, or enhancements to the Slocum glider. The first prototype of this glider was deployed off the coast of New Jersey in 1999, and Rutgers purchased their first commercially available Slocum Electric glider in 2003. By 2007, Slocum gliders had been declared a viable technology for sustained ocean observations [1]. With the largest fleet of Slocum gliders in the world outside of the U.S. Navy, Rutgers has gained valuable operational experience from over 400 deployments around the world. A first-ever Slocum-TREC (Thermal RECharging) deep ocean glider has been developed through a partnership between Teledyne Webb Research Corporation (TWRC) and the National Aeronautical Space Administration's Jet Propulsion Laboratory (NASA-JPL) for the Office of Naval Research (ONR). Slocum-TREC is a thermal-class glider that can harvest energy from the ocean thermoclines. A photo of the Slocum-TREC "Clark" is shown as Fig. 1. The Slocum-TREC ocean glider was deployed on June 9^{th} 14 miles off the coast of St. Thomas, U.S. Virgin Islands. The goal of Slocum-TREC is to demonstrate the feasibility of the thermal buoyancy drive and TREC energy harvesting system to power deep ocean floats that can operate autonomously for periods of up to 10 years.

978-0-933957-43-5 ©2015 MTS

Fig. 1: Photo of the Slocum-TREC Glider "Clark"

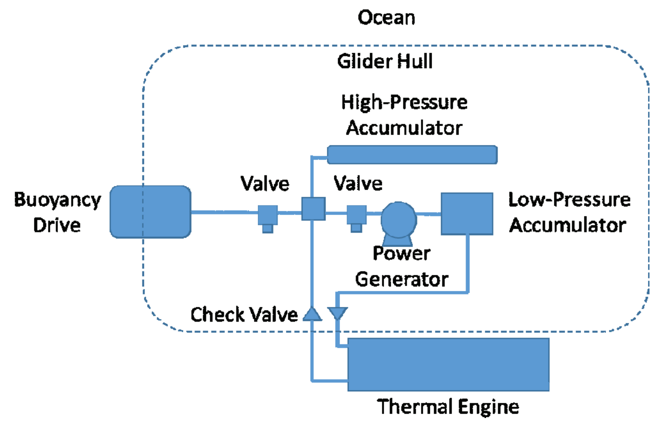

Fig. 2: Functional schematic of Slocum-TREC energy harvesting and thermal buoyancy drive

II. BACKGROUND

A. Glider Configuration

The Slocum-TREC glider is currently configured to operate with one scientific instrument to measure conductivity, temperature, and depth (CTD). Thermal-class gliders use a thermal engine to directly drive a buoyancy pump that controls the ocean glider's depth and ascent rate. It is capable of diving to 1200 meters and is currently programmed to dive up to 4 times a day. This ocean glider is not limited by battery energy storage.

1) Energy Harvesting System

A functional schematic of the Slocum-TREC energy harvesting and thermal buoyancy drive is shown as Fig. 2. As the glider travels through an ocean thermocline, a phase-change wax in the thermal engine undergoes a freeze-thaw cycle. As the phase-change wax is thawed, the expansion of the wax pressurizes the hydraulic oil in the thermal engine. As the hydraulic oil is pressurized, the energy from pressurization is captured in a high-pressure accumulator. The energy stored in the high-pressure accumulator can then be discharged to the gliders buoyancy drive to provide propulsion [2]. The energy storage in the high pressure accumulator can also be discharged to a power generator to be converted to electrical energy [3]. The electrical energy is used to provide electrical power to the glider to support hotel loads, science and communications. After the oil storage in the high-pressure accumulator is discharged, it is collected in the low-pressure accumulator and fed back to the thermal engine during the phase-change wax freeze cycle.

2) Field test, Energy Harvesting

The energy storage battery voltage of the TREC system during ocean testing is shown as Fig. 3. The TREC energy storage system is configured of two batteries, one battery is being charged by the energy harvested from the ocean by the TREC system, the other is used to provide electrical power to the Slocum-TREC ocean glider. The energy storage batteries are cycling between 13.2 and 13.4 Volts. These battery voltages correspond to approximately 40 to 75% state-of-charge (SOC). Operating the batteries in this SOC range will maximize battery cycle life to meet the program goals of 10 years of operation. The battery set points are controlled from land and can be changed to operate in a SOC range required by a specific mission. An example of a power generation cycle for the TREC system during ocean testing is shown as Fig. 4. A typical generation cycle runs between 40 to 45 seconds. The maximum charge power is approximately 220 Watts. The average energy generated by the TREC system per dive is approximately 1.8 Wh. The estimated energy storage is approximately 1.7 Wh/Dive, this includes the efficiency of the batteries under these charge conditions. In the present operating mode, a battery could deliver approximately 70 Wh electrical energy every 80 generation cycles. This energy can be delivered at power levels as high as 800 Watts. This capability can enable the operation of high-power science instruments on a Slocum-Class ocean glider with the persistence of years of operation.

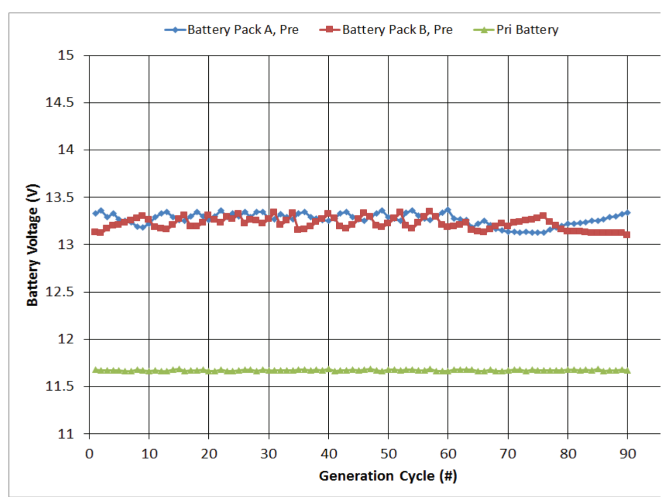

Fig. 3: Energy storage battery voltage of TREC system

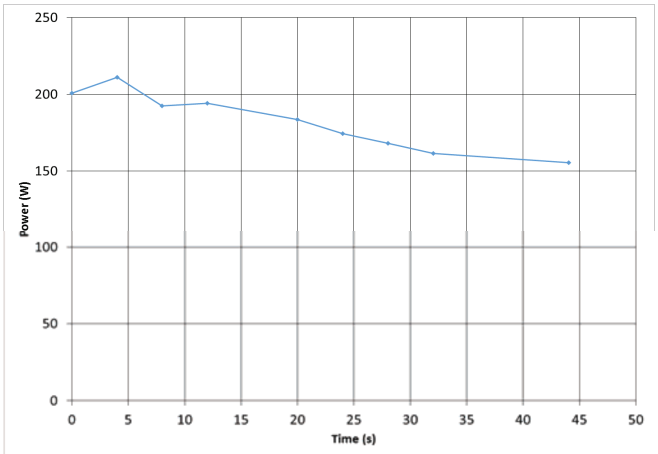

Fig. 4: TREC system energy generation cycle

B. Ballasting and Flight Dynamics

Engineers from TWRC, NASA-JPL, and Rutgers combined their expertise at the University of the Virgin Islands (UVI) in St. Thomas, USVI to assemble, ballast, and deploy the Slocum-TREC for a long duration test flight. The importance of stringent control of ballast is exacerbated by the buoyancy drive; too light and the glider cannot dive to the depths and temperatures it needs to reach to achieve a thermal charge, too heavy and the glider is unable to surface, which ultimately leads to the expulsion of an ejection weight and the end of the mission, requiring an emergency recovery.

Flight characteristics are generally similar to standard electric gliders, but volume and structural differences change the dynamics, giving the Slocum-TREC its own signature flight pattern and nuances. Ballasting was conducted in Brewers Bay, a relatively sheltered patch of water adjacent to UVI's dock, with only a moderate predominate wave and current field. Reliant upon the CTD attached to the Slocum-TREC, data were obtained, density calculations were made, and ballast was adjusted accordingly. Fine adjustments were made at sea, once flight parameters were analyzed following a test dive, by adding small ballast weights externally to achieve a symmetrical yo (dive and climb) pattern. Total symmetry in the yo could not, however, be obtained due to water mass layering. The decision was then made to aim for symmetry in the top water mass, allowing the glider's vertical velocity to slow in the deep water masses; the effects of which are mitigated by compaction of the carbon fiber hull resulting in a lesser volume, and therefore less buoyancy. Further flight dynamics adjustments required recovery and needed to be performed in the lab. Specifically, an inherent roll was noticed that would switch signs from the average on the dive and climb; rolling slightly to port on the dive and hard to port on the climb; this can be seen in the top plot of Fig. 5. A detailed inspection and measurements in the lab uncovered a slight twist between the hull and the thermal engines, effectively turning the entire glider into a rudder. The twist was corrected, and roll has been steady at less than -2 degrees as seen in the bottom plot of Fig. 5.

.

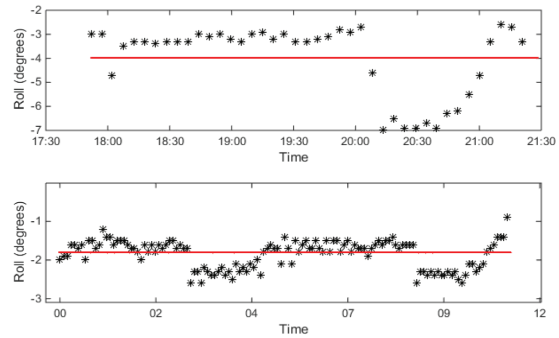

Fig. 5 – Roll before and after fixing the twist in the hull. Red is average roll; -4 degrees prior and less than -2 after.

III. Results

A. Characterization of physical structure – salinity, temperature, and density off the U.S. Virgin Islands

The Slocum-TREC is equipped with a Seabird Electronics (SBE) 41 CP CTD - a low power, 1 Hz continuously profiling flow-through cell CTD originally designed for profiling floats that has proven effective over long periods of unattended operations [4]. This allows for the continual collection of conductivity and temperature data, providing a clear picture of the physical structure of the water column. Initial analysis of the CTD data raised some concerns related to the calibration of the instrument, as results were atypical of the deep water column structure commonly seen in other areas. Once instrument calibration was verified by TWRC, a closer look was taken at the climatology of the area via the Caribbean Coastal Ocean Observing System (CariCOOS.org), a Rutgers partner through the Integrated Ocean Observing System (IOOS). The atypical structure is a subsurface peak of high salinity water nearly 37 psu sitting at a depth of almost 200 m known as the Subtropical Underwater (SUW) mass. The SUW is almost 2 psu higher than the deep water masses in the area, but is more than 15 degrees C warmer, ensuring a stable water column with no density inversions (Fig. 6). The lower salinity top water layer is known as the Caribbean Surface Water (CSW) mass, and, when time shifted, shares a decent correlation to the outflow of the Orinoco River basin in Venezuela [5]. Further freshwater input to the area comes from North Atlantic surface waters and the immense outflow of the Amazon River basin, resulting in a significantly less dense surface water in the top 100 m approximate depth [6]. The CSW exhibits a strong seasonal cycle between the summer and fall in both the depth and intensity of the halocline, corresponding to the lack of or abundance of freshwater input from South America [5]. It is this water mass and its fluctuations that makes its way onto the shelf and impacts marine life in and around the islands. The Slocum-TREC boasts its advantage as a superior platform for sustained ocean observing operations focusing on these types of measurements, as it has the ability to profile continuously for years while actively controlling its location as opposed to Lagrangian-style floats that must ride the predominate currents. Several seasonal cycles could be observed on a single Slocum-TREC deployment, closing data gaps and possibly raising correlations to related climatic cycles.

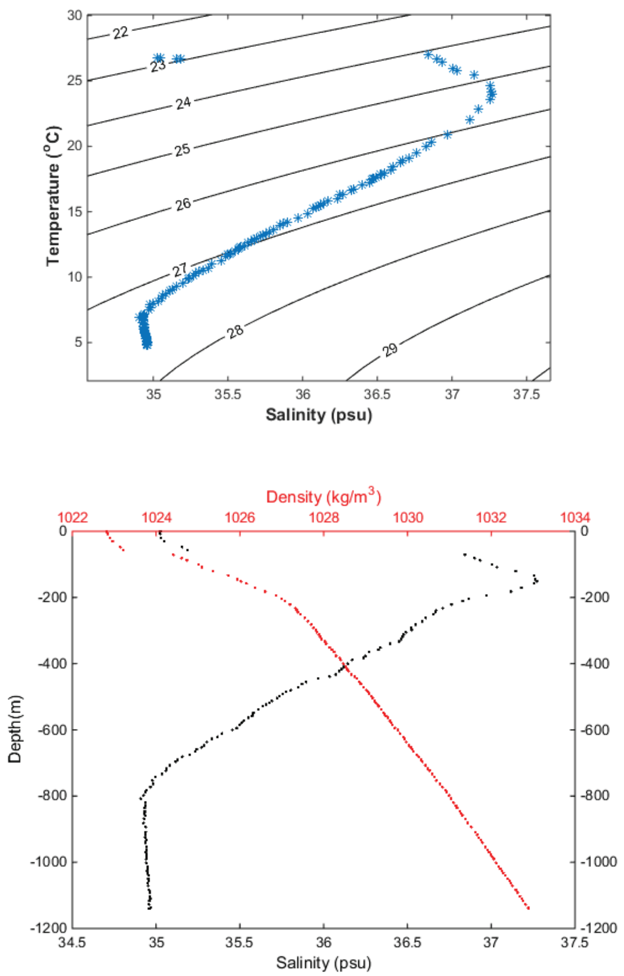

Fig. 6 – T-S diagram, salinity field and density structure showing water column stability. All data transmitted back from "Clark".

B. *Quantification of system design and limitations*

While the Slocum-TREC is currently deployed and fully operational, there are several components of the system that still require quantification. The thermal power generation and energy storage system developed by JPL has been thoroughly tested, measured, and documented, and is described above in detail. Thermal harvesting and power generation has, in fact, been so efficient that the Slocum-TREC has been shunting excess energy, and CTD horizontal resolution has been increased to sample on every dive. The overachieving nature of this system will likely lead to further design improvements as more energy intensive instruments can be integrated to further enhance ocean sampling. Initial musings include increasing sampling resolution in water masses of interest, along with integrating a pumped CTD such as the SBE GPCTD to improve thermal lag calculations in high vertical resolution sampling of strong thermoclines. The latitudinal limits of operation, however – how far north or south the glider can operate while continuing to obtain a thermal charge – are more difficult to discern. The glider requires a thermal difference of at least 12 degrees C between the surface and its maximum dive depth of 1200 m, spending approximately 120 minutes at <8 degrees C for the wax to freeze, plus an additional 120 minutes at >20 degrees C for the wax to melt in order to obtain a thermal charge. While oceanographic models may assist in determining general latitudinal limits, this can change in the short term as currents meander or eddies form and migrate. On a larger time scale, latitudinal limits may expand in the future as oceans continue to warm. One pressing limitation that the Slocum-TREC team has not addressed is a concept familiar to many who have conducted long duration oceanographic studies – biofouling. Ablative paints and other standard antifouling methods have proven ineffective over long durations, and newer technologies such as those resembling shark skin coatings are not yet commercially available. By continuously harvesting thermal energy, the Slocum-TREC has solved the propulsion and energy budget limitations, perhaps thrusting biofouling to the forefront of the list of issues facing long duration ocean sampling.

C. *Data Flow and Implications for the Future*

Currently, data collected by the Slocum-TREC "Clark" is transferred via the Iridium satellite constellation and routed directly to TWRC. This is then synced to a server at Rutgers where data is displayed on the web in near real-time. From Rutgers, this data is ported into the Global Telecommunications System (GTS) for ingestion into oceanographic models by operational modeling centers such as the National Centers or Environmental Prediction (NCEP) and the U.S. Navy (NAVO). NCEP's mission statement refers to delivering climate products essential to protecting life, property, and economic well-being, immediately vesting their interest in the expansion of the collection of accurate, high resolution ocean data. Through the GTS, data collected by gliders, floats, and other assets can be assimilated into models such as the Real-Time Ocean Forecasting System (RTOFS), a global operational model based on an eddy resolving 1/12° global HYCOM (Hybrid Coordinates Ocean Model) developed by the U.S. Navy [7]. Future plans for RTOFS include inputs to hurricane and climate forecast systems, further emphasizing the need for high resolution data collection in sparsely sampled areas. The strengths of the Slocum-TREC become apparent in this context, showcasing the ability to routinely gather high resolution data that can be regularly transmitted ashore for a cost that diminishes throughout the life of the glider. Daily assimilation into models can assist with improving ocean, terrestrial, hurricane and climate forecasting at a level that is unparalleled by any other oceanographic platform.

IV. CONCLUSIONS

Thus far, the Slocum-TREC deployment has been a resounding success. "Clark" has been continually operating in the Virgin Islands Trench, sending full-profile data ashore in user-configurable intervals of anywhere from 6-12 hours; further adjustable if desired. The ocean glider operators, dubbed pilots, since the glider does "fly", are currently in the process of optimizing and adjusting flight and energy storage parameters. The first stage of endurance testing will be complete after 90 consecutive days of deployment. The goal for the second stage of endurance testing is for continued operation greater than 200 days. After the second stage of endurance testing, the glider's flight and energy system data will be evaluated and an extended mission will be proposed. The third mission will likely traverse the Atlantic, including paths suggested by Rutgers undergraduates studying the global ocean models and working on detailed path-planning projects, allowing "Clark's" success to transcend the engineering community and enter the educational community as well.

ACKNOWLEDGMENTS

This work presented here was carried out by Rutgers and Teledyne Webb Research in conjunction with the Jet Propulsion Laboratory, California Institute of Technology under a contract with National Aeronautics and Space Administration. Funding for the project was provided by the Office of Naval Research.

REFERENCES

[1] O. Schofield, et.al. "Slocum gliders: Robust and ready," Journal of Field Robotics, Special Issue: Special Issue on Underwater Robotics, 24(6), 473-485.

[2] D. C. Webb, U. S. Patent No: 7,987,674, Autonomous propulsion within a volume of fluid. (1991)

[3] J. A. Jones, Y. Chao, T. I. Valdez, U. S. Patent No: 7,987,674, Phase change material thermal power generator. (2007)

[4] Riser, S.C. (1998). "The Distribution of 18-Degree Water in the North Atlantic During the Autumn of 1997 and the Winter of 1988", AGU 1998 Ocean Sciences Meeting Presentation OS11J-04.

[5] "Salinity Field." CariCOOS.org. Caribbean Regional Association, 1999. Accessed January 2015.

[6] Joanna Gyory, Arthur J. Mariano, Edward H. Ryan. "The Caribbean Current." Ocean Surface Currents. University of Miami, 2001-2013. Accessed August 2015.

[7] Chassignet, E.P., H.E. Hurlburt, E.J. Metzger, O.M. Smedstad, J. Cummings, G.R. Halliwell, R. Bleck, R. Baraille, A.J. Wallcraft, C. Lozano, H.L. Tolman, A. Srinivasan, S. Hankin, P. Cornillon, R. Weisberg, A. Barth, R. He, F. Werner, and J. Wilkin, 2009. U.S. GODAE: Global Ocean Prediction with the HYbrid Coordinate Ocean Model (HYCOM). Oceanography, 22(2), 64-75.

AGU PUBLICATIONS

JGR

Journal of Geophysical Research: Oceans

RESEARCH ARTICLE

10.1002/2014JC010474

Key Points:

- Underwater glider observes sediment transport in Hurricane Sandy
- Glider data are used to validate sediment transport modeling
- Model shows over 3 cm of erosion on the northern NJ shelf

Correspondence to:
T. Miles,
tnmiles@marine.rutgers.edu

Citation:
Miles, T., G. Seroka, J. Kohut, O. Schofield, and S. Glenn (2015), Glider observations and modeling of sediment transport in Hurricane Sandy, *J. Geophys. Res. Oceans*, *120*, doi:10.1002/2014JC010474.

Received 26 SEP 2014
Accepted 2 FEB 2015
Accepted article online 6 FEB 2015

Glider observations and modeling of sediment transport in Hurricane Sandy

Travis Miles[1], Greg Seroka[1], Josh Kohut[1], Oscar Schofield[1], and Scott Glenn[1]

[1]Center for Ocean Observing Leadership, Department of Marine and Coastal Sciences, School of Environmental and Biological Sciences, Rutgers University, New Brunswick, New Jersey, USA

Abstract Regional sediment resuspension and transport are examined as Hurricane Sandy made landfall on the Mid-Atlantic Bight (MAB) in October 2012. A Teledyne-Webb Slocum glider, equipped with a Nortek Aquadopp current profiler, was deployed on the continental shelf ahead of the storm, and is used to validate sediment transport routines coupled to the Regional Ocean Modeling System (ROMS). The glider was deployed on 25 October, 5 days before Sandy made landfall in southern New Jersey (NJ) and flew along the 40 m isobath south of the Hudson Shelf Valley. We used optical and acoustic backscatter to compare with two modeled size classes along the glider track, 0.1 and 0.4 mm sand, respectively. Observations and modeling revealed full water column resuspension for both size classes for over 24 h during peak waves and currents, with transport oriented along-shelf toward the southwest. Regional model predictions showed over 3 cm of sediment eroded on the northern portion of the NJ shelf where waves and currents were the highest. As the storm passed and winds reversed from onshore to offshore on the southern portion of the domain waves and subsequently orbital velocities necessary for resuspension were reduced leading to over 3 cm of deposition across the entire shelf, just north of Delaware Bay. This study highlights the utility of gliders as a new asset in support of the development and verification of regional sediment resuspension and transport models, particularly during large tropical and extratropical cyclones when in situ data sets are not readily available.

1. Introduction

At midnight on 29 October, Hurricane Sandy made landfall near Brigantine, NJ devastating New York and New Jersey coastal communities through a combination of high winds and historic storm surge [*Blake et al.*, 2013]. This storm caused significant coastal erosion [*Hapke et al.*, 2013], and showed a distinct seabed signature at an inner-shelf site [*Trembanis et al.*, 2013] but little is understood about broader regional sediment resuspension and transport on the continental shelf. A unique data set from a Teledyne-Webb Slocum glider equipped with a Nortek Aquadopp Current profiler deployed ahead of the storm in combination with the Regional Ocean Modeling System (ROMS) allow us to assess regional patterns of sediment resuspension and transport throughout Hurricane Sandy.

Storms are important episodic events that redistribute sediment on continental shelves [*Cacchione and Grant*, 1987; *Drake and Cacchione*, 1992; *Sherwood et al.*, 1994; *Ogston et al.*, 2000; *Keen and Glenn*, 2002; *Styles and Glenn*, 2005; *Teague et al.*, 2006; *Warner et al.*, 2008a]. Many of the field programs over the past two decades used benthic landers and tripods equipped with a suite of optical and acoustic sensors at a single location to understand sediment resuspension and transport dynamics [*Trowbridge and Nowell*, 1994; *Agrawal and Pottsmith*, 2000; *Harris et al.*, 2003; *Styles and Glenn*, 2005]. These sensor platforms have provided a wealth of information that have aided in the development of one-dimensional bottom boundary layer models (BBLMs) that take into account combined wave and current interactions [*Grant and Madsen*, 1979, 1986; *Glenn and Grant*, 1987; *Madsen and Wikramanayake*, 1991; *Madsen*, 1994; *Styles and Glenn*, 2000, 2002; *Warner et al.*, 2008b]. These one-dimensional models generally require input of wave and current data and a significant amount of tuning in order to accurately predict sediment resuspension and transport at a specific location.

In the past decade, these one-dimensional BBLMs have been coupled to three-dimensional hydrographic models to understand broader scale erosion and deposition at regional scales [*Blaas et al.*, 2007;

Papanicolaou and Elhakeem, 2008; *Warner et al*., 2008b; *Hu et al*., 2009]. With the development of these regional scale sediment resuspension and transport studies new technologies are necessary to supplement single point measurements of sediment resuspension and transport on continental shelves. Many of the sensors included on tripods and benthic landers have now been developed for autonomous platforms such as Teledyne-Webb Slocum gliders [*Davis et al*., 2003; *Schofield et al*., 2007; *Glenn et al*., 2008]. A study by *Glenn et al*. [2008] presented data from two gliders deployed on the New Jersey shelf during storm conditions, one during stratified summer months and the other after the fall transition to well-mixed winter conditions. The stratified summer deployment showed sediment resuspension throughout the bottom layer, restricted by thermal stratification, during a summer hurricane, while the deployment after the fall transition identified full water column sediment resuspension that followed a Rousian distribution [*McLean*, 1991], where suspended sediment concentration decreased logarithmically with height above the bed. A follow up study [*Miles et al*., 2013] used two simultaneously deployed gliders during a northeaster in fall of 2009 to identify spatial variability in sediment resuspension and transport.

The present work builds on previous sediment resuspension and transport work by using a combination of model predictions and glider observations to identify idealized broad spatial patterns of sediment resuspension, transport, and deposition on the New Jersey (NJ) continental shelf during Hurricane Sandy in October of 2012.

A detailed description of observational and model setup is given in section 2. The synoptic atmospheric and oceanic conditions, as well as the observed and modeled sediment resuspension and transport response along the glider track are detailed in section 3. Section 4 provides a broader regional look at sediment transport throughout the storm and highlights the atmospheric and wave forcing that lead to shelf wide patterns of erosion and deposition. A final summary and conclusions are provided in section 5.

2. Methods

2.1. Gliders

Teledyne-Webb Slocum gliders have become robust tools for sampling storm conditions [*Glenn et al*., 2008; *Ruiz et al*., 2012; *Miles et al*., 2013]. These instruments are mobile sensor platforms that profile through the water column using a combination of buoyancy and a set pitch angle to move vertically and horizontally in a sawtooth pattern. Data are logged every 2 s on downcast and upcast with vertical speeds of $\sim$20 cm/s resulting in high data density relative to traditional shipboard techniques. A single hour long sampling segment may include approximately 5–10 profiles depending on water column depth. After each segment is complete the glider surfaces and relays its position and data back to Rutgers using an Iridium satellite phone in the aft section of the glider. Further details of Rutgers glider operations can be found in *Schofield et al*. [2007].

The glider used in this study was RU23, a first generation shallow (100 m rated) glider equipped with a suite of oceanographic sensors. RU23 included three science sensors, a Seabird unpumped conductivity temperature and depth (CTD) sensor, two Wetlabs triplet sensors and an externally mounted Nortek Aquadopp current profiler. One Wetlabs triplet was an optical backscatter puck (bb3) that measured the volume scattering function (VSF) at three wavelengths 470, 532, and 660 nm in the 117° back direction. We converted from the VSF to estimated backscatter coefficients following *Boss and Pegau* [2001]. For our analysis, we use the 660 nm channel as it is less impacted by absorption effects than the shorter wavelength channels (E. Boss, personal communication, 2014). These instruments respond linearly to increased suspended particulate matter concentrations [*Boss et al*., 2009], but are also sensitive to variability in particle size, shape, and composition; similar sensors were used onboard previous glider observations of storm driven sediment resuspension and transport [*Glenn et al*., 2008; *Miles et al*., 2013]. The second Wetlabs triplet was an ecopuck that we used primarily to measure chlorophyll fluorescence.

The Nortek Aquadopp was a three-beam 2 MHz system with a 0.2 m blanking distance that collected data in 10 1 m bins in beam coordinates. The Aquadopp was externally mounted in an upward looking position, with a custom glider head that measured 0° pitch at a nominal glider pitch angle of 26.5°. Data were logged internally and downloaded postdeployment. This instrument served two purposes: the first was to estimate realistic water column velocities following a shear least squares method originally developed for lowered acoustic Doppler current profilers [*Visbeck*, 2002] and recently adapted to use on glider platforms [*Todd et al.*, 2011a, 2011b]. The shear least squared method is used to solve the following equation:

$$(u,v)_r=(u,v)_w-\ (u,v)_g \tag{1}$$

where $(u,v)_r$ is the measured water velocity relative to the glider, $(u,v)_w$ is the real ocean velocity, and $(u,v)_g$ is the velocity of the glider. The measured water velocity relative to the glider is taken directly from the vertical profile of the horizontal shear of the velocity profiles above the glider. Glider velocity is dead-reckoned [*Davis et al.*, 2003] using a combination of pre and postsegment GPS fixes, pitch angle, heading, and depth. These two measurements are then used to solve for the real ocean velocities using least squares, which are described in detail in Appendix B of *Todd et al.* [2011a].

The second purpose was to provide acoustic backscatter observations coincident with optical measurements. Acoustic return (*Amp*) strength along each beam was converted to echo level (*EL*), with units of decibels (dB) following *Lohrmann* [2001]:

$$EL=Amp\times 0.43+20\log_{10}(R)+2\alpha_w R+20R\int \alpha_p\times dr \tag{2}$$

where R is the range along each beam, α_w is the water absorption in db m^{-1}, and α_p is the particle attenuation in db m^{-1}. Previous studies [e.g., *Lynch et al.*, 1997] have used colocated optical and acoustic backscatter sensors on bottom tripods to assess the relative contribution of small and large sediment particles. The difference in acoustic and optical response to different size classes is most clearly illustrated in *Lynch et al.* [1997, Figure 4], with an optical backscatter sensor and a 1 and 5 MHz acoustic backscatter sensor. An Aquadopp is most sensitive to particles with a $k*a=1$, where k is the acoustic wave number and a is the particle radius [*Lohrmann*, 2001; *Thorne and Hanes*, 2002]. For a 2 MHz system, a k*a value is most sensitive to particles with a 0.25 mm diameter with a reduction in sensitivity raised to the fourth power for particles smaller than a and inversely proportional for particles with a diameter larger than a. Optical backscatter sensors generally respond to the cross-sectional area [*Bunt et al.*, 1999] and have been shown to have large increases in observed optical backscatter for similar concentrations of small versus large particles, thus in the presence of significant concentrations of small suspended particles these sensors are largely unresponsive to additional concentrations of large particles (C. Sherwood, personal communication, 2014).

As the glider was deployed over a broad spatial region with varying bottom types, sediment types and optical properties we did not attempt to calibrate either optical or acoustic backscatter sensors using in situ sediment, but rather focus on intercomparison of the suite of sensors to estimate sediment resuspension and transport throughout the deployment.

2.2. Additional Observational Assets

We use National Oceanographic and Atmospheric Association (NOAA) buoy 44025 and 44009 data to supplement glider data and validate numerical model results. NOAA buoy 44025 is located at 40.250°N and 73.167°W off of Long Island, New York, and NOAA buoy 44009 is located at 38.461°N and 74.703°W offshore of Delaware Bay (Figure 1). Buoy data included in this study are hourly wind speed and direction collected at a height of 4 m, barometric pressure, significant wave height, dominant wave period, wave spectra, and mean wave direction from buoy 44025 only.

2.3. Hydrodynamic Model

The Regional Ocean Modeling System (ROMS) [*Shchepetkin and McWilliams*, 2005, 2009; *Haidvogel et al.*, 2008] version 3.6 was used to simulate the ocean response to storm forcing. ROMS is a free surface, sigma coordinate primitive equation model that is widely used for coastal applications. The configuration here is a modified version of the Experimental System for Predicting Shelf and Slope Optics (ESPreSSO) (http://www.myroms.org/espresso/) with 5 km horizontal resolution and 36 vertical levels, which extends from Cape Cod, MA, to Cape Hatteras, NC, and near shore to beyond the shelf-break (Figure 2). The ESPreSSO domain has been used extensively on the MAB to study a diverse array of physical and biological processes [*Cahill et al.*, 2008; *Haidvogel et al.*, 2008; *Hofmann et al.*, 2008; *Zhang et al.*, 2009; *Wilkin and Hunter*, 2013; *Xu et al.*, 2013]. We used the original assimilative ESPreSSO four-dimensional variational data assimilations (IS4DVAR) output as an initial condition starting on 25 October and ran the model forward including boundary

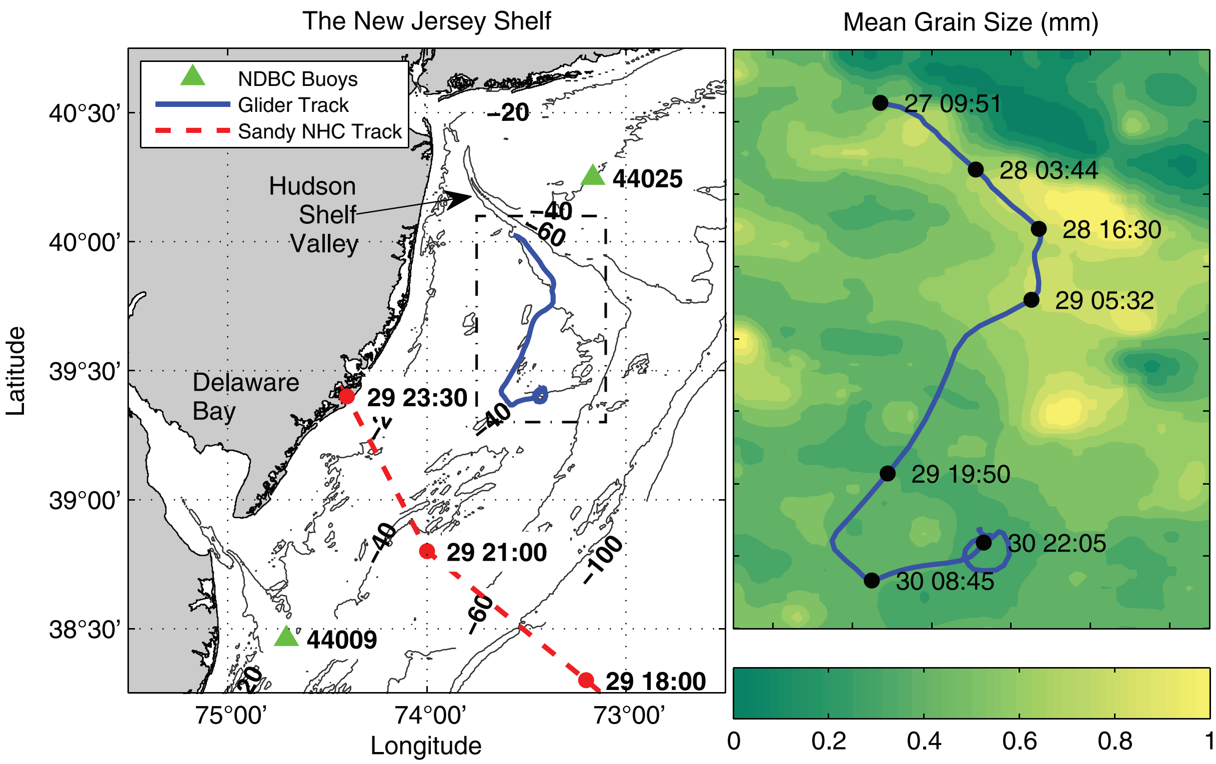

Figure 1. Map of the (a) New Jersey shelf, with locations of buoys (green diamonds) 44025 and 44009, (blue line) RU23 glider sampling track, the (red dashed line) Hurricane Sandy track from the National Hurricane Center (NHC) with associated time points. (b) A map of mean bed grain sizes over the area defined by the dashed box in Figure 1a in millimeters compiled from the usSEABED project, with a (blue line) track of the glider consistent with Figure 1a overlaid with times in the format of day hour:minute on 27 October through 30 October 2012.

conditions from HYCOM-NCODA (http://hycom.org/), tidal boundary conditions from the ADCIRC tidal model (http://adcirc.org/).

For this study, we modify the standard ESPreSSO setup in a number of ways: we replace the standard ESPreSSO atmospheric forcing from the National Center for Environmental Prediction (NCEP) North American Mesoscale (NAM) model with our own Weather Research and Forecasting (WRF) model detailed in section 2.4; by turning on the sediment features detailed in section 2.5; and the BBLM detailed in section 2.6; and drive this BBLM with the wave information from NOAAs, WAVEWATCH III model detailed in section 2.7. While numerous studies have used the Coupled Ocean Atmosphere Wave Sediment Transport (COAWST) system [*Warner et al*., 2010; *Olabarrieta et al*., 2012] for sediment transport, which includes a coupled wave and atmospheric model, for simplicity we use the Rutgers ROMS ESPreSSO domain as it has a robust history of reproducing realistic circulation over our study region [*Wilkin and Hunter*, 2013] and required minimal adjustment from the standard setup to run for the purposes of this study.

2.4. Atmospheric Model

Default atmospheric forcing for ROMS ESPreSSO is from the NCEP NAM model, which is an operational version of the WRF Nonhydrostatic Mesoscale Model (WRF-NMM) run at 12 km horizontal resolution with standard output every 3 h. In order to provide ROMS with higher spatial and temporal resolution atmospheric forcing, we used our own implementation of the Advanced Research WRF (WRF-ARW), Version 3.4 [*Skamarock et al*., 2008]. WRF-ARW is a fully compressible, nonhydrostatic, terrain-following coordinate, primitive equation atmospheric model that is used for many different weather and climate applications.

Our WRF-ARW simulations were run at 6 km horizontal resolution with 35 vertical levels, using the Global Forecast System (GFS) 0.5° model for lateral boundary conditions. To provide continuous near-analysis atmospheric forcing, we used hourly output from a series of six short 36 h WRF-ARW hindcasts. These hindcasts were initialized at 00:00 GMT each day starting on 25 October 2012. For each run, excluding the first

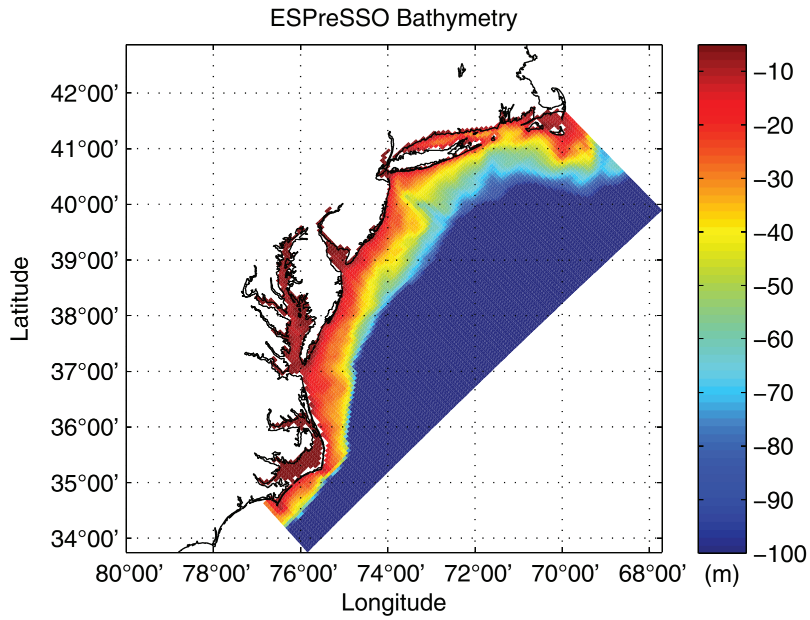

Figure 2. A map of bathymetry for the ESPreSSO model domain (gridded region) with the maximum plotted depth of 100 m. Depths beyond 100 m are present in the model domain but are plotted as blue here.

and last runs, only data from hours 7 to 30 were retained in an effort to minimize the impact of model reinitialization on wind forcing. The first run included hours 1 through 30 and the last run included hours 7 to 36 in an effort to maximize coverage.

For bottom boundary conditions over water, we used a high-resolution sea surface temperature (SST) composite product. This daily SST product has a resolution of 2 km and is a 3 day coldest dark pixel composite of regionally declouded daytime scans from the Advanced Very High Resolution Radiometer (AVHRR) aboard the NOAA-18 and NOAA-19 satellites. Through these techniques, normally unresolved coastal upwelling and tropical cyclone cold wake processes are preserved. For each simulation, we initialize SST with the daily composite described above and leave it fixed until the next simulation's initialization. Model validations in section 3.3 indicate that this model setup adequately represents storm forcing for our purposes, but future model runs may benefit from coupled ocean and atmospheric modeling.

ESPreSSO air-sea heat and momentum fluxes were calculated using the bulk formulae of *Fairall and Bradley* [1996] and *Fairall et al*. [2003] using the ESPreSSO model sea surface temperature and WRF-ARW sea level air temperature, precipitation, pressure, relative humidity, and 10 m winds.

2.5. Sediment Model

We used the Community Sediment Transport Model (CSTM) to simulate sediment resuspension and transport. A detailed description of the CSTM can be found in *Warner et al*. [2008b]. The CSTM requires input of user-defined sediment size classes, critical shear stress values, fall velocities, densities, and erodibility constants. We initialized with an idealized spatially uniform single, 15 m deep, bed layer with two noncohesive size classes of 0.1 mm and 0.4 mm to represent fine and medium grain size sands found in the glider sample region (Figure 1b). According to a map generated from data collected by the usSEABED project [*Goff et al*., 2008] on 29 October 2012 during peak storm conditions, the glider was sampling over a region with approximately 0.4 mm mean grain sizes. Additionally, a recent publication [*Trembanis et al*., 2013] collected grab samples on the southern region, near buoy 44009 and identified mean grain sizes of approximately 0.3 mm prior to Sandy impacting the region. Based on the 0.1 and 0.4 mm diameters and 2650 kg m^{-3} densities, we use settling velocities and critical shear stresses of 5.7 mm s^{-1} and 0.14 N m^{-2}, respectively, for the 0.1 mm sediment and 52 mm s^{-1} and 0.23 N m^{-2} for the 0.4 mm sediment and erodibility constants of 5×10^{-4} kg m^{-2} s^{-1} for both sediment types. This uniform bed setup is used to only generally represent sediment resuspension and transport on the continental shelf, and is primarily used for simplification of data interpretation and comparison of large and small grain size particles with glider data. This setup will not address the potential impact of realistic sediment distributions and bed armoring on sediment resuspension. For more detailed analysis, we recommend using a broader array of sediment types, higher spatial resolution model grids, and coupled ocean-atmosphere-wave model routines.

At each time step, the model uses sediment bed properties to calculate bed roughness at each grid point and passes this information to the bottom boundary layer model to calculate bottom stress (τ_{sf}) from combined waves and currents. If critical shear stresses (τ_{ce}) are exceeded sediment is resuspended into the water column and transported as a tracer similar to temperature and salinity, but with an additional source and sink term, based on the erosional source and settling velocity, respectively. From *Warner et al*. [2008b]:

$$C_{source,m} = \frac{\partial w_{s,m} C_m}{\partial s} + E_{s,m} \tag{3}$$

where s is the vertical coordinate for the advection diffusion equation in ROMS, w_s is the vertical settling velocity prescribed by the user for each size class m, C is sediment concentration, and E_s is the erosion source, which follows[*Ariathurai and Arulanandan*, 1978]:

$$E_{s,m} = E_{0,m}(1-\phi) \frac{\tau_{sf} - \tau_{ce,m}}{\tau_{ce,m}} \quad \tau_{sf} > \tau_{ce,m} \tag{4}$$

where again, s is the vertical coordinate in ROMS, E_s is the surface erosion mass flux, E_0 is a bed erodibility constant, ϕ is the bed porosity of the uppermost bed layer and τ_{sf} τ_{ce} are the defined above. For the purposes of this study, we only consider suspended load transport for direct comparison with glider observed suspended load transport, though for realistic studies of sediment transport bedload transport must be considered. Bedload transport routines are also available in ROMS [*Meyer-Peter and Müller*, 1948; *Soulsby and Damgaard*, 2005].

2.6. Bottom Boundary Layer Model

The standard ESPreSSO setup uses a quadratic drag law with a drag coefficient expression to represent bottom stress. For sediment resuspension and transport, a more detailed calculation of bottom stress is needed as realistically, large gradients in velocity and sediment concentration occur near the bed. For this study, we use the ssw_bbl model, which follows *Madsen* [1994] for combined waves and currents and the moveable bed routines from *Wiberg and Harris* [1994] and *Harris and Wiberg* [2002]. The ssw_bbl routine used in this study is covered in detail in *Warner et al*. [2008b]. Parameters required for the ssw_bbl model include sediment characteristics described in the previous section to determine bed roughness, near-bottom reference velocities, u and v taken as the velocity in the lowest model grid, wave orbital velocities u_b, wave period T, and wave direction θ.

2.7. Wave Model

The wave parameters used for this study are derived from the third generation NOAA WAVEWATCH III (WWIII) (http://polar.ncep.noaa.gov/waves/index2.shtml) operational wave model. We specifically use data from the hindcast reanalysis version 2.22, with 3 h output. We use two WWIII data sets for this study, with 4° and 10° min resolutions that cover the study region. The 4 min resolution data does not cover the entire ESPreSSO domain but provides higher resolution in near shore shallow water regions. Both the 4 and 10 min resolution data are interpolated to the standard ESPreSSO grid with a nominal 5 km horizontal resolution. While this may not be an ideal methodology for detailed analysis of coastal change or long-term studies on the continental shelf, interpolation of these readily available products were sufficient for a first-order comparison of glider optical data to modeled suspended sediment at the midshelf. WWIII model hindcasts do not include the full wave spectra as the operational and forward run products. To calculate bottom orbital velocities from WWIII data without spectral information, we use linear wave theory and follow the method of *Wiberg and Sherwood* [2008] using an assumed Joint North Sea Wave Project (JONSWAP) spectrum. Matlab® codes for this calculation are included in the reference and validation of the calculated product of both buoys is presented in section 3.3.

3. Results

3.1. Storm Conditions

On 28 October, when winds and waves began to steadily increase on the MAB (Figure 3) the center of Hurricane Sandy was located nearly due east of the Georgia and South Carolina. On 29 October, the storm began

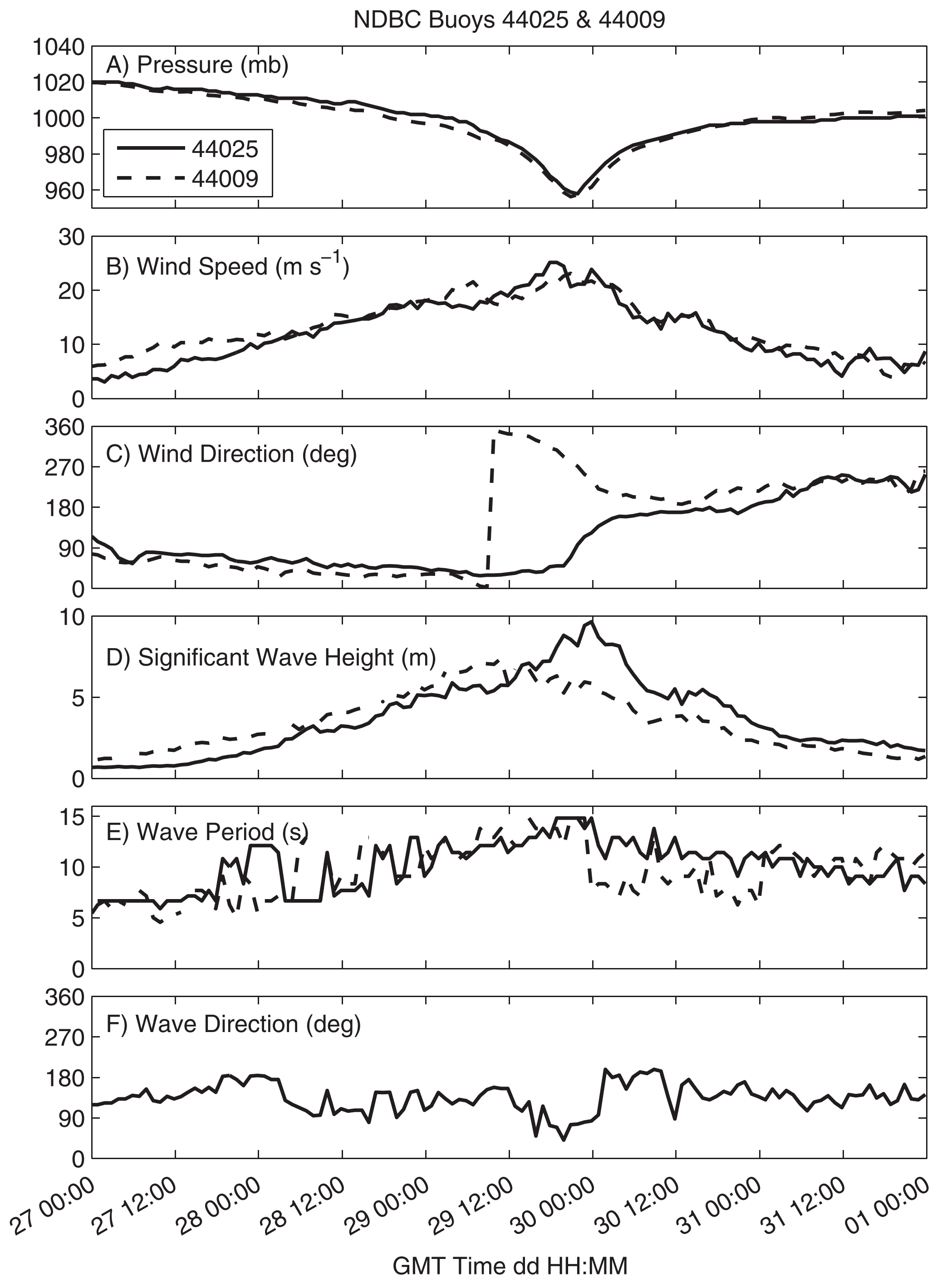

Figure 3. Buoy (solid line) 44025 and (dashed line) 44009 (a) pressure, (b) wind speed, (c) wind direction from north, (d) significant wave height, (e) wave period, and (f) wave direction from north at buoy 44025 only. The *x* axis is in days hour:minute for October 2012.

a left hand turn toward the New Jersey coastline and made landfall near Brigantine, New Jersey at 23:30 GMT (Figure 1a) [*Blake et al.*, 2013]. Buoy 44025 and 44009 were located to the north and south, respectively, of the storm track as it crossed the shelf (Figure 1a). Minimum sea-level pressure at 44025 and 44009 was below 960 at both locations, and maximum wind speeds peaked over 20 m s^{-1} (Figure 3). Winds were initially downwelling favorable from the northwest at 44025 and north at 44009. Winds shifted counterclockwise to be more northeasterly at 44009 on 29 October as the storm center crossed the shelf. Winds at 44025 maintained a northwesterly direction until just prior to landfall when they shifted clockwise to be

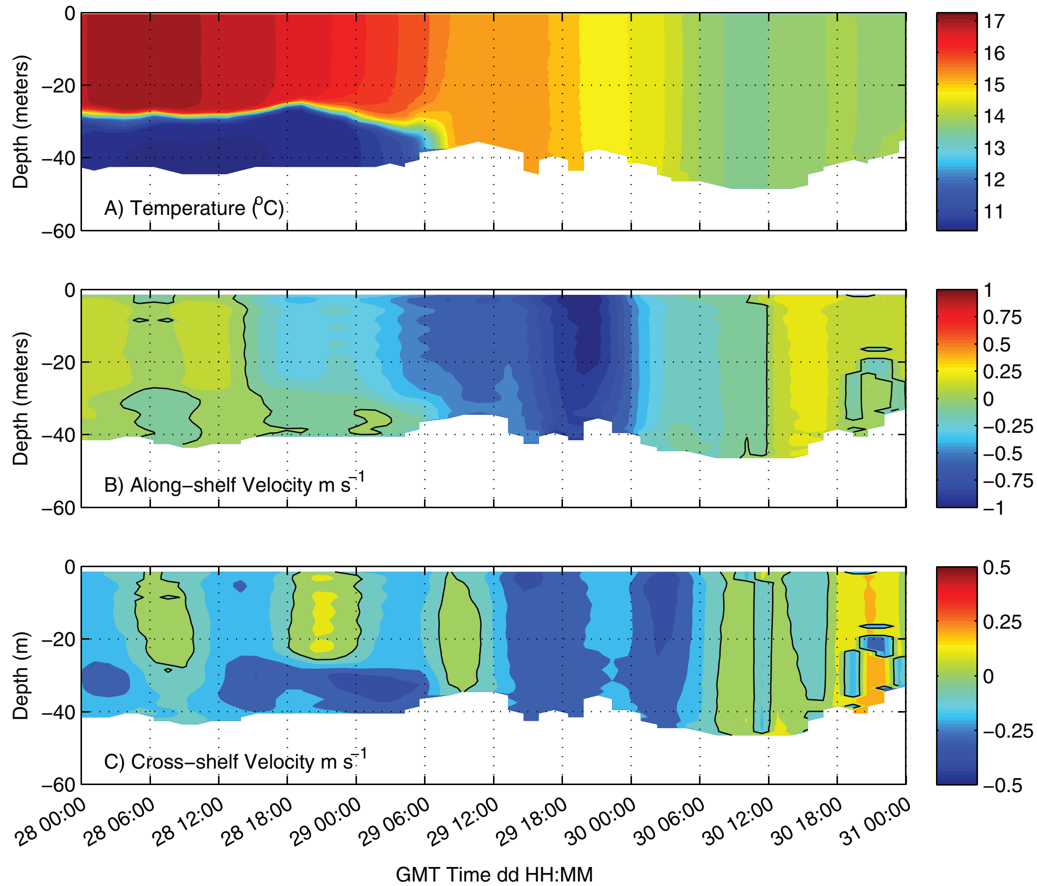

Figure 4. Cross sections along the glider track of (a) temperature, (b) along-shelf currents, and (c) cross-shelf currents with the black contour representing 0 m s^{-1}. Directions are toward and rotated 30° clockwise from north to be approximately along and cross-shelf, where positive is toward the northeast and offshore, respectively. Times on the *x* axis are as in Figure 3.

from the southwest as the eye passed between the two stations. Significant wave heights first peaked on the southern MAB at 44009 near 7 m approximately 12 h before they peaked at 44025 near 10 m. Dominant wave periods at both buoys reached 15 s near landfall. Wave periods dropped immediately following eye passage at 44009, likely due to the rapid shift in wind direction. While no wave direction data were available at 44009, mean wave direction at 44025 was generally in agreement with wind direction.

3.2. Glider Deployment

Glider RU23 was deployed on 25 October approximately 15 km off of northern New Jersey, on the southern flank of the Hudson Shelf Valley (Figure 1a). RU23 progressed southeastward in an effort to exit a coastal shipping lane prior to storm conditions. During the initial storm forcing period from 28 October at 00:00 GMT to the 29 October at 06:00 GMT, the water column observed by the glider was highly thermally stratified with surface temperatures of near 18°C and bottom temperatures as low as 10°C separated by a sharp thermocline (Figure 4a). During the stratified phase currents measured by the Nortek Aquadopp showed two-layer cross-shelf flow consistent with downwelling circulation on the shelf (Figures 4b and 4c), with offshore flow near the bottom and onshore flow near the surface. On 29 October at 06:00 GMT, the system transitioned from two to one-layer with a uniform water column temperature of ~15°C and strong alongshore flow toward the southwest. As glider horizontal speeds are on the order of 0.2–0.3 m s^{-1}, the glider was rapidly advected alongshore with the mean current until after the eye passed on 29 October at 23:30 GMT.

3.3. Model Validation

To validate the meteorological and wave forcing parameters, we calculated correlation coefficients and root-mean-square-error between modeled and observed winds, sea level pressure, wave height, and calculated bottom orbital velocities at buoy 44025 and 44009. We focused the comparison on the storm

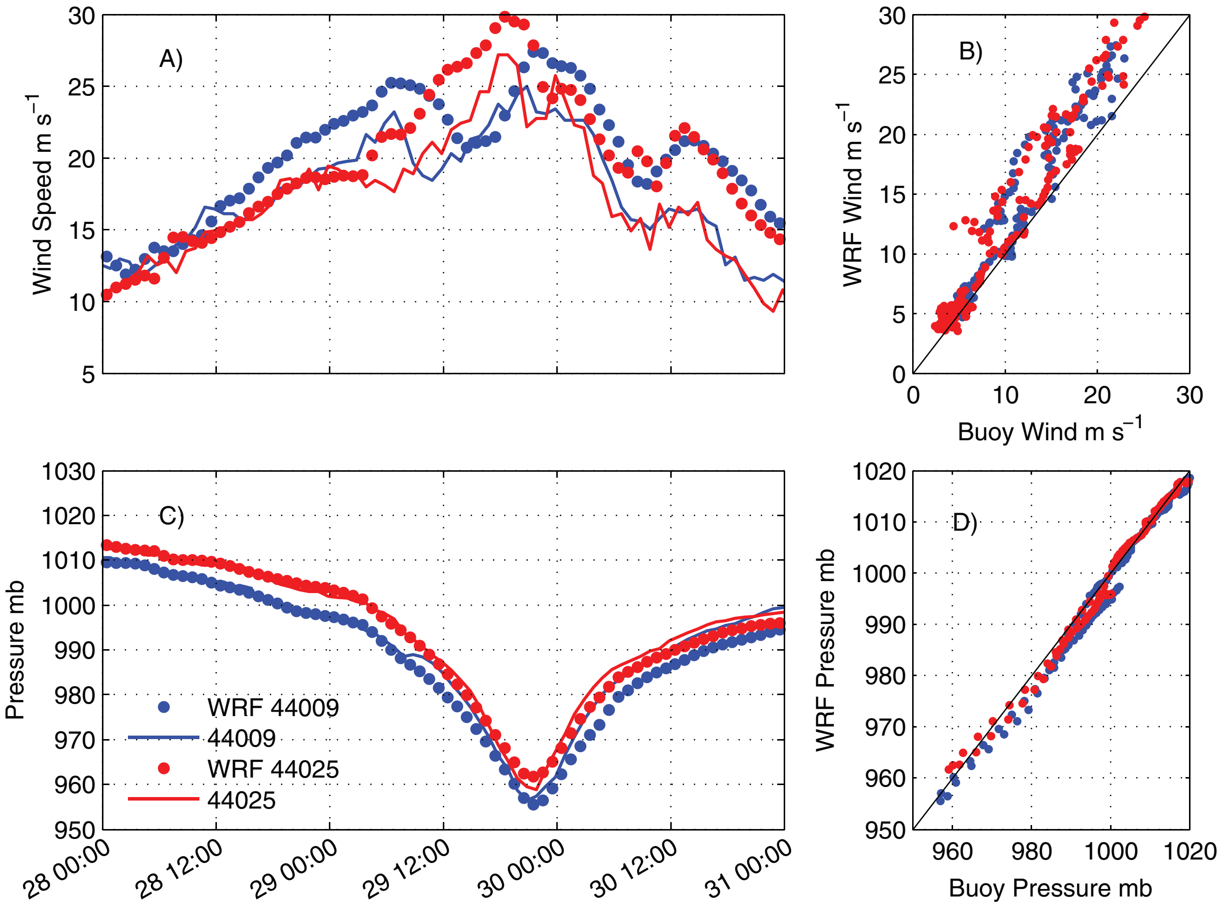

Figure 5. Comparisons of (dots) WRF and (lines) buoys (blue) 44009 and (red 44025) of (a and b) wind speed and (c and d) pressure during the storm forcing period. WRF versus buoy winds had a root mean square error (RMSE) of 4.25 and 4.14 m s^{-1} and correlation coefficients of 0.87 and 0.90 for 44009 and 44025, respectively. WRF versus buoy pressures had RMSE of 2.75 and 1.74 mb and correlation coefficients of 0.99 and 0.99 for 44009 and 44025, respectively. Time on the *x* axis is consistent with Figure 3.

forcing period between 28 October at 00:00 GMT and the 31 October at 00:00 GMT so as not to bias the validation to fair-weather conditions. Quantitative comparisons are detailed in the captions for Figures 5 and 6.

Qualitatively, the WRF hindcast wind speed and pressure (Figure 5) were in good agreement with observations at buoy 44025 and 44009. Modeled wind speeds (Figures 5a and 5b) appear to be overpredicted, likely due to WRF winds being instantaneous values extracted hourly while observed winds were hourly averages. Despite the high values, WRF winds followed along closely with the observations except for a late drop in winds at buoy 44009 on the 29 October at 12:00 GMT. Model predicted pressure was extremely close to the observations with similar trends and minimums below 960 millibars, indicating that the storm track and strength were well represented in the model.

WWIII simulated wave heights (Figures 6a and 6b) were underpredicted at both locations ahead of the storm, particularly at 44009, with peak observed wave heights occurring nearly 12 h ahead of peak modeled wave heights. Wave heights between 29 October at 12:00 GMT and 31 October at 00:00 GMT were well represented at both locations and peak modeled and observed wave heights occurred at approximately the same time at buoy 44025. Simulated bottom orbital velocities at 44025 were similarly underpredicted but generally in good agreement with the observations (Figures 6c and 6d). Differences between modeled and observed waves are likely due to the lack of spectral information included with the archived WWIII model data and coarse resolution. These properties would likely be improved by use of operational WWIII products with full spectral information or by using a modeling system such as COAWST, which includes three-way coupling between ROMS, the simulating waves near-shore (SWAN) model, and the weather research

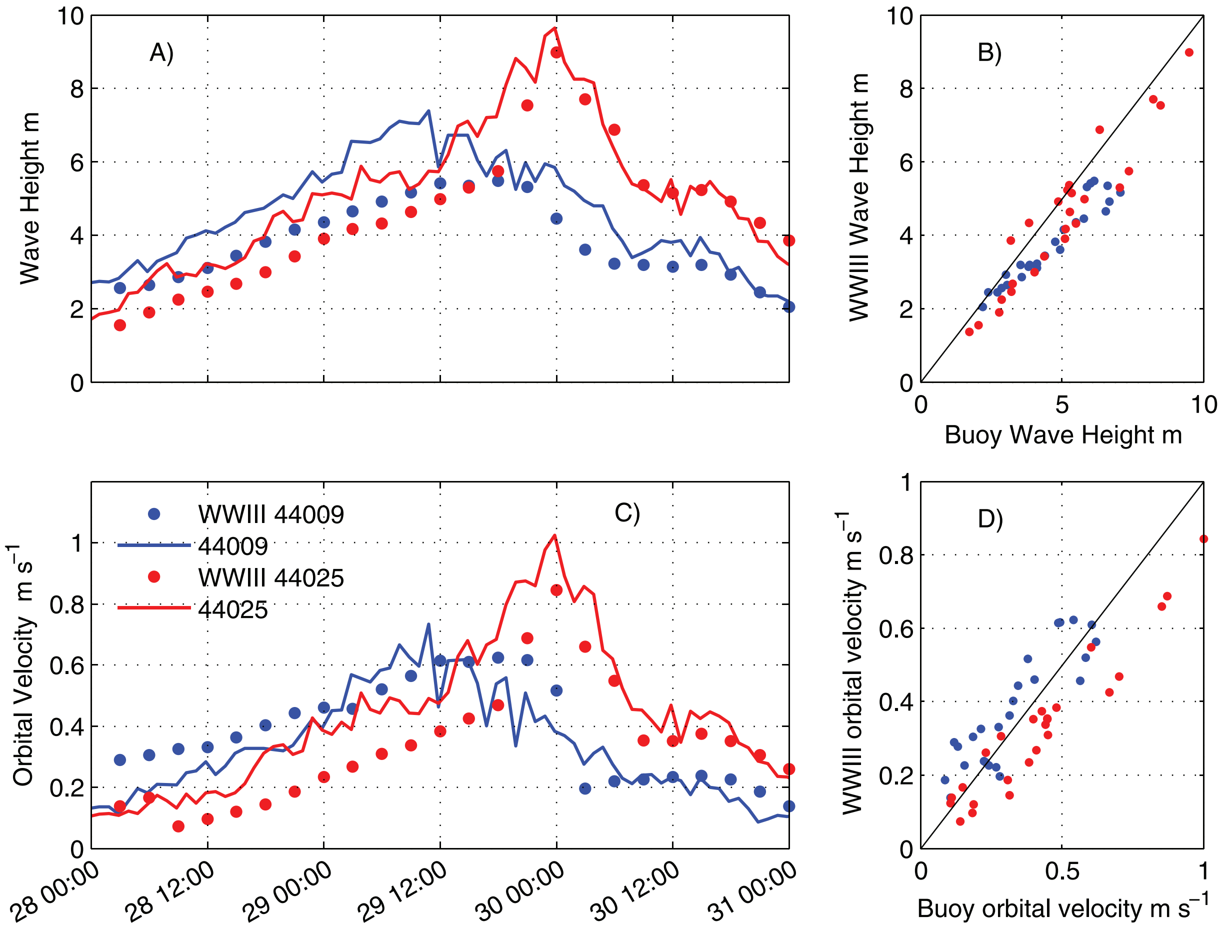

Figure 6. Comparisons of (dots) WWIII and (lines) buoys (blue) 44009 and (red 44025) of (a and b) wave height and (c and d) bottom orbital velocities during the storm. WWIII versus buoy waves had RMSE of 0.98 and 0.83 m and correlation coefficients of 0.96 and 0.95 for 44009 and 44025, respectively. WWIII versus buoy bottom orbital velocities had RMSE of 0.09 and 0.12 m s^{-1} and correlation coefficients of 0.88 and 0.96 for 44009 and 44025, respectively. Time on the *x* axis is consistent with Figure 3.

forecasting (WRF) model [*Warner et al.*, 2010]. Comparisons between the model and observations were sufficient for analysis of concurrent glider and model data north of the eye.

In order to assess modeled ESPreSSO currents, we compared depth-averaged values along the glider track to depth and time-averaged glider currents calculated using dead-reckoning [*Davis et al.*, 2003]. ESPreSSO currents were extracted hourly from the nearest grid point to each hourly glider surfacing. Both glider and ESPreSSO currents were rotated clockwise 30° from true north to align approximately alongshore and cross-shore at the glider location. ESPreSSO currents were in good agreement with the observed dead reckoned glider currents for the majority of the deployment (Figures 7a and 7b). The complex correlation coefficient between the model and glider was 0.90 with ROMS velocities rotated 8.1° counterclockwise of glider data. Cross-shore currents were generally well represented, though predicted velocities were slightly slower during the main forcing period from 29 October to at 00:00 GMT to the 30 October at 06:00 GMT. Both model predicted and observed alongshore velocities reached peak values near 1 m s^{-1} at landfall. Glider dead-reckoned currents are sensitive to accurate compass calibration. While, the compass was calibrated prior to flight and offsets from true compass direction were accounted for in postprocessing this remains a source of uncertainty in the model and observation comparisons and will require careful consideration in future deployments.

3.4. Glider and Modeled Sediment Resuspension and Transport

Typically validation of regional sediment resuspension and transport is done using poststorm surveys or using single point locations but little in situ validation over broad spatial regions and throughout the full

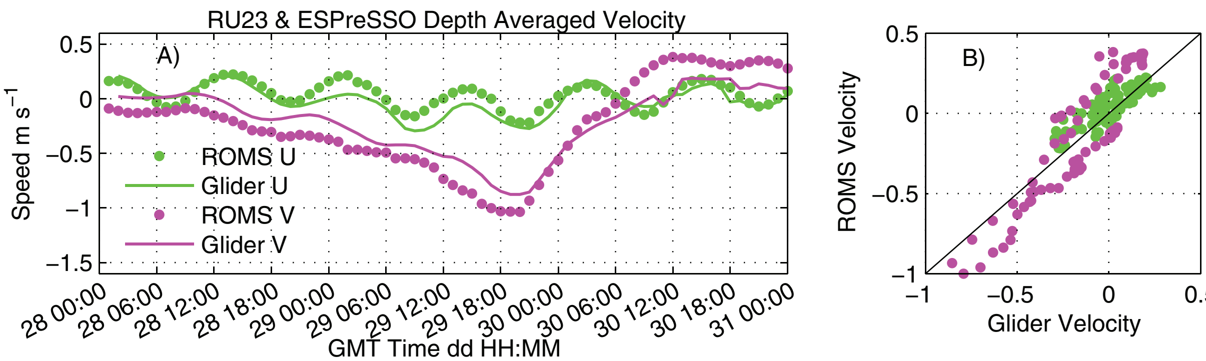

Figure 7. Comparisons of depth-averaged (dots) ROMS and (lines) glider depth-averaged currents calculated along the glider track in the (green) cross-shelf and (pink) along-shelf directions. Positive values indicate along-shelf (cross-shelf) toward the northeast (offshore). The complex correlation coefficient of ROMS versus RU23 depth-averaged currents is 0.90 with ROMS velocities rotated 8.1° counterclockwise of the glider data.

water column has previously been possible from a single set of profiling sensors. As our glider, RU23, was equipped with optical and acoustic sensors we compare along-track sediment resuspension and transport between the model and glider.

Cross sections of model suspended 0.4 and 0.1 mm sediment concentration along the glider track (Figures 8a and 8b) are compared with Aquadopp acoustic backscatter and bb3 optical backscatter (Figures 8c and 8d). Model cross sections of sediment resuspension along the glider track suggest 0.4 and 0.1 mm sediment resuspension initiate in response to storm forcing after 28 October at 12:00 GMT, with concentrations limited to within a few meters of the bed. Full water column resuspension is evident 24 h later, on the 29 October after 12:00 GMT, with large concentrations evident in the lower 10–15 m for 0.4 mm sediment, and throughout the entire water column to the surface for 0.1 mm sediment. Peak values for both grain sizes occur on the 29 October at 19:00 GMT, a few hours prior to landfall, following peak model predicted and observed wave heights and orbital velocities at buoy 44009 but prior to peak values at 44025 (Figures 5a and 5b). This is likely the timing of peak wave heights and orbital velocities at the glider location, which is approximately midway between the two buoys. Larger 0.4 mm particles fall out of suspension rapidly after the eye made landfall on 29 October at 23:30 GMT, while smaller particles had persistent elevated concentrations throughout the water column for 18 h following landfall. Acoustic backscatter (Figure 8c) was significantly different from model predicted values in two distinct ways. First, during early stages of the deployment, between 28 October at 06:00 GMT and 29 October at 00:00 GMT, there is a clear acoustic backscatter signal that fills the lower stratified (Figure 4a) region. Wave heights and orbital velocities were building during this period (Figures 6a and 6b) but were relatively weak compared to peak values. This feature was also present in optical backscatter values (Figure 8d), which indicates that the Aquadopp was likely responding to smaller fine grained sediment in the absence of a significant signal from larger grain sediments near the target 0.25 mm grain size. Cross sections of chlorophyll concentration (Figure 8e) derived from the fluorometer also suggest finer particles or biological material in this lower layer prior to transition from stratified to unstratified conditions. The second deviation from the model predicted suspended sediment is a persistent near surface acoustic backscatter signal, which peaks during peak wave and wind conditions on 29 October at 19:00 GMT. This signal is likely due to bubble entrainment in the surface boundary layer. In the lower portion of the water column acoustic backscatter qualitatively agrees with modeled 0.4 mm suspended sediment, with peak acoustic backscatter near 75 dB just prior to landfall coincident with model predicted peak concentrations. After the storm passed between 30 October at 00:00 GMT and the 31 October at 00:00 GMT, the persistent full water column acoustic backscatter near 55 dB is again likely due to fine particles that remained resuspended after coarse sand fell out of suspension. Cross sections of optical backscatter at 660 nm (Figure 8d) qualitatively agrees with concentrations of 0.1 mm sediment, which were elevated to the sea surface at nearly the same time as observed optical backscatter just prior to 29 October at 18:00 GMT, the peak in 0.1 mm concentrations and optical backscatter occurred in the model and observations similar to the acoustic and model 0.4 mm sand just prior to landfall at 19:00 GMT on 29 October. The optical signal remained high throughout the water column until 30 October near 18:00 GMT, persisting longer than modeled 0.1 mm sand. This suggests that there were likely smaller particles present than those modeled, which remained in

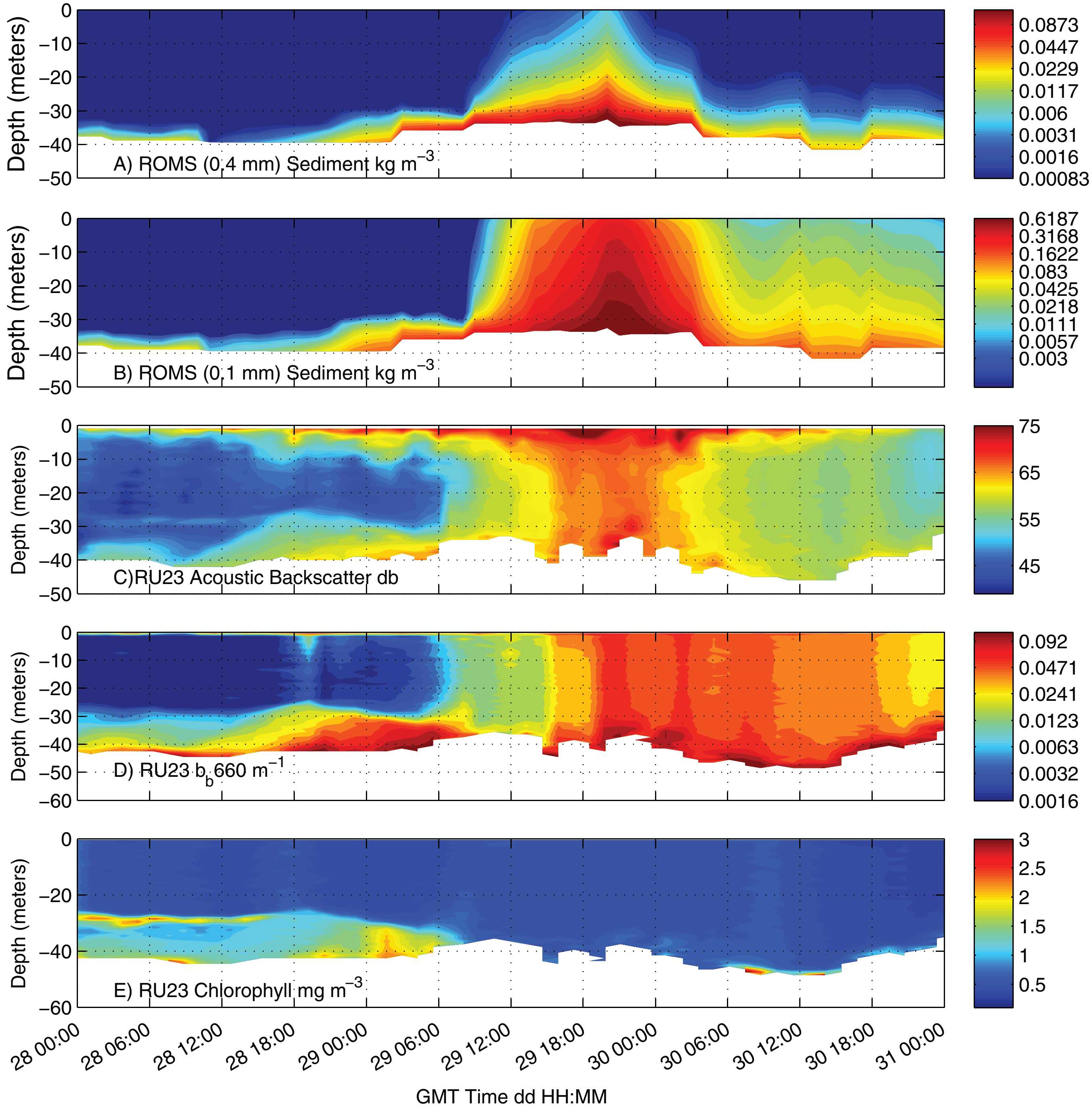

Figure 8. Cross sections of modeled sediment concentrations along the glider track for (a) 0.4 mm grain sizes, (b) 0.1 mm grain sizes and observed cross sections of (c) acoustic backscatter, (d) optical backscatter at 660 nm, and (e) chlorophyll concentration. Times along the *x* axis are as in Figure 3.

suspension well after the storm passed. Profiles extracted from each modeled, acoustic, and optical cross section (Figure 9) provide a more detailed comparison of sediment resuspension at three time periods, prior to the storm on 28 October at 06:00 GMT, just prior to landfall on 29 October at 21:00 GMT and 18 h after the storm on 30 October at 18:00 GMT. Shallow slopes were evident in modeled 0.1 and 0.4 mm grain sizes as well as acoustic and optical measurements prestorm, consistent with limited suspended sediment, though there were two features of the optical and acoustic profiles of note. The optics did not have a linear slope on a log-log scale. The subthermocline signal is likely related to organic material, detritus, chlorophyll, or other

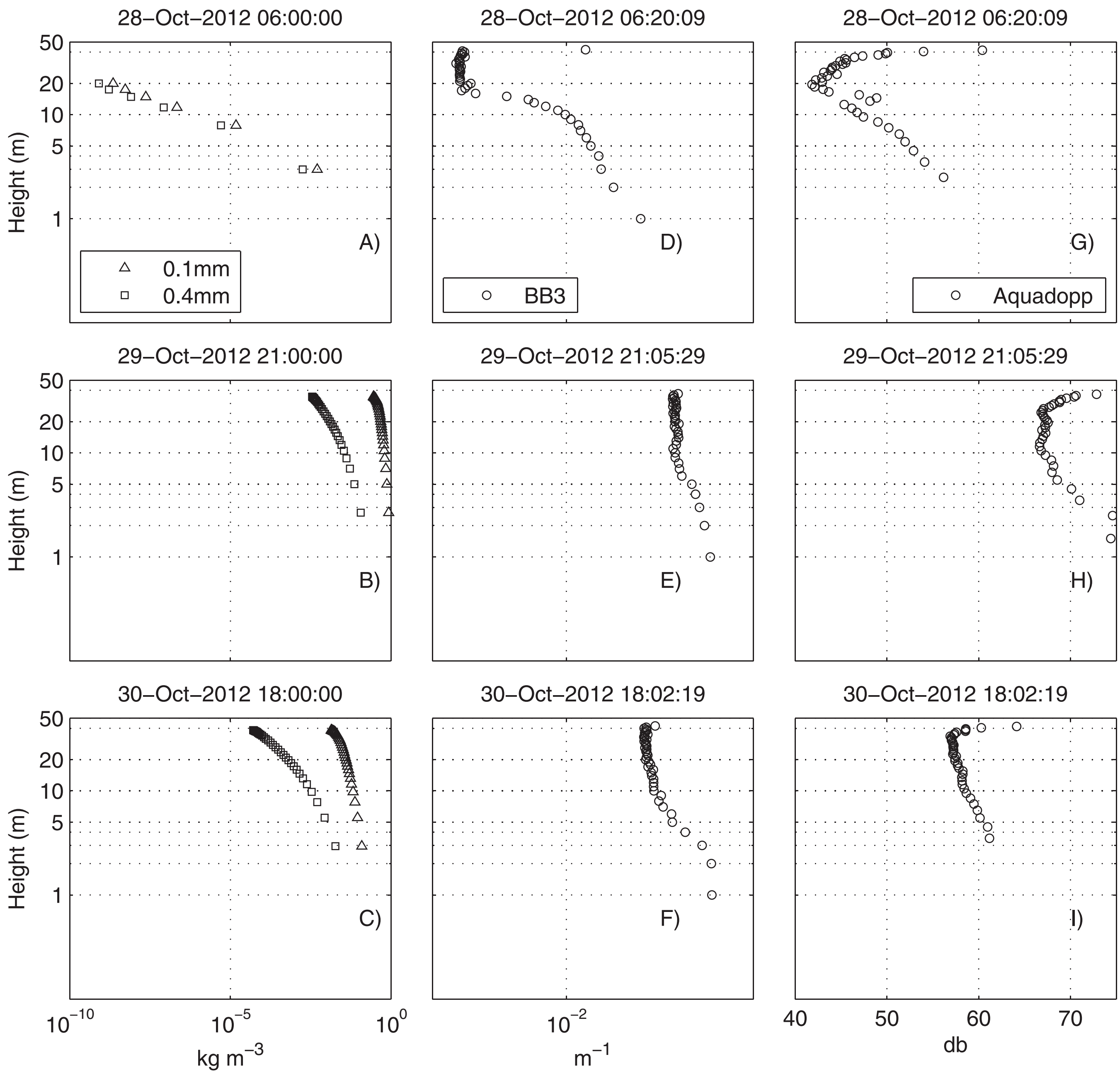

Figure 9. Log-log profiles of modeled 0.1 mm (triangles) and 0.4 mm (squares) (a–c) sediment concentration, (d–e) optical backscatter, and (g–i) semi-log profiles of acoustic backscatter. Acoustic backscatter has a logarithmic response to increased sediment concentration at the target frequency thus values are plotted on a linear db scale. Values below 10^{-10} kg m^{-3} are not plotted in Figures 9a–9c to more easily compare profiles across time points.

fine particulate matter rather than the larger cohesive sediment found on the bottom and was restricted by stratification at 20 m above the bed. Acoustics (Figure 9g) showed a positive slope above the thermocline likely due to bubbles as discussed above. During peak storm conditions model predicted and observed profiles were more vertical consistent with large concentrations of suspended sediment. Above 20 m off, the bed acoustics continued to show a positive slope likely due to bubbles and breaking waves (Figure 9h). Post-storm profiles were shallower than peak-storm but did not entirely return to prestorm conditions consistent with particles continuing to fall out of suspension.

Depth-integrated transport was calculated for modeled sediment concentrations and observed acoustic and optical backscatter. Acoustic backscatter responds logarithmically to increased observed concentration

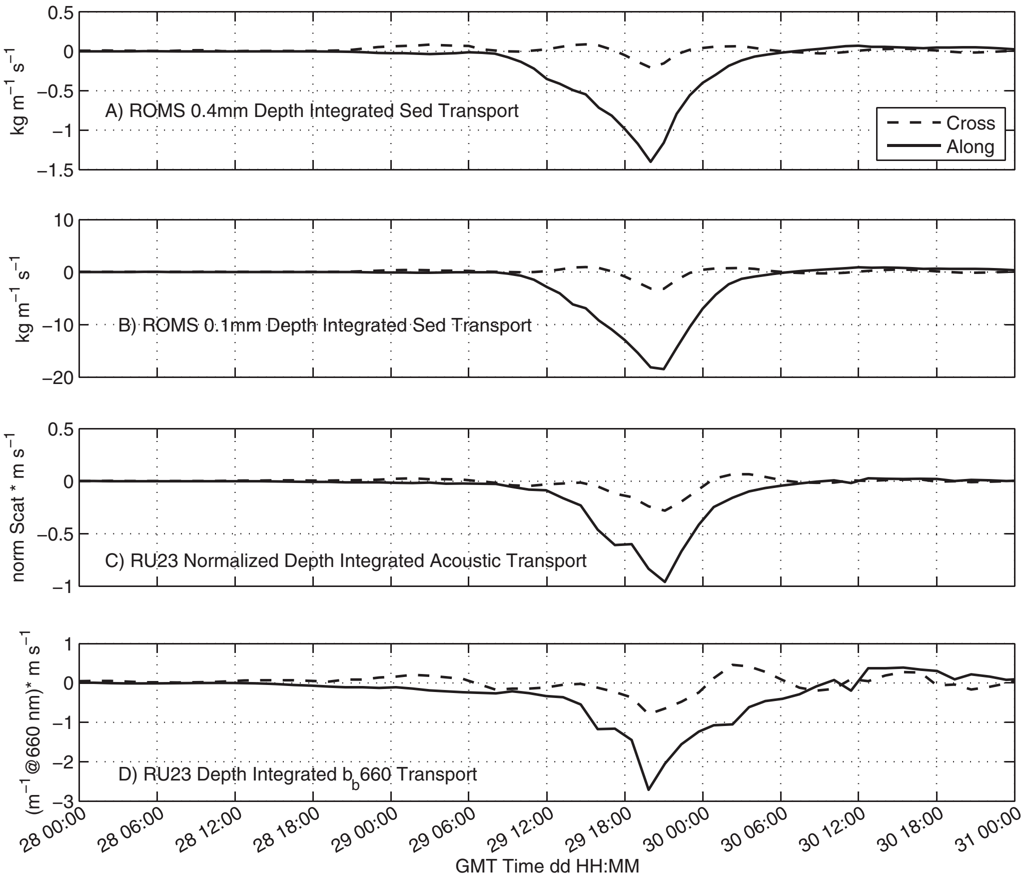

Figure 10. Depth-averaged transports calculated along the glider track for modeled (a) 0.4 mm sediment, (b) 0.1 mm sediment, (c) normalized depth-integrated acoustic transport, and depth-integrated optical backscatter transport in the (dashed) cross and (solid) along-shelf directions. Positive values indicate along-shelf (cross-shelf) toward the northeast (offshore).

[*Lohrmann*, 2001] so values were raised to the power of 10 and then normalized by dividing the maximum observed value. Additionally, acoustic backscatter shallower than 10 m were neglected from the depth integration to reduce the impact of bubble entrainment on relative transport estimates. The timing and direction of peak transport (Figure 10) were consistent between modeled and observed transports, with maximum values in the along-shelf direction on 29 October at 19:00 GMT. Inconsistency between the model predicted and observed cross-shelf currents (Figure 7) during the peak resuspension event is responsible for the limited modeled onshore transport relative to the observations on the 29 October at 19:00 GMT. The model and observations both captured the offshore cross-shelf transport immediately following landfall on 30 October at 3:00 GMT.

3.5. Regional Sediment Resuspension and Transport

Spatial maps (Figure 11) of the model predicted storm conditions over the final 12 h prior to landfall show snapshots of WRF winds (Figures 11a–11c) and WWIII waves (Figures 11d–11e) on 29 October at 12:00 GMT, 18:00 GMT and 30 October at 00:00 GMT. Winds were initially downwelling favorable and alongshore toward the southwest on the NJ shelf. WWIII model predicted wave heights were between 9 and 10 m offshore and decreased with proximity to land. As the storm approached, the coast winds shifted to a more onshore direction on the northern portion of the NJ shelf and offshore in the southern portion. Additionally, waves were near 10 m at the coastline on the northern NJ shelf, and decreased significantly to between 4 and 5 m on the southern NJ shelf as winds shifted toward the offshore direction.

As bottom orbital velocities and ambient currents are primarily responsible for sediment resuspension and transport, respectively, we present maps of the ROMS depth-averaged currents with tides retained (Figures 12a–12c) and WWIII bottom orbital velocities (Figures 12d–11f) on 29 October at 12:00 GMT, 18:00 GMT and

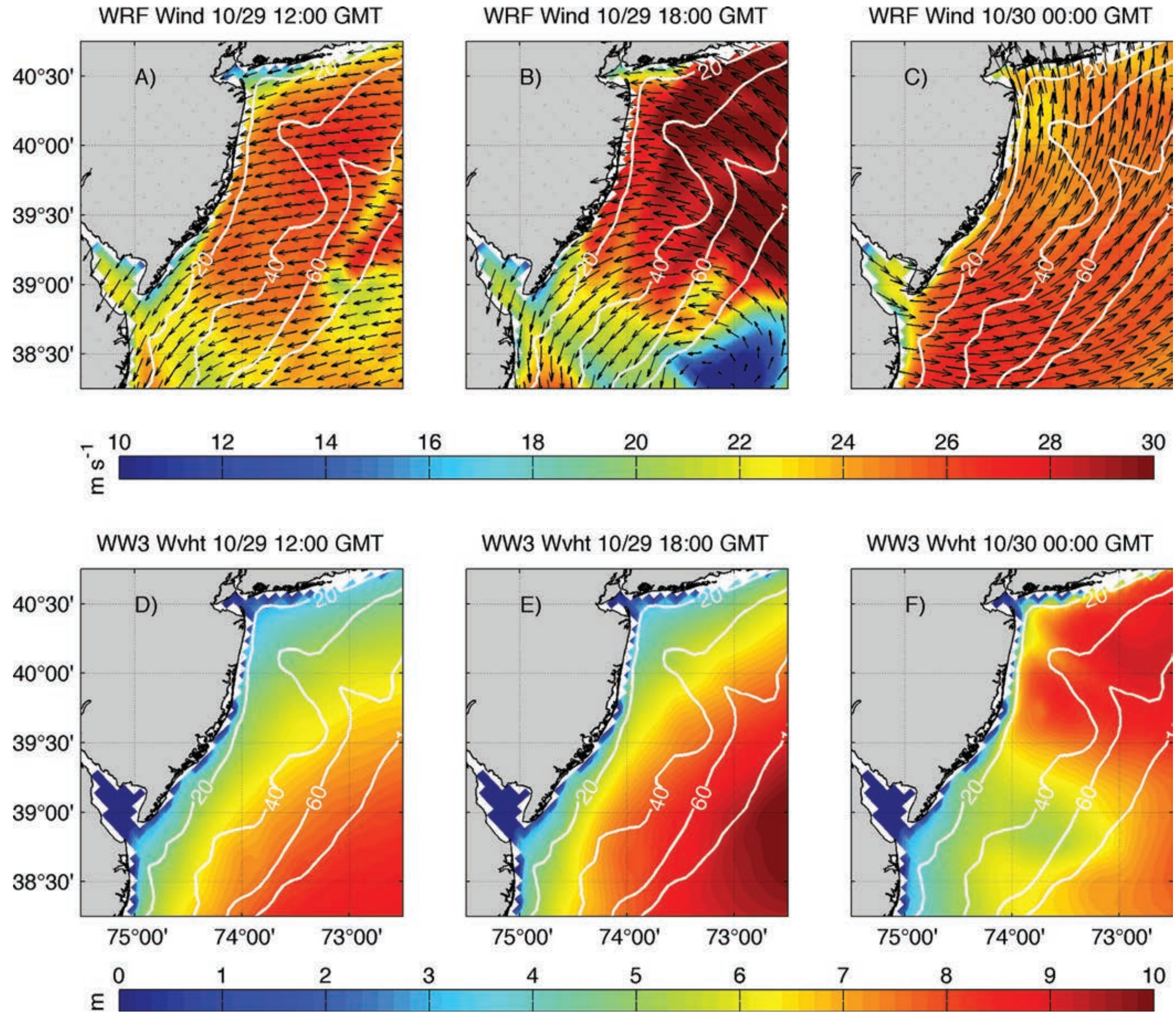

Figure 11. WRF wind on 29 October at (a) 12:00 GMT, (b) 18:00 GMT, and (c) 30 October at 00:00 GMT. WWII wave heights on 29 October at (d) 12:00 GMT, (e) 18:00 GMT, and (f) 30 October at 00:00 GMT.

30 October at 00:00 GMT. Early on 29 October, model predicted currents were highest south of the Hudson Shelf Valley and nearly uniform across the entire shelf except for a region of weak currents outside of Delaware Bay. As the storm crossed the shelf velocities were elevated to near 1 m s^{-1} across the entire domain. Current speeds were quickly reduced as the storm made landfall, likely due to the shift from alongshore winds to the southwest to weaker alongshore winds to the northeast (Figures 13a–11c). Bottom orbital velocities throughout the storm forcing duration were highest near shore south of the Hudson Shelf Valley with largest values, over 1.5 m s^{-1} near the glider deployment location on the northern side of the storm track.

Snapshots of depth-integrated suspended sediment concentration for the 0.4 mm (Figures 13a–13c) and 0.1 mm (Figures 13d–13f) are additionally mapped for the same time periods as in Figures 11 and 12 to show regional model estimates of sediment resuspension throughout the storm. On 29 October at 12:00 GMT, model predicted depth-integrated concentrations on the NJ continental shelf south of the Hudson Shelf Valley were near 1.2 and 10 kg m^{-2} for 0.4 and 0.1 mm, respectively, with highest values in the near-shore region for 0.4 mm and highest values on the central NJ shelf further offshore for the 0.1 mm

10.1002/2014JC010474

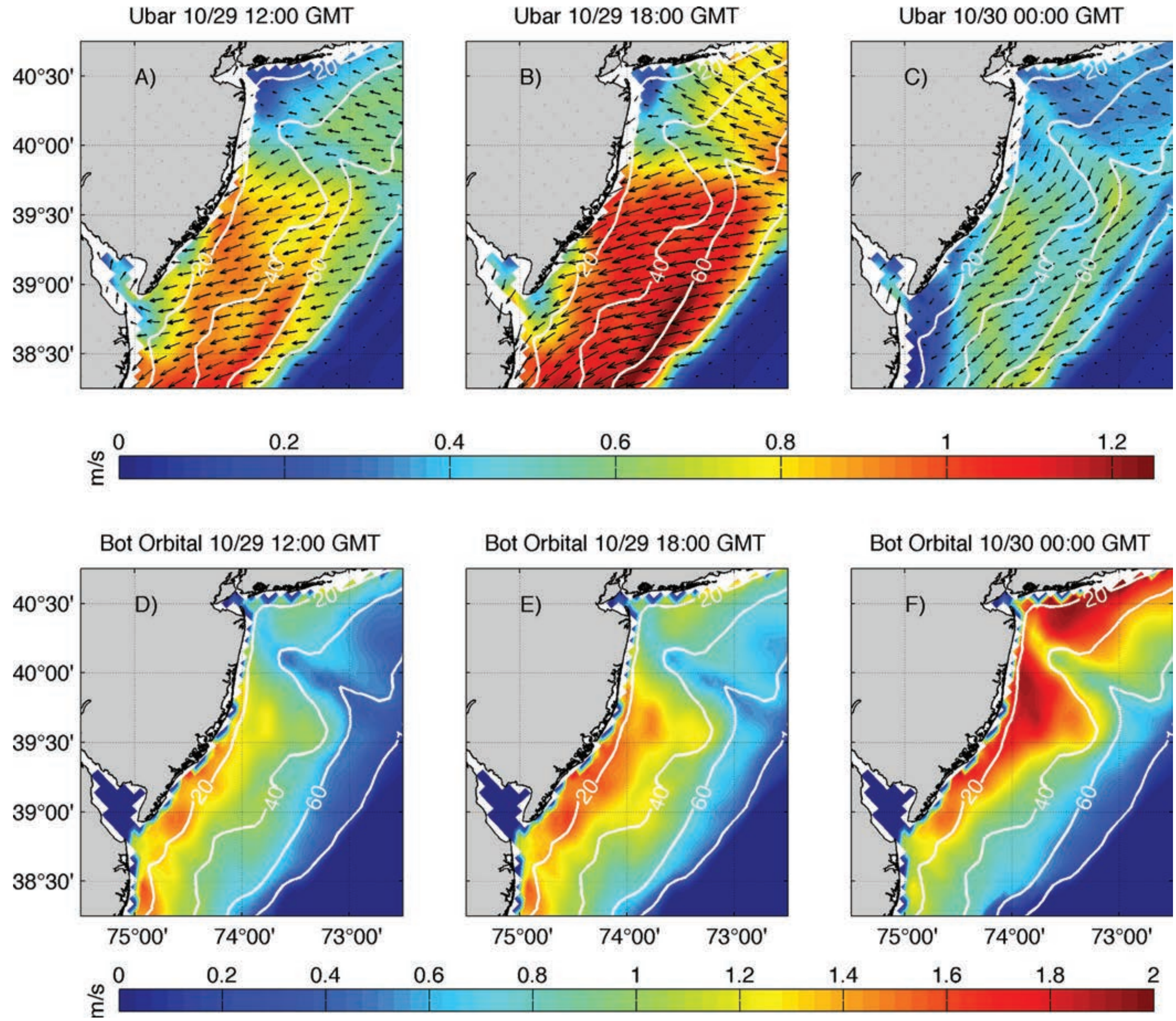

Figure 12. ROMS depth-averaged currents on 29 October at (a) 12:00 GMT, (b) 18:00 GMT, and (c) 30 October at 00:00 GMT. Bottom orbital velocities on 29 October at (d) 12:00 GMT, (e) 18:00 GMT, and (f) 30 October at 00:00 GMT.

sediment. On the 29 October at 18:00 GMT, 0.4 mm sand is resuspended along the entire inner shelf south of the Hudson Shelf Valley, while 0.1 mm sand is mobilized over the entire inner, middle, and outer shelf regions. As the storm made landfall near 30 October at 00:00 GMT, Figures 13c and 13f show that the 0.4 mm sand was resuspended coincident with peak orbital velocities (Figure 12f) and 0.1 mm sand was at a maximum across the entire northern portion of the shelf. Values for both 0.4 and 0.1 mm on the southern portion of the NJ shelf dropped significantly between 29 October at 18:00 GMT and 30 October at 00:00 GMT. This reduction was likely a result of the reduction in wave heights and orbital velocities associated with a reversal of wind direction as Sandy crossed the shelf.

Bed thickness change from the initialization to the end of the model run on 31 October at 08:00 GMT (Figure 14) predicts bed erosion of over 3 cm south of the Hudson Shelf Valley on the northern portion of the NJ shelf. This region is north of the storm track, which had highest waves, orbital velocities, and winds. Deposition of near 3 cm occurred toward the southwest in the direction of along-shelf transport (Figures 12a–12d).

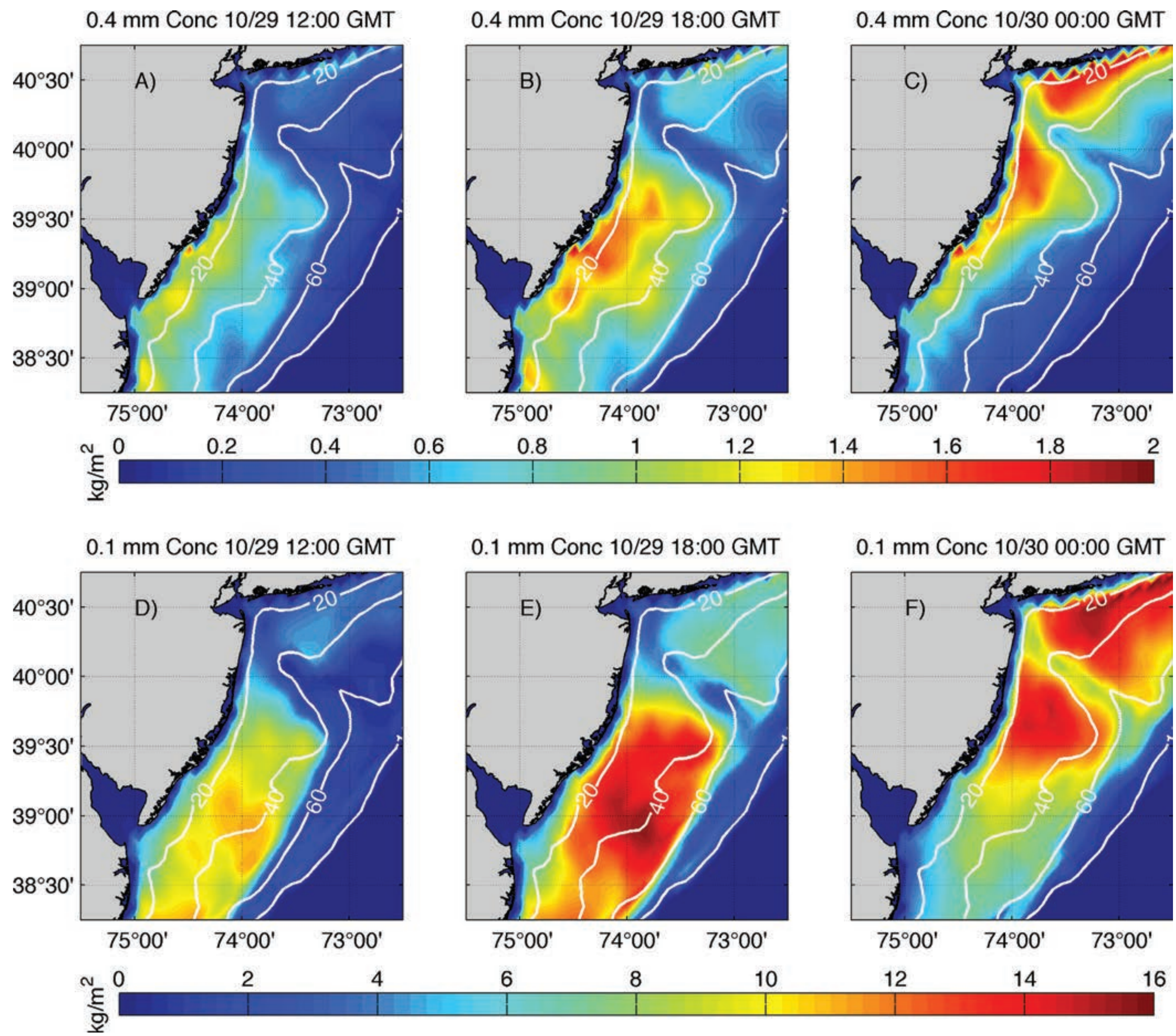

Figure 13. ROMS depth-integrated 0.4 mm sediment concentration on 29 October at (a) 12:00 GMT, (b) 18:00 GMT, and (c) 30 October at 00:00 GMT. ROMS depth-integrated 0.1 mm sediment concentration on 29 October at (d) 12:00 GMT, (e) 18:00 GMT, and (f) 30 October at 00:00 GMT.

4. Discussion

Previous studies have highlighted alongshore transport as the dominant feature of storm driven sediment transport on continental shelves [*Keen and Glenn*, 1995; *Ogston and Sternberg*, 1999; *Styles and Glenn*, 2005; *Miles et al.*, 2013], primarily during winter northeasters in the Mid-Atlantic. The typical offshore track of these storms leads to along-shelf wind stress toward the southwest and waves that increase across the entire NJ shelf [*Keim et al.*, 2004]. While Sandy initially had downwelling favorable along-shelf winds (Figures 11a and 11b), the unique cross-shelf track of the storm [*Hall and Sobel*, 2013] lead to a rotation to offshore winds on the southern portion of the NJ shelf in the 6 h before landfall. This shift on the southern NJ shelf reduced wave heights (Figures 3d and 11f), quickly reduced wave periods (Figure 3e) and ultimately reduced bottom orbital velocities (Figures 6c and 11f), which reduced bottom stress and allowed sediment that was continuing to be transported southwestward to fall out of suspension on the southern portion of the domain.

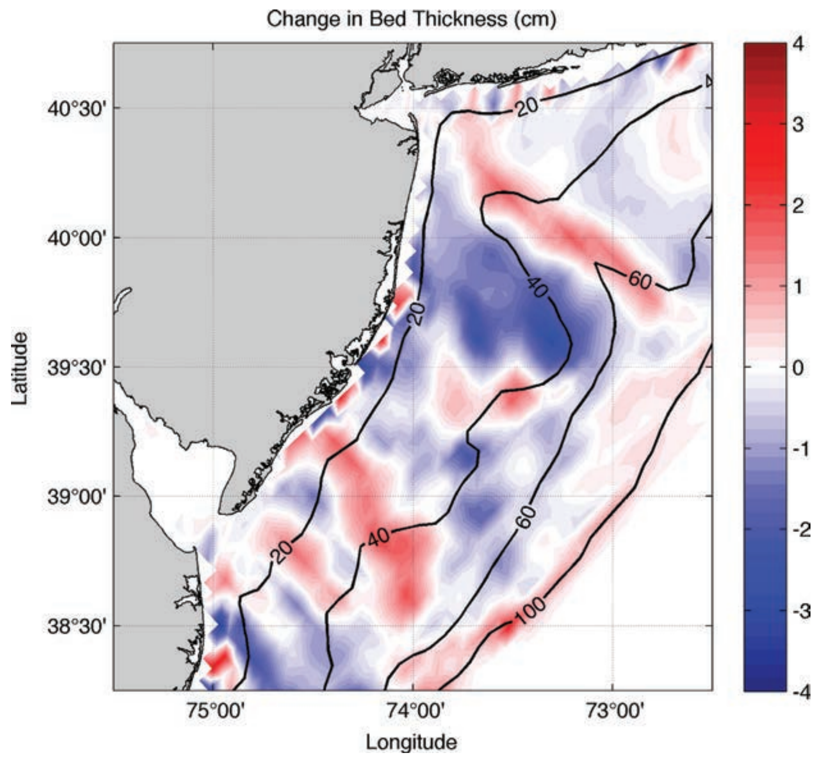

Figure 14. Change in bed thickness between the model initialization on 23 October 2012 at 00:00 GMT and 31 October at 11:00 GMT, with positive values indicating net deposition and negative values net erosion.

The modeled change in bed thickness of over + and − 3 cm on the northern and southern NJ shelf, respectively, should be approached with caution as the idealized model setup did not account for processes such as bed armoring [*Wiberg et al*., 1994], which may have reduced available fine grained sediment for resuspension, or bedload transport, which has been shown to be orders of magnitude larger than suspended sediment transport on the continental shelf [*Styles and Glenn*, 2005]. Regardless, the in situ observations from acoustic and optical sensors mounted on Slocum glider, RU23, support model predictions and suggest that a significant portion of the bed was likely eroded from the northern NJ shelf north of the storm track and deposited along the southern portion of the shelf. This modeled erosion and deposition pattern is likely rare on the New Jersey shelf as the estimated return rate, defined as the occurrence of a sandy-like track with a category 1 or greater under constant climate conditions, is 714 years with a 95% confidence range of 435–1429 years [*Hall and Sobel*, 2013].

Autonomous underwater vehicle and ship-based surveys showed partial recovery of the bed near buoy 44009 five weeks after Hurricane Sandy made landfall [*Trembanis et al*., 2013]. While this suggests that preservation of Sandy's sedimentary signature in the bed is not likely in the active nearshore region, the observed deposition toward the shelf break on the southern portion of the domain may be present as reworking in deeper waters is driven by more episodic wave processes [*Wiberg*, 2000].

While the onshore track, landfall, and resulting erosion and deposition patterns are likely atypical for the Mid-Atlantic, land-falling storms with onshore tracks are typical in other regions. In the Gulf of Mexico hurricanes Camille in 1969 [*Keen et al*., 2004], Hurricane Ivan in 2004 [*Teague et al*., 2006; *Smith et al*., 2013; *Zambon et al*., 2014], and Hurricanes Katrina and Rita in 2005 [*Horton et al*., 2009]. Maximum observed scours poststorm in Hurricane Ivan were as high as 36 cm at the 60 m isobath under the region of maximum winds on the right side of the eye. Along the coast of China typhoons, such as Typhoon Morakot [*Li et al*., 2012] also typically make landfall with an onshore track and resuspend and transport sediment. The continued development of sediment resuspension and transport models is critical to understanding coastal changes driven by land-falling storms across the world. Future studies of sediment resuspension and transport modeling and poststorm sediment analysis will benefit greatly from a suite of observing platforms that include in situ glider data to interpret results over a broad range continental shelves.

5. Summary and Conclusions

In this study, we successfully deployed a Teledyne-Webb Slocum glider in rapid response ahead of Hurricane Sandy on the New Jersey Shelf. This mobile profiling sensor platform proved invaluable in providing in situ sediment resuspension and transport model validation, as well as simultaneous validation of currents in the hydrodynamic models. Predicted resuspension and transport suggested erosion of over 3 cm on the northern portion of the New Jersey Shelf, north of the storm track where waves and currents were highest and deposition of over 3 cm on the southern NJ shelf just north of Delaware Bay. This erosion and deposition pattern was the result of the onshore track of Hurricane Sandy, which is not typical. This study provides a valuable assessment of suspended material in a major storm using coincident acoustic and optical sensors on a glider platform, which builds confidence in the communities' ability to model regional sediment resuspension and transport. Glider technologies now have the ability to compliment invaluable high-resolution near bed measurements from moored and bottom mounted sensors. Future advances that may improve sediment concentration estimates from glider platforms include downward facing acoustic sensors, which will reduce the impact of bubble entrainment near the surface, provide data near the bed where concentrations are highest, and allow for detailed estimates of bottom-stress in situ over a large spatial area.

Acknowledgments
Glider data used in this study are available through the MARACOOS assets page http://maracoos.org/data and http://marine.rutgers.edu/cool/auvs/index.php?did=369 with more detailed data sets available upon request to tnmiles@marine.rutgers.edu. Regional Ocean Modeling System and WRF model results are also available upon request to tnmiles@marine.rutgers.edu. Buoy data and WAVEWATCH III data sets are publicly available through http://www.ndbc.noaa.gov/ and http://polar.ncep.noaa.gov/waves/index2.shtml, respectively. We are grateful for the funding support provided by NOAA grant NA11NOS0120038 as part of MARACOOS, the regional partner of U.S. IOOS and NOAA grant NA13OAR4830233 as part of CINAR, the regional partner of the CIPO. We would also like to thank Teledyne-Webb Research for providing graduate student funding, NortekUSA for providing equipment through a student equipment grant. Additionally, we would like to thank the glider technicians and pilots of the Rutgers University Center for Ocean Observing Leadership; the help of John Wilkin and the research associates of the Rutgers Ocean Modeling group with help setting up the ocean model; and commentary and help setting up the sediment model from Chris Sherwood at the United States Geological Survey (USGS).

References

Agrawal, Y. C., and H. C. Pottsmith (2000), Instruments for particle size and settling velocity observations in sediment transport, *Mar. Geol.*, *168*(1-4), 89–114, doi:10.1016/s0025-3227(00)00044-x.

Ariathurai, R., and K. Arulanandan (1978), Erosion rates of cohesive soils, *J. Hydraul. Div. Am. Soc. Civ. Eng.*, *104*(2), 279–283.

Blaas, M., C. Dong, P. Marchesiello, J. C. McWilliams, and K. D. Stolzenbach (2007), Sediment-transport modeling on Southern Californian shelves: A ROMS case study, *Cont. Shelf Res.*, *27*(6), 832–853, doi:10.1016/j.csr.2006.12.003.

Blake, E. S., T. B. Kimberlain, R. J. Berg, P. C. John, and J. L. Beven II (2013), Tropical cyclone report: Hurricane Sandy, (AL182012) 22–29 October 2012. National Hurricane Center.

Boss, E., and W. Pegau (2001), Relationship of light scattering at an angle in the backward direction to the backscattering coefficient, *Appl. Opt.*, *40*(30), 5503, doi:10.1364/AO.40.005503.

Boss, E., et al. (2009), Comparison of inherent optical properties as a surrogate for particulate matter concentration in coastal waters, *Limnol. Oceanogr. Methods*, *7*, 803–810.

Bunt, J. A. C., P. Larcombe, and C. F. Jago (1999), Quantifying the response of optical backscatter devices and transmissometers to variations in suspended particulate matter, *Cont. Shelf Res.*, *19*(9), 1199–1220, doi:10.1016/S0278–4343(99)00018-7.

Cacchione, D., and W. Grant (1987), Storm-dominated bottom boundary layer dynamics on the Northern California continental shelf: Measurements and predictions, *J. Geophys. Res.*, *92*(C2), 1817–1827.

Cahill, B., O. Schofield, R. Chant, J. Wilkin, E. Hunter, S. Glenn, and P. Bissett (2008), Dynamics of turbid buoyant plumes and the feedbacks on near-shore biogeochemistry and physics, *Geophys. Res. Lett.*, *35*, L10605, doi:10.1029/2008GL033595.

Davis, R., C. Eriksen, and C. Jones (2003), Autonomous buoyancy-driven underwater gliders, in *Technology and Applications of Autonomous Underwater Vehicles*, edited by G. Griffiths, p. 37, Taylor and Francis, London, U. K.

Drake, D. E., and D. A. Cacchione (1992), Wave-current interaction in the bottom boundary layer during storm and non-storm conditions: Observations and model predictions, *Cont. Shelf Res.*, *12*(12), 1331–1352, doi:10.1016/0278–4343(92)90058-R.

Fairall, C., and E. Bradley (1996), Bulk parameterization of air-sea fluxes for Tropical Ocean-Global Atmosphere Coupled-Ocean Atmosphere Response Experiment, *J. Geophys. Res.*, *101*(C2), 3747–3764.

Fairall, C. W., E. F. Bradley, J. E. Hare, A. A. Grachev, and J. B. Edson (2003), Bulk parameterization of air-sea fluxes: Updates and verification for the COARE algorithm, *J. Clim.*, *16*(4), 571.

Glenn, S., C. Jones, M. Twardowski, L. Bowers, J. Kerfoot, J. Kohut, D. Webb, and O. Schofield (2008), Glider observations of sediment resuspension in a Middle Atlantic Bight fall transition storm, *Limnol. Oceanogr. Methods*, *53*(5 part 2), 2180–2196, doi:10.4319/lo.2008.53.5_part_2.2180.

Glenn, S. M., and W. D. Grant (1987), A suspended sediment stratification correction for combined wave and current flows, *J. Geophys. Res.*, *92*(C8), 8244–8264.

Goff, J. A., C. J. Jenkins, and S. J. Williams (2008), Seabed mapping and characterization of sediment variability using the usSEABED data base, *Cont. Shelf Res.*, *28*(4–5), 614–633, doi:10.1016/j.csr.2007.11.011.

Grant, W., and O. Madsen (1979), Combined wave and current interaction with a rough bottom, *J. Geophys. Res.*, *84*(8), 1797–1808.

Grant, W. D., and O. S. Madsen (1986), The continental-shelf bottom boundary layer, *Annu. Rev. Fluid Mech.*, *18*(1), 265–305, doi:10.1146/annurev.fl.18.010186.001405.

Haidvogel, D. B., et al. (2008), Ocean forecasting in terrain-following coordinates: Formulation and skill assessment of the Regional Ocean Modeling System, *J. Comput. Phys.*, *227*(7), 3595–3624, doi:10.1016/j.jcp.2007.06.016.

Hall, T. M., and A. H. Sobel (2013), On the impact angle of Hurricane Sandy's New Jersey landfall, *Geophys. Res. Lett.*, *40*, 2312–2315, doi:10.1002/grl.50395.

Hapke, B. C. J., O. Brenner, R. Hehre, B. J. Reynolds, S. Jewell, and U. S. G. Survey (2013), *Coastal Change from Hurricane Sandy and the 2012-13 winter storm season, US Geological Survey Open-File Report 1231, 37*, Fire Island, N. Y.

Harris, C., and P. Wiberg (2002), Across-shelf sediment transport: Interactions between suspended sediment and bed sediment, *J. Geophys. Res.*, *107*(C1), 3008, doi:10.1029/2000JC000634.

Harris, C. K., B. Butman, and P. Traykovski (2003), Winter-time circulation and sediment transport in the Hudson Shelf Valley, *Cont. Shelf Res.*, *23*(8), 801–820, doi:10.1016/S0278-4343(03)00025-6.

Hofmann, E., J.-N. Druon, K. Fennel, M. Friedrichs, D. Haidvogel, C. Lee, A. Mannino, C. McClain, R. Najjar, and J. O'Reilly (2008), Eastern US continental shelf carbon budget integrating models, data assimilation, and analysis, *Oceanography*, *21*(1), 86–104.

Horton, B. P., V. Rossi, and A. D. Hawkes (2009), The sedimentary record of the 2005 hurricane season from the Mississippi and Alabama coastlines, *Quat. Int.*, *195*, 15–30, doi:10.1016/j.quaint.2008.03.004.

Hu, K., P. Ding, Z. Wang, and S. Yang (2009), A 2D/3D hydrodynamic and sediment transport model for the Yangtze Estuary, China, *J. Mar. Syst.*, *77*(1–2), 114–136, doi:10.1016/j.jmarsys.2008.11.014.

Keen, T., and S. Glenn (2002), Predicting bed scour on the continental shelf during Hurricane Andrew, *J. Waterw. Port Coastal Ocean Eng.*, *128*(6), 249–257, doi:10.1061/(ASCE)0733-950X(2002)128:6(249).

Keen, T. R., and S. M. Glenn (1995), A coupled hydrodynamic-bottom boundary layer model of storm and tidal flow in the middle Atlantic Bight of North America, *J. Phys. Oceanogr.*, *25*(3), 391–406, doi:10.1175/1520-0485(1995)025<0391:ACHBLM>2.0.CO;2.

Keen, T. R., S. J. Bentley, W. C. Vaughan, and C. A. Blain (2004), The generation and preservation of multiple hurricane beds in the northern Gulf of Mexico, *Mar. Geol.*, *210*, 79–105, doi:10.1016/j.margeo.2004.05.022.

Keim, B. D., R. A. Muller, and G. W. Stone (2004), Spatial and temporal variability of coastal storms in the North Atlantic Basin, *Mar. Geol.*, *210*(1–4), 7–15, doi:10.1016/j.margeo.2003.12.006.

Li, Y., A. Wang, L. Qiao, J. Fang, and J. Chen (2012), The impact of typhoon Morakot on the modern sedimentary environment of the mud deposition center off the Zhejiang-Fujian coast, China, *Cont. Shelf Res.*, *37*, 92–100, doi:10.1016/j.csr.2012.02.020.

Lohrmann, A. (2001), Monitoring sediment concentration with acoustic backscattering instruments, *Nortek Tech. Note*, (I), 1–5.

Lynch, J. F., T. F. Gross, C. R. Sherwood, J. D. Irish, B. H. Brumley, and J. D. Irish (1997), Acoustical and optical backscatter measurements of sediment transport, Continental Shelf Research *17*(4), 337–366.

Madsen, O. (1994), Spectral wave-current bottom boundary layer flows, *Coastal Eng.*, *1*(24), 384–398.

Madsen, O., and P. Wikramanayake (1991), Simple models for turbulent wave current bottom boundary layer flow, U. S. Army Corps of Engineers, WES, Report No. DRP-91-1.

McLean, S. (1991), Depth-integrated suspended-load calculations, *J. Hydraul. Eng.*, *117*(11), 1440–1458.

Meyer-Peter, E., and R. Müller (1948), Formulas for bed-load transport, in *Proceedings of the 2nd Meeting of the International Association for Hydraulic Structures Research*, pp. 39–64.

Miles, T., S. Glenn, and O. Schofield (2013), Temporal and spatial variability in fall storm induced sediment resuspension on the Mid-Atlantic Bight, *Cont. Shelf Res.*, *63*, Supplement, S36–S49, doi:10.1016/j.csr.2012.08.006.

Ogston, A., D. Cacchione, R. Sternberg, and G. Kineke (2000), Observations of storm and river flood-driven sediment transport on the northern California continental shelf, *Cont. Shelf Res.*, *20*(16), 2141–2162, doi:10.1016/S0278-4343(00)00065-0.

Ogston, A. S., and R. W. Sternberg (1999), Sediment-transport events on the northern California continental shelf, *Mar. Geol.*, *154*, 69–82, doi:10.1016/S0025-3227(98)00104-2.

Olabarrieta, M., J. Warner, and B. Armstrong (2012), Ocean-atmosphere dynamics during Hurricane Ida and Nor'Ida: An application of the coupled ocean-atmosphere-wave-sediment transport (COAWST) modeling system, *Ocean Modell.*, *43–44*, 112–137, doi:10.1016/j.ocemod.2011.12.008.

Papanicolaou, A., and M. Elhakeem (2008), Sediment transport modeling review—Current and future developments, *J. Hydraul. Eng.*, *134*(1), 1–14.

Ruiz, S., L. Renault, B. Garau, and J. Tintoré (2012), Underwater glider observations and modeling of an abrupt mixing event in the upper ocean, *Geophys. Res. Lett.*, *39*, L01603, doi:10.1029/2011GL050078.

Schofield, O., et al. (2007), Slocum gliders: Robust and ready, *J. Field Robotics*, *24*(6), 473–485, doi:10.1002/rob.20200.

Shchepetkin, A., and J. McWilliams (2009), Computational kernel algorithms for fine-scale, multi-process, long-time oceanic simulations, *Comput. Methods*, *14*(8), 121–183, doi:10.1016/S1570-8659(08)01202-0.

Shchepetkin, A. F., and J. C. McWilliams (2005), The regional oceanic modeling system (ROMS): A split-explicit, free-surface, topography-following-coordinate oceanic model, *Ocean Modell.*, *9*(4), 347–404, doi:10.1016/j.ocemod.2004.08.002.

Sherwood, C. R., B. Butman, D. A. Cacchione, D. E. Drake, T. F. Gross, R. W. Sternberg, P. L. Wiberg, and A. J. Williams (1994), Sediment-transport events on the northern California continental shelf during the 1990–1991 STRESS experiment, *Cont. Shelf Res.*, *14*(10–11), 1063–1099, doi:10.1016/0278-4343(94)90029-9.

Skamarock, W., J. Klemp, J. Dudhia, D. O. Gill, D. M. Barker, M. G. Duda, X.-Y. Huang, W. Wang, and J. G. Powers (2008), A description of the advanced research WRF version 3, *NCAR Tech. Note NCAR/TN-475+STR*.

Smith, T. A., S. Chen, T. Campbell, P. Martin, W. E. Rogers, S. Gaberšek, D. Wang, S. Carroll, and R. Allard (2013), Ocean-wave coupled modeling in COAMPS-TC: A study of Hurricane Ivan (2004), *Ocean Modell.*, *69*, 181–194, doi:10.1016/j.ocemod.2013.06.003.

Soulsby, R. L., and J. S. Damgaard (2005), Bedload sediment transport in coastal waters, *Coastal Eng.*, *52*(8), 673–689, doi:10.1016/j.coastaleng.2005.04.003.

Styles, R., and S. Glenn (2000), Modeling stratified wave and current bottom boundary layers on the continental shelf, *J. Geophys. Res.*, *105*(C10), 24,119–24,139.

Styles, R., and S. Glenn (2002), An Optimized Combined Wave and Current Algorithm for Arbitrary Bed Roughness, Technical Report, Coastal Phys. Oceanogr. Lab, Dep. of Geol. Sci., Univ. of S. C., Columbia, S. C.

Styles, R., and S. M. Glenn (2005), Long-term sediment mobilization at a sandy inner shelf, *J. Geophys. Res.*, *110*, C04S90, doi:10.1029/2003JC002175.

Teague, W. J., E. Jarosz, T. R. Keen, D. W. Wang, and M. S. Hulbert (2006), Bottom scour observed under Hurricane Ivan, *Geophys. Res. Lett.*, *33*, L07607, doi:10.1029/2005GL025281.

Thorne, P. D., and D. M. Hanes (2002), A review of acoustic measurement of small-scale sediment processes, *Cont. Shelf Res.*, *22*(4), 603–632, doi:10.1016/S0278-4343(01)00101-7.

Todd, R. E., D. L. Rudnick, M. R. Mazloff, R. E. Davis, and B. D. Cornuelle (2011a), Poleward flows in the southern California Current System: Glider observations and numerical simulation, *J. Geophys. Res.*, *116*, C02026, doi:10.1029/2010JC006536.

Todd, R. E., D. L. Rudnick, R. E. Davis, and M. D. Ohman (2011b), Underwater gliders reveal rapid arrival of El Niño effects off California's coast, *Geophys. Res. Lett.*, *38*, L03609, doi:10.1029/2010GL046376.

Trembanis, A., C. DuVal, J. Beaudoin, V. Schmidt, D. Miller, and L. Mayer (2013), A detailed seabed signature from Hurricane Sandy revealed in bedforms and scour, *Geochem. Geophys. Geosyst.*, *14*, 4334–4340, doi:10.1002/ggge.20260.

Trowbridge, J. H., and A. R. M. Nowell (1994), An introduction to the Sediment TRansport Events on Shelves and Slopes (STRESS) program, *Cont. Shelf Res.*, *14*(10–11), 1057–1061, doi:10.1016/0278-4343(94)90028-0.

Visbeck, M. (2002), Deep velocity profiling useding lowered acoustic Doppler current profilers: Bottom track and inverse solutions, *J. Atmos. Oceanic Technol.*, *19*, 794–807.
Warner, J., B. Butman, and P. Dalyander (2008a), Storm-driven sediment transport in Massachusetts Bay, *Cont. Shelf Res.*, *28*(2), 257–282, doi:10.1016/j.csr.2007.08.008.
Warner, J. C., C. R. Sherwood, R. P. Signell, C. K. Harris, and H. G. Arango (2008b), Development of a three-dimensional, regional, coupled wave, current, and sediment-transport model, *Comput. Geosci.*, *34*(10), 1284–1306, doi:10.1016/j.cageo.2008.02.012.
Warner, J. C., B. Armstrong, R. He, and J. B. Zambon (2010), Development of a Coupled Ocean-Atmosphere-Wave-Sediment Transport (COAWST) modeling system, *Ocean Modell.*, *35*(3), 230–244, doi:10.1016/j.ocemod.2010.07.010.
Wiberg, P. (2000), A perfect storm: Formation and potential for preservation of storm beds on the continental shelf, *Oceanography*, *13*(3), 93–99, doi:10.5670/oceanog.2000.18.
Wiberg, P. L., and C. K. Harris (1994), Ripple geometry in wave-dominated environments, *J. Geophys. Res.*, *99*(C1), 775–789.
Wiberg, P. L., and C. R. Sherwood (2008), Calculating wave-generated bottom orbital velocities from surface-wave parameters, *Comput. Geosci.*, *34*(10), 1243–1262, doi:10.1016/j.cageo.2008.02.010.
Wiberg, P. L., D. E. Drake, and D. A. Cacchione (1994), Sediment resuspension and bed armoring during high bottom stress events on the northern California inner continental shelf: Measurements and predictions, *Cont. Shelf Res.*, *14*(10–11), 1191–1219, doi:10.1016/0278–4343(94)90034-5.
Wilkin, J., and E. Hunter (2013), An assessment of the skill of real-time models of Mid-Atlantic Bight continental shelf circulation, *J. Geophys. Res. Oceans*, *118*, 2919–2933, doi:10.1002/jgrc.20223.
Xu, Y., B. Cahill, J. Wilkin, and O. Schofield (2013), Role of wind in regulating phytoplankton blooms on the Mid-Atlantic Bight, *Cont. Shelf Res.*, *63* Supplement, S26–S35, doi:10.1016/j.csr.2012.09.011.
Zambon, J. B., R. He, and J. C. Warner (2014), Investigation of hurricane Ivan using the coupled ocean-atmosphere-wave-sediment transport (COAWST) model, *Ocean Dyn.*, *64*(11), 1535–1554, doi:10.1007/s10236-014-0777-7.
Zhang, W. G., J. L. Wilkin, J. C. Levin, and H. G. Arango (2009), An adjoint sensitivity study of buoyancy- and wind-driven circulation on the New Jersey inner shelf, *J. Phys. Oceanogr.*, *39*(7), 1652–1668, doi:10.1175/2009JPO4050.1.

Model Comparison for Transatlantic Ocean Glider Flight: Student Analysis of Modern Circumnavigation

Andrenette Morrison, Liam Ramsay, Martin Arroyo*, Kelsey Ashbrook*, Olivia Czerewko*, Stephanie Lee*, Caleb Lintz*, Erin Payne*, Josh Kohut, Scott Glenn, Oscar Schofield, and Travis Miles

Rutgers University
Center for Ocean Observing Leadership
New Brunswick, NJ, USA

*United States Naval Academy
Annapolis, MD, USA

***Abstract*- Oceanic forecast models are imperative to understand the Earth's ocean. Current oceanic forecasts assimilate satellite sea surface height and temperature data along with temperature and salinity profiles from Argo networks of over 3000 drifters. Even though assimilation of these datasets are reliable, they have limitations because areas that provide critical data to ocean forecast models are often under sampled. Autonomous Underwater Gliders (AUGs) can be used as a solution to reduce under sampled regions of the ocean. Over the last decade, AUGs have successfully been used to carry out regional deployments to conduct scientific expeditions throughout the Earth's Ocean. Through the Challenger Glider Mission, coordinated flights covering 128,000 kilometers are planned around the five ocean basins. A range of international institutions and agencies can participate in the mission using interactive tools developed by the U.S. Integrated Ocean Observing System (IOOS) and the education outreach tools of the U.S. National Science Foundation's (NSF) Ocean Observing Initiative (OOI). These interactive tools are programmed to display real time glider data with interactive browser-based access, enabling student participation in global ocean exploration and predictive skill experiments. During the summer of 2015, student research teams participated in the second leg of the South Atlantic Challenger Glider Mission (named RU29). The aim is to show the usefulness of RU29's in situ datasets in ocean forecasting by comparing salinity, temperature, and sea surface current observations to the predictive readings of ocean models (RTOFS, MyOcean) and data generated by the Argo Float program. The students' involvement contributes to the assessment of current scientific and oceanographic models, courtesy of the Challenger Glider Mission.**

Keywords – Ocean forecasting; Autonomous Underwater Gliders; Challenger Glider Mission

I. INTRODUCTION

In November 2013, Glider Mission RU29 was deployed in the South Atlantic. It was deployed off Cape Town South Africa, stopped in the Ascension Islands before it was recovered off Sao Paulo, Brazil, ending the 4,420 km crossing in May of 2014. During the summer of 2014, data from RU29 was used to analyze the skill of the American RTOFS ocean model and the European MyOcean ocean model. Students observed the differences between data collected from the glider and the data predicted by the models. This comparison is useful in analyzing oceanographic elements, such as the Brazil Current, that the glider might encounter during its second deployment.

On June 23, 2015, RU29 embarked on its second leg of its circumnavigation of

978-0-933957-43-5 ©2015 MTS

the South Atlantic Ocean. It was deployed from Ubatuba, Brazil and is traveling back to Cape Town, South Africa. This trip is expected to take one year, and will span at least 6,500 kilometers. The glider, subject to ocean currents and necessary energy efficiencies, can travel approximately 7,000 kilometers. If needed the glider will be able to stop at the remote island of Tristan da Cunha for repairs. In order to maximize distance traveled and minimize energy usage, a potential track will be determined for the glider to follow based on the currents predicted with global ocean models, as well as wind and wave forecasts. Throughout RU29's deployment, data collected will be compared to the output from two ocean models, RTOFS and MyOcean, as well as the Argo float program. Based on the analysis of these comparisons, a better understanding of the oceanic conditions within the South Atlantic will be provided to help the glider transit the entire South Atlantic Ocean.

II. METHODS

To assess the forecasting capabilities of existing international suite of oceanic models and devices, the comparison between the US Model, RTOFS, The European model, MyOcean, the Argo float data program and RU29 data was conducted. The collaboration between European countries such as the United Kingdom, France, Germany, and Denmark resulted in the development of the MyOcean model and RTOFS (Real Time Ocean Forecast System) is a United States model created by the National Center for Environmental Predication. Through primarily satellite data assimilation, RTOFS and MyOcean provides integrated oceanic information, which is accessible from internet databases.

In situ data from the Argo floats were compared to both glider and modeled profiles. Argo floats profile the ocean from the surface to as deep as 2000m once every 10 days. Each profile samples ocean temperature, salinity, and density along with other oceanic parameters based on the drifter configuration. There are thousands of Argo floats deployed around the world today including around the area along the glider's track. By comparing a glider and an Argo float profiles to each other, the quality of the glider's measurements of the water column can be determined. These comparisons between RU29 and an Argo float datasets verify the glider CTD data.

RU29 is a G2 glider equipped with a SeaBird pumped Conductivity, Temperature and Depth (CTD) sensor to collect temperature and salinity profiles. Using a process from Kerfoot et al. [5] to correct the thermal inertia of the conductivity sensor, the dataset of RU29 can be compared to an Argo float and sections of the RTOFS and MyOcean models taken along the glider's path (Figure 1). A series of MATLAB scripts facilitated the data processing and profile creations of the temperature and salinity data gathered by the models, the Argo float program and RU29.

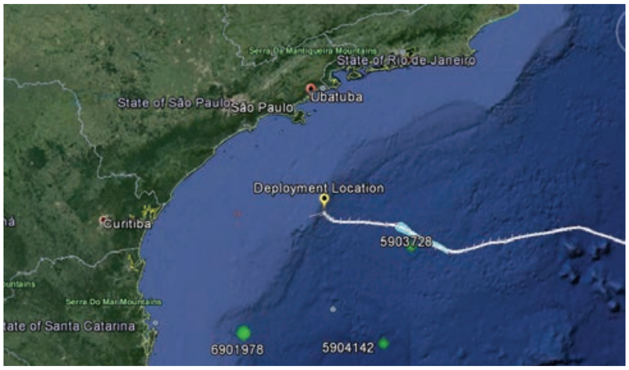

Figure 1: RU29's deployment location and the portion of its track off the coast of Brazil used for the comparison to the models and an Argo float.

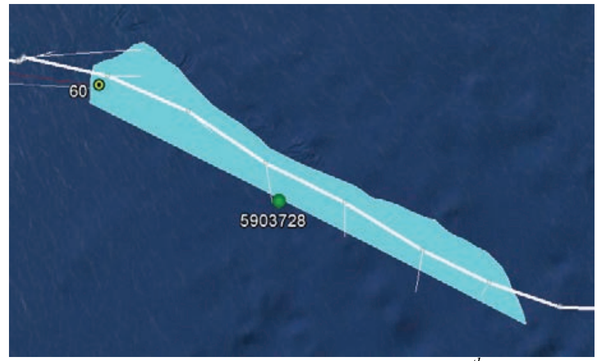

Figure 2: Argo# 5903728 completed its 60th cycle on July 1st approximately 3.44km from where RU29 surfaced on June 29th. The blue shading indicates where RU29's profiles were extracted.

III. RESULTS

On June 29th, RU29 passed by an Argo float (Argo#5903728) that completed its 60th cycle on July 1st several days later. These data were used to compare the glider CTD with RTOFS, MyOcean, and the Argo float (Figure 2). This study will focus on the deeper measurements below the more variable surface layer. In these deeper waters the spatial variability of temperature and salinity are longer. The temperature collected by Argo#5903728 and RU29 did not show any disparity but rather congruency throughout the water column (Figure 3). This cannot be said for salinity. While the profiles compared well in the beginning of the study, on June 30th the glider moved into a water mass with saltier water at depth. Glider profiles 18 to 20 are saltier at depth than the available Argo float data and the profiles sampled by the glider in the days prior (Figure 3).

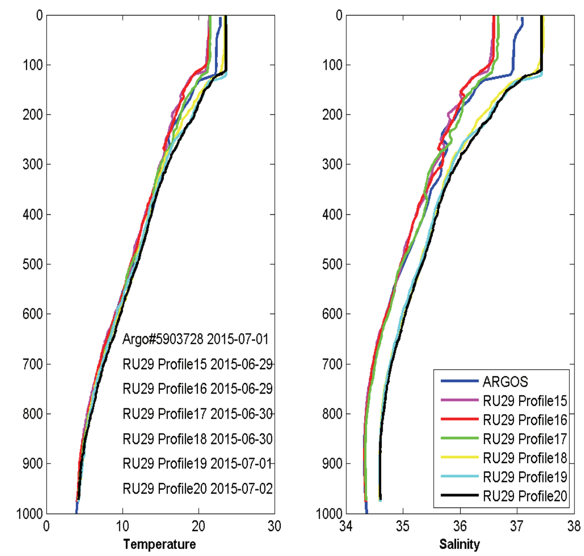

Figure 3: Temperature and salinity depth profile comparison between Argo#5903728 and RU29. Temperature on the left and salinity on the right

The glider highlights spatial changes in the deep water mass not captured by the closest ARGO profile. In the spatial comparisons of the Argo float, glider and models, RU29's profile 18 indicates that at the bottom a significant increase in salinity had occurred (Figure 4). Since Argo#5903728 did not move across this change sampled by the glider and the model grids are courser than the scale sampled by the glider, they could not detect the change. Additionally at the surface, RTOFS predicted lower temperature and salinity than RU29 while MyOcean predicted a slightly higher temperature and salinity than the glider (Figure 4). In the deep ocean, the temperature gradually increases while the salinity stayed constant as the glider continues to travel eastward (Figure 4). Furthermore, Argo#5903728 measured fresher water at depth than RTOFS, MyOcean and the glider and the float and the models report lower temperatures than RU29 (Figure 4). The South Atlantic is characterized with lower precipitation and saltier surface water with strong winds. The spatial comparisons of RU29, Argo#5903728, and the models show that the surface is warmer and saltier than the deep ocean, consistent with the climatology of the South Atlantic (Figure 4).

IV. DISCUSSION

According to observing System Simulation Experiments, additional profile data, especially profile data that cross frontal features, are the most influential at reducing forecast uncertainty. This is evident as RU29's profiles 18 to 20 showed temperature similarities with Argo#5903728 but not in salinity as the glider saw a drastic increase as it moved east along its path (Figure 5). The sudden change in salinity indicates that RU29 crossed a front that the Argo float did not pick up. Since the location of Argo drifters cannot be controlled after they are deployed, they typically do not cross fronts, rather they move along fronts.

Like the glider/ARGO float comparison, the two models and RU29 comparisons highlight the potential spatial considerations needed when evaluating with the higher resolution glider data. The RTOFS and MyOcean models had some similarities with RU29, but they both did not reproduce the frontal structure apparent in the in situ glider data (Figure 6). Since the output of RTOFS and MyOcean are courser than the glider profile data, they do not represent the higher resolution of the Glider or ARGO profile data.

Consequently, the models and RU29 data can show disassociation around sharp oceanic gradients. For instance, RTOFS' June 30th projected currents showed that the RTOFS output compared to the glider was taken in an area of weaker currents in a different feature than the closest glider data and MyOcean output in time and space. (Figure 7). This likely partially explains the difference between the glider and model output. In addition, RTOFS and MyOcean generates average temperature and salinity data of the grid, which limited their ability to resolve the front.

Autonomous Underwater Gliders can be used to assimilate into or evaluate ocean forecast models because of their ability to traverse previously under sampled frontal regions of the ocean. It is crucial to the future of ocean modeling that glider-collected data be incorporated especially where areas of disagreement between the models and an Argo float occur. Over the course of this glider mission we will continue to look at features resolved by the glider to understand how they are represented in the global models. This preliminary analysis focuses on the data deeper than 500 m. As we continue this line of research we will include surface waters associated with these features.

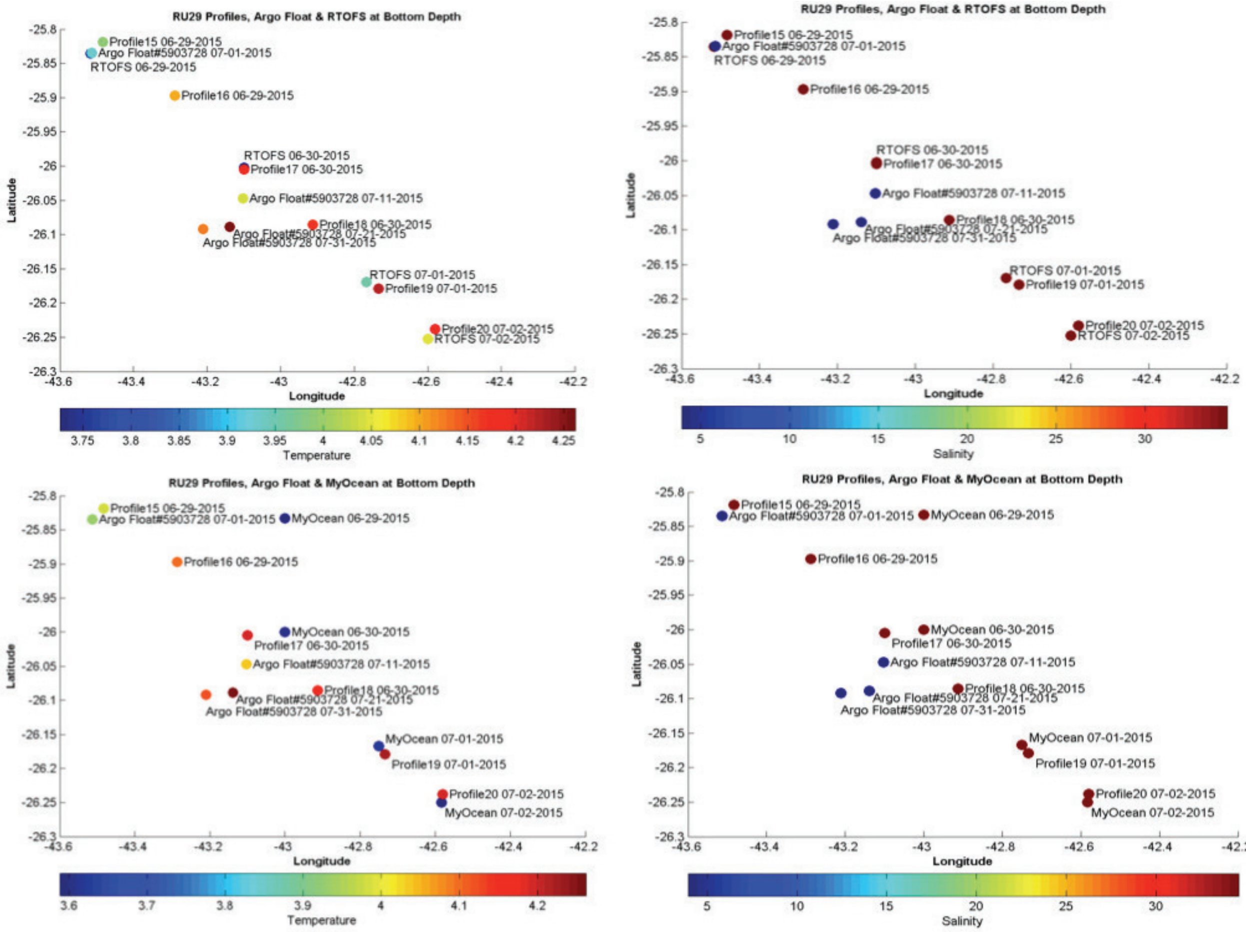

Figure 4: Location, time, and space for RU29, Argo and RTOFS (a and b) and MyOcean (c and d) model data. Time and Sources are indicated (a) bottom temperature with RTOFS, (b) bottom salinity with ROTFS, (c) bottom temperature with MyOcean, and (d) bottom salinity with MyOcean.

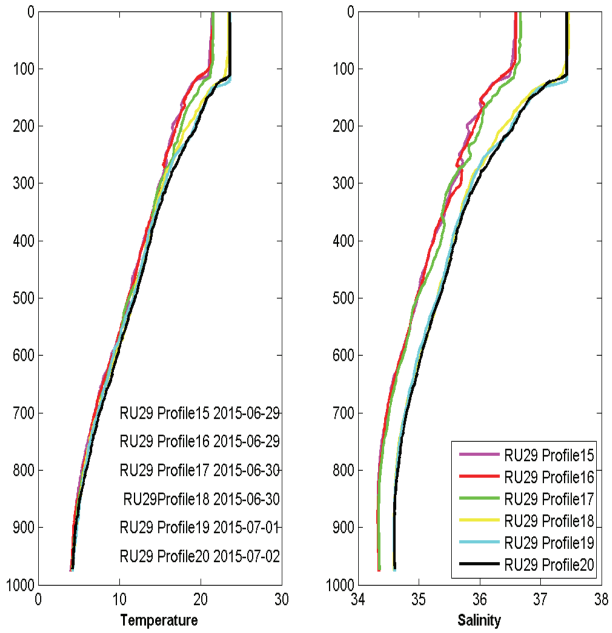

Figure 5: Temperature and salinity depth profile comparison between RU29 profiles #15-20. Temperature on the left and salinity on the right.

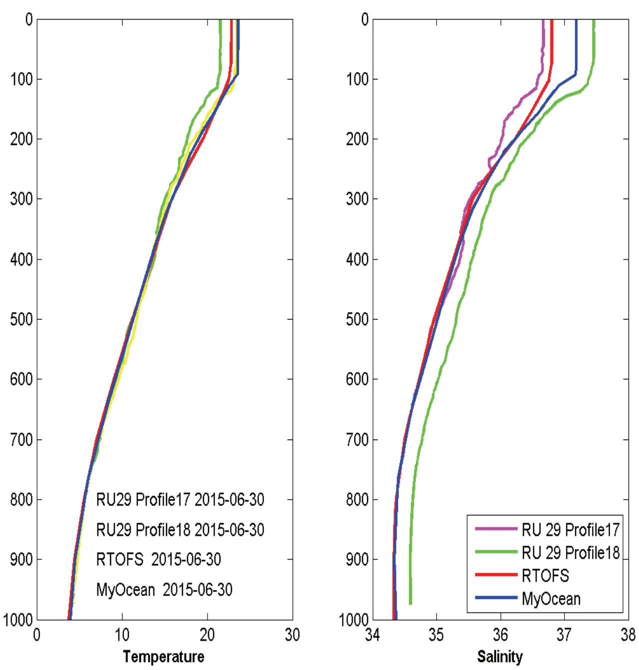

Figure 6: Temperature and salinity depth profile comparison between RU29 profiles #17& 18, RTOFS and MyOcean. Temperature on the left and salinity on the right.

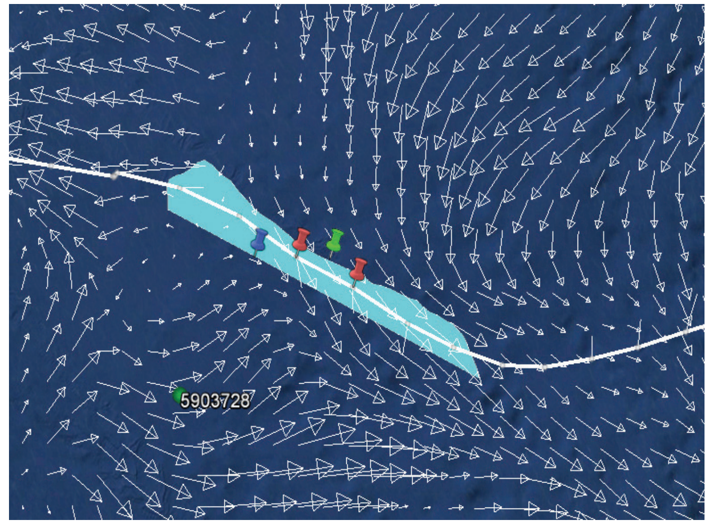

Figure 7: RTOFS projected current directions in the South Atlantic on June 30th. Pins indicate the location of where RTOFS (blue), MyOcean (green), and RU29 (red) data were taken on the glider path.

V. ACKOWNLEDGMENTS

The Challenger Gilder Mission is growing global partnership of gilder operators, scientists, educators and students coordinated by Rutgers University and endorsed by the Challenger Society. The results presented on this paper were initiated in a Rutgers research course and authored by two undergraduate summer interns (Andrenette Morrison and Liam Ramsay) supported by Teledyne Webb Research and six U.S. Naval Academy interns (Martin Arroyo, Kelsey Ashbrook, Olivia Czerewko, Stephanie Lee, Caleb Lintz and Erin Payne). Glider path planning and model/data comparison activities are led by Nilsen Strandskov (Rutgers) and Antonio Ramos (Universidad de Las Palma de Gran Canaria) with cyber infrastructure support provided by John Kerfoot and Sage Lichtenwalner (Rutgers). Glider operators include Chip Haldeman, Dave Aragon, Tina Haskin (Rutgers) and Ben Alsup (TWR). Argo data was collected and made freely available by International Argo Program and the national programs that contribute to it.

VI. REFERENCES

[1] *Challenger Glider Mission.* May 2014. <challenger.marine.rutgers.edu/mission/the-challenger-glider.mission.> (accessed June 8, 2015).

[2] Drévillon, M., and Coauthors, 2008: The GODAE/Mercator-Ocean global ocean forecasting system: results, applications and prospects. *J. Oper. Oceanogr.*, **1**, 51–57,doi:10.1080/1755876X.2008.11020095.

[3]Dobson, C., Mart, J., Strandskov, N., Kohut, J., Schofield, O., Glenn, S., Jones, C., Webb, D., Barrera, C., Ramos, A. 2013. The Challenger glider mission: a global ocean predictive skill experiment. Oceans'13 MTS/IEEE San Diego: 1-8.

[4] *How Argo floats work.* <http://www.argo.ucsd.edu/How_Argo_floats.html.> (accessed June 8, 2015)

[5] Kerfoot, J., S. Glenn, H. Arango, C., Haldeman, C. Jones and D. Pinkel, 2010. Correction and comparison of pumped and non-pumped CTS sensors on the Slocum Glider, EOS Transactions, AGU, 91(26), Ocean Sci. Meet. Suppl., Abstract IT35B-03

[6] Mehra, A., and I. Rivin, 2010: A Real Time Ocean Forecast System for the North Atlantic Ocean. *Terr. Atmos. Ocean. Sci.*, **21**, 211–228.

[7] Sacatelli, R., Schofield, T., Todoroff, K., Carandang, A., Eng, A., Lowry, I., Mather, H., Ramos, A., Swart, S., Dottori, M., Strandskov, N., Kohut, J., Schofield, O., Glenn, S. 2014. Ocean Predictive Skill Assessments in the South Atlantic: Crowd-Outsourcing of Student-Based Discovery: 1-6.

[8] Schofield, O., and Coauthors, 2007: Slocum Gliders: Robust and ready. *J. F. Robot.*, **24**, 473–485, doi:10.1002/rob.20200.

The Ocean is Our Classroom: A 4-Year Research Track for Undergraduate Exploration, Research and Discovery in Oceanography

Scott Glenn, Oscar Schofield, Grace Saba, Travis Miles, Hugh Roarty and Josh Kohut

Center for Ocean Observing Leadership, Rutgers University, New Brunswick, NJ, USA

***Abstract*—Mitigating and adapting to climate change while the global human population continues its projected growth will be the dominant choice challenge confronting the present generation of undergraduates over their professional lifetimes. Today's students should be prepared to develop solutions that will involve the sea, but life-changing at-sea research experiences for undergraduates are limited. The rapid expansion of ocean observatories provides a solution. We have demonstrated in our own observatory how undergraduate student research can be enabled as a year-round activity during a student's full undergraduate career starting on day 1. What began as the Challenger Glider Mission has spread to other observatory technology and science activities both locally and in remote polar regions.**

Keywords — Ocean Observing; Undergraduate Education; Autonomous Underwater Gliders; Challenger Glider Mission.

I. Introduction

Present and future generations will be challenged by the impacts of climate change, including melting of land and sea ice, rising sea levels, ocean acidification and deoxygenation, and increasing extreme weather. This will be combined with the challenges of energy, food and water security as global populations continue to grow while natural and living marine resources are increasingly depleted. An improved multi-disciplinary understanding of the global ocean and its many large marine ecosystems, combined with the ability to observe their present and forecast their future state, is central to providing human society with mitigation and adaptation strategies. A growing constellation of ocean-viewing satellites, and the evolving suite of climate, global and regional scale ocean models, are key advances. Despite the international success of the Argo program, physical, biological and chemical ocean profiles are still among the most sought after datasets for the subsurface ocean, typically requiring expensive ship time countries can no longer afford. Long-duration autonomous underwater gliders, combined with compact sensors on marine mammals, reptiles and fish, can augment the Argo program with additional valuable data to enable discovery, promote scientific understanding, and ultimately improve our ability to forecast the ocean.

Today's undergraduate students will confront the dual challenges of a changing climate and a growing global population over their professional careers, not only the small percentage continuing to graduate school, but increasingly the broader distribution of students as future members of interdisciplinary teams seeking innovative solutions to societal issues within economic constraints. Even though the benefits of undergraduate research experiences are well known, hands-on oceanography remains limited by the availability of time at sea. The global proliferation of ocean observatories provide a means to overcome this issue, increasing undergraduate access to the sea via the Internet.

II. Methods

At Rutgers, we have taken advantage of ocean observatories to provide undergraduates the opportunity to participate in a comprehensive oceanographic research program spanning their entire undergraduate career [1]. Based on the cognitive apprenticeship model, students progress through three levels of participation, frequently described in simple terms as "watch one, do one, teach one". As early as their first semester at Rutgers, interested students can participate in Oceanography House or one of several seminar courses taught by senior level faculty. The seminars introduce students to research opportunities the students may have never envisioned while they are still fulfilling general core course requirements. For those that have already chosen participation in ocean research as an undergraduate goal, Oceanography House provides hands on training in research skills that accelerates the student into the second level of participation, "do one". At the second level, students are

978-0-933957-43-5 ©2015 MTS

taking many of their oceanographic core courses, including a hands-on Ocean Methods and Data Analysis course that includes the use of modern observational technologies on student-directed ½ day research cruises. Additionally, a more data analysis intensive course uses ocean observatory data on student led research. Typical classes of 50-70 students each semester are organized into research teams of 5-7 people led by a more senior student mentor. The semester long research of each group is presented at the end of each semester in a science symposium that features a high level invited speaker to inspire the students in their own future careers. In the final phase, students are taking their oceanography elective courses, and are acting as near-peer mentors to the younger students in the research course. The older students gain valuable mentorship experience including training in how to be a good mentor.

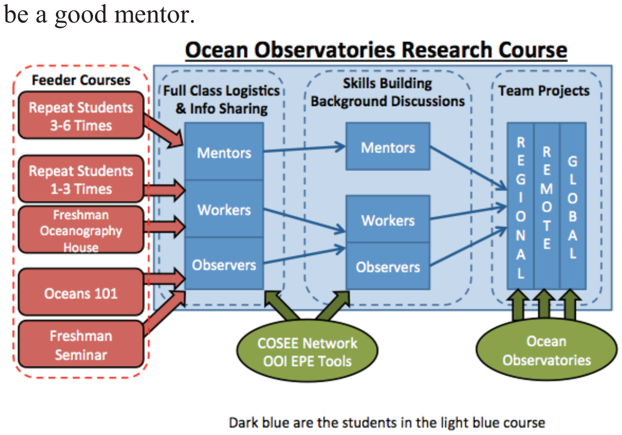

Figure 1: Ocean Observatories Research course that forms the core of the undergraduate research experience.

III. RESULTS

The Challenger Glider Mission is the core field component for the above observatories research course. Student involvement in undergraduate research is enabled by multiple gliders on simultaneous basin-scale missions that over several years are revisiting the historic track of the H.M.S. Challenger, the first dedicated scientific circumnavigation and the beginning of modern oceanography. The scientific questions to be investigated focus on a quality assessment and interpretation of the ensemble of available global-scale ocean models. The mission has already begun with one global-class G2 Slocum Electric glider deployed in the North Atlantic (Silbo) and a second deployed in the South Atlantic (RU29). These two gliders have already completed over 1100 days at sea covering more 22,000 km. The goal is to match the 128,000 km distance covered by the H.M.S Challenger with glider tracks around all 5 ocean basins. The Slocum Electric Gliders Silbo and RU29 will be joined by the Slocum Thermal Glider Clark during the summer of 2015.

The immediate scientific goals are to assess the current capabilities of the existing international suite of global ocean forecast models, and assess the forecast impact on ocean conditions in the vicinity of the glider. The existing global ocean forecast models assimilate satellite sea surface height and temperature data as well as temperature/salinity profiles from the Argo network of over 3,000 drifters. Still, Observing System Simulation Experiments routinely indicate that additional profile data, especially profile data that crosses frontal features, are the most influential at reducing forecast uncertainty. Since the location of Argo drifters cannot be controlled after they are deployed, some regions are critically under sampled, and strong boundary currents are often unresolved. Moreover, even with the SST, altimeter and Argo data, the mesoscale eddy field, the dominant energetic structures for most of the global ocean, are not uniquely or completely resolved by the existing global observation network. Additional data provided by gliders can augment these structures where needed.

A current example is presented here. Glider RU29 recently began Leg 3 of a circumnavigation of the south Atlantic gyre (Fig. 2). Leg 1 ran from Cape Town, South Africa to Ascension Island in 2013. Leg 2 from Ascension to Ubatuba, Brazil in 2014. RU29 is now heading back to Cape Town in 2015 along one of two lines. The orange line is the direct great-circle route back to Cape Town. The red line includes the potential for a stop at the remote island of Tristan da Cunha. The white line is the actual track and current location of RU29, flying somewhere between the red and orange lines.

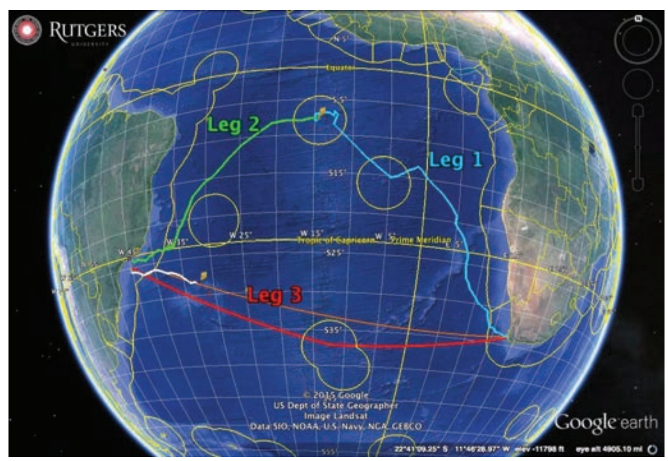

Figure 2: Glider RU29's circumnavigation of the South Atlantic Gyre, with Leg 1 (blue) begun in 2013, Leg 2 (green) in 2014, and potential Leg 3 lines, either directly across (orange) or with a stop in Tristan da Cunha (red). RU29's actual progress on Leg 3 in 2015 is shown in white.

Student-led comparisons between glider data and global ocean models along Legs 1 & 2 have already been reported at previous MTS meetings [2, 3]. Leg 3 is now in the navigation phase, where students must successfully pilot the glider across the basin and investigate interesting features along the way. Figure 4 zooms into the current location of the glider flying generally along the orange line directly towards Cape Town. The average current over the depth of the glider undulations as derived from the NOAA Real Time Ocean Forecast System (RTOFS) are plotted as the green vectors. If RU29 remains on this course along the orange line, RTOFS says it will soon encounter the southern side of a large clockwise rotating eddy (outlined in green) with its adverse currents.

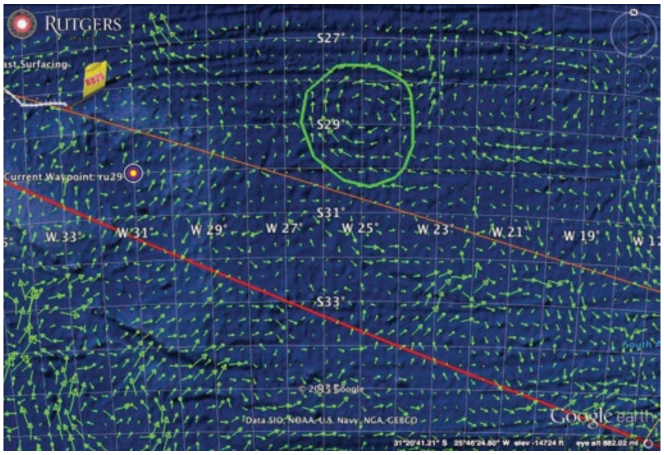

Figure 3: The U.S. RTOFS forecast depth average current field is shown in green. The large clockwise eddy along the orange track is circled with the green line.

However, if one examines the European Copernicus model for the same time period, the depth averaged currents (yellow) indicate a very different situation. Instead of a single clockwise eddy as found in RTOFS (green circle), there are two counterclockwise rotating eddies (yellow circles). The end result, a counter current near the orange direct path to Cape Town, but the reason is totally different. Even though both models are assimilating the same SST, Altimeter and Argo data, the end result on the energetic mesoscale is quite different.

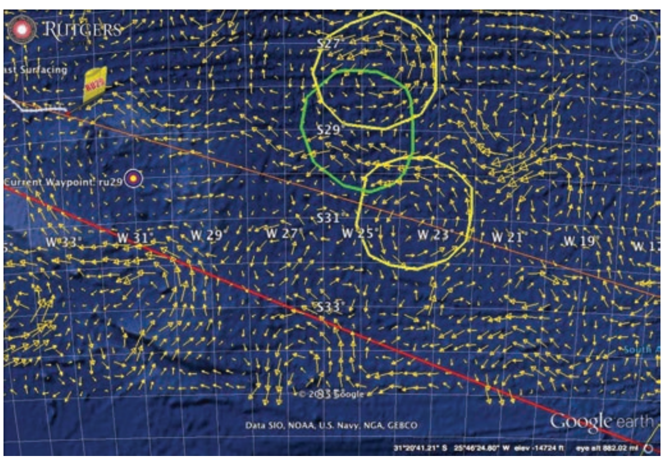

Figure 4: The European Copernicus forecast depth average current field is shown is yellow. The two counterclockwise eddies along the orange track are circled in yellow.

To investigate this, glider RU29 can be targeted to fly through the area of the greatest difference. While both structures produce a counter current to the west along the orange route, the structure between the two yellow eddies from Copernicus and across the middle of the green eddy from RTOFS will be very different. However, to get there, RU29 must first navigate through a field of seamounts (Figure 6), and then line up for a pass through the mesoscale eddies. Differences in the mesoscale eddy structure like this are common.

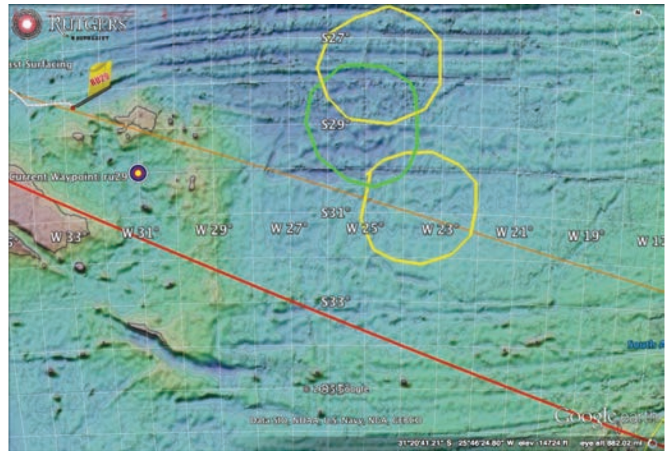

Figure 5: Bathymetry map showing the seamounts RU29 must initially navigate through before lining up for the survey of the differing mesoscale eddy field.

The growth in class size created a new demand for course research projects and intersession research internships. Research projects expanded to include the extensive observatory operated by the Mid Atlantic Regional Association Coastal Ocean Observing System (MARACOOS) as part of the U.S. Integrated Ocean Observing System (IOOS). Research participation ranged from technology improvements to the distributed glider network [4] and the extensive Mid-Atlantic High Frequency (HF) Radar network [5], to scientific applications of the data to homeland security [6.7], fisheries and offshore wind.

School-year research activities are augmented with more intensive hands-on undergraduate opportunities during class breaks. During the summer and winter intersessions, students can commit fulltime to hands-on research in ways not possible during the more class intensive semesters. The shorter winter break coincides with the southern hemisphere summer season. In the Southern Summer Research Institute, in collaboration with projects supported by the NSF Office of Polar Programs, undergraduates have the opportunity to participate in and contribute to research in Antarctica. Over the last 5 years, students have made significant contributions to research on polar research vessels and land based research stations. Students participating in the Northern Summer Research Institute are from Rutgers, the U.S. Naval Academy, and other universities around the country. They come to Rutgers each summer to work full time on team research projects that utilize ocean observatory data. Projects begun during the semester are often pursued in greater detail over the summer. Students are supported through a variety of mechanisms including university contributions, federal grants, and direct industry sponsorship. A major focal point of the Northern Summer Research Institute is the Challenger Glider Mission, where students work with researchers from around the world to validate global ocean models using basin-scale underwater glider missions. The Summer Research Institute uses the MTS/IEEE Oceans process to summarize and present results. Abstracts are submitted early in the summer, and results are documented in Proceedings papers submitted by the students at the end of the summer for presentation at the fall MTS/IEEE Oceans meeting. Over the last 3 years, 8 undergraduate student papers have been submitted to Oceans based on student research in the Summer Research Institute. Papers this year include optimizing glider flight parameters for long-duration missions, comparisons of basin-scale glider data with an ensemble of global ocean models, and the analysis of the first year of HF Radar data from the Western Antarctic Peninsula.

IV. Discussion

We have found that augmenting the standard Marine Science course track with a concurrent research track increases student involvement, retention and diversity. The success of this approach can be assessed by tracking student involvement in the research course established in the fall of 2007. Pre-course levels of undergraduates working in the research lab were consistently at the level of 1 to 3 people per year for 10 years. The research course started with 7 students who began the mission to be the first group to fly an underwater glider across an ocean basin. After the Trans-Atlantic's mission success and publicity in 2009, the course peaked in 2012 with 70 students. Since then, student involvement has leveled off, consistently remaining near 50 students per semester as we continue to fly gliders across ocean basins as part of the Challenger Glider Mission.

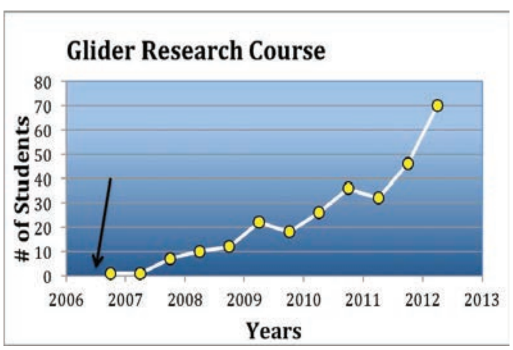

Figure 6: Student involvement in the Ocean Observatories Research course over time since the course was established in 2007.

As the number and diversity of ocean observatories grow worldwide, research courses like the one we teach at Rutgers can be put in place in more locations. One example will be the NSF Ocean Observatories Initiative (OOI). The OOI Education and Public Engagement (EPE) Implementing Organization has already built new software tools to enable undergraduate access to near real time data streams from the OOI. The tools are organized into a Concept Mapper that allows complex concepts to be deconstructed into more elemental components, Data Visualization tools launched from a web browser to reduce computer programming barriers to participation, and a Data Investigation Builder for teachers to produce custom guides for students.

V. Acknowledgements

The Challenger Glider Mission is growing global partnership of glider operators, scientists, educators and students coordinated by Rutgers University and partially supported by the U.S. Integrated Ocean Observing System (IOOS). RU29 mission support is currently provided by the G. Unger Vetlesen Foundation and ONR-Global. Student support is provided by NSF Research Internships in Ocean Science (RIOS) and Teledyne Webb Research. The Ocean Observatories Initiative Education and Public Engagement activities and the Antarctic research activities are supported by the National Science Foundation. The Mid-Atlantic Regional Association Coastal Ocean Observing System is funded by the U.S. Integrated Ocean Observing System through NOAA.

VI. References

[1] Glenn, S., Kohut, J., McDonnell, J., Seidel, D., Aragon, D., Haskins, T., Handel, E., Haldeman, C., Heifetz, I., Kerfoot, J., Lemus, E., Lictenwalder, S., Ojanen, L., Roarty, H., Atlantic Crossing Students, Jones, C., Webb, D., Schofield, O. 2011. The Trans-Atlantic Slocum glider expeditions: A catalyst for undergraduate participation in ocean science and technology. Marine Technology Society 45: 75-90.

[2] Dobson, C.; Mart, J.; Strandskov, N.; Kohut, J.; Schofield, O.; Glenn, S.; Jones, C.; Webb, D.; Barrera, C.; Ramos, A, "The Challenger Glider Mission: A global ocean predictive skill experiment," Oceans - San Diego, 2013 , vol., no., pp.1,8, 23-27 Sept. 2013.

[3] Sacatelli, R., Schofield, T., Todoroff, K., Carandang, A., Eng, A., Lowry, I., Mather, H., Ramos, A., Swart, S., Dottori, M., Strandskov, N., Kohut, J., Schofield, O., Glenn, S., Ocean Predictive Skill Assessments in the South Atlantic: Crowd-Sourcing of Student-Based Discovery MTS IEEE Oceans 2014 Proceedings

[4] Schofield, O., Kohut, J., Glenn, S., Morell, J., Capella, J., Corredor, J., Orcutt, J., Arrott, M., Krueger, I., Meisinger, M., Peach, C., Vernon, F., Chave, A., Chao, Y., Chien, S., Thompson, D., Brown, W., Oliver, M., Boicourt, W. 2010. A regional Slocum glider network in the Mid-Atlantic coastal waters leverages broad community engagement. Marine Technology Society 44(6): 64-74.

[5] Roarty, H.J., S. M. Glenn, J. T. Kohut, D. Gong, E. Handel, E. Rivera, T. Garner, L. Atkinson, W. Brown, C. Jakubiak, M. Muglia, S. Haines and H. Seim (2010) "Operation and Application of a Regional HF Radar Network in the Mid-Atlantic Bight" Marine Technology Society Journal, Vol. 45, No. 1, 52-67.

[6] Holenstein, K.; Dobson, C.; Smith, M.; Roarty, H.; Glenn, S.; Barrick, D.E., "Bistatic vessel detection from the CODAR SeaSonde," Oceans San Diego, 2013, pp.1,5, 23-27 Sept. 2013

[7] Dobson, C.; Holenstein, K.; Smith, M.; Roarty, H.; Glenn, S.; Welan, C.; Barrick, D.; Isaacson, J., "Mono static vessel detection statistics from the CODAR SeaSonde," Oceans San Diego, 2013, pp.1-4, 23-27 Sept. 2013

Hurricane Irene Sensitivity to Stratified Coastal Ocean Cooling

Greg Seroka and Travis Miles

Center for Ocean Observing Leadership, Department of Marine and Coastal Sciences, School of Environmental and Biological Sciences, Rutgers, The State University of New Jersey, New Brunswick, New Jersey

Yi Xu

State Key Laboratory of Estuarine and Coastal Research, East China Normal University, Shanghai, China

Josh Kohut, Oscar Schofield, and Scott Glenn

Center for Ocean Observing Leadership, Department of Marine and Coastal Sciences, School of Environmental and Biological Sciences, Rutgers, The State University of New Jersey, New Brunswick, New Jersey

(Manuscript received 29 December 2015, in final form 25 April 2016)

ABSTRACT

Cold wakes left behind by tropical cyclones (TCs) have been documented since the 1940s. Many questions remain, however, regarding the details of the processes creating these cold wakes and their in-storm feedbacks onto tropical cyclone intensity. This largely reflects a paucity of measurements within the ocean, especially during storms. Moreover, the bulk of TC research efforts have investigated deep ocean processes—where tropical cyclones spend the vast majority of their lifetimes—and very little attention has been paid to coastal ocean processes despite their critical importance to shoreline populations. Using Hurricane Irene (2011) as a case study, the impact of the cooling of a stratified coastal ocean on storm intensity, size, and structure is quantified. Significant ahead-of-eye-center cooling (at least 6°C) of the Mid-Atlantic Bight occurred as a result of coastal baroclinic processes, and operational satellite SST products and existing coupled ocean–atmosphere hurricane models did not capture this cooling. Irene's sensitivity to the cooling is tested, and its intensity is found to be most sensitive to the cooling over all other tested WRF parameters. Further, including the cooling in atmospheric modeling mitigated the high storm intensity bias in predictions. Finally, it is shown that this cooling—not track, wind shear, or dry air intrusion—was the key missing contribution in modeling Irene's rapid decay prior to New Jersey landfall. Rapid and significant intensity changes just before landfall can have substantial implications on storm impacts—wind damage, storm surge, and inland flooding—and thus, coastal ocean processes must be resolved in future hurricane models.

1. Introduction

While tropical cyclone (TC) track prediction has steadily improved over the past two decades, TC intensity prediction has failed to progress in a similarly substantial way (Cangialosi and Franklin 2013). Many environmental factors control TC intensity, including the storm track itself, wind shear, intrusion of dry air, and upper-ocean thermal evolution (Emanuel et al. 2004). The last factor underlies all other processes because it directly impacts the fundamental transfer of energy from the ocean to the atmosphere within the TC heat engine (Emanuel 1999; Schade and Emanuel 1999).

Hurricane models often account for track and large-scale atmospheric processes that affect intensity—wind shear, dry air intrusion, and interaction with midlatitude troughs (Emanuel et al. 2004). Some possible reasons include (i) greater attention to the atmosphere in modeling, and (ii) large-scale processes being resolved well, even with less advanced models. However, models do a comparatively less accurate job of representing oceanic processes that govern hurricane intensity because

Denotes Open Access content.

Corresponding author address: G. S. Seroka, Center for Ocean Observing Leadership, Department of Marine and Coastal Sciences, School of Environmental and Biological Sciences, Rutgers, The State University of New Jersey, New Brunswick, NJ 08901.
E-mail: greg.seroka@gmail.com

DOI: 10.1175/MWR-D-15-0452.1

they are data limited (Emanuel 1999, 2003; Emanuel et al. 2004).

A specific upper-ocean thermal phenomenon that consistently emerges after a TC has passed is a cold pool of water left in the wake of its path, termed a ''cold wake.'' This oceanic phenomenon has been observed behind TCs since at least the 1940s off the coast of Japan (Suda 1943) and since at least the 1950s in the Atlantic, Caribbean, and Gulf of Mexico (Fisher 1958). Observational studies continued into the 1960s (e.g., Leipper 1967) with investigation of potential processes causing the cold wakes, such as upwelling and turbulent entrainment of cold water into the warmer mixed layer. Studies in the late 1970s (Chang and Anthes 1979; Sutyrin and Agrenich 1979) began the use of idealized numerical simulations to investigate the effect of this oceanic cooling on TC intensity, but neglected TC movement. Then, numerical modeling studies in the 1980s (Price 1981; Sutyrin and Khain 1984) and 1990s (Khain and Ginis 1991; Bender et al. 1993; Price et al. 1994) incorporated TC movement and three-dimensional coupled ocean–atmosphere models to further examine the negative SST feedback on storm intensity.

Prior to the 1980s and 1990s, observations of the upper ocean beneath a TC were uncommon due to the unpredictable and dangerous winds, waves, and currents in the storms (D'Asaro 2003). At that point, ocean observations in TCs, summarized by Price (1981), occurred primarily as a result of targeted studies using air-deployed profilers (e.g., Sanford et al. 1987; Shay et al. 1992), long-term observations that happened to be close to a TC's track (e.g., Forristall et al. 1977; Mayer and Mofjeld 1981; Dickey et al. 1998) or hydrographic surveys in a TC's wake (e.g., Brooks 1983). The severe conditions of TCs hampered progress in determining physical processes leading to the previously observed cold wake, as well as specific timing and location of the ocean cooling relative to the TC core. In the 2000s, studies began to provide observational and model evidence that significant portions of this surface ocean cooling can occur ahead of the hurricane eye center (e.g., D'Asaro 2003; Jacob and Shay 2003; Jaimes and Shay 2009), proposing that such cooling is especially important for hurricane intensity.

Even today, the bulk of research efforts have investigated deep ocean processes and their feedback onto TC intensity; indeed, a TC typically spends the vast majority of its lifetime over deep, open waters. However, rapid and significant changes in intensity just before landfall and often in shallow water can have substantial implications on storm impacts (i.e., wind damage, storm surge, and inland flooding). For example, the statistical analysis by Rappaport et al. (2010) finds that category-3–5 hurricanes in the Gulf of Mexico weakened approaching landfall due to both vertical wind shear and hurricane-induced sea surface temperature reductions on the order of 1°C ahead of the storm center. Therefore, attention must be paid to coastal processes as well (Marks et al. 1998), which inherently differ from deep-water processes due to the influence of a shallow ocean bottom and coastal wall, and have been observed to produce SST cooling in TCs up to 11°C (Glenn et al. 2016).

This paper analyzes a recent landfalling storm, Hurricane Irene (2011), using a combination of unique datasets. Hurricane Irene is an ideal case study because in the days leading up to its landfall in New Jersey (NJ), its intensity was overpredicted by hurricane models (i.e., ''guidance'') and in resultant National Hurricane Center (NHC) forecasts (Avila and Cangialosi 2012). The NHC final report on the storm stated that there was a ''consistent high bias [in the forecasts] during the U.S. watch–warning period.'' NHC attributes one factor in this weakening to an ''incomplete eyewall replacement cycle'' and a resulting broad and diffuse wind field that slowly decayed as the storm moved from the Bahamas to North Carolina (NC)—over a warm ocean and in relatively light wind shear. Irene made landfall in NC as a category-1 hurricane, two categories below expected strength.

One hypothesis as to why Irene unexpectedly weakened between the Bahamas and NC involves both aerosols and ocean cooling (Lynn et al. 2016; Khain et al. 2016). Irene crossed a wide band of Sahara dust just north of the West Indies, initially causing convection invigoration in the simulated eyewall and fostering the hurricane's development (Lynn et al. 2016). However, as Irene approached the United States, continental aerosols intensified convection at the simulated storm's periphery. This intensification of convection at the TC periphery can lead to increases in TC central pressure and weakening of wind speed near the eyewall (Lynn et al. 2016 and references within).

This paper's focus is on Irene's time after its NC landfall (Fig. 1) and after it had weakened in intensity due to continental aerosol interaction with convection at the hurricane's periphery and the slight SST cooling in the South Atlantic Bight (SAB). The SST cooling over the Mid-Atlantic Bight (MAB) was at least 3–5 times greater than the SST cooling that occurred in the SAB (Figs. 2 and 3).

While energetic ocean mesoscale features can distort the structure of the TC cold wake (Walker et al. 2005; Jaimes and Shay 2010; Jaimes et al. 2011), during the direct forcing part of the storm, TC cooling in a deep ocean with no eddy features is frequently distributed

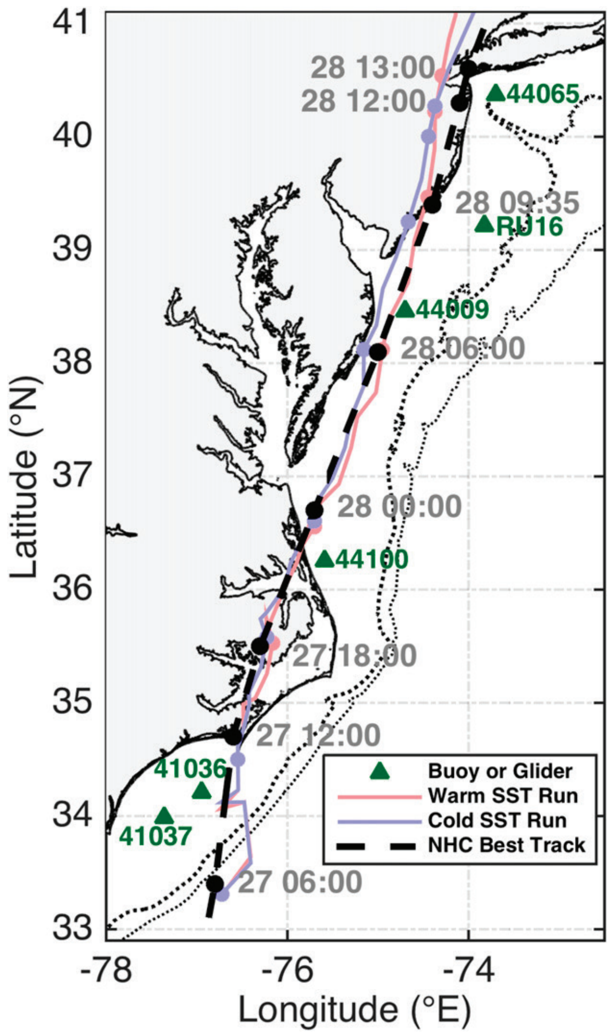

FIG. 1. NHC best-track data for Hurricane Irene in dashed black with timing (DD HH:MM August 2011) labeled in gray. Tracks for warm (red) and cold (blue) SST simulations are also plotted. NDBC buoy and glider RU16 locations are shown with green triangles. The 50- and 200-m isobaths are plotted in dotted black lines.

symmetrically between the front and back half of the storm (Price 1981). This does not include the inertial response in the cold wake. As will be shown in this paper, significant ahead-of-eye-center SST cooling (at least 6°C and up to 11°C, or 76%–98% of total in-storm cooling) was observed over the MAB continental shelf during Hurricane Irene, indicating that coastal baroclinic processes enhanced the percentage of cooling that occurred ahead of eye center (Glenn et al. 2016).

This paper will 1) explore how Irene's predictions change using a semi-idealized treatment of the ahead-of-eye-center cooling, 2) show that better treatment would have lowered the high bias in real-time predictions, and 3) conclude that this ahead-of-eye-center cooling observed in Irene was the missing contribution—not wind shear, track, or dry air intrusion—to the rapid decay of Irene's intensity just prior to NJ landfall.

2. Data and methods

a. Gliders

Teledyne-Webb Research (TWR) Slocum gliders are autonomous underwater vehicles (AUVs) that have become useful platforms for monitoring the ocean's response to storms (Glenn et al. 2008; Ruiz et al. 2012; Miles et al. 2013, 2015). Gliders can profile the water column from the surface to depths of up to 1000 m. They continuously sample every 2 s, providing a high temporal resolution time series from pre- to poststorm and complementing the spatial coverage that multiple concurrent airborne expendable bathythermograph (AXBT; Sessions et al. 1976; Sanabia et al. 2013) deployments can provide. Finally, gliders can be piloted, enabling more targeted profiling throughout the storm, in contrast to Argo (Gould et al. 2004; Roemmich et al. 2009) and Air-Launched Autonomous Micro-Observer (ALAMO; Sanabia and Jayne 2014; Sanabia et al. 2016) floats, which passively move with ocean currents. Because of this, gliders can be directed to steer into a storm and station-keep, providing a fixed-point Eulerian observation time series. A more detailed description of general capabilities of these gliders can be found in Schofield et al. (2007). For storm-specific capabilities of the gliders, see Miles et al. (2013, 2015) and Glenn et al. (2016).

Rutgers University Glider RU16 was used in this study. The glider was equipped with several science sensors, including a Seabird unpumped conductivity–temperature–depth (CTD) sensor, which measured temperature, salinity, and water depth. The top bin in the temperature profiles—0–1-m depth—is used to provide a measure of near-surface temperature at the glider location (Fig. 1). Thermal-lag-induced errors associated with the unpumped CTD were corrected before any data were used (Garau et al. 2011).

b. Buoys

1) NEAR-SURFACE TEMPERATURE

National Data Buoy Center (NDBC) buoys 41037 and 41036 in the SAB and buoys 44100, 44009, and 44065 in the MAB were used in this study (Fig. 1). Hourly water temperatures were used, which is measured at 0.6-m depth at all buoys except 0.46-m depth at 44100. These data provide near-surface water temperatures along and near the track of Hurricane Irene through the SAB and MAB.

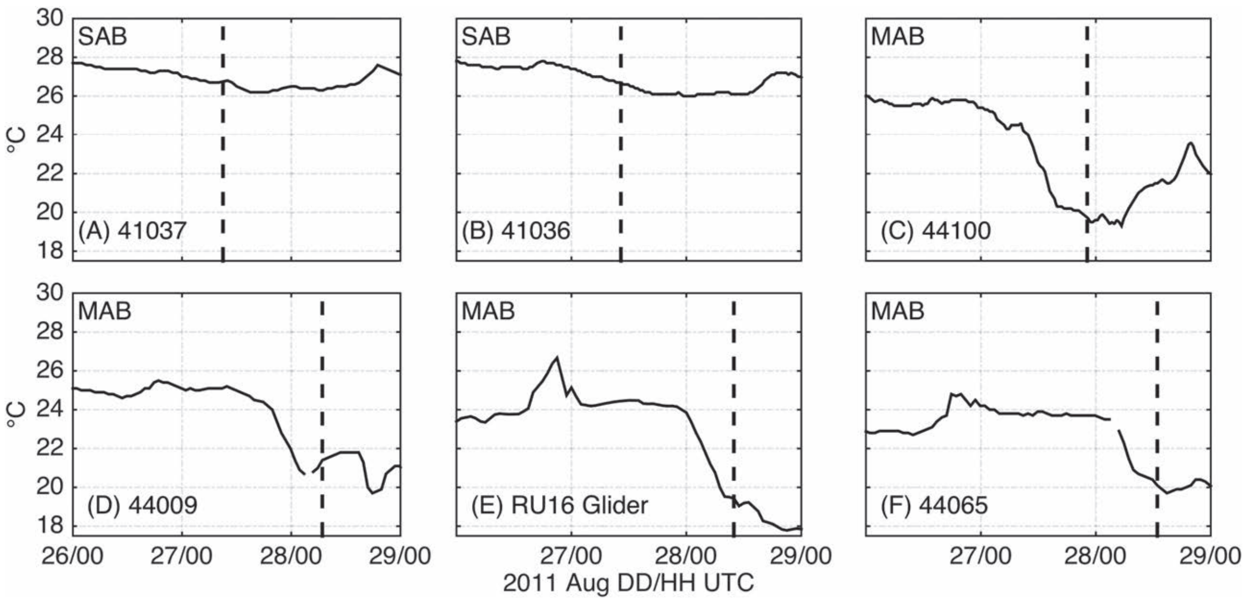

FIG. 2. NDBC buoy and glider near surface water temperature (°C) time series. South Atlantic Bight buoys (denoted by "SAB") from south to north are 41037 and 41036, and Mid-Atlantic Bight buoys and glider RU16 (denoted by "MAB") from south to north are 44100, 44009, glider RU16, and 44065. Timing of Irene's eye passage by the buoy or glider is denoted with vertical dashed line.

2) HEAT FLUXES

NDBC buoys 44009 and 44065 were used for latent and sensible heat flux calculations, which were estimated based on the "bulk formulas" (Fairall et al. 1996):

$$\text{Sensible heat flux:}\quad H = -(\rho c_p)C_H U(\theta - \theta_{\text{sfc}}), \tag{1}$$

$$\text{Latent heat flux:}\quad E = -(\rho L_v)C_Q U(q - q_{\text{sfc}}), \tag{2}$$

where ρ is density of air, c_p is specific heat capacity of air, C_H is sensible heat coefficient [see Eq. (5)], U is 5-m wind speed, θ is potential temperature of the air at 4 m and θ_{sfc} is potential temperature at the water surface, L_v is enthalpy of vaporization, C_Q is latent heat coefficient [see Eq. (6)], q is specific humidity of the air at 4 m, and q_{sfc} is interfacial specific humidity at the water surface.

Neither θ_{sfc} and q_{sfc} are directly computed from interfacial water temperature, but rather computed from buoy temperature measured at 0.6-m depth. During high wind conditions, the difference between skin temperature and temperature at 0.6-m depth is likely small enough to have a negligible effect on the computed bulk fluxes (Fairall et al. 1996).

c. Satellites

1) SEA SURFACE TEMPERATURE

The National Centers for Environmental Prediction (NCEP) Real-Time Global High-Resolution (RTG-HR) is a daily SST analysis used in this study. RTG-HR SST is operationally produced using in situ and AVHRR data on a 1/12° grid (Reynolds and Chelton 2010). The operational 13-km Rapid Refresh (RAP) and the 12-km North American Mesoscale Forecast System (NAM) and its inner nests, including the 4-km NAM continental U.S. (CONUS) nest, use fixed RTG-HR SST. Therefore, RTG-HR is the most relevant SST product for comparison with the 2-km SST composite described next.

Standard techniques to remove cloudy pixels in SST composites use a warmest pixel method because clouds are usually colder than the SST (Cornillon et al. 1987). This tends to reduce cloud contamination but results in a warm bias, which is unfavorable for capturing TC cooling. In this study, a 3-day "coldest dark-pixel" composite method is used to map regions of cooling from Irene. This technique, described in Glenn et al. (2016), filters out bright cloudy pixels while retaining darker ocean pixels.

2) WATER VAPOR

Satellites are also used for a spatial estimate of the intrusion of dry air into Irene's circulation. *Geostationary Operational Environmental Satellite-13 (GOES-13)* water vapor channel-3 brightness temperature imagery is used for these estimates.

d. Radiosondes

Radiosondes, typically borne aloft by a weather balloon released at the ground, directly measure temperature, humidity, and pressure, and derive wind speed and direction. To validate profiles of modeled wind shear and

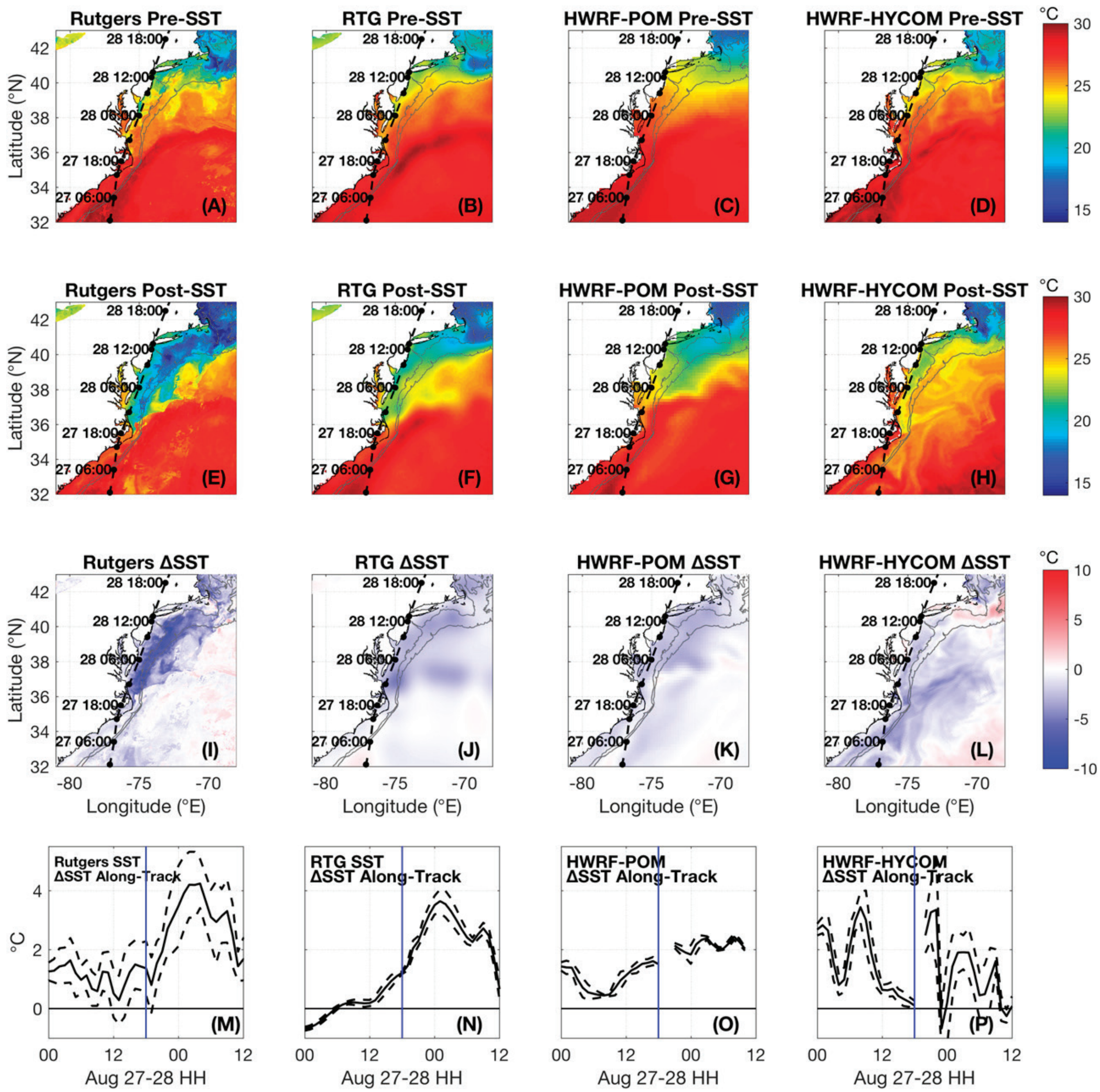

FIG. 3. SST plots (a)–(d) before Irene, (e)–(h) after Irene, (i)–(l) difference between before and after. (m)–(p) Along-track SST change (mean within 25 km of NHC best track in solid black, ±1 standard deviation in dashed black) time series with vertical blue line dividing the first part of the time series when Irene was over the SAB, and the second part of the time series when Irene was over the MAB. (a),(e),(i),(m) The new Rutgers SST composite, as described in section 2c(1); before Irene is coldest dark-pixel composite from 24 to 26 Aug 2011, after Irene is from 29 to 31 Aug 2011. (b),(f),(j),(n) The Real-Time Global High Resolution (RTG HR) SST product from NOAA; before Irene is from 26 Aug, after Irene is from 31 Aug. (c),(g),(k),(o) The operational HWRF-POM from 2011, simulation initialized at 0000 UTC 26 Aug 2011; before Irene is from 0000 UTC 26 Aug, after Irene is from 0000 UTC 31 Aug. (d),(h),(l),(p) The experimental HWRF-HYCOM from 2011, simulation initialized at 0000 UTC 26 Aug 2011; before Irene is from 0000 UTC 26 Aug, after Irene is from 0000 UTC 31 Aug.

dry air intrusion, radiosonde observations of u and v winds are used from Albany, New York (KALB); Chatham, Massachusetts (KCHH); and Wallops Island, Virginia (KWAL), and RH is used from KALB and KWAL.

e. North American Regional Reanalysis

The North American Regional Reanalysis (NARR) is a 32-km, 45 vertical layer atmospheric reanalysis produced by NCEP and provides a long-term (1979–present) set of consistent atmospheric data over North America (Mesinger et al. 2006). The data consist of reanalyses of the initial state of the atmosphere, which are produced by using a consistent data assimilation scheme to ingest a vast array of observational data into historical model hindcasts. NARR is used to evaluate modeled size and structure of Irene, modeled heat fluxes, and modeled wind shear, both horizontally and vertically.

f. Modeling and experimental design

1) Hurricane Weather Research and Forecasting

Output from two different versions of the Hurricane Weather Research and Forecast system [HWRF; Skamarock et al. (2008)] was used in this study: 1) the 2011 operational HWRF, which was the Weather Research and Forecasting (WRF) Model coupled to the feature-model-based Princeton Ocean Model [HWRF-POM; Blumberg and Mellor (1987)], and 2) the same HWRF atmospheric component but coupled to the Hybrid Coordinate Ocean Model [HWRF-HYCOM; Chassignet et al. (2007)].

For the operational 2011 hurricane season, POM for HWRF-POM was run at 1/6° resolution (~18 km), with 23 terrain-following sigma coordinate vertical levels. The three-dimensional POM output files contain data that are interpolated vertically onto the following vertical levels: 5-, 15-, 25-, 35-, 45-, 55-, 65-, 77.5-, 92.5-, 110-, 135-, 175-, 250-, 375-, 550-, 775-, 1100-, 1550-, 2100-, 2800-, 3700-, 4850-, and 5500-m depth (Tallapragada et al. 2011). Near-surface temperatures are pulled from the top level of POM, which occurs at 5 m.

The ocean model component of the 2011 HWRF-HYCOM system is the Real-Time Ocean Forecast System-HYCOM [RTOFS-HYCOM; Mehra and Rivin (2010)], which varies smoothly in horizontal resolution from ~9 km in the Gulf of Mexico to ~34 km in the eastern North Atlantic (Kim et al. 2014). Initial conditions are estimated from RTOFS-Atlantic (Mehra and Rivin 2010) 24-h nowcasts (Kim et al. 2014). RTOFS-HYCOM uses the Goddard Institute for Space Studies (GISS) vertical mixing and diffusion scheme (Canuto et al. 2001, 2002). Near-surface temperatures are pulled from the top layer of HYCOM, which ranges from less than 1 m in shallower regions (approximately 40-m water column depth or less) to 3 m in deeper regions (approximately 100-m water column depth or greater).

2) Regional Ocean Modeling System

The Regional Ocean Modeling System [ROMS; http://www.roms.org, Haidvogel et al. (2008)] is a free-surface, sigma coordinate, primitive equation ocean model that has been particularly used for coastal applications. Output is used from simulations run on the Experimental System for Predicting Shelf and Slope Optics (ESPreSSO) model (Wilkin and Hunter 2013) grid, which covers the MAB from Cape Hatteras to Cape Cod, from the coast to past the shelf break, at 5-km horizontal resolution and with 36 vertical levels.

3) WRF and experimental design

(i) Control simulation

The Advanced Research dynamical core of WRF [ARW, http://www.wrf-model.org, Skamarock et al. (2008)], version 3.4 is a fully compressible, nonhydrostatic, terrain-following vertical coordinate, primitive equation atmospheric model. This ARW domain extends from south Florida to Nova Scotia, and from Michigan to Bermuda (Glenn et al. 2016).

In the experiments, the control simulation has a horizontal resolution of 6 km with 35 vertical levels. The following physics options are used: longwave and shortwave radiation physics were both computed by the Rapid Radiative Transfer Model-Global (RRTMG) scheme, the Monin–Obukhov atmospheric layer model and the Noah land surface model were used with the Yonsei University planetary boundary layer (PBL) scheme, and the WRF double-moment 6-class moisture microphysics scheme (Lim and Hong 2010) was used for grid-scale precipitation processes. The control simulation did not include cumulus parameterization (Kain 2004); sensitivity to cumulus parameterization was tested in a subsequent simulation (see below and in Table 1).

It was critical to ensure that the control simulation had a track very similar to the NHC best track, so as to not include any additional land effects on Irene's intensity as it tracked closely along the coast. Also, because TC translation speed has a large impact on SST response and subsequent negative feedback on TC intensity (Mei et al. 2012), it was critical to closely simulate Irene's translation speed. Several different lateral boundary conditions and initialization times were experimented with before arriving at the best solution (after Zambon et al. 2014a). The resulting initial and lateral boundary conditions used are from the Global Forecast System (GFS) 0.5° operational cycle initialized at 0600 UTC 27 August 2011.

For the control simulation, RTG-HR SST from 0000 UTC 27 August 2011 is used for bottom boundary conditions over the ocean. This is 6 h prior to model initialization, to mimic NAM and RAP operational conditions. All simulations are initialized at 0600 UTC 27 August 2011 when Irene was just south of NC (Fig. 1) and end at 1800 UTC 28 August 2011. By initializing so late, the focus is only on changes in Irene's

TABLE 1. List of model sensitivities, grouped by type. Name of sensitivity is on left, details of sensitivity with WRF namelist option on right. Control run listed last.

Sensitivity	WRF namelist option
A. Model configuration	
1. Horizontal resolution (dx)	3 vs 6 km
2. Vertical resolution (e_vert, eta_levels)	51 vs 35 vertical levels
3. Adaptive time step (use_adaptive_time_step)	On vs off
4. Boundary conditions (update frequency, interval_seconds)	3 vs 6 h
5. Digital filter initialization (DFI, dfi_opt)	On (dfi_nfilter = 7) vs off
B. Atmospheric–model physics	
6–7. Microphysics (mp_physics)	6 (WRF single-moment 6-class) vs 16 (WRF double-moment 6-class) vs 30 (HUJI spectral bin microphysics, "fast")
8–9. Planetary boundary layer scheme (bl_pbl_physics)	5 (Mellor–Yamada–Nakanishi–Niino level 2.5) vs 7 (ACM2) vs 1 (Yonsei University)
10. Cumulus parameterization (cu_physics)	1 (Kain–Fritsch, cudt = 0, cugd_avedx = 1) vs 0 (off)
11. SST skin (sst_skin)	On vs off
12–14. Longwave radiation (ra_lw_physics)	1 (RRTM) vs 5 (new Goddard) vs 99 (GFDL) vs 4 (RRTMG)
15–17. Shortwave radiation (ra_sw_physics)	1 (Dudhia) vs 5 (new Goddard) vs 99 (GFDL) vs 4 (RRTMG)
18–19. Latent heat flux < 0 over water (in module_sf_sfclay)	On vs off (warm SST) On vs off (cold SST)
20. Land surface physics (sf_surface_physics)	1 (5-layer thermal diffusion) vs 2 (Noah)
C. Advanced Hurricane WRF (AHW) options	
21–22. Air–sea flux parameterizations (isftcflx)	1 vs 0 (warm SST) (control run: isftcflx = 2) 1 vs 0 (cold SST) (control run: isftcflx = 2)
D. Sea surface temperature	
23–25. SST	Cold vs warm (isftcflx = 2) Cold vs warm (isftcflx = 1) Cold vs warm (isftcflx = 0)
E. Advanced Hurricane WRF (AHW) options (12-h later initialization)	
26. Digital filter initialization (DFI, dfi_opt)	On (dfi_nfilter = 7) vs off
27–28. 1D ocean mixed layer model (sf_ocean_physics = 1)	On (isothermal warm initial conditions) vs on (glider stratified initial conditions) vs off
29–30. 3D ocean Price–Weller–Pinkel model (sf_ocean_physics = 2)	On (HWRF-HYCOM initial conditions) vs on (glider stratified initial conditions) vs off

intensity occurring in the MAB. Further, as will be shown below, model spinup was a quick 6 h, so the model is already in a state of statistical equilibrium (Brown and Hakim 2013) under the applied dynamical forcing by the time Irene enters the MAB.

A two-part experiment, detailed below, is performed to investigate why model guidance did not fully capture the rapid decay of Irene just prior to NJ landfall. First, >140 simulations are conducted for sensitivities of Irene's intensity, size, and structure to various model parameters, physics schemes, and options, including horizontal and vertical resolution, microphysics [including a simulation with WRF spectral bin microphysics (Khain et al. 2010) to test sensitivity to aerosols], PBL scheme, cumulus parameterization, longwave and shortwave radiation, land surface physics, air–sea flux parameterizations, coupling to a 1D ocean mixed layer (OML) model, coupling to a 3D ocean Price–Weller–Pinkel (PWP) model, and SST (Table 1). These simulations quantify and contextualize the sensitivities of Irene's modeled intensity, size, and structure to SST. Second, a model assessment is performed, specifically evaluating the control run's treatment of track, wind shear, and dry air intrusion.

To conclude the data and methods section, details are provided on a few key sensitivities. These are the following: SST, air–sea flux parameterizations, 1D OML model, 3D PWP model, and latent heat flux < 0 over water.

(ii) Sensitivity to SST

To quantify the maximum impact of the ahead-of-eye-center SST cooling on storm intensity, the control run using a static warm prestorm SST (RTG-HR SST) is compared to a simulation using static observed cold poststorm SSTs. For this cold SST, the 29–31 August 2011 3-day coldest dark-pixel SST composite (described above) is used (Fig. 3e). According to underwater glider and NDBC buoy observations along Irene's entire MAB track (Fig. 1), almost all of the SST cooling in the MAB occurred ahead of Irene's eye center (Figs. 2c–f). The SAB also experienced ahead-of-eye-center SST cooling, but values are on the order of 1°C or less (Figs. 2a,b). Also, the model simulations include only 6 h of storm presence over the SAB. Therefore, the SST simulations described above quantify the sensitivity of Irene to ahead-of-eye-center cooling that occurred only in the MAB.

(iii) Sensitivity to air–sea flux parameterizations

The bulk formulas for sensible and latent heat fluxes are listed above in the buoy heat flux description. The following is the equation for momentum flux:

$$\text{Momentum flux:} \quad \tau = -\rho C_D U^2, \tag{3}$$

where ρ is density of air, C_D is drag coefficient, and U is 10-m wind speed.

Three options exist in ARW version 3.0 and later for air–sea flux parameterizations (WRF namelist option isftcflx = 0, 1, and 2). These parameterization options change the momentum (z_0), sensible heat (z_T), and latent heat (z_Q) roughness lengths in the following equations for drag, sensible heat, and latent heat coefficients:

$$\text{Drag coefficient:} \quad C_D = \kappa^2/[\ln(z_{\text{ref}}/z_0)]^2, \tag{4}$$

$$\text{Sensible heat coefficient:} \quad C_H = (C_D^{1/2})[\kappa/\ln(z_{\text{ref}}/z_T)], \tag{5}$$

$$\text{Latent heat coefficient:} \quad C_Q = (C_D^{1/2})[\kappa/\ln(z_{\text{ref}}/z_Q)], \tag{6}$$

where κ is the von Kármán constant and z_{ref} is a reference height (usually 10 m).

The reader is encouraged to refer to Green and Zhang (2013) for a detailed look at the impact of isftcflx = 0, 1, and 2 on roughness lengths, exchange coefficients, and exchange coefficient ratios C_H/C_D, C_Q/C_D, and C_K/C_D, where $C_K = C_H + C_Q$. Some key points from their paper are that, at wind speeds of $33\,\text{m}\,\text{s}^{-1}$ or greater, isftcflx = 1 has the largest C_K/C_D ratio and shares with isftcflx = 2 the lowest C_D. As a result, they found that for Hurricane Katrina (2005), using isftcflx = 1 produced the most intense storm in terms of minimum SLP and maximum winds.

Therefore, our SST sensitivity effectively changes the variables θ_{sfc} and q_{sfc} in Eqs. (1)–(3) above, while our air–sea flux parameterization sensitivities change the equations for the momentum, sensible heat, and latent heat coefficients [Eqs. (4)–(6)] going into the respective flux Eqs. (1)– (3). Because isftcflx = 1 and isftcflx = 2 both include a term for dissipative heating and isftcflx = 0 does not in WRFv3.4 (Green and Zhang 2013), the air–sea flux parameterization sensitivity between isftcflx = 0 and 1, and between isftcflx = 0 and 2 also test the effect of turning on and off dissipative heating in the model. Although the dissipative heating term was removed as of WRFv3.7.1 due to controversy within the wind-wave modeling community, dissipative heating is still considered an important issue in high wind regimes, and it has been shown to be capable of increasing TC intensity by 10%–20% as measured by maximum sustained surface wind speeds (Liu et al. 2011).

For the air–sea flux parameterization sensitivities, simulations are conducted with isftcflx = 0, 1, and 2 using both the warm (control) and cold SST boundary conditions.

(iv) Sensitivities coupling WRF to 1D and 3D ocean models

Pollard et al.'s [1972; described in WRF context by Davis et al. (2008)] 1D ocean mixed layer model was used to test the sensitivity of Irene to 1D ocean processes. Two different initializations of the 1D ocean model were initially performed: 1) *coastal stratification*: initializing the mixed layer depth (MLD) everywhere to 10 m and the slope of the thermocline everywhere to $1.6°\text{C}\,\text{m}^{-1}$ according to glider RU16's observations (Glenn et al. 2016), and 2) *HYCOM stratification:* initializing the MLD and top 200-m mean ocean temperature spatially using HYCOM. However, there were major issues using both of these options to accurately determine sensitivity to 1D ocean processes. The issue with the first option is its requirement that the initialization is nonvariant in space; the Gulf Stream, which is included in the model domain, is very warm and well mixed down to 100–200 m (Fuglister and Worthington 1951). Initializing the Gulf Stream MLD to 10 m would result in cold water only 10 m deep being quickly mixed to the surface. The issue with the second option of using HYCOM is that due to its poor initialization, the HYCOM simulation used here did not resolve the abundant bottom cold water over the MAB continental shelf that was observed by glider RU16 prior to Irene (Glenn et al. 2016) and that is typical of the summer MAB cold pool (Houghton et al. 1982).

The 3D ocean PWP model (Price et al. 1986, 1994) was used to test the sensitivity of Irene to 3D open-ocean, deep-water processes, including Ekman pumping–upwelling and mixing across the base of the mixed layer caused by shear instability. While the 3D PWP model contains 3D dynamics and is fully coupled to WRF, it does not have bathymetry or a coastline (Lee and Chen 2014); water depth is uniform across the model grid. Therefore, any 3D PWP model run will not simulate the coastal baroclinic processes that were observed in Irene over the MAB continental shelf due to the presence of the coastline (Glenn et al. 2016). In addition, like in the 1D ocean model, initialization must be nonvariant in x–y space.

To ameliorate the issue with mixing the Gulf Stream and still conduct sensitivities on nonstatic 1D and 3D ocean processes, an initialization time 12 h later—1800

UTC 27 August instead of 0600 UTC 27 August—was used for the WRF-1D OML and WRF-3D PWP simulations, because Irene by then was already north of the Gulf Stream and thus would not interact with it, and still south of the MAB (see Fig. 1). Four sensitivities with this initialization time were tested with various configurations of the 1D OML and 3D PWP models. First, the 1D OML model was initialized using the prestorm coldest dark-pixel composite for SST and with a MLD of 200 m, to simulate isothermal warm ocean conditions and the effect of air–sea heat fluxes. Second, the 1D OML model was initialized everywhere using RU16 observed stratification, as described above; this simulated the effect of 1D deep-water mixing processes (the 1D OML model does not have an ocean bottom). Third, the 3D PWP model was initialized everywhere using the same RU16 observed stratification that was used for the 1D OML model simulation but with 400-m full water column depth, to simulate the effect of 3D deep-water processes. Fourth, the 3D PWP model was initialized everywhere using HWRF-HYCOM stratification at the RU16 glider location at 0000 UTC 26 August and again with 400-m full water column depth, to test the sensitivity to a poor ocean initialization. These simulations are summarized in Table 1.

(v) Sensitivity to latent heat flux < 0 over water

In the WRF surface layer scheme code, a switch exists that disallows any latent heat flux $< 0\,\mathrm{W\,m^{-2}}$. (There is also a switch that disallows any sensible heat flux less than $-250\,\mathrm{W\,m^{-2}}$.) WRF convention for negative heat flux is downward, or from atmosphere to land or water surface. This sensitivity involves removing the switch disallowing negative latent heat flux. This switch removal only results in changes in latent heat flux over water, because the subsequent WRF land surface scheme modifies fluxes and already allows for latent heat flux to be negative over land.

3. Results

Sensitivity tests

1) MOTIVATION

Hurricane Irene developed into a tropical storm just east of the Lesser Antilles on 20 August 2011, strengthening into a category-1 hurricane just after landfall in Puerto Rico 2 days later. Irene continued to move northwest over the Bahamas, intensifying into a category-3 hurricane on 23 August. Soon after, a partial eyewall replacement cycle occurred and Irene was never able to fully recover, eventually weakening into a category-1 hurricane on 27 August as it neared NC. Irene remained at hurricane strength over the MAB until it made landfall in NJ as a tropical storm at 0935 UTC 28 August. As stated above, the NHC final report on Irene (Avila and Cangialosi 2012) conveyed a ''consistent high bias [in the forecasts] during the U.S. watch–warning period,'' which consisted of the time period when Irene was traversing the SAB and MAB (Avila and Cangialosi 2012).

The coastal track of Irene (Fig. 1) over the relatively highly instrumented mid-Atlantic allowed for a comprehensive look into the details and timing of coastal ocean cooling. All in-water instruments employed here provide fixed point data within 70 km from Irene's eye, including station-keeping RU16, providing an Eulerian look at the ahead-of-eye-center cooling occurring near the storm's inner core. RU16 profiled the entire column of water over the MAB continental shelf, providing a view of the full evolution of the upper-ocean response. The rapid two-layer shear-induced coastal mixing process that led to ahead-of-eye-center cooling is described in detail in Glenn et al. (2016).

The buoys in the SAB (41037 and 41036) documented ~1°C SST cooling in the storm's front half, with total SST cooling less than 2°C (Fig. 2). Eye passage at each buoy is indicated by a vertical dashed line and represents the minimum sea level pressure (SLP) observed. For RU16, minimum SLP taken from the nearby WeatherFlow Tuckerton coastal meteorological station was used to calculate eye passage time, and for 44100, linearly interpolated NHC best-track data was used for eye passage time. In contrast to the SAB, the MAB buoys (44100, 44009, and 44065) as well as RU16 observed 4°–6°C SST ahead-of-eye-center cooling, with only slight cooling after eye passage of less than 2°C (Fig. 2). Therefore, the buoys and glider provide detailed evidence that significant ahead-of-eye-center cooling—76%–98% of the total observed in-storm cooling (Glenn et al. 2016)—occurred in the MAB.

While the buoys provided information on the timing of SST cooling, the high-resolution coldest dark-pixel SST composite showed the spatial variability of the cooling, revealing that the cooling was not captured by basic satellite products and some models used to forecast hurricane intensity. The improved 3-day coldest dark-pixel SST composite showed prestorm (24–26 August 2011; Fig. 3a) and poststorm (29–31 August 2011; Fig. 3e) SST conditions along the U.S. East Coast. SST cooling to the right of the storm track in the SAB approached 2°C, and in the MAB approached 11°C at the mouth of the Hudson Canyon (Fig. 3i). Under the TC inner core, within 25 km of Irene's track, SST cooling in the SAB ranged from 0.5° to 1.5°C, while in the MAB cooling ranged from ~2° to ~4°C (Fig. 3m). It is important

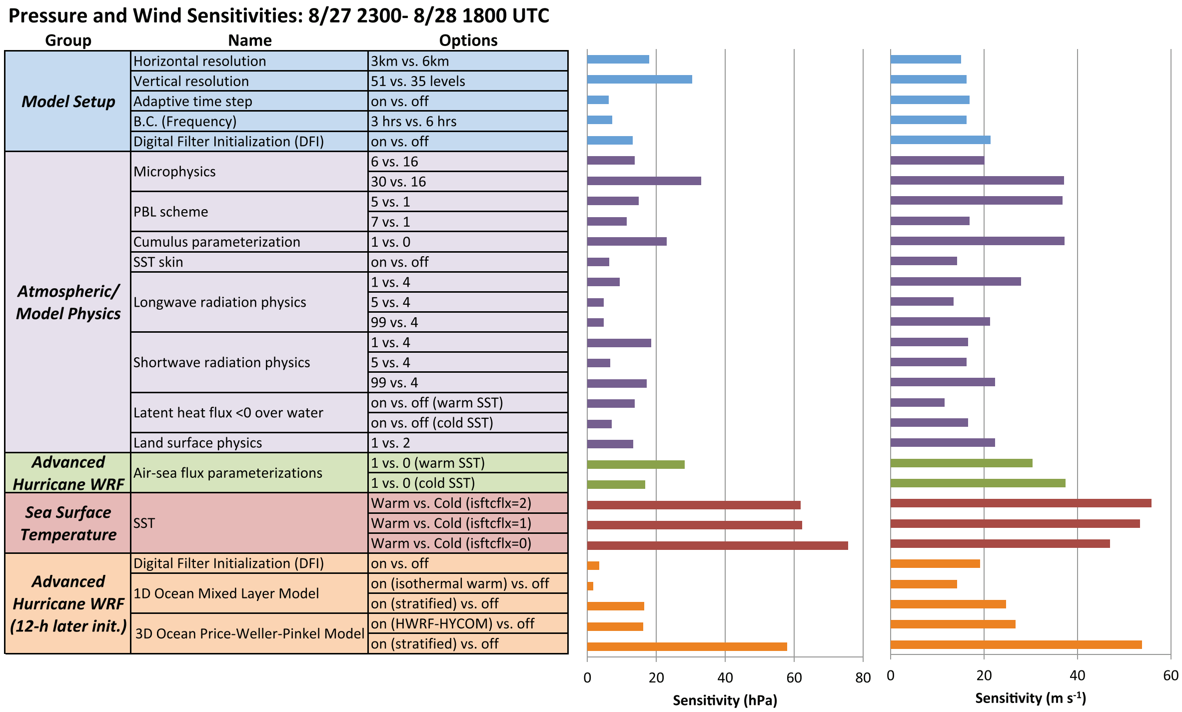

FIG. 4. Cumulative model sensitivity results from 2300 UTC 27 Aug 2011 (entrance of Irene's eye center over MAB) to 1800 UTC 28 Aug 2011 (end of simulation). (left) Group, name, and WRF namelist options with control run namelist option listed last for each sensitivity. (middle) Minimum sea level pressure (hPa) sensitivity and (right) maximum sustained 10-m wind (m s^{-1}) sensitivity.

to note that the SST composite from 3 days after storm passage was used for poststorm conditions. There were, indeed, large cloud-free areas over the MAB 1 day after storm passage, but it took an additional 2 days to fill in the remaining areas over the MAB and attain a cloud-free composite for input into WRF. In the persistently clear areas during this 3-day stretch, no additional SST cooling occurred during the poststorm inertial mixing period after the direct storm forcing.

RTG-HR SST pre- (26 August; Fig. 3b), poststorm (31 August; Fig. 3f), and difference (31 August minus 26 August; Fig. 3j) plots show spatially similar cooling patterns to the coldest dark-pixel SST composite, but cooling magnitudes are lower, especially to the right of the storm track in both the SAB and MAB (Fig. 3j). Similarly, there was no significant additional MAB cooling in RTG-HR SST from 1 day after (not shown) to 3 days after (Fig. 3f) storm passage.

HWRF-POM (Figs. 3c,g,k,o) and HWRF-HYCOM (Figs. 3d,h,l,p) model results are also shown as examples of coupled ocean–atmosphere hurricane models. Prestorm (0000 UTC 26 August) and poststorm (0000 UTC 31 August) times for both model results are coincident with the coldest dark-pixel SST composite and RTG-HR SST composite times, and both model simulations shown are initialized at 0000 UTC 26 August. Therefore, the poststorm SST conditions are 5-day forecasts in both models. Again, there are no significant differences in MAB SST cooling between immediately after and 3 days after Irene's passage in both HWRF-POM and HWRF-HYCOM. Like RTG-HR poststorm SST (Fig. 3f), HWRF-POM (Fig. 3g) and HWRF-HYCOM (Fig. 3h) poststorm SSTs in the MAB are several degrees too warm—the coldest SSTs are 20°–23°C, where they should be 17°–20°C. Therefore, these coupled atmosphere–ocean models designed to predict TCs did not fully capture the magnitude of SST cooling in the MAB that resulted from Hurricane Irene.

2) SENSITIVITY RESULTS

Over 140 WRF simulations were conducted to test the sensitivity of modeled Irene intensity to the observed ahead-of-eye-center cooling and to other model parameters. Only those simulations with tracks within 50 km of NHC best track were retained, leaving 30 simulations (Table 1).

To quantify cumulative model sensitivities, the sum of the absolute value of the hourly difference between the control run minimum SLP (and maximum sustained 10-m winds) and experimental run minimum SLP (and maximum 10-m winds) was taken, but only from 2300 UTC 27 August to the end of the simulation.

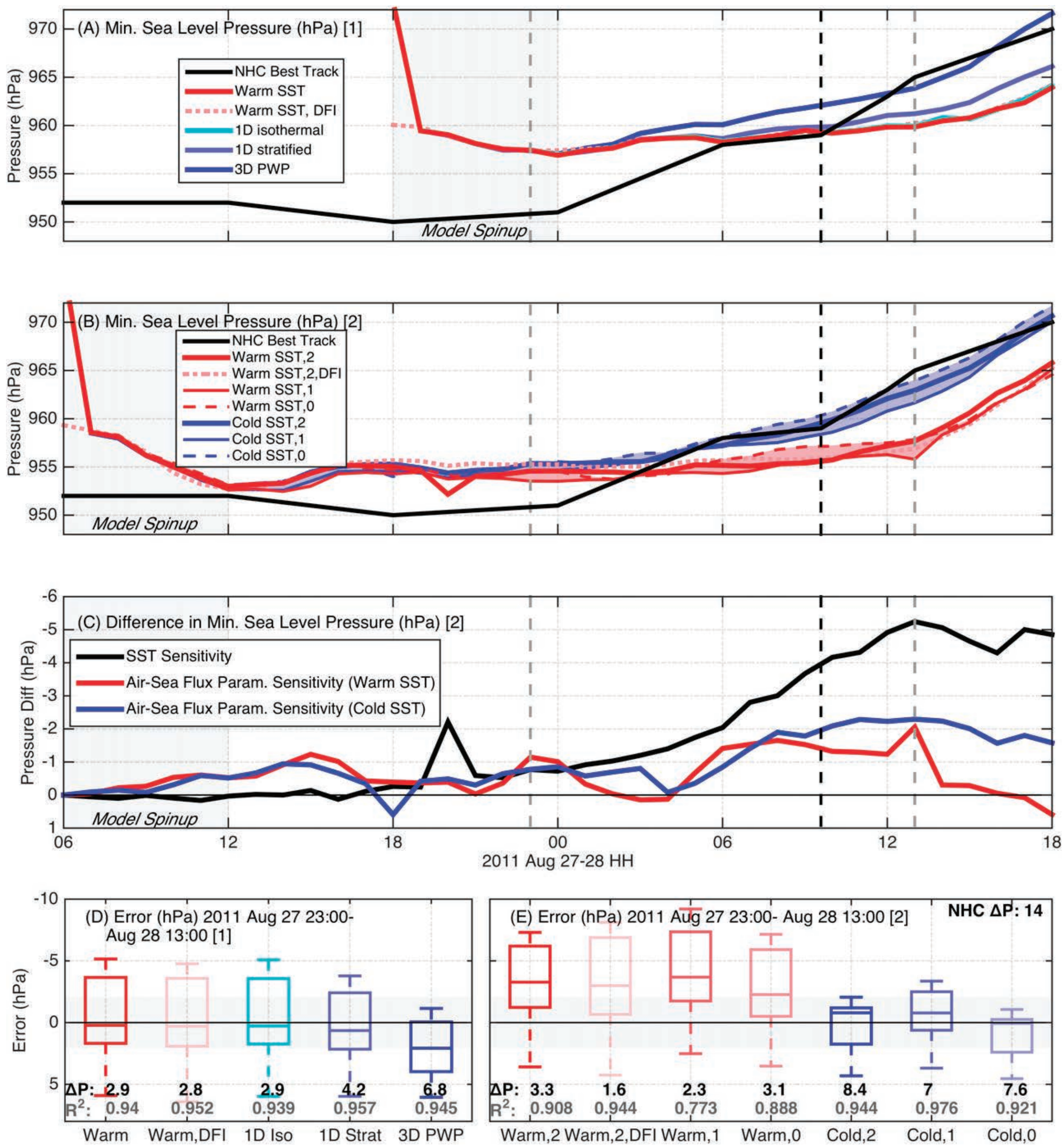

FIG. 5. Minimum SLP (hPa) time series for (a) WRF nonstatic ocean runs with NHC best track in black, warm SST in red, warm SST with DFI in dotted red, 1D ocean with isothermal warm initialization in cyan, 1D ocean with stratified initialization in light blue, and 3D PWP ocean in dark blue. (b) As in (a), but for WRF static ocean runs, with warm SST with isftcflx = 2 in red, warm SST with DFI in dotted red, warm SST with isftcflx = 1 in thin red, warm SST with isftcflx = 0 in dashed red, the three cold SST runs the same as warm SST but in blue lines. Vertical dashed gray lines depict start and end of Irene's presence over the MAB (2300 UTC 27 Aug–1300 UTC 28 Aug), with vertical dashed black line depicting Irene's landfall in NJ. Model spinup indicated as first 6 simulation hours with gray box. Difference in central pressure (c) between WRF static ocean warm and cold SST runs with isftcflx = 2 in black, between isftcflx = 0 and 1 for warm SST in red, and between isftcflx = 0 and 1 for cold SST in blue. (d) Box-and-whisker plots of errors vs NHC best-track data for WRF static ocean runs and (e) nonstatic ocean during Irene's MAB presence with R^2 values in gray and ΔP between 2300 UTC 27 Aug and 1300 UTC 28 Aug in black. NHC best-track ΔP in top right of (e), and uncertainty in pressure from NHC best-track data indicated by gray horizontal ribbon ±0 in (d) and (e).

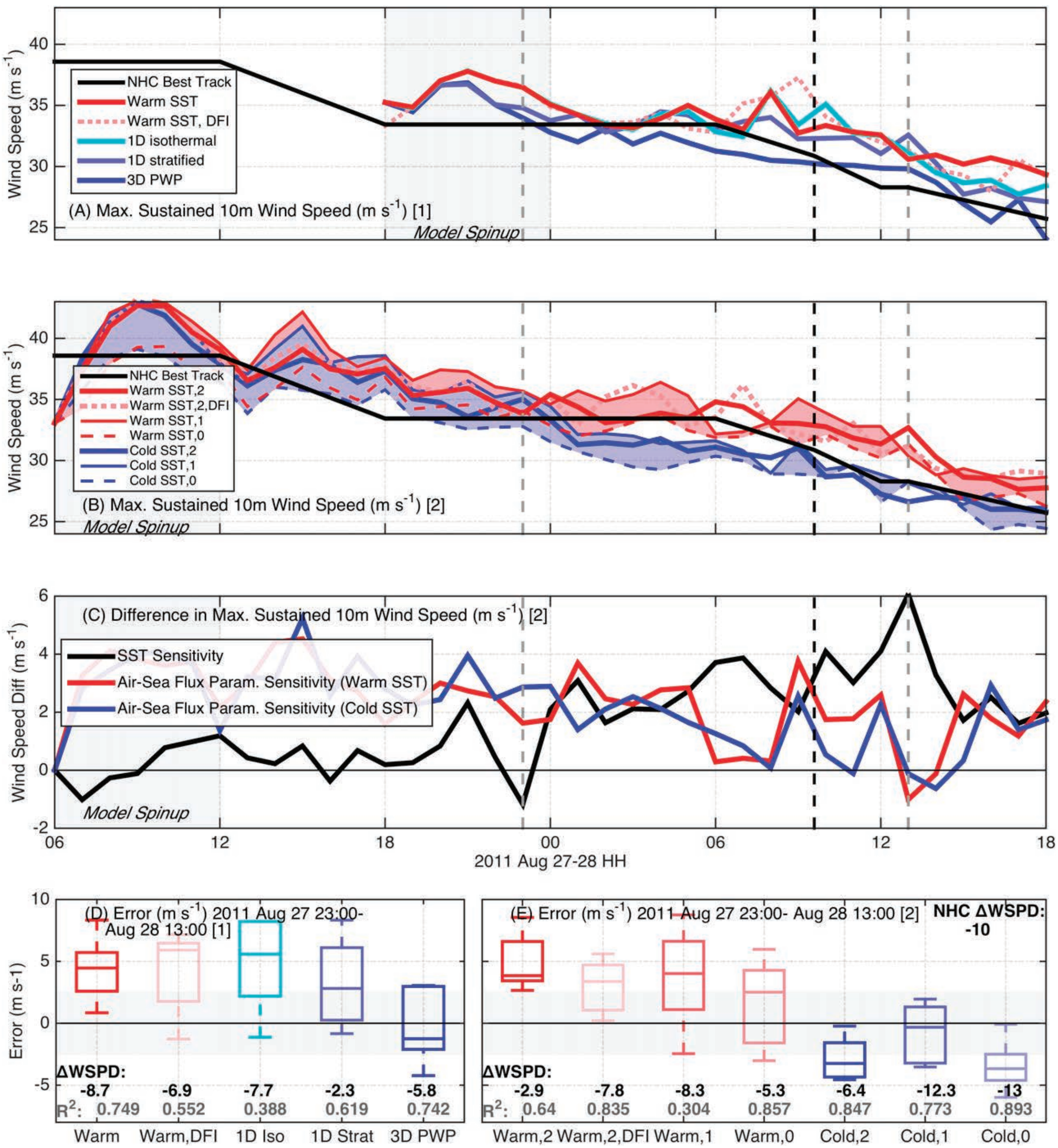

FIG. 6. As in Fig. 5, but for maximum sustained 10-m winds ($m\,s^{-1}$).

This confines the sensitivity to the time period of Irene's presence over the MAB and thereafter. The equation is as follows:

$$\sum_{i=2300\mathrm{UTC27Aug}}^{i=1800\mathrm{UTC28Aug}} |\min \mathrm{SLP}[\mathrm{control}(\mathrm{at\ hour}\ i)] - \min \mathrm{SLP}[\exp(\mathrm{at\ hour}\ i)]|. \quad (7)$$

Figure 4 shows the model sensitivities as measured by minimum SLP (left) and maximum 10-m wind speeds (right). Over the 19 h calculated, the three largest sensitivities when considering both intensity metrics were due to SST with the three WRF air–sea flux parameterization options (isftcflx = 0, 1, 2). On average, for SST over the three options, pressure sensitivity was 66.6 hPa over the 19 h (3.5 $hPa\,h^{-1}$) and wind sensitivity was 52.0 $m\,s^{-1}$ over

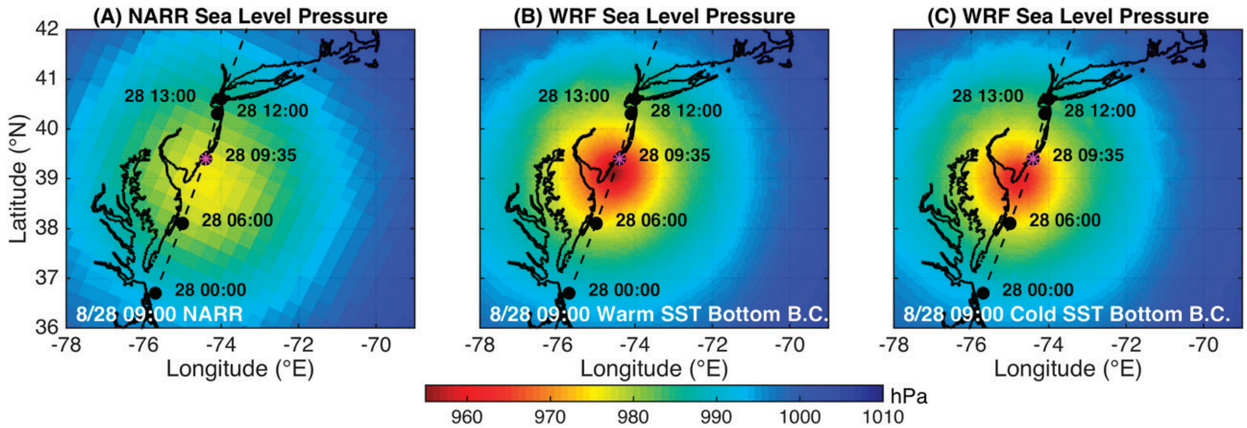

FIG. 7. Spatial plot of SLP (hPa) at 0900 UTC 28 Aug just prior to NJ landfall, with Irene's NHC best track in dashed black: (a) NARR, (b) WRF with warm SST bottom boundary conditions, and (c) WRF with cold SST bottom boundary conditions.

the 19 h (2.7 m s^{-1} h^{-1}). Sensitivity to 3D open-ocean, deep-water processes through the use of the 3D PWP model was comparatively large (Fig. 4). However, caution must be taken with this simulation because the 3D PWP model does not have a coastline and bathymetry, and ended up producing more in storm SST cooling than was observed by glider RU16 (not shown).

The Advanced Hurricane WRF sensitivities for the 12-h later initialization (1D warm isothermal, 1D stratified, and 3D PWP) are presented in time series in Figs. 5a and 6a. The black line indicates NHC best-track estimates of intensity, while the red solid line indicates the fixed prestorm warm SST control run. Note that minimum SLP at initialization is about 973 hPa whereas NHC best track indicates 950 hPa at that time; this difference is due to issues with WRF's vortex initialization (Zambon et al. 2014a), and it only takes 6 h for the model to adjust and drop 13 hPa to 959 hPa. The dotted red line indicates a sensitivity with digital filter initialization (DFI) turned on, which removes ambient noise at initialization. DFI resulted in initial min SLP (maximum winds) to be ~960 hPa (33 m s^{-1})—a reduction of 12 hPa (2 m s^{-1})—with downstream sensitivity negligible, demonstrating that the seemingly significant initialization issue likely has little significant effect on downstream intensity. The remaining sensitivities in Figs. 5a and 6a are the 1D ocean with isothermal warm initial conditions (effect of air–sea fluxes) in cyan, the 1D ocean with stratified initial conditions (effect of 1D mixing processes) in light blue, and the 3D PWP deep ocean with stratified initial conditions (effect of 3D deep-water processes) in dark blue. The air–sea fluxes have a negligible effect on intensity, while the 1D ocean mixing and 3D deep-water processes have a gradually larger negative effect on intensity.

The air–sea flux parameterization sensitivities with the standard initialization time are shown in Figs. 5b and 6b. Again, the black line indicates NHC best-track estimates of intensity, and the simulations have issues with vortex initialization. The DFI sensitivity for this set of runs (dotted red) again effectively resolves this issue. The red lines indicate the three WRF air–sea flux parameterization options using the warm prestorm SST with the area between the isftcflx = 0 and 1 options shaded in red, and the blue lines and blue shading indicate the same but for the cold poststorm SST. Consistent with the results found by Green and Zhang (2013), isftcflx=1 produced the most intense storm using both minimum SLP and maximum winds intensity metrics, for both the warm prestorm SST and cold poststorm SST; again, isftcflx = 1 has the largest C_K/C_D ratio and shares with isftcflx = 2 the lowest C_D.

Figures 5c and 6c show the time evolution of three sensitivities: 1) SST, warm versus cold (black), 2) air–sea flux parameterization with warm SST, isftcflx = 0 versus 1 (red), and 3) air–sea flux parameterization with cold SST, isftcflx = 0 versus 1 (blue). For both intensity metrics, sensitivity to SST gradually increases from about equal to flux parameterization sensitivity upon entrance to the MAB (first gray vertical dashed line) to almost triple it (~5 hPa vs ~2 hPa, 6 m s^{-1} vs ~0–2 m s^{-1}) upon exit out of the MAB (second gray vertical dashed line). Finally, Figs. 5d,e and 6d,e show box-and-whisker plots of simulation error as compared to NHC best track, only during MAB presence (2300 UTC 27 August–1300 UTC 28 August), with uncertainty in NHC best-track data (Torn and Snyder 2012; Landsea and Franklin 2013) shown with gray shading. Correlation coefficient (R^2) values are shown at the bottom in gray, and ΔP and ΔWSPD are shown in black, with NHC ΔP and ΔWSPD values shown in the top right of Figs. 5e and 6e. These delta values, a measure of weakening rate, are calculated by taking the difference in

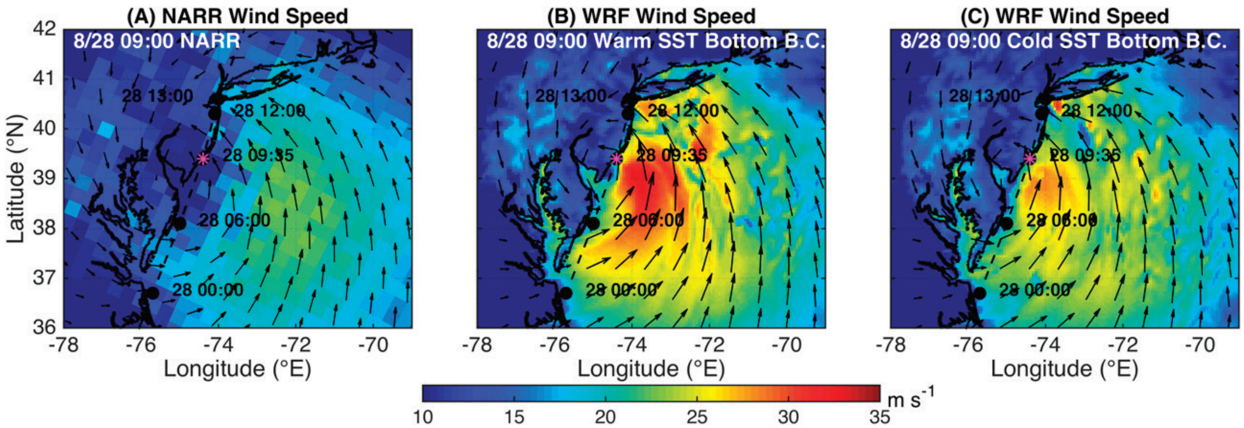

FIG. 8. As in Fig. 7, but for 10-m wind speeds and vectors (m s^{-1}).

pressure and wind speed between exit out of, and entrance into, the MAB.

Although the errors in minimum SLP for the simulations in Fig. 5d are low and the R^2 values are high, the errors in maximum winds are higher and the R^2 values are much lower in Fig. 6d. The four warm SST simulations (Figs. 5e and 6e) have a minimum SLP too low and maximum wind speed too high, while the three cold SST simulations have a minimum SLP closer to NHC best track and a maximum wind speed slightly lower than NHC best track. Because of the high uncertainty (4–5 m s^{-1} for nonmajor hurricanes) associated with NHC best-track wind estimates (Torn and Snyder 2012; Landsea and Franklin 2013), errors from the pressure metric are used. Minimum SLP is also a more certain measure of intensity because it is always at the TC eye center. The highest R^2 values and the ΔP values closest to NHC best-track ΔP were found with the three cold SST simulations. This indicates that a more accurate representation of the ahead-of-eye-center cooling via fixed cold poststorm SSTs lowers the high bias in our model's prediction of intensity. Further, the low ΔP–weakening rate attained using the 3D deep-water PWP simulation (ΔP: 6.8 hPa; rate: 0.5 hPa h^{-1})—which again did not have a coastline or appropriately shallow ocean bottom—suggests that coastal baroclinic processes were responsible for the cooling that contributed to Irene's observed larger ΔP–weakening rate (ΔP: 14 hPa; rate: 1 hPa h^{-1}). These coastal baroclinic processes, which are investigated in detail in Glenn et al. (2016), can be summarized as follows:

(i) front half of Irene's winds were onshore toward the mid-Atlantic coastline;
(ii) ocean currents in the surface layer above the sharp, shallow thermocline were aligned with the winds and also directed onshore over the MAB continental shelf;
(iii) water piled up along the mid-Atlantic coast, setting up a pressure gradient force directed offshore;
(iv) responding to the coastal piling of water, currents in the bottom layer below the sharp, shallow thermocline were directed offshore; and
(v) opposing onshore surface layer and offshore bottom layer currents led to large shear across the thermocline and turbulent entrainment of abundant bottom cold water to the surface; this enhancement of shear and SST cooling occurred in the front half of Irene as long as the winds were directed onshore (hence the term "ahead-of-eye-center cooling").

Therefore, without the coastline in simulations, 1) the coastal piling of water, 2) the offshore bottom counterflow, 3) the enhanced shear at the thermocline, and 4) the rapid surface cooling would not be simulated.

Finally, the deep ocean simulations using the 1D ocean and the 3D ocean PWP model initialized with stratified conditions produced 32% and 56% of the in-storm ahead-of-eye-center cooling at the RU16 glider location, respectively (not shown). Meanwhile, 76% of the observed in-storm cooling at the RU16 glider location—and 82%, 90%, and 98% at 44009, 44065, and 44100,

TABLE 2. Radius of maximum 10-m winds (in km). Warm SST and cold SST simulations compared to b-deck data from the ATCF system database.

	Radius of max wind (km)		
Time	b-deck	Warm SST	Cold SST
0600 UTC 27 Aug	111	107	107
1200 UTC 27 Aug	83	80	80
1800 UTC 27 Aug	83	102	104
0000 UTC 28 Aug	83	72	85
0600 UTC 28 Aug	185	74	74
1200 UTC 28 Aug	185	213	280

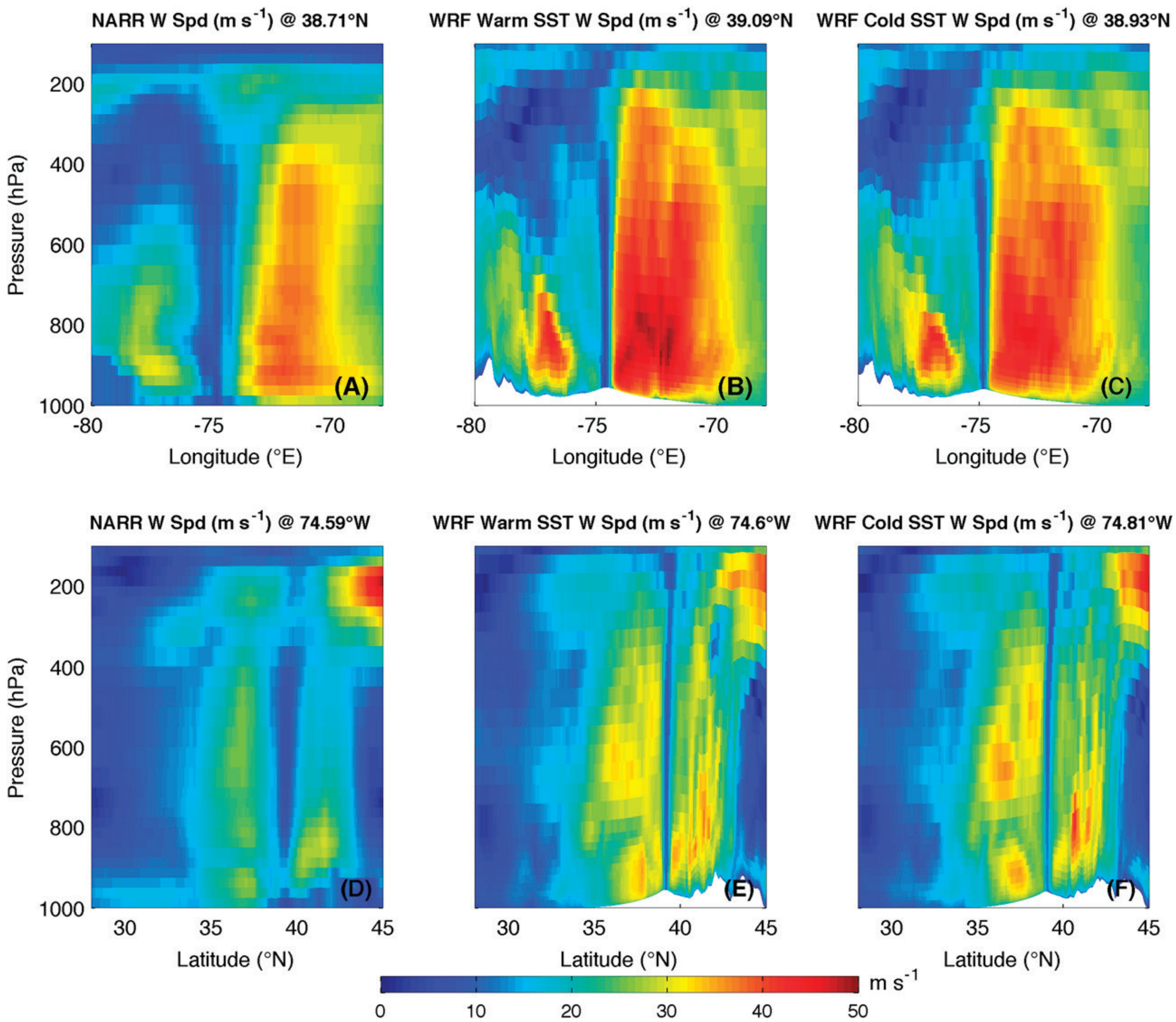

FIG. 9. Vertical cross sections of wind speed through Irene's eye at 0900 UTC 28 Aug, just prior to NJ landfall. (a)–(c) west–east cross sections and (d)–(f) south–north cross sections. For each, the latitude and longitude of eye is determined by locating the minimum SLP for (a),(d) NARR; (b),(e) WRF with warm SST bottom boundary conditions; and (c),(f) WRF with cold SST bottom boundary conditions.

respectively—occurred ahead of the eye center (Fig. 2), further indicating that the nonsimulated coastal baroclinic processes enhanced the percentage of ahead-of-eye-center cooling in Irene.

How sensitive are Irene's size and structure to SST? To spatially evaluate WRF results, NARR SLP and winds are used (Fig. 7). Spatial plots of SLP are shown from NARR (Fig. 7a), WRF warm SST (Fig. 7b), and WRF cold SST (Fig. 7c) runs, at just before NJ landfall. Only slight differences exist between WRF simulations, mainly in Irene's central pressure (warm SST: 955.4 hPa, cold SST: 959.1 hPa); overall size and structure of the storm is very similar between runs. The WRF simulations also compare well in size and shape to NARR SLP, but do not in central pressure (NARR: 975.9 hPa). This is likely due to lower NARR resolution, as the NHC best-track estimate of central pressure at landfall, only 35 min after, is 959 hPa. NARR, at 32-km resolution, is far too coarse to resolve inner-eyewall processes (Gentry and Lackmann 2010; Hill and Lackmann 2009).

Similar results are shown in spatial plots of 10-m winds (Fig. 8). General size and structure, especially over land, agree well among NARR, warm SST, and cold SST runs, but major differences exist over the MAB waters. NARR shows a maximum wind speed of 22.7 m s^{-1}, whereas the WRF warm SST (33.0 m s^{-1}) and cold SST (31.0 m s^{-1}) simulations are much closer to NHC best-track estimate of 30.9 m s^{-1}. Besides a general overall reduction in wind speed in the cold SST simulation, little difference is noted in size of Irene between warm and

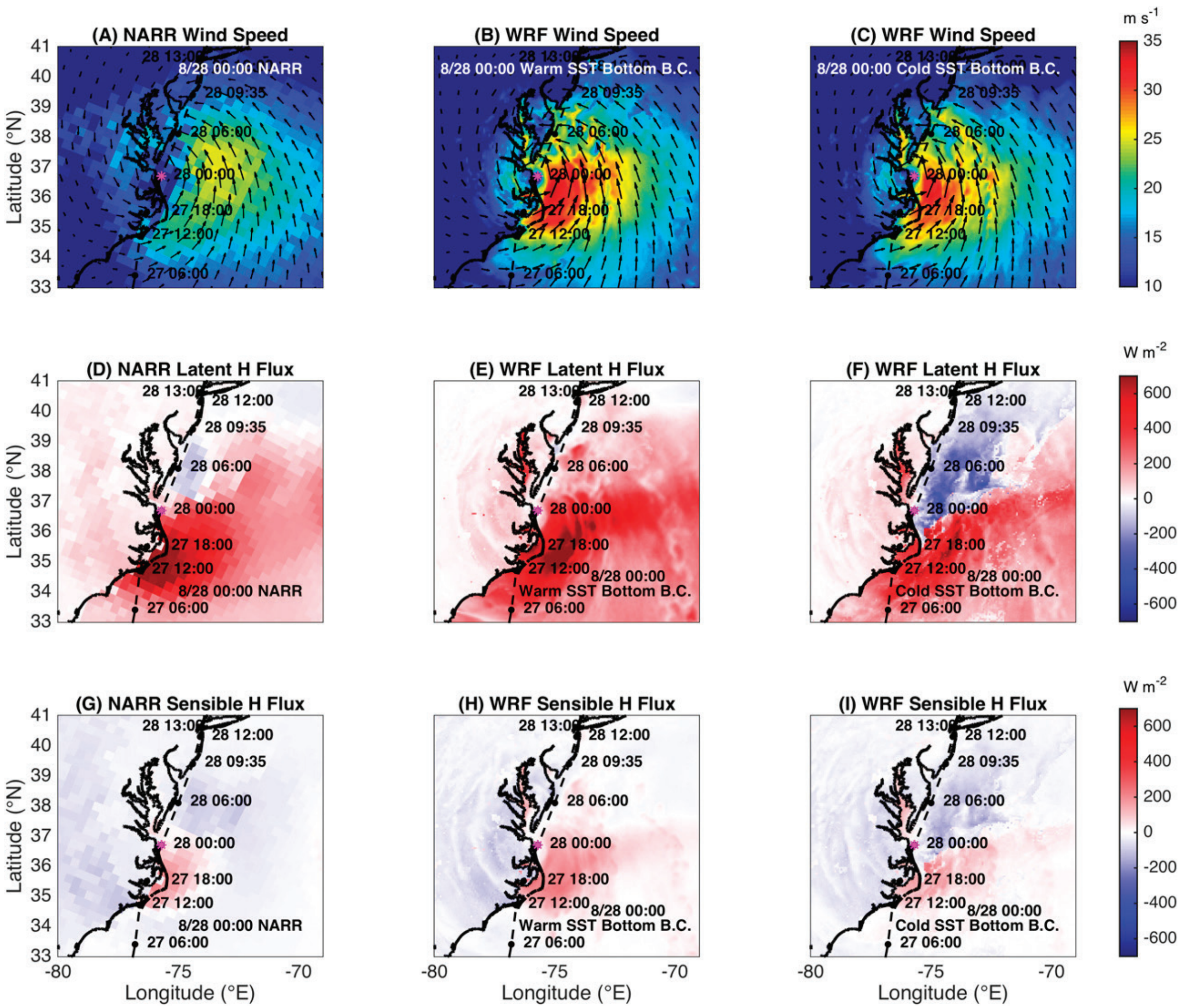

FIG. 10. (a)–(c) Spatial plots of 10-m wind speeds and vectors (m s^{-1}), (d)–(f) latent heat flux at the surface (W m^{-2}), and (g)–(i) sensible heat flux at the surface (W m^{-2}), at 0000 UTC 28 Aug. Fluxes are positive directed from water or land to atmosphere. (a),(d),(g) NARR is shown with fluxes shown as 3-h averages ending at 0000 UTC 28 Aug; (b),(e),(h) WRF is shown with warm SST bottom boundary conditions, with fluxes shown as instantaneous; and (c),(f),(i) WRF is shown with cold SST bottom boundary conditions (with negative latent heat flux allowed), with fluxes also shown as instantaneous.

cold SST. This is verified by a radius of maximum wind (RMW) comparison between the warm and cold SST simulations and b-deck data from the Automated Tropical Cyclone Forecast [ATCF; Sampson and Schrader (2000)] system database (Table 2). The data files within ATCF are within three decks known as a, b, and f decks. The b-deck data for Irene, available every 6 h, shows good agreement with both warm and cold SST simulations, with 13 km or less difference in RMW between warm and cold SST for the first 24 h of simulation, and 21 km or less difference in RMW between model and "observed" b-deck radii for the first 18 h of simulation. At 1200 UTC 28 August, the cold SST simulation shows a much larger RMW, likely due to the strongest winds occurring in an outer band thunderstorm and indicating more rapid enlargement of storm size.

Vertical east–west (Figs. 9a–c) and north–south (Figs. 9d–f) cross sections of wind speeds through the eye of Irene at 0900 UTC 28 August, just before landfall, tell the same story—that NARR has issues reproducing the higher wind speeds not only at 10 m but through the entire atmosphere, and that there are only slight differences in wind speed structure between the warm and cold SST simulations. Both simulations show an asymmetric storm west–east with the core of the strongest winds over water, on the right side of the eye, extending all the way up to the tropopause at about 200 hPa (Figs. 9b and 9c), with the warm SST run showing much higher wind speeds

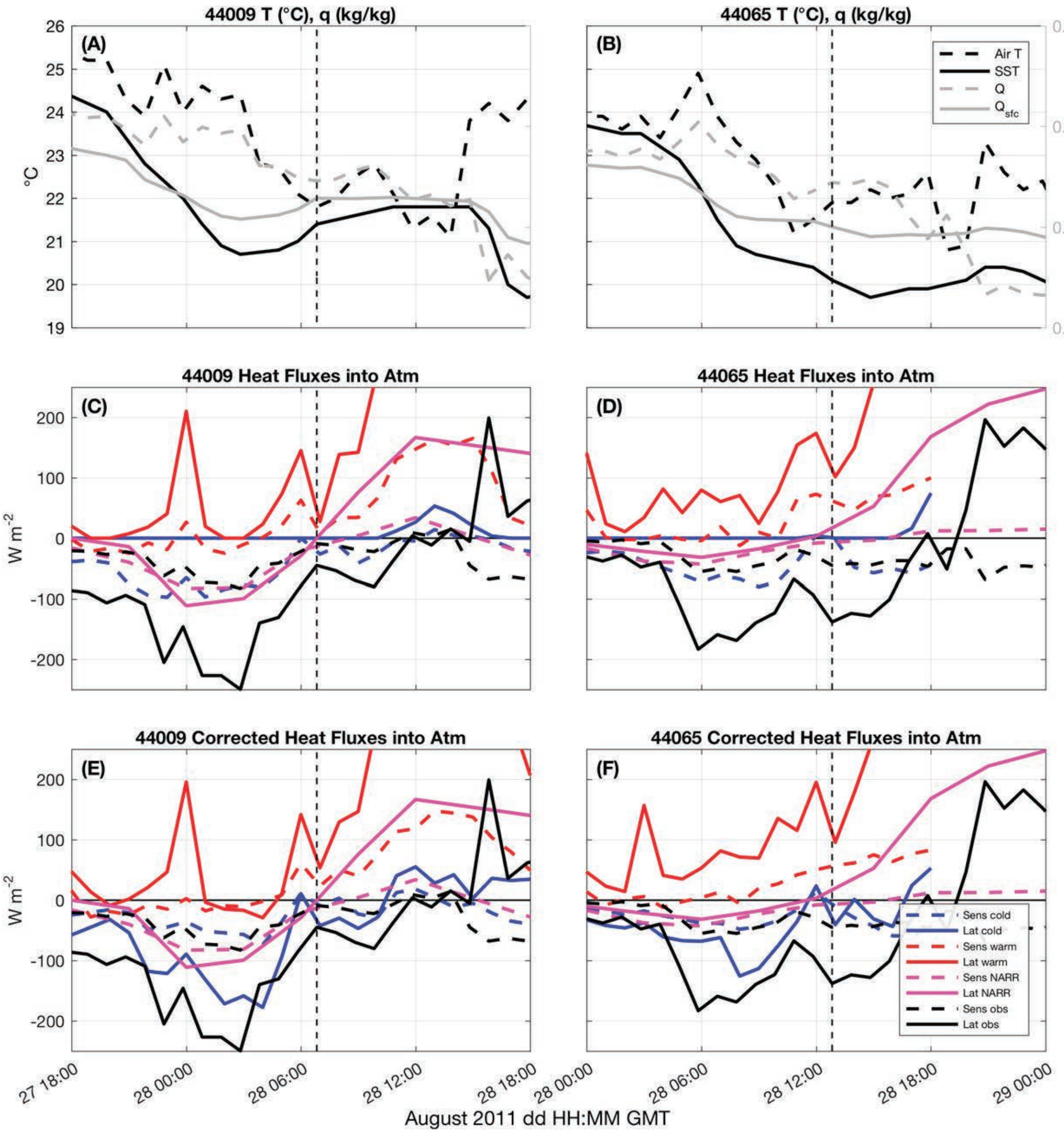

FIG. 11. Time series of air temperature (°C, black dashed), near-surface water temperature (°C, black solid), air specific humidity (kg kg^{-1}, gray dashed), and specific humidity at water surface (kg kg^{-1}, gray solid) at buoy (a) 44009 and (b) 44065, with vertical dashed line indicating timing of eye passage by that buoy (note the time axes are different for each buoy). (c) Sensible (dashed) and (d) latent (solid) heat fluxes (W m^{-2}) are shown for observed (black), NARR (magenta, 3-h flux averages), warm SST (red), and cold SST (blue). Fluxes are positive from ocean to atmosphere. (e),(f) The same fluxes are shown for observed and NARR as in (c),(d), but WRF fluxes are corrected to allow for negative latent heat flux over water.

from ~950 to 700 hPa. On the left side of the eye, the strongest winds extend only up to 700–800 hPa and the core is much narrower from west to east. The north–south cross sections show a more symmetric storm, as well as the outer edges of the jet stream at about 200 hPa and 45°N.

Because air–sea heat fluxes drive convection, TC circulation, and thus resulting TC intensity, a closer look at the sensible and latent heat fluxes, specifically to determine just how sensitive they are to a change in SST, is warranted. The fluxes are plotted spatially at 0000 UTC 28 August in Fig. 10, and temporally at two MAB buoys in Fig. 11. The largest modeled latent and sensible heat fluxes correlate well spatially with the strongest winds in NARR, warm SST, and cold SST runs (Fig. 10).

However, there are large differences in both latent and sensible heat fluxes between the warm and cold SST runs, most notably over the MAB where a reverse in the sign of both latent and sensible heat flux occurs. In some locations over the MAB, the warm SST run shows a few hundred watts per meters squared in latent heat flux directed from the ocean to the atmosphere (Fig. 10e), whereas the cold SST run shows several hundred watts per meters squared in the opposite direction (Fig. 10f). NARR also shows slightly negative latent heat flux over the MAB (NARR fluxes are 3-h averages). Similar patterns are evident in sensible heat flux, but at a much smaller magnitude. It is again important to note that a negative latent heat flux over water—directed from the atmosphere to the ocean—is disallowed in WRF (similarly, sensible heat fluxes $< -250\,\mathrm{W\,m^{-2}}$ are also disallowed over water). What is shown for the cold SST (warm SST) run in Fig. 10 is the cold SST (warm SST) simulation from sensitivity number 19 (18) (Table 1), with latent heat flux < 0 allowed over water. When negative latent heat flux is not allowed, all negative latent heat fluxes (e.g., the blue areas in Fig. 10f) become zero (not shown).

The negative latent heat fluxes were also ''observed'' at both buoys at which they were calculated—44009 and 44065. At both buoys, for almost the entire times shown, air temperature was greater than SST—in some cases over 4.5°C warmer—and air specific humidity was greater than specific humidity at water surface (Figs. 11a,b). The largest temperature and specific humidity differences occurred either during or right at the end of the SST cooling at each buoy, and coincided with the largest calculated observed negative sensible heat fluxes (–50 to $-100\,\mathrm{W\,m^{-2}}$) and negative latent heat fluxes (-200 to $-250\,\mathrm{W\,m^{-2}}$) at both buoys (Figs. 11c,d). These negative values are in stark contrast to the positive enthalpy fluxes (latent + sensible heat fluxes) of $O(1000)$ $\mathrm{W\,m^{-2}}$ found under normal and rapid TC intensification scenarios (Lin et al. 2009; Jaimes and Shay 2015). At this time, NARR latent heat fluxes approached $-120\,\mathrm{W\,m^{-2}}$ at 44009 and $-40\,\mathrm{W\,m^{-2}}$ at 44065. The cold SST simulation shows latent heat fluxes zeroed out this whole time period (Figs. 11c,d), and approached $-180\,\mathrm{W\,m^{-2}}$ at 44009 and $-130\,\mathrm{W\,m^{-2}}$ at 44065 when negative latent heat fluxes are allowed (Figs. 11e,f). Meanwhile, the warm SST simulation shows latent heat fluxes with opposite sign, approaching $470\,\mathrm{W\,m^{-2}}$ toward the end of the simulation at 44009 and $530\,\mathrm{W\,m^{-2}}$ at 44065. Further, heat flux sensitivity to air–sea flux parameterizations was low, especially when compared to its sensitivity to warm versus cold SST. This evaluation of air–sea heat fluxes confirms that the cold SST simulation not only begins to resolve the negative latent heat fluxes that have been indicated by observations, but also approaches negative values that significantly affect storm intensity.

TABLE 3. Track error (in km) as compared to NHC best-track data, for the warm and cold SST simulations.

	Track error (km)	
Time	Warm SST	Cold SST
0600 UTC 27 Aug	12	12
1200 UTC 27 Aug	23	23
1800 UTC 27 Aug	13	11
0000 UTC 28 Aug	16	10
0600 UTC 28 Aug	5	14
0935 UTC 28 Aug[a]	8	28
1200 UTC 28 Aug	25	44
1300 UTC 28 Aug	26	48

[a] Landfall in NJ.

3) Validation of track, wind shear, and dry air intrusion

To test our hypothesis that upper ocean thermal structure and evolution in the MAB was the missing contribution to Irene's decay just before NJ landfall, the control run's treatment of track, wind shear, and dry air intrusion was evaluated.

Track was handled very well by the simulations, remaining within 30 km for the entire time series for the control run and until landfall for the cold SST sensitivity (Fig. 1, Table 3). As Irene tracked so close to shore, this was critical for teasing out any potential impact from land interactions. In addition, control run translation speed over the MAB ($\sim 10\,\mathrm{m\,s^{-1}}$) and cold SST sensitivity translation speed over the MAB ($\sim 10\,\mathrm{m\,s^{-1}}$) were consistent with NHC best-track translation speed for Irene over the MAB ($\sim 10\,\mathrm{m\,s^{-1}}$). For context, typical TC translation speed at 36°–40°N (approximate MAB latitude range) is 8–$10\,\mathrm{m\,s^{-1}}$ (Mei et al. 2012).

Wind shear values within and ahead of Irene during its MAB presence were similarly handled well by the simulations. At the time of entrance into the MAB, 200–850-hPa wind shear values in NARR, WRF warm SST, and WRF cold SST runs approached $60\,\mathrm{m\,s^{-1}}$ in the near vicinity ahead of Irene's eye (Figs. 12a,c,e). Radiosonde launches from KALB, KCHH, and KWAL at the same time showed 200–850-hPa wind shear values of about 38, 34, and $15\,\mathrm{m\,s^{-1}}$, respectively, which matched well with NARR (44, 29, and $22\,\mathrm{m\,s^{-1}}$) and both WRF simulations (41, 33, and $17\,\mathrm{m\,s^{-1}}$ for warm SST; 39, 32, and $19\,\mathrm{m\,s^{-1}}$ for cold SST); furthermore, simulated u and v wind profiles across the entire atmospheric column correlated well with observed profiles (Figs. 12g,i,k). Twelve hours later, wind shear values ahead of Irene in NARR and both WRF simulations again approached $60\,\mathrm{m\,s^{-1}}$, and observed wind shear at all three radiosonde sites

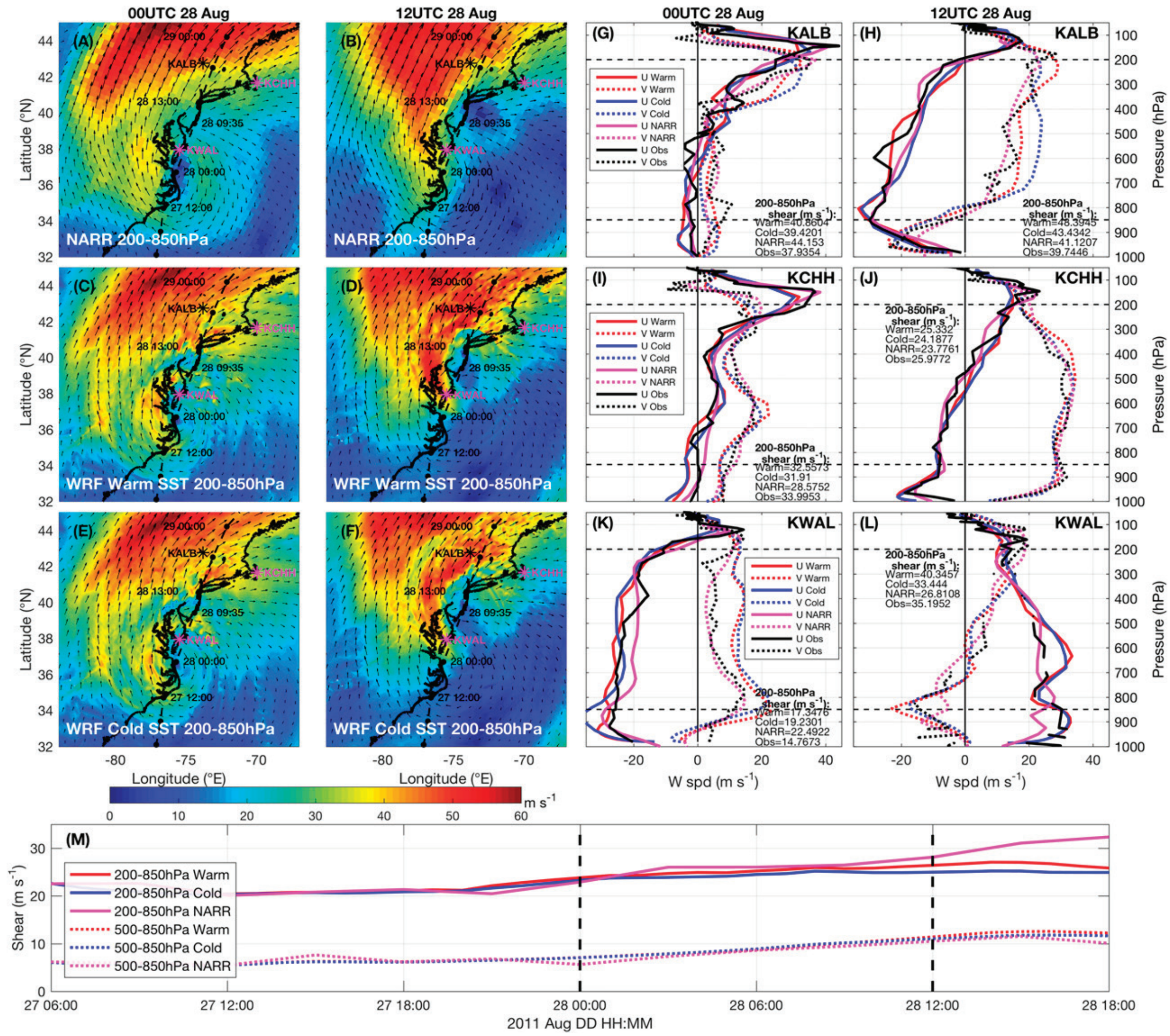

FIG. 12. Wind shear validation (a),(c),(e),(g),(i),(k) at 0000 UTC 28 Aug and (b),(d),(f),(h),(j),(l) at 1200 UTC 28 Aug. Spatial plots are the 200–850-hPa wind shear magnitude and vectors (m s^{-1}) with (a),(b) NARR; (c),(d) WRF warm SST; and (e),(f) WRF cold SST. KALB, KCHH, and KWAL indicated by labeled stars on maps and upper air radiosonde data at (g),(h) KALB; (i),(j) KCHH; and (k),(l) KWAL plotted, with solid lines for u winds (positive from west) and dashed lines for v winds (positive from south), and observed in black, NARR in magenta, WRF cold SST in blue, and WRF warm SST in red. The 200–850-hPa wind shear values (m s^{-1}) are labeled on graphs for observed, NARR, and WRF (cold and warm) simulations. (m) Time series of 200–850 hPa (solid) and 500–850 hPa (dotted) vertical shear (m s^{-1}) for WRF warm SST (red), WRF cold SST (blue), and NARR (magenta), with vertical dashed lines indicating times of (a)–(l).

correlated well with NARR and WRF (Figs. 12h,j,l). Finally, time series of 200–850- and 500–850-hPa wind shear values for NARR and WRF simulations were calculated by averaging wind shear values within an annulus 200–800 km from Irene's center (Rhome et al. 2006; Zambon et al. 2014b). The 200–850-hPa wind shear values increase from approximately 20 m s^{-1} at 1200 UTC 27 August to 25–30 m s^{-1} by the end of the simulation. These wind shear values were likely extremely detrimental to Irene's intensity. Our WRF simulations accurately reproduced these very high values and thus our model captured this important contribution to Irene's decay.

Finally, a snapshot of RH at 200 and 700 hPa from WRF at 1200 UTC 28 August shows an intrusion of dryer air into the southeast quadrant of Irene, agreeing well with a *GOES-13* water vapor image 12 min later (Figs. 13a–e). This *GOES-13* image indicates dry upper levels (~200 hPa) and moist lower levels (~700 hPa) in the southern half of the storm. In the northern half of the storm there are moist upper and lower levels. Our WRF simulations match well in both halves. WRF simulations

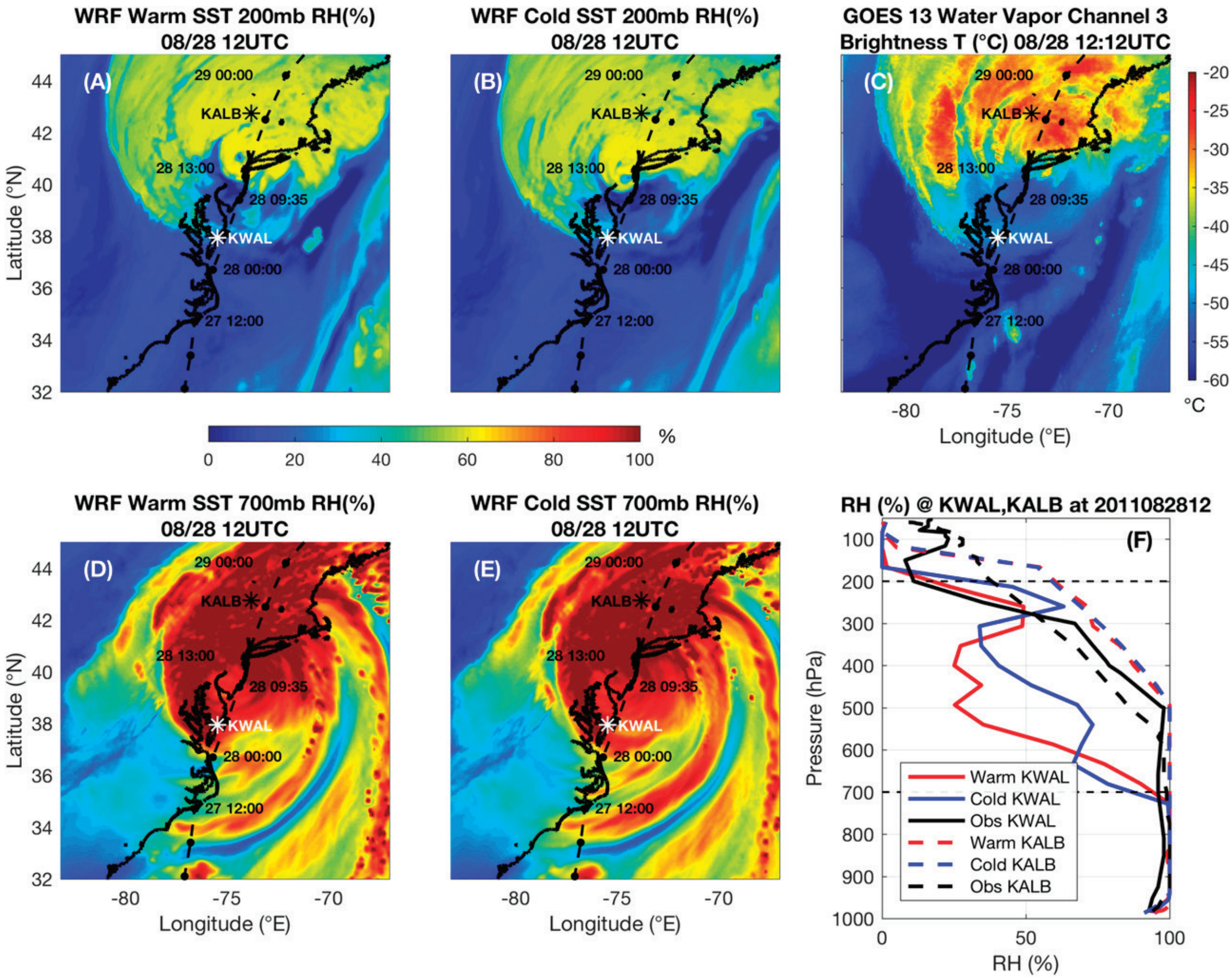

FIG. 13. Dry air intrusion validation (relative humidity, RH, %) at 1200 UTC 28 Aug with (a),(d) WRF warm SST; (b),(e) cold SST; and (c),(f) observations. (c) *GOES-13* water vapor channel-3 brightness temperature (°C) at 1212 UTC 28 Aug and (f) upper air radiosonde relative humidity (%) at KWAL (KALB in dashed) with observed in black, WRF warm SST in red, and WRF cold SST in blue. (a), (b) WRF RH (%) at 200 mb for upper atmosphere, and (d),(e) WRF RH (%) at 700 mb for mid- to lower atmosphere. KWAL (KALB) location is shown in white (black), and the NHC best track is shown in black in spatial plots.

are also consistent with observations from a KALB radiosonde (Fig. 13f, dashed lines), which was in the storm's northern half at this time and showed moist lower levels and relatively moist upper levels. Comparisons with a KWAL radiosonde (Fig. 13f, solid lines), which was in the storm's southern half at this time, showed WRF actually drying out the atmosphere more than observed between approximately 700 and 300 hPa. Overdrying the midlevels would result in additional decreases in storm intensity, so it is clear that dry air intrusion was also not a neglected contribution to Irene's decay.

4. Discussion

In summary, significant ahead-of-eye-center SST cooling (at least 6°C and up to 11°C, or 76%–98% of in-storm cooling) was observed over the MAB continental shelf during Hurricane Irene. Standard coupled ocean–atmosphere hurricane models did not resolve this cooling in their predictions, and operational satellite SST products did not capture the result of the cooling. In this paper, the sensitivity of Irene's intensity, size, and structure to the ahead-of-eye-center SST cooling was quantified. The intensity sensitivity to the ahead-of-eye-center cooling turned out to be the largest among tested model parameters, surpassing sensitivity to the parameterization of air–sea fluxes themselves. Storm size and structure sensitivity to the ahead-of-eye cooling was comparatively low.

Furthermore, accounting for the ahead-of-eye-center SST cooling in our modeling through the use of a fixed cold poststorm SST that captured the cooling mitigated the high bias in model predictions. Validation of modeled

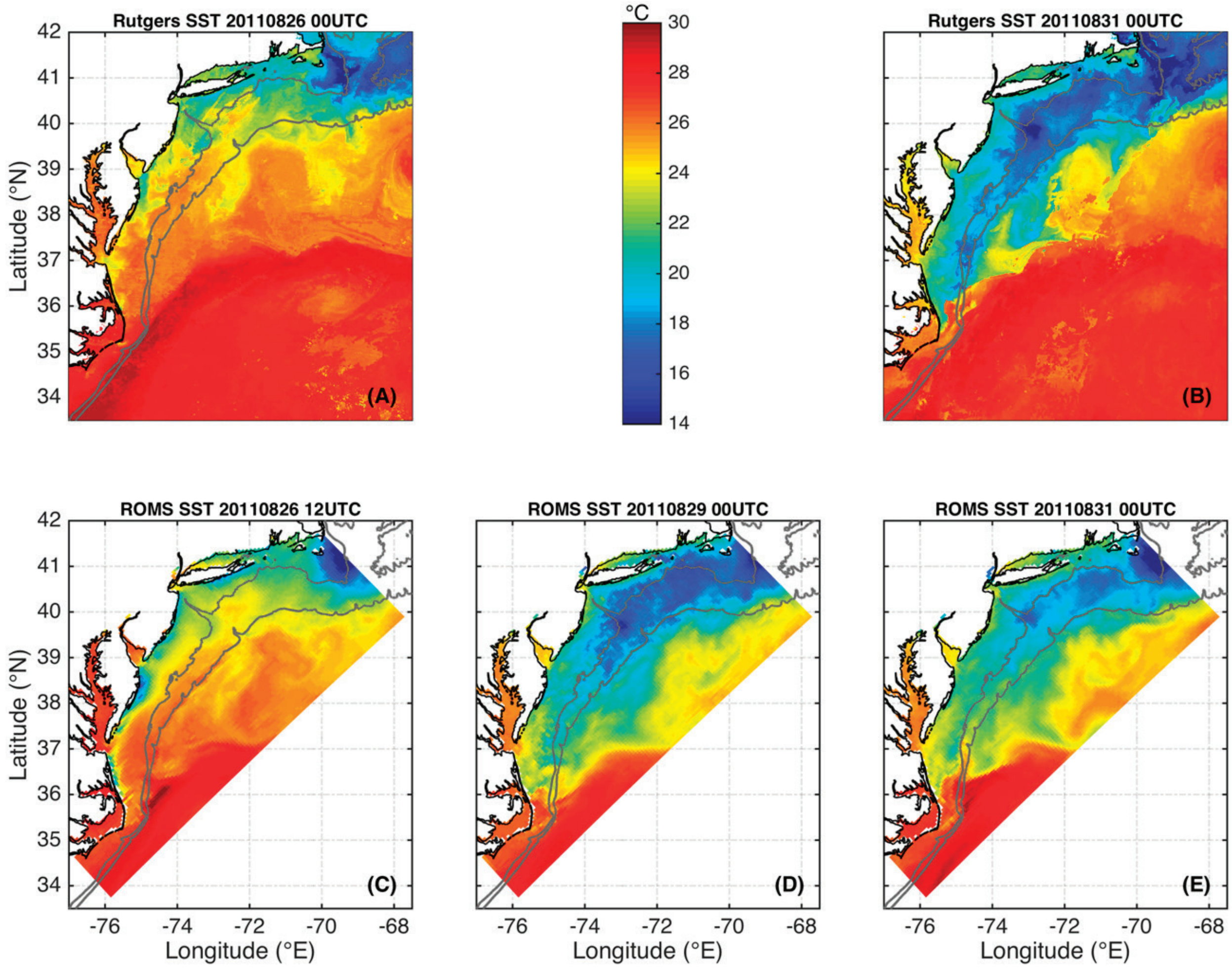

FIG. 14. SST from the new Rutgers SST composite in (a) from before Irene at 0000 UTC 26 Aug to (b) after Irene at 0000 UTC 31 Aug. The water temperature of top layer from a simulation using the ROMS ESPreSSO grid, (c) before Irene at 1200 UTC 26 Aug (simulation initialization), (d) just after Irene at 0000 UTC 29 Aug, and (e) well after Irene at 0000 UTC 31 Aug.

heat fluxes indicated that the cold SST simulation accurately reversed the sign of latent heat flux over the MAB as observed by two NDBC buoys. This would confirm the use of poststorm SST fixed through simulation so that Irene would propagate over the colder ''premixed'' waters, even though some slight cooling did indeed occur after eye passage. Finally, the simulations handled track, wind shear, and dry air intrusion well, indicating that upper ocean thermal evolution was the key missing contribution to Irene's decay just prior to NJ landfall.

Simplistic 1D ocean models are incapable of resolving the 3D coastal baroclinic processes responsible for the ahead-of-eye-center cooling observed in Irene, consistent with Zambon et al. (2014a) in their study of Hurricane Ivan (2004). Rather, a 3D high-resolution coastal ocean model, such as ROMS, nested within a synoptic- or global-scale ocean model like HYCOM and initialized with realistic coastal ocean stratification, could begin to spatially and temporally resolve this evidently important coastal baroclinic process (as described above in the ''results'' section), adding significant value to TC prediction in the coastal ocean—the last hours before landfall where impacts (storm surge, wind damage, and inland flooding) are greatest and are most closely linked with changes in storm intensity.

A ROMS simulation at 5-km horizontal resolution over the MAB not specifically designed for TCs can begin to resolve this ahead-of-eye-center cooling spatially (Fig. 14). This moderately accurate treatment of TC cooling, however, was arrived at through the combination of weak wind forcing from NAM (maximum winds $\sim 10\,\mathrm{m\,s^{-1}}$ too low) and a broad initial thermocline, thus providing a right answer for the wrong reasons. Some issues with SST cooling from ROMS remain, including insufficient cooling in the southern MAB and surface waters warming too quickly poststorm. Further improvements may be realized with:

1) Better initialization to resolve and maintain the sharp initial thermocline and abundant bottom cold water.
2) Better mixing physics/turbulence closure schemes to accurately widen and deepen the thermocline upon storm forcing.
3) More accurate wind forcing and air–sea flux coefficients.

These suggestions are consistent with the recommendations of Halliwell et al. (2011), who studied Hurricane Ivan (2004) in detail as it moved over the relatively deeper and less stratified waters of the Gulf of Mexico. Future research will be conducted to test these ocean model improvements.

Other future work is threefold. First, better ocean data (e.g., more coastal ocean profile time series from flexible platforms like underwater gliders), will be needed to better spatially validate ocean models and identify critical coastal baroclinic processes. Second, Glenn et al. (2016) identified 10 additional MAB hurricanes since 1985, as well as Super Typhoon Muifa (2011) over the Yellow Sea, that exhibited ahead-of-eye-center cooling in stratified coastal seas. In-depth investigation of these storms, the response of the coastal baroclinic ocean, and the feedbacks to storm intensities will be crucial. Finally, movement toward a fully coupled modeling system is critical. Studies like this help isolate specific processes that components of coupled models should simulate.

Acknowledgments. Support was provided by New Jersey Board of Public Utilities (2010RU-COOL, BP-070), the Environmental Protection Agency (EP-11-C-000085), New Jersey Department of Environmental Protection (WM13-019-2013), National Oceanic and Atmospheric Administration (NOAA) led Integrated Ocean Observing System through the Mid-Atlantic Regional Association Coastal Ocean Observing System (MARACOOS, NA11NOS0120038), NOAA Cooperative Institute for the North Atlantic Region (NA13OAR4830233, Disaster Recovery Act), Teledyne Webb Research, and Rutgers University. We thank Hyun-Sook Kim and Zhan Zhang of the HWRF team at NCEP for providing the HWRF-POM and HWRF-HYCOM data. We also thank John Wilkin at Rutgers University for his suggestions regarding the ocean modeling and upper-air validation, the Rutgers Ocean Modeling research associates for their ROMS help, and the RU COOL group for their support and ideas. We thank Louis Bowers for his help with WRF, Hugh Roarty for his ocean observational guidance, and Rich Dunk for his helpful meteorological discussions and ideas. Finally, we thank David Titley, Jim Price, Joe Zambon, and the anonymous reviewers for their useful comments.

REFERENCES

Avila, L. A., and J. Cangialosi, 2012: Tropical Cyclone Report: Hurricane Irene. National Hurricane Center Tropical Cyclone Rep. AL092011, 45 pp. [Available online at http://www.nhc.noaa.gov/data/tcr/AL092011_Irene.pdf.]

Bender, M. A., I. Ginis, and Y. Kurihara, 1993: Numerical simulations of tropical cyclone-ocean interaction with a high-resolution coupled model. *J. Geophys. Res.*, **98**, 23 245–23 263, doi:10.1029/93JD02370.

Blumberg, A. F., and G. L. Mellor, 1987: A description of a three-dimensional coastal ocean circulation model. *Three-Dimensional Coastal Ocean Models*, N.S. Heaps, Ed., Amer. Geophys. Union, 1–16.

Brooks, D. A., 1983: The wake of Hurricane Allen in the western Gulf of Mexico. *J. Phys. Oceanogr.*, **13**, 117–129, doi:10.1175/1520-0485(1983)013<0117:TWOHAI>2.0.CO;2.

Brown, B. R., and G. J. Hakim, 2013: Variability and predictability of a three-dimensional hurricane in statistical equilibrium. *J. Atmos. Sci.*, **70**, 1806–1820, doi:10.1175/JAS-D-12-0112.1.

Cangialosi, J. P., and J. L. Franklin, 2013: 2012 National Hurricane Center Forecast Verification Report. National Hurricane Center, 79 pp. [Available online at http://www.nhc.noaa.gov/verification/pdfs/Verification_2012.pdf.]

Canuto, V. M., A. Howard, Y. Cheng, and M. S. Dubovikov, 2001: Ocean turbulence. Part I: One-point closure model—Momentum and heat vertical diffusivities. *J. Phys. Oceanogr.*, **31**, 1413–1426, doi:10.1175/1520-0485(2001)031<1413:OTPIOP>2.0.CO;2.

——, ——, ——, and ——, 2002: Ocean turbulence. Part II: Vertical diffusivities of momentum, heat, salt, mass, and passive scalars. *J. Phys. Oceanogr.*, **32**, 240–264, doi:10.1175/1520-0485(2002)032<0240:OTPIVD>2.0.CO;2.

Chang, S. W., and R. A. Anthes, 1979: The mutual response of the tropical cyclone and the ocean. *J. Phys. Oceanogr.*, **9**, 128–135, doi:10.1175/1520-0485(1979)009<0128:TMROTT>2.0.CO;2.

Chassignet, E. P., H. E. Hurlburt, O. M. Smedstad, G. R. Halliwell, P. J. Hogan, A. J. Wallcraft, R. Baraille, and R. Bleck, 2007: The HYCOM (HYbrid Coordinate Ocean Model) data assimilative system. *J. Mar. Syst.*, **65**, 60–83, doi:10.1016/j.jmarsys.2005.09.016.

Cornillon, P., C. Gilman, L. Stramma, O. Brown, R. Evans, and J. Brown, 1987: Processing and analysis of large volumes of satellite-derived thermal infrared data. *J. Geophys. Res.*, **92**, 12 993–13 002, doi:10.1029/JC092iC12p12993.

D'Asaro, E. A., 2003: The ocean boundary layer below Hurricane Dennis. *J. Phys. Oceanogr.*, **33**, 561–579, doi:10.1175/1520-0485(2003)033<0561:TOBLBH>2.0.CO;2.

Davis, C., and Coauthors, 2008: Prediction of landfalling hurricanes with the Advanced Hurricane WRF Model. *Mon. Wea. Rev.*, **136**, 1990–2005, doi:10.1175/2007MWR2085.1.

Dickey, T., and Coauthors, 1998: Upper-ocean temperature response to Hurricane Felix as measured by the Bermuda testbed mooring. *Mon. Wea. Rev.*, **126**, 1195–1201, doi:10.1175/1520-0493(1998)126<1195:UOTRTH>2.0.CO;2.

Emanuel, K. A., 1999: Thermodynamic control of hurricane intensity. *Nature*, **401**, 665–669, doi:10.1038/44326.

——, 2003: Tropical cyclones. *Annu. Rev. Earth Planet. Sci.*, **31**, 75–104, doi:10.1146/annurev.earth.31.100901.141259.

——, C. DesAutels, C. Holloway, and R. Korty, 2004: Environmental control of tropical cyclone intensity. *J. Atmos. Sci.*, **61**, 843–858, doi:10.1175/1520-0469(2004)061<0843:ECOTCI>2.0.CO;2.

Fairall, C. W., E. F. Bradley, D. P. Rogers, J. B. Edson, and G. S. Young, 1996: Bulk parameterization of air-sea fluxes for Tropical Ocean-

Global Atmosphere Coupled-Ocean Atmosphere Response Experiment. *J. Geophys. Res.*, **101**, 3747, doi:10.1029/95JC03205.

Fisher, E. L., 1958: Hurricanes and the sea-surface temperature field. *J. Meteor.*, **15**, 328–333, doi:10.1175/1520-0469(1958)015<0328:HATSST>2.0.CO;2.

Forristall, G. Z., R. C. Hamilton, and V. J. Cardone, 1977: Continental shelf currents in Tropical Storm Delia: Observations and theory. *J. Phys. Oceanogr.*, **7**, 532–546, doi:10.1175/1520-0485(1977)007<0532:CSCITS>2.0.CO;2.

Fuglister, F. C., and L. V. Worthington, 1951: Some results of a multiple ship survey of the Gulf Stream. *Tellus*, **3**, 1–14, doi:10.1111/j.2153-3490.1951.tb00771.x.

Garau, B., S. Ruis, W. G. Zhang, A. Pascual, E. Heslop, J. Kerfoot, and J. Tintore, 2011: Thermal lag correction on Slocum CTD glider data. *J. Atmos. Oceanic Technol.*, **28**, 1065–1071, doi:10.1175/JTECH-D-10-05030.1.

Gentry, M. S., and G. M. Lackmann, 2010: Sensitivity of simulated tropical cyclone structure and intensity to horizontal resolution. *Mon. Wea. Rev.*, **138**, 688–704, doi:10.1175/2009MWR2976.1.

Glenn, S., and Coauthors, 2016: Stratified coastal ocean interactions with tropical cyclones. *Nat. Commun.*, **7**, 10887, doi:10.1038/ncomms10887.

——, C. Jones, M. Twardowski, L. Bowers, J. Kerfoot, J. Kohut, D. Webb, and O. Schofield, 2008: Glider observations of sediment resuspension in a Middle Atlantic Bight fall transition storm. *Limnol. Oceanogr.*, **53**, 2180–2196, doi:10.4319/lo.2008.53.5_part_2.2180.

Gould, W. J., and Coauthors, 2004: Argo profiling floats bring new era of in situ ocean observations. *Eos, Trans. Amer. Geophys. Union*, **85**, 185–191, doi:10.1029/2004EO190002.

Green, B. W., and F. Zhang, 2013: Impacts of air–sea flux parameterizations on the intensity and structure of tropical cyclones. *Mon. Wea. Rev.*, **141**, 2308–2324, doi:10.1175/MWR-D-12-00274.1.

Haidvogel, D. B., and Coauthors, 2008: Ocean forecasting in terrain-following coordinates: Formulation and skill assessment of the Regional Ocean Modeling System. *J. Comput. Phys.*, **227**, 3595–3624, doi:10.1016/j.jcp.2007.06.016.

Halliwell, G. R., L. K. Shay, J. K. Brewster, and W. J. Teague, 2011: Evaluation and sensitivity analysis of an ocean model response to Hurricane Ivan. *Mon. Wea. Rev.*, **139**, 921–945, doi:10.1175/2010MWR3104.1.

Hill, K. A., and G. M. Lackmann, 2009: Analysis of idealized tropical cyclone simulations using the Weather Research and Forecasting Model: Sensitivity to turbulence parameterization and grid spacing. *Mon. Wea. Rev.*, **137**, 745–765, doi:10.1175/2008MWR2220.1.

Houghton, R. W., R. Schlitz, R. C. Beardsley, B. Butman, and J. L. Chamberlin, 1982: The Middle Atlantic Bight cold pool: Evolution of the temperature structure during summer 1979. *J. Phys. Oceanogr.*, **12**, 1019–1029, doi:10.1175/1520-0485(1982)012<1019:TMABCP>2.0.CO;2.

Jacob, S. D., and L. K. Shay, 2003: The role of oceanic mesoscale features on the tropical cyclone–induced mixed layer response: A case study. *J. Phys. Oceanogr.*, **33**, 649–676, doi:10.1175/1520-0485(2003)33<649:TROOMF>2.0.CO;2.

Jaimes, B., and L. K. Shay, 2009: Mixed layer cooling in mesoscale oceanic eddies during Hurricanes Katrina and Rita. *Mon. Wea. Rev.*, **137**, 4188–4207, doi:10.1175/2009MWR2849.1.

——, and ——, 2010: Near-inertial wave wake of Hurricanes Katrina and Rita over mesoscale oceanic eddies. *J. Phys. Oceanogr.*, **40**, 1320–1337, doi:10.1175/2010JPO4309.1.

——, and ——, 2015: Enhanced wind-driven downwelling flow in warm oceanic eddy features during the intensification of Tropical Cyclone Isaac (2012): Observations and theory. *J. Phys. Oceanogr.*, **45**, 1667–1689, doi:10.1175/JPO-D-14-0176.1.

——, ——, and G. R. Halliwell, 2011: The response of quasigeostrophic oceanic vortices to tropical cyclone forcing. *J. Phys. Oceanogr.*, **41**, 1965–1985, doi:10.1175/JPO-D-11-06.1.

Kain, J. S., 2004: The Kain–Fritsch convective parameterization: An update. *J. Appl. Meteor.*, **43**, 170–181, doi:10.1175/1520-0450(2004)043<0170:TKCPAU>2.0.CO;2.

Khain, A. P., and I. Ginis, 1991: The mutual response of a moving tropical cyclone and the ocean. *Contrib. Atmos. Phys.*, **64**, 125–141.

——, B. Lynn, and J. Dudhia, 2010: Aerosol effects on intensity of landfalling hurricanes as seen from simulations with the WRF Model with spectral bin microphysics. *J. Atmos. Sci.*, **67**, 365–384, doi:10.1175/2009JAS3210.1.

——, ——, and J. Shpund, 2016: High resolution WRF simulations of Hurricane Irene: Sensitivity to aerosols and choice of microphysical schemes. *Atmos. Res.*, **167**, 129–145, doi:10.1016/j.atmosres.2015.07.014.

Kim, H. S., C. Lozano, V. Tallapragada, D. Iredell, D. Sheinin, H. L. Tolman, V. M. Gerald, and J. Sims, 2014: Performance of ocean simulations in the coupled HWRF-HYCOM model. *J. Atmos. Oceanic Technol.*, **31**, 545–559, doi:10.1175/JTECH-D-13-00013.1.

Landsea, C. W., and J. L. Franklin, 2013: Atlantic hurricane database uncertainty and presentation of a new database format. *Mon. Wea. Rev.*, **141**, 3576–3592, doi:10.1175/MWR-D-12-00254.1.

Lee, C.-Y., and S. S. Chen, 2014: Stable boundary layer and its impact on tropical cyclone structure in a coupled atmosphere–ocean model. *Mon. Wea. Rev.*, **142**, 1927–1945, doi:10.1175/MWR-D-13-00122.1.

Leipper, D. F., 1967: Observed ocean conditions and Hurricane Hilda, 1964. *J. Atmos. Sci.*, **24**, 182–186, doi:10.1175/1520-0469(1967)024<0182:OOCAHH>2.0.CO;2.

Lim, K.-S. S., and S.-Y. Hong, 2010: Development of an effective double-moment cloud microphysics scheme with prognostic cloud condensation nuclei (CCN) for weather and climate models. *Mon. Wea. Rev.*, **138**, 1587–1612, doi:10.1175/2009MWR2968.1.

Lin, I.-I., C.-H. Chen, I.-F. Pun, W. T. Liu, and C.-C. Wu, 2009: Warm ocean anomaly, air sea fluxes, and the rapid intensification of Tropical Cyclone Nargis (2008). *Geophys. Res. Lett.*, **36**, L03817, doi:10.1029/2008GL035815.

Liu, B., H. Liu, L. Xie, C. Guan, and D. Zhao, 2011: A coupled atmosphere–wave–ocean modeling system simulation of the intensity of an idealized tropical cyclone. *Mon. Wea. Rev.*, **139**, 132–152, doi:10.1175/2010MWR3396.1.

Lynn, B. H., and Coauthors, 2016: The sensitivity of Hurricane Irene to aerosols and ocean coupling: Simulations with WRF spectral bin microphysics. *J. Atmos. Sci.*, **73**, 467–486, doi:10.1175/JAS-D-14-0150.1.

Marks, F. D., and Coauthors, 1998: Landfalling tropical cyclones: Forecast problems and associated research opportunities. *Bull. Amer. Meteor. Soc.*, **79**, 305–323.

Mayer, D. A., and H. O. Mofjeld, 1981: Near-inertial internal waves observed on the outer shelf in the Middle Atlantic Bight in the wake of Hurricane Belle. *J. Phys. Oceanogr.*, **11**, 87–106, doi:10.1175/1520-0485(1981)011<0087:NIIWOO>2.0.CO;2.

Mehra, A., and I. Rivin, 2010: A real time ocean forecast system for the North Atlantic Ocean. *Terr. Atmos. Oceanic Sci.*, **21**, 211–228, doi:10.3319/TAO.2009.04.16.01(IWNOP).

Mei, W., C. Pasquero, and F. Primeau, 2012: The effect of translation speed upon the intensity of tropical cyclones over the tropical ocean. *Geophys. Res. Lett.*, **39**, L07801, doi:10.1029/2011GL050765.

Mesinger, F., and Coauthors, 2006: North American Regional Reanalysis. *Bull. Amer. Meteor. Soc.*, **87**, 343–360, doi:10.1175/BAMS-87-3-343.

Miles, T., S. Glenn, and O. Schofield, 2013: Temporal and spatial variability in fall storm induced sediment resuspension on the Mid-Atlantic Bight. *Cont. Shelf Res.*, **63**, S36–S49, doi:10.1016/j.csr.2012.08.006.

——, G. N. Seroka, J. T. Kohut, O. Schofield, and S. M. Glenn, 2015: Glider observations and modeling of sediment transport in Hurricane Sandy. *J. Geophys. Res. Ocean*, **120**, 1771–1791, doi:10.1002/2014JC010474.

Pollard, R. T., P. B. Rhines, and R. O. Thompson, 1972: The deepening of the wind-mixed layer. *Geophys. Astrophys. Fluid Dyn.*, **4**, 381–404, doi:10.1080/03091927208236105.

Price, J. F., 1981: Upper ocean response to a hurricane. *J. Phys. Oceanogr.*, **11**, 153–175, doi:10.1175/1520-0485(1981)011<0153:UORTAH>2.0.CO;2.

——, R. A. Weller, and R. Pinkel, 1986: Diurnal cycling: Observations and models of the upper ocean response to diurnal heating, cooling, and wind mixing. *J. Geophys. Res.*, **91**, 8411–8427, doi:10.1029/JC091iC07p08411.

——, T. B. Sanford, and G. Z. Forristall, 1994: Forced stage response to a moving hurricane. *J. Phys. Oceanogr.*, **24**, 233–260, doi:10.1175/1520-0485(1994)024<0233:FSRTAM>2.0.CO;2.

Rappaport, E. N., J. L. Frankling, M. DeMaria, L. K. Shay, and E. J. Gibney, 2010: Tropical cyclone intensity change before U.S. Gulf Coast landfall. *Wea. Forecasting*, **25**, 1380–1396, doi:10.1175/2010WAF2222369.1.

Reynolds, R. W., and D. B. Chelton, 2010: Comparisons of daily sea surface temperature analyses for 2007–08. *J. Climate*, **23**, 3545–3562, doi:10.1175/2010JCLI3294.1.

Rhome, J. R., C. A. Sisko, and R. D. Knabb, 2006: On the calculation of vertical shear: An operational perspective. *27th Conf. on Hurricanes and Tropical Meteorology*, Monterey, CA, Amer. Meteor. Soc., 14A.4. [Available online at https://ams.confex.com/ams/27Hurricanes/techprogram/paper_108724.htm.]

Roemmich, D., and Coauthors, 2009: The Argo Program: Observing the global ocean with profiling floats. *Oceanography*, **22**, 34–43, doi:10.5670/oceanog.2009.36.

Ruiz, S., L. Renault, B. Garau, and J. Tintoré, 2012: Underwater glider observations and modeling of an abrupt mixing event in the upper ocean. *Geophys. Res. Lett.*, **39**, L01603, doi:10.1029/2011GL050078.

Sampson, C. R., and A. J. Schrader, 2000: The Automated Tropical Cyclone Forecasting System (version 3.2). *Bull. Amer. Meteor. Soc.*, **81**, 1231–1240, doi:10.1175/1520-0477(2000)081<1231:TATCFS>2.3.CO;2.

Sanabia, E. R., and S. R. Jayne, 2014: Evolution of the upper-ocean thermal structure beneath Hurricanes Iselle and Julio (2014). *2014 Fall Meeting*, San Francisco, CA, Amer. Geophys. Union, Abstract A11O-07.

——, B. S. Barrett, P. G. Black, S. Chen, and J. A. Cummings, 2013: Real-time upper-ocean temperature observations from aircraft during operational hurricane reconnaissance missions: AXBT demonstration project year one results. *Wea. Forecasting*, **28**, 1404–1422, doi:10.1175/WAF-D-12-00107.1.

——, S. R. Jayne, W. Swick, S. Chen, and J. Cummings, 2016: Variability in upper-ocean thermal structure beneath tropical cyclones as observed by air-deployed profiling floats. *32nd Conf. on Hurricanes and Tropical Meteorology*, San Juan, Puerto Rico, Amer. Meteor. Soc., 3B.4. [Available online at https://ams.confex.com/ams/32Hurr/webprogram/Paper293996.html.]

Sanford, T. B., P. G. Black, J. R. Haustein, J. W. Feeney, G. Z. Forristall, and J. F. Price, 1987: Ocean response to a hurricane. Part I: Observations. *J. Phys. Oceanogr.*, **17**, 2065–2083, doi:10.1175/1520-0485(1987)017<2065:ORTAHP>2.0.CO;2.

Schade, L. R., and K. A. Emanuel, 1999: The ocean's effect on the intensity of tropical cyclones: Results from a simple coupled atmosphere–ocean model. *J. Atmos. Sci.*, **56**, 642–651, doi:10.1175/1520-0469(1999)056<0642:TOSEOT>2.0.CO;2.

Schofield, O., and Coauthors, 2007: Slocum gliders: Robust and ready. *J. F. Robot.*, **24**, 473–485, doi:10.1002/rob.20200.

Sessions, M. H., T. P. Barnett, and W. S. Wilson, 1976: The airborne expendable bathythermograph. *Deep-Sea Res. Oceanogr. Abstr.*, **23**, 779–782, doi:10.1016/S0011-7471(76)80021-6.

Shay, L. K., P. G. Black, A. J. Mariano, J. D. Hawkins, and R. L. Elsberry, 1992: Upper ocean response to Hurricane Gilbert. *J. Geophys. Res.*, **97**, 20 227–20 248, doi:10.1029/92JC01586.

Skamarock, W. C., and Coauthors, 2008: A description of the Advanced Research WRF version 3. NCAR Tech. Note NCAR/TN-475+STR, 113 pp., doi:10.5065/D68S4MVH.

Suda, K., 1943: *Ocean Science*. Kokin-Shoin, 770 pp.

Sutyrin, G. G., and E. A. Agrenich, 1979: Interaction of the boundary layers of the ocean and atmosphere in a tropical cyclone. *Meteor. Gidrol.*, **2**, 45–56.

——, and A. P. Khain, 1984: Effect of the ocean–atmosphere interaction on the intensity of a moving tropical cyclone. *Atmos. Oceanic Phys.*, **20**, 697–703.

Tallapragada, V., and Coauthors, 2011: Hurricane Weather Research and Forecasting (HWRF) model: 2011 scientific documentation. Developmental Testbed Center, 81 pp. [Available online at http://www.dtcenter.org/HurrWRF/users/docs/scientific_documents/HWRFScientificDocumentation_August2011.pdf.]

Torn, R. D., and C. Snyder, 2012: Uncertainty of tropical cyclone best-track information. *Wea. Forecasting*, **27**, 715–729, doi:10.1175/WAF-D-11-00085.1.

Walker, N. D., R. R. Leben, and S. Balasubramanian, 2005: Hurricane-forced upwelling and chlorophyll α enhancement within cold-core cyclones in the Gulf of Mexico. *Geophys. Res. Lett.*, **32**, L18610, doi:10.1029/2005GL023716.

Wilkin, J. L., and E. J. Hunter, 2013: An assessment of the skill of real-time models of Mid-Atlantic Bight continental shelf circulation. *J. Geophys. Res. Ocean*, **118**, 2919–2933, doi:10.1002/jgrc.20223.

Zambon, J. B., R. He, and J. C. Warner, 2014a: Investigation of Hurricane Ivan using the Coupled Ocean–Atmosphere–Wave–Sediment Transport (COAWST) model. *Ocean Dyn.*, **64**, 1535–1554, doi:10.1007/s10236-014-0777-7.

——, ——, and ——, 2014b: Tropical to extratropical: Marine environmental changes associated with Superstorm Sandy prior to its landfall. *Geophys. Res. Lett.*, **41**, 8935–8943, doi:10.1002/2014GL061357.

CHAPTER

c0018 # New Sensors for Ocean Observing: The Optical Phytoplankton Discriminator

18

J. Shapiro[1,*], L.K. Dixon[1], O.M. Schofield[2], B.A. Kirkpatrick[1,3], Gary J. Kirkpatrick[1,*]

Mote Marine Laboratory, Sarasota, FL, USA[1]; Institute of Marine and Coastal Sciences, Rutgers University, New Brunswick, NJ, USA[2]; Gulf of Mexico Coastal Ocean Observing System, College Station, TX, USA[3]

[**AU5**] **Corresponding authors: Email: gkirkpat@mote.org; shapiro@mote.org*

CHAPTER OUTLINE

s0010 ## 1. INTRODUCTION

p0010 Phytoplankton are integral to complex natural processes such as the carbon cycling, food web dynamics, coastal hypoxia events, and harmful algal blooms (HABs). Identification and quantification of phytoplankton are listed as high-priority measurements needed to address six of the seven societal goals identified in the Integrated Ocean Observing System (IOOS) Summit[1] and were listed as core variables for observatory systems.[2,3] Similarly, chromophoric dissolved organic matter (CDOM) is the primary constituent that is absorbing light in the ocean and often exceeds even the light absorbed by phytoplankton.[4] As a result, CDOM dominates ocean color, plays a critical role in photobiology and photochemistry, photoproduction of CO_2,[5] as well as controlling the absorption of light energy and subsequent impacts on heat flux[6] and other ocean−climate interactions. The IOOS Summit[1] included CDOM among its 26 high-priority variables required to address three of its seven societal goals. The Optical Phytoplankton Discriminator

Coastal Ocean Observing Systems. http://dx.doi.org/10.1016/B978-0-12-802022-7.00018-3

organic matter (FDOM) as a proxy for CDOM. Fluorescence-based CDOM instruments, however, measure only a small subset of DOM molecules that have the aromaticity and conjugation to fluoresce. The FDOM:CDOM relationship varies with the source of CDOM, its lability, and its light exposure history. Significantly, FDOM cannot provide spectral slope information.

p0040 Unlike FDOM determinations, spectrophotometric CDOM absorption measurements directly quantify the desired light absorption properties in both coastal and oceanic waters, provided adequate sensitivity and accuracy are obtained. Spectral slope data can be readily derived from full spectrum absorption. Conventional path lengths of both laboratory spectrophotometers and field absorption instrumentation are typically limited to 10 or 25 cm, respectively, which limits some open ocean applications. Corrections for salinity, temperature, and scattering[31] are also applied for the most exacting work. The most sensitive commercially available CDOM absorption instrument and the OPD utilize liquid-core waveguide (LCW) technology, in which the difference in refractive index between sample and waveguide wall results in a highly efficient internal reflection, permitting an illumination of the core to be transmitted through a coiled waveguide and resulting in path lengths of 200 cm or more. Operational issues common to all LCW instruments include fragility of silica capillary, bubble artifacts, condensation, and clogging of small lumen apertures. Additionally, because light transmission through the LCW is a function of the sample refractive index in addition to the sample absorption,[32] data collection requires careful accounting for temperature and salinity differences between references and samples. The commercial LCW instrument, though limited to manual benchtop operation, has advanced the sensitivity of CDOM analysis and resulting knowledge.[4,32,33] The OPD provides similar absorption measurement sensitivity with the additional feature of unattended, in situ, automated operation.

s0015 2. HISTORY OF THE OPD

p0045 In a set of laboratory experiments, Millie et al.[34] utilized in vivo absorbance spectra to discriminate different light acclimation states of *K. brevis* cultures grown under differing light levels. Results from those experiments on a single species provided evidence that there might be utility in the use of absorbance spectra to discriminate multiple taxonomic groups of phytoplankton. Subsequently, taxonomic groups were discriminated in theoretical mixes of absorbance spectra collected from multiple monospecific cultures.[35] A stepwise discriminant analyses was used to differentiate mean-normalized absorbance spectra for laboratory cultures of *K. brevis* from absorbance spectra of a diatom, a prasinophyte, and peridinin-containing dinoflagellates. Wavelengths delineated by the stepwise techniques were associated with the accessory carotenoids. Unfortunately, the comparative absorption by the carotenoids in the green, yellow, and orange wavelengths was much less than the absorption by chlorophyll in the blue and red wavelengths, limiting the sensitivity of that approach. Furthermore, the absorbance attributable to class-specific groupings of accessory

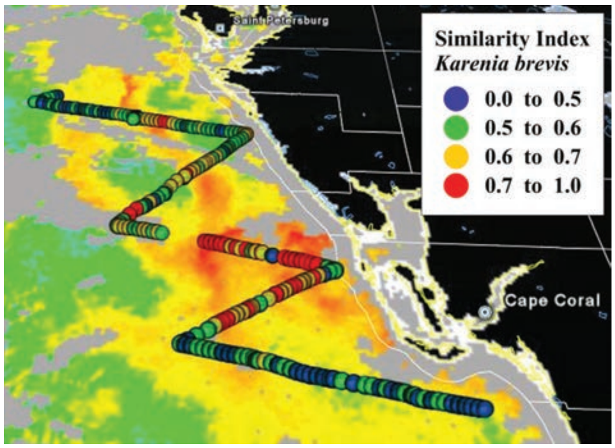

f0015 **FIGURE 2**

The near surface *Karenia* sp. similarity indexes (SI) determined by a shipboard OPD on November 8, 2005. Background image is MODIS remote sensing fluorescence line height.
Remote sensing image courtesy of USF-IMARS.

s0020 3. METHODOLOGY

p0060 Photopigments of plants and algae are light-harvesting molecules that function to channel light energy into the photochemical pathway for photosynthesis or to shunt excess light energy away from the photochemical pathway when there is a risk of damage from too much light energy.[45] There are approximately 45 known plant pigments found in marine microalgae, each with a slightly different molecular structure.[46] These differences in molecular structure yield differences in the shapes of light absorption spectra for each pigment. The absorption spectrum of an individual plant pigment can be modeled as the sum of a set of Gaussian curves centered at wavelengths of maximum absorption by the light-absorbing chemical structures. The absorption spectrum of any phytoplankton cell is the sum of the absorption spectra of all the pigments making up the cells pigment complement modified by factors such as cell size and the concentration of pigments within the cell (pigment-packaging effects).

p0065 The OPD method is a computational means of highlighting the absorption characteristics of plant photopigments, removing or minimizing the absorption and scattering characteristics of nonpigmented components of the bulk sample, and then fitting a set of known taxonomic class photopigment signatures to the highlighted photopigment absorption characteristics. To accomplish this, the bulk water particle absorbance spectrum is subjected to derivative analysis, and then that derivative spectrum is compared to the derivative spectrum of the known target taxa yielding a similarity index (SI).

p0090 Absorption by CDOM is determined using the standard approach where the natural logarithm of the ratio of the light transmission through the CDOM containing water sample to the light transmission through "pure" water is scaled by the optical path length of the water-containing cell. CDOM absorption is an exponential function of wavelength and can be expressed as follows:

$$a_{CDOM}(\lambda) = a_{CDOM}(\lambda_S) * e^{-S*(\lambda-\lambda_s)} \quad (1)$$

where $a_{CDOM}(\lambda_S)$ is the absorption value at a "standard" wavelength (λ_S), typically 400 or 440 nm), and S is the exponential slope of the CDOM absorption spectrum at λ_S. By accepting the standard form of the CDOM absorption spectrum (Eqn (1)), it is possible to completely describe a CDOM absorption spectrum by reporting just $a_{CDOM}(\lambda_S)$ and S. To determine those two parameters for any CDOM absorption spectrum, first, the spectral absorption values are transformed by the natural log (ln), and then a least squares linear regression is fit to the transformed absorption values over the wavelength range from 380 to 500 nm. The best fit linear coefficients, intercept and slope, then represent $\log_e(a_{CDOM}(\lambda_S))$ and S, respectively. During every sample cycle, the CDOM absorption is calculated.

s0025 4. SYSTEMS LEVEL INTEGRATION

p0095 The OPD is a system of fluidic, optical, and computational systems that obtains a water sample, illuminates the sample with a calibrated light source, and measures the transmission spectrum through the water sample (Figure 3). There are two

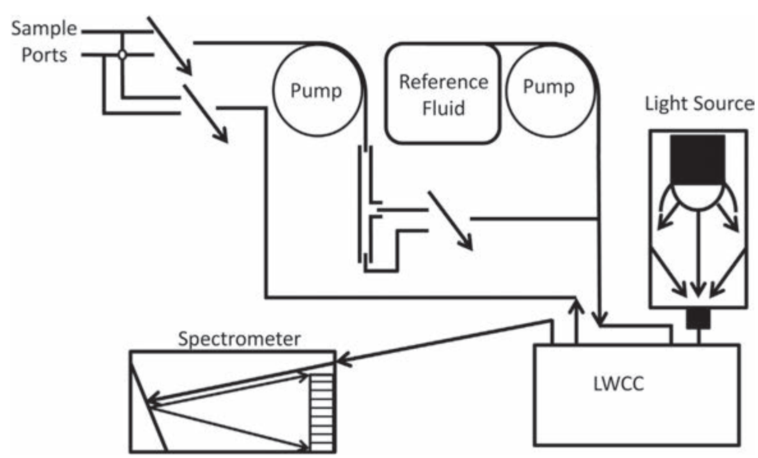

f0020 **FIGURE 3**

Schematic of major OPD components including the fluidic pathways.

and a whole water transmission spectrum ($I(\lambda)_w$) is collected. For this sample, a dark spectrum is not collected because it follows immediately after the previous filtered (CDOM) sample. Calculation of SI and CDOM absorption spectra are completed, and results are stored and transmitted as specified by the user. If the OPD is ~~set~~ configured
~~up~~ to continuously cycle, only the portion of cycle described ~~that comes after~~ the proceeding
CDOM reference is repeated. The CDOM reference cycle is repeated on an adjustable schedule, but usually every 8 to 10 cycles to account for the development of fouling in the LWCC, changes in the light source spectrum, and drift in the spectrometer. Additionally, if there will be a delay before the next cycle, a small volume of CDOM reference water is pumped into the LWCC to displace fouling organisms and compounds and to inhibit growth.

p0110 Computational, electronic, fluidic, and optical systems are controlled by a low-power Persistor Instruments, Inc. CF2 microcontroller. This processor handles all data management, processing, and communications capabilities of the OPD. Communications with host systems, which can include external communications systems (LP units) or independent control and communications systems (HP units on AUVs), are handled by RS232 serial standard protocol.

p0115 The Optical Phytoplankton Detector provides a relatively low-cost way to monitor phytoplankton community structure and CDOM. On a systems level, an LP OPD capable of operating unattended for approximately one month has a purchase price of under \$30,000. Operating costs are on the order of \$1000 per deployment, including costs of operating marine vessels to deploy and recover units. A single trained operator is capable of maintaining approximately four instruments. An HP OPD for deployment on an AUV has a purchase cost on the order of \$40,000, in addition to the cost of the AUV, and it can run with minimal user intervention on the order of two weeks. In comparison, shipboard survey work costs on the order of \$10,000−20,000 per day for vessel operations and personnel, plus the cost of scientific staff on board, and sample processing costs once grab samples are returned to shore. For the purpose of regional HAB monitoring, the OPD is capable of identifying domains of interest for shipboard surveys without the cost associated with large-scale surveys.

s0030 5. APPLICATIONS

p0120 The OPD is a modular instrument, in that components can be adapted for different water types with varying optical transmission properties and phytoplankton concentrations. In offshore environments, namely oligotrophic waters, planktonic and CDOM concentrations can be extremely low, requiring an increase in instrument sensitivity. This can be achieved by increasing the sample volume and path length, for planktonic and CDOM detection, respectively, to result in a measurable change in absorbance. Similarly, in extremely turbid waters, absorbance by CDOM in the water can extinguish the characteristic transmission spectra of planktonic cells contained within the sample volume, necessitating a shortened waveguide.

instrument for continuous position information in time and space. Variants of the CDOM mapper have been designed that incorporate updated sensor components to prevent obsolesce, to measure conductivity and temperature for refractive index modeling and correction, and to prevent and remove bubbles in the sampling pathway. The most recent variant of the CDOM mapper has increased ease of operation to make it possible to integrate into the SeaKeeper Discovery Yachts Program, increasing available deployments to include both scientific research vessels and private vessels of opportunity.

s0035 6. VALIDATION AND RESULTS

p0135 Because of the remote, unattended nature of OPD deployments, it was often not feasible to directly verify the results telemetered back to the laboratory. Data from several projects that employed the OPD (Table History1) were used in the validation of the method. To accurately conduct a validation exercise, it was necessary to assure that the OPD and the comparison method utilized the same water sample very
closely in ~~close to the~~ same time. Phytoplankton communities, especially at bloom concentra-
very spatially tions, can be ~~spatially very~~ patchy. Photo-acclimation of photopigments can change pigment compliments and the resulting absorbance signature on minute time scales. Fortunately, there have been studies, both laboratory and field, that conducted simultaneous sampling and processing. Additionally, comparison methods are subject to their own inaccuracies, making it necessary to place caveats on validation results. For instance, the use of optical microscope enumeration of phytoplankton taxonomic classes has been the de facto standard method for many years. Although the optical microscope is a powerful tool when used by skilled taxonomists, it is very time consuming and problematic when identifying very small cells. Because *Karenia* sp. cells are large and very distinctly shaped, optical microscope enumeration provides very accurate data for comparison to the OPD estimations of *Karenia* sp. However, the diatom class, for instance, includes a wide range of species with varying sizes and shapes. Some are large and uniquely shaped, making practical the use of microscopic enumeration for numerous samples. Conversely, very small-sized diatom species with nondescript shapes (at optical microscope resolution) are difficult to enumerate accurately by optical microscopes in large numbers of samples. The upshot of these issues in optical microscope enumeration is that there were no complete taxonomic enumerations of community structure to use in validation of the OPD community structure estimates. There are molecular techniques for identification of taxonomic groups, but few simultaneously provide comprehensive coverage of all the possible groups. Chemotaxonomic classification of class-level taxonomy, utilizing high-performance liquid chromatography (HPLC), is a widely accepted approach to dealing with relatively large numbers of samples and for including the full complement of taxonomic classes in natural water samples.

s0040 7. FUTURE DEVELOPMENT/PLANS

p0165 The OPD has been developed for over a decade and has been implemented across a broad geographic range including North America, from the Eastern Pacific to the Western Atlantic, around the Gulf of Mexico, and in the Great Lakes. An OPD has made its way across the Mediterranean, around the Arctic, and there have been deployments in Mexico. With this experience, there are several developmental pathways that will enhance future development. Improvements fall into the domains of expanding species identification capabilities, enhancing CDOM measurement, and expanding the user base.

p0170 To identify plankton species and allocate species to a community structure using the OPD, characteristic fourth derivative spectra must be maintained on file. These spectra are obtained by running isolated plankton samples through the OPD. Typically, plankton are collected during bloom conditions, or they are isolated and grown in culture to detectable levels. A rigorous effort to generate absorption spectra from cultured samples must be conducted and verified by testing plankton from both culture and wild blooms. Additional validation of OPD results against known samples of mixed cultures and against ambient samples determined through more complete molecular and microscopic methods is desirable. The present library of species files would benefit from including phytoplankton from different geographic regions, and a database of libraries would enable researchers and operators of monitoring stations to access and share species files.

p0175 The OPD has demonstrated success in responding to naturally varying levels of CDOM in the natural sampling environment. For OPD to provide CDOM measurements as absorption coefficients (m^{-1}) for research purposes, remote sensing validation, and generating hybrid in situ remote sensing products, a thorough validation and calibration of CDOM measurement must be demonstrated. Simultaneous analyses of CDOM via OPD and benchtop spectroscopy would be performed on estuarine samples that cover a range of both CDOM and salinity values, as well as a matrix of constructed, fixed CDOM-varying salinity samples. The resulting dataset would allow an algorithm to correct measured absorbance with actual CDOM absorption coefficients by accounting for variations in refractive index between sample and reference salinity. The successful algorithm to compensate CDOM absorbance for changing salinity would motivate that integration of a conductivity cell within the OPD, similar to that designed as part of CDOM mapper, as well as the integration of this algorithm into the automated sampling sequence.

p0180 To integrate additional sensors, such as a conductivity cell and thermistor into the OPD, as well as to maintain compatibility with the upcoming generations of ocean sampling platforms, it will eventually be desirable to convert the OPD hardware from the Persistor CF2 processor to an ARM Linux architecture. This would enable a more flexible computing infrastructure and additional computing power to calculate plankton community structure and chlorophyll *a* biomass contributions in real time. It has already been determined that the Slocum Glider will make a similar transition from the Persistor series of processors to the more flexible Linux architecture.

p0185 In the Gulf of Mexico, the Gulf of Mexico Coastal Ocean Observation System (GCOOS) currently supports a number of OPD installations in the eastern Gulf. In addition, GCOOS is currently seeking to expand observing systems including, among other systems, an extended harmful algal bloom monitoring system, of which the OPD could be an integral component. The Sarasota Operations of the Coastal Ocean Observation Laboratories (SO-COOL) model of combining fixed and mobile HAB monitoring instruments with real-time data telemetry and distribution to end users can easily be extend to accommodate additional sampling sites. An effective model would be an instrument exchange program that would support sites around the Gulf, maintaining continuous OPD operations with minimal instrument/site downtime and minimal replication of technical expertise.

REFERENCES

1. *U.S. IOOS summit report: a new decade for the integrated ocean observing system*. Interagency Ocean Observation Committee; Copyright © 2013.
2. U.S. Commission on Ocean Policy. *An ocean blueprint for the 21st century*. 2004. Final Report. Washington, DC. ISBN: 09759462-X.
3. Ocean.US. *The first U.S. integrated ocean observing system (IOOS) development plan*. No. 9. The National Office for Integrated and Sustained Ocean Observations; 2006.
4. Nelson NB, Siegel DA. The global distribution and dynamics of chromophoric dissolved organic matter. *Ann Rev Mar Sci* 2013;**5**:447−76. http://dx.doi.org/10.1146/annurev-marine-120710-100751.
5. Clark CD, Hiscock WT, Millero FJ, Hitchcock G, Brand L, Miller WL, et al. CDOM distribution and CO_2 production on the Southwest Florida Shelf. *Mar Chem* 2004;**89**. http://dx.doi.org/10.1016/j.marchem.2004.02.011.
6. Hill V. Impacts of chromophoric dissolved organic material on surface ocean heating in the Chukchi Sea. *J Geophys Res* 2008;**113**(C7). http://dx.doi.org/10.1029/2007JC004119.
7. Sosik HM, Olson RJ. Automated taxonomic classification of phytoplankton sampled with imaging-in-flow cytometry. *Limnol Oceanogr Methods* 2007;**5**. http://dx.doi.org/10.4319/lom.2007.5.204.
8. Campbell L, Olson RJ, Sosik HM, Abraham A, Henrichs DW, Hyatt CJ, et al. First harmful *Dinophysis* (Dinophyceae, Dinophysiales) bloom in the U.S. is revealed by automated imaging flow cytometry. *J Phycol* 2010;**46**. http://dx.doi.org/10.1111/j.1529-8817.2009.00791.x.
9. See JH, Campbell JL, Richardson T, Pickney JL, Shen R, Guinasso NL. Combining new technologies for determination of phytoplankton community structure in the Northern Gulf of Mexico. *J Phycol* 2005;**41**. http://dx.doi.org/10.1111/j.1529-8817.2005.04132.x.
10. Buskey EJ, Hyatt CJ. Use if the FlowCAM® for semi-automated recognition of red tide cells (*Karenia brevis*) in natural plankton samples. *Harmful Algae* 2006;**5**(6). http://dx.doi.org/10.1016/j.hal.2006.02.003.
11. Greenfield D, Marin III R, Doucette GJ, Mikulski C, Jones K, Jenson S, et al. Field applications of the second generation environmental sample processor (ESP) for remote detection of harmful algae: 2006−2007. *Limnol Oceanogr Methods* 2008;**6**. http://dx.doi.org/10.4319/lom.2008.6.667.

AGU PUBLICATIONS

Journal of Geophysical Research: Oceans

RESEARCH ARTICLE

10.1002/2016JC011650

Mixing and phytoplankton dynamics in a submarine canyon in the West Antarctic Peninsula

Filipa Carvalho[1], Josh Kohut[1], Matthew J. Oliver[2], Robert M. Sherrell[1,3], and Oscar Schofield[1]

[1]Department of Marine and Coastal Sciences, Rutgers University, New Brunswick, New Jersey, USA, [2]College of Earth, Ocean and Environment, University of Delaware, Lewes, Delaware, USA, [3]Department of Earth and Planetary Sciences, Rutgers University, Piscataway, New Jersey, USA

Key Points:
- Underwater gliders observe phytoplankton dynamics in Antarctic coastal seas
- Mixed layer depth and water stability as key driver of seasonal phytoplankton blooms
- Contrary to what was initially hypothesized, mUCDW does not seem to play an important role in the phytoplankton spring bloom in the canyon

Correspondence to:
F. Carvalho,
filipa@marine.rutgers.edu

Citation:
Carvalho, F., J. Kohut, M. J. Oliver, R. M. Sherrell, and O. Schofield (2016), Mixing and phytoplankton dynamics in a submarine canyon in the West Antarctic Peninsula, *J. Geophys. Res. Oceans*, *121*, 5069–5083, doi:10.1002/2016JC011650.

Received 14 JAN 2016
Accepted 1 JUL 2016
Accepted article online 5 JUL 2016
Published online 24 JUL 2016

Abstract Bathymetric depressions (canyons) exist along the West Antarctic Peninsula shelf and have been linked with increased phytoplankton biomass and sustained penguin colonies. However, the physical mechanisms driving this enhanced biomass are not well understood. Using a Slocum glider data set with over 25,000 water column profiles, we evaluate the relationship between mixed layer depth (MLD, estimated using the depth of maximum buoyancy frequency) and phytoplankton vertical distribution. We use the glider deployments in the Palmer Deep region to examine seasonal and across canyon variability. Throughout the season, the ML becomes warmer and saltier, as a result of vertical mixing and advection. Shallow ML and increased stratification due to sea ice melt are linked to higher chlorophyll concentrations. Deeper mixed layers, resulting from increased wind forcing, show decreased chlorophyll, suggesting the importance of light in regulating phytoplankton productivity. Spatial variations were found in the canyon head region where local physical water column properties were associated with different biological responses, reinforcing the importance of local canyon circulation in regulating phytoplankton distribution in the region. While the mechanism initially hypothesized to produce the observed increases in phytoplankton over the canyons was the intrusion of warm, nutrient enriched modified Upper Circumpolar Deep Water (mUCDW), our analysis suggests that ML dynamics are key to increased primary production over submarine canyons in the WAP.

1. Introduction

The cross-shelf canyon systems in the West Antarctic Peninsula (WAP) are considered biological "hotspots" because they are associated with penguin chick rearing locations [*Erdmann et al.*, 2011; *Fraser and Trivelpiece*, 1996]. The association of penguin colonies with deep submarine canyons has led to the hypothesis that phytoplankton productivity is enhanced as a result of water column dynamics in the canyon heads [*Schofield et al.*, 2013]. The presence of the UCDW has been linked to increased phytoplankton productivity [*Kavanaugh et al.*, 2015; *Prézelin et al.*, 2000; *Prézelin et al.*, 2004] which supports a productive regional food web [*Schofield et al.*, 2010], yet the physical mechanisms driving phytoplankton blooms in these canyons are not well understood.

The canyons in the WAP are shelf-incising [*Harris and Whiteway*, 2011], and often connect the off-shelf region to the coast. Heat transport facilitated by cross-shelf canyons/troughs is enhanced by mixing particularly due to tides [*Allen and de Madron*, 2009]. Small-scale roughness in canyons can be responsible for much of the internal tidal energy [*Kunze et al.*, 2002], which tends to be enhanced in canyons. Additionally these regions have enhanced internal waves with periods shorter than that of tides, and has been associated with the vertical mixing over the slope and shelf waters [*Bruno et al.*, 2006]. Tides in these canyons also appear to be important for penguin foraging behavior [*Oliver et al.*, 2013] and krill swarms [*Bernard and Steinberg*, 2013].

These canyons allow UCDW to penetrate across the shelf, providing warmer [*Martinson and McKee*, 2012; *Martinson et al.*, 2008] and nutrient-enriched water to mix with coastal surface waters [*Arrigo et al.*, 2015; *Prézelin et al.*, 2000; *Prézelin et al.*, 2004]. The presence of these canyons has been connected to locally increased sea surface temperature (SST), reduced sea ice coverage, and increased diatom biomass [*Kavanaugh et al.*, 2015]. Using a model, *Allen et al.* [2001] showed that the formation of an eddy over the head of a canyon trapped passive particles such as phytoplankton and small zooplankton in that location.

Globally, light and nutrients are key drivers of a bloom, but their relative importance in primary production depends on the region and the role of local stratification. Light is a key factor regulating phytoplankton growth in polar regions, including the WAP. Several studies have linked shallower mixed layer depths (MLD), which increases the overall light available to phytoplankton [*Holm-Hansen and Mitchell*, 1991; *Mitchell and Holm-Hansen*, 1991; *Moline and Prezelin*, 1996; *Sakshaug et al*., 1991], with increased phytoplankton biomass, especially diatoms [*Fragoso and Smith*, 2012]. Increased irradiance and vertical stratification have also been positively correlated with increased diatom biomass [*Mitchell and Holm-Hansen*, 1991; *Nelson and Smith*, 1991], especially during early spring season [*Fragoso and Smith*, 2012]. Macronutrients are generally abundant throughout the WAP [*Ducklow et al*., 2012; *Serebrennikova and Fanning*, 2004] and although they show marked seasonality [*Clarke et al*., 2008], in most cases they do not seem to limit phytoplankton growth [*Holm-Hansen and Mitchell*, 1991]. Micronutrients such as iron do not seem to limit primary production in the coastal waters of the WAP where canyon heads are located either [*Annett et al*., 2015; *Helbling et al*., 1991; *Martin et al*., 1990], but available data are limited.

It is important to understand the link between some of the physical drivers, like stratification and MLD, and phytoplankton dynamics as the higher trophic levels are dependent on primary producers [*Schofield et al*., 2010]. In this work, we characterize the phytoplankton dynamics in submarine canyons in the WAP using Palmer Deep Canyon (PD) as a focused study area. Here we describe, both temporally and spatially, the phytoplankton spring bloom at PD, using a 6 year Slocum glider dataset. The high spatial and temporal resolution sampling provides a detailed analysis of the phytoplankton and physical dynamics at the head of a submarine canyon in the WAP. While the mechanism initially hypothesized to produce the observed increases in phytoplankton over the canyons was the intrusion of warm, nutrient-enriched mUCDW [*Prézelin et al*., 2000; *Prézelin et al*., 2004; *Schofield et al*., 2013], our analysis suggests that ML dynamics are key to increased primary production over submarine canyons in the WAP.

2. Materials and Methods

2.1. Slocum Gliders

Slocum electric gliders are a robust tool to map in high-resolution the upper water column properties in different environments [*Schofield et al*., 2007] including polar regions [*Kohut et al*., 2013; *Oliver et al*., 2013; *Schofield et al*., 2013]. These 1.5 m torpedo-shaped buoyancy-driven autonomous underwater vehicles provide high-resolution surveys of the physical and bio-optical properties of the water column [*Schofield et al*., 2007]. Data were collected using both shallow (100 m depth range) and deep (1000 m) gliders. However, only data above 100 m were considered for this analysis as we are focusing on processes within the euphotic zone. All gliders were equipped with a Seabird Conductivity-Temperature-Depth (CTD) sensor and WET Labs Inc. Environmental Characterization Optics (ECO) pucks, which measured chlorophyll-*a* fluorescence, and optical backscatter at 470, 532, 660, and 700 nm. Glider based conductivity, temperature, and depth measurements were compared with a calibrated ship CTD sensor on deployment and recovery to ensure data quality, as well as with a calibrated laboratory CTD prior to deployment. Glider profiles were binned into 1 m bins and assigned a midpoint latitude and longitude.

2.2. Sampling Overview

Our analysis includes all available concurrent glider physical and biological profiles in the WAP region (Figure 1) where bathymetric depressions have been linked to deep-water intrusion onto the shelf, with a focus on the dynamics at PD. Overall, the data include 26,455 profiles, 265 deployment days, and 3,937 km flown. For comparison purposes, the WAP-shelf analysis excluded all the points in PD region (purple rectangle in Figure 1).

The deployments on the shelf along the WAP were part of the NSF Palmer-Long-Term Ecological Research Project (PAL-LTER) [*Ducklow et al*., 2007] effort, with the goal of understanding changes (1) in the entire WAP ecosystem with 26 deployments conducted throughout the peninsula from Anvers Island to Charcot Island ($-64°$ to $-69°$ latitude) and (2) with a focus on the PD region where Palmer Station is located. In the PD region (Figure 1, right), data were collected during six field seasons (2010–2015) over the austral summer as part of the NSF PAL-LTER and one field season (2014–2015) as part of the NSF CONVERGE Project [*Kohut et al*., 2014]. Gliders were deployed from Palmer Station (Anvers Island) with the goal of characterizing PD, focusing on the head of the canyon.

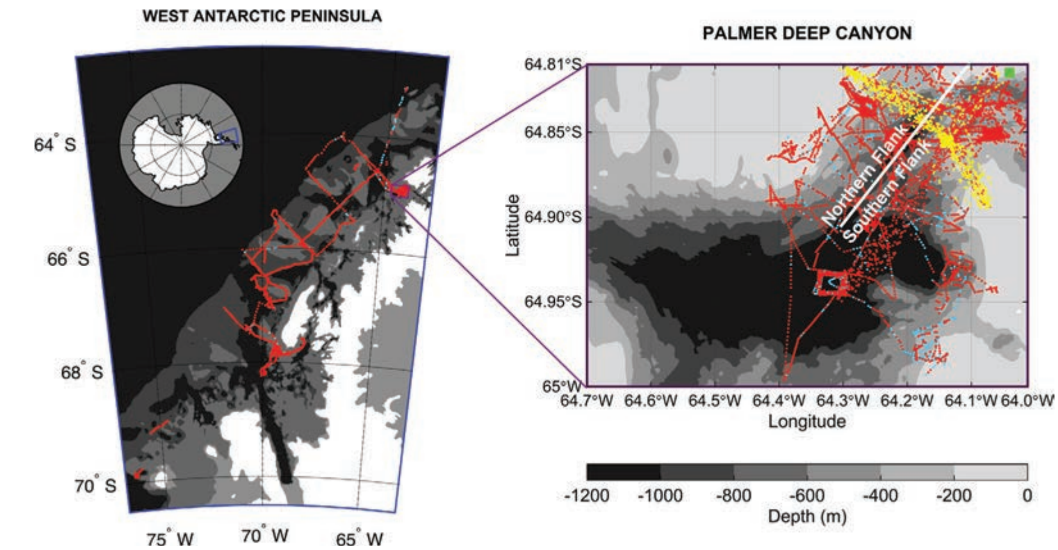

Figure 1. Bathymetry maps overlaid with location of the glider profiles (red – MLD Quality index (QI) > 0.5; blue dots, remaining profiles where MLD was not determined and therefore not included in the analysis, i.e., QI < 0.5) for the regions, (left) WAP and (right) PD. Cross-canyon transects highlighted in yellow from the 2015 mission (gliders ru05 and ud134). White line separates the head of the canyon into northern and southern flanks. Green square indicates location of Station E where dissolved iron data were collected.

PD (Figure 1, right), a cross-shelf canyon bathymetrically similar to others in the WAP, is associated with large penguin colonies [*Fraser and Trivelpiece*, 1996; *Schofield et al*., 2013]. PD extends approximately 22 km in length and 10 km across with a maximum depth of 1420 m. Over the head of the canyon, there is evidence of increased primary production [*Kavanaugh et al*., 2015] and localized penguin foraging [*Oliver et al*., 2013]. Our study will describe glider data collected over varying spatial scales from the WAP shelf, to PD, and, at the smallest scale, the head of PD.

2.3. Mixed Layer Depth Estimation

For each profile, MLD was determined by finding the depth of the maximum water column buoyancy frequency, max (N^2). A quality index (Equation 1) following *Lorbacher et al*. [2006] was used to quantify the uncertainty in the MLD estimate, and to filter out profiles where MLD was not resolved. Using

$$QI = 1 - \frac{rmsd(\rho_k - \overline{\rho})|_{(H_1, H_{MLD})}}{rmsd(\rho_k - \overline{\rho})|_{(H_1, 1.5\times H_{MLD})}} \tag{1}$$

where ρ_k is the density at a given depth (k) and rmsd () denotes the standard deviation of from the vertical mean $\overline{\rho}$ from H_1, the first layer near the surface, to the MLD or 1.5xMLD. This index evaluates the quality of the MLD computation, where MLD was determined with certainty (QI > 0.8), determined but with some uncertainty (0.5 < QI < 0.8) or not determined (QI < 0.5). This index does not take into account the strength of stratification, rather it indicates that there is a homogeneous layer present and the MLD calculated is close to the lower boundary of that vertically uniform surface layer. Higher QI are observed during summer and fall, where sharp gradients at the base of the seasonal mixed layer are present [*Lorbacher et al*., 2006].

MLD criteria were tested and matched against the chlorophyll fluorescence data to evaluate whether the MLD definition chosen was capturing the biological observations (Figure 2). ML-averaged temperature and salinity were calculated by averaging all 1-m binned data points from the surface to the base of the ML.

2.4. Optical Measurements

2.4.1. ML-Averaged and Integrated Chlorophyll

Chlorophyll-*a* (chl-*a*) fluorescence, as measured by the glider ECO pucks, is our indicator of phytoplankton biomass. Discrete in situ water samples were collected from eight depths (0, 5, 10, 20, 35, 50, and 60 m) from CTD casts during each glider deployment and recovery. Water samples were filtered onto 25 mm Whatman GF/F filters and extracted using 90% acetone. Chl-*a* concentration was then measured using a fluorometer and compared to its correspondent glider profiles. QA/QC methods were applied to the data to ensure data quality. Concurrent measurements of optical backscatter and chl-*a* fluorescence were used to

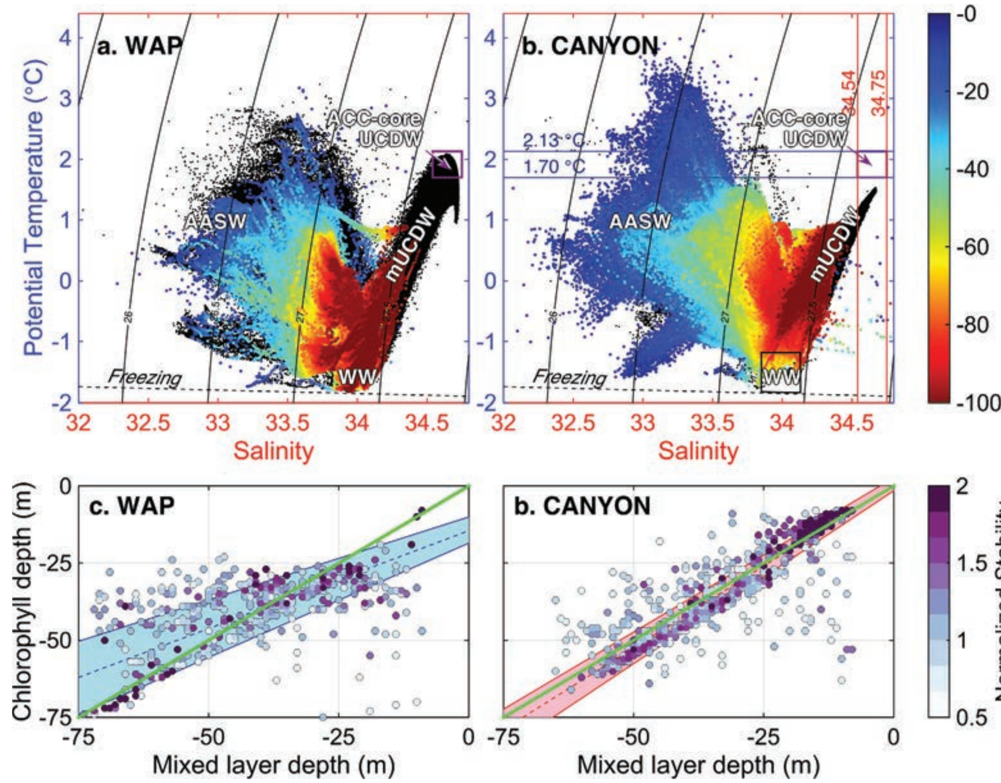

Figure 2. (top row) θ-S for the two areas shown in Figure 1: (a, c) WAP, and (b, d) Palmer Deep Canyon. All data collected below 100 m are plotted in black. Color indicates depth of the water column measurement (upper 100 m of the water column). Primary water masses sampled are indicated and labeled (WW = Winter Water; AASW = Antarctic (summer) Surface Water; mUCDW = modified Upper Circumpolar Deep Water; and the regional ACC-core UCDW. (bottom row) Scatter plots comparing depth of the mixed layer (MLD) with the depth of the lower boundary of the chlorophyll profile for all glider profiles with Quality Index (QI) over 0.5. Shaded region represents 95% confidence intervals (CI) for each region. Trend lines are shown for each area and each quality index. Line 1:1 shown in green. A quality index of 0.5 was also applied to chlorophyll (QI_{chl}) profiles and only profiles with $QI_{chl} > 0.5$ are shown above. Color of the dots represents normalized stability, i.e., the stability frequency at the depth of the ML divided by the median stability of that region.

correct for light-dependent effects. Given the high linear correlation found between backscatter and chlorophyll-*a* fluorescence (R^2 between 0.76 and 0.95 for all deployments), a correction was applied to the latter to account for nonphotochemical quenching [*Behrenfeld et al*., 2005]. Linear regressions were calculated by deployment using all the measurements taken between 20 and 40 m, below the light influenced chl-*a* values and above the possible sedimentary (deep) sources of backscatter. Slope and intercept were calculated and used to correct chlorophyll from the surface to the chlorophyll maximum in each profile. No chlorophyll maxima were found shallower than 15 m.

Integrated and averaged chlorophyll from our defined MLD to the surface were determined using the trapezoid method. Chl-*a* concentration was calculated for each 1 m bin and a cumulative value from the surface down to the MLD was calculated to determine the ML-integrated chlorophyll. The ML-averaged chlorophyll was determined by dividing the ML-integrated chlorophyll by the depth of the mixed layer.

2.4.2. Chlorophyll Depth

A model-2 regression was used to compare the MLD with the lower boundary of the surface chlorophyll fluorescence layer. Following a method adapted from the maximum angle principle [*Chu and Fan*, 2011], the depth of lower boundary of chlorophyll was estimated (referred to as chlorophyll depth in Figure 2). Here we apply the same principle using the maximum angle, as we are interested in calculating the depth at which the chlorophyll profile starts decreasing. Using a vector of n = 7 data points, the depth of the max ($\tan_\theta$) of the chlorophyll profile was determined and used as the chlorophyll depth.

2.5. Climatology

One of the main goals of this study is to characterize the physical setting and to map the seasonal phytoplankton dynamics at the head of the PD by taking advantage of the high spatial and temporal glider coverage. Using a 6 year data set of glider deployments (13,972 profiles after all filters applied), MLDs were calculated for each individual profile and daily MLD averages were calculated for temperature, salinity and chlorophyll by averaging all the values between the surface and the base of the MLD.

Wind and Photosynthetic Available Radiation (PAR) data were collected from an automated weather station (AWS) at Palmer Station, on Anvers Island. Daily averages were calculated using 2 min data.

2.6. Seawater Iron Methods

Surface water was collected at LTER Station E (6.5 km NE of the head of PD), at eight time points between 5 January and 9 March 2015. Samples were cleanly collected in duplicate from a Zodiac inflatable boat using all-polypropylene syringes and filtered directly into 60 mL LDPE bottles (Nalge®) using 25mm Acrodisc (Pall®) 0.45 μm pore size syringe filters, within minutes of sample collection. The resulting samples were stored at 4°C until arrival at Rutgers University, where they were acidified to pH∼2.0 with ultrapure HCl (Fisher Optima®, concentration in seawater 0.012 *M*). The mean of the duplicates is reported if they agree within 15% (difference about the mean), otherwise the lower of the two values is reported.

Seawater samples were prepared for analysis of dissolved Fe and other trace metals at Rutgers University using the commercially available version of an automated preconcentration and matrix elimination system (SeaFAST pico®, ESI, Omaha, NB) which operates on the same principle as reported in *Lagerström et al.* [2013], and employs the method of isotope dilution, but collects eluates offline rather than directly analyzing online.

The eluate solutions, 25-fold concentrates of the trace metals in the sample but with greatly reduced major ion concentrations, were analyzed in medium resolution on a Thermo Element-1 HR-ICP-MS. Determined process blanks for Fe typically averaged 0.040 n*M* and precision was 1–3% standard deviation about the mean. Accuracy was verified by repeated analysis of reference seawater materials (SAFe S and D2, GEOTRACES S, and D), which showed agreement within one standard deviation of the consensus values.

2.7. Cross-Canyon Analysis

To better understand the across canyon spatial variability in MLD and chlorophyll, a 1 month long glider mission was designed with a repeated transect (yellow, Figure 1) that crossed the head of the canyon perpendicularly to its deep channel axis (64°48.7′S and 64°17.9′W to 64°53.7′S and 64°4.2′W, corresponding to the northern and southernmost extreme of the transect, respectively). Gliders used for this temporal/spatial study were both shallow gliders (ru05 and ud134) rated to 100 m. The first glider (ud134) was deployed 6 January 2015 and performed six full transects before ru05 took over its mission of surveying the head of the canyon. The second glider was recovered, brought back to Palmer Station, and redeployed twice more during its mission to replace batteries and resume the cross-canyon mission. Final recovery took place on 8 February 2015. Gliders repeated transects across the head of the canyon 39 times throughout their missions, taking an average of 16 h to complete each cross section. The orientation of PD was used to divide (Figure 1, white line) the head of the canyon into two regions, the northern and the southern flanks.

3. Results

3.1. Physical Properties Around the Palmer Deep Canyon

Gliders were able to map many of the key water masses during the austral summer in the WAP shelf and PD region (top plots of Figure 2). The glider profiles over six field seasons identified the Antarctic Surface Water (AASW), Winter Water (WW), and modified Upper Circumpolar Deep Water (mUCDW). The core-UCDW seen immediately offshore of the WAP shelf ($1.7 \leq T \leq 2.13$; $34.54 \leq S \leq 34.7$, following *Martinson et al.* [2008]) was not present in the canyon; instead the canyon was characterized by a modified colder and fresher mUCDW water mass. This mUCDW extended to depths below 100 m. A second water mass present in PD was the WW (or T_{min}, minimum temperature), defined by $T \leq -1.2$°C and $33.85 \leq S \leq 34.13$. The WW represents the remnants of the mixed-layer water from the previous winter [*Martinson et al.*, 2008] and was found over a range of depths. Above the WW was the AASW (seen in the blue colors of Figure 2). In the canyon, AASW showed a wider range of temperature, salinity, and depth. In both the WAP and PD, this water mass was freshest of all the water masses present. The main differences between the PD and the WAP shelf (PD profiles were excluded from the latter) were the absence of core-UCDW and fresh surface waters at PD. WW was found at greater depths in the WAP compared to the canyon.

We evaluated the relationship between the MLD and chlorophyll depth with a model-2 linear regression (Figures 2c and 2d). In the canyon, the MLD-chlorophyll relationship was close to a 1:1 line with 95% confidence levels with the tightest regression associated with the profiles with the highest stability. Generally the PD had shallower MLD than the WAP. Although more profiles in the WAP fell away from the 1:1 line, there were no significant differences (with a 95% CI) from that line for MLDs below 23 m.

3.2. Coupled Dynamics at Palmer Deep Canyon

3.2.1. Seasonal Climatology of MLD and Chlorophyll

A seasonal climatological analysis of the MLD properties (Figure 3) was conducted by averaging the data between the surface and the corresponding ML for temperature, salinity, and chlorophyll-*a* fluorescence. Generally, MLD shoaled in December, reaching its shallowest depth ($\overline{MLD} = -11 \pm 0.76$ m) in the beginning of January. MLD remained fairly constant (above 20 m) throughout most of January, then started to deepen at the end of this month. The ML in January was generally fresher and colder and as it deepened it became warmer and saltier. Wind speed was fairly constant and low until late January. From then, there was increasing wind speed until the end of the growing season. The summer MLD reached its maximum depth ($\overline{MLD} = -52 \pm 0.66$ m) during the first week of February and then started shoaling again in early March. Both the temperature (Figure 3a) and salinity (Figure 3c) showed a very clear temporal signal. Secondary shoaling of the ML in mid-February was accompanied by a freshening and slight cooling of the ML. The ML-averaged chlorophyll (Figure 3b) was highest when MLD was shallowest, i.e., throughout January. Going into February, when MLD was deepest, chlorophyll concentrations were low. ML-averaged chlorophyll showed a direct relationship with MLD ($y = 0.136x + 7.03$; $r^2 = 0.42$; $p < 0.0002$), with higher chl-*a* when MLD is shallow and lower chl-*a* when deeper. An increase in chlorophyll was observed when MLD shoaled again later in the season. Surface dissolved iron (Fe) concentrations (Figure 3d) at a station 6.5 km from the

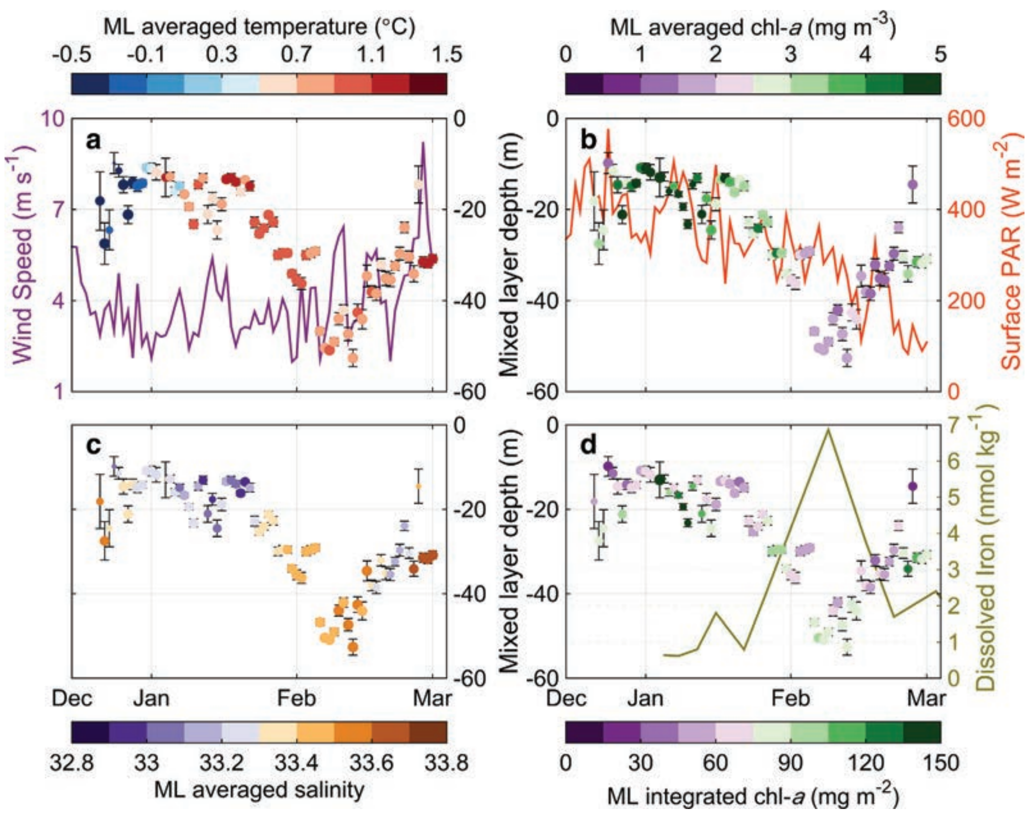

Figure 3. Mixed Layer Depth (MLD) in the Palmer Deep region showing evolution on MLD throughout the spring/summer season. Color denotes ML-averaged: (a) temperature, (b) chlorophyll, (c) salinity, and (d) ML-integrated chlorophyll. Marker size represents the standard error of the variable in color (larger marker represents lower standard error, and vice-versa). Standard error of depth MLD is shown in the vertical bars. Averages were calculated using 13,972 individual glider profiles collected during 2010–2015 deployments. Daily averages of wind and surface PAR are shown in Figures 3a and 3b, respectively. Surface iron measurements at Station E are shown in Figure 3d from 2014–2015 season.

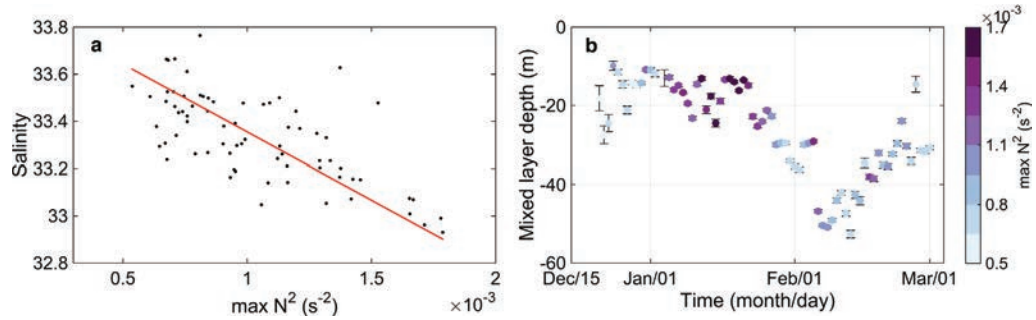

Figure 4. Water stability in the Palmer Deep region using daily averages: (a) salinity and maximum of stability frequency (max N^2); (b) seasonal climatology of MLD with max(N^2). Averages were calculated using 13,972 individual glider profiles collected during 2010–2015 deployments.

canyon head, exhibited an inverse relationship with chlorophyll, reaching maximum values when MLD was deepest. Throughout the season, Fe concentrations at this station never fell below 0.6 nmol kg^{-1}.

The strength of water column stratification at the depth of the ML (max N^2) was seen to vary through the season (Figure 4). In January, when chlorophyll concentrations were high, the water column was more stable (Figure 4b) and over the season the water column stability decreased. Stability was inversely correlated with salinity ($R^2 = -0.77$, $p < 0.0001$), with higher stability associated with shallower MLD and lower salinities (Figure 4a) suggesting the importance of sea ice melt and potentially glacial melt in phytoplankton primary productivity.

3.2.2. Cross-Canyon Variability

Four glider deployments, conducted over 1 month, collected high-resolution data across the head of the canyon in PD with the goal of understanding the dynamics of the water masses in the canyon over the summer season. The mission characterized the spatial variability between the northern and southern regions of PD (Figure 1). A temporal and spatial analysis of the θ-S plot is shown in Figure 5. The AASW, represented by the shallowest depths (blue), was cold and fresh in the beginning of January. As the month progressed, surface water became warmer and saltier. Winter water ($T < -1.2$°C), was present in the beginning of January and was found in deeper waters as time progressed. Deeper water (reds) was warmer and saltier in the beginning of January. The AASW was warmer at the beginning of February (Figure 5, last column).

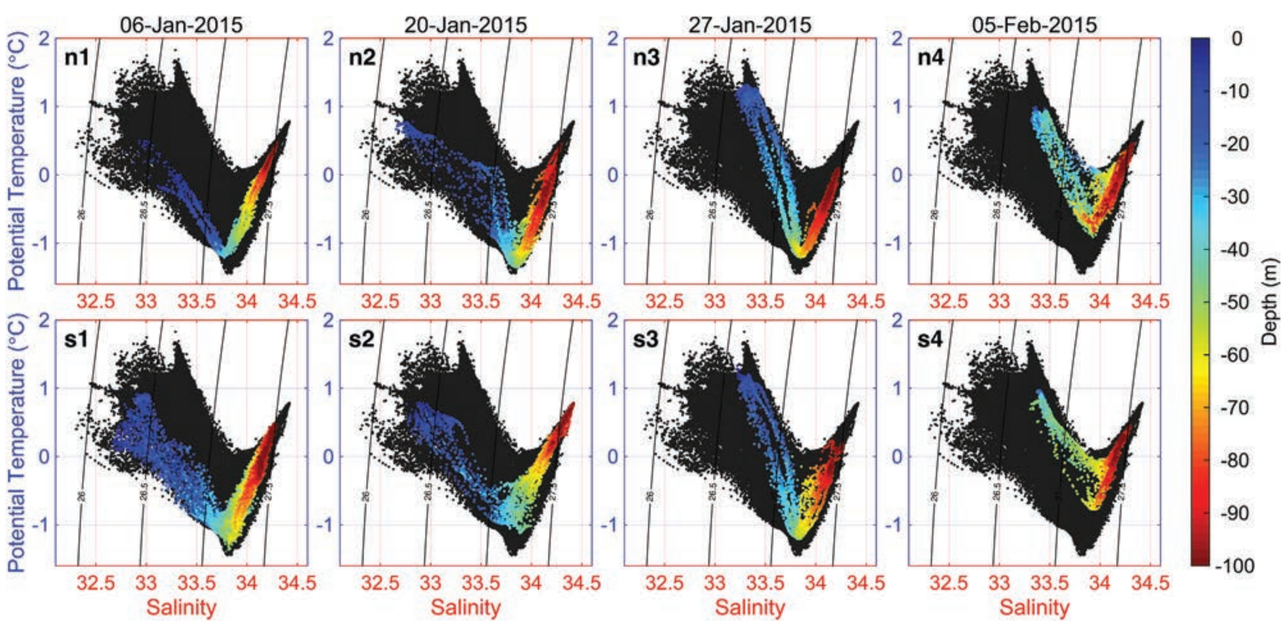

Figure 5. θ-S scatter plots from ru05/ud134 gliders, comparing the water masses of Northern (N, top) and Southern (S, bottom) flanks of the head of the Palmer Deep canyon through time (plots left to right). Black dots represent all glider measurements (both areas) for the entire deployment. Color denotes depth of the water column measurement.

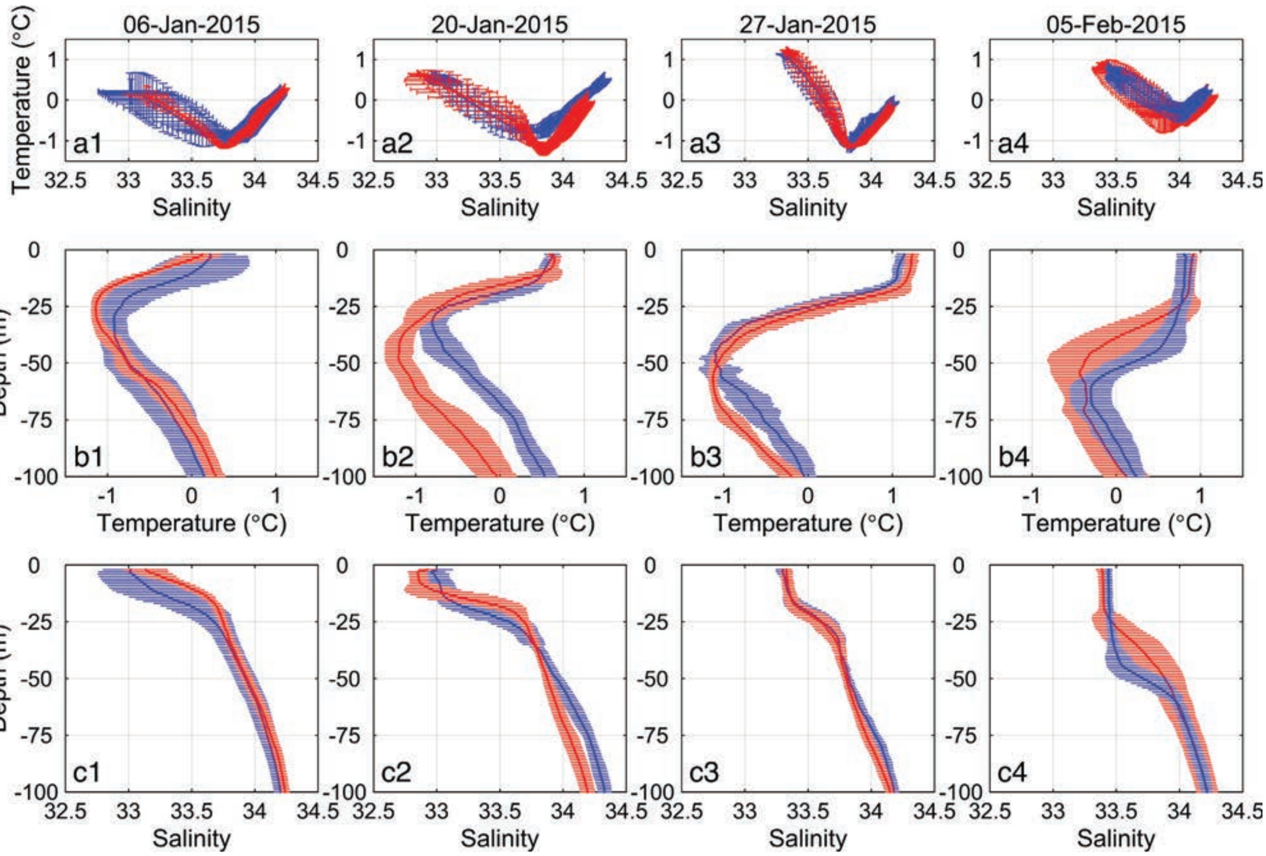

Figure 6. Decomposition of the θ-S diagrams from Figure 5, for Northern (red) and Southern (blue) flanks of the head of the Palmer Deep canyon: (a1–a4) average θ-S diagram with average (center points) and standard deviation (horizontal bars for salinity; vertical bars for temperature), (b1–b4) average temperature profile, (c1–c4) average salinity profile, with standard deviation (shaded area), per depth for each time point.

Given the importance of ML structure in driving the chlorophyll, the θ-S plots in Figure 5 were decomposed into average depth profiles (Figure 6). The average temperature (b plots, middle row) and salinity (c plots, bottom row) depth profiles for each time point, were calculated and then compared between the two regions (blue and red) at the head of the PD canyon. The top row in Figure 6 is for the average distribution and respective standard deviation for the temperature and salinity for each depth and different time periods over the month. The southern region (blue, Figure 6a1) showed overall a wider range in temperature and salinity in the beginning of January. This increased variance was especially marked in AASW, which was characterized by lower salinities. This trend reversed over the month with the northern region of the canyon (red) showing a wider variance in surface water properties (both temperature and salinity). Observed differences were more influenced by temperature (Figures 6b1−6b4) than by salinity (Figures 6c1−6c4). Although surface temperatures were similar between regions, below the MLD, the northern region (red) had consistently lower temperatures (Figures 6b1−6b4) compared to the southern region. Differences of over 0.5°C, sometimes almost up to 1°C, were found at depth on 20 January (Figure 6b2). Both areas showed similar salinity profiles in January. The only salinity differences found were in February and were mostly due to deeper MLDs in the southern region.

The ML-averaged and integrated chlorophyll were calculated for each profile and plotted against its corresponding MLD (Figure 7). Here we define the end of the bloom (21/22 January) by evaluating the evolution of individual profiles of chlorophyll and the change of the trends between MLD and chl-*a* through time. This date separated two time periods, one during bloom conditions (blue, from 5 to 21 January) and the second during postbloom conditions (red, from 22 January to 9 February). Bloom conditions were characterized by a clear progression from a moderately shallow (30 m) and highly productive MLD (dark blue) to an even shallower (8 m) and less productive ML (light blue). Both ML-integrated (Figure 7a) and averaged chlorophyll (Figure 7b) showed similar trends. While ML-averaged chlorophyll decreased with the deepening of

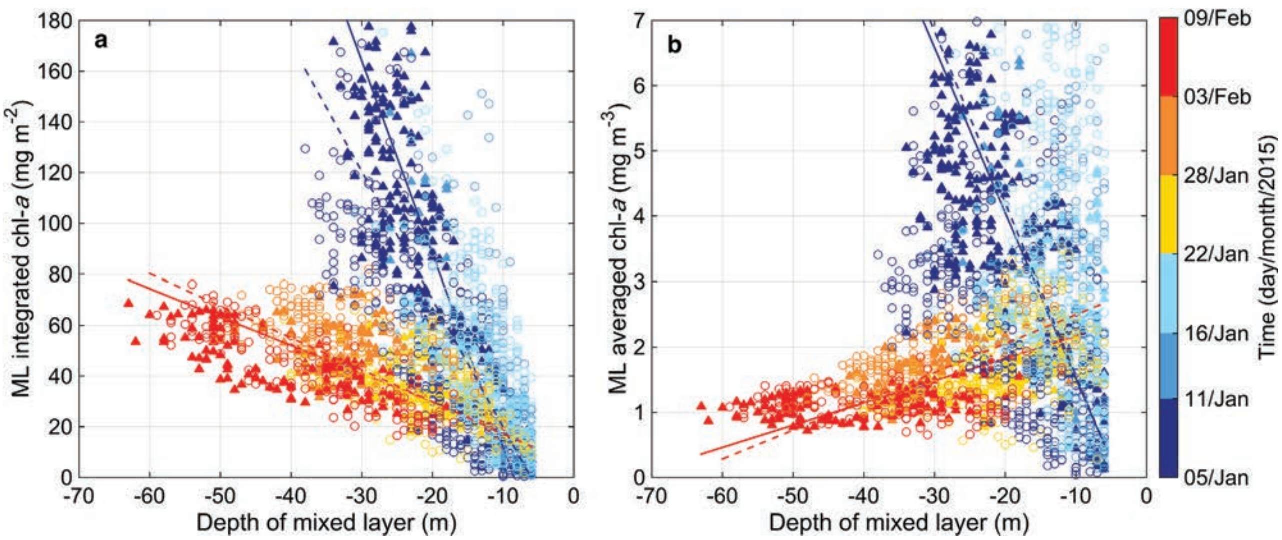

Figure 7. Relationship between the depth of the mixed layer (defined by the maximum water column buoyancy frequency, N^2) and: (a) ML-integrated or (b) ML-averaged chlorophyll concentrations. Comparison between the northern (filled marker, solid line) and southern (open marker, dashed line) flanks. The colors indicate time. Lines represent the trends seen between 6 January to 21 January (blue) and 22 January to 9 February (red).

the ML and consequent ending of the bloom, ML-integrated chlorophyll increased during this postbloom condition (Figures 7 and 9e). When comparing the two regions (northern-solid line; southern-dashed line), few differences were found.

Sustained cross-canyon sampling in 2015 allowed for an analysis for the spatial differences within the canyon. The time-averaged transect (6–28 January 2015) for temperature and salinity is shown in Figures 8a and 8b. While the warm surface layer appears uniform in both regions, a thicker and colder layer (light blue), with a tongue of colder ($T < -1°C$; dark blue) water at mid depths of 45-70 m was evident in the northern region. The southern region showed warmer and saltier water at depths below the colder layer. A fresher layer was evident in the surface few meters in the northern region. The bottom plot of Figure 8 shows a time-averaged mixed layer depth (blue dotted line) and upper 100 m integrated chlorophyll (solid green line) for each 1 km along the transect line. Northern region was characterized by shallower MLD

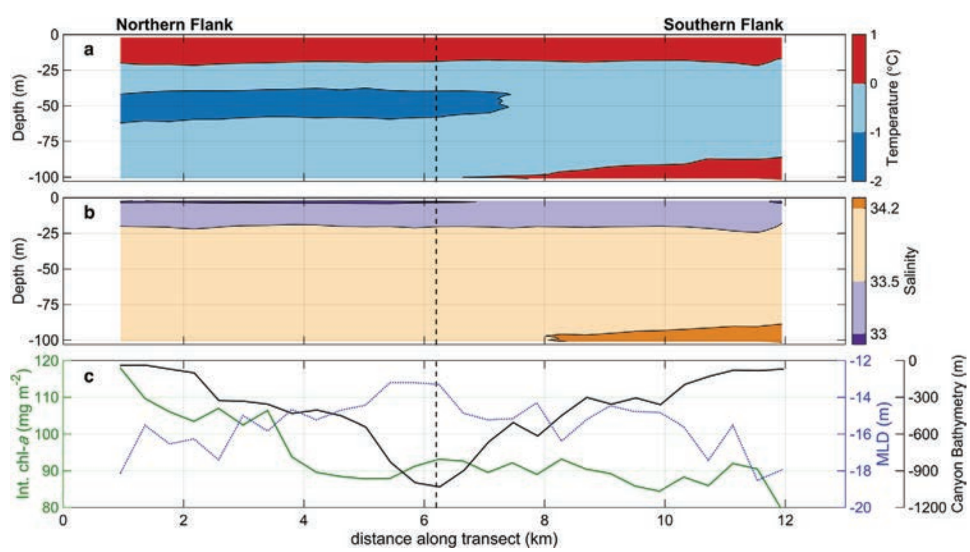

Figure 8. Time-averaged transect (6 January to 28 January 2015). Northern and Southern regions are separated by the dashed vertical line at km 6.2 in the along-track distance. Variables plotted are time-averaged transect of: (a) temperature, where warm layer at the surface represents AASW, dark blue denotes WW, bottom layer in red indicates possibly mUCDW intrusion; (b) salinity and (c) mixed layer depth (MLD; blue-dotted line) with integrated chlorophyll (upper 100 m; green solid line) and canyon bathymetry (black solid line).

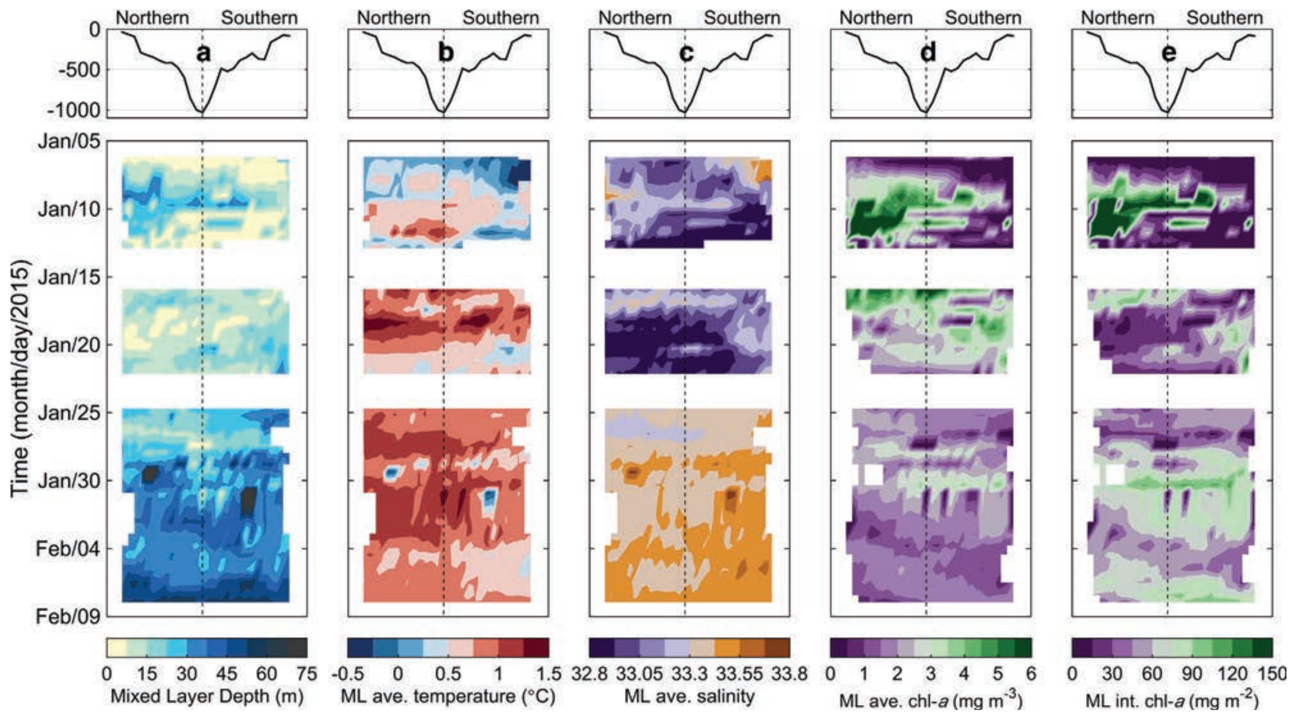

Figure 9. (top) Bathymetry of the cross-canyon transect performed by ru05 (yellow, Figure 1). (bottom) Hovmöller diagram of the temporal evolution of each transect by ru05 regarding: (a) mixed layer depth, (b–d) ML-averaged (b) temperature, (c) salinity, (d) chlorophyll, and (e) ML-integrated chlorophyll. Dashed line separates northern and southern flanks of the head of the Palmer Deep canyon.

and increased integrated chlorophyll in the upper 100 m of the water column while the southern region showed overall deeper MLD and slightly lower integrated chlorophyll concentrations.

A repeated glider section across the head of the canyon captured the temporal and spatial variability of the phytoplankton (Figure 9). Each glider cross section was interpolated through space and time with a resolution of 500 m and 16 h, respectively. Temporal gaps in Figure 9 correspond to glider recovery and redeployment after battery exchange. The top plot shows bathymetry of the two regions (northern and southern) being fairly symmetrical, going from deeper (~1000 m) depths at the center to shallower depths (~100 m) when moving away from the deep trough.

Again, the temporal signal is the most evident across all five plots. Early in January, the MLD was shallow, colder, and fresher. This period was also characterized by increased chlorophyll (both ML-integrated and averaged chlorophyll). As January progressed, the MLD (Figure 9a) deepened, accompanied by warming (Figure 9b) and increased salinity (Figure 9c) in the upper ML with a decrease in the chlorophyll concentration (Figures 9d and 9e). An increase in ML-integrated chlorophyll (Figure 9e) late in the mission is also present in the climatology (Figure 3).

The magnitude of the spatial variability was less than the temporal variability observed over the entire summer season, yet differences were observed, particularly in the physical properties of the water. The MLD was overall shallower in the northern region. This is especially true for the second and fourth deployments. Warmer temperatures and lower salinities also characterized this region. This pattern was also clear when looking at the homogeneous surface ML later in the season (Figures 6b4 and 6c4).

4. Discussion

The WAP ecosystem is characterized by high interannual phytoplankton variability [*Smith et al*., 2008], with chlorophyll-*a* showing a wide range in both time and space [*Moline et al*., 1997; *Montes-Hugo et al*., 2008; *Smith et al*., 1998]. Chlorophyll concentrations are highest near shore with a decreasing gradient moving offshore [*Vernet et al*., 2008]. The canyons are known hotspots for penguin foraging [*Kahl et al*., 2010; *Oliver et al*., 2012; *Schofield et al*., 2013] with increased chlorophyll compared to coastal regions with shallow bathymetry [*Kavanaugh et al*., 2015]. While previous studies have focused on the primary productivity over the entire WAP [*Moline and Prezelin*, 1996; *Montes-Hugo et al*., 2010; *Prézelin et al*., 2004], the high-resolution sampling capabilities introduced with gliders, allowed us to conduct a detailed analysis of the canyon primary production focusing on the physical forcing of the increased production observed over submarine canyons.

4.1. The Seasonal Cycle at Palmer Deep Canyon

4.1.1. Primary Water Masses

A fundamental question regarding phytoplankton dynamics in the region [*Schofield et al*., 2013] involves the supply of heat and nutrients from the warm, deep water (UCDW) found at depth off the shelf. Canyons provide a conduit for this water to move across the shelf [*Martinson et al*., 2008]. No direct pathways have been found of ACC-core UCDW onto the Palmer Deep Canyon, so no ACC-core UCDW is present in the canyon, but by looking at T_{max} at depth, we find a modified-UCDW (relatively colder and fresher than pure UCDW) at depth. Because the bulk of the mUCDW is found at deeper depths and the gliders are usually only sampling the upper 100 m of the water column, we are only partially capturing this intrusion onto the canyon. This intrusion however is not observed to reach the euphotic zone until after the growing season. Therefore it is unlikely that it plays an important role in supplying nutrients to primary producers over the canyon during the growing season.

The WW, identified by T_{min} in the profile, was found above mUCDW. This water mass is the remnant surface water from the preceding winter season and is typically found at 50–60 m. WW has a very clear seasonal pattern (Figure 5), showing a well-defined and strong presence early in the season, followed by erosion by mixing with warmer water from above and below as the season progresses. The increase in solar radiation and winds, typical of the late summer season in the region, deepens the MLD, further mixing AASW with the WW below. As the latter, saltier water mass is slowly eroded, together with the decrease in freshwater input later in the season due to the reduction in sea ice meltwater, a marked increase in the overall salinity of surface water is observed.

4.1.2. Phytoplankton Seasonal Dynamics

In the WAP, chlorophyll-*a* variability has been correlated with local physical forcing such as wind, water column stability, and sea ice [*Saba et al*., 2014]. The relationship between sea ice dynamics and biological productivity is complex. While decreasing sea ice cover can remove the shading effect of ice resulting in higher productivity, as seen in the southern region of the WAP [*Montes-Hugo et al*., 2009; *Saba et al*., 2014], at the same time, the decrease in fresh water input from melting sea ice will result in lower stratification and likely deeper MLDs, which should lead to decreased primary production resulting from decreasing average light levels [*Vernet et al*., 2008].

The high variability in the timing of the sea ice retreat [*Stammerjohn et al*., 2008] matches the high variability seen in the MLD (*y*-axis, Figure 3) in late December. Shallower MLDs in the early growing season show both increased stability (Figure 4) and decreased salinity (Figure 3d). They have been associated with low wind speeds over weekly timescales [*Moline*, 1998; *Moline and Prezelin*, 1996], freshwater input from glacial and sea ice melt [*Meredith et al*., 2008], and surface warming from incoming solar energy. The input of fresh water from glacial and sea ice melting shoals the MLD, increases the stability of the water column [*Garibotti et al*., 2003] and restricts deep mixing. This creates a stable upper water column in which phytoplankton cells are allowed to remain in a favorable light regime [*Garibotti et al*., 2003; *Vernet et al*., 2008]. In addition, the canyon's proximity to land shelters the canyon head from storms and strong winds seen offshore [*Hofmann et al*., 1996], helping to maintain the observed shallow and stable MLD. Modeling work by *Mitchell and Holm-Hansen* [1991] concluded that intense phytoplankton blooms develop when MLD is shallower than 25 m, there is no limitation by nutrients and specific loss rate is $\sim$0.3–0.35 d^{-1}, with grazing and respiration comprising over 2/3 of this loss. Although we do not have direct measurements of nutrients or loss rates at the same time as the glider profiles, our MLD and chlorophyll data match this model, with high concentrations of chlorophyll observed in MLD of 25–30 m or shallower and declining when the MLD is deeper. Note that there was a decrease in ML-averaged chlorophyll when MLD shoals to values close to 10 m (Figure 7), suggesting some photoinhibition processes due to high light or light limitation by self-shading [*Moline et al*., 1996].

The mechanisms driving the chlorophyll decrease later in the growing season remain an open question. Data show that decreases in ML-averaged chl-*a* are accompanied by a deepening of the ML (Figures 3 and 7). Decrease in freshwater input together with increased vertical mixing from wind forcing causes MLD to deepen and water stability to decrease. Another contributor to this decreased water column stability is the warming of WW by vertical mixing with intruding mUCDW from below. The deepening of the ML can decrease the ML-averaged chl-*a* concentrations by diluting a high concentration of phytoplankton over a larger depth interval; this idea is also supported by the increase in ML-integrated chl-*a* as MLD deepens (red line; Figure 7a), indicating there are phytoplankton below the MLD. While the deepening of the ML alone could drive down the ML-averaged chl-*a* concentrations as it also decreases the mean light levels required for phytoplankton photosynthesis [*Mitchell and Holm-Hansen*, 1991], other factors, such as nutrient limitation and grazing, can also play a role in this decrease. Although gliders do not provide in situ measurements of the nutrient concentrations in the water column, an inspection of historical nutrient data from the LTER Station E (6.5 km NE of the sampled area) shows that no macronutrient limitation is observed throughout the season [*Ducklow et al*., 2012]. The scarce micronutrient (trace metal) studies in the region make it difficult to evaluate the micronutrient limitation question, especially regarding iron deficiency after a bloom. Iron is known to be a limiting factor controlling primary productivity in the Southern Ocean, mainly due to the lack of efficient supply mechanisms [*Boyd et al*., 2012]. However, recent studies have shown that regions in close proximity to the coast in Antarctica, such as canyon heads, are not iron limited, and that in certain parts of the WAP there is enough iron to allow the potential utilization of all macronutrients available [*Annett et al*., 2015]. Surface dissolved Fe:PO_4 ratios measured at Station E were always above 1.1 mmol mol^{-1}, much higher than cellular Fe:P$\sim$0.2 mmol mol^{-1} measured in Fe-limited Southern Ocean waters [*Twining and Baines*, 2013]. In addition, dissolved Fe was always $>$0.5 nmol/kg (Figure 3), higher than dissolved Fe concentrations $\sim$0.1 nmol kg^{-1} typical of Fe-limited waters [*Sedwick et al*., 2008], further supporting our inference that Fe is not limiting phytoplankton production at the head of Palmer Canyon. Increases in surface dissolved Fe concentrations at Station E (Figure 3) are concurrent with the deepening of the ML, indicating a potential source of iron to the surface waters. The presence of WW, acting as a physical barrier between the AASW and mUCDW implies that this Fe source is likely related to vertical mixing from shallow sediments or lateral advection of surface inputs such as glacial meltwater. Losses by grazing are likely a contributing cause of chl-*a* decline as canyons are known to aggregate zooplankton prey for the apex predators [*Bernard and Steinberg*, 2013], however, we do not have concurrent zooplankton data to address this question.

The timing of a secondary shoaling of the MLD in late February/early March is matched with a freshening of the ML and a small increase in water column stability. The rising air temperatures in the summer months drive the increased fresh, glacial meltwater input onto the surface coastal waters. Concurrent with this, a secondary peak in chl-*a* is observed, consistent with previous work by *Moline and Prezelin* [1996], and a reduction of dissolved Fe to intermediate values, presumably a result of decreased supply from below and increased Fe removal in association with the chl-a increase, balancing the increased supply of Fe from glacial meltwater.

4.2. Palmer Deep Cross-Canyon Spatial Analysis

While most phytoplankton studies in the WAP canyons have focused on the temporal (seasonal and interannual) variability [*Kavanaugh et al*., 2015; *Moline and Prezelin*, 1996], little is known about what is driving the high small-scale spatial variability observed in the foraging behavior of penguins [*Oliver et al*., 2013]. Spatial differences in phytoplankton are also likely to occur as a cyclonic eddy feature is expected to dominate the upper water column circulation over the canyon and to aggregate small nonmigratory species at the head of canyons, particularly at the downstream side of the canyon [*Allen et al*., 2001].

Preliminary analysis of CODAR High-Frequency Radar (HFR) data at PD [*Kohut et al*., 2014], which provides surface maps of ocean currents, shows on average for the months of January and February, a strong Northeastward (onshore) current toward the Bismarck Straight that crosses the southern region of this study, with average speeds an order of magnitude faster than the flow that crosses the northern region. On the other hand, although a less prominent feature, a weaker Southeastward (offshore) coastal current crosses the northern flank of the transect. Initial analysis of the mean current standard deviation shows higher variability in the flow that crosses the southern region [*Todoroff et al*., 2015]. This highly energetic and variable flow can explain the increased variability in the water properties in that region as seen in Figures 5 and 6. This variability decreases with the temporal evolution of the water masses, with surface water becoming warmer and saltier and with WW being warmed both from above and below. Main spatial differences in water properties can be found at depth, with the northern region showing overall colder temperatures, as evident by the presence of WW until later in the season. The southern flank shows intrusions of warm, salty, deep water likely from the onshore current forcing mUCDW onto the shelf that then mixes upward, weakening the signal of WW from below (Figure 8). The northern flank shows a strong presence of winter water and a fresh water lens that comes from glacial and sea ice melt brought by the coastal current. The differences in magnitude and the variability of the currents between the two regions are likely to contribute to the stability of the MLD dynamics on local scales. With less energetic currents, the water in the northern region is likely to show higher residence times, ideal for local primary production to occur. On the other hand, southern region mean currents show higher variability and magnitude that can potentially impede local production to fully thrive as the timescales of the mean currents are shorter than the doubling time of Antarctic phytoplankton.

Another factor known to control primary production is the availability of iron [*Twining and Baines*, 2013]. Although there are several potential sources of iron to surface waters (glacial melt, sea-ice melt, seawater interaction with shallow sediments, atmospheric input and deep water upwelling), glacial meltwater has been identified as one of the most important [*Dierssen et al*., 2002; *Hawkings et al*., 2014], by its volume flux and because of the continuous yet variable supply during the growing season [*Meredith et al*., 2008]. The close proximity of canyon head systems on the WAP to the coast where glaciers are prominent features, may also contribute favorably to the increased production seen in the canyon as the increased glacial meltwater input (and pushed by the coastal current) contributes to increased water column stability and is a potential source of iron to the system [*Alderkamp et al*., 2015; *Annett et al*., 2015; *Arrigo et al*., 2015]. While mUCDW upwelling enriched with iron from sediments has been proposed as a potential source of iron to coastal WAP regions [*Annett et al*., 2015], at Ryder Bay (340 km south of Palmer Deep) it was found to account for very little of the iron input due to the highly stratified waters during the growth season. It is however identified as an important source of iron over annual or longer time-scales. The same seems true for the overall nutrient budget. Glider observations during the austral spring and summer show no evidence of this mUCDW upwelling reaching surface waters during the growth season as there is a clear layer of WW physically separating surface waters from the deep waters below while the bloom is present. However, this water mass is slowly warming throughout the season due to vertical mixing from above and below, contributing to the decreased water column stability. While there is no evidence of the surface waters at PD being limited by macro or micronutrients at any point, a drawdown in the nutrient pool is apparent while the bloom is thriving [*Ducklow et al*., 2012]. After the growth season, as the stratification weakens, mUCDW intrusions from below will replenish the surface water with both micro and macronutrients required for the following year's spring phytoplankton bloom.

5. Conclusions

Understanding the spatial and temporal variability of phytoplankton is important, especially to assess the dynamics of higher trophic levels as they are dependent on primary producers for food source. The high-resolution capabilities of gliders allow sampling and coverage at appropriate scales to evaluate phytoplankton dynamics. Using the 6 year glider observations over PD, we were able to describe the fine temporal and spatial variability of the phytoplankton seasonal cycle and relate it to its main physical drivers, namely MLD and water stability. Although interannual variability was observed in the data, the shoaling of the MLD in late spring matching increased chlorophyll concentration was a pattern observed in all years sampled (2010–2015), as more light becomes available to the phytoplankton community. Following this period, a summer (February) deepening of the MLD was accompanied by decreased chlorophyll concentration.

Observations showed that MLD dynamics and chlorophyll variability were tightly coupled in both time and space. Spatial variability was evaluated by glider transects across the head of the canyon. While MLD dynamics was similar in the northern and southern canyon regions, the physical setting observed in different regions of the canyon, such as water column stratification and water masses present, explain some of the observed chlorophyll variability. Preliminary analysis of surface currents provides an insight on what could be driving some of the observed differences in water column structure that are key for phytoplankton development. The northern region with increased chlorophyll showed a more coastal influence, with increased freshwater input, slower currents, and increased stratification, while the southern region with lower chlorophyll showed more influence from offshore with faster currents and more intrusions of mUCDW from below. However, further sampling and analysis is necessary to evaluate whether water column physics is driving the spatial differences in chlorophyll concentrations alone or if iron supply plays a role in the system at any point in the growth season.

Acknowledgments
We thank the two anonymous reviewers whose suggestions helped improve and clarify this manuscript. The research was supported by the National Science Foundation grants ANT-0823101 (Palmer-LTER), ANT-1327248 and ANT-1326541 (CONVERGE) and ANT-1142250 (iron WAP). Filipa Carvalho was funded by a Portuguese doctoral fellowship from Fundação para a Ciência e Tecnologia (DFRH-SFRH/BD/72705/2010). Glider data can be accessed at ERDDAP server at http://erddap.marine.rutgers.edu/erddap/info/. Weather data can be access at http://oceaninformatics.ucsd.edu/datazoo/data/pallter/datasets.

References

Alderkamp, A., G. L. van Dijken, K. E. Lowry, T. L. Connelly, M. Lagerström, R. M. Sherrell, C. Haskins, E. Rogalsky, O. Schofield, and S. E. Stammerjohn (2015), Fe availability drives phytoplankton photosynthesis rates during spring bloom in the Amundsen Sea Polynya, Antarctica, *Elementa*, *3*(1), 000043.

Allen, S. E., and X. D. de Madron (2009), A review of the role of submarine canyons in deep-ocean exchange with the shelf, *Ocean Sci.*, *5*(4), 607–620.

Allen, S. E., C. Vindeirinho, R. E. Thomson, M. G. G. Foreman, and D. L. Mackas (2001), Physical and biological processes over a submarine canyon during an upwelling event, *Can. J. Fish. Aquat. Sci.*, *58*(4), 671–684, doi:10.1139/cjfas-58-4-671.

Annett, A. L., M. Skiba, S. F. Henley, H. J. Venables, M. P. Meredith, P. J. Statham, and R. S. Ganeshram (2015), Comparative roles of upwelling and glacial iron sources in Ryder Bay, coastal western Antarctic Peninsula, *Mar. Chem.*, *176*, 21–33, doi:10.1016/j.marchem.2015.06.017.

Arrigo, K. R., G. L. van Dijken, and A. L. Strong (2015), Environmental controls of marine productivity hot spots around Antarctica, *J. Geophys. Res. Oceans*, *120*, 5545–5565, doi:10.1002/2015JC010888.

Behrenfeld, M. J., E. Boss, D. A. Siegel, and D. M. Shea (2005), Carbon-based ocean productivity and phytoplankton physiology from space, *Global Biogeochem. Cycles*, *19*, GB1006, doi:10.1029/2004GB002299.

Bernard, K. S., and D. K. Steinberg (2013), Krill biomass and aggregation structure in relation to tidal cycle in a penguin foraging region off the Western Antarctic Peninsula, *ICES J. Mar. Sci.*, *70*(4), 834–849, doi:10.1093/icesjms/fst088.

Boyd, P. W., K. R. Arrigo, R. Strzepek, and G. L. van Dijken (2012), Mapping phytoplankton iron utilization: Insights into Southern Ocean supply mechanisms, *J. Geophys. Res.*, *117*, C06009, doi:10.1029/2011JC007726.

Bruno, M., A. Vazquez, J. Gomez-Enri, J. M. Vargas, J. G. Lafuente, A. Ruiz-Canavate, L. Mariscal, and J. Vidal (2006), Observations of internal waves and associated mixing phenomena in the Portimao Canyon area, *Deep Sea Res., Part II*, *53*(11–13), 1219–1240, doi:10.1016/j.dsr2.2006.04.015.

Chu, P. C., and C. W. Fan (2011), Maximum angle method for determining mixed layer depth from seaglider data, *J. Oceanogr.*, *67*(2), 219–230, doi:10.1007/s10872-011-0019-2.

Clarke, A., M. P. Meredith, M. I. Wallace, M. A. Brandon, and D. N. Thomas (2008), Seasonal and interannual variability in temperature, chlorophyll and macronutrients in northern Marguerite Bay, Antarctica, *Deep Sea Res., Part II*, *55*(18–19), 1988–2006, doi:10.1016/j.dsr2.2008.04.035.

Dierssen, H. M., R. C. Smith, and M. Vernet (2002), Glacial meltwater dynamics in coastal waters west of the Antarctic peninsula, *Proc. Natl. Acad. Sci. U. S. A.*, *99*(4), 1790–1795, doi:10.1073/pnas.032206999.

Ducklow, H. W., K. Baker, D. G. Martinson, L. B. Quetin, R. M. Ross, R. C. Smith, S. E. Stammerjohn, M. Vernet, and W. Fraser (2007), Marine pelagic ecosystems: The west Antarctic Peninsula, *Philos. Trans. R. Soc. B*, *362*(1477), 67–94.

Ducklow, H. W., A. Clarke, R. Dickhut, S. C. Doney, H. Geisz, K. Huang, D. G. Martinson, M. P. Meredith, H. V. Moeller, and M. Montes-Hugo (2012), The Marine System of the Western Antarctic Peninsula, in *Antarctic Ecosystems: An Extreme Environment in a Changing World*, edited by A. D. Rogers, et al., pp. 121–159, John Wiley & Sons, Ltd., Chichester, U. K., doi:10.1002/9781444347241.ch5.

Erdmann, E. S., C. A. Ribic, D. L. Patterson-Fraser, and W. R. Fraser (2011), Characterization of winter foraging locations of Adelie penguins along the Western Antarctic Peninsula, 2001-2002, *Deep Sea Res., Part II*, *58*(13–16), 1710–1718, doi:10.1016/j.dsr2.2010.10.054.

Fragoso, G. M., and W. O. Smith (2012), Influence of hydrography on phytoplankton distribution in the Amundsen and Ross Seas, Antarctica, *J. Mar. Syst.*, *89*(1), 19–29, doi:10.1016/j.jmarsys.2011.07.008.

Fraser, W. R., and W. Z. Trivelpiece (1996), Factors controlling the distribution of seabirds: Winter-summer heterogeneity in the distribution of adélie penguin populations, *Antarct. Res. Ser.*, *70*, 257–272.

Garibotti, I. A., M. Vernet, M. E. Ferrario, R. C. Smith, R. M. Ross, and L. B. Quetin (2003), Phytoplankton spatial distribution patterns along the western Antarctic Peninsula (Southern Ocean), *Mar. Ecol. Prog. Ser.*, *261*, 21–39, doi:10.3354/meps261021.

Harris, P. T., and T. Whiteway (2011), Global distribution of large submarine canyons: Geomorphic differences between active and passive continental margins, *Mar. Geol.*, *285*(1–4), 69–86, doi:10.1016/j.margeo.2011.05.008.

Hawkings, J. R., J. L. Wadham, M. Tranter, R. Raiswell, L. G. Benning, P. J. Statham, A. Tedstone, P. Nienow, K. Lee, and J. Telling (2014), Ice sheets as a significant source of highly reactive nanoparticulate iron to the oceans, *Nat. Commun.*, *5*, 3929, doi:10.1038/ncomms4929.

Helbling, E. W., V. Villafane, and O. Holmhansen (1991), Effect of Iron on Productivity and Size Distribution of Antarctic Phytoplankton, *Limnol. Oceanogr.*, *36*(8), 1879–1885.

Hofmann, E. E., J. M. Klinck, C. M. Lascara, and D. A. Smith (1996), Water mass distribution and circulation west of the Antarctic Peninsula and including Bransfield Strait, in *Foundations for Ecological Research West of the Antarctic Peninsula*, edited by R. M. Ross, E. E. Hofmann and L. B. Quetin, AGU, Washington, D. C., doi:10.1029/AR070p0061.

Holm-Hansen, O., and B. Mitchell (1991), Spatial and temporal distribution of phytoplankton and primary production in the western Bransfield Strait region, *Deep Sea Res. Part A*, *38*(8), 961–980.

Kahl, L. A., O. Schofield, and W. R. Fraser (2010), Autonomous gliders reveal features of the water column associated with foraging by adelie penguins, *Integr. Comp. Biol.*, *50*(6), 1041–1050, doi:10.1093/icb/icq098.

Kavanaugh, M. T., F. N. Abdala, H. Ducklow, D. Glover, W. Fraser, D. Martinson, S. Stammerjohn, O. Schofield, and S. C. Doney (2015), Effect of continental shelf canyons on phytoplankton biomass and community composition along the western Antarctic Peninsula, *Mar. Ecol. Prog. Ser.*, *524*, 11–26, doi:10.3354/meps11189.

Kohut, J., E. Hunter, and B. Huber (2013), Small-scale variability of the cross-shelf flow over the outer shelf of the Ross Sea, *J. Geophys. Res. Oceans*, *118*, 1863–1876, *doi*:10.1002/jgrc.20090.

Kohut, J., K. Bernard, W. Fraser, M. J. Oliver, H. Statscevvich, P. Winsor, and T. Miles (2014), Studying the impacts of local oceanographic processes on adelie penguin foraging ecology, *Mar. Technol. Soc. J.*, *48*(5), 25–34.

Kunze, E., L. K. Rosenfeld, G. S. Carter, and M. C. Gregg (2002), Internal waves in Monterey Submarine Canyon, *J. Phys. Oceanogr.*, *32*(6), 1890–1913, doi:10.1175/1520-0485(2002)032 < 1890:IWIMSC>2.0.CO;2.

Lagerström, M., M. Field, M. Séguret, L. Fischer, S. Hann, and R. Sherrell (2013), Automated on-line flow-injection ICP-MS determination of trace metals (Mn, Fe, Co, Ni, Cu and Zn) in open ocean seawater: Application to the GEOTRACES program, *Mar. Chem.*, *155*, 71–80.

Lorbacher, K., D. Dommenget, P. P. Niiler, and A. Köhl (2006), Ocean mixed layer depth: A subsurface proxy of ocean-atmosphere variability, *J. Geophys. Res.*, *111*, C07010, doi:10.1029/2003JC002157.

Martin, J. H., S. E. Fitzwater, and R. M. Gordon (1990), Iron deficiency limits phytoplankton growth in Antarctic waters, *Global Biogeochem. Cycles*, *4*(1), 5–12.

Martinson, D. G., and D. C. McKee (2012), Transport of warm upper circumpolar deep water onto the western Antarctic Peninsula continental shelf, *Ocean Sci.*, *8*(4), 433–442, doi:10.5194/os-8-433-2012.

Martinson, D. G., S. E. Stammerjohn, R. A. Iannuzzi, R. C. Smith, and M. Vernet (2008), Western Antarctic Peninsula physical oceanography and spatio-temporal variability, *Deep Sea Res., Part II*, *55*(18–19), 1964–1987, doi:10.1016/j.dsr2.2008.04.038.

Meredith, M. P., M. A. Brandon, M. I. Wallace, A. Clarke, M. J. Leng, I. A. Renfrew, N. P. Van Lipzig, and J. C. King (2008), Variability in the freshwater balance of northern Marguerite Bay, Antarctic Peninsula: Results from hwater b, *Deep Sea Res., Part II*, *55*(3), 309–322.

Mitchell, B. G., and O. Holm-Hansen (1991), Observations of modeling of the Antartic phytoplankton crop in relation to mixing depth, *Deep Sea Res., Part A*, *38*(8), 981–1007.

Moline, M. A. (1998), Photoadaptive response during the development of a coastal Antarctic diatom bloom and relationship to water column stability, *Limnol. Oceanogr.*, *43*(1), 146–153.

Moline, M. A., and B. B. Prezelin (1996), Long-term monitoring and analyses of physical factors regulating variability in coastal Antarctic phytoplankton biomass, in situ productivity and taxonomic composition over subseasonal, seasonal and interannual time scales, *Mar. Ecol. Prog. Ser.*, *145*(1–3), 143–160, doi:10.3354/meps145143.

Moline, M. A., B. B. Prezelin, and H. Claustre (1996), Light-saturated primary production in antarctic coastal waters, *Antarct. J. U. S.*, *31*(5), 105–107.

Moline, M. A., B. B. Prezelin, O. Schofield, and R. C. Smith (1997), Temporal dynamics of coastal Antarctic phytoplankton: Environmental driving forces and impact of 1991/92 summer diatom bloom on the nutrient regimes, in *Antarctic Communities: Species, Structure and Survival*, edited by B. Battaglia, J. Valencia, and D. W. H. Walton, pp. 67–72, Cambridge Univ. Press, Cambridge.

Montes-Hugo, M. A., M. Vernet, D. Martinson, R. Smith, and R. Iannuzzi (2008), Variability on phytoplankton size structure in the western Antarctic Peninsula (1997-2006), *Deep Sea Res., Part II*, *55*(18–19), 2106–2117, doi:10.1016/j.dsr2.2008.04.036.

Montes-Hugo, M. A., S. C. Doney, H. W. Ducklow, W. Fraser, D. Martinson, S. E. Stammerjohn, and O. Schofield (2009), Recent changes in phytoplankton communities associated with rapid regional climate change along the western Antarctic Peninsula, *Science*, *323*(5920), 1470–1473, doi:10.1126/science.1164533.

Montes-Hugo, M. A., C. Sweeney, S. C. Doney, H. Ducklow, R. Frouin, D. G. Martinson, S. Stammerjohn, and O. Schofield (2010), Seasonal forcing of summer dissolved inorganic carbon and chlorophyll a on the western shelf of the Antarctic Peninsula, *J. Geophys. Res.*, *115*, C03024, doi:10.1029/2009JC005267.

Nelson, D. M., and W. Smith (1991), The role of light and major nutrients, *Limnol. Oceanogr.*, *36*, 1650–1661.

Oliver, M. J., M. A. Moline, I. Robbins, W. Fraser, D. Patterson, and O. Schofield (2012), Letting penguins lead: Dynamic modeling of penguin locations guides autonomous robotic sampling, *Oceanography*, *25*(3), 120–121.

Oliver, M. J., A. Irwin, M. A. Moline, W. Fraser, D. Patterson, O. Schofield, and J. Kohut (2013), Adelie penguin foraging location predicted by tidal regime switching, *PLoS One*, *8*(1), e55163, doi:10.1371/journal.pone.0055163.

Prézelin, B. B., E. E. Hofmann, C. Mengelt, and J. M. Klinck (2000), The linkage between Upper Circumpolar Deep Water (UCDW) and phytoplankton assemblages on the west Antarctic Peninsula continental shelf, *J. Mar. Res.*, *58*(2), 165–202.

Prézelin, B. B., E. E. Hofmann, M. Moline, and J. M. Klinck (2004), Physical forcing of phytoplankton community structure and primary production in continental shelf waters of the Western Antarctic Peninsula, *J. Mar. Res.*, *62*(3), 419–460.

Saba, G. K., et al. (2014), Winter and spring controls on the summer food web of the coastal West Antarctic Peninsula, *Nat. Commun.*, *5*, 4318, doi:10.1038/ncomms5318.

Sakshaug, E., G. Johnsen, K. Andresen, and M. Vernet (1991), Modeling of light-dependent algal photosynthesis and growth: Experiments with the Barents sea diatoms *Thalassiosira nordenskioldii* and *Chaetoceros furcellatus*, *Deep Sea Res., Part A*, *38*(4), 415–430.

Schofield, O., et al. (2007), Slocum gliders: Robust and ready, *J. Field Robot*, *24*(6), 473–485, doi:10.1002/rob.20200.

Schofield, O., H. W. Ducklow, D. G. Martinson, M. P. Meredith, M. A. Moline, and W. R. Fraser (2010), How do polar marine ecosystems respond to rapid climate change?, *Science*, *328*(5985), 1520–1523.

Schofield, O., et al. (2013), Penguin biogeography along the west antarctic peninsula testing the canyon hypothesis with Palmer LTER observations, *Oceanography*, *26*(3), 204–206.

Sedwick, P. N., A. R. Bowie, and T. W. Trull (2008), Dissolved iron in the Australian sector of the Southern Ocean (CLIVAR SR3 section): Meridional and seasonal trends, *Deep Sea Res., Part I*, *55*(8), 911–925, doi:10.1016/j.dsr.2008.03.011.

Serebrennikova, Y. M., and K. A. Fanning (2004), Nutrients in the Southern Ocean GLOBEC region: Variations, water circulation, and cycling, *Deep Sea Res., Part II*, *51*(17–19), 1981–2002, doi:10.1016/j.dsr2.2004.07.023.

Smith, R. C., K. S. Baker, and M. Vernet (1998), Seasonal and interannual variability of phytoplankton biomass west of the Antarctic Peninsula, *J. Mar. Syst.*, *17*(1–4), 229–243, doi:10.1016/S0924-7963(98)00040-2.

Smith, R. C., D. G. Martinson, S. E. Stammerjohn, R. A. Iannuzzi, and K. Ireson (2008), Bellingshausen and western Antarctic Peninsula region: Pigment biomass and sea-ice spatial/temporal distributions and interannual variabilty, *Deep Sea Res., Part II*, *55*(18–19), 1949–1963, doi:10.1016/j.dsr2.2008.04.027.

Stammerjohn, S. E., D. G. Martinson, R. C. Smith, and R. A. Iannuzzi (2008), Sea ice in the western Antarctic Peninsula region: Spatiotemporal variability from ecological and climate change perspectives, *Deep Sea Res., Part II*, *55*(18-19), 2041–2058, doi:10.1016/j.dsr2.2008.04.026.

Todoroff, K., J. Kohut, P. Winsor, and H. Statscewich (2015), Spatial circulation patterns over Palmer Deep canyon and the effects on Adélie Penguin foraging, paper presented at OCEANS 2015-MTS/IEEE Washington, IEEE, Washington, D. C., 19–22 Oct.

Twining, B. S., and S. B. Baines (2013), The trace metal composition of marine phytoplankton, *Ann. Rev. Mar. Sci.*, *5*, 191–215, doi:10.1146/annurev-marine-121211-172322.

Vernet, M., D. Martinson, R. Iannuzzi, S. Stammerjohn, W. Kozlowski, K. Sines, R. Smith, and I. Garibotti (2008), Primary production within the sea-ice zone west of the Antarctic Peninsula: I-Sea ice, summer mixed layer, and irradiance, *Deep Sea Res., Part II*, *55*(18–19), 2068–2085, doi:10.1016/j.dsr2.2008.05.021.

Comparison between glider-derived geostrophic velocities and shipboard ADCP measurements

Nicole Couto, Oscar Schofield, Josh Kohut
Department of Marine and Coastal Science
Rutgers University
New Brunswick, NJ USA
ncouto@marine.rutgers.edu

***Abstract*— On the continental shelf of the west Antarctic Peninsula (WAP), waters below the permanent pycnocline are strongly influenced by intrusions of water masses shed from the Antarctic Circumpolar Current. These intrusions carry relatively warm water toward the coast and to glacier grounding lines, but intrusion locations, mechanisms, and pathways by which this water moves on the shelf are still poorly understood. Dozens of deployments of autonomous underwater vehicles (gliders) in the vicinity of Palmer Deep, a biologically productive canyon on the WAP, have collected temperature and salinity data at extremely high spatial resolution. These data can be used to calculate geostrophic currents in the across-glider-track direction, and this would provide an extensive dataset to study circulation on the WAP shelf, but the relative importance of the geostrophic component to the total current field must first be determined.**

Here, we present a comparison between one ADCP transect and several repeat glider transects along the same line. Velocities measured by the ADCP are difficult to compare to geostrophic velocities because the shallowest ADCP bin is 46 m below the surface, while geostrophic velocities are referenced to dead-reckoned velocities with a significant contribution from surface currents. Despite limitations, depth-averaged geostrophic currents show promise in being a useful proxy for total depth-average currents on the WAP. The depth-averaged currents from glider deployments show significant day-to-day variability in both magnitude and direction, but the glider transect timed most closely to the ADCP transect showed a similar pattern. Vertical shear is predominantly directed onshore, and measurements of shear below the permanent pycnocline are small compared to those at the surface.

***Keywords*— geostrophic velocity, thermal wind, glider, vertical shear. Antarctic**

I. Introduction

Palmer Deep is a canyon on the continental shelf of the west Antarctic Peninsula (WAP) considered to be a hot spot of biological activity. The high productivity of the region has been attributed to the presence of a deep nutrient-rich water mass called Upper Circumpolar Deep Water (UCDW) [1] which originates offshore within the Antarctic Circumpolar Current. A modified form of UCDW (mCDW) is always present deep within the canyon, but the pathways by which it travels from the shelfbreak are poorly understood.

Understanding the pathways by which UCDW travels across the shelf and becomes mCDW is important to our understanding of how circulation affects biological activity. These pathways are linked to residence time on the shelf, mixing with other water masses, and the formation areas of convergence and divergence at the surface where phytoplankton bloom. Intrusions of UCDW are also important in delivering heat to the WAP [2]. This region of the world is one of the fastest warming on Earth and the rising temperatures are thought to be driven more by the ocean than the atmosphere [3]-[5]. Upper Circumpolar Deep Water is the source of heat to the WAP. It is known to enter the shelf via canyons at depths between about 200 and 500 m, but the frequency and magnitude of these intrusions are mostly unknown.

Although circulation is thought to be an important driver of productivity on the WAP, and it plays a critical role in regulating the heat budget, its patterns are still not well mapped. Data collection is limited by harsh weather conditions and the extent of sea ice during winter. During the summer months (October – March), the United States Antarctic Program conducts research cruises along the peninsula. Water velocity measurements are often taken on these cruises by a hull-mounted Acoustic Doppler Current Profiler (ADCP), and these data have been used to explain the general circulation patterns on the WAP [6], but the detailed mechanisms by which UCDW reaches Palmer Deep and circulates within it remain undescribed.

Geostrophic current calculations have long been used to understand circulation patterns where velocity data are limited. They rely on the geostrophic balance between a pressure gradient and the Coriolis force. Differences in the density profile between two locations in the ocean lead to a pressure difference which forces water to move between the two locations. The effect of the Coriolis force introduces a rotation to the motion such that, when a current is in geostrophic balance, it flows perpendicular to the pressure gradient. Any two density profiles, therefore, can be used to calculate the geostrophic velocity between them, as long as one reference velocity somewhere on the profile is known (otherwise, only relative velocity is calculated).

Since 2010, the Rutgers University Center for Coastal Observation Leadership (RUCOOL) has conducted dozens of glider deployments within and near Palmer Deep. The gliders were deployed from Palmer Station, a research outpost situated at the head of Palmer Deep (Fig. 1), and

978-1-5090-1537-5/16/$31.00 ©2016 IEEE

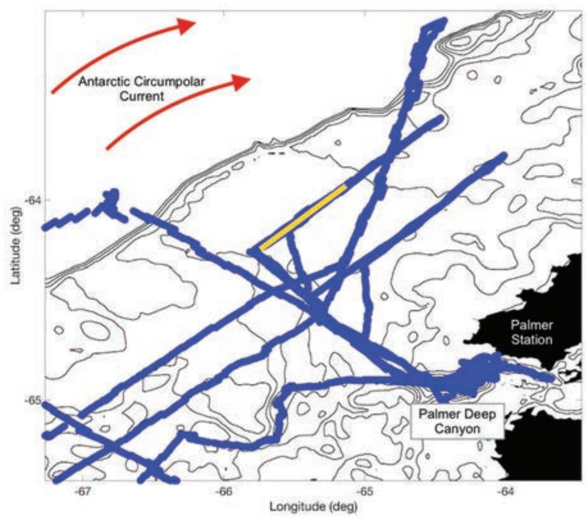

Fig 1. Map of Palmer Deep vicinity with RUCOOL glider deployments in blue. The ADCP transect is shown in yellow, overlapping eight repeat transects of one glider deployment.

were equipped with a variety of sensors depending on the purpose of each individual mission. The gliders do not directly measure current speeds, but every glider measured density. Additionally, the gliders calculated a depth-averaged current between every surfacing based on dead-reckoning. This information, combined with the density profiles can be used to calculate geostrophic velocities everywhere the gliders flew.

The spatial extent and resolution of this dataset provides an exciting opportunity to map circulation patterns within and near Palmer Deep. But first, in order to assess the utility of these measurements, a comparison between glider-calculated geostrophic currents and known currents must be

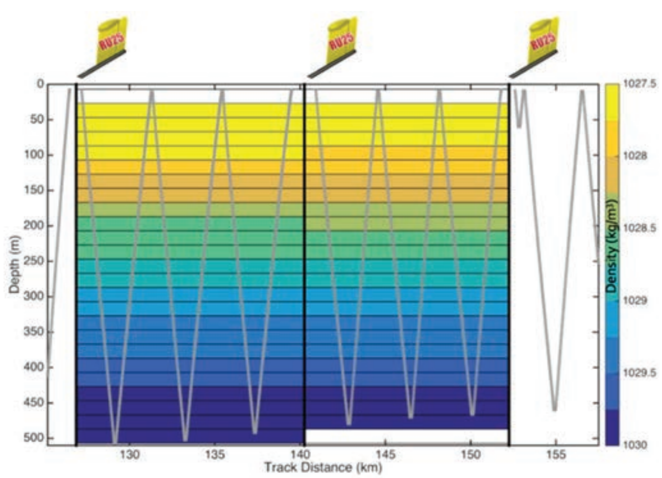

Fig. 2. Example of two neighboring averaged profiles used to calculate geostrophic velocities. Each time the glider surfaces (indicated by tail icons), it calculates a depth-integrated dead-reckoned current velocity between the present and previous surfacing location. All profiles between surfacings are averaged into 10-meter depth bins and the average profiles are used to calculate northward and eastward velocities.

performed. Geostrophic currents describe only the baroclinic component of velocity, so the simultaneous measurement of true velocity is important for understanding the relative contributions of the baroclinic and barotropic components in this region. Here we compare several repeat transects of a glider to the same transect measured by shipboard ADCP. The ADCP data is considered the true velocity field, including both the barotropic and baroclinic velocities. The differences between the two types of measurements reveal some circumstances under which geostrophic currents can describe the circulation near Palmer Deep.

II. METHODS

A Teledyne Webb glider was used in this study to measure temperature and salinity profiles on the WAP continental shelf. Gliders are buoyancy-driven autonomous underwater vehicles that sample the water column from the surface of the ocean to the bottom in a see-saw pattern as they travel between operator-specified waypoints (Fig. 2). They move slowly (~1 km/hr) and, as a result, sample the ocean with very high spatial resolution. The glider used here was deployed from Palmer Station in late December 2014 and flew to the mouth of a canyon that extends from the shelf break to Palmer Deep (Fig. 1). It made eight repeat transects across the mouth of this canyon on its northeastern side (Fig. 1). The glider traveled parallel to, and approximately 45 km away from, the shelf break. This location was chosen because it was through to be a possible intrusion point for UCDW onto the shelf. Studies of a different canyon on the WAP shelf have shown that warm water tends to intrude along its northeastern wall [7]. These eight passes were made between January 2, and January 18, 2015.

The glider was equipped with a conductivity, temperature, and depth sensor. These variables were measured four times per second and were used to calculate density. Each time a glider surfaces it gets a GPS fix. Using the difference in its position between surfacings and its own measurement of heading and speed, the glider calculates the depth-averaged velocity between its previous and present position.

Density profiles were averaged between glider surfacings and into 10-meter depth bins, and vertical shear was calculated between every pair of averaged profiles according to the geostrophic relationship:

$$\frac{\partial v}{\partial z} = \frac{g}{f\rho_0}\frac{\partial \rho}{\partial x}, \tag{1}$$

where x is distance in the along-track direction, and v is the geostrophic velocity in the across-track direction. The integrated form of the equation:

$$v = \int_z^0 \frac{g}{f\rho_0}\frac{\partial \rho}{\partial x}dz + \text{constant} \tag{2}$$

$$= \text{depth-averagred velocity}$$

reflects the across-track component of velocity, resulting from the density structure. Here, ρ is the density of a given depth bin, ρ_0 is a reference density, set as the average of all measured densities, g is the acceleration to due gravity, f is the Coriolis parameter, and z is depth. The integrated shear profiles are scaled using a constant offset so that the total depth-integrated shear matches the across-track component of the depth-averaged current experienced by the glider.

The research vessel *Laurence M. Gould* made a transect along the glider path on January 9, 2015. The vessel was equipped with a hull-mounted ADCP operating at 38 kHz. This frequency allowed for measurements of velocity between 46 m and 1462 m water depth with depth bins of 24 m. Corrections for heading and speed of sound were applied by Dr. Teresa Chereskin at the Scripps Institute of Oceanography. These data were interpolated into 10 m depth bins and averaged hourly resulting in a total of four water velocity profiles calculated along the transect. The processed and interpolated data was acquired from the Joint Archive for Shipboard ADCP.

To facilitate comparison between all transects, velocity data from the eight glider sections and one ship section were interpolated onto a grid with a vertical spacing of 10 m and a horizontal spacing of approximately 5 km.

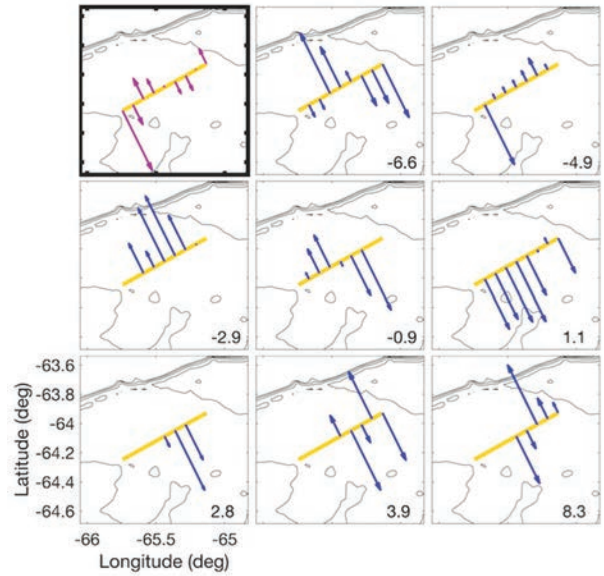

Fig. 3 The depth-averaged across-track component of velocity measured by the Gould ADCP is shown in the upper left plot. The other eight plots show the depth-averaged across-track geostrophic velocities calculated by the glider. The number of days between the ship transect and the glider transect is given in the lower right corner of each plot. Starting from the middle of the top row and moving left to right, the first four glider transects occurred before the ship transect and the last four occurred after it.

III. Results

Velocity profiles measured by the shipboard ADCP were rotated into along- and across-track coordinates, where the track was defined as the line passing through the first and last ADCP profiles. Working in the coordinate system defined by the track is important to be able to directly compare the ADCP velocities to those measured by the glider. Since the glider was not equipped with its own ADCP, geostrophic velocities were calculated instead. Using the geostrophic relationship, across-track currents are calculated from along-track pressure differences, but nothing is known of the magnitude of geostrophic velocity in the along-track direction. Depth-averaged across-track currents measured by the ADCP and the glider are shown in Fig. 3. Glider transects were made over the course of sixteen days, and there is significant variability in the geostrophic

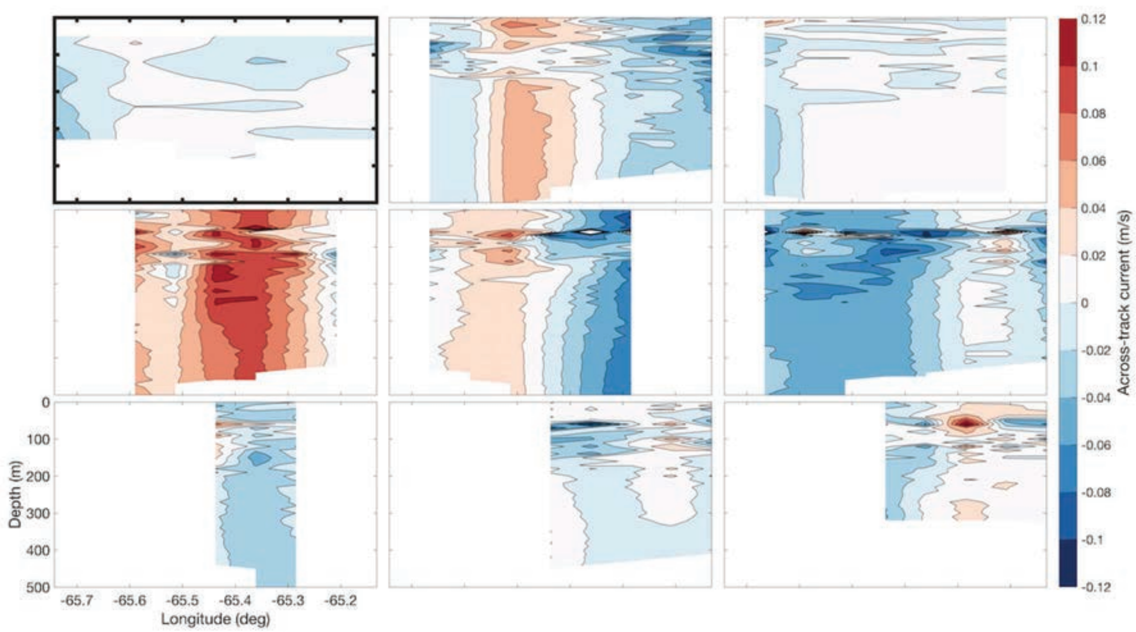

Fig. 4. Across-track component of velocity measured by the Gould ADCP is show in the upper left plot. The other eight plots show the across-track geostrophic velocities calculated from density measurements on the eight repeat glider transects that covered the same path.

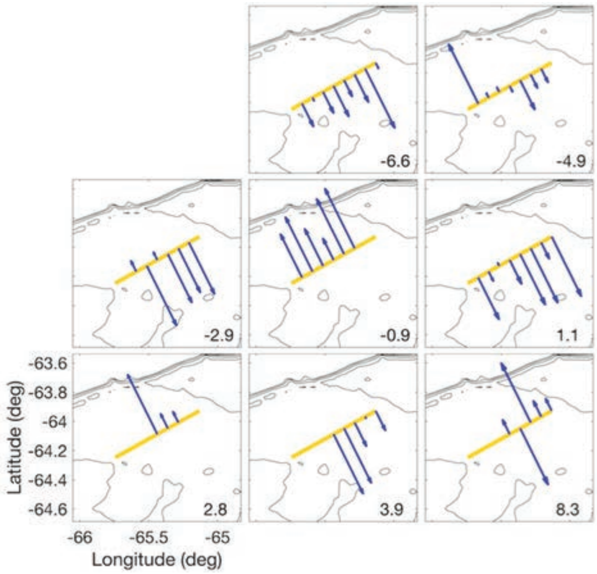

Fig. 5. The depth averaged vertical shear measured by the glider on its eight repeat transects. Each pass is shown in the same position as in Fig. 3.

currents measured over this time (Fig. 3).

The overall direction of geostrophic flow measured by the glider is slightly in the southeast direction (onshore). Fifty-four percent of the total across-track depth-averaged flow measured by the glider was onshore while 46% was offshore. Most of the flow across the ADCP track was also directed onshore, but this was mainly due to a strong onshore flow along the southwest edge of the canyon. The northeastern side of the track showed a surface-intensified onshore flow and a subsurface offshore flow that was smaller in magnitude (Fig. 4).

Unfortunately none of the glider transects happened at exactly the same time as the ADCP transect which is serving as the ground truth for velocity measurements. Simultaneous measurements are difficult to achieve because 1) the glider moves much slower than the ship and 2) the glider is kept away from ships whenever possible to avoid the possibility of collision. The fourth pass of the glider was closest in time to the ADCP transect: the glider completed the transect slightly less than one day earlier than the ship. The depth-averaged geostrophic currents on this pass look most similar to depth-averaged velocity from the ADCP track (Fig. 3, center panel). Flow was onshore on the northeast side of the canyon and offshore on the southwest side of the canyon.

The magnitude of the geostrophic currents in this and most other glider passes was greater than the magnitude of currents measured by the shipboard ADCP, but this is likely due to the fact that ADCP velocity measurements began at 46 m depth while currents are generally strongest at the surface. The depth-averaged current is used to shift the shear profile so that its mean value is equal to the depth-averaged value. With stronger currents at the surface, a depth-averaged current that includes the upper 46 m is likely to be greater than one that does not. A velocity measurement taken deeper in the water column would be a more appropriate reference point for comparisons to depth-averaged ADCP velocities between 46 m and the bottom, but the glider dead-reckoned current was the only reference available here.

Vertical shear profiles reflect the baroclinic component of velocity throughout the water column. They are relative velocities, unshifted by a reference velocity. Depth-averaged shear profiles are shown in Fig. 5, mapped the same way as in Fig. 3. In contrast to the geostrophic currents, shear is predominantly directed onshore, suggesting that the baroclinic component of velocity through the canyon is generally onshore and total currents are influenced by other

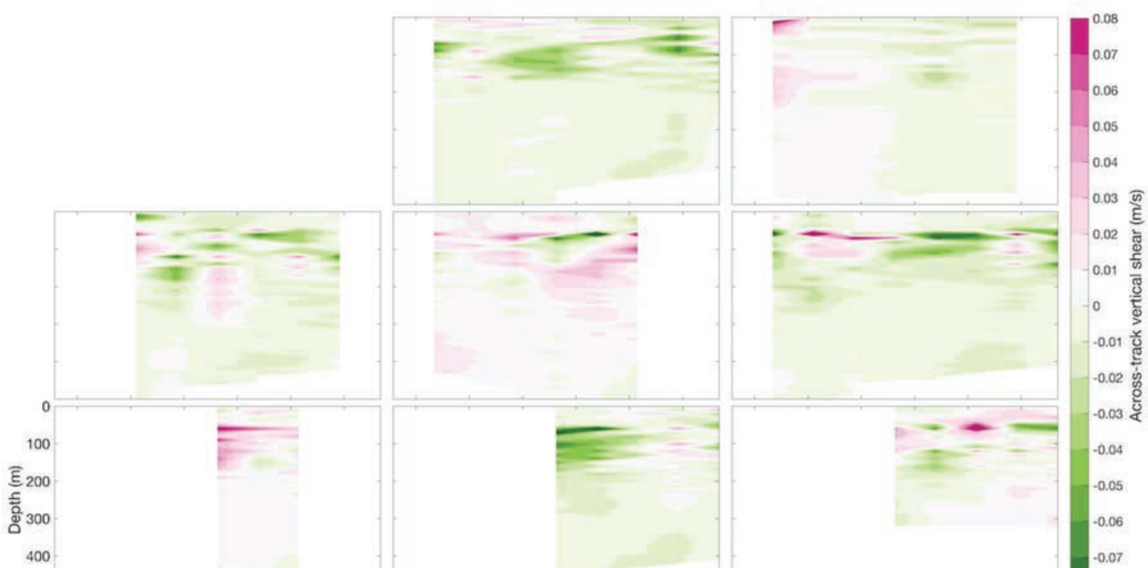

Fig. 6. Vertical shear due to along-track density gradients. Each of the eight glider transects are shown in the same subplots as in Fig. 3 and 4. The first pass is shown in the middle plot on the top row and the last is shown in the bottom right plot.

factors (ex. tides, weather) on daily timescales.

Shear tends to be surface intensified suggesting that the greatest lateral density differences are at the surface and deeper waters are more homogenous (Fig. 6). Surface intensity extends to a depth of about 200 m, which is the approximate depth of the permanent pycnocline in this region. The vertical shear pattern seen in the fourth glider pass (the pass closest in time to the ADCP transect) is similar to the pattern seen in the ADCP data with a localized surface intensification on the northeast side of the canyon. This suggests that a significant portion of the total velocity may be explained by the baroclinic component.

IV. Conclusions

Geostrophic currents measured by gliders show promise as being a useful proxy for total currents in this region of the ocean, but more direct comparisons with total velocities measured by ADCP would be helpful in determining their relative importance Since the completion of this deployment the RUCOOL group has completed a few glider deployments within Palmer Deep with glider-mounted ADCPs. Continued research on the relative importance of baroclinic and barotropic components of velocity in this region will be conducted using these new datasets.

The ability to map the velocities on the WAP is critical for understanding the regional circulation patterns. The transport of UCDW to Palmer Deep is known to be important, but its pathways are unclear. Paired with temperature measurements made by the gliders, geostrophic velocities could be used to better understand these transport pathways.

Acknowledgement

ADCP data was processed by Dr. Teresa K. Chereskin at the Scripps Institute of Oceanography and made available at the Joint Archive for Shipboard ADCP: http://ilikai.soest.hawaii.edu/sadcp. Thanks to the RUCOOL glider technicians for their support during the glider deployment and thanks to the field team and staff at Palmer Station for successful deployment and recovery of the glider.

References

[1] B. B. Prézelin, E. E. Hofmann, C. Mengelt, and J. M. Klinck, "The linkage between Upper Circumpolar Deep Water (UCDW) and phytoplankton assemblages on the west Antarctic Peninsula continental shelf," *Journal of Marine Research*, vol. 58, pp. 165–202, 2000.

[2] D. G. Martinson, S. E. Stammerjohn, and R. A. Iannuzzi, "Western Antarctic Peninsula physical oceanography and spatio–temporal variability," *Deep Sea Research …*, vol. 55, no. 18, pp. 1964–1987, 2008.

[3] A. Jenkins, P. Dutrieux, S. S. Jacobs, S. D. McPhail, J. R. Perrett, A. T. Webb, and D. White, "Observations beneath Pine Island Glacier in West Antarctica and implications for its retreat," *Nature Geoscience*, vol. 3, no. 7, pp. 468–472, Jun. 2010.

[4] H. D. Pritchard, S. R. M. Ligtenberg, H. A. Fricker, D. G. Vaughan, M. R. van den Broeke, and L. Padman, "Antarctic ice-sheet loss driven by basal melting of ice shelves," *Nature*, vol. 484, pp. 502–505, Apr. 2012.

[5] E. Rignot and S. S. Jacobs, "Rapid Bottom Melting Widespread near Antarctic Ice Sheet Grounding Lines," *Science*, vol. 296, no. 5575, pp. 2020–2023, Jun. 2002.

[6] D. K. Savidge and J. A. Amft, "Circulation on the West Antarctic Peninsula derived from 6 years of shipboard ADCP transects," *Deep Sea Research Part I: Oceanographic Research Papers*, vol. 56, no. 10, pp. 1633–1655, Oct. 2009.

[7] D. G. Martinson and D. C. McKee, "Transport of warm Upper Circumpolar Deep Water onto the western Antarctic Peninsula continental shelf," *Ocean Science Discussions*, vol. 8, pp. 433–442, 2012.

Interannual variability and trends in the Middle Atlantic Bight cold pool

Samuel J. Coakley, Travis Miles, Josh Kohut, and Hugh Roarty
Department of Marine and Coastal Sciences
Rutgers University
New Brunswick, United States
Sjc244@scarletmail.rutgers.edu

Abstract— **The Middle Atlantic Bight (MAB) exhibits one of the largest seasonal cycles of temperature in the global ocean. During the summer, the water column is strongly stratified with warm surface waters separated from much colder bottom waters by a strong, shallow thermocline. The bottom water that remains cold in the summer months is referred to as the 'cold pool'. The cold pool is formed as the stratification sets up in late spring and it remains until fall mixing breaks down the seasonal thermocline with each passing storm; it usually breaks down in September or October. The cold pool is an important feature of the MAB as it influences the surrounding waters, the intensity of storms, and fish assemblages over the MAB. We use various data sources to explore interannual variability and long-term climatic trends in summer stratification and cold pool source water. Annual trawls conducted by the National Oceanic and Atmospheric Administration National Marine Fisheries Services (NOAA NMFS) provide temperature and salinity measurements consistently from 1980 to the present. Slocum gliders have been regularly deployed along New Jersey shelf since 2003 and collect data for various organizations such as Rutgers University and the Environmental Protection Agency. NOAA's National Data Buoy Center provides several buoys in the region that have been collecting data since the early 1980's. A better understanding of the cold pool can lead to a better understanding of ocean and storm interactions in the MAB and of potential climate change impacts on the region.**

Keywords— Ocean observing systems, Autonomous underwater vehicles

I. Introduction

The Middle Atlantic Bight (MAB) is the region off of the Northeastern coast of the United States that extends ~1000 km from Cape Hatteras, North Carolina to Cape Cod, Massachusetts. The MAB is characterized by a shallow sloping continental shelf that is at its narrowest (50 km) off of North Carolina and its widest (~200 km) east of New Jersey and west of Long Island, New York. The New York Metropolitan area adjacent to the MAB has a population of over 19 million people and accounts for close to 10% of the US GDP. This region is important for fishing, shipping, and recreational use, and is also highly vulnerable to coastal storms, including frequent nor'easters in winter and fall as well as tropical cyclones in summer months (Glenn et al., 2016). Due to its large population and highly concentrated population at the coastline it is highly vulnerable to changing climates and sea level rise. The coastal ocean of the MAB is unique as it has one of the largest intra-annual temperature ranges. In winter the water column is subject to salinity dominated stratification but in the spring, the surface water is warmed by solar heating. This warming causes the creation of a strong thermocline, trapping cold water along the bottom of the shelf (Castelao, Glenn, & Schofield, 2010; Houghton, Schlitz, Beardsley, Butman, & Chamberlin, 1982). This thermal stratification persists through summer and into the fall when storm induced vertical mixing breaks down the thermocline. Surface cooling in the fall has been shown to not be the dominant process in the breakdown of the thermocline (Castelao et al., 2008; Lentz, 2003).

The cold water that gets trapped by the thermal stratification is referred to as the 'cold pool'. The cold pool is defined as any water inside the 10° Celsius isotherm over the shelf, and is typically located between the 40 and 200 meter isobaths. During the summer, the cold pool migrates south along the coast but remains over the shelf. The stratification and formation of the cold pool starts in the Gulf of Maine and then moves south with a speed of approximately 5 cm/sec and the flow rate is .15 Sv (Flagg, Wallace, & Kolber, 1997). The cold pool stretches along the length of the MAB and has been shown to be relatively uniform with respect to temperature. The time frame the cold pool exists is not rigid because it is dependent on atmospheric influences (Lentz, 2003). The formation and breakdown of the cold pool is heavily influenced by local and remote sources. As source waters, like the Labrador Sea, are affected by climate change, the cold pool reflects these changes.

The dominant factor in the break down of the thermocline, and the subsequent dissolution of the cold pool, is strong wind events. In summer, when tropical cyclones follow a northward track along the MAB, studies have found that intense leading-edge winds can drive shear-induced mixing of the water column, which has implications in atmospheric models. As a storm moves north through the MAB, the water ahead of the storm is cooled because of the induced mixing (Glenn et al., 2016). Thus the storm's intensity is reduced, as there is no longer warm water to give the storm strength. This 'ahead of eye cooling' phenomenon was missing from atmospheric

978-1-5090-1537-5/16/$31.00 ©2016 IEEE

models, which led to an under-prediction of Hurricane Irene's intensity just prior to landfall. The characteristics and tendencies of the cold pool are still widely unknown and unrepresented in simulations, which remains a critical challenge for hurricane intensity forecasters in the region.

The Mid-Atlantic Bight is an economically important region because of fishing. Certain species of fish such as winter flounder, *Pseudopleuronectes americanus*, depend on the cold pool during the summers. As surface temperatures in New Jersey estuaries rise during the summer, winter flounder migrate to the ocean with the goal of finding colder water (Able, Grothues, Morson, & Coleman, 2014). The cold pool provides these flounder with cooler water and when the seasons change and the thermocline fades, the flounder migrate back in shore. Yellow tail flounder, *Limanda ferruginea*, is another fished species in the MAB that is dependent the coldest, deepest water of the MAB to thrive. Another ecologically important species is the glacier lantern fish, *Benthosema glaciale*, which thrives in the benthic region over the shelf in most of the north Atlantic (Grothues & Cowen, 1999).

A number of recent studies have identified warming trends in the surface waters of the MAB showing increasing temperatures of 0.0026 $^{\circ}C\ yr^{-1}$ from 1977 to 2013 with an increase to 0.11 $^{\circ}C\ yr^{-1}$ in more recent years (Forsyth, Andres, & Gawarkiewicz, 2015). Additionally, Mountain et al., 2003 showed MAB shelf waters were 1°C warmer in the 1990s than 1977 to 1987. Despite the importance of resolving and understanding the dynamics and long-term trends of the cold pool, due to the high cost of ship-based monitoring there are limited observations over climate scales. In this study we aggregate over 38 years of National Marine Fisheries datasets and 10 years of high spatial and temporal resolution autonomous underwater glider data on the New Jersey continental shelf, south of the Hudson Shelf Valley.

II. Methods

For this analysis we define a study area based on depth and distance from the Hudson Shelf Valley as well as an area where gliders and ship-based surveys had significant overlap. The study area is defined as the polygon shown in Figure 1. The red shapes represent the location of static NDBC buoys and although they are not in the defined study area, because of their proximity, they still provide an estimate of the surface conditions in the study area. Future work will involve analyzing historic Advanced Very High Resolution Radiometer satellite data over the study area.

Teledyne-Webb Research Slocum gliders have been deployed on the MAB since as early as 2003. Gliders are autonomous underwater vehicles that move through the water

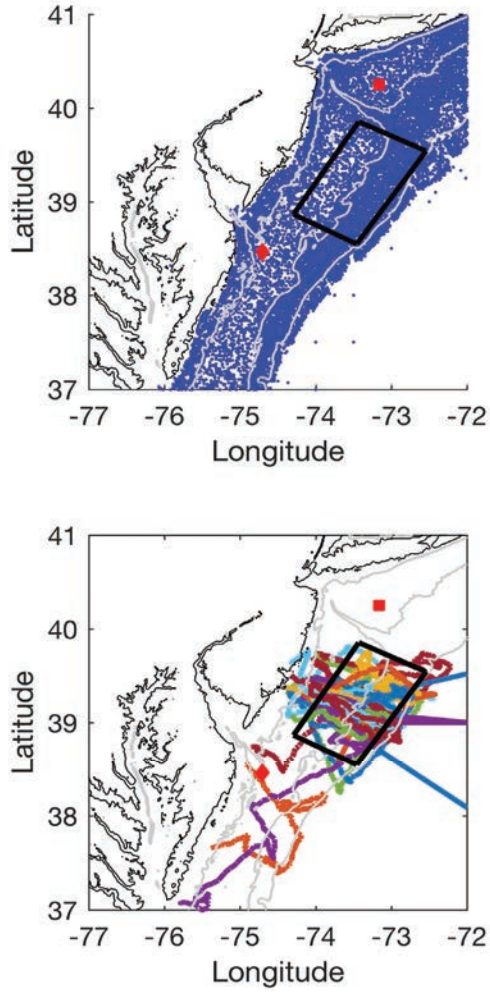

Figure 1 **Map showing the study area represented by the black polygon. The red shapes symbolize the two National Data Buoy Center buoys. a) Data from the National Marine Fisheries Society is shown in blue. b) Each color represents a different Slocum glider deployment that was used in this study.**

column by small changes in buoyancy. The glider is programmed to move the position of a pump, taking in or expelling seawater, to make the glider more or less dense than the water when it needs to dive or climb respectively. As the glider dives and climbs, it collects hydrographic data continuously and after surfacing transmits that data to shore, resulting in high temporal and vertical resolution data over broad spatial areas. Data collected from 49 glider deployments were used in this study (Figure 1b).

The data analysis for this study was supported by a Teledyne Webb Research undergraduate research fellowship.

Island, and 44009, off of the coast of Delaware, were used in this study.

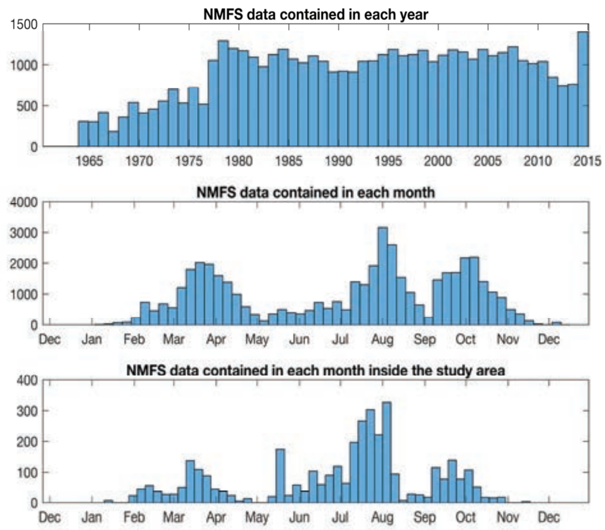

Figure 2 **Histograms showing the quantity of data collected by the NMFS surveys (a through c from the top down). a) Illustrates the number of data points collected in each month across all years. b) Illustrates the number of data points collected in each month across all years. c) Illustrates the number of data points collected inside the study area, each month, across all years.**

The National Oceanic and Atmospheric Administration's (NOAA) National Marine Fisheries Service (NMFS) has conducted seasonal trawls in the MAB as part of fish stock assessments since 1965. Before 1987, temperature was the only hydrographic data collected and it was measured using reversing thermometers. In this same time frame, there were 90 pre-selected stations that data was collected at during each survey. Not every station would be utilized every year but no data was collected anywhere but these stations. After 1987, a stratified random station design was implemented and now NMFS starts every trawl in a specified region and records the exact position (Mountain, 2003). Salinity data was not collected consistently until 1996. Before each trawl began, a CTD was dropped and surface and bottom data were recorded, where the bottom is defined as 5m above the sea floor. The area sampled is consistent from year to year but the time that each specific region is sampled is not always the same because of complications such as weather and malfunctioning equipment. These surveys provided a nearly continuous time series of temperature and salinity in the MAB over the last 50 years but this study only used data collected during or later than 1974. Figure 2 shows the annual and seasonal distribution of profiles of this dataset and the portion that falls within the study region.

NOAA's National Data Buoy Center buoy's are static buoys that continuous collect surface climatological data. This data was used to confirm the data collected by the NMFS surveys and to fill in the times when the NMFS surveys were not collecting data. Buoys 44025, off of the coast of Long Island, and 44009, off of the coast of Delaware, were used in this study.

III. Results

The minimum temperature in the study region at any time was defined as the temperature of the cold pool (Houghton et al., 1982). Weekly minimum temperatures were taken from both NMFS and glider data sets individually from every year of each data set. The data was limited using three standard deviations from the mean of each early and late data separately. This provides a time series of the cold pool throughout one year.

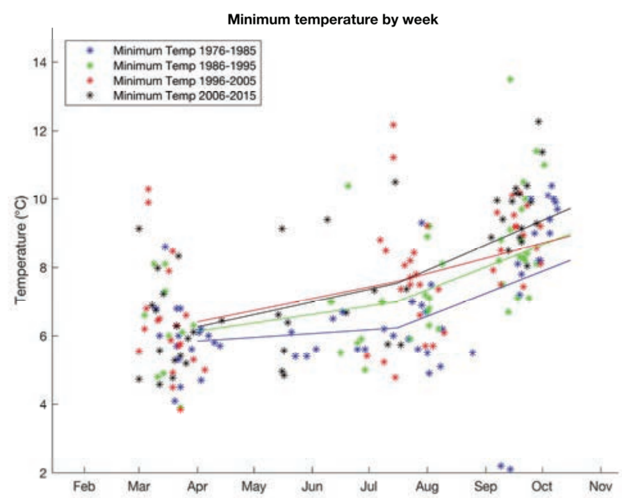

Figure 3 **The minimum temperatures displayed were found by taking the weekly minimum temperature inside the study region from both the NMFS and the glider data sets. These minimums were then limited to only include points within three standard deviations of the mean. The lines represent the decadal seasonal means, found by taking the average minimum in the time ranges of 1 March – 31 May, 1 June – 31 August, and 1 September – 31 November. The colors correspond to the colors of the data points, for example the blue line corresponds to the 1976-1985 decade.**

Figure 3 shows all of the bottom temperature readings separated into four decades starting with 1976 and ending in 2015. The absolute minimum temperatures recorded in each of the four decades were 2.1°C, 3.9°C, 3.84°C, and 4.58°C and were recorded 14 September, 23 March, 23 March, and 12 March respectively. The times associated with the latter three decades' minimum temperatures were as expected because the thermocline develops in the spring and the cold pool has no source of cooling after its formation (Houghton et al., 1982). In the earliest decade, the drop in temperature in September is under further investigation, as it may be an outlier. The large grouping of data points at and above the 10°C isotherm starting in September is a sign of the cold pool undergoing fall transition due to mixing with the upper layers of the water column. The points before September that fall above the 10°C isotherm were most likely a product of a mixing events, but not due to the full fall transition.

Table 1 **The table shows the data represented in Figure 3 by the colored lines. The means were calculated from the weekly minimums of both NMFS and glider data. The minimums were found for every year and the means were found decadally.**

Mean of the minimum bottom temperatures (°C)				
	1976-1985	1986-1995	1996-2005	2006-2015
1 March – 31 May	5.84	6.13	6.41	6.26
1 June – 31 August	6.23	7.00	7.59	7.54
1 September – 30 November	8.21	8.98	8.92	9.72

The minimum temperatures were averaged by season; 1 March-31 May, 1 June-31 August, 1 September-30 November. This average was calculated four times across the forty years of data. This data is displayed in Table 1. All time periods show increase in minimum temperature throughout one year. A warming across the four individual time periods is also shown. The absolute minimum average, 5.84°C, appears in the spring of the earliest time frame. The absolute maximum mean, 9.72°C, appears in the fall of the most recent time frame.

Figure 4 shows the difference between the annual mean bottom temperature and the mean of the bottom temperature throughout all years of the data set. The time frame of each year was limited to 1 March – 31 December to ensure that the cold pool is present within the time frame and to exclude the cold water in January and February from analysis. The largest differences from the mean bottom temperature occurred in 1977, -4.45°C, and in 2009, +4.45°C. The largest differences from the mean bottom salinity occurred in 1996, -1.10 PSU, and in 2015, 1.19 PSU. The mean difference for bottom temperature and bottom salinity were 1.27°C and 0.39 PSU respectively.

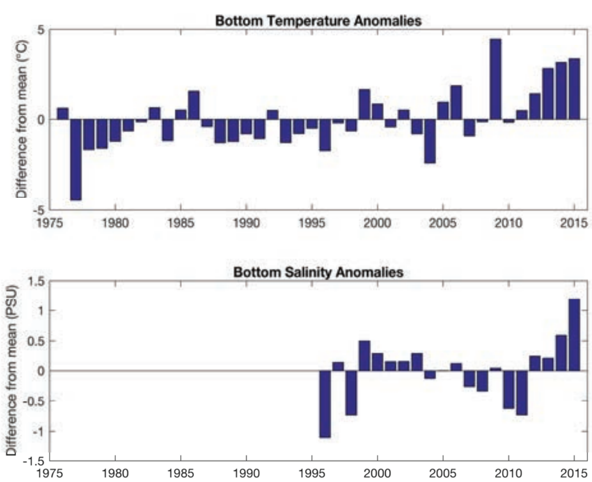

Figure 5 **The mean was calculated for all years of both the NMFS and glider data sets and then the yearly means were calculated. For the glider data, the bottom was defined as the maximum depth reached in each individual profile and was limited to only include profiles that reached depths greater than 35m.**

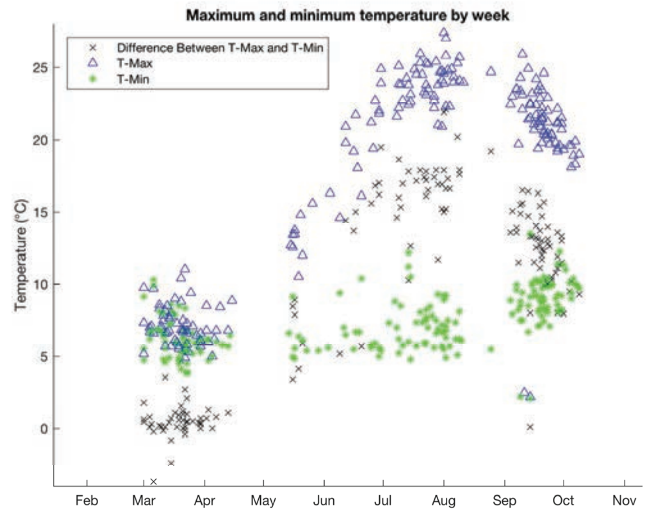

Figure 4 **The maximum temperature was found using an identical method to the method previously described for the minimum temperature, where the weekly maximums from each data set were found for each year of the data set. Both the maximum and the minimum were limited to only display data within three standard deviations of their respective means. The difference was calculated by subtracting the minimum from the maximum only for weeks when there was data recorded for each the maximum and the**

The minimum temperatures from every week over the forty year data set were subtracted from the maximum temperatures from every week over the same time. This provides maximum difference in temperature between the surface and the bottom serves as a proxy for thermal stratification. The largest positive difference between surface and bottom occurred on 2 August. The surface temperature was 22.1°C warmer than the bottom temperature. It is clear that the difference between the two water masses fluctuates throughout the year as the cold pool forms and is separated from the surface. The absolute smallest values of both maximum and minimum temperature are 2.2°C and 2.1°C respectively. This was most likely due to some error in the sensor used to take the readings. NMFS and glider data were compiled and then limited to contain three standard deviations above and below the mean.

IV. Discussion

Two warming trends can be seen in the analysis of the minimum bottom temperature. The first is the seasonal warming of T-min. Across each decade displayed in both Figure 3 and Table 1, there is a warming trend from spring to fall but the largest difference between fall and is seen in the most recent decade with an increase of ~3.5°C. This is reasonable considering the warm anomalies occurring in recent years shown in Figure 4. A previous study has shown a ~1°C across every month, starting in February (Houghton et al., 1982). Their study area encompassed a wider span of the MAB and they only focused on one year of data.

The second warming trend shown is the warming of each season across the forty year span. Each season's mean has increased from the beginning to the end of the data set by

~1°C. This is supported, again, by the anomaly data presented in Figure 4. Bottom temperature has been warming overall but the warming that has occurred with respect to each season varies. The fall has shown the largest change in mean temperature across the full length of the data set. The fall showed the most variability because the bottom temperature in the fall is dependent on what the surface temperature was in the summer. Fall is when the mixing begins to occur; the surface temperature has a strong influence on bottom temperature. Another factor in the variability of fall bottom temperature is the time at which the stratification is broken down. If there are strong mixing events early in the fall then the bottom starts to warm earlier causing the minimum temperature to rise early in the year.

Over the last forty years, a warming trend of the bottom water can be seen in Figure 4. The anomalies show a warming trend as the anomalies start below the mean and move more toward the mean and then above the mean as the data approaches the present. There is a higher density of data in the later years, starting in 2005, due to the glider data set that has helped illustrate this trend.

A similar analysis of bottom temperature was conducted by Mountain et al., 2003. Their study showed a smaller anomalous range from the mean. This study and theirs agree that the anomalies tend to be positive in the latter half of the time frame than in the earlier. The time frames of the two studies overlap but the anomalies do not agree. This is most likely due this study's wider time frame. Mountain's study area was not limited to anything but the MAB and looked at the full time frame of the year, not just from March to December like this study. The mean of this time frame includes the warmer recent years. This would also explain why this study has a larger range of anomalies. Although the two studies do not agree directly, the trend seen is similar.

The salinity anomalies shown in Figure 4 were found using the salinity associated with the bottom temperature reading recorded in each data set. No significant trend is evident in the data. However, the addition of the glider data in 2005 shows no impact on any potential trend in the data, further strengthening the argument that the amount of the glider data did not skew the means.

The difference between surface and bottom temperatures was used as an indicator of thermal stratification. The maximum and minimum temperatures recorded were used to represent surface and bottom temperatures respectively. A trend can be seen in the maximum temperature of warming in spring until the fall when it starts to cool again. This is because of seasonal changes in time exposed to the heating from the sun and storm activity. From Late August onwards, storms cause mixing of the water column in the region with strong winds (Lentz, 2003). The minimum temperature shows little variability in comparison to the maximum temperature. This caused the difference between the two to follow the trend of the maximum. This trend shows that thermal stratification is not present in March and April but is strong in the summer as the minimum temperature warms slightly and the maximum temperature rises quickly. The difference starts to decrease during the end of August as the frequency of mixing events increases.

Both the maximum and minimum temperature reach their minimum values in the same annual time period. This is when there is no or little thermal stratification, in winter and spring. This study has expanded the work of Lentz in 2003 by including forty years of data as opposed to his time series of two years. Utilizing the larger data set gives a more comprehensive picture of what can be expected to happen. Lentz showed that in the time frame they analyzed, there were major mixing events that led to a significant drop in the difference between surface and bottom temperature.

V. Conclusion

The major stages of the life of the cold pool are reflected in the changes of the minimum temperature in a region over the course of a year. It is important to understand when the cold pool is formed and when it breaks down. After it has formed, certain species of fish depend on its cold water to live in. The break down of the cold pool is important to understand because of the impact it has on storm predictions.

In terms of interannual trends, the bottom temperature's increase of ~1°C across all seasons is significant because of the ecological implications it holds. If the bottom temperature becomes too warm, the stratification that holds the cold pool on the bottom will no longer form or it may be weaker. This could lead to more vertical mixing in the water column during the summer, which may lead to stronger storms. This is ongoing research and in the future a more precise signal of the formation and destruction of the stratification will be pursued. If these signals are found, the exact state of the cold pool could be known at anytime which would aid in storm predictions.

The bottom temperature in the Middle Atlantic Bight has been shown to be rising over the last forty years. By analyzing the anomalies over a long time frame, an expected range of variability from the mean has been established for the bottom temperature in the region. As the bottom temperature warms, the impact the cold pool has on the ecosystem will diminish. Populations of fishes that depend on the cold pool for it's cold water may begin to diminish or they may just leave the region in search of colder water. The cold pool is also crucial in the disspiation of storms in the region. However, as it gets warmer, it will be less effective at this. As we continue this research, we will also study the effects of El Niño Southern Osciallation and North Atlantic Oscillation on the surface and bottom temperatures of the region.

By analyzing the maximum and minimum temperatures, as representative values for surface and bottom temperatures, on an intra-annual scale a standard of what the stratification should look like in the region is shown. It shows a time frame of when the stratification should develop and break down over the course of one year. By using a large data set, a standard of when the development and breakdown should happen is shown. To further develop this in the future, buoy data will be incorporated to determine a time frame where mixing events usually occur and that will be analyzed alongside the surface and bottom temperatures. This is with the hope of aligning drops in the difference between the surface and bottom with the time frame where mixing events usually occur.

ACKNOWLEDGMENTS

Glider data used in this study is available through the MARACOOS assets page http://maracoos.org/data and http://marine.rutgers.edu/cool/auvs/index.php?did=369. Buoy data used is available at http://www.ndbc.noaa.gov/ . NMFS data used is available at http://www.nefsc.noaa.gov/epd/ocean/MainPage/ioos.html. Thank you to Teledyne Webb Research for undergraduate fellowship research funding. We would like to thank all of my fellow undergraduates in the RU COOL Room as well as Laura Nazzaro for their continued helped and support.

REFERENCES

[1] Able, K. W., Grothues, T. M., Morson, J. M., & Coleman, K. E. (2014). Temporal variation in winter flounder recruitment at the south margin of their range: is the decline due to increasing temperatures? *ICES Journal of Marine Science*, 2186–2197.

[2] Castelao, R., Glenn, S., & Schofield, O. (2010). Temperature, salinity, and density variability in the central Middle Atlantic Bight. *Journal of Geophysical Research: Oceans*, *115*(10), 1–14. http://doi.org/10.1029/2009JC006082

[3] Castelao, R., Glenn, S., Schofield, O., Chant, R., Wilkin, J., & Kohut, J. (2008). Seasonal evolution of hydrographic fields in the central Middle Atlantic Bight from glider observations. *Geophysical Research Letters*, *35*(3), 6–11. http://doi.org/10.1029/2007GL032335

[4] Flagg, C.N., Wallace, D., & Kolber, Z. (1997). Cold anticyclonic eddies formed from cold poolwater in the southern Middle Atlantic Bight. Pergamon, 17(15), 1839-1867.

[5] Forsyth, J. S. T., Andres, M., & Gawarkiewicz, G. (2015). Journal of Geophysical Research : Oceans. *J. Geophys. Res.*, *120*(3), 2370–2384. http://doi.org/10.1002/2014JC010516.Received

[6] Glenn, S. M., Miles, T. N., Seroka, G. N., Xu, Y., Forney, R. K., Yu, F., … Kohut, J. (2016). Stratified coastal ocean interactions with tropical cyclones. *Nature Communications*, *7*(May 2015). http://doi.org/10.1038/ncomms10887

[7] Grothues, T. M., & Cowen, R. K. (1999). Larval fish assembladges and water mass history in a major faunal transition zone. *Continental Shelf Research*, *19*, 1171–1198.

[8] Houghton, R. W., Schlitz, R., Beardsley, R. C., Butman, B., & Chamberlin, J. L. (1982). The Middle Atlantic Bight Cold Pool: Evolution of the Temperature Structure During Summer 1979. *Journal of Physical Oceanography*, *12*(10), 1019–1029. http://doi.org/10.1175/1520-0485(1982)012<1019:TMABCP>2.0.CO;2

[9] Lentz, S. (2003). Evolution of stratification over the New England shelf during the Coastal Mixing and Optics study, August 1996–June 1997. *Journal of Geophysical Research*, *108*(June 1997), 1–14. http://doi.org/10.1029/2001JC001121

[10] Mountain, D. G. (2003). Variability in the properties of Shelf Water in the Middle Atlantic Bight, 1977–1999. *Journal of Geophysical Research*, *108*(C1), 1–11. http://doi.org/10.1029/2001JC001044

Lessening biofouling on long-duration AUV flights: Behavior modifications and lessons learned

Clinton D. Haldeman III, David K. Aragon, Travis Miles, Scott M. Glenn
Center for Ocean Observing Leadership Rutgers, The State University of New Jersey 71 Dudley Rd., New Brunswick, NJ 08901

Antonio G. Ramos
Universidad de Las Palmas de Gran Canaria Division of Robotic and Computational Oceanography (IUSIANI-ULPGC) Las Palmas de Gran Canaria, Las Palmas, Spain

***Abstract*—With recent developments in battery technology and ocean energy harvesting systems, biological fouling, or biofouling, a process referring to the gradual accumulation of organisms on underwater surfaces, has gained a foothold as the primary adversary in long-duration autonomous underwater vehicle (AUV) flights of the Challenger glider mission. Limiting biofouling on long-duration AUVs is essential to the success of the flight. Inverse relationships and correlations were drawn between biofouling, vertical velocity of the AUV, and in turn, steering capability. As organisms settle and grow on the AUV, the hydrodynamics of the vessel changed, resulting in larger volume and more drag, adding buoyancy discrepancies as well. The increased drag results in a lower vertical velocity, and therefore less water flow over the rudder, or fin, directly causing the reduction in steering capability. Additionally, the organisms were not evenly distributed about the AUV, causing an imbalance in the drag. The fin then needed to maintain an offset to counteract this imbalance, resulting in less overall range in fin movement, further reducing the ability to steer. Analysis of the data from four separate legs of ocean basin crossings has shown that as the AUV begins to foul, it needs to maintain a vertical velocity of greater than 12 cm/s to maintain viable steering. Overall the fin will move more as it attempts to compensate for biofouling, which will use additional power throughout the duration of the flight, bringing power budgets back into the equation.**

Although the biofouling issues facing long-duration AUVs are subject to the same settling processes as boats and ships, porting commercially available antifoulant technologies from larger, faster vessels to the AUVs has proven challenging. Non-like metals combined with biofilms can result in increased galvanic corrosion, so copper coating compounds on steel components and aluminum AUV hull are not ideal, particularly with limited space and weight for sacrificial anodes. Ablative paints, by design, can wear away, causing possible ballast issues while failing to prevent fouling. Biocides, for obvious reasons, have not been in the list of candidates for consideration in the ongoing battle against biological growth. We introduced some behavioral modifications in the flight characteristics of the AUV that provided some assistance. For example, we avoided the majority of the warmer and illuminated euphotic zone, where primary production occurred, or zones above a certain temperature range that could hamper organism growth, even if it was not possible to prevent settling. This paper will explore the differences in biofouling, flight environment, preventative measures, and lessons learned on the four legs of ocean basin crossings completed by two separate Slocum electric gliders, part of the Rutgers AUV fleet.

Keywords—gliders, long duration AUV, biofouling, flight characteristics

I. Introduction

Developed in the early days of the National Oceanographic Partnership Program, Slocum gliders have become a common, robust tool in oceanographic research [1]. Users from glider centers in the United States, Brazil, South Africa, Australia, the United Kingdom, Spain, and more now deploy these gliders in ocean basins worldwide, collecting both physical and biological parameters with an ever-expanding available sensor suite. Since the first test flight off the New Jersey coast in 1999, these autonomous underwater vehicles (AUVs) have gone through several iterations, upgrades, and "hardening" to ensure their durability at sea. Rutgers University has partnered with Teledyne Webb Research since the inception, and has often been a testbed - and the catalyst - for new designs. In 2007, Rutgers technicians began experimenting with lengthening the gliders to accommodate additional batteries, as well as exploring other battery technologies that offer more available power. This resulted in a larger onboard "fuel tank", opening the door for long duration underwater flights and potential sustained monitoring operations. Rutgers has since attempted five long duration flights; of which the last four consecutive have completed successfully. These flights comprise several firsts, including the first AUV to cross an ocean basin under its own power, and more recently, the first AUV to circumnavigate an ocean basin – all the while collecting and returning valuable physical data that can be ingested by global ocean models. These accomplishments have not come without their challenges, but they have provided Rutgers glider pilots with data and experience to both prepare gliders prior to deployment and fine-tune flight mechanics to sustain long-endurance missions.

II. Background

In 2008, Slocum glider RU17, with many of its parts fabricated from excess materials in the Rutgers machine shop, was launched off the New Jersey coast in an effort to cross the North Atlantic Ocean basin. After 160 days at sea, the glider sank, approximately 200 miles west of the Azores, presumably caused primarily by a large animal interaction. Although a wealth of valuable information was lost, many lessons were also learned along the way. While large animal encounters cannot be foreseen or necessarily avoided, potentially

978-1-5090-1537-5/16/$31.00 ©2016 IEEE

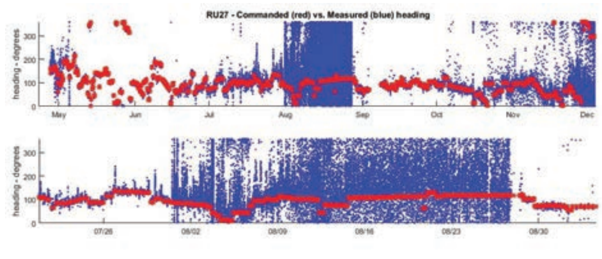

Fig. 1. Glider commanded (red) vs. measured (blue) heading. Bottom plot: August 2009 zoom.

problematic issues such as galvanic corrosion resulting from immersing non-like metals in seawater can be addressed in the lab prior to launch. Later that year, with the help of the manufacturer, a hardened version of the Slocum glider was assembled, taking note of issues observed during the previous deployment. Dubbed RU27, in April of 2009 this 200 m glider was once again launched off the New Jersey coast and headed across the Atlantic. After four months of flight in the summertime waters of the North Atlantic, RU27 could no longer maintain a heading in the intended direction of travel, even utilizing the full 25 degree extent of the rudder's range of travel. Fig. 1 shows RU27's commanded heading in red vs. measured heading in blue, highlighting the period between August and September where the glider had little to no control of its heading in the lower panel. Prior to August, there was little variation between the measured and commanded heading, but small spikes in the measured heading were becoming more noticeable as time passed. A 94% correlation in heading during the month of July dropped to less than 23% throughout August. RU27 was practically inoperable for, at this point, reasons unknown, and glider flight engineering data was doing little to aid the diagnosis.

III. Biofouling

Changes to the glider's buoyancy drive and pitch angle were made in an attempt to increase vertical velocity, but no amount of adjustment of flight parameters could bring RU27 back to operational status from afar, so a visit to the glider became imperative. Toward the end of August 2009, a small group was assembled to intercept RU27 at sea. Intentions were to provide a diagnosis and, if possible, repair the glider and allow it to continue on its mission. What met the intervention team was a rather unexpected adversary: Biofouling. Defined as the gradual accumulation of organisms on underwater surfaces, a plethora of research exists on the topic. The settling process has been well-cataloged - the initial adhesion of bacterial biofilms, followed by the settling of microorganisms (diatoms, fungi, and protozoans), and finally the settling of macroorganisms such as barnacles, polychaetes, and coelenterates [2,3,4,5]. Biofouling rates are highly dependent upon the environment; and can vary drastically between locales. Typically, areas with higher temperatures will experience a higher degree of biofouling, as temperature can determine breeding periods and growth rates [6].

Funded in part by The G. Unger Vetlesen Foundation, NOAA IOOS, University of Sao Paulo, University of Cape Town, and Rutgers, The State University of New Jersey

Fig. 2. Biofouling on University of South Florida glider after 28 days at sea

For example, Rutgers technicians experience is that a standard glider deployment off the coast of New Jersey of approximately one month duration will see little to no biofouling. Biofilms are typical of the fouling on these deployments, but barnacle growth and other macroorganism fouling is rare. Conversely, a deployment by the University of South Florida in the Gulf of Mexico will often see degradation of optical sensors within 10 days and a complete coating of fouling on the glider by the end of a one month mission [7]. (Fig. 2) Although this glider had fouled enough to compromise the quality of the data collected, it had not fouled enough to severely affect flight performance. Quite the contrary, RU27 had experienced macrofouling to such an extent that it was no longer able to function properly. Upon arrival at the glider's location approximately 200 nm west of the Azores, the intervention team noticed a fairly significant colony of Pollicipes pollicipes, or Goose Neck Barnacles, attached to various portions of the hulls of the glider. (Fig. 3) These barnacles are a common marine organism found in the mid latitudes that often attach themselves to flotsam or other debris adrift in the water column. Studies have shown that not only can these macroorganisms choose their settlement substrate on the basis of topography and/or water flow, they are also able to crawl toward their preferred location [8,9]. On RU27, these processes resulted in several distinct areas of significant growth, primarily around the joints of the glider, where the discontinuities in the smooth hull create microturbulent structures, allowing for settlement of macroorganism larvae [10]. As filter feeders, P. pollicipes have a number of cirri, which protrude from the oral cavity with the intention of collecting food. However, when a number of these organisms latch on to the hull of the Slocum Gliders, they have proven to be detrimental to missions – and especially the long duration missions - as the surface area of these foreign protrusions produces a large amount of drag. Occurrences such as these have the potential to reduce the velocity of a glider to <10% as seen with RU27. (Fig. 4)

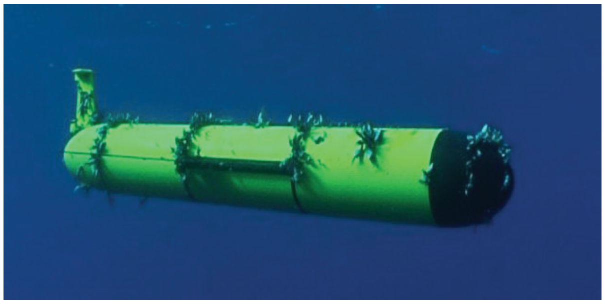

Fig. 3. P. pollicipes attached to glider RU27, primarily near joint areas (1st Atlantic glider crossing, 2009)

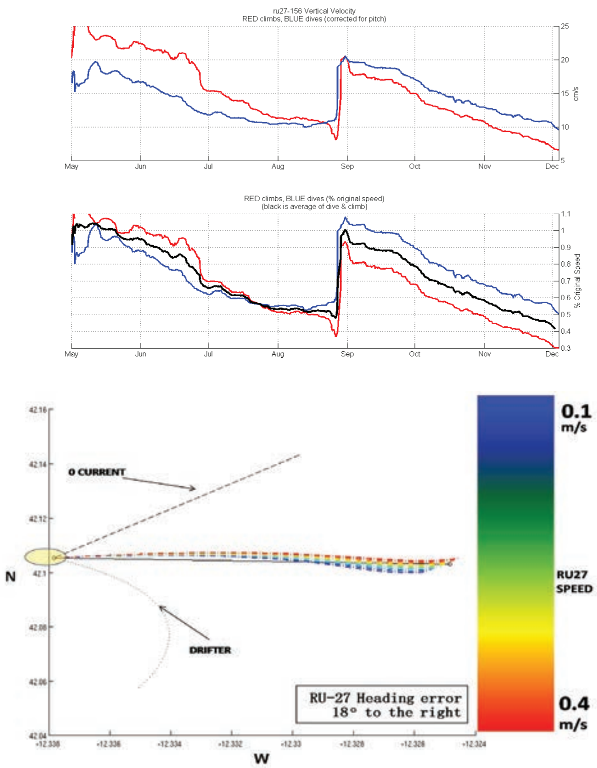

Fig. 4. RU27 vertical velocity (red – dives blue - climbs). Noticeable decay observed. The heading error was of 18º (1st Atlantic glider crossing, 2009)

Once the vertical velocity of a Slocum glider is reduced, hydrodynamic flow past the rudder is lessened, causing an associated reduction in steering ability. Although actual values can vary dependent upon glider size and configuration, these long duration flights have shown that any vertical velocity less than approximately 12 cm/s and increased drag from biofouling can result in the complete loss of ability to steer.

As depicted in Fig. 4, it does not take an excessive amount of growth to reach this threshold. Perhaps most surprising is that growth amassed despite antifouling measures taken into account prior to launch. The hull sections were covered in ClearSignal, a rubberized coating designed to be used on acoustic streamers used in surveys in the oil and gas industry [11]. An antifoulant paint provided by Epaint, EP-SN-1, was applied to the nosecone, fore stem, wings, wing rails, aft cap, tail stem, CTD (conductivity, temperature, depth sensor), and the aluminum rings between hull sections. More on antifoulant techniques will be discussed later in this paper. During the at-sea rendezvous, although it was never pulled from the water, RU27 was cleaned of all visible biofouling, and tests were conducted to ensure flight performance had been restored. With drag decreased, RU27's flight characteristics returned to normal, and the glider proceeded to make its way to Baiona, Spain. Upon recovery, it was discovered that the glider was once again fouled with P. pollicipes, albeit to a slightly lesser extent.

Colleagues from University of Las Palmas de Gran Canaria conducted a post-flight analysis of the vertical velocity decline showing that the rate of change of vertical velocity coincided with the changes in the average temperature of the water column in which RU27 was flying. Three separate episodes of velocity decline were considered, where Vmax is the initial velocity at t0, Vt is the velocity and time t (days), and k is the rate of change in days-1:

$$Vt = Vmax^{*}e^{-k(t-t0)}$$

In water with an average temperature just 1°C higher, the rate of velocity decay was an order of magnitude higher. (Fig. 5) The initial velocity decline (episode 1) encompassed 92 days – May, June, and July - and several flight parameter adjustments (increased pump throw, pitch changes, etc.). Prior to the start of episode 2, all mechanical changes to increase glider speed had been exhausted, and the next decline took a mere 12 days to reach 10% of an already reduced maximum velocity. Episode 3 encompasses the flight time after the glider had been cleaned at sea until recovery, a total of 98 days. The rate of velocity decay shows that the glider had a total of 160 days until it reached the 10% velocity threshold; a 2 month cushion, but the fouling had already begun to affect flight dynamics. This direct correlation between average water column temperature and rate of vertical velocity decay is an important consideration in long duration mission planning.

Analysis of rostrum width of P. pollicipes applied to the von Bertalanffy growth model has also provided a method to back out possible events during the glider's flight that may have contributed to barnacle attachment and speed lost. Several examples have correlated well with glider system aborts or extended analyses of flight data, where the glider had spent a considerable amount of time at the surface. Surfacing events greater than 1 hour in duration can aid in the protein polymerization, or the setting of the barnacle's "glue" [12,13,14].

IV. RU29 – CASE STUDY

RU27's success crossing the Atlantic Ocean while collecting data for global ocean models opened the door for sustained at-sea data gathering operations, and the continuance of the Challenger mission, initially proposed by Dr. Richard Spinrad, to recreate the H.M.S. Challenger's global mission w/ AUVs. To do so would require careful planning, taking note of lessons learned from RU27, as the next leg of the Challenger mission was slated for an even more remote location. The

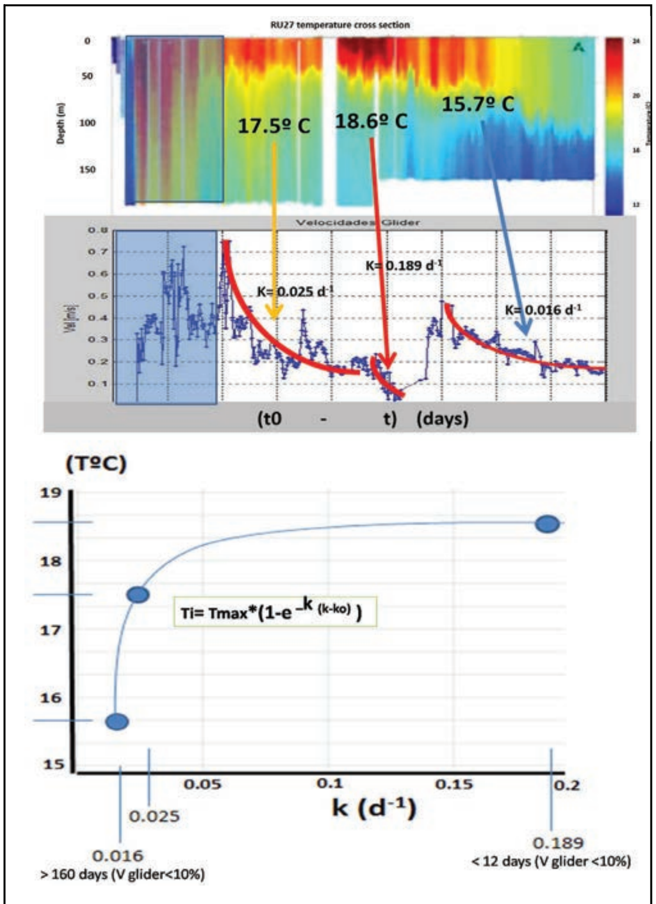

Fig. 5. Velocity decay (k in days-1) and average water column temperature correlation. (1st Atlantic glider crossing, 2009)

glider was scheduled to be launched in South Africa in January of 2013, passing near Ascension Island, and continuing on to Brazil as leg 1, with leg 2 being the return trip from Brazil to South Africa. Following is an analysis of what became 3 legs of the mission as related to background provided by RU27's maiden crossing.

A. Glider improvements – design and antifoulant techniques

RU27 was a first generation (G1) glider. The glider had anodized aluminum hulls, a flowthrough CTD, and a shallow buoyancy-drive pump rated to maximum depth of 200 m. This meant that RU27's entire flight was spent in the relatively higher productivity zones of the open ocean where light can penetrate. In addition, RU27's extended length was a product of replacing the science bay with a standard aft or fore hull. This increased the size of the glider without increasing the size of the buoyancy drive or the fin, resulting in a glider that is inherently slower than a standard sized glider. Battery packs also had to be purchased individually and soldered together to create a one-of-a-kind custom pack. For power savings, the onboard science computer was removed, and the CTD was wired back to the mainboard, similar to past Slocum glider designs, prior to the addition of a standalone science bay computer. Antifoulant protections included painting exposed parts with antifoulant paint provided by Epaint and coating the hulls with ClearSignal antifouling coating. Additional anodes were added to prevent the additional corrosion likely to be seen due to duration and the ability of marine biofilms to create additional ionic transport, thereby enhancing corrosion [15].

In contrast, RU29 is a second generation (G2) glider with several notable improvements. The extended energy bay, now a commercially available product, is simply an add-on section that allows standard battery pack fitment. Its buoyancy drive is an oil-filled bladder, ultimately resulting in both an additional 60 cc's of buoyancy drive and deeper rating, up to a maximum depth of 1000 m. It includes a standard science bay with a pumped CTD instead of flowthrough, which allows for flight characteristic (primarily pitch) changes without compromising data integrity and thermal lag calculations. Software improvements have given rise to a "low power mode", effectively allowing the glider to turn off between sampling intervals. Further updates included this feature for the standalone science computer as well, which was used to save power on leg 3, from Brazil to South Africa. Antifoulant measures again included an Epaint product on the CTD, wings, tail cone, and aft cap. Trilux 33 was used on the fore section, nosecone, and wing rails for leg 2. Paint choice was based more on color than compound at that stage. Extra zinc anodes were again added to combat biofouling-enhanced corrosion. The hull sections were coated only with the standard paint, but an additional step was taken to prevent larval settlement amidst the joints. A polyurethane "seam tape" was used to smooth out the joints and reduce the resulting microturbulent features.

B. Leg 1 – Cape Town, South Africa to Ascension Island, U.K.

Leg 1 saw the deployment of RU29 off the coast of Cape Town, South Africa, in January of 2013. The glider was deployed nearshore, in the cooler, nutrient-rich upwelled waters off the coast. Inside of the first week, RU29 had made its way toward Cape Canyon and off the shelf into the deeper waters of the South Atlantic. Eddies off the coast can push the warm surface waters down several hundred meters (Fig. 6), but the average temperature of the water column in which RU29 was able to fly (top 1000 m) was 9.75°C versus the 18°C average waters that RU27 traversed; nearly half as warm. Not wanting to pass up on lessons learned from RU27, the team at Rutgers soon decided to change RU29's top inflection depth from the surface to a depth of 125 m in an attempt to stay below the 15°C mark, and out of the euphotic zone. Average temperature of the water column from 125 m to 1000 m over the course of the deployment was 8.17°C, even with the deepening of the thermocline as the glider made its way closer to the equator. This vertical creep by the thermocline did, however, cause the top inflection depth of 125 m to be slightly over the 15°C threshold; a number chosen

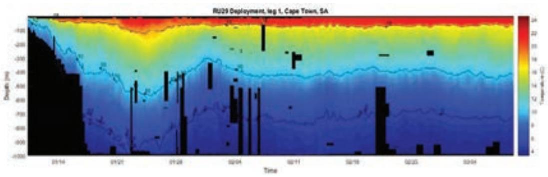

*Fig. 6. **Eddies of the Cape Town coast bring warm surface waters to depth*** (RU-29 1st South Atlantic Circumnavigation, Challenger mission (January 2013-March 2016)

to keep barnacle growth at a minimum, keeping the vertical velocity decay rate (k) less than .016/day, translating to approximately 3.5% of glider speed lost per month. Approximately halfway through the deployment RU29 fell victim to a software glitch, causing the glider to reset underwater, triggering a software bug that caused it to become stuck in a loop flying in the surface waters for the next 10 days without attempting to call in. Surprisingly, a similar software glitch allowed control to be regained, but the detrimental effects of RU29's hiatus had already begun to exhibit in the data. Running at full power in shallow water had burnt nearly 1.5 months of power in low power mode, and P. lepas, a South Atlantic species of the Goose Neck Barnacle, had colonized the glider, reducing its vertical velocity nearly 50% in less than 2 weeks, highlighting the perils of time spent at the surface. (Fig. 7) This reduction in velocity manifested itself again in the glider's inability to maintain a heading, even utilizing the full buoyancy drive and full extent of the fin's range of motion. In the true spirit of an international collaborative effort, help was enlisted from South Africa and U.K. to transport a satellite phone to an individual that was willing to sail out to the glider and clean it off – in similar fashion to RU27's initial crossing. This at-sea intervention restored the glider's vertical velocity to pre-hiatus levels, a faster rate of decay was noticed throughout the remainder of the mission. (Fig. 8) Rate of decay is presumed to be higher toward the end of the mission as the glider entered warmer surface waters near the equator, favorable to both growth and breeding rates of barnacles. Leg 1 ended with a recovery by Ascension Island residents just as the glider's battery expired. This recovery is noteworthy as it brings to light another method of biofouling; albeit more episodic as opposed to the typical chronic fouling over time. The glider had drifted overnight in relatively warm surface waters near the equator. Flying Fish, several species of which are common in the area, tend to lay their filamentous eggs on flotsam, as the eggs are negatively buoyant [16]. RU29 was fouled in mats of these filamentous eggs upon recovery. (Fig. 8) While likely not so thick and dense as to scuttle the glider, possible buoyancy discrepancies and certainly additional drag are issues to consider. The common theme throughout biofouling experiences becomes the primary lesson – keep the glider off the surface.

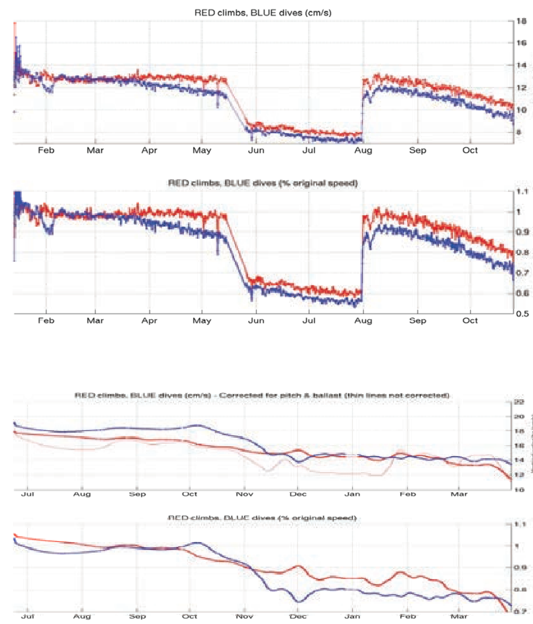

Fig. 7. (Top) RU29 vertical velocity corrected for pitch and ballast. Drastic reduction after hiatus; restored to nearly full vertical velocity after at-sea cleaning. Significantly faster rate of decay evident after cleaning, potentially due to warmer surface waters near equator. (Bottom) RU29 vertical velocity from leg 3; a more typical curve without any significant fouling events. RU-29 Challenger glider mission (January 2013-March 2016)

C. Leg 2 – Ascension Island to Ubatuba, Brazil

Leg 2 of RU29's ocean basin circumnavigation was initially unplanned, as Ascension Island was only an emergency bail-out point that became a necessity. A small team from Rutgers eventually made their way to the island with only enough field equipment to repair and redeploy the glider. Aside from replacing a damaged fin, it was no more than a routine servicing – rebattery, repaint, new anodes, and prepare for redeployment. RU29 was going in near the equator, in already warm waters, and flying throughout the southern hemisphere's summer, so biofouling concerns were forefront. Post-deployment, RU29 showed an average water column temperature of 10°C between 125-1000 m from Ascension Island to Brazil, with a significant deepening of the thermocline approximately midway through; the 18°C mark reaching as deep as 200 m between February and March. (Fig. 9) Heeding lessons learned during the two previous deployments, RU29 was deployed in deep water off the coast of Ascension Island, and was able to nearly immediately dive to full depth. With the "stay off the surface" protocol in mind, one further change was added to the glider's behavior – more yo's. Defined as a dive and a climb, adding a yo between surfacings will keep the glider underwater for several more hours. At this stage, the glider was only surfacing 1-2 times

Fig. 8. Mats of negatively buoyant flying fish eggs covering the glider (RU-29 1st South Atlantic Circumnavigation, Challenger mission (January 2013-March 2016)

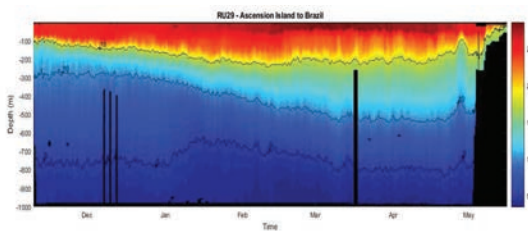

Fig. 9. Temperature transect, Ascension Island to Brazil. Noticeable deepening of the thermocline near the midway mark. (RU-29 1st South Atlantic Circumnavigation, Challenger mission (January 2013-March 2016)

daily (every 12-14 hours). A comparatively uneventful and short 6 months after deployment, RU29 was recovered off Ubatuba, Brazil – but not before collecting a wealth of data on a persistent eddy off the coast of the aptly named Cabo Frio.

D. Leg 3 – Ubatuba, Brazil to Cape Town, South Africa

Leg 3 of RU29's mission was initially slated to begin in July of 2014, but twice the glider leaked at depth only a few days after deployment. Once a miniscule scratch in the carbon fiber hull was finally located, the hull was replaced and the glider was ready for its return trip to South Africa. The glider was deployed in June of 2015, in an ocean basin averaging over 13°C, with warm surface waters comprising the top 200 m of the water column, and nearly 7000 km to traverse. (Fig. 10). Tristan de Cunha, a small island in the South Atlantic, was the only possible bailout point. Reachable only by vessel, it is not an ideal endpoint. But with experience gained, confidence levels were high. Precautions were taken during RU29's dry-dock time, and several pieces, including the bellows in the buoyancy pump, were replaced. An oddity with the persistor caused concern, and was promptly replaced. RU29 was redeployed off the shelf, where it could immediately reach full depth, in an attempt to avoid biological growth. Becoming typical of the midpoint of long duration flights, a valve on the buoyancy pump began to slip, causing oil to leak back until the pump reached an "out of deadband" phase, and turned on to pump the oil back out. This "slippage" of oil and the resulting double pumping while flying to 1000 m brought the energy usage up to a level that was not sustainable to make it across the ocean basin. The solution was to limit flight depth to 500 m, the point at which slippage would occur, but the glider would inflect prior to restarting the pump. This once again raised concerns of biofouling as the glider no longer had the ability to remain in the colder temperatures of the deep ocean. Antifoulant protection was nearly identical to previous flights; Epaint on various exposed parts of the glider, seam tape around the joints, with one additional measure taken. A number of seagoing technicians use Desitin or similar zinc oxide creams on moored instrumentation arrays with varying degrees of effectiveness, so the decision was made to add that around seams that could not be taped or painted effectively, such as where the aft cap meets the rear hull, and where the fore section tapers down to meet the nosecone. Upon recovery off

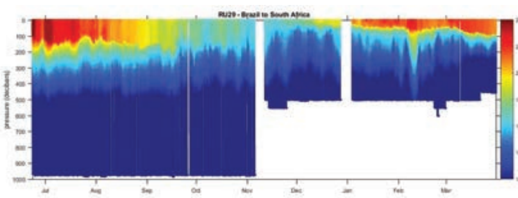

Fig. 10. RU29's temperature profile from Brazil to South Africa (Jun 2015-Mar 2016), clearly exhibiting the time spent limiting flight depth to 500 m depth (RU-29 1st South Atlantic Circumnavigation, Challenger mission (January 2013-March 2016)

the coast of South Africa, overall biofouling was minimal, confirming the effectiveness partially of antifoulant methods used prior to deployment, but primarily due to glider behavioral modifications. Adjusting flight parameters accordingly is a key component to the success of long duration flights.

Barnacles recovered along with the glider that were able to survive transport, handling, and sorting were once again analyzed by Antonio Ramos and other colleagues at University of Las Palmas de Gran Canaria. The barnacles were grouped into 3 primary size groups as measured by the width across the rostrum. Based on their sizes and estimated growth rates, their attachment date could be estimated. Results are summarized in table 1.

Table 1. Estimated barnacle settling date

Barnacle Size	Barnacle Count	Estimated Settling Date
0 to 0.75 cm	13	12/20/2015-1/15/2016
0.75 to 1.0 cm	12	10/31/2015-11/25/2015
1.0 to 1.75 cm	5	8/15/2015 (majority)

On a previous mission by another glider, Silbo, which flew almost 2000 km from the Azores Islands to the Canary Islands, a preliminary analysis of barnacle size and attachment dates was attempted. This lead to several observations that potentially long surfacing times could lead to increased barnacle settling. A typical surfacing interval (where the glider sits 1/4 above water and 3/4 in the top .5 meter) lasts 5-20 minutes. 10 minutes is typical for trans-oceanic missions. The dates in Table 1 above correlated to 2 specific events and a third sequence of events. For the smallest and largest barnacles, the singular event was an unintended reset of the computer system. This results in the vehicle performing short, shallow default missions until the glider can be retasked. In these examples, several hours passed prior to being able to retask the glider to dive deeper and stay underwater longer. The medium-sized barnacles correlated to an approximately 1 month long collection of surfacings after having switched to shallow missions due to buoyancy pump problems. These long surfacings and shallow dives were in effort to troubleshoot buoyancy engine issues and involved longer transfers of engineering data.

V. Conclusions

Advances is battery technology and other power systems have shifted biofouling to the forefront of issues facing long duration flights. Corrosion-enhancing biofilms and flight performance-hampering macrofouling can all contribute to the detriment of the project, and perhaps even the untimely demise of the vehicle. Thus antifoulant measures need to be taken both prior to launch and throughout the duration of the flight.

A. Antifoulants

Preparations for any glider flight longer than 1-2 months typically include a combination of antifoulant paints, a polyurethane seam tape, and some type of zinc oxide cream. There are 2 primary points of consideration for selection of an antifoulant paint – ablation and composition. While the vast majority of antifoulant paints on the market are ablative, this is not a desirable attribute for long duration AUVs. Typical speeds are much too slow for the ablation to prevent biofouling, and the loss of weight from this process could potentially contribute to ballasting complications. Paint composition must also be considered, as copper compounds have been the standard formula for many years. While effective against biofouling, in this particular two-metal system, aluminum becomes the anode. Galvanic corrosion could sacrifice the integrity of aluminum components, potentially causing a leak and the eventual loss of the vehicle. This reasoning led to the selection of Epaint's compounds and Interlux's Trilux 33, as both are purportedly aluminum safe antifoulant compounds. Most external components of the glider receive at least one coat of paint, including the nosecone, tail cone, wings, etc. Overall effectiveness appears marginal, and there is no protection for parts in proximity to these paints.

Polyurethane seam tape is used to cover the areas where the glider is joined together, with small holes poked around the perimeter to aid in allowing air to escape. This tape seals off the areas that cause microturbulent features that can allow barnacle larvae to settle and also prevents them from being able to crawl and settle in the joints. Thus far, this seam tape appears to be quite effective, as there has not been significant growth near areas where the tape was used. Experience with zinc oxide creams is limited to only one (albeit the longest) leg of the circumnavigation of the South Atlantic basin. This was applied to seams that were difficult to tape such as where the nosecone meets the fore section and where the tail cone meets the aft cap. Little to no growth was seen in areas where the zinc oxide cream was used.

In the case of an aborted mission, the glider should be cleaned and scrubbed thoroughly prior to being redeployed in an effort to remove any larvae that may have already settled. Barnacle attachment needs to be avoided and prevented for as long as possible.

Throughout the duration of the flight, behavioral modifications and flight parameter adjustments tend to be most critical and are perhaps the most effective tool for preventing biofouling. Whether event-based like a flying fish spawn or the more standard accumulation of biomass over time, keeping the vehicle out of the surface layer is a key component to mission success. Data returns are decimated to include only what is necessary for science and vehicle status monitoring in an effort to keep the time spent at the surface to a minimum. If the glider is adrift for greater than one hour, protein polymerization occurs and barnacles will likely remain attached for the duration of the flight. Avoiding long surfacings is paramount. CTD data is typically gathered on the following dive to ensure a full water column profile, but surface inflection depth is then adjusted to 125 m for several ensuing cycles. Keeping the glider out of the euphotic zone changes the photoperiod of barnacles that may already be attached, increases the average barometric pressure experienced, and reduces their feeding capabilities in the cooler water at depth. 125 m was chosen initially as the inflection depth as it coincided with the 15°C mark where barnacle growth rates remain slow enough as to provide a manageable decline in glider speed. These behavioral adjustments provide the best chance of success, and should be instituted as default parameters to avoid surfacings in the event of a system reset.

Continuing research in biomimicry (e.g. sharkskin paints) and liquefied surfaces could have significant future implications in the fight against biofouling, but as of this paper these products are not commercially available.

References

[1] O. Schofield, et al., "Slocum gliders: Robust and ready," *Journal of Field Robotics, Special Issue: Special Issue on Underwater Robotics,* vol. 24, no. 6, pp. 473-485, 2007.

[2] S. Cao, J.D. Wang, & H.S. Chen, "Progress of marine biofouling and antifouling technologies," *Chinese Science Bulletin,* vol. 56, no. 7, pp. 598-612, 2011.

[3] E.W. Knight-Jones, "Laboratory experiments on gregariousness during setting in Balanus Balanoides and other barnacles," *Journal of Experimental Biology,* vol. 30, pp. 584-598, 1953.

[4] D.J. Crisp, "The behaviour of barnacle cyprids in relation to water movement over a surface," *Journal of Experimental Biology,* vol. 32, pp. 569-590, 1955.

[5] D.J. Crisp, "Territorial behaviour in barnacle settlement," *Journal of Experimental Biology,* vol. 38, pp. 429-446, 1961.

[6] V. J. D. Rascio, "Antifouling coatings: Where do we go from here?," *Corros. Rev.,* vol. 18, pp. 133-154, 2000.

[7] C. Lembke, *pers. comm.,* University of South Florida, 2016.

[8] B. K. Jakob, et al., "Antifouling enzymes and the biochemistry of marine settlement," *Biotechnol Adv,* vol. 26, pp. 471-481, 2008.

[9] N. Lagersson & J. Hoeg, "Settlement behavior and antennary biomechanics in cypris larvae of Balanus amphitrite (Crustacea: Thecostraca: Cirripedia)," *Marine Biology,* vol. 141, pp. 513-526, 2002.

[10] H. Fuchs, *pers. comm.,* Rutgers University, 2010.

[11] H. Lobe, C. Haldeman, & S. Glenn, "ClearSignal coating controls biofouling on the Rutgers glider crossing," *Sea Technology,* vol. 51, no. 5, pp. 31-36, 2010.

[12] K. Oding et al., "An in vivo study of exocytosis of cement proteins from barnacle Balanus improvisus (D.) cyprid larva," *Journal of Experimental Biology,* vol. 209, no. 5, pp. 956-964, 2006.

[13] H.E. Pagett et al, "Structural characherisation of the N-glycan moiety of the barnacle settlement-inducing protein complex (SIPC)," *Journal of Experimental Biology,* vol. 215, no. 7, pp. 1192-1198, 2012.

[14] K. Matsumura et al., "Larval vision contributes to gregarious settlement in barnacles: adult red fluorescence as a possible visual signal," *Journal of Experimental Biology,* vol. 217, no. 5, pp. 743-750, 2014.

[15] S. Dexter & J. LaFontaine, "Effect of natural marine biofilms on galvanic corrosion," *Corrosion,* vol. 54, no. 11, pp. 851-861, 1998.

[16] W. Hunte, H. Oxenford, & R. Mahon, "Distribution and relative abundance of flyingfish (Exocoetidae) in the eastern Caribbean. II. Spawning substrata, eggs and larvae," *Marine Ecology Progress Series,* vol. 117, pp. 25-37, 1995.

Mapping Antarctic phytoplankton physiology using autonomous gliders

Filipa Carvalho, Josh Kohut, Maxim Gorbunov and Oscar Schofield
Department of Marine and Coastal Sciences
Rutgers University
New Brunswick, NJ, USA
filipa@marine.rutgers.edu

Matthew J. Oliver
College of Earth, Ocean and Environment
University of Delaware
Lewes, Delaware, USA

Keywords: gliders, phytoplankton, physiology, Antarctica, fluorescence induction and relaxation (FIRe) sensor

I. Introduction

Environmental factors, such as nutrient availability and irradiance, play the key role in phytoplankton physiology. Phytoplankton growth and marine primary production depend on physiological performance of phytoplankton that in turn respond to varying environmental conditions. The use of variable fluorescence kinetics has increasingly become a vital method in oceanographic studies; however, its use within the community is limited by the complexity of physiological data interpretation and the cost of available instruments. Physiological responses also span across different scales that are hard to record with the discrete manual sampling methods available.

The Quantum Yield of Photosynthesis (ϕ) is defined as the ratio of oxygen evolved in photosynthesis (or carbon assimilated) to the number of photons absorbed in the process [1]. Evaluating the Quantum Yield of Photosynthesis *in vivo* provides an alternate approach to C^{14} uptake, for example, for investigating how photosynthetic processes are affected by environmental factors, as it is highly sensitive to environmental stresses. The variable fluorescence [2] is the most sensitive signal detected from the ocean, which provides considerable insight into the photophysiology of phytoplankton, in particular the structure and function of Photosystem II (PSII). In the field, the maximum yield of photochemistry in PSII (Fv/Fm) has been widely used as a diagnostic tool to rapidly assess the health of phytoplankton and infer potential stresses or primary production controls [3].

Traditional sampling strategies such as the pump-and-probe, Fast Repetition Rate Fluorometers (FRRF) and more recently the Fluorescence Induction and Relaxation (FIRe) sensor [4] have been employed to characterize and understand the factors controlling phytoplankton physiology and primary production in the ocean. While continuous automated acquisition of physiological parameters is commonly used for surface waters using different fluorometers, repeated depth measurements over diel cycles are less often reported. When available, depth profiles have been built from discrete samples collected in bottles and ran on the benchtop instrument. Besides being a destructive sampling method, it is also constrained by the fact that the water collection and instrument run need to be done manually. Another benefit of measuring variable fluorescence *in situ* lies in the fact that the assessment of the photo-physiological properties of phytoplankton happens in the actual light fields in which these organisms are growing [5]. An important point since these physiological properties are highly sensitive to the ambient light fields.

Phytoplankton developed photoadaptation mechanisms to overcome light-induced stresses [6] i.e. to optimize light absorption under low light conditions or reducing total photon absorption under supra-optimal irradiances. These mechanisms, reflecting changes in the functional absorption cross-section of PSII (σ_{PSII}), are short-term light adaptation mechanisms such as Non-Photochemical Quenching (state transition, energy dependent and photoinhibition) and long term modifications in the light harvesting complex of phytoplankton (i.e. photoacclimation) [1]. The integration of an instrument, such as the FIRe sensor, that is capable of evaluating depth-dependent phytoplankton physiology in situ and in high resolution is an important step to fully understand phytoplankton dynamics and marine primary production.

II. Materials and Methods

A. Slocum gliders

Slocum electric gliders are a robust tool to map, with high spatial and temporal resolution, the upper water column properties in different environments [7], including polar regions. These 1.5 m torpedo-shaped buoyancy driven autonomous underwater vehicles provide high-resolution surveys of the physical and bio-optical properties of the water column [7].

Glider used for these deployments (ru24) was equipped with a Seabird Conductivity-Temperature-Depth (CTD) sensor. Glider based conductivity, temperature and depth measurements were compared with a calibrated ship CTD sensor on deployment and recovery to ensure data quality, as well as with a calibrated laboratory CTD prior to deployment.

978-1-5090-1537-5/16/$31.00 ©2016 IEEE

Glider profiles were binned into 1-meter bins and assigned a mid-point latitude and longitude. For each profile, Mixed Layer Depth (MLD) was determined by finding the depth of the maximum water column buoyancy frequency, max (N^2). An upward facing Photosynthetic Active Radiation (PAR) sensor was also integrated in the glider to record PAR in the range of 400-700 nm.

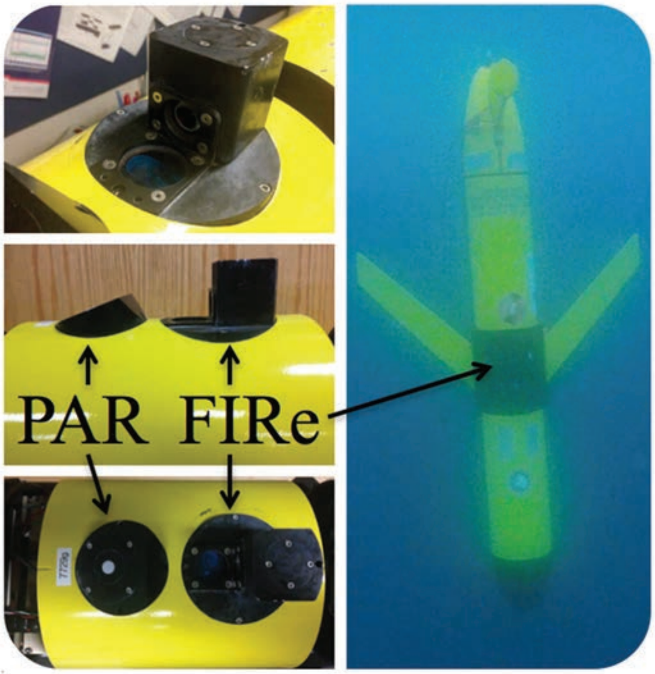

Figure 1: Fluorescence Induction and Relaxation (FIRe) and PAR sensors integrated into a Slocum glider.

B. FIRe sensor

In order to evaluate physiological responses of phytoplankton to physical forcing, ru24 was equipped with a FIRe sensor [8], the first sensor of its kind to be integrated in a glider. This allowed a high-resolution continuous mapping of the phytoplankton physiological responses to variable light regimes in the water column.

The FIRe sensor [4] provides a comprehensive suite of photosynthetic characteristics of the organisms, such as the minimum (F_o) and maximum (F_m) fluorescence yields corresponding to open and closed reaction centers of PSII, respectively, variable fluorescence component (F_v) and the functional absorption cross section of PSII (σ_{PSII}). This is accomplished by employing a sequence of excitation flashes of light with controlled intensity, duration and interval between flashes. The maximum quantum yield (efficiency) of photochemistry in PSII, denoted by ϕ_{PSII}, is given by the ratio F_v/F_m, i.e. $[F_m\text{-}F_o]/F_m$. Dark-adapted F_v/F_m has been widely used as an algal "health" parameter, which is responsive to the short-term (hours) light and nutrient history of the cells [9]. By definition, the actual quantum yield of photochemistry in PSII at a given PAR level is denoted Fv'/F_m'. A cap was used to cover the FIRe sample chamber so the signal was measured in the dark (the prime (') symbol after the variable denotes any light acclimated sample measured in darkness [10]). At low irradiance (under 100 $\mu E/m^2/s$, which comprises over 98% of the data points), Fv'/Fm' approaches Fv/Fm, and so for simplicity, Fv'/Fm' will be referred to as photosynthetic efficiency for the remaining of the manuscript.

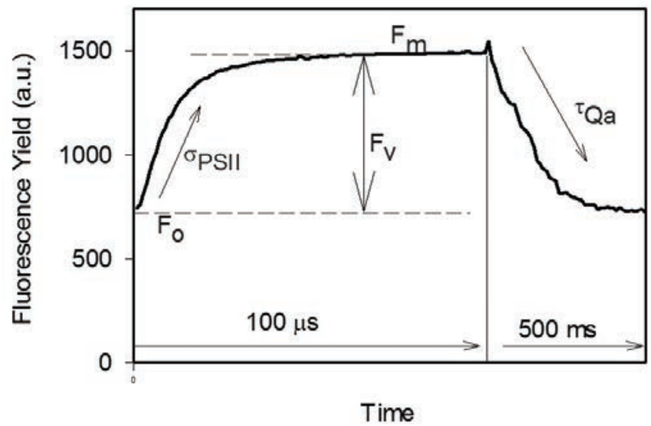

Figure 2: FIRe parameters from the Single Turnover Flash (STF) protocol. Minimum (Fo) and maximum (Fm) fluorescence yields corresponding to open and closed reaction centers of PSII, respectively, variable fluorescence component (Fv, where Fv=Fm-Fo), the quantum yield of photochemistry in PSII (Fv/Fm) and the functional absorption cross-section of PSII (σ_{PSII}).

C. FIRe glider data post-deployment processing

Several steps comprise the FIRe glider post-deployment processing. After the glider is recovered, raw data are downloaded from the onboard FIRe memory. Binary raw data is run through the Satlantic software and converted to ascii format. Data was then corrected for gain of the detector before applying any other corrections:

a) Blanks

"Blank" is the background signal recorded from the sample without phytoplankton in it. The blank signal includes a small amount of fluorescence from dissolved organic matter (DOM) and phytoplankton degradation products dissolved in water. As in any fluorometer, blanks must be removed from fluorescence signals (only Fm and Fo, as other FIRe parameters are blank-independent) to get accurate, blank-corrected values of chlorophyll fluorescence. Although blanks in the FIRe sensors are usually relatively small and may be neglected in many cases, the blank correction procedure will be critical in waters with high amount of DOM and/or small amount of phytoplankton (e.g. oligotrophic regions or deep layers below the euphotic zone).

As it is not possible to collect blanks while the glider is deployed, discrete *in situ* water samples were collected from the surface and at a depth well below the deep chlorophyll maximum (DCM), several times before and after the glider deployments. Surface and deep water samples were filtered and measured using the FIRe glider. Average surface and deep values were calculated and subtracted from the FIRe glider fluorescence signals during the deployment from the surface up to the DCM and below the DCM, respectively.

b) Functional absorption cross-section of PSII (σ_{PSII})

In order to convert the measured σ_{PSII} (in relative units) into absolute units (Å^2 quantum^{-1}), a correction coefficient was determined by cross-calibrating the FIRe glider against a "standard" calibrated benchtop FIRe instrument. A correction factor of 1650 was determined for the FIRe sensor RU24.

c) Converting FIRe Fm to chlorophyll-a concentrations

Discrete water samples at 8 different depths within the euphotic zone were collected during each glider deployment and recovery to further convert the measured Fm (maximum fluorescence intensities, in relative units) into absolute chlorophyll concentration (μg L^{-1}), a variable measured by other sensors, facilitating further comparisons with other studies. Chlorophyll-*a* (chl-*a*) is a proxy of phytoplankton biomass. Water samples were filtered onto 25 mm Whatman GF/F filters and extracted using 90% acetone.

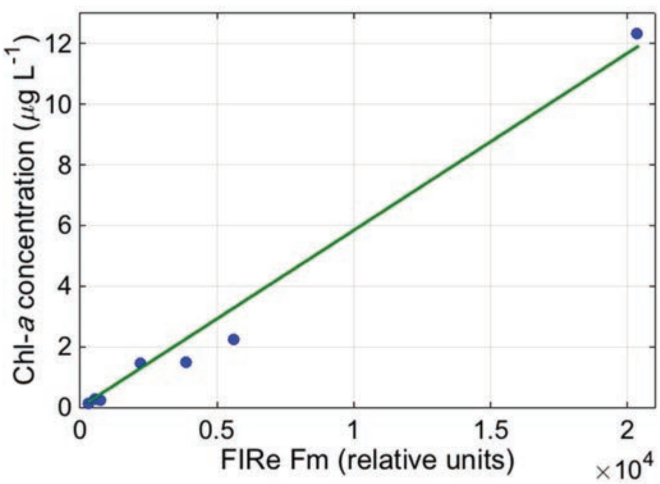

Figure 3: Scatter plot and respective linear trend from discrete water samples measured by the FIRe sensor (FIRe Fm) and chlorophyll-*a* concentrations obtained by the fluorometric method.

As a linear correlation is expected between FIRe Fm and chl-*a* concentration, the same sample was also run through the FIRe glider and its Fm measurement recorded. FIRe Fm throughout the deployment was then converted into chl-*a* concentration (Equation 1) using the high linear correlation (r^2=0.98) found between the 2 variables:

$$Chl = Fm \times 5.84 \times 10^{-4} \quad (1)$$

where *Chl* is the derived chlorophyll concentration and *Fm* is the maximum fluorescence measured by the FIRe sensor, after gain and blank corrections. QA/QC methods were applied to the data to ensure data quality.

D. Sampling overview

Palmer Deep (PD) is one of the cross-shelf canyons located in the West Antarctic Peninsula (WAP) where there is evidence of increased primary production [11, 12] and localized penguin foraging [13]. The National Science Foundation (NSF) funded Palmer Long Term Ecological Research (PAL-LTER) project [14] has been monitoring this ecosystem since 1991. The dependence of higher trophic levels on primary producers has led to increased efforts to try to understand the link between some of the physical drivers (such as stratification and mixed layer depth, MLD) and phytoplankton dynamics [12, 15, 16].

Part of this project has been focusing on understanding the phytoplankton physiological responses due to physical forcing. Until recently, sampling methods were restricted to discrete samples taken by a rosette or go-flo bottles collected from the ship or zodiac, respectively. This method provides insight into the depth dependent response of phytoplankton physiology, however it requires manual water collection at certain depths and times. A second shipboard method measures physiological parameters continuously using the onboard flow-through system at 5 m depth. This provides higher resolution horizontal maps, but lacks the depth component. The integration of a FIRe system into a glider allowed us to overcome these constrains and to sample *in situ* phytoplankton physiological responses in high-resolution both vertically and horizontally.

By measuring changes in maximal (F_m') and minimal (F_o') fluorescence in the same water mass over a diel cycle, one can get fluorescence values representative of a darkened adapted and relaxed state [17]. Evaluating diel cyles will also allow us to better understand the light effect on phytoplankton physiology by isolating the effect of supra-irradiance during peak daytime hours.

Here we present the results of two FIRe glider missions that have been designed to evaluate physiological responses at different temporal and spatial scales:

a) Temporal evolution – "the drift mission"

b) Spatial variability – "the station keeping mission"

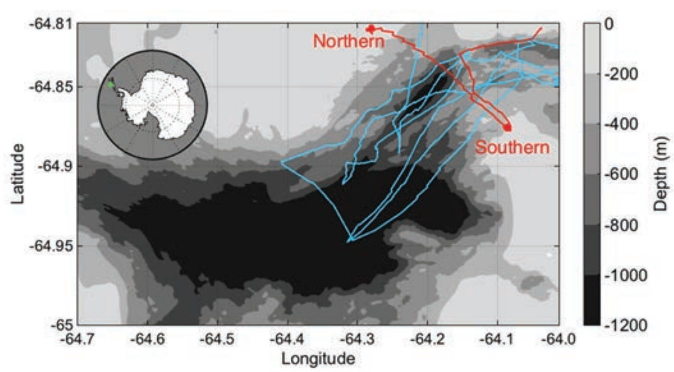

Figure 4: Bathymetry map of Palmer Deep canyon (green dot) in the WAP, Antarctica with the 2 sampling strategies used in the study: 1) drift mission (blue) to evaluate temporal changes in phytoplankton physiology and 2) station keeping mission (red) to evaluate spatial variability in phytoplankton physiology due to physical forcing.

III. EVALUATING TEMPORAL CHANGES

Previous studies have shown that the community structure, such as phytoplankton cell size and taxonomy, has influence on the photosynthetic rates, and therefore on the variable fluorescence signal [18]. In order to better isolate the temporal signal in phytoplankton photosynthetic efficiency, a mission was designed (Figure 4, blue) where the same water mass would be followed. This would allow a better characterization of physiological changes of the same community over time. The principle behind this mission was to conduct drift missions starting southwest of the canyon head as the dominant currents would push the glider towards the head of the canon. Every hour, the glider would perform a corkscrew dive and climb (fin set all the way to starboard side), while drifting at the surface in between dives. This way the same water mass was being followed and, by default, the same phytoplankton community would be evaluated during that drift. Four drift transects were conducted that lasted around 2 diel cycles each.

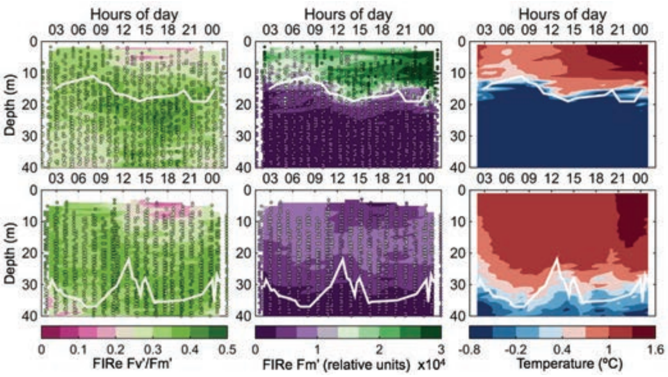

Figure 5: Averaged diel cycles of Fv'/Fm' (Photosynthetic efficiency), Fm' (proxy for phytoplankton biomass) and temperature for 2 different MLD (white line) regimes. Dots represent actual in FIRe glider measurements.

Phytoplankton acclimate to light levels averaged over the MLD. As stratification increases during spring/summer time, cells start to acclimate to the light intensity at each depth. Shallow MLDs provide a relatively stable light environment that allows phytoplankton to photoacclimate on the timescale of 1-2 days [19]. Intense mixing can bring dim-light adapted phytoplankton to the upper MLD where phytoplankton get exposed to supra-optimal irradiances and a decrease in Fm and Fv/Fm is recorded. Non-Photochemical Quenching (NPQ) is evident from reduction in both Fv'/Fm' and Fm' during daytime hours. Under higher irradiance (11:00-22:00 GMT), both Fv/Fm and Fm decrease, with the lowest values and deeper light penetration during peak irradiance hours (15:00-18:00 GMT). NPQ signal is more marked (Fv'/Fm'<0.1) when MLD is deeper as phytoplankton cells are acclimated to a mid-MLD light level, and therefore show higher light stress under supra-optimal irradiances.

IV. EVALUATING SPATIAL VARIABILITY

Spatial variability in the water column structure has been recorded across the head of the canyon [12]. In order to evaluate whether phytoplankton physiological responses are related to physical forcing, a mission was designed (Figure 4, red) where diel cycles of FIRe parameters were recorded at each location together with the standard CTD measurements. The station keeping glider recorded 2 consecutive diel cycles at each location (Figure 6), where at least one out of three dives/climbs would record FIRe data (approximately one FIRe dive an hour). In the remaining dives, the glider would only capture water column physical parameters.

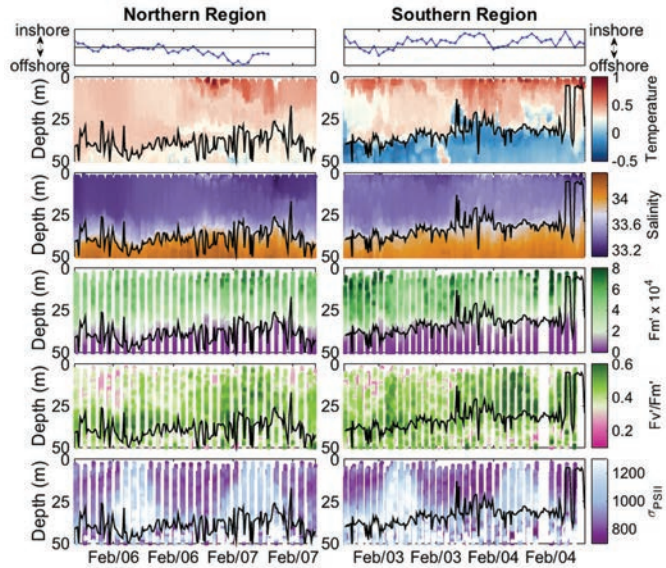

Figure 6: Comparison of 2 diel cycles at each region. Top row indicates dominant surface currents: inshore (oceanic "warm" influence) and offshore (coastal "cold" current). Temperature (°C), Salinity and FIRe parameters Fm' (relative units), Fv'/Fm' and σ_{PSII} (functional absorption cross-section of PSII, Å^2 quantum^{-1}) are presented for both regions. Black line denotes MLD.

V. EVALUATING PHOTOACCLIMATION MECHANISMS

Phytoplankton developed photo-adaptation mechanisms to overcome light-induced stresses, i.e. to optimize light absorption under low light conditions or to reduce total photon utilization under supra-optimal irradiances. Our preliminary analyses have shown different photoacclimation responses resulting from different MLD dynamics due to different solar radiation exposure conditions (both time and intensity).

An exponential relationship was found between Fv'/F_m' and PAR (Figure 7, left). Under low light (nighttime periods and deeper depths) Fv'/F_m' was maximum and equal to F_v/F_m, while under high light (high PAR) Fv'/F_m' decreased, an evidence of light-induced down regulation of PSII. A power fit curve (Equation 2) was applied to the FIRe data to evaluate differences in photoacclimation regimes under two different MLD conditions:

$$\frac{Fv'}{Fm'} = a\, e^{-\frac{PAR}{E_k}} \qquad (2)$$

where Fv'/F_m' is photosynthetic efficiency and PAR is Photosynthetic Available Radiance, both measured by the glider, E_k is light saturation parameter and a is a constant.

By comparing E_k values calculated for each depth/PAR bin, we can begin to distinguish between similar photo-physiologic communities, i.e. communities that have similar photoacclimation regimes and different photo-physiological communities and relate that to the depth of the ML.

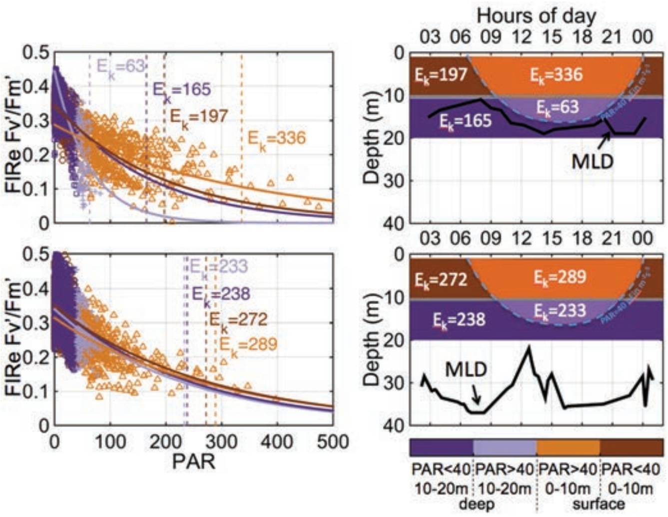

Figure 7: (left) Scatter plots of Fv'/F_m' and PAR with power curve fits for each PAR and depth bins highlighted in the legend. E_k values for each fitting are also presented; (right) schematics on difference in photoacclimation regimes presented in the plots on the left, evaluating the light saturation parameter in relation to the MLD (black line).

When MLD is shallow (Figure 7, top), the two layers show different E_k values. The much higher E_k, seen at the surface, gives an indication of phytoplankton acclimated to high irradiances while the lower E_k seen below the MLD shows low light acclimation. On the other hand, when MLD is deeper, and the 2 layers (0-20 m) fall within the ML, E_k values are much more similar, indicating that phytoplankton have similar photoacclimation regimes in the 2 layers. Note that the E_k of both layers when ML is deeper also fall between the first 2 E_k, indicative of a mid-light level acclimation.

Table 1: Summary on depth-dependent photoacclimation regimes in a nutrient replete environment.

MLD (m)	Stratification max[N^2], s^{-2}	Biomass (FIRe Fm')	Layer 0-10m	Layer 10-20m
Shallow ($\overline{MLD} \approx 16$)	High ($\overline{N^2} \approx 2x10^{-3}$)	High	High-light acclimated (higher E_k)	Low-light acclimated (lower E_k)
Deeper ($\overline{MLD} \approx 32$)	Low ($\overline{N^2} \approx 6.7x10^{-4}$)	Low	Mid-light (MLD) acclimated E_k(0-10m) ≈ E_k(10-20m)	

VI. Conclusions

The integration of a FIRe sensor into a glider allows us to map, with high temporal and spatial resolution, phytoplankton physiological responses to physical forcing. Different missions were designed to evaluate the temporal and spatial variability of phytoplankton physiology by using a drift and a station keeping mission, respectively. Diel cycles collected show a clear diurnal variations driven by incident radiation, with both maximal fluorescence and photosynthetic efficiency (in any light adapted phytoplankton) showing reduced values only in the upper 10-15 meters of the water column at the highest irradiances. Further analyses comparing different MLD regimes have shown different photoacclimation responses (light saturation parameter, E_k) resulting from differences in solar radiation exposure conditions (both time and intensity), reflected in the depth of the ML. Further analyses include determining a method to correct the FIRe glider fluorescence profiles in the upper ocean during daytime by comparing the maximum fluorescence during the highest irradiance (daytime) with the lowest irradiance (nighttime).

Acknowledgments

We would like to thank the Rutgers glider team, Palmer Station personnel and ARSV Laurence M. Gould crew for support in deployments and recoveries. Filipa Carvalho was funded by a Portuguese doctoral fellowship from Fundação para a Ciência e Tecnologia (DFRH - SFRH/BD/72705/2010).

References

[1] P. G. Falkowski and J. A. Raven, *Aquatic photosynthesis*: Princeton University Press, 2007.

[2] P. Falkowski and Z. Kolber, "Variations in chlorophyll fluorescence yields in phytoplankton in the world oceans," *Functional Plant Biology,* vol. 22, pp. 341-355, 1995.

[3] M. J. Behrenfeld, K. Worthington, R. M. Sherrell, F. P. Chavez, P. Strutton, M. McPhaden*, et al.*, "Controls on tropical Pacific Ocean productivity revealed through nutrient stress diagnostics," *Nature,* vol. 442, pp. 1025-1028, 2006.

[4] M. Y. Gorbunov and P. G. Falkowski, "Fluorescence induction and relaxation (FIRe) technique and instrumentation for monitoring photosynthetic processes and primary production in aquatic ecosystems," in *Photosynthesis: Fundamental Aspects to Global Perspectives"-Proc. 13th International Congress of Photosynthesis, Montreal, Aug*, 2004, pp. 1029-1031.

[5] D. J. Suggett, O. Prášil, and M. A. Borowitzka, *Chlorophyll a Fluorescence in Aquatic Sciences*: Springer, 2011.

[6] Z. Dubinsky and O. Schofield, "From the light to the darkness: thriving at the light extremes in the oceans," *Hydrobiologia,* vol. 639, pp. 153-171, 2009.

[7] O. Schofield, J. Kohut, D. Aragon, L. Creed, J. Graver, C. Haldeman*, et al.*, "Slocum gliders: robust and ready," *Journal of Field Robotics,* vol. 24, pp. 473-485, Jun 2007.

[8] C. Haskins and O. Schofield, "Glider measurements of phytoplankton physiology in penguin foraging zones along

the Western Antarctic Peninsula," in *OCEANS 2015 - MTS/IEEE Washington*, Washington, DC, 2015, pp. 1-4.

[9] J. A. Berges, D. O. Charlebois, D. C. Mauzerall, and P. G. Falkowski, "Differential effects of nitrogen limitation on photosynthetic efficiency of photosystems I and II in microalgae," *Plant Physiology,* vol. 110, pp. 689-696, 1996.

[10] O. Vankooten and J. F. H. Snel, "The Use of Chlorophyll Fluorescence Nomenclature in Plant Stress Physiology," *Photosynthesis Research,* vol. 25, pp. 147-150, Sep 1990.

[11] M. T. Kavanaugh, F. N. Abdala, H. Ducklow, D. Glover, W. Fraser, D. Martinson*, et al.*, "Effect of continental shelf canyons on phytoplankton biomass and community composition along the western Antarctic Peninsula," *Marine Ecology Progress Series,* vol. 524, pp. 11-26, Mar 30 2015.

[12] F. Carvalho, J. Kohut, M. J. Oliver, R. M. Sherrell, and O. Schofield, "Mixing and phytoplankton dynamics in a submarine canyon in the West Antarctic Peninsula," *Journal of Geophysical Research: Oceans,* 2016.

[13] M. J. Oliver, A. Irwin, M. A. Moline, W. Fraser, D. Patterson, O. Schofield*, et al.*, "Adelie penguin foraging location predicted by tidal regime switching," *PLoS One,* vol. 8, p. e55163, 2013.

[14] H. W. Ducklow, K. Baker, D. G. Martinson, L. B. Quetin, R. M. Ross, R. C. Smith*, et al.*, "Marine pelagic ecosystems: the west Antarctic Peninsula," *Philos Trans R Soc Lond B Biol Sci,* vol. 362, pp. 67-94, Jan 29 2007.

[15] O. Holm-Hansen, B. Mitchell, C. Hewes, and D. Karl, "Phytoplankton blooms in the vicinity of Palmer Station, Antarctica," *Polar Biology,* vol. 10, pp. 49-57, 1989.

[16] M. A. Moline and B. B. Prezelin, "Long-term monitoring and analyses of physical factors regulating variability in coastal Antarctic phytoplankton biomass, in situ productivity and taxonomic composition over subseasonal, seasonal and interannual time scales," *Marine Ecology Progress Series,* vol. 145, pp. 143-160, Dec 1996.

[17] J. W. Runcie and M. J. Riddle, "Distinguishing downregulation from other non-photochemical quenching of an Antarctic benthic macroalga using in situ fluorometry," *European Journal of Phycology,* vol. 46, pp. 171-180, 2011.

[18] D. J. Suggett, C. M. Moore, A. E. Hickman, and R. J. Geider, "Interpretation of fast repetition rate (FRR) fluorescence: signatures of phytoplankton community structure versus physiological state," *Marine Ecology Progress Series,* vol. 376, pp. 1-19, 2009.

[19] O. Schofield, M. A. Moline, and B. B. Prezelin, "Palmer LTER: Photoacclimation in a coastal phytoplankton bloom," *Biological Sciences,* p. 130, 1995.

nature COMMUNICATIONS

ARTICLE

Received 21 May 2015 | Accepted 29 Jan 2016 | Published 8 Mar 2016

DOI: 10.1038/ncomms10887 OPEN

Stratified coastal ocean interactions with tropical cyclones

S.M. Glenn[1], T.N. Miles[1], G.N. Seroka[1], Y. Xu[2], R.K. Forney[1], F. Yu[3], H. Roarty[1], O. Schofield[1] & J. Kohut[1]

Hurricane-intensity forecast improvements currently lag the progress achieved for hurricane tracks. Integrated ocean observations and simulations during hurricane Irene (2011) reveal that the wind-forced two-layer circulation of the stratified coastal ocean, and resultant shear-induced mixing, led to significant and rapid ahead-of-eye-centre cooling (at least 6 °C and up to 11 °C) over a wide swath of the continental shelf. Atmospheric simulations establish this cooling as the missing contribution required to reproduce Irene's accelerated intensity reduction. Historical buoys from 1985 to 2015 show that ahead-of-eye-centre cooling occurred beneath all 11 tropical cyclones that traversed the Mid-Atlantic Bight continental shelf during stratified summer conditions. A Yellow Sea buoy similarly revealed significant and rapid ahead-of-eye-centre cooling during Typhoon Muifa (2011). These findings establish that including realistic coastal baroclinic processes in forecasts of storm intensity and impacts will be increasingly critical to mid-latitude population centres as sea levels rise and tropical cyclone maximum intensities migrate poleward.

[1] Center for Ocean Observing Leadership, Department of Marine and Coastal Sciences, School of Environmental and Biological Sciences, Rutgers University, 71 Dudley Road, New Brunswick, New Jersey 08901, USA. [2] State Key Laboratory of Estuarine and Coastal Research, East China Normal University, 3663 Zhongshan Road North, Shanghai 200062, China. [3] Institute of Oceanology, Chinese Academy of Sciences, 7 Nanhai Road, Qingdao 266071, China. Correspondence and requests for materials should be addressed to S.G. (email: glenn@marine.rutgers.edu).

Tropical cyclones are among the most destructive weather phenomena on Earth[1]. Declines in hurricane related mortalities[2] reflect improvements in global atmospheric and ensemble modelling approaches[3] that have reduced hurricane track forecast errors by factors of 2–3 (ref. 4). Despite two decades of progress in hurricane track prediction, improvements in hurricane-intensity forecast skill have lagged significantly[4]. The predictions, public response and unexpected devastation patterns related to Hurricane Irene exemplify this dichotomy. Accurate track forecasts days in advance provided time for preparations and coastal evacuations, but Irene's official forecast maximum wind speeds along the Mid-Atlantic coast were consistently $\sim 5\,\mathrm{m\,s^{-1}}$ too high[5]. Irene instead caused catastrophic inland flooding because of heavy rainfall[5], making it the eighth costliest cyclone to hit the United States since 1900 (ref. 6), with damages of $\sim$\$16 billion (ref. 5). These intensity forecast uncertainties have significant negative consequences, ranging from unnecessary preparation costs to future public skepticism[7].

Improved tropical cyclone intensity predictions include dependencies on the rapid space–time evolution of the atmosphere–ocean responses and feedbacks[8]. Coupled atmosphere–ocean models demonstrate that small shifts in sea surface temperature (SST) and stratification, even on small (100 km) horizontal scales, can have significant impacts on storm intensity[9–11]. Several studies have noted[12–16] the relationship between warm and cold mesoscale features in the deep ocean and rapid changes in intensity, but the coastal ocean has received much less attention.

Here, utilizing an ocean observing network to inform ocean and atmospheric model simulations, the role of baroclinic processes on a stratified coastal ocean and their impact on the intensity of Hurricane Irene was quantified. The high percentage of ahead-of-eye-centre[14,17,18] cooling (76–98%) observed in Irene is not reproduced by standard open ocean models that exclude these coastal baroclinic processes. Atmospheric model sensitivity studies indicate that intense in-storm sea surface cooling over a strongly stratified coastal regime is the missing contribution required to reproduce the rapid decay of Hurricane Irene's intensity. The 30-year historical buoy record shows an average of 73% of the in-storm cooling occurs ahead-of-eye-centre on the Mid-Atlantic Bight (MAB) in the stratified season. A Yellow Sea buoy observed up to 85% of in-storm cooling ahead-of-eye-centre during Super Typhoon Muifa (2011). The results demonstrate the importance of rapid ahead-of-eye-centre vertical shear-induced mixing processes and the ensuing ocean–atmosphere feedbacks for generating more accurate simulations of storm intensity.

Results

Synoptic conditions. Hurricane Irene formed east of the Caribbean's Windward Islands on 22 August 2011 and made initial United States landfall in North Carolina as a Category 1 hurricane on 27 August. It re-emerged over the ocean in the MAB before a second landfall in New Jersey as a tropical storm on 28 August (ref. 5), closely following the historical northeastward tracks of hurricanes along the northeast United States[19]. Irene accelerated and lost intensity as it crossed the MAB, moving parallel to the coast with the eye over inner-continental shelf waters (Fig. 1a). Propagation was rapid at $30–40\,\mathrm{km\,h^{-1}}$, requiring only $\sim$9.5 h to cross from North Carolina to New Jersey landfall. Cloud bands extended over 600 km from the eye centre, obscuring the ocean from satellite infrared SST sensors during passage. Differencing 3-day composites of cloud-free satellite imagery before (24–26 August) from after (29–31 August) Irene reveals the regional pattern of MAB sea surface cooling (Fig. 1a and Supplementary Fig. 1A,B). The largest

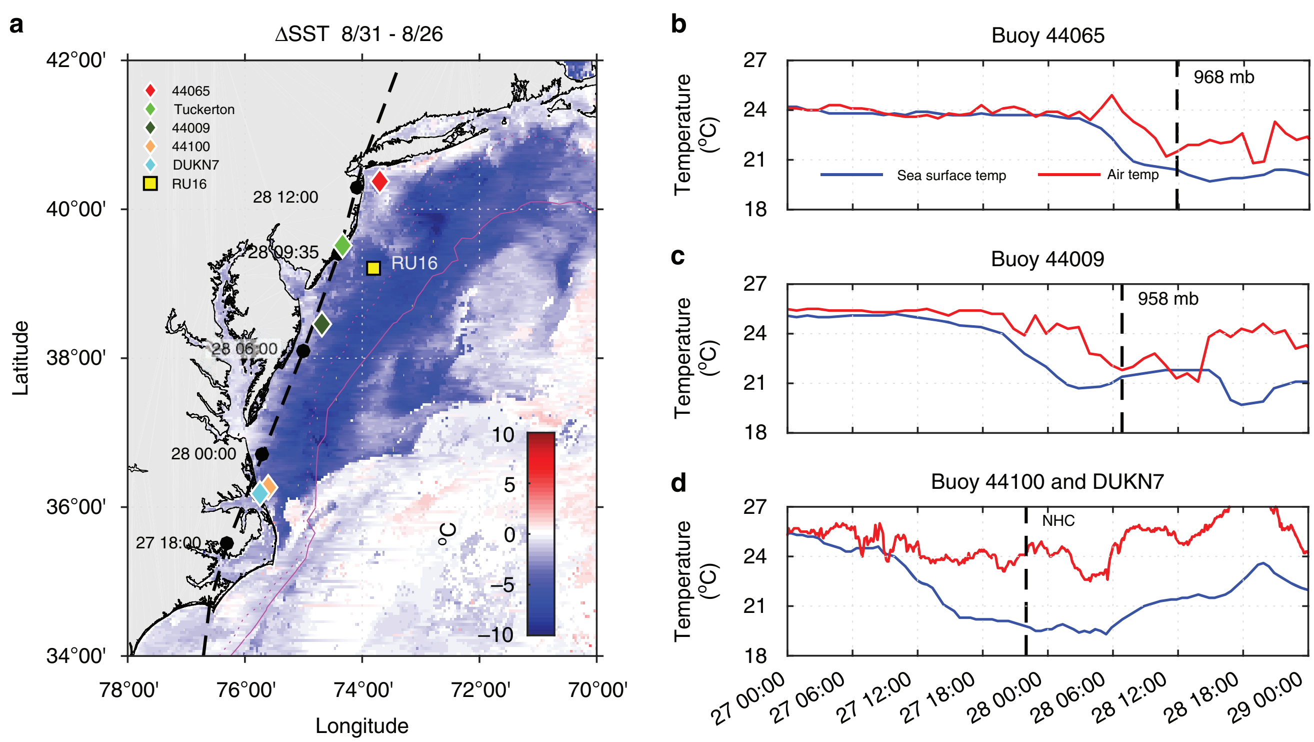

Figure 1 | Map of the study domain with satellite and buoy data. (**a**) SST difference map post-Irene (8/31) minus pre-Irene (8/26) with NHC best track (black dots connected by dashed line labelled with August date and UTC time), weather buoys/stations (coloured diamonds), underwater glider RU16 location during storm (yellow square) and bathymetry at 50 m (dotted magenta) and 200 m (solid magenta). (**b**–**d**) Buoy/station observed SST (blue) and air temperature (red) with vertical black dashed line/label indicating the time/value of minimum air pressure (**b**,**c**), and time of eye passage according to NHC best track data (**d**). The individual SST three-day composite maps for 24–26 August and 29–31 August are provided in Supplementary Fig. 1A,B.

cooling (5–11 °C) was observed to the right of the eye centre over the MAB's middle to outer shelf. Inner shelf cooling was slightly less, with averages of 3–5 °C of cooling within the 25-km radius eye wall (Supplementary Fig. 1C). Cooling was much less significant on the shelf seas to the south of the MAB, in the deep ocean to the east and, as previously noted in other hurricanes[20], along the very shallow unstratified coast, bays and sounds.

Observations. National Data Buoy Center (NDBC) buoys 44009 and 44065 recorded peak wind speeds (Supplementary Fig. 2) near 20 m s^{-1} from offshore as Irene approached. At these NDBC buoys and at 44100, water temperatures dropped rapidly by 3.8–6.3 °C ahead of eye centre passage (Fig. 1b–d), representing 82–98% of the in-storm cooling at these locations (Supplementary Fig. 3). At Irene's fast propagation speed, the eye was still 150–200 km to the south after the most rapid cooling was complete. As the ocean surface cooled, observed air temperatures were greater than SSTs, indicating air–sea-sensible heat fluxes were from the atmosphere into the ocean.

Atmospheric conditions (Fig. 2a) were recorded just inshore of a Slocum autonomous underwater glider[21,22] measuring subsurface ocean conditions[23] during Irene at the location shown in Fig. 1a (see Supplementary Fig. 4 for a plot of the complete glider track well before, during and after the storm). Winds initially from offshore (90°), with speeds near 20 m s^{-1} ahead of the eye, rotated rapidly to blow from onshore (270°) after the eye passed. Glider-observed subsurface temperatures (Fig. 2b) indicate that initially, typical MAB summer stratification[24] was present, with a seasonally warmed surface layer ($\sim$24 °C) above the MAB Cold Pool[25] ($<$10 °C) separated by a sharp ($<$8 m thick) thermocline. Significant cooling of the surface layer (5.1 °C) and deepening of the thermocline ($>$15 m) was observed under the leading edge of the storm. Little change in thermocline depth and much less cooling (1.6 °C) of the upper layer was observed after eye passage. Thus, ahead-of-eye-centre cooling represents 76% of in-storm cooling observed at the glider (Fig. 2b). Both the glider and buoy data suggest that much of the satellite observed SST cooling (over $\sim$100,000 km^2 of continental shelf) occurred ahead-of-eye-centre.

Ocean surface currents measured by a CODAR high-frequency (HF) radar[26] network[27] illustrated the rapid response of the thin surface layer (Supplementary Fig. 5) to the changing wind direction (Fig. 2a). Time-series of the cross-shelf components of the currents (Fig. 2c) at the glider location, with positive values towards land, indicate that the onshore surface currents began building before the eye entered the MAB, increasing to a peak value $>$50 cm s^{-1} towards the coast before the eye passage. Along-shelf currents throughout the water column were weak (Fig. 2d). After the eye, the winds changed direction and within a few hours, the cross-shelf surface currents switched to offshore. Despite the strong observed surface currents, the depth-averaged current (Fig. 2c) reported by the glider remained small during the storm's duration, with peaks barely exceeding 5 cm s^{-1}. As in deep water, the current response is baroclinic[28,29], but the low depth-averaged current implies a strong offshore flow in the bottom layer. These bottom layer currents were estimated based on the relative layer thicknesses and the requirement that the combined surface and bottom layer-averaged currents matched the glider-observed dead-reckoned depth-averaged current. The estimated bottom layer currents accelerated in the offshore direction as the eye approached, causing significant shear between the two layers at the same time the surface layer was deepening and cooling.

Ocean model simulations. Coastal ocean three-dimensional (3D) model simulations of Irene using the Regional Ocean Modeling System (ROMS) in the MAB[30,31] successfully reproduced the thermocline deepening and surface layer cooling (Fig. 3a) similar to the glider observations (Fig. 2b). The modelled cross-shelf velocity component (Fig. 3b) also has similarities to the combined glider and HF radar data (Fig. 2c). The surface layer flow accelerated shoreward for 12 h until eye passage, while the bottom layer responded more slowly with an offshore counter-flow. A few hours after eye passage, the cross-shelf flows reversed, also consistent with observations. The dominant terms in the cross-shelf momentum balance (Fig. 3g) indicate that the surface wind stress increased as the eye approached and decreased as it receded. Before the eye centre arrival, the presence of a coastline produced an offshore-directed pressure gradient that nearly balanced the wind stress and accelerated the offshore jet in the bottom layer. After the storm passage, the cross-shelf surface current switched to offshore; the cross-shelf pressure gradient also switched sign and was redirected towards the coast. At this point in the storm, the dominant cross-shelf momentum balance was nearly geostrophic (Fig. 3g) with a northward along-shelf surface current (Fig. 3d).

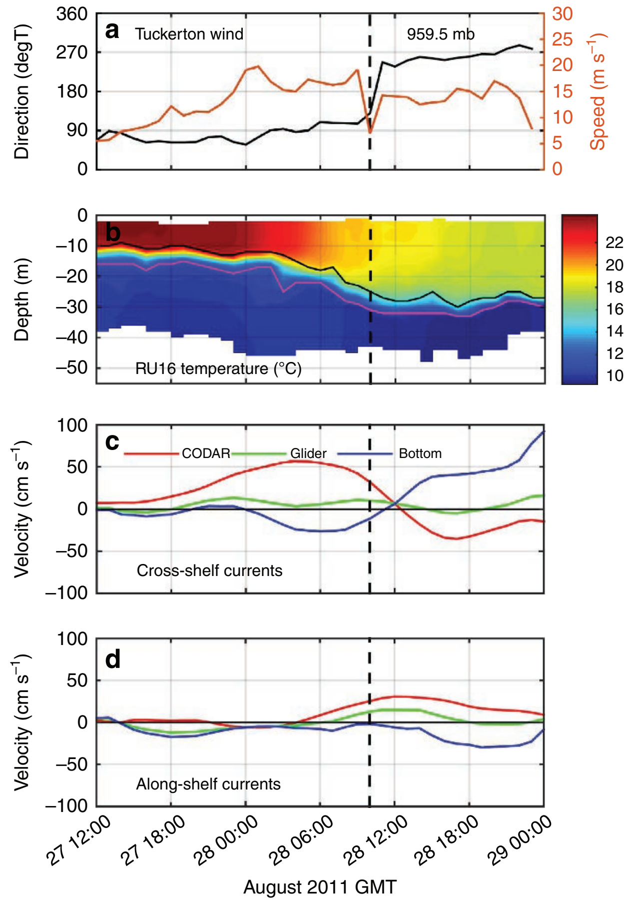

Figure 2 | Data from a local meteorological station, glider and HF radar. (**a**) Tuckerton WeatherFlow, Inc. station 10 m wind speed (orange) and direction from (black) with vertical black dashed line/label indicating the time/value of the minimum air pressure corresponding to landfall time on 28 August at 935 GMT. (**b**) Temporal evolution and vertical structure of the glider temperature during storm conditions with lines indicating top (black) and bottom (magenta) of thermocline. (**c**) Cross-shelf currents (positive onshore, negative offshore) for the surface layer (red) from CODAR HF Radar, depth-averaged (green) from the glider and bottom layer (blue) calculated from the depth-weighted average of the HF radar and glider velocities. (**d**) Same as **c** but for along-shelf currents (positive up-shelf northeastward and negative down-shelf southwestward).

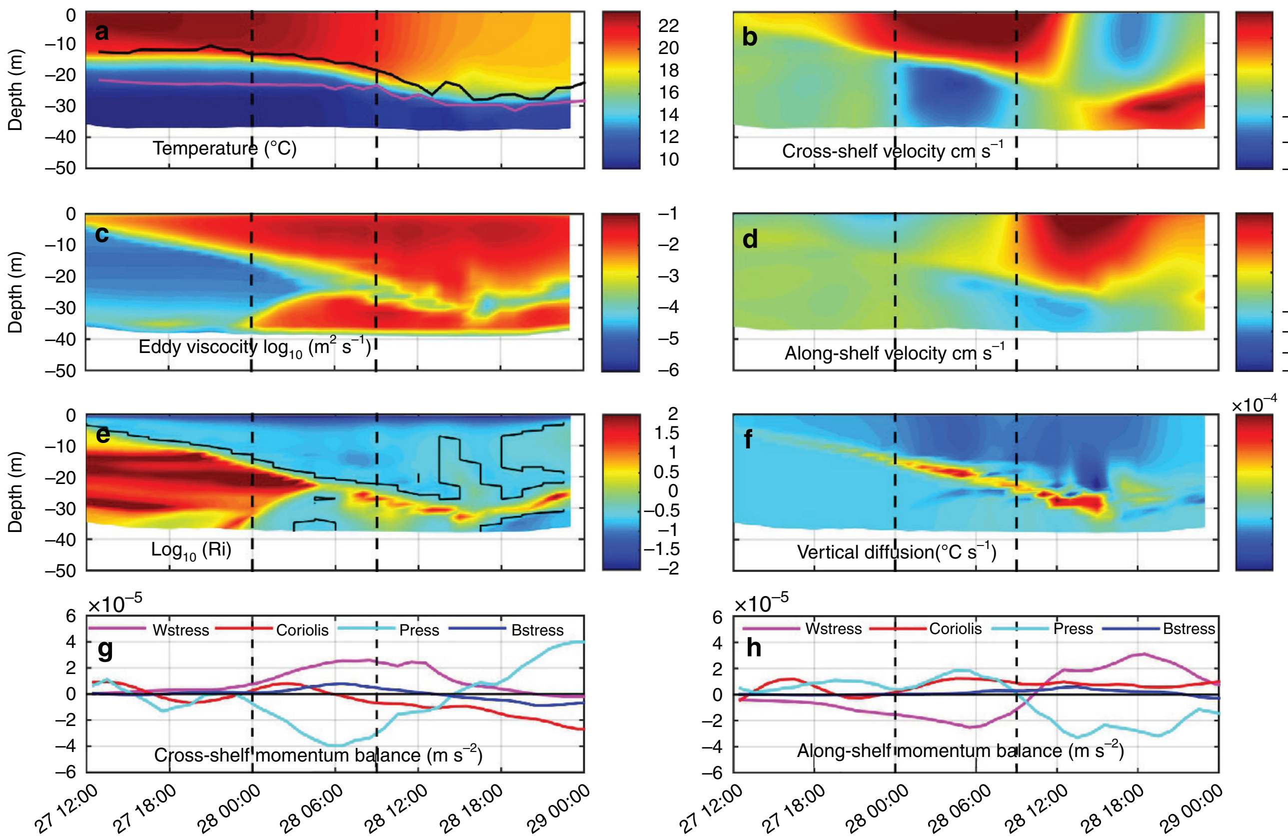

Figure 3 | ROMS ocean simulation results at the glider location. ROMS ocean simulation results at the glider location during the storm period, with first vertical black dashed line indicating initiation of the coastal baroclinic response and second vertical black dashed line indicating eye passage. (**a**) Temperature with top (black) and bottom (magenta) of thermocline as in Fig. 2b. (**b**) Cross-shelf velocity (red/yellow onshore; blue offshore). (**c**) Eddy viscosity. (**d**) Along-shelf velocity (red/yellow northward; blue southward). (**e**) $\mathrm{Log_{10}}$(Richardson number) with black contour indicating Richardson number of 0.25. (**f**) Vertical diffusion temperature diagnostic equation term, showing warming (positive, red/yellow) and cooling (negative, dark blue). (**g**) Dominant depth-averaged cross-shelf momentum balance terms (positive onshore and negative offshore) from wind stress (wstress, magenta), Coriolis force (coriolis, red), pressure gradient (press, cyan) and bottom stress (bstress, blue). (**h**) Same as **g** but for along-shelf momentum balance terms (positive northward, negative southward).

The subsurface cross-shelf circulation within the two-layer coastal ocean had a significant influence on vertical mixing as illustrated by the Richardson number (Fig. 3e) and the vertical eddy viscosity (Fig. 3c). The Richardson number and the eddy viscosity show that the surface layer deepened to meet the stratification at the top of the thermocline as the surface layer accelerated with the approaching storm. As the offshore counter current accelerated in the bottom boundary layer, the lower layer Richardson number also decreased and eddy viscosity increased until the two layers interacted. The most rapid ahead-of-eye-centre cooling and deepening of the surface layer occurred when the small Richardson numbers and large vertical eddy viscosities from the surface and bottom boundary layers overlapped. The model's temperature diagnostic equation indicates that vertical diffusion (Fig. 3f) was the dominant term (Supplementary Fig. 6) acting to deepen the thermocline and cool the surface layer during the event.

Atmospheric model simulations. Atmospheric model simulations of Irene used the Weather Research and Forecasting (WRF)[32] model as applied to the US East Coast for tropical cyclone forecasting[33]. Typical surface boundary approaches in uncoupled atmospheric models use satellite SSTs over water that remain fixed when new data is not available because of cloud cover. A matrix of over 130 simulations revealed ahead-of-eye-centre cooling of the ocean's surface layer has a significant impact on intensity as reflected in the hurricane pressure (Fig. 4) and wind fields (Supplementary Fig. 7). Examining the ensemble of simulations with track errors less than one eye-wall radius, the largest wind and pressure intensity sensitivities were generated using fixed warm pre-storm and cold post-storm SST boundary conditions (Supplementary Figs 8,9). The sea level pressure (SLP) fields at landfall indicate the warm (Fig. 4a) versus the cold (Fig. 4b) SST changed the centre SLP by 7–8 hPa, with the maximum wind speed reduced by $>5\,\mathrm{m\,s^{-1}}$ due to the cooler SST (Supplementary Fig. 7). The minimum SLP time history (Fig. 4c) of selected model runs can be compared with the National Hurricane Center (NHC) best track parameters. The best track central pressure remains constant near 952 hPa until the eye enters the MAB (28 August at about 00 h), followed by a steady increase in the central pressure to 965 hPa 13 h later as the eye leaves the MAB. Once Irene's eye entered the MAB, the cold SST air–sea flux parameterization sensitivities all produce a reduction in intensity that cluster with the best track analysis, while the warm SST air–sea flux parameterization sensitivities maintain a lower minimum SLP with little change nearly until landfall.

The top three model sensitivities are quantified by the envelope width for the minimum SLP (Fig. 4d). For both warm and cold SSTs, sensitivities to the three standard WRF air–sea flux formulations range from 0 to 2 hPa for the 13 h after the eye entered the MAB. The sensitivity to warm and cold SST

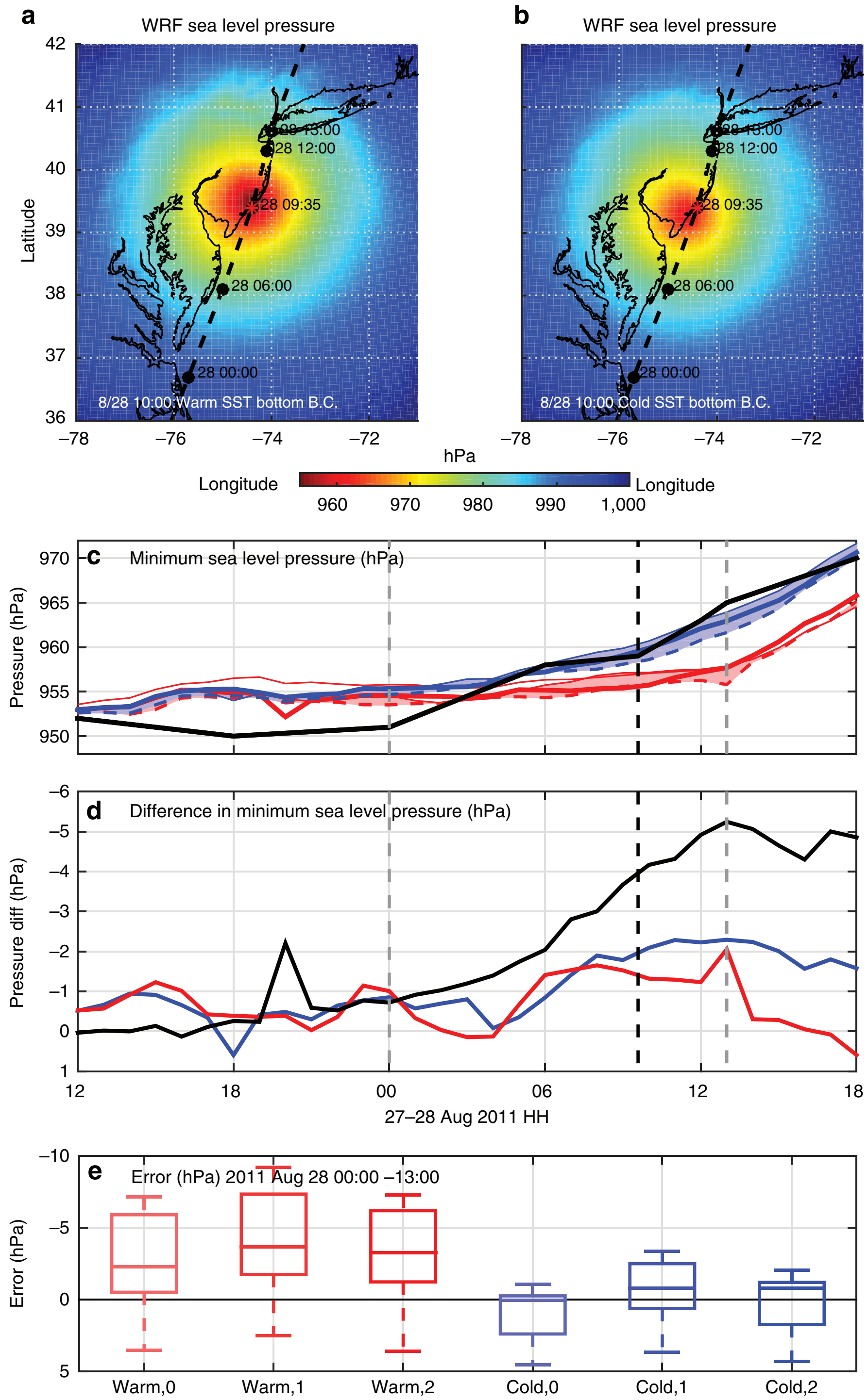

Figure 4 | WRF atmospheric model simulation results. (**a**) WRF model SLP (with surface flux option 2) at landfall (red star) for the warm SST boundary condition with NHC best track drawn as in Fig. 1a. (**b**) Same as **a** but for the cold SST. (**c**) Minimum SLP for NHC best track (black), and WRF's three air–sea flux parameterization options isftcflx = 0 (thin line); 1 (dotted line); and 2 (thick line) for the warm (red) and cold (blue) SST. Vertical grey and black dashed lines indicate eye enters MAB, makes landfall and leaves MAB. (**d**) Model SLP sensitivity to SST (black, warm minus cold SST for isftcflx = 2), and to flux parameterizations (isftcflx = 1 minus isftcflx = 0) for warm (red) and cold (blue) SST. (**e**) Box and whisker plots of SLP deviations from NHC best track when eye is over MAB for warm (red) and cold (blue) SST.

begins growing as the storm nears the MAB, climbing steadily to 5 hPa as it leaves the MAB. Statistical comparisons of each model run to the NHC best track over the MAB are quantified by the box and whisker plots (Fig. 4e) showing the median, inter-quartile range and outliers. The three warm SST air–sea flux sensitivities consistently over-predict the intensity with minimum SLPs that are too low, while the three cold SST air–sea flux sensitivities more accurately reflect the intensity reduction for all of the air–sea flux options.

Table 1 | Sea surface temperature cooling in coastal tropical cyclones.

Storm name	Buoy	Water depth (m)	Ahead-of-eye-centre cooling (°C)	In-storm cooling (°C)	% Ahead-of-eye-centre
Arthur (2014)	44014	48	1.4	2.4	58%
Irene (2011)	44009	26	4.5	5.5	82%
Barry (2007)	ALSN6	29	5.1	5.1	100%
Hermine (2004)	44009	31	0.9	1.1	82%
Allison (2001)	CHLV2	14	2.3	2.6	88%
Bonnie (1998)	CHLV2	14	4.2	4.2	100%
Danny (1997)	44009	31	2.1	3.6	58%
Arthur (1996)	44009	31	2.3	3.5	66%
Emily (1993)	44014	48	2.3	2.8	82%
Bob (1991)	44025	41	2.1	4.6	46%
Charley (1986)	44009	31	2.7	5.4	50%
Average		**31**	**2.7**	**3.7**	**73%**
Standard deviation		**11**	**1.3**	**1.4**	**19%**
Irene (2011)	44065	25	3.8	4.2	90%
Irene (2011)	RU16	37-46	5.1	6.7	76%
Irene (2011)	44100	26	6.3	6.4	98%
Muifa (2011)	37.045 N 122.66 E	31	4.1	4.8	85%

Ahead-of-eye-centre cooling (°C), in-storm cooling (°C) and % ahead-of-eye-centre observed at nearshore MAB buoys for 11 tropical cyclones that traversed the MAB continental shelf during summer stratified conditions since 1985, additional data from Hurricane Irene and Super Typhoon Muifa.

Discussion

Using Hurricane Irene as a diagnostic case study, a new feedback mechanism on storm intensity in the coastal ocean has been identified. The strong onshore winds occurring ahead-of-eye-centre in tropical cyclones and the coastal wall set up a down-welling circulation that limits the storm surge and results in significant shear across the thermocline. This shear leads to turbulent entrainment of abundant cold bottom water and mixing with warmer surface water. The resulting ocean cooling reduces surface heat fluxes to the atmosphere, weakening the storm.

Rapid tropical cyclone intensity changes over the deep ocean have been correlated with storm passage over warm and cold core eddies[12–16,34]. Also in the deep ocean, SST changes of as little as 1 °C are noted to significantly impact storm intensity[9,35]. During Hurricane Irene, ahead-of-eye-centre cooling of 3.8–6.3 °C was observed with nearshore buoys (Supplementary Fig. 3) and 5.1 °C was observed with a mid-shelf glider (Fig. 2). Storm-induced cooling in deep water is often equally distributed between the front and back half of the storm[36]. Deep ocean simulations of Irene with both a 1D ocean mixed layer model and the 3D Price–Weller–Pinkel[37] model produced 32 and 56% of the in-storm cooling ahead-of-eye-centre, respectively. In Hurricane Irene, 76% (glider) to 98% (buoy 44100) of the in-storm cooling occurred ahead-of-eye-centre, indicating that coastal baroclinic processes are enhancing the percentage of ahead-of-eye-centre cooling in Irene.

To verify that enhanced ahead-of-eye-centre coastal ocean cooling is not unique to Irene, 30 years of historical nearshore buoy data throughout the MAB were investigated. During that time period, ahead-of-eye-centre cooling was observed in all 11 tropical cyclones that tracked northeastward over the MAB continental shelf during the highly stratified summer months (June–August)[24,38] (Table 1 and Supplementary Figs 10–12). The maximum continental shelf buoy observed ahead-of-eye-centre cooling for these 11 storms averages 2.7 ± 1.3 °C, representing an average of 73% of the in-storm cooling.

An 11-year global satellite climatology[39] reveals that the shallow mid-latitude Yellow Sea and northern East China Sea also experience a large 20 °C seasonal SST cycle, similar to the MAB but over three times larger in area. A 1986 Yellow Sea shipboard conductivity temperature and depth survey reports surface to bottom temperature differences approaching 15 °C (ref. 40), also similar to the stratified summer MAB. Maps of western Pacific typhoon tracks (coast.noaa.gov/hurricanes) indicate 26 typhoons have tracked across the northern East China Sea and Yellow Sea during June–August since 1985. Like Irene, the landfalling intensity of Super Typhoon Muifa (2011) was over-predicted by standard models[41]. Satellite SST maps indicate Muifa caused significant in-storm cooling (up to 7 °C) across ~300,000 km^2 of the continental shelf[41]. Nearshore buoy observations show cooling of 4.1 °C (85% of the in-storm cooling observed at that location) was ahead-of-eye-centre (Table 1, Supplementary Fig. 13).

Globally, over the past 30 years, tropical cyclone maximum intensities have migrated poleward[42]. In the North Atlantic, hurricane intensities have increased since the early 1980s and are projected to continue to increase as the climate warms[43–46]. Combined with rapid sea level rise[47], mid-latitude population centres will experience heightened vulnerability to storm surge and inundation from increasingly powerful storms. To mitigate these risks, improved forecasting of tropical cyclone intensity over mid-latitude stratified coastal seas is vital, and will require realistic 3D ocean models to forecast enhanced ahead-of-eye-centre cooling.

Methods

Data source. The Mid-Atlantic Regional Association Coastal Ocean Observing System (MARACOOS) is a sustained regional component of the US Integrated Ocean Observing System (IOOS)[48]. Its integrated observation network of satellites, buoys, coastal meteorological stations, HF radar and autonomous underwater gliders provided the data used in this study[49].

Satellite remote sensing. National Oceanographic and Atmospheric Administration (NOAA) Advanced Very High-Resolution Radiometer (AVHRR) satellite data (Supplementary Fig. 1) were acquired through a SeaSpace TeraScan L-Band satellite ground station at Rutgers University. AVHRR data are converted to SST using the multi-channel SST algorithm[50]. To specifically map areas of rapid cooling, a 'coldest-dark-pixel' composite technique is used to identify and remove bright cloud covered pixels while retaining the darker ocean pixels. This is accomplished through the following series of tests performed on AVHRR channels 4 and 2 scans. Pixels are considered contaminated by clouds and removed if (1) AVHRR channel 4 (10.3–11.3 μm) temperatures are <5 °C (3.5 °C) in summer (winter); or (2) near infrared albedo in daytime AVHRR Channel 2 (0.725–1 μm) exceeds 2.3% (an empirically derived threshold specific to the MAB). Further tests are performed on 3 × 3 km grid boxes to account for large changes in temperature over short distances typical of cloud edges. Centre pixels are flagged as potential cloud edges and removed if (1) temperature changes in AVHRR channel 4 scans are $>1\,°C$ across the centre point of each 3×3 grid data; or (2) the change in infrared albedo across the centre of each 3×3 grid box is $>0.15\%$. After declouding is performed, the resulting 3 days of scans between 12:00 to 17:00 GMT are composited with the NASA (National Aeronautics and Space Administration) short-term Prediction Research and Transition centre (SPoRT) 2 km blended 7-day SST product. At each pixel the coldest value is retained between all daytime AVHRR scans for the past 3 days and the SPoRT SST product for that day to ensure retention of coastal upwelling zones and regions that underwent rapid mixing. Consistent with real-time processing protocols, the date assigned to each composite corresponds to the final day of the data window.

Meteorological observations. Meteorological observations were obtained from NOAA NDBC buoys, coastal towers and pier stations, and a WeatherFlow Inc. meteorological tower located in Tuckerton, New Jersey (Fig. 1a). Buoys 44009 (38.461° North and 74.703° West) and 44065 (40.369° North and 73.703° West) included wind speed and direction measured at a height of 5 m, air temperature at a height of 4 m and ocean temperatures at 0.6 m depth. Buoy 44100 (36.255° North and 75.591° West) is a Waverider buoy managed by Scripps Institution of Oceanography that measured ocean temperatures at 0.46 m depth. Station DUKN7 (36.184° North and 75.746° West) is a coastal station that measures air temperature at 15.68 m above mean sea level. The Tuckerton WeatherFlow Inc. meteorological tower (39.52° North and 74.32° West) measured wind speed and direction at 12 m. Meteorological data is plotted at the standard frequencies and averaging intervals reported by these stations.

High frequency radar. A network of over 40 CODAR Ocean Sensors SeaSonde HF Radar stations[26] are deployed along the MAB coast by a consortium of institutions coordinated through MARACOOS[27]. The stations transmit HF radio waves that are scattered off the ocean surface waves and then received back on shore. The Doppler shift in the Bragg peaks of the received signal are used to map the radial components of the total surface velocity field in front of each station[51]. Radial components from multiple stations are combined using an optimal interpolation scheme[52] to produce 1 h centre-averaged hourly surface current maps[53] with a nominal 6 km spatial resolution (Supplementary Fig. 5).

Autonomous underwater gliders. Teledyne Webb Research Slocum gliders are buoyancy-driven underwater vehicles that act as mobile sensor platforms[22]. These instrument platforms adjust small amounts of buoyancy in order to glide through the water column at 20–30 $cm\,s^{-1}$ in a sawtooth pattern. At pre-programmed intervals the gliders come to the surface and transfer data back to Rutgers University in near real-time. The glider used in this study, RU16, was equipped with an un-pumped Seabird conductivity temperature and depth sensor that logged data every 4 s on downcasts and upcasts. Depth- and time-averaged velocity calculations were performed using a dead-reckoning technique typical for such platforms[22,54,55]. The measured pitch angle, fall velocity and a model of glider flight to estimate angle of attack are used to calculate an underwater horizontal displacement during each dive segment. The difference between the calculated horizontal displacement from the final pre-dive location and the actual surfacing location divided by the time underwater provides an estimate of depth- and time-averaged velocity.

A combination of dead-reckoned depth-averaged glider currents and HF radar surface currents are used to estimate bottom currents along the glider track (Fig. 2c). The following algorithm assumes that the HF radar surface currents are representative of the surface layer above the thermocline (defined as the maximum vertical temperature gradient along each profile) and requires that the depth-weighted average surface and bottom layer currents must equal the total depth-averaged glider current:

$$U_b = \frac{U_g(H_s+H_b)}{H_b} - \frac{U_sH_s}{H_b} \tag{1}$$

$$V_b = \frac{V_g(H_s+H_b)}{H_b} - \frac{V_sH_s}{H_b} \tag{2}$$

where H_s and H_b are the layer thicknesses above and below the thermocline, respectively, U_g and V_g are along- and cross-shelf depth-averaged currents, respectively, from glider dead-reckoning, U_s and V_s are surface layer-averaged currents from HF radar, and U_b and V_b are the calculated bottom layer-averaged currents (Fig. 2).

ROMS model setup. The numerical simulations were conducted using the ROMS[31], a free-surface, sigma coordinate, primitive equation ocean model (code available at http://www.myroms.org) that has been widely used in a diverse range of coastal applications. The ESPreSSO (Experimental System for Predicting Shelf and Slope Optics) model[56] covers the MAB from the centre of Cape Cod southward to Cape Hatteras, from the coast to beyond the shelf break and shelf/slope front. Gridded bathymetric data is used to construct a model grid with a horizontal resolution of 5 km (Supplementary Fig. 4) and 36 vertical levels in a terrain-following s-coordinate system. The initial conditions were developed from the same domain ROMS run with strong constrained four-dimensional variational (4D-Var) data assimilation[57]. The meteorological forcing is from the North American Mesoscale (NAM) model 12 km 3-hourly forecast data. Reanalyses of surface air temperature, pressure, relative humidity, 10 m vector winds, precipitation, downward longwave radiation and net shortwave radiation were used to specify the surface fluxes of momentum and buoyancy based on the COARE bulk formulae[58]. Boundary conditions are daily two-dimensional surface elevation, as well as three-dimensional velocity, temperature, and salinity fields from the Hybrid Coordinate Ocean Model Navy Coupled Ocean Data Assimilation forecast system. Inflows for the seven largest rivers are from daily average United States Geological Survey discharge data. Tidal boundary conditions are from the The ADvanced CIRCulation tidal model. The general length scale method k-kl type vertical mixing scheme[59,60] is used to compute vertical turbulence diffusivity.

ROMS momentum balance analysis. We extracted depth-averaged momentum balance terms from ROMS (Fig. 3g–h) at the glider sampling location in order to diagnose the dominant forces during the storm, where the acceleration terms are balanced by a combination of horizontal advection, pressure gradient, surface and bottom stresses and the Coriolis force (horizontal diffusion was small and neglected in this case):

$$\underbrace{\frac{\partial u}{\partial t}}_{\text{Acceleration}} = \underbrace{-\frac{\partial(uu)}{\partial x} - \frac{\partial(vu)}{\partial y}}_{\text{Horizonal advection}} \underbrace{-\frac{1}{\rho_0}\frac{\partial P}{\partial x}}_{\text{Pressure gradient}} + \underbrace{\left(\underbrace{\frac{\tau_s^x}{h\rho_0}}_{\text{Surface}} - \underbrace{\frac{\tau_b^x}{h\rho_0}}_{\text{Bottom}}\right)}_{\text{Stress}} + \underbrace{fv}_{\text{Coriolis}} \tag{3}$$

$$\underbrace{\frac{\partial v}{\partial t}}_{\text{Acceleration}} = \underbrace{-\frac{\partial(uv)}{\partial x} - \frac{\partial(vv)}{\partial y}}_{\text{Horizonal advection}} \underbrace{-\frac{1}{\rho_0}\frac{\partial P}{\partial y}}_{\text{Pressure gradient}} + \underbrace{\left(\underbrace{\frac{\tau_s^y}{h\rho_0}}_{\text{Surface}} - \underbrace{\frac{\tau_b^y}{h\rho_0}}_{\text{Bottom}}\right)}_{\text{Stress}} - \underbrace{fu}_{\text{Coriolis}} \tag{4}$$

where u and v are the along-shelf and cross-shelf components of velocity respectively, t is time, P is pressure, ρ_o is a reference density, τ_s and τ_b are surface and bottom stresses, h is water column depth and f is the latitude-dependent Coriolis frequency.

ROMS heat balance analysis. *Heat balance analysis*. The general conservation expression for the temperature budget in ROMS is given by

$$\frac{\partial T}{\partial t} = -\frac{\partial(uT)}{\partial x} - \frac{\partial(vT)}{\partial y} - \frac{\partial(wT)}{\partial z} + \frac{\partial A_{kt}\frac{\partial T}{\partial z}}{\partial z} + \mathcal{D}_T + \mathcal{F}_T \tag{5}$$

with the following surface and bottom boundary conditions:

$$\left(A_{kt}\frac{\partial T}{\partial z}\right)_{z=0} = \frac{Q_{net}}{\rho_0 C_p} \tag{6}$$

$$\left(A_{kt}\frac{\partial T}{\partial z}\right)_{z=-h} = 0 \tag{7}$$

Here, T is the temperature, t is time, u, v and w are the along-shelf, cross-shelf and vertical components of velocity. A_{kt} is the vertical diffusivity coefficient, $\mathcal{D}_T$ is the horizontal diffusion term and $\mathcal{F}_T$ is friction. Q_{net} is the surface net heat flux, $\rho_0 = 1025\,kg\,m^{-3}$ is a reference density, $C_p = 3985\,J\,(kg\,°C)^{-1}$ is the specific heat capacity of seawater and h is the water depth.

The ROMS conservation of heat equation was used to diagnose the relative contributions of the different terms responsible for the modelled temperature change. Time-series of the vertical temperature diagnostic terms were investigated along the glider track with emphasis on the temperature evolution between the top of the thermocline depth (the shallowest location where the vertical temperature gradient exceeded $0.4\,°C\,m^{-1}$, black contour in Fig. 3a and Supplementary Fig. 6) and the transition layer depth (the deepest location where the vertical temperature gradient exceeded $0.7\,°C\,m^{-1}$, magenta contour in Fig. 3a and Supplementary Fig. 6). Term-by-term analysis of equation 5 offered additional insights on the temperature source and sink terms. Supplementary Fig. 6A shows the temperature rate of change, which is the sum of the vertical diffusion term (Supplementary Fig. 6B) and advection term (Supplementary Fig. 6C), in which the advection term is separated into along-shelf advection (Supplementary Fig. 6D), cross-shelf advection (Supplementary Fig. 6E) and vertical advection (Supplementary Fig. 6F). The horizontal diffusion term's order of magnitude is much smaller than other terms and is not plotted. The dominant term influencing the surface mixed layer temperature change was the vertical diffusion, which is plotted in Fig. 3f.

WRF-ARW model setup. The Weather Research and Forecasting Advanced Research (WRF-ARW) dynamical core (code available at http://www.wrf-model.org)[32], Version 3.4 was used for the atmospheric simulations in this study. WRF-ARW is a fully compressible, non-hydrostatic, terrain-following coordinate, primitive equation atmospheric model. Our WRF-ARW domain extends from South Florida to Nova Scotia (Supplementary Fig. 14), with grid resolution of 6 km in the horizontal and 35 vertical levels. Lateral boundary conditions used are from the Global Forecast System (GFS) 0.5° initialized at 06 UTC on 27 August 2011.

Our simulations begin at 06 UTC on 27 August 2011 when Hurricane Irene was south of North Carolina (NC) over the South-Atlantic Bight (SAB) and end at 18

UTC on 28 August 2011 as the storm moved into New England. Simulation results shown (Fig. 4c,d and Supplementary Fig. 7C,D) begin at 12 UTC on 27 August 2011, at NC landfall time, after the model has 6 h to adjust to vortex initialization. WRF's digital filter initialization (DFI) was run to determine the sensitivities to different realizations of the GFS initializations. DFI deepened the initial vortex central pressure by over 10–960 hPa, which matches GFS initial central pressure (Supplementary Fig. 15). However, downstream sensitivity to DFI beyond 2 h was minimal.

For our control run, the following are used: longwave and shortwave radiation physics were both computed by the Rapid Radiative Transfer Model-Global scheme; the Monin–Obukhov atmospheric layer model and the Noah Land Surface Model were used with the Yonsei University planetary boundary layer scheme; and the WRF Double-Moment 6-class moisture microphysics scheme was used for grid-scale precipitation processes.

WRF sensitivity to SST. The model was run over 130 times to compare the sensitivity of certain parameter tuning. All sensitivities were compared to the control run (described above), which for surface boundary conditions over the ocean, that is, SST, used the Real-Time Global High-Resolution (RTG HR) SST analysis from 00 UTC on 27 August 2011 fixed throughout the simulation. This is the warm pre-storm SST, and has temperatures across the model domain similar to the AVHRR coldest-dark-pixel composite a day earlier (Supplementary Fig. 1A). By having the control run use Real-Time Global High-Resolution SST fixed throughout the simulation, we are consistent with what the operational NAM 12 km model used for bottom boundary conditions over the ocean.

To show the maximum impact of the ahead-of-eye-centre SST cooling on storm intensity, we compared our control run with a simulation using observed cold post-storm SST. For this, we used our AVHRR coldest-dark-pixel composite, which includes data from 29 to 31 August 2011 (Supplementary Fig. 1B). According to underwater glider and NDBC buoy observations along Irene's entire MAB track, almost all of the SST cooling occurred ahead of Irene's eye centre (Fig. 1b–d). NDBC buoy observations near Irene's track in the SAB (41013, 41036, 41037) also show ahead-of-eye-centre SST cooling, but values are on the order of 1 °C or less (Fig. 1a). Because our model simulations include only 6 h of storm presence over the SAB before NC landfall, and SST cooling in the SAB was significantly less than observed in the MAB (Fig. 1), we can conclude that the main result from our SST sensitivity is due to the ahead-of-eye-centre cooling in the MAB.

WRF sensitivity to air-sea flux parameterizations. The equations for the momentum (τ), sensible (H) and latent heat fluxes (E) are as follows:

$$\tau = -\rho C_D U^2 \tag{8}$$

$$H = -(\rho c_p) C_H U(\theta_{2m} - \theta_{sfc}) \tag{9}$$

$$E = -(\rho L_v) C_Q U(q_{2m} - q_{sfc}) \tag{10}$$

where ρ is density of air, C_D is drag coefficient, U is 10 m wind speed, c_p is specific heat capacity of air, C_H is sensible heat coefficient, θ_{2m} is potential temperature at 2 m and θ_{sfc} is potential temperature at the surface, L_v is enthalpy of vaporization, C_Q is latent heat coefficient, q_{2m} is specific humidity at 2 m and q_{sfc} is interfacial specific humidity at the surface.

Three options exist in WRF-ARW Version 3.0 and later for air–sea flux parameterizations (WRF namelist option isftcflx = 0, 1, and 2; see (ref. 61) for more details). These parameterization options change the momentum (z_0), sensible heat (z_T) and latent heat roughness lengths (z_Q) in the following equations for drag (C_D), sensible heat (C_H) and latent heat (C_Q) coefficients:

$$C_D = K^2/[\ln(z_{ref}/z_0)]^2 \tag{11}$$

$$C_H = \left(C_D^{1/2}\right)[K/\ln(z_{ref}/z_T)] \tag{12}$$

$$C_Q = \left(C_D^{1/2}\right)[K/\ln(z_{ref}/z_Q)] \tag{13}$$

where K is the von Kármán constant and z_{ref} is a reference height (usually 10 m).

Therefore, our SST sensitivity effectively changes the variables θ_{sfc} and q_{sfc} in equations 8–10 above, while our air–sea flux parameterization sensitivities change the equations for the momentum, sensible heat and latent heat coefficients (equations 11–13) going into the respective flux equations 8–10.

For our air–sea flux parameterization sensitivities in this study, we ran isftcflx = 0, 1, and 2 with both the warm (control) and cold SST boundary conditions.

Additional WRF sensitivities. We have discussed SST and air–sea flux parameterizations. WRF-ARW was run over 130 times in total, with various model configuration and physics options turned on and off.

We examined the ensemble of simulations with space/time track errors <25 km (one eye-wall radius) from available NHC best track positional data. Only preserving those simulations with accurate tracks is important because Hurricane Irene tracked close to and parallel to the Mid-Atlantic coast. The remaining sensitivities are shown in central pressure (Supplementary Fig. 8) and maximum winds (Supplementary Fig. 9). These are cumulative hourly sensitivities during Irene's presence over the MAB and NY Harbor (28 August 00-13 UTC). Supplementary Table 1 shows a list of these sensitivities, with the WRF namelist option number alongside its name (control run listed last for each sensitivity).

The sensitivity titled 'latent heat flux <0 over water' requires a brief explanation. In the WRF surface layer scheme code, there is a switch that disallows any latent heat flux less than 0 W m^{-2} (similarly, there is a switch that disallows any sensible heat flux less than -250 W m^{-2}). WRF convention for negative heat flux is downward, or atmosphere to land/water. We run WRF after removing the line of code disallowing negative latent heat flux, and compare to the control run. This switch removal only changes latent heat flux and allows it to be negative over water, as the subsequent WRF land surface scheme modifies fluxes and allows for negative latent heat flux over land.

Ahead-of-eye-centre and in-storm cooling calculations. Ahead-of-eye-centre cooling (Table 1) at NDBC buoys (Supplementary Figs 10–12) and the Yellow Sea buoy (Supplementary Fig. 13) was calculated by taking the difference between the maximum water temperature as the winds increased above 5 m s^{-1} and the minimum water temperature before or at the minimum observed SLP. In-storm cooling was determined as the difference between the same maximum water temperature as the winds increased above 5 m s^{-1} and the minimum water temperature while winds remained above 5 m s^{-1} after the pressure minimum. To calculate the average and standard deviation of cooling for the 11 storms passing through the MAB since 1985, we selected the one buoy on the continental shelf that recorded wind speed, pressure and water temperature and exhibited the greatest ahead-of-eye-centre cooling. For completeness we show Irene cooling statistics (Table 1) and time-series (Supplementary Fig. 3) for buoys 44065 and 44100 used in Fig. 1.

Data availability. Buoy meteorological data used in this study are available through the National Data Buoy Center. Glider and HF Radar data can be found through the MARACOOS THREDDS server at http://maracoos.org/data. Tuckerton meteorological data are supported by WeatherFlow Inc. and can be made available upon request to the corresponding authors. WRF and ROMS model simulations are stored locally at the Rutgers Department of Marine and Coastal Sciences and will be made available upon request to the corresponding authors. The Yellow Sea buoy data are stored at the Institute of Oceanology, Chinese Academy of Sciences.

References

1. Keim, B. D., Muller, R. A. & Stone, G. W. Spatiotemporal patterns and return periods of tropical storm and hurricane strikes from Texas to Maine. *J. Clim.* **20,** 3498–3509 (2007).
2. Walker, N. *et al.* Hurricane prediction a century of advances. *Oceanography* **19,** 24–36 (2006).
3. Krishnamurti, T. N. *et al.* Improved weather and seasonal climate forecasts from multimodel superensemble. *Science* **285,** 1548–1550 (1999).
4. Cangialosi, J. P. & Franklin, J. L. *2012 National Hurricane Center Forecast Verification Report* pp. 79 (National Hurricane Center, 2013).
5. Avila, L. A. & Cangialosi, J. P. *Tropical Cyclone Report: Hurricane Irene* (2012); pp. 45.
6. Blake, E. S., Landsea, C. W. & Gibney, E. J. *The Deadliest, Costliest, and Most Intense United States Tropical Cyclones from 1851 to 2010* (National Weather Service National Hurricane Center, 2011) pp. 47.
7. Considine, T. J., Jablonowski, C., Posner, B. & Bishop, C. H. The value of hurricane forecasts to oil and gas producers in the Gulf of Mexico. *J. Appl. Meteorol.* **43,** 1270–1282 (2004).
8. Emanuel, K., DesAutels, C., Holloway, C. & Korty, R. Environmental control of tropical cyclone intensity. *J. Atmos. Sci.* **61,** 843–858 (2004).
9. Emanuel, K. Tropical cyclones. *Annu. Rev. Earth Planet. Sci.* **31,** 75–104 (2003).
10. Schade, L. R. & Emanuel, K. A. The ocean's effect on the intensity of tropical cyclones: results from a simple coupled atmosphere–ocean model. *J. Atmos. Sci.* **56,** 642–651 (1999).
11. Jaimes, B. & Shay, L. K. Enthalpy and momentum fluxes during Hurricane Earl relative to underlying ocean features. *Mon. Weather Rev.* **143,** 111–131 (2015).
12. Ma, Z., Fei, J., Liu, L., Huang, X. & Cheng, X. Effects of the cold core eddy on tropical cyclone intensity and structure under idealized air–sea interaction conditions. *Mon. Weather Rev.* **141,** 1285–1303 (2012).
13. Emanuel, K. A. Thermodynamic control of hurricane intensity. *Nature* **401,** 665–669 (1999).
14. Jaimes, B. & Shay, L. K. Mixed layer cooling in mesoscale oceanic eddies during Hurricanes Katrina and Rita. *Mon. Weather Rev.* **137,** 4188–4207 (2009).
15. Shay, L. K., Goni, G. J. & Black, P. G. Effects of a warm oceanic feature on Hurricane Opal. *Mon. Weather Rev.* **128,** 1366–1383 (2000).
16. Walker, N. D., Leben, R. R. & Balasubramanian, S. Hurricane-forced upwelling and chlorophyll a enhancement within cold-core cyclones in the Gulf of Mexico. *Geophys. Res. Lett.* **32,** 1–5 (2005).

17. Jacob, S. D. & Shay, L. K. The role of oceanic mesoscale features on the tropical cyclone–induced mixed layer response: a case study. *J. Phys. Oceanogr.* **33,** 649–676 (2003).
18. D'Asaro, E. The ocean boundary layer below Hurricane Dennis. *J. Phys. Oceanogr.* **31,** 561–579 (2003).
19. Hall, T. & Yonekura, E. North American tropical cyclone landfall and SST: a statistical model study. *J. Clim.* **26,** 8422–8439 (2013).
20. Cornillon, P., Stramma, L. & Price, J. F. Satellite measurements of sea surface cooling during Hurricane Gloria. *Nature* **326,** 373–375 (1987).
21. Schofield, O. *et al.* A regional Slocum Glider network in the mid-Atlantic bight leverages broad community engagement. *Mar. Technol. Soc. J.* **44,** 185–195 (2010).
22. Schofield, O. *et al.* Slocum gliders: robust and ready. *J. F. Robot.* **24,** 473–485 (2007).
23. Kohut, J. T., Haldeman, C. & Kerfoot, J. *Monitoring Dissolved Oxygen in New Jersey Coastal Waters Using Autonomous Gliders*. EPA/600/R-13/180 (US Environmental Protection Agency, Washington, DC, 2014).
24. Castelao, R., Glenn, S. & Schofield, O. Temperature, salinity, and density variability in the central middle Atlantic Bight. *J. Geophys. Res.* **115,** C10005 (2010).
25. Houghton, R. W., Schlitz, R., Beardsley, R. C., Butman, B. & Chamberlin, J. L. The Middle Atlantic Bight cold pool: evolution of the temperature structure during summer 1979. *J. Phys. Oceanogr.* **12,** 1019–1029 (1982).
26. Barrick, D. E., Evans, M. W. & Weber, B. L. Ocean surface currents mapped by radar. *Science* **198,** 138–144 (1977).
27. Roarty, H. *et al.* Operation and application of a regional high-frequency radar network in the Mid-Atlantic Bight. *Mar. Technol. Soc. J.* **44,** 133–145 (2010).
28. Shay, L. K., Chang, S. W. & Elsberry, R. L. Free surface effects on the near-inertial ocean current response to a hurricane. *J. Phys. Oceanogr.* **20,** 1405–1424 (1990).
29. Teague, W. J., Jarosz, E., Wang, D. W. & Mitchell, D. A. Observed oceanic response over the upper continental slope and outer shelf during Hurricane Ivan. *J. Phys. Oceanogr.* **37,** 2181–2206 (2007).
30. Wilkin, J. L. & Hunter, E. J. An assessment of the skill of real-time models of Mid-Atlantic Bight continental shelf circulation. *J. Geophys. Res. Ocean* **118,** 2919–2933 (2013).
31. Haidvogel, D. B. *et al.* Ocean forecasting in terrain-following coordinates: formulation and skill assessment of the Regional ocean modeling system. *J. Comput. Phys.* **227,** 3595–3624 (2008).
32. Skamarock, W. *et al. A description of the advanced research WRF version 3, NCAR Technical Note*, NCAR/TN–475 + STR (NCAR, Boulder, CO, USA, 2008).
33. Seroka, G. *et al.* in *Proceedings of the OCEANS MTS/IEEE Conference*, 1–4 (Rutgers University Coastal Ocean Observation Laboratory (RU-COOL) Hampton Roads, North Carolina, USA, 2012).
34. Lin, I.-I., Wu, C.-C., Pun, I.-F. & Ko, D.-S. Upper-ocean thermal structure and the Western North Pacific Category 5 Typhoons. Part I: ocean features and the category 5 typhoons' intensification. *Mon. Weather Rev.* **136,** 3288–3306 (2008).
35. Cione, J. J. & Uhlhorn, E. W. Sea surface temperature variability in hurricanes: implications with respect to intensity change. *Mon. Weather Rev.* **131,** 1783–1796 (2003).
36. Price, J. F. Upper ocean response to a hurricane. *J. Phys. Oceanogr.* **11,** 153–175 (1981).
37. Price, J. F. & Weller, R. A. Diurnal cycling: observations and models of the upper ocean response to diurnal heating, cooling, and wind mixing. *J. Geophys. Res.* **91,** 8411–8427 (1986).
38. Gong, D., Kohut, J. & Glenn, S. Seasonal climatology of wind-driven circulation on the New Jersey Shelf. *J. Geophys. Res. Ocean* **115,** 953–968 (2010).
39. Schofield, O. *et al.* The decadal view of the mid-Atlantic Bight from the COOLroom: is our coastal system changing? *Oceanography* **21,** 108–117 (2008).
40. Chen, C., Beardsley, R. C., Limeburner, R. & Kim, K. Comparison of winter and summer hydrographic observations in the Yellow and East China Seas and adjacent Kuroshio during 1986. *Cont. Shelf Res.* **14,** 909–929 (1994).
41. Sun, M. *et al.* Simulation of typhoon Muifa using a mesoscale coupled atmosphere-ocean model. *Acta Oceanol. Sin.* **33,** 123–133 (2014).
42. Kossin, J. P., Emanuel, K. A. & Vecchi, G. A. The poleward migration of the location of tropical cyclone maximum intensity. *Nature* **509,** 349–352 (2014).
43. Walsh, J. *et al. Our Changing Climate*. Synopsis of Climate Change Impacts in the United States. The Third National Climate Assessment, Natl Clim. Team Staff (2014).
44. Knutson, T. R. Dynamical downscaling projections of twenty-first-century Atlantic Hurricane activity: CMIP3 and CMIP5 model-based scenarios. *J. Clim.* **26,** 6591–6617 (2013).
45. Knutson, T. R. *et al.* Tropical cyclones and climate change. *Nat. Geosci.* **3,** 157–163 (2010).
46. Seneviratne, S. *et al.* in *Managing the Risk of Extreme Events and Disasters to Advance Climate Change Adaptation* (eds Field, C. *et al.*) 109–230 (Cambridge University Press, 2012).
47. Miller, K. G. *et al.* Sea-level rise in New Jersey over the past 5000 years: Implications to anthropogenic changes. *Glob. Planet. Change* **66,** 10–18 (2009).
48. Briscoe, M. G., Martin, D. L. & Malone, T. C. Evolution of regional efforts in international GOOS and US IOOS. *Mar. Technol. Soc. J.* **42,** 4–9 (2008).
49. Glenn, S. & Schofield, O. Growing a distributed ocean observatory: our view from the COOL Room. *Oceanography* **22,** 128–145 (2009).
50. McClain, E. P., Pichel, W. G., Walton, C. C., Paul, E. & Pichel, G. Comparative performance of AVHRR-based multichannel sea surface temperatures. *J. Geophys. Res. Ocean* **90,** 11587–11601 (1985).
51. Kohut, J. T. & Glenn, S. M. Improving HF Radar surface current measurements with measured antenna beam patterns. *J. Atmos. Ocean. Technol.* **20,** 1303 (2003).
52. Kohut, J., Roarty, H., Randall-Goodwin, E., Glenn, S. & Lichtenwalner, C. S. Evaluation of two algorithms for a network of coastal HF radars in the Mid-Atlantic Bight. *Ocean Dyn.* **62,** 953–968 (2012).
53. Roarty, H., Baskin, C., Smith, M. & Glenn, S. in *Proceedings of the OCEANS MTS/IEEE Conference* (Rutgers University Coastal Ocean Observation Laboratory (RU-COOL) New Brunswick, New Jersey, USA, 2014).
54. Davis, R., Eriksen, C. & Jones, C. in *Technology and Applications of Autonomous Underwater Vehicles* (ed. Griffiths, G.) 37 (Taylor & Francis, 2003).
55. Sherman, J., Davis, R. E., Owens, W. B. & Valdes, J. The autonomous underwater glider 'Spray'. *IEEE J. Ocean. Eng.* **26,** 437–446 (2001).
56. Wilkin, J. & Hunter, E. An assessment of the skill of real-time models of Mid-Atlantic Bight continental shelf circulation. *J. Geophys. Res.* **118,** 2919–2933 (2013).
57. Moore, A. M. *et al.* The Regional Ocean Modeling System (ROMS) 4-dimensional variational data assimilation systems. *Prog. Oceanogr.* **91,** 34–49 (2011).
58. Fairall, C. W., Bradley, E. F., Hare, J. E., Grachev, A. A. & Edson, J. B. Bulk Parameterization of air–sea fluxes: updates and verification for the COARE algorithm. *J. Clim.* **16,** 571 (2003).
59. Warner, J. C., Sherwood, C. R., Arango, H. G. & Signell, R. P. Performance of four turbulence closure models implemented using a generic length scale method. *Ocean Model.* **8,** 81–113 (2005).
60. Umlauf, L. & Burchard, H. A generic length-scale equation for geophysical turbulence models. *J. Mar. Res.* **61,** 235–265 (2003).
61. Green, B. W. & Zhang, F. Impacts of air–sea flux parameterizations on the intensity and structure of tropical cyclones. *Mon. Weather Rev.* **141,** 2308–2324 (2013).

Acknowledgements
Support was provided by the National Oceanic and Atmospheric Administration (NOAA) led Integrated Ocean Observing System (IOOS) through the Mid-Atlantic Regional Association Coastal Ocean Observing System (MARACOOS, NA11NOS0120038), the Environmental Protection Agency (EP-11-C-000085), the New Jersey Department of Environmental Protection (WM13-019-2013) and Board of Public Utilities (2010RU-COOL) and the NOAA Cooperative Institute for the North Atlantic Region (CINAR, NA13OAR4830233), Disaster Recovery Act. The authors thank Teledyne Webb Research and Rutgers University for student support, and the NOAA National Centers for Environmental Prediction for student engagement. We further thank David Titley, Jim Price and an anonymous reviewer for their useful comments.

Author contributions
S.M.G. synthesized and analysed the multiple data sets and wrote the manuscript in collaboration with the other authors. T.N.M. assisted in the synthesis of the *in situ* oceanographic data. G.N.S. contributed the atmospheric and storm sensitivity studies. Y.X. contributed the ocean simulations and analysis. R.K.F. performed historical buoy data and storm track analysis. F.Y. provided plots of buoy data beneath Super Typhoon Muifa. H.R. provided the observational data from the HF Radars. O.S. was involved in data collections and involved in analysis and manuscript preparation. J.K. contributed the Slocum data and was involved in analysis and manuscript preparation. All authors reviewed and edited this manuscript.

Additional information
Supplementary Information accompanies this paper at http://www.nature.com/naturecommunications

Competing financial interests: The authors declare no competing financial interests.

Reprints and permission information is available online at http://npg.nature.com/reprintsandpermissions/

How to cite this article: Glenn, S. M. *et al.* Stratified coastal ocean interactions with tropical cyclones. *Nat. Commun.* 7:10887 doi: 10.1038/ncomms10887 (2016).

Project CONVERGE: Impacts of local oceanographic processes on Adélie penguin foraging ecology

Josh Kohut and Travis Miles
Rutgers University

Matt Oliver and Megan Cimino
University of Delaware

Kim Bernard
Oregon State University

Peter Winsor and Hank Statscewich
University of Alaska, Fairbanks

William Fraser and Donna Patterson-Fraser
Polar Oceans Research Group

Erick Fredj
Jerusalem College of Technology

Abstract- **The Palmer Deep submarine canyon on the Western Antarctic Peninsula provides a conduit for upwelling of relatively warm, nutrient rich waters which enhance local primary production and support a food web productive enough to sustain a large top predator biomass. In an analysis of ten years of satellite-tagged penguins, showed that circulation features associated with tidal flows may be a key driver of nearshore predator distributions. During diurnal tides, the penguins feed close to their breeding colonies and during semi-diurnal tides, the penguins make foraging trips to the more distant regions of Palmer Deep. It is hypothesized that convergent features act to concentrate primary producers and aggregate schools of krill that influence the behavior of predator species. The initial results from a six month deployment of a High Frequency Radar network in Palmer Deep are presented in an attempt to characterize and quantify convergent features. During a three month period from January through March 2015, we conducted in situ sampling consisting of multiple underwater glider deployments, small boat acoustic surveys of Antarctic krill, and penguin ARGOS-linked satellite telemetry and time-depth recorders (TDRs). The combination of real-time surface current maps with adaptive in situ sampling introduces High Frequency Radar to the Antarctic in a way that allows us to rigorously and efficiently test the influence of local tidal processes on top predator foraging ecology**

Index Terms—Ocean observing, Polar ecosystems, Physical oceanography

I. Introduction

Physical processes in the coastal ocean are highly variable in space and time and play a critical role in coupled biological and chemical processes. From events lasting several hours to days on through inter-annual and decadal scales, the variability in the fluid itself structures marine ecological systems. The rapid evolution of the Integrated Ocean Observation System (IOOS) made possible through interdisciplinary partnerships and networked data sharing provides descriptions of coastal ocean hydrography and hydrodynamics at fine scales of space and time and regional spatial extents. These ocean observing networks now sample across these important time and space scales to better understand the physical ocean that structures marine ecosystems. For over a decade ocean observing technologies have been deployed, developed and applied to serve societal goals around US coastal waters. These services include supporting search and rescue, fisheries management, storm response, among others. These coastal observatories are built on regional scale observation and modeling that integrates satellite, HF radar, moored, and autonomous glider networks. The capabilities developed

978-1-5090-1537-5/16/$31.00 ©2016 IEEE

and tested in the coastal waters of the US are now migrating to the poles. Project CONVERGE, funded by the NSF Office of Polar programs, deployed an ocean observing network similar to the US networks in the Antarctic to better understand ecosystem function [1].

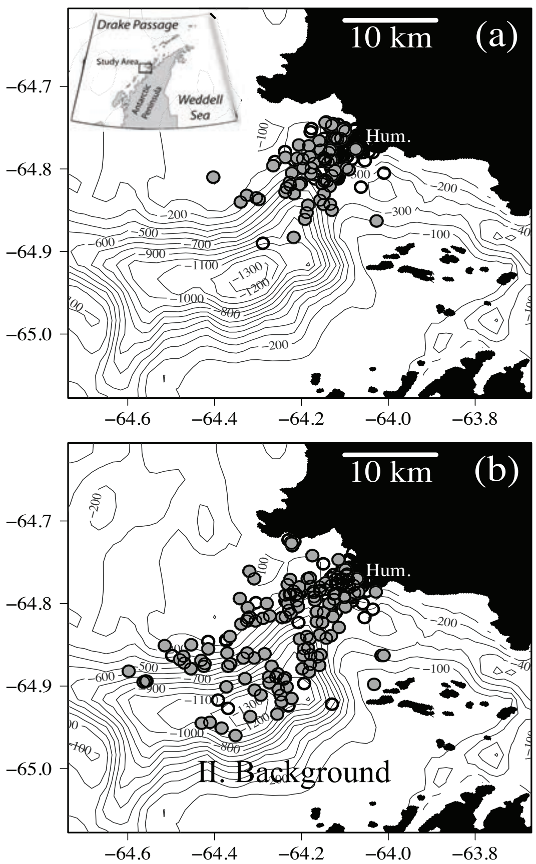

Figure 1. Penguin locations corresponding to diving (filled symbols) and non-diving behavior (open symbols) for diurnal (a) and semi-diurnal (b) tidal regimes for the 2011 season.

II. Background

Food resources in the ocean are extremely diffuse and must be either physically or biologically concentrated to support top trophic levels [2]. Resource concentrating features may include bathymetrically or tidally driven convergence zones [3, 4, 5], the formation of phytoplankton thin layers [6], or swarming and schooling behavior of consumers [7]. Since these concentrating features are ephemeral, marine ecosystems are often characterized by patchy spatial and temporal distributions of both primary producers and their consumers. In the coastal Western Antarctic Peninsula (WAP), the food web is short and characterized by intense phytoplankton blooms that are grazed by krill, a primary prey source for penguins and other predators. Averaged over decades to centuries, penguin hotspots are spatially coherent with submarine canyons and nearshore deep bathymetry [8, 9, 10]. However, within these hotspots (spatial scales <10 km), penguin foraging locations are highly variable, reflecting a patchy distribution of prey resources [11]. Adélie penguin foraging patterns determined from tag data collected over the same season appear to be correlated with the tides [12]. During the diurnal tidal regime, penguins tended to forage within 6 km of their breeding site on Humble Island. As the tidal regime switched to a semi-diurnal regime, the penguins typically remained close to shore for the first 4 days, but then began to move further off, into the head of the Palmer Deep, approximately 12 km away [Figure 1]. The spatial coherence between penguin colonies and deep canyons suggests that resources are preferentially transported to, and/or concentrated within these hotspots. Therefore, hotspots may serve as local refugia that buffer the impact of regional climate change through the persistence of the circulation features that transport and concentrate prey resources. Nearshore canyons and their associated dynamics play disproportionately important roles as biological hotspots and are critical for our understanding of WAP marine ecosystem structure and function.

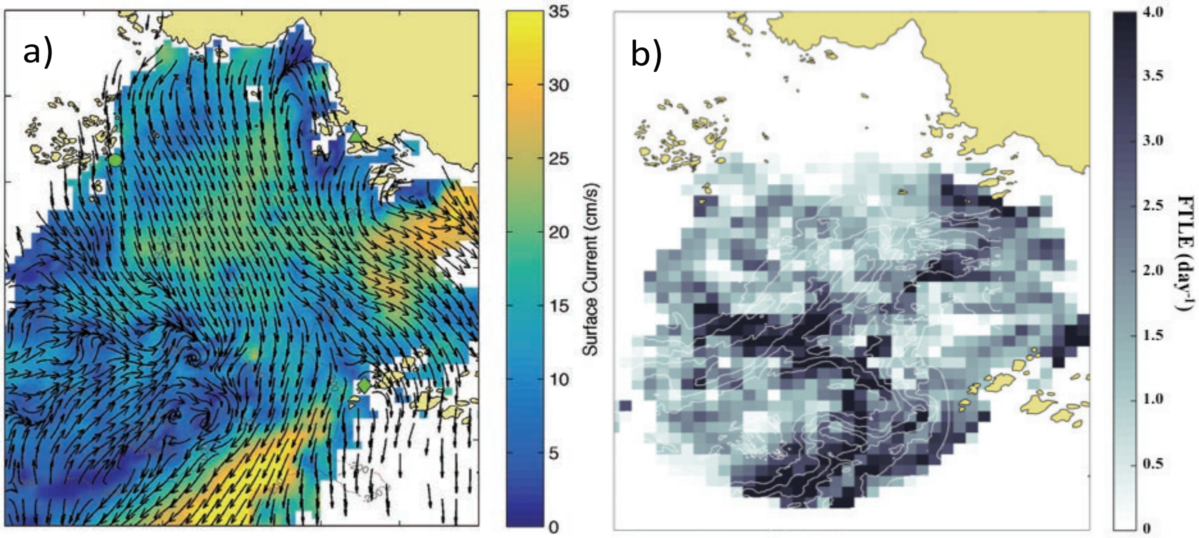

Figure 2. a) Hourly surface current map, January 27, 08:00 GMT 2015. The HF radar sites located at Palmer Station (green triangle) and the Wauwermans (green diamond) and Joubin (green square) island groups are also shown. b) Map of FTLE derived from the trajectories of simulated drifters released in hourly HFR maps (January 27, 2015).

During the austral summer of 2014-2015, project CONVERGE deployed a multi-platform network to sample the Adélie penguin foraging hotspot associated with Palmer Deep Canyon along the Western Antarctic Peninsula. The focus of CONVERGE was to assess the impact of prey-concentrating ocean circulation dynamics on Adélie penguin foraging behavior. Food web links between phytoplankton and zooplankton abundance and penguin behavior were examined to better understand the within-season variability in Adélie foraging ecology.

III. Approach

A. High Frequency Radar Network

A three-site HFR network was deployed in November 2014 at Palmer Deep [Figures 2]. The first site deployed at Palmer Station was powered by the station facilities. The two other sites deployed in the Joubin and Wauwermans Island chains relied on remote power systems that were constructed on site, lightered to shore via zodiac with ship support. The Remote Power Modules (RPMs) generate the required power for the HFRs through a combination of small-scale micro wind turbines and a photovoltaic array with a 96-hour battery backup. The remote power system consisted of a single watertight enclosure, used to house power distribution equipment, the HFR, and the communication gear. Built in redundancies within the power module, wind charging/resistive loads, solar, and independent battery banks ensure that should any one component fail, the unit was able to adjust autonomously. Each site also had 15-minute meteorological measures of air temperature, wind, relative humidity, and solar radiation. Communication between the two remote sites and Palmer Station was with line of sight radio modems (Freewave), which enabled remote site diagnostics and maintenance and provided a real-time data link.

B. Underwater Gliders

Electric gliders were a key component to successfully map in high resolution the upper water column properties

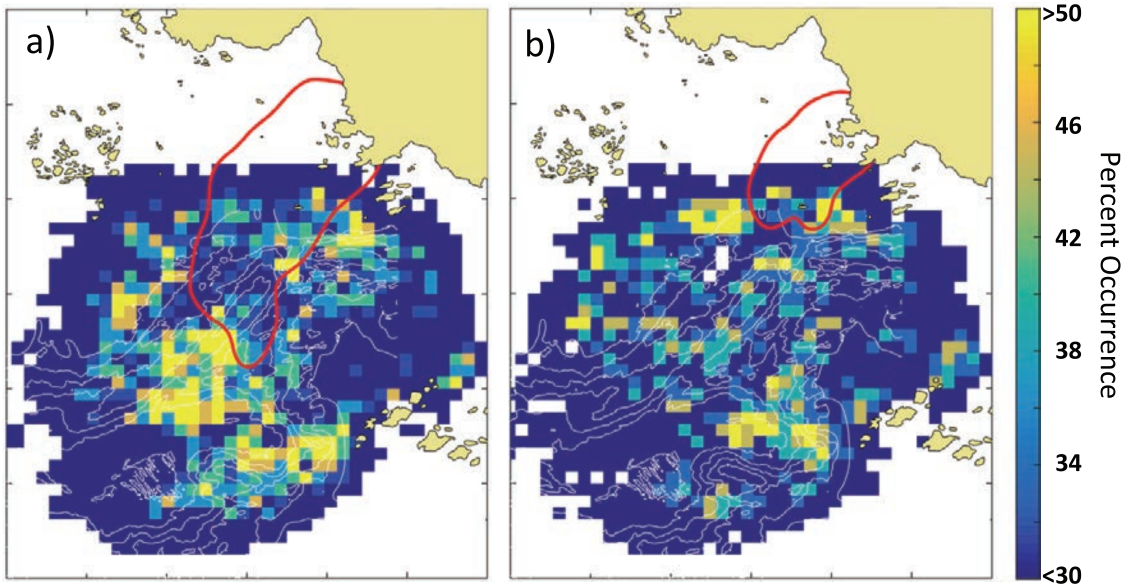

Figure 3. Maps of the percent of occurrence of the strongest quarter of all observed convergent fronts during a) semi-diurnal and b) diurnal days. The spatial density kernels (red contours) based on 10 years of tagged penguin data are shown in panel a for the semi-diurnal days and in panel b for diurnal days (Oliver et al., 2013).

relative to the convergent features identified by the HFR. Glider based sampling provided a continuous presence, through all weather conditions, over the critical spatial domain identified by the HFR network. Simultaneous measurements of physical and biological variables (phytoplankton and krill) from the gliders sampled the spatial and temporal variability over Palmer Deep. We deployed 3 gliders each equipped with a sensor suite to characterize the ecosystem's physical structure (Seabird C, T, D), *in situ* phytoplankton fluorescence and particle backscatter (Wet Labs Eco Triplet configured to measure backscatter of light at 470 nm and 532 nm as well as chlorophyll *a* fluorescence). Three gliders operated as a coordinated fleet to isolate temporal variability captured by a stationary 100 m glider from spatial and temporal variability captured by an along canyon (200 m) and cross canyon (100 m) lines. Both the station keeping glider and the along canyon 200m rated glider carried an additional aquadopp sensor operating at 1 and 2 MHz respectively.

IV. Ecological Connections

A. Mapping Convergent Features

Eddies and fronts were mapped hourly by a High Frequency Radar (HFR) network [Figure 2]. Simulated passive particles released in these hourly maps were used to identify the location and intensity of convergent features during days with diurnal and semi-diurnal tides. Lagrangian Coherent Structures (LCS, specifically Finite Time Lyapunov Exponent [FTLE]) derived from the particle trajectories were used to estimate the location of concentrating features [Figure 2b]. Broadly, Lagrangian Coherent Structures (LCSs) are boundaries in a fluid that distinguish regions of differing dynamics [13]. LCSs are often associated with filaments and mesoscale features, such as eddies, jets and fronts. The location frequency of the strongest fronts associated with the semi-diurnal and diurnal tidal regimes are shown in Figure 3. During the semi-diurnal tidal regime, frontal features are more frequently located offshore, consistent with the offshore Adélie penguin foraging locations. During the diurnal tidal regime, the overlap moves inshore, closer to the colony.

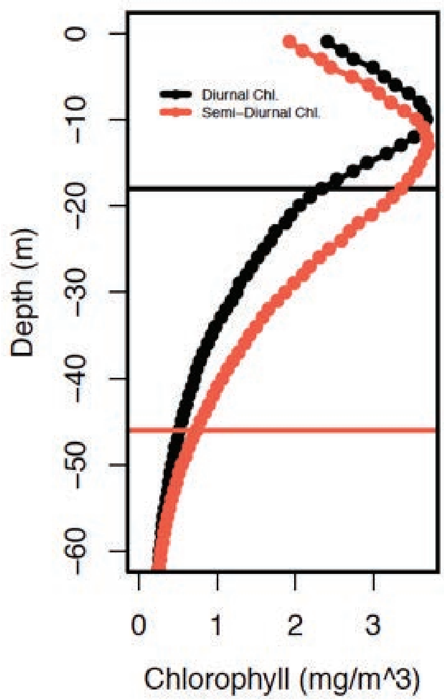

Figure 4. Average profiles of Chlorophyll Fluorescence averaged over all diurnal (Black) and semi-diurnal days (Red) measured from a single glider line along the main axis of Palmer Deep during the Austral Summer of 2014-2015. The horizontal lines indicate the depth of maximum buoyancy frequency from the density profile averaged over all diurnal (black) and semi-diurnal (red) days.

B. Vertical Patterns Linked to Local Tides

The link between the occurrence of these features and the behavior of the satellite-tagged penguins raises important questions about the coupling mechanisms operating throughout the entire food web, including phytoplankton and krill. Concurrent glider sampling shows that the influence of the tidal regime may extend to phytoplankton. The vertical structure in chlorophyll sampled by an along-canyon glider mission in January and February 2014-2015 shows that during days with diurnal tides, the average phytoplankton biomass was more compressed toward the surface than during days with semi-diurnal tides [Figure 4].

C. Anatomy of a Front

While Adélie penguin foraging locations and the occurrence of convergent features covary with tidal regime [Figure 3], it is on the scale of the individual physical features themselves that food web focusing occurs. On January 27, 2015 a glider sampled a convergent front identified in the HFR estimated FTLE field that was also targeted by two foraging penguins [Figure 5]. Hours before the penguins arrived, the glider sampled the sub-surface ocean associated with the convergent feature. The vertical sections of the glider across the front highlight the strong thermal gradient associated with the feature. This front had elevated chlorophyll concentrations associated with a surface bloom [Figure 5c]. While concurrent profiles of the acoustic return crossing the front suggest a peak that could be related to krill feeding on the observed bloom, the frequency (1 MHz) was not ideal for detecting krill [Figure 5d].

V. Conclusions

The spatial coherence between penguin colonies and deep canyons suggests that resources are preferentially transported to, and/or concentrated within these hotspots. Therefore, circulation features associated with the Palmer Deep canyon may enable enhanced food web transfer, termed “trophic focusing” [14]. The tight coupling from the hydrography through the phytoplankton to foraging penguins gives strong inference for the critical role that these physical features may have on food web focusing. Therefore, hotspots may serve as local refugia that buffer the impact of regional climate change through the persistence of the circulation features that transport and concentrate prey resources.

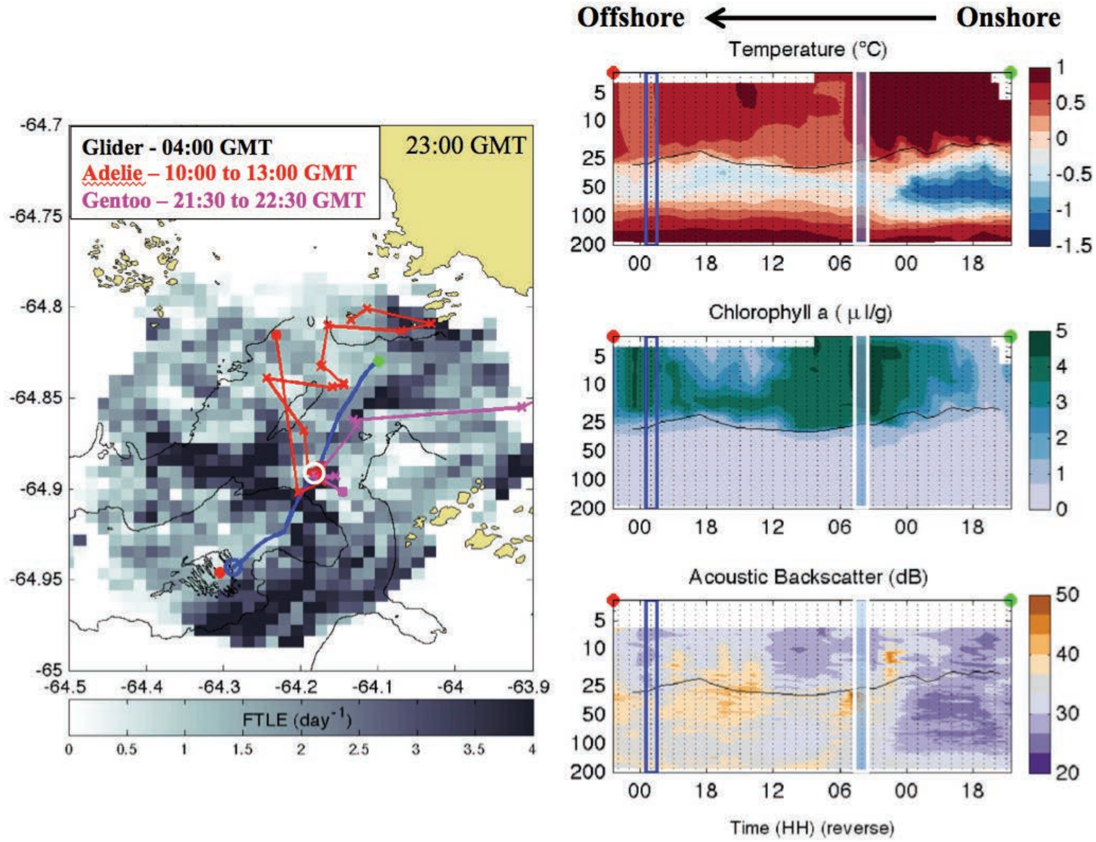

Figure 5. (left) Map showing the location of convergent features in the surface current fields mapped on January 27th, 2015. The track of the glider (blue) and the path of an Adélie (Red) and gentoo (Pink) are also shown. The cross-section data sampled by the glider as it moved offshore along the line highlighted in the map for (Upper Right) Temperature, (Middle Right) Chlorophyll Fluorescence, and Acoustic Backscatter. The glider location that overlaps the penguin foraging is highlighted as a white circle on the map and a white rectangle on the three cross-section plots on the right. The position of the glider at 23:00 GMT is shown as a blue circle on the map and a blue rectangle on the three cross-section plots on the right.

Nearshore canyons and their associated dynamics play disproportionately important roles as biological hotspots and are critical for our understanding of WAP marine ecosystem structure and function.

References

[1] Kohut, J., Bernard, K., Fraser, W., Oliver, M. J., Statscewich, H., Winsor, P., Miles, T. 2014.Studying the impacts of local oceanographic processes on Adélie penguin foraging ecology. *Marine Technology Society Journal*. doi: dx.doi.org/10.4031/MTSJ.48.5.10

[2] Lasker, R. 1978. The relationship between oceanographic conditions and larval anchovy food in the California Current: Identification of factors contributing to recruitment failure. *Rapports et Procs-Verbaux des Runions du Conseil International pour I'Exploration de la Mer* 173: 212–230.

[3] Hunt Jr, G. L., Russell, R. W., Coyle, K. O., Weingartner, T. 1998. Comparative foraging ecology of planktivorous auklets in relation to ocean physics and prey availability. *Marine Ecology Progress Series* 167: 241–259, doi: 10.3354/meps167241

[4] Cotté C, Simard Y. 2005. Formation of dense krill patches under tidal forcing at whale feeding hot spots in the St. Lawrence Estuary. *Marine Ecology Progress Series* 288: 199–210. doi: 10.3354/meps288199.

[5] Vlietstra L. S., Coyle K. O., Kachel N. B., Hunt Jr G. L. 2005. Tidal front affects the size of prey used by a top marine predator, the short-tailed shearwater (*Puffinus tenuirostris*). *Fisheries Oceanography* 14: 196–211, doi: 10.1111/j.1365-2419.2005.00369.x

[6] Dekshenieks, M. M., Donaghay, P. L., Sullivan, M., Rines, J. E. B, Osborn, T. R., Twardowski, M. S. 2001. Temporal and spatial occurrence of phytoplankton thin layers in relation to physical processes. *Marine Ecology Progress Series* 223: 61–71

[7] Benoit-Bird, K. J., Cowles, T. J., Wingard, C. E. 2009. Edge gradients provide evidence of ecological interactions in planktonic thin layers. *Limnology and Oceanography* 54(4): 1382–1392.

[8] Fraser, W. R., Trivelpiece, W. Z. 1996. Factors controlling the distribution of seabirds: winter-summer heterogeneity in the distribution of Adélie penguin populations. In: Ross, R., Hofmann, E. E. and Quetin, L. (eds). *Foundations for Ecological Research West of the Antarctic Peninsula, Antarctic Research Series* 70: 257-252.

[9] Ducklow, H. W., Baker, K., Martinson, D. G., Quentin, L. B., Ross, R. M., Smith, R. C., Stammerjohn, S. E., Vernet, M., Fraser, W. 2007. Marine ecosystems: The West Antarctic Peninsula. *Philosophical Transactions of the Royal Society of London* 362(1477):67-94.

[10] Erdmann, E. S., Ribic, C. A., Patterson-Fraser, D. L., Fraser, W. R. 2011. Characterization of winter foraging locations of Adélie penguins along the Western Antarctic Peninsula. *Deep Sea Research II* 58: 1710-1718.

[11] Bernard K. S., Steinberg D. K. 2013. Krill biomass and aggregation structure in relation to tidal cycle in a penguin foraging region off the Western Antarctic Peninsula. *ICES Journal of Marine Science* 70(4): 834-849.

[12] Oliver, M. J., Irwin, A. J., Moline, M. A., Fraser, W., Patterson, D., Schofield, O., Kohut, J. 2013. Adélie penguin foraging location predicted by tidal regime switching. *PLoS One*, doi: 10.1371/journal.pone.0055163.

[13] Haller, G. 2015. Lagrangian Coherent Structures. Annual Review of Fluid Mechanics. Vol. 47: 137-162 DOI: 10.1146/annurev-fluid-010313-141322

[14] Genin, A. 2004. Bio-physical coupling in the formation of zooplankton and fish aggregations over abrupt topographies. *Journal of Marine Systems* 50: 3-20.

Oliver et al. Anim Biotelemetry (2017) 5:14
DOI 10.1186/s40317-017-0129-8

Animal Biotelemetry

TELEMETRY CASE REPORT

Open Access

Factors affecting detection efficiency of mobile telemetry Slocum gliders

Matthew J. Oliver[1*], Matthew W. Breece[1], Danielle E. Haulsee[1], Megan A. Cimino[2], Josh Kohut[3], David Aragon[3] and Dewayne A. Fox[4]

Abstract

Background: Acoustic biotelemetry sensors have been fully integrated into a broad range of mobile autonomous platforms; however, estimates of detection efficiency in different environmental conditions are rare. Here, we examined the role of environmental and vehicle factors influencing detection range for two common acoustic receivers, the VEMCO mobile transceiver (VMT) and a VEMCO cabled receiver (VR2c) aboard a Teledyne Slocum glider. We used two gliders, one as a mobile transmitting glider and one as a mobile receiving glider during the fall in the mid-Atlantic coastal region.

Results: We found distance between gliders, water depth, and wind speed were the most important factors influencing the detection efficiency of the VMT and the VR2c receivers. Vehicle attitude and orientation had minimal impacts on detection efficiency for both the VMT and VR2c receivers, suggesting that the flight characteristics of the Slocum glider do not inhibit the detection efficiency of these systems. The distance for 20% detection efficiency was approximately 0.4 and 0.6 km for the VMT and VR2c, respectively. The VR2c receivers had significantly lower detection efficiencies than the VMT receiver at distances <0.1 km, but higher detection efficiencies than the VMT at distances >0.1 km.

Conclusions: Slocum gliders are effective biotelemetry assets that serve as sentinels along important animal migration corridors. These gliders can help elucidate the relationships between telemetered organisms and in situ habitat. Therefore, estimating the detection ranges of these common telemetry instruments provides an important metric for understanding the spatial scales appropriate for habitat selection inferences.

Keywords: Slocum glider, VMT, VR2c, Range test, VEMCO, Acoustic telemetry

Background

Acoustic biotelemetry is commonly used to monitor the presence and movement of organisms in aquatic environments [1], supporting both regional and international conservation efforts [2]. Location information for acoustic biotelemetry observations is tied to the location of the receiver and its detection range. The detection range of acoustic receivers depends on in situ listening conditions, which are linked to environmental conditions. Tides, currents, winds, stratification, and listening array configuration can impact detection efficiency, thus impacting the study of the presence and movement of organisms using acoustic biotelemetry [3–5].

The issue of acoustic range is further complicated by the use of telemetered autonomous underwater vehicles (AUVs) and other mobile platforms that transit different listening environments. While AUVs often measure environmental conditions that could impact listening conditions [6], moving platforms and dynamic environments create new range of testing challenges. One solution to this challenge is near-real-time triangulation of the acoustic signal using a combination synthetic aperture and known test tag locations [7]. Another solution is using a combination of stereo receivers and near-real-time particle filtering [8], and multiple AUVs to geolocate the acoustic tag on meter scales [9]. These approaches

*Correspondence: moliver@udel.edu
[1] School of Marine Science and Policy, College of Earth Ocean and Environment, University of Delaware, Lewes, DE, USA
Full list of author information is available at the end of the article

can be highly effective for geolocating acoustic signals, but require high-performance, propeller-driven AUVs that are able to precisely control their positions in the water. However, because these propellered AUVs require more energy to operate, they are limited to relatively short deployments due to battery life (<2 days). These propelled platforms are not designed to conduct continuous long-term searches, listening for telemetry signals of dispersed animals.

Observations of acoustically telemetered animals can be infrequent in the ocean environment; therefore, low-power AUVs such as Slocum and wave gliders can play the supporting role of environmental sentinel, targeting ocean features and discovering new areas used by telemetered organisms outside of fixed acoustic arrays with missions that last weeks to months [10–14]. Gliders are easily outfitted with externally mounted, self-contained VEMCO mobile transceivers (VMT) [10, 15], or with vehicle-integrated VEMCO cabled receivers (VR2c) [11, 14]. Critical to their sentinel role is the ability to associate in situ environmental data with acoustic detections, allowing inferences to be made about habitat associations [11]. However, this requires estimates of the range of acoustic detections over the large spatial scales (hundreds of km) covered by these long-lived AUV missions, which is difficult to obtain with moored test tags. In this study, we estimate the detection range of an integrated VR2c and externally mounted VMT on Slocum gliders during the fall along the mid-Atlantic Bight. We used a combination of vehicle attitude, in situ oceanographic data and meteorological observations from nearby NOAA buoys to determine which factors affected the detection efficiency of these common telemetry systems.

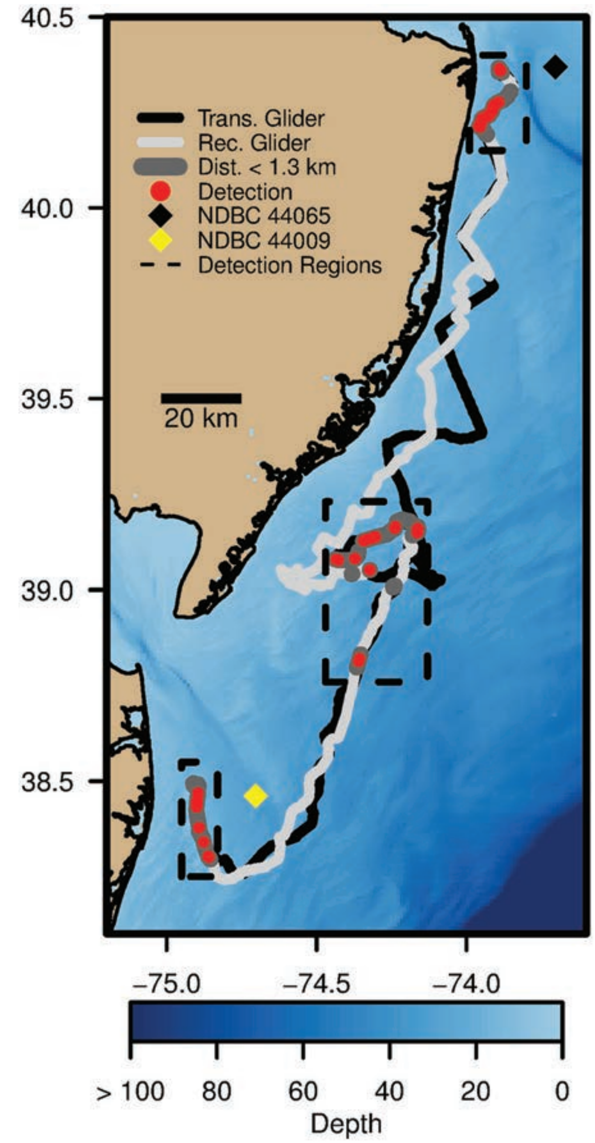

Fig. 1 Paths of the transmitting and receiving glider along New Jersey, Delaware, and Maryland coasts. The gliders transited very similar paths, but were not always close together. *Dark gray* regions indicate when the gliders were within 1.3 km of each other within study boxes, and *red dots* indicate when the receiving glider detected the transmitting glider. *The diamonds* are the location of NDBC buoys used to determine wind speeds. *Dashed boxes* indicate the three regions the receiving glider detected the transmitting glider

Methods

Glider deployments

Slocum gliders are buoyancy-driven vehicles that dive and climb at a nominal 26° angle and travel in a vertical "sawtooth" pattern between predetermined surface events [16]. While the glider is underway, it collects vertical profiles of physical (temperature, salinity), chemical (oxygen), and biological properties (chlorophyll-*a* fluorescence). Two Slocum gliders (Teledyne Webb Research) were deployed off of Sandy Hook, New Jersey, USA, on September 17, 2015, and were recovered off the coast of Delaware, USA, on October 7, 2015 (Fig. 1). For this 20-day mission in the mid-Atlantic coastal ocean, one glider (transmitting glider) was equipped with an externally mounted VEMCO mobile transceiver (VMT, VEMCO Ltd.) programmed to transmit coded acoustic signals (69 kHz, 156 dB) [10]. The second glider (receiving glider) was equipped with an externally mounted VMT programmed to only receive coded acoustic signals, and two hull integrated (1 top and 1 bottom) VEMCO VR2c acoustic receivers [11]. The hydrophones of the integrated VR2c's were normal to the major axis of the glider (pointed upward and downward), while the VMT hydrophone was mounted facing forward, and along the major axis of the glider (Fig. 2). The gliders record vehicle pitch, roll, depth, heading, and total water depth at

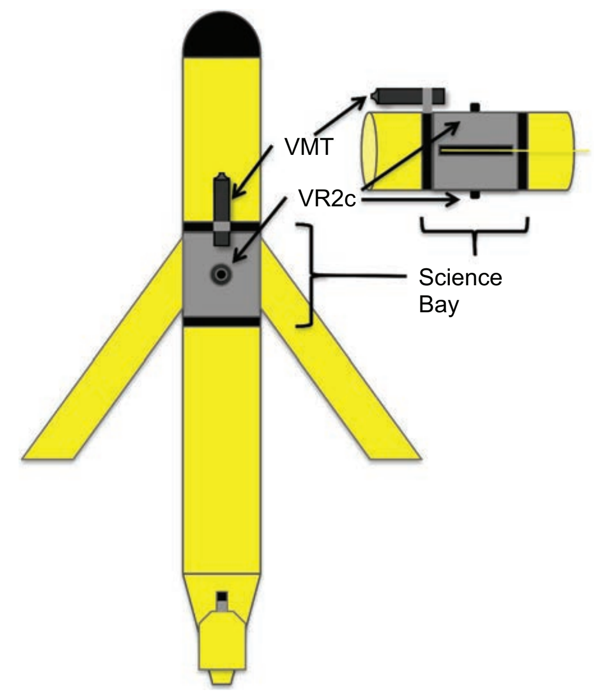

Fig. 2 The mounting orientation of the VMT and VR2c's on the receiving glider from the dorsal (*left*) and the lateral (*right*) view. Two VR2c's are integrated into the central science bay, one pointing up and the other down. The VMT was mounted in a bracket forward of the top VR2c, with its receiver pointing toward the nose of the glider. The transmitting glider had a VMT mounted in a same way

1 Hz throughout the mission. The gliders also estimate depth integrated water currents between surface events by comparing surface GPS locations with dead-reckoning subsurface navigation. The transmitting glider's primary mission objective was to measure full water column dissolved oxygen in the coastal ocean. The receiving glider, deployed at the same time and location, was testing an automated glider path-planning tool. Given these primary objectives, these gliders also served as mobile platforms of opportunity to test the influence of environmental and vehicle factors on acoustic signal detection in the mid-Atlantic coastal ocean. The receiving glider was within 1.3 km (the longest distance of detection between gliders) of the transmitting glider during three distinct time periods, each with different environmental conditions (Fig. 3).

Environmental and vehicle predictors of detection efficiency

The VMT mounted on the transmitting glider was scheduled to transmit a coded acoustic signal at 69 kHz (156 dB) on average every 110 s (range 70–150 s). We hypothesized that reception of coded acoustic signals by either the VMT or integrated VR2c's on the receiving glider would be affected by the distance between gliders, depth of the water, wind speed, current speed, depth of the receiving glider, water column density, pitch and roll of the receiving glider, and the bearing of the transmitting glider to the receiving glider. We computed the distance between the gliders using the rdist.earth function in the fields R package [17]. We used wind speeds measured at NDBC buoys 44065 and 44009 as proxies for wind speeds at the glider locations (Fig. 1). The wind records at these buoys are different, but strongly correlated ($r = 0.81$) (Fig. 3a). We used wind speed from NDBC 44065 as a proxy for wind speed for the northernmost region where the receiving glider was detecting the transmitting glider, and NDBC 44009 for the middle and southernmost regions. We derived water density using the equation of state (temperature, salinity, pressure) measured by each glider [18]. We estimated water column stratification by differencing surface and bottom density. We eliminated predictors that were highly collinear ($|r| > 0.7$). For example, depth of the glider was highly correlated to the altitude of the glider from the bottom because the gliders were in relatively similar depths throughout the mission. Also, the relative depths of the transmitting gliders were not considered because the vertical depth differences were only 2% (max of 30 m) of the horizontal depth differences of detection (up to 1.3 km).

Generalized additive mixed model analyses

To test which predictor variables influenced detection efficiency, we used a generalized additive mixed model (GAMM) framework in the R gamm4 package [19]. A GAMM sums smoother functions (penalized regression splines) to model the binomial presence/absence of telemetry detections compared to the expected number of detections from the transmitting glider. We implemented penalized shrinkage smoothers as an automatic alternative to model selection of environmental predictors. Shrinkage smoothers incorporate a penalty, which may shrink all of the coefficients to zero, effectively penalizing the variable out of the model [20]. We used penalized thin plate regression splines (ts) for non-cyclic predictors and penalized cubic regression splines for cyclic predictors (cc) using the mgcv package in R. We limited the number of knots for each smooth variable in our model to five to prevent overfitting. Model analysis was limited to mission times when the transmitting glider was within 1.3 km of the receiving glider. This was the furthest distance the receiving glider detected the transmitting glider. The receiving and transmitting gliders were within 1.3 km in three distinct regions (northern NJ, southern NJ, and Delaware coasts) (Fig. 1). Therefore, we added these locations as random effects to account for unknown differences inherent to these three locations that are otherwise unaccounted for in our analysis. Finally, we used fivefold cross-validation on these models to determine if the model was

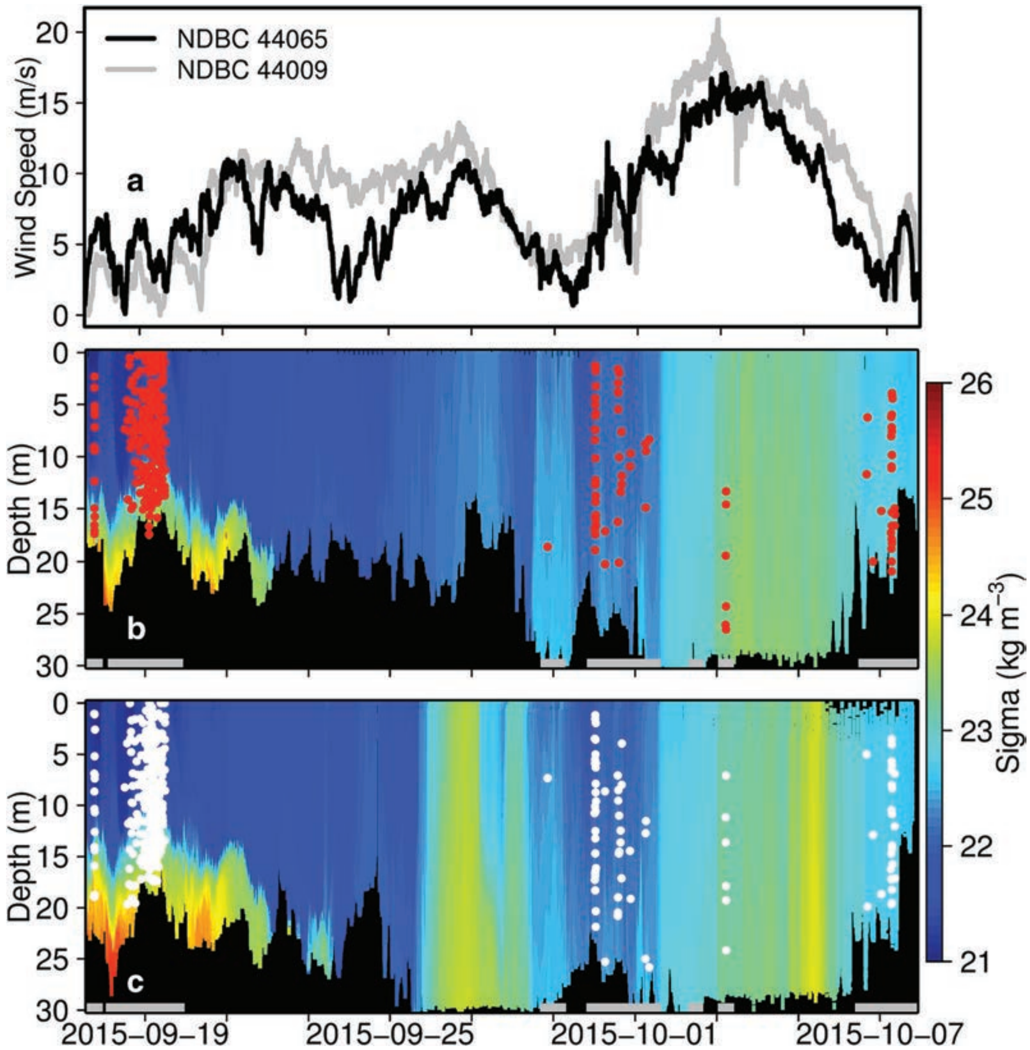

Fig. 3 **a** Wind velocities at the NDBC buoys during the deployment. Sigma (density-1000) cross section of the receiving (**b**) and transmitting (**c**) glider. *Points* indicate the depth of the receiving glider (*red*) and transmitting glider (*white*) when detections were recorded. *Gray bars* indicate when the gliders were within 1.3 km of each other

overfit and to test the performance of the model without each fold of data. This was done by splitting the data randomly into five subsets, reiteratively fitting the model to four of the five subsets (training dataset), and then predicting on the remaining subset (test dataset) to verify the robustness of the models [21]. We estimated the relative predictor importance of these cross-validated models using the BIOMOD2 package [22, 23].

Results

Environmental conditions

The transmitting and receiving gliders made similar, but not identical southward paths starting in coastal NJ waters and ending in DE waters (Fig. 1). These gliders encountered three prolonged wind events >10 m s^{-1} (Fig. 3a), presumably changing the subsurface noise conditions [3]. Stratification of the water column is most pronounced early in the mission, with up to a 4 sigma (4 kg m^{-3}) difference in density between surface and bottom waters. Data collected by the receiving (Fig. 3b) and transmitting (Fig. 3c) gliders show the erosion of the pycnocline and a general increase in density due to cooling over the study period. This erosion of the strong summer pycnocline is well known in this region as a result of seasonal cooling and storm activity [24].

Acoustic detections

The two gliders were within 1.3 km of each other for 90.7 h and got as close as 15 m. Within this distance range, the transmitting glider emitted 2177 coded acoustic signals. The VMT receiver successfully decoded 124 detections (5.6%) of the transmitting glider. The top integrated VR2c receiver decoded 188 detections (8.6%), while the bottom integrated VR2c receiver decoded 175 detections (8.0%). Forty-eight of the transmissions were detected by both the top and bottom integrated VR2c receivers. Treating the integrated VR2c receivers as a single receiving apparatus, removing double detection counts, the integrated VR2c receivers recorded 264 detections (12.1%) of the transmitting glider. There were six other tags detected during this experiment; however, these detections were not intermingled with the detections of the transmitting glider. Therefore, we believe that false-positive detections are not a major factor in this study.

Detection efficiency for the VMT receiver was highest when the distance to the transmitting glider was <0.1 km and decreased with distance (Fig. 4). At distances >0.4 km, VMT receiver detections were sparse. In contrast, the integrated VR2c receivers performed poorly at distances <0.1 km, but were comparable to or better than the VMT at the further distances. Peak detection efficiencies for the integrated VR2c receivers were at 0.2–0.3 km, but dropped markedly past 0.6 km. The low detection efficiencies at distances <0.1 km by the integrated VR2c receivers are likely a result of close proximity detection interference, where the power of the transmission (156 dB in our case) overwhelms the hydrophone and is known to occur in these systems. These detection efficiency patterns create different expectations for the distance of a received transmission by these two sensors known as the "doughnut effect" (Fig. 4) [25]. The integrated VR2c's have a much larger detection area, which scales with the square of the distance between the transmitter and receiver.

Environmental and vehicle attitude predictors of detections

GAMMs were developed for predicting both VMT and integrated VR2c detections using penalized smoothers for continuous predictors. We observed strong stratification during the first glider encounter, but the water column was thoroughly mixed for the rest of the experiment. Models predicting the presence/absence of detections on the VMT and the integrated VR2c receivers (Table 1) had AUC values of 0.96 and 0.89, respectively, indicating good model performance. Fivefold cross-validation of these models had AUC values of 0.95 and 0.89 indicating that these models were not overfit. Variable importance for these models followed similar patterns for the VMT and the integrated VR2c's (Fig. 5). Distance between gliders was the most important predictor of detections for both the VMT (54.2%) receiver and the integrated VR2c (69.6%) receivers (Fig. 5). Wind speed (19.0%) and water depth (15.3%) were similarly important for predicting detections on the VMT receiver; however water depth (16.5%) was more important than wind speed (4.4%) for

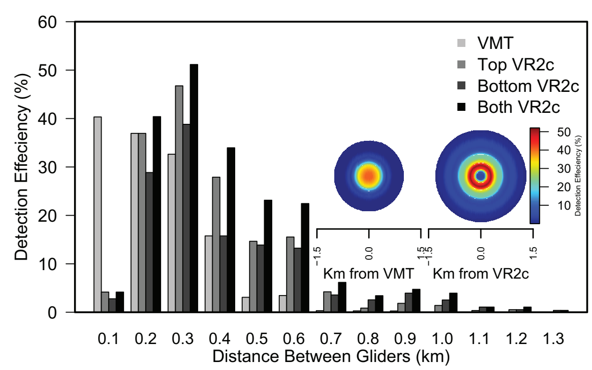

Fig. 4 Detection efficiency of the VMT and integrated VR2c receivers on the receiving glider at distance bins away from the transmitting glider. *The figure inset* is a visual aid for the circular distribution of detection efficiency for the VMT and both integrated VR2c receivers, illustrating the "doughnut effect" [25]

Table 1 GAMMs evaluated to predict the likelihood of acoustic transmission detection by a VMT and integrated VR2c receivers based on environmental conditions

	GAMMs (binomial, knots = 5, penalized smoothers)	Adj. R^2	AIC	AUC
VMT	VMT ~ s(Dist.) + s(Wind) + s(W. Depth) + s(Cur.) + s(Strat.) + s(Bearing) + s(Depth) + s(Pitch) + s(Roll) + s(Den.) + 1| Region	0.385	473.9	0.96
VR2c	VR2c ~ s(Dist.) + s(Wind) + s(W. Depth) + s(Cur.) + s(Strat.) + s(Bearing) + s(Depth) + s(Pitch) + s(Roll) + s(Den.) + 1| Region	0.277	1090.6	0.89

Dist. is the distance between gliders, Wind is wind speed from the nearest NDBC buoy, W. Depth is the depth of the water estimated by the receiving glider altimeter, Density is the density of the sea water measured by the receiving glider, Strat. is the difference between surface and bottom densities measured by the receiving glider, Cur. is the glider estimated depth integrated currents, Depth is the depth of the receiving glider, Pitch is the angle of descent of the receiving glider, Bearing is the bearing of the transmitting glider in relation to the receiving glider, Roll is the roll of the receiving glider, and Region refers to the three major geographic areas where detections occurred in Fig. 1

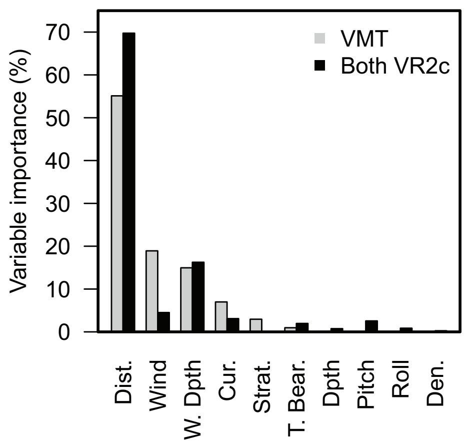

Fig. 5 The relative importance of environmental and vehicle attitude predictors affecting acoustic detections. See Fig. 1 caption for variable abbreviations

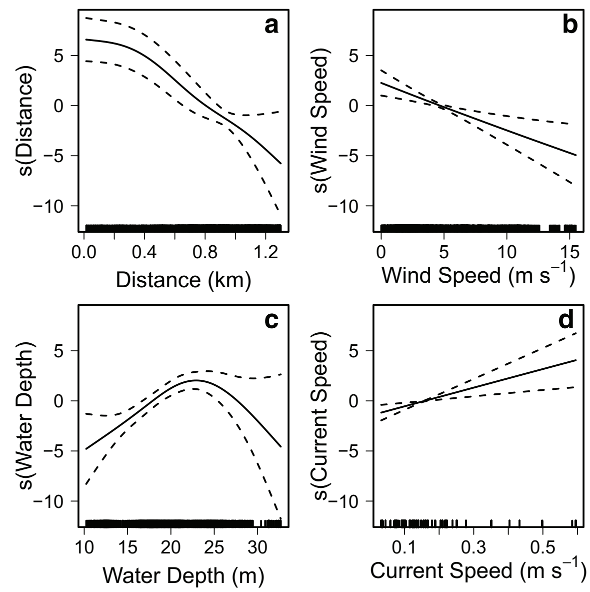

Fig. 6 VMT model response functions of the four most important variables (**a** Distance between gliders, **b** Wind speed, **c** Water depth, **d** Current speed) affecting likelihood of detections on VMT receiver. *Dashed lines* indicate confidence intervals, and *rug plots* indicate observations. *Positive values* indicate conditions that enhance detection efficiency, and *negative values* indicate conditions that suppress detection efficiency

the VR2c model (Fig. 5). Current speed (7.5, 3.1%) was somewhat important for both models, with the rest of the predictors, including vehicle attitude, having less than 3% importance (Fig. 5). Distance, wind speed, water depth, current speed, stratification, and target bearing were significant ($p < 0.05$) predictors of VMT detections (Additional file 1: Table S1). For the integrated VR2c's all predictors were significant except for stratification, AUV depth, and water density (Additional file 1: Table S2).

The response curves of the four most important predictors of detections by the VMT (Fig. 6) and the integrated VR2c's (Fig. 7) exhibit different responses for these two acoustic telemetry systems, especially with respect to distance between the gliders. VMT model predictors showed the expected decline in detection likelihood as distance between the gliders increased (Fig. 6a); however, the VR2c model did not illustrate the same monotonic decline (Fig. 7a). Instead, the response curve showed that the VR2c's were not as effective at very close distances, similar to the results in Fig. 4. Both the VMT receiver and integrated VR2c receivers performed better at low wind speeds, indicating that noise generated by windy conditions might affect detection efficiency (Figs. 6b, 7b). However, confidence intervals around the partial residual plot of the effect of wind on detection efficiency for the VR2c receivers always encompass zero, and therefore, there is low confidence in this relationship. Both the VMT receiver and integrated VR2c receivers performed better as water depth increased; however, deeper than 20 m, the standard error estimates of the response curves increase substantially, making judgments about the response curve in deeper waters difficult (Fig. 6b). This is likely because

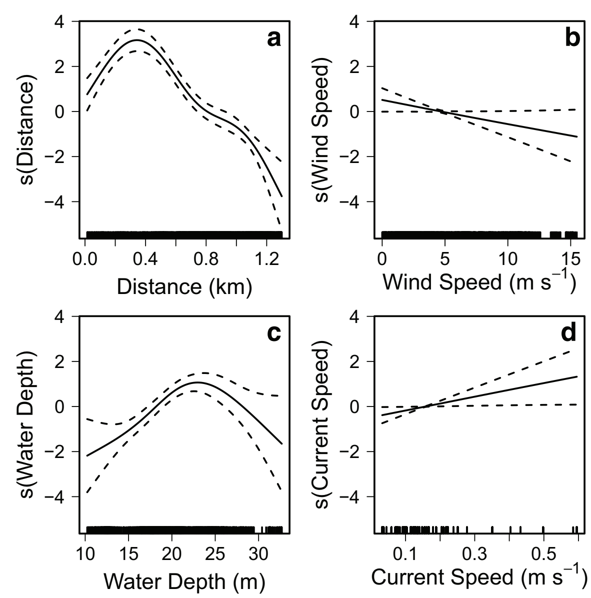

Fig. 7 Model 4 response functions of the four most important variables (**a** Distance between gliders, **b** Wind speed, **c** Water depth, **d** Current speed) affecting likelihood of detection on integrated VR2c receivers. *Dashed lines* indicate confidence intervals, and *rug plots* indicate observations. *Positive values* indicate conditions that enhance detection efficiency, and *negative values* indicate conditions that suppress detection efficiency

only 2.5% of our observations were in waters deeper than 30 m, increasing the spread of the confidence intervals. In addition, the confidence intervals for the effect of current speeds on the detection efficiency of VR2c receivers always included zero, making interpretation of the effects inconclusive (Fig. 7d). Water column stratification played a statistically significant but minor role in VMT detections (Fig. 5; Additional file 2, Additional file 1: Table S1). Stronger stratification reduced the likelihood of VMT detection; however, the confidence intervals include zero, making it difficult to interpret the stratification effect. Vehicle attitude parameters in general were nonsignificant predictors of detection efficiency for the VMT, with the exception of the effect of target bearing being weak but significant (Additional file 1: Table S1). For the integrated VR2c's, vehicle roll, pitch, and target bearing were statistically significant, but weak predictors of detection efficiency (Fig. 5; Additional file 3, Additional file 1: Table S2).

Discussion

The major predictors of detection efficiency for both receiver assets were distance between transmitter and receiver, wind, and water depth (Fig. 5). This is generally in line with previous studies [3–5]. We suspect more studies are necessary during highly stratified periods to estimate the full impact of a stratified water column on acoustic detection efficiency, as stratification played only a minor role in detection efficiency for the VMT. Increased wind speeds decreased detection efficiency for the VMT and VR2c (Figs. 5b, 6b); however, the effect was more pronounced with the VMT. Wind stress has been shown to decrease detection efficiencies of VMTs [26]; however, we do not know why the VR2c appears to be less sensitive to wind in this study. Encouragingly, vehicle attitude and sensor orientation seemed to play a minor role in detection efficiency, indicating that Slocum gliders can play an important role in biotelemetry studies without major concerns of orientation affecting detection efficiency. The effect of target bearing is probably related to the orientation and position of the mounted receivers (Fig. 2). As a result, the VMT receiver had slightly higher detection efficiency when the bearing of transmitting glider was not near 180° (behind the receiving glider). The VMT was mounted slightly forward of the top integrated VR2c receiver, which may have caused some signal blocking from the transmitting glider. For example, the detection efficiency of the integrated VR2c receivers was slightly reduced when the bearing of the transmitting glider was near 0° (ahead of the receiving glider). We view these effects as conditional on the mounting relationship between the VMT and the integrated VR2c's, which could be changed.

The externally mounted VMT and integrated VR2c's had different effective detection ranges. The results of our study suggest the effective detection range to be ~0.4 and ~0.6 km for the VMT and integrated VR2c receivers, respectively, comparable to previous findings for detecting high-power tags (69 kHz, 161 dB) [25]. In addition, our range testing results are similar to estimates using a Slocum glider with integrated VR2c receivers passing by a moored test tag [11]. Studies using VMTs as receivers on AUVs and as animal-borne sensors are becoming more common and often have experimental designs that make range testing impractical [27–29]. Our study gives an upper bound on the scales of interaction that can be inferred between telemetered organisms and their environment as they move through the coastal ocean, outside of established fixed acoustic receiver arrays. Detection efficiency of the VMT and integrated VR2c's differed depending on the distance between the receiver and transmitter. At 0.1–0.2 km, the detection efficiencies of the VMT and VR2c receivers were near 30–40%, which is similar to the mean detection efficiency (33%) reported by fixed arrays in a shallow coastal ocean [3]. However, our detection efficiency was much lower than the 80–90% detection efficiency by high-power tags reported by arrays in an Arctic embayment, fresh water lake, and a subtropical marine reef [25]. A possible strategy to estimate detection efficiency using gliders throughout their mission would be to fly them in formation, one acting as a transmitter and the other as a receiver to estimate the detection efficiency distance decay curve. The detection efficiency "doughnut effect" we observed with the integrated VR2c receivers indicates that one system (VMT vs. integrated VR2c) might be preferable over the other depending on the science question. If the science question depends on localization, then the VMT might be preferred; however, if the science question depends on broader scale presence or absence, then the integrated VR2c receivers may be better suited as a result of their larger detection range.

Conclusion

Our analysis suggests that Slocum gliders can operate as effective and efficient acoustic telemetry sentinels outside fixed receiver arrays, whether they are using VMT or integrated VR2c receiver technology. The effective range for the VMT and VR2c receivers does not appear to be affected by vehicle attitude, but rather distance between transmitter and receiver, and environmental conditions. With the expectation that more Slocum gliders will be being used to map habitat associations of telemetered fishes during their migrations outside fixed receiver arrays, these estimates should provide valuable insights into study design and increase the precision of estimates.

This study outlines important length scales when considering the inferred relationships between telemetered organisms and their habitat.

Additional files

Additional file 1. GAMM model results for the VMT and VR2c Model in Table 1.

Additional file 2. VMT model response functions of the less important variables affecting VMT detections. Dashed lines indicate confidence intervals, and rug plots indicate observations. Of these predictors, only target bearing was statistically significant (Additional file 1: Table S1). Positive values indicate conditions that enhance detection efficiency and negative values indicate conditions that suppress detection efficiency.

Additional file 3. VR2c response functions of the less important variables affecting VR2c detections. Dashed lines indicate confidence intervals, and rug plots indicate observations. Of these predictors, density and pitch were not statistically significant (Additional file 1: Table S2). Positive values indicate conditions that enhance detection efficiency and negative values indicate conditions that suppress detection efficiency.

Abbreviations
AUV: autonomous underwater vehicle; VMT: VEMCO mobile transceiver; VR2c: VEMCO cabled receiver.

Authors' contributions
MO, MB, DH, and JK designed the experiment. MO, MB, DA, and JK collected the data for the experiment. MO, MB, and MC analyzed data for the experiment. MO, MB, DH, MC, JK, and DF wrote the manuscript. All authors read and approved the final manuscript.

Author details
[1] School of Marine Science and Policy, College of Earth Ocean and Environment, University of Delaware, Lewes, DE, USA. [2] Scripps Institute of Oceanography, University of California, San Diego, CA, USA. [3] Department of Marine and Coastal Sciences, Rutgers University, New Brunswick, NJ, USA. [4] Department of Agriculture and Natural Resources, Delaware State University, Dover, DE, USA.

Acknowledgements
None.

Competing interests
The authors declare that they have no competing interests.

Availability of data and materials
The datasets used and/or analyzed during the current study are available from the corresponding author on reasonable request.

Funding
National Ocean Service (NOS), National Oceanic and Atmospheric Administration (NOAA) NOAA-NOS-IOOS-20160204378; New Jersey Department of Environmental Protection (NJDEP) WM13-019 2013; Lenfest Ocean Program 00026773; Robertson Fund. These funding bodies did not design, collect, analyze, nor interpret the data presented in this manuscript. These funding bodies did not write any portion of this manuscript.

Received: 6 March 2017 Accepted: 5 June 2017
Published online: 20 June 2017

References
1. Hussey NE, Kessel ST, Aarestrup K, Cooke SJ, Cowley PD, Fisk AT, et al. Aquatic animal telemetry: a panoramic window into the underwater world. Science. 2015;348:1255642.
2. Block BA, Holbrook CM, Simmons SE, Holland KN, Ault JS, Costa DP, et al. Toward a national animal telemetry network for aquatic observations in the United States. Anim Biotelem. 2016;4:1–8.
3. Mathies NH, Ogburn MB, McFall G, Fangman S. Environmental interference factors affecting detection range in acoustic telemetry studies using fixed receiver arrays. Mar Ecol Prog Ser. 2014;495:27–38.
4. Welsh JQ, Fox RJ, Webber DM, Bellwood DR. Performance of remote acoustic receivers within a coral reef habitat: implications for array design. Coral Reefs. 2012;31:693–702.
5. How JR, de Simon L. Acoustic tracking: issues affecting design, analysis and interpretation of data from movement studies. Mar Freshw Res. 2012;63:312–24.
6. Grothues TM, Dobarro J, Eiler J. Collecting, interpreting, and merging fish telemetry data from an AUV: remote sensing from an already remote platform. In: Autonomous underwater vehicles (AUV), 2010 IEEE/OES; 2010. doi:10.1109/AUV.2010.5779658.
7. Grothues TM, Dobarro J, Ladd J, Higgs A, Niezgoda G, Miller D. Use of a multi-sensored AUV to telemeter tagged Atlantic sturgeon and map their spawning habitat in the Hudson River, USA. In: Autonomous underwater vehicles, 2008, AUV 2008 IEEE/OES; 2008. doi:10.1109/AUV.2008.5347597.
8. Clark CM, Forney C, Manii E, Shinzaki D, Gage C, Farris M, et al. Tracking and following a tagged leopard shark with an autonomous underwater vehicle. J Field Robot. 2013;30:309–22.
9. Lin Y, Hsiung J, Piersall R, White C, Lowe CG, Clark CM. A multi-autonomous underwater vehicle system for autonomous tracking of marine life. J Field Robot. 2016. doi:10.1002/rob.21668.
10. Oliver MJ, Breece MW, Fox DA, Haulsee DE, Kohut JT, Manderson J, et al. Shrinking the haystack: using an AUV in an integrated ocean observatory to map Atlantic Sturgeon in the coastal ocean. Fisheries. 2013;38:210–6.
11. Haulsee DE, Breece MW, Miller DC, Wetherbee BM, Fox DA, Oliver MJ. Habitat selection of a coastal shark species estimated from an autonomous underwater vehicle. Mar Ecol Prog Ser. 2015;528:277–88.
12. Breece MW, Fox DA, Dunton KJ, Frisk MG, Jordaan A, Oliver MJ. Dynamic seascapes predict the marine occurrence of an endangered species: Atlantic Sturgeon *Acipenser oxyrinchus oxyrinchus*. Methods Ecol Evol. 2016. doi:10.1111/2041-210X.12532.
13. Whoriskey FG. The ocean tracking network: a global partnership uses electronic tagging technologies to track the movements of aquatic animals, answer science questions, stimulate new technology development and assist with sustainable development of the ocean. In: OCEANS 2015, MTS/IEEE Washington; 2015. doi:10.23919/OCEANS.2015.7404513.
14. Carlon R. Tracking tagged fish using a wave glider. In: OCEANS'15 MTS/IEEE Washington; 2015. doi:10.23919/OCEANS.2015.7404617.
15. Crowley M, Schofield O, Glenn S, Whoriskey F. Gliderpalooza 2013 to modelpalooza2014: Joint U.S. & Canadian ocean glider operations supporting multidisciplinary scientific research and education. 2014 Oceans, St John's; 2014. doi:10.1109/OCEANS.2014.7003124.
16. Schofield O, Kohut J, Aragon D, Creed L, Graver J, Haldeman C, et al. Slocum gliders: robust and ready. J Field Robot. 2007;24:473–85.
17. Nychka D, Furrer R, Sain S. fields: tools for spatial data. R package version 691. 2013.
18. Pond S, Pickard GL. Introductory dynamical oceanography. 2nd ed. Oxford: Pergamon Press; 1983.
19. Wood S, Scheipl F. gamm4: generalized additive mixed models using mgcv and lme4. R package version 02-3. 2014.
20. Marra G, Wood SN. Practical variable selection for generalized additive models. Comput Stat Data Anal. 2011;55:2372–87.
21. Wegmann M, Leutner B, Dech S. Remote sensing and GIS for ecologists: using open source software. Exeter: Pelagic Publishing; 2016.
22. Thuiller W, Lafourcade B, Engler R, Araujo MB. BIOMOD—a platform for ensemble forecasting of species distributions. Ecography. 2009;32:369–73.
23. Thuiller W, Georges D, Engler R, Breiner F. biomod2: ensemble platform for species distribution modeling. R package version 33-7. 2016.

24. Castelao R, Glenn S, Schofield O, Chant R, Wilkin J, Kohut J. Seasonal evolution of hydrographic fields in the central Middle Atlantic Bight from glider observations. Geophys Res Lett. 2008. doi:10.1029/2007GL032335.
25. Kessel ST, Hussey NE, Webber DM, Gruber SH, Young JM, Smale MJ, et al. Close proximity detection interference with acoustic telemetry: the importance of considering tag power output in low ambient noise environments. Anim Biotelem. 2015;3:1.
26. Baker LL, Jonsen ID, Flemming JEM, Lidgard DC, Bowen WD, Iverson SJ, et al. Probability of detecting marine predator-prey and species interactions using novel hybrid acoustic transmitter-receiver tags. PLoS ONE. 2014;9:e98117.
27. Lidgard DC, Bowen WD, Jonsen ID, Iverson SJ. Animal-borne acoustic transceivers reveal patterns of at-sea associations in an upper-trophic level predator. PLoS ONE. 2012;7:1–8.
28. Stuart C, Joanna MF. Seal encounters at sea: a contemporary spatial approach using R-INLA. Ecol Model. 2014;291:175–81.
29. Haulsee DE, Fox DA, Breece MW, Brown LM, Kneebone J, Skomal GB, et al. Social network analysis reveals potential fission–fusion behavior in a shark. Sci Rep. 2016;6:34087.

AGU PUBLICATIONS

Geophysical Research Letters

RESEARCH LETTER
10.1002/2016GL071205

Key Points:
- Underwater glider observes phytoplankton distribution in Antarctic coastal seas
- Glider data are used to determine ecologically relevant mixed-layer depth
- Maximum of buoyancy frequency is ecologically relevant mixed-layer depth

Supporting Information:
- Supporting Information S1
- Figure S1
- Figure S2

Correspondence to:
F. Carvalho,
filipa@marine.rutgers.edu

Citation:
Carvalho, F., J. Kohut, M. J. Oliver, and O. Schofield (2017), Defining the ecologically relevant mixed-layer depth for Antarctica's coastal seas, *Geophys. Res. Lett.*, *44*, doi:10.1002/2016GL071205.

Received 13 SEP 2016
Accepted 2 JAN 2017
Accepted article online 5 JAN 2017

Defining the ecologically relevant mixed-layer depth for Antarctica's coastal seas

Filipa Carvalho[1], Josh Kohut[1], Matthew J. Oliver[2], and Oscar Schofield[1]

[1]Department of Marine and Coastal Sciences, Rutgers University, New Brunswick, New Jersey, USA, [2]College of Earth, Ocean, and Environment, University of Delaware, Lewes, Delaware, USA

Abstract Mixed-layer depth (MLD) has been widely linked to phytoplankton dynamics in Antarctica's coastal regions; however, inconsistent definitions have made intercomparisons among region-specific studies difficult. Using a data set with over 20,000 water column profiles corresponding to 32 Slocum glider deployments in three coastal Antarctic regions (Ross Sea, Amundsen Sea, and West Antarctic Peninsula), we evaluated the relationship between MLD and phytoplankton vertical distribution. Comparisons of these MLD estimates to an applied definition of phytoplankton bloom depth, as defined by the deepest inflection point in the chlorophyll profile, show that the maximum of buoyancy frequency is a good proxy for an ecologically relevant MLD. A quality index is used to filter profiles where MLD is not determined. Despite the different regional physical settings, we found that the MLD definition based on the maximum of buoyancy frequency best describes the depth to which phytoplankton can be mixed in Antarctica's coastal seas.

1. Introduction

The surface mixed layer is a portion of the upper ocean where turbulent mixing processes form an upper density layer distinct from the layer below. The depth of these layers varies greatly across the world's ocean in time and space and plays an important role in interpreting the environmental factors driving phytoplankton blooms [*Behrenfeld and Boss*, 2014]. Mixed-layer depth (MLD) is therefore a central metric for understanding phytoplankton dynamics [*Sverdrup*, 1953] especially in Antarctica's coastal seas [*Fragoso and Smith*, 2012; *Venables et al.*, 2013]. The depth of the surface mixed-layer can regulate the amount of solar radiation available to the phytoplankton community [*Denman and Gargett*, 1983; *Mitchell et al.*, 1991]. From below, water column stability at the base of the ML has been linked to the flux of nutrients to the surface layer [*Ducklow et al.*, 2007; *Prézelin et al.*, 2000; *Prézelin et al.*, 2004]. A recent study by *Smith and Jones* [2015] showed that vertical mixing and phytoplankton biomass in the Ross Sea are consistent with the critical depth concept formalized by *Sverdrup* [1953]. This critical depth is a function of incoming radiation, which in the poles shows a marked seasonality, and is an important factor controlling phytoplankton dynamics in polar seas [*Smith and Sakshaug*, 2013]. Similar conclusions relating the critical depth hypothesis with phytoplankton growth were found for the West Antarctic Peninsula [*Carvalho et al.*, 2016; *Cimino et al.*, 2016; *Vernet et al.*, 2008].

While seasonal mixed-layers have been widely used to better understand the critical links between the physical structure of the water column and primary production, there are a wide range of methods and metrics used to estimate this important parameter. MLD calculations are based on temperature, salinity, or density. Common methods used in MLD calculations in Antarctic waters are based on either a difference or gradient in the target variable, and every study justifies their specific method. Estimates of MLD from a difference measured at two depths use a range of values. Temperature thresholds vary from 0.8°C [*Kara et al.*, 2000] to 0.2°C [*de Boyer Montégut et al.*, 2004; *Dong et al.*, 2008], while potential density thresholds vary from 0.01 kg m^{-3} [*Smith and Jones*, 2015], 0.03 kg m^{-3} [*Sallée et al.*, 2010], and 0.05 kg m^{-3} [*Venables et al.*, 2013]. The reference depths over which these differences are estimated can vary from the near surface [*Venables et al.*, 2013] to as deep as 10 m [*Smith and Jones*, 2015]. All these differences in criteria and method can potentially yield different estimates of MLD. This is especially troublesome when trying to compare results between studies and distributed seas within which local physical conditions lead to different optimal methods to estimate local MLD. In this study, we use concurrent profiles of hydrography and chlorophyll *a* (chl *a*) fluorescence during the austral spring/summer season in three coastal regions around Antarctica and propose a standard and ecologically relevant metric of

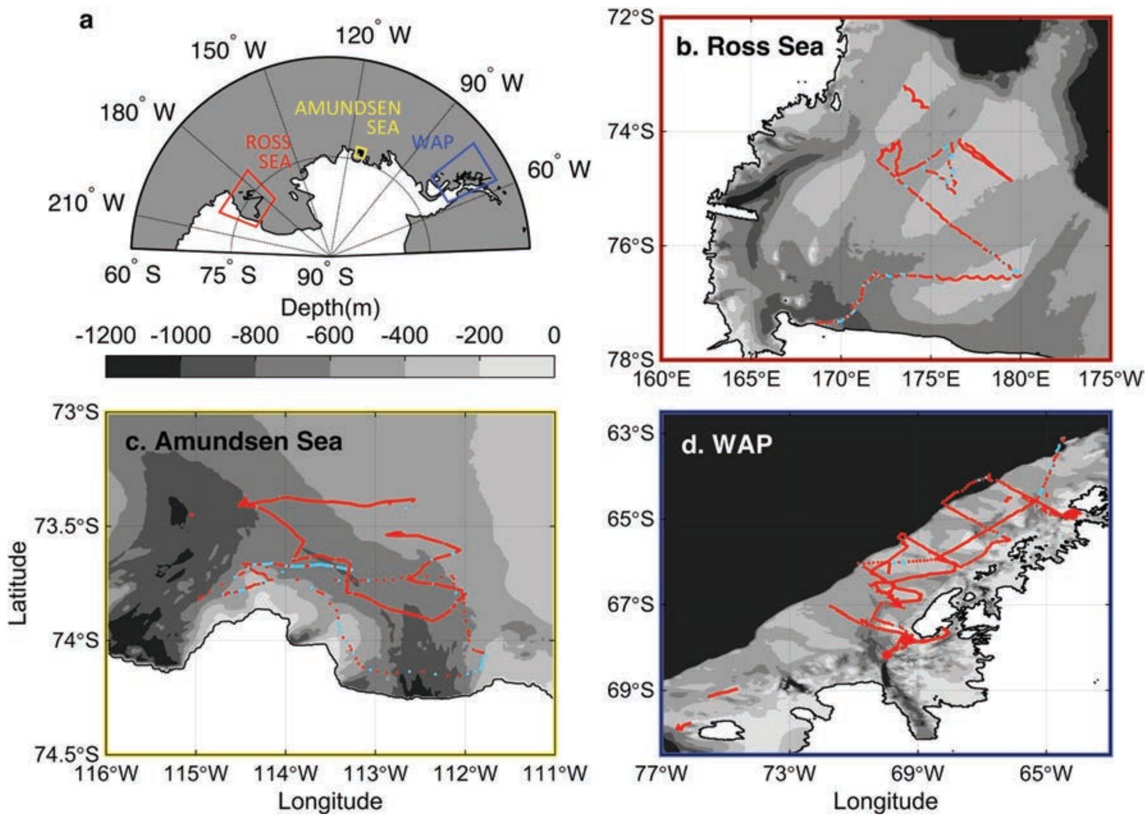

Figure 1. Location of glider data used in the analysis: (a) glider tracks in the three main regions. (b–d) Bathymetry maps overlaid with the detailed location of each individual glider profile (dots) for the regions shown in Figure 1a: (b) Ross Sea, (c) Amundsen Sea, and (d) WAP. Red dots: MLD quality index (QI) > 0.5 (see section 2.2 for details); blue dots: remaining profiles not considered for the MLD analysis (QI < 0.5).

MLD as it consistently captures the lower vertical limit of phytoplankton distribution across the Amundsen Sea (AS), the Ross Sea (RS), and the shelf along the Western Antarctic Peninsula (WAP) that facilitate comparisons between studies.

2. Data and Methods

2.1. Slocum Gliders

Slocum electric gliders are 1.5 m torpedo-shaped buoyancy-driven autonomous underwater vehicles that provide high-resolution surveys of the physical and bio-optical properties of the upper water column [*Schofield et al.*, 2007]. All gliders used in this analysis were equipped with a Seabird conductivity-temperature-depth (CTD) sensor and carried WET Labs Inc. Environmental Characterization Optics (ECO) pucks, which measured chl *a* fluorescence. Glider-based conductivity, temperature, and depth measurements were compared with a calibrated ship CTD sensor on deployment and recovery to ensure data quality, as well as with a calibrated laboratory CTD prior to deployment (as described in *Kohut et al*. [2014]). Each glider profile was averaged into 1 m bins and assigned a midpoint latitude and longitude. Only profiles with 50 bins or more were considered for the analysis. Glider profiles start at 2–4 m depth. In the AS, three missions collected 2247 profiles (December 2010 to February 2011 and January 2015). In the RS, three missions collected 2212 profiles (December 2010 to January 2011). Along the WAP, 26 missions collected 16,673 profiles (December–March, 2009 through 2015). Overall, these data include 21,132 profiles, 465 days at sea and 9836 km flown during the austral spring/summer (Figure 1).

2.2. Mixed-Layer Depth

We evaluated an ecologically relevant MLD definition based on comparisons with concurrent chl *a* fluorescence profiles (described below). We show a detailed analysis on the MLD estimated based

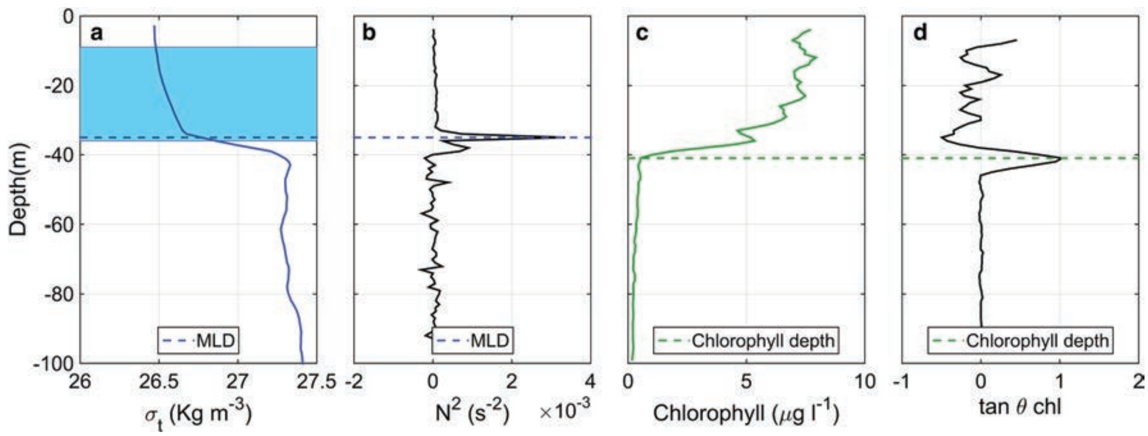

Figure 2. Determination of mixed-layer depth (MLD) and chl *a* depth (Z_{chl}) from a glider profile (located at 64.827°S, 64.286°W at GMT 4:29 on 6 January 2014). (a) Density profile (solid blue line) with MLD (blue dashed line) calculated by max (N^2) and range of MLD (shaded blue) calculated using methods described in Table 1; (b) calculated buoyancy frequency (N^2) profile and MLD; (c) chl *a* profile (solid green line) with Z_{chl} (green dashed line) defined by the maximum angle method [*Chu and Fan*, 2011], or the max ($\tan_{\theta(chl)}$), and (d) calculated $\tan_{\theta(chl)}$ and Z_{chl}.

on the maximum of buoyancy frequency (max(N^2) or stability frequency). For each profile (Figures 2a and 2b), MLD was determined by finding the depth of the maximum water column buoyancy frequency. The same analysis was conducted for the most commonly used estimates of MLD in Antarctica's coastal seas and presented in the supporting information as a comparison against our proposed MLD definition.

The determination of MLD is based on the principle that there is a near-surface layer characterized by quasi-homogeneous properties with a standard deviation of the property within this layer close to zero. Below the MLD, the variance of the property should increase rapidly. To clarify the relationship between MLD and chl *a* in such a high-resolution data set, a quality index (QI) (equation (1)) by *Lorbacher et al*. [2006] was used to evaluate our MLD calculations and filter out profiles where MLD could not be resolved:

$$\mathrm{QI} = 1 - \frac{\mathrm{rmsd}(\rho_k - \overline{\rho})|_{(Z_1, Z_{\mathrm{MLD}})}}{\mathrm{rmsd}(\rho_k - \overline{\rho})|_{(Z_1, 1.5 \times Z_{\mathrm{MLD}})}} \tag{1}$$

where ρ_k is the density at a given depth (k), Z_1 is the first layer near the surface, and rmsd() denotes the standard deviation from the vertical mean $\overline{\rho}$ from Z_1 either to the MLD or $1.5 \times$ MLD. This index evaluates the quality of the MLD computation. Using this, MLDs can be characterized into estimates determined with certainty (QI > 0.8), determined but with some uncertainty ($0.5 <$ QI < 0.8) or not determined (QI < 0.5). Example of profiles for data removed from the analysis (QI < 0.5) can be found in the supporting information (Figure S2). This QI metric does not consider the strength of stratification, just homogeneity of the surface layer above the defined MLD. Therefore, by definition, the MLD estimate is close to the lower boundary of that vertically uniform layer. Following the thresholds set by *Lorbacher et al*. [2006], for the analyses presented in this study, a quality index of 0.5 was used to reasonably warrant a calculation of MLD. The quality index threshold of 0.5 was determined based on the insensitivity of the slope of the trend lines using higher QI values (0.8).

Apart from the depth of the ML, stratification also plays an important role in phytoplankton dynamics [*Holm-Hansen and Mitchell*, 1991; *Mitchell et al*., 1991]. The differences in the vertical physical structure setting seen in the temperature (T) and salinity (S) plots (Figure 3) result in differences in stratification. To identify the profiles with the highest stability at the base of the MLD in each region, stability was normalized independently for each region by dividing the buoyancy frequency at the base of MLD of that profile by the regional average of buoyancy frequency at the base of the MLD. The normalized stability was calculated to find the magnitude of each point as it relates to the overall stability in each region. This allows the regional differences due to the vertical structure of the water column to be removed.

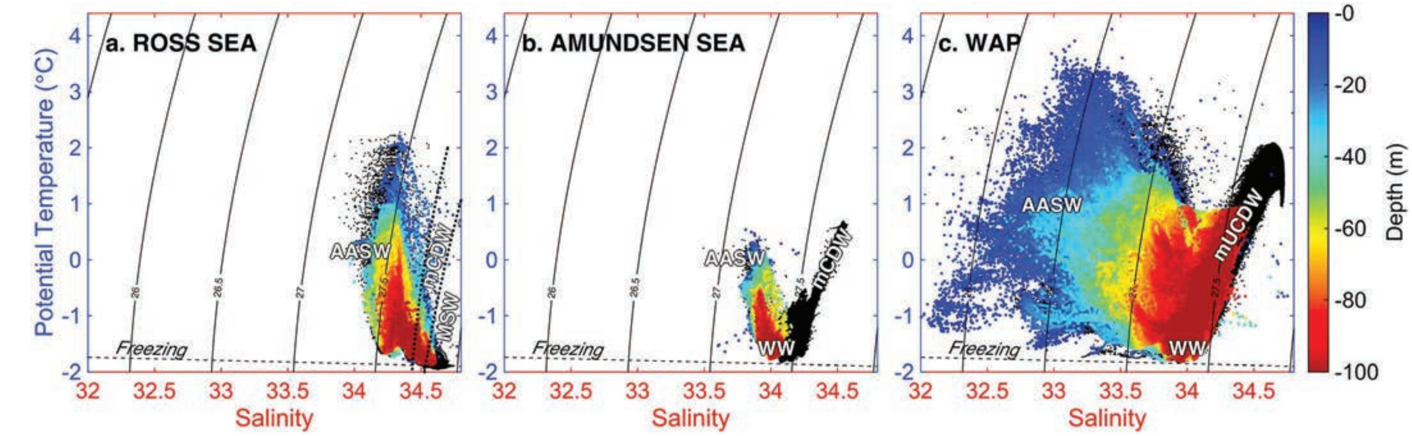

Figure 3. The θ-S scatters plots for all three areas shown in Figure 1: (a) Ross Sea, (b) Amundsen Sea, and (c) WAP. Color indicates depth of the water column measurement in the upper 100 m of the water column. All data between 100 and 1000 m are plotted in black. Primary water masses sampled are indicated and labeled (WW = Winter Water; MSW = Modified Shelf Water; AASW = Antarctic (summer) Surface Water; mUCDW = modified Upper Circumpolar Deep Water.

2.3. Chlorophyll *a* Fluorescence

Chl *a* fluorescence, as measured by the glider ECO pucks, is our indicator of phytoplankton biomass. Discrete in situ water samples were collected from several depths from casts during each glider deployment and recovery. Water samples were filtered onto 25 mm Whatman GF/F filters and extracted using 90% acetone, and chl *a* concentration was then measured using a fluorometer. For each deployment, the structure and magnitude of chl *a* measured by the glider puck was verified against both the independent discrete measurements and an independent calibrated fluorometer deployed from a collocated ship station. While the complex relation between fluorescence versus biomass was not fully evaluated, we provide an accurate characterization of the observed fluorescence, fully realizing that our measurements may not accurately represent phytoplankton biomass. Also, since our analysis focuses on the bottom of the phytoplankton biomass layer, daily nonphotochemical quenching of chl *a* fluorescence is not a factor in our analysis.

Following a method adapted from the maximum angle principle used to calculate MLD [*Chu and Fan*, 2011], the depth of lower boundary of chl *a* was estimated, referred to as chlorophyll depth (Z_{chl}) in the analysis. This method is based on three main steps: (1) fitting the profile data with a vector (pointing downward and with n points) from shallower depths to a certain depth k and a second vector from that depth to deeper depth ($k + 1 + n$); (2) identifying the tangent angle ($\tan_\theta$) between the two vectors for each depth k; and (3) defining the MLD by determining the maximum angle in each profile. Here we apply the same principle using the maximum angle, as we are interested in calculating the depth of the deepest inflection point in the chl *a* profile. Using a vector of $n = 7$ data points, the depth of the max($\tan_\theta$) of the chl *a* profile was determined and used as the Z_{chl} (Figures 2c and 2d). A quality index (QC) (equation (2)) was also applied to the chlorophyll data to evaluate the Z_{chl} computation. A modification to equation (1) was made to account for the homogeneity occurring below the Z_{chl} and not above:

$$\mathrm{QC} = 1 - \frac{\mathrm{rmsd}\left(\mathrm{CHL}_k - \overline{\mathrm{CHL}}\right)\big|_{(Z_{\mathrm{chl}}, Z_D)}}{\mathrm{rmsd}\left(\mathrm{CHL}_k - \overline{\mathrm{CHL}}\right)\big|_{(Z_D - 1.5(Z_D - Z_{\mathrm{chl}}),\ Z_D,)}} \qquad (2)$$

As both variables have errors in them and linear relationships are expected between both variables [*Holm-Hansen and Mitchell*, 1991; *Mitchell et al.*, 1991], model 2 regressions were applied to concurrent MLD and Z_{chl} calculations to evaluate the MLD determination of the definitions chosen by comparing it to a 1:1 line.

3. Results and Discussion

Each region had a different distribution of water masses as indicated in temperature (*T*) and salinity (*S*) space (Figure 3). Surface water in the RS and AS were similar, but quite different from the WAP while at depth, AS and WAP showed similarities. Compared to the WAP, both Ross and Amundsen Seas showed overall colder and saltier waters with the latter being on average saltier. The warmer, saltier and deep modified Upper

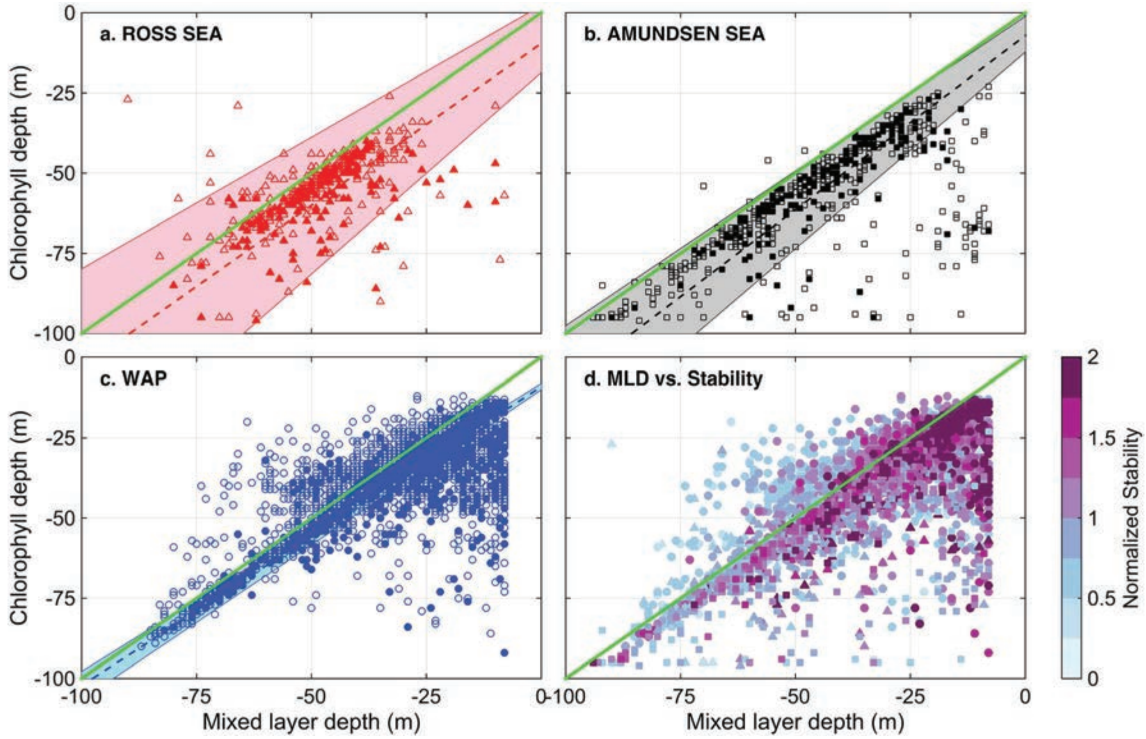

Figure 4. Correlation between MLD and Z_{chl} for all glider profiles with quality index (QI) over 0.5 (open marker) and over 0.8 (filled marker) for all three regions: (a) Ross Sea (triangle); (b) Amundsen Sea (square); (c) WAP (circle); (d) comparison between all three Antarctic regions (QI > 0.5) with normalized stability frequency colored. Ninety-five percent confidence intervals (shaded area) and model 2 regression line are shown for QI > 0.8 (dashed line). A quality index of 0.5 was also applied to chl *a* (QI_{chl}) profiles, and only profiles with $QI_{chl} > 0.5$ are shown above. Line 1:1 is shown in green.

Circumpolar Deep Water (mUCDW) found at shallower depths in the WAP was not seen in the upper 100 m (colored dots in Figure 3) in RS and AS. In both the latter regions, T_{min} was found generally in the deepest sampled waters (red). The WAP (Figure 3c), with the widest range of T-S properties as it is located at lower latitudes, spans entire seasonal cycles due to more sustained sampling and is more influenced by coastal inputs.

We compared our MLD estimation based on N^2 and chlorophyll depth, described in section 2.3, across each of the coastal regions. Profiles with QI and QC values less than 0.5 [*Lorbacher et al.*, 2006] were removed as MLD and Z_{chl} were not clearly defined. The remaining profiles were characterized as "estimated with uncertainty" ($0.5 < QI < 0.8$; Figure 4, open markers) and "estimated with certainty" ($QI > 0.8$; Figure 4, filled markers). A linear, model 2 regression was applied to each regional data set, and the line and corresponding R^2 are reported in the supporting information (Table S2). Although some regional differences were found in the MLD ranges, all three regions showed an MLD-chl *a* relationship close to 1:1 with 95% confidence (compare dashed trend lines with green), i.e., the deeper the MLD, the deeper the lower boundary of the chl *a* profile. The observed differences in the depth of the ML across regions (Figure 4) were mostly influenced by the timing of the measurements, i.e., uneven sampling in time in different regions. Nevertheless, the MLD calculations are within range of those reported for each region [*Schofield et al.*, 2015; *Smith et al.*, 2014; *Vernet et al.*, 2008].

Given the disproportionately greater number of profiles collected in the WAP (Figure 4c), this region showed the widest range of MLDs estimated with certainty ($QI > 0.8$) of all three regions, ranging from 8 to 65 m of depth. It showed, on average, the shallowest MLD ($\overline{MLD}$ = -33 m ± 13) and a trend line ($y = 0.93175x - 9.0415$; $R^2 = 0.82$; $p < 0.0001$) close to the 1:1 line (green line). The RS (Figure 4a) showed the deepest MLD ($\overline{MLD}$ = -49 m ± 9), but regardless, the relationship between MLD and chl *a* ($y = 1.0098x - 9.5745$; $R^2 = 0.60$; $p < 0.0001$) was similar to those seen in the other two regions. The AS that exhibited the smallest number of data points, however, showed a high R^2 ($y = 1.0849x - 7.125$; $R^2 = 0.78$;

Table 1. Examples of Criteria Used to Define MLD in Waters Around Antarctica

Author	Area studied	MLD Threshold Criterion
Kara et al. [2000]	Global ocean	$\Delta T = 0.8°C \Delta\sigma_\theta = \sigma_\theta (T + \Delta T,S) - \sigma_\theta (T,S)$ with $\Delta T = 0.8°C$
de Boyer Montégut et al. [2004]	Global ocean	$\Delta T = 0.2°C \Delta\sigma_\theta = 0.03$ kg m^{-3}
Dong et al. [2008]	Southern Ocean (open ocean)	$\Delta\rho = 0.03$ kg m^{-3} $\lvert\Delta T\rvert = 0.2°C$
Sallée et al. [2010]	Southern Ocean (open ocean)	$\Delta\sigma_\theta = 0.03$ kg m^{-3}
Long et al. [2012]	Ross Sea	$\Delta\sigma_\theta = 0.05$ kg m^{-3}
Smith and Jones [2015]	Ross Sea	$\Delta\sigma_\theta = 0.01$ kg m^{-3}
Fragoso and Smith [2012]	Ross and Amundsen Seas	$\Delta\sigma_\theta = 0.01$ kg m^{-3}
Schofield et al. [2015]	Amundsen Sea	max(N^2)
Vernet et al. [2008]; *Prézelin et al.* [2004]	WAP	Not specified
Venables et al. [2013]	Margarite Trough (WAP)	$\Delta\sigma_\theta = 0.05$ kg m^{-3}
Moline et al. [1997]; *Cimino et al.* [2016]	Anvers Island (WAP)	max($\partial\rho/\partial z$)
Walsh et al. [2001]	Northern WAP	Not specified
Mitchell and Holm-Hansen [1991]	SW Bransfield Strait (WAP) and Drake Passage	$\Delta\sigma_\theta = 0.05$ kg m^{-3} (in 5 m window)

$p < 0.0001$) for both quality indices used. This region shows again a wider range of MLD comparatively to the Ross Sea, but has also, on average, deeper MLDs ($\overline{MLD}$ = -41 m ± 13) than the WAP. All three regions showed slopes not significantly different than the 1:1 line (Table S2).

Comparing the trends obtained using both indices (QI > 0.8 compared to QI > 0.5, corresponding to 26–31% and 80–87% of the profiles, respectively) showed little differences (Table S2). Higher QIs are observed during summer and fall, where sharp gradients at the base of the seasonal mixed layer are present [*Lorbacher et al.*, 2006]. A maximum MLD difference of 3 m for the AS was observed when using QI > 0.5 compared to a higher MLD quality index, QI > 0.8; and overall, this difference was much smaller for the remaining two regions. This ensures that even though we are using a lower quality index to include more data in the analysis (QI > 0.5, the minimum threshold set by *Lorbacher et al.* [2006] for determining MLD), we are capturing the same patterns. Points that are closer to the trend line show, on average, much higher water stability (Figure 4d), with the shallowest MLD showing the highest water stability due to freshwater input from meltwater [*Martinson and Iannuzzi*, 1998]. Since our gliders measurements start at a minimum of 2 m depth and our Z_{chl} computation relies on a 7-point vector, it was not possible to evaluate the biophysical relationship in this study within the upper 7 m. This is a constraint on our method of evaluating the correlation between MLD and chlorophyll depth and not on the actual MLD determination. Studies in the region have also shown that most Z_{chl} occur deeper than 7 m [*Moline et al.*, 1997; *Smith et al.*, 2013]. Note that, as this method captures the maximum stability frequency of the water column profile, its accuracy depends both on the vertical resolution and the vertical extent of the measurements. This is especially important in the presence of meltwater lenses in the surface layer, which our gliders were not able to capture. This method relies on the implicit assumption of a two-layer ocean. Cases where the surface ocean has a well-defined (and deeper) ML and a surface active mixing layer [*Brainerd and Gregg*, 1995], this method will capture the depth of the strongest water column stability and therefore a lower QI may be determined based on this two-step surface ML if the base of the ML has a stronger N^2 value.

To determine the value of our combined method linking physical MLD with chl *a* depth, we evaluated several MLD methodologies. The most commonly used MLD criteria in polar waters (Table 1) were tested for each individual profile and matched against the Z_{chl}. The range of MLD calculated using the different criteria are presented for a representative profile as the shaded area in Figure 2a.

Using a model 2 linear regression, we were able to evaluate the various MLD definitions (Table S1 and Figure S1 in the supporting information) and concluded that the most ecologically relevant MLD determination method across all regions based on the strength of the correlation with the lower boundary of the chl *a* profile was the maximum of buoyancy frequency (section 2).

Independent of the different water mass compositions and dynamics present in each region, the biophysical relationship between MLD and chl *a* remains the same in all three regions. With slopes not significantly different from the 1:1 line (within the 95% confidence intervals of the model 2 regression fit) in all three regions suggests that the MLD definition we are using is a good predictor of the depth of the inflection point in the chl *a* profile (lower boundary of the chl *a* patch in the water column) and is therefore an important parameter in phytoplankton dynamics studies.

4. Conclusions

Understanding the spatial and temporal variability of phytoplankton is important, especially to assess ecological dynamics of marine food webs. Historically different MLD calculations have been applied in Antarctic continental shelves and linked to phytoplankton dynamics [*Mitchell and Holm-Hansen*, 1991; *Smith and Jones*, 2015; *Vernet et al*., 2008]. These calculations were based on different subjective thresholds (sometimes linked to local hydrography) for the same regions. This leads to significant variability in MLD estimations, making comparisons between studies and regions problematic. MLDs calculated from buoyancy frequency were similarly correlated with our adapted estimate of Z_{chl} across all three coastal regions. Given the variability in water mass distribution and volume between the RS, AS, and along the WAP, this biophysical relationship was similar in all regions, which suggests that the maximum of stability frequency (or max(N^2)) is an appropriate and robust metric to compare and contrast biophysical processes across all three Antarctic regions.

Acknowledgments
We thank the crews of R/V Nathaniel B. Palmer, ARSV Laurence M. Gould, R/V Araon, Palmer Station support staff, and the Rutgers glider team for facilitating our long-term data collection efforts. We also wish to thank five anonymous reviewers for their suggestions regarding the analysis in this paper. The research was supported by the National Science Foundation grants ANT-0823101 (Palmer-LTER), ANT-1327248, and ANT-1326541 (CONVERGE), ANT-0839039 (SEAFAReRS), ANT-0838995 (ASPIRE), and the Korean Polar Research Institute grant PP1502 (KOPRI). Filipa Carvalho was funded by a Portuguese doctoral fellowship from Fundação para a Ciência e Tecnologia (DFRH - SFRH/BD/72705/2010). Glider data can be accessed at ERDDAP server at http://erddap.marine.rutgers.edu/erddap/info/.

References

Behrenfeld, M. J., and E. S. Boss (2014), Resurrecting the ecological underpinnings of ocean plankton blooms, *Annu. Rev. Mar. Sci.*, *6*, 167–194.

Brainerd, K. E., and M. C. Gregg (1995), Surface mixed and mixing layer depths, *Deep Sea Res., Part I*, *42*(9), 1521–1543.

Carvalho, F., J. Kohut, M. J. Oliver, R. M. Sherrell, and O. Schofield (2016), Mixing and phytoplankton dynamics in a submarine canyon in the West Antarctic Peninsula, *J. Geophys. Res. Oceans*, *121*, 5069–5083, doi:10.1002/2016jc011650.

Chu, P. C., and C. W. Fan (2011), Maximum angle method for determining mixed layer depth from seaglider data, *J. Oceanogr.*, *67*(2), 219–230, doi:10.1007/s10872-011-0019-2.

Cimino, M. A., M. A. Moline, W. R. Fraser, D. L. Patterson-Fraser, and M. J. Oliver (2016), Climate-driven sympatry may not lead to foraging competition between congeneric top-predators, *Sci. Rep.*, *6*, doi:10.1038/srep18820.

de Boyer Montégut, C., G. Madec, A. S. Fischer, A. Lazar, and D. Iudicone (2004), Mixed layer depth over the global ocean: An examination of profile data and a profile-based climatology, *J. Geophys. Res.*, *109*, C12003, doi:10.1029/2004JC002378.

Denman, K., and A. Gargett (1983), Time and space scales of vertical mixing and advection of' phytoplankton in the upper ocean, *Oceanography*, *28*(5), 801–815.

Dong, S., J. Sprintall, S. T. Gille, and L. Talley (2008), Southern Ocean mixed-layer depth from Argo float profiles, *J. Geophys. Res.*, *113*, C06013, doi:10.1029/2006JC004051.

Ducklow, H. W., K. Baker, D. G. Martinson, L. B. Quetin, R. M. Ross, R. C. Smith, S. E. Stammerjohn, M. Vernet, and W. Fraser (2007), Marine pelagic ecosystems: The west antarctic peninsula, *Philos. Trans. R. Soc. Lond. B Biol. Sci.*, *362*(1477), 67–94.

Fragoso, G. M., and W. O. Smith (2012), Influence of hydrography on phytoplankton distribution in the Amundsen and Ross Seas, Antarctica, *J. Mar. Syst.*, *89*(1), 19–29, doi:10.1016/j.jmarsys.2011.07.008.

Holm-Hansen, O., and B. Mitchell (1991), Spatial and temporal distribution of phytoplankton and primary production in the western Bransfield Strait region, *Deep Sea Res. Part A. Oceanogr. Res. Pap.*, *38*(8), 961–980.

Kara, A. B., P. A. Rochford, and H. E. Hurlburt (2000), An optimal definition for ocean mixed layer depth, *J. Geophys. Res.*, *105*, 16,803–16,821, doi:10.1029/2000JC900072.

Kohut, J., C. Haldeman, and J. Kerfoot (2014), Monitoring dissolved oxygen in New Jersey Coastal waters using autonomous gliders, *Tect. EPA/600/R-13/180*, U.S. Environmental Protection Agency, Washington, D. C.

Long, M. C., L. N. Thomas, and R. B. Dunbar (2012), Control of phytoplankton bloom inception in the Ross Sea, Antarctica, by Ekman restratification, *Global Biogeochem. Cycles*, *26*, GB1006, doi:10.1029/2010GB003982.

Lorbacher, K., D. Dommenget, P. P. Niiler, and A. Köhl (2006), Ocean mixed layer depth: A subsurface proxy of ocean-atmosphere variability, *J. Geophys. Res.*, *111*, C07010, doi:10.1029/2003JC002157.

Martinson, D. G., and R. A. Iannuzzi (1998), Antarctic Ocean-Ice Interaction: Implications from Ocean Bulk Property Distributions in the Weddell Gyre, in *Antarctic Research Series, Antarctic Sea Ice: Physical Processes, Interactions and Variability*, edited by M. Jeffries, pp. 243–271, AGU, Boston, Mass.

Mitchell, B. G., and O. Holm-Hansen (1991), Observations of modeling of the Antartic phytoplankton crop in relation to mixing depth, *Deep Sea Res. Part A. Oceanogr. Res. Pap.*, *38*(8), 981–1007.

Mitchell, B. G., E. A. Brody, O. Holm-Hansen, C. McClain, and J. Bishop (1991), Light limitation of phytoplankton biomass and macronutrient utilization in the Southern Ocean, *Limnol. Oceanogr.*, *36*(8), 1662–1677.

Moline, M. A., B. B. Prezelin, O. Schofield, and R. C. Smith (1997), Temporal dynamics of coastal Antarctic phytoplankton: Environmental driving forces and impact of 1991/92 summer diatom bloom on the nutrient regimes, in *Antarctic Communities: Species, Structure and Survival*, edited by B. Battaglia, J. Valencia, and D. W. H. Walton, pp. 67–72, Cambridge Univ. Press, Cambridge.

Prézelin, B. B., E. E. Hofmann, C. Mengelt, and J. M. Klinck (2000), The linkage between Upper Circumpolar Deep Water (UCDW) and phytoplankton assemblages on the west Antarctic Peninsula continental shelf, *J. Mar. Res.*, *58*(2), 165–202.

Prézelin, B. B., E. E. Hofmann, M. Moline, and J. M. Klinck (2004), Physical forcing of phytoplankton community structure and primary production in continental shelf waters of the Western Antarctic Peninsula, *J. Mar. Res.*, *62*(3), 419–460.

Sallée, J. B., K. G. Speer, and S. R. Rintoul (2010), Zonally asymmetric response of the Southern Ocean mixed-layer depth to the Southern Annular Mode, *Nat. Geosci.*, *3*(4), 273–279, doi:10.1038/ngeo812.

Schofield, O., et al. (2007), Slocum gliders: Robust and ready, *J. Field Robot.*, *24*(6), 473–485, doi:10.1002/rob.20200.

Schofield, O., T. Miles, A.-C. Alderkamp, S. Lee, C. Haskins, E. Rogalsky, R. Sipler, R. M. Sherrell, and P. L. Yager (2015), In situ phytoplankton distributions in the Amundsen Sea Polynya measured by autonomous gliders, *Elementa: Sci. Anthropocene*, *3*(1), 000,073.

Smith, W., and R. M. Jones (2015), Vertical mixing, critical depths, and phytoplankton growth in the Ross Sea, *ICES J. Mar. Sci.: J. du Conseil*, *72*(6), 1952–1960, doi:10.1093/icesjms/fsu234.

Smith, W., and E. Sakshaug (2013), 9. Polar phytoplankton, in *Polar Oceanography: Chemistry, Biology, and Geology*, edited by W. Smith, pp. 477–526, Acad. Press, San Diego, Calif.

Smith, W., S. Tozzi, M. C. Long, P. N. Sedwick, J. A. Peloquin, R. B. Dunbar, D. A. Hutchins, Z. Kolber, and G. R. DiTullio (2013), Spatial and temporal variations in variable fluoresence in the Ross Sea (Antarctica): Oceanographic correlates and bloom dynamics, *Deep Sea Res., Part I*, *79*, 141–155.

Smith, W., D. G. Ainley, K. R. Arrigo, and M. S. Dinniman (2014), The oceanography and ecology of the Ross Sea, *Annu. Rev. Mar. Sci.*, *6*, 469–487.

Sverdrup, H. (1953), On conditions for the vernal blooming of phytoplankton, *J. Conseil*, *18*(3), 287–295.

Venables, H. J., A. Clarke, and M. P. Meredith (2013), Wintertime controls on summer stratification and productivity at the western Antarctic Peninsula, *Limnol. Oceanogr.*, *58*(3), 1035–1047.

Vernet, M., D. Martinson, R. Iannuzzi, S. Stammerjohn, W. Kozlowski, K. Sines, R. Smith, and I. Garibotti (2008), Primary production within the sea-ice zone west of the Antarctic Peninsula: I—Sea ice, summer mixed layer, and irradiance, *Deep Sea Res., Part II*, *55*(18-19), 2068–2085, doi:10.1016/j.dsr2.2008.05.021.

Walsh, J. J., D. A. Dieterle, and J. Lenes (2001), A numerical analysis of carbon dynamics of the Southern Ocean phytoplankton community: The roles of light and grazing in effecting both sequestration of atmospheric CO2 and food availability to larval krill, *Deep Sea Res., Part I*, *48*(1), 1–48.

Flight Dynamics of Slocum Gliders in Intermediate-Water Hurricane

Rutgers University Center for Ocean Observing Leadership (RU COOL)

Cassidy Gonzalez-Morabito, David Aragon, Travis Miles, Josh Kohut, Scott Glenn
Rutgers University Department of Marine & Coastal Sciences
New Brunswick, NJ
Cmg348@rutgers.edu Dkaragon@marine.rutgers.edu

***Abstract*— The new and emerging use of Slocum gliders in oceanographic data collection has brought about a progressive new way to record in-situ oceanic data. This piece of technology has been used by the Rutgers University Department of Marine Science through over 400 deployments, including a deployment during Hurricane Sandy in late October 2012. Data being collected during this deployment was done by Slocum glider RU23, which recorded measurements such as backscatter, fluorescence, water velocity, conductivity, temperature and depth. The dynamics of water motion RU23 flew in caused an unforeseen additional dataset to be collected by the glider. Because RU23 flew during intermediate type ocean waves, the orbital motion of the water potentially caused fluctuations seen in the dive and climb profiles of RU23's pressure record. Analysis can be done on the signal seen in the pressure record, by viewing its pressure fluctuation in the frequency spectrum. From this, wave period can be extracted. Accuracy of the glider's extracted wave period will be done by comparing the glider wave period to recorded wave period done by nearby NDBC buoys. Also analyzed was the glider's response to the turbulent water dynamics gauged by its performance in its attitude measurements.**

***Keywords*—Slocum gliders; intermediate-water hurricane; wave period; particle motion; power spectral density analysis**

I. INTRODUCTION

Due to its higher latitude, the New Jersey region historically has a low probability of being hit with a major hurricane. With only three category 1 hurricanes (74-95 mph wind speeds) hitting the New Jersey region in the past century, it is no surprise that Hurricane Sandy of late October 2012 was given the name 'Superstorm Sandy'. At its peak, Sandy was classified as a category 3 hurricane, and when it made landfall in New Jersey, it had wind speeds recorded around 80mph. An unusual characteristic of Hurricane Sandy was its perpendicular path to the eastern coast when it made landfall in New Jersey, meaning the storm moved inland cross-shelf, vs. parallel to the coastline. Statistical simulations show Hurricane Sandy's actual path having a probability of happening once every 700 years [1]. This hurricane was the most destructive and one of the rarest natural disasters New Jersey has faced on record, while also being the second costliest hurricane in United States history. Its infliction of billions of dollars' worth of damage includes 346,000 homes being destroyed and erosion across the entire New Jersey coastline [2].

To mitigate the intensity uncertainty associated with these hurricanes and tropical cyclones, Rutgers University's COOL group (Center for Ocean Observing Leadership) deploys Teledyne Webb Research Slocum gliders during these events to collect oceanographic data about the storm. From CTDs measuring conductivity, temperature & depth, to acoustic current profilers, measuring water column current profiles, to ECO (Environmental Characterization Optics) pucks measuring fluorescence, backscatter, and more, the Slocum gliders provide a plethora of in-situ data to be used and distributed throughout the oceanographic and meteorological community. Rutgers has utilized the capabilities of oceanographic observing with gliders in all 7 continents, from Antarctica to Svalbard, Norway. Though using gliders for science is relatively new, this new perspective of the oceanic and atmospheric interaction can help further improve hurricane forecasting and data collecting.

Operating gliders in storm conditions, notably intermediate water conditions, which is based off of water depth and wavelength, has brought about observations concerning the gliders flight dynamics. How well the glider flies, ways to improve this flight for future, and measurements derived from how the glider and the surrounding water interact will be the focus of this paper. This paper will review how well Slocum glider 'RU23' flew during Hurricane Sandy by looking statistically at how much has changed in its flight dynamics before, during, and after the storm passed over the glider. Also to be discussed will be new variables, such as dominant wave period, which can potentially be derived from the gliders unique flight dynamics during intermediate water storms. This will be done by assessing the frequency spectrum of the signal caused by the passing wave in RU23s pressure record. From this, the dominant wave period can be extracted for each dive and climb profile this signal is present in, and a time series of wave period can be created. This time series will be compared to nearby National Oceanic and Atmospheric Association (NOAA) National Data Buoy Center (NDBC) stations and an assessment of the extracted wave period from RU23 will be done. Finally, this paper will review the limits of acquiring wave period from Slocum gliders based off the required environment conditions, the sampling rate of the glider, and more.

II. METHODS

A. Slocum Gliders

978-0-692-94690-9/$31.00 ©2017 MTS

Gliders are remotely operated underwater vehicles which have become an important tool concerning oceanographic data collection. They can be deployed remotely and can continue to be controlled from a desktop computer in the comfort of an office or home. They are essential when during dangerous and long duration missions, like collecting data during hurricanes or sampling in the middle of the ocean 1000 meters deep, as a human not need be present for this piece of technology to be operated. A glider will sample a planned mission autonomously until it is complete, while sending a mission report periodically as an update to its flight engineer. This is to benefit during a storm where loss of contact due to high waves becomes prevalent.

Slocum gliders also have the opportunity to be customized to a mission's needs. If the turbidity of the water must be measured during a mission, the glider can be equipped with an ECO puck and measure exactly this. On the other hand, if this measurement is not needed for a subsequent mission, the ECO puck can be removed, or turned off to conserve battery. The way a Slocum glider moves and collects data is primarily through a change in density, ascending and descending the height of the water column to a predetermined depth. The flight path of a Slocum glider thus looks similar to a zig-zagged triangle profile, as seen as the black line in Fig. 5.

Before Hurricane Sandy hit New Jersey, Slocum glider RU23 was deployed at 19:44 UTC on 25 October 2012 from Rutgers University for approximately 10.92 days, until 17:44 UTC on 5 November 2012. During its deployment, RU23 was equipped to measure CDOM (colored dissolved organic matter), chlorophyll, fluorescence, backscatter (700 nm), temperature, conductivity, and depth, and was outfitted with an Aquadopp current meter. Some differences will arise in the way data are collected by the glider due to there being two computers operating the glider. The two data collection methods are first through the science bay computer, collecting scientific data such as CDOM and current velocities, and second through the flight controller, collecting engineering and flight performance data such as pitch and roll. This causes repeated measurements, such as for time, and depth, with different sampling rates — an average sampling rate of 2.02 seconds for science bay and an approximate sampling rate of 4-5 seconds for flight bay.

B. *Statistical Analysis*

Statistical analysis of the collected data from RU23 is done in MATLAB. RU23's DbdGroup is loaded into MATLAB and the "not a number" (NaN) data points are filtered accordingly. Next, a two-dimensional grid, using the array of time, from RU23's collected data during the entirety of its Hurricane Sandy mission, and the array of water depth, from the top inflection depth to the bottom inflection depth per profile, is created to produce the coordinates of a rectangular grid. After this, an analyzed moving window standard deviation function is applied. This function creates a size 3 windowed standard deviation of the statistical array to be analyzed (i.e. this will find a moving standard deviation of pitch or roll during RU23's flight). The size of the window is determined by the appropriate amount of smoothing required to analyze this dataset. The statistic gridded on a time and depth axis can now be plotted using colored plots to be analyzed in upcoming sections of this paper.

C. *Wave Type and Particle Motion*

Wave theories will be used to determine the type of wave motion felt by RU23 during its Hurricane Sandy mission. The trajectories of a particle's motion, induced by a wave, is dependent on the wave type. The limits of applicability of types of waves will be bases off the book, *Introduction to Physical Oceanography* by John A. Knauss, and Newell Garfield. In this book, it is stated that the limits of applicability depend on the ratio of depth of water 'h' to wave length 'L' as shown in Fig. 1 [3]. The ratio of water depth to wavelength must be greater than 0.25 to be classified as a deep-water wave, whereas this ratio must be less than 0.05 to be classified as a shallow-water wave. If the ratio falls in between the previous two, from 0.25 to 0.05, the wave is classified as an intermediate-water wave.

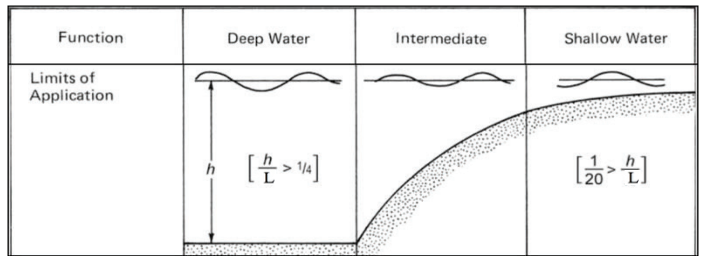

Figure 1: Limits of applicability for determining the classification of a wave [3]. Wavelength is represented as 'L' and water depth is represented as 'h'.

The average water depth RU23 flew in during its Hurricane Sandy mission was approximately 43 meters (approximately 141 feet), according to the total water column depth data collected from RU23. The closest NDBC buoy to RU23, station 44025, recorded the average wave period as 12.14 seconds. These data used to determine this average were collected and made freely available by the NOAA NDBC. The wave period calculated from the NDBC buoy is the average wave period over the number of days a signal from Hurricane Sandy is present in RU23's data, from approximately 05:48 UTC on 29 Oct 2012 to the 21:32 UTC on 30 Oct 2012. From this, the ratio of water depth to wavelength can be approximated using methods from the Shore Protection Manual [4]. Initially, a deep-water wavelength, L_0 must be calculated using the following equation:

$$L_0 = \frac{g \cdot T^2}{2\pi} \tag{1}$$

In (1), T is the known wave period, 12.14 seconds, and g is the gravitational acceleration constant, 9.81 m/sec^2 (32.2 ft/sec^2). Solving gives the deep-water wavelength (L_0) equal to 230.19m (755.23 feet). Next, the water depth to deep-water wavelength ratio (h/L_0) can be calculated as 0.19, using 43 meters (141.1 feet) as h. An approximation can now be determined graphically for the ratio of wavelength to water depth as a function of h/L_0 by referencing a figure from *Coastal Protection* not shown in this paper [5]. This gives a ratio as approximately h/L = 0.20, therefore, RU23 felt intermediate-water waves during its Hurricane Sandy mission. Further investigation into determining the wave period in the pressure record from RU23 will be done under the conclusion that RU23s mission was performed in intermediate-type waves.

The characteristics of motion a particle will feel in deep, intermediate, and shallow water waves differs in shape, from circular to elliptical, as shown in Fig. 2 [3, 6]. In an intermediate-water scenario, the shape is elliptical, with the minor radius decaying with depth until it reaches zero. The major radius will also decay with depth, but does not reach zero. This wave signal increases intensity with depth, as shown in Fig. 3, as the elliptical motion shape horizontally flattens more greatly with depth. The Results section will discuss this concept in more detail. The signal received in the pressure record from RU23 will be what is analyzed and compared to NDBC buoys. Shown in the left subplots of Fig. 3 is a typical dive profile of depth for a Slocum glider. As the sample number representing time progressed, the glider descends in depth on a fairly straight dive plane. However, noticed during Hurricane Sandy the pressure record becomes erratic. We surmise that this is from the types of motion induced by the wave field above the glider and wish to analyze the resulting pressure record fluctuation through frequency analysis.

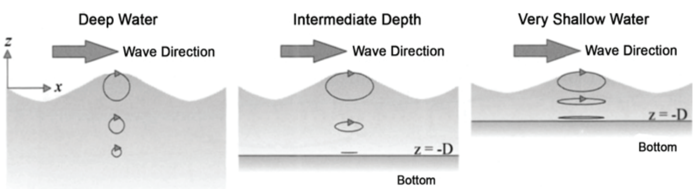

Figure 2: Orbital motion of a particle in deep, intermediate, and shallow water type waves. 'z' represents bottom depth and 'D' represents depth in water column [6].

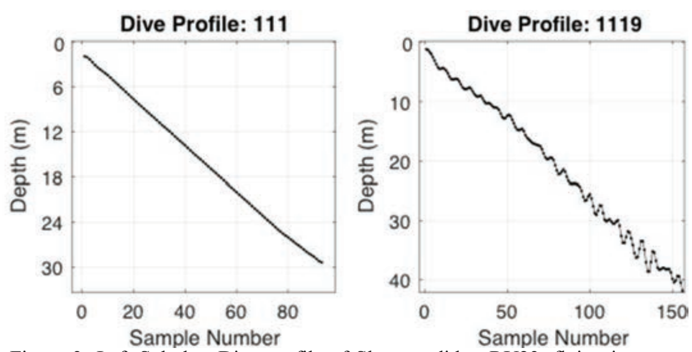

Figure 3: Left Subplot: Dive profile of Slocum glider, RU23, flying in water undisturbed by waves. Right Subplot: Dive profile of RU23 flying in intermediate-type waves, which signal is present in pressure data.

D. Signal Processing

The frequency analysis of the periodic signal, present in RU23's pressure data, is extracted and analyzed using Welch's overlapped averaging estimator. A power spectral density for the pressure record, recorded by the science bay, is determined for each dive and climb profile RU23 performed, using the function 'pwelch' from MATLAB. Inputs into this function are determined individually based on characteristics of each profile to limit bias.

Once the power spectral density is found per profile, a filter is applied to determine the dominant wave period felt during the dive or climb. This filter removes the signal created from the inflection and deflection pattern of the glider's vertical flight path. A demonstration of this power spectrum density plot for dive profile 1119, before the filter is applied, is shown in Fig. 4, where 'f' is the frequency. Here, it can be seen that the dominant signal is 15.6 seconds, or 0.6Hz.

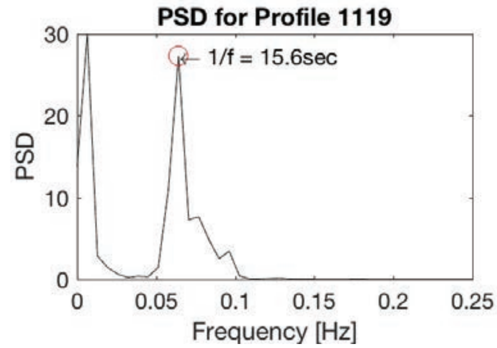

Figure 4: Power spectral density for the signal found in the pressure record of profile 1119 from RU23. 'f' indicated frequency. The circled peak correlates to a recorded signal of 15.6 seconds.

III. Results

A. Glider Performance

Understanding the dynamics of the Slocum gliders flight performed during its mission is important for understanding the data the glider collects. Some background information must be established first. The pitch, roll, and yaw of an aeronautical vehicle are the principle axis of rotation. The pitch of a Slocum glider can be controlled via adjusting a weight in the fore of the body, the yaw can be controlled via adjusting the rudder at the rear, and the roll of the glider cannot be controlled. The Slocum glider is ballasted as close to 0° in roll as possible, and change to this axis while in flight can only be done through the influence of an outside force. An example of the standard roll, pitch and depth profiles recorded from a glider, vs. examples during a storm or turbulent water, are seen in Fig. 5.

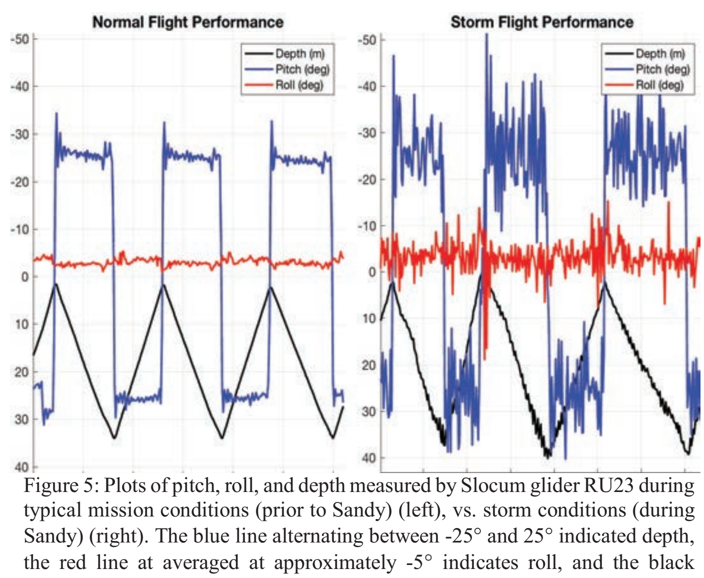

Figure 5: Plots of pitch, roll, and depth measured by Slocum glider RU23 during typical mission conditions (prior to Sandy) (left), vs. storm conditions (during Sandy) (right). The blue line alternating between -25° and 25° indicated depth, the red line at averaged at approximately -5° indicates roll, and the black triangle shape line indicates depth.

In the left subplot, the standard record of pitch, in blue, is stable at -25° and 25° when RU23 transitions to and from a dive position and climb position during typical flight conditions. Roll can be seen in the same plot during the same conditions as the red line, remaining stable near -5°, and the pressure record, indicating depth, can be seen as the black line, remaining steady as the glider ascends and descends the water column. In the right subplot, the three variables are all influences significantly by the outside environmental force of the storm, causing extreme variability in the measurements.

If change in roll is seen in the gliders flight data, then it is known that there is an outside influence on the glider. This could indicate mixing, turbulence, or another outside force. The extent to which a change in roll is seen in the glider data, could show how deep the mixing is, and to which depths the water column is being affected by the storm. A plot of the standard deviation of roll from RU23 is shown in Fig. 6 as the top subplot. This plot also includes a record of wind intensity, in knots, collected from the nearby NDBC station 44025 as the overlaid solid line. As the intensity of wind increases, caused by the approaching Hurricane Sandy, the standard deviation of roll increases. One benefit to this is the ability to measure potential mixing or turbulence without the need for an additional sensor, and the extent of depth to which this is occurring.

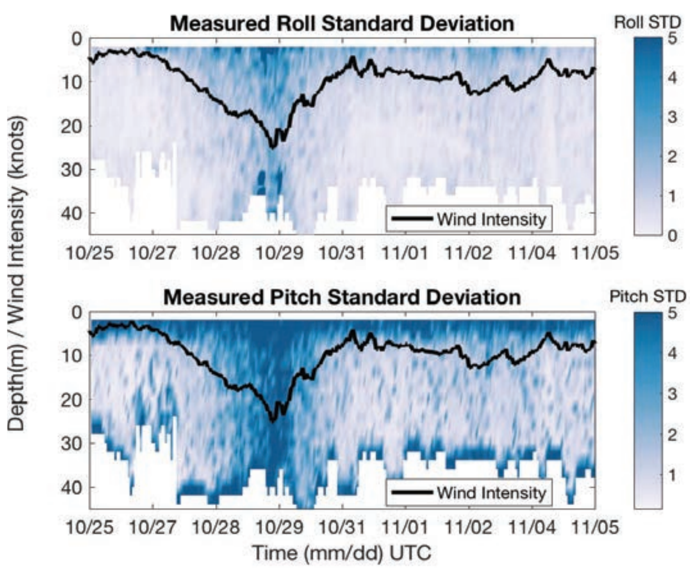

Figure 6: Top: Plot of the standard deviation of roll with depth recorded from RU23. Bottom: Plot of the standard deviation of measured pitch with depth recorded from RU23. Record overlaid on the standard deviation plot is wind intensity recorded from NDBC station 44025, with a peak at 25kt on 29 Oct 2012.

Worth noting is that gliders are considered a quite stable platform. However, during storms we have continuously noticed they are often affected by the surrounding water to varying degrees. Not only in pressure as analyzed before, but in attitude as well [7]. This could make attitude related sensors, such as turbulence probes, current profilers, and acoustic sampling devices, more difficult to operate.

The pitch of Slocum gliders is expected to only change at each inflection and deflection during its mission, but, as with roll, the surrounding environment can have an effect. Because Slocum gliders have the ability measure and change its pitch, readjustments were made by RU23 during its Hurricane Sandy mission when an error in pitch was too significant. The standard deviation of measured pitch recorded from RU23 can be seen as the bottom subplot in Fig. 6. This shows that as the intensity of wind increases, there is greater fluctuation in the measured pitch angle from RU23. It is important to keep in mind this change in pitch when analyzing the fluctuating pressure record. Suspicion that the fluctuation is caused by the changes in pitch will be discussed in the next section. Similar to the changes seen in roll, changes seen in pitch can indicate how deep mixing or turbulence is felt throughout the depths of the water column.

B. Wave Period

Besides the pressure from incoming waves, a possibility which could cause the fluctuations in the pressure record, as seen in the right subplot in Fig. 3, is the change in pitch angle caused by a turbulent environment. Slocum gliders detect an error in pitch, and if the error is too significant, a commanded adjustment to its pitch angle will be made. Changes to pitch, either caused by the environment, or due to commands, increases or decreases the flight angle of the glider. To rule out the possibility that the fluctuations in the pressure record are due to the change in pitch, the dive and climb profiles of RU23 are recreated based off the pitch angle, assuming a constant velocity per profile. Doing so accurately displays the dive and climb profiles of RU23, but fluctuations in depths are no longer present in this representation. Had the changes in pitch been the cause to the fluctuating pressure record, the signal would have continued to be present in the recreated dive and climb profiles. Therefore, suspicion that the fluctuation in pressure is due to changes in pitch can be ruled out, further indicating the likelihood that these observed pressure changes are induced by waves.

In a case where deep-water waves are present, no signal from the above passing waves can be seen in the pressure record from a glider, as noted from previous glider deployments done by Rutgers University's COOL group. As a wave passes over the glider, the glider moves with the wave in a circular motion, as seen in Fig. 2. This mimicking orbital motion done by the glider in a deep-water wave, cancels any additional pressure brought on by the passing wave, therefore, no flux in the pressure record is present. The vertical motion is the important reasoning behind a wave signal present, or not present, in a pressure record. If the vertical displacement of the glider is the same as the vertical flux of water caused by the passing wave, then detection of this wave will not be present in the data. In a case where intermediate-water waves are present, as the circumstance for RU23s Hurricane Sandy mission, the vertical displacement of the glider is not equal to the vertical influx of water from the wave, therefore some additional pressure brought on by the wave is present in the data, as seen in Fig. 3.

Analysis can be done on this fluctuating pressure record to determine the wave period. This is done by evaluating the frequency spectrum of the signal from the pressure record. Doing so for each dive and climb profile from RU23 with a present wave signal can give a time series of wave period. Accuracy of this wave period time series from RU23 is determined by a comparison with nearby NDBC buoys. Discrepancies in wave period between RU23 and nearby NDBC buoys could result from either fault in the methods of extracting wave period, or differences in environment from the locations of the buoys to that of RU23. Fig. 7 displays the track of RU23 as a solid blue line, in addition to the track of Hurricane Sandy as a dashed red line, and the location of the NDBC buoys as green triangles [8]. Note the substantial geographic difference in location of the NDBC buoys in comparison to the track of RU23. This can contribute to errors seen in the comparison of wave period data, with the closest NDBC buoy being 38km away near the start of RU23s mission [8].

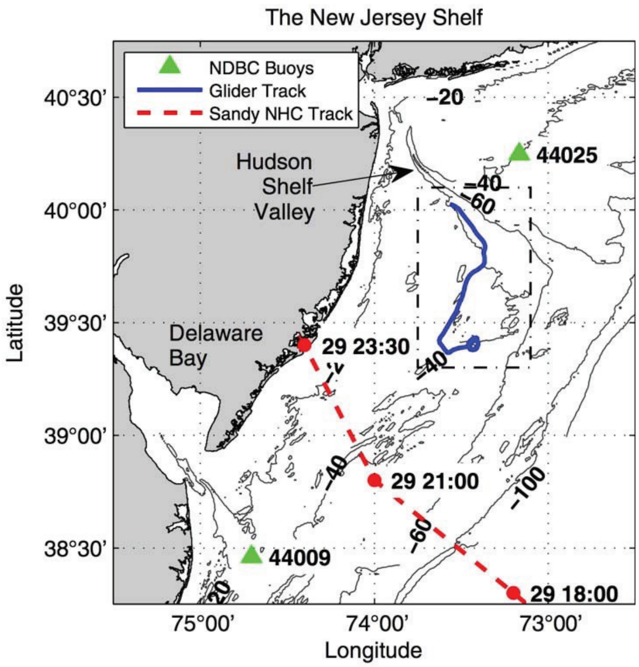

Figure 7: Plot of the New Jersey shelf with bathymetric contours measured in meters. Dashed red line indicates track of Hurricane Sandy; red dots on the dashed lines indicate corresponding times Hurricane Sandy is at each location. The solid blue line shows the mission track of Slocum glider RU23. The green triangles show locations of two nearby NDBC stations [8].

Visualization of the extracted wave period data from RU23, in comparison with two NDBC stations, can be seen in Fig. 8. Within the figure, similarities in trends are revealed, and matching peaks and valleys in data can be seen. If a discrepancy in RU23's wave period data is seen in comparison to Station 44025 during a certain time, it is likely that at this same time, an agreement in data can be seen with Station 44009, and vice versa. An example of this is demonstrated in Fig. 8 on 28 October 2012, at approximately 21:00 and on 29 October 2012, at approximately 11:00. Reason for this difference between the glider and Station 44009 is likely due to Station 44009 being located on the opposite side of the storm track as RU23. The winds are blowing in the opposite direction at Station 44009 compared to where RU23 flew, and the location of Station 44025, and thus rapidly reduced the wave period by blowing against to the mean wave direction. Station 44025 was on the same side of the storm as the glider, and therefore the results are more consistent. Overall, there is considerable agreement between the NDCB station's wave period data and the extracted RU23 wave period data. What is interesting about the buoy's data are the large changes in measured wave periods from 13 seconds to 9 seconds in a short time span. RU23's pressure record does not show these short span changes. It would be worth investigating why wave period would change rapidly only to return to its previous values.

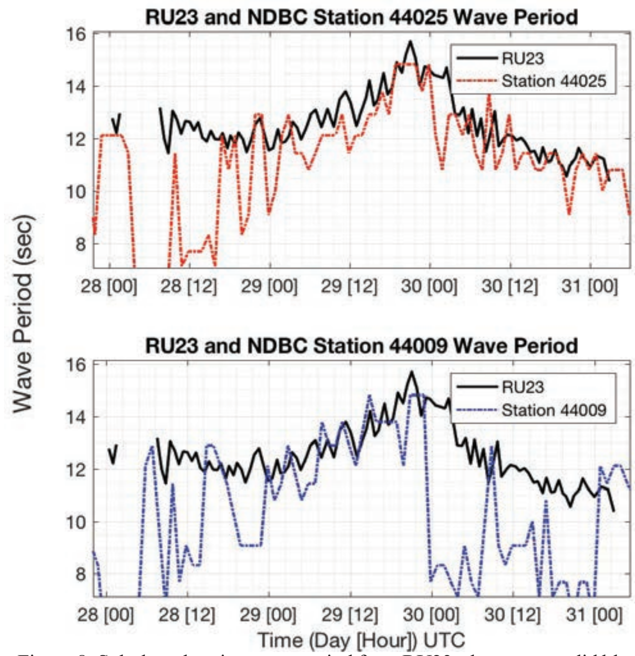

Figure 8: Subplots showing wave period from RU23, shown as a solid black line, and from NDBC Stations, shown as a dashed red or blue line. Top subplot shows data from Station 44025 (red) in comparison with RU23, and bottom subplot shows data from Station 44009 (blue) in comparison with RU23.

C. Limitations for Sampling

Acquiring wave period from Slocum gliders is limited to restrictions in glider sampling rates, and certain required environmental characteristics. The restrictions in glider sampling rates due to the Nyquist frequency will determine which signals the glider can and cannot detect. For example, if a device were to sample something that occurs at 1Hz, this device would need to sample at 2Hz, or twice as fast, minimum. To put this into the context of the paper, if the glider were to sample a 15 second wave period ($0.0\overline{6}$ Hz), the minimum sampling rate the glider must have would be 7.5 seconds ($0.1\overline{3}$Hz). This frequency is the minimum frequency a device must record at to see frequencies double to the recording frequency, without drastic error. Because the Slocum glider's science bay records at 0.5Hz, or every 2 second as mentioned previously, theoretically, the glider should be able to detect 4 second period waves, or waves passing at 0.25Hz. This is not reflected in the data, as shown in Fig. 8. We surmise that the shorter period waves were caused by smaller waves, which were not large enough to cause a signal in the glider's pressure record.

The minimum wave period RU23 was able to detect during this mission was near 10-11 seconds. Periods recorded by RU23 lower than this, as determined by the NDBC buoys, are recorded as errors, or are not present in the extracted wave period data. Reasoning behind this could be due to changing dynamics of orbital partial motion, from intermediate-water waves to deep-water waves, thus allowing the glider to fly smoother through the water column during these periods. This change in orbital motion will lessen the additional pressure felt on the glider by the waves, thus changing its pressure profile from the right subplot in Fig. 3 to the left subplot in the same figure, therefore causing the signal to be lost. When wave heights were below 4 m, as per the NDBC stations, the signal for detecting the wave period in the pressure record appeared to diminish to undetectable states. This loss of signal can be the reason why no data is present from approximately 03:00 28 October 2012 to 06:00 28 October 2012 in Fig. 7. An alternative reasoning behind the lack of accuracy in low period waves could be due to fault in methods for extracting wave period from each dive and climb pressure profile, as explained in the methods section of this paper.

IV. Conclusions

Slocum gliders are useful in many situations. They can collect in-situ oceanographic data in the roughest conditions without the need for a human to be present. Examples of data a Slocum glider can collect include water velocity, particle size, backscatter, flouresence, and more. In certain conditions though, Slocum gliders can also collect wave period using its pressure sensor by methods described in this paper. Though wave periods below 10-11 seconds inflict error in the extracted wave period data, wave periods above this threshold were recorded with considerable accuracy in the conditions RU23 faced during its Hurricane Sandy mission in October of 2012. The benefits to this ability to extract wave period during certain conditions include the lack of need for an additional instrument on the glider, because a Slocum glider is always equipped with a pressure sensor in its CTD, and an additional measurement of wave period for comparison with surrounding instruments. Further work is being done to see if any kind of wave height measurements can be calculated using wave theories from the vehicle's pressure record. Water depth, wave period, wavelength are known. Also it would be interesting to see if wave period can be measured for smaller waves in more shallow water. There is a variety of storm data available, typically Nor'Easters which could facilitate this investigation.

Acknowledgment

Great appreciation goes out to the COOL team at Rutgers University for the unlimited amount of assistance and guidance during this research project, and all other projects I have had the fortunate opportunity to work on with. Special thanks go out to Dave who help step me through this project, everyone who were nice enough to help me through this writing process, including persons at Rutgers University, and Texas A&M University.

References

[1] S. Charley, "What Made Hurricane Sandy so Unusual -- Was It Climate Change?," GeoSpace: American Geophysical Union, 04 June 2013. [Online]. [Accessed 25 May 2017].

[2] D. G. Buchanan, "Damage Assesment Report on the Effects of Hurricane Sandy on the State of New Jersey's Natural Resources," Office of Science: New Jersey Department of Environmental Protection , Trenton, 2015.

[3] J. A. Knauss and N. Garfield, Introduction to Physical Oceanography, 3rd Edition ed., Long Grove, Illinois: Waveland Press, 2016, pp. 202-204.

[4] Department of The Army: US Army Corps of Engineers, Shore Protection manual, 4th Edition ed., vol. I, Vicksburg, Mississippi: Coastal Engineering Research Center, 1984.

[5] Pile Buck, Coastal Protection, Lulu, 2012.

[6] L. H. Holthuijsen, Waves in Oceanic and Coastal Waters, 1st Edition ed., New York: Cambridge University Press, 2007.

[7] D. Aragon, S. Glenn, T. Miles, and R. Curry, "Glider Performance During Hurricane Gonzalo," *Oceans 2015- MTS/IEEE Washington,* IEEE, New York, 2015.

[8] T. Miles, G. Seroka, J. Kohut, O. Schofield and S. Glenn, "Glider observations and modeling of sediment transport in Hurricane Sandy," Journal of Geophysical Research: Oceans, vol. 120, no. 3, pp. 1771-1791, March 2015. doi:10.1002/2014JC010474

AGU PUBLICATIONS

JGR

Journal of Geophysical Research: Oceans

RESEARCH ARTICLE

10.1002/2017JC012840

Distribution of Upper Circumpolar Deep Water on the warming continental shelf of the West Antarctic Peninsula

Nicole Couto[1], Douglas G. Martinson[2], Josh Kohut[1], and Oscar Schofield[1]

[1]Department of Marine and Coastal Sciences, Rutgers University, New Brunswick, New Jersey, USA, [2]Lamont-Doherty Earth Observatory, Columbia University, Palisades, New York, USA

Key Points:

- Autonomous underwater vehicles provide measurements of mesoscale features (~10 km) in the Antarctic with high-spatial resolution
- Mesoscale eddy-like features contribute significantly to the heat budget of the west Antarctic Peninsula continental shelf
- Upper Circumpolar Deep Water consistently intrudes onto the WAP shelf in bathymetric depressions

Correspondence to:
N. Couto,
ncouto@marine.rutgers.edu

Citation:
Couto, N., D. G. Martinson, J. Kohut, and O. Schofield (2017), Distribution of Upper Circumpolar Deep Water on the warming continental shelf of the West Antarctic Peninsula, *J. Geophys. Res. Oceans*, *122*, 5306–5315, doi:10.1002/2017JC012840.

Received 28 FEB 2017
Accepted 31 MAY 2017
Accepted article online 5 JUN 2017
Published online 3 JUL 2017

Abstract We use autonomous underwater vehicles to characterize the spatial distribution of Upper Circumpolar Deep Water (UCDW) on the continental shelf of the West Antarctic Peninsula (WAP) and present the first near-synoptic measurements of mesoscale features (eddies) containing UCDW on the WAP. Thirty-three subsurface eddies with widths on the order of 10 km were detected during four glider deployments. Each eddy contributed an average of 5.8×10^{16} J to the subpycnocline waters, where a cross-shelf heat flux of 1.37×10^{19} J yr^{-1} is required to balance the diffusive loss of heat to overlying winter water and to the near-coastal waters. Approximately two-thirds of the heat coming onto the shelf diffuses across the pycnocline and one-third diffuses to the coastal waters; long-term warming of the subpycnocline waters is a small residual of this balance. Sixty percent of the profiles that contained UCDW were part of a coherent eddy. Between 20% and 53% of the lateral onshore heat flux to the WAP can be attributed to eddies entering Marguerite Trough, a feature in the southern part of the shelf which is known to be an important conduit for UCDW. A northern trough is identified as additional important location for eddy intrusion.

1. Introduction

Most of the glaciers along the West Antarctic Peninsula (WAP) have retreated since the early 1950s [*Cook et al.*, 2005], and the rate at which ice sheets have been losing mass has accelerated over the past decade [*Rignot et al.*, 2014]. The glacial retreat has been attributed to calving events, linked to warming atmospheric temperatures, and melting from below, attributed to the onshore transport of warmer ocean water [*Rignot and Jacobs*, 2002; *Jenkins et al.*, 2010; *Pritchard et al.*, 2012; *Cook et al.*, 2016]. Atmospheric temperatures over the WAP have warmed at an approximate rate of 0.5°C per decade since the 1950s [*Meredith and King*, 2005; *Turner et al.*, 2006; *Bromwich et al.*, 2013], although recent observations show a reversal of the warming trend since the late 1990s, consistent with the large variability of the system [*Turner et al.*, 2016]. Summertime upper ocean water temperatures rose by more than 1°C between the mid-1950s and mid-1990s [*Meredith and King*, 2005] and continued to increase at a rate of 0.1–0.3°C per decade since the 1990s [*Schmidtko et al.*, 2014]. This warming reflects the effects of changes in atmospheric temperatures. Recent observations, however, suggest that glacier retreat on the WAP is driven primarily by deep ocean temperatures [*Cook et al.*, 2016] which can also supply heat to the atmosphere [*Venables et al.*, 2016].

Upper Circumpolar Deep Water (UCDW) is the largest source of ocean heat to the WAP continental shelf [*Hofmann et al.*, 1996]. This water mass is characterized by potential temperatures exceeding 1.7°C and salinities greater than 34.54 [*Martinson et al.*, 2008], and is the warmest deep water mass observed on the WAP continental shelf. UCDW is found just off the shelf at depths between 200 and 600 m within the Antarctic Circumpolar Current (ACC), an eastward-flowing current that runs directly along the continental slope of the WAP [*Klinck*, 1998; *Klinck et al.*, 2004]. While surface water properties on the continental shelf vary seasonally with the growth and melting of sea ice and variable wind mixing [*Hofmann et al.*, 1996], water below the permanent pycnocline is kept warm throughout the year by frequent intrusions of UCDW from the offshore ACC [*Smith et al.*, 1999; *Martinson et al.*, 2008].

Overlying the relatively warm deep water on the shelf is Winter Water. This cold water mass is generated from a combination of sea ice growth, sensible heat loss to the atmosphere, and deep vertical mixing driven by winds during the winter and is persistent in most parts of the shelf throughout the summer. In the winter, it extends from the surface to around 200 m. Beginning in the spring, relatively fresh sea ice meltwater creates a shallow surface layer that overlies the Winter Water and warms throughout the summer. As UCDW intrudes onto the shelf, it loses heat to the surrounding water and overlying Winter Water through both diapycnal and isopycnal mixing [*Smith et al*., 1999]. Over the course of the year on the continental shelf, there is a net flux of heat out of the surface ocean with a magnitude estimated between 6 W m^{-2} (using data from 1993 only) [*Smith and Klinck*, 2002] and 19 W m^{-2} (averaged over 1993–2004) [*Martinson et al*., 2008]. The cross-pycnocline heat flux from UCDW-warmed water into the Winter Water balances this heat loss to the atmosphere. The temperature gradient that drives this vertical diffusion of heat is preserved by subpycnocline along-isopycnal heat transport from off the shelf [*Klinck et al*., 2004].

Several mechanisms have been suggested for delivering UCDW to the WAP. Upwelling of offshore UCDW is evidenced in hydrographic data by shoaling of the permanent pycnocline [*Martinson et al*., 2008]. Topographically induced or wind-driven upwelling events have been linked to large diatom blooms on the shelf [*Prézelin et al*., 2000]. However, shoaling may not always indicate upwelling; it can also be produced when a subsurface eddy moves onto the shelf and deflects isopycnals [*Martinson and McKee*, 2012]. Indeed, with the high-temporal resolution of mooring observations in Marguerite Trough and the neighboring shelf, and the increased spatial resolution of regional models, mesoscale eddies have emerged as the most prominent mechanism of heat delivery to the WAP shelf [*Dinniman et al*., 2011; *Martinson and McKee*, 2012]. While upwelling has not been ruled out as a potential delivery mechanism [*Martinson and McKee*, 2012], the apparent shelf-wide flooding of UCDW documented in coarsely resolved hydrographic surveys [*Prézelin et al*., 2004] was shown to actually be the result of coherent eddies moving on to the shelf and dissipating heat [*Moffat et al*., 2009; *Dinniman et al*., 2011; *Martinson and McKee*, 2012].

Eddies are carried onto the shelf during episodic advective intrusions of UCDW, which may occur during periods of intense wind stress [*Dinniman et al*., 2011]. Modeling studies and observations indicate that, with a strong enough forcing, when the mean shelf break flow encounters curving bathymetry, some of the water flowing in the ACC along the shelf break is carried by momentum onto the shelf [*Dinniman and Klinck*, 2004; *Klinck et al*., 2004]. Evidence from a high-resolution model also suggests that Rossby waves at the shelf break can interact with a trough to produce features consistent with eddies [*St-Laurent et al*., 2013].

Moorings in Marguerite Trough and on the surrounding shelf have recorded eddies passing by at rates of three to four per month [*Moffat et al*., 2009; *Martinson and McKee*, 2012], but presence elsewhere on the shelf is largely unknown. Existing data sets in the region were collected using traditional shipboard sampling, with measurements typically made at coarser resolution than that required to resolve mesoscale eddies on the WAP. Weak subsurface stratification of the shelf combined with the effects of high-latitude result in a small radius of deformation which determines the length scale of eddy dynamics [*Chelton et al*., 1998]. Eddies shed from the ACC have diameters of $\sim$10–20 km [*Klinck and Dinniman*, 2010].

Here we use data from four deployments of Slocum-Webb autonomous underwater vehicles (gliders) to map the spatial distribution of UCDW on the shelf. Some of the UCDW is contained in subsurface mesoscale eddies with widths on the order of 10 km. Glider profiles are 1 km apart, on average, providing sufficient spatial resolution to define the horizontal boundaries of mesoscale features. These data allow us to identify previously undetected pathways of intrusion for eddies onto the shelf, and allow us to estimate their relative importance to the WAP continental shelf heat budget.

We place these glider deployments in the context of annual shelf-wide hydrographic data from repeat cruises conducted each January from 1993 to 2008 [*Smith et al*., 1995; *Ducklow et al*., 2012]. Hydrographic stations occupied during these cruises were rarely closer than 20 km apart, so they lack the spatial resolution to detect eddies on the shelf, but they allow us to construct a subpycnocline heat budget from which we can estimate the contribution of subsurface eddies carrying UCDW and discuss their impact on the warming trend observed across the shelf over the last several decades.

2. Methods

This study uses data obtained from four deployments of Slocum Webb deep gliders from Palmer Station, Antarctica (64°46′S, 64°03′W) during austral summers 2010–2011, 2011–2012, and 2012–2013. Deployments lasted between 29 and 62 days and covered distances up to 1600 km in the coastal waters west of the

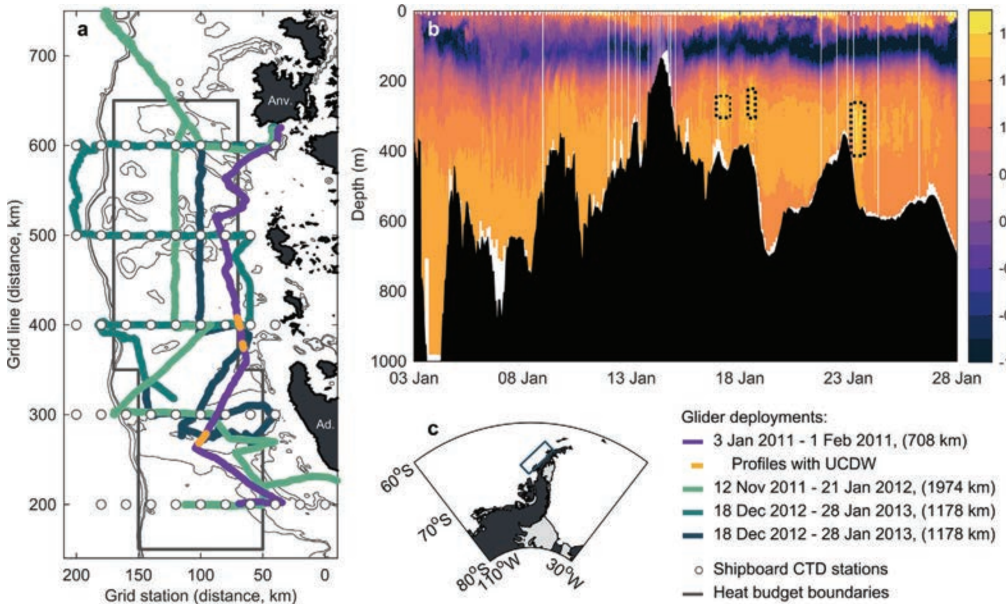

Figure 1. (a) The region of the WAP continental shelf discussed in this analysis. Shipboard CTD profile locations used in the heat budget calculations are shown as circles. The gray box encloses stations used to calculate the change in shelf heat over time and the vertical heat flux to the winter water layer. Lateral diffusion is measured across the right box boundary and lateral onshore heat flux is calculated across the left box boundary. Green and purple lines show tracks of the four glider deployments. Temperature data from the purple track are shown in Figure 1b with yellow dots indicating profiles where UCDW was found. Bathymetry contours are plotted at the 500, 600, and 1000 m isobaths. Anvers (Anv.) and Adelaide (Ad.) Islands are labeled. (b) Temperature section from the glider deployment shown in purple in Figure 1a. Dotted boxes show the extent of UCDW in the three mesoscale features detected on this deployment. (c) Regional map, with boundaries of plot a shown.

Antarctica Peninsula (Figure 1). Gliders are buoyancy-driven autonomous underwater vehicles that move from the surface to a depth of up to 1000 m with an average horizontal speed of 1 km h^{-1} [*Davis et al*., 2002; *Schofield et al*., 2007]. All gliders used in this study were equipped with a Seabird CTD to measure conductivity, temperature, and depth with a sampling resolution of 4–6 measurements per vertical meter. Data from each dive or climb were averaged into 1 m depth bins and the latitude/longitude of the entire profile was set to the average latitude/longitude of the climb or dive.

In each of the four deployments, gliders traveled generally southward along the peninsula. We restrict our focus to profiles taken on the continental shelf, which we define as shoreward of the 600 m isobath (Figure 1a). Among the shelf profiles, UCDW ($T > 1.7$°C and $S > 34.54$, *Martinson et al*. [2008]) was often encountered below the permanent pycnocline as part of distinct boluses with characteristics consistent with subsurface eddies (Figure 1b).

Studies of subsurface eddies in the North Pacific [*Pelland et al*., 2013] and North Atlantic [*Bower et al*., 2013] suggest that a Gaussian distribution model is appropriate for defining the horizontal boundaries of those features. We use it to measure chord lengths of the eddy-like boluses encountered by the gliders. From here forward, we will refer to the boluses as "eddies." The model assumes that the cross section of an eddy along an isopycnal is circular and that its temperature is greatest at its center and decays in the radial direction. This geometry is described by the following equation:

$$T' = T_{\max} \cdot e^{-\left(\frac{(x-x_0)}{r}\right)^2}, \tag{1}$$

where T' is the temperature anomaly at position x, T_{max} is the maximum value of the anomaly at the eddy center, x_0, and r is the eddy radius.

Following the methods of *Zhang et al*. [2015], who calculated widths of subthermocline eddies in the North Pacific using Argo float profiles, we interpolated temperature profiles onto surfaces of constant potential density separated by 0.01 kg m^{-3}. For each isopycnal surface, using only observations on the shelf, we calculated the mean temperature and anomalies from the mean. We then identified every shelf profile that

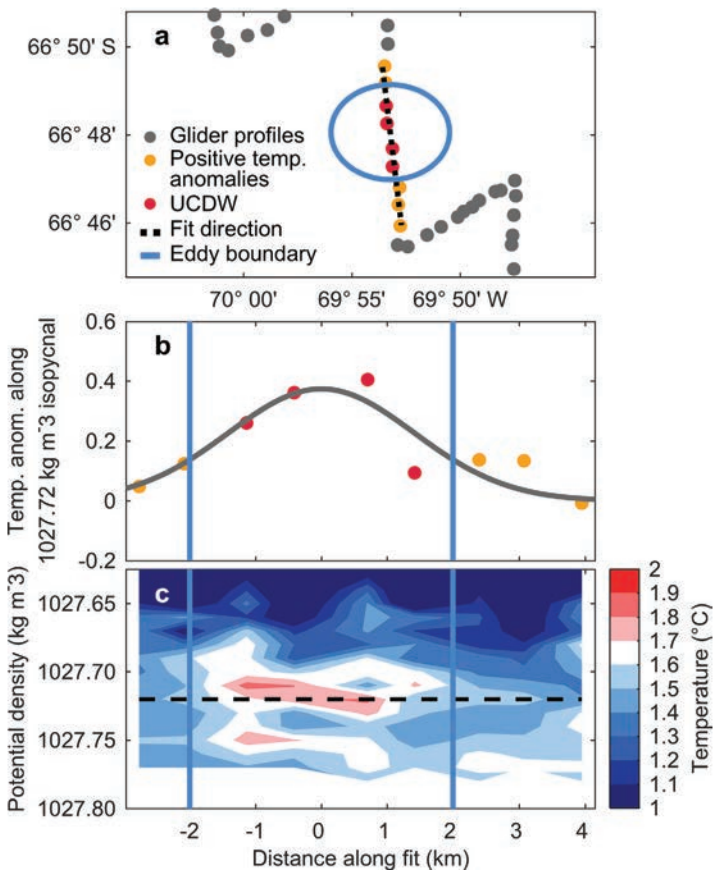

Figure 2. Example of method used to define eddy width. (a) Profiles containing UCDW at any depth are identified based on temperature and salinity values (red dots). One isopycnal surface is selected and the surrounding profiles that contain positive temperature anomalies along that surface are identified (yellow dots). A least-squares line is fit to these profiles (black dashed line). (b) A Gaussian curve is fit to the positive temperature anomalies along the chosen isopycnal in the direction of the least squares fit. Eddy width is defined by equation (1) as twice the radius, enclosing 84.3% of the heat (vertical blue lines). (c) Temperature section with vertical blue lines showing the calculated eddy width. Dots in Figures 2a and 2b show the locations of each glider profile (a single dive or climb).

contained UCDW at any depth and fit Gaussian curves to the positive temperature anomalies surrounding these profiles on each of fifteen isopycnal surfaces between 1027.63 kg m^{-3} (approximating the base of the winter mixed layer and the shallowest isopycnal where UCDW was found) and 1027.77 kg m^{-3} (the deepest isopycnal that at least 50% of glider profiles extended to).

We used the MATLAB "fit" function to calculate the radii of the eddies according to equation (1) (Figure 2). Distances (x) were measured along the least squares fit line through all points on the isopycnal surrounding the UCDW profile that had positive temperature anomalies (Figure 2a). This method was repeated for every profile containing UCDW and every potential density surface between 1027.63 and 1027.77 kg m^{-3}, resulting in several fits to the same feature; we chose the best as the fit with the lowest rms/mean. Isopycnals representing the best fits ranged from 1027.70 to 1027.76 kg m^{-3}.

Eddy chord lengths were defined according to equation (1) as twice the radius, r, which encloses 84.3% of the temperature anomaly in the fit (Figure 2b). These lengths are used as an estimate for eddy width, but since we do not know how closely the glider passed through eddy centers, nor do we know the direction of eddy movement, there is error in this estimate. Drawing random lines through a stationary circle to measure the diameter would result in an average estimate that is 68% of the true diameter, but eddies are not assumed to be stationary during the time the glider spent sampling them. Width is likely to have been underestimated (overestimated) during times when the glider passed through an eddy as it was carried by the mean flow in the opposite (same) direction as the glider motion.

The heat content of each eddy was calculated relative to the average shelf temperature, T_{ref}:

$$Q = \int_{z_1}^{z_2} (T - T_{ref}) \rho_z c_p \pi r^2 dz, \tag{2}$$

where z_1 and z_2 are the shallowest and deepest depths where UCDW was observed within a single eddy. These depths averaged 221 and 346 m on the shelf across all glider deployments. The reference temperature, T_{ref}, was calculated as the average potential temperature below the permanent pycnocline of all non-UCDW profiles on the shelf and had a value of 1.2°C. Since the reference temperature includes every profile where the maximum potential temperature was below 1.7°C and does not demand that the profile be cooled any further, heat calculated relative to this temperature represents a lower bound of the heat delivered to the shelf by eddies.

Temperature profiles were also taken during annual cruises in January 1993 and 1995–2015 as part of the Palmer Long Term Ecological Research (LTER) project. The LTER grid is made up of lines running along the peninsula spaced 100 km apart and stations running perpendicular to the shelf spaced 20 km apart (Figure 1a). The lines are named according to distance from a point south of this particular study area: the 200 line extends out from south of Adelaide Island and, 400 km northeast of that, the 600 line extends out from south of Anvers Island (Figure 1). The same temperature and salinity criteria ($T \geq 1.7°C$, $S \geq 34.54$) used to identify UCDW in the glider data were used to identify UCDW in the shipboard CTD data, and the same potential density surfaces were used to calculate the heat content of every profile. These data were used to investigate the spatial patterns of UCDW on the shelf. They were also used to create a volume-averaged heat budget for the WAP shelf in order to determine the importance of the subsurface eddies as a source of heat to the shelf.

3. Results and Discussion

3.1. Locations of UCDW Intrusions

Hydrographic measurements on the WAP, taken from both traditional ship platforms and glider deployments, reveal a consistent pattern of intrusion locations onto the shelf (Figure 3). Both data sets show a heightened presence of UCDW on the shelf in deep areas, mostly confined to the region around Marguerite Trough (300 and 400 lines). In both data sets, observations of UCDW drop off with distance from the shelf break toward the coast, as expected, since processes on the shelf lead to the modification of UCDW.

Ocean gliders have significantly improved the spatial resolution of hydrographic measurements along the Antarctic Peninsula, allowing us to resolve features smaller than the spacing of a typical ship-based survey [*Heywood et al.*, 2014; *Erickson et al.*, 2016]. The increased sampling resolution of the gliders increases the likelihood of encountering the small-scale features containing UCDW. The glider data confirm our understanding of UCDW intrusion locations but indicate that studies based solely on hydrographic surveys with profiles separated by 20 km or more have underestimated the quantity of unmixed UCDW on the shelf (Figure 3, blue bars versus red bars). During some LTER cruises, no UCDW was seen on the shelf, but it easily could have been missed; a single CTD cast from a ship is meant to represent a 20 km $\times$ 100 km area of ocean, within which it is possible for several mesoscale features to exist but go undetected. Glider surveys consistently encountered more UCDW per unit effort (profiles measured) than did shipboard surveys.

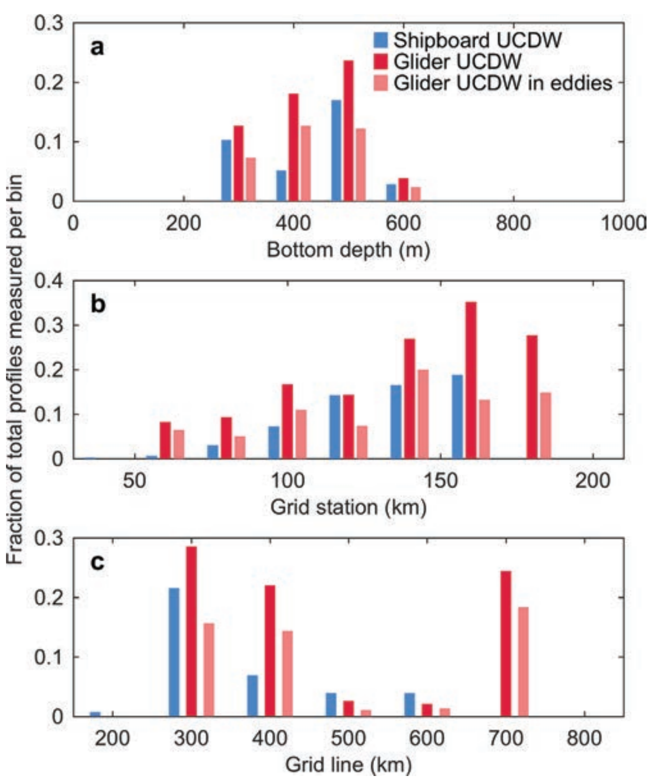

Figure 3. Fractions of (blue) total shipboard CTD profiles that contained UCDW, (red) total glider CTD profiles that contained UCDW, and (pink) total glider CTD profiles that were part of an eddy, that were found in bins of (a) bottom depth, (b) grid station, and (c) grid line. Eddy profiles were identified by fitting Gaussian curves to temperature anomalies, as described in section 2.

The glider data allow us to separate UCDW that appears in coherent eddies from UCDW present outside eddy-like structures. Coherent features carrying UCDW were seen in each of the four glider deployments. Of all profiles containing UCDW, 60% occurred as part of eddies (Figure 3, pink bars versus red bars). The UCDW found outside of eddies was present either near the shelf break spread over tens of kilometers, which may be evidence of a mean advection across the shelf break,

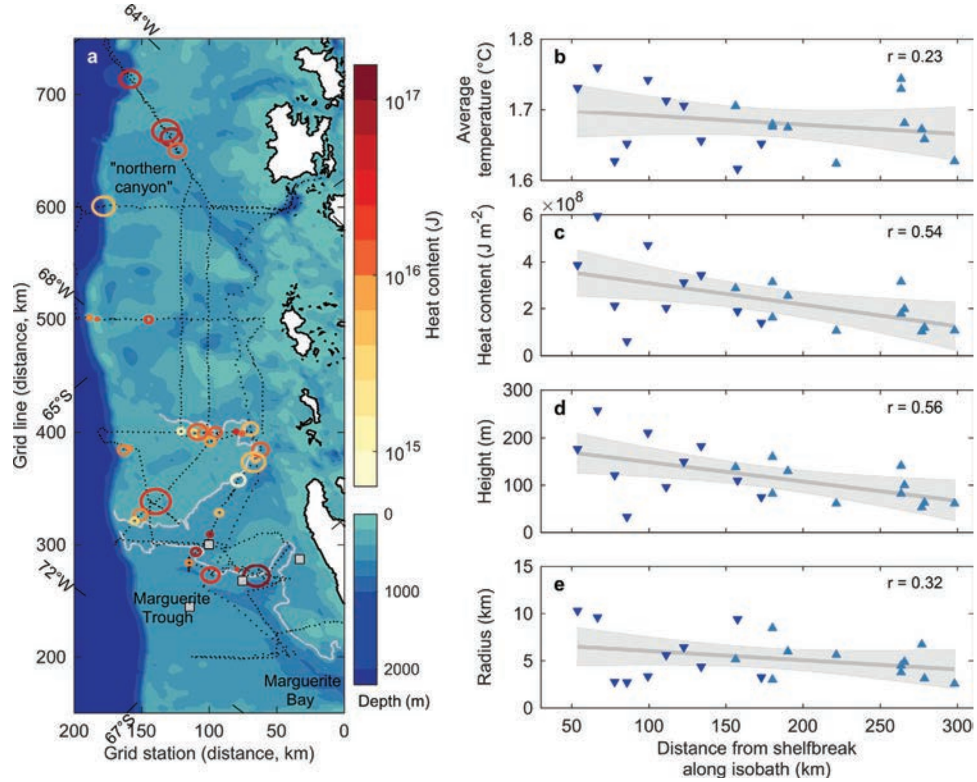

Figure 4. (a) Map of WAP continental shelf with overlaid eddies detected by the gliders, colored by the average heat content of the profiles measured within them. Dotted black lines show glider tracks. Gray squares show the locations of SO GLOBEC moorings [*Moffat et al.*, 2009] and LTER [*Martinson and McKee*, 2012] moorings that have been used in previous studies to measure frequency of eddy intrusion into Marguerite Bay. Gray lines trace the (top) 400 m and (bottom) 500 m bathymetric contours representing "upper" and "lower" paths of Marguerite Trough. Dark blue downward-pointing triangles in Figures 4b–4e show data from eddies lying along lower contour, and light blue upward-pointing triangles show data from eddies lying along upper contour. Gray lines and shading in Figures 4b–4e represent least squares fit to data and 95% confidence bounds. Correlation coefficients are given.

or as isolated profiles near the locations where eddies were found, which may represent remnants of larger features that had dissipated or instances of interleaving.

Mooring observations from the vicinity of Marguerite Trough previously identified eddies there [*Moffat et al.*, 2009; *Martinson and McKee*, 2012]. Glider observations confirm that this canyon is important for the advection of eddies onto the shelf and identify an additional, previously undetected, intrusion pathway to the north. The "northern canyon" (Figure 4a) is a cross-shelf canyon that lies outside the boundaries of the LTER grid, so no observations of UCDW had been made there in LTER time series. Mesoscale features containing UCDW were found along the northern wall of this canyon. Similarly, UCDW eddies were found along the northern wall of the entrance to Marguerite Trough. Eddies that enter the shelf at Marguerite Trough appear to follow one of two pathways onto the shelf: an upper pathway follows the 400 m isobaths to the northeast and a lower pathway follows the 500 m isobaths the southeast (Figure 4a). The highest percentage of UCDW on the shelf was measured in areas with depths near 500 m (Figure 3a), which is the approximate depth of both Marguerite Trough and the northern canyon where they cross the shelf break.

3.2. Properties of UCDW Eddies

Overall, 14% of the profiles measured by the gliders on the shelf contained UCDW. Of these, 60% were contained in 33 coherent Gaussian features with properties consistent with subsurface eddies. The majority of these features were found in or around Marguerite Trough, but the northern canyon also appears to be a conduit for transport of eddies onto the shelf (Figure 3a). Fewer observations were made in that canyon than in Marguerite Trough.

The mean value of all chord lengths was 11.3 ± 5.1 km with a median value of 10.3 km. It is important to note that eddy widths measured here are an estimate of true diameters since we do not know how close the glider came to the center or the direction of eddy travel. However, these estimates are within the range of eddy sizes predicted by the internal deformation radius [*Chelton et al*., 1998] and are similar to the size of eddies measured by moorings on the shelf [*Moffat et al*., 2009; *Martinson and McKee*, 2012].

Subsurface eddies entering the shelf contained as much as 1.93×10^{17} J of heat relative to the reference temperature (1.2°C). Eddies lose heat to the overlying winter water and to the cooler shelf waters as they are carried in the mean flow. In the general circulation pattern in the southern half of the grid, water enters onto the shelf through Marguerite Trough and makes a counter-clockwise loop following the northern branch of the canyon [*Smith et al*., 1999; *Dinniman and Klinck*, 2004; *Savidge and Amft*, 2009]. A second branch carries water into Marguerite Bay via the southern branch of the canyon [*Klinck et al*., 2004]. The properties of eddies detected by the gliders are consistent with this pattern.

In Figure 4, plots b–e show properties of eddies that enter Marguerite Trough as a function of distance from the shelf break along one of two isobaths. Heat content per unit area and height are most strongly correlated with distance. Eddy height is defined as the vertical distance separating the shallowest and deepest observations of UCDW within the eddy. Radius and average temperature are weakly correlated with distance. Again, the interpretation of these relationships must include a consideration of the chord-length sampling error. An eddy that a glider passed through the edge of would appear to have a shorter radius and a cooler average temperature than if the eddy had been sampled through the middle. The observations suggest that subsurface eddies enter onto the shelf with widths on the order of 10 km and are modified as they travel along an isobaths. They dissipate most of their heat vertically and less of it laterally. Slower rates of lateral diffusion and the resulting effects of lateral spreading may explain the weak correlation between eddy width and distance traveled.

3.3. Heat Balance on the WAP

A simple two-dimensional heat budget was constructed for the region of the WAP shelf where glider and CTD observations were made (Figure 5). This region extends 500 km along the coast and 100 km across the continental shelf (Figure 1a). Vertical limits are between the depth of the permanent pycnocline, which has an average depth of 160 m and generally corresponds to the 1027.63 kg m^{-3} isopycnal, and the seafloor, which are separated by an average distance of 280 m. The height of the heat budget box is defined as this average distance. Following the assumption of *Klinck et al*. [2004], we assume the alongshore advection is

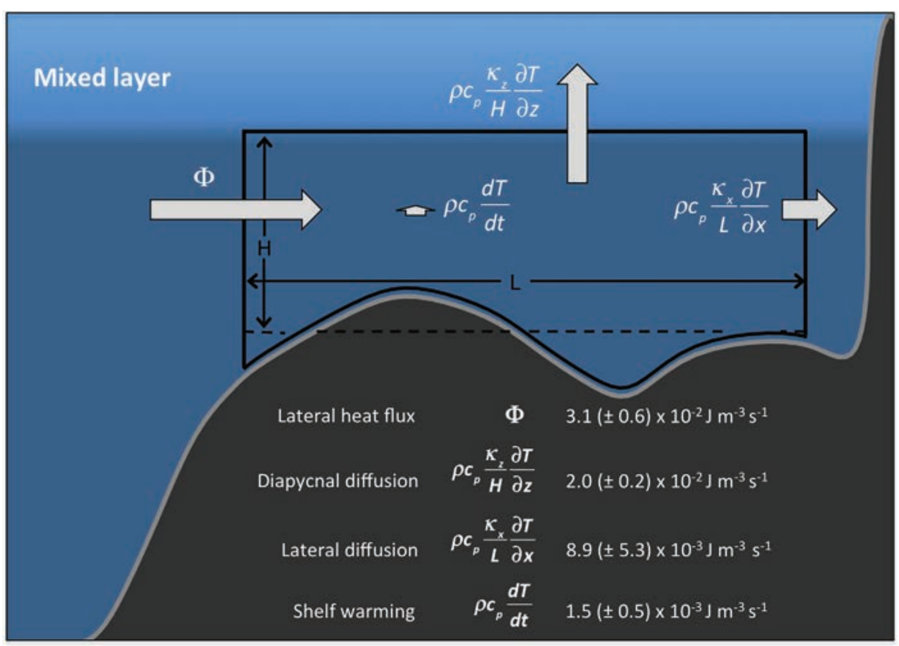

Figure 5. Schematic illustrating the components of the heat budget on the WAP continental shelf. Values shown are calculated using $\kappa_x = 100$ m^2 s^{-1}. All other values are listed in Table 1. We use the average bottom depth of the WAP, indicated by the dashed line, as height, *H*. Arrow lengths are proportional to the relative contributions of each term to the heat budget.

Table 1. Coefficients and Variables Used Throughout the Text

Symbol	Description	Value
T_{ref}	Reference seawater temperature	1.2°C
P	Reference seawater density	1027.7 kg m^{-3}
c_p	Specific heat of seawater	4000 J kg^{-1}°C^{-1}
H	Height of heat budget box	280 m
L	Across-shelf extent of heat budget box	100 km
W	Along-shelf extent of heat budget box	500 km
κ_z	Vertical diffusivity	10^{-4} m^2 s^{-1}
κ_x	Lateral diffusivity	100 (37,200) m^2 s^{-1}
$\frac{\partial T}{\partial t}$	Time rate of change of shelf temperature	3.61 ($\pm$1.15) $\times$ 10^{-10}°C s^{-1}
$\frac{\partial T}{\partial x}$	Midshelf to inner-shelf temperature gradient	2.18 ($\pm$1.28) $\times$ 10^{-6}°C m^{-1}
$\frac{\partial T}{\partial z}$	Diapycnal temperature gradient	0.014 $\pm$ 0.002°C m^{-1}

small and that there is no heat flux at the bottom or directly at the coast, although we do calculate lateral diffusion between the midshelf and nearshore stations. The heat balance below the permanent pycnocline on the shelf is the sum of lateral fluxes across the shelf break, diapycnal diffusion into the overlying winter water, and isopycnal diffusion across the shoreward box boundary (Figure 1a). Here we extend the analysis to include all years between 1993 and 2008, during which the overall heat content of the shelf increased [*Martinson et al.*, 2008]. Therefore, we also include a shelf warming term. Temperatures below the permanent pycnocline on the WAP shelf during the 1993–2008 sampling period warmed at an average rate of 0.01°C per year.

We integrate the advection-diffusion equation over the width (L) and depth (H) of the shelf, ignoring vertical advection and including a warming trend. We then divide by the width and depth to arrive at the volume-averaged heat budget equation:

$$\Phi-\rho c_p\left(\frac{\kappa_z}{H}\frac{\partial T}{\partial z}+\frac{\kappa_x}{L}\frac{\partial T}{\partial x}\right)=\rho c_p\frac{dT}{dt}. \tag{3}$$

The lateral temperature gradient, $\frac{\partial T}{\partial x}$ is the time series average gradient of temperatures between midshelf and inner-shelf stations. Similarly, $\frac{\partial T}{\partial z}$ is the shelf-wide time-averaged temperature gradient across the permanent pycnocline at each station. H is the average vertical distance between the permanent pycnocline and the seafloor and Φ is the total flux across the shelf break. Values for all heat budget terms are listed in Table 1.

Values for the lateral and vertical diffusivities, κ_x and κ_z, respectively, are taken from the literature. *Howard et al*. [2004] estimated a shelf-wide average diapycnal diffusivity of 10^{-5} m^2 s^{-1} based on fall and winter cruises in 2001, however this value is thought to underestimate the true mixing on the shelf which is dominated by isolated wind events [*Howard et al*., 2004]. Estimates based on shelf-wide budgets suggest a value closer to 10^{-4} m^2 s^{-1} [*Klinck*, 1998; *Smith et al*., 1999; *Smith and Klinck*, 2002; *Martinson et al*., 2008] and not exceeding 7.7 $\times$ 10^{-4} m^2 s^{-1} [*Klinck et al*., 2004]. As the shelf waters have warmed, the magnitude of κ_z has decreased [*Martinson et al*., 2008]. We use 10^{-4} m^2 s^{-1} as an average value for the shelf over the time series, which leads to an appropriate eddy-decay time scale of eddies advected with the mean flow in Marguerite Trough [*Moffat et al*., 2009]. Estimates of isopycnal diffusivity on the shelf range from 37 m^2 s^{-1} [*Klinck*, 1998] to 200 m^2 s^{-1} [*Smith et al*., 1999] to an unrealistic maximum of 1600 m^2 s^{-1} [*Klinck et al*., 2004]. According to mixing length arguments, lateral diffusivity scales as κ vl [*Prandtl*, 1925]. Using a typical subpycnocline current speed of 1–5 cm s^{-1} [*Howard et al*., 2004; *Klinck et al*., 2004] and a typical eddy width of 10 km, mixing length arguments indicate that lateral diffusivity should be on the order of 100–500 m^2 s^{-1}. This gives us confidence to use the 37–200 m^2 s^{-1} range in our calculations.

Using values listed in Table 1, we calculate the average diapycnal diffusion across the permanent pycnocline, the average lateral diffusion across the inner heat box boundary, and the rate of shelf warming over the 1993–2008 shipboard sampling period. The magnitude of diapycnal diffusion is about twice that of lateral diffusion and the shelf warming term is, comparatively, very small. Of the heat that enters the shelf below the permanent pycnocline, approximately two-thirds is diffused vertically across the permanent pycnocline and one-third reaches the coastal waters by lateral diffusion.

We calculate the horizontal lateral flux, Φ, required to balance the other terms, to be 1.36×10^{19} J yr^{-1} (ranging from 0.97×10^{19} to 2.23×10^{19} J yr^{-1} depending on the lateral diffusivity, and including error estimates). This value is found by multiplying Φ in equation (3) by the volume of the heat budget box, and represents the total lateral heat flux from various mechanisms, including eddies transported onto the shelf. The average heat content of eddies observed near the shelf break is 5.8×10^{16} J. The total annual heat flux onto the shelf is equivalent to 150–342 eddies with an average temperature of 1.7°C across a diameter of 12 km (the average temperature and width of observed eddies within 50 km of the shelf break) coming onto the shelf each year.

Year-round mooring observations at a fixed location north of Marguerite Trough led to estimates that 35–40 eddies containing UCDW passed by the mooring location each year during 2007, 2008, and 2010 [*Martinson and McKee*, 2012]. Observations from a mooring shoreward of that location, within the trough itself, showed similar numbers of eddies passing there [*Moffat et al*., 2009]. Our results show that eddies occur at similar densities to the north and south of the Marguerite Trough entrance so, assuming the trough is a conduit for 70–80 eddies per year, it alone could serve as the entryway for 20–53% of the necessary heat flux to the shelf. The northern canyon appears to be an additional location of eddy intrusion, although further observations there will be necessary to quantify its contribution as an eddy delivery pathway. In 186 days on the shelf, our gliders encountered 33 eddies suggesting that a lower-limit estimate of eddy intrusions onto the WAP shelf each year is around 64, which would account for 19–43% of the range of lateral heat flux estimates.

4. Conclusions

High-resolution measurements from Slocum Webb deep gliders deployed along the west Antarctic Peninsula confirm that warm water from the ACC is intruding onto the continental shelf as distinct mesoscale features [*Moffat et al*., 2009; *Martinson and McKee*, 2012; *St-Laurent et al*., 2013; *Graham et al*., 2016]. The high-spatial resolution of the glider data allows us to present the first near-synoptic cross sections of mesoscale eddies on the WAP. We estimate the eddy-like boluses to be on the order of 10 km wide and 125 m thick. Intrusions tend to occur at Marguerite Trough and a second cross-shelf canyon in the northern part of the study area. The annual shipboard CTD measurements also indicate these two canyons act as primary conduits for heat transport, but they are unable to resolve the spatial extent of the intrusions.

Glider measurements have allowed us to capture warm water features over a larger area of the WAP continental shelf than was previously available, but we still lack information about the mechanism by which the warm deep water, once on the shelf, reaches the coastal surface waters. Recent research using gliders suggests that bathymetry plays an important role in local mixing of deep and surface waters and may be important in the transformation of water masses across the entire shelf [*Venables et al*., 2016]. Melting of the glaciers on the West Antarctic Peninsula could raise global sea levels by up to 69 ± 5 mm [*Huss and Farinotti*, 2014] and most of the glacier retreat since the 1990s can be attributed to interactions with the ocean [*Cook et al*., 2016]. Understanding the rate at which heat contained in the ocean is melting the ice is crucial to predicting how much ice will be lost in the warming climate. The UCDW features described here may account for up to 50% of the onshore heat flux, with the remainder likely to come from upwelling and advection of the ACC onto the shelf. Future efforts will focus on a better understanding of the eddy dissipation processes and the mechanisms responsible for bringing the remaining heat to the shelf.

Acknowledgments
Glider data used in this study are available through the Rutgers University Center for Ocean Observing Leadership (RUCOOL) webpage http://marine.rutgers.edu/cool/auvs/ and the MARACOOS assets page http://maracoos.org/data. Data sets are also available upon request to ncouto@marine.rutgers.edu. We gratefully acknowledge support from the National Science Foundation (NSF/PLR Award 0823101), from Teledyne Webb Research for providing graduate student funding and from the RUCOOL glider technicians and pilots for their tireless work during deployments. We would also like to thank Darren McKee for several productive conversations and our anonymous reviewers for their careful criticism that helped to improve the manuscript.

References

Bower, A. S., R. M. Hendry, D. E. Amrhein, and J. M. Lilly (2013), Direct observations of formation and propagation of subpolar eddies into the Subtropical North Atlantic, *Deep Sea Res., Part II*, *85*, 15–41, doi:10.1016/j.dsr2.2012.07.029.

Bromwich, D. H., J. P. Nicolas, A. J. Monaghan, M. A. Lazzara, L. M. Keller, G. A. Weidner, and A. B. Wilson (2013), Central West Antarctica among the most rapidly warming regions on Earth, *Nat. Geosci.*, *6*, 139–145.

Chelton, D. B., R. A. deSzoeke, M. G. Schlax, K. El Naggar, N. Siwertz, D. B. Chelton, R. A. deSzoeke, M. G. Schlax, K. El Naggar, and N. Siwertz (1998), Geographical variability of the first baroclinic Rossby radius of deformation, *J. Phys. Oceanogr.*, *28*(3), 433–460, doi:10.1175/1520-0485(1998)028 < 0433:GVOTFB>2.0.CO;2.

Cook, A. J., A. J. Fox, D. G. Vaughan, and J. G. Ferrigno (2005), Retreating Glacier Fronts on the Antarctic Peninsula over the Past Half-Century, *Science*, *308*(5721), 541–544, doi:10.1126/science.1104235.

Cook, A. J., P. R. Holland, M. P. Meredith, T. Murray, A. Luckman, and D. G. Vaughan (2016), Ocean forcing of glacier retreat in the western Antarctic Peninsula, *Science*, *353*(6296), 283–286, doi:10.1126/science.aae0017.

Davis, R. E., C. C. Eriksen, and C. P. Jones (2002), Autonomous buoyancy-driven underwater gliders, in *The Technology and Applications of Autonomous Underwater Vehicles*, edited by G. Griffiths, pp. 37–58, Taylor and Francis, London.
Dinniman, M. S., and J. M. Klinck (2004), A model study of circulation and cross-shelf exchange on the west Antarctic Peninsula continental shelf, *Deep Sea Res., Part II*, *51*, 2003–2022.
Dinniman, M. S., J. M. Klinck, and W. O. Smith Jr. (2011), A model study of Circumpolar Deep Water on the West Antarctic Peninsula and Ross Sea continental shelves, *Deep Sea Res., Part II*, *58*(13–16), 1508–1523, doi:10.1016/j.dsr2.2010.11.013.
Ducklow, H., et al. (2012), The marine system of the Western Antarctic Peninsula, in *Antarctic Ecosystems an Extreme Environment in a Changing World*, edited by A. D. Rogers et al., Blackwell, London.
Erickson, Z. K., A. F. Thompson, N. Cassar, J. Sprintall, and M. R. Mazloff (2016), An advective mechanism for deep chlorophyll maxima formation in southern Drake Passage, *Geophys. Res. Lett.*, *43*, 10,846–10,855, doi:10.1002/2016GL070565.
Graham, J. A., M. S. Dinniman, and J. M. Klinck (2016), Impact of model resolution for on-shelf heat transport along the West Antarctic Peninsula, *J. Geophys. Res. Oceans*, *121*, 7880–7897, doi:10.1002/2016JC011875.
Heywood, K. J., et al. (2014), Ocean processes at the Antarctic continental slope, *Philos. Trans. R. Soc. A*, *372*(2019), 20130047, doi:10.1098/rsta.2013.0047.
Hofmann, E. E., J. M. Klinck, C. M. Lascara, and D. A. Smith (1996), Water mass distribution and circulation west of the Antarctic Peninsula and including Bransfield Strait, in *Foundations for Ecological Research West of the Antarctic Peninsula*, edited by R. M. Ross, E. E. Hofmann, and L. B. Quentin, pp. 61–80, AGU, Washington, D. C.
Howard, S. L., J. Hyatt, and L. Padman (2004), Mixing in the pycnocline over the western Antarctic Peninsula shelf during Southern Ocean GLOBEC, *Deep Sea Res., Part II*, *51*(17–19), 1965–1979, doi:10.1016/j.dsr2.2004.08.002.
Huss, M., and D. Farinotti (2014), A high-resolution bedrock map for the Antarctic Peninsula, *The Cryosphere*, *8*, 1261–1273.
Jenkins, A., P. Dutrieux, S. S. Jacobs, S. D. McPhail, J. R. Perrett, A. T. Webb, and D. White (2010), Observations beneath Pine Island Glacier in West Antarctica and implications for its retreat, *Nat. Geosci.*, *3*(7), 468–472, doi:10.1038/ngeo890.
Klinck, J. M. (1998), Heat and salt changes on the continental shelf west of the Antarctic Peninsula between January 1993 and January 1994, *J. Geophys. Res*, *103*, 7617–7636, doi:10.1029/98JC00369.
Klinck, J. M., and M. S. Dinniman (2010), Exchange across the shelf break at high southern latitudes, *Ocean Sci. Discuss.*, *6*, 513–524, doi:10.5194/os-6-513-2010.
Klinck, J. M., E. E. Hofmann, R. C. Beardsley, B. Salihoglu, and S. Howard (2004), Water-mass properties and circulation on the west Antarctic Peninsula Continental Shelf in Austral Fall and Winter 2001, *Deep Sea Res., Part II*, *51*, 1925–1946, doi:10.1016/j.dsr2.2004.08.001.
Martinson, D. G., and D. C. McKee (2012), Transport of warm Upper Circumpolar Deep Water onto the western Antarctic Peninsula continental shelf, *Ocean Sci. Discuss.*, *8*, 433–442, doi:10.5194/os-8-433-2012.
Martinson, D. G., S. E. Stammerjohn, R. A. Iannuzzi, R. C. Smith, and M. Vernet (2008), Western Antarctic Peninsula physical oceanography and spatio-temporal variability, *Deep Sea Res., Part II*, *55*(18–19), 1964–1987, doi:10.1016/j.dsr2.2008.04.038.
Meredith, M. P., and J. C. King (2005), Rapid climate change in the ocean west of the Antarctic Peninsula during the second half of the 20th century, *Geophys. Res. Lett.*, *32*, L19604, doi:10.1029/2005GL024042.
Moffat, C., B. Owens, and R. C. Beardsley (2009), On the characteristics of Circumpolar Deep Water intrusions to the west Antarctic Peninsula Continental Shelf, *J. Geophys. Res.*, *114*, C05017, doi:10.1029/2008JC004955.
Pelland, N. A., C. C. Eriksen, and C. M. Lee (2013), Subthermocline Eddies over the Washington Continental Slope as Observed by Seagliders, 2003–09, *J. Phys. Oceanogr.*, *43*, 2025–2053, doi:10.1175/JPO-D-12-086.1.
Prandtl, L. (1925), Bericht über Untersuchungen zur ausgebildeten Turbulenz, *Z. Angew. Math. Mech.*, *5*(2), 136–139.
Prézelin, B. B., E. E. Hofmann, C. Mengelt, and J. M. Klinck (2000), The linkage between Upper Circumpolar Deep Water (UCDW) and phytoplankton assemblages on the west Antarctic Peninsula continental shelf, *J. Mar. Res.*, *58*, 165–202.
Prézelin, B. B., E. E. Hofmann, M. Moline, and J. M. Klinck (2004), Physical forcing of phytoplankton community structure and primary production in continental shelf waters of the Western Antarctic Peninsula, *J. Mar. Res.*, *62*(3), 419–460, doi:10.1357/0022240041446173.
Pritchard, H. D., S. R. M. Ligtenberg, H. A. Fricker, D. G. Vaughan, M. R. van den Broeke, and L. Padman (2012), Antarctic ice-sheet loss driven by basal melting of ice shelves, *Nature*, *484*, 502–505, doi:10.1038/nature10968.
Rignot, E., and S. S. Jacobs (2002), Rapid bottom melting widespread near Antarctic ice sheet grounding lines, *Science*, *296*(5575), 2020–2023, doi:10.1126/science.1070942.
Rignot, E., J. Mouginot, M. Morlighem, H. Seroussi, and B. Scheuchi (2014), Widespread, rapid grounding line retreat of Pine Island, Thwaites, Smith, and Kohler glaciers, West Antarctica, from 1992 to 2011, *Geophys. Res. Lett.*, *41*, 3502–3509, doi:10.1029/2011GL046583.
Savidge, D. K., and J. A. Amft (2009), Circulation on the West Antarctic Peninsula derived from 6 years of shipboard ADCP transects, *Deep Sea Res., Part I*, *56*(10), 1633–1655, doi:10.1016/j.dsr.2009.05.011.
Schmidtko, S., K. J. Heywood, A. F. Thompson, and S. Aoki (2014), Multidecadal warming of Antarctic waters, *Science*, *346*, 1227–1231, doi:10.1126/science.1256117.
Schofield, O., et al. (2007), Slocum Gliders: Robust and ready, *J. Field Robotics*, *24*(6), 473–485, doi:10.1002/rob.20200.
Smith, D. A., and J. M. Klinck (2002), Water properties on the west Antarctic Peninsula continental shelf: A model study of effects of surface fluxes and sea ice, *Deep Sea Res., Part II*, *49*, 4863–4886, doi:10.1016/S0967-0645(02)00163-7.
Smith, D. A., E. E. Hofmann, J. M. Klinck, and C. M. Lascara (1999), Hydrography and circulation of the West Antarctic Peninsula Continental Shelf, *Deep Sea Res., Part I*, *46*, 925–949.
Smith, R. C., et al. (1995), The Palmer LTER: A long-term ecological research program at Palmer Station, Antarctica, *Oceanography*, *8*, 77–86.
St-Laurent, P., J. M. Klinck, and M. S. Dinniman (2013), On the role of coastal troughs in the circulation of warm Circumpolar Deep Water on Antarctic shelves, *J. Phys. Oceanogr.*, *43*, 51–64, doi:10.1175/JPO-D-11-0237.1.
Turner, J., T. A. Lachlan-Cope, S. Colwell, G. J. Marshall, and W. M. Connolley (2006), Significant warming of the Antarctic winter troposphere, *Science*, *311*, 1914–1917, doi:10.1126/science.1121652.
Turner, J., H. Lu, I. White, J. C. King, T. Phillips, J. S. Hosking, T. J. Bracegirdle, G. J. Marshall, R. Mulvaney, and P. Deb (2016), Absence of 21st century warming on Antarctic Peninsula consistent with natural variability, *Nature*, *535*(7612), 411–415, doi:10.1038/nature18645.
Venables, H. J., M. P. Meredith, and J. A. Brearley (2016), Modification of deep waters in Marguerite Bay, western Antarctic Peninsula, caused by topographic overflows, *Deep Sea Res., Part II*, doi:10.1016/j.dsr2.2016.09.005.
Zhang, Z., P. Li, L. Xu, C. Li, W. Zhao, J. Tian, and T. Qu (2015), Subthermocline eddies observed by rapid-sampling Argo floats in the subtropical northwestern Pacific Ocean in Spring 2014, *Geophys. Res. Lett.*, *42*, 6438–6445, doi:10.1002/2015GL064601.

AGU PUBLICATIONS

Journal of Geophysical Research: Oceans

RESEARCH ARTICLE

10.1002/2017JC013031

Coastal ocean circulation during Hurricane Sandy

Travis Miles[1], **Greg Seroka**[2], **and Scott Glenn**[1]

[1]Department of Marine and Coastal Sciences, Rutgers University Center for Ocean Observing Leadership, New Brunswick, New Jersey, USA, [2]Ocean Prediction Center, NOAA/NWS/NCEP, College Park, Maryland, USA

Key Points:

- Tropical cyclones can have a large impact on coastal ocean circulation
- Sandy was an extreme event that drastically altered the water column characteristics through cross-shelf advective processes
- Integrated ocean observing systems and regional modeling are critical tools to resolve coastal ocean circulation in tropical cyclones

Correspondence to:
T. Miles,
tnmiles@marine.rutgers.edu

Citation:
Miles, T., G. Seroka, and S. Glenn (2017), Coastal ocean circulation during Hurricane Sandy, *J. Geophys. Res. Oceans*, *122*, 7095–7114, doi:10.1002/2017JC013031.

Received 26 APR 2017
Accepted 20 JUL 2017
Accepted article online 26 JUL 2017
Published online 5 SEP 2017

Abstract Hurricane Sandy (2012) was the second costliest tropical cyclone to impact the United States and resulted in numerous lives lost due to its high winds and catastrophic storm surges. Despite its impacts little research has been performed on the circulation on the continental shelf as Sandy made landfall. In this study, integrated ocean observing assets and regional ocean modeling were used to investigate the coastal ocean response to Sandy's large wind field. Sandy's unique cross-shelf storm track, large size, and slow speed resulted in along-shelf wind stress over the coastal ocean for nearly 48 h before the eye made landfall in southern New Jersey. Over the first inertial period (~18 h), this along-shelf wind stress drove onshore flow in the surface of the stratified continental shelf and initiated a two-layer downwelling circulation. During the remaining storm forcing period a bottom Ekman layer developed and the bottom Cold Pool was rapidly advected offshore ~70 km. This offshore advection removed the bottom Cold Pool from the majority of the shallow continental shelf and limited ahead-of-eye-center sea surface temperature (SST) cooling, which has been observed in previous storms on the MAB such as Hurricane Irene (2011). This cross-shelf advective process has not been observed previously on continental shelves during tropical cyclones and highlights the need for combined ocean observing systems and regional modeling in order to further understand the range of coastal ocean responses to tropical cyclones.

Plain Language Summary Hurricane Sandy (2012) was the second costliest tropical cyclone to impact the United States and resulted in numerous lives lost due to its high winds and catastrophic storm surges. Despite its impacts little research has been performed on the circulation of the coastal ocean as Sandy made landfall. In this study integrated ocean observing assets and regional ocean modeling were used to investigate the coastal ocean response to Sandy's large wind field. Sandy's unique cross-shelf storm track, large size, and slow speed resulted in powerful alongshore winds over the coastal ocean for nearly 48 h before the eye made landfall in southern New Jersey. These winds transported cold bottom waters offshore and left the coastal ocean uniformly warm and mixed. This circulation pattern has not been observed previously during tropical cyclones and highlights the need for a continued focus on coastal ocean observing systems and numerical modeling during storm events.

1. Introduction

Tropical cyclones (TCs) are among the deadliest and costliest natural hazards on earth. In the US alone they are responsible for nearly half of all billion dollar natural disasters, and account for over 3000 deaths between 1980 and 2016 (https://www.ncdc.noaa.gov/billions/). Globally, individual storms can be extremely deadly such as Nargis, which lead to over 100,000 fatalities in Myanmar in 2008 [*Fritz et al*., 2009]. TC track forecasts have improved dramatically since 1970, yet similar dramatic progress has not been made in TC intensity prediction [*DeMaria et al*., 2014; *Cangialosi and Franklin*, 2016]. Predictions of TC rapid intensification or deintensification just before landfall remain a critical challenge within this intensity gap. Rapid intensification in the hours before landfall has the potential to catch coastal communities off guard, while unexpected rapid deintensification may erode future forecast credibility among the public [*Considine et al*., 2004]. Uncertain modeling of the ocean response to and feedback on TCs remains a critical factor that has limited improvement in intensity forecasts [*Emanuel et al*., 2004; *Yablonsky and Ginis*, 2009; *Emanuel*, 2016], particularly in the coastal ocean just prior to landfall [*Glenn et al*., 2016; *Seroka et al*., 2016]. This manuscript contributes to a growing body of work that details the response of the coastal ocean to TCs. Specifically, this work focuses on the stratified coastal ocean response ahead of and during Hurricane Sandy, the second costliest storm to impact the US (~$68 billion USD in damages and 159 lives lost https://www.ncdc.noaa.gov/billions/).

Small changes in sea surface temperature (SST)—~1°C—can impact TC intensity [*Price*, 1981; *Emanuel*, 1999; *Bender and Ginis*, 2000; *Emanuel et al*., 2004; *Yablonsky and Ginis*, 2008], as the ocean provides a source of heat for atmospheric convection [*Black et al*., 2007; *Jaimes and Shay*, 2015]. In the deep ocean, TCs have been found to drive upwelling and mixing of cold nutrient rich water to the sea surface since the mid 1900s [*Hidaka and Akiba*, 1955; *Fisher*, 1958; *Leipper*, 1967]. These events, frequently referred to as "cold wakes," are typically observable by satellite [*Stramma et al*., 1986; *Cornillon et al*., 1987] and can produce large phytoplankton blooms in the days following storm passage [*Wang and Zhao*, 2008]. Focused field campaigns such as the Coupled Boundary Layer Air-Sea Transfer Experiment (CBLAST) have used a combination of atmosphere and ocean observations and modeling to show that storm-driven mixing over the deep ocean can reduce heat transfer to the atmosphere [*Black et al*., 2007; *Chen et al*., 2007]. Extensive literature exists detailing both the deep ocean response to TCs as well as storm surge impacts, yet comparatively little work has been done over continental shelves. One of these few studies has indicated that in some coastal regions rapid intensification is expected to increase as the planet warms [*Emanuel*, 2016]. Others have focused on TCs entering midlatitudes, and have shown that rapid deintensification occurs when storms cross the highly stratified continental shelves [*Glenn et al*., 2016]. Existing operational coupled atmosphere-ocean TC models have failed to accurately capture the ocean response that leads to this rapid deintensification.

The source of the cold water on the Mid Atlantic (MAB) Bight shelf, which can be mixed to the surface and lead to rapid storm deintensification [*Glenn et al*., 2016; *Seroka et al*., 2016], is a seasonal feature known as the summer Cold Pool [*Houghton et al*., 1982]. The Cold Pool is a near bottom water mass that extends from the southern edge of Georges Bank along the MAB continental midshelf and outer-shelf to Cape Hatteras, NC. The Cold Pool is formed in the spring as thermal heating develops a seasonal thermocline over cold remnant winter water. This thermocline reaches its peak strength in July and August when surface to bottom temperature differences can exceed 15°C and the surface mixed layer is typically between 10 and 20 m thick across the shelf [*Castelao et al*., 2008]. This stratification begins to break down in September through a combination of reduced solar heating, falling atmospheric temperatures, and most notably fall transition storms, which periodically vertically mix the water column [*Houghton et al*., 1982; *Lentz*, 2003, 2017; *Glenn et al*., 2008].

Hurricane Irene in 2011 was a relatively heavily sampled storm that impacted the MAB continental shelf and serves as an ideal case study of rapid deintensification. Irene made landfall in New Jersey in late August of 2011 [*Avila and Cangialosi*, 2012] when MAB stratification was near its peak. A study by *Glenn et al*. [2016] showed that onshore winds forced the surface mixed layer toward the NJ coastline setting up an offshore-directed pressure gradient that forced an offshore bottom layer flow, enhancing vertical shear and mixing over the midshelves and outer-shelves where stratification was greatest. SSTs were reduced ahead-of-eye-center by over ~4.5°C at a coastal buoy, accounting for 82% of the total storm cooling at that location. This study showed that out of the 11 storms that have traversed the MAB between 1985 and 2016 during the summer stratified season, 73% of the overall cooling across all storms at selected coastal buoy locations occurred ahead-of-eye-center with an average cooling of 2.7°C. In Irene, this cooling represented the largest factor contributing to the storm's deintensification just prior to its NJ landfall—not track, wind shear, or dry air intrusion [*Seroka et al*., 2016].

Hurricane Sandy made landfall in New Jersey 14 months after Irene in nearly the same location [*Blake et al*., 2013]. Despite its catastrophic damages, Hurricane Sandy also weakened and was designated as posttropical as it crossed the continental shelf of the MAB. Unlike Irene, MAB SSTs during Sandy were only reduced by ~2°C. Coupled ocean-atmosphere model hindcasts [*Zambon et al*., 2014] showed Sandy's weakening was linked to large-scale synoptic atmospheric circulation and was insensitive to air-sea coupling. This study hypothesized that the MAB had already undergone its fall transition, limiting the impact of the MAB ocean on atmospheric processes. Yet, observations from an autonomous underwater glider deployed ahead of Sandy showed the Cold Pool and stratification was still present on the MAB shelf, although to a lesser degree than in Irene [*Miles et al*., 2015]. The dichotomy between the ocean's impact on the intensities of Irene and Sandy indicates that more focused studies of the stratified coastal ocean response to a wide range of landfalling TCs are critical. In this manuscript, we investigate the coastal ocean response of the

Cold Pool to Sandy's powerful and long-lasting winds as the storm crossed the MAB continental shelf. We use a unique data set from a Teledyne Webb Slocum autonomous underwater glider and process-focused numerical simulations with the Regional Ocean Modeling System (ROMS). Understanding these processes will be critical to improving and building confidence in short-term forecasts of storm intensity as storms cross continental shelves and approach increasingly vulnerable population centers [*Miller et al*., 2009; *Kossin et al*., 2014].

2. Methods

Ocean observing systems have developed into critical networks of instruments capable of sampling the coastal ocean in three dimensions before, during, and after storm events [*Kohut et al*., 2006; *Miles et al*., 2013, 2015; *Domingues et al*., 2015; *Glenn et al*., 2016]. Hurricane Sandy made landfall after crossing through the Mid Atlantic Regional Association Coastal Ocean Observing System (MARACOOS), a certified Regional Information Coordination Entity (RICE) of the U.S. Integrated Ocean Observing System (IOOS) [*Briscoe et al*., 2008]. These systems typically include a range of technologies such as satellite observations, high frequency (HF) Radars, met-ocean buoys, autonomous underwater gliders, among many others and support regional ocean data products and forecasts through data assimilation and model validation. Technologies used in this study and described below include autonomous underwater gliders, HF Radar, and numerical model technologies that were developed and supported through MARACOOS over the past decade.

2.1. Gliders

Autonomous underwater gliders have become reliable technologies for sampling the ocean in extreme weather conditions [*Glenn et al*., 2008, 2016; *Ruiz et al*., 2012; *Miles et al*., 2013, 2015; *Domingues et al*., 2015; *Swart et al*., 2015; *Nicholson et al*., 2016; *du Plessis et al*., 2017]. The ability of Teledyne Webb Research manufactured Slocum gliders to access shallow ($<$100 m) continental shelves and their modular science bay design make them uniquely suited for rapid deployment to sample coastal storm events. Slocum gliders move vertically through the water column by using a pump in the fore section to change volume and shifting ballast to alter pitch to dive and climb at $\sim$15–20 cm s^{-1}. The glider body shape, wings, and nominal pitch angle of $\pm$26.5° result in forward motion of $\sim$20 km d^{-1} relative to the moving water column. Integrated sensors typically collect data at 0.5 Hz and send data back to shore in near real-time through an Iridium Satellite cellphone in the tail section. Rutgers University glider RU23 data were used in this study to investigate the evolution of the thermal structure and water column velocities on the continental shelf during Hurricane Sandy storm conditions. Previously these data were also used to investigate sediment resuspension and transport in Sandy by *Miles et al*. [2015]. RU23 was programmed to surface at 2 h intervals in order to provide high temporal resolution data during the storm. This glider was equipped with an unpumped Seabird glider conductivity, temperature, and depth (CTD) sensor; two Wetlabs, Inc. Eco Triplets with two channels measuring chlorophyll fluorescence, colored dissolved organic matter, and four channels of optical backscatter; and an externally mounted internally logging 2 MHz transducer Nortek Aquadopp current profiler.

Thermal inertia of the conductivity cell has remained a challenge for calculating high-quality salinity and density parameters with unpumped glider CTDs in regions with large temperature gradients such as those found on the MAB. Attempts at thermal lag correction to conductivity and subsequent salinity and density calculations following the *Garau et al*. [2011] minimization technique were unsuccessful. This is likely due to the exceptionally large thermal stratification, which exceeds what was successfully tested in that study, as well as the difficulty in finding consistent time offsets with the unpumped glider CTD. To address this issue, we calculate density by removing salinity data after large temperature changes in each profile (e.g., below the thermocline on glider dives and above the thermocline on the subsequent climb) and utilize the nearest-bottom salinity on dives and nearest-surface salinity on climbs to represent that layer's salinity for density calculations. While crude, this approach maintains water column stability. Further, the MAB density structure is dominated by temperature rather than salinity, so there is a limited impact on final density calculations. Temperature and corrected salinity and density fields were binned into 2 m bins. With the glider fall velocity of $\sim$15–20 cm s^{-1} and CTD sample rate at 0.5 Hz this resulted in over 10 points per bin. These binned data were used to estimate buoyancy frequency as:

$$N^2 = \frac{g}{\rho_o} \frac{\partial \sigma_\theta}{\partial z} \quad (1)$$

where N is the buoyancy frequency, g is gravity, ρ_o is a reference density of 1025 kg m^{-3}, σ_θ is potential density anomaly, and z is depth.

The Nortek Aquadopp current profiler was an externally mounted and independently logging three-beam 2 MHz instrument. It was mounted in an upward looking orientation for practical deployment and recovery purposes and to not block downward looking optical sensors. The transducer head was custom made to be oriented vertically at a glider pitch angle of 26.5°. Data collection was configured with 10 1 m bins and a 0.2 m blanking distance, and samples in beam coordinates were collected at 1 Hz. To rotate beam coordinates into east, north, and up (ENU) pitch and roll were used from the Nortek Aquadopps internal sensor, while heading information after timestamp alignment was interpolated from the glider compass. This was done to minimize magnetic interference from the moving battery pack and pump system in the fore section of the glider, which was closer to the mounting location of the Aquadopp than the aft mounted glider compass. To estimate realistic water column velocities a method typically used for lowered acoustic Doppler current profilers [*Visbeck*, 2002], and which has been adapted for use on Spray [*Todd et al*., 2011a, 2011b] and Slocum [*Miles et al*., 2015] gliders was used. This method uses the Aquadopp to determine water column vertical shear during a glider segment (glider dive and surfacing) and constrains these shear velocities with the glider dead-reckoned depth averaged current [*Davis et al*., 2002] to determine the absolute water column velocity. The time resolution of these currents is dependent on the length of time between each glider surfacing, which can vary. In this case, the glider surfaced approximately every 2 h as stated above in an effort to resolve tidal variability as well as the rapidly changing currents induced by Sandy.

2.2. HF Radar

The MAB has one of the largest continuous networks of CODAR HF Radar stations globally, ranging from North Carolina to Massachusetts. HF Radar uses the Doppler shift of backscattered radio frequencies from surface waves to measure the radial component of ocean surface currents, i.e. toward or away from each station [*Barrick*, 1971a,1971b; *Teague*, 1971]. Radial data are collected continuously and overlapping radials are combined via an optimal interpolation method to produce hourly total surface current maps hourly [e.g., *Kohut et al*., 2012]. The network in the MAB, managed through MARACOOS, consists of nested 5, 13, and 25 MHz networks [*Roarty et al*., 2010]. The 5 MHz network used in this study is capable of measuring surface currents out to the shelf-break, approximately 150 km offshore in ideal wave conditions and has a nominal spatial resolution of 6 km. The MARACOOS HF Radar network was operating at full capacity during Sandy's approach, but storm surges destroyed numerous stations reducing data coverage and quality starting at 3:00 GMT on 31 October 2012.

2.3. Atmospheric Model

The atmospheric model used in this study was the RUCOOL implementation of the Weather Research and Forecasting Advanced Research WRF (WRF-ARW) model developed at NCAR [*Skamarock et al*., 2008]. The forcing was previously used in *Miles et al*. [2015] and is configured with 6 km horizontal resolution, 35 vertical levels, horizontal boundary conditions from the Global Forecasting System (GFS) 0.5° operational configuration at the time, and a coldest-pixel composite SST bottom boundary condition from the Advanced Very High Resolution Radiometer (AVHRR) and NASA SPoRT [*Glenn et al*., 2016]. The SST bottom boundary condition is held static within each 36 h hindcast cycle, since there were very few new datapoints to add to each composite interval due to Sandy's extensive cloud cover. This static bottom boundary is appropriate based on the limited impact of air-sea coupling affecting Sandy's wind field [*Zambon et al*., 2014]. This WRF product is similar to the one used in previous studies [*Georgas et al*., 2014; *Glenn et al*., 2016; *Seroka*, 2016] and covers the entire MAB (Figure 1). Data were output hourly from a series of six 36 h forecast runs reinitialized at 00:00 GMT daily starting on 25 October. We combined hourly output from hour 7 to 30 and removed hours 0 to 6 to minimize the impact of model spin-up time on the final continuous hourly forcing. Please see *Miles et al*. [2015] for further details of the WRF atmospheric model configuration used in this study.

The WRF model output used in this study was previously compared with buoys 44009 and 44025 in *Miles et al*. [2015]. This comparison showed that simulated winds and pressure compared qualitatively well with

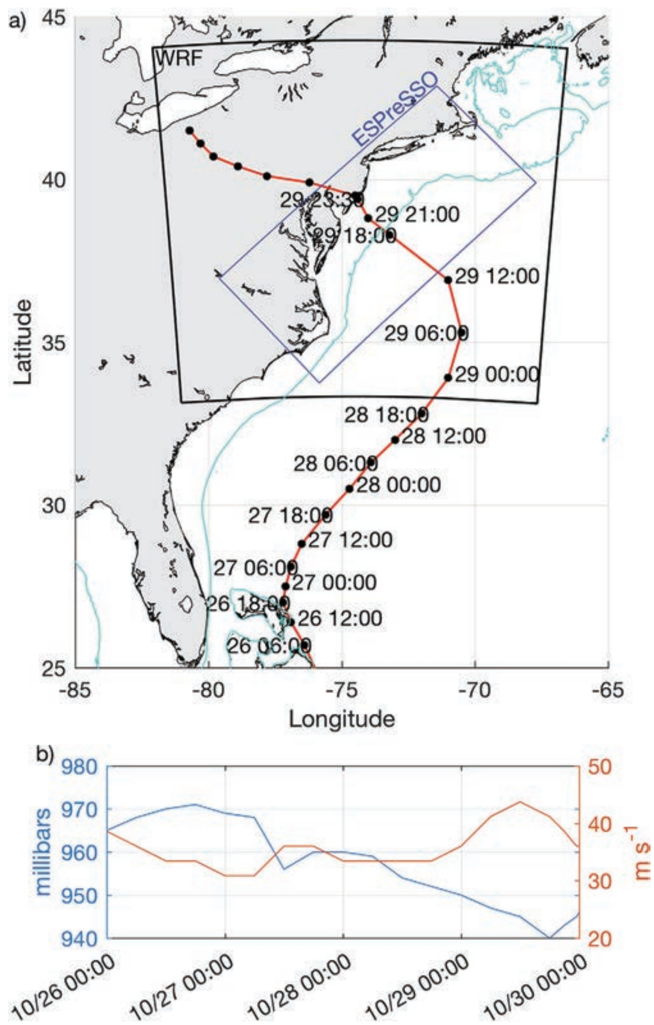

Figure 1. A map (a) of the WRF model domain (black box), ROMS ESPreSSO model domain (blue box), NHC best track positions (red line) and times (dd HH:MM in black), and the 100 m isobath (teal line). A time series (b) of the NHC best track pressure (blue) and maximum wind speed (orange).

observations and had correlation coefficients of 0.87 and 0.90 with winds at 44009 and 44025, respectively, and 0.99 with pressure at both buoys. Sandy track comparisons between modeled minimum pressure and the NHC best track estimates as the eye transited across the continental shelf (Figure 2) show the modeled track staying slightly north of the NHC best track until the final hour before landfall. The maximum separation between the two tracks during this time period is less than 35 km and was less than 10 km at landfall, well within the NHC best track estimate uncertainties of 80 to 30 km for tropical depressions and category 4 to 5 hurricanes, respectively, in the Atlantic Basin [*Torn and Snyder*, 2012].

2.4. Hydrodynamic Model

We performed numerical model simulations of the coastal ocean response to Sandy using the Regional Ocean Modeling System (ROMS) [*Shchepetkin and McWilliams*, 2005, 2009a, 2009b; *Haidvogel et al*., 2008] with the Experimental System for Predicting Shelf and Slope Optics (ESPreSSO) domain [*Cahill et al*., 2008; *Haidvogel et al*., 2008; *Hofmann et al*., 2008; *Zhang et al*., 2009; *Xu et al*., 2013]. ROMS is a free surface, sigma-coordinate, primitive equation numerical ocean model that has been used extensively to investigate regional ocean processes globally. The ESPreSSO domain (Figure 1) includes the entire MAB from within bays out past the shelf-break with 5 km horizontal resolution and 36 vertical levels. ESPreSSO uses

Four-dimensional variational (4D-Var) data assimilation to obtain the best state estimate of the coastal ocean in near real-time [*Moore et al*., 2011] and has been running nearly continuously since 2006. The standard ESPreSSO configuration uses boundary conditions from the Hybrid Coordinate Ocean Model (HYCOM) Navy Coupled Ocean Data Assimilation (NCODA) forecast system (http://hycom.org/), tides from the Advanced CIRCulation (ADCIRC) tidal model (http://adcirc.org/), and river discharge from the United States Geological Survey (USGS). Surface fluxes derived from the WRF-ARW simulation mentioned above were calculated using the COARE bulk formulae [*Fairall et al*., 2003]. The generic length scale k-kl vertical mixing scheme was used for water column turbulent mixing parameterization [*Umlauf and Burchard*, 2003; *Warner et al*., 2005]. The Sandy hindcast simulation was initialized at 00:00 GMT on 25 October 2012 and run forward until 31 October 2012 07:00 GMT with hourly output. *Miles et al*. [2015] previously used this model configuration and setup to investigate sediment resuspension and transport processes during Sandy on the MAB.

Depth-average momentum balance terms were extracted from standard ROMS output and are represented by the following equations:

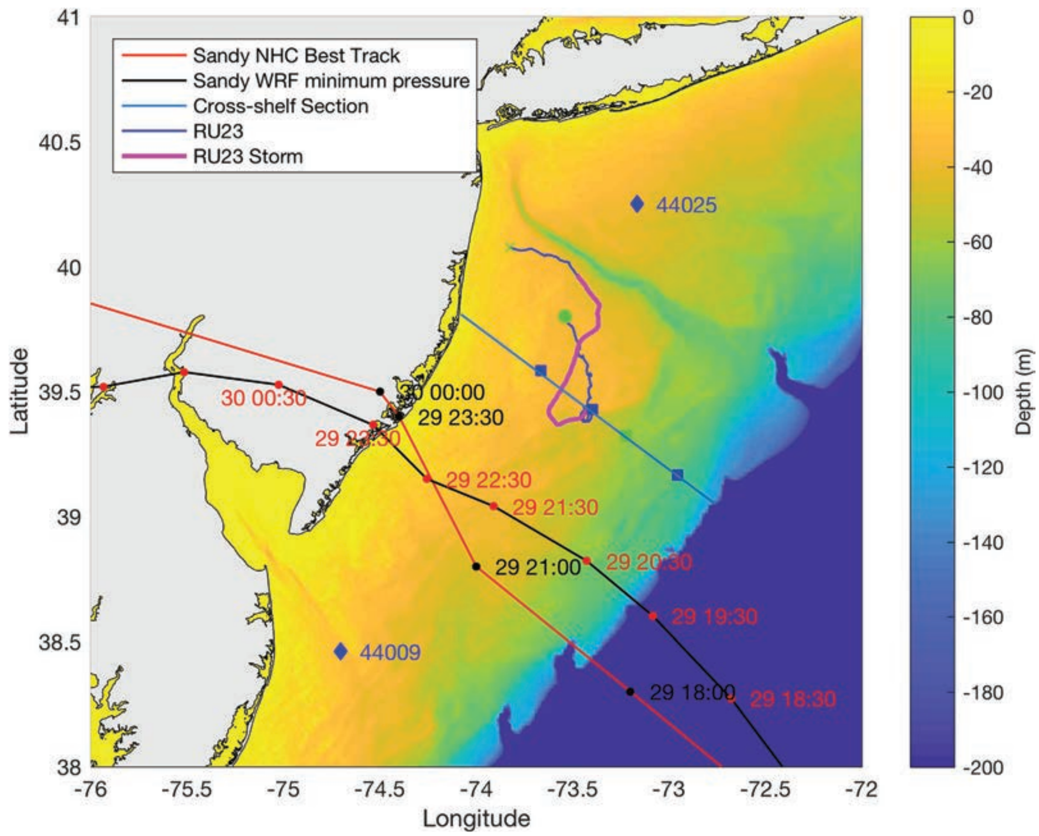

Figure 2. A zoomed in map of the New Jersey continental shelf and bathymetry with the NHC best track positions (red line) and times (dd HH:MM in black), and the WRF modeled track (black line) and times (dd HH:MM in red). The full glider RU23 track (blue) is plotted with the start location (green x) and recovery location (green circle) and the storm sampling period of 00:00 GMT on 28 October to 00:00 GMT on 31 October 2012 (magenta). NDBC buoys 44025 and 44009 are plotted with blue diamonds. The cross-shelf section used for Figures 7–12 is plotted in blue and the points for data extraction used in Figure 11 are plotted as blue squares. The third farthest extraction point from land at the 60 m isobath (green square) is used for Figure 6.

$$\underbrace{\frac{\partial u}{\partial t}}_{acceleration} = \underbrace{-\frac{\partial (uu)}{\partial x} - \frac{\partial (vu)}{\partial y}}_{horizontal\ \ advection} - \underbrace{\frac{1}{\rho_o}\frac{\partial P}{\partial x}}_{pressure\ \ gradient} + \left(\underbrace{\frac{\tau_s^x}{h\rho_o}}_{\substack{surface\\stress}} - \underbrace{\frac{\tau_b^x}{h\rho_o}}_{\substack{bottom\\stress}}\right) + \underbrace{fv}_{Coriolis} \tag{2}$$

$$\underbrace{\frac{\partial v}{\partial t}}_{acceleration} = \underbrace{-\frac{\partial (uv)}{\partial x} - \frac{\partial (vv)}{\partial y}}_{horizontal\ \ advection} - \underbrace{\frac{1}{\rho_o}\frac{\partial P}{\partial y}}_{pressure\ \ gradient} + \left(\underbrace{\frac{\tau_b^x}{h\rho_o}}_{\substack{surface\\stress}} - \underbrace{\frac{\tau_b^y}{h\rho_o}}_{\substack{bottom\\stress}}\right) - \underbrace{fu}_{Coriolis} \tag{3}$$

where t is time u and v are depth-averaged velocity in the x and y direction rotated into along-shelf and cross-shelf, P is pressure, ρ_o is a reference density of 1025 kg m^{-3}, τ_s^x and τ_s^y are wind stress, τ_b^x and τ_b^y are bottom stress, f is the Coriolis frequency. The horizontal viscosity terms were small in both the along and cross-shelf directions and were not included in equation (2) or (3). The temperature change rate equation was used to investigate the relative impact of mixing and advection on thermal changes throughout the water column as Sandy crossed the MAB shelf. Direct output from ROMS was used and is represented by:

$$\frac{\partial T}{\partial t} = -\frac{\partial (uT)}{\partial x} - \frac{\partial (vT)}{\partial y} - \frac{\partial (wT)}{\partial z} + \frac{\partial A_{kt}\frac{\partial T}{\partial z}}{\partial z} + D_T + F_T \tag{4}$$

with surface and bottom boundary conditions of:

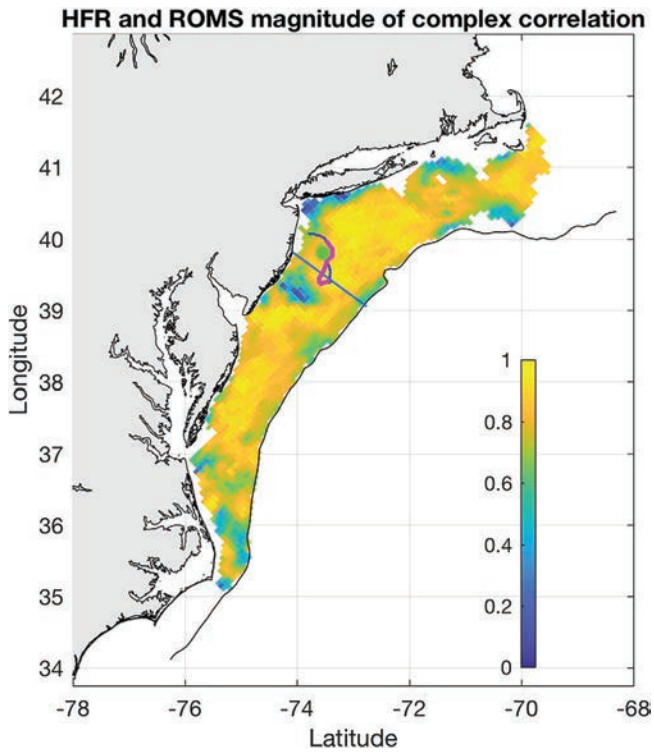

Figure 3. A map of the magnitude of the complex correlation between HF Radar hourly center-averaged surface currents and ROMS surface currents after interpolation to the nearest HF Radar grid point within the 150 m isobath (black contour). Correlation coefficients were made from model initialization at 00:00 GMT on 25 October to 00:00 GMT on 29 October 2012. The cross-shelf section used for Figures 7–12 is plotted in blue. The full glider RU23 track (blue) is plotted with the start location (green x) and recovery location (green circle) and the storm sampling period of 00:00 GMT on 28 October to 00:00 GMT on 31 October 2012 (magenta)

$$\left(A_{kt}\frac{\partial T}{\partial z}\right)_{z=0}=\frac{Q_{net}}{\rho_o C_P} \tag{5}$$

$$\left(A_{kt}\frac{\partial T}{\partial z}\right)_{z=-h}=0 \tag{6}$$

where, variables are as above in (2) and (3) in addition to T as temperature, D_T as the horizontal diffusion term, F_T is friction, A_{kt} is the vertical eddy diffusivity, h is depth, Q_{net} is the surface net heat flux, and C_p is the specific heat capacity of seawater as 3985 J (kg C)$^{-1}$.

The ROMS-ESPreSSO model output has been extensively validated and performed well compared to numerous other regional models [*Wilkin and Hunter*, 2013]. A portion of the results section is dedicated to comparisons between the model output and water column glider data at a single location. Here we also include additional verification using hourly averaged HF Radar output starting at model initialization time of 00:00 GMT on 25 October to 00:00 GMT 29 October 2012 prior to station loss as Sandy made landfall. For this comparison, complex correlation coefficients were calculated between hourly time series of each ROMS-ESPreSSO grid point and nearest HF Radar grid point on the continental shelf (onshore of the 150 m isobath). Complex correlation coefficients showed that the ROMS model simulated surface currents well throughout the majority of the domain (Figure 3) while HF Radar data were available. In particular, the ROMS model simulated surface currents well in the vicinity of the deployed glider and cross-shelf transect used for analysis in Figures 7–12.

3. Results

3.1. Storm Conditions

NHC best track estimates show Hurricane Sandy moved along the southeastern coast of the United States on 26 October 2012 in a relatively weak state with a minimum pressure of 970 m bar and maximum sustained wind speeds of 35 m s^{-1} (Figure 1). Sandy moved parallel to the US East Coast through the 27th and 28th with pressure gradually falling and maximum sustained wind speeds staying near 35 m s^{-1}. Just before midnight on 28 October and into the 29, wind speeds began to increase rapidly and Sandy began to make a northwestward turn toward the MAB. Wind speeds continued to increase, reaching a peak over 40 m s^{-1} at approximately 12:00 GMT on 29 October and a minimum pressure of 940 mbar a few hours later. Maximum sustained wind speeds decreased back to 35 m s^{-1} just before landfall in southern NJ at 23:30 GMT on 29 October Sandy's eye entered the WRF model domain (Figure 4) on 29 October just after midnight GMT. Modeled 10 m winds were directed alongshore toward the southwest along the MAB coastline at over 20 m s^{-1}. Winds continued in the alongshore direction toward the southwest on the NJ shelf until landfall, while in the southern MAB winds were directed offshore toward the south and southeast. At landfall in southern NJ winds rapidly shifted offshore over Delaware, alongshore toward the northeast on the NJ continental shelf, and onshore toward Long Island, NY farther north. As Sandy crossed the MAB

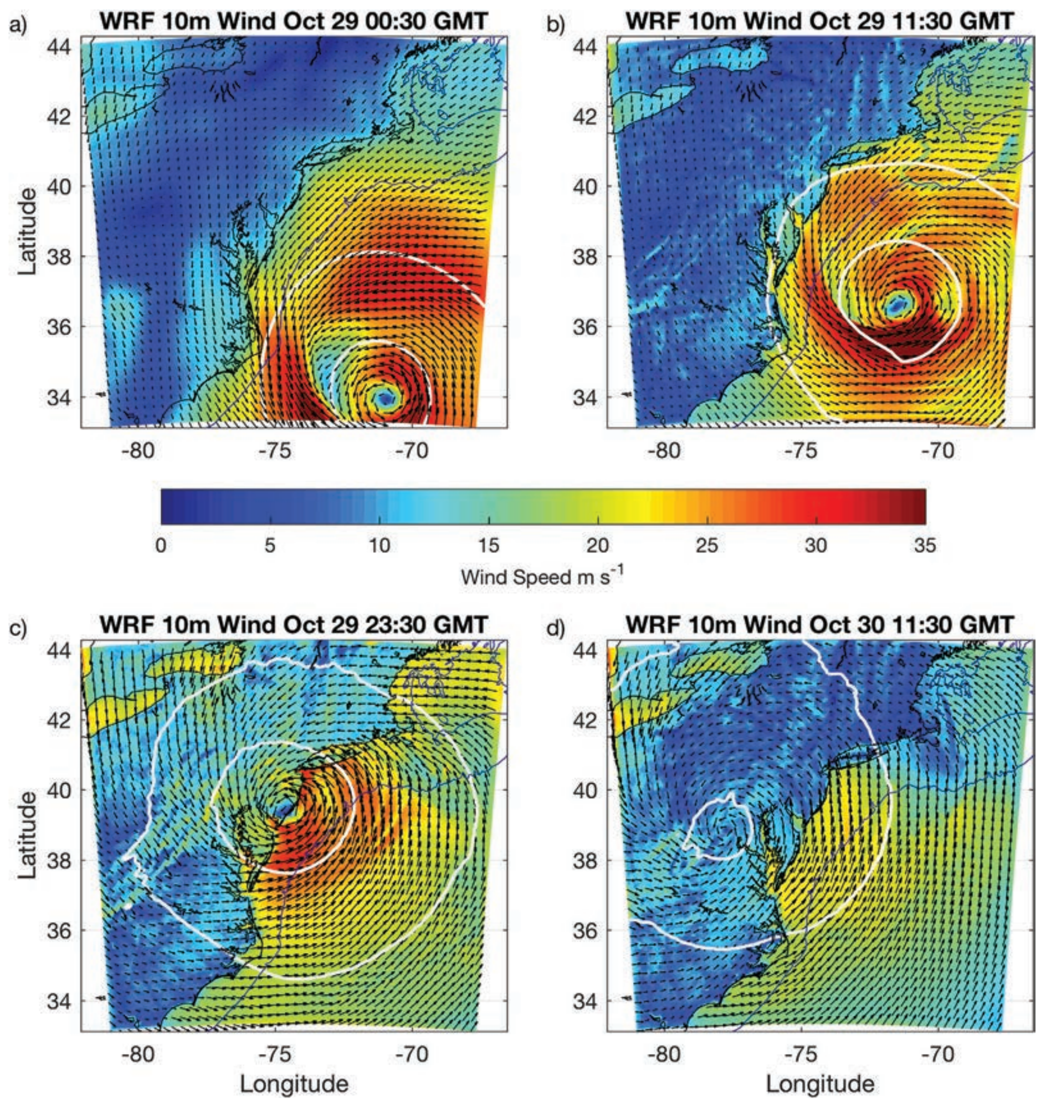

Figure 4. Maps of the WRF 10 m wind speed (colors) and direction (arrows) with the 990 (outer white contour) and 970 (inner white contour) millibar surface pressures at (a) 00:30 GMT, (b) 11:30 GMT, (c) 23:30 GMT on 29 October, and 11:30 GMT on 30 October.

continental shelf (Figure 2) it made its closest approach to the south of glider RU23 at 21:00 GMT on 29 October while also passing between the two NOAA NDBC buoys 44025 to the north and 44009 to the south.

3.2. Glider Water Column Observations

Glider RU23 was deployed on 25 October just south of the Hudson Shelf Valley off the northern NJ coastline (Figure 2). It was piloted offshore out to the 40 m isobath prior to the storm in order to avoid being forced by strong currents into the coastline. During the storm forcing period the glider was pushed toward the southwest over 60 km. Regardless of this alongshore advection the glider stayed near the 40 m isobaths, and on the northern side of the storm track. With the shelf-wide scale of storm forcing we interpret RU23 glider output as a time series of vertical profiles (Figure 5), though alongshore variability in water column properties may exist. These time series show four distinct time periods. The initial stratified period between 00:00 and 12:00 GMT on 28 October showed warm surface temperatures of over 17°C in the upper 30 m and 10°C temperatures below the thermocline, uniform to the bottom. Glider mounted Aquadopp derived cross-shelf currents were mostly vertically uniform and reflected the barotropic tide, with a slight bottom intensification in the offshore direction. Along-shelf flow was vertically uniform and southwestward at near

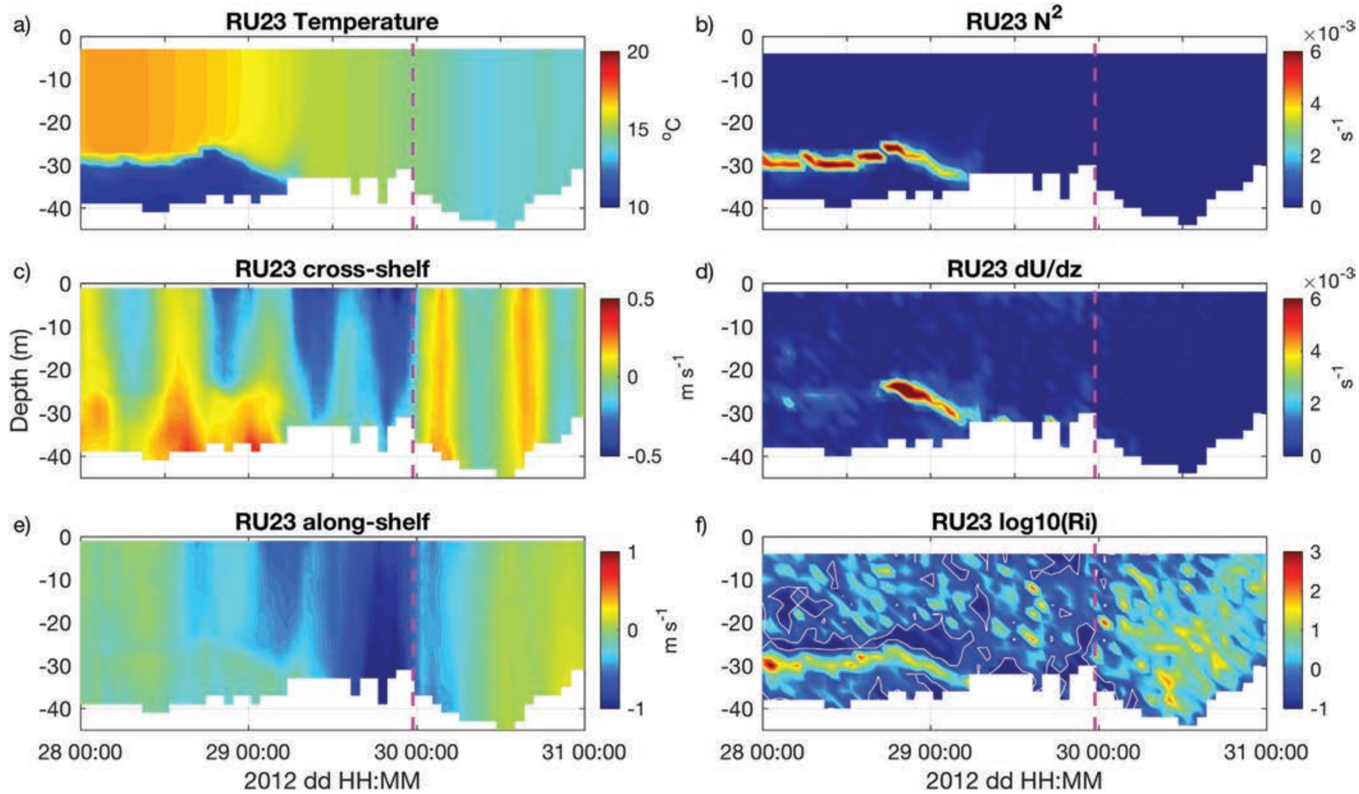

Figure 5. RU23 glider time series of vertical profiles extracted during the storm forcing period (track on magenta line shown in Figure 2). The vertical magenta line indicates Sandy landfall time. Variables plotted include (a) temperature, (c) cross-shelf velocity, (e) along-shelf velocity, (b) buoyancy frequency, (d) vertical shear of the horizontal velocity, and (f) the log10 of the Richardson number with Richardson number of 0.25 plotted with white contours. Velocity color bars are different in Figures 5c and 5e to highlight larger along-shelf magnitudes.

0.1 m s^{-1}. The sharp thermal stratification (>5°C m^{-1}) resulted in a stable pycnocline and large buoyancy frequencies. There was little vertical shear and the Richardson numbers remained large at the thermocline.

During the second time period between 12:00 GMT on 28 October and 06:00 GMT on the 29, the thermocline initially rose and then deepened dramatically, reaching the bottom in 12 h. Along-shelf currents increased to nearly 0.5 m s^{-1} in the surface layer and remained low in the bottom layer similar to during the initial stratified period. In the cross-shelf direction currents were onshore in the surface over 0.2 m s^{-1} while in the lower layer currents were offshore and near 0.4 m s^{-1} at 00:00 GMT on 29 October. While the thermocline deepened, vertical shear increased significantly, yet Richardson numbers remained above 0.25, indicating stable stratification was maintained up until the system transitioned from a two-layer to one-layer system by 06:00 GMT. During these 12 h the glider was advected ~12 km southward and remained on the northern side of the storm track, which indicates that much of the observed variability was temporal rather than spatial.

Between 06:00 GMT on 29 October and landfall at 23:30 GMT the water column responded to wind stress as a single layer. As the two-layer to one-layer transition occurred, the full water column cooled to just over 15°C, cross-shelf and along-shelf currents became relatively vertically uniform with primarily onshore flow with peak values near 0.2 m s^{-1}. Along-shelf flow was directed toward the southwest and reached near 1 m s^{-1} in the direction of the wind forcing. With a vertically well-mixed water column and uniform flow both buoyancy frequency and vertical shear were low and gradient Richardson numbers were variable throughout the water column. Following landfall storm-driven cross-shelf currents rapidly slowed and reflected the barotropic tide, while along-shelf currents slowed rapidly.

3.3. Hydrodynamic Model Output

ROMS output was extracted from a single location at the 60 m isobath (Figure 2) for comparison to glider cross sections (Figure 6). The model did not adequately represent the Cold Pool at the 40 m isobath where the glider was piloted but rather had a more defined Cold Pool farther offshore near the 60 m isobath.

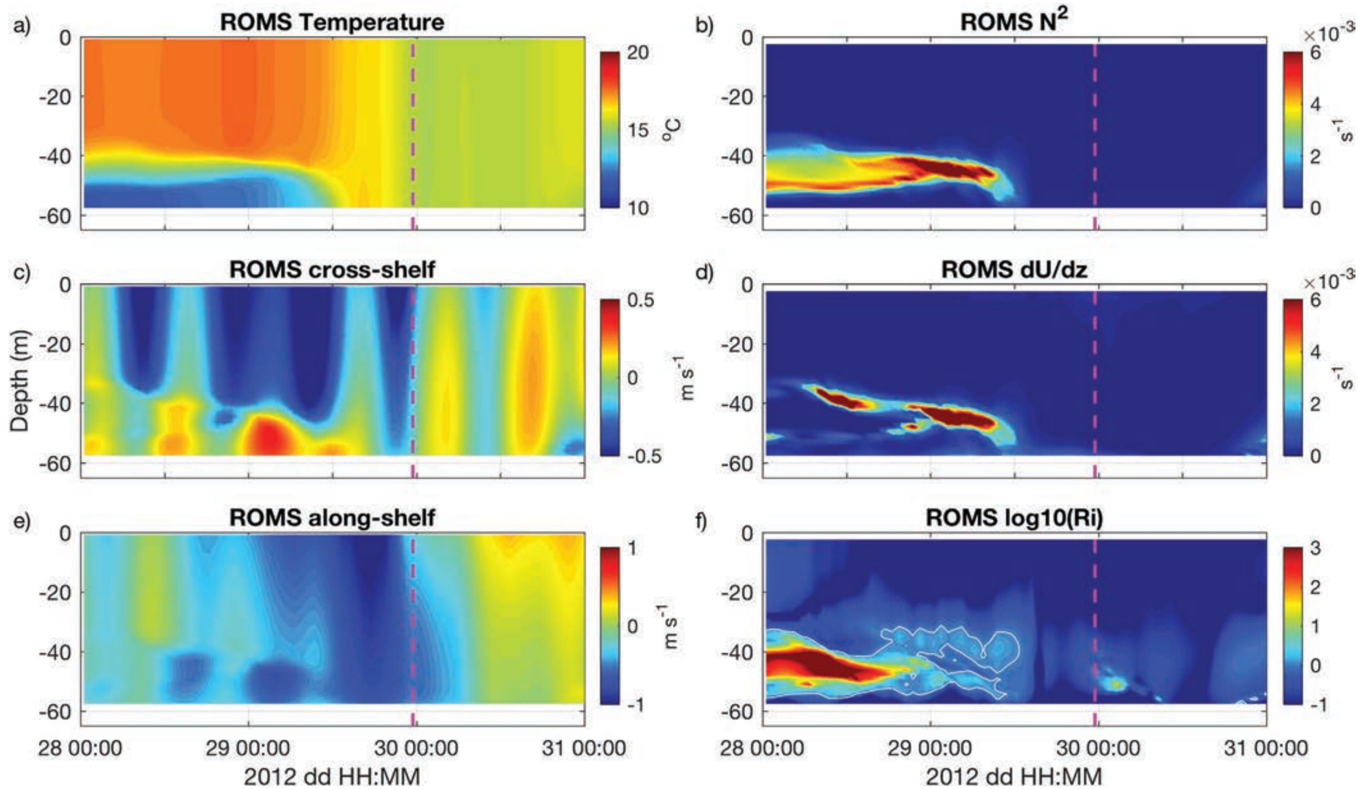

Figure 6. ROMS time series of vertical profiles extracted during the storm forcing period (green square plotted at the 60 m isobath shown in Figure 2). The vertical magenta line indicates Sandy landfall time. Variables plotted include (a) temperature, (c) cross-shelf velocity, (e) along-shelf velocity, (b) buoyancy frequency, (d) vertical shear of the horizontal velocity, and (f) the $\log_{10}$ of the Richardson number with Richardson number of 0.25 plotted with white contours. Velocity color bars are different in Figures 6c and 6e to highlight larger along-shelf magnitudes.

During the initial stratified period from 00:00 GMT and 12:00 GMT on 28 October modeled surface temperatures were only slightly warmer than observations, near 18°C while bottom temperatures were warmer than observations at11.5°C with a total difference of 6.5°C compared to 7°C observed by the glider. Currents were similar to glider sampled velocities with bottom intensified offshore flow in the cross-shelf direction and weak and variable along-shelf flow. At this farther offshore location stratification persisted until 12:00 GMT on 29 October, 6 h later than at the glider location. While the surface and bottom temperatures were similar to observations the thermocline was much thicker and weaker with a vertical temperature gradient of $\sim$0.3°C m^{-1} resulting in lower buoyancy frequencies than those observed by the glider over a broader vertical area, yet Richardson numbers remained above 0.25 throughout the storm forcing period. As stratification persisted longer in the model at this location flow was two-layer during the main storm forcing period with strong onshore flow near 0.5 m s^{-1} in the surface layer and offshore flow near 0.2 m s^{-1} near the bottom. Along-shelf southwestward flow did not reach its peak until after stratification eroded at 12:00 GMT on 29 October. While the thermocline deepened, N^2 remained elevated despite increasing vertical shear and, while Richardson numbers in the thermocline were reduced, they continued to remain above 0.25 until the system transitioned from two-layers to one. Despite differences between the glider observations and model output the observed water column features and transition from a two-layers to one-layer circulation are well represented.

Cross-shelf sections of the model simulated temperature and velocity were extracted along the transect shown in Figure 2 for three times, 12:30 GMT on 28 October, 00:30 GMT on 29 October, and 12:30 GMT on 29 October (Figure 7). At 12:30 GMT on 28 October a thin-layer of partially mixed Cold Pool water was present inshore up to the 20 m isobath with core Cold Pool water extending over a thicker bottom layer out to the shelf-break. Cross-shelf currents were directed offshore within the bottom Cold Pool layer and onshore in the surface layer. Along-shelf velocities were low throughout the water column at this time. Vertical velocities show downwelling at the inshore edge of the Cold Pool and over the deep ocean with upwelling

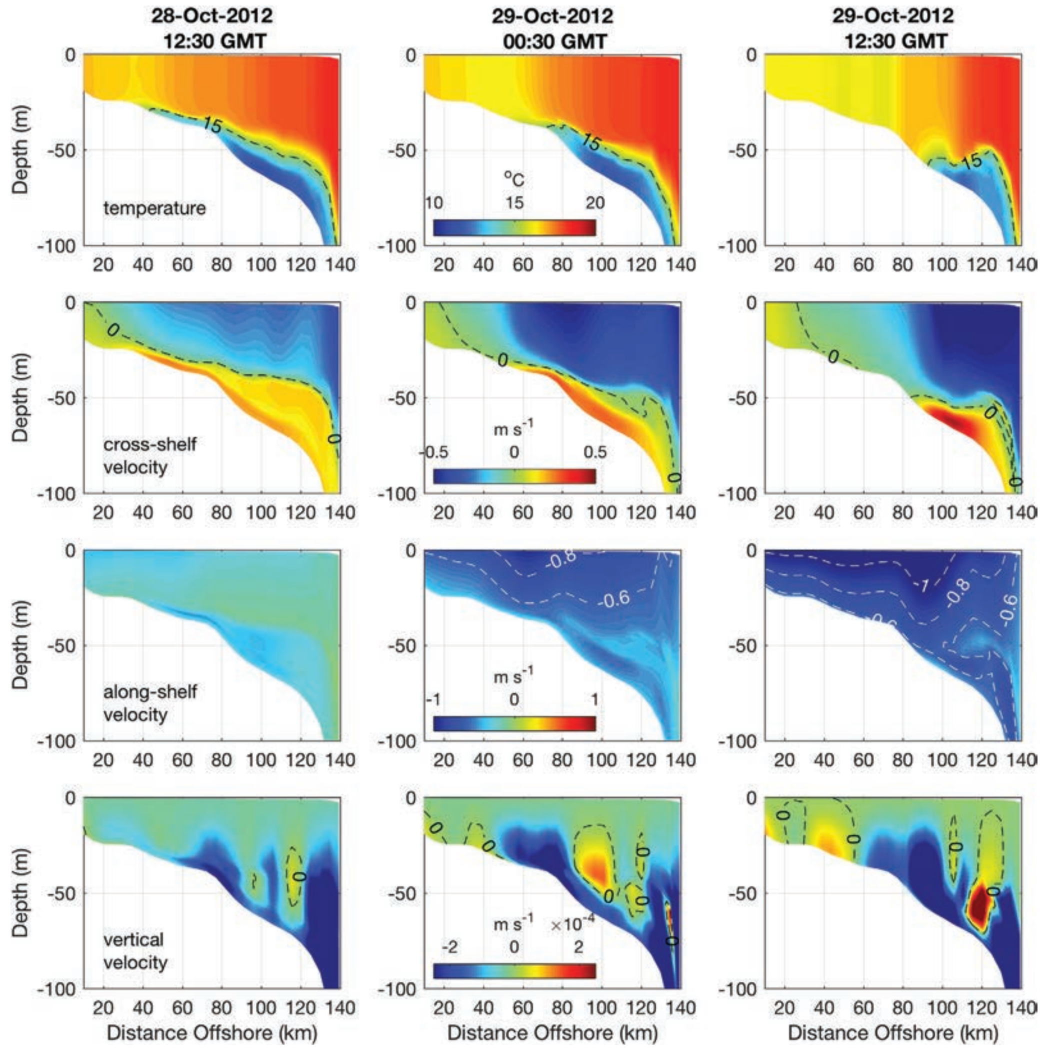

Figure 7. Cross-shelf sections of temperature (row 1), cross-shelf velocity (row 2), along-shelf velocity (row 3), and vertical velocity (row 4) extracted from the cross-shelf section shown in Figure 2. Times extracted include 12:30 GMT on 28 October, 00:30 GMT on 29 October, and 12:30 GMT on 29 October. Contours are used to show the approximate Cold Pool extent (row 1), to provide 0 crossing reference for velocities in rows 2 and 4, and to highlight the along-shelf southwestward velocities of 1, 0.8, and 0.6 m s^{-1} (row 3). Velocity color bars are different in rows 2–4.

within the core Cold Pool offshore. Over the next 24 h, a clear frontal region developed with vertically uniform temperatures that expanded across the innershelf. Cross-shelf velocities were onshore in the surface layer over the stratified region and slowed as they approached the unstratified innershelf. Bottom intensified offshore flow was evident within the Cold Pool and downwelling offshore flow occurred throughout the entire Cold Pool. Over the innershelf along-shelf velocities were toward the southwest throughout the entire water column, and were enhanced in an along-shelf jet toward the southwest at the downwelling front just above the innershelf edge of the Cold Pool at 12:30 GMT on 29 October.

Hovmöller diagrams of temperature and velocity were plotted along the same cross-shelf section to continuously track the temporal evolution of the surface and bottom layers (Figure 8). At 00:00 GMT on the 28th surface (Figure 8a) and bottom (Figure 8b) temperatures are similar out to 25 km offshore representing the well-mixed region inshore of the Cold Pool shown in Figure 7. The inshore edge of the Cold Poolis hereafter referred to as the Cold Pool Front and is defined by the cross-shelf temperature gradient in the bottom layer. The Cold Pool extended across the shelf between approximately 40 km and over 130 km offshore. Over the next 48 h until landfall the Cold Pool Front moved offshore by over 70 km. Within the innershelf bottom temperatures remained near 16°C throughout the duration of the storm while surface temperatures

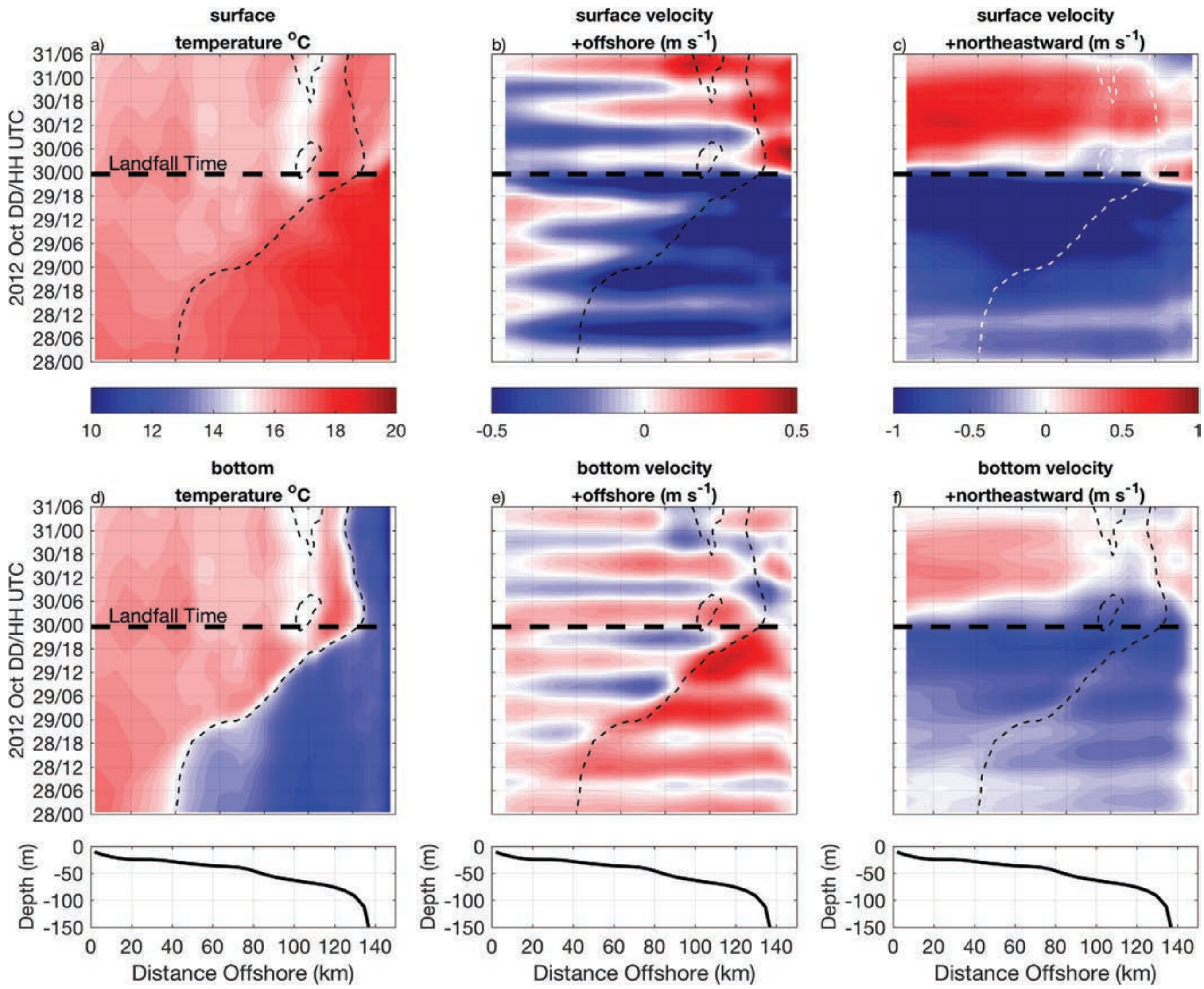

Figure 8. Hovmöller diagrams of hourly ROMS output extracted from the cross-shelf section shown in Figure 2. Extracted variables include (a) surface temperature, (b) surface cross-shelf velocity, (c) surface along-shelf velocity, (d) bottom temperature, (e) bottom cross-shelf velocity, and (f) bottom along-shelf velocity. Cross-shelf and along-shelf velocities are positive in the offshore and northeastward directions. Black dashed contours represent the 15°C bottom temperature or the approximate position of the Cold Pool Front. Horizontal dashed lines represent Sandy's landfall time. The bottom three plots are the bathymetry and distance offshore extracted from the cross-shelf line.

cooled by approximately 1°C out to 100 km offshore on the landward side of the Cold Pool Front. Enhanced cooling (warming) of the surface (bottom) occurred at landfall time 100 km offshore down (up) to 14.5°C. Landward of the Cold PoolFront, cross-shelf surface velocities were directed offshore. Seaward of the Cold Pool Front surface currents were directed onshore indicating a surface convergence zone and downwelling at the Cold Pool Front consistent with Figure 7. In the bottom layer, cross-shelf currents landward of the Cold Pool front were weak and directed onshore, while cross-shelf currents seaward of the Cold Pool front were strong and directed offshore indicating a region of divergence and offshore Cold Pool advection. Along-shelf currents during the ahead-of-eye period were consistently in the southwestward direction and were $\sim$1 m s^{-1} in the surface layer. Along-shelf bottom currents were in the same direction as surface currents but weaker until the main storm forcing period between 06:00 GMT on 29 October and just after landfall at 03:00 GMT on 30 October.

To further investigate the processes responsible for the observed and simulated coastal ocean response to Sandy, a time series of depth-averaged momentum balance terms are shown in Figures 9 and 10, with each term defined in equation (2) and (3) for cross-shelf and along-shelf directions respectively. The horizontal

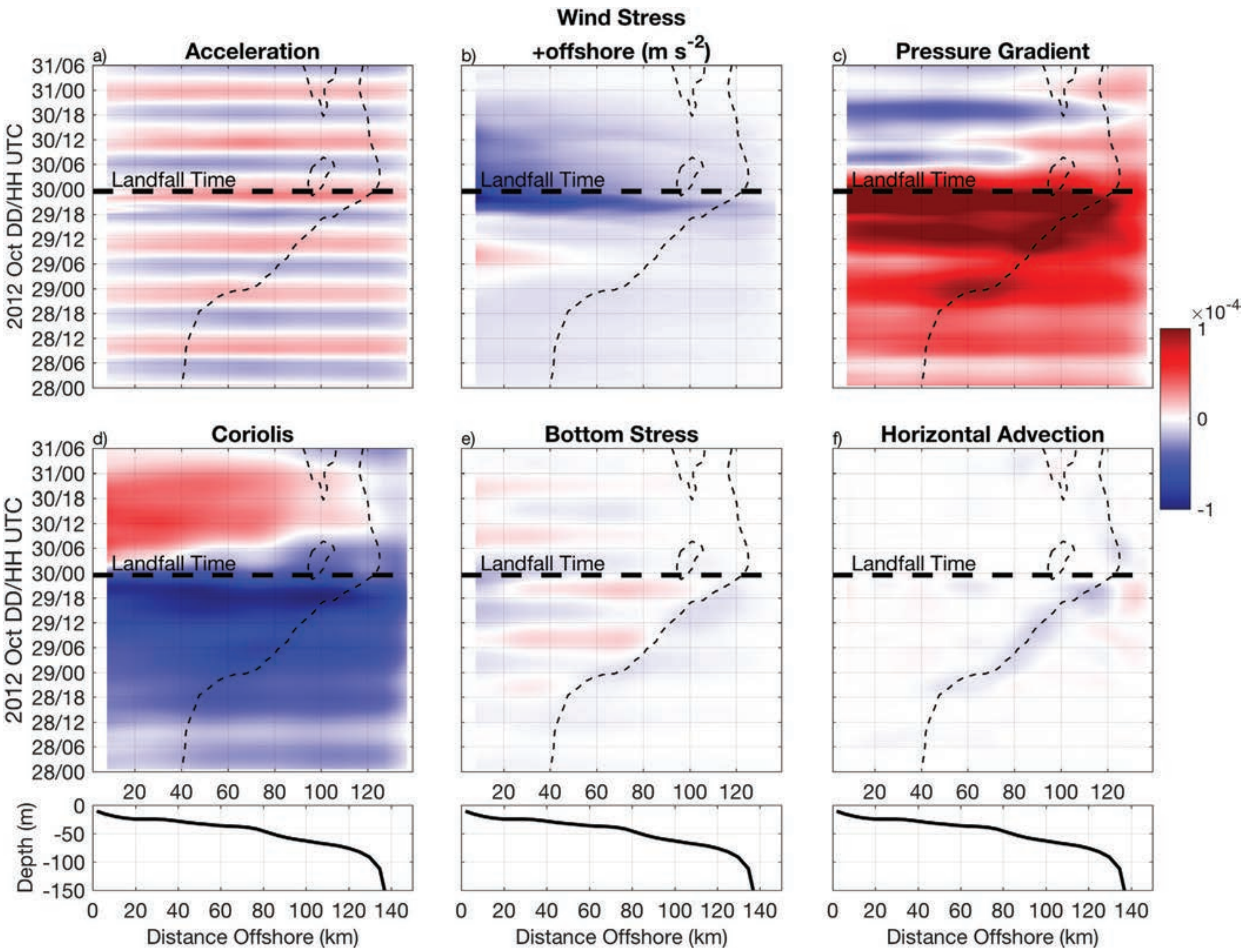

Figure 9. Hovmöller diagrams of hourly ROMS output of the depth-averaged cross-shelf momentum balance terms (equation (2)) extracted from the cross-shelf section shown in Figure 2. Extracted variables include (a) acceleration, (b) wind stress, (c) pressure gradient, (d) Coriolis, (e) bottom stress, and (f) horizontal advection. Positive is in the offshore directions Black dashed contours represent the 15°C bottom temperature or the approximate position of the Cold Pool Front. Horizontal dashed lines represent Sandy's landfall time. The bottom three plots are the bathymetry and distance offshore extracted from the cross-shelf line.

viscosity term was negligible and was not included. In both the cross-shelf and along-shelf directions the acceleration is tidally dominated with enhanced northeastward acceleration as Sandy made landfall. Wind stress was consistent with observed wind fields (Figure 4) alongshore toward the southwest and slightly offshore prior to landfall and rotated to northeastward and slightly onshore after landfall. The pressure gradient term was one of the dominant cross-shelf terms prior to landfall and was positive indicating an offshore directed sea-surface slope, or sea-surface setup along the coastline. This cross-shelf pressure gradient was balanced by a negative Coriolis term prior to landfall indicating that the coastal ocean over much of the shelf was nearly in geostrophic balance prior to Sandy making landfall. On the landward side of the Cold Pool Front, where the water column was vertically uniform, bottom stress was large and northeastward ahead of landfall, opposing the southwestward bottom currents. Depth-averaged horizontal advection terms in both the cross-shelf and along-shelf directions were small.

To quantitatively assess the impact of mixing and advection on the destratification of the continental shelf water column, we plotted time series profiles (Figure 11) of the temperature rate of change, combined temperature horizontal and vertical advection, and temperature vertical diffusion terms from equation (4). Data were extracted from four points on the cross-shelf transect shown in Figure 2 representing the approximate 20, 40, 60, and 80 m isobaths with the 60 m point aligning with the data extracted from ROMS in Figure 6. Tidal influences can be seen at all four locations in the total temperature rate and advection terms,

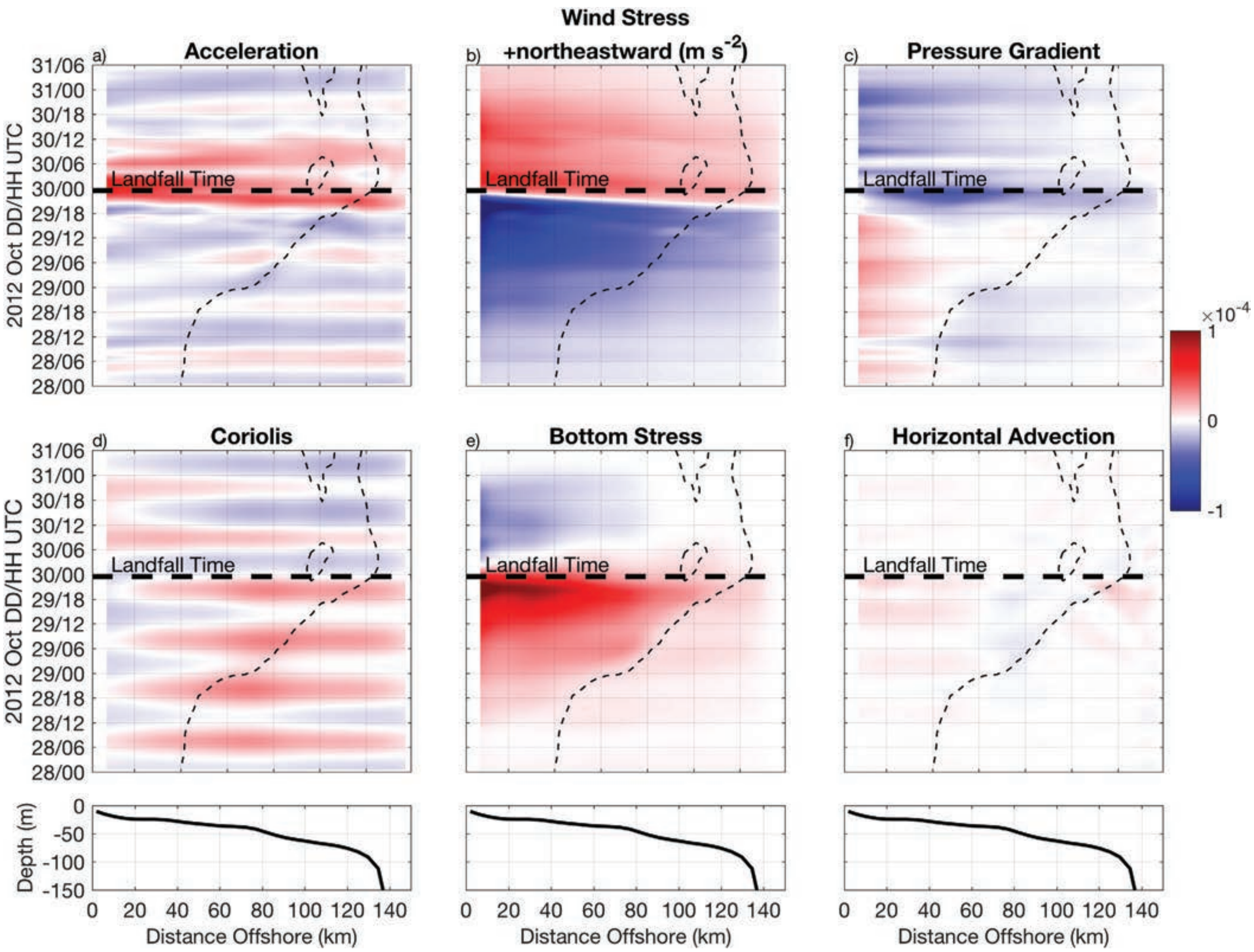

Figure 10. Hovmöller diagrams of hourly ROMS output of the depth-averaged along-shelf momentum balance terms (equation (3)) extracted from the cross-shelf section shown in Figure 2. Extracted variables include (a) acceleration, (b) wind stress, (c) pressure gradient, (d) Coriolis, (e) bottom stress, and (f) horizontal advection. Positive is in the southwestward direction. Black dashed contours represent the 15°C bottom temperature or the approximate position of the Cold Pool Front. Horizontal dashed lines represent Sandy's landfall time. The bottom three plots are the bathymetry and distance offshore extracted from the cross-shelf line.

particularly in the surface layer but not in vertical diffusion terms. While these tidal features are ubiquitous they are small relative to the large storm-driven advective terms and only represent changes on the order of 0.1°C at each given location. Aside from the tidally driven advection the inner shelf point exhibits little change throughout the storm forcing period and no vertical diffusion of temperature as temperature is vertically uniform. At the 40 m isobath cooling is evident at 00:00 GMT on the 29th in the surface layer and warming near the bottom. Cooling in the surface layer was driven by vertical diffusion of Cold Pool water while warming near the bottom was a combination of both advection and vertical diffusion. At the 60 m isobath a similar and more obvious pattern is evident with cooling in the surface layer and warming and deepening of the bottom layer between 00:00 GMT and landfall at 23:30 GMT on 29 October. Negative vertical diffusion of temperature is evident throughout the surface layer while positive vertical diffusion is only evident at the top of Cold Pool waters indicating erosion of the top of the Cold Pool into the surface layer. Within the Cold Pool, temperature advection was positive and dominated the temperature rate of change indicating that Cold Pool water was exported consistent with offshore flow observed in the near bottom layer in Figures 5 (glider time series), 6 (model time series), 7 model cross-shelf section), and 8 (model Hovmöller). At the offshore location there is a distinct periodic warming and cooling at the top of the Cold Pool by temperature advection, potentially linked with internal wave dynamics, though the period of the signal is unclear due to the short duration of the response. A distinct positive advective signal was again evident

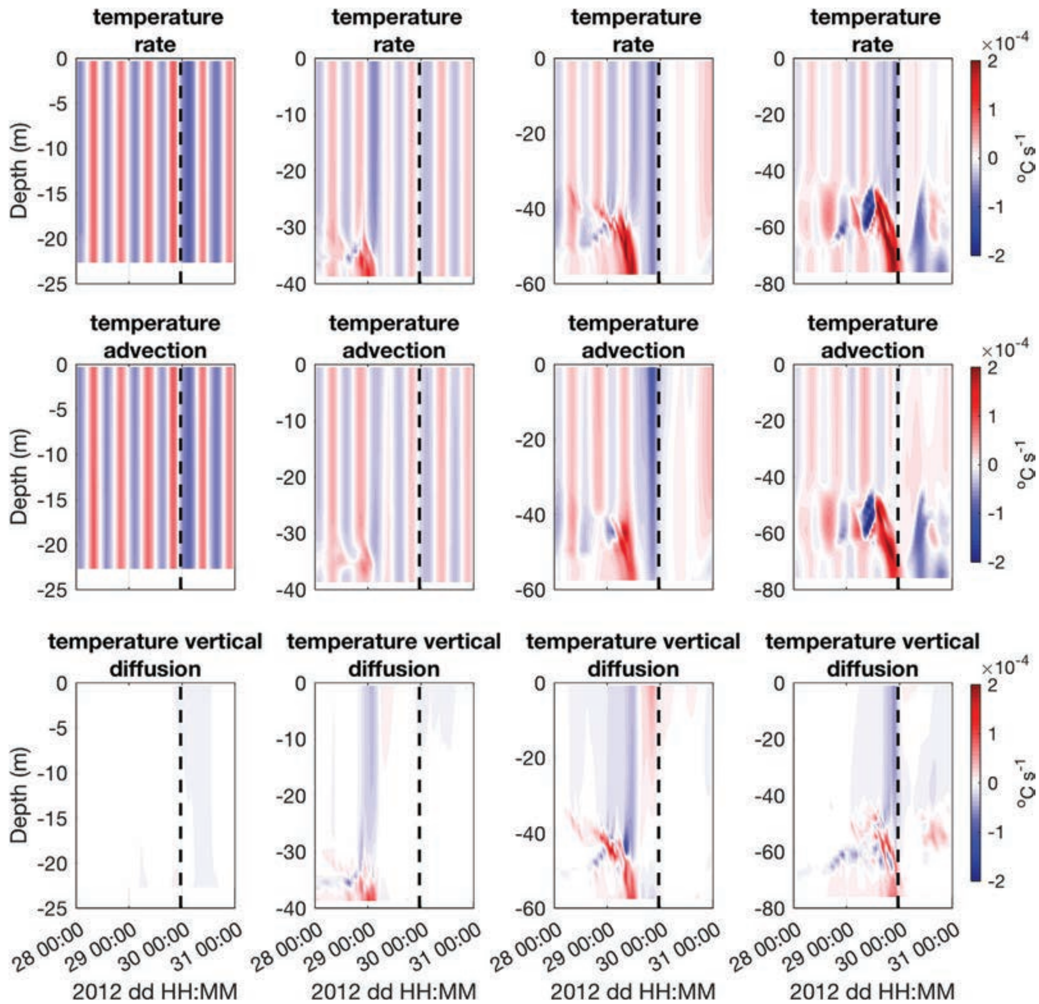

Figure 11. Time series of vertical profiles of the temperature diagnostic terms (equation (4)) extracted from the 4 cross-shelf points shown in Figure 2. Variables include the temperature rate of change (row 1), combined horizontal and vertical advection terms (row 2), and temperature vertical diffusion terms (row 3). The dashed vertical black line is Sandy's landfall time at 23:30 GMT on 29 October 2012.

near bottom at, and just after, landfall consistent with offshore advection of the Cold Pool seen at the shallower 60 m location. Vertical diffusion of temperature is limited and irregular pre-landfall while cooling is seen in the sea-surface after landfall when winds and currents reverse direction.

4. Discussion

The observed and modeled offshore bottom velocities, stable water column, momentum balance terms, and temperature diagnostics indicate that mixing processes alone were not sufficient for the seaward progression of the Cold Pool Front ~70 km offshore ahead of Sandy's landfall in New Jersey. The observed ahead-of-eye-center surface cooling was similar to previous studies of tropical cyclones that impacted the MAB during the stratified season such as Irene [*Glenn et al.*, 2016; *Seroka et al.*, 2016] and Barry [*Seroka*, 2017]. However, unlike these previous storms Sandy induced an extreme coastal ocean response to a tropical cyclone with the offshore advection of the Cold Pool Front. Three features of Sandy contributed to this coastal ocean response. (1) Sandy's cross-shelf track: typically tropical cyclones enter the stratified MAB from the south and travel alongshore toward the northeast [*Hall and Yonekura*, 2013] leading to initially onshore leading edge winds that rotate into alongshore southward or northward as a storm passes depending on its inshore or offshore track. Synthetic tropical cyclones that followed a similar cross-shelf track to Sandy was found to have a return rate of greater than 700 years for the MAB region [*Hall and Sobel*, 2013], and only five storms of tropical storm strength or greater have crossed nearly perpendicular to the NJ shelf since 1889 (https://coast.noaa.gov/hurricanes/). (2) Sandy was an exceptionally large storm: After exiting the Caribbean and passing the Bahamas, Sandy's radius of maximum winds increased to over 185 km, a large size it maintained until landfall [*Blake et al.*, 2013]. This large size is nearly 4 times the average radius of maximum wind for typical U.S. landfalling storms [*Hsu and Yan*, 1998]. 3) Sandy was a slow moving storm: Typical storms within the MAB region have translation speeds of approximately 40 km h^{-1} [*Landsea et al.*, 2015], while Sandy had an average translation speed between 00:00 GMT on 28 October to 23:30 GMT on 29 October of 27 km h^{-1} [*Blake et al.*, 2013].

The above three factors combined to produce a prolonged exposure of the stratified coastal ocean to alongshore southwestward downwelling favorable wind stress for nearly 48 h, or over 2.5 inertial periods, which are approximately 18 hours on the central MAB. The idealized two-dimensional downwelling response of a stratified coastal ocean to alongshore wind stress has been described for the Oregon [*Allen and Newberger*, 1996] and Mid Atlantic [*Austin and Lentz*, 2002] continental shelves. In *Austin and Lentz* [2002], they used an idealized version of the Princeton Ocean Model to represent a gently sloping continental shelf with a highly stratified water column typical of the Northeastern U.S. in summer. Downwelling favorable winds of $\sim$8 m s^{-1} were ramped up over one inertial period and held constant for nearly 2 weeks. They simulated onshore Ekman transport in the surface that deepened the pycnocline in the nearshore region until it intersected the bottom and was advected offshore. In their simulation they found that over the first inertial period alongshore wind stress resulted in onshore Ekman transport in the surface layer and led to a barotropic response that advected the bottom downwelling front seaward. For two-dimensional cross-shelf circulation they assumed that the vertically integrated transport was zero and could be divided into the surface Ekman transport, the barotropic interior, and the bottom Ekman transport. In the initial forcing period when the bottom Ekman layer is not spun up the cross-shelf balance is between the surface Ekman transport and the barotropic interior flow [*Dever*, 1997]. From *Austin and Lentz* [2002], the offshore displacement of the front for the barotropic response scaled with:

$$x_{baro}(t)= \sqrt{\int_0^t \frac{2U^s}{\alpha}dt+X_0^2} \tag{7}$$

where x_{baro} is the cross-shelf displacement, t is time, α is the slope of the shelf, X_0 is the initial front position, and U^s is the surface Ekman transport such that $U^s=\tau/\rho f$ where τ is the alongshore wind stress, ρ is a reference density, and f is the Coriolis frequency. The limited along-shelf bottom stress, elevated alongshelf wind stress, and elevated cross-shelf pressure gradient components of the momentum balance (Figure 9 and 10) during the first inertial period starting at 00:00 GMT on 28 October 2012 support this. In *Austin and Lentz* [2002], after the first inertial period the bottom Ekman layer develops and the bottom Ekman transport approximately equals the surface Ekman transport and the offshore displacement of the front scaled with:

$$x_{ek}(t)= X_0+\sqrt{\int_0^t \frac{2U^s}{\alpha}dt} \tag{8}$$

which is also supported by the increased along-shelf bottom stress matching the along-shelf wind stress at 06:00 GMT on 29 October 2012 (Figure 10).

To determine if the Cold Pool Front displacement in Sandy fits with the theoretical scaling in *Austin and Lentz* [2002] we used constants of $\alpha = 0.00055$, $X_0 = 40$ km, $f = 10^{-4}$ s^{-1}, $\rho = 1025$ kg m^{-3}. The alongshore wind stress from WRF was averaged along the cross-shelf section in Figure 2 hourly. The winds between 00:00 to 18:00 GMT 28 October were used with equation (7) and during the remaining time period until landfall 18:00 GMT on 28 October to 23:30 GMT on 29 October with equation (8). The frontal displacement from concatenating the results from equations (7) and (8) is shown in Figure 12 along with the offshore displacement of the 15°C isotherm which was previously shown in Figures 8–10 to represent the Cold Pool Front. The 15°C isotherm position and estimated frontal displacement were in good agreement with a barotropic displacement of $\sim$10 km in the first inertial period and an Ekman driven offshore displacement of $\sim$60 km in the remaining 1.5 inertial periods until landfall at the top of Figure 12. Key assumptions necessary for the *Austin and Lentz* [2002] scaling to be valid include (1) that conservation of mass is a strong constraint on the flow, (2) along-shelf variability in the flow is small compared to the cross-shelf variability, or

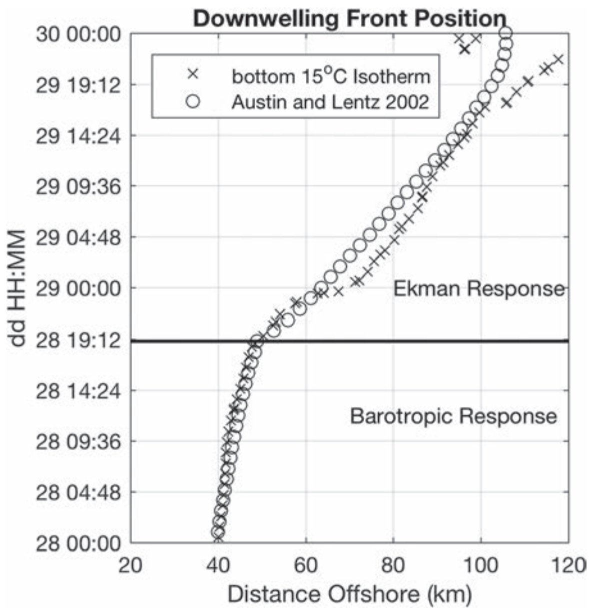

Figure 12. A Hovmöller diagram showing the offshore position of the 15°C bottom contour (x's) extracted from the ROMS model to represent the approximate position of the Cold Pool Front, and the position estimated from [*Austin and Lentz*, 2002] using the barotropic response (Equation 7) for the first inertial period and the Ekman response (equation (8)) for the remainder of Sandy's storm forcing period (o's). The solid horizontal line indicates the end of the first inertial period.

that the flow is approximately two-dimensional, (3) Ekman transport in the surface layer is well established and independent of turbulent closure schemes; and (4) deepening of the mixed-layer is limited.

This coastal ocean response to a tropical cyclone in the stratified MAB is unique to Hurricane Sandy. Alongshore winds measured at buoy 44025 (Figure 2) for Sandy showed that winds steadily increased from 5 to over 20 m s^{-1} and persisted for over 48 h ahead of landfall. An analysis of along-shelf wind speed from buoy 44025 from 1985 to present, which included the 11 storms that impacted the MAB during the stratified season highlighted in *Glenn et al*. [2016] show that no tropical cyclones resulted in alongshore wind stress that exceeded 18 h, thus none were capable of inducing the offshore Ekman response observed on the shelf during Sandy. While cross-shelf tracking storms are not typical over the MAB, NOAA storm track maps (coast.noaa.gov/hurricanes) show the southeastern coast of China and the Yellow Sea, regions with highly stratified water columns in summer [*Chen et al*., 1994; *Li et al*., 2012], are frequently impacted by cross-shelf tracking storms that may induce significant alongshore wind stress prior to landfall. A sediment resuspension and transport study on Typhoon Morakot in 2009 [*Li et al*., 2012] shows seaward displacement of cold bottom waters offshore. While not explicitly tested, the offshore advection of the Cold Pool ahead-of-eye-center may have been a contributing factor to the limited deintensification observed in Hurricane Sandy and more research on the coastal ocean response to tropical cyclones is needed.

In addition to the impacts on the water column structure, the observed and modeled offshore advection of the downwelling front ahead-of-eye-center also had implications for sediment resuspension and transport. Sandy had a large impact on coastal sediment resuspension and transport throughout the MAB [*Trembanis et al*., 2013; *Miles et al*., 2015; *Warner et al*., 2017]. The 70 km cross-shelf advection of the Cold Pool reduced water column stability on the innershelf and allowed for significant sediment resuspension and transport. On the offshore side of the downwelling front, where the water column was stratified, bottom stress was limited and subsequently sediment resuspension and transport along with cross-shelf currents was limited. On the inshore side of the downwelling front bottom stress was enhanced, sediment was resuspended throughout the full water column, and along-shelf flow transported sediment from the northern portion of the NJ Shelf near the Hudson Shelf Valley to the southern portion of the NJ Shelf near Delaware bay [*Miles et al*., 2015]. This rapid resuspension and resorting of shelf sediments in a few hours, which was on the scale of trawling and dredging impacts, has potential implications for benthic habitats [*Fanning et al*., 1982; *Thrush and Dayton*, 2002] and for prediction of the fate and effects of pollutants introduced at the coastline [*Biscaye et al*., 1988]. In addition to changes in sediment character, downwelling circulation on the NJ shelf has previously also been found to redistribute surfclam larvae across the shelf and may have implications for their settlement and recruitment among other macrofaunal communities [*Grassle et al*., 2006]. Also, rapid temperature changes with the passage of a warm downwelling front may have negative physiological impacts on benthic organisms [*Thiyagarajan et al*., 2000].

5. Conclusions

In this study we use an integrated ocean observing system that consists of an HF Radar network, Teledyne-Webb Slocum gliders, buoys, and regional ocean and atmospheric modeling to detail the coastal ocean response to Hurricane Sandy. Many studies have detailed the impact of tropical cyclones on the upper ocean, particularly while these storms transit over the deep sea [*Price*, 1981; *Price et al.*, 1994; *Zedler et al.*, 2002; *D'Asaro*, 2003; *Jaimes and Shay*, 2009; *Jaimes et al.*, 2011; *Sanford et al.*, 2011]. While many of these studies have focused on shear-driven vertical mixing, a study by *Yablonsky and Ginis* [2009] showed that modeling three-dimensional upwelling processes is necessary to accurately represent sea surface cooling induced by tropical cyclones over the deep ocean. More recent studies [*Glenn et al.*, 2016; *Seroka et al.* 2017; *Seroka et al.*, 2016] have shown three-dimensional coastal ocean processes can contribute to rapid sea-surface cooling through enhanced vertical shear ahead-of-eye center. This paper adds to that growing knowledge by detailing an additional case-study where ahead-of-eye-center downwelling circulation can advect the Cold Pool offshore and reduce stratification on the shallow inner shelf before eye-passage. While to-date this is a unique process observed during hurricane Sandy there is evidence that oceanographic conditions and storm tracks off of Southeastern China may result in similar dynamics. The results of this study continue to highlight the need for combined ocean observing systems and regional modeling in order to further understand the range of coastal ocean responses to tropical cyclones and potential feedbacks on storm intensity.

Acknowledgments
Glider data used in this study are available through the U.S. IOOS glider DAC https://data.ioos.us/gliders/erddap/tabledap/ru23-20121025T1944.html. Regional Ocean Modeling System and WRF model output are available at ftp://boardwalk.marine.rutgers.edu/tnmiles/JGR_Sandy_2017/. Buoy data and HF Radar data are publicly available through http://www.ndbc.noaa.gov/andhttp://tds.marine.rutgers.edu/thredds/cool/catalog.html, respectively. Funding support was provided by the National Oceanic and Atmospheric Administration (NOAA) led Integrated Ocean Observing System (IOOS) through the Mid-Atlantic Regional Association Coastal Ocean Observing System (MARACOOS, NA11NOS0120038), the New Jersey Board of Public Utilities (2010RU-COOL), and the NOAA Cooperative Institute for the North Atlantic Region (CINAR, NA13OAR4830233), Disaster Recovery Act. The authors thank Teledyne Webb Research and Rutgers University for student support, the NOAA National Centers for Environmental Prediction for student engagement. Additionally, we would like to thank the glider technicians and pilots of the Rutgers University Center for Ocean Observing Leadership; the help of John Wilkin and the research associates of the Rutgers Ocean Modeling group with help setting up the ocean model; and two anonymous reviewers for their helpful comments.

References

Allen, J. S., and P. A. Newberger (1996), Downwelling circulation on the Oregon continental shelf. Part I: Response to idealized forcing, *J. Phys. Oceanogr.*, *26*(10), 2011–2035, doi:10.1175/1520-0485(1996)026 < 2011:DCOTOC>2.0.CO;2.
Austin, J., and S. Lentz (2002), The inner shelf response to wind-driven upwelling and downwelling., *J. Phys. Oceanogr.*, *32*, 2171–2193.
Avila, L. A., and J. P. Cangialosi (2012), Tropical Cyclone Report: Hurricane Irene, National Hurricane Center Tropical Cyclone Rep. AL092011, 45 pp. [Available online at http://www.nhc.noaa.gov/data/tcr/AL092011_Irene.pdf.]
Barrick, D. E. (1971a), Theory of HF and VHF propagation across the rough sea. 1: The effective surface impedance for a slightly rough highly conducting medium at grazing incidence, *Radio Sci.*, *6*(5), 517–526, doi:10.1029/RS006i005p00517.
Barrick, D. E. (1971b), Theory of HF and VHF propagation across the rough sea. 2: Application to HF and VHF propagation above the sea, *Radio Sci.*, *6*(5), 527–533, doi:10.1029/RS006i005p00527.
Bender, M., and I. Ginis (2000), Real-case simulations of hurricane-ocean interaction using a high-resolution coupled Model: Effects on hurricane intensity, *Mon. Weather Rev.*, *128*, 917–946.
Biscaye, P. E., R. F. Anderson, and B. L. Deck (1988), Fluxes of particles and constituents to the eastern United States continental slope and rise: SEEP—I, *Cont. Shelf Res.*, *8*(5–7), 855–904
Black, P. G., E. A. D'Asaro, T. B. Sanford, W. M. Drennan, J. A. Zhang, J. R. French, P. P. Niiler, E. J. Terrill, and E. J. Walsh (2007), Air-sea exchange in hurricanes: Synthesis of observations from the coupled boundary layer air-sea transfer experiment, *Bull. Am. Meteorol. Soc.*, *88*(3), 357–374, doi:10.1175/BAMS-88-3-357.
Blake, E. S., T. B. Kimberlain, R. J. Berg, P. C. John, and J. L. Beven II (2013), Tropical cyclone report: Hurricane sandy, *Natl. Hurric. Cent.*, *12*, 1–157.
Briscoe, M. G., D. L. Martin, and T. C. Malone (2008), Evolution of regional efforts in international GOOS and US IOOS, *Mar. Technol. Soc. J.*, *42*(3), 4–9.
Cahill, B., O. Schofield, R. Chant, J. Wilkin, E. Hunter, S. Glenn, and P. Bissett (2008), Dynamics of turbid buoyant plumes and the feedbacks on near-shore biogeochemistry and physics, *Geophys. Res. Lett.*, *35*, L10605, doi:10.1029/2008GL033595.
Cangialosi, J. P., and J. L. Franklin (2016), National Hurricane Center Forecast VErification Report: 2015 Hurricane Season, Miami, Fla.
Castelao, R., S. Glenn, O. Schofield, R. Chant, J. Wilkin, and J. Kohut (2008), Seasonal evolution of hydrographic fields in the central Middle Atlantic Bight from glider observations, *Geophys. Res. Lett.*, *35*, L03617, doi:10.1029/2007GL032335.
Chen, C., R. C. Beardsley, R. Limeburner, and K. Kim (1994), Comparison of winter and summer hydrographic observations in the Yellow and East China Seas and adjacent Kuroshio during 1986, *Cont. Shelf Res.*, *14*(7–8), 909–929, doi:10.1016/0278-4343(94)90079-5.
Chen, S. S., J. F. Price, W. Zhao, M. A. Donelan, and E. J. Walsh (2007), The CBLAST-Hurricane program and the next-generation fully coupled atmosphere-wave-ocean models for hurricane research and prediction, *Bull. Am. Meteorol. Soc.*, *88*(3), 311–317, doi:10.1175/BAMS-88-3-311.
Considine, T. J., C. Jablonowski, B. Posner, and C. H. Bishop (2004), The value of hurricane forecasts to oil and gas producers in the Gulf of Mexico, *J. Appl. Meteorol.*, *43*, 1270–1282.
Cornillon, P., L. Stramma, and J. F. Price (1987), Satellite measurements of sea surface cooling during hurricane Gloria, *Nature*, *326*(6111), 373–375, doi:10.1038/326373a0.
D'Asaro, E. A. E. (2003), The ocean boundary layer below hurricane dennis, *J. Phys. Oceanogr.*, *33*(3), 561–579, doi:10.1175/1520-0485(2003)033 < 0561:TOBLBH>2.0.CO;2.
Davis, R., C. Eriksen, and C. Jones (2002), Autonomous buoyancy-driven underwater gliders, in *Technology and Applications of Autonomous Underwater Vehicles*, edited by G. Griffiths, pp. 37–58, Taylor and Francis, London.
DeMaria, M., C. R. Sampson, J. A. Knaff, and K. D. Musgrave (2014), Is tropical cyclone intensity guidance improving?, *Bull. Am. Meteorol. Soc.*, *95*(3), 387–398, doi:10.1175/BAMS-D-12-00240.1.
Dever, E. P. (1997), Wind-forced cross-shelf circulation on the Northern California shelf, *J. Phys. Oceanogr.*, *27*(8), 1566–1580, doi:10.1175/1520-0485(1997)027 < 1566:WFCSCO>2.0.CO;2.
Domingues, R., G. Goni, F. Bringas, S.-K. Lee, H.-S. Kim, G. Halliwell, J. Dong, J. Morell, and L. Pomales (2015), Upper ocean response to Hurricane Gonzalo (2014): Salinity effects revealed by targeted and sustained underwater glider observations, *Geophys. Res. Lett.*, *42*, 7131–7138, doi:10.1002/2015GL065378.
du Plessis, M., S. Swart, I. J. Ansorge, and A. Mahadevan (2017), Submesoscale processes accelerate seasonal restratification in the Subantarctic Ocean, *J. Geophys. Res. Oceans*, *122*, 2960–2975, doi:10.1002/2016JC012494.
Emanuel, K. (2016), Will global warming make hurricane forecasting more difficult?, *Bull. Am. Meteorol. Soc.*, *98*(3), 495–501, doi:10.1175/BAMS-D-16-0134.1.

Emanuel, K., C. DesAutels, C. Holloway, and R. Korty (2004), Environmental control of tropical cyclone intensity, *J. Atmos. Sci.*, *61*(7), 843–858, doi:10.1175/1520-0469(2004)061 < 0843:ECOTCI > 2.0.CO;2.
Emanuel, K. A. (1999), Thermodynamic control of hurricane intensity, *Nature*, *401*(6754), 665–669.
Fairall, C. W., E. F. Bradley, J. E. Hare, A. A. Grachev, and J. B. Edson (2003), Bulk parameterization of air-sea fluxes: Updates and verification for the COARE algorithm, *J. Clim.*, *16*(4), 571–591.
Fanning, K. A., K. L. Carder, and P. R. Betzer (1982), Sediment resuspension by coastal waters: A potential mechanism for nutrient re-cycling on the ocean's margins, *Deep Sea Res., Part A*, *29*(8), 953–965, doi:10.1016/0198-0149(82)90020-6.
Fisher, E. L. (1958), Hurricanes and the sea-surface temperature field, *J. Meteorol.*, *15*(3), 328–333, doi:10.1175/1520-0469(1958)015 < 0328:HATSST > 2.0.CO;2.
Fritz, H. M., C. D. Blount, S. Thwin, M. K. Thu, and N. Chan (2009), Cyclone Nargis storm surge in Myanmar, *Nat. Geosci.*, *2*(7), 448–449, doi:10.1038/ngeo558.
Garau, B., S. Ruiz, W. G. Zhang, A. Pascual, E. Heslop, J. Kerfoot, and J. Tintoré (2011), Thermal lag correction on slocum CTD glider data, *J. Atmos. Oceanic Technol.*, *28*(9), 1065–1071, doi:10.1175/JTECH-D-10-05030.1.
Georgas, N., P. Orton, A. Blumberg, L. Cohen, D. Zarrilli, and L. Yin (2014), The impact of tidal phase on hurricane Sandy's flooding around New York City and Long Island Sound, *J. Extrem. Events*, *1*(1), Article 1450006, doi:10.1142/S2345737614500067.
Glenn, S., C. Jones, M. Twardowski, L. Bowers, J. Kerfoot, J. Kohut, D. Webb, and O. Schofield (2008), Glider observations of sediment resuspension in a Middle Atlantic Bight fall transition storm, *Limnol. Oceanogr. Methods*, *53*(5 part 2), 2180–2196, doi:10.4319/lo.2008.53.5_part_2.2180.
Glenn, S. M., T. N. Miles, G. N. Seroka, Y. Xu, R. K. Forney, F. Yu, H. Roarty, O. Schofield, and J. Kohut (2016), Stratified coastal ocean interactions with tropical cyclones, *Nat. Commun.*, *7*, Article 10887, 1–10, doi:10.1038/ncomms10887.
Grassle, J. P., H. Ma, and R. J. Chant (2006), Vertical distribution of bivalve larvae along a cross-shelf transect during summer upwelling and downwelling, *Mar. Biol.*, *149*(5), 1123–1138, doi:10.1007/s00227-006-0287-3.
Haidvogel, D. B., et al. (2008), Ocean forecasting in terrain-following coordinates: Formulation and skill assessment of the Regional Ocean Modeling System, *J. Comput. Phys.*, *227*(7), 3595–3624, doi:10.1016/j.jcp.2007.06.016.
Hall, T., and E. Yonekura (2013), North American tropical cyclone landfall and SST: A statistical model study, *J. Clim.*, *26*(21), 8422–8439, doi:10.1175/JCLI-D-12-00756.1.
Hall, T. M., and A. H. Sobel (2013), On the impact angle of Hurricane Sandy's New Jersey landfall, *Geophys. Res. Lett.*, *40*, 2312–2315, doi:10.1002/grl.50395.
Hidaka, K., and Y. Akiba (1955), Upwelling induced by a circular wind system, *Rec. Ocean. Work. Jpn.*, *2*, 7–18.
Hofmann, E., J.-N. Druon, K. Fennel, M. Friedrichs, D. Haidvogel, C. Lee, A. Mannino, C. McClain, R. Najjar, and J. O'Reilly (2008), Eastern US continental shelf carbon budget integrating models, data assimilation, and analysis, *Oceanography*, *21*(1), 86–104.
Houghton, R. W., R. Schlitz, R. C. Beardsley, B. Butman, and J. L. Chamberlin (1982), The Middle Atlantic bight cold pool: Evolution of the temperature structure during summer 1979, *J. Phys. Oceanogr.*, *12*(10), 1019–1029, doi:10.1175/1520-0485.
Hsu, S. A., and Z. Yan (1998), A note on the radius of maximum wind for hurricanes, *J. Coast. Res.*, *14*(2), 667–668.
Jaimes, B., and L. K. Shay (2009), Mixed layer cooling in mesoscale oceanic eddies during hurricanes Katrina and Rita, *Mon. Weather Rev.*, *137*(12), 4188–4207, doi:10.1175/2009MWR2849.1.
Jaimes, B., and L. K. Shay (2015), Enthalpy and momentum fluxes during hurricane earl relative to underlying ocean features, *Mon. Weather Rev.*, *143*(1), 111–131, doi:10.1175/MWR-D-13-00277.1.
Jaimes, B., L. K. Shay, and G. R. Halliwell (2011), The response of quasigeostrophic oceanic vortices to tropical cyclone forcing, *J. Phys. Oceanogr.*, *41*(10), 1965–1985, doi:10.1175/JPO-D-11-06.1.
Kohut, J., H. Roarty, E. Randall-Goodwin, S. Glenn, and C. S. Lichtenwalner (2012), Evaluation of two algorithms for a network of coastal HF radars in the Mid-Atlantic Bight, *Ocean Dyn.*, *62*(6), 953–968, doi:10.1007/s10236-012-0533-9.
Kohut, J. T., S. M. Glenn, and J. D. Paduan (2006), Inner shelf response to Tropical Storm Floyd, *J. Geophys. Res.*, *111*, C09S91, doi:10.1029/2003JC002173.
Kossin, J. P., K. A. Emanuel, and G. A. Vecchi (2014), The poleward migration of the location of tropical cyclone maximum intensity, *Nature*, *509*(7500), 349–352.
Landsea, C. W., J. L. Franklin, and J. L. Beven (2015), The revised Atlantic hurricane database (HURDAT2), Sponsor National Oceanographic and Atmospheric Administration, National Hurricane Center. [Available at http://www.nhc.noaa.gov/data/hurdat/hurdat2-format-atlantic.pdf.]
Leipper, D. F. (1967), Observed ocean conditions and hurricane Hilda, 1964, *J. Atmos. Sci.*, *24*(2), 182–186, doi:10.1175/1520-0469(1967)024 < 0182:OOCAHH > 2.0.CO;2.
Lentz, S. (2003), Evolution of stratification over the New England shelf during the Coastal Mixing and Optics study, August 1996–June 1997, *J. Geophys. Res.*, *108*(C1), 3008, doi:10.1029/2001JC001121.
Lentz, S. J. (2017), Seasonal warming of the Middle Atlantic Bight Cold Pool, *J. Geophys. Res. Oceans*, *122*, 941–954, doi:10.1002/2016JC012201.
Li, Y., A. Wang, L. Qiao, J. Fang, and J. Chen (2012), The impact of typhoon Morakot on the modern sedimentary environment of the mud deposition center off the Zhejiang-Fujian coast, China, *Cont. Shelf Res.*, *37*, 92–100, doi:10.1016/j.csr.2012.02.020.
Miles, T., S. Glenn, and O. Schofield (2013), Temporal and spatial variability in fall storm induced sediment resuspension on the Mid-Atlantic Bight, *Cont. Shelf Res.*, *63*, S36–S49.
Miles, T., G. Seroka, J. Kohut, O. Schofield, and S. Glenn (2015), Glider observations and modeling of sediment transport in Hurricane Sandy, *J. Geophys. Res. Oceans*, *120*, 1771–1791, doi:10.1002/2014JC010474.
Miller, K. G., P. J. Sugarman, J. V. Browning, B. P. Horton, A. Stanley, A. Kahn, J. Uptegrove, and M. Aucott (2009), Sea-level rise in New Jersey over the past 5000 years: Implications to anthropogenic changes, *Global Planet. Change*, *66*(1–2), 10–18, doi:10.1016/j.gloplacha.2008.03.008.
Moore, A. M., H. G. Arango, G. Broquet, B. S. Powell, A. T. Weaver, and J. Zavala-Garay (2011), The Regional Ocean Modeling System (ROMS) 4-dimensional variational data assimilation systems, *Prog. Oceanogr.*, *91*(1), 34–49, doi:10.1016/j.pocean.2011.05.004.
Nicholson, S.-A., M. Lévy, J. Llort, S. Swart, and P. M. S. Monteiro (2016), Investigation into the impact of storms on sustaining summer primary productivity in the Sub-Antarctic Ocean, *Geophys. Res. Lett.*, *43*, 9192–9199, doi:10.1002/2016GL069973.
Price, J. F. (1981), Upper Ocean Response to a Hurricane, *J. Phys. Oceanogr.*, *11*(2), 153–175, doi:10.1175/1520-0485(1981)011 < 0153:UORTAH > 2.0.CO;2.
Price, J. F., T. B. Sanford, and G. Z. Forristall (1994), Forced stage response to a moving hurricane, *J. Phys. Oceanogr.*, *24*(2), 233–260, doi:10.1175/1520-0485(1994)024 < 0233:FSRTAM > 2.0.CO;2.

Roarty, H., et al. (2010), Operation and application of a regional high-frequency radar network in the Mid-Atlantic Bight, *Mar. Technol. Soc. J.*, *44*(6), 133–145.
Ruiz, S., L. Renault, B. Garau, and J. Tintoré (2012), Underwater glider observations and modeling of an abrupt mixing event in the upper ocean, *Geophys. Res. Lett.*, *39*, L01603, doi:10.1029/2011GL050078.
Sanford, T. B., J. F. Price, and J. B. Girton (2011), Upper-ocean response to hurricane Frances (2004) observed by profiling EM-APEX Floats, *J. Phys. Oceanogr.*, *41*(6), 1041–1056, doi:10.1175/2010JPO4313.1.
Seroka, G. (2016), Stratified coastal ocean interactions with hurricanes and the sea breeze in the U.S. Mid-Atlantic.
Seroka, G., T. Miles, Y. Xu, J. Kohut, O. Schofield, and S. Glenn (2016), Hurricane Irene sensitivity to stratified coastal ocean cooling, *Mon. Weather Rev.*, *144*(9), 3507–3530, doi:10.1175/MWR-D-15-0452.1.
Seroka, G., T. Miles, Y. Xu, J. Kohut, O. Schofield, and S. Glenn (2017), Rapid shelf-wide cooling response of a stratified coastal ocean to hurricanes, *J. Geophys. Res. Ocean.*, doi:10.1002/2017JC012756.
Shchepetkin, A. F., and J. C. McWilliams (2005), The regional oceanic modeling system (ROMS): A split-explicit, free-surface, topography-following-coordinate oceanic model, *Ocean Modell.*, *9*(4), 347–404, doi:10.1016/j.ocemod.2004.08.002.
Shchepetkin, A. F., and J. McWilliams (2009a), Computational kernel algorithms for fine-scale, multi-process, long-time oceanic simulations, *Handbook Numer. Anal.*, *14*(8), 121–183, doi:10.1016/S1570-8659(08)01202-0.
Shchepetkin, A. F., and J. C. McWilliams (2009b), Correction and commentary for "Ocean forecasting in terrain-following coordinates: Formulation and skill assessment of the regional ocean modeling system" by Haidvogel et al., J. Comp. Phys. 227, pp. 3595–3624, J. Comput. Phys., 228(24), 8985–9000, doi:10.1016/j.jcp.2009.09.002.
Skamarock, W., J. Klemp, J. Dudhia, D. O. Gill, D. M. Barker, M. G. Duda, X.-Y. Huang, W. Wang, and J. G. Powers (2008), A description of the advanced research WRF version 3, NCAR Tech. Note NCAR/TN–475+STR, 475 pp., Natl. Cent. for Atmos. Res., Boulder, Colo.
Stramma, L., P. Cornillon, and J. Price (1986), Satellite observations of sea surface cooling by hurricanes, *J. Geophys. Res.*, *91*, 5031–5035.
Swart, S., S. J. Thomalla, and P. M. S. Monteiro (2015), The seasonal cycle of mixed layer dynamics and phytoplankton biomass in the Sub-Antarctic Zone: A high-resolution glider experiment, *J. Mar. Syst.*, *147*, 103–115, doi:10.1016/j.jmarsys.2014.06.002.
Teague, C. C. (1971), *High Frequency Resonant Scattering Techniques for the Observation of Directional Ocean Wave Spectra*, Dep. of Electr. Eng., Stanford Univ., Stanford, Calif.
Thiyagarajan, V., Y. Nancharaiah, V. Venugopalan, K. V. Nair, and T. Subramoniam (2000), Relative tolerance of cirripede larval stages to acute thermal shock: A laboratory study, *J. Therm. Biol.*, *25*(6), 451–457, doi:10.1016/S0306-4565(00)00010-3.
Thrush, S. F., and P. K. Dayton (2002), Disturbance to marine benthic habitats by trawling and dredging: Implications for marine biodiversity, *Annu. Rev. Ecol. Syst.*, *33*(1), 449–473, doi:10.1146/annurev.ecolsys.33.010802.150515.
Todd, R. E., D. L. Rudnick, M. R. Mazloff, R. E. Davis, and B. D. Cornuelle (2011a), Poleward flows in the southern California Current System: Glider observations and numerical simulation, *J. Geophys. Res.*, *116*, C02026, doi:10.1029/2010JC006536.
Todd, R. E., D. L. Rudnick, R. E. Davis, and M. D. Ohman (2011b), Underwater gliders reveal rapid arrival of El Niño effects off California's coast, *Geophys. Res. Lett.*, *38*, L03609, doi:10.1029/2010GL046376.
Torn, R. D., and C. Snyder (2012), Uncertainty of tropical cyclone best-track information, *Weather Forecasting*, *27*(2006), 715–729, doi: 10.1175/WAF-D-11-00085.1.
Trembanis, A., C. DuVal, J. Beaudoin, V. Schmidt, D. Miller, and L. Mayer (2013), A detailed seabed signature from Hurricane Sandy revealed in bedforms and scour, *Geochem. Geophys. Geosyst.*, *14*, 4334–4340, doi:10.1002/ggge.20260.
Umlauf, L., and H. Burchard (2003), A generic length-scale equation for geophysical turbulence models, *J. Mar. Res.*, *61*(2), 235–265.
Visbeck, M. (2002), Deep velocity profiling using lowered acoustic doppler current profilers: Bottom track and inverse solutions, *J. Atmos. Oceanic Technol.*, *19*, 794–807.
Wang, D., and H. Zhao (2008), Estimation of phytoplankton responses to Hurricane Gonu over the Arabian Sea based on ocean color data, *Sensors*, *8*(8), 4878–4893, doi:10.3390/s8084878.
Warner, J. C., C. R. Sherwood, H. G. Arango, and R. P. Signell (2005), Performance of four turbulence closure models implemented using a generic length scale method, *Ocean Modell.*, *8*(1–2), 81–113, doi:10.1016/j.ocemod.2003.12.003.
Warner, J. C., W. C. Schwab, J. H. List, I. Safak, M. Liste, and W. Baldwin (2017), Inner-shelf ocean dynamics and seafloor morphologic changes during Hurricane Sandy, *Cont. Shelf Res.*, *138*, 1–18, doi:10.1016/j.csr.2017.02.003.
Wilkin, J. L., and E. J. Hunter (2013), An assessment of the skill of real-time models of Mid-Atlantic Bight continental shelf circulation, *J. Geophys. Res. Oceans*, *118*, 2919–2933, doi:10.1002/jgrc.20223.
Xu, Y., B. Cahill, J. Wilkin, and O. Schofield (2013), Role of wind in regulating phytoplankton blooms on the Mid-Atlantic Bight, *Cont. Shelf Res.*, *63*(Mld), S26–S35, doi:10.1016/j.csr.2012.09.011.
Yablonsky, R. M., and I. Ginis (2008), Improving the ocean initialization of coupled hurricane-ocean models using feature-based data assimilation, *Mon. Weather Rev.*, *136*(7), 2592–2607, doi:10.1175/2007MWR2166.1.
Yablonsky, R. M., and I. Ginis (2009), Limitation of one-dimensional ocean models for coupled hurricane-ocean model forecasts, *Mon. Weather Rev.*, *137*(12), 4410–4419, doi:10.1175/2009MWR2863.1.
Zambon, J. B., R. He, and J. C. Warner (2014), Tropical to extratropical: Marine environmental changes associated with Superstorm Sandy prior to its landfall, *Geophys. Res. Lett.*, *41*, 8935–8943, doi:10.1002/2014GL061357.
Zedler, S. E., T. D. Dickey, S. C. Doney, J. F. Price, X. Yu, and G. L. Mellor (2002), Analyses and simulations of the upper ocean's response to Hurricane Felix at the Bermuda Testbed Mooring site: 13–23 August 1995, *J. Geophys. Res.*, *107*(C12), 3232, doi:10.1029/2001JC000969.
Zhang, W. G., J. L. Wilkin, and R. J. Chant (2009), Modeling the pathways and mean dynamics of river plume dispersal in the New York Bight, *J. Phys. Oceanogr.*, *39*(5), 1167–1183, doi:10.1175/2008JPO4082.1.

AGU PUBLICATIONS

JGR

Journal of Geophysical Research: Oceans

RESEARCH ARTICLE
10.1002/2017JC012756

Special Section:
Oceanic Responses and Feedbacks to Tropical Cyclones

Key Points:
- Observations, models reveal similar processes governing stratified coastal ocean cooling response to Hurricane Irene, Tropical Storm Barry
- Robust shear-induced mixing produced rapid ahead-of-eye-center cooling in TCs on opposite ends of track and seasonal stratification envelope
- Coupled TC models capable of predicting processes leading to rapid cooling of stratified coastal oceans critical for populated coastlines

Correspondence to:
G. Seroka,
gregory.seroka@noaa.gov

Citation:
Seroka, G., T. Miles, Y. Xu, J. Kohut, O. Schofield, and S. Glenn (2017), Rapid shelf-wide cooling response of a stratified coastal ocean to hurricanes, *J. Geophys. Res. Oceans*, *122*, 4845–4867, doi:10.1002/2017JC012756.

Received 30 JAN 2017
Accepted 12 MAY 2017
Accepted article online 20 MAY 2017
Published online 15 JUN 2017

Rapid shelf-wide cooling response of a stratified coastal ocean to hurricanes

Greg Seroka[1,2], Travis Miles[1], Yi Xu[3], Josh Kohut[1], Oscar Schofield[1], and Scott Glenn[1]

[1]Center for Ocean Observing Leadership, Department of Marine and Coastal Sciences, School of Environmental and Biological Sciences, Rutgers University, New Brunswick, New Jersey, USA, [2]I.M. Systems Group, Inc., and Ocean Prediction Center, NOAA/NWS/NCEP, College Park, Maryland, USA, [3]State Key Laboratory of Estuarine and Coastal Research, East China Normal University, Shanghai, China

Abstract Large uncertainty in the predicted intensity of tropical cyclones (TCs) persists compared to the steadily improving skill in the predicted TC tracks. This intensity uncertainty has its most significant implications in the coastal zone, where TC impacts to populated shorelines are greatest. Recent studies have demonstrated that rapid ahead-of-eye-center cooling of a stratified coastal ocean can have a significant impact on hurricane intensity forecasts. Using observation-validated, high-resolution ocean modeling, the stratified coastal ocean cooling processes observed in two U.S. Mid-Atlantic hurricanes were investigated: Hurricane Irene (2011)—with an inshore Mid-Atlantic Bight (MAB) track during the late summer stratified coastal ocean season—and Tropical Storm Barry (2007)—with an offshore track during early summer. For both storms, the critical ahead-of-eye-center depth-averaged force balance across the entire MAB shelf included an onshore wind stress balanced by an offshore pressure gradient. This resulted in onshore surface currents opposing offshore bottom currents that enhanced surface to bottom current shear and turbulent mixing across the thermocline, resulting in the rapid cooling of the surface layer ahead-of-eye-center. Because the same baroclinic and mixing processes occurred for two storms on opposite ends of the track and seasonal stratification envelope, the response appears robust. It will be critical to forecast these processes and their implications for a wide range of future storms using realistic 3-D coupled atmosphere-ocean models to lower the uncertainty in predictions of TC intensities and impacts and enable coastal populations to better respond to increasing rapid intensification threats in an era of rising sea levels.

1. Introduction

Although substantial progress in the prediction of tropical cyclone (TC) tracks has been realized globally over the past few decades, TC intensity prediction skill has remained comparatively flat across all TC ocean basins [*DeMaria et al.*, 2014; *Sopko and Falvey*, 2014; *Cangialosi and Franklin*, 2016]. This intensity gap can be traced to high-resolution requirements for TC models, poor understanding and modeling of the atmospheric boundary layer, difficulty for many existing assimilation techniques to ingest observations of small but intense features, and—most importantly for this study—challenges in modeling the upper ocean response to TCs [*Emanuel*, 2017, and references therein]. Large uncertainty in predicting the strength of TCs thus remains, which has its most significant implications for landfalling TCs where impacts to life and property—via storm surge, wind damage, and inland flooding—are greatest. These storms must first traverse the shallow, coastal ocean before making landfall. The number of studies in the literature investigating shallow, coastal ocean TC responses, indeed, pales in comparison to the number examining deep, open ocean TC responses [*Seroka et al.*, 2016]. Further, the differences between the deep, open ocean processes and the coastal processes are stark due to the influence of the bottom boundary layer and coastal wall in shallow water [*Glenn et al.*, 2016; *Seroka et al.*, 2016]. It is critical to close this gap, with the goal of improving the simulation of coastal ocean physics in coupled TC intensity models [e.g., *Zambon et al.*, 2014; *Warner et al.*, 2017].

In the summer hurricane season, the shallow Mid-Atlantic Bight (MAB) off the U.S. East Coast is one of the most seasonally stratified regions in the world [*Schofield et al.*, 2008], characterized by a sun-heated warm (>25°C) and thin (10 m or less) surface layer and a cold (<10°C) bottom layer termed the "Cold Pool"

[*Houghton et al*., 1982]. When Hurricane Irene traversed the highly stratified, shallow MAB waters in August 2011 before making landfall in New Jersey, rapid surface cooling caused by mixing processes resulting from the two-layer baroclinic circulation in the MAB were observed by an underwater glider and several National Data Buoy Center (NDBC) buoys; these intense mixing processes and the surface cooling (up to 11°C) response in the MAB are described in detail in *Glenn et al*. [2016]. Because the magnitude of the cooling was so significant, it led to a reversal in the direction of air-sea latent and sensible heat fluxes—from the ocean providing heat to the storm when using a fixed prestorm warm sea surface temperature (SST) bottom boundary condition to the ocean acting as a heat sink when using the fixed poststorm cold SST condition [*Seroka et al*., 2016].

This cooling was also found to primarily occur ahead of Irene's eye center—critical for direct impact on storm intensity—as the storm traversed northeastward along the MAB coastline. The cascade of processes responsible were strong ahead-of-eye-center onshore winds and surface currents, coastal setup with water piling up along the coast, offshore bottom currents in response to the resulting offshore pressure gradient, and larger shear-driven turbulence, mixing, and entrainment of cold bottom water to the surface due to directly opposing onshore surface and offshore bottom currents.

The ahead-of-eye-center cooling signal that resulted from these baroclinic coastal ocean mixing processes was found to be present in the 10 additional storms since 1985 that traversed northeastward across the MAB in the summer stratified season, and also in Super Typhoon Muifa (2011) in the similarly highly stratified Yellow Sea between eastern China and Korea. Further, this ahead-of-eye-center cooling was found to have a large impact on Hurricane Irene's intensity, larger than any other Weather Research and Forecasting (WRF) parameter tested [*Seroka et al*., 2016].

Many questions remain. First, it is not known to what extent the ahead-of-eye-center cooling impacted the intensities of the other 10 MAB storms and Typhoon Muifa. Extensive sensitivity studies like the one performed by *Seroka et al*. [2016] would need to be conducted for each storm to investigate these intensity impacts.

Second, it is not known if the same or different cooling processes occurred in the other 10 MAB storms and in Typhoon Muifa. To improve understanding of TC coastal ocean response, the dominant momentum balances that occurred in these storms as well as mixing versus advective processes that led to the ahead-of-eye-center cooling signals should be investigated in detail. It is also critical to understand the spatial—cross-shelf and along-shelf, shallow and deep water—variability of the cooling processes, for a wider range of storms including Irene. Previous studies focused on these processes at the underwater glider location and not elsewhere on the MAB continental shelf [i.e., *Glenn et al*., 2016]. These research gaps will guide this paper's work.

Standard operational model annual performance metrics are based on the mean across all storms simulated during one or several hurricane seasons [e.g., *Kim et al*., 2014; *Tallapragada et al*., 2014; *Cangialosi and Franklin*, 2016]. While this method is effective in testing overall performance of a model, it tends to wash out any unique storm characteristics in both the atmosphere and the ocean. The full range of storm characteristics represents the full range of storm air-sea feedbacks that coupled models should capture and resolve. Therefore, it is critical to not only improve models incrementally based on the mean in an operational environment [e.g., *Kim et al*., 2014; *Tallapragada et al*., 2014; *Cangialosi and Franklin*, 2016] but also to investigate individual case studies and processes that models may or may not be correctly resolving [e.g., *D'Asaro et al*., 2007; *Lin et al*., 2009; *Jaimes and Shay*, 2015; *Glenn et al*., 2016; *Seroka et al*., 2016].

In order to better understand the baroclinic ocean response for different storms, further investigation was performed on Irene and Tropical Storm Barry (2007), 1 of the other 10 MAB storms listed in *Glenn et al*. [2016]. A map of National Hurricane Center (NHC) best tracks for Irene and Barry show both storms traversing northeastward over the MAB, with Irene traveling 600 km from eastern North Carolina (NC) to New York City in 19 h in late August 2011 (~32 km/h translation speed), and Barry traveling 700 km from eastern NC to just south of Montauk Point, NY in 18 h in early June 2007 (~39 km/h translation speed, Figure 1, left). Typical translation speeds at MAB latitudes are 29–36 km/h [*Mei et al*., 2012]. Intensity time series show Irene weakening throughout its MAB crossing using both wind and pressure intensity metrics and show Barry weakening—at a lesser rate than Irene—over its last 12 h across the MAB using both metrics (Figure 1, right). Both storms had a radius of maximum wind (RMW) reported in the Automated Tropical Cyclone Forecast (ATCF) [*Sampson and Schrader*, 2000] system database of ~74 km 30 h prior to storm presence

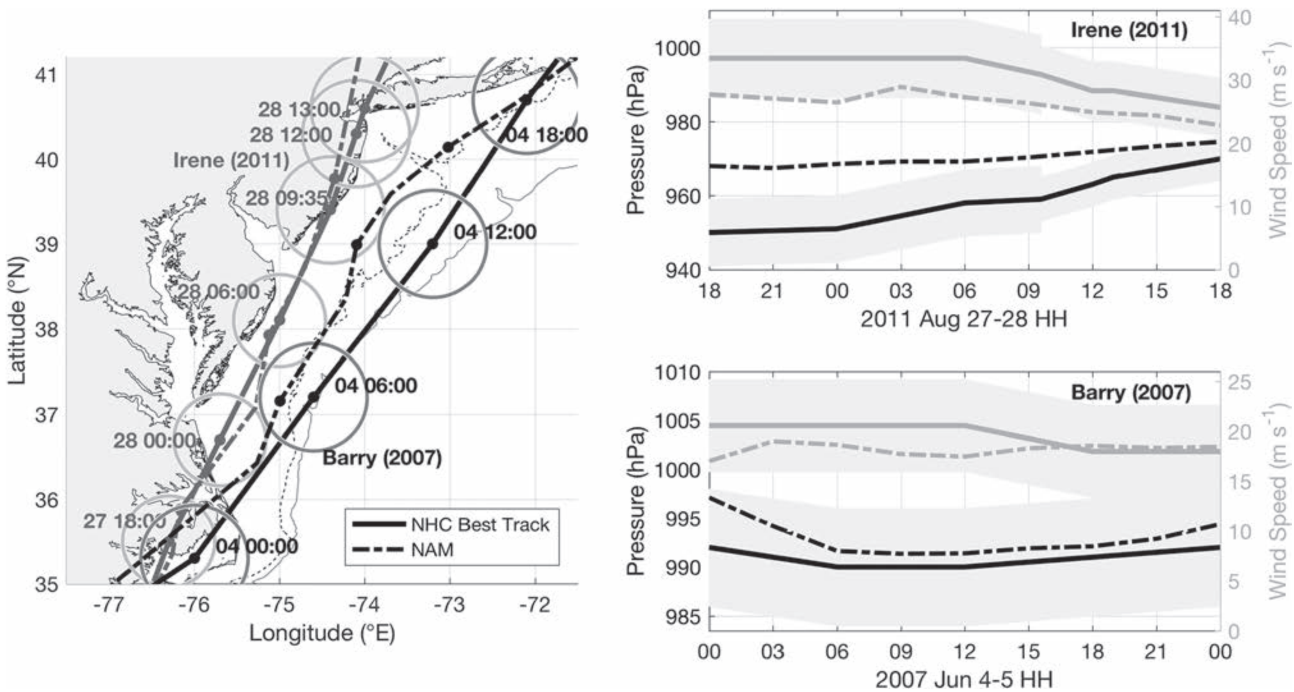

Figure 1. Irene and Barry. NHC best track spatial map (left) for Irene (gray solid line) and Barry (black solid line), with position uncertainty circles plotted at each NHC best track position for each storm. NAM in dash-dotted line for Irene (gray) and Barry (black). 50 and 200 m isobaths are in dotted contours. Date and time are in format 2011 MM HH:MM for Irene and 2007 MM HH:MM for Barry. NHC best track intensity time series for Irene (top right) and Barry (bottom right), with minimum central pressure (hPa) in solid black line and maximum sustained 10 m wind speeds (m s^{-1}) in solid gray line and intensity uncertainty in shaded gray. NAM in black dash-dotted lines for minimum central pressure and gray dash-dotted lines for maximum winds. NHC best track position and intensity uncertainties are from [*Torn and Snyder*, 2012] and depend on the intensity of the TC. All times are in UTC.

over eastern NC, with Irene's RMW increasing to 185 km 36 h later when the storm was over the MAB. For context, the average RMW for hurricanes making landfall in the U.S. from 1893 to 1979 was 47 km [*Hsu and Yan*, 1998].

For both of these storms, Rutgers University underwater gliders were deployed on the MAB continental shelf. Irene had a more inshore track northward through the MAB and Barry tracked farther offshore along the shelf break (Figure 1). Irene occurred in late August toward the end of the MAB summer stratified season, while Barry occurred in early June, during the beginning of the summer stratified season. However, the intent is not to perform direct comparisons between the two storms, as this would introduce several uncontrollable variables and not be a fully controlled experiment. Rather, the objective is to better understand the conditions in both the atmosphere and ocean that may lead to the baroclinic coastal ocean cooling processes, ahead-of-eye-center cooling, and impact on storm intensities for two extremes in the storm track—one nearshore and one well offshore—and two extremes in summer stratification—one near the end and one near the beginning of the season. This paper will investigate the details of and variability in the dominant baroclinic coastal ocean processes—in both the cross-shelf and along-shelf directions—for both Irene and Barry. By studying the spatiotemporal variability in these baroclinic coastal ocean cooling TC processes, the aim will be to improve the modeling of the full range of stratified coastal ocean TC responses.

2. Data and Methods

2.1. High Frequency (HF) Radar

Hourly surface ocean current data, 1 h center-averaged, from a network of CODAR Ocean Sensors SeaSonde HF Radar stations [*Roarty et al.*, 2010] along the MAB coast were used in this paper. Surface current map data have a nominal 6 km spatial resolution (Figure 1).

2.2. Gliders

Teledyne-Webb Research (TWR) Slocum gliders, autonomous underwater vehicles (AUVs), were used in this paper [*Schofield et al.*, 2007; *Glenn et al.*, 2008, 2016; *Ruiz et al.*, 2012; *Miles et al.*, 2013, 2015]. Rutgers

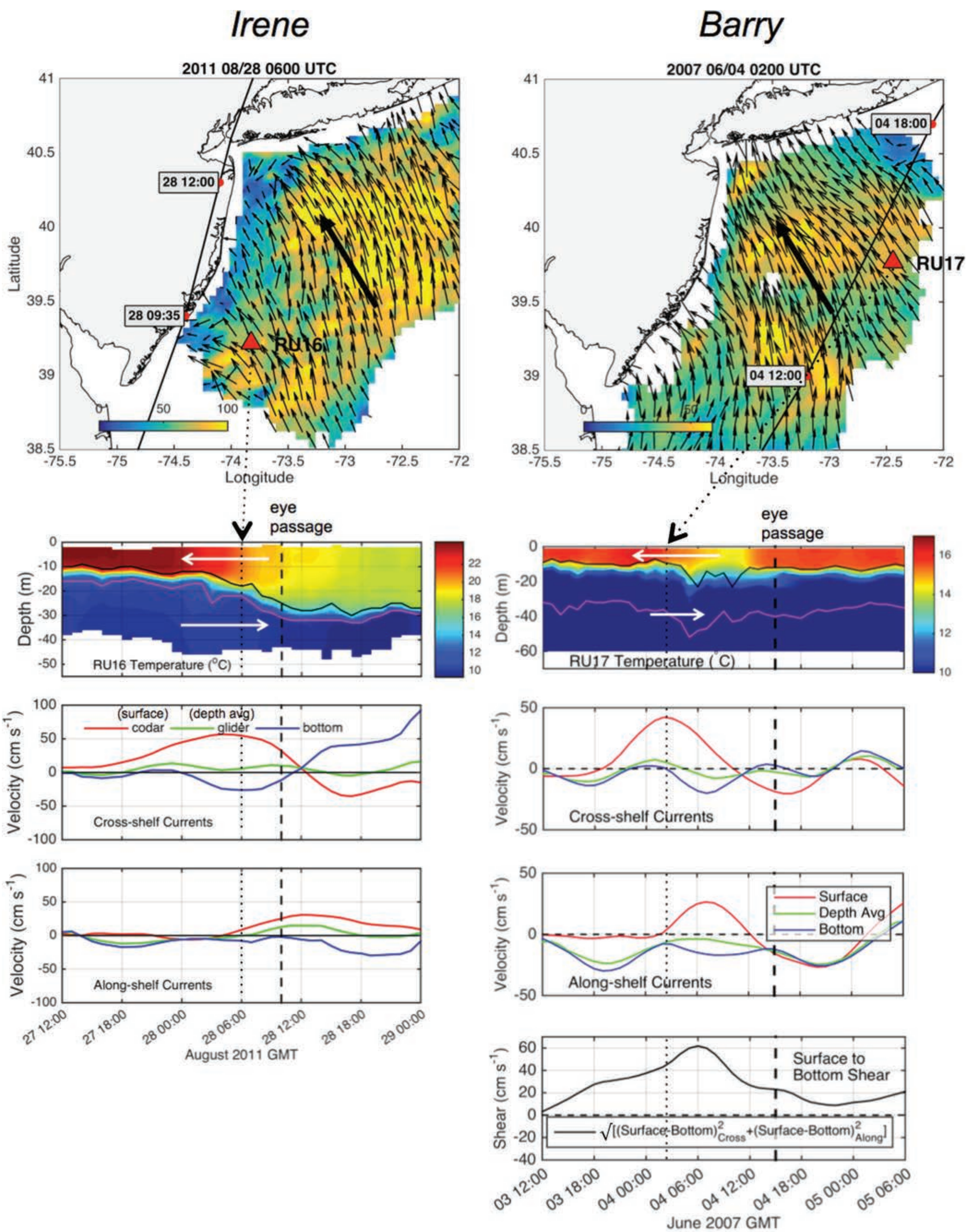
Irene
Barry
2011 08/28 0600 UTC
2007 06/04 0200 UTC
28 12:00
28 09:35
RU16
04 18:00
04 12:00
RU17
Latitude
Longitude
eye passage
RU16 Temperature (°C)
RU17 Temperature (°C)
Depth (m)
(surface) codar
(depth avg) glider
bottom
Cross-shelf Currents
Along-shelf Currents
Velocity (cm s-1)
Surface
Depth Avg
Bottom
August 2011 GMT
June 2007 GMT
Shear (cm s-1)
Surface to Bottom Shear
√[(Surface-Bottom)²Cross+(Surface-Bottom)²Along]

Figure 2.

University Gliders RU16 (Irene) and RU17 (Barry) data were analyzed. Both gliders were equipped with a Seabird unpumped conductivity, temperature, and depth (CTD) sensor.

Depth and time-averaged velocity calculations were performed using a dead-reckoning technique, a method typically used for underwater gliders [*Sherman et al*., 2001; *Davis et al*., 2002; *Schofield et al*., 2007]. To estimate bottom layer currents at the glider location, a combination of dead-reckoned depth-averaged glider currents and HF radar surface currents is used (Figure 2). This method assumes that the HF radar surface currents are representative of the currents in the surface mixed layer above the thermocline. See *Glenn et al*. [2016] for detailed methods and equations used to calculate bottom layer currents.

2.3. Bathymetry

U.S. Coastal Relief Model data from the NOAA National Centers for Environmental Information were used for water depth and coastlines throughout this paper [*NOAA National Centers for Environmental Prediction*, 2016].

2.4. Satellite SST

Advanced Very High Resolution Radiometer (AVHRR) data were used for ocean model SST verification. Techniques empirically derived for the MAB to remove bright cloud covered pixels and retain darker ocean pixels were used to decloud AVHRR data but preserve the rapid TC cooling signal, following *Glenn et al*. [2016].

2.5. Regional Ocean Modeling System (ROMS): ESPreSSO

Ocean model simulations were conducted using ROMS [*Haidvogel et al*., 2008], a free-surface, sigma coordinate, primitive equation ocean model (code available at http://www.myroms.org). ROMS has been used for a wide variety of coastal applications. Specifically, the ESPreSSO (Experimental System for Predicting Shelf and Slope Optics) model [*Wilkin and Hunter*, 2013], covering the MAB from Cape Cod to south of Cape Hatteras, and from the inland bays to beyond the shelf break, was used for simulations. In an assessment of skill of real-time ocean models over the MAB continental shelf for 2010–2011, ESPreSSO performed well as compared to global models and other regional models, indicating its usefulness for simulating coastal ocean circulations across a wide range of conditions, including Hurricane Irene which also occurred in 2011 [*Wilkin and Hunter*, 2013].

The ESPreSSO grid has a horizontal resolution of 5 km and 36 vertical levels in a terrain-following *s*-coordinate system. Initial conditions here were developed from an ESPreSSO grid ROMS reanalysis with strong constrained four-dimensional variational (4D-Var) data assimilation, including assimilation of sea surface height, SST, HF radar surface currents, and in situ temperature and salinity observations. For atmospheric forcing, North American Mesoscale (NAM) 12 km 3 hourly forecast data from its daily 00Z cycles were used. Only short-term forecast hours f03–f27 were used to limit any longer-term forecast error, with the f00 analysis skipped to allow for model spin-up. NAM surface air temperature, pressure, relative humidity, 10 m vector winds, precipitation, downward longwave radiation, and net shortwave radiation were used to specify the surface momentum and buoyancy fluxes based on the COARE bulk formulae [*Fairall et al*., 2003].

The NAM track map and intensity time series as assembled here for both Irene and Barry are compared to the NHC best track analyses (Figure 1). NHC best track uncertainty estimates depend on the intensity of the TC, with the uncertainty increasing as the intensity decreases [*Torn and Snyder*, 2012]. For both storms, the NAM tracks are all well within or just outside the best track uncertainties, and the NAM maximum wind intensities are within or at the best track uncertainties (Figure 1). For Barry, the minimum central pressure intensities are well within the uncertainties, and for Irene, they are at or just outside the uncertainties. The wind rather than central pressure intensities are most relevant for this study, as the winds provide the momentum fluxes forcing the TC ocean response. Overall, the NAM tracks properly represent the typical MAB track envelope, with Irene propagating along the inner shelf and Barry along the mid to outer shelf.

Figure 2. Irene and Barry. HF radar surface ocean current 1 h center-averaged maps for Irene and Barry before eye passage by RU16 (Irene, top left) and RU17 (Barry, top right). NHC best track in black, with large black arrow indicating general direction of surface currents. Location of RU16 and RU17 shown with red triangles. Time series at glider locations of temperature with thermocline depth in black contour, transition layer depth (see *Glenn et al*. [2016] for definitions) in magenta contour, and large white arrows indicating general direction of layer currents (second row from top); cross-shelf currents (third row from top); along-shelf currents (fourth row); and surface to bottom shear for Barry (bottom right). Currents and shear are smoothed using the MATLAB "smooth" function using a span of 8.

Boundary conditions were daily two-dimensional surface elevation and three-dimensional velocity, temperature, and salinity fields from the Hybrid Coordinate Ocean Model (HYCOM) Navy Coupled Ocean Data Assimilation (NCODA) forecast system. River inflows were from the seven largest rivers, using daily average U.S.G.S. discharge data. Tidal boundary conditions were from the ADvanced CIRCulation (ADCIRC) tidal model. Finally, vertical turbulence diffusivity was determined using the general length-scale method k-kl type vertical mixing scheme [*Umlauf and Burchard*, 2003; *Warner et al*., 2005].

For Barry, the ROMS ESPreSSO simulation was initialized at 1200 UTC on 29 May 2007 and ended at 1200 UTC on 8 June 2007, with storm eye passage by glider RU17 at 1700 UTC on 4 June 2007, just over 5 days into the simulation to allow for model spin-up. For Irene, the ROMS ESPreSSO simulation was initialized at 1200 UTC on 24 August 2011 and ended at 0000 UTC on 3 September 2011, with storm eye passage by glider RU16 at 1200 UTC on 28 August 2011, exactly 4 days into the simulation.

The depth-averaged momentum balance terms were direct output from the ROMS simulations, and the equations are as follows:

$$\underbrace{\frac{\partial u}{\partial t}}_{\text{acceleration}} = \underbrace{-\frac{\partial(uu)}{\partial x}-\frac{\partial(vu)}{\partial y}}_{\text{horizontal advection}} \underbrace{-\frac{1}{\rho_0}\frac{\partial P}{\partial x}}_{\text{pressure gradient}} + \left(\underbrace{\frac{\tau_s^x}{h\rho_0}}_{\text{surface stress}} - \underbrace{\frac{\tau_b^x}{h\rho_0}}_{\text{bottom stress}}\right) + \underbrace{fv}_{\text{Coriolis}}, \tag{1}$$

$$\underbrace{\frac{\partial v}{\partial t}}_{\text{acceleration}} = \underbrace{-\frac{\partial(uv)}{\partial x}-\frac{\partial(vv)}{\partial y}}_{\text{horizontal advection}} \underbrace{-\frac{1}{\rho_0}\frac{\partial P}{\partial y}}_{\text{pressure gradient}} + \left(\underbrace{\frac{\tau_s^y}{h\rho_0}}_{\text{surface stress}} - \underbrace{\frac{\tau_b^y}{h\rho_0}}_{\text{bottom stress}}\right) - \underbrace{fu}_{\text{Coriolis}}, \tag{2}$$

where u and v are the along-shelf and cross-shelf components of depth-averaged velocity, respectively, t is time, P is depth-averaged pressure, ρ_o is a reference density, τ_s and τ_b are surface (wind) and bottom stresses, h is water column depth, and f is the latitude-dependent Coriolis frequency. Horizontal diffusion was small and neglected here.

The temperature rate equation terms to diagnose advection versus mixing were also direct output from ROMS. The equation is as follows:

$$\frac{\partial T}{\partial t} = -\frac{\partial(uT)}{\partial x}-\frac{\partial(vT)}{\partial y}-\frac{\partial(wT)}{\partial z}+\frac{\partial A_{kt}\frac{\partial T}{\partial z}}{\partial z}+D_T+F_T, \tag{3}$$

with the following surface and bottom boundary conditions, respectively:

$$\left(A_{kt}\frac{\partial T}{\partial z}\right)_{z=0} = \frac{Q_{net}}{\rho_0 C_p}, \tag{4}$$

$$\left(A_{kt}\frac{\partial T}{\partial z}\right)_{z=0} = 0. \tag{5}$$

Here T is the temperature, t is time, u, v, and w are the along-shelf, cross-shelf, and vertical components of velocity. A_{kt} is the vertical diffusivity coefficient, D_T is the horizontal diffusion term, and F_T is friction. Q_{net} is the surface net heat flux, $\rho_0 = 1025$ kg m^{-3} is a reference density, $C_p = 3985$ J (kg °C)$^{-1}$ is the specific heat capacity of seawater, and h is the water depth. Horizontal diffusion again was small and neglected here.

3. Results

3.1. Observations

Glenn et al. [2016] used HF radar and glider RU16 data to determine surface, depth-averaged, and bottom currents at the glider location during Irene. Part of the time series is repeated here in Figure 2 for ease of comparison to a similar analysis for Barry. At 0600 UTC on 28 August 2011, less than 4 h before Irene's NJ landfall and eye passage by glider RU16, surface ocean currents were directed onshore and upshelf, aligning close to the onshore winds ahead of Irene's eye (Figure 2, top left). Current magnitudes at this time approached 1 m s^{-1}. At 0200 UTC on 4 June 2007, a full 15 h before Barry's eye passage by glider RU17, surface ocean currents were in a very similar direction, onshore and upshelf.

Time series of temperature profiles at the glider locations below the surface current maps indicate initially very strong stratification and an eventual breakdown in stratification upon storm forcing. For Irene in late August, surface mixed-layer temperatures approached 25°C to ~10–15 m depth, and bottom MAB Cold Pool temperatures were less than 10°C. For Barry in early June, surface mixed-layer temperatures down to ~10–15 m depth were approaching 16°C with bottom MAB Cold Pool temperatures again less than 10°C, approaching 5°C. For Irene, the thermocline (black contour) deepened to ~30 m depth and surface mixed-layer temperatures cooled to ~17°C, with much (~5°C, or ~75%) of the cooling occurring ahead-of-eye-center. For Barry, the thermocline (black contour) deepened briefly to 25 m depth and surface mixed-layer temperatures cooled to nearly 14°C, with 100% of the cooling at RU17 occurring ahead-of-eye-center.

Cross-shelf and along-shelf surface (red), depth-averaged (green), and bottom (blue) current time series are depicted in the two figures below the temperature time series in Figure 2. For Irene, currents in Earth coordinates are rotated 31° clockwise from north to attain cross-shelf and along-shelf components. For Barry, currents in Earth coordinates are rotated 50° clockwise from north to attain cross-shelf and along-shelf components. For both Irene and Barry, red surface currents peaked onshore ahead-of-eye-center, and blue bottom currents peaked offshore at the same time yet with a bit of a lag in setup. For Irene, along-shelf currents were very small ahead-of-eye-center, but for Barry, along-shelf surface currents to the northeast peaked ahead-of-eye-center and bottom currents peaked just before. For both storms, observations indicate a two-layer circulation, with cross-shelf surface currents onshore and cross-shelf bottom currents offshore, enhancing the shear and resultant mixing and cooling. For Barry, a similar surface to bottom shear profile occurred in the along-shelf direction. Figure 2 (bottom right) shows a calculation of surface to bottom shear, combining both the along-shelf and cross-shelf components for Barry due to the large observed along-shelf component. Maximum shear occurred at the same time as maximum surface cooling and thermocline deepening, and well before eye passage.

3.2. Modeling

In order to investigate the details of the baroclinic processes and mixing that occurred in Irene and Barry, including momentum balance analysis and the temperature diagnostic equation for mixing versus advection comparisons, ROMS ESPreSSO simulations were performed as described in section 2.5 above.

3.2.1. ROMS Simulation Validation: Hurricane Irene (2011)

A prestorm map of SST over the MAB from AVHRR at 0742 UTC on 24 August 2011 (Figure 3, top left) shows coastal upwelling along the NJ, DE, and MD coastlines, with a warm tongue of SST through the southern MAB and extending offshore of the 50 m isobath and into the northern MAB north of the Hudson Canyon. The ROMS ESPreSSO rerun SST ~4 h later (Figure 3, top right) shows very good agreement with AVHRR, capturing the coastal upwelling, warm tongue, Gulf Stream, and colder waters south of Rhode Island and Nantucket.

A poststorm map of SST over the MAB from AVHRR at 0828 UTC on 29 August 2011 (Figure 3, middle left) shows a much different story, with cold <18°C SST from the mouth of the Hudson Canyon and northward, and a corridor of colder water at the 50 m isobath and offshore in the southern MAB. The ROMS ESPreSSO rerun SST (Figure 3, middle right) again shows very good agreement with AVHRR, with perhaps the only minor issue being not as cold water at the mouth of the Delaware Bay and in the southern MAB.

A difference map of poststorm minus prestorm AVHRR SST (Figure 3, bottom left) shows maximum cooling (approaching 11°C) at the mouth of the Hudson Canyon and across the MAB, with less cooling in the shallow regions of the shelf and offshore in the deep water. Again, ROMS (Figure 3, bottom right) agrees very well with the AVHRR cooling map, capturing the maximum in cooling at the Hudson Canyon mouth.

Finally, RU16 glider temperature profile time series (Figure 4, left) shows the same deepening of the thermocline and cooling of the surface layer as shown in Figure 2. ROMS (Figure 4, right) taken at the closest grid cell to the average position of RU16 during the storm period shows an initial thermocline ~10–15 m too deep but with correct surface mixed layer and bottom layer temperatures. Although the simulated

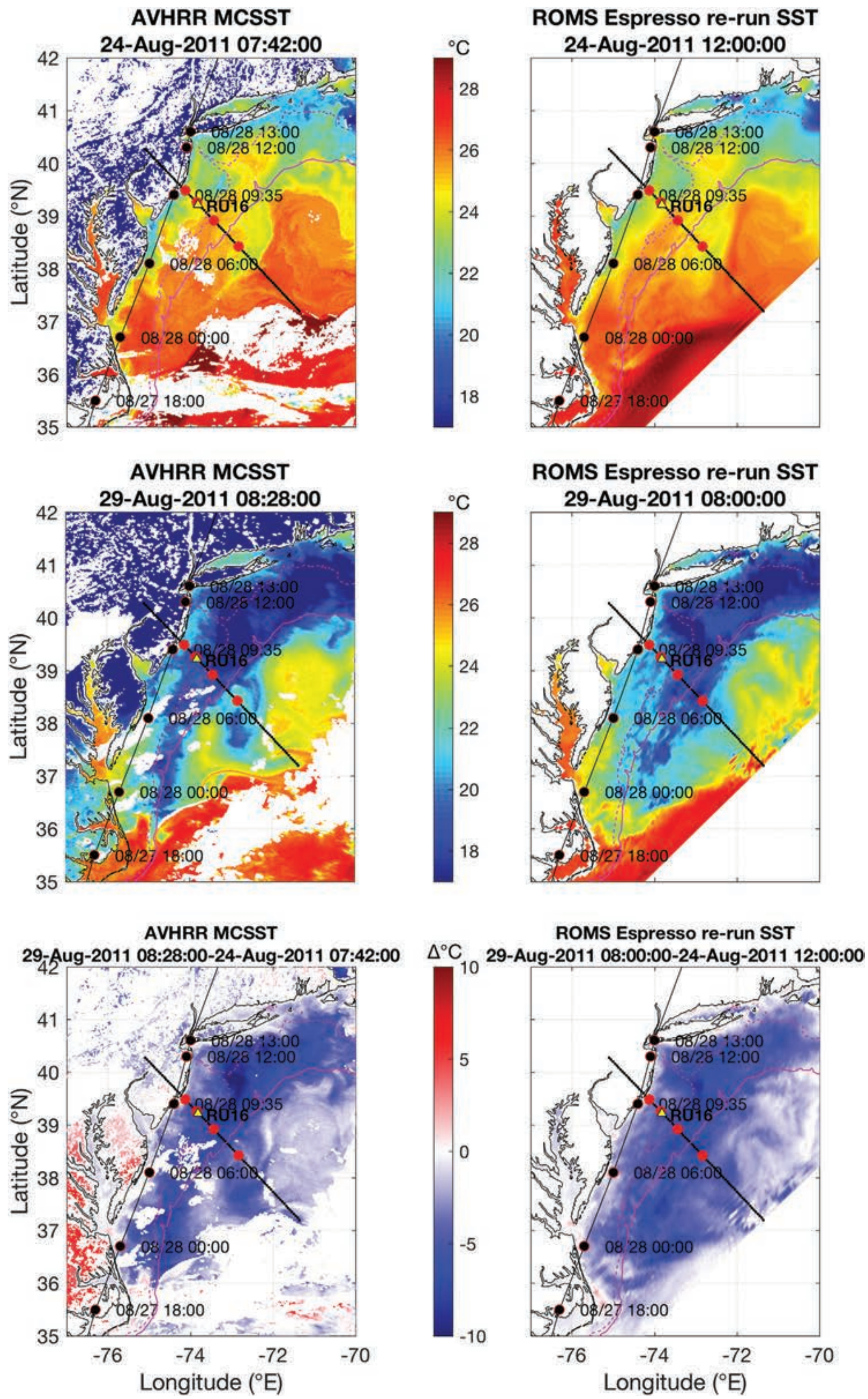

Figure 3. Irene. AVHRR Multi-Channel SST (MCSST) (top left) and ROMS ESPreSSO rerun SST (top right) prestorm for Irene; the same for poststorm in middle figures, and for poststorm minus prestorm in bottom figures. Dashed magenta contour is 50 m isobath, and solid magenta contour is 200 m isobath. RU16 location throughout the storm period plotted as yellow triangle, NHC best track for Irene in black with red outlined dots, small black dots in line northwest to southeast indicating cross-section location taken for Hövmoller figures below, and large red dots along this black line indicating profile locations taken for temperature diagnostic Figure 15.

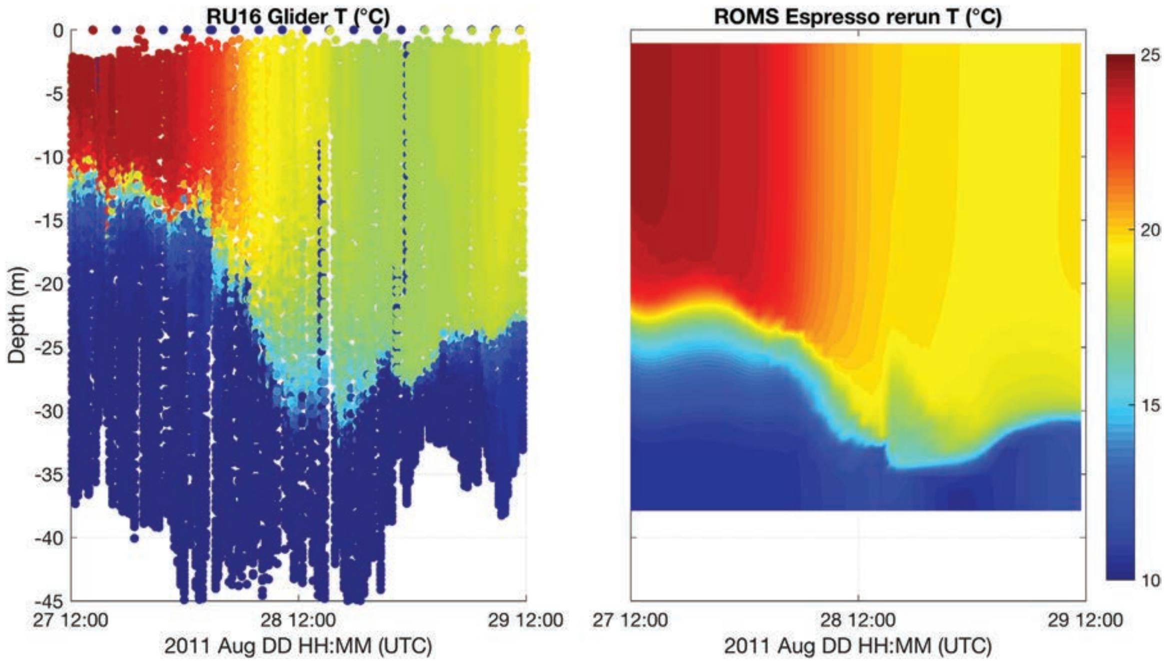

Figure 4. Irene. RU16 glider temperature (°C) (left) and ROMS ESPreSSO rerun temperature (°C) (right) at the closest ESPreSSO grid point to the average RU16 glider location during the storm.

thermocline is deeper than observed, the two-layer structure is present to support the relevant processes. Upon storm forcing, the ROMS thermocline deepens to the correct depth, but the surface does not sufficiently cool, likely due to the inadequate supply of cold bottom water at the start. Insufficient surface ocean cooling in model simulations due to an excessively thick surface layer has also been found to occur in other recent TC studies [e.g., *Zhang et al*., 2016], and is likely a common deficiency in numerical model simulations of TC ocean response. Despite deficiencies in the details, the overall storm response characteristics—two-layer structure at the start, deepening of the thermocline, and rapid and intense cooling of the surface mixed layer—are present and adequate for determining dominant force balances and diagnosing the causes of SST cooling.

3.2.2. ROMS Simulation Validation: Tropical Storm Barry (2007)

A prestorm map of SST over the MAB from AVHRR at 0559 UTC on 2 June 2007 (Figure 5, top left) is partially blocked by clouds but shows a warm Gulf Stream offshore, a couple Gulf Stream rings to the northwest in the slope water, a ribbon of colder water along the shelf break at 200 m, a ribbon of warmer water inshore of the 50 m isobath, and coastal upwelling east of Cape May, NJ, at the mouth of Delaware Bay, and along the Delmarva Peninsula. ROMS (Figure 5, top right) shows good agreement with AVHRR, with a warm Gulf Stream, cold water to the north, NJ and Delaware Bay coastal upwelling, warmer midshelf MAB waters, and a hint of the warm Gulf Stream filament approaching the 200 m isobath.

A poststorm map of SST over the MAB from AVHRR at 0207 UTC on 5 June 2007 (Figure 5, middle left) with the same color bar in Figure 5 (top) shows cooler water over the northern MAB, and ROMS at the same time (Figure 5, middle right) provides a similar picture. The difference maps of poststorm minus prestorm AVHRR SST (Figure 5, bottom left), ROMS rerun at the same time difference (Figure 5, bottom middle), and ROMS rerun to maximize cooling (Figure 5, bottom right) highlight the cooling and warming patterns across the MAB. Although clouds block parts of the map, AVHRR shows a pattern of warming in the southern MAB and offshore, and cooling in the northern MAB and offshore. Both ROMS rerun difference maps show more widespread cooling, with slight warming offshore NJ and off the Delmarva Peninsula, and where the Gulf Stream meanders moved through time.

Finally, the profile time series of temperature at the RU17 glider location (Figure 6, left) again shows surface mixed-layer cooling and deepening during the storm period, as in Figure 2. ROMS ESPreSSO rerun (Figure 6, right) shows a thermocline initially 15–20 m too deep, but surface and bottom temperatures overall correct.

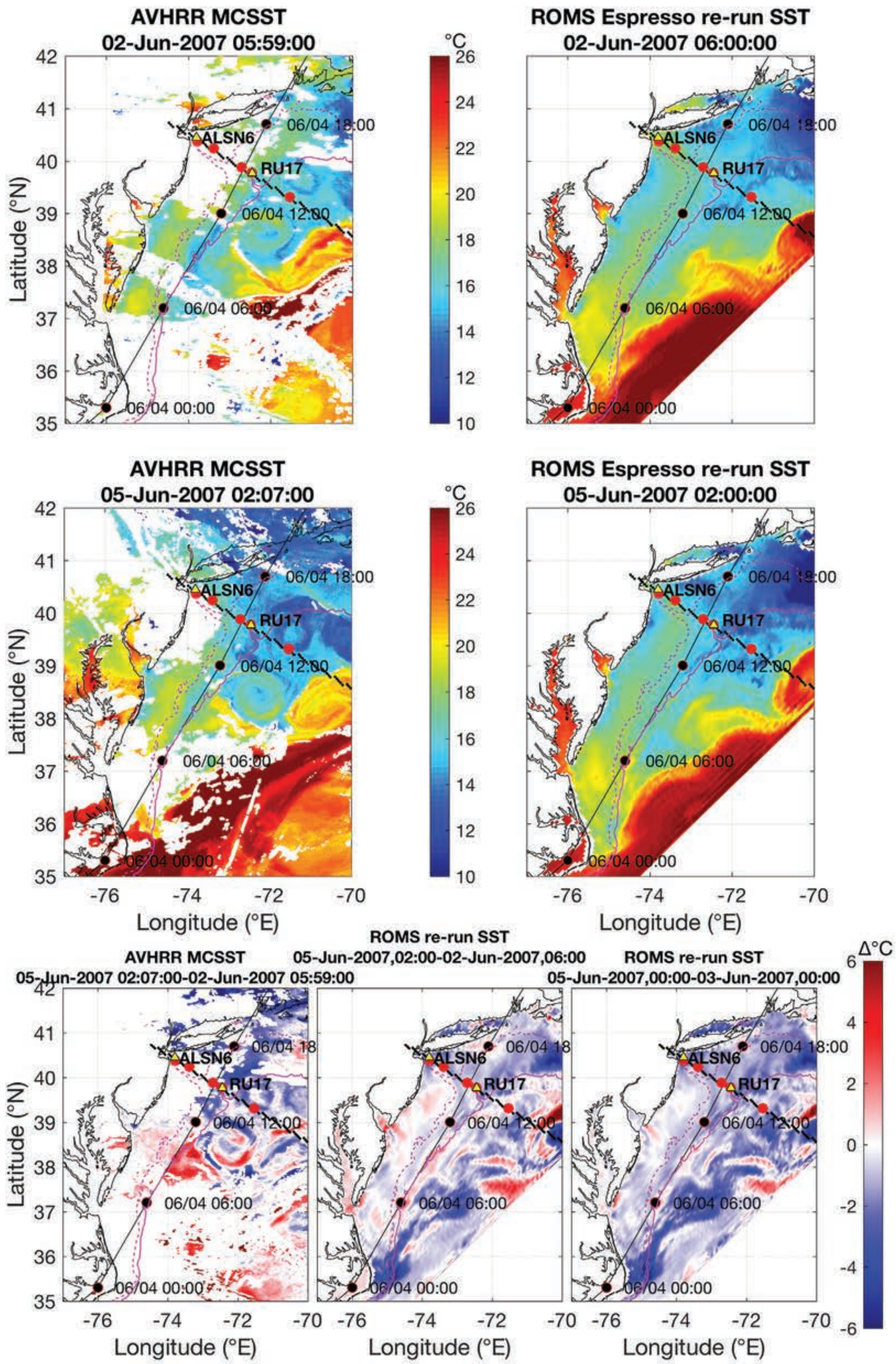

Figure 5. Barry. The same as Figure 3, but for Barry. NDBC station ALSN6 and RU17 glider locations indicated with yellow triangles. Northern cross-section location used for Barry plotted as west-northwest to east-southeast black dots just north of the Hudson Canyon, and large red dots along this black line indicating profile locations taken for temperature diagnostic Figure 16. A third figure on bottom (bottom right) is added for Barry with poststorm minus prestorm time difference chosen to maximize the cooling across the map in the ROMS ESPreSSO rerun.

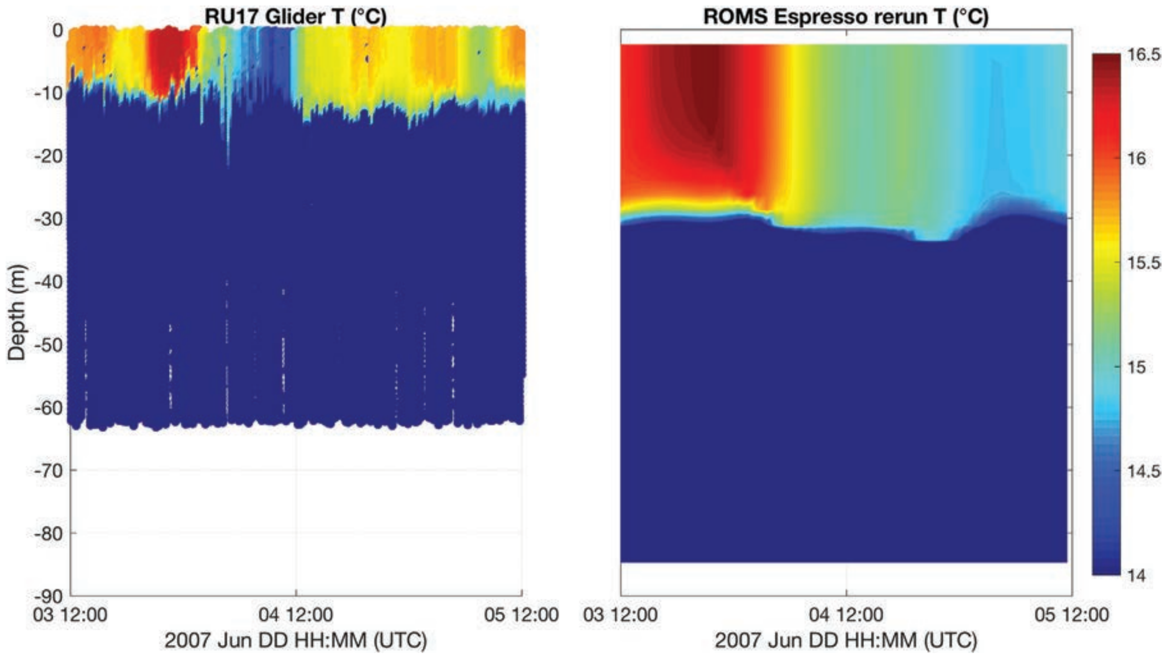

Figure 6. Barry. The same as Figure 4, but for RU17 glider in Barry. RU17 only sampled to ~60 m even though full water column depth was >80 m.

The resulting cooling of the surface layer occurs at about the correct time, but the surface layer warming poststorm does not occur.

3.2.3. Temperature, Current, Shear, and Momentum Balance Spatial Time Series: Irene

At the cross-section location near RU16 noted by the northwest to southeast black dots in Figure 3, Hövmoller diagrams of time (increasing up) versus distance offshore were produced. Surface temperature (Figure 7, top left) shows initially warm surface water stretching from the edge of the coastal upwelling to >200 km offshore. Then, SST rapidly cools across the shelf and in deep water, so that any cooling after eye passage (from NAM—two hours later than observed) is minimal. No SST cooling occurred within the nearshore coastal upwelling region. Bottom temperature (Figure 7, bottom left) shows a warm downwelling bulge during the storm, starting at the coastline and extending to close to 50 km offshore. The core of the MAB Cold Pool can be seen around 100 km offshore. Four sample locations are noted with the vertical solid lines labeled (1) in the upwelling region, (2) near RU16, (3) in the core of the Cold Pool, and (4) in deep water. These four locations will be used in the temperature diagnostic analysis (section 3.2.5).

A Hövmoller of cross-shelf surface currents (Figure 7, top middle) show onshore currents increasing at about 0000 UTC on 28 August, from about 50 km offshore across the shelf and into some of the deeper water. For Irene model results, currents in Earth coordinates are again rotated 31° clockwise from north to attain cross-shelf and along-shelf components. The onshore surface currents peak at around 0300 UTC and then decrease a few hours before eye passage. Bottom currents (Figure 7, bottom middle) are opposing offshore across the shelf and weaker than the onshore surface currents. The bottom onshore currents begin again at about 0000 UTC on 28 August and last until eye passage. After eye passage, surface currents switch to offshore, with the switch nearshore occurring a few hours after eye passage likely due to tidal influence (not shown). Bottom currents switch to onshore after eye passage almost immediately. Maximum shear from this plot occurred roughly from 0000 to 1200 UTC on 28 August and reversed from 1500 UTC on 28 August to 0000 UTC on 29 August.

The along-shelf surface current Hövmoller (Figure 7, top right) shows northeastward currents ahead of and after eye passage, with southwestward surface currents after eye passage in deeper water. Bottom currents (Figure 7, bottom right) are southwestward ahead of eye passage and immediately after, then northeastward later at 0000 UTC on 29 August. Maximum shear from this plot occurred roughly from 0600 to 1500 UTC on 28 August.

A bulk surface to bottom shear Hövmoller diagram, comprised the cross-shelf and along-shelf components, is shown in Figure 8 (left). This bulk shear Hövmoller shows a symmetric ~50% ahead and 50% behind eye

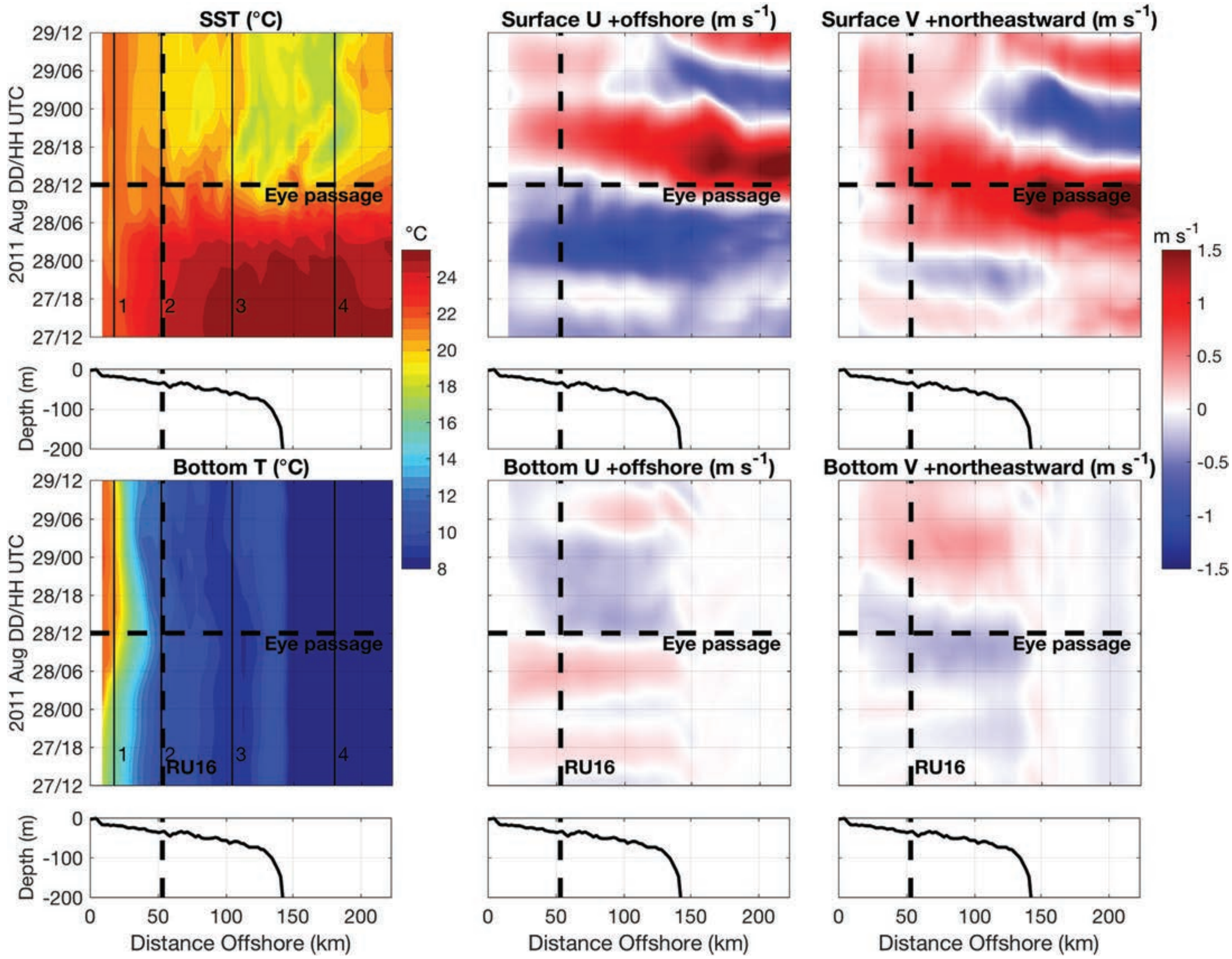

Figure 7. Irene. Hövmollers of ROMS ESPreSSO rerun SST (°C, top left), surface cross-shelf currents (m s^{-1}, top middle), and surface along-shelf currents (m s^{-1}, top right), with positive reds offshore/northeastward and negative blues onshore/southwestward for cross-shelf/along-shelf currents. Bottom row the same as top row but for the bottom of the water column. Eye passage in NAM atmospheric forcing marked with the horizontal dashed line, and RU16 glider location marked with the vertical dashed line. Vertical solid lines in left figure labeled 1 (upwelling), 2 (near RU16), 3 (in Cold Pool core), and 4 (in deep water) are locations where temperature diagnostics are performed in Figure 15. Water depth (m) along the cross section is plotted in the figures below the Hövmoller figures.

shear pattern in deep water, consistent with *Price* [1981]. In the shallow water over the continental shelf, shear is skewed ahead-of-eye-center. Because in deep water the bottom layer is quiescent and in shallow water the bottom layer is moving, only qualitative comparisons between deep and shallow water can be made. Additionally, bottom currents in shallow water are affected by opposing bottom stress, restricting any quantitative comparisons between deep and shallow water. By changing bottom currents to 0, a more evenly distributed shear pattern between ahead of and behind eye passage results (Figure 8, right), showing that the opposing bottom currents in the two-layer circulation has an influence on the shear pattern.

The ahead-of-eye-center cooling due to this shear is greater than behind-eye cooling (Figure 7, top left), potentially because (1) behind the eye center the water column is already mixed, and the surface layer is already deeper, (2) there are weaker backside offshore winds than frontside onshore winds due to frictional land effects—supported by observations at NDBC buoys 44014, 44009, and 44065, and at a WeatherFlow Inc. coastal land station at Tuckerton, NJ, and (3) the frontside of Irene cools the SST, the eye moves over the cooler water and weakens the storm, and the backside is weaker (Figure 1). As will be shown in the following momentum balance Hövmollers, the dominant cross-shelf momentum terms are onshore wind

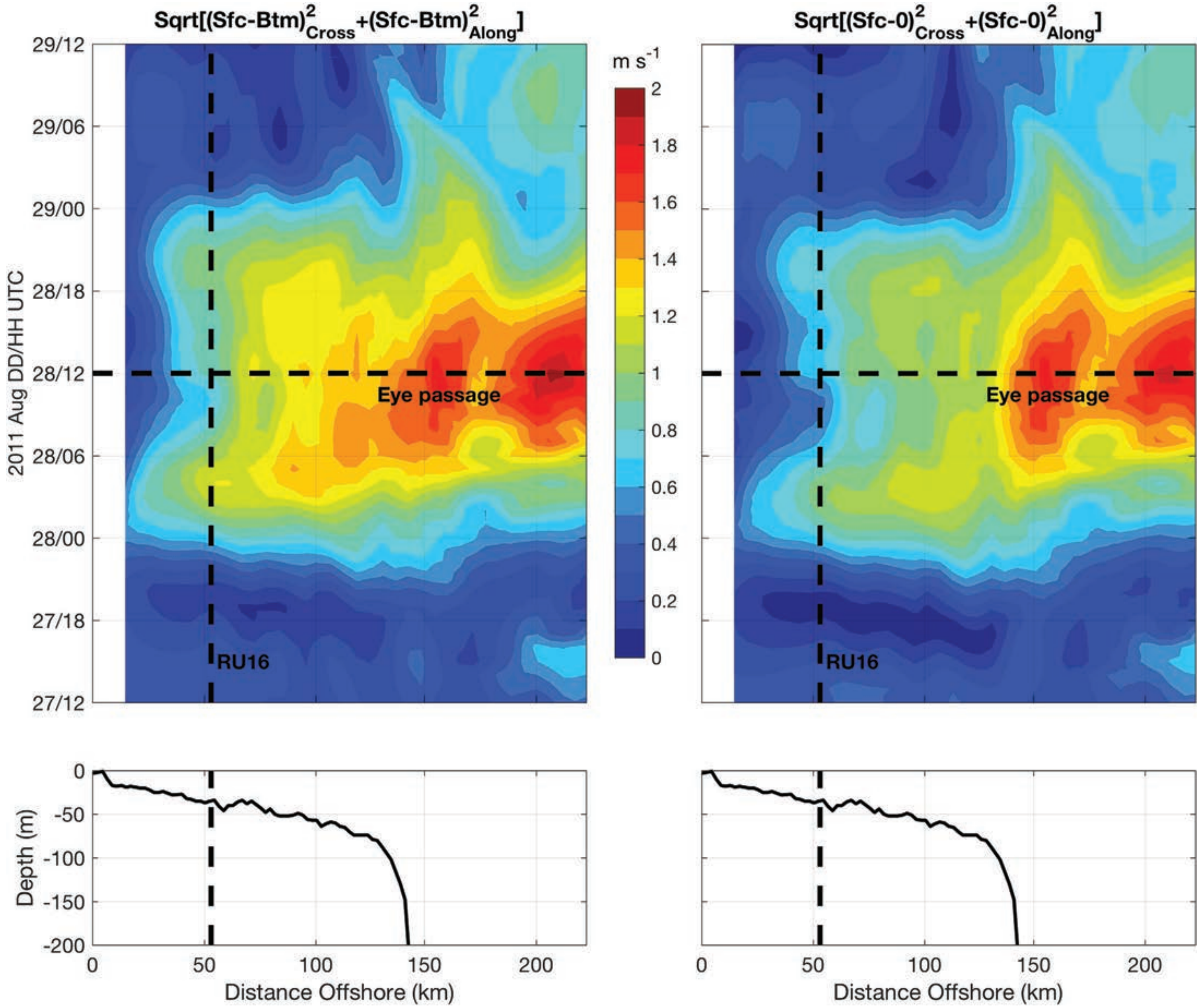

Figure 8. Irene. Same formatted Hövmoller as in Figure 7, but for bulk surface to bottom cross- and along-shelf shear (left, m s^{-1}). This bulk shear is calculated according to the equation in the header: square root of the sum of the squares of the surface to bottom cross-shelf and along-shelf shears. Right figure is the same as left but for 0 substituted for bottom currents.

stress balanced by offshore pressure gradient force ahead-of-eye-center, and offshore wind stress balanced by onshore pressure gradient force behind-eye-center. This balance is likely due to the presence of the coastline and shallow bottom, in which onshore surface winds ahead-of-eye-center pile water at the coast and result in the offshore bottom current, and offshore surface winds behind-eye-center push water away from the coast and result in the onshore bottom current. In both cases—ahead-of-eye-center and behind-eye-center—a two-layer circulation occurs due to the presence of the coastline, shallow bottom, and stratified water column.

The depth-averaged cross-shelf momentum balance time series (Figure 9) depicts all terms except for horizontal viscosity, which was very small. Acceleration shows a strongly tidal signal, with less onshore acceleration just before eye passage. Wind stress is strongly onshore ahead-of-eye passage, and switches to offshore after. Pressure gradient force is offshore ahead-of-eye-center from the coast all the way to the shelf break, and then switches to onshore midshelf first and then both nearshore and near the shelf break second; this pressure gradient pattern is due to coastal setup ahead-of-eye and coastal set down behind-eye.

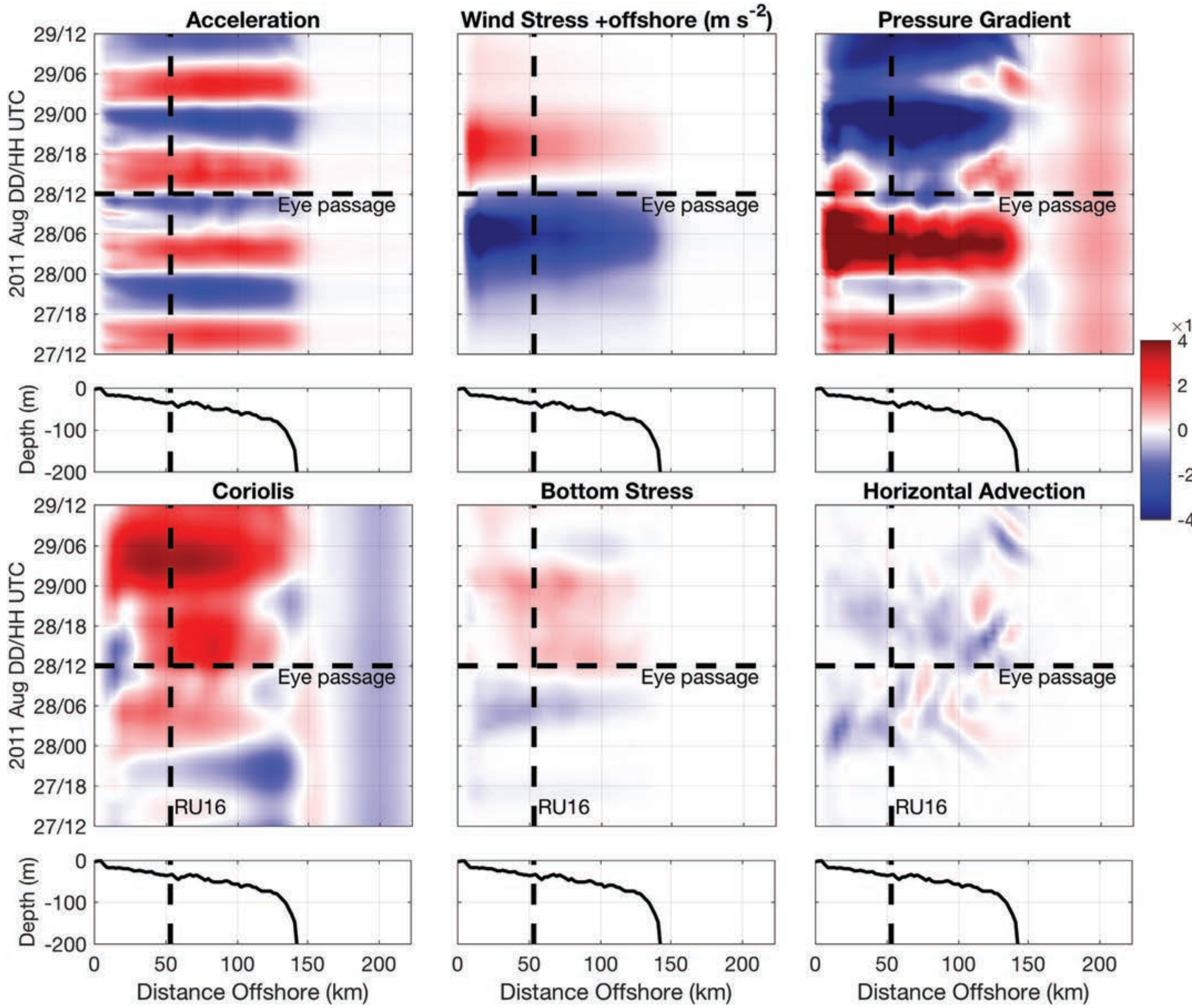

Figure 9. Irene. Hövmollers of the cross-shelf depth-averaged momentum balance terms (m s^{-2}), with positive reds offshore and negative blues onshore. Horizontal diffusion was small and thus not plotted.

Coriolis is offshore, increasing after the eye. Bottom stress is onshore opposing the offshore bottom currents ahead-of-eye, and then switches sign after eye. Finally, advection is small and noisy, with a response near the inertial period especially near the shelf break. The dominant cross-shelf force balance progresses from onshore wind stress balanced by offshore pressure gradient ahead-of-eye-center, to offshore wind stress and Coriolis balanced by onshore pressure gradient after eye passage until 0000 UTC on 29 August, and finally to a geostrophic balance of offshore Coriolis balanced by onshore pressure gradient.

In the along-shelf direction, depth-averaged momentum balance terms (Figure 10) are generally smaller than the cross-shelf terms. Again, acceleration has a tidal signal, but so does Coriolis. The dominant along-shelf force balance progresses from southwestward wind stress balanced by northeastward pressure gradient and Coriolis, to northeastward wind stress balanced by southwestward pressure gradient and Coriolis, and finally to alternating southwestward and northeastward pressure gradient balanced by Coriolis (tidal periodicity).

3.2.4. Temperature, Current, Shear, and Momentum Balance Spatial Time Series: Barry

The time series of SST for Barry (Figure 11, top left) was taken at the northern WNW to ESE cross-section location just north of the Hudson Canyon as indicated by the black dots in Figure 5. This northern location

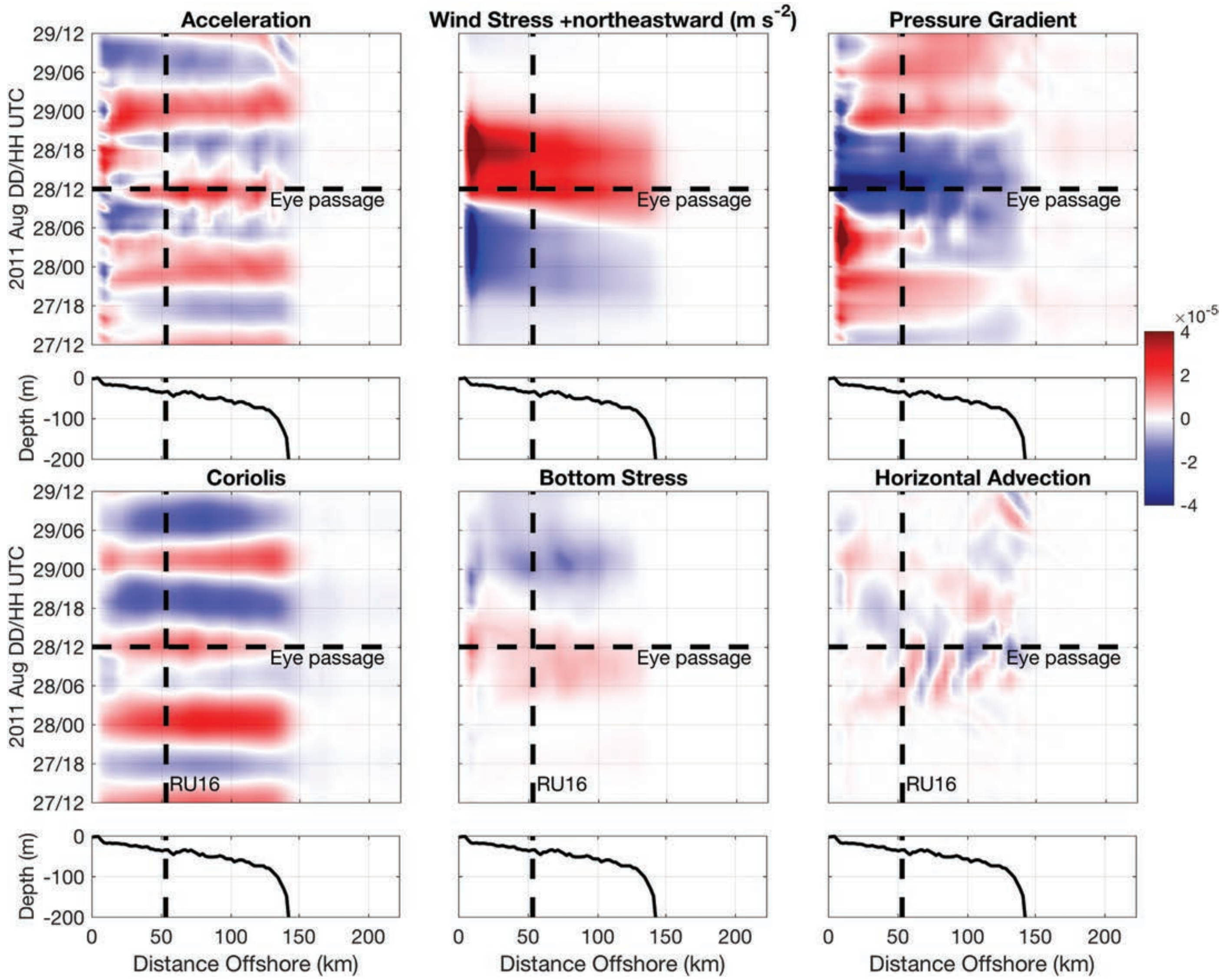

Figure 10. Irene. Same as Figure 9 but for along-shelf depth-averaged momentum balance terms (m s^{-2}), with positive reds northeastward and negative blues southwestward.

was chosen to target the greatest SST cooling in Barry. A similar cooling signal is apparent across the shelf and even in deep water. At National Data Buoy Center (NDBC) station ALSN6, the Barry station used by *Glenn et al*. [2016] for the ahead-of-eye-center cooling signal, cooling (~3.5°C) was greatest. At the warm strip of water indicated by the vertical line labeled "2," and in the deep water, total cooling was less than 1°C. The bottom temperature spatial time series (Figure 11, bottom left) shows a similar but more subtle downwelling bulge from the coast as was evident in Irene. Five sample locations are noted with the vertical solid lines labeled (1) in the nearshore maximum cooling and near ALSN6, (2) in the warm strip of water, (3) in the core of the Cold Pool, (4) near RU17, and (5) in deep water. These five locations will be used in the temperature diagnostic analysis (section 3.2.6).

The cross-shelf surface current time series (Figure 11, top middle) shows onshore surface currents peaking 12–18 h prior to eye passage, but remaining weakly onshore until eye passage. For Barry model results, currents in Earth coordinates are again rotated 51° clockwise from north to attain cross-shelf and along-shelf components. Bottom currents (Figure 11, bottom middle) show a primarily tidal signal, with alternative offshore and onshore bottom currents. Maximum shear was roughly 0600 to 1200 UTC on 4 June. This maximum shear occurs when the bottom offshore currents (mainly tidal) oppose the onshore surface currents. Because the storm forcing is weaker than in Irene, the tidal signal dominates the bottom current forcing.

 10.1002/2017JC012756

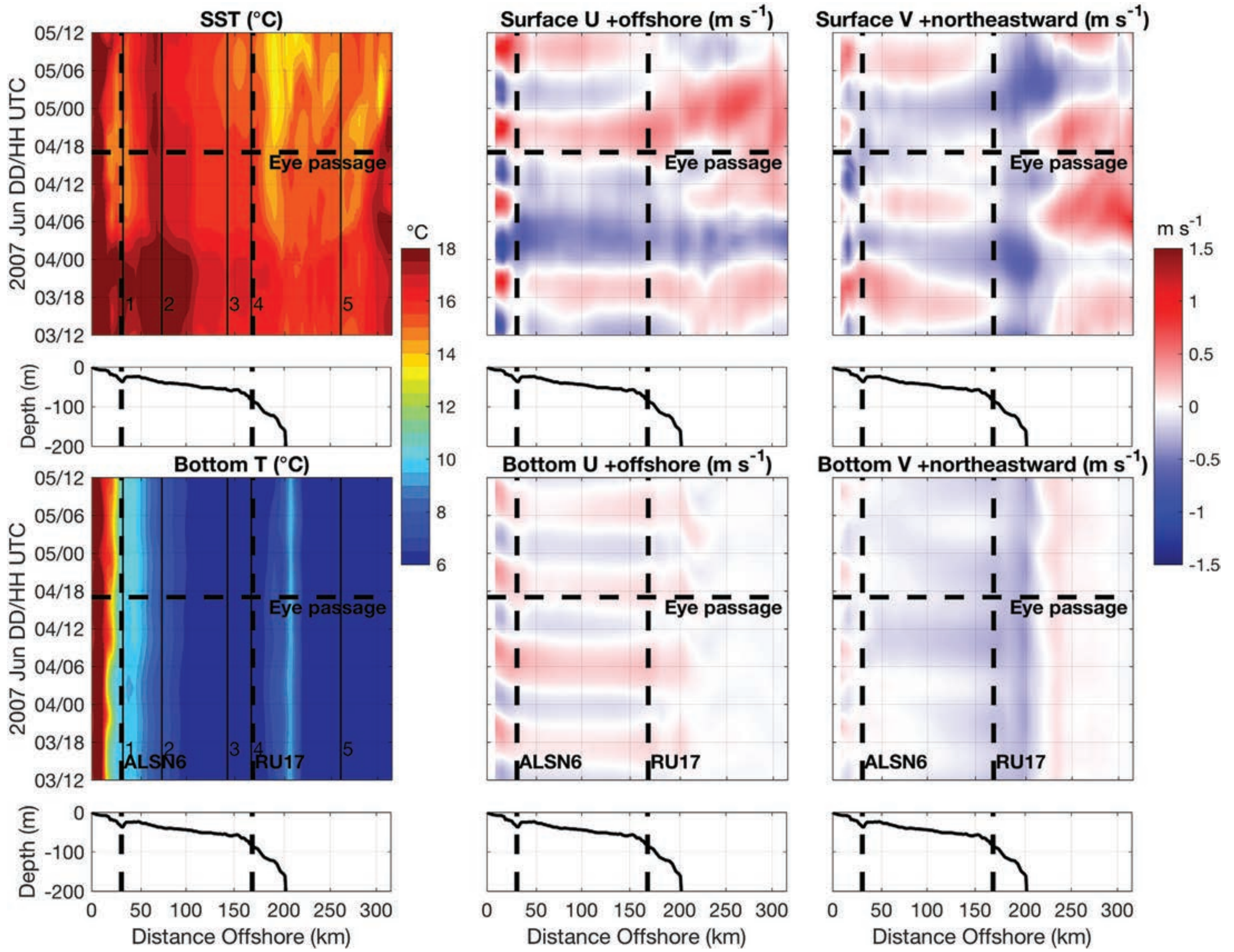

Figure 11. Barry. Same as Figure 7 but for Barry, with ALSN6 and RU17 locations plotted as vertical dashed lines. Vertical solid lines in left figures labeled 2 (near ALSN6), 2 (in warm strip), 3 (in Cold Pool core), 4 (near RU17), and 5 (in deep water) are locations where temperature diagnostics are performed in Figure 16.

This is consistent with the findings of *Keen and Glenn* [1995], who found that during a storm crossing the MAB in October 1990, the tidal signal dominated the bottom current forcing, and storm sedimentation was directly related to the tidal flow.

In the along-shelf direction, surface currents were northeastward before eye passage and southwestward after (Figure 11, top right). Bottom currents were southwestward the entire storm period, both before and after eye passage. A similar analysis just south of the Hudson Canyon may help answer why this occurred. One potential reason is that the Hudson Canyon acted as a barrier, blocking bottom currents from crossing the large bathymetric gradients.

The bulk surface to bottom shear Hövmoller for Barry, comprised the cross-shelf and along-shelf shears, is shown in Figure 12 (left). This bulk shear Hövmoller again shows a roughly symmetric ~50% ahead and 50% behind eye shear pattern in deep water if the time period of 0000 UTC on 4 June to 0600 UTC on 5 June is used. Again, like for Irene, shear is skewed ahead-of-eye passage in the shallow water, and by substituting 0 for bottom currents, a more (but not quite fully) symmetric shear pattern in shallow water results (Figure 12, right).

The Hövmoller cross-shelf depth-averaged momentum balance terms (Figure 13) show a strongly tidal signal in the acceleration, pressure gradient, and Coriolis terms across the shelf, and in the bottom stress and

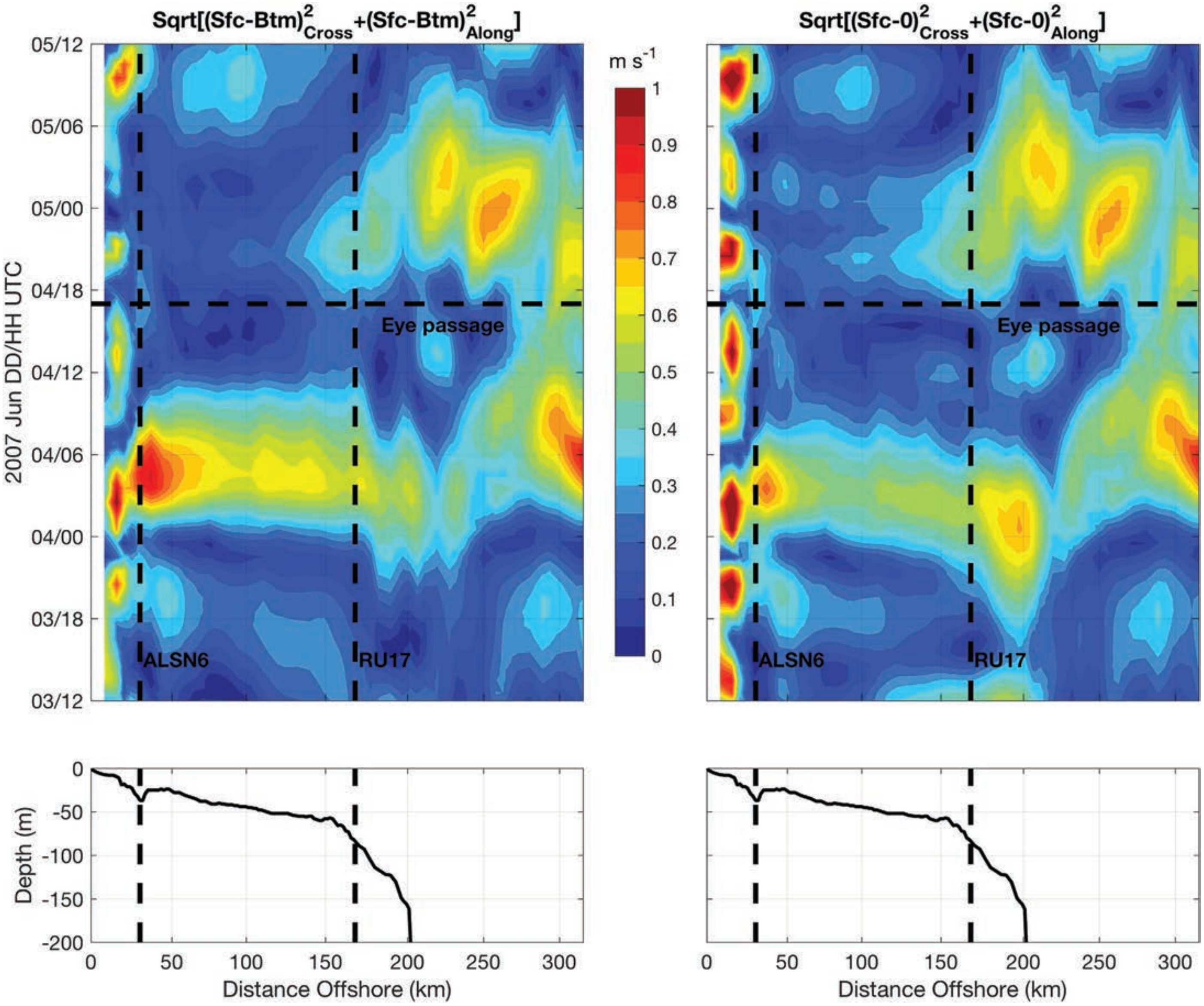

Figure 12. Barry. Same as Figure 8 (bulk surface to bottom shear analysis), but for Barry.

horizontal advection terms very near shore. Wind stress was directed onshore ahead of eye passage and weakly offshore after. Pressure gradient was primarily tidal, with more positive offshore values along the shelf break just ahead of eye passage as compared to after eye passage. Coriolis was largely tidal and onshore, with the maximum again at the shelf break. Bottom stress was mostly tidal, but mostly negative opposing the offshore bottom currents at about 0600 UTC on 4 June ahead of eye, when the downwelling circulation aligned with the tidal signal. Finally, horizontal advection was mostly small. The dominant depth-averaged cross-shelf force balance progressed from onshore wind stress balanced by offshore pressure gradient ahead of eye passage, to offshore wind stress balanced by alternating onshore/offshore Coriolis and pressure gradient (tidal periodicity) just after eye passage, to quasi-geostrophic balance with alternating onshore/offshore Coriolis balanced by pressure gradient (again tidal).

The Hövmoller along-shelf depth-averaged momentum balance terms (Figure 14) show a mostly tidally forced signature. Acceleration was mostly tidal, with slightly more negative onshore (or less positive offshore) acceleration ahead of eye passage from 0000 to ~0900 UTC on 4 June. Wind stress was southwestward ahead of eye passage and northeastward after. Pressure gradient and Coriolis terms were primarily

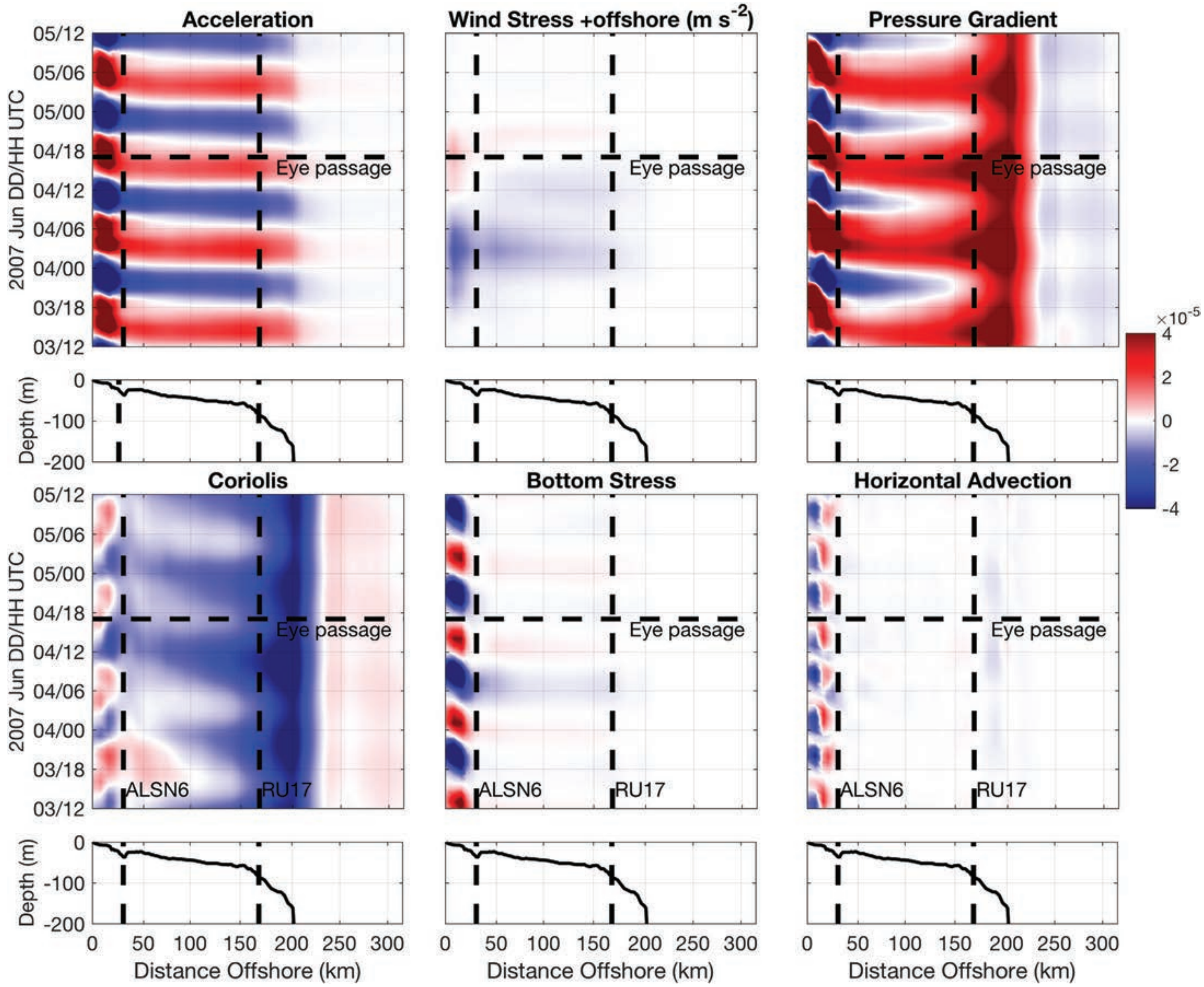

Figure 13. Barry. Same as Figure 9 (Hövmoller cross-shelf depth-averaged momentum balance terms), but for Barry.

tidal, bottom stress was always northeastward opposing the southwestward bottom currents, and horizontal advection was small. The dominant along-shelf depth-averaged momentum balance progressed from southwestward wind stress balanced by northeastward bottom stress and a residual in the alternating northeastward/southwestward pressure gradient term and Coriolis term ahead of eye passage, to northeastward wind stress balanced by alternating northeastward/southwestward Coriolis and pressure gradient behind eye passage.

The shelf break maxima in the pressure gradient and Coriolis terms could be due to the presence of a warm core ring starting prestorm just north of the Hudson Canyon and the northern cross-section location (Figure 5, top left) and moving southeastward by poststorm (Figure 5, middle left). This ring, moving along the shelf break and beginning to impinge onto the shelf, forces a geostrophic circulation at the shelf break front [*Zhang and Gawarkiewicz*, 2015], which is evident at the shelf break in both the cross-shelf and along-shelf momentum balance Hövmollers (Figures 12 and 13).

3.2.5. Advection Versus Mixing Temperature Response: Irene

The temperature diagnostic equation terms were plotted for Irene (Figure 15) at the points indicated by the large red dots in Figure 3 and by the vertical solid black lines in Figure 7 (left) to determine the primary

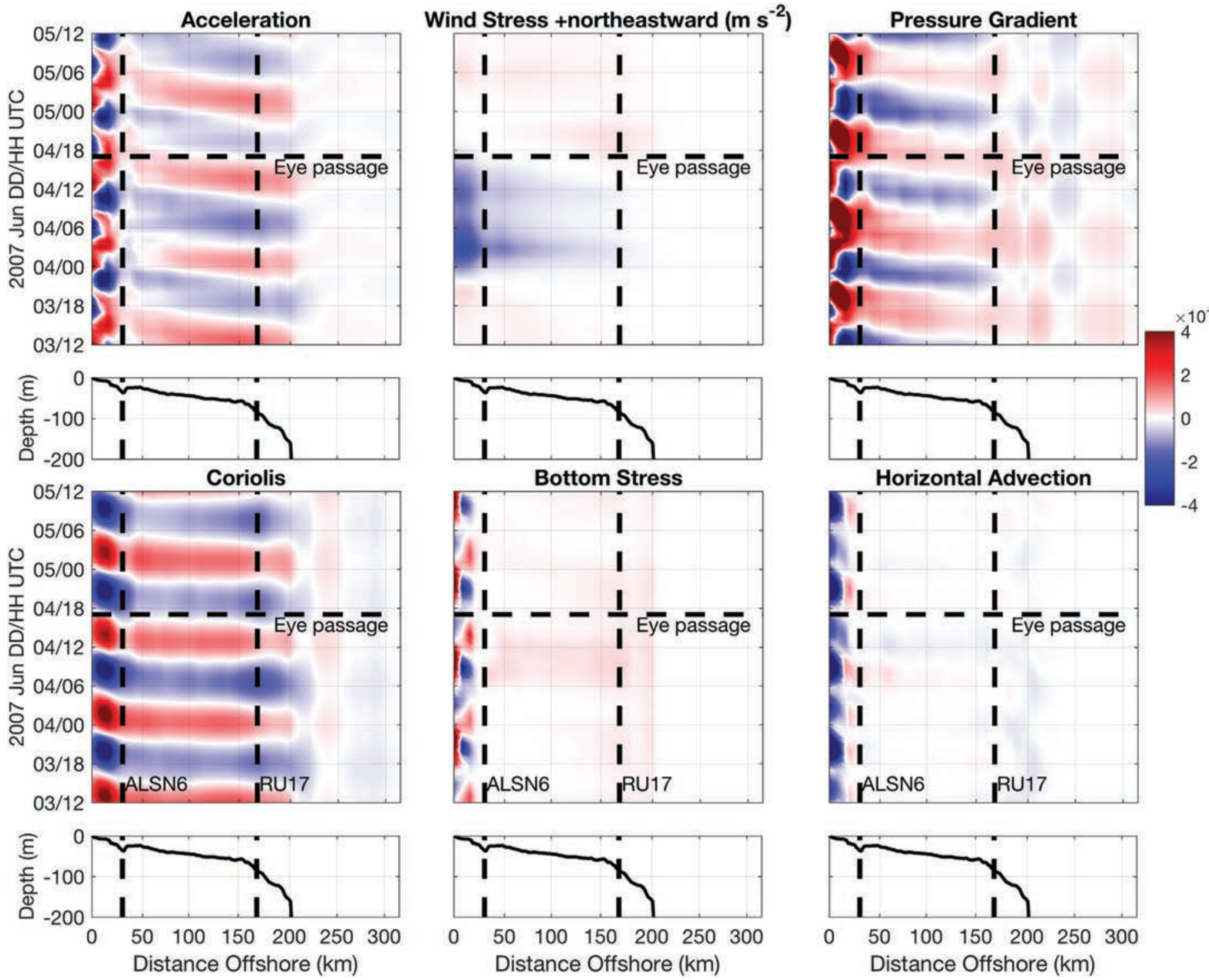

Figure 14. Barry. Same as Figure 10 (Hövmoller along-shelf depth-averaged momentum balance terms), but for Barry.

cause of cooling. The left figure is within the upwelling region, the second is at RU16, the third is in the MAB Cold Pool core, and the fourth is in deep water. At the top is the full temperature rate term, in the middle is the vertical diffusion term, and at the bottom are the vertical plus horizontal advection terms. Horizontal diffusion was not plotted, as it was very small. First, a general tidal signal is apparent in the full temperature rate term, primarily due to advection at all four locations. Cooling in the mixed layer was due to vertical diffusion at all four points, with ahead-of-eye-center cooling occurring at points 1–3. At point 1 within the upwelling, surface mixed-layer cooling stopped once the thermocline reached the bottom of the water column, as the source of cold water was removed (Figure 15, left middle). At point 2 near RU16, ahead-of-eye-center cooling was caused by vertical diffusion cooling being skewed ahead-of-eye-center. At point 3 in the Cold Pool core, vertical diffusion cooling was also skewed ahead-of-eye-center, with advection warming after eye passage. Finally, at point 4 in the deep water, a deep, cold quiescent bottom allowed for some cold water to entrain into the thick ~200 m surface mixed-layer ahead-of-eye passage, with an advective signal dominating after eye passage.

3.2.6. Advection Versus Mixing Temperature Response: Barry

The temperature diagnostic equation terms plotted for Irene at four locations in Figure 15 were also plotted for Barry at five locations in Figure 16. These five locations are indicated by the large red dots in Figure 5

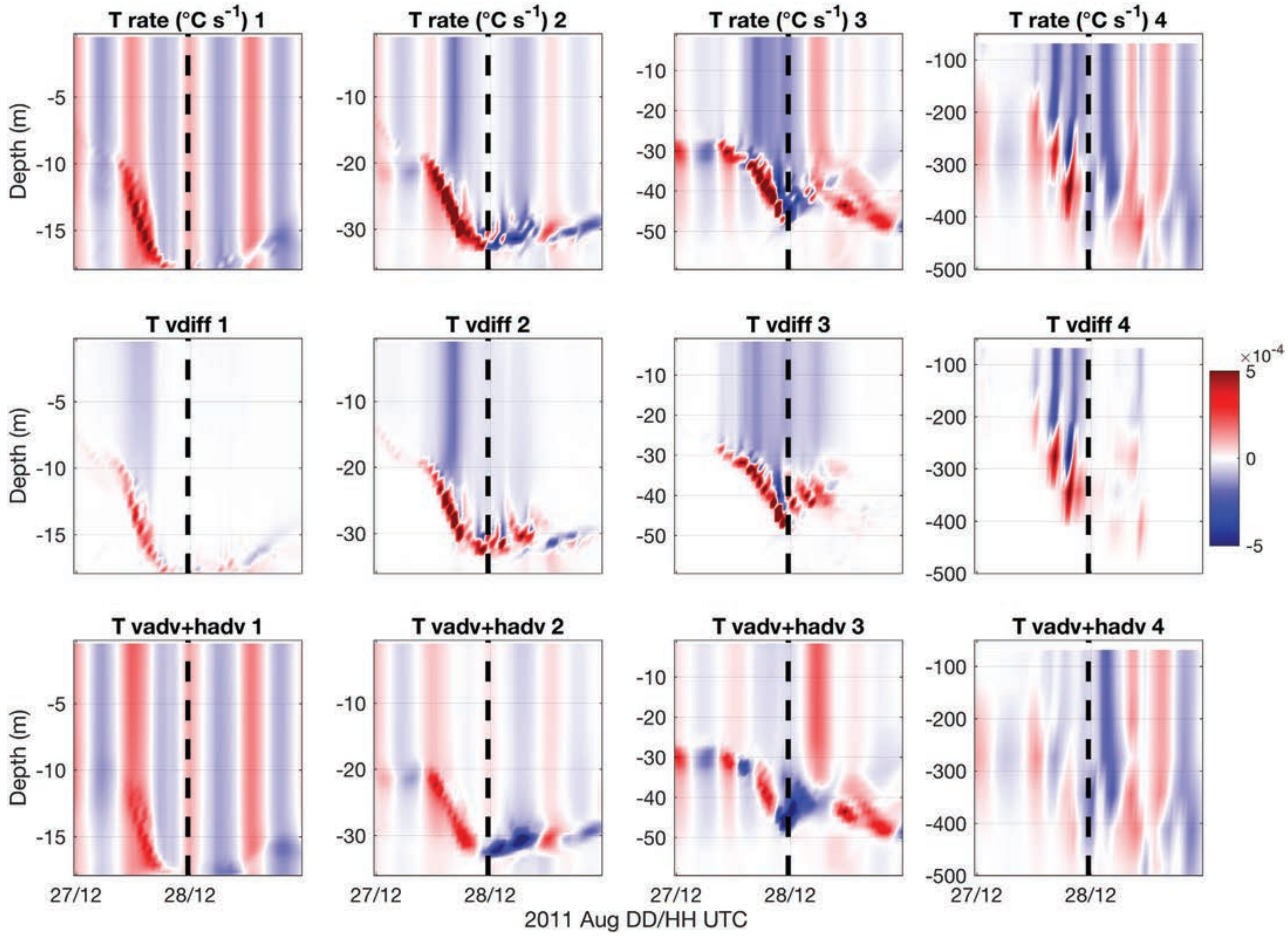

Figure 15. Irene. Temperature diagnostic equation terms at points 1–4 marked in Figure 3 red dots ordered 1–4 northwest to southeast, and in Figure 7 (left), with full temperature rate term at top, vertical diffusion in middle, and vertical + horizontal advection at bottom (°C s^{-1}). Horizontal diffusion is small and thus not plotted. Eye passage marked with vertical dashed line. At point 4, only the top 500 m of the water column is plotted.

and the vertical solid black lines in Figure 11 (left). For Barry, Figure 16 (left) is near ALSN6, the second figure is within the warm strip of water, the third figure is within the Cold Pool core, the fourth is near RU17, and the fifth is in deep water. Again, a tidal advection signal is apparent, with vertical diffusion not exhibiting any tidal cooling/warming signal. Vertical diffusion again caused cooling in the mixed layer except at point 5 in the deep water. Point 5 looks primarily advective with a deep quiescent bottom. At points 1–4 the tidal advection cooling/warming periodicity was modulated by the vertical diffusion cooling, which looks to be skewed ahead-of-eye passage during the greatest shear period (Figure 12, left).

4. Summary

Baroclinic coastal ocean cooling processes were investigated in detail for Hurricane Irene (2011) and Tropical Storm Barry (2007), two summer TCs, both with rapid ahead-of-eye-center cooling, but with different tracks and occurring at different times in the summer season. Cross-shelf variability in the depth-averaged momentum balance terms demonstrated that the dominant force balance driving the baroclinic circulation was the same across the entire MAB shelf. Cross-shelf variability in the temperature diagnostic equations showed that the resultant ahead-of-eye-center cooling of the surface layer in both storms was dominated by mixing rather than advection.

For Irene, it was previously found that cross-shelf two-layer surface to bottom opposing current shear was large and along-shelf surface to bottom shear was small at the RU16 glider location [*Glenn et al.*, 2016]. Here

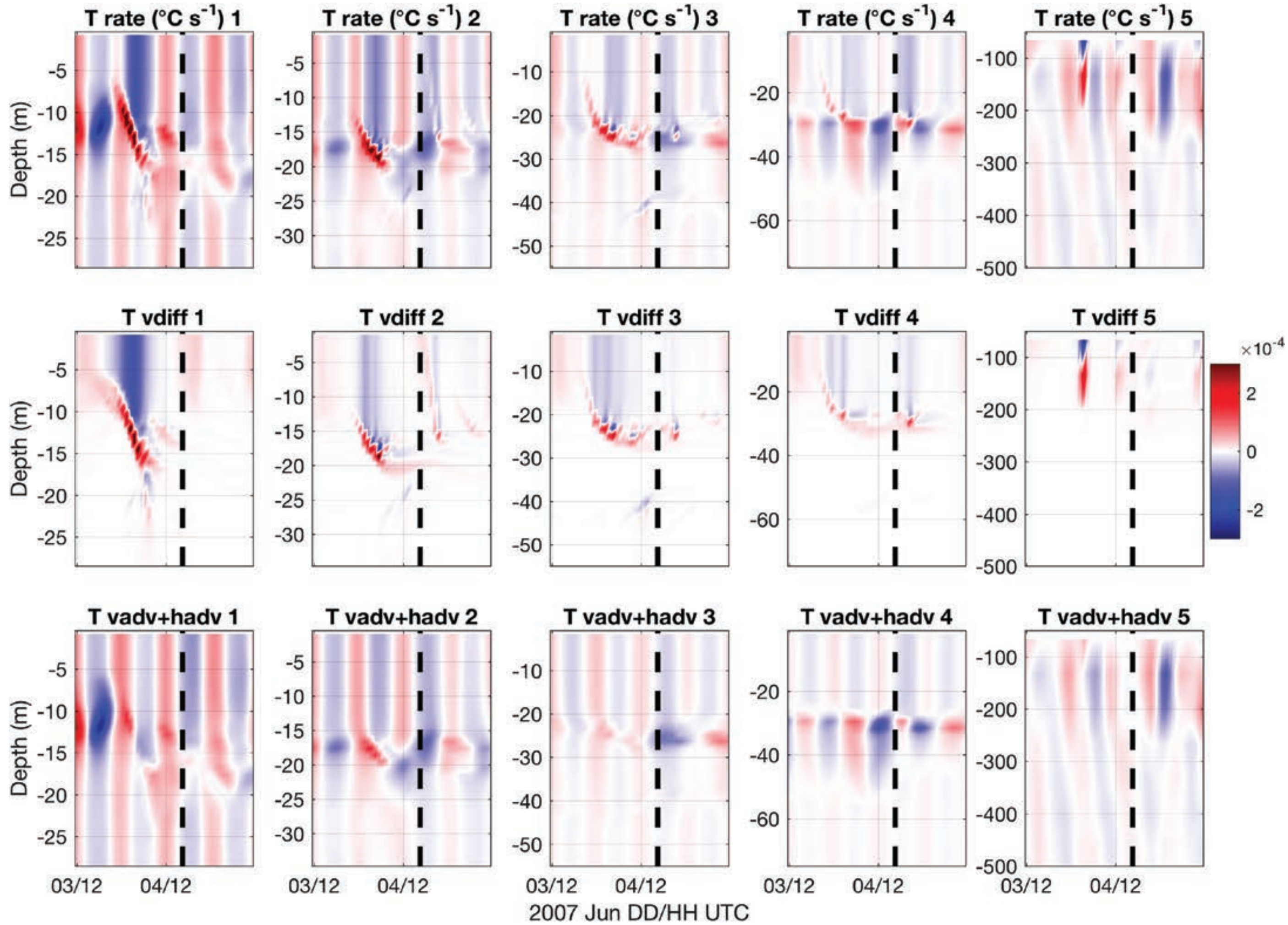

Figure 16. Barry. Same as Figure 15 (temperature diagnostic equation terms) but for Barry. Points 1–5 are marked in Figure 5 red dots ordered 1–5 west-northwest to east-southeast, and in Figure 11 (left).

for Barry, it was found that both the cross-shelf and along-shelf components of the surface to bottom opposing current shear contributed to the mixing and cooling observed at the RU17 glider location. For both storms, analysis of bulk shear (including both cross-shelf and along-shelf shear components) indicated a symmetric 50% ahead and 50% behind eye shear pattern in deep water, but with maximum shear skewed ahead-of-eye-center in the shallow water over the continental shelf. This ahead-of-eye-center skewing of the vertical shear was found to occur not only due to opposing bottom currents over the shelf before the eye, but also due to weaker winds and a deeper surface layer after the eye.

For Irene, the dominant force balance ahead of eye passage was onshore wind stress balanced by offshore pressure gradient, and the large offshore pressure gradient term stretched across the entire shelf. The wind stress and pressure gradient terms switched directions right after eye passage and eventually the force balance evolved to geostrophic long after the storm. For Barry, the dominant force balance on the shelf ahead of eye passage was modulated by the tides but also had the onshore wind stress term balanced by offshore pressure gradient, and again the large offshore pressure gradient term extended all the way across the shelf. The along-shelf force balance also played a role for Barry, potentially due to the location of the cross section relative to the changing slopes of the bathymetry just north of the Hudson Canyon. In both the cross-shelf and along-shelf directions, independent of the wind forcing, there was a maximum in the pressure gradient and Coriolis terms near the shelf break, which coincided with a warm eddy moving southwestward along the shelf slope front with a geostrophic circulation.

Finally, cross-shelf variability in the temperature change diagnostic terms was investigated. For both storms in the shallow water on the shelf, vertical diffusion was the main cause of the mostly ahead-of-eye-center cooling in the surface mixed layer. Tidal periodicity of cooling/warming was apparent in the combined vertical and horizontal advection terms. Cooling in the surface layer due to vertical diffusion did occur within the coastal upwelling during Irene, and the cooling stopped once the thermocline hit the bottom of the water column as the bottom cold water was also removed. In deep water, vertical diffusion and advection were important drivers of mixed-layer cooling for Irene, whereas for Barry in deep water, advection was the main driver in the periodic and alternating warming/cooling near the surface.

The drivers for the major differences in coastal ocean response between Irene and Barry were storm track, structure, intensity, and time of year. Irene had a more inshore MAB track during the late summer stratified season, whereas Barry was weaker with a farther offshore track during the early summer stratified season. Due to the offshore track, MAB surface winds for Barry had a more along-shelf component than the primarily cross-shelf winds during Irene, leading to both cross-shelf and along-shelf components playing a larger role in the coastal ocean response for Barry, and a primarily cross-shelf response for Irene.

5. Discussion

Glenn et al. [2016] identified 11 summer storms that traversed northeastward across the MAB and that exhibited a range of ahead-of-eye-center cooling. Here we selected two extreme cases—both with an underwater glider deployed—from this envelope: one with an offshore track and the other with an inshore one. One was near the beginning of the summer stratified season and the other near the end. Indeed, differences in the details exist between the two storm extremes—from the along-shore component playing a larger role in Barry's force balance, to the alternating warming/cooling advective tidal signal playing a larger role in Barry's temperature response. Nevertheless, both storms exhibited a two-layer baroclinic circulation, forced by an offshore pressure gradient opposing the onshore wind stress ahead-of-eye-center and extending across the entire MAB shelf. Cooling in both storms was mostly ahead-of-eye-center and dominated by vertical shear-induced mixing. These commonalities across the two storm extremes indicate that the process is robust and can be expected on stratified continental shelves over a wide range of TC scenarios.

Because this process is robust across these two extreme cases drawn from the 30 year envelope of MAB summer cyclones, it will be critical to resolve and forecast the same process for future storms, with the goal of lowering the uncertainty in predictions of TC impacts. Realistic 3-D coupled models that assimilate coastal observatory data and that are capable of predicting the ahead-of-eye-center stratified coastal ocean cooling processes will be critical [e.g., *Zambon et al.*, 2014; *Warner et al.*, 2017]. The increasingly populated [*Peduzzi et al.*, 2012] at-risk coastlines—the Northeast U.S. and northeastern China and Korea—adjacent to the two most stratified seas in the world—the MAB and Yellow Sea—will be increasingly vulnerable to TCs as sea levels rise [*Hansen et al.*, 2016], as TCs more frequently and severely undergo rapid intensification just before landfall [*Emanuel*, 2017], and if maximum TC intensities continue to migrate poleward [*Kossin et al.*, 2014]. By lowering uncertainty in coastal TC intensity forecasts through models that resolve these stratified coastal ocean cooling processes, these populations can better prepare for and respond to these rising threats.

Acknowledgments
HF Radar, glider, and satellite SST data used in this study are available through the MARACOOS assets page http://maracoos.org/data, https://rucool.marine.rutgers.edu/data, and http://marine.rutgers.edu/cool/auvs/index.php?did=369 with more detailed data sets available upon request to gregory.seroka@noaa.gov. Regional Ocean Modeling System results are also available upon request to gregory.seroka@noaa.gov. NAM data sets are publicly available through https://www.ncdc.noaa.gov/data-access/model-data/model-datasets/north-american-mesoscale-forecast-system-nam. Support was provided by New Jersey Board of Public Utilities (2010RU-COOL, BP-070), the Environmental Protection Agency (EP-11-C-000085), New Jersey Department of Environmental Protection (WM13–019-2013), National Oceanic and Atmospheric Administration (NOAA) led Integrated Ocean Observing System through the Mid-Atlantic Regional Association Coastal Ocean Observing System (MARACOOS, NA11NOS0120038), NOAA Cooperative Institute for the North Atlantic Region (NA13OAR4830233), and Rutgers University. We would like to thank John Wilkin and Julia Levin at Rutgers University for their suggestions regarding the ocean modeling, the Rutgers Ocean Modeling research associates for their ROMS help, and Rich Dunk for his helpful meteorological discussions and ideas.

References

Cangialosi, J. P., and J. L. Franklin (2016), National Hurricane Center forecast verification report: 2015 hurricane season, National Hurricane Center, Miami, Fla.

D'Asaro, E., T. B. Sanford, P. P. Niiler, and E. J. Terrill (2007), Cold wake of Hurricane Frances, *Geophys. Res. Lett.*, *34*, L15609, doi:10.1029/2007GL030160.

Davis, R. E., C. C. Eriksen, and C. P. Jones (2002), Autonomous Buoyancy-driven underwater gliders, in *Technology and Applications of Autonomous Underwater Vehicles*, edited by G. Griffiths, pp. 37–58, CRC Press, London, New York.

DeMaria, M., C. R. Sampson, J. A. Knaff, and K. D. Musgrave (2014), Is tropical cyclone intensity guidance improving?, *Bull. Am. Meteorol. Soc.*, *95*(3), 387–398, doi:10.1175/BAMS-D-12-00240.1.

Emanuel, K. (2017), Will global warming make hurricane forecasting more difficult?, *Bull. Am. Meteorol. Soc.*, March 2017, pp. 495–502, doi:10.1175/BAMS-D-16-0134.1.

Fairall, C. W., E. F. Bradley, J. E. Hare, and A. A. Grachev (2003), Bulk parameterization of air-sea fluxes: Updates and verification for the COARE algorithm, *J. Clim.*, *16*(4), 571–591.

Glenn, S., C. Jones, M. Twardowski, L. Bowers, J. Kerfoot, J. Kohut, D. Webb, and O. Schofield (2008), Glider observations of sediment resuspension in a Middle Atlantic Bight fall transition storm, *Limnol. Oceanogr.*, *53*(5), 2180–2196, doi:10.4319/lo.2008.53.5_part_2.2180.

Glenn, S. M., T. N. Miles, G. N. Seroka, Y. Xu, R. K. Forney, F. Yu, H. Roarty, O. Schofield, and J. Kohut (2016), Stratified coastal ocean interactions with tropical cyclones, *Nat. Commun.*, *7*, 1–10, doi:10.1038/ncomms10887.
Haidvogel, D. B. et al. (2008), Ocean forecasting in terrain-following coordinates: Formulation and skill assessment of the Regional Ocean Modeling System, *J. Comput. Phys.*, *227*(7), 3595–3624, doi:10.1016/j.jcp.2007.06.016.
Hansen, J. et al. (2016), Ice melt, sea level rise and superstorms: Evidence from paleoclimate data, climate modeling, and modern observations that 2°C global warming could be dangerous, *Atmos. Chem. Phys.*, *16*(6), 3761–3812, doi:10.5194/acp-16-3761-2016.
Houghton, R. W., R. Schlitz, R. C. Beardsley, B. Butman, and J. L. Chamberlin (1982), The Middle Atlantic Bight cold pool: Evolution of the temperature structure during summer 1979, *J. Phys. Oceanogr.*, *12*(10), 1019–1029, doi:10.1175/1520-0485.
Hsu, S. A., and Z. Yan (1998), A note on the radius of maximum wind for hurricanes, *J. Coastal Res.*, *14*(2), 667–668.
Jaimes, B., and L. K. Shay (2015), Enhanced wind-driven downwelling flow in warm oceanic Eddy features during the intensification of Tropical Cyclone Isaac (2012): Observations and theory, *J. Phys. Oceanogr.*, *45*(6), 1667–1689, doi:10.1175/JPO-D-14-0176.1.
Keen, T. R., and S. M. Glenn (1995), A coupled hydrodynamic-bottom boundary layer model of storm and tidal flow in the Middle Atlantic Bight of North America, *J. Phys. Oceanogr.*, *25*(3), 391–406.
Kim, H. S., C. Lozano, V. Tallapragada, D. Iredell, D. Sheinin, H. L. Tolman, V. M. Gerald, and J. Sims (2014), Performance of ocean simulations in the coupled HWRF-HYCOM model, *J. Atmos. Oceanic Technol.*, *31*(2), 545–559, doi:10.1175/JTECH-D-13-00013.1.
Kossin, J. P., K. Emanuel, and G. Vecchi (2014), The poleward migration of the location of tropical cyclone maximum intensity, *Nature*, *509*(7500), 349–352, doi:10.1038/nature13278.
Lin, I.-I., C.-H. Chen, I.-F. Pun, W. T. Liu, and C.-C. Wu (2009), Warm ocean anomaly, air sea fluxes, and the rapid intensification of Tropical Cyclone Nargis (2008), *Geophys. Res. Lett.*, *36*, L03817, doi:10.1029/2008GL035815.
Mei, W., C. Pasquero, and F. Primeau (2012), The effect of translation speed upon the intensity of tropical cyclones over the tropical ocean, *Geophys. Res. Lett.*, *39*, L07801, doi:10.1029/2011GL050765.
Miles, T., S. Glenn, and O. Schofield (2013), Temporal and spatial variability in fall storm induced sediment resuspension on the Mid-Atlantic Bight, *Cont. Shelf Res.*, *63*, S36–S49.
Miles, T. N., G. N. Seroka, J. T. Kohut, O. Schofield, and S. M. Glenn (2015), Glider observations and modeling of sediment transport in Hurricane Sandy, *J. Geophys. Res. Oceans*, *120*, 1771–1791, doi:10.1002/2014JC010474.
NOAA National Centers for Environmental Information (2016), U.S. coastal relief model, NOAA, Boulder, Colo. [Available at http://www.ngdc.noaa.gov/mgg/coastal/crm.html.]
Peduzzi, P., B. Chatenoux, H. Dao, A. De Bono, C. Herold, J. Kossin, F. Mouton, and O. Nordbeck (2012), Global trends in tropical cyclone risk, *Nat. Clim. Change*, *2*(4), 289–294, doi:10.1038/nclimate1410.
Price, J. F. (1981), Upper ocean response to a hurricane, *J. Phys. Oceanogr.*, *11*(2), 153–175, doi:10.1175/1520-0485(1981)011<0153:UOR-TAH>2.0.CO;2.
Roarty, H. et al. (2010), Operation and Application of a Regional High-Frequency Radar Network in the Mid-Atlantic Bight, *Mar. Technol. Soc. J.*, *44*(6), 133–145, doi:10.4031/MTSJ.44.6.5.
Ruiz, S., L. Renault, B. Garau, and J. Tintoré (2012), Underwater glider observations and modeling of an abrupt mixing event in the upper ocean, *Geophys. Res. Lett.*, *39*, L01603, doi:10.1029/2011GL050078.
Sampson, C. R., and A. J. Schrader (2000), The automated tropical cyclone forecasting system (version 3.2), *Bull. Am. Meteorol. Soc.*, *81*(6), 1231–1240, doi:10.1175/1520-0477(2000)081<1231:TATCFS>2.3.CO;2.
Schofield, O., et al. (2007), Slocum gliders: Robust and ready, *J. F. Robot.*, *24*(6), 473–485, doi:10.1002/rob.20200.
Schofield, O., R. J. Chant, B. Cahill, and R. Castelao (2008), The decadal view of the Mid-Atlantic Bight from the COOLroom: Is our coastal system changing?, *Oceanography*, *21*(4), 108–117.
Seroka, G. N., T. N. Miles, Y. Xu, J. T. Kohut, O. Schofield, and S. M. Glenn (2016), Hurricane Irene sensitivity to stratified coastal ocean cooling, *Mon. Weather Rev.*, *144*(9), 3507–3530, doi:10.1175/MWR-D-15-0452.1.
Sherman, J., R. E. Davis, W. B. Owens, and J. Valdes (2001), The autonomous underwater glider ''spray,'' *IEEE J. Oceanic Eng.*, *26*(4), 437–446.
Sopko, S. P., and R. J. Falvey (2014), Annual tropical cyclone report 2014: Joint Typhoon Warning Center, Joint Typhoon Warning Center, Pearl Harbor, Hawaii.
Tallapragada, V., C. Kieu, Y. Kwon, S. Trahan, Q. Liu, Z. Zhang, and I.-H. Kwon (2014), Evaluation of storm structure from the operational HWRF during 2012 implementation, *Mon. Weather Rev.*, *142*(11), 4308–4325, doi:10.1175/MWR-D-13-00010.1.
Torn, R. D., and C. Snyder (2012), Uncertainty of tropical cyclone best-track information, *Weather Forecast.*, *27*(3), 715–729, doi:10.1175/WAF-D-11-00085.1.
Umlauf, L., and H. Burchard (2003), A generic length-scale equation for geophysical turbulence models, *J. Mar. Res.*, *61*(2), 235–265, doi:10.1357/002224003322005087.
Warner, J. C., C. R. Sherwood, H. G. Arango, and R. P. Signell (2005), Performance of four turbulence closure models implemented using a generic length scale method, *Ocean Modell.*, *8*(1–2), 81–113, doi:10.1016/j.ocemod.2003.12.003.
Warner, J. C., W. C. Schwab, J. H. List, I. Safak, M. Liste, and W. Baldwin (2017), Inner-shelf ocean dynamics and sea floor morphologic changes during Hurricane Sandy, *Cont. Shelf Res.*, *138*(2017), 1–18, doi:10.1016/j.csr.2017.02.003.
Wilkin, J. L., and E. J. Hunter (2013), An assessment of the skill of real-time models of Mid-Atlantic Bight continental shelf circulation, *J. Geophys. Res. Oceans*, *118*, 2919–2933, doi:10.1002/jgrc.20223.
Zambon, J. B., R. He, and J. C. Warner (2014), Tropical to extratropical: Marine environmental changes associated with Superstorm Sandy prior to its landfall, *Geophys. Res. Lett.*, *41*, 8935–8943, doi:10.1002/2014GL061357.
Zhang, H., D. Chen, L. Zhou, X. Liu, T. Ding, and B. Zhou (2016), Upper ocean response to typhoon Kalmaegi (2014), *J. Geophys. Res. Oceans*, *121*, 6520–6535, doi:10.1002/2016JC012064.
Zhang, W. G., and G. G. Gawarkiewicz (2015), Dynamics of the direct intrusion of Gulf Stream ring water onto the Mid-Atlantic Bight shelf, *Geophys. Res. Lett.*, *42*, 7687–7695, doi:10.1002/2015GL065530.

Workforce Development for the Blue Economy: Rutgers Masters in Integrated Ocean Observing

Scott Glenn
Center for Ocean Observing Leadership
Rutgers University
New Brunswick, NJ 08904 USA
glenn@marine.rutgers.edu

Oscar Schofield
Center for Ocean Observing Leadership
Rutgers University)
New Brunswick, NJ 08904 USA
oscar@marine.rutgers.edu

Josh Kohut
Center for Ocean Observing Leadership
Rutgers University
New Brunswick, NJ 08904 USA
kohut@marine.rutgers.edu

Janice McDonnell
Center for Ocean Observing Leadership
Rutgers University
New Brunswick, NJ 08904 USA
mcdonnel@marine.rutgers.edu

Travis Miles
Center for Ocean Observing Leadership
Rutgers University
New Brunswick, NJ 08904 USA
tnmiles@marine.rutgers.edu

Grace Saba
Center for Ocean Observing Leadership
Rutgers University
New Brunswick, NJ 08904 USA
saba@marine.rutgers.edu

Hugh Roarty
Center for Ocean Observing Leadership
Rutgers University
New Brunswick, NJ 08904 USA
hroarty@marine.rutgers.edu

Michael Crowley
Center for Ocean Observing Leadership
Rutgers University
New Brunswick, NJ 08904 USA
crowley@marine.rutgers.edu

***Abstract*—The global need for sustainable development has never been greater. Solutions to provide food, water, energy and economic security to a growing global population that is increasingly coastal will necessarily involve the ocean. Every coastal country should be able to monitor their own waters, share their data as appropriate, and respond to actionable forecasts and information that supports a sustainable and resilient blue economy. This will require a new workforce trained in the operation of new ocean observing technologies capable of widespread distribution that can broaden participation by all nations. Towards this end, Rutgers University has developed a new Operational Masters in Integrated Ocean Observing to bridge the training gap between Ph.D. scientists and efforts to develop an ocean-literate public. The 15-month program begins with a summer software bootcamp to spin-up a common toolkit for data access. The fall and spring semesters feature 2-semester course sequences in (a) Integrated Ocean Observatories, (b) an Ocean Observing Field and Laboratory course, and (c) an Ocean Observing Cyber Lab. The capstone is an operational Masters thesis that leverages the MTS/IEEE Oceans meetings, and the local MTS student chapter. The initial class will begin in the summer of 2018.**

Keywords—education, ocean observatories, marine technology.

I. Introduction – Growing Global Demand

Today's students will be challenged over their professional lifetimes with providing 60% more food, 55% more water and 80% more energy to a growing global population forecast to approach 10 billion by 2050. Our students will be required to meet this challenge while the climate is warming, sea level is rising, the ocean is acidifying, coastal waters are more often hypoxic, and extreme weather events are increasing. Sustainable solutions that provide for basic human needs, minimize climatic impacts, and build resilient societies will require increasingly efficient green and blue economies on land and at sea. A sustainable blue economy requires information to support decisions that enable maritime sector industries while maintaining safety, improving the environment, and supporting the ecosystem. This can only be realized through scientific understanding that applies emerging technologies to optimize sustained observations and forecasts.

An ocean that is physically complex, biologically diverse, and inadequately sampled challenges the lofty goal of a sustainable blue economy. New at-sea sampling and land-based cyber technologies are required to bridge this gap. Scientific advancement may be supported by a few select academic groups of early adopters, but the compact scales of the energetic mesoscale, and the diversity of coastal large marine ecosystems, demand that we enhance multi-disciplinary spatial observations at regional scales globally. These observing systems can be organized into global networks for efficiency, but ultimately, they must be locally implemented and sustained at the relevant regional scale, requiring significant capacity development across the globe.

II. Program Design – Requirements and Experience

A. New Workforce Requirements

The Global Ocean Observing System's (GOOS) uses the Framework for Ocean Observing (FOO) to provide a structure by which societal goals can be met through the integration of a

XXX-X-XXXX-XXXX-X/XX/$XX.00 ©20XX IEEE
978-0-692-94690-9/$31.00 ©2017 MTS

wide variety of ocean observing technologies. Key integrated ocean observing gaps identified by the FOO process include lack of a global High Frequency Radar network, lack of a global underwater glider network, and the need for numerous biological and chemical sensors that can be effectively deployed on autonomous platforms. Global implementation will requires a new workforce with a variety of skills capable of working together as a team to operate new observing technologies in frontier areas, curate the data flow, and produce forecasts with quantifiable uncertainties appropriate to inform decision makers. They will be faced with real data and imperfect models, and will be required to turn what they have into actionable information.

Guidance to educators interested in workforce development for the blue economy was gathered through a discussion panel at the 2017 Oceanology International North America conference. Specific guidance included that workers must understand both *why* they are collecting data (a collaborative skill) as well as *how* to accomplish the goal (a technical skill). That data is never perfect, and one must see the sensors and platforms, and understand how they work, to fully understand their limitations. It was noted in the discussion that many of today's oceanographers have not gone to sea, yet our need for oceanographers has grown beyond our ability to train everyone at sea. Students therefore must gain this experience through new approaches. Present training approaches need to be more experiential, where students are encouraged to ask questions, and to determine if a piece of critical data makes sense. Individuals should be trained to collect and review the data, understand it, and work collaboratively to understand what it really means as a launching point for where to go next. Ultimately, to be employable in the marine sector, the students need to have worked with real data and be ready for action. This is rarely the case in undergraduate education, but a full 5+ year Ph.D. experience is overkill. A shorter but intensive program that goes beyond the necessary general undergraduate education to focus on operational needs is what is missing. To be accepted in their future positions, the operational students will be drawn from and resemble a cross section of the communities they serve. This will move new frontier technologies beyond the scientific early adopters into widespread use.

B. *Proven Educational Expertise*

Rutgers developed and delivered since 2006 a new hands-on undergraduate research program in ocean observatories to compliment its existing Marine Science major [1]. The centerpiece of the program is a flexible research experience that can begin as early as freshman year and can continue over a student's full undergraduate career. The research follows the cognitive apprenticeship model, where more experienced students lead small teams of student researchers using real data collected in operational ocean observatories to investigate research questions they formulate [2][3]. The program enables students to gain experience working with real data, promotes teamwork, and provides near-peer mentorship opportunities in modern ocean and coastal observing networks (Fig.1). The program has grown to involve an average of 30-50 students in research projects each semester. Over the last decade, undergraduate Marine Science student involvement in research has increased by an order of magnitude and the percentage of minority students has doubled [4].

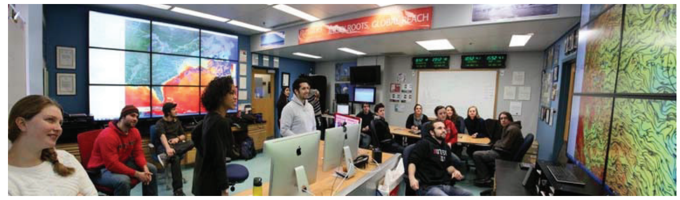

Fig. 1. The U.S. IOOS-certified ocean observing operations center at Rutgers University.

III. A GLOBALLY UNIQUE MASTERS PROGRAM

The Rutgers University Center for Ocean Observing Leadership (RU COOL), an international leader in the development and sustained operation of new observing system technologies as an integrated network, has designed a new Operational Masters in Integrated Ocean Observing to begin in the summer of 2018. The compact 15-month program, that includes 2 semesters of coursework sandwiched between two summers of research, can fulfill all the requirements for a Rutgers Masters degree if 6 credits of graduate work can be drawn from the student's undergraduate coursework (Table 1). The preferred 6 credits are the equivalents of Rutgers' Introduction to Physical Oceanography and Introduction to Biological Oceanography courses that are cross-listed as both undergraduate and graduate courses. This ensures that the students have at least a basic background level of experience and are familiar with the ontology of oceanography so that they can proceed quickly with the more technical aspects of the Masters. For Rutgers students, this is effectively a 4+1 Bachelors+Masters degree program.

TABLE I.

Masters in Integrated Ocean Observatories - Course Sequence		
Semester	**Course Title**	**Credits C=Course R=Research**
Equivalent Undergraduate Experience	Intro to Physical Oceanography	3 C
	Intro to Biological Oceanography	3 C
Summer 1	Software Bootcamp	3 R
Fall	Integrated Ocean Observatories I	3 C
	Ocean Observing Field Lab I	3 C
	Ocean Observing Cyber Lab I	3 C
Spring	Integrated Ocean Observatories II	3 C
	Ocean Observing Field Lab II	3 C
	Ocean Observing Cyber Lab II	3 C
Summer 2	Thesis Completion and Defense	3 R
Total		**24 C, 6 R**

Students in the Masters program will occupy year-round open-concept desk space in the operations center of a U.S. IOOS-certified ocean observatory (Fig. 1) so that they spend their entire day inculcated by operational activities on a college campus fueled by technology development and scientific discovery. The first summer includes a Software Bootcamp, where students are spun up on typical data analysis tools like R, Matlab and Python, the typical oceanographic data formats such as netCDF and ERDDAP, and available oceanographic processing toolkits for data and model analysis. A new coastal research vessel provides on-campus access to the Raritan Estuary and Bay so that at sea training can begin immediately (Fig. 2).

Fig. 2. The R/V Rutgers can dock at the on-campus Rutgers boathouse, providing students easy access to salt water conditions for instrument testing and deployments. Photo by Sean O'Grady.

The school year includes a series of three 6-credit courses encompassing both fall (part I) and spring (part II) semesters. The Integrated Ocean Observing I & II course sequence runs across both semesters and introduces students to the wide variety of Eulerian and Lagrangian platforms and sensors that comprise a modern observing network. Each type of platform or sensor has a series of at least 3 classes that first introduce the sensor itself and quality assurance protocols, a second class that accesses actual data for homework and the application of specific quality control measures, and a third class where students orally presents the results of their homework to the rest of the class for discussion in a supportive environment designed to enhance oral communications skills. The course is interspersed with coaching classes on best practices in data visualization techniques, and how to communicate with data. A second two-semester sequence is the Ocean Observing Field Lab. Here students have hands-on opportunities to prepare (Fig. 2), quality assure, deploy/recover (Figs. 2 & 4), operate, quality control and curate data they acquire within an operating ocean observatory. Some of this data may contribute directly to student theses. A third two-semester sequence is the Ocean Observing Cyber Lab, where data analysis techniques and forecast models for winds, waves and currents are introduced. Model validation with data and the impacts of data assimilation are included.

Fig. 3. The Glider Lab where the annual Rutgers Glider School is taught serves as a staging area for the Ocean Observatories Field Lab.

The capstone is an Operational Masters thesis conducted during the spring and final summer based on the MTS/IEEE Oceans conference. Students work with a faculty advisor to submit an abstract to the semi-annual Oceans conference as their thesis proposal. Their research is completed over the spring and summer, and culminates with the submission of an MTS/IEEE Oceans conference proceedings paper. During a student's second summer, they also serve as mentors to the students entering their first summer, transferring their knowledge of software and their analysis programs to the new students, building an operational software toolkit that is constantly being updated and will remain publicly accessible throughout their future career. In an end of summer research symposium, each student presents their 15-minute MTS/IEEE Oceans oral presentation they will eventually present at the conference if accepted.

Fig. 4. A local HF Radar beach deployment site used for training.

Applications for the class of Masters students will be accepted in January of 2018, with the first summer semester beginning in June of 2018. As the courses are matured, international accreditation by the UK-based IMarEST will be sought to ensure that the courses meet the educational needs of the maritime sector.

ACKNOWLEDGMENT

Support provided by the Rutgers School of Environmental and Biological Sciences, the Rutgers Department of Marine and Coastal Sciences, the Rutgers Student Glider Endowment, and Teledyne Webb Research.

REFERENCES

[1] Glenn, S., Kohut, J., McDonnell, J., Seidel, D., Aragon, D., Haskins, T., Handel, E., Haldeman, C., Heifetz, I., Kerfoot, J., Lemus, E., Lictenwalder, S., Ojanen, L., Roarty, H., Atlantic Crossing Students, Jones, C., Webb, D., Schofield, O. 2011. The Trans-Atlantic Slocum glider expeditions: A catalyst for undergraduate participation in ocean science and technology. Marine Technology Society 45: 75-90.

[2] Dobson, C., Mart, J., Strandskov, N., Schofield, O., Glenn, S., Jones, C., Webb, D., Barrera, C., Ramos, A.G., December 2012. The Challenger Mission: A global ocean predictive skill experiment. OCEANS'12 MTS/IEEE San Diego, CA, USA.

[3] Sacatelli, R., T. Schofield, K. Todoroff, A. Carandang, A. Eng, I. Lowry, H. Mather, A. Ramos, S. Swart, M. Dottori, N. Strandskov, J. Kohut, O. Schofield, S. Glenn, 2014. Ocean predictive skill assessments in the South Atlantic: Crowd-sourcing of student-based discovery, OCEANS'14, MTS/IEEE St. Johns, Canada. 10.1109/Oceans 2014.7003134.

[4] Glenn, S., Schofield, O., Saba, G., Miles, T., Roarty, H., Kohut, J. 2015. The ocean is our classroom: A 4-year research track for undergraduate exploration, research and discovery in oceanography, OCEANS'15 MTS/IEEE Washington, DC, USA, pp. 1-5.

THE OFFICIAL MAGAZINE OF THE OCEANOGRAPHY SOCIETY
Oceanography

CITATION

Greer, A.T., A.M. Shiller, E.E. Hofmann, J.D. Wiggert, S.J. Warner, S.M. Parra, C. Pan, J.W. Book, D. Joung, S. Dykstra, J.W. Krause, B. Dzwonkowski, I.M. Soto, M.K. Cambazoglu, A.L. Deary, C. Briseño-Avena, A.D. Boyette, J.A. Kastler, V. Sanial, L. Hode, U. Nwankwo, L.M. Chiaverano, S.J. O'Brien, P.J. Fitzpatrick, Y.H. Lau, M.S. Dinniman, K.M. Martin, P. Ho, A.K. Mojzis, S.D. Howden, F.J. Hernandez, I. Church, T.N. Miles, S. Sponaugle, J.N. Moum, R.A. Arnone, R.K. Cowen, G.A. Jacobs, O. Schofield, and W.M. Graham. 2018. Functioning of coastal river-dominated ecosystems and implications for oil spill response: From observations to mechanisms and models. *Oceanography* 31(3):90–103, https://doi.org/10.5670/oceanog.2018.302.

DOI

https://doi.org/10.5670/oceanog.2018.302

Functioning of Coastal River-Dominated Ecosystems and Implications for Oil Spill Response

FROM OBSERVATIONS TO MECHANISMS AND MODELS

By Adam T. Greer, Alan M. Shiller, Eileen E. Hofmann, Jerry D. Wiggert, Sally J. Warner, Sabrina M. Parra, Chudong Pan, Jeffrey W. Book, DongJoo Joung, Steven Dykstra, Jeffrey W. Krause, Brian Dzwonkowski, Inia M. Soto, M. Kemal Cambazoglu, Alison L. Deary, Christian Briseño-Avena, Adam D. Boyette, Jessica A. Kastler, Virginie Sanial, Laura Hode, Uchenna Nwankwo, Luciano M. Chiaverano, Stephan J. O'Brien, Patrick J. Fitzpatrick, Yee H. Lau, Michael S. Dinniman, Kevin M. Martin, Peng Ho, Allison K. Mojzis, Stephan D. Howden, Frank J. Hernandez, Ian Church, Travis N. Miles, Su Sponaugle, James N. Moum, Robert A. Arnone, Robert K. Cowen, Gregg A. Jacobs, Oscar Schofield, and William M. Graham

ABSTRACT. Coastal river-dominated oceans are physically complex, biologically productive, and intimately connected to human socioeconomic activity. The Deepwater Horizon blowout and subsequent advection of oil into coastal waters of the northern Gulf of Mexico (nGOM) highlighted the complex linkages among oceanographic processes within this river-dominated system and knowledge gaps about it that resulted in imprecise information on both oil transport and ecosystem consequences. The interdisciplinary research program implemented through the CONsortium for oil exposure pathways in COastal River-Dominated Ecosystems (CONCORDE) is designed to identify and quantitatively assess key physical, biological, and geochemical processes acting in the nGOM, in order to provide the foundation for implementation of a synthesis model (coupled circulation and biogeochemistry) of the nGOM shelf system that can ultimately aid in prediction of oil spill transport and impacts. CONCORDE field and modeling efforts in 2015–2016 focused on defining the influence of freshwater input from river plumes in the nGOM. In situ observations, combined with field-deployed and simulated drifters, show considerable variability in the spatial extent of freshwater influence that is related to wind direction and strength. Increased primary production and particle abundance (a proxy for secondary production) was observed during the spring when nGOM shelf waters were becoming stratified. Zooplankton and marine snow displayed intense vertical and horizontal patchiness during all seasons, often aggregating near the halocline. Simulations of a neutrally buoyant tracer released offshore of the Mississippi Bight showed surface advection of low tracer concentrations onto the inner shelf under high river discharge, high stratification, and variable wind conditions compared to almost no advection onto the inner shelf under low discharge, negligible stratification, and generally northeasterly winds. The interconnectedness of environmental variables and biological activity indicate that multiple factors can affect the transport of oil and the resulting ecological impacts. The process-oriented understanding provided by CONCORDE is necessary to predict ecosystem-level impacts of oil spills, and these results are applicable to other river-dominated coastal systems worldwide that often support oil extraction activities.

BACKGROUND

The April 2010 explosion of the Deepwater Horizon (DWH) drilling rig resulted in the loss of 11 lives, as well as the release into the Gulf of Mexico of ~5 million barrels of oil, 1.7×10^{11} g of methane, and other gaseous hydrocarbons from the Macondo well located at ~1,500 m depth (Reddy et al., 2012). The unprecedented magnitude of this 87-day spill eventually led to oil washing up along the northern Gulf of Mexico (nGOM) coast from Louisiana to Florida, producing substantial environmental damage (Michel et al., 2013; Murawski et al., 2016). Wind-driven circulation interacting with complex freshwater flows derived from numerous river inputs influenced the trajectory of oil on the shelf (Kourafalou and Androulidakis, 2013; Özgökmen et al., 2016) and made predictions of oil transport and impacts difficult (Joye et al., 2016; Özgökmen et al., 2016). The ability to forecast the movement of the oil was further complicated by river diversions that augmented river discharge in an attempt to keep oil from coming ashore in certain areas (O'Connor et al., 2016).

The challenges of predicting DWH spill effects were exacerbated by the three-dimensional (3-D) movement of the oil from depth. Approximately half of the released oil reached the surface (Federal Interagency Solutions Group, 2010; Passow and Hetland, 2016) as a weathered, reddish-brown substance, less cohesive compared to crude oil (Peterson et al., 2012). The other half formed a deepwater plume that settled at approximately 1,100 m (Diercks et al., 2010), where it was advected by midwater and deep-sea currents (Camilli et al., 2010). Marine snow particles provided a mechanism to export some of this midwater oil to depth (Hazen et al., 2010; Valentine et al., 2014; Daly et al., 2016; Passow and Ziervogel, 2016), where it likely had an impact on sensitive and poorly studied deep-sea ecosystems (Schrope, 2011; Fisher et al., 2014). Surface oil was observed in the Mississippi Bight (MacDonald et al., 2015) and reached the nearby coastlines (Nixon et al., 2016), yet there are no reliable estimates of the exact percentage of spilled oil that was transported to the coast, which necessitates approximations in oil fate budgets accounting for oil recovery/burning, evaporation, microbial degradation, sedimentation, and advection (Passow and Hetland, 2016). Because biological production and fisheries activity is concentrated on the nGOM shelf and in coastal habitats (Grimes, 2001), oil in this region can have a disproportionately strong ecological impact that is directly connected to human social and economic well-being.

The Mississippi Bight region of the nGOM (Figure 1) represents a critical intermediary between the DWH oil spill site and coastal ecosystems. Flanked by the Mobile Bay outflow to the east and barrier islands to the north and west, this region is characterized by dynamic river- and wind-influenced flows. In addition to the substantial freshwater discharge from Mobile Bay (annual average of ~2,200 $m^3\ s^{-1}$; Gelfenbaum and Stumpf, 1993), numerous smaller rivers empty directly into Mississippi Sound (shallow waters north of the barrier islands) or enter indirectly through Lake Pontchartrain, totaling ~928 $m^3\ s^{-1}$ (Sikora and Kjerfve, 1985). While an estimated 47% of the Mississippi River discharge travels east and offshore (Dinnel and Wiseman, 1986), the amount that moves toward the inner shelf of the Mississippi

FACING PAGE. Surface convergence at a density front near Main Pass at the mouth of Mobile Bay. Exchange between fresher estuarine and saltier shelf waters can generate these features, which are common in the northern Gulf of Mexico shelf ecosystem and influence the distributions of biogeochemical constituents. *Photo credit: Brian Dzwonkowski*

Bight has not been quantified. Under circumstances when the Mississippi River reaches flood stage near New Orleans, as it did in January 2016, the Bonnet Carré Spillway is used to divert river water into Lake Pontchartrain, which then flows into Mississippi Sound.

The wide and shallow nGOM shelf receives a seasonally variable supply of nutrients and particulates from the rivers that flow into Mississippi Sound and Mobile Bay, or directly onto the shelf. This riverine input is essential to maintaining the high primary production (Lohrenz et al., 1997) and fertile fishing grounds (Grimes, 2001) that characterize the nGOM. Circulation near the shelf edge and beyond is influenced by winds, river plumes, and mesoscale eddies spawned by and interacting with the Loop Current (Sturges and Leben, 2000; Ohlmann et al., 2001; Oey et al., 2005). The physical processes that affect nGOM shelf circulation act at a range of spatiotemporal scales, making accurate forecasting of oil transport patterns challenging. The biological and chemical processes that impact oil fate and toxicity contribute additional complexity to these challenges.

The clear need to understand transport and oil exposure pathways in the pulsed, river-dominated Mississippi Bight led to the implementation of the CONsortium for oil spill exposure pathways in COastal River-Dominated Ecosystems (CONCORDE). The CONCORDE research agenda centers on three scientific objectives: (1) to characterize the complex, 3-D physical oceanographic setting in order to understand potential oil pathways; (2) to describe spatiotemporal distributions of planktonic organisms, as well as geochemical and bio-optical parameters at scales relevant to processes transporting oil; and (3) to generate a synthesis model (Box 1) to predict oil transport on continental shelves and potential ecological impacts during future spill events for pulsed, river-dominated coastal ecosystems that incorporates new information on physical,

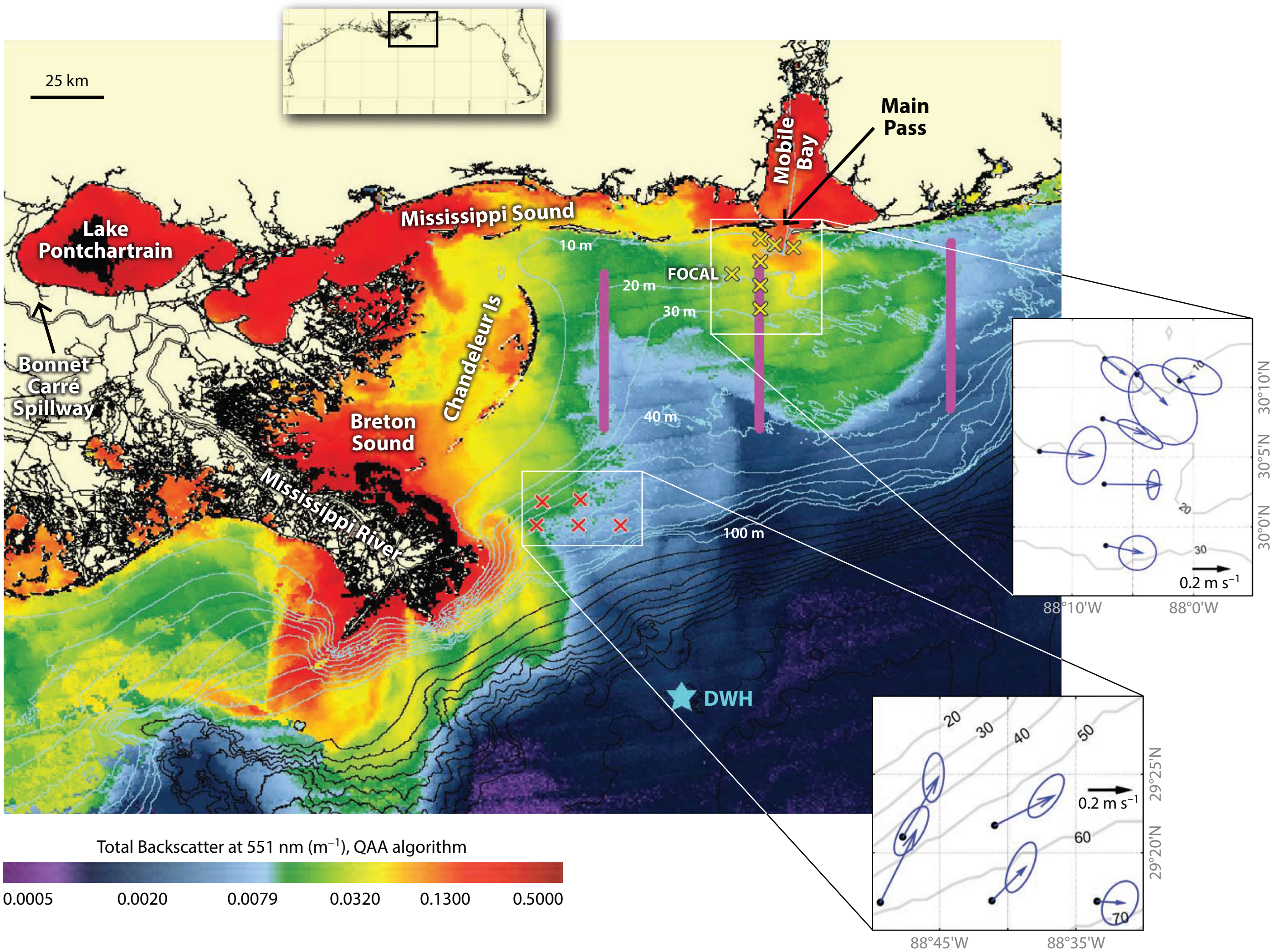

FIGURE 1. Map of the CONCORDE (CONsortium for oil exposure pathways in COastal River-Dominated Ecosystems) study region showing field sampling corridors within the Mississippi Bight (magenta lines, samples between corridors not shown) and the locations of moored instruments (red and yellow Xs). The color shading shows surface optical backscatter (a proxy for relative chlorophyll-*a* distribution obtained from the Visible Infrared Imaging Radiometer Suite, VIIRS) on April 5, 2016, corresponding to a high river discharge event. Inset maps for the mooring arrays show the depth-averaged current vectors with ellipses encompassing, on average, 93% of the current variability for April 5, 2016. The blue star marks the location of the Deepwater Horizon (DWH) drilling platform.

Box 1. Synthesis Model

The CONCORDE synthesis model, which simulates various oceanographic conditions by incorporating several data sources, can be used for assessment and prediction of the effects of future oil spills entering the Mississippi Bight. The circulation model is based on a 400 m resolution implementation of the Regional Ocean Modeling System (ROMS; Shchepetkin and McWilliams, 2005; Haidvogel et al., 2008) within the Coupled Ocean-Atmosphere-Wave-Sediment Transport (COAWST) modeling system (Warner et al., 2010). The model encompasses Mobile Bay and the Mississippi Sound and Bight, extending to 87.30°W and 29.25°N. Boundary conditions are from the 1 km resolution Navy Coastal Ocean Model (NCOM), with river discharge estimated from US Geological Survey data. The biogeochemical model is based on a nitrogen, phytoplankton, zooplankton, detritus model (Fennel et al., 2006; Hofmann et al., 2008; Druon et al., 2010) and simulates nitrogen in various states (dissolved organic nitrogen, nitrate, ammonium, inorganic suspended particulate matter) using two size classes of phytoplankton and detritus, three size classes of zooplankton, and larval fish, all of which can be used to estimate dissolved oxygen concentrations (following Wiggert et al., 2017). CONCORDE field measurements and routine in situ data sets provide calibrations and verification of the ecosystem parameter settings.

Atmospheric forcing is from an hourly 0.01° gridded meteorological reanalysis product composed of several parameters. The Real-Time Mesoscale Analysis (RTMA; De Pondeca et al., 2011) provides surface momentum and thermodynamic atmospheric data. Radiation parameters and total cloud cover percentage are from North American Mesoscale Forecast System (NAM) fields. Hourly precipitation is provided by the Next Generation Weather Radar Level-III (NEXRAD). Gridded sea surface temperature fields (SST) are computed daily using a 10-day running mean of the Advanced Very High-Resolution Radiometer (AVHRR) SST product. The Coupled Ocean-Atmosphere Response Experiment (COARE) flux algorithm calculates sensible heat flux and surface momentum stresses (Fairall et al., 2003).

The CONCORDE synthesis model examines responses to oceanographic conditions and river plume dynamics, providing insights into ecosystem impacts from oil reaching the shelf and nearshore waters. The simulations are designed to evaluate several processes, including (1) environmental controls (e.g., river discharge) on retention/flushing of plankton and dissolved constituents in the study region; (2) physical-biological controls on organism distributions; and (3) suspended particle dynamics and its role in particle aggregation and sinking, with emphasis on toxin transport, removal/retention, and resuspension. Additional simulations consider climate change or management responses (e.g., spillway openings, agricultural practices) that modify freshwater discharge, nutrient forms, and concentrations of terrigenous particulates into coastal waters of the nGOM.

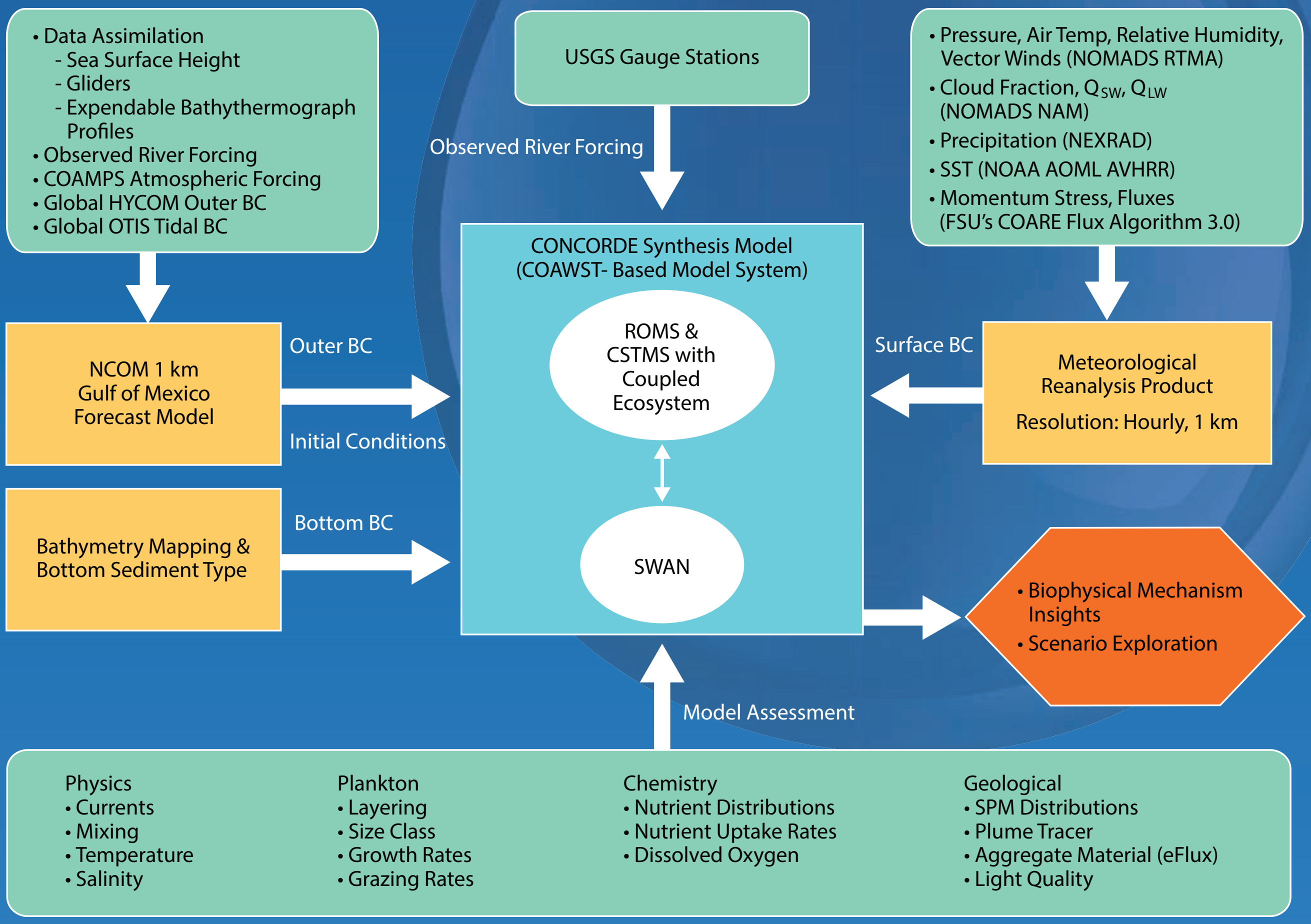

FIGURE B1-1. Conceptual diagram showing the data (green boxes) informing the initial and boundary conditions (BC; tan boxes) for the 4-D synthesis model. Field-collected data (green box at the bottom) are used for model assessment and validation. SWAN (Simulating WAves Nearshore) and the CSTMS (Community Sediment Transport Modeling System) simulate the impact of surface wave-current interactions and suspended sediment fields, respectively, within the coupled physical-biogeochemical model. The model runs under different oceanographic conditions to examine mechanisms of oil impact on the nGOM ecosystem (orange hexagon).

biological, and biogeochemical processes. This effort includes outreach activities designed to disseminate findings and build public trust in scientific information related to the DWH spill (see Box 2).

CONCORDE results are directly applicable to risk assessment, coastal system management, and examination of how ecosystem-level oil impacts may vary depending on the season when an oil spill occurs. Here, we highlight new information generated from sampling different zones of freshwater influence, and we explore how this information supports an emerging oil spill response paradigm (Graham et al., 2011; Peterson et al., 2012) that involves the use of four-dimensional (4-D) descriptions (3-D spatial plus temporal) to predict transport patterns and ecosystem impacts. The processes elucidated from this research are relevant to other ecologically and economically important river-dominated coastal ecosystems found throughout the world.

CONCORDE APPROACH

Research Cruises

The CONCORDE field research approach combined continuous observations from satellites, moored platforms, and autonomous gliders with seasonal ship-based field sampling campaigns in 2015 and 2016 under differing vertical stratification regimes and shifts in wind direction/intensity (Figure 2, Table 1). The ship-based sampling, which focused on zones in the Mississippi Bight with varying degrees of freshwater influence, consisted of fixed surveys and adaptive sampling to document fine-scale processes that influence oil transport and exposure of organisms (e.g., river plumes, fronts, layers with high plankton concentrations).

Physical Oceanography

Physical oceanographic measurements were obtained using a variety of instruments deployed from small boats, moorings, autonomous gliders, and research vessels, providing a 4-D description of the physical dynamics. The moored (fixed position) observations were supplemented by three deployments of autonomous underwater gliders prior to and during cruises. Small boat surveys were conducted to examine the freshwater pulses exiting Main Pass at the mouth of Mobile Bay, an example of a major tidal inlet associated with the barrier islands found in the nGOM. The near-field physical properties (e.g., plume depth, spreading rate, and frontal features) and their impact on the overall fate of freshwater discharge and particulate export along the coastal boundary of the CONCORDE sampling domain were determined from drifter releases and CTD and Laser In Situ Scattering and Transmissometer casts (for suspended particulates).

Moorings were deployed in two regions to capture the freshwater flows over different seasons (Figure 1). During the fall, a season typically characterized by low freshwater discharge, five line and bottom moorings were placed near the shelf break on the western side of the study area, where Mississippi River plumes were most likely to traverse (Figure 1, red Xs). Line moorings with sensors measuring temperature, salinity, and turbulence were deployed for the month of November 2015. Bottom moorings with upward-looking acoustic Doppler current profilers (ADCPs) and pressure sensors remained until mid-April 2016. In the spring, an array of six bottom moorings and three line moorings (Figure 1, yellow Xs) was placed just south of the Main Pass of Mobile Bay to observe plume dynamics and exchanges onto the shelf. This mooring array near the Mobile Bay outflow supplemented existing long-term observations by the Fisheries Oceanography in Coastal Alabama (FOCAL) mooring, allowing better resolution of the complex plume structure. Turbulence was estimated using bottom ADCPs and high-resolution thermistors and pitot-static tubes on χ-pods (Moum and Nash, 2009) tethered to line moorings.

Research vessels collected high-resolution measurements over broad

Box 2. Outreach Program

Because CONCORDE research is directly applicable to several environmental and economic issues affecting the nGOM coast (e.g., fisheries, hypoxia, tourism), outreach activities are organized to distill research findings in order to make them accessible to a broader audience. Outreach activities targeted to specific audiences include (1) a seminar series about scientific progress in the nGOM five years after the Deepwater Horizon spill, (2) teacher professional development, and (3) a citizen science initiative with multi-ethnic fishing community members from the nGOM coast.

Three teacher workshops coincided with the deployment of several autonomous underwater vehicles (known as the "AUV Jubilee") and aircraft in July 2015. In the first workshop, participating teachers worked with CONCORDE researchers and external scientists to conduct a synchronous data collection event in the nGOM to explore basic concepts in oceanography. At the end of this workshop, each teacher submitted a lesson plan based on concepts relating to the nGOM oil spill. Teachers in subsequent workshops offered input on the lessons, which are being distributed as a high school science curriculum.

Members of the fishing community are engaged with the CONCORDE project by learning to collect oceanographic data (e.g., YSI CastAway portable CTD) that can be used to validate model outputs. During training sessions, scientists and fishermen interact with the objective of improving trust in scientific findings within the fishing community, which is frequently at odds with regulatory agencies. Additionally, local knowledge provided by the fishing community may inspire new lines of scientific inquiry, and scientists provide advice on effective participation in local decision-making. These efforts are examples of fruitful collaboration among public, research, and regulatory groups.

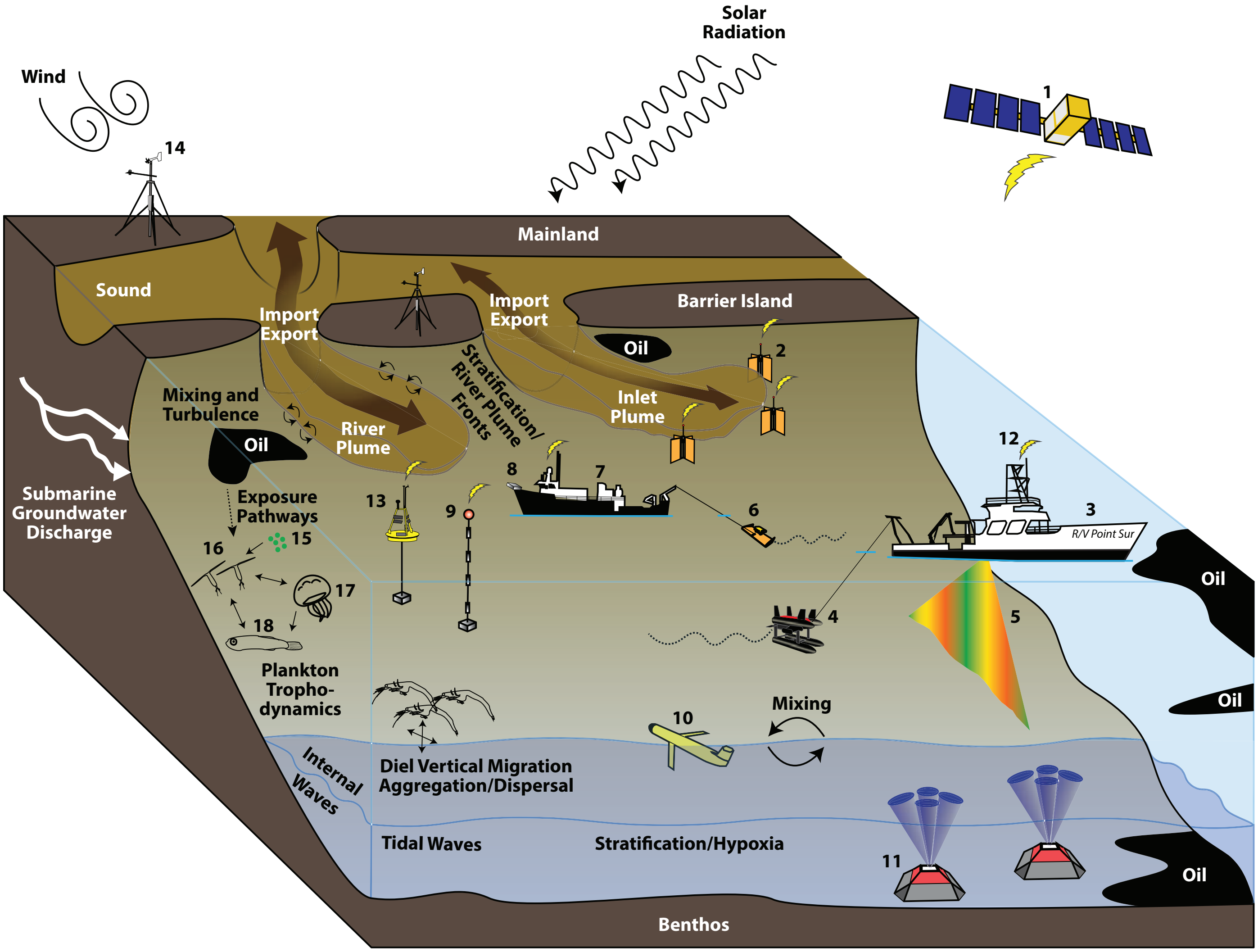

FIGURE 2. Schematic representation of the dynamic processes in the nGOM that influence the distribution, transport, and exposure pathways of oil in the planktonic community. Measurements related to these processes were collected with (1) the Suomi National Polar-Orbiting Partnership satellite equipped with a Visible Infrared Imaging Radiometer Suite; (2) surface drifters; (3) R/V *Point Sur* equipped with a CTD rosette, a sediment multicorer, a BIONESS multi-net system sampling at different depths, and an incubator as well as (4) an In Situ Ichthyoplankton Imaging System (ISIIS) and (5) Reson multibeam acoustics; (6) a Scanfish system shown being towed by (7) R/V *Pelican*, which is equipped with a CTD, a Chameleon microstructure profiler, and (8) ship-based Lidar; (9) a line mooring with sensors measuring current velocity, temperature, salinity, dissolved oxygen, turbulence, and optical properties; (10) an autonomous underwater glider; (11) bottom moorings with ADCPs and bottom pressure sensors; (12) satellite communication; (13) a Central Gulf of Mexico Ocean Observing System (CenGOOS) buoy and Fisheries Oceanography in Coastal Alabama (FOCAL) moorings; and (14) weather stations that include anemometers and various samplers for measuring biological properties of the plankton community, which includes (15) phytoplankton, (16) micro- and mesozooplankton, (17) gelatinous zooplankton, and (18) ichthyoplankton.

spatial and short temporal scales compared to moored and glider observations, which were limited in their spatial coverage. R/V *Point Sur* towed the undulating In Situ Ichthyoplankton Imaging System (ISIIS; Cowen and Guigand, 2008), which provided measurements of temperature, salinity, depth, dissolved oxygen, and downwelling irradiance while collecting in situ images of planktonic organisms. In conjunction with the ISIIS tows, a Reson SeaBat 7125 multibeam sonar was used to map the bathymetry of the study region and to collect water column backscatter data to detect physical and biological features. R/V *Pelican* towed a Scanfish to measure temperature, salinity, depth, and bio-optical properties in the water column. In the spring, R/V *Pelican* also deployed the Chameleon microstructure profiler (Moum et al., 1995), which measured microscale turbulence, temperature, conductivity, optical backscatter (800 nm), and fluorescence throughout

TABLE 1. Dates for the CONCORDE field sampling campaigns.

Expedition	Dates	Research Vessels
Fall Cruise	October 28–November 7, 2015	*Point Sur* & *Pelican*
Bonnet Carré Spillway Cruise	February 11–February 13, 2016	*Point Sur*
Spring Cruise	March 29–April 11, 2016	*Point Sur* & *Pelican*
Summer Cruise	July 24–July 30, 2016	*Point Sur*

the water column from the surface to within 2 cm of the seafloor. The resultant 4,201 Chameleon profiles were combined with acoustic imaging, radar tracking of fronts, shipboard ADCP, and a near-surface towed temperature-conductivity chain to yield a detailed view of river plume dynamics and corresponding oceanographic changes.

Shelf Biological Productivity, Plankton Distributions, and Nutrients

The ISIIS acquired images with two cameras in ~0.06 second intervals, capturing planktonic organisms between ~400 µm and ~13 cm in size using a shadowgraph lighting technique, with no discernible bias in detectability among zooplankton groups (Cowen et al., 2013). The ISIIS images were processed following methods similar to those described in Greer et al. (2015). Images from the smaller camera (4.3 cm field of view, 8.9 cm depth of field, ~40 µm pixel resolution) were automatically segmented, a process that extracted particles greater than 500 pixels in cross-sectional area (~1.0 mm equivalent spherical diameter). These high-resolution images were supplemented with depth-discrete and surface plankton net tows, both of which provided biological samples needed for verification of the image classifications and further laboratory analyses.

Discrete water samples were used to characterize lower trophic level biological processes and nutrient concentrations. Rates of primary production, nitrate-based uptake, and biogenic silica production were measured from shipboard incubations. Chlorophyll (>0.6 µm and >5.0 µm size fractions) concentrations, bulk particulate organic carbon, and particulate organic nitrogen concentrations (among other parameters) were obtained from the water samples. Microplankton (20–200 µm) assemblage composition, size distribution, and abundances were described by imaging water samples with a FlowCAM® Benchtop B3 Series.

Chemical Tracers of Water Masses

Seawater samples for chemical tracer analysis were collected at the surface to characterize the freshwater river input, at midwater depth, and at the bottom to investigate the development of hypoxia based on evidence of previous hypoxic events that occurred in the Mississippi Bight (Brunner et al., 2006). The sampling and analysis strategies follow the methodology previously applied on the Louisiana Shelf (Joung and Shiller, 2014). Conservative parameters such as water isotopes (δ^{18}O and δD) and molybdenum (Mo) and cesium (Cs) concentrations were measured to identify the sources of freshwater to the Mississippi Bight. Barium (Ba) concentrations and radium isotopes (Ra) provided an estimate of the role submarine groundwater discharge plays in the development of bottom water hypoxia (Moore, 2010; Peterson et al., 2016).

Remote Sensing and Circulation Model

Satellite-derived products were combined with circulation model forecasts to characterize daily nGOM biophysical properties. The ocean circulation forecast fields, obtained from a 1 km horizontal resolution implementation of the Navy Coastal Ocean Model (NCOM), were used in planning portions of the CONCORDE field sampling campaigns. The three-hourly circulation fields were integrated with daily satellite-derived temperature and ocean color to provide visualization of environmental conditions that were used to optimize cruise and glider sampling in near-real time. This approach allowed for targeting features of interest, such as fronts and river plumes.

The effects of different environmental scenarios on transport pathways were evaluated with the CONCORDE synthesis model (Box 1) using simulations in which a neutral tracer (neutrally buoyant, passively following the current field) was released continuously throughout the water column along the southernmost boundary of the CONCORDE model domain. Simulations illustrated the fate of the tracer released over 21 days in the fall (October 1–October 21, 2015) and the spring (March 18–April 7, 2016). The integrated tracer concentration in the shallowest 1 m was used to determine surface transport patterns. This depth range was chosen because the mixed layer is shallow in the Mississippi Bight, and using a fixed depth allows for a comparison that is independent of seasonal and spatial changes in mixed layer depth. The tracer was designed to simulate surface water transport that could contain surface crude oil or droplets mixed just below the air-sea interface. Wind roses at 88.5°W, 29.4°N (near the southern boundary of the model domain) were calculated from the wind analysis field.

RESULTS AND DISCUSSION

River Plume Transport

Results from one survey day (April 10, 2016) illustrate some physical processes and transport mechanisms involving the Mobile Bay plume. River plumes flowing into the nGOM contribute to vertical stratification that varies in strength throughout the year. The highest freshwater input occurs in spring, resulting in a stratified system with high-salinity shelf water at depth, an intermediate layer of old plume water that has been mixed over time with deeper waters (Figure 3a), and the occasional presence of a thin surface plume from the Mobile Bay outflow (Dzwonkowski et al., 2015). The strong stratification between layers limits vertical exchange of passive constituents such as sediments (as observed in optical backscatter, Figure 3b) and chlorophyll-*a* (inferred from fluorescence, Figure 3c). To counteract the effects of stratification, opposing current velocities (surface vs. bottom, Figure 3e) create vertical shear, inducing turbulence via shear instability (Figure 3d; Smyth and Moum, 2012) that drives a Fickian-like diffusion of salt and other constituents between layers (Shroyer et al., 2016). The depth-integrated change in salinity over time (dS/dt) within the intermediate layer (thickness H) correlates with the turbulent salt flux across the pycnocline (depicted in Figure 3f as the product of turbulence diffusivity, K_ρ, and the vertical salinity gradient). This correlation suggests that turbulent mixing can account for the exchange of passive constituents between layers despite the stratification that opposes this exchange. Strong winds, which enhance mixing, would erode stratification and homogenize the water column in the absence of periodic injections of freshwater by river plumes.

Secondary lateral currents also impact the transport of these constituents (Figure 3e). Southeasterly winds can drive a current in the intermediate layer to the northeast, forcing the intermediate layer toward shore. Consequently, constituents near the surface are advected toward shore, while deeper waters are advected offshore due to the pressure head of the outflow and downwelling wind. Mixing between layers defines a more complex pathway in which initially deep constituents are mixed upward and then transported shoreward. Lateral transport is further complicated by the presence of tidally reversing currents and rotating inertial oscillations, the clockwise turning near the local inertial frequency (~24-hour period at nGOM latitudes) caused by Earth's rotation.

In mid-April, the river plume was advected along the coast, but its position varied in response to other environmental conditions. Under weaker wind conditions, plume-tracking drifters moved offshore and to the west, consistent with a buoyancy-driven plume (Figure 4a). However, the stronger upwelling conditions (westerly winds) forced the plume offshore where it continued to be pushed eastward by shelf currents (Figure 4b). The trajectories of simulated drifters are similar to those of observed drifters under different wind forcing conditions, indicating the model skill in resolving the Mobile Bay plume response to winds. The observed and simulated drifter pathways show that the eastern-most CONCORDE sampling transect (87.53°W, Figure 1) can receive freshwater input derived from Mobile Bay during periods of upwelling wind.

Additional drifter releases simulated by the circulation model (Box 1) show transport pathways for different prevailing wind, tidal, and freshwater discharge conditions. Transport depicted from drifter simulations for the winter cruise (during the period of the Bonnet Carré Spillway opening) agreed with water mass distributions determined from underway bio-optical measurements.

Oxygen isotope analysis showed that the Mississippi River plays a surprisingly small role in freshwater input to the Mississippi Bight (relative to freshwater from Mobile Bay and other sources). The Bonnet Carré Spillway opening was an exceptional freshwater discharge event where Mississippi River water entered through Lake Pontchartrain, north of the main Mississippi River Delta, with a seemingly more direct connection to the Bight. Even under these circumstances, only waters in the westernmost part of the Bight showed Mississippi River influence. Chemical tracers also indicated

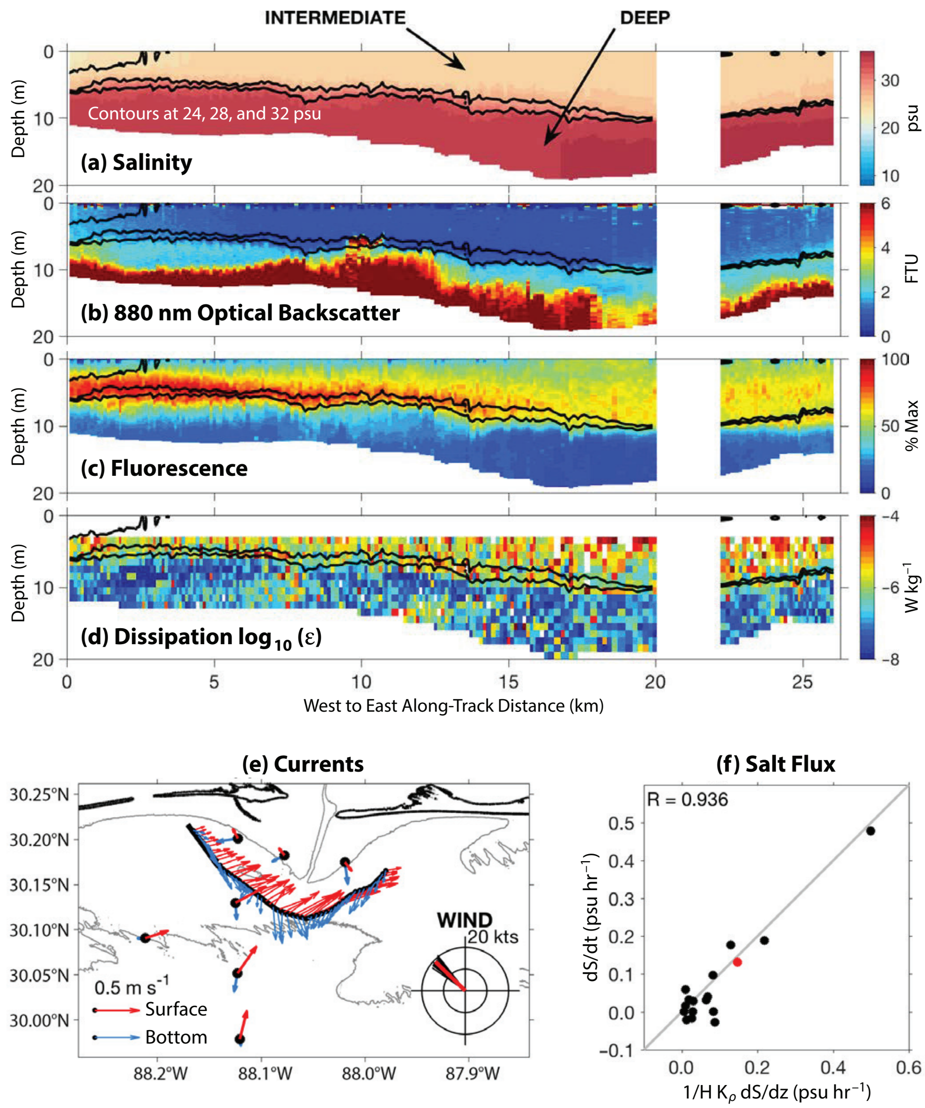

FIGURE 3. Observed distribution of (a) salinity, (b) 880 nm optical backscatter, (c) chlorophyll fluorescence, and (d) turbulent kinetic energy dissipation rate measured with the Chameleon microstructure profiler during the evening of April 10, 2016, along the semicircular transect shown in (e), located ~5 km south of Mobile Bay. (e) Near-surface (red) and near-bottom (blue) currents measured by a 1,200 kHz shipboard ADCP along the transect path, and current vectors at the mooring locations averaged over the 4.5 hours it took to complete the shipboard transect. Inset shows average wind direction (southeasterly) and speed (20 knots). (f) Turbulent salt flux divergence across the intermediate layer (x-axis) compared with the measured change in salt in the intermediate layer (y-axis). The transect shown in a–d is plotted in red.

transport of local river waters, including Mobile Bay outflow, to the western part of Mississippi Sound during this event. Most of the Mississippi River water (from both the Delta and the Bonnet Carré Spillway) appears to hug the Louisiana coast and move toward the south and west, leaving the Bight to be primarily influenced by Mobile Bay outflow and smaller rivers. This oxygen isotope data set, indicating strong south and eventually westward trajectory of the Mississippi River outflow, provides an approach for assessing the skill of the simulated circulation patterns.

Shelf Circulation and Transport Pathways

Throughout the sampling period between fall 2015 and spring 2016, mooring arrays (Xs in Figure 1) provided a broader context for the higher-resolution physical and biogeochemical measurements. Currents near the Mississippi River Delta were generally oriented along the isobaths, with typical variation ranging between 30 cm s^{-1} and 50 cm s^{-1} in both along-isobath directions (e.g., Figure 1, lower inset), while mean speeds were an order of magnitude smaller at 2–5 cm s^{-1}. The large difference between the variations and mean suggests that there is no dominant orientation for the currents east of the Mississippi River Delta from fall to spring. Currents often oscillated with a near-inertial frequency (clockwise rotation), primarily forced by the passage of cold fronts through this region that occur every 2–15 days. Despite its proximity, the Mississippi River outflow did not play a significant role in driving weekly variations of currents during the study period. Rather, local southeasterly winds drove southwestward currents with slight offshore fluxes, and northwesterly winds drove northeastward currents with slight onshore fluxes.

The potential pathways that result in oil exposure on the nGOM continental shelf and their variability were assessed with the circulation model using simulations that tracked the concentration of a continuously released neutral tracer throughout the model domain. Tracers were released during the fall and spring for a 21-day period. The fall tracer release (October 1–October 21, 2015) shows consistent surface transport from west to northeast, with little northward advection into the inner shelf region of the Mississippi Bight (Figure 5a). In contrast, the spring release (March 18–April 7, 2016) shows the tracer transported northward to the nGOM inner shelf region, as well as surface spreading of the tracer over most of the CONCORDE model domain (Figure 5b). Major differences between these two cases include the winds (Figure 5c,d—stronger speed peaks and greater directional variability in the spring period relative to the fall), the stratification (stronger in spring), and the river discharge (higher in spring). The fall and spring simulated tracer patterns indicate that the timing of an oil spill can greatly influence its distribution on the shallow nGOM shelf, and high river discharge does not necessarily obstruct the onshore transport of surface water constituents to the shelf and coastal habitats. These simulations provide a basis for further studies that address the effects of environmental complexity and uncertainty on oil transport in the nGOM and on ecosystem processes.

Biological Production and Aggregation on the Shelf

Biological constituents responded to variable salinities and nutrient inputs from nearby rivers. During the fall, minimal freshwater input led to a well-mixed

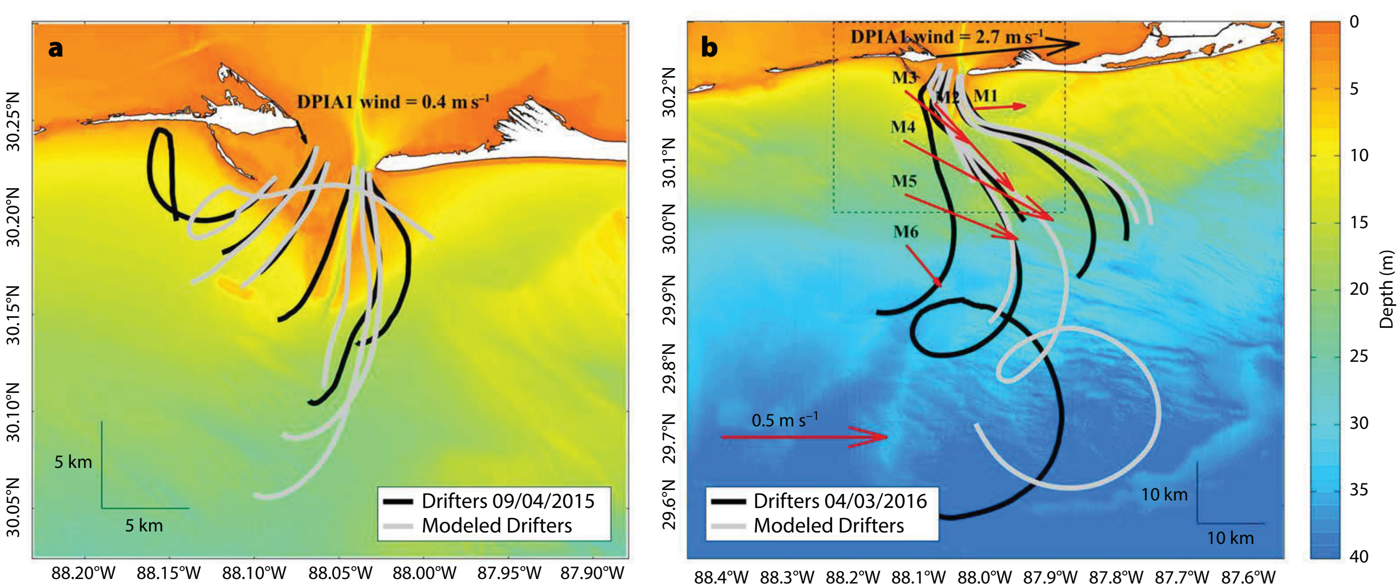

FIGURE 4. Example trajectories for observed (black) and simulated (gray) drifter releases on (a) September 4, 2015, during a weak sea breeze cycle, and (b) April 3, 2016, after a frontal passage. The drifters were released at Main Pass approximately a quarter of the way into the ebb tide; however, the drifter recovery varied from 5 hours to 60 hours, resulting in extended trajectories for some drifters. Wind vectors (black) at Main Pass show average wind speed and direction during drifter releases (NOAA/NDBC station DPIA1). Red vectors (panel b only) indicate the near-surface currents at the moorings averaged over the duration of the drifter release.

water column with relatively high salinity (Cambazoglu et al., 2017) and low biological productivity (Figure 6a,b), as measured by both primary production and zooplankton abundances (Dzwonkowski et al., 2017). The water column underwent a dramatic change as spring rains led to increased river discharge from Mobile Bay, directly affecting large portions of the shelf and producing a large vertical salinity range (salinity of ~24 at surface and ~36 at depth). These nutrient-rich river discharges produced higher biological productivity, with the zooplankton and marine snow particle distributions closely following the halocline (Figure 6c,d). The mooring near the northern end of the transect (southernmost yellow X in Figure 1) showed two-layer cross-shelf transport caused by an inertial oscillation likely created by a wind event. During the inertial cycle, currents were oriented offshore in the surface layer and onshore in the lower layer. They slowly turned clockwise in each layer to reverse course over the next 12 hours, reaching the opposite pattern of onshore flow in the surface layer and offshore flow at depth. These currents then slowly turned clockwise over the next 12 hours to return to the original flow pattern (the period of inertial oscillations is diurnal at these latitudes). This is an example of differential advection set up by stratified conditions, which has implications for understanding oil transport in this region.

During summer, the vertical salinity range was lower, but the halocline was strongest with apparent vertical oscillations (i.e., internal waves; Figure 6e,f). The zooplankton and marine snow distributions were confined to a narrow range of intermediate salinity levels, but the peak concentrations were not as high as those measured during spring. The spring to summer halocline strengthening appeared to correspond to vertically confined distributions of zooplankton, as well as to a reduced capacity for ventilation of the deeper shelf waters that generates favorable conditions for the development of hypoxia. In summer, bottom waters showed radium enrichment, a key indicator of submarine groundwater

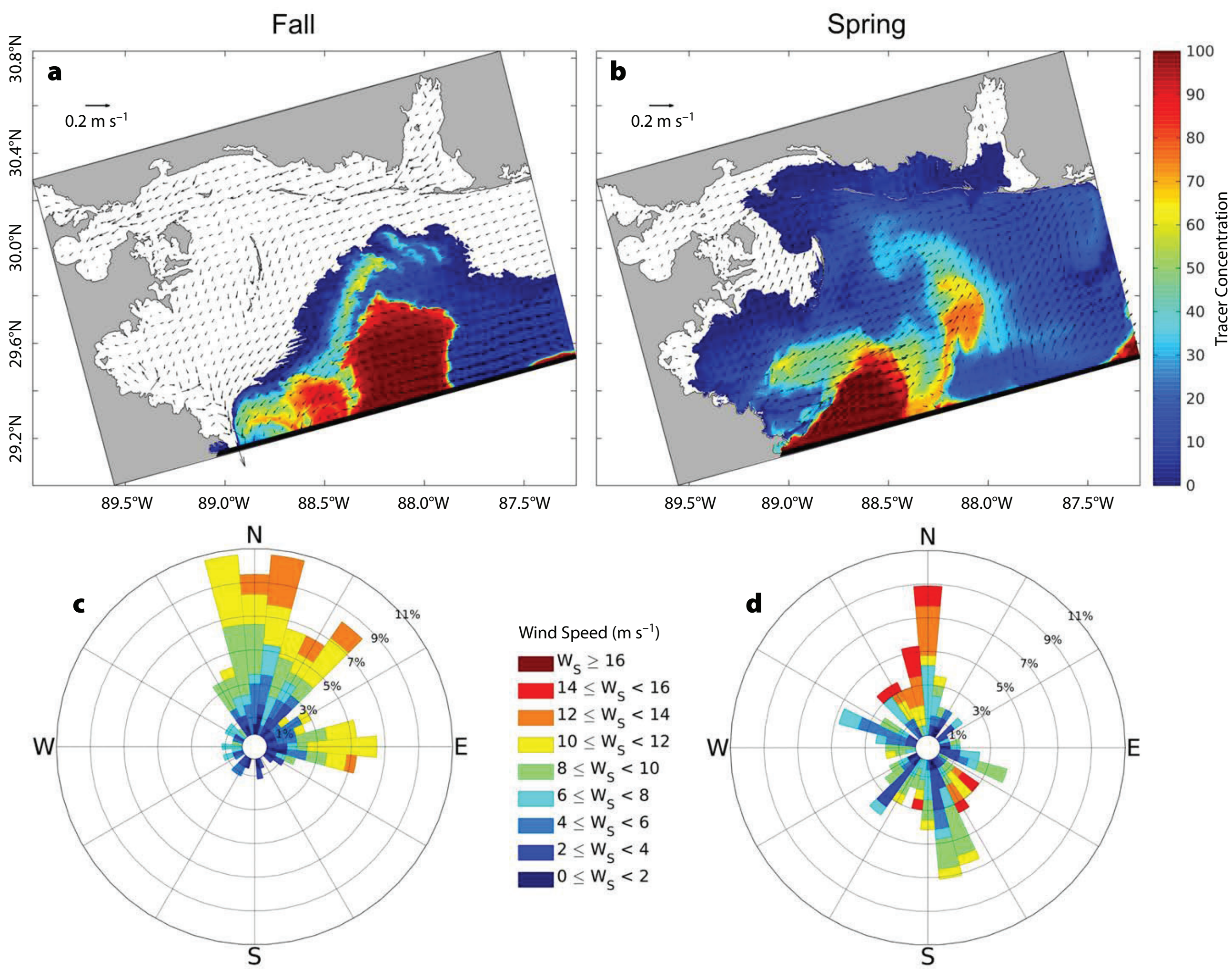

FIGURE 5. Simulated neutrally buoyant tracer release (color shading) at the southern edge of the CONCORDE model domain in the Mississippi Bight. Tracer distribution (integrated 1 m surface concentration in arbitrary units ranging from 0 to 100—concentration is 100 at the site of the release) is shown after 21 days of continuous release and passive advection during (a) fall (October 1–21) and (b) spring (March 18–April 7) seasons, respectively (see online supplemental material for tracer advection animation). Regions with tracer concentrations <0.1 (white areas) and current vectors (simulation day 21) are also shown. Wind roses (showing direction wind is coming from) were produced from the wind analysis field (meteorological reanalysis product – see Box 1) from the (c) fall and (d) spring during the same 21-day period near the southern boundary of the model domain (29.4°N, 88.5°W).

discharge, and this was correlated with high dissolved silica, inorganic nitrogen, and phosphate, and low dissolved oxygen. Thus, in addition to river discharge, submarine groundwater appears to play a role in nutrient delivery in the Mississippi Bight, with possible concomitant effects on productivity and bottom water hypoxia.

The intense aggregation of plankton and marine snow, particularly during spring and summer, has important implications for the propagation of oil and contaminants throughout the food web (Figure 6b,d,f). Sinking marine snow provides a mechanism for transport of oil to depth and potentially serves as a trophic exposure pathway for oil into the planktonic food web (reviewed by Daly et al., 2016). The association between seasonal changes in salinity structure and zooplankton/marine snow distributions provides requisite data for quantifying spatial overlap (e.g., Greer and Woodson, 2016) and contact rates between marine snow particles and various zooplankton groups, along with information about behavioral interactions (e.g., orientation and predation events; see Figure 6g–m for example images). These measurements can be used to generate taxon-specific understanding of vulnerability to oil exposure and of detailed trophic pathways for oil incorporation into the planktonic food web (Graham et al., 2010; Buskey et al., 2016).

SUMMARY AND FUTURE APPLICATIONS OF CONCORDE

Analysis of high-resolution, near-synoptic measurements that cross traditional oceanographic disciplines has improved

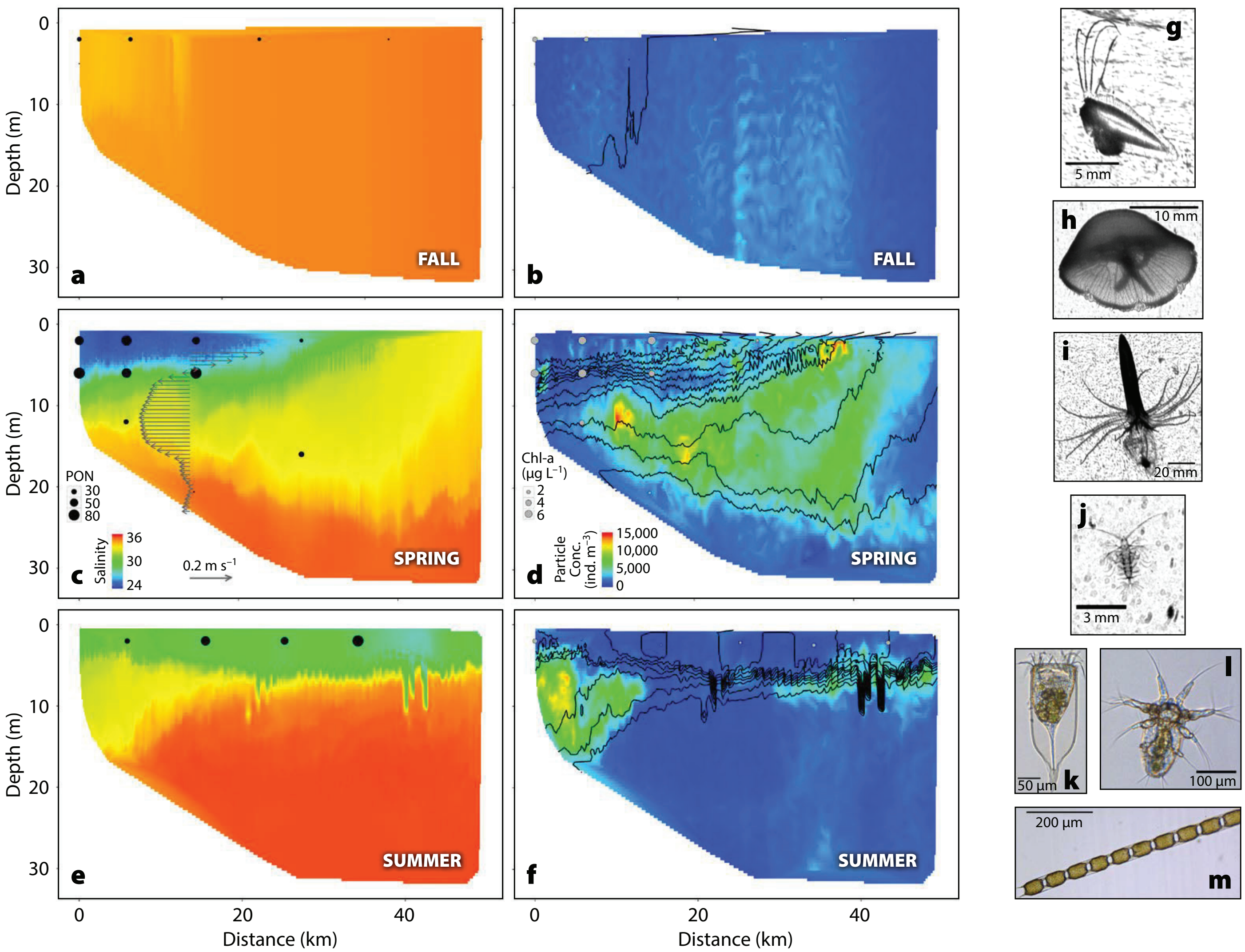

FIGURE 6. Measured salinity versus distance from start of the ISIIS transect (left is north) in (a) fall (October 30, 2015), (c) spring (April 4, 2016), and (e) summer (July 25, 2016) along the middle sampling corridor (Figure 1) and measured particulate organic nitrogen concentrations (black dots). Panel c shows the current vectors from a mooring averaged between 10:00 and 12:00 CDT on April 4, 2016 (southernmost yellow X in Figure 1). Particle concentrations (zooplankton and marine snow) during (b) fall, (d) spring, and (f) summer, with measured chlorophyll-*a* (Chl-a) concentrations (gray dots) along the same sampling corridors. Salinity between 25 and 35 is indicated by black lines in 1 unit increments. The legend for (c) also applies to (a) and (e), and (d) contains the legend for (b) and (f). Example images of fauna captured with the ISIIS and within the size range of particles show (g) a larval flatfish, (h) a juvenile moon jelly (*Aurelia* spp.), (i) a larval tube anemone consuming a salp, and (j) a eucalanoid copepod. Images k–m, captured with the FlowCAM®, show (k) a tintinnid ciliate, (l) a copepod nauplius, and (m) a diatom chain (*Odontella sinensis*) that were all below the ~1 mm size threshold of plankton plotted in (b), (d), and (f).

our understanding of the Mississippi Bight, a critical region separating offshore oil drilling sites and coastal habitats. Complex physical processes in this river-influenced region of the nGOM contribute to the structuring of ecological communities, but measurements on scales appropriate for resolving many processes relevant to oil transport (hourly temporal scales and centimeter to meter spatial scales), and the interactions of oil with biological and other chemical components, have been lacking. Several new findings have emerged from this research, including the discovery of both direct and indirect transport pathways driven by the wind and consistent plankton aggregations that track salinity variations.

Wind has a major influence on transport of river plume waters, which in turn impacts other ecosystem properties. Mooring observations suggest that wind is the dominant control on the currents to the east of the Mississippi Delta, and wind variations can move Mississippi River water along the shelf break and into or out of the Bight. However, chemical distributions indicate that Mississippi River water actually makes up a relatively small proportion of the freshwater entering the Bight, suggesting that much of the Mississippi River water that flows eastward is advected either along the shelf break or offshore. Wind can also drive the Mobile Bay plume westward or eastward and plays an indirect role in setting up the shear observed in the Mobile Bay plume, producing the observed mixed layer salinity changes and generating inertial oscillations that diurnally advect plumes after a wind event. Biological sampling demonstrates that strong salinity gradients influence the distributions of zooplankton, marine snow, and nutrients. The distributions of plankton and geochemical constituents are therefore connected to wind speed and direction, as the wind forcing modulates the halocline through mixing and impacts plume fronts through advection. These connections, which can only be revealed with an interdisciplinary approach, show that different, seasonally dependent environmental factors structure the distribution of constituents and can also influence oil advection and the magnitude of oil spill impacts on the ecosystem.

Improved forecasting of oil spill transport and impacts requires understanding oceanographic processes that change with depth. Although most oil spill transport research has focused on atmospheric forcing and circulation near the sea surface, the Deepwater Horizon blowout demonstrates that understanding oil transport and interactions should be considered a 4-D problem, with depth adding a complex new dimension that is difficult to observe (Peterson et al., 2012). This understanding is becoming critical given that oil extraction is taking place in deeper, offshore sites (Graham et al., 2011). Accurate prediction of ecosystem-level impacts from oil spills is the foundation for effective response planning, so observations and modeling must be extended to include interactions throughout the water column between oil (and dispersants) and the biological and geochemical constituents that serve as a mechanistic link to bulk ecological and economic impacts. The dynamics of pulsed river plumes adds an additional degree of complexity for predicting physical advection and chemical-biological interactions. Even though river-dominated shelf ecosystems are relatively shallow, their physical, chemical, and biological properties can change dramatically with depth. CONCORDE provides detailed new information on river-dominated systems, as spilled oil traversing these regions directly threatens coastal habitats and human populations.

River-influenced coastal systems found throughout the world are productive habitats for a variety of culturally and economically important marine species. Oil drilling has resulted in repeated spills and significant environmental damage in areas such as the Niger River Delta (Ite et al., 2013) and will continue to threaten similar habitats globally (Figure 7). Principles derived, and patterns described, from CONCORDE's interdisciplinary approach to identifying and quantitatively assessing key physical, biological, and geochemical processes acting in the nGOM are applicable to other pulsed, river-dominated systems, even though there may be differing ecological communities, volumes of river discharge, and degrees of oil extraction activities relative to the nGOM. Moreover, many of these oil reserves near river mouths are currently relatively unexploited, such as those on the Alaskan shelf.

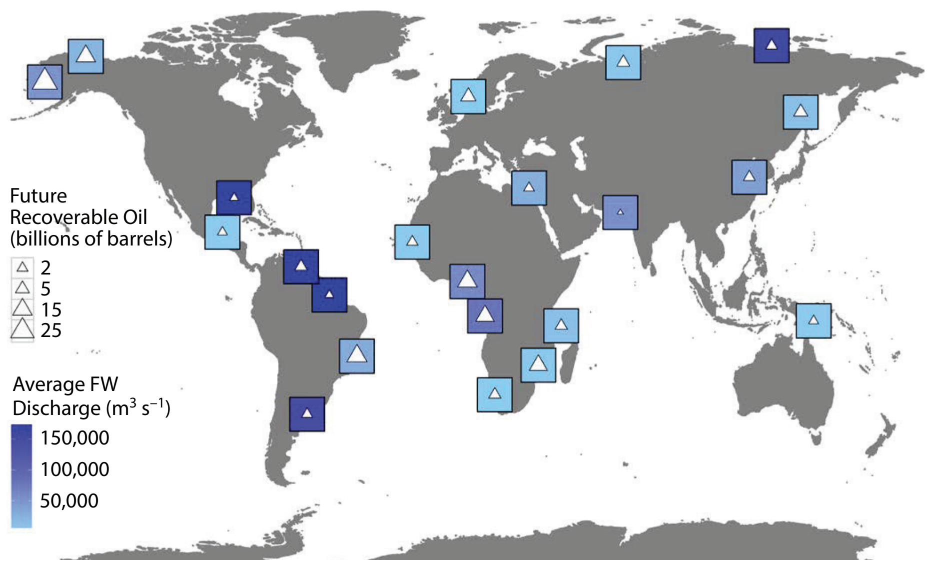

FIGURE 7. Locations of coastal river-dominated ecosystems around the world with nearby oil extraction activities that are similar to the CONCORDE domain. Color corresponds to the average freshwater (FW) river discharge, and the size of the triangle represents the current extent of oil reserves (see supplementary material data sets and references used to generate the figure).

Because accidents can have such dire consequences, as demonstrated during the Deepwater Horizon spill, understanding the physical pathways for oil and distributions of biological and chemical constituents under different oceanographic conditions must be a priority *before* extraction begins. This information provides the basis for oil spill transport modeling and estimation of exposure rates for planktonic organisms that can then be utilized in formulating response plans aimed at preserving the vital ecological functioning of the system.

SUPPLEMENTARY MATERIALS

An animation of simulated neutrally buoyant tracer release at the southern edge of the CONCORDE model domain, Gulf of Mexico is available at https://youtu.be/9FjC1bBnMSA. More information on global oil production in river-dominated ecosystems and the reference data sets used to generate Figure 7 and are available at https://doi.org/10.5670/oceanog.2018.302.

REFERENCES

Brunner, C.A., J.M. Beall, S.J. Bentley, and Y. Furukawa. 2006. Hypoxia hotspots in the Mississippi Bight. *Journal of Foraminiferal Research* 36(2):95–107, https://doi.org/10.2113/36.2.95.

Buskey, E.J., H.K. White, and A.J. Esbaugh. 2016. Impact of oil spills on marine life in the Gulf of Mexico: Effects on plankton, nekton, and deep-sea benthos. *Oceanography* 29(3):174–181, https://doi.org/10.5670/oceanog.2016.81.

Cambazoglu, M.K., I.M. Soto, S.D. Howden, B. Dzwonkowski, P.J. Fitzpatrick, R.A. Arnone, G.A. Jacobs, and Y.H. Lau. 2017. Inflow of shelf waters into the Mississippi Sound and Mobile Bay estuaries in October 2015. *Journal of Applied Remote Sensing* 11(3):032410, https://doi.org/10.1117/1.JRS.11.032410.

Camilli, R., C.M. Reddy, D.R. Yoerger, B.A.S. Van Mooy, M.V. Jakuba, J.C. Kinsey, C.P. McIntyre, S.P. Sylva, and J.V. Maloney. 2010. Tracking hydrocarbon plume transport and biodegradation at Deepwater Horizon. *Science* 330:201–204, https://doi.org/10.1126/science.1195223.

Cowen, R.K., A.T. Greer, C.M. Guigand, J.A. Hare, D.E. Richardson, and H.J. Walsh. 2013. Evaluation of the In Situ Ichthyoplankton Imaging System (ISIIS): Comparison with the traditional (bongo net) sampler. *Fishery Bulletin* 111:1–12.

Cowen, R.K., and C.M. Guigand. 2008. In Situ Ichthyoplankton Imaging System (ISIIS): System design and preliminary results. *Limnology and Oceanography: Methods* 6:126–132, https://doi.org/10.4319/lom.2008.6.126.

Daly, K.L., U. Passow, J. Chanton, and D. Hollander. 2016. Assessing the impacts of oil-associated marine snow formation and sedimentation during and after the Deepwater Horizon oil spill. *Anthropocene* 13:18–33, https://doi.org/10.1016/j.ancene.2016.01.006.

De Pondeca, M.S.F.V., G.S. Manikin, G. DiMego, S.G. Benjamin, D.F. Parrish, R.J. Purser, W.-S. Wu, J.D. Horel, D.T. Myrick, Y. Lin, and others. 2011: The real-time mesoscale analysis at NOAA's National Centers for Environmental Prediction: Current status and development. *Weather Forecasting* 26:593–612, https://doi.org/10.1175/WAF-D-10-05037.1.

Diercks, A., R.C. Highsmith, V.L. Asper, D. Joung, Z. Zhou, L. Guo, A.M. Shiller, S.B. Joye, A.P. Teske, N. Guinasso, T.L. Wade, and S.E. Lohrenz. 2010. Characterization of subsurface polycyclic aromatic hydrocarbons at the Deepwater Horizon site. *Geophysical Research Letters* 37, L20602, https://doi.org/10.1029/2010GL045046.

Dinnel, S.P., and W.J. Wiseman Jr. 1986. Fresh water on the Louisiana and Texas shelf. *Continental Shelf Research* 6:765–784, https://doi.org/10.1016/0278-4343(86)90036-1.

Druon, J., A. Mannino, S. Signorini, C. McClain, M. Friedrichs, J. Wilkin, and K. Fennel. 2010. Modeling the dynamics and export of dissolved organic matter in the Northeastern US Continental Shelf. *Estuaries Coastal and Shelf Science* 88:488–507, https://doi.org/10.1016/j.ecss.2010.05.010.

Dzwonkowski, B., A.T. Greer, C. Briseño-Avena, J.W. Krause, I.M. Soto, F.J. Hernandez, A.L. Deary, J.D. Wiggert, D. Joung, P.J. Fitzpatrick, and others. 2017. Estuarine influence on biogeochemical properties of the Alabama shelf during the fall season. *Continental Shelf Research* 140:96–109, https://doi.org/10.1016/j.csr.2017.05.001.

Dzwonkowski, B., K. Park, and R. Collini. 2015. The coupled estuarine-shelf response of a river-dominated system during the transition from low to high discharge. *Journal of Geophysical Research* 120:6,145–6,163, https://doi.org/10.1002/2015JC010714.

Fairall, C.W., E.F. Bradley, J.E. Hare, A.A. Grachev, and J.B. Edson. 2003. Bulk parameterization of air-sea fluxes: Updates and verification for the COARE algorithm. *Journal of Climate* 16:571–591, https://doi.org/10.1175/1520-0442(2003)016<0571:BPOASF>2.0.CO;2.

Federal Interagency Solutions Group. 2010. *Oil Budget Calculator:* Deepwater Horizon. Technical Documentation: A Report to the National Incident Command, 217 pp.

Fennel, K., J. Wilkin, J. Levin, J. Moisan, J. O'Reilly, and D. Haidvogel. 2006. Nitrogen cycling in the Middle Atlantic Bight: Results from a three-dimensional model and implications for the North Atlantic nitrogen budget. *Global Biogeochemical Cycles* 20, GB3007, https://doi.org/10.1029/2005GB002456.

Fisher, C.R., A.W.J. Demopoulos, E.E. Cordes, I.B. Baums, H.K. White, and J.R. Bourque. 2014. Coral communities as indicators of ecosystem-level impacts of the Deepwater Horizon spill. *Bioscience* 64:796–807, https://doi.org/10.1093/biosci/biu129.

Gelfenbaum, G., and R.P. Stumpf. 1993. Observations of currents and density structure across a buoyant plume front. *Estuaries* 16(1):40–52, https://doi.org/10.2307/1352762.

Graham, W.M., R.H. Condon, R.H. Carmichael, I. D'Ambra, H.K. Patterson, L.J. Linn, and F.J. Hernandez Jr. 2010. Oil carbon entered the coastal planktonic food web during the Deepwater Horizon oil spill. *Environmental Research Letters* 5, 045301, https://doi.org/10.1088/1748-9326/5/4/045301.

Graham, B., W.K. Reilly, F. Beinecke, D.F. Boesch, T.D. Garcia, C.A. Murray, and F. Ulmer. 2011. *Deep Water: The Gulf Oil Disaster and the Future of Offshore Drilling*. Report to the President by the National Commission on the BP Deepwater Horizon Oil Spill and Offshore Drilling, 398 pp.

Greer, A.T., R.K. Cowen, C.M. Guigand, and J.A. Hare. 2015. Fine-scale planktonic habitat partitioning at a shelf-slope front revealed by a high-resolution imaging system. *Journal of Marine Systems* 142:111–125, https://doi.org/10.1016/j.jmarsys.2014.10.008.

Greer, A.T., and C.B. Woodson. 2016. Application of a predator-prey overlap metric to determine the impact of sub-grid scale feeding dynamics on ecosystem productivity. *ICES Journal of Marine Science* 73:1,051–1,061, https://doi.org/10.1093/icesjms/fsw001.

Grimes, C.B. 2001. Fishery production in the Mississippi River discharge. *Fisheries* 26:17–26, https://doi.org/10.1577/1548-8446(2001)026<0017:FPATMR>2.0.CO;2.

Haidvogel, D.B., H. Arango, W.P. Budgell, B.D. Cornuelle, E. Curchitser, E. Di Lorenzo, K. Fennel, W.R. Geyer, A.J. Hermann, L. Lanerolle, and others. 2008. Ocean forecasting in terrain-following coordinates: Formulation and skill assessment of the regional ocean modeling system. *Journal of Computational Physics* 227:3,595–3,624, https://doi.org/10.1016/j.jcp.2007.06.016.

Hazen, T.C., E.A. Dubinsky, T.Z. Desantis, G.L. Andersen, Y.M. Piceno, N. Singh, J.K. Jansson, A. Probst, S.E. Borglin, J.L. Fortney, and others. 2010. Deep-sea oil plume enriches indigenous oil-degrading bacteria. *Science* 330:204–208, https://doi.org/10.1126/science.1195979.

Hofmann, E., J.N. Druon, K. Fennel, M. Friedrichs, D. Haidvogel, C. Lee, A. Mannino, C. McClain, R. Najjar, J. O'Reilly, and others. 2008. Eastern US continental shelf carbon budget integrating models, data assimilation, and analysis. *Oceanography* 21(1):86–104, https://doi.org/10.5670/oceanog.2008.70.

Ite, A.E., U.J. Ibok, M.U. Ite, and S.W. Petters. 2013. Petroleum exploration and production: Past and present environmental issues in the Nigeria's Niger Delta. *American Journal of Environmental Protection* 1(4):78–90, https://doi.org/10.12691/env-1-4-2.

Joung, D., and A.M. Shiller. 2014. Dissolved barium behavior in Louisiana Shelf waters affected by the Mississippi/Atchafalaya River mixing zone. *Geochimica et Cosmochimica Acta* 141:303–313, https://doi.org/10.1016/j.gca.2014.06.021.

Joye, S.B., A. Bracco, T.M. Özgökmen, J.P. Chanton, M. Grosell, I.R. MacDonald, E.E. Cordes, J.P. Montoya, and U. Passow. 2016. The Gulf of Mexico ecosystem, six years after the Macondo Oil Well blowout. *Deep Sea Research Part II* 129:4–19, https://doi.org/10.1016/j.dsr2.2016.04.018.

Kourafalou, V.H., and Y.S. Androulidakis. 2013. Influence of Mississippi River induced circulation on the Deepwater Horizon oil spill transport. *Journal of Geophysical Research* 118(8):3,823–3,842, https://doi.org/10.1002/jgrc.20272.

Lohrenz, S., G. Fahnenstiel, D. Redalje, G.A. Lang, X.G. Chen, and M.J. Dagg. 1997. Variations in primary production of northern Gulf of Mexico continental shelf waters linked to nutrient inputs from the Mississippi River. *Marine Ecology Progress Series* 155:45–54, https://doi.org/10.3354/meps155045.

MacDonald, I.R., O. Garcia-Pineda, A. Beet, S. Daneshgar Asl, L. Feng, G. Graettinger, D. French-McCay, J. Holmes, C. Hu, F. Huffer, and others. 2015. Natural and unnatural oil slicks in the Gulf of Mexico. *Journal of Geophysical Research* 120:8,364–8,380, https://doi.org/10.1002/2015JC011062.

Michel, J., E.H. Owens, S. Zengel, A. Graham, Z. Nixon, T. Allard, W. Holton, P.D. Reimer, A. Lamarche, M. White, and others. 2013. Extent and degree of shoreline oiling: Deepwater Horizon oil spill, Gulf of Mexico, USA. *PLoS ONE* 8(6):e65087, https://doi.org//10.1371/journal.pone.0065087.

Moore, W.S. 2010. The effect of submarine groundwater discharge on the ocean. *Annual Review of Marine Science* 2:59–88, https://doi.org/10.1146/annurev-marine-120308-081019.

Moum, J.N., M.C. Gregg, R.C. Lien, and M.E. Carr. 1995: Comparison of turbulence kinetic energy dissipation rate estimates from two ocean microstructure profilers. *Journal of Atmospheric and Oceanic Technology* 12(2):346–366, https://doi.org/10.1175/1520-0426(1995)012<0346:COTKED>2.0.CO;2.

Moum, J.N., and J.D. Nash. 2009. Mixing measurements on an equatorial ocean mooring. *Journal of Atmospheric and Oceanic Technology* 26(2):317–336, https://doi.org/10.1175/2008JTECHO617.1.

Murawski, S.A., J.W. Fleeger, W.F. Patterson III, C. Hu, K. Daly, I. Romero, and G.A. Toro-Farmer. 2016. How did the Deepwater Horizon oil spill affect coastal and continental shelf ecosystems of the Gulf of Mexico? *Oceanography* 29(3):160–173, https://doi.org/10.5670/oceanog.2016.80.

Nixon, Z., S. Zengel, M. Baker, M. Steinhoff, G. Fricano, S. Rouhani, and J. Michel. 2016. Shoreline oiling from the Deepwater Horizon oil spill. *Marine Pollution Bulletin* 107:170–178, https://doi.org/10.1016/j.marpolbul.2016.04.003.

O'Connor, B.S., F.E. Muller-Karger, R.W. Nero, C. Hu, and E.B. Peebles. 2016. The role of Mississippi River discharge in offshore phytoplankton blooming in the northeastern Gulf of Mexico during August 2010. *Remote Sensing of the Environment* 173:133–144, https://doi.org/10.1016/j.rse.2015.11.004.

Oey, L.-Y., T. Ezer, and H.-C. Lee. 2005. Loop current, rings, and related circulation in the Gulf of Mexico: A review of numerical models and future challenges. Pp. 31–56 in *Circulation in the Gulf of Mexico: Observations and Models*. W. Sturges, and A. Lugo-Fernandez, eds, Geophysical Monograph Series 161, American Geophysical Union, Washington, DC, https://doi.org/10.1029/161GM04.

Ohlmann, J.C., P.P. Niiler, C.A. Fox, and R.R. Leben. 2001. Eddy energy and shelf interactions in the Gulf of Mexico. *Journal of Geophysical Research* 106:2,605–2,620, https://doi.org/10.1029/1999JC000162.

Özgökmen, T.M., E.P. Chassignet, C.N. Dawson, D. Dukhovskoy, G. Jacobs, J. Ledwell, O. Garcia-Pineda, I.R. MacDonald, S.L. Morey, M.J. Olascoaga, and others. 2016. Over what area did the oil and gas spread during the 2010 Deepwater Horizon oil spill? *Oceanography* 29(3):96–107, https://doi.org/10.5670/oceanog.2016.74.

Passow, U., and R.D. Hetland. 2016. What happened to all of the oil? *Oceanography* 29(3):88–95, https://doi.org/10.5670/oceanog.2016.73.

Passow, U., and K. Ziervogel. 2016. Marine snow sedimented oil released during the Deepwater Horizon spill. *Oceanography* 29(3):118–125, https://doi.org/10.5670/oceanog.2016.76.

Peterson, C.H., S.S. Anderson, G.N. Cherr, R.F. Ambrose, S. Anghera, S. Bay, M. Blum, R. Condon, T.A. Dean, W.M. Graham, and others. 2012. A tale of two spills: Novel science and policy implications of an emerging new oil spill model. *Bioscience* 62:461–469, https://doi.org/10.1525/bio.2012.62.5.7.

Peterson, R.N., W.S. Moore, S.L. Chappel, R.F. Viso, S.M. Libes, and L.E. Peterson. 2016. A new perspective on coastal hypoxia: The role of saline groundwater. *Marine Chemistry* 179:1–11, https://doi.org/10.1016/j.marchem.2015.12.005.

Reddy, C.M., J.S. Arey, J.S. Seewald, S.P. Sylva, K.L. Lemkau, R.K. Nelson, C.A. Carmichael, C.P. McIntyre, J. Fenwick, G.T. Ventura, and B.A. Van Mooy. 2012. Composition and fate of gas and oil released to the water column during the Deepwater Horizon oil spill. *Proceedings of the National Academy of Sciences of the United States of America* 109(50):20,229–20,234, https://doi.org/10.1073/pnas.1101242108.

Schrope, M. 2011. Oil spill: Deep wounds. *Nature* 472:152–154, https://doi.org/10.1038/472152a.

Shchepetkin, A.F., and J.C. McWilliams. 2005. The regional oceanic modeling system (ROMS): A split-explicit, free-surface, topography-following-coordinate oceanic model. *Ocean Modelling* 9:347–404, https://doi.org/10.1016/j.ocemod.2004.08.002.

Shroyer, E.L., D.L. Rudnick, J.T. Farrar, B. Lim, S.K. Venayagamoorthy, L.C. St. Laurent, A. Garanaik, and J.N. Moum. 2016. Modification of upper-ocean temperature structure by subsurface mixing in the presence of strong salinity stratification. *Oceanography* 29(2):62–71, https://doi.org/10.5670/oceanog.2016.39.

Sikora, W.B., and B. Kjerfve. 1985. Factors influencing the salinity regime of Lake Pontchartrain, Louisiana, a shallow coastal lagoon: Analysis of a long-term data set. *Estuaries* 8:170–180, https://doi.org/10.2307/1351866.

Smyth, W.D., and J.N. Moum. 2012. Ocean mixing by Kelvin-Helmholtz instability. *Oceanography* 25(2):140–149, https://doi.org/10.5670/oceanog.2012.49.

Sturges, W., and R. Leben. 2000. Frequency of ring separations from the Loop Current in the Gulf of Mexico: A revised estimate. *Journal of Physical Oceanography* 30:1,814–1,819, https://doi.org/10.1175/1520-0485(2000)030<1814:forsft>2.0.co;2.

Valentine, D.L., G.B. Fisher, S.C. Bagby, R.K. Nelson, C.M. Reddy, S.P. Sylva, and M.A. Woo. 2014. Fallout plume of submerged oil from Deepwater Horizon. *Proceedings of the National Academy of Sciences of the United States of America* 111(45):15,906–15,911, https://doi.org/10.1073/pnas.1414873111.

Warner, J.C., B. Armstrong, R.Y. He, and J.B. Zambon. 2010. Development of a Coupled Ocean-Atmosphere-Wave-Sediment Transport (COAWST) modeling system. *Ocean Modelling* 35(3):230–244, https://doi.org/10.1016/j.ocemod.2010.07.010.

Wiggert, J.D., R.R. Hood, and C.W. Brown. 2017. Modeling hypoxia and its ecological consequences in Chesapeake Bay. Pp. 119–147 in *Modeling Coastal Hypoxia: Numerical Simulations of Patterns, Controls and Effects of Dissolved Oxygen Dynamics*. D. Justic, R.D. Hetland, K.A. Rose, and K. Fennel, eds, Springer.

ACKNOWLEDGMENTS

We would like to thank Captain Nic Allen, Captain Tad Berkey, and the crews of R/V *Point Sur* and R/V *Pelican* for their assistance during the CONCORDE field sampling campaigns. Charles Cousin and Cedric Guigand (Bellamare, LLC) guided the initial setup and field trials of the plankton imaging system. Thanks also to numerous technicians and graduate students for their involvement with CONCORDE cruise logistics, field data collection, and sample processing. We would also like to thank two anonymous reviewers and Andy Kough for comments that improved an earlier version of the manuscript. This research was made possible by a grant from the Gulf of Mexico Research Initiative. All data are publicly available through the Gulf of Mexico Research Initiative Information & Data Cooperative (GRIIDC) at https://data.gulfresearchinitiative.org (https://doi.org/10.7266/N77D2SJ5, https://doi.org/10.7266/N7QF8R84, https://doi.org/10.7266/N7KP80JS, https://doi.org/10.7266/N79C6VGW, https://doi.org/10.7266/N7TX3CFP, https://doi.org/10.7266/N7697236, https://doi.org/10.7266/N7542M3W, https://doi.org/10.7266/N79Z930H, https://doi.org/10.7266/N7416V4D, https://doi.org/10.7266/N7Z036JW).

AUTHORS

Adam T. Greer (adam.greer@usm.edu) is Postdoctoral Research Associate, and **Alan M. Shiller** is Professor, Division of Marine Science, University of Southern Mississippi (USM), Stennis Space Center, MS, USA. **Eileen E. Hofmann** is Professor, Center for Coastal Physical Oceanography, Old Dominion University, Norfolk, VA, USA. **Jerry D. Wiggert** is Associate Professor, Division of Marine Science, USM, Stennis Space Center, MS, USA. **Sally J. Warner** is Research Associate, College of Earth, Ocean, and Atmospheric Sciences, Oregon State University, Corvallis, OR, USA. **Sabrina M. Parra** is American Society for Engineering Education Postdoctoral Fellow, US Naval Research Laboratory (NRL), Stennis Space Center, MS, USA. **Chudong Pan** is Postdoctoral Research Associate, Division of Marine Science, USM, Stennis Space Center, MS, USA. **Jeffrey W. Book** is Oceanographer, US NRL, Stennis Space Center, MS, USA. **DongJoo Joung** is Postdoctoral Research Associate, Division of Marine Science, USM, Stennis Space Center, MS, USA. **Steven Dykstra** is PhD Candidate, **Jeffrey W. Krause** is Assistant Professor, and **Brian Dzwonkowski** is Assistant Professor, University of South Alabama and Dauphin Island Sea Lab, Dauphin Island, AL, USA. **Inia M. Soto** is Postdoctoral Research Associate, and **M. Kemal Cambazoglu** is Research Associate, both in the Division of Marine Science, USM, Stennis Space Center, MS, USA. **Alison L. Deary** is Postdoctoral Research Associate, Division of Coastal Sciences, Gulf Coast Research Laboratory, USM, Ocean Springs, MS, USA. **Christian Briseño-Avena** is Postdoctoral Research Associate, Hatfield Marine Science Center, Oregon State University, Newport, OR, USA. **Adam D. Boyette** is PhD Candidate, Division of Marine Science, USM, Stennis Space Center, MS, USA. **Jessica A. Kastler** is Coordinator of Program Development, Gulf Coast Research Laboratory, USM, Ocean Springs, MS, USA. **Virginie Sanial** is Postdoctoral Research Associate, **Laura Hode** is a graduate student, and **Uchenna Nwankwo** is a graduate student, all in the Division of Marine Science, USM, Stennis Space Center, MS, USA. **Luciano M. Chiaverano** is Research Associate, Gulf Coast Research Laboratory, USM, Ocean Springs, MS, USA. **Stephan J. O'Brien** is PhD Candidate, Division of Marine Science, USM, Stennis Space Center, MS, USA. **Patrick J. Fitzpatrick** is Associate Research Professor, and **Yee H. Lau** is Research Associate, both at Mississippi State University Science and Technology Center, Stennis Space Center, MS, USA. **Michael S. Dinniman** is Research Scientist, Center for Coastal Physical Oceanography, Old Dominion University, Norfolk, VA, USA. **Kevin M. Martin** is Research Staff, **Peng Ho** is PhD Candidate, **Allison K. Mojzis** is Research Staff, **Stephan D. Howden** is Associate Professor, all in the Division of Marine Science, USM, Stennis Space Center, MS, USA. **Frank J. Hernandez** is Assistant Professor, Gulf Coast Research Laboratory, USM, Ocean Springs, MS, USA. **Ian Church** is Assistant Professor, Department of Geodesy and Geomatics Engineering, University of New Brunswick, Fredericton, NB, Canada. **Travis N. Miles** is Assistant Research Professor, Department of Marine and Coastal Sciences, Rutgers University, New Brunswick, NJ, USA. **Su Sponaugle** is Professor, Department of Integrative Biology, Hatfield Marine Science Center, Oregon State University, Newport, OR, USA. **James N. Moum** is Professor, College of Earth, Ocean, and Atmospheric Sciences, Oregon State University, Corvallis, OR, USA. **Robert A. Arnone** is Research Professor, Division of Marine Science, USM, Stennis Space Center, MS, USA. **Robert K. Cowen** is Director, Hatfield Marine Science Center, Oregon State University, Newport, OR, USA. **Gregg A. Jacobs** is Oceanographer, US NRL, Stennis Space Center, MS, USA. **Oscar Schofield** is Distinguished Professor, Department of Marine and Coastal Sciences, Rutgers University, New Brunswick, NJ, USA. **William M. Graham** is Professor, Division of Marine Science, USM, Stennis Space Center, MS, USA.

ARTICLE CITATION

Greer, A.T., A.M. Shiller, E.E. Hofmann, J.D. Wiggert, S.J. Warner, S.M. Parra, C. Pan, J.W. Book, D. Joung, S. Dykstra, J.W. Krause, B. Dzwonkowski, I.M. Soto, M.K. Cambazoglu, A.L. Deary, C. Briseño-Avena, A.D. Boyette, J.A. Kastler, V. Sanial, L. Hode, U. Nwankwo, L.M. Chiaverano, S.J. O'Brien, P.J. Fitzpatrick, Y.H. Lau, M.S. Dinniman, K.M. Martin, P. Ho, A.K. Mojzis, S.D. Howden, F.J. Hernandez, I. Church, T.N. Miles, S. Sponaugle, J.N. Moum, R.A. Arnone, R.K. Cowen, G.A. Jacobs, O. Schofield, and W.M. Graham. 2018. Functioning of coastal river-dominated ecosystems and implications for oil spill response: From observations to mechanisms and models. *Oceanography* 31(3):90–103, https://doi.org/10.5670/oceanog.2018.302.

SCIENTIFIC REPORTS

OPEN

Received: 4 October 2017
Accepted: 6 March 2018
Published online: 15 March 2018

Lagrangian coherent structure assisted path planning for transoceanic autonomous underwater vehicle missions

A. G. Ramos[1], V. J. García-Garrido[2,3], A. M. Mancho[2], S. Wiggins[4], J. Coca[1], S. Glenn[5], O. Schofield[5], J. Kohut[5], D. Aragon[5], J. Kerfoot[5], T. Haskins[5], T. Miles[5], C. Haldeman[5], N. Strandskov[5], B. Allsup[6], C. Jones[6] & J. Shapiro[6]

Transoceanic Gliders are Autonomous Underwater Vehicles (AUVs) for which there is a developing and expanding range of applications in open-seas research, technology and underwater clean transport. Mature glider autonomy, operating depth (0–1000 meters) and low energy consumption without a CO_2 footprint enable evolutionary access across ocean basins. Pursuant to the first successful transatlantic glider crossing in December 2009, the Challenger Mission has opened the door to long-term, long-distance routine transoceanic AUV missions. These vehicles, which glide through the water column between 0 and 1000 meters depth, are highly sensitive to the ocean current field. Consequently, it is essential to exploit the complex space-time structure of the ocean current field in order to plan a path that optimizes scientific payoff and navigation efficiency. This letter demonstrates the capability of dynamical system theory for achieving this goal by realizing the real-time navigation strategy for the transoceanic AUV named Silbo, which is a Slocum deep-glider (0–1000 m), that crossed the North Atlantic from April 2016 to March 2017. Path planning in real time based on this approach has facilitated an impressive speed up of the AUV to unprecedented velocities resulting in major battery savings on the mission, offering the potential for routine transoceanic long duration missions.

Silbo, a deep Slocum glider in the Challenger mission was deployed in Massachusetts on the 13th April 2016 and was recovered at the South of Ireland on March 9th 2017. He completed 6506.8 km, gliding across the North Atlantic by following a saw tooth trajectory (see Fig. 1) through the top 1000 meters of the water column in 330 days by consuming 1.5 A · h/*day* (or 22.5 W · h/*day* at 15 V) from its lithium batteries (see https://marine.rutgers.edu/cool/auvs/index.php?gid=46).

Silbo's flight demonstrated that autonomous underwater deep gliders will play a preeminent role in transoceanic ocean observation in coming years[1–3]. Expectations for transoceanic gliders are high due to their ability to map and monitor the marine environment without requiring direct human control. For this reason, they provide opportunities for data acquisition in areas of the ocean otherwise difficult, dangerous or impossible to access, including areas beneath tropical cyclones or ice sheets in polar regions[3,4]. Glider's generate propulsion by modulating their buoyancy at specified depths (shallow or deep glider) and transferring a component of the induced vertical acceleration forward by means of a lifting body and swept wings. They are designed to have long endurance (months, years) and to navigate autonomously, being controlled by periodically surfacing for GPS fixes, data telemetry and opportunity for shore side operators to update the vehicle's mission. One operational consequence of designing for endurance is that the effective but low horizontal speed (0.2–0.4 m/s) makes them extremely sensitive to the current fields that they experience. As underactuated vehicles, gliders are not necessarily capable

[1]División de Robótica y Oceanografía Computacional (IUSIANI), Universidad de Las Palmas de Gran Canaria, Las Palmas de Gran Canaria, Spain. [2]Instituto de Ciencias Matemáticas, CSIC-UAM-UC3M-UCM, C/Nicolás Cabrera 15, Campus de Cantoblanco UAM, 28049, Madrid, Spain. [3]U.D. Matemáticas, Universidad de Alcalá, 28871, Alcalá de Henares, Spain. [4]School of Mathematics, University of Bristol, Bristol, BS8 1TW, United Kingdom. [5]Rutgers University Center of Ocean Observing Leadership, School of Environmental and Biological Sciences, Rutgers University, New Brunswick, NJ, 08901, USA. [6]Teledyne Webb Research, North Falmouth, MA, 02566, USA. Correspondence and requests for materials should be addressed to A.M.M. (email: a.m.mancho@icmat.es)

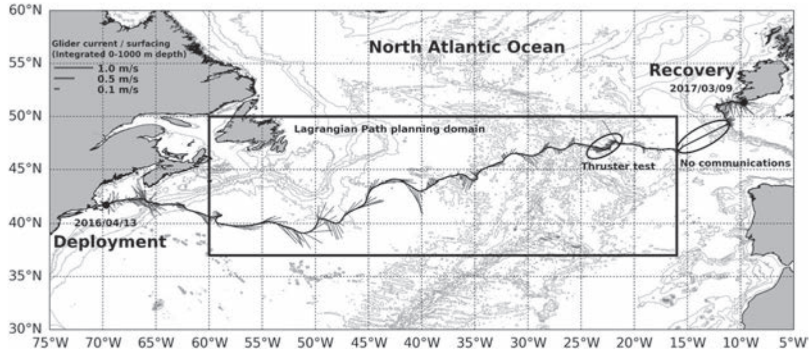

Figure 1. Silbo NE Atlantic crossing path. Silbo was deployed in Massachusetts on the 13th April 2016 and was recovered at the South of Ireland on the 9th March 2017 after completing a transect between 0–1000 meters depth of 6506.8 km in 330 days. The figure was created using python 3.5.2, matplotlib[36] module 1.5.1 (https://www.python.org/downloads/release/python-352/). Bathymetry data was obtained from Gebco[37] 2014 30 arc-second grid (http://www.gebco.net). Glider track and currents were derived from glider log navigation files. Coastlines were obtained from GSHHG - A Global Self-consistent, Hierarchical, High-resolution Geography Database (https://www.ngdc.noaa.gov/mgg/shorelines/gshhs.html).

of following an arbitrary trajectory to reach a required location. In this context, it would be a significant advantage to utilize the ocean current field in a way that could optimize the mission of the glider.

Typical conventional glider path planning methodologies for determining optimal paths have demonstrated their effectiveness in regional environments. Among these methodologies are linear programming, probabilistic sampling, potential fields or genetic algorithms and artificial intelligence methods such as A^* (see[5–11]). Some of these methods require the use of Regional Ocean Models (ROMs) forecast datasets with high space-time resolution (1/32^o, hourly). Nowadays in the open ocean only low space-time resolution models are available (1/12^o, daily) and therefore these techniques are not implementable in transoceanic glider crossing missions. In this regard if global models in the future would increase their resolution and accuracy it could be that regional methods provide efficient solutions also in these missions, but this is not the case for the current state of the art. Some attempts in this direction are references[12,13] that describe the path planning A* technique used at the end of the first Atlantic glider crossing, once it approached the Iberian coast. In particular the method was implemented with the ROM ESEOO Iberian domain data (1/32°, hourly, +72 h). Additional regional path planning requirements, as for instance the demand of environmental obstacles by the Theta algorithm, are not available at global scale, or the need of a rather stable environment just subjected to small perturbations, a must for incremental methods such as D* and Phi*, does not work in a highly dynamic and changing environment like that found in the open ocean. Long-term long-distance path planning missions require guiding techniques that are useful for highly dynamic open-sea areas, and thus they must be based on robust and fundamental ocean features.

Transoceanic Slocum glider missions are relatively recent and until now there has been only a few of them. The first successful North East transatlantic mission was achieved by the Scarlet Knight RU27 glider in 2009[1]. This mission was preceded in 2008 by the RU17 glider attempt, which was unfortunately lost just off the coast of the Azores. Other subsequent missions have been performed by Cook, Drake, Silbo and RU29 gliders[2]. Missions have been an adventurous path to learning about a completely unexplored terrain and to gain information about many different aspects of the missions, ranging from glider flight dynamics, battery consumption, resets, bathymetry risks, aborts, piloting error, physical and biological impediments (such as barnacles adhesion and fouling) and their effects on long term navigation, etc. In the Silbo mission described in this article, navigation has been in the 0–1000 m depth range, however the 2009 Scarlet Knight RU 27 flew between 0–200 meters depth range and this allowed taking a maximum advantage of the Gulf stream speed, aligned with the direction of the voyage. In other missions, with gliders Drake and Cook, deep flying has been shown to be an effective way to fight unfavorable currents since at large depths currents are weaker. Since the first missions, in order to gain insights into the ocean landscape, different approaches have been considered. The first missions were flown using Sea Surface Temperature (SST) fields as a primary reference for mesoscale flow features, and waypoints were programmed according to the displayed structures. SST was chosen for its global availability, its relatively fast update cycle from AVHRR satellite data, and its ability to resolve many surface flow features. Alternatives to this product have been currents derived from the Sea Level Anomaly, 3D current fields from models, etc. In this letter, we demonstrate the success and promise of a new approach to path planning for future AUV crossing missions that was implemented for Silbo. This is the dynamical systems approach to transport that involves using the space-time structure of the ocean current field in a way that optimizes the propulsion of the glider in a manner that promotes sustainable missions. More specifically, the methodology proposed in this mission for supporting the waypoint selection uses Lagrangian Coherent Structures (LCS). This is not disconnected from velocity fields, but based on them since LCS provide a time dependent Lagrangian pattern (i.e. based on fluid particle trajectories) which at each day encompasses information from the velocity field in past and future days, and therefore is suitable for advising about Lagrangian paths, such as those followed by gliders. Eulerian velocity fields or instantaneous temperature fields used in previous missions are more rudimentary in this regard.

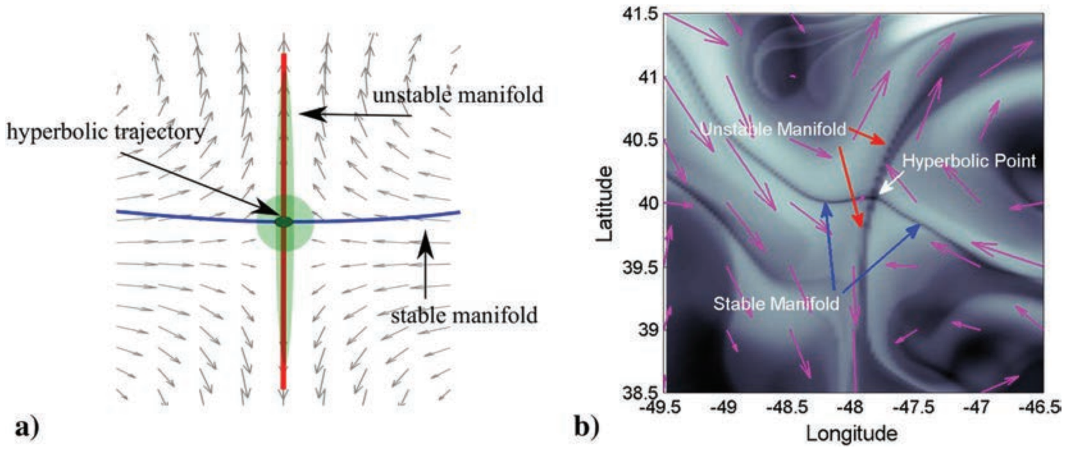

Figure 2. (**a**) A hyperbolic trajectory in a vector field. Particles at successive times evolve by approaching the hyperbolic point along the stable direction (blue) and getting away from it along the unstable direction (red). Green blobs illustrate this behavior. (**b**) Visualization of a hyperbolic point by means of the function M evaluated on Copernicus data on the 17th June 2016. The current field is drawn with magenta arrows.

The idea of exploiting natural dynamics for vehicle transport has been previously used in space mission design. The work is similar in spirit to our work in the ocean in the sense that the gravitational field of the planetary system is used to determine a desired mission trajectory for a spacecraft with low thrust capabilities[14,15]. These ideas have also been previously proposed in oceanic setting, for planning glider routes through ocean currents[16], but they have not been applied to transoceanic missions in the way that we have done for the Silbo mission.

Results

Silbo's control mechanisms allow the glider to control its heading so as to pass through manually defined waypoints (WPs) with or without compensating for local depth average current. Our goal is to extract information from the oceanic currents, in particular, about the natural dynamics of particle trajectories advected by ocean currents, since we expect that this knowledge will inform the choice of WPs. In the ocean, particles follow trajectories $\mathbf{x}(t)$ that evolve according to the dynamical system:

$$\frac{d\mathbf{x}}{dt} = \mathbf{v}(\mathbf{x}(t),\, t), \tag{1}$$

where $\mathbf{v}(\mathbf{x}, t)$ is the velocity field of the ocean in the region of interest. In our analysis we will assume that the motion of particles is mainly horizontal. Many LCS studies have been performed in a two-dimensiolnal scenario in which is assumed that fluid parcels remain on surfaces of constant density (isopycnals), which are quasi-horizontal[17–22]. We will discuss deviations from horizontal motion afterwards.

A challenge here is that even flows with smooth velocity fields may exhibit complex particle trajectories. An approach for exploiting this complexity derives from the methodology of nonlinear dynamical systems theory. Rather than seeking to understand the behavior of large ensembles of particle trajectories, this approach is based on finding geometrical structures, known as Lagrangian Coherent Structures (LCSs) that divide the ocean into regions corresponding to qualitatively distinct particle motions[23–25]. The boundaries or barriers between these regions are time dependent material surfaces (which, mathematically, are invariant manifolds). This spatio-temporal template can be constructed with a recent technique referred to as Lagrangian Descriptors (LDs). The particular LD that we use is a function referred to as M[26–28] which is defined as follows:

$$M(\mathbf{x}_0,\, t_0,\, \tau) = \int_{t_0-\tau}^{t_0+\tau} \|\mathrm{v}(\mathbf{x}(t;\, \mathbf{x}_0),\, t)\|\, dt, \tag{2}$$

where $\|\cdot\|$ stands for the modulus of the velocity vector. At a given time t_0, function $M(\mathbf{x}_0, t_0, \tau)$ measures the arclength of trajectories starting at $\mathbf{x}(t_0) = \mathbf{x}_0$ as they evolve forwards and backwards in time for a time interval τ. Large M values, represented in white color (see Fig. 2), are related to regions of high speed fluid (such as straight or circular jets), while dark colors denote calm regions. One expects that large M values will favor glider propulsion, as far as the commanded-glider trajectory is aligned with the current, and that calm ocean regions will be related to slower glider motions.

The pattern displayed by the function M depends on τ. For small τ, the function M has a smooth output, while as the parameter τ is increased, sharp features and structures emerge highlighting LCS. Typically patterns provided by very large τ values reveal a more detailed description of the dynamical history of the system. In our setting we use data from the Global Ocean Model provided by Copernicus that has forecasts for 10 days, and thus this value fixes the operational upper threshold for the forward time integration period. In practice the integration period necessary to display the required LCS depends on the characteristics of each velocity field. We have verified that $\tau = 8$ days is a sufficient choice for our data, and from the physical point of view this is consistent

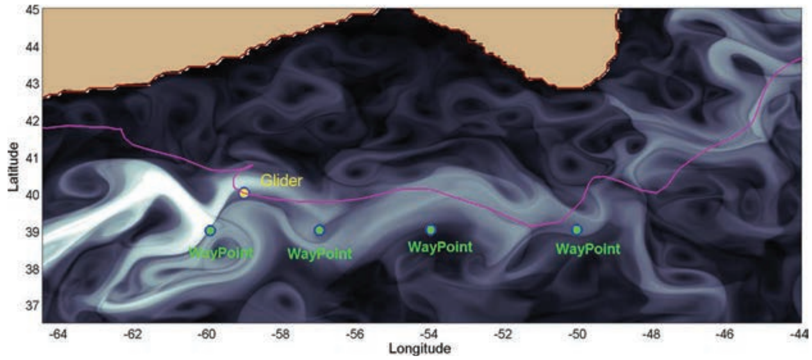

Figure 3. Lagrangian structures on the 30th May 2016 at 12:00 UTC in the NW Atlantic highlighted by the M function for $\tau = 8$ days from CMEMS velocities averaged across depths 0–902 m. The glider Lagrangian path planning panel shows WPs used to cross the Gulf Stream (27th May–27th July 2016) (see video S1). This figure was created with MATLAB version R2010b (https://es.mathworks.com). The map shown is generated with a mask of values included in the CMEMS velocity field dataset. This mask indicates regions which correspond to continental shelf and sea.

with the time required by the glider to navigate distances equivalent to the size of mesoscale ocean structures. In this way when the function M is computed for this sufficiently large τ it provides a detailed landscape from which it is possible to relate glider accelerations directly to the topography of this landscape. Of particular interest are features highlighting hyperbolic trajectories that are responsible for deflecting the grider's trajectory. Regions in the fluid characterized by high expansion and contraction rates generate the stable and unstable structures in the flow field that characterize hyperbolic trajectories. Figure 2a illustrates how blobs in the neighborhood of these trajectories evolve, contracting along the stable direction and expanding along the unstable direction. Curves associated with the stable and unstable directions of these hyperbolic trajectories are referred to as stable and unstable manifolds and they indicate optimal paths for approaching and leaving the vicinity of these trajectories. Hyperbolic trajectories are recognizable in the pattern of M as the crossing points of singular features that highlight stable and unstable manifolds. For instance, an evaluation of M on a typical data set used in this study for $\tau = 8$ days on the 17 June 2016 is displayed in Fig. 2b. Blue arrows mark the position of a stable manifold along which particles approach the hyperbolic trajectory at high speed and red arrows mark the position of an unstable manifold along which particles move away from the hyperbolic trajectory at high speed. Fluid particles slow their motion in the neighborhood of the hyperbolic trajectory. Magenta arrows representing the velocity field overlapped with the M pattern supports this interpretation of the stable and unstable directions. Next we describe how these effects, which are observed in the natural dynamics of particle trajectories advected by ocean currents, are also observed along the glider path. Given that hyperbolic points are objects for which there exist optimal pathways, they are a natural choice to be used as WPs for glider guidance. We describe next how this choice has proven to be effective.

The success of the described approach depends on how well the available velocity data represents the ocean state in the area in the domain of operation. The assessment of the ocean data with Lagrangian tools has been addressed in recent studies[20–22]. In particular[22], shows the success of the Copernicus Marine Environment Monitoring Service (CMEMS) data (available at http://marine.copernicus.eu/) for monitoring oil spill events in real time, thus supporting this product as reliably representing ocean transport and confirming its high quality. Our study supports those findings, since the Copernicus Global Ocean and Iberia-Biscay-Ireland sea models have provided data which successfully supported the guidance of Silbo.

During the Trans-Atlantic mission, Silbo navigated at depths ranging from the surface to 900 meters following a saw tooth trajectory. This means that during navigation Silbo experienced currents at different depths from the upper Atlantic layers. Fully 3D studies performed in quasi 2D flows such as the ocean or the stratosphere have shown that 3D Lagrangian structures are close to those obtained by a'vertical extension' of the evolving structures calculated in the 2D plane approximation[19,29,30]. Across most of this water column, Lagrangian patterns have a vertical curtain-like structure with only slight differences in each horizontal plane. Our approach to this problem then has been to study the 2D problem in Equation (1), by means of a representative 2D velocity field of the upper layers. To this end we have considered vertical averages of the instantaneous horizontal velocities components supplied by the model in the range 0–902 meters. We have compared these results with those obtained just by considering velocities at the 453 meters sigma layer, which is the mid layer of the total vertical range swept by the glider, and also averaged velocities over the water column 0–453 meters. We have found that Lagrangian structures are very similar in all cases, and we proceed to report results mainly with the first choice, i.e. averages across the range 0–902 meters. This choice is also supported by our observational experience as agrees well with the glider derived current field. Additional results with the other choices are also reported for comparative purposes.

Figure 3 shows the operational panel used for glider path planning. The integration period for these patterns is $\tau = 8$ days. Waypoints are introduced according to the hyperbolic trajectories observed in Lagrangian patterns highlighted in the background, by looking for favorable navigation routes between hyperbolic trajectories towards the final destination of the glider. Stable and unstable manifolds associated to the hyperbolic trajectories

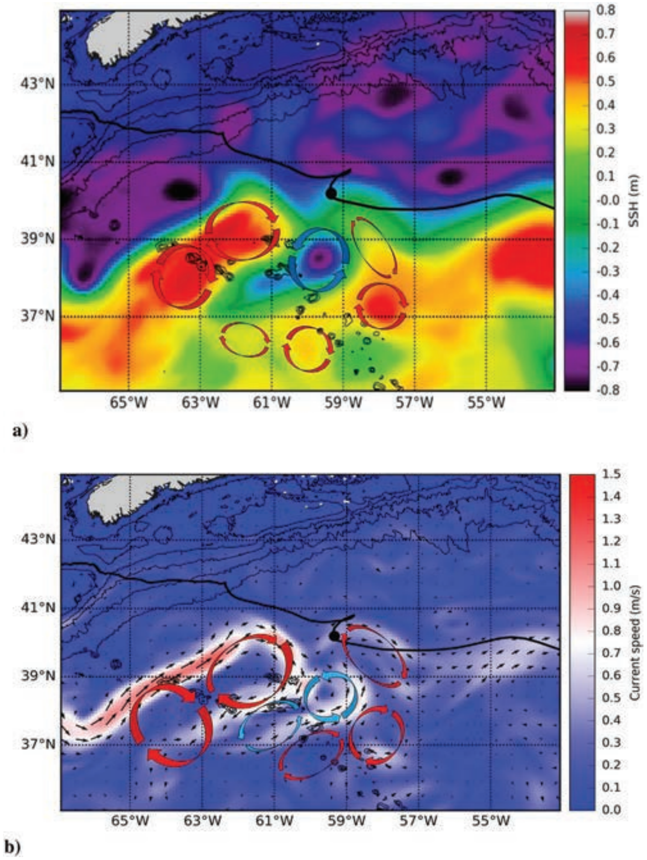

Figure 4. Glider path and Eulerian Gulf Stream description with the CMEMS dataset illustrating warm and cold vortex cores on the 30th May 2016. (**a**) Sea surface height (SSH) above geoid. (**b**) Velocity fields and averaged current speed (0–902 m). The figure was created using python 3.5.2, matplotlib[36] module 1.5.1 (https://www.python.org/downloads/release/python-352/). Bathymetry data was obtained from Gebco[37] 2014 30 arc-second grid (http://www.gebco.net). Glider track was extracted from glider log navigation files. Coastlines were obtained from GSHHG - A Global Self-consistent, Hierarchical, High-resolution Geography Database (https://www.ngdc.noaa.gov/mgg/shorelines/gshhs.html). SSH and current fields were obtained from Operational Mercator global ocean analysis and forecast (GLOBAL_ANALYSIS_FORECAST_PHY_001_024 product in Copernicus marine segment, http://marine.copernicus.eu).

are recognised as singular lines in the background. Hyperbolic trajectories are suitable to select as waypoints supporting glider bearing since these objects have invariant manifolds which provide an optimal path for reaching the WPs. Eulerian fields shown in Fig. 4 do not display such objects and therefore it is more difficult to find a criterion for fixing waypoints using solely Eulerian information.

The major findings of this work are summarized in the movie S1, which runs from the 15th April 2016 until the 1st November 2016. This animation overlaps the Lagrangian pattern provided by function *M* (obtained from velocities averaged in the 0–902 m range), with Silbo's speed at different points along the glider path. Additionally, the movie displays instantaneous averaged velocity fields and the waypoint positions at different times.

The analysis of the movie S1 confirms that the exploitation of natural dynamics efficiently optimizes glider transport. Alternatively, if the glider is forced to fly against this natural dynamic, speeds of the glider are notoriously small. We describe two events in the movie supporting the first assertion, and two events supporting the second one. Table 1 summarizes these findings. Between the 14th-17th of June and the 18th-23rd June 2016 two successive events (Events 1 and 2 in Table 1) take place which demonstrate the enhancement of glider speed due to the presence, in an appropriate configuration, of geometrical dynamical objects described as hyperbolic trajectories and their stable and unstable invariant manifolds. In these two events the glider shows high performance (high velocities) while it approaches to a hyperbolic trajectory (HT) through its stable manifold (SM) and when it leaves its neighborhood through the unstable direction (UM). In the vicinity of the HT the glider reduces its speed. Figure 5 supports this description by specifically selecting areas of the movie S1 at days 19th, 20th and 23rd June 2016 which encompass the glider and the hyperbolic point. In particular, Fig. 5a shows the glider position and its speed while approaching a hyperbolic point along its stable manifold on the 19th June 2016. Figure 5b confirms the speed reduction at the closest position to the hyperbolic point on the 20th June 2016. Figure 5c shows the glider moving away from the hyperbolic point through the unstable manifold on the 23rd June 2016. Remarkably, this day the glider speed achieves a record velocity (1.04 m/s), which is unprecedented for this type of missions, since typical operational velocities for this type of gliders are below 0.5 m/s. These findings confirm

Event	Time interva	Day/Glider speed (m/s)/Configuration	Day/Glider speed (m/s)/ Configuration	Day/Glider speed (m/s)/Configuration	Day/Glider speed (m/s)/Configuration
1	14–17 June 2016	14 June/0.95/(SM)	15 June/0.48/(SM)	16 June/0.23/(HT)	17 June/0.34/(UM)
2	19–23 June 2016	19 June/0.56/(SM)	20 June/0.41/(HT)	22 June/0.70/(UM)	23 June/1.04/(UM)
3	7–16 Sept 2016	7 Sept/0.16/(HT)	10 Sept/0.08/(SM)	11 Sept/0.06/(SM)	16 Sept/0.06/(SM)
4	17–29 Sept 2016	18 Sept/0.05/(UM)	22 Sept/0.03/(UM)	26 Sept/0.06/(UM)	29 Sept/0.11/(HT)

Table 1. Detailed description of five events with special configurations that propel or slow down glider motion. Each event is described by the day, the glider speed and its position with respect to the dynamical objects: hyperbolic trajectories (HT) and their stable (SM) and unstable (UM) manifolds. Sequences SM-HT-UM provide high speed along manifolds and reductions in the vicinity of HT. Configurations such as HT-SM or UM-HT force the glider to move against the natural dynamics resulting in a slowing down of the motion along manifolds.

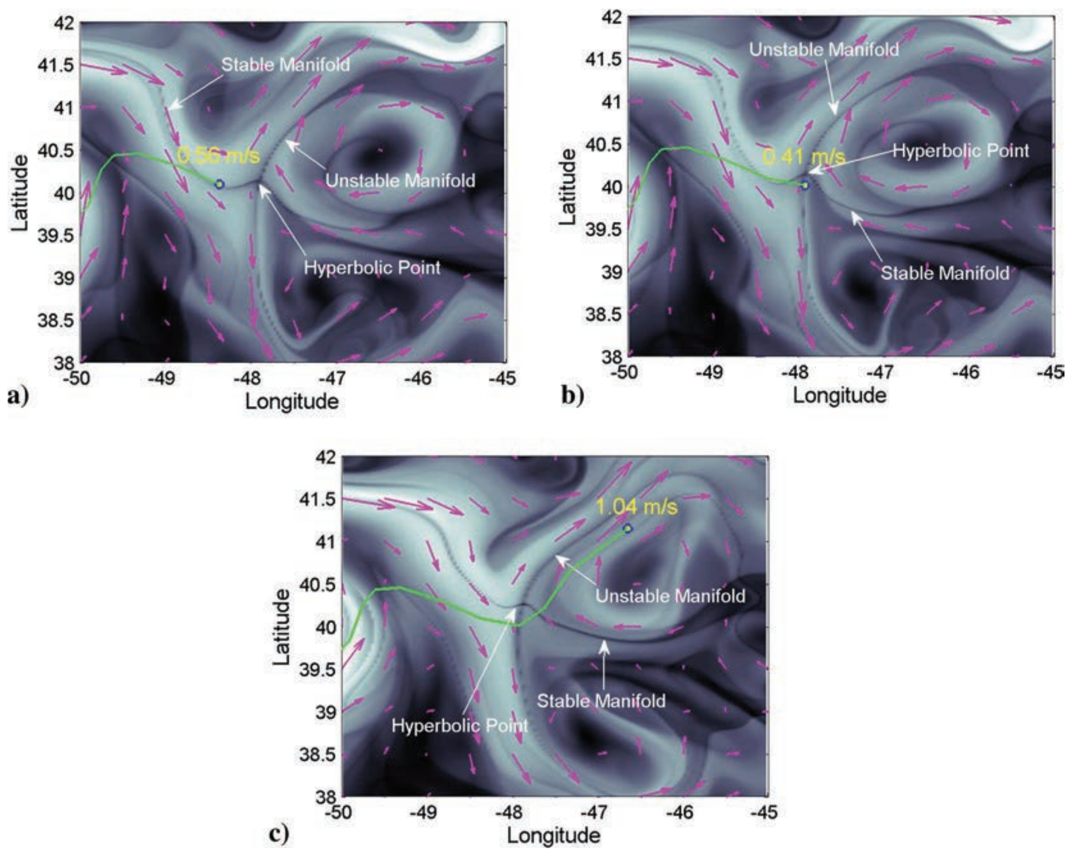

Figure 5. Glider path and Eulerian velocity fields in the neighborhood of a hyperbolic trajectory highlighted by the function M. (**a**) 19th June 2016. (**b**) 20th June 2016. (**c**) 23rd June 2016.

that stable manifolds (SM) are optimal paths towards the HT, i.e. the glider approaches to the HT very efficiently along this direction. On the other hand, unstable manifolds (UM) are the optimal path for moving away from the HT. In the neighborhood of the HT the glider slows down. Consequently, an optimal path to navigate is to follow the dynamical sequence SM-HT-UM. To avoid excessive slow down near the HT, it is appropriate that before approaching it to closely, the WP placed there is moved to a new HT. This HT must be selected in such as a way that its SM is aligned with the UM of the previous HT, so that the new WPs force the glider to leave the neighborhood of the previous HT along the direction of the UM. An appropriate navigation sequence thus would concatenate: SM-HT-UM/SM-HT-UM. This results in a wave-shape path with the glider moving alternatively from stable to unstable manifolds, as visible from Fig. 3. The video also shows that Silbo described this waving-path when it speeded up to 1 m/s and flied out the NE American waters heading to the open North Atlantic waters.

In order to make a correct interpretation of the stable and unstable directions of an HT the instantaneous depth-averaged current field must be superimposed onto the M field so that the direction of the manifolds is revealed. It is not possible to distinguish these directions just from the function M template. If a glider were to approach a HT along an unstable manifold, it would slow down since it would be navigating in a counter-current flow. Two events of this kind are described next.

Events 3 and 4 in Table 1 correspond to a period in which the glider was flown against the current to test its propulsion mechanism. In these events the glider navigates towards the HT along its unstable manifold or leaves the HT along its stable manifold. Therefore the glider follows inverse paths to those described above as it moves along manifolds that do not support its displacement. In this case the glider shows extremely low speeds when it is at positions along the manifolds, and speeds slightly increases in the neighborhood of the HT.

We also remark that during the mission, typically, Silbo navigated with the current correction mode off. Thus it was sensitive to strong currents as it was not forced to approach the WPs following a straight line. There exist days, visible from the movie, in which currents deviate the glider from a rectilinear path, at stages in which the glider is still far from the WP, however these deviations are not an obstacle to approaching the WPs.

Movie S2 and S3 represent, respectively, Lagrangian structures for velocities averaged in the range 0–453 m and at the 453 m depth layer. These movies support similar conclusions to the ones obtained from S1, thus confirming assumptions about the robustness of the Lagrangian structures and their ability to provide a fundamental ocean landscape for navigation in spite of uncertainties.

Conclusions

Long-time, long-distance transoceanic glider path planning is now possible using dynamical systems methodologies and techniques that have been used before in astronautics (e.g. the Mariner 10, Voyager 1, and Rosetta missions[31–33]) to support the flight of low cost space missions based on gravity assisted trajectories. However, the implementation of path planning based on dynamical systems ideas in the oceanic context, presents new challenges. The described dynamical analysis relies on the quality of the velocity fields (geometrical objects such as hyperbolic trajectories and their invariant manifolds depend upon knowledge of the flow field). Ocean motions are turbulent in nature, thus obtaining trusted ocean current forecast and analysis remains a challenge. The success of the application of the dynamical systems methodology to the Silbo transoceanic mission confirms the high reliability of Copernicus Global Data to accurately represent the ocean state across the North Atlantic, since the identified hyperbolic trajectories and their stable and unstable manifolds are indeed present in the ocean and visible to the glider, providing effective navigation routes on which the glider has reached exceptionally high speeds which have no precedent in this context. We expect that the described methodology and tools will contribute to the discovery of new underwater clean-transport pathways for crossing oceans. Effective path planning in transoceanic glider missions will open new possibilities for improving the quality and increasing the density of measurements in under-sampled open-ocean deep regions (0–1 km depth), which could be assimilated and incorporated into global operational marine forecasting systems. This, in turn, will positively impact the diagnostic of deep sea observed changes due to global climate change.

Methods

Glider Data. Silbo. North Atlantic crossing 2016–17. Challenger Glider Mission.

Ocean Data. The ocean velocity fields used in this work were obtained from the Copernicus Marine Environment Monitoring Service (CMEMS) available at http://marine.copernicus.eu/. In particular, we have used the datasets provided by the high resolution Global Ocean Model[34] for most of the mission (the global analysis and forecast product GLOBAL_ANALYSIS_FORECAST_PHY_001_024). The system contains daily 3D global ocean current field data. The horizontal resolution of the model is 1/12° (approximately 8 km) with regular longitude/latitude equirrectangular projection and 50 vertical geopotential levels ranging from 0 to 5500 meters. In particular, to perform the Lagrangian path planning simulations, the daily operational velocity fields have been derived from the dataset by averaging the currents over the water column that extends from 0 to 902 meters depth (glider diving depth).

Mathematical Model. We consider the trajectories of passive fluid particles in a two-dimensional surface (quasi-horizontal approximation) described by Equation (1). In particular, we consider the equations of motion written in spherical coordinates on a sphere of radius $R = 6371\, km$, which are given by:

$$\frac{d\lambda}{dt} = \frac{u(\lambda, \phi, t)}{R \cos\phi}, \quad \frac{d\phi}{dt} = \frac{v(\lambda, \phi, t)}{R}, \tag{3}$$

where λ is longitude and ϕ latitude, u and v represent respectively the eastward and northward components of the velocity field provided by the dataset. The computation of fluid particle trajectories is necessary in order to evaluate the function M in Equation (2). Trajectories are calculated by integrating Equation (3), and since ocean currents are provided on a discrete space-time grid, we need to deal with the issue of interpolation. We have used for that purpose bicubic interpolation in space and third order Lagrange polynomials in time according to the details given in[20,35].

References

1. Glenn, S. *et al*. The trans-Atlantic Slocum glider expeditions: A catalyst for undergraduate participation in ocean science and technology. *Marine Technology Society* **45**, 75–90 (2011).
2. Sacatelli, R. *et al*. Ocean predictive skill assessments in the South Atlantic: Crowd-sourcing of student-based discovery. In *2014 Oceans - St. John's*, 1–7, https://doi.org/10.1109/OCEANS.2014.7003134 (2014).
3. Glenn, S. *et al*. Stratified coastal ocean interactions with tropical cyclones. *Nature Communications* **7**, https://doi.org/10.1038/ncomms10887 (2016).
4. Bellingham, J. G. *et al*. An Arctic basin observational capability using AUVs. *Oceanography* **13**, 64–70 (2000).
5. Hart, P. E., Nilsson, N. J. & Raphael, B. A formal basis for the heuristic determination of minimum cost paths. *IEEE Transactions on Systems Science and Cybernetics* **4**, 100–107, https://doi.org/10.1109/TSSC.1968.300136 (1968).

6. Carroll, K. P. *et al*. AUV path planning: an A* approach to path planning with consideration of variable vehicle speeds and multiple, overlapping, time-dependent exclusion zones. In *Proceedings of the 1992 Symposium on Autonomous Underwater Vehicle Technology*, 79–84 https://doi.org/10.1109/AUV.1992.225191 (1992).
7. Koenig, S. & Likhachev, M. D* lite. In *Eighteenth National Conference on Artificial Intelligence*, 476–483 (2002).
8. Nash, A., Daniel, K., Koenig, S. & Felner, A. Theta*: Any-angle path planning on grids. *Journal of Artificial Intelligence Research* **39**, 533–579 (2010).
9. Zhang, W., Inanc, T., Ober-Blobaum, S. & Marsden, J. E. Optimal trajectory generation for a glider in time-varying 2D ocean flows B-spline model. *IEEE International Conference on Robotics and Automation* 1083–1088 (2008).
10. Yilmaz, N. K., Evangelinos, C., Lermusiaux, P. F. J. & Patrikalakis, N. M. Path planning of autonomous underwater vehicles for adaptive sampling using mixed integer linear programming. *IEEE Journal of Oceanic Engineering* **33**, 522–537 (2008).
11. Walsh, K. & Banerjee, B. Fast A* with iterative resolution for navigation. *International Journal on Artificial Intelligence Tools* **19**, 101–119 (2010).
12. Fernández-Perdomo, E. *et al*. Path planning for gliders using Regional Ocean Models: Application of Pinzón path planner with the ESEOAT model and the RU27 trans-Atlantic flight data. In *OCEANS 2010 IEEE - Sydney*, 1–10 https://doi.org/10.1109/OCEANSSYD.2010.5603684 (2010).
13. Fernández-Perdomo, E. Adaptive bearing sampling for a constant-time surfacing A* path planning algorithm for gliders. In *2011 IEEE International Conference on Robotics and Automation*, 2350–2355, https://doi.org/10.1109/ICRA.2011.5980137 (2011).
14. Koon, W. S., Lo, M. W., Marsden, J. E. & Ross, S. D. Low energy transfer to the moon. *Celestial Mechanics and Dynamical Astronomy* **81**, 63–73 (2001).
15. Marsden, J. E. & Ross, S. D. New methods in celestial mechanics and mission design. *Bulletin of the American Mathematical Society* **43**, 43–73 (2006).
16. Inanc, T., Shadden, S. C. & Marsden, J. E. Optimal trajectory generation in ocean flows. In *Proceedings of the 2005, American Control Conference*. 674–679, https://doi.org/10.1109/ACC.2005.1470035 (2005).
17. d'Ovidio, F., Fernández, V., Hernández-García, E. & López, C. Mixing structures in the Mediterranean Sea from finite-size Lyapunov exponents. *Geophys. Res. Lett.* **31**, L12203 (2004).
18. d'Ovidio, F., Isern-Fontanet, J., López, C., Hernández-García, E. & García-Ladona, E. Comparison between Eulerian diagnostics and finite-size Lyapunov exponents computed from altimetry in the Algerian basin. *Deep Sea Res. I* **56**, 15–31 (2009).
19. Branicki, M., Mancho, A. M. & Wiggins, S. A Lagrangian description of transport associated with a front–eddy interaction: Application to data from the North-Western Mediterranean Sea. *Physica D* **240**, 282–304 (2011).
20. Mendoza, C., Mancho, A. M. & Wiggins, S. Lagrangian descriptors and the assessment of the predictive capacity of oceanic data sets. *Nonlinear Processes in Geophysics* **21**, 677–689 (2014).
21. García-Garrido, V. J., Mancho, A. M., Wiggins, S. & Mendoza, C. A dynamical systems approach to the surface search for debris associated with the disappearance of flight MH370. *Nonlinear Processes in Geophysics* **22**, 701–712 (2015).
22. García-Garrido, V. J., Ramos, A., Mancho, A. M., Coca, J. & Wiggins, S. A dynamical systems perspective for a real-time response to a marine oil spill. *Marine Pollution Bulletin* **112**, 201–210 (2016).
23. Wiggins, S. The dynamical systems approach to Lagrangian transport in oceanic flows. *Annual Review of Fluid Mechanics* **37**, 295–328 (2005).
24. Samelson, R. & Wiggins, S. *Lagrangian Transport in Geophysical Jets and Waves*. (Springer-Verlag, New York, 2006).
25. Mancho, A. M., Small, D. & Wiggins, S. A tutorial on dynamical systems concepts applied to Lagrangian transport in oceanic flows defined as finite time data set: Theoretical and computational issues. *Physics Reports* **437**, 55–124 (2006).
26. Madrid, J. A. J. & Mancho, A. M. Distinguished trajectories in time dependent vector fields. *Chaos* **19**, https://doi.org/10.1063/1.3056050 (2009).
27. Mendoza, C. & Mancho, A. M. The hidden geometry of ocean flows. *Physical Review Letters* **105** (2010).
28. Mancho, A. M., Wiggins, S., Curbelo, J. & Mendoza, C. Lagrangian descriptors: A method for revealing phase space structures of general time dependent dynamical systems. *Communications in Nonlinear Science and Numerical Simulation* **18**, 3530–3557 (2013).
29. Bettencort, J. H., López, C. & Hernández-García, E. Oceanic three-dimensional Lagrangian coherent structures: A study of a mesoscale eddy in the Benguela upwelling region. *Ocean Modelling* **51** (2012).
30. Curbelo, J. *et al*. Insights into the three-dimensional Lagrangian geometry of the Antarctic polar vortex. *Nonlinear Processes in Geophysics* **24**, 379–392 (2017).
31. Mariner 10 mission. https://www.jpl.nasa.gov/missions/mariner-10/. Accessed: 2017-09-30.
32. Voyager 1 mission. https://saturn.jpl.nasa.gov/https://saturn.jpl.nasa.gov/. Accessed: 2017-09-30.
33. Rosetta mission. http://www.esa.int/Education/Teach_with_Rosetta/Rosetta_timeline/. Accessed: 2017-09-30.
34. von Schuckmann, K. *et al*. The Copernicus Marine Environment Monitoring Service Ocean State Report. *Journal of Marine Operational Oceanography* **9**, 235–320 (2017).
35. Mancho, A. M., Small, D. & Wiggins, S. Computation of hyperbolic trajectories and their stable and unstable manifolds for oceanographic flows represented as data sets. *Nonlinear Processes in Geophysics* **11**, 17–33 (2004).
36. Hunter, J. D. Matplotlib: A 2D graphics environment. *Computing In Science & Engineering* **9**, 90–95, https://doi.org/10.1109/MCSE.2007.55 (2007).
37. IOC, IHO & BODC. In *Centenary Edition of the GEBCO Digital Atlas, Published on CD-ROM on Behalf of the Intergovernmental Oceanographic Commission and the International Hydrographic Organization as Part of the General Bathymetric Chart of the Oceans*. (British Oceanographic Data Centre, Liverpool, UK, 2003).

Acknowledgements

V. J. García-Garrido and A. M. Mancho are supported by MINECO grant MTM2014-56392-R and ONR grant N00014-17-1-3003. The research of S. Wiggins is supported by ONR grant No. N00014- 01-1-0769. Thanks are owed to CESGA and ICMAT for computing facilities and to Teledyne Webb Research and the Challenger Glider Mission for the access to the glider dataset during the whole mission. We acknowledge to the Physical Oceanography Department (Puertos del Estado, Spain) for providing assistance with the ROM IBI/Copernicus data during the last part of the mission.

Author Contributions

A.G.R. conceived the idea for the paper and proposed waypoints during the mission; V.J.G.-G. did the Lagrangian coherent structure simulations and prepared Figures 2b, 3 and 5 and the Movies S1, S2 and S3; A.M.M. prepared Figure 2a and Table 1; A.G.R., V.J.G.-G., A.M.M. and S.W. wrote the paper; J.C. prepared Figures 1 and 4; A.G.R., S.G., O.S., J.K., D.A., J.K., T.H., T.M., C.H., N.S., B.A., C.J., J.S. contributed to the glider mission.

Additional Information

Supplementary information accompanies this paper at https://doi.org/10.1038/s41598-018-23028-8.

Competing Interests: The authors declare no competing interests.

Origin and Attenuation of Mesoscale Structure in Circumpolar Deep Water Intrusions to an Antarctic Shelf

DARREN C. MCKEE AND DOUGLAS G. MARTINSON

Division of Ocean and Climate Physics, Lamont–Doherty Earth Observatory of Columbia University, Palisades, and Department of Earth and Environmental Sciences, Columbia University, New York, New York

OSCAR SCHOFIELD

Center for Ocean Observing Leadership, Department of Marine and Coastal Sciences, School of Environmental and Biological Sciences, Rutgers, The State University of New Jersey, New Brunswick, New Jersey

(Manuscript received 25 June 2018, in final form 17 February 2019)

ABSTRACT

Cross-isobath transport of Upper Circumpolar Deep Water (UCDW) provides a major source of heat to the Antarctic continental shelves. Adaptive sampling with a Slocum glider revealed that the UCDW regularly intrudes onto the western Antarctic Peninsula shelf within mesoscale eddies, and a linear stability analysis of the shelf-break current upstream confirmed eddy length scales and vertical structure are consistent with the baroclinic instability of the current. The properties of the most unstable mode are insensitive to current orientation but sensitive to bottom slope in accordance with modified Eady theory. Once on the shelf, the eddies' core properties mix with ambient shelf water to form modified CDW (mCDW). Concurrent shipboard CTD and ADCP data are used to diagnose the responsible mixing processes and highlight the importance of thermohaline intrusions. The genesis mechanism of the interleaving layers cannot be confirmed, however a simple analytic model suggests the upper limit contribution of advection by internal waves cannot account for the observed temperature variance unless the cross-eddy temperature gradient is large. Data-adaptive sampling of an eddy with the glider revealed it lost heat across two isopycnals and a fixed radius at a rate of 7×10^9 J s^{-1} over 3.9 days. This rate is corroborated by a diffusion model initialized with the eddy's initial hydrographic properties and informed by the heat fluxes parameterized from the shipboard data. The results suggest eddies predominately lose heat laterally and downward, which preserves subsurface heat for melting of marine-terminating glaciers.

1. Introduction

The West Antarctic Peninsula (WAP) is bordered by the Antarctic Circumpolar Current (ACC), which flows along the continental slope. Below the surface layer, the ACC advects a warm mass of Circumpolar Deep Water (CDW) with significant heat content relative to the in situ freezing point. The CDW spans a range of properties, though Gordon (1971) distinguishes between an upper (UCDW) and lower (LCDW) variety defined by temperature and salinity maxima, respectively. The southern boundary of the ACC is defined as the southernmost presence of UCDW (Orsi et al. 1995) and, unique compared to the rest of Antarctica, near the WAP the ACC flows immediately adjacent to the shelf break, making UCDW readily available to the shelf (Fig. 1).

The WAP is undergoing rapid climate change and the ocean is a primary heat source, particularly in winter when there is no direct radiative forcing. The marginal seas of West Antarctica are warming (Schmidtko et al. 2014) and the increase in heat content along the WAP margin has been attributed to a warming of the UCDW T_{max} (Martinson et al. 2008). Cook et al. (2016) confirm an oceanic role in glacier retreat along the WAP by demonstrating an asymmetry in glacial advance/retreat: southern marine-terminating glaciers that have access to warm subpycnocline waters are retreating whereas northern glaciers under the influence of much colder Bransfield Strait waters are not. More and/or warmer CDW has also left its imprint on the atmosphere. The northern portion of the WAP is undergoing rapid winter warming (Turner et al. 2013), presumably related to

Corresponding author: Darren C. McKee, dmckee@ldeo.columbia.edu

DOI: 10.1175/JPO-D-18-0133.1

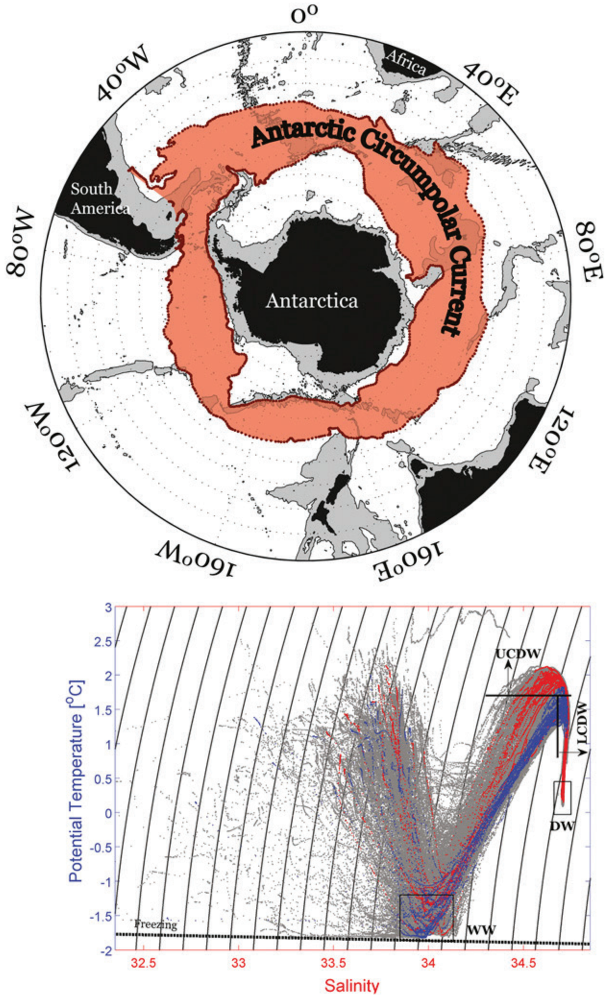

FIG. 1. (top) Location of climatological ACC (Orsi et al. 1995), transporting warm UCDW. Bathymetry shallower than 3 km is shaded. (bottom) Potential temperature–salinity properties within the LTER sampling grid (gray) highlighting those from a shelf station (300.100, blue) and a slope station (200.160, red) to emphasize the difference in UCDW properties. UCDW is identified as a potential temperature greater than 1.7°C, LCDW is identified as a salinity greater than 34.68 (with potential temperature less than 1.7°C), and WW and Deep Water (DW) are defined as in Martinson et al. (2008). The DW is a definition used by Martinson et al. (2008) in order to define a local end member for a water mass mixing analysis and is not an actual water mass of the Southern Ocean (and is not discussed here).

lighter sea ice cover venting ocean heat to the atmosphere. The reduced sea ice cover, in turn, may be related to changes in the winds and their effect on UCDW delivery and mixing across the pycnocline (Dinniman et al. 2012).

The myriad consequences of UCDW heat have made the exchange of CDW with the WAP shelf an active area of research (Klinck 1998; Smith et al. 1999; Klinck et al. 2004; Dinniman and Klinck 2004; Moffat et al. 2009; Dinniman et al. 2011, 2012; Martinson and McKee 2012; Spence et al. 2014, 2017; Graham et al. 2016; Couto et al. 2017), which is summarized in a recent review by Moffat and Meredith (2018). Various processes have been implicated in driving the cross-isobath transport of CDW onto the WAP shelf, each of which may dominate on different time and/or space scales. The importance of the mesoscale has been argued for by theoretical means (Stewart and Thompson 2015), demonstrated in high-resolution numerical models (St-Laurent et al. 2013; Graham et al. 2016; Stewart et al. 2018), and observed (Moffat et al. 2009; Martinson and McKee 2012; Couto et al. 2017). Warm-core, subpycnocline, primarily anticyclonic eddy-like features have been found within several tens of kilometers from the shelf break, particularly in the vicinity of Marguerite Trough, and are steered along isobaths. The hydrographic properties of the eddies indicate an injection of UCDW as it is found on the continental slope and their length scale is as large as or slightly larger than the first baroclinic Rossby radius, which near the shelf break is about 5 km. Decorrelation lengths of physical and geochemical scalars on the WAP shelf are also about 5 km (Eveleth et al. 2017), suggesting mesoscale eddies may dominate tracer stirring. The eddies' large heat content relative to surrounding waters indicates a potentially large onshore heat flux. For example, in numerical models, cumulative onshore heat transport is reduced by as much as 50% when model grid spacing is increased from 1 to 2 km (St-Laurent et al. 2013).

Still, very little is known about the origin of the eddies. Their core hydrographic properties and stratification suggest an origin along the continental slope and their observation along isobaths suggests they are, at least in part, advected within the mean flow. Consistent with the former, an idealized numerical model with a continental slope straddled by a jet similar to that observed along the WAP suggests that the jet soon becomes unstable and a Rossby wave containing alternating warm anticyclones and cold cyclones emerges (St-Laurent et al. 2013). Additionally, it is important to understand the processes that attenuate the mesoscale variability and work toward setting the larger-scale shelf stratification. Once UCDW intrudes onto the shelf it mixes to become modified CDW (mCDW), but attempts to understand UCDW transformation have been based on shelf-integrated budgets and have been process independent (Klinck 1998; Smith et al. 1999; Klinck et al. 2004).

In this study we seek to both understand the origin of mesoscale eddies observed on the WAP shelf and then identify and quantify the major processes responsible for their heat loss. Our focus is on the southern grid region of the Palmer Long Term Ecological Research project (Pal LTER; Smith et al. 1995) and in particular the vicinity of Marguerite Trough as this is a region of frequent eddy activity, is close in proximity to the shelf-break jet that we hypothesize generates the eddies, and contains well-defined bathymetric pathways by which to steer the eddies. We primarily use data from a novel Slocum glider survey designed to sample a known pathway for CDW exchange, documenting gradients along the axis of advection for any eddies encountered along the way, and then identify and track an eddy in real time through data-adaptive sampling. This allows, for the first time, high-spatial and temporal resolution transects directly through some of these eddies and a real-time quantification of the attenuation of their core properties. We supplement this with shipboard CTD and ADCP data used to quantify the mixing processes in the WAP environment around and within the eddies and to diagnose the instability that generates the eddies. Ultimately, we simulate the evolution of the eddy as documented by the glider with a simple diffusion model informed by our parameterized mixing processes.

2. Data and observations

The principal dataset used in this study is a set of temperature and salinity profiles collected by a Teledyne–Webb Slocum glider (Schofield et al. 2007) equipped with an unpumped Sea-Bird CTD. Slocum gliders traverse the water column (to 1000 m) in a sawtooth pattern by changing their buoyancy, traveling with average horizontal speed of $0.35\,\mathrm{m\,s^{-1}}$. There is a hysteresis effect apparent in the up versus down traces that we correct by applying the thermal lag correction of Garau et al. (2011). We also empirically correct for a salinity bias by regressing glider-recorded salinity against ship-recorded salinity, each averaged in subpycnocline temperature bins, for five stations that were occupied by both platforms (maximum temporal separation of 12 days). To facilitate analysis, all corrected up and down traces are binned into 1-m profiles whose latitude, longitude, and time coordinates are taken as the average of all intraprofile samples.

The glider was deployed at Palmer Station at the head of Palmer Deep Canyon (PD) and traveled downgrid before reaching grid station 400.100 (see Fig. 2 for grid convention and physical setting), at which point it began the first of two phases of sampling. In the first phase, the glider flew against the mean current within the anticyclonic cell extending out of Marguerite Trough in order to sample any eddies being advected across the shelf and to identify lateral gradients in their properties. In the second phase, after reaching station 290.115 within Marguerite Trough, it waited to come across an eddy in order to track it in real time. The sampling strategy and basic observations of each of these stages are described below.

a. *Glider survey: Advective Path*

1) SAMPLING STRATEGY

The Advective Path (highlighted in Fig. 2) refers to the anticyclonic cell extending out of Marguerite Trough that carries upwelled UCDW to the northern portion of the grid. This path was confirmed to carry UCDW by Martinson and McKee (2012), and its width and central location were inferred from the depth-averaged currents and CDW dye transport in Dinniman et al. 2011 (their currents superimposed on our Fig. 2). Because the width of the current is about the same as the expected diameter of the eddies we were confident that by flying straight through it we would be able to cross any existing eddies traversing the shelf. Nominal glider profile spacing is 1 km, which should afford several profiles through each eddy.

2) EDDY CHARACTERISTICS

As the glider flew upstream (downgrid), it encountered five eddies imbedded within the subpycnocline $T_{\max}$ layer. We define a mCDW temperature profile as the along-isopycnal average of all profiles whose $T_{\max}$ is <1.55°C and then compute heat content per unit area Q of the eddy profiles relative to this mCDW profile by differencing the two and integrating between $\sigma_{\mathrm{shal}} = 1027.64\,\mathrm{kg\,m^{-3}}$ and $\sigma_{\mathrm{deep}} = 1027.76\,\mathrm{kg\,m^{-3}}$. We use neighboring mCDW as our reference profile because we are interested in how the eddies mix with their surroundings. We choose these isopycnals since 1) they encompass a positive temperature anomaly within eddies, 2) σ_{shal} is relatively stable within the permanent pycnocline, and 3) σ_{deep} is near, but does not intersect, the bottom. Series of temperature, salinity, heat content per unit area, and geostrophic current at 280 dbar relative to the bottom are shown in Fig. 3, with the eddies labeled A–E (geographic locations of eddies A–E shown in Fig. 2). Fundamental statistics for each eddy developed and discussed below are given in Table 1.

To quantify the dimensions, gradients, and heat content of these eddies, we obtain an analytical representation for the eddy in terms of a Gaussian function that is fit to the data via nonlinear regression. Specifically, we

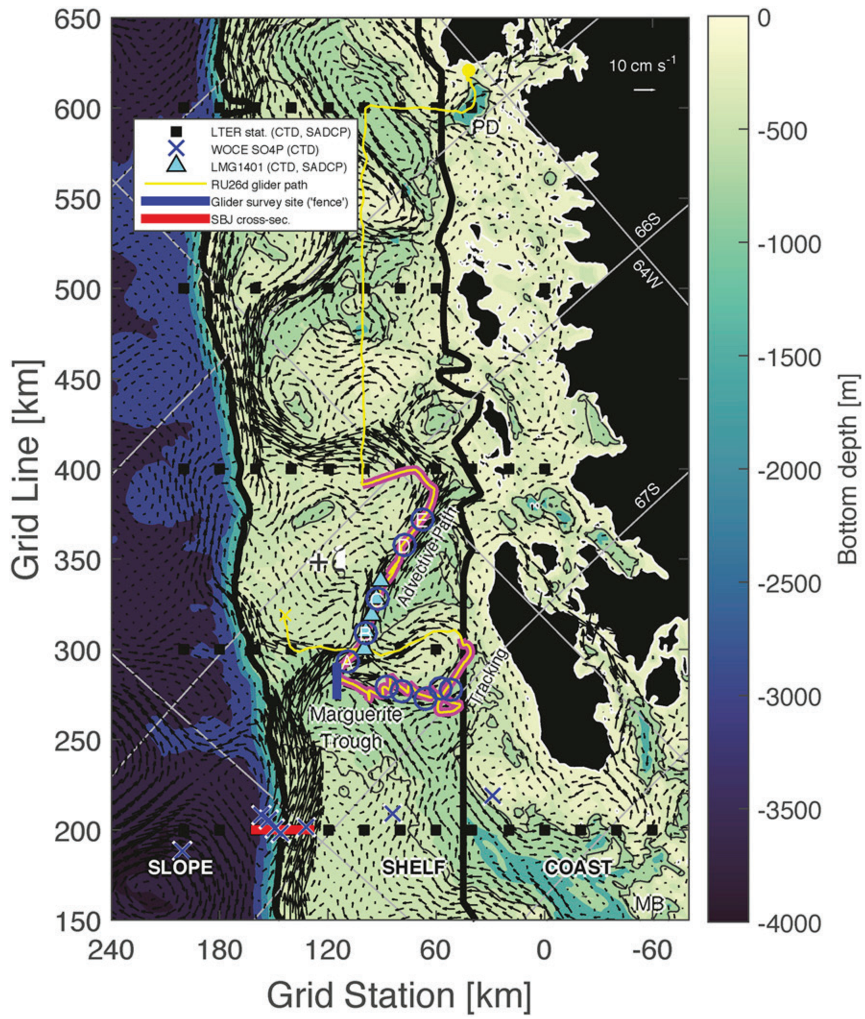

FIG. 2. Map of study region and all data used. LTER sampling grid (shipboard CTD, ADCP) shown as black squares (100 grid line is not shown but is used). All locations in the paper use the LTER coordinate system and are given as GGG.SSS where GGG is the grid line (km) and SSS the grid station (km). Origin 000.000 is at ~69.0°S, ~73.6°W, near Alexander Island. WOCE S04P CTD locations are shown as "x" symbols, and they are gridded onto the 200 line (red line, see text). Additional CTD casts taken in January 2014 are shown as triangles. The flight of glider RU26d is indicated by the yellow line (beginning at circle), and the survey fence is denoted by the blue line perpendicular to the eastern wall of Marguerite Trough. The two stages of the glider mission are described in section 2, are emphasized with a magenta outline, and are labeled; the eddies encountered are indicated by blue circles. Finally, for reference we present a snapshot of the depth-averaged currents during a CDW upwelling event from the model run of Dinniman et al. (2011) with reference vector in upper right corner. Marguerite Trough, which cuts across the center of the shelf into Marguerite Bay, is labeled along with Marguerite Bay (MB) and Palmer Deep (PD). The center of the anticyclonic cell extending out of Marguerite Trough is labeled $+\zeta$. Grid bathymetry is shaded between contours at 0, 200, 350, 500, and 750 m and then at 750-m intervals until 3750 m. The 480-m isobath, which is continuous between Marguerite Trough and the Advective Path, is indicated in black. The bold black lines separate the Slope, Shelf, and Coast regimes.

identify intraeddy profiles via positive heat content and assign them an along-eddy coordinate χ along an axis determined via orthogonal regression of profile grid line against grid station. This allows inversion of the following model

$$Q(\chi) = Q_{\max} \exp\left[-\left(\frac{\chi - \chi_0}{R}\right)^2\right], \qquad (2.1)$$

for core heat content per unit area $Q_{\max}$, center χ_0, and radius R. Implicit in this model is the assumption of

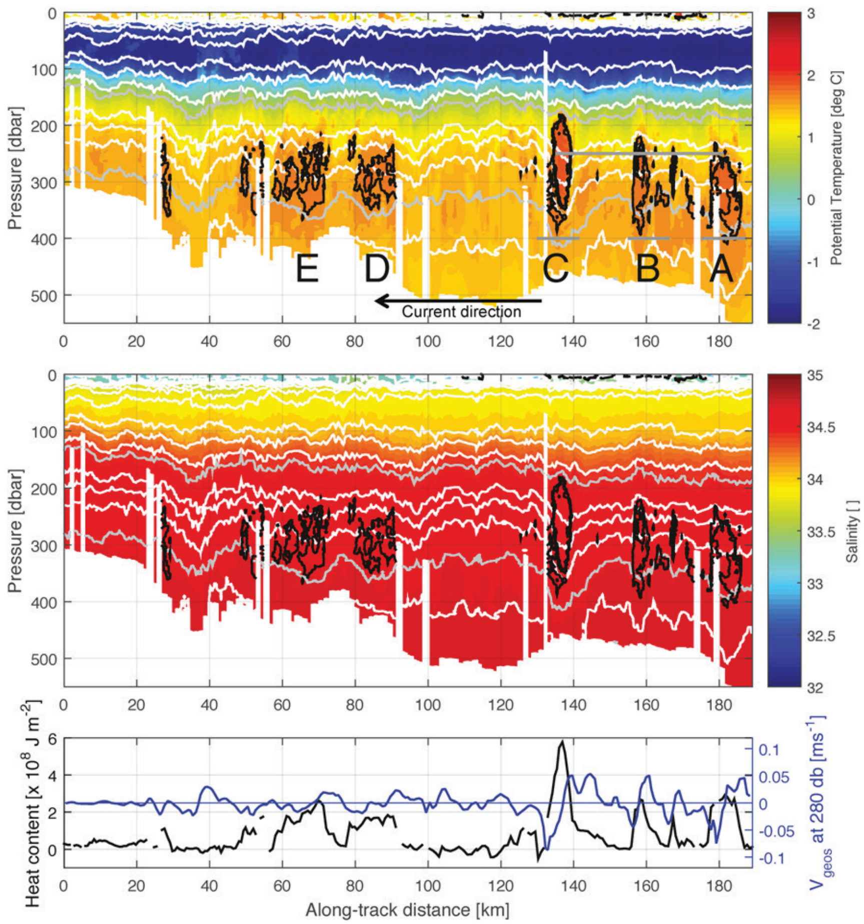

FIG. 3. Summary of glider observations over the Advective Path. (top) Potential temperature (colors) with the 1.7° and 1.8°C isotherms (black) and isopycnals (white; σ_{shal} and σ_{deep} in gray) indicated. Eddies are labeled A–E, alphabetically increasing with distance from shelf break. Scales and separation distance of the upstream (at right) eddies are indicated with thick gray lines. (middle) As in the top panel, but for salinity. (bottom) Heat content relative to mCDW integrated between σ_{shal} and σ_{deep} (black) and geostrophic current at 280 dbar relative to seafloor (blue).

axisymmetry, which we maintain throughout the paper. Our model is similar to those used by other authors (Couto et al. 2017), however we fit the function to integrated heat content as opposed to along-isopycnal temperature anomalies since integration smooths over some of the locally high temperature variance that can reduce the quality of fit. The total eddy heat content is given by the radial and azimuthal integrals of Q:

$$Q_{\mathrm{tot}} = 2\pi \int_{\chi_0}^{\chi_0+R} (\chi - \chi_0) Q(\chi)\, d\chi. \tag{2.2}$$

TABLE 1. Fundamental statistics for eddies sampled by glider along Advective Path, where gl_0 and gs_0 are the grid line and grid station coordinates, respectively, at χ_0.

	R (km)	R_{TD} (km)	H (m)	$Q_{\max}$ (10^8 J m^{-2})	Q_{tot} (10^{16} J)	gl_0 (km)	gs_0 (km)	V_{g} (m s^{-1})	$\partial T/\partial z\vert_{\mathrm{top}}$ (10^{-2} °C m^{-1})	$\partial T/\partial z\vert_{\mathrm{bot}}$ (10^{-3} °C m^{-1})	$\partial T/\partial r\vert_R$ (10^{-4} °C m^{-1})
A	3.3	5.7	195.7	3.08	0.67	293.6	109.3	0.07	1.66	−1.03	1.36
B	2.2	5.3	178.0	2.48	0.23	309.4	99.2	0.05	2.00	−1.09	0.69
C	2.8	5.5	222.5	5.46	0.88	328.0	92.6	0.09	3.38	−1.25	1.53
D	6.8	8.5	177.3	1.81	1.67	358.0	77.7	0.02	2.01	−1.60	0.32
E	7.1	10.4	188.8	2.25	2.25	372.3	67.9	0.02	1.90	−1.22	0.37

It is important to note that radii (and heat content) determined from this method are underestimates because the glider may not be going straight through the eddy (they are half chord lengths) but also because the glider is deliberately flying against the mean flow which is advecting the eddy through the glider during sampling. Therefore, we provide an additional measure of eddy size as half the along-track distance spanned by intraeddy profiles (R_{TD}), which tends to be slightly larger.

The cores of the eddies contain as much as $5.5 \times 10^8\,\mathrm{J\,m^{-2}}$ relative to the reference profile. In T–S space, the properties of these eddies are consistent with UCDW. Particularly so, eddy C contains water disjoint from neighboring water, consistent with UCDW as found upstream on the continental slope and indicating warm-core isolation. The upstream eddies A–C are narrower than their downstream counterparts D–E, having radii R ~3 km (R_{TD} ~5 km) compared to R ~7 km (R_{TD} ~9 km). Eddies D–E are broader than the upstream eddies but do not have a substantially smaller heat content per unit area and in fact tend to have more total heat. The large discrepancy in upstream versus downstream total heat content might be more reflective of a sampling bias (offset trajectory through eddy center and stronger head current encountered through eddies A–C) as opposed to an actual difference in heat content. The injection of UCDW into the shelf water column means that the eddies are associated with a downward deflection of isopycnals and anticyclonic shear (Fig. 3). The deflection of isopycnals is largest in the weakly stratified portion of the water column at and below the T_{max}, which leads to a cross-track geostrophic velocity signal. To quantify this, we evaluate the geostrophic current at 280 dbar relative to the bottom. We choose this depth as it is the approximate depth of the moored current meters used by Martinson and McKee (2012) upstream where they found the largest eddy signal. A composite over all of the eddies (Fig. 4) reveals a well-defined signature of anticyclonic rotation centered about a warm core, similar to the composites of Moffat et al. (2009).

We measure temperature gradients at the eddy boundaries via a least squares approach. We define $\partial T/\partial z|_{top}$ by regressing a straight line to the portion of the temperature profile spanning 10 m above and below the depth of σ_{shal} and then averaging the slopes laterally across all profiles within $\chi_0 \pm R$. We define $\partial T/\partial z|_{bot}$ similarly, considering the region 40 m above and below the depth of σ_{deep}. To estimate $\partial T/\partial r|_R$, we fit a straight line on each isopycnal to the

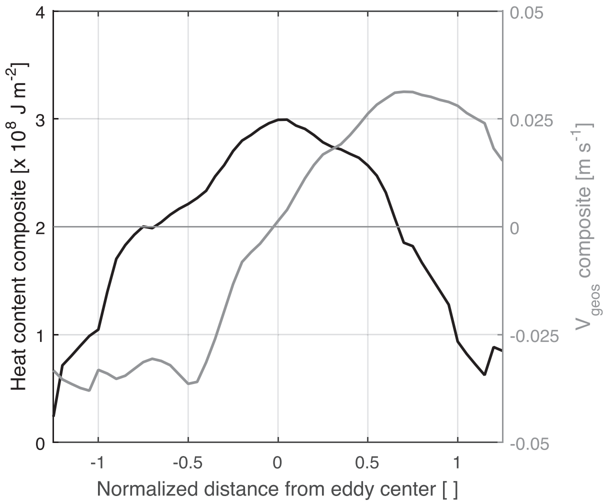

FIG. 4. Composite heat content per unit area (black) and geostrophic current at 280 dbar relative to bottom (gray) for eddies A–E. To account for different eddy sizes, each is first stretched or squeezed by interpolating onto a dimensionless grid with values −1 and +1 at the downstream and upstream edges $\chi_0 - R$ and $\chi_0 + R$, respectively.

temperature value at the profile nearest to $\chi_0 \pm R$ and up to two values on either side of that profile and then average the slopes between σ_{shal} and σ_{deep} and across both hemispheres. Owing to the nature of glider sampling, for the same reasons radius estimates are underestimates, lateral gradient estimates are overestimates. Vertical gradients are similar for all eddies while lateral gradients are larger for the three upstream eddies.

b. Glider survey: Tracking Stage

1) SAMPLING STRATEGY

We conducted transects along a ''fence'' perpendicular to the eastern wall of Marguerite Trough (Fig. 2, blue line) to find an eddy and then track it via real-time adaptive sampling. Given the local Rossby radius (~5 km), the mean flow speed, an assumption that eddies are advected within the mean flow, and the lateral deviation of the mean flow, we determined that the fence should be 15 km wide and that it should be surveyed back to back in a 24 h period, which is within the operational constraints of the glider. During sampling, profiles were inspected for a $T_{max} \geq 1.8°C$ as evidence of a UCDW-core eddy and, if found, trajectories were forecast by integrating along both the vector of 24-h mean glider depth-averaged currents and along a streamline fit to the Dinniman et al. (2011) model time–depth-averaged currents, both of which generally agreed within one Rossby radius. We encountered an eddy shortly after initiating sampling and crossed it five

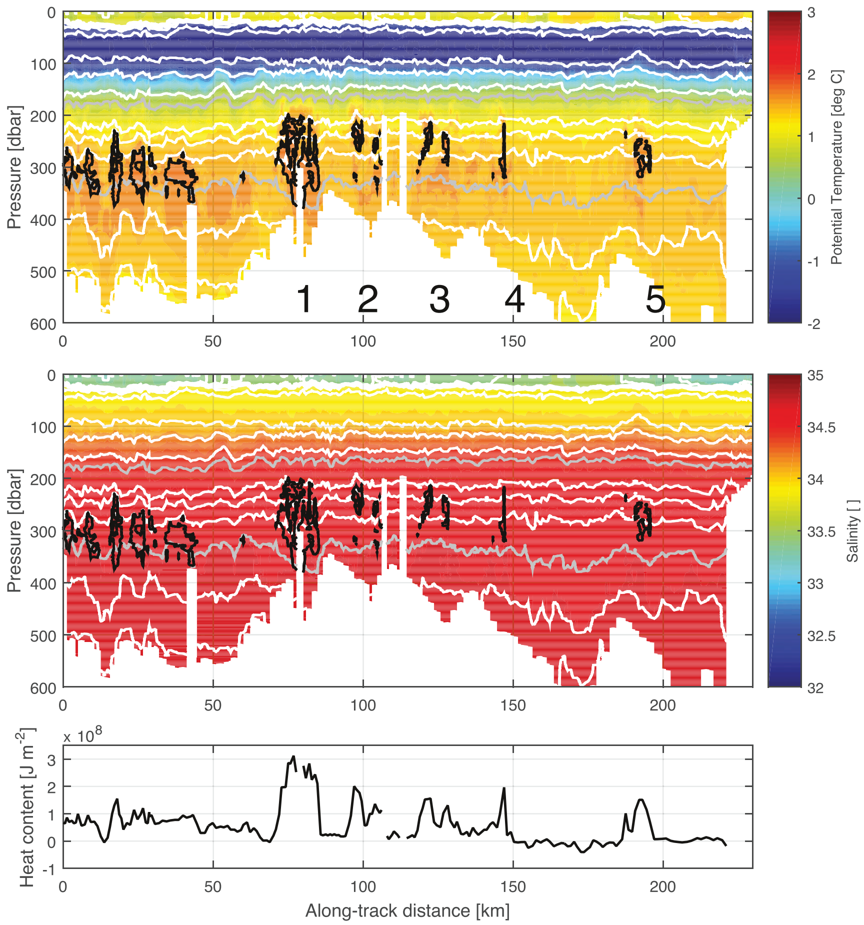

FIG. 5. As in Fig. 3, but showing data for the Tracking Stage. The repeat glider crossings of the single tracked eddy are numbered 1–5. Since the glider path did not always cleanly intersect the eddy, geostrophic currents do not provide a meaningful measure of azimuthal velocity and they are not shown.

times over 4 days. The trajectory followed the eastern wall of Marguerite Trough, consistent with the eddy-like features observed by Moffat et al. (2009).

2) EDDY CHARACTERISTICS

We define a local reference profile in the same manner as before and subtract it in order to obtain Q. Analogous to the Advective Path, sections of data are shown in Fig. 5. However, unlike in that stage, we are not confident that we consistently crossed the eddy via a chord length. Connecting spatial end-members of threshold $T_{\max}$ along a line perpendicular to isobaths leads to an estimated mean diameter of 8.5 km, similar to the eddies observed on the Advective Path. There is, in general, a decrease in heat content per unit area over time. Anticyclonic shear is less apparent beyond the first few crossings, and the vertical structure of temperature and salt anomalies is much more complicated. We will quantify the heat loss of this eddy in section 5.

c. *Shipboard data*

1) PAL LTER CTD AND SADCP

Shipboard data are used to supplement the glider data and to apply mixing parameterizations. CTD profiles are collected as part of the standard sampling on the annual cruises to the WAP each austral Summer since 1993 and are currently (since 1999) collected with a dual-pumped Sea-Bird 911+ CTD system (see Martinson et al. 2008 for details). The standard grid locations are indicated as black squares in Fig. 2. The entire grid was occupied until 2008 whereas now only a subset of stations is occupied (nominally one coastal, shelf, and slope station per grid line), though this is generally complemented by various process-study

CTD casts at nongrid locations that are not plotted but are utilized here.

Processed, high-resolution (5 min in time, 8 m in vertical) velocity profiles from the ARSV *L. M. Gould*'s hull-mounted RDI 150 kHz narrowband instrument were obtained from the Joint Archive for Shipboard ADCP (SADCP). The 150 kHz instrument provides velocity profiles good to about 300 m (depending on weather and sea state) when the vessel is on station. For mixing parameterizations we need concurrent shear and stratification profiles, so only the overlapping portion of the database is used (Januaries 2000–15; SADCP installed in mid-1999). For those applications, the hydrographic data are bin-averaged onto the same 8-m grid of the velocity data. Stratification and shear are computed as first differences on the 8-m grid as $N^2 = -(g/\rho)(\Delta\rho/\Delta z)$ and $S^2 = (\Delta U/\Delta z)^2 + (\Delta V/\Delta z)^2$. For bins with very weak stratification ($N^2 < 1 \times 10^{-6}\,\mathrm{s}^{-2}$), N^2 is set to a constant value ($1 \times 10^{-6}\,\mathrm{s}^{-2}$).

2) Casts on Advective Path

We draw special attention to 5 CTD casts collected in January 2014 along the Advective Path that was sampled by the glider the year prior (triangles in Fig. 2). These casts fortuitously sampled one or more eddies and indicate substantial interleaving structure, particularly in the pycnocline (Fig. 6). The layering connects cores of injected slope-type UCDW to the surrounding cooler pycnocline. These data are used to assess the importance and origin of thermohaline intrusions into the eddies.

3) S04P casts across continental slope

We suspect the eddies are generated along the continental slope. To diagnose the structure and stability of the shelf-break current upstream of Marguerite Trough we use CTD data from the WOCE S04P cruise in February 1992 (''x'' symbols in Fig. 2). Though it is possible that the hydrographic structure over the continental slope has changed in the long interim period, we use these data as they provide a high spatial resolution transect across the slope, slightly finer than the 2011 reoccupation of the line. The stations are ''moved'' from their original location to the 200 line by tracing the isobath at the actual station location to the 200 line, a small correction (a few kilometers). Neutral density is computed using the Jackett and McDougall (1997) software and profiles of neutral density, temperature, and salinity are filtered with a third-order Butterworth filter with width 100 dbar to remove noise and filter out Charney-type instabilities. We choose to do this because surface-trapped Charney-type instabilities do not convert significant available potential energy (APE) to eddy kinetic energy (EKE) compared to the pycnocline-level instabilities we are seeking (Smith 2007). Geopotential anomaly is calculated from the smoothed temperature and salinity profiles and is linearly extrapolated to handle bottom triangles. Both neutral density and geopotential anomaly are mapped with a Gaussian weighting function to a two-dimensional grid across the slope using the WOCE global climatology vertical grid (Gouretski and Koltermann 2004) and uniform 5-km horizontal spacing.

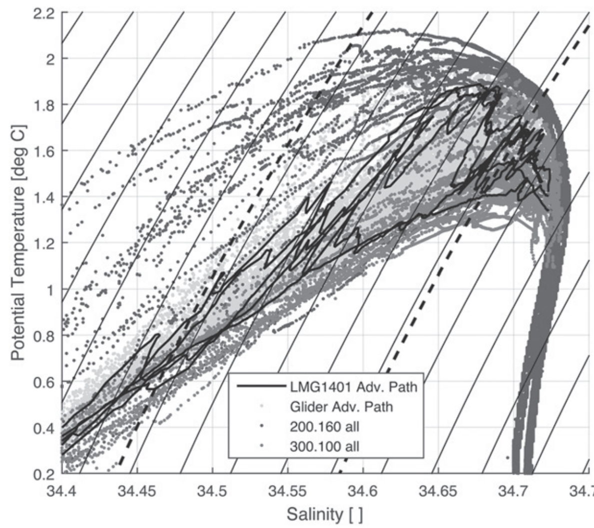

FIG. 6. Potential temperature–salinity diagram zoomed in to the UCDW region showing the five CTD casts along the Advective Path (black lines) along with all historic casts from a slope station (200.160; dark gray) and a shelf station (300.100; medium gray). The interleaving layers join slope-type UCDW with cooler, shelf-type pycnocline waters. Isopycnals σ_{shal} and σ_{deep} used for integrations are indicated as black dashed lines, and the glider profiles in the same region are shown as light gray dots.

3. Origin of mesoscale structure

a. QG model and background state

To understand the theoretical characteristics of eddies on the WAP, we begin by diagnosing the stability of the shelf-break current upstream of where UCDW intrudes onto the shelf. We follow the inviscid quasigeostrophic model of Smith (2007), assuming a local, slowly varying mean stratification N and horizontal flow $\mathbf{U}$ depending only on z. Assuming plane-wave solutions $\Re\{\hat{\psi}(z)\exp[i(kx + ly - \omega t)]\}$ where $\hat{\psi}$ is the complex amplitude of the perturbation streamfunction,

ω the complex perturbation frequency, and $\mathbf{k} = (k, l)$ the wavevector, the linearized quasigeostrophic equations in geographic coordinates lead to the eigenvalue problem

$$\left.\begin{aligned}
&(\mathbf{k}\cdot\mathbf{U}-\omega)(\Gamma-\mathbf{k}\cdot\mathbf{k})\hat{\psi} = -\left(k\frac{\partial Q}{\partial y} - l\frac{\partial Q}{\partial x}\right)\hat{\psi}, && -H < z < 0\\
&(\mathbf{k}\cdot\mathbf{U}-\omega)\frac{\partial\hat{\psi}}{\partial z} = \left[k\left(\frac{\partial U}{\partial z} - \frac{N^2\alpha^y}{f}\right) + l\left(\frac{\partial V}{\partial z} + \frac{N^2\alpha^x}{f}\right)\right]\hat{\psi}, && z = -H\\
&(\mathbf{k}\cdot\mathbf{U}-\omega)\frac{\partial\hat{\psi}}{\partial z} = \left(k\frac{\partial U}{\partial z} + l\frac{\partial V}{\partial z}\right)\hat{\psi}, && z = 0
\end{aligned}\right\}. \tag{3.1}$$

Here, $\Gamma = (\partial/\partial z)[(f^2/N^2)(\partial/\partial z)]$ is the potential vorticity stretching operator and $\alpha^{x,y}$ are the bottom slopes. We caution that the assumption of a linearly growing wave in a stable background state that is steady in time is highly idealized. Surely interactions with the evolving turbulence field of the ACC are relevant for the dynamics of the shelf-break flow. Nevertheless, we suspect that the regularity of the eddies and their common statistical metrics (Figs. 3, 4; Moffat et al. 2009; Couto et al. 2017) demonstrate that there is a preferential length scale and vertical structure for instabilities in this environment.

The background state is defined by the gridded stratification and geostrophic velocity profiles at grid location 200.150. This site is chosen as it is located midway across the slope and the geostrophic shear there agrees well with climatological SADCP shear. The current is assumed to flow parallel to isobaths, specifically at an angle of 40° north of east. The local bottom slope is calculated by fitting a 2D plane to all ETOPO1 bathymetry data (Amante and Eakins 2009) within a radius of 0.25° about the grid location.

One assumption of this model is that the background state varies slowly in the horizontal. Since there is clearly lateral shear in the shelf-break current, we need to justify excluding the potential of barotropic instability. For a generic, mixed baroclinic–barotropic instability, the contribution to the growth rate from baroclinic instability scales as $\sigma_{\mathrm{BC}} \sim (fL/ND)|\partial U/\partial z|$ and the contribution from barotropic instability scales as $\sigma_{\mathrm{BT}} \sim |\partial U/\partial y|$ (Pedlosky 1987). For these data, the latter is one order of magnitude smaller than the former ($\sigma_{\mathrm{BC}} \sim 13\,\mathrm{day}^{-1}$, $\sigma_{\mathrm{BT}} \sim 2\,\mathrm{day}^{-1}$). This is corroborated by Stern et al. (2015) who found baroclinic instability to grow much faster than barotropic instability in their QG model of a similar shelf-slope configuration, though their model was fully turbulent and not limited to the linear growth stage.

b. Most unstable mode

The equation is discretized as in Smith (2007) and solved for a range of wavenumbers. For each wavenumber, the most unstable mode is that with the largest imaginary part of ω. We find the overall most unstable mode to have an inverse wavenumber $|\mathbf{k}_{\max}|^{-1} = 4.4\,\mathrm{km}$ and growth rate $0.4\,\mathrm{day}^{-1}$ (Fig. 7). Over the wavenumber space evaluated, this is both the global and only local maximum. The mode's vertical structure is characterized by nonzero amplitude below the permanent pycnocline in the CDW depth range with a maximum at about 600 m and a secondary maximum at about 350 m. Specifically, this depth range spans the water column presence of UCDW ($T \geq 1.7°\mathrm{C}$) and LCDW ($S = S_{\max}$) within the four profiles across the slope. The instability appears to be qualitatively similar to a Phillips type instability (Phillips 1954) for the following reasons: 1) vertical structure seems to be dictated by interior sign changes in the potential vorticity gradient, 2) ~33° phase shift within the amplitude maximum indicates APE release there, and 3) horizontal scale obeys $L \approx (N/f)h_{\mathrm{pycnocline}} \approx 5\,\mathrm{km}$.

Overall these findings are in very good agreement with the glider observations over the Advective Path (Fig. 3). First, the vertical structure of the mode is concentrated within and below the permanent pycnocline, which is where the eddies exist. Second, the observed diameters of eddies A–C upstream and average crest-to-crest separation are ~8.3 km (averages of $2R$ and $2R_{\mathrm{TD}}$) and 22.3 km, respectively, which are comparable to the theoretical diameters $2|\mathbf{k}_{\max}|^{-1} = 8.8\,\mathrm{km}$ and crest-to-crest separation $2\pi|\mathbf{k}_{\max}|^{-1} = 27.8\,\mathrm{km}$ for eddies spun off of an unstable Rossby wave. Temperature anomalies relative to mCDW and geostrophic currents provide some evidence for a cold cyclone between eddies B–C, though in general, only warm anticyclones tend to be found on the shelf. The eddies D–E downstream on the path are broader than A–C but have a similar separation. With the caveat that this is a linear model, note that the wavelength implies delivery of (365 days) × $u|\mathbf{k}_{\max}|/2\pi$ = 57–114 eddies per year (for typical shelf

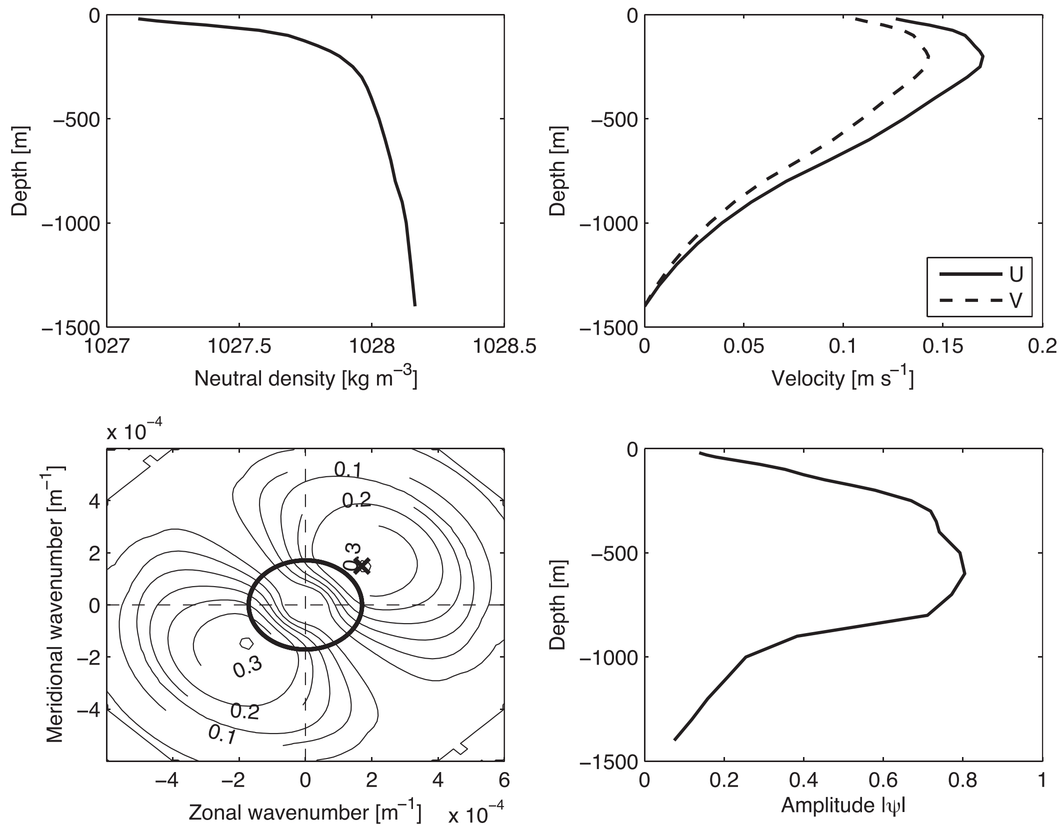

FIG. 7. Profiles used for linear stability analysis and results. (top) Profiles of (left) neutral density and (right) geostrophic velocities used. (bottom left) Perturbation growth rates as a function of wavenumber. The overall most unstable mode is indicated with black x. Locus of points $|k| = L_R^{-1}$ is given by solid black circle. (bottom right) Amplitude structure of the most unstable mode.

currents of 0.05 or 0.10 m s^{-1}), which could account for the totals observed by Moffat et al. (2009) and Martinson and McKee (2012).

c. Roles of bottom slope and current orientation

Exploring the parameter space of bottom slopes and current orientations allows us to simultaneously understand the sensitivity of the most unstable mode's structure and growth rate to these parameters and to understand how generalizable these results are to other regions around Antarctica. Using the same geostrophic shear and stratification profiles, we repeat the above analysis for all bottom slopes between −0.15 and +0.15 at increments of 0.01 and for all current orientations between 0° (zonal) and 90° (meridional) counterclockwise from east at 10° increments and examine changes in the growth rate, wave vector, and structure of the most unstable modes. Evaluating positive and negative bottom slopes effectively allows consideration of both prograde (isopycnals slope in same sense as bathymetry; e.g., WAP) and retrograde (isopycnals slope in opposite sense as bathymetry; e.g., Ross Sea) jets.

Figure 8 shows the growth rate and inverse wavenumber of the most unstable mode over the entire parameter space. The orientation of the current has essentially no effect on the instability. This is likely because the planetary beta effect is so small at this latitude that potential vorticity gradients are dominated by the stretching term and bottom slope. Indeed the topography plays a large role in determining the strength and properties of the most unstable mode. It is found that negative bottom slopes are stabilizing while increasing positive bottom slopes are destabilizing to a point and then stabilizing. Blumsack and Gierasch (1972) demonstrate that the relevant parameter for the stability problem under QG scaling is not the bottom slope itself but rather the ratio of the bottom slope to the isopycnal slope, $\delta \equiv \alpha/s$ (Blumsack and Gierasch 1972; Poulin et al. 2014). In the QG model of Smith (2007) that we use, the bottom slope only enters the problem as a boundary condition in the bottom layer's potential

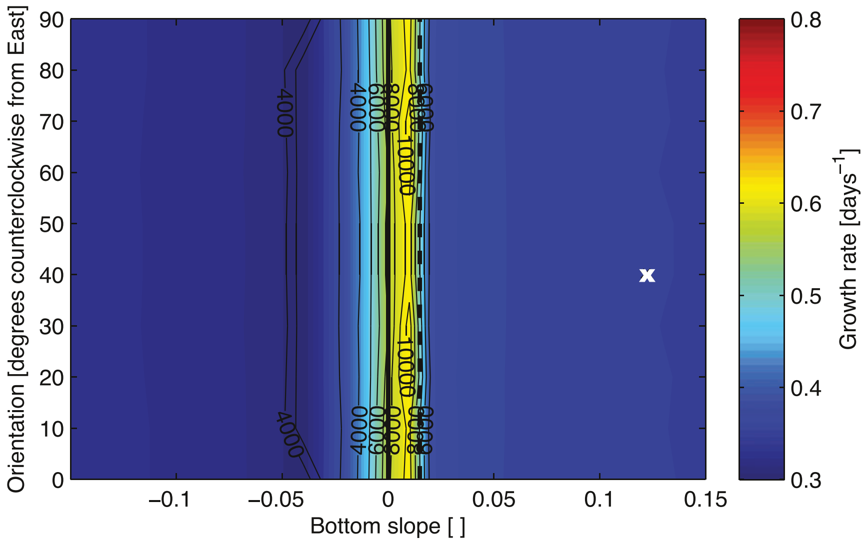

FIG. 8. Growth rate (color) and inverse wavenumber (contours) of most unstable mode for various bottom slopes and current orientations. All cases use the same shear and stratification from Fig. 7 and assume that the current flows exactly parallel to the shelf break. Slope of the 1028.0 kg m^{-3} neutral surface is indicated by a black dashed line. Actual bottom slope and current orientation indicated as white "x."

vorticity gradient. When the bottom slope exceeds the slope of the 1028.0 kg m^{-3} neutral surface, the potential vorticity gradient vanishes in the lower layer which has the effect of suppressing the growth rate in accordance to the Charney–Stern criteria (Pedlosky 1987). Nevertheless, this does not change the fact that there are still sign changes in the interior potential vorticity gradient and therefore instability persists where $\delta > 1$ or $\delta < 0$ (Isachsen 2011). These regions of weaker instability with inverse wavenumbers of 4–5 km all have similar vertical structure as the most unstable mode obtained in the realistic scenario analyzed earlier.

The fastest growing modes for prograde currents with relatively flat bottoms ($0 \leq \delta \leq 1$) are qualitatively consistent with Eady modes for the following reasons: 1) they have amplitude maxima at both ~350 m and near the bottom; 2) they have an inverse wavenumber $L \approx NH/(1.6f) \approx 9.4$ km, probably since the weakly varying N is dynamically similar enough to the uniform N of Eady's model. These modes have a pronounced spike at ~350 m near the UCDW temperature maximum and, in regions with a flatter bottom slope than the WAP, could also be expected to contribute to exchange of CDW. The region between $-2 \leq \delta < 0$ represents a sort of transition between the Eady-type modes and the Phillips-type modes. They have smaller length scales (~2 km) and are bottom-boundary trapped. This trend fits the qualities described by Blumsack and Gierasch (1972) for increasingly negative slope parameter, namely decreasing length scale and boundary trapping.

4. Attenuation of mesoscale structure

Having identified a plausible origin for the UCDW eddies, we here consider the processes responsible for their decay. Box inversions of steady heat budgets on the WAP point to diapycnal mixing between overlying remnant winter mixed layer Winter Water (WW) and a constantly replenished CDW layer as the maintenance of the permanent pycnocline. For some context, using a steady advective–diffusive balance, Klinck et al. (2004) place an upper bound on the vertical (lateral) diffusivity of heat at 7.7×10^{-4} m^2 s^{-1} (1600 m^2 s^{-1}) in the limit of no lateral (vertical) mixing. In an earlier study, Klinck (1998) used seasonal changes in water properties and a similar integrated budget to find a vertical (lateral) diffusivity of heat as 1×10^{-4} m^2 s^{-1} (37 m^2 s^{-1}). Martinson et al. (2008) used interannual variability of WW heat content and assumed a UCDW replenishing time to suggest a vertical diffusivity of 8.5×10^{-5} m^2 s^{-1}. Our study, however, focuses on how the properties of the subpycnocline "box" are set by the mixing of advected parcels of UCDW, within which the vertical and lateral gradients are quite different from those used in mean-shelf balances.

a. Shear-driven instability

Shear-driven instability is thought to be important in maintaining the permanent pycnocline and is thought to yield larger heat fluxes on the WAP than double-diffusive instabilities (Howard et al. 2004). Regarding sources of shear, internal tides are likely not important but near-inertial waves may be. Howard et al. (2004) suggest the semidiurnal tide is weak, as is the stratification, making baroclinic conversion unlikely. Further, Beardsley et al. (2004) use rotary spectral analysis of drifter velocity to show power in the semidiurnal band is two orders of magnitude less than that in the near-inertial. In general, we might expect that vertical mixing should be elevated over seamounts or within cross-cutting canyons. At seamounts, internal waves with frequency at the critical slope may be generated whereas in canyons internal waves may become trapped and focused toward the canyon head (Gordon and Marshall 1976).

Because we do not have microstructure measurements within eddies or on the surrounding midshelf, our approach is to use SADCP and CTD data to estimate diffusivities, temperature gradients, and heat fluxes across the permanent pycnocline, which we define globally to be between 98 and 250 m. We exclude grid stations below the 000 grid line as the hydrography there is very different (very deep and cold remnant winter mixed layers). Note that winter mixing by entrainment of the thermocline during brine rejection is not considered here, but is important in the annual heat budget (Martinson and Iannuzzi 1998).

1) General shear-driven instability

The method of Pacanowski and Philander (1981, hereafter PP81) computes a diffusivity $K_z(z)$ as a function of the Richardson number, with the idea being that when shear overcomes stratification, instability and mixing result. This method was developed for steady currents in equatorial ocean models and assumes nothing about the underlying sources of shear. Nevertheless, it has been applied to the WAP (Howard et al. 2004) and other high latitude environments (Dewey et al. 1999). For every 8-m binned CTD cast we have we pair it with all concurrent on-station SADCP profiles and compute a time-averaged Richardson number $\overline{\mathrm{Ri}} = \langle N^2/S^2 \rangle$. Because this is essentially a space–time-averaged Ri based on finite-differenced data, it is best interpreted as a probabilistic measure of potential instability at space (and time) scales lower than the differencing (and averaging) scales. The PP81 parameterization is

$$K_z = 10^{-5} + \frac{5\times 10^{-3} + 10^{-4}(1+5\overline{\mathrm{Ri}})^2}{(1+5\overline{\mathrm{Ri}})^3}\,\mathrm{m^2\,s^{-1}}, \tag{4.1}$$

and a vertical heat flux can then be calculated at each depth as

$$Q_f = \rho_0 c_p K_z \partial T/\partial z. \tag{4.2}$$

2) Internal wave parameterizations

Various authors have modeled the energy transfer through the steady Garrett–Munk (GM; Garrett and Munk 1975) internal wave vertical wavenumber spectrum via nonlinear interactions down to dissipation scales and turbulence production by scaling the GM shear spectrum by observed shear variance (e.g., Gregg 1989, hereafter G89). By assuming a steady turbulent kinetic energy balance and assuming a constant mixing efficiency ($\Gamma = 0.2$), one can then estimate a diffusivity coefficient from parameterized dissipation via the relation $K_z = \Gamma\varepsilon/N^2$. We use a modified version of the G89 parameterization, which is

$$K_z(z) = K_0 \frac{\langle S^4 \rangle}{\langle S^4_{\mathrm{GM}} \rangle} h(R_\omega) j(f, N). \tag{4.3}$$

In this expression, $\langle S^4 \rangle$ is the 8-m SADCP shear squared, multiplied by 2 (correcting for the finite-difference filter; Gregg and Sanford 1988), and then squared again and averaged in time; $\langle S^4_{\mathrm{GM}} \rangle$ is the GM shear spectrum (with local scaling parameters for the WAP shelf; see appendix) integrated up to a cutoff wavenumber $\beta = 0.2\pi$ rad m^{-1}, squared, and then multiplied by 2 (assuming Gaussian statistics); and $K_0 = 5.6 \times 10^{-6}\,\mathrm{m^2\,s^{-1}}$ is a nominal diffusivity for the underlying internal wave spectrum (see appendix). The functions h and j are corrections added later and are not part of the original G89 model.

First, $h(R_\omega)$ is a polynomial function of R_ω, the N^2-normalized-shear–strain variance ratio, which is designed to adapt the model to non-GM wave fields with different aspect ratios and frequency content:

$$h(R_\omega) = \frac{3(R_\omega + 1)}{2\sqrt{2}R_\omega\sqrt{R_\omega - 1}}. \tag{4.4}$$

The GM spectrum has $R_\omega = 3$ ($h = 1$), and larger values of R_ω indicate elevated importance of near-inertial waves. Most of the open ocean has $R_\omega \sim 7$ (Kunze et al. 2006), and values in the Southern Ocean are generally between 8 and 12 (Thompson et al. 2007; Naveira Garabato et al. 2004). Calculating shear and strain spectra for each cast as in Kunze et al. (2006), we find $R_\omega = 9$ ($h = 0.42$) averaged over the LTER grid, and, owing to the difficulty involved in estimating strain, we use that constant value for all casts.

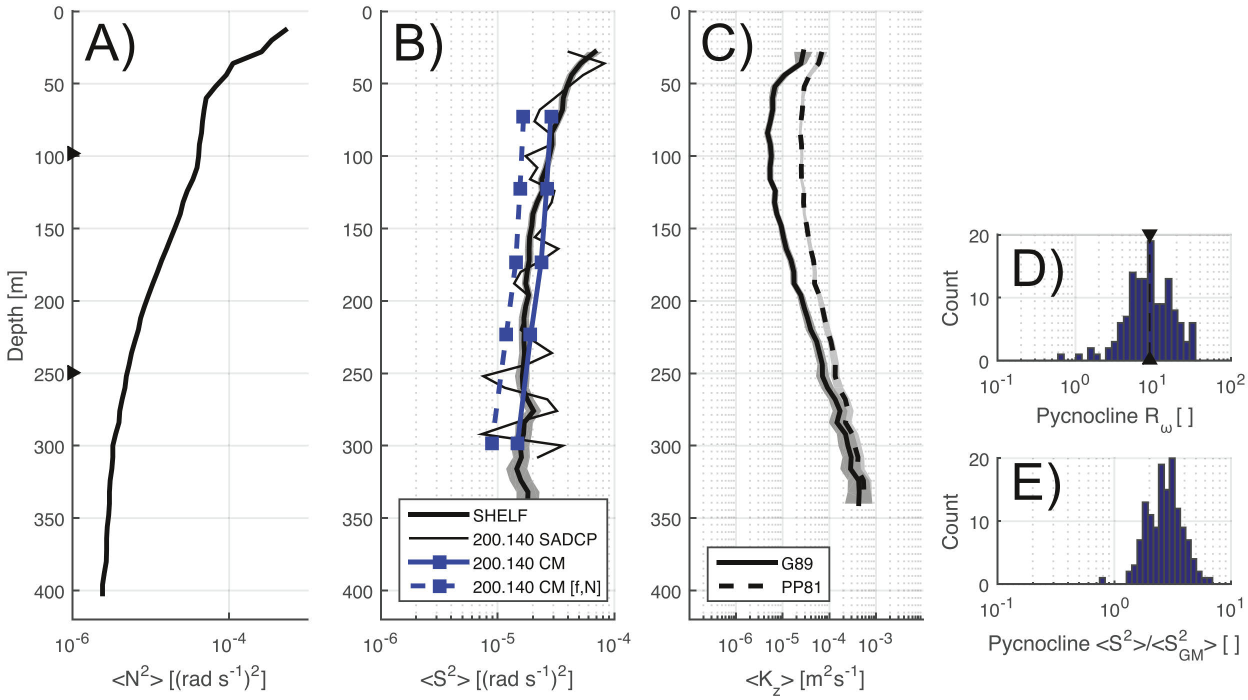

FIG. 9. Summary of vertical mixing parameterizations for Shelf region. (a) The N^2 calculated on shelf-averaged density profile (see appendix). Range of the permanent pycnocline as defined in the text indicated with black wedges. (b) Composite S^2 profile from all SADCP profiles log-averaged on depth coordinates (bold black) with $\pm$ 2 log standard errors (gray shading); composite S^2 profile from all SADCP profiles at station 200.140 log-averaged on depth coordinates (thin black); log-averaged total (solid blue) and internal wave band (dashed blue) S^2 from moored current meters at station 200.140. (c) Composite K_z profiles log-averaged on depth coordinates (G89 solid; PP81 dashed) along with $\pm$2 log standard errors (gray shading). (d) Histogram of shear-to-strain variance ratios for all Shelf profiles with complete pycnocline coverage; $R_\omega = 9$ indicated with black dashed line. (e) Histogram of observed-to-GM pycnocline shear variance ratios for all Shelf profiles with complete pycnocline coverage.

The second term $j(f, N)$ is a correction for latitude arising because the rate at which waves are Doppler shifted depends on the ratio of their horizontal and vertical wavenumbers, which depends on Coriolis frequency f (Gregg et al. 2003):

$$j(f, N) = \frac{f\,\text{acosh}(N/f)}{f_{30}\,\text{acosh}(N_0/f_{30})}. \tag{4.5}$$

This dependence was in the scaling used by G89, but he held $f\,\text{acosh}(N/f)$ to be constant. We use a typical latitude for the WAP (66.5°S) for all casts. After developing a diffusivity profile, a heat flux profile is calculated from Eq. (4.2).

3) RESULTS AND INTERPRETATION

Fundamental results are presented in the form of profiles of N^2, S^2, and K_z averaged over the Shelf region (see Fig. 2 for regional boundaries) in Fig. 9. In general, S^2 decreases more slowly with depth than does N^2, becoming nearly white below the pycnocline and yielding diffusivities that increase with depth. To confirm that the apparently unusual behavior of S^2 with depth is real, we compare the SADCP shear at station 200.140 to the shear calculated from a set of six moored current meter records at that site [corrected for finite differencing following Gregg and Sanford (1988) using local GM scaling]. The current meter shear (bold blue line) and SADCP shear (thin black line) at site 200.140 agree remarkably well, suggesting that, at least at this site, the large shear variance (and hence the large diffusivities) at depth is real (Fig. 9b).

While the SADCP shear variance represents an integral across all frequencies, we can bandpass filter the current meter observations between $[f, N_0]$ to retain only shear in the internal wave band. Doing so (dashed blue line in Fig. 9b) suggests that the internal wave band shear profile has the same shape as the total shear profile but that SADCP shear might be overestimating internal wave shear by a factor of ~1.6. Because we cannot evaluate this relation at other sites, we do not attempt to make any correction for non-internal wave shear. The histogram of $\langle S^2\rangle/\langle S^2_{GM}\rangle$ in the pycnocline depth range (Fig. 9e) suggests observed shear variances are generally a factor of 2–3 greater than GM. Spectra of shear and strain in the pycnocline confirm that

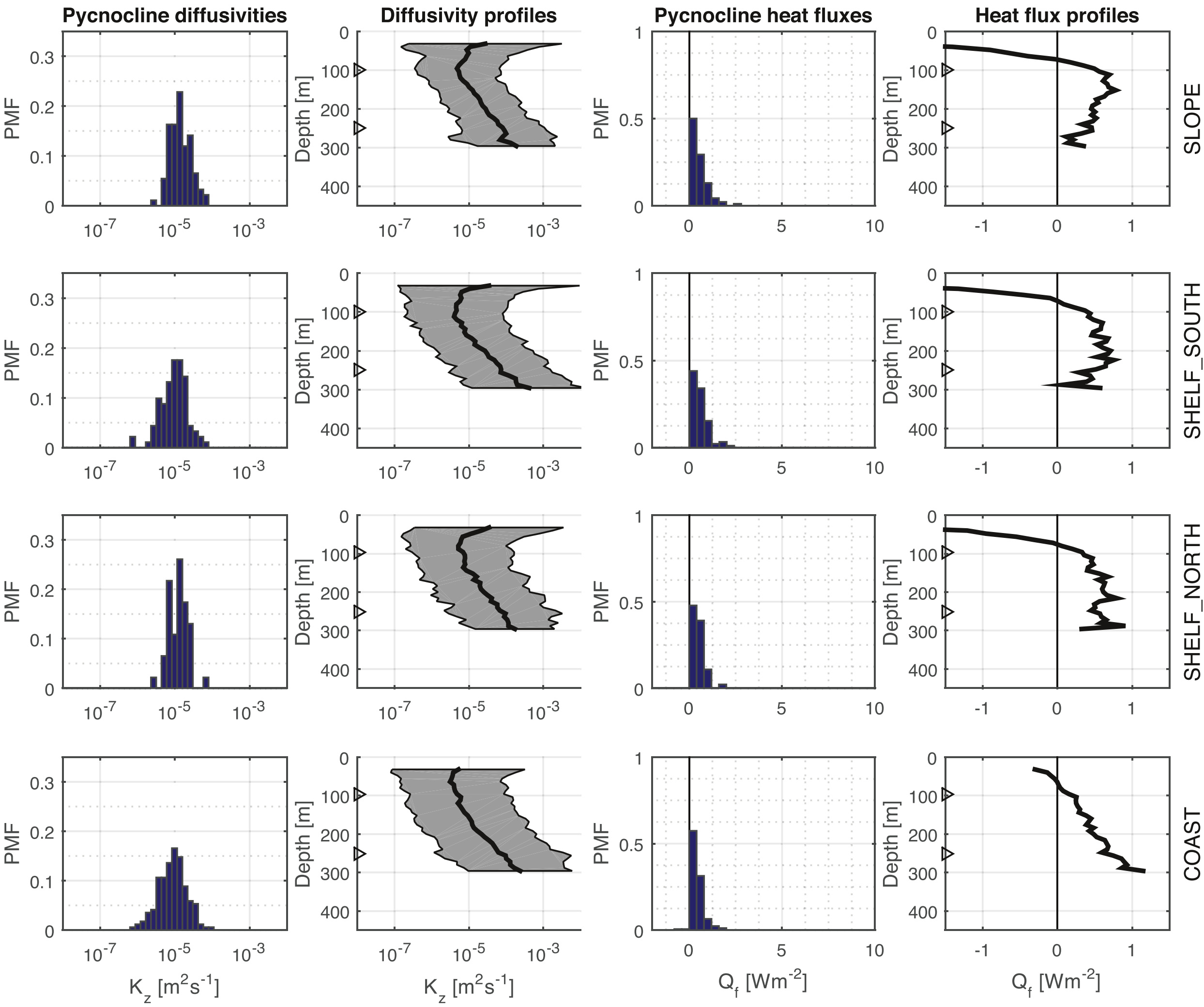

FIG. 10. Summary of regional variability of vertical diffusivities and heat fluxes. Rows indicate different regions (Shelf, Slope, and Coast indicated in Fig. 2; North Shelf and South Shelf are separated by 450 grid line). (first column) Histograms of G89 K_z, log-averaged over depth of pycnocline (blue bars). (second column) Profile of G89 K_z, log-averaged across all profiles at each depth. Gray shading indicates two log standard deviations. (third column) As in the first column, but for vertical heat fluxes, where depth-reduction is accomplished by using the median. (fourth column) As in the second column, but for vertical heat fluxes, where space reduction is accomplished by using the median. Because the heat fluxes do not follow a simple distribution, error bars are not shown. In total there are 1073 CTD casts north of the 000 grid line matched to an SADCP profile. Of those, 963 contain at least one good N^2 and S^2 value (used for composite profiles), 859 contain at least one good value within the pycnocline, and 398 contain good values throughout the pycnocline (used for depth-reduced histograms).

$R_\omega = 9$ is a good fit on the WAP shelf (Fig. 9d) and reveal an elevated importance of near-inertial waves in comparison to a standard GM spectrum.

Both the G89 and PP81 diffusivities increase with depth for reasons discussed above. Diffusivity values in the permanent pycnocline are small ($<10^{-5}$ m^2 s^{-1}), so much so that the asymptotic lower limit of the PP81 method renders it inapplicable there (Fig. 9c). Although the two methods agree better deeper in the water column, all further analyses will exclusively consider the G89 parameterization. The shear (Fig. 9b) and diffusivity (Fig. 9c) profiles are presented as means with the shaded region enclosing two standard errors, where both the means and standard errors are computed on log-transformed data. Owing to the large number of stations sampled, uncertainty in the mean is small.

To get a sense of how diffusivity and vertical heat fluxes vary regionally, Fig. 10 shows composite profiles of diffusivity and heat flux for data partitioned by region alongside histograms of the pycnocline-averaged quantities. The small diffusivities that characterize the permanent pycnocline operating on the background T profile yield vertical heat fluxes across the permanent pycnocline of $<1\,\mathrm{W\,m^{-2}}$ which is smaller than values reported by Howard et al. (2004), who used PP81. Diffusivities increase approximately log-linearly with depth to about $10^{-4}\,\mathrm{m^2\,s^{-1}}$ at 300 m (Fig. 10), which is as deep as the SADCP yields useable data.

As in Fig. 9, the central values are computed on log-transformed data, however now the spread is indicated by two standard deviations in order to indicate potential values instead of uncertainty in the mean. While the central values are small, the spread at any given depth is large and spans about two orders of magnitude, suggesting that the potential for strong mixing at any depth is high and that mixing is intermittent. Pycnocline diffusivities are significantly different between the Shelf and Slope, the Shelf and Coast, and between the Northern Shelf and Southern Shelf at an $\alpha = 10\%$ level. The variance seems to be larger in the Coast. The larger variance there is driven by larger variance in the shear. We also constructed two composites that should be more representative of the environment that most of the eddies are in. The first averages all profiles in the subregion of the Southern Shelf that is bounded by the 250 and 450 lines between stations 030 and 130 (the vicinity of Marguerite Trough) and the second averages only those profiles in that domain with a $T_{\max} \geq 1.55°\mathrm{C}$. The heat fluxes in those regions are qualitatively different with a much greater heat flux divergence centered about the $T_{\max}$ but are statistically indistinguishable from the more comprehensive Southern Shelf in terms of cross-pycnocline metrics. However, compared to the Northern Shelf, the Southern Shelf and both Marguerite Trough composites have significantly lower pycnocline diffusivities, significantly lower shear variance ratios, and insignificantly larger pycnocline heat fluxes. The results suggest that any enhanced vertical heat flux within an eddy compared to its surroundings is due to the altered gradients of the temperature profiles and not the shear.

While the SADCP does not allow for estimates of diffusivity or heat flux below about 300 m, extrapolating the log-linear trend in K_z with depth and using observed temperature gradients suggests that below the $T_{\max}$, the vertical temperature gradient is about one order of magnitude smaller than that in the permanent pycnocline, however the diffusivity should be about two orders of magnitude larger. This combines for a heat flux about 10 times greater below the eddy, and the spatial variability in the heat flux profiles is consistent with this scaling. The stratification on the Slope and Southern Shelf is dominated by pure UCDW and a middepth temperature maximum as in the eddies. The middepth maximum in temperature results in an upward heat flux above the $T_{\max}$ and a downward heat flux below, the former of which is apparent in the observed profiles and the latter of which is implied by the trend toward a $\sim 0\,\mathrm{W\,m^{-2}}$ heat flux at 300 m (Fig. 10). Because the downward heat flux is about 10 times greater than the upward heat flux, the temperature maximum is mixed downward in the water column as the UCDW is advected northward and shoreward. This is consistent with the positive vertical heat flux increasing with depth on the Northern Shelf and Coast stations (Fig. 10).

b. Thermohaline intrusions

Four of the five CTD casts taken along the Advective Path reveal that within and surrounding the eddies there is substantial along-isopycnal temperature and salinity variance associated with thermohaline intrusions (Fig. 6). Those data are plotted as profiles of temperature in Fig. 11 along with a background profile, which is constructed as a running median in density space with a window size of $0.015\,\mathrm{kg\,m^{-3}}$. The UCDW eddies are essentially moving fronts. Joyce (1977) derived a model in which medium-scale advection of heat and salt across a density-compensated large-scale front is balanced by small-scale diffusion across thermohaline intrusions, attenuating their T–S characteristics. The medium-scale advection is taken to be in the form of alternating interleaving structures, initiated by velocity perturbations with the energy source coming from thermoclinic energy of the cross-frontal property contrasts. His model makes no distinction as to what small-scale processes conduct the mixing.

The model balance leads to an effective cross-frontal diffusivity for T of

$$K_h = \overline{K_z^T\left(\frac{\partial T'}{\partial z}\right)^2} \Bigg/ \left(\frac{\partial \overline{T}}{\partial r}\right)^2, \qquad (4.6)$$

where primes indicate small-scale variance, overbars indicate large-scale averages (scales larger than intrusions), and the vertical eddy diffusivity is taken to encompass all mixing processes. To apply Eq. (4.6) we estimate the cross-frontal temperature gradient from the glider data along the Advective Path by averaging the lateral gradients of the 5 eddies encountered (A–E; $8.5 \times 10^{-5}\,°\mathrm{C\,m^{-1}}$). The small-scale intrusion variance in the vertical is derived from the CTD profiles at approximately the same location: the background profile is subtracted and the variance of the derivative of the residual is calculated. We calculate K_h in two ways: once using a constant K_z typical of the midwater column ($10^{-4}\,\mathrm{m^2\,s^{-1}}$; Hebert et al. 1990, Pelland et al. 2013) and once using the diffusivities as parameterized from the modified G89 method. The results are 3.2 ± 1.4 and $7.9 \pm 4.2\,\mathrm{m^2\,s^{-1}}$, respectively (two standard errors indicated).

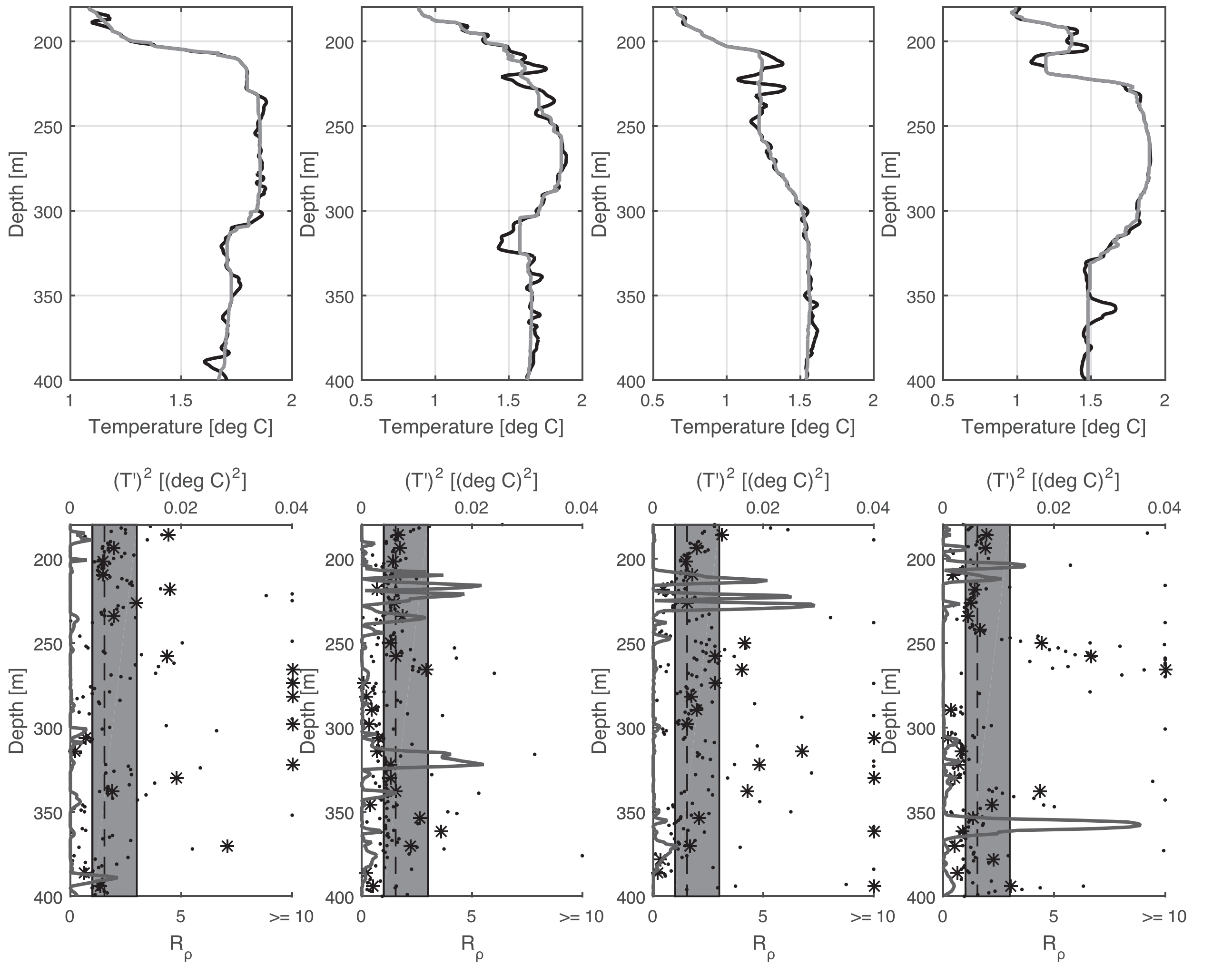

FIG. 11. Summary of temperature variance in the four out of five Advective Path CTD casts that indicate substantial thermohaline intrusions (time and downstream-distance increase from left to right). (top) Full temperature profile (black) along with background temperature profile (gray; see text for definition). (bottom) Temperature anomaly squared (gray line) along with density ratio computed on 8-m profiles (stars) and on 1-m profiles (dots). Axes are saturated so that depths with $R_\rho > 10$ are shown at 10 and doubly stable and statically unstable values are not shown. The shaded region indicates highly diffusively unstable region [1, 3], and the dashed line indicates the critical threshold of Bormans (1992a) below which diffusive stratification contributes significantly to cross-frontal heat fluxes.

We now consider processes that may be responsible for generating the thermohaline intrusions.

1) Double-diffusive growth

Theories for the growth of thermohaline intrusions (e.g., McDougall 1985a,b) in a region of density-compensated thermohaline gradients depend on one of the components of density being unstably stratified in order for an infinitesimal disturbance to grow to finite length. Figure 11 shows that the WAP water column between the WW $T_{\min}$ and the UCDW $T_{\max}$ is diffusively unstable and that the layer immediately below the UCDW core can be salt finger unstable. One way to quantify how much the unstably stratified component contributes to the stability of the water column is via the density ratio $R_\rho = (\beta\partial S/\partial z)(\alpha\partial T/\partial z)^{-1}$. A statically stable column is diffusively unstable if $1 < R_\rho < \infty$, salt finger unstable if $0 < R_\rho < 1$, and doubly stable if $R_\rho < 0$. As the ratio approaches 1, double-diffusive fluxes increase because the effect of the gravitationally unstable gradient is increasingly canceled by that of the stably stratified component's gradient. Bormans (1992a) found that diffusively unstable fronts had lateral intrusion heat fluxes significantly exceeding those of doubly-stable fronts only when R_ρ went below 1.54. Values in the lower pycnocline/eddy upper hemisphere occasionally breach that threshold, and there is a correspondence between the locations of largest temperature variance and the locations of density ratio nearest to 1 (Fig. 11, lower panels).

2) Internal wave advection

Another possibility is that the intrusion-scale temperature variance is caused by advection due to internal waves. If we consider the simplest advection equation and the square of its Fourier transform,

$$\frac{\partial \tilde{T}}{\partial t}(z) = u_r(z)\frac{\partial \overline{T}}{\partial r} \Leftrightarrow \omega^2 \Phi_{\tilde{T}} = \Phi_{u_r}\left(\frac{\partial \overline{T}}{\partial r}\right)^2, \quad (4.7)$$

we can rearrange it to construct an inequality for the maximum contribution by internal waves to the intrusion-scale (tilde) temperature variance:

$$\Phi_{\tilde{T}_z} \le \frac{1}{f^2}\left(\frac{\partial \overline{T}}{\partial r}\right)^2 \Phi_{u_z}. \quad (4.8)$$

Here we have assumed that all waves are purely horizontal (inertial waves) and we have differentiated in depth by multiplying each side by β^2, the vertical wavenumber squared. Shear spectra are calculated over our defined pycnocline range and temperature spectra are calculated over [180, 400] m, encompassing the eddy itself, the range of intrusions, and avoiding remnant diffusive staircases. The large-scale (overbar) temperature gradient is again the average across eddies A–E (Table 1). Figure 12 shows the two sides of Eq. (4.8) and it implies that observed temperature variance is greater than the maximum contribution of internal waves acting on the cross-eddy temperature gradient. It is worth noting, however, that if we instead use the lateral temperature gradient of only the three upstream eddies (A–C; 1.2×10^{-4}°C m^{-1}) then the 90% error bars in Fig. 12 begin to overlap in the range of intrusion thicknesses.

3) Geostrophic turbulence

Under geostrophic turbulence, the steep roll-off of energy spectra in comparison to the more gradual roll-off of potential enstrophy and tracer variance spectra means that the density field is dominated by the large, low-mode energy containing eddies that stir along isopycnals (such as the first-mode baroclinic instability; section 3) whereas the T–S variance is dominated by small-scale filamentary features that must be density compensated (Smith and Ferrari 2009). The cascade of tracer variance is halted at high vertical wavenumbers by vertical mixing, which counters the variance production by mesoscale stirring. If the along-isopycnal passive tracer variance surrounding the eddies was generated by their own stirring, we would expect their sizes to match the eddy length scale associated with

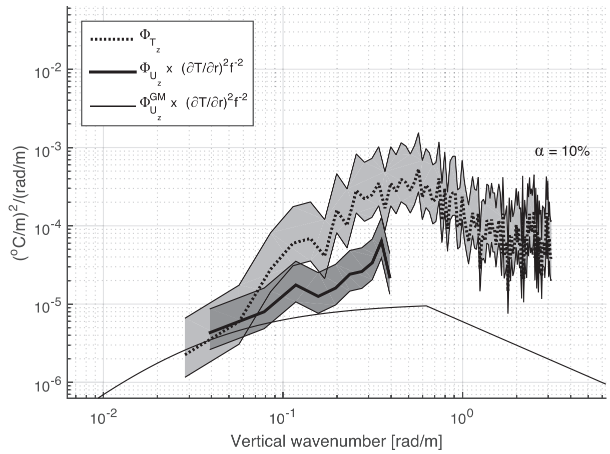

FIG. 12. Spectra of vertical derivatives of medium-scale temperature anomalies (dashed) and shear times $(\partial\overline{T}/\partial r)^2 f^{-2}$ for observations (bold black) and local GM (thin black). Error bars at the $\alpha = 10\%$ level are indicated by the shaded regions. If internal waves could account for all medium-scale temperature variance then the solid spectrum would exceed the dashed.

tracer variance generated by stirring across a mean gradient in accordance with mixing length theory (Tennekes and Lumley 1972):

$$L_{\mathrm{mix}} = \frac{(\overline{C'C'})^{1/2}}{\partial\overline{C}/\partial x}, \quad (4.9)$$

where C is some passive tracer, x is the cross-slope coordinate, and overlines indicate an average in time or space.

To unite density-compensated variations into a single variable we consider spice (Flament 2002) which effectively serves as a quantification of distance in T–S space orthogonal to isopycnals. We compute spice profiles $C(z)$ from the glider data along the Advective Path in addition to high-passed spice profiles $C_{\mathrm{HP}} = C - C_{\mathrm{LP}}$, which are the total profiles minus a filtered profile (triangular filter with width 25 m), thus retaining only the interleaving layers. Inspection of composites of $\overline{C'_{\mathrm{HP}}C'_{\mathrm{HP}}}$ across eddies A–E, where the over line indicates averaging in the vertical between [σ_{shal}, σ_{deep}], reveals that thermohaline variance is indeed largest at the eddy edges (Fig. 13). To visualize how spice variance is distributed more generally along the Advective Path, Fig. 14a shows a section of C on isopycnals and Fig. 14b collapses along-isopycnal variations into profiles of $\overline{C'C'}$ and $\overline{C'_{\mathrm{HP}}C'_{\mathrm{HP}}}$, where now primes are relative to the along-isopycnal mean and the products of anomalies are averaged on each isopycnal. Unsurprisingly, $\overline{C'C'}$ exhibits largest values in between [σ_{shal}, σ_{deep}], being overwhelmed by the presence or absence of warm core eddies. On the other hand, $\overline{C'_{\mathrm{HP}}C'_{\mathrm{HP}}}$ is less affected by the

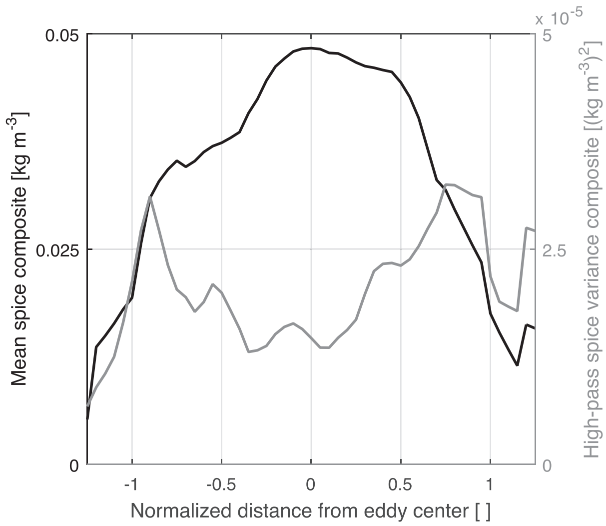

FIG. 13. Composite depth-mean spice anomaly (black) and high-pass-filtered spice variance (gray) between σ_{shal} and σ_{deep} for eddies A–E. Horizontal coordinate is stretched as in Fig. 4.

presence of eddies, making it much smaller within [σ_{shal}, σ_{deep}] but of comparable magnitude above.

Estimation of the mixing length requires knowledge of the mean spice gradient that is presumably stirred. Figure 14c shows time-averaged spice $\overline{C}$ along the 300 line (location of Marguerite Trough) as computed from the historic Pal LTER CTD data. There is a very strong gradient at the continental slope (180 station; gray line in Fig. 14d), however, unlike other grid lines, on the 300 line there is also a secondary region of large cross-slope spice gradient within [σ_{shal}, σ_{deep}] near the shoreward 130 station (blue line in Fig. 14d). We suspect that the gradient there is associated with the quasi-permanent diversion of the shelf-break current onto the shelf upon interacting with Marguerite Trough (Fig. 2).

Importantly, it is not known whether the interleaving layers are generated locally or remotely, so it is not obvious which is the relevant gradient to be stirred. Likewise, it is not immediately clear whether the relevant variance is $\overline{C'C'}$ or $\overline{C'_{HP}C'_{HP}}$ (i.e., should the high spice cores of the eddies be removed?). A conservative estimate is to assume that the variance is strictly that of the interleaving layers and that the gradient that is stirred is the local gradient within Marguerite Trough. That would suggest $L_{mix} = (\overline{C'_{HP}C'_{HP}})^{1/2}(\partial\overline{C}/\partial x\,|_{x=130})^{-1} = 5.6\,\mathrm{km}$ averaged between [σ_{shal}, σ_{deep}] (with range 3.4–7.5 km). An alternate perspective is to treat the warm eddy cores themselves as filamentary structures associated with stirring of the larger cross-slope gradient. In that case, $L_{mix} = (\overline{C'C'})^{1/2}(\partial\overline{C}/\partial x\,|_{x=180})^{-1} = 11.1\,\mathrm{km}$ (with range 3.4–17.2 km). Either way, the estimates are of the same order of magnitude as R and $|\mathbf{k}_{max}|^{-1}$. This suggests that the observed eddies are of sufficient size to generate the observed spice variance by stirring the mean spice gradient.

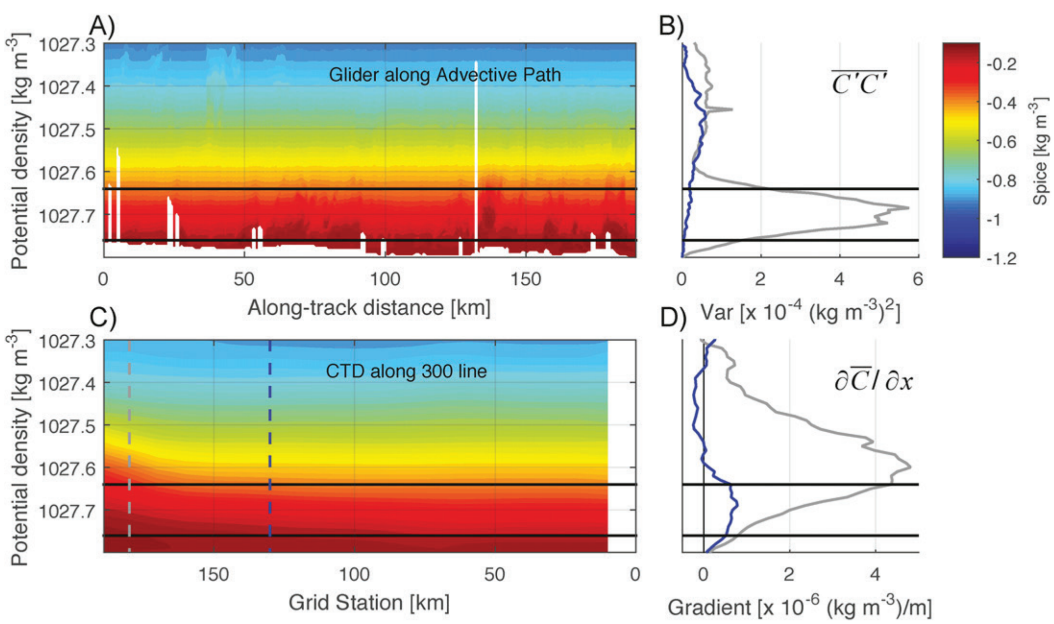

FIG. 14. (a) Spice C on isopycnals along Advective Path from glider. (b) Along-isopycnal variance of spice C (gray) and of high-pass-filtered spice C_{HP} (blue) for section in (a). (c) Cross-slope section of mean spice from climatological CTD data across the continental shelf at the 300 line. (d) Magnitude of the cross-slope spice gradient on isopycnals at the locations of the dashed lines in (c). In all panels σ_{shal} and σ_{deep} are indicated with black lines.

4) DISCUSSION

It is not obvious what causes the interleaving. Internal waves cannot provide enough temperature variance unless the lateral temperature gradient is on the larger end of those observed and the internal wave field is strongly biased toward inertial waves (which it somewhat is with $R_\omega = 9$). On the other hand, double diffusion, while qualitatively consistent with the vertical structure of the observations, tends to have slow growth rates. A more likely candidate appears to be stirring by the eddies of the cross-shelf temperature gradient within Marguerite Trough. Spice variance is largest at the eddy edges and its magnitude is consistent with the eddy sizes in accordance with mixing length theory. Thermohaline intrusions appear to be important for the decay of the eddies, particularly in their upper hemispheres, as cold neighboring water is brought inwards and warm slope water is ejected.

c. *Frictional spindown*

What appears to be cooling of the eddies may instead be redistribution of heat via a change in the buoyancy distribution of the eddy. Under the assumptions of a strictly vertical exchange of both mass and momentum, spindown of a geostrophically balanced along-front (or azimuthal) flow in the ocean interior leads to a secondary radial circulation that redistributes buoyancy so as to flatten isopycnals (Garrett 1982; Bormans 1992b). The potential vorticity equation takes the form of a diffusion equation in which the local time evolution of buoyancy B is balanced by a viscous spreading and a diapycnal diffusion of mass:

$$\frac{\partial B}{\partial t} = \frac{N^2}{f^2}\frac{\partial}{\partial r}\left(\nu\frac{\partial B}{\partial r}\right) + \frac{\partial}{\partial z}\left(K_z\frac{\partial B}{\partial z}\right). \tag{4.10}$$

Our data are incapable of being used to invert such a model, but we can make a few comments. The geostophic shear we calculate is evaluated at approximately the depth of the eddy core and is relative to the bottom, a depth range where we have previously shown there is strong potential for diapycnal mixing. It is possible that the turbulent mixing itself flattens isopycnals without the need for friction to reduce the azimuthal geostrophic flow. We do not know the Prandtl number $\mathrm{Pr} = \nu/K_z$ within these eddies, but it is generally thought to be of order 1. Assuming that it is 7 (canonical seawater value), an upper bound for a middepth value of the effective viscous spreading coefficient is of order $1\,\mathrm{m^2\,s^{-1}}$, which is comparable to the lateral diffusivity estimated in the previous section. There is insufficient evidence to confirm or refute any role of spindown in the eddies' decay.

5. Validation

Here we use a simple diffusion model informed by the results of the previous section to simulate the total heat loss of the eddy we tracked over crossings 1–5. We would like to emphasize that we do not expect to reproduce the small-scale structure of the eddy's cooling but instead aim to capture the bulk heat loss. The geometry of the first crossing gives us confidence that we passed directly through the eddy's center and through its entire diameter, therefore we set the initial condition as the hydrographic structure of the eddy as sampled on crossing 1. We identify the eddy's geographic center (x_1, y_1) and radius ($R_1 = 3.4\,\mathrm{km}$) as the mean and standard deviation, respectively, of a 2D Gaussian fit to the field of heat content per unit area integrated between σ_{shal} and σ_{deep}. We then assign each profile a radial distance from that center and grid the T and S on each isopycnal to construct a 3D field for the eddy. Outside of the eddy the domain is populated by the mCDW profile.

a. *Diffusion model*

We treat temperature and salinity as passive tracers and allow the eddy to diffuse in a domain $x = [-10\,\mathrm{km}, +10\,\mathrm{km}]$, $y = [-10\,\mathrm{km}, +10\,\mathrm{km}]$, and $z = [0\,\mathrm{m}, 480\,\mathrm{m}]$ with 250-m grid spacing in the horizontal and 2.5-m grid spacing in the vertical. The equation for temperature is

$$\left.\begin{aligned}
&\rho_0 c_p\frac{\partial T}{\partial t} = \rho_0 c_p K_h\left(\frac{\partial^2 T}{\partial x^2} + \frac{\partial^2 T}{\partial y^2}\right) + \rho_0 c_p\frac{\partial}{\partial z}\left[K_z(z)\frac{\partial T}{\partial z}\right],\\
&\frac{\partial T}{\partial z}(0) = \frac{\partial T}{\partial z}(-H) = 0,\\
&K_h = 3.2\,\mathrm{m^2\,s^{-1}},\\
&K_z(z) = \begin{cases} K_{\mathrm{top}} = 2.11\times10^{-5}\,\mathrm{m^2\,s^{-1}}, & z < 120\,\mathrm{m}\\ \text{log-linear increase between } K_{\mathrm{top}} \text{ and } K_{\mathrm{bot}}, & 120 \le z \le 400\,\mathrm{m}\\ K_{\mathrm{bot}} = 2.44\times10^{-3}\,\mathrm{m^2\,s^{-1}}, & z > 400\,\mathrm{m}\end{cases}
\end{aligned}\right\}, \tag{5.1}$$

and it is integrated for 4.5 days with a time step of 150 s using a finite-difference control volume approach. The diffusivity values are constant in time and are based on those parameterized in the previous section. The southern shelf composite K_z profile (Fig. 10) increases log linearly with depth from a value of $4.23 \times 10^{-6}\,\mathrm{m^2\,s^{-1}}$ at 120 m, however we found better results are achieved if we set K_{top} to be 5 times that value, which is within the reported 95% confidence interval.

b. Fit to data

We use a diffusion-only equation because the eddy's geographic coordinates $[x(t), y(t)]$ are additional unknowns. Therefore we assume that the eddy is advected by a depth-invariant current and seek an optimal $[x(\tau_i), y(\tau_i)]$ at each crossing i. We do this by performing a grid search by moving the modeled eddy to each location in a grid encompassing the glider track and then subsampling the modeled field along the glider track and calculating the depth-integrated heat content along the track. The position k that minimizes the root-mean-square (RMS) error between $Q^{\mathrm{obs}}(\tau_i)$ and $Q^{\mathrm{model},k}(\tau_i)$ defines the eddy center's location at time τ_i. On each crossing, there are a few profiles where thermohaline intrusions significantly attenuate that profile's heat per unit area and the presumed symmetry of the eddy and therefore they are excluded in the RMS fit (but are included when evaluating total along-track heat content).

To place error bars on our modeled heat content, we perturb the best fit eddy location by 1.2 km radially, again subsample the modeled field along the glider track, and then compute total along-track (x) and vertically (z) integrated heat content:

$$Q_{\mathrm{along}}(\tau_i) = \int_{x_{\mathrm{enter}}}^{x_{\mathrm{exit}}} \int_{z_{\sigma_{\mathrm{deep}}}}^{z_{\sigma_{\mathrm{shal}}}} \rho_0 c_p T_{\mathrm{anom}}(x, z, \tau_i)\, dz\, dx. \tag{5.2}$$

The spread in $Q_{\mathrm{along}}(\tau_i)$ provides a measure of uncertainty in the heat content of the best-fit eddy.

c. Results and interpretation

The best fit locations and modeled heat content are shown in Fig. 15. The predicted eddy track flows counter clockwise about the seamount east of Marguerite Trough (near 300.060), consistent with the mean flow, and the glider's excursion to the south confirms that this eddy did not go into Marguerite Bay. We are confident that the glider was indeed sampling the same eddy. Simulated particle trajectories (not shown) originating at $[x(\tau_1), y(\tau_1)]$ and using all possible 4-day sequences of the time-varying, depth-averaged current fields from Dinniman et al. (2011) confirm that parcels of water can follow the best-fit trajectory and can traverse the proposed distance traveled by the eddy over the total observation time.

In general, there is good agreement between the time series of observed and modeled along-track heat content (Fig. 15b). Particularly, the agreement is good near the edge of the eddy which contributes more to the integral of total heat content. There is a wide variety of intrusions, filimentation, and other submesoscale variability along the track. For example, the fourth crossing appears to skirt the eddy edge but contains a profile of water ejected from the eddy core. The second and third crossings appear to show the eddy core "split" by the cool layer that began penetrating the eddy during the first crossing. Obviously the model does not simulate these processes though it does seem capable of parameterizing their consequences. The total integrated heat contents fall within the range of perturbed model fits (Fig. 15c).

The results can be used to estimate the rate of heat loss of the eddy between crossings 1 and 5. The total heat content of the eddy during crossing 1 is easily obtained by integrating the model initial condition (itself a fit to the data) vertically between σ_{shal} and σ_{deep}, and then laterally out to R_1. At crossing 5, we obtain $Q_{\mathrm{max,chord}}$ and R_{chord} by fitting Eq. (2.1) to the data but to calculate the total heat content we need a cross section through the eddy center. Simple trigonometry shows that $R_{\mathrm{real}} = \sqrt{R_{\mathrm{chord}}^2 + D^2}$ and $Q_{\mathrm{max,real}} = Q_{\mathrm{max,chord}} \exp[+(D/R_{\mathrm{real}})^2]$, where D is the distance between the true eddy center and the chord-length center. Using $D = 2.5$ km (Fig. 15a), the total heat content is then obtained from Eq. (2.2) by using $Q_{\mathrm{max,real}}$ and R_{real} and integrating out to R_1. The initial and final heat contents are $Q_{\mathrm{tot}}(\tau_1) = 7.9 \times 10^{15}$ J and $Q_{\mathrm{tot}}(\tau_5) = 5.5 \times 10^{15}$ J, implying a cooling rate $\partial Q/\partial t = 7.0 \times 10^9\,\mathrm{J\,s^{-1}}$. It is worth noting that the modeled heat content on crossing 5 is 5.6×10^{15} J, only 2% greater than observed.

6. Discussions and conclusions

The first goal of this study was to understand the origin of UCDW eddies on the shelf. We conducted a linear stability analysis of the shelf-break current to show that its most unstable mode has a CDW-level amplitude maximum and an inverse wavenumber of 4.4 km. Glider observations confirmed that UCDW eddies on the shelf have diameters and crest-to-crest separation consistent with that metric and their anomalies are confined to the subpycnocline layer. The strong shear and weak stratification allow for sign changes in the interior potential vorticity gradient which cause instabilities smaller than the Rossby radius to persist

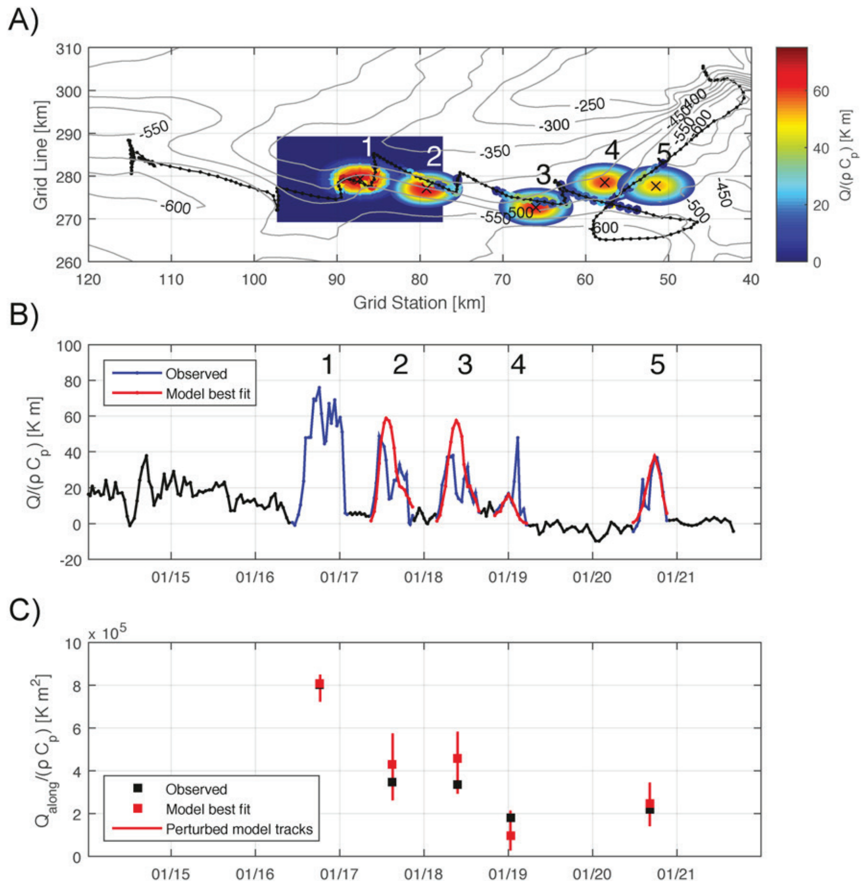

FIG. 15. Forward model results in comparison with glider data. (a) Glider track during the Tracking Stage (black line) where profiles containing the eddy are color coded by the vertically integrated heat content per unit area (dots). The contours are the diffusion model vertically integrated heat content per unit area at the time step of the crossing, situated at the geographic location that minimizes RMS error between the observed along-track series and the model field subsampled along the glider track. The first crossing shows the full model domain for scale. (b) Time series of observed (blue) and modeled (red) along-track heat content per unit area for each crossing of the eddy. (c) Time series of vertically and along-track-integrated heat content for each eddy. Observations are shown in black and the best fit model result is shown in red, along with error bars constructed by perturbing the model's best fit eddy location and then subsampling along the glider track and integrating.

even when Eady modes are suppressed by the bottom slope. This, in combination with the insensitivity to the planetary beta effect, suggests to us that similar UCDW eddies should be common around the Antarctic margins. However, we must be cautious with any broad extensions. While we have shown that either eastward or westward currents can support eddies, westward currents are often associated with the Antarctic Slope Front and very different stratification. The demonstrated sensitivity of eddy fluxes of CDW to other parameters that were not considered here, such as depth of the continental shelf or prominence of the Antarctic Slope Front (Stewart and Thompson 2015), restrict any generalizations and suggest eddy fluxes are still likely highly localized (Stewart et al. 2018) with one region of importance being the WAP.

The second goal of this study was to identify the major mixing processes that disperse eddy heat into surrounding water. Shipboard CTD and SADCP measurements were used to show cross-pycnocline diffusive fluxes should on average be $<1\ \mathrm{W\,m^{-2}}$ while fluxes below the eddy $T_{\max}$ should be an order of magnitude larger. CTD and glider profiles reveal that interleaving layers and thermohaline intrusions are ubiquitous, particularly in the lower pycnocline/eddy upper hemispheres where they link warm slope-type UCDW to the cooler waters within the adjacent water column's broad pycnocline. This water is most quickly

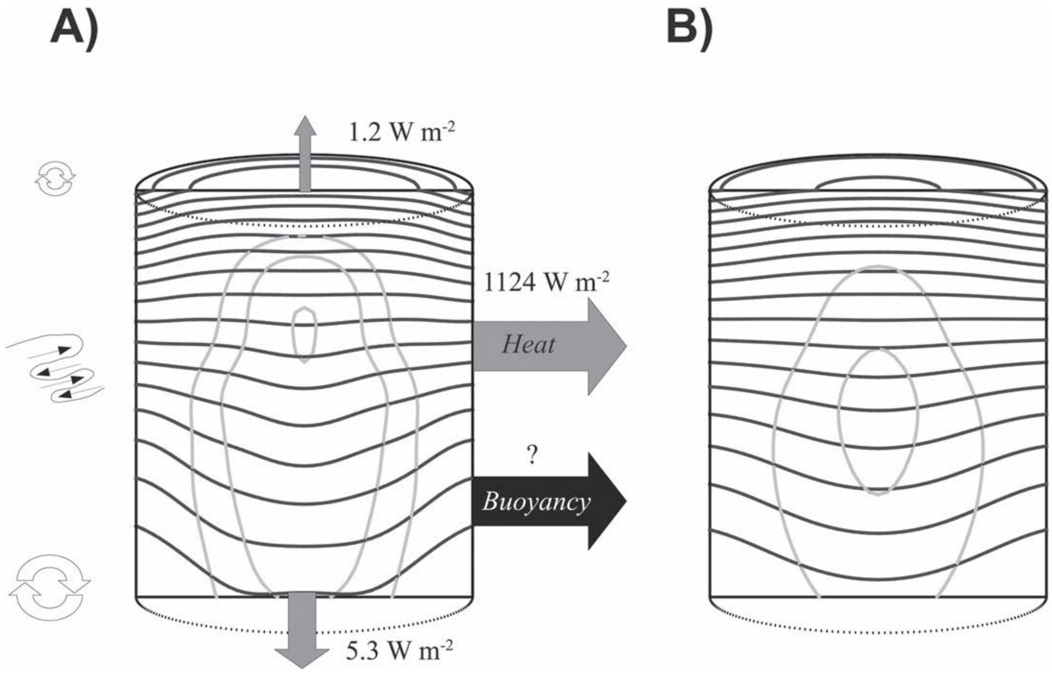

FIG. 16. Schematic summary of eddy heat loss processes and typical values for their fluxes based on the values in Table 1. The eddy is presented as a cylinder as in the integrated, averaged heat budget in the text. Isopycnals are shown as black lines, and three isotherms are shown as gray lines. (a) A schematic representation of the tracked eddy's initial condition and (b) schematic representation of the modeled eddy 4.5 days later. The same isolines are shown on each plot, suggesting that the temperature maximum is both eroded and mixed downward and that the geostrophic current is reduced. Lateral spreading of buoyancy by frictional spindown must occur, but its amount cannot be quantified with the glider data.

eroded over the Advective Path while the deeper, core $T_{\max}$ at ~250 m persists longer. The erosion of the core heat content per unit area is more apparent than that of the temperature maximum, implying erosion at the eddy boundaries and/or a redistribution of heat within the eddy interior. Consistent with this, high-pass-filtered spice variance is largest at the eddy edges.

The origin of the thermohaline intrusions is ambiguous. The magnitude of their thermal variance is larger than would be expected if due solely to internal wave shear, although this conclusion is highly dependent on the magnitude of the lateral temperature gradient across the eddy. In addition, thermal variance is largest above and just below the eddy core, both regions susceptible to double-diffusive instabilities. Instead, given the observed along-isopycnal spice variance, the mean spice gradient, and the size of the first-mode instability, a more plausible explanation for the origin of the interleaving layers may be stirring by the eddies themselves. A recent modeling study (Stewart et al. 2018) suggests that eddies may transfer heat across the Antarctic slope primarily by along-isopycnal stirring as opposed to advection by their overturning streamfunction. This also supports stirring as an explanation for the thermohaline variance.

The flexibility afforded by Slocum gliders allows for real-time, data-adaptive sampling. One of the novel aspects of this study is the collection of cross sections through an eddy as it traversed the shelf, providing a first estimate of the eddies' rate of cooling, which is consistent with that of a 3D diffusion model applied to the initial crossing. A lower limit on the time required to eliminate all heat relative to the mCDW profile within one radius from the eddy center is given by $Q_{\text{tot}}(\tau_1)/(\partial Q/\partial t) = 13.1$ days which assumes that the gradients are constant in time. Because lateral mixing dominates, an alternate cooling time is given by the solution to the two-dimensional diffusion equation with homogeneous lateral boundary conditions at infinity and a Gaussian initial condition of radius R. That solution implies that the heat content per unit area at the eddy center decreases as $R^2/(R^2 + 4K_h t)$. For the tracked eddy a 50% decrease is achieved after 10.3 days. For a typical eddy ($R = |\mathbf{k}_{\max}|^{-1}$), a 50% decrease takes 17.5 days.

We can synthesize these results with a heat budget integrated over a homogeneous eddy whose dimensions and gradients do not change in time:

$$\frac{1}{\rho_0 c_p}\frac{\partial Q_{\text{total}}}{\partial t} = 2\pi RHK_h \frac{\partial T}{\partial r}\bigg|_{r=R} + \pi R^2\left(K_z\frac{\partial T}{\partial z}\bigg|_{z=\text{top}} - K_z\frac{\partial T}{\partial z}\bigg|_{z=\text{bottom}}\right) + \varepsilon. \tag{6.1}$$

In this formulation, ε collects the mismatch between the left and right hand sides. It is meant to represent the effects of noise in the data but also captures the effects of processes that restructure the eddy. Because we only know $\partial Q/\partial t$ for the tracked eddy ($7.0 \times 10^9\,\mathrm{J\,s^{-1}}$), we balance the budget with that eddy's gradients and geometry averaged across crossings 1 and 5. For the tracked eddy, $R = 3.4\,\mathrm{km}$, $H = 188\,\mathrm{m}$, $\langle \partial T/\partial z|_{\text{top}}\rangle = 0.019°\,\mathrm{C\,m^{-1}}$, $\langle \partial T/\partial z|_{\text{bot}}\rangle = -0.0014°\,\mathrm{C\,m^{-1}}$, $\langle \partial T/\partial r|_{r=R}\rangle = 1.1 \times 10^{-4}\,°\mathrm{C\,m^{-1}}$, and the diffusivities are those used in the model, evaluated at the average depths of σ_{shal} and σ_{deep}. The balance implies the following conceptual model of eddy cooling. About 2% of initial heat loss occurs diapycnally through the permanent pycnocline; about 3% occurs diapycnally through the bottom and 95% occurs laterally. The lateral heat loss, which occurs in part through thermohaline intrusions, directly warms the surrounding pycnocline base and middepth waters. The diapycnal mixing through the bottom also works to flatten isopycnals at and below the $T_{\max}$ which reduces the azimuthal geostrophic current. The mismatch $\varepsilon/(\partial Q/\partial t) = 10\%$ is small, suggesting redistribution processes such as viscous spreading are of secondary importance compared to lateral mixing. To place this number in context, if the lateral diffusivity was increased from 3.2 to $3.6\,\mathrm{m^2\,s^{-1}}$ (which is within one standard error) then ε goes to zero. The budget is shown schematically in Fig. 16 with fluxes estimated for a more typical eddy (gradients and geometry from Table 1).

Importantly, a preference for the eddies to mix laterally and downward suggests that the eddies are good at redistributing heat rather than immediately venting it to the atmosphere. This sheltering has implications for the ability of intra and subpycnocline heat to persist and make its way shoreward toward marine-terminating glaciers even as the eddies themselves cease to remain coherent structures.

Acknowledgments. McKee and Martinson were supported by NSF Grants OPP-08-23101 and PLR-1440435; Schofield was supported by NSF Grant ANT-08-23101 and NASA Grant NNX14AL86G. Richard Iannuzzi processed the CTD and glider data, made Fig. 1, and provided valuable comments. We thank David Aragon and the Rutgers COOL group for deploying the glider and providing logistical support. We also thank Pat Caldwell at the JASADCP for culling and providing the SADCP data and Mike Dinniman for providing model current fields. We also acknowledge the captains and crews of the *L.M. Gould* and the *N.B. Palmer* for their efforts in acquiring many years of LTER data. Insightful comments from the editor and two anonymous reviewers greatly improved this manuscript. This is LDEO contribution 8310 and Palmer LTER contribution 620.

APPENDIX

The Garrett–Munk Spectrum on the WAP Continental Shelf

The Garrett–Munk (GM; Garrett and Munk 1975) spectrum provides an empirical description of the internal wave field in a flat-bottom open ocean away from boundaries and is frequently used to provide a statistical measure of internal wave variability in mixing parameterizations of nonlinear wave–wave interactions (e.g., G89). The GM spectrum ignores the presence of upper and lower boundaries and vertical structure in the wave field is manifested through a series of modal structures. Two fundamental parameters that scale the spectrum are a nondimensional energy E (canonically 6.3×10^{-5}) and a stratification depth b (canonically 1300 m). The GM shear spectrum is

$$\Phi_{\text{shear}} = \frac{Eb^3}{2\pi j_*}\left(\frac{N_0}{N}\right)\frac{\beta^2}{(1+\beta/\beta_*)^2}, \tag{A.1}$$

where β is the vertical wavenumber ($\mathrm{rad\,m^{-1}}$), $\beta_* = (\pi j_*/b)(N/N_0)$ is a reference wavenumber, $N_0 = 0.0052\ \mathrm{rad\,s^{-1}}$ is the canonical reference stratification, and $j_* = 3$ is the canonical mode number. A roll-off of -1 is imposed at wavenumbers greater than $\beta_c = 0.2\pi\ \mathrm{rad\,m^{-1}}$.

On the WAP continental shelf with typical bottom depths of ~400 m, the nondimensional energy E and the stratification scale b are likely quite different from canonical values (Levine 2002). Here we maintain the GM functional form (thus neglecting vertical boundaries) but adjust E and b in accordance with the environment of the WAP. One way to do so (section 4c of Levine 2002) is to first estimate the product $N_0 b$ from the observed stratification $N(z)$ and then to estimate the energy density in the internal wave band. We estimate $N(z)$ by first computing an average density profile from all summertime (January and February) Shelf CTD casts. For all casts, the depths of a set of evenly spaced isopycnals are calculated via linear interpolation and each isopycnal is assigned its mean depth. The resulting potential density profile is then interpolated to an 8-m grid and finite-differenced in order to obtain a profile of mean $N(z)$. The product $N_0 b$, which scales the wavenumber bandwidth, is defined as

$$N_0 b = \int_{404\,\mathrm{m}}^{24\,\mathrm{m}} N(z)\,dz = 1.5\,\mathrm{m\,s^{-1}}, \tag{A.2}$$

so that $b = 288\,\mathrm{m}$. The profile of mean N squared is shown in Fig. 9a. The lower integration bound is chosen as an average depth of all shelf stations and the upper integration bound is chosen as a typical seasonal mixed layer depth since overturns in the averaged density profile become apparent shallower than that [because the depth of the seasonal mixed layer varies regionally and interannually, the mean $N(z)$ profile is quasi-exponential with no apparent seasonal mixed layer]. Parameters N_0 and j_* are left at their canonical values.

To estimate the nondimensional energy density, we first estimate the kinetic energy density KE via baroclinic energy spectra from the moored current meter data of Martinson and McKee (2012). Their current meter data generally sample once per hour, however in 2007 they have one year-long record at site 300.100 that sampled once every 20 min with two current meters spanning the permanent pycnocline (one each nominally at $T_{\min}$ and $T_{\max}$). We define the barotropic current as the average of the two records and subtract that out. Then, the spectrum of the residual baroclinic current at each depth is calculated via squaring the Fourier transform of the complex time series, is averaged in the vertical, and is integrated over $[f, N_0]$. While the Nyquist frequency for this sampling is $0.5N_0$, the -2 roll-off in the internal wave band reveals that most of the contribution to the integral comes from the lower portion of the band. The depth average of the two integrated spectra times 1/2 yields the kinetic energy density (KE) and the nondimensional energy density is given by

$$E = \mathrm{KE}/(N_0 b)^2 = 3.0 \times 10^{-4}. \tag{A.3}$$

We now consider how the modified GM spectrum translates to parameterized diffusivities. Dissipation in the G89 model is given by

$$\varepsilon = \left[1.96\left(\frac{1.67}{\pi}\right) j_*^2 b^2 N_0^2 E^2 f_0 \operatorname{acosh}(N_0/f_0)\right]\left(\frac{N^2}{N_0^2}\right)\left(\frac{S^4}{S_{\mathrm{GM}}^4}\right)$$
$$= \varepsilon_0 \left(\frac{N^2}{N_0^2}\right)\left(\frac{S^4}{S_{\mathrm{GM}}^4}\right), \tag{A.4}$$

where the constant ε_0 is derived from wave–wave interactions in the GM energy flux spectrum. The assumption of a steady turbulent kinetic energy balance and a constant mixing ratio yields the relation for the diffusivity

$$K_z = \frac{\Gamma\varepsilon_0}{N^2}\left(\frac{N^2}{N_0^2}\right)\left(\frac{S^4}{S_{\mathrm{GM}}^4}\right) = K_0\left(\frac{S^4}{S_{\mathrm{GM}}^4}\right) \tag{A.5}$$

as presented in the text [but here without the corrections h and j; Eqs. (4.4) and (4.5)]. Under the canonical GM spectrum, $K_0 = 5.0 \times 10^{-6}\,\mathrm{m^2\,s^{-1}}$ whereas for the local parameters derived above $K_0 = 5.6 \times 10^{-6}\,\mathrm{m^2\,s^{-1}}$, which is a small difference. In addition, compared to shear variances using canonical GM parameters, integrated shear variances using the corrected GM parameters yield diffusivities that are generally up to a factor of 2 greater in the upper water column but almost equal near the $T_{\max}$. Given that the G89 method is demonstrated to be accurate within a factor of 2, all of this suggests that the improvements afforded by the corrected GM spectrum are small.

REFERENCES

Amante, C., and B. W. Eakins, 2009: ETOPO1 1 Arc-Minute Global Relief Model: Procedures, data sources and analysis. NOAA Tech. Memo. NESDIS NGDC-24, National Geophysical Data Center, 25 pp., https://www.ngdc.noaa.gov/mgg/global/relief/ETOPO1/docs/ETOPO1.pdf.

Beardsley, R. C., R. Limeburner, and B. W. Owens, 2004: Drifter measurements of surface currents near Marguerite Bay on the western Antarctic Peninsula shelf during austral summer and fall, 2001 and 2002. *Deep-Sea Res. II*, **51**, 1947–1964, https://doi.org/10.1016/j.dsr2.2004.07.031.

Blumsack, S. L., and P. J. Gierasch, 1972: Mars: The effects of topography on baroclinic instability. *J. Atmos. Sci.*, **29**, 1081–1089, https://doi.org/10.1175/1520-0469(1972)029<1081:MTEOTO>2.0.CO;2.

Bormans, M., 1992a: Effect of density ratio on double diffusive interleaving. *Deep-Sea Res.*, **39**, 871–884, https://doi.org/10.1016/0198-0149(92)90126-E.

——, 1992b: An experimental study on the formation and survival of stratified subsurface eddies. *J. Geophys. Res.*, **97**, 20 155–20 167, https://doi.org/10.1029/92JC01973.

Cook, A. J., P. R. Holland, M. P. Meredith, T. Murray, A. Luckman, and D. G. Vaughan, 2016: Ocean forcing of glacier retreat in the western Antarctic Peninsula. *Science*, **353**, 283–286, https://doi.org/10.1126/science.aae0017.

Couto, N., D.G. Martinson, J. Kohut, and O. Schofield, 2017: Distribution of Upper Circumpolar Deep Water on the warming continental shelf of the West Antarctic Peninsula. *J. Geophys. Res. Oceans*, **122**, 5306–5315, https://doi.org/10.1002/2017JC012840.

Dewey, R., R. Muench, and J. Gunn, 1999: Mixing and vertical heat flux estimates in the Arctic Eurasian Basin. *J. Mar. Syst.*, **21**, 199–205, https://doi.org/10.1016/S0924-7963(99)00014-7.

Dinniman, M. S., and J. M. Klinck, 2004: A model study of circulation and cross-shelf exchange on the west Antarctic Peninsula continental shelf. *Deep-Sea Res. II*, **51**, 2003–2022, https://doi.org/10.1016/j.dsr2.2004.07.030.

——, ——, and W. O. Smith Jr., 2011: A model study of Circumpolar Deep Water on the West Antarctic Peninsula and Ross

Sea continental shelves. *Deep-Sea Res. II*, **58**, 1508–1523, https://doi.org/10.1016/j.dsr2.2010.11.013.

——, ——, and E. E. Hofmann, 2012: Sensitivity of circumpolar deep water transport and ice shelf basal melt along the West Antarctic Peninsula to changes in the winds. *J. Climate*, **25**, 4799–4816, https://doi.org/10.1175/JCLI-D-11-00307.1.

Eveleth, R., N. Cassar, S. C. Doney, D. R. Munro, and C. Sweeney, 2017: Biological and physical controls on O_2/Ar, Ar, and pCO_2 variability at the Western Antarctic Peninsula and in the Drake Passage. *Deep-Sea Res. II*, **139**, 77–88, https://doi.org/10.1016/j.dsr2.2016.05.002.

Flament, P., 2002: A state variable for characterizing water masses and their diffusive stability: Spiciness. *Prog. Oceanogr.*, **54**, 493–501, https://doi.org/10.1016/S0079-6611(02)00065-4.

Garau, B., S. Ruiz, W. G. Zhang, A. Pascual, E. Heslop, J. Kerfoot, and J. Tintoré, 2011: Thermal lag correction on Slocum CTD glider data. *J. Atmos. Oceanic Technol.*, **28**, 1065–1071, https://doi.org/10.1175/JTECH-D-10-05030.1.

Garrett, C., 1982: On spindown in the ocean interior. *J. Phys. Oceanogr.*, **12**, 989–993, https://doi.org/10.1175/1520-0485(1982)012<0989:OSITOI>2.0.CO;2.

——, and W. Munk, 1975: Space-time scales of internal waves: A progress report. *J. Geophys. Res.*, **80**, 291–297, https://doi.org/10.1029/JC080i003p00291.

Gordon, A. L., 1971: Oceanography of Antarctic waters. *Antarct. Res. Ser.*, **15**, 169–203, https://doi.org/10.1029/AR015p0169.

Gordon, R. L., and N. F. Marshall, 1976: Submarine canyons: Internal wave traps? *Geophys. Res. Lett.*, **3**, 622–624, https://doi.org/10.1029/GL003i010p00622.

Gouretski, V. V., and K. P. Koltermann, 2004: WOCE global hydrographic climatology: A technical report. Bundesamt für Seeschifffahrt und Hydrographie Rep. 35, 52 pp.

Graham, J. A., M. S. Dinniman, and J. M. Klinck, 2016: Impact of model resolution for on-shelf heat transport along the West Antarctic Peninsula. *J. Geophys. Res.*, **121**, 7880–7897, https://doi.org/10.1002/2016JC011875.

Gregg, M. C., 1989: Scaling turbulent dissipation in the thermocline. *J. Geophys. Res.*, **94**, 9686–9698, https://doi.org/10.1029/JC094iC07p09686.

——, and T. B. Sanford, 1988: The dependence of turbulent dissipation on stratification in a diffusively stable thermocline. *J. Geophys. Res.*, **93**, 12 381–12 392, https://doi.org/10.1029/JC093iC10p12381.

——, ——, and D. P. Winkel, 2003: Reduced mixing from the breaking of internal waves in equatorial waters. *Nature*, **422**, 513–515, https://doi.org/10.1038/nature01507.

Hebert, D., N. Oakey, and B. R. Ruddick, 1990: Evolution of a Mediterranean salt lens: Scalar properties. *J. Phys. Oceanogr.*, **20**, 1468–1483, https://doi.org/10.1175/1520-0485(1990)020<1468:EOAMSL>2.0.CO;2.

Howard, S. L., J. Hyatt, and L. Padman, 2004: Mixing in the pycnocline over the western Antarctic Peninsula Shelf during Southern Ocean GLOBEC. *Deep-Sea Res. II*, **51**, 1965, https://doi.org/10.1016/j.dsr2.2004.08.002.

Isachsen, P. E., 2011: Baroclinic instability and eddy tracer transport across sloping bottom topography: How well does a modified Eady model do in primitive equation simulations? *Ocean Modell.*, **39**, 183–199, https://doi.org/10.1016/j.ocemod.2010.09.007.

Jackett, D. R., and T. J. McDougall, 1997: A neutral density variable for the world's oceans. *J. Phys. Oceanogr.*, **27**, 237–263, https://doi.org/10.1175/1520-0485(1997)027<0237:ANDVFT>2.0.CO;2.

Joyce, T. M., 1977: A note on the lateral mixing of water masses. *J. Phys. Oceanogr.*, **7**, 626–629, https://doi.org/10.1175/1520-0485(1977)007<0626:ANOTLM>2.0.CO;2.

Klinck, J. M., 1998: Heat and salt changes on the continental shelf west of the Antarctic Peninsula between January 1993 and January 1994. *J. Geophys. Res.*, **103**, 7617–7636, https://doi.org/10.1029/98JC00369.

——, E. E. Hofmann, R. C. Beardsley, B. Salihoglu, and S. Howard, 2004: Water-mass properties and circulation on the West Antarctic Peninsula continental shelf in austral fall and winter 2001. *Deep-Sea Res. II*, **51**, 1925–1946, https://doi.org/10.1016/j.dsr2.2004.08.001.

Kunze, E., E. Firing, J. M. Hummon, T. K. Chereskin, and A. M. Thurnherr, 2006: Global abyssal mixing inferred from lowered ADCP shear and CTD strain profiles. *J. Phys. Oceanogr.*, **36**, 1553–1576, https://doi.org/10.1175/JPO2926.1.

Levine, M. D., 2002: A modification of the Garrett–Munk internal wave spectrum. *J. Phys. Oceanogr.*, **32**, 3166–3181, https://doi.org/10.1175/1520-0485(2002)032<3166:AMOTGM>2.0.CO;2.

Martinson, D. G., and R. A. Iannuzzi, 1998: Antarctic ocean-ice interaction: Implications from ocean bulk property distributions in the Weddell Gyre. *Antarctic Sea Ice: Physical Processes, Interactions and Variability*, M. Jeffries, Ed., Antarctic Research Series, Vol. 74, Amer. Geophys. Union, 243–271.

——, and D. C. McKee, 2012: Transport of warm Upper Circumpolar Deep Water onto the western Antarctic Peninsula continental shelf. *Ocean Sci.*, **8**, 433–442, https://doi.org/10.5194/os-8-433-2012.

——, S. E. Stammerjohn, R. A. Iannuzzi, R. C. Smith, and M. Vernet, 2008: Western Antarctic Peninsula physical oceanography and spatio-temporal variability. *Deep-Sea Res. II*, **55**, 1964–1987, https://doi.org/10.1016/j.dsr2.2008.04.038.

McDougall, T. J., 1985a: Double-diffusive interleaving. Part I: Linear stability analysis. *J. Phys. Oceanogr.*, **15**, 1532–1541, https://doi.org/10.1175/1520-0485(1985)015<1532:DDIPIL>2.0.CO;2.

——, 1985b: Double-diffusive interleaving. Part II: Finite amplitude steady state interleaving. *J. Phys. Oceanogr.*, **15**, 1542–1556, https://doi.org/10.1175/1520-0485(1985)015<1542:DDIPIF>2.0.CO;2.

Moffat, C., and M. Meredith, 2018: Shelf-ocean exchange and hydrography west of the Antarctic Peninsula: A review. *Philos. Trans. Roy. Soc. A.*, **376**, 20170164, https://doi.org/10.1098/rsta.2017.0164.

——, B. Owens, and R. C. Beardsley, 2009: On the characteristics of Circumpolar Deep Water intrusions to the west Antarctic Peninsula Continental Shelf. *J. Geophys. Res.*, **114**, C05017, https://doi.org/10.1029/2008JC004955.

Naveira Garabato, A. C., K. L. Polzin, B. A. King, K. J. Heywood, and M. Visbeck, 2004: Widespread intense turbulent mixing in the Southern Ocean. *Science*, **303**, 210–213, https://doi.org/10.1126/science.1090929.

Orsi, A. H., T. Whitworth, and W. D. Nowlin, 1995: On the meridional extent and fronts of the Antarctic Circumpolar Current. *Deep-Sea Res. I*, **42**, 641–673, https://doi.org/10.1016/0967-0637(95)00021-W.

Pacanowski, R. C., and S. G. H. Philander, 1981: Parameterization of vertical mixing in numerical models of tropical oceans. *J. Phys. Oceanogr.*, **11**, 1443–1451, https://doi.org/10.1175/1520-0485(1981)011<1443:POVMIN>2.0.CO;2.

Pedlosky, J., 1987: *Geophysical Fluid Dynamics*. 2nd ed. Springer-Verlag, 710 pp.

Pelland, N. A., C. C. Eriksen, and C. M. Lee, 2013: Subthermocline eddies over the Washington continental slope as observed by seagliders, 2003–09. *J. Phys. Oceanogr.*, **43**, 2025–2053, https://doi.org/10.1175/JPO-D-12-086.1.

Phillips, N. A., 1954: Energy transformations and meridional circulations associated with simple baroclinic waves in a two-level, quasi-geostrophic model. *Tellus*, **6**, 273–286, https://doi.org/10.1111/j.2153-3490.1954.tb01123.x.

Poulin, F. J., A. Stegner, M. Hernandez-Arencibia, A. Marrero-Diaz, and P. Sangra, 2014: Steep shelf stabilization of the Bransfield coastal current: linear stability analysis. *J. Phys. Oceanogr.*, **44**, 714–732, https://doi.org/10.1175/JPO-D-13-0158.1.

Schmidtko, S., K. J. Heywood, A. F. Thompson, and S. Aoki, 2014: Multidecadal warming of Antarctic waters. *Science*, **346**, 1227–1231, https://doi.org/10.1126/science.1256117.

Schofield, O., and Coauthors, 2007: Slocum gliders: Robust and ready. *J. Field Robot.*, **24**, 473–485, https://doi.org/10.1002/rob.20200.

Smith, D. A., E. E. Hofmann, J. M. Klinck, and C. M. Lascara, 1999: Hydrography and circulation of the West Antarctic Peninsula Continental Shelf. *Deep-Sea Res. I*, **46**, 925–949, https://doi.org/10.1016/S0967-0637(98)00103-4.

Smith, K. S., 2007: The geography of linear baroclinic instability in Earth's oceans. *J. Mar. Res.*, **65**, 655–683, https://doi.org/10.1357/002224007783649484.

——, and R. Ferrari, 2009: The production and dissipation of compensated thermohaline variance by mesoscale stirring. *J. Phys. Oceanogr.*, **39**, 2477–2501, https://doi.org/10.1175/2009JPO4103.1.

Smith, R. C., and Coauthors, 1995: The Palmer LTER: A long-term ecological research program at Palmer Station, Antarctica. *Oceanography*, **8**, 77–86, https://doi.org/10.5670/oceanog.1995.01.

Spence, P., S. M. Griffies, M. H. England, A. M. C. Hogg, O. A. Saenko, and N. C. Jourdain, 2014: Rapid subsurface warming and circulation changes of Antarctic coastal waters by poleward shifting winds. *Geophys. Res. Lett.*, **41**, 4601–4610, https://doi.org/10.1002/2014GL060613.

——, R. M. Holmes, A. M. Hogg, S. M. Griffies, K. D. Stewart, and M. H. England, 2017: Localized rapid warming of West Antarctic subsurface waters by remote winds. *Nat. Climate Change*, **7**, 595–603, https://doi.org/10.1038/nclimate3335.

Stern, A. A., D. M. Holland, and L. P. Nadeau, 2015: Instability of ocean jets along the Antarctic continental slope. *J. Phys. Oceanogr.*, **45**, 2315–2338, https://doi.org/10.1175/JPO-D-14-0213.1.

Stewart, A. L., and A. F. Thompson, 2015: Eddy-mediated transport of warm Circumpolar Deep Water across the Antarctic Shelf Break. *Geophys. Res. Lett.*, **42**, 432–440, https://doi.org/10.1002/2014GL062281.

——, A. Klocker, and D. Menemenlis, 2018: Circum-Antarctic shoreward heat transport derived from an eddy- and tide-resolving simulation. *Geophys. Res. Lett.*, **45**, 834–845, https://doi.org/10.1002/2017GL075677.

St-Laurent, P., J. M. Klinck, and M. S. Dinniman, 2013: On the role of coastal troughs in the circulation of warm Circumpolar Deep Water on Antarctic shelves. *J. Phys. Oceanogr.*, **43**, 51–64, https://doi.org/10.1175/JPO-D-11-0237.1.

Tennekes, H., and J. L. Lumley, 1972: *A First Course in Turbulence*. 1st ed. MIT Press, 300 pp.

Thompson, A. F., S. T. Gille, J. A. MacKinnon, and J. Sprintall, 2007: Spatial and temporal patterns of small-scale mixing in Drake Passage. *J. Phys. Oceanogr.*, **37**, 572–592, https://doi.org/10.1175/JPO3021.1.

Turner, J., T. Maksym, T. Phillips, G. J. Marshall, and M. P. Meredith, 2013: The impact of changes in sea ice advance on the large winter warming on the western Antarctic Peninsula. *Int. J. Climatol.*, **33**, 852–861, https://doi.org/10.1002/joc.3474.

frontiers in Marine Science

REVIEW
published: 02 October 2019
doi: 10.3389/fmars.2019.00422

OceanGliders: A Component of the Integrated GOOS

Pierre Testor[1], Brad de Young[2], Daniel L. Rudnick[3], Scott Glenn[4], Daniel Hayes[5], Craig M. Lee[6], Charitha Pattiaratchi[7], Katherine Hill[8], Emma Heslop[9], Victor Turpin[1], Pekka Alenius[10], Carlos Barrera[11], John A. Barth[12], Nicholas Beaird[4], Guislain Bécu[13], Anthony Bosse[14], François Bourrin[15], J. Alexander Brearley[16], Yi Chao[17], Sue Chen[18], Jacopo Chiggiato[19], Laurent Coppola[20], Richard Crout[21], James Cummings[18], Beth Curry[6], Ruth Curry[22], Richard Davis[23], Kruti Desai[24], Steve DiMarco[25], Catherine Edwards[26], Sophie Fielding[16], Ilker Fer[14], Eleanor Frajka-Williams[27], Hezi Gildor[28], Gustavo Goni[29], Dimitri Gutierrez[30], Peter Haugan[14,31], David Hebert[32], Joleen Heiderich[33,34], Stephanie Henson[27], Karen Heywood[35], Patrick Hogan[36], Loïc Houpert[27,37], Sik Huh[38], Mark E. Inall[37], Masso Ishii[39], Shin-ichi Ito[40], Sachihiko Itoh[40], Sen Jan[41], Jan Kaiser[35], Johannes Karstensen[42], Barbara Kirkpatrick[43], Jody Klymak[44], Josh Kohut[4], Gerd Krahmann[42], Marjolaine Krug[45], Sam McClatchie[46], Frédéric Marin[47], Elena Mauri[48], Avichal Mehra[49], Michael P. Meredith[16], Thomas Meunier[50], Travis Miles[4], Julio M. Morell[51], Laurent Mortier[52], Sarah Nicholson[45], Joanne O'Callaghan[53], Diarmuid O'Conchubhair[54], Peter Oke[55], Enric Pallàs-Sanz[50], Matthew Palmer[27], JongJin Park[56], Leonidas Perivoliotis[57], Pierre-Marie Poulain[58], Ruth Perry[59], Bastien Queste[35], Luc Rainville[6], Eric Rehm[13], Moninya Roughan[60], Nicholas Rome[24], Tetjana Ross[61], Simon Ruiz[62], Grace Saba[4], Amandine Schaeffer[60], Martha Schönau[63], Katrin Schroeder[19], Yugo Shimizu[63], Bernadette M. Sloyan[55], David Smeed[27], Derrick Snowden[64], Yumi Song[56], Sebastian Swart[65,66], Miguel Tenreiro[50], Andrew Thompson[67], Joaquin Tintore[68], Robert E. Todd[34], Cesar Toro[69], Hugh Venables[16], Taku Wagawa[70], Stephanie Waterman[71], Roy A. Watlington[72] and Doug Wilson[72]*

[1] CNRS-Sorbonne Universités (UPMC Univ. Pierre et Marie Curie, Paris 06)-CNRS-IRD-MNHN, UMR 7159, Laboratoire d'Océanographie et de Climatologie (LOCEAN), Institut Pierre Simon Laplace (IPSL), Observatoire Ecce Terra, Paris, France, [2] Department of Physics and Physical Oceanography, Memorial University, Memorial University of Newfoundland, St. John's, NL, Canada, [3] Scripps Institution of Oceanography, San Diego, CA, United States, [4] Department of Marine and Coastal Sciences, Rutgers University, New Brunswick, NJ, United States, [5] Oceanography Centre, University of Cyprus (OC-UCY), Nicosia, Cyprus, [6] Applied Physics Laboratory, University of Washington, Seattle, WA, United States, [7] Oceans Graduate School, The University of Western Australia, Perth, WA, Australia, [8] World Meteorological Organization, Geneva, Switzerland, [9] UNESCO, Paris, France, [10] Finnish Meteorological Institute, Helsinki, Finland, [11] Oceanic Platform of the Canary Islands, Telde, Spain, [12] College of Earth, Ocean, and Atmospheric Sciences, Oregon State University, Corvallis, OR, United States, [13] Takuvik, Quebec, QC, Canada, [14] Geophysical Institute, University of Bergen, Bergen, Norway, [15] CEFREM, Perpignan, France, [16] British Antarctic Survey, Cambridge, United Kingdom, [17] Seatrec, Monrovia, CA, United States, [18] Naval Research Laboratory, Monterey, CA, United States, [19] CNR- Institute of Marine Sciences (ISMAR), Venice, Italy, [20] Laboratoire d'Océanographie de Villefranche (LOV), UMR7093 (Sorbonne Université/CNRS), Institut de la Mer de Villefranche (IMEV), Villefranche-sur-Mer, France, [21] Naval Research Laboratory, Stennis, MS, United States, [22] Bermuda Institute of Ocean Sciences, Saint George, Bermuda, [23] Department of Oceanography, Dalhousie University, Halifax, NS, Canada, [24] OceanLeadership, Washington, DC, United States, [25] Department of Oceanography, Texas A&M University, College Station, TX, United States, [26] Skidaway Institute of Oceanography, University of Georgia, Athens, GA, United States, [27] National Oceanography Centre, Southampton, United Kingdom, [28] Institute of Earth Sciences, The Hebrew University of Jerusalem, Jerusalem, Israel, [29] NOAA Atlantic Oceanographic and Meteorological Laboratory, Miami, FL, United States, [30] Institute of the Sea of Peru, Callao, Peru, [31] Institute of Marine Research, Bergen, Norway, [32] Department of Fisheries and Oceans, Bedford Institute of Oceanography, Dartmouth, NS, Canada, [33] Massachusetts Institute of Technology, Cambridge, MA, United States, [34] Woods Hole Oceanographic Institution, Woods Hole, MA, United States, [35] School of Environmental Sciences, Centre for Ocean and Atmospheric Sciences, University of East Anglia, Norwich, United Kingdom, [36] United States Naval Research Laboratory, Washington, DC, United States, [37] Scottish Association for Marine Science, Oban, United Kingdom, [38] Korea Institute of Ocean Science and Technology, Ansan-si, South Korea, [39] Meteorological Research Institute, Tsukuba, Japan, [40] Atmosphere and Ocean Research Institute, The University of Tokyo, Chiba, Japan, [41] Institute of Oceanography, National Taiwan University, Taipei, Taiwan, [42] GEOMAR Helmholtz Center for Ocean Research Kiel, Kiel, Germany, [43] Gulf of Mexico Coastal Ocean Observing System, College Station, TX, United States

OPEN ACCESS

Edited by:
Amos Tiereyangn Kabo-Bah, University of Energy and Natural Resources, Ghana

Reviewed by:
Yanhui Wang, Tianjin University, China
Shuxin Wang, Tianjin University, China

****Correspondence:***
Pierre Testor
testor@locean-ipsl.upmc.fr

Specialty section:
This article was submitted to Ocean Observation, a section of the journal Frontiers in Marine Science

Received: *31 October 2018*
Accepted: *05 July 2019*
Published: *02 October 2019*

[44] Ocean Physics Group, University of Victoria, Victoria, BC, Canada, [45] Council for Scientific and Industrial Research, Cape Town, South Africa, [46] FishOcean Enterprises, Auckland, New Zealand, [47] LEGOS/IRD, Toulouse, France, [48] Istituto Nazionale di Oceanografia e di Geofisica Sperimentale, Trieste, Italy, [49] NOAA National Centers for Environmental Prediction, College Park, MD, United States, [50] Ensenada Center for Scientific Research and Higher Education, Ensenada, Mexico, [51] Department of Marine Sciences, University of Puerto Rico at Mayagüez, Mayagüez, Puerto Rico, [52] ENSTA/LOCEAN, Palaiseau, France, [53] National Institute of Water and Atmospheric Research, Wellington, New Zealand, [54] Marine Institute, Galway, Ireland, [55] CSIRO, Oceans and Atmosphere, Hobart, TAS, Australia, [56] School of Earth System Sciences, Kyungpook National University, Daegu, South Korea, [57] Hellenic Center for Marine Research, Heraklion, Greece, [58] Centre for Maritime Research and Experimentation, La Spezia, Italy, [59] Shell, Houston, TX, United States, [60] School of Mathematics and Statistics, University of New South Wales, Sydney, NSW, Australia, [61] Department of Fisheries and Oceans, Institute of Ocean Sciences, Sidney, BC, Canada, [62] Instituto Mediterráneo de Estudios Avanzados, CSIC-UIB, Esporles, Spain, [63] Applied Ocean Science, Fairfax Station, VA, United States, [64] National Oceanic and Atmospheric Administration, Washington DC, United States, [65] Department of Marine Sciences, University of Gothenburg, Gothenburg, Sweden, [66] Department of Oceanography, University of Cape Town, Cape Town, South Africa, [67] California Institute of Technology, Pasadena, CA, United States, [68] SOCIB and IMEDEA (CSIC-UIB), Palma de Mallorca, Spain, [69] IOC-UNESCO, IOCARIBE, Paris, France, [70] Japan Fisheries Research and Education Agency, Yokohama, Japan, [71] Department of Earth, Ocean and Atmospheric Sciences, University of British Columbia, Vancouver, BC, Canada, [72] Caribbean Coastal Ocean Observing System, Mayagüez, Puerto Rico

The *OceanGliders* program started in 2016 to support active coordination and enhancement of global glider activity. *OceanGliders* contributes to the international efforts of the Global Ocean Observation System (GOOS) for Climate, Ocean Health, and Operational Services. It brings together marine scientists and engineers operating gliders around the world: (1) to observe the long-term physical, biogeochemical, and biological ocean processes and phenomena that are relevant for societal applications; and, (2) to contribute to the GOOS through real-time and delayed mode data dissemination. The *OceanGliders* program is distributed across national and regional observing systems and significantly contributes to integrated, multi-scale and multi-platform sampling strategies. *OceanGliders* shares best practices, requirements, and scientific knowledge needed for glider operations, data collection and analysis. It also monitors global glider activity and supports the dissemination of glider data through regional and global databases, in real-time and delayed modes, facilitating data access to the wider community. *OceanGliders* currently supports national, regional and global initiatives to maintain and expand the capabilities and application of gliders to meet key global challenges such as improved measurement of ocean boundary currents, water transformation and storm forecast.

Keywords: *in situ* ocean observing systems, gliders, boundary currents, storms, water transformation, ocean data management, autonomous oceanic platforms, GOOS

INTRODUCTION

The ocean is an important component of the global earth system influencing the global/regional climate, weather, ecosystems, living resources and biodiversity. The ocean plays a major role in many human activities including coastal protection, tourism, search and rescue, defense and security, shipping, aquaculture and fisheries, offshore industry and marine renewable energy. Ocean observation serves to enable us to better understand ocean functions and to meet the societal needs related to these activities. The Intergovernmental Oceanographic Commission (IOC of UNESCO) developed the Global Ocean Observing System (GOOS) more than two decades ago to coordinate the different national efforts in terms of sustained ocean observations throughout the world and to maximize the societal benefits of ocean observations. The GOOS has three observation panels for the development of observing strategies for climate, biogeochemistry and biology/ecosystems and the Observation Coordination group (OCG) of the World Meteorological Organization (WMO)/Intergovernmental Oceanographic Commission (IOC) Joint Commission on Oceanography and Marine Meteorology (JCOMM) for technical coordination of on-going observations. GOOS also serves as the ocean component of the Global Climate Observing system (GCOS). It is implemented through GOOS Regional Alliances and supported by a wide range of bodies, such as the Committee on Earth Observing Satellites (CEOS), the Partnership for Observation of the Global Ocean (POGO) and the GEO Blue Planet initiative.

The OceanObs'99 conference stimulated the first design of the GOOS and 10 years later, the OceanObs'09 conference assessed the progress made in implementing the GOOS. At that time, an international consensus was reached on how the GOOS should continue to evolve. Discussions around the GOOS highlighted the tremendous potential value for physical, biogeochemical, and biological observations, particularly in the transition between the open ocean and the coastal environment, which is a key area for societal issues, economical applications and at the same time is a prime area for autonomous underwater glider (Davis et al., 2002) observations. Gliders were considered in this global framework from the very beginning. Developed in the 1980–1990s (Lee and Rudnick, 2018), they arose from the vision that a network of small, intelligent, mobile and cheap observing platforms could fill sampling gaps left by the other ocean observing platforms (Stommel, 1989). This idea was first discussed at OceanObs'99 (see Conference Statement[1]), when the technology was immature, and further developed at OceanObs'09, when the technology was still maturing but poised to make a substantial contribution to global ocean observing (Testor et al., 2010). It was agreed that gliders could fill important gaps left by other observing systems and thus greatly enhance the GOOS if fully integrated into the system, and recommendations were made for the next decade.

Progress Over the Last Decade

Since OceanObs'09, autonomous underwater gliders have reached a mature state and are now operated routinely. They offer persistent fine resolution observations in the coastal and open ocean, even at high latitudes (at least during summer months). Typically, gliders profile from the surface to the bottom, or to 200–1,000 m depth, taking 0.5–6 h to complete a cycle from the surface to depth and back. During that time they travel 0.5–6 km horizontally at speeds of about 1 km/h, even during very severe weather conditions. Deployments of about a year are now possible, with deployments of 3–6 months now routine, and survey tracks extending over 1,000s kilometers. Sensors on gliders measure physical variables such as pressure, temperature, salinity, currents, turbulence and wind speed (Cauchy et al., 2018), biological variables relevant to phytoplankton and zooplankton, and ecologically important chemical variables such as dissolved oxygen, irradiance, carbon dioxide, pH (Saba et al., 2018), nitrate and hydrocarbon. Gliders have been developed to sample under-sea ice and ice shelves (Webster et al., 2015; Nelson et al., 2016; Lee et al., 2017), to recover data from other deep instruments via acoustic telemetry and send them to land while at the surface (Send et al., 2013), to detect acoustic tags on fishes (Oliver et al., 2013, 2017) and marine mammals. Improved gliders have reached depths of up to 6,000 m (Osse and Eriksen, 2007). All these improvements greatly open up the range of possible applications.

Their unique sampling capacities (high resolution and long term) are especially suitable for some key oceanic phenomena. They have yielded major scientific breakthroughs, revealing new insights into ocean physical, biogeochemical and biological processes. In particular, there are new results on (1) high latitudes oceanography, air-sea-ice interactions and intermediate/deep convection, (2) the variability of boundary currents, (3) (sub)mesoscale processes, (4) phytoplankton phenology and biogeochemistry, (5) higher trophic levels and biology, (6) shallow and marginal seas, (7) climate and variability of the water column, (8) internal waves, turbulence, tides, diffusivity and vertical mixing, and (9) particles fluxes and sedimentology (see **Table 1**).

Glider data are used for many applications in ocean physics, chemistry and biology (Rudnick, 2016). Glider data management by the scientific community has made data available to the public in real time for classical measured variables. Ocean numerical modeling and forecast activities already benefit from these data (**Table 1**). Models of ocean circulation, particularly for regional and coastal domains, have benefited from glider data in terms of validation and data assimilation, particularly in regional and coastal models. Glider data can improve hurricane intensity forecast models and has led to major results in ocean forecasting, weather forecasting including hurricane intensity, climatologies, and state estimates.

Underwater gliders will enable us to enter a new era of ocean observation and state estimates more effectively, meeting the needs of society and marine researchers. Gliders are a vital component in the portfolio of ocean observing platforms for most of the national ocean observation agencies. These agencies have invested in developing glider observing capability, and there are now about 400–500 gliders in the world actively being used to better observe the ocean (it is difficult to have exact numbers but based on our community knowledge we estimate ∼250 gliders in the USA; ∼100 in Europe; ∼50 in China; ∼30 in Australia; ∼30 in Canada; 9 in Mexico; 9 in South Korea; 5 in South Africa; 3 in Israel; 3 in Peru; 2 in New Zealand; 2 in India, 2 in Taiwan, etc.). Glider technology has also been used by the private sector during the last decade for applications in pollution events, defense, environment, and the offshore industry (Fragoso et al., 2016).

The Evolution of a Glider Observing Community-OceanGliders

Today, underwater gliders are operated by many teams around the world that have developed end-to-end systems able to steer their gliders and collect their data through their own facilities and Iridium satellite-based communications. Glider deployments are challenging because they must be managed in real-time throughout their deployment with the two-way communications needed for active piloting by the different operating teams. Glider technology requires a high level of expertise on the scientific and technological aspects in order to effectively operate the vehicles. Thanks to networking, coordination and capacity-building, training, liaison between providers and users, advocacy, and provision of expert advice, the global glider community has become more organized, grown rapidly, and responded to some of the system challenges. The idea for a glider community emerged in October 2005 at the first "EGO (Everyone's Gliding Observatories) Workshop and Glider School" and since then, collaborations have further developed. EGO Workshops and Glider Schools have been organized on an annual basis, to present and discuss scientific and technological issues, and to train and engage new users and countries worldwide. The formation of a user group and global coordination has improved glider operational reliability and data management, and resulted in improved glider monitoring, ocean observing and developments of the glider platform. Over the last decade, this coordination

[1]http://www.oceanobs09.net/work/oo99.php

TABLE 1 | Highlights on results during the past decade using the glider technology.

High latitudes oceanography, air-sea-ice interactions, or intermediate/deep convection	Beszczynska-Möller et al., 2011; Frajka-Williams et al., 2011; Beaird et al., 2012, 2013; Evans et al., 2013; Fan et al., 2013; Høydalsvik et al., 2013; Kohut et al., 2013; Queste et al., 2013; Guihen et al., 2014; Heywood et al., 2014; Carvalho et al., 2016; Houpert et al., 2016; Nelson et al., 2016; Azaneu et al., 2017; Couto et al., 2017; Jones and Smith, 2017; Lee et al., 2017; Timmermans and Winsor, 2013; Weingartner et al., 2013; Thompson et al., 2014; Ullgren et al., 2014; Venables and Meredith, 2014; Schofield et al., 2015; Swart et al., 2015; Thomalla et al., 2015; Testor et al., 2018; Våge et al., 2018; Viglione et al., 2018
Variability of boundary currents	Pascual et al., 2010; Pattiaratchi et al., 2010, 2017; Ramp et al., 2011; Todd et al., 2011a,b, 2016, 2018; Albretsen et al., 2012; Davis et al., 2012; McClatchie et al., 2012; Sherwin et al., 2012; Høydalsvik et al., 2013; Johnston et al., 2013; Lien et al., 2014, 2015; Pietri et al., 2014; Schaeffer and Roughan, 2015; Schönau et al., 2015; Yang et al., 2015; Lee et al., 2016; Mensah et al., 2016; Schaeffer et al., 2016a; Zaba and Rudnick, 2016; Andres et al., 2017; Anutaliya et al., 2017; Durand et al., 2017; Todd, 2017; Todd and Locke-Wynn, 2017; Aulicino et al., 2018; Houpert et al., 2018; Krug et al., 2018; Seim and Edwards, 2019
Mesoscale and submesoscale processes	Bouffard et al., 2010, 2012; Baird et al., 2011; Baird and Ridgway, 2012; Heslop et al., 2012; Mahadevan et al., 2012; Ruiz et al., 2012; Todd et al., 2012, 2013; Alvarez et al., 2013; Pelland et al., 2013, 2014, 2016, 2018; Pietri et al., 2013; Piterbarg et al., 2013; Timmermans and Winsor, 2013; Caldeira et al., 2014; Hristova et al., 2014; Bosse et al., 2015, 2016; Everett et al., 2015; Farrar et al., 2015; Omand et al., 2015; Schönau and Rudnick, 2015, 2017; Sherwin et al., 2015; Borrione et al., 2016; Caballero et al., 2016; Freitas et al., 2016; Mauri et al., 2016; Thompson et al., 2016; Thomsen et al., 2016; Brannigan et al., 2017; Buffett et al., 2017; Du Plessis et al., 2017; Gourdeau et al., 2017; Itoh and Rudnick, 2017; Karstensen et al., 2017; Kokkini et al., 2017; Krug et al., 2017; Mancero-Mosquera et al., 2017; Margirier et al., 2017; Morrow et al., 2017; Pascual et al., 2017; Ruan et al., 2017; Yu et al., 2017; Zacharia et al., 2017; Gula et al., 2019
Phytoplankton phenology and biogeochemistry	Asper et al., 2011; Briggs et al., 2011; Martin et al., 2011; Xu et al., 2011; Alkire et al., 2012, 2014; Cetinić et al., 2012, 2015; Pierce et al., 2012; Gower et al., 2013; Zhao et al., 2013; Foloni-Neto et al., 2014; Kaufman et al., 2014, 2017; Olita et al., 2014, 2017; Biddle et al., 2015; Evans et al., 2015; Hemsley et al., 2015; Nicholson et al., 2015; Queste et al., 2015; Seegers et al., 2015; Adams et al., 2016; Cotroneo et al., 2016; Fiedler et al., 2016; Jacox et al., 2016; Loginova et al., 2016; Pizarro et al., 2016; Porter et al., 2016; Schaeffer et al., 2016b; Schuette et al., 2016; Thomsen et al., 2016; Bosse et al., 2017; Hemming et al., 2017; Mayot et al., 2017; Ross et al., 2017; Thomalla et al., 2017; Little et al., 2018
Higher trophic levels and biology	Kahl et al., 2010; Klinck et al., 2012; McClatchie et al., 2012; Powell and Ohman, 2012, 2015; Wall et al., 2012; Baumgartner et al., 2013, 2014; Ohman et al., 2013; Oliver et al., 2013; Guihen et al., 2014; Kohut et al., 2014a; Pelland et al., 2014; Ainley et al., 2015; Goericke and Ohman, 2015; Swart et al., 2016; Kusel et al., 2017; Taylor and Lembke, 2017; Benoit-Bird et al., 2018; Chave et al., 2018
Shallow and marginal seas	Castelao et al., 2010; Shulman et al., 2010; Karstensen et al., 2014; Kohut et al., 2014b; Mazzini et al., 2014; Schaeffer et al., 2014; Piero Mazzini et al., 2015; Qiu et al., 2015; Dever et al., 2016; Mahjabin et al., 2016; Saldias et al., 2016; Heslop et al., 2017; Zarokanellos et al., 2017
Climate and variability of the water column	Cole and Rudnick, 2012; Schlundt et al., 2014; Domingues et al., 2015; Farrar et al., 2015; Houpert et al., 2015; Damerell et al., 2016; Schaeffer et al., 2016a; Rudnick et al., 2017; Portela et al., 2018
Internal waves, turbulence, tides, diffusivity and vertical mixing	Alford et al., 2012; Thorpe, 2012; Beaird et al., 2013; Johnston et al., 2013; Rainville et al., 2013, 2017; Fer et al., 2014; Peterson and Fer, 2014; Boettger et al., 2015; Cronin et al., 2015; Johnston and Rudnick, 2015; Palmer et al., 2015; Klymak et al., 2016; Hall et al., 2017; Schultze et al., 2017; St Laurent and Merrifield, 2017; Todd, 2017; Evans et al., 2018; Ma et al., 2018; Scheifele et al., 2018
Particles fluxes and sedimentology	Briggs et al., 2011; Miles et al., 2013; Bourrin et al., 2015; Omand et al., 2015; Many et al., 2016; Churnside et al., 2017; Durrieu de Madron et al., 2017
Ocean forecasting, climatology, and state estimates	Dobricic et al., 2010; Oke et al., 2010, 2015; Zhang et al., 2010a,b; Chudong et al., 2011; Ramp et al., 2011; Todd et al., 2011a, 2012; Yaremchuk et al., 2011; Jones et al., 2012; Melet et al., 2012; Mourre and Alvarez, 2012; Gangopadhyay et al., 2013; L'Heveder et al., 2013; Li et al., 2013; Rayburn and Kamenkovich, 2013; Wilkin and Hunter, 2013; Alvarez and Mourre, 2014; Chen et al., 2014; Drillet et al., 2014; Mourre and Chiggiato, 2014; Ngodock and Carrier, 2014; Pan et al., 2014, 2017; Durski et al., 2015; Miles et al., 2015; Rudnick et al., 2015; Estournel et al., 2016a,b; Fragoso et al., 2016; Kerry et al., 2016, 2018; Chao et al., 2017a,b; Damien et al., 2017; Dong et al., 2017; Goni et al., 2017; Halliwell et al., 2017; Kurapov et al., 2017; Onken, 2017; Todd and Locke-Wynn, 2017; Verdy et al., 2017

activity has also developed nationally and regionally. Many national facilities have been established to serve their national communities such as the IMOS (Integrated Marine Observing System) Ocean Gliders facility, Ocean Gliders Canada, GMOG (Grupo de Monitoreo Oceanográfico con Gliders) in Mexico, MARS (Marine Autonomous and Robotic Systems) in the UK, Norwegian National Facility for Ocean Gliders (NorGliders) in Norway, "Parc National de Gliders" in France, etc. Glider groups have also been set up for coordination within integrated ocean observation initiatives such as the Integrated Ocean Observing System (IOOS), the Integrated Marine Observing System (IMOS) and the European Ocean Observing System (EOOS)/EuroGOOS. There are now several levels of coordination and this greatly facilitates scientific and technological exchanges between glider operators and users, in academia and industry.

Building on this diverse community, the *OceanGliders* program started in September 2016 at the 7th EGO conference. It was set up in recognition of the maturity of the glider systems and their potential role in the GOOS in coming years. The *OceanGliders* program as a component of the GOOS was approved by the Joint WMO-IOC Technical Commission for Oceanography and Marine Meteorology (JCOMM) at their 5th Intergovernmental Session in October 2017 and the *OceanGliders* Steering Team reports to OCG. Here we review the progress made in implementing a glider component of the GOOS, one of the key recommendations from OceanObs'09, present the recently established program and components, and offer a vision for the coming decade.

MOVING FROM THE REGIONAL TO THE GLOBAL

The progress of gliders in moving from a developing to a mature technology is exemplified by the programs that have been run continuously for over 10 years, for example, in the California Current (Adams et al., 2016; Rudnick et al., 2017), and the Solomon Sea (Davis et al., 2012). Long-term observations lasting several years are becoming widespread (Heslop et al., 2012; Schaeffer et al., 2016a; Yu et al., 2017; Du Plessis et al., 2019). The capability to sustain these programs relies on the improved dependability of gliders (Brito et al., 2014; Rudnick et al., 2016a; Brito and Griffiths, 2018) and the experience, skill and confidence of the operators. The success of these projects can be summarized in the likelihood of a glider completing a desired mission, and the fraction of the time that a glider is in the water. Typical success rates of 0.9 have been achieved by experienced teams. The delivery of data from gliders in real time has become routine, with main glider data assembly centers in Europe (EGO/Coriolis[2]), Australia (IMOS[3]), and the USA (IOOS[4]).

Underwater gliders play a special role in observing systems designed to support regional modeling activities, because gliders generate many profiles at controlled locations. The potential for glider development was recognized quite early on, leading to the influential Autonomous Ocean Sampling Network (Ramp et al., 2009). Glider data are often used with models for two purposes: (1) verification, meaning to evaluate model output for fidelity to the ocean; and/or, (2) assimilation, the use of data to constrain model output (Edwards et al., 2015; Hayes et al., 2019). Models can either (1) forecast ocean variables in advance of any access to data for verification; or (2) hindcast to deliver state estimates that use data to create a complete set of ocean variables. Many combinations of using glider data for verification or assimilation of forecast or hindcast models have been tried in many regions around the world. For example, off California, Kurapov et al. (2017) used glider data (Rudnick et al., 2017) to verify a forecast model, while Chao et al. (2018) assimilated the same glider data to create forecasts. Temperature and salinity data from these gliders were assimilated into a state estimate (Todd et al., 2011a, 2012; Zaba et al., 2018), while velocity data were not assimilated so they could be used for verification. In the Mediterranean, Dobricic et al. (2010) showed the large-scale impact of the repetition of a glider section and in particular when depth-average currents were also assimilated while Mourre and Chiggiato (2014) and Onken (2017) assimilated glider data for a forecast and verified against data from a ship survey. A state estimate of the tropical Pacific (Verdy et al., 2017) was verified against withheld glider observations on either side of the Pacific basin. These examples illustrate the character of recent work. Ongoing work is expected to improve regional observing modeling in the coming decade.

Underwater gliders are especially well-suited for sustained, fine-spatial-resolution observations near the ocean boundaries. They allow cross-front measurements to help resolve mesoscale/sub-mesoscale fronts and associated shear-driven instabilities in both the coastal and open ocean. The long times for deployments of gliders are possible because they move slowly (10s cm/s) and because energy lost to drag is proportional to the cube of the speed through water. Gliders must profile continuously in order to make way through water, so fine resolution in the order of a few kilometers is common. Gliders can be deployed and recovered from small boats, thereby minimizing costs and allowing flexible operation. Sustained, fine-resolution operations near boundaries are ideal for monitoring the regional effects of climate variability. Gliders fill the gap between the coast and the open ocean, as tracks of thousands of kilometers are typical, making traversing the 200 nautical mile Exclusive Economic Zone practical. Gliders could revolutionize regional oceanographic observing just as Argo did for observing the open ocean over the last two decades.

OceanGliders Terms of Reference

The international *OceanGliders* program was created as a component of the GOOS with the broad goals of strengthening the glider community (users, scientists, engineers, operators, manufacturers) and facilitating the sustained worldwide use of gliders for the benefit of society and science[5]. An initial structure and set of governance rules were agreed upon, as well as more detailed ways to maintain and develop the program, briefly summarized in **Table 2**. Because of their proven ability to fill gaps and needs in the existing observation system, gliders are on the cusp of a transition from isolated, regional use by a few expert teams, to widespread use around the globe by coordinated groups with a wider range of applications. The glider community has realized the many benefits of sharing expertise, best practices, data, and even infrastructure components among existing and new members. Providing a global program, in which new ideas can be discussed and coordinated for larger-scale adoption, will turn regional efforts into integrated global efforts. This fits perfectly into the GOOS mission to promote feasible, high-impact observing programs.

Data Management

OceanGliders targets high-impact, societally-relevant, science-based observing through a number of initial scientific Task Teams (*OceanGliders* TT). They are developed in the following section, but one Task Team in particular relates to the smooth, coordinated functioning of each TT with each other and with the rest of the GOOS: the data management TT. This team aims to address the needs of long-term observation aspects of data management, benefiting the wider community, supporting and encouraging scientists designing and executing process studies, as well as engineers developing new gliders, sensors, and computing

[2]http://www.coriolis.eu.org/Data-Products/Catalogue#/metadata/589bfa51-2219-4cc8-a19e-83f3c3f27bb4
[3]https://portal.aodn.org.au/
[4]https://gliders.ioos.us/data/
[5]https://www.ego-network.org/dokuwiki/doku.php?id=public:goosgstt

TABLE 2 | Summary of *OceanGliders* terms of reference and objectives.

Purpose	To provide scientific leadership to promote and strengthen the glider community and facilitate their sustained use globally in order to respond to the integrated requirements of the Global Ocean Observing system (GOOS). Oversee the development and implementation of a global-scale glider array for observing key regions of the ocean on the long term, based on national and regional projects (https://www.ego-network.org/dokuwiki/lib/exe/fetch.php?media=public:gst:glider-st_tor.pdf)
Membership	Anyone willing to contribute to the different Task Teams is considered as a member, keeping in mind the focus on developing sustained glider activity and the "Framework for Ocean Observing."
Steering Team	Reflect and represent the sustained glider activity and to drive *OceanGliders* toward its goal of filling gaps in GOOS/GCOS
Exec Committee	Chair, co-Chair, Task Teams Leaders and GOOS advisor
Task Teams	Design network, define targets for Task Teams missions (optimum strategy)
	Define science implementation plans
	Describe scientific requirements and societal requirements
	Describe the global costs and cost-effectiveness
	Define the contribution of Task Teams in a multi-platform system designed to address scientific and societal issues, including unique roles of gliders
Meetings	Annual Steering Committee meetings

technologies to participate in metadata and data management. Data management implies not only data repositories of a certain standard, but the guidance and coordination in the development of new standards and best practices (Pearlman et al., 2019) for data collection, processing, and quality control. Data management requires metadata and its description, storage, and access. One of the benefits of coordination will be improved and sustained quality control of glider data.

Network Monitoring and Data Dissemination

One main goal for glider operators is to make data publicly available and in particular to publish data in near-real time on the GTS (Global Telecommunication System) and in CF (Climate and Forecast) compliant formats for operational services. They provide their metadata and data to a Data Assembly Center (DAC) in charge of the data management and linked to a Global Data Assembly Center (GDAC) for further dissemination and archive. Three *de facto* GDACs are currently operating: Australia (IMOS), Europe and partners (EGO/Coriolis), and the United States (IOOS). Each GDAC has adopted similar strategies and conventions: CF-compliant NetCDF observation file formats can be uploaded by operators, and public sites and tools are provided for downloading and visualization. There are minor differences in formats, and the implementation of tools for raw file conversion, discovery, download and visualization varies widely. Numerous regional and local efforts have developed important tools but this has made it painfully obvious that coordination is needed for global-scale visibility and availability of ocean observations of known quality control. Initial efforts by IMOS, EGO/Coriolis and IOOS at collecting daily glider data illustrate some of the extent of glider activity worldwide over the past decade (**Figures 1**, **2**). This also represents the commitments from glider teams that have fed these systems, showing most of the glider deployments carried out so far in the world. The next step of unifying and providing data seamlessly from any region through one portal must be simpler. Already, the three GDACs have shared detailed information on how to upload, discover, download, and visualize using their tools. Simplifications have been made to provide easy access among the GDACs. This information will be centralized as in **Figure 3** and accessible on the *OceanGliders* website www.oceangliders.org and will be an important tool to monitor global glider activity and promote its objectives.

The first dedicated global glider data management meeting has stimulated further developments (Genova, Italy, 17–19 September, 2018). Besides sharing expertise and latest developments at the regional level, this meeting produced a global consensus about how glider data can be made more useful to society, considering both historical and near real time data sets, now and in the future. Short-term goals include: setting up a solution to access all glider data in a single format; define indices for glider activity monitoring; handling the real time and delayed mode quality controls and assessments at the global level. Further development and sharing of best practices on data and metadata management are key for the *OceanGliders* Data Management Task Team. To that end, there is now a new central directory at www.oceanbestpractices.net, hosted by IODE, for *OceanGliders*.

Glider-specific tools have been developed at the GDAC and regional/institutional (or DAC) level to complement the other elements of the GOOS. The unique trajectory character of glider data, and of the wide range of metadata can cause these tools to be quite complex. Even the familiar concepts of "cruise," "mission," "transect," and "profile" do not adequately describe the nature of glider flight and programmable behavior in real time.

There are too many to exhaustively list here, but notable examples include: GliderScope[6] (Hanson et al., 2017), IOOS[7], EGO GFCP[8], NorGliders GliderPage[9], SOCIB[10] (Troupin et al., 2015), MARS[11], and GANDALF[12]. Going forward, standardized data and metadata interfaces will benefit the future development of such tools and enable easier, global access to the full set of quality-controlled glider data and metadata [e.g., the Sensor Web Enablement framework and associated standards (Bröring et al., 2017)].

Emerging Requirements

Glider data management will need to encompass developments within the glider networks, the GOOS and outside of the oceanographic domain in order to anticipate future changes in global data management. The implementation of Findable-Accessible-Interoperable-Reusable (FAIR) data principles is a

[6]http://imos.org.au/gliderscope/
[7]https://gliders.ioos.us/map/
[8]https://www.ego-network.org/dokuwiki/doku.php
[9]http://gp.gfi.uib.no
[10]http://www.socib.eu/?seccion=observingFacilities&facility=glider
[11]https://mars.noc.ac.uk/
[12]http://gandalf.gcoos.org

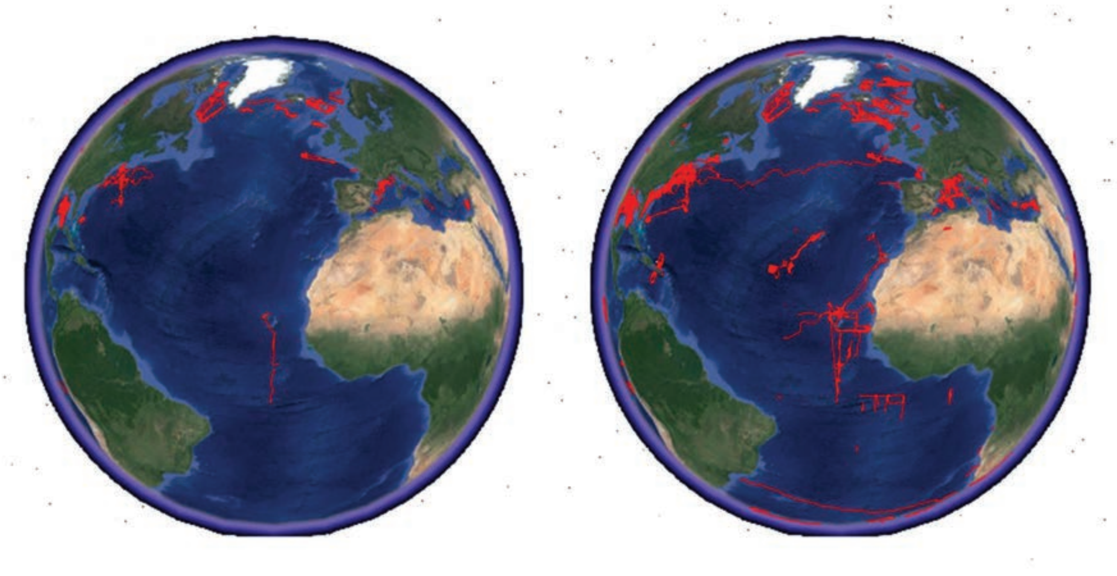

FIGURE 1 | Development of the glider activity over the past decade. Gliders tracks of past deployments **(left)** until December 2009 (OceanObs'09) and **(right)** until October 2018 (OceanObs'19 submissions), as can be viewed using google-earth.

common theme in environmental data management and will place demands for development on glider data infrastructure (Tanhua et al., 2019). The integration of data from different networks within the GOOS and the implementation of new Essential Ocean Variables (EOVs) are also emerging as requirements. Furthermore, additional demands on data management will emerge with such as automated piloting (e.g., Chang et al., 2015; Smedstad et al., 2015) and operational glider network monitoring technologies.

ADDRESSING GLOBAL OBSERVING NEEDS

The *OceanGliders* group met to discuss possible areas of focus and beyond the central need for improved data management, identified three key areas of focus for the developing program. These areas of interest were organized into Task Teams (TT) whose goals are to address the societal needs for ocean data and to entrain the community into discussions around the role of gliders in meeting these needs. It is expected that the mission-based TTs will organically develop by organizing the different initiatives into integrated and coordinated global efforts.

Boundary Currents

Society experiences changes in the global ocean at the ocean's boundaries. These boundary regions are the nexus of societal use of the ocean for fisheries, transportation, and recreation. The boundary regions are also where the intense ocean currents are key to the transport of mass, heat, salt, biogeochemical variables and plankton. In the large ocean basins, the subtropical western boundary currents dominate the surface poleward transport of warm water or equatorward transport of cold water at depth and are major drivers of climate variability. Subtropical eastern boundary currents are often upwelling systems that comprise some of the most biologically productive regions in the world and host the world's Oxygen Minimum Zones (OMZ). Subpolar eastern boundary currents induce significant poleward heat transport in the downwelling eastern part of the subpolar gyres. Boundary currents in marginal seas provide the major means of exchange with the open ocean and impact regional ecosystems. Finally, the communication between the coast and open ocean is regulated by the boundary currents that flow along the continental slopes, affecting ecosystems, flood levels, erosion and commercial activity. To summarize, there is a great need for sustained observations of these highly dynamic boundary current regions.

Underwater gliders are particularly effective at measuring and monitoring subsurface biogeochemical fields that are both key to marine ecosystem productivity and involved in some of the most pressing ocean challenges like ocean acidification and hypoxia. For instance, glider capabilities are well-suited to sample the upwelling source waters transported to the edge of the continental shelf by eastern boundary currents. Recent studies in the Pacific and Atlantic reveal details of the spatial structure and time evolution of, for example, low-oxygen zones in such regions (Pierce et al., 2012; Pietri et al., 2013; Adams et al., 2016; Pizarro et al., 2016; Thomsen et al., 2016; Karstensen et al., 2017).

From their earliest conception, underwater gliders were viewed as components of observing/modeling systems, and progress over the past decade has proven the efficacy of this approach. The data provided by underwater gliders are a natural match for regional models of coastal ocean circulation. These regional models are necessary, as the currents and water properties in the coastal ocean vary on the relatively small scales

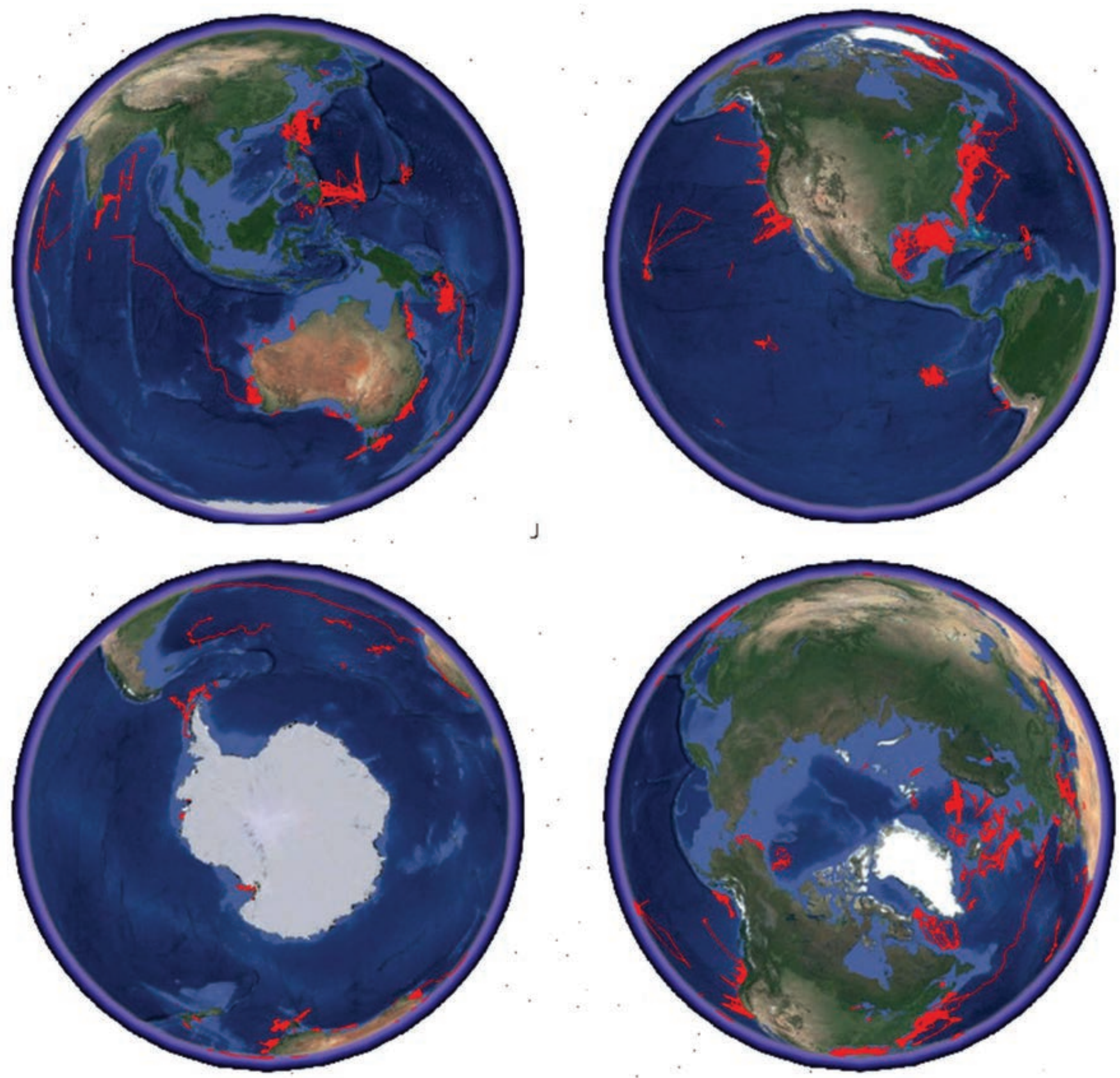

FIGURE 2 | Gliders tracks of past deployments until October 2018 (OceanObs'19 submissions), as can be viewed using google-earth from different locations.

set by topography. Accurate forecasting depends on initialization on these small scales, which can be satisfied by a network of gliders.

The most widespread application of sustained glider programs has been in boundary currents. These efforts range from the significant western boundary currents, to the highly productive eastern boundary upwelling systems, to regionally important boundary currents in marginal seas. Initial targets are often the mean and variability of velocity, temperature, and salinity, and now moving to include biogeochemical and biological variables. As the sustained time series increase in length, interannual climate variability is resolved. The remarkable increase in sustained glider observations in the last 10 years is summarized below and illustrated by **Figures 4–6**.

Sustained projects in the Atlantic include observations on the western, eastern and northern boundaries of the North Atlantic. The marginal seas of the Atlantic, including the Mediterranean and the Gulf of Mexico are also home to long-term observations.

- The Davis Strait was observed repeatedly during 2005–2014 to quantify the exchange between the Arctic Ocean/Baffin Bay and the subpolar North Atlantic (**Figure 5A**; Beszczynska-Möller et al., 2011; Curry et al., 2014; Webster et al., 2015). Although this effort succeeded in collecting year-round observations across the seasonally ice-covered strait, challenging logistics, harsh operating conditions and funding prevented continuous occupation of the section over the entire 2005–2014 period.
- The warm water paths of the North Atlantic Current over the Rockall-Hatton Plateau at 58°N are being observed using repeat glider sections between 15 and 21°W as part of OSNAP since 2014 (**Figure 5E**; Houpert et al., 2018; Lozier et al., 2019).

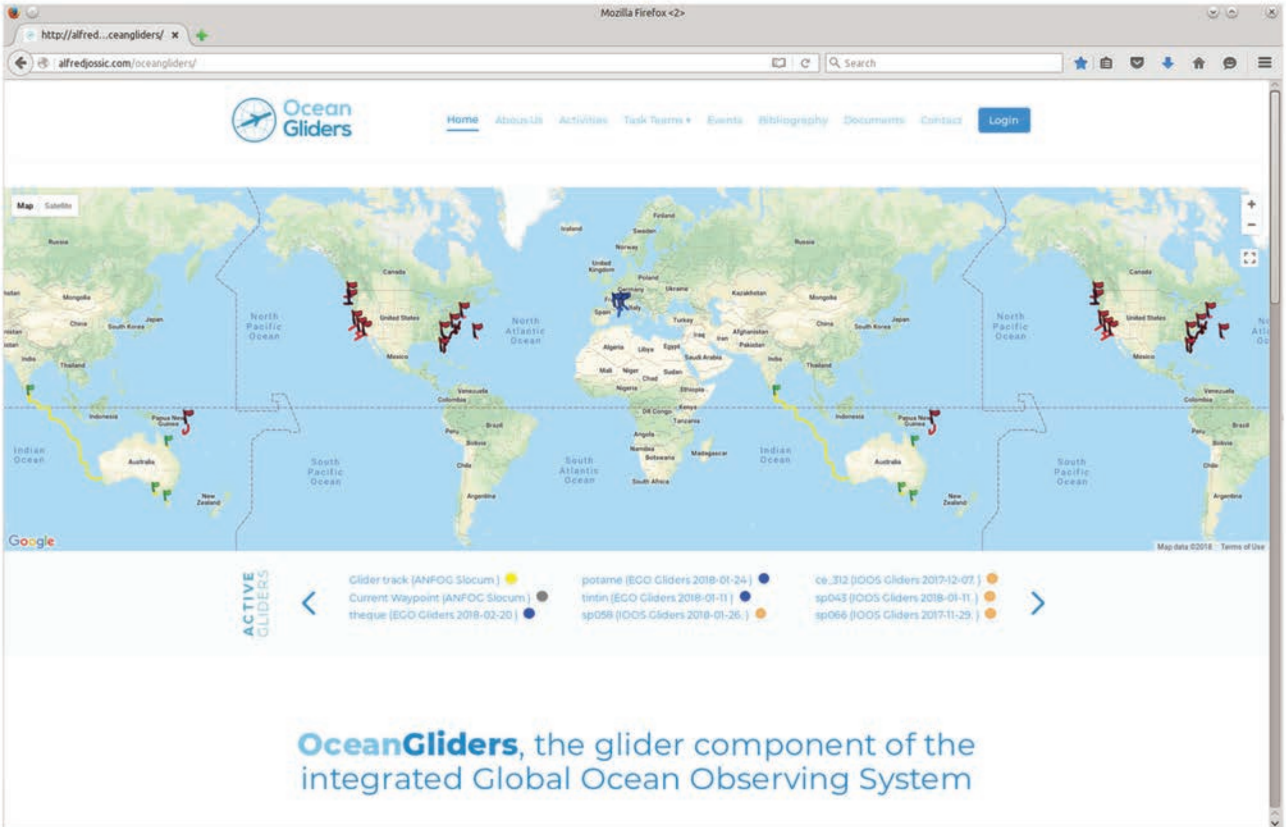

FIGURE 3 | The global active glider fleet trajectory map, updated daily (from http://anfog.ecm.uwa.edu.au/index.php?page=global_gliders, accessed 23 August, 2018).

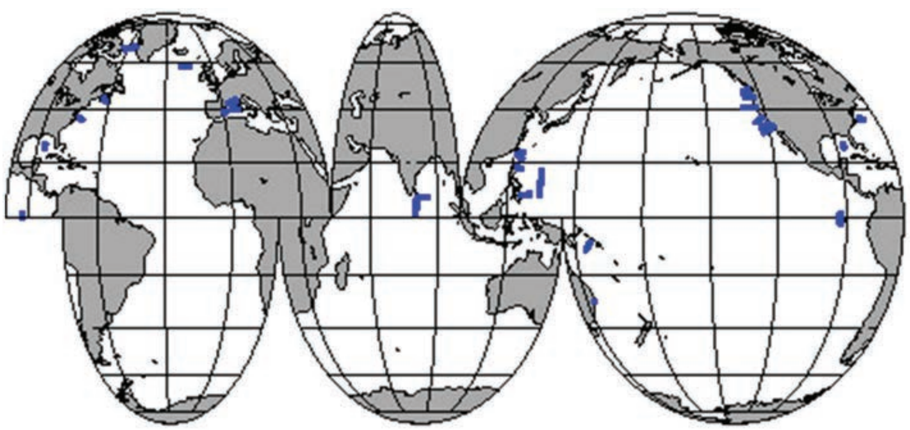

FIGURE 4 | Sustained observations of boundary currents of duration from at least one to over a dozen years. Mean sections of absolute geostrophic velocity are a unique product of underwater gliders, calculated by combining geostrophic shear with directly measured depth-average velocity. These sections at the locations in this figure are shown in **Figures 5**, **6**.

- The Nova Scotia Current was observed during 2011–2014 by repeat glider sections as part of the Ocean Tracking Network (**Figure 5B**; Dever et al., 2016) and re-established by Fisheries and Oceans Canada in 2018 as part of its monitoring programs.
- Along the East Coast of the United States, a program of routine glider surveys across the Gulf Stream is underway. Commanded to steer across strong currents of the western boundary current, gliders are able to occupy cross-Gulf Stream transects as they are advected downstream (**Figure 5C**; Todd

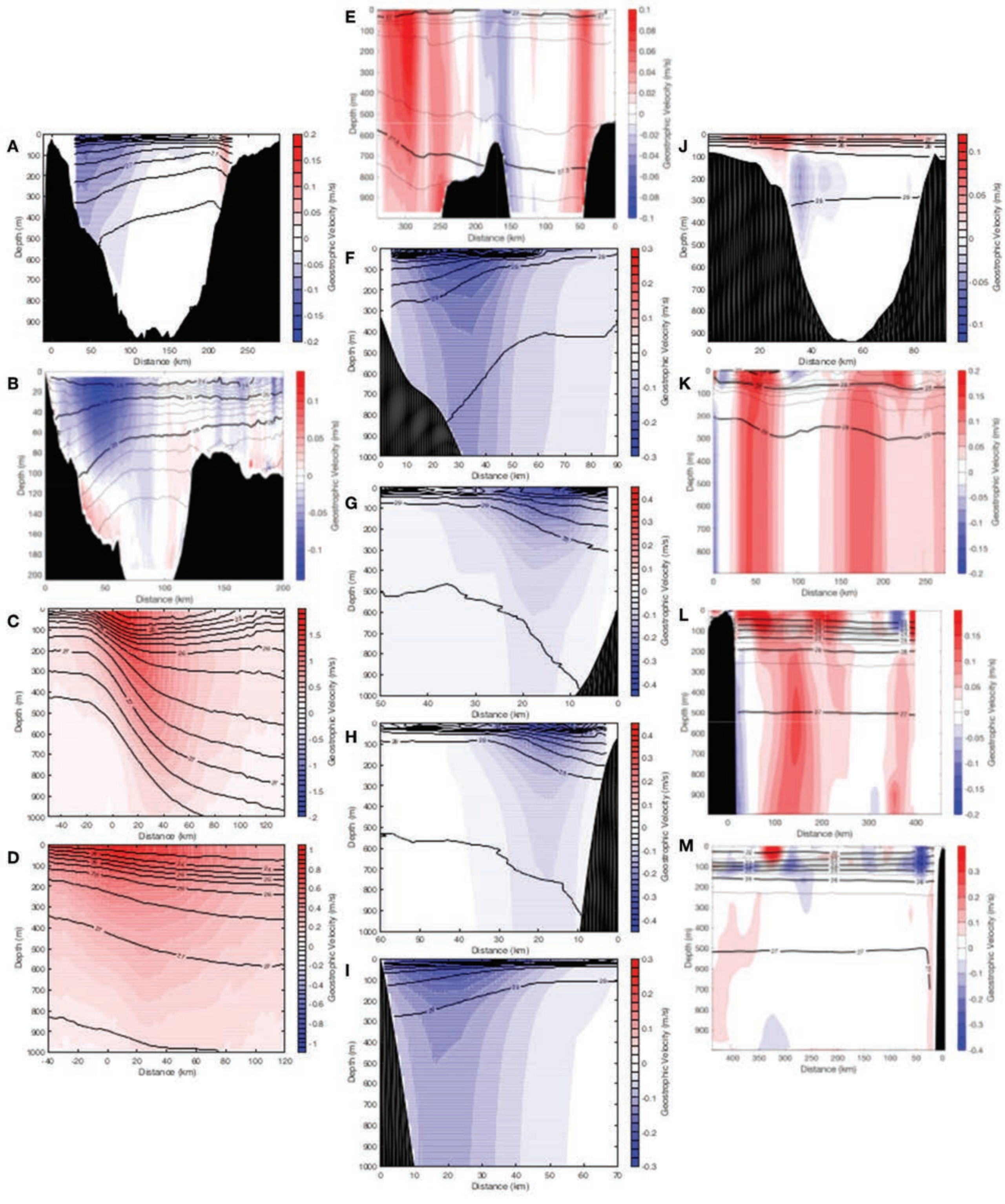

FIGURE 5 | Mean sections of geostrophic velocity from the Atlantic, Mediterranean and Indian Ocean. Sections in the Atlantic include **(A)** the Davis Strait, **(B)** the Nova Scotia Current off the east coast of Canada, **(C)** the Gulf Stream off the eastern US coast, **(D)** the Gulf of Mexico Loop Current, and **(E)** the North Atlantic Current west of the UK. Sections in the Northern Current System of the Mediterranean Sea are **(F–I)** along the southern coast of France, **(J)** between the Spanish coast and the island of Ibiza, and **(K)** between Sardinia Island and Menorca. In the Indian Ocean, sections are off the **(L)** east and **(M)** south coast of Sri Lanka. The sections are oriented generally west to east or south to north, and positive geostrophic velocity is primarily northward or eastward.

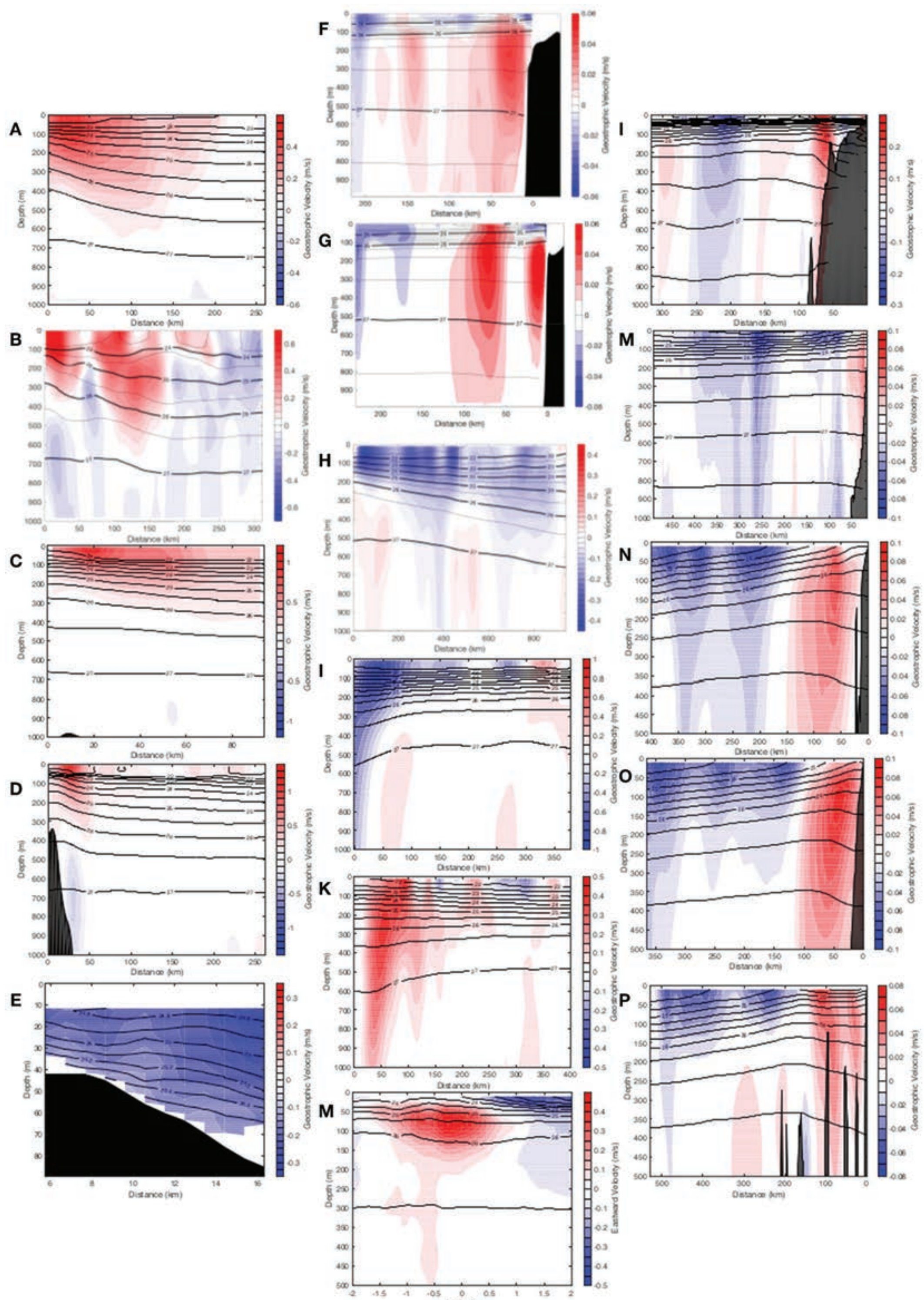

FIGURE 6 | Mean sections of geostrophic velocity from the Pacific. Sections in the western Pacific include the Kuroshio offshore of **(A,B)** Taiwan and **(C,D)** Luzon, and in **(E)** the East Australian Current, **(H)** the North Equatorial Current, **(I)** the Mindanao Current, and **(J)** the New Guinea Coastal Current of the Solomon Sea. Sections in the eastern Pacific include **(F,G)** two off Washington, **(L)** one off Oregon and four off the California coast at **(M)** Trinidad Head, **(N)** Monterey Bay, **(O)** Point Conception, and **(P)** Dana Point. A mean section across the equator at 93°W off the Galapagos **(K)** was measured by acoustic Doppler profilers, as geostrophy fails at the equator. The sections are oriented generally west to east or south to north, and positive velocity is primarily northward or eastward.

et al., 2016, 2018; Todd, 2017; Todd and Locke-Wynn, 2017; Gula et al., 2019).

- The Gulf of Mexico Loop Current was observed starting in 2007, and continuously during 2011–2014 with a focus on mean structure, eddies and separation processes (**Figure 5D**; Rudnick et al., 2015; Todd et al., 2016). Along-gradient glider trajectories of mesoscale eddies ubiquitous in the central and western Gulf of Mexico have been repeatedly carried out since May 2016 to present as a component of a quasi-continuous (90% of time) monitoring program conducted by GMOG.
- European Slope Current at 56.5N as part of the sustained Ellett Line program. Gliders have been occupying this section in winter since 2009, and several times per year since 2015 (Sherwin et al., 2015).
- In the Western Mediterranean, repeat glider transects have been conducted to monitor the variability of the Northern Current System, over 10 years in the north of the basin (**Figures 5E–H**; Testor et al., 2018), for 6 years at a circulation "choke" point (**Figure 5I**; Heslop et al., 2012), for 8 years at the Mallorca Channel (Barceló-Llul et al., 2019) and more recently between Sardinia and Balearic Islands (**Figure 5J**) and between Mallorca Island and the African coast (Cotroneo et al., 2016; Aulicino et al., 2018).
- The Norwegian Atlantic Current Observatory has undertaken long term glider monitoring across 2 transects over 4 years, monitoring northward flow to the Arctic regions (Høydalsvik et al., 2013). Gliders have been used to monitor the topographic steering of warm Atlantic waters toward Arctic tidewater glaciers on the west Spitsbergen margin (Fraser et al., 2018).
- Since 2012, gliders have been deployed in the Subantarctic Zone of the South Atlantic each year, as part of the Southern Ocean Seasonal Cycle Experiments (SOSCEx; Swart et al., 2012). Deployment have covered all seasons except late austral autumn to assess bio-physical interactions from sub seasonal to seasonal scales (Du Plessis, 2015; Swart et al., 2015; Thomalla et al., 2015; Little et al., 2018; Du Plessis et al., 2019).
- Repeated sections were carried out off Cape Verde Islands as part of the Collaborative Research Center 754 (DFG; Oschlies et al., 2018), Senegal (Kolodziejczyk et al., 2018) and Angola, primarily to study the OMZ.

Projects in the Indian Ocean range from the Bay of Bengal to the currents that connect to the Southern Ocean:

- Gliders in the Bay of Bengal off the east and south coasts of Sri Lanka (**Figures 5K,L**; Lee et al., 2016).
- Repeated sections in the Agulhas Current since 2017 as part of Gliders IN the Agulahas (GINA, Krug et al., 2018) following the Shelf Agulhas Glider Experiment (SAGE) in 2015. Initial results include observations of cyclones on the inshore edge of the current (Krug et al., 2017).
- Many cross sections of the Leeuwin Current, the poleward flowing eastern boundary current in the southern Indian Ocean (Pattiaratchi et al., 2017).

Projects in the Pacific include sustained observations in the eastern boundary current of the North Pacific, and both the midlatitude and low-latitude western boundary currents of the North and South Pacific:

- The Kuroshio off Taiwan (**Figures 6A–D**; Lien et al., 2014; Yang et al., 2015), the North Equatorial Current north of Palau (**Figure 6H**; Schönau and Rudnick, 2015) and the Mindanao Current off the Philippines (**Figure 6I**; Schönau and Rudnick, 2017) were occupied continuously from 2007 to 2014 to quantify transports and water masses as part of the project Origins of the Kuroshio and Mindanao Current (OKMC). Observations began again in 2017 with a line off Taiwan.
- Repeated sections across Solomon Sea were made for nearly a decade to monitor the low latitude western boundary current that feeds the Pacific equatorial current system from the Southern Hemisphere (**Figure 6J**; Davis et al., 2012).
- The California Underwater Glider Network has occupied three lines in the California Current System for the past decade with a primary goal of monitoring the regional effect of climate variability as caused by El Niño (**Figures 6N–P**; Rudnick et al., 2017). A fourth line off northern California has been occupied for 2 years (**Figure 6M**).
- The inshore edge of the East Australian Current (EAC) has had repeated sections run since 2010 (**Figure 6E**) to observe the separation of the current, and the momentum balance at that point (Schaeffer and Roughan, 2015), the hydrographic structure of the current (Schaeffer et al., 2016a), the biogeochemistry (Schaeffer et al., 2016b).
- Sections across the California Current, immediately south of the West Wind Drift bifurcation region, were occupied continuously from 2003 to 2009, and then annually, for 6–9 months per year, from 2010 to 2015 (**Figures 6F,G**). These observations provide data to advance the understanding of the regional response to climate variability and California Undercurrent Eddies (Pelland et al., 2013).
- The Ocean Observatories Initiative began occupying 5 sections off Oregon and Washington, starting in 2014 to address the influence of climate variability on eastern boundary ecosystems. One of these lines, off Oregon, has been occupied continuously since spring 2006 (**Figure 6L**; Mazzini et al., 2014).
- Repeated sections off Peru started in 2008 (Pietri et al., 2013) to study the Humbolt system.
- Repeated sections off Chile (Pizarro et al., 2016) primarily to study the OMZ.
- Repeated sections in the Coral Sea adjacent to the north Queensland coast (Australia) have been used to estimate boundary current transport (Ridgway and Godfrey, 2015).
- The Equatorial Current System was observed during 2013–2016 using acoustic Doppler profilers (Todd et al., 2017; **Figure 6H**), as geostrophy fails at the equator. These measurements were undertaken as part of the Repeat Observations by Gliders in the Equatorial Region (ROGER) program (Rudnick, 2016).
- Glider transects at 37.9°N across the East Korean Warm Current along the Korean Peninsula have been conducted since 2017.

Underwater gliders can measure absolute geostrophic velocity. The geostrophic shear may be calculated from glider sections by estimating the horizontal gradient of density. This shear is referenced to the depth-average velocity that is calculated by dead reckoning between navigational fixes at the beginning and end of dives. This absolute, depth-dependent geostrophic velocity normal to the glider section allows calculation of the transport of mass, heat and salt. These transports are the fundamental quantities needed for baseline monitoring of boundary currents. Much work has been done to quantify the scales resolved and the accuracy of the velocity. For example, high frequency motions, such as internal waves, are projected into spatial variability in a glider section, with the result that horizontal wavelengths longer than 30 km are resolved in midlatitudes (Rudnick and Cole, 2011). The accuracy of the depth-average velocity, is of order 0.01 ms^{-1}, as inferred in early design studies, and confirmed by decades of observations (Rudnick et al., 2018). The sustained observations have produced several estimates of the boundary currents (**Figures 4–6**).

The goal of the *OceanGliders* Boundary Ocean Observing Network (BOON) is to provide coordination for a global observing program. Because boundary currents invariably reside in EEZs, their observation must depend on regional efforts respectful of the coastal countries. The goal of BOON is to sustain observations year-round. The result will be a global network of regional networks that monitor boundary current variability across international borders to the world's benefit.

The *OceanGliders* BOON complements existing ocean observing networks. Argo has transformed ocean science with its global coverage. BOON connects Argo's observations of the open ocean with the coastal ocean by operating the transects that are required to monitor boundary currents. BOON expands the footprint of site-specific moorings of OceanSites by repeated sections that may connect to mooring locations. Repeated surveys by ships form the backbone for many existing regional efforts, in some cases going back decades. BOON will step change our ability to observe boundary current variability in real-time, across all seasons and in difficult conditions and locations, building on the historical record and improving temporal and spatial resolution by overlapping with these ship surveys. BOON will identify gaps in the observation of boundary currents, with the goal of filling them by the most appropriate technology (Todd et al., 2019).

Storms

Tropical and extra-tropical storms are among the most destructive natural events on Earth. Tropical storms cause an average of 10,000 deaths per year and will potentially cost the global economy more than $9.7 trillion over the next century. Growing coastal populations, urbanization, and rising sea levels magnify our vulnerabilities to storms, escalating the need for more accurate storm tracking, intensity and impact forecasts. Tropical storm tracking forecasting has shown steady improvement over the past 25 years due, in part, to the improvements in the global atmospheric forecast ensembles. But similar improvements in tropical storm intensity forecasts have lagged, in part due to the paucity of upper ocean data defining its pre-storm heat content, the inability of operational ocean models to forecast with sufficient accuracy the rapid changes in upper ocean heat content in conditions of extreme forcing, and the uncertainty in the processes that influence the transfer of heat between the ocean and atmosphere. Tropical storm impacts, such as wind and storm surge, require accurate tracking and intensity forecasts.

Gliders have been the critical observing system element for two study areas in particular, one focused on an area of potential rapid intensification surrounding the Caribbean Islands, and another in the Mid Atlantic Bight where rapid intensity reductions have challenged forecasters.

In the tropical Atlantic and Caribbean Sea, early research carried out by NOAA/AOML, NOAA/NHC, and University of Miami scientists has demonstrated that the upper ocean is linked to hurricane intensification and/or weakening provided that the appropriate atmospheric conditions are present (Shay et al., 2000). For example, several studies have shown how major hurricanes, including Hurricane *Katrina* (2005), rapidly intensified while traveling over a warm Loop Current and Eddy feature in the Gulf of Mexico (Mainelli et al., 2008). Studies carried out for other Atlantic hurricanes have shown the close link between the upper ocean heat content and the intensity changes observed in Cat 3 and above hurricanes. Since this link has been established in this region, efforts are now geared toward improving hurricane intensification forecasts of numerical operational and experimental models to produce a correct representation of the upper ocean density (temperature and salinity) structure. For example, recent research has shown that the appropriate initialization of the ocean component within the HYCOM-HWRF intensity forecast model has improved the representation of the upper ocean while reducing the error of the intensity forecast of Hurricane *Gonzalo* (2014) by almost 50% (Dong et al., 2017; **Figure 7**). In this case, underwater glider data were critical to improving the hurricane forecast because they were the only ocean observations that captured the salinity-stratified barrier layer that inhibited the mixing of colder subsurface waters and subsequent upper ocean cooling ultimately allowing for hurricane intensification (Domingues et al., 2015).

NOAA OAR research has established the relationship between hurricane intensity and the Mid Atlantic's two-layer water column. The missing essential ocean feature is the unseen bottom Cold Pool. This vast (1,000 km long × 100 km wide) cold water mass (∼10°C) lies below a thin warm layer (>28°C) during the Atlantic hurricane season and is unobservable by satellites. By deploying autonomous underwater gliders ahead of Mid Atlantic land-falling hurricanes, the Cold Pool was mapped and its evolution monitored, leading to the discovery of rapid storm induced mixing that cooled the ocean ahead-of-eye-center by up to 11°C (Glenn et al., 2016). This new ahead-of-eye-center cooling process was shown to be region-wide in multiple hurricanes (Seroka et al., 2017) and is responsible for over 75% of the observed storm-driven cooling in the Mid Atlantic since 1985 (Glenn et al., 2016). Furthermore, the cooling of the surface ocean by the entrainment of the sub-surface Cold Pool was the missing component required to accurately forecast

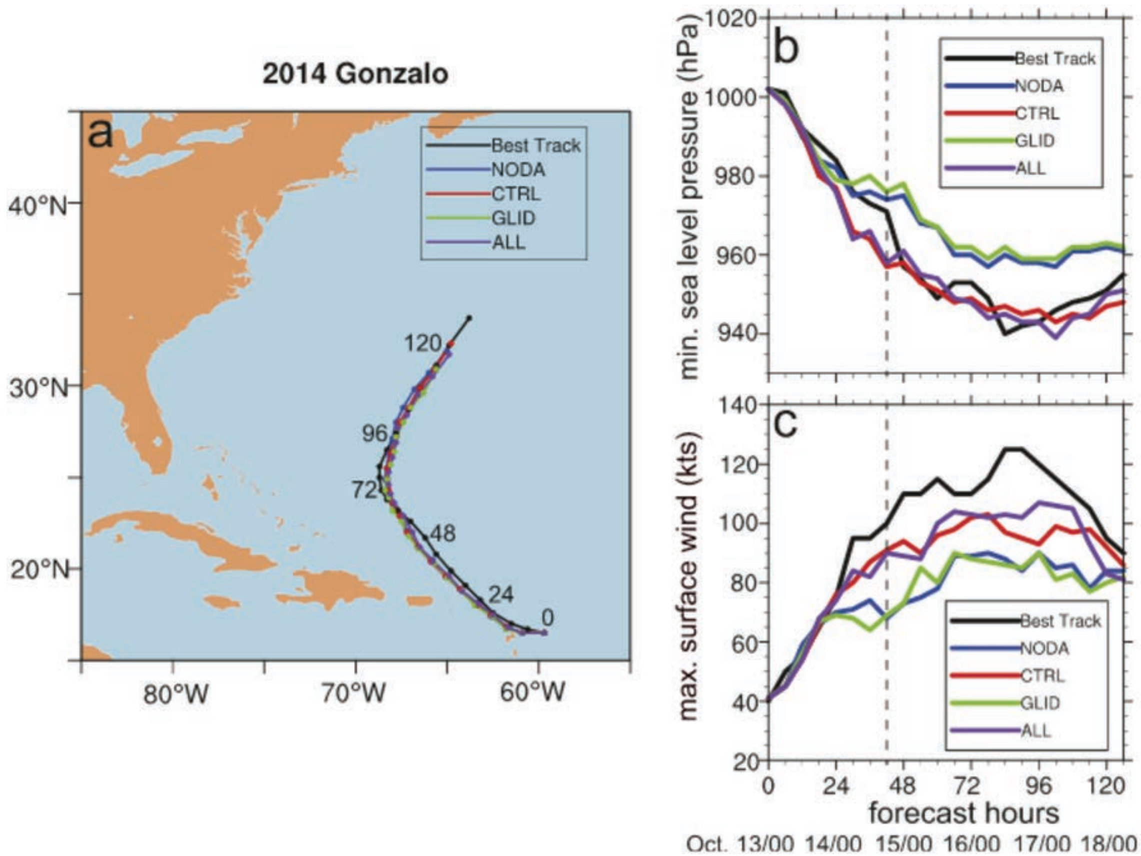

FIGURE 7 | (a) Hurricane Gonzalo track forecast, **(b)** minimum sea level pressure (center pressure), and **(c)** maximum wind forecasts, along with the best track. Gliders improve hurricane forecast. The dashed line denotes the track location closest to the glider at 0000 UTC 13 Oct 2014. (Figure 12 from Dong et al., 2017).

the rapid de-intensification of Hurricane *Irene* (Seroka et al., 2016). In stark contrast, gliders deployed ahead of Superstorm *Sandy* revealed a different Cold Pool response and impact on intensity. The onshore track, large wind field, and slow approach forced the Cold Pool more than 70 km offshore. This removed the bottom Cold Pool water and resulted in limited surface cooling and little storm weakening ahead of Sandy's historic storm surge in the region (Miles et al., 2017). The warm surface layer and the bottom Cold Pool, and their rapid evolution during hurricanes, must be well-resolved to reduce the uncertainty of hurricane intensity predictions. This can only be accomplished with underwater gliders reporting whatever the sea conditions are, and real-time subsurface profiles over the GTS, since operational ocean models cut off satellite altimeter data assimilation for water depths <150 m, leaving satellite Sea Surface Temperature (SST) as the only operational data contribution on continental shelves.

Picket lines of subsurface gliders sustained for the hurricane season in areas of rapid intensity change where identified as the most critical addition to the integrated ocean observations required to improve the ocean component of coupled ocean-atmosphere forecast models. A U.S. collaborative effort between NOAA, Navy, NSF, Industry and Academia implemented the hurricane glider picket line concept for the first time during the 2018 hurricane season. Data flow from individual glider operators to the GTS was coordinated through the U.S. IOOS Glider Data Assembly Center (DAC). The system was tested in September when 3 hurricanes were simultaneously present in the North Atlantic, each with gliders deployed in their path. This included Hurricane *Florence*, a category 4 storm at its peak that impacted the eastern seaboard of the US (**Figure 8**). The glider data transmitted over the GTS were used as input to the operational Ocean Heat Content maps that were used to help with NHC forecast intensity decisions.

OceanGliders supports the development of sustained glider observations to address hurricane issues worldwide as well as additional ones related to extra-tropical storms. Extra-tropical storms, also referred to as mid-latitude cyclones, are large scale (>1,000 km) low pressure weather systems that occur in middle and high latitudes and are associated with frontal systems. The wind speeds of these storms can be as high as those associated with tropical storms but their impacts last longer because of their greater spatial extent. Due to the large-scale features, extra-tropical storms are well-represented in atmospheric models. Hence, ocean gliders have mainly contributed to understanding the impacts of the storms on the ocean and coastal environments, particularly in terms of changes to the heat content (e.g., rapid

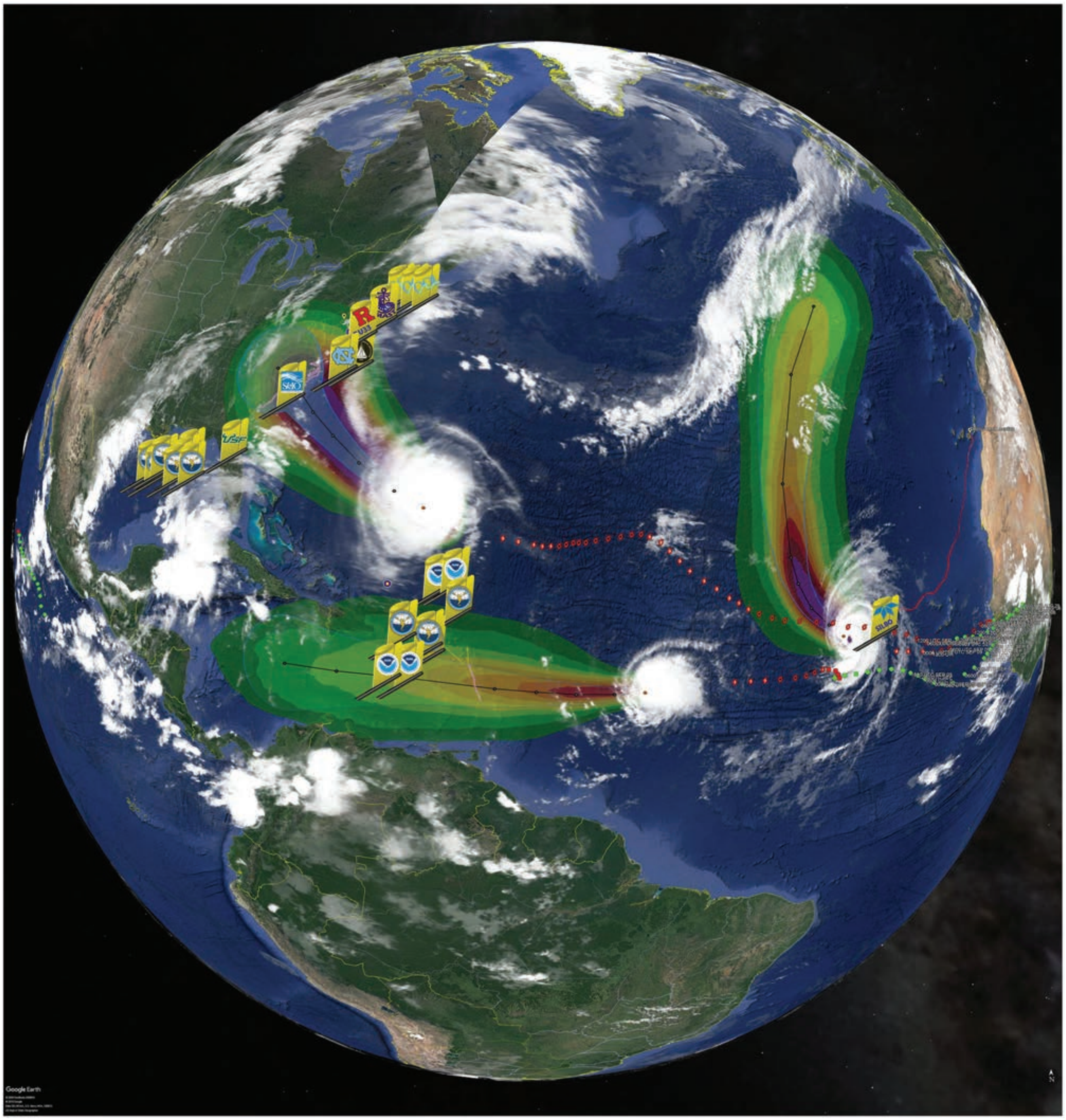

FIGURE 8 | Hurricane Florence, Isaac and Helene cloudtops (left to right) on September 11, 2018, with NHC best tracks behind each hurricane, NHC probability of tropical storm force winds ahead of each hurricane, and the tails of the diverse fleet of ocean glider in the picket lines transmitting upper ocean data in near-real time to forecasters.

cooling), its feedback on storm intensity, sediment resuspension and transport processes, and ecosystem response.

Ocean gliders are complementary to other storm sampling systems in their ability to relatively rapidly profile the upper ocean and transmit data to land even during the most severe storm conditions (Domingues et al., 2019). They provide unique datasets for studies of rapid upper ocean evolution and high-value profile data for assimilation in both operational forecast and research models before, during and after storms. Ocean glider measurements have revealed rapid changes in the distribution of water properties (temperature, salinity), and suspended sediment and chlorophyll (proxy for phytoplankton

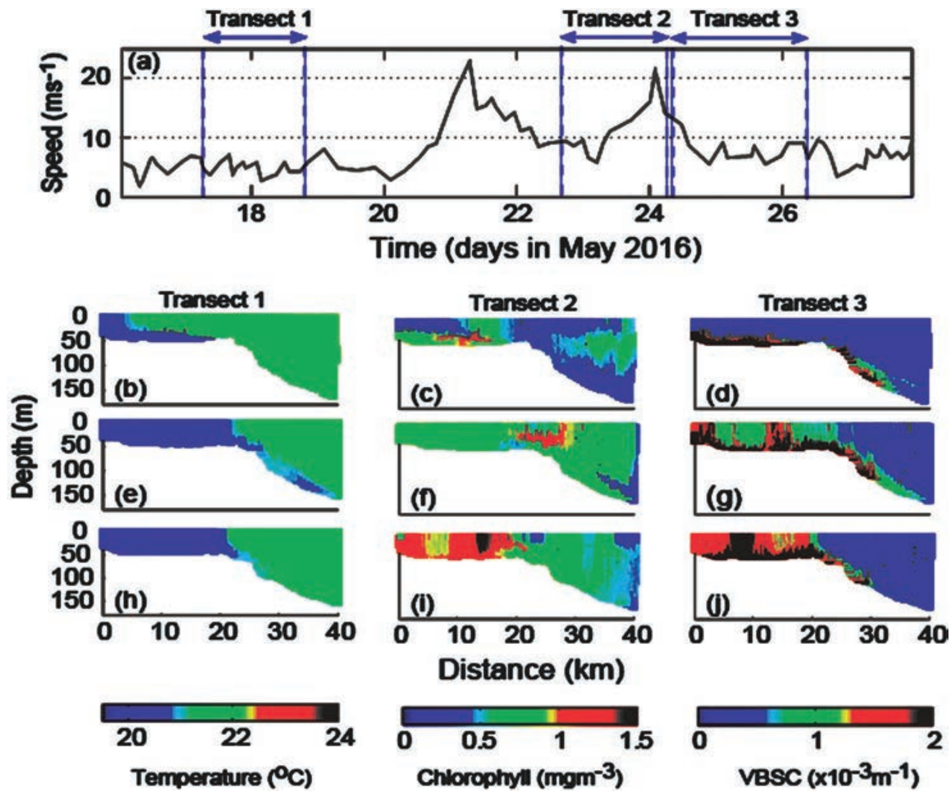

FIGURE 9 | (a) Wind speed and direction at Rottnest Island, south-west Australia. The vertical dashed lines represent timing of the ocean glider transects; Ocean glider vertical cross-sections of: **(b,e,h)** temperature (°C); **(c,f,i)** chlorophyll (mg·m^{-3}); and, **(d,g,j)** backscatter (x10^{-3}m^{-1}) across the Rottnest continental shelf. The time series of wind indicate calm winds (speeds ~5 m·s^{-1}) followed by two winter storms (speeds >20 m·s^{-1}). The wind speeds reduced to ~7 m·s^{-1} on 23 May before increasing again to >20 m·s^{-1}. There were 3 cross-shore ocean glider transects during this period. During the calm period (17–18 May 2016), a well-mixed water column with cooler (~20°C) water was present on the inner-shelf region to 5 km from the coast. Seaward of 5 km, a dense shelf water cascade (DSWC, Pattiaratchi et al., 2011) was present and extended along the sea bed to the shelf break. On the inner shelf, chlorophyll concentrations and backscatter values were higher within the DSWC and low in the surface layer. The two storms vertically mixed the continental shelf resulting in a well-mixed water column, increased suspended sediment elevated chlorophyll concentrations (modified from Chen et al., in review).

biomass) concentrations. Gliders with turbulence packages are being used to quantify the strength of storm driven mixing and its relevance in supporting prolonged phytoplankton production (Swart et al., 2015; Nicholson et al., 2016) as also highlighted by data collected on the inner continental shelf along the Rottnest continental shelf in south-west Australia (**Figure 9**).

Water Transformation

Physical, chemical, and biological properties are imported, redistributed, mixed and exported in substantial amounts by the oceanic circulation and processes. Any attempt to understand, model, and predict the evolution of the global and regional climates and marine ecosystems must include observations of their variability and their local and remote sensitivities to external changes. Indeed, fluctuation in any aspect is to lead to changes in the others, with the potential for feedback loops between them. While average conditions of the oceanic circulation and processes have been studied and assessed, little is known about the shifts in the system because of difficulties in observing water transformation phenomena directly and determining their (physical, chemical, biological) impacts.

Water transformation processes occur at relatively small scales and high frequencies not presently addressed by the GOOS. They are critical phenomena, however, that need to be assessed to better understand and model the evolution of the global/regional oceans, and in particular, their deep reservoirs of heat, salt, nutrients, etc. We do not know how these ocean processes influence change in these water properties. To fill this gap, the *OceanGliders* program proposes the long term and sustained observation of these phenomena with gliders whose unique capabilities (including under ice operations) and versatility allow the monitoring of such processes, in combination with other observing techniques, with sufficient accuracy. *OceanGliders* aims to address the two following global needs in ocean observations, by considering several key regions where water transformation processes that are important for the global (physical, chemical and biological) ocean occur.

Open Sea and Shelf Water Formation

Much of what is known about the oceanic circulation derives from the fundamental concept of water mass. The global/regional ocean is composed of a limited number of water masses that are formed (or transformed) in particular regions because of favorable local conditions (atmospheric regimes, stratification, topography, general circulation and major currents interactions) that can trigger buoyancy changes and the vertical mixing of the resident water masses in the surface and/or bottom boundary layers. Due to preconditioning effects (bottom topography, atmospheric forcing, stratification) the water formation processes lead to large mixed patches (100s km) presenting quasi-homogeneous (physical, chemical and biological) properties, and intermediate (100s of m, shelf/slope bottom) or sometimes deep (1–2 km, bottom) mixed layer depths, or thick (100s of m) bottom boundary layers.

The buoyancy decrease can be due to strong air-sea interactions (Swart et al., 2015; Houpert et al., 2016), sea ice and polynya formation in winter (Queste et al., 2015; Schofield et al., 2015), rough bottom topography (Beaird et al., 2013; Ruan et al., 2017), and major current instabilities (Schaeffer and Roughan, 2015). The water formation processes are common in winter in the subpolar gyres and high latitudes leading to the formation of the open ocean and shelf waters (Pattiaratchi et al., 2011; Durrieu de Madron et al., 2013; Bourrin et al., 2015; Peterson et al., 2017—**Figure 9**). It is so-called deep convection in few areas in the world where the mixing can reach great depths and ventilate the deep layers of the ocean due to peculiar and regional conditions (Testor et al., 2018). Later, in spring, these regions restratify, while the new water masses spread (or cascade on the ocean bottom) and mix with their surroundings. During this phase, intense blooms occur as the vertical mixing brought a large amount of nutrients in the euphotic layer and this can be sustained for a while by restratification processes (Queste et al., 2015; Schofield et al., 2015; Mayot et al., 2017), while the impacts on the benthic ecosystems can be important because of resuspended sediments. Mixing due to rough topography can also occur in overflow regions (Antarctic, Mediterranean, Denmark Strait) leading to the formation of new water masses and sediment resuspension (Durrieu de Madron et al., 2013, 2017; Venables et al., 2017) and through upwelling dynamics. The ice edge, presently in retreat toward the shelf, is a region of particular interest for water mass transformation, and gliders are ideal tools for exploring the marginal ice zone, as demonstrated in studies close to Greenland (Lee and Thomson, 2017; Våge et al., 2018).

These processes lead to the formation of water masses that move (together with their properties) through the oceanic basins interacting at the large scale with other water masses. This mixing can "buffer" or "memorize" climatic (physical, biogeochemical and biological) signals for long periods of time, until these water masses are mixed again vertically in the following years/decades/centuries, possibly far away (1,000s of km) from their formation areas. This water mass transformations can lead to rapid changes in the ocean, both locally and in remote places (Schroeder et al., 2017; Bosse et al., 2018).

Presently the large-scale formation of mode waters in winter is relatively well-covered by the present GOOS, but not by other open sea and shelf water mass formations that are more constrained by the regional scale. These processes are critical to the ventilation of the ocean and the evolution of the marine ecosystem, and this limits our understanding of the present state and evolution of the ocean and marine ecosystem. They occur sometimes in local patches on the shelf and in open sea, and on an intermittent basis, and are consequently not well resolved (temporally and spatially) at present. In addition, they generally result from different oceanic and atmospheric factors that encompass at least a year, owing to preconditioning effects (Durrieu de Madron et al., 2011; Bosse et al., 2018). This implies that sustained *in-situ* observing efforts must often be carried out in relatively large areas throughout the year to fully grasp the phenomena, with efforts occurring at a high frequency, and with high horizontal resolution to resolve the features that are involved. Moreover, in case of strong air-sea interactions in winter/spring, it is challenging to carry out traditional *in situ* measurements due to severe conditions at sea, for example winter convection in the Labrador Sea (deYoung et al., 2018). The observation of such phenomena remained a challenge until the use of autonomous underwater gliders, in combination with more classical ocean observing techniques. Much progress has been made during the last decade thanks to these relatively new platforms as demonstrated by many new publications on that subject (see introduction) and has led to a paradigm shift for deep convection (**Figure 10**). *OceanGliders* supports initiatives to fill these observational gaps in regions of water mass transformation in the coastal and open ocean.

Mesoscale and Submesoscale Phenomena

Mesoscale eddies (10–100 km horiz.) occur throughout the ocean and are not well-resolved by the present GOOS, particularly their vertical structure. They are responsible for large fluxes of energy and matter in the ocean. Depending on whether they rotate cyclonically or anticyclonically, they can be rich or poor in nutrients and can provide favorable or unfavorable conditions for phytoplankton and other organisms. They can be surface constrained, centered at intermediate depths or even extend down to the bottom (even the abyssal plain) and resuspend sea-floor sediments (Durrieu de Madron et al., 2017). Between their cores and their surroundings, temperature can vary by several degrees and practical salinity by 1 g/kg or more, while biogeochemical properties such as oxygen saturation can vary from 0 to 100% and pH by more than 1 (Bosse et al., 2017; Karstensen et al., 2017—**Figure 11**).

Mesoscale eddies can have a sub-surface expression, typical of the water mass composing their cores, and some are undetectable by satellite which makes their observation a challenge. They can be very coherent and dissipate mainly through very small-scale processes (diffusion, microturbulence) making their lifetimes extend to months or even years (Yu et al., 2017). They are able to transport the physical, biogeochemical, and biological properties of the waters composing their cores over great distances (1,000s km) after their formation before they finally dissipate (Fan et al., 2013; Pelland et al., 2013; Bosse et al., 2015, 2016, 2017; Meunier et al., 2018a). They can dissipate due to dramatic events like vertical mixing driven by atmospheric forcing reaching into their cores or by interactions with other eddies, currents or topography. Their properties, particularly their biological ones, can also change drastically throughout their lifetime due to such

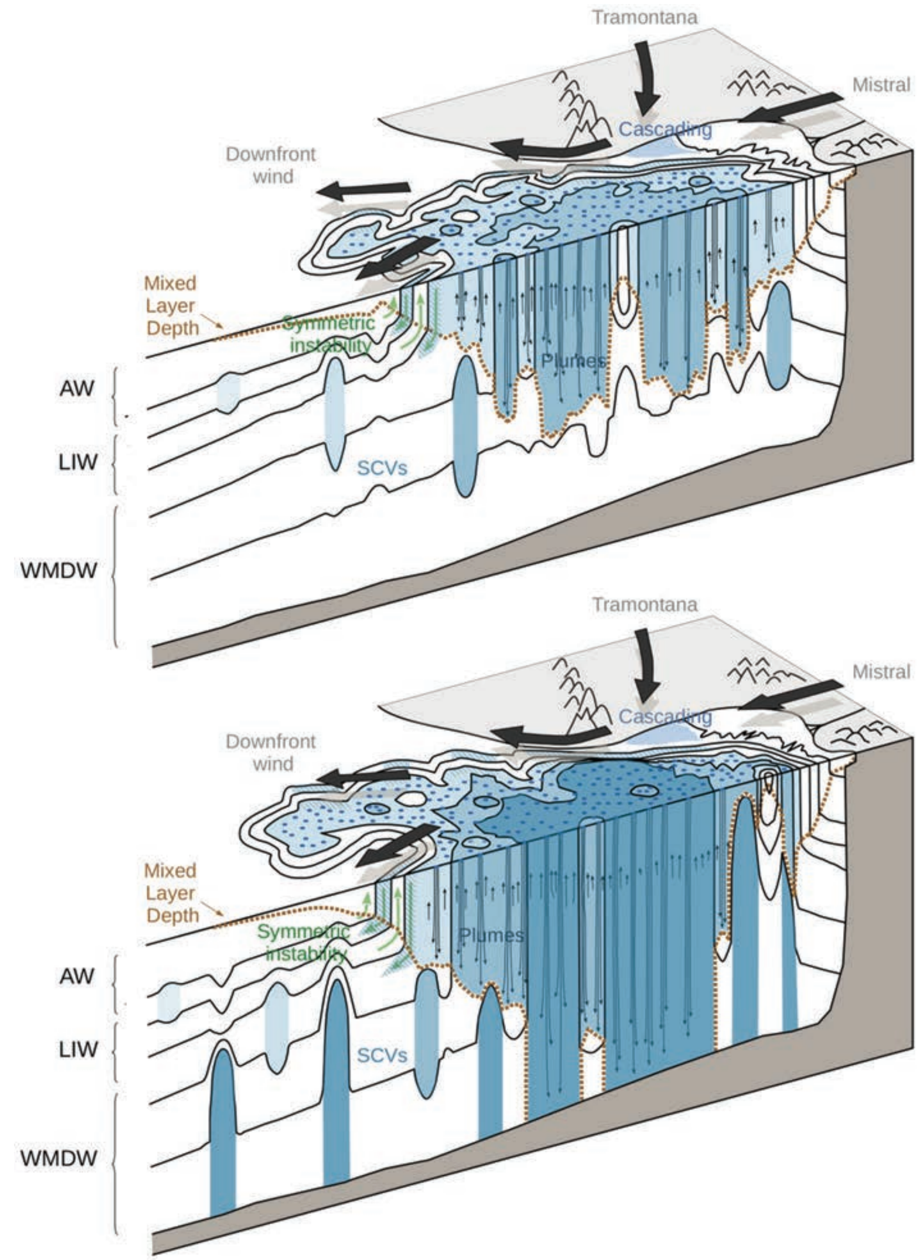

FIGURE 10 | Schematic diagram of the evolution of the convection area during the violent mixing phase in a period of 1–2 weeks. Underlying stratification/outcrop is shown by selected isopycnals (continuous black lines). The volume of fluid just mixed by convection is shaded and color coded according to potential density classes. (Figure 13 from Testor et al., 2018). Numerous glider deployments have allowed to objectively map the (physical and biogeochemical) evolution of the deep convection area on a 10-days basis for quantitative estimates while high resolution measurements allowed to investigate the small scale processes at stake.

external factors (McClatchie et al., 2012; Ainley et al., 2015; Villar et al., 2015; Durrieu de Madron et al., 2017). The impact of such factors on the properties of the eddy cores clearly depends on their vertical structure which in turn, depends on the oceanic (and atmospheric) conditions at their formation.

Mesoscale eddies can be formed through vertical mixing (due to air-sea-ice interactions or induced by rough topography, major current barotropic/baroclinic instabilities and/or detachments from the boundary circulation due to the continental slope curvature (Caldeira et al., 2014) and/or other effects like upwelling (Bosse et al., 2015). Mesoscale eddies can be classified according to their formation mechanism because they present similar characteristics and core properties. It has been shown that a number of different types of eddies (Loop Current Eddies, Agulhas rings, Dead Zone Eddies, Gulf Stream rings, Meddies, Suddies, Weddies, Algerian/Sardinian Eddies, deep

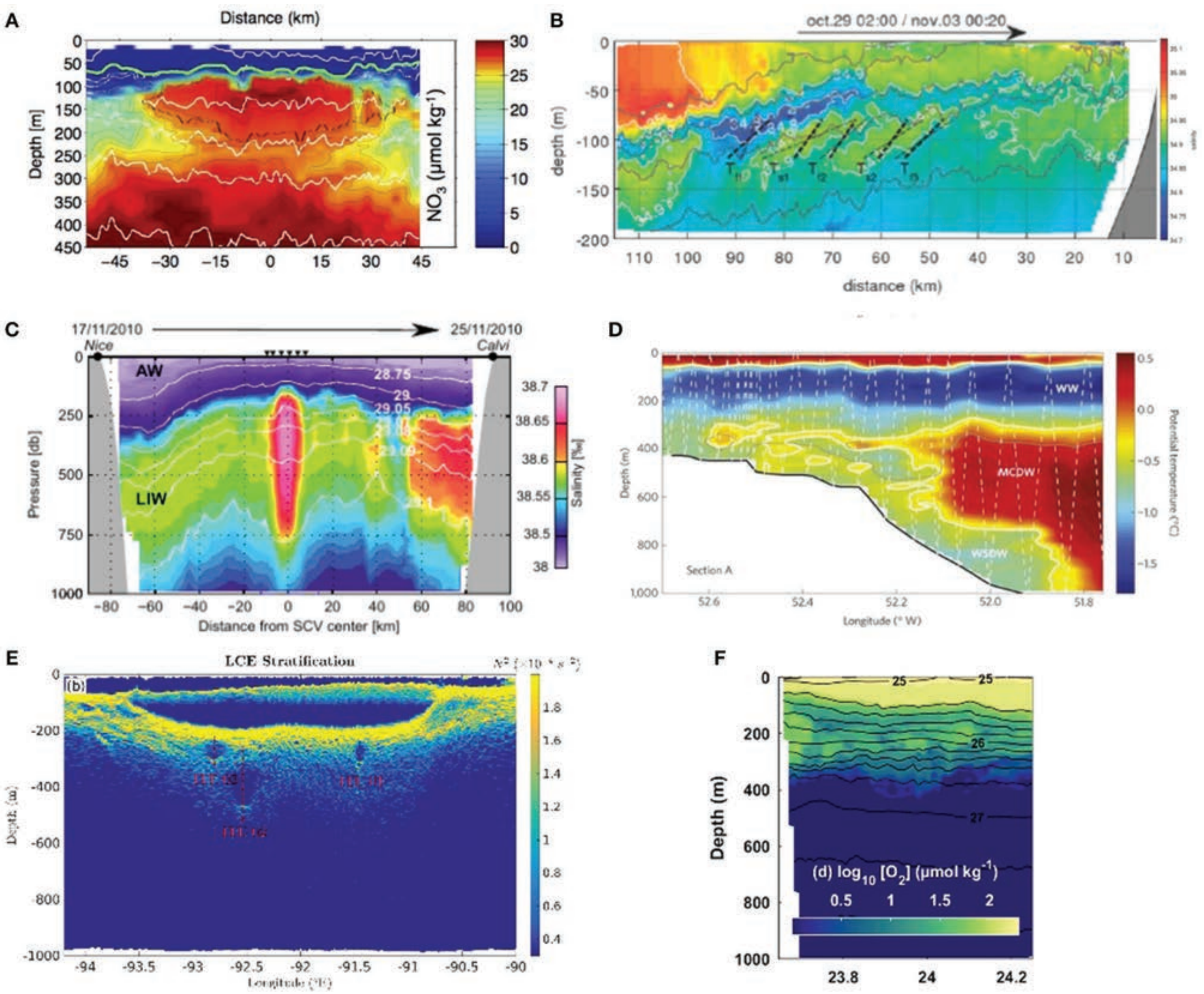

FIGURE 11 | Some highlights of (sub)mesoscale oceanic processes revealed by gliders that have been identified as important for the functioning of the physical, chemical and biological ocean: **(A)** Vertical section across a Dead Zone Eddy (DZE) showing its lens-like structure in nitrate concentrations (from Figure 7 of Karstensen et al., 2017); **(B)** Vertical section of salinity across the upwelling front off Peru (from Figure 7 of Pietri et al., 2013); **(C)** Vertical section across a SCV "Suddy" (from Figure 2 of Bosse et al., 2015); **(D)** Vertical section across the shelf of Antarctica peninsula (from Figure 1 of Thompson et al., 2014); **(E)** Vertical section across a LCE showing intrathermocline eddies (ITE) within (from Figure 11 of Meunier et al., 2018b); **(F)** Vertical section of dissolved oxygen in the Persian Gulf (from Figure 2 of Queste et al., 2013).

convection SCVs, ITEs…) can have a great impact on the ocean circulation/ecosystem state and evolution through their particular structures and transport mechanisms. Other fine scale processes are clearly involved in the ocean mixing, like microturbulence (Fer et al., 2014; Palmer et al., 2015; Schultze et al., 2017) or frontogenesis, filamentation due to stirring or symmetric instability (**Figure 11** and Ruiz et al., 2012; Thompson et al., 2014, 2016; Thomsen et al., 2016; Pietri et al., 2013; Brannigan et al., 2017; Buffett et al., 2017; Du Plessis et al., 2017; Pascual et al., 2017; Kolodziejczyk et al., 2018) that can lead to significant vertical velocities and fluxes. However, the extent and variability of their impact over long periods of time still needs to be assessed. The "mesoscale" dynamics and associated "submesoscale" features are important contributors to the ocean state and are of crucial importance for biogeochemical and biological processes in the ocean. Gliders offer a new high-resolution lens for observing the full seasonal cycle, a dominant mode of the earth system, in their ability to observe the physical-biological coupling at sub-seasonal and sub-mesoscale (Martin et al., 2009; Swart et al., 2012, 2015; Monteiro et al., 2015; Thomalla et al., 2015; Du Plessis et al., 2017).

It is difficult for an *in situ* ocean observing system to capture all these important but relatively small circulation features, but a regular (annual) statistical assessment of the numbers and properties (and impact) of the main families of eddies and smaller processes can be achieved through subsurface, continuous and sustained glider observations of sufficient horizontal resolution. The time and space resolution of the glider sampling, for a variety of different sensors, make gliders essential observing platforms for studies and continuous assessments of the role of (sub)mesoscale processes in the ocean circulation and ecosystem. Over the last decade, a remarkable number of articles on (sub)mesoscale dynamics and smaller scale mixing processes based on underwater glider data and their impact on biogeochemistry and biology has been published (see introduction). The importance of Submesoscale Coherent Vortices (SCV), filaments along fronts and around mesoscale eddies, and induced vertical movement, has been demonstrated from ground truth and their impact can now be monitored on the long term in key regions with gliders (Hristova et al., 2014; Bosse et al., 2016; Yu et al., 2017).

Underwater gliders do sample the vertical structure of the ocean in an unprecedented way, with high resolution along the horizontal over long periods of time. Gliders also transmit the observational data in near real-time. This remote access to observational data that resolves the (sub)mesoscale can improve forecasting the ocean dynamics, biogeochemistry and ecosystem. The glider data is a perfect match for assimilation in regional/coastal numerical models, providing ocean state estimates at small scales with increased accuracy benefiting societal applications. Gliders can map the subsurface ocean at high resolution and provide powerful tools for monitoring previously inaccessible ecological processes. *OceanGliders* promotes and supports all physical, biogeochemical and biological studies focusing on these small-scale processes and encourages long-term continuation of these studies. The anomalies caused by these (sub)mesoscale variabilities exceed by one order of magnitude those attributed to changes in large scale circulation and marine ecosystem variability brought about by a warming planet, as assessed by the IPCC (Bates et al., 2018) and must be considered to further our understanding and monitoring of the physical, biogeochemical and biological ocean.

END-USER BENEFITS

In section Addressing global observing needs, we have detailed the unique "oceanographic" monitoring space that gliders occupy. Here we describe how this translates to benefit for the end users of a fully integrated observing system, i.e., what key roles (primary and supporting) a global sustained glider network can play in delivering services for both science and society.

Gliders can make sustained observations at high resolution, bringing temporal and spatial scales, hourly to sub seasonal and from 10 m to 1,000 km's, relevant for a number of key ocean processes within economic reach. They are navigable and can be directed to sample ocean phenomena in real-time and with a fleet of gliders monitoring can be continuous, if required, and operational. Glider sensor payloads are expanding and their unique role in acoustic monitoring is already being exploited. They can sample in extreme conditions and to increasing depths, from surface to 6,000 m depth.

Gliders require pilots; however navigation is increasingly automated as a result of advances in platform reliability, community experience and piloting support tools. Glider observations require careful data processing protocols, an area that is being actively resolved, with tools and services emerging, and standard products from several deployments (e.g., gridded sections, geostrophic currents, etc.) that could be more accessible to non-expert users, many of which are from the *OceanGliders* community. Although gliders are relatively "slow" samplers, this is not an impediment to providing sampling capability at key space and time scales for the global observing system.

Gliders are uniquely poised to deliver sustained and responsive observations to the GOOS in the following areas:

- Connecting coast to open ocean: key for monitoring the regional effects of climate variability, and of processes (circulation, currents, upwelling) that have an impact on regional ecosystems.
- Boundary current monitoring: key to the transport of heat, salt, biogeochemical variables (nutrients) and plankton, they influence ecosystems and therefore variability in ocean productivity, and impact flood levels, erosion and commercial activity.
- The observation of ocean state variables at a high density in time and space in order to gain insight into the variability/statistical distribution of these variables locally given the turbulent nature of ocean flows.
- Surface to deep profiles in extreme conditions: observing ocean structure that affects the strength of violent storms (e.g., hurricanes) and of violent ocean mixing.
- Sustained observations in the polar regions where ship persistence is challenging due to ice and harsh conditions.
- Fast deployment and real-time navigation enabling delivery of vital information for environmental disaster management.

Looking at these key sampling capabilities under the GOOS theme areas of climate, operational services and ocean health, it is clear that sustained glider monitoring, as part of a fully integrated global ocean observing system, delivers a range of benefits.

Climate

- Monitoring boundary currents delivers knowledge on sub-seasonal variability and long-term trends that affect climate, leading to improved climate prediction. This information is used for adaptation to climatic change.
- Sustained 3D observations of deep and shelf water formation, a key component of our climate and ocean circulation system, provide knowledge to assess deep storage of heat, salt, nutrients and carbon sequestration. They uniquely can aid our understanding of variability in water formation and the impact of this on the global ocean budgets.
- Monitoring the subsurface development of climate oscillations (e.g., el Niño) aid prediction, support advanced warning capability and improved parameterization of climate patterns that affect seasonal forecasts.

Operational Services

- Monitoring lines across key coast-to-open ocean transects (often boundary current regions) increase the accuracy of regional ocean forecasts, which have economic impact (e.g., offshore wind, powerful eddies that affect oil platform drilling, flood hazard warnings, abundance and location of commercial

species) supporting reanalysis and prediction models, good for getting real time data back to inform the next modeling cycle.
- Glider deployments in the path of hurricanes and violent storms (tropical and extratropical) provide *in situ* water profiles of ocean structure and heat/salt content assimilated real-time into models, significantly increasing the accuracy of the storm intensity prediction, which is vital to regional government and emergency services.
- Speedy deployments of gliders at pollution events, provide simultaneous data on ocean circulation and pollutants, either to track the pollutants or to improve ocean forecasts by providing data for assimilation. This supports decision making by better disaster management services and thus can reduce environmental impact.
- Speedy and flexible deployments of gliders can enable co-located measurements with other air/ocean observing systems, which are key for advancing scientific understanding of marine biogeochemical-physical interactions and/or air-sea flux interactions across the oceanic surface. These can also help provide precious data points for future coupled data assimilation methods under active consideration for balanced initialization of coupled earth system models.
- Sustained ocean sound monitoring delivers real time information on key marine mammal species, for ship avoidance decisions. Increasingly, this is a must for conservation of populations as new shipping routes increasingly intersect with marine mammal habitats.
- Monitoring boundary currents or water transformation in key areas delivers knowledge on ocean changes, both sub-seasonal variability and long-term trends, that affect climate. Real-time information on these key components of the global circulation better constrain models and are used, for example, to increase the accuracy of forecasts for coastal regions.

Ocean Health

- Sustained transects from coastal to open ocean, including boundary currents and water transformation areas, are key for monitoring the regional effects of ocean variability on regional ecosystems. Physical, chemical and biological information from these sections improves understanding of ecosystem response to environmental stressors (e.g., low dissolved oxygen, ocean acidification), aids regional ecosystem management and can provide ocean health monitoring indicators.
- Sustained acoustic (fish tags, passive acoustics for mammals, active acoustics for zooplankton) and video monitoring from coast to open ocean, deliver information assessing distributions and stocks as well as behaviors of marine organisms and response to environmental conditions that enables improved physical/ecosystem modeling, prediction, and resource management.

THE WAY FORWARD

At present, global glider operations are still at the pilot stage and are not fully developed. There are some regional operations, e.g., the repeated glider transects off the west coast of the United States, that are well-established and fully operational but full coordination of glider missions at the regional, basin or global scale, as discussed, remain in the planning stages. There has been enough activity to prove that we have the capability to conduct such operations but the development of clear scientific and operational goals for the proposed network remains under discussion. Indeed, this white paper is a contribution to that discussion and is meant to further stimulate consideration of the potential opportunities to fill gaps in the present networks of global ocean sampling.

Further developments should be framed with clear measurement goals and analysis of the appropriate technological solutions to address the observational challenges. There are now many different options to address the three themes of the GOOS: Climate, Operational Services and Ocean Health, including autonomous surface and underwater craft, drifters, subsurface moorings, ships of opportunity and research ships and satellite systems. All of the options should be considered to determine which solution, or mix of platforms, best meets the observational goals. We have some of the tools needed for this analysis but also need to work together as a community to optimize the design of the global observing system.

Ocean gliders, and other autonomous marine vehicles, are evolving and improving at a remarkable pace. Their endurance, related to battery capacity and sensor performance, continues to improve, as does their range of operations in both the coastal and open sea environments. It is now possible to sample the deep ocean with gliders, with developments that will enable us to routinely reach depths of 6,000 m, while missions of many months or longer are now routine. There is also a growing range of private companies building these systems providing a wider range of options. This diversity shows the wide interest in these platforms and builds our confidence in their further development and availability, which is a key aspect of sustainability. Performance in extreme conditions, such as winter conditions, and navigation under sea-ice, is improving, and there are very few places on the planet where they cannot operate. Autonomy continues to develop, while full operational independence is still quite a few years away. As with many new platforms, in the first few years enormous effort is required to setup and deploy them. After two decades of operation, the learning curve for new users is not as steep as it was because of technological improvements and because the global community supports new users. Internationally, the *OceanGliders* program will help the glider community focus on the GOOS requirements. It builds on several long-term glider observational programs that exist in Europe, Australia, Canada, the United States, Mexico, Peru, Chile, South Africa, New Zealand, etc. Further development and coordination among these initiatives, and new ones that form, will provide support for coordinated global operations.

Global observing systems have shifted from a primarily physical focus to expanded measurements, spanning biological and biogeochemical variables. Essential Ocean Variables (EOV) within the GOOS now span a wide range, including biogeochemistry, biology and ecosystems. There has been a lot of progress in developing such sensors for gliders, for example, fluorometers for measuring phytoplankton have been in development for a long-time. So too have active/passive multi-frequency acoustic sensors been deployed on gliders to measure oceanic currents, surface wind intensity, zooplankton, and to detect acoustic small/large fish tags, marine mammals, sharks etc. Other sensors include imagery, as well as nitrate, oxygen and pH, carbon dioxide sensors, and various optical sensors to detect light, backscatter, attenuation, particles, harmful algal blooms and ocean acidification. However, the battery capacity of the gliders still limits the total range of sensors that can be deployed on a single vehicle. It is clear that further battery and sensor developments will enable a wider range of possibilities and demonstrate that the platform has potential for making an even wider range of observations than at the moment.

Data from ocean gliders are presently being used in operational ocean models and operational weather forecast models. The data are typically streamed in real-time through the GTS and are then available to all operational users. They have been used in research or pre-operational systems and improved weather forecast modeling and operational global and regional ocean forecasts such as Mercator Ocean, FOAM (Met Office), MFS (Mediterranean Forecasting System), BLUELink (Bureau of Meteorology, Australia), CONCEPTS (Fisheries and Oceans, Environment and Climate Change Canada and Department of National Defence, Canada), HYCOM/NCODA (USA), NAVOCEANO (US Naval Oceanographic Office), REMO (Brazil), TOPAZ/NERSC (Norway). Observation impact studies show the value of sub-surface hydrographic observations, such as those from gliders, in improving prediction. Moreover, data products can be created, such as data aggregations and mean fields, that are easily usable for model validation and assessment. In this paper we have presented plans to deploy gliders in the waters near hurricanes, in ocean boundary currents and in key areas of water transformation. Data from such deployments could provide critical information to improve the performance of ocean forecast models as ocean dynamics in such regions remains a modeling challenge for the next decade. Improved prediction at sub-seasonal to seasonal (S2S) scales requires use of ensembles (or super-ensembles) including those from ocean models. These ensembles can also provide a good representation of quantified uncertainty in time and space which could be targeted by future flexible positioning of underwater gliders in real-time or near real-time. Having a large network of gliders, potentially with different sensor packages and/or different measurement goals, will lead to piloting challenges on a day-to-day basis for individuals. Eventually the sampling patterns might be autonomously determined through use of data-assimilating models, remote sensing products, and other *in situ* measurements.

The increasing operational interest in gliders and glider teams' capability suggests that the applications mentioned in section End-user benefits could all become operationally routine within a decade. Looking further ahead there is much capacity for the use of gliders to expand, particularly in relation to ocean health and human pressures.

We envision that:

- Increase in sensor capability of gliders will increase their use for early warning of environmental stress or pollution (Verfuss et al., 2019), for example to manage compliance areas of ecosystem sensitivity.
- The weather/modeling community may invest in gliders in key ocean areas to support improved prediction, perhaps with artificial intelligence, smart models autopiloting the gliders in real-time in the regions of greatest uncertainty.
- Deep gliders will deliver the same insight on deep variability of currents, water mass, heat, salt, biogeochemical and biological variables, fundamentally changing our ability to model deep flow and thus climate scale predictions and seasonal forecasts. They will also be our cost-effective eyes and ears on the deep, policing infringement of deep mining and reporting on deep ecosystem health.
- Increasing battery life, introducing novel energy sources, and improving solutions to bio-fouling, will lower costs and extend glider operation time. This will allow for the monitoring of open ocean areas at low cost (there will still be a need to deploy them from small boats).
- International consortia will share sites for recovery/deployment, facilities for refurbishment, and even pilots to optimize operations worldwide and reduce the costs of operation and the loss probability.
- The cost of the gliders will decline as their numbers increase and the number of users worldwide increase.
- The glider's payload space will increase enabling them to carry a wider range of sensors and/or a different battery configuration.

In considering the application of gliders to problems such as boundary currents, water transformations or storms, a careful analysis of the measurement challenge should include consideration of other approaches to ocean observation. Gliders have strengths and limitations, as do all platforms and sensors, and both should be taken into account when designing an observing solution to address critical gaps in our global ocean observing strategy. Formal design exercises must be carried out with the other components of the GOOS considering its 3 themes: Climate, Operational Services and Ocean Health. Such design studies must consider all the societal benefits and needs of GOOS applications, including human impact, ecosystem, biodiversity and pollution assessments as well as sustainable management and marine hazard response (cf. GOOS strategic mapping[13]).

Numerical simulation experiments, using sophisticated coupled ocean-atmosphere models to determine the best mix of platforms and the tradeoffs in ocean sampling that result from deploying different systems should be carried out. However, this must be done while keeping a critical eye on the model's performances and this must not be the only basis when producing a design. While gliders may fill a critical role for a particular system, for example a particular boundary current, it

[13]http://www.goosocean.org/index.php?option=com_content&view=article&id=120&Itemid=277

may still be the case that a mix of moorings, drifters and other platforms would provide the best observational solution because of logistical constraints. It could be that biological requirements balance the needs of operational services, in a particular region in terms of resources optimization or the contrary, and so on.

The *OceanGliders* program can contribute to societal development and sustainability, and there are many examples of this potential already being achieved. These can be exemplified by activities that contribute toward achieving the United Nations Sustainable Development Goals (SDGs)[14], of which SDG2 (Zero Hunger), SDG13 (Climate Action) and SDG14 (Life Below Water) are arguably most germane. Examples of glider networks making such contributions include deployments in climatically sensitive regions that are also important breeding and nursery grounds for foodwebs, and the focus of a significant fishing industry. Sustained glider missions in these areas conducted as part of whole-ecosystem research programs provide the underpinning scientific knowledge for ecosystems-based fishery management. Glider networks provide enhanced data collection and improved transfer of knowledge to policymakers, so as to support such societally-relevant sustainability activities.

It is important to consider the targeted phenomena, their space/time scales and EOV since they will impose requirements in terms of sampling. The different *OceanGliders* TT will define what "operational" means for them. The Boundary Currents TT requirements of sampling the seasonal cycle implies that "operational" means having gliders in water year-round, while Storms requirements imply having gliders in the water only during the storm periods, and Water Transformation requirements could be year-round or focus only on the winter/summer period depending on the water transformation phenomenon that is considered. Other requirements will emerge as the program develops with TT on biogeochemistry or polar regions for instance.

The world ocean will change. We need to assess those changes appropriately and must not underestimate what could be done with gliders. Without doubt, there will be more end-user engagements, new technologies on board, more connectivity, more sensors, more gliders and more users to address that. The flexibility of gliders allows complementarity, and this is an asset for their integration in the GOOS. The challenge for the next decade will be to build a GOOS glider component that will help the GOOS reach the right balance between its different components to deliver products for societal benefits and applications, through the monitoring of the required oceanic phenomena and EOV.

VISION

Our vision is for a mature sustained global glider observing network by 2030. It will not only support regional, sustained operational deployment of gliders serving the present societal needs around operational services, ocean health and climate, but also solely allow new ocean observing applications in this framework. The outstanding capacity of gliders to play a role as an agent of integration, across scales, from the coast to the open ocean, and from physics to biology, needs to be used to enhance the GOOS, integrating with its other components (*in situ* and satellites). These global glider operations will likely have different schedules of operation, carry different sensors, and serve different needs but will have a shared support system through the *OceanGliders* program that will allow them to work together efficiently, to govern and support the system, coordinating global glider operations and ensuring that the needs of society for ocean data are best met.

OceanGliders will support global standards and best practices to ensure that the operations and the data delivered can be monitored at the global scale. Improved data interfaces and standardized data will ensure quality-controlled data are easily found and effectively used. By 2030 one should be able to effortlessly, perhaps unknowingly, find and acquire quality-controlled physical, biogeochemical and biological data from gliders alongside an already huge range of earth observations and use them to address scientific, commercial, or policy initiatives. Attaining our vision would ensure that the value of observations to society will never be lost, indeed, will increase over time as they are used and reused and in new ways not originally imagined.

Here, we have identified three key areas for the *OceanGliders* program to focus on: Boundary Currents, Storms and Water Transformation. These represent interests heard from the glider and user community, but we expect more to develop, as the *OceanGliders* program matures. Moving forward, *OceanGliders* will have, together with a wide range or stakeholders and participants, to conduct a value-chain assessment to explore further needs of users to ensure that the network continues to be fit-for-purpose, as discussed in the Framework on Ocean Observing. Through this paper, we have sought to demonstrate, through exploration of some key thematic examples, the opportunities and potential benefits of coordinated deployment of ocean gliders to fill some key gaps in the existing ocean observation system. The precise form of such activity requires a comprehensive and integrated analysis of the needs for observation, that is the most broadly defined societal needs, and an assessment of the different approaches to observation, just one of which is ocean gliders. Such an assessment will have to address needs related to the three key thematic areas of the GOOS: Ocean health, Operational services and Climate.

In his seminal paper, Stommel (1989), foresaw an operational fleet of 300–550 gliders at any time evolving in the world ocean to support the GOOS by 2025. Only a substantial increase in global resources would yield such an outcome by 2030. We propose a more modest implementation of the *OceanGliders* global program for the next decade. Sustained observations of boundary currents are perhaps the most established capability of gliders relevant to the GOOS. A sensible goal is to have continuously 100 gliders in a sustained Boundary Ocean Observing Network within the next 10 years, with some additional gliders addressing Storms and Water Transformation issues where and when this fleet would not already do so. We are confident that operation of such a fleet of 100 gliders is achievable. Further development will rely on capacity building and would be driven by a combination

[14]https://sustainabledevelopment.un.org/?menu=1300

of need and demonstrated benefit of the glider program. We have presented results from 25 boundary current sections sustained for a minimum of 1 year, and for as long as 12 years. While not all these 25 sections are currently sustained, the proof that they are operable has been made. An increase in this sampling by a factor of 4 is a relatively reasonable worldwide goal. The operational cost to keep one glider in the water for 1 year is approximately $200K, thus 100 gliders would cost $20M per year, a relatively affordable cost for a global component of the GOOS.

AUTHOR CONTRIBUTIONS

The editorial team for this paper (PT, BY, DR, SG, DHa, CL, CP, KHi, EH, and VT) has collected the contributions of the other co-authors and coordinated the writing of the paper.

ACKNOWLEDGMENTS

The editorial team would like to recognize the support of the global glider community to this paper. Our requests for data and information were met with enthusiasm and welcome contributions from around the globe, clearly demonstrating to us a point made in this paper that there are many active and dedicated teams of glider operators and users. We should also acknowledge the support that OceanGliders has received from the WMO/IOC JCOMM-OCG and JCOMMOPS that have allowed this program to develop, encouraging us to articulate a vision for the role of gliders in the GOOS. We acknowledge support from the EU Horizon 2020 AtlantOS project funded under grant agreement No. 633211 and gratefully acknowledge the many agencies and programs that have supported underwater gliders: AlterEco, ANR, CFI, CIGOM, CLASS Ellet Array, CNES, CNRS/INSU, CONACyT, CSIRO, DEFRA, DFG/SFB-754, DFO, DGA, DSTL, ERC, FCO, FP7, and H2020 Europen Commission, HIMIOFoTS, Ifremer, IMOS, IMS, IOOS, IPEV, IRD, Israel MOST, JSPS, MEOPAR, NASA, NAVOCEANO (Navy), NERC, NFR, NJDEP, NOAA, NRC, NRL, NSF, NSERC, ONR, OSNAP, Taiwan MOST, SANAP-NRF, SENER, SIMS, Shell Exploration and Production Company, Sorbonne Université, SSB, UKRI, UNSW, Vettleson, Wallenberg Academy Fellowship, and WWF.

REFERENCES

Adams, K.A., Barth, J. A., and Shearman, R. K. (2016). Intraseasonal cross-shelf variability of hypoxia along the Newport, Oregon, hydrographic line. *J. Phys. Oceanogr*. 46, 2219–2238. doi: 10.1175/JPO-D-15-0119.1

Ainley, D. G., Ballard, G., Jones, R. M., Jongsomjit, D., Pierce, S. D., Smith, W. O. Jr., et al. (2015). Trophic cascades in the western Ross Sea, Antarctica: revisited. *Marine Ecol. Progr. Series* 534, 1–16. doi: 10.3354/meps11394

Albretsen, J., Aure, J., Sætre, R., and Danielssen, D. S. (2012). Climatic variability in the Skagerrak and coastal waters of Norway. *ICES J. Mar. Sci*. 69, 758–776. doi: 10.1093/icesjms/fsr187

Alford, M. H., Mickett, J. B., Zhang, S., MacCready, P., Zhao, Z., and Newton, J. (2012). Internal waves on the Washington continental shelf. *Oceanography* 25, 66–79. doi: 10.5670/oceanog.2012.43

Alkire, M.B., D'Asaro, E., Lee, C. M., Perry, M. J., Gray, A., Cetinic, I., et al. (2012). Estimates of net community production and export using high-resolution, Lagrangian measurements of O_2, NO_3^-, and POC through the evolution of a spring diatom bloom in the North Atlantic. *Deep Sea Res. Part 1 Oceanogr. Res. Papers* doi: 10.1016/j.dsr.2012.01.012

Alkire, M. B., Lee, C. M., D'Asaro, E. A., Perry, M. J., Briggs, N., Cetinić, I., et al. (2014). Net community production and export from Seaglider measurements in the North Atlantic after the spring bloom. *J. Geophys. Res.* 119, 6121–6139. doi: 10.1002/2014JC010105

Alvarez, A., Chiggiato, J., and Schroeder, K. (2013). Mapping sub-surface geostrophic currents from altimetry and a fleet of gliders. *Deep Sea Res. Part I Oceanogr. Res. Papers* 74, 115–129. doi: 10.1016/j.dsr.2012.10.014

Alvarez, A., and Mourre, B. (2014). Cooperation or coordination of underwater glider networks? An assessment from observing system simulation experiments in the Ligurian sea. *J. Atmos. Ocean. Technol.* 31, 2268–2277. doi: 10.1175/JTECH-D-13-00214.1

Andres, M., Mensah, V., Jam, S., Chang, M.-H., Yang, Y.-J., Lee, C. M., et al. (2017). Downstream evolution of the Kuroshio's time-varying transport and velocity structure. *J. Geophys. Res. Oceans* 122, 3519–3542. doi: 10.1002/2016JC012519

Anutaliya, A., Send, U., McClean, J. L., Sprintall, J., Rainville, L., Lee, C. M., et al. (2017). An undercurrent off the east coast of Sri Lanka. *Ocean Sci.* 13, 1035–1044. doi: 10.5194/os-13-1035-2017

Asper, V., Smith, W., Lee, C., Gobat, J., Heywood, K., Queste, B., et al. (2011). "Using gliders to study a phytoplankton bloom in the Ross Sea, Antarctica," in *MTS/IEEE Kona Conference, OCEANS'11* (Kona, HI).

Aulicino, G., Cotroneo, Y., Ruiz, S., Sánchez Román, A., Pascual, A., Fusco, G., et al. (2018). Monitoring the Algerian Basin through glider observations, satellite altimetry and numerical simulations along a SARAL/AltiKa track. *J. Marine Syst.* 179, 55–71. doi: 10.1016/j.jmarsys.2017.11.006

Azaneu, M., Heywood, K. J., Queste, B. Y., and Thompson, A. F. (2017). Variability of the Antarctic slope current system in the Northwestern Weddell sea. *J. Phys. Oceanogr.* 47, 2977–2997. doi: 10.1175/JPO-D-17-0030.1

Baird, M. E., and Ridgway, K. R. (2012). The southward transport of sub-mesoscale lenses of Bass Strait Water in the centre of anti-cyclonic mesoscale eddies. *Geophys. Res. Lett.* 39:L02603. doi: 10.1029/2011GL050643

Baird, M. E., Suthers, I. M., Griffin, D. A., Hollings, B., Pattiaratchi, C., Everett, J. D., et al. (2011). The effect of surface flooding on the physical-biogeochemical dynamics of a warm-core eddy off southeast Australia. *Deep Sea Res. Part II Top. Stud. Oceanogr.* 58, 592–605. doi: 10.1016/j.dsr2.2010.10.002

Barceló-Llul, B., Pascual, A., Ruiz, S., Escudier, R., Torner, M., and Tintoré, J. (2019). Temporal and spatial hydrodynamic variability in the Mallorca channel (western Mediterranean Sea) from eight years of underwater glider data. *J. Geophys. Res.: Oceans* 124, 2769–2786. doi: 10.1029/2018JC014636

Bates, A. E., Helmuth, B., Burrows, M. T., Duncan, M. I., Garrabou, J., Guy-Haim, T., et al. (2018). Biologists ignore ocean weather at their peril. *Nature* 560, 299–301. doi: 10.1038/d41586-018-05869-5

Baumgartner, M. F., Fratantoni, D. M., Hurst, T. P., Brown, M. W., Cole, T. V. N., Van Parijs, S. M., et al. (2013). Real-time reporting of baleen whale passive acousticdetections from ocean gliders. *J. Acoust. Soc. Am.* 134, 1814–1823. doi: 10.1121/1.4816406

Baumgartner, M. F., Stafford, K. M., Winsor, P., StatScewich, F., and Fratantoni, D. M. (2014). Glider-based passive acoustic monitoring in the Arctic. *Mar. Technol. Soc. J.* 48, 40–51. doi: 10.4031/MTSJ.48.5.2

Beaird, N., Fer, I., Rhines, P., and Eriksen, C. (2012). Dissipation of turbulent kinetic energy inferred from seagliders: an application to the eastern Nordic seas overflows. *J. Phys. Oceanogr.* 42, 2268–2282. doi: 10.1175/JPO-D-12-094.1

Beaird, N. L., Rhines, P. B., and Eriksen, C. C. (2013). Overflow waters at the Iceland-Faroe ridge observed in multiyear seaglider surveys. *J. Phys. Oceanogr.* 43, 2334–2351. doi: 10.1175/JPO-D-13-029.1

Benoit-Bird, K. J., Patrick Welch, T., Waluk, C. M., Barth, J. A., Wangen, I., McGill, P., et al. (2018). Equipping an underwater glider with a new echosounder to explore ocean ecosystems. *Limnol. Oceanogr. Methods* 16, 734–749. doi: 10.1002/lom3.10278

Beszczynska-Möller, A., Woodgate, R. A., Lee, C., Melling, H., and Karcher, M. (2011). A synthesis of exchanges through the main oceanic gateways to the Arctic Ocean. *Oceanography* 24, 82–99. doi: 10.5670/oceanog.2011.59

Biddle, L. C., Kaiser, J., Heywood, K. J., Thompson, A. F., and Jenkins, A. (2015). Ocean glider observations of iceberg-enhanced biological production in the northwestern Weddell Sea. *Geophys. Res. Lett.* 42, 459–465. doi: 10.1002/2014GL062850

Boettger, D., Robertson, R., and Rainville, L. (2015). Characterizing the semidiurnal internal tide off Tasmania using glider data. *J. Geophys. Res. Oceans* 120, 3730–3746. doi: 10.1002/2015JC010711

Borrione, I., Falchetti, S., and Alvarez, A. (2016). Physical and dynamical characteristics of a 300 m-deep anticyclonic eddy in the Ligurian Sea (Northwest Mediterranean Sea): evidence from a multi-platform sampling strategy. *Deep Sea Res. Part I Oceanogr. Res. Papers* 116, 145–164. doi: 10.1016/j.dsr.2016.07.013

Bosse, A., Fer, I., Søiland, H., and Rossby, T. (2018). Atlantic water transformation along its poleward pathway across the Nordic Seas. *J. Geophys. Res. Oceans* 123, 6428–6448. doi: 10.1029/2018JC014147

Bosse, A., Testor, P., Houpert, L., Damien, P., Prieur, L., Hayes, D., et al. (2016). Scales and dynamics of Submesoscale Coherent Vortices formed by deep convection in the northwestern Mediterranean Sea. *J. Geophys. Res. Oceans* 121, 7716–7742. doi: 10.1002/2016JC012144

Bosse, A., Testor, P., Mayot, N., Prieur, L., D'Ortenzio, F., Lavigne, H., et al. (2017). A submesoscale coherent vortex in the Ligurian Sea: from dynamical barriers to biological implications. *J. Geophys. Res. Oceans* 122, 6196–6217. doi: 10.1002/2016JC012634

Bosse, A., Testor, P., Mortier, L., Prieur, L., Taillandier, V., d'Ortenzio, F., et al. (2015). Spreading of Levantine Intermediate Waters by submesoscale coherent vortices in the northwestern Mediterranean Sea as observed with gliders. *J. Geophys. Res. Oceans* 120, 1599–1622. doi: 10.1002/2014JC010263

Bouffard, J., Pascual, A., Ruiz, S., Faugere, Y., and Tintore, J. (2010). Coastal and mesoscale dynamics characterization using altimetry and gliders: a case study in the Balearic Sea. *J. Geophys. Res. Oceans* 115:C10029. doi: 10.1029/2009jc006087

Bouffard, J., Renault, L., Ruiz, S., Pascual, A., Dufau, C., and Tintore, J. (2012). Sub-surface small-scale eddy dynamics from multi-sensor observations and modeling. *Progr. Oceanogr.* 106, 62–79. doi: 10.1016/j.pocean.2012.06.007

Bourrin, F., Many, G., de Madron, X. D., Martín, J., Puig, P., Houpert, L., et al. (2015). Glider monitoring of shelf suspended particle dynamics and transport during storm and flooding conditions. *Cont. Shelf Res.* 109, 135–149. doi: 10.1016/j.csr.2015.08.031

Brannigan, L., Marshall, D. P., Garabato, A. C. N., Nurser, A. J. G., and Kaiser, J. (2017). Submesoscale instabilities in mesoscale eddies. *J. Phys. Oceanogr.* 47, 3061–3085. doi: 10.1175/JPO-D-16-0178.1

Briggs, N., Perry, M. J., Cetinic, I., Lee, C., D'Asaro, E., Gray, A. M., et al. (2011). High-resolution observations of aggregate flux during a sub-polar North Atlantic spring bloom. *Deep Sea Res. Part I Oceanogr. Res. Papers* 58, 1031–1039. doi: 10.1016/j.dsr.2011.07.007

Brito, M., Smeed, D., and Griffiths, G. (2014). Underwater glider reliability and implications for survey design. *J. Atmos. Ocean. Technol.* 31, 2858–2870. doi: 10.1175/JTECH-D-13-00138.1

Brito, M. P., and Griffiths, G. (2018). Updating autonomous underwater vehicle risk based on the effectiveness of failure prevention and correction. *J. Atmos. Ocean. Technol.* 35, 797–808. doi: 10.1175/JTECH-D-16-0252.1

Bröring, A., Schmid, S., Schindhelm, C., Khelil, A., Kabisch, S., Kramer, D., et al. (2017). Enabling IoT ecosystems through platform interoperability. *IEEE Softw. Gener.* 34, 54–61. doi: 10.1109/MS.2017.2

Buffett, G. G., Krahmann, G., Klaeschen, D., Schroeder, K., Sallares, V., Papenberg, C., et al. (2017). Seismic oceanography in the Tyrrhenian sea: thermohaline staircases. *Eddies, and internal waves. J. Geophys. Res. Oceans* 122, 8503–8523. doi: 10.1002/2017JC012726

Caballero, A., Rubio, A., Ruiz, S., Le Cann, B., Testor, P., Mader, J., et al. (2016). South-eastern Bay of Biscay eddy-induced anomalies and their effect on chlorophyll distribution. *J. Mar. Syst.* 162, 57–72. doi: 10.1016/j.jmarsys.2016.04.001

Caldeira, R., Stegner, A., Couvelard, X., Araújo, I. B., Testor, P., and Lorenzo, A. (2014). Evolution of an oceanic anticyclone in the lee of Madeira Island*: in situ* and remote sensing survey. *J. Geophys. Res.* 119, 1195–1216. doi: 10.1002/2013JC009493

Carvalho, F., Kohut, J., Oliver, M. J., Sherrell, R. M., and Schofield, O. (2016). Mixing and phytoplankton dynamics in a submarine canyon in the West Antarctic Peninsula. *J. Geophys. Res. Oceans* 121, 5069–5083. doi: 10.1002/2016JC011650

Castelao, R., Glenn, S., and Schofield, O. (2010). Temperature, salinity, and density variability in the central Middle Atlantic Bight. *J. Geophys. Res.* 115;C10005. doi: 10.1029/2009JC006082

Cauchy, P., Heywood, K. J., Merchant, N. D., Queste, B. Y., and Testor, P. (2018). Wind speed measured from underwater gliders using passive acoustics. *J. Atmos. Oceanic Technol.* 35, 2305–2321. doi: 10.1175/JTECH-D-17-0209.1

Cetinić, I., Perry, M. J., Briggs, N. T., Kallin, E., D'Asaro, E. A., and Lee, C. M. (2012). Particulate organic carbon and inherent optical properties during 2008 North Atlantic bloom experiment. *J. Geophys. Res.* 117:C06028. doi: 10.1029/2011JC007771

Cetinić, I., Perry, M. J., D'Asaro, E., Briggs, N., Poulton, N., Sieracki, M. E., et al. (2015). A simple optical index shows spatial and temporal heterogeneity in phytoplankton community composition during the 2008 North Atlantic Bloom experiment. *Biogeosciences* 12, 2179–2194. doi: 10.5194/bg-12-2179-2015

Chang, D., Zhang, F., and Edwards, C. R. (2015). Real-time guidance of underwater gliders assisted by predictive ocean models. *J. Atmos. Ocean. Tech*. 32, 562–578. doi: 10.1175/JTECH-D-14-00098.1

Chao, Y., Farrara, J. D., Bjorkstedt, E., Chai, F., Chavez, F., Rudnick, D. L., et al. (2017a). The origins of the anomalous warming in the California coastal ocean and San Francisco Bay during 2014-2016. *J. Geophys. Res. Oceans* 122, 7537–7557. doi: 10.1002/2017JC013120

Chao, Y., Farrara, J. D., Zhang, H., Armenta, K. J., Centurioni, L., Chavez, et al. (2018). Development, implementation, and validation of a California coastal ocean modeling, data assimilation, and forecasting system. *Deep Sea Research Part II: Topical Studies in Oceanography* 151, 49–63. doi: 10.1016/j.dsr2.2017.04.013

Chao, Y., Farrara, J. D., Zhang, H., Armenta, K. J., Centurioni, L., Chavez, F., et al. (2017b). Development, implementation and validation of a California coastal ocean modeling, data assimilation and forecasting system. *Deep Sea Res. Part II Top. Stud. Oceanogr*. 151, 49–63. doi: 10.1016/j.dsr2.2017.04.013

Chave, R., Buermans, J., Lemon, D., Taylor, J.C., Lembke, C., DeCollibus, C., et al. (2018). "Adapting multi-frequency echo-sounders for operation on autonomous vehicles," in *OCEANS'18 MTS/IEEE* (Charleston, SC), 1–6.

Chen, K., He, R., Powell, B. S., Gawarkiewicz, G. G., Moore, A. M., and Arango, H. G. (2014). Data assimilative modeling investigation of Gulf Stream Warm Core Ring interaction with continental shelf and slope circulation. *J. Geophys. Res. Oceans* 119, 5968–5991. doi: 10.1002/2014JC009898

Chudong, P., Max, Y., Dmitri, N., and Hans, N. (2011). Variational assimilation of glider data in Monterey Bay. *J. Mar. Res.* 69, 331–346. doi: 10.1357/002224011798765259

Churnside, J. H., Marchbanks, R. D., Lembke, C., and Beckler, J. (2017). Optical backscattering measured by airborne lidar and underwater glider. *Remote Sens.* 9:379. doi: 10.3390/rs9040379

Cole, S. T., and Rudnick, D. L. (2012). The spatial distribution and annual cycle of upper ocean thermohaline structure. *J. Geophys. Res. Oceans* 117:C02027. doi: 10.1029/2011JC007033

Cotroneo, Y., Aulicino, G., Ruiz, S., Pascual, A., Budillon, G., Fusco, G., et al. (2016). Glider and satellite high resolution monitoring of a mesoscale eddy in the algerian basin: effects on the mixed layer depth and biochemistry. *J. Mar. Syst.* 162, 73–88. doi: 10.1016/j.jmarsys.2015.12.004

Couto, N., Martinson, D. G., Kohut, J., and Schofield, O. (2017). Distribution of upper circumpolar deep water on the warming continental shelf of the West Antarctic Peninsula. *J. Geophys. Res. Oceans* 122, 5306–5315. doi: 10.1002/2017JC012840

Cronin, M. F., Pelland, N. A., Emerson, S. R., and Crawford, W. R. (2015). Estimating diffusivity from the mixed layer heat and salt balances in the North Pacific. *J. Geophys. Res. Oceans* 120, 7346–7362. doi: 10.1002/2015JC011010

Curry, B., Lee, C. M., Petrie, B., Moritz, R., and Kwok, R. (2014). Multiyear volume, liquid freshwater, and sea ice transports through Davis Strait, 2004–10. *J. Phys. Oceanogr*. 44, 1244–1266. doi: 10.1175/JPO-D-13-0177.1

Damerell, G. M., Heywood, K. J., Thompson, A. F., Binetti, U., and Kaiser, J. (2016). The vertical structure of upper ocean variability at the Porcupine Abyssal Plain during 2012-2013. *J. Geophys. Res. Oceans* 121, 3075–3089. doi: 10.1002/2015JC011423

Damien, P., Bosse, A., Testor, P., Marsaleix, P., and Estournel, C. (2017). Modeling post-convective submesoscale coherent vortices in the Mediterranean Sea. *J. Geophys. Res*. 122, 9937–9961. doi: 10.1002/2016JC012114

Davis, R., Eriksen, C., and Jones, C. (2002). "Autonomous Buoyancy-driven underwater gliders," in *The Technology and Applications of Autonomous Underwater Vehicles*', ed G. Griffiths (London: Taylor and Francis), 37–58.

Davis, R. E., Kessler, W. S., and Sherman, J. T. (2012). Gliders measure western boundary current transport from the south pacific to the equator. *J. Phys. Oceanogr.* 42, 2001–2013. doi: 10.1175/JPO-D-12-022.1

Dever, M., Hebert, D., Greenan, B. J. W., Sheng, J., and Smith, P. C. (2016). Hydrography and Coastal circulation along the halifax line and the connections with the Gulf of St. Lawrence. *Atmos. Ocean* 54, 199–217. doi: 10.1080/07055900.2016.1189397

deYoung, B., Oppeln-Bronikowski, N. J., Matthews, J.B.R., and Bachmayer, R. (2018). Glider operations in the Labrador sea. *J. Ocean Technol.* 13, 106–120.

Dobricic, S., Pinardi, N., Testor, P., and Send, U. (2010). Impact of data assimilation of glider observations in the Ionian Sea (Eastern Mediterranean). *Dyn. Atmos. Oceans 50,* 78–92. doi: 10.1016/j.dynatmoce.2010.01.001

Domingues, R., Goni, G., Bringas, F., Lee, S.-K., Kim, H.-S., Halliwell, G., et al. (2015). Upper ocean response to Hurricane Gonzalo, 2014: Salinity effects revealed by targeted and sustained underwater glider observations. *Geophys. Res. Lett.* 42, 7131–7138. doi: 10.1002/2015GL065378

Domingues, R., Kuwano-Yoshida, A., Cardon-Maldonado, P., Todd, R.E., Halliwell, G., Kim, H.-S., et al. (2019). Ocean observations in support of studies and forecasts of tropical and extratropical cyclones. *Front. Mar. Sci*. 6:446. doi: 10.3389/fmars.2019.00446

Dong, J., Domingues, R., Goni, G., Halliwell, G., Kim, H.-S., Lee, S.-K., et al. (2017). Impact of assimilating underwater glider data on Hurricane Gonzalo 2014 forecast. *Weather Forecast.* 32, 1143–1159. doi: 10.1175/WAF-D-16-0182.1

Drillet, Y., Lellouche, J. M., Levier, B., Drevillon, M., Le Galloudec, O., Reffray, G., et al. (2014). Forecasting the mixed-layer depth in the Northeast Atlantic: an ensemble approach, with uncertainties based on data from operational ocean forecasting systems. *Ocean Sci.* 10, 1013–1029. doi: 10.5194/os-10-1013-2014

Du Plessis, M. (2015). *Dynamics and Variability of the Subantarctic Mixed-Layer as Determined From a High Resolution Glider Dataset.* Cape Town: University of Cape Town.

Du Plessis, M., Swart, S., Ansorge, I. J., and Mahadevan, A. (2017). Submesoscale processes promote seasonal restratification in the Subantarctic Ocean. *J. Geophys. Res. Oceans* 122, 2960–2975. doi: 10.1002/2016JC012494

Du Plessis, M. D., Swart, S., Ansorge, I. J., Mahadevan, A., and Thompson, A. F. (2019). Southern Ocean seasonal restratification delayed by submesoscale wind-front interactions.. *J. Phys. Oceanogr.* 49, 1035–1053. doi: 10.1175/JPO-D-18-0136.1

Durand, F., Marin, F., Fuda, J.-L., and Terre, T. (2017). The east caledonian current: a case example for the intercomparison between altika and *in situ* measurements in a boundary current. *Mar. Geodesy* 40, 1–22. doi: 10.1080/01490419.2016.1258375

Durrieu de Madron, X., Guieu, C., Sempéré R., Conan, P., Cossa, D., D'Ortenzio, F., et al. (2011). Marine ecosystems' responses to climatic and anthropogenic forcings in the Mediterranean. *Progr. Oceanogr*. 91, 97–166. doi: 10.1016/j.pocean.2011.02.003

Durrieu de Madron, X., Houpert, L., Puig, P., Sanchez-Vidal, A., Testor, P., Bosse, A., et al. (2013). Interaction of dense shelf water cascading and open-sea convection in the northwestern Mediterranean during winter 2012. *Geophys. Res. Lett.* 40, 1379–1385. doi: 10.1002/grl.50331

Durrieu de Madron, X., Ramondenc, S., Berline, L., Houpert, L., Bosse, A., Martini, S., et al. (2017). Deep sediment resuspension and thick nepheloid layer generation by open-ocean convection. *J. Geophys. Res. Oceans* 122, 2291–2318. doi: 10.1002/2016JC012062

Durski, S. M., Kurapov, A. L., Allen, J. S., Kosro, P. M., Egbert, G. D., Shearman, R. K., et al. (2015). Coastal ocean variability in the US Pacific Northwest region: seasonal patterns, winter circulation, and the influence of the 2009-2010 El Nio. *Ocean Dyn.* 65, 1643–1663. doi: 10.1007/s10236-015-0891-1

Edwards, C. A., Moore, A. M., Hoteit, I., and Cornuelle, B. D. (2015). Regional ocean data assimilation. *Annu. Rev. Mar. Sci.* 7, 21–42. doi: 10.1146/annurev-marine-010814-015821

Estournel, C., Testor, P., Damien, P., D'Ortenzio, F., Marsaleix, P., Conan, P., et al. (2016b). High resolution modelling of dense water formation in the north-western Mediterranean: impacts of initial conditions and atmospheric forcing, heat and salt budget of the convection zone. *J. Geophys. Res*. 5367–5392. doi: 10.1002/2016JC011935

Estournel, C., Testor, P., Taupier-Letage, I., Bouin, M. N., Coppola, L., Durand, P., et al. (2016a). HyMeX-SOP2, the field campaign dedicated to dense water formation in the northwestern Mediterranean. *Oceanography* 29, 196–206. doi: 10.5670/oceanog.2016.94

Evans, D.G., Lucas, N., Hemsley, V., Frajka-Williams, E., Naveira Garabato, A., Martin, A., et al. (2018). Annual cycle of turbulent dissipation estimated from Seagliders. *Geophys. Res. Let.* 45, 10560–10569. doi: 10.1029/2018GL079966

Evans, W., Hales, B., Strutton, P. G., Shearman, R. K., and Barth, J., A. (2015). Failure to bloom: intense upwelling results in negligible phytoplankton response and prolonged CO2 outgassing over the Oregon shelf. *J. Geophys. Res. Oceans* 120, 1446–1461. doi: 10.1002/2014JC010580

Evans, W., Mathis, J. T., Winsor, P., Statscewich, H., and Whitledge, T. E. (2013). A regression modeling approach for studying carbonate system variability in the northern Gulf of Alaska. *J. Geophys. Res. Oceans* 118, 476–489. doi: 10.1029/2012JC008246

Everett, J. D., Macdonald, H. S., Baird, M. E., Humphries, J., Roughan, M., and Suthers, I. M. (2015). Cyclonic entrainment of pre-conditioned shelf waters into a Frontal Eddy. *J. Geophys. Res. Oceans* 120, 677–691. doi: 10.1002/2014JC010301

Fan, X., Send, U., Testor, P., Karstensen, J., and Lherminier, P. (2013). Observations of Irminger sea anticyclonic eddies. *J. Phys. Oceanogr.* 43, 805–823. doi: 10.1175/JPO-D-11-0155.1

Farrar, J. T., Rainville, L., Plueddemann, A. J., Kessler, W. S., Lee, C., Hodges, B. A., et al. (2015). Salinity and temperature balances at the SPURS central mooring during fall and winter. *Oceanography* 28, 56–65. doi: 10.5670/oceanog.2015.06

Fer, I., Peterson, A. K., and Ullgren, J. E. (2014). Microstructure measurements from an underwater glider in the turbulent faroe bank channel overflow. *J. Atmos. Oceanic Technol.* 31, 1128–1150. doi: 10.1175/JTECH-D-13-00221.1

Fiedler, B., Grundle, D. S., Schütte, F., Karstensen, J., Löscher, C. R., Hauss, H., et al. (2016). Oxygen utilization and downward carbon flux in an oxygen-depleted eddy in the eastern tropical North Atlantic. *Biogeosciences* 13, 5633–5647. doi: 10.5194/bg-13-5633-2016

Foloni-Neto, H., Tanaka, M., Joshima, H., and Yamazaki, H. (2014). Contribution to the themed section: advances in plankton modelling and biodiversity evaluation. A comparison between quasi-horizontal and vertical observations of phytoplankton microstructure. *J. Plankton Res.* 38, 944–945. doi: 10.1093/plankt/fbv075

Fragoso, M. D. R., de Carvalho, G. V., Soares, F. L. M., Faller, D., Toste, R., Sancho, L., et al. (2016). A 4D-variational ocean data assimilation application for Santos Basin, Brazil. *Ocean Dyn.* 66, 419–434. doi: 10.1007/s10236-016-0931-5

Frajka-Williams, E., Eriksen, C. C., Rhines, P. B., and Harcourt, R. R. (2011). Determining vertical water velocities from seaglider. *J. Atmos. Oceanic Technol.* 28, 1641–1656. doi: 10.1175/2011JTECHO830.1

Fraser, N. J., Skogseth, R., Nilsen, F., and Inall, M. E. (2018). Circulation and exchange in a broad Arctic fjord using glider-based observations. *Polar Res.* 37:1. doi: 10.1080/17518369.2018.1485417

Freitas, F. H., Siegel, D. A., Washburn, L., Halewood, S., and Stassinos, E. (2016). Assessing controls on cross-shelf phytoplankton and suspended particle distributions using repeated bio-optical glider surveys. *J. Geophys. Res. Oceans* 121, 7776–7794. doi: 10.1002/2016JC011781

Gangopadhyay, A., Schmidt, A., Agel, L., Schofield, O., and Clark, J. (2013). Multiscale forecasting in the western North Atlantic: sensitivity of model forecast skill to glider data assimilation. *Cont. Shelf Res.* 63, S159–S176. doi: 10.1016/j.csr.2012.09.013

Glenn, S. M., Miles, T. N., Seroka, G. N., Xu, Y., Forney, R. K., Yu, F., et al. (2016). Stratified coastal ocean interactions with tropical cyclones. *Nat. Commun.* 7:10887. doi: 10.1038/ncomms10887

Goericke, R., and Ohman, M. D. (2015). Introduction to CCE-LTER: responses of the California current ecosystem to climate forcing. *Deep Sea Res. Part Ii Top. Stud. Oceanogr.* 112, 1–5. doi: 10.1016/j.dsr2.2014.12.001

Goni, G. J., Todd, R. E., Jayne, S. R., Halliwell, G., Glenn, S., Dong, J., et al. (2017). Autonomous and Lagrangian ocean observations for Atlantic tropical cyclone studies and forecasts. *Oceanography* 30, 92–103. doi: 10.5670/oceanog.2017.227

Gourdeau, L., Verron, J., Chaigneau, A., Cravatte, S., and Kessler, W. (2017). Complementary use of Glider Data, altimetry, and model for exploring Mesoscale Eddies in the Tropical Pacific Solomon Sea. *J. Geophys. Res. Oceans* 122, 9209–9229. doi: 10.1002/2017JC013116

Gower, J., King, S., Statham, S., Fox, R., and Young, E. (2013). The Malaspina Dragon: a newly-discovered pattern of the early spring bloom in the Strait of Georgia, *British Columbia, Canada. Progr. Oceanogr.* 115, 181–188. doi: 10.1016/j.pocean.2013.05.024

Guihen, D., Fielding, S., Murphy, E. J., Heywood, K. J., and Griffiths, G. (2014). An assessment of the use of ocean gliders to undertake acoustic measurements of zooplankton: the distribution and density of Antarctic krill (*Euphausia superba*) in the Weddell Sea. *Limnol. Oceanogr. Methods* 12, 373–389. doi: 10.4319/lom.2014.12.373

Gula, J., Blacic, T. M., and Todd, R. E. (2019). Submesoscale coherent vortices in the Gulf Stream. *Geophys. Res. Lett*. 46, 2704–2714. doi: 10.1029/2019GL081919

Hall, R. A., Aslam, T., and Huvenne, V. A. I. (2017). Partly standing internal tides in a dendritic submarine canyon observed by an ocean glider. *Deep Sea Res. Part I Oceanogr. Res. Papers* 126, 73–84. doi: 10.1016/j.dsr.2017.05.015

Halliwell, G. R. Jr., Mehari, M. F., Le Henaff, M., Kourafalou, V. H., Androulidakis, I. S., Kang, H. S., et al. (2017). North Atlantic Ocean OSSE system: evaluation of operational ocean observing system components and supplemental seasonal observations for potentially improving tropical cyclone prediction in coupled systems. *J. Oper. Oceanogr.* 10, 154–175. doi: 10.1080/1755876X.2017.1322770

Hanson, C. E., L., Mun, Woo, P. L., Thomson, G., and Pattiaratchi, C. B. (2017). Observing the ocean with gliders: techniques for data visualization and analysis. *Oceanography* 30, 222–227. doi: 10.5670/oceanog.2017.210

Hayes, D., Dobricic, S., Gildor, H., Matsikaris, A., et al. (2019). Operational assimilation of glider temperature and salinity for an improved description of the Cyprus eddy. *Deep Sea Res. Part II Topical Stud. Oceanogr.* 164, 41–53. doi: 10.1016/j.dsr2.2019.05.015

Hemming, M. P., Kaiser, J., Heywood, K. J., Bakker, D. C. E., Boutin, J., Shitashima, K., et al. (2017). Measuring pH variability using an experimental sensor on an underwater glider. *Ocean Sci.* 13, 427–442. doi: 10.5194/os-13-427-2017

Hemsley, V. S., Smyth, T. J., Martin, A. P., Frajka-Williams, E., Thompson, A. F., Damerell, G., et al. (2015). Estimating oceanic primary production using vertical irradiance and chlorophyll profiles from ocean gliders in the North Atlantic. *Environ. Sci. Technol. 49,* 11612–11621. doi: 10.1021/acs.est.5b00608

Heslop, E. E., Ruiz, S., Allen, J., J., Luis Lopez-Jurado, Renault, L., and Tintore, J. (2012). Autonomous underwater gliders monitoring variability at "choke points" in our ocean system: a case study in the Western Mediterranean Sea. *Geophys. Res. Lett.* 39:L20604. doi: 10.1029/2012GL053717

Heslop, E. E., Sanchez-Roman, A., Pascual, A., Rodriguez, D., Reeve, K. A., Faugere, Y., et al. (2017). Sentinel-3A views ocean variability more accurately at finer resolution. *Geophys. Res. Lett. 44,* 12367–12374. doi: 10.1002/2017GL076244

Heywood, K. J., Schmidtko, S., Heuzé, C., Kaiser, J., Jickells, T. D., Queste, B. Y., et al. (2014). Ocean processes at the Antarctic continental slope. *Philos Trans A Math Phys Eng Sci.* 372:20130047. doi: 10.1098/rsta.2013.0047

Houpert, L., Inall, M. E., Dumont, E., Gary, S., Johnson, C., Porter, M., et al. (2018). Structure and transport of the North Atlantic Current in the eastern subpolar gyre from sustained glider observations. *J. Geophys. Res.* 123, 6019–6038. doi: 10.1029/2018JC014162

Houpert, L., Testor, P., de Madron, X. D., Somot, S., D'Ortenzio, F., Estournel, C., et al. (2015). Seasonal cycle of the mixed layer, the seasonal thermocline and the upper-ocean heat storage rate in the Mediterranean Sea derived from observations. *Progr. Oceanogr.* 132, 333–352. doi: 10.1016/j.pocean.2014.11.004

Houpert, L., X., Durrieu de Madron, Testor, P., Bosse, A., D'Ortenzio, F., Bouin, M. N., et al. (2016). Observations of open-ocean deep convection in the northwestern Mediterranean Sea: seasonal and interannual variability of mixing and deep water masses for the 2007-2013 period. *J. Geophys. Res. Oceans* 121, 8139–8171. doi: 10.1002/2016JC011857

Høydalsvik, F., Mauritzen, C., Orvik, K. A., LaCasce, J. H., Lee, C. M., and Gobat, J. (2013). Transport estimates of the Western Branch of the Norwegian Atlantic Current from glider surveys. *Deep Sea Res. Part I Oceanogr. Res. Papers* 79, 86–95. doi: 10.1016/j.dsr.2013.05.005

Hristova, H. G., Kessler, W. S., McWilliams, J. C., and Molemaker, M. J. (2014). Mesoscale variability and its seasonality in the Solomon and Coral Seas. *J. Geophys. Res. Oceans* 119, 4669–4687. doi: 10.1002/2013JC009741

Itoh, S., and Rudnick, D. L. (2017). Fine-scale variability of isopycnal salinity in the California current system. *J. Geophys. Res. Oceans* 122, 7066–7081. doi: 10.1002/2017JC013080

Jacox, M. G., Hazen, E. L., Zaba, K. D., Rudnick, D. L., Edwards, C. A., Moore, A. M., et al. (2016). Impacts of the 2015-2016 El Nino on the california current system: early assessment and comparison to past events. *Geophys. Res. Lett.* 43, 7072–7080. doi: 10.1002/2016GL069716

Johnston, T. M. S., and Rudnick, D. L. (2015). Trapped diurnal internal tides, propagating semidiurnal internal tides, and mixing estimates in the California Current System from sustained glider observations, 2006-2012, Deep-Sea Research Part Ii-Topical Studies. *Oceanography* 112, 61–78. doi: 10.1016/j.dsr2.2014.03.009

Johnston, T. M. S., Rudnick, D. L., Alford, M. H., Pickering, A., and Simmons, H. L. (2013). Internal tidal energy fluxes in the South China Sea from density and velocity measurements by gliders. *J. Geophys. Res. Oceans* 118, 3939–3949. doi: 10.1002/jgrc.20311

Jones, E. M., Oke, P. R., Rizwi, F., and Murray, L. (2012). Assimilation of glider and mooring data into a coastal ocean model. *Ocean Modell* 47,1–13. doi: 10.1016/j.ocemod.2011.12.009

Jones, R. M., and Smith, W. O. Jr. (2017). The influence of short-term events on the hydrographic and biological structure of the southwestern Ross Sea. *J. Marine Syst.* 166, 184–195. doi: 10.1016/j.jmarsys.2016.09.006

Kahl, L. A., Schofield, O., and Fraser, W. R. (2010). "Autonomous gliders reveal features of the water column associated with foraging by adelie penguins. integrative and comparative biology," in *Annual Meeting of the Society-for-Integrative-and-Comparative-Biology* (Seattle, WA), 1041–1050.

Karstensen, J., Liblik, T., Fischer, J., Bumke, K., and Krahmann, G. (2014). Summer upwelling at the Boknis Eck time-series station (1982 to 2012) – a combined glider and wind data analysis. *Biogeosciences* 11, 3603–3617. doi: 10.5194/bg-11-3603-2014

Karstensen, J., Schütte, F., Pietri, A., Krahmann, G., Fiedler, B., Grundle, D., et al. (2017). Upwelling and isolation in oxygen-depleted anticyclonic modewater eddies and implications for nitrate cycling. *Biogeosciences* 14, 2167–2181. doi: 10.5194/bg-14-2167-2017

Kaufman, D. E., Friedrichs, M. A. M., Smith, W. J. Jr., Queste, B. Y., and Heywood, K. J. (2014). Biogeochemical variability in the southern Ross Sea as observed by a glider deployment. *Deep Sea Res. Part I Oceanogr. Res. Papers* 92, 93–106. doi: 10.1016/j.dsr.2014.06.011

Kaufman, D. E., Friedrichs, M. A. M., Smith, W. O. Jr., Hofmann, E. E., Dinniman, M. S., and Hemmings, J. C. P. (2017). Climate change impacts on southern Ross Sea phytoplankton composition, productivity, and export. *J. Geophys. Res. Oceans* 122, 2339–2359. doi: 10.1002/2016JC012514

Kerry, C. G., Powell, B., Roughan, M., and Oke, P. (2016). Development and evaluation of a high-resolution reanalysis of the East Australian Current region using the Regional Ocean Modelling System (ROMS 3.4) and Incremental Strong-Constraint 4-Dimensional Variational data assimilation (IS4D-Var). *Geosci. Model Dev*. 9, 3779–3801 doi: 10.5194/gmd-9-3779-2016

Kerry, C. G., Roughan, M., and Powell, B. (2018). Observation impact in a regional reanalysis of the East Australian Current System. *J. Geophys. Res. Oceans* 123, 7511–7528. doi: 10.1029/2017JC013685

Klinck, H., Mellinger, D.K., Klinck, K., Bogue, N.M., Luby, J.C., et al. (2012). Near-real-time acoustic monitoring of beaked whales and other cetaceans using a seaglider^{TM}. *PLoS ONE.* 7:e36128. doi: 10.1371/journal.pone.0036128

Klymak, J. M., Simmons, H. L., Braznikov, D., Kelly, S., MacKinnon, J. A., Alford, M. H., et al. (2016). Reflection of linear internal tides from realistic topography: the tasman continental slope. *J. Phys. Oceanogr.* 46, 3321–3337. doi: 10.1175/JPO-D-16-0061.1

Kohut, J., Bernard, K., Fraser, W., Oliver, M. J., Statscevvich, H., Winsor, P., et al. (2014a). Studying the impacts of local oceanographic processes on adelie penguin foraging ecology. *Marine Technol. Soc. J.* 48, 25–34. doi: 10.4031/MTSJ.48.5.10

Kohut, J., Haldeman, C., and Kerfoot, J. (2014b). *Monitoring Dissolved Oxygen in New Jersey Coastal Waters Using Autonomous Gliders*. Washington, DC: U.S. Environmental Protection Agency.

Kohut, J., Hunter, E., and Huber, B. (2013). Small-scale variability of the cross-shelf flow over the outer shelf of the Ross Sea. *J. Geophys. Res. Oceans* 118, 1863–1876. doi: 10.1002/jgrc.20090

Kokkini, Z., Gerin, R., Poulain, P.-M., Mauri, E., Pasarić Z., Janeković I., et al. (2017). A multiplatform investigation of Istrian Front dynamics (north Adriatic Sea) in winter 2015. *Mediterranean Marine Sci.* 18/2, 344–354. doi: 10.12681/mms.1895

Kolodziejczyk, N., Testor, P., Lazar, A., Echevin, V., Krahmann, G., Chaigneau, A., et al. (2018). Subsurface fine-scale patterns in an anticyclonic eddy off Cap-Vert peninsula observed from glider measurements. *J. Geophys. Res. Oceans* 123, 6312–6329. doi: 10.1029/2018JC014135

Krug, M., Swart, S., and Gula, J. (2017). Submesoscale cyclones in the Agulhas current. *Geophys. Res. Lett.* 44, 346–354. doi: 10.1002/2016GL071006

Krug, M., Swart, S., and Hermes, J. (2018). Ocean gliders ride the research wave in the Agulhas Current. *Eos 99*. Available online at: https://eos.org/science-updates/ocean-gliders-ride-the-research-wave-in-the-agulhas-current

Kurapov, A. L., Pelland, N. A., and Rudnick, D. L. (2017). Seasonal and interannual variability in along-slope oceanic properties off the US West Coast: inferences from a high-resolution regional model. *J. Geophys. Res. Oceans* 122, 5237–5259. doi: 10.1002/2017JC012721

Kusel, E. T., Munoz, T., Siderius, M., Mellinger, D. K., and Heimlich, S. (2017). Marine mammal tracks from two-hydrophone acoustic recordings made with a glider. *Ocean Sci.* 13, 273–288. doi: 10.5194/os-13-273-2017

Lee, C.M., S., Jinadasa, U. P., Anutaliya, A., Centurioni, L. R., H., et al. (2016). Collaborative observations of boundary currents, water mass variability, and monsoon response in the southern Bay of Bengal. *Oceanography* 29, 102–111. doi: 10.5670/oceanog.2016.43

Lee, C.M., Thomson, J., and the Marginal Ice Zone, and Arctic Sea State Teams. (2017). An autonomous approach to observing the seasonal ice zone in the western Arctic. *Oceanography* 30, 56–68. doi: 10.5670/oceanog.2017.222

Lee, C. M., and Rudnick, D. L. (2018). "Underwater gliders," in *Observing the Oceans in Real Time*, eds R. Venkatesan, A. Tandon, E. A. D'Asaro, and M. A. Atmanand (Cham: Springer), 123–139. doi: 10.1007/978-3-319-66493-4_7

Lee, C. M., and Thomson, J. (2017). An autonomous approach to observing the deasonal ice zone in the Western Arctic. *Oceanography* 30, 56–68. doi: 10.5670/oceanog.2017.222

L'Heveder, B., Mortier, L., Testor, P., and Lekien, F. (2013). A glider network design study for a synoptic view of the oceanic mesoscale variability. *J. Atmos. Oceanic Technol.* 30, 1472–1493. doi: 10.1175/JTECH-D-12-00053.1

Li, Z., Chao, Y., Farrara, J. D., and McWilliams, J. C. (2013). Impacts of distinct observations during the 2009 Prince William Sound field experiment: a data assimilation study. *Continental Shelf Res.* 63, S209–S222. doi: 10.1016/j.csr.2012.06.018

Lien, R.-C., Ma, B., Lee, C. M., Sanford, T. B., Mensah, V., Centurioni, L. R., et al. (2015). The kuroshio and luzon undercurrent east of luzon Island. *Oceanography* 28, 54–63. doi: 10.5670/oceanog.2015.81

Lien, R. C., Ma, B., Cheng, Y. H., Ho, C. R., Qiu, B., Lee, C. M., et al. (2014). Modulation of Kuroshio transport by mesoscale eddies at the Luzon Strait entrance. *J. Geophys. Res. Oceans* 119, 2129–2142. doi: 10.1002/2013JC009548

Little, H., Vichi, M., Thomalla, S., and Swart, S. (2018). Spatial and temporal scales of chlorophyll variability using high-resolution glider data. *J. Mar. Syst.* 187, 1–12. doi: 10.1016/j.jmarsys.2018.06.011

Loginova, A. N., Thomsen, S., and Engel, A. (2016). Chromophoric and fluorescent dissolved organic matter in and above the oxygen minimum zone off Peru. *J. Geophys. Res. Oceans* 121, 7973–7990. doi: 10.1002/2016JC011906

Lozier, M.S., Li, F., Bacon, S., Bahr, F., Bower, A. S., Cunningham, S. A., et al. (2019). A sea change in our view of overturning in the subpolar North Atlantic. *Science* 363, 516–521. doi: 10.1126/science.aau6592

Ma, W., Wang, Y., Yang, S., Wang, S., and Xiu, Z. (2018). Observation of internal solitary waves using an underwater glider in the northern south china sea. *J. Coastal Res.* 34, 1188–1195 doi: 10.2112/JCOASTRES-D-17-00193.1

Mahadevan, A., D'Asaro, E., Lee, C. M., and Perry, M. J. (2012). Eddy-driven stratification initiates the NorthAtlantic Spring Bloom. *Science* 337, 54–58. doi: 10.1126/science.1218740

Mahjabin, T., Pattiaratchi, C., and Hetzel, Y. (2016). "Factors influencing the occurrence of Dense Shelf Water Cascades in Australia, Journal of Coastal Research," in *14th International Coastal Symposium (ICS)* (Sydney, NSW), 527–531.

Mainelli, M., DeMaria, M., Shay, L., and Goni, G. (2008). Application of oceanic heat content estimation to operational forecasting of recent Atlantic category 5 hurricanes. *Weather Forecast* 23, 3–16. doi: 10.1175/2007WAF2006111.1

Mancero-Mosquera, I., Poulain, P.-M., Gerin, R., Mauri, E., Hayes, D., Testor, P., et al. (2017). Analysis of frequency content of glider data via fourier and wavelet transforms. *Bollettino di Geofisica Teorica ed Applicata*, 58, 137–156. doi: 10.4430/bgta0194

Many, G., Bourrin, F., Durrieu de Madron, X., Pairaud, I., Gangloff, A., Doxaran, D., et al. (2016). Particle assemblage characterization in the Rhone River ROFI. *J. Marine Syst.* 157, 39–51. doi: 10.1016/j.jmarsys.2015.12.010

Margirier, F., Bosse, A., Testor, P., L'Heveder, B., Mortier, L., and Smeed, D. (2017). Characterization of convective plumes associated with oceanic deep convection in the northwestern mediterranean from high-resolution *in situ* data collected by gliders. *J. Geophys. Res. Oceans* 122, 9814–9826. doi: 10.1002/2016JC012633

Martin, J. P., Lee, C. M., Eriksen, C. C., Ladd, C., and Kachel, N. B. (2009). Glider observations of kinematics in a Gulf of Alaska eddy. *J. Geophys. Res.* 114:C12021. doi: 10.1029/2008JC005231

Martin, P., Lampitt, R. S., Perry, M. J., Sanders, R., Lee, C. M., and D'Asaro, E. (2011). Export and mesopelagic particle flux during a north atlantic spring diatom bloom. *Deep Sea Res.* 58, 338–349. doi: 10.1016/j.dsr.2011.01.006

Mauri, E., Gerin, R., and Poulain, P.-M. (2016). Measurements of water-mass properties with a glider in the South-western Adriatic Sea. *J. Operational Oceanogr.* 9(Suppl. 1), 3–9. doi: 10.1080/1755876X.2015.1117766

Mayot, N., D'Ortenzio, F., Taillandier, V., Prieur, L., de Fommervault, O. P., Claustre, H., et al. (2017). Physical and biogeochemical controls of the phytoplankton blooms in north western mediterranean sea: a multiplatform approach over a complete annual cycle (2012-2013 DEWEX Experiment). *J. Geophys. Res. Oceans* 122, 9999–10019. doi: 10.1002/2016JC012052

Mazzini, P. L. F., Barth, J. A., Shearman, R. K., and Erofeev, A. (2014). Buoyancy-driven coastal currents off oregon during fall and winter. *J. Phys. Oceanogr.* 44, 2854–2876. doi: 10.1175/JPO-D-14-0012.1

McClatchie, S., Cowen, R., Nieto, K., Greer, A., Luo, J. Y., Guigand, C., et al. (2012). Resolution of fine biological structure including small narcomedusae across a front in the Southern California Bight. *J. Geophys. Res. Oceans* 117. doi: 10.1029/2011JC007565

Melet, A., Verron, J., and Brankart, J. M. (2012). Potential outcomes of glider data assimilation in the Solomon Sea: control of the water mass properties and parameter estimation. *J. Marine Syst.* 94, 232–246. doi: 10.1016/j.jmarsys.2011.12.003

Mensah, V., Andres, M., R.-C., Lien, Ma, B., Lee, C. M., and Jan, S. (2016). Combining observations from multiple platforms across the Kuroshio northeast of Luzon: a highlight on PIES data. *J. Atmospheric Oceanic Technol.* 33, 2185–2203. doi: 10.1175/JTECH-D-16-0095.1

Meunier, T., Pallàs-Sanz, E., Tenreiro, M., Portela, E., Ochoa, J., Ruíz-Angulo, A., et al. (2018a). The vertical structure of a Loop Current Eddy. *J. Geophys. Res.* 123, 6070–6090. doi: 10.1029/2018JC013801

Meunier, T., Tenreiro, M., Pallàs-Sanz, E., Ochoa, J., Ruíz-Angulo, A., Portela, E., et al. (2018b). Intrathermocline eddies embedded within an anticyclonic vortex ring. *Geophys. Res. Lett.* 45, 7624–7633. doi: 10.1029/2018GL077527

Miles, T., Glenn, S. M., and Schofield, O. (2013). Temporal and spatial variability in fall storm induced sediment resuspension on the Mid-Atlantic Bight. *Continental Shelf Res.* 63, S36–S49. doi: 10.1016/j.csr.2012.08.006

Miles, T., Seroka, G., and Glenn, S. (2017). Coastal ocean circulation during Hurricane Sandy. *J. Geophys. Res. Oceans.* 122, 7095–7114. doi: 10.1002/2017JC013031

Miles, T., Seroka, G., Kohut, J., Schofield, O., and Glenn, S. (2015). Glider observations and modeling of sediment transport in Hurricane Sandy. *J. Geophys. Res. Oceans* 120, 1771–1791. doi: 10.1002/2014JC010474

Monteiro, P. M. S., Gregor, L., Lévy, M., Maenner, S., Sabine, C. L., and Swart, S. (2015). Intraseasonal variability linked to sampling alias in air-sea CO2 fluxes in the Southern Ocean. *Geophys. Res. Lett.* 42, 8507–8514. doi: 10.1002/2015GL066009

Morrow, R., Carret, A., Birol, F., Nino, F., Valladeau, G., Boy, F., et al. (2017). Observability of fine-scale ocean dynamics in the northwestern Mediterranean Sea. *Ocean Sci.* 13, 13–29. doi: 10.5194/os-13-13-2017

Mourre, B., and Alvarez, A. (2012). Benefit assessment of glider adaptive sampling in the Ligurian Sea. *Deep Sea Res. Part I Oceanogr. Res. Papers* 68, 68–78. doi: 10.1016/j.dsr.2012.05.010

Mourre, B., and Chiggiato, J. (2014). A comparison of the performance of the 3-D super-ensemble and an ensemble Kalman filter for short-range regional ocean prediction. *Tellus A: Dynamic Meteorol. Oceanogr.* 66, 21640. doi: 10.3402/tellusa.v66.21640

Nelson, M. J. S., Queste, B. Y., Smith, I. J., Leonard, G. H., Webber, B. G. M., and Hughes, K. G. (2016). Measurements of Ice Shelf Water beneath the front of the Ross Ice Shelf using gliders. *Ann. Glaciol.* 58, 41–50. doi: 10.1017/aog.2017.34

Ngodock, H., and Carrier, M. (2014). A 4DVAR system for the navy coastal ocean model. Part II: strong and weak constraint assimilation experiments with real observations in monterey bay. *Monthly Weather Rev.* 142, 2108–2117. doi: 10.1175/MWR-D-13-00220.1

Nicholson, D. P., Wilson, S. T., Doney, S. C., and Karl, D. M. (2015). Quantifying subtropical North Pacific gyre mixed layer primary productivity from Seaglider observations of diel oxygen cycles. *Geophys. Res. Lett.* 42, 4032–4039. doi: 10.1002/2015GL063065

Nicholson, S.-A., Lévy, M., Llort, J., Swart, S., and Monteiro, P. M. S. (2016). Investigation into the impact of storms on sustaining summer primary productivity in the Sub-Antarctic Ocean. *Geophys. Res. Lett.* 43, 9192–9199. doi: 10.1002/2016GL069973

Ohman, M. D., Chekalyuk, R., Davis, D. L., Feely, A., Kahru, R. E., Kim, R. A., et al. (2013). Autonomous ocean measurements in the California Current Ecosystem. *Oceanography* 26, 18–25. doi: 10.5670/oceanog.2013.41

Oke, P. R., Larnicol, G., Jones, E. M., Kourafalou, V., Sperrevik, A. K., Carse, F., et al. (2015). Assessing the impact of observations on ocean forecasts and reanalyses: part 2, regional applications. *J. Operational Oceanogr.* 8, S63–S79. doi: 10.1080/1755876X.2015.1022080

Oke, P. R., Sakov, P., and Schulz, E. (2010). A comparison of shelf observation platforms for assimilation in an eddy-resolving ocean model. *Dyn. Atmospheres Oceans* 48, 121–142. doi: 10.1016/j.dynatmoce.2009.04.002

Olita, A., Capet, A., Mahadevan, A., Claret, A., Ruiz, S., Tintor,é, J., et al. (2017). Frontal dynamics boost primary production in the summer stratified Mediterranean Sea. *Ocean Dynamics* 67, 767–782. doi: 10.1007/s10236-017-1058-z

Olita, A., Sparnocchia, S., Cusi, S., Fazioli, L., Sorgente, R., Tintore, J., et al. (2014). Observations of a phytoplankton spring bloom onset triggered by a density front in NW Mediterranean. *Ocean Sci.* 10, 657–666. doi: 10.5194/os-10-657-2014

Oliver, M. J., Breece, M. W., Fox, D. A., Haulsee, D. E., Kohut, J. T., Manderson, J., et al. (2013). Shrinking the Haystack: using an AUV in an Integrated Ocean Observatory to map Atlantic Sturgeon in the Coastal Ocean. *Fisheries* 38, 210–216. doi: 10.1080/03632415.2013.782861

Oliver, M. J., Breece, M. W., Haulsee, D. E., Cimino, M. A., Kohut, J., Aragon, D., et al. (2017). Factors affecting detection efficiency of mobile telemetry Slocum gliders. *Animal Biotelemet.* 14:1. doi: 10.1186/s40317-017-0129-8

Omand, M. M., D'Asaro, E. A., Lee, C. M., Perry, M. J., Briggs, N., Cetinic, I., et al. (2015). Eddy-driven subduction exports particulate organic carbon from the spring bloom. *Science* 348, 222–225. doi: 10.1126/science.1260062

Onken, R. (2017). Forecast skill score assessment of a relocatable ocean prediction system, using a simplified objective analysis method. *Ocean Sci.* 13, 925–945. doi: 10.5194/os-13-925-2017

Oschlies, A., Brandt, P., and Schmidtko, L., S. (2018). Drivers and mechanisms of ocean deoxygenation. *Nat. Geosci.* 11, 467–473. doi: 10.1038/s41561-018-0152-2

Osse, T. J., and Eriksen, C. C. (2007). "The deepglider: a full ocean depth glider for oceanographic research," in *OCEANS 2007* (Vancouver, BC), 1–12.

Palmer, M. R., Stephenson, G. R., Mall, M. E., Balfour, C., Duesterhus, A., and Green, J. (2015). Turbulence and mixing by internal waves in the Celtic Sea determined from ocean glider microstructure measurements. *J. Marine Syst.* 144, 57–69. doi: 10.1016/j.jmarsys.2014.11.005

Pan, C., Jiang, M., Dalgleish, F. R., and Reed, J. K. (2017). Modeling the impacts of the Loop Current on circulation and water properties over the Pulley Ridge region on the Southwest Florida shelf. *Ocean Model.* 112, 48–64. doi: 10.1016/j.ocemod.2017.02.009

Pan, C., Zheng, L., Weisberg, R. H., Liu, Y., and Lembke, C. E. (2014). Comparisons of different ensemble schemes for glider data assimilation on West Florida Shelf. *Ocean Model.* 81, 13–24. doi: 10.1016/j.ocemod.2014.06.005

Pascual, A., Ruiz, S., Olita, A., Troupin, C., Claret, M., Casas, B., et al. (2017). A multiplatform experiment to unravel meso- and submesoscale processes in an intense front (AlborEx). *Front. Mar. Sci.* 4:39. doi: 10.3389/fmars.2017.00039

Pascual, A., Ruiz, S., and Tintor,é, J. (2010). Combining new and conventional sensors to study the Balearic current. *Sea Techn.* 51, 32–36.

Pattiaratchi, C., Woo, L. M., Thomson, P. G., Hong, K. K., and Stanley, D. (2017). Ocean glider observations around australia. *Oceanography* 30, 90–91. doi: 10.5670/oceanog.2017.226

Pattiaratchi, C. B., Hollings, B., Woo, M., and Hanson, C. (2010). "Oceanographic observations of the Australian continental shelf and slope waters using autonomous ocean gliders," in *Proceedings of OceanObs'09: Sustained Ocean Observations and Information for Society Conference/, 2009,* eds J. Hall, D. E. Harrison, and D. Stammer (Venice: ESA publication WPP-306).

Pattiaratchi, C. B., Hollings, B., Woo, M., and Welhena, T. (2011). Dense shelf water formation along the south-west Australian inner shelf. *Geophys. Res. Lett.* 38:L10609. doi: 10.1029/2011GL046816

Pearlman, J., Bushnell, M., Coppola, L., Buttigieg, P. L., Chandler, C., Pearlman, F., et al. (2019). Evolving and sustaining ocean best practices and standards for the next decade. *Front. Marine Sci.* 6:277. doi: 10.3389/fmars.2019.00277

Pelland, N., Bennett, J., Steinberg, J. M., and Eriksen, C. E. (2018). Automated glider tracking of a california undercurrent eddy using the extended kalman filter. *J. Atmos. Oceanic Technol.* 35, 2241–2264. doi: 10.1175/JTECH-D-18-0126.1

Pelland, N. A., Eriksen, C. C., and Cronin, M. F. (2016). Seaglider surveys at ocean station papa: circulation and water mass properties in a meander of the North Pacific Current. *J. Geophys. Res. Oceans* 121, 6816–6846. doi: 10.1002/2016JC011920

Pelland, N. A., Eriksen, C. C., and Lee, C. M. (2013). Subthermocline eddies over the washington continental slope as observed by seagliders, 2003-09. *J. Phys. Oceanogr.* 43, 2025–2053. doi: 10.1175/JPO-D-12-086.1

Pelland, N. A., Sterling, J. T., Lea, M.-A., Bond, N. A., Ream, R. R., Lee, C. M., et al. (2014). Fortuitous encounters between seagliders and adult female northern fur seals (*Callorhinus ursinus*) off the Washington (USA) coast: upper ocean variability and links to top predator behavior. *PLoS ONE.* 9:0101268. doi: 10.1371/journal.pone.0101268

Peterson, A., and Fer, I. (2014). Dissipation measurements using temperature microstructure from an underwater glider. *Methods Oceanogr.* 10, 44–69. doi: 10.1016/j.mio.2014.05.002

Peterson, I., Greenan, B., Gilbert, D., and Hebert, D. (2017). Variability and wind forcing of ocean temperature and thermal fronts in the Slope Water region of the Northwest Atlantic. *J. Geophys. Res. Oceans* 122, 7325–7343. doi: 10.1002/2017JC012788

Pierce, S. D., Barth, J. A., Shearman, R. K., and Erofeev, A. Y. (2012). Declining oxygen in the northeast pacific. *J. Phys. Oceanogr.* 42, 495–501. doi: 10.1175/JPO-D-11-0170.1

Piero Mazzini, L. F., Craig Risien, M., John Barth, A., Stephen Pierce, D., Erofeev, A., Dever, E. P., et al. (2015). Anomalous near-surface low-salinity pulses off the central Oregon coast. *Sci Rep.* 5:17145. doi: 10.1038/srep17145

Pietri, A., Echevin, V., Testor, P., Chaigneau, A., Mortier, L., Grados, C., et al. (2014). Impact of a coastal-trapped wave on the near? Coastal circulation of the Peru upwelling system from glider data. *J. Geophys. Res.* 119, 2109–2120. doi: 10.1002/2013JC009270

Pietri, A., Testor, P., Echevin, V., Chaigneau, A., Mortier, L., Eldin, G., et al. (2013). Finescale vertical structure of the upwelling system off southern peru as observed from glider data. *J. Phys. Oceanogr.* 43, 631–646. doi: 10.1175/JPO-D-12-035.1

Piterbarg, L., Taillandier, V., and Griffa, A. (2013). Investigating frontal variability from repeated glider transects in the Ligurian Current (North West Mediterranean Sea). *J. Mar. Sys.* 129, 381–395. doi: 10.1016/j.jmarsys.2013.08.003

Pizarro, O., Ramirez, N., Castillo, M. I., Cifuentes, U., Rojas, W., and Pizarro-Koch, M. (2016). Underwater glider observations in the oxygen minimum zone off central chile. *Bull. Am. Meteorol. Soc.* 97, 1783–1789. doi: 10.1175/BAMS-D-14-00040.1

Portela, E., Tenreiro, M., Pallàs-Sanz, E., Meunier, T., Ruiz-Angulo, A., Sosa-Gutiérrez, R., et al. (2018). Hydrography of the central and western Gulf of Mexico. *J. Geophys. Res. Oceans* 123, 5134–5149. doi: 10.1029/2018JC013813

Porter, M., Inall, M. E., Hopkins, J., Palmer, M. R., Dale, A. C., Aleynik, D., et al. (2016). Glider observations of enhanced deep water upwelling at a shelf break canyon: a mechanism for cross-slope carbon and nutrient exchange. *J. Geophys. Res. Oceans* 121, 7575–7588. doi: 10.1002/2016JC012087

Powell, J. R., and Ohman, M. D. (2012). Use of glider-class acoustic Doppler profilers for estimating zooplankton biomass. *J. Plankton Res.* 34, 563–568. doi: 10.1093/plankt/fbs023

Powell, J. R., and Ohman, M. D. (2015). Covariability of zooplankton gradients with glider-detected density fronts in the Southern California Current System. *Deep Sea Res. II* 112, 79–90. doi: 10.1016/j.dsr2.2014.04.002

Qiu, C., Mao, H., Yu, J., Xie, Q., Wu, J., Lian, S., et al. (2015). Sea surface cooling in the Northern South China Sea observed using Chinese sea-wing underwater glider measurements. *Deep Sea Res. Part I Oceanogr. Res. Papers* 105, 111–118. doi: 10.1016/j.dsr.2015.08.009

Queste, B. Y., Fernand, L., Jickells, T. D., Karen J. H. (2013). Spatial extent and historical context of North Sea oxygen depletion in August 2010. *Biogeochemistry* 113, 53–68. doi: 10.1007/s10533-012-9729

Queste, B. Y., Heywood, K. J., Smith, W. O. Jr., Kaufman, D. E., Jickells, T. D., and Dinniman, M. S. (2015). Dissolved oxygen dynamics during a phytoplankton bloom in the Ross Sea polynya. *Antarctic Sci*. 27, 362–372. doi: 10.1017/S0954102014000881

Rainville, L., Gobat, J. I., Lee, C. M., and Shilling, G. B. (2017). Multi-month dissipation estimates using microstructure from autonomous underwater gliders. *Oceanography* 30, 49–50. doi: 10.5670/oceanog.2017.219

Rainville, L., Lee, C. M., Rudnick, D. L., and Yang, K.-C. (2013). Propagation of internal tides generated near Luzon Strait: observations from autonomous gliders. *J. Geophys. Res. Oceans* 118, 4125–4138. doi: 10.1002/jgrc.20293

Ramp, S. R., Davis, R. E., Leonard, N. E., Shulman, I., Chao, Y., Robinson, A. R., et al. (2009). Preparing to predict: the Second Autonomous Ocean Sampling Network (AOSN-II) experiment in the Monterey Bay. *Deep Sea Res. Part II Topical Stud. Oceanogr.* 56, 68–86. doi: 10.1016/j.dsr2.2008.08.013

Ramp, S. R., Lermusiaux, P. F. J., Shulman, I., Chao, Y., Wolf, R. E., and Bahr, F. L. (2011). Oceanographic and atmospheric conditions on the continental shelf north of the Monterey Bay during August 2006. *Dynam. Atmospheres Oceans* 52, 192–223. doi: 10.1016/j.dynatmoce.2011.04.005

Rayburn, J. T., and Kamenkovich, V. M. (2013). Comparison of the observed mixed layer depth in the lee of the hawaiian island to the modeled mixed layer depth of the regional navy coastal ocean model. *Marine Technol. Soc. J.* 47, 55–66. doi: 10.4031/MTSJ.47.1.3

Ridgway, K. R., and Godfrey, J. S. (2015). The source of the Leeuwin Current seasonality. *J. Geophys. Res. Oceans* 120, 6843–6864. doi: 10.1002/2015JC011049

Ross, T., Craig, S. E., Comeau, A., Davis, R., Dever, M., and Beck, M. (2017). Blooms and subsurface phytoplankton layers on the Scotian Shelf: insights from profiling gliders. *J. Marine Syst.* 172, 118–127. doi: 10.1016/j.jmarsys.2017.03.007

Ruan, X., Thompson, A. F., Flexas, M. M., and Sprintall, J. (2017). Contribution of topographically generated submesoscale turbulence to Southern Ocean overturning. *Nat. Geosci.* 10, 840. doi: 10.1038/ngeo3053

Rudnick, D. L. (2016). Ocean research enabled by underwater gliders. *Ann. Rev. Marine Sci.* 8, 519–541. doi: 10.1146/annurev-marine-122414-033913

Rudnick, D. L., and Cole, S. T. (2011). On sampling the ocean using underwater gliders. *J. Geophys. Res.* 116:C08010. doi: 10.1029/2010JC006849

Rudnick, D. L., Davis, R. E., and Sherman, J. T. (2016a). Spray underwater glider operations. *J. Atmospheric Oceanic Technol.* 33, 1113–1122. doi: 10.1175/JTECH-D-15-0252.1

Rudnick, D. L., Gopalakrishnan, G., and Cornuelle, B. D. (2015). Cyclonic Eddies in the Gulf of Mexico: observations by underwater gliders and simulations by numerical model. *J. Phys. Oceanogr.* 45, 313–326. doi: 10.1175/JPO-D-14-0138.1

Rudnick, D. L., Owens, B., Johnston, S., and Karnauskas, K. (2016b). *Underwater Glider Observations of the Ongoing El Niño*. New Orleans, LA: Ocean Sciences Meeting.

Rudnick, D. L., Sherman, J. T., and Wu, A. P. (2018). Depth-average velocity from Spray underwater gliders. *J. Atmospheric Oceanic Technol.* 35,1665–1673. doi: 10.1175/JTECH-D-17-0200.1

Rudnick, D. L., Zaba, K. D., Todd, R. E., and Davis, R. E. (2017). A climatology of the California Current System from a network of underwater gliders. *Progr. Oceanogr.* 154, 64–106. doi: 10.1016/j.pocean.2017.03.002

Ruiz, S., Renault, L., Garau, B., and Tintore, J. (2012). Underwater glider observations and modeling of an abrupt mixing event in the upper ocean. *Geophys. Res. Lett.* 39:L01603. doi: 10.1029/2011GL050078

Saba, G. K., Wright-Fairbanks, E., Chen, B., Cai, W.-J., Barnard, A. H., Jones, C. P., et al. (2018). "Developing a profiling glider pH sensor for high resolution coastal ocean acidification monitoring," in *OCEANS'18 MTS/IEEE.* (Charleston, SC), 1–8.

Saldias, G. S., Shearman, R. K., Barth, J. A., and Tufillaro, N. (2016). Optics of the offshore Columbia River plume from glider observations and satellite imagery. *J. Geophys. Res. Oceans* 121, 2367–2384. doi: 10.1002/2015JC011431

Schaeffer, A., and Roughan, M. (2015). Influence of a western boundary current on shelf dynamics and upwelling from repeat glider deployments. *Geophys. Res. Lett.* 42, 121–128. doi: 10.1002/2014GL062260

Schaeffer, A., Roughan, M., Austin, T., Everett, J. D., Griffin, D., Hollings, B., et al. (2016a). Mean hydrography on the continental shelf from 26 repeat glider deployments along Southeastern Australia. *Sci. Data*, 3:160070. doi: 10.1038/sdata.2016.70

Schaeffer, A., Roughan, M., Jones, E. M., and White, D. (2016b). Physical and biogeochemical spatial scales of variability in the East Australian Current separation from shelf glider measurements. *Biogeosciences* 13, 1967–1975. doi: 10.5194/bg-13-1967-2016

Schaeffer, A., Roughan, M., and Wood, J., E. (2014). Observed bottom boundary layer transport and uplift on the continental shelf adjacent to a western boundary current. *J. Geophys. Res. Oceans* 119, 4922–4939. doi: 10.1002/2013JC009735

Scheifele, B., Waterman, S., Merckelbach, L., and Carpenter, J. (2018). Measuring the dissipation rate of turbulent kinetic energy in strongly stratified, low-energy environments: a case study from the Arctic Ocean. *J. Geophys. Res. Oceans* 123, 5459–5480. doi: 10.1029/2017JC013731

Schlundt, M., Brandt, P., Dengler, M., Hummels, R., Fischer, T., Bumke, K., et al. (2014). Mixed layer heat and salinity budgets during the onset of the 2011 Atlantic cold tongue. *J. Geophys. Res. Oceans* 119, 7882–7910. doi: 10.1002/2014JC010021

Schofield, O., Miles, T., Alderkamp, A.-C., Lee, S., Haskins, C., Rogalsky, E., et al. (2015). *In situ* phytoplankton distributions in the Amundsen Sea Polynya measured by autonomous gliders. *Elementa Sci. Anthropocene* 3, 1–17. doi: 10.12952/journal.elementa.000073

Schönau, M. C., and Rudnick, D. L. (2015). Glider observations of the North Equatorial Current in the western tropical Pacific. *J. Geophys. Res. Oceans* 120, 3586–3605. doi: 10.1002/2014JC010595

Schönau, M. C., and Rudnick, D. L. (2017). Mindanao current and undercurrent: thermohaline structure and transport from repeat glider observations. *J. Phys. Oceanogr.* 47, 2055–2075. doi: 10.1175/JPO-D-16-0274.1

Schönau, M. C., Rudnick, D. L., Cerovecki, I., Gopalakrishnan, G., Cornuelle, B. D., McClean, J. L., et al. (2015). The mindanao current mean structure and connectivity. *Oceanography* 28, 34–45. doi: 10.5670/oceanog.2015.79

Schroeder, K., Chiggiato, J., Josey, S. A., Borghini, M., Aracri, S., and Sparnocchia, S. (2017). Rapid Response to Climate Change in a Marginal Sea. Scientific *Reports* 7:4065. doi: 10.1038/s41598-017-04455-5

Schuette, F., Karstensen, J., Krahmann, G., Hauss, H., Fiedler, B., Brandt, P., et al. (2016). Characterization of 'dead-zone' eddies in the eastern tropical North Atlantic. *Biogeosciences* 13, 5865–5881. doi: 10.5194/bg-13-5865-2016

Schultze, L. K. P., Merckelbach, L. M., and Carpenter, J. R. (2017). Turbulence and mixing in a shallow shelf sea from underwater gliders. *J. Geophys. Res. Oceans* 122, 9092–9109. doi: 10.1002/2017JC012872

Seegers, B. N., Birch, J. M., Marin, R. III, Scholin, C. A., Caron, D. A., Seubert, E. L., Howard, M. D. A., et al. (2015). Subsurface seeding of surface harmful algal blooms observed through the integration of autonomous gliders, moored environmental sample processors, and satellite remote sensing in southern California. *Limnol. Oceanogr.* 60, 754–764. doi: 10.1002/lno.10082

Seim, H. E., and Edwards, C. R. (2019). Upper-slope jets and Gulf Stream filaments inshore of the Charleston Bump during Winter 2012. *J. Phys. Oceanogr.* 49, 1423–1438. doi: 10.1175/JPO-D-18-0205.1

Send, U., Regier, L., and Jones, B. (2013). Use of underwater gliders for acoustic data retrieval from subsurface oceanographic instrumentation and bidirectional communication in the deep ocean. *J. Atmos. Oceanic Technol.* 30, 984–998. doi: 10.1175/JTECH-D-11-00169.1

Seroka, G., Miles, T., Xu, Y., Kohut, J., Schofield, O., and Glenn, S. (2016). Hurricane Irene sensitivity to stratified coastal ocean cooling. *Mon. Weather Rev*. 144, 3507–3530. doi: 10.1175/MWR-D-15-0452.1

Seroka, G., Miles, T., Xu, Y., Kohut, J., Schofield, O., and Glenn, S. (2017). Rapid shelf-wide cooling response of a stratified coastal ocean to hurricanes. *J. Geophys.Res. Oceans* 122, 4845–4867. doi: 10.1002/2017JC012756

Shay, L. K., Goni, G. J., and Black, P. G. (2000). Effects of warm oceanic features on hurricane opal. *Mon. Weather Rev*. 128, 131–148. doi: 10.1175/1520-0493(2000)128<1366:EOAWOF>2.0.CO;2

Sherwin, T. J., Aleynik, D., Dumont, E., and Inall, M. E. (2015). Deep drivers of mesoscale circulation in the central Rockall Trough. *Ocean Sci.* 11, 343–359. doi: 10.5194/os-11-343-2015

Sherwin, T. J., Read, J. F., Holliday, N. P., and Johnson, C. (2012). The impact of changes in North Atlantic Gyre distribution on water mass characteristics in the Rockall Trough. *ICES J. Marine Sci.* 69, 751–757. doi: 10.1093/icesjms/fsr185

Shulman, I., Anderson, S., Rowley, C., DeRada, S., Doyle, J., and Ramp, S. (2010). Comparisons of upwelling and relaxation events in the Monterey Bay area. *J. Geophys. Res. Oceans* 115:C06016. doi: 10.1029/2009JC005483

Smedstad, L. F., Barron, C. N., Bourg, R. N., Brooking, M. W., Bryant, D. A., Carr, R. J., et al. (2015). "An expansion of glider observation strategies to systematically transmit and analyze preferred waypoints of underwater gliders, ocean sensing and monitoring VIII," in *Proceedings SPIE*, Vol. 9459, eds W. Hou and R. Arnone (Baltimore, MD: SPIE Defense + Security), 1–12. doi: 10.1117/12.2176560

St Laurent, L., and Merrifield, S. (2017). Measurements of near-surface turbulence and mixing from autonomous ocean gliders. *Oceanography* 30, 116–125. doi: 10.5670/oceanog.2017.231

Stommel, H. (1989). The slocum mission. *Oceanography* 22–25. doi: 10.5670/oceanog.1989.26

Swart, S., Thomalla, S. J., and Monteiro, P. M. S. (2015). The seasonal cycle of mixed layer dynamics and phytoplankton biomass in the Sub-Antarctic Zone: a high-resolution glider experiment. *J. Mar. Syst.* 147, 103–115. doi: 10.1016/j.jmarsys.2014.06.002

Swart, S., Thomalla, S. J., Monteiro, P. M. S., and Ansorge, I. J. (2012). Mesoscale features and phytoplankton biomass at the GoodHope line in the Southern Ocean during austral summer. *African J. Marine Sci.* 34, 511–524. doi: 10.2989/1814232X.2012.749811

Swart, S., Zietsman, J. J., Coetzee, J. C., Goslett, D. G., Hoek, A., Needham, D., et al. (2016). Ocean robotics in support of fisheries research and management. *Afr. J. Mar. Sci.* 38, 525–538. doi: 10.2989/1814232X.2016.1251971

Tanhua, T., Pouliquen, S., Hausman, J., O'brien, K., Bricher, P., Bruin, T. D., et al. (2019). Ocean FAIR data services. *Front. Marine Sci*. 6:440. doi: 10.3389/fmars.2019.00440

Taylor, J. C., and Lembke, C. (2017). Echosounder for biological surveys using ocean gliders extending fishery ecosystem assessments to remote places. *Sea Technol.* 58, 35–38.

Testor, P., Bosse, A., Houpert, L., Margirier, F., Mortier, L., Legoff, H., et al. (2018). Multi-scale observations of deep convection in the northwestern Mediterranean Sea during winter 2012-2013 using multiple platforms. *J. Geophys. Res.* 123, 1745–1776. doi: 10.1002/2016JC012671

Testor, P., Meyers, G., Pattiaratchi, C., Bachmayer, R., Hayes, D., Pouliquen, S., et al. (2010). "Gliders as a component of future observing systems," in *Proceedings of OceanObs'09: Sustained Ocean Observations and Information for Society (Vol. 2),* eds J. Hall, D. E. Harrison, and D. Stammer (Venice: ESA Publication), 21–25.

Thomalla, S. J., Ogunkoya, A. G., Vichi, M., and Swart, S. (2017). Using optical sensors on gliders to estimate phytoplankton carbon concentrations and chlorophyll-to-carbon ratios in the southern ocean. *Front. Mar. Sci.* 4:34. doi: 10.3389/fmars.2017.00034

Thomalla, S. J., Racault, M.-F., Swart, S., and Monteiro, P. M. S. (2015). High-resolution view of the spring bloom initiation and net community production in the Subantarctic Southern Ocean using glider data. *J. Marine Sci.* 72, 1999–2020. doi: 10.1093/icesjms/fsv105

Thompson, A. F., Heywood, K. J., Schmidtko, S., and Stewart, A. L. (2014). Eddy transport as a key component of the Antarctic overturning circulation. *Nat. Geosci.* 7, 879–884. doi: 10.1038/ngeo2289

Thompson, A. F., Lazar, A., Buckingham, C., Naveira Garabato, A. C., Damerell, G. M., and Heywood, K. J. (2016). Open-ocean submesoscale motions: a full seasonal cycle of mixed layer instabilities from gliders. *J. Phys. Oceanogr.* 46, 1285–1307. doi: 10.1175/JPO-D-15-0170.1

Thomsen, S., Kanzow, T., Colas, F., Echevin, V., Krahmann, G., and Engel, A. (2016). Do submesoscale frontal processes ventilate the oxygen minimum zone off Peru. *Geophys. Res. Lett.* 43, 8133–8142.doi: 10.1002/2016GL070548

Thorpe, S. A. (2012). Measuring overturns with gliders. *J. Marine Res*. 70, 93–117. doi: 10.1357/002224012800502417

Timmermans, M.-L., and Winsor, P. (2013). Scales of horizontal density structure in the Chukchi Sea surface layer. *Continental Shelf Res.* 52, 39–45. doi: 10.1016/j.csr.2012.10.015

Todd, R. E. (2017). High-frequency internal waves and thick bottom mixed layers observed by gliders in the Gulf Stream. *Geophys. Res. Lett*., 44, 6316–6325. doi: 10.1002/2017GL072580

Todd, R. E., Asher, T. G., Heiderich, J., Bane, J. M., and Luettich, R. A. (2018). Transient response of the Gulf Stream to multiple hurricanes in 2017. *Geophys. Res. Lett*. 45, 10,509–10,519. doi: 10.1029/2018GL079180

Todd, R. E., Chavez, F. P., Clayton, S., Cravatte, S., Goes, M., Graco, M., et al. (2019). Global perspectives on observing ocean boundary current systems. *Front. Mar. Sci.* 6:423. doi: 10.3389/fmars.2019.00423

Todd, R. E., Gawarkiewicz, G. G., and Owens, W. B. (2013). Horizontal scales of variability over the middle atlantic bight shelf break and continental rise from finescale observations. *J. Phys. Oceanogr*. 43, 222–230. doi: 10.1175/JPO-D-12-099.1

Todd, R. E., and Locke-Wynn, L. (2017). Underwater glider observations and the representation of western boundary currents in numerical models. *Oceanography* 30, 88–89. doi: 10.5670/oceanog.2017.225

Todd, R. E., Owens, W. B., and Rudnick, D. L. (2016). Potential vorticity structure in the North Atlantic western boundary current from underwater glider observations. *J. Phys. Oceanogr.* 46, 327–348. doi: 10.1175/JPO-D-15-0112.1

Todd, R. E., Rudnick, D. L., Davis, R. E., and Ohman, M. D. (2011b). Underwater gliders reveal rapid arrival of El Niño effects off California's coast. *Geophys. Res. Lett.* 38:L03609. doi: 10.1029/2010GL046376

Todd, R. E., Rudnick, D. L., Mazloff, M. R., Cornuelle, B. D., and Davis, R. E. (2012). Thermohaline structure in the California Current System: observations and modeling of spice variance. *J. Geophys. Res. Oceans* 117:C02008. doi: 10.1029/2011JC007589

Todd, R. E., Rudnick, D. L., Mazloff, M. R., Davis, R. E., and Cornuelle, B. D. (2011a). Poleward flows in the southern california current system: glider observations and numerical simulation. *J. Geophys. Res.* 116:C02026. doi: 10.1029/2010JC006536

Todd, R. E., Rudnick, D. L., Sherman, J. T., Owens, W. B., and George, L. (2017). Absolute velocity estimates from autonomous underwater gliders equipped with Doppler current profilers. *J. Atmos. Oceanic Technol.* 34, 309–333. doi: 10.1175/JTECH-D-16-0156.1

Troupin, C., Beltran, J. P., Heslop, E., Torner, M., Garau, B., Allen, J., and Ruiz,S. J. (2005). A toolbox for glider data processing and management. *Methods Oceanogr.* 13–14, 13–23. doi: 10.1016/j.mio.2016.01.001

Ullgren, J. E., Fer, I., Darelius, E., and Beaird, N. (2014). Interaction of the faroe bank channel overflow with iceland basin intermediate waters. *J. Geophys. Res. Oceans* 119, 228–240. doi: 10.1002/2013JC009437

Våge, K., Papritz, L., Håvik, L., Spall, M. A., and Moore, G. W. K. (2018). Ocean convection linked to the recent ice edge retreat along east Greenland. *Nat. Commun.* 9:1287. doi: 10.1038/s41467-018-03468-6

Venables, H. J., and Meredith, M. P. (2014). Feedbacks between ice cover, ocean stratification, and heat content in Ryder Bay, western Antarctic Peninsula. *J. Geophys. Res. Oceans* 119, 5323–5336. doi: 10.1002/2013JC009669

Venables, H. J., Meredith, M. P., and Brearley, J. A. (2017). Modification of deep waters in Marguerite Bay, western Antarctic Peninsula, caused by topographic overflows. *Deep Sea Res. Part II Topical Stud. Oceanogr.* 139, 9–17. doi: 10.1016/j.dsr2.2016.09.005

Verdy, A., Cornuelle, B., Mazloff, M. R., and Rudnick, D. L. (2017). Estimation of the tropical pacific ocean state 2010-13. *J. Atmospheric Oceanic Technol.* 34, 1501–1517. doi: 10.1175/JTECH-D-16-0223.1

Verfuss, U. K., Aniceto, A. S., Harris, D. V., Gillespie, D., Fielding, S., Jiménez, G., Johnston, P., et al. (2019). A review of unmanned vehicles for the detection and monitoring of marine fauna. *Marine Pollut. Bull.* 140, 17–29. doi: 10.1016/j.marpolbul.2019.01.009

Viglione, G. A., Thompson, A. F., Flexas, M. M., Sprintall, J., and Swart, S. (2018). Abrupt transitions in submesoscale structure in southern drake passage: glider observations and GCM results. *J. Phys. Oceanogr.* 48, 2011–2017.

Villar, E., Farrant, G. K., Follows, M., Garczarek, L., Speich, S., Audic, S., et al. (2015): Environmental characteristics of Agulhas rings affect interocean plankton transport. *Science.* 348:6237. doi: 10.1126/science.1261447

Wall, C. C., Lembke, C., and Mann, D. A. (2012). Shelf-scale mapping of sound production by fishes in the eastern Gulf of Mexico, using autonomous glider technology. *Mar. Ecol. Prog. Ser*. 449, 55–64. doi: 10.3354/meps09549

Webster, S. E., Freitag, L. E., Lee, C. M., and Gobat, J. I. (2015). "Towards real-time under-ice acoustic navigation at mesoscale ranges," in *Proceedings, IEEE International Conference on Robotics and Automation (ICRA)* (Seattle, WA), 1–8.

Weingartner, T., Dobbins, E., Danielson, S., Winsor, P., Potter, R., and Statscewich, H. (2013). Hydrographic variability over the northeastern Chukchi Sea shelf in summer-fall 2008-2010. *Continental Shelf Res.* 67, 5–22. doi: 10.1016/j.csr.2013.03.012

Wilkin, J. L., and Hunter, E. J. (2013). An assessment of the skill of real-time models of Mid-Atlantic Bight continental shelf circulation. *J. Geophys. Res. Oceans* 118, 2919–2933. doi: 10.1002/jgrc.20223

Xu, Y., Chant, R., Gong, D., Castelao, R., Glenn, S., and Schofield, O. (2011). Seasonal variability of chlorophyll a in the Mid-Atlantic Bight. *Continental Shelf Res.* 31, 1640–1650. doi: 10.1016/j.csr.2011.05.019

Yang, K. C., Wang, J., Lee, C. M., Ma, B., Lien, R. C., Jan, S., et al. (2015). Two Mechanisms cause dual velocity maxima in the kuroshio east of taiwan. *Oceanography* 28, 64–73. doi: 10.5670/oceanog.2015.82

Yaremchuk, M., Nechaev, D., and Pan, C. (2011). A hybrid background error covariance model for assimilating glider data into a coastal ocean model. *Monthly Weather Rev.* 139, 1879–1890. doi: 10.1175/2011MWR3510.1

Yu, L. S., A., Bosse, I., Fer, K. A., Orvik, E. M., Bruvik, I., et al. (2017). The Lofoten Basin eddy: three years of evolution as observed by Seagliders. *J. Geophys. Res. Oceans* 122, 6814–6834. doi: 10.1002/2017JC012982

Zaba, K., Rudnick, D. L., Cornuelle, B., Gopalakrishnan, G., and Mazloff, M. (2018). Annual and interannual variability in the California Current System: comparison of an assimilating state estimate with a network of underwater gliders. *J. Phys. Oceanogr.* 48, 2965–2988. doi: 10.1175/JPO-D-18-0037.1

Zaba, K. D., and Rudnick, D. L. (2016). The 2014-2015 warming anomaly in the Southern California Current System observed by underwater gliders. *Geophys. Res. Lett.* 43, 1241–1248. doi: 10.1002/2015GL067550

Zacharia, S., Seshasayanan, R., Sudhakar, T., Atmanand, M. A., and Rao, R. R. (2017). Observed variability of surface layer in the Central Bay of Bengal: results of measurements using glider. *Curr. Sci.* 113, 2151–2159. doi: 10.18520/cs/v113/i11/2151-2159

Zarokanellos, N. D., Papadopoulos, V. P., Sofianos, S. S., and Jones, B. H. (2017). Physical and biological characteristics of the winter-summer transition in the Central Red Sea. *J. Geophys. Res. Oceans* 122, 6355–6370. doi: 10.1002/2017JC012882

Zhang, W. G., Wilkin, J. L., and Arango, H. G. (2010a). Towards an integrated observation and modeling system in the New York Bight using variational methods. Part I: 4DVAR data assimilation. *Ocean Model.* 35, 119–133. doi: 10.1016/j.ocemod.2010.08.003

Zhang, W. G., Wilkin, J. L., and Levin, J. C. (2010b). Towards an integrated observation and modeling system in the New York Bight using variational methods. Part II: repressenter-based observing strategy evaluation. *Ocean Model.* 35, 134–145. doi: 10.1016/j.ocemod.2010.06.006

Zhao, J., Hu, C., Lenes, J. M., Weisberg, R. H., Lembke, C., English, D., et al. (2013). Three-dimensional structure of a Karenia brevis bloom: observations from gliders, satellites, and field measurements. *Harmful Algae* 29, 22–30. doi: 10.1016/j.hal.2013.07.004

Conflict of Interest: YC, SM, RP, and MS were employed by companies Seatrec, FishOcean, Shell, and Applied Ocean Sciences respectively.

The remaining authors declare that the research was conducted in the absence of any commercial or financial relationships that could be construed as a potential conflict of interest.

Citation: Testor P, de Young B, Rudnick DL, Glenn S, Hayes D, Lee CM, Pattiaratchi C, Hill K, Heslop E, Turpin V, Alenius P, Barrera C, Barth JA, Beaird N, Bécu G, Bosse A, Bourrin F, Brearley JA, Chao Y, Chen S, Chiggiato J, Coppola L, Crout R, Cummings J, Curry B, Curry R, Davis R, Desai K, DiMarco S, Edwards C, Fielding S, Fer I, Frajka-Williams E, Gildor H, Goni G, Gutierrez D, Haugan P, Hebert D, Heiderich J, Henson S, Heywood K, Hogan P, Houpert L, Huh S, E. Inall M, Ishii M, Ito S-i, Itoh S, Jan S, Kaiser J, Karstensen J, Kirkpatrick B, Klymak J, Kohut J, Krahmann G, Krug M, McClatchie S, Marin F, Mauri E, Mehra A, Meredith MP, Meunier T, Miles T, Morell JM, Mortier L, Nicholson S, O'Callaghan J, O'Conchubhair D, Oke P, Pallàs-Sanz E, Palmer M, Park J, Perivoliotis L, Poulain PM, Perry R, Queste B, Rainville L, Rehm E, Roughan M, Rome N, Ross T, Ruiz S, Saba G, Schaeffer A, Schönau M, Schroeder K, Shimizu Y, Sloyan BM, Smeed D, Snowden D, Song Y, Swart S, Tenreiro M, Thompson A, Tintore J, Todd RE, Toro C, Venables H, Wagawa T, Waterman S, Watlington RA and Wilson D (2019) OceanGliders: A Component of the Integrated GOOS. Front. Mar. Sci. 6:422. doi: 10.3389/fmars.2019.00422 frontiers in Marine Science

METHODS
published: 30 October 2019
doi: 10.3389/fmars.2019.00664

The Development and Validation of a Profiling Glider Deep ISFET-Based pH Sensor for High Resolution Observations of Coastal and Ocean Acidification

Grace K. Saba[1], Elizabeth Wright-Fairbanks[1], Baoshan Chen[2], Wei-Jun Cai[2], Andrew H. Barnard[3], Clayton P. Jones[4], Charles W. Branham[3], Kui Wang[2] and Travis Miles[1]*

[1] Center for Ocean Observing Leadership, Department of Marine and Coastal Sciences, School of Environmental and Biological Sciences, Rutgers University, New Brunswick, NJ, United States, [2] School of Marine Science and Policy, University of Delaware, Newark, DE, United States, [3] Sea-Bird Scientific, Philomath, OR and Bellevue, WA, United States, [4] Teledyne Webb Research, North Falmouth, MA, United States

OPEN ACCESS

Edited by:
Leonard Pace,
Schmidt Ocean Institute,
United States

Reviewed by:
Vassilis Kitidis,
Plymouth Marine Laboratory,
United Kingdom
Philip Andrew McGillivary,
United States Coast Guard Pacific
Area, United States

***Correspondence:**
Grace K. Saba
saba@marine.rutgers.edu

Specialty section:
This article was submitted to
Ocean Observation,
a section of the journal
Frontiers in Marine Science

Received: 14 December 2018
Accepted: 10 October 2019
Published: 30 October 2019

Citation:
Saba GK, Wright-Fairbanks E,
Chen B, Cai W-J, Barnard AH,
Jones CP, Branham CW, Wang K and
Miles T (2019) The Development
and Validation of a Profiling Glider
Deep ISFET-Based pH Sensor
for High Resolution Observations
of Coastal and Ocean Acidification.
Front. Mar. Sci. 6:664.
doi: 10.3389/fmars.2019.00664

Coastal and ocean acidification can alter ocean biogeochemistry, with ecological consequences that may result in economic and cultural losses. Yet few time series and high resolution spatial and temporal measurements exist to track the existence and movement of water low in pH and/or carbonate saturation. Past acidification monitoring efforts have either low spatial resolution (mooring) or high cost and low temporal and spatial resolution (research cruises). We developed the first integrated glider platform and sensor system for sampling pH throughout the water column of the coastal ocean. A deep ISFET (Ion Sensitive Field Effect Transistor)-based pH sensor system was modified and integrated into a Slocum glider, tank tested in natural seawater to determine sensor conditioning time under different scenarios, and validated *in situ* during deployments in the U.S. Northeast Shelf (NES). Comparative results between glider pH and pH measured spectrophotometrically from discrete seawater samples indicate that the glider pH sensor is capable of accuracy of 0.011 pH units or better for several weeks throughout the water column in the coastal ocean, with a precision of 0.005 pH units or better. Furthermore, simultaneous measurements from multiple sensors on the same glider enabled salinity-based estimates of total alkalinity (A_T) and aragonite saturation state (Ω_{Arag}). During the Spring 2018 Mid-Atlantic deployment, glider pH and derived A_T/Ω_{Arag} data along the cross-shelf transect revealed higher pH and Ω_{Arag} associated with the depth of chlorophyll and oxygen maxima and a warmer, saltier water mass. Lowest pH and Ω_{Arag} occurred in bottom waters of the middle shelf and slope, and nearshore following a period of heavy precipitation. Biofouling was revealed to be the primary limitation of this sensor during a summer deployment, whereby offsets in pH and A_T increased dramatically. Advances in anti-fouling coatings and the ability to routinely clean and swap out sensors can address this challenge. The data presented here demonstrate the ability for gliders to routinely provide high resolution water column data on regional scales that can be applied to acidification monitoring efforts in other coastal regions.

Keywords: ocean acidification, pH, glider, monitoring, U.S. Northeast Shelf, Mid-Atlantic

INTRODUCTION

Ocean acidification (OA) has presented great research challenges and has significant societal ramifications that range from economic losses due to the decreased survival of commercially important organisms to the ecological consequences associated with altered ecosystems (Cooley et al., 2009; Doney, 2010). Particular areas of the coastal ocean are more susceptible to sustained, large increases in carbon dioxide (CO_2), including those in upwelling zones (Feely et al., 2008, 2010a), bays (Thomsen et al., 2010), and areas with high riverine and/or eutrophication influence (Salisbury et al., 2008; Cai et al., 2011). Yet few observations exist to track upwelling and movement of low pH water.

Past OA monitoring efforts have been limited to surface buoys equipped with sensors that measure pH and/or $p\mathrm{CO}_2$ (the concentration of CO_2 in seawater measured as partial pressure of the gas), flow-through $p\mathrm{CO}_2$ systems utilized by research vessels, and water column sampling during large field campaigns (e.g., U.S. Joint Ocean Global Flux Study, Bermuda Atlantic Time Series, Hawaiian Ocean Times Series) with low spatial resolution (mooring) or with low temporal resolution and high cost (research cruises). Only a fraction of these efforts include the U.S. continental shelves (e.g., Gulf of Mexico Ecosystems and Carbon Cycle Cruises [GOMECC], East Coast Ocean Acidification [ECOA] cruises) (Jiang et al., 2008; Wang et al., 2013, 2017; Wanninkhof et al., 2015), commercially important coastal regions where finfish, lobster, and wild stocks of shellfish are present (Hales et al., 2005; Feely et al., 2008; Vandemark et al., 2011; Xue et al., 2016). Furthermore, very few sampling locations (spatial and temporal scale) include more than one of the four measureable carbonate chemistry parameters (pH; dissolved inorganic carbon concentration, or DIC; total alkalinity, or A_T; and $p\mathrm{CO}_2$). At least two out of the four are necessary in order to fully characterize the marine carbonate system, including determinations of aragonite saturation state (Ω_{Arag}), an approximate measure of whether calcium carbonate (in the form of aragonite) will dissolve or precipitate in calcifying organisms (Lee et al., 2006; Cai et al., 2010; Johnson, 2010; Wang et al., 2013).

The recent development of sensors for *in situ* measurements of seawater pH has resulted in a growing number of autonomous pH monitoring stations in the United States (Seidel et al., 2008; Martz et al., 2010). New pH sensors that can rapidly respond to pH change and also withstand higher pressure (depth) show great value in monitoring coastal systems. A Deep-Sea ISFET (Ion Sensitive Field Effect Transistor) profiling pH sensor was recently developed by Monterey Bay Aquarium Research Institute (MBARI) and Honeywell and has been successful in collecting high quality data on a depth-profiling mooring (Johnson et al., 2009, 2016; Martz et al., 2010). These recent measurements in the open and coastal ocean have shown that the pH varies greatly in time and space, reflecting complex circulation patterns that are likely due to the influence of low pH deep water through mixing and the intrusion of low pH, fresh and/or estuarine water (Dore et al., 2009; Byrne et al., 2010; Hofmann et al., 2011; Yu et al., 2011). Earlier, an innovative approach of combined *in situ* pumping and shipboard measurements of $p\mathrm{CO}_2$ also demonstrated rapid spatial variations of the CO_2 system in the upwelling margin offshore Oregon, United States (Hales et al., 2005). These fluctuations may lead to large ecological and economic impacts, thus reinforcing the need for reliable high-resolution observations of the full water column.

Significant improvements could be immediately achieved with the implementation of a real-time monitoring network that quantifies the spatial location, duration, and transport of the low pH/Ω_{Arag} water in coastal regions (Feely et al., 2010b; Martz et al., 2010). The spatial, temporal, and depth resolution achieved from Teledyne Webb Slocum glider data far exceeds that from traditional sampling from ships and moorings (Rudnick et al., 2004; Schofield et al., 2007). These systems can sample in depths as shallow as 4 meters and as deep as 1000 m and have been used in a broad range of challenging environments including near ice shelves in the Antarctic, beneath hurricanes and coastal storms, and on river dominated continental shelves. Recent calls for a national (Baltes et al., 2014) and international observational network for OA identified underwater gliders as a potential pH monitoring instrument that "could resolve shorter space-time scale variability of the upper ocean" (Feely et al., 2010b; Martz et al., 2010). A variety of sensors have successfully been mounted on Slocum gliders. To date, however, no direct measurements of ocean pH have been collected by pH sensors integrated into these gliders.

We present here the recent development of the first integrated glider platform and sensor system for collecting pH data in the water column of the coastal ocean on a regional scale. Specifically, we modified and integrated a deep-depth rated version of the ISFET-based pH sensor system (Johnson et al., 2009, 2016; Martz et al., 2010), into a Slocum G2 glider science bay. In addition to pH, the glider is equipped with sensors that provided profiles of conductivity, temperature, depth, spectral backscatter, chlorophyll fluorescence, and dissolved oxygen (DO) that enabled the mapping of ocean pH against the other variables and the calculation of A_T and Ω_{Arag}. Here, we describe the performance of the new sensor from seawater tank tests and from the first *in situ* deployments within the U.S. Northeast Shelf (NES), one of the nation's most economically valuable coastal fishing regions. Water column pH measurements in this region are sorely lacking; hence, the glider deployments presented here deliver a much-needed full characterization of water column pH dynamics in this coastal region from the nearshore to the shelf-break and demonstrate the application of glider-based acidification monitoring in other coastal regions.

EXPERIMENTAL SECTION

pH Sensor Integration

The deep ISFET-based pH sensor was modified by Sea-Bird Scientific, and its integration into a Slocum Webb G2 glider (200 m) was a coordinated effort between Rutgers, Sea-Bird Scientific, and Teledyne Webb Research. To optimize the performance of the pH sensor for use on a glider Sea-Bird Scientific significantly modified the original design of Deep-Sea DuraFET, and ISFET-based sensor developed by MBARI (Johnson et al., 2016). Given the light sensitivity of the sensor and desire to be closely coupled with CTD (conductivity, temperature, depth) data acquisition, the deep ISFET-based sensor was reconfigured by Sea-Bird Scientific to fit into the existing rectangular glider CTD port utilizing a shared pumped system to pull seawater in past both the pH and CTD sensor elements (**Figure 1A**). Prior to integration with the glider CTD, the deep ISFET-based pH sensor was calibrated in a custom temperature-controlled pressure vessel filled with 0.01 N HCl over the range of 5–35°C and 0–3000 psi (Johnson et al., 2016). After the temperature and pressure calibration was completed, the pH sensor was integrated with the glider SBE41CP pumped CTD and conditioned in natural seawater for 1 week (Johnson et al., 2016). Based on the laboratory data collected at Sea-Bird Scientific the current specifications for the glider-based Deep-Sea DuraFET pH sensor are ±0.05 pH units in accuracy and ±0.001 pH units in precision. The resulting streamlined version utilizes the same mounting form factor as the SBE41CP pumped CTD, the standard model presently installed in Slocum gliders. Teledyne Webb Research facilitated the integration of the new deep ISFET pH/CTD unit into a standard glider science bay hull section (**Figure 1B**). This standalone science bay was also outfitted with a Sea-Bird Scientific ECO puck (BB2FL) configured for simultaneous fluorescence, CDOM, and optical backscatter measurements, and complimented the existing Aanderaa optode integrated into the aft of the glider for measuring DO. Teledyne Webb Research environmentally cycled (pressure and temperature), bench tested, and performed in-water tests on the completed assembly prior to deployment. A proglet was written for the glider science processor to ingest, store, and make available the data at each surface interval.

After the sensor calibrations and pre-deployment tests were completed by Sea-Bird Scientific and Teledyne Webb Research, the science sensor bay was assembled into the glider (**Figure 1C**) and placed in a natural seawater tank at Rutgers University for a minimum of 1 week at room temperature and pressure in order for the pH sensor to condition to seawater off the coast of Atlantic City, New Jersey (Bresnahan et al., 2014; Johnson et al., 2016).

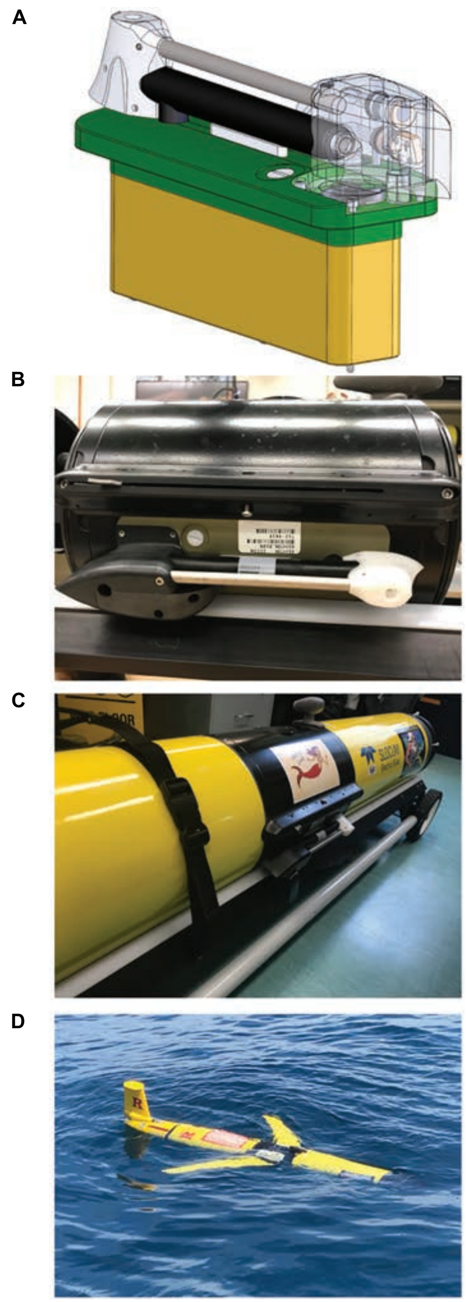

FIGURE 1 | DeepISFET-based pH sensor integration into a glider. Deep ISFET-based pH sensor integrated with pumped CTD **(A)**, Coupled pH and CTD integrated into a standalone science bay **(B)**, completely assembled in the glider **(C)**, and deployed in the Mid-Atlantic **(D)**.

pH Data Analysis

pH_{total} was calculated using the glider-measured reference voltage, pressure, sea water temperature, salinity, and sensor-specific calibration coefficients. Calculations were completed in Matlab (Johnson et al., 2017), and the code is provided in the **Supplementary Material**. The final equation used to calculate pH (below) was derived and modified from previous efforts

(Khoo et al., 1977; Millero, 1983; Dickson et al., 2007; Martz et al., 2010; Johnson et al., 2016):

$$pH_{total} = \frac{V_{ref} - k_0 - k_2 * t - f(p)}{S_{nernst}} + \log(Cl_T) + 2 * \log(\gamma HCl)_{T,P} - \log\left(1 + \frac{S_T}{K_{STP}}\right) - \log\left(\frac{1000 - 1.005 * S}{1000}\right)$$

Where:

$$S_{nernst} = \frac{R * T * \ln(10)}{F}$$

$$\log(\gamma HCl)_{T,P} = \log(\gamma HCl)_T + \left(\frac{V_{HCl^*p}}{\ln(10)\,RT}\right)/2$$

R is the universal gas constant = 8.314472 J/(mol*K);
t is the temperature in °C;
T is the temperature in K;
S is salinity in psu;
P is the pressure in dbar;
p is the pressure in bar;
F is the Faraday constant = 96485.3415 C/mol;
k_0 is the cell standard potential offset;
k_2 is the cell standard temperature slope;
$f(p)$ is the sensor pressure response function;
V_{ref} is the reference voltage;
V_{HCl} is the partial molar volume of HCl;
Cl_T is total chloride;
$(\gamma HCl)_T$ is the HCl activity coefficient at T;
$(\gamma HCl)_{T,P}$ is the HCl activity coefficient at T and p;
S_T is total sulfide;
K_{STP} is the acid dissociation constant of $HSO_{4,T\&P}$.

Tank Tests to Determine Sensor Conditioning Time

We conducted a series of tests October 17-November 6, 2018 to determine ISFET sensor conditioning time (**Figure 2A**). First, the glider was placed in a tank filled with natural seawater collected from nearshore waters near Atlantic City, NJ, United States. The pH/CTD sensors were immediately turned on with data continuously recording and transmitting in real-time using a Freewave modem linked to Teledyne Webb Slocum Fleet Mission Control software. This test defined the time required of an "off the shelf" pH sensor to condition or equilibrate to local seawater. A second set of tests investigated the response of the pH sensor to various wet/dry exposure time frames, representing scenarios wherein the sensor may be kept dry for periods of a few hours to days, such as during local, overnight, or distant transit from the laboratory facility to the field prior to a deployment (**Figures 2B–E**). Specifically, the second set of tests determined conditioning period after: (1) the glider was turned off for 2 h while the pH sensor remained submerged in the tank, then turned back on (**Figure 2B**); (2) the glider was removed from the tank and the pH sensor dried for 3 h, then the glider was placed back in the tank and turned on (**Figure 2C**); (3) the glider was removed from the tank and the pH sensor dried for 1 day then the glider was placed back in the tank and turned on (**Figure 2D**); and (4) the glider was removed from the tank and the pH sensor dried for 3 days then the glider was placed back in the tank and turned on (**Figure 2E**). The pH sensor was considered conditioned for each set of tests after the pH measurements stabilized with minimum drift (±0.0001 pH units hour^{-1} or ±0.003 pH units day^{-1}).

During the tank tests, discrete seawater samples were collected from the tank next to the glider at least three times daily and measured immediately on a spectrophotometric pH system set up next to the seawater tank. Accuracy of the glider pH sensor was determined as the pH measurement offset between glider pH and pH measured spectrophotometrically after the pH glider sensor was conditioned.

First Glider Deployments

After the sensor integration, factory calibration, testing, and conditioning was complete, we tested the capability of the glider sensor package in two deployments in coastal waters along the U.S. Northeast Shelf. Slocum gliders operate by increasing and decreasing volume with a buoyancy pump to dive and climb in repeat sawtooth sampling patterns. Wings, a pitch battery, and the shape of the glider body result in forward motion with an aft rudder and internal compass maintaining a pre-programed heading while underwater. At pre-programed surface intervals the glider acquires new location information, downloads new mission parameters, and sends back real time data. The glider, RU30, used in this study was a coastal glider with a 200 m rated pump. Coastal gliders profile vertically at 10–15 cm s^{-1} and travel horizontally at speeds of ∼20 km day^{-1}. Science sensors sample at 0.5 Hz resulting in measurements at every 20–30 cm intervals vertically.

We first deployed the glider on May 2, 2018 ∼9 km off the coast of Atlantic City, NJ (17 m water depth) (**Figures 1D, 3**, magenta track). This glider was powered by alkaline battery pack which supports a typical deployment for 3–4 weeks. Upon deployment, we conducted a CTD hydrographic profile and several individual casts with a 5 L Niskin bottle to sample discrete seawater samples for validating the sensor (see below) while the glider was conducting dives 50–100 m from the vessel. Once water sampling was completed, the glider was sent toward its next offshore waypoint to begin its cross-shelf transect. The glider completed a full cross-shelf transect in 20 days, and was recovered on May 22, 2018 ∼24 km off the coast of Atlantic City, NJ (25 m water depth). A subset of the full glider datasets were sent to shore in near real time via Iridium satellite cell phone located in the glider tail. After each glider sampling segment the glider surfaces, inflates an air bladder in the tail section, and connects to shore via iridium satellite cell phone. These datasets included all science variables necessary to calculate pH. This allowed for initial data quality checks while the glider was deployed, and ensured that if the glider was lost critical science data was still collected. After the glider was recovered, the full datasets were downloaded from the science memory cards stored onboard and are the datasets used throughout this publication. We have made

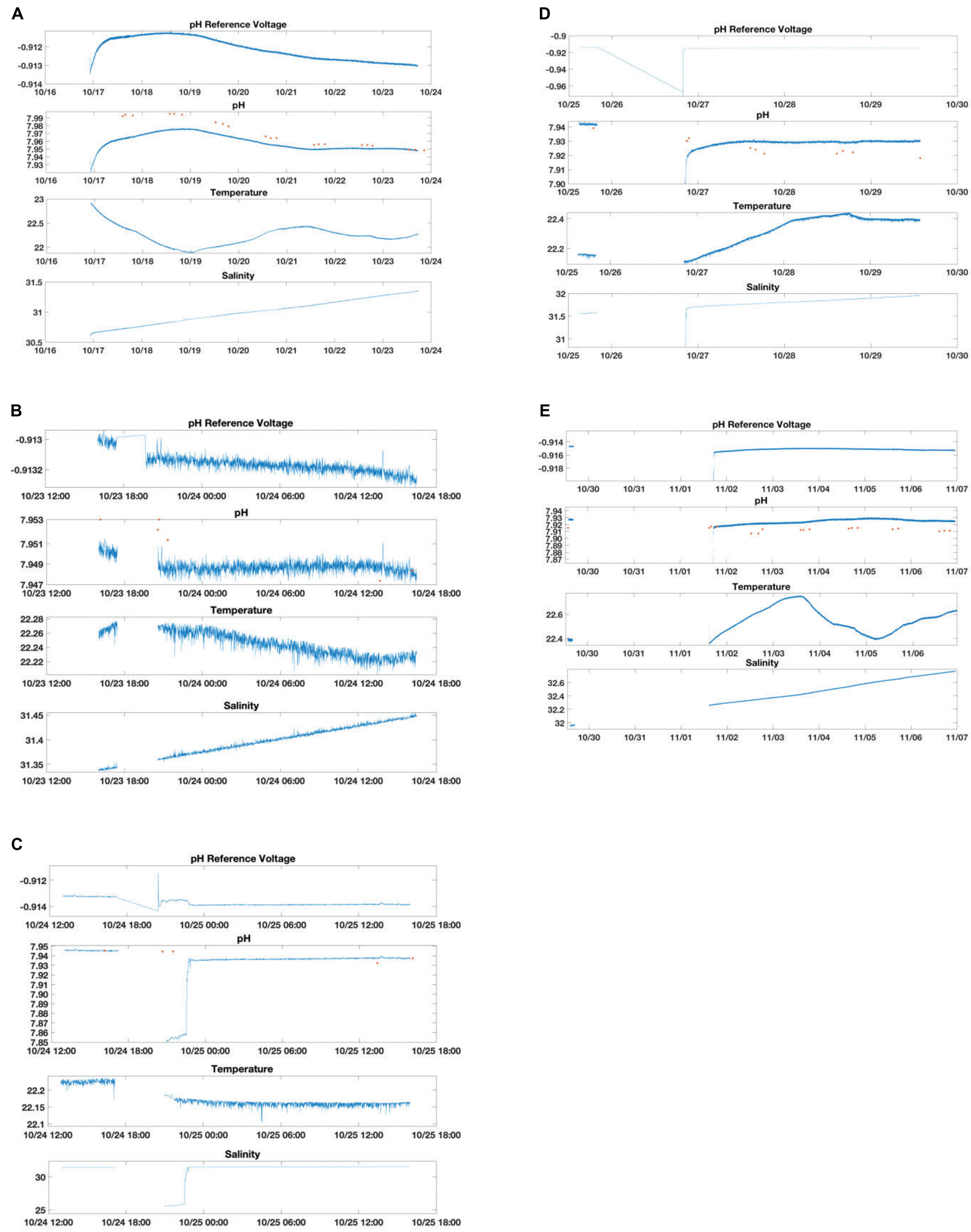

FIGURE 2 | Glider pH and discrete (spectrophotometric) pH tank test conditioning experiments. Data shown includes pH reference voltage measurements, calculated pH, temperature and salinity over time (month/day, for longer conditioning periods; month/day time, for shorter conditioning periods). The glider was placed in a saltwater tank and the pH/CTD sensor was turned on to determine times for initial conditioning from a sensor "off the shelf" **(A)**; conditioning after pH/CTD sensor turned off for 3 h while submerged in tank then turned back on **(B)**; conditioning after glider removed from tank and sensor dry for 2 h then placed back in the tank and turned on **(C)**; conditioning after glider removed from tank and sensor dry for 1 day then placed back in the tank and turned on **(D)**; conditioning after glider removed from tank and sensor dry for 3 days then placed back in the tank and turned on **(E)**. Data gaps represent the dry/off period.

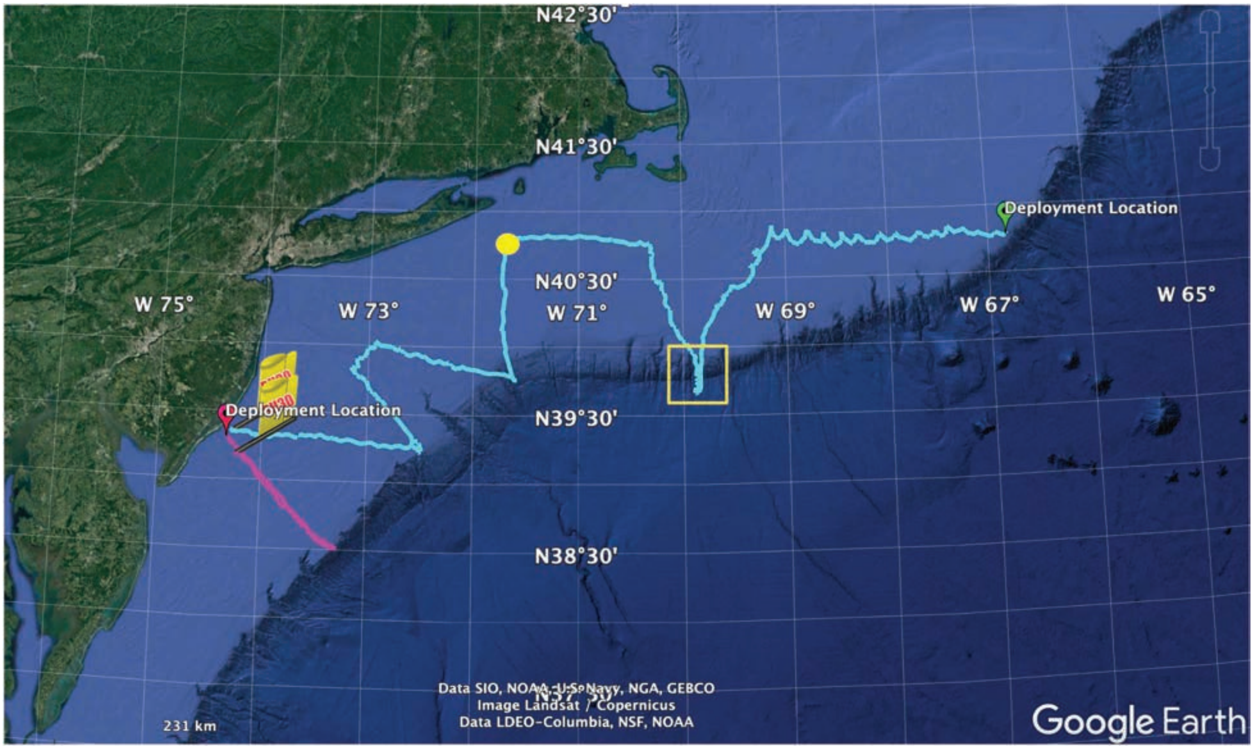

FIGURE 3 | Map showing location of first pH glider deployments. For the first deployment (magenta track), the glider was deployed off the coast of Atlantic City, New Jersey on May 2, 2018 and took measurements of pH and other variables from nearshore to the continental shelf break and back where it was recovered on May 22, 2018. For the second deployment (cyan track), the glider was deployed east of Georges Bank on July 5, 2018 and took measurements of pH and other variables during its transit until it was recovered off the coast of Atlantic City on August 28, 2018. During this deployment the glider was entrained into a warm core ring for nearly 5 days (yellow box). Concerned about biofouling due to this extended period in warm water, we intercepted the glider south of Montauk, NJ, United States on July 31, 2018 (yellow dot) to clean and re-deploy the glider and collect additional discrete water samples for sensor validation.

the glider variable data available and openly accessible on the ERDDAP server. The delayed mode time-series that contains all of the data as present in the source data files is accessible at: http://slocum-data.marine.rutgers.edu/erddap/tabledap/ru30-20180502T1355-trajectory-raw-delayed.html. The raw profile dataset that contains the data but broken up by glider profiles (not a time-series) is accessible at: http://slocum-data.marine.rutgers.edu/erddap/tabledap/ru30-20180502T1355-profile-raw-delayed.html. The science dataset that contains only scientifically relevant variables is accessible at: http://slocum-data.marine.rutgers.edu/erddap/tabledap/ru30-20180502T1355-profile-sci-delayed.html. Glider data processing, including analyses for sensor time lag corrections (below), was conducted using Slocum Power Tools available at: https://github.com/kerfoot/spt.

A second glider deployment occurred on the eastern edge of Georges Bank on July 5, 2018 (**Figure 3**, cyan track). This glider was powered by a lithium battery pack (configuration was 78 DD cells in a three series) which supports a typical deployment for nearly 60 days. At the time of this deployment, discrete seawater samples were collected in surface waters within 5 m from the pH/CTD glider sensor. After which the glider was sent west over Georges Bank. During a 4–5 days period (July 18–22), the glider was entrained in a warm core ring on the shelf break in waters off southern New England (**Figure 3**, yellow box). Concerned about biofouling due to this extended period in warm water, we intercepted the glider south of Montauk, NJ on July 31, 2018 (**Figure 3**, yellow dot) to clean the glider and collect additional discrete water samples for sensor validation. The glider was moderately biofouled and included biofouling inside the sensor intake (**Figure 4**). The glider and sensor were cleaned as much as possible by flushing with seawater and using brushes and cloth, but we were unable to remove biofouling in the far reaches of the internal sensor surfaces. The glider was re-deployed and continued on its transit where it was recovered off the coast of Atlantic City, NJ, United States on August 28, 2018. Due the evidence of biofouling during this summer deployment, we do not present here the full datasets and only report biofouling impacts on pH measurements and derived A_T.

Sensor Time Lag Corrections

Thermal lag corrections were applied to conductivity measurements prior to calculating pH. In a standard Sea-Bird CTD temperature is measured outside of the conductivity cell while conductivity is measured inside of the cell resulting in a mismatch in the measurements then used to calculate salinity, density, and subsequently pH (Garau et al., 2011). Thermal lag typically results in incorrect salinity and density estimates

FIGURE 4 | Biofouling on the glider deep ISFET-based pH sensor after 26 days during the July–August, 2018 deployment. The glider was intercepted, cleaned, and re-deployed south of Montauk, NJ, United States on July 31, 2018.

when the glider profiles through sharp interfaces. To address the thermal lag, temperature and conductivity data were binned in 0.25 m increments. Sequential temperature and conductivity profile pairs (one upcast and one downcast) were averaged together and the average profile was interpolated back to the original sampling depths. Salinity was calculated based on the corrected temperature and conductivity profiles.

Reference voltage and derived pH measurements exhibited a time lag during deployment, identified as skewed shifts in upcast and downcast measured (reference electrode) and derived pH (**Figures 5A,B**). To correct this lag, we first identified all upcast/downcast pairs (where there is an upcast followed by a downcast during the deployment). To determine the time shift that best matches the location of the clines, in this case typically a halocline, in an upcast and subsequent downcast, each pair was run through iterations of time shifts from 0 to 120 s at 5 s intervals. Optimal time shift was identified as the shift that minimized the difference of reference voltage in the two arms of the inverse V trajectory (upcast and subsequent downcast). We plotted optimal time shift for each upcast/downcast pair over time (**Figure 5C**) and optimal time shifts throughout full deployment as a histogram to determine shift peaks over time (**Figure 5D**). We observed 2 peaks during the May 2018 deployment, so one shift (47 s) was applied to first 1/3 of the deployment and a second shift (30 s) was applied to the last 2/3 (**Figures 5A,B**). July had 3 peaks (46, 81, 104 s) which were applied to those corresponding sections of deployment (data not shown).

Total Alkalinity Estimations and Aragonite Saturation State Calculations

To complement our glider pH measurements and to fully resolve the carbonate system, A_T was estimated from simultaneous glider salinity measurements. A_T exhibits near-conservative behavior with respect to salinity in the Atlantic along the east coast of the United States (Cai et al., 2010; Wang et al., 2013). To estimate A_T, we used the following linear regression equation, determined from the salinity-A_T relationship at three cross-shelf transects along the U.S NES (Massachusetts, New Jersey, and Delaware) sampled during the ECOA-1 cruise (summer 2015) (total 170 pairs of A_T and salinity data, $R^2 = 0.99$).

$$A_T = 50.04^* x + 564.08$$

Where x is salinity.

Final carbonate system parameters, including Ω_{Arag}, were calculated in Matlab using CO2SYS (van Heuven et al., 2011), with glider measured temperature, salinity, pressure, and pH and glider-derived salinity-based A_T as inputs. We used total pH scale (mol/kg-SW), K1 and K2 constants (Mehrbach et al., 1973) with refits (Dickson and Millero, 1987), and the acid dissociation constant of $KHSO_4$ in seawater (Dickson, 1990).

Quality Assurance and Quality Control (QA/QC)

The hydrographic (CTD) and DO data collected during the glider missions follows the QA/QC procedures outlined in an approved EPA Quality Assurance Project Plan (QAPP) that was developed specifically for glider observations of DO along the New Jersey coast (Kohut et al., 2014). The procedures include pre- and post-deployment steps for each sensor to ensure data quality for each deployment. Beyond these common measurements, the science bay of the glider was outfitted with an ECO puck and the profiling deep ISFET-based pH sensor. QA/QC procedures for each sensor are described in detail below.

CTD

The hydrographic data for each mission was sampled with a pumped CTD specifically engineered for this glider. Based on manufacturer specifications, the CTD was factory calibrated by SeaBird Scientific upon completion of the CTD-pH sensor integration. The QAPP requires a two-tier approach to verify the temperature and conductivity data from the glider CTD (Kohut et al., 2014). The first-tier test is a pre- and post-deployment verification between the glider CTD and a factory calibrated Sea-Bird-19 CTD in our ballast tank at Rutgers University in New Brunswick, NJ, United States. The second-tier test is an *in situ* verification at both the deployment and recovery of the glider. For each deployment and recovery, we lowered a manufacturer calibrated SeaBird-19 CTD to compare to the concurrent glider profile. This second-tier test gives an *in situ* comparison within the hydrographic conditions of the mission.

Aanderaa Optode

The DO data was sampled with an optical sensor unit manufactured by Aanderra Instruments called an optode. Like the CTD, we deployed a glider optode that is factory calibrated at least once per year. In addition to these annual calibrations, we also completed pre- and post- deployment verifications. To do this we compared optode observations to concurrent Winkler titrations of a sample at both 0

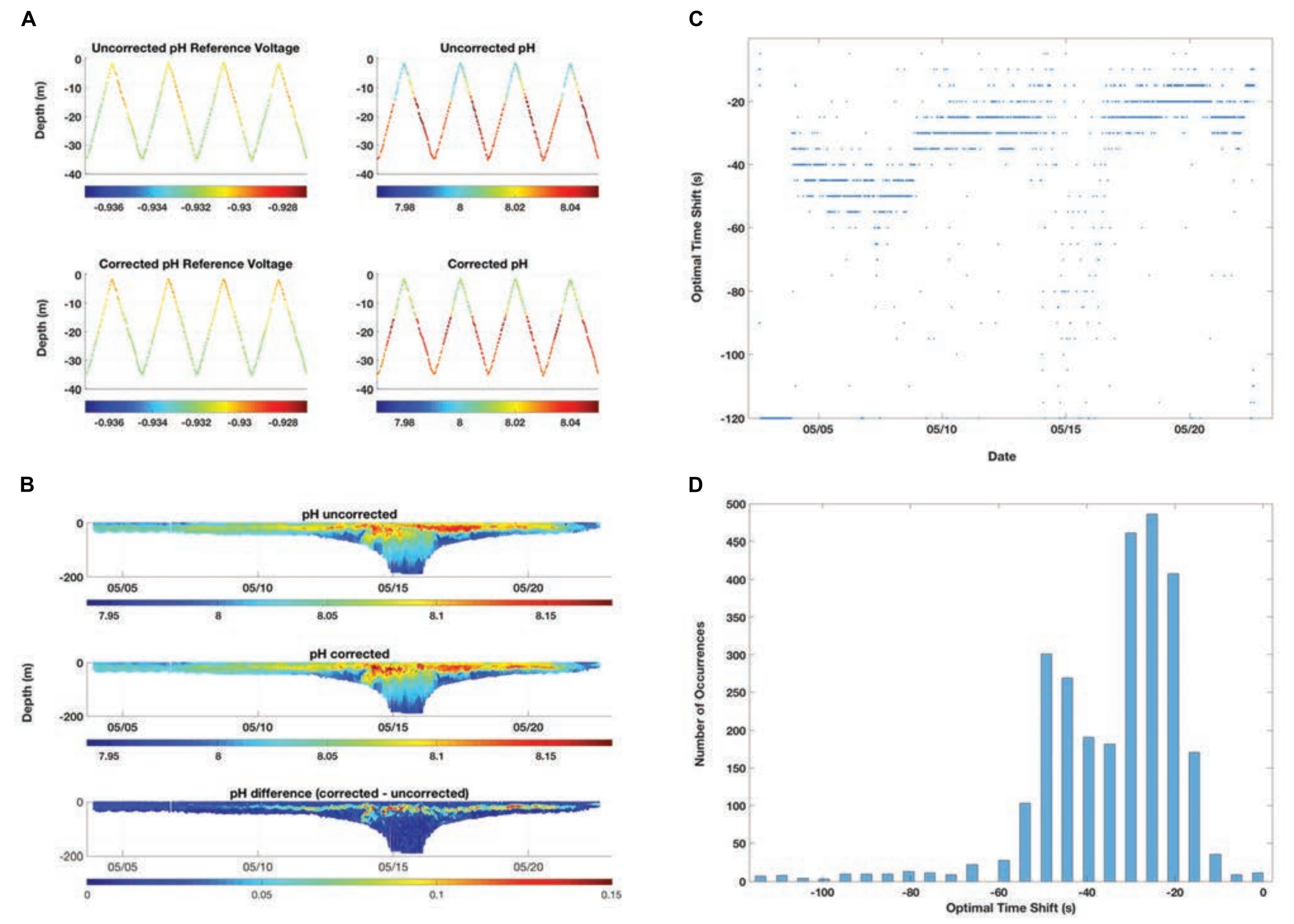

FIGURE 5 | pH response time lag corrections. Optimal time shift was identified as the shift that minimized the difference of reference voltage in the two arms of the inverse V trajectory (upcast and subsequent downcast). Example segments of uncorrected and corrected time lag observed in glider pH reference voltage and calculated pH data during the May 2018 deployment are shown in panel **(A)**. The time lag correction adjusted the measurements of pH reference voltage (left columns), and hence the calculations of pH (right columns). These were expanded to include uncorrected [top], corrected [middle], and the difference between the corrected and uncorrected pH [bottom] for the full May 2018 deployment **(B)**. The optimal time shift observed for upcast and downcast pairs over time **(C)** and the histogram of optimal time shifts **(D)** during the May deployment are presented here. Peaks were applied to shift time of pH reference voltage readings in order to minimize separation between glider up and downcasts.

and 100% saturation. The verification for this deployment met the QAPP requirement that all optode measurements are within 5% saturation of the results of the Winkler titrations for both the 0 and 100% saturation samples (Kohut et al., 2014).

BB2FL ECO Puck

The puck we deployed was standard factory calibration from WET Labs (recommended every 1–2 years for pucks in gliders).

Profiling Deep ISFET-Based pH Sensor

We followed Best Practices for autonomous pH measurements with the DuraFET, including the recommended rigorous calibration and ground truthing procedure (Bresnahan et al., 2014; Martz et al., 2015; Johnson et al., 2016). Using a 5 L Niskin bottle aboard the vessel during deployment and recovery, replicate water samples were collected near the glider from multiple depths (0.5 m, depth of thermocline, and 2 m from bottom; see **Table 1**). During this 1–2 h sampling procedure, the glider sampled the water column near the vessel. Water samples were collected for pH, DIC, and A_T analysis from the Niskin bottle into two 250 mL borosilicate glass bottles for a specific depth, with one bottle for DIC and A_T and another bottle for pH. Sampling involved overflow of seawater for at least one to two volumes, after which bottles were gently filled completely to avoid gas exchange with surrounding air. One mL of sample was removed to create a small headspace to allow for seawater expansion. The sample was then poisoned with 50 μL of saturated mercuric chloride, sealed with a pre-greased glass stopper and rubber band, and stored in a cool, dark location until analysis at Cai's laboratory (University of Delaware). Discrete sample pH was measured spectrophotometrically at 25° Celsius on the total

TABLE 1 | Comparisons between glider pH and derived total alkalinity (A_T) and discrete pH and A_T measured from seawater samples during the spring glider deployment (May 2018).

Date	Depth (m)	Glider pH	Discrete pH	pH Difference (Glider – Discrete)	Glider A_T	Discrete A_T	A_T Difference (Glider – Discrete)
May 2	0.5	7.945	7.977	−0.032	2119.3	2149.7	−30.4
May 2	0.5	7.945	7.975	−0.030	2119.3	2149.8	−30.5
May 2	0.5	7.945	7.976	−0.031	2119.3	2147.6	−28.3
May 2	11	7.947	7.938	0.009	2130.1	2154.3	−24.2
May 2	11	7.947	7.941	0.006	2130.1	2154.1	−24.0
May 2	11	7.947	7.942	0.005	2130.1	2155.0	−24.9
May 2	15	7.973	7.958	0.015	2141.3	2153.8	−12.5
May 2	15	7.973	7.972	0.001	2141.3	2154.1	−12.8
May 2	14	7.972	7.955	0.017	2138.9	2152.7	−13.8
May 22	0.5	8.010	8.026	−0.016	2079.8	2091.7	−11.9
May 22	0.5	8.010	8.024	−0.014	2079.8	2091.0	−11.2
May 22	9	7.988	8.001	−0.013	2094.0	2108.2	−14.2
May 22	9	7.988	8.002	−0.014	2094.0	2106.9	−12.9
May 22	23	7.987	7.998	−0.011	2142.1	2155.0	−12.9
May 22	23	7.987	7.993	−0.006	2142.1	2155.1	−13.0

At glider deployment (May 2) and recovery (May 22), water samples were collected from various depths using a 5 L Niskin bottle, preserved, and returned to the laboratory for determination of pH, A_T, and Dissolved Inorganic Carbon (DIC). During this 1–2 h water sampling procedure, the glider sampled the water column in proximity to the vessel. Values displayed here are replicate discrete pH measurements (corrected for in situ temperature and salinity) and glider pH measurements averaged at each sample depth (±0.5 m) over the sampling period. Additionally, glider A_T (μmol kg^{-1}) was calculated using a linear regression determined from the salinity-A_T relationship at three cross-shelf transects along the U.S Northeast Shelf (Massachusetts, New Jersey, and Delaware) sampled during the ECOA-1 cruise (summer 2015).

pH scale using purified M-Cresol Purple purchased from R. Byrne at the University of South Florida (Clayton and Byrne, 1993; Liu et al., 2011). Cai's lab has built a spec-pH unit similar to the Dickson Lab (Carter et al., 2013). The accuracy of pH data was verified against *Tris* buffers (Millero, 1986; DelValls and Dickson, 1998) purchased from Andrew Dickson at UCSD Scripps Institute of Oceanography and through joining inter-laboratory comparisons. A_T titrations were performed using open cell Gran titration and Apollo Scitech A_T titrator AS-ALK2 following previously described methods (Cai et al., 2010; Huang et al., 2012; Chen et al., 2015). DIC was measured using an Apollo Scitech DIC analyzer AS-C3, which acidifies a small volume of seawater (1.0 mL) and quantifies the released CO_2 with a LI-7000 Non-Dispersive InfraRed analyzer (Huang et al., 2012; Chen et al., 2015). Precision of A_T and DIC are better than ±0.1%. Measurements of A_T and DIC were quality controlled using CRMs obtained from Andrew Dickson at UCSD Scripps Institute of Oceanography. The internal consistency was first evaluated among DIC, A_T, and pH using the Excel version of CO2SYS (Pierrot et al., 2006). Then we conducted temperature correction for the measured pH values to the *in situ* conditions using the same Excel version of CO2SYS the guidelines for input (analysis) and output (*in situ*) temperature, a total pH scale (mol/kg-SW), K_1 and K_2 constants (Mehrbach et al., 1973) with refits (Dickson and Millero, 1987), and the acidity constant of $KHSO_4$ in seawater (Dickson, 1990). These discrete samples were compared to the glider deep ISFET pH measurements. Discrete pH and A_T measurements collected during this work are available below and in the **Supplementary Material**. Final carbonate system parameters on the discrete water samples were calculated using CO2SYS (Pierrot et al., 2006).

RESULTS AND DISCUSSION

Sensor Conditioning Time and Performance

Two processes occur when the Deep-Sea pH sensor is introduced to a new sample of seawater. First, the external electrode equilibrates with the new ionic concentration of the seawater or conditioning. This conditioning can take minutes to days depending on how different the ionic composition of the seawater is from the seawater the pH sensor was calibrated in at Sea-Bird (Pacific seawater collected near Hawaii). Second, the ISFET and counter electrode polarize. This polarization can take minutes to hours to complete. Once the conditioning of the pH sensor is complete, if sensor power is removed or the connection between the ISFET and the counter electrode is broken (e.g., a drying period) the sensor will need to repolarize again. We conducted a series of tests to determine sensor conditioning time initially (**Figure 2A**), and conditioning after variable time periods when the sensor was either turned off and kept wet or removed from tank and kept dry (**Figures 2B–E**). In the initial test, pH determined from the new sensor conditioned and reached within 0.005 pH units from the discrete pH values after 4–5 days of soak time in the natural seawater tank (**Figure 2A** and **Supplementary Material**). This is most likely due to the sensor equilibrating to the new seawater for the first time.

After this initial conditioning time, the pH/CTD sensor was turned off for 2 h while submerged in the tank then turned back on with the pH measurements stabilizing immediately and the offset between glider and discrete pH returning to within 0.003 pH units (**Figure 2B** and **Supplementary Material**). The glider and sensor were then turned off and removed from tank and kept dry for 3 h then placed back in the tank and turned on. The pH measurements stabilized and the offset returned to within 0.002 pH units within 17 h, and this likely occurred much sooner but discrete samples were not collected during the overnight period to confirm (**Figure 2C** and **Supplementary Material**). This conditioning was likely due to either a bubble trapped on the sensor that was cleared shortly after it was turned back on or the sensor repolarizing after being dried. The glider and sensor were then turned off and removed from tank and kept dry for 24 h then placed back in the tank and turned on. The pH sensor conditioned within 17 h, but the pH offset stabilized (±0.003 pH units) between 0.006 and 0.008 pH units for the next few days (**Figure 2D** and **Supplementary Material**). This test was repeated, except the dry period lasted 3 days prior to placing the glider/sensor back in the tank. The pH offsets stabilized (±0.003 pH units) after nearly 3 days, but this final offset between glider and discrete pH measurements was larger (0.012 – 0.015 pH units) (**Figure 2E** and **Supplementary Material**).

It is likely that after the 4–5 days of initial sensor stabilization, the sensor continued to condition or drift but at slower, gradual rate until reaching an average pH offset from discrete samples of 0.013 ± 0.001 after 18 days. This pH offset was similar to that seen *in situ* after initial sensor conditioning during the 3-week May 2018 glider deployment in the Mid-Atlantic Bight (absolute value range: 0.001–0.017; mean ± SD: 0.011 ± 0.005, n = 12). Therefore prior to a glider deployment, we recommend a minimum of 5 days of soak time in natural seawater collected from the field location. Another possibility for the gradual increase in pH offset between the glider and the discrete samples could be biofouling in the tank. The tank was filled with coarsely filtered, unsterilized natural seawater and kept at room temperature (not temperature-controlled). Although it was not visibly apparent, it is possible that a biofilm layer could have developed during the 18-day trial and contributed to or primarily caused the gradual sensor drift.

Nonetheless, an accuracy of 0.013 pH units achieved in the tank test (and 0.011 pH units in the field; see below) exceeded our expectations given the current specifications for this deep ISFET-based pH sensor are ±0.05 pH units in accuracy and ±0.001 pH units in precision.

In situ Glider and Discrete Sample pH and A_T Comparisons

On the first deployment (May 2018), absolute pH differences observed between glider pH and pH measured spectrophotometrically from discrete samples were quite variable, ranging from 0.001 to 0.032 pH units (**Table 1**). Discrepancies in the surface water at deployment were largest (mean ± SD: 0.031 ± 0.001, n = 3) compared to surface water at recovery and subsurface water at both deployment and recovery (absolute value range: 0.001–0.017; mean ± SD: 0.011 ± 0.005, n = 12). We attribute the large pH discrepancies in the surface at the start of the deployment and water sample collection to the sensor not yet being stabilized or conditioned after being out of the tank for 4–5 h during transit from the lab to the field. Offsets observed in surface water at recovery and subsurface water at both deployment and recovery might represent the logistical challenges faced when attempting to collect discrete water samples next to the glider, resulting in either salinity inputs, depth, and/or sampling time differences between glider pH measurement and pH in discrete seawater samples.

The Niskin sampling bottle used for seawater collection did not have a CTD attached which posed two challenges. First, to calculate pH using the spectrophotometric method, temperature and salinity data at target depths from the initial CTD cast conducted prior to Niskin water bottle sampling commenced were used as inputs to calculate pH. Therefore, potential salinity (and pH) changes at target depths between the CTD cast and water sampling (0.5 – 1.5 h) could have occurred due to boat drift and/or currents. Second, cable metered markings were relied upon to reach target depths, and currents or slack on the cable could have resulted in sampling at depths above the target causing mismatch between glider pH and spec pH measurements. This is supported also by high variability observed in discrete pH between replicate Niskin casts/bottle samples at certain depths (May 2, 15 m: discrepancy of 0.014 pH units; **Table 1**). Improvements in sampling techniques are now being employed. For example, upon deployment on July 2, surface seawater samples were collected using a Niskin water bottle deployed adjacent to the glider just after its deployment from the vessel (within a 5 m distance from the glider pH sensor), which greatly reduced the discrepancies between glider pH and discrete pH seen in the first deployment (range: 0.001–0.004 pH units; **Table 2**). Further improvements in water sampling technique could be made, specifically for subsurface seawater pH comparison, by using a CTD mounted on a rosette frame with multiple Niskin bottles to ensure sampling occurs at target depth and simultaneous measurements of salinity and temperature with each depth-specific sample collection.

The greatest challenge with *in situ* sensor validation was obtaining subsurface water samples next to the glider. During the time water sampling was being conducted on board (1–2 h), the pH glider conducted repetitive dives to sample the full water column near the vessel. While water sampling was conducted in proximity to the glider (within ∼100 m), it could have occurred far enough away that different patches were sampled by the two methods creating the offset in pH measurements. Simply, the two different sampling techniques were not measuring pH (glider) or collecting seawater for pH measurements (Niskin/discrete) at the same depths at the same place and at the same time. Future missions should test different sampling techniques (e.g., attaching glider to CTD rosette) to improve subsurface sensor validation that will minimize discrepancies at depth.

During multiple deployment and recovery practices in the U.S NES, glider salinity-based estimations of A_T were consistently lower than A_T measured in discrete samples (**Tables 1–3**). Overall, the differences in water column showed similar ranges of −11.2 to −30.5μmol kg^{-1} for the spring deployment and recovery (**Table 1**) and of −7.3 to −41.8μmol kg^{-1} and −6.0 to −34.8μmol kg^{-1} for summer deployments and recoveries (**Tables 2**, **3**), with averages of −18.5±7.5, −22.9±11.1, and −26.5±10.9 μmol kg^{-1}, respectively. The discrepancies between glider salinity-based estimates and discrete A_T likely reflect differences in water properties and/or water masses measured

TABLE 2 | Comparisons between glider pH and derived total alkalinity (A_T) and discrete pH and A_T measured from seawater samples during the summer glider deployment (July/August 2018).

Date	Depth (m)	Glider pH	Discrete pH	pH Difference	Glider A_T (Glider – Discrete)	Discrete A_T	A_T Difference (Glider – Discrete)
July 5	0.5	8.043	8.042	0.001	2270.8	2278.1	−7.3
July 5	0.5	8.043	8.039	0.004	2270.8	2279.3	−8.5
August 28	0.5	7.716	7.934	−0.218	2100.1	2120.2	−20.1
August 28	0.5	7.716	7.965	−0.249	2100.1	2119.6	−19.5
August 28	0.5	7.716	7.936	−0.220	2100.1	2119.8	−19.7
August 28	8.5	7.705	7.858	−0.153	2099.5	2128.5	−29.0
August 28	8.5	7.705	7.885	−0.180	2099.5	2112.2	−12.7
August 28	8.5	7.705	7.850	−0.145	2099.5	2125.0	−25.5
August 28	18	7.766	7.752	0.014	2108.2	2140.4	−32.2
August 28	15	7.766	7.732	0.034	2108.2	2143.5	−35.3
August 28	16	7.766	7.682	0.084	2108.2	2150.0	−41.8

At glider deployment (July 5) and recovery (August 28), water samples were collected from various depths using a 5 L Niskin bottle, preserved, and returned to the laboratory for determination of pH, A_T, and Dissolved Inorganic Carbon (DIC). During this 1–2 h water sampling procedure, the glider sampled the water column in proximity to the vessel. Values displayed here are replicate discrete pH measurements (corrected for in situ temperature and salinity) and glider pH measurements averaged at each sample depth (±0.5 m) over the sampling period. Additionally, glider A_T (μmol kg^{-1}) was calculated using a linear regression determined from the salinity-A_T relationship at three cross-shelf transects along the U.S Northeast Shelf (Massachusetts, New Jersey, and Delaware) sampled during the ECOA-1 cruise (summer 2015).

TABLE 3 | Biofouling impacts on glider pH measurements.

Depth (m)	Glider pH pre-clean	Glider pH post-clean	Discrete pH	pH Difference pre-clean (Glider – Discrete)	pH Difference post-clean (Glider – Discrete)	Glider A_T pre-clean	Glider A_T post-clean	Discrete A_T	A_T Difference pre-clean (Glider – Discrete)	A_T Difference post-clean (Glider – Discrete)
1	7.966	7.969	8.000	−0.034	−0.031	2171.4	2145.6	2178.3	−6.9	−32.7
8	7.952	7.984	8.033	−0.081	−0.049	2180.6	2177.7	2183.7	−3.1	−6.0
20	8.070	7.957	8.091	−0.021	−0.134	2154.6	2174.3	2199.2	−44.6	−24.9
30	8.016	7.902	7.872	0.144	0.030	2180.8	2179.8	2214.6	−33.8	−34.8
35	7.997	7.929	7.917	0.080	0.012	2187.0	2187.1	2213.5	−26.5	−26.4
55	7.926	7.848	7.893	0.033	−0.045	2193.5	2194.4	2228.6	−35.1	−34.2

During deployment in July 2018, the pH glider experienced moderate biofouling. On July 31, the glider was intercepted off of Long Island, NY, United States. Upon glider retrieval, seawater samples were collected at various depths and preserved for later analysis for comparison of glider and discrete pH and total alkalinity (A_T) measurements. An attempt was made to clean the glider and pH/CTD sensor unit before the glider was re-deployed. The data shown here are comparisons between glider pH and derived total alkalinity (A_T), just before (pre-clean) and after (post-clean) attempted cleaning of biofouling, and discrete pH and A_T measured from seawater samples. Glider pH measurements were averaged at each sample depth (±0.5 m) over the sampling period. Glider A_T (μmol kg^{-1}) was calculated using a linear regression determined from the salinity-A_T relationship at three cross-shelf transects along the U.S Northeast Shelf (Massachusetts, New Jersey, and Delaware) sampled during the ECOA-1 cruise (summer 2015).

during these glider deployments and the summer 2015 ECOA-1 cruise (where/when the salinity-A_T relationship was derived). These include seasonal differences in low-salinity end-member and nearshore organic alkalinity input, and ultimately, challenges for sampling and validation in this dynamic environment. The offsets between glider-derived and discrete A_T yielded lower glider-estimated Ω_{Arag}, offset from discrete Ω_{Arag} by −0.010 to −0.025 for surface waters during the Spring deployment (see **Supplementary Material**). Further work is needed for better evaluation of the relationship between A_T and salinity at nearshore lower salinity waters and different water masses in order to reduce the uncertainty that is propogated in the calculations of Ω_{Arag} using CO2SYS.

Sensor Time Lags

Two patterns emerged from the pH sensor time lag correction analyses. First, there was a change in time lag throughout the deployment in May 2018 (47 s during first week, 30 s for last 2 weeks) (**Figures 5C,D**). This may indicate a pH sensor conditioning period, wherein the sensor was acclimating to new seawater conditions. Second, the time shift had the greatest effect in areas of abrupt water type transition, specifically in the thermocline and halocline and offshore where we encountered a warmer, saltier water mass (**Figure 5B**). The glider moved rapidly (10–15 cm s^{-1}) through these vertically narrow transition zones without acclimating completely, which possibly increased pH sensor response time and caused the increased time lag observed at these depths. This could be due to either a lag in the thermal equilibration of the sensor or salinity response of the reference electrode or relatively slow flushing of the cell by the CTD pump. Further investigations on sensor conditioning, response time, and variability are recommended in order to improve this initial lag correction method. Additionally, modifications in CTD pump flow rate or glider dive approaches in highly stratified periods in coastal systems, including slower dives or step-wise vertical descents/ascents, should be considered.

Carbonate Chemistry Dynamics in the Mid-Atlantic Bight

The pH and Ω_{Arag} ranges observed during this Spring (May 2018) deployment were 7.906–8.205 and 1.48–2.22 respectively. pH was frequently observed highest in subsurface waters and was associated with the depth of chlorophyll and oxygen maximums (**Figure 6**). Higher pH values in the chlorophyll maximum throughout the transect ranged between 7.993 and 8.127. During primary production, photosynthesis increases pH due to the uptake of CO_2. So, while the observed association between pH and chlorophyll was not surprising, the ability to resolve the subsurface pH peak from the high-resolution vertical sampling with the glider provides a valuable perspective from which to not only evaluate concurrent vertical distributions of pelagic organisms, but also to put into context past pH monitoring efforts that mostly sample surface waters (Boehme et al., 1998; Wang et al., 2013, 2017; Wanninkhof et al., 2015; Xu et al., 2017). Higher pH in offshore slope waters was also associated with a warmer, saltier water mass and suggests mixing processes could play a major role in driving pH dynamics on the shelf. During the deployment, the glider measured warmer water in the upper mixed layer on its return transect, depicting the strengthening of seasonal summer stratification in the upper mixed-layer due to incident solar radiation. These warm surface waters on the return transect were associated with increased pH values (**Figure 6**). Higher Ω_{Arag} values were consistently observed in surface waters throughout the deployment, and highest values were associated with the warm, salty, higher alkaline water mass (**Figure 6**).

The lowest pH typically occurred in bottom waters of the middle shelf and slope and nearshore following a period of heavy precipitation (**Figure 6**). Lower pH values in the mid-shelf and slope bottom waters ranged between 7.918 and 8.027. Lower pH in mid-shelf bottom water occurred in the Cold Pool as defined by remnant winter water in the Mid-Atlantic Bight centered between the 40 and 70 m isobaths (Lentz, 2017). The Cold Pool is fed by Labrador Sea slope water and is isolated when vernal warming of the surface water sets up the seasonal thermocline. The annual formation of Cold Pool water means its carbonate chemistry should reflect near real-time increases in atmospheric CO_2 and pCO_2 in its Labrador source water which is weakly buffered and exhibits lower pH and Ω_{Arag} (Wanninkhof et al., 2015). Thus, the dominant drivers of low pH, as well as high DIC and low Ω_{Arag} (Wang et al., 2013), in shelf bottom water were likely a combination of stratification, biological activity (i.e., higher respiration at depth), and the inflow of Labrador Sea slope water into the Cold Pool. Nearshore, lower pH was associated with lower salinity from freshwater input that was most substantial during a high period of precipitation near the end of the deployment, whereby 4.45 inches of rainfall was recorded at Atlantic City Marina, NJ, between May 12–22 (NJ Weather & Climate Network[1]; **Figure 6**). This storm event resulted in the freshening of the entire water column near shore (30 m; **Figure 6**). River runoff has low pH from the equilibration with atmospheric CO_2 concentrations, and its zero salinity and low/zero alkalinity greatly reduces buffering capacity to offset changes in pCO_2 and contributes to low Ω_{Arag} (Salisbury et al., 2008; Johnson et al., 2013). Lowest Ω_{Arag} values consistently occurred in bottom waters on the shelf (**Figure 6**). This was likely driven by lower pH in these bottom waters.

When pH is plotted as a function of temperature and salinity (**Figure 7**), the pH characteristics of specific water masses become more apparent. For example, the fresher nearshore surface waters and surface water over the mid-shelf are distinctively different in pH (**Figure 7**). Thus, carbonate chemistry variability in this system over a range of scales will be driven by: (1) episodic storm mixing, upwelling, and precipitation events; (2) Mixing of water masses and the degree of horizontal intrusion of offshore water masses onto the shelf; (3) Seasonal stratification and vertical mixing/overturning processes; and (4) a combination of biological and physical drivers on the shelf and in shelf source waters. Both the horizontal and vertical gradients of pH observed were, at times, particularly sharp, and this new glider pH sensor suite demonstrated the ability to characterize the variability and drivers of this variability in these critical zones.

Current Limitations and Need for Future Research and Development

Comparative results between the glider deep ISFET-based pH sensor and pH measured spectrophotometrically from discrete seawater samples indicate that the glider pH sensor is capable of accuracy of 0.011 pH units or better for several weeks throughout the water column in the coastal ocean, with a precision of 0.005 pH units or better. These values are similar to those reported for the Deep-Sea DuraFET sensor deployed on moorings in Johnson et al. (2016).

However, in addition to the logistical issues related to sampling seawater next to the glider for *in situ* validation described above, the primary limitation we encountered and foresee is glider and sensor biofouling during deployments. Glider batteries have been evolving over time, from alkaline to lithium one-time use to rechargeable lithiums that have greatly improved the endurance capability of gliders and glider sensors. But as the potential deployment time for gliders has increased, the chance of biofouling is increased. Biofouling can impact glider flight behavior (e.g., increased drag and reduced efficiency; Rudnick, 2016) and greatly reduce sensor performance, as was observed in the SeaFET on week to month timescales (Bresnahan et al., 2014).

During our July deployment, we experienced moderate biofouling after about 3 weeks (**Figure 4**), which degraded the pH measurements over deployment time (**Tables 2**, **3**). This suggests that, at a minimum, the sensor unit was impacted, yielding unreliable pH voltage data and subsequent calculations of pH. This biofouling was likely intensified when the glider was entrained in a warm core ring for a 4–5 days period. After this event, the glider was intercepted south of Montauk, NY, United States. Seawater samples collected near the glider showed

[1]https://www.njweather.org/data/daily/272

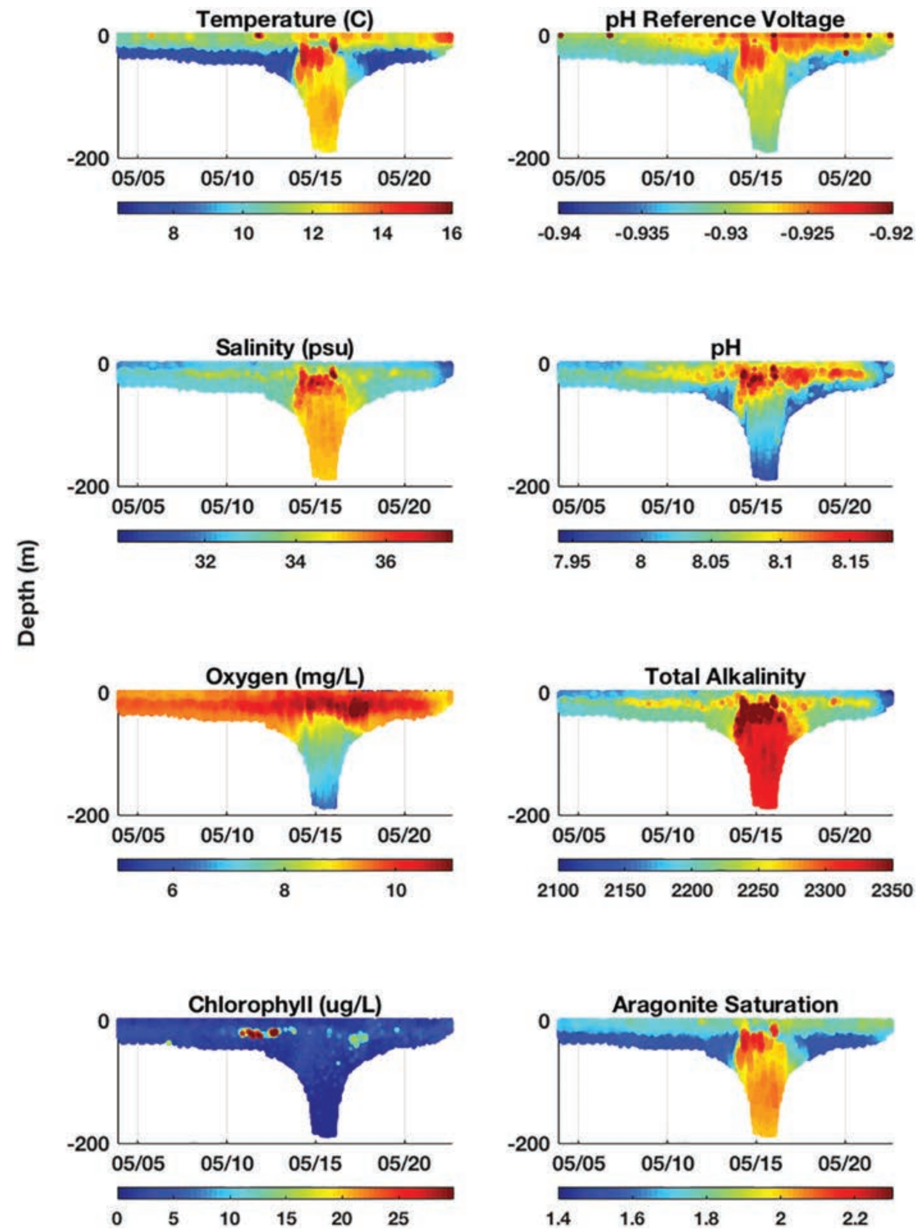

FIGURE 6 | Complete cross-sections of variables measured by the glider and calculated from glider measurements during deployment in May 2018. The glider's on-board scientific instruments measure temperature, conductivity (used to calculate salinity), dissolved oxygen concentration, chlorophyll fluorescence, and pH reference voltage (used to calculate pH). Salinity was used to estimate total alkalinity (TA) throughout deployment (see Methods). TA and pH were used as inputs into CO2SYS to resolve all carbonate system parameters, including aragonite saturation state, shown here.

the pH offsets between the glider and discrete samples were much higher compared to those at deployment (**Tables 2**, **3**). Offsets between glider and discrete pH ranged from −0.144 to 0.081 pH units (**Table 3**). We made an attempt to clean the glider and sensor by flushing the sensor with seawater and using brushes of various sizes on the outer structures of the glider and sensor unit, but biofouling in the internal structure of the pH sensor unit that we could not access was still evident. Nonetheless the glider was redeployed after this cleaning process. The offsets between glider and discrete pH, ranging from −0.03 to 0.134 pH units, remained unsatisfactory (**Table 3**). These offsets worsened rapidly over time, and when the glider was recovered on August 28, offsets in pH measurements ranged from −0.084 to 0.249 pH units (**Table 2**). The magnitude and the variability of the offsets resulting from heavy biofouling yielded pH data not acceptable for OA research. The biofouling impact seems specific to the pH sensor and not the CTD, specifically the conductivity sensor. Comparisons of salinity between the glider CTD profiles and the hand-lowered SeaBird-19 CTD conducted at each glider deployment and recovery passed the *in situ* verification process.

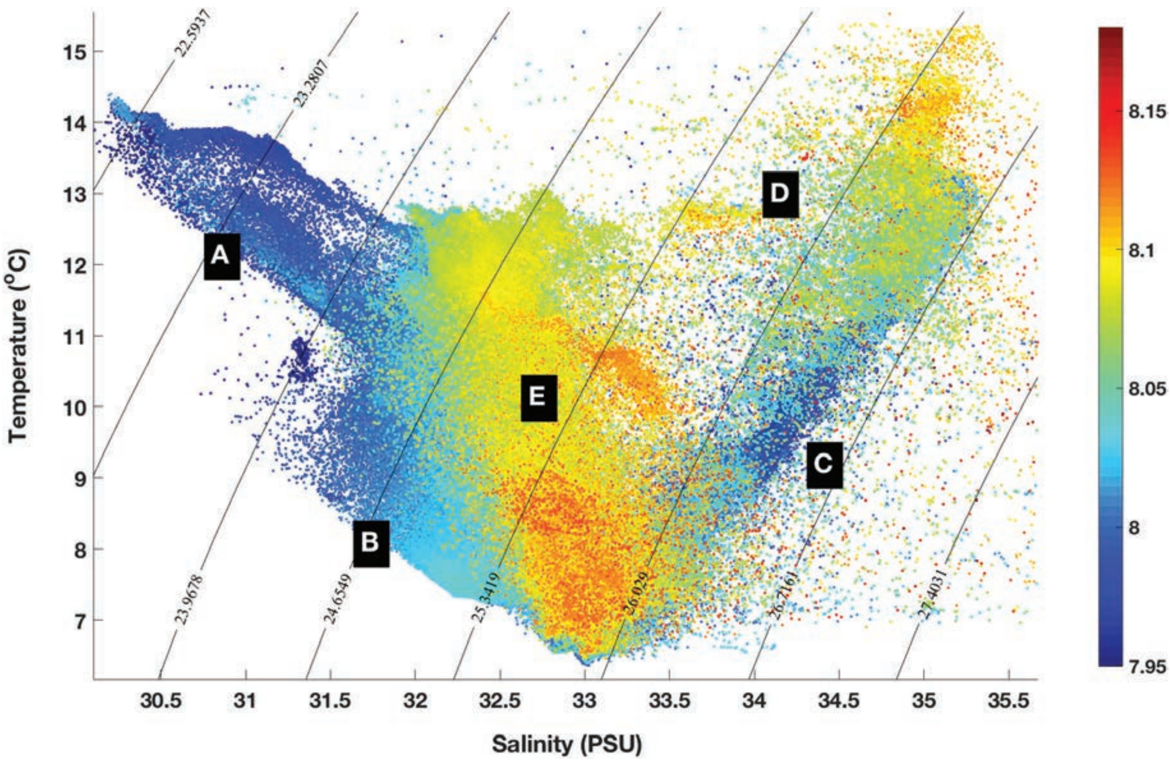

FIGURE 7 | Temperature/Salinity plot of pH. During the May 2018 deployment, lower pH water was found in fresher nearshore surface waters **(A)** and bottom waters of the colder mid-shelf **(B)** and shelf break **(C)**. Higher and more variable pH was found in surface water of the shelf break **(D)** and mid-shelf **(E)**.

Furthermore, the offsets between glider derived salinity-based calculations of A_T and discrete A_T on July 31 (when the glider was intercepted and re-deployed; 24.8 ± 14.3, $n = 20$) and August 28 (when the glider was recovered; 26.2 ± 9.2, $n = 9$) were similar to those from the May deployment (18.5 ± 7.5, $n = 15$). It is likely that biofouling impacted pH sensor response time, as indicated by the increasing sensor time lag corrections that were applied to the glider data from the start of the deployment on July 5 to recovery on August 28 (46–81–104 s).

Current biofouling prevention measures for this sensor are the enclosure of the coupled pH/CTD sensor to block light, an anti-fouling cartridge in the pH sensor's intake, and the active seawater pumping capability of the CTD that flushes water through the sensor package continuously during deployment. However, advances to improve anti-fouling mechanisms would greatly improve sensor performance, durability, endurance, and applicability. Approaches could include installation of an additional anti-fouling cartridge in the sensor intake and turning the glider CTD pump off at regular intervals during deployment to facilitate diffusion, concentration, and exposure of the anti-fouling agent into the water chamber surrounding the pH sensor. Furthermore, to enable sustained glider-based acidification monitoring in a coastal system, especially in warm and shallow conditions, researchers will require the ability to routinely clean and/or swap out sensors to prevent data degradation over time from biofouling.

Additionally, investigation of the mechanism that impacts pH measurements (i.e., affects on sensor response time or reference voltage readings) needs to be conducted. Finally, the current salinity-A_T relationship in the U.S. NES is only based on summer data. This relationship may be subject to change with time, particularly during other seasons, and under different conditionsthat impact freshwater influx and/or the presence of distinctive water masses in this dynamic coastal region. We recommend to determine a salinity-A_T relationship in collected water samples before and after the glider survey in order to use the salinity-based A_T together with the glider pH to reduce the uncertainty of estimating Ω_{Arag}.

SIGNIFICANCE

This new glider pH sensor suite has demonstrated its potential to: (1) Provide high resolution measurements of pH in a coastal region; (2) Determine natural variability that will provide a framework to better study organism response and design more realistic experiments; and (3) Identify and monitor high-risk areas that are more prone to periods of reduced pH and/or high pH variability to enable better management of essential habitats in future, more acidic oceans. The first glider deployment reported here provided data in habitats of commercially important fisheries in the U.S. Northeast Shelf, and allowed for the examination of temporal and spatial pH variability, the identification of areas and periods of lower pH water, better understanding of how mixing events and circulation impact pH across the shelf, and the creation of a baseline to track changes over time during future, scheduled deployments. Furthermore, the integration of simultaneous measurements from multiple sensors on the glider provides the ability to not only distinguish interactions between the physics, chemistry, and biology of the ecosystem, but also to conduct salinity- and temperature-based estimates of A_T in order to derive Ω_{Arag}. As such, if made commercially available, this sensor suite could undoubtedly be integrated in the planned national glider network (Baltes et al., 2014; Schofield et al., 2015; Rudnick, 2016) to provide the foundation of what could become a national coastal OA monitoring network serving a wide range of users including academic and government scientists, monitoring programs including those conducted by OOI, IOOS, NOAA and EPA, water quality managers, and commercial fishing companies. Finally, data resulting from this project and future applications can help build and improve biogeochemical and ecosystem models. A range of data validated and data assimilative modeling systems has matured rapidly over the last decade in the ocean science community. Many of these systems are being configured to assimilate glider data (temperature and salinity) (i.e., ROMs). The technology produced from this project will contribute to efforts to develop coastal forecast models with the capability to predict the variability and trajectory of the low pH water.

AUTHOR CONTRIBUTIONS

GS introduced the research ideas and led the proposal that funded this work. AB and CB developed and finalized the glider deep ISFET-based pH sensor design and provided technical support for the duration of this project. CJ worked with AB and CB on the deep ISFET-based pH sensor integration into the glider to ensure seamless hardware and software compatibility. EW-F and TM led glider data analysis efforts and figure production. BC, W-JC, and KW analyzed all discrete samples for pH, A_T, and DIC. GS wrote the draft. All authors contributed to the writing of the manuscript.

FUNDING

This project was funded by the National Science Foundation's Ocean Technology and Interdisciplinary Coordination Program (NSF OCE1634520). EW-F received support from the Rutgers University Graduate School Excellence Fellowship.

ACKNOWLEDGMENTS

We thank the Rutgers University Center for Ocean Observing Leadership (RU COOL) glider technicians David Aragon, Nicole Waite, and Chip Haldeman for glider preparation, deployment planning, and piloting glider missions. We also thank Rutgers undergraduate students Brandon Grosso and Laura Wiltsee for glider-based laboratory and field support, and RU COOL faculty Oscar Schofield, Josh Kohut, Scott Glenn, and Michael Crowley for facility support. We acknowledge Dave Murphy, Cristina Orrico, Vlad Simontov, and Dave Walter at Sea-Bird Scientific and Christopher DeCollibus, Clara Hulburt, and staff at Teledyne Webb Research for technical assistance. This original work was presented in October 2018 at the OCEANS'18 MTS/IEEE meeting in Charleston, SC, United States and in May 2019 at the 8th EGO meeting and International Glider Workshop in New Brunswick, NJ, United States.

SUPPLEMENTARY MATERIAL

The Supplementary Material for this article can be found online at: https://www.frontiersin.org/articles/10.3389/fmars.2019.00664/full#supplementary-material

REFERENCES

Baltes, B., Rudnick, D., Crowley, M., Schofield, O., Lee, C., Barth, J., et al. (2014). *Toward A U.S. IOOS Underwater Glider Network Plan: Part of a Comprehensive Subsurface Observing System*. Silver Spring, MD: NOAA.

Boehme, S. E., Sabine, C. L., and Reimers, C. E. (1998). CO2 fluxes from a coastal transect: a time series approach. *Mar. Chem.* 63, 49–67. doi: 10.1016/s0304-4203(98)00050-4

Bresnahan, P., Martz, T. R., Takeshita, Y., Johnson, K. S., and LaShomb, M. (2014). Best practices for autonomous measurement of seawater PH with the honeywell durafet. *Methods Oceanogr.* 9, 44–60. doi: 10.1016/j.mio.2014.08.003

Byrne, R. H., Mecking, S., Feely, R. A., and Liu, X. (2010). Direct observations of basin-wide acidification of the North Pacific Ocean. *Geophys. Res. Lett.* 37:L02601.

Cai, W.-J., Hu, X., Huang, W.-J., Jiang, L.-Q., Wang, Y., Peng, T.-H., et al. (2010). Alkalinity distribution in the western North Atlantic Ocean margins. *J. Geophys. Res.* 115:C08014.

Cai, W.-J., Hu, X., Huang, W.-J., Murrell, M. C., Lehrter, J. C., Lohrenz, S. E., et al. (2011). Acidification of subsurface coastal waters enhanced by eutrophication. *Nat. Geosci.* 4, 766–770. doi: 10.1021/es300626f

Carter, B. R., Radich, J. A., Doyle, H. L., and Dickson, A. G. (2013). An automated system for spectrophotometric seawater pH measurements. *Limnol. Oceanogr. Methods* 11, 16–27. doi: 10.4319/lom.2013.11.16

Chen, B., Cai, W.-J., and Chen, L. (2015). The marine carbonate system of the Arctic Ocean: assessment of internal consistency and sampling considerations, summer 2010. *Mar. Chem.* 176, 174–188. doi: 10.1016/j.marchem.2015.09.007

Clayton, T. D., and Byrne, R. H. (1993). Spectrophotometric seawater pH measurements: total hydrogen ion concentration scale calibration of m-cresol purple and at-sea results. *Deep Sea Res. I* 40, 2115–2129. doi: 10.1016/0967-0637(93)90048-8

Cooley, S. R., Kite-Powell, H. L., and Doney, S. C. (2009). Ocean acidification's potential to alter global marine ecosystem services. *Oceanography* 22, 172–181. doi: 10.5670/oceanog.2009.106

DelValls, T. A., and Dickson, A. G. (1998). The pH of buffers based on 2-amino-2-hydroxymethyl-1,3-propanediol ('tris') in synthetic sea water. *Deep Sea Res. Part I* 45, 1541–1554. doi: 10.1016/s0967-0637(98)00019-3

Dickson, A. G. (1990). Standard potential of the reaction AgCl(s) +0.5H2(g) = Ag(s) + HCl(aq) and the standard acidity constant of the ion HSO4– in synthetic sea water from 273.15 to 318.15 K. *J. Chem. Thermodynam.* 22, 113–127. doi: 10.1016/0021-9614(90)90074-z

Dickson, A. G., and Millero, F. J. (1987). A comparison of the equilibrium constants for the dissociation of carbonic acid in seawater media. *Deep Sea Res. Part A* 34, 1733–1743. doi: 10.1016/0198-0149(87)90021-5

Dickson, A. G., Sabine, C. L., and Christian, J. R. (2007). Guide to best practices for ocean CO2 measurements. *PICES Spec. Publ.* 3:191.

Doney, S. C. (2010). The growing human footprint on coastal and open-ocean biogeochemistry. *Science* 328, 1512–1516. doi: 10.1126/science.1185198

Dore, J. E., Lukas, R., Sadler, D. W., Church, M. J., and Karl, D. M. (2009). Physical and biogeochemical modulation of ocean acidification in the central North Pacific. *Proc. Natl. Acad. Sci. U.S.A.* 106, 12235–12240. doi: 10.1073/pnas.0906044106

Feely, R. A., Alin, S. R., Newton, J., Sabine, C., Warner, M., Devol, A., et al. (2010a). The combined effects of ocean acidification, mixing, and respiration on pH and carbonate saturation in an urbanized estuary. *Estuar. Coast Shelf Sci.* 88, 442–449. doi: 10.1016/j.ecss.2010.05.004

Feely, R. A., Fabry, V. J., Dickson, A. G., Gattuso, J.-P., Bijma, J., Riebesell, U., et al. (2010b). "An international observational network for ocean acidification," in *Proceedings of OceanObs'09: Sustained Ocean Observations and Information for Society*, eds J. Hall, D. E. Harrison, and D. Stammer, (Auckland: ESA Publication).

Feely, R. A., Sabine, C. L., Hernandez-Ayon, J. M., Ianson, D., and Hales, B. (2008). Evidence for upwelling of corrosive 'acidified' water onto the continental shelf. *Science* 320, 1490–1492. doi: 10.1126/science.1155676

Garau, B., Ruiz, S., Zhang, W. G., Pascual, A., Heslop, E., Kerfoot, J., et al. (2011). Thermal lag correction on slocum CTD glider data. *J. Atmos. Ocean. Technol.* 28, 1065–1071. doi: 10.1175/JTECH-D-10-05030.1

Hales, B., Takahashi, T., and Bandstra, L. (2005). Atmospheric CO2 uptake by a coastal upwelling system. *Glob. Biogeochem. Cycles* 19:GB1009.

Hofmann, G. E., Smith, J. E., Johnson, K. S., Send, U., Levin, L. A., Micheli, F., et al. (2011). High-frequency dynamics of ocean pH: a multi-ecosystem comparison. *PLoS One* 6:e28983. doi: 10.1371/journal.pone.0028983

Huang, W.-J., Wang, Y., and Cai, W.-J. (2012). Assessment of sample storage techniques for total alkalinity and dissolved inorganic carbon in seawater. *Limnol. Oceanogr. Methods* 10, 711–717. doi: 10.4319/lom.2012.10.711

Jiang, L.-Q., Cai, W.-J., Wang, Y., Wanninkhof, R., and Lüger, H. (2008). Air-sea CO2 fluxes on the U.S. South Atlantic bight: spatial and seasonal variability. *J. Geophys. Res.* 113:C07019. doi: 10.1029/2007JC004366

Johnson, K. S. (2010). Simultaneous measurements of nitrate, oxygen, and carbon dioxide on oceanographic moorings: observing the redfield ratio in real time. *Limnol. Oceanogr.* 55, 615–627. doi: 10.4319/lo.2010.55.2.0615

Johnson, K. S., Berelson, W. M., Boss, E. S., Chase, Z., Claustre, H., Emerson, S. R., et al. (2009). Observing biogeochemical cycles at global scales with profiling floats and gliders: prospects for a global array. *Oceanography* 22, 216–225. doi: 10.5670/oceanog.2009.81

Johnson, K. S., Jannasch, H. W., Coletti, L. J., Elrod, V. A., Martz, T. R., Takeshita, Y., et al. (2016). Deep-Sea DuraFET: a pressure tolerant pH sensor designed for global sensor networks. *Anal. Chem.* 88, 3249–3256. doi: 10.1021/acs.analchem.5b04653

Johnson, K. S., Plant, J. N., and Maurer, T. L. (2017). *Processing BGC-Argo pH Data at the DAC Level*. Plouzané: Ifremer.

Johnson, Z. I., Wheeler, B. J., Blinebry, S. K., Carlson, C. M., Ward, C. S., and Hunt, D. E. (2013). Dramatic variability of the carbonate system at a temperate coastal ocean site (Beaufort, North Carolina, USA) is regulated by physical and biogeochemical processes on multiple timescales. *PLoS One* 8:e85117. doi: 10.1371/journal.pone.0085117

Khoo, K. H., Ramette, R. W., Culberson, C. H., and Bates, R. G. (1977). Determination of hydrogen ion concentrations in seawater from 5 to 40 degree C: standard potentials at salinities from 20 to 45%. *Anal. Chem.* 49, 29–34. doi: 10.1021/ac50009a016

Kohut, J., Haldeman, C., and Kerfoot, J. (2014). "Monitoring dissolved oxygen in new jersey coastal waters using autonomous gliders," in *Proceedings of the U.S. Environmental Protection Agency*, Washington, DC.

Lee, K., Tong, L. T., Millero, F. J., Sabine, C. L., Dickson, A. G., Goyet, C., et al. (2006). Global relationships of total alkalinity with salinity and temperature in surface waters of the world's oceans. *Geophys. Res. Lett.* 33:L19605.

Lentz, S. J. (2017). Seasonal warming of the middle atlantic bight cold pool. *J. Geophys. Res. Oceans* 122, 941–954. doi: 10.1002/2016jc012201

Liu, X., Patsavas, M. C., and Byrne, R. H. (2011). Purification and characterization of meta-cresol purple for spectrophotometric seawater pH measurements. *Environ. Sci. Technol.* 45, 4862–4868. doi: 10.1021/es200665d

Martz, T., McLaughlin, K., and Weisberg, S. B. (2015). *Best Practices for Autonomous Measurement of Seawater pH With the Honeywell Durafet pH Sensor*. California: California Current Acidification Network (C-CAN).

Martz, T. R., Connery, J. G., and Johnson, K. S. (2010). Testing the honeywell durafet® for seawater pH applications. *Limnol. Oceanogr. Methods* 8, 172–184. doi: 10.4319/lom.2010.8.172

Mehrbach, C., Culberson, C. H., Hawley, J. E., and Pytkowicz, R. M. (1973). Measurement of the apparent dissociation constants of carbonic acid in seawater at atmospheric pressure. *Limnol. Oceanogr.* 18, 897–907. doi: 10.4319/lo.1973.18.6.0897

Millero, F. J. (1983). Influence of pressure on chemical processes in the sea. *Chem. Oceanogr.* 8, 1–88. doi: 10.1016/b978-0-12-588608-6.50007-9

Millero, F. J. (1986). The pH of estuarine waters. *Limnol. Oceanogr.* 31, 839–847. doi: 10.4319/lo.1986.31.4.0839

Pierrot, D. E., Lewis, E., and Wallace, D. W. R. (2006). *MS Excel Program Developed for CO2 System Calculations Oak Ridge National Laboratory, Carbon Dioxide Information Analysis Center*. Oak Ridge: US Department of Energy.

Rudnick, D. L. (2016). Ocean research enabled by underwater gliders. *Ann. Rev. Mar. Sci.* 8, 519–541. doi: 10.1146/annurev-marine-122414-033913

Rudnick, D. T., Davis, R. E., Eriksen, C. C., Fratantoni, D. M., and Perry, M. J. (2004). Underwater gliders for ocean research. *Mar. Technol. Soc. J.* 38, 48–59.

Salisbury, J., Green, M., Hunt, C., and Campbell, J. (2008). Coastal acidification by rivers: a threat to shellfish? *Eos Transl. Am. Geophys. Union* 89, 513–528.

Schofield, O., Jones, C., Kohut, J., Kremer, U., Miles, T., Saba, G., et al. (2015). Developing Coordinated Communities of Autonomous Gliders for Sampling Coastal Ecosystems. *Mar. Tech. Soc. J.* 49, 9–16. doi: 10.4031/mtsj.49.3.16

Schofield, O., Kohut, J., Aragon, D., Creed, L., Graver, J., Haldeman, C., et al. (2007). Slocum gliders: robust and ready. *J. Field Robot.* 24, 1–14.

Seidel, M. P., DeGrandpre, M. D., and Dickson, A. G. (2008). A sensor for in situ indicator-based measurements of seawater pH. *Mar. Chem.* 109, 18–28. doi: 10.1016/j.marchem.2007.11.013

Thomsen, J., Gutowska, M. A., Saphörster, J., Heinemann, A., Trübenbach, K., Fietzke, J., et al. (2010). Calcifying invertebrates succeed in a naturally CO2-rich coastal habitat but are threatened by high levels of future acidification. *Biogeoscience* 7, 3879–3891. doi: 10.5194/bg-7-3879-2010

van Heuven, S., Pierrot, D., Rae, J. W. B., Lewis, E., and Wallace, D. W. R. (2011). *MATLAB Program Developed for CO2 System Calculations. ORNL/CDIAC-105b. Carbon Dioxide Information Analysis Center*. Oak Ridge: U.S. Department of Energy.

Vandemark, D., Salisbury, J. E., Hunt, C. W., Shellito, S. M., Irish, J. D., McGillis, W. R., et al. (2011). Temporal and spatial dynamics of CO2 air-sea flux in the Gulf of Maine. *J. Geophys. Res.* 116:C01012.

Wang, H., Hu, X., Cai, W.-J., and Sterba-Boatwright, B. (2017). Decadal fCO2 trends in global ocean margins and adjacent boundary current-influenced areas. *J. Geophys. Res.* 44, 8962–8970. doi: 10.1002/2017GL074724

Wang, Z. A., Wanninkhof, R., Cai, W.-J., Byrne, R. H., Hu, X., Peng, T.-H., et al. (2013). The marine inorganic carbon system along the Gulf of Mexico and Atlantic coasts of the United States: Insights from a transregional coastal carbon study. *Limnol. Oceanogr.* 58, 325–342. doi: 10.4319/lo.2013.58.1.0325

Wanninkhof, R., Barbero, L., Byrne, R., Cai, W.-J., Huang, W.-J., Zhang, J.-Z., et al. (2015). Ocean acidification along the Gulf Coast and East Coast of the USA. *Cont. Shelf Res.* 98, 54–71. doi: 10.1016/j.csr.2015.02.008

Xu, Y.-Y., Cai, W.-J., Gao, Y., Wanninkhof, R., Salisbury, J., Chen, B., et al. (2017). Short-term variability of aragonite saturation state in the central Mid-Atlantic Bight. *J. Geophys. Res. Oceans* 122, 4274–4290. doi: 10.1002/2017JC012901

Xue, L., Cai, W.-J., Hu, X., Sabine, C., Jones, S., Sutton, A. J., et al. (2016). Sea surface carbon dioxide at the georgia time series site (2006–2007): Air–sea flux and controlling processes. *Prog. Oceanogr.* 140, 14–26. doi: 10.1016/j.pocean.2015.09.008

Yu, P. C., Matson, P. G., Martz, T. R., and Hofmann, G. E. (2011). The ocean acidification seascape and its relationship to the performance of calcifying marine invertebrates: laboratory experiments on the development of urchin larvae framed by environmentally-relevant pCO2/pH. *J. Exp. Mar. Biol. Ecol.* 400, 288–295. doi: 10.1016/j.jembe.2011.02.016

Conflict of Interest: AB and CB were employed by Sea-Bird Scientific/WET Labs. CJ was employed by Teledyne Webb Research.

The remaining authors declare that the research was conducted in the absence of any commercial or financial relationships that could be construed as a potential conflict of interest.

Impact of Glider Data Assimilation on the Global Ocean Forecasting System during the 2018 Hurricane Season

1st Maria Aristizábal Vargas, Travis Miles and Scott Glenn
Center for Ocean Observing Leadership
Department of Marine and Coastal Sciences
Rutgers University
New Brunswick, NJ 08901, USA
aristizabal@marine.rutgers.edu

2th Patrick Hogan
Naval Research Laboratory
Stennis Space Center
MS 39529

3th W. Douglas Wilson
Ocean and Coastal Observing - Virgin Islands
St. Thomas, USVI

4th Roy Watlington
CARICOOS
Lajas, PR 00667

5th Benjamin LaCour
NOAA/IOOS Program
Silver Spring, MD 20910, USA

***Abstract*—Accurate ocean initial conditions are necessary to improve hurricane intensity forecast. We assessed qualitatively the impact of glider data assimilation on the Global Ocean Forecasting System (GOFS 3.1), which provides the initial conditions to the NOAA hurricane forecasting models. For this assessment we used temperature data from two gliders that were within the range of influence of hurricane Michael and Florence. We conclude that the assimilation of glider data in GOFS 3.1 was crucial to improve the pre-storm vertical stratification during Michael. However, the assimilation frequency in the current setup, once a day, was insufficient to capture the rapid cooling of the surface layer. During Florence, GOFS 3.1 did not predict the evolution of the sea surface temperature because the model did not capture the extend of the MAB cold pool.**

***Index Terms*—autonomous underwater glider, GOFS, data assimilation, hurricanes**

I. Introduction

During the last three decades hurricane forecast track errors have been reduced substantially but intensity forecast errors have seen only limited improvement [7]. Operational hurricane forecasting models such as the Hurricane Weather Research and Forecasting model (HWRF) and the Hurricanes in a Multi-scale Ocean-coupled Non- hydrostatic model (HMON) coupled to the Hybrid Coordinate Ocean Model (HYCOM), run by NOAA EMC, require accurate ocean initial conditions in order to better forecast storm intensity [4]. Currently the ocean initial conditions for these models are provided by the Real Time Ocean Forecast System (RTOFS), which in turn is initialized by the Navy's Global Ocean Forecasting System (GOFS 3.1) that implements the 3DVar Navy Coupled Ocean Data Assimilation (NCODA) System. With the purpose of evaluating the initial conditions provided to the NOAA hurricane forecasting models, we conducted a qualitative assessment of the impact of glider data assimilation on the performance of GOFS 3.1. We did our assessment during the 2018 hurricane season for two storms: hurricane Florence and hurricane Michael. we used temperature data from a fleet of sentinel gliders deployed in the North Atlantic.

II. Methods

The glider data was accessed through the Integrated Ocean Observing System (IOOS) glider data assembly center (DAC) (https://data.ioos.us/gliders/erddap), with a total of 62 deployments during the 2018 hurricane season (Jun 1-Nov 30) (Fig. 1). These gliders were deployed collaboratively with gliders supplied by the U.S. Navy, U.S. IOOS, NOAA, NSF, academic institutions, state agencies and private companies. All the glider data reported to the IOOS glider DAC is subsequently sent to the Global Telecommunication System (GTS) where it is accessed by GOFS 3.1 and a number of numerical models for data assimilation purposes.

In this work we show temperature transects from two gliders, Ramses and ng288, that were closest to the track of hurricane Florence and hurricane Michael respectively. We obtained the corresponding along-track temperature glider-transects from the Navy operational ocean model GOFS 3.1 by interpolating the glider position and time onto the model grid and output timestamp. The model output corresponds to the hindcast output from Jan-1 2018 to present (https://tds.hycom.org/thredds/dodsC/GLBv0.08/expt_93.0/ts3z.html).

GOFS 3.1 is a global model based on the Hybrid Coordinate Ocean model (HYCOM). It has 41 vertical levels and a horizontal resolution of 0.08^o from 40^o south to 40^o north of latitude, and 0.04^o for locations poleward of 40^o. The output frequency is 3 hourly. The GOFS 3.1 system implements NCODA [6], a 3DVar data assimilation algorithm that uses satellite altimeter data, satellite and in-situ surface temperature, in-situ vertical temperature and salinity from Argo floats,

978-0-578-57618-3 ©2019 MTS

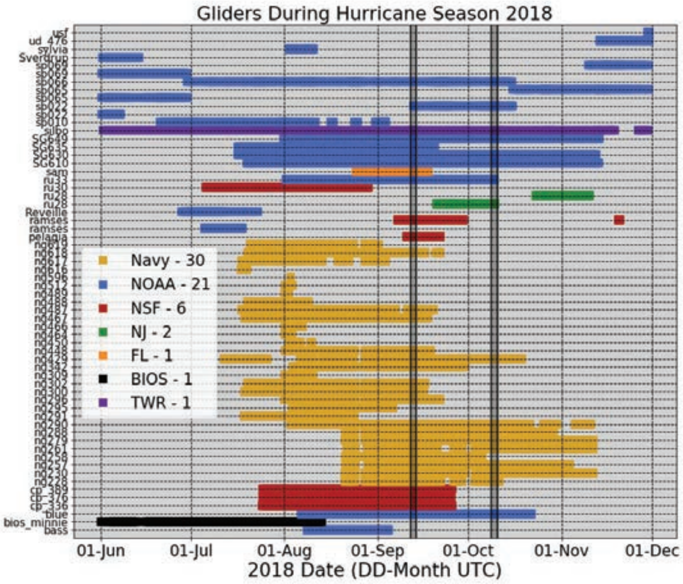

Fig. 1. Deployment period for the gliders reporting to the IOOS glider DAC during the 2018 hurricane season (Jun 1-Nov 30). The different colors indicate the institutions in charge of the deployments: U.S Navy, NOAA, NSF, New Jersey Department of Environmental Protection (NJ), State of Florida in collaboration with Florida Fish and Wildlife Conservation Commission (FL), the Simons Foundation International (BIOS) and Teledyne Web Research Corporation (TWR). In the legend, the number next to the institution is the number of glider deployments by that institution. The two grey vertical bars show the time period for hurricane Florence (Sep 11-Sep 14) and hurricane Michael (Oct 7-Oct 11).

buoys, gliders and XBTs (only temperature). NCODA uses a 24 hours update cycle centered at 12Z. For profile and altimetry data, it currently uses data within the 24 hours window but looks back up to 4 days and 5 days, respectively, due to data latency. The 3DVAR system selects data based on receipt time instead of observation time [2]. In this way all the data received since the previous assimilation cycle is used in the next assimilation cycle. As a consequence, non-synoptic measurements (more than 24 hours apart) are used in an assimilation cycle introducing errors in the analysis. This error is reduced using the First Guess at Appropriate Time (FGAT) technique. FGAT reduces the error by comparing observations against time-dependent background fields. More details about GOFS 3.1/NCODA system can be found in the GOFS 3.1 validation test report [6].

The code used to retrieve the glider data, model output and perform the interpolation between the glider position and time onto the model grid and time step is available at https://github.com/MariaAristizabal/glider_model_comparisons_Python.

III. Results

A. Hurricane Michael

In the Gulf of Mexico during the passage of hurricane Michael there were seven Navy gliders deployed in this region (Fig. 2). The eye of Hurricane Michael passed within 36 km of Navy glider ng288 on Oct 10 at 06:00 UTC. The oceanic response to Michael, a category 5 hurricane at landfall, was characterized by a 30 meter deepening of the surface layer that can be seen in the temperature and salinity profiles (Fig. 3). As the surface layer deepened, there was a cooling of about 0.8 degrees in the top 50 meters of the water column. There were also internal-inertial waves generated at the thermocline depth, defined here as the depth of the 26 degrees isotherm, that can be seen in the ng288 transect after the passage of Michael (Fig. 4 (a), Fig. 6 (b)), which are a typical response of the ocean to hurricane winds [8], [10].

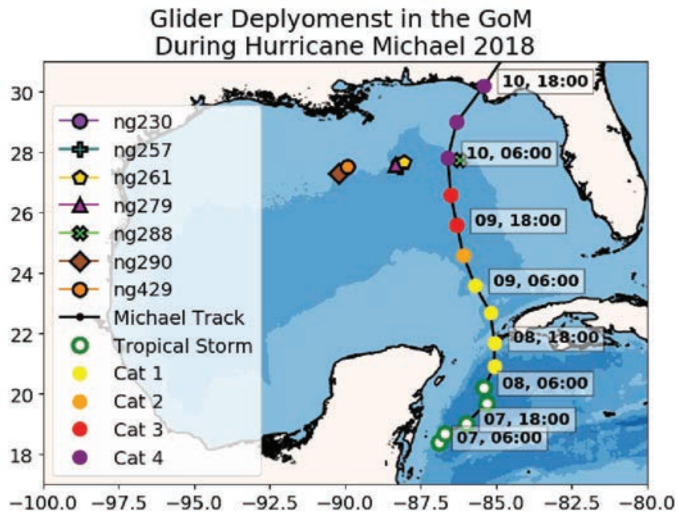

Fig. 2. Mean position of the gliders deployed in the Gulf of Mexico during the passage of hurricane Michael (Oct 7-Oct 10). The black line and colored circles show the trajectory and intensity in the Saffir-Simpson scale of hurricane Michael.

Five days before the eye of Michael passed closest to ng288, the depth of the thermocline estimated by GOFS 3.1 was deepened after every data assimilation cycle in order to match the glider data (Fig. 4 (b)). Two days previous to landfall, the thermocline had reached a stable depth (Fig. 4 (b) and (c)), though it was still a little shallower than the observed depth. As a result, the time series of temperature at 100 m from GOFS 3.1 exhibited positive jumps right after almost every increment insertion window (Fig. 4 (c)) when the NCODA algorithm was attempting to deepen the thermocline.

The spatial distribution of the temperature increments from the NCODA analysis at 100 meters depth on Oct 10 2018 revealed that the largest positive increments happen around the locations of the gliders (Fig. 5) and this is consistent with the positive temperature jumps that the model temperature experienced at 100 m (Fig. 4 (c)).

At the surface two days before landfall, the modeled and observed sea surface temperature (SST) agreed extremely well (Fig. 6 (c)), with both decreasing gradually. As the eye of Michael passed closest to ng288, the observed surface temperature decreased more rapidly. However, the modeled SST increased abruptly after the increment insertion window on Oct 10, driving the SST away from the observed value. We will discuss a possible explanation of why the data

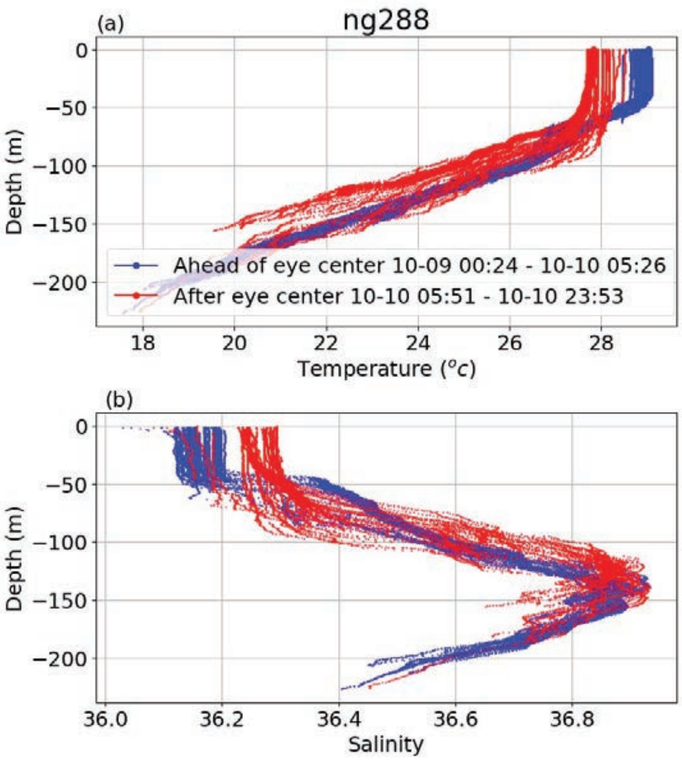

Fig. 3. (a) Temperature and (b) salinity profiles from glider ng288 during hurricane Michael. The blue (red) dots show profiles before (after) the eye of hurricane Michael was closest to glider ng288. The passage times next to the trajectory are in UTC.

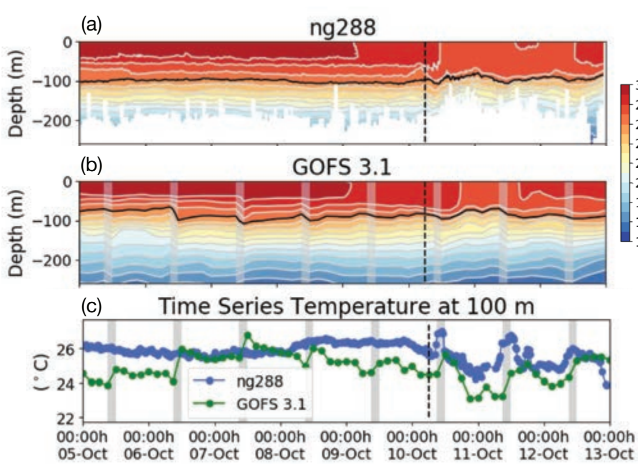

Fig. 4. (a) Temperature transect for ng288 from Oct 5 to Oct 13 2018. (b) The same along-track transect as for ng288 but interpolated onto GOFS 3.1 grid and timestamp. The black contour in (a) and (b) shows the 26 degrees isotherm. (c) Time series of the along-track temperature at 100 meters depth for ng288 and GOFS 3.1. The grey vertical rectangles in (b) and (c) show the increments insertion window (09Z to 12Z). The vertical dashed line in all panels show the time when the eye of hurricane Michael was closest to the ng288 location: Oct 10 06:00 UTC.

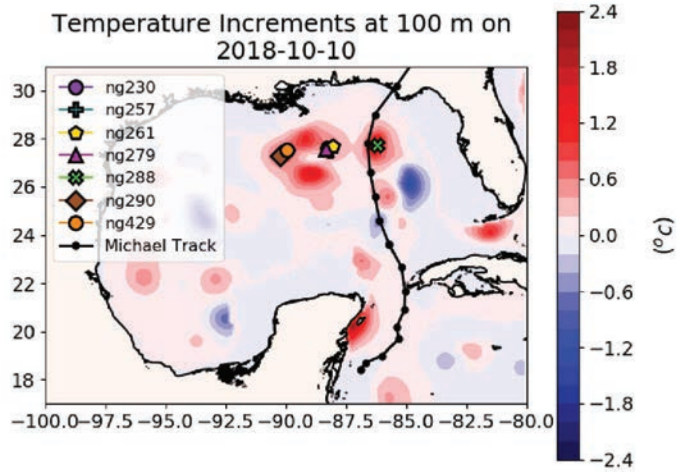

Fig. 5. Temperature increments at 100 meters depth from the GOFS 3.1/NCODA analysis on Oct 10 2018. The color markers show the mean position of the gliders deployed in the Gulf of Mexico during the passage of hurricane Michael (Oct 7-Oct 10) and the black line is the trajectory of hurricane Michael.

assimilation algorithm is failing to bring the model SST closer to observations.

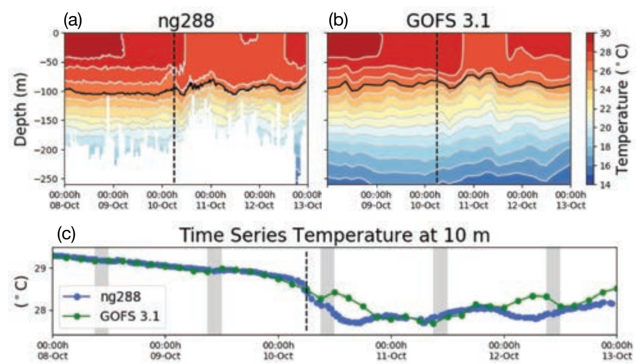

Fig. 6. (a) Temperature transect for ng288 from Oct 8 to Oct 13 2018. (b) The same along-track transect as for ng288 but interpolated onto GOFS 3.1 grid and timestamp. The black contour in (a) and (b) shows the 26 degrees isotherm. (c) Time series of the along-track temperature at 10 meters depth for ng288 and GOFS 3.1. The vertical dashed line in all panels show the time when the eye of hurricane Michael was closest to the ng288 location: Oct 10 06:00 UTC.

B. Hurricane Florence

In the Middle Atlantic Bight (MAB) there were a total of 9 gliders during the passage of hurricane Florence (Sep 11-Sep 15) (Fig. 7). The closest glider to the eye of hurricane Florence was Ramses, located 188 km north from the eye on Sep 14 00:00Z. At this shallow location, the water column mixed completely before and during the passage of Florence with a decrease in SST of 5 degrees (Fig. 8 (a)). This dramatic drop in temperature is comparable with the temperature change during hurricane Irene [3] and it is caused by the intense vertical mixing, either wind-induced or shear-induced, and the presence of the cold pool, a cold bottom layer of water that characterizes the Middle Atlantic Bight at this time of the year [1], [5]. The along-track temperature in GOFS 3.1 (Fig. 8 (b)) shows that the model captures the main features of the cold pool during the first part of the track (Sep 8-Sep 12), such as the bottom to surface temperature difference and the depth of the 26 degrees isotherm. But the model fails to produce the extend of the cold pool around Cape Hatteras, where Ramses was located during the passage of Florence. Instead the model shows a water column that is warm top to bottom. As a result, the model cannot produce the drop in SST because there is not cold bottom water to mix vertically.

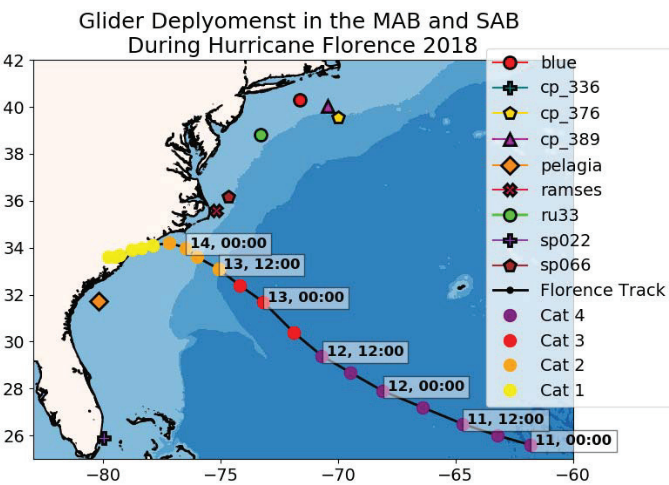

Fig. 7. Mean position of the gliders deployed in the Mid and South Atlantic Bight during the passage of hurricane Florence (Sep 11-Sep 14). The black line and colored circles show the trajectory and intensity in the Saffir-Simpson scale of hurricane Florence. The passage times next to the trajectory are in UTC.

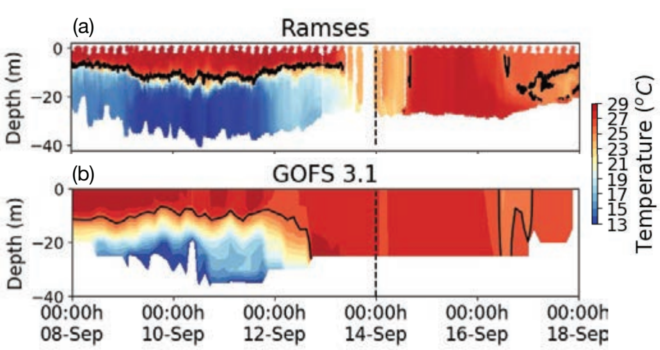

Fig. 8. (a) Temperature transect for Ramses from Sep 8 to Sep 18 2018. (b) The same along-track transect as for Ramses but interpolated onto GOFS 3.1 grid and timestamp. The black contour in both panels shows the 26 degrees isotherm. The vertical dashed line in both panels shows the time when the eye of hurricane Florence was closest to the Ramses location: Sep 14 00:00 UTC.

IV. Discussion and Conclusions

During hurricane Michael, ocean data assimilation in GOFS 3.1 proved to be critical to improve the pre-storm vertical stratification. This is important for hurricane forecasting because the deepening of the thermocline, caused by the storm-induced vertical mixing, and subsequent surface cooling are controlled by the pre-storm vertical stratification. It is crucial to correctly estimate the change in SST under the passage of a storm as this change in temperature controls the direction and magnitude of the heat fluxes [9]. These heat fluxes can significantly contribute to the weakening or strengthening of a storm. This result highlights the importance of deploying a glider fleet ahead of possible storms in order to capture the pre-storm subsurface conditions.

On the other hand, at the surface the data assimilation algorithm degraded the modeled SST by driving the SST away from observations during the period of rapid surface cooling. We think that the reason for this is that GOFS 3.1/NCODA system has a 1-day data assimilation cycle. This means that for the data assimilation cycle centered on Oct 10 12Z, NCODA assimilated data before the start of the rapid cooling and this may have shifted the SST towards warmer values. This suggests that the 1-day data assimilation cycle used by NCODA is not adequate to capture the rapid cooling during a storm.

During hurricane Florence, the closest glider to the eye of the storm shows that there was a cooling of about 5 degrees in the SST before and during the passage of the storm. This cooling happened thanks to the presence of the MAB cold pool and therefore it is an important feature that controls the magnitude of the cooling in this region [3]. GOFS 3.1 did not capture the extend of the cold pool, inhibiting a realistic prediction of the evolution of the SST.

To model the evolution of the SST during a storm is essential for coupled atmosphere-ocean hurricane models, as the heat fluxes are controlled by the SST differences between the upper ocean and the atmosphere. In the open ocean, the cooling is mostly controlled by the wind-induced vertical mixing [9]. In the shelf, there are other processes that can take place like shear-induced vertical mixing at the base of the thermocline driven by a two-layer cross-shelf circulation [3]. In either case, the coupled atmosphere-ocean hurricane models need to capture first the pre-storm vertical stratification as a necessary condition to improve the hurricane forecast intensity.

Acknowledgment

The author Maria Aristizábal Vargas was supported by the Mid Atlantic Regional Association Coastal Ocean Observing (MARACOOS), NOAA award number NA16NOS0120020. We thank to the U.S. Navy, all the institutions and researchers that provided their glider data to the IOOS glider DAC. We also thank John Kerfoot for his technical support to the IOOS glider DAC.

References

[1] Bigelow, Henry Bryant, ”Studies of the waters on the continental shelf, Cape Cod to Chesapeake Bay. I. The cycle of temperature”, Papers in Physical Oceanography and Meteorology, v.2, no.4, 1933. DOI:10.1575/1912/1144, https://hdl.handle.net/1912/1144

[2] Cummings J. A., and Smedstad O. M, ”Ocean data Impacts in global Hycom”, Journal of Atmospheric and Oceanic Technology, Vol 31, 2014. DOI: 10.1175/JTECH-D-14-00011.1
[3] Glenn, S.M., Miles, T.N., Seroka, G.N., Xu, Y., Forney, R.K., Yu, F., Roarty, H., Schofield, O. and Kohut, J., ”Stratified coastal ocean interactions with tropical cyclones”, Nature communications, 7, 2016, p.10887.
[4] Halliwell Jr, G.R., Shay, L.K., Jacob, S.D., Smedstad, O.M. and Uhlhorn, E.W., ”Improving ocean model initialization for coupled tropical cyclone forecast models using GODAE nowcasts”, Monthly Weather Review, 136(7), 2008, pp.2576-2591.
[5] Houghton, R.W., Schlitz, R., Beardsley, R.C., Butman, B. and Chamberlin, J.L., ”The Middle Atlantic Bight cold pool: evolution of the temperature structure during summer 1979”, Journal of Physical Oceanography, 12(10), 1982, pp.1019-1029.
[6] Metzger, E.J, Helber, R.W., Hogan, P.J., Posey, Thoppil, P.G., Townsend, T.L., Wallcraft, A.J., Smedstad, O.M., Franklin, D.S., Zamudio-Lopez, L., Phelps, M.W, ”Global Ocean Forecasting System 3.1, validation test”, Naval Research Laboratoty. 2017, NRL/MR/7320—17-9722.
[7] “National hurricane center forecast verification”. National Hurricane Center and Central Pacific Hurricane Center. 04 April 2017. https://www.nhc.noaa.gov/verification/verify5.shtml
[8] Price, J.F., ”Upper ocean response to a hurricane”, Journal of Physical Oceanography, 11(2), 1981, pp.153-175.
[9] Price, J. F., ”Metrics of hurricane-ocean interaction: vertically-integrated or vertically-averaged ocean temperature?”, Ocean Science, 5(3), 2009, 351-368.
[10] Sanford, T. B., J. F. Price, J. B. Girton, and D. C.Webb, ”Highly resolved observations and simulations of the ocean response to a hurricane”, Geophys. Res. Lett., 34, 2007, L13604, doi:10.1029/2007GL029679.

SCIENTIFIC REPORTS

OPEN

Central place foragers select ocean surface convergent features despite differing foraging strategies

Received: 10 November 2017
Accepted: 9 November 2018
Published online: 17 January 2019

Matthew J. Oliver[1], Josh T. Kohut[2], Kim Bernard[3], William Fraser[4], Peter Winsor[5], Hank Statscewich[5], Erick Fredj[6], Megan Cimino[7], Donna Patterson-Fraser[4] & Filipa Carvalho[8]

Discovering the predictors of foraging locations can be challenging, and is often the critical missing piece for interpreting the ecological significance of observed movement patterns of predators. This is especially true in dynamic coastal marine systems, where planktonic food resources are diffuse and must be either physically or biologically concentrated to support upper trophic levels. In the Western Antarctic Peninsula, recent climate change has created new foraging sympatry between Adélie (*Pygoscelis adeliae*) and gentoo (*P. papua*) penguins in a known biological hotspot near Palmer Deep canyon. We used this recent sympatry as an opportunity to investigate how dynamic local oceanographic features affect aspects of the foraging ecology of these two species. Simulated particle trajectories from measured surface currents were used to investigate the co-occurrence of convergent ocean features and penguin foraging locations. Adélie penguin diving activity was restricted to the upper mixed layer, while gentoo penguins often foraged much deeper than the mixed layer, suggesting that Adélie penguins may be more responsive to dynamic surface convergent features compared to gentoo penguins. We found that, despite large differences in diving and foraging behavior, both shallow-diving Adélie and deeper-diving gentoo penguins strongly selected for surface convergent features. Furthermore, there was no difference in selectivity for shallow- versus deep-diving gentoo penguins. Our results suggest that these two mesopredators are selecting surface convergent features, however, how these surface signals are related to subsurface prey fields is unknown.

Optimal foraging theory suggests central place foragers consider external cues like food quality, distance to food patch, and revisit times to food patches to maximize fitness[1]. The end result of the feedback between prey patch characteristics and the desire and ability of the predator to find food is manifested as random walks[2], Lévy walks[3], or other diffusive[4] or multi-modal movements. Interpreting the ecological significance of these movement modes necessitates an understanding of the dynamic nature of the available environmental cues, the relative response of predators and prey to these cues, and how organisms remember these cues[5]. For example, many organisms appear to exhibit Lévy walks, which are documented to optimize foraging success of random searchers[6]. However, the selective interactions that lead to the emergence of these patterns are often unknown, hence in the absence of an understanding of selective cues between the environment and the focal individual, alternative movement modes may equally explain observed movement patterns[7,8]. Therefore, it is not enough to only establish a movement mode to understand the ecological significance of foraging behaviors or how these behaviors might change in dynamic environmental conditions. Discovering the environmental predictors of foraging locations is equally important, yet can be challenging and is often the critical missing piece for interpreting the ecological significance of observed movement patterns of predators. It is difficult to map environmental cues at the appropriate scale to

[1]University of Delaware, College of Earth, Ocean and Environment, 700 Pilottown Road, Lewes, DE, 19958, USA. [2]Rutgers, The State University of New Jersey, Department of Marine and Coastal Sciences, 71 Dudley Road, New Brunswick, NJ, 08901, USA. [3]Oregon State University, College of Earth, Ocean, and Atmospheric Sciences, 104 CEOAS Admin Bldg, Corvallis, OR, 97330, USA. [4]Polar Oceans Research Group, P.O. Box 368, Sheridan, MT, 59749, USA. [5]University of Alaska, Fairbanks, College of Fisheries and Ocean Sciences, 905 Koyukuk Dr. Suite 245 O'Neill Bldg., Fairbanks, AK, 99775–7220, USA. [6]The Jerusalem College of Technology, Computer Science Department, 21 Havaad Haleumi St., P.O. Box 16031, Jerusalem, 91160, Israel. [7]Scripps Institution of Oceanography, University of California, San Diego, Coastal Observing R&D Center, 9500 Gilman Drive #0214, La Jolla, CA, 92093, USA. [8]National Oceanography Centre, European Way, Southampton, SO14 3ZH, United Kingdom. Correspondence and requests for materials should be addressed to J.T.K. (email: kohut@marine.rutgers.edu)

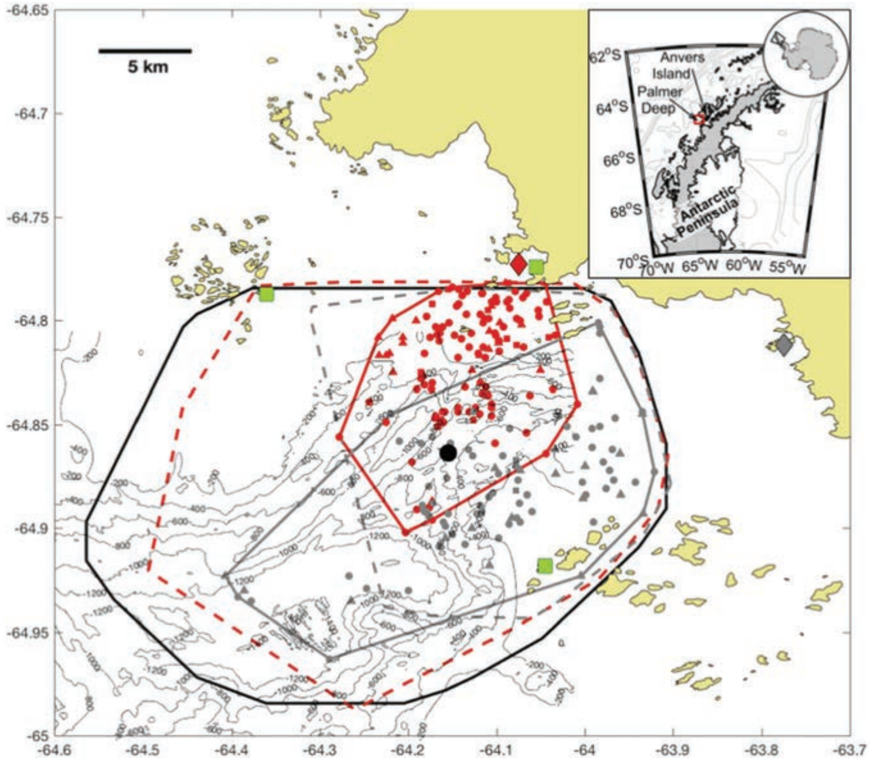

Figure 1. Map of the study site over Palmer Deep. Locations of tagged Adélie (red) and Gentoo Penguin (grey) forage dives (circles), search dives (squares) and transits (triangles) for 2015 study season are shown. The convex spatial hulls are shown for the tagged (thin red) and simulated (red dashed) Adélie and the tagged (thin grey) and simulated (grey dashed) Gentoo Penguins for the 2015 study season. Also shown is the Adélie colony at Torgersen (red diamond) and the gentoo colony at Biscoe Point (grey diamond); the HFR sites (green squares); the HFR data footprint (thin black line); and the glider time series (black circle). The maps were generated by the authors J.K. and H.S. using Matlab version R2016b (www.mathworks.com).

determine if they are being selected[9,10], especially in a fluid marine environment. In the coastal Western Antarctic Peninsula (WAP), the food web is short and characterized by intense phytoplankton blooms that are grazed by Antarctic krill (*Euphausia superba*, referred to hereafter as "krill"), a primary prey source for penguins and other predators. Although krill aggregations occur throughout the WAP[11], their distribution is extremely patchy even on scales less than 1 km[12,13]. Krill have intermediate Reynolds numbers (~10^2–10^3), compared to drifting phytoplankton (~10^{-2}) and swimming penguins (~10^6), which means they can make directed movements, even though they are also heavily influenced by local circulation.

Lagrangian convergent features are representations of time-dependent concentrating ocean dynamics at scales relevant to marine predator foraging ecology. Broadly, they are regions that concentrate neutrally buoyant particles and are often associated with filaments and mesoscale features, such as eddies, jets and fronts. Convergent features, identified by time varying concentrations of buoyant particle densities, may be proxies for the mechanisms by which sparse food resources move through marine trophic levels by collapsing the essential components of the food web in time and space. Realistic particle simulations show that convergent features have much higher concentrations of zooplankton[14]. Seabirds have also been associated with convergent features such as mesoscale eddies[15], and their flight paths are coherent with dynamic convergent features[16]. Macaroni penguins have been shown to associate with convergent features at relatively large scales (10–100 km), presumably because they concentrate prey resources[17]. These studies have focused on relatively large-scale associations using infrequent satellite composites of ocean features. However, convergent features are dynamic in space and time, and therefore should optimally be examined at space and time scales relevant to predator foraging behaviors.

At our study site, Adélie penguin (*Pygoscelis adeliae*) populations have decreased rapidly over the last three decades, while numbers of gentoo penguins (*P. papua*) have increased[18]. These population changes have resulted in relatively recent sympatry between these two congeneric central place foragers in our study site, where they also exhibit partially overlapping foraging ranges over the Palmer Deep canyon (Fig. 1). In this study, we determine if these two species select convergent features in a similar way to guide their foraging behavior. To do this, we used an integrated ocean observatory (Fig. 1) to estimate the relationship between surface convergent features and the foraging behavior of these two mesopredators.

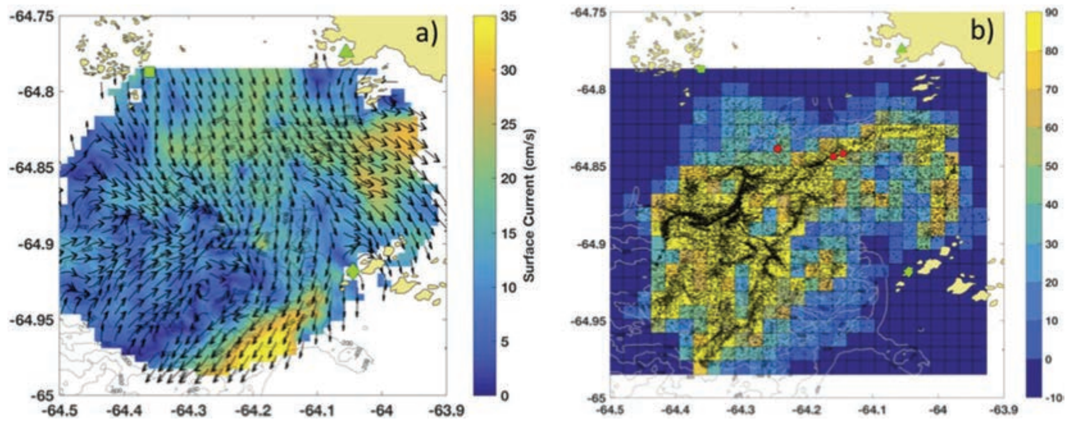

Figure 2. Convergent features near penguin foraging. (**a**) Hourly surface current map, January 27, 08:00 GMT 2015. The HFR sites located at Palmer Station (green triangle) and the Wauwermans (green diamond) and Joubin (green square) island groups are also shown. (**b**) Map showing the distribution of particles on January 27, 08:00 GMT (black dots) overlaid on the particle density metric (number of particles within each 1 × 1 km cell minus the median across all cells). The location of penguins is also shown (red circles). The maps were generated by the corresponding author J.K. using Matlab version R2016b (www.mathworks.com).

Species	Time Window (minutes)	Transiting	Search Diving	Forage Diving
Adélie	1	**0.001 (N = 32)**	**$\ll$0.001 (N = 18)**	**$\ll$0.001 (N = 74)**
	2.5	**$\ll$0.001 (N = 22)**	**0.004 (N = 8)**	**$\ll$0.001 (N = 94)**
	5	**0.004 (N = 16)**	**0.004 (N = 7)**	**$\ll$0.001 (N = 101)**
	15	0.184 (N = 2)	0.307 (N = 4)	**$\ll$0.001 (N = 118)**
Gentoo	1	**0.009 (N = 49)**	0.760 (N = 7)	0.309 (N = 42)
	2.5	0.373 (N = 22)	0.460 (N = 4)	0.063 (N = 72)
	5	0.547 (N = 10)	0.836 (N = 2)	**0.007 (N = 86)**
	15	0.835 (N = 2)	N = 0	**0.009 (N = 94)**

Table 1. The p-value and number of observations for KS tests comparing the field RPD to Adélie and gentoo ARGOS locations classified into transiting, search diving and forage diving behavior. The classifications were based on 1, 2.5, 5, and 15 minute windows before and after the ARGOS hit to classify the location. Bold text indicates that ARGOS locations had higher RPD than the field RPD.

Results

Penguin Locations Relative to Ocean Features. During the austral summer of 2014–2015, we mapped penguin foraging patterns relative to sea surface currents derived each hour from a High Frequency Radar (HFR) network over Palmer Deep canyon (Fig. 2a)[19]. Simulated passive particles released in the hourly surface current maps were used to identify the location and intensity of convergent features that may locally concentrate prey biomass during penguin foraging days. Maps of Relative Particle Densities (RPD) derived from particles released each hour across the HFR footprint were used to estimate the location of convergent features each hour between January 1st and March 1st 2015, where higher RPD values were indicative of convergence (Fig. 2b).

For 11 Adélie and 7 gentoo penguins, there was a total of 124 and 98 ARGOS class 1–3 locations representing 27 and 17 foraging trips, respectively. These locations were spatially matched to hourly RPD (Tables 1 and 2). ARGOS locations were classified as transiting, searching or foraging based on their dive profiles within 1, 2.5, 5, and 15 minutes of the ARGOS location (Tables 1 and 2). Adélie penguin dives associated with ARGOS locations had significantly higher RPD values compared to RPD values across the entire HFR field and significantly higher RPD values compared to the RPD values sampled by simulated Adélie penguins ($p \ll 0.001$ and $p \ll 0.001$, two-sample Kolmogorov-Smirnov tests respectively, Fig. 3a). Gentoo penguin locations had higher RPD values compared to RPD values across the entire HFR field but these were weakly significant ($p = 0.03$, two-sample Kolmogorov-Smirnov tests respectively, Fig. 3b). However, compared to RPD values sampled by simulated gentoo penguins, tagged gentoo penguins showed a significant selection for higher values as well ($p \ll 0.001$, two-sample Kolmogorov-Smirnov tests, Fig. 3b).

Both simulated and tagged penguins covered different areas of the HFR field during our experiment, and therefore experienced different RPD. However, simulated penguins within the convex hull of their tagged counterparts still showed significantly lower RPD values compared to tagged Adélie and gentoo penguins ($p = 0.02$ and $p = 0.0005$, respectively). To test the sensitivity of these results to the effects of individual trips or individual penguins, we resampled these ARGOS locations, systematically leaving out one foraging trip or one penguin (represented by the grey envelope in Fig. 3a,b). In all resampling cases, the Adélie and gentoo ARGOS RPD

Species	Time Window (minutes)	Transiting	Search Diving	Forage Diving
Adélie	1	0.075 (N = 32)	**0.001 (N = 18)**	**≪0.001 (N = 74)**
	2.5	**0.028 (N = 22)**	**0.017 (N = 8)**	**≪0.001 (N = 94)**
	5	0.057 (N = 16)	**0.021 (N = 7)**	**≪0.001 (N = 101)**
	15	0.294 (N = 2)	0.543 (N = 4)	**≪0.001 (N = 118)**
Gentoo	1	**≪0.001 (N = 49)**	0.339 (N = 7)	**0.025 (N = 42)**
	2.5	0.120 (N = 22)	0.189 (N = 4)	**≪0.001 (N = 72)**
	5	0.466 (N = 10)	0.821 (N = 2)	**≪0.001 (N = 86)**
	15	0.874 (N = 2)	N = 0	**≪0.001 (N = 94)**

Table 2. The p-value and number of observations for KS tests comparing the RPD of simulated Adélie or gentoo penguins to Adélie or gentoo ARGOS locations classified into transiting, search diving and forage diving behavior. The classifications were based on 1, 2.5, 5, and 15 minute windows before and after the ARGOS hit to classify the location. Bold text indicates that ARGOS locations had higher RPD than the simulated penguins RPD.

values were significantly higher than both the field and simulated penguin RPD values ($p \ll 0.001$, two-sample Kolmogorov-Smirnov tests). As a result, it is likely that both Adélie and gentoo penguins were systematically selecting for higher RPD.

We partitioned the ARGOS locations by behavior classification within the above mentioned time intervals (Tables 1 and 2). For Adélie penguins, ARGOS locations classified as foraging and search diving behavior occurred in significantly higher RPD compared to both the background RPD and the simulated penguin RPD. The exception was for the search diving behavior classified with a 15 minute time window, likely due to a low sample size ($n = 4$). Adélie penguin ARGOS locations classified as transiting had higher RPD compared to the background RPD, except when using a 15 minute time window due to low sample size ($n = 2$). Furthermore, only RPD for transiting Adélie penguins classified with the 2.5 minute window were significantly higher than the simulated penguins, although it should be noted that for the shorter time window of 1 minute the p-value was 0.075. For the tagged gentoo penguins, only ARGOS locations classified as forage diving had significantly higher RPD compared to the simulated penguin RPD for all time classifications. Search diving behavior had very few samples. The largest sample size for ARGOS locations classified as transiting with a 1 minute time window had significantly higher RPD compared to both background and simulated penguin RPD, while the longer time windows with fewer samples did not have significantly higher RPDs compared to both the background and simulated RPD. Overall, only ARGOS locations classified as forage diving had significantly higher RPD compared to simulated penguin RPD across both species and all time windows (Table 2).

Adélie and gentoo penguins displayed markedly different diving behaviors relative to oceanographic features. Adélie penguins foraged in waters above the mixed layer at depths between 5 and 50 m, where the surface layer is sensitive to atmospheric forcing, while gentoo penguins foraged both above and below the mixed layer, at depths between 5 and 100 m (Fig. 3c,d). The mixed layer depth (MLD), estimated from the maximum buoyancy frequency[20], was ~30 m during the time period that Adélie penguins were tagged and deepened to ~50 m during the period gentoos were tagged, which accords with natural seasonal changes[21]. We partitioned the gentoo data by dive depth relative to MLD. Gentoo penguins diving shallower than the MLD selected for higher RPD values than the simulated gentoo penguins ($p = 0.028$). Gentoo penguins diving deeper than the MLD also selected for higher RPD values compared to the simulated gentoo penguins ($p \ll 0.001$). The distributions of RPD targeted by the shallow and deep diving penguins were not significantly different ($p = 0.1$), indicating that gentoo selectivity of surface RPD was not dependent on penguin foraging depth.

Relative Particle Density Values in Diurnal and Semi-Diurnal Tidal Regimes. Prior work has shown that local tides are coherent with Adélie penguin ARGOS locations over Palmer Deep[22]. The dominant tidal constituent near Palmer Station is the diurnal K_1 followed closely by another diurnal constituent, O_1. The two prominent semi-diurnal constituents, K_2 and M_2, are smaller in magnitude[23]. The interaction of these constituents leads to a unique mixed tide that is slightly diurnal-dominated based on tide gauge data collected at Palmer Station[23]. The result is a tidal forcing and response that transitions from a diurnal to semi-diurnal regime approximately every two weeks. A long-term (2002–2011) record of Adélie penguin foraging distances showed that Adélies foraged at greater distances from shore during semi-diurnal tides, compared to diurnal tides (Fig. 4)[22]. In 2015, Adélie ARGOS locations expanded to the south and east during semi-diurnal tides, while gentoo ARGOS locations translated to the north and west during semi-diurnal tides. During the austral summer of 2014–2015, we mapped the location of strong convergent features based on the hourly RPD maps partitioned by days with semi-diurnal and diurnal tides. The convergent features were defined as grid cells with particle counts, normalized by subtracting the spatial median, greater than 100. The location frequency of these strongest fronts associated with the semi-diurnal and diurnal tidal regimes are shown in Fig. 4. During the semi-diurnal tidal regime, the highest occurrence of convergent features was located offshore over the central canyon (Fig. 4a), consistent with the offshore historic Adélie penguin foraging locations observed during semi-diurnal tides. During the diurnal tidal regime, the location of the highest percentage of convergent features moved south and inshore (Fig. 4b), closer to the penguin colonies. We suggest that the predictability of the locations of convergent features associated

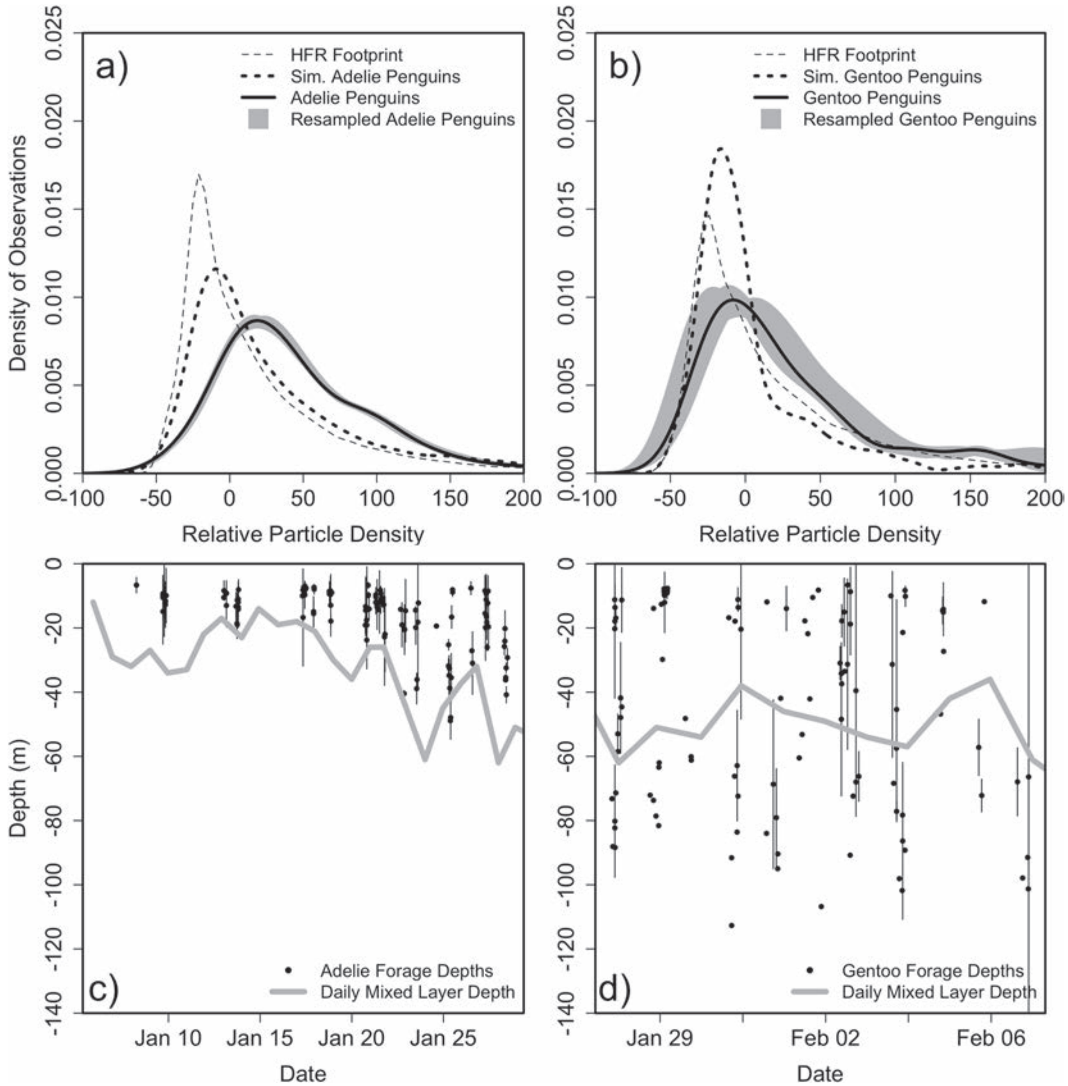

Figure 3. Penguin selectivity relative to convergent ocean features. Distribution of observed field PD values available to the penguins (grey dashed) and distribution of PD values at the tagged (solid black) and simulated (black dashed) penguin dive location for the (**a**) Adélie and (**b**) Gentoo Penguins. The range of solutions with of the resampled penguins by individual and by foraging trip is shown as a gray shade. Foraging dive depths (black dots) with one standard deviation and daily mixed layer depth determined from the station keeping glider (grey line) for the (**c**) Adélie and (**d**) gentoo penguins.

with the changing tidal regimes combined with their selection for these convergent features provides a mechanistic explanation for the variability in historic foraging locations observed in Adélie penguins[22].

Discussion

The outer and mid WAP continental shelf is characterized by irregular, episodic intrusions of Upper Circumpolar Deep Water (UCDW)[24,25] that drive intense phytoplankton blooms that may be advected into coastal regions[26,27]. These blooms are fed on by krill, which show a high degree of interannual variability in their abundance[28,29], both along the shelf and into coastal regions[30–32]. Palmer Deep canyon supports enhanced phytoplankton production[33] and is considered a biological hotspot that is home to Adélie, gentoo and chinstrap penguins[34]. This region is also a common feeding ground for humpback whales (*Megaptera novaeangliae*)[35], indicating that it is a place where upper trophic levels are persistently linked to primary producers through krill and other zooplankton. What is not known are the specific physical mechanisms that concentrate the various levels of the food web at the scales of the individual predators.

Within the Palmer Deep hotspot, a historical analysis (10 years) of Adélie penguin foraging locations demonstrated a correlation to local tidal regimes, indicating that individual penguins may track tidally-driven features, such as convergent zones, associated with the diurnal and semi-diurnal tides[19,22]. Here we show that as the tidal regime shifts from diurnal to semi-diurnal, the spatial patterns in the occurrence of strong convergent features is matched by similar shifts in penguin foraging locations. While penguin foraging locations and the occurrence

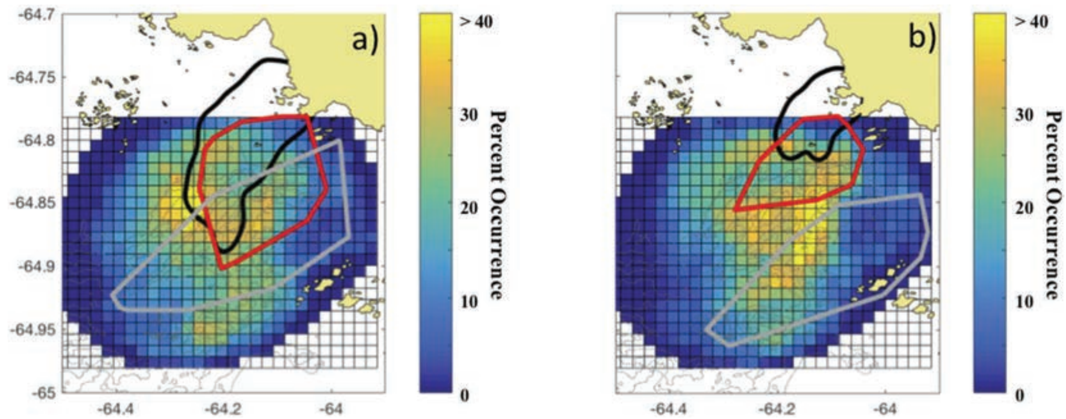

Figure 4. Maps of the percent of occurrence of the convergent features based on RPD (number of particles minus median > 100) observed during (**a**) semi-diurnal and (**b**) diurnal days. The spatial density kernels (black contours) based on 10 years of tagged Adélie data are shown in panel a) for the semi-diurnal days and in panel b) for diurnal days[25]. The convex hulls for the 2015 Adélie (red) and gentoo (grey) ARGOS locations are also shown. In 2015, Adélie penguins also foraged closer to their home colony during diurnal, compared to semi-diurnal tides. The maps were generated by the corresponding author J.K. using Matlab version R2016b (www.mathworks.com).

of convergent features covaried with tidal regime (Fig. 4), we show that both Adélie and gentoo penguins were specifically selecting for stronger surface convergent zones than were available based on simulations, suggesting the importance of these features at the scale of the individual. Despite the different typical dive depths exhibited by these two species, both the shallow-diving Adélie and deeper-diving gentoo penguins selected for surface convergent features (Fig. 3).

Penguins in the Palmer Deep canyon region travel relatively short distances (~8–25 km) during foraging trips compared to penguins breeding in many other locations, where foraging distances may reach up to 100 km[36]. These short foraging distances are also combined with the persistence of foraging locations across both tidal regimes, suggesting that these penguins may not need to use environmental cues to initiate foraging behavior; that is, they are simply returning to the same general location to find prey because the prey field spans the entire area. However, we argue that this is not always the case. Although the prey-scape was not spatially resolved in this study, previous vessel and AUV acoustic surveys in the region report typical krill patch length scales on the order of 40 m[12,37]. These patches are dispersed hundreds of meters apart across the +20 km foraging range of the local Adélie and gentoo colonies[12]. This spacing by itself might suggest that both Adélie and gentoo penguins could return to the same foraging ground and be successful, independent of foraging cues. However, measurements of the residence time of this region indicate that the surface layer is replaced on average every two days, and can be as short as 18 hours[38]. This leads to a very patchy and rapidly evolving prey environment within the penguin foraging range that is simultaneously targeted by other species including whales and seals. Therefore, the rapid replacement of the surface layer may necessitate individual foraging responses triggered by oceanographic conditions at the scale of the individual, along with memory of recent successful foraging trips, or social cues from other foragers[5].

At Palmer Station, Adélie penguins are often relatively shallow divers (<50 m)[39] compared to gentoo penguins that often dive deeper (<100 m)[37,40]. Gentoo penguins are the larger of the two species and consequently have a greater scope for maximum diving depth, even though Adélie penguins are capable of dives to similar depths[41]. During our study, Adélie penguins not only selected for stronger surface convergent features compared to their availability, but their foraging was also limited to the surface mixed layer. In contrast, gentoo penguins foraged both above and below the surface mixed layer, with some dives as deep as 150 m, yet also selected for stronger surface convergent features. We suggest that despite the variable foraging dive depths relative to the mixed layer, both species use surface layer convergent features as foraging cues.

ARGOS locations associated with foraging behavior for both species had consistently higher RPD compared to simulated penguins and background RPD suggesting that convergent features may cue foraging behavior. What is less clear is the impact of higher RPD for transiting Adélie and gentoo penguins. Gentoo penguins showed little selectivity for increased RPD during transiting behavior, with only one exception, suggesting that perhaps gentoo penguins are using past foraging experiences to get to a general foraging region before selecting for higher RPD values at finer spatial scales. Transiting Adélie penguins, however, showed some selectivity for higher RPD compared to background concentrations. As the time window we used to behaviorally classify ARGOS locations widened (Table 1), all but two ARGOS locations were considered to be associated with foraging behavior, suggesting foraging behavior could be interspersed throughout a foraging trip. It has been shown previously that ARGOS locations without diving behavior were strongly coherent with ARGOS locations with diving behavior in this location for Adélie penguins[22].

The link between the occurrence of strong convergent features and the foraging behavior of satellite-tagged penguins raises important questions about the coupling mechanisms operating throughout the entire food web. These convergent features may coincidently concentrate or attract krill in the surface layer, and trigger penguin foraging behavior, irrespective of whether penguins are shallow- or deep-diving. This would be consistent with a penguin that repeatedly dives in the same location once a prey patch is found[5]. Alternatively, there may be different physical mechanisms that concentrate prey above and below the mixed layer. For example, barotropic tides influence the entire water column, while the seasonal surface mixed layer circulation is likely driven by local winds[38] but retains a tidal signal when integrated over the foraging season. Below the mixed layer, circulation is likely driven by the bathymetric steering of density currents along isobaths (i.e. along f/H contours), suggesting the influence of the Palmer Deep canyon. Critically, these depth-dependent features could be co-located with deeper gentoo prey aggregations, thus explaining why deep-diving gentoos appear to be selecting for higher surface convergence, even though they are feeding well below the surface mixed layer. Another speculative possibility that could explain why deep diving penguins selected for higher surface RPD, is that they may select convergent features independently of visual prey detection. Dimethylsulphoniopropionate is released from grazed phytoplankton, which is volatilized in the ocean surface as dimethyl sulphide (DMS)[42], and is not necessarily correlated to surface phytoplankton concentrations[43]. Krill-consuming chinstrap penguins (*P. antarctica*), for example, have been shown to be attracted to DMS[44], and African penguins (*Spheniscus demersus*) have been shown to use DMS as a foraging cue[45]. If surface RPD values are a proxy for higher DMS, this may explain why deep diving gentoo penguins select for higher RPD values.

Given our results, we believe that physical factors like surface convergent features are an important mechanism that influences penguin foraging locations, and are therefore a critical feature influencing the maintenance of the Palmer Deep biological hotspot for penguins. Convergent fronts likely concentrate krill, the primary prey of penguins[46] in this region. This example of tight coupling from the hydrography through the lower trophic levels to foraging penguins shows the important role that these physical features may have on the coastal Antarctic food web. If these features are commonly targeted by predators, they may represent a key physical mechanism that is critical for the persistence of the Palmer Deep biological hotspot over the last 1000 years[34], despite known climate and environmental variability. However, because this study did not simultaneously resolve the distribution of krill and all of their major predators, there is still much work to be done to understand how important prey convergence is relative to other factors affecting prey distributions. Even though both penguin species selected, on average, for higher convergence zones, both also utilized a wide range of particle densities. This suggests to us that there are other important factors, in addition to surface convergence, affecting foraging behavior. One possibility is the top-down impact of other krill predators. For example, Adélie penguins at Cape Crozier in the Ross Sea increased their foraging duration and dove deeper as krill were removed by predation near the colony[47], suggesting a significant top-down control on penguin foraging location. In our study, we also observed a deepening of forage depths by Adélie penguins (Fig. 3c). Because this study did not resolve the distribution of krill, or account for other krill predators like whales, it is difficult for us to tell if prey depletion was an important factor in this study. One important difference between the colonies at Cape Crozier and those at Palmer Deep is that of colony size; the colonies in the Ross Sea that showed the prey depletion effect are two orders of magnitude larger than those near Palmer Deep. Because of this, we speculate that top-down effects like prey depletion play a relatively smaller role in determining foraging location near Palmer Deep. However, the relative importance of bottom up physical concentration factors and top down biological factors on penguin foraging remains an open and important question for understanding how these ecosystems may change in the future.

Materials and Methods

High Frequency Radar (HFR). HFR systems, typically deployed along the coast use Bragg peaks within a transmitted signal (3~30 MHz) scattered off the ocean surface to calculate radial components of the surface velocity at a given location[48]. Individual sites, composed of electronics, cables and a transmit and receive antenna, generate maps of surface component vectors directed toward the antenna with range resolution of 500 m horizontally and 5 degrees in azimuth. To provide sufficient coverage over the penguin foraging grounds associated with Palmer Deep, a three-site HFR network was deployed in November 2014 (Fig. 2). The first site was deployed at and powered by Palmer Station. The other two sites, deployed at the Joubin and Wauwermans Islands, relied on remote power systems that were constructed on site, lightered to shore via zodiac with ship support. Remote Power Modules (RPMs) generated the required power for the HFRs through a combination of small-scale micro wind turbines and a photovoltaic array with a 96-hour battery backup[19]. The RPMs consisted of a single watertight enclosure, used to house power distribution equipment, the HFR, and the communication gear. Built-in redundancies within the RPMs, including wind charging/resistive loads, solar energy, and independent battery banks ensured that, should any one component fail, the unit would be able to adjust autonomously. Each site also collected 15-minute meteorological measurements of air temperature, wind, relative humidity, and solar radiation. Communication between the two remote sites and Palmer Station was with line of sight radio modems (Freewave), which enabled remote site diagnostics and maintenance and provided a real-time data link.

The three-site network collected hourly measurements of ocean surface current component vectors throughout the penguin foraging season (November 2014 through March 2015). Every hour, the radial components from each site were combined into two-dimensional vector maps using the optimal interpolation algorithm of[49]. Throughout the time of active penguin foraging, a roughly 1,500 km2 area of ocean over Palmer Deep was covered greater than 80% of the time with hourly maps of surface ocean circulation. The evolution of these current fields was used to identify convergent features, including fronts and eddies, relative to known penguin foraging.

Surface Convergent Features. Various metrics have been used to map ocean convergent features. Maps of Lagrangian Coherent Structures (LCS), specifically Finite-Time Lyapunov Exponent (FTLE) and Finite-Space Lyapunov Exponent (FSLE) have seen greater application to marine ecological studies[14,16,50,51]. While these metrics often delineate boundaries in a fluid that distinguish regions with differing dynamics[52] they are based on an assumption that the input velocity fields are horizontally non-divergent (i.e. zero vertical velocity). The highly resolved current maps provided by the HFR network deployed over Palmer Deep display complex currents that do not meet this important criterium for both FTLE and FSLE. Consequently, we define a more appropriate metric to map the convergent features within our study site consistent with the dynamics captured by the HFR surface current maps.

To objectively map the time and location of convergent ocean features in the mapped surface current time series, we used a metric derived from simulated particle releases in the HFR surface current fields. Our relative particle density (RPD) metric is calculated based on the movement of simulated particles released in the HFR footprint and tracked over time. Each hour, we released simulated particles over a 200 × 200 m grid over the HFR footprint. The Lagrangian particles were advected in the HFR velocity field with a 4th-order Runge-Kutta integration scheme for a period of 48 hours. In our application, we compute hourly maps of RPD from t_1 = December 31, 2014, to t_N = February 19, 2015 (spanning the date range that penguins were tagged and actively foraging).

The hourly RPD was determined by the number of particles within 1 × 1 km boxes within the overlapping HFR coverage and penguin foraging grounds (Fig. 2b). To minimize the effect of the grid on the particle densities, only particles in the field for at least 6 hours were included in the count. To correct for time varying residence time of particles throughout the study period[38], each count was normalized by subtracting the median count across all 1 km boxes within the field for each time step (Fig. 2b), termed RPD for the purposes of this analysis.

Slocum Glider. Gliders are buoyancy driven vehicles that dive and climb at a nominal 26° angle and travel in a vertical "sawtooth" pattern between predetermined surface events 49. Glider-based sampling provided a continuous presence, through all weather conditions, over the spatial domain identified by the HFR network. Simultaneous measurements of physical and biological variables from the gliders sampled the spatial and temporal variability over Palmer Deep. A glider was programmed to complete a mission as a virtual mooring between January 5, 2015 to February 26, 2015 (Fig. 1), diving between the surface and 100 m. The glider was equipped with a sensor suite to characterize the ecosystem's physical structure (Seabird C, T, D). This glider provided the time series of mixed layer depth throughout the penguin foraging time period used in this analysis[20].

Penguin Tagging and Dive Analysis. From January 5 to 28, 2015, we deployed ARGOS satellite transmitters on 12 Adélie penguins (8 female, 4 male) that nested on Torgersen Island (64°46′S, 64°5′W), and from January 27 to February 7, 2015, we deployed satellite transmitters on 7 gentoo penguins (2 female, 5 male) at Biscoe Point (64°49′S, 63°46′W). All protocols were carried out in accordance with the approved guidelines of the Columbia University Institutional Animal Care and Use Committee (Assurance #AAAH8959). Tagged penguins were paired and had brood-stage nests containing two chicks. Penguins were equipped with SPOT 5 satellite transmitters (Wildlife Computers Redmond, WA, USA) and Lotek LAT1400 time-depth recorder (Lotek Wireless, Inc, St. John's Canada; resolution of 0.05 m, accuracy of 2 m) sampling at 2 Hz. Dive depths less than 5 m were not recorded to save space on the memory cards. Transmitters were attached to the anterior feathers on the lower dorsal region using waterproof tape and small plastic zip ties. Transmitters were removed and rotated to new penguins every 3–5 days dependent on weather conditions. Penguin locations were filtered to remove inaccurate location data due to erroneous terrestrial positions, unreasonable locations based on swimming speed and coastal geometry, following published the data processing methods[37]. We time-matched dive records to location data and the maximum dive depth was determined for each dive. Penguin dives were classified into transit, search and foraging dives, where foraging dives consisted of wiggles, plateaus or bottom time where prey was likely pursued (see[37] for more information). The convex hulls of penguin locations were computed using chull in the grDevices package[53].

Penguin Habitat Selectivity Statistical Tests. We compared the distribution of penguin ARGOS locations to distributions of available RPD values using two-sided Kolmogorov-Smirnov tests (ks.test in the stats package)[53] to test for habitat selectivity. Penguin selectivity is inferred from the distributional differences between RPD values at penguin ARGOS locations. Several considerations are needed for comparing penguin ARGOS locations to RPD simulations. For this analysis, we used ARGOS classes 1–3 (estimated accuracy is 350–1000 m, 150–350 m and <150 m, respectively), which have errors similar to, or smaller than the RPD grid cells. Penguins periodically haul-out on sea ice or islands during their foraging trips, so we restricted our analysis to ARGOS locations where the wet sensors were triggered and were within the field of computed RPD values. We used two estimates of available habitat for Adélie and gentoo penguins. The first estimate of available RPD habitat is the entire RPD HFR field over Palmer Deep during the times the penguins were foraging, because both Adélie and gentoo penguins are capable of traversing the entire RPD field in a single foraging trip. The second estimate of available RPD habitat was based on simulated Brownian motion of central place foragers (simm.bb in the adehabitatLT R package)[54], nesting at the Adélie and the gentoo penguin colonies (Fig. 1). We simulated two penguins per day from each colony, which was similar to the tagging effort during the field season. A 10-year analysis of foraging trip duration showed that these penguins take forage trips up to 48 hours, but most are 6–24 hr[22]. Simulated foraging trip duration was limited to 24 hr in one hour time steps, and the simulated penguin speeds were normally distributed around a mean of 4 km hr^{-1}, and a maximum of 8 km hr^{-1} to mimic Adélie and gentoo penguin swimming speeds[55]. Brownian motion is an uncorrelated movement that represents random foragers not selecting for environmental features, remembering previous feeding locations, or cuing off of other environmental proxies. We used these simulated penguin locations as a null metric of available RPD values by a non-selecting central place forager originating from the Adélie and gentoo penguin nesting sites.

The possibility of individual effects in tagging studies is a persistent problem reflected in their foraging trips or individual behavior. To deal with the possibility of foraging trip level effects driving the results of the of the

Kolmogorov-Smirnov tests, we systematically withheld individual foraging trips and individual penguins from our analysis to test the sensitivity of our results to individuals foraging trips being withheld from the analysis.

Data Availability

The HFR datasets are archived and accessible through the United States National HF radar archive housed at the National Oceanic and Atmospheric Administration (NOAA) National Data Buoy Center (NDBC): http://hfradar.ndbc.noaa.gov/. Additionally, the post-processed raw and de-tided total vector maps can be accessed via the Rutgers HFR Environmental Research Division Data Access Program (ERRDAPP) Service: http://hfr.marine.rutgers.edu/. The other datasets including the glider and penguin tagged data are available from the corresponding author on reasonable request, as some of these data are still in use for student dissertations.

References

1. Pyke, G. H. Optimal foraging theory: a critical review. *Annu Rev Ecol Syst* **15**, 523–575 (1984).
2. Berg, H. C. *Random Walks in Biology* (Princeton University Press, Princeton, NJ, 1983).
3. Klafter, J. & Sokolov, I. M. Anomalous diffusion spreads its wings. *Physics world* **18**, 29 (2005).
4. Okubo, A. & Levin, S. A. *Diffusion and ecological problems: modern perspectives* (Springer, New York, 2001).
5. Ford, R. G. *et al*. Testing assumptions of central place foraging theory: a study of Adélie penguins Pygoscelis adeliae in the Ross Sea. *J Avian Biol* **46**, 193–205 (2015).
6. Viswanathan, G. M., Buldyrev, S. V., Havlin, S. & Da Luz, M. G. E. Optimizing the success of random searches. *Nature* **401**, 911 (1999).
7. Palyulin, V. V., Chechkin, A. V. & Metzler, R. Lévy flights do not always optimize random blind search for sparse targets. *Proc Natl Acad Sci USA* **111**, 2931–2936 (2014).
8. Benhamou, S. How many animals really do the Levy walk. *Ecology* **88**, 1962–1969 (2007).
9. Nathan, R. *et al*. A movement ecology paradigm for unifying organismal movement research. *Proc Natl Acad Sci USA* **105**, 19052–19059 (2008).
10. Reynolds, A. M. & Rhodes, C. J. The Lévy flight paradigm: random search patterns and mechanisms. *Ecology* **90**, 877–887 (2009).
11. Atkinson, A. *et al*. Oceanic circumpolar habitats of Antarctic krill. *Mar Ecol Prog Ser* **362**, 1–23 (2008).
12. Bernard, K. S. *et al*. Factors that affect the nearshore aggregations of Antarctic krill in a biological hotspot. *Deep-Sea Res Part I* **126**, 139–147 (2017).
13. Bernard, K. S. & Steinberg, D. K. Krill biomass and aggregation structure in relation to tidal cycle in a penguin foraging region off the Western Antarctic Peninsula. *ICES J Mar Sci* **70**, 834–849 (2013).
14. Harrison, C. S., Siegel, D. A. & Mitarai, S. Filamentation and eddy— eddy interactions in marine larval accumulation and transport. *Mar Ecol Prog Ser* **472**, 27–44 (2013).
15. Hyrenbach, K. D., Veit, R. R., Weimerskirch, H. & Hunt, G. L. Seabird associations with mesoscale eddies: the subtropical Indian Ocean. *Mar Ecol Prog Ser* **324** (2006).
16. Kai, E. T. *et al*. Top marine predators track Lagrangian coherent structures. *Proc Natl Acad Sci USA* **106**, 8245–8250 (2009).
17. Bon, C. *et al*. Influence of oceanographic structures on foraging strategies: Macaroni penguins at Crozet Islands. *Mov Ecol* **3**, 32 (2015).
18. Schofield, O. *et al*. How do polar marine ecosystems respond to rapid climate change? *Science* **328**, 1520 (2010).
19. Kohut, J. *et al*. Studying the impacts of local oceanographic processes on Adélie Penguin foraging ecology. *Mar Technol Soc J* **48**, 25–34 (2014).
20. Carvalho, F., Kohut, J., Oliver, M. J. & Schofield, O. Defining the ecologically relevant mixed-layer depth for Antarctica's coastal seas. *Geophys Res Lett* **44**, 338–345 (2017).
21. Carvalho, F., Kohut, J., Oliver, M. J., Sherrell, R. M. & Schofield, O. Mixing and phytoplankton dynamics in a submarine canyon in the West Antarctic Peninsula. *J Geophys Res C* **121**, 5069–5083 (2016).
22. Oliver, M. J. *et al*. Adélie Penguin Foraging Location Predicted by Tidal Regime Switching. *PloS One* **8**, e55163 (2013).
23. Amos, A. F. RACER: the tides at Palmer Station. *Antarct J US* **28**, 162–164 (1993).
24. Moffat, C., Owens, B. & Beardsley, R. C. On the characteristics of Circumpolar Deep Water intrusions to the west Antarctic Peninsula continental shelf. *J Geophys Res C* **114** (2009).
25. Martinson, D. G. & McKee, D. C. Transport of warm Upper Circumpolar Deep Water onto the western Antarctic Peninsula continental shelf. *Ocean Sci* **8**, 433 (2012).
26. Dinniman, M. S. & Klinck, J. M. A model study of circulation and cross-shelf exchange on the west Antarctic Peninsula continental shelf. *Deep Sea Research Part II: Topical Studies in Oceanography* **51**, 2003–2022 (2004).
27. Prézelin, B. B., Hofmann, E. E., Moline, M. & Klinck, J. M. Physical forcing of phytoplankton community structure and primary production in continental shelf waters of the Western Antarctic Peninsula. *J Mar Res* **62**, 419–460 (2004).
28. Saba, G. K. *et al*. Winter and spring controls on the summer food web of the coastal West Antarctic Peninsula. *Nat Commun* **5**, https://doi.org/10.1038/ncomms5318 (2014).
29. Steinberg, D. K. *et al*. Long-term (1993–2013) changes in macrozooplankton off the Western Antarctic Peninsula. *Deep-Sea Res Part I* **101**, 54–70 (2015).
30. Hofmann, E. E., Klinck, J. M., Locarnini, R. A., Fach, B. & Murphy, E. Krill transport in the Scotia Sea and environs. *Antarct Sci* **10**, 406–415 (1998).
31. Piñones, A., Hofmann, E. E., Daly, K. L., Dinniman, M. S. & Klinck, J. M. Modeling environmental controls on the transport and fate of early life stages of Antarctic krill (Euphausia superba) on the western Antarctic Peninsula continental shelf. *Deep-Sea Res Part I* **82**, 17–31 (2013).
32. Piñones, A., Hofmann, E. E., Daly, K. L., Dinniman, M. S. & Klinck, J. M. Modeling the remote and local connectivity of Antarctic krill populations along the western Antarctic Peninsula. *Mar Ecol Prog Ser* **481**, 69–92 (2013).
33. Kavanaugh, M. T. *et al*. Effect of continental shelf canyons on phytoplankton biomass and community composition along the western Antarctic Peninsula. *Mar Ecol Prog Ser* **524**, 11–26 (2015).
34. Emslie, S. D., Fraser, W., Smith, R. C. & Walker, W. Abandoned penguin colonies and environmental change in the Palmer Station area, Anvers Island, Antarctic Peninsula. *Antarct Sci* **10**, 257–268 (1998).
35. Friedlaender, A.S., Fraser, W. R., Patterson-Fraser, D. L., Qian, S. S., & Haplin, P. N. The Effects of Prey Demography on Cetacean Community Structure Around the Western Antarctic Peninsula. *Polar Biol* in press (2008).
36. Williams, T. D. *The penguins* (Oxford University Press, 1995).
37. Cimino, M. A., Moline, M. A., Fraser, W. R., Patterson-Fraser, D. L. & Oliver, M. J. Climate-driven sympatry may not lead to foraging competition between congeneric top-predators. *Sci Rep* **6**, https://doi.org/10.1038/srep18820 (2016).
38. Kohut, J. T. *et al*. Variability in summer surface residence time within a West Antarctic Peninsula biological hotspot. *Philosophical Transactions of the Royal Society A*, https://doi.org/10.1098/rsta.2017.0165 (2018).

39. Chappell, M. A., Shoemaker, V. H., Janes, D. N., Bucher, T. L. & Maloney, S. K. Diving behavior during foraging in breeding Adelie penguins. *Ecology* **74**, 1204–1215 (1993).
40. Croxall, J. P., Davis, R. W. & O'Connell, M. J. Diving patterns in relation to diet of gentoo and macaroni penguins at South Georgia. *Condor* 157–167 (1988).
41. Schreer, J. F. & Kovacs, K. M. Allometry of diving capacity in air-breathing vertebrates. *Can J Zool* **75**, 339–358 (1997).
42. Dacey, J. W. H. & Wakeham, S. G. Oceanic dimethylsulfide: production during zooplankton grazing on phytoplankton. *Science* **233**, 1314–1316 (1986).
43. Kwint, R. L. J. & Kramer, K. J. M. Annual cycle of the production and fate of DMS and DMSP in a marine coastal system. *Mar Ecol Prog Ser* 217–224 (1996).
44. Amo, L., Rodríguez-Gironés, M. Á. & Barbosa, A. Olfactory detection of dimethyl sulphide in a krill-eating Antarctic penguin. *Mar Ecol Prog Ser* **474**, 277–285 (2013).
45. Wright, K. L. B., Pichegru, L. & Ryan, P. G. Penguins are attracted to dimethyl sulphide at sea. *J Exp Biol* **214**, 2509–2511 (2011).
46. Cimino, M. A., Fraser, W. R., Patterson-Fraser, D. L., Saba, V. S. & Oliver, M. J. Large-scale climate and local weather drive interannual variability in Adélie penguin chick fledging mass. *Mar Ecol Prog Ser* **513**, 253 (2014).
47. Ainley, D. G. *et al*. Trophic cascades in the western Ross Sea, Antarctica: revisited. *Mar Ecol Prog Ser* **534**, 1–16 (2015).
48. Barrick, D. E., Evans, M. W. & Weber, B. L. Ocean surface currents mapped by radar. *Science* **198**, 138–144 (1977).
49. Kim, S. Y., Terrill, E. & Cornuelle, B. Objectively mapping HF radar-derived surface current data using measured and idealized data covariance matrices. *J Geophys Res C* **112** (2007).
50. Della Penna, A., De Monte, S., Kestenare, E., Guinet, C. & d'Ovidio, F. Quasi-planktonic behavior of foraging top marine predators. *Sci Rep* **5** (2015).
51. Maps, F. *et al*. Linking acoustics and finite-time Lyapunov exponents reveals areas and mechanisms of krill aggregation within the Gulf of St. Lawrence, eastern Canada. *Limnol Oceanogr* **60**, 1965–1975 (2015).
52. Haller, G. Lagrangian coherent structures. *Annu Rev Fluid Mech* **47**, 137–162 (2015).
53. R Development Core Team. *R: A language and environment for statistical computing* (R Foundation for Statistical Computing, Vienna, Austria, 2014).
54. Calenge, C. The packaged adehabitat for the R software: a tool for the analysis of space and habitat use by animals. *Ecol Model* **197**, 516–519 (2006).
55. Ainley, D. G. *The Adélie Penguin: Bellwether of Climate Change* (Cambridge University Press, New York, 2002).

Acknowledgements

This project was funded through the National Science Foundation, award # ANT 1327248, with additional support provided by award # OPP-1440435 to WRF. We are grateful to the Antarctic Support Contractor and their teams, both in Denver, CO, aboard the ARSV Laurence M. Gould, and at Palmer Station, without whom a project such as ours would be impossible. We also thank the students and field assistants for their valued involvement in the CONVERGE project. Finally, we thank the Palmer Antarctica Long-Term Ecological Research team, for their advice, suggestions and collaboration.

Author Contributions

H.F. radar data collection and analysis was done by J.K., P.W., H.S. and F.C., and E.F. M.O., W.F., D.P.-F., and, K.B., and M.C. lead the penguin data analysis relative to the HFR and glider observations. All authors contributed text to and reviewed the complete document.

Additional Information

Competing Interests: The authors declare no competing interests.

Publisher's note: Springer Nature remains neutral with regard to jurisdictional claims in published maps and institutional affiliations.

Large-Aspect-Ratio Structures in Simulated Ocean Surface Boundary Layer Turbulence under a Hurricane

CLIFFORD WATKINS[a] AND DANIEL B. WHITT[b]

[a] Department of Marine and Coastal Sciences, Rutgers, The State University of New Jersey, New Brunswick, New Jersey
[b] Climate and Global Dynamics Laboratory, National Center for Atmospheric Research, Boulder, Colorado

(Manuscript received 18 June 2020, in final form 29 September 2020)

ABSTRACT: A large-eddy simulation (LES) initialized and forced using observations is used to conduct a process study of ocean surface boundary layer (OSBL) turbulence in a 2-km box of ocean nominally under Hurricane Irene (2011) in 35 m of water on the New Jersey shelf. The LES captures the observed deepening, cooling, and persistent stratification of the OSBL as the storm approaches and passes. As the storm approaches, surface-intensified Ekman-layer rolls, with horizontal wavelengths of about 200 m and horizontal-to-vertical aspect and velocity magnitude ratios of about 20, dominate the kinetic energy and increase the turbulent Prandtl number from about 1 to 1.5 due partially to their restratifying vertical buoyancy flux. However, as the storm passes, these rolls are washed away in a few hours due to the rapid rotation of the wind. In the bulk OSBL, the gradient Richardson number of the mean profiles remains just above (just below) 1/4 as the storm approaches (passes). At the base of the OSBL, large-aspect-ratio Kelvin–Helmholtz billows, with Prandtl number below 1, intermittently dominate the kinetic energy. Overall, large-aspect-ratio covariance modifies the net vertical fluxes of buoyancy and momentum by about 10%, but these fluxes and the analogous diffusivity and viscosity still approximately collapse to time-independent dimensionless profiles, despite rapid changes in the forcing and the large structures. That is, the evolutions of the mean temperature and momentum profiles, which are driven by the net vertical flux convergences, mainly reflect the evolution of the wind and the initial ocean temperature profile.

KEYWORDS: Coastal flows; Turbulence; Boundary layer; Oceanic mixed layer; Large eddy simulations

1. Introduction

Observations (e.g., Savelyev et al. 2018b) and simulations (e.g., Hamlington et al. 2014) show that ocean surface boundary layer (OSBL) turbulence sometimes includes a continuum of horizontal length scales characterized by a negative power spectral slope without a peak in variance near the length scale of the OSBL depth. In particular, prominent large-aspect-ratio[1] structures with horizontal scales larger than the OSBL depth coexist with more isotropic structures with scales similar to and smaller than the OSBL depth. Generically, these large-aspect-ratio structures can be generated in the OSBL by extracting energy from the mean profile (e.g., via an instability) and via nonlinear transfers of variance from other scales of variability, or they can propagate into the OSBL from below.

Prior work has loosely classified observed large-aspect-ratio structures into a few categories: 1) wind/wave/buoyancy-driven Langmuir circulations that are characterized by horizontally anisotropic rolls and streaks approximately aligned with the wind vector and perpendicular to surface wave crests (Langmuir 1938; Leibovich 1983; Smith 1992; Thorpe 2004; Kukulka et al. 2009), mostly with cross-roll length scales less than 4 times the OSBL depth but with some notable larger exceptions (Marmorino et al. 2005; Gargett et al. 2004; Sundermeyer et al. 2014; Gargett and Savidge 2020); 2) internal waves (Elachi and Apel 1976; Wijesekera and Dillon 1991; Shaun-Johnston and Rudnick 2009); 3) stratified shear instabilities such as the Kelvin–Helmholtz (KH) mode (Seim and Gregg 1994; Chang et al. 2016); and 4) submesoscale vortex and frontal dynamics (Munk et al. 2000; Savelyev et al. 2018a; D'Asaro et al. 2018; Marmorino and Chen 2019).

Other boundary layers also contain prominent large-aspect-ratio structures, which exhibit some similarities to their OSBL cousins. For example, numerous observations reveal roll vortices and associated streaks characteristic of shear instabilities in the atmospheric boundary layer (ABL) (Lemone 1973, 1976; Etling and Brown 1993; Young et al. 2002). In addition, laboratory measurements and direct numerical simulations reveal long streaks extending up to 10 times the BL height approximately aligned with the shear in high-Reynolds number wall-bounded flows with and without rotation and/or stratification (Tatro and Mollo-Christensen 1967; Marusic et al. 2010; Smits et al. 2011; Hutchins et al. 2012; Sous et al. 2013; Deusebio et al. 2014).

However, the role of large-aspect-ratio structures in OSBL turbulence and their implications for larger-scale ocean dynamics remains to be fully understood. Here, we build understanding

[1] Unless otherwise specified, we define large-aspect ratio to mean that the characteristic horizontal length scale is larger than the characteristic vertical length scale (no specific physical process is implied). Confusingly, many features of interest are also elongated and anisotropic in the horizontal plane. Hence, unless otherwise specified, the characteristic horizontal length scale of a structure refers to the shortest possible characteristic horizontal scale that can be derived.

Supplemental information related to this paper is available at the Journals Online website: https://doi.org/10.1175/JPO-D-20-0134.s1.

Corresponding author: Daniel B. Whitt, dwhitt@ucar.edu

DOI: 10.1175/JPO-D-20-0134.1

by reporting on a large-eddy simulation (LES) that models the rapid turbulent entrainment and sea surface temperature (SST) cooling observed on the New Jersey shelf during the passage of Hurricane Irene in 2011 (Glenn et al. 2016; Seroka et al. 2016) and contains vigorous large-aspect-ratio structures, which participate with smaller-scale turbulence in driving the entrainment and surface cooling.

Many previous studies have used LES to investigate transient and unsteady OSBL dynamics. LES provides a local perspective on OSBL turbulence that is generated by the surface forcing, dynamical instabilities and nonlinear transfers across the resolved scales, without the convoluting effects of lateral advection or propagation from remote locations or local transfers of energy from scales that are unresolved on the grid. However, only a few studies have used LES to study OSBL turbulence including horizontal wavelengths greater than 10 times the OSBL depth. Most of these studies have used large-aspect-ratio domains to study the interactions between submesoscale vortex and frontal dynamics and smaller-scale turbulence (e.g., Skyllingstad and Samelson 2012; Hamlington et al. 2014; Sundermeyer et al. 2014; Taylor 2016; Smith et al. 2016; Whitt and Taylor 2017; Skyllingstad et al. 2017; Callies and Ferrari 2018; Sullivan and McWilliams 2018, 2019). Comparatively little work has been devoted to investigating the role of such large-aspect-ratio structures in OSBLs forced simply by wind, before considering buoyancy and/or surface gravity wave effects. However, previous LES studies have noted interactions between surface boundary layer turbulence and short internal waves (Polton et al. 2008; Czeschel and Eden 2019). Sullivan et al. (2012) noted that it was necessary to use a 1500-m-wide domain (12.5 times the maximum OSBL depth) in order to resolve some spontaneously generated internal waves under hurricane forcing. Others (Sundermeyer et al. 2014; Skyllingstad et al. 2017) found large-aspect-ratio Ekman-layer rolls with horizontal scales 5–10 times the OSBL depth in both observations and LES, regardless of whether surface wave effects were included in the LES. Although ABL LES is limited by the similar computational challenges, previous studies have repeatedly simulated large structures approximately aligned with the geostrophic flow in the Ekman ABL (e.g., Moeng and Sullivan 1994; Khanna and Brasseur 1998; Fang and Porté-Agel 2015). However, it is still not well known how large-aspect-ratio structures contribute to the net fluxes and mean evolution of the OSBL under time-variable wind. But, it seems likely that large structures are important in some circumstances.

The purpose of this paper is to describe the simulated large-aspect-ratio structures and their role in OSBL turbulence under a hurricane in a large-aspect-ratio oceanic domain in which the OSBL depth ranges from 1/200 to 1/55 the horizontal domain length. The simulation is realistic in that it is initialized with observed temperature and salinity vertical profiles just before the storm and forced by a time-dependent 3-hourly surface wind stress, heat flux, and penetrative radiative heating derived from atmospheric reanalysis. On the other hand, the simulation is idealized in that all other processes are omitted, including the effects of ocean surface gravity waves and the larger-scale ocean circulation. The expectation is not that these other processes or their interactions with wind- and buoyancy-forced OSBL turbulence are not important. Rather, the expectation is that it is necessary to study these different processes both in isolation and in combination to obtain a full understanding of OSBL dynamics. This paper is a step toward that broader goal. After a description of the model, the results include two parts: the first is a descriptive analysis of the life cycle and characteristics of the simulated large-aspect-ratio structures. The second demonstrates how the evolution of the large-scale structures relates to and impacts the evolution of the mean profiles of momentum and buoyancy via the turbulent vertical fluxes that drive the evolution of the mean profiles.

2. Model configuration

a. Model description and initial conditions

The numerical model is similar to that used in Whitt and Taylor (2017) [and described in more detail by Taylor (2008)]. Briefly, the evolution of the resolved flow is obtained by time-stepping the rotating Boussinesq equations on a traditional f plane with Coriolis frequency $f = 9.3 \times 10^{-5}\,\mathrm{s}^{-1}$ using a mixed method, in which the Crank–Nicholson scheme advances the vertical viscous/diffusive terms, a third-order Runge–Kutta scheme advances all other terms, and the projection method is used to enforce incompressibility and update the pressure. Spatial derivatives are discretized using a pseudospectral approach in the horizontal and second-order central differences in the vertical. The fluid density ρ and buoyancy $b = -g\rho/\rho_0$ depend on both temperature and salinity via a linear equation of state $\rho = \rho_0[1 + \alpha(T - T_0) + \beta(S - S_0)]$, where $\rho_0 = 1022.8\,\mathrm{kg\,m^{-3}}$, $T_0 = 17.0°\mathrm{C}$, $S_0 = 31.5$ psu, $\alpha = -0.000\,281\,°\mathrm{C}^{-1}$, and $\beta = 0.000\,766\,\mathrm{psu}^{-1}$, and $g = 9.81\,\mathrm{m\,s^{-2}}$. Subgrid-scale (SGS) momentum fluxes are obtained using a modified Smagorinsky approach (Kaltenbach et al. 1994). The subgrid-scale fluxes of salt and temperature are represented by a down-gradient diffusion, where the diffusivities of heat and salt are equal but vary spatially and temporally with the subgrid-scale viscosity and Prandtl number, that is $\kappa_{\mathrm{SGS}} = \nu_{\mathrm{SGS}}\mathrm{Pr}_{\mathrm{SGS}}^{-1}$. As in Whitt and Taylor (2017), $\mathrm{Pr}_{\mathrm{SGS}}^{-1} = 1/(1 + \mathrm{Ri}_{\mathrm{GS}}/0.94)^{1.5}$ (Anderson 2009) and the gridscale gradient Richardson number $\mathrm{Ri}_{\mathrm{GS}} = \delta z\delta b/(\delta u^2 + \delta v^2)$, where δ denotes the difference between two vertically adjacent grid cells and u and v denote the horizontal components of the velocity vector.

The numerical solution is obtained in a horizontally periodic domain that is 1958 m × 1958 m × 35 m and spanned by a mesh with 2304 × 2304 × 85 grid points that are evenly spaced 0.85 m × 0.85 m × 0.42 m apart. A study of the sensitivity of the LES solutions to the domain size is not pursued here. However, we note that horizontal domains of 245, 122, and 41 m with the same horizontal and vertical grid spacings were also attempted. In the larger two of three domains, the simulations revealed dominant domain-scale structures and intermittency in the statistics, both of which were deemed undesirable. These issues were somewhat mitigated in the smallest domain, but the statistics in that case are not very robust with so few points.

The time step is varied dynamically so that the Courant number remains sufficiently small and the time stepping

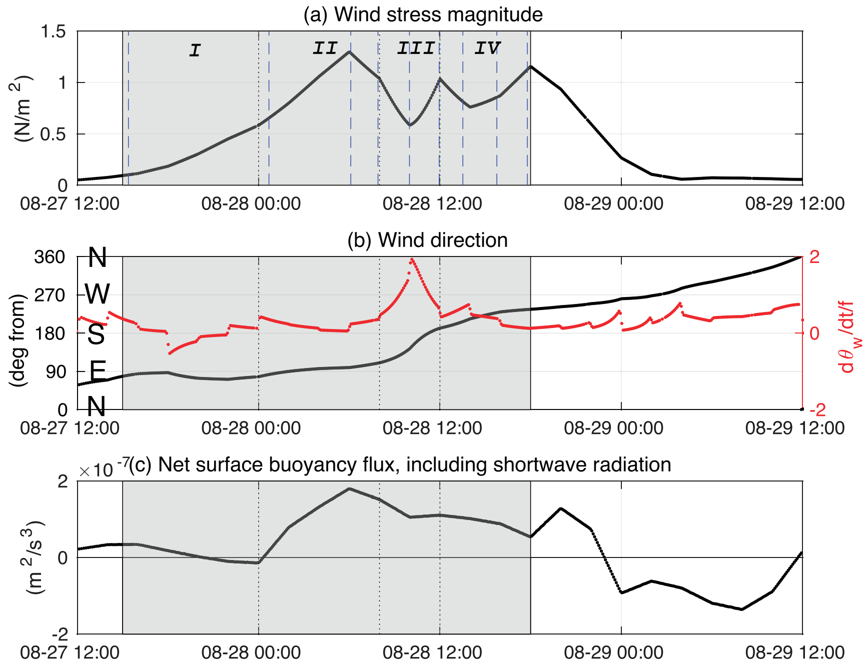

FIG. 1. Ocean surface fluxes during the storm. The surface stress has (a) magnitude $|\boldsymbol{\tau}|$ and (b) direction θ_w (left axis) and rate of rotation normalized by the Coriolis frequency $d\theta_w/dt/f$ (right axis). (c) The net surface buoyancy flux, which is (atypically) injecting buoyancy into the ocean during most of the storm, includes the penetrating shortwave, net longwave, latent, and sensible heat fluxes. Surface freshwater/salinity fluxes are set to zero for simplicity. This paper focuses on the gray-shaded time period and separates that period into four phases, as described in the text.

scheme remains stable. Due to the strong currents during the storm, the time step drops below 0.15 s late in the storm. Hence, the simulation requires about 370 000 time steps to reach the end of phase IV in Fig. 1a. The depth of the domain is chosen to be approximately the same as the ocean bottom depth roughly 100 km east of Cape May, New Jersey (about half way from the coast to the shelf break), where glider observations of temperature and salinity profiles were available before and during the storm; the glider maintained station-keeping operations near the 40-m isobath as shown in Fig. 2 with surfacing for upload of data every 3 h (Glenn et al. 2016).

The velocity field is initialized with a small-amplitude random kick in each grid cell with root-mean-square of order 10^{-4} m s^{-1}, and the temperature and salinity are initialized with horizontally uniform profiles that are defined by analytic functions designed to approximately match observed temperature and salinity profiles obtained by a glider on the New Jersey shelf just before the storm (Fig. 3) [for details about the observations, see Glenn et al. (2016)]. The simulation begins at 0000 UTC 27 August 2011 and runs through 1800 UTC 29 August, but the atmospheric forcing is modest until 1500 UTC 27 August, when our analysis begins (Fig. 1).

b. Atmospheric forcing and boundary conditions

The surface and bottom boundary conditions for vertical velocity are $w = 0$; temperature, salinity, and horizontal velocity are horizontally uniform but time-dependent vertical gradients. At the top, the vertical gradients of horizontal velocity, e.g., $\nu_{SGS}\partial\mathbf{u}/\partial z = \boldsymbol{\tau}/\rho_0$ where $\nu_{SGS} = 10^{-6}$ m^2 s^{-1}, and temperature are defined by 3-hourly surface wind stress and heat fluxes (excluding penetrating shortwave) derived from a regional ocean model published by Glenn et al. (2016) (Fig. 1). That regional ocean model in Glenn et al. (2016) is initialized from a state obtained via data assimilation and forced by the 3-hourly/12-km resolution reanalysis from the North American Mesoscale forecast model, and the surface fluxes are calculated using the COARE algorithm (Fairall et al. 2003). As in the regional ocean model of Glenn et al. (2016), shortwave radiation penetrates and acts as an interior heat source in the LES that follows a modified Jerlov type II two-component exponential profile (Paulson and Simpson 1977) with the first e-folding depth scale $\zeta_1 = 5$ m instead of 1.5 m to avoid a collapse of turbulence near the surface under stabilizing buoyancy forcing and weak wind before the storm. This approach is ad hoc and may need to be reconsidered in future work, but it is plausibly justified based on observations that the top few meters are sometimes more turbulent than expected from the wind stress and buoyancy flux alone due to surface wave effects (e.g., Anis and Moum 1995).

To aid in the latter description, we separate the forcing into four phases of interest as shown in Fig. 1a. In phase I, there is a period of rising but modest ($|\boldsymbol{\tau}| < 0.5$ N m^{-2}) and consistently easterly wind as the storm approaches from the south along the U.S. east coast. Then, in phase II there is a period of stronger

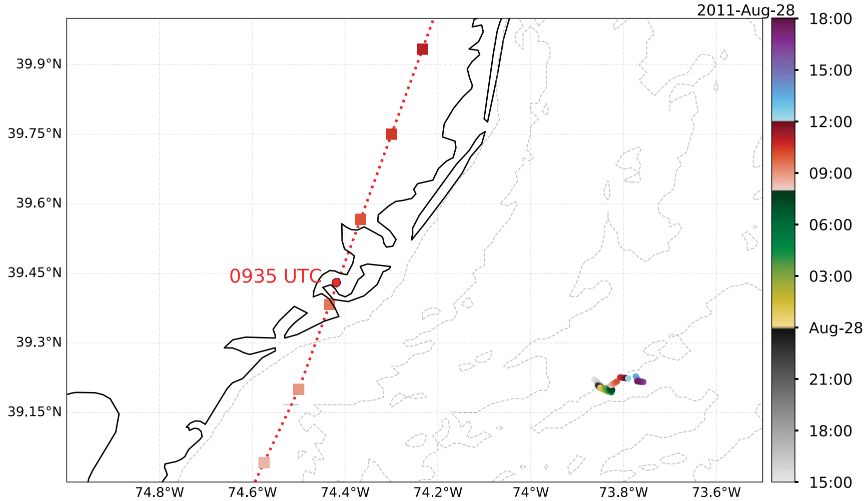

FIG. 2. The track of a profiling buoyancy glider (small dots) and bathymetry contours (dotted lines every 10 m). Color indicates the time (UTC), which is separated into four phases: I (black), II (green), III (red), and IV (blue) (see Fig. 1). The approximate location of the hurricane's eye is indicated by squares, which are spaced every 30 min and are colored to indicate the time, similar to the glider track. The red dot on the hurricane track indicates the time and location of landfall (Glenn et al. 2016).

winds from the east ($|\boldsymbol{\tau}| > 0.5\,\mathrm{N\,m^{-2}}$), which is punctuated by the maximum wind stress ($1.2\,\mathrm{N\,m^{-2}}$) at 0600 UTC 28 August. Phase III includes the eye passage, when winds are strong but weaker than the maximum ($1 > |\boldsymbol{\tau}| > 0.5\,\mathrm{N\,m^{-2}}$) and the stress vector rotates rapidly. Since the LES domain is situated to the right of the eye track, the wind stress vector rotates clockwise from a westward stress (easterly winds) to a northeastward stress (southwesterly winds) as the eye passes (Fig. 1b). Finally, phase IV represents the period of strong and persistently southwesterly wind after the eye passes. The subsequent periods of decaying winds and low poststorm winds are not considered in this paper.

Atypically, the net heat flux is into the ocean during most of the storm and during almost all of 28 August (Fig. 1c). During phases II and III, as the wind ramps up and eventually the eye passes at about 0900 UTC 28 August, the turbulent heat and buoyancy fluxes and the corresponding vertical temperature gradient at the surface boundary of the LES are positive (injecting heat into the ocean) during nighttime (Figs. 1b,c). During phase IV and the remainder of 28 August after the eye passage, there are weak turbulent heat losses from the ocean and a negative surface temperature gradient at the top boundary of the LES, but solar radiation makes the net heat flux positive until nearly nightfall at roughly 0000 UTC 29 August. This unusual situation, in which the turbulent surface latent and sensible heat fluxes are into the ocean, is thought to have been caused by the rapid entrainment-driven ahead-of-eye cooling of the SST, which contributed to the observed rapid decay of the hurricane during this period (Glenn et al. 2016; Seroka et al. 2016).

Before proceeding, consider the relative importance of the surface buoyancy flux $F_b(0)$ (Fig. 1c) and momentum flux $\mathbf{F}_m(0) = \boldsymbol{\tau}/\rho_0$ for the OSBL turbulence using Monin–Obukhov similarity theory (e.g., Monin and Obukhov 1954; Businger et al. 1971; Lombardo and Gregg 1989). First, the Monin–Obukhov length $L_{\mathrm{MO}} = |\mathbf{F}_m(0)|^{3/2}/[k|F_b(0)|] > 300\,\mathrm{m}$, where $k = 0.4$ is the von Kármán constant. And, the boundary layer is only 10–30 m deep. So, the conditions are generally near neutral, that is $|z/L_{\mathrm{MO}}| < 0.1$ and the wind-driven turbulence is expected to be only modestly impacted by the stable surface buoyancy flux at all depths and throughout the duration of the analysis (i.e., the shaded gray area in Fig. 1).

During the analysis period reported here (the gray shaded area in Fig. 1), the bottom layer remains nearly motionless and stratified on average, and the magnitude of the bottom stress never exceeds $10^{-4}\,\mathrm{N\,m^{-2}}$, so the details of the bottom gradient conditions and the associated wall model are thought to be unimportant and omitted for brevity although the bottom may still be significant, e.g., due to the trapping of internal wave energy that might otherwise radiate downward in the open ocean.

3. Visualization and description

We begin by reporting the results of flow visualizations and describe the dominant large turbulent structures in the OSBL, which we separate from more quiescent water below by the depth of maximum stratification $z = -D_{N^2}$, where the stratification is defined by $\langle N^2\rangle_{x,y} = \langle \partial b/\partial z\rangle_{x,y}$ (here, $\langle\rangle_{x,y}$ denotes an average over the horizontal dimensions x and y). This section is separated into two parts to facilitate a description of the two types of large structure that are, conveniently, dominant at two distinct depth levels: the first is a discussion of the near-surface layer, and the latter is focused on the base of the OSBL (i.e., just above D_{N^2}).

a. Near surface

Plan views of the simulated currents at 5-m depth early on 28 August (the beginning of phase II) reveal striking anisotropic

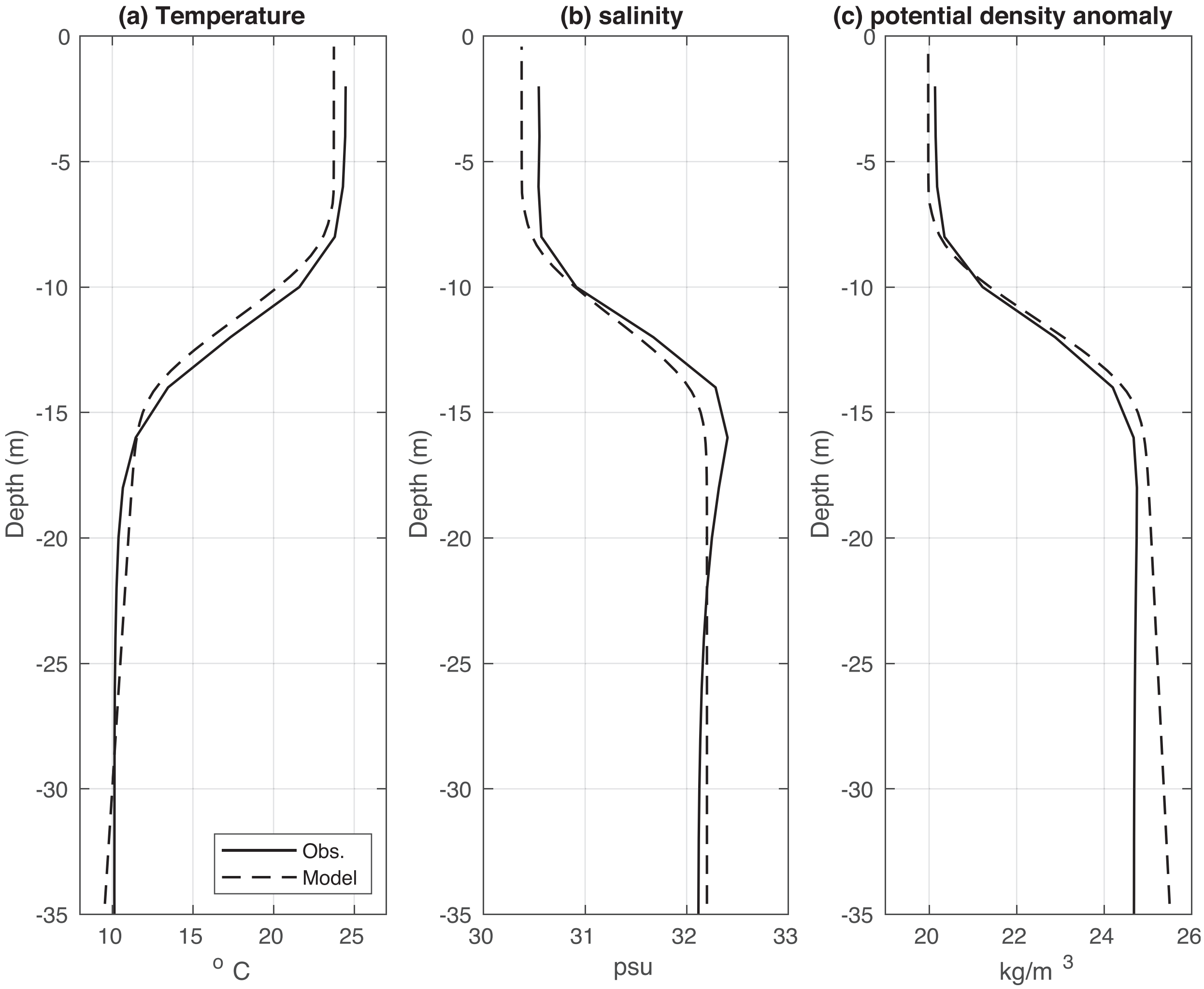

FIG. 3. A comparison between the modeled and observed (a) temperature, (b) salinity, and (c) potential density profiles just before the storm at 1200 UTC 27 Aug 2011, when the glider was at 39.24°N, 73.88°W.

streaks that are elongated in the wind direction (Fig. 4). We begin with a chronological description of the life cycle of these structures. Then we describe the spatial structure in more detail using vertical sections of several key variables in a streak–roll coordinate system.

It may be noted that the features are reminiscent of Ekman layer rolls [for stratified linear stability analysis, see Kaylor and Faller (1972), Brown (1972), and Asai and Nakasuji (1973); for atmospheric observations, see Lemone (1973, 1976); for recent oceanic perspective, see Sundermeyer et al. (2014), Duncombe (2017), and Skyllingstad et al. (2017)], but comparisons between the associated theory, prior observations, and the structures reported here are deferred to the discussion section.

1) CHRONOLOGY

To begin with, it is notable that it takes about 15–24 h for the streaks shown in Fig. 4 to first emerge as dominant features of the turbulence during phase I (which begins 15 h into the simulation at 1500 UTC 27 August), either because it takes this long for the wind to reach sufficient strength and/or because the motions take this long to achieve finite amplitude via another dynamic mechanism such as a linear instability. In particular, the power spectrum of kinetic energy as a function of time at 5-m depth and at large-scale wavelengths $\lambda > 3D_{N^2}$ exhibits approximately exponential growth in time $e^{t/\tau}$ with $\tau \sim 10^4$ s. At the same time, the wind stress magnitude and the associated magnitude of the mean wind-driven currents in the OSBL also increase approximately exponentially at about the same rate as the storm approaches. However, the largest of the large scales ($\sim$1 km) are energized somewhat more slowly than the smaller of the large scales ($\sim$0.1 km) (not shown; but the netCDF files with the spectra are published in Watkins and Whitt 2020). As a result, the fraction of the horizontal kinetic energy associated with wavelengths longer than 3 times $D_{N^2} \approx 10$ m is less than 25% of the total variance before 2000 UTC 27 August (Figs. 5a–c). In addition, the maxima in the radially integrated horizontal wavenumber spectra of both horizontal and vertical kinetic energy are both at about 0.1 cycles per meter

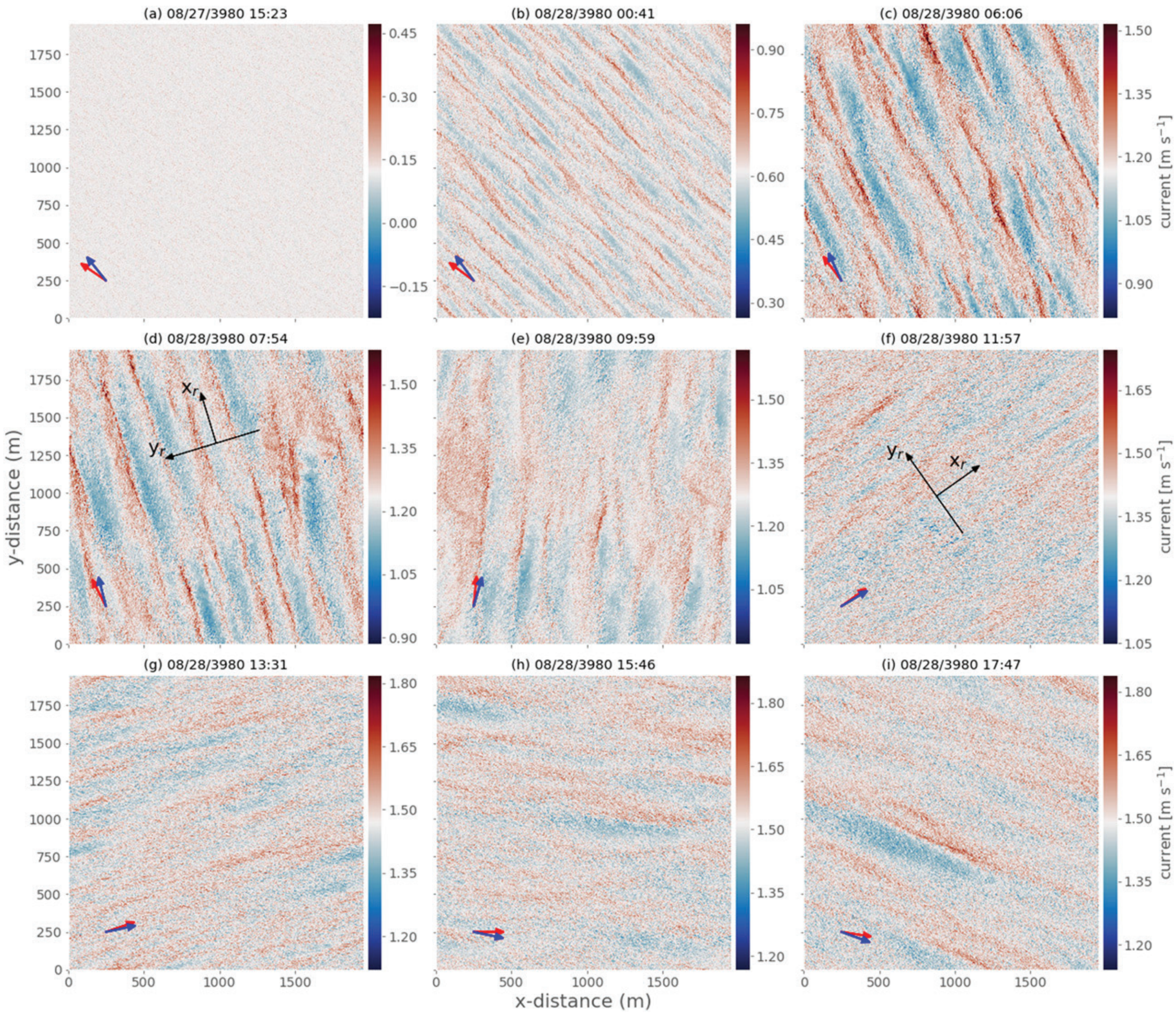

FIG. 4. Snapshots showing the speed of the horizontal current 5 m below the surface at nine times during phases (a) I, (b)–(d) II, (e),(f) III, and (g)–(i) IV of the storm; the time points are indicated by blue dashed lines in Fig. 1a. The diverging color bar is centered on the horizontal average to highlight the current anomalies. The domain is rotated counterclockwise 45° from the geographic coordinates referenced in Fig. 1b. Hence, winds initially from the east flow from the bottom right to the top left over the domain. As the eye of the storm passes during phase III [(d)–(f)], the source direction of the wind quickly rotates clockwise around the bottom of the domain to the left side, i.e., the southwest. The directions of the surface stress $\boldsymbol{\tau}$ and horizontally averaged shear vector at 5 m $\langle \partial \mathbf{u}_h/\partial z \rangle_{x,y}$ are indicated by the red and blue arrows, respectively, in the bottom-left corners. The roll coordinate charts used in Figs. 7 and 8 are overlaid in black.

at 5-m depth before 1500 UTC 27 August (see Watkins and Whitt 2020). Hence, the dominant large turbulent eddies are nearly isotropic with a characteristic scale similar to the OSBL depth during most of 27 August.

As the wind strengthens during the first half of 28 August (phase II), variance in both the horizontal currents and buoyancy increases at horizontal wavelengths $\lambda > 3D_{N^2}$ associated with large aspect ratios. In particular, horizontal kinetic energy at wavelengths $\lambda > 3D_{N^2}$ increases to more than half of the total horizontal kinetic energy at 5-m depth (Figs. 5a–c). And, the anomalous current speed in the streaks reaches a maximum characteristic magnitude of about 10 cm s^{-1}, which is roughly 10% of the mean speed, which grows from about 0.5 to 1.3 m s^{-1} during phase II. At the same time, the buoyancy variance at wavelengths $\lambda > 3D_{N^2}$ comes to represent more than 75% of the total variance shallower than 5-m depth (Figs. 5g–i). Hence, qualitatively similar streaks are visible in the plan views of temperature at 5 m, like the currents (cf. Figs. 4d and 6a), and the characteristic temperature anomalies in the streaks are a few tenths of a degree Celsius. The vertical kinetic energy also increases at wavelengths $\lambda > 3D_{N^2}$ during phase II (Figs. 5d–f). However, this large-scale vertical kinetic energy remains about two to three orders of magnitude weaker than the corresponding large-scale horizontal kinetic energy, as expected based on the aspect ratio of the flow structures. In addition, this large-scale vertical kinetic energy remains a small

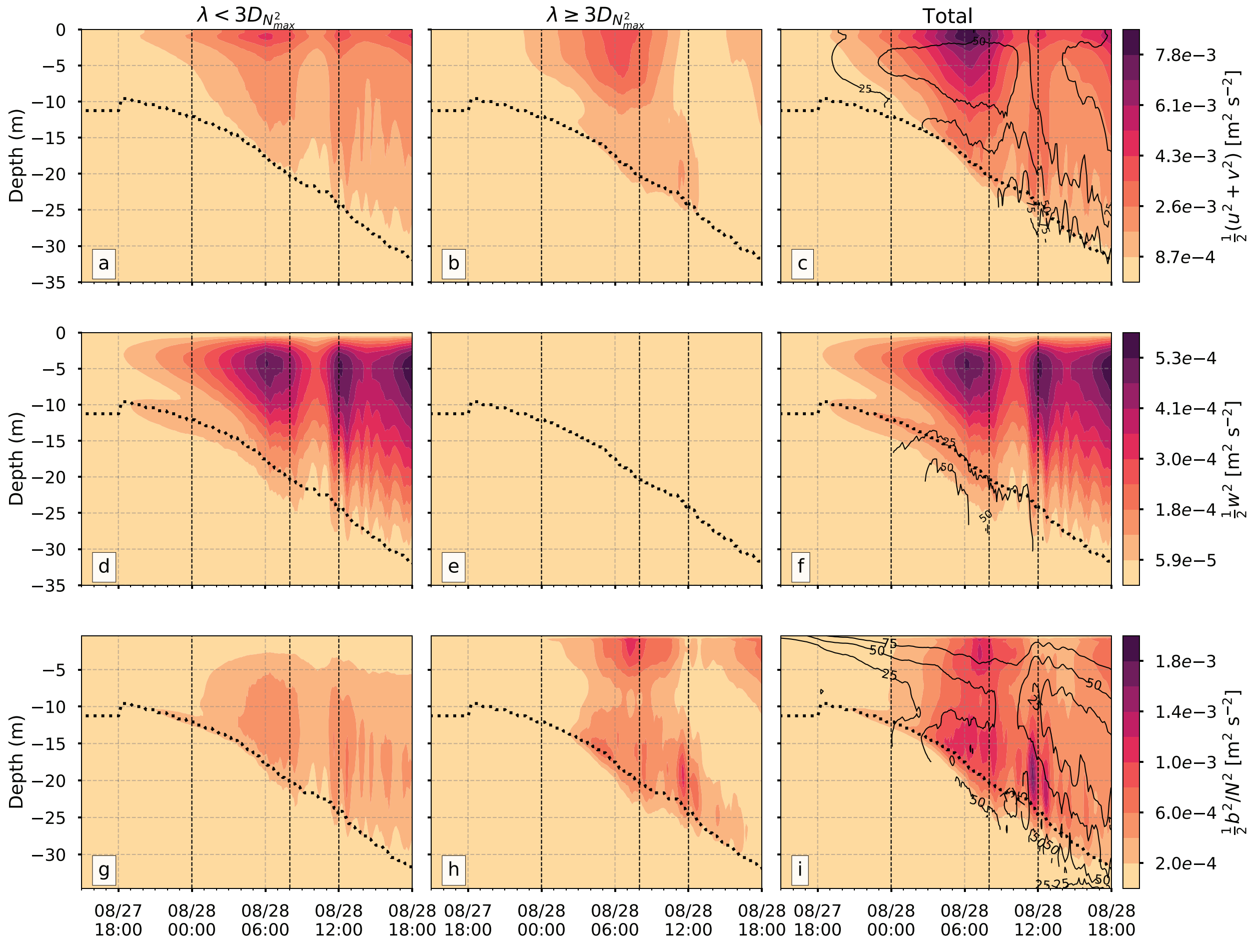

FIG. 5. (a)–(c) Horizontal and(d)–(f) vertical kinetic energy of the perturbations from the horizontally averaged flow, and (g)–(i) the buoyancy variance normalized by twice the mean vertical buoyancy gradient $\langle N^2 \rangle_{x,y}$. All three are decomposed using Fourier methods into wavelengths λ greater (center column) and smaller (left column) than 3 times D_{N^2}, the depth of maximum $\langle N^2 \rangle_{x,y}$, which is marked by a black dotted line. The black contours (every 25%) in the right column indicate the percentage of the variance accounted for by large scales (shown in the center column).

fraction of the total vertical kinetic energy, which remains dominated by wavelengths $\lambda < 3D_{N^2}$ typical of more isotropic OSBL turbulence.

Although the large-aspect-ratio streaks are prominent throughout phase II, when the wind is strong and persistently easterly, the streaks are not static. First, the streaks propagate at speeds comparable to the mean flow $\sim$1 m s^{-1}, such that their characteristic time scale measured at a fixed position is of order 100 s. For example, at the beginning of phase III, the streaks propagate to the northwest in about the same direction as mean surface current, which points at an angle about 45° to the right of the wind (the mean flow will be discussed in later sections). However, in a reference frame following the mean flow in the upper 10 m, the streaks are nearly stationary and evolve with a much longer characteristic time scale more appropriately measured in hours than seconds, consistent with the time scale over which they initially emerge (see videos in the online supplemental material, https://doi.org/10.1175/JPO-D-20-0134.s1). Second, the dominant cross-streak wavelength λ_r increases with time during phase II, from approximately 100 to 300 m (Fig. 4). Perhaps not coincidentally, the depth D_{N^2} deepens from about 12 to 20 m at the same time (Fig. 5), such that the ratio λ_r/D_{N^2} remains in a narrower range of about 8–15. However, the orientation of the along-streak axis remains fairly consistent during phase II: it is rotated slightly clockwise $\sim$10° from the wind vector (Fig. 4), which rotates slowly clockwise during phase II. As the wind rotates more quickly during phase III, the streaks also rotate more quickly clockwise with the wind. However, the amplitude of the current and temperature anomalies associated with the large-aspect-ratio streaks decays in both absolute terms and as a percentage of the total variance. The most obvious factor associated with the washing out of the streaks/rolls is the rate of rotation of the surface wind stress, which exceeds the local Coriolis frequency during eye passage in phase III. Thereafter, the streaks are not dominant features of the flow (Fig. 4), although the large-scale variance does increase toward the end of phase IV as the wind rotation slows and the direction stabilizes becoming consistently

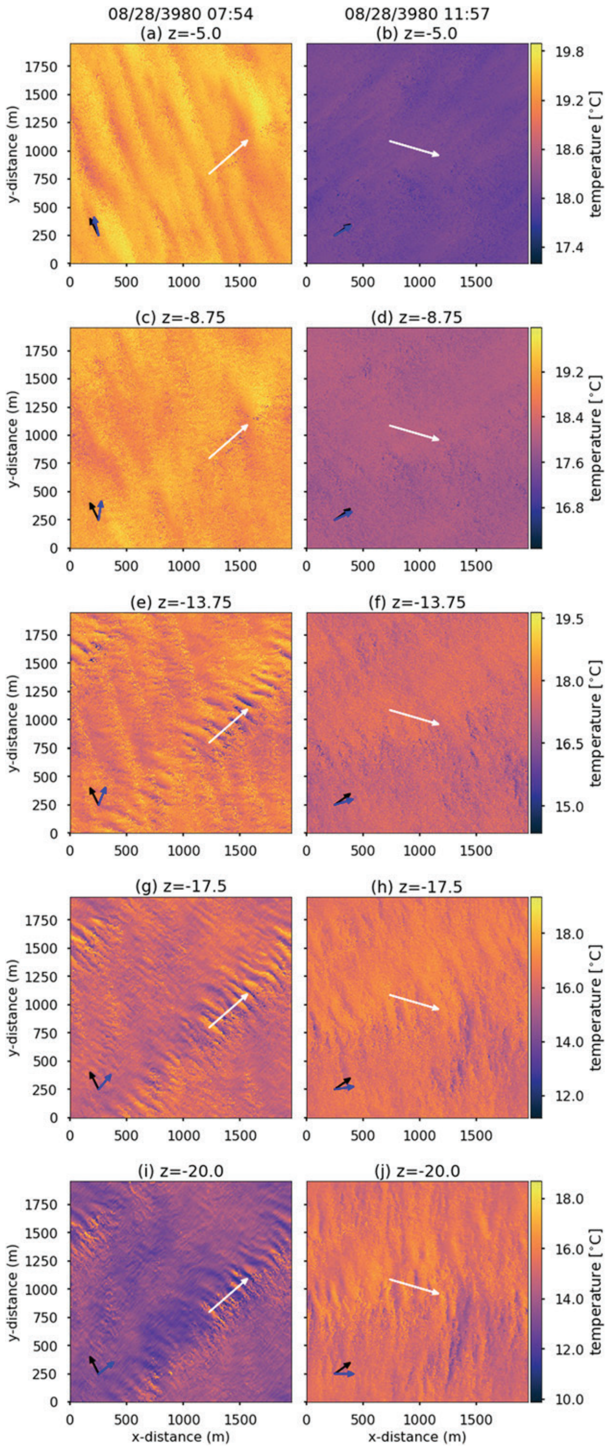

FIG. 6. Snapshots of temperature at both the (left) beginning and (right) end of phase III and at several depths (from top to bottom). The arrows in the bottom-left corner indicate the direction of the surface stress $\boldsymbol{\tau}$ (black) and the horizontally averaged shear vector $\langle \partial \mathbf{u}_h / \partial z \rangle_{x,y}$ at that depth. The white lines indicate the location of the vertical sections in Fig. 9.

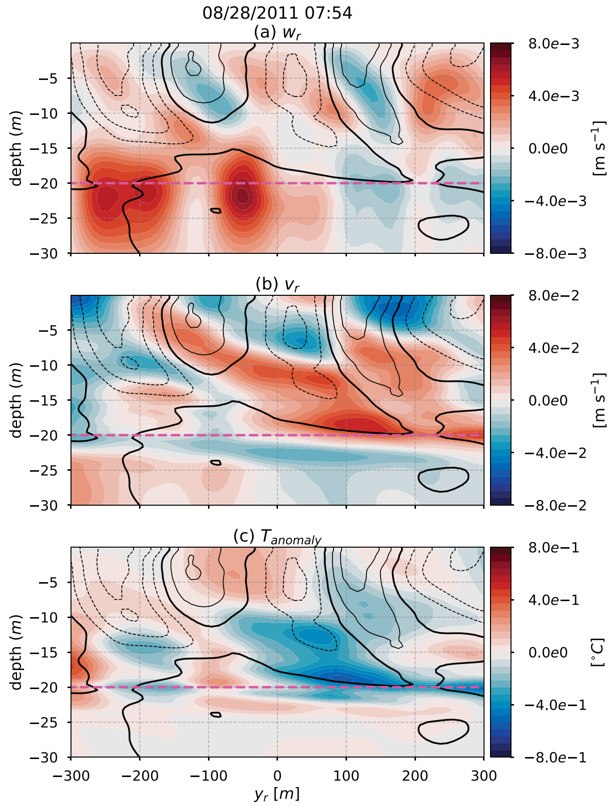

FIG. 7. (a) Vertical sections of vertical velocity, (b) cross-roll horizontal velocity, and (c) temperature, all of which are anomalies relative to the horizontal domain average. Overlaid is the along-roll streak velocity u_r (black contours every 4 cm s^{-1} have positive values marked by thin solid lines, negative values marked by thin dashed lines, and zero marked by the thick solid line) and D_{N^2} (magenta). The sections are along the cross-roll coordinate y_r shown in Fig. 4d, after smoothing with a 25-m Gaussian filter.

southwesterly to westerly (Figs. 4g–i and 5b,h), and the spinup time scale of the streaks in phase IV seems similar to their initial spinup time scale before the eye passes.

2) VERTICAL SECTIONS OF ROLLS/STREAKS IN ROLL COORDINATES

Vertical sections oriented perpendicular to the streak axis at the end of phase II highlight several key characteristics of the streaks/rolls and their impact on smaller-scale OSBL turbulence. We find that the cross-streak v_r and vertical w_r velocities form tilted rolls (Fig. 7) that are associated with the streaks u_r shown at 5-m depth in Fig. 4. The amplitude of the streaks/rolls decays rapidly with depth below 10 m, but their orientation in the horizontal plane does not rotate with depth despite substantial rotation of the mean shear vector (see Figs. 6 and 7). The simulated roll vertical velocity anomalies w_r have a characteristic scale of a few millimeters per second, and the corresponding cross-streak roll velocities v_r are a few centimeters per second, that is $v_r \sim 10 w_r$ consistent with the aspect ratio of about 10. The simulated horizontal cross-streak roll velocity v_r is about 3 times weaker than the along-roll streak velocity u_r.

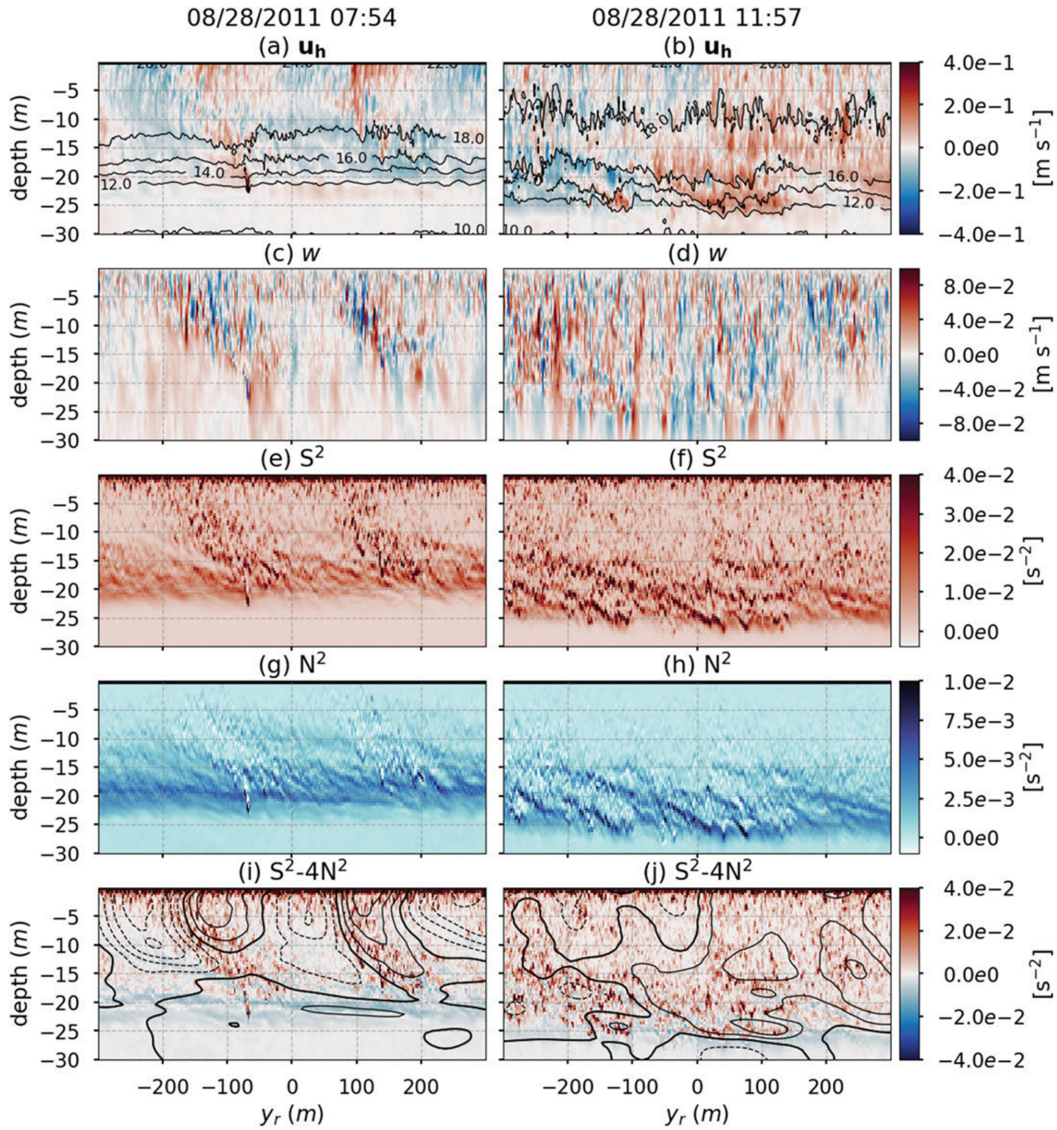

FIG. 8. As in Fig. 7, but without smoothing: (a),(b) anomaly in the horizontal speed $|\mathbf{u}_h|$, (c),(d) vertical velocity w, (e),(f) squared vertical shear of horizontal velocity S^2, (g),(h) stratification N^2, and (i),(j) reduced shear $S^2 - 4N^2$, just before (left) and just after (right) the eye. For reference, temperature contours are overlaid in (a) and (b) and smoothed u_r (also shown in Fig. 7) is overlaid in (i) and (j). The coordinate systems for before-eye and after-eye are plotted in Figs. 4d and 4f, respectively.

Thus, v_r stands out less prominently from other variability and appears less organized than u_r.

In addition, we find systematic correlations between the roll/streak variables, and thus an indication of net vertical transport by the streaks/rolls. In particular, the simulated streak velocity u_r is negatively correlated with w_r, although they are not perfectly aligned. The phase shift ϕ_r that minimizes the lagged correlation (to about -0.8) between $u_r(y_r)$ and $w_r(y_r + \phi_r)$ occurs at from $\phi_r \approx -20$ to -40 m or about $-0.1\lambda_r$. Conversely, temperature anomalies T_r are positively correlated with w_r, but the correlation coefficient is maximum (about $+0.6$) for a phase shift applied to w_r from $\phi_r \approx +10$ to $+40$ m or about $+0.1\lambda_r$. Thus, the results suggest that the roll-streak system may be associated with a downgradient momentum flux and positive shear production and upgradient buoyancy flux and positive buoyancy production. In a later section, we will separate by length scale and compare the turbulent vertical transport of momentum and buoyancy by these and all other structures and thereby explicitly quantify the impact of these structures on the evolution of the mean current and buoyancy profiles during the storm.

3) MODULATION OF SMALLER TURBULENCE

The vertical section plots in Fig. 8 show that the streaks modulate smaller-scale turbulence as well as the shear and stratification that influence the energetics of smaller scales. In particular, the region of strongest $\partial u_r/\partial z$, which is to the left (lower

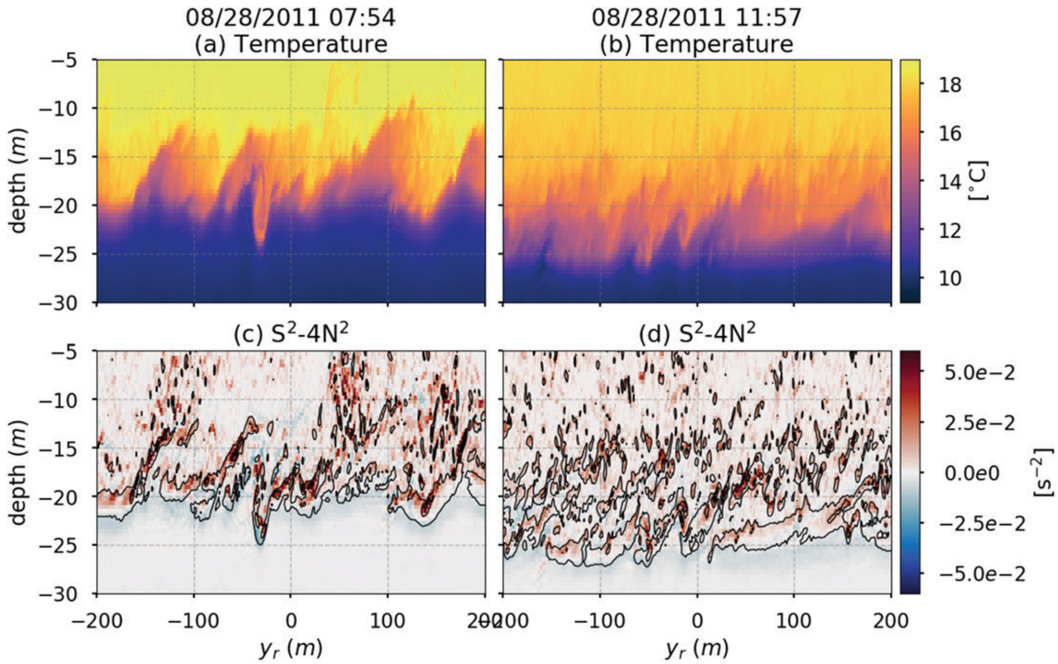

FIG. 9. (a),(b) Temperature and (c),(d) reduced shear with contours of vorticity (in x_r) overlaid in black along the white coordinate lines in Fig. 6.

y_r in roll coordinates) of and below positive streak anomalies ($u_r > 0$), is associated with a tongue of enhanced vertical velocity w variance, squared shear $S^2 = (\partial u/\partial z)^2 + (\partial v/\partial z)^2$ variance and stratification N^2 variance that extends downward and under the positive u_r anomaly, from the surface to the thermocline. In addition, the enhanced turbulence coincides with roll-scale downdrafts $w_r < 0$, which occur 20–40 m to the left of the streaks (toward lower y_r) and are correlated with cold temperature anomalies. This enhanced turbulence coincides with and is plausibly explained by strongly positive reduced shear, $S^2 - 4N^2 > 0$, in these regions (Fig. 8i), which is indicative of both a gradient Richardson number $\mathrm{Ri}_g = N^2/S^2 < 1/4$, hence the necessary conditions for instability are met (Miles 1961; Howard 1961; Hazel 1972), and substantial energy is available to the turbulence via shear production (Turner 1979; Rohr et al. 1988; Holt et al. 1992). Conversely, below the low-speed negative streak velocity anomalies ($u_r < 0$) turbulence is particularly weak and generally the reduced shear is negative and $\mathrm{Ri}_g \geq 1/4$. For comparison, a similar set of sections is shown after the eye passage in Fig. 8 in order to highlight the remarkable degree of periodicity imposed upon the turbulence by the streaks/rolls before the eye, under strong surface forcing.

b. Thermocline

Do the streaks and rolls discussed in the previous section, or large-aspect-ratio structures more generally, influence the entrainment of cold water from the thermocline and thereby the SST in the LES?

To begin addressing this question, we describe the characteristics of the dominant large structures in the turbulence near the thermocline, where the cold water enters the surface boundary layer. There, large scales $\lambda > 3D_{N^2}$ represent a majority of the horizontal kinetic energy and buoyancy variance between phases II and III (Fig. 5). In addition, plan views of temperature at different depths in Fig. 6 show that the characteristics of the large structures are qualitatively different at the thermocline compared to the surface-layer streaks/rolls. At the thermocline, the large-scale variance is dominated by smaller ~100-m-scale wave-like structures with crests and troughs perpendicular to the local shear vector $\partial\langle\mathbf{u}\rangle_{x,y}/\partial z$, which is rotated about 90° to the right of the wind stress. These wave-like features are reminiscent of organized KH billows (Fig. 9), so we refer to them as such before explicitly comparing to theory and prior observations in the discussion section below.

The significant spatial modulation of the KH billows is a feature of particular interest in such a large-aspect-ratio model domain. At the beginning of phase III, these features are organized into bands that are approximately parallel to the local shear vector, a few hundred meters wide, and spaced 1 km apart (Fig. 6g). Each band is associated with an undulation in the thermocline and horizontal velocity (e.g., it is warmer on the bottom-right and cooler on the top-left side of each band in Fig. 6g). These larger thermocline undulations are plausibly due to internal waves, but since these 1-km structures are not always this organized, we do not pursue a simple explanation for this kilometer-scale modulation. Nevertheless, the simulated axial coherence of the rolls (along lines of constant phase) is often at least several wavelengths, which is qualitatively consistent with existing albeit limited knowledge of axial coherence of KH-like billows observed in the atmosphere and laboratory (Thorpe 2002).

Although we do not explicitly plot the time evolution of the billows, we note that similar structures are prominent with

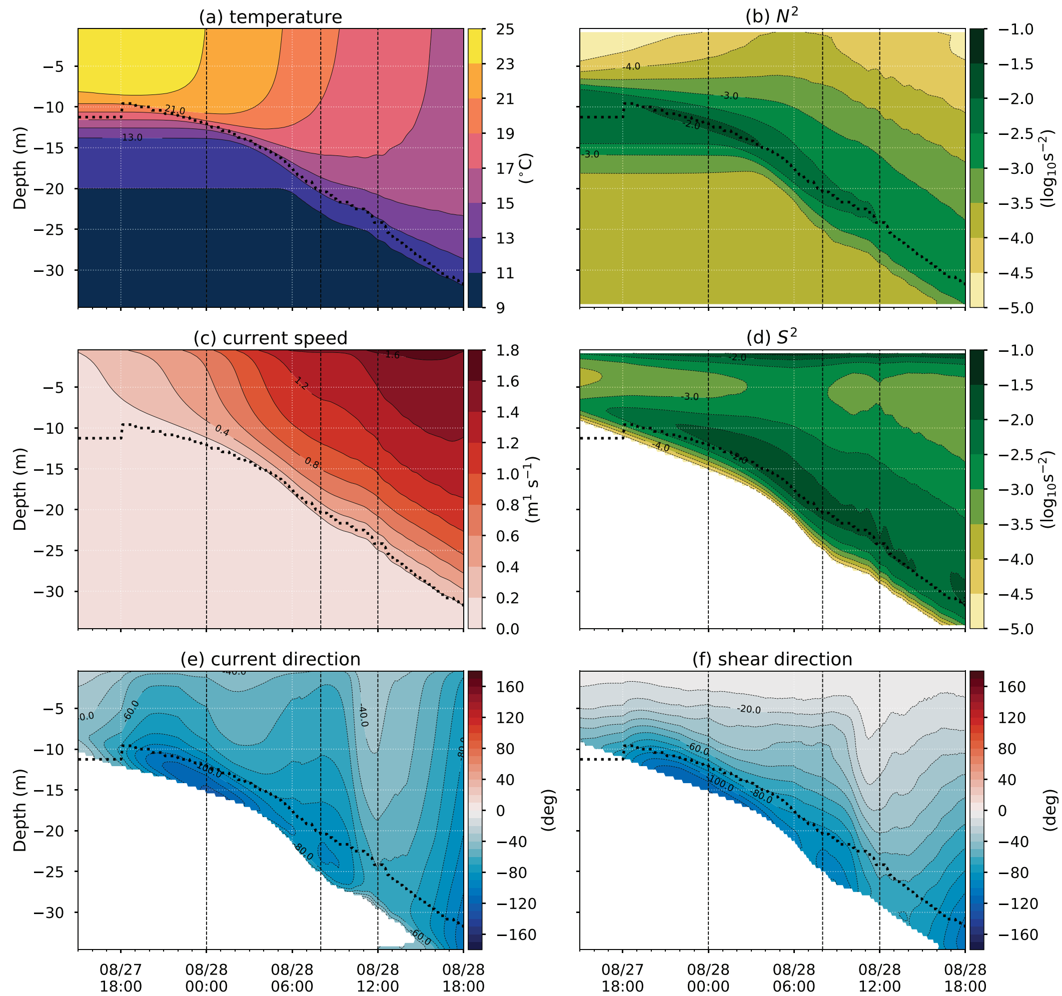

FIG. 10. (a) Mean vertical profiles of temperature, (b) vertical buoyancy gradient N^2, (c) horizontal current speed $|\mathbf{u}_h|$, (d) squared vertical shear of horizontal velocity S^2, (e) horizontal current direction, and (f) shear direction. Both of the angles in (e) and (f) indicate the direction the vector points and are given in degrees counterclockwise relative to the direction that the wind points. The angles are mostly negative and smaller than 90°, which indicates the current and shear vectors are to the right of the wind vector, as expected. Angles are only shown for speeds and shears greater than $10^{-3}\,\mathrm{m\,s^{-1}}$ and $\mathrm{s^{-1}}$, respectively. The dashed black line indicates the depth of maximum stratification D_{N^2}.

different degrees of organization at most times in phases II–IV (cf. Figs 9a and 9c with Figs. 9b and 9d; see also Fig. 6). In addition, the temporal evolution of the radially integrated horizontal wavenumber spectra of buoyancy variance and vertical kinetic energy at the time-dependent depth $z = -D_{N^2}$ both contain distinct local maxima at a wavelength λ that increases slowly from about 10–20 m at 1500 UTC 27 August to about 100 m at 0754 UTC 28 August (the beginning of phase III), during which time the depth D_{N^2} increases from about 10 to 20 m. Hence, unlike the surface streaks/rolls, which are more ephemeral and sensitive to the time-variability of the mean flow/forcing, the presence of organized wave-like or billow structures at the top of the thermocline is relatively robust to variations in the large scale conditions, although their precise spatial orientation and organization, characteristic scale, and magnitude varies.

4. Evolution of the mean profiles

The temporal evolution of the large-aspect-ratio structures is both dependent on and impacts the evolution of the mean profiles of momentum, temperature, salinity, and hence buoyancy. This section describes the temporal evolution of the horizontally averaged profiles of temperature, buoyancy, and momentum and then quantifies the net effects of the turbulence, including at large scales, on the mean profiles of momentum and buoyancy via vertical fluxes.

a. Mean profiles and comparisons to observations

In addition to generating the turbulence, the hurricane forcing also drives the evolution of the mean profiles, including the acceleration, deepening, and cooling of the OSBL (Figs. 10a,c).

For example, the forcing accelerates a sheared and surface-intensified mean current with speeds in excess of $1\,\mathrm{m\,s^{-1}}$ and shears in excess of $10^{-1}\,\mathrm{s^{-1}}$ (Figs. 10c,d). Even though the wind and currents are unsteady, the mean surface current vector points about $45° \pm 20°$ to the right of the wind vector until late in phase IV (Fig. 10e), and the current vector rotates clockwise with increasing depth throughout phases I–IV, as in an idealized steady Ekman layer (Ekman 1905). In phase III, the wind rotates rapidly clockwise at an angular frequency of about $2f$ while fluctuating in speed as the eye passes (Fig. 1). As a result, the simulated angle between the ocean surface current vector and the wind vector is briefly reduced (Fig. 10e), as the wind rotates clockwise faster than the ocean surface current. In phase IV, the current angle decreases throughout the OSBL at a rate of about 15°–20° $\mathrm{h^{-1}}$ as the wind direction stabilizes, as in an idealized inertial oscillation (Ekman 1905; Pollard and Millard 1970).

The simulated OSBL depth begins deepening at the beginning of phase II and continues to deepen from about 10 to 30 m through the end of phase IV (Figs. 10a,b). In addition, the overall extent of the deepening as well as the time of most rapid deepening, which occurs just ahead of the eye passage at the beginning of phase III, are reasonably similar to the observations (Fig. 11). In addition, the deepening is reasonably consistent with the theoretical model of wind-driven mixed layer deepening without a bottom by Pollard et al. (1972), whose Eq. (6.1) suggests a poststorm mixed layer depth of 34 m based on just the initial stratification profile and the maximum wind stress.

As the OSBL deepens, the simulated SST cools by more than 4°C ahead of the eye during phase II and by more than 6°C by the end of phase IV, similar to observations (see Fig. 2 of Glenn et al. 2016). In addition, the most rapid SST cooling occurs before the eye passage and earlier than the most rapid OSBL deepening, as observed (Glenn et al. 2016).

Interestingly, the mean OSBL profiles remain stratified ($\langle N^2\rangle_{x,y} \sim 10^{-5}$–$10^{-4}\,\mathrm{s^{-2}}$) as well as sheared ($\langle S\rangle^2_{x,y} \sim 10^{-4}$–$10^{-3}\,\mathrm{s^{-2}}$) throughout the storm (Figs. 10b,d and 11). In addition, the mean shear and stratification within the OSBL evolve similarly so that the mean profiles contain a region of approximately marginal stability within the OSBL (e.g., Thorpe and Liu 2009; Smyth et al. 2019), where $\mathrm{Ri}_g = \langle N^2\rangle_{x,y}/\langle S\rangle^2_{x,y} \approx 1/4$ from about 5-m depth to about D_N^2 (Fig. 12). Above 5 m, Ri_g remains positive, but it is much less than 1/4 due to the strong surface layer shear near the air–sea interface. During the eye passage, the mean shear and stratification in the OSBL weaken, and Ri_g decreases suddenly from just above 1/4 to just below 1/4 (Fig. 12a). Thereafter, the Ri_g profile remains relatively consistent through the end of phase IV. A statistical measure of the spatial variability in Ri_g (Fig. 12) connects back to Fig. 8; the modulation of the reduced shear by the rolls occurs in conjunction with a reduced percentage (50%–75%) of the area from 5 m to the pycnocline that is locally unstable ($\mathrm{Ri}_g < 1/4$). In contrast, without the rolls and after the eye, more than 75% of the area is locally unstable through most of the OSBL.

The reasonably good comparison between the simulated and observed OSBL depth and SST response suggests that the

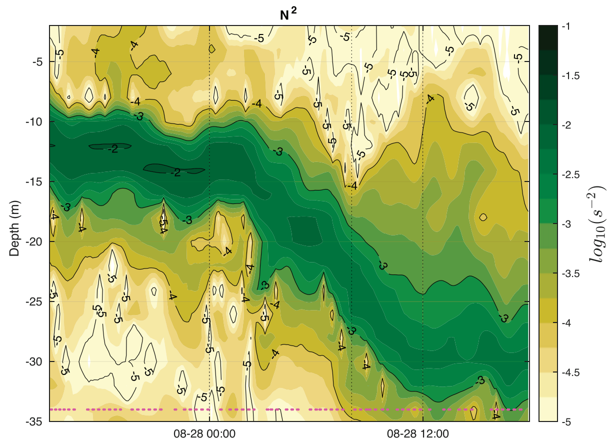

FIG. 11. Observed vertical buoyancy gradient N^2 in the region and time simulated by LES. Magenta dots at 34 m indicate the times of glider profiles sampled at 5-s resolution. The data have been linearly interpolated to a uniform 6 min × 2 m grid and smoothed with a forward-and-backward moving average with a 1-h (10-point) boxcar window and zero phase shift in an attempt to approximately mimic the spatial averaging that is applied in the analysis of the large-eddy simulation.

simulated turbulent transport processes that drive these changes in the LES may be relevant to and important in the real ocean. However, although the evolution of the simulated surface current direction is similar to observations (in Fig. 2 of Glenn et al. 2016), and observed and simulated differences between top and bottom velocities are within about a factor of two, the magnitude of the simulated surface current is sometimes stronger than observed by more than a factor of 2. We attribute the stronger surface currents and weaker bottom currents in the LES to the absence of a pressure-gradient-driven flow opposed to the wind-driven surface current, which Glenn et al. (2016) found was significant via numerical simulations. In addition, it is notable that the observed mean stratification of the OSBL at the beginning of phase III is somewhat weaker than simulated ($\langle N^2\rangle_{x,y} \sim 10^{-5}$ versus $10^{-4}\,\mathrm{s^{-2}}$; cf. Fig. 11 and Fig. 10b). In this case, it is plausible that the relatively strong simulated stratification is attributable to missing surface gravity wave effects, but missing large-scale processes may also contribute to this stratification bias as well. We will return to a discussion of these missing processes below.

b. Momentum flux

In this idealized simulation, the horizontally averaged velocity vector $\langle \mathbf{u}_h\rangle_{x,y}$ only evolves due to the Coriolis force and the convergence of turbulent vertical fluxes of momentum, that is

$$\frac{\partial\langle \mathbf{u}_h\rangle_{x,y}}{\partial t} + \mathbf{f}\times\langle \mathbf{u}_h\rangle_{x,y} = \frac{\partial \mathbf{F}_m}{\partial z},$$

where $\mathbf{f} = (0, 0, f)$ is the traditional Coriolis frequency in vector form. This section complements the previous description of the evolution of $\langle \mathbf{u}_h\rangle_{x,y}$ with a description of the turbulent momentum flux, $\mathbf{F}_m = \langle \nu_{\mathrm{SGS}}\partial\mathbf{u}_h/\partial z - w\mathbf{u}_h\rangle_{x,y}$, which is dominated

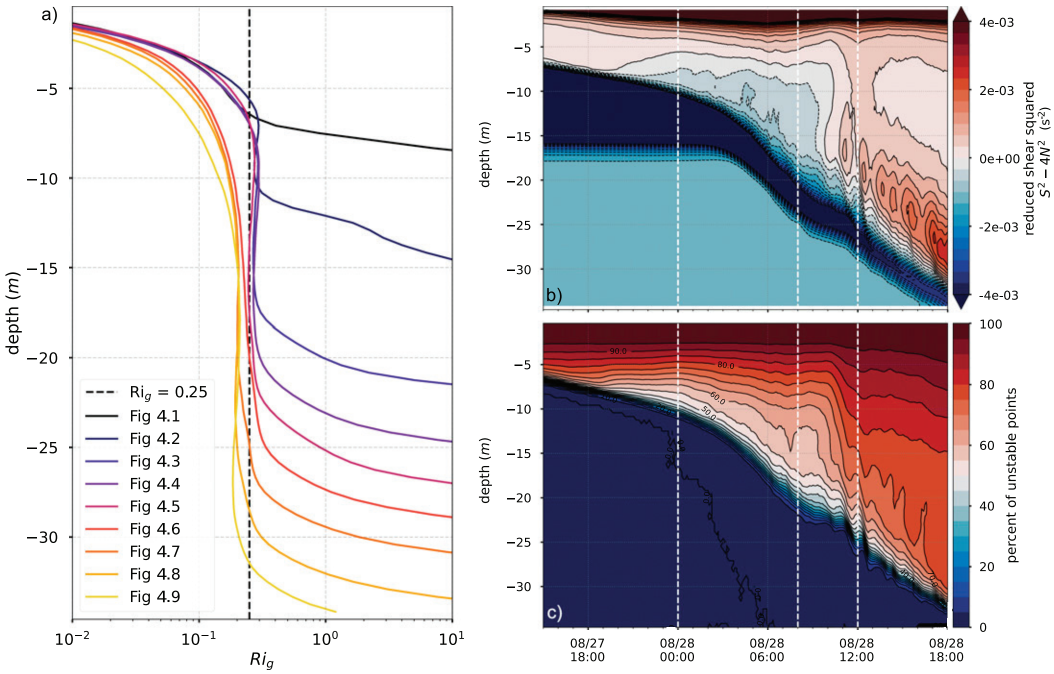

FIG. 12. Profiles of (a) the gradient Richardson number $\mathrm{Ri}_g = N^2/S^2$ and (b) the reduced shear $S^2 - 4N^2$ (s^{-2}) associated with the mean velocity and buoyancy profiles. (c) The percent of all points where the reduced shear is positive at each depth. The profiles all cluster into two regimes that separate by time: before and after eye passage, which occurs at about 0900 UTC 28 Aug (see Figs. 1 and 2).

by the resolved flux $-\langle w\mathbf{u}_h\rangle_{x,y}$ throughout most of the OSBL.[2] We characterize this flux in terms of its magnitude and direction, and we decompose it into two scales: smaller and larger than $3D_{N^2}$ (with subgrid-scale fluxes lumped with small scales). In addition, we quantify the effective turbulent viscosity profile, which we define by

$$\nu_t = \frac{\mathbf{F}_m \cdot \partial\langle \mathbf{u}_h\rangle_{x,y}/\partial z}{|\partial\langle \mathbf{u}_h\rangle_{x,y}/\partial z|^2}. \tag{1}$$

This definition of the scalar turbulent viscosity ν_t does not account for the nonlocal component of $\mathbf{F}_m$, i.e., the component of $\mathbf{F}_m$ that is perpendicular to $\partial\langle \mathbf{u}_h\rangle_{x,y}/\partial z$ (e.g., Large et al. 2019), which modifies ν_t by 3% or less in this scenario. Nevertheless, we still quantify the nonlocal component of $\mathbf{F}_m$ via the angle Ω between $\mathbf{F}_m$ and $\partial\langle \mathbf{u}_h\rangle_{x,y}/\partial z$ (e.g., Large et al. 2019), since the magnitude of the nonlocal flux is as large as 25% of $|\mathbf{F}_m|$ and thus may significantly influence the evolution of $\langle \mathbf{u}\rangle_{x,y}$ but is not accounted for in some OSBL mixing parameterizations (e.g., Large et al. 1994).

In this strongly forced regime, the magnitude of the shear is always positive, and the evolution of the momentum flux is controlled by the surface stress (see Fig. 1), which sets the surface value of $\mathbf{F}_m$. We also find that $|\mathbf{F}_m|$ decays approximately linearly with depth from the surface to about $z = -D_{N^2}$ while entrainment is occurring during phases II–IV (Figs. 13 and 14). Deviations from a linear $\mathbf{F}_m(z)$ profile do occur, but they have a magnitude of only about $0.2u_*^2$ where the friction velocity $u_* = \sqrt{|\boldsymbol{\tau}|/\rho_0}$. In addition, the turbulent viscosity collapses to a virtually time-independent vertical profile when ν_t is made dimensionless by dividing by $ku_*D_{N^2}$ and the depth z is divided by D_{N^2} (e.g., Large et al. 1994).

The decomposition of $\mathbf{F}_m$ into large and small scales (Fig. 14) shows that the flux is dominated by small wavelengths $\lambda < 3D_{N^2}$ at all depths and times. However, larger scales are nonnegligible, particularly during phase II and the beginning of phase III in the top 10 m, where the streaks and rolls are prominent and large scales account for about 10%–20% of the total flux. Just above the thermocline ($z = -D_{N^2}$), the large scale contribution to the flux is more intermittent and relatively weaker; it only just reaches 10% of the total flux at the beginning of phase III.

After the eye passage during phases III–IV, the acceleration of the OSBL continues, but the large-scale contribution to the flux is substantially smaller in percentage terms than before the eye. In addition, $|\mathbf{F}_m|$ briefly exhibits a relatively large ($\sim 0.2u_*^2$) positive deviation from the linear profile in the middle of the

[2] The subgrid-scale terms are only significant within a few meters of the surface and in the thermocline, hence the mean response and large-scale structures are expected to be fairly insensitive to refining the grid resolution (e.g., Whitt et al. 2019). Although it is prohibitively costly to significantly increase the resolution and test this in the large domain considered here, we confirmed this expectation by refining the grid resolution by a factor of 2 in all dimensions in a smaller domain.

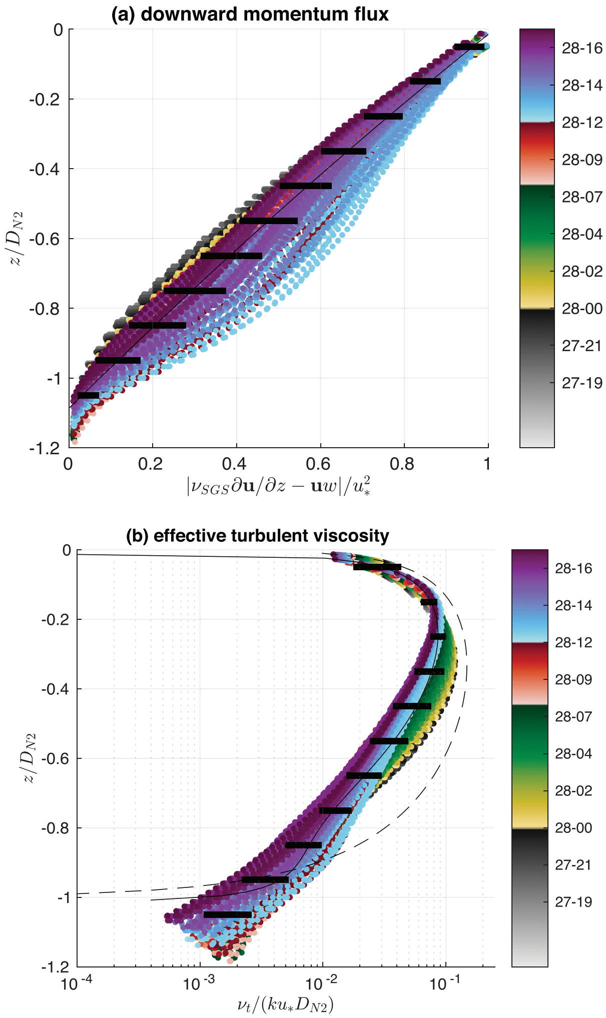

FIG. 13. (a) The momentum flux scaled by the friction velocity u_* decays nearly linearly with decreasing z/D_{N^2} at all times when entrainment is occurring (color bar, day-hour). The correlation coefficient between z/D_{N^2} and $|\mathbf{F}_m|$, where $\mathbf{F}_m = \langle \nu_{\mathrm{SGS}}\partial\mathbf{u}/\partial z - \mathbf{u}w\rangle_{x,y}$, is 0.98. The best fit quadratic (for $z/D_{N^2} > -1.2$) has coefficients -0.11, 1.18, and 1.09 (beginning with the highest-order term). (b) The effective turbulent viscosity, $\nu_t = \mathbf{F}_m \cdot \langle\partial\mathbf{u}_h/\partial z\rangle_{x,y}/|\langle\partial\mathbf{u}_h/\partial z\rangle_{x,y}|^2$, collapses when scaled by $ku_*D_{N^2}$, where $k = 0.4$ is the von Kármán constant. The best-fit quadratic (for $z/D_{N^2} > -1$) has coefficients -1.28, 3.41, -3.09, 0.97, and -0.01 and explains 88% of the variance for $z/D_{N^2} > -1$. Standard deviations in 11 bins are indicated by thick black bars. The dashed line in (b) is the empirical function $-z/D_{N^2}(1 + z/D_{N^2})^2$; a similar function is used in the K-profile parameterization scheme of Large et al. (1994).

OSBL (at about 1200 UTC 28 August, perhaps because the wind is particularly strong and well aligned with the shear, as shown in Fig. 10f) but thereafter returns to a nearly linear profile that persists through the end of phase IV.

The angle Ω between the momentum flux and the mean shear vector is also plotted as a function of time and scale in Fig. 14. In both the total and small-scale part of $\mathbf{F}_m$, Ω is small but nonnegligible, reaching maxima of about 15° and 10°, respectively, between about 5–10 m at the end of phase II (for reference, this implies that the nonlocal component of $\mathbf{F}_m$ is 17%–26% of the magnitude $|\mathbf{F}_m|$). With respect to the total and small-scale fluxes, Ω is very slightly negative at the surface, but positive throughout most of the OSBL during phase II. That is, the corresponding $\mathbf{F}_m$ vector is rotated counterclockwise relative to the local shear $\partial\langle\mathbf{u}_h\rangle_{x,y}/\partial z$ and toward the wind stress vector $\boldsymbol{\tau}$ in most of the OSBL.

It may be noted that the total and small-scale nonlocal fluxes are correlated in time with large-scale nonlocal fluxes, which are associated with much greater Ω, particularly in the middle of the OSBL. Hence, we consider the hypothesis that the nonlocal momentum flux, i.e., the occurrence of $\Omega \neq 0°$ in Figs. 14d–f, is due to the presence and modulating effects of the large-scale rolls/streaks. The evidence in support of this hypothesis is as follows. First, the magnitude ($w_r u_r \sim 10^{-4}\,\mathrm{m^2\,s^{-2}}$), depth range (top 10 m), and angle Ω of the large-scale fluxes (Figs. 14c,f) are consistent with the roll structures described in section 3 (Fig. 7). In particular, Ω (Fig. 14f) is slightly negative near the surface, where the streaks are rotated to the right of the wind stress and local shear, but Ω increases with depth as the mean shear vector rotates clockwise but the rolls and streaks remain at a fixed angle (see Figs. 6 and 7). Second, the temporal evolution of the nonlocal fluxes at small scales (Fig. 14e) is similar to the temporal evolution of the streaks as well as the associated large-scale fluxes (cf. to Figs. 5b,h and 14c). In particular, both the magnitude of the large-scale streaks/rolls and the small-scale nonlocal fluxes are largest during phase II and abruptly transition to much smaller values as the eye passes. Further, the small-scale turbulence is modulated by and more intense below the streaks ($u_r > 0$) (Figs. 8c,e,i), where the large-scale shear vector is rotated counterclockwise relative to the mean shear vector. To the extent this relationship is significant and strong, a positive Ω at small scales (Fig. 14e) is expected at the base of the streaks while they are present. Together, all of this evidence suggests that the nonlocal momentum flux, at large and small scales, is directly or indirectly due to the presence of the large-aspect-ratio streaks and rolls. In addition, explicit models of these large-aspect-ratio structures may be necessary to model nonlocal fluxes in OSBL mixing parameterizations.

Thus, we conclude that the large-aspect-ratio structures fundamentally alter the direction and magnitude of the momentum flux and thus the evolution of the mean momentum profile in this scenario, but the magnitudes of these modifications are relatively small (~10%) compared to the fraction of turbulent kinetic energy in these large scales (>50%).

c. *Entrainment and buoyancy flux*

The rapid SST cooling and the associated impacts on the hurricane are driven by entrainment and the downward turbulent buoyancy flux as the OSBL penetrates into the cold thermocline. In particular, since the OSBL is approximately mixed and the mean buoyancy profile is highly correlated with the mean temperature profile (Fig. 3), the evolution of the SST is governed by the evolution of the buoyancy averaged over $z > -D_{N^2}$ (Stevenson and Niiler 1983), which evolves according to

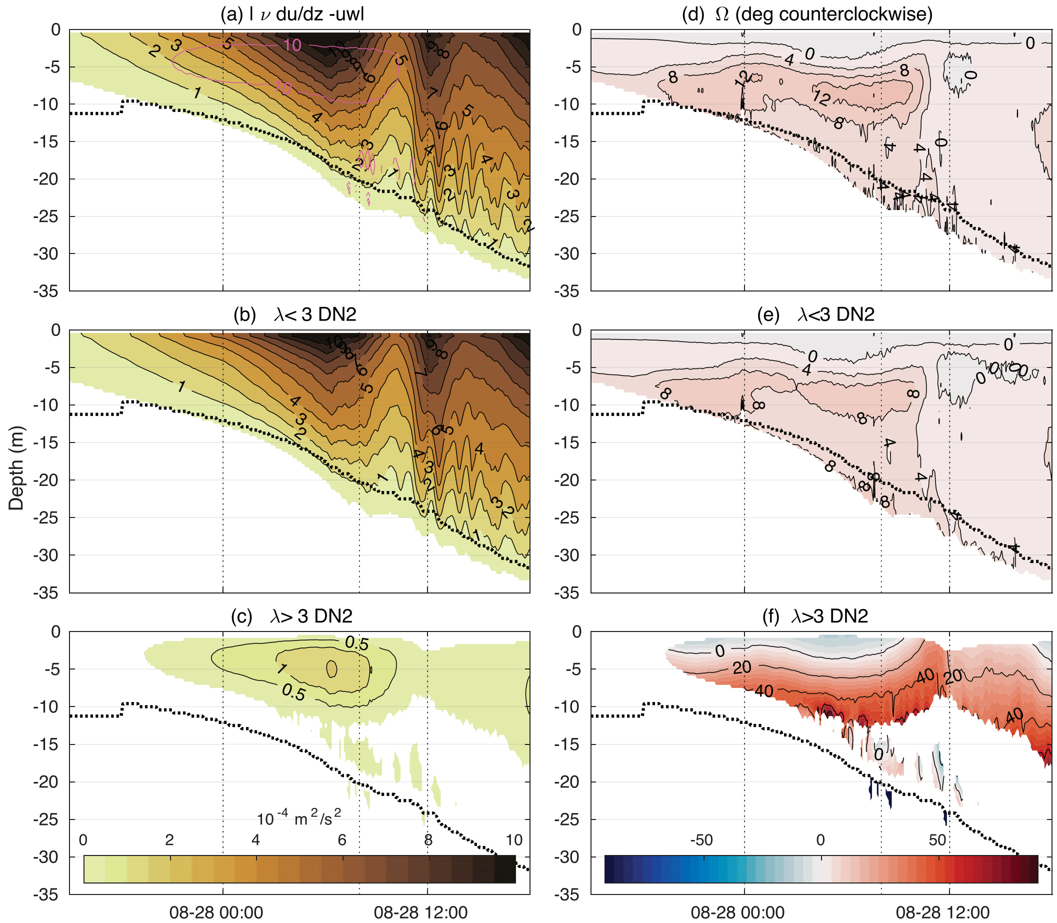

FIG. 14. The (left) magnitude and (right) direction of the downward vertical momentum flux vector $\mathbf{F}_m = \langle \nu_{\rm SGS}\partial \mathbf{u}_h/\partial z - w\mathbf{u}_h\rangle_{x,y}$. The direction is given relative to the local mean shear vector $\langle \partial \mathbf{u}_h(z,t)/\partial z\rangle_{x,y}$, which is shown in Fig. 10f. (a) The total flux is also decomposed, via Fourier transforms, into (b) small scales, that is, horizontal wavelengths $\lambda < 3D_{N^2}$ including subgrid scales, and (c) large scales, that is, horizontal wavelengths $\lambda > 3D_{N^2}$. For reference, the black dotted line indicates D_{N^2}. The magenta contours in (a), marked every 10%, indicate the percentage of the total flux that is attributable to large scales.

$$\frac{\partial}{\partial t}\left(\langle b\rangle_{x,y,D_{N^2}}\right) = \frac{F_b(z=0) - F_b(z=-D_{N^2})}{D_{N^2}} - \frac{\Delta b}{D_{N^2}}\frac{\partial D_{N^2}}{\partial t}, \quad (2)$$

where $\Delta b = \langle b\rangle_{x,y,z>-D_{N^2}} - \langle b\rangle_{x,y}(z=-D_{N^2})$ and

$$F_b = \langle \kappa_{\rm SGS}\partial b/\partial z - wb\rangle_{x,y}.$$

In addition, the evolution of the mean buoyancy profile is governed by

$$\frac{\partial\langle b\rangle_{x,y}}{\partial t} = \frac{\partial F_b}{\partial z}.$$

Therefore, this section quantifies F_b and the related entrainment flux $F_e = -\Delta b \partial D_{N^2}/\partial t$ in order to evaluate the impact of the storm-driven OSBL turbulence, and the large-aspect-ratio structures in particular, on the evolution of the mean buoyancy and stratification profiles, entrainment, and SST cooling.

First, it is notable that the buoyancy flux profile F_b collapses when divided by F_e (Fig. 15c). The maximum of F_b is found at $z \approx -3D_{N^2}/4$ throughout the storm, and the magnitude of this maximum is approximately equal to $3F_e/4$ on average (Figs. 15a,c). About 80% of the temporal variance in the maximum of F_b (Fig. 15a) can be explained by variations in the rate of entrainment F_e. In addition, a similarly large fraction of the temporal variance in F_e (and F_b) can be explained by the rate of working on the surface current by the wind stress $\boldsymbol{\tau}\cdot\mathbf{u}$ ($z = 0$) divided by D_{N^2} (Fig. 16).[3] During the end of phase III and the beginning of phase IV, when the angle between the wind and the current is relatively small (Fig. 10e), the dot product in $\boldsymbol{\tau}\cdot\mathbf{u}$ ($z = 0$) is particularly crucial; it is only at this time that the conventional friction

[3] As Bill Large suggested to us, the shear production averaged above D_{N^2} explains F_e about as well as the wind work. Motivated by that suggestion, we also find that the surface stress dotted into the average shear above D_{N^2}, i.e., $\tau\cdot\langle\partial\mathbf{u}_h/\partial z\rangle_{x,y,z>-D_{N^2}}$ explains the entrainment about equally well too.

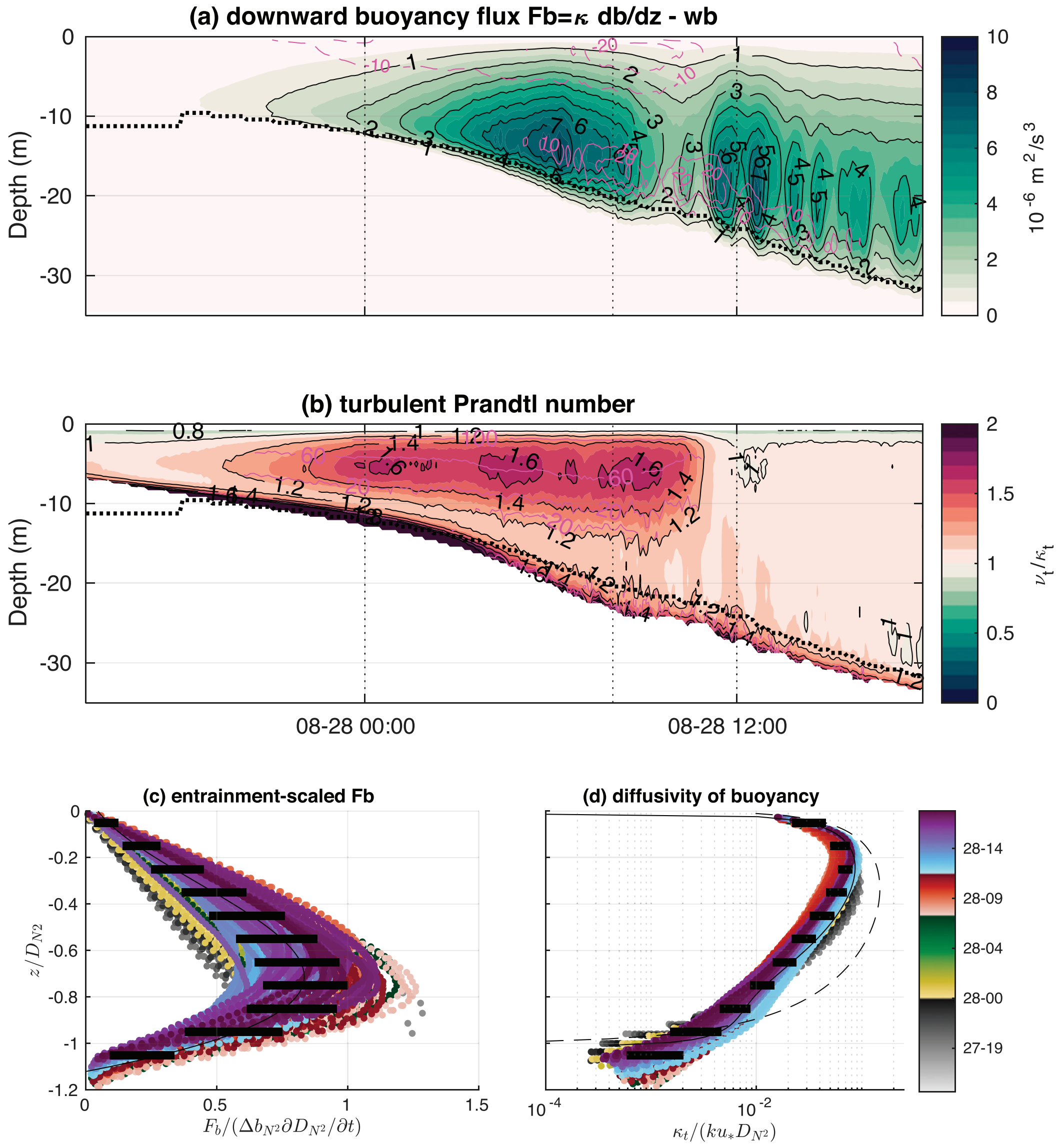

FIG. 15. (a) The vertical buoyancy flux $F_b = \langle \kappa_{SGS}\partial b/\partial z - bw\rangle_{x,y}$, which is collapsed in (c) by dividing by the entrainment buoyancy flux $F_e = \Delta b \partial D_{N^2}/\partial t$, where Δb is the difference between the depth-averaged buoyancy above D_{N^2} and the buoyancy at D_{N^2}. The color bar in (c) and (d) indicates the time (day-hour). The best-fit cubic in (c) (solid black line), which explains 86% of the variance of F_b, has coefficients −3.07, 2.82, 0.65, and 0.05 (from highest to lowest order). The turbulent diffusivity profile $\kappa_t = F_b/N^2$ in (d) is very similar to the turbulent viscosity profile ν_t (plotted in Fig. 13b), but the turbulent Prandtl number $\mathrm{Pr}_t = \nu_t/\kappa_t$ systematically differs from 1, as shown in (b). For reference, magenta contours in (a) and (b) quantify the percentage of F_b and $\mathrm{Pr}_t - 1 > 0.2$, respectively, that are attributable to fluctuations with wavelengths greater than $3D_{N^2}$. In both (c) and (d), horizontal black bars indicate standard deviations in 11 depth bins. For reference, the depth D_{N^2} (dotted black) is overlaid in (a) and (b), and the solid black and dashed black curves in (d) are the same dimensionless viscosity model profiles as in Fig. 13b.

velocity scaling u_*^3/D_{N^2}, which works reasonably well in phases I–III and late in phase IV, is too weak (Fig. 16). Hence, the rapid ahead-of-eye SST cooling in the LES is due to two factors: 1) the relatively large injection of kinetic energy from the wind to the OSBL ahead of the eye passage in phase II (due to the large friction velocity; see Fig. 16), and 2) the relatively small D_{N^2} at that time. The latter effect is quadratically important, since $\partial\langle b\rangle_{x,y,D_{N^2}}/\partial t \sim F_e/D_{N^2} \sim \boldsymbol{\tau}\cdot\mathbf{u}(z=0)/D_{N^2}^2$ [see Eq. (2)].

Second, it is notable that F_b has a relatively large magnitude in the OSBL throughout the storm. Specifically, the flux Richardson number (Osborn 1980)

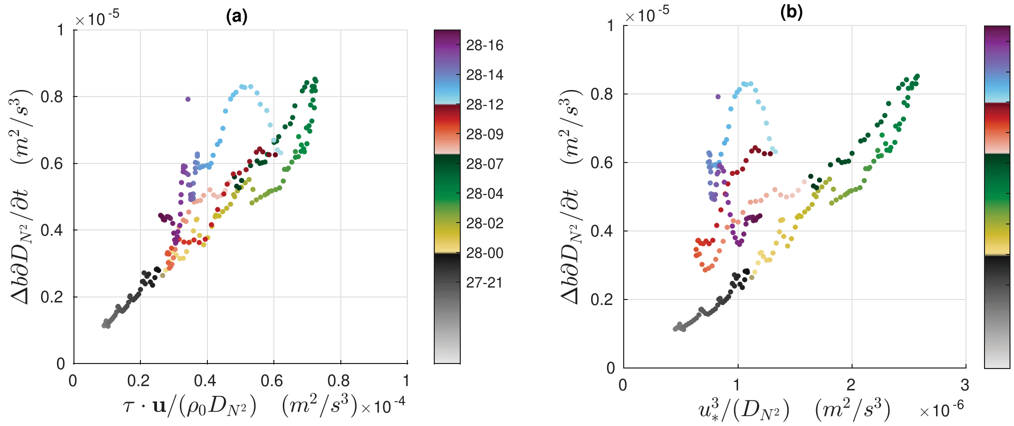

FIG. 16. The relationship between the entrainment flux F_e and the rate of working on the surface current by (a) the wind stress ($r^2 = 0.75$, linear regression slope = 0.1) and (b) the friction velocity u_*^3 ($r^2 = 0.37$, linear regression slope = 2.0) during entrainment. The color bar indicates the time (day-hour).

$$\mathrm{Ri}_f = \frac{F_b}{\mathbf{F}_m \cdot \partial \langle \mathbf{u} \rangle_{x,y} / \partial z} \sim 0.1$$

throughout most of the OSBL. In particular, $\mathrm{Ri}_f \sim \mathrm{Ri}_g$ (Fig. 17), and hence the buoyancy flux is 10% or more of the shear production where $\mathrm{Ri}_g \gtrsim 0.1$. That is, the strong wind makes buoyancy relevant to the turbulence energetics via entrainment, even though the Monin–Obukhov length is at least an order of magnitude greater than D_{N^2}, and the surface buoyancy flux $F_b(z = 0) \ll \max_z(F_b)$ is relatively small (cf. Figs. 1c and 15a).

Third, F_b is composed mostly of small scales $\lambda < 3D_{N^2}$, but large scales $\lambda > 3D_{N^2}$ make a nonnegligible contribution to the total F_b (similar to $\mathbf{F}_m$) (cf. Figs. 15a and 14). Specifically, the large scales are responsible for a countergradient flux $F_b < 0$, which is equal in magnitude to 10%–30% of the total $|F_b|$ in the upper 5–10 m during phases II–III. And, large scales are responsible for a downgradient flux equal to 10%–20% of the total F_b just above the thermocline during phases II–IV (Fig. 15a). Plots of F_b as a function of horizontal wavelength and depth at the beginning and end of phase III in Figs. 18a and 18b highlight the spatial and spectral localization of the large-scale buoyancy fluxes as well as the abrupt decay of the near-surface streaks/rolls and the associated large-scale fluxes during phase III. These spectra also provide explicit quantitative support for the hypothesis implicitly espoused in section 3: that there are a small number of distinct structures that dominate the large-scale dynamics, rather than a turbulent continuum at large scales. That is, although a scale separation is an imperfect way of separating the large-aspect-ratio rolls and billows from the turbulent continuum, the scale separation effectively achieves that end in this case. Most of the large-scale contribution to F_b can essentially be attributed to either the near-surface rolls/streaks in the top 10 m or the KH-like billows just above D_{N^2}, as described in section 3. Nevertheless, a cautious interpretation is still warranted: some of the flux associated with the KH-like billows is apparently categorized as small scale (to the right of the red line in Fig. 18), and some of the large-scale flux is evidently not associated with the dominant large structures described in section 3.

Finally, it is notable that although the buoyancy flux varies systematically with the momentum flux such that the turbulent Prandtl number $\mathrm{Pr}_t = \nu_t/\kappa_t$ is always near 1 [ν_t and κ_t are defined as in Eq. (1)], there are also persistent deviations $\mathrm{Pr}_t > 1$ (Figs. 15b and 17). In addition, these positive deviations in Pr_t coincide with and are partially attributable to: 1) the presence of the Ekman-layer rolls, which increase the overall Pr_t by reducing κ_t and increasing ν_t (see Figs. 18a,c,e; cf. Figs. 17a,b), 2) the increased mean-profile Ri_g, which is associated with higher $\mathrm{Pr}_t = \mathrm{Ri}_g/\mathrm{Ri}_f$ and lower Ri_f relative to Ri_g for $\mathrm{Ri}_g \approx 0.25$ (see Figs. 12 and 17), and 3) the nonlocal momentum flux during phase II, which does not directly modify Pr_t more than a few percent but is thought to be another consequence of the Ekman-layer rolls (Fig. 14). Conversely, the KH-like structures do not directly increase Pr_t. Just above the thermocline, the scale-dependent Prandtl number is generally positive but less than 1/2 over the depth range and wavelengths characteristic of the KH-like billows, which are more effective at transporting buoyancy than momentum and thus directly contribute to lowering Pr_t and increasing Ri_f (ignoring the indirect effects of these structures on Pr_t via smaller wavelengths; see Fig. 18).

In summary, although entrainment and SST cooling is controlled to a first approximation by the mean dynamics [i.e., it is a response to the wind work on the mean flow, as in Pollard et al. (1972)], the large-aspect-ratio structures contribute ~10% to the vertical buoyancy flux and thus may modify the SST response by ~10% (i.e., a few tenths or possibly even a whole degree Celsius).

5. Discussion

Before concluding, we briefly compare our simulation study with a few prior observational studies focused on the instabilities of both the Ekman boundary layer and stratified shear layers, which are thought to be relevant to the near-surface streaks/rolls and the KH-like billows near the thermocline, respectively. In the second section below, we explicitly discuss the possible significance and implications of two omitted processes, surface gravity waves and larger-scale ocean dynamics.

a. Comparisons with prior studies

1) Ekman layer rolls

Perhaps the most plausible dynamical causes of the simulated near-surface streaks and rolls are the linear instabilities of the Ekman layer (Kaylor and Faller 1972; Brown 1972; Asai and Nakasuji 1973; Lemone 1973; Duncombe 2017; Skyllingstad et al. 2017). These instabilities produce helical rolls/streaks approximately aligned with the geostrophic wind in the atmosphere and surface stress in the ocean (often tilted at some small angle $\sim 10°$ relative to the wind or stress) that are qualitatively similar to the near-surface streaks and rolls described in section 3 [e.g., compare Fig. 7 with Fig. 4a of Lemone (1973)]. In particular, the roll circulation (v_r, w_r) as shown in Fig. 7 is typically surface intensified and inclined in the cross-roll-vertical plane. In addition, the cross-roll wavelength $\lambda_r \sim 10D_{\mathrm{Ek}}$, where $D_{\mathrm{Ek}} = \sqrt{2\nu_t/f} \approx 15$ to 30 m and $\nu_t \sim 0.1ku_*D_{N^2}$ as in Fig. 13b (e.g., Lemone 1973; Asai and Nakasuji 1973; Sous et al. 2013).

There are also some notable similarities between the simulated streaks/rolls and observations of such features in the ABL, as reported by Lemone (1973, 1976). In both this LES and the ABL observations, the roll-streak system is associated with a downgradient momentum flux and positive shear production and upgradient buoyancy flux and positive buoyancy production. Further, the simulated roll-scale modulation of small-scale turbulence, which is enhanced in roll downdrafts $w_r < 0$ that correspond with cold temperature anomalies, is qualitatively analogous to the ABL observations, in which turbulence is enhanced in roll updrafts that correspond with warm temperature anomalies.

There are also some notable differences between our simulated rolls/streaks and those observed by Lemone (1973, 1976). For example, the cross-roll velocity v_r was stronger and more organized than the streak velocity u_r in their ABL observations, whereas the streak velocity u_r is stronger and more organized than the cross-roll velocity v_r in these ocean LES. Second, Lemone (1973) only observed the regime where $D_{\mathrm{Ek}} \ll D_{N^2}$ and thus found that $\lambda_r \sim D_{N^2}$, whereas in the LES $\lambda_r \sim 10D_{N^2}$ and w_r is thus much weaker than v_r, unlike their ABL observations. Further, Lemone (1976) finds that the observed modulation of smaller-scale turbulence in the ABL is explained by roll-scale vertical transport of small-scale turbulence via w_r in the absence of strong coherent streaks u_r. Although vertical transport of turbulence plausibly contributes to the observed roll-scale modulation of turbulence in the LES, the strong simulated streaks and the close relationship between positive reduced shear (below $u_r > 0$) and enhanced turbulence in the LES suggests that the strong streaks also contribute energy to the smaller-scale turbulence via shear production and thereby the overall roll-scale modulation of small-scale turbulence in the LES.

The favorable comparisons between the LES and ABL observations is encouraging, but the lack of direct observations of such rolls in the OSBL under Hurricane Irene means the realism of the simulated turbulence cannot be verified observationally. Direct comparisons to oceanic observations of the turbulence derived from the glider are not pursued here as the observations required to estimate vertical velocity variance (e.g., Merckelbach et al. 2019) were unavailable since the glider was lost before recovery. Temperature, conductivity, and pressure data were recorded at 5-s intervals and sent via the Iridium connections approximately every 3 h or every 5–7

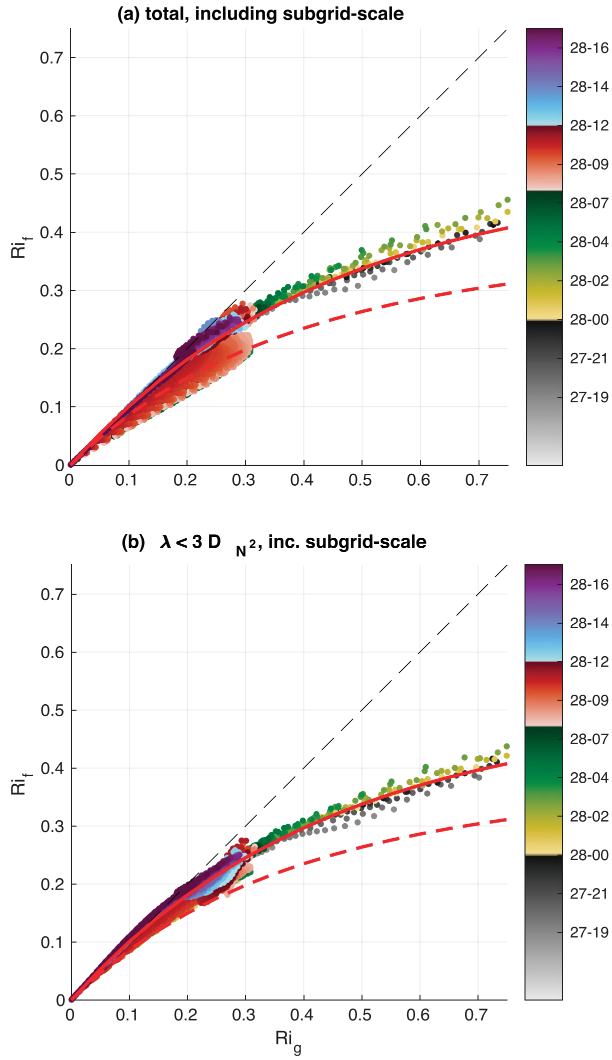

FIG. 17. The relationship between the gradient Richardson number Ri_g and flux Richardson number Ri_f above the depth of maximum stratification D_{N^2} where Ri_f is either as simulated (dots) or determined from Ri_g via $\mathrm{Ri}_f = 0.5(1 - e^{-2.25\mathrm{Ri}_g})$ (the solid red curve), which explains 93% and 98% of the variance in (a) and (b), respectively (e.g., Venayagamoorthy and Koseff 2016). In (a), the simulated Ri_f is calculated using the total buoyancy and momentum fluxes (including the subgrid scales), whereas in (b) the simulated Ri_f is calculated using only the wavelengths $\lambda < 3D_{N^2}$ (and the subgrid scales). The dashed red curve is a parameterization based on the ABL measurements (Anderson 2009), which parameterizes the subgrid-scale Ri_f in the LES (see section 2). The color bar indicates the time (day-hour).

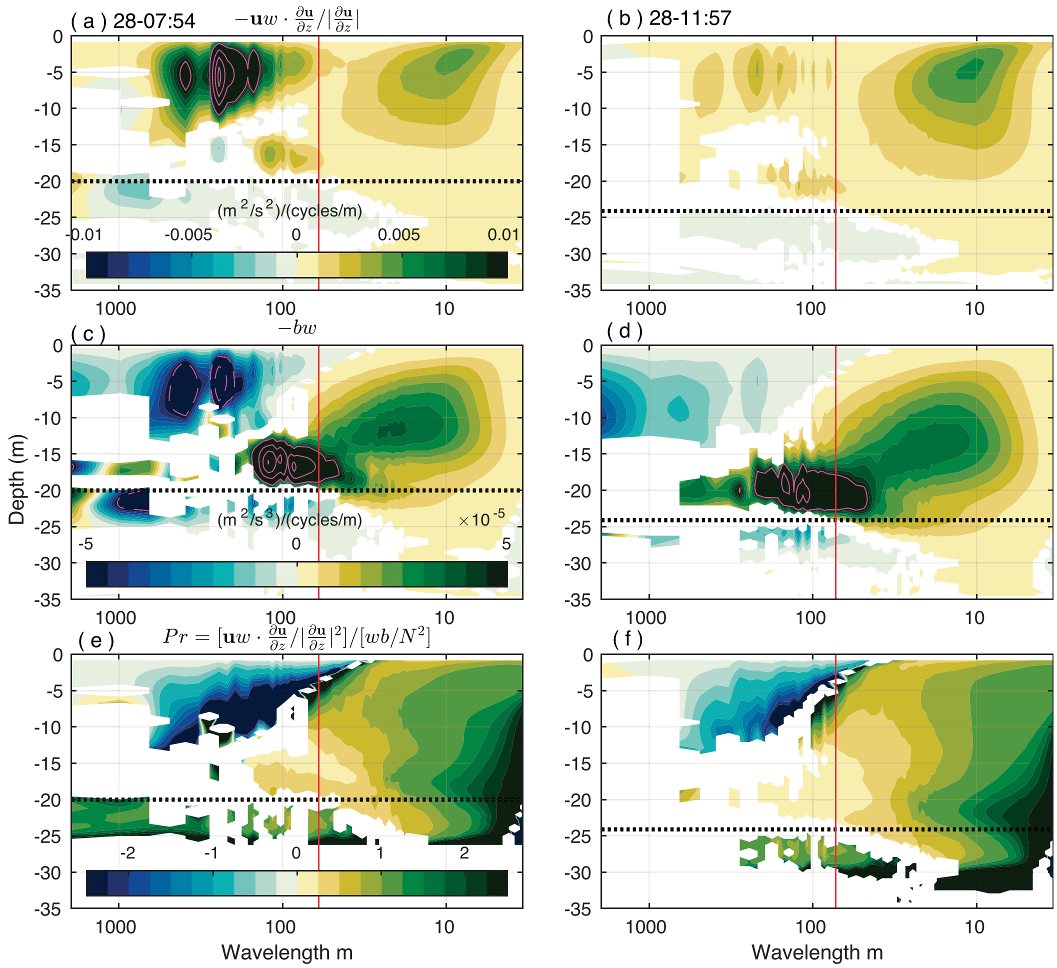

FIG. 18. Momentum and buoyancy flux cospectra at each depth averaged over 2-h windows centered at the (left) beginning and (right) end of phase III (see Fig. 1). Magenta contours, which are given every 0.01 m^2 s^{-2} (cycles per meter) in (a) and 0.000 05 m^2 s^{-3} (cycles per meter) in (c) and (d), respectively, highlight regions and wavelengths of particularly strong covariance before and after eye passage. Areas where the covariance is not significantly different from zero are blanked. The dotted black horizontal lines indicate the depth D_{N^2}, and the vertical red lines indicate the wavelength $3D_{N^2}$. The ratio of the relevant covariances, i.e., the flux Richardson number Ri_f, is decomposed by horizontal wavelength λ and written as a turbulent Prandtl number $\mathrm{Pr} = \mathrm{Ri}_g/\mathrm{Ri}_f$ in (e) and (f), where $\mathrm{Ri}_g = \langle N^2 \rangle_{x,y}/\langle S \rangle_{x,y}^2$ is the gradient Richardson number of the horizontally averaged velocity and density profiles.

downcast–upcast cycles. In summary, we lack the spatiotemporal resolution to isolate the roll structures or other features of interest in the turbulence that would allow for a useful direct comparison between the simulated and observed turbulence under Hurricane Irene.

Nevertheless, there are numerous observational indications of helical rolls such as those simulated in the LES in the ocean [going back to, e.g., Langmuir (1938); see section 1]. And some of these observed OSBL rolls/streaks have been simulated in LES and are qualitatively insensitive to the effects of surface gravity waves, which are omitted here (see Sundermeyer et al. 2014). Thus, the simulated large-aspect-ratio structures are plausibly realistic, even without surface gravity waves or larger-scale processes. However, we only explicitly compare the LES to the particularly relevant, intriguing, and recent observations of Gargett and Savidge (2020). They report observations of the coastal ocean boundary layer in 31 m of water under a hurricane on the South Atlantic Bight. As in the simulation reported above, they observed the oceanic response to a hurricane that moved approximately northward and passed to the west of the observing tower over about a day. The maximum stress in their case is perhaps 50% weaker than in ours, but the temporal evolution is quite similar. The winds come from a fairly consistent direction as the storm approaches, they rotate rapidly and weaken as the eye passes, and then the winds stabilize their direction and intensify after the eye before weakening again.

Most interestingly, Gargett and Savidge (2020) also find coherent large rolls, which they attribute to Langmuir supercells that are strong as the storm approaches, wash away during the eye passage, and then reemerge after the eye. The observed disappearance of the large rolls during the eye passage is qualitatively similar to the LES results above, although the observed forcing is dominated by waves whereas the LES forcing is dominated by winds, and their water column is essentially unstratified whereas ours is strongly stratified. A key conclusion of theirs, which our results seem to qualitatively endorse, is that steady-state nondimensional parameters may be insufficient to qualitatively or quantitatively characterize some features of OSBL turbulence under rapidly variable forcing. They also speculate that the disappearance of the large structures during the eye passage may reflect a sharp sensitivity to a ratio of two time scales: a time scale over which the large structures grow, and a time scale over which the mean flow or forcing evolves. This hypothesis is plausibly relevant in our LES as well, although the growth time scale of Ekman layer instabilities is thought to be much longer than Langmuir cells, and future work is necessary to test this hypothesis. We return to a discussion of the potential implications of missing surface waves in the LES below.

2) Kelvin–Helmholtz billows

The simulated large-scale structures just above the thermocline are also qualitatively similar to various oceanic observations of billows associated with shear instabilities in that they reveal temperature overturns wrapped by broken braids of strong vorticity that in some (rare) cases form cat's-eye patterns consistent with finite-amplitude Kelvin–Helmholtz billows in regions with a mean-profile $\mathrm{Ri}_g \approx 1/4$ (Seim and Gregg 1994; Chang et al. 2016). The crests and troughs of the simulated billows are oriented perpendicular to the mean shear vector at the depth of the thermocline, and their wavelength (about 125 m at the beginning of phase III) is consistent with the fastest growing linear KH instability on a canonical $\tanh(z/L)$ stratified shear layer with $L \approx 10$ m (Hazel 1972). However, the dominant-scale mode is also plausibly a result of merging or some other dynamical interaction and thereby associated with KH modes of a similar but different size [e.g., with half the wavelength and $L \approx 5$ m; see, e.g., Seim and Gregg (1994), Smyth and Moum (2000), and Smyth (2003)]. But, an exact match to theory is neither expected nor pursued since the observed mean shear and stratification are not exactly consistent with the canonical tanh profiles and the KH billows coexist with finite amplitude variance due to a range of other processes and scales (e.g., ambient turbulence lofted down from higher in the boundary layer; see Kaminski and Smyth 2019). Finally, it is worth reiterating that these billow-like structures are more the exception than the norm, although they are still directly responsible for ~10% of the covariances.

b. Missing processes

1) Surface gravity waves

Even though the SST cooling and rapid entrainment response to Hurricane Irene is qualitatively represented in the LES, one missing process that might significantly impact the OSBL turbulence described above is surface gravity waves. A future study with the Craik–Leibovich (CL) equations (e.g., McWilliams et al. 1997; Tejada-Martinez and Grosch 2007; Sullivan et al. 2012; Van Roekel et al. 2012; Large et al. 2019) might elucidate some effects of the time-dependent and misaligned waves and winds. Our omission of the wave effects captured by the CL equations might be cast as an assumption that the turbulent Langmuir number, i.e., $\mathrm{La}_t = \sqrt{u_*/u_s}$, where u_s is the surface Stokes velocity (Li et al. 2005), is sufficiently large. Although calculating the Stokes velocity for the wave field under Hurricane Irene is beyond the scope of this paper, La_t is likely within the range of 0.1–1 most of the time (e.g., as in the scenarios studied by Sullivan et al. 2012; Gargett and Savidge 2020), and thus CL effects are probably nonnegligible and likely dominant at some times. However, since the dominant waves (in the WaveWatch III simulation of Hurricane Irene; https://polar.ncep.noaa.gov/waves/hindcasts/prod-multi_1.php; Chawla et al. 2013) were often misaligned with the winds, which rotate rapidly, La_t itself may overestimate the CL effects (Van Roekel et al. 2012). In addition, there are other wave effects not captured by the CL equations that make it difficult to conjecture about the impact of waves in this scenario. For example, one issue is that the peak significant wave height is 8 m (in the WaveWatch III model) in 35 m of water, and the wave dynamics are in the intermediate regime (with peak wave periods ranging from about 14 to 7 s) where they are substantially modified by the shallow bottom. Further, wave-driven bottom boundary layer dynamics may also impact the evolution of the mean profiles (Grant and Madsen 1979, 1986) in ways not accounted for in either the LES reported here or an analogous simulation of the CL equations.

2) Pressure gradient forces and large-scale circulation

A second mechanism that may cause the OSBL turbulence to differ in the real ocean compared to the LES is the large-scale dynamics. In comparison to the surface waves, the effect of this process on the OSBL turbulence is more indirect, although probably more significant for the mean profile evolution and fluxes. In particular, pressure-gradient-driven flows arise due to the interactions of the wind-driven flow with the coastal boundary (e.g., Kundu et al. 1983; Glenn et al. 2016; Kelly 2019). As reported by Glenn et al. (2016), this process is likely responsible for both the observed stronger bottom velocity and weaker surface velocity relative to LES. In addition, the strong bottom flow activates the bottom boundary layer. Hence, mixing of the thermocline will occur both from below and above. Since the pressure gradient flows can induce a baroclinic response, they can both increase and decrease the vertical shear at the thermocline and could therefore reduce or increase mixing. Future work might evaluate the impact of the lateral pressure gradient forces on the OSBL turbulence in this scenario by imposing these forces, as simulated in the ocean model of Glenn et al. (2016), on the LES, and thereby build on the surface fluxes imposed in the control integration discussed here.

6. Conclusions

Hurricane Irene passed over the New Jersey Shelf on 28 August 2011. Ahead of the eye, wind-driven turbulent mixing led to rapid cooling of the SST by over 4°C, which contributed to energy loss via air–sea heat flux from the hurricane to the ocean and the resulting rapid decay from category 3 to category 1 during 28 August (Glenn et al. 2016; Seroka et al. 2016). Here, we report a large-eddy simulation of the ocean turbulence at horizontal scales from 2 km to 1 m in a box of ocean just to the right of where the eye passed in the middle of the New Jersey shelf. The simulation was forced by our best estimates of the time-evolving air–sea heat and momentum fluxes during the storm and the analysis focuses on the period of time when the winds strengthen and then rapidly rotate as the storm approaches and passes; the poststorm period when the winds decay and the simulated surface boundary layer extends to the bottom is left for future work.

Despite the omission of surface gravity wave effects and large scale ocean circulation dynamics, the simulation captures the observed rapid ahead-of-eye cooling of SST and deepening of the surface mixed layer. The results show that the rapid ahead-of-eye cooling was due to two factors: 1) the shallow and sharp thermocline before the storm, which facilitates both a relatively rapid SST response for a given entrainment rate, as well as a relatively rapid entrainment rate for a given wind forcing, and 2) the magnitude of the wind stress, which supplies the energy for entrainment. However, the most striking feature of the simulation and the focus of the analysis is on ephemeral large coherent structures with aspect ratios ~10 that dominated the turbulent kinetic energy and buoyancy variance at various times and depths within the OSBL.

A descriptive analysis shows that the large-aspect-ratio structures have many similarities and some differences to the classic helical Ekman layer rolls in the top 5–10 m and Kelvin–Helmholtz billows just above the thermocline, both of which have been previously observed in the atmosphere and ocean and have a well-developed basis in linear instability theory. The simulated rolls have a peak characteristic speed of $\sim$10 cm s^{-1} and a wavelength of about 300 m just before the eye, only to be washed away by the rapid rotation of the wind as the eye passes. In addition, there is striking kilometer-scale spatial modulation of the KH billows in the thermocline, which are present to some degree at most times but have a growing dominant horizontal wavelength, are far from spatially ubiquitous, and have variable orientations and degrees of organization.

Analysis of the horizontal wavenumber spectra and cospectra allow us to separate and quantify the contribution of the large-scale structures to the turbulent kinetic energy and net vertical fluxes. We find that the large structures directly contribute more than half of the kinetic energy and buoyancy variance, ~10% of the total fluxes of momentum and buoyancy, and they may modify the turbulent Prandtl number by up to 50% (from say 1 to 1.5). Although these impacts on the mean profiles are substantial, the relatively small contribution of large scales to the total fluxes suggests that the large structures probably only modestly alter the mean profile evolution (by ~10%). Consistent with this suggestion, profiles of momentum flux, buoyancy flux, and the corresponding turbulent viscosity and diffusivity nearly collapse to time-independent profiles when appropriately nondimensionalized, despite the transient nature of the dynamics. Nevertheless, if the SST evolution in a similar model scenario is desired to within better than perhaps 0.5° (or about 10%), then the large-aspect-ratio structures are probably important to account for explicitly. The simulated large turbulent structures have some qualitative similarities to known linear instability models. Thus, these linear models may be a useful starting point for parameterization development, but future LES in other parts of parameter space are probably necessary to provide guidance and validation.

Finally, since this LES is an idealized process simulation, which omits potentially important surface gravity wave effects and larger-scale ocean circulation dynamics, caution should be exercised in extrapolating from these results to the real ocean. Although there are encouraging qualitative similarities between the LES and the observations of Gargett and Savidge (2020) of the coastal ocean response to a different hurricane, future simulations exploring the impacts of the missing processes in the LES as well as observational validation of the results presented here would be necessary to make robust conclusions about the dynamics of the large-aspect-ratio structures such as those simulated here under a hurricane. As mentioned above, such future efforts may be warranted if models of the SST evolution under a hurricane are desired to within 10% accuracy.

Acknowledgments. This material is based upon work supported by the National Center for Atmospheric Research, which is a major facility sponsored by the National Science Foundation (NSF) under Cooperative Agreement 1852977. Computing and data storage resources, including the Cheyenne supercomputer (doi:10.5065/D6RX99HX), were provided by the Computational and Information Systems Laboratory at NCAR. CEW acknowledges support from Rutgers University through the School of Environmental and Biological Sciences Excellence Fellowship and the Teledyne Webb Research Graduate Fellowship. CEW also appreciates the guidance and patience of his advisor Scott Glenn as well as the insights of Bill Large, Bob Chant, Melissa Moulton, Jenessa Duncombe, and Sonya Legg into the dynamics of the system. DBW acknowledges support from the NSF, via OPP-1501993 and OCE-1658541, NOAA, via NA18OAR4310408, and NASA, via 80NSSC19K1116.

Data availability statement. All data used in this paper are publicly available in a cited reference or in Watkins and Whitt (2020); https://doi.org/10.6084/m9.figshare.12486056.v5.

REFERENCES

Anderson, P. S., 2009: Measurement of Prandtl number as a function of Richardson number avoiding self-correlation. *Bound.-Layer Meteor.*, **131**, 345–362, https://doi.org/10.1007/s10546-009-9376-4.

Anis, A., and J. Moum, 1995: Surface wave–turbulence interactions. scaling ε (z) near the sea surface. *J. Phys. Oceanogr.*, **25**, 2025–2045, https://doi.org/10.1175/1520-0485(1995)025<2025:SWISNT>2.0.CO;2.

Asai, T. and I. Nakasuji, 1973: On the stability of Ekman boundary layer flow with thermally unstable stratification. *J. Meteor.*

Soc. Japan, **51**, 29–42, https://doi.org/10.2151/jmsj1965.51.1_29.

Brown, R. A., 1972: On the inflection point instability of a stratified Ekman boundary layer. *J. Atmos. Sci.*, **29**, 850–859, https://doi.org/10.1175/1520-0469(1972)029<0850:OTIPIO>2.0.CO;2.

Businger, J. A., J. C. Wyngaard, Y. Izumi, and E. F. Bradley, 1971: Flux-profile relationships in the atmospheric surface layer. *J. Atmos. Sci.*, **28**, 181–189, https://doi.org/10.1175/1520-0469(1971)028<0181:FPRITA>2.0.CO;2.

Callies, J., and R. Ferrari, 2018: Baroclinic instability in the presence of convection. *J. Phys. Oceanogr.*, **48**, 45–60, https://doi.org/10.1175/JPO-D-17-0028.1.

Chang, M.-H., S.-Y. Jheng, and R.-C. Lien, 2016: Trains of large Kelvin-Helmholtz billows observed in the Kuroshio above a seamount. *Geophys. Res. Lett.*, **43**, 8654–8661, https://doi.org/10.1002/2016GL069462.

Chawla, A., D. M. Spindler, and H. L. Tolman, 2013: Validation of a thirty year wave hindcast using the Climate Forecast System Reanalysis winds. *Ocean Modell.*, **70**, 189–206, https://doi.org/10.1016/j.ocemod.2012.07.005.

Czeschel, L., and C. Eden, 2019: Internal wave radiation through surface mixed layer turbulence. *J. Phys. Oceanogr.*, **49**, 1827–1844, https://doi.org/10.1175/JPO-D-18-0214.1.

D'Asaro, E. A., and Coauthors, 2018: Ocean convergence and the dispersion of flotsam. *Proc. Natl. Acad. Sci. USA*, **115**, 1162–1167, https://doi.org/10.1073/pnas.1718453115.

Deusebio, E., G. Brethouwer, P. Schlatter, and E. Lindborg, 2014: A numerical study of the unstratified and stratified Ekman layer. *J. Fluid Mech.*, **755**, 672–704, https://doi.org/10.1017/jfm.2014.318.

Duncombe, J. R., 2017: Linear theory of roll instabilities in the ocean surface layer. M.S. thesis, Dept. of Ocean, Earth, and Atmospheric Sciences, Oregon State University, 76 pp.

Ekman, V. W., 1905: On the influence of the earth's rotation on ocean currents. *Ark. Mat. Astr. Fys.*, **2**, 1–52.

Elachi, C., and J. R. Apel, 1976: Internal wave observations made with an airborne synthetic aperture imaging radar. *Geophys. Res. Lett.*, **3**, 647–650, https://doi.org/10.1029/GL003i011p00647.

Etling, D., and R. Brown, 1993: Roll vortices in the planetary boundary layer: A review. *Bound.-Layer Meteor.*, **65**, 215–248, https://doi.org/10.1007/BF00705527.

Fairall, C. W., E. F. Bradley, J. Hare, A. A. Grachev, and J. B. Edson, 2003: Bulk parameterization of air–sea fluxes: Updates and verification for the COARE algorithm. *J. Climate*, **16**, 571–591, https://doi.org/10.1175/1520-0442(2003)016<0571:BPOASF>2.0.CO;2.

Fang, J., and F. Porté-Agel, 2015: Large-eddy simulation of very-large-scale motions in the neutrally stratified atmospheric boundary layer. *Bound.-Layer Meteor.*, **155**, 397–416, https://doi.org/10.1007/s10546-015-0006-z.

Gargett, A. E., J. Wells, A. Tejada-Martinez, and C. Grosch, 2004: Langmuir supercells: A mechanism for sediment resuspension and transport in shallow seas. *Science*, **306**, 1925–1928, https://doi.org/10.1126/science.1100849.

——, and D. K. Savidge, 2020: Winds, waves, and turbulence on a shallow continental shelf during passage of a tropical storm. *J. Phys. Oceanogr.*, **50**, 1341–1364, https://doi.org/10.1175/JPO-D-20-0024.1.

Glenn, S., and Coauthors, 2016: Stratified coastal ocean interactions with tropical cyclones. *Nat. Commun.*, **7**, 10887, https://doi.org/10.1038/ncomms10887.

Grant, W. D., and O. S. Madsen, 1979: Combined wave and current interaction with a rough bottom. *J. Geophys. Res.*, **84**, 1797–1808, https://doi.org/10.1029/JC084iC04p01797.

——, and ——, 1986: The continental-shelf bottom boundary layer. *Annu. Rev. Fluid Mech.*, **18**, 265–305, https://doi.org/10.1146/annurev.fl.18.010186.001405.

Hamlington, P. E., L. P. VanRoekel, B. Fox-Kemper, K. Julien, and G. Chini, 2014: Langmuir–submesoscale interactions: Descriptive analysis of multiscale frontal spindown simulations. *J. Phys. Oceanogr.*, **44**, 2249–2272, https://doi.org/10.1175/JPO-D-13-0139.1.

Hazel, P., 1972: Numerical studies of the stability of inviscid stratified shear flows. *J. Fluid Mech.*, **51**, 39–61, https://doi.org/10.1017/S0022112072001065.

Holt, S. E., J. R. Koseff, and J. H. Ferziger, 1992: A numerical study of the evolution and structure of homogeneous stably stratified sheared turbulence. *J. Fluid Mech.*, **237**, 499–539, https://doi.org/10.1017/S0022112092003513.

Howard, L. N., 1961: Note on a paper of John W. Miles. *J. Fluid Mech.*, **10**, 509–512, https://doi.org/10.1017/S0022112061000317.

Hutchins, N., K. Chauhan, I. Marusic, J. Monty, and J. Klewicki, 2012: Towards reconciling the large-scale structure of turbulent boundary layers in the atmosphere and laboratory. *Bound.-Layer Meteor.*, **145**, 273–306, https://doi.org/10.1007/s10546-012-9735-4.

Kaltenbach, H.-J., T. Gerz, and U. Schumann, 1994: Large-eddy simulation of homogeneous turbulence and diffusion in stably stratified shear flow. *J. Fluid Mech.*, **280**, 1–40, https://doi.org/10.1017/S0022112094002831.

Kaminski, A., and W. Smyth, 2019: Stratified shear instability in a field of pre-existing turbulence. *J. Fluid Mech.*, **862**, 639–658, https://doi.org/10.1017/jfm.2018.973.

Kaylor, R., and A. J. Faller, 1972: Instability of the stratified Ekman boundary layer and the generation of internal waves. *J. Atmos. Sci.*, **29**, 497–509, https://doi.org/10.1175/1520-0469(1972)029<0497:IOTSEB>2.0.CO;2.

Kelly, S. M., 2019: Coastally generated near-inertial waves. *J. Phys. Oceanogr.*, **49**, 2979–2995, https://doi.org/10.1175/JPO-D-18-0148.1.

Khanna, S., and J. G. Brasseur, 1998: Three-dimensional buoyancy- and shear-induced local structure of the atmospheric boundary layer. *J. Atmos. Sci.*, **55**, 710–743, https://doi.org/10.1175/1520-0469(1998)055<0710:TDBASI>2.0.CO;2.

Kukulka, T., A. J. Plueddemann, J. H. Trowbridge, and P. P. Sullivan, 2009: Significance of Langmuir circulation in upper ocean mixing: Comparison of observations and simulations. *Geophys. Res. Lett.*, **36**, L10603, https://doi.org/10.1029/2009GL037620.

Kundu, P. K., S.-Y. Chao, and J. P. McCreary, 1983: Transient coastal currents and inertio-gravity waves. *Deep-Sea Res.*, **30A**, 1059–1082, https://doi.org/10.1016/0198-0149(83)90061-4.

Langmuir, I., 1938: Surface motion of water induced by wind. *Science*, **87**, 119–123, https://doi.org/10.1126/science.87.2250.119.

Large, W. G., J. C. McWilliams, and S. C. Doney, 1994: Oceanic vertical mixing: A review and a model with a nonlocal boundary layer parameterization. *Rev. Geophys.*, **32**, 363–403, https://doi.org/10.1029/94RG01872.

——, E. G. Patton, and P. P. Sullivan, 2019: Nonlocal transport and implied viscosity and diffusivity throughout the boundary layer in LES of the Southern Ocean with surface waves. *J. Phys. Oceanogr.*, **49**, 2631–2652, https://doi.org/10.1175/JPO-D-18-0202.1.

Leibovich, S., 1983: The form and dynamics of Langmuir circulations. *Annu. Rev. Fluid Mech.*, **15**, 391–427, https://doi.org/10.1146/annurev.fl.15.010183.002135.

Lemone, M. A., 1973: The structure and dynamics of horizontal roll vortices in the planetary boundary layer. *J. Atmos. Sci.*, **30**, 1077–1091, https://doi.org/10.1175/1520-0469(1973)030<1077:TSADOH>2.0.CO;2.

——, 1976: Modulation of turbulence energy by longitudinal rolls in an unstable planetary boundary layer. *J. Atmos. Sci.*, **33**, 1308–1320, https://doi.org/10.1175/1520-0469(1976)033<1308:MOTEBL>2.0.CO;2.

Li, M., C. Garrett, and E. Skyllingstad, 2005: A regime diagram for classifying turbulent large eddies in the upper ocean. *Deep-Sea Res. I*, **52**, 259–278, https://doi.org/10.1016/j.dsr.2004.09.004.

Lombardo, C., and M. Gregg, 1989: Similarity scaling of viscous and thermal dissipation in a convecting surface boundary layer. *J. Geophys. Res.*, **94**, 6273–6284, https://doi.org/10.1029/JC094iC05p06273.

Marmorino, G., and W. Chen, 2019: Use of WorldView-2 along-track stereo imagery to probe a Baltic Sea algal spiral. *Remote Sens.*, **11**, 865, https://doi.org/10.3390/rs11070865.

——, G. Smith, and G. Lindemann, 2005: Infrared imagery of large-aspect-ratio Langmuir circulation. *Cont. Shelf Res.*, **25** (1), 1–6, https://doi.org/10.1016/j.csr.2004.08.002.

Marusic, I., B. J. McKeon, P. A. Monkewitz, H. M. Nagib, A. J. Smits, and K. R. Sreenivasan, 2010: Wall-bounded turbulent flows at high Reynolds numbers: Recent advances and key issues. *Phys. Fluids*, **22**, 065103, https://doi.org/10.1063/1.3453711.

McWilliams, J. C., P. P. Sullivan, and C.-H. Moeng, 1997: Langmuir turbulence in the ocean. *J. Fluid Mech.*, **334**, 1–30, https://doi.org/10.1017/S0022112096004375.

Merckelbach, L., A. Berger, G. Krahmann, M. Dengler, and J. R. Carpenter, 2019: A dynamic flight model for slocum gliders and implications for turbulence microstructure measurements. *J. Atmos. Oceanic Technol.*, **36**, 281–296, https://doi.org/10.1175/JTECH-D-18-0168.1.

Miles, J. W., 1961: On the stability of heterogeneous shear flows. *J. Fluid Mech.*, **10**, 496–508, https://doi.org/10.1017/S0022112061000305.

Moeng, C.-H., and P. P. Sullivan, 1994: A comparison of shear-and buoyancy-driven planetary boundary layer flows. *J. Atmos. Sci.*, **51**, 999–1022, https://doi.org/10.1175/1520-0469(1994)051<0999:ACOSAB>2.0.CO;2.

Monin, A. S., and A. M. Obukhov, 1954: Basic laws of turbulent mixing in the surface layer of the atmosphere. *Tr. Geofiz. Inst., Akad. Nauk SSSR*, **24**, 163–187.

Munk, W., L. Armi, K. Fischer, and F. Zachariasen, 2000: Spirals on the sea. *Proc. Roy. Soc. London*, **456A**, 1217–1280, https://doi.org/10.1098/rspa.2000.0560.

Osborn, T., 1980: Estimates of the local rate of vertical diffusion from dissipation measurements. *J. Phys. Oceanogr.*, **10**, 83–89, https://doi.org/10.1175/1520-0485(1980)010<0083:EOTLRO>2.0.CO;2.

Paulson, C. A., and J. J. Simpson, 1977: Irradiance measurements in the upper ocean. *J. Phys. Oceanogr.*, **7**, 952–956, https://doi.org/10.1175/1520-0485(1977)007<0952:IMITUO>2.0.CO;2.

Pollard, R. T., and R. C. Millard, 1970: Comparison between observed and simulated wind-generated inertial oscillations. *Deep-Sea Res. Oceanogr. Abstr.*, **17**, 813–821, https://doi.org/10.1016/0011-7471(70)90043-4.

——, P. B. Rhines, and R. Thompson, 1972: The deepening of the wind-mixed layer. *Geophys. Fluid Dyn.*, **4**, 381–404, https://doi.org/10.1080/03091927208236105.

Polton, J. A., J. A. Smith, J. A. MacKinnon, and A. E. Tejada-Martínez, 2008: Rapid generation of high-frequency internal waves beneath a wind and wave forced oceanic surface mixed layer. *Geophys. Res. Lett.*, **35**, L13602, https://doi.org/10.1029/2008GL033856.

Rohr, J., E. Itsweire, K. Helland, and C. Van Atta, 1988: Growth and decay of turbulence in a stably stratified shear flow. *J. Fluid Mech.*, **195**, 77–111, https://doi.org/10.1017/S0022112088002332.

Savelyev, I., and Coauthors, 2018a: Aerial observations of symmetric instability at the north wall of the Gulf Stream. *Geophys. Res. Lett.*, **45**, 236–244, https://doi.org/10.1002/2017GL075735.

——, and Coauthors, 2018b: Airborne remote sensing of the upper ocean turbulence during CASPER-East. *Remote Sens.*, **10**, 1224, https://doi.org/10.3390/rs10081224.

Seim, H. E., and M. C. Gregg, 1994: Detailed observations of a naturally occurring shear instability. *J. Geophys. Res.*, **99**, 10 049–10 073, https://doi.org/10.1029/94JC00168.

Seroka, G., T. Miles, Y. Xu, J. Kohut, O. Schofield, and S. Glenn, 2016: Hurricane Irene sensitivity to stratified coastal ocean cooling. *Mon. Wea. Rev.*, **144**, 3507–3530, https://doi.org/10.1175/MWR-D-15-0452.1.

Shaun-Johnston, T. M., and D. L. Rudnick, 2009: Observations of the transition layer. *J. Phys. Oceanogr.*, **39**, 780–797, https://doi.org/10.1175/2008JPO3824.1.

Skyllingstad, E. D., and R. Samelson, 2012: Baroclinic frontal instabilities and turbulent mixing in the surface boundary layer. Part I: Unforced simulations. *J. Phys. Oceanogr.*, **42**, 1701–1716, https://doi.org/10.1175/JPO-D-10-05016.1.

——, J. Duncombe, and R. M. Samelson, 2017: Baroclinic frontal instabilities and turbulent mixing in the surface boundary layer. Part II: Forced simulations. *J. Phys. Oceanogr.*, **47**, 2429–2454, https://doi.org/10.1175/JPO-D-16-0179.1.

Smith, J. A., 1992: Observed growth of Langmuir circulation. *J. Geophys. Res.*, **97**, 5651–5664, https://doi.org/10.1029/91JC03118.

Smith, K. M., P. E. Hamlington, and B. Fox-Kemper, 2016: Effects of submesoscale turbulence on ocean tracers. *J. Geophys. Res.*, **121**, 908–933, https://doi.org/10.1002/2015JC011089.

Smits, A. J., B. J. McKeon, and I. Marusic, 2011: High-Reynolds number wall turbulence. *Annu. Rev. Fluid Mech.*, **43**, 353–375, https://doi.org/10.1146/annurev-fluid-122109-160753.

Smyth, W., J. Nash, and J. Moum, 2019: Self-organized criticality in geophysical turbulence. *Sci. Rep.*, **9**, 3747, https://doi.org/10.1038/s41598-019-39869-w.

Smyth, W. D., 2003: Secondary Kelvin–Helmholtz instability in weakly stratified shear flow. *J. Fluid Mech.*, **497**, 67–98, https://doi.org/10.1017/S0022112003006591.

——, and J. N. Moum, 2000: Length scales of turbulence in stably stratified mixing layers. *Phys. Fluids*, **12**, 1327–1342, https://doi.org/10.1063/1.870385.

Sous, D., J. Sommeria, and D. Boyer, 2013: Friction law and turbulent properties in a laboratory Ekman boundary layer. *Phys. Fluids*, **25**, 046602, https://doi.org/10.1063/1.4802045.

Stevenson, J. W., and P. P. Niiler, 1983: Upper ocean heat budget during the Hawaii-to-Tahiti shuttle experiment. *J. Phys. Oceanogr.*, **13**, 1894–1907, https://doi.org/10.1175/1520-0485(1983)013<1894:UOHBDT>2.0.CO;2.

Sullivan, P. P., and J. C. McWilliams, 2018: Frontogenesis and frontal arrest of a dense filament in the oceanic surface boundary layer. *J. Fluid Mech.*, **837**, 341–380, https://doi.org/10.1017/jfm.2017.833.

——, and ——, 2019: Langmuir turbulence and filament frontogenesis in the oceanic surface boundary layer. *J. Fluid Mech.*, **879**, 512–553, https://doi.org/10.1017/jfm.2019.655.

——, L. Romero, J. C. McWilliams, and W. K. Melville, 2012: Transient evolution of Langmuir turbulence in ocean boundary layers driven by hurricane winds and waves. *J. Phys. Oceanogr.*, **42**, 1959–1980, https://doi.org/10.1175/JPO-D-12-025.1.

Sundermeyer, M. A., E. Skyllingstad, J. R. Ledwell, B. Concannon, E. A. Terray, D. Birch, S. D. Pierce, and B. Cervantes, 2014: Observations and numerical simulations of large-eddy circulation in the ocean surface mixed layer. *Geophys. Res. Lett.*, **41**, 7584–7590, https://doi.org/10.1002/2014GL061637.

Tatro, P. R., and E. Mollo-Christensen, 1967: Experiments on Ekman layer instability. *J. Fluid Mech.*, **28**, 531–543, https://doi.org/10.1017/S0022112067002289.

Taylor, J. R., 2016: Turbulent mixing, restratification, and phytoplankton growth at a submesoscale eddy. *Geophys. Res. Lett.*, **43**, 5784–5792, https://doi.org/10.1002/2016GL069106.

——, 2008: Numerical simulations of the stratified oceanic bottom boundary layer. Ph.D. dissertation, University of California, San Diego, 230 pp.

Tejada-Martinez, A., and C. Grosch, 2007: Langmuir turbulence in shallow water. Part II. Large-eddy simulation. *J. Fluid Mech.*, **576**, 63–108, https://doi.org/10.1017/S0022112006004587.

Thorpe, S., 2002: The axial coherence of Kelvin–Helmholtz billows. *Quart. J. Roy. Meteor. Soc.*, **128**, 1529–1542, https://doi.org/10.1002/qj.200212858307.

——, 2004: Langmuir circulation. *Annu. Rev. Fluid Mech.*, **36**, 55–79, https://doi.org/10.1146/annurev.fluid.36.052203.071431.

——, and Z. Liu, 2009: Marginal instability? *J. Phys. Oceanogr.*, **39**, 2373–2381, https://doi.org/10.1175/2009JPO4153.1.

Turner, J. S., 1979: *Buoyancy Effects in Fluids*. Cambridge University Press, 368 pp.

Van Roekel, L., B. Fox-Kemper, P. Sullivan, P. Hamlington, and S. Haney, 2012: The form and orientation of Langmuir cells for misaligned winds and waves. *J. Geophys. Res.*, **117**, C05001, https://doi.org/10.1029/2011JC007516.

Venayagamoorthy, S. K., and J. R. Koseff, 2016: On the flux Richardson number in stably stratified turbulence. *J. Fluid Mech.*, **798**, R1, https://doi.org/10.1017/jfm.2016.340.

Watkins, C., and D. Whitt, 2020: Data for large-aspect-ratio structures in simulated ocean surface boundary layer turbulence under a hurricane. Figshare, accessed 16 June 2020, https://doi.org/10.6084/m9.figshare.12486056.v5.

Whitt, D. B., and J. R. Taylor, 2017: Energetic submesoscales maintain strong mixed layer stratification during an autumn storm. *J. Phys. Oceanogr.*, **47**, 2419–2427, https://doi.org/10.1175/JPO-D-17-0130.1.

——, M. Lévy, and J. R. Taylor, 2019: Submesoscales enhance storm-driven vertical mixing of nutrients: Insights from a biogeochemical large eddy simulation. *J. Geophys. Res. Oceans*, **124**, 8140–8165, https://doi.org/10.1029/2019JC015370.

Wijesekera, H. W., and T. M. Dillon, 1991: Internal waves and mixing in the upper equatorial Pacific Ocean. *J. Geophys. Res.*, **96**, 7115–7125, https://doi.org/10.1029/90JC02727.

Young, G. S., D. A. Kristovich, M. R. Hjelmfelt, and R. C. Foster, 2002: Rolls, streets, waves, and more: A review of quasi-two-dimensional structures in the atmospheric boundary layer. *Bull. Amer. Meteor. Soc.*, **83**, 997–1002, https://doi.org/10.1175/1520-0477(2002)083<0997:RSWAMA>2.3.CO;2.

Applied Ocean Research 101 (2020) 102191

Contents lists available at ScienceDirect

Applied Ocean Research

journal homepage: www.elsevier.com/locate/apor

Modeling for the performance of navigation, control and data post-processing of underwater gliders

Mike Eichhorn*,[a], David Aragon[b], Yuri A.W. Shardt[a], Hugh Roarty[b]

[a] Department of Automation Engineering, Technische Universität Ilmenau, Helmholtzplatz 5, Ilmenau 98693, Germany
[b] Center for Ocean Observing Leadership, Rutgers, The State University of New Jersey, 71 Dudley Rd., New Brunswick, NJ 08901, USA

ARTICLE INFO

Keywords:
Underwater glider
Glider flight model
Nonlinear regression
Angle of attack
Long-term missions
Biofouling
Depth-average velocity

ABSTRACT

Underwater gliders allow efficient monitoring in oceanography. In contrast to buoys, which log oceanographic data at individual depths at only one location, gliders can log data over a period of up to one year by following predetermined routes. In addition to the logged data from the available sensors, usually a conductivity-temperature-depth (CTD) sensor, the depth-average velocity can also be estimated using the horizontal glider velocity and the GPS update in a dead-reckoning algorithm. The horizontal velocity is also used for navigation or planning a long-term glider mission. This paper presents an investigation to determine the horizontal glider velocity as accurately as possible. For this, Slocum glider flight models used in practice will be presented and compared. A glider model for a steady-state gliding motion based on this analysis is described in detail. The approach for estimating the individual model parameters using nonlinear regression will be presented. In this context, a robust method to accurately detect the angle of attack is presented and the requirements of the logged vehicle data for statistically verified model parameters are discussed. The approaches are verified using logged data from glider missions in the Indian Ocean from 2016 to 2018. It is shown that a good match between the logged and the modeled data requires a time-varying model, where the model parameters change with respect to time. A reason for the changes is biofouling, where organisms settle and grow on the glider. The proposed method for deciphering an accurate horizontal glider velocity could serve to improve the dead-reckoning algorithm used by the glider for calculating depth-average velocity and for understanding its errors. The depth-average velocity is used to compare ocean current models from CMEMS and HYCOM with the glider logged data.

1. Introduction

Today, underwater gliders are an inherent part of monitoring oceans. These platforms have proven their efficiency and robustness in the collection of oceanographic data in the last two decades [1–3]. The first operational underwater gliders, called “legacy gliders”, were the *Seaglider* [4] built by the University of Washington, the *Spray* [5] built at the Scripps Institution of Oceanography, and the *Slocum* [6] developed by the Webb Research Corporation. This paper focuses on the Slocum glider. It should be noted that the equations and methods presented are also applicable to other glider types. The data used are from the Center for Ocean Observing Leadership (COOL) at Rutgers University [7]. The Rutgers glider team started with the first Slocum glider missions in 2003 [8]. Since that time, the team has conducted 505 missions, which have mapped ocean properties over 252,944 km during 13,563 days at sea. The team is also involved in the Challenger Glider Mission, which is an international science effort to navigate a fleet of gliders on a global mission of discovery [9,10]. The gliders will retrace the path of the *HMS Challenger*, measuring temperature, salinity and current. The four-year voyage of the *HMS Challenger* that began in 1872 sought to answer significant questions about the world’s oceans. The measurements of the present day Challenger Glider Mission will be used to assess the capabilities of the most recent Ocean General Circulation Models. The Mission has completed the survey of the South Atlantic Ocean and is in the middle of the Indian Ocean leg as of publication. The data used in this paper is taken from the Indian Ocean transect.

Accurate determination of the glider states during a mission is a prerequisite for its control and the derivation of in-situ ocean current data. This requires an accurate glider model that should reflect the glider behavior in the current environmental conditions, such as salinity, temperature, pressure, bathymetry, and ocean current. The wing

* Corresponding author.
E-mail addresses: mike.eichhorn@tu-ilmenau.de, mike.eichhorn@ieee.org (M. Eichhorn), dkaragon@marine.rutgers.edu (D. Aragon), yuri.shardt@tu-ilmenau.de (Y.A.W. Shardt), hroarty@marine.rutgers.edu (H. Roarty).

https://doi.org/10.1016/j.apor.2020.102191
Received 12 December 2019; Received in revised form 16 April 2020; Accepted 3 May 2020
Available online 13 June 2020

configuration [11], the fitted sensors [12] and biofouling [13] also have an important influence on the glider model and should be considered.

The angle of attack is of crucial importance in glider modeling. It will be used for the calculation of the horizontal and vertical glider velocity. The horizontal glider velocity is required for dead-reckoning navigation during a mission [14] and for estimating the depth-average velocity [15]. The depth-average velocity results from the difference between the glider velocity over ground and the horizontal glider velocity through water. The horizontal velocity is also applied in the planning for long-term glider missions to find an optimal/passable path from a defined start to a goal and to get information about the feasibility of the mission with regards to energy consumption and the estimated arrival time at the goal [16]. The difference between the vertical glider velocity and the depth rate was used in [17] to determine the vertical current velocity.

Section 2 presents the glider flight model with relations and dependencies of the angle of attack and the horizontal glider velocity, which are based on the analysis of Slocum glider models presented in Section 3. The order of the sections (first: glider model used, second: relevant glider models) relates to the fact that many issues presented in Section 3 are explained in Section 2. Approaches to estimate the model parameters and to determine the angle of attack will be described in Section 4. Section 5 presents the results of the parameter identification for various parameter sets. Requirements regarding the logged data in order to determine trustworthy model parameters will be discussed. Horizontal glider velocities from a long-term mission are used in Section 6 to calculate the depth-average velocities which are used for the comparison of ocean current models from CMEMS [18] and HYCOM [19] with the glider data.

2. Glider flight model

A generally used glider model for a steady-state gliding motion will be described in the following sections.

2.1. Calculation of the horizontal glider velocity

Fig. 1 shows a schematic illustration of a glider with the defined reference frame, angles, velocities and forces.

It should be noted that the angle relations in Fig. 1 correspond to real glider conditions where a glider has a positive angle of attack α during the dive phase and a negative angle of attack during the climb phase.

The navigation of a glider, the planning of a long term glider mission or the in-situ estimation of the ocean current conditions during a mission require information about the correct horizontal glider velocity v_x. This velocity is dependent on the vertical glider velocity v_z and the glide path angle ξ, which is the result of the relation between the pitch angle θ and the angle of attack α

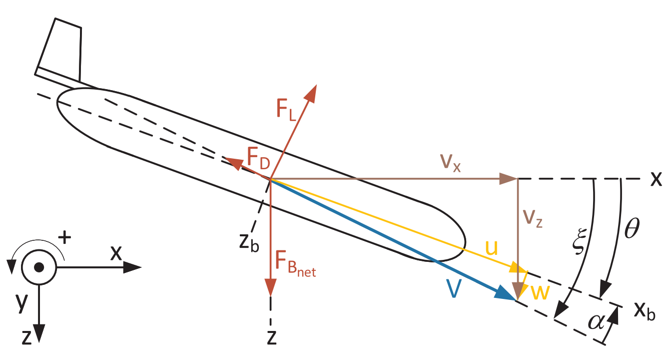

Fig. 1. Illustration of the defined reference frame, angles, velocities and forces for a glider.

$$\xi = \theta - \alpha \tag{1}$$

The angle of attack α is defined as the angle between the projection of the total velocity vector of the glider $\mathbf{V} = [u, v, w]$ onto a vertical plane, formed by the body-fixed x_b- and z_b-axes ($x_b - z_b$ plane), and the body-fixed x_b-axis. The angle α can be defined with the body-fixed velocities u and w as

$$\alpha = \tan^{-1}\left(\frac{w}{u}\right) \tag{2}$$

Assuming that the glider has zero roll and no yaw moment, this vertical plane can be used for a simplified glider flight model when the glider moves only in this plane. This assumption and the requirement for a symmetrical glider body will form the basis for the following modeling steps. This way, the resulting glide speed V can be calculated with the two body-fixed velocities u and w as

$$V = \sqrt{u^2 + w^2} \tag{3}$$

which can also be described with the horizontal and vertical glider velocity through water v_x, v_z as

$$V = \sqrt{{v_x}^2 + {v_z}^2} \tag{4}$$

and as function of the glide path angle ξ

$$V = -\frac{v_z}{\sin(\xi)} = -\frac{v_z}{\sin(\theta - \alpha)} \tag{5}$$

The horizontal glider velocity v_x, which is of interest, can be computed as

$$\begin{aligned} v_x &= -\frac{v_z}{\tan(\xi)} = -\frac{v_z}{\tan(\theta - \alpha)} \\ &= V\cos(\xi) = V\cos(\theta - \alpha) \end{aligned} \tag{6}$$

The vertical glider velocity (through water) v_z results from the difference between the depth rate (vertical velocity over ground) $\dot{z}$ and the vertical current velocity $v_{z_{current}}$, which is generally assumed to be zero

$$v_z = \dot{z} - v_{z_{current}} \overset{v_{z_{current}}=0}{\Rightarrow} v_z = \dot{z} \tag{7}$$

In contrast to the variables vertical glider velocity v_z and pitch angle θ, which can be directly derived from the logged glider data during the steady-state gliding, the angle of attack α has to be detected using additional glider parameters. The necessary steps and relationships for this are described below.

2.2. Force-velocity relations

The horizontal and vertical force equations for the glider in the vertical plane at equilibrium steady glides are

$$F_D\cos(\xi) + F_L\sin(\xi) = 0 \tag{8}$$

$$-F_D\sin(\xi) + F_L\cos(\xi) = F_{B_{net}} \tag{9}$$

where F_D is the drag force, F_L is the lift force, ξ is the glide path angle and $F_{B_{net}}$ is the net buoyancy force of the glider given by $F_{B_{net}} = m_0 g$, the product of the excess mass m_0 and the acceleration due to gravity g. The excess mass m_0 can be defined using the total vehicle mass m_v and the mass of displaced fluid m as $m_0 = m_v - m$. For a neutral buoyancy trimmed glider, m_0 corresponds to the variable ballast mass m_b. For safety reasons, a glider is often trimmed slightly light, so that it floats when the buoyancy engine is set to $m_b = 0$. Therefore, a buoyancy trim offset Δm_0 has to be added to the resulting excess mass:

$$m_0 = m_b + \Delta m_0 \tag{10}$$

Re-arranging Eqs. (8) and (9) into a separate description for F_D and F_L gives the buoyancy force components

$$F_D = -m_0 g\sin(\xi) \tag{11}$$

$$F_L = m_0 g\cos(\xi) \tag{12}$$

The hydrodynamic forces are modeled as

$$F_D = \frac{1}{2}\rho C_D(\alpha) A V^2 \tag{13}$$

$$F_L = \frac{1}{2}\rho C_L(\alpha) A V^2 \tag{14}$$

where C_D and C_L are the non-dimensional drag and the lift coefficients which refer to the reference area A, ρ is the density of water, and V is the glide speed.

2.3. Angle of Attack relations

The coefficients C_D and C_L are functions of the angle of attack α and will be generally modeled as

$$C_D = C_{D_0} + C_{D_2}\alpha^2 \tag{15}$$

$$C_L = C_{L_1}\alpha \tag{16}$$

Using the horizontal force Eq. (8) and the hydrodynamic force Eqs. (13) and (14), the glide path angle ξ can be calculated as

$$\tan(\xi) = \frac{\sin(\xi)}{\cos(\xi)} = \tan(\theta - \alpha) = -\frac{F_D}{F_L} = -\frac{C_D(\alpha)}{C_L(\alpha)} \tag{17}$$

The necessary steps to solve α numerically will be presented in Section 4.2.

A characteristic value to describe the gliding flight is the lift-to-drag ratio L/D which can be described using Eqs. (13)-(16) as

$$L/D = \frac{F_L}{F_D} = \frac{C_L(\alpha)}{C_D(\alpha)} = \frac{C_{L_1}\alpha}{C_{D_0} + C_{D_2}\alpha^2} \tag{18}$$

There is a maximum in L/D [20] at

$$\alpha_{(L/D)\max} = \pm\sqrt{\frac{C_{D_0}}{C_{D_2}}} \tag{19}$$

with a value of

$$(L/D)_{\max} = \frac{C_{L_1}}{2C_{D_0}}\sqrt{\frac{C_{D_0}}{C_{D_2}}} \tag{20}$$

The smallest glide angle $\xi_{\min}$ is at $(L/D)_{\max}$ and can be calculated as

$$\xi_{\min} = \xi_{(L/D)\max} = \pm\cot^{-1}\left(\frac{C_{L_1}}{2C_{D_0}}\sqrt{\frac{C_{D_0}}{C_{D_2}}}\right) \tag{21}$$

where $\cot^{-1}$ is the arccotangent.

Using Eq. (11) in (13) or (12) in (14), the glide speed V can be described as function of the related buoyancy force component to the hydrodynamic force as

$$V = \sqrt{-\frac{2m_0 g\sin(\xi)}{\rho A C_D(\alpha)}} \tag{22}$$

or

$$V = \sqrt{\frac{2m_0 g\cos(\xi)}{\rho A C_L(\alpha)}} \tag{23}$$

The vertical glider velocity v_z can be calculated by substituting Eq. (23) and a sine relation of the glide path angle ξ in Eq. (17) into Eq. (5)

$$v_z = \underbrace{\sqrt{\frac{2m_0 g\cos(\xi)}{\rho A C_L(\alpha)}}}_{V}\underbrace{\frac{C_D(\alpha)}{C_L(\alpha)}\cos(\xi)}_{-\sin(\xi)} = \sqrt{\frac{2m_0 g\cos(\xi)^3 C_D(\alpha)^2}{\rho A C_L(\alpha)^3}} \cong \sqrt{\frac{2m_0 g C_D(\alpha)^2}{\rho A C_L(\alpha)^3}} \tag{24}$$

Eq. (24) allows the calculation of the angle of attack for minimum vertical glider velocity $\alpha_{v_z,\min}$ by maximizing the term $C_L(\alpha)^3/C_D(\alpha)^2$ in the simplified equation, where the cosine term is ignored [21]. For typical, small glide angles ξ is the term $cos(\xi)^3$ close to one and constant. The solution of the extreme value problem

$$\frac{\partial}{\partial\alpha}\left(\frac{C_L(\alpha)^3}{C_D(\alpha)^2}\right) = \frac{\partial}{\partial\alpha}\left(\frac{{C_{L_1}}^3\alpha^3}{(C_{D_0} + C_{D_2}\alpha^2)^2}\right) = 0 \tag{25}$$

results in

$$\alpha_{v_z,\min} = \pm\sqrt{\frac{3C_{D_0}}{C_{D_2}}} \tag{26}$$

whereby the glide angle $\xi_{v_z,\min}$ can be calculated as

$$\xi_{v_z,\min} = \pm\cot^{-1}\left(\frac{C_{L_1}}{4C_{D_0}}\sqrt{\frac{3C_{D_0}}{C_{D_2}}}\right) \tag{27}$$

In analogy to the approach described above it is possible to determine the glide path angle where the horizontal glider velocity v_x has its maximum. Substitute Eq. (22) into (6)

$$v_x = \sqrt{-\frac{2m_0 g sin(\xi)}{\rho A C_D(\alpha)}}\cos(\xi) = \sqrt{-\frac{2m_0 g sin(\xi)\cos(\xi)^2}{\rho A C_D(\alpha)}} \cong \sqrt{-\frac{2m_0 g sin(\xi)\cos(\xi)^2}{\rho A C_{D_{const}}}} \tag{28}$$

and maximize the term $\sin(\xi)\cos(\xi)^2$ in the simplified Eq. (28), where the drag coefficient $C_D(\alpha)$ for small angles of attack is nearly constant. The extreme value problem for

$$\frac{\partial}{\partial\xi}(\sin(\xi)\cos(\xi)^2) = \cos(\xi)^2 - 2\sin(\xi)^2 = 0 \tag{29}$$

has one solution at

$$\xi_{v_x,\max} = \pm\cot^{-1}(\sqrt{2}) = \pm 35.3^\circ \tag{30}$$

The value $\xi_{v_x,\max} = 35.3^\circ$ is valid for all types of gliders and independent of hydrodynamic coefficients [22].

Fig. 2 shows a graphical representation of the glider velocities v_x and x_z for dive. This form of representation corresponds to the glide

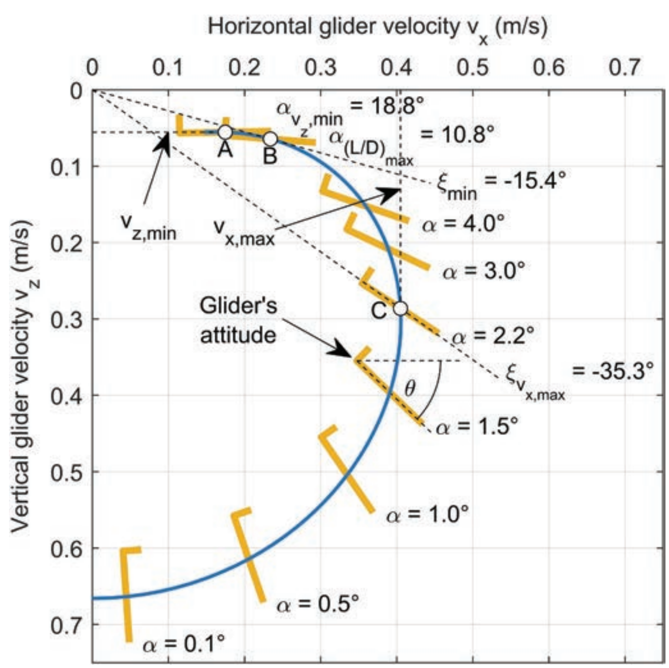

Fig. 2. Glide polar for a Slocum glider using the hydrodynamic coefficients of [14] for a excess mass $m_0 = 250g$. (A) minimum vertical glider velocity $v_{z,\min}$, (B) smallest glide angle $\xi_{\min}$, (C) maximum horizontal glider velocity $v_{x,\max}$.

polar of a sailplane [23] and can be used for graphical analysis and to determine the glider velocities v_x and v_z and angles α, ξ and θ for the operation point of interest. This plot is mirrored on the abscissa to the commonly used glide polar representation for a glider [22,24,25]. A glider should be flown within a glide angle range between $\xi_{\min}$ and $\xi_{x,\max}$ and between the operation points B and C. Here the slowest glide slope is defined at the maximum lift-to-drag ratio and results in the minimum specific energy consumption of the glider [22]. This slope is called stall glide slope in [25]. Flying at higher angles of attack will enable the lowest sink rate of a glider $v_{z,\ \min}$ in operation point A. Because the linear relation of the lift curve $C_L(\alpha)$ is not guaranteed for high angles of attack, this operation range should be avoided. The lift curve is dependent on the structural design of the glider and is mainly influenced by the shape of the wings. High angles of attack result in boundary layer separation and the wings stall [26].

3. Relevant work about slocum glider models

This section presents relevant work about the modeling of Slocum gliders. The interested reader will find information about model design, strategies to find the model parameters and relations between the individual models.

3.1. Relevant work

Vehicle Control Technologies, Inc. (VCT) [27] used computational fluid dynamics (CFD) computations to determine the coefficients C_D and C_L of the Slocum glider. These results are published in [24] and [26]. In this work, the coefficients C_D and C_L are normalized by the square length of the hull of 1.789 m. The reference area A is thus $(1.789\ \text{m})^2 = 3.2\ \text{m}^2$.

Graver [28] directly used the lift coefficient from [27] with a rescaling in his reference area, i.e. the frontal area of the vehicle for his glider flight model. With a glider diameter of 0.2127 m the reference area is $A = 0.0355\ \text{m}^2$. The drag coefficient was determined using the glider logging data and the given lift coefficient. An estimation of the buoyancy trim offset Δm_0 was necessary to avoid an asymmetrical drag coefficient curve.

Bhatta [29] used hydrodynamic force equations by analogy with Eqs. (37) and (38) so that the reference area definition could be omitted. Some parameters were estimated using glider logging data from sea trials in [28] and wind tunnel experiments in [26].

Williams et al. [30] used an iterative scheme to obtain estimates for the parameters C_{D_0}, C_{D_2} and C_{L_1} for the lift and drag coefficients. The individual parameters were determined sequentially in a loop using the logged glider data: pitch angle θ, vertical glider velocity v_z and the net buoyancy $F_{B_{net}}$. This loop is stopped when all parameters converge to a stable set. Here the reference area A is the frontal area of the glider. The values of the estimated parameters during dive are different from the values during climb. According to [30] this is due to the ballasting procedure. Williams's work also includes a detailed hydrodynamical analysis of a hull with a length-to-diameter ratio similar to a Slocum glider tested in a towing tank.

Merckelbach et al. [17] consider the hull and wings of a Slocum glider separately for the parameters of the lift and drag coefficients. The individual parameters for hull and wings are added together to give the total coefficients, so that they can be used in Eqs. (15) and (16). The buoyancy force calculation used considered the additional influences of water pressure P and water temperature T on the volume of the displaced fluid

$$F_B = g\rho\{V_g[1 - \varepsilon P + a_T(T - T_0)] + \Delta V_{bp}\} \tag{31}$$

where V_g is the glider volume at atmospheric pressure, ε is the compressibility of the hull, a_T is the thermal expansion coefficient, and ΔV_{bp} is the volume change resulting from the buoyancy engine. Therefore, the parameters V_g and ε are estimated using the logged glider data. An additional estimated parameter is C_{D_0} in Eq. (15). All other parameters in Eqs. (15) and (16) are the result of experiments or empirical formulas as described below. The determined parameters C_{D_2} and C_{L_1} from hull tow tests in Williams et al. [30] were used for the hull segment. Since these parameters refer to the frontal area A_F, rescaling is applied. The reference area in this work is the wing surface area $A_W = 0.1\ \text{m}^2$. The rescale factor is therefore $A_F/A_W = 0.038/0.1 = 0.38$. The parameter C_{L_1} for the lift coefficient of the wings is the result of a semiempirical formula [31] for a lift-curve slope using the aspect ratio $\mathcal{R}$, and the wing sweep angle Λ. (A detailed analysis and comparison of possible formulas for a lift-curve slope for a Slocum glider is given in [32].) Prandtl's lifting line theory was used for modeling the drag coefficient of the wings. In this theory the drag coefficient C_D has two terms, a parasitic drag C_{D_0} as a result of the form drag or pressure drag, the skin friction drag and the interference drag and an inducted drag C_{D_i} calculated using Prandtl's lifting-line theory

$$C_D = C_{D_0} + C_{D_i} = C_{D_0} + K{C_L}^2 \tag{32}$$

where

$$K = \frac{1}{\pi e \mathcal{R}} \tag{33}$$

The aspect ratio $\mathcal{R}$ is calculated as b^2/A_W, where b is the wing span and A_W is the wing area. The span efficiency parameter e in Eq. (33) allows the consideration of a real lift distribution, which is usually disturbed through the addition of fuselage, engine nacelles or other parts [33]. It should be noted that some of the relations used to describe the hydrodynamic vehicle behavior are based on aerodynamic studies where there is a wealth of experience. Another name for this factor is the Oswald efficiency factor. (A wide range of approaches to calculate this factor are presented in [34].)

Mahmoudian [35] also used Eq. (32) to describe the drag coefficient of the entire glider. The parameters used for the lift and drag coefficient in this model are from Bhatta [29].

Cooney [14] used exclusively empirical formulas from [33] to describe the glider behavior. Analogous to Merckelbach [17], a separate consideration of the hull and wings of a Slocum glider is conducted. The calculation of the drag coefficient is based on Eq. (32) where the parasitic drag C_{D_0} is exclusively the result of the pressure drag. The calculation of the pressure drag is based on Hoerner [33] (3–12 equation (25))

$$C_{D_0} = 0.44\frac{D}{L} + 4C_f(\text{Re})\frac{L}{D} + 4C_f(\text{Re})\sqrt{\frac{D}{L}} \tag{34}$$

where D is the hull diameter, L is the characteristic length and $C_f(\text{Re})$ is the skin-friction drag coefficient for a flat plate in laminar flow which is a function of Reynolds number Re

$$C_f = \frac{1.328}{\sqrt{\text{Re}}} \tag{35}$$

The Reynolds number Re represents the ratio of the dynamic forces relative to the friction forces [33] as

$$\text{Re} = \frac{VL}{\nu} \tag{36}$$

where V is the glide speed, L is the characteristic length and ν the fluid kinematic viscosity, which is taken to be $1.35\times 10^{-6}\ \text{m}^2/\text{s}$ at 10 °C. The speed-dependent behavior of the drag coefficient is a unique feature compared to the other models presented. Fig. 3 shows the pressure drag C_{D_0} as a function of glide speed V. Thus, a lower glide speed V leads to a greater drag coefficient C_D. The lift coefficient C_L due to the wings is determined using the lifting-line theory of swept wings. The parameters of the empirical formula are the aspect ratio $\mathcal{R}$ and the wing sweep angle Λ.

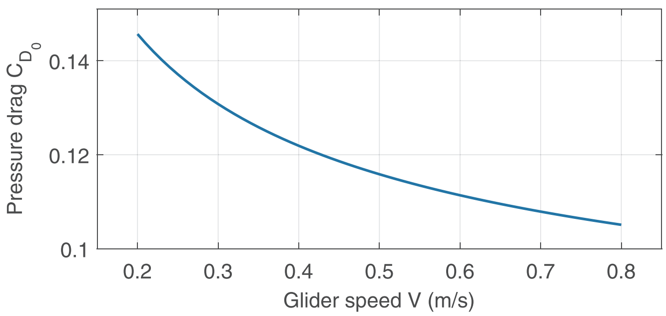

Fig. 3. Pressure drag C_{D_0} as function of glide speed V.

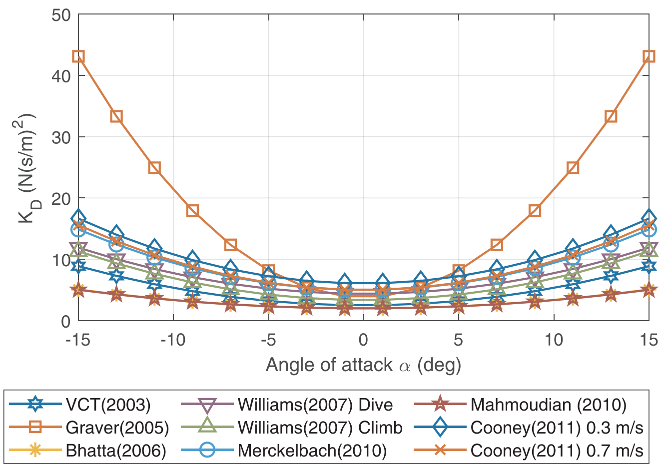

Fig. 4. Drag coefficient K_D of the individual models.

3.2. Comparison of the models

Although the models presented above describe the lift and drag coefficients for a Slocum glider, it is difficult to compare the individual parameters. The reasons for this are the different definition for the reference area A in Eqs. (13) and (14), different analytical equations to describe the drag and the lift coefficients, different types of Slocum glider and wing configurations. To compare the parameters used in the individual models, the following hydrodynamic force equations with the dimensioned lift and drag coefficients K_L and K_D will be used

$$F_D = \frac{\rho}{\rho_{fw}} K_D V^2 = \frac{\rho}{\rho_{fw}} \left(\underbrace{K_{D0}}_{\frac{1}{2}\rho_{fw} A C_{D0}} + \underbrace{K_{D_2}\alpha^2}_{\frac{1}{2}\rho_{fw} A C_{D_2}} \right) V^2 \tag{37}$$

$$F_L = \frac{\rho}{\rho_{fw}} K_L V^2 = \frac{\rho}{\rho_{fw}} \left(\underbrace{K_{L_1}}_{\frac{1}{2}\rho_{fw} A C_{L_1}} \alpha \right) V^2 \tag{38}$$

where p_{fw} is the density of freshwater 1000 kg/m^3. The relations of the dimensioned parameters K_{L_1}, K_{D_0} and K_{D_2} to the non-dimensioned parameters C_{L_1}, C_{D_0} and C_{D_2} in Eqs. (13) and (14) are located below the underbraces. This form of equation will also be used in this paper. Table 1 shows the individual parameters K_{L_1}, K_{D_0} and K_{D_2} and the characteristic values $\alpha_{(L/D)_{\max}}$, $(L/D)_{\max}$ and $\xi_{\min}$ calculated from it for the individual models.

It should be noted that the lift coefficient in VCT [27] and Graver [28] is defined as

$$C_L = C_{L_1}\alpha + C_{L_2}\alpha|\alpha| \tag{39}$$

which does not allow a direct comparison with the other models. In these cases, a linear regression can be used to estimate a linear coefficient C_{L_1} for Eq. (16). Therefore, the data points for α will be created ranging from 0° to 10°, which form the elements of the regression matrix $\mathcal{A}$. The lift coefficient values for Eq. (39) can now be calculated using these data points. These calculated values form the output variable y in the regression. This results in a parameter K_{L_1} equal to 219.93 ± 0.17 kg/m/rad for VCT and 219.43 ± 0.17 kg/m/rad for Graver.

To use a fixed drag coefficient for Cooney's work [14], two operating points, a glide speed $V = 0.3$ and $V = 0.7$ m/s, were chosen in Eq. (34). These give two K_{D_0} values of 6.06 and 5 kg/m which allow a direct comparison with the other models.

Table 1 shows a wide dispersion of the parameters and characteristic values. This also is evident in Figs. 4 and 5, which show the drag and lift coefficients as a function of α for the models. The curves of lift-to-drag ratio in Fig. 6 as well as the curves of glide path angle in Fig. 7 for dive, where the angle of attack α is positive show four characteristic groups (The curves for negative angles of attack are mirrored in the diagonal quadrant.). The corresponding group number is shown to the right of the curves.

The first group includes the work from VCT [27], Bhatta [29], Merckelbach [17] and Mahmoudian [35] where the maximum in L/D lies between 5.7 and 7.2 for α between 9.4° and 12.2°. The second group contains the results from Cooney [14] where the maximum in L/D lies between 3.5 and 3.8 for α between 10.3° and 11.3°. A third group contains the results of Williams [30]. The L/D curves for the dive and climb are similar, but the maximum in L/D lies at 1.8, which equals approximately one-third of the value of the first group. A reason for this could be in the initial configuration for the iterative scheme, which includes parameters only of the glider hull detected in the towing tank tests. The α values are again similar to the first group. The last group includes Graver's model. The maximum in L/D is 2.35 at an α of 4.7°. There is also a significant difference in the drag coefficient curve in Fig. 4 compared to the other models. Possible explanations for the high drag coefficient used by Graver [28] are complex geometry through wing deformation and a CTD sensor in real or bad data logging conditions due to a sideslip angle caused by a static roll.

Fig. 8 shows the determined angle of attack α and the resulting horizontal glider velocity v_x using mean values for the pitch angle θ and the vertical glider velocity v_z in Table 2 for all dives and climbs in the

Table 1
Parameters and characteristic values for the individual models.

Work	K_{L_1} (kg/m/rad)	K_{D0} (kg/m)	K_{D_2} (kg/m/rad^2)	$\alpha_{(L/D)\max}$ (deg)	$(L/D)_{\max}$	$\xi_{\min}$ (deg)
VCT(2003) [27]	219.93	2.5	93.24	9.38	7.21	7.9
Graver(2005) [28]	219.43	3.8	573.32	4.66	2.35	23.04
Bhatta(2006) [29]	135	2	45	12.08	7.12	8
Williams(2007) Dive [30]	82.98	4.37	109.82	11.43	1.89	27.84
Williams(2007) Climb	70.37	3.36	116.21	9.74	1.78	29.31
Merckelbach(2010) [17]	305	5	144	10.68	5.68	9.98
Mahmoudian(2010) [35]	135.52	1.99	44.23	12.16	7.22	7.89
Cooney(2011) V = 0.3 m/s [14]	212.28	6.06	154.39	11.35	3.47	16.08
Cooney(2011) V = 0.7 m/s	212.28	5	154.39	10.31	3.82	14.67

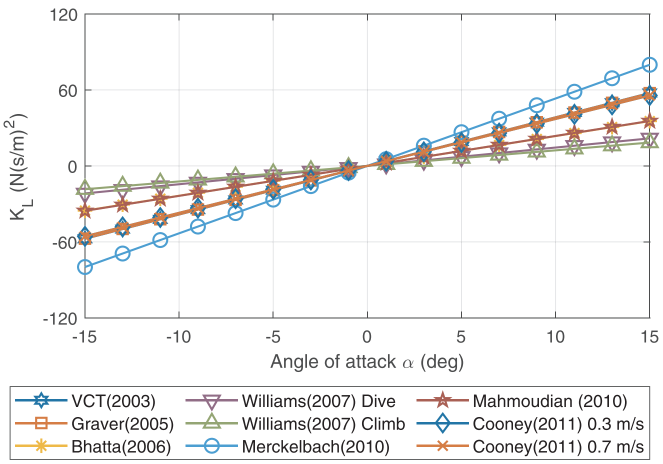

Fig. 5. Lift coefficient K_L of the individual models.

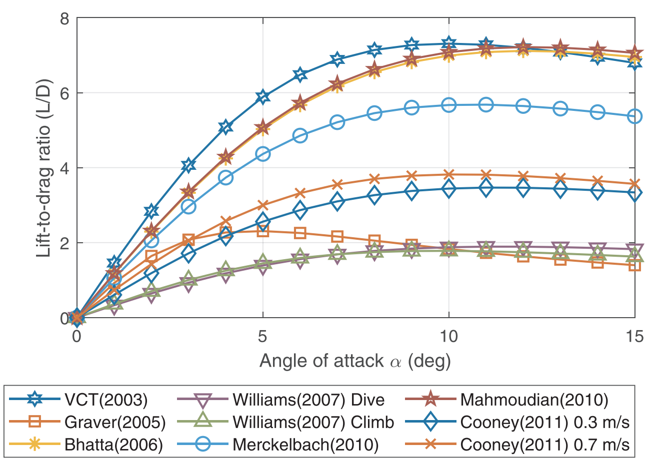

Fig. 6. Lift-to-drag ratio L/D of the individual models.

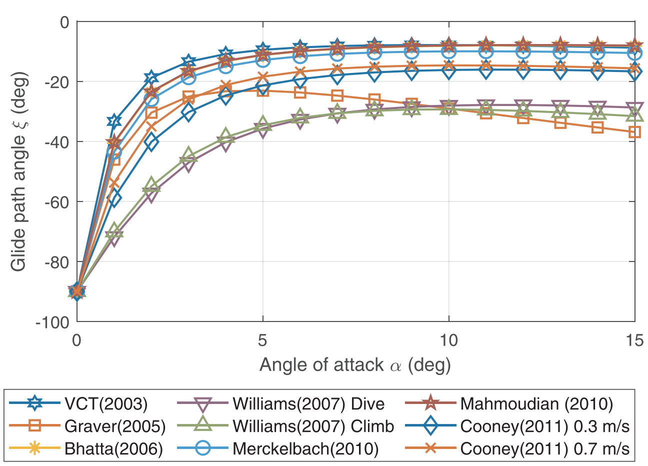

Fig. 7. Glide path angle ξ of the individual models.

period from 2018-09-05 to 2018-09-18 for the glider mission RU29-550 from Sri Lanka to Mauritius. As Fig. 8 shows, there is a maximal difference of 8% in the horizontal glider velocity in all models, except Williams. Although the models compared here have different parameters and L/D curves, the calculated horizontal vehicle velocities are close. The maximal difference in the horizontal glider velocity between Williams and the other models is around 20%.

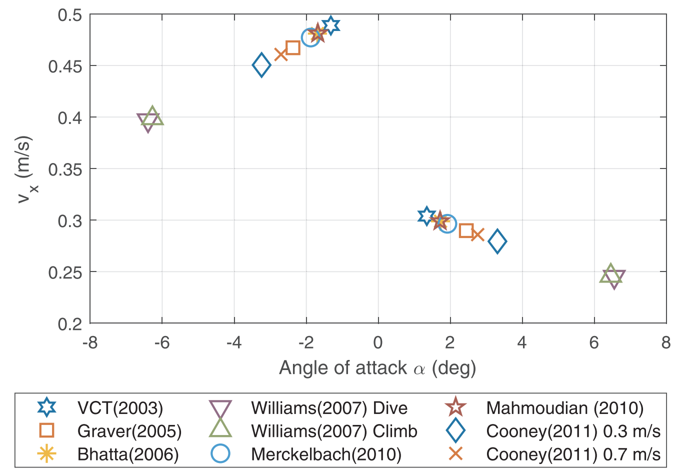

Fig. 8. Determined angle of attack α (see Section 4.2) and calculated horizontal glider velocity v_x from Eq. (6) for the individual models using the pitch angles θ and the vertical glider velocities v_z in Table 2.

Table 2
Mean values from the RU29-550 mission.

Mean Value	Dive		Climb
Pitch angle θ (deg)	−24.922		25.397
Vertical glider velocity v_z (ms^{-1})	0.150		−0.246
Variable ballast mass m_b (kg)	0.271		−0.269
Water density ρ (kg/m^3)		1029.23	

4. Parameter identification

4.1. Background

This section describes an approach to estimating the parameters for the lift and drag coefficients to determine α which is used in Eq. (6) for calculating the horizontal glider velocity v_x. The idea is to minimize the difference between the logged vertical glider velocity v_z, derived from the depth z, and the modeled vertical glider velocity $\hat{v}_z$ using estimated parameters. The vertical force Eq. (9) is used for modeling the vertical glider velocity v_z. Combining Eqs. (5), (37) and (38) into (9) gives

$$- \sin(\xi)\frac{\rho}{\rho_{fw}}(K_{D_0} + K_{D_2}\alpha^2)\left(\frac{v_z}{\sin(\xi)}\right)^2 + \cos(\xi)\frac{\rho}{\rho_{fw}}(K_{L_1}\alpha)\left(\frac{v_z}{\sin(\xi)}\right)^2 = (m_b + \Delta m_0)g \tag{40}$$

Solving for $\hat{v}_z$ gives

$$\hat{v}_z = -\sin(\theta - \alpha)\sqrt{\frac{\rho_{fw}(m_b + \boldsymbol{\Delta m_0})g}{\rho((\boldsymbol{K_{L_1}}\alpha)\cos(\theta - \alpha) - (\boldsymbol{K_{D_0}} + \boldsymbol{K_{D_2}}\alpha^2)\sin(\theta - \alpha))}} \tag{41}$$

The estimated parameters are marked in bold and summarized in the parameter vector β

$$\boldsymbol{\beta} = \langle K_{L_1}, K_{D_0}, K_{D_2}, \Delta m_0 \rangle^T \tag{42}$$

In addition to the parameters for the lift and drag coefficients, the buoyancy trim offset Δm_0 is a further parameter to be estimated. This is necessary since the lift and drag coefficients are used for the modeled vertical glider velocity in both the dive and the climb. Without calibration of the buoyancy trim offset Δm_0, the modeled lift and drag coefficients for the individual dive and climb lie above or below the ideal lines. The parameter vector β can be estimated using a search method to minimize the cost function C given by

$$C(\beta) = \frac{1}{n}\sum_{i=1}^{n}(v_{z_i} - \hat{v}_{z_i})^2 \tag{43}$$

which corresponds to the mean squared error (MSE) where n is the number of all logged dives and climbs within a defined time period. The values ρ, θ and m_b used in Eq. (41) are average values computed for each dive and climb.

4.2. Determination of the angle of attack

The calculation of the lift and drag coefficient in Eq. (41) requires a known angle of attack α. This angle can be solved numerically by inserting Eqs. (37) and (38) into Eq. (17) to give

$$\tan(\theta - \alpha)(K_{L_1}\alpha) + (K_{D_0} + K_{D_2}\alpha^2) = 0 \tag{44}$$

A bisection or bracketing method can be used to solve this one-dimensional optimization task. A bracketing method works without derivatives and finds the minimum through iterative decreasing of the interval until the desired tolerance ϵ is achieved, where the minimum lies. In this approach the bisection method in MATLAB `fzero` and the bracketing methods Golden section search [36], Fibonacci search [37] and Brent's method [38] were tested. Brent's method was used as it requires lesser cost function calls compared to the other methods. On average, 7–9 cost function calls are needed to determine the angle of attack. The MATLAB function name for this bracketing method is `fminbnd`. This method requires a cost function $f(x)$ and a fixed interval $[xl, xu]$ wherein the search parameter x lies. The cost function is defined as

$$f(x) = (\tan(\theta - \alpha)(K_{L_1}\alpha) + (K_{D_0} + K_{D_2}\alpha^2))^2 \tag{45}$$

Good interval values can be found by using a quadratic approximation of Eq. (44) to determine α where the function $tan(x)$ is approximated with x

$$(\theta - \alpha)(K_{L_1}\alpha) + (K_{D_0} + K_{D_2}\alpha^2) = 0 \tag{46}$$

The resulting quadratic equation is therefore

$$\alpha^2 + \frac{K_{L_1}\theta}{(K_{D_2} - K_{L_1})}\alpha + \frac{K_{D_0}}{(K_{D_2} - K_{L_1})} = 0 \tag{47}$$

The approximated angle of attack α can be solved using the discriminant *disc*. An evaluation of the real roots gives

$$\begin{aligned}
&disc = \frac{K_{L_1}{}^2\theta^2}{4(K_{D_2}-K_{L_1})^2} - \frac{K_{D_0}}{(K_{D_2}-K_{L_1})}\\
&\text{if } (disc < 0) \text{ then } disc = 0\\
&\alpha_{1,2} = -\frac{K_{L_1}\theta}{2(K_{D_2}-K_{L_1})} \pm \sqrt{disc}\\
&\alpha = \min(|\alpha_1|, |\alpha_2|)
\end{aligned} \tag{48}$$

In cases that $|K_{D_2} - K_{L_1}| < 10^{-9}$, the quadratic Eq. (47) reduces to a linear equation, where α can be calculated using

$$\alpha = -\frac{K_{D_0}}{K_{L_1}\theta} \tag{49}$$

The resulting interval is calculated using α from Eq. (48) or (49) by

$$\begin{aligned} x_l &= \alpha - \Delta\alpha\\ x_u &= \alpha + \Delta\alpha \end{aligned} \tag{50}$$

where $\Delta\alpha$ was chosen as 3°. This value worked well for all examined glider missions. The cost function $C(\beta)$ in Eq. (43) thus includes an internal search procedure to detect the corresponding angle of attack α for every dive or climb.

4.3. Initial parameters setting

To guarantee a good convergence and to find the global minimum, initial parameters have to be defined. The parameters for the lift and drag coefficients K_{L_1}, K_{D_0}, and K_{D_2} from Cooney [14] were used as initial parameters in this paper (The parameter K_{D_0} corresponds to the mean value of this parameter in Table 1). The initial parameter for the buoyancy trim offset Δm_0 can be calculated by inserting Eq. (11) into Eq. (37) with the assumption of similar drag coefficients for all dives and climbs as follows

$$V_{dive} = \frac{v_{z\,dive}}{\sin(\xi_{dive})} \qquad V_{climb} = \frac{v_{z\,climb}}{\sin(\xi_{climb})} \tag{51}$$

$$\Delta m_0 = \frac{\bar{m}_{b_{\text{dive}}}\overline{\sin(\theta_{\text{dive}})}\bar{\rho}_{\text{climb}}\bar{V}_{\text{climb}}{}^2 - \bar{m}_{b_{\text{climb}}}\overline{\sin(\theta_{\text{climb}})}\bar{\rho}_{\text{dive}}\bar{V}_{\text{dive}}{}^2}{\overline{\sin(\theta_{\text{climb}})}\bar{\rho}_{\text{dive}}\bar{V}_{\text{dive}}{}^2 - \overline{\sin(\theta_{\text{dive}})}\bar{\rho}_{\text{climb}}\bar{V}_{\text{climb}}{}^2} \tag{52}$$

where the unknown parameter angle of attack α in ξ was set to zero and mean values of all dives and climbs were used.

5. Results

Logged glider data from the Challenger Glider Mission [9,10] was used to evaluate the parameter identification approach presented in Section 4. The goal is the accurate determination of the horizontal glider velocity v_x during a mission using the identified lift and drag coefficients K_{L_1}, K_{D_0} and K_{D_2}. The glider data used in Eq. (41) is the mean values of the water density ρ, the pitch angle θ and the variable ballast mass m_b computed for each dive and climb in the defined time period. The nonlinear regression function `nlinfit` from MATLAB was used to estimate the coefficients. This function uses the Levenberg-Marquardt nonlinear least squares algorithm and allows an easy determination of the confidence intervals for the coefficients using the MATLAB function `nlparci` after the minimization. The independent variable matrix **X**, the parameter vector $\boldsymbol{\beta}$ and the output vector **y** can be written as

$$\mathbf{X} = \begin{bmatrix} \theta_1 & m_{b_1} & \rho_1\\ \theta_2 & m_{b_2} & \rho_2\\ \vdots & \vdots & \vdots\\ \theta_n & m_{b_n} & \rho_n \end{bmatrix} \tag{53}$$

$$\boldsymbol{\beta} = \langle K_{L_1}, K_{D_0}, K_{D_2}, \Delta m_0\rangle^T \tag{54}$$

$$\mathbf{y} = \langle v_{z_1}, v_{z_2}, \ldots, v_{z_n}\rangle^T \tag{55}$$

5.1. Minimizations for different parameter sets

The first tests used data from the glider mission RU29-550 from Sri Lanka to Mauritius for a time period of two weeks from 2018-09-05 to 2018-09-18. The data of the glider state during the time period is shown in Fig. 9.

Five minimizations with different Parameter Sets *PS** to be minimized were executed. The placeholder character * includes the positions of the estimated parameters in the parameter vector in Eq. (54). For example - PS24 means only parameter K_{D_0} and Δm_0 will be estimated, parameter K_{L_1} and K_{D_2} have fixed values and will not be estimated. The estimated parameters and their 95% confidence intervals are shown as black text, while the unestimated parameters are shown in gray text in Table 3. An underlined parameter value represents a statistically insignificant value, where the corresponding confidence interval includes zero.

The unestimated parameters correspond to the parameters from Cooney [14]. The buoyancy trim offset Δm_0 was an estimated parameter in every minimization. The results for all minimizations is similar around −120 g (positively buoyant). This means that the glider is trimmed slightly light, which makes sense for safety reasons. The resulting drag and lift coefficients as a function of α for the individual minimizations are shown in Figs. 10 and 11.

All minimizations found solutions where the modeled vertical glider velocity $\hat{v}_z$ agrees well with the logged vertical glider velocity v_z, as

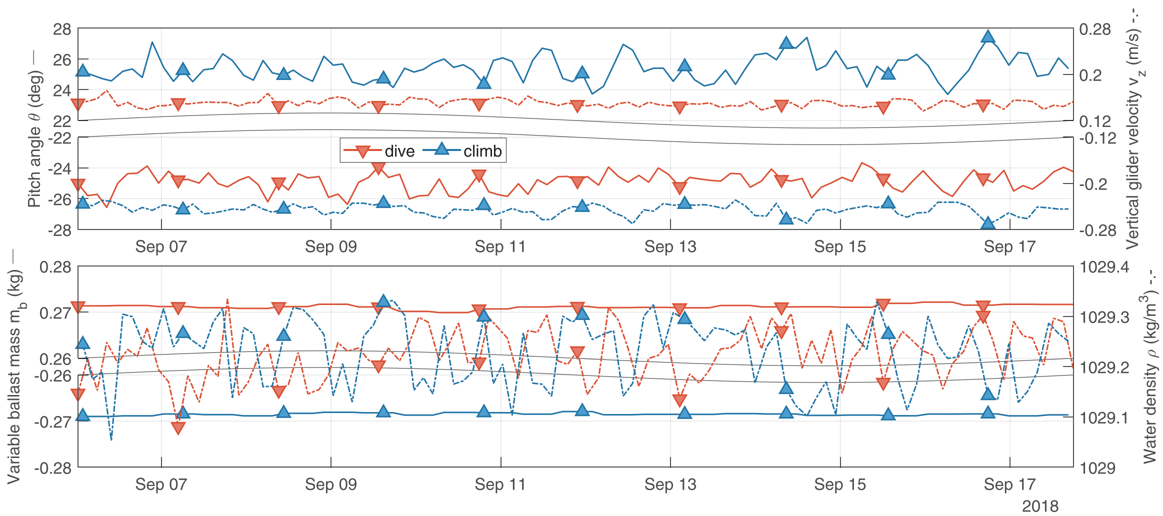

Fig. 9. Glider data used for the minimization: pitch angle θ, vertical glider velocity v_z, ballast mass m_b, water density ρ.

Table 3
Estimated parameters and their confidence intervals (CI).

Minimization	K_{L_1} (95% CI) (kg/m/rad)	K_{D0} (95% CI) (kg/m)	K_{D_2} (95% CI) (kg/m/rad^2)	Δm_0 (95% CI) (kg)
PS14	444.87 [416.67, 473.07]	5.53	154.39	−0.1197 [−0.1215, −0.1180]
PS24	212.28	6.30 [6.24, 6.35]	154.39	−0.1203 [−0.1220, −0.1186]
PS34	212.28	5.53	373.62 [360.63, 386.61]	−0.1198 [−0.1215, −0.1180]
PS234	212.28	7.21 [5.79, 8.63]	−109.54 [−519.36, 300.29]	−0.1207 [−0.1224, −0.1190]
PS1234	126.77 [-2100.06, 2353.59]	6.88 [1.52, 12.23]	169.90 [−1242.60, 1582.39]	−0.1207 [−0.1225, −0.1190]

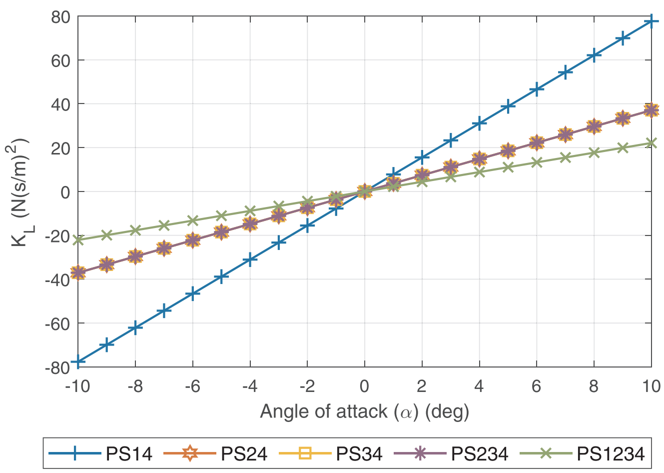

Fig. 11. Lift coefficient K_L for the minimizations.

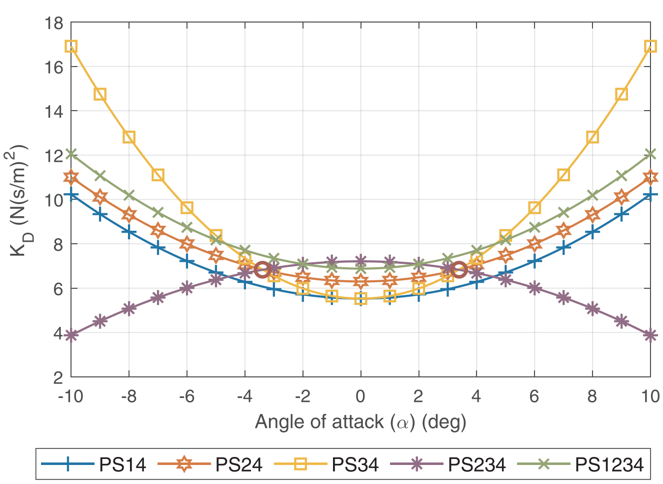

Fig. 10. Drag coefficient K_D for the minimizations.

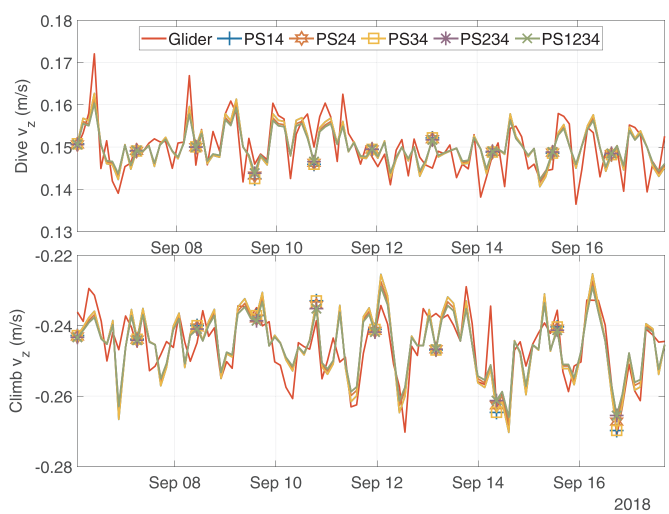

Fig. 12. Logged and modeled vertical velocities v_z for all minimizations for dive and climb.

shown in Fig. 12.

Likewise, the calculated drag and lift coefficients K_D and K_L, found using the logged glider data by substituting Eqs. (5) and (11) into Eq. (37)

$$K_D = -m_0 g \sin(\xi) \frac{\rho_{fw} \sin(\xi)^2}{\rho {v_z}^2} \tag{56}$$

and by substituting Eqs. (5) and (12) into Eq. (38)

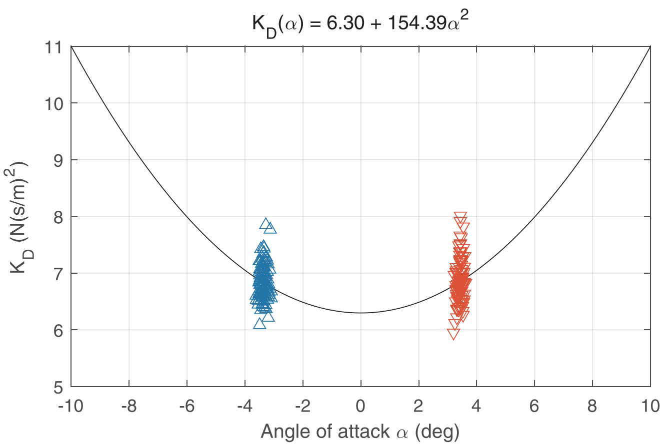

Fig. 13. Drag coefficient K_D estimated from PS24.

$$K_L = m_0 g \cos(\xi) \frac{\rho_{fw} \sin(\xi)^2}{\rho {v_z}^2} \tag{57}$$

lie along the fitted curves created by the estimated parameters for all minimizations. This can clearly be seen in Figs. 13 and 14, which show the results of the minimization PS24.

Although not all possible parameters were estimated in the first four minimizations, the good correlation between the logged and modeled data in Fig. 12 is remarkable. In addition to a good agreement between the chosen unestimated parameters and the real system parameters is another reason for the good correlation the cluster-like distribution of the logged data. This can be seen in Figs. 9, 18 and 19, where all logged data for the pitch angle θ and the vertical velocity v_z are concentrated around two individual points, one for the dives (θ = -24.922°, v_z = 0.15 m/s) and one for the climbs (θ = 25.397°, v_z = -0.246 m/s). For such a data constellation multiple settings exist for an angle of attack α to model these operating points. Figs. 15 and 16 show possible settings for the lift and drag coefficients for the dive operating point using Eqs. (56) and (57). In the case that the parameters of only one coefficient need to be optimized, the parameters result from the intersection of the given coefficient curve and the curve to describe possible settings of α for the operating point. This can be seen for the first minimization PS14 in Fig. 15, where the intersection of the given drag coefficient curve and the curve to describe possible settings of α results in an angle of attack α of around 1.46°. The three minimizations PS24, PS34 and PS234 use a given lift coefficient and estimate one or both parameters of the drag coefficient. This corresponds to Graver's work, where the lift coefficient was used from VCT [27] and only the drag coefficient was determined. Although the values found for K_{D_0} and K_{D_2} in Table 3 are

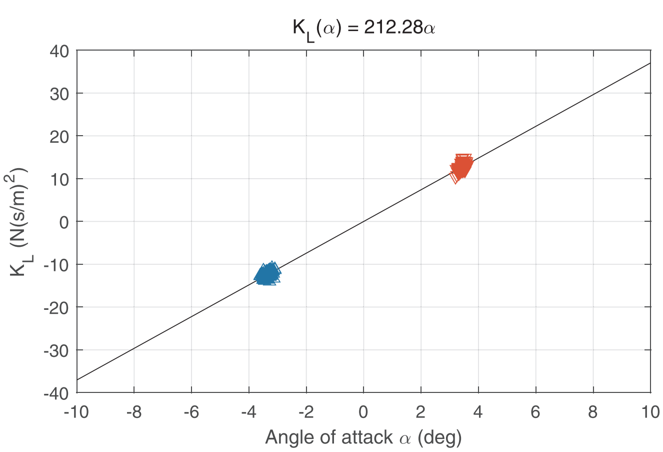

Fig. 14. Lift coefficient K_L estimated from PS24.

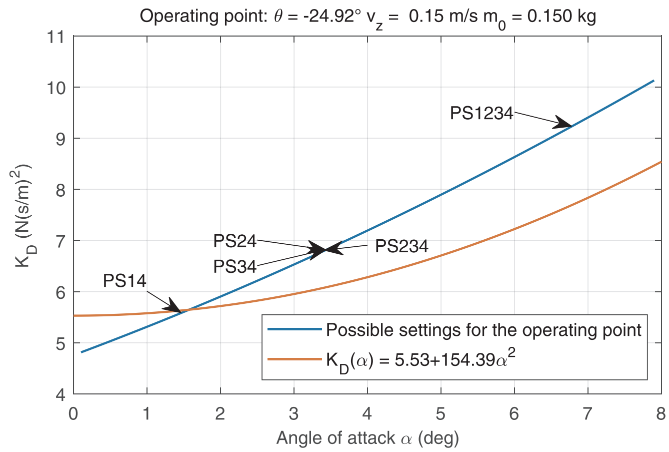

Fig. 15. Possible settings for the angle of attack α and the drag coefficient K_D for the defined operating point for dive.

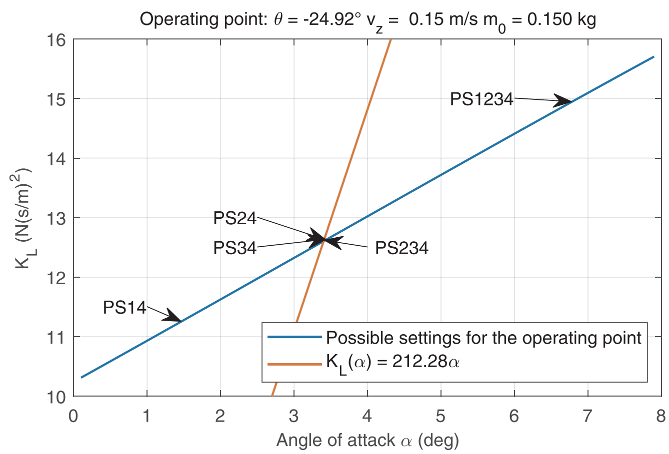

Fig. 16. Possible settings for the angle of attack α and the lift coefficient K_L for the defined operating point for dive.

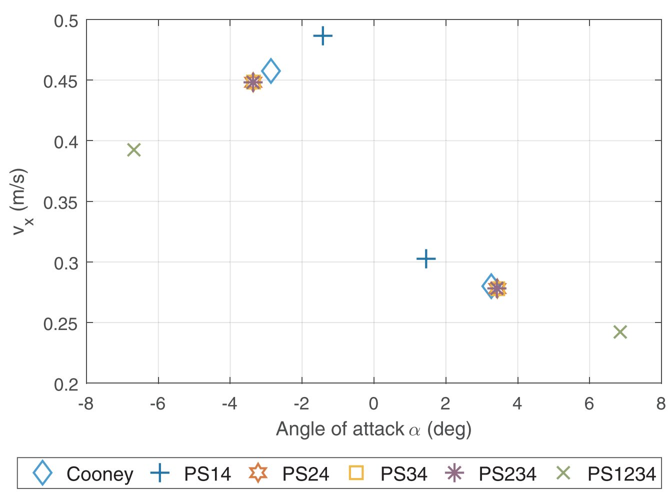

Fig. 17. Determined angle of attack α (see Section 4.2) and calculated horizontal glider velocity v_x using Cooney's approach and the individual minimizations for the pitch angles θ and the vertical glider velocities v_z in Table 2.

very different, the calculated angles of attack α and the horizontal glider velocities v_x in Fig. 17 are similar.

The reason for this is the cluster-like distribution of the logged data, which leads to an operating point of α = 3.4° and K_D = 6.8 N(s/m)^2 using the intersection method for the lift coefficient in Fig. 16 described

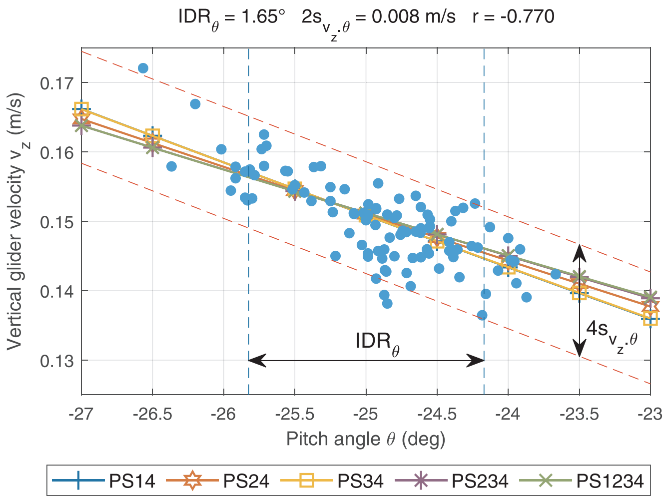

Fig. 18. Scatter plot of the logged pitch angle θ against vertical glider velocity v_z and the curves $v_z = f(\theta, K_{L_1}, K_{D0}, K_{D_2}, \Delta m_0)$ using the estimated parameters from minimizations in Eq. (41) for given pitch angles in the range [-27°, -23°] for dives.

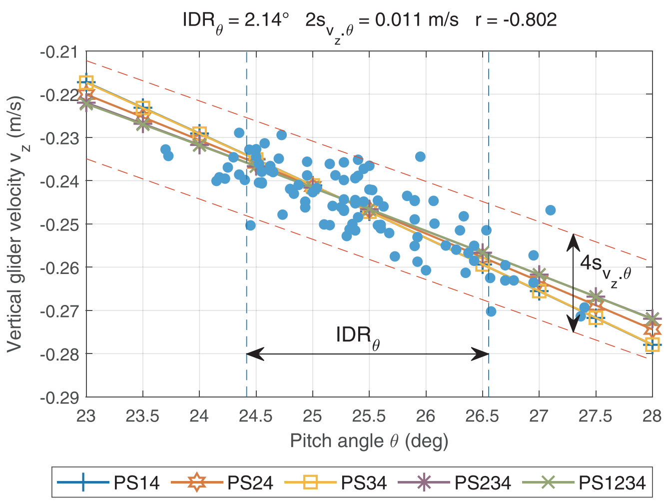

Fig. 19. Scatter plot of the logged pitch angle θ against vertical glider velocity v_z and the curves $v_z = f(\theta, K_{L_1}, K_{D0}, K_{D_2}, \Delta m_0)$ using the estimated parameters from minimizations in Eq. (41) for given pitch angles in the range [23°, 28°] for climbs.

above. This operating point can be modeled by various quadratic function curves, which is clearly shown in Fig. 10, where this operating point corresponds to the intersection point of the curves PS24, PS34 and PS234 (red circles). It should be noted that the negative value for the estimated parameter K_{D_2} obtained for minimization PS234 is a result of the cluster-like distribution of the logged data. A negative value for the parameter is impossible from the physical point of view, but it leads to the minimal cost for $C(\beta)$ in Eq. (43) using the logged data.

The minimization PS1234 has no limitations regarding the lift or drag coefficient curve used. This means that the lift and drag coefficients used to model the operating point are the result of a defined angle of attack α on the possible setting curves in Figs. 15 and 16. Multiple combinations for K_D and K_L are thus possible. The parameter set found leads to an angle of attack of around 6.8° for dives. This value is twice as high as the results of Cooney's approach (see Fig. 8) or the other minimizations (see Fig. 17) and is not trustworthy when using data with a cluster-like distribution around an operating point.

This data distribution is shown in Figs. 18 and 19 where the data samples are greatly scattered around the ideal curves.

The shape of these data distributions can be described by the scale parameters *interdecile range* (IDR) between the 10th and 90th percentiles for the pitch angle θ and the *residual standard deviation* of a linear regression $s_{y.x}$ for the vertical velocity v_z. A linear regression model $v_z = \beta_0 + \beta_1\theta$ is admissible for a pitch angle between $\pm$ 15° and $\pm$ 35° where the ideal curves in Figs. 18 and 19 can be assumed as linear. The using of IDR instead of a standard deviation results from the fact that the pitch angle data is not normally distributed and multimodal in practice. The MATLAB call for IDR is `IDR=diff(prctile(x,[10 90]))`. The residual standard deviation is defined as

$$s_{y.x} = \sqrt{\frac{\sum_{i=1}^{n}(y_i - \hat{y}_i)^2}{n-2}} \tag{58}$$

where n is the sample size, y_i are the individual output data samples and $\hat{y}_i$ are the modeled output values from the regression. The lower and the upper bounds of the distribution are defined by two standard deviations $s_{y.x}$ from the regression line. Another possible parameter to describe these distributions is *Pearson's correlation coefficient r* [39]. This coefficient is a measure of the linear correlation between two variables x and y and is defined as

$$r_{xy} = \frac{\sum_{i=1}^{n}(x_i - \bar{x})(y_i - \bar{y})}{\sqrt{\sum_{i=1}^{n}(x_i - \bar{x})^2}\sqrt{\sum_{i=1}^{n}(y_i - \bar{y})^2}} = \frac{\sum_{i=1}^{n}(x_i - \bar{x})(y_i - \bar{y})}{(n-1)s_x s_y} \tag{59}$$

where n is the sample size, x_i and y_i are the individual data samples, $\bar{x}$ and $\bar{y}$ are the sample means and s_x and s_y are the standard deviations. The variables x and y correspond here to the pitch angle θ and the vertical glider velocity v_z. A linear relation between the vertical glider velocity v_z and the pitch angle θ leads to a correlation coefficient of -1. The calculated coefficients for the dives and climbs using the logged data are -0.77 and -0.802. A reason for these distributions could be an existing vertical current velocity $v_{z_{current}}$ in Eq. (7) caused by internal waves. This is also discussed in [15] as a possible influencing factor on the measurement accuracy of depth-average velocity.

5.2. Sensitivity and topographical analysis of the cost function

For a better understanding of the influence of the parameters β_i on the cost function $C(\beta)$ in Eq. (43), and thus on modeling the vertical glider velocity v_z in Eq. (41), a global sensitivity analysis is carried out. The method used is based on cumulative distribution functions (CDFs) and is described in detail in [40]. The key idea is to analyze the differences between the conditional and unconditional CDFs of the output y using the Kolmogorov-Smirnov (KS) statistic as a measure of their distances. This distance correlates to the sensitivity of the input x_i to the output y. The unconditional CDF is the result when all inputs vary simultaneously in defined ranges, whereas the conditional CDFs result when varying all inputs except x_i, which is fixed at a defined value. The KS statistic provides a curve of sensitivity over all defined fixed values of x_i. A new density-based sensitivity index, called PAWN was presented in [40], where a defined statistic such as the *maximum, mean* or *median* extracts a single value T_i from the KS curve for every input x_i. This value varies between 0 and 1. A low value of T_i implies a smaller influence of x_i on y.

In this paper, the inputs x_i of the sensitivity analysis are the parameters β_i and the output y is the cost function value $C(\beta)$. The data used corresponds to that of the previous section. The Sensitivity Analysis for Everybody (SAFE) Toolbox for MATLAB [41] was used for the analysis. The curves for the KS statistic in Fig. 20 show a high sensitivity for the parameters K_{D_0} and Δm_0. The parameters K_{L_1} and K_{D_2} have low sensitivity within the whole range and lie under the critical level for a confidence level α of 0.05. This can explain the large confidence intervals for these parameters in Table 3 and their uncertain estimation in Section 5.1. An interesting point is the increase in the middle of the KS curves of the parameters K_{D_0} and Δm_0 in Fig. 20 that correspond to the estimated parameters. These parameter areas show a higher sensitivity

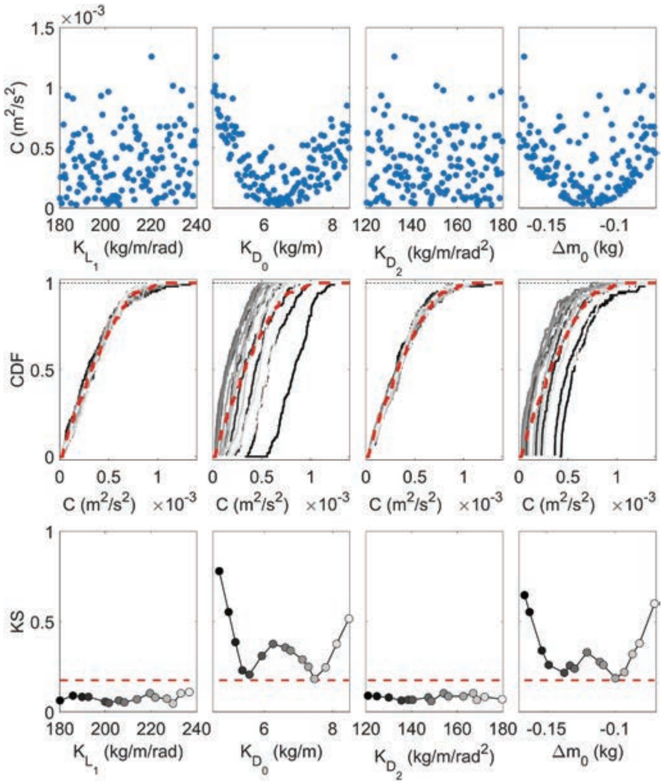

Fig. 20. *Top panels:* Scatter plots of the cost function $C(\beta)$ of Eq. (43) using the logged data from RU29-550 and the random samples of the parameters. *Middle panels:* Cumulative distribution functions (CDFs) of the cost function $C(\beta)$. The red dashed line is the empirical unconditional distribution function $\hat{F}_C(\cdot)$ of the cost function $C(\beta)$ and the gray lines are the empirical conditional distribution functions $\hat{F}_{C|\beta_i}(\cdot)$. *Bottom panels:* Kolmogorov-Smirnov statistic $\hat{KS}(\beta_i)$ at different conditioning values of β_i. The red dashed line is the critical level of the KS statistic for a confidence level of 0.05. [Experimental setup: sampling strategy: Latin Hypercube; number of samples used as conditioning values for the parameters β_i $n = 15$; number of samples used to create the empirical unconditional CDF $N_u = 150$; number of samples used to create the empirical conditional CDFs $N_c = 100$]. (For interpretation of the references to colour in this figure legend, the reader is referred to the web version of this article.)

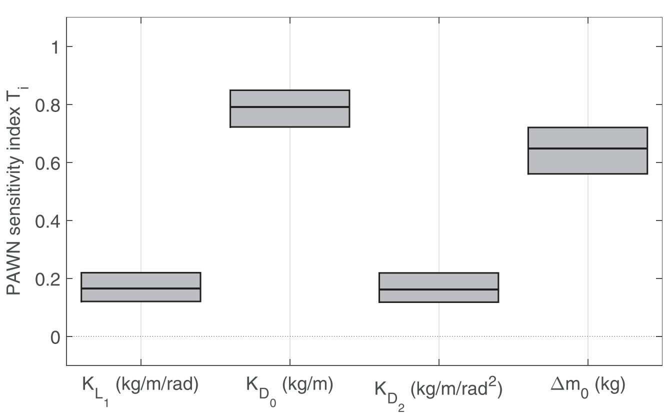

Fig. 21. PAWN sensitivity indices for the cost function $C(\beta)$ of Eq. (43) using the logged data from RU29-550. The boxes are formed by confidence intervals as a result of bootstrapping. The middle lines show the mean value of the PAWN index. [Experimental setup: sampling strategy: Latin Hypercube; $n = 15$; $N_u = 150$; $N_c = 100$; number of bootstrap resamples: 100; statistic used in the PAWN index calculation: *maximum*].

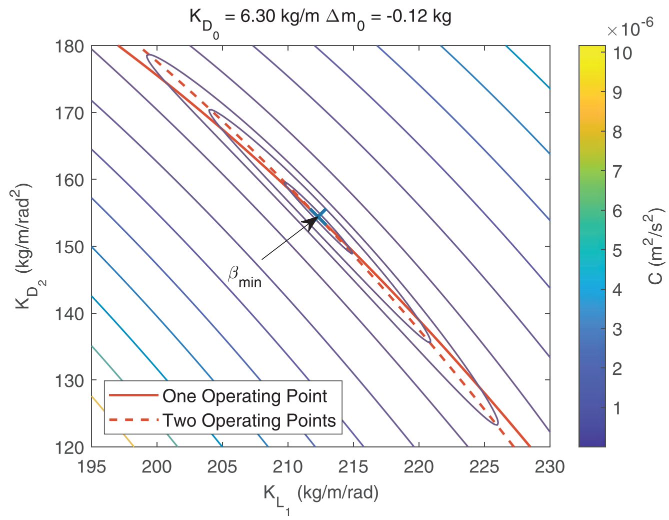

Fig. 22. Topology of the cost function with respect to the parameters K_{L_1} and K_{D_2} for the two operating points scenario. The parameters K_{D_0} and Δm_0 are fixed at their optimal value for the parameter set of minimization PS24. The red lines correspond to the minimum of the valley for a defined parameter K_{D_2} for one and two operating points. (For interpretation of the references to colour in this figure legend, the reader is referred to the web version of this article.)

to the cost function because they characterize the area of the cost function minimum. Fig. 21 shows the resulting PAWN sensitivity indices for the four parameters and their confidence intervals. It shows clearly that the most influential parameters of the cost function $C(\beta)$ are K_{D_0} and Δm_0.

The analysis of the cost function topography may also shed light on the influence of the parameters β_i on the cost function $C(\beta)$. To additionally examine the influence of the data distribution on the cost function topography, simulated data was generated. The parameter set of minimization PS24 in Table 3 was used to calculate the vertical glider velocities v_z in Eq. (41) and define thus the minimum of the cost function. Two scenarios were examined. The first scenario includes one operating point for dive and climb where the pitch angles θ, the variable ballast masses m_b and the water density ρ in Table 2 were used for the calculations in Eq. (41). The second scenario includes an additional operating point where the pitch angles θ are 7° smaller than in the first scenario. Fig. 22 shows the contour plot for the cost function $C(\beta)$ with respect to the parameters K_{L_1} and K_{D_2} when the parameters K_{D_0} and Δm_0 are fixed at their optimal values for the two operating points scenario. The minimum lies inside a long flat valley. Using the cost function for one operating point results in a similar valley without significant minimumarea. This can clearly be seen in Fig. 23, which shows the parameter K_{L_1} and the minimum of the valley $C_{\min}$ with

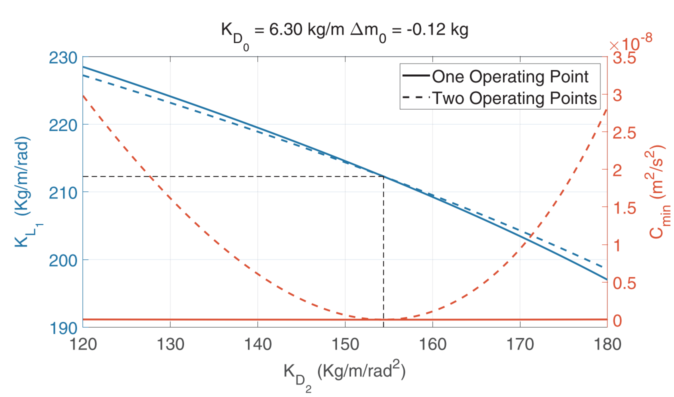

Fig. 23. Values for K_{L_1} and the minimum of the valley $C_{\min}$ with respect to the parameter K_{D_2} for one and two operating points.

respect to the parameter K_{D_2} for one and two operating points. The minimum of the valley $C_{\min}$ for two operating points shows a significant minimumarea, whereas the minimum curve $C_{\min}$ of one operating point is very flat, which makes it difficult or impossible to converge to the minimum. Multiple combinations of K_{L_1} and K_{D_2} are possible to fulfill the cost function requirement. This result is confirmed by the analysis of the minimization PS1234 in Section 5.1.

5.3. Requirements in parameter estimation

In order to detect the correct curve characteristics of the lift and the drag coefficient, it is necessary to use samples for dives and climbs which result in significantly variable angles of attack. This means using data with maximal informativeness about the system. This is a basic requirement in system identification or machine learning to create models which are valid for the whole operational area [42]. Tests with artificially generated noisy data using a parameter set assumed to be known in Eq. (41) and normally distributed pseudo-random numbers were carried out for minimization PS234 and PS1234.

These tests show that the minimization PS234 delivers significant parameters with a maximal 10% error to the given parameter K_{D_2} and a maximal 1% error to K_{D0} and Δm_0 with an interdecile range IDR_θ of at least 8° by two residual standard deviations $2s_{v_z,\theta}$ of 0.01 m/s corresponding to the logged data. In such a data distribution, the Pearson's correlation coefficient r is -0.99. Such a data distribution can be achieved by defining two operating points for the dives and climbs, where the pitch angles differ by about 7°. This is in line with [12] where three operating points $\theta = 16°, 19°, 27°$ for the dives and climbs were defined to detect the induced drag C_{D_2} in Eq. (15). Such a requirement contradicts the energy optimal control of a glider during long-term missions. A compromise has to be reached between the energy optimality and the correct estimation of all glider model parameters during a mission. It would be sufficient when the glider is operated with non optimal operation point for two or three days, to collect enough samples.

Finding significant parameters for all four parameters in minimization PS1234 requires in addition to an interdecile range IDR_θ of at least 8° a two residual standard deviations $2s_{v_z,\theta}$ of less than 0.001 m/s for the vertical velocity v_z which corresponds to a tenth of the observed deviation in the logged data. Pearson's correlation coefficient r is here -1.0. This requirement is difficult to realize in practice (existing vertical current velocity $v_{z_{current}}$ and measurement and detection errors in θ and v_z), which makes the estimation of all four parameters impossible. Another alternative is to use known model parameters and estimate the unknown ones, which is described in Section 5.4.1.

5.4. Depth-average velocity analysis for RU29-492

The logged data from the glider mission RU29-492 from Perth, Australia to Sri Lanka [47] for a time period of seven months from 2016-11-17 to 2017-06-24 was used to analyze the depth-average velocity during a long-term mission which is described in Section 6. The horizontal glider velocity required for this could be calculated with time-invariant and time-varying model parameters. The time-varying model allows the assessment of biofouling during the mission. The individual steps to determine the horizontal glider velocity v_x using a time-invariant and a time-varying model are shown in Fig. 24. The time-invariant model uses only one parameter set as result of the minimization of Eq. (43) using all logged glider data for the dives and climbs of the whole mission period, whereas the time-varying model estimates a parameter set for each dive and climb at time $t(i)$ using only logged glider data which lie in a sliding window defined by a time interval between $t(i) - 0.5t_{window}$ and $t(i) + 0.5t_{window}$. The length of the sliding window is t_{window}.

The data of the glider state during the time period is shown in Fig. 25. For most of this period, the glider was programmed to fly four

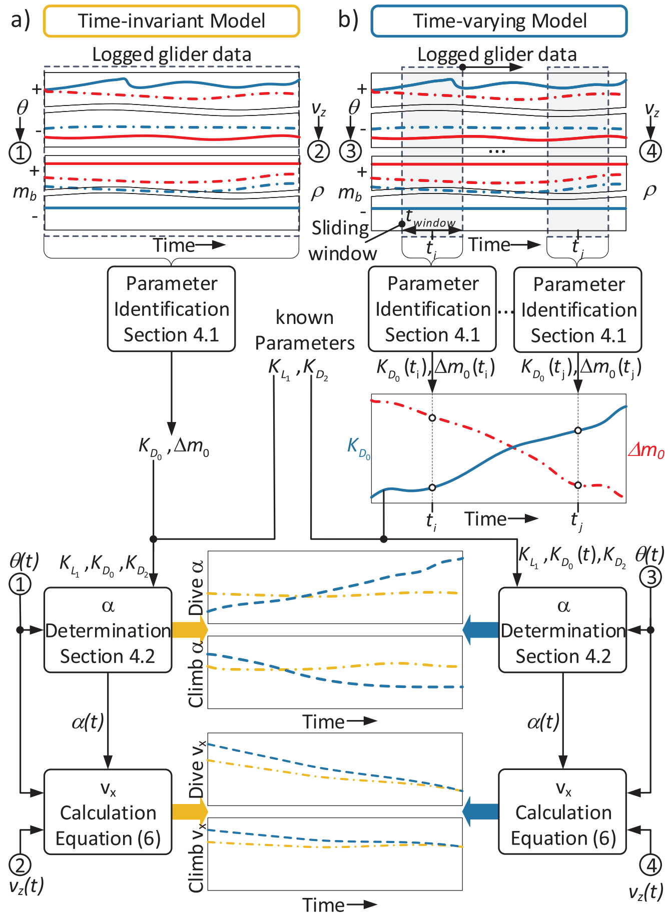

Fig. 24. Individual steps to determine the horizontal glider velocity v_x for a time-invariant (a) and a time-varying model (b).

yo profiles, starting from the surface and diving to 980 m, climbing to 100 m, diving again to 980 m, repeating this two additional times and returning to the surface. During the surface period of normally 10 min the glider sends the logged data via satellite to the Dockserver, the land- or ship-based glider communication center, and receives new instructions for command and control for the next dive period.

5.4.1. Parameter estimation

Due to the existing distribution of the logged data a reliable parameter estimation for all parameters in Eq. (41) is not appropriate (see Section 5.3). Therefore, the quadratic parameter K_{D_2} in drag coefficient Eq. (37) and the linear parameter K_{L_1} in lift coefficient Eq. (38) are assumed to be known and were used from Cooney [14] (see Table 1). This strategy is equivalent to the minimization set PS24 in Section 5.1 and corresponds to the works of Graver [28] and Merckelbach [17] where only a part of the model parameters were estimated. A close look at factors that influence both parameters shows that a change in value as a result of biofouling is unlikely. The linear parameter K_{L_1} only depends on constructive parameters/relations (aspect ratio $\mathcal{R}$, wing sweep angle Λ) where biofouling has no influence. Since in the lifting-line theory, the quadratic parameter K_{D_2} is calculated using the lift coefficient K_L (see Eqs. (32) and (33)) and the aspect ratio $\mathcal{R}$, a change in value as a result of biofouling is therefore also unlikely.

The approach described in Section 4.1 was used to estimate the unknown parameters K_{D0} and Δm_0. The first minimization estimates these two parameters using all logged data for the dives and climbs of the 7-month mission period in Eq. (43). This results in two single model parameters $K_{D0} = 7.355$ kg/m and $\Delta m_0 = -0.085$ g, which are time-invariant during the whole mission period. The modeled vertical glider

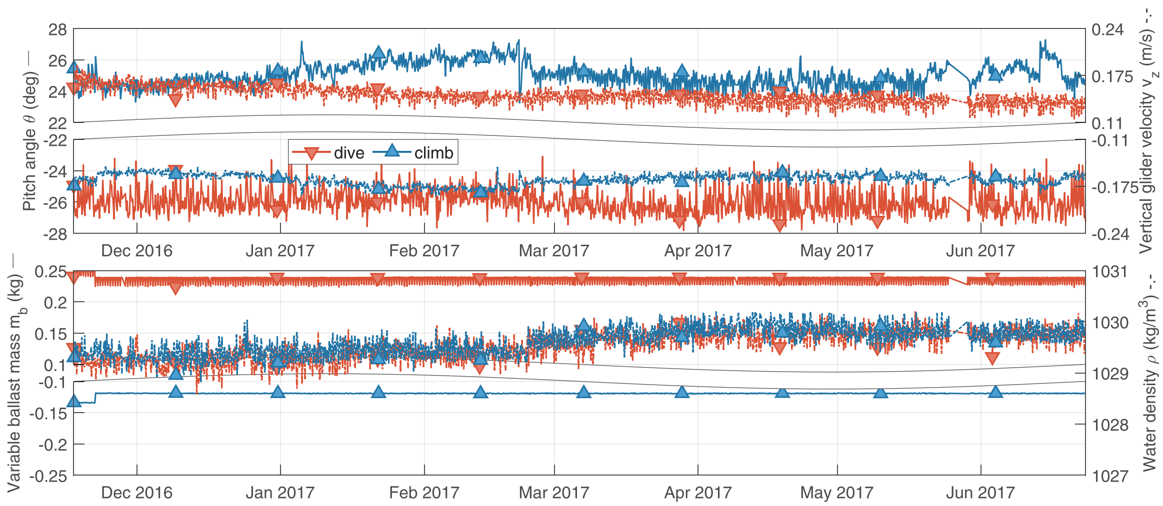

Fig. 25. Glider data used for the minimization: pitch angle θ, vertical glider velocity v_z, ballast mass m_b, water density ρ.

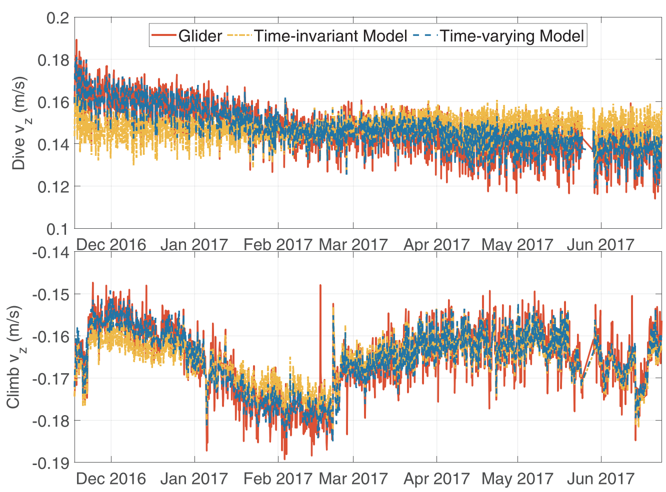

Fig. 26. Logged and modeled vertical glider velocity v_z for a time-invariant and time-varying model for dive and climb.

velocity v_z for dive and climb using these parameters in Eq. (41) are shown in curve “Time-invariant Model” in Fig. 26. The comparison of the logged and the modeled vertical glider velocity between dive and climb shows differences. There is a good match of the curves for climb for the whole mission period, where the vertical glider velocity is approximately equal to 0.16 m/s during the whole mission period. The modeled curve for the dive shows a relatively constant progression of 0.14 m/s, whereas the logged vertical glider velocity has larger values at the first half of the mission and smaller values in the second part of the mission. The real progression can be approximated as a linear slope starting at 0.17 m/s and ending at 0.14 m/s. The consistent commanded pitch angle θ and the variable ballast mass m_b (see Fig. 25) cannot explain the contradictory progression of the vertical glider velocity for the dive (time-varying progression) and the climb (time-invariant progression) during the mission.

To analyze the time-varying behavior of the vertical glider velocity for dive, an extended minimization process will be performed. In this process, the minimization will be executed for every mission day using the logged data over a sliding window of 3 weeks in Eq. (43). The resulting curves for the parameter K_{D_0} and Δm_0 are shown in Fig. 27. The glider was trimmed slightly, which results in a buoyancy trim offset of Δm_0 = -65 g at the start of the mission. This was necessary to compensate for the lower density of surface waters starting at Sumatra and most likely near Sri Lanka. The line “Time-varying Model” in Fig. 26 shows the course of the vertical glider velocity v_z using these parameters in Eq. (41).

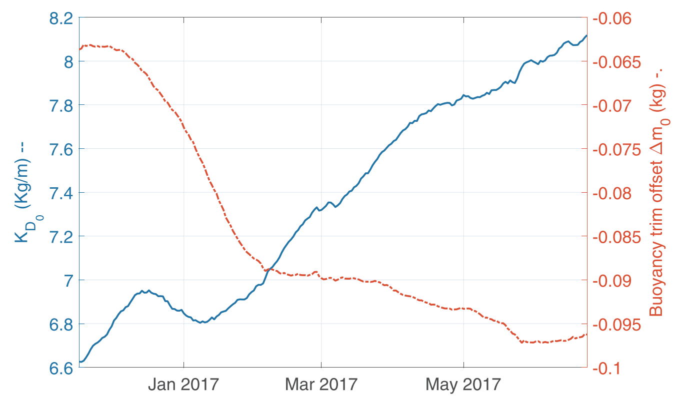

Fig. 27. Results of the moving minimization process for the parameters K_{D_0} and Δm_0.

Now both modeled curves for dive and climb match very well with the real glider behavior. The reason for this good match is the trends of the parameters K_{D_0} and Δm_0 during the mission. The parameter K_{D_0}, which corresponds to the parasitic drag coefficient and the negative buoyancy trim offset Δm_0 increase with time. Biofouling could be responsible for this behavior. The biofouling grows during the mission, which increases the skin friction drag and generates an additional buoyancy. This is also described in [13], where the influence of biofouling on the glider behavior during long-term missions is explained in detail. The 0.4 kg/m^3 increase in water density during the mission (see Fig. 25) can also explain the increase of Δm_0 by about 30 g. (The used glider had an extended energy bay, which results in a glider volume of 72.2 l. This volume leads to an additional buoyancy of 28.88 g = 0.4 kg/m^3 $\cdot$ 0.0722 m^3 during the mission.) These two effects, a larger drag coefficient and a larger negative buoyancy trim offset, add up during dive and reduce the glide speed. A larger negative buoyancy leads to a larger glide speed during climb. This effect will be compensated for by the larger drag coefficient, which decreases the glide speed. The result is an approximately equal glide speed for climb during the mission.

5.4.2. Resulting velocities

Fig. 28 shows the horizontal glider velocity and an estimated linear trend for dive and climb using the parameters from the time varying model. The estimated linear trend equations, computed with regression,

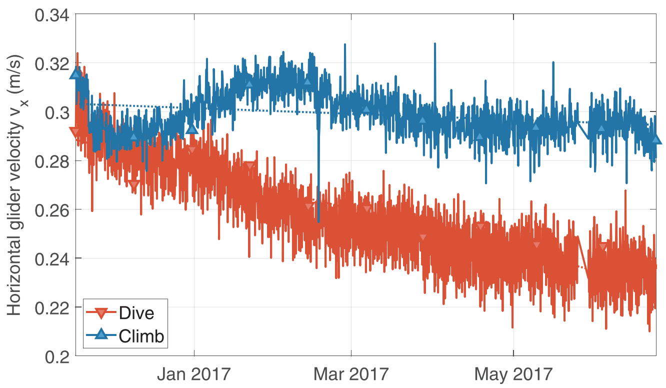

Fig. 28. Horizontal glider velocity v_x for dive and climb.

are

$$v_{x_{dive}} = 0.289\frac{m}{s} - 0.000275\frac{m}{s{\cdot}d}t_{mission} \tag{60}$$

$$v_{x_{climb}} = 0.303\frac{m}{s} - 0.0000396\frac{m}{s{\cdot}d}t_{mission} \tag{61}$$

where $t_{mission}$ is the mission duration in days. It is clear that the difference between the horizontal velocity for dive and climb will increase with increasing mission duration. The curves in Figs. 27 and 28 show three important facts which should be considered in connection with planning and navigation of long-term missions:

- The model parameter K_{D_0} and Δm_0 can be time-varying;
- The horizontal glider velocity v_x can decrease over the course of the mission;
- The horizontal glider velocity v_x for dive and climb can be different.

This means to obtain a similar horizontal glider velocity for dive and climb during the mission the current buoyancy trim offset Δm_0 needs to be detected as accurately as possible. A good estimate of this parameter can be achieved using Eq. (51). Fig. 29 shows the curves estimated using this approach ("Calculated Parameter") and the results of the moving minimization ("Estimated Parameter") as described above. The sliding window for the logged data is 3 weeks in both approaches. Since the maximum error between the curves is only 3.9 g, the calculated buoyancy trim offset is a good guide to determine the right variable balance mass m_b for climb and dive during the mission. A more accurate result can be achieved using an angle of attack α in Eq. (51).

Fig. 30 shows the calculated angle of attack courses using the model parameters from Cooney, a time-invariant and a time-varying model and the logged pitch angle θ in the angle of attack determination presented in Section 4.2. The angle of attack α is approximately equal to $\pm$ 4° during the mission using the parameters from the time-invariant

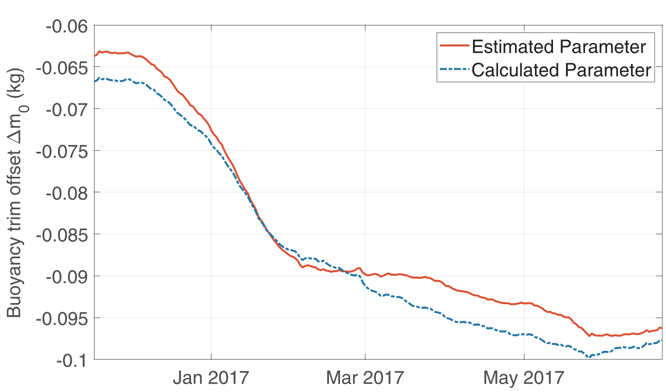

Fig. 29. Estimated and calculated buoyancy trim offset Δm_0.

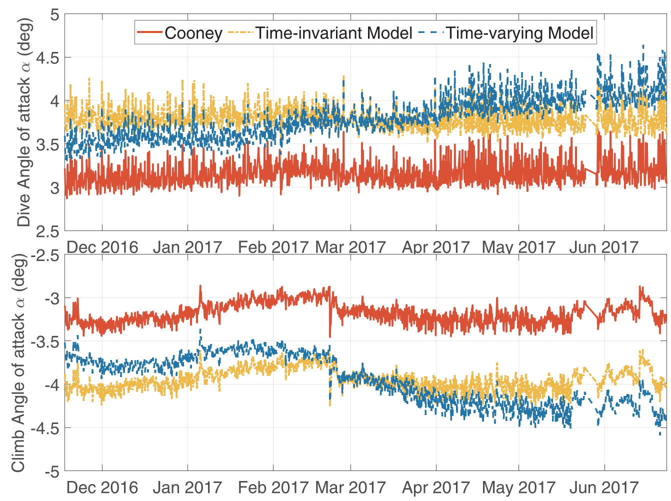

Fig. 30. Angle of attack α courses using the parameters from Cooney, a time-invariant and a time-varying model for dive and climb.

model. Using the time-varying model, the angle of attack will increase from $\pm$ 3.6° to $\pm$ 4.4° during the mission. Although Cooney's model does not include time-varying parameters a slight increase of the angle of attack α is observed for dives during the mission. The reason is the inclusion of the glide speed V in the pressure drag C_{D_0} calculation in Eq. (34), which is used in the angle of attack determination. The glide speed V is decreased for dives and remains constant for climbs during the mission.

Fig. 31 shows the calculated horizontal glider velocity v_x using the angles of attack in Fig. 30, the vertical glider velocity v_z and the pitch angle θ in Eq. (6). All curves have a similar trend, which is determined by the trend of the logged vertical glider velocity v_z for dive and climb. The calculated velocity values using Cooney's model are 0.005 to 0.015 m/s (1.7% to 5.0%) larger than the velocity values calculated with the time-varying model. The velocity values from the time-invariant model lie around the velocity curve of the time-varying model whereas the values are smaller in the first half of the mission ($-$0.005 to 0 m/s (1.7% to 0%)) and larger in the second part of the mission (0 to 0.005 m/s (0% to 1.7%)).

6. Evaluation of the depth-average velocity

The depth-average velocity is a unique calculated quantity in the

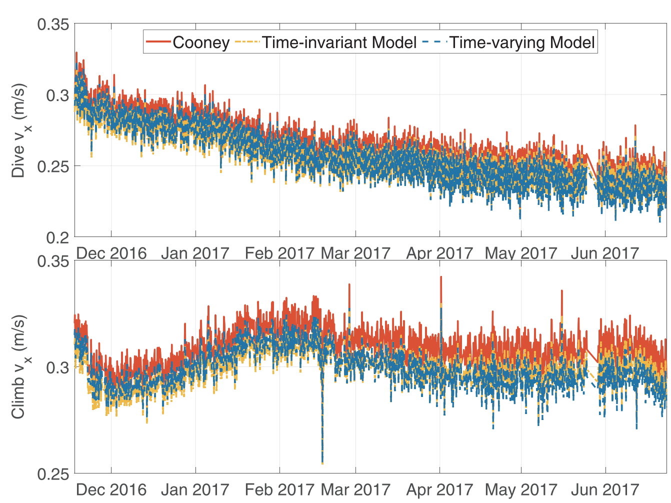

Fig. 31. Horizontal glider velocity v_x courses using the parameters from Cooney, a time-invariant and a time-varying model for dive and climb.

operating area of underwater gliders. It is used for glider navigation or as a score to evaluate the quality of ocean current models in and near the operating area of the glider. The evaluation of the ocean current models can help to choose a suitable current model for navigation during the mission. Another application for evaluation is the data post-processing, where the depth-average velocities of the individual dive segments in a mission will be compared with ocean current models. This evaluation can help to determine the confidence in new data sources, to improve the ocean models using the spatial and temporal anomalies between modeled and observed data, and to modify an ocean model with additional data/information from a glider or calculation methods from ocean models with a better correlation to the logged data. The individual steps for an evaluation process are presented below.

6.1. Calculation of depth-average velocity

To evaluate the depth-average velocity of an ocean current model with that of a glider requires their previous calculation. Both calculation methods for a glider and an ocean model will be described in detail below.

6.1.1. Depth-average velocity of a glider

The depth-average velocity of a glider $\mathbf{v}_{c_{Glider}}$ is the difference between the velocity over ground $\mathbf{v}_g$ and the horizontal glider velocity through water $\mathbf{v}_h$ [15]

$$\mathbf{v}_{c_{Glider}} = \mathbf{v}_g - \mathbf{v}_h \tag{62}$$

The velocity over ground $\mathbf{v}_g$ is the result of the GPS fixes at the beginning $\mathbf{x}_{start}$ and the end $\mathbf{x}_{end}$ of a dive segment and the time required for it

$$\mathbf{v}_g = \frac{\mathbf{x}_{end} - \mathbf{x}_{start}}{t_{end} - t_{start}} \tag{63}$$

The horizontal glider speed through water $\mathbf{v}_h$ can be described by its magnitude, the horizontal glider velocity v_x, and its direction, the logged glider heading ψ

$$\mathbf{v}_h = \begin{bmatrix} v_{east} \\ v_{north} \end{bmatrix} = \begin{bmatrix} v_x \cos(\psi) \\ v_x \sin(\psi) \end{bmatrix} \tag{64}$$

As shown in Section 5.4.1, there are two different horizontal glider velocities for dive $v_{x_{dive}}$ and climb $v_{x_{climb}}$. To calculate an exclusive horizontal velocity v_x used in Eq. (64) a temporal weighting where the velocities are active is necessary. The horizontal glider velocity for dive would be underestimated and the horizontal glider velocity for climb would be overestimated using a simple mean calculation, because the dive time period is larger than the climb time period. The vertical glider velocities $v_{z_{dive}}$ and $v_{z_{climb}}$ will be used for temporal weighting

$$v_x = \frac{|v_{z_{climb}}|}{v_{z_{dive}} + |v_{z_{climb}}|} v_{x_{dive}} + \frac{v_{z_{dive}}}{v_{z_{dive}} + |v_{z_{climb}}|} v_{x_{climb}} \tag{65}$$

6.1.2. Depth-average velocity of an ocean model

The depth-average velocity can be understood as the mean ocean current in the operation area of the glider during the time period for a considered dive segment. Such a segment can consist of one or more yo profiles. To calculate this value, the ocean current conditions $\mathbf{v}_c$ have to be detected at the position $\mathbf{x}_{start}$, at the time t_{start} and at the position $\mathbf{x}_{end}$, at the time t_{end} in several depth layers for the dive segment. Therefore, a defined number n of depth layers are equidistantly distributed between the surface and the dive-to depth which is shown in Fig. 32. The number n is taken to be 20. Finally, the mean value for all these ocean current components will be calculated according to the following equation

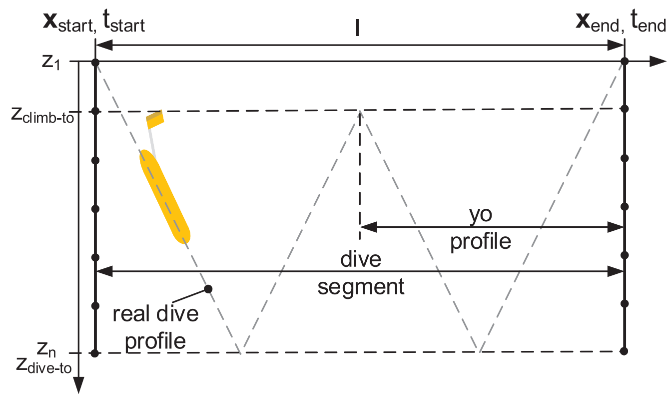

Fig. 32. Defined depth layers on the start and end position of a dive segment.

$$\mathbf{v}_{c_{Model}} = \frac{1}{2}\left(\begin{bmatrix} \mathbf{v}_c(\mathbf{x}_{start}, z_1, t_{start}) \\ \vdots \\ \mathbf{v}_c(\mathbf{x}_{start}, z_n, t_{start}) \end{bmatrix} + \begin{bmatrix} \mathbf{v}_c(\mathbf{x}_{end}, z_1, t_{end}) \\ \vdots \\ \mathbf{v}_c(\mathbf{x}_{end}, z_n, t_{end}) \end{bmatrix}\right) \tag{66}$$

Since the ocean current data, coming from the Ocean General Circulation Models (OGCM) as data files, will be provided only at discrete positions, depths and times with a nonlinear depth scale and a coarser time and length scale, so that the ocean current information cannot be taken directly from the files. Hence, a multi-dimensional interpolation scheme will be used to extract the desired ocean current data. Additional information about the interpolation scheme is presented in [16].

This approach is a simplification and works well for easy current conditions. In case of complex current conditions or to determine the depth-average velocity more accurately, a glider simulation should be used. Therefore, the exact yo movement of the glider in the current field of the ocean model using the commanded heading, pitch and dive profile for the dive segment will be simulated. The resulting surfacing position and the simulated horizontal glider velocity can then be used in Section 6.1.1 to determine the depth-average velocity.

6.2. Goodness-of-fit indicators

Two goodness-of-fit indicators were used for the evaluation. Both indicators use the distance information d between the calculated end positions using the depth-average velocity of the ocean model $\mathbf{v}_{c_{Model}}$ and the glider $\mathbf{v}_{c_{Glider}}$ after a defined time period Δt.

$$d = \|\mathbf{v}_{c_{Model}} - \mathbf{v}_{c_{Glider}}\|\Delta t \tag{67}$$

It should be noted that the horizontal glider velocity through water $\mathbf{v}_h$ has no influence on Eq. (67) because this vector will be used in both calculations for glider and for ocean model, and thus will be offset.

The first indicator is a non-dimensional skill score (ss) presented in [43]. This skill score was developed to compare simulated with observed drifter trajectories and has to be adapted for single dive segments. It has been applied in a variety of work [44–46] in the last decade. To overcome the difficulties with dive segments of different lengths a non-dimensional index s will be used to normalize the distance d with the length l of the dive segment

$$s = \frac{d}{l} \tag{68}$$

This index is used to calculate the skill score ss

$$ss = \begin{cases} 1 - \frac{s}{n}, & (s \leq n) \\ 0, & (s \geq n) \end{cases} \tag{69}$$

where n is a tolerance threshold. A skill score of 1 implies a perfect match between model and glider.

The second indicator is novel and uses a time period Δt of 24 hours in Eq. (67). The result of this indicator $Da24h$ is given in km. This makes

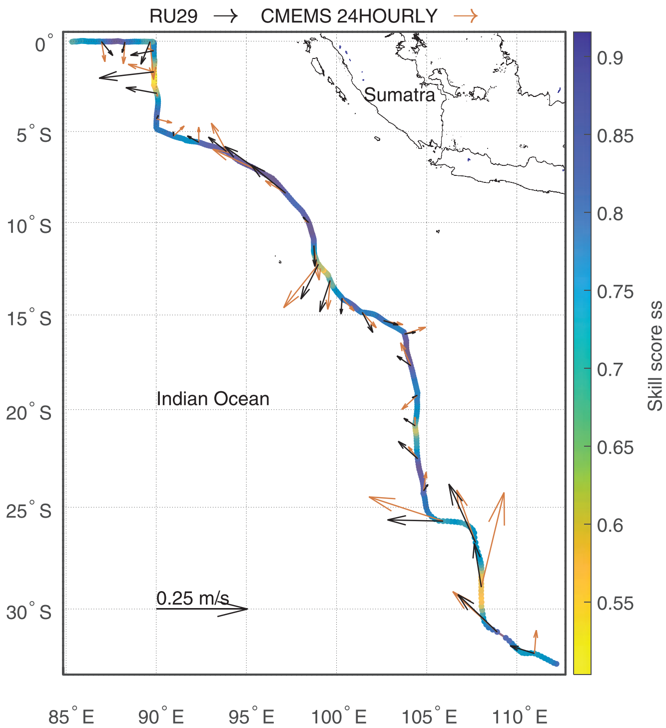

Fig. 33. Skill score *ss* and current vectors for the observed (RU29) and modeled (CMEMS 24HOURLY) depth-average velocities along the mission. The current vectors correspond to the weekly mean values.

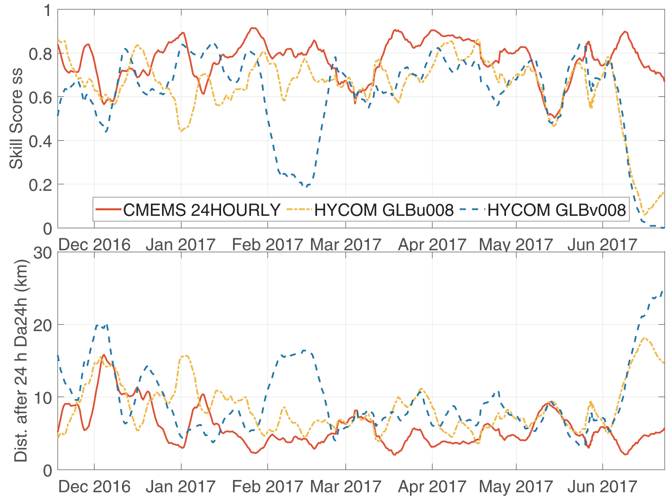

Fig. 34. Skill score *ss* and distance after 24h *Da24h* curves for the three ocean models: 24 hourly global-analysis-forecast-phys-001-024 model of CMEMS (CMEMS 24HOURLY), GLBu008 (HYCOM GlBu008) and GLBv008 (HYCOM GLBv008) of HYCOM.

it possible to overcome the difficulties with dive segments of different time periods. Likewise, this parameter can be imagined easily, as it corresponds to the distance between the modeled and the real surfacing position of the glider after 24 hours. A small distance means a good match between model and glider.

6.3. Evaluation

Three ocean current models were chosen for the comparison of the modeled with the observed depth-average velocities along the mission route. The models used are GLBu008 (GOFS 3.0) and GLBv008 (GOFS 3.1) of HYCOM [19] and the 24 hourly global-analysis-forecast-phys-001-024 model of the Copernicus Marine Environment Monitoring Service (CMEMS) [18]. Fig. 33 shows a map with the mission route of RU29-492 from Perth, Australia to Sri Lanka with the weekly mean depth-average velocity vectors from the glider RU29 (blue) using the calculated horizontal glider velocity v_x of the time-varying model and the 24 hourly CMEMS ocean model (red) for the several dive segments. This map includes additionally the smoothed skill score *ss* values for the several dive segments. A moving average algorithm with a sliding window of seven days was used for smoothing. There is a good match between the observed and modeled depth-average velocities for most of the mission period where the skill score *ss* is larger than 0.7. There are four regions during the mission with a bad evaluation:

- 28°-30°S and 108°E start of December 2016
- 21°S and 104°E start of January 2017
- 12.5°S and 99.25°E start of March 2017
- 2°S and 89.9°E middle of May 2017.

Fig. 34 shows the smoothed courses of the two goodness-of-fit indicators: skill score *ss* and distance after 24h *Da24h* for the three ocean current models using the calculated horizontal glider velocity v_x of the time-varying model. The distance after 24h *Da24h* shows an inverse behavior to the skill score *ss*. The HYCOM models show a worse evaluation in comparison to the CMEMS model. As shown in Table 4, which includes the mean values of the indicators, the GLBv008 model has a slightly worse evaluation in comparison to the GLBu008 model. The bad evaluation of the HYCOM models in the area are noticeable:

- 14.5°-15.5°S and 101°-103°E start of February 2017 (only GLBv008)
- 0°S and 85.5°-87°E middle of June 2017.

Table 4
Calculated mean values for skill score *ss* and distance after 24h *Da24h* for the three ocean models: 24 hourly global-analysis-forecast-phys-001-024 model of CMEMS, GLBu008 and GLBv008 of HYCOM and the three methods to detect the horizontal glider velocity v_x.

Score	Model	CMEMS	GLBu008	GLBv008
ss	Cooney	0.766	0.636	0.594
	Time-invariant	0.767	0.64	0.602
	Time-varying	0.768	0.641	0.603
Da24h (km)	Cooney	5.8	8.758	9.986
	Time-invariant	5.765	8.668	9.763
	Time-varying	5.762	8.646	9.754

Table 4 shows that the mean values of the two indicators for the methods used to detect horizontal glider velocity v_x are very similar. The higher model accuracy of the time-varying model does not lead to other significant results. The reason is the small differences in the calculated horizontal glider velocities in the individual methods (maximal 5%) (see Fig. 31). The CMEMS has a 20% better quality in *ss* and a 33% better quality in *Da24h* than the indicators of the HYCOM models. The GLBu008 shows a 6% better quality in *ss* and a 11% better quality in *Da24h* than the GLBv008 model.

7. Conclusions

This paper examines the need for an accurate glider model in navigation, control and data post-processing. A model which is generally used for a Slocum glider was presented in detail. The calculation of the horizontal glider velocity v_x based on an accurate angle of attack detection was discussed in this context. A robust minimization approach to detect the model parameters and its limitations due to the available logged glider data were described. The correct parameter estimation requires a large data distribution in the whole operation range of a glider which contradicts the energy optimal control of a glider during long-term missions. The analysis of RU29-492 from Perth, Australia to Sri Lanka shows an increase in the drag coefficient over the course of the mission caused by biofouling, which leads to an increase of the angle of attack of about 1° using similar pitch commands. In addition, an increase in the buoyancy trim offset as result of biofouling and changing salinity conditions during the mission could also be observed. This should be considered for the navigation and control of a glider through an online model parameter estimation during the mission. The decrease of the horizontal glider velocity from 0.3 to 0.26 m/s within 7 months should be considered in the global path planning.

The comparison of the depth-average velocity of ocean current models from CMEMS and HYCOM with the observed velocity from the glider using chosen goodness-of-fit indicators allows a spatial and temporal model evaluation along the mission route. In this context, one question arises: How should the evaluation results be processed so that they can be used in ocean model design?

CRediT authorship contribution statement

Mike Eichhorn: Conceptualization, Methodology, Software, Writing - original draft. **David Aragon:** Data curation, Software, Writing - original draft. **Yuri A.W. Shardt:** Writing - review & editing. **Hugh Roarty:** Resources, Validation, Writing - review & editing.

Declaration of Competing Interest

The authors declare that they have no known competing financial interests or personal relationships that could have appeared to influence the work reported in this paper.

References

[1] D.L. Rudnick, R.E. Davis, C.C. Eriksen, D.M. Fratantoni, M.J. Perry, Underwater gliders for ocean research, Mar. Technol. Soc. J. 38 (1) (2004) 48–59.
[2] O. Schofield, J. Kohut, D. Aragon, L. Creed, J. Graver, C. Haldeman, J. Kerfoot, H. Roarty, C. Jones, D. Webb, S. Glenn, Slocum gliders: robust and ready, J. Field Rob. 24 (6) (2007) 473–485, https://doi.org/10.1002/rob.20200.
[3] D. Meyer, Glider technology for ocean observations: areview, Ocean Sci. Discuss. 2016 (2016) 1–26, https://doi.org/10.5194/os-2016-40.
[4] C.C. Eriksen, T.J. Osse, R.D. Light, T. Wen, T.W. Lehman, P.L. Sabin, J.W. Ballard, A.M. Chiodi, Seaglider: a long-range autonomous underwater vehicle for oceanographic research, IEEE J. Oceanic Eng. 26 (4) (2001) 424–436, https://doi.org/10.1109/48.972073.
[5] J. Sherman, R.E. Davis, W.B. Owens, J. Valdes, The autonomous underwater glider ”Spray”, IEEE J. Oceanic Eng. 26 (4) (2001) 437–446, https://doi.org/10.1109/48.972076.
[6] D.C. Webb, P.J. Simonetti, C.P. Jones, SLOCUM: An underwater glider propelled by environmental energy, IEEE J. Oceanic Eng. 26 (4) (2001) 447–452, https://doi.org/10.1109/48.972077.
[7] Center for Ocean Observing LeadershipRutgers, Active deployments, (2019).
[8] O. Schofield, D. Aragon, C. Jones, J. Kohut, H. Roarty, G. Saba, X. Yi, S. Glenn, Maturing glider technology providing a modular platform capable of mapping ecosystems in the ocean, in: E. Delory, J. Pearlman (Eds.), Challenges and Innovations in Ocean In Situ Sensors - Measuring Inner Ocean Processes and Health in the Digital Age, Elsevier, 2018, pp. 173–181.
[9] C. Dobson, J. Mart, N. Strandskov, J. Kohut, O. Schofield, S. Glenn, C. Jones, D. Webb, C. Barrera, A. Ramos, The challenger glider mission: A global ocean predictive skill experiment, 2013 OCEANS - San Diego, (2013), pp. 1–8, https://doi.org/10.23919/OCEANS.2013.6741236.
[10] RUCOOL, The challenger glider mission, (2019).
[11] A. Alvarez, Redesigning the SLOCUM glider for torpedo tube launching, IEEE J. Oceanic Eng. 35 (4) (2010) 984–991, https://doi.org/10.1109/JOE.2010.2057170.
[12] L. Merckelbach, A. Berger, G. Krahmann, M. Dengler, J.R. Carpenter, A dynamic flight model for slocum gliders and implications for turbulence microstructure measurements, J. Atmos. Oceanic Technol. 36 (2) (2019) 281–296, https://doi.org/10.1175/JTECH-D-18-0168.1.
[13] C.D. Haldeman, D.K. Aragon, T. Miles, S.M. Glenn, A.G. Ramos, Lessening biofouling on long-duration auv flights: behavior modifications and lessons learned, OCEANS 2016 MTS/IEEE Monterey, (2016), pp. 1–8, https://doi.org/10.1109/OCEANS.2016.7761236.
[14] L. Cooney, Angle of attack and slocum vehicle model, Technical Report, Teledyne Webb Research, 2011.
[15] D.L. Rudnick, J.T. Sherman, A.P. Wu, Depth-average velocity from spray underwater gliders, J. Atmos. Oceanic Technol. 35 (8) (2018) 1665–1673, https://doi.org/10.1175/JTECH-D-17-0200.1.
[16] M. Eichhorn, Optimal routing strategies for autonomous underwater vehicles in time-varying environment, Rob. Auton. Syst. 67 (2015) 33–43, https://doi.org/10.1016/j.robot.2013.08.010.
[17] L. Merckelbach, D. Smeed, G. Griffiths, Vertical water velocities from underwater gliders, J. Atmos. Oceanic Technol. 27 (3) (2010) 547–563, https://doi.org/10.1175/2009JTECHO710.1.
[18] CMEMS, (2019).
[19] HYCOM, Data server, (2019).
[20] J. Tung, M. Guo, J. Guo, F. Chiu, S. Cheng, Design of an underwater glider with fore and aft buoyancy engines, 2007 Symposium on Underwater Technology and Workshop on Scientific Use of Submarine Cables and Related Technologies, (2007), pp. 446–450, https://doi.org/10.1109/UT.2007.370770.
[21] D. Raymer, Aircraft Design: A Conceptual Approach, Sixth Edition, American Institute of Aeronautics and Astronautics, Inc., 2018, https://doi.org/10.2514/4.104909.
[22] S.A. Jenkins, G. D'Spain, Autonomous underwater gliders, in: M.R. Dhanak, N.I. Xiros (Eds.), Springer Handbook of Ocean Engineering, Springer International Publishing, Cham, 2016, pp. 301–322, , https://doi.org/10.1007/978-3-319-16649-0_12.
[23] F. Irving, The paths of soaring flight, PUBLISHED BY IMPERIAL COLLEGE PRESS AND DISTRIBUTED BY WORLD SCIENTIFIC PUBLISHING CO., 1999, https://doi.org/10.1142/p045.
[24] S.A. Jenkins, D.E. Humphreys, J. Sherman, J. Osse, C. Jones, N. Leonard, J. Graver, R. Bachmayer, T. Clem, P. Carroll, P. Davis, J. Berry, P. Worley, Underwater glider system study, Scripps Institution of Oceanography Technical Report No. 53, Technical Report, Office of Naval Research, 2003.
[25] C. Eriksen, Gliders, in: J.H. Steele (Ed.), Encyclopedia of Ocean Sciences (Second Edition), second edition, Academic Press, Oxford, 2009, pp. 59–66, , https://doi.org/10.1016/B978-012374473-9.00728-1.
[26] S. Bergman, Comparison of the lift, drag and pitch moment coefficients of a Slocum glider wind tunnel model with computational results by Vehicle Control Technologies, Inc - MAE 222 Final Report, Technical Report, Princeton University, Princeton, NJ, 2003.
[27] D.E. Humphreys, N.S. Smith, A.V. Roup, K.W. Watkinson, Validation of the Hydrodynamics & Maneuvering Model for the Webb Research Corporation Slocum Glider - VCT Technical Report #70, Technical Report, Vehicle Control Technologies, Inc., Reston, VA, 2003.
[28] J.G. Graver, Underwater Gliders: Dynamics, Control and Design, Princeton University, Princeton, NJ, 2005 Ph.D. thesis.
[29] P. Bhatta, Nonlinear Stability and Control of Gliding Vehicles, Princeton University, Princeton, NJ, 2006 Ph.D. thesis.
[30] C.D. Williams, R. Bachmayer, B. deYoung, Progress in predicting the performance of ocean gliders from at-sea measurements, OCEANS 2008, Quebec City, QC, Quebec, Canada, (2008), pp. 1–8, https://doi.org/10.1109/OCEANS.2008.5152068.
[31] B. Etkin, L.D. Reid, Dynamics of flight - stability and control, 3rd, Wiley, New York, 1996.
[32] J.D. Rodgers, J.M. Wharington, Hydrodynamic implications for submarine launched underwater gliders, OCEANS'10 IEEE SYDNEY, (2010), pp. 1–8, https://doi.org/10.1109/OCEANSSYD.2010.5603616.
[33] S.F. Hoerner, Fluid-dynamic drag - practical information on aerodynamic drag and hydrodynamic resistance, Midland Park, N.J., 1965.
[34] M. Niţă, D. Scholz, Estimating the Oswald factor from basic aircraft geometrical parameters, in: D.G. für Luft-und Raumfahrt Lilienthal-Oberth e.V. (Ed.), Deutscher Luft- und Raumfahrtkongress 2012, Deutsche Gesellschaft für Luft- und Raumfahrt - Lilienthal-Oberth e.V., Berlin, Germany, 2012, pp. 1–19.
[35] N. Mahmoudian, J. Geisbert, C. Woolsey, Approximate analytical turning conditions for underwater gliders: implications for motion control and path planning, IEEE J. Oceanic Eng. 35 (1) (2010) 131–143, https://doi.org/10.1109/JOE.2009.2039655.
[36] J. Kiefer, Sequential minimax search for a maximum, Proc. Am. Mathematical. Soc. 4 (3) (1953) 502–506, https://doi.org/10.2307/2032161.
[37] D.E. Ferguson, Fibonaccian searching, Commun. ACM 3 (12) (1960), https://doi.org/10.1145/367487.367496. 648–
[38] R.P. Brent, Algorithms for minimization without derivatives, Prentice-Hall, Englewood Cliffs,NJ, 1973.
[39] M. Trauth, MATLAB®Recipes for earth sciences, Springer, Berlin, Heidelberg, 2015.
[40] F. Pianosi, T. Wagener, A simple and efficient method for global sensitivity analysis based on cumulative distribution functions, Environ. Modell. Softw. 67 (2015) 1–11, https://doi.org/10.1016/j.envsoft.2015.01.004.
[41] F. Pianosi, F. Sarrazin, T. Wagener, A matlab toolbox for global sensitivity analysis, Environ. Modell. Softw. 70 (2015) 80–85, https://doi.org/10.1016/j.envsoft.2015.04.009.
[42] Y. Shardt, Statistics for Chemical and Process Engineers : A Modern Approach, Springer, Berlin, Heidelberg, 2015.
[43] Y. Liu, R.H. Weisberg, Evaluation of trajectory modeling in different dynamic regions using normalized cumulative lagrangian separation, J. Geophys. Res. 116 (C9) (2011), https://doi.org/10.1029/2010JC006837.
[44] M.D. Dominicis, S. Falchetti, F. Trotta, N. Pinardi, L. Giacomelli, E. Napolitano, L. Fazioli, R. Sorgente, P.J. Haley Jr., P.F. J. Lermusiaux, F. Martins, M. Cocco, A relocatable ocean model in support of environmental emergencies, Ocean Dyn. 64 (5) (2014) 667–688, https://doi.org/10.1007/s10236-014-0705-x.
[45] H. Roarty, S. Glenn, A. Allen, Evaluation of environmental data for search and rescue, OCEANS 2016 - Shanghai, (2016), pp. 1–3, https://doi.org/10.1109/OCEANSAP.2016.7485535.
[46] Y.-W. Nam, Y.-H. Kim, Prediction of drifter trajectory using evolutionary computation, Discrete Dyn. Nat. Soc. 2018 (2018) 1–15, https://doi.org/10.1155/2018/6848745.
[47] J. Kerfoot, D. Aragon, Long duration underwater glider dataset: Indian Ocean from Perth, Australia to Mirissa, Sri Lanka, Data Brief (2020) 105752, https://doi.org/10.1016/j.dib.2020.105752.

LIMNOLOGY
and
OCEANOGRAPHY: METHODS

Limnol. Oceanogr.: Methods 2020

doi: 10.1002/lom3.10380

FIRe glider: Mapping in situ chlorophyll variable fluorescence with autonomous underwater gliders

Filipa Carvalho,[1]* **Maxim Y. Gorbunov**,[2] **Matthew J. Oliver**,[3] **Christina Haskins**,[2,4] **David Aragon**,[2] **Josh T. Kohut**,[2] **Oscar Schofield**[2]

[1]National Oceanography Centre, Southampton, UK
[2]Department of Marine and Coastal Sciences, Rutgers University, New Brunswick, New Jersey
[3]School of Marine Science and Policy, College of Earth, Ocean and Environment, University of Delaware, Lewes, Delaware
[4]Department of Applied Ocean Physics & Engineering, Woods Hole Oceanographic Institution, Woods Hole, Massachusetts

Abstract

Nutrient and light availability regulate phytoplankton physiology and photosynthesis in the ocean. These physiological processes are difficult to sample in time and space over physiologically and ecologically relevant scales using traditional shipboard techniques. Gliders are changing the nature of data collection, by allowing a sustained presence at sea over regional scales, collecting data at resolution not possible using traditional techniques. The integration of a fluorescence induction and relaxation (FIRe) sensor in a Slocum glider allows autonomous high-resolution and vertically-resolved measurements of photosynthetic physiological variables together with oceanographic data. In situ measurements of variable fluorescence under ambient light allows a better understanding of the physical controls of primary production (PP). We demonstrate this capability in a laboratory setting and with several glider deployments in the Southern Ocean. Development of these approaches will allow for the in situ evaluation of phytoplankton light stress and photoacclimation mechanisms, as well as the role of vertical mixing in phytoplankton dynamics and the underlying physiology, especially in remote locations and for prolonged duration.

Phytoplankton are the foundation of all aquatic ecosystems and their photosynthetic activity and production of organic carbon not only supports highly productive ocean/lake ecosystems but also plays a significant role in shaping the chemistry of the Earth (Falkowski and Knoll 2007). Phytoplankton populations are highly dynamic with high turnover rates driven by a suite of environmental factors such as light, macronutrients, micronutrients, grazing and temperature (Falkowski and Raven 2007). Since the pioneering work by Lorenzen (1966), chlorophyll fluorometers have been widely adopted by the oceanographic community and provide sensitive non-intrusive estimates of phytoplankton biomass. While chlorophyll fluorescence is routinely used for estimating chlorophyll concentrations, conventional fluorometers do not provide insight into the physiological state of phytoplankton or their photosynthetic rates. The pump-and-probe technique (Kolber et al. 1988), the fast repetition rate (FRR) fluorometer (Kolber et al. 1998), and the fluorescence induction and relaxation (FIRe) sensors (Gorbunov and Falkowski 2005) have been developed to study phytoplankton physiology and evaluate the environmental controls of ocean primary production. Variable fluorescence signals provide a sensitive tool to measure the optical cross-sections for photosynthesis, the quantum yields of photochemistry, and rates of photosynthetic electron transfer in phytoplankton (Falkowski et al. 2004). Variable fluorescence measurements have allowed the oceanographic community to study the underlying mechanisms and factors regulating the physiological state and growth of phytoplankton (Suggett et al. 2010). However, the application of this technology has been largely limited to sampling from ships (Lin et al. 2016), airborne (Chekalyuk et al. 2000) or diving (Gorbunov et al. 2000; Gorbunov et al. 2001) approaches, which limits when, where and how much data is collected.

Observations of horizontal distributions of near-surface phytoplankton photosynthetic properties (such as the quantum yield for electron transport) using ship-based underway fluorometers (Lin et al. 2016) and LIDARs (Light Detection and Ranging) (Chekalyuk and Gorbunov 1993) have revealed horizontal variability in these properties on meso- to micro scales which are relevant to phytoplankton dynamics. This variability increases dramatically in highly dynamic and

*Correspondence: filipa.carvalho@noc.ac.uk

marine ecosystems, such as the coastal Southern Ocean (Lin et al. 2016). Although ship-based underway sampling was instrumental to document the variability and factors controlling photosynthetic rates in the near-surface layer, the use of underwater autonomous vehicles, such as gliders, provides an important practical tool to explore a high-resolution 3D structure of photosynthetic fluorescence properties in the water column. Airborne LIDAR fluorescence based techniques from planes and satellites can be used to overcome some of the gaps left by satellites, but data is limited on subsurface phytoplankton biomass (Churnside and Marchbanks 2015) or surface only photosynthetic characteristics (Chekalyuk et al. 2000).

Recent years have seen the rapid development of buoyancy-driven autonomous underwater vehicles (AUV) for oceanographic research (Griffiths et al. 2007). Some classes of the AUVs (buoyancy vehicles) can conduct sustained missions from weeks to a year (Schofield et al. 2007; Rudnick 2016) and are capable of carrying a wide range of sensors (Schofield et al. 2015). Here we report on the development of a variable fluorescence sensor for an autonomous buoyancy vehicle offering the potential for collecting phytoplankton photophysiology data remotely, in situ, under ambient light with high spatial and temporal resolution. This technology was demonstrated during a series of deployments (Haskins and Schofield 2015; Carvalho et al. 2016*a*) in the coastal waters off the West Antarctica Peninsula, a region which is experiencing a rapid environmental change (Schofield et al. 2010).

Integrating a FIRe sensor on a glider provides sampling advantages over ships. These include: (1) Gliders allow sampling at the very near surface where ships (especially large ones) have difficulty sampling. Thus gliders have the ability to measure the physiology of a natural population that can be used to ground-truth algorithms developed to evaluate phytoplankton physiology from space. (2) The small footprint of a glider allows the collection of data without the ship-shadow effect that is significant when collecting shipboard measurements using instruments on a wire. (3) Gliders can be used in a semi-Lagrangian, water mass tracking mode to evaluate in situ physiological response (e.g., photoacclimation) of a phytoplankton community to local physical forcing, such as a gradual or abrupt deepening of the mixed layer, and provides a relatively cheap and reliable way to follow a water mass, collecting physical and biogeochemical properties over time in the same population. Pairing these data with turbulence measurements (which gliders are also capable of collecting) allow further evaluation at microscales. (4) Sustained spatial physiological observations for long periods is cost-effective for gliders. Given the proven reliability of gliders to provide sustained observations for months at a time, a FIRe on a glider would allow the collection of 3D maps of phytoplankton physiology across different scales (time and space) allowing us to assess the physical drivers of phytoplankton physiology over meso- and micro-scales.

This work showcases the FIRe glider as a new tool that will complement shipboard phytoplankton physiological measurements. It highlights some of the advantages and capabilities of miniaturizing and integrating an already established FIRe sensor on an autonomous platform. We characterize the instrument by running a series of comparisons to a benchtop mini-FIRe instrument and present some field demonstration deployments in the West Antarctic Peninsula. Finally, we describe and suggest a series of best practices when deploying this instrument on the field.

Materials and procedures

Autonomous platform

Teledyne Webb Research (TWR) Slocum electric gliders are a robust AUV platform capable of mapping properties within the upper water column (Schofield et al. 2007) that are increasingly filling mesoscale sampling needs for ocean science. Gliders maneuver across the ocean at a forward speed of 20–30 cm s^{-1} in a triangle-shaped diving trajectory, deriving its forward propulsion by means of a buoyancy change and steering by means of a tail fin rudder. Pitch is regulated by shifting batteries back and forth within the glider. A depth sensor enables pre-programmed sampling of depth ranging from a minimum $\sim$2–3 m (about 10 for deep gliders) to 1000 m on the downcast or on multiple successive dives without surfacing. On single dives, and especially on the upcast, Slocum gliders are capable of sampling all the way to the surface. Sensors carried by the gliders continuously record data during the glider descents/ascents, and a typical mission can collect thousands of vertical profiles. This allows the glider to collect high-resolution data in both time and space. Another great advantage of gliders over ships is the ability to sample both in Lagrangian or Eulerian mode, on demand. The glider can be set in drift mode, following this way the same water mass and record changes over the same population or operate virtual mooring (Clark et al. 2020), where the glider station keeps at one location (see Section "*Field evaluation and applications*" for specifically designed missions for the FIRe glider).

Integrating variable fluorescence measurements into a glider

Bio-optical measurements of photosynthetic rates and physiological characteristics of phytoplankton are based on the use of variable fluorescence techniques (Huot and Babin 2010), including the FIRe technique (Gorbunov and Falkowski 2005). FIRe measurements are sensitive, fast, nondestructive, and can be performed in real-time (Gorbunov et al. 2020). The parameters (Table 1) derived from Kolber et al. (1998), are used to quantify the phytoplankton-specific photosynthetic performance in natural assemblages in aquatic ecosystems (Dubinsky and Schofield 2009) and provide a background for modeling the rates of primary production in the water column (Hughes et al. 2018; Ko et al. 2019).

Table 1. Notation of FIRe variables. See Cosgrove and Borowitzka (2010) for more details and synonyms.

Abr.	Description	Abr.	Description
σ_{PSII}	Functional absorption cross section of PSII in a dark-adapted state (Å^2)	σ_{PSII}'	Functional absorption cross section of PSII in a light-adapted state (Å^2)
F_o, F_m	Minimum and maximum yields of Chl *a* fluorescence (arbitrary units)	F_o', F', F_m'	Minimum, steady-state, and maximum of Chl *a* fluorescence measured under ambient light (arbitrary units)
F_v	Variable fluorescence, $F_m - F_o$	F_v'	Variable fluorescence measured under ambient light, $F_m' - F_o'$
F_v/F_m	Maximum quantum yield of photochemistry in PSII, measured in a dark-adapted state (dimensionless)	$\Delta F'/F_m'$	Quantum yield of photochemistry in PSII, measured under ambient light, $F_m' - F'/F_m'$ (dimensionless)
E_k	Light-saturation parameter (μmol quanta m^{-2} s^{-1})	$\Delta F'$	Change in the fluorescence yield measured under ambient light, $F_m' - F'$
$'$	Prime indicates that measurements are collected under ambient light	$\Delta F'/F_v'$	Coefficient of photochemical quenching characterizing the fraction of open reaction centres in a light-adapted state

Fluorescence signals are excited by flashes from 450 nm light emitting diodes (LEDs), isolated by a 680 nm interference filter and detected by a sensitive avalanche photodiode module (Gorbunov and Falkowski 2005). The computer-controlled LED driver delivers pulses with varied duration from 0.5 μs to 50 ms, which ensures fast saturation of PSII within a single photosynthetic turnover (STF, < 100 μs). In partnership with Teledyne Webb Research and Satlantic, a FIRe sensor was miniaturized and integrated into the Slocum glider science payload bay (Fig. 1), from now on referred to as a FIRe glider. Merging these two platforms allows for high-resolution continuous and vertically resolved mapping of phytoplankton physiological parameters in the water column. This prototype was integrated into a Slocum G1 glider, a "shallow glider" rated for 100 m. Given the slow speeds of a glider, during the STF protocol, the glider only moves about 0.02–0.03 mm, so it is a fair assumption to consider the excitation constrained to a fixed sample in space relative to the detector, so no artifacts should be introduced by this moving platform, as long as only parameters from the 100 μs burst are being used in the analyses.

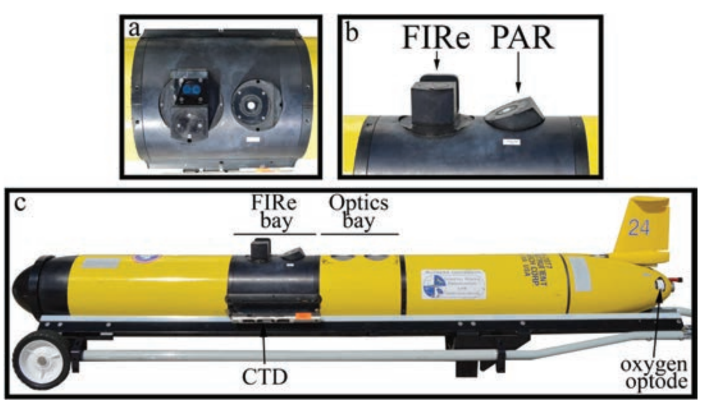

Fig. 1. Top **(a)** and side **(b)** view of the Fluorescence Induction and Relaxation (FIRe) and photosynthetic active radiation (PAR) sensors integrated into a Slocum glider FIRe bay (black section). (**c**) Extended Slocum glider with double science bay configuration with FIRe bay in front and optics bay with Seabird WET Labs ECO puck (measuring chlorophyll fluorescence, backscatter and/or colored dissolved organic matter), Seabird conductivity-temperature depth (CTD) sensor and Aanderaa dissolved oxygen optode in the aft. The glider is shown without its two lateral wings that connect to the black FIRe bay.

Other sensors

A photosynthetically active radiation (PAR) sensor is also incorporated in the FIRe science bay and is critical to the interpretation of the FIRe data. The standard Seabird Conductivity–Temperature–Depth (CTD) package in all gliders allows a high-resolution characterization of the physical setting, which provides critical data to relate physiological patterns associated with water column stability and mixed layer depth (Carvalho et al. 2017). The FIRe bay can be paired with an optional second science bay carrying a WET Labs Environmental Characterization Optics (ECO) pucks, measuring chlorophyll fluorescence, backscatter at several wavelengths, and/or colored dissolved organic matter (CDOM) fluorescence. Given the modular nature of Slocum gliders, other sensor pairings may be available on a second science bay or an extra stack-on bay, including extra energy bay to extend the deployment duration.

Assessment and discussion

Laboratory evaluation

Silsbe et al. (2015) highlights the importance of calibrations and understanding sensor behavior given the inherent variability within instruments. Bench testing was conducted to characterize this instrument and to understand how it compares to conventional benchtop instrument, i.e., mini-FIRe. We: (1) evaluated the relationship between the maximum fluorescence, F_m, and standard measurements of extracted chlorophyll concentration; (2) evaluated the effect of incident light on the measurement sensitivity and signal-to-noise; (3) characterized pure water, filtered seawater and deep in situ blanks; and (4) characterized instrument behavior in pure water.

Reference profile calibration

Like the bench-top FIRe instrument, the FIRe glider sensor requires a reference excitation profile, which is used to normalize the collected fluorescence intensities and to deduce fluorescence yields. This reference profile is acquired using a fluorescent dye (Rose Bengal) and is saved as a reference file. The reference profile reflects the actual shape of excitation intensity and has no variable fluorescence component. When processing the data collected during the deployment, the FIRe processing program will use this profile to calculate fluorescence yields. Given the high stability (< 0.5%) of this reference profile, due to the extremely stable and reproducible LEDs source, it is recommended the reference profile to be updated every 6 to 12 months.

Relationship between FIRe F_m and chlorophyll concentration

Like any fluorometer, the FIRe glider records fluorescence yields in arbitrary units. For these data to be used to assess phytoplankton biomass, maximum fluorescence yield (F_m) needs to be calibrated against standard extracted measurements of chlorophyll concentration (mg m^{-3}), to provide a proxy for phytoplankton biomass. These samples should be collected when and where the glider is being deployed as chlorophyll fluorescence yields may vary with community compositions.

Discrete samples were collected and evaluated in the (1) FIRe desktop, followed by the (2) FIRe glider, and finally (3) chlorophyll concentrations was estimated by filtering samples onto 25 mm Whatman GF/F filter and pigments extracted using 90% acetone, following the fluorometric method for phytoplankton chlorophyll determination (Yentsch and Menzel 1963). The filtered sample was then run again on both FIRe systems to evaluate blanks. A set of dilution experiments were conducted using water samples collected a few miles off Atlantic City (red, Fig. 2a,b) to increase the number of points and dynamic range in the F_m to chlorophyll concentration regression. Two sets of water sample calibrations from field deployments in the West Antarctic Peninsula were included in this analysis to add sample points with potentially different community compositions. F_m is less susceptible to variations in phytoplankton physiological state than F_o thus providing the best proxy for chlorophyll concentration. Comparison between FIRe glider measured F_m and chlorophyll concentrations is shown in Fig. 2a. Correlation between the two variables was evaluated using a Model-II geometric mean linear regression $y = 5.81x$ (5.44, 6.17) – 0.07 (–1.21, 1.06); $r^2 = 0.98$; $N = 43$).

To further characterize the custom-made glider integrated FIRe sensor, we ran the same discrete samples, in parallel, on the benchtop mini-FIRe, with filtered seawater (FSW) blank corrections applied for each system. To evaluate the correlation between F_v/F_m measured in each instrument, a model-2 major axis linear regression $y = 1.07$ (0.90, 1.24) - 0.10 (–0.22, 0.02), $r^2 = 0.92$ was calculated. Given that the order of the individual replicates in each system is not correlated (3 per sample in each system), only sample averages were used in this analysis. Nevertheless, standard errors are shown in error bars in Fig. 2c. Some of the variability may reflect that the FIRe system on the glider is significantly older then mini-FIRe which has been developed more recently, where increased sensitivity is due to the improvement of electronic circuitries and the use of a more sensitive detector (Gorbunov et al. 2020).

Blank correction

A “blank” is the background signal recorded from the sample, i.e., the signal associated with the absence of the property being studied, in this case, without chlorophyll fluorescence. In clear waters, the importance of blank collections has been highlighted (Cullen and Davis 2003; Bibby et al. 2008; Laney and Letelier 2008) because of fluorescence from dissolved organic matter (DOM) and phytoplankton degradation products (Benner and Strom 1993). In some instruments, electronic artifacts (Laney et al. 2001) and the effect of scatter by water itself (Laney et al. 2001) can present problems. The contribution of the latter two factors can be eliminated by improving the electronic and optical design. Although the magnitude and variability of the “blank” is usually small compared to chlorophyll fluorescence signals from phytoplankton in FIRe systems (Bibby et al. 2008), blanks should be routinely collected and subtracted from the fluorescence signals. However, in DOM-rich, low chlorophyll waters the blank correction may become critical for accurate retrievals of photosynthetic parameters (Bibby et al. 2008).

DI water blanks collected using this FIRe sensor integrated on the glider were overall very small (blank$_{\text{DI water}}$ = 39 ± 3.4, standard error), compared to the average chlorophyll fluorescence signal, corresponding to less than 3% of the lowest fluorescence recorded for a sample (i.e., F_m = 1200 a.u.). Furthermore, the amount of incident light did not affect the signal when exposing the DI water at varying irradiances. The “standard” blanks using filtered seawater (FSW) were collected to evaluate the effect of dissolved organic matter in the recorded fluorescence signal. Apart from the two lowest concentrations tested (chlorophyll concentration < 0.5 mg m^{-3}),

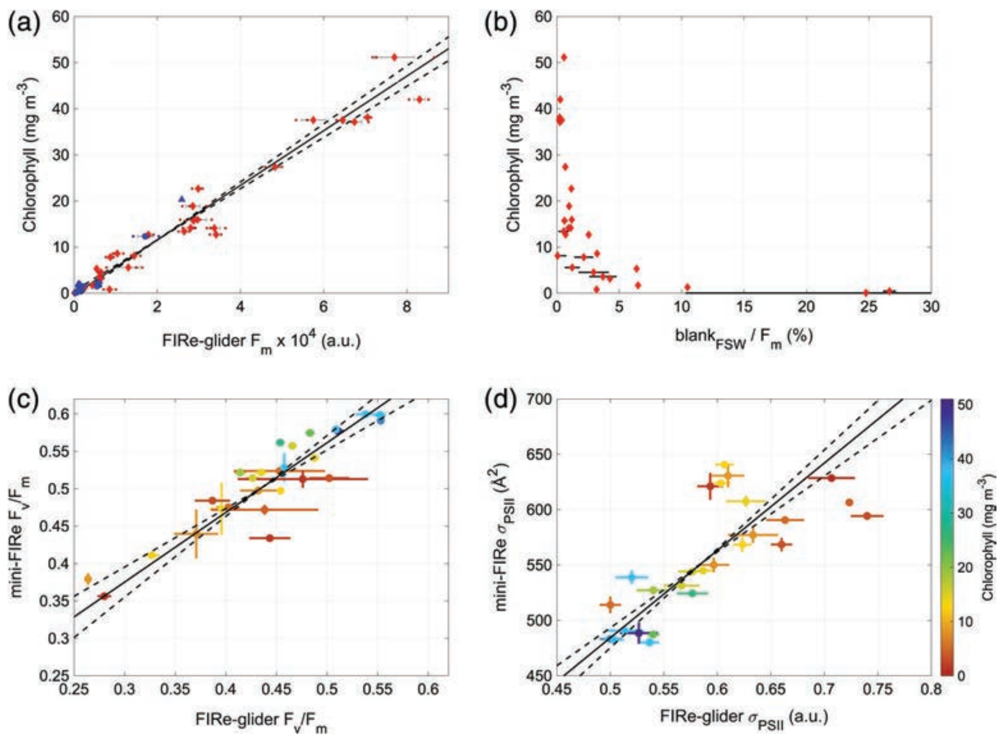

Fig. 2. Instrument calibration and characterization based on cross-comparison with the benchtop mini-FIRe instrument and discrete samples. (**a**) Relationship between maximum fluorescence (F_m' measured by the FIRe glider) and extracted chlorophyll concentration from in situ discrete samples. Different colors indicate different locations where water samples were collected (blue: West Antarctic Peninsula; red: New Jersey coastal waters). Individual measurements are shown in small colored dots, with averages shown in the large marker and standard errors for F_m in the horizontal bars. Model-II linear relationship (r^2 = 0.98) and slope uncertainty (2 standard errors) are shown in solid and dashed lines, respectively. Triple FIRe replicates were used individually against a single chlorophyll concentration from that sample (N = 43) for the regression analysis. (**b**) Ratio of freshwater (FSW) blank signal to F_m, against in situ chlorophyll concentration. Standard errors are shown in horizontal error bars. (**c**) Comparison of photosynthetic efficiency (F_v/F_m) measured using the mini-FIRe and the FIRe-glider. Model-II linear regression (r^2 = 0.92) and slope uncertainty (2 standard errors) of sample averages (N = 29) are shown in solid and dashed lines, respectively. Error bars indicate standard errors shown for each sample measured in each instrument and are colored based on chlorophyll concentration. (**d**) Cross-calibration of the functional absorption cross-section (σ_{PSII}). Comparison of sample averages (3 replicates each) between the FIRe-glider and the mini-FIRe with standard error bars for both instruments. Model-II linear regression (r^2 = 0.77) and 2 standard errors of the slope uncertainty shown in solid and dashed lines.

the magnitude of the fluorescence of the blank normalized to the F_m was less than 5% for average chlorophyll concentration found in the upper ocean (Fig. 2b).

While it is impossible to measure appropriate in situ blanks concurrently with the FIRe glider measurements during deployment, in situ discrete water samples should be collected and analyzed in the lab bench before and after deployment. This will allow the evaluation of region-specific blanks as well as potential effect of biofouling during long deployments. No significant signs of biofouling were found after up to 3-week long deployments in coastal Antarctica, even though the instrument does not use any anti-biofouling technology such as copper plating. Although biofouling itself is unavoidable during long-term deployments, the impact of biofouling on the measured signals is dramatically reduced by the improved optical design of the glider FIRe sensor. The optical design employs a two-window configuration, which includes excitation and emission windows. Thereby, the collimated excitation light does not reach the emission optical window and thus does not induce background fluorescence from biofouling material accumulated on this window. At the same time, fluorescence from biofouling accumulated on the excitation window does not reach the detector.

In all glider deployments conducted using the FIRe integration in coastal Antarctica, blanks corresponded to less than 1% of the chlorophyll fluorescence signal. Deep blanks, i.e., average signal in deep waters where we expect to find no phytoplankton, have been previously used when there is no chance to collect discrete in situ blanks. Using data from the field deployments, we found that the average "blank" signal at depth was higher (~ 450 a.u.) than the discrete blanks ran in the lab (~ 330 a.u.), likely due to the shallow profiling (100 m), constrained by the depth rating of the glider where this sensor was fitted to.

Functional absorption cross-section calibration

The functional absorption cross-section of Photosystem II (σ_{PSII}) is a product of the optical absorption cross section of

PSII (i.e., the size of the PSII antennae) and the quantum yield of photochemistry in PSII (Falkowski et al. 2004). This biophysical parameter is controlled by photoacclimation status and nutrient availability, as well as affected by the community composition (Suggett et al. 2009). σ_{PSII} is calculated from the rate of fluorescence rise during the single turnover flash (STF), as this rate is proportional to the product of σ_{PSII} and the excitation intensity (Gorbunov and Falkowski 2005). Accurate calibration of the excitation intensity within the sounding volume of the FIRe sensor is critical for retrievals of σ_{PSII} in absolute units, Angstrom squared (Å^2). Such calibration is conducted as part of the standard calibration procedure of the FIRe sensor. Because the spatial distribution of excitation intensity in the sounding volume of the underwater glider FIRe sensor is less uniform than that in the benchtop instrument, the benchtop instrument is much easier and more accurate to be calibrated. To convert the measured σ_{PSII}, collected in relative units, into absolute units, angstrom squared (Å^2), a correction coefficient must be determined by cross-calibrating the FIRe glider sensor against a "standard" calibrated benchtop FIRe instrument. A model-II linear regression $y = 789.2x$ (581.02, 997.45) + 89.66 (−33.25, 212.56) was calculated, with $r^2 = 0.77$ (Fig. 2d).

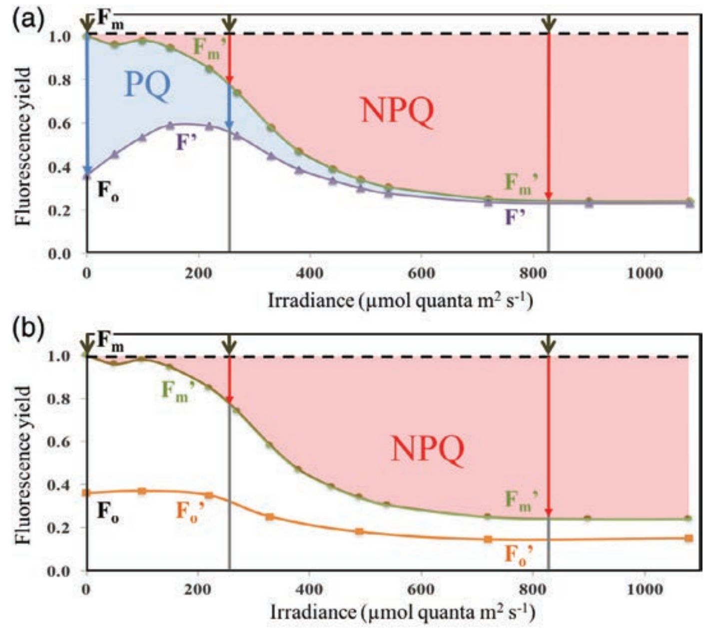

Fig. 3. Schematic of irradiance dependence of chlorophyll fluorescence yields. Measurements in: (**a**) light-adapted state, i.e., during daytime and (**b**) dark-adapted state, i.e., during night time. F_o and F_m are minimum (open reaction centres) and maximum (closed reaction centres) fluorescence yields measured in dark-adapted cells. F_o' and F_m' are the minimum and maximum fluorescence yields in a light adapted state. F' is the actual fluorescence yield measured under ambient light. PQ and NPQ are photochemical quenching and non-photochemical quenching, respectively. Top gray arrows indicate example irradiances and its corresponding fraction of NPQ and PQ.

Field evaluation and applications

The FIRe glider capabilities were evaluated in the field by three coastal deployments off the West Antarctic Peninsula (Fig. 5), in Palmer Deep Canyon (Carvalho et al. 2016*b*) near Palmer Station. The following sub-sections demonstrate some of the applications of such integration, some field experiments and some operational recommendations.

Non-Photochemical quenching (NPQ)

One of the biggest advantages of the FIRe integration on a glider is the ability to make measurements under ambient light. Daytime profiles reflect the physiological status resulting from high light during peak irradiance hours while night-time profiles can be used as a dark-adapted state. While capturing a "true" dark-adapted state is usually a problem in many FRRf studies, the sampling under ambient light by the FIRe glider allows the evaluation of the gradual relaxation of NPQ, but also understand when the true reversal of the daytime inactivation caused by supra-optimal irradiances. The physiological characteristics available under these two conditions are presented in Fig. 3 and described in Table 1.

In this situation, nutrient stress can be assessed using night-time profiles only and both Non-Photochemical Quenching (NPQ), a physiological mechanism to protect the photosynthetic apparatus from photodamage, where excess energy is dissipated as heat (Muller et al. 2001; Milligan et al. 2012) and Photochemical Quenching (PQ) can be evaluated throughout the deployment. The NPQ parameter (Bilger and Bjorkman 1990) gives a straightforward estimate of the portion of thermally dissipated photon flux (i.e., the quantum yield of nonphotochemical quenching).

To determine F_m we can use the night-time profile where F_m' is maximal (finding the maximum F_m' between 22:00 and 6:00) the night immediately before or after the daytime period being considered. This relies on the assumption that the glider has not moved into a different water mass, which is more valid when sampling in a Lagrangian way, which gliders are capable of. A specific semi-Lagrangian mission designed for the FIRe glider is further detailed in section "Evaluate the physiological responses of the same phytoplankton community to changes in water column dynamics".

The high resolution capability of gliders allows not only the timeseries analysis of NPQ at a particular depth (Fig. 4, left panels, in this case at 8 m depth), but also the characterization of a depth-resolved NPQ (Fig. 4, middle and right), important in situations where potentially different physiological communities react differently to varying irradiance. The two quenching components, non-photochemical quenching component (qN) and photochemical quenching component (qP), are defined in Kooten and Snel (1990). While the data is lacking in the upper 5-7 m for this example due to the deployment setup, the glider does have the capability to sample this

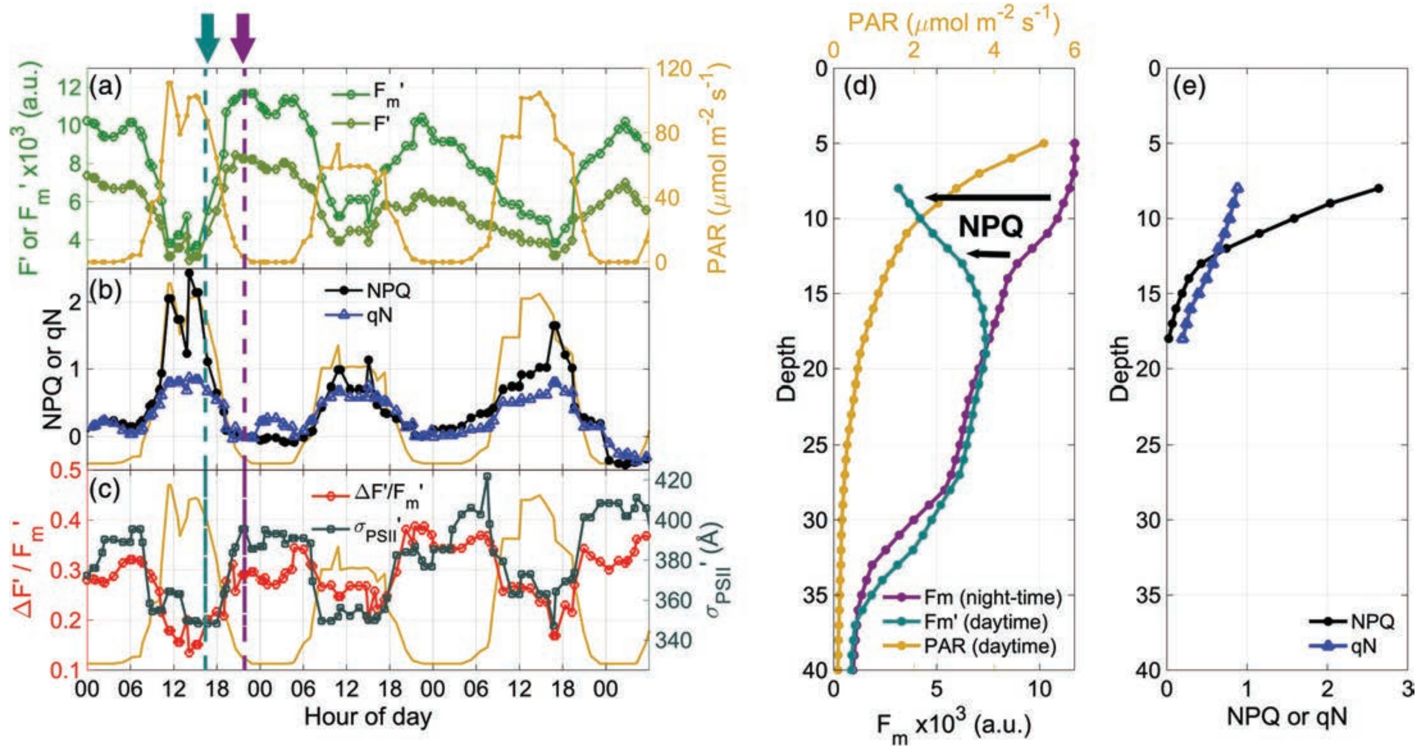

Fig. 4. Three diel cycles from a coastal deployment off the West Antarctic peninsula at 8 m depth of (**a**) fluorescence at steady-state (F', light green) and maximum (F_m', dark green) levels with factory calibrated photosynthetic active radiation (PAR, gold), (**b**) non-photochemical quenching (NPQ, black) and NPQ component (qN, blue); (**c**) the quantum yield of photochemistry in PSII ($\Delta F'/F_m'$, red) and functional absorption cross section for PSII (σ_{PSII}', gray). Vertical panels represent depth profiles of (**d**) F_m' during night-time (purple), determined by the maximum night-time fluorescence between 22:00 and 06:00) and a F_m' daytime example (teal) and (**e**) respective NPQ and qN.

layer and better inform the fluorescence kinetics where irradiance is highest.

Performance under low phytoplankton biomass conditions

Data collected over three different deployments in the West Antarctic Peninsula was used to evaluate the sensor sensitivity as a function of chlorophyll. Maximum fluorescence (F_m') was converted to chlorophyll using in situ discrete samples collected before and after deployments. For lower values of chlorophyll, there was more scatter, predominantly toward the negative values in F_v/F_m as, under low biomass (i.e., low signal-noise ratio), it gets increasingly difficult to distinguish first F_o, then F_m, from zero. Under low chlorophyll concentrations, poor fits of the biophysical model to the data were observed during the processing using the supplied Satlantic/Seabird software, resulting in still accurate F_m values (as shown by the good F_m:chl regression fit in Fig. 2a), but less certain estimates of F_o, where in most cases, F_o becomes negative. We will further on refer to these as "bad points," but note that it is due to the poor model fit and not bad data collected. To further assess the minimum chlorophyll concentration in which we can accurately collect physiological data, bad points (7% of the data, of a total of 41,445 data points) were identified when $F_v/F_m < 0$ (i.e., F_o was either higher than F_m or negative) or F_v/F_m was higher than is commonly found in natural populations ($F_v/F_m > 0.66$). Theoretically, F_o cannot be higher than F_m as in the scenario where the reaction centres are fully closed, F_o would equal F_m. Most "bad points" corresponded to $F_v/F_m < 0$ (94%, matching low chlorophyll concentrations), while only a very small percentage corresponded to $F_v/F_m > 0.66$ (6%). Fewer points in the scatter cloud were collected under high irradiance, with the majority being found below 50 m, under low light and where the signal-to-noise ratio was low. Applying a simple 3-point median filter to remove spikes resulted in a decrease of the "bad points" to 3.6% where a higher percentage (98.7%) corresponded to $F_v/F_m < 0$. Minimum chlorophyll concentration was calculated assuming different percentages of acceptable "bad points": when considering 10% "bad points" acceptable using untreated/raw data (data with median filter applied in parenthesis), minimum chlorophyll concentration is 0.26 (0.23) mg m^{-3}, while for 5 and 1% are 0.32 (0.26) and 0.44 (0.38) mg m^{-3}, respectively, with results improving with a larger window on the median filter. While these results could be indicative of low sensitivity of the instrument, after a careful visual analysis of the output of the fitting software under low concentrations, we believe the increasing number of bad

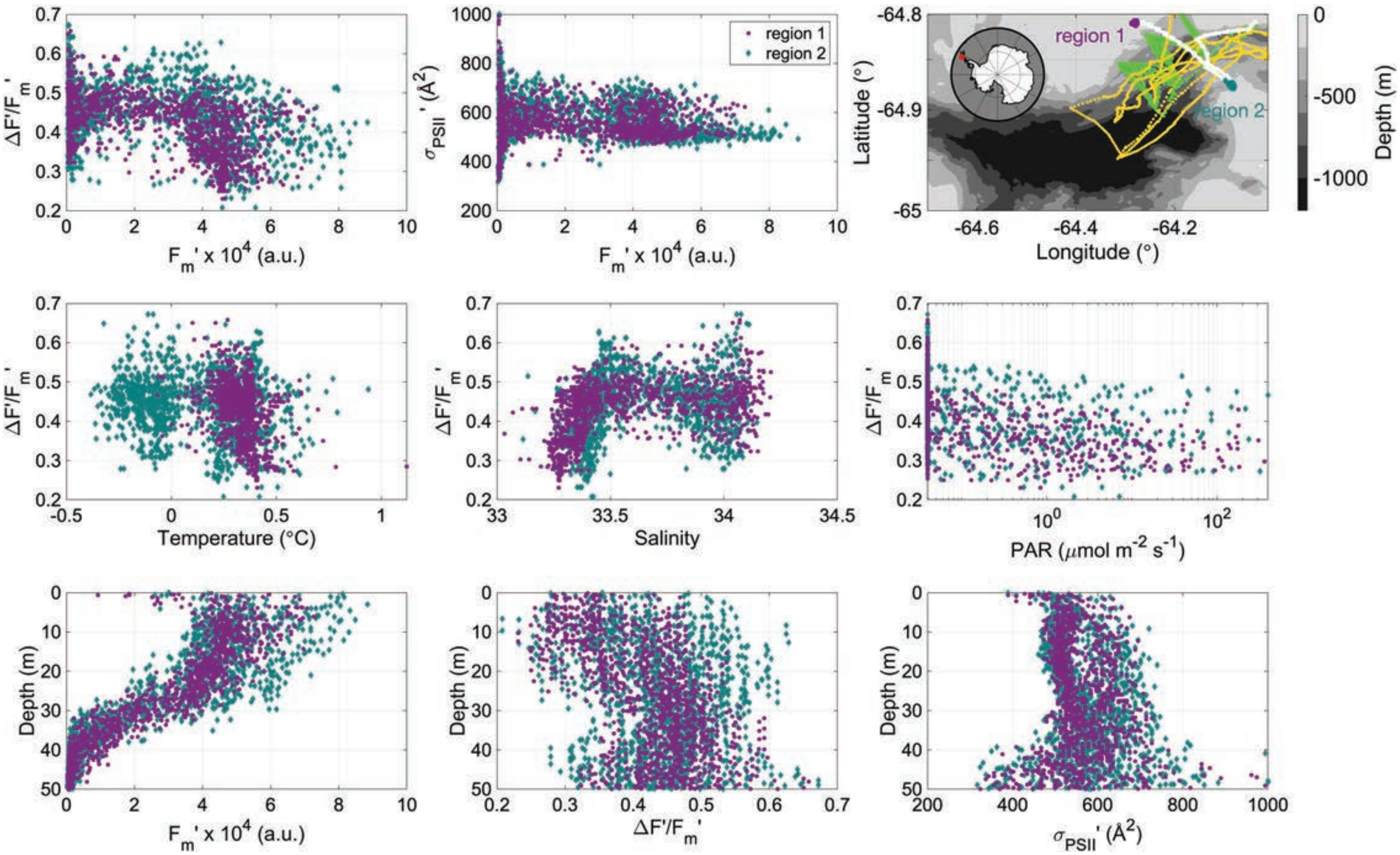

Fig. 5. Location of the three coastal deployments off the West Antarctic Peninsula shown in this manuscript, illustrating the station keeping mission (white, purple and teal for transit, region 1 and region 2, respectively), drift mission (yellow) and a zigzag mission (green). Scatter plots from the station keeping mission from Fig. 6 with the two diel cycles from each region showing different physiological responses to physical forcing: (top) Photosynthetic efficiency ($\Delta F'/F_m'$) and functional absorption cross-section of PSII (σ_{PSII}') as a function of phytoplankton biomass (F_m'); (middle) $\Delta F'/F_m'$ as a functional of temperature, salinity, and PAR; (bottom) depth profiles of F_m', $\Delta F'/F_m'$ and σ_{PSII}' for the two regions.

points at low concentrations are due to the poor curve fitting using the provided processing software. We believe this "sensitivity" can be further improved, if data is fitted manually (i.e., not using the provided software), as we found that misfits often resulted from just one potential outlier in the fluorescence induction curve. Unfortunately, the raw data files collected by the glider-integrated FIRe system are in a proprietary binary format which we were incapable of decoding, despite several unsuccessful attempts to interface with both Satlantic/Seabird, the commercial FIRe manufacturer, and Teledyne Webb Research, the glider manufacturer. Each file is individually processed on the software, where FIRe variables (Table 1) are derived; however, no statistics are reported for the quality fit of the biophysical model, so we are unable to fully characterize the robustness of the model fit. Given this constraint we were not able to demonstrate the reason for the poorer results low chlorophyll concentrations is not the instrument itself, instead it reflected issues with the proprietary software provided by Satlantic. Despite this problem, it represented only a small proportion of the data (7% of the raw data) and future development efforts will be should be able to resolve this issue. However, given the high-resolution capabilities of the gliders, under low chlorophyll concentration, signal can be isolated from scatter/noise by averaging and using low-pass filters, as shown previously. The amount of data points from the glider would still surpass, by far, the ones collected manually, using discrete samples.

Two missions have been designed to evaluate physiological responses at different temporal and spatial scales: (1) compare and contrast physiological responses of phytoplankton to different physical forcing settings using Eulerian sampling ("station keeping mission"), white, purple and teal dots in the map from Fig. 5) and (2) evaluate the physiological responses of the same phytoplankton community to changes in water column dynamics ("drift mission", yellow dots in the map from Fig. 5). A third mission was also conducted at the same location in a zigzag pattern (green dots in the map from Fig. 5) to increase the number of data points in the field assessment analyses.

Compare and contrast physiological responses of phytoplankton to different physical forcing ("station keeping mission")

Often, the irradiance regime experienced by phytoplankton is a result of the complex interaction between incident irradiation, turbulent mixing and variations in the water column vertical structure (i.e., changes in the water column stability and MLD due to varying wind stress and water mass types as well as heat from insolation) (Neale et al. 2003). For a given temperature and nutrient status, phytoplankton regulate photosynthetic rates based on their light field by altering their photosynthetic apparatus. For example, the cellular chlorophyll content is usually higher when the cells have been growing under low light (Lewis et al. 1984; MacIntyre et al. 2000). It is then informative to analyze phytoplankton physiology in the context of their physical setting (Hughes et al. 2020).

The ability of the FIRe glider to collect, at high resolution, physiological data together with physical oceanographic parameters allows further analyses on the physical drivers of primary production. Gliders also offer an advantage compared to other oceanographic platforms in providing more flexibility in how, when and where they sample. It is sometimes beneficial to use gliders as virtual moorings when the scientific question involves a spatial comparison. An Eulerian approach allows data collection that isolates the temporal signal by removing space from the equation. Deploying the FIRe glider in station keeping (virtual mooring) mode in locations with different physical settings, one can infer how environmental variables are associated with phytoplankton physiology over time (Fig. 6). The degree with which the same population is being sampled depends on the local circulation. This mission was conducted in an area where physical and biological regional differences had been previously documented (Carvalho et al. 2016*b*; Kohut et al. 2018). Different water masses and degrees of stratification can be identified between the two regions (Figs. 5, 6), where overall higher $\Delta F'/F_m'$, F_m' and σ_{PSII}' can be observed in region 2, an area with lower temperatures, increased PAR and higher salinity. Together with higher $\Delta F'/F_m'$ across all PAR range, a clear diel signal is evident in σ_{PSII}' (showing high values during night-time and a decrease during daytime, Fig. 6). Ranges of measured σ_{PSII}' are shown in Figs. 5, 6 are in accordance with previous studies (Behrenfeld and Kolber 1999; Suggett et al. 2009; Alderkamp et al. 2015).

Evaluate the physiological responses of the same phytoplankton community to changes in water column dynamics ("drift mission")

The properties of phytoplankton community structure, such as cell size and taxonomy, influence photosynthetic rates and therefore variable fluorescence signals (Suggett et al. 2009). When evaluating the temporal pattern (e.g., diel cycles) in the photosynthetic efficiency of a phytoplankton community in situ, it is important to make sure that the measurements are constrained to the same phytoplankton community. The best way to accomplish this in situ is to use a Lagrangian approach and follow the same water mass over time. While gliders are a platform capable of collecting a large amount of high-resolution profiles autonomously, one of its main constraints is the active movement into a potentially different water mass as they fly through the water column on their standard flight configuration. To stay within the same water mass and evaluate physiological changes of a phytoplankton community through time, a new mission was designed to avoid actively changing water masses. A glider cycle ("yo," including a dive and a climb back to the surface) takes around 20 min. On this custom mission design, a "yo" was done every hour, where the rudder (steering) was set all the way to one side, resulting in a corkscrew dive and climb. The remaining time, in between the hourly dives, the glider would drift at the surface following the phytoplankton community present in the same water mass. This setup allows the collection of at least 24 profiles to characterize a diel cycle within the same water mass.

Stratification, mixed layer depth (MLD) and rates of vertical mixing have been identified as controls on primary production and phytoplankton dynamics (Lewis et al. 1984; Mitchell and Holm-Hansen 1991; MacIntyre et al. 2000). In a strongly mixed surface layer, phytoplankton acclimate to light levels averaged over the MLD (Lewis et al. 1984), so a relatively stable light environment as a result of a shallow MLD allows phytoplankton to photoacclimate on timescales of 1–2 d (Schofield et al. 1995). During intense mixing events, dim-light adapted phytoplankton may be brought toward the surface where they are exposed to supra-optimal irradiances, which leads to a decrease in both F_m' and $\Delta F'/F_m'$.

Photoadaptive parameters respond to changes in irradiance at different rates. Photoinhibition can be assessed in the fluorescence signal on time-scales of seconds to minutes while it takes several hours for the photosynthetic capacity to be compromised (Lewis et al. 1984). Effects of high irradiance periods (hours 10–16) shown by the yellow colors in the Photosynthetically Active Radiation (Fig. 7, bottom) are evident by the low values seen in the photosynthetic efficiency ($\Delta F'/F_m'$, Fig. 7) maximum fluorescence (F_m' or proxy for chlorophyll concentration (Fig. 7), and in the functional absorption cross-section (σ_{PSII}', Fig. 7). This is evidence of NPQ, with the deepest penetration occurring during peak irradiance (hour 13–14). Increased fluorescence signal was found under shallower MLD. NPQ was more marked in the deeper MLD (lower F_m', Fig. 7) regime where phytoplankton are acclimated to lower light. The collection of high-resolution photo-physiology parameters over a diel cycle permits the evaluation of NPQ under supra-irradiances as seen by a decrease in $\Delta F'/F_m'$, F_m', and σ_{PSII}', as compared to their dark-adapted values.

Light-induced mechanisms used to prevent photodamage under high irradiance, such as NPQ, result in changes in the functional absorption cross-section of PSII (σ_{PSII}') (Krause and Weis 1991; Falkowski et al. 1994). This decrease in σ_{PSII} can be

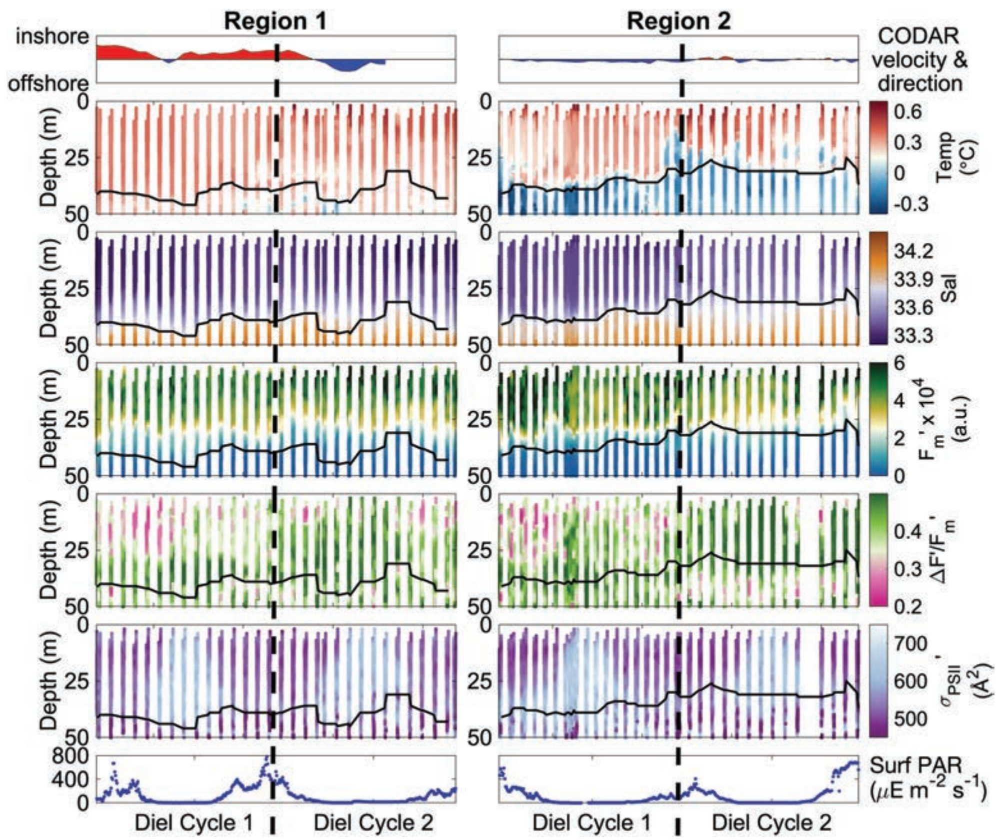

Fig. 6. Two diel cycles separated by the black vertical dotted line (as outlined in the surface PAR, bottom) collected in two regions with different oceanographic conditions. Direction and magnitude of the dominant surface currents (top, from HF radars) are in part responsible for changes in the vertical structure of the water column as demonstrated by the temperature and salinity panels and the depth of the mixed layer (black line). Remaining rows report FIRe measurements—F_m' (relative units), $\Delta F'/F_m'$ (dimensionless) and σ_{PSII}' (functional absorption cross-section of PSII, Å^2). Adapted from Carvalho et al. (2016a).

close to 50%, implying a matching reduction in the excitation delivery to the reaction centres of Photosystem II and a shift of E_k to higher values as seen in left σ_{PSII}' panel in Fig. 7 and left panels in Fig. 8.

Photoacclimation mechanisms evaluation

To cope with high light-induced stresses (i.e., to optimize light absorption under low light conditions or even to reduce total photon utilization under supra-optimal irradiances) phytoplankton have developed a suite of photoadaptation mechanisms. Using the drift mission data, we can compare the different photoacclimation responses to MLD dynamics (e.g., shallow vs. deep mixed layer). When cells photoacclimate, they adjust their photosynthetic machinery to operate at the highest quantum yield possible that allows for the maximal rate of photosynthesis. This occurs at the inflection point in the photosynthesis irradiance curve, the light saturation parameter (E_k) (Dubinsky and Schofield 2009). Bio-optical models (Webb et al. 1974; Jassby and Platt 1976) describe the relationship between photosynthesis and irradiance. The hyperbolic tangent model has become one of the most widely used models for predicting photosynthetic rates in natural phytoplankton assemblages. The photosynthetic rates (P) as a function of PAR are described by the following equation (Jassby and Platt 1976):

$$P = P_{\max}\left[\tanh\left(\frac{\text{PAR}}{E_k}\right)\right] \tag{1}$$

where PAR is photosynthetically active radiation, $P_{\max}$ is the maximum rate achieved at saturating light, and E_k is the light saturation parameter. The quantum yield ($\Delta F'/F_m'$) is, by definition, proportional to the ratio of P to PAR:

$$\frac{\Delta F'}{F_m'} = c\,\frac{E_k}{\text{PAR}}\left[\tanh\left(\frac{\text{PAR}}{E_k}\right)\right] \tag{2}$$

where $\Delta F'/F_m'$ is the quantum yield of photochemistry in PSII, measured under ambient light and c is a constant that corresponds to F_v/F_m measured in a dark-adapted state at PAR = 0, essentially α in a P–E curve. Changes in E_k values provide insight on photoacclimation regimes due to a combination of

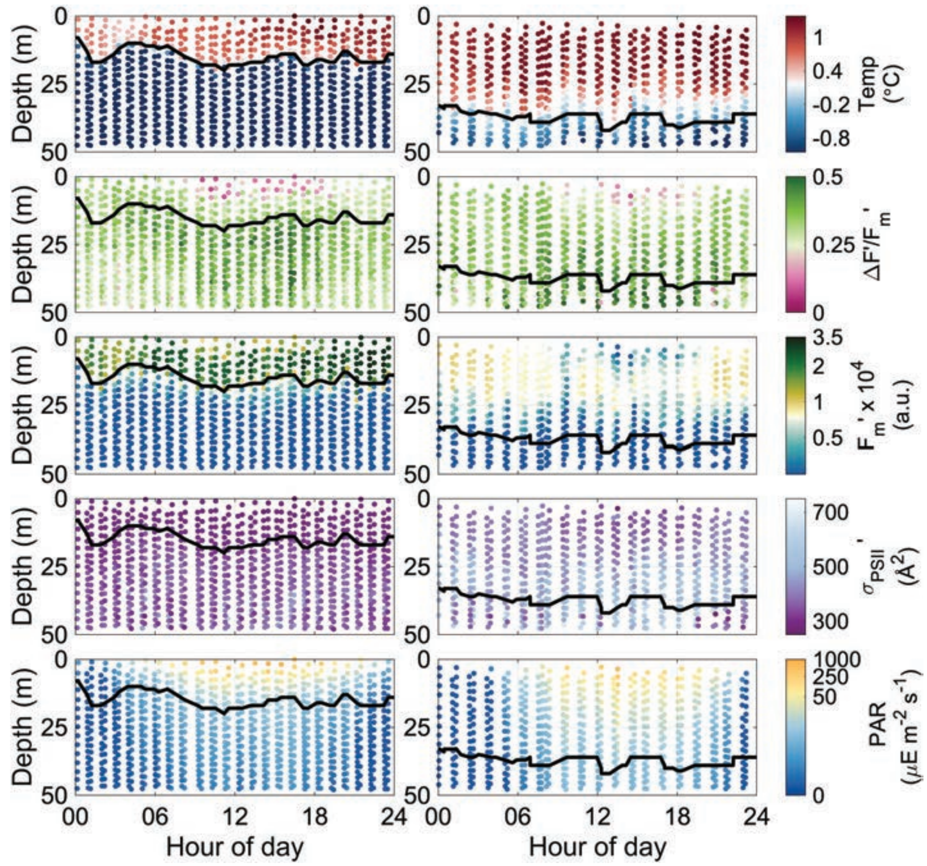

Fig. 7. Example of diel cycles collected during the drift mission for shallow (left panels) and deeper (right panels) mixing regimes. The depth of the mixed layer is shown with a black line. Gaps in data show times where glider was drifting at the surface. One profile was collected every hour. Effects of high irradiance periods (hours 10–16) shown in yellow in the Photosynthetically active radiation panels are evident by the low values seen in $\Delta F'/F_m'$ (photosynthetic efficiency), F_m' (proxy for biomass) and σ_{PSII}' (functional absorption cross-section). A warming of the upper ocean (temperature) is also seen during the highest irradiances. Adapted from Carvalho et al. (2016a).

the light field that phytoplankton are exposed and the mixing scales that can dominate the kinetics of primary productivity over the time-course of a day. This method can also be useful to evaluate the role of mixing in the competition between algal species (Falkowski and Woodhead 2013).

Applying this model (Eq. 2) to the high-resolution data from the FIRe glider during the drift mission we can estimate E_k and explain photoacclimatory responses of phytoplankton to changes in different MLD dynamics regimes (Figs. 7, 8).

Under a shallow MLD regime (Figs. 7, 8, left panel), where the light penetration reaches closer to the bottom of the ML, there is likelihood of two potential different physiological communities (i.e., communities with different photoacclimation regimes) as evaluated by the different E_k (compare orange and purple layers in Fig. 8). The much higher E_k seen at the surface gives an indication of phytoplankton acclimated to high irradiances while the lower E_k seen below the MLD shows lower light acclimation. Under deeper MLD conditions, E_k values are much closer (compare orange with purple box within the same MLD regime) indicating photoacclimation is similar between the two layers (Fig. 8). These measurements and the derived depth dependent variability of the light saturation parameter are difficult to measure using standard ship-based sampling strategies and cannot provide sustained measurements over time. The glider approach allows for these processes to be directly measured under ambient light and data collected over the deployment allows the rates of photoacclimation for natural populations to be measured as the physical features, such as the mixed layer depth, evolve over time, which are important controls on primary production.

The current configuration of the glider FIRe prototype allows the collection of an average induction curve every 2.5–3 m. This vertical resolution is constrained by the maximum sampling rate and by fixed pitch flying due to the configuration of the PAR sensor. Only upcast data are used for accurate PAR measurements, since the mounted PAR sensor is upward looking angled at -20° (Fig. 1). Multiple profiles are needed to increase the signal-to-noise ratio and provide a statistically significant fit to estimate E_k. For this dataset it required a

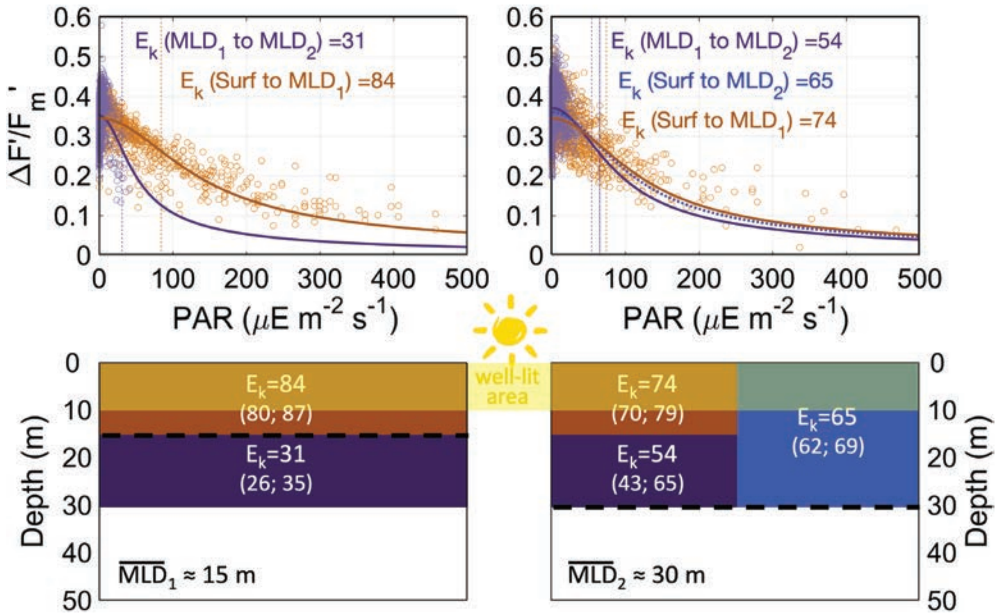

Fig. 8. (Top) Scatter plots of $\Delta F'/F_m'$ and PAR with curve fits (Eq. 2) for the two MLD regimes collected during the drift mission shown on Fig. 7 (upcast data only), highlighting the effect of MLD on phytoplankton photoacclimation. (left) average MLD$_1$ is 15 m, i.e., shallower. (right) average MLD$_2$ is 30 m, i.e., deeper. Three depth bins (surface to MLD$_1$—Orange, MLD$_1$ to MLD$_2$—purple, and surface to MLD$_2$—blue) were created to evaluate potential different phytoplankton photoacclimation regimes. Light saturation parameters, E_k, for each fitting are also presented. (bottom) Simple box model schematic with different depth bins, highlighting the different photoacclimation regimes presented in the plots on top, by comparing the E_k in each box, in relation to the MLD (black dashed line). Given PAR profiles from the glider, well-lit region of the upper ocean is shaded in yellow (top 10 m). 95% confidence intervals are presented in brackets for the E_k parameter estimation.

minimum of ~ 700 points, which corresponds to ~ 20 profiles using the current setup, all collected over a single diel cycle, to estimate a robust depth resolved E_k value. This number was obtained by evaluating the minimum number of points necessary to include in the analysis for the E_k to converge to a stable estimate.

Operational recommendations

Note that power is probably the biggest constrain when fitting a FIRe sensor on a glider. The factory estimated power consumption of the sensor is 5.88 W, but field data shows power consumption closer to 5.5 W, depending on the sampling rate, whether the instrument is on all the time and other fitted sensors. From our field experience, a deployment with the FIRe integration, where the sensors are kept always on, lasts about 10 and 36 d, using an alkaline and a lithium primary battery pack, respectively. In practice, given that shallow gliders collect one profile every 10–15 min, a reduction in profile frequency can extend the deployment length and maximize data collection. Sampling just on the upcast (as downcasts lack FIRe data in the upper 6-8 m given the time needed for the instrument to turn on and given the positioning of the PAR sensor), or even every other upcast still provides 2–3 profiles every hour and can double the deployment length. Depending on the science focus, namely nutrient limitation studies, sampling only during night-time can make a big difference in power consumption. Our planned station-keeping mission meant, contrary to the drift mission, that the glider is flying and collecting physical data continuously. A FIRe "yo" (upcast and downcast) every hour or so is a good compromise between the collection of high-resolution diel cycles of phytoplankton physiology and the mission longevity. Keep in mind, the ability to communicate with the glider means the duty cycle can be adjusted during the mission.

Comments and recommendations

Underwater gliders have proven to be a robust technology for autonomous high-resolution collection of oceanographic data. The integration of a FIRe sensor in a Slocum glider allows the evaluation of phytoplankton physiology in relation to the physical conditions. It also has the additional advantage of collecting in situ data under ambient light. Such data is fundamental for modeling instantaneous rates of primary production and the water-column integrated primary production (Ko et al. 2019). Using variable chlorophyll fluorescence, physiological parameters can be used to assess environmental factors controlling phytoplankton productivity. Gliders offer an added sampling flexibility in terms of both steering and endurance, by providing an opportunity to design missions to target specific scientific goals such as assessing the progression of a phytoplankton population through time or evaluating how different physical settings influence physiological responses. The high-resolution capabilities in both time and space permit the collection of diel cycles that allow a better understanding how phytoplankton react to variations in irradiance over different timescales.

Analysis of the irradiance dependencies of variable fluorescence signals provides insight into photoacclimation responses of phytoplankton to variations in vertical mixing regimes. While we realize that analyzing data from this FIRe sensor integration entails several assumptions and comes from a prototype, this study demonstrates the potential applications of this technology in autonomous platforms. Future plans include improving the sensor sensitivity to allow the use of the FIRe glider in oligotrophic regions. Increased flexibility to sample from different sensors independently from the FIRe sensor would be another helpful modification as it would allow extra data to be collected. The current integrated PAR sensor restricts the amount of data points collected during the profile as we cannot change the pitch to slow down the glider. Integrating a scalar irradiance PAR response would allow not only downcast sampling, but changing the pitch to slow the glider resulting in increased vertical resolution of photoacclimation parameters. Still, at a rate of ~ 0.4 measurements per metre, in a single 2-week mission, 592 profiles of FIRe data were collected, including over 17,000 induction curves, which corresponds to about 30 points per 100 m profile.

Another improvement would be integration of an ultra-high sensitive multi-color FIRe sensor (Gorbunov et al. 2020) onto the glider that allows selective excitation of different functional groups of phytoplankton, spectrally resolved functional absorption cross-sections of PSII. Such an integration would offer the potential to enhance sampling resolution, as well as to monitor changes in taxonomic composition of phytoplankton communities.

References

Alderkamp, A.,, G. L. van Dijken, K. E. Lowry, and T. L. Connelly. 2015. Fe availability drives phytoplankton photosynthesis rates during spring bloom in the Amundsen Sea Polynya, Antarctica. Elementa: Science of the Anthropocene. **3**: 000043. doi: 10.12952/journal.elementa.000043

Behrenfeld, M. J., and Z. S. Kolber. 1999. Widespread iron limitation of phytoplankton in the south pacific ocean. Science **283**: 840–843. doi:10.1126/science.283.5403.840

Benner, R., and M. Strom. 1993. A critical evaluation of the analytical blank associated with DOC measurements by high-temperature catalytic oxidation. Mar. Chem. **41**: 153–160. doi:10.1016/0304-4203(93)90113-3

Bibby, T. S., M. Y. Gorbunov, K. W. Wyman, and P. G. Falkowski. 2008. Photosynthetic community responses to upwelling in mesoscale eddies in the subtropical North Atlantic and Pacific oceans. Deep-Sea Res. II Top. Stud. Oceanogr. **55**: 1310–1320. doi:10.1016/j.dsr2.2008.01.014

Bilger, W., and O. Bjorkman. 1990. Role of the xanthophyll cycle in photoprotection elucidated by measurements of light-induced absorbance changes, fluorescence and photosynthesis in leaves of *Hedera canariensis*. Photosynth. Res. **25**: 173–185. doi:10.1007/BF00033159

Carvalho, F., J. Kohut, M. Gorbunov, O. Schofield, and M. J. Oliver. 2016a. Mapping Antarctic phytoplankton physiology using autonomous gliders, p. 1-6. *In* Mapping Antarctic phytoplankton physiology using autonomous gliders. OCEANS 2016 MTS/IEEE Monterey. doi:10.1109/OCEANS.2016.7761193

Carvalho, F., J. Kohut, M. J. Oliver, and O. Schofield. 2017. Defining the ecologically relevant mixed-layer depth for Antarctica's coastal seas. Geophys. Res. Lett. **44**: 338–345. doi:10.1002/2016gl071205

Carvalho, F., J. Kohut, M. J. Oliver, R. M. Sherrell, and O. Schofield. 2016b. Mixing and phytoplankton dynamics in a submarine canyon in the West Antarctic peninsula. J. Geophys. Res. Oceans **121**: 5069–5083. doi:10.1002/2016jc011650

Chekalyuk, A., and M. Y. Gorbunov. 1993. Laser remote sensing of Phytoplankton Photosynthetic Activity In-Situ. Int. Arch. Photogramm. Remote Sens. **29**: 897–900.

Chekalyuk, A. M., F. E. Hoge, C. W. Wright, R. N. Swift, and J. K. Yungel. 2000. Airborne test of laser pump-and-probe technique for assessment of phytoplankton photochemical characteristics. Photosynth. Res. **66**: 45–56. doi:10.1023/A:1010764420934

Churnside, J. H., and R. D. Marchbanks. 2015. Subsurface plankton layers in the Arctic Ocean. Geophys. Res. Lett. **42**: 4896–4902. doi:10.1002/2015gl064503

Clark, E. B., and others. 2020. Station-keeping underwater gliders using a Predictive Ocean circulation model and applications to SWOT calibration and validation. IEEE J. Oceanic Eng. **45**: 371–384. doi:10.1109/joe.2018.2886092

Cosgrove, J., and M. A. Borowitzka. 2010. Chlorophyll fluorescence terminology: An introduction, p. 1–17. *In* D. J. Suggett, O. Prášil, and M. A. Borowitzka [eds.], Chlorophyll a fluorescence in aquatic sciences: Methods and applications. Netherlands: Springer.

Cullen, J. J., and R. F. Davis. 2003. The blank can make a big difference in oceanographic measurements. Limnol. Oceanogr. Bull. **12**(2): 29–35. doi: 10.1002/lob.200312229

Dubinsky, Z., and O. Schofield. 2009. From the light to the darkness: Thriving at the light extremes in the oceans. Hydrobiologia **639**: 153–171. doi:10.1007/s10750-009-0026-0

Falkowski, P. G., R. M. Greene, and Z. Kolber. 1994. Light utilization and photoinhibition of photosynthesis in marine phytoplankton. *In* N. R. Baker and J. R. Bowyer [eds.], Photoinhibition of Photosynthesis from Molecular Mechanisms to the Field. Oxford: Bios Scientific Publishers. 409–434.

Falkowski, P. G., and A. H. Knoll. 2007. An Introduction to Primary Producers in the Sea: Who They Are, What They Do, and When They Evolved. *In* P. G. Falkowski and A. H. Knoll [eds.], Evolution of primary producers in the sea, p. 1–6. Burlington, MA, USA: Elsevier Academic Press.

Falkowski, P. G., M. Koblizek, M. Gorbunov, and Z. Kolber. 2004. Development and application of variable chlorophyll fluorescence techniques in marine ecosystems, p. 757–778. *In* Chlorophyll a fluorescence. Springer.

Falkowski, P. G., and J. A. Raven. 2007. Aquatic photosynthesis. Princeton, NJ: Princeton University Press. 488.

Falkowski, P. G., and A. D. Woodhead. 2013. Primary productivity and biogeochemical cycles in the sea. Boston, MA: Springer; 550. doi: 10.1007/978-1-4899-0762-2

Gorbunov, M. Y., and P. G. Falkowski. 2005. Fluorescence induction and relaxation (FIRe) technique and instrumentation for monitoring photosynthetic processes and primary production in aquatic ecosystems, p. 1029–1031. *In* A. van der Est and D. Bruce [eds.], Photosynthesis: Fundamental Aspects to Global Perspectives—Proc. 13th International Congress of Photosynthesis, Montreal, Aug 29 – Sep 3. Montreal: Allen Press.

Gorbunov, M. Y., P. G. Falkowski, and Z. S. Kolber. 2000. Measurement of photosynthetic parameters in benthic organisms in situ using a SCUBA-based fast repetition rate fluorometer. Limnol. Oceanogr. **45**: 242–245. doi:10.4319/lo.2000.45.1.0242

Gorbunov, M. Y., Z. S. Kolber, M. P. Lesser, and P. G. Falkowski. 2001. Photosynthesis and photoprotection in symbiotic corals. Limnol. Oceanogr. **46**: 75–85. doi:10.4319/lo.2000.45.1.0242

Gorbunov, M. Y., E. Shirsin, E. Nikonova, V. V. Fadeev, and P. G. Falkowski. 2020. A multi-spectral fluorescence induction and relaxation (FIRe) technique for physiological and taxonomic analysis of phytoplankton communities. Mar. Ecol. Prog. Ser. **644**: 1–13. doi:10.3354/meps13358

Griffiths, G., C. Jones, J. Ferguson, and N. Bose. 2007. Undersea gliders. J. Ocean Technol. **2**: 64–75.

Haskins, C., and O. Schofield. 2015. Glider measurements of phytoplankton physiology in penguin foraging zones along the Western Antarctic Peninsula. *In* OCEANS 2015—MTS/IEEE Washington. doi: 10.23919/OCEANS.2015.7404376

Hughes, D. J., and others. 2018. Roadmaps and detours: Active chlorophyll- a assessments of primary productivity across marine and freshwater systems. Environ. Sci. Technol. **52**: 12039–12054. doi:10.1021/acs.est.8b03488

Hughes, D. J., J. R. Crosswell, M. A. Doblin, K. Oxborough, P. J. Ralph, D. Varkey, and D. J. Suggett. 2020. Dynamic variability of the phytoplankton electron requirement for carbon fixation in eastern Australian waters. J. Mar. Syst. **202**: 103252. doi:10.1016/j.jmarsys.2019.103252

Huot, Y., and M. Babin. 2010. Overview of Fluorescence Protocols: Theory, Basic Concepts, and Practice, p. 31–74. *In* D. J. Suggett, O. Prášil, and M. A. Borowitzka [eds.], Chlorophyll a fluorescence in aquatic sciences: Methods and applications. Netherlands: Springer. doi:10.1007/978-90-481-9268-7_3

Jassby, A. D., and T. Platt. 1976. Mathematical formulation of the relationship between photosynthesis and light for phytoplankton. Limnol. Oceanogr. **21**: 540–547. doi:10.4319/lo.1976.21.4.0540

Ko, E., J. Park, M. Y. Gorbunov, and S. Yoo. 2019. Uncertainties in variable fluorescence and 14C methods to estimate primary production: A case study in the coastal waters off the Korean peninsula. Mar. Ecol. Prog. Ser. **627**: 13–31. doi:10.3354/meps13083

Kohut, J. T., P. Winsor, H. Statscewich, M. J. Oliver, E. Fredj, N. Couto, K. Bernard, and W. Fraser. 2018. Variability in summer surface residence time within a West Antarctic peninsula biological hotspot. Philos. Trans. R. Soc. A: Math. Phys. Eng. Sci. **376**: 20170165. doi:10.1098/rsta.2017.0165

Kolber, Z., O. Prášil, and P. G. Falkowski. 1998. Measurements of variable chlorophyll fluorescence using fast repetition rate techniques: Defining methodology and experimental protocols. Biochim. Biophys. Acta (BBA)-Bioenergetics **1367**: 88–106. doi:10.1016/S0005-2728(98)00135-2

Kolber, Z., J. Zehr, and P. Falkowski. 1988. Effects of growth irradiance and nitrogen limitation on photosynthetic energy conversion in photosystem II. Plant Physiol. **88**: 923–929. doi:10.1104/pp.88.3.923

Kooten, O., and J. F. Snel. 1990. The use of chlorophyll fluorescence nomenclature in plant stress physiology. Photosynth. Res. **25**: 147–150. doi:10.1007/BF00033156

Krause, G. H., and E. Weis. 1991. Chlorophyll fluorescence and photosynthesis: The basics. Annu. Rev. Plant Phys. **42**: 313–349. doi:10.1146/annurev.pp.42.060191.001525

Laney, S., R. Letelier, R. Desiderio, M. R. Abbott, D. Kiefer, and C. Booth. 2001. Measuring the natural fluorescence of phytoplankton cultures. J. Atmos. Oceanic Tech. **18**: 1924–1934. doi:10.1175/1520-0426(2001)018<1924:MTNFOP>2.0.CO;2

Laney, S. R., and R. M. Letelier. 2008. Artifacts in measurements of chlorophyll fluorescence transients, with specific application to fast repetition rate fluorometry. Limnol. Oceanogr.: Methods **6**: 40–50. doi:10.4319/lom.2008.6.40

Lewis, M. R., J. J. Cullen, and T. Piatt. 1984. Relationships between vertical mixing and photoadaptation of phytoplankton: Similarity criteria. Mar. Ecol. Prog. Ser. **15**: 141–149. doi:10.3354/meps015141

Lin, H., F. I. Kuzminov, J. Park, S. Lee, P. G. Falkowski, and M. Y. Gorbunov. 2016. Phytoplankton. The fate of photons absorbed by phytoplankton in the global ocean. Science **351**: 264–267. doi:10.1126/science.aab2213

Lorenzen, C. J. 1966. A method for the continuous measurement of in vivo chlorophyll concentration. Deep Sea Res. Oceanogr. Abstr. **13**(2): 223–227. doi: 10.1016/0011-7471(66)91102-8

MacIntyre, H. L., T. M. Kana, and R. J. Geider. 2000. The effect of water motion on short-term rates of photosynthesis by marine phytoplankton. Trends Plant Sci. **5**: 12–17. doi:10.1016/s1360-1385(99)01504-6

Milligan, A. J., U. A. Aparicio, and M. J. Behrenfeld. 2012. Fluorescence and nonphotochemical quenching responses to simulated vertical mixing in the marine diatom *Thalassiosira weissflogii*. Mar. Ecol. Prog. Ser. **448**: 67–78. doi:10.3354/meps09544

Mitchell, B. G., and O. Holm-Hansen. 1991. Observations of modeling of the Antarctic phytoplankton crop in relation to mixing depth. Deep-Sea Res. I Oceanogr. Res. Pap. **38**: 981–1007. doi:10.1016/0198-0149(91)90093-U

Muller, P., X. P. Li, and K. K. Niyogi. 2001. Non-photochemical quenching. A response to excess light energy. Plant Physiol. **125**: 1558–1566. doi:10.1104/pp.125.4.1558

Neale, P. J., E. W. Helbling, and H. E. Zagarese. 2003. Modulation of UVR exposure and effects by vertical mixing and advection, p. 107–134. *In* E. W. Helbling and H. E. Zagarese [eds.], UV effects in aquatic organisms and ecosystems. Comprehensive Series in Photochemical & Photobiological Sciences. Cambridge: The Royal Society of Chemistry. doi:10.1039/9781847552266-00107

Rudnick, D. L. 2016. Ocean research enabled by underwater gliders. Ann. Rev. Mar. Sci. **8**: 519–541. doi:10.1146/annurev-marine-122414-033913

Schofield, O., H. W. Ducklow, D. G. Martinson, M. P. Meredith, M. A. Moline, and W. R. Fraser. 2010. How do polar marine ecosystems respond to rapid climate change? Science **328**: 1520–1523. doi:10.1126/science.1185779

Schofield, O., C. Jones, J. Kohut, U. Kremer, T. Miles, G. Saba, D. Webb, and S. Glenn. 2015. Developing coordinated communities of autonomous gliders for sampling coastal ecosystems. Mar. Technol. Soc. J. **49**: 9–16. doi:10.4031/MTSJ.49.3.16

Schofield, O., and others. 2007. Slocum gliders: Robust and ready. J. Field Robot. **24**: 473–485. doi:10.1002/rob.20200

Schofield, O., M. A. Moline, and B. B. Prezelin. 1995. Palmer LTER: Photoacclimation in a coastal phytoplankton bloom. Antarctic Journal of the United States. **30**(5): 260–262.

Silsbe, G. M., and others. 2015. Toward autonomous measurements of photosynthetic electron transport rates: An evaluation of active fluorescence-based measurements of photochemistry. Limnol. Oceanogr.: Methods **13**: e10014. doi:10.1002/lom3.10014

Suggett, D. J., C. M. Moore, and R. J. Geider. 2010. Estimating aquatic productivity from active fluorescence measurements, p. 103–127. *In* Chlorophyll a fluorescence in aquatic sciences: Methods and applications. Springer.

Suggett, D. J., C. M. Moore, A. E. Hickman, and R. J. Geider. 2009. Interpretation of fast repetition rate (FRR) fluorescence: Signatures of phytoplankton community structure versus physiological state. Mar. Ecol. Prog. Ser. **376**: 1–19. doi:10.3354/meps07830

Webb, W. L., M. Newton, and D. Starr. 1974. Carbon dioxide exchange of *Alnus rubra*. Oecologia **17**: 281–291. doi:10.1007/BF00345747

Yentsch, C. S., and D. W. Menzel. 1963. A method for the determination of phytoplankton chlorophyll and phaeophytin by fluorescence. Deep Sea Res. Oceanogr. Abstr. **10**(3): 221–231. doi:10.1016/0011-7471(63)90358-9

Acknowledgments

The authors would like to thank Rutgers field team (in particular to Nicole Couto, Nicole Waite, Mike Brown, and Chip Haldeman), Palmer Station personnel and ARSV Laurence M. Gould crew for support during deployments and recoveries. We would like to thank Kevin Wyman for his comments on the manuscript, Nathan Briggs for helpful discussions over data analyses and several anonymous reviewers for constructive comments. This work was supported by National Science Foundation (NSF Palmer LTER program, grant 0823101), National Oceanographic Partnership Program (NOPP, grant NA05OAR4601089), and NASA Ocean Biology and Biogeochemistry Program (grants NNX16AT54G and 80NSSC18K1416). Filipa Carvalho was funded by a Portuguese doctoral fellowship from Fundação para a Ciência e Tecnologia (FCT, grant DFRH - SFRH/BD/72705/2010), a Teledyne Marine Graduate Fellowship and a European Research Council Consolidator grant (GOCART, agreement number 724416).

Conflict of Interest

None declared.

Submitted 10 January 2020
Revised 21 June 2020
Accepted 24 June 2020

Associate editor: David Suggett

JGR Oceans

RESEARCH ARTICLE
10.1029/2020JC016505

Key Points:
- A Slocum glider with an integrated deep-sea pH sensor collected high-resolution carbonate chemistry data in the Mid-Atlantic Bight
- Highest pH occurred in winter shelf and fall shelf break water, while lowest pH was seen in nearshore surface and Cold Pool bottom water
- Seasonal and spatial carbonate chemistry dynamics were influenced by stratification, freshwater input, biology, and water mass mixing

Supporting Information:
- Supporting Information S1
- Table S1
- Table S2
- Table S3

Correspondence to:
E. K. Wright-Fairbanks,
ekw31@marine.rutgers.edu

Citation:
Wright-Fairbanks, E. K., Miles, T. N., Cai, W.-J., Chen, B., & Saba, G. K. (2020). Autonomous observation of seasonal carbonate chemistry dynamics in the Mid-Atlantic Bight. *Journal of Geophysical Research: Oceans*, *125*, e2020JC016505. https://doi.org/10.1029/2020JC016505

Received 16 JUN 2020
Accepted 17 OCT 2020
Accepted article online 22 OCT 2020

Autonomous Observation of Seasonal Carbonate Chemistry Dynamics in the Mid-Atlantic Bight

Elizabeth K. Wright-Fairbanks[1], Travis N. Miles[1], Wei-Jun Cai[2], Baoshan Chen[2], and Grace K. Saba[1]

[1]Department of Marine and Coastal Sciences, School of Environmental and Biological Sciences, State University of New Jersey at Rutgers, New Brunswick, NJ, USA, [2]School of Marine Science and Policy, University of Delaware, Newark, DE, USA

Abstract Ocean acidification alters the oceanic carbonate system, increasing potential for ecological, economic, and cultural losses. Historically, productive coastal oceans lack vertically resolved high-resolution carbonate system measurements on time scales relevant to organism ecology and life history. The recent development of a deep ion-sensitive field-effect transistor (ISFET)-based pH sensor system integrated into a Slocum glider has provided a platform for achieving high-resolution carbonate system profiles. From May 2018 to November 2019, seasonal deployments of the pH glider were conducted in the central Mid-Atlantic Bight. Simultaneous measurements from the glider's pH and salinity sensors enabled the derivation of total alkalinity and calculation of other carbonate system parameters including aragonite saturation state. Carbonate system parameters were then mapped against other variables, such as temperature, dissolved oxygen, and chlorophyll, over space and time. The seasonal dynamics of carbonate chemistry presented here provide a baseline to begin identifying drivers of acidification in this vital economic zone.

Plain Language Summary Seawater chemistry affects the ability of organisms to survive in the ocean. Past monitoring of seawater chemistry has missed key times and locations that are important to natural life cycles. In order to fill in those gaps, we put a chemical sensor into a deep-sea robot that we can control from land. This robot, called a Slocum glider, glides from the top of the ocean down to 200-m depth and collects ocean chemistry data along the way. We used our Slocum glider to measure how seawater chemistry differs between seasons in the Mid-Atlantic, which will help us understand how organisms might be affected by water conditions.

1. Introduction

Ocean acidification (OA) results from the uptake of atmospheric carbon dioxide (CO_2), which alters oceanic carbonate chemistry (Doney et al., 2009; Gledhill et al., 2015; Orr et al., 2005). The ocean has absorbed approximately one third of the CO_2 emitted by human activities since the Industrial Revolution (Gruber et al., 2019). During this time, atmospheric CO_2 has risen from approximately 280 parts per million (ppm) to 410 ppm (Dlugokencky & Tans, 2020). When CO_2 is absorbed by the ocean, it reacts with seawater and results in complex chemical reactions that reduce seawater pH and calcium carbonate saturation state, Ω. Saturation states governing the formation and dissolution of the two mineral forms of calcium carbonate, calcite and aragonite, are expressed as Ω_{cal} and Ω_{arag}, respectively. A saturation state above 1 indicates carbonate supersaturation and thermodynamic favorability of carbonate calcification, while a saturation state below 1 indicates carbonate undersaturation and thermodynamic favorability of carbonate dissolution. However, carbonate saturation states approaching 1, and as high as 1.92, have been shown to cause negative impacts on calcifying organisms, despite carbonate supersaturation (Gazeau et al., 2007; Gledhill et al., 2015; Gobler & Talmage, 2013, 2014; Hettinger et al., 2012; Talmage & Gobler, 2009, 2010; Waldbusser et al., 2014), likely due to impacts on metabolism and increases in the energetic cost of mitigating stress (Melzner et al., 2019; Miller et al., 2009; Pan et al., 2015).

The rate of oceanic uptake of atmospheric CO_2 has increased in the last two decades due to increasing levels of atmospheric CO_2 (Intergovernmental Panel on Climate Change [IPCC], 2019). The global ocean is acidifying at unprecedented rates, with open ocean surface water pH decreasing by 0.017–0.027 pH units per decade since the late 1980s (Gledhill et al., 2015; IPCC, 2019; Sutton et al., 2016; Zeebe, 2012). Global surface ocean pH is predicted to decline by up to 0.29 pH units by 2081–2100 relative to 2006–2015 under RCP8.5 (IPCC, 2019). In addition to global changes in pH, the rate of change in global Ω_{arag} since the Industrial Revolution has been 5 times greater than natural variability over the last millennium (Friedrich et al., 2012; Gattuso et al., 2015). Under RCP8.5, there will be no ocean water with Ω_{arag} greater than 3.0, and the total volume of water with Ω_{arag} less than 1.0 will increase from 76% (1990 value) to 91%, by 2100 (Gattuso et al., 2015).

In coastal oceans, carbonate chemistry is influenced by a range of drivers including productivity-respiration cycles, nutrient loading, freshwater inputs, and other coastal processes (Gledhill et al., 2015; Saba, Goldsmith, et al., 2019). Because of its multiple contributors, acidification in coastal zones can be highly variable and episodic both spatially and temporally (Baumann & Smith, 2017). The hydrodynamic and biological processes influencing coastal environments can vary on the order of minutes to days (Runcie et al., 2018; Xu et al., 2017). These extreme short-term events likely have a more immediate impact on carbonate-dependent organisms compared to gradual change due to increases in atmospheric CO_2 (Baumann & Smith, 2017; Cai et al., 2011; Waldbusser & Salisbury, 2014). However, a global increase in atmospheric CO_2 will increase the frequency of extreme acidification events, pushing organisms past critical survival thresholds more regularly (Gledhill et al., 2015). Furthermore, acidification can cooccur with other metabolic stressors, including low dissolved oxygen (DO) and warm temperatures (Cai et al., 2011, 2017; Saba, Goldsmith, et al., 2019).

The Mid-Atlantic Bight (MAB), located within the U.S. Northeast Shelf (NES), is an ecologically and economically vital coastal zone. This region is home to some of the most profitable commercial and recreational fisheries in the United States (Colvocoresses & Musick, 1984; Hare et al., 2016; NEFSC, 2020), ecosystems that protect coastal communities from inundation, storms, and erosion (NRC, 2010), and offshore wind energy development sites (Musial et al., 2013; NEFSC, 2020). The MAB is prone to acidification due to freshwater sources (primarily riverine), eutrophication and photosynthesis-respiration cycles, coastal upwelling, and other influences. Coastal inputs and biological activity alter carbonate chemistry more quickly than gas equilibrium and therefore play a major role in determining the carbonate system, specifically the partial pressure of CO_2 (pCO_2) and pH (Cai et al., 2020). Mid-Atlantic coastal waters are acutely affected by seasonal changes in temperature and inputs from shore. Because MAB oceanography is highly variable between seasons, it is necessary to monitor changes in the carbonate system seasonally (Huret et al., 2018). While there may be no net change in pH or Ω_{arag} over a full annual cycle, seasonal changes operate under a time scale that could affect biological processes in the nearshore (Gledhill et al., 2015; Waldbusser & Salisbury, 2014). Monitoring seasonal changes also provide a basis for identifying long-term changes in carbonate chemistry due to shifts in salinity, temperature, atmospheric CO_2, and coastal inputs (Gledhill et al., 2015; Goldsmith et al., 2019; Xu et al., 2020).

Acidification monitoring efforts to date are limited in temporal and spatial resolution and lacking in economically important coastal regions including the MAB (Goldsmith et al., 2019). Traditionally, monitoring in the MAB has been conducted through large field campaigns every few years. These ship-based surveys depict large spatial variability and decadal changes of surface water carbonate chemistry in the U.S. NES but lack seasonal resolution across the system (Cai et al., 2020; Z. A. Wang et al., 2013; Wanninkhof et al., 2015). In addition to cruise campaigns, there are few fixed (moored) stations monitoring carbonate system parameters on the MAB shelf. These fixed stations are capable of characterizing temporal changes in carbonate chemistry but lack spatial resolution in terms of location and depth. Additionally, many existing MAB monitoring stations measure only one of the four carbonate system parameters (pH, dissolved inorganic carbon [DIC], total alkalinity [TA], and pCO_2), two of which are necessary to fully characterize the carbonate system (Pimenta & Grear, 2018). Along with cruise campaigns and surface-fixed stations, satellite imagery can be used to estimate a suite of surface water carbon system factors, including biological productivity, pCO_2, salinity-derived carbonate parameters, and large-scale coastal inputs (Salisbury et al., 2015; H. Wang et al., 2017).

The ability to monitor carbonate chemistry in high resolution throughout the water column is critical in order to detect low pH in water masses and to derive relationships between physical, biological, and carbonate system variability. Autonomous underwater gliders, capable of collecting data in highly variable

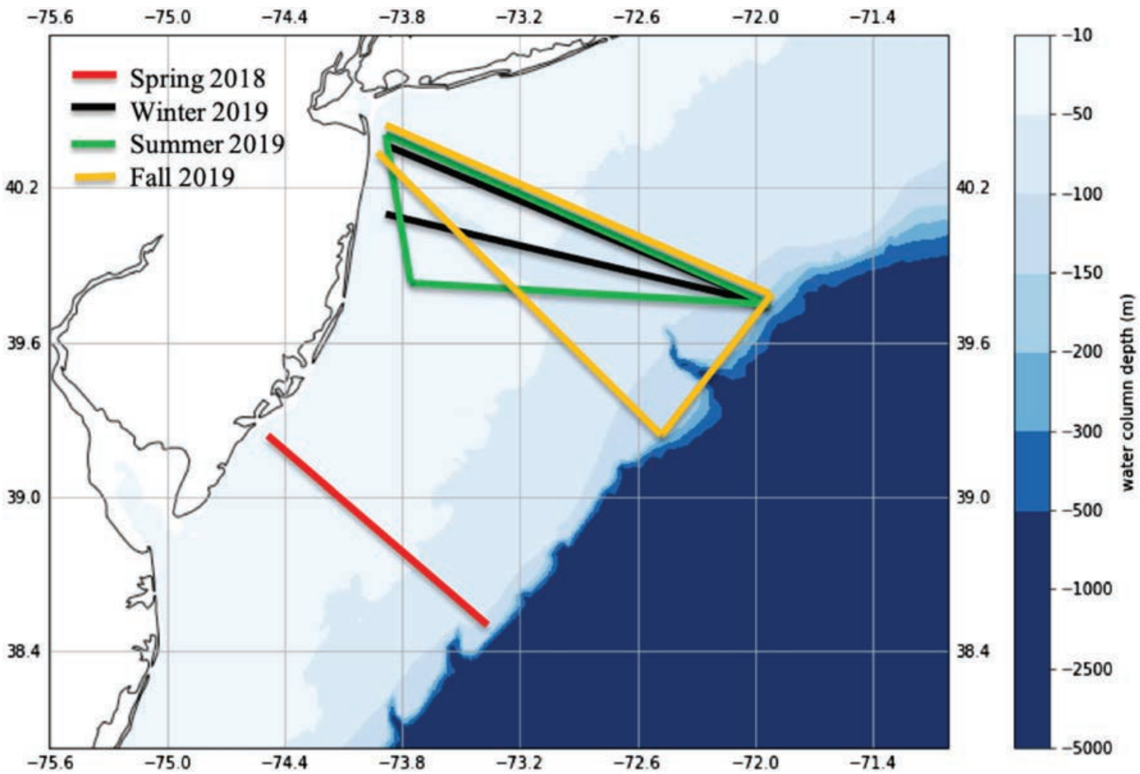

Figure 1. Seasonal glider deployments completed between May 2018 and November 2019.

currents in water depths up to 1,000 m, are a reliable platform that fulfill this role (Rudnick, 2016; Schofield et al., 2007). A deep ion-sensitive field-effect transistor (ISFET) pH sensor was recently developed and integrated into a Teledyne-Webb Slocum G2 glider (Saba, Wright-Fairbanks, et al., 2019). In addition to measuring pH, this glider has a suite of sensors that provide profiles of conductivity, temperature, DO, chlorophyll fluorescence, and spectral backscatter. This allows users to compare seawater pH to other ocean properties and conduct salinity-based estimates of TA in order to constrain the carbonate system. Here, we present data from four seasonal deployments of the pH glider in the central MAB, which have produced the first spatially and temporally high-resolution characterization of seasonal carbonate system dynamics in this region.

2. Materials and Methods

2.1. Seasonal Deployments

The pH glider was deployed on four seasonal missions in the MAB (2–22 May 2018 [spring], 1–19 February 2019 [winter], 17 July to 12 August 2019 [summer], and 15 October to 6 November 2019 [fall]; Figure 1). Before deployment, the glider pH sensor was fully conditioned following the guidelines described in Saba, Wright-Fairbanks, et al. (2019). After deployment from the small vessel R/V Rutgers, the glider was sent on a shallow mission during discrete water sample collection (see below). Once discrete sampling was completed, the glider was sent to its first offshore waypoint. The winter, summer, and fall missions followed a cross-shelf transect starting ~15 km off Sandy Hook, New Jersey, traveling 200 km eastward to the shelf break. The glider then completed various transects and triangles back to shore, covering a total of 469.6 km in winter, 503.5 km in summer, and 471.4 km in fall. The spring mission followed an established glider observation line from Atlantic City, New Jersey, 140 km eastward to the shelf break and back, for a total of 317.0 km.

Timing for sensor repairs and recalibrations prevented four sequential seasonal deployments on the Sandy Hook transect line. A mission planned for spring of 2019 on the Sandy Hook line was postponed due to technological difficulties and rough seas, and the postponed mission was terminated within hours of deployment due to a glider pump failure. The spring deployment was rescheduled for April 2020 but was canceled due to research restrictions during the coronavirus disease 2019 (COVID-19) pandemic.

Upon each deployment and recovery of the pH glider, discrete water samples were collected following best practice guidelines for autonomous pH measurements with DuraFET sensors (Bresnahan et al., 2014; Johnson et al., 2016; Martz et al., 2015; Saba, Wright-Fairbanks, et al., 2019). Discrete samples were collected near the glider at various depths either by a hand-lowered 5-L Niskin (spring and winter; within 5 m of glider) or using an SBE55 6-bottle rosette with an SBE19 conductivity, temperature, and depth sensor (CTD) attached (summer and fall; within 100 m of glider). Samples were collected into 250-ml borosilicate glass bottles and preserved with 50 μl of saturated mercuric chloride then transported to the Cai laboratory (University of Delaware) for analysis (section 2.2.3).

2.2. Sensor QA/QC

2.2.1. Glider CTD, Oxygen, and Chlorophyll Sensors

The glider was equipped with a pumped CTD modified for integration with an ISFET pH sensor, an Aanderaa oxygen optode, and a Sea-Bird Scientific BB2FL ECO puck to measure chlorophyll fluorescence, colored dissolved organic matter (CDOM), and optical backscatter. The CTD and DO data were run through quality assurance/quality control (QA/QC) guidelines outlined in an Environmental Protection Agency (EPA) QA Project Plan for glider deployments along the coast of New Jersey (Kohut et al., 2014). Both sensors are factory calibrated annually, and data were verified predeployment and postdeployment (Saba, Wright-Fairbanks, et al., 2019). The BB2FL ECO puck is factory calibrated by WET labs every 1–2 years. Between each seasonal deployment, the integrated CTD/pH sensor was cleaned and recalibrated by the manufacturer (Sea-Bird Scientific).

2.2.2. Glider pH Sensor

Each time the glider surfaced throughout a mission, a subset of collected data was sent to shore via an Iridium satellite phone located in the tail of the glider. This allowed for preliminary inspection of all science data and software metrics to assess glider functionality. Full data sets were collected postrecovery from memory cards stored in the glider. Data were processed using Slocum Power Tools (https://github.com/kerfoot/spt/) and analyzed using MATLAB data analysis software (version R2019a).

pH data were initially inspected for sensor time lags, which were identified as skewed upcast and downcast profiles in pH reference voltage data and were often associated with areas of steep gradients in salinity or temperature. To correct for sensor lag, upcast and downcast pairs were run through potential time shifts from 0 to 60 s at 1-s intervals. The optimal time shift minimized the difference between reference voltage at a certain depth in an upcast/downcast pair (Saba, Wright-Fairbanks, et al., 2019).

After time shifts were applied, pH data were run through QA/QC measures based on the Integrated Ocean Observing System (IOOS) Manual for Real-Time Quality Control of pH Data Observations (IOOS, 2019). pH reference voltage data were flagged and removed in instances where more than 1 hr has passed between observations ($\ll$1% of observations) or in instances without a valid time stamp (~20% of observations). Next, observations of other scientific variables without both a corresponding pH reference voltage and pressure value were removed (~40% of observations). Observations outside of the latitude and longitude bounds of the MAB were flagged and removed ($\ll$1% of observations). pH values were validated in a gross range test, flagging and removing values outside the calibration bounds of the glider pH sensor (pH $<$ 6.5 and pH $>$ 9; $\ll$1% of observations). As more deployments of the pH glider provide a mean climatology for the MAB, the gross range test can be restricted to a user-specified local or seasonal pH range. Next, a spike test identified and removed single value spikes in pH reference voltage observations ($\ll$1% of observations). Lastly, data were inspected visually for unrealistic rates of change, flat-lining, and attenuated signals, which would indicate sensor failure. Tests for multivariate failure and comparisons to nearby pH sensors were not applicable to these deployments, but should be considered in future pH glider deployments.

2.2.3. Discrete Samples

Discrete sample pH was measured spectrophotometrically at 25°C using purified *meta*-Cresol Purple dye (Clayton & Byrne, 1993; Liu et al., 2011). pH accuracy was determined against Tris buffers (DelValls & Dickson, 1998; Millero, 1986). Additionally, discrete TA and DIC measurements were used to calculate pH and check the internal accuracy of spectrophotometric measurements. TA titrations were run via open cell Gran titration on an Apollo Scitech TA titrator AS_ALK2 (Cai et al., 2010; B. Chen et al., 2015;

Huang et al., 2012). DIC was quantified using a nondispersive infrared method on an Apollo Scitech DIC Analyzer AS-C3 (B. Chen et al., 2015; Huang et al., 2012). TA and DIC accuracies were determined using certified reference materials (CRMs) from Andrew Dickson's group at the Scripps Institution of Oceanography.

Discrete pH measurements were converted to in situ pH values using in situ, depth-specific temperature and salinity measured by SBE19 CTD. Discrete pH was then compared to glider ISFET measurements at the same, or closest, depth from the glider's first profile at deployment and its last profile before recovery. Groundtruthing offsets were determined as glider pH—discrete pH at each depth. Glider agreement was calculated as the average absolute offset between all depths at deployment or recovery. Uncertainty in glider agreement was calculated as one standard deviation between glider pH measurements in the surface layer during the discrete sampling period. Because there was little variation in temperature and salinity in the surface layer over a short period of time, variation in glider pH introduced by the environment was small. Glider pH science bays were sent to SeaBird Scientific for postdeployment analysis, cleaning, and recalibration between deployments.

2.3. Data Analysis

Salinity was calculated based on glider-measured conductivity, temperature, and pressure. TA and salinity exhibit a conservative relationship in U.S. East Coast waters (Cai et al., 2010; Z. A. Wang et al., 2013); thus, TA is estimated using glider-derived salinity (Saba, Wright-Fairbanks, et al., 2019). In each season, a linear regression to estimate TA from salinity was derived from a combination of discrete samples taken at glider deployment/recovery and discrete samples from transects across the U.S. NES during the East Coast Ocean Acidification (ECOA)-1 cruise in summer 2015 (supporting information Text S1). Discrete samples from glider deployments and the ECOA-1 cruise were both analyzed by the Cai group using the same method. Sampling during glider deployments and recoveries took place only in relatively low salinity nearshore waters (Figure S1). Conversely, the ECOA-1 cruise sampled across the entire shelf to the shelf break but missed lower salinity areas. Using both seasonal discrete samples and shelf-wide ECOA samples ensured that seasonal TA-salinity regressions accounted for the entire scope of salinities the glider encountered in the MAB while minimizing uncertainty due to seasonal differences in TA-salinity relationships. Full-deployment salinity-estimated TA was also compared to TA derived using the CANYON-B algorithm, which is trained on GLODAPv2 and GO-SHIP bottle samples, and calculates carbonate system parameters using measured latitude, longitude, time, depth, temperature, salinity, and oxygen (Bittig et al., 2018).

Glider pH was calculated on the total hydrogen concentration scale using glider-measured reference voltage, salinity, pressure, temperature, and sensor-specific calibration coefficients (Johnson et al., 2017; Saba, Wright-Fairbanks, et al., 2019). The remaining carbonate system parameters were calculated using CO2SYS for MATLAB (v3.0) with glider temperature, salinity, pressure, pH, and salinity-derived TA as inputs (Lewis & Wallace, 1998; Sharp et al., 2020; van Heuven et al., 2011). Other CO2SYS inputs included total pH scale (mol kg^{-1}-SW), K_1 and K_2 constants of Mehrbach et al. (1973) with refits by Dickson and Millero (1987), KSO_4 dissociation constant of Dickson (1990), KHF dissociation constant of Uppstrom (1974), and borate-to-salinity ratio of Perez and Fraga (1987). Carbonate system parameters reported here are pH, Ω_{arag}, and ratio of TA to DIC (TA:DIC). TA:DIC provides context for the CO_2 buffering capacity of seawater. Oceanic buffering capacity for CO_2 reaches a minimum at TA:DIC = 1, meaning water with TA:DIC closest to 1 is most susceptible to acidification (Cai et al., 2020; Egleston et al., 2010; Z. A. Wang et al., 2013).

Slocum gliders are propelled by purposeful changes in buoyancy, allowing the glider to dive and climb in a sawtooth pattern from surface to bottom waters. The pH glider system used here was equipped with a 200-m pump, allowing it to operate in depths as shallow as 4 m and as deep as 200 m. Coastal gliders travel approximately 20 km day^{-1} horizontally, while profiling vertically at 10–15 cm s^{-1}. Sensors sample at 0.5 Hz, providing observations at 20- to 30-cm intervals vertically. All measured and derived variables were bin-averaged into 1-m depth by 1-km-distance bins. At a sampling rate of 0.5 Hz and vertical profiling velocity of 10–15 cm s^{-1}, a 1-m depth average incorporated three to five measurements, minimizing the effect of small-scale physical and biological water column dynamics. At a horizontal speed of 20 km day^{-1}, a 1-km-distance bin averaged 1.2 hr of data, which could include between 3 and 30 individual profiles depending on water column depth.

Brunt-Vaisala frequency squared (N^2) was calculated between adjacent 1-m layers in each depth- and distance-binned profile. The mixed-layer depth (MLD) for each binned profile was determined as the depth of maximum N^2 ($\max(N^2)$) (Carvalho et al., 2017). Each profile's mixed layer was assigned a quality index (QI), which indicates the significance of the stratification index based on relative homogeneity in and below the mixed layer (Carvalho et al., 2017; Lorbacher et al., 2006). Profiles with QI < 0.5 were considered well mixed and removed from MLD analysis.

For analysis, deployment data were split into spatial and depth-defined regions. Distinctions between surface and bottom waters were made using the mean MLD in each season, with surface waters defined as surface to MLD, and bottom waters from MLD to the bottom. During winter, there was no significant MLD (QI < 0.5). Therefore, winter surface and bottom parameters were represented by an average of the top 5 m and bottom 5 m of the water column, respectively. The nearshore region was defined as extending from shore to the 35-m isobath, where sea slope begins to increase in the central MAB, or 1–40 km offshore (Levin et al., 2018). Midshelf was defined from the 35- to 100-m isobaths or 40–160 km offshore (40–120 km offshore in the spring). The shelf break was defined as beyond the continental shelf (>160 km offshore or >120 km offshore in spring), where depth increases to >100 m.

Significances of regional and seasonal comparisons of measured and derived variables were calculated using a Kruskal-Wallis analysis with Dunn post hoc, unless otherwise noted. Significance is reported as a p value, with $p < 0.05$ demonstrating a significant difference between the values being compared. All averages are presented as mean ±1 standard deviation, and a table of averages is included in the supporting information (Table S1). Along with being depth-averaged into 1-m bins, chlorophyll and oxygen concentrations were integrated to 35-m depth to analyze mixed layer productivity. Integration to 35 m, as opposed to full-water column integration, ensured that the majority of mixed layer productivity in each season was captured while minimizing skewed integrations that could arise due to seasonal differences in profile depths. The 35-m integrated chlorophyll and oxygen are presented along with 1-m depth-averaged chlorophyll and oxygen.

To visualize the spread of data in each season, box-and-whisker plots displaying medians, 25th and 75th percentiles, minimums, and maximums were created for glider-measured and derived variables. To summarize carbonate system interactions with the development and degradation of seasonal stratification and chlorophyll maxima, physical, biological, and carbonate system properties from the first cross-shelf transect of each deployment were plotted on common color axes. Finally, full-deployment carbonate parameters were plotted as a function of distance from shore and season in order to visualize spatial differences in carbonate system seasonality.

3. Results

3.1. Sensor Performance

A full record of groundtruthing offsets is available in Tables S2 and S3. Seasonal mean glider agreement ranged from 0.005 to 0.042 pH units and within-mixed-layer variability ranged from 0.001 to 0.027 pH units. Given these observations, we believe that glider pH measurements are accurate to better than 0.05 pH units, which agrees with the manufacturer accuracy specification for this sensor (±0.05 pH units). Short-term reproducibility is likely significantly better than 0.03 because the source of error is short-term, within-mixed layer repeatability. This conclusion is supported by the manufacturer precision specification for this sensor (±0.001 pH units), which implies that spatial variability along a section can be resolved to ±0.001 pH units. Therefore, pH is reported here to the third decimal place.

pH sensor time lag varied seasonally. No shift was necessary for the winter mission, while 47- and 30-s shifts were applied to the spring mission, a 36-s shift was applied to the summer mission, and a 45-s shift was applied to the fall mission. Spring required two lag corrections because of a shift in the sensor lag between the first third and last two thirds of deployment, likely due to a shift in water column structure (Saba, Wright-Fairbanks, et al., 2019).

The magnitude of uncertainty in derived variables varied based on the accuracy of TA estimation. Average absolute differences between discrete TA and estimated TA ranged from 5.5 (winter) to 27.4 μmol kg^{-1} (summer). Average uncertainty in Ω_{arag} and TA:DIC due to TA offsets ranged from 0.005 to 0.024 and 0.0001 to 0.0003, respectively (Table S4). A full analysis of TA offsets, as well as a list of seasonal

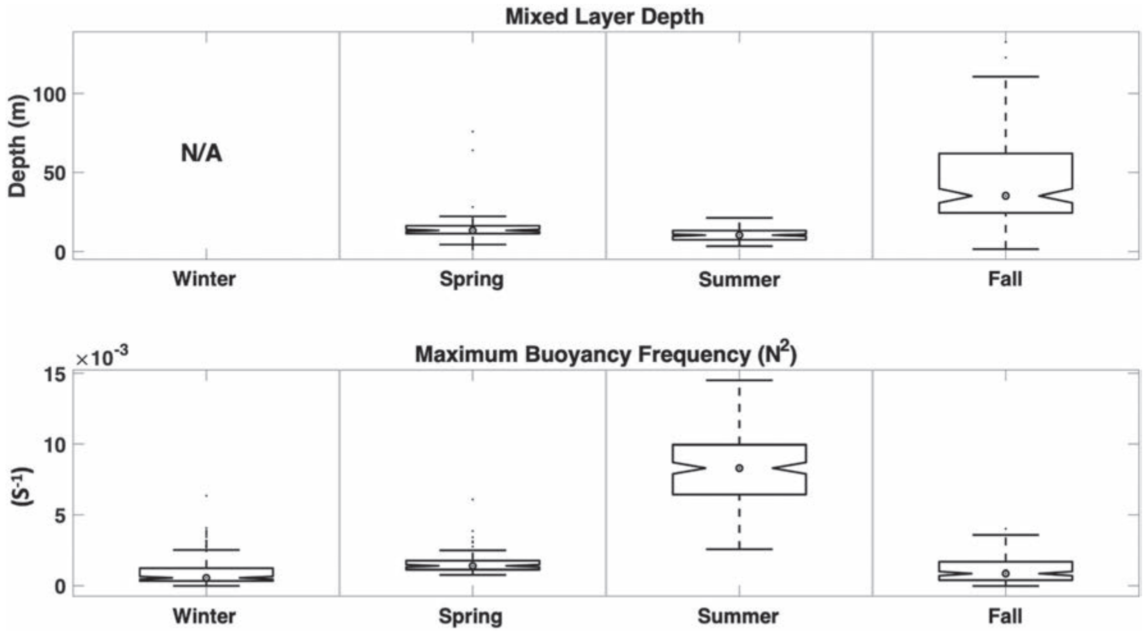

Figure 2. Comparisons of mixed layer depth (MLD) and maximum buoyancy frequency (max(N^2)) during seasonal glider deployments. Targets indicate median values, box limits indicate the 25th to 75th percentiles, and whiskers represent the full range of data. Data points beyond 1.5 times the interquartile range away from the top or bottom of the box were identified as outliers and are shown as black dots extending from the whiskers. Notches depict the 95% confidence interval around the median. If notches do not overlap, there is 95% confidence that the medians are different ($p < 0.05$). Winter had a well-mixed water column with insignificant MLD QI values; thus, no data are shown for winter MLD.

TA-salinity regressions, can be found in the supporting information (Text S1 and Tables S4 and S5). Full-deployment salinity-derived TA was similar to CANYON-B algorithm estimates of TA, differing at most by a seasonal average of 2.0 ± 4.3 μmol kg^{-1} (~0.1%).

3.2. Seasonal and Spatial Water Column Dynamics

The winter mission collected 4,933 profiles of science data over 19 days, spring collected 6,426 profiles over 20 days, summer collected 6,948 profiles over 26 days, and fall collected 5,333 profiles over 22 days. On average, about 270 profiles were generated per day. Although the four seasonal deployments were not sequential, they highlight stratification and mixing patterns typical of the MAB, revealing seasonal transitions in physical, biological, and chemical characteristics described in detail below.

3.2.1. Physical Dynamics

Seasonal changes in stratification occurred in the MAB (Figures 2 and 3). The winter water column was cold (<13°C) and well mixed, with no significant MLD (QI < 0.5) and the lowest observed max(N^2) (0.0010 ± 0.0010 s^{-1}, $n = 187$, $p < 0.001$). Surface waters were warmer in the spring compared to winter ($p < 0.001$), resulting in stronger stratification (max(N^2) = 0.0015 ± 0.0005 s^{-1}, $n = 129$, $p < 0.001$) and MLD of 14.4 ± 8.2 m ($n = 129$). Surface temperature peaked in the summer (23.64 ± 1.13°C, $n = 188$, $p < 0.001$), while bottom waters remained cold, resulting in continued shoaling of MLD to 10.4 ± 3.7 m ($n = 188$) and the greatest max(N^2) observed seasonally (0.0082 ± 0.0025 s^{-1}, $n = 188$, $p < 0.001$). Strong stratification in the spring and summer trapped a cold (<12°C) water mass below the mixed layer, which was consistent with the well-known summer Cold Pool (Z. Chen et al., 2018; Houghton et al., 1982). Surface waters cooled in the fall, causing a lower max(N^2) (0.0011 ± 0.0009, $n = 358$), and a deep MLD (44.7 ± 27.7 m, $n = 180$).

Surface and bottom water salinity were significantly lower in the nearshore than at the shelf break in every season ($p < 0.001$; Figures 3 and 4). With the exception of spring (full water column) and summer bottom water, surface and bottom temperature also increased from nearshore to the shelf break in each season ($p < 0.004$; Figures 3 and 4). The lowest salinities were recorded in nearshore summer surface waters ($p < 0.001$), averaging 30.06 ± 0.37 PSU ($n = 28$). In the summer, midshelf surface waters were also significantly fresher than the other seasons ($p < 0.001$), due to heavy rainfall during the mission. The highest

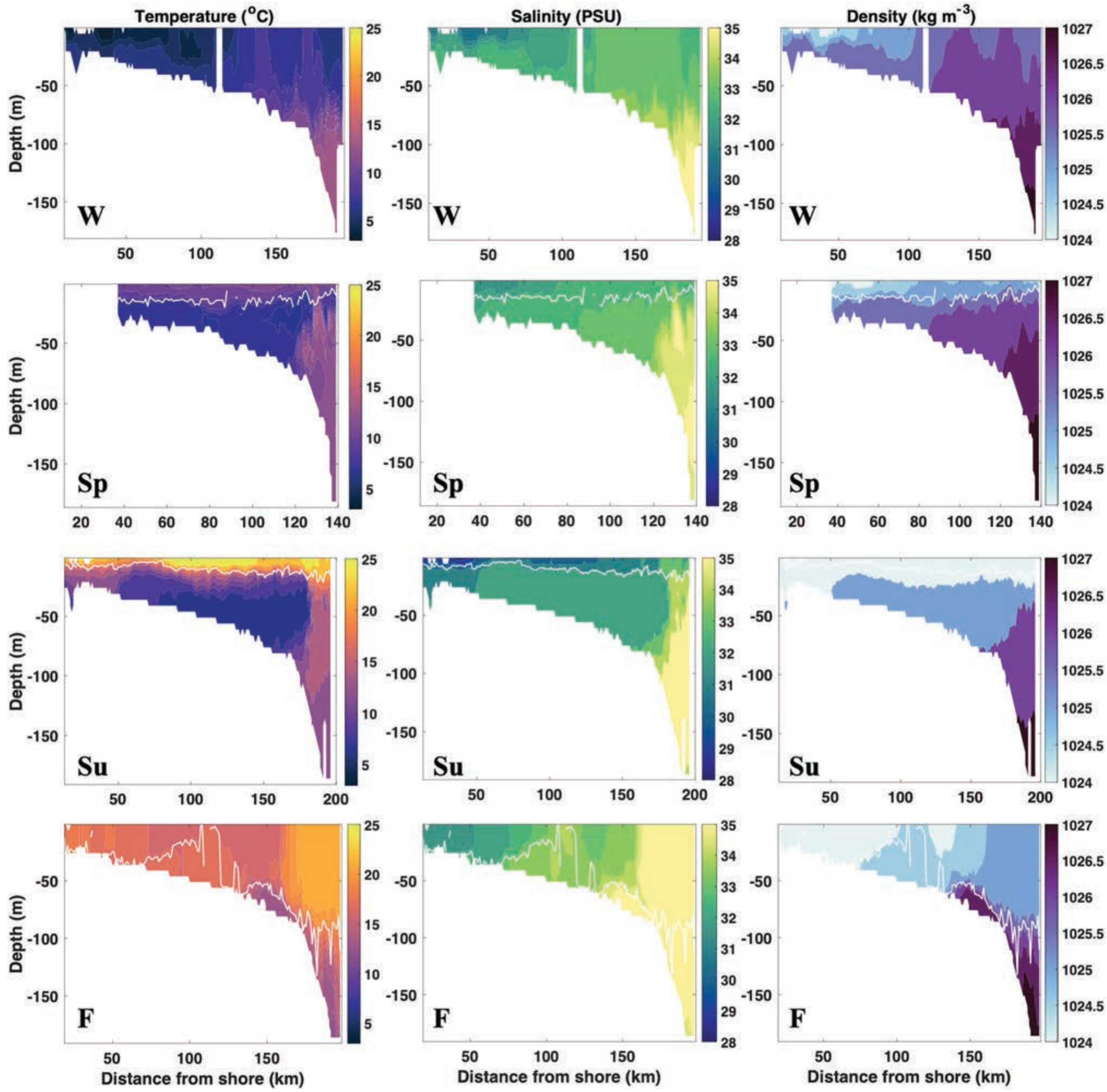

Figure 3. Contour plots of temperature, salinity, and density from four seasonal glider deployments in the MAB (W = winter, Sp = spring, Su = summer, and F = fall). Data shown are from the first cross-shelf transect of each deployment. Mixed layer depth (MLD) for each binned profile is plotted in white. Winter had no significant mixed layer. The nearshore region was defined as 1–40 km offshore, midshelf was 40–160 km offshore (40–120 km in spring), and the shelf break was >160 km offshore (>120 km offshore in spring).

salinities were recorded in fall shelf break surface and bottom waters ($p < 0.001$), averaging 35.66 ± 0.26 PSU ($n = 38$) and 35.37 ± 0.17 PSU ($n = 38$).

3.2.2. Biological Characteristics

Phytoplankton biomass varied seasonally as water column structure changed in the MAB (Figures 4 and 5). The deeply mixed fall water column and the productive spring water column had the highest 35-m integrated chlorophyll concentrations of 43.39 ± 11.23 mg m^{-2} ($n = 180$) and 42.82 ± 19.79 mg m^{-2} ($n = 129$), respectively ($p < 0.001$). Fall and spring integrated chlorophyll levels were not significantly different from one another. Winter and summer had significantly lower 35-m integrated chlorophyll concentrations than the seasons preceding them ($p < 0.001$).

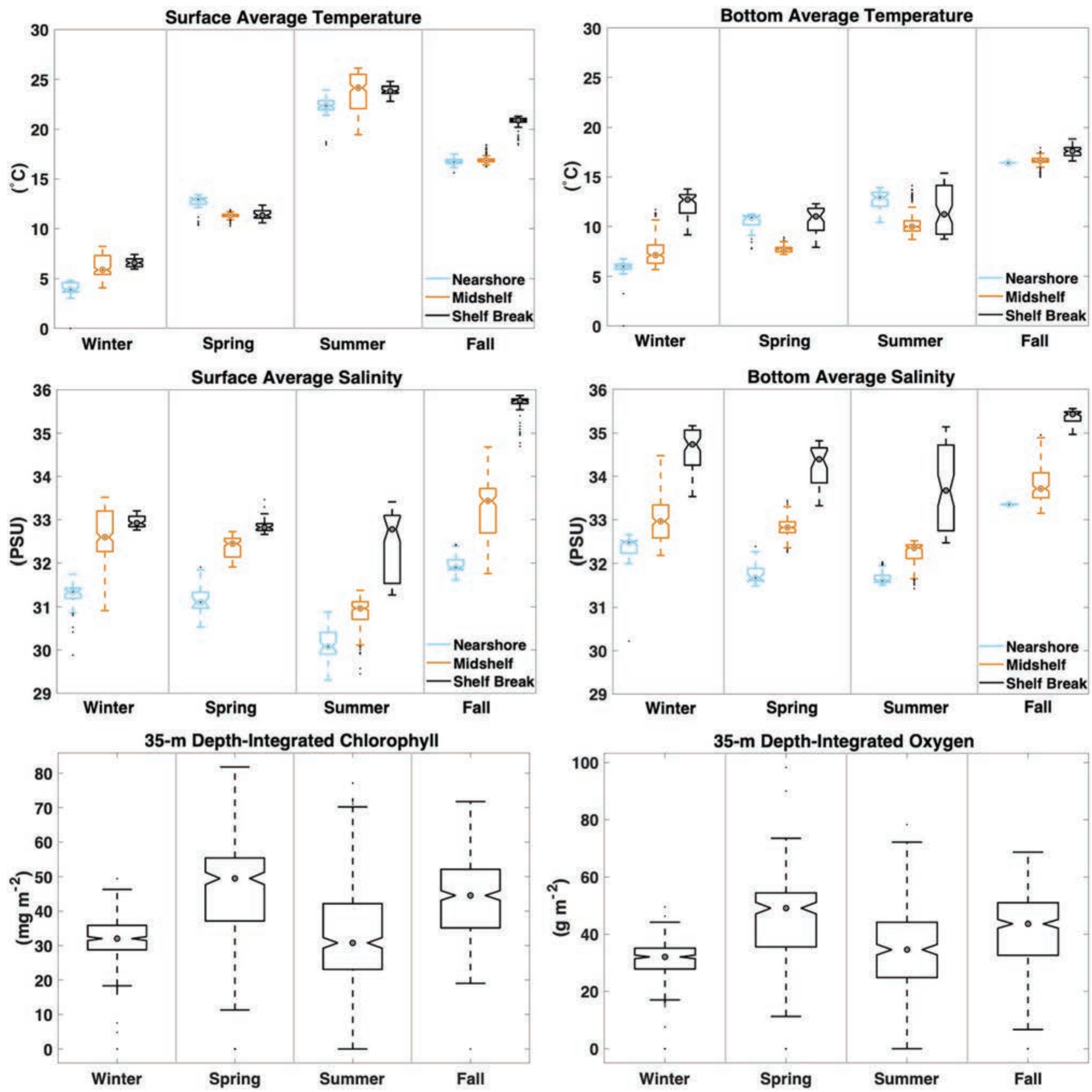

Figure 4. Comparisons of physical, biological, and chemical ocean properties during seasonal glider deployments. Targets indicate median values, box limits indicate the 25th to 75th percentiles, and whiskers represent the full range of data. Data points beyond 1.5 times the interquartile range away from the top or bottom of the box were identified as outliers, and are shown as black dots extending from the whiskers. Notches depict the 95% confidence interval around the median. If notches do not overlap, there is 95% confidence that the medians are different ($p < 0.05$).

In each binned profile, the chlorophyll maximum was identified as the 1-m depth bin with the highest 1-m depth-averaged chlorophyll concentration. Depth-averaged chlorophyll concentrations at the chlorophyll maximum were 1.55 ± 0.48 mg m^{-3} ($n = 187$) in winter, 3.35 ± 2.16 mg m^{-3} ($n = 129$) in spring, 2.52 ± 0.88 mg m^{-3} ($n = 188$) in summer, and 1.80 ± 0.58 ($n = 180$) mg m^{-3} in fall.

In each season, surface and bottom depth-averaged chlorophyll was highest in the nearshore and lowest at the shelf break ($p < 0.001$), except in fall bottom water which saw no significant spatial change (Figure 5). The highest depth-averaged chlorophyll concentrations occurred in nearshore spring bottom water (2.86 ± 0.49 mg m^{-3}, $n = 13$, $p < 0.001$), which captured the spring chlorophyll maximum layer. High

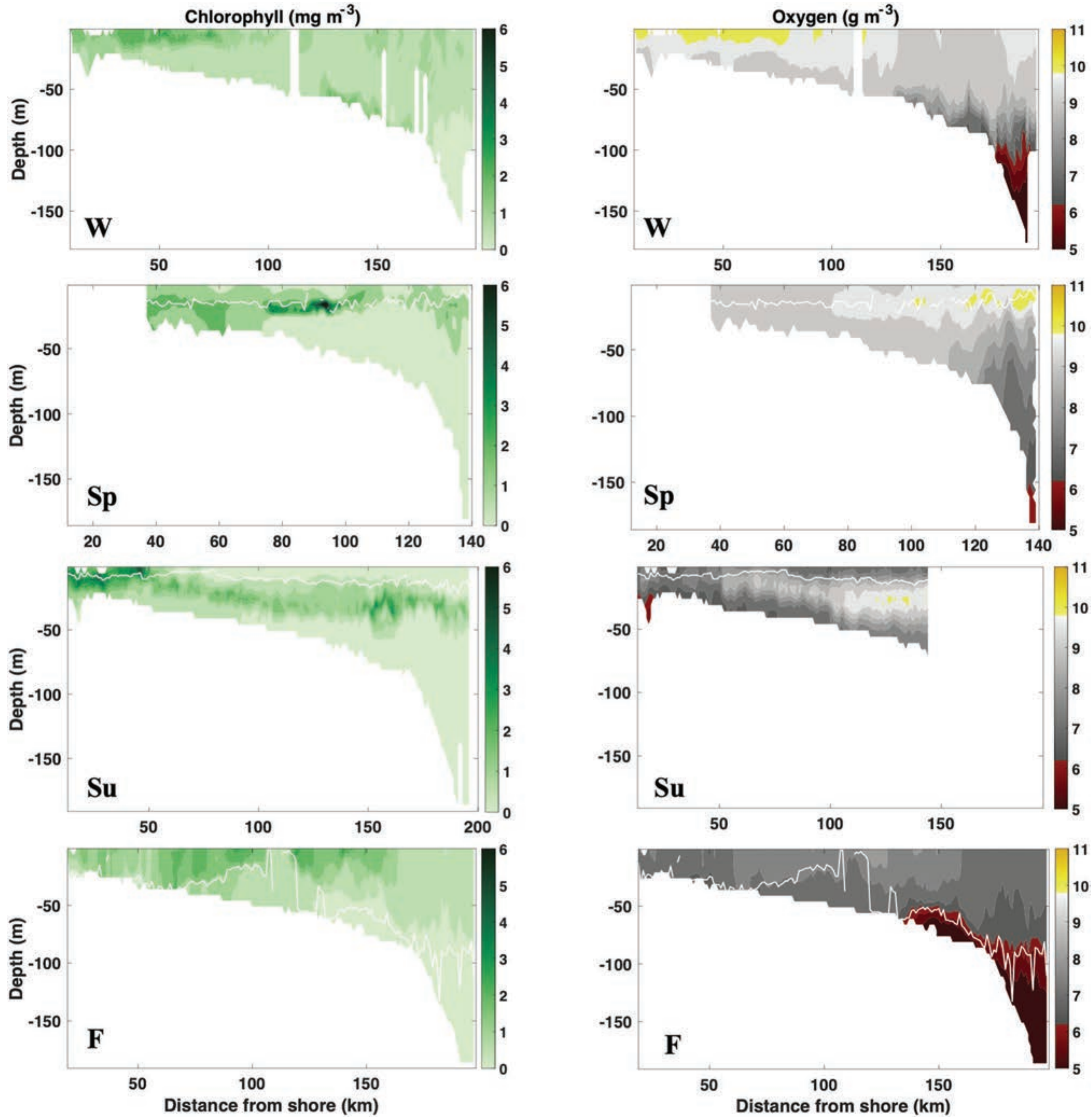

Figure 5. Contour plots of depth-averaged chlorophyll and oxygen from four seasonal glider deployments in the MAB (W = winter, Sp = spring, Su = summer, and F = fall). Data shown are from the first cross-shelf transect of each deployment. Mixed layer depth (MLD) for each binned profile is plotted in white. Winter had no significant mixed layer. The nearshore region was defined as 1–40 km offshore, midshelf was 40–160 km offshore (40–120 km in spring), and the shelf break was >160 km offshore (>120 km offshore in spring).

depth-averaged chlorophyll was also present in spring and summer nearshore surface waters, averaging 2.13 ± 0.71 mg m^{-3} ($n = 13$) and 2.30 ± 0.45 mg m^{-3} ($n = 28$), respectively.

3.2.3. Chemical Dynamics

3.2.3.1. Oxygen

The chlorophyll-rich, stratified spring and deeply mixed fall water columns exhibited the highest 35-m integrated DO concentrations of 41.55 ± 20.12 g m^{-2} ($n = 129$) and 41.86 ± 12.46 g m^{-2} ($n = 180$) ($p < 0.001$;

Figures 4 and 5). Like chlorophyll concentration, winter and summer 35 m integrated oxygen levels were significantly lower than both fall and spring ($p < 0.001$).

In spring, summer, and fall, high depth-averaged DO was observed at the chlorophyll maximum depth (Figure 5). Shelf break bottom waters exhibited the lowest depth-averaged DO concentrations in winter, spring, and fall ($p < 0.001$), averaging 6.20 ± 0.88 g m^{-3} ($n = 35$), 8.20 ± 0.49 g m^{-3} ($n = 20$), and 6.32 ± 0.36 g m^{-3} ($n = 39$), respectively. The DO optode malfunctioned shortly after summer deployment, so summer shelf break measurements are not available.

3.2.3.2. Carbonate System

Figures 6 and 7 display seasonal and spatial differences in the carbonate system. Full water column pH ranged from 7.701 to 8.166 throughout all seasons, while Ω_{arag} ranged from 0.83 to 3.72, and TA:DIC ranged from 1.019 to 1.180. Deployment-averaged pH was highest in winter and lowest in summer (Table S6). Deployment-averaged Ω_{arag} and TA:DIC were highest in fall and lowest in summer (Table S6). Areas that differed from the means were localized in space and time. For example, areas of high pH were associated with the chlorophyll maximum in spring and summer, and areas of high pH, Ω_{arag}, and TA:DIC were found at the shelf break in all seasons (Figure 6). Conversely, areas of low pH, Ω_{arag}, and TA:DIC were associated with the nearshore region in spring, summer, and fall, and with shelf bottom waters in the summer (Figure 6).

In summer and fall, surface and bottom pH, Ω_{arag}, and TA:DIC were lowest in the nearshore and significantly higher at the shelf break ($p < 0.001$; Figure 7). The highest spring pH, Ω_{arag}, and TA:DIC values were also present at the shelf break ($p < 0.005$, Figure 7). Winter followed a different spatial pattern, with surface and bottom pH highest in the nearshore and significantly lower at the shelf break ($p < 0.001$). Winter surface Ω_{arag} and TA:DIC were highest in the midshelf region ($p < 0.05$), while bottom Ω_{arag} and TA:DIC increased from nearshore to shelf break ($p < 0.002$).

In the nearshore, surface and bottom pH were highest in winter, averaging 8.124 ± 0.007 ($n = 31$) and 8.080 ± 0.014 (n = 31) respectively ($p < 0.005$; Figures 6 and 7). The lowest nearshore pH occurred in summer bottom waters ($p < 0.001$), averaging 7.827 ± 0.029 ($n = 28$). Bottom waters also reached a minimum in Ω_{arag} and TA:DIC in summer ($p < 0.03$), averaging 1.29 ± 0.11 and 1.048 ± 0.007 respectively ($n = 28$). Contrary to seasonal patterns in pH, nearshore surface water saw the highest Ω_{arag} and TA:DIC in the summer/fall and lowest in the winter/spring ($p < 0.001$).

In the midshelf, the highest seasonal pH occurred in well mixed, cold winter surface water ($p < 0.002$; Figures 3, 6, and 7). Average winter midshelf surface pH was 8.107 ± 0.013 ($n = 121$). Conversely, winter midshelf surface waters had low Ω_{arag} and TA:DIC, averaging 1.84 ± 0.09 and 1.082 ± 0.004, respectively ($n = 121$). The lowest midshelf pH occurred in summer surface and bottom water, averaging 7.934 ± 0.016 in the surface and 7.922 ± 0.053 in the bottom ($p < 0.001$, $n = 120$). Low pH summer bottom water was associated with the Cold Pool bottom water mass and also exhibited the lowest Ω_{arag} and TA:DIC in the midshelf (1.47 ± 0.15 and 1.059 ± 0.009, respectively; $p < 0.001$; $n = 120$). While summer midshelf bottom water had the lowest seasonal Ω_{arag} and TA:DIC, summer midshelf surface water had the highest values in the region, averaging 2.30 ± 0.18 and 1.101 ± 0.008 respectively ($p < 0.001$, $n = 120$), though these values were not significantly different than fall.

At the shelf break, a warm, salty water mass persisted throughout all four seasons (Figure 3). The highest shelf break Ω_{arag} and TA:DIC occurred in fall ($p < 0.001$), when this water mass mixed into the surface layer (Figure 6). There, Ω_{arag} averaged 3.13 ± 0.12 ($n = 39$) and TA:DIC averaged 1.138 ± 0.006 ($n = 39$). The lowest shelf break Ω_{arag} and TA:DIC occurred in winter surface waters ($p < 0.05$), averaging 1.73 ± 0.06 and 1.075 ± 0.003 ($n = 35$), respectively. The lowest seasonal shelf break pH occurred in summer surface waters ($p < 0.001$), averaging 7.969 ± 0.014 ($n = 39$).

4. Discussion

High-resolution data resulting from deployments of a glider equipped with novel pH sensor technology highlight seasonal and spatial carbonate chemistry dynamics in the MAB for the first time. Results underscore the importance of seasonality, water mass mixing, biological production, and freshwater inputs in controlling the carbonate system in the MAB.

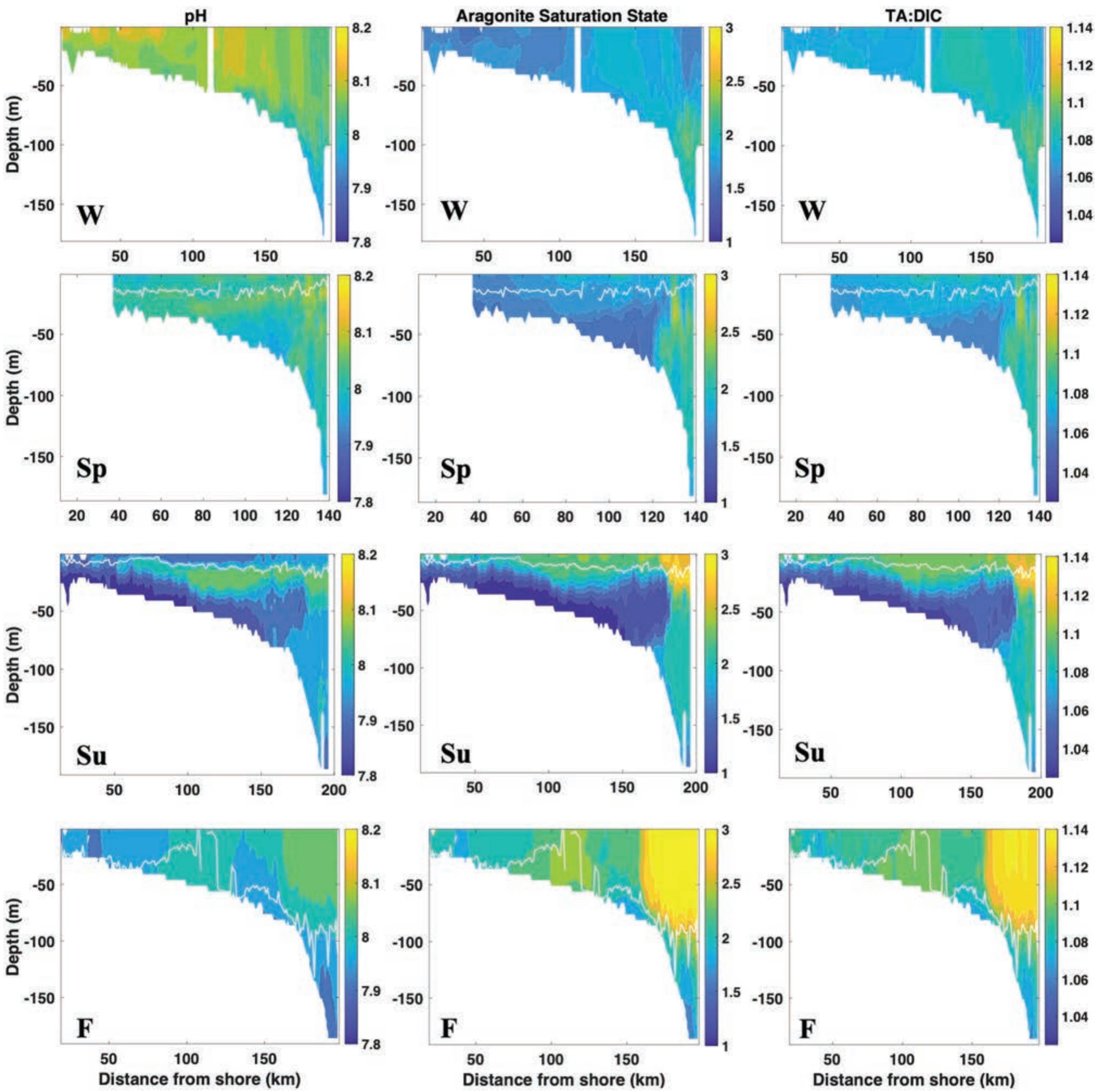

Figure 6. Contour plots of in situ pH, Ω_{arag}, and TA:DIC from four seasonal glider deployments in the MAB (W = winter, Sp = spring, Su = summer, and F = fall). Data shown are from the first cross-shelf transect of each deployment. Mixed layer depth (MLD) for each binned profile is plotted in white. Winter had no significant mixed layer. The nearshore region was defined as 1–40 km offshore, midshelf was 40–160 km offshore (40–120 km in spring), and the shelf break was >160 km offshore (>120 km offshore in spring).

4.1. Drivers of MAB Seasonality

Seasonal glider deployments recorded physical water column changes caused by intense MAB seasonality. Observations aligned with established MAB physical climatology (Castelao et al., 2010, 2008). Warming of surface waters in the spring and summer, combined with freshening of surface waters, increased the strength of stratification and trapped a Cold Pool water mass below the mixed layer. Cold Pool bottom water generally contains relatively fresh (<34 PSU) and cold (<10°C) water, with source water likely originating from the Labrador Sea (Z. Chen et al., 2018). Wind- and storm-driven seasonal overturn in the fall caused surface and Cold Pool bottom waters to mix, resulting in a cool, well-mixed water column that persisted through winter.

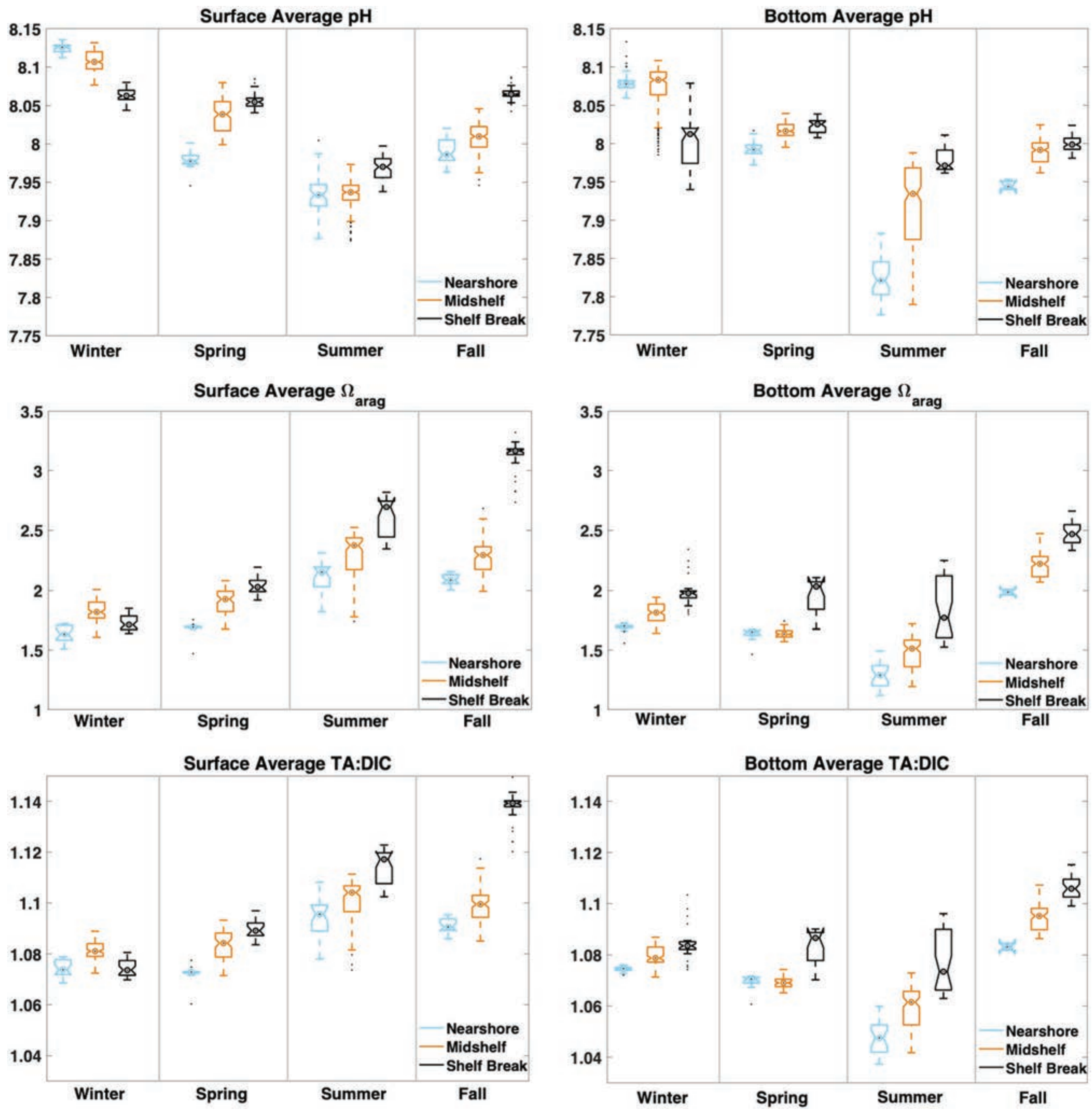

Figure 7. Comparisons of carbonate system parameters measured during and derived from seasonal glider deployments. Targets indicate median values, box limits indicate the 25th to 75th percentiles, and whiskers represent the full range of data. Data points beyond 1.5 times the interquartile range away from the top or bottom of the box were identified as outliers and are shown as black dots extending from the whiskers. Notches depict the 95% confidence interval around the median. If notches do not overlap, there is 95% confidence that the medians are different ($p < 0.05$).

The occurrence of low surface water Ω_{arag} and TA:DIC in winter and high Ω_{arag} and TA:DIC in summer surface waters supports the findings of Cai et al. (2020) who concluded that surface water Ω_{arag} and DIC are controlled additively by thermodynamic equilibrium and air-sea gas exchange in the MAB. Unlike Ω_{arag} and TA:DIC, shelf surface water pH during glider deployments exhibited a decoupling from the effect of gas exchange, with the highest pH recorded in winter and lowest pH values in summer. This indicated a more complicated system of seasonal surface pH drivers, including freshwater input (summer) and biological removal of CO_2 (winter), which acted on a time scale faster than gas equilibrium (Cai et al., 2020).

In areas and periods of dense chlorophyll biomass, primary producers remove CO_2 from the water, increasing DO and pH (Kemp et al., 1994). Fall and spring glider missions captured the highest seasonal integrated chlorophyll levels, due to high phytoplankton biomass. High fall integrated chlorophyll supports the findings of Y. Xu et al. (2011), who identified a bimodal cycle of biological production in the MAB, in which a dominant fall-winter phytoplankton bloom between the 20- and 60-m isobaths accounts for almost 60% of the region's annual chlorophyll production. This bloom forms when fall overturn injects nutrient-rich bottom water into the surface, promoting phytoplankton production. High productivity captured in the fall deployment led to high integrated DO and increased surface pH in the nearshore and midshelf. The second mode of MAB phytoplankton production described by Y. Xu et al. (2011) indicates a less dominant spring-summer bloom triggered by stratification, which allows phytoplankton to overcome light limitation caused by deep mixing during the winter. Spring and summer glider deployments captured the development of strong seasonal stratification, isolating a chlorophyll maximum just below the mixed layer predominantly in the midshelf region that was colocated with high pH (Figure 6).

High depth-integrated chlorophyll and DO in the fall and spring were followed by periods of lower integrated chlorophyll and DO in the winter and summer. In summer, this was likely influenced by Cold Pool bottom water, where respiration of surface-derived particulate carbon produces CO_2 and reduces DO. Once seasonal stratification is set up, the Cold Pool has little ventilation to seawater above the thermocline, and accumulation of respired CO_2 reduces pH, Ω_{arag}, and buffering capacity for CO_2 (Cai et al., 2011, 2017; Waldbusser & Salisbury, 2014; Wootton et al., 2008). Our summer mission captured the full extent of low bottom water pH, Ω_{arag}, and TA:DIC associated with stratification and the Cold Pool (Figures 6 and 7).

In summer nearshore surface and bottom waters, high-low-high cycles in pH, Ω_{arag}, and TA:DIC appeared in ~20-km increments (Figure 8). Cycles observed there align with the glider's average horizontal movement of 20 km day^{-1}, indicating potential diel variability in pH, Ω_{arag}, and TA:DIC. Daily swings in surface water pH were as large as 0.145 pH units, corresponding to swings in surface Ω_{arag} of 0.52 and TA:DIC of 0.033. These pH swings were about half the amplitude of those observed previously in nearby Mid-Atlantic estuaries, which can exhibit swings of up to 0.26 pH units day^{-1}, attributed to high productivity and shallow waters (Baumann & Smith, 2017). The pattern of daily variability was not always consistent (day vs. night), suggesting that these complex carbonate chemistry dynamics are likely driven by a combination of biological productivity, temperature swings, fluctuations in salinity, and mixing. For example, pH and Ω_{arag} in nearshore bottom water exhibited strong positive correlations with temperature and chlorophyll (Spearman's $r > 0.75$, $p < 0.001$) and strong negative correlations with salinity (Spearman's $r < -0.67$, $p < 0.001$). In nearshore surface water, these correlations were weaker and, in one case, the direction of the correlation flipped (Spearman's r between Ω_{arag} and chlorophyll $= -0.50$, $p < 0.001$). Therefore, trends in pH and Ω_{arag} cannot be explained by any one driver. Additional observations are needed in order to thoroughly analyze and establish the relative importance of these drivers to diel variability.

4.2. Year-Round Water Column Features

In every season, nearshore waters experienced the lowest surface salinities, highlighting the influence of freshwater inputs to the coastal system (Castelao et al., 2010). During the summer, freshening extended into the midshelf due to heavy rainfall and typical seasonal freshening due to peak seasonal runoff from the Hudson River (Castelao et al., 2010; Richaud et al., 2016). Freshwater inputs from rivers and storms introduce low TA water into the coastal system, decreasing CO_2 buffering capacity (Siedlecki et al., 2017; Waldbusser & Salisbury, 2014). Spring, summer, and fall exhibited their lowest respective pH, Ω_{arag}, and TA:DIC in nearshore waters compared to the midshelf and shelf break regions. Summer nearshore and midshelf surface waters had the lowest seasonal pH, pointing to freshwater input as a major driver of pH there. However, as discussed in section 4.1, summer nearshore and midshelf surface waters had the highest seasonal Ω_{arag} and TA:DIC, indicating that thermodynamic control was a stronger influence on Ω_{arag} and TA:DIC than salinity. These complex carbonate system dynamics indicate that freshwater influence is a complicated but important driver of the carbonate system on the shelf.

Throughout all seasonal deployments, a warm (>12°C), salty (>35 PSU) water mass persisted at the continental shelf break. This slope water mass signified that the glider traveled through a shelf-break front, formally called the MAB shelf-break jet, which is influenced by warm, saline Gulf Stream waters entrained into

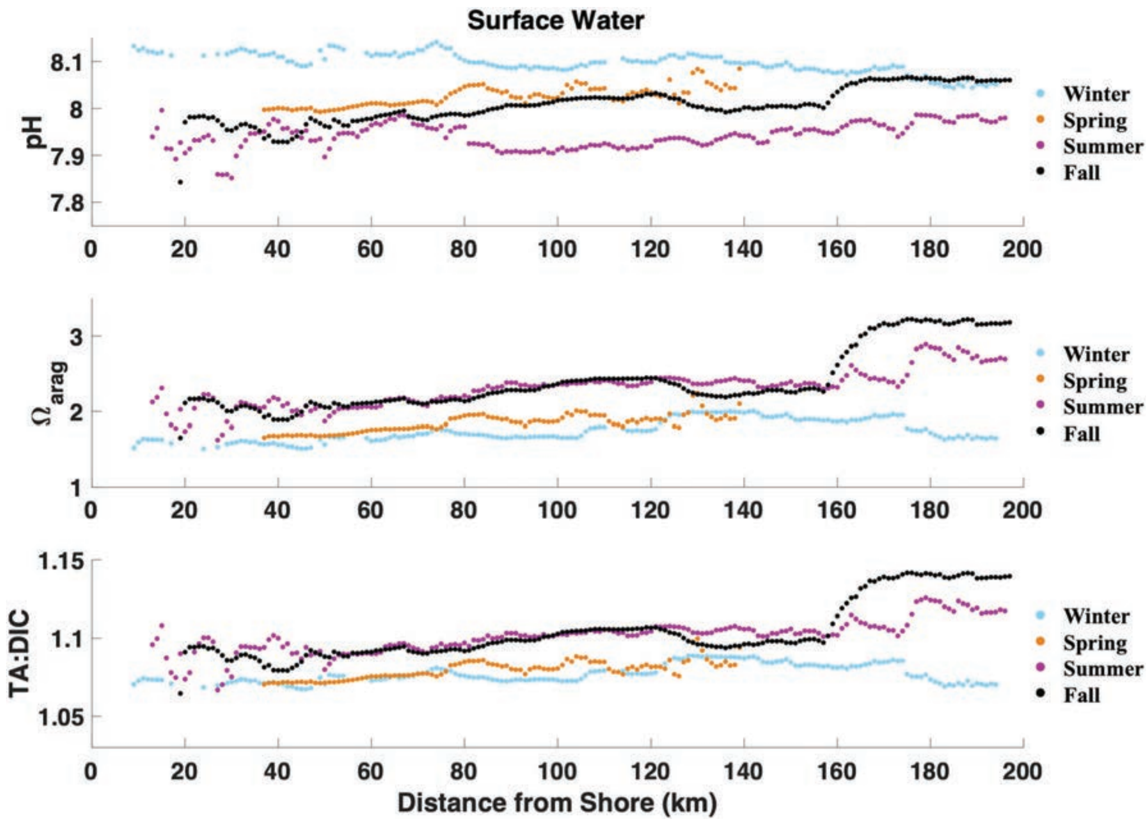

Figure 8. Seasonal differences in surface water pH (top), Ω_{arag} (middle), and TA:DIC (bottom) expressed as a function of distance from shore. Surface water is defined as above MLD in spring, summer, and fall, and as the top 5 m in winter. Data presented are from the entire deployment and are 1 m depth and 1 km distance binned.

the MAB by eddies (K. Chen & He, 2010; Fratantoni et al., 2001; Linder & Gawarkiewicz, 1998; Wanninkhof et al., 2015). The front was pushed progressively farther off-shelf with the onset and persistence of seasonal stratification and infiltrated back onto the shelf during fall overturn, following MAB shelf-break jet climatology described by Linder and Gawarkiewicz (1998). The deepest water sampled at the shelf break (>150 m) exhibited the lowest depth-averaged oxygen levels in each deployment, suggesting that this water mass is not well ventilated to the atmosphere, and ongoing respiration there depletes oxygen and adds CO_2. Despite ongoing respiration, shelf break jet deep water had high Ω_{arag} and TA:DIC, reflecting its Gulf Stream source and consistently high salinity levels. High TA:DIC indicated that this water mass had a high buffering capacity for CO_2 and therefore had high pH in spring, summer, and fall, regardless of high net respiration.

The intrusion of the highly buffered shelf break jet onto the shelf during fall overturn, along with the high fall phytoplankton biomass and a decrease in freshwater input, resulted in a well-mixed water column with high pH, Ω_{arag}, and TA:DIC. High pH persisted through winter, while thermodynamic interactions led to low winter Ω_{arag} and TA:DIC after the fall bloom. This suggests that seasonal intrusion of the shelf break jet could be an important mitigator of acidification on the MAB shelf during fall.

4.3. Potential Ecological Implications

It is important to consider natural seasonal, spatial, and depth variability when investigating MAB habitat suitability. Surface water pH, Ω_{arag}, and TA:DIC exhibited seasonal differences across the MAB shelf, with Ω_{arag} and TA:DIC diverging to a greater extent at the shelf break (Figure 8). Bottom water pH exhibited seasonal swings on the MAB shelf, but values converged at the continental shelf break, while bottom water Ω_{arag} and TA:DIC saw seasonal divergence at the shelf break (Figure 9). Seasonality in pH, Ω_{arag}, and TA:DIC across the shelf and shelf break demonstrated seasonal and spatial fluctuations in carbonate system drivers in the MAB.

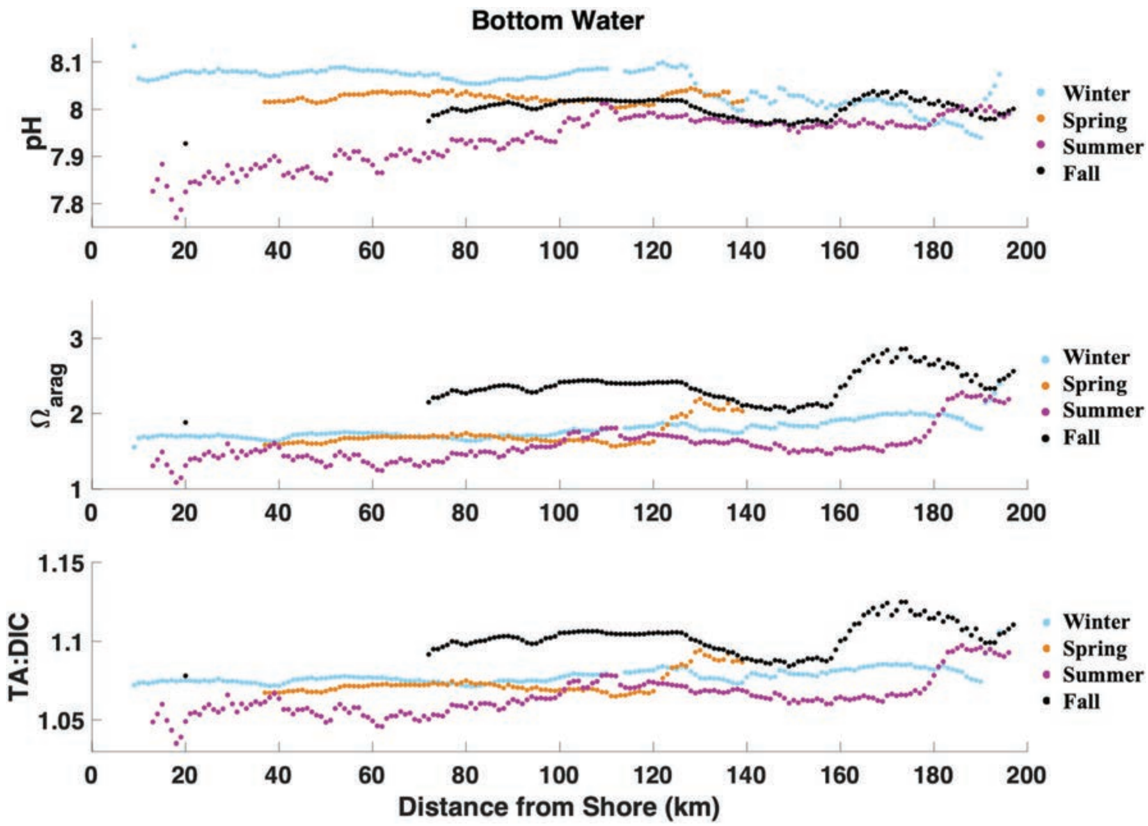

Figure 9. Seasonal differences in bottom water pH (top), Ω_{arag} (middle), and TA:DIC (bottom) expressed as a function of distance from shore. Bottom water is defined as below MLD in spring, summer, and fall, and as the bottom 5 m in winter. Data presented are from the entire deployment and are 1 m depth and 1 km distance binned.

Shelf water masses, specifically the MAB Cold Pool, have been linked to the distribution and recruitment of economically important fish species, including the calcifying shellfish Atlantic sea scallop (*Placopecten magellanicus*) and Atlantic surfclam (*Spisula solidissima*), which are vulnerable to acidification (Colvocoresses & Musick, 1984; Cooley et al., 2015; Steves et al., 2000; Sullivan et al., 2000; Weinberg, 2005). These organisms are able to survive and reproduce through observed seasonal swings in carbonate chemistry on the MAB shelf, but the extent to which survival and reproduction may be negatively impacted by current levels of pH and Ω_{arag} is unknown. Potential vulnerability of these organisms during late summer/early fall spawning events on the MAB shelf should be a consideration for future fishery management.

4.4. Limitations and Benefits

While the pH glider has undergone significant field testing for robustness, it is not exempt from limitations common to autonomous underwater vehicles (AUVs) and other sensors used in oceanographic field work. Gliders deployed in areas of high productivity are subject to biofouling over time, which can increase offsets between glider and discrete pH measurements (Saba, Wright-Fairbanks, et al., 2019). Increased offsets from deployment to recovery in winter, summer, and fall might indicate biofouling throughout deployment. Primary production associated with algal biofouling near the sensor intake would remove CO_2 from water in close vicinity to the glider, thereby increasing pH. Additionally, biofouling from barnacles or juvenile bivalves can occur on gliders. Saba, Wright-Fairbanks, et al. (2019) reported an instance of biofouling by a juvenile clam which settled onto the glider pH sensor intake valve. In that case, respiration would decrease pH around the sensor. Increases in offsets over time can also occur due to pH sensor drift. Sensor drift generally arises due to a lack of full conditioning to Br^- anion in seawater and is a common issue for autonomous pH monitoring platforms (Johnson et al., 2016).

Seasonal TA-salinity relationships derived from discrete samples perform generally well when compared to the CANYON-B algorithm and discrete sample TA values. Large offsets between discrete and regression-based TA corresponded to a break in the TA-salinity relationship at approximately 30–31 PSU (Figure S1). These offsets were particularly large in summer and fall, with discrete and calculated TA differing by up to 51.1 and 87.6 μmol kg^{-1} respectively (Table S5). Uncertainty in Ω_{arag} and TA:DIC due to TA uncertainty was as extreme as −0.08 and 0.0013 (fall; Table S4). However, the difference between CANYON-B-estimated TA and salinity-derived TA was quite small, averaging ~0.1%. Because of this, we are confident that seasonal TA-salinity regressions are applicable to full glider deployments.

While none of the seasonal deployment pH offsets described here exceeded manufacturer specifications for the sensor, changes in offsets over time underscore the importance of taking discrete samples at each glider deployment and recovery to ensure continued accuracy and data quality. These missions therefore require a vessel with water sampling capabilities, but the data provided during the otherwise automated 30- to 60-day missions far outweigh the cost to collect data of this resolution during major research cruises (Schofield et al., 2010). Furthermore, gliders have proven their effectiveness for high-quality observations in a range of coastal and open ocean environments, including locations that are not conducive to vessel operation or human presence (e.g., polar environments and hurricane seas) (Testor et al., 2019).

5. Significance

The work presented here highlights the distinct capability of an autonomous Slocum glider equipped with a deep-ISFET based pH sensor to make highly accurate, high-resolution observations of the marine carbonate system. The use of pH glider technology can be scaled up to address regional, national, and global OA observing needs. Using this glider sensor suite, we have observed seasonal patterns in the carbonate system directly associated with changes in other physical, biological, and chemical properties. While it is beyond the scope of this paper to quantify the relative importance of different carbonate system drivers, these data make clear that several drivers impact the strength of acidification. These include air-sea CO_2 exchange, seasonal stratification, biological activity, and freshwater input, as well as physical mixing of the MAB shelf break front. Importantly, data presented here describe the typical seasonal patterns of carbonate system dynamics in the MAB, but absolute values will change from year-to-year due to differences in regional climate, temperature, precipitation, wind patterns, and storm activity. Continued seasonal glider observation efforts, together with other carbonate monitoring platforms, will assist in developing a mean carbonate chemistry climatology for the MAB. This will help to inform the design of laboratory experiments investigating the response of commercially important species to acidification using realized carbonate system values and variability (Goldsmith et al., 2019; Saba, Goldsmith, et al., 2019). Furthermore, ongoing monitoring efforts can be used to identify areas or time periods prone to acidification due to interaction with other potential stressors, and the derivation of synergistic relationships between these variables. Continued simultaneous collection of chemical, physical, and biological metrics will allow the development of algorithms linking carbonate chemistry to other ocean properties. These quantitative relationships are necessary to develop broader predictive forecast models for the coastal ecosystem, which will ultimately aid in fisheries management planning and mitigation of short-term acidification events in the MAB.

Acknowledgments
We thank Rutgers University Center for Ocean Observing Leadership (RU COOL) glider technicians: David Aragon, Nicole Waite, Chip Haldeman, Laura Nazzaro, and John Kerfoot for their efforts in glider preparation, deployment logistics, fieldwork, mission piloting, and data management. We also thank Rutgers undergraduate alumni Brandon Grosso and Laura Wiltsee for their dedicated work with gliders in the field and lab. We acknowledge RU COOL faculty Oscar Schofield, Scott Glen, Josh Kohut, and RU COOL manager Michael Crowley for facility support. We appreciate Yui Takeshita (Monterey Bay Aquarium Research Institute) for his support on data interpretation. Finally, we thank our colleagues at SeaBird Scientific including Dave Murphy, Cristina Orrico, Vlad Simontov, and Dave Walter, along with Clara Hulburt and Christopher DeCollibus at Teledyne Webb Research for their technical expertise and support. This project was funded by National Science Foundation's Ocean Technology and Interdisciplinary Coordination program (National Science Foundation [NSF] OCE1634520 and OCE1634582). E. W-F. received support from the Mid-Atlantic Sea Grant/NOAA OAP Graduate Research Fellowship (NA18OAR4170087) and the Rutgers University School of Environmental and Biological Sciences Excellence Fellowship.

Data Availability Statement

Data supporting the conclusions made in this paper can be obtained online (at http://slocum-data.marine.rutgers.edu/erddap/search/index.html?page=1&itemsPerPage=1000&searchFor=ru30).

References

Baumann, H., & Smith, E. M. (2017). Quantifying metabolically driven pH and oxygen fluctuations in US nearshore habitats at diel to interannual time scales. *Estuaries and Coasts*, *41*(4), 1102–1117. https://doi.org/10.1007/s12237-017-0321-3

Bittig, H. C., Steinhoff, T., Claustre, H., Fiedler, B., Williams, N. L., Sauzède, R., et al. (2018). An alternative to static climatologies: Robust estimation of open ocean CO_2 variables and nutrient concentrations from T, S, and O_2 data using Bayesian neural networks. *Frontiers in Marine Science*, *5*. https://doi.org/10.3389/fmars.2018.00328

Bresnahan, P. J., Martz, T. R., Takeshita, Y., Johnson, K. S., & LaShomb, M. (2014). Best practices for autonomous measurement of seawater pH with the Honeywell Durafet. *Methods in Oceanography*, *9*, 44–60. https://doi.org/10.1016/j.mio.2014.08.003

Cai, W.-J., Hu, X., Huang, W.-J., Jiang, L.-Q., Wang, Y., Peng, T.-H., & Zhang, X. (2010). Alkalinity distribution in the western North Atlantic Ocean margins. *Journal of Geophysical Research*, *115*, C08014. https://doi.org/10.1029/2009JC005482

Cai, W.-J., Hu, X., Huang, W.-J., Murrell, M. C., Lehrter, J. C., Lohrenz, S. E., et al. (2011). Acidification of subsurface coastal waters enhanced by eutrophication. *Nature Geoscience*, *4*(11), 766–770. https://doi.org/10.1038/ngeo1297

Cai, W.-J., Huang, W. J., Luther, G. W. 3rd, Pierrot, D., Li, M., Testa, J., et al. (2017). Redox reactions and weak buffering capacity lead to acidification in the Chesapeake Bay. *Nature Communications*, *8*(1), 369. https://doi.org/10.1038/s41467-017-00417-7

Cai, W.-J., Xu, Y. Y., Feely, R. A., Wanninkhof, R., Jonsson, B., Alin, S. R., et al. (2020). Controls on surface water carbonate chemistry along North American ocean margins. *Nature Communications*, *11*(1), 2691. https://doi.org/10.1038/s41467-020-16530-z

Carvalho, F., Kohut, J., Oliver, M. J., & Schofield, O. (2017). Defining the ecologically relevant mixed-layer depth for Antarctica's coastal seas. *Geophysical Research Letters*, *44*, 338–345. https://doi.org/10.1002/2016GL071205

Castelao, R., Glenn, S., & Schofield, O. (2010). Temperature, salinity, and density variability in the central Middle Atlantic Bight. *Journal of Geophysical Research*, *115*, C10005. https://doi.org/10.1029/2009JC006082

Castelao, R., Glenn, S., Schofield, O., Chant, R., Wilkin, J., & Kohut, J. (2008). Seasonal evolution of hydrographic fields in the central middle Atlantic bight from glider observations. *Geophysical Research Letters*, *35*, L03617. https://doi.org/10.1029/2007GL032335

Chen, B., Cai, W.-J., & Chen, L. (2015). The marine carbonate system of the Arctic Ocean: Assessment of internal consistency and sampling considerations, summer 2010. *Marine Chemistry*, *176*, 174–188. https://doi.org/10.1016/j.marchem.2015.09.007

Chen, K., & He, R. (2010). Numerical investigation of the Middle Atlantic Bight shelfbreak frontal circulation using a high-resolution ocean hindcast model. *Journal of Physical Oceanography*, *40*(5), 949–964. https://doi.org/10.1175/2009jpo4262.1

Chen, Z., Curchitser, E., Chant, R., & Kang, D. (2018). Seasonal variability of the cold pool over the Mid-Atlantic Bight continental shelf. *Journal of Geophysical Research: Oceans*, *123*, 8203–8226. https://doi.org/10.1029/2018JC014148

Clayton, T. D., & Byrne, R. H. (1993). Spectrophotometric seawater pH measurements: Total hydrogen ion concentration scale calibration of m-cresol purple and at-sea results. *Deep-Sea Research*, *40*(10), 2115–2129.

Colvocoresses, J. A., & Musick, J. A. (1984). Species associations and community composition of Middle Atlantic Bight continental shelf demersal fishes. VIMS Articles, 625.

Cooley, S. R., Rheuban, J. E., Hart, D. R., Luu, V., Glover, D. M., Hare, J. A., & Doney, S. C. (2015). An integrated assessment model for helping the United States sea scallop (*Placopecten magellanicus*) fishery plan ahead for ocean acidification and warming. *PLoS ONE*, *10*(5), e0124145. https://doi.org/10.1371/journal.pone.0124145

DelValls, T. A., & Dickson, A. G. (1998). The pH of buffers based on 2-amino-2-hydroxymethyl-1,3-propanediol ('tris') in synthetic sea water. *Deep Sea Research*, *45*, 1541–1554.

Dickson, A. (1990). Standard potential of the reaction: AgCl(s) + 1/2H2(g) = Ag(s) + HCl (aq), and the standard acidity constant of the ion HSO4- in synthetic sea water from 273.15 to 318.15 K. *Journal of Chemical Thermodynamics*, *22*, 113–127.

Dickson, A., & Millero, F. J. (1987). A comparison of the equilibrium constants for the dissociation of carbonic acid in seawater media. *Deep-Sea Research*, *34*(10), 1733–1743.

Dlugokencky, E., & Tans, P. (2020). Trends in atmospheric carbon dioxide. NOAA Earth System Research Laboratory.

Doney, S. C., Fabry, V. J., Feely, R. A., & Kleypas, J. A. (2009). Ocean acidification: The other CO_2 problem. *Annual Review of Marine Science*, *1*, 169–192. https://doi.org/10.1146/annurev.marine.010908.163834

Egleston, E. S., Sabine, C. L., & Morel, F. M. M. (2010). Revelle revisited: Buffer factors that quantify the response of ocean chemistry to changes in DIC and alkalinity. *Global Biogeochemical Cycles*, *24*, GB1002. https://doi.org/10.1029/2008GB003407

Fratantoni, P. S., Pickart, R. S., Torres, D. J., & Scotti, A. (2001). Mean structure and dynamics of the shelfbreak jet in the Middle Atlantic Bight during fall and winter. *Journal of Physical Oceanography*, *31*, 2135–2156.

Friedrich, T., Timmermann, A., Abe-Ouchi, A., Bates, N. R., Chikamoto, M. O., Church, M. J., et al. (2012). Detecting regional anthropogenic trends in ocean acidification against natural variability. *Nature Climate Change*, *2*(3), 167–171. https://doi.org/10.1038/nclimate1372

Gattuso, J., Magnan, A., Bille, R., Cheung, W. W. L., Howes, E. L., Joos, F., et al. (2015). Contrasting futures for ocean and society from different anthropogenic CO_2 emissions scenarios. *Science Magazine*, *349*(6243). https://doi.org/10.1126/10.1126/science.aac4722

Gazeau, F., Quiblier, C., Jansen, J. M., Gattuso, J.-P., Middelburg, J. J., & Heip, C. H. R. (2007). Impact of elevated CO_2 on shellfish calcification. *Geophysical Research Letters*, *34*, L07603. https://doi.org/10.1029/2006GL028554

Gledhill, D., White, M., Salisbury, J., Thomas, H., Misna, I., Liebman, M., et al. (2015). Ocean and coastal acidification off New England and Nova Scotia. *Oceanography*, *25*(2), 182–197. https://doi.org/10.5670/oceanog.2015.41

Gobler, C. J., & Talmage, S. C. (2013). Short- and long-term consequences of larval stage exposure to constantly and ephemerally elevated carbon dioxide for marine bivalve populations. *Biogeosciences*, *10*(4), 2241–2253. https://doi.org/10.5194/bg-10-2241-2013

Gobler, C. J., & Talmage, S. C. (2014). Physiological response and resilience of early life-stage eastern oysters (*Crassostrea virginica*) to past, present and future ocean acidification. *Conservation Physiology*, *2*(1), cou004. https://doi.org/10.1093/conphys/cou004

Goldsmith, K. A., Lau, S., Poach, M. E., Sakowicz, G. P., Trice, T. M., Ono, C. R., et al. (2019). Scientific considerations for acidification monitoring in the U.S. Mid-Atlantic Region. *Estuarine, Coastal and Shelf Science*, *225*. https://doi.org/10.1016/j.ecss.2019.04.023

Gruber, N., Clement, D., Carter, B. R., Feely, R. A., van Heuven, S., Hoppema, M., et al. (2019). THe oceanic sink for anthropogenic CO_2 from 1994 to 2007. *Science*, *363*, 1193–1199.

Hare, J. A., Morrison, W. E., Nelson, M. W., Stachura, M. M., Teeters, E. J., Griffis, R. B., et al. (2016). A vulnerability assessment of fish and invertebrates to climate change on the northeast U. S. continental shelf. *PLoS ONE*, *11*(2), e0146756. https://doi.org/10.1371/journal.pone.0146756

Hettinger, A., Sanford, E., Hill, T. M., Russell, A. D., Sato, K. N. S., Hoey, J., et al. (2012). Persisten carry-over effects of planktonic exposure to ocean acidification in the Olympic oyster. *Eology*, *93*(12), 2758–2768.

Houghton, R. W., Shlitz, R., Beardsley, R. C., Butman, B., & Chamberlin, J. L. (1982). The Middle Atlantic Bight Cold Pool: Evolution of the temperature structure during summer 1979. *American Meteoroligcal Society*, *12*, 1019–1029.

Huang, W.-J., Wang, Y., & Cai, W.-J. (2012). Assessment of sample storage techniques for total alkalinity and dissolved inorganic carbon in seawater. *Limnology and Oceanography: Methods*, *10*(9), 711–717. https://doi.org/10.4319/lom.2012.10.711

Huret, M., Bourriau, P., Doray, M., Gohin, F., & Petitgas, P. (2018). Survey timing vs. ecosystem scheduling: Degree-days to underpin observed interannual variability in marine ecosystems. *Progress in Oceanography*, *166*, 30–40. https://doi.org/10.1016/j.pocean.2017.07.007

IOOS. (2019). Manual for real-time quality control of pH data observations: A guide to quality control and quality assurance for pH observations. https://doi.org/10.25923/111k-br08

IPCC. (2019). Summary for policymakers. IPCC special report on the ocean and cryosphere in a changing climate.

Johnson, K. S., Jannasch, H. W., Coletti, L. J., Elrod, V. A., Martz, T. R., Takeshita, Y., et al. (2016). Deep-Sea DuraFET: A pressure tolerant pH sensor designed for global sensor networks. *Analytical Chemistry*, *88*(6), 3249–3256. https://doi.org/10.1021/acs.analchem.5b04653

Johnson, K. S., Plant, J. N., & Maurer, T. L. (2017). Processing BGC-Argo ph data at the DAC level. https://doi.org/10.13155/57195

Kemp, P. F., Falkowski, P. G., Flagg, C. N., Phoel, W. C., Smith, S. L., Wallace, D. W. R., & Wirick, C. D. (1994). Modeling vertical oxygen and carbon flux during stratified spring and summer conditions on the continental shelf, Middle Atlantic Bight, eastern U. S. A. *Deep Sea Research*, *41*(2/3), 629–655.

Kohut, J., Haldeman, C., & Kerfoot, J. (2014). Monitoring dissolved oxygen in New Jersey coastal waters using autonomous gliders. Environmental Protection Agency Office of Research and Developmoent.

Levin, J., Wilkin, J., Fleming, N., & Zavala-Garay, J. (2018). Mean circulation of the Mid-Atlantic Bight from a climatological data assimilative model. *Ocean Modelling*, *128*, 1–14. https://doi.org/10.1016/j.ocemod.2018.05.003

Lewis, E., & Wallace, D. W. R. (1998). Program developed for CO_2 system calculations.

Linder, C. A., & Gawarkiewicz, G. (1998). A climatology of the shelfbreak front in the Middle Atlantic Bight. *Journal of Geophysical Research*, *103*(C9), 18,405–18,423. https://doi.org/10.1029/98JC01438

Liu, X., Patsavas, M. C., & Byrne, R. H. (2011). Purification and characterization of meta-cresol purple for spectrophotometric seawater pH measurements. *Environmental Science & Technology*, *45*(11), 4862–4868. https://doi.org/10.1021/es200665d

Lorbacher, K., Dommenget, D., Niiler, P. P., & Köhl, A. (2006). Ocean mixed layer depth: A subsurface proxy of ocean-atmosphere variability. *Journal of Geophysical Research*, *111*, C07010. https://doi.org/10.1029/2003JC002157

Martz, T. R., McLaughlin, K., & Weisberg, S. (2015). Best Practices for autonomous measurement of seawater pH with the Honeywell Durafet pH sensor. California Current Acidification Network (C-CAN).

Mehrbach, C., Culberson, C. H., Hawley, J. E., & Pytkowicz, R. M. (1973). Measurement of the apparent dissociation constants of carbonic acid in seawater at atmospheric pressure. *Limnology and Oceanography*, *18*(6), 897–907.

Melzner, F., Mark, F. C., Seibel, B. A., & Tomanek, L. (2019). Ocean acidification and coastal marine invertebrates: Tracking CO_2 effects from seawater to the cell. *Annual Review of Marine Science*, *12*, 12.11–12.25. https://doi.org/10.1146/annurev-marine-010419-010658

Miller, A. W., Reynolds, A. C., Sobrino, C., & Riedel, G. F. (2009). Shellfish face uncertain future in high CO_2 world: Influence of acidification on oyster larvae calcification and growth in estuaries. *PLoS ONE*, *4*(5), e5661. https://doi.org/10.1371/journal.pone.0005661

Millero, F. J. (1986). The pH of estuarine waters. *Limnology and Oceanography*, *31*(4), 839–847.

Musial, W., Elliott, D., Fields, J., Parker, Z., Scott, G., & Draxl, C. (2013). Assessment of offshore wind energy leasing areas for the BOEM New Jersey wind energy area. National Renewable Energy Laboratory Technical Reports.

NEFSC. (2020). State of the ecosystem 2020: Mid-Atlantic. NOAA Fisheries Reports.

NRC (2010). *Ocean acidification: A national strategy to meet the challenges of a changing ocean*. New York: The National, Academies Press. https://doi.org/10.17226/12904

Orr, J. C., Fabry, V. J., Aumont, O., Bopp, L., Doney, S. C., Feely, R. A., et al. (2005). Anthropogenic ocean acidification over the twenty-first century and its impact on calcifying organisms. *Nature*, *437*(7059), 681–686. https://doi.org/10.1038/nature04095

Pan, T. C., Applebaum, S. L., & Manahan, D. T. (2015). Experimental ocean acidification alters the allocation of metabolic energy. *Proceedings of the National Academy of Sciences of the United States of America*, *112*(15), 4696–4701. https://doi.org/10.1073/pnas.1416967112

Perez, F. F., & Fraga, F. (1987). Association constant of fluoride and hydrogen ions in seawater. *Marine Chemistry*, *21*(2), 161–168. https://doi.org/10.1016/0304-4203(87)90036-3

Pimenta, A. R., & Grear, J. S. (2018). Guidelines for measuring changes in seawater pH and associated carbonate chemistry in coastal environments of the eastern United States. United States Environmental Protection Agency.

Richaud, B., Kwon, Y.-O., Joyce, T. M., Fratantoni, P. S., & Lentz, S. J. (2016). Surface and bottom temperature and salinity climatology along the continental shelf off the Canadian and U.S. East Coasts. *Continental Shelf Research*, *124*, 165–181. https://doi.org/10.1016/j.csr.2016.06.005

Rudnick, D. L. (2016). Ocean research enabled by underwater gliders. *Annual Review of Marine Science*, *8*, 519–541. https://doi.org/10.1146/annurev-marine-122414-033913

Runcie, J. W., Krause, C., Torres Gabarda, S. A., & Byrne, M. (2018). Technical note: Continuous fluorescence-based monitoring of seawater pH in situ. *Biogeosciences*, *15*(13), 4291–4299. https://doi.org/10.5194/bg-15-4291-2018

Saba, G. K., Goldsmith, K. A., Cooley, S. R., Grosse, D., Meseck, S. L., Miller, A. W., et al. (2019). Recommended priorities for research on ecological impacts of ocean and coastal acidification in the U.S. Mid-Atlantic. *Estuarine, Coastal and Shelf Science*, *225*, 106188. https://doi.org/10.1016/j.ecss.2019.04.022

Saba, G. K., Wright-Fairbanks, E., Chen, B., Cai, W.-J., Barnard, A. H., Jones, C. P., et al. (2019). The development and validation of a profiling glider deep ISFET-based pH sensor for high resolution observations of coastal and ocean acidification. *Frontiers in Marine Science*, *6*. https://doi.org/10.3389/fmars.2019.00664

Salisbury, J., Vandemark, D., Jönsson, B., Balch, W., Chakraborty, S., Lohrenz, S., et al. (2015). How can present and future satellite missions support scientific studies that address ocean acidification? *Oceanography*, *25*(2), 108–121. https://doi.org/10.5670/oceanog.2015.35

Schofield, O., Kohut, J., Aragon, D., Creed, L., Graver, J., Haldeman, C., et al. (2007). Slocum gliders: Robust and ready. *Journal of Field Robotics*, *24*(6), 473–485. https://doi.org/10.1002/rob.20200

Schofield, O., Kohut, J., Glenn, S., Morell, J. M., Capella, J., Corredor, J., et al. (2010). A regional Slocum glider network in the Mid-Atlantic Bight leverages broad community engagement. *Marine Technology Society Journal*, *44*(6).

Sharp, J. D., Pierrot, D., Humphreys, M. P., Epitalon, J.-M., Orr, J. C., Lewis, E., & Wallace, D. W. R. (2020). CO_2-System-Extd, v3.0, MATLAB (MathWorks).

Siedlecki, S. A., Pilcher, D. J., Hermann, A. J., Coyle, K., & Mathis, J. (2017). The important of freshwater to spatial variability of aragonite saturation state in the Gulf of Alaska. *Journal of Geophysical Research: Oceans*, *122*, 8482–8502. https://doi.org/10.1002/2017JC012791

Steves, B. P., Cowen, R. K., & Malchoff, M. H. (2000). Settlement and nursery habitats for demersal fishes on the continental shelf of the New York Bight. *Fishery Bulletin*, *98*(1), 167–188.

Sullivan, M. C., Cowen, R. K., Able, K. W., & Fahay, M. P. (2000). Spatial scaling of recruitment in four continental shelf fishes. *Marine Ecology Progress Series*, *207*, 141–154.

Sutton, A. J., Sabine, C. L., Feely, R. A., Cai, W.-J., Cronin, M. F., McPhaden, M. J., et al. (2016). Using present-day observations to detect when anthropogenic change forces surface ocean carbonate chemistry outside preindustrial bounds. *Biogeosciences*, *13*(17), 5065–5083. https://doi.org/10.5194/bg-13-5065-2016

Talmage, S. C., & Gobler, C. J. (2009). The effects of elevated carbon dioxide concentrations on the metamorphosis, size, and survival of larval hard clams (*Mercenaria mercenaria*), bay scallops (*Argopecten irradians*), and Eastern oysters (*Crassostrea virginica*). *Limnology and Oceanography*, *54*(6), 2072–2080.

Talmage, S. C., & Gobler, C. J. (2010). Effects of past, present, and future ocean carbon dioxide concentrations on the growth and survival of larval shellfish. *Proceedings of the National Academy of Sciences of the United States of America*, *107*(40), 17,246–17,251. https://doi.org/10.1073/pnas.0913804107

Testor, P., de Young, B., Rudnick, D. L., Glenn, S., Hayes, D., Lee, C. M., et al. (2019). OceanGliders: A component of the integrated GOOS. *Frontiers in Marine Science*, *6*. https://doi.org/10.3389/fmars.2019.00422

Uppstrom, L. (1974). The boron/chlorinity ratio of deep-sea water from the Pacific Ocean. *Deep-Sea Research*, *21*(2).

van Heuven, S., Pierrot, D., Rae, J. W. B., Lewis, E., & Wallace, D. W. R. (2011). MATLAB program developed for CO_2 system calculations. ORNL/CDIAC-105b. Carbon Dioxide Information Analysis Center, Oak Ridge National Laboratory, U.S. Department of Energy, Oak Ridge, Tennessee. https://doi.org/10.3334/CDIAC/otg.CO2SYS_MATLAB_v1.1

Waldbusser, G. G., Hales, B., Langdon, C. J., Haley, B. A., Schrader, P., Brunner, E. L., et al. (2014). Saturation-state sensitivity of marine bivalve larvae to ocean acidification. *Nature Climate Change*, *5*(3), 273–280. https://doi.org/10.1038/nclimate2479

Waldbusser, G. G., & Salisbury, J. E. (2014). Ocean acidification in the coastal zone from an organism's perspective: Multiple system parameters, frequency domains, and habitats. *Annual Review of Marine Science*, *6*, 221–247. https://doi.org/10.1146/annurev-marine-121211-172238

Wang, H., Hu, X., Cai, W.-J., & Sterba-Boatwright, B. (2017). Decadal fCO_2 trends in global ocean margins and adjacent boundary current-influenced areas. *Geophysical Research Letters*, *44*, 8962–8970. https://doi.org/10.1002/2017GL074724

Wang, Z. A., Wanninkhof, R., Cai, W.-J., Byrne, R. H., Hu, X., Peng, T.-H., & Huang, W.-J. (2013). The marine inorganic carbon system along the Gulf of Mexico and Atlantic coasts of the United States: Insights from a transregional coastal carbon study. *Limnology and Oceanography*, *58*(1), 325–342. https://doi.org/10.4319/lo.2013.58.1.0325

Wanninkhof, R., Barbero, L., Byrne, R., Cai, W.-J., Huang, W.-J., Zhang, J.-Z., et al. (2015). Ocean acidification along the Gulf Coast and East Coast of the USA. *Continental Shelf Research*, *98*, 54–71. https://doi.org/10.1016/j.csr.2015.02.008

Weinberg, J. R. (2005). Bathymetric shift in the distribution of Atlantic surfclams: Response to warmer ocean temperature. *ICES Journal of Marine Science*, *62*(7), 1444–1453. https://doi.org/10.1016/j.icesjms.2005.04.020

Wootton, J. T., Pfister, C. A., & Forester, J. D. (2008). Dynamic patterns and ecological impacts of declining ocean pH in a high-resolution multi-year dataset. *Proceedings of the National Academy of Sciences of the United States of America*, *105*(48), 18,848–18,853. https://doi.org/10.1073/pnas.0810079105

Xu, Y., Chant, R., Gong, D., Castelao, R., Glenn, S., & Schofield, O. (2011). Seasonal variability of chlorophyll a in the Mid-Atlantic Bight. *Continental Shelf Research*, *31*(16), 1640–1650. https://doi.org/10.1016/j.csr.2011.05.019

Xu, Y.-Y., Cai, W.-J., Gao, Y., Wanninkhof, R., Salisbury, J., Chen, B., et al. (2017). Short-term variability of aragonite saturation state in the central Mid-Atlantic Bight. *Journal of Geophysical Research: Oceans*, *122*, 4274–4290. https://doi.org/10.1002/2017JC012901

Xu, Y. Y., Cai, W. J., Wanninkhof, R., Salisbury, J., Reimer, J., & Chen, B. (2020). Long-term changes of carbonate chemistry variables along the north American East Coast. *Journal of Geophysical Research: Oceans*, *125*(7), e2019JC015982. https://doi.org/10.1029/2019JC015982

Zeebe, R. E. (2012). History of seawater carbonate chemistry, atmospheric CO_2, and ocean acidification. *Annual Review of Earth and Planetary Sciences*, *40*(1), 141–165. https://doi.org/10.1146/annurev-earth-042711-105521

Monitoring ocean biogeochemistry with autonomous platforms

Fei Chai, Kenneth S. Johnson, Hervé Claustre, Xiaogang Xing, Yuntao Wang, Emmanuel Boss, Stephen Riser, Katja Fennel, Oscar Schofield and Adrienne Sutton

Abstract | Human activities have altered the state of the ocean, leading to warming, acidification and deoxygenation. These changes impact ocean biogeochemistry and influence ecosystem functions and ocean health. The long-term global effects of these changes are difficult to predict using current satellite sensing and traditional in situ observation techniques. Autonomous platforms equipped with biogeochemical sensors allow for the observation of marine biogeochemical processes and ecosystem dynamics, covering a wide range of spatial and temporal scales. The international Biogeochemical-Argo (BGC-Argo) project is currently building a global, multidisciplinary ocean-observing network of autonomous Argo floats equipped with an extensive range of biogeochemical sensors. Other autonomous platforms, such as gliders and surface vehicles, have also incorporated such sensors, mainly operating on regional scales and near the ocean surface. Autonomous mobile assets, along with remotely sensed data, will provide the 4D information required to improve model simulations and forecasts of ocean conditions and ecosystem health.

Anthropogenic activities are rapidly changing the oceans, contributing to ocean warming, acidification, eutrophication, pollution, deoxygenation, nutrient flux reduction, vital habitat destruction, declining fishery resources and an increasing number of endangered marine species[1]. Recent observation-based estimates show that the ocean has been undergoing rapid warming over the past few decades, and that the rate of warming has increased[2]. Ocean warming has been linked to increases in rainfall intensity in tropical regions, declines in ice sheets, glaciers and ice caps in the polar regions, rising sea levels, enhancement of ocean stratification and a decrease in primary production[3]. Ocean-ecosystem health responds to anthropogenic activities in general through transforming the dynamics of marine organisms, altering the rate of the carbon cycle and changing marine-animal behaviour[4].

The upcoming United Nations (UN) Decade of Ocean Science for Sustainable Development marks a global push towards collecting comprehensive observational data for biogeochemical processes in order to encourage the sustainable development of the ocean. However, marine ecosystems and biogeochemical cycles are complex, involving a range of physical processes, such as wind-driven mixing, convective mixing, upwelling, downwelling, isopycnal mixing, diapycnal diffusion and horizontal advection, chemical processes, such as air–sea CO_2 exchange, ocean acidification and deoxygenation, and biological processes, such as primary production, phytoplankton growth and loss, and zooplankton grazing[5–8]. Many of these complex processes cannot be observed using only traditional observation platforms, such as ships and moorings.

To address the limitations of existing observation methods, new sensor technologies for conducting biological and biogeochemical measurements are being developed and equipped on novel observational platforms, such as autonomous mobile platforms[9]. Together with more traditional observation methods, these new platforms can collect data to assess the changes in biogeochemical and physical properties of the ocean on global and decadal scales[10,11].

In this Perspective, we explore the application of autonomous platforms in assessing ocean biogeochemistry and ecosystem health. We first review traditional methods used for observing ocean biogeochemistry. Then, we discuss the demand for conducting observations to resolve marine biogeochemical and ecosystem spatial and temporal variations. We present current examples of the use of multiple autonomous mobile platforms and how different platforms are used synergistically. Finally, we describe the approaches for applying 4D data to monitor and forecast ocean biogeochemistry and ecosystem health.

Traditional ocean observations and challenges

The use of observing platforms has evolved over the past century (FIG. 1). Early motivations for using such platforms were to investigate the productivity of the ocean, and fisheries in particular, to mitigate marine destructive events, such as typhoons and tsunamis, and to study geography[12]. Whereas ships and moorings were the platforms of choice to survey the ocean, recently, the application of remote sensing has greatly improved the spatial coverage of the entire ocean to near real-time. In this section, we describe existing ocean-observing platforms and their related applications and challenges.

Shipborne observations. Oceanographers historically collected data from the ocean and seafloor using ships during cruises of limited duration. This expeditionary research approach has resulted in major advances in our understanding of the global ocean. The *HMS Challenger* expedition in the 1870s pioneered the concept of a systematic global survey of the subsurface ocean, measuring the physics and chemistry of seawater and collecting biological samples at hundreds of sites. Later efforts, such as the Geochemical Ocean Sections Study (GEOSECS) in the 1970s, the World Ocean Circulation Experiment (WOCE) in the 1980s and 1990s, and the ongoing Global Ocean Ship-Based Hydrographic Investigations Program (GO-SHIP) (FIG. 1), have improved global coverage and included measurements of

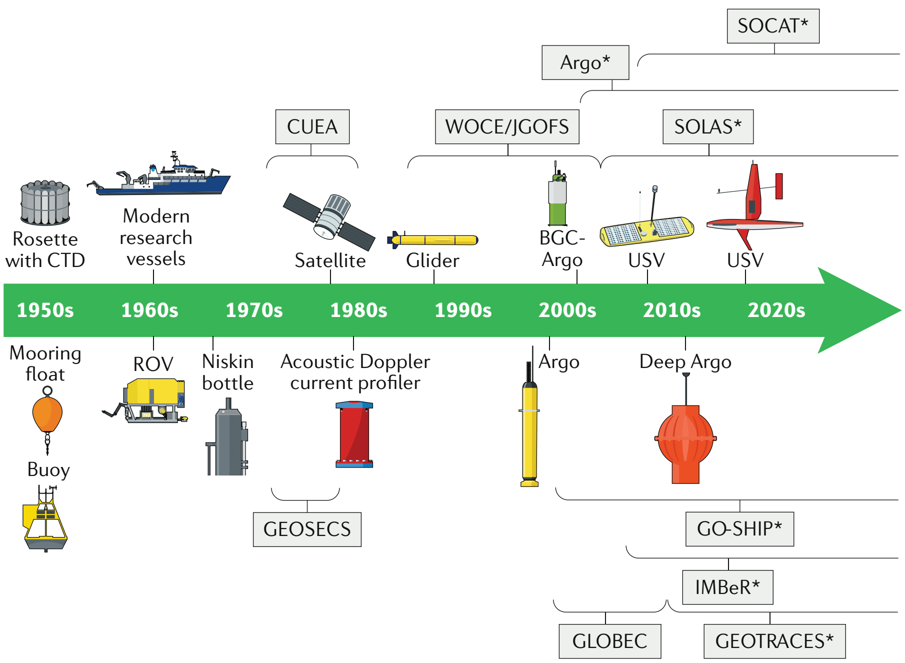

Fig. 1 | **Timeline of oceanographic observation platforms and international projects measuring marine biogeochemistry.** International project durations are indicated with brackets. Ongoing projects are denoted with an asterisk (*). BGC-Argo, Biogeochemical-Argo; CTD, conductivity, temperature and depth; CUEA, Coastal Upwelling Ecosystems Analysis; GEOSECS, Geochemical Ocean Sections Study; GLOBEC, Global Ocean Ecosystem Dynamics; GO-SHIP, Global Ocean Ship-based Hydrographic Investigations Program; IMBeR, Integrated Marine Biosphere Research; JGOFS, Joint Global Ocean Flux Study; ROV, remotely operated underwater vehicle; SOCAT, Surface Ocean CO_2 Atlas; SOLAS, Surface Ocean Lower Atmosphere Study; USV, unmanned surface vehicle; WOCE, World Ocean Circulation Experiment.

biogeochemical variables, such as nutrient concentrations and the carbonate system[13]. Research and industry partnerships have also supported networks of autonomous physical and chemical measurements on ships of opportunity, such as in the Surface Ocean CO_2 Atlas (SOCAT) since 2007 (REF.[14]). Shipborne observations have allowed the discovery of large spatial variations in productivity through the identification of phenomenon such as high-nutrient, low-chlorophyll zones[15] and the oligotrophic gyres[16]. More recently, the GEOTRACES programme has identified processes and quantified fluxes that control the distributions of key trace elements and isotopes in the oceans[17], and the Tara Oceans project has shown the enormous taxonomic diversity of photosynthetic microorganisms in the surface ocean[18].

However, ship-based observations are limited by their spatial and temporal coverage, and can be prohibitively expensive, such that only a limited number of cruises can be conducted at any given time. Cruises can also be constrained by extreme weather conditions, particularly during winter; as a result, ship-based observations can be sparse and strongly biased towards summer-season sampling.

Sustained, fixed-location observations. Modern ocean moorings have evolved from the weather stations established in the 1940s (REF.[19]). By the 1980s, moorings had become critical platforms, enabling studies into ocean biogeochemistry and the role of the ocean in influencing climate and weather[20]. Data from historical stations such as Ocean Station Papa and ALOHA revealed ecosystem responses to the El Niño–Southern Oscillation events[21], global warming[22] and ocean acidification[5]. Moorings now provide the backbone of many of the global ocean networks used for studying ocean–atmosphere interactions[23,24] and for characterizing marine-ecosystem changes[25,26], particularly in coastal waters[27]. OceanSITES, a worldwide system of open-ocean reference stations, coordinates time series of global mooring observations and serves as a global long-term network[26].

Fixed-location moorings will continue to be a key element of ocean-observing infrastructure, providing high-frequency subsurface data to supplement data collected by ships, autonomous vehicles and satellite remote sensing. A disadvantage of these systems is their high maintenance cost, which severely limits the number of systems that can be deployed. Furthermore, sensors are often located at fixed depths, and instruments near the surface are subject to biofouling. Thus, despite being an ideal platform for collecting high-resolution times series, fixed-location moorings are ineffective at providing large-scale spatial coverage or tracing the movement of different water masses.

Remote sensing. Satellites are an important innovation in oceanographic technology[28]. A range of satellite observing systems is available, including active scatterometers, microwave spectrometers, radiometers, microwave imagers, altimeters and probes for advanced gravity missions. Ocean-colour satellite observation systems started with the launch of the Coastal Zone Color Scanner (CZCS) in the late 1970s, which provided the first global view of phytoplankton distribution[29]. Global ocean-colour data have been recorded continuously since the SeaWiFS project began in 1997, sustained by the MODIS-Aqua, MERIS, VIIRS and OLCI sensors[30]. In the past four decades, satellite observations have resulted in numerous advances in our fundamental understanding of the ocean through resolving global features associated with the mesoscale circulation of physical and biological properties[30,31].

Satellite observations can be used to estimate long-term trends in marine-ecosystem change at both basin and global scales. Satellite remote sensing has shown that global chlorophyll *a* is decreasing (REF.[32]), especially in the subtropical gyres[33], and that oligotrophic areas of all oceans are expanding[34]. The response of primary producers to climatic oscillations, ranging from intraseasonal[35] to multidecadal scales[36], has been clearly shown by satellite imaging, in particular, following El Niño–Southern Oscillation[37]. Unfortunately, satellites have limited capabilities for resolving features below the ocean surface. The presence of clouds can also interfere with some satellite sensors; this is especially problematic for cloudy regions, such as high-latitude oceans, which play a predominant role in driving global biogeochemistry[38]. At high latitudes, data from ocean-colour satellites often contain large gaps in winter, owing to low sun angle and increased cloudiness[39].

Needs in ocean observation

Due to the limitations of traditional observing systems, there is a need for new systems capable of resolving complex, multiscaled biogeochemical phenomena.

Observing the ocean requires large spatial coverage, high temporal sampling frequency and capability to conduct measurements at depth with high vertical resolution.

Spatial coverage. Compared with traditional in situ observations by ships and moorings, the greatest strength of autonomous-platform networks is their capacity to conduct multiscale and cross-disciplinary measurements. Such resolution is critical, as biogeochemical processes and associated dynamics can vary largely in scales; for example, basin-scale phytoplankton growth can be influenced by the atmospheric transport and deposition of Asian dust-associated iron tens of thousands of kilometres away[40].

In recent years, mesoscale and sub-mesoscale data have been increasingly acquired by Biogeochemical-Argo (BGC-Argo) project floats, gliders and unmanned surface vehicles (USVs)[41–47] (FIG. 2). Data from such autonomous platforms have rapidly improved our understanding of relationships between physical and biogeochemical processes. This is particularly true for observations from gliders, as they are capable of adaptive sampling through eddies and fronts. Based on glider data and model interpretations, Mahadevan et al.[47] showed that mixed-layer dynamics can be driven by sub-mesoscale processes and, conversely, patchy blooms can be triggered when the mixed-layer depth is abruptly shoaled due to eddy-driven restratification. Another study combining BGC-Argo and glider observations found that sub-mesoscale physical processes are also likely to affect algal-community composition, as more diatoms appeared in the patchy bloom areas than outside them[43]. BGC-Argo float and glider data have shown that sub-mesoscale subduction induced by eddy pumping can contribute to the biological carbon pump, transferring dissolved and particulate organic matter from the surface into the mesopelagic zone[45,48]. Integration of meteorological measurements with biogeochemical measurements by USVs can also help to determine how strong atmospheric forcing and mesoscale physical processes drive ocean biogeochemistry[49].

A global array of 1,000 BGC-Argo floats can capture a snapshot of the global upper-layer biogeochemical and ecosystem state every 10 days, which is higher in sampling frequency and much less costly than ship-based surveys[50]. For example, the Global Ocean Data Analysis Project Version 2 (GLODAPv2), a ship-based survey comprised of 724 cruises between 1972 and 2013, collected data from 52,317 stations globally[51]; a global BGC-Argo array would be able to surpass this total number of temperature, salinity, chlorophyll *a*, nitrate concentration, pH and oxygen profiles in only 2 years[11].

Some high-density networks capable of wide-ranging spatiotemporal coverage are already active on a regional scale. In the Southern Ocean, 35 BGC-Argo floats have revealed discrepancies in air–sea CO_2 fluxes in various sub-provinces and during different seasons[52]. In the Mediterranean Sea, data taken from 39 BGC-Argo floats between 2012 and 2017 have improved the performance of a pre-existing regional biogeochemical model[53]. On a global scale, more than 100 BGC-Argo floats produced the first global bio-optical data set (chlorophyll *a*, particulate backscatter and spectral radiometry) in order to address differences in regional distribution in bio-optical properties[54], regional discrepancies in photoacclimation effects on phytoplankton chlorophyll-to-carbon ratios[55] and global distribution of non-algal particles[56]. The large-scale observations made by the BGC-Argo array allowed characterization of biogeochemical provinces and biomes, and potentially provides data for improving biogeochemical model performance, as well as the calibration and validation of satellite measurement systems.

Vertical coverage. As ocean satellite measurements are limited to the surface ocean, there is a need to extend biogeochemical observations throughout the water column[57]. For example, the biological carbon pump has an important role in transferring atmospheric CO_2 from the sea surface, through the water column

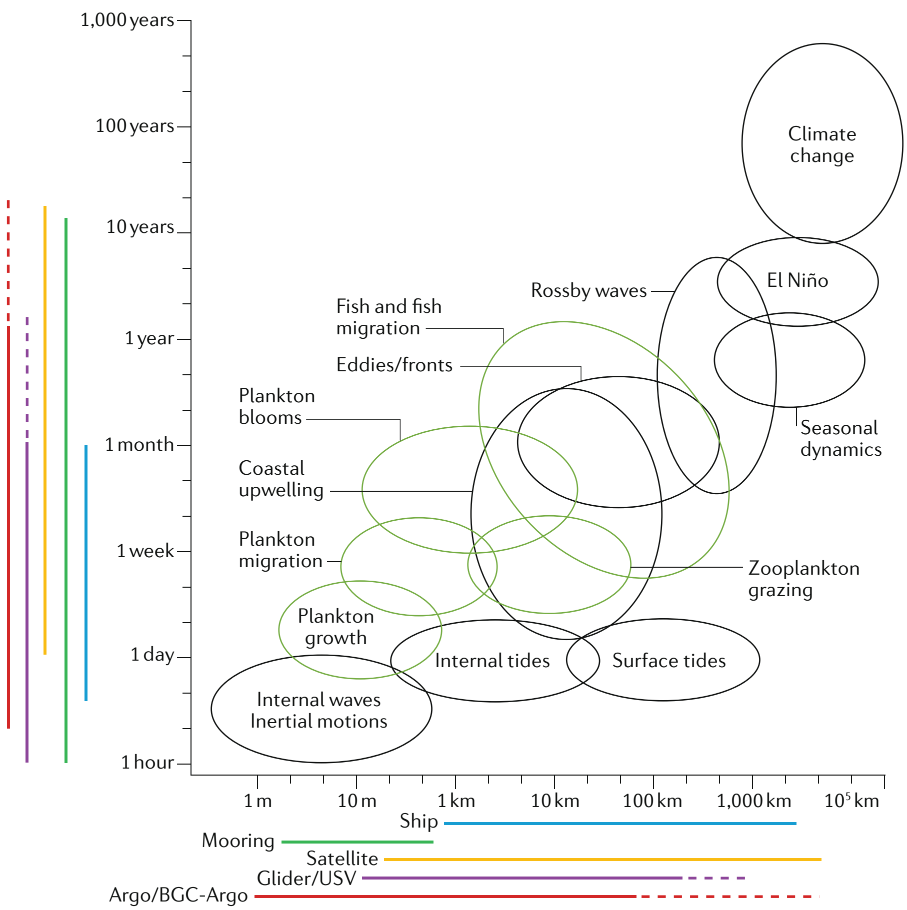

Fig. 2 | **Measuring across spatiotemporal scales in marine systems.** Spatial and temporal scales of marine dynamic and ecosystem processes, and the measurement capabilities of different observational platforms. Dynamic and/or physical processes are represented by black circles and biological and/or ecological processes by green circles. The presence of new autonomous platforms, such as Biogeochemical-Argo (BGC-Argo) floats (red line) and gliders and similar unmanned surface vehicles (USVs) (purple line), fill the cross-discipline and cross-scale observational gaps left by traditional observation methods such as remote sensing by satellite (yellow line), moorings (green line) or ship-based observations (blue line). Dashed lines indicate potential extension of an observational network. Data from REF.[179]. Adapted with permission from REF.[180], Elsevier.

and into the ocean interior, and, thus, is responsible for modulating climate change and supporting deep-ocean ecosystems. Studies on the efficiency of the pump, and related physical–biogeochemical coupling processes, now rely heavily on the observations from autonomous platforms[58–63]. BGC-Argo and gliders are excellent tools for resolving physical and biogeochemical variables in various oceanic conditions, as they are operational in both open and deep oceans (>1,000 m), and gliders can also operate in marginal seas (<1,000 m). Moreover, autonomous platforms equipped with transmissometers can operate in drifting mode as 'optical sediment traps' and can directly and accurately observe particle sedimentation on daily to weekly scales with higher frequency than traditional sediment traps that operate at monthly scales[64].

Temporal coverage. Autonomous platforms can fill some of the important temporal continuity gaps inherent with traditional platforms, improving observation frequency in the open ocean from monthly or seasonal to daily and weekly timescales. USVs such as saildrones and Wave Gliders can perform continuous observation of sea-surface biogeochemical properties, such as $p\mathrm{CO_2}$, dissolved oxygen, pH, chlorophyll *a* concentration and air–sea carbon flux[65,66]. As autonomous platforms can operate in harsh environments, even operating underneath sea ice[52,67,68], they are capable of recording continuous time series at high latitudes under all-weather conditions; these data can fill the temporal gaps seen during winter using satellite-based observations[52,69–71].

Rapid weather changes can lead to transient ecosystem responses not captured by ships or satellites. For example, a large number of BGC-Argo observations have revealed that rapid changes in mixed-layer depth could efficiently pump particles from the surface ocean into deep waters[59,60]. A BGC-Argo float in the Bay of Bengal recorded subsurface chlorophyll *a* enhancement after a tropical cyclone induced regional upwelling and turbulent mixing; the surface chlorophyll *a* bloom was attributed to the combined effect of subsurface chlorophyll *a* entrainment and nutrient injection[6].

Autonomous platforms

The presence of new autonomous platforms, such as Argo floats, gliders and USVs, fill the cross-disciplinary and cross-scale observational gaps described above, providing revolutionary insights into ocean biogeochemistry and marine ecosystems.

Argo floats. The profiling float, a modern instrument that is complementary to ship-based systems, was first used in prototype form, carrying only temperature and pressure sensors, during the WOCE[72]. Large-scale deployments with commercially prepared instruments commenced in 1999 (REF.[73]). The float uses an inflatable, oil-filled bladder to change its buoyancy, in order to vertically profile from the sea surface to depths of 1,000–2,000 m, a process that occurs over the course of ~10 days[72]. Data are reported in near real-time using a satellite link and recent versions are outfitted with conductivity, temperature and depth (CTD) instrumentation. Presently, ~4,000 profiling floats are collecting publicly available, real-time observations, providing a synoptic view of the ocean interior every few days as part of the international Argo programme[74]. Some profiling floats have also been adapted to extend observations to deeper oceans or shallower marginal seas, including deep Argo floats reaching 6,000 m (REF.[75]) and coastal Argo floats with fast observation time and anti-drift capabilities[76].

Modern versions of Argo floats (FIG. 3a) used in the BGC-Argo network are equipped with a variety of additional physical, chemical and bio-optical sensors, such as an optode for oxygen sensing, ultraviolet spectrophotometers for measuring nitrate concentrations, electrochemical sensors for pH measurements, chlorophyll *a* fluorometers, scatterometers and radiometers[77]. Throughout the ocean, including in ice-covered regions, floats can operate for between 2 and 7 years after launch, depending on battery usage[50,78]. Using a global network of sensors greatly enhances the probability of encountering transient phenomenon such as carbon export by mixed-layer pump processes during the late winter–spring transition[60,79], episodic responses of dissolved oxygen during tropical cyclones[8] and blooms induced by restratification[80]. Recently, the first observational evidence of a hydrothermal-vent-triggered bloom was captured by BGC-Argo floats in the Southern Ocean, revealing that iron from hydrothermal vents can play an important role in modulating surface primary production[7].

Profiling floats can also be used for long-term data collection. A recent study on nitrate measurements, using data collected from Ocean Station Papa in the North Pacific, demonstrated interannual changes in nitrate concentration, which lead to significant changes in ecosystem functions[81]. They enable predictions of ocean health, including fishery yields. However, Argo floats are limited by the available sensor technology[82] and by sensor offsets and drifts[77]. Moreover, unlike moorings, Argo floats drift passively and, therefore, cannot remain at a fixed location, making long-term observations of a single location difficult.

Gliders. Gliders (FIG. 3b) are similar to Argo floats and operate using similar buoyancy engines[83]. Some gliders are equipped with wings that can translate some vertical movement through the water column into horizontal movement; an adjustable weight inside the glider allows the platform to be steered automatically in order to fulfil spatial requirements for measurements. Gliders use the Iridium global telecommunications network to transmit data to shore-based servers and receive commands for future actions from shore-based personnel when at the surface[84]. Consequently, gliders can conduct uninterrupted missions for up to a year; however, most deployments are shorter in duration, as these systems generally operate continuously, whereas profiling floats sleep for up to 10 days between profiles.

With the ability to carry many diverse sensors (TABLE 1), gliders effectively collect and integrate information related to the physics, chemistry and biology of the ocean[85]. Unlike Argo networks, gliders mainly sample on continental shelves and reveal energetic features of the coastal oceans. Furthermore, their adaptive capabilities allow for sampling of subsurface ocean features that cannot be observed from satellites, such as thermoclines, nutriclines and the deep chlorophyll maximum[41]. Gliders can even collect and transmit ocean data from within hurricanes[86], making them well suited for storm research. Much of the uncertainty in storm forecasts is caused by storm-induced ocean mixing processes, which can alter the storm's intensity at landfall[86]. Given that gliders can adjust their positions dynamically, national agencies are now exploring how gliders might provide a network that can be adaptively positioned during a storm's approach to fill data gaps from traditional methods. Use of gliders in this way could allow more accurate forecasting of storm trajectory and intensity. However, operational time during deployment is limited by the glider's battery life[87].

Unmanned surface vehicles. USVs, including saildrones and Wave Gliders, are capable of basin-scale observations of meteorological variables and surface ocean conditions. A number of USVs are in various stages of development and use (FIG. 1), with the majority of testing done by the Tropical Pacific Observing System (TPOS) and Innovative Technology for Arctic Exploration (ITAE)[66].

A saildrone (FIG. 3c) is a 7-m-long USV with a 5-m-high wing, which uses wind for propulsion and solar energy for powering its sensors[44]. Meteorological sensors are mounted on the wing of the saildrone, and oceanographic sensors are present in the hull and keel. Saildrones are capable of measuring air temperature, barometric pressure, relative humidity, solar irradiance, wind speed and direction, sea-surface temperature and salinity, ocean colour, dissolved oxygen, pH, and atmospheric and seawater pCO_2, and can use active acoustics to measure currents, bathymetry and fish, and passive acoustics to measure ocean noise caused by marine mammals and subsea volcanoes. Adaptations can be made for extreme environments; the current fleet of ~70 saildrones, active since 2015, has been operating in the Arctic[49,88,89], Southern Ocean, western boundary currents and coastal waters.

New USV designs such as Wave Gliders (FIG. 3d) show promise for operating in extreme currents, wind and wave conditions in western boundary currents and high latitudes, where air–sea observations are currently undersampled[90,91]. The surface float of the Wave Gliders that hold the sensor package are 2–3 m long and are propelled by the conversion of ocean wave energy into forward thrust independent of wave direction through subsurface wings at 8 m depth tethered to the float. Wave Gliders have been utilized on several repeat observing missions[92], but, although subsurface measurements have been made on the Wave Glider's 8-m-depth wings, sampling of subsurface waters is a current limitation of surface vehicles.

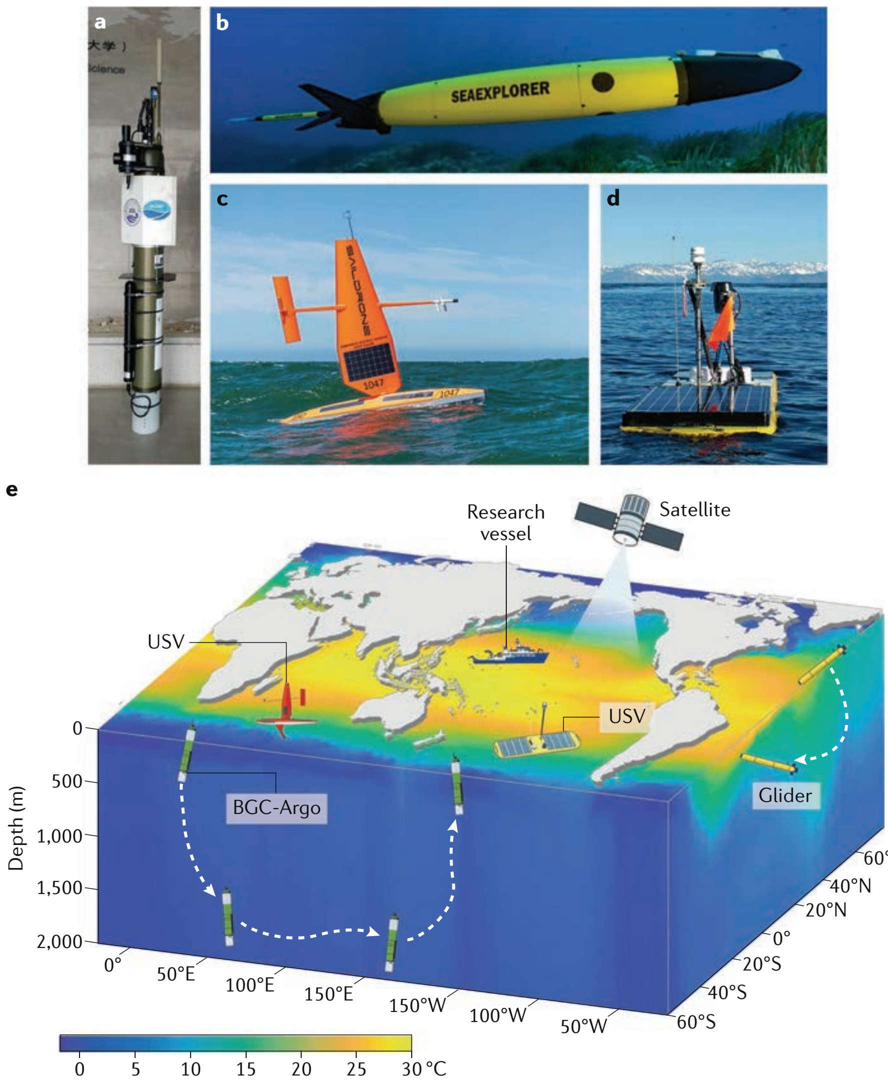

Fig. 3 | **Four available ocean-observation platforms and example areas of operation. a** | A typical Biogeochemical-Argo (BGC-Argo) float. **b** | A glider. **c** | A saildrone (a type of unmanned surface vehicle (USV)). **d** | A Wave Glider (a type of USV). **e** | A schematic diagram of ocean-observation-platform operations, along with research vessels and satellites. Traditional shipborne platforms provide fundamental reference data for many biogeochemical variables across all platforms, and satellite sensing provides the continuous spatiotemporal coverage of sea-surface variables. The Argo and BGC-Argo arrays measure ocean variables through the water column, with all floats reaching up to 2,000 m. Gliders are more suitable for observation at various depths in coastal and shallow oceans, whereas USVs provide air–sea flux data. Panel **b** reprinted with permission from ALSEAMAR. Panel **c** reprinted courtesy of Saildrone. Panel **d** reprinted with permission from NOAA PMEL/Evans (Hakai Institute).

Biogeochemical sensors on autonomous platforms. A novel ensemble of biogeochemical sensors capable of operating on floats, gliders and USVs is now available (FIG. 3e) and has been used on hundreds of profiling floats[93,94] and regional and global networks of gliders[85,95]. Some other sensors have also been equipped on gliders[96,97] and USVs in specific cases[98]. Available sensors are listed in TABLE 1.

New sensors are currently in development; alkalinity sensors[99], for example, could complement already operational pH sensors to robotically estimate CO_2 flux with lower uncertainty than present statistical methods[100,101]. Imaging techniques, as well as active acoustic systems, are presently being developed and tested to better quantify organisms in higher trophic levels, such as zooplankton and mesopelagic fishes. Their applications in the near future could help investigate critically undersampled components of ecosystems and biogeochemical cycles, potentially representing neglected biomass and food resources[102,103]. Finally, passive acoustic sensors have the potential to measure meteorological properties[104,105], as well as anthropogenic noise and mammal presence[89,106–108]. A global integrated observational system, equipped with a large variety of sensors, is now capable of fulfilling the need for multifunctional and multidisciplinary sampling from marginal seas to open oceans and from the surface to the deep ocean.

Current mobile platform networks

The establishment and development of global and regional observation arrays of multiple autonomous platforms will aid

Table 1 | **Major observed biogeochemical properties on mobile platforms**

Observed property	Sensor	Platforms applied	Ref.
Dissolved oxygen	Luminescence lifetime optode sensor	All autonomous platforms	138
pCO_2	NDIR spectrometer	USVs	98
	Equilibration-based infrared gas analyser	USVs	66
Nitrate	Ultraviolet spectrophotometer	Argo floats, gliders	175
pH	Ion-sensitive field-effect transistor	All autonomous platforms	176
Particulate backscattering coefficient	Optical backscatter	All autonomous platforms	82
Particulate beam attenuation coefficient	Optical transmissometer	Argo floats	64
Chlorophyll *a* concentration	Fluorometer	All autonomous platforms	144
Single-channel CDOM fluorescence	Fluorometer	All autonomous platforms	177
Multichannel CDOM fluorescence	Fluorometer	Gliders	97
Downwelling irradiance and PAR	Radiometer	Argo floats, gliders	54
Presence of zooplankton, fish and mammals	Echo sounder	Gliders and USVs	96
Zooplankton size and species	UVP	Argo floats	178

CDOM, coloured dissolved organic matter; NDIR, non-dispersive infrared; PAR, photosynthetically available radiation; pCO_2, carbon dioxide partial pressure; USV, unmanned surface vehicle; UVP, Underwater Vision Profiler.

the development of 4D data sets to inform and constrain oceanographic models.

Global BGC-Argo array. The BGC-Argo programme is in charge of planning and managing global deployment of BGC-Argo floats, with the goal of conducting global measurements of biogeochemistry and ecosystems. The science and implementation plan identified from the Biogeochemical-Argo Planning Group[93] proposed that an initial step was to carry optical and chemical sensors to support the assessment of biogeochemistry and ecosystems in a changing ocean. At OceanObs'19, a multidisciplinary global ocean-observation-system conference, the specifics of BGC-Argo implementation were refined. The revised plan aims for better interaction and synergy with the global Argo programme, allowing the development of a long-term vision for Argo, defined as 'global, full-depth, and multidisciplinary'[11,50].

The initial target size for the BGC-Argo array is 1,000 floats[93], a goal based on modelling[109] and in situ data analysis[110,111]. The BGC-Argo array currently consists of over 350 floats reporting data regularly, fostering interdisciplinary studies that range from the tropics to high latitudes (FIG. 4). It is becoming an essential component of the global observing network proposed for the next decade and will transform our ability to systematically observe, document and understand changes of ocean environment and marine ecosystems. However, there are some drawbacks associated with the BGC-Argo array. As Argo floats move passively with currents, it is possible floats could drift into an exclusive economic zone (EEZ), which can cause legal issues that could delay data transfer. Moreover, operation of Argo floats is expensive; the average lifetime of a float is ~4 years, and the yearly global cost of a sustained BGC-Argo array is estimated to be ~US $30 million[93]. Improving Argo technology to extend its average working lifetime is an important target for the future and could proportionally reduce running costs[50].

Regional arrays of other autonomous platforms. Similar to BGC-Argo, gliders are being used by an international community through the Boundary Ocean Observing Network (BOON)[95], which is also in the initial phases of incorporating USVs into the network[112] (FIG. 4). In the northeast Pacific, two regular glider lines have operated since spring 2006 (REFS[113,114]), supported by the Ocean Observatories Initiative (OOI). These gliders measure major biogeochemical variables, such as oxygen, chlorophyll *a*, coloured dissolved organic matter (CDOM) fluorescence and particulate backscattering[115]. Sustained glider deployments also monitor upper-ocean conditions in areas frequently impacted by tropical cyclones[116–118], which have been an important part of the NOAA Hurricane Field Program[119]. The OOI also sustains a long-term glider line in the USA east coast, focusing on frontal processes[120,121]. Gliders have been deployed in high-latitude oceans and all over the Southern Ocean, including in the Antarctic Circumpolar Current (ACC)[122–124], continental shelves[125–129], near ice shelves[117,130,131] and in the Arctic Ocean[23]. Also, in the Mediterranean Sea, more than five glider endurance lines are currently in operation[132].

USVs are also filling a growing need for surface-based observations in the Southern Ocean (FIG. 4e), assessing physical air–sea fluxes[133,134] and gas air–sea fluxes, notably, CO_2 (REF.[92]). While existing USV missions are primarily regional, saildrones and other USVs are designed and have been used for basin-scale observations[46,66]. Given the ability to actively navigate USVs, they present an opportunity for sampling in regions where ships do frequent less. For example, USV-based seawater pCO_2 observations covering observing gaps of open-ocean missions from the tropical Pacific to the South Pacific Gyre are being incorporated into the 2020 version of the SOCAT.

Multiplatform synergy

Generally, ship-based measurements are of very high quality and include key variables that cannot presently be measured by floats or gliders, for example, levels of silicon, phosphorus, iron, ammonia, bacteria, total dissolved organic carbon (DOC) concentration and phytoplankton species[135]. Moreover, remote sensing offers a large-scale snapshot of the ocean surface, which cannot be covered by individual autonomous platforms. Therefore, autonomous platforms could complement these observation methods by extending observations into full seasonal cycles, or from open-ocean to coastal regions, and by providing the three-dimensional real-time data needed for operational models.

Synergy between autonomous and ship platforms. Although ship-based observations are infrequent and biased to summer months, well-calibrated shipborne data provide, by far, the most important reference for in situ validation of autonomous platforms[77]. For the delayed-mode quality control of autonomous platforms in particular, climatological data captured by ships can validate previously acquired oceanographic measurements. NO_3^- and pH measurements by autonomous platforms may be biased by sensor offsets and drifts[77]. The high-quality GLODAP data set, generated from ship-based measurements, includes deep (>1,000 m) NO_3^- and pH measurements that can be used as reference values to correct the sensor offsets and drifts. Methods for using GLODAPv2 to produce reference measurements at float geolocations are based on multiple linear-regression analyses[136] and neural networks[137,138]. These regressions and neural networks are driven with data from CTD and O_2 sensors on the floats. Similarly, observation of other platforms (ships, buoys and USVs) in the Surface Ocean CO_2 Network (SOCONET)[24] can provide the reference measurements for calculated pCO_2 based on BGC-Argo observations[139].

Synergy between autonomous and satellite platforms. Variables measured by autonomous platforms, for example, chlorophyll *a*, backscattering and photosynthetically available radiation (PAR), can be used to validate satellite platforms[140–142] and evaluate calibration of in situ sensors[143,144]. Several recent studies also present prototype floats that can be used as calibration platforms for ocean-colour satellites through acquiring high-quality radiometric measurements[145,146]. The combination of in situ BGC-Argo observations with ocean-colour remote sensing can be assisted by machine-learning techniques; this approach has been used to develop a 4D global map of the backscattering coefficient, a proxy for measuring particulate organic carbon[11,79].

The calibrated sensor data from floats and gliders can be used to evaluate satellite observation platforms. Recent studies using this approach showed that NASA's chlorophyll *a* and POC algorithms perform without significant mean bias in the Southern Ocean[77,141], despite several publications suggesting the opposite[147–149].

Multiplatform experiments. Comprehensive data sets can be collected by combining data from autonomous platforms, ship, buoy and satellite observations. Increasingly, oceanographic experiments and observation networks are being conducted across multiple platforms. The OOI not only supports two regular glider lines as mentioned above but also hosts several surface and profiler moorings[121]. Early-stage, multiplatform experiments included the in situ iron-enrichment experiment IronEx-I in 1993 (REF.[150]), the CLIVAR Mode Water Dynamics Experiment (CLIMODE) in 2006–2007, the North Atlantic Bloom experiment (NAB08) in 2008 (REF.[58]) and the coastal experiment in the eastern Alboran Sea, AlborEx, in 2014 (REF.[151]). These studies have greatly improved our understanding of phytoplankton physiology and impacts of mesoscale and sub-mesoscale dynamics on regulating primary production, among other biogeochemical phenomena[43,47].

In 2016 and 2017, the Salinity Processes in the Upper-Ocean Regional Study (SPURS-2)[152] and the Northern Arabian Sea Circulation-Autonomous Research (NASCar)[153] coordinated almost all autonomous platforms (including Argo floats, gliders and USVs) and moorings focused on targeted mesoscale eddy. These studies demonstrated the use of multiple platforms to resolve physical

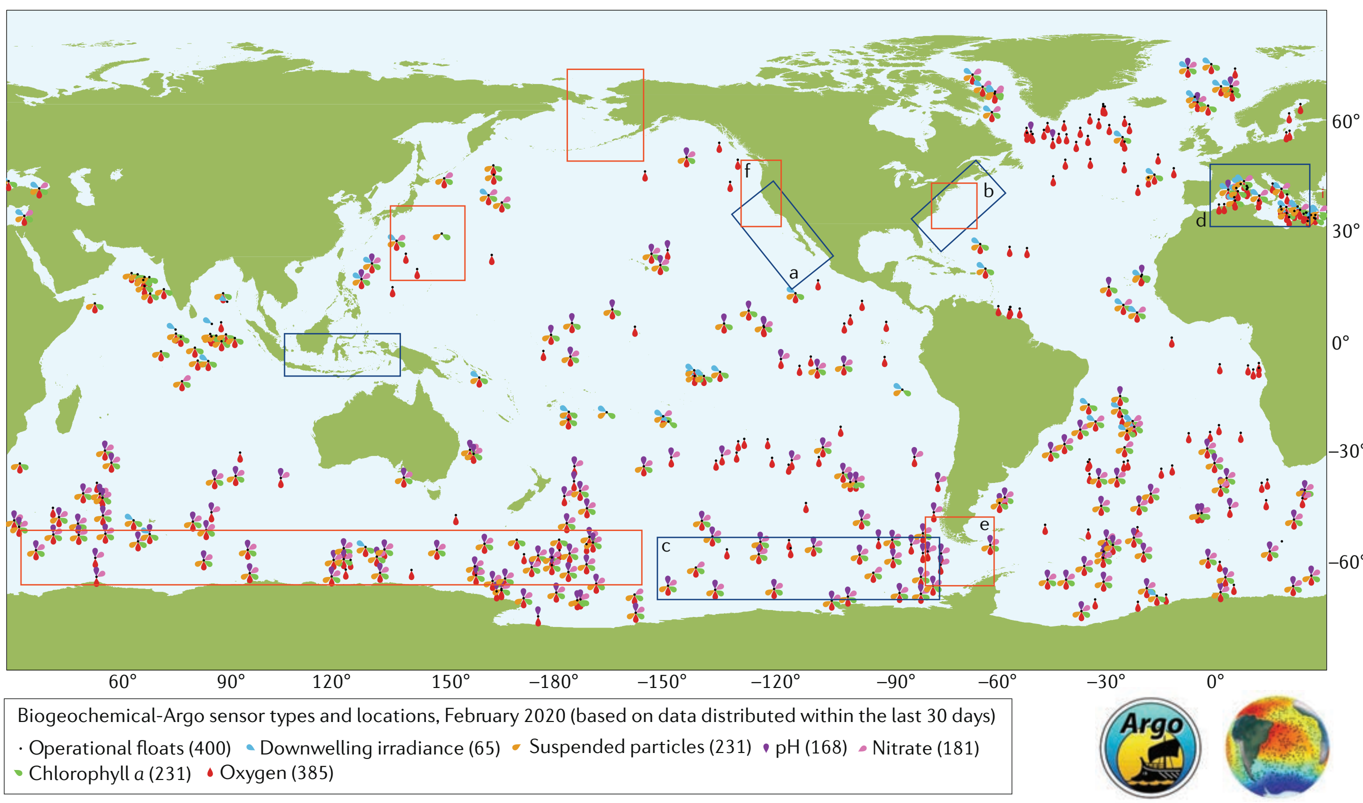

Fig. 4 | **Locations of recent autonomous ocean observations.** A map of the global array of Biogeochemical-Argo floats with various sensors in February 2020, with locations based on data distributions over 30 days. Boxes indicate areas that have been observed frequently by gliders (blue) or unmanned surface vehicles (red). Data in a obtained from REF.[115]; data in b from REF.[119]; data in c from REFS[124,130]; data in d from REF.[132]; data in e from REF.[133]; and data in f from REF.[112]. Adapted with permission from jcommops.org.

oceanography, and their approaches could be used for measuring biogeochemistry in the future. The EXport Processes in the Ocean from Remote Sensing (EXPORTS) project is currently developing a predictive understanding of the export and fate of global ocean net primary production and its implications for present and future climates, based on BGC-Argo floats, gliders and satellites[154]. These experiments and projects suggest a multiplatform future for marine biogeochemical research, in which synergic observations are capable of providing comprehensive 4D oceanographic information at a high spatiotemporal resolution.

The future of modelling and forecasting

Data from integrated observational platforms can be applied to evaluate and improve existing numerical models, ensuring model reliability for predicting marine biogeochemical processes (FIG. 5).

Reliable modelling for ocean biogeochemistry and ecosystem. Biogeochemical models can guide assessments of the current state of the ocean, elucidate ongoing trends and shifts, anticipate impacts of climate change and management policies, and maintain ocean ecosystem health (see a recent overview by Fennel et al.[155]). Such modelling capabilities can only be achieved in combination with comprehensive ocean biogeochemical observations, such as those provided by autonomous platforms.

Presently, biogeochemical modelling applications lag behind physical ocean modelling and prediction, mainly because traditional biogeochemical observation streams are too sparse for comprehensive validation, initialization and optimization of biogeochemical models[155]. Improved biogeochemical models can be used to estimate system properties that are not directly observable, such as lateral NO_3^- supply and air–sea exchange of CO_2 in the Southern Ocean[156]. They further offer spatial and temporal coverage not attainable by direct observations. The technological readiness for assimilating observations from BGC-Argo data into biogeochemical models has been demonstrated for state estimation[53,156,157], as well as parameter optimization[158].

Assimilation of physical observations in biogeochemical models can significantly reduce model biases[157]. BGC-Argo observations provide much better constraints than traditional observation streams on the dynamics and vertical structures of biogeochemical properties, as shown by a forecasting system for the Mediterranean Sea[53] and a biogeochemical-parameter-optimization study for the Gulf of Mexico[158]. New observations might also elucidate previously unrecognized shortcomings in biogeochemical models and satellite-based data products, and prompt modifications and refinements of model structures, parameterizations and algorithms for data products.

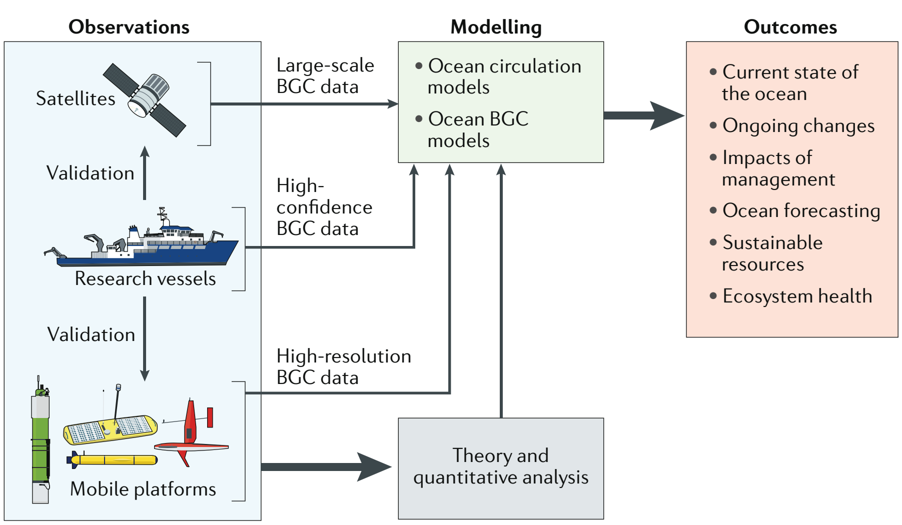

Fig. 5 | **Relationships between new observation technologies, biogeochemical models and ecosystem health management.** Mobile platforms, as an important component of global ocean-observing systems, provide high-resolution biogeochemical data. The data sets acquired by multiple platforms, including also ships and satellite sensors, are crucial to improving ocean biogeochemical models, and, in turn, to better evaluating the current state of ocean ecosystems and forecast its changes. BGC, biogeochemical.

Forecasting systems to support decision-making. A major focus in delivering the UN's sustainable development goals and aims set out in the Paris Agreement[2] is the construction of a reliable and comprehensive forecasting system. Forecasting systems are fundamental for facilitating the decision-making process, and there is great potential for BGC-Argo and other autonomous platforms to be at the forefront of these systems.

4D data sets can optimize forecasting system parameters[71,104]. Autonomous platforms have been used in marginal seas during spring blooms to measure nutrient content in high temporal frequency and vertical resolution, in order to resolve anomalous NO_3^- drawdown[159]. The implementation of high-spatiotemporal-resolution observational data into ocean models can fill observational gaps and help make reliable predictions for biogeochemical cycles, ocean primary production and fishery resource[160,161]. The behaviours of fishes, such as tuna in the tropical Pacific, can be better understood and simulated using accurate observational data to fit the likelihood of spawning, model migration patterns and improve stock assessment[162]. An ecosystem-based modelling procedure could also refine fishing policies adaptively, mitigating stressors induced by anthropogenic activities and guarding ecosystem health by informing sustainable resource use[163,164].

One of the major expectations from the UN Decade of Ocean Science for Sustainable Development is a well-predicted ocean, which relies on a sustainable ocean-observing system[165]. The major bottleneck for the development of biogeochemical models is the lack of observations; the use of in situ biochemical data from floats, gliders and USVs is, therefore, expected to be important for increasing the capability and credibility of ocean models[166]. Well-established models are anticipated to steer sustainable development of human society and can optimize approaches for assessing the responses of marine ecosystems to stress conditions, for example, algal blooms and storms, and help stakeholders make reasonable decisions[167].

Machine learning and artificial intelligence could be used to handle the autonomous-platform data sets[168]. These new approaches can extract spatial and temporal patterns from geospatial data to construct a hybrid model, systematically describing the multidisciplinary marine system[169]. A technique integrating a near real-time data-transmission system and data processing can enable the forecasting system to predict the ocean state in a comprehensive manner[170]. Improved forecasting models based on observational data streaming and cutting-edge data sciences are predicted to help explore the carbon cycle and underlying Earth systems[171]. An accurate forecasting system could, therefore, reduce the threats on climate and marine ecosystems through refining the decision-making process.

Conclusions

Many notable observations of ocean biogeochemistry and ecosystems have been made over the past century using traditional observation methods. However, these methods are now proving inadequate for capturing the varied temporal and spatial scales of biogeochemistry[11]. Autonomous platforms will play an important role in filling the observational gaps in monitoring and forecasting marine ecosystems. Argo floats and other autonomous platforms have also been considered as the most effective way to globally acquire vertical profiles of key environmental, biogeochemical and ecosystem variables[13,82]. They represent a new era of modern oceanographic observations, with great potential to provide new Essential Climate Variables and Essential Ocean Variables (ECVs and EOVs, respectively) related to ecosystem health and resource management[1]. There are ongoing developments in merging satellite and in situ robotic measurements for constructing a global three-dimensional view of biogeochemically relevant variables[79], and, in the near future, these three-dimensional fields will likely become essential parts of the data set for the initialization and/or validation of global biogeochemical models.

Currently, the implementation of integrated observation systems has primarily been addressed by the physical community[172,173]. It is now obvious that the scope of observational networks has to expand to include ocean biogeochemical and ecosystem components, and to integrate efforts across these scientific disciplines. The methodology for developing physical observational systems should serve as a guideline for the development of their biogeochemical and ecosystem counterparts[24]. The integration of biogeochemical and ecosystem components into an already existing physical observational system, however, is not just a matter of adding new sensors[77]. The implementation strategy of these new components will have to be discussed and organized by the physical, biogeochemical and ecosystem components[66].

BGC-Argo and other emerging autonomous platforms equipped with biogeochemical sensors are essential components for global observations of ocean conditions on multiple temporal and spatial scales. These global and regional networks of autonomous platforms, along with remotely sensed data, will provide the 4D information required to improve model simulations and forecasts of ocean conditions and ecosystem health. The success of any future ocean-observation system will strongly depend on the capability of the observing community to improve interactions between physical, chemical and biological oceanographic disciplines and integrate in situ, satellite and modelling components[174].

Fei Chai[1,2]✉, Kenneth S. Johnson[3], Hervé Claustre[4], Xiaogang Xing[1], Yuntao Wang[1], Emmanuel Boss[2], Stephen Riser[5], Katja Fennel[6], Oscar Schofield[7] and Adrienne Sutton[8]

[1]State Key Laboratory of Satellite Ocean Environment Dynamics (SOED), Second Institute of Oceanography, Ministry of Natural Resources, Hangzhou, China.

[2]School of Marine Sciences, University of Maine, Orono, ME, USA.

[3]Monterey Bay Aquarium Research Institute (MBARI), Moss Landing, CA, USA.

[4]Sorbonne Université & CNRS, Laboratoire d'Océanographie de Villefranche (LOV), Villefranche-sur-Mer, France.

[5]School of Oceanography, University of Washington, Seattle, WA, USA.

[6]Department of Oceanography, Dalhousie University, Halifax, Nova Scotia, Canada.

[7]Department of Marine and Coastal Sciences, Rutgers University, New Brunswick, NJ, USA.

[8]NOAA Pacific Marine Environmental Laboratory (PMEL), Seattle, WA, USA.

✉*e-mail: fchai@maine.edu*

https://doi.org/10.1038/s43017-020-0053-y
Published online: 21 May 2020

1. Lotze, H. K. et al. Global ensemble projections reveal trophic amplification of ocean biomass declines with climate change. *Proc. Natl Acad. Sci. USA* **116**, 12907–12912 (2019).
2. Cheng, L., Abraham, J., Hausfather, Z. & Trenberth, K. E. How fast are the oceans warming. *Science* **363**, 128–129 (2019).
3. Intergovernmental Panel on Climate Change. Climate Change 2013: the physical science basis (IPCC, 2013).
4. Rombouts, I. et al. Evaluating marine ecosystem health: case studies of indicators using direct observations and modelling methods. *Ecol. Indic.* **24**, 353–365 (2013).
5. Dore, J. E., Lukas, R., Sadler, D. W., Church, M. J. & Karl, D. M. Physical and biogeochemical modulation of ocean acidification in the central North Pacific. *Proc. Natl Acad. Sci. USA* **106**, 12235–12240 (2009).
6. Chacko, N. Chlorophyll bloom in response to tropical cyclone Hudhud in the Bay of Bengal: Bio-Argo subsurface observations. *Deep Sea Res. Part I Oceanogr. Res. Pap.* **124**, 66–72 (2017).
7. Ardyna, M. et al. Hydrothermal vents trigger massive phytoplankton blooms in the Southern Ocean. *Nat. Commun.* **10**, 2451 (2019).
8. Xu, H., Tang, D., Sheng, J., Liu, Y. & Sui, Y. Study of dissolved oxygen responses to tropical cyclones in the Bay of Bengal based on Argo and satellite observations. *Sci. Total Environ.* **659**, 912–922 (2019).
9. Bishop, J. K. B., Davis, R. E. & Sherman, J. T. Robotic observations of dust storm enhancement of carbon biomass in the North Pacific. *Science* **298**, 817–821 (2002).
10. Johnson, K. S. et al. Observing biogeochemical cycles at global scales with profiling floats and gliders: prospects for a global array. *Oceanography* **22**, 216–225 (2009).
11. Claustre, H., Johnson, K. S. & Takeshita, Y. Observing the global ocean with Biogeochemical-Argo. *Annu. Rev. Mar. Sci.* **12**, 23–48 (2020).
12. Shattuck, G. B. The expedition to the Bahama Islands of the Geographical Society of Baltimore. *Science* **18**, 427–432 (1903).
13. Sloyan, B. M. et al. The Global Ocean Ship-based Hydrographic Investigations Program (GO-SHIP): a platform for integrated multidisciplinary ocean science. *Front. Mar. Sci.* **6**, 445 (2019).
14. Bakker, D. C. E. et al. A multi-decade record of high-quality fCO_2 data in version 3 of the Surface Ocean CO_2 Atlas (SOCAT). *Earth Syst. Sci. Data* **8**, 383–413 (2016).
15. Martin, J. H. et al. Testing the iron hypothesis in ecosystems of the equatorial Pacific Ocean. *Nature* **371**, 123–129 (1994).
16. Lewis, M. R., Hebert, D. L., Harrison, W. G., Platt, T. & Oakey, N. S. Vertical nitrate fluxes in the oligotrophic ocean. *Science* **234**, 870–873 (1986).
17. Anderson, R. F. GEOTRACES: accelerating research on the marine biogeochemical cycles of trace elements and their isotopes. *Annu. Rev. Mar. Sci.* **12**, 49–85 (2020).
18. Pierella Karlusich, J. J., Ibarbalz, F. M. & Bowler, C. Phytoplankton in the Tara Ocean. *Annu. Rev. Mar. Sci.* **12**, 233–265 (2020).
19. Freeland, H. A short history of Ocean Station Papa and Line P. *Prog. Oceanogr.* **75**, 120–125 (2007).
20. Steinberg, D. K. et al. Overview of the US JGOFS Bermuda Atlantic Time-series Study (BATS): a decade-scale look at ocean biology and biogeochemistry. *Deep Sea Res. Part II Top. Stud. Oceanogr.* **48**, 1405–1447 (2001).
21. Karl, D. M. et al. Ecosystem changes in the North Pacific subtropical gyre attributed to the 1991–92 El Niño. *Nature* **373**, 230–234 (1995).
22. Signorini, S. R., McClain, C. R., Christian, J. R. & Wong, C. S. Seasonal and interannual variability of phytoplankton, nutrients, TCO_2, pCO_2, and O_2 in the eastern subarctic Pacific (ocean weather station Papa). *J. Geophys. Res.* **106**, 31197–31215 (2001).
23. Smith, G. C. et al. Polar ocean observations: a critical gap in the observing system and its effect on environmental predictions from hours to a season. *Front. Mar. Sci.* **6**, 429 (2019).
24. Wanninkhof, R. et al. A surface ocean CO_2 reference network, SOCONET and associated marine boundary layer CO_2 measurements. *Front. Mar. Sci.* **6**, 400 (2019).
25. Sutton, A. et al. Using present-day observations to detect when anthropogenic change forces surface ocean carbonate chemistry outside preindustrial bounds. *Biogeosciences* **13**, 5065–5083 (2016).
26. Benway, H. M. et al. Ocean time series observations of changing marine ecosystems: an era of integration, synthesis, and societal applications. *Front. Mar. Sci.* **6**, 393 (2019).
27. Bailey, K. et al. Coastal mooring observing networks and their data products: recommendations for the next decade. *Front. Mar. Sci.* **6**, 180 (2019).
28. Munk, W. in *Elsevier Oceanography Series, 63. Satellites, Oceanography and Society* Ch. 1 (ed. Halpern, D.) 1–4 (Elsevier, 2000).
29. Gordon, H. R., Clark, D. K., Mueller, J. L. & Hovis, W. A. Phytoplankton pigments from the Nimbus-7 Coastal Zone Color Scanner: comparisons with surface measurements. *Science* **210**, 63–66 (1980).
30. Groom, S. et al. Satellite ocean colour: current status and future perspective. *Front. Mar. Sci.* **6**, 485 (2019).
31. Halpern, D. (ed.) *Elsevier Oceanography Series, 63. Satellites, Oceanography and Society* (Elsevier, 2000).
32. Gregg, W. W., Conkright, M. E., Ginoux, P., O'Reilly, J. E. & Casey, N. W. Ocean primary production and climate: Global decadal changes. *Geophys. Res. Lett.* **30**, 1809 (2003).
33. Signorini, S. R. & McClain, C. R. Subtropical gyre variability as seen from satellites. *Remote. Sens. Lett.* **3**, 471–479 (2012).
34. Polovina, J. J., Howell, E. A. & Abecassis, M. Ocean's least productive waters are expanding. *Geophys. Res. Lett.* **35**, L03618 (2008).
35. Resplandy, L., Vialard, J., Lévy, M., Aumont, O. & Dandonneau, Y. Seasonal and intraseasonal

biogeochemical variability in the thermocline ridge of the southern tropical Indian Ocean. *J. Geophys. Res.* **114**, C07024 (2009).
36. Martinez, E., Antoine, D., D'Ortenzio, F. & Gentili, B. Climate-driven basin-scale decadal oscillations of oceanic phytoplankton. *Science* **326**, 1253–1256 (2009).
37. Behrenfeld, M. J. et al. Climate-driven trends in contemporary ocean productivity. *Nature* **444**, 752–755 (2006).
38. Fabry, V. J., McClintock, J. B., Mathis, J. T. & Grebmeier, J. M. Ocean acidification at high latitudes: the bellwether. *Oceanography* **22**, 160–171 (2009).
39. Gregg, W. W. & Casey, N. W. Sampling biases in MODIS and SeaWiFS ocean chlorophyll data. *Remote. Sens. Environ.* **111**, 25–35 (2007).
40. Letelier, R. M. et al. Climate-driven oscillation of phosphorus and iron limitation in the North Pacific Subtropical Gyre. *Proc. Natl Acad. Sci. USA* **116**, 12720–12728 (2019).
41. Niewiadomska, K., Claustre, H., Prieur, L. & d'Ortenzio, F. Submesoscale physical-biogeochemical coupling across the Ligurian current (northwestern Mediterranean) using a bio-optical glider. *Limnol. Oceanogr.* **53**, 2210–2225 (2008).
42. Ascani, F. et al. Physical and biological controls of nitrate concentrations in the upper subtropical North Pacific Ocean. *Deep Sea Res. Part II Top. Stud. Oceanogr.* **93**, 119–134 (2013).
43. Cetinic´, I. et al. A simple optical index shows spatial and temporal heterogeneity in phytoplankton community composition during the 2008 North Atlantic Bloom Experiment. *Biogeosciences* **12**, 2179–2194 (2015).
44. Meinig, C., Lawrence-Slavas, N., Jenkins, R. & Tabisola, H. M. The use of Saildrones to examine spring conditions in the Bering Sea: vehicle specification and mission performance. *Proc. MTS/IEEE Oceans* **2015**, 1–6 (2015).
45. Llort, J. et al. Evaluating Southern Ocean carbon eddy-pump from biogeochemical-Argo floats. *J. Geophys. Res.* **123**, 971–984 (2018).
46. Zhang, D. et al. Comparing air-sea flux measurements from a new unmanned surface vehicle and proven platforms during the SPURS-2 field campaign. *Oceanography* **32**, 122–133 (2019).
47. Mahadevan, A., D'Asaro, E., Lee, C. & Perry, M. J. Eddy-driven stratification initiates North Atlantic spring phytoplankton blooms. *Science* **337**, 54–58 (2012).
48. Omand, M. M. et al. Eddy-driven subduction exports particulate organic carbon from the spring bloom. *Science* **348**, 222–225 (2015).
49. Cokelet, E. D. et al. The use of Saildrones to examine spring conditions in the Bering sea. *Proc. MTS/IEEE Oceans* **2015**, 1–7 (2015).
50. Roemmich, D. et al. On the future of Argo: A global, full-depth, multi-disciplinary array. *Front. Mar. Sci.* **6**, 439 (2019).
51. Olsen, A. et al. The Global Ocean Data Analysis Project version 2 (GLODAPv2) – an internally consistent data product for the world ocean. *Earth Syst. Sci. Data* **8**, 297–323 (2016).
52. Gray, A. R. et al. Autonomous biogeochemical floats detect significant carbon dioxide outgassing in the high-latitude Southern Ocean. *Geophys. Res. Lett.* **45**, 9049–9057 (2018).
53. Cossarini, G. et al. Towards operational 3D-Var assimilation of chlorophyll Biogeochemical-Argo float data into a biogeochemical model of the Mediterranean Sea. *Ocean Model.* **133**, 112–128 (2019).
54. Organelli, E. et al. Bio-optical anomalies in the world's oceans: an investigation on the diffuse attenuation coefficients for downward irradiance derived from Biogeochemical Argo float measurements. *J. Geophys. Res. Oceans* **122**, 3543–3564 (2017).
55. Barbieux, M. et al. Assessing the variability in the relationship between the particulate backscattering coefficient and the chlorophyll *a* concentration from a global Biogeochemical-Argo database. *J. Geophys. Res.* **123**, 1229–1250 (2017).
56. Bellacicco, M. et al. Global variability of optical backscattering by non-algal particles from a Biogeochemical-Argo data set. *Geophys. Res. Lett.* **46**, 9767–9776 (2019).
57. Martin, A. et al. The oceans' twilight zone must be studied now, before it is too late. *Nature* **580**, 26–28 (2020).
58. Briggs, N. et al. High-resolution observations of aggregate flux during a sub-polar North Atlantic spring bloom. *Deep Sea Res. Part I Oceanogr. Res. Pap.* **58**, 1031–1039 (2011).
59. Lacour, L. et al. Unexpected winter phytoplankton blooms in the North Atlantic subpolar gyre. *Nat. Geosci.* **10**, 836–839 (2017).
60. Lacour, L., Briggs, N., Claustre, H., Ardyna, M. & Dall'Olmo, G. The intraseasonal dynamics of the mixed layer pump in the subpolar North Atlantic Ocean: A Biogeochemical-Argo float approach. *Global Biogeochemical Cycles* **33**, 266–281 (2019).
61. Rembauville, M. et al. Plankton assemblage estimated with BGC-Argo floats in the Southern Ocean: Implications for seasonal successions and particle export. *J. Geophys. Res.* **122**, 8278–8292 (2017).
62. Boyd, P. W., Claustre, H., Levy, M., Siegel, D. & Weber, T. Multi-faceted particle pumps drive carbon sequestration in the ocean. *Nature* **568**, 327–335 (2019).
63. Briggs, N., Dall'Olmo, G. & Claustre, H. Major role of particle fragmentation in regulating biological sequestration of CO_2 by the oceans. *Science* **367**, 791–793 (2020).
64. Estapa, M., Feen, M. & Breves, E. Direct observations of biological carbon export from profiling floats in the subtropical North Atlantic. *Global Biogeochem. Cycles* **33**, 282–300 (2019).
65. Willcox, S. et al. An autonomous mobile platform for underway surface carbon measurements in open-ocean and coastal waters. *Proc. IEEE Oceans* **2010**, 1–8 (2010).
66. Meinig, C. et al. Public–private partnerships to advance regional ocean-observing capabilities: a saildrone and NOAA-PMEL case study and future considerations to expand to global scale observing. *Front. Mar. Sci.* **6**, 448 (2019).
67. Wong, A. P. S. & Riser, S. C. Profiling float observations of the upper ocean under sea ice off the Wilkes Land coast of Antarctica. *J. Phys. Oceanogr.* **41**, 1102–1115 (2011).
68. Mayot, N. et al. Assessing phytoplankton activities in the seasonal ice zone of the Greenland Sea over an annual cycle. *J. Geophys. Res.* **123**, 8004–8025 (2018).
69. Boss, E. et al. Observations of pigment and particle distributions in the western North Atlantic from an autonomous float and ocean color satellite. *Limnol. Oceanogr.* **53**, 2112–2122 (2008).
70. Xing, X. et al. Seasonal variations of bio-optical properties and their interrelationships observed by Bio-Argo floats in the subpolar North Atlantic. *J. Geophys. Res.* **119**, 7372–7388 (2014).
71. Mignot, A., Ferrari, R. & Claustre, H. Floats with bio-optical sensors reveal what processes trigger the North Atlantic bloom. *Nat. Commun.* **9**, 190 (2018).
72. Davis, R. E., Regier, L. A., Dufour, J. & Webb, D. C. The Autonomous Lagrangian Circulation Explorer (ALACE). *J. Atmos. Ocean. Technol.* **9**, 264–285 (1992).
73. Intergovernmental Oceanographic Commission. The Argo project: IOC assembly resolution XX-6 (IOC, 1999).
74. Riser, S. C. et al. Fifteen years of ocean observations with the global Argo array. *Nat. Clim. Change* **6**, 145–153 (2016).
75. Zilberman, N. V. Deep Argo: sampling the total ocean volume in state of the climate in 2016. *Bull. Am. Meteorol. Soc.* **98**, S73–S74 (2017).
76. Vilibic´, I. & Mihanovic´, H. Observing the bottom density current over a shelf using an Argo profiling float. *Geophys. Res. Lett.* **40**, 910–915 (2013).
77. Johnson, K. S. et al. Biogeochemical sensor performance in the SOCCOM profiling float array. *J. Geophys. Res.* **122**, 6416–6436 (2017).
78. Riser, S. C., Swift, D. D. & Drucker, R. Profiling floats in SOCCOM: technical capabilities for studying the southern ocean. *J. Geophys. Res.* **123**, 4055–4073 (2018).
79. Sauzède, R. et al. A neural network-based method for merging ocean color and Argo data to extend surface bio-optical properties to depth: retrieval of the particulate backscattering coefficient. *J. Geophys. Res. Ocean.* **121**, 2552–2571 (2016).
80. Bishop, J. K. B. & Wood, T. J. Year-round observations of carbon biomass and flux variability in the Southern Ocean. *Global Biogeochem. Cycles* **23**, GB2019 (2009).
81. Bif, M. B., Siqueira, L. & Hansell, D. A. Warm events induce loss of resilience in organic carbon production in the northeast Pacific Ocean. *Global Biogeochem. Cycles* **33**, 1174–1186 (2019).
82. Graff, J. R. et al. Analytical phytoplankton carbon measurements spanning diverse ecosystems. *Deep Sea Res. Part I Oceanogr. Res. Pap.* **102**, 16–25 (2015).
83. Davis, R. E., Eriksen, C. C. & Jones, C. P. in *Technology and Applications of Autonomous Underwater Vehicles* (ed. Griffiths, G.) 37–58 (Taylor & Francis, 2002).
84. Schofield, O. et al. Slocum gliders: Robust and ready. *J. Field Robot.* **24**, 473–485 (2007).
85. Rudnick, D. L. Ocean research enabled by underwater gliders. *Annu. Rev. Mar. Sci.* **8**, 519–541 (2016).
86. Glenn, S. et al. Stratified coastal ocean interactions with tropical cyclones. *Nat. Commun.* **7**, 10887–10887 (2016).
87. Chao, Y. Autonomous underwater vehicles and sensors powered by ocean thermal energy. *Proc. IEEE Oceans* **2016**, 1–4 (2016).
88. Cross, J. N. et al. Innovative technology development for Arctic exploration. *Proc. IEE Oceans* **2015**, 1–8 (2015).
89. Mordy, C. W. et al. Advances in ecosystem research: Saildrone surveys of oceanography, fish, and marine mammals in the Bering Sea. *Oceanography* **30**, 113–115 (2017).
90. Bourassa, M. A. et al. High-latitude ocean and sea ice surface fluxes: challenges for climate research. *Bull. Am. Meteorol. Soc.* **94**, 403–423 (2013).
91. Todd, R. E. et al. Global perspectives on observing ocean boundary current systems. *Front. Mar. Sci.* **6**, 423 (2019).
92. Monteiro, P. M. S. et al. Intraseasonal variability linked to sampling alias in air-sea CO_2 fluxes in the Southern Ocean. *Geophys. Res. Lett.* **42**, 8507–8514 (2015).
93. Biogeochemical-Argo Planning Group. The scientific rationale, design, and implementation plan for a Biogeochemical-Argo float array (eds Johnson K. & Claustre H.) (Biogeochemical-Argo, 2016).
94. Bittig, H. C. et al. A BGC-Argo guide: Planning, deployment, data handling and usage. *Front. Mar. Sci.* **6**, 502 (2019).
95. Testor, P. et al. OceanGliders: a component of the integrated GOOS. *Front. Mar. Sci.* **6**, 422 (2019).
96. Guihen, D., Fielding, S., Murphy, E. J., Heywood, K. J. & Griffiths, G. An assessment of the use of ocean gliders to undertake acoustic measurements of zooplankton: the distribution and density of Antarctic krill (*Euphausia superba*) in the Weddell Sea. *Limnol. Oceanogr. Methods* **12**, 373–389 (2014).
97. Cyr, F. et al. A new glider-compatible optical sensor for dissolved organic matter measurements: test case from the NW Mediterranean Sea. *Front. Mar. Sci.* **4**, 89 (2017).
98. Jiang, Z.-P. et al. Application and assessment of a membrane-based pCO_2 sensor under field and laboratory conditions. *Limnol. Oceanogr. Methods* **12**, 264–280 (2014).
99. Briggs, E. M. et al. Solid state sensor for simultaneous measurement of total alkalinity and pH of seawater. *ACS Sens.* **2**, 1302–1309 (2017).
100. Williams, N. L. et al. Calculating surface ocean pCO2 from biogeochemical Argo floats equipped with pH: An uncertainty analysis. *Global Biogeochem. Cycles* **31**, 591–604 (2017).
101. Bittig, H. C. et al. Oxygen optode sensors: principle, characterization, calibration, and application in the ocean. *Front. Mar. Sci.* **4**, 429 (2018).
102. Irigoien, X. et al. Large mesopelagic fishes biomass and trophic efficiency in the open ocean. *Nat. Commun.* **5**, 3271–3271 (2014).
103. John, M. A. S. et al. A dark hole in our understanding of marine ecosystems and their services: perspectives from the mesopelagic community. *Front. Mar. Sci.* **3**, 31 (2016).
104. Riser, S. C. & Johnson, K. S. Net production of oxygen in the subtropical ocean. *Nature* **451**, 323–325 (2008).
105. Yang, J., Riser, S. C., Nystuen, J. A., Asher, W. & Jessup, A. T. Regional rainfall measurements: using the Passive Aquatic Listener during the SPURS field campaign. *Oceanography* **28**, 124–133 (2015).
106. Suberg, L. et al. Assessing the potential of autonomous submarine gliders for ecosystem monitoring across multiple trophic levels (plankton to cetaceans) and pollutants in shallow shelf seas. *Methods Oceanogr.* **10**, 70–89 (2014).
107. Wall, C. C. et al. Mapping the soundscape off the southeastern USA by using passive acoustic glider technology. *Mar. Coast. Fish.* **9**, 23–37 (2017).
108. Guihen, D. & Hewitt, J. High-resolution acoustic surveys with diving gliders come at a cost of aliasing moving targets. *PLoS One* **13**, e0201816 (2018).

109. Delworth, T. L. et al. Simulated climate and climate change in the GFDL CM2.5 high-resolution coupled climate model. *J. Clim.* **25**, 2755–2781 (2012).
110. Jones, S. D., Le Quéré, C. & Rödenbeck, C. Autocorrelation characteristics of surface ocean pCO_2 and air-sea CO_2 fluxes. *Global Biogeochem. Cycles* **26**, GB2042 (2012).
111. Majkut, J. D. et al. An observing system simulation for Southern Ocean carbon dioxide uptake. *Philos. Trans. A Math. Phys. Eng. Sci.* **372**, 20130046 (2014).
112. Voosen, P. Saildrone fleet could help replace aging buoys. *Science* **359**, 1082–1083 (2018).
113. Adams, K. A., Barth, J. A. & Shearman, R. K. Intraseasonal cross-shelf variability of hypoxia along the Newport, Oregon, hydrographic line. *J. Phys. Oceanogr.* **46**, 2219–2238 (2016).
114. Saldías, G. S., Shearman, R. K., Barth, J. A. & Tufillaro, N. Optics of the offshore Columbia River plume from glider observations and satellite imagery. *J. Geophys. Res.* **121**, 2367–2384 (2016).
115. Barth, J. A. et al. Better regional ocean observing through cross-national cooperation: a case study from the Northeast Pacific. *Front. Mar. Sci.* **6**, 93 (2019).
116. Domingues, R. et al. Upper ocean response to Hurricane Gonzalo (2014): Salinity effects revealed by targeted and sustained underwater glider observations. *Geophys. Res. Lett.* **42**, 7131–7138 (2015).
117. Miles, T., Seroka, G., Kohut, J., Schofield, O. & Glenn, S. Glider observations and modeling of sediment transport in Hurricane Sandy. *J. Geophys. Res.* **120**, 1771–1791 (2015).
118. Todd, R. E., Asher, T. G., Heiderich, J., Bane, J. M. & Luettich, R. A. Transient response of the Gulf Stream to multiple hurricanes in 2017. *Geophys. Res. Lett.* **45**, 10,509–10,519 (2018).
119. Domingues, R. et al. Ocean observations in support of studies and forecasts of tropical and extratropical cyclones. *Front. Mar. Sci.* **6**, 446 (2019).
120. Gawarkiewicz, G. et al. The changing nature of shelf-break exchange revealed by the OOI Pioneer Array. *Oceanography* **31**, 60–70 (2018).
121. Trowbridge, J. et al. The Ocean Observatories Initiative. *Front. Mar. Sci.* **6**, 74 (2019).
122. Swart, S., Thomalla, S. J. & Monteiro, P. M. S. The seasonal cycle of mixed layer dynamics and phytoplankton biomass in the Sub-Antarctic Zone: A high-resolution glider experiment. *J. Mar. Syst.* **147**, 103–115 (2015).
123. Cheng, L., Abraham, J., Hausfather, Z. & Trenberth, K. E. How fast are the oceans warming? *Science* **363**, 128–129 (2019).
124. Viglione, G. A., Thompson, A. F., Flexas, M. M., Sprintall, J. & Swart, S. Abrupt transitions in submesoscale structure in southern Drake Passage: glider observations and model results. *J. Phys. Oceanogr.* **48**, 2011–2027 (2018).
125. Kahl, L. A., Schofield, O. & Fraser, W. R. Autonomous gliders reveal features of the water column associated with foraging by Adelie penguins. *Integr. Comp. Biol.* **50**, 1041–1050 (2010).
126. Schofield, O. et al. Penguin biogeography along the West Antarctic Peninsula: Testing the canyon hypothesis with Palmer LTER observations. *Oceanography* **26**, 204–206 (2013).
127. Thompson, A. F., Heywood, K. J., Schmidtko, S. & Stewart, A. L. Eddy transport as a key component of the Antarctic overturning circulation. *Nat. Geosci.* **7**, 879–884 (2014).
128. Carvalho, F., Kohut, J., Oliver, M. J., Sherrell, R. M. & Schofield, O. Mixing and phytoplankton dynamics in a submarine canyon in the West Antarctic Peninsula. *J. Geophys. Res.* **121**, 5069–5083 (2016).
129. Carvalho, F., Kohut, J., Oliver, M. J. & Schofield, O. Defining the ecologically relevant mixed-layer depth for Antarctica's coastal seas. *Geophys. Res. Lett.* **44**, 338–345 (2017).
130. Schofield, O. et al. In situ phytoplankton distributions in the Amundsen Sea Polynya measured by autonomous gliders. *Elementa* **3**, 1–17 (2015).
131. Garabato, A. C. N. et al. Vigorous lateral export of the meltwater outflow from beneath an Antarctic ice shelf. *Nature* **542**, 219–222 (2017).
132. Tintoré, J. et al. Challenges for sustained observing and forecasting systems in the Mediterranean Sea. *Front. Mar. Sci.* **6**, 568 (2019).
133. Thomson, J. & Girton, J. B. Sustained measurements of Southern Ocean air-sea coupling from a wave glider autonomous surface vehicle. *Oceanography* **30**, 104–109 (2017).
134. Schmidt, K. M., Swart, S., Reason, C. & Nicholson, S. A. Evaluation of satellite and reanalysis wind products with in situ wave glider wind observations in the Southern Ocean. *J. Atmos. Ocean. Technol.* **34**, 2551–2568 (2017).
135. Talley, L. D. et al. Changes in ocean heat, carbon content, and ventilation: a review of the first decade of GO-SHIP global repeat hydrography. *Annu. Rev. Mar. Sci.* **8**, 185–215 (2016).
136. Williams, N. L. et al. Assessment of the carbonate chemistry seasonal cycles in the Southern Ocean from persistent observational platforms. *J. Geophys. Res.* **123**, 4833–4852 (2018).
137. Sauzède, R. et al. Estimates of water-column nutrient concentrations and carbonate system parameters in the global ocean: a novel approach based on neural networks. *Front. Mar. Sci.* **4**, 128 (2017).
138. Bittig, H. C. et al. An alternative to static climatologies: robust estimation of open ocean CO_2 variables and nutrient concentrations from T, S, and O_2 data using Bayesian neural networks. *Front. Mar. Sci.* **5**, 328 (2018).
139. Pfeil, B. et al. A uniform, quality controlled Surface Ocean CO_2 Atlas (SOCAT). *Earth Syst. Sci. Data* **5**, 125–143 (2012).
140. Villareal, T. A. & Wilson, C. A comparison of the Pac-X trans-Pacific wave glider data and satellite data (MODIS, Aquarius, TRMM and VIIRS). *PLoS One* **9**, e92280 (2014).
141. Haentjens, N., Boss, E. & Talley, L. D. Revisiting Ocean Color algorithms for chlorophyll *a* and particulate organic carbon in the Southern Ocean using biogeochemical floats. *J. Geophys. Res.* **122**, 6583–6593 (2017).
142. Wojtasiewicz, B. et al. Use of bio-optical profiling float data in validation of ocean colour satellite products in a remote ocean region. *Remote. Sens. Environ.* **209**, 275–290 (2018).
143. Lavigne, H., D'Ortenzio, F., Claustre, H. & Poteau, A. Towards a merged satellite and in situ fluorescence ocean chlorophyll product. *Biogeosciences* **9**, 2111–2125 (2012).
144. Roesler, C. et al. Recommendations for obtaining unbiased chlorophyll estimates from in situ chlorophyll fluorometers: A global analysis of WET Labs ECO sensors. *Limnol. Oceanogr. Methods* **15**, 572–585 (2017).
145. Gerbi, G. P. et al. Validation of ocean color remote sensing reflectance using autonomous floats. *J. Atmos. Ocean. Technol.* **33**, 2331–2352 (2016).
146. Leymarie, E. et al. ProVal: A new autonomous profiling float for high quality radiometric measurements. *Front. Mar. Sci.* **5**, 437 (2018).
147. Dierssen, H. M. & Smith, R. C. Bio-optical properties and remote sensing ocean color algorithms for Antarctic Peninsula waters. *J. Geophys. Res.* **105**, 26301–26312 (2000).
148. Kahru, M. & Mitchell, B. G. Blending of ocean colour algorithms applied to the Southern Ocean. *Remote. Sens. Lett.* **1**, 119–124 (2010).
149. Guinet, C. et al. Calibration procedures and first data set of Southern Ocean chlorophyll a profiles collected by elephant seals equipped with a newly developed CTD-fluorescence tags. *Earth Syst. Sci. Data* **5**, 15–29 (2013).
150. Coale, K. H. et al. IronEx-I, an in situ iron-enrichment experiment: Experimental design, implementation and results. *Deep Sea Res. Part II Top. Stud. Oceanogr.* **45**, 919–945 (1998).
151. Pascual, A. et al. A multiplatform experiment to unravel meso- and submesoscale processes in an intense front (AlborEx). *Front. Mar. Sci.* **4**, 39 (2017).
152. Lindstrom, E. J. et al. Autonomous multi-platform observations during the salinity processes in the upper-ocean regional study. *Oceanography* **30**, 38–48 (2017).
153. Centurioni, L. R. et al. Northern Arabian Sea Circulation-Autonomous Research (NASCar): a research initiative based on autonomous sensors. *Oceanography* **30**, 74–87 (2017).
154. Siegel, D. et al. Prediction of the export and fate of global ocean net primary production: The EXPORTS science plan. *Front. Mar. Sci.* **3**, 22 (2016).
155. Fennel, K. et al. Advancing marine biogeochemical and ecosystem reanalyses and forecasts as tools for monitoring and managing ecosystem health. *Front. Mar. Sci.* **6**, 89 (2019).
156. Verdy, A. & Mazloff, M. R. A data assimilating model for estimating Southern Ocean biogeochemistry. *J. Geophys. Res.* **122**, 6968–6988 (2017).
157. Yu, L., Fennel, K., Bertino, L., El Gharamti, M. & Thompson, K. R. Insights on multivariate updates of physical and biogeochemical ocean variables using an Ensemble Kalman Filter and an idealized model of upwelling. *Ocean Model.* **126**, 13–28 (2018).
158. Wang, B., Fennel, K., Yu, L. & Gordon, C. Assessing the value of Argo profiles versus satellite observations for biogeochemical model optimization in the Gulf of Mexico. *Biogeosciences Discuss*. https://doi.org/10.5194/bg-2020-137 (2020).
159. Vincent, A. G. et al. Nitrate drawdown during a shelf sea spring bloom revealed using a novel microfluidic in situ chemical sensor deployed within an autonomous underwater glider. *Mar. Chem.* **205**, 29–36 (2018).
160. Buitenhuis, E. T., Hashioka, T. & Le Quéré, C. Combined constraints on global ocean primary production using observations and models. *Global Biogeochem. Cycles* **27**, 847–858 (2013).
161. Subramanian, A. C. et al. Ocean observations to improve our understanding, modeling, and forecasting of subseasonal-to-seasonal variability. *Front. Mar. Sci.* **6**, 427 (2019).
162. Lehodey, P., Senina, I., Nicol, S. & Hampton, J. Modelling the impact of climate change on South Pacific albacore tuna. *Deep Sea Res. Part II Top. Stud. Oceanogr.* **113**, 246–259 (2015).
163. Barange, M. et al. Impacts of climate change on marine ecosystem production in societies dependent on fisheries. *Nat. Clim. Change* **4**, 211–216 (2014).
164. Koenigstein, S., Mark, F. C., Gößlingreisemann, S., Reuter, H. & Poertner, H. Modelling climate change impacts on marine fish populations: process-based integration of ocean warming, acidification and other environmental drivers. *Fish Fish.* **17**, 972–1004 (2016).
165. Ryabinin, V. et al. The UN Decade of Ocean Science for Sustainable Development. *Front. Mar. Sci.* **6**, 470 (2019).
166. Zhang, X., Wang, L., Jiang, X. & Zhu, C. (eds) *Modeling with Digital Ocean and Digital Coast* (Springer, 2017).
167. Zhang, W.-Z., Wang, H., Chai, F. & Qiu, G. Physical drivers of chlorophyll variability in the open South China Sea. *J. Geophys. Res.* **121**, 7123–7140 (2016).
168. Yu, Y., Gu, L. L. & Wu, X. Q. The application of artificial intelligence in ocean development. *Adv. Mater. Res.* **864–867**, 2116–2119 (2014).
169. Reichstein, M. et al. Deep learning and process understanding for data-driven Earth system science. *Nature* **566**, 195–204 (2019).
170. Liu, Y., Qiu, M., Liu, C. & Guo, Z. Big data challenges in ocean observation: a survey. *Pers. Ubiquitous Comput.* **21**, 55–65 (2017).
171. Runge, J. et al. Inferring causation from time series in Earth system sciences. *Nat. Commun.* **10**, 2553 (2019).
172. Le Traon, P. Y. From satellite altimetry to Argo and operational oceanography: three revolutions in oceanography. *Ocean. Sci.* **9**, 901–915 (2013).
173. Gasparin, F. et al. Requirements for an integrated *in situ* Atlantic Ocean observing system from coordinated observing system simulation experiments. *Front. Mar. Sci.* **6**, 83 (2019).
174. Le Traon, P. Y. et al. From observation to information and users: the Copernicus Marine Service perspective. *Front. Mar. Sci.* **6**, 234 (2019).
175. Johnson, K. S. et al. Long-term nitrate measurements in the ocean using the In Situ Ultraviolet Spectrophotometer: sensor integration into the Apex profiling float. *J. Atmos. Ocean. Technol.* **30**, 1854–1866 (2013).
176. Johnson, K. S. et al. Deep-Sea DuraFET: a pressure tolerant pH sensor designed for global sensor networks. *Anal. Chem.* **88**, 3249–3256 (2016).
177. Cetinic´, I., Toro-Farmer, G., Ragan, M., Oberg, C. & Jones, B. H. Calibration procedure for Slocum glider deployed optical instruments. *Opt. Express* **17**, 15420–15430 (2009).
178. Haëntjens, N. et al. Detecting mesopelagic organisms using biogeochemical-Argo floats. *Geophys. Res. Lett.* **47**, e2019GL086088 (2020).
179. Bushinsky, S. M., Takeshita, Y. & Williams, N. L. Observing changes in ocean carbonate chemistry: our autonomous future. *Curr. Clim. Change Rep.* **5**, 207–220 (2019).
180. Ruhl, H. A. et al. Societal need for improved understanding of climate change, anthropogenic impacts, and geo-hazard warning drive development of ocean observatories in European Seas. *Prog. Oceanogr.* **91**, 1–33 (2011).

Acknowledgements
F.C., X.X. and Y.W. were supported by the National Key Research and Development Program of China (2016YFC1401600), the National Natural Science Foundation of China (41730536) and the Scientific Research Fund of the Second Institute of Oceanography, Ministry of Natural Resources, China (14283). K.S.J. was supported by the David and Lucile Packard Foundation and by the NSF's Southern Ocean Carbon and Climate Observations and Modeling project (SOCCOM) under the NSF award PLR-1425989, with additional support from the NOAA and NASA. H.C. was supported by funding from a European Research Council Advanced Grant (REFINE, no. 834177). BGC-Argo data are collected and made freely available by the international Argo programme and the national programmes that contribute to it (http://www.argo.ucsd.edu, http://argo.jcommops.org). The Argo programme is part of the Global Ocean Observing System (GOOS). This is Pacific Marine Environmental Laboratory (PMEL) contribution #5058.

Author contributions
F.C., X.X. and Y.W. researched data for the article. F.C., K.S.J., H.C., X.X., K.F., O.S. and A.S. all contributed to the writing of the article. F.C., X.X., Y.W., E.B. and S.R. contributed to reviewing and editing the manuscript prior to submission. All authors made a substantial contribution to the discussion of content.

Competing interests
The authors declare no competing interests.

Peer review information
Nature Reviews Earth & Environment thanks Burton Jones, Tetsuichi Fujiki, Zhaohui Aleck Wang and the other, anonymous, reviewer for their contribution to the peer review of this work.

RELATED LINKS
Biogeochemical-Argo programme: https://biogeochemical-argo.org/
OceanObs'19: http://www.oceanobs19.net/
United Nations Decade of Ocean Science for Sustainable Development: https://www.oceandecade.org/

Validation of the HWRF-POM and HWRF-HYCOM hurricane forecasting systems during Hurricane Dorian using glider observations

1st Maria F. Aristizabal-Vargas, 3rd Travis Miles,
4th Scott Glenn
Department of Marine and Coastal Sciences
Rutgers University
New Brunswick, NJ 08901
1st maria.aristizabal@marine.rutgers.edu
3rd tnmiles@marine.rutgers.edu
4th glenn@marine.rutgers.edu

2nd Hyun-Sook Kim, 5nd Avichal Mehra
NOAA-NCEP
5830 University Research Ct, College Park, MD 20740
2nd hyun.sook.kim@noaa.gov
5nd avichal.mehra@noaa.gov

Global Oceans 2020: Singapore - U.S. Gulf Coast | 978-1-7281-5446-6/20/$31.00 ©2020 IEEE | DOI: 10.1109/IEEECONF38699.2020.9389066

Abstract*—Hurricane Dorian devastated the Bahamas in August 2019 when it underwent rapid intensification and transitioned from a category 4 to a category 5 storm. The operational hurricane forecasting models consistently under predicted the intensity evolution of Dorian. It has been shown that an accurate representation of the upper ocean processes that affect air-sea heat fluxes in coupled atmospheric-ocean models is necessary for an accurate hurricane intensity forecast. In this work, we evaluate several ocean surface metrics that are relevant to air-sea heat fluxes in one of NOAA's operational hurricane forecasting systems during the 2019 hurricane season: HWRF2019-POM initialized from climatology, and two experimental hurricane forecasting models: HWRF2020-POM and HWRF2020-HYCOM, both initialized from the Real Time Ocean Forecasting System (RTOFS). For this, we use temperature and salinity data from a fleet of autonomous underwater gliders, dedicated to hurricane research and operations, during the passage of Hurricane Dorian through the Caribbean. We contrast our results with estimates from a data assimilative model, the Global Ocean Forecasting System (GOFS 3.1). We found that even though all the models have a good skill in predicting temperature and salinity over the full water column, the model's skill considerably deteriorates for the ocean surface metrics evaluated. We also found that of the three hurricane forecasting models, HWRF2020-HYCOM is the model with the highest skill for the ocean surface metrics. All the models also show a cold bias in the mixed layer temperature and a deficit in the ocean heat content with respect to the glider observations. These results demonstrate that the implementation of HYCOM as the ocean model underneath the hurricane forecasting models, will significantly improve the representation of key quantities that are important for the air-sea heat fluxes during tropical cyclones.

***Index Terms*—Hurricane Dorian, HWRF-POM, HWRF-HYCOM, Underwater Gliders**

I. Introduction

It has been demonstrated that the sea surface thermal structure plays a very important role in the intensification of storms [4], [9] and that an accurate representation of the upper ocean processes that affect air-sea heat fluxes in ocean-atmosphere coupled models is necessary for an accurate intensity forecast [6], [8], [18]. In the last three decades there has been significant progress reducing the error in the storm track in the operational hurricanes forecasting models, however the error reduction in the intensity has been marginal [15].

In August 2019, Hurricane Dorian developed from a tropical wave off the west coast of Africa and moved through the Caribbean gaining strength. Dorian continued its way into the Atlantic and made landfall in Great Abaco Island on September 1 as a category 5 hurricane, becoming the strongest hurricane in record to make landfall in the Bahamas. None of the hurricane forecasting models captured the intensity evolution five days prior to Dorian reaching its maximum strength [1].

We evaluated three upper ocean metrics that have been identified as having an effect on the intensification and/or weakening of storms in four different models: the HWRF2019-POM operational, the HWRF2020-POM experimental, the HWRF2020-HYCOM experimental and GOFS 3.1 during the passage of Hurricane Dorian through the Caribbean. The first metric evaluated is the surface mixed layer temperature. The surface mixed layer is the surface portion of the water column where turbulent processes, such as wind-driven mixing, make water density nearly uniform [3]. The second metric is the ocean heat content (OHC), defined as the amount of heat in the surface ocean above the 26 degrees isotherm. OHC is a Metric that has been shown to be correlated with the intensification of storms in the open ocean [11]–[13]. The last metric is the depth average temperature in the top 100 meters (T100). T100 was proposed as a metric that quantifies the resulting sea surface temperature (SST) after the passage of a hurricane that fully mixes the top 100 meters, somehow accounting for the effect of cold subsurface water and the strength of vertical stratification on storm weakening [17].

978-1-7281-5446-6/20/$31.00 ©2020 IEEE

II. Methods

A. Observational Data Sources

A fleet of underwater gliders was deployed in the Caribbean Sea, Gulf of Mexico, the South and Middle Atlantic Bight during the 2019 hurricane season as part of the National Oceanic and Atmospheric Administration (NOAA) hurricane underwater glider project and operations [16]. During the passage of Hurricane Dorian through the Caribbean, there were six underwater gliders deployed in the region north and south of Puerto Rico. These gliders were deployed by the NOAA Atlantic Oceanographic and Meteorological Laboratory (AOML) and the Integrated Ocean Observing Systems (IOOS) from July 15 to November 15 2019 (Fig. 1) The gliders collected temperature and salinity with an approximate frequency of 2 hours and reaching a maximum depth of 900 meters. The glider data is publicly available through the IOOS glider data assembly center (DAC) (https://data.ioos.us/gliders/erddap)

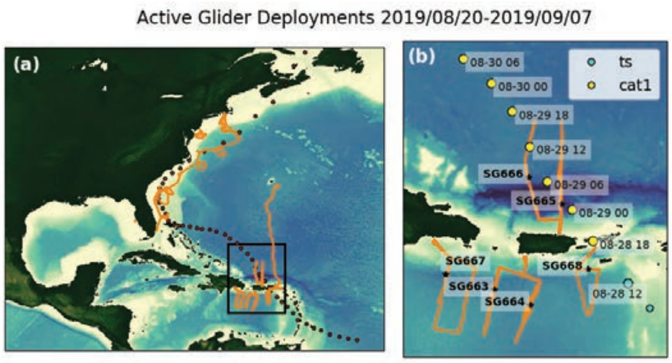

Fig. 1. (a) North Atlantic map showing the path of hurricane Dorian (red dots) and the glider trajectories between Aug 20 to Sept 7 2019 (yellow lines). (b) Detail of the Caribbean Sea around Puerto Rico showing the path and category (red symbols) and the glider trajectories (yellow lines).

B. Numerical Data Sources

The Hurricane Weather and Forecasting model (HWRF) coupled to the Message Passing Interface Princeton Ocean Model - Tropical Cyclone (MPIPOM-TC) is one of the hurricane forecasting systems run by NOAA National Centers for Environmental Prediction (NCEP) [2]. Hereon we will call this couple system HWRF2019-POM and it is one of the models that was used by the National Hurricane Center (NHC) to guide their official track and intensity hurricane forecast in the North Atlantic Basin during 2019. The ocean component of HWRF2019-POM was initialized from climatology and a feature-based model. In this study, we also accessed the output of an experimental version of the coupled system, HWRF2020-POM, with the ocean component initialized from the Real Time Ocean Forecasting system (RTOFS). In addition, we evaluated another experimental system, HWRF coupled to the Hybrid Coordinate Ocean Model, HWRF2020-HYCOM, with ocean initialization from RTOFS [10].

The Global Ocean Forecasting System, GOFS 3.1, is the US Navy operational ocean model. It is a global model based on the Hybrid Coordinate Ocean model (HYCOM). GOFS 3.1 implements a 3DVar data assimilation algorithm, called NCODA that uses satellite altimeter data, satellite and in-situ surface temperature, in-situ vertical temperature and salinity from Argo floats, buoys, gliders and XBTs (only temperature). More details about GOFS 3.1/NCODA system can be found in the GOFS 3.1 validation test report [14]. The hindcast output for GOFS 3.1 used here can be accessed at https://tds.hycom.org/thredds/dodsC/GLBv0.08/expt 93.0/ts3z.html.

C. Surface Ocean Metrics

The mixed layer was estimated as the surface portion of the water column that presents very small changes in vertical stratification. We used two different criteria, a density criteria (2) and a temperature criteria (1).

$$T - T_{10} \leq 0.2^o \tag{1}$$

$$\rho_{10} - \rho \leq 0.125 \frac{kg}{m^3} \tag{2}$$

where ρ_{10} is the water density at 10 meters depth and ρ is density at different depths.

The average Temperature and salinity within the mixed layer are calculated as the average temperature and salinity of every profile that is within the mixed layer.

Ocean heat content is defined as the depth integrated heat content between the depth of the 26 ^{o} isotherm to the surface (Eq. 3).

$$OHC = C_p \rho_0 \int_{Z_{26^o}}^{0} (T - 26) dz \tag{3}$$

Where C_p is the heat capacity of sea water, ρ_0, is the mean density of water column down to the 26^o isotherm and T is temperature at different depths in degrees Celsius.

The depth average temperature in the top 100 meters (T100) is a metric that estimates the resulting SST after the passage of a hurricane due to vertical mixing processes in the ocean interior [17].

D. Taylor Diagrams and Mean Bias

In order to quantify the model's skill, we estimated the normalized standard deviation and correlation between the observational data and the model's output. We used all the available temperature and salinity profiles from the fleet of gliders present north and south of Puerto Rico when Hurricane Dorian was transiting through that region (Fig. 1). We obtained the corresponding along-track temperature and salinity glider-transects in the ocean models by interpolating the glider position and time onto the model grid and output timestamp. The normalized standard deviation and correlation for all the different metrics can be visualized together by constructing a Taylor diagram [19], giving us a compact way to assess the model's skills.

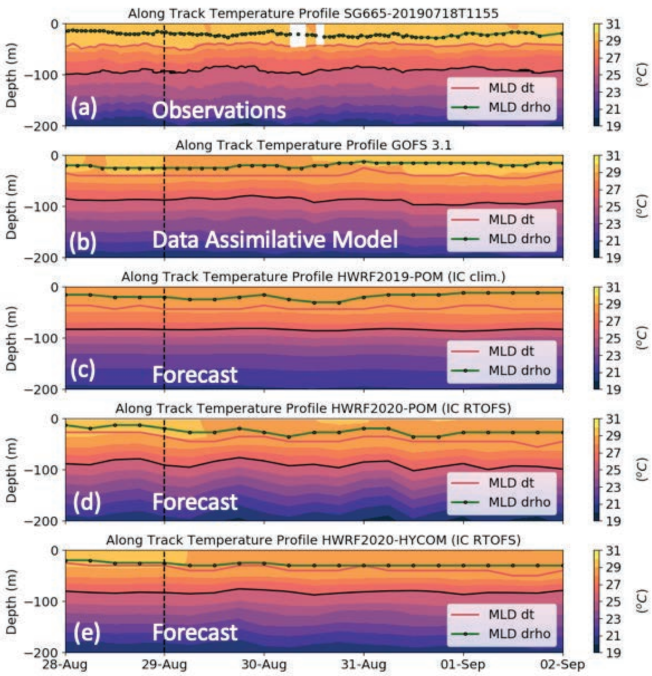

Fig. 2. (a) Temperature transects for glider SG665 from Aug 29 to Sep 2. (b), (c), (d), (e) The same along-track transect as for SG665 but interpolated onto the respective model grid and timestamp. MLD dt and MLD drho stands for mixed layer depth based on the temperature criteria and density criteria respectively. The dash vertical line in all figures shows the time when Hurricane Dorian was the closest glider SG665.

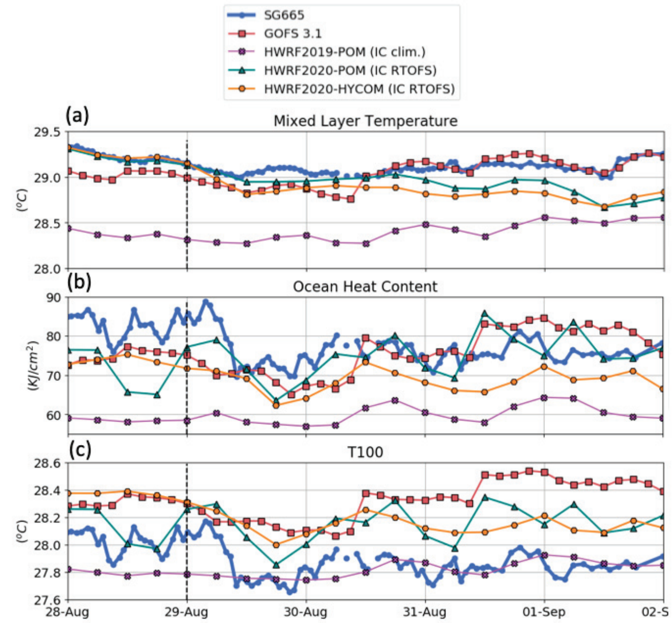

Fig. 3. Time series of (a) mixed layer temperature, (b) ocean heat content and (c) T100 for glider SG665 (blue), GOFS 3.1 (red), HWRF2019-POM (IC clim.) (purple), HWRF2020-POM (IC RTOFS) (green) and HWRF2020-HYCOM (IC RTOFS) (orange). The dash vertical line in all figures shows the time when Hurricane Dorian was the closest glider SG665.

Another statistical quantity that is not represented in a Taylor Diagram is the mean bias. We estimated the mean bias percentage of the different metrics as

$$Bias\% = \frac{\overline{X_{obs}} - \overline{X_{model}}}{\overline{X_{obs}}} \times 100\% \tag{4}$$

Where $\overline{X_{obs}}$ is the mean value of a specific metric from the observations and $\overline{X_{model}}$ is the mean value of the same metric from the different model's output.

III. Results

The temperature transects from the glider observations show that the surface temperature at the end of August north of Puerto Rico was close to $30^oC$and that the 26^oC isotherm is approximately at 100 meters depth (Fig. 2 (a)). The mixed layer depth (MLD) based on the temperature criteria (MLD dt) (Eq. 1) is consistently deeper than the mixed layer depth based on the density criteria (MLD drho) (Eq. 2). A qualitative comparison of the glider transect for the SG665 glider from Aug. 28 to Sep. 2 2019 shows that the temperature fields in the four ocean models agree well with the glider observations (Fig. 2 (b)-(e)). In all the models the MLD based on the density criteria is shallower than the MLD based on the temperature criteria and the 26^oC isothermal is approximately at the same depth or slightly shallower than the observations. The discrepancy in the MLD using the two different criteria is caused by the so called barrier layer, a fresh surface layer

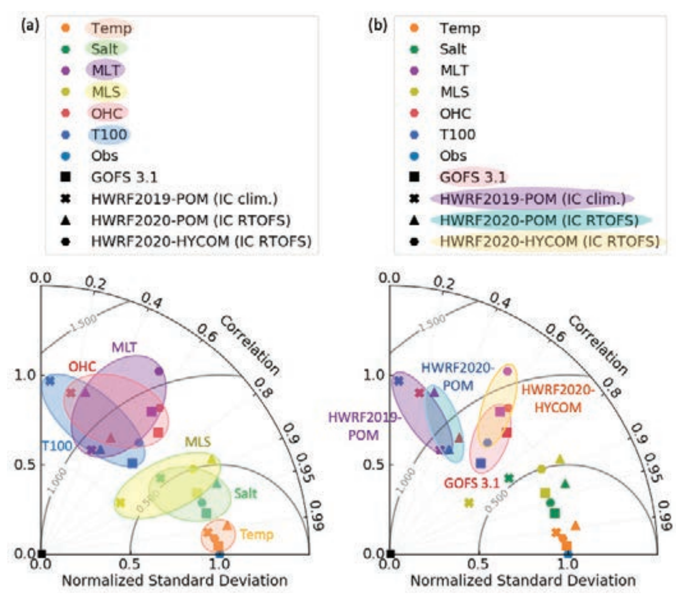

Fig. 4. Taylor diagram showing the model skill for the four models evaluated: GOFS 3.1, HWRF2019-POM (IC clim.), HWRF2020-POM (IC RTOFS) and HWRF2020-HYCOM (IC RTOFS). in (a) The ellipses group the skill by the different quantities and in (b) The ellipses group the skill according to the different models.

that characterizes the Caribbean Sea and is produced by the spreading of the Amazon and Orinoco river plumes [7]. As a consequence, salinity rather than temperature controls vertical stratification at the surface in the Caribbean Sea. For this reason, we will use the estimate of the mixed layer based on the density criteria from now on in our analysis.

Despite the general agreement in the temperature fields, there are obvious differences between the observed mixed layer temperature based on the density criteria and the one estimated from the models (Fig. 3 (a)). HWRF2019-POM, initialized by climatology, is about 1^oC colder than observations. HWRF2020-POM and HWRF2020-HYCOM, both initialized from RTOFS, have almost the same temperature as the observations during the first 24 hours of the forecast, but beyond this point the mixed layer temperature gets progressively colder. GOFS 3.1, the data assimilative model, starts colder than the glider temperature but it approaches it on Aug. 30 12Z, after a jump in temperature that could have been caused by the data assimilation algorithm. The measured ocean heat content (OHC) is well above $60Kj/cm^2$ (Fig. 3 (b)), the OHC level that is considered minimum to favor storm intensification [13]. The OHC in HWRF2019-POM is well below the observed value but the other models match better the measured OHC, although HWRF2020-HYCOM is consistently lower than the glider estimate. In contrast, T100 from HWRF2019-POM is the closest to the observational value, while the other models exhibit higher values (Fig. 3 (c)).

The previous qualitative assessments are quantified estimating the normalized Taylor diagrams and mean bias between the glider observations and the different models. (Fig. 4 (a)). The normalized Taylor diagram shows that all the models have a good skill in the temperature (Temp) and salinity (Salt) of the entire water column. However the three metrics relevant for the air-sea heat fluxes: temperature in the surface mixed layer (MLT) based on the density criteria, ocean heat content (OHC) and depth average temperature in the top 100 m (T100), are poorly represented in all models. In particular, HYCOM2019-POM, initialized from climatology, and HYCOM2020-POM, initialized from RTOFS, have very low skill for the surface metrics (Fig. 4 (b)). But these metrics are fairly represented in HWRF2020-HYCOM, initialized from RTOFS, and GOFS 3.1. The fact that HWRF2020-HYCOM, is close in skill to the data assimilative model GOFS 3.1, gives us confidence that of the three air-sea coupled hurricane forecasting models evaluated, HWRF2020-HYCOM is the one that better represents the ocean surface conditions.

The mean percentage bias (Table I) for the MLT shows that all the models are colder than observations within the ocean surface mixed layer, with HWRF2019-POM initialized from climatology being the coldest. We see a similar pattern for the OHC. HWRF2019-POM presents a 22% deficit with respect to the observations in the OHC while GOFS 3.1 has only a deficit of 3.6%. From the hurricane coupled models, HWRF2020-HYCOM has the lowest OHC bias.

TABLE I
MEAN BIAS PERCENTAGE BETWEEN THE OBSERVATIONS AND THE DIFFERENT MODELS FOR THE MIXED LAYER TEMPERATURE (MLT), OCEAN HEAT CONTENT (OHC) AND DEPTH AVERAGE TEMPERATURE IN THE TOP 100 METERS (T100).

	GOFS 3.1	HWRF19-POM (IC Clim.)	HWRF20-POM (IC RTOFS)	HWRF20-HYCOM (IC RTOFS)
MLT	-0.40 %	-3.0 %	-0.94 %	-0.62%
OHC	-3.6 $	-22 %	-17 %	-8.7 %
T100	1.4 %	-0.46 %	0.49 %	1.2 %

IV. Conclusion

The ocean-atmosphere coupled hurricane models HWRF2019-POM, HWRF2020-POM and HWRF2020-HYCOM, have a good skill in the temperature and salinity over the full water column when Hurricane Dorian was transitioning from tropical storm to category 1 hurricane. However, their skill is significantly reduced for the upper ocean metrics that are relevant to the air-sea heat fluxes such as temperature in the mixed layer, ocean heat content and average temperature in the top 100 meters. However the skill of HRWR2020-HYCOM was the best of the three coupled models and comparable to the data assimilative model GOFS 3.1. This shows that HRWR2020-HYCOM is the coupled model that best represents the ocean surface metrics that are important for the air-sea heat fluxes during storms.

Acknowledgment

The author Maria Aristizábal Vargas was supported by the NOAA Integrated Ocean Observing System (IOOS), NOAA award number NA16NOS0120020. We thank Ben LaCour for his help to get access to the NOAA machines. We also thank all the institutions and researchers that provided their glider data to the IOOS glider DAC.

References

[1] Avila, L., Stewart, S., Berg, R., and AB, H, "Tropical cyclone report hurricane dorian (al052019) 24 august–7 september 2019". 2020. National Hurricane Center.

[2] Biswas M. K., S. Abarca, L. Bernardet, I. Ginis, E. Grell, M. Iacono, E. Kalina, B. Liu, Q. Liu, T. Marchok, A. Mehra, K. Newman, J. Sippel, V. Tallapragada, B. Thomas, W. Wang, H. Winterbottom, and Z. Zhang, 2018: Hurricane Weather Research and Forecasting (HWRF) Model: 2018 Scientific Documentation, Available at https://dtcenter.org/HurrWRF/users/docs/index.php

[3] DE Ruijter, W. P., "Effects of velocity shear in advective mixed-layer model", Journal of Geophysical Research, 13, 1983, pp.1589-1599.

[4] Emanuel, K. A, "Thermodynamic control of hurricane intensity". Nature, 401(6754), 1999, pp.665–669.

[5] Metzger, E.J, Helber, R.W., Hogan, P.J., Posey, Thoppil, P.G., Townsend, T.L., Wallcraft, A.J., Smedstad, O.M., Franklin, D.S., Zamudio-Lopez, L., Phelps, M.W, "Global Ocean Forecasting System 3.1, validation test", Naval Research Laboratoty. 2017, NRL/MR/7320—17-9722.

[6] Jr, G., Shay, L. K., Brewster, J., and Teague, W. J. (2011). Evaluation and sensitivity analysis of an ocean model response to hurricane Ivan. Monthly Weather Review, 139(3), pp.921–945.

[7] Hu, C., Montgomery, E.T., Schmitt, R.W. and Muller-Karger, F.E., "The dispersal of the Amazon and Orinoco River water in the tropical Atlantic and Caribbean Sea: Observation from space and S-PALACE floats". Deep Sea Research Part II: Topical Studies in Oceanography, 51(10-11), 2004, pp.1151-1171.

[8] Jaimes, B., Shay, L. K., and Halliwell, G. R., "The response of quasigeostrophic oceanic vortices to tropical cyclone forcing". Journal of physical oceanography, 41(10), 2011, pp.1965–1985.

[9] Jaimes, B., Shay, L. K.,and Uhlhorn, E. W., " Enthalpy and momentum fluxes during hurricane earl relative to underlying ocean features". Monthly Weather Review, 143(1), 2015, pp.111–131.
[10] Kim, H.S., Lozano, C., Tallapragada, V., Iredell, D., Sheinin, D., Tolman, H.L., Gerald, V.M. and Sims, J., "Performance of ocean simulations in the coupled HWRF–HYCOM model". Journal of Atmospheric and Oceanic Technology, 31(2), 2014, pp.545-559.
[11] Leipper, D. F., and Volgenau, D., "Hurricane heat potential of the Gulf of Mexico". Journal of Physical Oceanography, 2(3), 1972, pp.218–224.
[12] Lin, I.-I., Chen, C.-H., Pun, I.-F., Liu, W. T., and Wu, C.-C., "Warm ocean anomaly, air sea fluxes, and the rapid intensification of tropical cyclone Nargis". Geophysical Research Letters, 36(3), 2008.
[13] Mainelli, M., DeMaria, M., Shay, L. K., and Goni, G., "Application of oceanic heat content estimation to operational forecasting of recent Atlantic category 5 hurricanes". Weather and Forecasting, 23(1), 2008, pp.3–16.
[14] Metzger, E.J, Helber, R.W. ,Hogan, P.J., Posey, Thoppil, P.G., Townsend, T.L., Wallcraft, A.J., Smedstad, O.M., Franklin, D.S., Zamudio-Lopez, L., Phelps, M.W, "Global Ocean Forecasting System 3.1, validation test", Naval Research Laboratory. 2017, NRL/MR/7320—17-9722.
[15] "National hurricane center forecast verification". National Hurricane Center and Central Pacific Hurricane Center. 04 April 2017. https://www.nhc.noaa.gov/verification/verify5.shtml
[16] The NOAA hurricane underwater glider project and operations. "https : //www.aoml.noaa.gov/phod/goos/gliders/index.php". (Accessed: 2020/05/05)
[17] Price, J. F., "Metrics of hurricane-ocean interaction: vertically-integrated or vertically-averaged ocean temperature?", Ocean Science, 5(3), 2009, 351-368.
[18] Shay, L. K., and Brewster, J. K. (2010). Oceanic heat content variability in the eastern pacific ocean for hurricane intensity forecasting. Monthly Weather Review, 138(6), 2110–2131.
[19] Taylor, K. E., "Summarizing multiple aspects of model performance in a single diagram". Journal of Geophysical Research: Atmospheres, 106(D7), 2001, pp.7183–7192.

On the Development of SWOT In Situ Calibration/Validation for Short-Wavelength Ocean Topography

Jinbo Wang,[a] Lee-Lueng Fu,[a] Bruce Haines,[a] Matthias Lankhorst,[b] Andrew J. Lucas,[b,c] J. Thomas Farrar,[d] Uwe Send,[b] Christian Meinig,[e] Oscar Schofield,[f] Richard Ray,[h] Matthew Archer,[a] David Aragon,[f] Sebastien Bigorre,[d] Yi Chao,[g] John Kerfoot,[f] Robert Pinkel,[b] David Sandwell,[b] and Scott Stalin[e]

[a] *Jet Propulsion Laboratory, California Institute of Technology, Pasadena, California*
[b] *Scripps Institution of Oceanography, University of California, San Diego, La Jolla, California*
[c] *Department of Mechanical and Aerospace Engineering, University of California, San Diego, La Jolla, California*
[d] *Woods Hole Oceanographic Institution, Woods Hole, Massachusetts*
[e] *Pacific Marine Environmental Laboratory, National Oceanic and Atmospheric Administration, Seattle, Washington*
[f] *Rutgers, The State University of New Jersey, New Brunswick, New Jersey*
[g] *Remote Sensing Solutions, Monrovia, California*
[h] *NASA Goddard Space Flight Center, Greenbelt, Maryland*

(Manuscript received 7 April 2021, in final form 10 November 2021)

ABSTRACT: The future Surface Water and Ocean Topography (SWOT) mission aims to map sea surface height (SSH) in wide swaths with an unprecedented spatial resolution and subcentimeter accuracy. The instrument performance needs to be verified using independent measurements in a process known as calibration and validation (Cal/Val). The SWOT Cal/Val needs in situ measurements that can make synoptic observations of SSH field over an $O(100)$ km distance with an accuracy matching the SWOT requirements specified in terms of the along-track wavenumber spectrum of SSH error. No existing in situ observing system has been demonstrated to meet this challenge. A field campaign was conducted during September 2019–January 2020 to assess the potential of various instruments and platforms to meet the SWOT Cal/Val requirement. These instruments include two GPS buoys, two bottom pressure recorders (BPR), three moorings with fixed conductivity–temperature–depth (CTD) and CTD profilers, and a glider. The observations demonstrated that 1) the SSH (hydrostatic) equation can be closed with 1–3 cm RMS residual using BPR, CTD mooring and GPS SSH, and 2) using the upper-ocean steric height derived from CTD moorings enable subcentimeter accuracy in the California Current region during the 2019/20 winter. Given that the three moorings are separated at 10–20–30 km distance, the observations provide valuable information about the small-scale SSH variability associated with the ocean circulation at frequencies ranging from hourly to monthly in the region. The combined analysis sheds light on the design of the SWOT mission postlaunch Cal/Val field campaign.

KEYWORDS: Internal waves; Ocean dynamics; Small scale processes; Altimetry; Global positioning systems (GPS); In situ oceanic observations; Ship observations

1. Introduction

The Surface Water and Ocean Topography (SWOT) mission is a pathfinder mission that will demonstrate the next-generation satellite altimeter based on a Ka-band radar interferometer (KaRIn) (Durand et al. 2010; Fu and Ubelmann 2014). The major thrusts of the mission are the low noise and wide-swath sea surface height (SSH) measurements of the KaRIn instrument. After its launch in 2022, understanding the performance of the KaRIn instrument against a ground truth of dynamical SSH is crucial for subsequent scientific applications. This emphasizes the importance of the mission's ocean topography calibration and validation (Cal/Val), which focuses on the wavenumber spectrum of SWOT SSH measurement errors.

In the past, the ground truth for satellite altimeters was typically produced using point measurements from ground stations such as tide gauges, a method that has been used successfully for all previous nadir-altimeter missions, such as the Jason-series altimeters (e.g., Haines et al. 2021; Bonnefond et al. 2019; Quartly et al. 2021). However, the SWOT mission requires a new approach for calibration and validation because the SWOT science requirement is specified in terms of the wavenumber spectrum over 15–1000 km wavelengths (Fig. 1; Desai et al. 2018). As such, validation of the sensor requires capturing a synoptic SSH field along a line covering 15–1000 km wavelengths. Validation of wavelengths ranging from ~120 to 1000 km will be accomplished by the onboard Jason-class altimeter (Wang and Fu 2019), whose performance in wavenumber space is known (e.g., Dufau et al. 2016). The ground truth over the short wavelength (15–150 km) may be achieved by airborne instruments such as lidar (Melville et al. 2016) for geodetic validation and in situ oceanographic measurements (Wang et al. 2018) for oceanographic validation. For the latter, we need an observing approach designed specifically for SSH wavenumber spectrum validation at scales between 15 and 150 km with subcentimeter accuracy.

Corresponding author: Jinbo Wang, jinbo.wang@jpl.nasa.gov

DOI: 10.1175/JTECH-D-21-0039.1

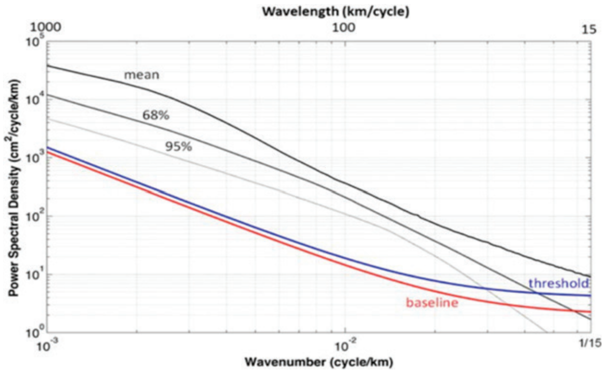

FIG. 1. The SSH baseline requirement spectrum (red line) as a function of wavenumber (Desai et al. 2018). The thick black line is the mean spectrum of the *Jason-2* altimeter track 159, which extends from the Southern Ocean to North Pacific. The 68th and 95th percentiles are marked by the thin black line and the gray line; i.e., 68% and 95% of the spectra are above the corresponding curve. The red curve defines the baseline requirement represented by $E(k) = 2 + 0.001\,25k^{-2}(\mathrm{cm}^2\ \mathrm{cpkm}^{-1})$. The blue curve represents the threshold requirement $E(k) = 4 + 0.0015k^{-2}(\mathrm{cm}^2\ \mathrm{cpkm}^{-1})$.

An observing system simulation experiment (OSSE) was conducted as a first step to evaluate the feasibility of an array of moorings to meet the Cal/Val requirement (Wang et al. 2018). Based on the OSSE, the top challenges in reconstructing the small-scale synoptic SSH field over a 150 km distance come from the emerging dominance of superinertial high-frequency SSH variability at spatial scales <150 km, and the weak SSH signal itself at those scales. These challenges led to a series of field campaigns to identify the relevant ocean processes at the Cal/Val site (near 35.6°N, 125°W) and to evaluate the performance of different in situ platforms and instruments in meeting the SWOT requirement.

Here we report the results from a recent field campaign conducted between September 2019 and January 2020. The rest of the paper is organized as follows. Section 2 summarizes the past development of SWOT oceanographic Cal/Val and the in situ field campaigns. The summary provides the background and motivation of this study. Section 3 discusses the instrumentation of the 2019/20 field campaign. Results are shown in section 4. Uncertainties in the observations and quantifications exist and are discussed in section 5. Summaries are presented in section 6.

2. The development of SWOT SSH Cal/Val

This section reviews the previous work in developing an in situ observing array for the SWOT oceanographic Cal/Val. Section 2a introduces the nature of the SWOT SSH Cal/Val. Section 2b discusses the theoretical basis for conducting oceanographic Cal/Val through in situ mooring platforms. Section 2c reviews the previous OSSE results. Section 2d discusses the transformation of the measurement errors from wavenumber spectrum to time series measurement at a single point and provides accuracy requirements imposed on individual observing platforms used in the field campaign. Section 2e briefly reviews a pilot field campaign that took place prior to the recent 2019/20 field campaign.

a. SWOT SSH Cal/Val

After the SWOT satellite launch, the first 90 days will be dedicated to instrument hardware checkout. The second 90 days will be for the mission Cal/Val along a 1-day-repeat orbit (Desai et al. 2018). The 90-day Cal/Val orbit provides more frequent SSH measurements at certain locations for both the validation of the instrument and to develop an understanding of the SWOT measurements from an oceanographic perspective at a very early stage. The SWOT mission Cal/Val has two aspects: 1) characterizing the performance of the instrument KaRIn from a *geodetic* perspective and 2) characterizing the SWOT-observed variability from an *oceanographic* perspective.

Recent studies have shown that the superposition of eddies and internal gravity waves in SSH may make the interpretation of SWOT observations complicated (Rocha et al. 2016; Qiu et al. 2018; Torres et al. 2018; Morrow et al. 2019). When considering the exploratory nature of the SWOT mission as the next-generation altimeter, it is crucially important that we use this 1-day repeat fast-sampling period, in which the satellite will overfly ground-track crossover region twice a day. The results will shed light on the connection of the SWOT SSH to the dynamics of ocean circulation beneath the sea surface (e.g., d'Ovidio et al. 2019), which is the mission's ultimate science goal for oceanography.

b. Closing the SSH budget using in situ observations

The ocean dynamics governing the large and mesoscale SSH variability have been the subject of intensive research over the past few decades, stimulated in part by satellite altimetry (e.g., Fu and Cazenave 2001). The SSH signal that has spatial scales smaller than mesoscale, however, has not yet been fully explored, largely because of lack of observations. The first task is to understand the observability of SSH at scales of ~150 km and smaller. To what level of accuracy can we close the SSH budget (formulated below) using available in situ instruments and platforms?

Integrating the hydrostatic equation $dp/dz = \rho g$ from the ocean floor to the free surface, the SSH budget equation can be written as

$$p(-H) = \int_{-H}^{\eta} g\rho(z)\, dz + p_a,$$

in which $-H$ is the depth of the ocean floor, η is the free sea surface height, p_a is the atmospheric pressure. We are interested in the temporal variability. Decomposing each term into a temporal mean (overline) and an anomaly (prime) gives

$$\begin{aligned} \overline{p}(-H) &= \int_{-H}^{0} g\overline{\rho(z)}\, dz + g\rho_0\overline{\eta} + \overline{p_a}, \\ p'(-H) &= \int_{-H}^{0} g\rho'\, dz + g\rho_0\eta' + p'_a, \end{aligned} \tag{1}$$

where ρ_0 the reference density, ρ' the in situ density anomaly, η' the sea surface height anomaly referenced to $\overline{\eta}$, p'_a the atmospheric pressure anomaly. The term $g\eta'\rho'$ is second order and neglected. $\overline{\eta}\rho'$ is implicitly included in the first term on the right hand by taking $z = 0$ at $\overline{\eta}$. The four terms in Eq. (1) represent temporal anomalies of bottom pressure, dynamic height, sea surface pressure due to the free surface, and atmospheric pressure. These terms from left to right can be assessed by bottom pressure recorders (BPR), moorings with CTDs, GPS buoys, and barometers, respectively. We test the closure of Eq. (1) using GPS, BPR, and mooring CTDs in section 4b.

Note that the dominant variability in both the bottom pressure and the free sea surface elevation is nonsteric, such as the barotropic tides. The steric component is much weaker, typically only on the order of a few centimeters.

Denote the steric and nonsteric components of the sea surface height and bottom pressure as η', η'_{ns}, p'_{bs}, and p'_{bns}, respectively. We further expand Eq. (1) into

$$p'_{\text{bs}} + p'_{\text{bns}} = \int_{-H}^{0} g\rho'\,dz + g\rho_0 s'_\eta + g\rho_0\eta'_{\text{ns}} + p'_a. \tag{2}$$

The cancellation of the nonsteric components is written as $p'_{\text{bns}} = g\rho_0\eta'_{\text{ns}} + p'_a$. After removing the nonsteric components, Eq. (2) becomes

$$p'_{\text{bs}} - g\rho_0\eta'_s = \int_{-H}^{0} g\rho'\,dz. \tag{3}$$

Equation (3) means that the dynamic height due to the density change can be calculated directly from density profiles or indirectly calculated from bottom pressure and steric sea surface height (after the atmospheric pressure correction). In reality, the steric and nonsteric components are impossible to separate from bottom pressure or GPS free sea surface based on a single mooring as a result of an underdetermined problem. Equation (3) is only used to illustrate the meaning of the closure of the SSH equation. It is worth noting that deriving $O(1)$ cm steric height from $O(100)$ cm GPS SSH and BP-derived SSH requires extreme accuracy in both instruments. For this reason, one of the objectives of the SWOT prelaunch campaigns (sections 2e and 3) was to examine the closure of the hydrostatic equation [Eq. (1)] and to quantify the errors associated with different platforms and instruments.

c. An OSSE

An OSSE was first conducted to understand the SSH signal at SWOT scales and the performance of different instruments and platforms in meeting the SWOT requirement (Wang et al. 2018). We used a tide-resolving high-resolution global ocean simulation as a virtual ocean and simulated the performance of several instruments/platforms commonly used in modern observational physical oceanography, i.e., underway CTDs (UCTD), gliders, fixed-CTD moorings, pressure inverted echo sounders (PIES). The model simulation is the high-resolution global ocean simulation using MITgcm with 1/48° horizontal resolution, llc4320, used in several recent studies (e.g., Rocha et al. 2016; Torres et al. 2018; Su et al. 2018; Yu et al. 2019). One conclusion was that in the Cal/Val region (near 35.7°N, 124.7°W) the total SSH over the 15–150 km wavelength range (SWOT scale) can be represented by the upper-ocean steric height after the large-scale barotropic signal and inverted barometer (IB) influence are removed through a high-pass filter. The residual is well below the mission error requirement shown in the error wavenumber spectrum in the OSSE study.

The OSSE study also found that internal gravity waves and internal tides (IGW) might be strong enough to mask the eddy field SSH signal over the small spatial scales and impose an observational challenge (Wang et al. 2018). This dominance of IGWs over small scales is simply because the SSH wavenumber spectrum of eddies (balanced motions) is steeper than that of IGWs (Qiu et al. 2018; Chereskin et al. 2019; Callies and Wu 2019). The presence of internal gravity wave motions on these scales poses a challenge for designing an in situ observational network. For example, through the OSSE we found that slow platforms such as ship-towed UCTD are unable to meet the Cal/Val requirement. An array of station-keeping gliders can marginally meet the requirements, but the errors are mostly over small spatial scales (~50 km) due to the high-frequency motions. PIES can empirically convert the travel time of an acoustic signal to steric height but have about 5 cm uncertainty (D. R. Watts 2016, personal communication; Wang et al. 2018), which is larger than SWOT's subcentimeter requirement. The OSSE study concluded that an array of CTD-equipped moorings could produce a steric height field that is sufficiently accurate to meet the requirement.

The numerical ocean simulation used in the OSSE, however, has excessive tidal energy (C. Wunsch 2017, personal communication; Savage et al. 2017; Yu et al. 2019), which introduces large uncertainties in the OSSE results. It is also not clear how well the deep-ocean variability is reproduced. Field experiments are necessary to test the performance of different platforms and instruments. In addition, while the OSSE focused on oceanographic Cal/Val, the geodetic SSH such as measured by GPS buoys needs to be evaluated to synthesize the oceanographic and geodetic objectives. It led to two objectives of the field campaigns: 1) quantify the performance of oceanographic in situ platforms and 2) test the GPS measurements and their relationship with those derived from hydrographic measurements.

d. SWOT measurement error requirement

In the two field campaigns described in the next section, we do not have a full-scale mooring array that enables a wavenumber spectrum calculation. To evaluate the performance of an in situ instrument, the SWOT error requirement in wavenumber space needs to be integrated over a range of wavenumbers $\int E(k)$ to assess time series in situ measurement. The mission requirement is specified between 15 and 1000 km wavelengths. The baseline error[1] is

[1] The "baseline error" is the error the mission currently plans to achieve. The "threshold error" is the error level that the mission must achieve to address the minimum science goals.

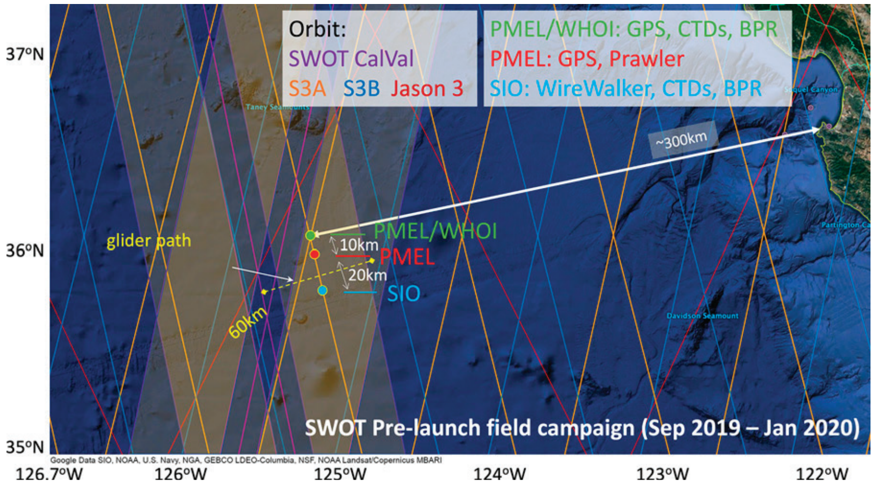

FIG. 2. Map of the field campaign instrumentation. The three moorings are marked by the three colored dots. From north to south, they are the PMEL/WHOI mooring, the PMEL Prawler mooring with GPS on the buoy, and the SIO full-depth mooring. The separation distance is 10 and 20 km. The dashed yellow line is the glider target path of 60 km wide. Two bottom pressure recorders were deployed near the PMEL/WHOI and SIO moorings.

$E(k) = 4\ \text{cm}^2\ \text{cpkm}^{-1} + 0.00125k^{-2}$, where k is the wavenumber with a unit of cycle km^{-1} (cpkm) and 2 cm^2 cpkm^{-1} is the KaRIn instrument noise averaged across a swath over 7.5 km distance for significant wave height (SWH) of 2 m (Fig. 1, red line). The threshold error requirement is similar: $E(k) = 4\ \text{cm}^2\ \text{cpkm}^{-1} + 0.0015k^{-2}$ (Fig. 1, blue line).

For the spatial range between 15 and 1000 km, an integration of the error based on the requirement is $\int_{1\times10^{-3}}^{1/15} E(k)\,dk = 1.36\ \text{cm}^2$, i.e., 1.17 cm RMS. If only the 15–150 km range is considered, the total integrated error has 0.29 cm^2 variance (0.54 cm RMS), the integrated random KaRIn noise is 0.12 cm^2 (0.35 cm RMS), and the integrated correlated error (cpkm) is 0.17 cm^2 (0.41 cm RMS). The 0.54 cm number represents a target accuracy needed for validating SSH measurements in the presence of oceanographic "noise," i.e., an upper limit for errors in observing ocean processes including those which are correlated on the scales of interest. These are the signals analyzed in this study. The 0.35 cm value is a requirement for inherent sensor/platform/sampling error at a single location that is uncorrelated from platform to platform.

The postlaunch Cal/Val approach involves calculating the wavenumber spectrum of the difference between the SWOT SSH measurement and the mooring-derived SSH during the SWOT overflight of the mooring array. A spatial linear trend over the length of the mooring array will be removed before calculating the wavenumber spectrum. This detrending operation minimizes the effects of the scales longer than those of the in situ Cal/Val. Such a difference spectrum is considered a snapshot of the measurement error spectrum, which will be averaged over the 90-day Cal/Val period to achieve statistical assessment of the SWOT performance.

Ideally, we would like to test the mooring capability using an array of moorings covering ~150 km. However, owing to the limited budget, we deployed three moorings spanning 30 km (Fig. 2). The evaluation of the mooring capability discussed in the following sections will be unavoidably influenced by the large-scale signals that are irrelevant to SWOT short-wavelength Cal/Val. It is thus difficult to rigorously define measurement requirement for a single mooring. However, from analysis of ocean model simulations (Torres et al. 2018), the temporal scales corresponding to 15–150 km wavelengths are roughly 2–14 days. We therefore impose the following for the requirement for the in situ SSH observations: Integrated over periods of 2–14 days, the RMS error shall not exceed 0.54 cm. A caveat is that this criterion is not rigorously derived due to insufficient mooring measurements and is only used as a guideline. The spatial–temporal separation can be directly calculated during the postlaunch Cal/Val where an order of 10 moorings will be deployed along a line under a SWOT swath (section 5).

e. The 2017 pilot field campaign

The first field campaign was conducted in Monterey Bay, California, during June/July 2017. Two gliders, one BPR, and a GPS buoy (Haines et al. 2017) were deployed near the Monterey Bay Aquarium Research Institute (MBARI) M_1 mooring. The two gliders sampled the upper 500 m near the mooring at 36.75°N, 122.03°W. The first objective was to quantify the capability of station-keeping gliders in constructing the high-resolution steric height derived from a fixed instrumented mooring. The second objective was to examine the connection between GPS-observed SSH that resembles spaceborne measurements and steric height that represents the ocean circulation.

The 2017 pilot campaign successfully tested the first objective, but not the second one. In particular, the results have not yet yielded satisfying closure between the GPS-derived SSH and upper-ocean steric height. The campaign took place 20 km from the shore, with the GPS buoy situated over the steep walls of the Monterey submarine canyon. One of the challenges was the large mean sea surface (geoid) gradient, which contributes to the time variation in GPS-derived SSH as the buoy meandered over the canyon wall and within the watch circle. This nearshore location was also dominated by nonsteric processes, making the site less representative of the open-ocean conditions expected near the SWOT Cal/Val crossover location. The campaign, however, shed new light on the challenges of reconciling SSH (from surface GPS or satellites such as SWOT) with steric height (from gliders and moorings), and the outcomes helped to inform the architecture of the subsequent 2019/20 prelaunch campaign reported in this paper. The next section provides the general information about this campaign.

3. The 2019/20 prelaunch field campaign

The 2019/20 prelaunch field campaign was conducted near the SWOT Cal/Val crossover location, about 300 km west of Monterey, California (Fig. 2), between September 2019 and January 2020. It was designed to mainly 1) test the closure of the SSH equation, which was not satisfactorily addressed in the 2017 field campaign, and 2) quantify the error in steric height using different platforms. There are six specific objectives: 1) test the SSH budget closure with GPS buoy, CTD mooring, and BPR following Eq. (1); 2) evaluate the vertical scale of SSH at the SWOT scales for different frequency bands; 3) evaluate the role of bottom pressure in SWOT SSH signals; 4) evaluate the small-scale steric height information; 5) evaluate the reconstruction of the upper-ocean circulation; and 6) provide information for the design of the postlaunch in situ observing system. We will mainly focus on 1–4 in this paper. The outcome will aid the design of the postlaunch in situ field campaign for SWOT Cal/Val.

Six institutions participated in the campaign: Jet Propulsion Laboratory, NOAA Pacific Marine Environmental Laboratory, Wood Hole Oceanographic Institution, Scripps Institution of Oceanography, Rutgers, and Remote Sensing Solutions. Three moorings and two BPRs were deployed between 1 and 7 September 2019, and recovered between 16 and 21 January 2020. One Slocum glider was deployed from Monterey Bay and piloted to the mooring locations around mid-September 2019.

The three moorings are 1) the PMEL/WHOI (*northern mooring*) configured with a GPS buoy and 18 fixed CTDs from surface to the bottom, 2) the PMEL GPS mooring (*middle mooring*) with a Prawler (Osse et al. 2015) sampling the upper-500-m temperature and salinity (*T*/*S*), and 3) the Scripps Institution of Oceanography (SIO) mooring (*southern mooring*) with a Wirewalker (Pinkel et al. 2011) sampling the top 500 m and fixed, real-time telemetered CTDs between 500 m and ocean floor. The mooring array was placed along a *Sentinel-3A* ground track, which fortuitously was in the middle of a SWOT swath along the Cal/Val orbit. The separation distances are 10 and 20 km for the northern and southern pairings, respectively, to support testing of small-scale SSH variability not resolved by conventional satellite altimeters. During the first phase of the campaign, the glider sampled a 60-km-long section perpendicular to the mooring line (Fig. 2) with a 1000 m dive depth, which was chosen to minimize the travel time for the 60 km section. During the second phase, the glider performed station keeping near the three moorings for cross calibration. The glider stayed at each mooring for about 5 days. The PMEL BPR is near the northern mooring and a PIES was deployed at the southern mooring location.

a. GPS measurements of SSH

A modular, low-power, high-accuracy GNSS measurement system was designed for long-term, continuous, and autonomous measurements of SSH on ocean- and cryosphere-observing platforms (Haines et al. 2017; Guthrie et al. 2020). It results from a joint project between NASA JPL, NOAA PMEL, and the University of Washington. The project aims to probe the limit of new kinematic precise-point positioning (PPP) techniques for accurately determining sea surface height and recovering neutral and charged atmosphere characteristics; and explore the potential scientific benefits—in the fields of physical oceanography, weather, and space weather—of accurate GNSS observations from a global ocean network of floating platforms. It integrates a Septentrio dual-frequency GPS receiver and a PMEL buoy. The receiver is low power (~1 W) and is accompanied by a miniaturized digital compass (for attitude information) and a load cell (to measure force on the mooring line). The buoy communicates using Iridium, and the payload is adaptable to multiple floating platforms such as surface buoys, wave gliders. When coupled with advanced precise point positioning techniques (Bertiger et al. 2010), the observations collected by the GPS buoy enable geodetic-quality solutions in remote locations without nearby reference stations.

The GPS level-2 data have 1-Hz temporal frequency, processed to accurate 3D positions using the GipsyX software (Bertiger et al. 2020) with units of meters for the height component. These high-frequency data were binned to hourly average to remove the surface gravity waves (Fig. 3). The hourly data were then corrected for an apparent systematic sea-state bias (estimated empirically), solid tides, line tension, mean sea surface (MSS), and IB effect. The MSS correction is important for comparing GPS-SSH with steric height because the horizontal displacement of the GPS buoy within its watch circle can project geoid variations into the GPS time series. This spatial-to-temporal projection is especially significant over steep bathymetry, which was the case during the 2017 field campaign, where the GPS buoy was placed near the Monterey submarine canyon and the spatial geoid variations were as large as 10 cm within the mooring watch circle of 2 km radius, but less significant over the prelaunch campaign region where ocean bathymetry is rather flat. The IB correction (Wunsch and Stammer 1997) follows IB (mm) = $-9.948p'$, where p' is the sea level pressure anomaly. The final derived SSH after the MSS and IB corrections was then detrended over the 4-month period (mid-September 2019 to mid-January 2020).

The GPS buoy system has developed from campaigns undertaken in progressively more challenging conditions.

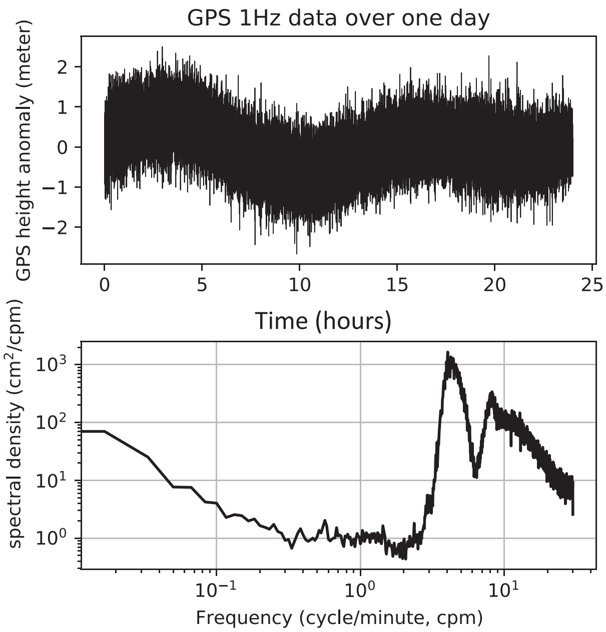

FIG. 3. (top) The 1-Hz GPS measurement of SSH. (bottom) The frequency spectrum of the 1-Hz GPS SSH.

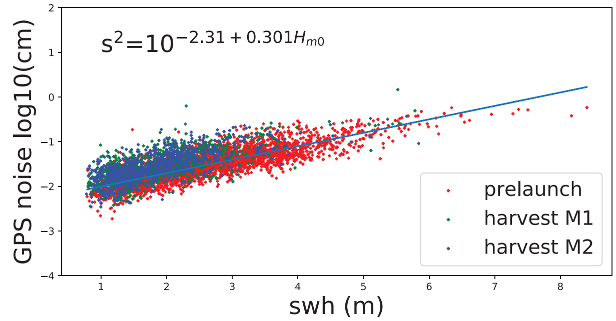

FIG. 4. The GPS error as a function of SWH derived from two SWOT prelaunch field campaigns described in section 2. The red dots are from the 2019 prelaunch field campaign and the green and blue dots are from the two GPS buoys of the 2017 pilot field campaign.

Nearly 1000 buoy days of data have been successfully collected since 2015, over SWH ranging from calm to 9 m. The GPS buoys have been an integral part of the SWOT pilot experiment in 2017 (Monterey Bay) and the prelaunch field campaign (2019/20). An example of the processed 1-Hz data is shown in Fig. 3. The 1-Hz sampling frequency is high enough to reveal detailed expressions of surface waves. The amplitude of the high-rate (1-Hz) height estimates reach 5 m for this day. The frequency spectrum illustrates the wind wave and swells by the two spectral peaks. SWH can also be derived from this 1-Hz data following SWH = 4 × RMS(SSH), where SSH is high-pass filtered with a cutoff frequency of 1 cycle min^{-1}.

We tried to estimate the GPS measurement errors in the context of the SWOT requirements. Without a true reference, we need to make assumptions in order to derive the error from the GPS measurement itself. We assume the minimum in the spectrum near 1 cycle min^{-1} reflects random instrument noise. As we are interested in ocean signals that are of periods longer than 1 h, the GPS error can be estimated by integrating the random noise spectrum, assumed constant taken as the value of the spectrum minimum near 1 cycle min^{-1}, over the frequency range (0–1 cycle h^{-1}). The SWH can be derived from the surface wave spectrum. We can split a long time series into 1-h-long segments, then derive an empirical relationship between GPS error and SWH. Based on the two SWOT prelaunch field tests, there is a clear relationship between SWH and GPS errors following a logarithmic function as shown in Fig. 4. The relationship is $S^2 = 10^{-2.31+0.3H_{m0}}$, where H_{m0} represents the SWH, and S^2 is the noise variance. Under these assumptions, the GPS error from a single buoy meets the SWOT mission geodetic requirement, i.e., 0.13 cm^2 for SWH < 4.1 m, which corresponds to 2 cm^2 cpkm^{-1} instrument noise in the wavenumber space (Fig. 1).

Other errors exist in addition to those induced by the surface waves. Those errors are correlated but difficult to unravel with a single GPS buoy. They will contribute to the total error presented in section 4. Residual atmospheric refraction delays are one of the dominant correlated error sources. As the ionospheric refraction is corrected to first order using the two GPS frequencies, the primary concern here is refraction from the troposphere. Taking advantage of mapping functions, the wet troposphere delay in the zenith direction is estimated along with the buoy position. Despite the relatively small magnitude, the wet component of the troposphere delay is highly variable and sometimes difficult to capture, especially during intense weather fronts with large atmospheric gradients. Other important systematic errors for the buoy technique are related to the platform altitude and to the force on the mooring line, both of which impact accurate modeling of the buoy's waterline and thus the SSH (Zhou et al. 2020). Here we use, respectively, the digital compass and load cell data from our payload package to mitigate these errors.

b. Hydrographic measurements

1) MOORINGS WITH FIXED-DEPTH CTD INSTRUMENTATION

The fixed-depth CTD mooring is one of the most conventional in situ platforms for observational oceanography. The CTDs used in the campaign are the Sea-Bird Electronics, model SBE-37. The SBE-37 can be configured with and without a pressure sensor. The pressures for those instruments without the corresponding sensors (from the northern mooring) were determined through interpolating from the next instruments above or below, using the known wire lengths between the instruments. For these fixed-depth CTDs, the distances between instruments along the mooring line are fixed, but the actual depths of the CTD instruments change over time. The amount of vertical excursion depends on the currents and winds as well as the mooring design: the northern mooring was a "slack mooring" (i.e., mooring line much longer than water depth) of an inverse catenary design with vertical sensor excursions up to about 300 m, while the southern mooring had a taut lower section that limited vertical excursions to about 60 m. The nominal depths of the fixed CTDs are (505, 618, 810, 1182, 1690, 2365, 3202, 4384) m on the southern mooring and (20, 30, 59, 107, 174, 261, 367, 492, 609, 805, 1180, 1408, 1692, 1909, 2189, 2488, 2750, 4545) m on the northern mooring.

A climatological mean in situ density profile is removed before the density anomalies are interpolated onto a uniform vertical grid to avoid interpolation error in calculating steric height. We have also used the mean profile constructed from all the measurements in the campaign instead of the climatological mean. No quantitative difference is observed. This procedure removes the spurious deep-ocean variability introduced by the vertical-to-temporal projection due to the vertical movement of the CTD sensors. The bottom CTD on the northern mooring was corrupted so the full-depth steric height was calculated with the assumption that the ocean below 3000 m has no temperature and salinity variability.

2) MOORINGS WITH PROFILERS

Two moorings had profilers with CTD instruments. The middle mooring had a Prawler that covered the upper 500 m with a Sea-Bird Electronics (SBE-PRAWLER) CTD, and the southern mooring had a Wirewalker in the upper 500 m with an RBR Concerto CTD. Profiling methods are not subject to errors due to vertical resolution, but the temporal resolution is less favorable. The Prawler was set to 8 profiles per day on average during the 2019/20 campaign. The number of profiles per day can be higher, but was chosen to test the endurance of the Prawler mooring. The Wirewalker on the southern mooring yielded about 80 up- and downcast profiles per day (i.e., ~7000 profiles, or 3500 vertical kilometers profiled over 86 days of deployment). The profiler CTDs pass through vertical gradients of temperature and conductivity in the upper ocean, which requires data processing to remove spikes in salinity, and to adjust for lagged sensor responses. After this alignment, vertical profiles of density with 1 and 0.25 m vertical resolution over the upper 500 m are produced for the Prawler and Wirewalker, respectively.

Below the profiler, the southern mooring featured additional, vertical fixed instrumentation. It used a taut mooring between the seafloor and 600 m, connected to the surface buoy via a reverse catenary inductive connection and the Wirewalker profiling wire. The taut mooring has a very small watch circle (<250 m) and so the fixed instruments stay within a narrow depth range. The inductive connection allowed real-time data from the fixed instruments all the way to the seafloor. This experimental mooring design is less tested, and the catenary wire parted after 86 days of the intended 90-day deployment.

3) UNDERWATER GLIDERS

The hydrography data collected by the gliders are similar to the moored profilers. Vertical resolution is high and requires no additional interpolation steps, although the same precautions against mismatched sensor response times and resulting spikes in salinity data need to be taken. Gliders have the advantage of mobility, but they may experience large horizontal deviation from target locations due to strong currents. A station-keeping glider can act as a virtual mooring. A glider that performs station keeping at different mooring locations can also be used for cross-mooring calibration and validation. The Slocum glider used in this campaign has a vertical speed of about 18–20 cm s^{-1} yielding ~30 profiles per day for 500 m dives.

4) APPROACH TO CALIBRATION AND VALIDATION OF CTD DATA

An effort was made to cross calibrate all CTD data to a common reference. For the fixed-depth, moored CTD instruments, this was done by attaching the mooring instruments to a recently calibrated, ship-based CTD and Rosette system, and then collecting vertical profiles with 10 min stops at several depths. At these dwell depths, water samples were taken for laboratory salinity measurements to provide an absolute salinity reference. This approach was carried out for mooring instruments both before mooring deployment and after mooring recovery. The method is described by Kanzow et al. (2006), and has the key advantage that all three sensors (conductivity, temperature, pressure) are adjusted independently of one another. Over the course of the mooring deployment, the corrections applied to the mooring data are shifted linearly from the predeployment to the postrecovery values. For temperature data, the adjustments are offsets added to the raw data. For conductivity data, the adjustments are gain factors multiplied by the raw data. For pressure data, the adjustments are a combination of a gain factor and an additive offset (Kanzow et al. 2006).

The glider was flown to the vicinity of each mooring on several occasions. A comparison of the glider data against the fixed-depth, cross-calibrated moored CTDs was used to adjust the glider conductivity with a gain factor, such that the temperature–salinity curves derived from the glider would best match those from the nearby mooring. This assumes that the glider temperature and pressure sensors are correct.

For the two moored profilers, two different approaches were done: The Prawler conductivity data were adjusted against the (adjusted) glider data, based on nudging the conductivity such that the temperature–salinity curves would be matched. For the Wirewalker on the southern mooring, a spare fixed-depth instrument that had the ship-based corrections was attached to the profiling body. The profiler conductivity was nudged against the data from this collocated instrument, again to best match the temperature–salinity relationship, but the comparison was restricted to deeper depths because the fixed-depth instrument does not have a sensor response time suitable for the upper-ocean profiles. For both moored profilers, the result is that the conductivity data are adjusted, while the temperature and pressure data are assumed correct, as for the gliders.

c. *Ocean bottom pressure*

There were two ocean bottom pressure instruments: the northern one was a system based on the DART tsunami detection technology (Meinig et al. 2005), and the southern one a PIES (pressure-sensing inverted echo sounder) (Watts and Rossby 1977). The actual pressure sensors are identical in the two systems (Paroscientific Digiquartz) that are operated at about 15-s acquisition times. The DART-based systems operate nearly continuously, while the PIES have a 10-min sampling interval. When subsampling a near-continuous DART-like record at 10-min resolution, hourly averages can be reproduced to about 0.5 mm accuracy. Availability of the data in near–real time depends on the available underwater communication systems, which typically operate acoustically at low bandwidth. For PIES, hourly data were telemetered on an irregular schedule during the 2017 field campaign, typically with several days' latency. The data transfer uses the nearby glider as a communication device. The northern ocean bottom pressure data were telemetered four times per day during the 2019/20 field campaign using an acoustic modem.

The absolute magnitudes of the pressure data are not particularly useful in the context of SWOT Cal/Val, for two reasons: first, calibration uncertainties typically result in offsets to the data, which are not constant but drift with time; second, the exact depths where the sensors are on the seafloor are not known, i.e., one cannot assign a known vertical coordinate to the data. Therefore, a time mean that includes sensor drift is subtracted from the record. Following Eble and Gonzalez (1991), the preferred trend removal involves the sum of an exponentially decaying function and a linear trend. The variability in the residuals is then dominated by tidal signals. From comparing different tide removal algorithms, such as harmonic fits with different tidal constituents as well as low-pass filters of the data, coherent tidal signals can be removed.

d. *Auxiliary datasets*

GPS measures total SSH, so it is the closest equivalence of SWOT SSH. GPS SSH and SWOT SSH will share the same MSS and IB corrections. For the MSS correction, we used an MSS height model (MSSCNESCLS19), which is based on all available radar altimeter data (Schaeffer et al. 2018) with 16–20 km spatial resolution. The hourly ERA5 atmospheric pressure (Copernicus Climate Change Service 2017; Hersbach et al., 2020) used for IB correction and the gridded DUACS-DT2018 L4 SSH product (Pujol et al. 2016; Taburet et al. 2019) and *Sentinel-3A* L2P data are provided by Copernicus Climate Change Service (2017).

4. Results

a. *Large and mesoscale background during the campaign*

The campaign was conducted in the California Current system, a typical eastern boundary current system that comprises a wind-driven coastal upwelling and equatorward surface current. It is one of the best-studied and longest-observed regions in the world oceans (e.g., Hickey 1979; Flament et al. 1985; Ikeda and Emery 1984; Capet et al. 2008a,b; Collins et al. 2013; Rudnick et al. 2017; and many others). The coastal upwelling driven by the equatorward alongshore wind during summer brings cold waters to the surface (Fig. 5d), which introduces strong thermal fronts next to the warmer open ocean to form a southward California Current. This upwelled water also contains abundant nutrients to support the dynamic ecosystem indicated by the high chlorophyll concentration (Fig. 5e).

Mesoscale and submesoscale eddies are ubiquitous in the California Current System (CCS). The cold coastal water often pinches off from the coastal current and drifts westward into the open ocean supporting the coastal–open-ocean exchange of water masses (e.g., Strub and James 2000, among numerous others). Meanwhile, this offshore transport of mass and heat is balanced by the onshore transport of the deep open-ocean water that feeds the upwelling and the horizontal onshore transport by mesoscale and submesoscale eddies.

During the period of the 2019/20 prelaunch field campaign, the mooring array observed the formation of a warm-core anticyclonic mesoscale eddy. The process started from a southward flow meander at the beginning of the campaign around early September 2019 (Fig. 5a). The meander started to stretch and fold, a typical evolution of baroclinic instability, during October 2019 (Fig. 5b), which eventually detached from the initial meander to form a coherent mesoscale eddy near the end of the campaign (Fig. 5c). The mature mesoscale eddy trapped the warm, nutrient-scarce open-ocean water and drifted shoreward to resupply and mix with coastal water. During this evolution, the three moorings were within the meander at the start of the deployment and on the edge of the formed eddy by the end of the deployment. From the mesoscale perspective, then, the observations during the campaign were skewed toward ocean dynamics of a meander and the edge of a mesoscale eddy in CCS. Detailed in-depth analyses of the underlying mesoscale dynamics are not a focus of this paper and will be reported elsewhere.

b. *SSH closure*

As discussed in section 2b, one can derive an equivalent full-depth steric height from GPS, BPR, and atmospheric pressure through the hydrostatic equation. The derived full-depth steric height is then compared with the steric height derived from hydrographic measurements through mooring CTDs. Their differences contain the errors in both GPS-derived and CTD-derived steric heights.

Figure 6 shows the hourly steric height derived from GPS/BPR (red) and 6-min-resolution steric height from hydrographic measurements (blue). The top panel shows the full-time series for four months. The bottom panel shows the details of the time series over a 10-day period. The two independently derived steric height time series agree over low frequencies (top panel) and over major tidal frequencies (bottom panel). Note that the barotropic tides are eliminated by the difference between the GPS SSH and BPR-derived SSH, leaving the residuals at tidal frequencies, the baroclinic internal tides.

The total RMSE between the two derived steric heights is 2 cm, but they also depend on the sea state as shown by the single GPS analyses (Fig. 4). To our knowledge, this is the first demonstration that the GPS-/BPR-derived sea surface height is equivalent to the steric height measured concurrently in

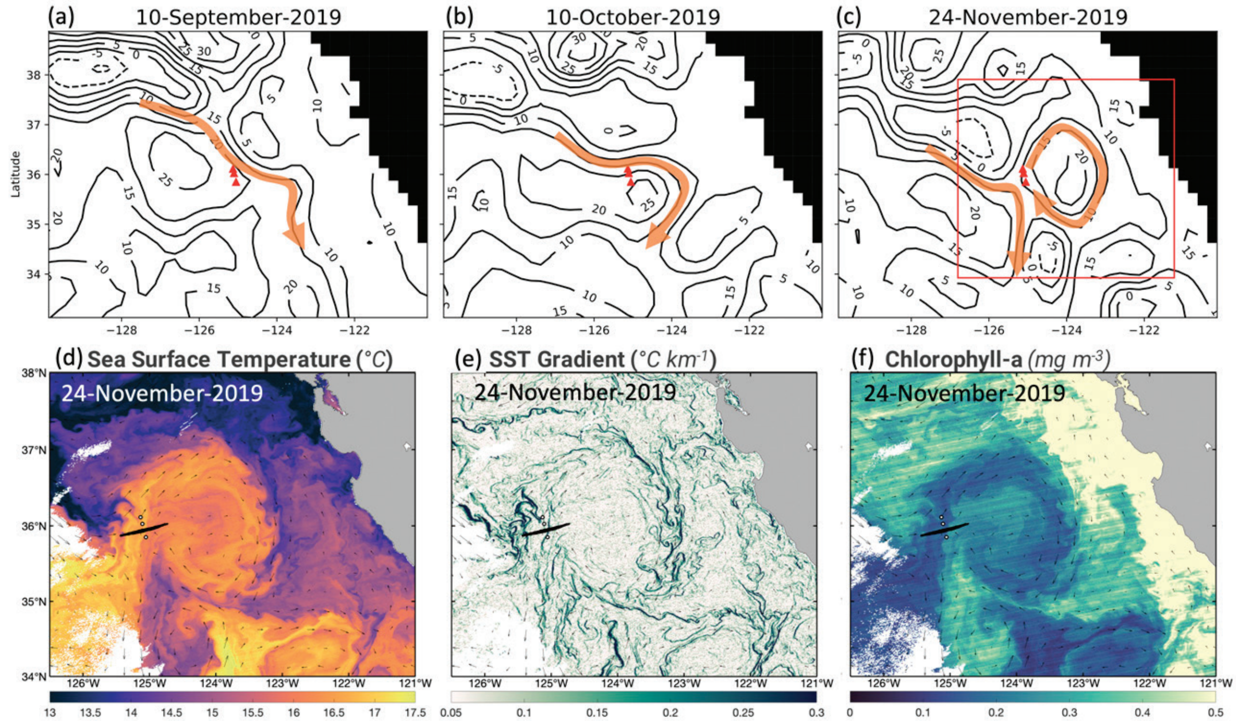

FIG. 5. (a)–(c) The altimetric sea level anomaly (SLA) on 10 Sep, 10 Oct, and 24 Nov 2019 corresponding to the beginning, middle, and end of the campaign, respectively. The thick orange arrows show the pinch-off of mesoscale eddy from the meander of the California current. The three red triangles mark the three mooring locations. The red box in (c) marks the domain boundary for (d)–(f) he SST and surface chlorophyll-a after the eddy formed approximately on 24 Nov (an ascending 750 m resolution swath from VIIRS *Suomi NPP* L2 taken at 2100 UTC). The black lines (60 km long) in (d)–(f) mark the glider flight path.

situ, indicating that the GNSS GPS system is accurate enough to measure the oceanic baroclinic signals.

The difference between the two steric height time series is further binned into different sea states characterized by SWH. As expected, the RMS difference between the two is a function of sea state (Fig. 7). The RMS difference is about 1 cm for calm seas with SWH < 1 m, 1.7 cm for SWH = 2 m, and 3 cm for SWH > 6 m. These GPS errors may be of large scale and not contribute to 15–150-km-scale errors that are of primary interest here. Detailed discussions are given in section 5.

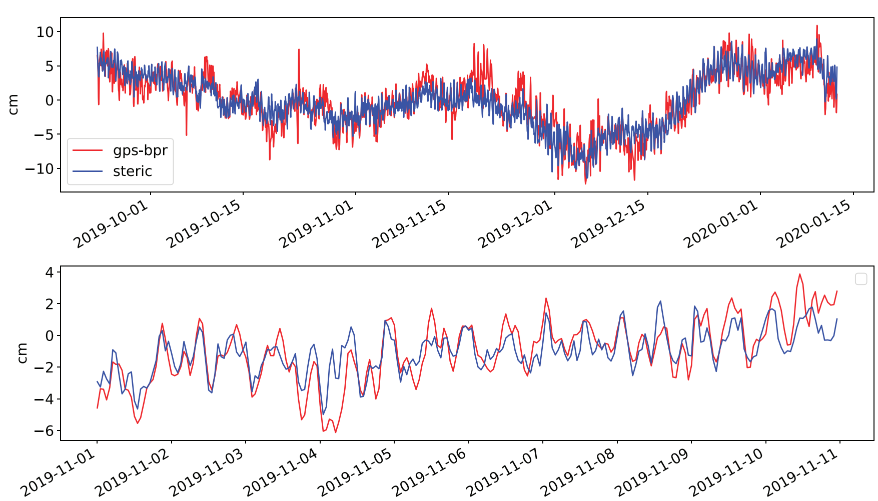

FIG. 6. (top) The steric height from the hydrographic measurements (blue) and the GPS-BPR-derived dynamic SSH. (bottom) As in the top panel, but for a short period (10 days).

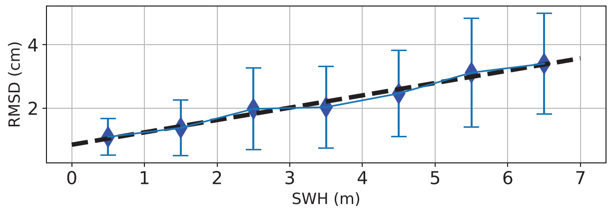

FIG. 7. The RMS difference (RMSD) between the steric heights derived from GPS/BPR and mooring CTDs as a function of significant wave height (SWH). The diamond symbols represent the mean RMSD binned to SWH values with a 1 m bin width. The error bars show the standard deviation of the absolute difference as an uncertainty measure. The line is the linear fit to the mean following RMSD=0.84 + 0.4SWH (cm).

The difference between GPS-derived and CTD-derived steric height can be scrutinized in frequency space, where we may identify the error sources. The GPS-based and CTD-based steric heights match at low frequencies with equal power spectral density within the 95% uncertainty bounds (Fig. 8). The major difference starts to show for periods less than 10 days, except for several major tidal periods such as M_2 and M_4 where the spectral peaks and coherence are significant. This is visible from the time series in Fig. 6. It is interesting to note that the coherence is high at 7.6-h period, which corresponding to the frequency of nonlinear interaction between inertial motions and semidiurnal tide denoted fM_2 (Mihaly et al. 1998).

The amplification of the differences over short periods less than 10 days is not fully understood, but could be related to the cadence of weather systems. The largest dispersions are sporadic in time (Fig. 6) and have a linear relationship with sea state (Fig. 7), and could also reflect refraction errors for the GPS systems. Errors in CTD-derived steric height exist but should not be a function of sea state and are less likely to be the dominant error source. The major difference between red and blue lines in Fig. 6 probably arises from the GPS-derived steric heights, which reflect not only GPS errors but also the errors in the IB correction through ERA5 and errors from MSS uncertainties. However, these errors may well be of large spatial scales that are less relevant to the SWOT in situ Cal/Val focus in this region (<150 km; Wang et al. 2018). If the GPS and IB related uncertainty/errors have large spatial scales, they can be removed through a spatial high-pass filter or simply by removing a linear trend along a 150 km distance as done in Wang et al. (2018).

c. *The vertical scale*

To minimize the cost of the postlaunch in situ Cal/Val, we may need to tolerate some uncertainties due to missing direct

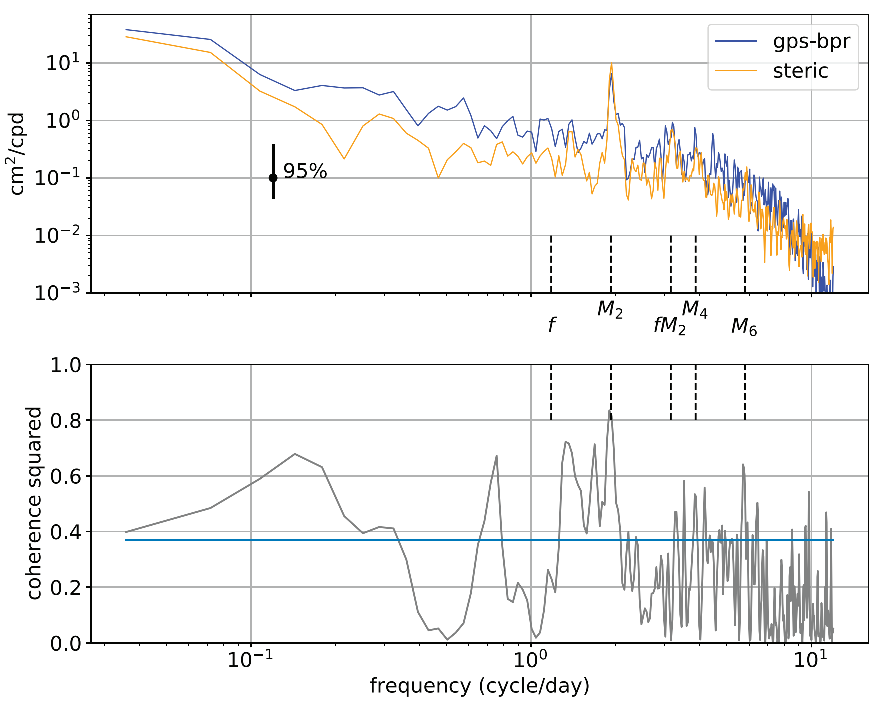

FIG. 8. (top) The frequency spectrum of the full-depth steric height (orange) [right-hand side of Eq. (3)] and the GPS-derived dynamic SSH (blue) [left-hand side of Eq. (3)]. The spectra are calculated using the Welch method with four nonoverlapped segments giving a degree of freedom (DOF) of 8. A Hanning windowing and linear-detrend operation were applied. The 95% significance level with DOF = 8 is shown by the black vertical bar. (bottom) The magnitude-squared coherence between the two time series using the Welch method with the same number of segments and DOF. The blue horizontal line marks the 95% significant level with DOF = 8.

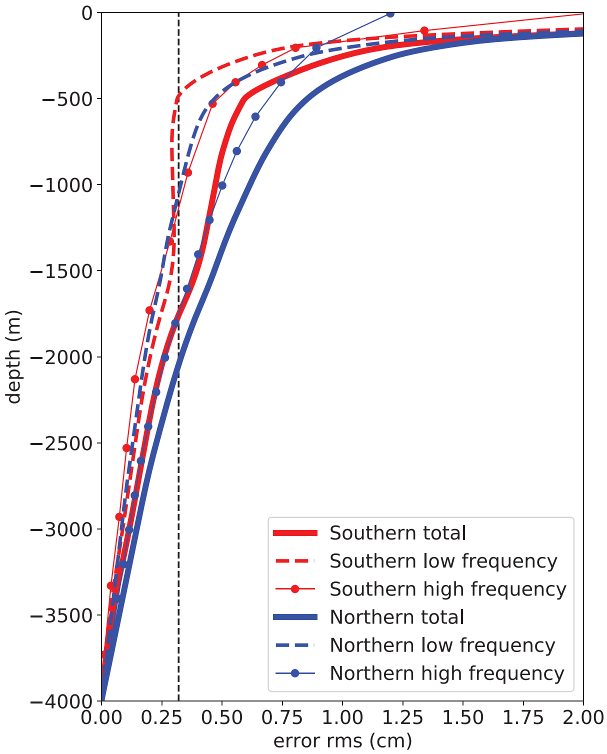

FIG. 9. The RMSE $\epsilon(z)$ of the upper-ocean steric height relative to full-depth steric height as a function of integration depth. Because the bottom CTD on the northern mooring was corrupted, we chose 4000 m as the deep-ocean reference for both moorings. By definition, the error decreases when the integration depth gets deeper and reaches zero at the bottom (4000 m in this case). The southern mooring is shown in red and the northern mooring in blue. The thick solid lines are for the total signals, the dashed lines for low frequency (>48 h), and the thin solid–dot lines for high frequencies (<48 h). The black dashed vertical line marks the 0.32 cm RMS level, which is derived from 2 cm^2 $cpkm^{-1}$ wavenumber spectrum noise level for stations separated by 10 km.

measurements of the deep ocean. How deep do we have to measure the ocean to generate a steric height accurate enough for SWOT Cal/Val?

The uncertainty introduced by missing deep-ocean measurement below a depth z is defined as the steric height integrated between ocean bottom and z:

$$\eta_{\mathrm{deep}}(z) = -\int_{-H}^{z} \frac{\rho'(z')}{\rho_{\mathrm{ref}}} \, dz',$$

where ρ' is the in situ density anomaly deviation from a time-mean density profile $\overline{\rho}(z)$, and ρ_{ref} is the mean in situ density (set to 1035 kg m^{-3} here). We quantify the uncertainty using the standard deviation of this deep-ocean steric height $\epsilon(z) = \mathrm{std}[(\eta_{\mathrm{deep}}(z))]$.

The results based on the northern and southern mooring are shown in Fig. 9. The $\epsilon(z)$ decreases toward the deeper ocean as defined but with a larger rate in the southern mooring (thick red) than the northern mooring (thick blue). The different vertical scales between the northern and the southern moorings may be caused by different dynamic regimes experienced by the two moorings. The 500 m depth is of particular interest because that is roughly the bottom depth of the Prawler and Wirewalker platform. Table 1 lists some relevant numbers about the errors $\epsilon(500)$. The total error $\epsilon(500)$, i.e., the error of missing the deep ocean below 500 m, is 0.61 ± 0.1 and 0.84 ± 0.17 cm for the southern and northern mooring, respectively. The errors represent the mean RMS and the standard deviation in a time series of $\epsilon(500)$ calculated based on segments of a 10-day duration subsampled from either the original or the filtered time series. The error amplitude changes over time. Most of these errors come from high-frequency processes with periods less than 2 days (we will use the format $T < 2$ d hereafter). They are 0.51 ± 0.06 and 0.67 ± 0.14 cm for the southern and northern moorings, respectively. The low-frequency (2–14 d) component on the other hand has errors less than 0.15 ± 0.1 cm for both moorings, accounting for less than 4% of total variance (Table 1). The deep-ocean (<−500 m) steric height has a 0.5–0.7 cm RMS values and accounts for 5% of the full-depth steric height for high frequencies with periods less than 2 days at the southern mooring. This ratio becomes 30% at the northern mooring. The northern mooring particularly presents a higher deep-ocean high-frequency variability. The causality cannot be confirmed without more independent observations. It may be caused by the topographically generated deep-ocean internal tide/wave signal that is strong for the northern mooring, or simply because of the errors in determining the depths of the deep CTDs, which have large vertical excursions.

The spectrum of the upper-500-m steric height and the full-depth steric height and their coherence are shown in Fig. 10. We used the Welch method with a Hanning window. The full time series is split into nonoverlapping segments. The steric heights of the upper 500 m (blue) and of the full depth (orange) agree well over subinertial frequencies with similar spectra density and high coherence for both moorings. The major difference comes from the superinertial frequencies, especially around the tidal frequencies at M_2 (and M_4 for the southern mooring). The errors are relatively high (green lines) but the coherence (red lines) is still large and significant

TABLE 1. Deep-ocean contribution to steric height ϵ(500 m) for the two moorings at different frequency bands. This represents the error by only measuring the upper 500 m.

	Total RMSE (cm)	2–14-day band (cm)	Variance percentage (2–14 days) (%)	High frequency (<2 days) (cm)	Variance percentage (<2 days) (%)
Southern	0.61 ± 0.1	0.14 ± 0.1	1	0.51 ± 0.06	5
Northern	0.83 ± 0.17	0.15 ± 0.07	3.4	0.67 ± 0.14	31

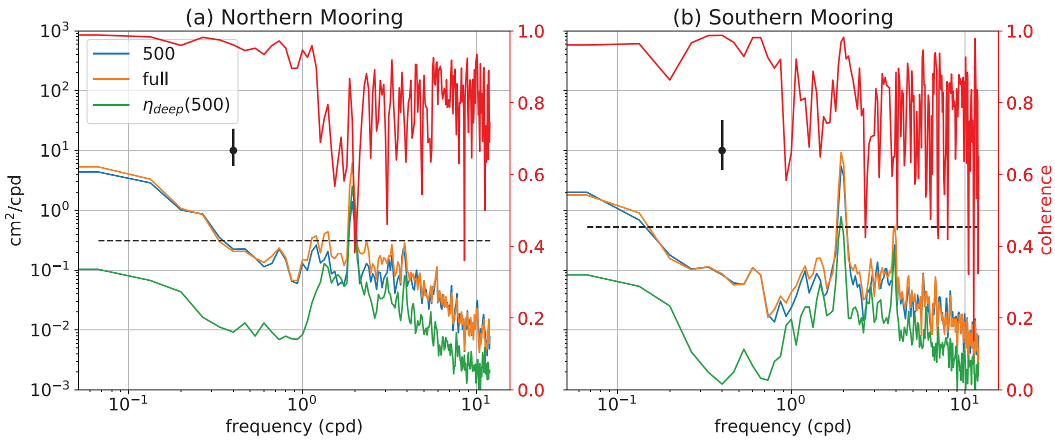

FIG. 10. The frequency spectra of 500 m (blue) and full-depth (orange) steric height and their difference (green) and the magnitude-squared coherence (red). The difference (green) is $\eta_{\text{deep}}(500)$. The spectra were calculated using Welch with nonoverlapping segments, each of which is of 15-day duration. The black error bar represents the 95% confidence interval. The degrees of freedom are 10 for the southern mooring and 18 for the northern mooring (due to its longer duration). The 95% significance level of the magnitude-squared coherence is shown by the dashed line: 0.31 and 0.53 for the northern and southern moorings, respectively.

(above 95% confidence level) for both moorings. This reflects that the superinertial motions, especially the semidiurnal internal tides, are of low baroclinic mode and reach deeper in depth than the subinertial submesoscale and mesoscale motions. [see also Lapeyre and Klein (2006) and LaCasce and Mahadevan (2006)].

The errors presented in this section include all spatial and temporal scales. Because of the SWOT focus on scales smaller than the mesoscale, correlated mesoscale scale error among the moorings can be removed, yielding a much smaller residual error budget. The high-frequency deep-ocean steric height with periods less than 2 days has 0.5–0.7 cm RMS and mostly from baroclinic tides (Fig. 10). If only the subinertial motions (2–14-day period) are considered, missing deep ocean introduce less than 2 mm error (Table 1), which is well below the KaRIn measurement error (0.54 cm RMS). These deep-ocean high-frequency signals require deep-reaching mooring CTDs.

d. Station-keeping glider as a virtual mooring

Gliders, unlike moorings, are mobile and add more flexibility to the campaign. We had one Slocum glider in the 2019/20 campaign for 1) testing the performance of a data assimilation system (Archer et al. 2022) and 2) testing the glider as a virtual mooring for the contingency of a failed mooring.

The glider vertical trajectories generally straight lines underwater, proceeding in a single direction fixed to a magnetic heading. This heading can be chosen to correct for ocean currents if one wishes to hold sampling lines. The downside of a single trajectory underwater means larger errors in station keeping and thus the ability to remain close to a single location. This is because of large distances traversed horizontally underwater, especially while diving deep.

To compensate for this and maintain a fixed position, the glider must have the ability to change heading underwater. It achieves this by maintaining a course of waypoints underwater which can be in any shape, for instance, a square, triangle, or even back and forth with two waypoints. Built into the underwater positioning is an algorithm to correct for estimated depth averaged current. This allows the underwater vehicle to continuously correct for current and maintain the same positions on Earth underwater for periods of several hours or more.

The Slocum glider's dive speed is about 18–20 cm s^{-1} yielding ~45 min per profile for a diving depth of 500 m. This will produce about 30 profiles a day. The capability of a station-keeping glider has been tested in our OSSE study (Wang et al. 2018) and the 2017 field campaign (Clark et al. 2018), where we confirmed that the glider-derived steric height matches the upper-ocean steric height from a nearby mooring for periods longer than 6 h with error-to-signal ratio smaller than 0.5 (figure not shown).

We tested the glider's station keeping again in the 2019/20 campaign and also used the glider as a conduit to connect and test the three moorings. The Slocum glider performed station keeping near the three moorings for three weeks between 27 November and 17 December 2019. The relative location of the glider flight path to three moorings are shown in Fig. 11. The glider stayed for about 3, 5.5, and 6.5 days around the southern, middle, and northern moorings, respectively. The associated mean glider–mooring distances are 1.2 ± 0.2 km, 0.8 ± 0.4 km, and 0.9 ± 0.2 km from south to north. The clusters of the glider surface locations have smaller circles referenced to its own center. The circles have a radius of 233, 350, and 520 m from north to south, respectively. The horizontal spread of the glider surface locations has a comparable size to the watch circle of the southern mooring during this period. A larger spread of the glider paths is expected for a longer duration and/or in a stronger flow field.

The Slocum glider's capability of being a virtual mooring was validated again in this campaign. The RMS difference

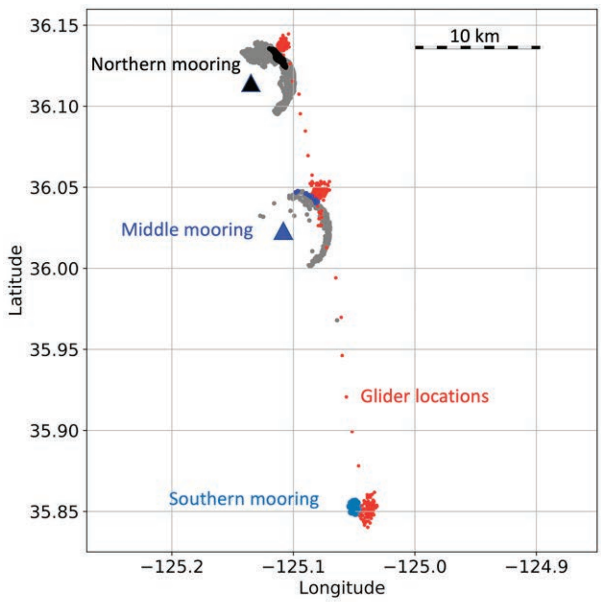

FIG. 11. The locations of the glider (red) and the northern mooring (black), the middle mooring (blue), and the southern mooring (navy blue) during the glider station-keeping phase, 27 Nov–17 Dec 2019. The mean separation distances during station keeping phase are 0.9 ± 0.2, 0.8 ± 0.4, and 1.2 ± 0.2 km for the northern, middle, and southern mooring, respectively. The two triangles show the anchor locations of the middle and northern moorings. The mooring watch circle shown by the gray dots has a radius of 4.5 km.

between glider and mooring upper-ocean (500 m) steric height is about 0.4–0.5 cm. Figure 12 (top panel) shows the time series of the upper-500 m steric height calculated from the glider (blue lines) and the moorings (orange lines). To avoid temporal interpolation errors, we used individual profiles to calculate the steric height without temporal interpolation between the subsurface temperature and salinity profiles. The time associated with the steric height of each profile was taken from the time at 250 m depth.

Figure 12 shows that the upper-500-m steric heights from glider and moorings are closely matched. The RMS differences are 0.4, 0.48, and 0.45 cm for the northern, middle, and southern mooring. The northern mooring has fixed CTDs binned to a 6-min grid close mooring–glider match confirms the capability of gliders to reproduce the upper-500-m steric height to time scales of several cycles per day.

The comparison of the glider to the northern mooring has the least RMS difference. The middle mooring was equipped with a Prawler, similar to a Wirewalker on the southern mooring, but was configured to sample about 8 profiles per day to test the endurance of the mooring. The larger RMS difference is mostly caused by the low temporal resolution (8 profiles per day) in mooring steric height (orange line/symbol in the top-center panel of Fig. 12). Because of the low temporal resolution, the middle mooring undersampled the internal tides especially the peaks that were captured by the glider. For example, the internal tidal variance at the beginning of 12 May 2019 is captured by the glider but not by the mooring (Fig. 12, top-center panel). This indicates the insufficiency of 8 profiles per day sampling frequency.

For the southern mooring comparison (top-right panel), there are superinertial variabilities in the mooring steric height largely captured by the glider except for the tidal peaks on 29 November. The glider dived to 1000 m at this location, so the temporal resolution is half that of the 500 m dives. The resulting lower temporal resolution in the glider steric height introduces an RMS difference 0.45 cm, which is larger than the 0.4 cm at the northern mooring. The time series comparison indicates that mapping the SSH variability due to the internal wave displacement of the density structure of the upper 500 m requires around 24 profiles per day. The spectral and coherence analyses shown in the bottom panel of Fig. 12 confirm the direct visual examination of the steric height time series discussed above. The glider steric height matches the northern mooring steric height in spectral density (bottom left, blue and orange lines) with high coherence (>0.6) down to approximately 5–6-h period (bottom left, purple line). For the middle mooring, because of the low temporal resolution in the mooring steric height, the glider–mooring only matches up to the M_2 tidal frequency, so ~8 profiles per day can resolve M_2 tides but not supertidal variabilities. For the southern mooring location (bottom-right panel), the mooring and glider match with high coherence (>0.6) down to a 6-h period.

In summary, the steric height derived from the glider matched the mooring upper-500-m steric height with 0.4–0.5 cm RMS difference. This largely validated the capability of gliders as a virtual mooring in the Cal/Val region with one caveat that the glider's error is referenced to the mooring's upper-ocean steric height, which itself carries about 0.6 cm uncertainty. Even though this uncertainty can be reduced by nearby deep-reaching CTD moorings with instruments in the deep ocean, the added uncertainty should be emphasized in a contingency scenario that a glider is needed to substitute a failed mooring.

e. *Spatial and temporal variability*

Each mooring produces a steric height time series. We can examine the temporal and frequency content of the signal. The spatial–temporal variabilities can be examined by combining the three moorings separated at 10 and 20 km even though a full wavenumber spectrum cannot be calculated across so few mooring separations.

1) TEMPORAL VARIABILITY

In the time domain, the mooring upper-500-m steric height closely follows the gridded SSH over long periods. Figure 13 shows the direct comparison between AVISO and the steric height of the northern and southern moorings (black solid and dashed lines). At the beginning of the campaign in early September 2019, the mooring steric heights and altimetric SSH are all at about approximately 76 cm level. This is associated with a south–north meandering current, whose SSH gradient is largest east–west perpendicular to the mooring array (Fig. 5a). When the meander curved toward the coast to form

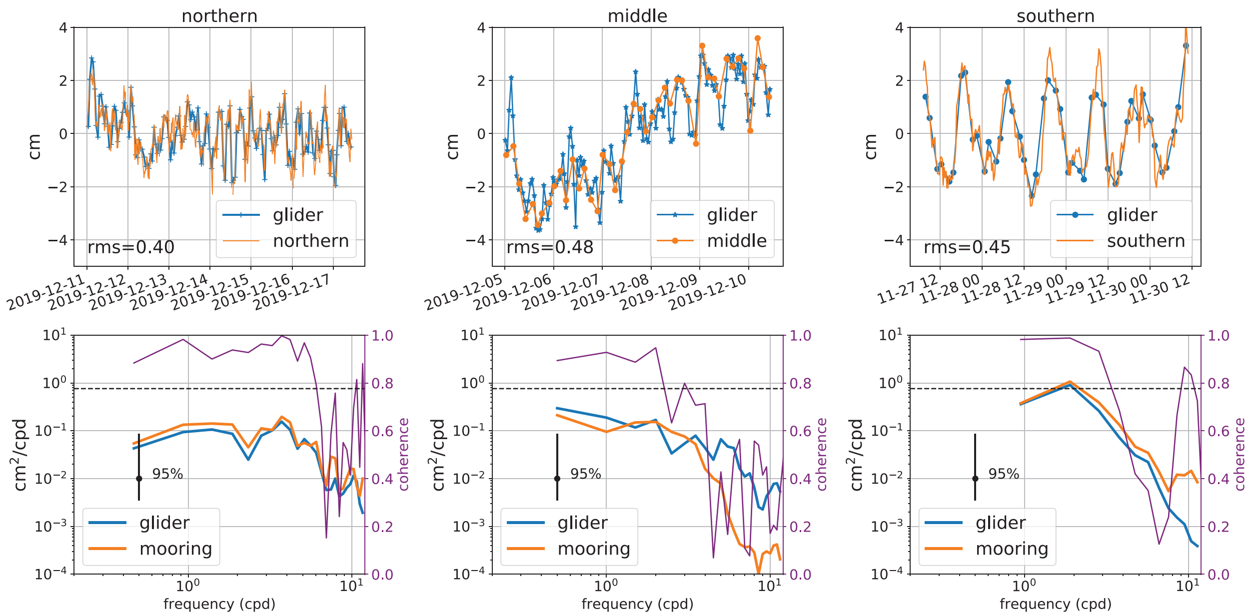

FIG. 12. (top) The upper-500-m steric height reconstructed from the glider (blue lines) and moorings (orange lines). (bottom) The frequency power spectral density for the glider (blue) and moorings (orange). The black vertical lines show the 95% confidence interval with 4 degrees of freedom (three nonoverlapping segments). The magnitude-squared coherence is shown in purple with the y axis on the right and the associated 95% confidence level marked by the dashed lines(left to right) The northern, middle, and southern moorings. The duration of the station-keeping phase was longest at the northern mooring (6.5 days) and shortest at the southern mooring (3.5 days).

an isolated mesoscale eddy during the eddy formation, the flow turned zonal (Fig. 5b) and the SSH differences between the three moorings can be as large as 10 cm between the southern and northern moorings, for example, at the end of October 2019 (Fig. 13, top panel). Near the end of November 2019, when the eddy was finally formed and detached (Fig. 5c), the meander regained its original north–south orientation with isolines oriented along the direction of the mooring array, resulting in a minimal SSH difference among the moorings. This eddy development can be seen from both altimetric SSH and mooring steric height, but the two-dimensional altimetric SSH field reveals more of the physical process than the one-dimensional array.

The gridded altimetry product and mooring have high coherence (>0.6) for periods longer than 20 days (figure not shown). The match between altimetric SSH and mooring upper-500-m steric height with less than 2 cm RMS error validates the upper-500-m steric height in representing satellite SSH over low frequencies. For periods shorter than ~20 days, the mooring steric height exhibits more variability than the gridded altimetric product, which is expected. From the example shown in the bottom panel of Fig. 13, the M_2 tide can be coherent and propagate from north to south shown by the gray arrow, but the coherency among the three moorings is intermittent. Over a 2-day period between 11 and 13 November, for example, the M_2 tidal peaks are less obvious at the northern mooring than at the southern mooring (Fig. 13, bottom panel).

The southern and northern mooring time series (Fig. 13, upper panel) reveal that the M_2 tide is stronger and more coherent at the southern mooring than the northern mooring. From a tidal analysis on the two steric height time series (figure not shown), the southern mooring has an M_2 steric height amplitude of 1.7 cm while the northern one has an amplitude of 0.7 cm. The M_2 baroclinic tide represented by the steric height is dominated by the first baroclinic mode that has a large wavelength longer than 100 km.

To address the question of why the M_2 tide is so different between two moorings separated by 30 km, we first eliminated the possibility that the difference comes from different mooring designs. The southern mooring uses a subsurface taut mooring connected to the profiler and surface buoy above by a reserve catenary. This design has a much smaller watch circle (250 m radius) than the northern slackline design mooring (~4 km radius). However, it is unlikely that this contributes to the difference in the M_2 signal at the different moorings, based on the glider results during its station-keeping phases shown in Fig. 12. The time variability at the M_2 tidal period is well characterized by the glider for both the southern and the northern moorings. During the 6-day period where the glider operated near the northern mooring, it confirmed the weak M_2 signal there. Likewise, at the southern mooring, the glider confirmed the elevated M_2 variability in steric height there. This mooring–glider comparison largely eliminates the influence of mooring design on the reconstruction of the coherent tides. As a result, the significantly different M_2 tide between the northern and the southern moorings appears to be real.

One possibility for the different tides between the northern and the southern moorings is that this small-scale difference is expected due to multiwave interference that has been

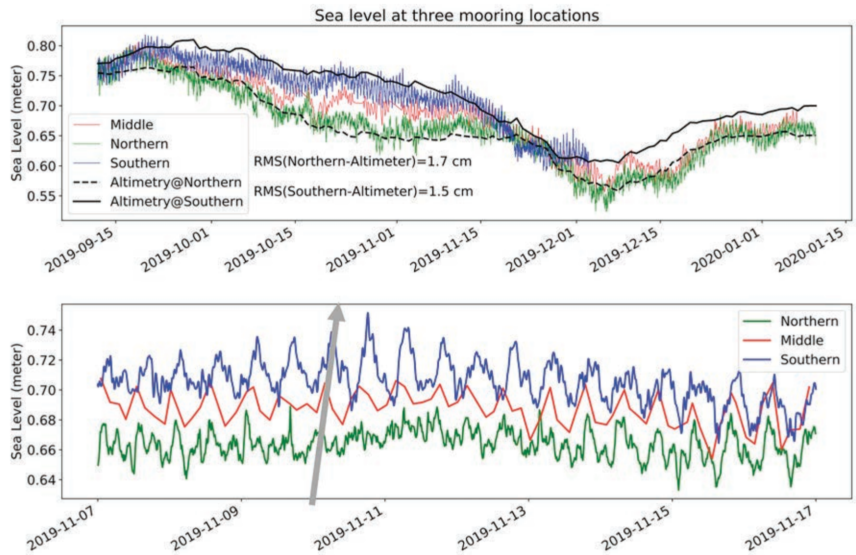

FIG. 13. (top) The time series of the upper-500-m steric height from three moorings (colored lines) offset by a constant 496.91 m, and the altimetric sea level anomaly interpolated at northern mooring (black solid) and southern mooring (black dashed). The RMS differences between WHOI mooring and SIO mooring steric height from their local altimetric sea level anomaly is 1.7 and 1.5 cm, respectively. (bottom) The same mooring steric height time series, but focusing on a 10-day window between 7 and 17 Nov 2019. The semitransparent gray arrow marked the propagation of the internal tides from the northern mooring through the middle mooring and to the southern mooring.

observed in the conventional altimetry (Zhao et al. 2019; Zaron 2019). An altimetry-based internal tide model that fits plane internal waves with multiple directions does also show similar amplitude variation of the mode-1 M_2 internal tide over the 30 km distance between the two moorings (Zaron 2019).

Another possibility is the modulation of coherent tides by balanced motions (e.g., Ponte and Klein 2015). The mesoscale and smaller mesoscale eddies are stronger at the northern mooring location than the southern mooring location, resulting in stronger eddy modulation of the tides and reduced tidal coherency. This can be seen from the frequency spectra of the steric height field of the three moorings (Fig. 14). The stronger M_2 tides at the southern mooring discussed above are illustrated in the frequency spectrum, i.e., the green line is much higher than the blue line at the M_2 frequency. The three moorings have matched energy on the low-frequency end with periods longer than 20 days. However, the spectral energy level at the southern mooring is drastically different from and one order of magnitude weaker than the other two moorings over 1–10-day periods. The gridded altimetry SSH maps (Fig. 5) show that the southern mooring is on the warm side of the meander and inside of the mature eddy at later stage, while the northern mooring spent more time on the further edge of the eddy where sharp horizontal fronts can be more prominent. This is confirmed by the horizontal gradient of SST, which is persistently stronger at the northern mooring location than at the southern mooring (figure not shown). This set of evidence points to the hypothesis that mesoscale eddies can modulate coherent low mode tides within a distance shorter than the tidal wavelength. The 2D SSH field to be observed by SWOT can be very useful to detect these small-scale eddy–wave interactions. Further proof of the hypothesis needs more observations or process-oriented numerical modeling studies and will be pursued elsewhere.

2) SPATIAL VARIABILITY

With two full-depth moorings at the northern and southern locations, we can start to examine the spatial variability from

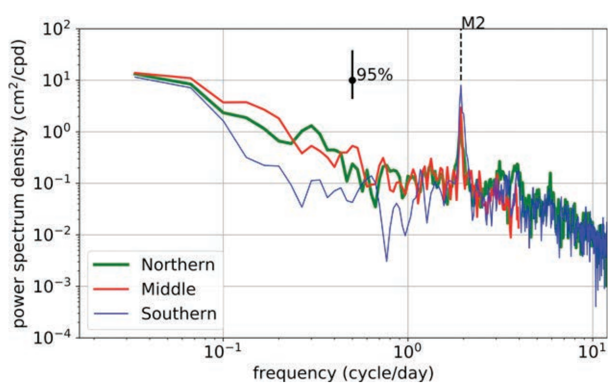

FIG. 14. The frequency spectra of the upper-500-m steric height from the northern (blue), middle (red), and the southern mooring (green). M_2 tidal frequency is marked by the dashed vertical line. The middle mooring spectrum (red) was cut at 4 cycles per day for its limited sampling frequency at 8 profiles per day.

TABLE 2. RMS differences between the northern and the southern moorings for the period 10 Sep–25 Nov 2019 when full-depth measurements are available at both sites. The temporal-scale separation is done in frequency space through Fourier analysis without windowing. The bottom row is done through a three-mooring scale separation described in the text representing a back-of-envelope calculation of the small-scale (<~30 km) variability. The unit for all values is cm.

	Full water column	0–500 m	500–4000 m
All frequencies	3.2	2.8	0.9
<14 days	1.6	1.4	0.8
2–14 days	0.7	0.7	0.2
<2 days	1.5	1.2	0.7
Anomalies to a linear function of the three moorings		0.2–0.7	

the mooring difference. Table 2 shows that the RMS difference over 30 km is 3.5 cm based on the full-depth steric height, among which 2.8 cm is due to the upper 500 m and 1 cm to the deeper ocean. These values include the influence of the wavelengths longer than 150 km, which is beyond the focus of the in situ Cal/Val. With only three moorings spanning 30 km, it is impossible to single out the signals with wavelength less than 150 km, but in general longer wavelengths are associated with longer periods. For example, these RMS differences are reduced for periods less than 14 days and significantly reduced for the 2–14-day band. The variability with periods less than 14 days is dominated by high frequencies (>1/2 cycle day^{-1}). This dependence of RMS difference on time scales is expected for a typical SSH frequency spectrum that is dominated by low-frequency (monthly and longer) variabilities and tidal peaks over high (superinertial) frequencies (e.g., Fig. 14).

The middle mooring does not have deep CTDs below the Prawler and samples only the upper 500 m. If we only focus on the upper-500-m steric height, the three moorings can be used to derive steric height difference for separation distances of 10 and 20 km. The standard deviations of the differences are 1.6 and 2.0 cm for 10 and 20 km, respectively.

These analyses with a single mooring (section 4c, Table 1) or two-mooring differences (Table 2) cannot distinguish different spatial scales, but we have used the above frequency filtering to isolate motions on SWOT spatial scales and thus could estimate the expected RMS differences due to these motions on the single spatial lag of 30 km. This is the size of SSH differences expected due to motions of interest to SWOT over such distances. In addition, with three moorings, we can begin to decipher the spatial–temporal variabilities due to the smallest-scale motions, even without the actual wavenumber spectrum. The main technique is discussed as follows.

Given three moorings with separation distances of 10 and 20 km, we have three points spanning 30 km distance. To examine small-scale signals, we removed the large-scale influence by removing a spatial linear trend through the three moorings for each hourly snapshot as shown in the schematic diagram in Fig. 15a. The middle mooring time series is linearly interpolated from 8 profiles per day to hourly, which inevitably introduces errors. The deviations from the fitted linear trend are considered the SSH anomaly at small scales.

The linear-trend removal is a crude spatial high-pass filter. The effectiveness of removing the local linear trend is evaluated using a Monte Carlo simulation to test a Hanning high-pass filter with different window sizes. We first generate 5000 128-km-long synthetic SSH profiles with certain wavenumber spectral slopes, then sample the profiles in the middle at three locations separated by 10 and 20 km, resembling the prelaunch campaign mooring placement. The synthetic mooring data are separated into large scale and small scale using the same method of fitting a three-point linear trend. The results are compared with results produced by a high-pass Hanning filter of different window widths. We find that for synthetic SSH profiles with k^{-4} wavenumber spectrum, the smallest difference between removing a local linear trend of the three moorings and a Hanning-window filtering occurs at 22 km Hanning-window width. For k^{-2} profiles, it is at 32 km. The SSH profile is "smoother" for steeper wavenumber spectrum, e.g., k^{-4}, so the local linear trend captures and removes large-scale signals more effectively. The anomalies after removing the local linear trend are mostly from spatial scales less than approximately 30 km. We denote these anomalies as "small scale" and the linear trend as "large scale" in the following paragraph. It is worth emphasizing again that this operation is a crude way of separating small and large scales, given the limitation of the spatial coverage of the data.

The derived small-scale variability is significantly weaker than the large-scale variability (Fig. 15b). The RMS values of the total upper-500-m steric height for the three moorings are 1.9, 1.3, and 1.9 cm from north to south. The corresponding large scales defined by the linear trend have RMS values of 1.7, 1.2, and 1.9 cm. The small-scale (<~30 km) steric height is 0.4, 0.7, 0.2 cm for the northern, middle, and southern moorings, respectively. These values for small scales are smaller or close to the SWOT KaRIn noise values around 0.54 cm (section 2d). It indicates that the SSH signal at the Cal/Val site can be weaker than the SWOT KaRIn noise for spatial scales 20–30 km and smaller. This result is consistent with Wang et al. (2019).

Note that the sum of small-scale and large-scale temporal variances is larger than the variance of the total signal. This provides evidence that this spatial filtering does not separate the signal in the temporal space. However, removing the local linear trend effectively removes most of the low-frequency variability that is visually obvious in the time series (Fig. 15b) and also clearly shown in the frequency spectra in Fig. 15c, where the power spectra of the total and large-scale signals converge over periods longer than 10 days (blue and orange lines). Removing the linear trend also effectively removes most of the M_2 baroclinic tides in the steric height, which means that the baroclinic tides have spatial scales larger than about 30 km. Even though the large-scale signal is more energetic than the smaller spatial signal over almost all

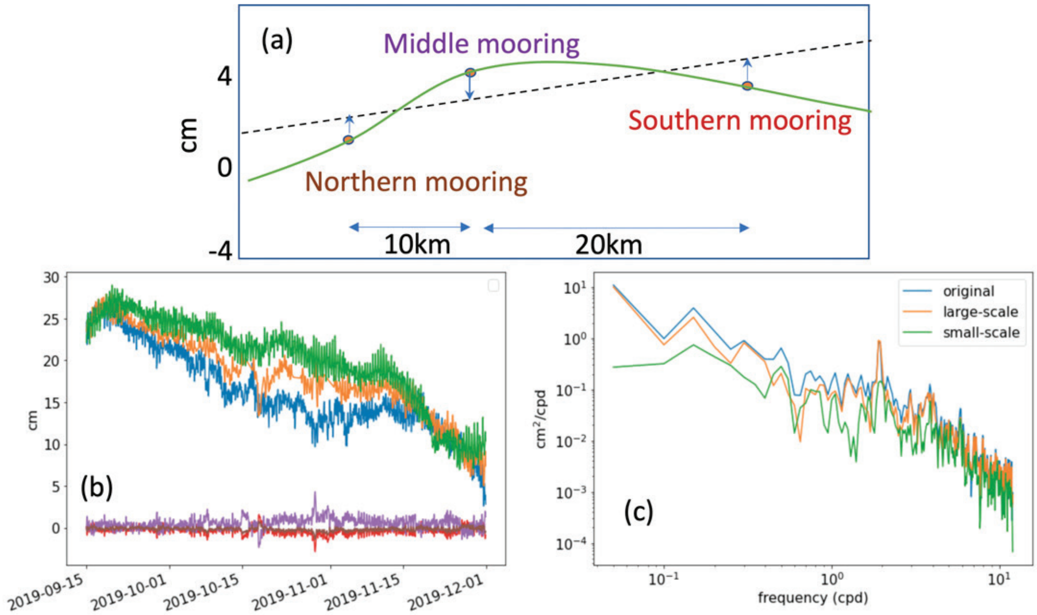

FIG. 15. (a) The schematic of deriving small-scale anomalies from three moorings. The linear trend (dashed line) was derived through the least squares method. The deviation of each mooring steric height from their linear trend is denoted as the small-scale component. Removing the linear trend over a 30 km segment is similar to high-pass filtering with a 20–30-km-wide Hanning window depending on the wavenumber slope of the signal. (b) The original steric height of each mooring (green, orange, and blue lines). The small-mesoscale signals defined in (a) are shown by purple, red, and brown lines for the three moorings. (c) The frequency spectra for the original steric height (blue), the linear trend representing the large-scale (orange), and the small-scale steric height (green) averaged over the spectra of the three moorings.

frequencies, the small-scale signal is particularly large over the period range of 2–5 days relative to the large scale. With a caveat of uncertain significance, we may tentatively associate <30 km spatial scales with 2–5-day temporal scales. This spatial–temporal-scale association may have a practical value for designing the optimal error covariance matrices in the data assimilation system with the multiscale approach, such as Li et al. (2019), D'Addezio et al. (2019), and Archer et al. (2022).

f. Comparison to Sentinel-3A *SSH*

The *Sentinel-3A* ground track was not a factor for the design of the SWOT Cal/Val orbit. It is rather fortunate that one of the *Sentinel-3A* (*S3A*) ground tracks is in the middle of a SWOT swath along the fast-repeating orbit. For this reason, the mooring array in the prelaunch field campaign was placed along the *S3A* ground track (Fig. 2). During the 2019/20 campaign period, *S3A* passed the mooring array five times (Fig. 16). The mooring steric heights (upper 500 m) match the *S3A* measurements within 2 cm RMS. There were two times when the steric heights and *S3A* values were different (the third and fifth rows). Despite the sizeable differences, the spatial structures in the mooring array steric heights resemble the spatial structures of the *S3A* SSH profiles. However, bias corrections of 2 and 6 cm were applied to 6 November 2019 and 2 January 2020 profiles, respectively. The nature of the bias is unknown at the time of writing and deferred to future investigations.

g. Bottom pressure

Bottom pressure recorders measure both the barotropic (due to additional water mass above the BPR) and baroclinic (due to interior temperature/salinity changes) signals on the ocean floor. The BPRs deployed in this campaign have enough precision to detect millimeter-level signals, but BPRs suffer from a large long-term drift that may be mistaken for a low-frequency signal in our ~90-day records. Ray (2013) analyzed a network of BPRs of this type, showing that the BPR-derived tide matches the altimetric tide model with about 5 mm RMS difference for the M_2 constituent. The BPRs used in the campaign should be accurate enough to detect deep baroclinic pressure signals even though separating them from much more energetic barotropic tides based on a single mooring is impossible (Ray 2013). The most prominent signal in the bottom pressure is the tide (Fig. 17a). We fit 53 tidal constituents to the measured bottom-pressure signal to produce a detided bottom pressure record (Fig. 17b) using the same tool from Ray (2013). The detided signals are relatively small (2.3–2.6 cm), but still potentially important. Unfortunately, we have little information about the spatial scale of the signals contributing to these residual bottom pressure signals. Taking the difference between the two detided bottom-pressure records can give us a vague sense of how small-scale signals

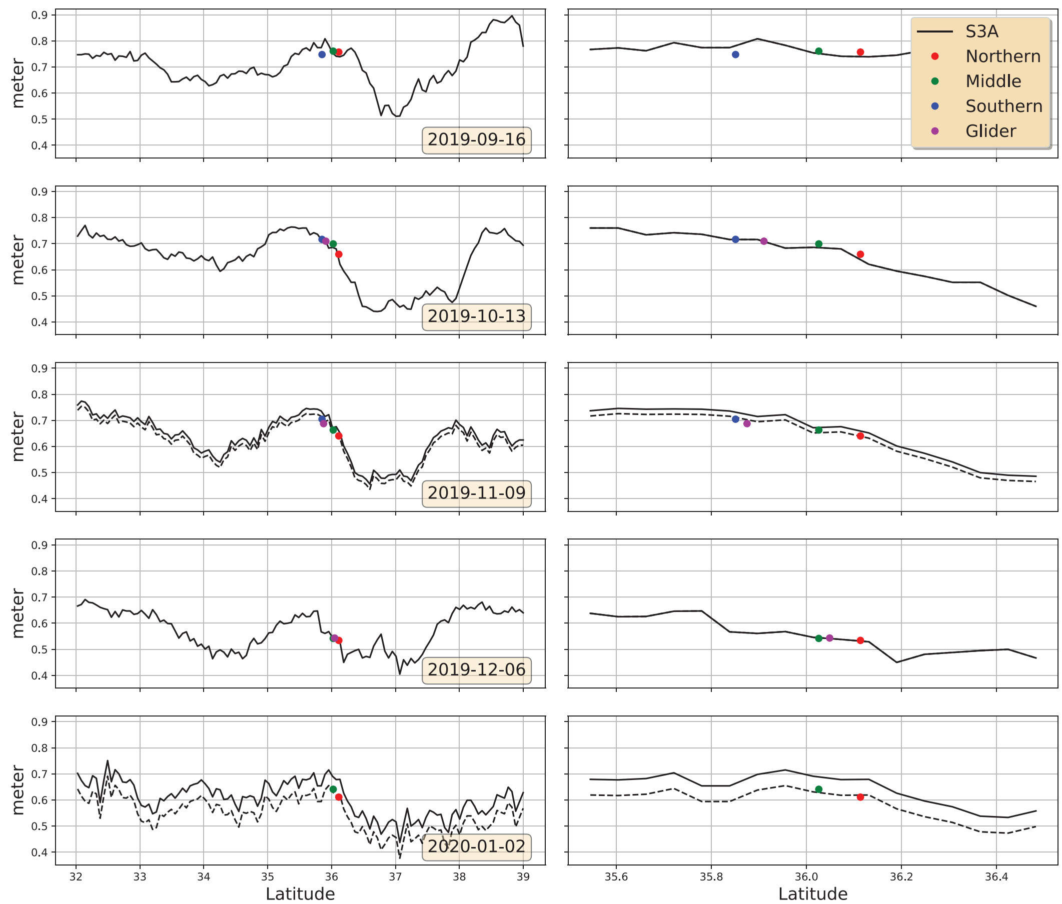

FIG. 16. The five *Sentinel-3A* SSH profiles during the 2019/20 campaign period that pass the mooring array (black lines). They are the L3 product with ocean (barotropic) tides, dynamic atmosphere correction (DAC), and long-wavelength-error (LWE) correction applied. The colored dots show the upper-500-m steric height from the northern (red), middle (green), and southern (blue) moorings and the glider (purple). (left) The 7° segment to show the large-scale context. (right) The same profile, but zooming in to focus on the mooring array within 100-km-wide segments. The dashed lines in the third and fifth rows are the black lines offset by 2 and 6 cm, respectively. The steric height is calculated from the original in situ density without removing the time mean, then offset by 496.385 m to match the *Sentinel-3A* profiles.

might contribute. This difference has an RMS amplitude of 0.6 cm based on the period of 1 October 2019–1 October 2020 when the bottom pressure drift becomes less obvious. It contains both barotropic and baroclinic signals, including several tidal frequencies and low-frequency variability, and the parabolic shape of the difference curve (Fig. 17b) suggests it may also be affected by differences in the low-frequency drift of the two bottom pressure recorders. Removing a quadratic fit to the difference between the two detided bottom-pressure records reduces the RMS difference to about 0.4 cm, which is below the SWOT KaRIn noise level derived in section 2d.

5. The design of a SWOT postlaunch campaign

The main purpose of the SWOT prelaunch campaign described in the paper is to provide information for the design of an effective yet affordable postlaunch SWOT ocean in situ observing system for the mission's calibration and validation. To validate the SWOT SSH, we need an array of observations for comparison with the nearly simultaneous measurement taken by the satellite in less than 23 s over 150 km. The resolution of SWOT in the California Cal/Val region is about 20 km in wavelength, below which the baroclinic SSH becomes less than KaRIn instrument noise (Wang et al. 2019). To meet the Nyquist wavelength requirement of 20 km, we need a measurement every 10 km. Although Wang and Fu (2019) indicated that the onboard nadir altimeter is able to validate SWOT at wavelengths longer than 120 km, we feel that, in order to reduce cost, it is acceptable to deploy an array of 11 moorings covering 100 km to meet the in situ Cal/Val objectives.

Based on the analysis presented in the paper, it is acceptable to sample only the upper 500 m for the low-frequency ocean variability. However, it is desirable to sample the ocean deeper than 500 m to capture the deep signals of internal tides and occasional deep eddies. Since the wavelengths of internal

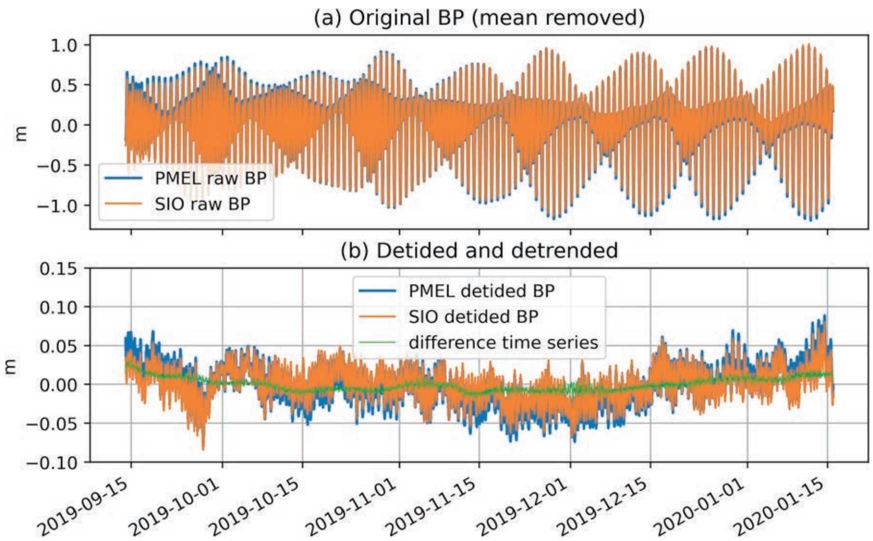

FIG. 17. (a) The original time series of the bottom pressure from the southern (orange) and the northern (blue) BPRs. (b) The residual after removing the fitted tides and linear trends. We fit 53 tidal constituents to the 4-month-long time series to reduce the residual. The remaining signal of each BPR still has 2.2–2.4 cm standard deviation.

tides are longer than 60 km (the two lowest modes of the M_2 tides; Zhao et al. 2019), the required Nyquist sampling interval for low-mode internal tides is 30 km. Shown in Fig. 18 is a baseline design of the postlaunch observing system. It contains 11 moorings with 4 of them (triangles) consisting of a Wirewalker and deep CTDs like the SIO system. The remaining 7 moorings are Prawler moorings like the PMEL system, sampling only the upper 500 m. These instruments will provide time series observations that allow the construction of the snapshots of steric height for comparison with the SWOT SSH measurement on a daily basis. The difference between the two observations will provide an assessment of the SWOT measurement errors for the small-wavelength range reconstructed by the in situ mooring array (20–100 km). Its wavenumber spectrum will be compared with the SWOT requirement (Fig. 1).

Based on the results from the prelaunch campaign, GPS buoys and BPRs are not critical for meeting the Cal/Val objectives. To make accurate IB correction for the SWOT SSH, one barometer at the center of the array is included in the design.

Two gliders are included to sample the cross-track ocean variability to aid the estimation of the two-dimensional state of the upper ocean for validating the science goals of the mission to determine the circulation of the upper ocean. If funding permits, more gliders would be highly desirable for achieving the science goals. As illustrated in the paper, the gliders, when operating in the station-keeping mode, will also serve as a contingency for any failed mooring.

Given the constraints of the mission's budget, this design presents a minimum system for meeting the mission's Cal/Val objectives. We look forward to opportunities of collaboration with other interested parties to expand this SWOT Cal/Val array into a larger-scope, submesoscale-focused experiment in this region.

6. Discussion and conclusions

It has been shown that observations from the moorings and the glider can be used to reconstruct a steric height field with accuracy at an RMS error below 1 cm at each location level. There are, however, remaining uncertainties in the accuracy of the horizontal wavenumber spectrum produced by an array of these moorings.

The moorings' large watch circles might be a source of uncertainty in making an SSH wavenumber calculation for the SWOT Cal/Val purpose. The watch circle can reach a 4 km radius. It may change the spacing between moorings and result in nonuniformly spaced mooring array. In addition, the deviation from the centerline of the mooring array (the middle of the SWOT swath) can also be as large as the watch circle radius. These along-track and cross-track drifts of the moorings will introduce errors and uncertainties, but we do not have a formal assessment of the error in this study. In any case, the size of the watch circle is less than the 15–20-km-wavelength resolution of SWOT in the Cal/Val region (Wang et al. 2019).

The deep-ocean steric height has variability and can contribute to the overall steric height signal. Based on the ~90 days of mooring observations collected during the 2019/20 campaign, the consequence of missing the deep-ocean steric height was about 0.6–0.8 cm standard deviation for each mooring, mostly arising from baroclinic tides (Fig. 10).

There is some evidence that eddies at and below 500 m occasionally occur in the Cal/Val region (Collins et al. 2013). Although Collins et al. (2013) do not report on the water

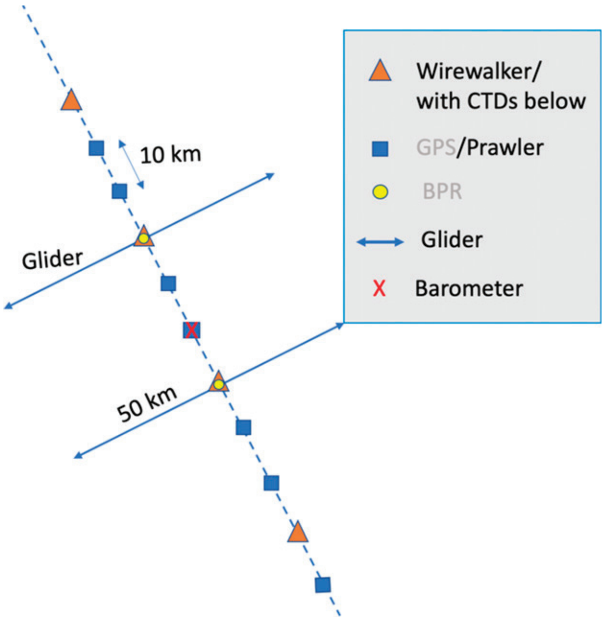

FIG. 18. A minimum baseline for the SWOT postlaunch ocean Cal/Val field campaign. The four hybrid moorings with full-depth *T*/*S* measurements can capture deep-reaching baroclinic tides with relatively longer wavelengths. The seven Prawlers will measure the upper-500-m steric height. Two gliders will sample the cross-swath direction and also serve as a contingency for failed moorings. The barometer will provide high-precision, high-frequency atmospheric pressure for IB correction. BPRs and GPS receivers are not part of the minimum baseline but will be a valuable upgrade.

column structure associated with the observed deep eddies, they could contribute to variability in steric height and to significant nonzero velocities at 500 m depth. For example, assuming a mode-1 structure, a 25-km-wide eddy at 1500 m with ~10 cm s^{-1} velocities as reported by Collins et al. (2013) would be associated with a ~1 cm change in steric height across its diameter. They also observed an eddy at 660 m depth with velocities that would correspond to 1.4 cm steric height signal across the eddy with a diameter of 54 km at that depth. However, deep eddies need not be associated with a mode-1 structure. For example, Gula et al. (2019) report on the presence of deep submesoscale coherent vortices (SCVs) in the Gulf Stream with diameters of 10–30 km. Those SCVs have a mode-2 like signature that would have little if any impact on steric height (e.g., Fig. 2d in Gula et al. 2019). Given the potential for deep eddies to contribute a small amount of steric height variability, a subset of moorings in the SWOT Cal/Val effort will monitor the deep ocean to account for these signals if they arise (Fig. 18).

Even though the error in GPS SSH from a single buoy (>1 cm RMS) is larger than SWOT mission requirements, much of this error is attributed to sea-state and water-line errors, and intrinsic GPS errors (e.g., from tropospheric refraction) that are spatially correlated over the campaign footprint. Significant cancellation of common mode errors can thus be expected from combined processing of observations of multiple buoys operating in the same campaign theater. This is supported by recent tandem buoy campaigns in the Bass Strait (Zhou et al. 2020) and near the Harvest platform (Haines et al. 2019), both of which suggest that errors (on ΔSSH between buoys in proximity) are reduced to less than 1 cm. Whether the accuracies achieved can approach the stringent requirements imposed by the validation of the SWOT wavenumber spectrum remains an open question (Zhou et al. 2020). Regardless, the GPS buoy technique has advanced significantly and already offers a powerful means of resolving discrepancies between steric height (as measured with hydrographic techniques) and geodetic SSH (as measured by SWOT).

We have shown that it is possible to measure the steric contribution to sea surface height to <1 cm RMS precision with several moorings and a glider. This allows confidence that an array of moorings and collocated glider lines (e.g., Fig. 18) will allow for a robust oceanographic calibration and validation of the KaRIn sensor on board the SWOT satellite during the planned 1-day fast-repeat period before the satellite is moved to its final orbit.

This is the first time when a combination of independent high-precision in situ instruments is used to analyze the SSH budget focusing on such small spatial scales (less than 30 km) and high frequencies (period less than monthly). The results shed light on the design of the SWOT postlaunch field campaign as well as the ocean physics over such small scales and high frequencies (periods ranging from hours to months).

We have shown that the ocean sea surface height measured by GPS, which is like altimeter/SWOT measurements, matches the steric height derived from the temperature and salinity measurements using CTDs after subtracting the bottom pressure and applying the inverted barometer correction. The consistency between the GPS-BPR and the mooring steric height validated the utility of the steric height as the ground truth for satellite calibration and validation. Even though the absolute RMS difference between GPS-BPR-derived steric height and CTD-derived steric height is larger than 1 cm, how much of the error is due to the large-scale common mode GPS error is unknown, but expected to be largely removable. The utility of GPS in the SWOT Cal/Val is still under investigation through the second GPS on the middle mooring. The major advantage of using steric height is the absence of the errors due to surface waves.

The variability in steric height is mostly due to the upper-ocean processes. For example, the deep-ocean ($z < -500$ m) steric height variability has a standard deviation of 0.6–0.8 cm, most of which comes from superinertial frequencies, especially around the semidiurnal M_2. If only subinertial variabilities with periods between 2 and 14 days are considered, missing deep ocean results in <2 mm uncertainty.

Small scales less than 30 km wavelength have very weak steric height variation, 0.2–0.7 cm standard deviation near the SWOT Cal/Val campaign region diagnosed from the 2019/20 campaign conducted in the wintertime. This small-scale variability is estimated based on the deviations of the three mooring steric heights from their spatial linear trend. This weak small-scale steric height signal underlines the challenge for

SWOT, but also highlights the opportunities provided by SWOT and the values of a full-scale array with a dozen CTD moorings in conducting the mission Cal/Val and studying the small-scale ocean circulation.

Acknowledgments. We are grateful to Anna Savage and R/V *Sally Ride* captain and crew for the unplanned recovery of the Wirewalker, and to Hong Zhang for providing ERA5 atmospheric pressure for the IB correction, Ed Zaron for the discussion on internal tides, and Marie Eble and George Mungov for the discussions on the tidal reconstruction from BP. The research was carried out at the Jet Propulsion Laboratory, California Institute of Technology, under a contract with the National Aeronautics and Space Administration (80NM0018D0004). All authors are supported by the SWOT project. J. T. Farrar was partially supported by NASA NNX16AH76G. The in-situ observations are available for download at https://podaac.jpl.nasa.gov/.

REFERENCES

Archer, M. R., Z. Li, J. Wang, and L.-L. Fu, 2022: Reconstructing fine-scale ocean variability via data assimilation of the SWOT pre-launch in situ observing system. *J. Geophys. Res. Oceans*, **127**, e2021JC017362, https://doi.org/10.1029/2021JC017362.

Bertiger, W., and Coauthors, 2010: Single receiver phase ambiguity resolution with GPS data. *J. Geod.*, **84**, 327–337, https://doi.org/10.1007/s00190-010-0371-9.

——, and Coauthors, 2020: GipsyX/RTGx: A new tool set for space geodetic operations and research. *Adv. Space Res.*, **66**, 469–489, https://doi.org/10.1016/j.asr.2020.04.015.

Bonnefond, P., and Coauthors, 2019: Corsica: A 20-yr multi-mission absolute altimeter calibration site. *Adv. Space Res.*, **68**, 1171–1186, https://doi.org/10.1016/j.asr.2019.09.049.

Callies, J., and W. Wu, 2019: Some expectations for submesoscale sea surface height variance spectra. *J. Phys. Oceanogr.*, **49**, 2271–2289, https://doi.org/10.1175/JPO-D-18-0272.1.

Capet, X., J. C. McWilliams, M. J. Molemaker, and A. F. Shchepetkin, 2008a: Mesoscale to submesoscale transition in the California Current system. Part I: Flow structure, eddy flux, and observational tests. *J. Phys. Oceanogr.*, **38**, 29–43, https://doi.org/10.1175/2007JPO3671.1.

——, ——, ——, and ——, 2008b: Mesoscale to submesoscale transition in the California Current system. Part III: Energy balance and flux. *J. Phys. Oceanogr.*, **38**, 2256–2269, https://doi.org/10.1175/2008JPO3810.1.

Chereskin, T. K., C. B. Rocha, S. T. Gille, D. Menemenlis, and M. Passaro, 2019: Characterizing the transition from balanced to unbalanced motions in the Southern California Current. *J. Geophys. Res. Oceans*, **124**, 2088–2109, https://doi.org/10.1029/2018JC014583.

Clark, E. B., and Coauthors, 2018: Station-keeping underwater gliders using a predictive ocean circulation model and applications to SWOT calibration and validation. *IEEE J. Oceanic Eng.*, **45**, 371–384, https://doi.org/10.1109/JOE.2018.2886092.

Collins, C. A., T. Margolina, T. A. Rago, and L. Ivanov, 2013: Looping RAFOS floats in the California Current system. *Deep Sea Res. II*, **85**, 42–61, https://doi.org/10.1016/j.dsr2.2012.07.027.

Copernicus Climate Change Service, 2017: ERA5: Fifth generation of ECMWF atmospheric reanalyses of the global climate. Copernicus Climate Change Service Climate Data Store, accessed 1 March 2020, https://cds.climate.copernicus.eu/cdsapp\#!/home.

D'Addezio, J. M., S. Smith, G. A. Jacobs, R. Helber, C. Rowley, I. Souopgui, and M. J. Carrier, 2019: Quantifying wavelengths constrained by simulated SWOT observations in a submesoscale resolving ocean analysis/forecasting system. *Ocean Modell.*, **135**, 40–55, https://doi.org/10.1016/j.ocemod.2019.02.001.

Desai, S., and Coauthors, 2018: Surface Water and Ocean Topography Mission (SWOT) project science requirements document. Jet Propulsion Laboratory Doc. JPL D-61923, revision B, 29 pp.

d'Ovidio, F., and Coauthors, 2019: Frontiers in fine-scale in situ studies: Opportunities during the SWOT fast sampling phase. *Front. Mar. Sci.*, **6**, 168, https://doi.org/10.3389/fmars.2019.00168.

Dufau, C., M. Orsztynowicz, G. Dibarboure, R. Morrow, and P. Traon, 2016: Mesoscale resolution capability of altimetry: Present and future. *J. Geophys. Res. Oceans*, **121**, 4910–4927, https://doi.org/10.1002/2015JC010904.

Durand, M., L.-L. Fu, D. P. Lettenmaier, D. E. Alsdorf, E. Rodriguez, and D. Esteban-Fernandez, 2010: The Surface Water and Ocean Topography mission: Observing terrestrial surface water and oceanic submesoscale eddies. *Proc. IEEE*, **98**, 766–779, https://doi.org/10.1109/JPROC.2010.2043031.

Eble, M. C., and F. I. Gonzalez, 1991: Deep-ocean bottom pressure measurements in the northeast Pacific. *J. Atmos. Oceanic Technol.*, **8**, 221–233, https://doi.org/10.1175/1520-0426(1991)008<0221:DOBPMI>2.0.CO;2.

Flament, P., L. Armi, and L. Washburn, 1985: The evolving structure of an upwelling filament. *J. Geophys. Res.*, **90**, 11 765–11 778, https://doi.org/10.1029/JC090iC06p11765.

Fu, L.-L., and A. Cazenave, 2001: *Satellite Altimetry and Earth Sciences.* Academic Press, 509 pp.

——, and C. Ubelmann, 2014: On the transition from profile altimeter to swath altimeter for observing global ocean surface topography. *J. Atmos. Oceanic Technol.*, **31**, 560–568, https://doi.org/10.1175/JTECH-D-13-00109.1.

Gula, J., T. M. Blacic, and R. E. Todd, 2019: Submesoscale coherent vortices in the Gulf Stream. *Geophys. Res. Lett.*, **46**, 2704–2714, https://doi.org/10.1029/2019GL081919.

Guthrie, J., and Coauthors, 2020: Preliminary results from the first deployments of the dynamic ocean topography buoy: In-situ observations of sea surface height in ice-covered seas. *AGU Ocean Sciences Meeting*, San Francisco, CA, Amer. Geophys. Union, Abstract HE14B-1930, https://agu.confex.com/agu/osm20/meetingapp.cgi/Paper/648899.

Haines, B., S. Desai, C. Meinig, and S. Stalin, 2017: CAL/VAL of the SWOT SSH spectrum: Moored GPS approach. *SWOT Science Team Meeting*, Toulouse, France, NASA, https://trs.jpl.nasa.gov/handle/2014/48164.

——, ——, A. Dodge, R. Leben, M. Shannon, C. Meinig, and S. Stalin, 2019: The Harvest experiment: New results from the platform and moored GPS buoys. *Ocean Surface Topography Science Team Meeting*, Chicago, IL, NASA.

——, ——, D. Kubitschek, and R. Leben, 2021: A brief history of the Harvest experiment: 1989–2019. *Adv. Space Res.*, **68**, 1161–1170, https://doi.org/10.1016/j.asr.2020.08.013.

Hersbach, H., and Coauthors, 2020: The ERA5 global reanalysis. *Quart. J. Roy. Meteor. Soc.*, **146**, 1999–2049, https://doi.org/10.1002/qj.3803.

Hickey, B. M., 1979: The California Current system—Hypotheses and facts. *Prog. Oceanogr.*, **8**, 191–279, https://doi.org/10.1016/0079-6611(79)90002-8.

Ikeda, M., and W. J. Emery, 1984: Satellite observations and modeling of meanders in the California Current system off Oregon and Northern California. *J. Phys. Oceanogr.*, **14**, 1434–1450, https://doi.org/10.1175/1520-0485(1984)014<1434:SOAMOM>2.0.CO;2.

Kanzow, T., U. Send, W. Zenk, A. D. Chave, and M. Rhein, 2006: Monitoring the integrated deep meridional flow in the tropical North Atlantic: Long-term performance of a geostrophic array. *Deep-Sea Res. I*, **53**, 528–546, https://doi.org/10.1016/j.dsr.2005.12.007.

LaCasce, J. H., and A. Mahadevan, 2006: Estimating subsurface horizontal and vertical velocities from sea surface temperature. *J. Mar. Res.*, **64**, 695–721, https://doi.org/10.1357/002224006779367267.

Lapeyre, G., and P. Klein, 2006: Dynamics of the upper oceanic layers in terms of surface quasigeostrophy theory. *J. Phys. Oceanogr.*, **36**, 165–176, https://doi.org/10.1175/JPO2840.1.

Li, Z., J. Wang, and L.-L. Fu, 2019: An observing system simulation experiment for ocean state estimation to assess the performance of the SWOT mission: Part 1—A twin experiment. *J. Geophys. Res. Oceans*, **124**, 4838–4855, https://doi.org/10.1029/2018JC014869.

Meinig, C., S. E. Stalin, A. I. Nakamura, and H. B. Milburn, 2005: Real-time deep-ocean tsunami measuring, monitoring, and reporting system: The NOAA DART II description and disclosure. NOAA NDBC Rep., 15 pp.

Melville, W. K., L. Lenain, D. R. Cayan, M. Kahru, J. P. Kleissl, P. Linden, and N. M. Statom, 2016: The Modular Aerial Sensing System. *J. Atmos. Oceanic Technol.*, **33**, 1169–1184, https://doi.org/10.1175/JTECH-D-15-0067.1.

Mihaly, S. F., R. E. Thomson, and A. B. Rabinovich, 1998: Evidence for nonlinear interaction between internal waves of inertial and semidiurnal frequency. *Geophys. Res. Lett.*, **25**, 1205–1208, https://doi.org/10.1029/98GL00722.

Morrow, R., and Coauthors, 2019: Global observations of fine-scale ocean surface topography with the Surface Water and Ocean Topography (SWOT) mission. *Front. Mar. Sci.*, **6**, 232, https://doi.org/10.3389/fmars.2019.00232.

Osse, T. J., C. Meinig, S. Stalin, and H. Milburn, 2015: The Prawler, a vertical profiler powered by wave energy. *OCEANS 2015*, Washington, DC, IEEE, https://doi.org/10.23919/OCEANS.2015.7404354.

Pinkel, R., M. A. Goldin, J. A. Smith, O. M. Sun, A. A. Aja, M. N. Bui, and T. Hughen, 2011: The Wirewalker: A vertically profiling instrument carrier powered by ocean waves. *J. Atmos. Oceanic Technol.*, **28**, 426–435, https://doi.org/10.1175/2010JTECHO805.1.

Ponte, A. L., and P. Klein, 2015: Incoherent signature of internal tides on sea level in idealized numerical simulations. *Geophys. Res. Lett.*, **42**, 1520–1526, https://doi.org/10.1002/2014GL062583.

Pujol, M. I., Y. Faugère, G. Taburet, S. Dupuy, C. Pelloquin, M. Ablain, and N. Picot, 2016: DUACS DT2014: The new multi-mission altimeter data set reprocessed over 20 years. *Ocean Sci.*, **12**, 1067–1090, https://doi.org/10.5194/os-12-1067-2016.

Qiu, B., S. Chen, P. Klein, J. Wang, H. Torres, L. Fu, and D. Menemenlis, 2018: Seasonality in transition scale from balanced to unbalanced motions in the World Ocean. *J. Phys. Oceanogr.*, **48**, 591–605, https://doi.org/10.1175/JPO-D-17-0169.1.

Quartly, G. D., G. Chen, F. Nencioli, R. Morrow, and N. Picot, 2021: An overview of requirements, procedures and current advances in the calibration/validation of radar altimeters. *Remote Sens.*, **13**, 125, https://doi.org/10.3390/rs13010125.

Ray, R. D., 2013: Precise comparisons of bottom-pressure and altimetric ocean tides. *J. Geophys. Res. Oceans*, **118**, 4570–4584, https://doi.org/10.1002/jgrc.20336.

Rocha, C., T. Chereskin, G. Gille, and D. Menemenlis, 2016: Mesoscale to submesoscale wavenumber spectra in Drake Passage. *J. Phys. Oceanogr.*, **46**, 601–620, https://doi.org/10.1175/JPO-D-15-0087.1.

Rudnick, D. L., K. D. Zaba, R. E. Todd, and R. E. Davis, 2017: A climatology of the California Current system from a network of underwater gliders. *Prog. Oceanogr.*, **154**, 64–106, https://doi.org/10.1016/j.pocean.2017.03.002.

Savage, A. C., and Coauthors, 2017: Spectral decomposition of internal gravity wave sea surface height in global models. *J. Geophys. Res. Oceans*, **122**, 7803–7821, https://doi.org/10.1002/2017JC013009.

Schaeffer, P., and Coauthors, 2018: What do we need to improve the next mean sea surface? *Ocean Surface Topography Science Team Meeting*, Ponta Delgado, Portugal, NASA.

Strub, P. T., and C. James, 2000: Altimeter-derived variability of surface velocities in the California Current system: 2. Seasonal circulation and eddy statistics. *Deep-Sea Res. II*, **47**, 831–870, https://doi.org/10.1016/S0967-0645(99)00129-0.

Su, Z., and Coauthors, 2018: Ocean submesoscales as a key component of the global heat budget. *Nat. Commun.*, **9**, 775, https://doi.org/10.1038/s41467-018-02983-w.

Taburet, G., A. Sanchez-Roman, M. Ballarotta, M. I. Pujol, J. F. Legeais, F. Fournier, Y. Faugere, and G. Dibarboure, 2019: DUACS DT-2018: 25 years of reprocessed sea level altimeter products. *Ocean Sci.*, **15**, 1207–1224, https://doi.org/10.5194/os-15-1207-2019.

Torres, H. S., P. Klein, D. Menemenlis, B. Qiu, Z. Su, J. Wang, S. Chen, and L. Fu, 2018: Partitioning ocean motions into balanced motions and internal gravity waves: A modeling study in anticipation of future space missions. *J. Geophys. Res. Oceans*, **123**, 8084–8105, https://doi.org/10.1029/2018JC014438.

Wang, J., and L.-L. Fu, 2019: On the long-wavelength validation of the SWOT KaRIn measurement. *J. Atmos. Oceanic Technol.*, **36**, 843–848, https://doi.org/10.1175/JTECH-D-18-0148.1.

——, ——, B. Qiu, D. Menemenlis, J. T. Farrar, Y. Chao, A. F. Thompson, and M. M. Flexas, 2018: An observing system simulation experiment for the calibration and validation of the Surface Water Ocean Topography sea surface height measurement using in situ platforms. *J. Atmos. Oceanic Technol.*, **35**, 281–297, https://doi.org/10.1175/JTECH-D-17-0076.1.

——, ——, H. S. Torres, S. Chen, B. Qiu, and D. Menemenlis, 2019: On the spatial scales to be resolved by the Surface Water and Ocean Topography Ka-band radar interferometer. *J. Atmos. Oceanic Technol.*, **36**, 87–99, https://doi.org/10.1175/JTECH-D-18-0119.1.

Watts, D., and H. T. Rossby, 1977: Measuring dynamic heights with inverted echo sounders: Results from MODE. *J. Phys. Oceanogr.*, **7**, 345–358, https://doi.org/10.1175/1520-0485(1977)007<0345:MDHWIE>2.0.CO;2.

Wunsch, C., and D. Stammer, 1997: Atmospheric loading and the oceanic inverted barometer effect. *Rev. Geophys.*, **35**, 79–107, https://doi.org/10.1029/96RG03037.

Yu, X., A. L. Ponte, S. Elipot, D. Menemenlis, E. D. Zaron, and R. Abernathey, 2019: Surface kinetic energy distributions in the global oceans from a high-resolution numerical model and surface drifter observations. *Geophys. Res. Lett.*, **46**, 9757–9766, https://doi.org/10.1029/2019GL083074.

Zaron, E. D., 2019: Baroclinic tidal sea level from exact-repeat mission altimetry. *J. Phys. Oceanogr.*, **49**, 193–210, https://doi.org/10.1175/JPO-D-18-0127.1.

Zhao, Z., and Coauthors, 2019: Decomposition of the multimodal multidirectional M_2 internal tide field. *J. Atmos. Oceanic Technol.*, **36**, 1157–1173, https://doi.org/10.1175/JTECH-D-19-0022.1.

Zhou, B., C. Watson, B. Legresy, M. King, J. Beardsley, and A. Deane, 2020: GNSS/INS-equipped buoys for altimetry validation: Lessons learnt and new directions from the Bass Strait validation facility. *Remote Sens.*, **12**, 3001, https://doi.org/10.3390/rs12183001.

Sediment Resuspension and Transport from a Glider-Integrated Laser in Situ Scattering and Transmissometry (LISST) Particle Analyzer

TRAVIS MILES,[a] WAYNE SLADE,[b] AND SCOTT GLENN[a]

[a] *Rutgers, The State University of New Jersey, New Brunswick, New Jersey*
[b] *Sequoia Scientific, Inc., Bellevue, Washington*

(Manuscript received 16 December 2020, in final form 28 April 2021)

ABSTRACT: Suspended particle size and concentration are critical parameters that are necessary to understand water quality, sediment dynamics, carbon flux, and ecosystem dynamics, among other ocean processes. In this study we detail the integration of a Sequoia Scientific, Inc., Laser In Situ Scattering and Transmissometry (LISST) sensor into a Teledyne Webb Research Slocum autonomous underwater glider. These sensors are capable of measuring particle size, concentration, and beam attenuation by particles in size ranges from 1.00 to 500 μm at a resolution of 1 Hz. The combination of these two technologies provides the unique opportunity to measure particle characteristics persistently at specific locations or to survey regional domains from a single profiling sensor. In this study we present the sensor integration framework, detail quality assurance and control procedures, and provide a case study of storm-driven sediment resuspension and transport. Specifically, Rutgers glider RU28 was deployed with an integrated LISST-Glider for 18 days in September of 2017. During this period, it sampled the nearshore environment off coastal New Jersey, capturing full water column sediment resuspension during a coastal storm event. A novel method for in situ background corrections is demonstrated and used to mitigate long-term biofouling of the sensor windows. In addition, we present a method for removing schlieren-contaminated time periods utilizing coincident conductivity temperature and depth, fluorometer, and optical backscatter data. The combination of LISST sensors and autonomous platforms has the potential to revolutionize our ability to capture suspended particle characteristics throughout the world's oceans.

SIGNIFICANCE STATEMENT: This study details the integration and deployment of an optical particle size and concentration system on an autonomous underwater vehicle. The unique combination of this sensor and platform will enable broad sampling of suspended particle characteristics across the coastal and global oceans, within extreme storm events, in coastal river plumes, and throughout the deep oceans' "twilight zones." This will greatly enhance our ability to monitor water quality, sediment mobilization, ecosystem dynamics, pollutant fate and effects, and carbon export flux, among other important ocean-observing applications.

KEYWORDS: Extratropical cyclones; In situ oceanic observations; Instrumentation/sensors; Profilers, oceanic; Sampling

1. Introduction

In situ ocean observations of suspended particle size and concentration are important to monitor and study water quality, sediment dynamics, carbon export flux, fate and effects of pollutants, light propagation, ecosystem dynamics, water column visibility, and to ground truth remote sensing observations among other applications. Methods for measuring particle characteristics typically require labor intensive water sampling and sieving, or careful calibration of optical and acoustic backscatter sensors (Boss et al. 2018a; Agrawal and Pottsmith 2000; Bunt et al. 1999; Lynch et al. 1994; Thorne et al. 1991; Holdaway et al. 1999; Thorne et al. 2007). These approaches are not easily scalable beyond discrete sampling by ships or highly localized instrument deployment where calibration procedures remain valid. Laser In Situ Scattering and Transmissometry (LISST) particle analyzers have been used to reliably estimate particle size and concentration over the past two decades (Agrawal and Pottsmith 2000). These systems use laser diffraction as a composition insensitive method for sizing ensembles of particles in a sample volume. The near forward scattering of light onto concentric detector rings paired with inversion algorithms can be used to estimate particle size distributions (PSD) and volume concentration. Applications of LISST systems include storm-driven sediment resuspension (Dickey et al. 1998; Chang et al. 2001), sediment resuspension in estuaries and bays (Yuan et al. 2008; Wang et al. 2013), suspended sediment flocculates (Mikkelsen and Pejrup 2001), particle aggregation and disaggregation (Slade et al. 2011), phytoplankton size distributions (Karp-Boss et al. 2007), coastal water quality (Ahn et al. 2005), in flow-through systems across ocean basins (Boss et al. 2018b), bottom boundary layer studies (Agrawal and Traykovski 2001; Curran et al. 2007), monitoring the effect of dispersants during oil spill response (Bejarano et al. 2013), among many others. LISSTs along with other optical and acoustic sensors for monitoring suspended particles, are typically deployed on moorings, benthic landers, tripods, and other fixed point platforms (Trowbridge and Nowell 1994; Agrawal and Pottsmith 2000; Harris et al. 2003; Styles and Glenn 2005) or ship based profilers and underway

Denotes content that is immediately available upon publication as open access.

Corresponding author: Travis Miles, tnmiles@marine.rutgers.edu

DOI: 10.1175/JTECH-D-20-0207.1

systems for regional surveys. In this study we demonstrate the use of a newly integrated LISST-Glider into a Teledyne Webb Research Slocum autonomous underwater glider. Pairing of these technologies enables new possibilities for sustained sampling of particle size and concentration at regional scales and in conditions and locations not readily accessible by ship-based surveys.

In nearshore regions autonomous underwater gliders are the ideal platforms for collecting physical and biological data persistently across local and regional scales (from tens to hundreds of kilometers). Gliders have proven to be uniquely suited for collection of persistent profiles of optical data during the initiation, transport, and clearance of suspended sediment during hurricanes, coastal storms, and discharge events (Glenn et al. 2008; Miles et al. 2013, 2015; Bourrin et al. 2015). One of the first studies using gliders to investigate storm-driven sediment resuspension and transport detailed the impact of stratification on sediment dynamics (Glenn et al. 2008). Specifically, this study found that even during hurricane events, stratification inhibits full water column resuspension in summer months on the U.S. Mid-Atlantic Bight (MAB) continental shelf. This strong stratification is formed seasonally on the MAB, driven by rapid surface warming isolating the summer cold pool near bottom (Houghton et al. 1982). Storms in the fall season that break down stratification or occur after it has eroded can resuspend sediment throughout the full water column. Similar results for fall conditions were found in a follow-on study (Miles et al. 2013). In that study a fleet of simultaneously deployed gliders highlighted how local variability in bottom type can influence shelf-scale sediment resuspension and transport. Glider studies focused on storm-driven sediment resuspension and the influence of river runoff on particle assemblages have also been carried out in the Mediterranean Sea (Bourrin et al. 2015; Many et al. 2016). While these studies have used multiple wavelength optical backscatter measurements, these sensors alone have limited capability in determining particle size in situ.

In an initial effort to broadly determine in situ particle size from gliders, Miles et al. (2015) measured acoustic backscatter from a Nortek Aquadopp deployed alongside a Wetlabs optical backscatter sensor. Differing particle size sensitivity for acoustic and optical sensors allows for partitioning of ''large'' and ''small'' particle concentrations (Lynch et al. 1997). This approach was used to observe resuspension during Hurricane Sandy and qualitatively evaluate patterns of resuspension in an application of the Regional Ocean Modeling System (ROMS) coupled to the Community Sediment Transport Model (CSTM). Quantitative suspended particle concentration estimates from optical backscatter sensors require calibration with local sediment samples to measure accurate water column sediment concentrations (Bunt et al. 1999) and cannot identify particle size distributions. Over the course of a glider mission this type of calibration has limited feasibility, as the glider may be sampling over a broad spatial area (10–100 km) with highly variable sediment characteristics.

To fill this gap, we have recently integrated the newly developed Sequoia Scientific, Inc., LISST-200X into a Teledyne Webb Research (TWR) Slocum glider. This approach combines two proven technologies to enable broad, quantitative, sampling of particle size and concentration across a diversity of environments and conditions. In this paper we detail the sensor integration approach, in situ calibration and correction procedures, and an example of storm-driven sediment resuspension in the nearshore region of the MAB.

2. Sensor integration and deployments

a. Sensor integration

Slocum gliders are robotic uncrewed underwater systems with a demonstrated operational maturity over the last 20 years (Schofield et al. 2016). These low-power buoyancy-driven systems can carry out sustained missions of weeks to more than a year in water depths of ~10–1000 m, allowing them to sample nearshore, coastal, and deep ocean environments. Their broad sampling range includes extreme environments such as beneath hurricanes (Glenn et al. 2016; Miles et al. 2017) in coastal riverine environments (Schofield et al. 2015), and in polar oceans (Kohut et al. 2015). Slocum gliders profile the water column in a sawtooth pattern with speeds in the vertical direction of 10–15 $\mathrm{cm\,s^{-1}}$ and in the horizontal plane of 20–25 $\mathrm{cm\,s^{-1}}$, resulting in high data density and full water column coverage. Gliders surface at preprogrammed intervals to obtain new GPS fixes, send data to shore, and receive new commands. Slocum gliders have modular payload bays located in the center section of the vehicle, which allow for customizable sensor loadouts and a flexible system for integrating new sensors.

Sequoia Scientific developed a LISST particle sizing instrument to fit within a Slocum second- (G2) and third-generation (G3) glider. The optical arrangement of the LISST-Glider is based on the Sequoia Scientific LISST-200X but mounted to fit within a Slocum glider hull section (Fig. 1). This system uses a ''monoblock'' optical head with the end cap machined as a solid component incorporating both receive and transmit windows for increased robustness of alignment under variations in temperature, pressure, and possible impacts. The basic measurement system is a sample volume exposed to ambient flow, flanked by a windowed pressure housing containing the laser source, and collimation optics, and the receive optics and detector array. The transmit optics consists of a fiber coupled 660-nm laser diode source with a beam splitter and reference photodetector and a lens providing a collimated source beam into the sample volume. The receive optics contains a focusing lens and a 36-element photodetector array placed at the focal plane of the lens. By the Fourier transform property of this lens, light scattered at a given angle at any point along the sample volume will be incident onto the ring detector plane at the same distance from the optical axis. A pinhole at the focal point allows transmitted light to be passed to a photodetector for measuring beam transmission. The LISST system is designed to measure the size distribution of particles from 1.00 to 500 μm in 36 size classes at 1 Hz (Agrawal and Pottsmith 2000; Agrawal et al. 2008).

The LISST-Glider was integrated into a Slocum glider short hull section, commonly referred to as a stack-on bay (Fig. 1). This configuration allows for the LISST to be rapidly installed or removed from an available glider with limited impact on other sensor loadouts. A tie-rod extension and wiring harness

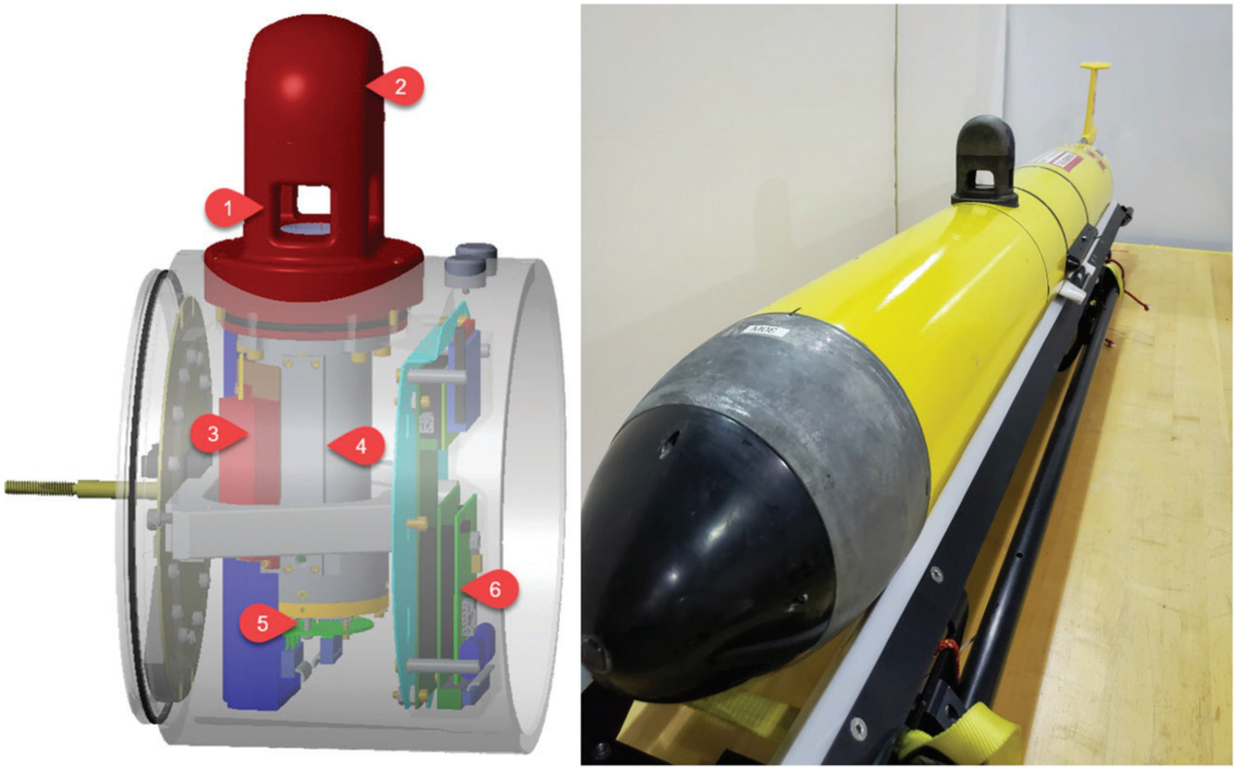

FIG. 1. (left) A schematic view of the LISST-Glider shows that the sample volume (label 1) is a 2.5-cm-pathlength scattering volume flanked with fused quartz windows for durability. The beam collimation optics and reference detector are also contained in the optical head (label 2), connected to a fiber coupled diode laser module (label 3). Scattered light is received through the lens tube (label 4), which also contains an extended detector array. The primary ring detectors and transmission sensor (label 5) are mounted on an XY stage that is used to adjust the instrument alignment, which can then be locked into place. An electronics section (label 6) digitizes the analog signals from the scattering detectors, controls the sampling process, logs the full scattering dataset, and calculates beam attenuation particle size metrics (i.e., mean size and total concentration). (right) A view of the LISST-Glider integrated into a G2 Slocum glider.

enable connection directly fore of the standard payload bay. During LISST-Glider production, quality control tests used bead standards to verify alignment and centration of the detector array. Factory clean water background measurements are stored on the instrument for use in data processing. These can be replaced by user-collected background measurements for both real-time onboard processing and with recovered datasets postdeployment following standard LISST-200X procedures. The resulting LISST-Glider payload bay underwent extensive pressure and thermal cycling at TWR. Currently, commercially available systems are rated to 600 m. Default sampling settings, and those used in this study, include 32 measurements averaged every second with full datasets saved on board.

New firmware was developed that allows the LISST-Glider to be controlled by the glider science controller. Raw laser scattering data are stored on board the instrument in binary files compatible with standard LISST-200X processing software. These raw files contain all ancillary data needed to process the raw scattering measurements to particle size distribution. In the default glider configuration, the LISST-Glider generates a separate binary file for each glider segment, the data collection period between each subsequent glider surfacing. As for the standard LISST-200X, the firmware also calculates beam attenuation from transmission measurements and estimates of particle volume concentration and Sauter mean diameter in real time (Agrawal and Mikkelsen 2009); these parameters are output to the glider and available for transfer to shore as standard real-time glider output variables in glider binary files. Stored full-resolution data can be downloaded upon glider recovery and processed using Sequoia Scientific software as in standalone LISST applications. Additionally, Sequoia Scientific provides Mathworks, Inc., MATLAB functions, which were used in this study to merge LISST recovered data with full-resolution Slocum glider data using Slocum Power Tools (https://github.com/kerfoot/spt/wiki).

b. *Glider configuration*

The LISST-Glider science bay used in this study was integrated into a TWR Slocum G2 glider, RU28. This glider was operated by the Rutgers University Center for Ocean Observing Leadership (RUCOOL) on behalf of the State of New Jersey Department of Environmental Protection (SNJ-DEP). These SNJ-DEP deployments are typically focused on mapping nearshore water quality, specifically nearshore hypoxic conditions that may impact critical fisheries and recreation in

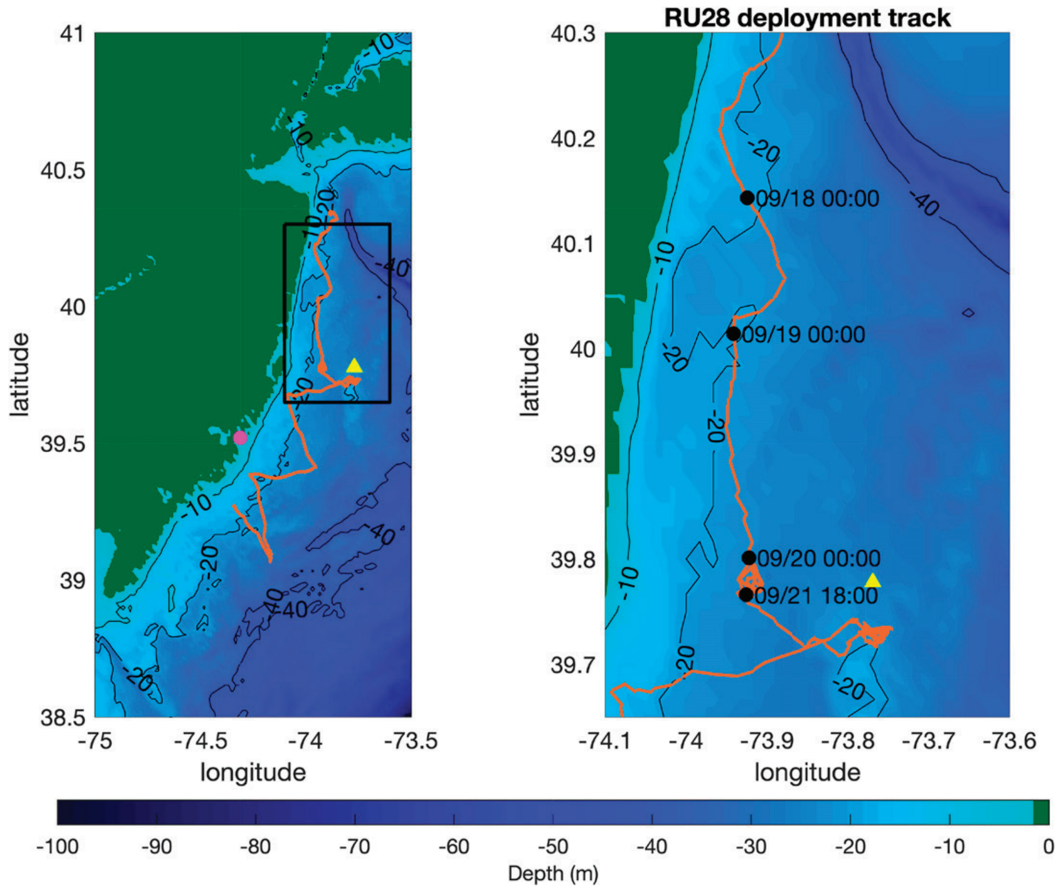

FIG. 2. (left) RU28's full deployment track in orange with the Rutgers University Marine Field Station Met Tower (magenta circle) and Buoy 44091 (yellow triangle); the black-outlined box represents (right) the zoomed area where the glider was located during the storm period.

New Jersey. These deployments target the autumn transition period (September–November) in late summer and early autumn. During this time, summer stratification leads to low oxygen in the bottom cold pool, a seasonal subsurface feature characterized by cold temperatures (<10°C) isolated from the atmosphere (Houghton et al. 1982). Extratropical cyclones, colloquially referred to as ''nor'easters'' or fall transition storms, pass through the region and incrementally erode stratification (Lentz 2017), redistribute oxygen and nutrients, and mobilize and transport sediment (Glenn et al. 2008).

Glider RU28 was a shallow water glider with a 30-m pump designed for rapid inflection at the surface and bottom. This gearing for shallow water allows it to maintain greater speeds at inflections and to more quickly return to a nominal flight speed. RU28 was equipped with a suite of sensors in addition to the LISST-Glider system. This included a Sea-Bird Scientific Co. pumped conductivity–temperature–depth (GPCTD) sensor; a Sea-Bird ECO Triplet that measured chlorophyll fluorescence, optical backscatter at 700 nm (bb700), and colored dissolved organic matter (CDOM); and an Aandera Data Instruments AS oxygen optode that measures oxygen concentration and saturation. These sensors are maintained and calibrated following an Environmental Protection Agency Quality Assurance Project Plan (QAPP) (Kohut et al. 2014) and following protocols detailed in the Mid-Atlantic Regional Association Coastal Ocean Observing System (MARACOOS) Regional Information Coordination Entities (RICE) certification (https://maracoos.org/certification.shtml). This includes factory calibrations of the GPCTD and optode following manufacturer recommendations (calibration every 1–2 years), predeployment comparisons with laboratory-based instruments and measurements, and comparisons with calibrated instruments in situ at deployment and recovery.

c. Glider deployment

Slocum glider RU28 was deployed on 15 September 2017 and recovered on 3 October 2017, near Sandy Hook and Atlantic City, New Jersey, respectively (Fig. 2a). The glider carried out a nearshore survey with onshore and offshore zigzags near the 20-m isobath as it transited southward along the New Jersey coast. RU28 was programmed to surface at ~2-h intervals to obtain new waypoints, telemeter real-time data, and calculate dead-reckoned current velocities at sufficient resolution to resolve tidal variability. This resulted in 201 segments over 18 days with a mean of 60 profiles collected per ~2-h segment. The glider was piloted to collect data while

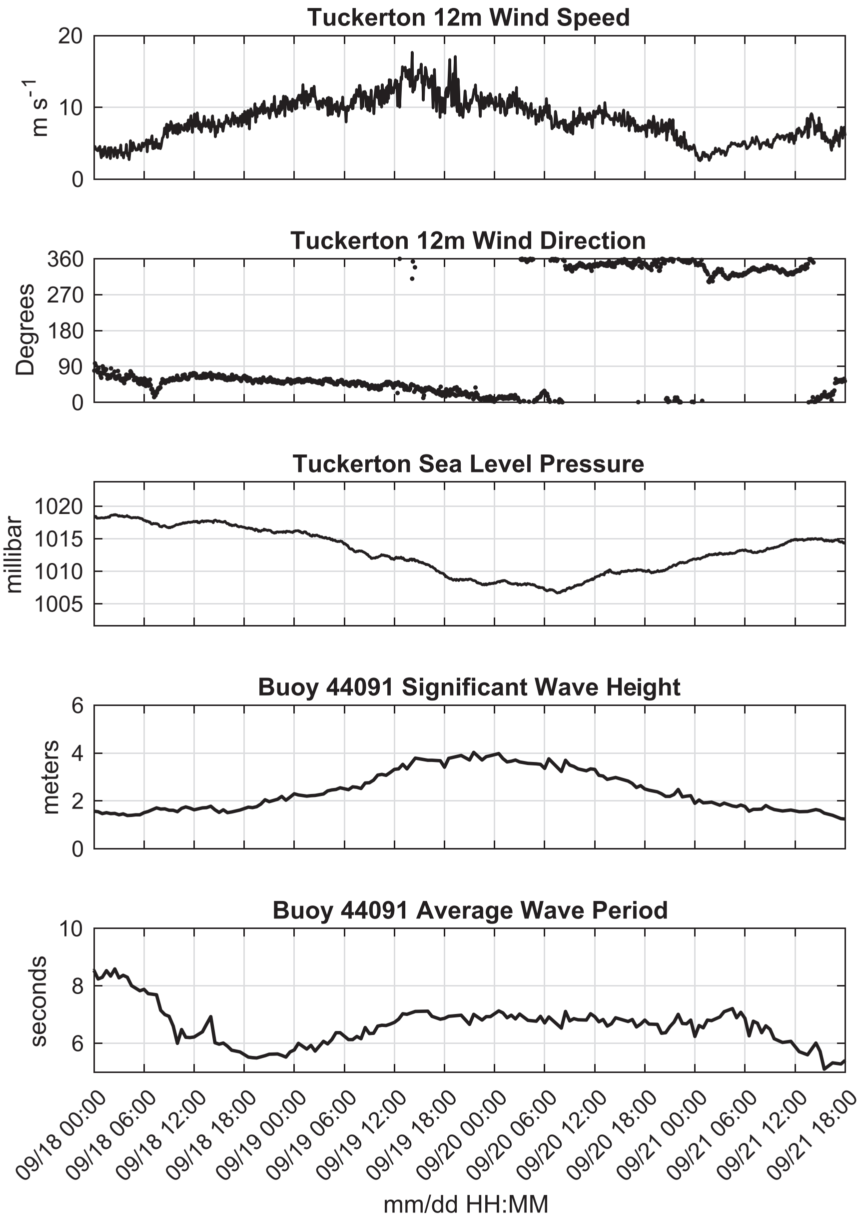

FIG. 3. The RUMFS Tuckerton Met Tower (top) wind speed, (top middle) wind direction from, and (middle) sea level pressure, and Buoy 44091 (bottom middle) significant wave height and (bottom) average wave period.

transiting for the majority of the deployment. However, a coastal storm event passed through the region on 18–22 September (Fig. 3). By 0000 UTC 20 September RU28 was programmed to hold position just offshore of the 20-m isobath at 39.78°N and 73.92°W (Fig. 2b) east of Barnegat Bay, New Jersey. This station-keeping location was approximately 45 km to the northeast of the Rutgers University Marine Field Station (RUMFS) Met Tower and 13 km west of National Data Buoy Center (NDBC) Buoy 44091. For the majority of this time period, the glider maintained a small watch circle (<2.5 km). Our analysis of the LISST-Glider output focuses on the short period from 0000 UTC 18 through 1800 UTC 21 September. This time period includes large vertical density gradients while the glider was in transit, and strong storm forcing during unstratified conditions while the glider was station keeping (Fig. 4).

d. Deployment site sediment characteristics

The sediment characteristics and resuspension processes throughout the region that RU28 sampled during the storm event has been extensively studied (Keen and Glenn 1995; Traykovski et al. 1999; Styles and Glenn 2002; Gargett et al. 2004; Styles and Glenn 2005; Glenn et al. 2008; Goff et al. 2008; Miles et al. 2013, 2015). These additionally include some of the earliest studies with the LISST (Agrawal and Pottsmith 2000; Agrawal 2005)

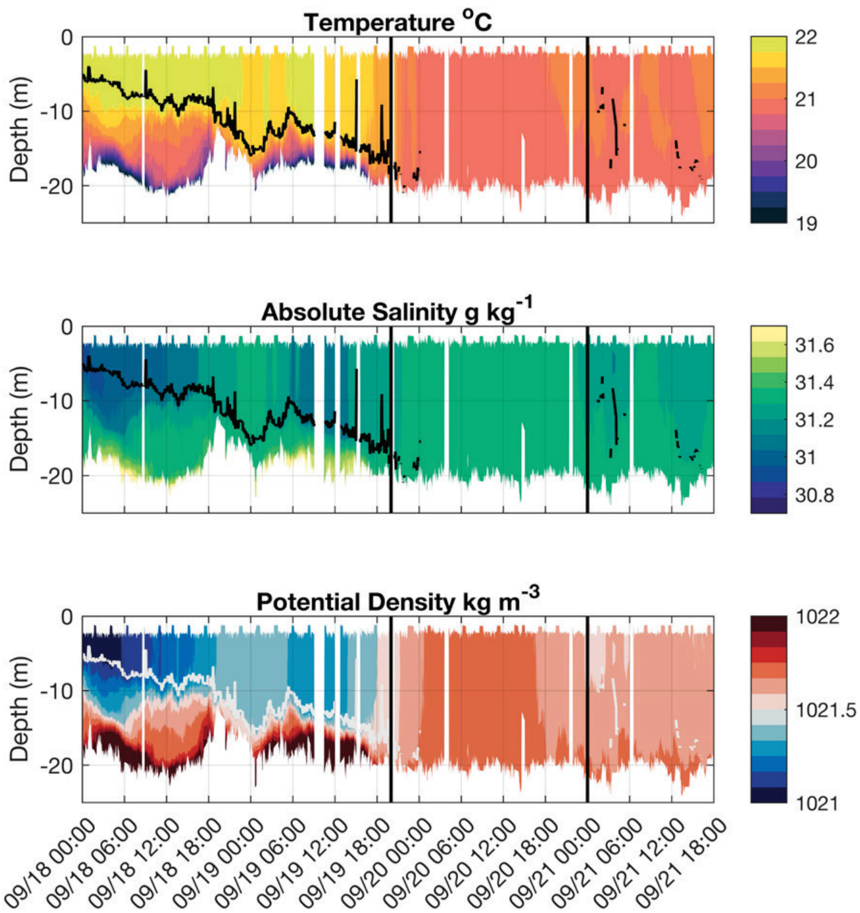

FIG. 4. Glider cross sections of (top) temperature, (middle) absolute salinity, and (bottom) potential density. Contour lines (black in the top and middle panels and gray in the bottom panel) represent the surface mixed layer depth. Vertical black lines represent the primary resuspension event time period.

deployed at the Long-term Ecosystem Observatory (LEO-15) site. These and other studies have characterized the New Jersey inner shelf as a region with a typically sandy bottom with median particle diameters of near 400 μm; however, significant patchiness exists (Goff et al. 2008; Miles et al. 2013) with typically larger grain sizes on the inner shelf to the north, and smaller to the south. For estimates of sediment transport in this study we assume particles during the main storm event are noncohesive sands with a density of 2650 kg m^{-3} when converting from volume concentration to mass concentration, ideally future LISST-Glider deployments should include in situ sampling of sediment type at deployment and recovery at a minimum, coincident with water column calibration information.

e. Meteorological and wave data

Wave data are from NDBC Buoy 44091 (39.78°N and 73.77°W), a Coastal Data Information Program (CDIP) buoy owned and operated by the U.S. Army Corp of Engineers with data provided by Scripps Institute of Oceanography. This system is a Datawell directional buoy (Mark 3) that collects wave energy, wave direction, and sea surface temperature. Significant wave height, wave period, and bottom orbital velocities were estimated following linear wave theory using measured spectra (Wiberg and Sherwood 2008), with bottom orbital velocities estimated at 20-m depth, the approximate water column depth during RU28's station-keeping time period.

Additionally, we use wind data from the RUCOOL-operated 12-m meteorological tower located near the RUMFS in Tuckerton, New Jersey. The tower is equipped with a suite of atmospheric sensors including an R. M. Young Co. sonic anemometer model 81000 mounted at 12 m above ground level. The sonic anemometer collects wind speed at 0.01 m s^{-1} resolution with an accuracy of 0.05 m^{-1} within the 0–30 m s^{-1} range. Wind direction measurements have a 0.1° resolution with a 2° accuracy at speeds of 1–30 m s^{-1}.

3. LISST-Glider postprocessing

a. Background correction

Typical ship-based LISST operations include clean water background measurements either before each profile, daily, or

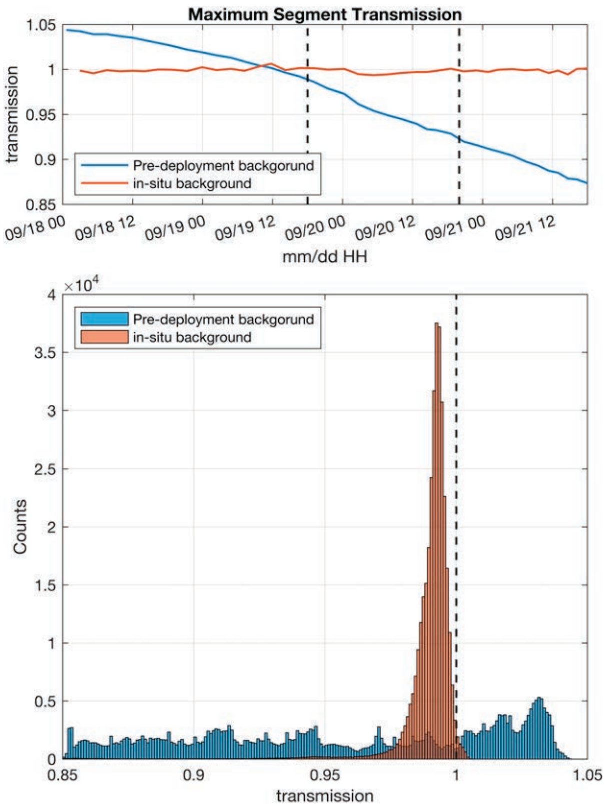

FIG. 5. (top) A comparison of the maximum transmission per ~2-h glider segment using only the predeployment background correction (blue) and the in situ correction method (red). The vertical black lines indicate the storm sediment resuspension time period. (bottom) Histograms of all transmission measurements using only the predeployment background correction (blue) and the in situ correction method (red). The vertical black line shows a value of 1 for reference.

as needed depending on environmental conditions. While this approach is not possible for an autonomously deployed vehicle, we demonstrate a method for carrying out in situ background corrections to account for biofouling and other mechanisms of sensor drift. LISST-Glider background measurements were taken in the laboratory predeployment on 13 September. The instrument windows were cleaned with lens paper and isopropyl alcohol, taking care not to scratch windows. The sample volume was covered with black tape to create a watertight dark chamber. In this case we used degassed deionized water for background measurements, although if it is available, for highest accuracy Sequoia Scientific recommends using filtered seawater from the study site, allowed to degas overnight if needed (Boss et al. 2018b; Agrawal and Pottsmith 2000). Sensor windows were visually inspected to ensure that no bubbles were present. Standard LISST background correction procedures were carried out according to the LISST-200X user's manual (https://www.sequoiasci.com). Three consecutive passing background measurements were taken before being saved to the instrument. Maximum transmission values using only the predeployment calibration from each segment are shown in Fig. 5 in blue. The resulting maximum transmission values show progressively decreasing transmission as well as initial transmission values greater than 1. The transmission values greater than 1 suggest poor laboratory calibration relative to in situ water clarity despite the methods noted above. The progressive decrease in transmission indicates some combination of fouling and sensor drift over time. Linear biofouling over time scales of a few weeks is not unexpected; see, for example, Manov et al. (2004). In their deployments with open sensors such as transmissometers and fluorometers without antifouling treatment, data showed level-1–3 biofouling over ~3 weeks, with stationary sensors.

To mitigate the progressive decrease in transmission, in postprocessing we utilize in situ data to carry out dynamic background corrections similar to those utilized by Barone et al. (2015). Specifically, for each glider segment we find the time point with the maximum transmission within each ~20-h period. If coincident bb700 measurements from the ECO Triplet were $< 0.005\,\mathrm{m^{-1}}$ the raw data were extracted and used as a background for that particular segment. Segments with coincident bb700 values $> 0.005\,\mathrm{m^{-1}}$ were contained to the main storm sediment resuspension period between 1800 UTC 19 and 2000 UTC 20 September. During this storm-sampling period, we interpolate background information linearly from the last segment before the resuspension event to the first clear segment following resuspension. The resulting values of maximum transmission are shown as a red line in (Fig. 5a), with the full distributions shown in the Fig. 5b. The maximum transmissions now plot at a horizontal line near one, and the full distribution of the in situ corrected data falls mostly between 0.95 and 1. Our focus for this study is on a large resuspension event; thus, we do not expect potential errors in in situ backgrounds to have significant impacts on our findings, and the correction far outweighs the alternative of using only the prestorm background correction. This approach should be used with caution when studying smaller concentrations in shallow water and will likely be more effective in deep ocean deployments with long durations of clear water measurements.

After background correction, we apply a four-point median filter on raw 1-s angular scattering data to remove measurements of spurious large particles. After filtering, angular scattering data were inverted into a volume PSD with a Sequoia Scientific–provided algorithm (Agrawal and Pottsmith 2000). We used the inversion kernel developed empirically for randomly shaped natural particles (Agrawal et al. 2008). All inversions were performed on the full-resolution datasets then linearly interpolated to align with glider science computer time stamps. The inverted solutions result in 36 log-spaced size classes from 1.00- to 500-μm diameters. We evaluate the impacts our correction method by comparing PSDs using only the predeployment background measurements, and after applying our dynamic in situ corrections. Volume concentrations are presented at three time points, ahead of the resuspension event at 1200 UTC 18 September, during peak sediment resuspension at 1200 UTC 19 September, and after sediment resuspension at 1200 UTC 21 September. Pre-event and postevent time points were bin averaged over 2 m at 5-m depth, and the storm time point was bin averaged at 19-m

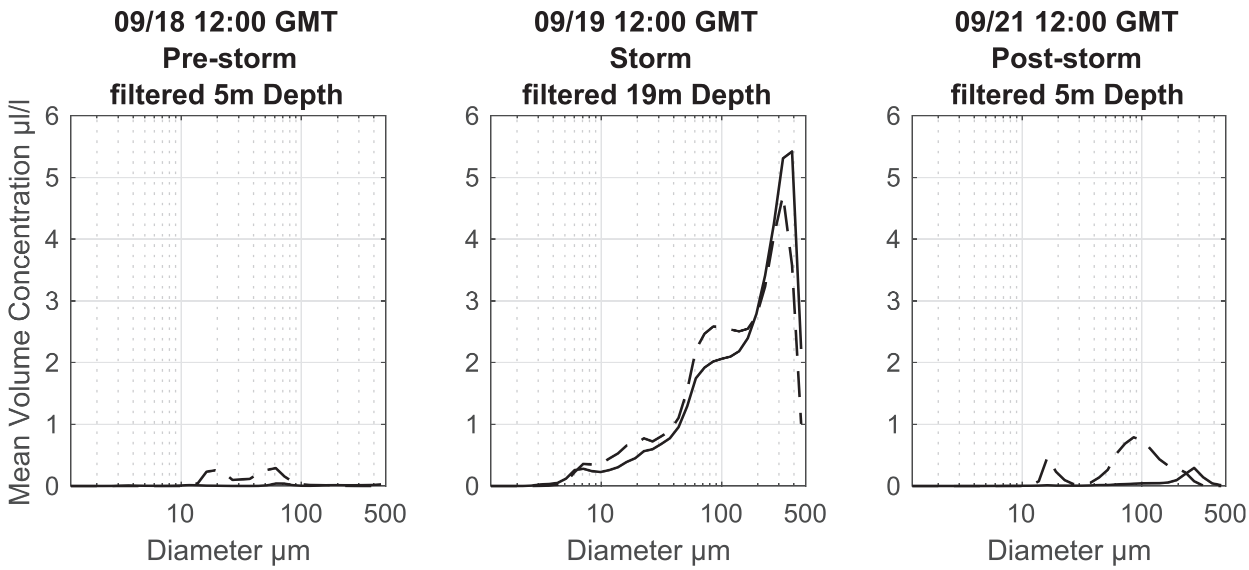

FIG. 6. Two-hourly and 2-m bin center-averaged mean volume concentrations at 5-m depth (left) ahead of and (right) after the storm event as well as (center) near the bottom at 19-m depth during the storm resuspension event.

depth, near the bed. Each bin was calculated as a center average in time over 2 h, containing between 44 and 96 samples each. These time periods and depths were selected in unstratified regions to limit potential schlieren impacts. Dynamic in situ background corrections show a clear removal with two peaks between 10 and 100 μm in all three time periods (Fig. 6). This persistent feature was likely due to contamination on the instrument windows during the prestorm background that was subsequently removed, or a scratch or persistent contamination throughout the deployment. Regardless of the correction, it is small relative to the observed resuspension signal shown in the middle time period (Fig. 6b). Future studies should utilize water and bottom sediment sampling at glider deployment and recovery to more clearly assess background corrections, specifically when sampling in time periods and locations with low concentrations. The remainder of this paper uses volume concentrations that have had the dynamic and interpolated in situ corrections applied.

b. Schlieren corrections

Microscale turbulent shear can lead to changes in index of refraction in proximity to large density gradients (Mikkelsen et al. 2008). This well-known effect, commonly referred to as schlieren, can result in measurement of forward scattering by optical instruments without the presence of suspended particles. In the LISST family of instruments this leads to elevated estimates of beam attenuation and the volume scattering function for the innermost ring detectors, corresponding with large particle sizes. Previous analyses have identified schlieren as contributing to increases in beam attenuation and increase in particle volume for buoyancy frequencies N ranging from 0.02 to 0.05 s^{-1} (Mikkelsen et al. 2008; Tao et al. 2017) with contamination likely outside these ranges in a variety of other field sites. A study (Styles 2006) using a type-C LISST identified schlieren effects on the nine innermost rings, corresponding to particle sizes greater than 128 μm. We calculate correlation coefficients of each of the 36 size bins with N during periods where N exceeded 0.02 s^{-1} to evaluate schlieren impacts on volume concentration estimates. This approach of calculating conditional correlation coefficients has similarities to Tao et al. (2017).

Total volume concentrations are plotted in (Fig. 7a). There are two distinct regions of elevated concentrations, beneath the pycnocline during stratified conditions (0000 UTC 18–2000 UTC 19 September), and throughout the unstratified time period during peak storm conditions (2000 UTC 19–0000 UTC 21 September). During the stratified time period, measurements of bb700 only show limited suspended particles ~1–2 m above bottom (mab) (Fig. 7c), while buoyancy frequencies are elevated throughout the entire bottom layer (Fig. 7b). This suggests that the observed total volume concentrations measured by the LISST in the bottom stratified layer may be contaminated by schlieren effects.

To evaluate particle size ranges that may be affected by schlieren, we compared volume concentrations from each LISST size bin with $N > 0.02\ s^{-1}$ (Fig. 8). During the full storm time period (0000 UTC 18–1800 UTC 21 September) correlation coefficients between volume concentrations and $N > 0.02\ s^{-1}$ (Fig. 8) were elevated between 0.2 and 0.6 for the four innermost rings, while all remaining sizes bins, both for $N < 0.02\ s^{-1}$ and $N > 0.02\ s^{-1}$, were uncorrelated (<0.1). These data indicate that schlieren effects are present during stratified conditions when bb700 values (not expected to be affected by schlieren) are low (Figs. 7b,c) and are not present when the water column becomes unstratified and the main storm-driven sediment resuspension event occurs. Scattering by density fluctuations scale with the Kolmogorov scale, mostly affecting inner rings. Thus, to mitigate the effects of schlieren on total volume concentration estimates, measurements from the four innermost ring detectors (particle diameters > 250 μm) were excluded from raw scattering data and inversion when N was

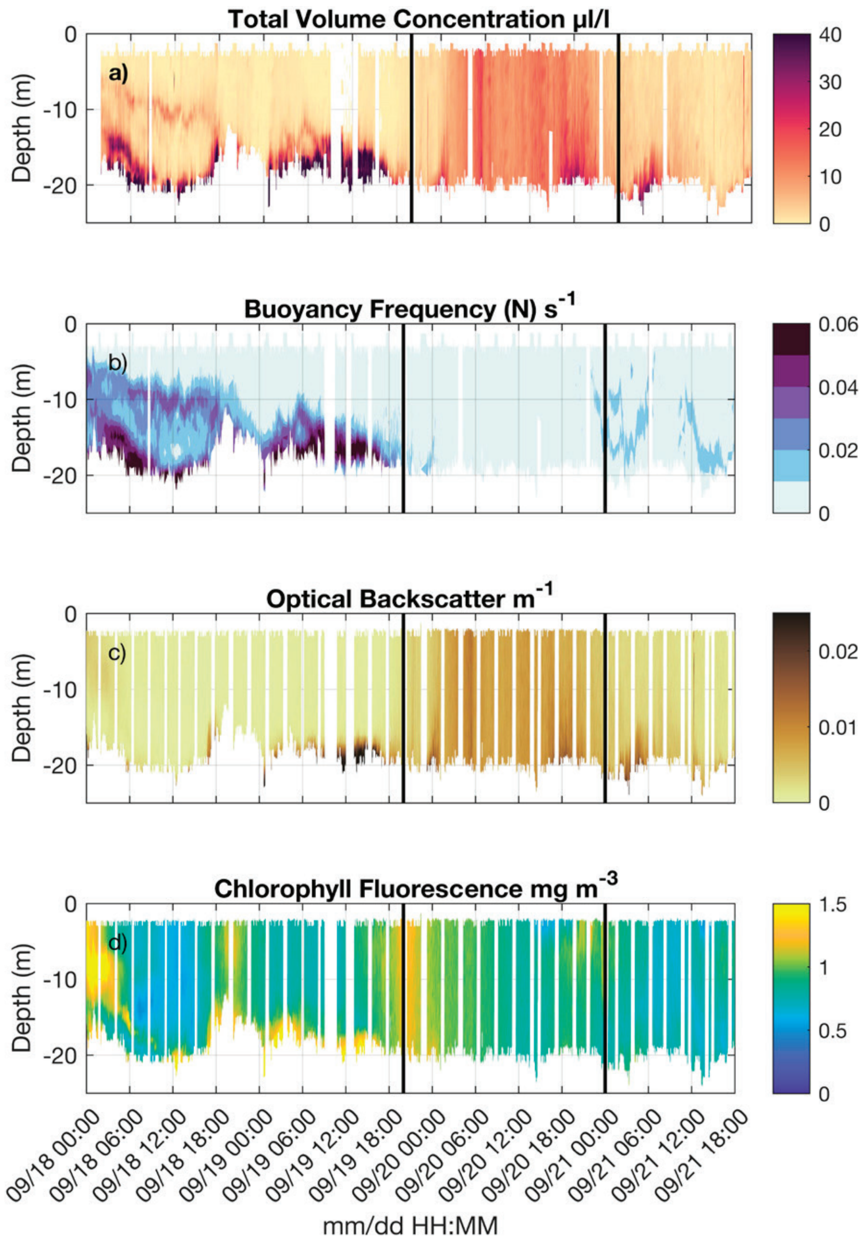

FIG. 7. Glider cross sections of (a) total volume concentration, (b) buoyancy frequencies, (c) optical backscatter, and (d) chlorophyll fluorescence. Vertical black lines represent the primary resuspension event time period.

greater than 0.02 (Fig. 9e) and thus are also not included as contributions to total volume concentrations throughout the remainder of the study (Fig. 9a).

4. Storm-driven sediment resuspension and transport

As described in section 2c, RU28 was programmed to station keep near Buoy 44091 and just offshore of the Tuckerton RUMFS meteorological station throughout the duration of an extratropical storm event. The storm event transited northeastward through the mid-Atlantic region typical of an early season nor'easter. Wind speeds (Fig. 3) measured at RUMFS showed an increase from 5 m s^{-1} on 0000 UTC 18 September to a peak near 15 m s^{-1} just after 1200 UTC 19 September. Winds rotated from due east to north throughout the storm event. Peak waves at Buoy 44091 coincided with peak winds, with significant wave heights reaching 4 m. Average wave periods were short, between 6 and 7 s, for the duration of the storm event. Wind and wave conditions gradually reduced to prestorm conditions throughout 20 and into 21 September.

During prestorm conditions at 0000 UTC 18 September the water column was vertically stratified (Fig. 4). The surface

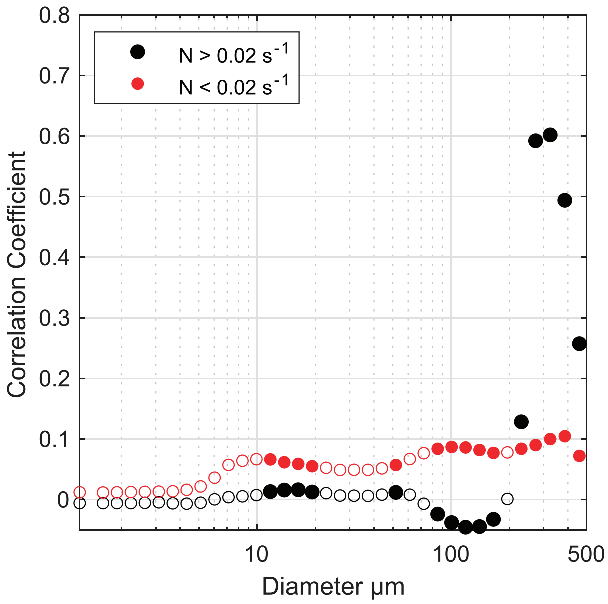

FIG. 8. Correlation coefficients between buoyancy frequency and scattering for each particle diameter measured. Analysis was separated out for values of $N < 0.02\,\mathrm{s}^{-1}$ (red) and $N > 0.02\,\mathrm{s}^{-1}$ (black). Closed circles are significant with $P > 0.05$.

mixed layer depth (SMLD) was calculated following Evans et al. (2018) using a vertical density gradient criteria of $0.1\,\mathrm{kg\,m^{-3}\,m^{-1}}$ to identify the base of the mixed layer. The surface mixed layer initially was found at 5-m depth on 0000 UTC 18 September and steadily fell until it reached the bottom on 1800 UTC 19 September. Above the SMLD temperature, salinity, and density were vertically uniform near 22°C, $30.9\,\mathrm{g\,kg^{-1}}$, and $1021\,\mathrm{kg\,m^{-3}}$, respectively. Below this surface layer the water column was continuously stratified with temperatures decreasing with depth to 19.5°C, salinities of $31.2\,\mathrm{g\,kg^{-1}}$, and densities of $1022\,\mathrm{kg\,m^{-3}}$. After 1800 UTC 19 September the temperature, salinity, and density were vertically uniform throughout the water column at 21°C, $31.1\,\mathrm{g\,kg^{-1}}$, and $1021.5\,\mathrm{kg\,m^{-3}}$ during this period. After 0000 UTC 21 September the water column began to restratify following the cessation of storm conditions. The near-bottom stratification ahead of the storm is characteristic of remnant bottom summer cold pool waters, which are seasonally eroded by storm-driven mixing and reductions in surface heat flux during the transition into autumn (Castelao et al. 2008).

With both background corrections applied and effects of schlieren removed we can now use the LISST-Glider data to evaluate storm-driven sediment resuspension and transport. Particle volume concentrations were binned according to phi unit size class ranges for silts (phi > 4 or grain sizes < 64 μm; Fig. 9b), very fine sands (phi 4–3 or 64–125 μm Fig. 9c), fine sands (phi 3–2 or 125–250 μm; Fig. 9d), and medium sands (phi 2–1 or 250–500 μm; Fig. 9e). On 2000 UTC 19 September, following water column destratification, total volume concentrations increased throughout the full water column (Fig. 9a) and remained elevated until 0000 UTC 21 September. Elevated concentrations were seen across silts, very fine, and fine sands, with little contribution from of medium sands to the total concentration. To demonstrate the uniformity of the distribution throughout the water column in more detail we calculate the mean particle size distribution in the surface (<10-m depth) and bottom (>10-m depth) during the initial peak resuspension period from 0000 to 1600 UTC 20 September. Distributions were nearly identical (Fig. 10a), suggesting either uniform turbulence throughout the water column, or more likely that turbulent buoyancy forces exceeded gravitational settling forces for the available sediment supply. During the end of the resuspension period between 1600 UTC 20 and 0000 UTC 21 September (Fig. 10b), surface and bottom particle size distributions showed elevated concentrations near the bottom and decreased concentrations in the surface layer for particle sizes > 72 μm. This indicates that, with weakening storm conditions, gravitational settling forces likely exceeded turbulent buoyancy forces for larger particles, and they began to fall out of suspension.

To evaluate the predicted ratio of turbulence to settling velocities we utilize the standard Rouse profile for resuspended sediment under neutral conditions (Glenn et al. 2008):

$$C(z) = C_r(z/z_r)^{[-\gamma w_f/(\kappa u_*)]}, \tag{1}$$

where $C(z)$ is sediment concentration at depth z, C_r is sediment concentration at a reference depth z_r, w_f is a settling velocity defined below, u_* is turbulent shear velocity, and γ and κ are constants. Von Kármán's κ is set 0.4, while γ is set to 0.8 (Glenn and Grant 1987). Equation (1) can be rearranged to solve for the ratio of settling and turbulent shear velocity:

$$w_f/u_* = -(\kappa/\gamma)\{\ln[C(z)/C_r]/\ln(z/z_r)\}. \tag{2}$$

The right-hand side of the equation can be obtained using the constants above and by taking the slope of a linear fit of the concentration profile in the unstratified region outside the bottom boundary layer. Two hourly-averaged profiles of potential density, total volume concentration, and bb700 are displayed at 3-hourly intervals between 2000 UTC 19 and 1700 UTC 21 September (Fig. 11) in semilog-y (density) and log–log (total volume concentration and bb700) space. We fit a line linearly in log–log space to values of the total volume concentration and bb700 in the bottom mixed layer, in this case contained to the lower 5 m of the water column. Profile fits where r-squared values were less than 0.3 (0500 and 1400 UTC 20 September) were not included. Settling velocities were estimated from the mean profile particle size at each time point (Fig. 11a) following the method of Soulsby (1997) for irregular grains:

$$w_f = \frac{\nu}{d}[(10.36^2 + 1.049D_*^3)^{1/2} - 10.36], \tag{3}$$

where ν is the kinematic viscosity of water, d is the grain diameter, and D_* is a dimensionless grain size:

$$D_* = \left[\frac{g(s-1)}{\nu^2}\right]^{1/3} d, \tag{4}$$

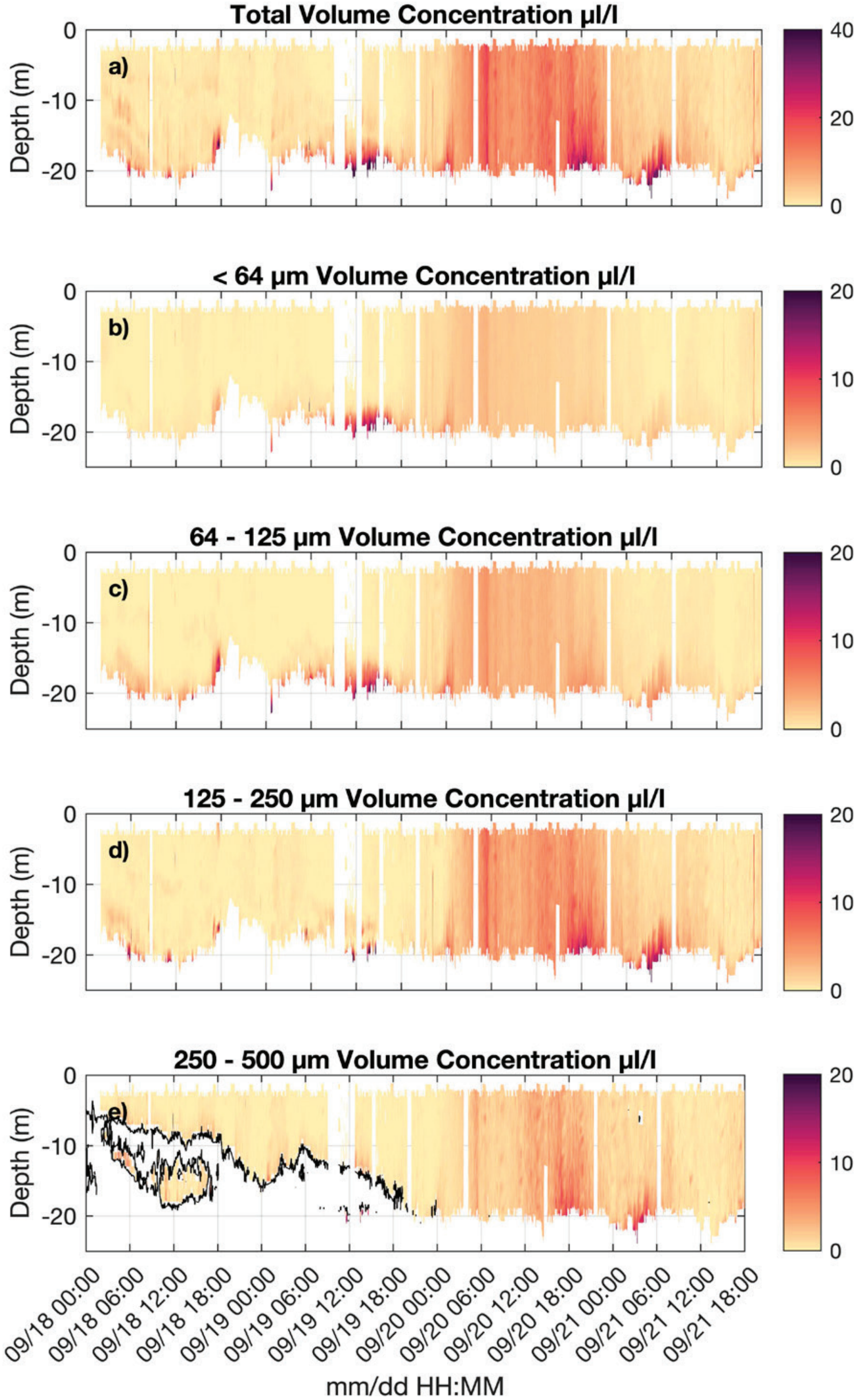

FIG. 9. Glider cross sections of (a) corrected total volume concentration and volume concentration (b) $< 64\,\mu$m, (c) between 64 and 125 μm, (d) between 125 and 250 μm, and (e) between 250 and 500 μm. The black contour in (e) denotes the region where $N > 0.02\,\mathrm{s}^{-1}$ and data were removed.

with g being the acceleration due to gravity and s the ratio of densities of sand and water. Solving w_f from the LISST mean grain size measurements and an assumed density of 2650 kg m^{-3} for the predominantly sandy site, leaves u_* as the only remaining unknown. We then solve Eq. (2) using slopes from both total volume concentration and bb700 fits for two estimates of u_*. Estimates of settling velocities for the fixed particle sizes of 150 μm (w_{f150}, the maximum observed mean particle size) and

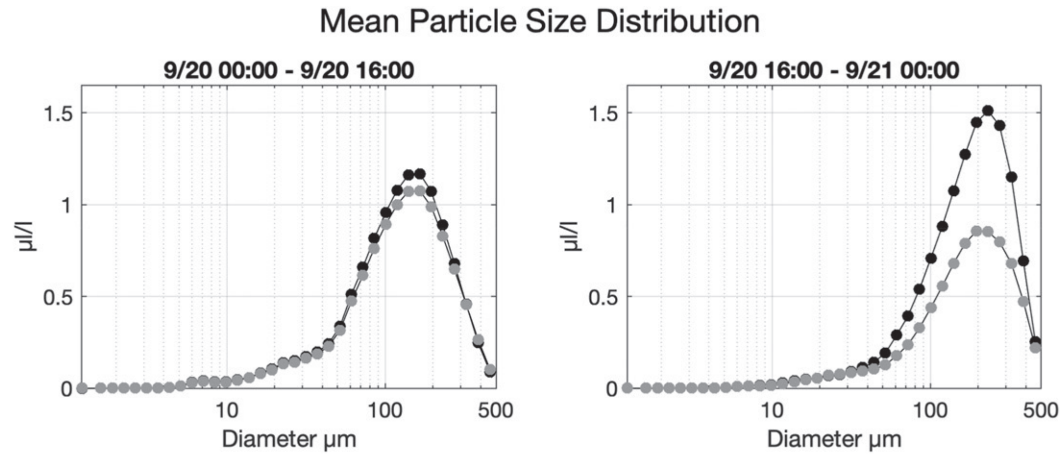

FIG. 10. Mean volume concentrations in the upper 10 m (gray) and below 10 m (black), showing (left) distributions during the initial resuspension phase and (right) distributions during the beginning of the settling phase.

500 μm (w_{f500}, the maximum size range sampled by the LISST-Glider) are plotted for reference on Fig. 11b.

There is good agreement between u_* estimates from both the LISST and ECO Triplet sensors for the majority of the storm forcing period with u_* reaching values of nearly 0.5 m s^{-1} at peak storm forcing. The good agreement between the slopes and u_* from the LISST and ECO Triplet suggest that both sensors have similar sensitivity to particle size for the unimodal sands sampled at this study site. This approach should be used with caution at other locations with different particle characteristics. At the first two time points (2000 and 2300 UTC 19 September), u_* was low below both w_{f150} and w_{f500}. Profiles show a limited bottom mixed layer extending up to 5 mab. Below this depth, slopes were shallow and the associated particle sizes were small, close to 50 μm. Between 0200 and 1400 UTC 20 September the bottom mixed layer extended throughout the full water column. Slopes of the total volume concentrations were steep and nearly vertical throughout this time period, corresponding to peak values of u_*, representing a significant increase in turbulence throughout the water column. As storm conditions are reduced after 1700 UTC 20 September the u_* values fall and profiles shallow consistent with sediment falling out of suspension. As mentioned above, these estimates of u_* and interpretation of the profiles are based on the solution for Eq. (1) under neutral conditions. As described in Glenn and Grant (1987), this assumption holds when the stability parameter z/L (with z being the depth and L the Monin–Obukhov length), multiplied by the constant $\beta \sim 4.7$ is $\ll$ than γ. We calculate $\beta(z/L)$ at the top and bottom of the fit profiles at 1 and 5 m following Eq. (43) presented in Glenn and Grant (1987) to evaluate the range of the potential stability parameters above the wave bottom boundary layer. The equation is adapted here where we use only the mean particle size estimate of fall velocity and the u_* estimated from the LISST-Glider only:

$$\frac{z}{L} = \frac{\kappa z}{u_*^3} g(s-1) w_f C(z). \quad (5)$$

Results are plotted in Fig. 11c and show that for all but four time points $\beta(z/L)$ at both depths is much less than γ, indicating that the neutral solutions are valid. Values of $\beta(z/L)$ were close to, or exceeded γ at four time points, 2000 UTC 19 and 0200, 1400, and 1700 UTC 21 September. All time points where assumptions of neutral conditions were invalid fell outside the main resuspension event, with the measurement 0200 UTC 21 September being associated with a peak in a secondary event (Fig. 9) seen across all size classes. This secondary event is an ideal candidate for future investigation of suspended sediment stratification, which is described in detail in Glenn and Grant (1987) but has not been previously observed in the field.

The above results and estimated sediment transport from the LISST-Glider are summarized in Fig. 12. Volume concentrations, plotted at three heights (5, 7, and 10 mab, Fig. 12a) show initially low concentrations despite high bottom orbital velocities (Fig. 12e), and high depth-averaged velocities (Fig. 12d). The elevated buoyancy frequencies (Fig. 12c) highlight that stratification likely restricts the full resuspension of sediment throughout the water column. As buoyancy frequency drops when the water column becomes unstratified, volume concentrations increase at all three depths. As bottom orbital velocities fall on 1400 UTC 20 September the concentrations at the three depths begin to separate, with elevated concentrations near the bed and reduced concentrations near the surface consistent with what was shown in Fig. 11 with sediment falling out of suspension. While all values fall by 0000 UTC 21 September, there is a brief increasing period for the near bed measurements that is timed with our findings that $\beta(z/L)$ exceeded γ, as described above. There are two main peaks in suspended load transport at 0300 UTC 20 September and approximately 12 h later at 1500 UTC 20 September. The peaks align with peak depth-averaged velocity and are consistent with the M_2 tidal period of 12.42 h, the dominant tidal constituent within the MAB. Tidal modulation of sediment transport is similar to what was observed in Glenn et al. (2008), with tidal forcing increasing resuspension and transport even after peak storm conditions. We do not expect these currents to be driven by inertial oscillations as the peaks appear with a frequency shorter than

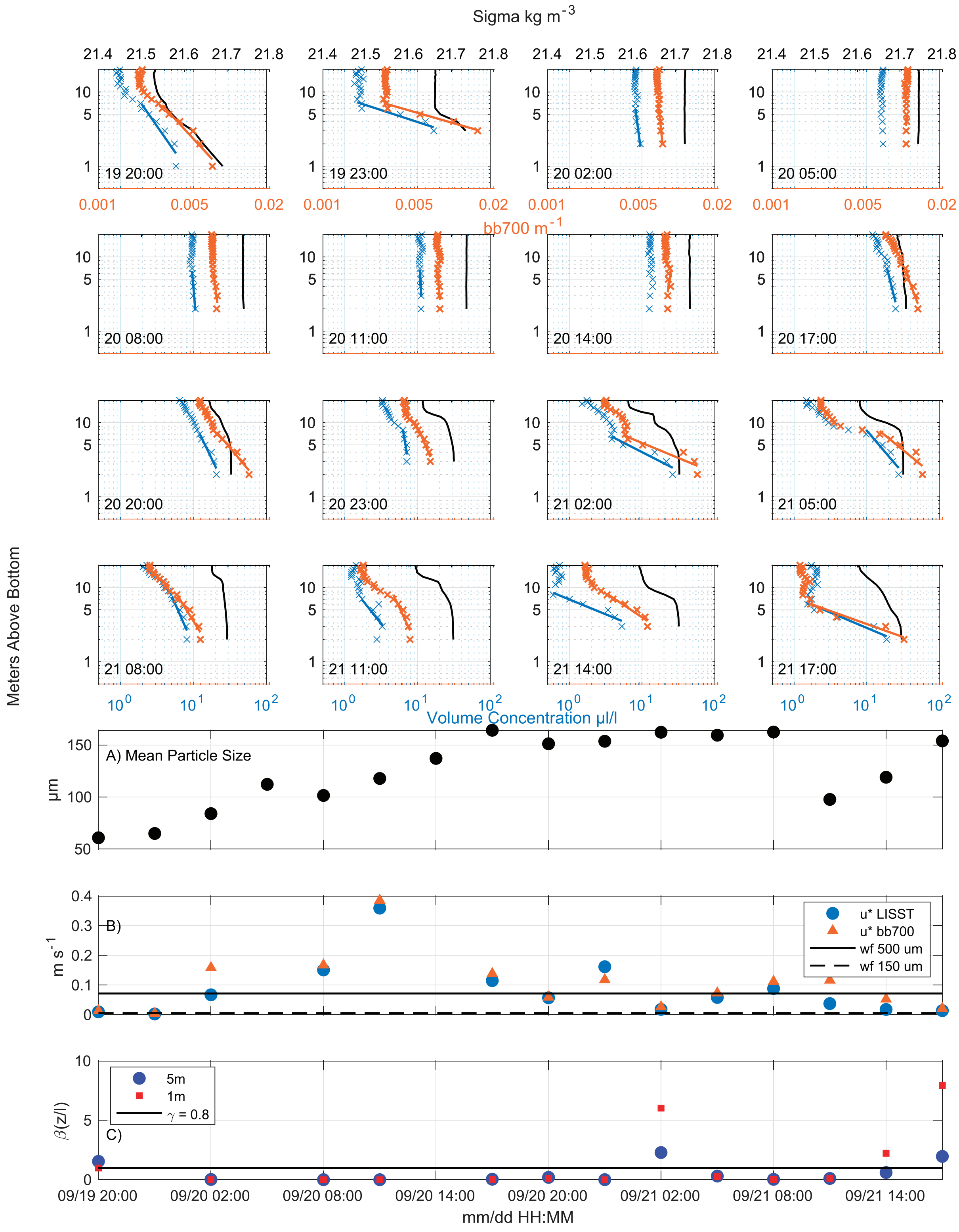

FIG. 11. (top) Hourly-averaged profiles at 3-h intervals of density in sigma units (black), bb700 (orange), and volume concentration (blue). Blue lines are linear regressions of volume concentration in the bottom mixed layer, excluding profiles where r-squared values are < 0.3. (a) The mean particle sizes averaged over the lower 5 m, (b) estimates of u_* derived from the linear fits to LISST total volume concentration profiles (blue) and bb700 (orange), with horizontal lines indicating fall velocities for particles of 500 (solid black) and 150 (dashed black line) μm, and (c) estimates of $\beta(z/L)$ at the 5-m depth (blue) and 1-m depth (red) with constant γ (horizontal black line).

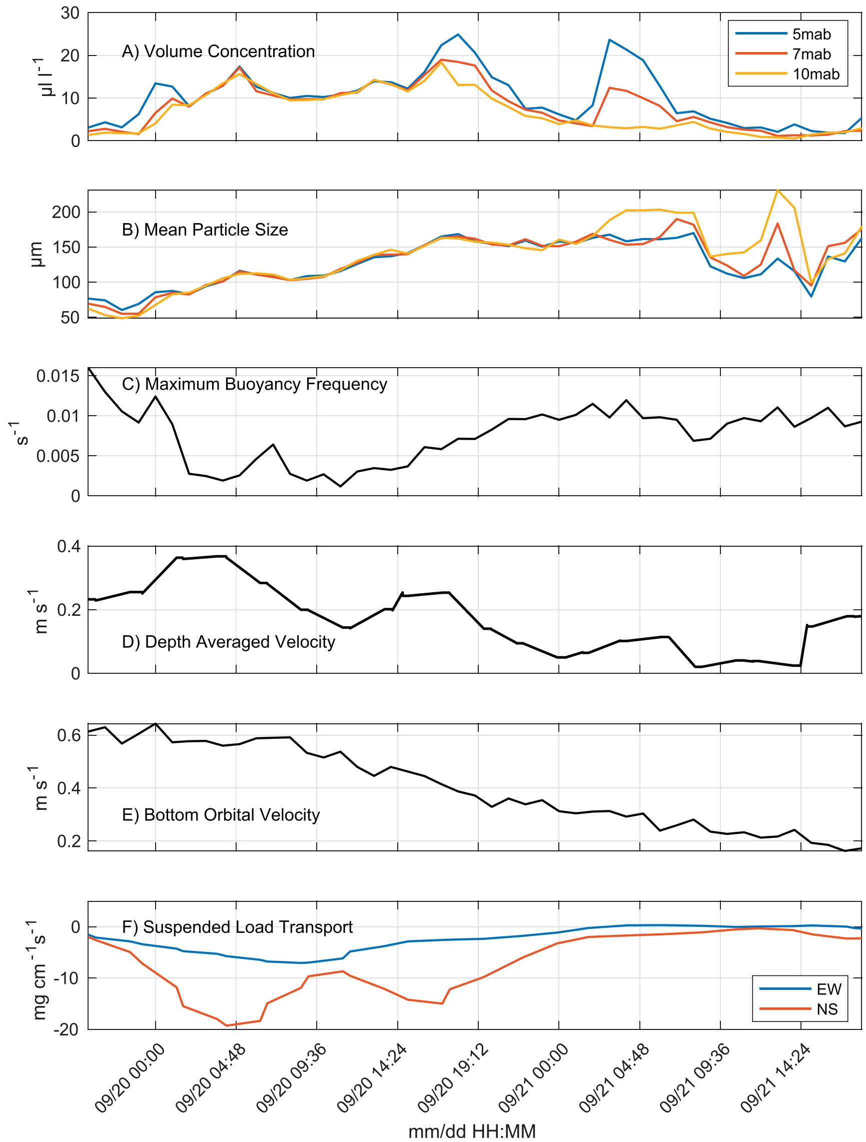

FIG. 12. Time series of (a) volume concentration and (b) mean particle size at depths of 5 (blue), 7 (red), and 10 (yellow) mab, (c) maximum buoyancy frequency, (d) depth-averaged velocity, (e) bottom orbital velocities at 44091, and (f) LISST-Glider estimated suspended load transport.

the local inertial period (~18 h). The total depth- and time-integrated suspended sediment load estimated for this particular event is 311 mg cm^{-1}, which is within the range of what has previously been estimated on the inner MAB shelf (Styles and Glenn 2005).

5. Discussion and conclusions

This study presents the first measurements from a Sequoia Scientific LISST integrated into an autonomous underwater glider and includes initial procedures for quality assurance and control on board this unique platform. This included implementation and demonstration of in situ background corrections similar to those for shipboard measurements (Barone et al. 2015). This combination of the LISST, along with additional optical sensors, on the glider platform allowed for a fuller description of the optical properties and sediment environment than previously deployed optical instruments on profiling gliders (Glenn et al. 2008; Miles et al. 2013; Many et al. 2016; Bourrin et al. 2015). This capability represents a significant advance in our ability to obtain detailed high-quality optical measurements from a single profiling sensor platform that was previously only possible from ship-based or moored platforms.

As an example of these capabilities, we characterized sediment resuspension and transport during a coastal storm on the MAB. A region regularly impacted by storm events and with a long history of sediment resuspension and transport studies (Styles and Glenn 2005; Agrawal 2005; Boss et al. 2004; Traykovski et al. 1999; Gargett et al. 2004). In addition to enabling in situ monitoring of sediment characteristics these data enabled us to infer bottom turbulent shear velocities based on the slope of the concentration and bb700 profiles combined with fall velocities from the mean particle size. These measurements and analyses will be particularly useful in calibrating sediment resuspension and transport models and their associated parameterizations, such as the Community Sediment Transport Model coupled to ROMS (Warner et al. 2010; Wu et al. 2011), which have been regularly used to study storm-driven sediment resuspension and transport (Warner et al. 2008; Ralston et al. 2013; Miles et al. 2015; Yang et al. 2015; Warner et al. 2017).

Despite these successes, limitations remain, in particular with regard to our ability to make regular background corrections with equivalent certainty as those used in shipboard or laboratory studies. Methods utilizing pre- and postdeployment background measurements and in situ data during optically clear conditions remain viable methods for determining vicarious background corrections and mitigating the effects of fouling over long-term deployments. Additional use of paired optical backscatter and fluorescence measurements are strongly encouraged to help interpret the effects of schlieren as well as to monitor potential biofouling, especially if LISST-Gliders are deployed for the full range of a glider's duration, from a month up to a year.

This study represents the first of these paired technologies, narrowly focused on storm-driven sediment resuspension. However, there are significant opportunities to expand these analyses with other paired bio-optical measurements to quantify additional particle characteristics, potentially including particle composition, shape, and color. In addition to other bio-optical sensors, coincident measurements with physical sensors such as glider-integrated acoustic Doppler current profilers or turbulent microstructure can enable better quantification of turbulent production and near bottom turbulent shear for resuspension studies. Even more promising is the use of LISST-Gliders as a distributed network to calibrate and validate satellite remote sensing over a broad array of conditions and environments for sustained periods. These advances will only be possible with continued collaboration and development among academic institutions, private companies, and a diverse set of federal and state funding agencies and laboratories.

Acknowledgments. This work was supported by the Office of Naval Research (ONR) Award N00014-16-1-2553 as well as a leveraged glider deployment supported by the New Jersey Department of Environmental Protection. The authors acknowledge the dedicated work of the engineers at both Sequoia Scientific, Inc., and Teledyne Webb Research in performing the sensor integration, as well as technicians at the Rutgers University Center for Ocean Observing Leadership. The Tuckerton Met Tower is maintained by Weatherflow, Inc. (https://weatherflow.com/), which includes biannual repair and maintenance. We give thanks to Oscar Schofield for providing commentary on early versions of the analysis presented herein. We also thank reviewers Emmanuel Boss, an anonymous reviewer, and the journal editor for their constructive and thoughtful comments and suggestions.

Data availability statement. Glider delayed-mode data, including onboard processed LISST data, are publicly available through a NOAA designed ERDDAP server hosted at the Rutgers University Center for Ocean Observing Leadership (http://slocum-data.marine.rutgers.edu/erddap/tabledap/ru28-20170915T1416-profile-sci-delayed.html). Real-time data from the deployment can be found within the NOAA Integrated Ocean Observing System (IOOS) glider Data Assembly Center (DAC; https://gliders.ioos.us/). Raw binary LISST data files were downloaded postdeployment and can be found via the open data repository Zenodo (https://doi.org/10.5281/zenodo.4325447).

REFERENCES

Agrawal, Y. C., 2005: The optical volume scattering function: Temporal and vertical variability in the water column off the New Jersey coast. *Limnol. Oceanogr.*, **50**, 1787–1794, https://doi.org/10.4319/lo.2005.50.6.1787.

——, and H. C. Pottsmith, 2000: Instruments for particle size and settling velocity observations in sediment transport. *Mar. Geol.*, **168**, 89–114, https://doi.org/10.1016/S0025-3227(00)00044-X.

——, and P. Traykovski, 2001: Particles in the bottom boundary layer: Concentration and size dynamics through events. *J. Geophys. Res.*, **106**, 9533–9542, https://doi.org/10.1029/2000JC900160.

——, and O. A. Mikkelsen, 2009: Shaped focal plane detectors for particle concentration and mean size observations. *Opt. Express*, **17**, 23 066–23 077, https://doi.org/10.1364/OE.17.023066.

——, A. Whitmire, O. A. Mikkelsen, and H. C. Pottsmith, 2008: Light scattering by random shaped particles and consequences on measuring suspended sediments by laser diffraction. *J. Geophys. Res.*, **113**, C04023, https://doi.org/10.1029/2007JC004403.

Ahn, J. H., S. B. Grant, C. Q. Surbeck, P. M. Digiacomo, N. P. Nezlin, and S. Jiang, 2005: Coastal water quality impact of stormwater runoff from an urban watershed in Southern California. *Environ. Sci. Technol.*, **39**, 5940–5953, https://doi.org/10.1021/es0501464.

Barone, B., R. R. Bidigare, M. J. Church, D. M. Karl, R. M. Letelier, and A. E. White, 2015: Particle distributions and dynamics in the euphotic zone of the North Pacific Subtropical Gyre. *J. Geophys. Res. Oceans*, **120**, 3229–3247, https://doi.org/10.1002/2015JC010774.

Bejarano, A. C., E. Levine, and A. J. Mearns, 2013: Effectiveness and potential ecological effects of offshore surface dispersant use during the Deepwater Horizon oil spill: A retrospective analysis of monitoring data. *Environ. Monit. Assess.*, **185**, 10 281–10 295, https://doi.org/10.1007/s10661-013-3332-y.

Boss, E., W. S. Pegau, M. Lee, M. Twardowski, E. Shybanov, G. Korotaev, and F. Baratange, 2004: Particulate backscattering ratio at LEO 15 and its use to study particle composition and distribution. *J. Geophys. Res.*, **109**, C01014, https://doi.org/10.1029/2002JC001514.

——, N. Haëntjens, T. K. Westberry, L. Karp-Boss, and W. H. Slade, 2018a: Validation of the particle size distribution obtained with the Laser in-Situ Scattering and Transmission (LISST) meter in flow-through mode. *Opt. Express*, **26**, 11 125–11 136, https://doi.org/10.1364/OE.26.011125.

——, C. R. Sherwood, P. Hill, and T. Milligan, 2018b: Advantages and limitations to the use of optical measurements to study sediment properties. *Appl. Sci.*, **8**, 2692, https://doi.org/10.3390/app8122692.

Bourrin, F., and Coauthors, 2015: Glider monitoring of shelf suspended particle dynamics and transport during storm and flooding conditions. *Cont. Shelf Res.*, **109**, 135–149, https://doi.org/10.1016/j.csr.2015.08.031.

Bunt, J. C., P. Larcombe, and C. F. Jago, 1999: Quantifying the response of optical backscatter devices and transmissometers to variations in suspended particulate matter. *Cont. Shelf Res.*, **19**, 1199–1220, https://doi.org/10.1016/S0278-4343(99)00018-7.

Castelao, R., S. Glenn, O. Schofield, R. Chant, J. Wilkin, and J. Kohut, 2008: Seasonal evolution of hydrographic fields in the central Middle Atlantic Bight from glider observations. *Geophys. Res. Lett.*, **35**, L03617, https://doi.org/10.1029/2007GL032335.

Chang, G. C., T. D. Dickey, and A. J. Williams, 2001: Sediment resuspension over a continental shelf during Hurricanes Edouard and Hortense. *J. Geophys. Res.*, **106**, 9517–9531, https://doi.org/10.1029/2000JC900032.

Curran, K. J., P. S. Hill, T. G. Milligan, O. A. Mikkelsen, B. A. Law, X. Durrieu de Madron, and F. Bourrin, 2007: Settling velocity, effective density, and mass composition of suspended sediment in a coastal bottom boundary layer, Gulf of Lions, France. *Cont. Shelf Res.*, **27**, 1408–1421, https://doi.org/10.1016/j.csr.2007.01.014.

Dickey, T. D., G. C. Chang, Y. C. Agrawal, A. J. Williams, and P. S. Hill, 1998: Sediment resuspension in the wakes of Hurricanes Edouard and Hortense. *Geophys. Res. Lett.*, **25**, 3533–3536, https://doi.org/10.1029/98GL02635.

Evans, D. G., and Coauthors, 2018: Annual cycle of turbulent dissipation estimated from Seagliders. *Geophys. Res. Lett.*, **45**, 10 560–10 569, https://doi.org/10.1029/2018GL079966.

Gargett, A., J. Wells, A. E. Tejada-Martínez, and C. E. Grosch, 2004: Langmuir supercells: A mechanism for sediment resuspension and transport in shallow seas. *Science*, **306**, 1925–1928, https://doi.org/10.1126/science.1100849.

Glenn, S. M., and W. D. Grant, 1987: A suspended sediment stratification correction for combined wave and current flows. *J. Geophys. Res.*, **92**, 8244–8264, https://doi.org/10.1029/JC092iC08p08244.

——, C. Jones, M. Twardowski, L. Bowers, J. Kerfoot, J. Kohut, D. Webb, and O. Schofield, 2008: Glider observations of sediment resuspension in a Middle Atlantic Bight fall transition storm. *Limnol. Oceanogr.*, **53**, 2180–2196, https://doi.org/10.4319/lo.2008.53.5_part_2.2180.

——, and Coauthors, 2016: Stratified coastal ocean interactions with tropical cyclones. *Nat. Commun.*, **7**, 10887, https://doi.org/10.1038/ncomms10887.

Goff, J., C. J. Jenkins, and S. Jeffress Williams, 2008: Seabed mapping and characterization of sediment variability using the usSEABED data base. *Cont. Shelf Res.*, **28**, 614–633, https://doi.org/10.1016/j.csr.2007.11.011.

Harris, C. K., B. Butman, and P. Traykovski, 2003: Winter-time circulation and sediment transport in the Hudson Shelf Valley. *Cont. Shelf Res.*, **23**, 801–820, https://doi.org/10.1016/S0278-4343(03)00025-6.

Holdaway, G. P., P. D. Thorne, D. Flatt, S. E. Jones, and D. Prandle, 1999: Comparison between ADCP and transmissometer measurements of suspended sediment concentration. *Cont. Shelf Res.*, **19**, 421–441, https://doi.org/10.1016/S0278-4343(98)00097-1.

Houghton, R. W., R. Schlitz, R. C. Beardsley, B. Butman, and J. L. Chamberlin, 1982: The Middle Atlantic Bight cold pool: Evolution of the temperature structure during summer 1979. *J. Phys. Oceanogr.*, **12**, 1019–1029, https://doi.org/10.1175/1520-0485(1982)012<1019:TMABCP>2.0.CO;2.

Karp-Boss, L., L. Azavedo, and E. Boss, 2007: LISST-100 measurements of phytoplankton size distribution: Evaluation of the effects of cell shape. *Limnol. Oceanogr. Methods*, **5**, 396–406, https://doi.org/10.4319/lom.2007.5.396.

Keen, T. R., and S. M. Glenn, 1995: A coupled hydrodynamic–bottom boundary layer model of storm and tidal flow in the Middle Atlantic Bight of North America. *J. Phys. Oceanogr.*, **25**, 391–406, https://doi.org/10.1175/1520-0485(1995)025<0391:ACHBLM>2.0.CO;2.

Kohut, J., C. Haldeman, and J. Kerfoot, 2014: Monitoring dissolved oxygen in New Jersey coastal waters using autonomous gliders. EPA Rep. EPA/600/R-13, 180 pp.

——, K. Bernard, W. Fraser, M. J. M. J. Oliver, H. Statscewich, P. Winsor, and T. Miles, 2015: Studying the impacts of local oceanographic processes on Adélie penguin foraging ecology. *Mar. Technol. Soc. J.*, **48**, 25–34, https://doi.org/10.4031/MTSJ.48.5.10.

Lentz, S. J., 2017: Seasonal warming of the Middle Atlantic Bight cold pool. *J. Geophys. Res. Oceans*, **122**, 941–954, https://doi.org/10.1002/2016JC012201.

Lynch, J. F., J. D. Irish, C. R. Sherwood, and Y. C. Agrawal, 1994: Determining suspended sediment particle size information from acoustical and optical backscatter measurements. *Cont. Shelf Res.*, **14**, 1139–1165, https://doi.org/10.1016/0278-4343(94)90032-9.

——, T. F. Gross, C. R. Sherwood, J. D. Irish, and B. H. Brumley, 1997: Acoustical and optical backscatter measurements of sediment transport in the 1988–1989 STRESS experiment. *Cont. Shelf Res.*, **17**, 337–366, https://doi.org/10.1016/S0278-4343(96)00041-6.

Manov, D. V., G. C. Chang, and T. D. Dickey, 2004: Methods for reducing biofouling of moored optical sensors. *J. Atmos. Oceanic Technol.*, **21**, 958–968, https://doi.org/10.1175/1520-0426(2004)021<0958:MFRBOM>2.0.CO;2.

Many, G., and Coauthors, 2016: Particle assemblage characterization in the Rhone River ROFI. *J. Mar. Syst.*, **157**, 39–51, https://doi.org/10.1016/j.jmarsys.2015.12.010.

Mikkelsen, O. A., and M. Pejrup, 2001: The use of a LISST-100 laser particle sizer for in-situ estimates of floc size, density and settling velocity. *Geo-Mar. Lett.*, **20**, 187–195, https://doi.org/10.1007/s003670100064.

——, T. G. Milligan, P. S. Hill, R. J. Chant, C. F. Jago, S. E. Jones, V. Krivtsov, and G. Mitchelson-Jacob, 2008: The influence of schlieren on in situ optical measurements used for particle characterization. *Limnol. Oceanogr. Methods*, **6**, 133–143, https://doi.org/10.4319/lom.2008.6.133.

Miles, T., S. Glenn, and O. Schofield, 2013: Temporal and spatial variability in fall storm induced sediment resuspension on the Mid-Atlantic Bight. *Cont. Shelf Res.*, **63**, S36–S49, https://doi.org/10.1016/j.csr.2012.08.006.

——, G. Seroka, J. Kohut, O. Schofield, and S. Glenn, 2015: Glider observations and modeling of sediment transport in Hurricane Sandy. *J. Geophys. Res. Oceans*, **120**, 1771–1791, https://doi.org/10.1002/2014JC010474.

——, ——, and S. Glenn, 2017: Coastal ocean circulation during Hurricane Sandy. *J. Geophys. Res. Oceans*, **122**, 7095–7114, https://doi.org/10.1002/2017JC013031.

Ralston, D. K., J. C. Warner, W. R. Geyer, and G. R. Wall, 2013: Sediment transport due to extreme events: The Hudson River estuary after Tropical Storms Irene and Lee. *Geophys. Res. Lett.*, **40**, 5451–5455, https://doi.org/10.1002/2013GL057906.

Schofield, O., C. Jones, J. Kohut, U. Kremer, T. Miles, G. Saba, D. Webb, and S. Glenn, 2015: Developing coordinated communities of autonomous gliders for sampling coastal ecosystems. *Mar. Technol. Soc. J.*, **49**, 9–16, https://doi.org/10.4031/MTSJ.49.3.16.

——, J. Kohut, U. Kremer, T. Miles, G. Saba, S. Glenn, C. Jones, and D. Webb, 2016: Gliders as maturing technology: Using gliderpalooza as means to develop an integrated glider community. *Oceans 2015*, Washington, DC, IEEE, https://doi.org/10.23919/OCEANS.2015.7404588.

Slade, W., E. Boss, and C. Russo, 2011: Effects of particle aggregation and disaggregation on their inherent optical properties. *Opt. Express*, **19**, 7945, https://doi.org/10.1364/OE.19.007945.

Soulsby, R. L., 1997: *Dynamics of Marine Sands.* Thomas Telford, 249 pp.

Styles, R., 2006: Laboratory evaluation of the LISST in a stratified fluid. *Mar. Geol.*, **227**, 151–162, https://doi.org/10.1016/j.margeo.2005.11.011.

——, and S. M. Glenn, 2002: Modeling bottom roughness in the presence of wave-generated ripples. *J. Geophys. Res.*, **107**, 3110, https://doi.org/10.1029/2001JC000864.

——, and ——, 2005: Long-term sediment mobilization at a sandy inner shelf. *J. Geophys. Res.*, **110**, C04S90, https://doi.org/10.1029/2003JC002175.

Tao, J., P. S. Hill, E. S. Boss, and T. G. Milligan, 2017: Evaluation of optical proxies for suspended particulate mass in stratified waters. *J. Atmos. Oceanic Technol.*, **34**, 2203–2212, https://doi.org/10.1175/JTECH-D-17-0042.1.

Thorne, P. D., C. E. Vincent, P. J. Hardcastle, S. Rehman, and N. Pearson, 1991: Measuring suspended sediment concentrations using acoustic backscatter devices. *Mar. Geol.*, **98**, 7–16, https://doi.org/10.1016/0025-3227(91)90031-X.

——, Y. C. Agrawal, and D. A. Cacchione, 2007: A comparison of near-bed acoustic backscatter and laser diffraction measurements of suspended sediments. *IEEE J. Oceanic Eng.*, **32**, 225–235, https://doi.org/10.1109/JOE.2007.890978.

Traykovski, P., A. E. Hay, J. D. Irish, and J. F. Lynch, 1999: Geometry, migration, and evolution of wave orbital ripples at LEO-15. *J. Geophys. Res. Oceans*, **104**, 1505–1524, https://doi.org/10.1029/1998JC900026.

Trowbridge, J. H., and A. R. M. Nowell, 1994: An introduction to the Sediment Transport Events on Shelves and Slopes (STRESS) program. *Cont. Shelf Res.*, **14**, 1057–1061, https://doi.org/10.1016/0278-4343(94)90028-0.

Wang, Y. P., G. Voulgaris, Y. Li, Y. Yang, J. Gao, J. Chen, and S. Gao, 2013: Sediment resuspension, flocculation, and settling in a macrotidal estuary. *J. Geophys. Res. Oceans*, **118**, 5591–5608, https://doi.org/10.1002/jgrc.20340.

Warner, J. C., B. Butman, and P. Dalyander, 2008: Storm-driven sediment transport in Massachusetts Bay. *Cont. Shelf Res.*, **28**, 257–282, https://doi.org/10.1016/j.csr.2007.08.008.

——, B. Armstrong, R. He, and J. B. Zambon, 2010: Development of a Coupled Ocean–Atmosphere–Wave–Sediment Transport (COAWST) modeling system. *Ocean Modell.*, **35**, 230–244, https://doi.org/10.1016/j.ocemod.2010.07.010.

——, W. C. Schwab, J. H. List, I. Safak, M. Liste, and W. Baldwin, 2017: Inner-shelf ocean dynamics and seafloor morphologic changes during Hurricane Sandy. *Cont. Shelf Res.*, **138**, 1–18, https://doi.org/10.1016/j.csr.2017.02.003.

Wiberg, P. L., and C. R. Sherwood, 2008: Calculating wave-generated bottom orbital velocities from surface-wave parameters. *Comput. Geosci.*, **34**, 1243–1262, https://doi.org/10.1016/j.cageo.2008.02.010.

Wu, L., C. Chen, P. Guo, M. Shi, J. Qi, and J. Ge, 2011: A FVCOM-based unstructured grid wave, current, sediment transport model, I. Model description and validation. *J. Ocean Univ. China*, **10**, 1–8, https://doi.org/10.1007/s11802-011-1788-3.

Yang, X., Q. Zhang, J. Zhang, F. Tan, Y. Wu, N. Zhang, H. Yang, and Q. Pang, 2015: An integrated model for three-dimensional cohesive sediment transport in storm event and its application on Lianyungang Harbor, China. *Ocean Dyn.*, **65**, 395–417, https://doi.org/10.1007/s10236-014-0806-6.

Yuan, Y., H. Wei, L. Zhao, and W. Jiang, 2008: Observations of sediment resuspension and settling off the mouth of Jiaozhou Bay, Yellow Sea. *Cont. Shelf Res.*, **28**, 2630–2643, https://doi.org/10.1016/j.csr.2008.08.005.

Observation-Large eddy simulation comparison of ocean mixing under Typhoon Soulik (2018)

Samuel Coakley
Department of Marine and Coastal Sciences
Rutgers University
New Brunswick, USA
sjc244@marine.rutgers.edu

Travis N. Miles
Department of Marine and Coastal Sciences
Rutgers University
New Brunswick, USA
tnmiles@marine.rutgers.edu

Scott Glenn
Department of Marine and Coastal Sciences
Rutgers University
New Brunswick, USA
glenn@marine.rutgers.edu

Hak Soo Lim
Marine Disaster Research Center
Korean Institute of Ocean Science and Technology
Busan, South Korea
hslim@kiost.ac.kr

***Abstract*— Ocean mixing by tropical cyclones (TC) can cool the sea surface and reduce heat flux from the ocean to the atmosphere ahead of the eye. This ahead of eye cooling has been shown to play a significant role in weakening as TCs translate over stratified, continental shelves. Typhoon Soulik weakened over the northern East China Sea prior to landfall at 8/23 14:00 UTC on the Korean Peninsula. This weakening was attributed to cooling of the sea surface ahead of the storm. Significant sea surface cooling was corroborated through a collaborative deployment of a Slocum underwater glider with the Korean Institute of Ocean Science and Technology. This glider collected data on the state of the ocean ahead of and throughout the duration of the forcing and observed 8°C of SST cooling. The glider was flown in the vicinity of a Korean Meteorological Association surface meteorological buoy, which collected data on wind and heat flux forcing on the ocean. This study investigates the physical mechanisms driving the ocean's response to this extreme forcing using the Price-Weller-Pinkel (PWP) one-dimensional ocean mixed layer model and an Oceananigans.jl Large Eddy Simulation (LES). An LES resolves turbulence in the flow field which allows for the study of its onset and evolution throughout the duration of the forcing. The configurations of PWP and the LES in this study are unable to capture the ocean's response to Typhoon Soulik which implies that there are processes critical to the response that are not captured by the models.**

Keywords—Underwater gliders, Large Eddy Simulation, Ocean mixing, Tropical Cyclones, Air-Sea interactions

I. Introduction

Tropical cyclones (TCs) are one of the costliest and deadliest natural disasters globally. In the US alone, damages have exceeded \$1 trillion USD and 6593 lives have been lost since 1980 [1]. Globally, the loss of life can be orders of magnitude larger with individual storms, such as Cyclone Nargis killing over 138000 people [2]. Coastal communities require days of advance notice to implement disaster mitigation plans such as coastal evacuations, thus it is vital that they have accurate information on both the track and intensity of approaching TCs. Over the last 40 years, there has been a marked improvement in forecasting TC tracks [3][4]. In spite of recent improvements in the accuracy of TC intensity forecasting in the US, the 72-hour forecast intensity error is ~15 knots which is equivalent to a difference between a Category 2 and a Category 3 hurricane on the Saffir Simpson Hurricane Wind Scale which is used to communicate risk to the public [5]. Additionally, these improvements have not been seen internationally by other TC forecasting agencies [3][6]. Error in intensity forecasts also leads to errors in prediction of storm surge and inundation caused by TCs.

TC intensity is coupled to the state of the surface ocean through fluxes of heat and momentum at the air-sea interface [7]. This heat and moisture cause local increases in buoyancy which incite convection in the eyewall of the TC, forming deep convective structures, and supporting intensification [8][9][10]. Surface wind speeds, the ocean state, and air-sea thermodynamic gradients control the magnitude of these fluxes to the TC [11][12][13]. TC intensity is also sensitive to atmospheric factors such as vertical wind shear and dry air intrusion [14][15][7], yet the state of the ocean and air-sea interactions remain a significant source of uncertainty in intensity forecasts of mature TCs [16].

While warm ocean temperatures can rapidly intensify TCs, ocean mixing can cool the sea surface and reduce heat flux from the ocean to the atmosphere ahead of the eye [11][17][18][19][20][21]. A cooled sea surface ahead of and under the eye can weaken the warm core of the TC which can weaken the storm [18][22][23]. Over stratified continental shelves, extreme ahead of eye cooling (> 6°C) has been shown to play a significant role in weakening TCs in the hours just before landfall [18][19][22]. In the case of Hurricane Irene, sea surface cooling was driven by entrainment processes including coastal downwelling causing shear at the pycnocline [18][20]. New studies using Large Eddy Simulations (LES) of the ocean under Hurricane Irene have additionally shown Ekman layer instabilities working to homogenize the surface layer with and Kelvin-Helmholtz instabilities at the pycnocline [24]. This rapid co-evolution of the ocean and TC intensity is a major challenge in TC intensity forecasting because the ocean and the storm change on the same time scale.

Typhoon Soulik (2018) translated across the Kuroshio Current into the East China Sea (ECS), eventually making landfall over the South Jeolla Province of the Republic of Korea [25][26]. The Kuroshio is a western boundary current with a deep, warm surface layer that persists year-round,

978-0-692-93559-0 ©2021 MTS

while the ECS is a seasonally thermally stratified, shallow sea located East of China and South of the Korean Peninsula [27]. Cold water produced during the winter in the Yellow Sea expands southward into the ECS forming Yellow Sea Bottom Cold Water. During the summer, surface heating enhances the thermal stratification in the ECS. The presence of the Yellow Sea Bottom Cold Water allowed Typhoon Soulik to cool the surface of the ECS by a maximum of 8.1°C [19]. Typhoon Soulik entered the ECS at its peak intensity of 950 mbar and weakened by 25 mbar as it slowly translated (Uh=~4 m/s) across the ECS toward land [25][26][19]. This weakening was attributed to the reversal of the enthalpy flux caused by cooling of the sea surface ahead of the storm's eye [19]. This cooling was driven in part by local mixing, but the drivers of the mixing have not been identified.

Ocean mixing under storm forcing is a long-studied topic that is still actively growing. A previous study in the open ocean has shown that ahead of eye cooling can be represented by a simple, one-dimensional shear mixing parametrization [28]. However, three-dimensional ocean models are required, in some cases, to capture TC-driven sea surface cooling because of the potentially important role of upwelling in slowly translating storms [29][30][21]. In this study, we propose that there are critical vertical mixing processes that drive the ocean's response to the forcing of Typhoon Soulik (2018) which are not captured by one-dimensional shear parameterizations. Typhoon Soulik induced significant ahead of eye sea surface cooling (7.4°C) which caused the storm to weaken [19]. We present novel observations of both the TC forcing, measured by a surface meteorological buoy, and the upper ocean cooling it caused, measured by an autonomous underwater glider. We employ both a one-dimensional mixed layer model and a three-dimensional Large Eddy Simulation to investigate what drove the ocean's response. Our aim is to identify the relevant physical processes that drove the observed sea surface cooling ahead of the eye of the storm which led to Typhoon Soulik's weakening hours before landfall.

II. Methods

A. Glider observations

Autonomous underwater gliders have been used in a number of studies to sample the ocean under extreme weather conditions [31][32]. Teledyne Webb Research (TWR) Slocum gliders move vertically through the water column at ~15-20 cm/s by adjusting their buoyancy using a pump in their fore section to draw in or expel ambient water. Wings and their nominal pitch angle of 26.5° allow them to use the changes in their buoyancy to move horizontally at a rate of ~20 km/d relative to the ambient current. As they glide through the water, they sample the ocean at a rate of 0.5 Hz, resulting in vertical data resolutions of < 1m. The glider used in the present study was a Slocum G1 system RU22 equipped with a Seabird Electronics (SBE) unpumped conductivity, temperature, depth (CTD) sensor; two SBE ECO-pucks with one measuring chlorophyll fluorescence, optical backscatter at 880nm, and colored dissolved organic matter concentration (CDOM); the second ECO-puck measured optical backscatter at 3-wavelengths (470,532, and 660 nm). The CTD was factory calibrated prior to deployment on March 17, 2017. The CTD data were used to calculate the potential temperature, practical salinity, and potential density using the GSW-Python package's implementation of the Thermodynamic Equation of Seawater 2010 (http://www.teos-10.org/publications.htm).

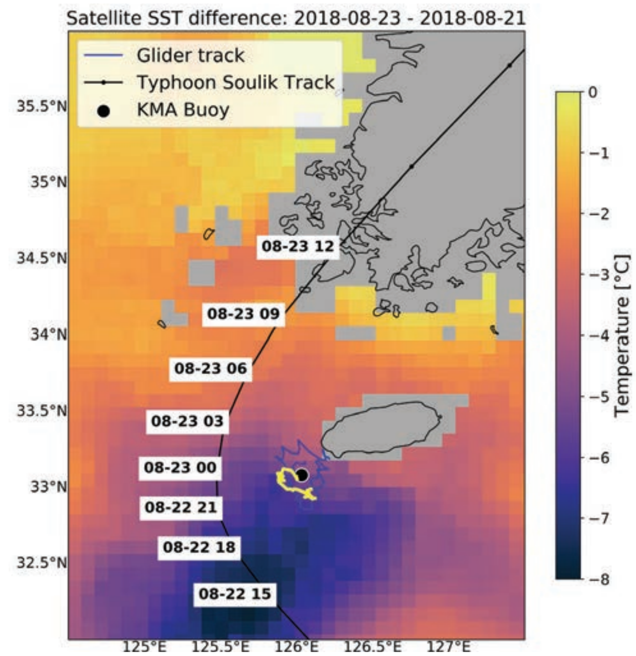

Fig. 1. A map of the study region with the track of Typhoon Soulik (black line), glider track (blue line) with the forced period highlighted (yellow line), buoy position (black circle), and change in SST from 8/21 to 8/23 in °C (color map) [25][26]

B. Additional observational datasets

The meteorological data presented in this study were collected by a Korean Meteorological Administration (KMA) buoy located southwest of Jeju Island Fig. 1. This buoy recorded hourly measurements of wind speed, wind direction, gust wind speed, atmospheric pressure, humidity, air temperature, sea surface temperature (SST), maximum wave height, significant wave height, average wave height, wave period, and wave direction. Based on the wind speed and atmospheric pressure data, we determined the forcing period of Typhoon Soulik at the buoy location to be 8/22/2018 00:00 UTC to 8/23/2018 04:00 UTC. Coefficients of drag and enthalpy flux were calculated from these data following [33][34][13]. Bulk thermodynamic fluxes of latent and sensible heat flux were calculated from these data following [35].

Satellite-derived SST provides a spatial context to the point observations of the glider and buoy. The satellite SST shown in Fig. 1 comes from a global, merged, multisensor, data product from Remote Sensing Systems (remss.com) following Fig. 1 in [19]. This product blends the through cloud measurements of microwave radiometers with the high resolution and near coastal infrared radiometer data. This is advantageous when assessing the change in SST under a large meteorological feature such as a TC. This product provides daily images of SST with a 9km resolution.

Identify applicable funding agency here. If none, delete this text box.

The best track data from the International Best Track Archive for Climate Stewardship (IBTrACS) were used to characterize the location and intensity of Typhoon Soulik over time [25][26].

C. Price-Weller-Pinkel model

This study employs the one-dimensional Price-Weller-Pinkel (PWP) ocean mixing model [36]. This idealized ocean mixing model has been used extensively to study ocean mixing during hurricane conditions [37][38][39][28][40]. PWP is initialized from user provided temperature and salinity profile and forced with either realistic or idealized wind stress, freshwater flux, heat flux, and current drag due to internal or inertial wave dispersion. The system uses both the bulk and gradient Richardson numbers to determine mixed layer stability and shear stability, respectively. The model uses the boundary conditions to solve the momentum equation for velocity, temperature, salinity. During the implementation of forcing, the model will check both stability criteria and if there is an instability present, the water column will be partially mixed until the criteria are satisfied.

In this study, one-dimensional PWP is forced at the surface by wind stress, latent heat flux, and sensible heat flux derived from the KMA buoy observations. The initial profiles of temperature and salinity are taken as the average profile of each parameter measured by the glider between 8/21 22:00 UTC and 8/22 00:25 UTC, averaged into 1m bins. The vertical resolution of the model is 1m with a full column depth of 100m and the model steps forward with 15-minute time steps. The model is not forced with freshwater flux due to data limitations. Model runs with drag from wave dispersion were tested, however results were insensitive to its inclusion and therefore are not described here.

D. Oceananigans.jl Large Eddy Simulation

This study utilizes the newly developed Oceananigans.jl Large Eddy Simulation (LES) (Ramadhan et al., 2020)(Oceananigans.jl) to investigate the physical mechanisms driving the ocean's response to the forcing of Typhoon Soulik. Oceananigans.jl is a flexible, user friendly flow solver based in the programming language Julia. Julia allows this modeling system to be controlled entirely through a script-based interface without the need for compiling or configuration files. Oceananigans.jl solves the Navier-Stokes equations under the Boussinesq approximation. Using an LES allows us to resolve the turbulence in the flow field and study its onset and evolution throughout the duration of the forcing. In this study, the Oceananigans.jl LES is forced at the surface by wind stress, latent heat flux, and sensible heat flux derived from the KMA buoy observations. These fluxes are applied uniformly over the horizontal extent of the domain. A no flux condition was used for salinity at the surface boundary. The initial profiles of temperature and salinity are taken as the average profile of each parameter measured by the glider between 8/21 22:00 UTC and 8/22 00:25 UTC, fit to the resolution of the model domain using a 1D spline interpolator. The full domain is initialized from the same initial profiles of temperature and salinity so there are no initial horizontal gradients. The vertical velocity was initialized with a random noise profile of $O(10^{-6})$ m/s to aid in model spin up. The domain extent in (x,y,z) is (32m, 32m, 84m) with a uniform resolution of 1m in each direction. For compactness and ease of comparison with PWP and the glider data, the LES output has been horizontally averaged at each time step. The maximum model timestep is set to 128s and the LES closure used is the Anisotropic Minimum Dissipation closure. The lateral boundary conditions are periodic. The model employs a linear equation of state to calculate buoyancy and we assume an f-plane because of the small horizontal scale of the domain.

III. Results

A. Observations

Glider RU22 was deployed off the southwest coast of Jeju Island, Republic of Korea on 8/14. The glider was deployed for 13 days and sampled in the vicinity of the KMA surface meteorological buoy Fig.1 throughout the duration of Typhoon Soulik's approach and landfall. At the buoy, wind speeds rose steadily starting from 8/22 00:00 UTC to 8/22 22:00 UTC reaching 24.3 m/s Fig. 2a and a minimum sea-level pressure of 975.9 hPa (data not shown). This coincides with the time of the closest proximity between Typhoon Soulik and buoy and we refer to this as eye passage [25][26]. Wind speeds begin to fall after eye passage. Both latent and sensible heat flux are positive (upward from the ocean to atmosphere) until 8/22 20:00 UTC, just two hours before eye passage, Fig. 2b. The glider observed 7.4°C of SST cooling ahead of the eye of the storm, Fig.2c. The most rapid period of cooling was 6 hours before eye passage, when the wind speed was near its peak value, Fig.2a.

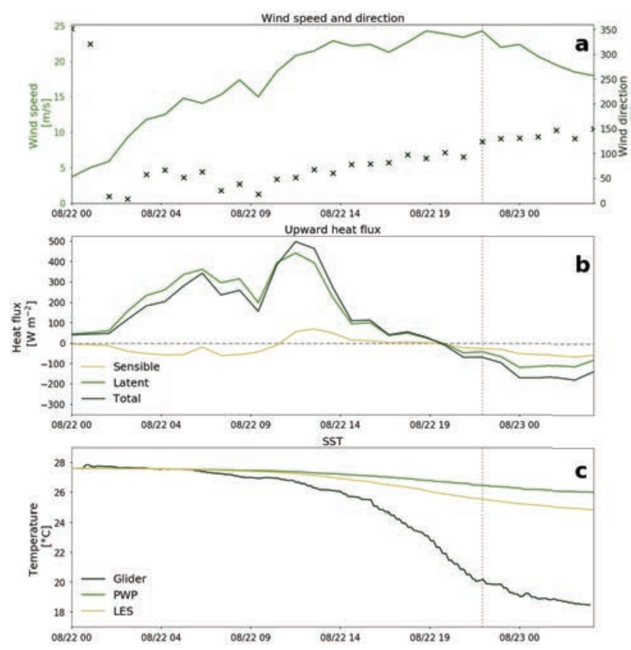

Fig. 2. Surface meteorological data from a Korean Meteorological Agency buoy deployed off the southwest coast of Jeju Island, Republic of Korea during the forcing period of Typhoon Soulik (2018). [a] Wind speed and wind direction reported as direction-from in degrees from North. [b] Sensible heat flux, latent heat flux, and their total enthalpy flux (positive into the atmosphere) with the horizontal dashed line indicating zero heat flux. [c] Sea surface temperature measured by the glider and modeled the PWP and LES experiments. In panels [a-c], the grey dotted line indicates the time of minimum Sea Level Pressure at the buoy location which coincides with the time of closest proximity to the TC.

The buoy and glider SST are misaligned ahead of eye as the buoy SST cools more slowly and steadily, but they converge 6 hours after eye passage.

Based on the observed glider profiles, Fig. 3b, we split the observed water column into three thermal layers separated by distinct thermoclines. To identify the depths of these thermoclines, we first average individual profiles into 1m depth bins and then calculate the vertical temperature gradient, $\partial T/\partial z$. We then employ a spike detection algorithm (scipy.signal.find_peaks) to identify local maxima in each profile of $\partial T/\partial z$. If any point in the profile has a value greater than both its neighboring points, it is labeled as a spike. We constrain this algorithm by requiring a minimum $\partial T/\partial z$ of 0.02°C/m [42] and that all spikes be at least 5m apart. This ensures that distinct thermoclines are detected. Now, with the list of distinct spikes, we chose the two most prominent spikes and recorded their position and magnitude which represent the depth and the strength of the thermoclines, respectively. We chose two spikes based on the observed, 3-layer structure of the initial temperature profiles.

We define the upper and middle layers by the interfaces shown in Fig. 3b. The upper layer deepened by 26m ahead of eye passage, while the middle interface oscillated, around 60m throughout the forced period. The mean layer temperature of the middle and bottom layers both remain nearly constant throughout the duration of the storm (data not shown).

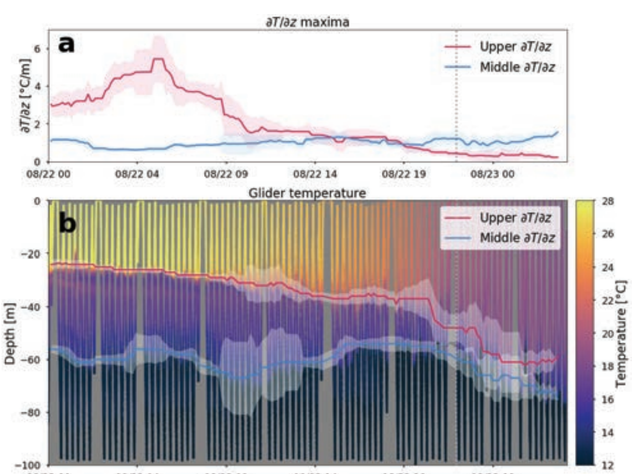

Fig. 3. [a] The maximum stratification at each interface over time with the upper interface in red and the middle interface in blue. These data were passed through a median filter with a 5-point moving window. [b] The observed temperature transect with the upper interface (red line) and the middle interface (blue line) depths marked for each profile. These interface depths were smoothed using a median filter with a 5 profile wide moving window. In both panels, the shading around each line indicates one standard deviation of each set of filtered points. Dotted line is as in Fig. 2.

Both the position and the strength of the interfaces are critical to understanding their evolution. Fig. 3a shows how the layers' stratification strength change over time. The upper interface reaches peak stratification at 8/22 06:00 UTC, 6 hours after forcing began. After its maximum, the stratification rapidly weakens until it falls below 1°C/m and the strength of the middle interface at 8/22 19:00. This is coincident with an increase in the standard deviation of the upper layer depth seen in Fig. 3b. The middle layer stratification remains relatively constant ahead of eye passage, near 1°C/m.

B. Model output

The maximum thermal stratification strength modeled by PWP, Fig. 4a, remains at its initial value until 10 hours into the experiment when it enters a cycle of strengthening and weakening. This cycle continues through eye passage and peak forcing (indicated by the vertical grey line) until it returns to its original value at 8/23 00:16. Both the PWP and the LES experiments showed a weaker SST cooling signal, Fig. 2c, and less change in the thermal structure of the profile, Fig. 4b and Fig. 5b, than was seen in the glider observations. The initial profile shows a maximum stratification at -25m, Fig. 4b, which indicates the upper layer depth. The upper layer begins to deepen 08/22 12:00 UTC and continues to deepen for the duration of the experiment, reaching -30m by eye passage, the dashed grey line in Fig. 4, and -35m by the end of the run at 08/23 04:00 UTC.

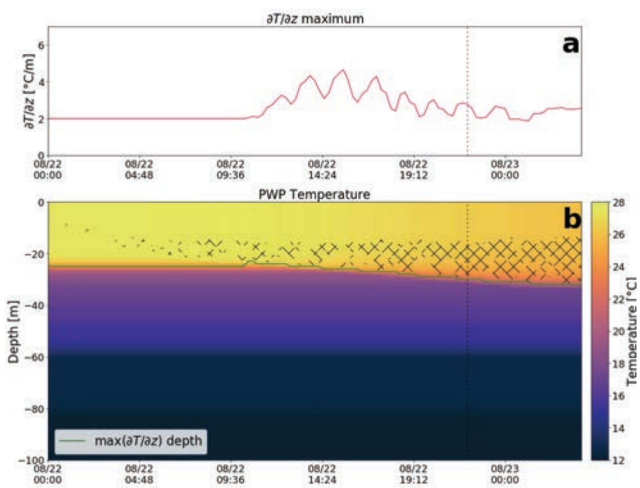

Fig. 4. [a] The maximum stratification strength in the PWP profile. [b] The temperature profile over time output by PWP. The depth of maximum stratification is indicated by the green line. The hatched area represents where the condition in (3) is met. Dotted line is as in Fig. 2.

Shear instabilities occur in PWP when the gradient Richardson number falls below 0.25. This criterion is transformed to (3) for convenience,

$$S^2 = (\partial u/\partial z)^2 + (\partial v/\partial z)^2 \quad (1)$$

$$N^2 = (g/\rho_0) * (\partial \rho/\partial z) \quad (2)$$

$$S^2 - 4N^2 > 0 \quad (3)$$

where g is the gravitational constant, 9.81 m/s^2, ρ_0 is a reference density of 1025 kg/m^3, ρ is the calculated density, and (u,v) are the velocities in the (x,y) direction. Areas of shear mixing are indicated by the hatched pattern in Fig. 4c. Shear mixing begins early in the run and the mixing region deepens and until 8/22 4:48. The mixing region then begins to widen, with the shallow extent maintain a depth near 15m and the deep extent tracking the depth of maximum stratification strength.

The maximum stratification strength captured by the LES experiment, Fig.5a, begins to weaken starting at 8/22 02:00 and reaches a minimum at 08/22 11:00. The LES shows the upper layer starting to deepen at 08/22 12:00, with a depth at eye passage of 35m, and a final depth of 39m by end of the run, Fig.5b. Shear mixing begins in the LES experiment immediately after the start in the surface 10m. The depth over which the mixing is occurring deepens until approaching the thermocline at 08/22 12:00 and then follows the thermocline depth until after eye passage.

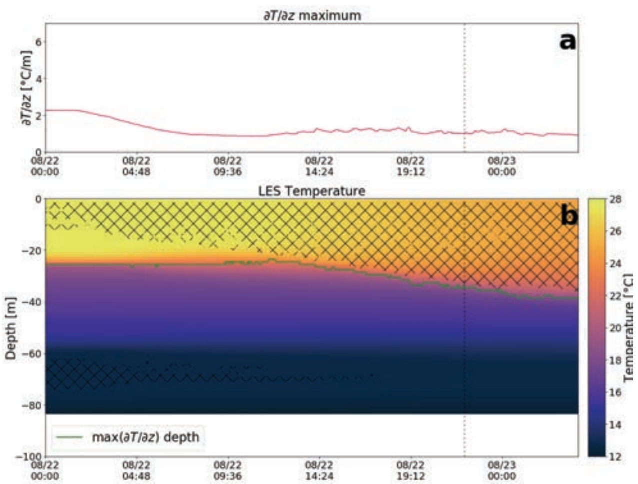

Fig. 5. [a] The maximum stratification strength in the mean LES profile. [b] The mean temperature profile over time output by the LES. The depth of maximum stratification is indicated by the green line. The hatched area represents where the condition in (3) is met. Dotted line is as in Fig. 2.

IV. Discussion

The observed and modeled responses of the ocean to Typhoon Soulik were vastly different. Both the PWP and LES experiments showed less SST cooling and less upper layer deepening than was observed by the glider. Additionally, neither model experiment captured the extent of the weakening of the observed upper layer thermocline with PWP showing an increase in the stratification strength over time and the LES experiment showing steady stratification after moderate weakening. These stark differences in the observed and modeled oceans' responses imply that there are processes causing changes in the upper layer that are not present in the model.

If we consider a one-dimensional water column, the initial observed profile can be described as a three-layer system with two thermoclines, shown in Fig. 3. Equation 4 details a temperature budget for the upper layer of this system, which is representative of the SST,

$$T_{upper,\,f} = Q/(c_p\, \rho_0\, a)\, \Delta t + 1/a\; K_T\, \partial T/\partial z\, \Delta t + F + T_{upper,\,i} \quad (4)$$

where Q is the total enthalpy flux at the surface in W/m^2, c_p is the specific heat of seawater 3850 J/(kg °C), ρ_0 is a reference density of 1025 kg/m^3, *a* is the upper layer depth, K_T is the thermal diffusivity, and Δt is change in time in seconds. The first term on the left-hand side (LHS) represents the change due to surface heat fluxes. Surface heat fluxes could cause warming or cooling of the upper layer, depending on the direction of the heat flux. The second term represents the change due to mixing across the interface between the upper and middle layers. *F* represents the change in the upper layer temperature due to advection, which we are not able to calculate directly from observations. $T_{upper,\,i}$ is the initial upper layer temperature. We will use this framework to identify the role of each process in the observed cooling of the upper layer.

Using the first term on the LHS from (4), a conservative estimate of the change in SST due to surface heat flux can be calculated by assuming the upper layer depth, *a*, is constant throughout the duration of the forcing. This is conservative because *a* deepens over time and the change in temperature due to heat flux is inversely proportional to *a*. The resulting change in the SST is on the order of 0.1°C. This shows that the role of the surface heat flux in changing SST in TC forcing is small.

In order to determine the role of vertical mixing in the change in the upper layer temperature, we employ a linear mixing model following [19],

$$T_{upper,\,f} = a/h\; T_{upper} + (h-a)/h\; T_{middle} \quad (5)$$

where *a* is the initial upper thermocline depth, *h* is the upper thermocline depth at eye passage, T_{upper} is the depth average temperature in the upper layer, and T_{middle} is the depth average temperature in the middle layer. $T_{upper,\,f}$ is the final average temperature of the upper layer after mixing. The linear mixing approach assumes that as the upper layer deepens, the entrained water is homogenized with the upper layer water. Using this model, the cooling due to vertical mixing is 5.1°C. This is more than double the cooling seen in the model results. This would imply that 2.3°C of the observed cooling was driven by other physical processes described in (4). However, if we take *h* to be the final depth of the middle layer then, the cooling due to vertical mixing is 7.4°C, which is the same amount of cooling observed in the glider SST. Approximately 3 hours before eye passage, the standard deviation of the upper layer depth begins to increase Fig. 3b as the strength of the stratification of the interface decreases, Fig. 3a. This indicates that the upper thermocline is less defined and may have been mixed away. These two linear mixing hypotheses provide us with a range of SST cooling due to vertical mixing of 5.1 - 7.4°C. Observations of the SST from the left-hand side of Typhoon Soulik show 6.2°C cooling with 70% attributed to vertical mixing [19].

Hurricane Irene was another case of storm driven mixing leading to massive ahead of eye SST cooling and weakening of the storm [18][20]. This ocean response was driven by coherent mixing structures working to (i) broaden the pycnocline and (ii) homogenize the upper layer [24]. Rapid rotation of the winds during the fast approach of Irene shut down the surface homogenization [24] but observations from Typhoon Soulik show a slow rotation of the wind vector, due to the slow translation speed of the storm, which may have allowed for the sustained surface homogenization seen throughout the duration of the forcing in Fig. 4d.

Although the PWP did not capture the observed response of the ocean to Typhoon Soulik, the experiment produced similar results as seen in [28] where a one-dimensional implementation of PWP captured the observed ocean's response to the wind forcing of Super Typhoon Nepartak. In both cases, shear mixing developed early in the experiment near the surface, the maximum stratification strength increased over the duration of the experiment, and the mixing region deepened and widened throughout the experiment. Super Typhoon Nepartak was a stronger and faster moving storm and the initial ocean profile had a deeper, broader initial pycnocline than in the Typhoon Soulik case [28]. These differences in initial conditions and forcing could explain the difference in the ability of PWP to capture the ocean's response. The shear in the wind driven flow was not able to overcome the stratification in the case of Typhoon Soulik. This implies that there were other sources of mixing such as surface gravity wave breaking, wave-current interactions, coherent mixing structures, or shear in the background flow. Future LES experiments on this case will investigate the roles of wave breaking, wave-current interactions, and coherent mixing structures.

V. Conclusions

In this study we see that Typhoon Soulik (2018) drove mixing that caused a massive amount of SST cooling ahead of the eye of the storm as observed by an underwater glider. The SST cooling, thermocline deepening, and thermocline weakening observed by the glider were not reproduced by the one-dimensional PWP or LES experiments. This leads us to conclude that processes not captured by these model experiments (i.e. surface gravity wave effects, coherent mixing structures, and shear in the ambient flow) were essential to the ocean's response to Typhoon Soulik. Our next steps will be to run LES experiments with surface gravity wave effects implemented.

Acknowledgments

The deployment of RU22 was possible through a collaboration between the Korean Institute of Ocean Science and Technology (KIOST) and the Rutgers University Center for Ocean Observing Leadership (RUCOOL) supported by a NOAA Joint Program Agreement (JPA) project. Satellite derived SST was acquired from http://www.remss.com/measurements/sea-surface-temperature/oisst-description/.

References

[1] NOAA National Centers for Environmental Information (NCEI) U.S. Billion-Dollar Weather and Climate Disasters (2021). https://www.ncdc.noaa.gov/billions/, DOI: 10.25921/stkw-7w73

[2] Fritz, H. M., Blount, C. D., Thwin, S., Thu, M. K., & Chan, N. (2009). Cyclone Nargis storm surge in Myanmar. *Nature Geoscience*, *2*(7), 448–449. https://doi.org/10.1038/ngeo558

[3] Bushnell, J. M., Cherrett, R. C., & Falvey, R. J. (2018). *JTWC Annual Tropical Cyclone Report*

[4] Cangialosi, J. P. (2020). *National Hurricane Center Forecast Verification Report 2019 Hurricane Season*. Retrieved from https://www.nhc.noaa.gov/verification/pdfs/Verification_2019.pdf

[5] Cangialosi, J. P., Blake, E., Demaria, M., Penny, A., Latto, A., Rappaport, E., & Tallapragada, V. (2020). Recent progress in tropical cyclone intensity forecasting at the national hurricane center. *Weather and Forecasting*, *35*(5), 1913–1922. https://doi.org/10.1175/WAF-D-20-0059.1

[6] *Annual Report on the Activities of the RSMC Tokyo - Typhoon Center 2019*. (2020).

[7] Emanuel, K. A. (1986). An Air-Sea Interaction Theory for Tropical Cyclones. Part I: Steady-State Maintenance. *Journal of the Atmospheric Sciences*, *43*(6), 585–605.

[8] Emanuel, K. A. (1991). The Theory Of Hurricanes. *Annual Review of Fluid Mechanics*, *23*(1), 179–196. https://doi.org/10.1146/annurev.fluid.23.1.179

[9] Montgomery, M. T., Persing, J., & Smith, R. K. (2015). Putting to rest WISHE-ful misconceptions for tropical cyclone intensification. *Journal of Advances in Modeling Earth Systems*, *7*(1), 92–109. https://doi.org/10.1002/2014MS000362

[10] Montgomery, M. T., & Smith, R. K. (2014). Paradigms for tropical cyclone intensification. *Australian Meteorological and Oceanographic Journal*, *64*(1), 37–66.

[11] Jaimes de la Cruz, B., Shay, L. K., Wadler, J. B., & Rudzin, J. E. (2021). On the Hyperbolicity of the Bulk Air-Sea Heat Flux Functions: Insights into the Efficiency of Air-Sea Moisture Disequilibrium for Tropical Cyclone Intensification. *Monthly Weather Review*, 1–58. https://doi.org/10.1175/MWR-D-20-0324.1

[12] Potter, H., Drennan, W. M., & Graber, H. C. (2017). Upper ocean cooling and air-sea fluxes under typhoons: A case study. *Journal of Geophysical Research: Oceans*, *122*(9), 7237–7252. https://doi.org/10.1002/2017JC012954

[13] Zhang, J. A., Black, P. G., French, J. R., & Drennan, W. M. (2008). First direct measurements of enthalpy flux in the hurricane boundary layer: The CBLAST results. *Geophysical Research Letters*, *35*(14), 2–5. https://doi.org/10.1029/2008GL034374

[14] Braun, S. A., Sippel, J. A., & Nolan, D. S. (2012). The impact of dry midlevel air on hurricane intensity in idealized simulations with no mean flow. *Journal of the Atmospheric Sciences*, *69*(1), 236–257. https://doi.org/10.1175/JAS-D-10-05007.1

[15] DeMaria, M. (1996). The Effect of Vertical Shear on Tropical Cyclone Intensity Change. *Journal of the Atmospheric Sciences*, *53*(14), 2076–2088. https://doi.org/10.1175/1520-0469(1996)053<2076:TEOVSO>2.0.CO;2

[16] Torn, R. D. (2016). Evaluation of atmosphere and ocean initial condition uncertainty and stochastic exchange coefficients on ensemble tropical cyclone intensity forecasts. *Monthly Weather Review*, *144*(9), 3487–3506. https://doi.org/10.1175/MWR-D-16-0108.1

[17] Bender, M. A., Ginis, I., & Kurihara, Y. (1993). Numerical simulations of tropical cyclone-ocean interaction with a high-resolution coupled model. *Journal of Geophysical Research*, *98*(D12), 245–263. https://doi.org/10.1029/93jd02370

[18] Glenn, S. M., Miles, T. N., Seroka, G., Xu, Y., Forney, R. K., Yu, F., … Kohut, J. (2016). Stratified coastal ocean interactions with tropical cyclones. *Nature Communications*, *7*(May 2015). https://doi.org/10.1038/ncomms10887

[19] Park, J., Yeo, D., Lee, K., Lee, H., Lee, S., Noh, S., … Nam, S. (2019). Rapid Decay of Slowly Moving Typhoon Soulik (2018) due to Interactions With the Strongly Stratified Northern East China Sea. *Geophysical Research Letters*, *46*(24), 14595–14603. https://doi.org/10.1029/2019GL086274

[20] Seroka, G., Miles, T., Xu, Y., Kohut, J., Schofield, O., & Glenn, S. (2017). Rapid shelf-wide cooling response of a stratified coastal ocean to hurricanes. *Journal of Geophysical Research: Oceans*, *122*, 4845–4867. https://doi.org/10.1002/2017JC012756

[21] Zhao, X., & Chan, J. C. L. (2017). Changes in tropical cyclone intensity with translation speed and mixed-layer depth: idealized WRF-ROMS coupled model simulations. *Quarterly Journal of the Royal Meteorological Society*, *143*(702), 152–163. https://doi.org/10.1002/qj.2905

[22] Seroka, G., Miles, T., Xu, Y., Kohut, J., Schofield, O., & Glenn, S. (2016). Hurricane Irene Sensitivity to Stratified Coastal Ocean Cooling. *Monthly Weather Review*, *144*(9), 3507–3530. https://doi.org/10.1175/MWR-D-15-0452.1

[23] Yao, J., Duan, W., & Qin, X. (2021). Which Features of the SST Forcing Error Most Likely Disturb the Simulated Intensity of Tropical Cyclones? *Advances in Atmospheric Sciences*, *38*(4), 581–602. https://doi.org/10.1007/s00376-020-0073-z

[24] Watkins, C., & Whitt, D. B. (2020). Large-Aspect-Ratio Structures in Simulated Ocean Surface Boundary Layer Turbulence under a Hurricane. *Journal of Physical Oceanography*, *50*(12), 3561–3584. https://doi.org/10.1175/JPO-D-20-0134.1

[25] Knapp, K., Diamond, H. J., Kossin, J., Kruk, M. C., & Schreck, C. (2018). International Best Track Archive for Climate Stewardship (IBTrACS) Project, Version 4. [West Pacific]. *NOAA National Centers for Environmental Information.* https://doi.org/https://doi.org/10.25921/82ty-9e16

[26] Knapp, K. R., Kruk, M. C., Levinson, D. H., Diamond, H. J., & Neumann, C. J. (2010). The International Best Track Archive for Climate Stewardship (IBTrACS). *Bulletin of the American Meteorological Society*, *91*(3), 363–376. https://doi.org/10.1175/2009BAMS2755.1

[27] Lie, H. J., & Cho, C. H. (2016). Seasonal circulation patterns of the Yellow and East China Seas derived from satellite-tracked drifter trajectories and hydrographic observations. *Progress in Oceanography*, *146*, 121–141. https://doi.org/10.1016/j.pocean.2016.06.004

[28] Yang, Y. J., Chang, M. H., Hsieh, C. Y., Chang, H. I., Jan, S., & Wei, C. L. (2019). The role of enhanced velocity shears in rapid ocean cooling during Super Typhoon Nepartak 2016. *Nature Communications*, *10*(1), 1–11. https://doi.org/10.1038/s41467-019-09574-3

[29] Bender, Morris A., & Ginis, I. (2000). Real-case simulations of hurricane-ocean interaction using a high-resolution coupled model: Effects on hurricane intensity. *Monthly Weather Review*, *128*(4), 917–946. https://doi.org/10.1175/1520-0493(2000)128<0917:RCSOHO>2.0.CO;2

[30] Yablonsky, R. M., & Ginis, I. (2009). Limitation of one-dimensional ocean models for coupled hurricane-ocean model forecasts. *Monthly Weather Review*, *137*(12), 4410–4419. https://doi.org/10.1175/2009MWR2863.1

[31] Merckelbach, L., Berger, A., Krahmann, G., Dengler, M., & Carpenter, J. R. (2019). A Dynamic Flight Model for Slocum Gliders and Implications for Turbulence Microstructure Measurements. *Journal of Atmospheric and Oceanic Technology*, *36*(2), 281–296. https://doi.org/10.1175/JTECH-D-18-0168.1

[32] Miles, T., Seroka, G., & Glenn, S. (2017). Coastal ocean circulation during Hurricane Sandy. *Journal of Geophysical Research: Oceans*, *122*(9), 7095–7114. https://doi.org/10.1002/2017JC013031

[33] Powell, M. D., Vickery, P. J., & Reinhold, T. A. (2003). Reduced drag coefficient for high wind speeds in tropical cyclones. *Nature*, *422*(6929), 279–283. https://doi.org/10.1038/nature01481

[34] Black, P. G., D'Asaro, E. A., Drennan, W. M., French, J. R., Niiler, P. P., Sanford, T. B., … Zhang, J. A. (2007). Air–Sea Exchange in Hurricanes: Synthesis of Observations from the Coupled Boundary Layer Air–Sea Transfer Experiment. *Bulletin of the American Meteorological Society*, *88*(3), 357–374. https://doi.org/10.1175/BAMS-88-3-357

[35] Fairall, C. W., Bradley, E. F., Rogers, D. P., Edson, J. B., & Young, G. S. (1996). Bulk parameterization of air-sea fluxes for tropical oceanglobal atmosphere coupled-ocean atmosphere response experiment. *Journal of Geophysical Research C: Oceans*, *101*(C2), 3747–3764. https://doi.org/10.1029/95JC03205

[36] Price, J. F., Weller, R. A., & Pinkel, R. (1986). Diurnal cycling: Observations and models of the upper ocean response to diurnal heating, cooling, and wind mixing. *Journal of Geophysical Research*, *91*(C7), 8411–8427. https://doi.org/10.1029/JC091iC07p08411

[37] Hlywiak, J., & Nolan, D. S. (2019). The influence of oceanic barrier layers on tropical cyclone intensity as determined through idealized, coupled numerical simulations. *Journal of Physical Oceanography*, *49*(7), 1723–1745. https://doi.org/10.1175/JPO-D-18-0267.1

[38] Rudzin, J. E., Shay, L. K., & Johns, W. E. (2018). The influence of the barrier layer on SST response during tropical cyclone wind forcing using idealized experiments. *Journal of Physical Oceanography*, *48*(7), 1471–1478. https://doi.org/10.1175/JPO-D-17-0279.1

[39] Wang, X. D., Han, G. J., Qi, Y. Q., & Li, W. (2011). Impact of barrier layer on typhoon-induced sea surface cooling. *Dynamics of Atmospheres and Oceans*, *52*(3), 367–385. https://doi.org/10.1016/j.dynatmoce.2011.05.002

[40] Zedler, S. E., Dickey, T. D., Doney, S. C., Price, J. F., Yu, X., & Mellor, G. L. (2002). Analyses and simulations of the upper ocean's response to Hurricane Felix at the Bermuda Testbed Mooring site: 13-23 August 1995. *Journal of Geophysical Research: Oceans*, *107*(12), 13–23. https://doi.org/10.1029/2001jc000969

[41] Ramadhan, A., Wagner, G., Hill, C., Campin, J.-M., Churavy, V., Besard, T., et al.. (2020). Oceananigans.jl: Fast and friendly geophysical fluid dynamics on GPUs. *Journal of Open Source Software*, *5*(53), 2018. https://doi.org/10.21105/joss.02018

[42] Dohan, K., & Davis, R. E. (2011). Mixing in the transition layer during two storm events. *Journal of Physical Oceanography*, *41*(1), 42–66. https://doi.org/10.1175/2010JPO4253.1

Uncrewed Ocean Gliders and Saildrones Support Hurricane Forecasting and Research

By Travis N. Miles, Dongxiao Zhang, Gregory R. Foltz, Jun A. Zhang, Christian Meinig, Francis Bringas, Joaquin Triñanes, Matthieu Le Hénaff, Maria F. Aristizabal Vargas, Sam Coakley, Catherine R. Edwards, Donglai Gong, Robert E. Todd, Matthew J. Oliver, W. Douglas Wilson, Kerri Whilden, Barbara Kirkpatrick, Patricia Chardon-Maldonado, Julio M. Morell, Debra Hernandez, Gerhard Kuska, Cheyenne D. Stienbarger, Kathleen Bailey, Chidong Zhang, Scott M. Glenn, and Gustavo J. Goni

INTRODUCTION

In the United States alone, hurricanes have been responsible for thousands of deaths and over US$1 trillion in damages since 1980 (https://www.ncdc.noaa.gov/billions/). These impacts are significantly greater globally, particularly in regions with limited hurricane early warning systems and where large portions of the population live at or near sea level. The high socioeconomic impacts of tropical cyclones will increase with a changing climate, rising sea level, and increasing coastal populations. To mitigate these impacts, efforts are underway to improve hurricane track and intensity forecasts, which drive storm surge models and evacuation orders and guide coastal preparations. Hurricane track forecasts have improved steadily over past decades, while intensity forecasts have lagged until recently (Cangialosi et al., 2020). Hurricane intensity changes are influenced by a combination of large-scale atmospheric circulation, internal storm dynamics, and air-sea interactions (Wadler et al., 2021, and references therein).

Components of the sustained ocean observing system (e.g., profiling floats, expendable bathythermographs, drifters, moorings) are useful for understanding the role of the ocean in hurricane intensity changes. However, gaps in the ocean observing system, particularly collection of data near the air-sea interface and in coastal regions, boundary currents (e.g., the Gulf Stream, Kuroshio, among others), and areas with complex currents and seafloor topography (e.g., the Caribbean Sea), have led to difficulties in accurately representing upper ocean features and processes in numerical ocean models. Employment of uncrewed ocean observing platforms has begun to fill these gaps by offering rapid relocation and adaptive sampling of regions and ocean features of interest. These platforms include autonomous underwater gliders (Figure 1; Testor et al., 2019) and surface vehicles (Meinig et al., 2019). Uncrewed surface vehicles (USVs), such as saildrones and wave gliders, are systems designed for data collection in hazardous conditions. Data collected by these platforms have improved our understanding of upper ocean temperature and salinity stratification and mixing processes and are becoming critical in improving operational ocean and coupled air-sea hurricane forecast models (Domingues et al., 2021).

This paper provides a broad overview of the ongoing US hurricane glider project and details of a new effort with the Saildrone USV during the 2021 hurricane season. While this article focuses on the US East Coast, Gulf of Mexico, and Caribbean Sea, similar efforts are underway in Korea, the Philippines, Japan, and China, among other countries.

THE OCEAN AND HURRICANES

The ocean influences hurricane development through the transfer of heat and momentum across the air-sea interface (Le Hénaff et al., 2021; Wadler et al., 2021, and references therein). Warm sea surface temperatures are conducive to hurricane intensification while cool temperatures often lead to weakening. Research shows that upper ocean temperature and salinity ahead of and during hurricanes can evolve rapidly (Glenn et al., 2016). The evolution of the upper ocean depends on various factors, including wind speed and direction, wave state, upper ocean stratification, and interactions with the coastal ocean, among others. To accurately forecast hurricane intensity in the western Atlantic, coupled ocean and atmosphere operational forecast models must resolve large-scale warm ocean currents (e.g., the Gulf Stream, the Gulf of Mexico Loop Current, and their associated meanders and eddies; Todd et al., 2018); freshwater layers from large rivers such as the Amazon-Orinoco and Mississippi (Domingues et al., 2021), which can inhibit ocean mixing and maintain warm upper ocean temperatures ahead of storms; and shallow

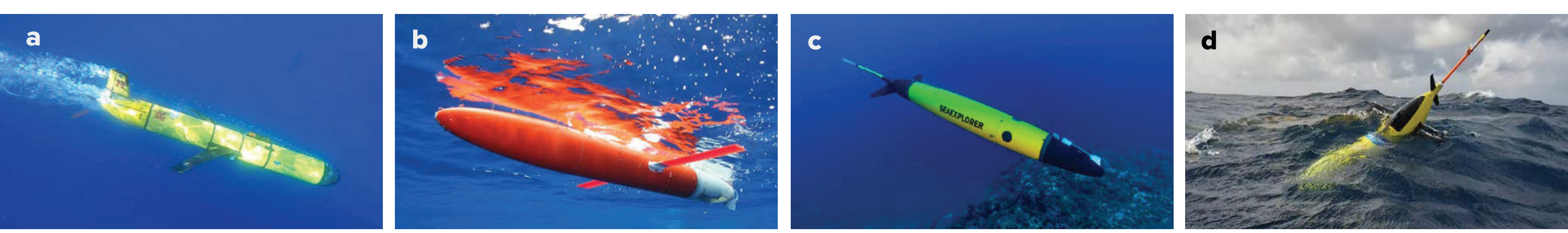

FIGURE 1. Underwater gliders: (a) Slocum. (b) Spray. (c) SeaExplorer. (d) Seaglider. For more information on gliders, go to https://ioos.noaa.gov/project/underwater-gliders/. *Photo credits: (a) Matt Souza, University of Virgin Islands (b) Robert E. Todd, WHOI (c) ALSEAMAR (d) NOAA AOML*

continental shelf features like the Mid-Atlantic Cold Pool, a cold bottom water mass that can rapidly mix to the surface and weaken storms before landfall (Glenn et al., 2016). New technologies such as uncrewed ocean gliders and surface vehicles, alongside more established components of the Global Ocean Observing System (e.g., Argo floats, air-launched expendable bathythermographs, and satellite sensors), will improve existing hurricane forecast and warning systems and support critical research to develop the next generation systems.

UNDERWATER GLIDERS

Gliders (Figure 1) have emerged as a major component of US and international multi-hazard warning systems. Since 2014, the operation of gliders for hurricane research and forecasts has been a joint effort by the US National Oceanic and Atmospheric Administration (NOAA), the US Integrated Ocean Observing System (IOOS) Regional Associations, academic institutions, the US Navy, the National Science Foundation, private companies, and other regional and international partners. Gliders are unique in their maneuverability, able to profile through the water column as deep as 1,000 m with vertical and horizontal speeds of ~10–20 cm/s and ~25 cm/s, respectively. Standard glider sensor packages include temperature, salinity, and density, while some gliders also collect profiles of water speed and direction. Biogeochemical measurements can include oxygen, phytoplankton, and particle concentration for water quality assessment. Numerous advanced sensor packages continue to be developed and integrated. Gliders can collect data as frequently as every two seconds, providing submeter-scale measurements in the vertical, though lower sample rates are typically used to conserve power and minimize surface time.

While opportunistic glider deployments were carried out for hurricane research in the first decade of this century, coordinated regional fleets were first used for hurricane research and operational model development in 2014. These experiments were supported by the congressionally authorized Disaster Recovery Act following the devastation of Superstorm Sandy in October 2012. Studies from this time period (Glenn et al., 2016; Domingues et al., 2021, and references therein) demonstrated the unique capabilities of gliders to contribute to our understanding of ocean feedbacks on hurricane intensity and to the improved accuracy of coupled hurricane model forecasts.

Following the coastal impacts of Hurricanes Irma and Maria in 2017, large multi-institution fleets of gliders have now been deployed to collect data. These efforts, and other leveraged glider observations, have resulted in over 280 deployments, collecting nearly 600,000 ocean profiles during 13,000 glider days in hurricane seasons from 2018 to 2021 in the open Atlantic Ocean, the Caribbean Sea, the Gulf of Mexico, and off the US East Coast (Figure 2).

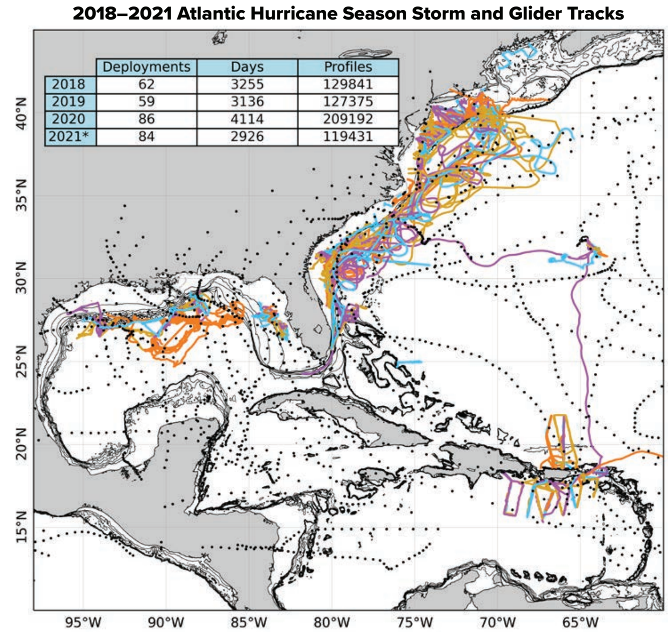

FIGURE 2. Glider tracks from the 2018 (orange), 2019 (purple), 2020 (yellow), and 2021* (blue) hurricane seasons (May to November) generated with data from the Integrated Ocean Observing System Glider Data Assembly Center (https://gliders.ioos.us), with an overlay of tropical cyclone tracks (black dots) from the International Best Track Archive for Climate Stewardship (IBTrACS, https://www.ncdc.noaa.gov/ibtracs/). The table in the upper left indicates the yearly breakdown of glider deployments, glider days at sea, and collected profiles. (*2021 data were extracted on 09/17/2021 prior to the completion of the Atlantic hurricane season.)

These gliders were strategically deployed in regions with high probabilities of hurricane passage, near ocean features that impact hurricane intensity, and near vulnerable coastal population centers.

Gliders have collected data in the ocean under more than 30 Atlantic tropical cyclones. These data are provided to the publicly accessible IOOS Glider Data Assembly Center (DAC; https://gliders.ioos.us), where they are accessed in real time and distributed through the World Meteorological Organization Global Telecommunication System (GTS). This distribution pathway allows NOAA to access the glider profiles for assimilation into the operational numerical models, such as the global Real Time Ocean Forecast System, used to initialize the ocean component of coupled hurricane forecast models such as the NOAA Hurricane Weather Research and Forecasting model.

A data impact study of Hurricane Maria (2017) showed that, out of the suite of in situ ocean observing platforms, glider data locally generate the largest error reduction in intensity forecasts within NOAA operational forecast models (Domingues et al., 2021). Additional model improvements were achieved when glider data were used alongside other ocean observations (Halliwell et al., 2020). Gliders have also contributed to new understanding of hurricane-forced coastal ocean circulation (Glenn et al., 2016), impacts on boundary currents (Todd et al., 2018), ahead-of-eye mixing processes (Glenn et al., 2016), and impacts of these processes on hurricane intensity. With the development of new sensors and public data repositories, gliders additionally contribute to the understanding of regional ecosystems, fisheries, water quality, harmful algal blooms, ocean warming and climate change, and renewable energy, among other coastal processes, stressors, and solutions.

A NEW UNCREWED SURFACE VEHICLE FOR HURRICANE OPERATIONS AND RESEARCH

To continue making significant progress toward understanding and predicting hurricane intensity changes, new technologies are being tested to provide improved estimates of air-sea fluxes in a hurricane environment. Efforts by public-private partnerships have rapidly advanced development of USVs into air-sea interaction observing platforms (Meinig et al., 2019). The use of renewable wind, surface wave, and solar energy for propulsion and instrumentation has increased USV endurance up to 12 months and enabled installation of more sensors (Zhang et al., 2019). Specifically, Saildrone USVs (Figure 3) are equipped with 15 sensor packages that measure 22 essential ocean and climate variables, such as sea surface temperature, salinity, oxygen, wave height and period, near-surface winds, air temperature, relative humidity, solar and longwave radiation, and barometric pressure (Zhang et al., 2019).

During the 2021 hurricane season, NOAA supported for the first time deployment and operation of five specially designed Saildrone USVs to measure air-sea interaction in regions where Atlantic tropical cyclones occur frequently. Compared to conventional Saildrone platforms, these extreme weather systems have shorter wings for increased stability, allowing them to operate in hurricane-force winds and in the presence of large breaking waves (Figure 3). For the 2021 mission, the five extreme weather Saildrone USVs were strategically located in regions of the western tropical Atlantic, the Caribbean, and near the US East Coast to maximize the probability of encountering at least one hurricane or tropical storm. The USVs continuously measured properties in the near-surface atmosphere and ocean and transmitted one-minute averaged data to the GTS and data centers in real time for assimilation into forecast models and for other public use.

The extreme weather Saildrone USVs travel at speeds of about 30–150 km per day, depending on winds and currents, and can be directed to locations directly in tropical cyclone paths. For example, during the 2021 mission, Saildrone SD-1031 traveled 35 km to the east during the 24 hours before the arrival of Hurricane Henri, bringing it within 50 km of the eye of the storm. The ability to move the USV into storm paths increases the chances of acquiring ocean-atmosphere measurements in high-wind conditions. These measurements are extremely valuable because the rates of heat and momentum exchange between the ocean and tropical cyclones, and storm dependence on the states of the ocean and atmosphere, are not well known, in part because there are so few measurements. The highlight of the mission was the passage of Category 4 Hurricane Sam directly over Saildrone SD-1045 on September 30 (Figure 4), when winds up to 56 m/s (at a height of 5 m) and waves as high as 14 m were recorded in the hurricane's northern eyewall. Saildrone SD-1045 then traveled across the eastern edge of the eye and through the southern eyewall, recording the first-ever video from the sea surface of the eyewall of a major hurricane (https://www.saildrone.com/press-release/ocean-drone-captures-video-inside-category-4-hurricane).

During the August–October 2021 Atlantic hurricane mission, two other tropical storms passed close to saildrones: Grace passed directly over Saildrone SD-1048 south of Puerto Rico, and Fred passed about 140 km to the north of the same saildrone. When they were not being directed toward tropical cyclones, the mission scientists worked with Saildrone Inc. pilots to keep four of the Saildrone USVs close to gliders to obtain nearly collocated measurements of the upper ocean and near-surface atmosphere (Figure 4). In addition, NOAA's hurricane reconnaissance aircraft acquired collocated profiles of atmospheric

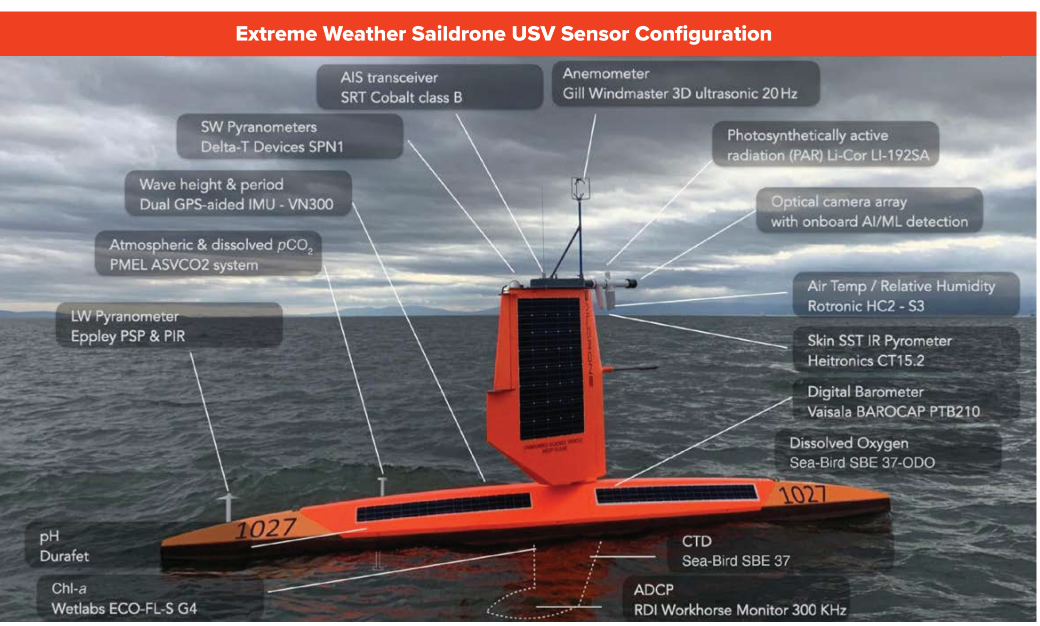

FIGURE 3. Extreme weather (short-wing) Saildrone and its measurement capabilities (https://www.saildrone.com/news/what-is-saildrone-how-work).

temperature, humidity, and winds from dropsondes together with ocean temperature profiles collected from air-launched expendable bathythermographs in Hurricane Henri. NASA aircraft also launched dropsondes near some of the Saildrone USVs during its Convective Processes Experiment – Aerosols & Winds (CPEX-AW) field campaign. These unique data sets will be valuable for advancing knowledge of interactions between the subsurface ocean and tropical cyclones.

CONCLUSIONS

Both autonomous underwater gliders and uncrewed surface vehicles such as saildrones represent advanced ocean observing technologies that are revolutionizing both our understanding of and ability to forecast hurricane track and intensity. To realize their full potential, these technologies will continue to be more closely integrated with established regional and global ocean and atmosphere observing platforms. One of the main objectives of these projects during the 2021 Atlantic hurricane season was to obtain collocated and simultaneous measurements of the upper ocean and air-sea coupling within a hurricane. These combined observations will provide new insights into the coevolution and coupling of the ocean and atmosphere to better predict storm intensity. Future hurricane observations should encourage more closely coordinated deployments of underwater, near-surface, and airborne observations in order to better understand rapid hurricane intensity changes. As ocean, atmosphere, and coupled model architecture and data assimilation capabilities continue to coevolve and improve, these observing systems and their shoreside cyberinfrastructure will become critical components of operational forecasting systems in the United States.

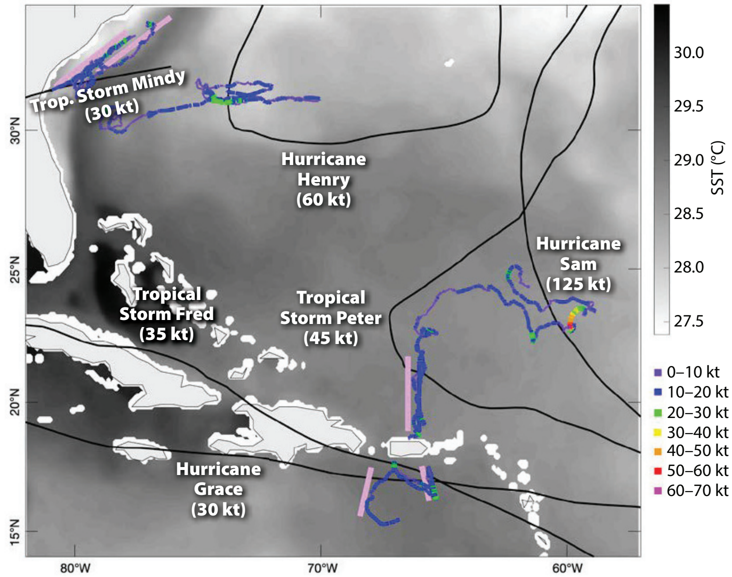

FIGURE 4. Colored Saildrone tracks during August to October 2021 represent one-hour averaged wind speed measured at a height of 5 m. Saildrone data from the mission are available at https://www.pmel.noaa.gov/saildrone-hurricane2021/. Black lines show tracks of tropical cyclones that passed close to one or more Saildrones. Storm names and their maximum sustained one-minute wind speeds at locations of closest approach to a Saildrone are also indicated. Thicker pink lines indicate repeat tracks of ocean gliders that obtained collocated measurements with Saildrones. Background shading is sea surface temperature averaged during August to September 2021.

REFERENCES

Cangialosi, J.P., E. Blake, M. Demaria, A. Penny, A. Latto, E. Rappaport, and V. Tallapragada. 2020. Recent progress in tropical cyclone intensity forecasting at the national hurricane center. *Weather and Forecasting* 35(5):1,913–1,922, https://doi.org/10.1175/WAF-D-20-0059.1.

Domingues, R., M. Le Hénaff, G.R. Halliwell, J.A. Zhang, F. Bringas, P. Chardon-Maldonado, H. Kim, J.M. Morell, and G.J. Goni. 2021. Ocean conditions and the intensification of three major Atlantic hurricanes in 2017. *Monthly Weather Review* 149(5):1,265–1,286, https://doi.org/10.1175/MWR-D-20-0100.1.

Glenn, S.M., T.N. Miles, G.N. Seroka, Y. Xu, R.K. Forney, F. Yu, H. Roarty, O. Schofield, and J. Kohut. 2016. Stratified coastal ocean interactions with tropical cyclones. *Nature Communications* 7:10887, https://doi.org/10.1038/ncomms10887.

Halliwell, G.R., G.J. Goni, M.F. Mehari, V.H. Kourafalou, M. Baringer, and R. Atlas. 2020. OSSE assessment of underwater glider arrays to improve ocean model initialization for tropical cyclone prediction. *Journal of Atmospheric and Oceanic Technology* 37(3):467–487, https://doi.org/10.1175/JTECH-D-18-0195.1.

Le Hénaff, M., R. Domingues, G. Halliwell, J.A. Zhang, H.S. Kim, M. Aristizabal, T. Miles, S. Glenn, and G. Goni. 2021. The role of the Gulf of Mexico ocean conditions in the intensification of Hurricane Michael (2018). *Journal of Geophysical Research: Oceans* 126(5):e2020JC016969, https://doi.org/10.1029/2020JC016969.

Meinig, C., E.F. Burger, N. Cohen, E.D. Cokelet, M.F. Cronin, J.N. Cross, S. de Halleux, R. Jenkins, A.T. Jessup, C.W. Mordy, and others. 2019. Public-private partnerships to advance regional ocean observing capabilities: A Saildrone and NOAA-PMEL case study and future considerations to expand to global scale observing. *Frontiers in Marine Science* 6:448, https://doi.org/10.3389/fmars.2019.00448.

Testor, P., B. de Young, D.L. Rudnick, S. Glenn, D. Hayes, C.M. Lee, C. Pattiaratchi, K. Hill, E. Heslop, V. Turpin, and others. 2019. OceanGliders: A component of the integrated GOOS. *Frontiers in Marine Science* 6:422, https://doi.org/10.3389/fmars.2019.00422.

Todd, R.E., T.G. Asher, J. Heiderich, J.M. Bane, and R.A. Luettich. 2018. Transient response of the Gulf Stream to multiple hurricanes in 2017. *Geophysical Research Letters* 45(19):10,509–10,519, https://doi.org/10.1029/2018GL079180.

Wadler, J.B., J.A. Zhang, R.F. Rogers, B. Jaimes, and L.K. Shay. 2021. The rapid intensification of Hurricane Michael (2018): Storm structure and the relationship to environmental and air–sea interactions. *Monthly Weather Review* 149(1):245–267, https://doi.org/10.1175/MWR-D-20-0145.1.

Zhang, D., M.F. Cronin, C. Meinig, J.T. Farrar, R. Jenkins, D. Peacock, J. Keene, A. Sutton, and Q. Yang. 2019. Comparing air-sea flux measurements from a new unmanned surface vehicle and proven platforms during the SPURS-2 field campaign. *Oceanography* 32(2):122–133, https://doi.org/10.5670/oceanog.2019.220.

ACKNOWLEDGMENTS

The Saildrone project work was supported by NOAA's Office of Marine and Aviation Operations (OMAO) and Office of Oceanic and Atmospheric Research (OAR): Weather Program Office (NA21OAR4590394), Atlantic Oceanographic and Meteorological Laboratory (AOML), Pacific Marine Environmental Laboratory (PMEL), Cooperative Institute for Climate, Ocean and Ecosystem Studies (CICOES/UW), and the Oceans Portfolio. The glider work was supported by NOAA (Integrated Ocean Observing System, Global Ocean Monitoring and Observing Program, IOOS Regional Associations—MARACOOS, CARICOOS, SECOORA, and GCOOS—made possible in part by supplemental funds from the Bipartisan Budget Act of 2018 and the 2019 Additional Supplemental Appropriations for Disaster Relief Act), the National Science Foundation, and Office of Naval Research. Support for the NOAA and US Navy glider partnership was made possible by NOAA OMAO. Rutgers researchers were also partially supported by NOAA (NA16NOS0120020). This is PMEL contribution # 5333.

ARTICLE DOI: https://doi.org/10.5670/oceanog.2021.supplement.02-28

AUTHORS

Travis N. Miles (tnmiles@marine.rutgers.edu), **Sam Coakley**, and **Scott M. Glenn**, Rutgers, The State University of New Jersey, Department of Marine and Coastal Sciences, USA. **Dongxiao Zhang**, NOAA Pacific Marine Environmental Laboratory, and Cooperative Institute for Climate, Ocean, and Ecosystem Studies, University of Washington, USA. **Gregory R. Foltz**, **Francis Bringas**, and **Gustavo J. Goni**, NOAA Atlantic Oceanographic and Meteorological Laboratory (AOML), USA. **Jun A. Zhang**, Cooperative Institute for Marine and Atmospheric Studies (CIMAS), University of Miami, USA. **Joaquin Triñanes**, Department of Electronics and Computer Science, Universidade de Santiago de Compostela, Spain. **Christian Meinig** and **Chidong Zhang**, NOAA Pacific Marine Environmental Laboratory, USA. **Matthieu Le Hénaff**, CIMAS, University of Miami, and NOAA/AOML, USA. **Maria F. Aristizabal Vargas**, IM Systems Group at NOAA Environmental Modeling Center, USA. **Catherine R. Edwards**, Skidaway Institute of Oceanography, University of Georgia, USA. **Donglai Gong**, Virginia Institute of Marine Science, College of William & Mary, USA. **Robert E. Todd**, Woods Hole Oceanographic Institution, USA. **Matthew J. Oliver**, School of Marine Science and Policy, University of Delaware, USA. **W. Douglas Wilson**, Ocean and Coastal Observing, Virgin Islands. **Kerri Whilden** and **Barbara Kirkpatrick**, Gulf of Mexico Coastal Ocean Observing System Regional Association, Texas A&M University, USA. **Patricia Chardon-Maldonado** and **Julio M. Morell**, Caribbean Coastal Ocean Observing System, Puerto Rico. **Debra Hernandez**, Southeast Coastal Ocean Observing Regional Association, USA. **Gerhard Kuska**, Mid Atlantic Regional Association Coastal Ocean Observing System, USA. **Cheyenne D. Stienbarger**, NOAA Global Ocean Monitoring and Observing Program, USA. **Kathleen Bailey**, NOAA US Integrated Ocean Observing System Office, USA.

ARTICLE CITATION

Miles, T.N., D. Zhang, G.R. Foltz, J. Zhang, C. Meinig, F. Bringas, J. Triñanes, M. Le Hénaff, M.F. Aristizabal Vargas, S. Coakley, C.R. Edwards, D. Gong, R.E. Todd, M.J. Oliver, W.D. Wilson, K. Whilden, B. Kirkpatrick, P. Chardon-Maldonado, J.M. Morell, D. Hernandez, G. Kuska, C.D. Stienbarger, K. Bailey, C. Zhang, S.M. Glenn, and G.J. Goni. 2021. Uncrewed ocean gliders and saildrones support hurricane forecasting and research. Pp. 78–81 in *Frontiers in Ocean Observing: Documenting Ecosystems, Understanding Environmental Changes, Forecasting Hazards.* E.S. Kappel, S.K. Juniper, S. Seeyave, E. Smith, and M. Visbeck, eds, A Supplement to *Oceanography* 34(4), https://doi.org/10.5670/oceanog.2021.supplement.02-28.

On the Development of SWOT In Situ Calibration/Validation for Short-Wavelength Ocean Topography

JINBO WANG,[a] LEE-LUENG FU,[a] BRUCE HAINES,[a] MATTHIAS LANKHORST,[b] ANDREW J. LUCAS,[b,c] J. THOMAS FARRAR,[d] UWE SEND,[b] CHRISTIAN MEINIG,[e] OSCAR SCHOFIELD,[f] RICHARD RAY,[h] MATTHEW ARCHER,[a] DAVID ARAGON,[f] SEBASTIEN BIGORRE,[d] YI CHAO,[g] JOHN KERFOOT,[f] ROBERT PINKEL,[b] DAVID SANDWELL,[b] AND SCOTT STALIN[e]

[a] *Jet Propulsion Laboratory, California Institute of Technology, Pasadena, California*
[b] *Scripps Institution of Oceanography, University of California, San Diego, La Jolla, California*
[c] *Department of Mechanical and Aerospace Engineering, University of California, San Diego, La Jolla, California*
[d] *Woods Hole Oceanographic Institution, Woods Hole, Massachusetts*
[e] *Pacific Marine Environmental Laboratory, National Oceanic and Atmospheric Administration, Seattle, Washington*
[f] *Rutgers, The State University of New Jersey, New Brunswick, New Jersey*
[g] *Remote Sensing Solutions, Monrovia, California*
[h] *NASA Goddard Space Flight Center, Greenbelt, Maryland*

(Manuscript received 7 April 2021, in final form 10 November 2021)

ABSTRACT: The future Surface Water and Ocean Topography (SWOT) mission aims to map sea surface height (SSH) in wide swaths with an unprecedented spatial resolution and subcentimeter accuracy. The instrument performance needs to be verified using independent measurements in a process known as calibration and validation (Cal/Val). The SWOT Cal/Val needs in situ measurements that can make synoptic observations of SSH field over an $O(100)$ km distance with an accuracy matching the SWOT requirements specified in terms of the along-track wavenumber spectrum of SSH error. No existing in situ observing system has been demonstrated to meet this challenge. A field campaign was conducted during September 2019–January 2020 to assess the potential of various instruments and platforms to meet the SWOT Cal/Val requirement. These instruments include two GPS buoys, two bottom pressure recorders (BPR), three moorings with fixed conductivity–temperature–depth (CTD) and CTD profilers, and a glider. The observations demonstrated that 1) the SSH (hydrostatic) equation can be closed with 1–3 cm RMS residual using BPR, CTD mooring and GPS SSH, and 2) using the upper-ocean steric height derived from CTD moorings enable subcentimeter accuracy in the California Current region during the 2019/20 winter. Given that the three moorings are separated at 10–20–30 km distance, the observations provide valuable information about the small-scale SSH variability associated with the ocean circulation at frequencies ranging from hourly to monthly in the region. The combined analysis sheds light on the design of the SWOT mission postlaunch Cal/Val field campaign.

KEYWORDS: Internal waves; Ocean dynamics; Small scale processes; Altimetry; Global positioning systems (GPS); In situ oceanic observations; Ship observations

1. Introduction

The Surface Water and Ocean Topography (SWOT) mission is a pathfinder mission that will demonstrate the next-generation satellite altimeter based on a Ka-band radar interferometer (KaRIn) (Durand et al. 2010; Fu and Ubelmann 2014). The major thrusts of the mission are the low noise and wide-swath sea surface height (SSH) measurements of the KaRIn instrument. After its launch in 2022, understanding the performance of the KaRIn instrument against a ground truth of dynamical SSH is crucial for subsequent scientific applications. This emphasizes the importance of the mission's ocean topography calibration and validation (Cal/Val), which focuses on the wavenumber spectrum of SWOT SSH measurement errors.

In the past, the ground truth for satellite altimeters was typically produced using point measurements from ground stations such as tide gauges, a method that has been used successfully for all previous nadir-altimeter missions, such as the Jason-series altimeters (e.g., Haines et al. 2021; Bonnefond et al. 2019; Quartly et al. 2021). However, the SWOT mission requires a new approach for calibration and validation because the SWOT science requirement is specified in terms of the wavenumber spectrum over 15–1000 km wavelengths (Fig. 1; Desai et al. 2018). As such, validation of the sensor requires capturing a synoptic SSH field along a line covering 15–1000 km wavelengths. Validation of wavelengths ranging from ~120 to 1000 km will be accomplished by the onboard Jason-class altimeter (Wang and Fu 2019), whose performance in wavenumber space is known (e.g., Dufau et al. 2016). The ground truth over the short wavelength (15–150 km) may be achieved by airborne instruments such as lidar (Melville et al. 2016) for geodetic validation and in situ oceanographic measurements (Wang et al. 2018) for oceanographic validation. For the latter, we need an observing approach designed specifically for SSH wavenumber spectrum validation at scales between 15 and 150 km with subcentimeter accuracy.

Corresponding author: Jinbo Wang, jinbo.wang@jpl.nasa.gov

DOI: 10.1175/JTECH-D-21-0039.1

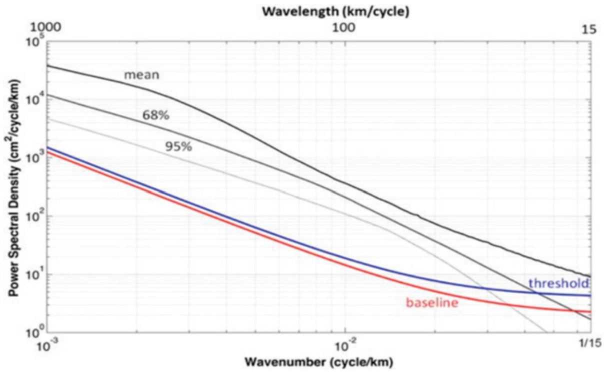

FIG. 1. The SSH baseline requirement spectrum (red line) as a function of wavenumber (Desai et al. 2018). The thick black line is the mean spectrum of the *Jason-2* altimeter track 159, which extends from the Southern Ocean to North Pacific. The 68th and 95th percentiles are marked by the thin black line and the gray line; i.e., 68% and 95% of the spectra are above the corresponding curve. The red curve defines the baseline requirement represented by $E(k) = 2 + 0.001\,25k^{-2}(\mathrm{cm}^2\ \mathrm{cpkm}^{-1})$. The blue curve represents the threshold requirement $E(k) = 4 + 0.0015k^{-2}(\mathrm{cm}^2\ \mathrm{cpkm}^{-1})$.

An observing system simulation experiment (OSSE) was conducted as a first step to evaluate the feasibility of an array of moorings to meet the Cal/Val requirement (Wang et al. 2018). Based on the OSSE, the top challenges in reconstructing the small-scale synoptic SSH field over a 150 km distance come from the emerging dominance of superinertial high-frequency SSH variability at spatial scales <150 km, and the weak SSH signal itself at those scales. These challenges led to a series of field campaigns to identify the relevant ocean processes at the Cal/Val site (near 35.6°N, 125°W) and to evaluate the performance of different in situ platforms and instruments in meeting the SWOT requirement.

Here we report the results from a recent field campaign conducted between September 2019 and January 2020. The rest of the paper is organized as follows. Section 2 summarizes the past development of SWOT oceanographic Cal/Val and the in situ field campaigns. The summary provides the background and motivation of this study. Section 3 discusses the instrumentation of the 2019/20 field campaign. Results are shown in section 4. Uncertainties in the observations and quantifications exist and are discussed in section 5. Summaries are presented in section 6.

2. The development of SWOT SSH Cal/Val

This section reviews the previous work in developing an in situ observing array for the SWOT oceanographic Cal/Val. Section 2a introduces the nature of the SWOT SSH Cal/Val. Section 2b discusses the theoretical basis for conducting oceanographic Cal/Val through in situ mooring platforms. Section 2c reviews the previous OSSE results. Section 2d discusses the transformation of the measurement errors from wavenumber spectrum to time series measurement at a single point and provides accuracy requirements imposed on individual observing platforms used in the field campaign. Section 2e briefly reviews a pilot field campaign that took place prior to the recent 2019/20 field campaign.

a. *SWOT SSH Cal/Val*

After the SWOT satellite launch, the first 90 days will be dedicated to instrument hardware checkout. The second 90 days will be for the mission Cal/Val along a 1-day-repeat orbit (Desai et al. 2018). The 90-day Cal/Val orbit provides more frequent SSH measurements at certain locations for both the validation of the instrument and to develop an understanding of the SWOT measurements from an oceanographic perspective at a very early stage. The SWOT mission Cal/Val has two aspects: 1) characterizing the performance of the instrument KaRIn from a *geodetic* perspective and 2) characterizing the SWOT-observed variability from an *oceanographic* perspective.

Recent studies have shown that the superposition of eddies and internal gravity waves in SSH may make the interpretation of SWOT observations complicated (Rocha et al. 2016; Qiu et al. 2018; Torres et al. 2018; Morrow et al. 2019). When considering the exploratory nature of the SWOT mission as the next-generation altimeter, it is crucially important that we use this 1-day repeat fast-sampling period, in which the satellite will overfly ground-track crossover region twice a day. The results will shed light on the connection of the SWOT SSH to the dynamics of ocean circulation beneath the sea surface (e.g., d'Ovidio et al. 2019), which is the mission's ultimate science goal for oceanography.

b. *Closing the SSH budget using in situ observations*

The ocean dynamics governing the large and mesoscale SSH variability have been the subject of intensive research over the past few decades, stimulated in part by satellite altimetry (e.g., Fu and Cazenave 2001). The SSH signal that has spatial scales smaller than mesoscale, however, has not yet been fully explored, largely because of lack of observations. The first task is to understand the observability of SSH at scales of ~150 km and smaller. To what level of accuracy can we close the SSH budget (formulated below) using available in situ instruments and platforms?

Integrating the hydrostatic equation $dp/dz = \rho g$ from the ocean floor to the free surface, the SSH budget equation can be written as

$$p(-H) = \int_{-H}^{\eta} g\rho(z)\, dz + p_a,$$

in which $-H$ is the depth of the ocean floor, η is the free sea surface height, p_a is the atmospheric pressure. We are interested in the temporal variability. Decomposing each term into a temporal mean (overline) and an anomaly (prime) gives

$$\begin{aligned} \overline{p}(-H) &= \int_{-H}^{0} g\overline{\rho(z)}\, dz + g\rho_0\overline{\eta} + \overline{p_a}, \\ p'(-H) &= \int_{-H}^{0} g\rho'\, dz + g\rho_0\eta' + p'_a, \end{aligned} \tag{1}$$

where ρ_0 the reference density, ρ' the in situ density anomaly, η' the sea surface height anomaly referenced to $\overline{\eta}$, p'_a the atmospheric pressure anomaly. The term $g\eta'\rho'$ is second order and neglected. $\overline{\eta}\rho'$ is implicitly included in the first term on the right hand by taking $z = 0$ at $\overline{\eta}$. The four terms in Eq. (1) represent temporal anomalies of bottom pressure, dynamic height, sea surface pressure due to the free surface, and atmospheric pressure. These terms from left to right can be assessed by bottom pressure recorders (BPR), moorings with CTDs, GPS buoys, and barometers, respectively. We test the closure of Eq. (1) using GPS, BPR, and mooring CTDs in section 4b.

Note that the dominant variability in both the bottom pressure and the free sea surface elevation is nonsteric, such as the barotropic tides. The steric component is much weaker, typically only on the order of a few centimeters.

Denote the steric and nonsteric components of the sea surface height and bottom pressure as η', $\eta'_{\rm ns}$, $p'_{\rm bs}$, and $p'_{\rm bns}$, respectively. We further expand Eq. (1) into

$$p'_{\rm bs} + p'_{\rm bns} = \int_{-H}^{0} g\rho'\,dz + g\rho_0 s'_\eta + g\rho_0\eta'_{\rm ns} + p'_a. \qquad (2)$$

The cancellation of the nonsteric components is written as $p'_{\rm bns} = g\rho_0\eta'_{\rm ns} + p'_a$. After removing the nonsteric components, Eq. (2) becomes

$$p'_{\rm bs} - g\rho_0\eta'_s = \int_{-H}^{0} g\rho'\,dz. \qquad (3)$$

Equation (3) means that the dynamic height due to the density change can be calculated directly from density profiles or indirectly calculated from bottom pressure and steric sea surface height (after the atmospheric pressure correction). In reality, the steric and nonsteric components are impossible to separate from bottom pressure or GPS free sea surface based on a single mooring as a result of an underdetermined problem. Equation (3) is only used to illustrate the meaning of the closure of the SSH equation. It is worth noting that deriving $O(1)$ cm steric height from $O(100)$ cm GPS SSH and BP-derived SSH requires extreme accuracy in both instruments. For this reason, one of the objectives of the SWOT prelaunch campaigns (sections 2e and 3) was to examine the closure of the hydrostatic equation [Eq. (1)] and to quantify the errors associated with different platforms and instruments.

c. An OSSE

An OSSE was first conducted to understand the SSH signal at SWOT scales and the performance of different instruments and platforms in meeting the SWOT requirement (Wang et al. 2018). We used a tide-resolving high-resolution global ocean simulation as a virtual ocean and simulated the performance of several instruments/platforms commonly used in modern observational physical oceanography, i.e., underway CTDs (UCTD), gliders, fixed-CTD moorings, pressure inverted echo sounders (PIES). The model simulation is the high-resolution global ocean simulation using MITgcm with 1/48° horizontal resolution, llc4320, used in several recent studies (e.g., Rocha et al. 2016; Torres et al. 2018; Su et al. 2018; Yu et al. 2019). One conclusion was that in the Cal/Val region (near 35.7°N, 124.7°W) the total SSH over the 15–150 km wavelength range (SWOT scale) can be represented by the upper-ocean steric height after the large-scale barotropic signal and inverted barometer (IB) influence are removed through a high-pass filter. The residual is well below the mission error requirement shown in the error wavenumber spectrum in the OSSE study.

The OSSE study also found that internal gravity waves and internal tides (IGW) might be strong enough to mask the eddy field SSH signal over the small spatial scales and impose an observational challenge (Wang et al. 2018). This dominance of IGWs over small scales is simply because the SSH wavenumber spectrum of eddies (balanced motions) is steeper than that of IGWs (Qiu et al. 2018; Chereskin et al. 2019; Callies and Wu 2019). The presence of internal gravity wave motions on these scales poses a challenge for designing an in situ observational network. For example, through the OSSE we found that slow platforms such as ship-towed UCTD are unable to meet the Cal/Val requirement. An array of station-keeping gliders can marginally meet the requirements, but the errors are mostly over small spatial scales (~50 km) due to the high-frequency motions. PIES can empirically convert the travel time of an acoustic signal to steric height but have about 5 cm uncertainty (D. R. Watts 2016, personal communication; Wang et al. 2018), which is larger than SWOT's subcentimeter requirement. The OSSE study concluded that an array of CTD-equipped moorings could produce a steric height field that is sufficiently accurate to meet the requirement.

The numerical ocean simulation used in the OSSE, however, has excessive tidal energy (C. Wunsch 2017, personal communication; Savage et al. 2017; Yu et al. 2019), which introduces large uncertainties in the OSSE results. It is also not clear how well the deep-ocean variability is reproduced. Field experiments are necessary to test the performance of different platforms and instruments. In addition, while the OSSE focused on oceanographic Cal/Val, the geodetic SSH such as measured by GPS buoys needs to be evaluated to synthesize the oceanographic and geodetic objectives. It led to two objectives of the field campaigns: 1) quantify the performance of oceanographic in situ platforms and 2) test the GPS measurements and their relationship with those derived from hydrographic measurements.

d. SWOT measurement error requirement

In the two field campaigns described in the next section, we do not have a full-scale mooring array that enables a wavenumber spectrum calculation. To evaluate the performance of an in situ instrument, the SWOT error requirement in wavenumber space needs to be integrated over a range of wavenumbers $\int E(k)$ to assess time series in situ measurement. The mission requirement is specified between 15 and 1000 km wavelengths. The baseline error[1] is

[1] The "baseline error" is the error the mission currently plans to achieve. The "threshold error" is the error level that the mission must achieve to address the minimum science goals.

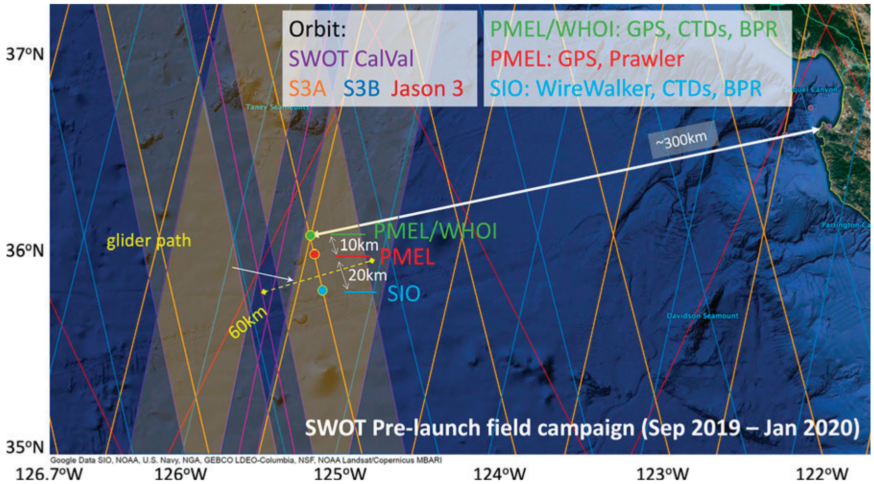

FIG. 2. Map of the field campaign instrumentation. The three moorings are marked by the three colored dots. From north to south, they are the PMEL/WHOI mooring, the PMEL Prawler mooring with GPS on the buoy, and the SIO full-depth mooring. The separation distance is 10 and 20 km. The dashed yellow line is the glider target path of 60 km wide. Two bottom pressure recorders were deployed near the PMEL/WHOI and SIO moorings.

$E(k) = 4\ \mathrm{cm}^2\ \mathrm{cpkm}^{-1} + 0.00125k^{-2}$, where k is the wavenumber with a unit of cycle km^{-1} (cpkm) and $2\ \mathrm{cm}^2\ \mathrm{cpkm}^{-1}$ is the KaRIn instrument noise averaged across a swath over 7.5 km distance for significant wave height (SWH) of 2 m (Fig. 1, red line). The threshold error requirement is similar: $E(k) = 4\ \mathrm{cm}^2\ \mathrm{cpkm}^{-1} + 0.0015k^{-2}$ (Fig. 1, blue line).

For the spatial range between 15 and 1000 km, an integration of the error based on the requirement is $\int_{1\times10^{-3}}^{1/15} E(k)\,dk = 1.36\ \mathrm{cm}^2$, i.e., 1.17 cm RMS. If only the 15–150 km range is considered, the total integrated error has 0.29 cm^2 variance (0.54 cm RMS), the integrated random KaRIn noise is 0.12 cm^2 (0.35 cm RMS), and the integrated correlated error (cpkm) is 0.17 cm^2 (0.41 cm RMS). The 0.54 cm number represents a target accuracy needed for validating SSH measurements in the presence of oceanographic "noise," i.e., an upper limit for errors in observing ocean processes including those which are correlated on the scales of interest. These are the signals analyzed in this study. The 0.35 cm value is a requirement for inherent sensor/platform/sampling error at a single location that is uncorrelated from platform to platform.

The postlaunch Cal/Val approach involves calculating the wavenumber spectrum of the difference between the SWOT SSH measurement and the mooring-derived SSH during the SWOT overflight of the mooring array. A spatial linear trend over the length of the mooring array will be removed before calculating the wavenumber spectrum. This detrending operation minimizes the effects of the scales longer than those of the in situ Cal/Val. Such a difference spectrum is considered a snapshot of the measurement error spectrum, which will be averaged over the 90-day Cal/Val period to achieve statistical assessment of the SWOT performance.

Ideally, we would like to test the mooring capability using an array of moorings covering ~150 km. However, owing to the limited budget, we deployed three moorings spanning 30 km (Fig. 2). The evaluation of the mooring capability discussed in the following sections will be unavoidably influenced by the large-scale signals that are irrelevant to SWOT short-wavelength Cal/Val. It is thus difficult to rigorously define measurement requirement for a single mooring. However, from analysis of ocean model simulations (Torres et al. 2018), the temporal scales corresponding to 15–150 km wavelengths are roughly 2–14 days. We therefore impose the following for the requirement for the in situ SSH observations: Integrated over periods of 2–14 days, the RMS error shall not exceed 0.54 cm. A caveat is that this criterion is not rigorously derived due to insufficient mooring measurements and is only used as a guideline. The spatial–temporal separation can be directly calculated during the postlaunch Cal/Val where an order of 10 moorings will be deployed along a line under a SWOT swath (section 5).

e. The 2017 pilot field campaign

The first field campaign was conducted in Monterey Bay, California, during June/July 2017. Two gliders, one BPR, and a GPS buoy (Haines et al. 2017) were deployed near the Monterey Bay Aquarium Research Institute (MBARI) M_1 mooring. The two gliders sampled the upper 500 m near the mooring at 36.75°N, 122.03°W. The first objective was to quantify the capability of station-keeping gliders in constructing the high-resolution steric height derived from a fixed instrumented mooring. The second objective was to examine the connection between GPS-observed SSH that resembles spaceborne measurements and steric height that represents the ocean circulation.

The 2017 pilot campaign successfully tested the first objective, but not the second one. In particular, the results have not yet yielded satisfying closure between the GPS-derived SSH and upper-ocean steric height. The campaign took place 20 km from the shore, with the GPS buoy situated over the steep walls of the Monterey submarine canyon. One of the challenges was the large mean sea surface (geoid) gradient, which contributes to the time variation in GPS-derived SSH as the buoy meandered over the canyon wall and within the watch circle. This nearshore location was also dominated by nonsteric processes, making the site less representative of the open-ocean conditions expected near the SWOT Cal/Val crossover location. The campaign, however, shed new light on the challenges of reconciling SSH (from surface GPS or satellites such as SWOT) with steric height (from gliders and moorings), and the outcomes helped to inform the architecture of the subsequent 2019/20 prelaunch campaign reported in this paper. The next section provides the general information about this campaign.

3. The 2019/20 prelaunch field campaign

The 2019/20 prelaunch field campaign was conducted near the SWOT Cal/Val crossover location, about 300 km west of Monterey, California (Fig. 2), between September 2019 and January 2020. It was designed to mainly 1) test the closure of the SSH equation, which was not satisfactorily addressed in the 2017 field campaign, and 2) quantify the error in steric height using different platforms. There are six specific objectives: 1) test the SSH budget closure with GPS buoy, CTD mooring, and BPR following Eq. (1); 2) evaluate the vertical scale of SSH at the SWOT scales for different frequency bands; 3) evaluate the role of bottom pressure in SWOT SSH signals; 4) evaluate the small-scale steric height information; 5) evaluate the reconstruction of the upper-ocean circulation; and 6) provide information for the design of the postlaunch in situ observing system. We will mainly focus on 1–4 in this paper. The outcome will aid the design of the postlaunch in situ field campaign for SWOT Cal/Val.

Six institutions participated in the campaign: Jet Propulsion Laboratory, NOAA Pacific Marine Environmental Laboratory, Wood Hole Oceanographic Institution, Scripps Institution of Oceanography, Rutgers, and Remote Sensing Solutions. Three moorings and two BPRs were deployed between 1 and 7 September 2019, and recovered between 16 and 21 January 2020. One Slocum glider was deployed from Monterey Bay and piloted to the mooring locations around mid-September 2019.

The three moorings are 1) the PMEL/WHOI (*northern mooring*) configured with a GPS buoy and 18 fixed CTDs from surface to the bottom, 2) the PMEL GPS mooring (*middle mooring*) with a Prawler (Osse et al. 2015) sampling the upper-500-m temperature and salinity (*T*/*S*), and 3) the Scripps Institution of Oceanography (SIO) mooring (*southern mooring*) with a Wirewalker (Pinkel et al. 2011) sampling the top 500 m and fixed, real-time telemetered CTDs between 500 m and ocean floor. The mooring array was placed along a *Sentinel-3A* ground track, which fortuitously was in the middle of a SWOT swath along the Cal/Val orbit. The separation distances are 10 and 20 km for the northern and southern pairings, respectively, to support testing of small-scale SSH variability not resolved by conventional satellite altimeters. During the first phase of the campaign, the glider sampled a 60-km-long section perpendicular to the mooring line (Fig. 2) with a 1000 m dive depth, which was chosen to minimize the travel time for the 60 km section. During the second phase, the glider performed station keeping near the three moorings for cross calibration. The glider stayed at each mooring for about 5 days. The PMEL BPR is near the northern mooring and a PIES was deployed at the southern mooring location.

a. GPS measurements of SSH

A modular, low-power, high-accuracy GNSS measurement system was designed for long-term, continuous, and autonomous measurements of SSH on ocean- and cryosphere-observing platforms (Haines et al. 2017; Guthrie et al. 2020). It results from a joint project between NASA JPL, NOAA PMEL, and the University of Washington. The project aims to probe the limit of new kinematic precise-point positioning (PPP) techniques for accurately determining sea surface height and recovering neutral and charged atmosphere characteristics; and explore the potential scientific benefits—in the fields of physical oceanography, weather, and space weather—of accurate GNSS observations from a global ocean network of floating platforms. It integrates a Septentrio dual-frequency GPS receiver and a PMEL buoy. The receiver is low power (~1 W) and is accompanied by a miniaturized digital compass (for attitude information) and a load cell (to measure force on the mooring line). The buoy communicates using Iridium, and the payload is adaptable to multiple floating platforms such as surface buoys, wave gliders. When coupled with advanced precise point positioning techniques (Bertiger et al. 2010), the observations collected by the GPS buoy enable geodetic-quality solutions in remote locations without nearby reference stations.

The GPS level-2 data have 1-Hz temporal frequency, processed to accurate 3D positions using the GipsyX software (Bertiger et al. 2020) with units of meters for the height component. These high-frequency data were binned to hourly average to remove the surface gravity waves (Fig. 3). The hourly data were then corrected for an apparent systematic sea-state bias (estimated empirically), solid tides, line tension, mean sea surface (MSS), and IB effect. The MSS correction is important for comparing GPS-SSH with steric height because the horizontal displacement of the GPS buoy within its watch circle can project geoid variations into the GPS time series. This spatial-to-temporal projection is especially significant over steep bathymetry, which was the case during the 2017 field campaign, where the GPS buoy was placed near the Monterey submarine canyon and the spatial geoid variations were as large as 10 cm within the mooring watch circle of 2 km radius, but less significant over the prelaunch campaign region where ocean bathymetry is rather flat. The IB correction (Wunsch and Stammer 1997) follows IB (mm) = $-9.948p'$, where p' is the sea level pressure anomaly. The final derived SSH after the MSS and IB corrections was then detrended over the 4-month period (mid-September 2019 to mid-January 2020).

The GPS buoy system has developed from campaigns undertaken in progressively more challenging conditions.

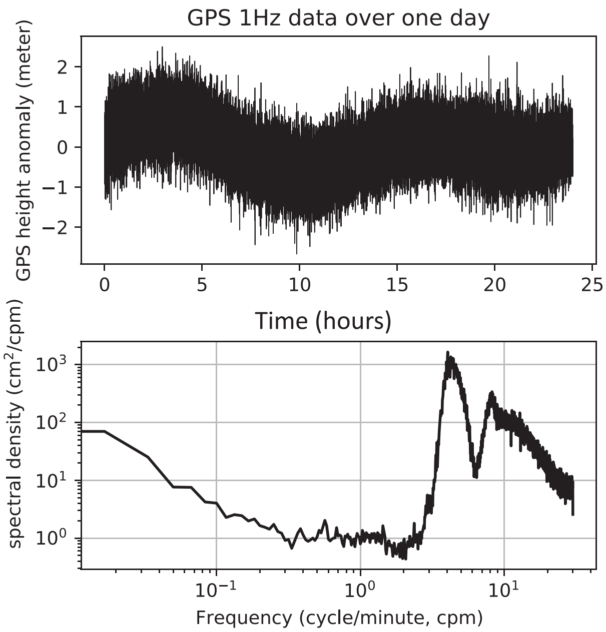

FIG. 3. (top) The 1-Hz GPS measurement of SSH. (bottom) The frequency spectrum of the 1-Hz GPS SSH.

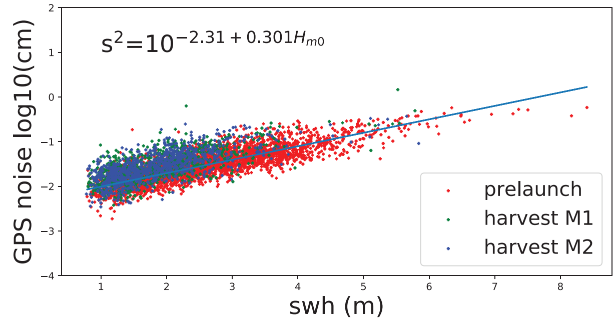

FIG. 4. The GPS error as a function of SWH derived from two SWOT prelaunch field campaigns described in section 2. The red dots are from the 2019 prelaunch field campaign and the green and blue dots are from the two GPS buoys of the 2017 pilot field campaign.

Nearly 1000 buoy days of data have been successfully collected since 2015, over SWH ranging from calm to 9 m. The GPS buoys have been an integral part of the SWOT pilot experiment in 2017 (Monterey Bay) and the prelaunch field campaign (2019/20). An example of the processed 1-Hz data is shown in Fig. 3. The 1-Hz sampling frequency is high enough to reveal detailed expressions of surface waves. The amplitude of the high-rate (1-Hz) height estimates reach 5 m for this day. The frequency spectrum illustrates the wind wave and swells by the two spectral peaks. SWH can also be derived from this 1-Hz data following SWH = 4 × RMS(SSH), where SSH is high-pass filtered with a cutoff frequency of 1 cycle min^{-1}.

We tried to estimate the GPS measurement errors in the context of the SWOT requirements. Without a true reference, we need to make assumptions in order to derive the error from the GPS measurement itself. We assume the minimum in the spectrum near 1 cycle min^{-1} reflects random instrument noise. As we are interested in ocean signals that are of periods longer than 1 h, the GPS error can be estimated by integrating the random noise spectrum, assumed constant taken as the value of the spectrum minimum near 1 cycle min^{-1}, over the frequency range (0–1 cycle h^{-1}). The SWH can be derived from the surface wave spectrum. We can split a long time series into 1-h-long segments, then derive an empirical relationship between GPS error and SWH. Based on the two SWOT prelaunch field tests, there is a clear relationship between SWH and GPS errors following a logarithmic function as shown in Fig. 4. The relationship is $S^2 = 10^{-2.31+0.3H_{m0}}$, where H_{m0} represents the SWH, and S^2 is the noise variance. Under these assumptions, the GPS error from a single buoy meets the SWOT mission geodetic requirement, i.e., 0.13 cm^2 for SWH < 4.1 m, which corresponds to 2 cm^2 cpkm^{-1} instrument noise in the wavenumber space (Fig. 1).

Other errors exist in addition to those induced by the surface waves. Those errors are correlated but difficult to unravel with a single GPS buoy. They will contribute to the total error presented in section 4. Residual atmospheric refraction delays are one of the dominant correlated error sources. As the ionospheric refraction is corrected to first order using the two GPS frequencies, the primary concern here is refraction from the troposphere. Taking advantage of mapping functions, the wet troposphere delay in the zenith direction is estimated along with the buoy position. Despite the relatively small magnitude, the wet component of the troposphere delay is highly variable and sometimes difficult to capture, especially during intense weather fronts with large atmospheric gradients. Other important systematic errors for the buoy technique are related to the platform altitude and to the force on the mooring line, both of which impact accurate modeling of the buoy's waterline and thus the SSH (Zhou et al. 2020). Here we use, respectively, the digital compass and load cell data from our payload package to mitigate these errors.

b. Hydrographic measurements

1) MOORINGS WITH FIXED-DEPTH CTD INSTRUMENTATION

The fixed-depth CTD mooring is one of the most conventional in situ platforms for observational oceanography. The CTDs used in the campaign are the Sea-Bird Electronics, model SBE-37. The SBE-37 can be configured with and without a pressure sensor. The pressures for those instruments without the corresponding sensors (from the northern mooring) were determined through interpolating from the next instruments above or below, using the known wire lengths between the instruments. For these fixed-depth CTDs, the distances between instruments along the mooring line are fixed, but the actual depths of the CTD instruments change over time. The amount of vertical excursion depends on the currents and winds as well as the mooring design: the northern mooring was a "slack mooring" (i.e., mooring line much longer than water depth) of an inverse catenary design with vertical sensor excursions up to about 300 m, while the southern mooring had a taut lower section that limited vertical excursions to about 60 m. The nominal depths of the fixed CTDs are (505, 618, 810, 1182, 1690, 2365, 3202, 4384) m on the southern mooring and (20, 30, 59, 107, 174, 261, 367, 492, 609, 805, 1180, 1408, 1692, 1909, 2189, 2488, 2750, 4545) m on the northern mooring.

A climatological mean in situ density profile is removed before the density anomalies are interpolated onto a uniform vertical grid to avoid interpolation error in calculating steric height. We have also used the mean profile constructed from all the measurements in the campaign instead of the climatological mean. No quantitative difference is observed. This procedure removes the spurious deep-ocean variability introduced by the vertical-to-temporal projection due to the vertical movement of the CTD sensors. The bottom CTD on the northern mooring was corrupted so the full-depth steric height was calculated with the assumption that the ocean below 3000 m has no temperature and salinity variability.

2) MOORINGS WITH PROFILERS

Two moorings had profilers with CTD instruments. The middle mooring had a Prawler that covered the upper 500 m with a Sea-Bird Electronics (SBE-PRAWLER) CTD, and the southern mooring had a Wirewalker in the upper 500 m with an RBR Concerto CTD. Profiling methods are not subject to errors due to vertical resolution, but the temporal resolution is less favorable. The Prawler was set to 8 profiles per day on average during the 2019/20 campaign. The number of profiles per day can be higher, but was chosen to test the endurance of the Prawler mooring. The Wirewalker on the southern mooring yielded about 80 up- and downcast profiles per day (i.e., ~7000 profiles, or 3500 vertical kilometers profiled over 86 days of deployment). The profiler CTDs pass through vertical gradients of temperature and conductivity in the upper ocean, which requires data processing to remove spikes in salinity, and to adjust for lagged sensor responses. After this alignment, vertical profiles of density with 1 and 0.25 m vertical resolution over the upper 500 m are produced for the Prawler and Wirewalker, respectively.

Below the profiler, the southern mooring featured additional, vertical fixed instrumentation. It used a taut mooring between the seafloor and 600 m, connected to the surface buoy via a reverse catenary inductive connection and the Wirewalker profiling wire. The taut mooring has a very small watch circle (<250 m) and so the fixed instruments stay within a narrow depth range. The inductive connection allowed real-time data from the fixed instruments all the way to the seafloor. This experimental mooring design is less tested, and the catenary wire parted after 86 days of the intended 90-day deployment.

3) UNDERWATER GLIDERS

The hydrography data collected by the gliders are similar to the moored profilers. Vertical resolution is high and requires no additional interpolation steps, although the same precautions against mismatched sensor response times and resulting spikes in salinity data need to be taken. Gliders have the advantage of mobility, but they may experience large horizontal deviation from target locations due to strong currents. A station-keeping glider can act as a virtual mooring. A glider that performs station keeping at different mooring locations can also be used for cross-mooring calibration and validation. The Slocum glider used in this campaign has a vertical speed of about 18–20 cm s^{-1} yielding ~30 profiles per day for 500 m dives.

4) APPROACH TO CALIBRATION AND VALIDATION OF CTD DATA

An effort was made to cross calibrate all CTD data to a common reference. For the fixed-depth, moored CTD instruments, this was done by attaching the mooring instruments to a recently calibrated, ship-based CTD and Rosette system, and then collecting vertical profiles with 10 min stops at several depths. At these dwell depths, water samples were taken for laboratory salinity measurements to provide an absolute salinity reference. This approach was carried out for mooring instruments both before mooring deployment and after mooring recovery. The method is described by Kanzow et al. (2006), and has the key advantage that all three sensors (conductivity, temperature, pressure) are adjusted independently of one another. Over the course of the mooring deployment, the corrections applied to the mooring data are shifted linearly from the predeployment to the postrecovery values. For temperature data, the adjustments are offsets added to the raw data. For conductivity data, the adjustments are gain factors multiplied by the raw data. For pressure data, the adjustments are a combination of a gain factor and an additive offset (Kanzow et al. 2006).

The glider was flown to the vicinity of each mooring on several occasions. A comparison of the glider data against the fixed-depth, cross-calibrated moored CTDs was used to adjust the glider conductivity with a gain factor, such that the temperature–salinity curves derived from the glider would best match those from the nearby mooring. This assumes that the glider temperature and pressure sensors are correct.

For the two moored profilers, two different approaches were done: The Prawler conductivity data were adjusted against the (adjusted) glider data, based on nudging the conductivity such that the temperature–salinity curves would be matched. For the Wirewalker on the southern mooring, a spare fixed-depth instrument that had the ship-based corrections was attached to the profiling body. The profiler conductivity was nudged against the data from this collocated instrument, again to best match the temperature–salinity relationship, but the comparison was restricted to deeper depths because the fixed-depth instrument does not have a sensor response time suitable for the upper-ocean profiles. For both moored profilers, the result is that the conductivity data are adjusted, while the temperature and pressure data are assumed correct, as for the gliders.

c. *Ocean bottom pressure*

There were two ocean bottom pressure instruments: the northern one was a system based on the DART tsunami detection technology (Meinig et al. 2005), and the southern one a PIES (pressure-sensing inverted echo sounder) (Watts and Rossby 1977). The actual pressure sensors are identical in the two systems (Paroscientific Digiquartz) that are operated at about 15-s acquisition times. The DART-based systems operate nearly continuously, while the PIES have a 10-min sampling interval. When subsampling a near-continuous DART-like record at 10-min resolution, hourly averages can be reproduced to about 0.5 mm accuracy. Availability of the data in near–real time depends on the available underwater communication systems, which typically operate acoustically at low bandwidth. For PIES, hourly data were telemetered on an irregular schedule during the 2017 field campaign, typically with several days' latency. The data transfer uses the nearby glider as a communication device. The northern ocean bottom pressure data were telemetered four times per day during the 2019/20 field campaign using an acoustic modem.

The absolute magnitudes of the pressure data are not particularly useful in the context of SWOT Cal/Val, for two reasons: first, calibration uncertainties typically result in offsets to the data, which are not constant but drift with time; second, the exact depths where the sensors are on the seafloor are not known, i.e., one cannot assign a known vertical coordinate to the data. Therefore, a time mean that includes sensor drift is subtracted from the record. Following Eble and Gonzalez (1991), the preferred trend removal involves the sum of an exponentially decaying function and a linear trend. The variability in the residuals is then dominated by tidal signals. From comparing different tide removal algorithms, such as harmonic fits with different tidal constituents as well as low-pass filters of the data, coherent tidal signals can be removed.

d. Auxiliary datasets

GPS measures total SSH, so it is the closest equivalence of SWOT SSH. GPS SSH and SWOT SSH will share the same MSS and IB corrections. For the MSS correction, we used an MSS height model (MSSCNESCLS19), which is based on all available radar altimeter data (Schaeffer et al. 2018) with 16–20 km spatial resolution. The hourly ERA5 atmospheric pressure (Copernicus Climate Change Service 2017; Hersbach et al., 2020) used for IB correction and the gridded DUACS-DT2018 L4 SSH product (Pujol et al. 2016; Taburet et al. 2019) and *Sentinel-3A* L2P data are provided by Copernicus Climate Change Service (2017).

4. Results

a. Large and mesoscale background during the campaign

The campaign was conducted in the California Current system, a typical eastern boundary current system that comprises a wind-driven coastal upwelling and equatorward surface current. It is one of the best-studied and longest-observed regions in the world oceans (e.g., Hickey 1979; Flament et al. 1985; Ikeda and Emery 1984; Capet et al. 2008a,b; Collins et al. 2013; Rudnick et al. 2017; and many others). The coastal upwelling driven by the equatorward alongshore wind during summer brings cold waters to the surface (Fig. 5d), which introduces strong thermal fronts next to the warmer open ocean to form a southward California Current. This upwelled water also contains abundant nutrients to support the dynamic ecosystem indicated by the high chlorophyll concentration (Fig. 5e).

Mesoscale and submesoscale eddies are ubiquitous in the California Current System (CCS). The cold coastal water often pinches off from the coastal current and drifts westward into the open ocean supporting the coastal–open-ocean exchange of water masses (e.g., Strub and James 2000, among numerous others). Meanwhile, this offshore transport of mass and heat is balanced by the onshore transport of the deep open-ocean water that feeds the upwelling and the horizontal onshore transport by mesoscale and submesoscale eddies.

During the period of the 2019/20 prelaunch field campaign, the mooring array observed the formation of a warm-core anticyclonic mesoscale eddy. The process started from a southward flow meander at the beginning of the campaign around early September 2019 (Fig. 5a). The meander started to stretch and fold, a typical evolution of baroclinic instability, during October 2019 (Fig. 5b), which eventually detached from the initial meander to form a coherent mesoscale eddy near the end of the campaign (Fig. 5c). The mature mesoscale eddy trapped the warm, nutrient-scarce open-ocean water and drifted shoreward to resupply and mix with coastal water. During this evolution, the three moorings were within the meander at the start of the deployment and on the edge of the formed eddy by the end of the deployment. From the mesoscale perspective, then, the observations during the campaign were skewed toward ocean dynamics of a meander and the edge of a mesoscale eddy in CCS. Detailed in-depth analyses of the underlying mesoscale dynamics are not a focus of this paper and will be reported elsewhere.

b. SSH closure

As discussed in section 2b, one can derive an equivalent full-depth steric height from GPS, BPR, and atmospheric pressure through the hydrostatic equation. The derived full-depth steric height is then compared with the steric height derived from hydrographic measurements through mooring CTDs. Their differences contain the errors in both GPS-derived and CTD-derived steric heights.

Figure 6 shows the hourly steric height derived from GPS/BPR (red) and 6-min-resolution steric height from hydrographic measurements (blue). The top panel shows the full-time series for four months. The bottom panel shows the details of the time series over a 10-day period. The two independently derived steric height time series agree over low frequencies (top panel) and over major tidal frequencies (bottom panel). Note that the barotropic tides are eliminated by the difference between the GPS SSH and BPR-derived SSH, leaving the residuals at tidal frequencies, the baroclinic internal tides.

The total RMSE between the two derived steric heights is 2 cm, but they also depend on the sea state as shown by the single GPS analyses (Fig. 4). To our knowledge, this is the first demonstration that the GPS-/BPR-derived sea surface height is equivalent to the steric height measured concurrently in

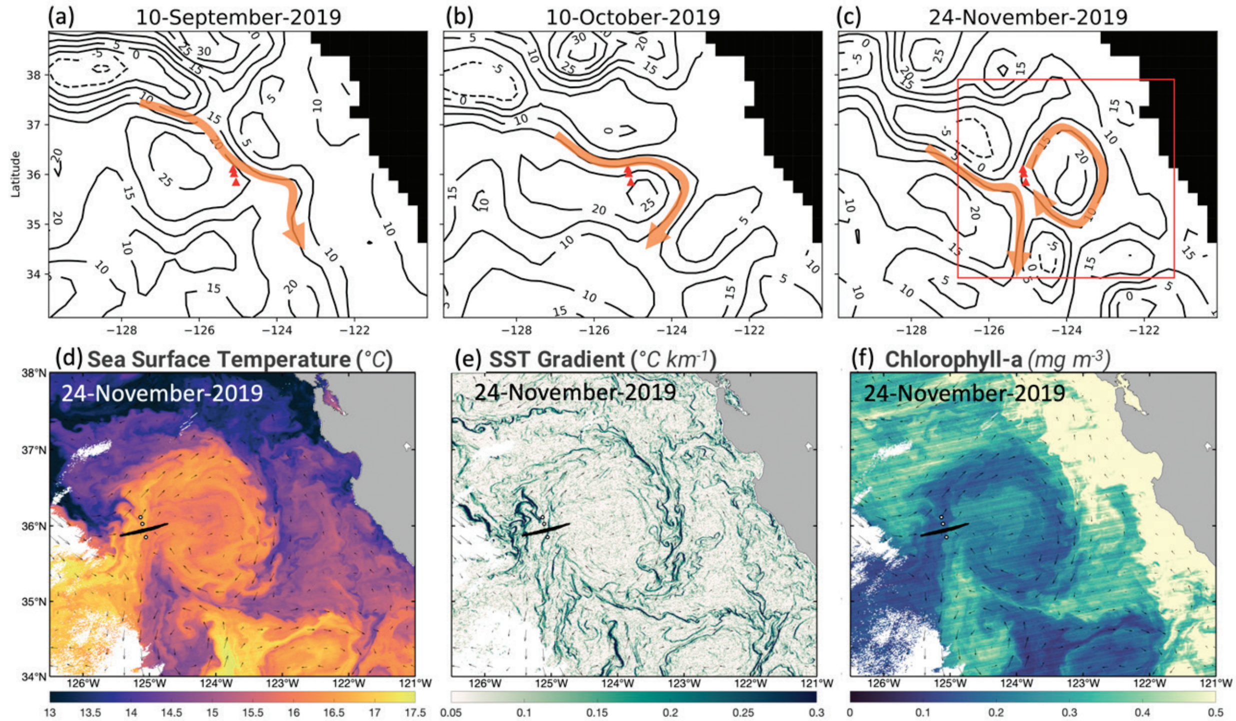

FIG. 5. (a)–(c) The altimetric sea level anomaly (SLA) on 10 Sep, 10 Oct, and 24 Nov 2019 corresponding to the beginning, middle, and end of the campaign, respectively. The thick orange arrows show the pinch-off of mesoscale eddy from the meander of the California current. The three red triangles mark the three mooring locations. The red box in (c) marks the domain boundary for (d)–(f) he SST and surface chlorophyll-a after the eddy formed approximately on 24 Nov (an ascending 750 m resolution swath from VIIRS *Suomi NPP* L2 taken at 2100 UTC). The black lines (60 km long) in (d)–(f) mark the glider flight path.

situ, indicating that the GNSS GPS system is accurate enough to measure the oceanic baroclinic signals.

The difference between the two steric height time series is further binned into different sea states characterized by SWH. As expected, the RMS difference between the two is a function of sea state (Fig. 7). The RMS difference is about 1 cm for calm seas with SWH $<$ 1 m, 1.7 cm for SWH = 2 m, and 3 cm for SWH $>$ 6 m. These GPS errors may be of large scale and not contribute to 15–150-km-scale errors that are of primary interest here. Detailed discussions are given in section 5.

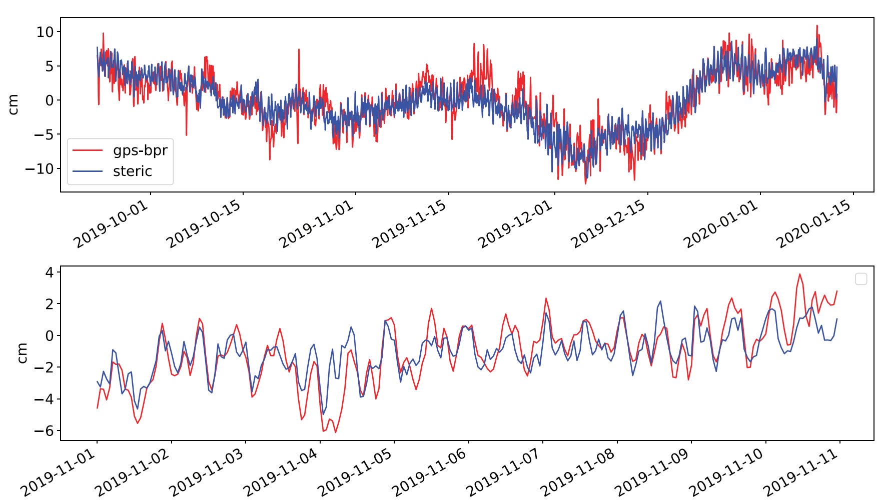

FIG. 6. (top) The steric height from the hydrographic measurements (blue) and the GPS-BPR-derived dynamic SSH. (bottom) As in the top panel, but for a short period (10 days).

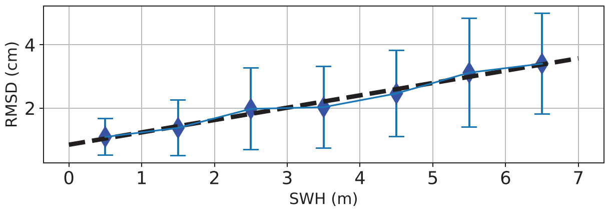

FIG. 7. The RMS difference (RMSD) between the steric heights derived from GPS/BPR and mooring CTDs as a function of significant wave height (SWH). The diamond symbols represent the mean RMSD binned to SWH values with a 1 m bin width. The error bars show the standard deviation of the absolute difference as an uncertainty measure. The line is the linear fit to the mean following RMSD=0.84 + 0.4SWH (cm).

The difference between GPS-derived and CTD-derived steric height can be scrutinized in frequency space, where we may identify the error sources. The GPS-based and CTD-based steric heights match at low frequencies with equal power spectral density within the 95% uncertainty bounds (Fig. 8). The major difference starts to show for periods less than 10 days, except for several major tidal periods such as M_2 and M_4 where the spectral peaks and coherence are significant. This is visible from the time series in Fig. 6. It is interesting to note that the coherence is high at 7.6-h period, which corresponding to the frequency of nonlinear interaction between inertial motions and semidiurnal tide denoted fM_2 (Mihaly et al. 1998).

The amplification of the differences over short periods less than 10 days is not fully understood, but could be related to the cadence of weather systems. The largest dispersions are sporadic in time (Fig. 6) and have a linear relationship with sea state (Fig. 7), and could also reflect refraction errors for the GPS systems. Errors in CTD-derived steric height exist but should not be a function of sea state and are less likely to be the dominant error source. The major difference between red and blue lines in Fig. 6 probably arises from the GPS-derived steric heights, which reflect not only GPS errors but also the errors in the IB correction through ERA5 and errors from MSS uncertainties. However, these errors may well be of large spatial scales that are less relevant to the SWOT in situ Cal/Val focus in this region (<150 km; Wang et al. 2018). If the GPS and IB related uncertainty/errors have large spatial scales, they can be removed through a spatial high-pass filter or simply by removing a linear trend along a 150 km distance as done in Wang et al. (2018).

c. *The vertical scale*

To minimize the cost of the postlaunch in situ Cal/Val, we may need to tolerate some uncertainties due to missing direct

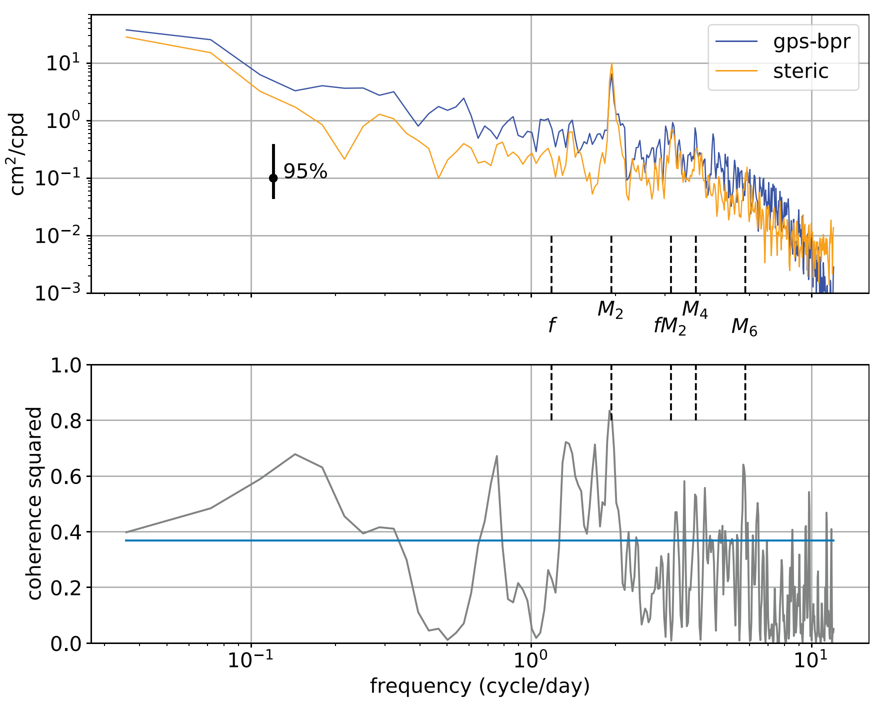

FIG. 8. (top) The frequency spectrum of the full-depth steric height (orange) [right-hand side of Eq. (3)] and the GPS-derived dynamic SSH (blue) [left-hand side of Eq. (3)]. The spectra are calculated using the Welch method with four nonoverlapped segments giving a degree of freedom (DOF) of 8. A Hanning windowing and linear-detrend operation were applied. The 95% significance level with DOF = 8 is shown by the black vertical bar. (bottom) The magnitude-squared coherence between the two time series using the Welch method with the same number of segments and DOF. The blue horizontal line marks the 95% significant level with DOF = 8.

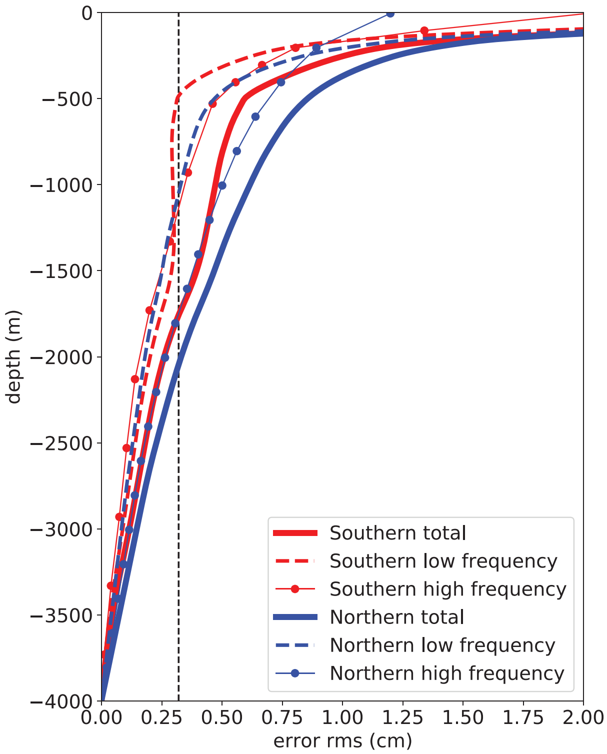

FIG. 9. The RMSE $\epsilon(z)$ of the upper-ocean steric height relative to full-depth steric height as a function of integration depth. Because the bottom CTD on the northern mooring was corrupted, we chose 4000 m as the deep-ocean reference for both moorings. By definition, the error decreases when the integration depth gets deeper and reaches zero at the bottom (4000 m in this case). The southern mooring is shown in red and the northern mooring in blue. The thick solid lines are for the total signals, the dashed lines for low frequency (>48 h), and the thin solid–dot lines for high frequencies (<48 h). The black dashed vertical line marks the 0.32 cm RMS level, which is derived from 2 cm^2 cpkm^{-1} wavenumber spectrum noise level for stations separated by 10 km.

measurements of the deep ocean. How deep do we have to measure the ocean to generate a steric height accurate enough for SWOT Cal/Val?

The uncertainty introduced by missing deep-ocean measurement below a depth z is defined as the steric height integrated between ocean bottom and z:

$$\eta_{\text{deep}}(z) = -\int_{-H}^{z} \frac{\rho'(z')}{\rho_{\text{ref}}}\ dz',$$

where ρ' is the in situ density anomaly deviation from a time-mean density profile $\overline{\rho}(z)$, and ρ_{ref} is the mean in situ density (set to 1035 kg m^{-3} here). We quantify the uncertainty using the standard deviation of this deep-ocean steric height $\epsilon(z) = \text{std}[(\eta_{\text{deep}}(z))]$.

The results based on the northern and southern mooring are shown in Fig. 9. The $\epsilon(z)$ decreases toward the deeper ocean as defined but with a larger rate in the southern mooring (thick red) than the northern mooring (thick blue). The different vertical scales between the northern and the southern moorings may be caused by different dynamic regimes experienced by the two moorings. The 500 m depth is of particular interest because that is roughly the bottom depth of the Prawler and Wirewalker platform. Table 1 lists some relevant numbers about the errors $\epsilon(500)$. The total error $\epsilon(500)$, i.e., the error of missing the deep ocean below 500 m, is 0.61 ± 0.1 and 0.84 ± 0.17 cm for the southern and northern mooring, respectively. The errors represent the mean RMS and the standard deviation in a time series of $\epsilon(500)$ calculated based on segments of a 10-day duration subsampled from either the original or the filtered time series. The error amplitude changes over time. Most of these errors come from high-frequency processes with periods less than 2 days (we will use the format $T < 2$ d hereafter). They are 0.51 ± 0.06 and 0.67 ± 0.14 cm for the southern and northern moorings, respectively. The low-frequency (2–14 d) component on the other hand has errors less than 0.15 ± 0.1 cm for both moorings, accounting for less than 4% of total variance (Table 1). The deep-ocean (<−500 m) steric height has a 0.5–0.7 cm RMS values and accounts for 5% of the full-depth steric height for high frequencies with periods less than 2 days at the southern mooring. This ratio becomes 30% at the northern mooring. The northern mooring particularly presents a higher deep-ocean high-frequency variability. The causality cannot be confirmed without more independent observations. It may be caused by the topographically generated deep-ocean internal tide/wave signal that is strong for the northern mooring, or simply because of the errors in determining the depths of the deep CTDs, which have large vertical excursions.

The spectrum of the upper-500-m steric height and the full-depth steric height and their coherence are shown in Fig. 10. We used the Welch method with a Hanning window. The full time series is split into nonoverlapping segments. The steric heights of the upper 500 m (blue) and of the full depth (orange) agree well over subinertial frequencies with similar spectra density and high coherence for both moorings. The major difference comes from the superinertial frequencies, especially around the tidal frequencies at M_2 (and M_4 for the southern mooring). The errors are relatively high (green lines) but the coherence (red lines) is still large and significant

TABLE 1. Deep-ocean contribution to steric height ϵ(500 m) for the two moorings at different frequency bands. This represents the error by only measuring the upper 500 m.

	Total RMSE (cm)	2–14-day band (cm)	Variance percentage (2–14 days) (%)	High frequency (<2 days) (cm)	Variance percentage (<2 days) (%)
Southern	0.61 ± 0.1	0.14 ± 0.1	1	0.51 ± 0.06	5
Northern	0.83 ± 0.17	0.15 ± 0.07	3.4	0.67 ± 0.14	31

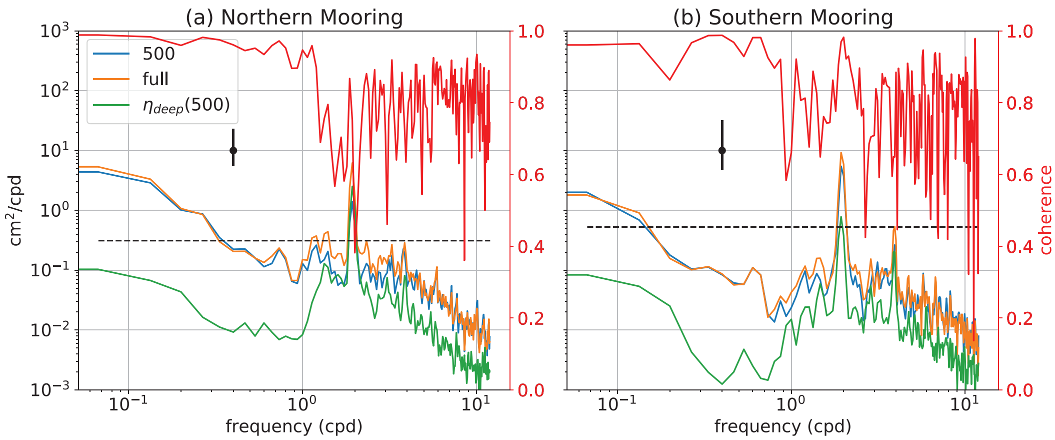

FIG. 10. The frequency spectra of 500 m (blue) and full-depth (orange) steric height and their difference (green) and the magnitude-squared coherence (red). The difference (green) is $\eta_{\text{deep}}(500)$. The spectra were calculated using Welch with nonoverlapping segments, each of which is of 15-day duration. The black error bar represents the 95% confidence interval. The degrees of freedom are 10 for the southern mooring and 18 for the northern mooring (due to its longer duration). The 95% significance level of the magnitude-squared coherence is shown by the dashed line: 0.31 and 0.53 for the northern and southern moorings, respectively.

(above 95% confidence level) for both moorings. This reflects that the superinertial motions, especially the semidiurnal internal tides, are of low baroclinic mode and reach deeper in depth than the subinertial submesoscale and mesoscale motions. [see also Lapeyre and Klein (2006) and LaCasce and Mahadevan (2006)].

The errors presented in this section include all spatial and temporal scales. Because of the SWOT focus on scales smaller than the mesoscale, correlated mesoscale scale error among the moorings can be removed, yielding a much smaller residual error budget. The high-frequency deep-ocean steric height with periods less than 2 days has 0.5–0.7 cm RMS and mostly from baroclinic tides (Fig. 10). If only the subinertial motions (2–14-day period) are considered, missing deep ocean introduce less than 2 mm error (Table 1), which is well below the KaRIn measurement error (0.54 cm RMS). These deep-ocean high-frequency signals require deep-reaching mooring CTDs.

d. Station-keeping glider as a virtual mooring

Gliders, unlike moorings, are mobile and add more flexibility to the campaign. We had one Slocum glider in the 2019/20 campaign for 1) testing the performance of a data assimilation system (Archer et al. 2022) and 2) testing the glider as a virtual mooring for the contingency of a failed mooring.

The glider vertical trajectories generally straight lines underwater, proceeding in a single direction fixed to a magnetic heading. This heading can be chosen to correct for ocean currents if one wishes to hold sampling lines. The downside of a single trajectory underwater means larger errors in station keeping and thus the ability to remain close to a single location. This is because of large distances traversed horizontally underwater, especially while diving deep.

To compensate for this and maintain a fixed position, the glider must have the ability to change heading underwater. It achieves this by maintaining a course of waypoints underwater which can be in any shape, for instance, a square, triangle, or even back and forth with two waypoints. Built into the underwater positioning is an algorithm to correct for estimated depth averaged current. This allows the underwater vehicle to continuously correct for current and maintain the same positions on Earth underwater for periods of several hours or more.

The Slocum glider's dive speed is about 18–20 cm s^{-1} yielding ~45 min per profile for a diving depth of 500 m. This will produce about 30 profiles a day. The capability of a station-keeping glider has been tested in our OSSE study (Wang et al. 2018) and the 2017 field campaign (Clark et al. 2018), where we confirmed that the glider-derived steric height matches the upper-ocean steric height from a nearby mooring for periods longer than 6 h with error-to-signal ratio smaller than 0.5 (figure not shown).

We tested the glider's station keeping again in the 2019/20 campaign and also used the glider as a conduit to connect and test the three moorings. The Slocum glider performed station keeping near the three moorings for three weeks between 27 November and 17 December 2019. The relative location of the glider flight path to three moorings are shown in Fig. 11. The glider stayed for about 3, 5.5, and 6.5 days around the southern, middle, and northern moorings, respectively. The associated mean glider–mooring distances are 1.2 ± 0.2 km, 0.8 ± 0.4 km, and 0.9 ± 0.2 km from south to north. The clusters of the glider surface locations have smaller circles referenced to its own center. The circles have a radius of 233, 350, and 520 m from north to south, respectively. The horizontal spread of the glider surface locations has a comparable size to the watch circle of the southern mooring during this period. A larger spread of the glider paths is expected for a longer duration and/or in a stronger flow field.

The Slocum glider's capability of being a virtual mooring was validated again in this campaign. The RMS difference

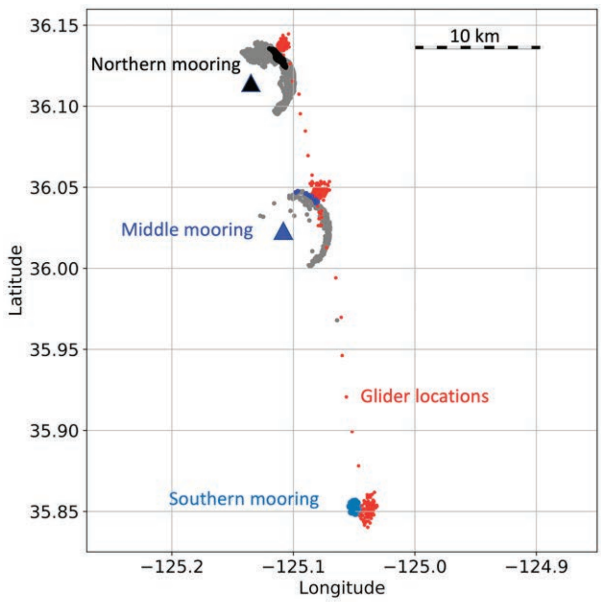

FIG. 11. The locations of the glider (red) and the northern mooring (black), the middle mooring (blue), and the southern mooring (navy blue) during the glider station-keeping phase, 27 Nov–17 Dec 2019. The mean separation distances during station keeping phase are 0.9 ± 0.2, 0.8 ± 0.4, and 1.2 ± 0.2 km for the northern, middle, and southern mooring, respectively. The two triangles show the anchor locations of the middle and northern moorings. The mooring watch circle shown by the gray dots has a radius of 4.5 km.

between glider and mooring upper-ocean (500 m) steric height is about 0.4–0.5 cm. Figure 12 (top panel) shows the time series of the upper-500 m steric height calculated from the glider (blue lines) and the moorings (orange lines). To avoid temporal interpolation errors, we used individual profiles to calculate the steric height without temporal interpolation between the subsurface temperature and salinity profiles. The time associated with the steric height of each profile was taken from the time at 250 m depth.

Figure 12 shows that the upper-500-m steric heights from glider and moorings are closely matched. The RMS differences are 0.4, 0.48, and 0.45 cm for the northern, middle, and southern mooring. The northern mooring has fixed CTDs binned to a 6-min grid close mooring–glider match confirms the capability of gliders to reproduce the upper-500-m steric height to time scales of several cycles per day.

The comparison of the glider to the northern mooring has the least RMS difference. The middle mooring was equipped with a Prawler, similar to a Wirewalker on the southern mooring, but was configured to sample about 8 profiles per day to test the endurance of the mooring. The larger RMS difference is mostly caused by the low temporal resolution (8 profiles per day) in mooring steric height (orange line/symbol in the top-center panel of Fig. 12). Because of the low temporal resolution, the middle mooring undersampled the internal tides especially the peaks that were captured by the glider. For example, the internal tidal variance at the beginning of 12 May 2019 is captured by the glider but not by the mooring (Fig. 12, top-center panel). This indicates the insufficiency of 8 profiles per day sampling frequency.

For the southern mooring comparison (top-right panel), there are superinertial variabilities in the mooring steric height largely captured by the glider except for the tidal peaks on 29 November. The glider dived to 1000 m at this location, so the temporal resolution is half that of the 500 m dives. The resulting lower temporal resolution in the glider steric height introduces an RMS difference 0.45 cm, which is larger than the 0.4 cm at the northern mooring. The time series comparison indicates that mapping the SSH variability due to the internal wave displacement of the density structure of the upper 500 m requires around 24 profiles per day. The spectral and coherence analyses shown in the bottom panel of Fig. 12 confirm the direct visual examination of the steric height time series discussed above. The glider steric height matches the northern mooring steric height in spectral density (bottom left, blue and orange lines) with high coherence (>0.6) down to approximately 5–6-h period (bottom left, purple line). For the middle mooring, because of the low temporal resolution in the mooring steric height, the glider–mooring only matches up to the M_2 tidal frequency, so ~8 profiles per day can resolve M_2 tides but not supertidal variabilities. For the southern mooring location (bottom-right panel), the mooring and glider match with high coherence (>0.6) down to a 6-h period.

In summary, the steric height derived from the glider matched the mooring upper-500-m steric height with 0.4–0.5 cm RMS difference. This largely validated the capability of gliders as a virtual mooring in the Cal/Val region with one caveat that the glider's error is referenced to the mooring's upper-ocean steric height, which itself carries about 0.6 cm uncertainty. Even though this uncertainty can be reduced by nearby deep-reaching CTD moorings with instruments in the deep ocean, the added uncertainty should be emphasized in a contingency scenario that a glider is needed to substitute a failed mooring.

e. *Spatial and temporal variability*

Each mooring produces a steric height time series. We can examine the temporal and frequency content of the signal. The spatial–temporal variabilities can be examined by combining the three moorings separated at 10 and 20 km even though a full wavenumber spectrum cannot be calculated across so few mooring separations.

1) TEMPORAL VARIABILITY

In the time domain, the mooring upper-500-m steric height closely follows the gridded SSH over long periods. Figure 13 shows the direct comparison between AVISO and the steric height of the northern and southern moorings (black solid and dashed lines). At the beginning of the campaign in early September 2019, the mooring steric heights and altimetric SSH are all at about approximately 76 cm level. This is associated with a south–north meandering current, whose SSH gradient is largest east–west perpendicular to the mooring array (Fig. 5a). When the meander curved toward the coast to form

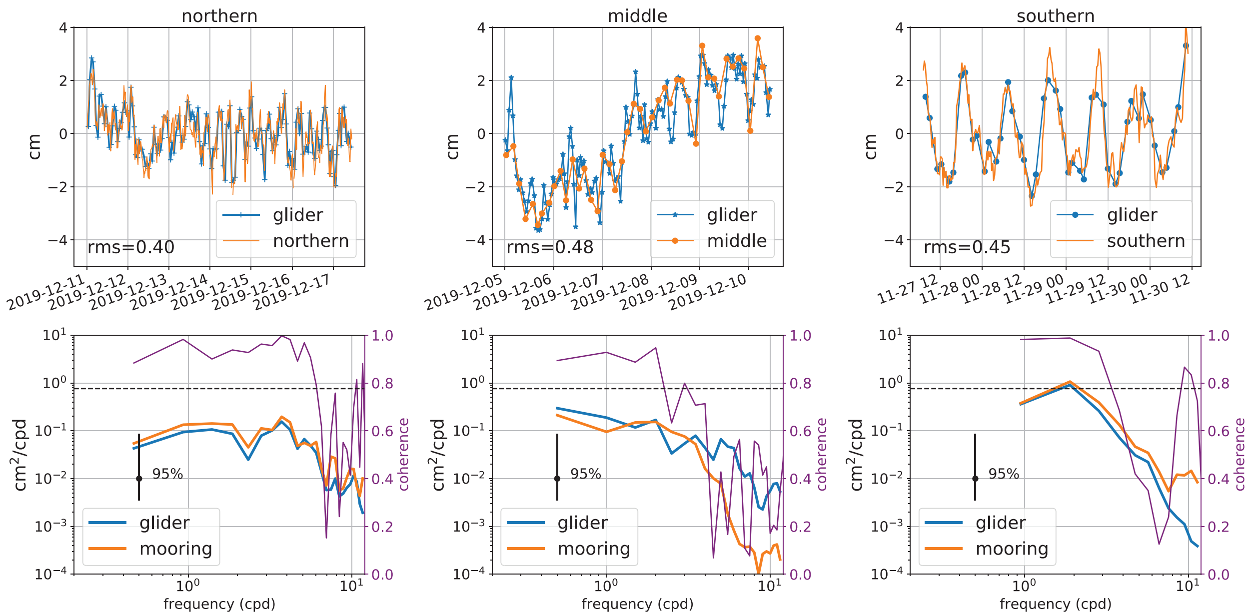

FIG. 12. (top) The upper-500-m steric height reconstructed from the glider (blue lines) and moorings (orange lines). (bottom) The frequency power spectral density for the glider (blue) and moorings (orange). The black vertical lines show the 95% confidence interval with 4 degrees of freedom (three nonoverlapping segments). The magnitude-squared coherence is shown in purple with the *y* axis on the right and the associated 95% confidence level marked by the dashed lines(left to right) The northern, middle, and southern moorings. The duration of the station-keeping phase was longest at the northern mooring (6.5 days) and shortest at the southern mooring (3.5 days).

an isolated mesoscale eddy during the eddy formation, the flow turned zonal (Fig. 5b) and the SSH differences between the three moorings can be as large as 10 cm between the southern and northern moorings, for example, at the end of October 2019 (Fig. 13, top panel). Near the end of November 2019, when the eddy was finally formed and detached (Fig. 5c), the meander regained its original north–south orientation with isolines oriented along the direction of the mooring array, resulting in a minimal SSH difference among the moorings. This eddy development can be seen from both altimetric SSH and mooring steric height, but the two-dimensional altimetric SSH field reveals more of the physical process than the one-dimensional array.

The gridded altimetry product and mooring have high coherence (>0.6) for periods longer than 20 days (figure not shown). The match between altimetric SSH and mooring upper-500-m steric height with less than 2 cm RMS error validates the upper-500-m steric height in representing satellite SSH over low frequencies. For periods shorter than ~20 days, the mooring steric height exhibits more variability than the gridded altimetric product, which is expected. From the example shown in the bottom panel of Fig. 13, the M_2 tide can be coherent and propagate from north to south shown by the gray arrow, but the coherency among the three moorings is intermittent. Over a 2-day period between 11 and 13 November, for example, the M_2 tidal peaks are less obvious at the northern mooring than at the southern mooring (Fig. 13, bottom panel).

The southern and northern mooring time series (Fig. 13, upper panel) reveal that the M_2 tide is stronger and more coherent at the southern mooring than the northern mooring. From a tidal analysis on the two steric height time series (figure not shown), the southern mooring has an M_2 steric height amplitude of 1.7 cm while the northern one has an amplitude of 0.7 cm. The M_2 baroclinic tide represented by the steric height is dominated by the first baroclinic mode that has a large wavelength longer than 100 km.

To address the question of why the M_2 tide is so different between two moorings separated by 30 km, we first eliminated the possibility that the difference comes from different mooring designs. The southern mooring uses a subsurface taut mooring connected to the profiler and surface buoy above by a reserve catenary. This design has a much smaller watch circle (250 m radius) than the northern slackline design mooring (~4 km radius). However, it is unlikely that this contributes to the difference in the M_2 signal at the different moorings, based on the glider results during its station-keeping phases shown in Fig. 12. The time variability at the M_2 tidal period is well characterized by the glider for both the southern and the northern moorings. During the 6-day period where the glider operated near the northern mooring, it confirmed the weak M_2 signal there. Likewise, at the southern mooring, the glider confirmed the elevated M_2 variability in steric height there. This mooring–glider comparison largely eliminates the influence of mooring design on the reconstruction of the coherent tides. As a result, the significantly different M_2 tide between the northern and the southern moorings appears to be real.

One possibility for the different tides between the northern and the southern moorings is that this small-scale difference is expected due to multiwave interference that has been

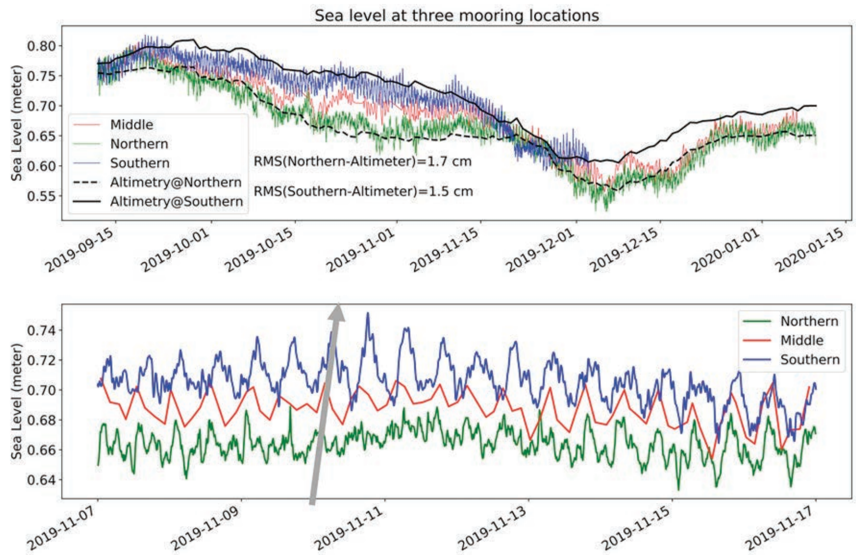

FIG. 13. (top) The time series of the upper-500-m steric height from three moorings (colored lines) offset by a constant 496.91 m, and the altimetric sea level anomaly interpolated at northern mooring (black solid) and southern mooring (black dashed). The RMS differences between WHOI mooring and SIO mooring steric height from their local altimetric sea level anomaly is 1.7 and 1.5 cm, respectively. (bottom) The same mooring steric height time series, but focusing on a 10-day window between 7 and 17 Nov 2019. The semitransparent gray arrow marked the propagation of the internal tides from the northern mooring through the middle mooring and to the southern mooring.

observed in the conventional altimetry (Zhao et al. 2019; Zaron 2019). An altimetry-based internal tide model that fits plane internal waves with multiple directions does also show similar amplitude variation of the mode-1 M_2 internal tide over the 30 km distance between the two moorings (Zaron 2019).

Another possibility is the modulation of coherent tides by balanced motions (e.g., Ponte and Klein 2015). The mesoscale and smaller mesoscale eddies are stronger at the northern mooring location than the southern mooring location, resulting in stronger eddy modulation of the tides and reduced tidal coherency. This can be seen from the frequency spectra of the steric height field of the three moorings (Fig. 14). The stronger M_2 tides at the southern mooring discussed above are illustrated in the frequency spectrum, i.e., the green line is much higher than the blue line at the M_2 frequency. The three moorings have matched energy on the low-frequency end with periods longer than 20 days. However, the spectral energy level at the southern mooring is drastically different from and one order of magnitude weaker than the other two moorings over 1–10-day periods. The gridded altimetry SSH maps (Fig. 5) show that the southern mooring is on the warm side of the meander and inside of the mature eddy at later stage, while the northern mooring spent more time on the further edge of the eddy where sharp horizontal fronts can be more prominent. This is confirmed by the horizontal gradient of SST, which is persistently stronger at the northern mooring location than at the southern mooring (figure not shown). This set of evidence points to the hypothesis that mesoscale eddies can modulate coherent low mode tides within a distance shorter than the tidal wavelength. The 2D SSH field to be observed by SWOT can be very useful to detect these small-scale eddy–wave interactions. Further proof of the hypothesis needs more observations or process-oriented numerical modeling studies and will be pursued elsewhere.

2) SPATIAL VARIABILITY

With two full-depth moorings at the northern and southern locations, we can start to examine the spatial variability from

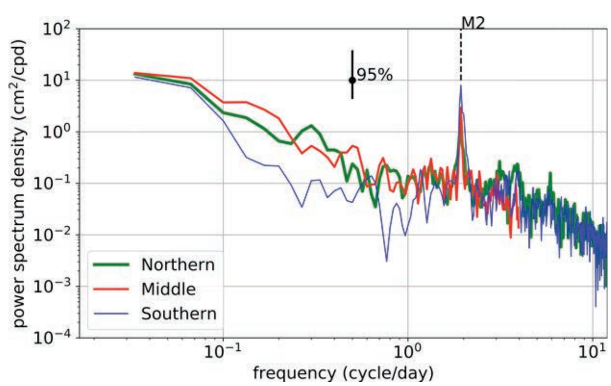

FIG. 14. The frequency spectra of the upper-500-m steric height from the northern (blue), middle (red), and the southern mooring (green). M_2 tidal frequency is marked by the dashed vertical line. The middle mooring spectrum (red) was cut at 4 cycles per day for its limited sampling frequency at 8 profiles per day.

TABLE 2. RMS differences between the northern and the southern moorings for the period 10 Sep–25 Nov 2019 when full-depth measurements are available at both sites. The temporal-scale separation is done in frequency space through Fourier analysis without windowing. The bottom row is done through a three-mooring scale separation described in the text representing a back-of-envelope calculation of the small-scale (<~30 km) variability. The unit for all values is cm.

	Full water column	0–500 m	500–4000 m
All frequencies	3.2	2.8	0.9
<14 days	1.6	1.4	0.8
2–14 days	0.7	0.7	0.2
<2 days	1.5	1.2	0.7
Anomalies to a linear function of the three moorings		0.2–0.7	

the mooring difference. Table 2 shows that the RMS difference over 30 km is 3.5 cm based on the full-depth steric height, among which 2.8 cm is due to the upper 500 m and 1 cm to the deeper ocean. These values include the influence of the wavelengths longer than 150 km, which is beyond the focus of the in situ Cal/Val. With only three moorings spanning 30 km, it is impossible to single out the signals with wavelength less than 150 km, but in general longer wavelengths are associated with longer periods. For example, these RMS differences are reduced for periods less than 14 days and significantly reduced for the 2–14-day band. The variability with periods less than 14 days is dominated by high frequencies (>1/2 cycle day^{-1}). This dependence of RMS difference on time scales is expected for a typical SSH frequency spectrum that is dominated by low-frequency (monthly and longer) variabilities and tidal peaks over high (superinertial) frequencies (e.g., Fig. 14).

The middle mooring does not have deep CTDs below the Prawler and samples only the upper 500 m. If we only focus on the upper-500-m steric height, the three moorings can be used to derive steric height difference for separation distances of 10 and 20 km. The standard deviations of the differences are 1.6 and 2.0 cm for 10 and 20 km, respectively.

These analyses with a single mooring (section 4c, Table 1) or two-mooring differences (Table 2) cannot distinguish different spatial scales, but we have used the above frequency filtering to isolate motions on SWOT spatial scales and thus could estimate the expected RMS differences due to these motions on the single spatial lag of 30 km. This is the size of SSH differences expected due to motions of interest to SWOT over such distances. In addition, with three moorings, we can begin to decipher the spatial–temporal variabilities due to the smallest-scale motions, even without the actual wavenumber spectrum. The main technique is discussed as follows.

Given three moorings with separation distances of 10 and 20 km, we have three points spanning 30 km distance. To examine small-scale signals, we removed the large-scale influence by removing a spatial linear trend through the three moorings for each hourly snapshot as shown in the schematic diagram in Fig. 15a. The middle mooring time series is linearly interpolated from 8 profiles per day to hourly, which inevitably introduces errors. The deviations from the fitted linear trend are considered the SSH anomaly at small scales.

The linear-trend removal is a crude spatial high-pass filter. The effectiveness of removing the local linear trend is evaluated using a Monte Carlo simulation to test a Hanning high-pass filter with different window sizes. We first generate 5000 128-km-long synthetic SSH profiles with certain wavenumber spectral slopes, then sample the profiles in the middle at three locations separated by 10 and 20 km, resembling the prelaunch campaign mooring placement. The synthetic mooring data are separated into large scale and small scale using the same method of fitting a three-point linear trend. The results are compared with results produced by a high-pass Hanning filter of different window widths. We find that for synthetic SSH profiles with k^{-4} wavenumber spectrum, the smallest difference between removing a local linear trend of the three moorings and a Hanning-window filtering occurs at 22 km Hanning-window width. For k^{-2} profiles, it is at 32 km. The SSH profile is "smoother" for steeper wavenumber spectrum, e.g., k^{-4}, so the local linear trend captures and removes large-scale signals more effectively. The anomalies after removing the local linear trend are mostly from spatial scales less than approximately 30 km. We denote these anomalies as "small scale" and the linear trend as "large scale" in the following paragraph. It is worth emphasizing again that this operation is a crude way of separating small and large scales, given the limitation of the spatial coverage of the data.

The derived small-scale variability is significantly weaker than the large-scale variability (Fig. 15b). The RMS values of the total upper-500-m steric height for the three moorings are 1.9, 1.3, and 1.9 cm from north to south. The corresponding large scales defined by the linear trend have RMS values of 1.7, 1.2, and 1.9 cm. The small-scale (<~30 km) steric height is 0.4, 0.7, 0.2 cm for the northern, middle, and southern moorings, respectively. These values for small scales are smaller or close to the SWOT KaRIn noise values around 0.54 cm (section 2d). It indicates that the SSH signal at the Cal/Val site can be weaker than the SWOT KaRIn noise for spatial scales 20–30 km and smaller. This result is consistent with Wang et al. (2019).

Note that the sum of small-scale and large-scale temporal variances is larger than the variance of the total signal. This provides evidence that this spatial filtering does not separate the signal in the temporal space. However, removing the local linear trend effectively removes most of the low-frequency variability that is visually obvious in the time series (Fig. 15b) and also clearly shown in the frequency spectra in Fig. 15c, where the power spectra of the total and large-scale signals converge over periods longer than 10 days (blue and orange lines). Removing the linear trend also effectively removes most of the M_2 baroclinic tides in the steric height, which means that the baroclinic tides have spatial scales larger than about 30 km. Even though the large-scale signal is more energetic than the smaller spatial signal over almost all

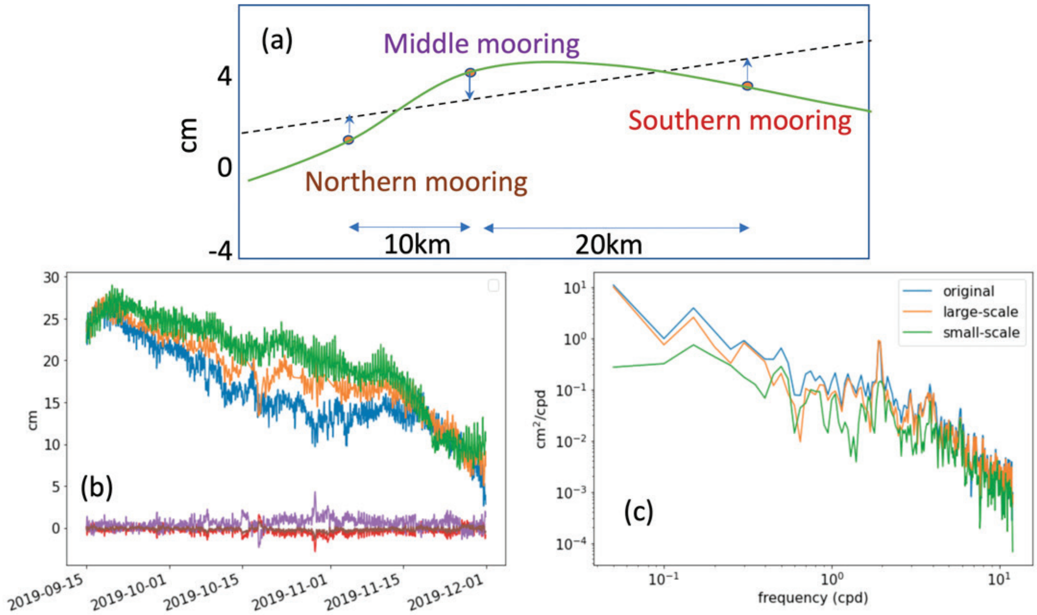

FIG. 15. (a) The schematic of deriving small-scale anomalies from three moorings. The linear trend (dashed line) was derived through the least squares method. The deviation of each mooring steric height from their linear trend is denoted as the small-scale component. Removing the linear trend over a 30 km segment is similar to high-pass filtering with a 20–30-km-wide Hanning window depending on the wavenumber slope of the signal. (b) The original steric height of each mooring (green, orange, and blue lines). The small-mesoscale signals defined in (a) are shown by purple, red, and brown lines for the three moorings. (c) The frequency spectra for the original steric height (blue), the linear trend representing the large-scale (orange), and the small-scale steric height (green) averaged over the spectra of the three moorings.

frequencies, the small-scale signal is particularly large over the period range of 2–5 days relative to the large scale. With a caveat of uncertain significance, we may tentatively associate <30 km spatial scales with 2–5-day temporal scales. This spatial–temporal-scale association may have a practical value for designing the optimal error covariance matrices in the data assimilation system with the multiscale approach, such as Li et al. (2019), D'Addezio et al. (2019), and Archer et al. (2022).

f. Comparison to Sentinel-3A *SSH*

The *Sentinel-3A* ground track was not a factor for the design of the SWOT Cal/Val orbit. It is rather fortunate that one of the *Sentinel-3A* (*S3A*) ground tracks is in the middle of a SWOT swath along the fast-repeating orbit. For this reason, the mooring array in the prelaunch field campaign was placed along the *S3A* ground track (Fig. 2). During the 2019/20 campaign period, *S3A* passed the mooring array five times (Fig. 16). The mooring steric heights (upper 500 m) match the *S3A* measurements within 2 cm RMS. There were two times when the steric heights and *S3A* values were different (the third and fifth rows). Despite the sizeable differences, the spatial structures in the mooring array steric heights resemble the spatial structures of the *S3A* SSH profiles. However, bias corrections of 2 and 6 cm were applied to 6 November 2019 and 2 January 2020 profiles, respectively. The nature of the bias is unknown at the time of writing and deferred to future investigations.

g. Bottom pressure

Bottom pressure recorders measure both the barotropic (due to additional water mass above the BPR) and baroclinic (due to interior temperature/salinity changes) signals on the ocean floor. The BPRs deployed in this campaign have enough precision to detect millimeter-level signals, but BPRs suffer from a large long-term drift that may be mistaken for a low-frequency signal in our ~90-day records. Ray (2013) analyzed a network of BPRs of this type, showing that the BPR-derived tide matches the altimetric tide model with about 5 mm RMS difference for the M_2 constituent. The BPRs used in the campaign should be accurate enough to detect deep baroclinic pressure signals even though separating them from much more energetic barotropic tides based on a single mooring is impossible (Ray 2013). The most prominent signal in the bottom pressure is the tide (Fig. 17a). We fit 53 tidal constituents to the measured bottom-pressure signal to produce a detided bottom pressure record (Fig. 17b) using the same tool from Ray (2013). The detided signals are relatively small (2.3–2.6 cm), but still potentially important. Unfortunately, we have little information about the spatial scale of the signals contributing to these residual bottom pressure signals. Taking the difference between the two detided bottom-pressure records can give us a vague sense of how small-scale signals

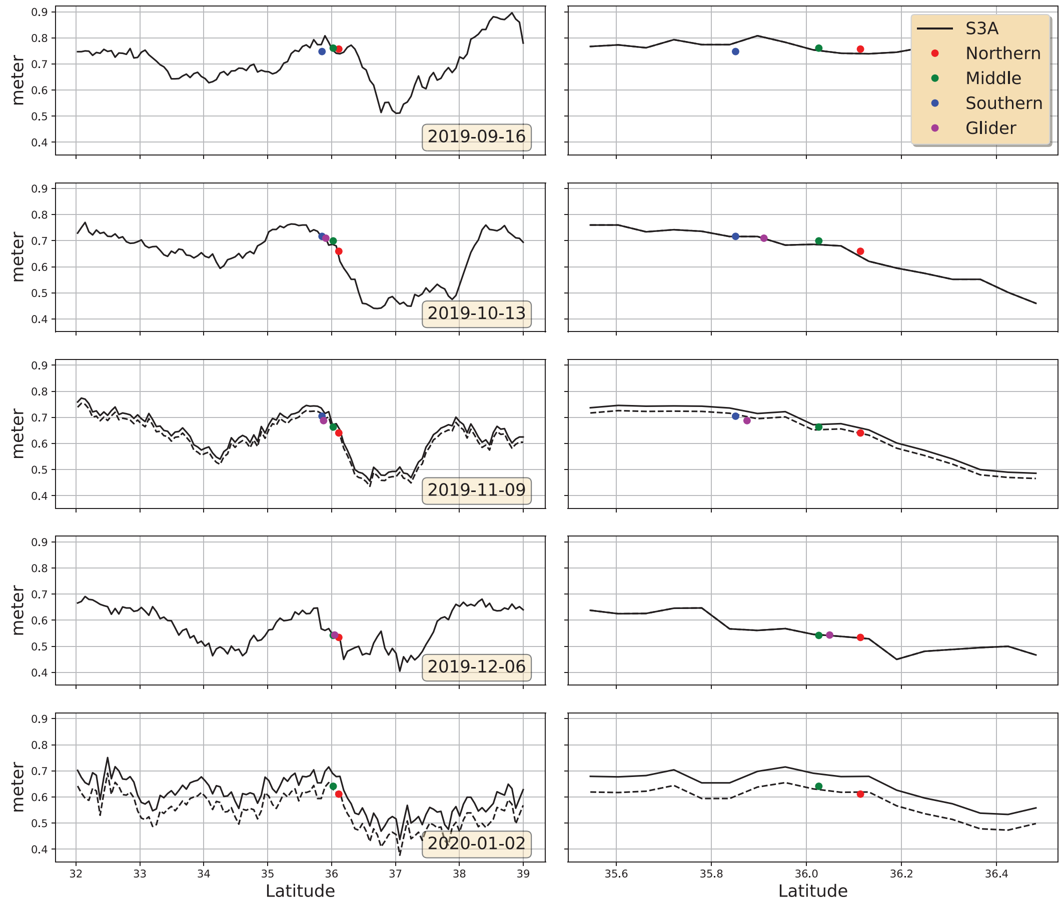

FIG. 16. The five *Sentinel-3A* SSH profiles during the 2019/20 campaign period that pass the mooring array (black lines). They are the L3 product with ocean (barotropic) tides, dynamic atmosphere correction (DAC), and long-wavelength-error (LWE) correction applied. The colored dots show the upper-500-m steric height from the northern (red), middle (green), and southern (blue) moorings and the glider (purple). (left) The 7° segment to show the large-scale context. (right) The same profile, but zooming in to focus on the mooring array within 100-km-wide segments. The dashed lines in the third and fifth rows are the black lines offset by 2 and 6 cm, respectively. The steric height is calculated from the original in situ density without removing the time mean, then offset by 496.385 m to match the *Sentinel-3A* profiles.

might contribute. This difference has an RMS amplitude of 0.6 cm based on the period of 1 October 2019–1 October 2020 when the bottom pressure drift becomes less obvious. It contains both barotropic and baroclinic signals, including several tidal frequencies and low-frequency variability, and the parabolic shape of the difference curve (Fig. 17b) suggests it may also be affected by differences in the low-frequency drift of the two bottom pressure recorders. Removing a quadratic fit to the difference between the two detided bottom-pressure records reduces the RMS difference to about 0.4 cm, which is below the SWOT KaRIn noise level derived in section 2d.

5. The design of a SWOT postlaunch campaign

The main purpose of the SWOT prelaunch campaign described in the paper is to provide information for the design of an effective yet affordable postlaunch SWOT ocean in situ observing system for the mission's calibration and validation. To validate the SWOT SSH, we need an array of observations for comparison with the nearly simultaneous measurement taken by the satellite in less than 23 s over 150 km. The resolution of SWOT in the California Cal/Val region is about 20 km in wavelength, below which the baroclinic SSH becomes less than KaRIn instrument noise (Wang et al. 2019). To meet the Nyquist wavelength requirement of 20 km, we need a measurement every 10 km. Although Wang and Fu (2019) indicated that the onboard nadir altimeter is able to validate SWOT at wavelengths longer than 120 km, we feel that, in order to reduce cost, it is acceptable to deploy an array of 11 moorings covering 100 km to meet the in situ Cal/Val objectives.

Based on the analysis presented in the paper, it is acceptable to sample only the upper 500 m for the low-frequency ocean variability. However, it is desirable to sample the ocean deeper than 500 m to capture the deep signals of internal tides and occasional deep eddies. Since the wavelengths of internal

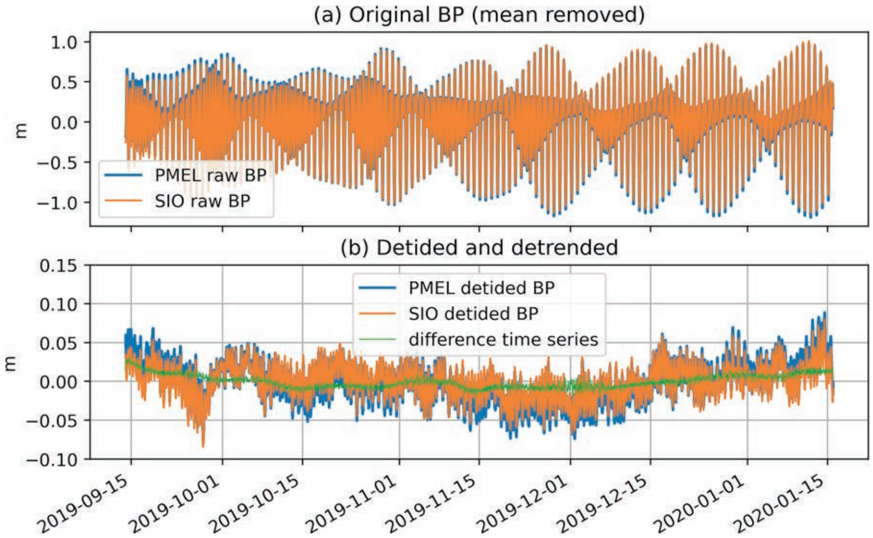

FIG. 17. (a) The original time series of the bottom pressure from the southern (orange) and the northern (blue) BPRs. (b) The residual after removing the fitted tides and linear trends. We fit 53 tidal constituents to the 4-month-long time series to reduce the residual. The remaining signal of each BPR still has 2.2–2.4 cm standard deviation.

tides are longer than 60 km (the two lowest modes of the M_2 tides; Zhao et al. 2019), the required Nyquist sampling interval for low-mode internal tides is 30 km. Shown in Fig. 18 is a baseline design of the postlaunch observing system. It contains 11 moorings with 4 of them (triangles) consisting of a Wirewalker and deep CTDs like the SIO system. The remaining 7 moorings are Prawler moorings like the PMEL system, sampling only the upper 500 m. These instruments will provide time series observations that allow the construction of the snapshots of steric height for comparison with the SWOT SSH measurement on a daily basis. The difference between the two observations will provide an assessment of the SWOT measurement errors for the small-wavelength range reconstructed by the in situ mooring array (20–100 km). Its wavenumber spectrum will be compared with the SWOT requirement (Fig. 1).

Based on the results from the prelaunch campaign, GPS buoys and BPRs are not critical for meeting the Cal/Val objectives. To make accurate IB correction for the SWOT SSH, one barometer at the center of the array is included in the design.

Two gliders are included to sample the cross-track ocean variability to aid the estimation of the two-dimensional state of the upper ocean for validating the science goals of the mission to determine the circulation of the upper ocean. If funding permits, more gliders would be highly desirable for achieving the science goals. As illustrated in the paper, the gliders, when operating in the station-keeping mode, will also serve as a contingency for any failed mooring.

Given the constraints of the mission's budget, this design presents a minimum system for meeting the mission's Cal/Val objectives. We look forward to opportunities of collaboration with other interested parties to expand this SWOT Cal/Val array into a larger-scope, submesoscale-focused experiment in this region.

6. Discussion and conclusions

It has been shown that observations from the moorings and the glider can be used to reconstruct a steric height field with accuracy at an RMS error below 1 cm at each location level. There are, however, remaining uncertainties in the accuracy of the horizontal wavenumber spectrum produced by an array of these moorings.

The moorings' large watch circles might be a source of uncertainty in making an SSH wavenumber calculation for the SWOT Cal/Val purpose. The watch circle can reach a 4 km radius. It may change the spacing between moorings and result in nonuniformly spaced mooring array. In addition, the deviation from the centerline of the mooring array (the middle of the SWOT swath) can also be as large as the watch circle radius. These along-track and cross-track drifts of the moorings will introduce errors and uncertainties, but we do not have a formal assessment of the error in this study. In any case, the size of the watch circle is less than the 15–20-km-wavelength resolution of SWOT in the Cal/Val region (Wang et al. 2019).

The deep-ocean steric height has variability and can contribute to the overall steric height signal. Based on the ~90 days of mooring observations collected during the 2019/20 campaign, the consequence of missing the deep-ocean steric height was about 0.6–0.8 cm standard deviation for each mooring, mostly arising from baroclinic tides (Fig. 10).

There is some evidence that eddies at and below 500 m occasionally occur in the Cal/Val region (Collins et al. 2013). Although Collins et al. (2013) do not report on the water

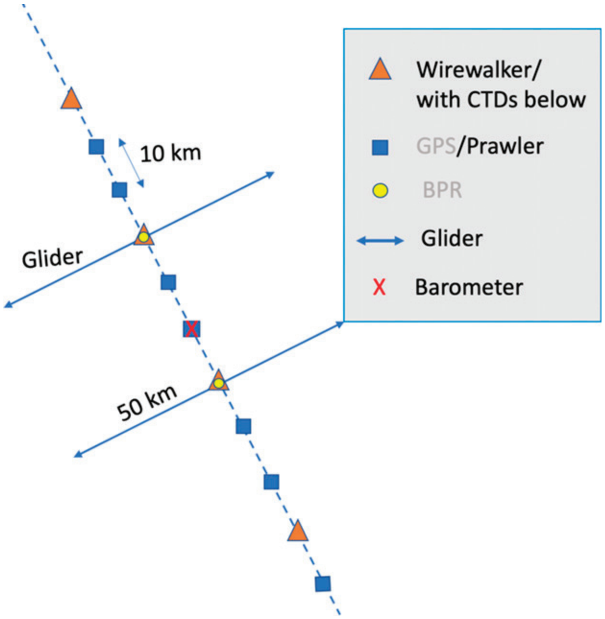

FIG. 18. A minimum baseline for the SWOT postlaunch ocean Cal/Val field campaign. The four hybrid moorings with full-depth *T*/*S* measurements can capture deep-reaching baroclinic tides with relatively longer wavelengths. The seven Prawlers will measure the upper-500-m steric height. Two gliders will sample the cross-swath direction and also serve as a contingency for failed moorings. The barometer will provide high-precision, high-frequency atmospheric pressure for IB correction. BPRs and GPS receivers are not part of the minimum baseline but will be a valuable upgrade.

column structure associated with the observed deep eddies, they could contribute to variability in steric height and to significant nonzero velocities at 500 m depth. For example, assuming a mode-1 structure, a 25-km-wide eddy at 1500 m with ~10 cm s^{-1} velocities as reported by Collins et al. (2013) would be associated with a ~1 cm change in steric height across its diameter. They also observed an eddy at 660 m depth with velocities that would correspond to 1.4 cm steric height signal across the eddy with a diameter of 54 km at that depth. However, deep eddies need not be associated with a mode-1 structure. For example, Gula et al. (2019) report on the presence of deep submesoscale coherent vortices (SCVs) in the Gulf Stream with diameters of 10–30 km. Those SCVs have a mode-2 like signature that would have little if any impact on steric height (e.g., Fig. 2d in Gula et al. 2019). Given the potential for deep eddies to contribute a small amount of steric height variability, a subset of moorings in the SWOT Cal/Val effort will monitor the deep ocean to account for these signals if they arise (Fig. 18).

Even though the error in GPS SSH from a single buoy (>1 cm RMS) is larger than SWOT mission requirements, much of this error is attributed to sea-state and water-line errors, and intrinsic GPS errors (e.g., from tropospheric refraction) that are spatially correlated over the campaign footprint. Significant cancellation of common mode errors can thus be expected from combined processing of observations of multiple buoys operating in the same campaign theater. This is supported by recent tandem buoy campaigns in the Bass Strait (Zhou et al. 2020) and near the Harvest platform (Haines et al. 2019), both of which suggest that errors (on ΔSSH between buoys in proximity) are reduced to less than 1 cm. Whether the accuracies achieved can approach the stringent requirements imposed by the validation of the SWOT wavenumber spectrum remains an open question (Zhou et al. 2020). Regardless, the GPS buoy technique has advanced significantly and already offers a powerful means of resolving discrepancies between steric height (as measured with hydrographic techniques) and geodetic SSH (as measured by SWOT).

We have shown that it is possible to measure the steric contribution to sea surface height to <1 cm RMS precision with several moorings and a glider. This allows confidence that an array of moorings and collocated glider lines (e.g., Fig. 18) will allow for a robust oceanographic calibration and validation of the KaRIn sensor on board the SWOT satellite during the planned 1-day fast-repeat period before the satellite is moved to its final orbit.

This is the first time when a combination of independent high-precision in situ instruments is used to analyze the SSH budget focusing on such small spatial scales (less than 30 km) and high frequencies (period less than monthly). The results shed light on the design of the SWOT postlaunch field campaign as well as the ocean physics over such small scales and high frequencies (periods ranging from hours to months).

We have shown that the ocean sea surface height measured by GPS, which is like altimeter/SWOT measurements, matches the steric height derived from the temperature and salinity measurements using CTDs after subtracting the bottom pressure and applying the inverted barometer correction. The consistency between the GPS-BPR and the mooring steric height validated the utility of the steric height as the ground truth for satellite calibration and validation. Even though the absolute RMS difference between GPS-BPR-derived steric height and CTD-derived steric height is larger than 1 cm, how much of the error is due to the large-scale common mode GPS error is unknown, but expected to be largely removable. The utility of GPS in the SWOT Cal/Val is still under investigation through the second GPS on the middle mooring. The major advantage of using steric height is the absence of the errors due to surface waves.

The variability in steric height is mostly due to the upper-ocean processes. For example, the deep-ocean ($z < -500$ m) steric height variability has a standard deviation of 0.6–0.8 cm, most of which comes from superinertial frequencies, especially around the semidiurnal M_2. If only subinertial variabilities with periods between 2 and 14 days are considered, missing deep ocean results in <2 mm uncertainty.

Small scales less than 30 km wavelength have very weak steric height variation, 0.2–0.7 cm standard deviation near the SWOT Cal/Val campaign region diagnosed from the 2019/20 campaign conducted in the wintertime. This small-scale variability is estimated based on the deviations of the three mooring steric heights from their spatial linear trend. This weak small-scale steric height signal underlines the challenge for

SWOT, but also highlights the opportunities provided by SWOT and the values of a full-scale array with a dozen CTD moorings in conducting the mission Cal/Val and studying the small-scale ocean circulation.

Acknowledgments. We are grateful to Anna Savage and R/V *Sally Ride* captain and crew for the unplanned recovery of the Wirewalker, and to Hong Zhang for providing ERA5 atmospheric pressure for the IB correction, Ed Zaron for the discussion on internal tides, and Marie Eble and George Mungov for the discussions on the tidal reconstruction from BP. The research was carried out at the Jet Propulsion Laboratory, California Institute of Technology, under a contract with the National Aeronautics and Space Administration (80NM0018D0004). All authors are supported by the SWOT project. J. T. Farrar was partially supported by NASA NNX16AH76G. The in-situ observations are available for download at https://podaac.jpl.nasa.gov/.

REFERENCES

Archer, M. R., Z. Li, J. Wang, and L.-L. Fu, 2022: Reconstructing fine-scale ocean variability via data assimilation of the SWOT pre-launch in situ observing system. *J. Geophys. Res. Oceans*, **127**, e2021JC017362, https://doi.org/10.1029/2021JC017362.

Bertiger, W., and Coauthors, 2010: Single receiver phase ambiguity resolution with GPS data. *J. Geod.*, **84**, 327–337, https://doi.org/10.1007/s00190-010-0371-9.

——, and Coauthors, 2020: GipsyX/RTGx: A new tool set for space geodetic operations and research. *Adv. Space Res.*, **66**, 469–489, https://doi.org/10.1016/j.asr.2020.04.015.

Bonnefond, P., and Coauthors, 2019: Corsica: A 20-yr multi-mission absolute altimeter calibration site. *Adv. Space Res.*, **68**, 1171–1186, https://doi.org/10.1016/j.asr.2019.09.049.

Callies, J., and W. Wu, 2019: Some expectations for submesoscale sea surface height variance spectra. *J. Phys. Oceanogr.*, **49**, 2271–2289, https://doi.org/10.1175/JPO-D-18-0272.1.

Capet, X., J. C. McWilliams, M. J. Molemaker, and A. F. Shchepetkin, 2008a: Mesoscale to submesoscale transition in the California Current system. Part I: Flow structure, eddy flux, and observational tests. *J. Phys. Oceanogr.*, **38**, 29–43, https://doi.org/10.1175/2007JPO3671.1.

——, ——, ——, and ——, 2008b: Mesoscale to submesoscale transition in the California Current system. Part III: Energy balance and flux. *J. Phys. Oceanogr.*, **38**, 2256–2269, https://doi.org/10.1175/2008JPO3810.1.

Chereskin, T. K., C. B. Rocha, S. T. Gille, D. Menemenlis, and M. Passaro, 2019: Characterizing the transition from balanced to unbalanced motions in the Southern California Current. *J. Geophys. Res. Oceans*, **124**, 2088–2109, https://doi.org/10.1029/2018JC014583.

Clark, E. B., and Coauthors, 2018: Station-keeping underwater gliders using a predictive ocean circulation model and applications to SWOT calibration and validation. *IEEE J. Oceanic Eng.*, **45**, 371–384, https://doi.org/10.1109/JOE.2018.2886092.

Collins, C. A., T. Margolina, T. A. Rago, and L. Ivanov, 2013: Looping RAFOS floats in the California Current system. *Deep Sea Res. II*, **85**, 42–61, https://doi.org/10.1016/j.dsr2.2012.07.027.

Copernicus Climate Change Service, 2017: ERA5: Fifth generation of ECMWF atmospheric reanalyses of the global climate. Copernicus Climate Change Service Climate Data Store, accessed 1 March 2020, https://cds.climate.copernicus.eu/cdsapp\#!/home.

D'Addezio, J. M., S. Smith, G. A. Jacobs, R. Helber, C. Rowley, I. Souopgui, and M. J. Carrier, 2019: Quantifying wavelengths constrained by simulated SWOT observations in a submesoscale resolving ocean analysis/forecasting system. *Ocean Modell.*, **135**, 40–55, https://doi.org/10.1016/j.ocemod.2019.02.001.

Desai, S., and Coauthors, 2018: Surface Water and Ocean Topography Mission (SWOT) project science requirements document. Jet Propulsion Laboratory Doc. JPL D-61923, revision B, 29 pp.

d'Ovidio, F., and Coauthors, 2019: Frontiers in fine-scale in situ studies: Opportunities during the SWOT fast sampling phase. *Front. Mar. Sci.*, **6**, 168, https://doi.org/10.3389/fmars.2019.00168.

Dufau, C., M. Orsztynowicz, G. Dibarboure, R. Morrow, and P. Traon, 2016: Mesoscale resolution capability of altimetry: Present and future. *J. Geophys. Res. Oceans*, **121**, 4910–4927, https://doi.org/10.1002/2015JC010904.

Durand, M., L.-L. Fu, D. P. Lettenmaier, D. E. Alsdorf, E. Rodriguez, and D. Esteban-Fernandez, 2010: The Surface Water and Ocean Topography mission: Observing terrestrial surface water and oceanic submesoscale eddies. *Proc. IEEE*, **98**, 766–779, https://doi.org/10.1109/JPROC.2010.2043031.

Eble, M. C., and F. I. Gonzalez, 1991: Deep-ocean bottom pressure measurements in the northeast Pacific. *J. Atmos. Oceanic Technol.*, **8**, 221–233, https://doi.org/10.1175/1520-0426(1991)008<0221:DOBPMI>2.0.CO;2.

Flament, P., L. Armi, and L. Washburn, 1985: The evolving structure of an upwelling filament. *J. Geophys. Res.*, **90**, 11 765–11 778, https://doi.org/10.1029/JC090iC06p11765.

Fu, L.-L., and A. Cazenave, 2001: *Satellite Altimetry and Earth Sciences.* Academic Press, 509 pp.

——, and C. Ubelmann, 2014: On the transition from profile altimeter to swath altimeter for observing global ocean surface topography. *J. Atmos. Oceanic Technol.*, **31**, 560–568, https://doi.org/10.1175/JTECH-D-13-00109.1.

Gula, J., T. M. Blacic, and R. E. Todd, 2019: Submesoscale coherent vortices in the Gulf Stream. *Geophys. Res. Lett.*, **46**, 2704–2714, https://doi.org/10.1029/2019GL081919.

Guthrie, J., and Coauthors, 2020: Preliminary results from the first deployments of the dynamic ocean topography buoy: In-situ observations of sea surface height in ice-covered seas. *AGU Ocean Sciences Meeting*, San Francisco, CA, Amer. Geophys. Union, Abstract HE14B-1930, https://agu.confex.com/agu/osm20/meetingapp.cgi/Paper/648899.

Haines, B., S. Desai, C. Meinig, and S. Stalin, 2017: CAL/VAL of the SWOT SSH spectrum: Moored GPS approach. *SWOT Science Team Meeting*, Toulouse, France, NASA, https://trs.jpl.nasa.gov/handle/2014/48164.

——, ——, A. Dodge, R. Leben, M. Shannon, C. Meinig, and S. Stalin, 2019: The Harvest experiment: New results from the platform and moored GPS buoys. *Ocean Surface Topography Science Team Meeting*, Chicago, IL, NASA.

——, ——, D. Kubitschek, and R. Leben, 2021: A brief history of the Harvest experiment: 1989–2019. *Adv. Space Res.*, **68**, 1161–1170, https://doi.org/10.1016/j.asr.2020.08.013.

Hersbach, H., and Coauthors, 2020: The ERA5 global reanalysis. *Quart. J. Roy. Meteor. Soc.*, **146**, 1999–2049, https://doi.org/10.1002/qj.3803.

Hickey, B. M., 1979: The California Current system—Hypotheses and facts. *Prog. Oceanogr.*, **8**, 191–279, https://doi.org/10.1016/0079-6611(79)90002-8.

Ikeda, M., and W. J. Emery, 1984: Satellite observations and modeling of meanders in the California Current system off Oregon and Northern California. *J. Phys. Oceanogr.*, **14**, 1434–1450, https://doi.org/10.1175/1520-0485(1984)014<1434:SOAMOM>2.0.CO;2.

Kanzow, T., U. Send, W. Zenk, A. D. Chave, and M. Rhein, 2006: Monitoring the integrated deep meridional flow in the tropical North Atlantic: Long-term performance of a geostrophic array. *Deep-Sea Res. I*, **53**, 528–546, https://doi.org/10.1016/j.dsr.2005.12.007.

LaCasce, J. H., and A. Mahadevan, 2006: Estimating subsurface horizontal and vertical velocities from sea surface temperature. *J. Mar. Res.*, **64**, 695–721, https://doi.org/10.1357/002224006779367267.

Lapeyre, G., and P. Klein, 2006: Dynamics of the upper oceanic layers in terms of surface quasigeostrophy theory. *J. Phys. Oceanogr.*, **36**, 165–176, https://doi.org/10.1175/JPO2840.1.

Li, Z., J. Wang, and L.-L. Fu, 2019: An observing system simulation experiment for ocean state estimation to assess the performance of the SWOT mission: Part 1—A twin experiment. *J. Geophys. Res. Oceans*, **124**, 4838–4855, https://doi.org/10.1029/2018JC014869.

Meinig, C., S. E. Stalin, A. I. Nakamura, and H. B. Milburn, 2005: Real-time deep-ocean tsunami measuring, monitoring, and reporting system: The NOAA DART II description and disclosure. NOAA NDBC Rep., 15 pp.

Melville, W. K., L. Lenain, D. R. Cayan, M. Kahru, J. P. Kleissl, P. Linden, and N. M. Statom, 2016: The Modular Aerial Sensing System. *J. Atmos. Oceanic Technol.*, **33**, 1169–1184, https://doi.org/10.1175/JTECH-D-15-0067.1.

Mihaly, S. F., R. E. Thomson, and A. B. Rabinovich, 1998: Evidence for nonlinear interaction between internal waves of inertial and semidiurnal frequency. *Geophys. Res. Lett.*, **25**, 1205–1208, https://doi.org/10.1029/98GL00722.

Morrow, R., and Coauthors, 2019: Global observations of fine-scale ocean surface topography with the Surface Water and Ocean Topography (SWOT) mission. *Front. Mar. Sci.*, **6**, 232, https://doi.org/10.3389/fmars.2019.00232.

Osse, T. J., C. Meinig, S. Stalin, and H. Milburn, 2015: The Prawler, a vertical profiler powered by wave energy. *OCEANS 2015*, Washington, DC, IEEE, https://doi.org/10.23919/OCEANS.2015.7404354.

Pinkel, R., M. A. Goldin, J. A. Smith, O. M. Sun, A. A. Aja, M. N. Bui, and T. Hughen, 2011: The Wirewalker: A vertically profiling instrument carrier powered by ocean waves. *J. Atmos. Oceanic Technol.*, **28**, 426–435, https://doi.org/10.1175/2010JTECHO805.1.

Ponte, A. L., and P. Klein, 2015: Incoherent signature of internal tides on sea level in idealized numerical simulations. *Geophys. Res. Lett.*, **42**, 1520–1526, https://doi.org/10.1002/2014GL062583.

Pujol, M. I., Y. Faugère, G. Taburet, S. Dupuy, C. Pelloquin, M. Ablain, and N. Picot, 2016: DUACS DT2014: The new multi-mission altimeter data set reprocessed over 20 years. *Ocean Sci.*, **12**, 1067–1090, https://doi.org/10.5194/os-12-1067-2016.

Qiu, B., S. Chen, P. Klein, J. Wang, H. Torres, L. Fu, and D. Menemenlis, 2018: Seasonality in transition scale from balanced to unbalanced motions in the World Ocean. *J. Phys. Oceanogr.*, **48**, 591–605, https://doi.org/10.1175/JPO-D-17-0169.1.

Quartly, G. D., G. Chen, F. Nencioli, R. Morrow, and N. Picot, 2021: An overview of requirements, procedures and current advances in the calibration/validation of radar altimeters. *Remote Sens.*, **13**, 125, https://doi.org/10.3390/rs13010125.

Ray, R. D., 2013: Precise comparisons of bottom-pressure and altimetric ocean tides. *J. Geophys. Res. Oceans*, **118**, 4570–4584, https://doi.org/10.1002/jgrc.20336.

Rocha, C., T. Chereskin, G. Gille, and D. Menemenlis, 2016: Mesoscale to submesoscale wavenumber spectra in Drake Passage. *J. Phys. Oceanogr.*, **46**, 601–620, https://doi.org/10.1175/JPO-D-15-0087.1.

Rudnick, D. L., K. D. Zaba, R. E. Todd, and R. E. Davis, 2017: A climatology of the California Current system from a network of underwater gliders. *Prog. Oceanogr.*, **154**, 64–106, https://doi.org/10.1016/j.pocean.2017.03.002.

Savage, A. C., and Coauthors, 2017: Spectral decomposition of internal gravity wave sea surface height in global models. *J. Geophys. Res. Oceans*, **122**, 7803–7821, https://doi.org/10.1002/2017JC013009.

Schaeffer, P., and Coauthors, 2018: What do we need to improve the next mean sea surface? *Ocean Surface Topography Science Team Meeting*, Ponta Delgado, Portugal, NASA.

Strub, P. T., and C. James, 2000: Altimeter-derived variability of surface velocities in the California Current system: 2. Seasonal circulation and eddy statistics. *Deep-Sea Res. II*, **47**, 831–870, https://doi.org/10.1016/S0967-0645(99)00129-0.

Su, Z., and Coauthors, 2018: Ocean submesoscales as a key component of the global heat budget. *Nat. Commun.*, **9**, 775, https://doi.org/10.1038/s41467-018-02983-w.

Taburet, G., A. Sanchez-Roman, M. Ballarotta, M. I. Pujol, J. F. Legeais, F. Fournier, Y. Faugere, and G. Dibarboure, 2019: DUACS DT-2018: 25 years of reprocessed sea level altimeter products. *Ocean Sci.*, **15**, 1207–1224, https://doi.org/10.5194/os-15-1207-2019.

Torres, H. S., P. Klein, D. Menemenlis, B. Qiu, Z. Su, J. Wang, S. Chen, and L. Fu, 2018: Partitioning ocean motions into balanced motions and internal gravity waves: A modeling study in anticipation of future space missions. *J. Geophys. Res. Oceans*, **123**, 8084–8105, https://doi.org/10.1029/2018JC014438.

Wang, J., and L.-L. Fu, 2019: On the long-wavelength validation of the SWOT KaRIn measurement. *J. Atmos. Oceanic Technol.*, **36**, 843–848, https://doi.org/10.1175/JTECH-D-18-0148.1.

——, ——, B. Qiu, D. Menemenlis, J. T. Farrar, Y. Chao, A. F. Thompson, and M. M. Flexas, 2018: An observing system simulation experiment for the calibration and validation of the Surface Water Ocean Topography sea surface height measurement using in situ platforms. *J. Atmos. Oceanic Technol.*, **35**, 281–297, https://doi.org/10.1175/JTECH-D-17-0076.1.

——, ——, H. S. Torres, S. Chen, B. Qiu, and D. Menemenlis, 2019: On the spatial scales to be resolved by the Surface Water and Ocean Topography Ka-band radar interferometer. *J. Atmos. Oceanic Technol.*, **36**, 87–99, https://doi.org/10.1175/JTECH-D-18-0119.1.

Watts, D., and H. T. Rossby, 1977: Measuring dynamic heights with inverted echo sounders: Results from MODE. *J. Phys. Oceanogr.*, **7**, 345–358, https://doi.org/10.1175/1520-0485(1977)007<0345:MDHWIE>2.0.CO;2.

Wunsch, C., and D. Stammer, 1997: Atmospheric loading and the oceanic inverted barometer effect. *Rev. Geophys.*, **35**, 79–107, https://doi.org/10.1029/96RG03037.

Yu, X., A. L. Ponte, S. Elipot, D. Menemenlis, E. D. Zaron, and R. Abernathey, 2019: Surface kinetic energy distributions in the global oceans from a high-resolution numerical model and surface drifter observations. *Geophys. Res. Lett.*, **46**, 9757–9766, https://doi.org/10.1029/2019GL083074.

Zaron, E. D., 2019: Baroclinic tidal sea level from exact-repeat mission altimetry. *J. Phys. Oceanogr.*, **49**, 193–210, https://doi.org/10.1175/JPO-D-18-0127.1.

Zhao, Z., and Coauthors, 2019: Decomposition of the multimodal multidirectional M_2 internal tide field. *J. Atmos. Oceanic Technol.*, **36**, 1157–1173, https://doi.org/10.1175/JTECH-D-19-0022.1.

Zhou, B., C. Watson, B. Legresy, M. King, J. Beardsley, and A. Deane, 2020: GNSS/INS-equipped buoys for altimetry validation: Lessons learnt and new directions from the Bass Strait validation facility. *Remote Sens.*, **12**, 3001, https://doi.org/10.3390/rs12183001.

Investigating the Overlap Between the Mid-Atlantic Bight Cold Pool and Offshore Wind Lease Areas

Rebecca Horwitz
Department of Geology and Environmental Studies
Carleton College
Northfield, USA
hhorwitzb@gmail.com

Travis N. Miles
Center for Ocean Observing Leadership (COOL)
Rugers University
New Brunswick, USA.
tnmiles@marine.rutgers.edu

Daphne Munroe
Department of Marine and Coastal Sciences
Rutgers University
New Brunswick, USA
dmunroe@hsrl.rutgers.edu

Josh Kohut
Center for Ocean Observing Leadership (COOL)
Rugers University
New Brunswick, USA.
kohut@marine.rutgers.edu

OCEANS 2022, Hampton Roads | 978-1-6654-6809-1/22/$31.00 ©2022 IEEE | DOI: 10.1109/OCEANS47191.2022.9977050

Abstract—— **The Mid-Atlantic Cold Pool is a seasonal mass of cold bottom water that extends throughout the Mid-Atlantic Bight (MAB). The Cold Pool forms from rapid surface warming in the spring and dissipates in the fall due to mixing events such as storms. The Cold Pool supports coastal ecosystems and economically valuable commercial and recreational fisheries along the MAB. Offshore wind energy has been rapidly developing within the MAB in recent years. Studies in Europe demonstrate that existing WEAs can impact seasonal stratification; however, there is limited information on how MAB wind development will affect the Cold Pool. Seasonal overlap between the Cold Pool and wind lease areas in the Southern New York Bight along coastal New Jersey was evaluated using a data assimilative ocean model. Results highlight overlap periods as well as a thermal gradient that persists after bottom temperatures warm above the threshold typically used to identify the Cold Pool. These results also support cross-shelf variability in Cold Pool evolution. This work highlights the need for more focused ocean modeling studies and observations of the Cold Pool and MAB wind lease area overlap.**

Keywords—Stratification, Bottom Temperature, Cold Pool, Offshore Wind, Mid-Atlantic Bight

I. Introduction

The Mid-Atlantic Cold Pool is a seasonal mass of cold bottom water extending throughout the Mid-Atlantic Bight (MAB) from Nantucket, MA to Cape Hatteras, NC, which results in one of the largest thermal gradients in the world (Fig.1). This stratification and the associated cold bottom temperatures and nutrient-rich environment support a diverse coastal ecosystem including economically important recreational and commercial fisheries [1]. Within the MAB, over 2.3 million acres of the MAB continental shelf has been leased for offshore wind energy projects that are under development, including sites that overlap with the seasonal Cold Pool [1,2]. Limited information exists about the extent of this overlap, as well as the impact of the turbines on the Cold Pool [1].

The Cold Pool develops in the winter as cold water from the Nantucket Shoals, north of the MAB, is transported southward to well-mixed MAB water [3,4]. In the spring, as surface water temperature increases and storm frequency decreases, a strong thermocline develops that isolates the cold, and relatively fresh bottom water, known as the Cold Pool [3, 5]. Stratification within the MAB is controlled and stabilized by salinity and temperature [6]. The strength of the thermocline, driven primarily by temperature, reaches a seasonal peak between July and August, when the Cold Pool also peaks [6]. As surface temperatures begin to decrease in the late summer and early fall, the thermocline weakens and fall storms eventually mix stratified surface waters to the bottom and the Cold Pool dissipates [3-8].

Seasonal Cold Pool evolution is integral to MAB ecosystem processes. Upwelling along the MAB occurs annually transporting Cold Pool waters further inshore and towards the coastal surface, which can drive phytoplankton blooms [9,10]. The presence of Cold Pool water allows species ranges to extend further south than would be anticipated by latitude, supporting many economically and culturally valuable finfish and shellfish fisheries [11–14].

The United States is anticipated to become one of the largest offshore energy markets by 2030 with an estimated 1.7 million acres under lease, and more than 2,100 turbine foundations to be installed [15]. The MAB region leads the nation in proposed offshore wind energy projects with regional offshore wind goals totaling more than 40,083 megawatts (MW) of energy within the next decade [2]. Offshore wind development in the United States is relatively new, while European offshore wind energy has been developed extensively and can provide insight into possible interactions between turbines, physical oceanographic processes, and biological systems despite key differences between the regions [16].

Funding provided by the National Science Foundation and the Science Center for Marine Fisheries

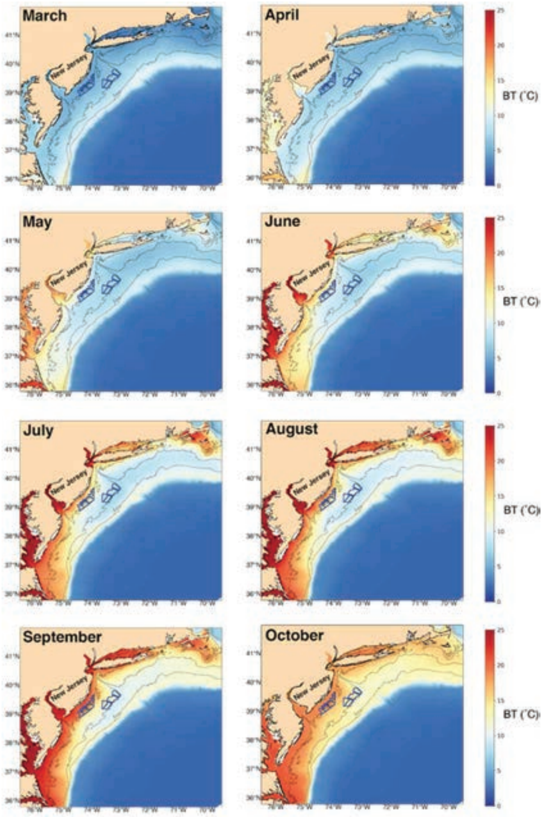

Fig.1. Monthly averaged bottom temperatures based on Doppio simulations spanning 2007 to 2020 within the MAB. Only peak Cold Pool months are included. The Cold Pool is highlighted with white and blue colors when the bottom temperature reaches below 10˚C. Wind lease areas included in this study are outlined in blue. The 25, 50 and 75m isobaths are shown in black.

While still applicable, results from European studies are more representative of conditions in the MAB during relatively weakly stratified periods, and do not represent Cold Pool conditions [1]. Likewise, many European lease areas use smaller turbines with different density and spacing, further adding to uncertainty about how relevant European research is to MAB conditions [16].

Wind turbines can directly impact the hydrodynamics within and around the site through their underwater infrastructure, and indirectly through changes in both the surface and atmospheric wind fields [17]. Structure-induced friction and blocking from flow past cylindrical structures often forms Von Kármán vortex streets, increasing the turbulence directly downstream of the turbine. In the context of the Cold Pool, this could lead to less stratified conditions [1]. It is unclear what the effects will be on the highly stratified system like the MAB Cold Pool if the area of increased turbulence is expanded [17-18]. Likewise, the extraction of atmospheric kinetic energy by turbines may be amplified by larger clusters of wind turbines in turn reducing shear-driven forcing at the sea surface and decreasing horizontal velocities, and turbulent mixing within several kilometers of the wind site [19]. This could potentially mean that within the MAB, offshore wind projects within the Cold Pool could strengthen stratification. The implications of offshore wind on the hydrodynamic features of the MAB require further study, however, because of the broader spatial extent of wind lease areas, the weaker tidal strength and increased storm frequency within the MAB versus Europe, as well as the technological differences in turbine design.

In this paper, we evaluate the extent and cross-shelf variability of spatial overlap between wind lease areas and the Cold Pool. We will focus on projects proposed in waters off the state of New Jersey to highlight trends in these differences. Specifically, we will evaluate the duration, strength, and variability of stratification where the Cold Pool overlaps with wind lease areas within the southern New York Bight, off of New Jersey (NJ) using output from a data assimilative regional ocean model known as Doppio [20].

II. Methods

Data used in this study was simulated by the Doppio model, a Regional Ocean Modeling System (ROMS) application of the MAB and the Gulf of Maine [20]. Doppio is computed using 4-Dimensional variational assimilation of satellites, HF-radar ocean surface currents and all available *in situ* observations from MARACOOS and NERACOOS regional associations of the U.S Integrated Ocean Observing System (IOOS). The model resolution is a uniform 7 km horizontal grid with 40 vertical layers. The output of Doppio used in this study is from a free-running regional model run with simulations spanning from 2007 to 2021. Data was accessed in March 2022 using the thredds link: (https://tds.marine.rutgers.edu/thredds/roms/doppio/catalog.html?dataset=DopAnV3R3-ini2007_da_monthly_averages).

The presence and location of the Cold Pool is defined as locations where the vertical temperature gradient is 0.2˚C/m or greater and the bottom temperature is 10˚C or less [1, 3, 7, 21–24]. The density stratification over the MAB region is primarily thermally controlled during the peak Cold Pool months, thus stratification is determined by calculating the temperature gradient:

$$0.2^\circ C/m \le \delta T/\delta z \ \& \ T \le 10^\circ C \qquad (1)$$

Seven wind lease areas (WLAs) were identified as the closest geographically to the New Jersey shoreline and were selected for this study (Fig. 2). Six study locations were selected approximately central within or at a boundary between the seven WLAs. Monthly averaged temperature values were obtained from Doppio simulations for each study location (Fig. 2). Using all 40 vertical layers of the monthly averaged temperature data, a monthly vertical temperature gradient was calculated for each location (n=180). The monthly average bottom temperature was also calculated for each location. Temporal trends and variability in Cold Pool evolution were determined using ensemble monthly averages (i.e the mean of all January temperature values from 2007-2021) and standard deviation calculated for both bottom temperature and temperature gradients for all 15 years at each study location.

III. RESULTS

Based on the temperature gradient and bottom temperature criteria, the Cold Pool was present at all six selected study locations within the seven wind lease areas (Fig. 3,Table I,Table II). Despite the fifteen-year temporal span of the ensemble monthly averages of bottom temperature and the temperature gradient, variability across the time series at each study point was limited. Bottom temperature during peak Cold Pool months varied by 0.13˚C (standard deviation) while temperature gradient varied by 0.02˚C/m (standard deviation) across all sites and years.

There were limited latitudinal differences in the duration or strength of the Cold Pool across the six study locations (Fig. 3,Table I,Table II). Four study points are offshore in 50m water depth, while two are relatively inshore at approximately 25m of depth. All four offshore study locations had bottom water temperature below 10˚C and a thermal gradient greater than 0.2˚C/m in the month of April signifying the presence of the Cold Pool (Fig. 3). The bottom temperature at these four offshore study points exceeded 10˚C in July meaning the Cold Pool duration there was approximately three months (Fig. 3,Table I). Despite the warming bottom temperatures in all four offshore sites, the thermal gradient value above 0.2˚C/m was maintained for two additional months dissipating in September (table I). In the four offshore sites, the minimum bottom water temperature occurred at approximately the same time as the temperature gradient exceeded 0.2˚C/m in either March or April (Fig. 3, Table I, Table II). The peak temperature gradient occurred simultaneously with bottom water warming above 10˚C (Fig. 3). The highest bottom temperatures occurred as stratification broke down around October or November (Fig. 3).

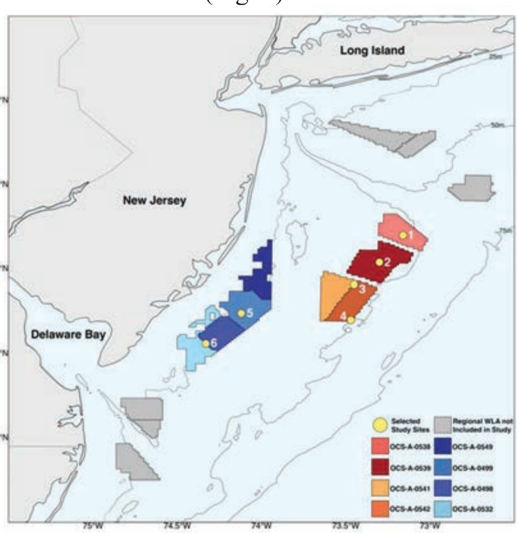

Fig. 2**.** Study locations are depicted with yellow circles and associated wind lease areas (WLA) are shown as colored blocks, with different colors for different lease blocks. Blue WLA correspond to nearshore study points while red WLA are offshore study points. Other WLA not included in this study are shown in gray. The 25, 50 and 75m isobaths are shown in black.

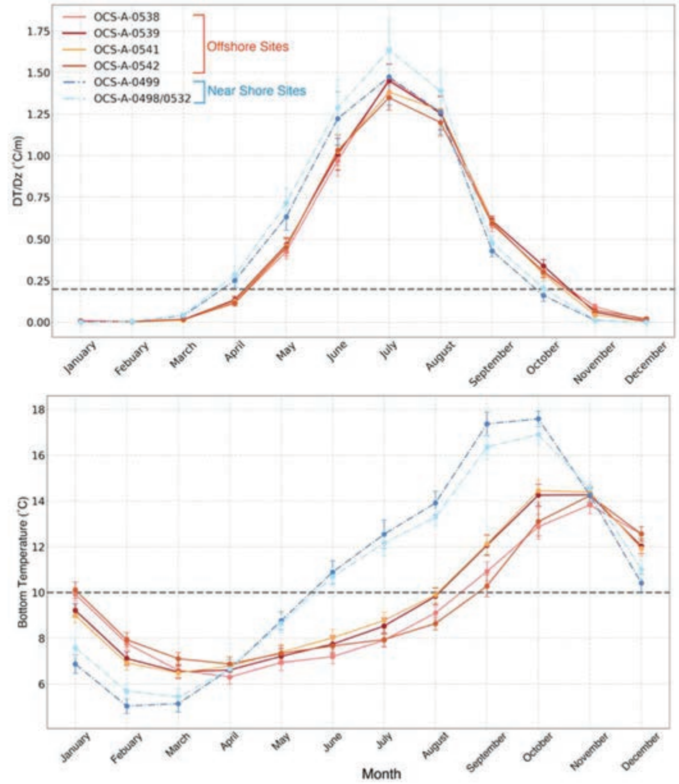

Fig.3. Monthly average bottom temperature (lower panel) and dt/dz values (upper panel) from 2007-2021 for study locations. Colors correspond to the specified wind lease area (Fig. 2). Blue colors represent nearshore sites while red colors symbolize offshore sites. The Cold Pool exists when bottom temperature values remain below the dashed grey line and when dt/dz values are above the above grey dashed line.

TABLE I. The duration of the Cold Pool based on ensemble averages from 2007-2021 according to the traditional definition as well as the duration of the thermal gradient above 0.2˚C/m for each study location. The Cold Pool start signifies the thermal gradient passing 0.2˚C/m and the Cold Pool end occurs when bottom temperatures surpass 10˚C. Wind lease area (WLA) names correspond to official lease call numbers.

Study Location	WLA Name (OCS-A-)	Cold Pool			dT/dz>0.2˚C/m	
		Start	*End*	*Length*	*End*	*Length*
1	0538	Apr.	Jul.	3	Sep.	5
2	0539	Apr.	Jul.	3	Sep.	5
3	0541	Apr.	Jul.	3	Sep.	5
4	0542	Apr.	Jul.	3	Sep.	5
5	0499	Mar.	Apr.	1	Sep.	7
6	0498/0532	Mar.	Apr.	1	Sep.	7

TABLE II. Minimum bottom temperature (BT) and maximum thermal gradient (dT/dz) values based on ensemble averages from 2007-2021 for each study location. Timing of each value is also shown. Wind lease area (WLA) names correspond to official lease call numbers.

Study Location	WLA Name (OCS-A-)	Min. BT (˚C)	Month	Max. dT/dz (˚C/m)	Month
1	0538	6.30	Apr.	1.46	Jul.
2	0539	6.53	Mar.	1.45	Jul.
3	0541	6.49	Mar.	1.38	Jul.
4	0542	6.87	Apr.	1.35	Jul.
5	0499	5.03	Feb.	1.47	Jul.
6	0498/0532	5.43	Mar.	1.64	Jul.

There are notable differences in the Cold Pool evolution between the nearshore and offshore points (Fig. 3, Table I,Table II). In the two nearshore study sites, the Cold Pool duration was shorter, spanning approximately one month, starting in March with increasing thermal gradient values and ending in April when the bottom temperature surpassed 10˚C (Fig. 3). Despite the short duration of the Cold Pool, the heightened thermal gradient values in these two nearshore sites lasted longer than at the four offshore sites (Fig. 3,Table I). In study sites five and six, the thermal gradient above the Cold Pool threshold extended for seven months (Fig. 3,Table I). Despite an earlier development in sites five and six, the thermal gradient dissipated at approximately the same time as the offshore sites (Fig. 3,Table I). In both nearshore sites, the minimum bottom temperature occurred at a similar time to the offshore sites but was more than 1˚C cooler than the offshore sites. Peak thermal gradients in both nearshore sites occurred in July, despite the bottom temperature warming above 10˚C in April. Bottom temperature and thermal gradients reached a greater maximum value at the nearshore sites.

IV. Discussion

Findings of regional Cold Pool trends offshore of New Jersey in this study are consistent with those of previous papers that discuss the spatial and temporal variability of the Cold Pool [3, 4, 6–8, 21, 23]. Nearshore bottom temperatures warmed more quickly (0.02˚C/day) than offshore bottom temperatures (0.06˚C/day) which is consistent with results from previous papers [7, 8]. Generally, the Cold Pool is shorter in duration at areas of relatively shallow depths [7,8]. Previous studies have defined the Cold Pool dissipation as the decrease in stratification strength in early fall [7,8]. While findings in this study support the strengthened thermal gradient extending into the early fall, bottom temperatures were consistently above the Cold Pool threshold after July. The thermal gradient in the southern New York Bight, where all six study sites are located, has been observed to be greater than in other areas of the MAB because of lower thermal diffusivity in the area [7,8]. Previous studies indicate the maximum temperature gradients to be around between 0.5 and 0.8 ˚C/m, while in both offshore and nearshore sites the values in this study exceeded 1˚C/m [7,8].

Cold Pool dissipation has previously been associated with bottom temperatures warming above 10˚C [3,7, 8]; however, we found that the thermal gradient remains above 0.2˚C/m well beyond when the bottom temperature warms. Even in the nearshore sites, stratification extends months after the bottom temperature warms and reaches higher maximum thermal gradient values than within the offshore sites. This finding is important as stratification is the buoyancy force that inhibits mixing by flow past structures such as wind turbines, and it maintains ecologically important habitat [1]Atlantic Surf clams, Ocean Quahogs and Sea Scallops are some of the most dominant and economically valuable fisheries within the larger MAB as well as within the state of New Jersey [1, 13, 25, 26]. These species are thermally sensitive and their distribution is often an indicator of changing bottom temperatures [13, 25].Thermal gradients and changes in bottom temperature could have direct impacts on these and other commercially and ecologically important species. Results indicate a larger spatial and temporal overlap between offshore NJ wind lease areas and the MAB Cold Pool versus near shore wind lease areas following traditional Cold Pool definition. It is still uncertain the extent to which impacts from WEA development will affect the Cold Pool. European studies have shown that wind lease areas do influence the hydrodynamic features of coastal environments [17–19]. These impacts, however, depend heavily on the spatial extent of the WEAs as well as the temporal and spatial variability of stratification and mixing [18-19]. The current wind lease areas within the German Bight occupy a significantly smaller area than those proposed along the MAB. The stratification within the German Bight is quantified as a 5-10˚C difference between surface and bottom water temperature and tidal currents in this region can reach near 1.0 m/s [18-19]. At the peak of thermal stratification in the German Bight during the year 2014, the bottom water temperature along the 25m isobath only reached 14˚C resulting in a maximum thermal gradient of 0.2˚C/m [18]. Local tidal forcing within the MAB is much weaker than the German Bight (>0.1 m/s) despite more frequent storms within the MAB [27]. The German Bight, therefore, has significantly weaker stratification than the MAB and stronger currents. Because of the spatial, technological, and environmental differences between the German Bight and the MAB, it is uncertain what the hydrodynamic impacts of offshore wind on the Cold Pool will be, however, the above characteristics of the MAB and findings of this study suggest that the impacts from turbines will be less than those found in the German Bight.

V. Conclusion

The MAB Cold Pool is an invaluable coastal ocean feature that supports some of the most economically and culturally valuable fisheries in the United States. The Cold Pool influences a variety of oceanographic processes, such as atmospheric and oceanic circulation, coastal primary productivity, and carbon sequestration. The development of offshore wind has been rapidly expanding off of coastal NJ. This study found that there is notable overlap between proposed offshore wind lease areas in NJ and the Cold Pool. In addition, it was found that thermal gradient values above the Cold Pool threshold extended past when bottom temperatures warmed above the Cold Pool criteria. Results also supported results from previous studies that nearshore bottom temperatures warm more rapidly than offshore, despite stronger thermal gradient values in nearshore sites. It is unclear from the technological, environmental, and spatial differences between the German Bight and the MAB what the impacts of the development of offshore wind on the Cold Pool will be. Future studies to determine the interdecadal trends of Cold Pool evolution is necessary to further evaluate the extent of overlap between the Cold Pool and the MAB wind lease areas are needed. Additional study is also necessary to determine the effects of newer turbine technology on the MAB seasonally stratified environment.

ACKNOWLEDGMENT

We thank the Rutgers University Department of Marine and Coastal Sciences, the Haskin Shellfish Research Lab at Rutgers University, and the Geology and Environmental Studies departments at Carleton College for their continued support. We also thank Julia Levin, John Wilkin and Alex Lòpez for their help with Doppio. Special thanks to Joe Gradone and Ailey Sheehan.

REFERENCES

[1] T. Miles, S. Murphy, J. Kohut, S. Borsetti, and D. Munroe, "Offshore Wind Energy and the Mid-Atlantic Cold Pool: A Review of Potential Interactions," Marine Technology Society Journal, vol. 55, no. 4, pp. 72–87, Jul. 2021, doi: 10.4031/MTSJ.55.4.8.

[2] W. Musial et al., "Offshore Wind Market Report: 2022 Edition," U.S Department of Energy Office of Energy Efficiency & Renewable Energy, DOE/GO-102022-5765, Aug. 2022. [Online]. Available: https://www.energy.gov/sites/default/files/2022-08/offshore_wind_market_report_2022.pdf

[3] R. Houghton, R. Schlitz, R. Beardsley, B. Butman, and J. Chamberlin, "The Middle Atlantic Bight Cold Pool: Evolution of the Temperature Structure During Summer 1979," Journal of Physical Oceanography, vol. 12, pp. 1019-1029,1982, doi: 10.1175/1520-0485(1982)012<1019:TMABCP>2.0.CO;2.

[4] H. W. Ou and R. Houghton, "A Model of the Summer Progression of the Cold-Pool Temperature in the Middle Atlantic Bight," Journal of Physical Oceanography, vol. 12, no. 10, pp. 1030–1036, Oct. 1982, doi: 10.1175/1520-0485(1982)012<1030:AMOTSP>2.0.CO;2.

[5] H. B. Bigelow, Studies of the waters on the continental shelf, Cape Cod to Chesapeake Bay. Cambridge, MA: Massachusetts Institute of Technology and Woods Hole Oceanographic Institution, 1933. doi: 10.1575/1912/1144.

[6] R. Castelao, S. Glenn, and O. Schofield, "Temperature, salinity, and density variability in the central Middle Atlantic Bight," Journal of Geophysical Research, vol. 115, no. C10, p. 2009JC006082, Oct. 2010, doi: 10.1029/2009JC006082.

[7] S. J. Lentz, "Seasonal warming of the Middle Atlantic Bight Cold Pool," Journal of Geophysical Research Oceans, vol. 122, no. 2, pp. 941–954, Feb. 2017, doi: 10.1002/2016JC012201.

[8] Z. Chen, E. Curchitser, R. Chant, and D. Kang, "Seasonal Variability of the Cold Pool Over the Mid-Atlantic Bight Continental Shelf," Journal of Geophysical Research Oceans, vol. 123, no. 11, pp. 8203–8226, Nov. 2018, doi: 10.1029/2018JC014148.

[9] S. Glenn and O. Schofield, "Observing the Oceans from the COOL Room: Our History, Experience and Opinions.," Journal of Oceanography, vol. 16(4):37–52, 2003, doi: https://doi.org/10.5670/oceanog.2003.07.

[10] S. Glenn et al., "Biogeochemical impact of summertime coastal upwelling on the New Jersey Shelf," Journal of Geophysical Research: Oceans, vol. 109, no. C12, 2004, doi: 10.1029/2003JC002265.

[11] W. L. Gabriel, "Persistence of Demersal Fish Assemblages Between Cape Hatteras and Nova Scotia, Northwest Atlantic," Journal of Northwest Atlantic Fishery Science, vol. 14, pp. 29–46, Dec. 1992, doi: 10.2960/J.v14.a2.

[12] S. Lucey and J. Nye, "Shifting species assemblages in the Northeast US Continental Shelf Large Marine Ecosystem," Marine Ecology Progress Series, vol. 415, pp. 23–33, Sep. 2010, doi: 10.3354/meps08743.

[13] K. D. Friedland, T. Miles, A. G. Goode, E. N. Powell, and D. C. Brady, "The Middle Atlantic Bight Cold Pool is warming and shrinking: Indices from in situ autumn seafloor temperatures," Fisheries Oceanography, vol. 31, no. 2, pp. 217–223, 2022, doi: 10.1111/fog.12573.

[14] T. Murray, "Economic Activity Associated with SCeMFiS Supported Fishery Products (Ocean Quahog & Atlantic Surfclams)," Jun. 2016. [Online]. Available: https://scemfis.org/wp-content/uploads/2020/02/Ec_Impact-tjm_rm2.pdf

[15] M. Shields et al., "The Demand for a Domestic Offshore Wind Energy Supply Chain," National Renewable Energy Laboratory (NREL), Denver, CO, Technical Report NREL/TP-5000-81602, Jun. 2022. [Online]. Available: (https://www.nrel.gov/docs/fy22osti/81602.pdf

[16] E. Methratta, A. Hawkins, B. Hooker, A. Lipsky, and J. Hare, "Offshore Wind Development in the Northeast US Shelf Large Marine Ecosystem: Ecological, Human, and Fishery Management Dimensions," Journal of Oceanography, vol. 33, no. 4, pp. 16–27, Dec. 2020, doi: 10.5670/oceanog.2020.402.

[17] J. van Berkel, H. Burchard, A. Christensen, L. Mortensen, O. Petersen, and F. Thomsen, "The Effects of Offshore Wind Farms on Hydrodynamics and Implications for Fishes," Journal of Oceanography, pp. 108–117, Dec. 2020.

[18] J. R. Carpenter, L. Merckelbach, U. Callies, S. Clark, L. Gaslikova, and B. Baschek, "Potential Impacts of Offshore Wind Farms on North Sea Stratification," PLOS ONE, vol. 11, no. 8, p. e0160830, Aug. 2016, doi: 10.1371/journal.pone.0160830.

[19] N. Christiansen, U. Daewel, B. Djath, and C. Schrum, "Emergence of Large-Scale Hydrodynamic Structures Due to Atmospheric Offshore Wind Farm Wakes," Frontiers in Marine Science, vol. 9, p. 818501, Feb. 2022, doi: 10.3389/fmars.2022.818501.

[20] A. G. López, J. L. Wilkin, and J. C. Levin, "Doppio – a ROMS (v3.6)-based circulation model for the Mid-Atlantic Bight and Gulf of Maine: configuration and comparison to integrated coastal observing network observations," Geoscientific Model Development, vol. 13, no. 8, pp. 3709–3729, Aug. 2020, doi: 10.5194/gmd-13-3709-2020.

[21] D. G. Mountain, "Variability in the properties of Shelf Water in the Middle Atlantic Bight, 1977–1999," Journal of Geophysical Research, vol. 108, no. C1, p. 3014, 2003, doi: 10.1029/2001JC001044.

[22] C. de Boyer Montégut, G. Madec, A. S. Fischer, A. Lazar, and D. Iudicone, "Mixed layer depth over the global ocean: An examination of profile data and a profile-based climatology," Journal of Geophysical Research: Oceans, vol. 109, no. C12, 2004, doi: 10.1029/2004JC002378.

[23] W. Brown et al., "Mapping the Mid-Atlantic Cold Pool evolution and variability with ocean gliders and numerical models," in 2012 Oceans, Hampton Roads, VA, Oct. 2012, pp. 1–6. doi: 10.1109/OCEANS.2012.6404970.

[24] Y. Li et al., "Spatio-temporal patterns of stratification on the Northwest Atlantic shelf," Progress in Oceanography, vol. 134, pp. 123–137, May 2015, doi: 10.1016/j.pocean.2015.01.003.

[25] E. N. Powell, A. M. Ewing, and K. M. Kuykendall, "Ocean quahogs (Arctica islandica) and Atlantic surfclams (Spisula solidissima) on the Mid-Atlantic Bight continental shelf and Georges Bank: The death assemblage as a recorder of climate change and the reorganization of

the continental shelf benthos," Palaeogeography, Palaeoclimatology, Palaeoecology, vol. 537, p. 109205, Jan. 2020, doi: 10.1016/j.palaeo.2019.05.027.
[26] D. M. Munroe et al., "Fishing and bottom water temperature as drivers of change in maximum shell length in Atlantic surfclams (Spisula solidissima)," Estuarine, Coastal and Shelf Science, vol. 170, pp. 112–122, Mar. 2016, doi: 10.1016/j.ecss.2016.01.009.
[27] K. Brunner and K. M. M. Lwiza, "Evidence of coastal trapped wave scattering using high-frequencyradar data in the Mid-Atlantic Bight," Remote Sensing/Current Field/Surface/Shelf Seas, preprint, Jul. 2020. doi: 10.5194/os-2020-46.

Typhoon-induced Full Vertical Mixing and Subsequent Intrusion of Yangtze Fresh Waters in the Southern Yellow Sea: Observation with an Underwater Glider and GOCI Ocean Color Imagery

Authors: Lim, Hak Soo, Kim, Dongha, Lee, Hee Jun, Kim, Minwoo, Jin, Seung Hwan, et al.

Source: Journal of Coastal Research, 114(sp1) : 171-175

Published By: Coastal Education and Research Foundation

URL: https://doi.org/10.2112/JCR-SI114-035.1

Journal of Coastal Research	SI	114	171–175	Coconut Creek, Florida	2021

Typhoon-induced Full Vertical Mixing and Subsequent Intrusion of Yangtze Fresh Waters in the Southern Yellow Sea: Observation with an Underwater Glider and GOCI Ocean Color Imagery

www.cerf-jcr.org

Hak Soo Lim†*, Dongha Kim†, Hee Jun Lee††, Minwoo Kim†††, Seung Hwan Jin†, Travis N. Miles††††, and Scott Glenn††††

†Marine Disaster Research Center
Korea Institute of Ocean Science & Technology
Busan, Republic of Korea

††Marine Active Fault Research Unit
Korea Institute of Ocean Science & Technology
Busan, Republic of Korea

†††Ocean Circulation and Climate Research Center
Korea Institute of Ocean Science & Technology
Busan, Republic of Korea

††††Department of Marine and Coastal Sciences
Rutgers University
New Brunswick, NJ, USA

www.JCRonline.org

ABSTRACT

Lim, H.S.; Kim, D.; Lee, H.J.; Kim, M.; Jin, S.H.; Miles, T.N., and Glenn, S., 2021. Typhoon-induced full vertical mixing and subsequent intrusion of Yangtze fresh waters in the Southern Yellow Sea: Observation with an underwater glider and GOCI ocean color imagery. *In:* Lee, J.L.; Suh, K.-S.; Lee, B.; Shin, S., and Lee, J. (eds.), *Crisis and Integrated Management for Coastal and Marine Safety*. *Journal of Coastal Research*, Special Issue No. 114, pp. 171–175. Coconut Creek (Florida), ISSN 0749-0208.

Typhoons have been regarded as an important forcing to control oceanographic phenomena, particularly in the Yellow and East China Seas. The influences of typhoons have become increasingly severe due to global warming. An autonomous underwater glider was deployed west of Jeju Island for 10 days from 15th to 25th August, 2018 to observe changes in physical environments induced by Typhoon Soulik. The glider data show that the stratified water masses were destroyed by the typhoon into a fully mixed stage of the entire water column. This de-stratification is manifested by many environmental parameters including temperature, salinity, chlorophyll-a, and suspended sediment concentrations. Accordingly, calculated parameters, density, and Richardson number, indicate de-stratification. The water column displayed, however, a rapid return to the stratification stage immediately after the typhoon passage. In addition, the GOCI geostationary ocean color imagery was analyzed that were obtained during and after the passage of Soulik between 15-25 August, 2018. These satellite images suggest that the discharge of the Yangtze River fresh water so increased during the typhoon that the intensified freshwater plume could move toward Jeju Island. As a result, observations with an autonomous glider may provide a promising means in analyzing oceanographic processes occurring during the peak of typhoons.

ADDITIONAL INDEX WORDS: *Typhoon-ocean interaction, ocean de-stratification, Yangtze diluted water, underwater glider, GOGI observation.*

INTRODUCTION

Recently, the threat of typhoons on the coast of the Korean Peninsula has been gradually increasing because of rising of sea water temperature and sea level due to global warming. The number of typhoons that influenced South Korea sharply increased from 2.5 a year on average in the last 10 years (2001-2010) to 5 in 2018 and 7 in 2019 (KMA, 2020). Many of the typhoons entering the Yellow Sea moved toward the southern coast of the Korean Peninsula through the coastal waters of Jeju Island (Figure 1a).

In addition, typhoons caused the surface water temperature to be dramatically changed producing a strong surface cooling. In August 2012, the passing of Typhoon Bolaven resulted in the surface water temperature dropping from 27-28 °C to 16-20 °C according to satellite observations from near the west coast of Jeju Island (Kim *et al.*, 2014). The passing of Typhoon Soulik also resulted in the surface water temperature decreasing from 27.5 °C to 16.5 °C according to underwater glider observation from the west coast of Jeju Island (Lim *et al.*, 2020). Both typhoons passed through west Jeju Island from the East China Sea in August 2012 and 2018, respectively. The study area is a critical alley of typhoons that enter the East China Sea (Figure 1a). This area is characterized by the Yellow Sea Cold Bottom Water and is frequently influenced by a low-salinity plume of the Yangtze fresh water in summer (Kim *et al.*, 2004). Prior to the Typhoon Soulik passage, strong summer stratification was observed to form due to substantial differences in temperature (11 °C) between the surface and bottom layers (Lim *et al.*, 2020). Similarly, the rapid surface cooling by Hurricane Irene also observed over the stratified coastal waters of northeast United States in August 2011 (Glenn *et al.*, 2016).

This study updates the preliminary results (Lim *et al.*, 2020) from the underwater glider observations in the western coastal waters of Jeju Island of Korea (Figure 1b). The observations were performed vertically through the water column down to 100 m during a 10-day period including the passage of Typhoon Soulik. The major goal of the present study is to illuminate details of the oceanographic changes induced by Typhoon Soulik. To do this, the glider data were carefully re-analyzed, and the GOCI (Geostationary Ocean Color Imager) imagery was used to monitor how the typhoon influenced the distributions of suspended matter in the study area.

DOI: 10.2112/JCR-SI114-035.1 received 20 November 2020; accepted in revision 18 January 2021.
*Corresponding author: hslim@kiost.ac.kr

METHODS

Typhoon Soulik formed on August 16, 2018 in the western North Pacific and rapidly intensified to the level of typhoon in two days. The typhoon slowly passed west of Jeju Island around 12:00 KST (3:00 UTC) on 23 August. On the same day, though somewhat weakened, it made landfall over the southwestern coast of the Korean Peninsula around 23:00 KST.

Underwater Glider

An underwater glider (RU22) was deployed in an area west of Jeju Island (Figure 1b) from 15th to 25th August 2018 (Lim *et al.*, 2020). The RU22 glider was equipped with CTD and optical BBFL2 sensors to measure various oceanographic parameters including temperature, salinity, density, chlorophyll-a, dissolved organic matter, and optical backscatter, a proxy of suspended sediment concentrations. The glider moved through the almost entire water column from the surface down to 100 m. Details on operation and measurements can be seen elsewhere (Lim *et al.*, 2020).

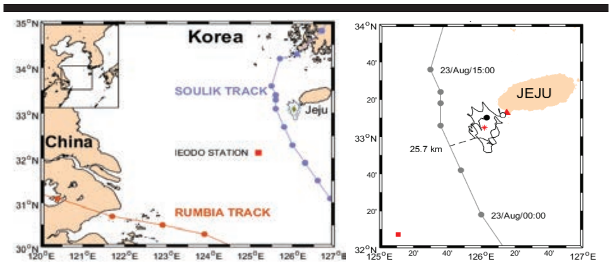

(a) Typhoon Tracks (b) Glider Tracks

Figure 1. (a) Track of Typhoon Rumbia (Red) and Soulik (Blue) in south Yellow Sea and (b) Track of glider observation for 10 days from 15th to 25th August 2018. Triangle = deployment site; circle = recovery site; star = Marado ocean buoy; square = Ieodo station.

GOCI Observation

GOCI obtains ocean color images every day during the daytime (Choi *et al.*, 2012). Some of GOCI images obtained during 21-26 August 2018 were chosen in this study to reveal distributional time-series of chlorophyll-a and suspended sediment concentration (SSC).

RESULTS

The vertical ocean mixing induced by Typhoon Soulik is evident in the distributions of temperature, salinity, and thus density (Figure 2). At the Soulik passage on 23 August, temperature dropped about 11 °C from 27.5 °C to 16.5 °C at the surface in contrast to the water depth of 100 m where it increased by 3 °C (from 11 °C to 14 °C) (Figure 2a). At the same time, salinity clearly shows a remarkable increase of about 1.8 psu at the surface, while it remained constant or barely increased (about 0.7 psu) at 100 m (Figure 2b). The Marado ocean buoy close to the glider area (Figure 1b) exhibits that significant wave heights measured 8 m during the typhoon; this buoy also measures tide. Immediately after the typhoon passage, however, salinity rapidly increase to about 34.3 psu in the bottom layer. Both the temperature and salinity display a thermocline and a halocline, respectively, around the water depths of 20-40 m before the typhoon (Figure 2a, b). Density follows well the patterns of temperature and salinity as the latter control density dominantly (Figure 2c). A pycnocline was therefore existent between 20 and 40 m. It is interesting that tidal fluctuations may affect the variations of these three parameters considerably, particularly in the mid-to-bottom water depths.

The typhoon effects on temperature, salinity, and density are more clearly shown in selected vertical profiles (Figure 3). All the profiles illustrate vertical mixing and hence the de-stratification of the entire water mass by Typhoon Soulik.

The degree of stratification can be evaluated using the Richardson number, *Ri* (Prandle, 2009):

$$Ri = \frac{g}{\rho} \frac{\partial \rho / \partial z}{\left(\partial u / \partial z \right)^2} \tag{1}$$

where, g is gravity, ρ is density of sea water, u is flow speed, and z is water depth. The condition, $Ri < 0.25$, was used to signal de-stratification. Flow speed was obtained on the assumption that the horizontal speeds of the glider and flows were identical to each other. Figure 4 shows full mixing at the typhoon passage and otherwise a consistent stratification in the water layer of 20-40 m.

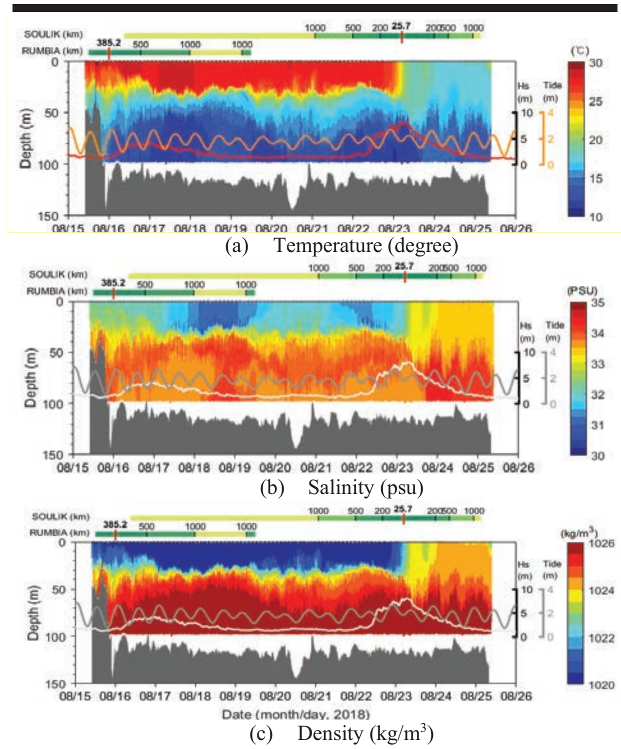

(a) Temperature (degree)
(b) Salinity (psu)
(c) Density (kg/m^3)

Figure 2. Time-series of vertical variations of (a) temperature (degree), (b) salinity (psu), and (c) density (kg/m^3) from the surface to the water depth of 100 m induced by Typhoon Soulik from 15th to 25th August, 2018. The significant wave height (red or white) and tide elevation derived from the Marado ocean buoy. For the buoy location, see Figure 1b. The gray shades show time-series of bottom bathymetry during the glider observation.

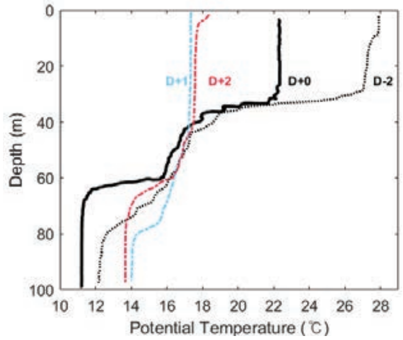

(a) Temperature profiles (degree)

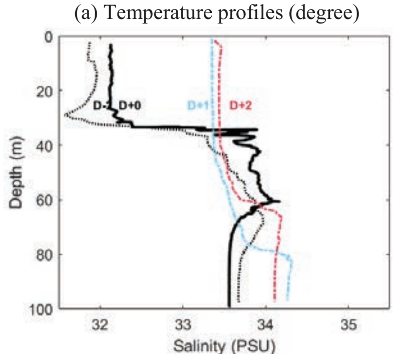

(b) Salinity profiles (psu)

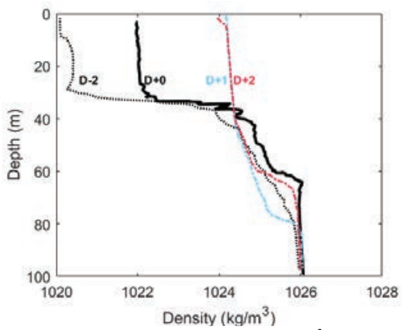

(c) Density profiles (kg/m^3)

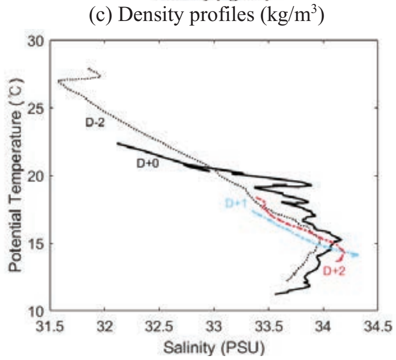

(d) Temperature-salinity diagram

Figure 3. Vertical profiles of (a) temperature (degree), (b) salinity (psu), and (c) density (kg/m^3) two days before the typhoon arrival (D-2), at the typhoon arrival (D+0), and one and two days after the typhoon arrival (D+1 and D+2, respectively). (d) temperature-salinity (T-S) diagram derived from the profiles shown in a and b.

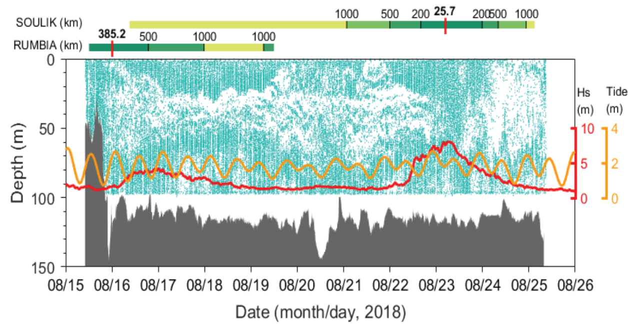

Figure 4. Time-series of vertical variation of the Richardson number (*Ri*) calculated by the horizontal speed of the underwater glider for 10 days from 15th to 25th August, 2018. A blue dot indicates *Ri* <0.25, the de-stratification state.

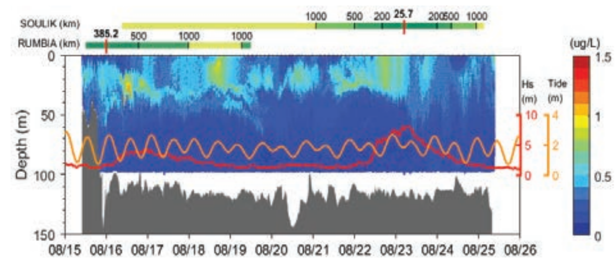

(a) Chlorophyll-a (ug/L)

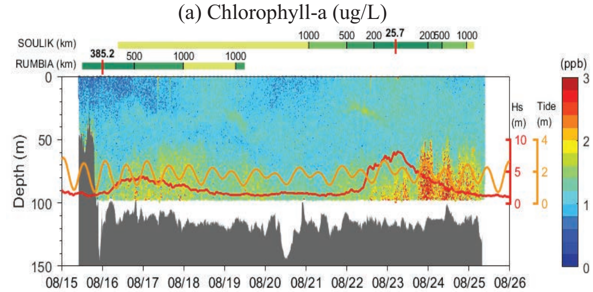

(b) CDOM (ppb)

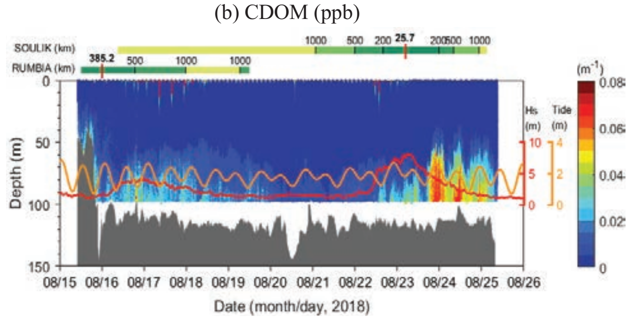

(c) Optical backscatter (b_b) at a wavelength of 880 nm (m^{-1})

Figure 5. Time-series of vertical variations of (a) chlorophyll-a (ug/L), (b) colored dissolved organic matter (ppb), and (c) optical backscatter at 880 nm (m^{-1}) for 10 days from 15th to 25th August, 2018. The significant wave height (red line) and tide elevation (brown line) were derived from the Marado ocean buoy.

Figure 5 shows time-series of chlorophyll-a, colored dissolved organic matter (CDOM) and optical backscatter. Chlorophyll-a also indicates vertical mixing processes by the typhoon (Figure 5a). Its concentrations were diluted in the surface layer but somewhat increased in the mid layer during the typhoon passage. The CDOM and optical backscatter display rapid increases by high waves of the typhoon in the bottom waters (Figure 5b, c). Such an increase continued after the typhoon waned. The concordant variations of these two parameters with tide suggest that tidal currents can resuspend seabed sediments in this area.

The GOCI ocean color images show the distribution of surface chlorophyll-a in the southern Yellow Sea before and after the Typhoon Soulik passage (Figure 6). A surface plume laden by chlorophyll-a came to move eastward from the Yangtze-river mouth to near Jeju Island as the Yangtze-river discharge greatly increased owing to heavy rainfall during the typhoon. The SSC distributions were quite similar to those of chlorophyll-a (Figure 7). Typhoon Soulik resulted in the Yangtz-river diluted fresh water extending to Jeju Island.

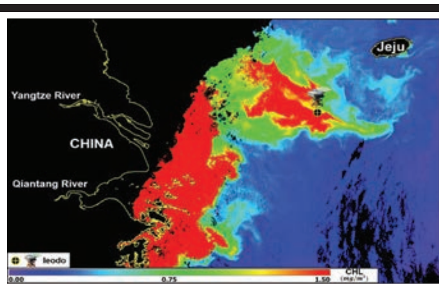

(a) 21 August 2018

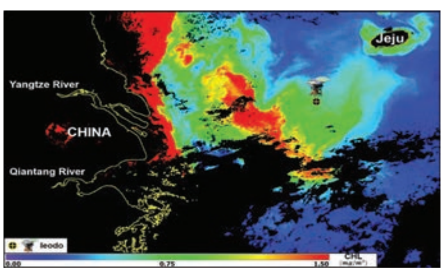

(b) 24 August 2018

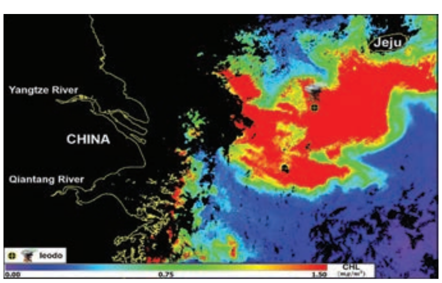

(c) 26 August 2018

Figure 6. Distribution of surface chlorophyll-a from GOCI images on August (a) 21, (b) 24, and (c) 26, 2018. A surface plume of Yangtze-river fresh waters was shown to move toward Jeju Island during Typhoon Soulik.

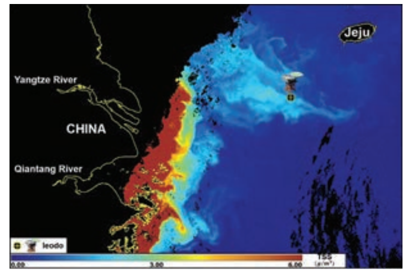

(a) 21 August 2018

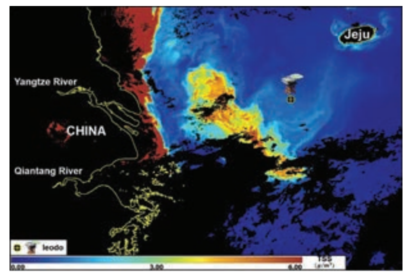

(b) 24 August 2018

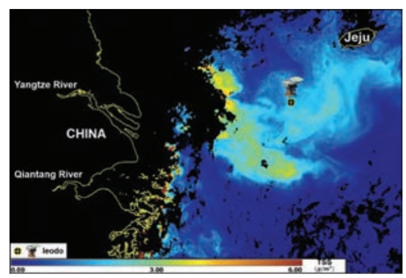

(c) 26 August 2018

Figure 7. Distribution of surface suspended sediment concentrations from GOCI images on August (a) 21, (b) 24 and (c) 26, 2018. A surface plume of Yangtze-river fresh waters was shown to move toward Jeju Island during Typhoon Soulik.

DISCUSSION

Typhoon Soulik created an extensive vertical mixing of the order of 100 m. That mixing destructed pre-typhoon ocean stratification that had been characterized by a thermocline and a pycnocline well established between water depths of 20-40 m near west Jeju Island, Korea. As a result, the bottom-water layer received a great amount of heat energies (equivalent to an increase of 3 ℃), whereas the surface layer was cooled significantly (a drop of 11 ℃). In this exchange of water masses, organic matters abundant in the surface layer were also dispersed down to the bottom layer. Such a scale of vertical mixing observed by underwater glider has not been demonstrated in the study area. Kang, Jo, and Kim (2020) also reported vertical mixing and fluctuation of the thermocline by Typhoon Soulik from Argo floats near the coastal waters of southwestern Korean Peninsula. However, the thermocline layer, where temperature range is 15-20 °C, was deepened from 20-30 m to 40-50 m by the typhoon.

The seabed sediments appear to be resuspended by tidal currents. The time-series data (Figure 5c) show that during spring tide the resuspension occurred in tidal modulation. However, Typhoon Soulik most probably agitated the seabed sediments in that optical-backscatter signals began to be recorded abruptly when waves heights rapidly increased (Figure 5c). Those data suggest that the threshold of the seabed sediments may be exceeded by typhoon- or storm-induced, 5-m-high waves. This finding may reflect that typhoon and storms play an important role in the mud flux and distribution in the Yellow Sea and adjacent seas (Lee and Chough, 1987). It is interesting that the optical backscatter further increased during the diminishing waves under the same tidal conditions unchanged. More detailed physical data from the near-bottom layer should be needed to resolve these resuspension processes.

The satellite data (Figures 6 and 7) have illuminated that the Yangtze fresh waters can reach the coastal zone of Jeju Island, not only during the summertime flooding seasons but also during a short period of heavy rainfalls by typhoons. Previous studies were mostly focused on the movements of a Yangtze diluted freshwater plume associated with the summer flooding (Bai *et al*., 2014). The present study clearly shows that the Yangtze fresh waters extended to near Jeju Island by Typhoon Soulik, although the summer flooding seasons of that year (2018) had already ended. The appearance of the Yangtze plume near Jeju Island is a critical issue to fishery industries of that region. Therefore, typhoons should be requisite to forecasting the plume formation and behavior accurately.

CONCLUSIONS

The vertical ocean mixing by the Typhoon Soulik over the highly stratified waters of west Jeju Island was re-analyzed with the oceanographic parameters including temperature, salinity, and density from CTD sensor and chlorophyll-a, dissolved organic matter, and optical backscatter from optical BBFL2 sensor equipped with the underwater glider. The change of surface distribution of chlorophyll-a and suspended sediment concentration which was derived from GOCI ocean color imagery was also analyzed for the Typhoon Soulik influence.

The ocean stratification in the water depth of 20-40 m before the typhoon was vertically fully mixed by the strong typhoon effect and tidal fluctuations. The typhoon-driven vertical ocean mixing also could affected the suspended sediment transport concentration in the mid-to-bottom water depths enhanced by the tidal effect. The Yangtze-river fresh water affected significantly not only the surface temperature and salinity but also the surface concentrations of chlorophyll-a, CDOM, and SSC during the typhoon passage.

ACKNOWLEDGMENTS

The authors thank to Dr. Young Baek Son and Dr. Jae-Seol Shim, Korea Institute of Ocean Science and Technology (KIOST), for supporting and facilitating the glider observation. This research was fully supported by the Ministry of Trade, Industry and Energy (MOTIE), Korea for its financial support of the project titled “The establishment of advanced marine industry open laboratory and development of realistic convergence content.” The authors are also grateful to the Ministry of Oceans and Fisheries (MOF), Korea for its administrative support of the project titled “Construction of ocean research stations and their application studies” with NOAA-MOF Joint Project Agreement.

LITERATURE CITED

Bai, Y.; He, X.; Pan, D.; Chen, C.T.; Kang, Y.; Chen, X., and Cai, W.-J., 2014. Summertime Changjiang River plume variation during 1998–2010. *Journal of Geophysical Research: Oceans*, 119, 6238–6257, DOI:10.1002/2014JC009866.

Choi, J.K.; Park, Y.J.; Ahn, J.H.; Lim, H.S.; Eom, J., and Ryu, J.H., 2012. GOCI, the world’s first geostationary ocean color observation satellite for the monitoring of temporal variability in coastal water turbidity. *Journal of Geophysical Research,* 117, C09004, DOI:10.1029/2012JC008046.

Glenn, S.M.; Miles, T.N.; Seroka, G.N.; Xu, Y.; Forney, R.K.; Yu, F.; Roarty, H.; Schofield, O., and Kohut, J., 2016. Stratified coastal ocean interactions with tropical cyclones. *Nature Communications*, DOI:10.1038/ncomms10887.

Kang, K.R.; Jo, H.J., and Kim, Y.J., 2020. Ocean responses to Typhoon Soulik (1819) around Korea. *Ocean Science Journal (2020)*, 55(3), 445-457.

Kim, C.S.; Lim, H.S.; Jeong, J.Y.; Shim, J.S.; Moon, I.J.; Oh, Y.J., and You, H.Y., 2014. Response of coastal waters in Yellow Sea to Typhoon Bolaven. *In:* Green, A.N. and Cooper, J.A.G. (eds.), *Proceedings 13th International Coastal Symposium* (Durban, South Africa). *Journal of Coastal Research*, Special Issue No. 70, pp. 278–283.

Kim, C.S.; Lim, H.S.; Yoon, J.J., and Chu, P.C., 2004. Numerical simulation of hydrodynamics and water properties in the Yellow Sea. I. Climatological inter-annual variability. *Journal of Korean Society of Oceanography*, 39(1), 72-95.

Korea Meteorological Administration (KMA), 2020. *Typhoon Information-development statistics*. http://www.weather.go.kr/weather/typoon/statistic.jsp (accessed October 15, 2020).

Lee, H.J. and Chough, S.K., 1987. Sediment distribution, dispersal and budget in the Yellow Sea. *Marine Geology,* 87, 195-205.

Lim, H.S.; Miles, T.N.; Scott, G.; Kim, D.H.; Kim, M.W.; Shim, J.S.; Chun, I., and Hwang, K.-N., 2020. Rapid ocean destratification by Typhoon Soulik over the highly stratified waters of west Jeju Island, Korea. *In:* Malvárez, G. and Navas, F. (eds.), *Global Coastal Issues of 2020*. *Journal of Coastal Research*, Special Issue No. 95, pp. 1480–1484.

Prandle, D., 2009. Estuaries: Dynamics, mixing, sedimentation and morphology. Cambridge, Cambridge University Press, 236 p.

Progress in Oceanography 219 (2023) 103130

Contents lists available at ScienceDirect

Progress in Oceanography

journal homepage: www.elsevier.com/locate/pocean

The Southern Ocean carbon and climate observations and modeling (SOCCOM) project: A review

Jorge L. Sarmiento [a], Kenneth S. Johnson [b,*], Lionel A. Arteaga [c,d], Seth M. Bushinsky [e], Heidi M. Cullen [b], Alison R. Gray [f], Roberta M. Hotinski [a], Tanya L. Maurer [b], Matthew R. Mazloff [g], Stephen C. Riser [f], Joellen L. Russell [h], Oscar M. Schofield [i], Lynne D. Talley [g]

[a] Program in Atmospheric and Oceanic Sciences, Princeton University, Princeton, NJ 08544, USA
[b] Monterey Bay Aquarium Research Institute, Moss Landing, CA 95039, USA
[c] Global Modeling and Assimilation Office, NASA Goddard Space Flight Center, Greenbelt, MD 20771, USA
[d] Goddard Earth Sciences, Technology and Research II, University of Maryland Baltimore County, Baltimore, MD 21250, USA
[e] Department of Oceanography, School of Ocean and Earth Science and Technology, University of Hawai'i at Mānoa, Honolulu, HI 96822, USA
[f] School of Oceanography, University of Washington, Seattle, WA 98195, USA
[g] Scripps Institution of Oceanography, University of California San Diego, La Jolla, CA 92093, USA
[h] Department of Geosciences, University of Arizona, Tucson, AZ 85721, USA
[i] Center of Ocean Observing Leadership, Department of Marine and Coastal Science, Rutgers University, New Brunswick, NJ 08901, USA

ARTICLE INFO

Keywords:
Biogeochemical-Argo
Southern Ocean
Carbon cycle
Oxygen
Nitrate
pH

ABSTRACT

The Southern Ocean serves as the primary gateway through which the intermediate, deep, and bottom waters of the ocean interact with the surface ocean (and thus the atmosphere), and it has a profound influence on the oceanic uptake of anthropogenic carbon and heat as well as nutrient resupply from the abyss to the surface. Yet it has been the least observed and understood region of the world ocean. The Southern Ocean Carbon and Climate Observations and Modeling (SOCCOM) project was implemented in 2014 with a goal to help remedy this deficit in observations and understanding. The SOCCOM project is based on two major advances that have the potential to transform understanding of the Southern Ocean. The first is the development of new biogeochemical sensors mounted on autonomous profiling floats that allow sampling of ocean biogeochemistry in 3-dimensional space. Floats may detect processes with a temporal resolution that ranges from hours to years. The second is that the climate modeling community finally has the computational resources and physical understanding to develop fully coupled climate models that can represent crucial, mesoscale processes in the Southern Ocean, as well as corresponding models that assimilate observations to produce a state estimate. The observational component, based on deployment of profiling floats with oxygen, nitrate, pH and bio-optical sensors, is generating vast amounts of new biogeochemical data that provide a year-round view of the Southern Ocean from the surface to 2000 m. The modeling effort is applying these observations and enhancing our understanding of the current ocean, and reducing uncertainty in projections of future carbon and nutrient cycles and climate. After nine years of operation, including a project renewal in the sixth year, the SOCCOM project has deployed more than 260 profiling floats. These floats have collected over 27,000 vertical profiles throughout the Southern Ocean. A data-assimilating biogeochemical state estimate model has been implemented. Here, the design of the SOCCOM project is reviewed and the scientific results that have been obtained are described. The project's capability to help meet the observing system priorities outlined for a notional UN Decade for Ocean Sciences Southern Ocean observing system is assessed.

* Corresponding author.
E-mail address: johnson@mbari.org (K.S. Johnson).

https://doi.org/10.1016/j.pocean.2023.103130
Received 1 March 2023; Received in revised form 14 June 2023; Accepted 26 September 2023
Available online 1 October 2023

1. Introduction

In 2014, the Southern Ocean Carbon and Climate Observations and Modeling (SOCCOM) project was initiated with a vision to enable a transformative shift in scientific and public understanding of the role of the Southern Ocean in global carbon biogeochemistry and the associated effects on climate. A strategic mix of innovative and sustained observations of the physical and biogeochemical elements of the carbon cycle, as well as mesoscale eddying model simulations linked to the observations formed the nucleus of the project. The project focused on the Southern Ocean because of its outsized role in regulating the global cycles of carbon and heat and the climate of the earth. Prior results suggested that:

- the Southern Ocean south of 44°S accounts for up to half of the annual oceanic uptake of anthropogenic carbon dioxide (CO_2) from the atmosphere (cf., Gruber et al., 2009);
- vertical exchange in the Southern Ocean south of about 40°S supplies nutrients that fertilize up to three-quarters of the biological production in the global ocean north of 30°S (Sarmiento et al., 2004; Marinov et al., 2006);
- the Southern Ocean is warming rapidly (Gille, 2002; Levitus et al., 2012) and recent work suggests that the region south of 30°S accounts for about 75%±22% of the excess heat that is transferred from the atmosphere into the ocean each year (Frölicher et al., 2015); and
- Southern Ocean winds and buoyancy fluxes are the principal source of energy for driving the global large-scale deep meridional overturning circulation (e.g., Toggweiler and Samuels, 1998; Marshall and Speer, 2012).

Model studies also projected that changes in the Southern Ocean would have a profound influence on future climate trends, with corresponding alteration of the ocean carbon cycle, heat uptake, and ecosystems. Projections included:

- due to acidification, the Southern Ocean south of ~ 60°S will become undersaturated in aragonitic calcium carbonate by ~ 2030 (McNeil and Matear, 2008; Feely et al., 2009), with potentially large impacts on calcifying organisms and Antarctic ecosystems (Bednaršek et al., 2012); and.
- The vertical exchange of deep and surface waters may either increase or decrease. Projected increases in winds over the Southern Ocean will decrease stratification and increase vertical exchange, whereas projected increases in rainfall and meltwater input will increase stratification and decrease vertical exchange. More vertical exchange would be expected to result in more anthropogenic carbon uptake from the atmosphere, but less storage of carbon through biological cycling (cf. Sarmiento et al., 1988), while its impact on heat uptake depends on whether it brings anomalously warm or cold waters to the ocean surface.

The two overarching goals of SOCCOM were:

- Goal 1: Quantify and understand the role of all regions of the Southern Ocean in carbon cycling, acidification, nutrient cycling including oxygen, and heat uptake, on seasonal, interannual, and longer time scales.
- Goal 2: Develop the scientific basis for projecting the contribution of the Southern Ocean to the future trajectory of carbon, acidification, nutrient cycling, and heat uptake.

To achieve these ends, we proposed a three-pronged approach, consisting of:

- a novel autonomous biogeochemical observing system for the Southern Ocean;
- high-resolution state estimation that would incorporate biogeochemical processes and assimilate the new data sets; and
- Earth System Model analyses, data/model assessment metrics, and development of a Southern Ocean Model Intercomparison Project.

The proposed observing system was to span all sectors of the Southern Ocean and extend from the surface to depths of two kilometers (Fig. 1). It was to be capable of measuring the processes outlined in Goal 1 with the skill needed for internally consistent observations spanning decades.

The modeling and state estimation components leveraged large external resources. The most expensive part of SOCCOM by far has been the observing system simply because of the cost of instrumentation, deployment, and data management. This observing system was necessary because, despite the significance of the Southern Ocean in the carbon cycle and climate-related processes (Martin et al., 1990), it has been one of the least observed basins of the global ocean (Bakker et al., 2016, Johnson et al., 2017b). To remedy this deficiency, the SOCCOM project proposed to deploy an array consisting of roughly 180 Biogeochemical-Argo (BGC-Argo) profiling floats (Johnson, 2017; Riser et al., 2018; Claustre et al., 2020) throughout the Southern Ocean over a 6-year interval beginning in 2014. The size of the array was based on several assessments described in Section 2.2. As floats are lost due to system failures or battery exhaustion, additional floats must be deployed to sustain the array. A subsequent renewal of the program funded an additional 120 floats over 4 years to maintain the array. This renewal began in 2020 and ends in 2024. Finally, the project aspired to educate a new generation of ocean scientists trained in both ocean observation and simulation, and to develop a sophisticated outreach effort to disseminate results to the broadest possible community.

As SOCCOM was developing, planning also began in 2017 for the United Nations Decade of Ocean Science, with the theme "the science we need for the ocean we want". In conjunction with the UN Decade, it was argued (Pendleton et al., 2020) that scientific research in the ocean has not kept pace with changing social and environmental conditions. Pendleton et al. (2020) called for fundamental changes in ocean science and ocean observing to equip society with the necessary information to manage marine systems. A UN Decade working group for the Southern Ocean (Hofmann et al., 2020) defined a series of priorities for an observing system in the Southern Ocean that would enable the UN goals to be achieved (Table 1). Many of the observing system priorities outlined in the UN report align closely with the design and objectives of the SOCCOM program. Given the significance of the UN Decade of Ocean Science effort, this review will incorporate the observing system priorities identified in the UN Decade Southern Ocean Workshop Report (Hofmann et al., 2020; hereafter UN Southern Ocean Report). This enables a comparison that serves, in part, as an assessment of the capability to build and operate an observing system compatible with UN Decade of Ocean Science goals and that would also achieve the goals outlined in the SOCCOM proposal.

The first part of this paper describes the SOCCOM observation and modeling implementation strategy followed by our major biogeochemical and modeling results, and then assessment of public outreach. This structure reflects the design of the SOCCOM project. SOCCOM operated with teams focused on observations, modeling, and broader impacts, rather than teams that might focus on a specific science topic, such as carbon cycling. This structure ensured that communications between groups always covered a broad range of topics, rather than permitting smaller groups with a single focus to become isolated. In each section that addresses a priority in the UN Southern Ocean Report (Table 1), those priorities are reiterated to emphasize the coherence between SOCCOM and the desired observing system. In a "SOCCOM in the Future" section, new applications of SOCCOM data are described.

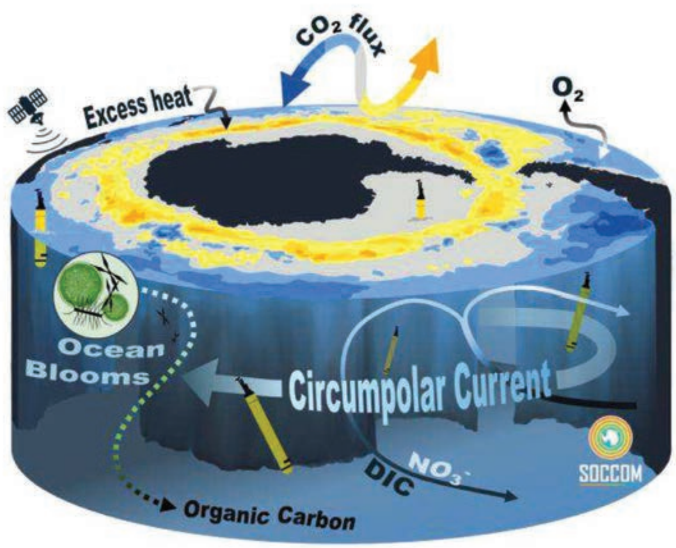

Fig. 1. The SOCCOM observing system concept. An array of profiling floats spanning all sectors of the Southern Ocean. The profiling floats would carry sensors that enable fluxes and stocks of carbon, oxygen, and nitrate to be assessed, along with the major biological and physical processes that contribute to the fluxes. Data would be delivered in real time, via satellite, for assimilation in state estimates and scientific analysis. Surface shading represents the air-sea CO_2 flux in August 2017 (Bushinsky et al. 2019a,b). Graphic by Emily Clark, MBARI.

Table 1
Priorities of the UN Decade of Ocean Science Southern Ocean Report (Hofmann et al., 2020) addressed by the SOCCOM project design.

Theme 1: Healthy and Resilient Ocean
Priority 1: Improve understanding of key drivers of change and their impacts on Southern Ocean species and food webs.
Priority 2: Improve understanding of sea ice, including its role in ecological processes of the Southern Ocean.
Priority 3: Improve understanding of Southern Ocean biogeochemical cycling. The Southern Ocean plays a key role in biogeochemical cycling, particularly in regulating air-sea exchange of carbon dioxide in the global carbon cycle.
Priority 4: Improve societal understanding of Southern Ocean issues and appreciation of the Southern Ocean for its global value in Earth systems and unique environment.
Theme 2: Predicted Ocean
Priority 1: Enhance and expand observational capability to support predictions.
Priority 2: Improve and enhance Southern Ocean modeling capability.
Theme 3: Sustainable Productive Ocean
Priority 1: Increase the suite, types and reliability of measurements, including those focused on ecosystem change, needed to inform management and policy.
Priority 3: Ensure science-based and effective MPAs and uphold sustainable fisheries management.
Cross Cutting Themes
Priority 3: Implement a coordinated, international, circumpolar observational program to elucidate processes that 1) allow life histories of key species in the Southern Ocean ecosystem to be quantified, 2) allow a total carbon budget to be developed, 3) provide coverage of the annual cycle, and 4) quantify the role of sea ice in regulating ecosystem productivity.
Priority 5: Enhance predictive skill across climate, circulation, cryosphere, and ecosystems. The Southern Ocean community can add scenarios, such as freshwater inputs in the Southern Ocean, to understand climate sensitivity. End-to-end integration across ecosystems is needed to improve estimations of carbon fluxes, understand the effects of multiple stressor on ecosystems, identify biological hotspots, and evaluate the effects of living resource extraction on biological productivity. This requires working across disciplines, comprehensive observational systems, community engagement, and resources.

2. SOCCOM implementation strategy

2.1. Observational strategy

The SOCCOM observational program was designed to provide circumpolar biogeochemical observations throughout the year, within the Southern Ocean (Talley et al., 2019), by deployment of a large array of BGC-Argo profiling floats (Fig. 2). The BGC-Argo program is described in Claustre et al. (2020). The quality controlled data would be served in real time (Maurer et al., 2021). The SOCCOM float array was also designed to provide crucial year-round profile data in the large seasonal sea ice zone south of 60°S. Argo-type profiling floats are free drifting, battery-powered platforms that cycle between 2000 m depth and the surface (Johnson, 2017; Riser et al., 2016, 2018; Roemmich et al., 2019). A typical profile cycle is shown in Fig. 3. Floats ascend from depths near 2000 m to the surface at defined time intervals (typically 10.08 days). Physical and chemical measurements are made during the ascent at programmed depth intervals (typically 70 depths for chemical measurements and every 2 m for physical measurements in SOCCOM floats). Once at the surface, the float position is determined by GPS, and the observed data are then transmitted via the Iridium communication system to a shore-based server. The data are immediately processed. This includes any necessary corrections for sensor calibration offsets or sensor drift (Maurer et al., 2021). Data suitable for scientific analysis are then made available through publicly accessible databases on the Internet (https://soccom.princeton.edu/content/data-access) and the Argo data system (Wong et al., 2020) within 24 h. The float then returns to a parking depth at 1000 m before repeating the cycle.

The current status of the SOCCOM BGC-Argo float array is shown in Fig. 4a. SOCCOM has achieved circumpolar coverage, with many floats operating in the Antarctic sea ice zone. SOCCOM also sought from the start to achieve sampling in all dynamical and BGC regimes of the Southern Ocean (Talley et al., 2019). The Antarctic Circumpolar Current (ACC) fronts are shown for context in Fig. 4a; SOCCOM has also achieved this regime-defined coverage which has enabled studies of the zonal and meridional dependence of carbon, productivity and air-sea fluxes. After 9 years of deployments, floats in the earliest years of SOCCOM have become inactive due to battery lifetime, such that about half of the floats deployed are active at this time (Fig. 4b).

The observing system implemented for the SOCCOM project aligns closely with the UN Southern Ocean Workshop Report priorities:

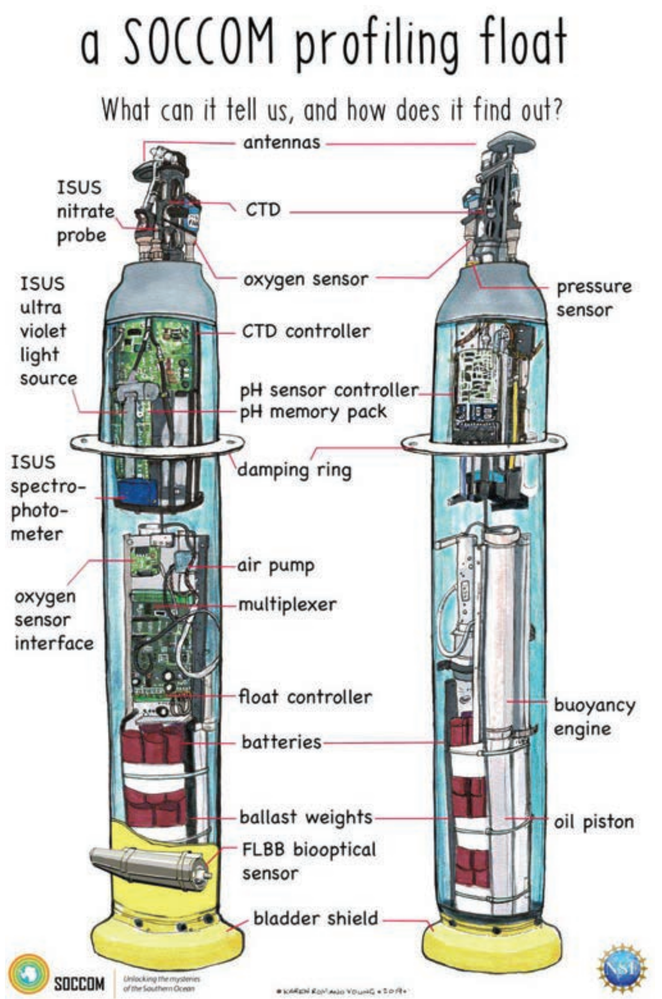

Fig. 2. Schematic of a SOCCOM profiling float showing component views of the float (left) and rotated by 180° (right). This sketch, created by Karen Romano Young, is widely used in SOCCOM's K-12 outreach program. The original drawing, with additional detail, was designed for a poster size and is available on the SOCCOM website (https://soccom.princeton.edu).

- *Enhance and expand observational capability to support predictions.*
- *Increase the suite, types and reliability of measurements, including those focused on ecosystem change, needed to inform management and policy.*

2.2. Array size

A variety of methods have been applied to assess the optimum number of floats in the SOCCOM array. One of the primary tools has been Observing System Simulation Experiments (OSSE). Majkut et al. (2014) sampled CO_2 fluxes in the GFDL-ESM2M 'historical' simulation (years 1995–2000) with synthetic floats. This OSSE found that a large uncertainty reduction in reconstruction of the air-sea CO_2 flux in the Southern Ocean (south of 30°S) was obtained with approximately 200 floats. Kamenkovich et al. (2017) subsampled oxygen in CM2.6 to assess observing system design and also identified 200 floats as being an optimal choice. Taking a different approach, Mazloff et al. (2018) estimated the correlation scales in the Southern Ocean for carbon flux and content on seasonal time-scales and longer using an ocean model. These findings suggest that, ideally, approximately 100 floats would be deployed with one every 20° longitude by 6° latitude. In practice, however, this deployment spacing is impossible to achieve due to advection that aggregates floats in some regions and removes them from others, making the required float number greater than 100. An additional caveat for all these studies is that constraining the higher frequency signals (i.e. subseasonal) may require far more than 200 floats. For example, Prend et al. (2022c) found that much of the Southern Ocean chlorophyll variability occurs at sub-seasonal time scales that would require a much larger float array to characterize. Chlorophyll has a very short turnover time that leads to a patchier distribution than tracers such as DIC (Mahadevan and Campbell, 2002). A float array cannot resolve the short length scales that characterize ocean chlorophyll. But the analysis of Mazloff et al (2018) shows that a float array can resolve the DIC length scales. This implies that a float array can quantify processes such as net community production from DIC (or nitrate) drawdown. Further, we have shown (Johnson and Bif, 2021) that float arrays can resolve primary productivity signals quantitatively, but at low spatial and temporal resolution.

The goal in the initial SOCCOM proposal was to deploy 180 floats south of 30°, based on Majkut et al.'s (2014) results. It was presumed that international partners would supply the remainder. A uniform distribution of floats was desired to meet the goals outlined in the BGC-Argo Science and Implementation Plan (Biogeochemical-Argo Planning Group, 2016) with floats in all basins of the Southern Ocean. Fig. 4b shows the number of SOCCOM floats that were operating in each year and the cumulative number deployed by the project. The highest population of active floats was achieved in year 6 of the project (2020) with 152 floats. This number fell short of the 180 float goal due a fault in APEX float (the primary float-type deployed) power management that led to premature failure of the float batteries at around 150 vertical profiles. The fault was not recognized until floats had been in the water nearly 4 years. The power management fault has since been resolved and APEX floats deployed since 2020 are capable of making $\sim$ 275 vertical profiles before battery depletion. The resolution of this problem was followed immediately by the Covid-19 pandemic, which limited production and deployment capabilities. The array population then fell to $\sim$ 120 floats operating each year. The number of operating floats, now at 137, will gradually increase at planned deployment rates of 30 floats per year.

Observing system design work continues with similar and expanded approaches, including the use of transition matrices to project information forward in time (Chamberlain et al., 2023). The prospect of utilizing covariance information from other observables to reduce observational demands is also being explored (Giglio et al., 2018; Liang et al., 2018). Finally, other groups have been applying OSSEs for other BGC variables. For example, Valsala et al. (2021) considered observing system design for pCO_2 in the Indian Ocean. Ford (2021) assessed the effect of assimilation for chlorophyll, oxygen, pH and nitrate in the global ocean. These studies all find significant reduction in error through use of a large array of biogeochemical floats.

2.3. SOCCOM float sensors

Major advances in sensor technology have enabled SOCCOM floats to measure nitrate and oxygen concentrations and bio-optical properties from profiling floats (Riser and Johnson, 2008; Johnson, 2017; Johnson et al., 2013, 2017b; Körtzinger et al., 2005; Boss et al., 2008; and Bittig et al., 2018a). Newly developed pH sensors have now been successfully integrated onto the profiling float platform with measurements to 2000 m depth (Johnson et al., 2016, 2017b; Williams et al., 2017).

Oxygen is measured with optode sensors that determine concentration from the effect of oxygen partial pressure on luminescence lifetime of an embedded fluorophore (Bittig et al., 2018a). The large number of deployments in SOCCOM have enabled a robust demonstration of the capability to recalibrate the optode sensors with air oxygen measurements (Johnson et al., 2015). Nitrate is measured using direct UV spectrophotometry (Johnson et al., 2013). pH is measured with an Ion Sensitive Field Effect Transistor (Johnson et al., 2016). Both the nitrate and pH sensor output must be corrected for offsets in the initial calibration that may arise during the many months between laboratory

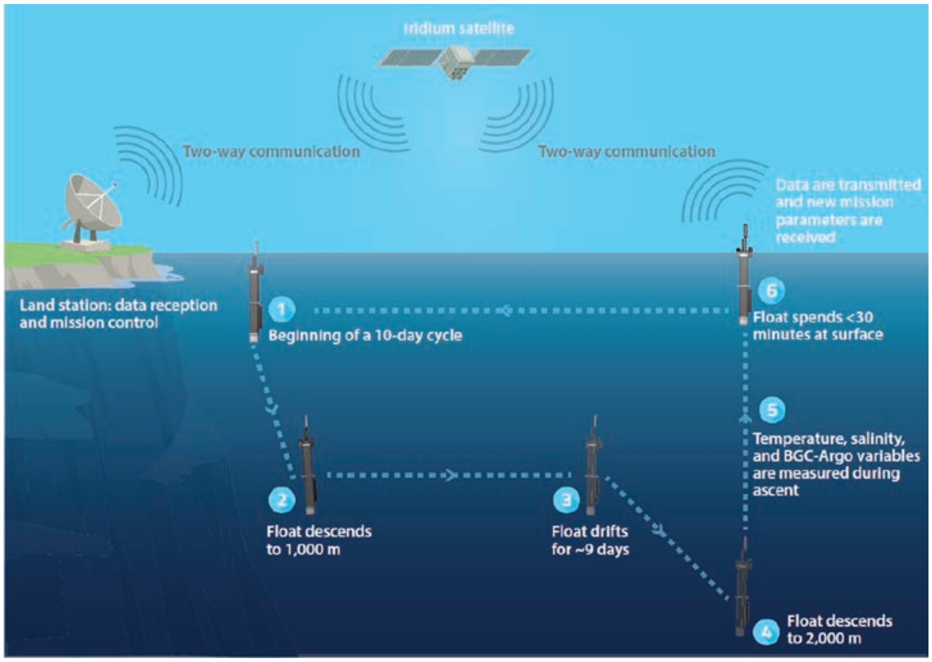

Fig. 3. Typical profile cycle for a SOCCOM Argo float. From Claustre et al. (2020).

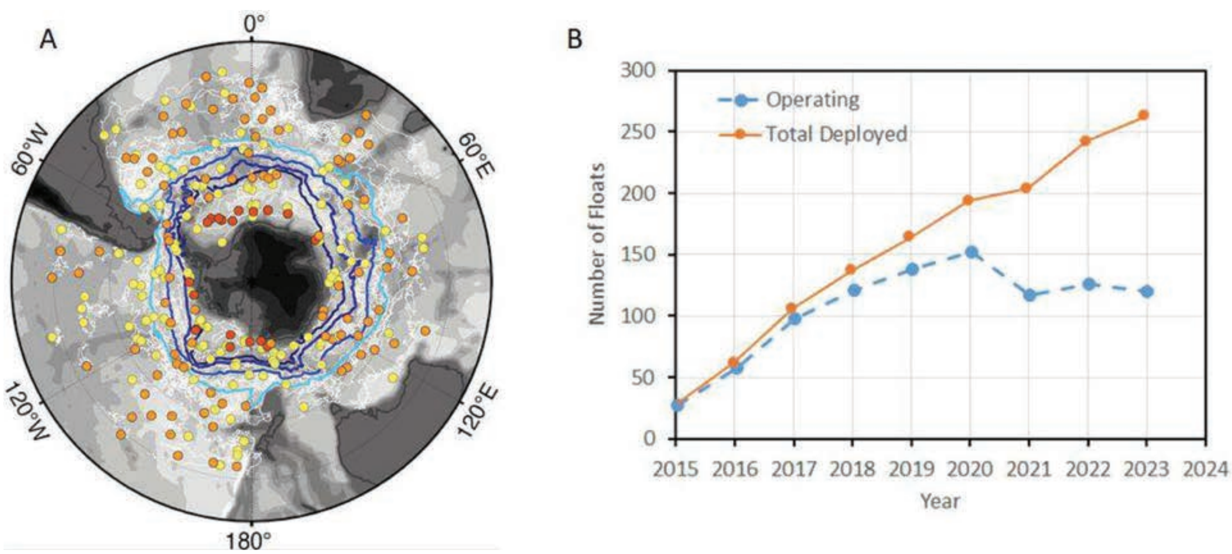

Fig. 4. A) SOCCOM float locations as of December 2022. Active floats: orange. Under-ice floats: dark orange. Inactive floats: yellow. Trajectories of all floats shown as white lines. Antarctic Circumpolar Current frontal positions are shown as solid lines: Subantarctic Front (light blue), Polar Front (medium blue), Southern ACC Front (dark blue), Southern Boundary of the ACC (black), from north to south (positions from Kim and Orsi, 2014). B) Number of floats operating in each year of the SOCCOM project and total number of floats deployed.

calibration and deployment, as well as correction for offsets or drifts that occur after deployment. Protocols were developed for these corrections (Johnson et al., 2017b; Maurer et al., 2021) and these are described further in Section 2.6.1. Particle abundance (primarily phytoplankton and their detritus in the open ocean; Graff et al., 2015) is measured using optical backscatter. Chlorophyll fluorescence is measured by in situ fluorometry (Roesler et al., 2017). These sensors are all capable of operating for years through the pressure and temperature extremes experienced by Argo floats (Johnson et al. 2017b). Fig. 5 shows one example of the data records in the upper 300 m from all of these sensors. This record spans four years on a SOCCOM float (WMO 5904468) operating in the seasonal ice zone of the Weddell Sea (Claustre et al., 2020).

2.4. Float performance

The SOCCOM project utilizes both APEX and Navis profiling floats. The APEX floats used in SOCCOM are constructed at the University of Washington from components purchased from Teledyne/Webb Corporation. They carry batteries capable of powering the floats for about 250 profiles to 2000 m. However, due to a power management fault in early floats used by the project, the batteries failed shortly after 150 cycles. This fault was corrected in floats that were built after 2019. The mortality of the floats used in SOCCOM is somewhat higher than analogous floats used throughout the world ocean in Argo and other programs (Riser et al., 2018). About 50% of the SOCCOM floats have survived about 4 years, or 150 profiles. For longer times, the survivability

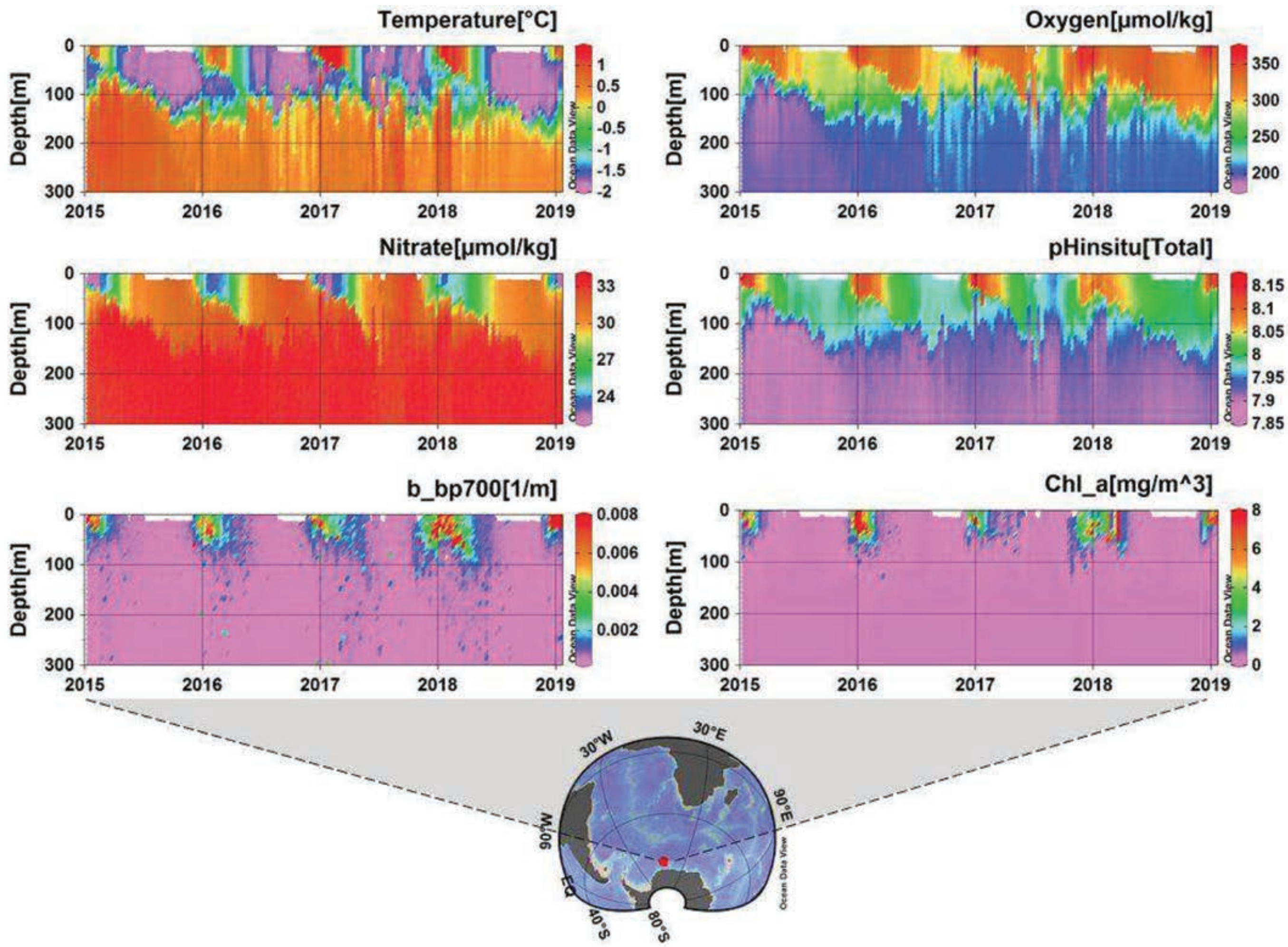

Fig. 5. Sensor data gathered by World Meteorological Organization (WMO) float number 5904468 in the upper 300 m of the Atlantic sector of the Southern Ocean. Note that the float acquired data under ice (during the periods identified by white sectors in the surface layer) and then transmitted them when the ocean surface became ice free (adapted from Claustre et al., 2020).

decreases, largely due to the power management fault, and only about 30% of the floats continue to operate for 250 profiles. The technical details and performance characteristics of the floats used in SOCCOM are discussed in Riser et al. (2018). The Navis floats are acquired in completed form from Sea-Bird Scientific and used after a thorough inspection that now includes disassembly of complete floats to check internal components.

Argo floats, including the BGC-Argo floats deployed by the SOCCOM project, are regularly operating under ice-covered water (Wong and Riser, 2011; Riser et al., 2018; Chamberlain et al., 2018). Sixty-six SOCCOM floats have operated under seasonal sea ice and collected over 2600 vertical BGC profiles in the seasonal ice zone. The survival rate for APEX floats operating in ice is moderately lower (93% survival/year) versus floats outside the seasonal ice zone (96%/year).

Like all Argo floats, SOCCOM floats cannot determine position from GPS when operating under ice. The Argo default is linear interpolation between available profiles with GPS fixes. Acoustic receivers have been added to limited sets of Argo floats for under-ice tracking in the insonified Weddell Sea (Klatt et al., 2007). However, the rough sea ice bottom interferes with acoustic range. As part of SOCCOM, Chamberlain et al. (2022a) developed a Kalman smoothing method for improved acoustic tracking and applied it to the Weddell Sea floats. While this work is promising, expansion of the existing Weddell array of moored sound sources to the full Southern Ocean is prohibitively expensive at present. Chamberlain et al. (2018) used a set of acoustically-tracked Argo floats to quantify the uncertainty in the linear interpolation of float locations. The location error is approximately 100 km for a 9-month sojourn under the ice. This is of comparable size to other sources of representation error (e.g. "eddy noise"). As a result, acoustic receivers have not been incorporated on SOCCOM floats.

2.5. Float deployments

SOCCOM has operated with essentially no dedicated ship time (Talley et al., 2019). Float deployments have occurred from ships of opportunity in nearly all cases. The primary exception has been the assignment of several days of ship time to SOCCOM for float deployments on US research vessels making transits between ports. At this time, floats have been deployed from 19 different ships. Fifteen of these ships have been from other nations, including Australia, Germany, Japan, Korea, New Zealand, Russia (on a Swiss charter), South Africa, Spain, and the United Kingdom. This international collaboration has been essential to the development of the SOCCOM array by providing access to all regions of the Southern Ocean.

Although SOCCOM has not used dedicated ships for the most part, the deployment platforms have played a key role in the success of the project. A SOCCOM policy was to collect a hydrocast with high quality measurements of oxygen, nitrate, carbonate parameters (pH, titration alkalinity, dissolved inorganic carbon), HPLC measurements of photosynthetic pigments, and particulate organic carbon whenever possible

(Talley et al., 2019). The shipboard chemical measurements are used to validate the data obtained from float sensors. Nearly all deployments have occurred from research vessels, as a result. Nearly 50% of the deployments have been on GO-SHIP cruises (Talley et al., 2016) to take advantage of the high quality data generated by this program. The data from these hydrographic stations taken at float deployment sites has provided convincing evidence of the quality of the float observations (Section 2.6.1). The validation data was also a key contribution to the development of the quality control methods by providing a quantitative metric for improvements to data processing. As sensors evolve, continued collection of validation data will be essential to demonstrate their improvement. The SOCCOM project encourages the collection of this type of supporting data whenever possible.

As batteries in a profiling float are depleted, the float is lost at depths near 2000 m when the external bladder can no longer be inflated to change its buoyancy. Each profiling float, with a mass near 30 kg, thus contributes to marine waste. However, when compared to the impacts from operation of an ocean going research vessel that may burn five tons of fuel each day, a 30 kg profiling float that operates 4 to 6 years is an extremely low impact observing system. A further assessment of the environmental impacts of Argo floats can be found in Riser and Wijffels (2020).

2.6. Data system

Parameters observed by SOCCOM floats (temperature, salinity, dissolved oxygen, nitrate, pH, chlorophyll and particulate backscatter) are Essential Ocean Variables (EOVs) and contribute to our understanding of the Southern Ocean and its response to a changing climate. Profiling float data are provided in real-time (<24 h) to the community with equal access to all. The SOCCOM website (https://soccom.princeton.edu) provides a direct link to these data resources. Although the SOCCOM data system was developed before the FAIR concept for data accessibility was published (Wilkinson et al., 2016), it adheres closely to the principles of findability, accessibility, interoperability, and reusability. The success of the SOCCOM system in achieving the FAIR principles can be assessed through the number of external publications that use the observations and model output, as described in Section 3.6. SOCCOM data are provided to users through multiple format options, including both NetCDF files and human-readable text files that contain estimates of derived carbon parameters (dissolved inorganic carbon (DIC), total alkalinity (TAlk), partial pressure of carbon dioxide (pCO2) and particulate organic carbon (POC)). The provision of such value-added products, calculated in a standardized way, facilitates analysis across a broad user base. A key objective of the SOCCOM program has been to supply the data in a way that fosters direct and efficient ingestion by users. SOCCOM scientists have collaborated with the sister Global Ocean Biogeochemistry Array (GO-BGC) to make toolboxes available in a variety of computer languages (Matlab, Python, R; https://go-bgc.org) to further facilitate data access. These toolboxes include instructional videos and examples.

SOCCOM is integrated into the larger One Argo program framework, a program that serves as the backbone to both the Global Ocean Observing System (GOOS) and Global Climate Observing System (GCOS) (Roemmich et al, 2019; Owens et al., 2022). SOCCOM deployments represent up to 15 percent of annual Argo deployments in the ocean south of 30°S and, on average, close to 70 percent of total BGC-Argo floats deployed in this region annually. This has established SOCCOM as an integral part of the Core Argo program to observe ocean temperature and salinity and of the BGC-Argo global networks. All SOCCOM data are delivered to Argo Global Data Assembly Centers via the US Argo Data Assembly Center within 24 h of successful transmission to shore. SOCCOM has become the dominant source of in situ biogeochemical observations in the Southern Ocean (Table 2). SOCCOM and partner international programs that comprise BGC-Argo have become essential for observing biogeochemical changes in the ocean interior as the amount of such data collected from ships has declined precipitously in recent decades (Fig. 6). The expanded ocean coverage in space and in time is enabling a transformation in ocean observing similar to the transformation Argo has provided for physical measurements (Wong et al., 2020). This was especially true during the COVID-19 pandemic when ship activity was constrained but deployed floats continued to collect data (Boyer et al., 2023).

Table 2
Number of profiles to at least 900 m depth over an 8-year span reported by SOCCOM floats or by ships. The float data includes only profiles with data quality marked good. Ship data was obtained from World Ocean Database (https://www.ncei.noaa.gov/products/world-ocean-database).

Property	SOCCOM 2015–2022	Ships South of 30°S 2010–2017	Ships North of 30°S 2010–2017
Oxygen	21,420	1,764	3,032
Nitrate	20,564	1,651	2,840
pH	12,603	1,054	1,976

2.6.1. Data quality

The goal of the SOCCOM float program is to produce a climate-quality data record for carbon, oxygen, and nitrate cycling. This is a "time series of measurements of sufficient length, consistency and continuity to determine climate variability and change" (National Research Council, 2004). Such a record requires sensors that are well characterized and calibrated to the property of interest before deployment, and whose calibration is assessed at deployment with high quality hydrographic measurements, or in which post-deployment calibration is possible. Meeting project goals requires continuous reviews to ensure that the profiling float data are of high quality and consistency. Further, as SOCCOM is one element of the BGC-Argo array, these efforts should be well documented and capable of implementation at all Argo Data Assembly Centers (DACs). To meet these sensor goals, novel methods were developed to ensure sensors were accurate and could be corrected for post-deployment drift in calibration (Maurer et al., 2021).

Körtzinger et al. (2005) and Bittig and Körtzinger (2015) demonstrated the potential for optical oxygen sensors to be calibrated in air when floats surface. This work was limited to a small number of floats. Using nearly 50 SOCCOM and Argo Canada floats, the SOCCOM project built on this work to establish that air oxygen calibration could reduce oxygen concentration errors below 1% of surface saturation values for large arrays (Johnson et al., 2015). These capabilities were built into a software package, the SOCCOM Assessment and Graphical Evaluation (SAGE-O2) tool, which is now in widespread use at Argo DACs (Maurer et al., 2021). The air oxygen measurements enable assessment of sensor calibration and calibration drift in time.

Errors arising in nitrate and pH sensor calibrations are corrected using methods that build on the techniques developed in the Core Argo program to assess change in salinity sensor calibration (Owens and Wong, 2009). Sensor measurements at depths between 1000 and 2000 dbar, where conditions change only slowly in time, are compared to high quality shipboard observations. Differences are assigned to sensor offsets or drifts. In the case of salinity, there are sufficient ship-based observations to use objective mapping to predict salinity values at float profile locations. There are too few ship-based observations of nitrate and pH to allow direct mapping of these observations to float profile locations. Instead, software was developed to interpolate shipboard observations using the well-known relationship between oxygen and nitrate or pH that is encapsulated in the Redfield Ratio (Anderson and Sarmiento, 1994). Initially, locally interpolated regressions (LIR) were built using the GLODAPv2 dataset (Carter et al., 2018). The LIRs allow nitrate and pH to be predicted at depth using profiling float oxygen, date, and position data with biases less than 0.00 ± 0.47 (1 SD) μmol kg^{-1} and 0.001 ± 0.006 pH at depths near 2000 m. Subsequent work using neural networks has provided improved spatial resolution in fitted

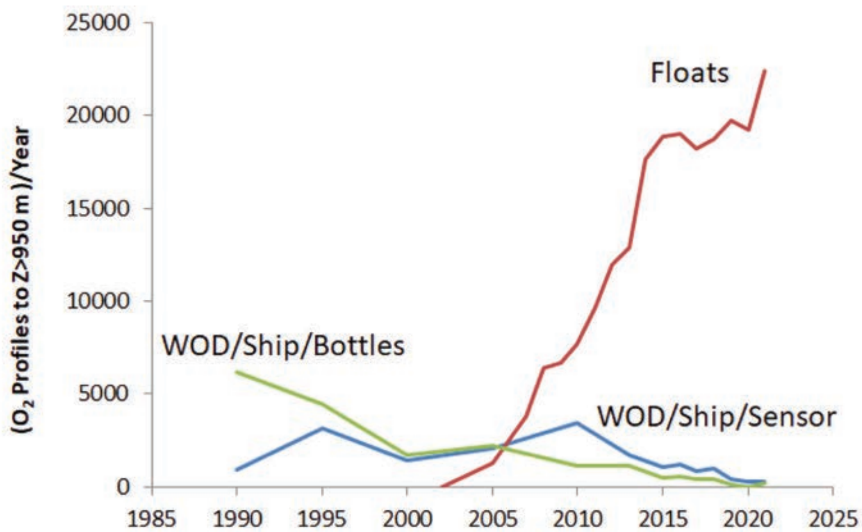

Fig. 6. Oxygen profiles in the global ocean to a depth of at least 950 m per year. Values for analyses of water collected on bottle casts (green) and for oxygen sensors on CTD casts from ships (blue) are from the NOAA/NCEI World Ocean Database. Values for Argo profiling floats are from the Argo Global Data Assembly Center and are for all BGC-Argo floats.

deep reference data (Bittig et al., 2018a,b; Carter et al., 2021). These tools are used in the SAGE software application to quality control and adjust nitrate and pH sensor data (Maurer et al., 2021).

The accuracy of the adjusted and quality-controlled data collected by SOCCOM floats has been assessed by comparing sensor values from the first float profile with data from standard laboratory analysis methods applied to water samples collected during a conventional hydrocast coincident with the float deployment. Such shipboard measurements of oxygen, nitrate, pH, HPLC pigments and particulate organic carbon (POC) have been made alongside nearly all SOCCOM float deployments. Note that SOCCOM sensor calibrations are made independently of the accompanying shipboard measurements. Oxygen sensors use air oxygen measured by the floats for the final sensor calibration (Johnson et al., 2015). pH and nitrate data are adjusted by applying an offset based on a deep, stable reference field (Johnson et al., 2013; 2016; 2017a, 2017b; Maurer et al., 2021) predicted with global algorithms fitted to high quality ship data (Carter et al., 2018; Bittig et al., 2018b). Both the raw and adjusted sensor data are always reported.

Statistical comparison of float sensor data with shipboard data (Fig. 7) yields the overall accuracies quoted for SOCCOM float BGC sensors (Maurer et al., 2021). Some of the statistical uncertainty in the validation comparisons is due to hydrographic differences between float and shipboard sampling times and locations. Validation matchups across the array are an average of 23 h and 8 km apart in time and space. Assuming that half of the standard deviation in the bottle minus float differences (Fig. 7) is from natural ocean variability, float data uncertainties are 3 μmol kg^{-1}, 0.5 μmol kg^{-1}, and 0.007 for oxygen, nitrate, and pH, respectively. These uncertainties correspond to coefficients of variation near 1.5% for oxygen and nitrate concentrations near their mean values. The assumption that half of the error is due to oceanographic processes is consistent with alternate assessments of data quality, such as a comparison of sensor nitrate concentrations in surface water with temperature >24 °C, excluding equatorial regions. The expected nitrate concentration in these conditions is near 0. The observed surface nitrate concentration for all profiles that meet these conditions from floats supported by the UW/MBARI group is 0.2 ± 0.5 μmol kg^{-1}. This standard deviation is similar to one half of the value for nitrate in Fig. 7. These uncertainties meet or exceed targets for sensor performance set in the original proposal.

Note that when chemical concentrations are near zero, both the oxygen and nitrate sensors will report negative values. A negative concentration is physically impossible. However, the values returned by a sensor are an estimate of concentration and estimates can be negative (Thompson, 1988). At concentrations near zero, half the estimates of concentration will be negative. The SOCCOM project has elected to retain these negative values in the dataset with a quality flag of good to

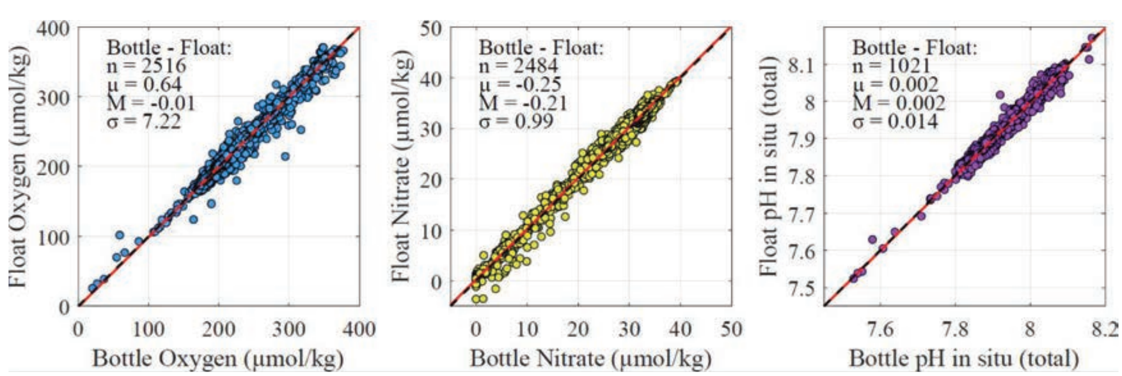

Fig. 7. Comparison of profiling float oxygen, nitrate, and pH sensor values versus values measured on board ship in samples collected from a hydrocast made near the time of float deployment. Statistics for number of comparisons (n), mean difference (μ), median difference (M), and standard deviation (σ) are shown for each property. Adapted from Maurer et al. (2021) after updating to all data available through 2022.

avoid a bias known as "left censoring" of the data (Newman et al., 1989). Left censoring results in unrealistic estimates of error near zero concentration. The user must make their own decision on how to utilize these negative values.

The long term stability of the adjusted sensor data has been assessed by comparing the quality controlled sensor values to shipboard profile measurements when floats pass within 20 km of a station in the GLODAPv2 database (Johnson et al., 2017b; Maurer et al., 2021). Offsets in the comparisons change with the age of the shipboard observations. The rate of change for both pH and oxygen are consistent with known ocean acidification or deoxygenation rates (Johnson et al., 2017b; Maurer et al., 2021). The nitrate comparisons are invariant with the age of the shipboard observations. These results indicate that the quality controlled float data are stable in time.

These statistical adjustments relative to deep ocean data that may slowly change in time require a continuous update of the deep, ship-based reference data. In essence, the float measurements provide a record of the large, seasonal changes in upper ocean chemistry (Fig. 5) relative to a deep, ship-based observational product. As such, projects such as SOCCOM require a decadal scale set of repeated hydrographic section measurements, such as those conducted in the GO-SHIP program (Talley et al., 2016), to produce a climate quality dataset.

In addition to the chemical sensor measurements, SOCCOM floats have also collected chlorophyll fluorescence and optical backscatter data. The conversion of chlorophyll fluorescence to chlorophyll concentration is fraught with uncertainty (Roesler et al., 2017). Measurements of chlorophyll pigments by High Performance Liquid Chromatography in samples collected at float deployment show large variability in the relationship between chlorophyll fluorescence and chlorophyll (Johnson et al., 2017b). Despite this uncertainty the chlorophyll fluorescence data have proven to be extremely useful in a variety of SOCCOM studies (e.g., Carranza et al., 2018; Haëntjens et al., 2017; Von Berg et al., 2020). The optical backscatter data show a robust relationship with Particulate Organic Carbon (POC) concentration in samples collected at float deployment (Johnson et al., 2017b). This has enabled estimates of POC throughout the Southern Ocean (Haëntjens et al., 2017; Johnson et al., 2017a; Arteaga et al., 2020).

2.7. Biogeochemical-Southern Ocean state estimate

An integral strategy in the SOCCOM design was to assimilate the observational data into a state estimate model. Data assimilating models are computationally expensive, especially for biogeochemistry. Ample and sustained data constraints are required in order to justify the task of operating a large-scale ocean model that assimilates data. The SOCCOM array has provided this data source. The Biogeochemical Southern Ocean State Estimate (B-SOSE; Verdy and Mazloff, 2017) assimilates physical and biogeochemical data into the MIT ocean general circulation model using an adjoint method developed by the consortium for Estimating the Climate and Circulation of the Ocean (ECCO; Stammer et al., 2002; Forget et al., 2015). The biogeochemical model in B-SOSE is the nitrogen version of the Biogeochemistry with LIght, Nutrients and Gases model (NBLING; evolved from Galbraith et al., 2010). B-SOSE provides a complete, budget-closing analysis of Southern Ocean biogeochemical and physical processes. Similar data assimilation efforts are now appearing elsewhere (Fennel et al., 2019).

The B-SOSE objective is to yield a baseline estimate of the large-scale Southern Ocean biogeochemical, sea ice, and physical properties, and a framework to understand this baseline. Nudging (i.e. reinitializing) models allows one to fit eddy signals, but the B-SOSE aim is to have closed budgets, and thus there is no nudging included. The gridded model solution aims to capture the seasonally varying properties by adjusting the atmospheric state and initial conditions, with eddies represented in a statistical sense. The first state estimate produced was a 1/3° resolution solution for the period 2008–2012. Validation, analysis, model inputs, code, and comprehensive diagnostics have been published. This demonstrates the maturity of BGC state estimation (Verdy and Mazloff, 2017). A subsequent 2013–2021 SOCCOM era state estimate was produced at higher-resolution (1/6°).

B-SOSE offers a gridded product consistent with model physics and constrained to the large-scale signals observed by the SOCCOM array. A first study with B-SOSE was an intensive analysis of the dissolved inorganic carbon budget (Rosso et al., 2017). B-SOSE has also had smaller regional models nested inside to inform the impact of resolution on the carbon cycle (e.g. Jersild et al., 2021; Swierczek et al., 2021a) and its predictability (Swierczek et al., 2021b). The B-SOSE resource has been used as an essential component of numerous studies, which are noted throughout the remainder of this review.

2.8. Earth system models

The Southern Ocean is notoriously difficult to simulate consistently. At every stage of the Coupled Model Intercomparison Project (CMIP), sponsored by the Intergovernmental Panel on Climate Change (IPCC), there have been significant inter-model differences as well as a lack of observationally-based metrics on which to discern the overall quality of each model (Russell et al. 2006a, 2006b, 2018; Meijers et al., 2012; Beadling et al. 2019, 2020; Kajtar et al., 2021; Bourgeois et al., 2022). To address this issue, a climate and biogeochemistry modeling component, including the Geophysical Fluid Dynamics Laboratory (GFDL) mesoscale eddying coupled climate models (e.g. "CM4") and Earth System Models (e.g., "ESM4"), has been a core SOCCOM element. This enables the program to translate our evolving understanding of the current ocean into a greatly improved projection of the future with an emphasis on the role of the Southern Ocean in the global climate. The benefits of the SOCCOM joint observation and modeling approach are clear, as important spatially- and temporally-resolved data have been assimilated into our state estimates and metrics of biogeochemical and physical ocean properties that provide consistent benchmarks have been established (Beadling et al., 2020).

The state estimation and global modeling components address the UN Southern Ocean Report priority:

- *Improve and enhance Southern Ocean modeling capability.*

3. Major SOCCOM biogeochemical results

Here we review SOCCOM results that improve our understanding of biogeochemical cycles in the Southern Ocean. These results advance the UN Southern Ocean Report priorities:

- *Improve understanding of Southern Ocean biogeochemical cycling. The Southern Ocean plays a key role in biogeochemical cycling, particularly in regulating air-sea exchange of carbon dioxide in the global carbon cycle.*
- *Implement a coordinated, international, circumpolar observational program to elucidate processes that 1) allow life histories of key species in the Southern Ocean ecosystem to be quantified, 2) allow a total carbon budget to be developed, 3) provide coverage of the annual cycle, and 4) quantify the role of sea ice in regulating ecosystem productivity.*

3.1. Southern Ocean air-sea gas fluxes

Autonomous profiling floats have enabled year-round observations of biogeochemical parameters such as oxygen, nitrate, pH, and bio-optics in large regions of the ocean that previously were under-sampled (Hennon et al. 2016; Briggs et al. 2018; Arteaga et al. 2019, 2020; Johnson and Bif 2021). In sufficient numbers, profiling floats can provide the quasi-continuous data needed to calculate air-sea gas exchange over broad regions through full annual cycles.

3.1.1. Oxygen fluxes

Bushinsky et al. (2017) demonstrated the capability to resolve basin-scale gas exchange processes by calculating air-sea oxygen fluxes in the major zones of the Southern Ocean using the data in Fig. 8. They found a Southern Ocean oxygen sink of -221 ± 57 Tmol O_2 yr^{-1} south of 30°S, nearly double prior estimates (Gruber et al., 2001). The increased sink is due, in part, to strong uptake in partially ice covered waters of the Seasonal Ice Zone.

3.1.2. CO_2 fluxes

Few autonomous vehicles have been deployed that are capable of constraining the carbonate system through the full water column (Bushinsky et al. 2019b). The deployment of autonomous profiling floats equipped with pH sensors requires one other carbon parameter to enable determination of the complete carbon system. Fortunately, titration alkalinity can be estimated with reasonable accuracy using a variety of models fitted to shipboard data sets such as GLODAPv2 (Olsen et al., 2020). pCO_2 values determined using pH are not particularly sensitive to the titration alkalinity estimate (Williams et al., 2017). Estimates of pCO_2 and Dissolved Inorganic Carbon (DIC) using measured pH and estimated alkalinity have the potential to greatly increase our understanding of the wintertime carbon cycle (Williams et al., 2018), spatial patterns of carbon uptake (Johnson et al., 2022), and the influence of sub-surface processes on gas fluxes (Prend et al., 2022b; Chen et al., 2022).

The first Southern Ocean study using float-based estimates of carbonate system parameters to explore the seasonal drivers of carbonate changes (Williams et al., 2018) found variable agreement with prior studies based on shipboard observations (Takahashi et al., 2014). There is reasonable agreement between float-based estimates of pCO_2 and DIC in the more northerly Subtropical and Subantarctic zones (Fig. 9; Williams et al. 2018). However, in the poorly sampled Polar Frontal Zone and Antarctic Southern Zone there are large offsets in pCO_2 (Fig. 9). These offsets were suspected to result from undersampling in the ship-based data. Fay et al. (2018) compared pCO_2 estimates from SOCCOM floats going through the Drake Passage with nearby, shipboard observations from the Drake Passage Time-series (Munro et al., 2015). They found that the float estimates of pCO_2 agreed, within their estimated relative error of 2.7%, with the shipboard observations.

Estimates of the air-sea CO_2 flux using data from the first 3 years of SOCCOM float observations led to a calculated Southern Ocean net annual flux south of 35°S of only -0.08 ± 0.55 Pg C yr^{-1} (negative into the ocean), relative to the ship-based estimate of approximately -1.1 Pg C yr^{-1} (Gray et al. 2018). To obtain a more comprehensive assessment, these float data were combined with Surface Ocean CO_2 Atlas (Bakker et al., 2016) observations and gridded using previously established mapping and interpolation methods. The merged data (Fig. 10a) yields a contemporary Southern Ocean flux of -0.75 ± 0.22 Pg C yr^{-1} (Bushinsky et al. 2019a). This represents an approximately 0.4 Pg C yr^{-1} reduction in the contemporary Southern Ocean sink, relative to estimates based only on SOCAT data. Independent estimates of the Southern Ocean anthropogenic carbon sink from observations of ocean interior carbon concentrations coupled with inverse modeling approaches indicate that the anthropogenic flux is -1.1 Pg C yr^{-1} (DeVries 2014; Mikaloff Fletcher et al. 2006; Gruber et al. 2019). A contemporary flux of -0.75 Pg C yr^{-1} implies that the Southern Ocean natural outgassing flux is likely positive and on the order of several tenths of a Pg yr^{-1}, changing the prior understanding of a neutral natural carbon flux with uptake in the subtropical north balancing upwelling-driven outgassing South of the Antarctic Circumpolar Current (ACC; Gruber et al. 2019).

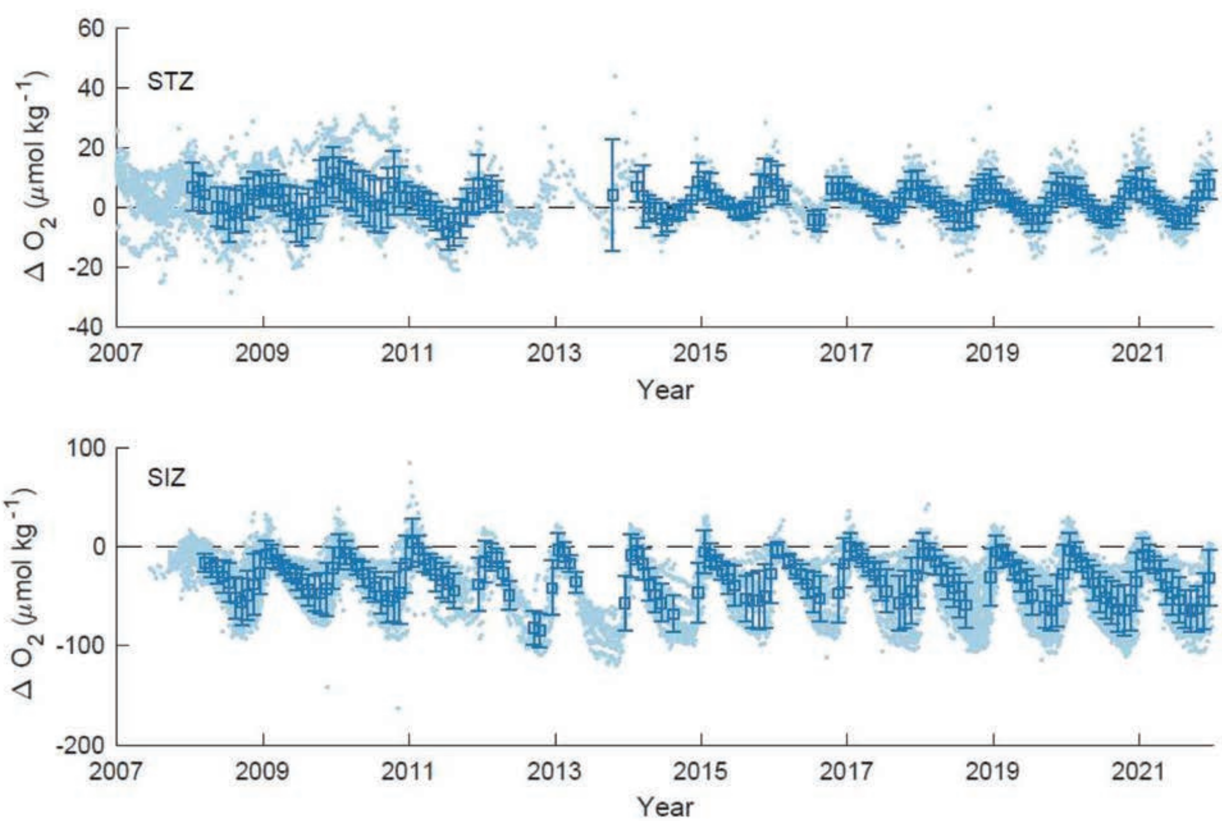

Fig. 8. Oxygen concentration difference from saturation ($\Delta O_2 = [O_2]_{measured} - [O_2]_{saturation}$) for the Subtropical Zone (STZ) and Sea ice Zone (SIZ). Updated from Bushinsky et al. (2017) with data through 2022. Light blue points indicate mixed layer concentrations from individual profile averages. Blue squares and error bars are monthly means ± 1 SD when average float temperature agreed with the NOAA Optimal Interpolation Sea Surface Temperature product as a check on data coverage.

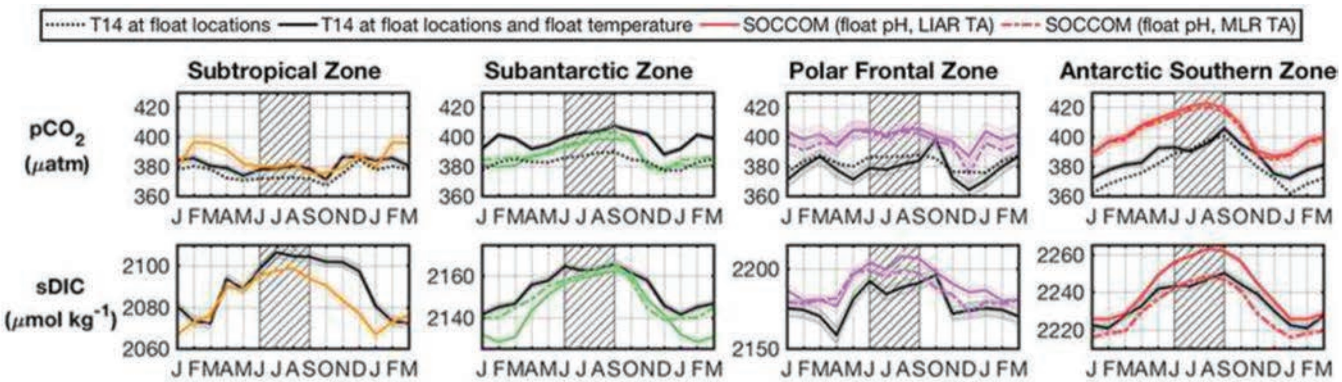

Fig. 9. Seasonal cycles of pCO_2 and salinity normalized DIC (sDIC) in the Subtropical, Subantarctic, Polar Frontal, and Antarctic Southern Zones. Float data are shown as solid, colored lines. The climatological values reported by Takahashi et al. (2014) for the year 2005 (T14 on figure), were adjusted to the present. The mean of all Takahashi et al. (2014) data at each float location are shown as black dotted lines and a filtered data set, with values selected only when float and climatology temperatures were similar, are shown as solid black lines.
Adapted from Williams et al. (2018)

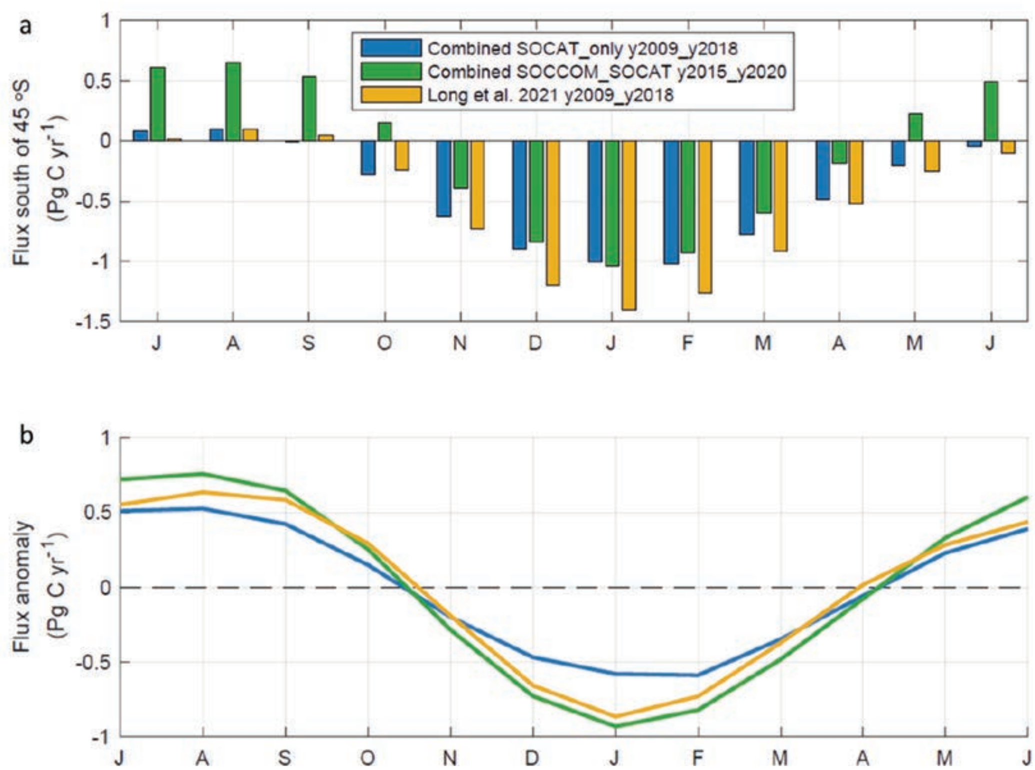

Fig. 10. Monthly mean sea to air CO_2 fluxes south of 45°S (positive values for flux from sea to air). (a) Values reported by Long et al. (2021) for 2009 to 2018 are shown as yellow bars. Values determined from the MPI SOM-FFN method (Landschützer et al., 2017) fitted to SOCAT shipboard data only for 2009 to 2018 are shown as blue bars. Values from the MPI SOM-FFN method fitted to the combined SOCAT and SOCCOM profiling float datasets (Bushinsky et al. 2019a,b) for 2015 to 2020 are shown as green bars. (b) The same data from panel a) are shown as monthly anomalies from the overall mean of each data set.

A recent study used aircraft and ground station measurements of atmospheric pCO_2 with atmospheric inversion models to develop a new constraint on air-sea CO_2 fluxes south of 45°S (Long et al. 2021). These fluxes, derived primarily from vertical gradients in atmospheric pCO_2 observations, agree more closely in annual magnitude with prior ship-only estimates. This may suggest a systematic bias in float based pCO_2 fluxes that would arise if float pH were consistently low around 0.005 to 0.010 pH. However, it is also clear that the flux based on the merged float and SOCAT data yield a seasonal cycle much closer to the values derived from atmospheric measurements than do the SOCAT only fluxes. This is shown by a plot of the anomaly from the annual mean in seasonal cycles from the atmospheric data, the shipboard only data and the shipboard plus float data (Fig. 10b). The SOCCOM float data appear to add significant information regarding the timing and amplitude of the seasonal cycle, relative to the SOCAT only dataset. The merged SOCCOM and SOCAT data yield a seasonal flux cycle that agrees closely with the aircraft data in seasonal amplitude and timing (Fig. 10b). The seasonal cycle would be difficult to obtain from sparse, shipboard observations in the Southern Ocean that are heavily biased to observations in summer (Bushinsky et al., 2019a).

Independent studies such as Long et al. (2021), Wu et al. (2022), and MacKay and Watson (2021) suggest that there may be a systematic offset in pCO_2 values that are derived from profiling floats of 5 to 10 μatm. It should be possible to identify and correct such a systematic error. Possible sources of systematic error include biases in carbon system thermodynamics (Fong and Dickson, 2019) or a systematic error in calibration protocols (Johnson et al., 2016). Resolving a potential bias will clearly lead to more precise and accurate air-sea CO_2 fluxes. The potential need for improvements in the profiling float pH and derived pCO_2 accuracy are reminiscent of the work required to make shipboard pCO_2 observations from different research groups consistent with each other (Körtzinger et al., 2000).

As the SOCCOM array has grown to cover the Southern Ocean in all of its most distinctive regimes, it has become possible to document regional differences within circumpolar regimes (Williams et al., 2018). These spatial and temporal variations can then be related to physical and biological processes. Chen et al. (2022) documented the connection of the deep water reservoirs of high carbon to the near-surface in the southern part of the Antarctic Circumpolar Current, using both SOCCOM float and historical hydrographic data (Olsen et al., 2020) and the property potential pCO_2 (PCO_2). The PCO_2 is the pCO_2 a parcel of water would have if raised to the sea surface (Broecker and Peng, 1982), and better characterizes the potential for air-sea exchange than the DIC concentration. Prend et al. (2022b) connected this high subsurface PCO_2 to the sea surface. Using SOCCOM air-sea carbon fluxes, they showed preferential outgassing in the Indian and Pacific sectors of the Southern Ocean compared with the Atlantic (Fig. 11). The initial hypothesis for the asymmetry was the lower PCO_2 observed for Atlantic deep water compared with Indo-Pacific Deep Water. However, Prend et al. (2022b) showed that stronger winter entrainment of high PCO_2 waters into the mixed layer is the proximate cause. Thus, a future with strengthening westerly winds and deepening mixed layers (e.g. Sallée et al., 2021)

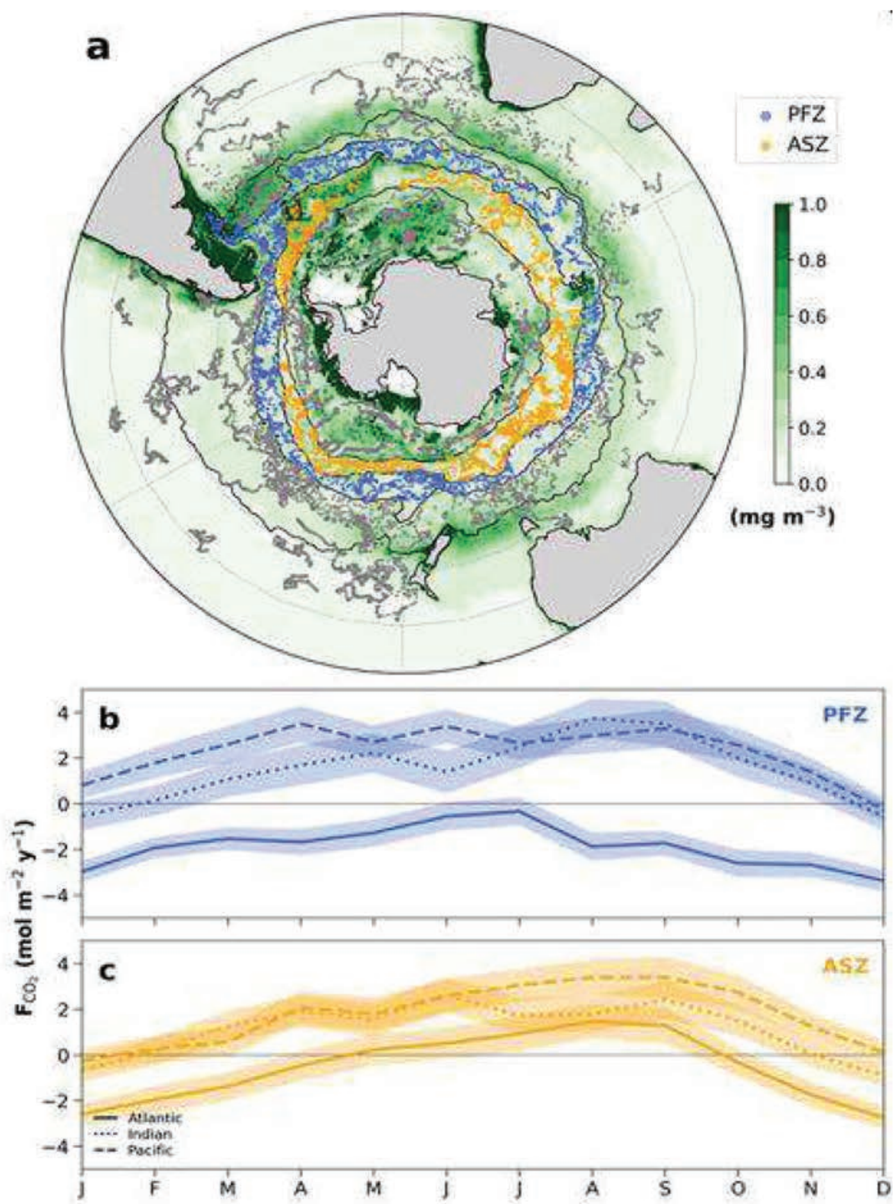

Fig. 11. (a) SOCCOM float profile locations sorted by frontal zone (PFZ: Polar Frontal Zone; ASZ: Antarctic Southern Zone). The color shading shows austral summer surface chlorophyll (mg/m3) from a 2002 to 2019 satellite ocean color climatology (NASA Goddard Space Flight Center, Ocean Ecology Laboratory, Ocean Biology Processing Group, 2018). (b) Monthly climatology of air-sea CO2 flux (mol C/m2/yr) in the PFZ from float profiles in the Atlantic, 65°W–25°E (solid line), Indian, 25°E – 150°E (dotted line), and Pacific, 150°E – 65°W (dashed line) sectors. Float profiles were made between 2014 and 2020. Panel (c) same as panel (b), but for the ASZ. Adapted from Prend et al. (2022b).

would lead to greater carbon outgassing.

Prend et al. (2022a) demonstrate the capability of SOCCOM profiling float pH observations to assess the processes that drive pCO_2 seasonal cycles. There is a change from a summer maximum of pCO_2 in the subtropics to a winter maximum in the polar regions. They find this shift is driven by a reduction in the amplitude of the seasonal temperature change at high latitudes, rather than biological processes.

3.2. Primary production and seasonal biomass cycles

3.2.1. Primary productivity

The transformation of dissolved inorganic to organic carbon during photosynthesis in the ocean, i.e., primary productivity, fuels marine ecosystems and plays an essential role in the global carbon cycle. Global marine net primary productivity (NPP) (defined as gross carbon fixation minus autotrophic respiration) is commonly inferred from ocean color remote sensing observations. Satellite observations provide information on water optical constituents and the available light field to infer phytoplankton biomass and division rates (Behrenfeld and Falkowski, 1997). The calibration of these satellite productivity models relies on scarce in situ observations of productivity determined from incubations of seawater samples with added $H^{14}CO_3^-$. The in situ observations are mostly constrained to low latitude regions (Buitenhuis et al., 2013; Marra et al., 2021).

Alternatively, primary productivity can be quantified by tracking the production of oxygen through photosynthesis. BGC-floats with oxygen sensors, including all floats within the SOCCOM array, permit the direct measurement of in situ gross oxygen production (GOP), albeit at coarse spatial scales. Although profiling floats cycle at ~ 10 day intervals, the diel cycle of oxygen can be detected by a float array if the individual floats surface at different times of the day (Fig. 12; Johnson and Bif, 2021). In this case, the set of profiling floats act as a dispersed chemical sensor array. The GOP computed from the diel cycle in oxygen concentration can then be converted to NPP, yielding a globally integrated value of 53 ± 7 (1 standard error) Pg C yr^{-1}. This value is consistent with the previous mean estimate of 50.7 Pg C yr^{-1} obtained from multiple ocean color and general circulation models (Carr et al., 2006). The diel oxygen method developed in SOCCOM has been extended to include diel cycles of particulate organic carbon in a study using SOCCOM data (Stoer and Fennel, 2022).

In addition to chemical sensors, SOCCOM floats have been equipped with bio-optical instruments that allow the estimation of phytoplankton chlorophyll and carbon biomass from measurements of fluorescence and particle backscattering that are combined with the models used to calculate productivity from remote sensing observations. These bio-optical observations are used to constrain phytoplankton physiology in response to nutrient and light limitation and to extend the computation of NPP beyond the mixed ocean surface and past the first optical depth (Arteaga et al., 2022), where most satellite sensors are unable to retrieve bio-optical information. Within the surface ocean observed by satellites, the increasing availability of float bio-optical observations is enabling the evaluation of ocean color remote sensing products (Bisson et al., 2019, 2021). For example, an assessment of estimates of chlorophyll and particulate organic carbon from NASA's Ocean Color Index (OCI) algorithm based on retrievals from the Moderate Resolution Imaging Spectroradiometer (MODIS) and (VIIRS) showed a good agreement with float-based estimates of these variables in the Southern Ocean (Haëntjens et al., 2017).

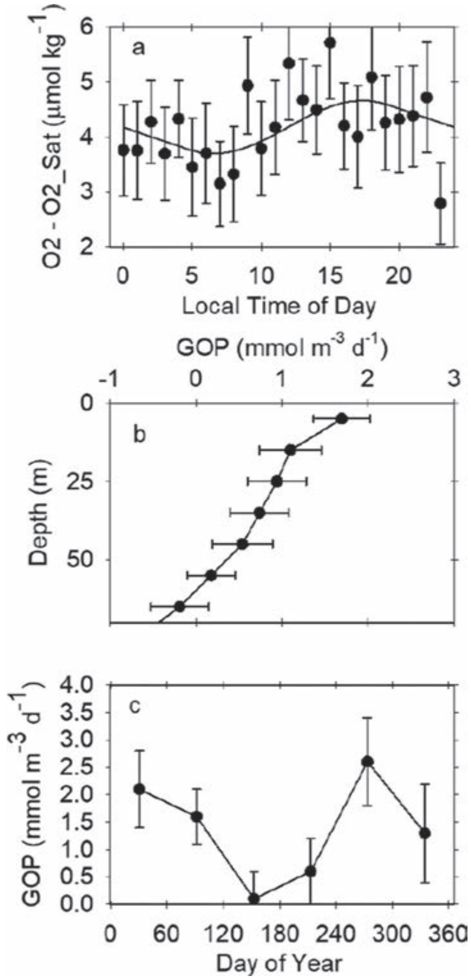

Fig. 12. Diel oxygen productivity from 30°S to 60°S following Johnson and Bif (2021). (a) Diel cycle of oxygen in the upper 20 m for all SOCCOM floats on days 0 to 61. (b) Vertical profile of Gross Oxygen Production (GOP). (c) Seasonal cycle of GOP in the upper 10 m. Error bars are 90% confidence intervals.

3.2.2. Bloom dynamics

The incorporation of bio-optical sensors together with the float's biogeochemical measurements has increased our capacity to assess the role of ocean physics in setting the necessary nutrient and light preconditions needed for phytoplankton to grow and blooms to develop. Prend et al. (2019) coupled float data with the B-SOSE model to show that the large bloom in the Scotia Sea is linked to an unusually shallow mixed layer. This is due to a Taylor column over a topographic feature supporting early bloom formation. von Berg et al. (2020) show that the initiation and magnitude of blooms in the seasonal ice zone are linked to the timing of sea ice retreat. Uchida et al. (2019) and Arteaga et al. (2020) examined the phenology of phytoplankton blooms from the in situ observations of SOCCOM floats, a complementary approach to prior satellite-based assessments. Over the last ten years, studies based on satellite information have suggested that the temporal evolution of phytoplankton blooms cannot be fully understood from abiotic environmental properties controlling phytoplankton division rates (Behrenfeld and Boss, 2018). In situ observations of phytoplankton biomass from SOCCOM float bio-optical sensors have revealed a temporal gap between the seasonal cycle of phytoplankton division rates and actual biomass accumulation, which highlights the role of biomass-loss processes (e.g., grazing, viruses, sinking) as important drivers of bloom initiation and termination (Arteaga et al., 2020).

3.2.3. Linking to elements of the global ocean observing system

Profiling floats operate in synergy with all elements of the global ocean observing system. They are dependent on ships for deployments, sensor validation, and mapped products for sensor adjustment (Maurer et al., 2021). They complement earth observing satellites such as ocean color sensors and altimeters by providing observations with vertical resolution under clouds and ice, and during dark winter periods. Satellite-based communication systems are required to transmit data.

These synergies are illustrated in Fig. 13. The figure emphasizes the role that floats add to the observing system. They extend ship-based observations in time. They extend satellite observations in depth. They provide a consistent set of in situ observations that can effectively link these systems. For example, Haëntjens et al. (2017) have demonstrated consistency between SOCCOM profiling float chlorophyll values and the concentrations determined from ocean color satellites. Arteaga et al. (2022) used SOCCOM profiling float bio-optical data to extend NPP values computed with the Carbon-Based Productivity Model (Westberry et al., 2008), developed to support ocean color satellites, into waters deeper than can be resolved by ocean color satellites. They find that the vertical extrapolations necessary with ocean color satellite data have systematic biases in the Southern Ocean that affect vertical integrals of NPP.

The spatial density of profiling float observations cannot approach that obtained by ocean color satellites. However, processes that operate at higher temporal and spatial scales than those that floats sample at are aliased into the float data. In many cases, these signals can be recovered from the analysis of large numbers of float profiles. In addition to the above example of diel oxygen production by phytoplankton (Johnson and Bif, 2021), Carranza et al. (2018) used SOCCOM profiling float bio-optical sensors and satellite wind sensors to examine the effects of Southern Ocean storms on the vertical structure of plankton communities and their ability to develop vertical structure during quiescent wind periods.

3.3. Biological carbon pump

The biological influence on air-sea carbon flux is controlled by the downward flux of organic matter produced by phytoplankton in the surface ocean. This export and transfer of carbon from the surface to depth is termed the biological carbon pump. It is one of the main regulators of global atmospheric CO_2 levels (Volk and Hoffert, 1985). In most cases, the amount of carbon exported by the biological carbon pump will equal the annually integrated net community production (NCP), where NCP is the amount of primary production minus respiration at all trophic levels. SOCCOM floats have observed NCP from the seasonal drawdown of nitrate (Johnson et al., 2017a; Arteaga et al., 2019) and DIC (Briggs et al., 2018) in all regions of the Southern Ocean, providing comprehensive assessments of the net carbon production that is subsequently exported. This work allows the first, systemwide rate observations with the potential for annual resolution.

These analyses of NCP and the biological carbon pump generally make simplifying assumptions regarding potential biases due to ocean physics. As the number of floats increase, more effective use of the observational data may be made by incorporating the results with data assimilating models such as B-SOSE. Such an approach was used to study the mismatches in NCP rates determined from DIC and nitrate that may occur in oligotrophic systems. Elevated rates of DIC uptake may occur without corresponding nitrate uptake (Johnson et al., 2022) in oligotrophic systems. This study, which merged observations of 234 seasonal cycles of nitrate and DIC from floats with the corresponding results in B-SOSE, implies that much of the DIC uptake north of about 40°S is due to the production of dissolved organic matter containing little or no nitrogen. Seasonal declines in oxygen concentration observed by SOCCOM floats in the mesopelagic zone (depths between 100 and 1000 m) have been used to determine consumption rates of exported carbon (Arteaga et al., 2018, 2019; Hennon et al., 2016). The decreases in oxygen are driven by respiration of sinking organic carbon.

The ocean near the Polar Front (~50° S), a region of extremely low iron concentrations, appears to be an area of elevated biogenic carbon export relative to the rest of the Southern Ocean (Arteaga et al., 2019; Johnson et al., 2017a; Fig. 14). Prior studies have suggested differences in the remineralization and grazing efficiency by bacteria and zooplankton as a potential driving mechanism (Cavan et al., 2015; Laurenceau-Cornec et al., 2015; Le Moigne et al., 2016). An alternative hypothesis derived from the analysis of SOCCOM float-based export estimates and satellite productivity algorithms is that iron limitation promotes silicification in diatoms, which is evidenced by the low silicate to nitrate ratio of surface waters around the Antarctic Polar Front

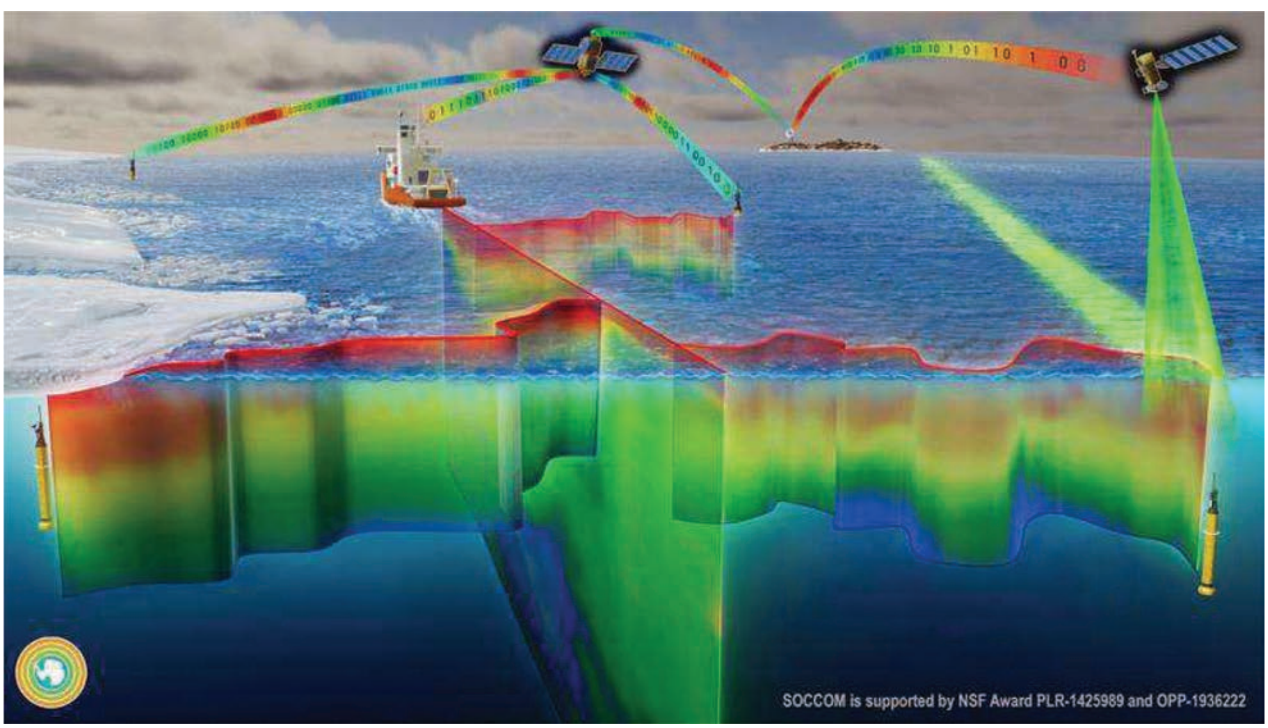

Fig. 13. Illustration of the SOCCOM float observing system embedded within the framework of ship-based observations and satellite remote sensing and communications. Floats deployed from the ship extend elements of the diverse laboratory data out in time. Floats extend the high spatial resolution of ocean color data in the first optical depth of the ocean down in the vertical, while depending on satellites for data communications. Credit: SOCCOM Project, Princeton University.

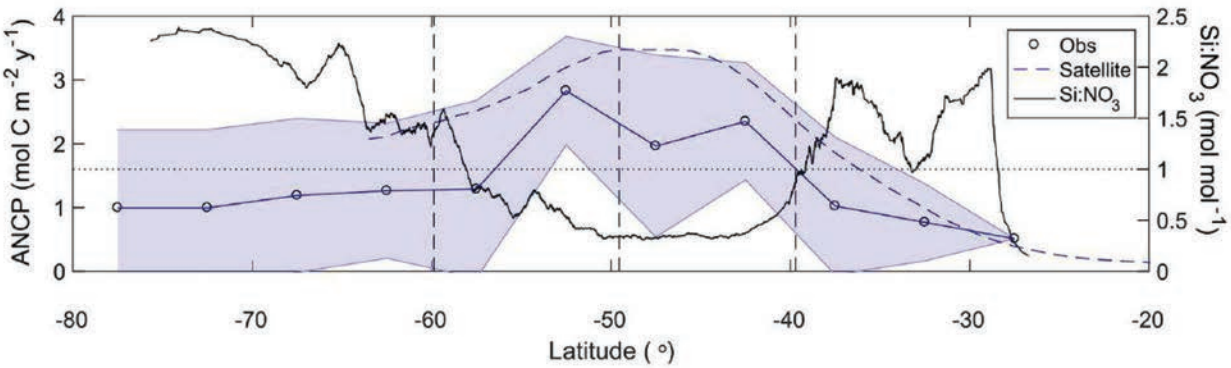

Fig. 14. Meridional pattern in export production (inferred from annual net community production - ANCP). Export production inferred from float oxygen and nitrate profiles (open blue circles and blue solid line), and satellite observations (blue dashed line). The Silicate to nitrate ratio (black solid line) was obtained from float nitrate observations and the World Ocean Atlas (2013) silicate climatology (Garcia et al., 2014).
Adapted from Arteaga et al. (2019)

(Arteaga et al., 2019). High diatom silicification increases the ballasting effect of particulate organic carbon and overall annual net community production in this region (Arteaga et al., 2019).

3.4. Floats in the seasonal ice zone

A hallmark of the Southern Ocean is the presence of seasonal sea ice south of about 60° S. Biogeochemical observations under sea ice have been rare, particularly during winter. SOCCOM has greatly improved sampling of both biogeochemistry and temperature/salinity in the sea-ice zone around the Antarctic continent with thousands of vertical profiles through all times of the year. These observations have allowed for unprecedented views of the under-ice water column properties in winter and the evolution of biogeochemical properties throughout an annual cycle (Briggs et al., 2018).

The SOCCOM floats operating in the seasonal ice zone enable a number of the observing system priorities identified in the UN Southern Ocean Report to be advanced. These include:

- *Improve understanding of sea ice, including its role in ecological processes of the Southern Ocean.*
- *Enhance predictive skill across climate, circulation, cryosphere, and ecosystems.*

3.4.1. Ice-ocean interactions

While SOCCOM was designed as a circumpolar observing system, its unprecedented year-round coverage has led to important contributions to more regional studies in the sea-ice zone as well (Wilson et al., 2019). In 2016 and again in 2017, a relatively large, open-ocean polynya appeared in the Weddell Sea region around Maud Rise (Campbell et al., 2019). This was in the same area occupied by the very large Weddell polynya of the mid-1970s. The 2016–17 polynya events were the largest since those observed in the mid-1970s (e.g. Gordon, 1978). SOCCOM floats over Maud Rise showed that the upper ocean in this region was only marginally statically stable during the events, with a mixed layer salinity approaching the limit for deep convection in late summer of both 2016 and 2017. The polynyas in both years were triggered by the passage of strong atmospheric storms, initiating mixing and heat loss from the subsurface ocean. Analysis of the stratification and climate forcing between the 1970s and 2016 indicated that this combination of weak stratification and strong climate forcing in the intervening years was rare (hence no polynya formation). The BGC sensors on the Maud Rise floats and in the northern Weddell Sea provided a comparison of productivity in the two regions, showing much higher productivity in the circulation trapped over Maud Rise, suggesting greatly enhanced vertical mixing that transports nutrients to the mixed layer.

Haumann et al. (2020) used a combination of under-ice profiles from both Core Argo floats and SOCCOM BGC-Argo floats, as well as ship-based and animal borne profiles, to investigate the details of temperature anomalies under and near sea ice. Surprisingly, a number of cases were found of water at temperatures below the in situ freezing point, termed supercooled, and water that would have been below the freezing point if it were raised to the sea surface, termed potential supercooled. Haumann et al. showed that nearly 6% of the profiles under the ice appeared to be supercooled, especially close to the Antarctic continent. The cause was attributed to melting of ice shelves and the existence of convective plumes during the formation of sea ice in winter. Such plumes might have important implications in the vertical transport of properties such as nutrients and carbon. An idealized modeling study nested in B-SOSE demonstrated the importance of ice shelf melt rates on spatial patterns of productivity (Twelves et al., 2021). These works suggest a need for a more focused observational study in these regions near the ice shelves.

3.4.2. Climatologies of BGC properties

The under-ice observations (from both Core Argo floats, with temperature and salinity data; and SOCCOM floats, with temperature, salinity, and BGC data) have been combined to produce a climatology of the wintertime under-ice regime around the continent, as can be seen in Fig. 15. Here we show the climatology in the wintertime surface mixed layer ($\sigma_\theta = 27.4$ and ~ 50 m deep in summer; $\sigma_\theta = 27.7$ and 100–120 deep in winter). The climatologies shown in this figure were formed by averaging and gridding the float data in an equal-area, scalable Earth projection, in order to avoid problems with convergence of meridians near the pole.

Mazloff et al. (2023) used the profiling float pH profiles and the B-SOSE model to create a monthly, mapped pH product for the Southern Ocean from 30°S to 70°S. The pH product was then compared to pH measurements made from ships prior to 2014. The differences in the climatology and shipboard measurements show that pH is decreasing most rapidly near the surface at a rate of -0.02 pH decade^{-1}, consistent with the rate of atmospheric CO_2 increase. The rate of decrease is not uniform horizontally, with some regions showing little change. The observed pattern of pH rate of change is consistent with the overturning circulation. Regions with low acidification rates are areas where Southern Ocean winds drive upwelling, which brings older, less acidified water to the surface and this decreases the rate at which pH declines.

3.4.3. Sea ice and phytoplankton

Sea ice plays a central role in structuring the productivity and

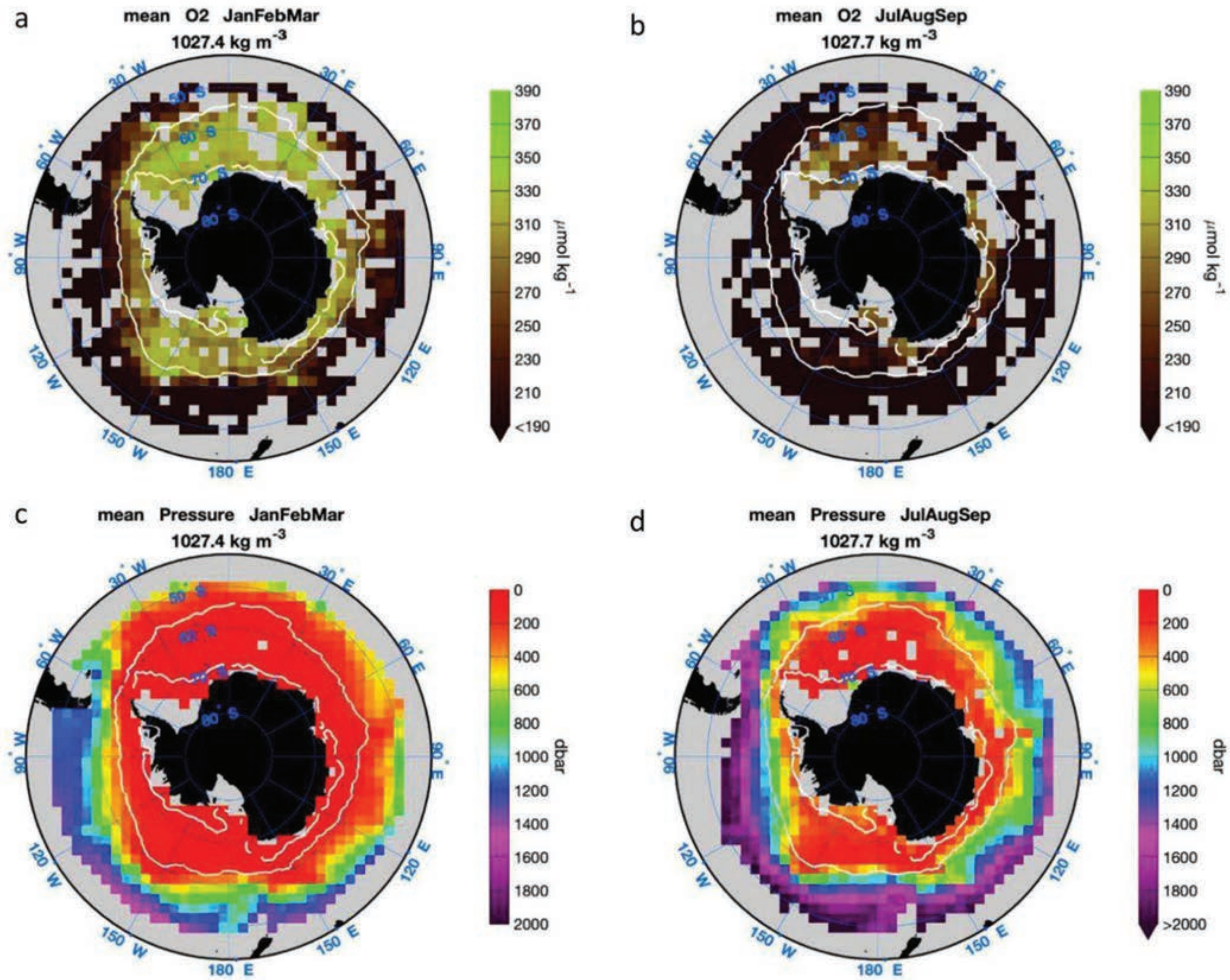

Fig. 15. Under ice climatology for oxygen. Dissolved O_2 (μmol kg^{-1}) determined from SOCCOM float data in summer (panel a) and winter (panel b) on the pressure (decibars) surfaces shown in panels c ($\sigma_\theta = 27.4$) and d ($\sigma_\theta = 27.7$). These pressure surface lie at the base of the mixed layer in summer and winter and the O_2 concentrations represent values in the surface mixed layer. The inner and outer white contours represent the summer and winter limits of the sea ice zone. The climatologies are gridded using an equal area scalable Earth projection that preserves the gridding in cells near the pole.

ecology of marine polar ecosystems. Observations in the Southern Ocean have long shown that sea ice communities are highly productive and diverse (Garrison 1991; Smith and Garrison, 1990). It has also been hypothesized that sea ice plays a critical role in adjacent pelagic communities (Smith and Nelson 1986), which represent a significant proportion of the annual primary productivity, and underpins trophic dynamics and biogeochemical cycles of the Southern Ocean (Arrigo et al. 2008).

Under-ice observations from SOCCOM floats revealed that Antarctic phytoplankton in ice covered regions begin to bloom (net increase in biomass accumulation) in early winter (Prend et al., 2019; von Berg et al., 2020; Arteaga et al., 2020), well before sea ice starts to retreat (Fig. 16). Under-ice blooming has been observed at local scales in the Arctic (Arrigo et al., 2012) and near Antarctica (Gibson and Trull, 1999; Arrigo et al., 2017), but the SOCCOM float dataset demonstrates that this phenomenon is a common feature of the seasonal ice zone. This is a remarkable event given the low light levels at which the bloom appears to begin (less than1 E m^{-2} d^{-1}). Biomass loss must be very low to permit phytoplankton to accumulate despite very low cellular division rates (Arteaga et al., 2020). These blooms deplete nitrate and DIC and, as light increases, they rapidly produce oxygen (Briggs et al., 2018). These observations show that respiration in winter nearly balances summer production with little net carbon export.

3.5. Circumpolar circulation

SOCCOM investigators worked on describing and understanding the pathways of the deep waters to the sea surface in the Southern Ocean (Morrison et al., 2015). This work was inspired by the findings of unexpectedly large carbon outgassing in the southern Antarctic Circumpolar Current (Section 3.1) that are driven by upwelling of high carbon deep waters. To explore the upwelling deep waters, Lagrangian tracking in multiple computer simulations revealed a southward and upward spiraling pathway (Tamsitt et al., 2017, 2018; Drake et al., 2019). Deep waters exiting the Atlantic, Pacific, and Indian Oceans were shown to be localized to the western and eastern boundaries and to mid-ocean ridges. These waters enter the eastward-flowing ACC, and mingle with each other and with ventilated waters from south of the ACC. While the net upward pathway is related to Ekman suction, most of the actual upwelling occurs in eddy fields at topographic features that are encountered by the ACC. This topographically-facilitated upwelling is active up to near the base of the surface mixed layers. The last step of

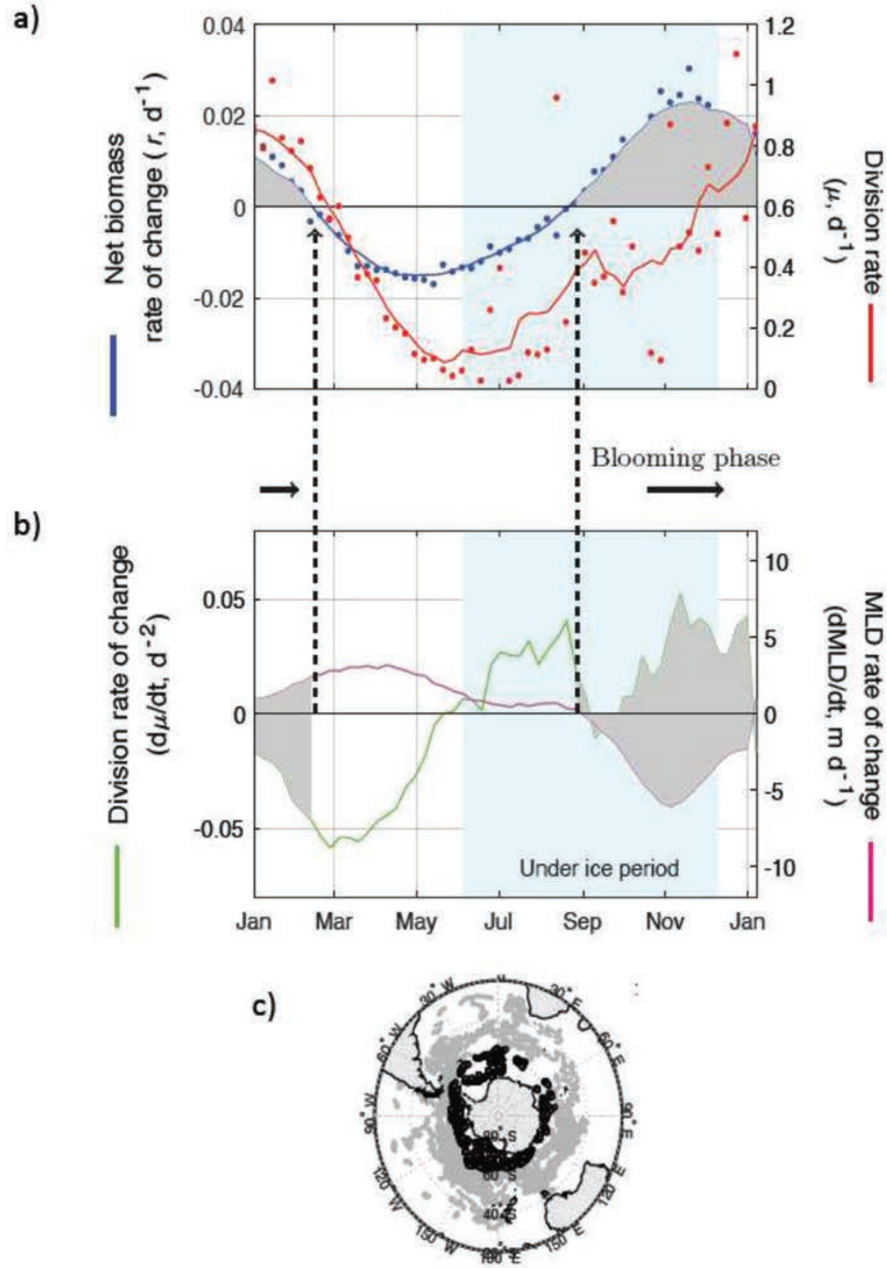

Fig. 16. Climatological phytoplankton bloom cycle in the Antarctic seasonal ice zone (SIZ). (a) Annual cycle of net phytoplankton biomass rate of change (r, blue line) and division rates (μ, red line). Individual points are weekly averaged observations and the continuous line is the result of a smoothing temporal filter. (b) Averaged time series of the temporal derivative of μ (dμ/dt, green line) and of the mixed layer depth (MLD) (dMLD/dt, magenta line). The blooming phase (r greater than 0) is highlighted by the gray shaded periods. The light blue shaded section indicates the period where 50% or more profiles were under ice. (c) Location of float profiles in the STZ and SIZ.
Adapted from Arteaga et al. (2020)

incorporation into the mixed layer is decoupled from these topographic features, and instead is dominated by surface-forced mixed layer entrainment. This process is most vigorous where winter mixed layers are deep, in the Indian and Pacific sectors of the ACC (Prend et al., 2022b).

Thus carbon outgassing in the southern ACC is driven by the conjunction of two processes – upwelling of high-carbon, northern deep waters to just below the surface layer, and vigorous winter entrainment that incorporates this water. There are many steps of this process that remain to be detailed, but the framework is now clear. After the northern deep waters upwell to near the sea surface, they split into the lower and upper limbs of the Southern Ocean's overturning circulation. The lower limb is fed by the densified surface layer, fueled by brine rejection from sea ice formation. In the upper limb, surface waters and sea ice are exported northward through Ekman transport. Freshwater from melted sea ice provides enough buoyancy to allow the upwelled water to move northward and warm, eventually reaching the northern ACC where it subducts into the thermocline (Haumann et al., 2016). This upper limb water carries high nutrients and carbon which become the source of nutrients for the thermocline (Sarmiento et al., 2004, Verdy and Mazloff 2017). This split between the upper and lower limbs has been quantified and localized in SOCCOM studies utilizing the B-SOSE output (Abernathey et al. 2016; Masich et al. 2018). Abernathey et al. 2016 showed the importance of freshwater transport via sea-ice in setting the structure of this overturning circulation (Fig. 17).

3.6. SOCCOM biogeochemical data as a community resource

A major focus of the SOCCOM program was to provide open access data to the community that was easily accessible outside of the program participants to ensure maximum influence. There are numerous publications by scientists outside the SOCCOM program who have used these data. Here we focus on just three topical examples; the effect of eddies on biogeochemical processes, studies of carbon export, and studies of plankton blooms under sea ice.

The open access SOCCOM dataset has played a seminal role in studies that illustrate the role of eddies on biogeochemical processes. This work has been performed completely by scientists outside of the project (Su et al., 2021; Cornec et al., 2021), illustrating both the Findability and Accessibility principles of a FAIR dataset (Wilkinson et al., 2016). These authors used the large SOCCOM dataset, as well as other floats in the BGC-Argo system, to assign float profiles to their location in cyclonic and anticyclonic mesoscale eddies that were mapped with satellite altimeters (an illustration of the FAIR Interoperability principle). This allowed them to test hypotheses regarding the role of eddy circulation in sustaining enhanced chlorophyll in these systems. Chlorophyll fluorescence in the deep chlorophyll maximum of eddies may increase due to biomass accumulation or photo-adaptation. Cornec et al. (2021) find, in a study with a global span, that in cyclonic eddies the fluorescence increase is primarily due to biomass accumulation, while in anti-cyclonic eddies it results primarily from photo-adaptation. Su et al. (2021) focused on the Indian Ocean sector of the Southern Ocean, where they found fluorescence increases generally resulted from both biomass accumulation and photo-adaptation. They show the importance of eddy pumping for sustaining elevated biomass in cyclonic eddies, as expected from prior studies. Supporting studies at the scale of eddies was not one of the original goals of SOCCOM, illustrating the FAIR principle of data Reusability.

SOCCOM floats have also played a significant role as a data source for studies of carbon export (Dall'Olmo et al., 2016; Stukel and Ducklow, 2017; Llort et al., 2018; Su et al., 2022). There is a growing appreciation that transport of organic carbon into the deep sea may occur by a variety of mechanisms (Boyd et al., 2019) in addition to the gravitational sinking of particles (the biological carbon pump; Ducklow et al., 2001). The broad distribution of SOCCOM floats allowed carbon export processes observed at the Long Term Ecological Research Station on the Palmer Peninsula to be extrapolated across the Southern Ocean (Stukel and Ducklow, 2017). Vertical mixing appeared to contribute one quarter of the biological carbon pump. In a global study, using many SOCCOM floats, Dall'Olmo et al. (2016) demonstrated that deep winter mixing is an important transport mechanism that detrains particles from surface waters to the deep-sea, a process labeled the seasonal mixed-layer pump. Llort et al. (2018) used SOCCOM floats to demonstrate that vertical motions along mesoscale eddies can further transport particulate carbon into the deep-sea, a process they termed the carbon eddy-pump. Su et al. (2022) used all of the available Southern Ocean oxygen profiles to compute oxygen consumption rates between the euphotic zone and 1000 m throughout the Southern Ocean. They obtained Annual Net Community Production rates by presuming the vertically integrated respiration rates are balanced by surface production and export. Their values are 1.1 to 2.8 times higher than found in prior studies.

The ability of the SOCCOM profiling floats to collect year-round data under sea ice has become a novel data resource that is being well utilized by the broader community. Jena and Pillai (2020) used SOCCOM floats, which fortuitously surfaced in the Weddell Polyna (Campbell et al., 2019), to examine the processes controlling plankton blooms in ice free regions of the seasonal ice zone. Hague and Vichi (2021) used SOCCOM float data to test the hypothesis that blooms in the seasonal ice zone form when meltwater stabilizes the water column. They found that significant growth occurred under ice and before there was a large salinity decrease. Bisson and Cael (2021) examined the relationship between phytoplankton abundance detected by SOCCOM floats and remotely sensed sea-ice properties to assess the role of ice in plankton growth. Horvat et al. (2022) used the SOCCOM data to demonstrate that under-

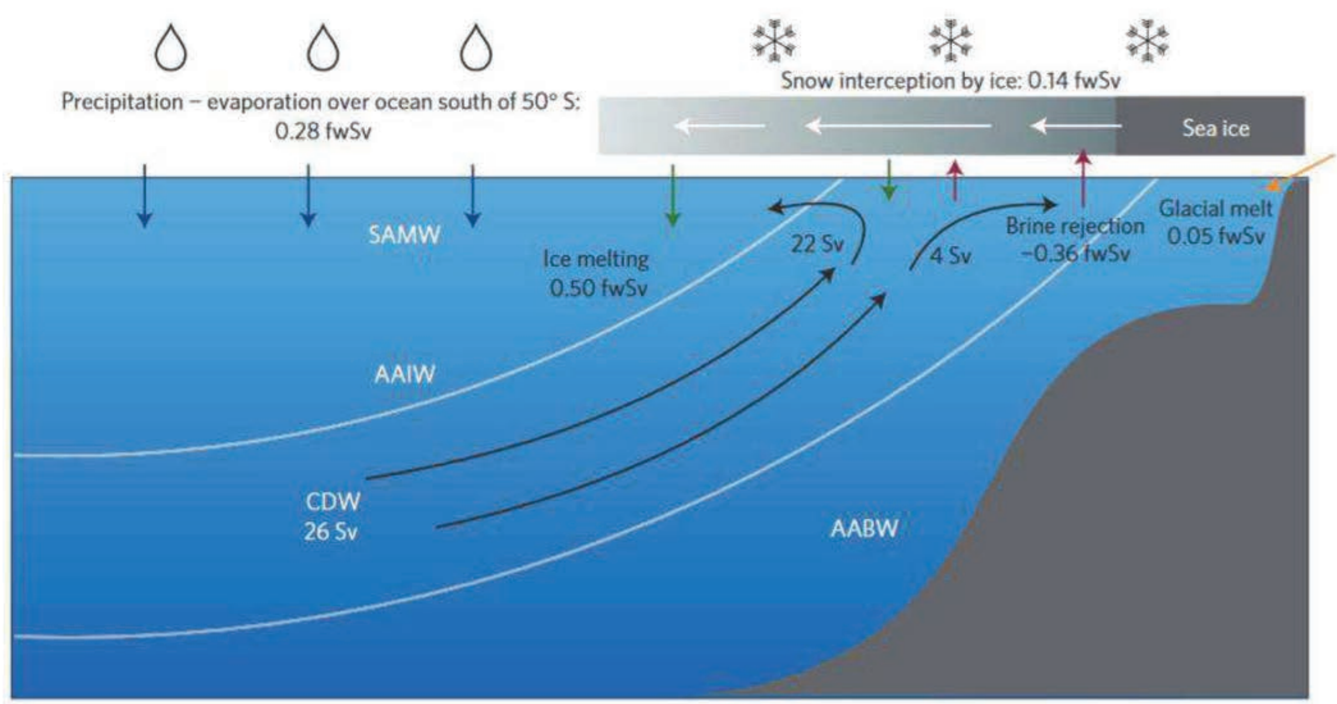

Fig. 17. Schematic depicting the various bulk contributions to the freshwater exchange at the ocean surface south of 50° S (positive downward). Net fluxes are given in units of freshwater sverdrups: 1 fwSv = 10^6 m^{-3} freshwater s^{-1} = 3.15 × 10^4 Gt freshwater per year. For reference, 1 fwSv = 1.9 mm d^{-1} of rainfall distributed over the region. From (Abernathey et al., 2016).

ice phytoplankton blooms are widespread in the Southern Ocean. Nearly all profiles under compact ice (80–100% coverage) showed large blooms during austral spring. Moreau et al. (2020) examined the fate of the carbon produced in ice-edge and under-ice blooms. Herbivory accounts for 90% of the losses and downward POC export is less than 10%.

These papers are just a subset of the analyses now produced by members of the ocean science community that are not directly associated with the program, but who are using the SOCCOM float data and B-SOSE output. They illustrate the role that SOCCOM is playing in becoming a major data resource that will enable both process studies and long-term assessments of the Southern Ocean response to climate forcing.

The SOCCOM observing system also fulfills a broader role through its synergism with other Southern Ocean observing systems and research programs. Examples of synergism with other programs include use of data from marine mammals that have been instrumented by the Marine Mammals Exploring the Oceans Pole to Pole (MEOP) program. The B-SOSE data assimilation system uses MEOP data as a constraint, which is particularly valuable in waters that are shallower than the 2000 m limit at which most floats are deployed. A SOCCOM study of the effect of storm driven mixing on bio-optical gradients used both profiling float and MEOP data (Carranza et al., 2018). Another SOCCOM study of the distribution of supercooled water used profiling float, MEOP, and ship-based measurements from the NOAA World Ocean Database (Haumann et al., 2020). Other major programs use the SOCCOM data in a variety of applications. For example, the Palmer Long Term Ecological Research (LTER) project is using SOCCOM float to provide an open ocean end member to assess the changes in shelf productivity driven by the precipitous declines in sea ice. Close interaction with focused programs such as Ocean Regulation of Climate by Heat and Carbon Sequestration and Transports (ORCHESTRA) resulted in benefit to both programs through float deployments and data exchange (Meredith et al., 2017). SOCCOM profiling float data have been used in Marine Ecosystem Assessment of the Southern Ocean (MEASO) to understand the ecological significance of subsurface chlorophyll maxima (Baldry et al., 2020). Of course, the SOCCOM program is closely intertwined with the international GO-SHIP program, which has deployed many of the SOCCOM floats and which is an irreplaceable source of validatation data for float sensors. These programs have formed an essential base for the success of the SOCCOM project.

4. Modeling the current and future state of the Southern Ocean and climate

Initial work with Earth System Models has focused on improving understanding of several important drivers of ocean change (Shi et al., 2018). This work addresses the UN Southern Ocean Report priority:

- *Improve understanding of key drivers of change and their impacts on Southern Ocean species and food webs.*

A critical component of SOCCOM modeling and the associated observations has been assessing the impacts of known model deficiencies and biases related to freshwater forcing, in addition to wind effects. Meltwater from the Antarctic Ice Sheet is projected to cause up to one meter of sea-level rise by 2100 under the highest greenhouse gas concentration trajectory (RCP8.5) considered by the Intergovernmental Panel on Climate Change (Oppenheimer et al., 2019). However, the effects of meltwater from the ice sheets and ice shelves of Antarctica are not included in the widely used CMIP5 or CMIP6 climate models, which may introduce bias into IPCC climate projections. Work using B-SOSE (Abernathey et al., 2016) highlights the importance of understanding and incorporating the effects of freshwater inputs on Southern Ocean circulation.

The Southern Hemisphere surface westerly winds are the main driver of the Southern Ocean circulation, mixing and air-sea exchanges. These strong westerly winds drive vertical mixing between surface and deep waters. An increase and poleward shift in these westerly winds, due to both the cooling of the stratosphere and the warming of the troposphere, has been inferred from reanalyses since 1980 (Swart and Fyfe 2012). The effects of meltwater provide a significant positive feedback on these changes. Models from both CMIP5 and CMIP6 still underestimate these historical trends (Beadling et al., 2020). The SOCCOM-led Southern Ocean Model Intercomparison Project (SOMIP) addresses this wind issue directly by imposing a “corrective perturbation” to the wind stress felt by the ocean.

4.1. Meltwater and wind

Antarctic Ice Sheet meltwater discharge into the Southern Ocean is generally neglected in most CMIP simulations (Pauling et al., 2016). Bronselaer et al. (2018), however, found that accounting for this discharge substantially affected the rest of the climate system. Including meltwater discharge slows the rate of global atmospheric warming, delaying the realization of both 1.5 °C and 2 °C warming by more than ten years. Ice sheet meltwater into the Southern Ocean during future simulations also drives a northward shift of the Inter-Tropical Convergence Zone (ITCZ), which results in reduced drying over Northern Hemisphere landmasses and enhanced drying in the Southern Hemisphere, relative to future simulations that neglect the meltwater. These SOCCOM results suggest that a feedback mechanism is in operation, whereby the meltwater added at the surface induces subsurface warming. That in turn leads to enhanced melting underneath ice shelves, potentially causing further meltwater-related climate effects (Fig. 18). The results demonstrate that meltwater discharge from the Antarctic Ice Sheet not only contributes to sea-level rise but also influences the global climate throughout most of the twenty-first century, emphasizing the importance of ocean and ice-sheet feedbacks on the climate system.

Wind increases and meltwater increases have opposing effects on Southern Ocean biogeochemistry. Additional meltwater causes a local reduction in ventilation that decreases subsurface oxygen levels. On the other hand, reduced ventilation increases subsurface nitrate concentrations along the continent through the accumulation of nutrients in more poorly ventilated waters and reduces nitrate export out of the Southern Ocean in newly formed intermediate water. The reduction in nitrate concentrations therefore propagates to low latitudes. In opposition, the wind-induced increase in ventilation causes an increase in oxygen concentrations throughout the upper 1,000 m of the Southern Ocean, while at the same time increasing surface nutrients and nutrient export through increased upwelling of deep, nutrient-rich waters. The balance between competing effects of wind and meltwater on ventilation will therefore influence future projections of ocean biogeochemistry.

Future climate change beyond 2100 is expected to cause nutrient trapping in the Southern Ocean through increases in surface stratification and poleward-shifting westerlies, starving the world-wide ocean of nutrients. Bronselaer et al. (2020) find that adding meltwater at the surface strongly amplifies Southern Ocean nutrient accumulation south of 60°S (Fig. 19). Previously, Pauling et al. (2016) concluded that adding meltwater at the surface or at ice shelves had little difference. Bronselaer et al. (2020) also find that increasing both wind and meltwater leads to significantly decreased nutrients north of 60°S as well (Fig. 19). While Southern Ocean nutrient trapping is found to be important in the twenty-second century, our results suggest that accounting for Antarctic meltwater and wind can cause similar effects in the twenty-first century, suppressing global biological productivity sooner than otherwise expected.

4.2. Buoyancy forcing, wind, and circulation changes

Strong westerly winds are a hallmark of the Southern Ocean and the primary driver of the ACC (Munk and Wunsch, 1998; Paparella and

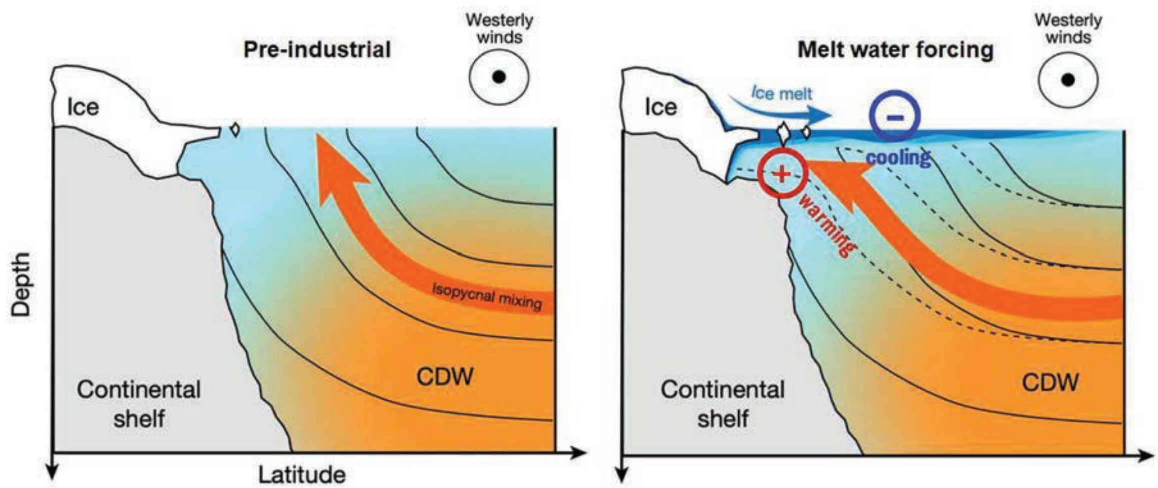

Fig. 18. Schematic showing subsurface warming in response to increased melt water is added to the surface of the Southern Ocean in an earth system model. After Bronselaer et al. (2018).

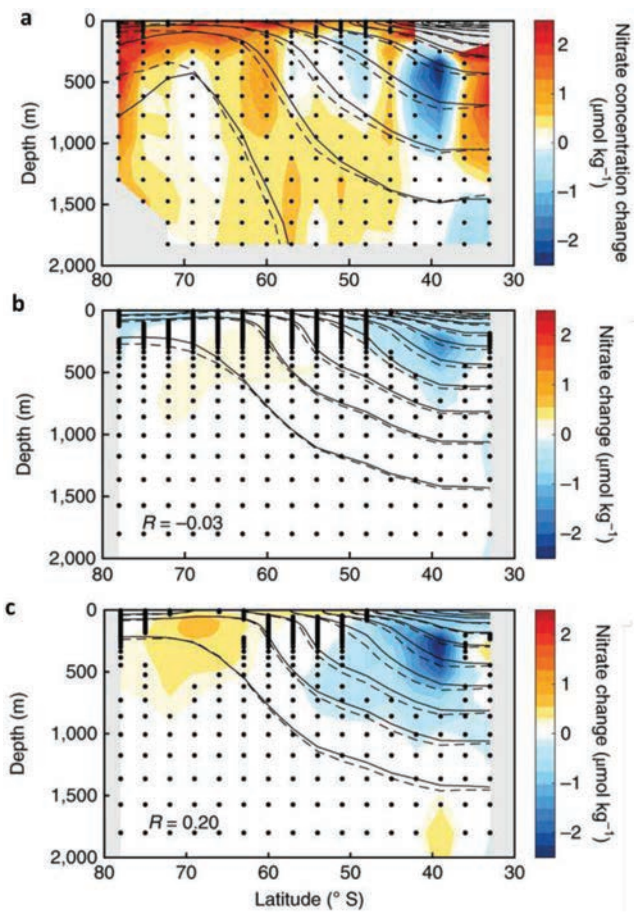

Fig. 19. Zonal-mean change in nitrate concentration. a) Observed nitrate change, SOCCOM float data 2014 to 2019 minus Ship data pre-2005. b) The decadal change of nitrate in the RCP 8.5 ESM2M simulation (2014 to 2019 mean minus 1985 to 2005 mean). c) The decadal change of nitrate in a SOMIP simulation with altered wind and meltwater (2005 to 2025 mean) minus the RCP 8.5 ESM2M simulation mean for 1985 to 2005. After Bronselaer et al. (2020).

Young, 2002). These winds are intensifying and shifting poleward, which may sustain an important feedback mechanism on the global carbon cycle (Russell et al., 2006b) and ocean warming (Armour et al., 2016). Much of the increased wind energy on the ocean appears in the mesoscale eddy field at locations determined by topographic interactions (Cai et al., 2022). Increased wind did not seem to appear in the mean flow. The weak effect on mean flow led to a concept known as eddy saturation (Straub, 1993; Munday et al., 2013).

In a SOCCOM supported study, Shi et al. (2020) used the Community Earth System Model (CESM) to examine climate driven controls on the ACC flow. They demonstrated that a changing buoyancy flux across the ACC was an important process regulating the ACC. To the north of the ACC, increasing ocean temperature produces a large buoyancy flux that has increased in time. Strong upwelling to the south of the ACC limits warming there. In a combined observational and modeling study, Shi et al. (2021) examined this process further. They used profiling floats, shipboard hydrography, and satellite altimetry with a careful statistical analysis to conclude that the zonally averaged ACC flow is accelerating, rather than remaining static. The increased baroclinicity due to the asymmetric buoyancy flux is a major driver of the increased flow, while strengthened wind stress is of secondary importance.

5. Broader impacts

SOCCOM's Broader Impacts vision is to transform training of oceanographers, expand public understanding of the Southern Ocean and its impact on climate change and living conditions on the planet, and enable broad access to the technology and findings of the SOCCOM initiative. The SOCCOM website, https://soccom.princeton.edu, was developed to enable much of this vision to be communicated to the public. The website includes access to profiling float data, model output, and a variety of multimedia resources including videos, photos, and graphics. Resources for an Adopt-A-Float program, including lesson plans for teachers are available. Some of these programs and resources are described in more detail below.

5.1. Public understanding

SOCCOM has a mission to drive a transformative shift in the scientific and public understanding of the outsized role of the ocean–and the Southern Ocean in particular–within our global climate system. In addition to deepening public understanding of the ocean's key role as a climate change buffer, the real-time monitoring of ocean health being done by SOCCOM provides critical information to policy makers, providing an ongoing assessment of carbon uptake and an independent way to effectively track progress on emission targets. This SOCCOM mission aligns with the UN Southern Ocean Report priority:

- *Improve societal understanding of Southern Ocean issues and appreciation of the Southern Ocean for its global value in Earth systems and unique environment.*

SOCCOM's Broader Impacts activities include use of social media, an Adopt-a-Float program, an array of multimedia content (lesson plans, videos, animations, and fact sheets), and capacity-building workshops to help researchers effectively apply float data (Matsumoto et al., 2022). The Adopt-a-Float program (Fig. 20) partners with teachers and classrooms around the world by enabling classes to adopt a profiling float with a goal to inspire and educate students about the Southern Ocean and climate change. Elementary- to college-level classes have the opportunity to give a soon-to-be-deployed float a name, and follow its progress at sea through online data visualizations and, sometimes, blogs written by their paired SOCCOM scientists. Students can find their float on the adopted floats table and explore data collected via a special Adopt-a-Float visualization application. Beginning with just one classroom in 2015, the program now has 180 adopted floats in classrooms across 42 states and seven countries (Chile, Canada, Australia, UK, Saudi Arabia, Japan, and Poland). Multimedia content is available through the SOCCOM YouTube channel that is linked on the SOCCOM website.

Outreach to communicate these key points has been part of the SOCCOM program since its inception and has helped scientists, teachers, students, and the public better understand the ocean's role in climate change while shining a light on the Southern Ocean.

5.2. Educating the next generation of Southern Ocean scientists

The SOCCOM project has contributed directly to the training and education of 19 postdocs, 22 graduate students, and 50 undergraduate students who have been actively engaged in our research program at SOCCOM institutions. Over half (59%) of these junior researchers have been female and nearly 9% have been participants from under-represented groups, with highest participation of under-represented groups at the undergraduate level. These students and postdocs are an integral part of the program. Many of the publications cited above are the direct result of research by postdocs, graduate students and undergraduates. As part of their training, SOCCOM early career personnel participate in regular research webinars as well as the SOCCOM annual meeting, where they present their research and take part in professional development activities. Ten SOCCOM-supported Ph.D. students have successfully defended their dissertations and have moved on to post-doctoral and faculty positions.

In addition to our program alumni, SOCCOM has established connections with dozens of ocean BGC researchers affiliated with the project partners through associate researcher and early career scientist groups. The program has also helped expand the community of BGC float and model data users through public training workshops on biogeochemical float and sensor technology, BGC data processing and QC, climate model data analysis and verification, and use and applications of the B-SOSE model.

5.3. SOCCOM in public policy

The SOCCOM program has been influential in shaping national

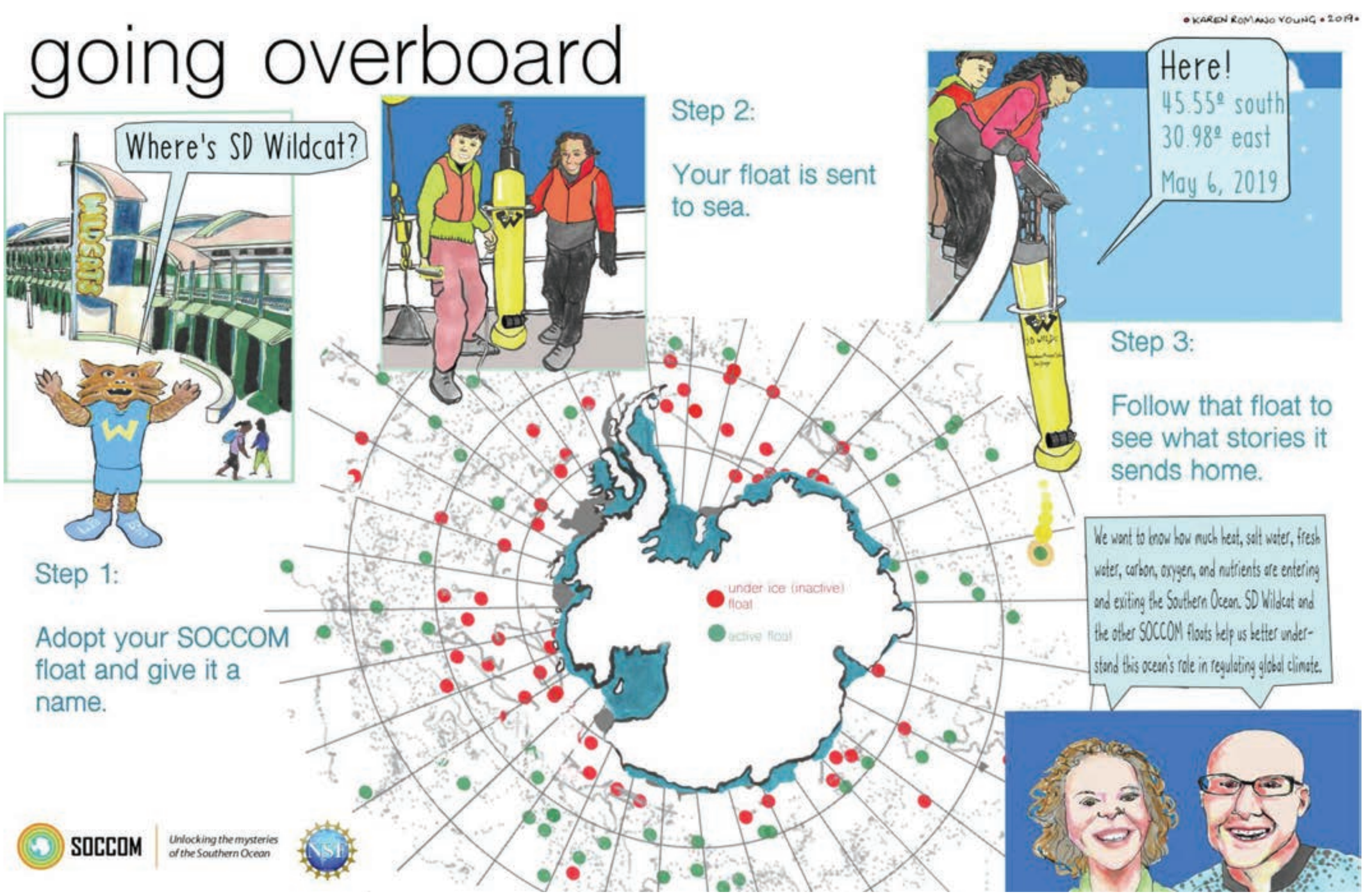

Fig. 20. The SOCCOM team partners with teachers and classrooms across the country to inspire and educate students about global ocean biogeochemistry and climate change through the "Adopt-A-Float" initiative. This illustration provides step-by-step instructions for adopting a float. Credit: Karen Romano Young for SOCCOM. The original drawing, with additional detail, was designed for a poster size and is available on the SOCCOM website (https://soccom.princeton.edu).

research policy. The second decadal plan for US ocean science, "Science and Technology for America's Oceans: A Decadal Vision" (NSTC, 2018), prominently features the SOCCOM project in the discussion on modernizing R&D infrastructure. The "Mid-Term Assessment of Progress on the 2015 Strategic Vision for Antarctic and Southern Ocean Research" (NAS, 2021) describes the role of SOCCOM in providing year-round observations of the Southern Ocean and the discoveries that have resulted. The role of SOCCOM in an international ocean carbon observing system has been discussed (IOC-R, 2021). Results from SOCCOM have been frequently included in the Bulletin of the American Meteorological Society Annual State of the Climate Assessment (Meredith et al., 2017; Swart et al., 2018; Meijers et al, 2019; Tamsitt et al., 2021).

6. SOCCOM in the future

The science performed in the SOCCOM program has evolved in scale as the profiling float array has grown. Initial studies were focused on one or a few floats (e.g., Williams et al., 2017; Briggs et al., 2018). The rapid growth of the array then enabled studies that encompassed the entire Southern Ocean, but without zonal resolution (e.g., Johnson et al., 2017a, 2017b; Bushinsky et al., 2017; Gray et al., 2018; Arteaga et al., 2019). As the array has progressed to more than 200 floats, studies with zonal resolution that reveal differences between processes in the Atlantic, Pacific, and Indian basins of the Southern Ocean are now possible (Prend et al., 2022b; Chen et al., 2022). Contrasting regional variability is also now possible. For example, Rosso et al. (2020) used machine learning techniques to classify profiles from the Indian Ocean sector of the Southern Ocean based on the vertical distribution of properties. The classification was then used to sort profiles into common groups. The grouping reproduced the expected frontal zone structure, but also showed significant differences with position relative to the Kerguelen Plateau. Such machine learning techniques will play an increasing role in studies of the growing SOCCOM dataset.

An immediate challenge for the SOCCOM system is sustaining the observations long enough to detect the effects of climate variability on biogeochemical processes. The time scales for detection of climate driven changes in biogeochemical cycles are typically greater than 15 years and often multiple decades (Henson et al., 2010; 2016; Schlunegger et al., 2020). The SOCCOM project has clearly established the capability to observe major elements of ocean biogeochemical cycles and their spatial variability over seasonal and internannual time scales (Bushinsky et al., 2017, 2019a; Johnson et al., 2017a, 2022; Gray et al., 2018; Arteaga et al., 2019; Prend et al., 2022a,b; Mazloff et al., 2023). However, with records that are typically less than 10 years in length, it is not yet reasonable to expect climate driven change to be detected unless float data is merged with prior, ship-based observations (Bronselaer et al., 2020; Mazloff et al., 2023). As the SOCCOM array operations are extended it will be critical to demonstrate that the data collected from profiling floats retain long-term consistency and can be used to directly detect climate driven change. Sustaining such a record will be a major challenge.

As the ocean warms (Roemmich et al., 2015, Cheng et al, 2022), it is likely that changes in primary productivity will result (Boyd et al., 2014) with significant effects throughout the ecosystem (IPCC, 2019). "Greening" of the Southern Ocean, quantified as an increase in chlorophyll detected by remote sensing (Del Castillo et al., 2019), has been suggested to result from warming. An enhanced focus on ecosystem properties, through bio-optical observations, is necessitated by these changes. Future SOCCOM efforts will continue to incorporate bio-optical sensors for both chlorophyll and optical backscatter, as well as adding downwelling irradiance. Each of these parameters provides information on changing biomass and phenology. A sustained array of these observations will provide a novel view of ecosystem change in the Southern Ocean.

Irradiance has not previously been a focus of SOCCOM. The radiometer, which is used to measure downwelling irradiance, will provide a scientifically valuable addition to the SOCCOM suite of measurements. The intensity of incident solar radiation varies substantially over the annual cycle in the Southern Ocean. In ice covered waters, there is considerable interest in the light level that enables the onset of the spring bloom (Horvat et al., 2022). The attenuation of downwelling irradiance is also a useful measure of integrated chlorophyll stocks (Xing et al., 2011). The combination of irradiance and chlorophyll fluorescence can be used to assess nutrient stress in phytoplankton (Schallenberg et al., 2022). The depth dependence of light attenuation also provides important insight into upper ocean heating (Ohlmann et al., 1996). Adding radiometers to the floats deployed in SOCCOM should provide valuable information on these issues across all zones of the Southern Ocean. Within a few years, most SOCCOM floats will carry radiometers, in addition to the five BGC sensors now carried. The addition of more advanced bio-optics, such as Underwater Vision Profilers (Picheral et al., 2022) and hyperspectral radiometers (Organelli et al., 2021), are being tested on profiling floats. These instruments provide additional capabilities for assessing higher trophic levels or plankton functional groups.

The SOCCOM project was explicitly designed as a program to examine the physical and chemical properties of the Southern Ocean at sites with depths in excess of 2000 m. Nearly all SOCCOM and Argo floats deployed to date in the Southern Ocean have adhered to this constraint. The program has the opportunity to expand these goals and objectives as a second renewal proposal is prepared. One of these future objectives is to expand the array into shallower, ice covered waters typical of the very highest latitudes in the Ross Sea, a core part of the Ross Sea Marine Protected Area (MPA). Buoyancy driven gliders are frequently deployed in this region (Jones and Smith, 2017; Kaufman et al., 2014; Meyer et al., 2022) and have provided valuable information on biological process including bloom dynamics and carbon export. However, glider deployments are generally limited to a few months, which requires ships to deploy and recover them. That presents significant logistical challenges if observations are to be sustained. Gliders also have carried a limited suite of sensors, typically bio-optics and oxygen sensors. While Argo floats are generally not intended to operate at depths less than 2000 m, eight UW-produced Argo floats were deployed on the Ross Sea shelf in a region less than 500 m deep late in 2013 (Porter et al., 2019). The float technology and ice-avoidance software proved to be robust, with seven of the floats continuing to operate on the shelf for 4 years or more. The resulting data yielded a unique view of the heat and freshwater budgets on the Antarctic continental shelf over an extended period of time, including new information on the contribution of land-based ice to these budgets (Porter et al., 2019).

These shallow, Ross Sea float deployments open the window for sustained, year-round profiling float operations in waters that had been accessible only in summer. They have led to questions of what such floats might observe if they were equipped with a full BGC sensor suite. In order to investigate the biogeochemical processes in this shelf region, and their links to the physical characteristics of the site, SOCCOM has deployed a set of 5 floats in the same region studied by Porter et al. (2019) that are equipped with O_2, NO_3, pH, Chl, and backscatter sensors, as well as a standard CTD. While both SOCCOM and GO-BGC are intended to be deep water observation networks, the continental shelf around the Antarctic continent is a unique region, where local water mass formation and carbon fluxes may have global implications. Thus, we hope to be able to observe these processes on the Ross Shelf in the near future using profiling float technology. Operation of floats in these shallow waters will provide a unique view into ecosystems, as there are few observations made year around.

The measurements in shallow waters of the Ross Sea MPA will support the UN Southern Ocean Report goal:

- *Ensure science-based and effective MPAs and uphold sustainable fisheries management.*

7. Conclusions

7.1. Lessons learned in operating a basin-scale array

Early planning for BGC-Argo, sponsored by the US Ocean Carbon and Biogeochemistry program, found that deployment of a regional profiling float array would be the next step towards a global system (Johnson et al., 2009). This regional project needed to demonstrate three essential capabilities. The float sensors had to generate "climate-research-quality" data. The system would have to be capable of inter-operating with other components of the ocean observing system including satellites, ships, and data-assimilating models. There had to be an integrated data management system operating in real-time. The SOCCOM project became an early model for this regional system. Along the way, a number of valuable lessons were learned about the effort to go to regional and then global arrays.

Lesson 1: Expanding operations involves many risks that do not manifest themselves until the expansion is well underway. A comment frequently made to SOCCOM personnel about the goal of expanding BGC-Argo to a much larger array was not to start until all aspects were ready. As practical as that advice seems, one cannot assess whether one is ready until the regional, and then global, arrays are built and relatively large numbers of sensors are deployed. For example, as a project transitions from small scale operations to something more akin to mass production a variety of new issues arise. Instruments that were hand built by the engineers and scientists who designed them must now be assembled by a less experienced production team. Inevitable miscommunications in construction of the platforms and sensors will arise with a detrimental effect on operations. When that is combined with an increasing demand for hardware to meet frequent cruise dates and data expectations from users, there will be system failures.

Lesson 2: Systemic failures will occur and vigilant monitoring of an expanding array is required to detect such failures as early as possible. Even in mature programs such as Core-Argo, very small manufacturing changes have resulted in widespread system failures in mature components such as pressure sensors (Barker et al., 2011; Wong et al., 2020) and salinity sensors (Wong et al., 2020). These systemic failures typically span multiple years before they are identified, understood, re-engineered, and then upgraded float deployments are resumed. In the case of pH sensors manufactured at MBARI, a modest manufacturing change resulted in widespread failures of pH sensors deployed in both 2017 and 2018, which illustrates the time scale of these problems. An unrelated problem is now affecting pH sensors manufactured at Sea-Bird Scientific. The extent of real-time monitoring and assessment of system operation which was required was a somewhat unexpected task. If the expectation is that such problems must be cured before basin to global-scale arrays are deployed, then no large scale system would be built.

Lesson 3: A rigorous approach to sensor data validation in the field is an extremely valuable contribution to program success. Much of the success in SOCCOM has resulted because of efforts such as collecting high quality hydrographic data to validate sensor performance (Section 2.6.1). These efforts also identified early sensor performance issues (Johnson et al., 2017b). The validation data guided our development of data adjustment procedures. Such efforts are essential to demonstrate the long-term stability of data.

Lesson 4: The cheapest way to obtain more high quality data is to transfer knowledge to the community. As lessons are learned while scaling up production and data processing, a very effective way to multiply this effort is to transfer that understanding as broadly and quickly as possible. In SOCCOM, several software tools, SAGE (SOCCOM Assessment and Graphical Evaluation) and SAGE-O2 were developed to streamline the quality control of nitrate and pH, and oxygen, respectively (Maurer et al., 2021). These tools are open source and they are now widely used in the BGC-Argo system. This contributes to the amount of high quality data available for research.

In parallel with this effort, a large amount of BGC-Argo data remained in the raw state at the start of SOCCOM without quality control or adjustments. Quality control of data in the Argo system is the responsibility of the principal investigator that deploys the float. However, Argo Data Assembly Centers set up to process Core-Argo temperature and salinity data may not have the complete expertise to quality control biogeochemical data. To mitigate this problem, SOCCOM developed the Argo Oxygen Audit. This program surveys all of the BGC-Argo data, performs an automated assessment of the consistency of the data through several metrics, computes sensor gain correction factors, and then reports these results to each Argo Data Assembly Center. This audit is performed 2 to 3 times per year. It has resulted in an increase in the percentage of quality controlled Argo oxygen data (Argo Adjusted Mode or Argo Delayed Mode data types) from 35% in 2019 to a value of 91% today.

Lesson 5: Expect the unexpected and have a strong management structure to enable rapid solutions. While the SOCCOM project could not anticipate an event such as the Covid-19 pandemic, they seem to find the program. Sole source components for instruments will become unavailable, requiring rushed research and engineering to find alternatives. Cruises will be canceled due to medical or engineering issues on ships. The SOCCOM Executive Team met weekly using remote video platforms from the beginning of the project. These meetings facilitated early recognition of unexpected events and the rapid development of solutions. The management structure helped prevent these problems from becoming frustrations.

7.2. Did SOCCOM meet its goals?

After nine years of operation, the SOCCOM project has established the observing system that was outlined in the initial proposal. Over 260 floats have been deployed. Thousands of profiles have been collected (Table 2) in all regions of the Southern Ocean (Fig. 4). The sensor data have been quality controlled, and made freely available (Maurer et al., 2021). These data extend observations in the Southern Ocean, particularly in the seasonal ice zone, throughout the year. A data-assimilating Biogeochemical Southern Ocean State Estimate has been developed and is now routinely assimilating SOCCOM profiling float data, as well as data from an array of other sources (Verdy and Mazloff, 2017). Insights from the profiling float data and B-SOSE have been used to understand factors that limit the performance of coupled climate models (Beadling et al., 2020, 2020; Bronselaer et al., 2018, 2020).

The profiling float data have been applied to studies of carbon, oxygen, and nitrate cycling, as well as a variety of ecosystem processes throughout the Southern Ocean and over complete annual cycles. More than 170 peer-reviewed papers acknowledge funding from the SOCCOM project. Dozens of papers have been written by scientists outside of the SOCCOM project using data generated by profiling floats of the SOCCOM array, as well as the products of the B-SOSE model. The access by scientists outside of the project demonstrates both the facile access to data and the confidence that the community has in this resource.

The SOCCOM array, and BGC-Argo (Claustre et al., 2020) in general, have demonstrated the robustness of autonomous observations during the height of a global pandemic. The onset of the Covid-19 pandemic led to a suspension of research ship operations in March of 2020. This included cancelation of the GO-SHIP A13.5 cruise, for which SOCCOM floats had already been shipped. Thus, float deployments were directly affected. However, the array of deployed robotic profiling floats continued to collect data (Boyer et al., 2023). The year 2020 will have few biogeochemical ocean records collected from ships. In comparison, there were 19,235 such oxygen profiles collected by all BGC-Argo floats in 2020.

While 2020 was an extraordinary year due to Covid-19, there is a continuing, downward trend over time in biogeochemical observations of essential ocean variables, such as oxygen, that are being reported from ships. Robotic observing systems are required to offset the lack of shipboard data, and the SOCCOM array demonstrates that such arrays can operate at the extent of an ocean basin. Operation of systems such as SOCCOM are an essential tool for observation of change in the ocean interior. Sustaining the operation of this system will be necessary to observe ocean change driven by climate processes.

In summary, SOCCOM has made very significant progress towards its very aspirational goals:

- Goal 1: Quantify and understand the role of all regions of the Southern Ocean in carbon cycling, acidification, nutrient cycling including oxygen, and heat uptake, on seasonal, interannual, and longer time scales.
- Goal 2: Develop the scientific basis for projecting the contribution of the Southern Ocean to the future trajectory of carbon, acidification, nutrient cycling, and heat uptake.

The project has met its three primary objectives to: generate climate research quality data, develop a system capable of inter-operating with the broader ocean observing system, and develop a data system that delivered science quality data in real-time. However, fully achieving the SOCCOM goals will require operating the system for longer periods of time to observe and quantify the emerging, climate driven signals that are expected.

The features of the SOCCOM system clearly address many of the priorities outlined in the UN Southern Ocean Report. While that report was largely aspirational, the SOCCOM project demonstrates that the development of comprehensive observing systems is possible. SOCCOM can stand as a model for observing systems in other basin-scale, sustained ocean observing systems.

Declaration of Competing Interest

The authors declare that they have no known competing financial interests or personal relationships that could have appeared to influence the work reported in this paper.

Data availability

All data sources are identified in the manuscript

Acknowledgements

The Southern Ocean Carbon and Climate Observations and Modeling (SOCCOM) Project is funded by the National Science Foundation, Division of Polar Programs (NSF PLR-1425989 and OPP-1936222), supplemented by NOAA Grant NA20OAR4320271, NASA Grant NNX14AP49G, and by the International Argo Program and the national programs that contribute to it (http://www.argo.ucsd.edu, http://argo.jcommops.org). The Argo Program is part of the Global Ocean Observing System. Work at MBARI is also supported by the David and Lucile Packard Foundation. We thank all of the personnel who have contributed to the construction of the profiling float array and data system, personnel who have assisted at sea in deployments, and the captains and crew of the vessels that have deployed these floats.

Data Availability

All profiling float data generated by the SOCCOM project are available in a permanent archive at the University of California San Diego digital library with a digital object identifier (10.6075/J0TX3C9X). The archive is updated approximately three times each year. The real-time, quality controlled data are also uploaded, typically within 24 hours of receipt, to the Argo data system where they are available from the Argo Global Data Assembly Centers. See https://argo.ucsd.edu/data/ for a description of the Argo data system. In addition, real-time data with added data products such as computed total alkalinity, dissolved inorganic carbon and pCO2 are available from ftp://ftp.mbari.org/pub/SOCCOM/FloatVizData/.

Shipboard observations made to validate SOCCOM float deployments are available from the CLIVAR and Carbon Hydrographic Data Office (CCHDO; https://cchdo.ucsd.edu) by searching on the keyword SOCCOM.

B-SOSE model output is available from http://sose.ucsd.edu.

References

Abernathey, R.P., Cerovecki, I., Holland, P.R., Newsom, E., Mazloff, M., Talley, L.D., 2016. Water-mass transformation by sea ice in the upper branch of the Southern Ocean overturning. Nat. Geosci. 9 (8), 596–601. https://doi.org/10.1038/ngeo2749.

Anderson, L.A., Sarmiento, J.L., 1994. Redfield ratios of remineralization determined by nutrient data analysis. Global Biogeochem. Cycles 8 (1), 65–80. https://doi.org/10.1029/93GB03318.

Armour, K.C., Marshall, J., Scott, J.R., Donohoe, A., Newsom, E.R., 2016. Southern Ocean warming delayed by circumpolar upwelling and equatorward transport. Nat. Geosci. 9, 549–554.

Arrigo, K.R., Perovich, D.K., Pickart, R.S., Brown, Z.W., Van Dijken, G.L., Lowry, K.E., Mills, M.M., Palmer, M.A., Balch, W.M., Bahr, F., Bates, N.R., 2012. Massive phytoplankton blooms under Arctic sea ice. Science 336 (6087). https://doi.org/10.1126/science.1215065, 1408–1408.

Arrigo, K.R., van Dijken, G.L., Bushinsky, S., 2008. Primary production in the Southern Ocean, 1997–2006. J. Geophys. Res. Oceans 113 (C8), C08004. https://doi.org/10.1029/2007JC004551.

Arrigo, K.R., van Dijken, G.L., Alderkamp, A.C., Erickson, Z.K., Lewis, K.M., Lowry, K.E., Joy-Warren, H.L., Middag, R., Nash-Arrigo, J.E., Selz, V., van de Poll, W., 2017. Early spring phytoplankton dynamics in the Western Antarctic Peninsula. J. Geophys. Res. Oceans 122 (12), 9350–9369. https://doi.org/10.1002/2017JC013281.

Arteaga, L., Haëntjens, N., Boss, E., Johnson, K.S., Sarmiento, J.L., 2018. Assessment of Export Efficiency Equations in the Southern Ocean Applied to Satellite-Based Net Primary Production. J. Geophys. Res. Oceans 123 (4), 2945–2964. https://doi.org/10.1002/2018JC013787.

Arteaga, L.A., Pahlow, M., Bushinsky, S.M., Sarmiento, J.L., 2019. Nutrient controls on export production in the Southern Ocean. Global Biogeochem. Cycles 33, 942–956. https://doi.org/10.1029/2019GB006236.

Arteaga, L.A., Boss, E., Behrenfeld, M.J., Westberry, T.K., Sarmiento, J.L., 2020. Seasonal modulation of phytoplankton biomass in the Southern Ocean. Nat. Commun. 11 (1), 1–10. https://doi.org/10.1038/s41467-020-19157-2.

Arteaga, L.A., Behrenfeld, M.J., Boss, E., Westberry, T.K., 2022. Vertical structure in phytoplankton growth and productivity inferred from Biogeochemical-Argo floats and the carbon-based productivity model. Global Biogeochem. Cycles 36, e2022GB007389. https://doi.org/10.1029/2022GB007389.

Bakker, D.C., Pfeil, B., Landa, C.S., Metzl, N., O'brien, K.M., Olsen, A., Smith, K., Cosca, C., Harasawa, S., Jones, S.D. and Nakaoka, S.I., 2016. A multi-decade record of high-quality fCO 2 data in version 3 of the Surface Ocean CO 2 Atlas (SOCAT). Earth Syst. Sci. Data 8(2), pp.383-413. doi:10.5194/essd-8-383-2016.

Baldry, K., Strutton, P.G., Hill, N.A., Boyd, P.W., 2020. Subsurface chlorophyll-a maxima in the Southern Ocean. Front. Mar. Sci. 7, 671. https://doi.org/10.3389/fmars.2020.00671.

Barker, P.M., Dunn, J.R., Domingues, C.M., Wijffels, S.E., 2011. Pressure sensor drifts in Argo and their impacts. J. Atmos. Oceanic Tech. 28 (8), 1036–1049. https://doi.org/10.1175/2011JTECHO831.1.

Beadling, R.L., Russell, J.L., Stouffer, R.J., Goodman, P.J., Mazloff, M., 2019. Assessing the quality of Southern Ocean circulation in CMIP5 AOGCM and Earth System Model simulations. J. Clim. 32, 5915–5940. https://doi.org/10.1175/JCLI-D-19-0263.1.

Beadling, R.L., Russell, J.L., Stouffer, R.J., Mazloff, M., Talley, L.D., Goodman, P.J., Sallée, J.B., Hewitt, H.T., Hyder, P., Pandde, A., 2020. Representation of Southern Ocean properties across coupled model intercomparison project generations: CMIP3 to CMIP6. J. Clim. 33 (15), 6555–6581. https://doi.org/10.1175/JCLI-D-19-0970.1.

Bednaršek, N., Tarling, G.A., Bakker, D.C.E., Fielding, S., Jones, E.M., Venables, H.J., Ward, P., Kuzirian, A., Lézé, B., Feely, R.A., Murphy, E.J., 2012. Extensive dissolution of live pteropods in the Southern Ocean. Nat. Geosci. 5 (12), 881–885. https://doi.org/10.1038/ngeo1635.

Behrenfeld, M.J., Boss, E.S., 2018. Student's tutorial on bloom hypotheses in the context of phytoplankton annual cycles. Glob. Change Biol. 24, 55–77. https://doi.org/10.1111/gcb.13858.

Behrenfeld, M.J., Falkowski, P.G., 1997. Photosynthetic rates derived from satellite-based chlorophyll concentration. Limnol. Oceanogr. 42, 1–20.

Biogeochemical-Argo Planning Group, 2016. The scientific rationale, design and implementation plan for a Biogeochemical-Argo float array. https://doi.org/10.13155/46601.

Bisson, K.M., Cael, B.B., 2021. How are under ice phytoplankton related to sea ice in the Southern Ocean? Geophys. Res. Lett. 48 (21), e2021GL095051 https://doi.org/10.1029/2021GL095051.

Bisson, K.M., Boss, E., Westberry, T.K., Behrenfeld, M.J., 2019. Evaluating satellite estimates of particulate backscatter in the global open ocean using autonomous

profiling floats. Opt. Express 27 (21), 30191–30203. https://doi.org/10.1364/OE.27.030191.
Bisson, K.M., Boss, E., Werdell, P.J., Ibrahim, A., Behrenfeld, 2021. Particulate backscattering in the global ocean: A comparison of independent assessments. Geophys. Res. Lett. 48, e2020GL090909 https://doi.org/10.1029/2020GL090909.
Bittig, H.C., Körtzinger, A., 2015. Tackling oxygen optode drift: Near-surface and in-air oxygen optode measurements on a float provide an accurate in situ reference. J. Atmos. Oceanic Tech. 32 (8), 1536–1543. https://doi.org/10.1175/JTECH-D-14-00162.1.
Bittig, H.C., Körtzinger, A., Neill, C., Van Ooijen, E., Plant, J.N., Hahn, J., Johnson, K.S., Yang, B., Emerson, S.R., 2018a. Oxygen optode sensors: principle, characterization, calibration, and application in the ocean. Front. Mar. Sci. 4, 429. https://doi.org/10.3389/fmars.2017.00429.
Bittig, H.C., Steinhoff, T., Claustre, H., Fiedler, B., Williams, N.L., Sauzède, R., Körtzinger, A., Gattuso, J.P., 2018b. An alternative to static climatologies: Robust estimation of open ocean CO_2 variables and nutrient concentrations from T, S, and O_2 data using Bayesian neural networks. Front. Mar. Sci. 5, 328. https://doi.org/10.3389/fmars.2018.00328.
Boss, E., Swift, D., Taylor, L., Brickley, P., Zaneveld, R., Riser, S., Perry, M.J., Strutton, P. G., 2008. Observations of pigment and particle distributions in the western North Atlantic from an autonomous float and ocean color satellite. Limnol. Oceanogr. 53, 2112–2122. https://doi.org/10.4319/lo.2008.53.5_part_2.2112.
Bourgeois, T., Goris, N., Schwinger, J., Tjiputra, J.F., 2022. Stratification constrains future heat and carbon uptake in the Southern Ocean between 30°S and 55°S. Nat Commun 13, 340. https://doi.org/10.1038/s41467-022-27979-5.
Boyd, P.W., Claustre, H., Levy, M., Siegel, D.A., Weber, T., 2019. Multi-faceted particle pumps drive carbon sequestration in the ocean. Nature 568 (7752), 327–335. https://doi.org/10.1038/s41586-019-1098-2.
Boyd, P.W., Sundby, S., Pörtner, H.O., 2014. Cross-chapter box on net primary production in the ocean. In Climate Change 2014: Impacts, Adaptation, and Vulnerability. Part A: Global and Sectoral Aspects. Contribution of Working Group II to the Fifth Assessment Report of the Intergovernmental Panel of Climate Change (pp. 133-136). Cambridge University Press. hdl:10013/epic.45154.d001.
Boyer, T., Zhang, H., O'Brien, K., Reagan, J., Diggs, S., Freeman, E., Garcia, H., Heslop, E., Hogan, P., Huang, B., Jiang, L., Kozyr, A., Liu, C., Locarnini, R., Mishonov, A.V., Paver, C., Wang, Z., Zweng, M., Alin, S., Barbero, L., Barth, J.A., Belbeoch, M., Cebrian, J., Connell, K., Cowley, R., Dukhovskoy, D., Galbraith, N.R., Goni, G., Katz, F., Kramp, M., Kumar, A., Legler, D., Lumpkin, R., McMahon, C.R., Pierrot, D., Plueddemann, A.J., Smith, E.A., Sutton, A., Turpin, V., Jiang, L., Suneel, V., Wanninkhof, R., Weller, R.A., Wong, A.P., 2023. Effects of the Pandemic on Observing the Global Ocean. Bull. Am. Meteorol. Soc. 104, E389–E410. https://doi.org/10.1175/BAMS-D-21-0210.1.
Briggs, E.M., Martz, T.R., Talley, L.D., Mazloff, M.R. and Johnson, K.S., 2018. Physical and biological drivers of biogeochemical tracers within the seasonal sea ice zone of the Southern Ocean from profiling floats. J. Geophys. Res.: Oceans, 123(2), pp.746-758. https:/doi.org/10.1002/2017JC012846.
Broecker, W.S., Peng, T.H., 1982. Tracers in the sea. Eldigio Press.
Bronselaer, B., Winton, M., Griffies, S.M., Hurlin, W.J., Rodgers, K.B., Sergienko, O.V., Stouffer, R.J., Russell, J.L., 2018. Change in future climate due to Antarctic meltwater. Nature 564 (7734), 53–58. https://doi.org/10.1038/s41586-018-0712-z.
Bronselaer, B., Russell, J.L., Winton, M., Williams, N.L., Key, R.M., Dunne, J.P., Feely, R. A., Johnson, K.S., Sarmiento, J.L., 2020. Importance of wind and meltwater for observed chemical and physical changes in the Southern Ocean. Nat. Geosci. 13 (1), 35–42. https://doi.org/10.1038/s41561-019-0502-8.
Buitenhuis, E.T., Hashioka, T., Quéré, C.L., 2013. Combined constraints on global ocean primary production using observations and models. Global Biogeochem. Cycles 27, 847–858. https://doi.org/10.1002/gbc.20074.
Bushinsky, S.M., Gray, A.R., Johnson, K.S., Sarmiento, J.L., 2017. Oxygen in the Southern Ocean from Argo floats: Determination of processes driving air-sea fluxes. J. Geophys. Res. Oceans 122. https://doi.org/10.1002/2017JC012923.
Bushinsky, S.M., Landschützer, P., Rödenbeck, C., Gray, A.R., Baker, D., Mazloff, M.R., Resplandy, L., Johnson, K.S., Sarmiento, J.L., 2019a. Reassessing Southern Ocean air-sea CO2 flux estimates with the addition of biogeochemical float observations. Global Biogeochem. Cycles 33 (11), 1370–1388. https://doi.org/10.1029/2019GB006176.
Bushinsky, S.M., Takeshita, Y., Williams, N.L., 2019b. Observing changes in ocean carbonate chemistry: our autonomous future. Curr. Climate Change Reports 5 (3), 207–220. https://doi.org/10.1007/s40641-019-00129-8.
Cai, Y., Chen, D., Mazloff, M.R., Lian, T., Liu, X., 2022. Topographic modulation of the wind stress impact on eddy activity in the Southern Ocean. Geophys. Res. Lett. 49, e2022GL097859 https://doi.org/10.1029/2022GL097859.
Campbell, E.C., Wilson, E.A., Moore, G.K., Riser, S.C., Brayton, C.E., Mazloff, M.R., Talley, L.D., 2019. Antarctic offshore polynyas linked to Southern Hemisphere climate anomalies. Nature 570 (7761), 319–325. https://doi.org/10.1038/s41586-019-1294-0.
Carr, M.E., Friedrichs, M.A., Schmeltz, M., Aita, M.N., Antoine, D., Arrigo, K.R., Asanuma, I., Aumont, O., Barber, R., Behrenfeld, M., Bidigare, R., 2006. A comparison of global estimates of marine primary production from ocean color. Deep Sea Res. Part II 53 (5–7), 741–770. https://doi.org/10.1016/j.dsr2.2006.01.028.
Carranza, M.M., Gille, S.T., Franks, P.J.S., Johnson, K.S., Pinkel, R., Girton, J.B., 2018. When Mixed Layers Are Not Mixed. Storm-Driven Mixing and Bio-optical Vertical Gradients in Mixed Layers of the Southern Ocean. J. Geophys. Res. Oceans 123 (10), 7264–7289. https://doi.org/10.1029/2018JC014416.
Carter, B.R., Feely, R.A., Williams, N.L., Dickson, A.G., Fong, M.B., Takeshita, Y., 2018. Updated methods for globally locally-interpolated estimation of alkalinity, pH, and Nitrate. Limnol. Oceanogr. Methods 16, 119–131. https://doi.org/10.1002/lom3.10232.
Carter, B.R., Bittig, H.C., Fassbender, A.J., Sharp, J.D., Takeshita, Y., Xu, Y.Y., Álvarez, M., Wanninkhof, R., Feely, R.A., Barbero, L., 2021. New and updated global empirical seawater property estimation routines. Limnol. Oceanogr. Methods 19 (12), 785–809. https://doi.org/10.1002/lom3.10461.
Cavan, E.L., Le Moigne, F.A., Poulton, A.J., Tarling, G.A., Ward, P., Daniels, C.J., Fragoso, G.M., Sanders, R.J., 2015. Attenuation of particulate organic carbon flux in the Scotia Sea, Southern Ocean, is controlled by zooplankton fecal pellets. Geophys. Res. Lett. 42 (3), 821–830. https://doi.org/10.1002/2014GL062744.
Chamberlain, P., Cornuelle, B., Talley, L.D., Speer, K., Hancock, C., Riser, S., 2022a. Acoustic float tracking with the Kalman smoother. J. Atmos. Oceanic Tech. 40, 15–35. https://doi.org/10.1175/JTECH-D-21-0063.1.
Chamberlain, P.M., Talley, L.D., Mazloff, M.R., Riser, S.C., Speer, K., Gray, A.R., Schwartzman, A., 2018. Observing the ice-covered Weddell Gyre with profiling floats: Position uncertainties and correlation statistics. J. Geophys. Res. Oceans 123, 8383–8410. https://doi.org/10.1029/2017JC012990.
Chamberlain, P., Talley, L.D., Mazloff, M., van Sebille, E., Gille, S., Tucker, T., Scanderbeg, M., Robbins, P., 2023. Using existing Argo trajectories to statistically predict future float positions with a Transition Matrix. J. Atm. Oceanic Tech. https://doi.org/10.1175/JTECH-D-22-0070.1.
Chen, H., Haumann, F.A., Talley, L.D., Johnson, K.S., Sarmiento, J.L., 2022. The deep ocean's carbon exhaust. Global Biogeochem. Cycles 36, e2021GB007156. https://doi.org/10.1029/2021GB007156.
Cheng, L., Abraham, J., Trenberth, K.E., Fasullo, J., Boyer, T., Mann, M.E., Zhu, J., Wang, F., Locarnini, R., Li, Y., Zhang, B., 2022. Another record: Ocean warming continues through 2021 despite La Niña conditions. Adv. Atmos. Sci. 39 (3), 373–385. https://doi.org/10.1007/s00376-022-1461-3.
Claustre, H., Johnson, K.S., Takeshita, Y., 2020. Observing the global ocean with biogeochemical-Argo. Ann. Rev. Mar. Sci. 12, 23–48. https://doi.org/10.1146/annurev-marine-010419-010956.
Cornec, M., Laxenaire, R., Speich, S., Claustre, H., 2021. Impact of mesoscale eddies on deep chlorophyll maxima. Geophys. Res. Lett. 48, e2021GL093470 https://doi.org/10.1029/2021GL093470.
Dall'Olmo, G., Dingle, J., Polimene, L., Brewin, R.J.W., Claustre, H., 2016. Substantial energy input to the mesopelagic ecosystem from the seasonal mixed-layer pump. Nat. Geosci. 9, 820–823. https://doi.org/10.1038/NGEO2818.
Del Castillo, C.E., Signorini, S.R., Karaköylü, E.M., Rivero-Calle, S., 2019. Is the Southern Ocean getting greener? Geophys. Res. Lett. 46, 6034–6040. https://doi.org/10.1029/2019GL083163.
DeVries, T., 2014. The oceanic anthropogenic CO 2 sink: Storage, air-sea fluxes, and transports over the industrial era. Global Biogeochem. Cycles 28, 631–647. https://doi.org/10.1002/2013GB004739.
Drake, H.F., Morrison, A.K., Griffies, S.M., Sarmiento, J.L., Weijer, W., Gray, A.R., 2019. Lagrangian timescales of Southern Ocean upwelling in a hierarchy of model resolutions. Geophys. Res. Lett. 45, 891–898. https://doi.org/10.1002/2017GL076045.
Ducklow, H.W., Steinberg, D.K., Buesseler, K.O., 2001. Upper ocean carbon export and the biological pump. Oceanography 14 (4), 50–58.
Fay, A.R., Lovenduski, N.S., McKinley, G.A., Munro, D.R., Sweeney, C., Gray, A.R., Landschützer, P., Stephens, B.B., Takahashi, T., Williams, N., 2018. Utilizing the Drake Passage Time-series to understand variability and change in subpolar Southern Ocean pCO 2. Biogeosciences 15 (12), 3841–3855. https://doi.org/10.5194/bg-15-3841-2018.
Feely, R.A., Doney, S.C., Cooley, S.R., 2009. Ocean acidification: Present conditions and future changes in a high-CO_2 world. Oceanography 22 (4), 36–47.
Fennel, K., Gehlen, M., Brasseur, P., Brown, C.W., Ciavatta, S., Cossarini, G., Crise, A., Edwards, C.A., Ford, D., Friedrichs, M.A., Gregoire, M., 2019. Advancing marine biogeochemical and ecosystem reanalyses and forecasts as tools for monitoring and managing ecosystem health. Front. Mar. Sci. 6, 89.
Fong, M.B., Dickson, A.G., 2019. Insights from GO-SHIP hydrography data into the thermodynamic consistency of CO2 system measurements in seawater. Mar. Chem. 211, 52–63. https://doi.org/10.1016/j.marchem.2019.03.006.
Ford, D., 2021. Assimilating synthetic Biogeochemical-Argo and ocean colour observations into a global ocean model to inform observing system design. Biogeosciences 18 (2), 509–534. https://doi.org/10.5194/bg-18-509-2021.
Forget, G., Campin, J.-M., Heimbach, P., Hill, C.N., Ponte, R.M., Wunsch, C., 2015. ECCO version 4: an integrated framework for non-linear inverse modeling and global ocean state estimation. Geosci. Model Dev. 8, 3071–3104. https://doi.org/10.5194/gmd-8-3071-2015.
Frölicher, T.L., Sarmiento, J.L., Paynter, D.J., Dunne, J.P., Krasting, J.P., Winton, M., 2015. Dominance of the Southern Ocean in anthropogenic carbon and heat uptake in CMIP5 models. J. Clim. 28 (2), 862–886. https://doi.org/10.1175/JCLI-D-14-00117.1.
Galbraith, E.D., Gnanadesikan, A., Dunne, J.P., Hiscock, M.R., 2010. Regional impacts of iron-light colimitation in a global biogeochemical model. Biogeosciences 7 (3), 1043–1064. https://doi.org/10.5194/bg-7-1043-2010.
Garcia, H.E., Locarnini, R.A., Boyer, T.P., Antonov, J.I., Baranova, O.K., Zweng, M.M., Reagan, J.R., Johnson, D.R., 2014. World Ocean Atlas 2013. Vol. 4: Dissolved Inorganic Nutrients (phosphate, nitrate, silicate). In: S. Levitus, A. Mishonov, Technical Ed., NOAA Atlas NESDIS76, (25 pp).
Garrison, D.L., 1991. Antarctic sea ice biota. Am. Zool. 31 (1), 17–34. https://doi.org/10.1093/icb/31.1.17.
Gibson, J.A., Trull, T.W., 1999. Annual cycle of fCO2 under sea-ice and in open water in Prydz Bay, East Antarctica. Mar. Chem. 66 (3–4), 187–200. https://doi.org/10.1016/S0304-4203(99)00040-7.

Giglio, D., Lyubchich, V., Mazloff, M.R., 2018. Estimating oxygen in the Southern Ocean using Argo temperature and salinity. J. Geophys. Res. Oceans 123 (6), 4280–4297. https://doi.org/10.1029/2017JC013404.

Gille, S.T., 2002. Warming of the Southern Ocean since the 1950s. Science 295 (5558), 1275–1277. https://doi.org/10.1126/science.1065863.

Gordon, A.L., 1978. Deep Antarctic convection west of Maud Rise. J. Phys. Oceanogr. 8, 600–612.

Graff, J.R., Westberry, T.K., Milligan, A.J., Brown, M.B., Dall'Olmo, G., van Dongen-Vogels, V., Reifel, K.M. and Behrenfeld, M.J., 2015. Analytical phytoplankton carbon measurements spanning diverse ecosystems. Deep Sea Research Part I, 102, pp.16-25. doi:10.1016/j.dsr.2015.04.006.

Gray, A.R., Johnson, K.S., Bushinsky, S.M., Riser, S.C., Russell, J.L., Talley, L.D., Wanninkhof, R., Williams, N.L., Sarmiento, J.L., 2018. Autonomous biogeochemical floats detect significant carbon dioxide outgassing in the high-latitude Southern Ocean. Geophys. Res. Lett. 45 (17), 9049–9057. https://doi.org/10.1029/2018GL078013.

Gruber, N., Gloor, M., Fan, S.-M., Sarmiento, J.L., 2001. Air-sea flux of oxygen estimated from bulk data: Implications For the marine and atmospheric oxygen cycles. Global Biogeochem. Cycles 15 (4), 783–803. https://doi.org/10.1029/2000GB001302.

Gruber, N., Gloor, M., Mikaloff Fletcher, S.E., Doney, S.C., Dutkiewicz, S., Follows, M.J., Gerber, M., Jacobson, A.R., Joos, F., Lindsay, K., Menemenlis, D., 2009. Oceanic sources, sinks, and transport of atmospheric CO2. Global Biogeochem. Cycles 23 (1). https://doi.org/10.1029/2008GB003349.

Gruber, N., Landschutzer, P., Lovenduski, N.S., 2019. The variable Southern Ocean carbon sink. Ann. Rev. Mar. Sci. 11 (1), 159–186. https://doi.org/10.1146/annurev-marine-121916-063407.

Haëntjens, N., Boss, E., Talley, L.D., 2017. Revisiting Ocean Color algorithms for chlorophyll a and particulate organic carbon in the Southern Ocean using biogeochemical floats. J. Geophys. Res. Oceans 122 (8), 6583–6593. https://doi.org/10.1002/2017JC012844.

Hague, M., Vichi, M., 2021. Southern Ocean Biogeochemical Argo detect under-ice phytoplankton growth before sea ice retreat. Biogeosciences 18 (1), 25–38. https://doi.org/10.5194/bg-18-25-2021.

Haumann, F.A., Moorman, R., Riser, S.C., Smedsrud, L.H., Maksym, T., Wong, A.P., Wilson, E.A., Drucker, R., Talley, L.D., Johnson, K.S., Key, R.M., 2020. Supercooled southern ocean waters. Geophys. Res. Lett. 47 (20), e2020GL090242 https://doi.org/10.1029/2020GL090242.

Haumann, F.A., Gruber, N., Münnich, M., Frenger, I., Kern, S., 2016. Sea-ice transport driving Southern Ocean salinity and its recent trends. Nature 537 (7618), 89–92. https://doi.org/10.1038/nature19101.

Hennon, T.D., Riser, S.C., Mecking, S., 2016. Profiling float-based observations of net respiration beneath the mixed layer. Global Biogeochem. Cycles 30 (6), 920–932. https://doi.org/10.1002/2016GB005380.

Henson, S.A., Sarmiento, J.L., Dunne, J.P., Bopp, L., Lima, I., Doney, S.C., John, J., Beaulieu, C., 2010. Detection of anthropogenic climate change in satellite records of ocean chlorophyll and productivity. Biogeosciences 7 (2), 621–640.

Henson, S.A., Beaulieu, C., Lampitt, R., 2016. Observing climate change trends in ocean biogeochemistry: when and where. Glob. Change Biol. 22 (4), 1561–1571. https://doi.org/10.1111/gcb.13152.

Hofmann, E., Biddle, L., de Bruin, T., Brooks, C., Corney, S., Haumann, A., et al., 2020. 1st Southern Ocean Regional Workshop for the UN Decade of Ocean Science for Sustainable Development Report. Geneva: Zenodo, doi: 10.5281/ZENODO.3973745.

Horvat, C., Bisson, K., Seabrook, S., Cristi, A., Matthes, L.C., 2022. Evidence of phytoplankton blooms under Antarctic sea ice. Front. Mar. Sci. 9, 2154. https://doi.org/10.3389/fmars.2022.942799.

IOC-R, 2021. Integrated Ocean Carbon Research: A Summary of Ocean Carbon Research, and Vision of Coordinated Ocean Carbon Research and Observations for the Next Decade. R. Wanninkhof, C. Sabine and S. Aricò (eds.). Paris UNESCO. 46 pp. (IOC Technical Series, 158 Rev.) doi:10.25607/h0gj-pq41.

IPCC, 2019. IPCC Special Report on the Ocean and Cryosphere in a Changing Climate [H.-O. Pörtner, D.C. Roberts, V. Masson-Delmotte, P. Zhai, M. Tignor, E. Poloczanska, K. Mintenbeck, A. Alegría, M. Nicolai, A. Okem, J. Petzold, B. Rama, N. M. Weyer (eds.)].

Jena, B., Pillai, A.N., 2020. Satellite observations of unprecedented phytoplankton blooms in the Maud Rise polynya, Southern Ocean. The Cryosphere 14 (4), 1385–1398. https://doi.org/10.5194/tc-14-1385-2020.

Jersild, A., Delawalla, S., Ito, T., 2021. Mesoscale eddies regulate seasonal iron supply and carbon drawdown in the Drake Passage. Geophys. Res. Lett. 48, e2021GL096020 https://doi.org/10.1029/2021GL096020.

Johnson, K.S., 2017. Developing chemical sensors to observe the health of the global ocean. IEEE Transducers 2017. https://doi.org/10.1109/TRANSDUCERS.2017.7993975.

Johnson, K.S., Bif, M.B., 2021. Constraint on net primary productivity of the global ocean by Argo oxygen measurements. Nat. Geosci. 14 (10), 769–774. https://doi.org/10.1038/s41561-021-00807-z.

Johnson, K.S., Coletti, L.J., Jannasch, H.W., Sakamoto, C.M., Swift, D.D., Riser, S.C., 2013. Long-term nitrate measurements in the ocean using the In Situ Ultraviolet Spectrophotometer: sensor integration into the APEX profiling float. J. Atmos. Oceanic Tech. 30 (8), 1854–1866. https://doi.org/10.1175/JTECH-D-12-00221.1.

Johnson, K.S., Berelson, W.M., Boss, E.S., Chase, Z., Claustre, H., Emerson, S.R., Gruber, N., Körtzinger, A., Perry, M.J. and Riser, S.C., 2009. Observing biogeochemical cycles at global scales with profiling floats and gliders: prospects for a global array. Oceanography, 22(3), pp.216-225. https://www.jstor.org/stable/24861005.

Johnson, K.S., Mazloff, M.R., Bif, M.B., Takeshita, Y., Jannasch, H.W., Maurer, T.L., Plant, J.N., Verdy, A., Walz, P.M., Riser, S.C., Talley, L.D., 2022. Carbon to nitrogen uptake ratios observed across the Southern Ocean by the SOCCOM profiling float array. J. Geophys. Res.: Oceans 127 (9), e2022JC018859. https://doi.org/10.1029/2022JC018859.

Johnson, K.S., Plant, J.N., Riser, S.C., Gilbert, D., 2015. Air oxygen calibration of oxygen optodes on a profiling float array. J. Atmos. Oceanic Tech. 32 (11), 2160–2172. https://doi.org/10.1175/JTECH-D-15-0101.1.

Johnson, K.S., Jannasch, H.W., Coletti, L.J., Elrod, V.A., Martz, T.R., Takeshita, Y., Carlson, R.J., Connery, J.G., 2016. Deep-Sea DuraFET: A pressure tolerant pH sensor designed for global sensor networks. Anal. Chem. 88 (6), 3249–3256. https://doi.org/10.1021/acs.analchem.5b04653.

Johnson, K.S., Plant, J.N., Dunne, J.P., Talley, L.D., Sarmiento, J.L., 2017a. Annual nitrate drawdown observed by SOCCOM profiling floats and the relationship to annual net community production. J. Geophys. Res.: Oceans 122, 6668–6683. https://doi.org/10.1002/2017jc012839.

Johnson, K.S., Plant, J.N., Coletti, L.J., Jannasch, H.W., Sakamoto, C.M., Riser, S.C., Swift, D.D., Williams, N.L., Boss, E., Haentjens, N., Talley, L.D., Sarmiento, J.L., 2017b. Biogeochemical sensor performance in the SOCCOM profiling float array. J. Geophys. Res. Oceans 122 (8), 6416–6436. https://doi.org/10.1002/2017JC012838.

Jones, R.M., Smith Jr., W.O., 2017. The influence of short-term events on the hydrographic and biological structure of the southwestern Ross Sea. J. Mar. Syst. 166, 184–195. https://doi.org/10.1016/j.jmarsys.2016.09.006.

Kajtar, J.B., Santoso, A., Collins, M., Taschetto, A.S., England, M.H., Frankcombe, 2021. CMIP5 intermodel relationships in the baseline Southern Ocean climate system and with future projections. Earth's Future 9, e2020EF001873. https://doi.org/10.1029/2020EF001873.

Kamenkovich, I., Haza, A., Gray, A.R., Dufour, C.O., Garraffo, Z., 2017. Observing System Simulation Experiments for an array of autonomous biogeochemical profiling floats in the Southern Ocean. J. Geophys. Res. Oceans 122 (9), 7595–7611. https://doi.org/10.1002/2017JC012819.

Kaufman, D.E., Friedrichs, M.A.M., Smith Jr., W.O., Queste, B.Y., Heywood, K.J., 2014. Biogeochemical variability in the southern Ross Sea as observed by a glider deployment. Deep-Sea Research I 92, 93–106. https://doi.org/10.1016/j.dsr.2014.06.011.

Kim, Y.S., Orsi, A.H., 2014. On the variability of Antarctic Circumpolar Current fronts inferred from 1992–2011 altimetry. J. Phys. Oceanogr. 44 (12), 3054–3071. https://doi.org/10.1175/JPO-D-13-0217.1.

Klatt, O., Boebel, O., Fahrbach, E., 2007. A profiling float's sense of ice. J. Atmos. Oceanic Tech. 24 (7), 1301–1308. https://doi.org/10.1175/JTECH2026.1.

Körtzinger, A., Mintrop, L., Wallace, D.W., Johnson, K.M., Neill, C., Tilbrook, B., Towler, P., Inoue, H.Y., Ishii, M., Shaffer, G., Saavedra, R.F.T., 2000. The international at-sea intercomparison of fCO2 systems during the R/V Meteor Cruise 36/1 in the North Atlantic Ocean. Mar. Chem. 72 (2–4), 171–192. https://doi.org/10.1016/j.marchem.2022.104085.

Körtzinger, A., Schimanski, J., Send, U., 2005. High quality oxygen measurements from profiling floats: A promising new technique. J. Atmos. Oceanic Tech. 22 (3), 302–308. https://doi.org/10.1175/JTECH1701.1.

Landschützer, P., Gruber, N., and Bakker, D. C. E., 2017. An updated observation-based global monthly gridded sea surface pCO2 and air-sea CO2 flux product from 1982 through 2015 and its monthly climatology (NCEI accession 0160558). version 2.2., NOAA National Centers for Environmental Information. Dataset [2017-07-11].

Laurenceau-Cornec, E.C., Trull, T.W., Davies, D.M., Bray, S.G., Doran, J., Planchon, F., Carlotti, F., Jouandet, M.P., Cavagna, A.J., Waite, A.M., Blain, S., 2015. The relative importance of phytoplankton aggregates and zooplankton fecal pellets to carbon export: insights from free-drifting sediment trap deployments in naturally iron-fertilised waters near the Kerguelen Plateau. Biogeosciences 12 (4), 1007–1027. https://doi.org/10.5194/bg-12-1007-2015.

Le Moigne, F.A., Henson, S.A., Cavan, E., Georges, C., Pabortsava, K., Achterberg, E.P., Ceballos-Romero, E., Zubkov, M., Sanders, R.J., 2016. What causes the inverse relationship between primary production and export efficiency in the Southern Ocean? Geophys. Res. Lett. 43 (9), 4457–4466. https://doi.org/10.1002/2016GL068480.

Levitus, S., Antonov, J.I., Boyer, T.P., Baranova, O.K., Garcia, H.E., Locarnini, R.A., Mishonov, A.V., Reagan, J.R., Seidov, D., Yarosh, E.S., Zweng, M.M., 2012. World ocean heat content and thermosteric sea level change (0–2000 m), 1955–2010. Geophys. Res. Lett. 39 (10) https://doi.org/10.1029/2012GL051106.

Liang, Y.C., Mazloff, M.R., Rosso, I., Fang, S.W., Yu, J.Y., 2018. A multivariate empirical orthogonal function method to construct nitrate maps in the Southern Ocean. J. Atmos. Oceanic Tech. 35 (7), 1505–1519. https://doi.org/10.1175/JTECH-D-18-0018.1.

Llort, J., Langlais, C., Matear, R., Moreau, S., Lenton, A., Strutton, P.G., 2018. Evaluating Southern Ocean carbon eddy-pump from biogeochemical-Argo floats. J. Geophys. Res. Oceans 123 (2), 971–984. https://doi.org/10.1002/2017JC012861.

Long, M.C., Stephens, B.B., McKain, K., Sweeney, C., Keeling, R.F., Kort, E.A., Morgan, E. J., Bent, J.D., Chandra, N., Chevallier, F., Commane, R., 2021. Strong Southern Ocean carbon uptake evident in airborne observations. Science 374 (6572), 1275–1280. https://doi.org/10.1126/science.abi4355.

Mackay, N., and Watson, A., 2021. Winter air-sea CO_2 fluxes constructed from summer observations of the polar southern ocean suggest weak outgassing. J. Geophys. Res.: Oceans, 126, e2020JC016600. https://doi.org/10.1029/2020JC016600.

Mahadevan, A., Campbell, J.W., 2002. Biogeochemical patchiness at the sea surface. Geophys. Res. Lett. 29 (19), 32-1. https://doi.org/10.1029/2001GL014116.

Majkut, J.D., Carter, B.R., Frölicher, T.L., Dufour, C.O., Rodgers, K.B., Sarmiento, J.L., 2014. An observing system simulation for Southern Ocean carbon dioxide uptake. Philos. Trans. R. Soc. A Math. Phys. Eng. Sci. 372 (2019), 20130046. https://doi.org/10.1098/rsta.2013.0046.

Marinov, I., Gnanadesikan, A., Toggweiler, J.R., Sarmiento, J.L., 2006. The southern ocean biogeochemical divide. Nature 441 (7096), 964–967. https://doi.org/10.1038/nature04883.
Marra, J.F., Barber, R.T., Barber, E., Bidigare, R.R., Chamberlin, W.S., Goericke, R., Hargreaves, B.R., Hiscock, M., Iturriaga, R., Johnson, Z.I., Kiefer, D.A., Kinkade, C., Knudson, C., Lance, V., Langdon, C., Lee, Z.-P., Perry, M.J., Smith, W.O., Vaillancourt, R., Zoffoli, L., 2021. A database of ocean primary productivity from the 14C method. Limnol. Oceanogr. Lett. 6, 107–111. https://doi.org/10.1002/lol2.10175.
Marshall, J., Speer, K., 2012. Closure of the meridional overturning circulation through Southern Ocean upwelling. Nat. Geosci. 5 (3), 171–180. https://doi.org/10.1038/ngeo1391.
Martin, J., Gordon, R.M., Fitzwater, S.E., 1990. Iron in Antartic waters. Nature 345, 156–158. https://doi.org/10.1038/345156a0.
Masich, J., Mazloff, M.R., Chereskin, T.K., 2018. Interfacial form stress in the Southern Ocean state estimate. J. Geophys. Res. Oceans 123, 3368–3385. https://doi.org/10.1029/2018JC013844.
Matsumoto, G.I., Johnson, K.S., Riser, S., Talley, L., Wijffels, S., Hotinski, R., 2022. The Global Ocean Biogeochemistry (GO-BGC) Array of Profiling Floats to Observe Changing Ocean Chemistry and Biology. Mar. Technol. Soc. J. 56 (3), 122–123. https://doi.org/10.4031/MTSJ.56.3.25.
Maurer, T.L., Plant, J.N., Johnson, K.S., 2021. Delayed-mode quality control of oxygen, nitrate, and pH data on SOCCOM biogeochemical profiling floats. Frontiers in Marine. Science 1118. https://doi.org/10.3389/fmars.2021.683207.
Mazloff, M.R., Cornuelle, B.D., Gille, S.T., Verdy, A., 2018. Correlation Lengths for Estimating the Large-Scale Carbon and Heat Content of the Southern Ocean. J. Geophys. Res. Oceans 123 (2), 883–901. https://doi.org/10.1002/2017JC013408.
Mazloff, M.R., Verdy, A., Gille, S.T., Johnson, K.S., Cornuelle, B.D., Sarmiento, J., 2023. Southern Ocean acidification revealed by Biogeochemical-Argo floats. J. Geophys. Res.: Oceans 128, e2022JC019530. https://doi.org/10.1029/2022JC019530.
McNeil, B.I., Matear, R.J., 2008. Southern Ocean acidification: A tipping point at 450-ppm atmospheric CO2. Proc. Natl. Acad. Sci. 105 (48), 18860–18864. https://doi.org/10.1073/pnas.0806318105.
Meijers, A., Sallée, J. B., Grey, A., Johnson, K. S., Arrigo, K., Swart, S., King, B., and Mazloff, M. 2019. Southern Ocean [in "State of the Climate in 2018"]. Bull. Amer. Meteor. Soc., 100 (9), S181–S185, doi:10.1175/2019BAMSStateoftheClimate.1.
Meijers, A.J.S., Shuckburgh, E., Bruneau, N., Sallee, J.-B., Bracegirdle, T.J., Wang, Z., 2012. Representation of the Antarctic Circumpolar Current in the CMIP5 climate models and future changes under warming scenarios. J. Geophys. Res. 117, C12008. https://doi.org/10.1029/2012JC008412.
Meredith, M.P., Sarmiento, J.L., Johnson, K.S., McDonagh, E.L., 2017. Advances in understanding the Southern Ocean's role in global climate: the ORCHESTRA and SOCCOM programs. Bull. Am. Meteorol. Soc. 98 (8), S168–S169. https://doi.org/10.1175/2017BAMSStateoftheClimate.1.
Meyer, M.G., Jones, R.M., Smith Jr., W.O., 2022. Quantifying Seasonal Particulate Organic Carbon Concentrations and Export Potential in the Southwestern Ross Sea Using Autonomous Gliders. J. Geophys. Res.: Oceans 127 (10), e2022JC018798. https://doi.org/10.1029/2022JC018798.
Mikaloff Fletcher, S.E., Gruber, N., Jacobson, A.R., Doney, S.C., Dutkiewicz, S., Gerber, M., Follows, M., Joos, F., Lindsay, K., Menemenlis, D., Mouchet, A., 2006. Inverse estimates of anthropogenic CO2 uptake, transport, and storage by the ocean. Global Biogeochem. Cycles 20 (2). https://doi.org/10.1029/2005GB002530.
Moreau, S., Boyd, P.W., Strutton, P.G., 2020. Remote assessment of the fate of phytoplankton in the Southern Ocean sea-ice zone. Nat. Commun. 11 (1), 1–9. https://doi.org/10.1038/s41467-020-16931-0.
Morrison, A.K., Frölicher, T.L., Sarmiento, J.L., 2015. Upwelling in the Southern Ocean. Phys. Today 68 (1), 27–32. https://doi.org/10.1063/PT.3.2654.
Munday, D.R., Johnson, H.L., Marshall, D.P., 2013. Eddy saturation of equilibrated circumpolar currents. J. Phys. Oceanogr. 43, 507–532. https://doi.org/10.1175/JPO-D-12-095.1.
Munk, W., Wunsch, C., 1998. Abyssal recipes II: Energetics of tidal and wind mixing. Deep Sea Res. Part I 45 (12), 1977–2010. https://doi.org/10.1016/S0967-0637(98)00070-3.
Munro, D.R., Lovenduski, N.S., Takahashi, T., Stephens, B.B., Newberger, T., Sweeney, C., 2015. Recent evidence for a strengthening CO2 sink in the Southern Ocean from carbonate system measurements in the Drake Passage (2002–2015). Geophys. Res. Lett. 42 (18), 7623–7630. https://doi.org/10.1002/2015GL065194.
NAS, 2021. Mid-Term Assessment of Progress on the 2015 Strategic Vision for Antarctic and Southern Ocean Research. National Academy of Sciences, Washington, DC. https://doi.org/10.17226/26338.
Newman, M.C., Dixon, P.M., Looney, B.B., Pinder III, J.E., 1989. Estimating mean and variance for environmental samples with below detection limit observations. J. Am. Water Resour. Assoc. 25, 905–916. https://doi.org/10.1111/j.1752-1688.1989.tb05406.x.
NRC, 2004. Climate data records from environmental satellites: Interim report. National Research Council, National Academies Press. https://doi.org/10.17226/10944.
NSTC, 2018. Science and technology for America's oceans: a decadal vision. Subcommittee on Ocean Science and Technology, National Science & Technology Council.
Ohlmann, J.C., Siegel, D.A., Gautier, C., 1996. Ocean mixed layer radiant heating and solar penetration: A global analysis. J. Clim. 9 (10), 2265–2280. https://doi.org/10.1175/1520-0442(1996)009<2265:OMLRHA>2.0.CO;2.
Olsen, A., Lange, N., Key, R.M., Tanhua, T., Bittig, H.C., Kozyr, A., Àlvarez, M., Azetsu-Scott, K., Becker, S., Brown, P.J., Carter, B.R., 2020. GLODAPv2. 2020–the second update of GLODAPv2. Earth Syst. Sci. Data 165. https://doi.org/10.5194/essd-2020-165.
Oppenheimer, M., Glavovic, B.C., Hinkel, J., van de Wal, R., Magnan, A.K., Abd-Elgawad, A., Cai, R., Cifuentes-Jara, M., DeConto, R.M., Ghosh, T., Hay, J., Isla, F., Marzeion, B., Meyssignac, B., Sebesvari, Z., 2019. Sea Level Rise and Implicationsfor Low-Lying Islands, Coasts and Communities. In: Roberts, D.C., Masson-Delmotte, V., Zhai, P., Tignor, M., Poloczanska, E., Mintenbeck, K., Alegría, A., Nicolai, M., Okem, A., Petzold, J., Rama, B., Weyer, N.M. (Eds.), IPCC Special Report on the Ocean and Cryosphere in a Changing Climate [H.-O. Pörtner]. Cambridge University Press, Cambridge, UK and New York, NY, USA, pp. 321–445. https://doi.org/10.1017/9781009157964.006.
Organelli, E., Leymarie, E., Zielinski, O., Uitz, J., D'ortenzio, F., Claustre, H., 2021. Hyperspectral radiometry on biogeochemical-argo floats: a bright perspective for phytoplankton diversity. Oceanography 90–91. https://doi.org/10.5670/oceanog.2021.supplement.02-33.
Owens, W.B., Wong, A.P.S., 2009. An improved calibration method for the drift of the conductivity sensor on autonomous CTD profiling floats by theta-S climatology. Deep-Sea Res. I 56 (3), 450–457. https://doi.org/10.1016/j.dsr.2008.09.008.
Owens, W.B., Zilberman, N., Johnson, K.S., Claustre, H., Scanderbeg, M., Wijffels, S., Suga, T., 2022. OneArgo: A New Paradigm for Observing the Global Ocean. Mar. Technol. Soc. J. 56 (3), 84–90. https://doi.org/10.4031/MTSJ.56.3.8.
Paparella, F., Young, W.R., 2002. Horizontal convection is non-turbulent. J. Fluid Mech. 466, 205–214. https://doi.org/10.1017/S0022112002001313.
Pauling, A.G., Bitz, C.M., Smith, I.J., Langhorne, P.J., 2016. The response of the Southern Ocean and Antarctic sea ice to freshwater from ice shelves in an Earth system model. J. Clim. 29 (5), 1655–1672. https://doi.org/10.1175/JCLI-D-15-0501.1.
Pendleton, L., Evans, K., Visbeck, M., 2020. Opinion: we need a global movement to transform ocean science for a better world. Proc. Natl. Acad. Sci. 117, 9652–9655. https://doi.org/10.1073/pnas.2005485117.
Picheral, M., Catalano, C., Brousseau, D., Claustre, H., Coppola, L., Leymarie, E., Coindat, J., Dias, F., Fevre, S., Guidi, L., Irisson, J.O., 2022. The Underwater Vision Profiler 6: an imaging sensor of particle size spectra and plankton, for autonomous and cabled platforms. Limnol. Oceanogr. Methods 20 (2), 115–129. https://doi.org/10.1002/lom3.10475.
Porter, D.F., Springer, S.R., Padman, L., Fricker, H.A., Tinto, K.J., Riser, S.C., Bell, R.E., ROSETTA-Ice Team, 2019. Evolution of the seasonal surface mixed layer of the Ross Sea, Antarctica, observed with autonomous profiling floats. J. Geophys. Res.: Oceans 124 (7), 4934–4953. https://doi.org/10.1029/2018JC014683.
Prend, C.J., Gille, S.T., Talley, L.D., Mitchell, B.G., Rosso, I. and Mazloff, M.R., 2019. Physical drivers of phytoplankton bloom initiation in the Southern Ocean's Scotia Sea. J. Geophys. Res.: Oceans, 124(8), pp.5811-5826. http://10.1029/2019JC015162.
Prend, C. J., Hunt, J. M., Mazloff, M. R., Gille, S. T., and Talley, L. D., 2022a. Controls on the boundary between thermally and non-thermally driven pCO2 regimes in the South Pacific. Geophys. Res. Lett. 49, e2021GL095797. 10.1029/2021GL095797.
Prend, C.J., Gray, A.R., Talley, L.D., Gille, S.T., Haumann, F.A., Johnson, K.S., Riser, S.C., Rosso, I., Sauvé, J. and Sarmiento, J.L., 2022b. Indo-Pacific sector dominates Southern Ocean carbon outgassing. Global Biogeochem. Cycles 36(7), p. e2021GB007226. 10.1029/2021GB007226.
Prend, C.J., Keerthi, M.G., Lévy, M., Aumont, O., Gille, S.T. and Talley, L.D., 2022c. Sub-Seasonal Forcing Drives Year-To-Year Variations of Southern Ocean Primary Productivity. Global Biogeochem. Cycles, 36(7), p.e2022GB007329. 10.1029/2022GB007329.
Riser, S.C., Wijffels, S., 2020. Environmental issues and the Argo array. https://argo.ucsd.edu/wp-content/uploads/sites/361/2020/05/final.Argo_Environmental_Impact.2020.05.10-1.pdf.
Riser, S.C., Freeland, H.J., Roemmich, D., Wijffels, S., Troisi, A., Belbéoch, M., Gilbert, D., Xu, J., Pouliquen, S., Thresher, A., Le Traon, P.Y., 2016. Fifteen years of ocean observations with the global Argo array. Nat. Clim. Chang. 6 (2), 145–153. https://doi.org/10.1038/nclimate2872.
Riser, S.C., Johnson, K.S., 2008. Net production of oxygen in the subtropical ocean. Nature 451 (7176), 323–325. https://doi.org/10.1038/nature06441.
Riser, S.C., Swift, D., Drucker, R., 2018. Profiling Floats in SOCCOM: Technical Capabilities for Studying the Southern Ocean. J. Geophys. Res.: Oceans 123 (6), 4055–4073. https://doi.org/10.1002/2017JC013419.
Roemmich, D., Church, J., Gilson, J., Monselesan, D., Sutton, P., Wijffels, S., 2015. Unabated planetary warming and its ocean structure since 2006. Nat. Clim. Chang. 5 (3), 240–245. https://doi.org/10.1038/nclimate2872.
Roemmich, D., Alford, M.H., Claustre, H., Johnson, K., King, B., Moum, J., Oke, P., Owens, W.B., Pouliquen, S., Purkey, S., Scanderbeg, M., 2019. On the future of Argo: A global, full-depth, multi-disciplinary array. Front. Mar. Sci. 6, 439. https://doi.org/10.3389/fmars.2019.00439.
Roesler, C., Uitz, J., Claustre, H., Boss, E., Xing, X., Organelli, E., Briggs, N., Bricaud, A., Schmechtig, C., Poteau, A., d'Ortenzio, F., 2017. Recommendations for obtaining unbiased chlorophyll estimates from in situ chlorophyll fluorometers: A global analysis of WET Labs ECO sensors. Limnol. Oceanogr. Methods 15 (6), 572–585. https://doi.org/10.1002/lom3.10185.
Rosso, I., Mazloff, M.R., Talley, L.D., Purkey, S.G., Freeman, N.M., Maze, G., 2020. Water mass and biogeochemical variability in the Kerguelen sector of the Southern Ocean: A machine learning approach for a mixing hot spot. J. Geophys. Res.: Oceans 125, e2019JC015877. https://doi.org/10.1029/2019JC015877.
Rosso, I., Mazloff, M.R., Verdy, A., Talley, L.D., 2017. Space and time variability of the Southern Ocean carbon budget. J. Geophys. Res. Oceans 122 (9), 7407–7432. https://doi.org/10.1002/2016JC012646.
Russell, J.L., Souffer, R.J., Dixon, K.W., 2006a. Intercomparison of the Southern Ocean circulations in the IPCC Coupled Model Control Simulations. J. Clim. 19 (18), 4560–4575. https://doi.org/10.1175/JCLI3869.1.

Russell, J.L., Dixon, K.W., Gnanadesikan, A., Stouffer, R.J., Toggweiler, J.R., 2006b. The Southern Hemisphere westerlies in a warming world: Propping open the door to the deep ocean. J. Clim. 19 (24), 6382–6390. https://doi.org/10.1175/JCLI3984.1.
Russell, J.L., Kamenkovich, I., Bitz, C., Ferrari, R., Gille, S.T., Goodman, P.J., Hallberg, R., Johnson, K., Khazmutdinova, K., Marinov, I., Mazloff, M., 2018. Metrics for the evaluation of the Southern Ocean in coupled climate models and earth system models. J. Geophys. Res. Oceans 123 (5), 3120–3143. https://doi.org/10.1002/2017JC013461.
Sallée, J.B., Pellichero, V., Akhoudas, C., Pauthenet, E., Vignes, L., Schmidtko, S., Garabato, A.N., Sutherland, P., Kuusela, M., 2021. Summertime increases in upper-ocean stratification and mixed-layer depth. Nature 591 (7851), 592–598. https://doi.org/10.1038/s41586-021-03303-x.
Sarmiento, J.L., Toggweiler, J.R., Najjar, R., 1988. Ocean carbon-cycle dynamics and atmospheric pCO2. Philos. Trans. Roy. Soc. London Series A, Math. Phys. Sci. 325 (1583), 3–21. https://doi.org/10.1098/rsta.1988.0039.
Sarmiento, J.L., Gruber, N., Brzezinski, M.A., Dunne, J.P., 2004. High-latitude controls of thermocline nutrients and low latitude biological productivity. Nature 427 (6969), 56–60. https://doi.org/10.1038/nature02127.
Schallenberg, C., Strzepek, R.F., Bestley, S., Wojtasiewicz, B., Trull, 2022. Iron limitation drives the globally extreme fluorescence/chlorophyll ratios of the Southern Ocean. Geophys. Res. Lett. 49, e2021GL097616 https://doi.org/10.1029/2021GL097616.
Schlunegger, S., K.B. Rodgers, J.L. Sarmiento, J.L., Ilyina, T., Dunne, J.P., Takano, Y., Christian, J.R., Long, M.C., Frölicher, T.L., Slater, R. and Lehner, F., 2020. Time of Emergence and Large Ensemble Intercomparison for Ocean Biogeochemical Trends. Global Biogeochem. Cycles 34, e2019GB006453. DOI:10.1029/2019GB006453.
Shi, J.R., Xie, S.P., Talley, L.D., 2018. Evolving relative importance of the Southern Ocean and North Atlantic in anthropogenic ocean heat uptake. J. Clim. 31 (18), 7459–7479. https://doi.org/10.1175/JCLI-D-18-0170.1.
Shi, J.R., Talley, L.D., Xie, S.P., Liu, W., Gille, S.T., 2020. Effects of buoyancy and wind forcing on Southern Ocean climate change. J. Clim. 33 (23), 10003–10020. https://doi.org/10.1175/JCLI-D-19-0877.1.
Shi, J.R., Talley, L.D., Xie, S.P., Peng, Q., Liu, W., 2021. Ocean warming and accelerating Southern Ocean zonal flow. Nat. Clim. Chang. 11 (12), 1090–1097. https://doi.org/10.1038/s41558-021-01212-5.
Smith, W.O., Garrison, D.L., 1990. Marine ecosystem research at the Weddell Sea ice edge: the AMERIEZ Program. Oceanography 3 (2), 22–29.
Smith, W.O., Nelson, D.M., 1986. Importance of ice edge phytoplankton production in the Southern Ocean. Bioscience 36 (4), 251–257. https://doi.org/10.2307/1310215.
Stammer, D., Wunsch, C., Giering, R., Eckert, C., Heimbach, P., Marotzke, J., Adcroft, A., Hill, C.N. and Marshall, J., 2002. Global ocean circulation during 1992–1997, estimated from ocean observations and a general circulation model. J. Geophys. Res.: Oceans, 107(C9), pp.1-1. doi:10.1029/ 2001JC000888.
Stoer, A.C., Fennel, K., 2022. Estimating ocean net primary productivity from daily cycles of carbon biomass measured by profiling floats. Limnol. Oceanogr. Lett. https://doi.org/10.1002/lol2.10295.
Straub, D.N., 1993. On the transport and angular momentum balance of channel models of the Antarctic Circumpolar Current. J. Phys. Oceanogr. 23, 776–782. https://doi.org/10.1175/1520-0485(1993)023<0776:OTTAAM>2.0.CO;2.
Stukel, M.R., Ducklow, H.W., 2017. Stirring up the biological pump: Vertical mixing and carbon export in the Southern Ocean. Global Biogeochem. Cycles 231, 1420–1434. https://doi.org/10.1002/2017GB005652.
Su, J., Schallenberg, C., Rohr, T., Strutton, P.G., Phillips, H.E., 2022. New estimates of Southern Ocean Annual Net Community Production revealed by BGC-Argo floats. Geophys. Res. Lett. 49 (15), p.e2021GL097372. https://doi.org/10.1029/2021GL097372.
Su, J., Strutton, P.G., Schallenberg, C., 2021. The subsurface biological structure of Southern Ocean eddies revealed by BGC-Argo floats. J. Mar. Syst. 220, 103569 https://doi.org/10.1016/j.jmarsys.2021.103569.
Swart, S., Johnson, K. S., Mazloff, M. R., Meijers, A., Meredith, M. P., Newman, L. and Sallée, J.-B. 2018. The Southern Ocean, [in "State of the Climate in 2017"]. Bull. Amer. Meteor. Soc., 99 (8), S185–S190, doi:10.1175/ 2018BAMSStateoftheClimate.1.
Swart, N.C., Fyfe, J.C., 2012. Ocean carbon uptake and storage influenced by wind bias in global climate models. Nat. Clim. Chang. 2 (1), 47–52. https://doi.org/10.1029/2012GL052810.
Swierczek, S., Mazloff, M. R., Morzfeld, M., Russell, J.L., 2021a. The effect of resolution on vertical heat and carbon transports in a regional ocean circulation model of the Argentine Basin. J. Geophys. Res.: Oceans, 126, e2021JC017235. 10.1029/ 2021JC017235.
Swierczek, S., Mazloff, M.R., Russell, J.L., 2021b. Investigating predictability of DIC and SST in the Argentine Basin through wind stress perturbation experiments. Geophys. Res. Lett. 48, e2021GL095504. 10.1029/2021GL095504.
Takahashi, T., Sutherland, S.C., Chipman, D.W., Goddard, J.G., Ho, C., Newberger, T., Sweeney, C., Munro, D.R., 2014. Climatological distributions of pH, pCO2, total CO2, alkalinity, and CaCO3 saturation in the global surface ocean, and temporal changes at selected locations. Mar. Chem. 164, 95–125. https://doi.org/10.1016/j.marchem.2014.06.004.
Talley, L.D., Feely, R.A., Sloyan, B.M., Wanninkhof, R., Baringer, M.O., Bullister, J.L., Carlson, C.A., Doney, S.C., Fine, R.A., Firing, E., Gruber, N., 2016. Changes in ocean heat, carbon content, and ventilation: a review of the first decade of GO-SHIP global repeat hydrography. Ann. Rev. Mar. Sci. 8 (1) https://doi.org/10.1146/annurev-marine-052915-100829.
Talley, L.D., Rosso, I., Kamenkovich, I., Mazloff, M.R., Wang, J., Boss, E., Gray, A.R., Johnson, K.S., Key, R.M., Riser, S.C., Williams, N.L., 2019. Southern Ocean biogeochemical float deployment strategy, with example from the Greenwich Meridian line (GO-SHIP A12). J. Geophys. Res. Oceans 124 (1), 403–431. https://doi.org/10.1029/2018JC014059.
Tamsitt, V., Drake, H.F., Morrison, A.K., Talley, L.D., Dufour, C.O., Gray, A.R., Griffies, S. M., Mazloff, M.R., Sarmiento, J.L., Wang, J., Weijer, W., 2017. Spiraling pathways of global deep waters to the surface of the Southern Ocean. Nat. Commun. 8 (1), 1–10. https://doi.org/10.1038/s41467-017-00197-0.
Tamsitt, V., Abernathey, R.P., Mazloff, M.R., Wang, J., Talley, L.D., 2018. Transformation of deep water masses along Lagrangian upwelling pathways in the Southern Ocean. J. Geophys. Res. Oceans 123 (3), 1994–2017. https://doi.org/10.1002/2017JC013409.
Tamsitt, V., Bushinsky, S., Li, Z., du Plessis, M., Foppert, A., Gille, S., Rintoul, S., Shadwick, E., Silvano, A., Sutton, A., Swart, S., Tilbrook, B., Williams, N.L., 2021. Southern Ocean [in "State of the Climate in 2020"]. Bull. Amer. Meteor. Soc., 102 (8), S341-S345, DOI:10.1175/BAMS-D-21-0081.1.
Thompson, M., 1988. Do we really need detection limits? Analyst 123, 405–407. https://doi.org/10.1039/A705702D.
Toggweiler, J.R., Samuels, B., 1998. On the ocean's large-scale circulation near the limit of no vertical mixing. J. Phys. Oceanogr. 28 (9), 1832–1852. https://doi.org/10.1175/1520-0485(1998)028<1832:OTOSLS>2.0.CO;2.
Twelves, A.G., Goldberg, D.N., Henley, S.F., Mazloff, M.R., Jones, D.C., 2021. Self-shading and meltwater spreading control the transition from light to iron limitation in an Antarctic coastal polynya. J. Geophys. Res.: Oceans 126, e2020JC016636. https://doi.org/10.1029/2020JC016636.
Uchida, T., Balwada, D., Abernathey, R., Prend, C.J., Boss, E., Gille, S.T., 2019. Southern Ocean phytoplankton blooms observed by biogeochemical floats. J. Geophys. Res. Oceans 124, 7328–7343. https://doi.org/10.1029/2019JC015355.
Valsala, V., Sreeush, M.G., Anju, M., Sreenivas, P., Tiwari, Y.K., Chakraborty, K., Sijikumar, S., 2021. An observing system simulation experiment for Indian Ocean surface pCO2 measurements. Prog. Oceanogr. 194, 102570. https://doi.org/10.1016/j.pocean.2021.102570.
Verdy, A., Mazloff, M.R., 2017. A data assimilating model for estimating Southern Ocean biogeochemistry. J. Geophys. Res. Oceans 122 (9), 6968–6988. https://doi.org/10.1002/2016JC012650.
Volk, T., and Hoffert, M., 1985. Ocean carbon pumps: Analysis of relative strengths and efficiencies in ocean-driven atmospheric co2 changes. In: Sundquist, E., Broecker, W. (Eds.), The carbon cycle and atmospheric CO 2: Natural variations Archean to present. Chapman conference papers, 1984 (Geophysical Monograph 32, pp. 99–110). Washington, DC: American Geophysical Union.
von Berg, L., Prend, C.J., Campbell, E.C., Mazloff, M.R., Talley, L.D., Gille, S.T., 2020. Weddell Sea phytoplankton blooms modulated by sea ice variability and polynya formation. Geophys. Res. Lett. 47, e2020GL087954 https://doi.org/10.1029/2020GL087954.
Westberry, T., Behrenfeld, M.J., Siegel, D.A., Boss, E., 2008. Carbon-based primary productivity modeling with vertically resolved photoacclimation. Global Biogeochem. Cycles 22 (2), GB2024. https://doi.org/10.1029/2007GB003078.
Wilkinson, M.D., Dumontier, M., Aalbersberg, I.J., Appleton, G., Axton, M., Baak, A., Blomberg, N., Boiten, J.W., da Silva Santos, L.B., Bourne, P.E., Bouwman, J., 2016. The FAIR Guiding Principles for scientific data management and stewardship. Sci. Data 3 (1), 1–9. https://doi.org/10.1038/sdata.2016.18.
Williams, N.L., Juranek, L.W., Feely, R.A., Johnson, K.S., Sarmiento, J.L., Talley, L.D., Dickson, A.G., Gray, A.R., Wanninkhof, R., Russell, J.L., Riser, S.C., 2017. Calculating surface ocean pCO2 from biogeochemical Argo floats equipped with pH: An uncertainty analysis. Global Biogeochem. Cycles 31 (3), 591–604. https://doi.org/10.1002/2016GB005541.
Williams, N.L., Juranek, L.W., Feely, R.A., Russell, J.L., Johnson, K.S., Hales, B., 2018. Assessment of the carbonate chemistry seasonal cycles in the Southern Ocean from persistent observational platforms. J. Geophys. Res. Oceans 1–20. https://doi.org/10.1029/2017JC012917.
Wilson, E.A., Riser, S.C., Campbell, E.C., Wong, A.P., 2019. Winter upper-ocean stability and ice–ocean feedbacks in the sea ice–covered Southern Ocean. J. Phys. Oceanogr. 49 (4), 1099–1117. https://doi.org/10.1175/JPO-D-18-0184.
Wong, A.P., Riser, S.C., 2011. Profiling float observations of the upper ocean under sea ice off the Wilkes Land coast of Antarctica. J. Phys. Oceanogr. 41 (6), 1102–1115. https://doi.org/10.1175/2011jpo4516.1.
Wong, A.P., Wijffels, S.E., Riser, S.C., Pouliquen, S., Hosoda, S., Roemmich, D., Gilson, J., Johnson, G.C., Martini, K., Murphy, D.J., Scanderbeg, M., 2020. Argo data 1999–2019: two million temperature-salinity profiles and subsurface velocity observations from a global array of profiling floats. Front. Mar. Sci. 7, 700. https://doi.org/10.3389/FMARS.2020.00700.
Wu, Y., Bakker, D.C., Achterberg, E.P., Silva, A.N., Pickup, D.D., Li, X., Hartman, S., Stappard, D., Qi, D., Tyrrell, T., 2022. Integrated analysis of carbon dioxide and oxygen concentrations as a quality control of ocean float data. Commun. Earth Environ. 3 (1), 1–11. https://doi.org/10.1038/s43247-022-00421-w.
Xing, X., Morel, A., Claustre, H., Antoine, D., Ortenzio, F.D., Poteau, A., Mignot, A., 2011. Combined processing and mutual interpretation of radiometry and fluorimetry from autonomous profiling Bio - Argo floats: Chlorophyll a retrieval. J. Geophys. Res. 116, C06020. https://doi.org/10.1029/2010JC006899.

Continental Shelf Research 264 (2023) 105040

Contents lists available at ScienceDirect

Continental Shelf Research

journal homepage: www.elsevier.com/locate/csr

Mid-Atlantic Bight cold pool based on ocean glider observations

W.S. Brown[a,*], O. Schofield[b], S. Glenn[b], J. Kohut[b], W. Boicourt[c]

[a] *School for Marine Science and Technology, University of Massachusetts Dartmouth, 706 S Rodney French Blvd., New Bedford, MA 02744, USA*
[b] *Coastal Ocean Observation Lab, Rutgers, State University of New Jersey, 71 Dudley Rd., New Brunswick, NJ 08901, USA*
[c] *Center for Environmental Science, University of Maryland, PO Box 775, Cambridge, MD 21613, USA*

ARTICLE INFO

Keywords:
Hydrography
Ocean glider
Mid-atlantic bight
Cold pool

ABSTRACT

During summer, distinctive, bottom-trapped, cold water mass of remnant local and remote winter water called Cold Pool Water (CPW) resides as a swath over the mid to outer continental shelf throughout much of the Mid-Atlantic Bight (MAB). This evolving CPW is important because it strongly influences the ecosystem, including several important fisheries. Thus, there is a priority to better understand the relevant ocean processes and develop CPW forecast capability. Over the past decade, repeated high-resolution Slocum glider measurements of ocean water properties along a New Jersey cross-shelf transect have helped to define the variability of the CPW structure off New Jersey. More recently the Mid-Atlantic Regional Association Coastal Ocean Observing System-supported ocean gliders have occupied a series of along-shelf zigzag trajectories from Massachusetts to New Jersey and New Jersey to Maryland. The comprehensive set of March through November 2007 glider measurements has been used to define the annual evolution of the 10 °C Cold Pool in terms of its distribution and water properties. The rather steady warming at the rate of 1 °C per month July through October 2007 is reflected in the 2007 CPW temperature (T) and salinity (S) properties. We describe how a three-glider fleet view of the September 2013 Cold Pool (a) confirmed the Lentz (2017) CPW cold patch and (b) the impingement of a Gulf Stream warm core ring warmed and salted the 2013 CPW. The Gulf Sream 2013 event forced our extension of the CPW T and S properties.

1. Introduction

The Cold Pool is a distinctive, highly-variable, bottom-trapped, cold water mass remnant of the local and remote winter water. It is found during summer over the mid and outer continental shelf between Cape Cod and Cape Hatteras – a region known as the Mid-Atlantic Bight (MAB).

The Cold Pool is an important element in the MAB habitat according to Malone et al. (1983) and Flagg et al. (1994), who have shown that it affects phytoplankton productivity; and Sullivan et al. (2005) and Weinberg (2005) who have shown that it affects the behavior and recruitment of pelagic and demersal fish on the shelf.

The distribution and characteristics of this Cold Pool water mass evolves significantly during its May through October lifetime (Ketchum and Corwin, 1964; Boicourt and Hacker, 1976; Beardsley et al., 1976; Beardsley and Boicourt, 1981). Lentz (2003) present the annual evolution of a MAB-averaged cross-shelf section of the climatological temperature. This sequence shows that well-mixed winter shelf waters cool between January and March. The May section shows how the vernal onset of temperature- and fresh water-induced stratification creates a bottom-trapped, Cold Pool water mass with minimum temperatures dependent on the severity of the previous winter's local cooling.

Once formed, this distinctive Cold Pool goes through a complex evolution during the rest of the spring and throughout the summer. For example, during May–June the northeastern MAB Cold Pool gets colder due to continued inflow of winter water from the Gulf of Maine/Georges Bank (GoM/GB) region (Brown and Irish, 1993; Hopkins and Garfield, 1979; Ramp et al., 1988). The Lentz (2017) map of the NMFS May 1979 data reveals a patch of the coldest waters (or *"cold patch"*) within the Cold Pool. Ou and Houghton (1982) note that locations of the *"cold patch"* during the summer 1979 is consistent with the well-documented general 5 cm/s (~5 km/day) southwestward along-shelf MAB flow.

During the summer, the Cold Pool Water mass (CPW) is warmed by turbulent processes acting on its surface (Chen et al., 2014) and along its inshore boundary (Kohut et al., 2004). The CPW is also heated and salted by a complex array of turbulent processes along its offshore boundary which is the shelf-break front (SBF) (Houghton et al., 1982; 2010). Candidate

* Corresponding author.
E-mail address: wbrown@umassd.edu (W.S. Brown).

https://doi.org/10.1016/j.csr.2023.105040
Received 20 June 2022; Received in revised form 15 February 2023; Accepted 26 May 2023
Available online 11 June 2023

across-SBF exchange processes result in episodic warm/salty intrusions into CPW by way of the interior and bottom boundary layers (Linder et al., 2004). Interactions between Gulf Stream Warm Core Rings (WCR) and the SBF undoubtedly contribute to such exchanges.

The cooling of northeast MAB CPW ceases in July, which is followed by a general warming of all the still distinct Cold Pool through September (Lentz, 2017). Then during autumn (primarily in October), the inevitable energetic storms mix the MAB water column well enough to erase the distinctiveness the Cold Pool by November, when and the following year's annual Cold Pool evolution cycle begins anew.

The mysteries of the Cold Pool and its importance to the MAB ecosystem prompt us to seek answers regarding these erosion processes. Such answers are now within our reach because of the newly available technologies, including ocean gliders, remote high frequency radar-derived surface current mapping, modern data-assimilation coastal ocean numerical models, and the development of the Integrated Ocean Observing System (IOOS; Bassett et al., 2010) and the Ocean Observatory Initiative (OOI): Pioneer Array. This paper describes what we have learned about the MAB Cold Pool from primarily glider observations.

2. Measuring the Cold Pool

Rutgers University researchers began deploying Teledyne/Webb Research (TWR) Slocum ocean gliders on the Mid-Atlantic Bight shelf in 2003 (Schofield et al., 2010). This earlier effort evolved into the effort of the Mid Atlantic Regional Association Coastal Ocean Observing System (MARACOOS) to deploy ongoing series of Slocum glider missions along a (a) cross-shelf transect off New Jersey called the Endurance Line (Fig. 1; Leg-6); (b) cross-shelf series of zigzags from Massachusetts to New Jersey in the northeastern part of MAB (NE-MAB; Legs 1–6); and (c) the southwestern part of MAB (SW-MAB; Legs 6–10) is series of cross-shelf zigzags from New Jersey to Maryland. The following description of the different phases of the Cold Pool is based primarily on glider measurements from the most extensive cross-shelf transects represented by Legs 1, 6, and 8, respectively.

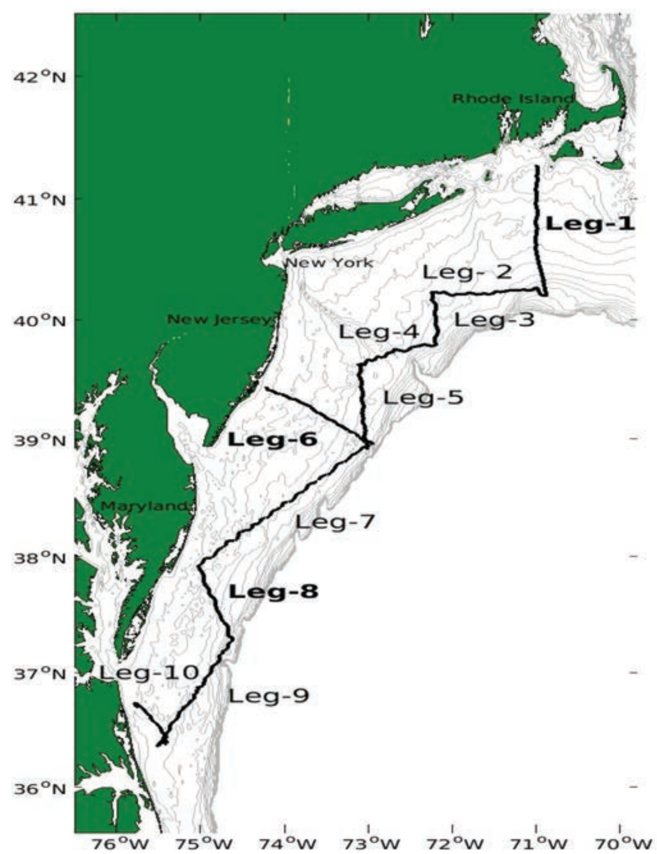

Fig. 1. The definition of the transect sections in this paper in terms of a composite of the May 2007 glider trajectory in the northeastern MAB (NE-MAB; Legs 1–6) and July 2007 in the southwestern MAB (SW-MAB; Legs 6–10). Leg-1, Leg-6 and Leg-8 are emboldened. Some of the MAB states are identified.

The Slocum glider sawtooths its way through the ocean (Schofield et al., 2010) with an average horizontal speed of about 0.25 m/s (½ kt.). A glider slant (27° rel. to horizontal) shelf profile consists of depths of about 3 m–3 m above the bottom. On the shelf, these Slocum gliders make about 20 sawtooth pairs of profiles in 3 h - our typical time between surfacings. We use the zigzag glider slices to estimate the extent and properties of the MAB Cold Pool during each of the glider missions. A typical zigzag run takes a typical 100 m Slocum glider (at ~25 km/day) about 3–4 weeks to transit from Massachusetts to New Jersey. All the gliders considered here measured a standard suite of measurements including pressure (P), temperature (T), pumped conductivity (C) (or derived salinity S), and an estimated glider inter-surfacing segment-averaged ocean velocity (V).

2.1. Pre-cold pool – Late Winter/Early Spring

The glider measurements between 13 March and 12 April 2007 define the MAB winter water mass, which is the basis for the 2007 Cold Pool Water (CPW). The cross-self glider transects show the expected vertically well-mixed "winter water". Leg-1 south of Massachusetts exhibits the coldest transect minimum temperature (T_{min}) at 2.87 °C (Table 1). The salinity at the Leg-1 T_{min} (S_{Tmin}) is 32.80 Practical Salinity Units (psu; see Appendix A for the way to covert those psu salinities into the more modern Absolute Salinity S_A). The Leg-6 transect off New Jersey is somewhat warmer with a T_{min} at 4.94 °C and saltier with a S_{Tmin} at 33.08 psu than the Leg-1 counterparts. The individual transect temperature minima T_{min} is a good proxy for the properties and location of the *core of the Cold Pool* of that section.

2.2. Proto-cold pool – Mid-Spring

Vernal warming of the MAB upper layer leads to the first definition of the 2007 Cold Pool off of New Jersey. This is shown by the 13–19 May 2007 Leg-6 glider measurements (Fig. 2) which contrast with the Leg-1 still well-mixed structure. However, both transect T_{min}s have warmed relative to the March T_{min}s. The along-shelf gradients in the Leg-1 versus Leg-6 water properties are typical of what we see even after the development of 2007 Cold Pool throughout the MAB as presented next.

2.3. Cold pool 2007 established – Spring 2007

The 23–27 May 2007 glider measurements (Fig. 3) show a surface layer that has warmed and freshened enough to isolate and thus define the 2007 Cold Pool Water throughout the MAB. However, note that T_{min} in both transects is somewhat cooler than that seen in April (and thus throughout the MAB). The along-MAB temperature gradients, with the Leg-6 waters generally warmer than the Leg-1 waters at corresponding depths define the cold patch in the northeastern MAB. We speculate that the cooler temperatures are due to the inflow of colder "upstream" waters from the Gulf of Maine/Georges Bank region.

2.4. Cold pool – Summer 2007

The 18–24 July Leg-6 reveals an increasingly distinct Cold Pool with a transect T_{min} of 5.60 °C (Fig. 4-upper). It compares well with the 11–15 June Leg-6 T_{min} of 5.32 °C (Fig. 3) and consistent with the expected translation of the temperature minimum patch. The 18–24 July Leg-6 S_{Tmin} compares well with the 11–15 June Leg-6 S_{Tmin} (Table 1) being only about 0.3 psu greater than its Leg-1 counterpart. The salinity difference is likely the signature of intrusion(s) of high salinity/warmer

Table 1
The 2007 section-minimum temperatures T_{min} and associated salinities S_{Tmin} are presented for a representative set of sections. For sub-thermocline waters ($T < 10$ °C), the means and standard deviations of *temperature departures* ($T_D = T - T_{min}$) and associated *salinity departures* ($S_D = S - S_{Tmin}$) are presented.

2007 Survey Month	Leg	Date	T_{min} (°C)	T_D Mean (°C)	T_D Std Dev (°C)	S_{Tmin} (PSU)	S_D Mean (PSU)	S_D Std Dev (PSU)
MAR	**Leg-1**	Mar16	2.872	1.70	0.81	32.801	0.23	0.16
	Leg-6	Apr 03	4.929	1.83	1.16	33.083	0.52	0.40
		Ave.	***3.901***	***1.77***	***0.99***	***32.942***	***0.38***	***0.28***
APR	**Leg-1**	Apr 28	4.843	1.30	0.82	32.815	0.01	0.24
	Leg-6	May 15	6.648	1.76	1.02	33.272	−0.00	0.23
		Ave.	***5.746***	***1.53***	***0.92***	***33.044***	***0.01***	***0.24***
		SPR. AVE.	***4.824***	***1.63***	***0.96***	***32.993***	***0.20***	***0.26***
MAY	**Leg-1**	May 27	4.780	3.17	2.18	32.739	0.09	0.24
	Leg-6	June 11	5.319	2.14	1.87	33.006	0.13	0.18
		Ave.	***5.050***	***2.66***	***2.03***	***32.873***	***0.11***	***0.21***
JUL	**Leg-6**	July 24	5.603	2.04	1.47	32.961	0.08	0.25
	Leg-8	Aug 03	6.331	2.10	1.10	33.028	0.22	0.21
		Ave.	***5.967***	***2.07***	***1.29***	***32.995***	***0.15***	***0.23***
		SUM. AVE.	***5.509***	***2.37***	***1.66***	***32.934***	***0.13***	***0.22***
SEP	**Leg-1**	Sep 30	7.711	1.24	0.54	33.006	0.03	0.28
	Leg-6	Oct 13	8.478	0.49	0.39	32.967	0.06	0.17
		Ave.	***8.095***	***0.87***	***0.47***	***32.987***	***0.05***	***0.23***
OCT	**Leg-6**	Oct 10	8.588	0.41	0.37	33.057	0.07	0.19
	Leg-8	Oct 25	9.902	0.04	0.03	33.201	0.07	0.08
		Ave.	***9.245***	***0.23***	***0.20***	***33.129***	***0.07***	***0.14***
		AUT. AVE.	***8.670***	***0.55***	***0.34***	***33.058***	***0.06***	***0.19***
		ASSA. AVE.	6.334	***1.52***	***0.99***	32.995	***0.13***	***0.22***

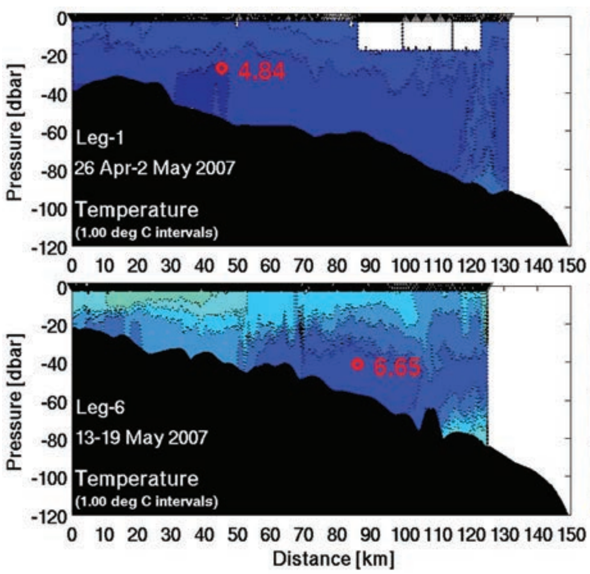

Fig. 2. NE-MAB PROTO-COLD POOL 2007: *Mid-Spring*. The 26 April–19 May 2007 glider RU06: *(upper)* Leg-1 temperature section, with section-minimum temperatures indicated (red). *(lower)* The same for Leg-6, with temperature (°C) legends to the right. (The missing data is due to our glider piloting, while crossing the east-west New York shipping lanes.)

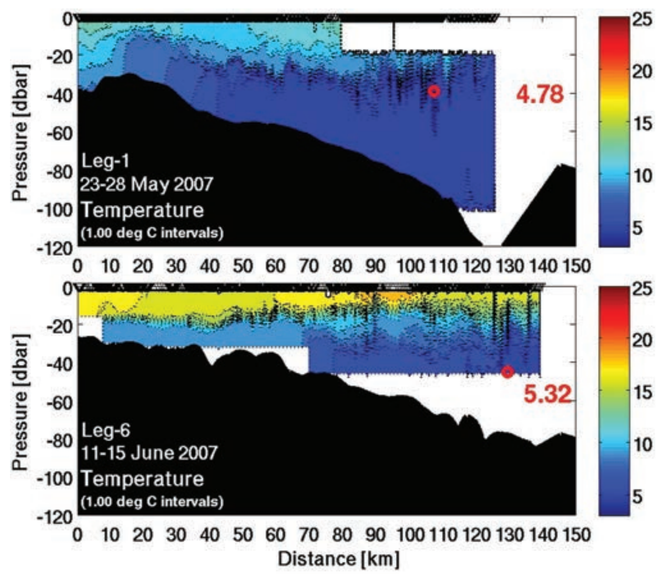

Fig. 3. NE-*MAB* COLD POOL 2007: *Spring*. The 23 May–15 June 2007 *glider RU17 (upper)* Leg-1 temperature section, with section-minimum temperatures indicated (red), and *(lower)* the same for Leg-6, with temperature (°C) legends to the right.

water intrusion across the shelf-break front. Repeated intrusions such as this are thought to be one of the mechanisms that warms/salts the seaward extremes of the Cold Pool during the summer (Gawarkiewiz et al., 2018). The strong vertical stratification with its downward intrusions (Fig. 4-lower) appears to be supporting a strong internal tide. Spatial glider measurements of the internal tide will always be aliased.

2.5. Cold pool – Autumn 2007

Glider measurements in the northeast MAB (Fig. 5) and southwest MAB (Fig. 6) define a still distinct Cold Pool that is even warmer than summer Cold Pool. The warming of T_{min} continues into late autumn (Fig. 7; Table 1); presumably by atmospheric cooling-induced mixing of the water column of the warm upper and cool lower layers. The winter cooling (to come) is forecast by the Leg-6 T_{min}, which in the New Jersey inshore.

There is mid-December evidence (Fig. 7) of the water column is beginning to cool. These measurements capture the beginning of the winter 2007–08 cooling phase of the MAB waters. After more atmospheric cooling of the coastal ocean in January through March, that water mass becomes part of the 2008 Cold Pool.

3. An evolving Cold Pool

This 2007 series of zigzag glider runs provide the most complete view of an annual realization of a clearly evolving MAB Cold Pool to date. With this high-resolution picture of an evolving Cold Pool, we now focus on the more complete set of Cold Pool water mass properties and their evolution. The *thermal cores* of the 2007 Cold Pool for both summer

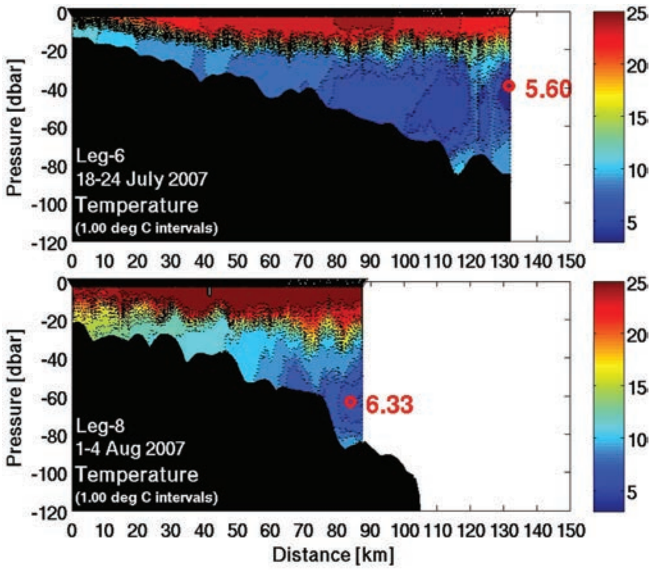

Fig. 4. *SW-MAB* COLD POOL 2007: *Summer*. The 18 July–4 August 2007 *glider RU01 (upper)* Leg-6 temperature section, with section-minimum temperatures indicated (red), and *(lower)* the same for Leg-8, with temperature (°C) legends to the right.

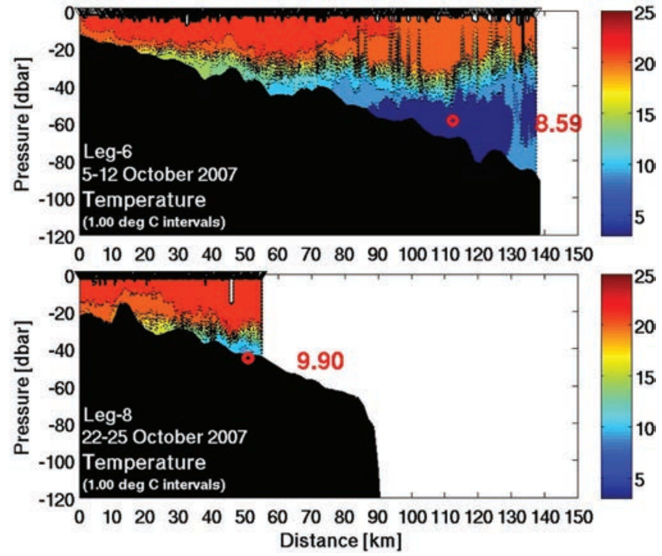

Fig. 6. *SW-MAB* COLD POOL 2007: *Autumn*. The 7–26 October 2007 *glider RU06 (upper)* Leg-6 temperature section, with section-minimum temperatures indicated (red), and *(lower)* the same for Leg-8, with temperature (°C) legends to the right.

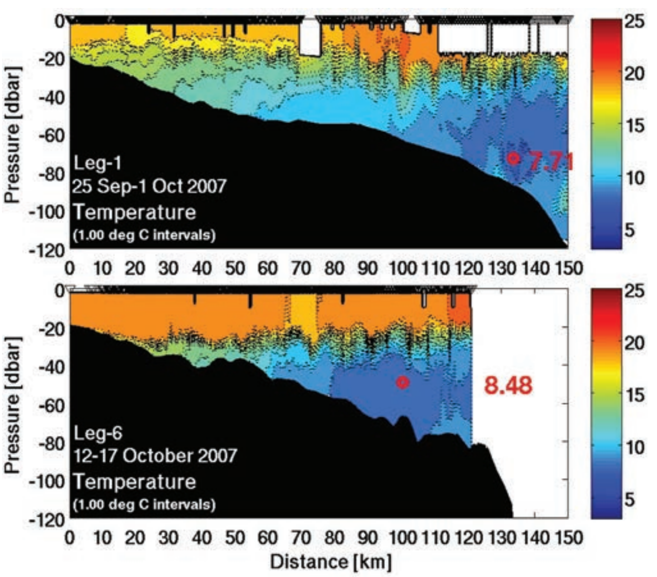

Fig. 5. *NE-MAB* COLD POOL 2007: *Autumn*. The 25 September–17 October 2007 *glider RU05 (upper)* Leg-1 temperature section, with section-minimum temperatures indicated (red), and *(lower)* the same for Leg-6, with temperature (°C) legends to the right.

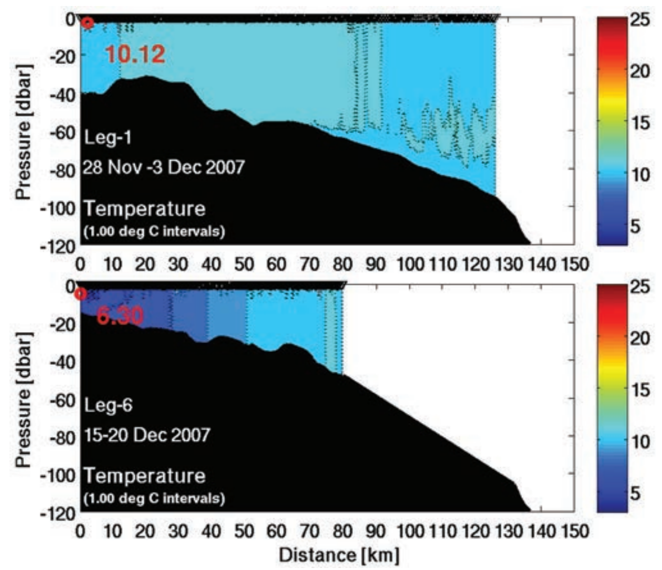

Fig. 7. NE-COLD POOL 2007: *Late Autumn*. The 28 Nov.–20 Dec. 2007*glider RU01 (upper)* Leg-1 temperature section, with section-minimum temperatures indicated (red), and *(lower)* the same for Leg-6, with temperature (°C) legends to the right.

and autumn are defined by the section temperature minimums T_{min}s, as we can see in Figs. 8 and 9. The locations of the T_{min} show that the Cold Pool core is near, if not in the shelf-break front (SBF) during both seasons. Thus, the Cold Pool hydrography geostrophically supports the SBF jet, which are exemplified by some of the fastest along-shelf flows. The fact that T_{min}s are usually 10 m–20 m above the bottom is consistent with the location of the SBF jet. Thus, the SBF jet advects the outer part of the Cold Pool generally from northeast to southwest along the outer shelf.

The section minimum temperature T_{min} is an excellent proxy for the seasonal variability of Cold Pool temperature at different sections of the MAB. For example, the T_{min} of Leg-1 and Leg-6 (two of more complete cross-shelf transects) warmed between March and April 2007 (Table 1). This *warming phase* was followed during May by a dramatic cooling of the Leg-6 waters. The fact that the Legs-1 through −4 tends to support the Lentz (2017) argument that a cold patch centered on the Hudson Valley is responsible for this observation. Consequently, the substantial Leg-6 T_{min} minus Leg-1 T_{min} difference of 2.0 °C at the beginning of May decreased rapidly to 0.7 °C by mid-June. The 2007 Cold Pool was established throughout the MAB at this time.

In early July, the MAB-wide Cold Pool Waters (CPW) began to warm at about a rate of ~1 °C/month. Estimates of the warming rates highlight the contrast between the *Spring* (Apr–May) cooling and *Summer* (May–October) warming in the northeastern segment of the MAB (NE-MAB) Cold Pool. The summer warming of the MAB Cold Pool (Fig. 10) could be

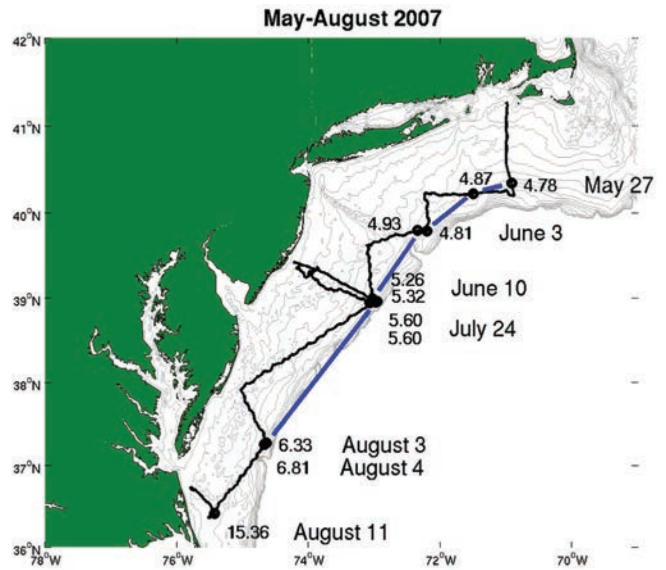

Fig. 8. The composite of the glider trajectories in the northeastern (NE) MAB *(RU17)* and the southwestern (SW) MAB *(RU01)* during the *summer* 2007. The section-minimum temperatures T_{min} (o) are highlighted by the blue line. The dates are located according to their alongshelf location of the gliders.

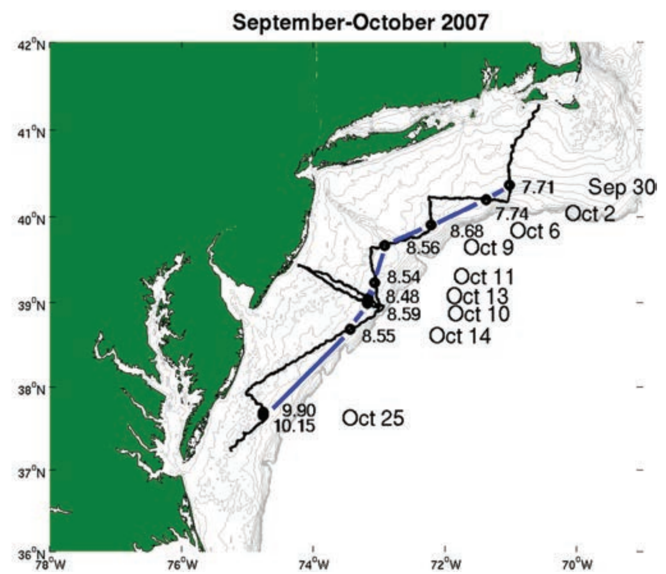

Fig. 9. The composite of the glider trajectories in *autumn* 2007: NE MAB *(RU05)* and SW MAB *(RU06)*. The section-minimum temperatures T_{min} (o) are highlighted by the blue line. The dates are located according to their alongshelf location of the gliders.

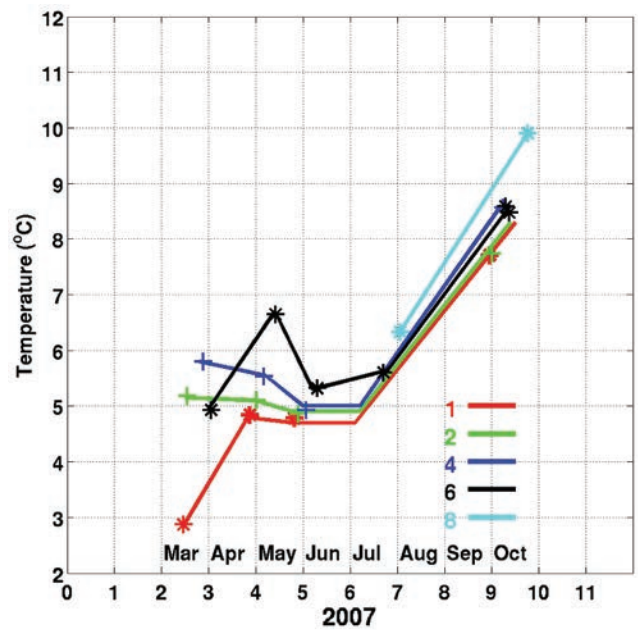

Fig. 10. The 2007 section-minimum temperature T_{min} versus time for Legs-1 (red *), 2 (green +), 4 (blue +), 6 (black *) and 8 (cyan *). Note that the Apr.–May 2007 cooling rates, which range from largest at Leg-6 and smallest at Leg-1, are followed by a shelf-wide average Jun.–Oct. 2007 warming rate of 1.05 °C/month.

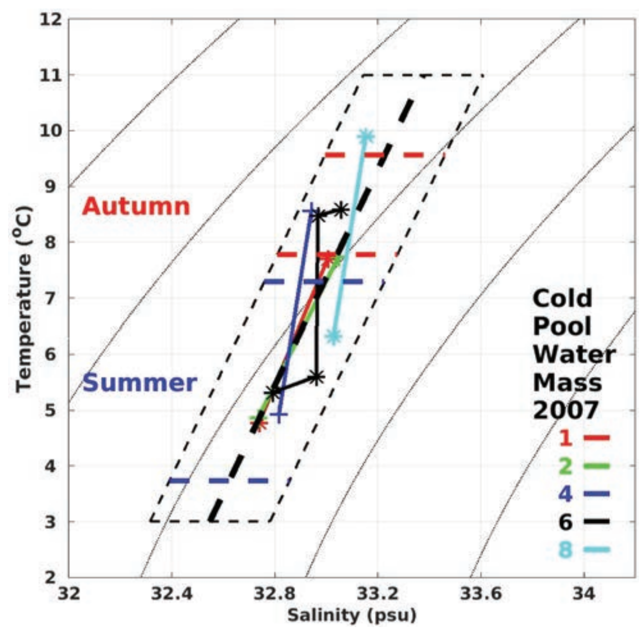

Fig. 11. A statistical definition of 2007 Cold Pool Water properties (CPW; black dashed trapezoid) is based on the average 2007 section T_{min}–S_{Tmin} relation (bold dashed line); which is a linear statistical fit to the May–October 2007 T_{min}/S_{Tmin} observations for the Legs-1 (red*), 2 (green+), 4 (blue+), 6 (black*), and 8 (cyan*). The trapezoid width is a constant $\pm$ S_D standard deviation (σ) of all sub-10 °C waters (see main text). The 2007 summer (blue dashed) and autumn (red dashed) CPW temperature bounds are shown.

due to several processes including turbulent transport of heat from the (a) surface layer above, (b) offshore waters beyond the shelf-break front (SBF), and (c) landward boundary via upwelling/downwelling exchange. The question of which of these processes dominate during the different phases of the Cold Pool evolution will be addressed below.

The 2007 T_{min}/S_{Tmin} are used to define the Cold Pool's TS water properties between 3 °C and 11 °C (Fig. 11) for several representative transects. A linear fit to the observed T_{min}/S_{Tmin} represents the average 2007 T_{min}–S_{Tmin} relationship (Fig. 11; bold dashed line). This T_{min}–S_{Tmin} relationship shows as the Cold Pool core waters warm their salinity increases. The trend toward higher temperatures during the summer could be due to the processes mentioned above. However, the trend of this T_{min}–S_{Tmin} relationship toward higher salinities is only consistent with exchange between the Cold Pool and Slope Sea water across the SBF.

Sub-thermocline Cold Pool water properties through mixing with other adjacent water masses (e.g., Slope Sea and MAB shelf waters). The extents of the Cold Pool Water properties on a specific transect T^t and S^t in Fig. 11 were determined by the statistics of their respective departure properties T_D/S_D computed according to:

$$T_D\ (x, s, z) = T^t\ (x, s, z) - T_{min}(s)$$

and

$$S_D\ (x, s, z) = S^t\ (x, s, z) - S_{Tmin}\ (s),$$

where T^t/S^t is any temperature/salinity pair in the transect with respect to T_{min} (s)/S_{Tmin} (s); "*x*" is an inshore coordinate referenced to the alongshore location of the "s" and "*z*" is upward.

Thus, for measured sub-thermocline water temperatures (<10 °C), we computed the departure of temperatures from T_{min} (T_D); and salinities from the corresponding S_{Tmin} (S_D). Note in Table 1 that the S_D standard deviations are virtually constant throughout the summer (1σ ~ 0.24 psu). That is the basis for the dashed lines on either side of the average T_{min}–S_{Tmin} relationship in Fig. 11. In contrast to the salinities, the T_D statistics are seasonal – reflecting the warming noted before. Thus, we use a average $T_{min} \pm T_D$ 1σ window to define the Cold Pool Water (CPW) mass in the region of a specific cross-shelf section with a specified T_{min}. Examples of the temperature boundaries ± 1σ relative the average T_{min} for the respective *summer* and *autumn 2007* are given in Fig. 11.

4. Cold Pool 2007 Water masses

A few glider measured-transects can be used to define the seasonal cycle of the bathymetric extent of properties of the 2007 MAB Cold Pool. We determine the footprint of the of the *summer* 2007, sub-10 °C Cold Pool from a composite of measurements by (a) glider RU17 in the northeastern MAB during *late May-early June* and (b) glider RU01 in the southwestern MAB during *late July–early August*. The traditional approach in defining the Cold Pool extent is to use the 10 °C isotherm. Following this approach, we locate the inshore intersection of the 10 °C isotherm with the bottom – "the bottoming" – in each temperature section.

In addition, we built a model for estimating the Cold Pool volume. We wrote a Matlab program to estimate the Cold Pool (CP) volume using real estimated bathymetry. The inputs are the glider-measured/estimated geometry of the sub-10 °C (or sub-12 °C based glider missions) Cold Pool and the uniform-thickness warm layer above the Cold Pool. Then, we ran the estimation model, with a various warm layer thicknesses (based glider measurements) for the different cases. For each case, the CP volume mean ± one standard deviation are given.

4.1. *Summer 2007 Cold Pool: 10 °C isotherm*

Both the RU17 and the RU01 glider missions just did not go far enough offshore to pierce the Shelf-Break Front (SBF; Linder et al., 2004). However, the SBF hovers around the 100 m isobath, and contains the 10 °C isotherm. Therefore, we assume that the seaward boundary of the 2007 10 °C Cold Pool to coincides with 100 m isobath. We built a crude model to estimate the Cold Pool volume (4119 ± 9 km^3) and the bottom footprint of the *summer 2007 sub-10 °C Cold Pool* map (Fig. 12). The error involved with the assumption stated above was small.

4.2. *Autumn 2007 Cold Pool: 10 °C isotherm*

We construct a map of the *autumn 2007 sub-10 °C Cold* map (Fig. 13) following the above approach with the September/October 2007 glider RU05 and RU06 transects (see Brown et al., 2015). Note that gliders RU05 and RU06 occupied the New Jersey transect - Leg-6 - within a week of each other and measured very similar 10 °C isotherm bottoming locations and T_{min}s. The footprint of the *autumn 2007* Cold Pool is clearly smaller, about 3 °C warmer and 0.1 psu saltier than the *summer 2007 CPW*. The *autumn 2007* Cold Pool does not go inshore, as much as its *summer* counterpart. However, it does indicate an off-shelf escape

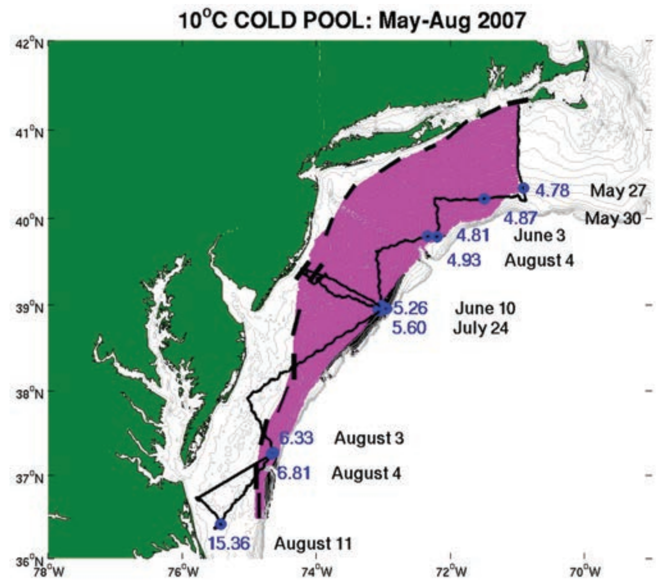

Fig. 12. The *summer* 2007, sub-10 °C Cold Pool Water (CPW) footprint (pink) is defined by *glider RU17/RU01* survey measurements. The section-minimum temperatures (blue o) – defining the Cold Pool core – are located. Estimated CPW Volume = 4119 ± 9 km^3.

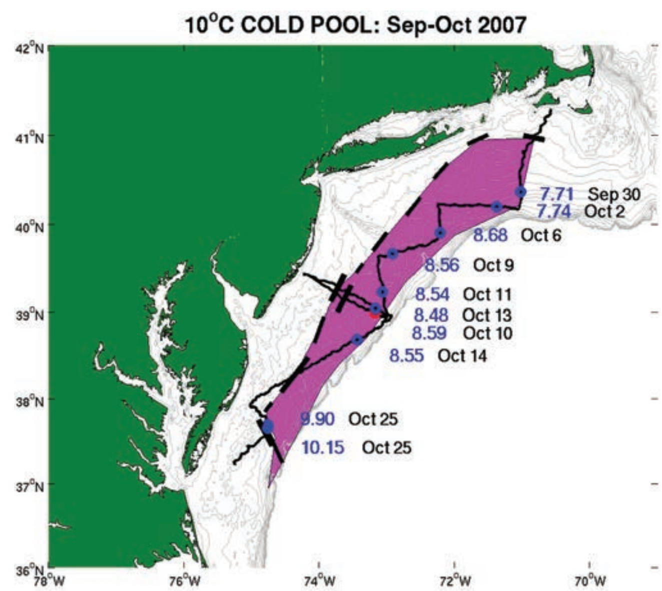

Fig. 13. The *autumn* 2007, sub-10 °C CPW footprint (pink) is defined by *glider RU05/RU06* survey measurements. The section-minimum temperatures (blue o) – defining the Cold Pool core – are located. Estimated CPW Volume = 2310 ± 45 km^3.

route offshore of the mouth of the Chesapeake Bay. We have assumed a uniform depth of 30 m for the thermocline, which contains the 10 °C isotherm and estimated the volume of the autumn 2007, sub-10 °C Cold Pool to be 2310 ± 45 km^3.

4.3. *September 2013 Cold Pool: 10 °C isotherm*

MARACOOS organized a 9-glider deployment consisting of glider operations all along the American coastal ocean between Nova Scotia and Florida – *GliderPalooza 2013*. We focus on a three-glider subset of missions in the Mid-Atlantic Bight (MAB) consisting of the almost simultaneous glider Blue, RU-23 and RU-22 missions (Fig. 14). The

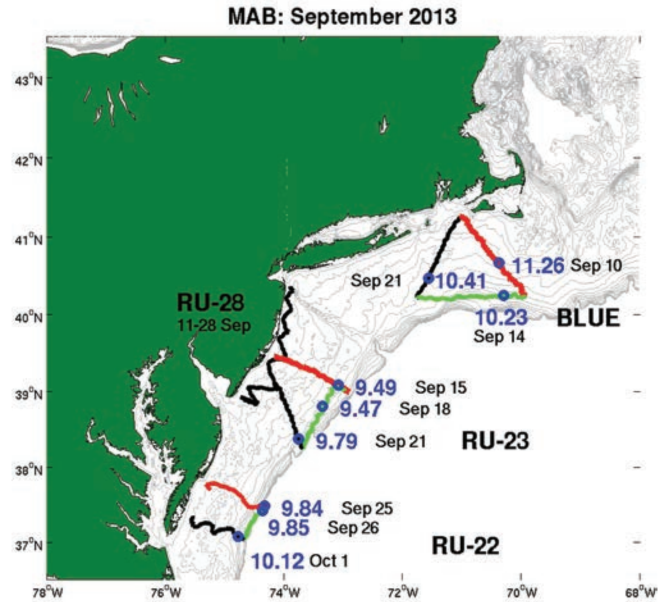

Fig. 14. The MAB trajectories of *gliders BLUE, RU-23, RU-22, and RU-28*. The glider Blue triangle in the Southern New England Bight consists of Legs-1 (red), -2 (green), and -3 (black); as was the *glider RU-23* trajectory off New Jersey (NJ); as was the *glider RU-22* trajectory east of Maryland (MD). The *glider RU-28* trajectory (blk), inside of the 30 m isobath, completed the triangle in the NJ region. The Leg-T_{min}/dates are indicated.

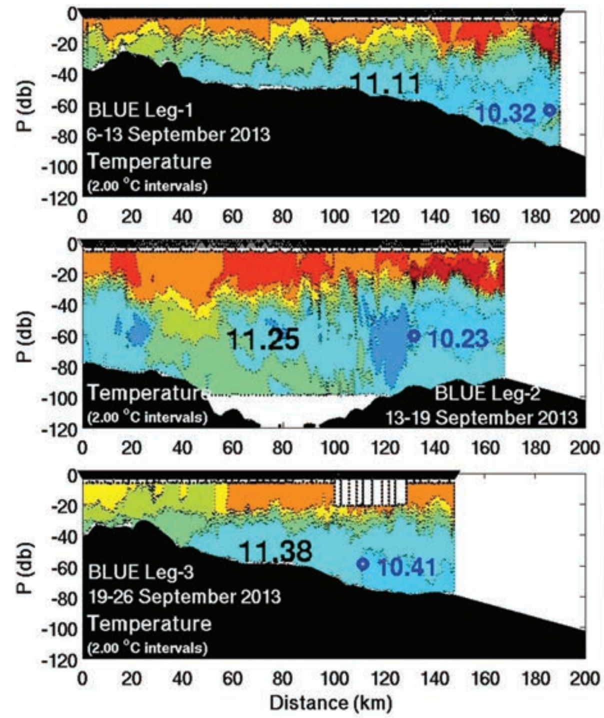

Fig. 15. Glider Blue's temperature (T°C) sections for *(upper)* Leg-1; *(middle)* Leg-2; and *(lower)* Leg-3 are presented. Section minimum temperatures T_{min} (blue) are located and the average lower-layer temperatures ≤12 °C (black) are indicated. The missing data in Leg-3's upper layer is because we restricted the glider's maximum depth to 17 db in the New York's east-west shipping lanes except for surfacing (lines).

September 2013 Cold Pool was warmer than the autumn 2007 Cold Pool.

Glider Blue's conducted its mission in the Southern New England Bight just south of Rhode Island (SNEB). The near-equilateral triangular trajectory sliced through the cold water (a redefined Cold Pool – see below) twice (Fig. 14). During glider Blue's east-west Leg-2 penetrated the shelf-break front (SBF) once. The middle panel of the three-leg display of glider Blue's contoured temperatures (Fig. 15) shows the measuring temperatures above 12 °C (green).

Almost simultaneously, glider RU23 penetrated beyond the SBF as it sliced through the Cold Pool twice (Fig. 15). This coldest patch of Cold Pool water in the New Jersey sector of the MAB. RU-28 patrolled the inner shelf in water depths less than 30 m along the NJ coast at the same time. These gliders also tested the hypothesis that triangular patterns are particularly effective for data-assimilation numerical modeling of MAB flow with a general 5 km/day southwestward flow.

A week or so later, glider RU22 was deployed at an inshore site off Maryland. RU22 sliced through the Cold Pool and SBF twice (with a non-triangular trajectory). Notice that the glider RU23 section minimum temperatures (Figs. 14 and 16) were clearly colder than those of either gliders Blue to the north and RU22 to the south.

The September 2013 glider Blue leg T_{min}s are greater than sub-10 °C (in the SNEB region of the MAB) were warmer than the 10 °C waters in September–October 2007. The gliders in the NJ and MD measured leg T_{min}s were sub-10 °C. So, the Sep.–Oct. 2013 sub-10 °C Cold Pool footprint (Fig. 17) is smaller than its autumn 2007 counterpart. The sub-10 °C CPW volume 1132 ± 47 km^3 is about half as much as the comparable Cold Pool volume in Sep.–Oct. 2007 (2310 ± 46 km^3).

We have concluded that the Cold Pool waters were being warmed by the cross-SBF mixing with the warmer/saltier waters of the Sep. 2013 Gulf Stream warm core ring (GS-WCR; Fig. 18). Gulf Stream water core rings influence the MAB in all seasons; systematically warming and salting Cold Pool properties.

The influence of the GS-WCR on the Cold Pool temperature prompted us to reconsider using a sub-10 °C definition for Cold Pool. Based on the observations described below, we expanded the "typical" Cold Pool

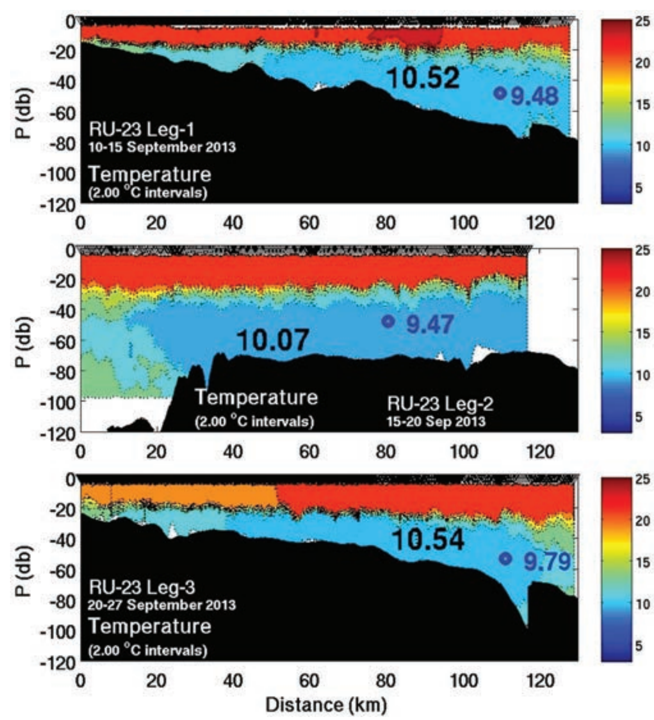

Fig. 16. Glider RU23's temperature (T°C) sections for *(upper)* Leg-1; *(middle)* Leg-2; and *(lower)* Leg-3 are presented. The blue lines at the ends of Legs1 & 2 mark "duplicate" sections. Section minimum temperatures T_{min} (blue) are located and the average lower-layer temperature T ≤ 12 °C (black) is indicated.

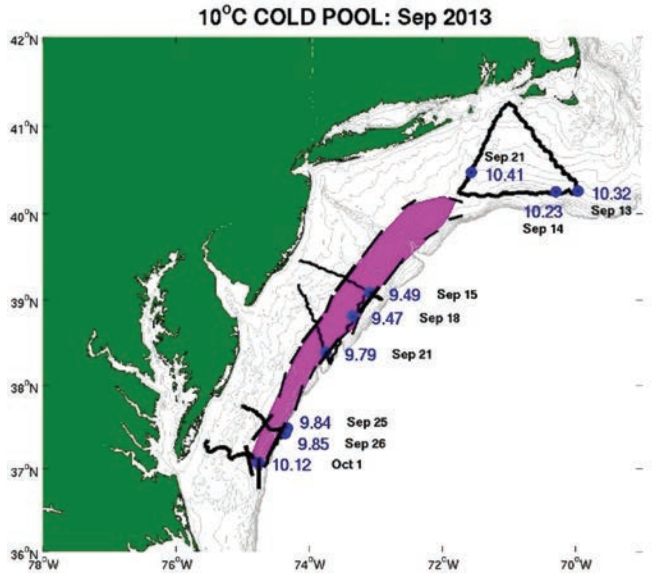

Fig. 17. The sub-10 °C MAB Cold Pool (pink) for September 2013 is defined by the trio of glider measurements: *glider Blue* in the northeast MAB, *glider RU23* in mid-shelf MAB and *glider RU22* in the southwest MAB. The section-minimum temperatures T_{min} (blue o) are located. *Estimated CPW Volume* = 1132 ± 47 km^3.

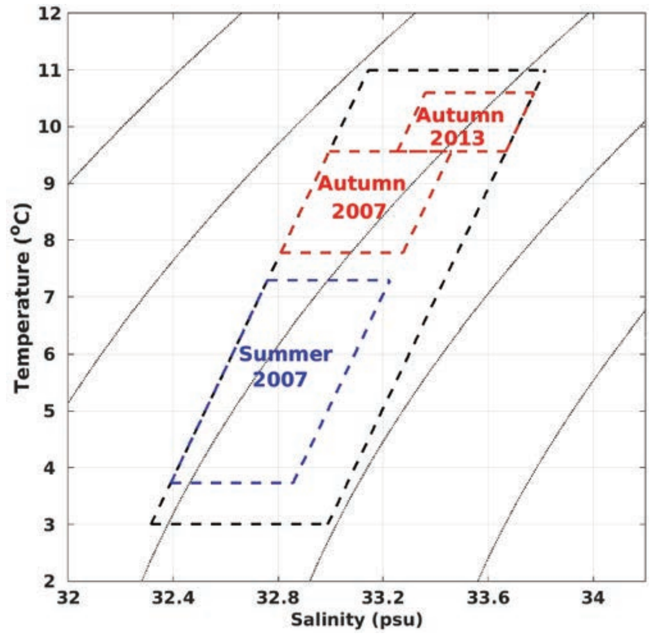

Fig. 19. The "global" definition of the Cold Pool water mass (blk dashed) includes seasonal sub-definitions: Spring/Summer 2007, Autumn 2007 and Autumn 2013.

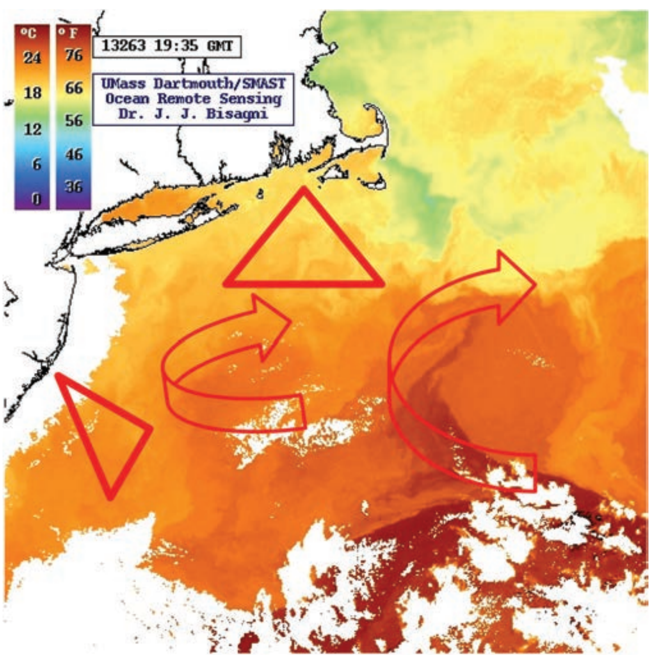

Fig. 18. A NOAA-18 AVHRR SST image of a warm ring and streamer that are influencing the MAB region on Sep. 20, 2013. The anti-cyclonic circulation around Gulf Stream warm core ring and streamer are indicated.

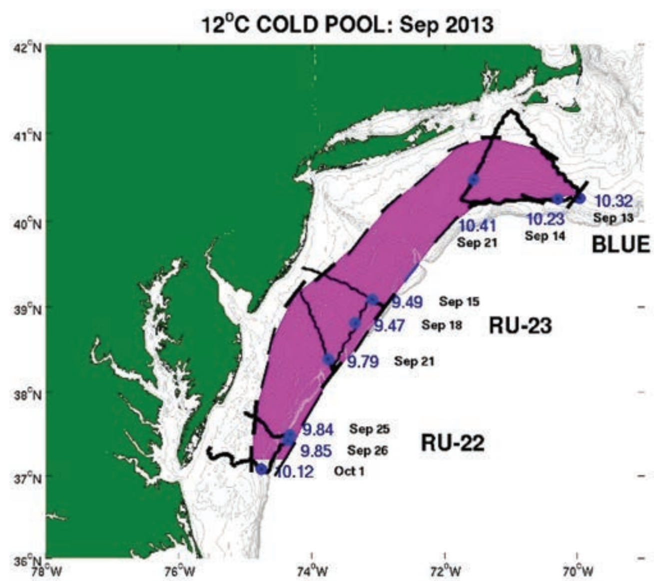

Fig. 20. The sub-12 °C MAB Cold Pool (pink) for September 2013 is defined by the trio of glider measurements: Blue (SNEB sector), RU23 (NJ sector) and RU22 (MD sector). The section-minimum temperatures T_{min} (blue o) are located.

water mass properties to higher salinities (Fig. 19). Rather we used a sub-12 °C definition for the CPW for the 2013 season. All MAB glider-derived temperature sections during Sep. 2013 displayed a distinctive sub-12 °C Cold Pool (Figs. 15 and 16). This sub-12 °C definition of CPW properties, allowed us to define the 2013 CPW mass shown in Fig. 20. The CPW "footprint" is shown in Fig. 20 is associated with an estimated the CPW mass volume to be 4109 ± 15 km^3.

Estimated CPW Volume = 4109 ± 15 km^3

The extent of the sub-12 °C CPW is shown in Fig. 20. Embolden short lines mark where the glider's measurements indicated the 12 °C isotherm intersected with bottom on the inshore end of the leg. The seaward end of the 12 °C isotherm is assumed to in the SBF, which is assumed to run along the 100 m isobath. The details for the SNEB (Blue), NJ (RU23) and MD (RU22) are presented next.

4.3.1. SNEB region

At the inshore end of glider Blue's Leg-1 temperature section (Fig. 15), the 12 °C isotherm intersects with the bottom near the 40 m isobath. Glider Blue measurements along Leg-2 indicate seaward end of the 12 °C isotherm extends 20–30 km beyond the shelf-break in the westward direction. At the Blue's Leg-2 near the western end, we see the Cold Pool water extension of Leg-3 and the signature (Fig. 15 -green) of the SBF at about 100 m isobath. Within the SBF, the 12 °C isotherm intersects with the bottom near the 85 m isobath. At the Leg-3 seaward end of glider Blue's Leg-2 section, the 12 °C isotherm intersects the bottom at 45 m.

4.3.2. NJ region

At the inshore end of Leg-1 temperature section (Fig. 16), the 12 °C isotherm intersects with the bottom near the 25 m isobath. Glider RU-23 did not go far enough to cross the SBF on Leg-1. Most of Leg-2 is less 80 m and the temperature data indicates the Cold Pool Water extends seaward. It is toward the southwestern end of Leg-2 that it deeper 80 m and the 12 °C isotherm in SBF intersects with the bottom near the 85 m isobath. At the seaward end of Leg-3, we also see the 12 °C isotherm in SBF intersects with the bottom near the 85 m isobath. At the inshore end of Leg-3 section, the 12 °C isotherm/bottom intersection occurs at a depth of about 30 m.

4.3.3. MD region

At the inshore ends of temperature sections of Leg-1 and Leg-3, the 12 °C isotherm with the bottom near the 35 m isobath (not shown). The seaward temperature data (not presented) is consistent with a at least part of the Cold Pool is leaving shelf here.

The September 2013 glider-measured water properties are consistent with our Cold Pool water mass definition. For both the SNEB and NJ regions, the T_{min} station T/S profiles intersect our Cold Pool water mass definition (Fig. 21). The SNEB/Blue region of the TS diagram suggests that the deepest Cold Pool waters mix with warm slope water (WSW). Also, the TS diagram information indicates that inshore water properties are strongly influenced by lateral mixing with Cold Pool waters (Fig. 21). These results suggest that a quantitative water mass analysis – beyond the scope of this effort – could lead to cross-SBF mixing rates.

5. Summary of results

A series of Slocum glider observation missions in 2007 and 2013 have been used to define the time-space variable Cold Pool between Cape Cod and Cape Hatteras. We describe the time-space evolution of the 2007 Cold Pool in terms of a spring/autumn series of *single glider* zig-zag missions with from northeast to southwest down the shelf. The Cold Pool was defined by the thermocline at the bottom of warm upper layer, which varied spatially from 25 to 45 m.We used the 2007 glider water property measurements to define sub-10 °C Cold Pool – an important, evolving habitat feature of the Mid-Atlantic Bight (MAB). Based on the 2007 glider measurements, we found that a trapezoidal T–S definition of Cold Pool Water, highlighted by an increased about 1 °C warming/mon. and 0.11 psu salting/month after June (Fig. 11). This all happened to Cold Pool, while the MAB water were flowing southwestward at an average velocity of 5 km/day.

The 2007 glider measurements show that the core of the Cold Pool (defined by the transect minimum temperatures – T_{min}) hugs the outer shelf in the vicinity of the well-known Shelf-Break Front (SBF; Figs. 8 and 9). The Cold Pool salts due to exchanges with Slope Sea waters as the Cold Pool waters flow from northeast to southwest along the MAB. The vertical mixing caused by autumn storms gradually erase the temperature distinctiveness of the Cold Pool. The vertical mixing late November–early December 2007 produce the vertically well mixed temperature profiles in Fig. 7. The intense winter cooling is hinted at in the inshore profiles of Leg-6 of Fig. 7.

Our early summer 2007 mapping, based on only two zigzag glider measurements of a *sub-10 °C waters,* ranging from full shelf-width CPW in the SNEB region to a very narrow strip southwestward in locations off Maryland (Fig. 12). We estimated the summer 2007 Cold Pool volume to be 4119 ± 9 km^3. The warming of CPWs in the MAB continued throughout summer leading to a decrease in CPW volume. This reduced autumn 2007 estimated volume of 2310 ± 46 km^3 (Fig. 13). This loss of sub-10 °C CPW volume is associated with increased salinity (Table 1) and is consistent with the southwestward average flow 5 km per day.

During September–October 2013, we have also explored the Mid-Atlantic Cold Pool with the contemporaneous *trio of glider* missions highlighted in Fig. 14. With that set of nearly simultaneous glider measurements, we showed that the *September 2013* Cold Pool in the NJ region was colder than in 2007 than the rest of 2013 Cold Pool.

We also showed that the SNEB region the *2013 Cold Pool* was warmer than the 2007 Cold Pool in this region. That warming of the SNEB region of the Cold Pool was probably due to the influence of a nearby Gulf Stream Warm Core Ring (Fig. 18). This led us to widen of the trapezoidal T–S definition of Cold Pool Water properties -salinity in particular (Fig. 19). We changed from the sub-10 °C cold Pool definition to a 12 °C definition for the 2013 Cold Pool. This resulted in a *sub-12°C* 2013 Cold Pool has an estimated volume of 4109 ± 15 km^3 (Fig. 20).

The September/October 2013 glider measurements (as well as in October 2007) document the autumn Cold Pool 2013, during which the Cold Pool loses its distinctiveness due to storm mixing. [Of course, the SNEB region 2013 Cold Pool water properties are consistent with our redefined trapezoid of Cold Pool water properties (Fig. 21)]. All three sub-regions – SNEB, NJ and MD – exhibited inshore water properties that reflected mixtures with the local Cold Pool waters. The T_{min} T–S relationships indicated deeper water properties that hinted at slope water influence. The possibility CPW origins of "upstream" from the Gulf of Maine is explored in Appendix B. The inter-annual variability of Cold Pool Waters was explored through glider measurements of autumn

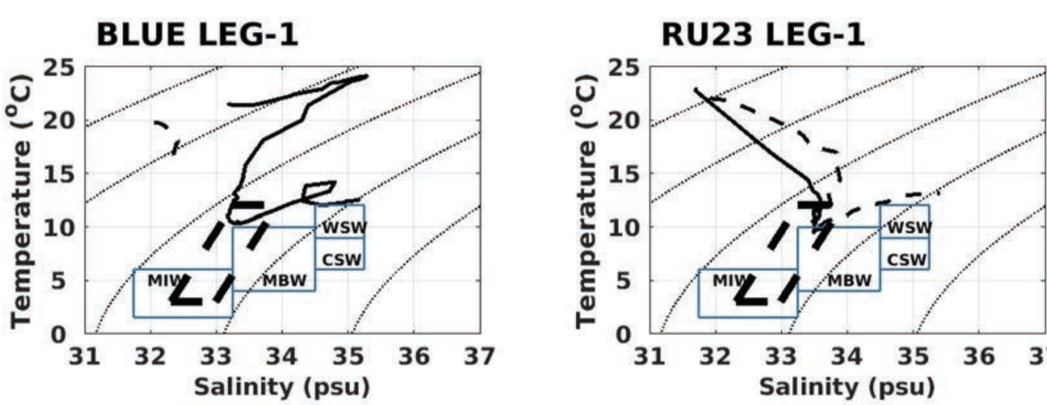

Fig. 21. The (left) SNEB region glider Blue Leg-1 and (right) NJ region glider RU23 Leg-1 T–S relations for the T_{min} station (solid) and most shoreward station (dashed) for the September 2013 measurements. The global Cold Pool water mass is defined by the dashed trapezoid. The rectangular boxes define the Brown and Irish (1993) Gulf of Maine water masses – MIW and MBW and the warm (WSW) and cold slope water (CSW).

2013. The nearly simultaneous 2013 trio of glider measurements (Fig. 14) were used to show how the 2013 MAB Cold Pool Waters in the northeastern sector were warmed and salted by the impingement of a Gulf Stream Warm Core Ring. However, these results suggest that a quantitative water mass analysis – beyond the scope of this effort – could lead to cross shelfbreak front mixing rates.

Declaration of competing interest

The authors declare that they have no known competing financial interests or personal relationships that could have appeared to influence the work reported in this paper.

Data availability

Data will be made available on request.

Acknowledgments

This research has benefitted from the assistance provided by Richard Arena. The contributions to this paper made James Bisagni is acknowledged. The research has been supported in part through a NOAA grant NA07NOS4730221for the implementation of the Mid Atlantic Regional Association Coastal Ocean Observing System (MARACOOS).

Appendix A. Covert Practical Salinity to Absolute Salinity (S_A)

We expressed salinities in this paper as PSS-78 Practical Salinities (S_P); with units as psu). Pawlowicz (2013) maintains that "However, for all purposes S_A (Absolute Salinity) according to the TEOS-10 definition is required". Determining S_A from S_P requires the following.

(1) For waters in the "Neptuian" range (i.e., $2 < S_P < 42$; $-2\ ^\circ C <$ ITS-10 temperature $<35\ ^\circ C$), a Reference Salinity S_R on the Reference Composition Salinity Scale (Millero et al., 2008) be estimated as

$$S_R \Big/ \left(\mathrm{g\ kg^{-1}}\right) = \frac{35.16504}{35} \times S_P$$

The Reference Salinity is the mass fraction of solute in an artificial seawater with a precisely defined Reference Composition.

(2) "Because the composition of seawater is not exactly constant, this Reference Salinity is not exactly as the same as the actual Absolute Salinity. Instead, they differ by a small correction factor δS_A:

$$S_A = S_R + \delta S_{A.}$$

This correction factor is usually, but always positive." It can be large as 0.02 g/kg in the open ocean, and as 0.09 g/kg in some coastal areas. Pawlowicz (2013) recommends estimate $\delta S_A = 0$ for coastal regimes such as we have here and states in ignoring this correction is roughly equivalent to using the PSS78/EOS80 approach.

Appendix B. Cold Pool Water Origins

We have used the New England Shelf Flux Experiment (NSFE) data (Ramp et al., 1988) to characterize the inflow variability to the Mid Atlantic Bight (MAB) Cold Pool through a section south of Nantucket during spring/summer 1979. The multi-mooring array configuration is shown Fig. B1. The variability of the westward transport of waters of less than 10 °C through the NSFE (N1–N4) section in Fig. B2 shows that the sub-10 °C water inflow ceased by the end of June 1979.

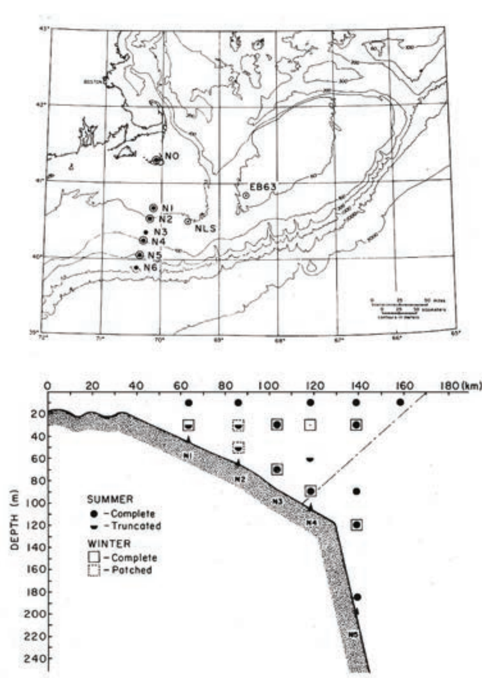

Fig. B1. *(upper)* A map the NSFE mooring array: N1 (depth = *46m*), N2 (*66m*), N3 (*88m*), N4 (*105m*), N5 (*196m*) and N6 (*250m*). *(lower)* The temperature and current measurements making up the year long NSFE. The focus of our interest in the "summer" measurements. (from Ramp et al., 1988).

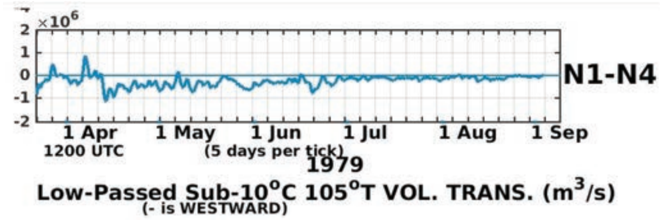

Fig. B2. The major portion of the volume transport of sub-10 °C waters (in 10^6 m^3/s) (spans moorings N1 and N4) normal (105°T) to the 1979 NSFE mooring array. Negative transport is toward the MAB (185°T).

This typical April–June process leaves a distinctive pocket of very cold water that is advected west and southwestward along the MAB. This cold water pocket feeds the evolving Cold Pool, which warms from July onward … as described above in the main text.

What is the origins of the springtime cold water inflow to the MAB Cold Pool? One possibility is that Gulf of Maine Intermediate Water (MIW) escape to feed the MAB Cold Pool. Another possibility is that the Cold Water derives from the Scotian Shelf via the south flank of Georges Bank. We explore both of those possibilities below.

This study tracks MIW outflow from Wilkinson Basin through the set of hydrographic transects (henceforth RIM) from the Gulf of Maine 1986–87 Experiment (Fig. B3 – Brown and Irish, 1993). In particular, note the similar-looking T–S diagrams of the T_{min} stations in each of the transects. The corresponding T–S diagram is shown in Fig. B4. It indicates the presence of Maine Bottom Water (MBW), which Brown and Irish (1993) and others have shown is a mixture between Maine Intermediate Water (MIW characterized by T_{min}) and Slope Water after its entry into the Gulf of Maine (GoM) through the Northeast Channel (NEC). From this evidence, we conclude that significant amounts of MIW, which we know is produced in Wilkinson Basin in the western GoM, is flowing out of the Gulf at a depth in and around 100 m - below the minimum depth of the sill in the great South Channel.

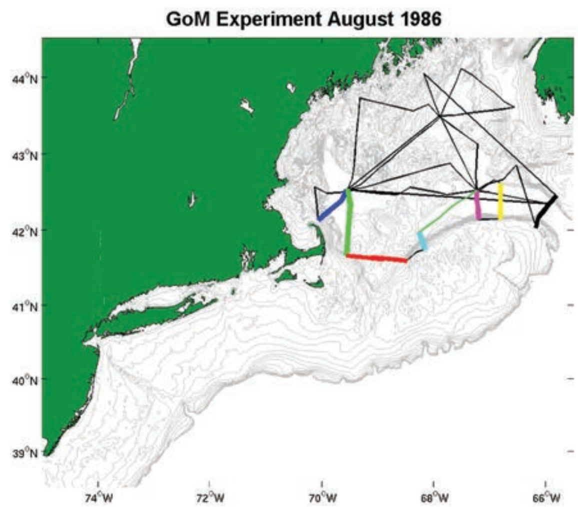

Fig. B3. Composite of the August 1986 Hydrographic Survey Color-Coded RIM Transects: Leg-6a (blue), Leg-1b (green), Leg-7 (red), Leg-7a (cyan/green), Leg-4a (maroon), Leg-3 (yellow), and Leg-5 (black).

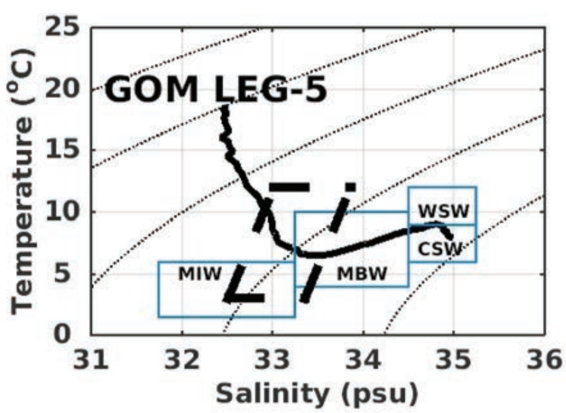

Fig. B4. The T–S diagram for the T_{min} station of the Aug 1986 RIM transect 5 (in Fig. B-3 – black). The global Cold Pool water mass properties is defined (dashed trapezoid). The rectangular boxes define the Brown and Irish (1993) Gulf of Maine water masses – MIW and MBW and the warm (WSW) and cold slope water (CSW).

References

Bassett, R., Beard, R., Burnett, W., Crout, R., Griffith, B., Jensen, R., Signell, R., 2010. Implementing the national Integrated Ocean Observing System (IOOS): from the federal agency perspective. Mar. Technol. Soc. J. 44 (6), 32–41.

Beardsley, R.C., Boicourt, W.C., 1981. On estuarine and continental-shelf circulation in the Middle Atlantic Bight. In: Warren, B.A., Wunsch, C. (Eds.), Evolution of Physical Oceanography. The MIT Press, Cambridge, MA, pp. 198–233.

Beardsley, R.C., Boicourt, W.C., Hansen, D.V., 1976. Physical oceanography of the middle atlantic Bight. The middle atlantic continental Shelf and New York Bight, november 3-5, 1975, New York, N.Y. American society of limnology and oceanography. Special Symposium Series 2, 20–34.

Boicourt, W.C., Hacker, P.W., 1976. Circulation on the atlantic continental shelf of the United States, Cape may to Cape Hatteras. In: Nihoul, J.C.J. (Ed.), Memoires de la Societe Royale des Sciences de Liege. Univ. of Liege, Liege, Belgium, pp. 187–200.

Brown, W.S., Irish, J.D., 1993. The annual variation of water mass structure in the Gulf of Maine. J. Mar. Res. 51, 53–107.

Brown, W.S., Schofield, O., Glenn, S., Kohut, J., Boicourt, W., 2015. The Evolution of the Mid-Atlantic Bight Cold Pool Based on Ocean Glider Observations. SMAST Technical Report 15-03-01, p.35. http://www.smast.umassd.edu/OCEANOL/reports.php.

Chen, K., Gawarkiewicz, G.G., Lentz, S.J., Bane, J., 2014. Diagnosing the warming of the Northeastern U.S. Coastal Ocean in 2012: a linkage between the atmospheric jet stream variability and ocean response. J. Geophys. Res. 119 (1), 218–222. https://doi.org/10.1002/2013JC009393.2014.

Flagg, C.N., Wirick, C.D., Smith, S.L., 1994. The interaction of phytoplankton, zooplankton and currents from 15 months of continuous data in the Mid-Atlantic Bight. Deep Sea Res. 41, 411–436.

Gawarkiweiz, G., Todd, R.E., Zhang, W., Partida, J., Gangopadhyay, A., Monim, M., Fratantoni, P., Mercer, A.M., Dent, M., 2018. The changing nature of shelf-break exchange revealed by the OOI pioneer. Array 31 (1), 60–70.

Hopkins, T.S., Garfield III, N., 1979. Gulf of Maine intermediate water. J. Mar. Res. 37, 103–139.

Houghton, R., Schlitz, R., Beardsley, R.C., Butman, B., Chamberlin, J.L., 1982. The Middle Atlantic Bight cold pool: evolution of the temperature structure during summer 1979. J. Phys. Oceanogr. 12, 1019–1029.

Ketchum, B.H., Corwin, N., 1964. The persistence of winter water on the continental shelf south of Long Island, New York. Limnol. Oceangr. 9, 467–475.

Kohut, J.T., Glenn, S.M., Chant, R.J., 2004. Seasonal current variability on the New Jersey inner shelf. J. Geophys. Res. 109, C07S07. https://doi.org/10.1029/2003JC001963.

Lentz, S.J., 2003. A climatology of salty intrusions over the continental shelf from Georges Bank to Cape Hatteras. J. Geophys. Res. 108 (C10), 3326. https://doi.org/10.1029/2003JC001859, 2003.

Lentz, S.J., Shearman, R.K., Plueddemann, A.J., 2010. Heat and salt balances over the New England continental shelf, August 1996 to June 1997. J. Geophys. Res. 115 (C7) https://doi.org/10.1029/2009JC006073, 2010.

Lentz, S.J., 2017. Seasonal warming of the middle atlantic Bight cold pool. J. Geophys. Res. Oceans 122, 941–954. https://doi.org/10.1002/2016JC012201.

Linder, C.A., Gawarkiewicz, G.G., Pickart, R.S., 2004. Seasonal characteristics of bottom boundary layer detachment at the shelfbreak front in the Middle Atlantic Bight. J. Geophys. Res. 109, C03049 https://doi.org/10.1029/2003JC002032.

Malone, T.C., Hopkins, T.S., Falkowski, P.G., Whitledge, T.E., 1983. Production and transport of phytoplankton biomass over the continental shelf of the New York Bight. Continent. Shelf Res. 1, 305–337.

Ou, H.W., Houghton, R., 1982. A model of the summer progression of the cold-pool temperature in the Middle Atlantic Bight. J. Phys. Oceanogr. 12, 1030–1036.

Pawlowicz, R., 2013. What Every Oceanographer Needs to Know about TEOS-10 (The TEOS-10 Primer). http://www.teos-10.org/pubs/TEOS-10_Primer.pdf.

Ramp, S.R., Brown, W.S., Beardsley, R.C., 1988. The Nantucket shoals flux experiment (NSFE79). Part 3: the alongshelf transport of volume, heat, salt and nitrogen. J. Geophys. Res. 93 (C11), 14039–14054.

Schofield, O., Kohut, J., Glenn, S., Morell, J., Capella, J., Corredor, J., Orcutt, J., Arrott, M., Krueger, I., Meisinger, M., Peach, C., Vernon, F., Chave, A., Chao, Y., Chien, S., Thompson, D., Brown, W., Oliver, M., Boicourt, W., 2010. A regional Slocum glider network in the Mid-Atlantic coastal waters leverages broad community engagement. Mar. Tech. Soc. 44 (6), 64–74.

Sullivan, M.C., Cowen, R.K., Steves, B.P., 2005. Evidence for atmosphere-ocean forcing of yellowtail flounder (*Limanda ferruginea*) recruitment in the Middle Atlantic Bight. Fish. Oceanogr. 14, 386–399.

Weinberg, J.R., 2005. Bathymetric shift in the distribution of Atlantic surf clams: response to warmer ocean temperature. ICES J. Mar. Sci. 62, 1444–1453.

An examination of salinity effect on Hurricane Sally (2020)

1st Senam Tsei
School of Ocean Science and Engineering
The University of Southern Mississippi
Stennis Space Center, MS
senam.tsei@usm.edu

2nd Stephan Howden
School of Ocean Science and Engineering
The University of Southern Mississippi
Stennis Space Center, MS
Stephan.Howden@usm.edu

3rd Arne Diercks
School of Ocean Science and Engineering
The University of Southern Mississippi
Stennis Space Center, MS
arne.diercks@usm.edu

4th Jun Zhang
NOAA/AOML/Hurricane Research Division with University of Miami/CIMAS
jun.zhang@noaa.gov

5th Travis Miles
School of Environmental and Biological Sciences
Rutgers University
New Jersey, USA
tnmiles@marine.rutgers.edu

6th Kevin Martin
School of Ocean Science and Engineering
The University of Southern Mississippi
Stennis Space Center, MS
kevin.m.martin@usm.edu

***Abstract*— On September the 15th of 2020, Hurricane Sally traveled within 35 km from the location of NOAA NDBC Sea-glider (SG) 601 situated south of De Soto canyon. In this study, upper ocean observations from SG601 were compared to Hybrid Coordinated Ocean Model (HYCOM) and Navy Coastal Ocean Model for American Seas (NCOM-AmSeas or NCOM), coupled atmospheric-ocean models mainly used in hurricane science. Results from this study show that water temperatures, from the HYCOM simulations, were >29°C in the upper 30m and differ from SG observations by a 1°C. On HYCOM modelled upper ocean salinity, the differences (2-3PSU) are noticeable on two days (09/15 and 09/16). NCOM simulations, on the other hand, show a difference of 0.5-1°C (1.5-2PSU) in upper ~30 m water temperatures (salinity) of 09/15. Furthermore, when a 1D PWP model was initialized with a temperature and salinity profile with a barrier layer (barrier layer removed) to evaluate the influence of barrier layer on Hurricane Sally (HS), a 0.1-0.15°C (0.15°C-0.20°C) cooling of the mixed layer was noticed on 09/15.**

Keywords—upper ocean water temperature and salinity; salinity stratification; barrier layer

I. Introduction

In 2020, the poorly predicted, both in intensity and track, Hurricane Sally (HS), produced hurricane force winds along the coasts of Mississippi, Alabama, and western Florida. On 09/15, HS began a rapid intensification with an increase in intensity from 80 mph at 1800 UTC to 109 mph by the morning of the following day [1]. A NOAA report on HS [1], indicated that the upper-level atmospheric divergence increased by twofold on 09/15, which led to the observed intensification despite the deep layer vertical shear in the atmosphere near HS [1]. Between 0500-0600 UTC of 09/16, HS began moving onshore and affected Baldwin County (Alabama) within the next 3hours. HS made landfall at 09:45 UTC at Gulf Shores, Alabama with maximum sustained winds of ~110 mph.

Understanding the ocean environment and the complex two-way responses, between the ocean and atmosphere, that favor rapid intensification is critical to providing more accurate hurricane forecasts to the gulf coast communities. The path of HS, fortuitously, came across that of NOAA NDBC Sea glider, SG601. SG 601 provides an observational perspective of the upper ocean under HS low pressure system. Hence, inthis study, we compared the SG601 observations to numerical experiments (NCOM-AmSeas or NCOM, Navy Coastal Ocean Model; HYCOM, Hybrid Coordinated Ocean Model) and analyzed the extent to which the observed salinity stratification potentially suppressed surface ocean cooling and promoted the observed intensification of HS on late 09/15/2020.

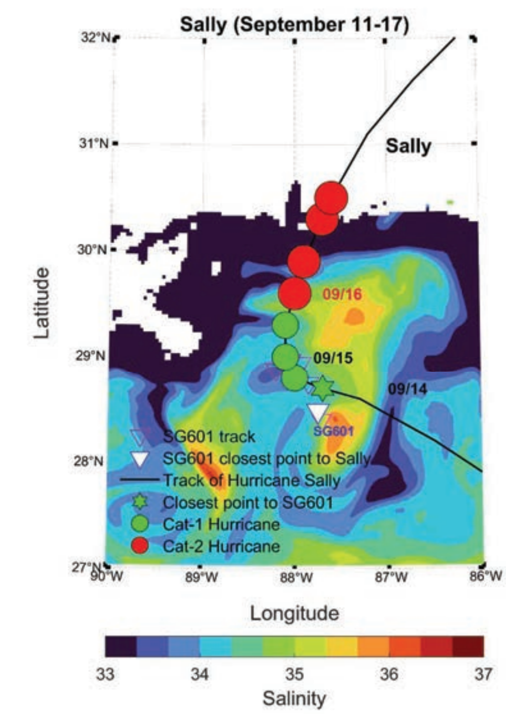

Figure 1: describing the study area, dominated by fresh sea surface salinity (underlying colormap) from NCOM-AmSeas (or NCOM) experiments. The circles, green and red, represent respectively, the intensities and position of HS. Figure 1 also describes the track of HS (black track plot), downward pointing (white) triangle and the track of SG601 (downward pointing, magenta, triangle). Furthermore, figure 1 shows where SG 601 was closest to HS track.

II. Data and Methods

The Hybrid Coordinated Ocean Model (HYCOM) for the Gulf of Mexico (GoM), is a 1/25° regional model and discussed extensively in [2]. Hence in this study, a short description is provided. HYCOM is a nested grid modelling system, with a fine resolution of inner model embedded inside the coarser outer model [2]. HYCOM extends northward from 18.1˚ and westward from -77.4˚. The inner model's resolution is twice the outer (1/12˚). HYCOM has 20 hybrid layers vertically. Many studies have used HYCOM analyses to examine the upper ocean response to tropical cyclones and hurricanes in the Gulf of Mexico [2]–[5].

NCOM-AmSeas (or NCOM) is the Navy Coastal Ocean Model for the Gulf of Mexico and Caribbean Sea, which is operated by the Fleet Numerical Meteorology and Oceanography Center (FNMOC). NCOM-AmSeas has a ~3km horizontal resolution. Information on this product is available at https://www.ncei.noaa.gov/products/weather-climate-models/fnmoc-regional-navy-coastal-ocean. NCOM uses NCODA (Navy Coupled Data Assimilation) to assimilate quality controlled ocean observations from the GoM, including glider datasets, satellite derived temperature and heights of the sea surface [6], [7]. NCOM together with HYCOM were compared to SG601 data to evaluate the performance of these coupled atmosphere-ocean models in modelling the upper ocean.

Upper ocean surveys ahead of HS were conducted using NOAA sea glider, SG601. SG601 is a buoyancy driven autonomous underwater vehicle. SG601 profiles the ocean vertically down to 1000m. Glider observations presented here were extracted from the Integrated Ocean Observing System (IOOS) Glider Assembly Center (GDAC). Moreover, SG601 observations from the IOOS-GDAC were quality controlled [8] to the best international practices. To examine the extent to which the observed salinity stratification suppressed sea surface cooling during HS, two experiments (one with a barrier layer and other without a barrier layer) were conducted utilizing a 1D ocean mixing model, Price-Weller-Pinkel one-dimensional model, [9]. [10], [11] have used the PWP 1D model in studying ocean mixing during a hurricane. PWP includes shear driven mixing and buoyancy forcing processes [9]. PWP 1D uses three stability criteria (static instability, bulk, and gradient Richardson number) to account for vertical mixing. The bulk and gradient Richardson number were set to 0.65 and 0.25, respectively, to stability criteria. The 1D model was further forced with wind and surface heat fluxes from the North American Mesoscale Forecast System analysis. Moreover, the temperature and salinity profile close to the track of HS were used in the 1D model. This initial profile was evaluated for the presence of a barrier layer. The barrier layer was calculated using the methods of [12], [13] using
$\Delta\sigma\theta = \sigma\theta\,(T_o - \Delta T, S_o) - \sigma\theta\,(T_o, S_o)$, where To and So are, respectively, the 2m temperature and salinity. ΔT is 0.8°C as in [13].

III. Results and Analyses

HYCOM and SG601 water temperature and salinity sections (figure 2) depict contrary descriptions of the upper ocean. On 09/14, in the upper 30m, the HYCOM simulations of the water temperature appear analogous to that of SG601. However, the variations began at the later hours of 09/14. These observed variations continued into the hours of 09/15. Figure 2 (upper middle panel), SG601, shows water temperatures were >29°C in the upper 30m and differ from the HYCOM simulations (upper right panel) by 1°C. Observations from SG601 indicates that water temperatures stayed above 26°C, even after the passage of HS on the 09/15. About the upper ocean salinity, there is a striking divergence in the upper ocean salinity between SG601 and HYCOM. Figure 2 (lower panel) describes that the salinity values of the upper 30m in HYCOM range from 35.5-36PSU while SG601 indicates 34-36PSU at the same depth range. Evident in figure 2 (lower right panel) are the differences in salinity between HYCOM and SG601. Figure 2 (lower right panel) shows that these differences are noticeable on two days (09/15 and 09/16). Above all, the variations in the upper ocean sallinit appear reaching ~60 m depth.

The NCOM-AmSeas (or NCOM) simulations, left upper panel (figure 3), depict temperatures of 29°C in the upper ~30 m from 09/14 to 09/16 while water temperatures in depths >40m appear like those of SG601. The difference in water temperatures between NCOM simulations and that of SG601 (right upper panel, figure 3) shows a range of 0.5-1°C in the upper ~30 m on 09/15. These differences suggest that NCOM simulations of upper ocean water temperatures appear more comparable to the observations (SG601) than HYCOM. The lower panel of figure 3 shows the water salinities (34-35.5PSU). Salinities in NCOM simulations appear fresher in the upper ~30m than what is observed in SG601. Moreover, the observed low salinities (center lower panel, figure 3), SG601, appear shallower than what is modelled in NCOM. This difference raised the question on how riverine inputs are assimilated into both HYCOM and NCOM. According to [14], HYCOM riverine inputs are inter-annual flows, while in the case of NCOM, rivers inflows are based on monthly means because real time river discharges are difficult to obtain in the time frame needed for operational modelling [15]. Furthermore, using a monthly mean river discharge has improved upon simulations in global NCOM [15]. Despite the differences between NCOM and HYCOM, both stimulations point to a salinity stratified upper ocean.

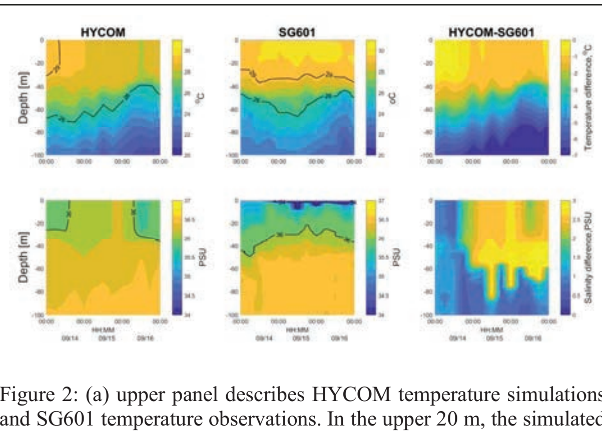

Figure 2: (a) upper panel describes HYCOM temperature simulations and SG601 temperature observations. In the upper 20 m, the simulated temperatures appear analogous to the observations of SG601 on 09/14. However, on the 09/15, temperature simulations in the upper 30m drift away from SG601's temperatures; and these differences (1°C) are evident in the right upper panel. Furthermore, the differences between HYCOM and SG601 indicate that the modelled temperatures at depths >40m are close to the observed temperatures. (b) lower panel describes the HYCOM simulations of salinity. The lower panel describes a noticeable divergence in upper ocean salinity. The HYCOM modelled salinity ranges from 35.5PSU to 36PSU while SG601 indicates salinity range of 34-36PSU in the upper 30m.

The question therefore is whether this physical feature (salinity stratification or barrier layer) potentially influenced HS.

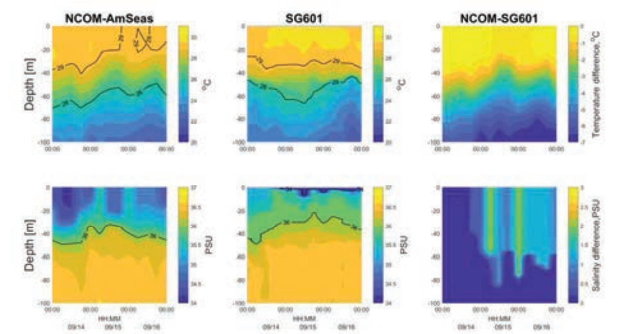

Figure 3: (a) upper panel describes NCOM-AmSeas (or NCOM) temperature simulations depict a 29°C in the upper ~30 m from 09/14 to 09/16 while water temperatures in depths >40m appear alike to that of SG601. The difference in water temperatures, between NCOM simulations and that of SG601, shows a 0.5-1°C temperature difference in upper ~30 m of 09/15. (b) lower panel describes the NCOM simulations of upper ocean salinity. The NCOM modelled salinity ranges from 34PSU to 35.5PSU while SG601 indicates salinity range of 34-36PSU in the upper 30m.

Figure 4 illustrates two experiments in the 1D PWP model, used to analyze the potential effect of the barrier layer on HS intensification. The first experiment (upper panel) describes the upper ocean response to HS when a barrier layer is present. In this experiment, the barrier layer is responsible for 0.1-0.15°C cooling of the mixed layer while the second experiment (lower panel), without a barrier layer, shows that the mixed layer cooled from 0.15°C to 0.20°C on 09/15. The reduced cooling exhibited in the first experiment attests to the hypothesis that salinity stratification (or barrier layer) inhibits cooling of the upper ocean [10], [11], [16], [17]. Although the modelled 1D PWP cooling, in this study, is small (0.05°C) compared to 0.3°C and 0.4-0.8°C of previous studies [11], [17] respectively, the potential impact of salinity stratification on HS was apparent. Above all, the low cooling is also connected to the low intensity (higher Category 1) of HS [10] on the 09/15.

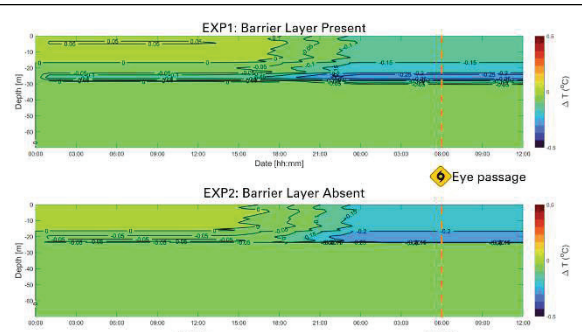

Figure 4: (a) the upper panel describes an experiment in PWP with temperature and salinity profile (with a barrier layer). In this experiment, the barrier layer is responsible for 0.1-0.15°C cooling of the mixed layer on 09/15. (b) the lower panel, on the other hand, describes an experiment in PWP with temperature and salinity profile (without a barrier layer, or barrier layer removed). In this experiment the mixed layer cooled from -0.15°C to -0.20°C.

IV. Conclusion

This study highlights the influence of the river discharge in modulating hurricane driven SST cooling in our region of interest. Although the HYCOM simulation showed striking differences between the observed and the modelled upper ocean salinity, both NCOM and HYCOM demonstrate the influence of freshwater on upper ocean stratification. In this study, using a 1D PWP model, the salinity stratification has been demonstrated to affect SST development, which in turn has an influence on tropical storm intensity. This finding agrees with previous studies that had used the same 1D PWP to study barrier layers and their influences on tropical cyclones and provides further evidence of the importance of fluvial inputs for tropical cyclone intensification in the northern Gulf of Mexico.

Acknowledgment

This study sincerely appreciates Shell corporation and NOAA NDBC for, respectively, funding and providing the observational platform, SG601, the sole observing platform in the study area during Hurricane Sally.

References

[1] B. W. Klotz and D. S. Nolan, “SFMR Surface Wind Undersampling over the Tropical Cyclone Life Cycle,” *Mon. Weather Rev.*, vol. 147, no. 1, pp. 247–268, Jan. 2019, doi: 10.1175/MWR-D-18-0296.1.

[2] T. G. Prasad and P. J. Hogan, “Upper-ocean response to Hurricane Ivan in a 1/25° nested Gulf of Mexico HYCOM,” *J. Geophys. Res.*, vol. 112, no. C4, p. C04013, Apr. 2007, doi: 10.1029/2006JC003695.

[3] E. J. Metzger *et al.*, “US Navy Operational Global Ocean and Arctic Ice Prediction Systems,” *Oceanography*, vol. 27, no. 3, pp. 32–43, Sep. 2014, doi: 10.5670/oceanog.2014.66.

[4] M. M. Gierach, B. Subrahmanyam, and P. G. Thoppil, “Physical and biological responses to Hurricane Katrina (2005) in a 1/25° nested Gulf of Mexico HYCOM,” *J. Mar. Syst.*, vol. 78, no. 1, pp. 168–179, Aug. 2009, doi: 10.1016/j.jmarsys.2009.05.002.

[5] M. M. Gierach and B. Subrahmanyam, “Biophysical responses of the upper ocean to major Gulf of Mexico hurricanes in 2005,” *J. Geophys. Res.*, vol. 113, no. C4, p. C04029, Apr. 2008, doi: 10.1029/2007JC004419.

[6] C. N. Barron, L. F. Smedstad, J. M. Dastugue, and O. M. Smedstad, “Evaluation of ocean models using observed and simulated drifter trajectories: Impact of sea surface height on synthetic profiles for data assimilation,” *J. Geophys. Res.*, vol. 112, no. C7, p. C07019, Jul. 2007, doi: 10.1029/2006JC003982.

[7] A. B. Kara, C. N. Barron, P. J. Martin, L. F. Smedstad, and R. C. Rhodes, “Validation of interannual simulations from the 1/8° global Navy Coastal Ocean Model (NCOM),” *Ocean Model.*, vol. 11, no. 3–4, pp. 376–398, Jan. 2006, doi: 10.1016/j.ocemod.2005.01.003.

[8] M. Bushnell *et al.*, “Quality Assurance of Oceanographic Observations: Standards and Guidance Adopted by an International Partnership,” *Front. Mar. Sci.*, vol. 6, p. 706, Nov. 2019, doi: 10.3389/fmars.2019.00706.

[9] J. F. Price, R. A. Weller, and R. Pinkel, “Diurnal cycling: Observations and models of the upper ocean

response to diurnal heating, cooling, and wind mixing," *J. Geophys. Res.*, vol. 91, no. C7, p. 8411, 1986, doi: 10.1029/JC091iC07p08411.
[10] Y. Yan, L. Li, and C. Wang, "The effects of oceanic barrier layer on the upper ocean response to tropical cyclones: EFFECTS OF THE BARRIER LAYER ON TCs," *J. Geophys. Res. Oceans*, vol. 122, no. 6, pp. 4829–4844, Jun. 2017, doi: 10.1002/2017JC012694.
[11] J. E. Rudzin, L. K. Shay, and W. E. Johns, "The Influence of the Barrier Layer on SST Response during Tropical Cyclone Wind Forcing Using Idealized Experiments," *J. Phys. Oceanogr.*, vol. 48, no. 7, pp. 1471–1478, Jul. 2018, doi: 10.1175/JPO-D-17-0279.1.
[12] C. De Boyer Montégut, J. Mignot, A. Lazar, and S. Cravatte, "Control of salinity on the mixed layer depth in the world ocean: 1. General description," *J. Geophys. Res.*, vol. 112, no. C6, p. C06011, Jun. 2007, doi: 10.1029/2006JC003953.
[13] A. B. Kara, P. A. Rochford, and H. E. Hurlburt, "Mixed layer depth variability and barrier layer formation over the North Pacific Ocean," *J. Geophys. Res. Oceans*, vol. 105, no. C7, pp. 16783–16801, Jul. 2000, doi: 10.1029/2000JC900071.
[14] J. A. Cummings, "Operational multivariate ocean data assimilation," *Q. J. R. Meteorol. Soc.*, vol. 131, no. 613, pp. 3583–3604, Oct. 2005, doi: 10.1256/qj.05.105.
[15] C. N. Barron and L. F. Smedstad, "Global River Inflow within the Navy Coastal Ocean Model".
[16] X. Wang, G. Han, Y. Qi, and W. Li, "Impact of barrier layer on typhoon-induced sea surface cooling," *Dyn. Atmospheres Oceans*, vol. 52, no. 3, pp. 367–385, Dec. 2011, doi: 10.1016/j.dynatmoce.2011.05.002.
[17] K. Balaguru *et al.*, "Ocean barrier layers' effect on tropical cyclone intensification," *Proc. Natl. Acad. Sci.*, vol. 109, no. 36, pp. 14343–14347, Sep. 2012, doi: 10.1073/pnas.1201364109.

Dodging Ships: Is New Jersey Vessel Traffic a Threat to Underwater Gliders?

Leslie Birch
Department of Marine and Coastal Sciences
Rutgers University
New Brunswick, U.S.
lbirch@marine.rutgers.edu

Thomas Grothues
Department of Marine and Coastal Sciences
Rutgers University
New Brunswick, U.S.
grothues@marine.rutgers.edu

Josh Kohut
Department of Marine and Coastal Sciences
Rutgers University
New Brunswick, U.S.
kohut@marine.rutgers.edu

Alex Lopez
Department of Marine and Coastal Sciences
Rutgers University
New Brunswick, U.S.
alopez@marine.rutgers.edu

Abstract—**Global ocean observing systems utilize autonomous underwater vehicles (AUVs) to monitor coastal ocean conditions. These vehicles collect data while facing challenges of shallow waters, changing currents, and stratification. In addition to these natural challenges, AUVs share the waters with increased marine traffic, leading to potentially catastrophic ship strikes. Autonomous vehicles lack the ability to sense vessels, creating a need for a ship detection system leading to evasive maneuvers. Before vessel avoidance behaviors can be effectively implemented, baseline analysis is needed to understand the proximity of vessels to deployed AUVs. This research examines vessel traffic in New Jersey during an underwater glider mission using Automatic Identification System (AIS) mapped vessel movement, and glider data from Rutgers University. We quantify the probability of vessel co-location with a glider by distance, and vessel characteristics including their type and draft. Results show that most ships were not an immediate threat to the glider, with most in the range of 35–110 km. During the mission, less than 0.6% of ship position reports were within 20 km. Many ships were fishing vessels with a distance over 35 km from the glider. The average ship draft was 8 m with a maximum of 19 m. While most vessels were found beyond 35 km of the glider, there was a small but significant number of vessels that could be avoided if the glider were equipped with a ship detection system to make evasive actions.**

Keywords—underwater glider, AUV, path planning, collision avoidance, AIS, vessel traffic, acoustic

I. Introduction

Autonomous underwater vehicles (AUVs) are sensor platforms of the Global Ocean Observing System. Their data are used for tracking environmental changes, ocean floor mapping, hurricane prediction, wildlife tracking, marine archaeology, geologic formations, and search and rescue [1, 2, 3, 4, 5]. Oil and gas industries are using autonomous vehicles for inspection and repair of infrastructure [6]. The Blue Economy is creating more opportunities for AUV obtained data including wave forecasting, recreational fishing, commercial shipping, aquaculture, and mariculture [7].

Underwater gliders are a type of AUV capable of longer missions (~month to months). These vehicles use a buoyancy pump to move vertically through the water in a sawtooth motion [8]. Their pump and wings make them energy efficient. They rely on the global positioning system (GPS) for navigation and can only transmit data and receive commands through satellite when they surface [8]. These robots lack the ability to sense ships and react to the potential danger of ship strikes. Large cargo ships are not the only threat, as even a small pleasure craft can damage a glider fin or wing, causing a mission failure and a potential expensive loss. Many glider missions focus on coastal waters near busy ports and estuaries as seen in [9, Fig. 1]. During these deployments, remotely situated glider pilots face the challenge of navigating busy shipping lanes and dense recreational boat traffic with little strategy other than pilot commands that restrict a glider to deeper depths.

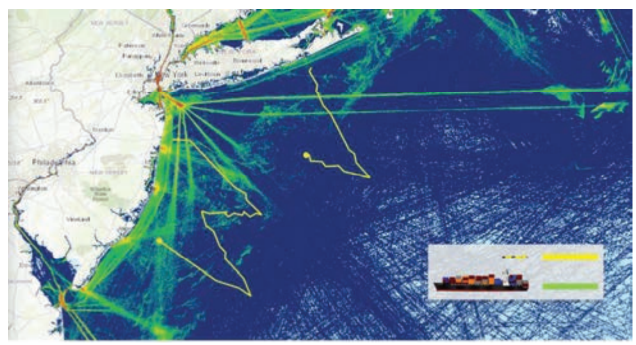

Fig. 1. Typical glider paths and shipping lanes of New Jersey/New York.

Our research establishes the level of vessel traffic risk as it pertains to an underwater glider in busy New Jersey coastal waters. It identifies the probability of a ship encountering the glider during a typical mission and the distance between ships and glider. Details of encountered vessels, including type of ship and draft are evaluated. Our interest is whether a future ship detection system may be able to thwart a ship strike. We hope this information is beneficial for improving navigation strategies for glider pilots and improving safety in waterways.

A. Background

The New Jersey coast offers a rich test site, with abundant glider missions from Rutgers University and other regional partners, and busy shipping lanes serving ports in New York and New Jersey. Automatic Information System (AIS) data provide a time series of reported vessel positions in the area. AIS is a

New Jersey Research and Monitoring Initiative, Ørsted ECOPAM

979-8-218-14218-6 ©2023 MTS

shipboard broadcast system that uses a VHF channel to share travel information [10]. Ships transmit key data including ship name, GPS, time, vessel type, and draft. Ships also receive AIS data for the surrounding area, aiding navigation. AIS data for New Jersey in [11, Fig. 2] confirms that vessels transit throughout the coastal waters.

Fig. 2. Recent AIS data.

Large types include tankers, cargo, passenger, and dredging vessels. In 2022, the New York-New Jersey seaport ranked 2nd highest in the nation with a 27% increase over 2019 due to rerouting of ships from COVID [12]. This busy vessel area overlaps with many Rutgers glider missions monitoring the oceanographic and ecological characteristics of the coastal ocean.

B. Review of Literature

Vessel movement is not just a concern for glider pilots. The Port Authority of New York and New Jersey monitors activities of cargo vessels and marine traffic as it relates to economy and safety (https://www.panynj.gov/). Offshore wind development has a need to understand marine traffic before and after construction with researchers looking at "near misses" of vessels on the Atlantic Coast [13]. The number of whale ship strikes is a growing concern, with studies in the New York Bight comparing sightings with AIS data to understand vessel risk [14].

Although ship strikes are of interest, there is a lack of research on potential collisions with AUVs. The potential loss of gliders due to ship strike in the German Bight has been analyzed using probability models and Monte Carlo simulations [15]. An estimate of damage to a small ship colliding with a glider at a speed over 7.5 m/s shows an outcome of severe hull damage [16]. There are numerous studies on path planning for AUVs utilizing algorithms and modeling [17, 18, 19]. One of the challenges of this research is determining which factors to include for algorithms and modeling. Speed, time, heading, obstacles, currents, and other environmental hazards may be considered. Another challenge is dealing with the difference between gliders and ships, both in their shapes and the depths they occupy. Lastly, for path planning information to be helpful, it must be based on data from the specific area of interest.

In the next section, we discuss the methods used to obtain and prepare data. Following the methods, we introduce the results, showing plots of vessel and glider data. A discussion follows with implications of the study, as well as a conclusion summarizing the findings.

II. Methodology

To better understand the interaction between marine traffic and coastal glider activity, we compared a concurrent glider mission to ship traffic off the busy New Jersey coast. Glider data were procured from the Ørsted ECO-PAM project [20]. The ECO-PAM project was led by Rutgers University in partnership with Woods Hole Oceanographic Institution and the University of Rhode Island [21]. A key component of the project was to deploy glider missions in and around the Ocean Wind 1 offshore wind lease area to monitor North Atlantic right whales (*Eubalaena glacialis*) [21]. The gliders are equipped with hydrophones, which can detect the sound of marine life and anthropogenic noise. This analysis focuses on a single mission deployed from February 15–March 15, 2022, transecting the New Jersey coast near Atlantic City to the shelf break. This mission is representative of a typical coastal glider deployment based on mission duration and lack of mechanical errors. Matching AIS data for the New Jersey coast for the same period were downloaded from https://marinecadastre.gov/ais [22].

Data were processed using Python 3 and its libraries, NumPy, Panda, and Matplotlib. A library developed at Rutgers University, Cool Maps (https://github.com/rucool/cool_maps), facilitated map plots. Files were sorted by time to the nearest minute, and missing data treated as not-a-number (NaN), as opposed to zero. Plots were created showing the glider mission path and probability of a ship in the area. Distance between vessels and glider were calculated based on GPS coordinates. Distribution of types of vessels encountered during the mission, and drafts for the types of vessels were also considered.

III. Results

A. Percentage Vessel Likelihood

A comparison of glider and AIS data reveals information about the proximity of the glider and surrounding ships. The glider mission shown in Fig. 3 includes an east-west transect to the shelf break, returning close to the same track during its mission. The likelihood of a ship off the coast of New Jersey to be in any one location at a given time is predominately 6% or less during the mission as shown in Fig. 4. Points above 10% are frequently in higher trafficked shipping lanes.

B. Distance of Ships to Glider

To understand encounters, we used AIS data to determine the distance between the glider and all ship positions reported during the mission. Fig. 5 shows ship position reports were predominately 35–110 km from the glider. 0.6% of ship position reports were in the 20 km range during the mission. The largest category of ships encountered in the 20 km range was fishing vessels, followed by cargo/tanker ships.

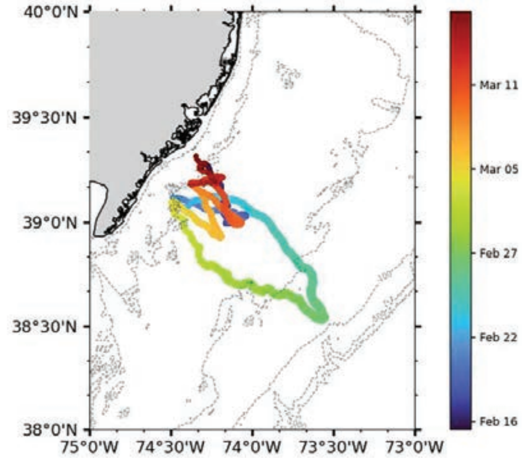

Fig. 3. Glider path mission near New Jersey coast.

C. Glider Depth With Distance to Ships

Plotting the glider depth in relation to ship traffic shows a similar range of 35–110 km as shown in Fig. 6. Ship positions reported were primarily 40–70 km from the glider. The average ship draft was 8 m, and the maximum draft was 19 m.

D. Ship Drafts

Further examination of ship draft in Fig. 7 reveals cargo/tanker ships with the largest draft at 5–18.5 m. Passenger ships have the second largest draft at 2.4–10.5 m. The "Other" category had many outliers, due to the varied assortment of boats and ships. Ships encountered in the 20 km range from the glider are likely fishing vessels or cargo/tanker ships, which creates a split between small drafts and exceptionally large drafts.

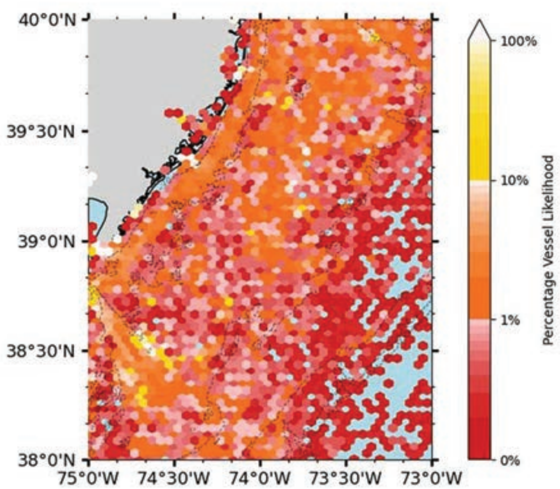

Fig. 4. Percentage vessel likelihood during mission.

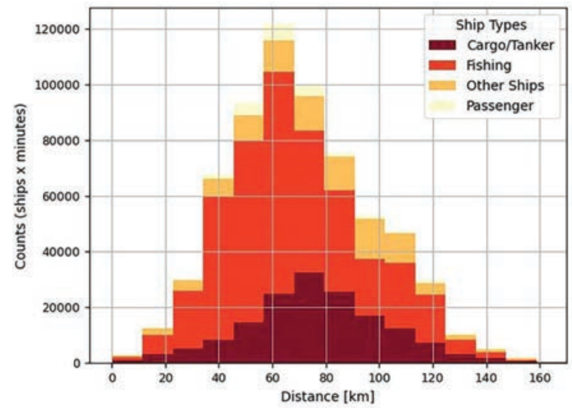

Fig. 5. Distance of ships to glider. This bar plot shows the cumulative distance of vessels to glider during the mission by ship type. The category "Other Ships" includes towing, dredging, diving ops, military ops, sailing, pleasure craft, high-speed craft, pilot vessel, search/rescue, tug, port tender, anti-pollution, law enforcement, non-combatant, and medical transport.

IV. Discussion

Ships and gliders must coexist in coastal waters, and both are growing. We must find ways to minimize interactions, starting with an understanding of the frequency of interactions and vessel classes. Data show 0.6% of total ship position reports are within 20 km of the glider during the mission. Most ships are found at a distance greater than 35 km. The results suggest there is a small, but significant number of ships that may be avoidable with a ship detection system. The ships of concern are likely fishing vessels that have a small draft, although cargo ships and tankers may also pose a threat. The small draft of fishing ships allows gliders the opportunity to dive to safety. Cargo/tanker ships have a large draft and lack maneuverability, creating a challenge for gliders.

Crossing shipping lanes is a navigation concern. Our research clarifies the risk of a glider moving east–west, with shipping lanes positioned north–south. This parallels research by Merckelbach [15], in which he concluded that east–west transects in the German Bight were a greater risk than north-south. While we do not yet have a simulation to prove our

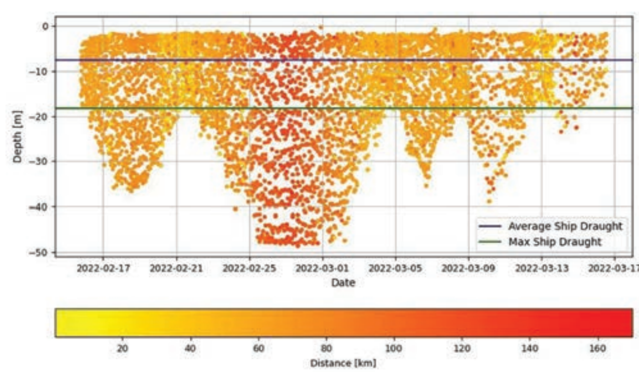

Fig. 6. Glider depth with distance to ships. Average ship draft and maximum ship draft are based on ships in the area during the glider mission.

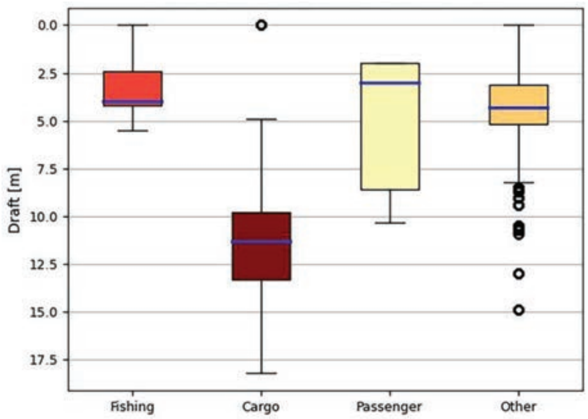

Fig. 7. Ship drafts during glider mission.

situation in New Jersey, our view of ship distances is a step towards understanding the risk. Another aspect of navigation concern is the reverse premise of our research—the threat of gliders to boats. According to Drücker et al. [16], there is more concern for a glider impacting a boat than there is for a boat impacting a glider. This is a point well taken, and our research also contributes to this focus of work since the goal is to understand the risk of collision.

Limitations of this research fall into two categories—data challenges and researcher challenges. The data are skewed in favor of the glider evading ships. Glider pilots are aware of shipping lanes and program gliders to stay deeper and surface less frequently when crossing. Results were based only on distances calculated using GPS points of the glider and ships. Breithaupt et al. [13] used a more complete calculation in their analysis of navigation conflicts between ships, using speed and heading. They also described the type of encounter as "crossing", "overtaking", or "head-on" [13]. Another data challenge in our research is the simplification of ship categories. We combined multiple classes of ships in the "Other" category when numbers were determined to be low. "Ghost ships", vessels that do not provide their information to AIS, also pose a risk, and were not considered in this analysis. Researcher challenges include a constraint on project time which only allowed one glider mission to be analyzed. These limitations result in research that is a "first look" at the risk gliders may face in New Jersey waters.

There is more information to absorb from this analysis, particularly the depth of the glider compared to distances of ship positions shown in Fig. 6. The light yellow/orange shaded areas near the beginning and end of the mission may coincide with shipping lanes. At the end of the mission, a pilot confines the glider to a location near the coast for recovery. The glider may travel back and forth between multiple waypoints, placing it at risk near shipping lanes. It would be helpful to compare the GPS coordinates for the shipping lanes and time stamps of the mission.

Future work should tackle the means for a glider to obtain ship data for a detection system. Hydrophones are frequently used on gliders for marine mammal tracking and other acoustic surveys [23, 24]. Data for our research include the hydrophone's acoustic files for the same period. Acoustic files are stored and compressed on a Digital Acoustic Monitoring (DMON) instrument that works in conjunction with the hydrophone [25]. Files can be converted to spectrograms which show audio signals of the environment. These signals are used to identify whale species and anthropogenic noise. Using machine learning, it may be possible to use acoustic signals to isolate ships that risk the glider mission. A machine learning model processing acoustic files from moored hydrophones classified large ships with an accuracy of 98.04% [26].

An alternate method for ship detection capitalizes on AIS data. Researchers have proposed relaying data to the glider from a nearby ship or beacon using a modem [27]. Another potential method is for the glider to receive AIS data directly from a VHF antenna. There are challenges to overcome with both acoustic and AIS methods. A glider's CPU (central processing unit) is limited by memory and processing capability [28]. Energy consumption must be kept at a minimum [28], and any attachments such as antennas or extra hardware may affect performance.

V. Conclusion

In this research we examined whether New Jersey vessel traffic is a threat to underwater gliders. The findings suggest the threat of vessel traffic is low. Distances of ship positions to the glider were calculated using AIS data. We found the occurrence of reported ship positions within 20 km of the glider to be 0.6% of the total mission, while most reported ship positions were found over 30 km. The greatest number of ships encountered were fishing vessels, while cargo/tanker ships were also a concern. The median ship draft was 8 m, and the maximum was 19 m.

The low, but nonzero, occurrence of vessels close to a coastal glider indicates a glider may benefit from a ship detection system. Future research should focus on methods for the glider to obtain ship data for a detection system. Two potential methods include using a hydrophone for acoustic data, and an antenna or modem for receiving AIS data.

Some limitations of our research include skewed data from effective glider piloting, lack of data due to ships that do not report their AIS information, and time constraints. The main limitation is the basic distance calculation which does not include other variables such as ship size, speed and heading. Although our method is simplistic, it relates to research in Germany examining the possibility of ships colliding with gliders [15]. Our work also shares an interest in gliders colliding with ships [16]. Together researchers must continue to work on a solution to protect lives and marine assets with the growing New Blue Economy.

Acknowledgment

The authors acknowledge and respect the ancestral territory of the Lenape people where Rutgers University, New Jersey, is located. The authors would like to thank Ørsted and Rutgers University for providing glider data. Additional thanks given to Marine Cadastre for AIS data.

References

[1] "What is an AUV? : Ocean Exploration Facts: NOAA Office of Ocean Explorationand Research." https://oceanexplorer.noaa.gov/facts/auv.html (accessed Jul. 15, 2023).

[2] W. D. Wilson, S. Glenn, T. Miles, A. Knap, and C. Toro, "Transformative Ocean Observing for Hurricane Forecasting, Readiness, and Response in the Caribbean Tropical Storm Corridor," *Marine Technology Society Journal*, vol. 55, no. 3, pp. 90–91, May 2021, doi: 10.4031/MTSJ.55.3.43.

[3] J. H. Eiler, T. M. Grothues, J. A. Dobarro, and R. Shome, "Tracking the Movements of Juvenile Chinook Salmon using an Autonomous Underwater Vehicle under Payload Control," *Applied Sciences*, vol. 9, no. 12, Art. no. 12, Jan. 2019, doi: 10.3390/app9122516.

[4] M. Xanthidis, B. Joshi, J. M. O'Kane, and I. Rekleitis, "Multi-Robot Exploration of Underwater Structures," *IFAC-PapersOnLine*, vol. 55, no. 31, pp. 395–400, Jan. 2022, doi: 10.1016/j.ifacol.2022.10.460.

[5] C. Cai, J. Chen, Q. Yan, and F. Liu, "A Multi-Robot Coverage Path Planning Method for Maritime Search and Rescue Using Multiple AUVs," *Remote Sensing*, vol. 15, no. 1, Art. no. 1, Jan. 2023, doi: 10.3390/rs15010093.

[6] "5 new advancements in AUV technology for oil and gas," May 17, 2020. https://energydigital.com/utilities/5-new-advancements-auv-technology-oil-and-gas (accessed Jul. 15, 2023).

[7] R. W. Spinrad, "Chapter 6 - The new blue economy," in *Preparing a Workforce for the New Blue Economy*, L. Hotaling and R. W. Spinrad, Eds., Elsevier, 2021, pp. 87–111. doi: 10.1016/B978-0-12-821431-2.00042-1.

[8] https://www.teledynemarine.com/en-us/products/product-line/Pages /Autonomous-Underwater-Glider.aspx (Accessed Jul. 29, 2023).

[9] "OceansMap–MARACOOS."https://maracoos.org/index.php/ oceansmap/ (accessed Jul. 29, 2023).

[10] "Automatic Identification System (AIS) Overview | Navigation Center." https://www.navcen.uscg.gov/automatic-identification-system-overview (accessed Jul. 29, 2023).

[11] "Free AIS Ship Tracker–VesselFinder." https://www.vesselfinder.com/ (accessed Jul. 30, 2023).

[12] "Port Authority Reports Highest Cargo Activity in its History," *New Jersey Business Magazine*. https://njbmagazine.com/njb-news-now/port-authority-reports-highest-cargo-activity-in-its-history/ (accessed Jun. 21, 2023).

[13] S. A. Breithaupt, M. Bensi, and A. Copping, "AIS-based characterization of navigation conflicts along the US Atlantic Coast prior to development of wind energy," *Ocean Engineering*, vol. 264, p. 112235, Nov. 2022, doi: 10.1016/j.oceaneng.2022.112235.

[14] D. M. Brown, "An Analysis of Opportunistic Data to Investigate Humpback Whale (*Megaptera novaeangliae*) Sighting Patterns and Vessel Risk in the Northwestern New York Bight," Thesis, 2020. Accessed: Jul. 16, 2023. [Online]. Available: https://mars.gmu.edu /handle/1920/11051.

[15] L. Merckelbach, "On the probability of underwater glider loss due to collision with a ship," *J Mar Sci Technol*, vol. 18, no. 1, pp. 75–86, Mar. 2013, doi: 10.1007/s00773-012-0189-7.

[16] S. Drücker, D. Steglich, L. Merckelbach, A. Werner, and S. Bargmann, "Finite element damage analysis of an underwater glider–ship collision," *J Mar Sci Technol*, vol. 21, no. 2, pp. 261–270, Jun. 2016, doi: 10.1007/s00773-015-0349-7.

[17] F. Jalal and F. Nasir, "Underwater Navigation, Localization and Path Planning for Autonomous Vehicles: A Review," in *2021 International Bhurban Conference on Applied Sciences and Technologies (IBCAST)*, Jan. 2021, pp. 817–828. doi: 10.1109/IBCAST51254.2021.9393315.

[18] M. Li, J. Mou, R. (Rachel) Liu, P. Chen, Z. Dong, and Y. He, "Relational Model of Accidents and Vessel Traffic Using AIS Data and GIS: A Case Study of the Western Port of Shenzhen City," *Journal of Marine Science and Engineering*, vol. 7, no. 6, Art. no. 6, Jun. 2019, doi: 10.3390 /jmse7060163.

[19] T. Yao, T. He, W. Zhao, and A. Y. M.Sani, "Review of Path Planning for Autonomous Underwater Vehicles," in *Proceedings of the 2019 International Conference on Robotics, Intelligent Control and Artificial Intelligence*, in RICAI '19. New York, NY, USA: Association for Computing Machinery, Sep. 2019, pp. 482–487. doi: 10.1145/3366194. 3366280.

[20] "ru34-20220215T1926Deployment."https://marine.rutgers.edu /cool/data/gliders/deployments/deployment.php?deployment=ru34-20220215T1926 (accessed Jul. 31, 2023).

[21] "Orsted ECO-PAM." https://orsted-eco-pam-web-portal.srv.axds.co/ (accessed Nov. 27, 2022).

[22] "MarineCadastre.gov." https://marinecadastre.gov/data/ (accessed Nov. 27, 2022).

[23] S. M. Van Parijs *et al.*, "NOAA and BOEM Minimum Recommendations for Use of Passive Acoustic Listening Systems in Offshore Wind Energy Development Monitoring and Mitigation Programs," *Frontiers in Marine Science*, vol. 8, 2021, Accessed: Jul. 12, 2023. [Online]. Available: https://www.frontiersin.org/articles/10.3389/fmars.2021.760840.

[24] M. F. Baumgartner *et al.*, "Near real-time detection of low-frequency baleen whale calls from an autonomous surface vehicle: Implementation, evaluation, and remaining challenges," *The Journal of the Acoustical Society of America*, vol. 149, no. 5, pp. 2950–2962, May 2021, doi: 10.1121/10.0004817.

[25] M. F. Baumgartner *et al.*, "Real-time reporting of baleen whale passive acoustic detections from ocean gliders," *The Journal of the Acoustical Society of America*, vol. 134, no. 3, pp. 1814–1823, Sep. 2013, doi: 10.1121/1.4816406.

[26] A. Alvaro, F. Schwock, J. Ragland, and S. Abadi, "Ship detection from passive underwater acoustic recordings using machine learning," *The Journal of the Acoustical Society of America*, vol. 150, no. 4, pp. A124–A124, Oct. 2021, doi: 10.1121/10.0007848.

[27] S. Imbert, C. Laot, A.-O. Boudraa, and J.-J. Szkolnik, "Performance Optimization of Underwater Communication Links at Different Ranges for AIS Relay to AUV," *Applied Sciences*, vol. 12, no. 9, Art. no. 9, Jan. 2022, doi: 10.3390/app12094166.

[28] H. C. Woithe *et al.*, "Slocum Glider energy measurement and simulation infrastructure," in *OCEANS'10 IEEE SYDNEY*, May 2010, pp. 1–8. doi: 10.1109/OCEANSSYD.2010.5603909.

frontiers | Frontiers in Marine Science

TYPE Original Research
PUBLISHED 18 August 2023
DOI 10.3389/fmars.2023.1224609

OPEN ACCESS

EDITED BY
Won Sang Lee,
Korea Polar Research Institute,
Republic of Korea

REVIEWED BY
Karthik Balaguru,
Pacific Northwest National Laboratory
(DOE), United States
Sok Kuh Kang,
Korea Institute of Ocean Science and
Technology (KIOST), Republic of Korea

*CORRESPONDENCE
Travis N. Miles
tnmiles@marine.rutgers.edu

RECEIVED 17 May 2023
ACCEPTED 01 August 2023
PUBLISHED 18 August 2023

CITATION
Miles TN, Coakley SJ, Engdahl JM, Rudzin JE, Tsei S and Glenn SM (2023) Ocean mixing during Hurricane Ida (2021): the impact of a freshwater barrier layer. *Front. Mar. Sci.* 10:1224609. doi: 10.3389/fmars.2023.1224609

Ocean mixing during Hurricane Ida (2021): the impact of a freshwater barrier layer

Travis N. Miles[1]*, Samuel J. Coakley[1], Julia M. Engdahl[1], Johna E. Rudzin[2], Senam Tsei[3] and Scott M. Glenn[1]

[1]Rutgers University Center for Ocean Observing Leadership, Department of Marine and Coastal Sciences, Rutgers University, New Brunswick, NJ, United States, [2]Department of Geosciences, Northern Gulf Institute, Mississippi State University, Starkville, MS, United States, [3]School of Ocean Science and Engineering, Division of Marine Science, University of Southern Mississippi, John C. Stennis Space Center, MS, United States

Tropical cyclones are +ne of the costliest and deadliest natural disasters globally, and impacts are currently expected to worsen with a changing climate. Hurricane Ida (2021) made landfall as a category 4 storm on the US Gulf coast after intensifying over a Loop Current eddy and a freshwater barrier layer. This freshwater layer extended from the coast to the open ocean waters south of the shelf-break of the northern Gulf of Mexico (GoM). An autonomous underwater glider sampled this ocean feature ahead of Hurricane Ida operated through a partnership between NOAA, Navy, and academic institutions. In this study we evaluate hurricane upper ocean metrics ahead of and during the storm as well as carry out 1-D shear driven mixed layer model simulations to investigate the sensitivity of the upper ocean mixing to a barrier layer during Ida's intensification period. In our simulations we find that the freshwater barrier layer inhibited cooling by as much as 57% and resulted in enhanced enthalpy flux to the atmosphere by as much as 11% and an increase in dynamic potential intensity (DPI) of 5 m s^{-1} (~9.72 knots) in the 16 hours leading up to landfall. This highlights the utility of new ocean observing systems in identifying localized ocean features that may impact storm intensity ahead of landfall. It also emphasizes the northern Gulf of Mexico and the associated Mississippi River plume as a region and feature where the details of upper ocean metrics need to be carefully considered ahead of landfalling storms.

KEYWORDS

hurricanes, barrier layers, uncrewed systems, ocean observing networks, and upper ocean mixing

1 Introduction

Tropical cyclones (TCs) are one of the costliest and deadliest natural disasters on the planet (Smith, 2020). The ability to forecast TC intensity has improved recently (Cangialosi et al., 2020), however intensity forecast errors remain large (~12 kts at 72 hours). The primary controls of the intensity of mature TCs are vertical wind shear, dry air intrusion,

10.3389/fmars.2023.1224609

and the fluxes of enthalpy and momentum between the surface ocean and atmosphere (Emanuel, 1986). Numerous studies have shown that the upper ocean can evolve rapidly beneath TCs and feedback on storm intensity (Cione and Uhlhorn, 2003; Black et al., 2007; D'Asaro et al., 2007; Zedler et al., 2009; Mrvaljevic et al., 2013; Steffen and Bourassa, 2020) among many others therein. Recent studies have focused on coastal ocean processes and their feedbacks on storm intensity, including coastal upwelling, downwelling, and enhanced shear-driven mixing (Glenn et al., 2016; Seroka et al., 2016; Miles et al., 2017; Seroka et al., 2017; Zhang et al., 2018; Dzwonkowski et al., 2021; Gramer et al., 2022), with a particular focus on highly stratified water columns. A common hurricane intensity forecasting challenge in regions with large river runoff are upper ocean salinity barrier layers (Lukas and Lindstrom, 1991; Sprintall and Tomczak, 1992; Foltz and McPhaden, 2009; Grodsky et al., 2012; Steffen and Bourassa, 2018). Generally, stratification can inhibit vertical mixing and limit entrainment of cool subsurface waters into the mixed layer during TC passage (e.g. Rudzin et al., 2018). These ocean features are found on continental shelves, near river outflows (Sengupta et al., 2008), and over the open ocean with offshore transport of freshwater (Pailler et al., 1999; Grodsky et al., 2012). Barrier layers increase the potential energy gradient, inhibit sea surface temperature (SST) cooling, and can support enhanced enthalpy fluxes into the atmosphere during hurricanes (Wang et al., 2011; Balaguru et al., 2012; Rudzin et al., 2018; Rudzin et al., 2019; Balaguru et al., 2020; Rudzin et al., 2020; Sanabia and Jayne, 2020). Only a few observations and studies have explicitly focused on the interactions of TCs passing over the Mississippi river-induced salinity barrier layer (Le Hénaff et al., 2021; John et al., 2023). This barrier layer is a product of the largest river outflow in the US from the Mississippi River, in a region where strong hurricanes make landfall and coastal communities have repeatedly been devastated by powerful landfalling hurricanes, including Hurricane Ida in the summer of 2021.

Hurricane Ida (2021) underwent rapid intensification (RI) over the warm waters of the Gulf of Mexico (GoM) (Figure 1), with an increase in maximum wind speed of 60 kts (~30 m/s) in 24 hours (Beven et al., 2022). Ida continued to intensify as it passed over the continental shelf before making landfall as a category 4 hurricane in Louisiana on August 29th (Figure 1) as the second costliest storm to make landfall in the region after Hurricane Katrina (2005); (Smith, 2020). A recent study (Zhu et al., 2022) identified that nearshore SSTs ahead of Ida were >30°C, above the mean SSTs (28.7°C) that other major hurricanes crossed over in the region. They also

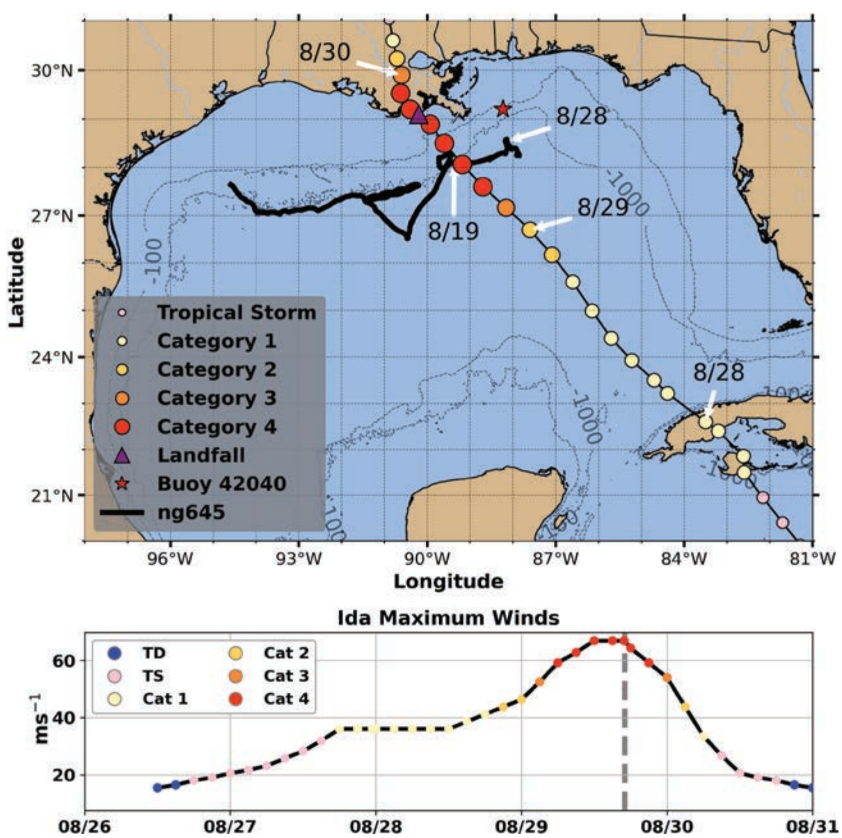

FIGURE 1
A map (top) of Hurricane Ida's NHC best track with colored circles denoting the storm's category in three-hour increments, with an additional purple triangle denoting landfall. Arrows pointing to track locations indicate Ida's position on 8/28, 8/29, and 8/30 for reference. The black line indicates the NG645 glider track, with additional arrows indicating the glider position on 8/19 and 8/28 for reference to profiles used to initialize our PWP experiments. NDBC Buoy 42040 is represented by the red star. A time-series (bottom) of Ida's NHC best track maximum wind speed and intensity (colored circles) as well as the storms landfall time (dashed grey line).

indicated that slow translation speeds kept the backside of the storm over these warm and fresh waters for an extended duration, contributing to Ida's slow weakening after landfall. While there is a large body of research on freshwater plume, or salinity barrier layer, impacts on hurricane intensity there are only a few focused on the Mississippi River plume (Le Hénaff et al., 2021; John et al., 2023). Despite major hurricanes regularly transiting this region, there are limited upper ocean observations during storm events in this region. For example, in the highly dynamic region where Ida rapidly reached and maintained category 4 (Figure 1) from 27.5° to 30° N and between 91° and 88.5° W only 20 Argo floats and 252 profiles are available in the last 20 years (~13 profiles/year) during hurricane season (https://erddap.ifremer.fr/erddap/index.html).

According to Beven et al. (2022), official forecasts for Hurricane Ida (2021) generally outperformed guidance and the previous five year mean official forecasts for the full storm period. However, few models or official forecasts captured Ida's peak winds at landfall including as Ida rapidly intensified over the warm waters of the central GoM and fresh Mississippi River plume coastal waters (Figures 2, 3). Fortunately, as part of the 2021 Hurricane Glider Program (Miles et al., 2021) a Navy operated and NOAA coordinated autonomous underwater glider, NG645, was deployed ahead of and during Ida's eye passage over the region (Figures 1–3). Ahead of the storm, in the deep ocean (>100m depth) just south of the GoM northern escarpment NG645 observed (Figure 2) warm sea surface temperatures, low salinity, and heat content near a threshold (60 kJ cm^{-2}) typically conducive for intensification (Mainelli et al., 2008). The presence of the freshwater barrier layer and elevated SSTs suggest that, even with marginal ocean heat content, these ocean conditions are conducive to storm intensification. In this study we investigate upper ocean metrics for storm intensification in the region Hurricane Ida (2021) passed over, as well as the sensitivity of SST cooling to the strong vertical salinity stratification in the region ahead of landfall. To carry out this work we combine the *in-situ* observations from NG645 and satellite remote sensing with a 1-D mixed layer model sensitivity experiments to evaluate the impact of barrier layer presence and absence with the Price-Weller-Pinkel (PWP) model (Price et al., 1986).

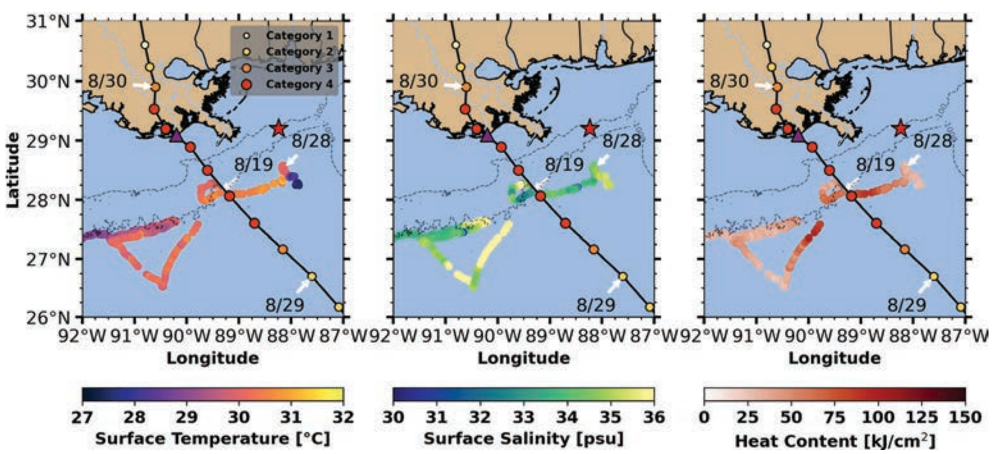

FIGURE 2
Maps of upper ocean metrics calculated from NG645. From left to right, scatter plot of NG645 sea surface temperature (SST), sea surface salinity (SSS), ocean heat content (OHC), respectively, represented by colored markers. Hurricane Ida's storm track as-in Figure 1, with an additional time reference arrow at 8/29.

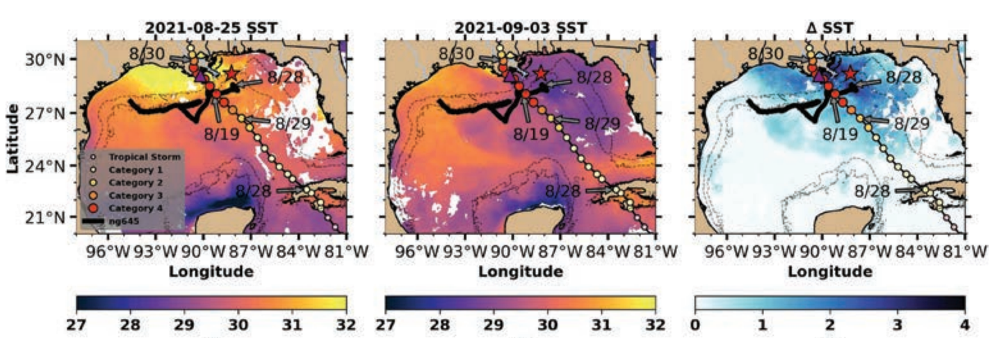

FIGURE 3
Maps of Sea Surface Temperature (SST) from GOES16 SST daily composite SST on 8/25 (left) and 9/3 (middle). The right panel is the difference (8/25 – 9/3) in SST with positive values indicating ocean cooling. Hurricane Ida's storm track as-in Figure 1, with an additional time reference arrow at 8/29.

2 Methods

Ocean observations ahead of and during Hurricane Ida were obtained from Slocum glider (Schofield et al., 2007) NG645, operated by the Naval Oceanographic office in close collaboration with the Integrated Ocean Observing System (IOOS) Hurricane Glider Program. Slocum gliders are buoyancy driven uncrewed underwater vehicles that can profile vertically (up to 1000 m at ~20 cm s^{-1}) and horizontally (~ 20 km day^{-1}). They typically collect data at up-to 2 second intervals, resulting in high (<1m) vertical resolution. These systems have been used over the past decade to study upper ocean processes during TCs (Domingues et al., 2015; Glenn et al., 2016; Seroka et al., 2016; Miles et al., 2017; Seroka et al., 2017; Lim et al., 2020) and to provide near real-time data for assimilation into operational hurricane forecast models (Miles et al., 2021). NG645 specifically was operated as part of an agreement between NOAA and the Navy with the goal of providing real-time *in-situ* glider observations to improve and inform hurricane intensity forecasts.

NG645 was deployed on June 13th, 2021, offshore of the continental shelf at 27.6°N and 94.6°W. In mid-August the glider was navigated eastward south of the escarpment of the northern GoM (Figures 1–3), through the northwestern edge of a loop current eddy (LCE) and into a gap region south of the continental shelf, but north of the LCE. The glider transited in the deep (>1000 m) of water off the continental shelf for the duration of the mission. NG645 crossed ahead of Ida's track at 89.23°W and 28.12°N on August 19th, 60 km from the shelf-break and 100 km from the nearest land point. The glider did not station keep at this location but was piloted to collect a broad swath of data further eastward before station keeping on August 27th ahead of the storm at 88.17°W and 28.57°N. The region to the east of Ida's track was a gap region between the continental shelf to the north and the LCE to the south. In this study we present data from NG645 through August 31st, however the glider continued sampling through September 24th in further support of hurricane forecast models. NG645 was equipped with a standard Seabird Scientific, Inc. (SBE) pumped conductivity, temperature, and depth sensor (CTD), which reported data in at ~8s intervals. The Naval Oceanographic Office submitted data in near real-time and for archiving via the IOOS Glider Data Assembly Center (DAC). However, post-deployment data was not made available, thus intermittent data transmission issues resulted in periodic data gaps.

2.1 Upper ocean metrics

Upper ocean metrics relevant to hurricane intensity and salinity barrier layers were calculated from NG645 CTD data extracted from the IOOS GDAC (https://gliders.ioos.us/erddap/tabledap/index.html). This includes sea surface temperature and salinity and metrics described below starting with Ocean Heat Content (OHC). OHC, introduced by Leipper and Volgenau (1972), and used in operational hurricane forecasting is the vertical integral of heat from the 26°C isotherm to the surface calculated as:

$$Q = \rho_o c_p \int_{Z_{26}}^{0} (T - 26) dz$$

Where ρ_o=1025 kg m^{-3} and $c_p = 4 \times 10^3$ J kg^{-1}°C^{-1} and Z_{26} is the depth of the 26°C isotherm. The 26°C isotherm has historically been chosen to represent average subtropical atmospheric boundary layer temperatures, implying that ocean temperatures and associated heat warmer than that value would be available for flux into the relatively cooler atmosphere during a storm event, leading to storm intensification. Mainelli et al. (2008) found that in statistical hurricane intensity predictions, OHC values greater than 60 kJ cm^{-2} were predictive of storm intensification, while OHC below this threshold were predictive of weakening. However, Mainelli et al. (2008) also proposed that the larger OHC was not the direct cause of storm intensification, but rather larger OHC were related to deeper warm temperatures and thus limited SST cooling throughout storms. Other OHC value thresholds have been discussed for intensification (Jaimes et al., 2016), however for simplicity we use 60 kJ cm^{-2} as a reference throughout this work. More recent work (Balaguru et al., 2018; Potter and Rudzin, 2021) has also shown that pre-storm SST and OHC are not always a good predictor of storm intensity, particularly when there are shallow mixed layers present. Price (2009) detailed an alternative upper ocean average temperature metric T_d, where d = 100m over the deep ocean (indicated as a typical depth of mixing for a category 3 tropical cyclone) or d = the water column depth on shallow continental shelves. As NG645 was located off the continental shelf in more than 100m of water for the duration of its deployment we calculate T_d metric to 100m (T100).

Price (2009) briefly discussed necessary modifications of T_d for salinity stratified water columns, where mixing would not reach 100m in deep ocean cases or the bottom on continental shelves, and alternative dynamic temperature metrics (Balaguru et al., 2018) have been used to represent upper ocean temperatures down to the 26°C isotherm. To evaluate the role of salinity stratification in the case of Hurricane Ida we additionally calculate the potential energy anomaly (PEA), ϕ, which is the amount of energy required to vertically redistribute the mass of the water column from stratified to fully mixed (Simpson and Hunter, 1974; Simpson et al., 1981), represented by the equations:

$$\phi = \frac{1}{h} \int_{-h}^{0} (\bar{\rho} - \rho) g z dz; \quad \bar{\rho} = \frac{1}{h} \int_{-h}^{0} \rho dz$$

In this case h is equal to the 100m water depth, ρ is the density measured at a given depth z, and g is the gravitational constant. We limit the PEA to the upper 100m for similar reasons as T100, e.g. we expect TC induced upper ocean mixing to be limited to water shallower than 100m. While PEA is a useful water column metric, we also calculate barrier layer thickness (BLT) as the difference between the isothermal layer depth (ILD) and mixed layer depth (MLD). Each glider profile was evaluated for the presence of a barrier layer where the MLD was defined following de Boyer Montégut et al. (2007) using the potential density:

$$\Delta\sigma_\theta = \sigma_\theta(T_\circ - \Delta T, S_\circ) - \sigma_\theta(T_\circ, S_\circ)$$

where $T_{\circ}$ and $S_{\circ}$ are the 2m temperature and salinity, respectively. ΔT is 0.5°C. We calculated the ILD as the shallowest depth where the temperature is 0.5°C less than the $T_{\circ}$, and the BLT as the distance between the ILD and the MLD. The 0.5°C criterion is larger than that used by de Boyer Montégut et al. (2007) however it is aligned with Rudzin et al. (2017), which adapted the criteria for salinity barrier layers.

2.2 1-D mixed layer experiments

Upper ocean mixing experiments were carried out with twin PWP model simulations at two sites to investigate the role of salinity stratification in shear-driven upper ocean mixing as Ida (2021) approached and made landfall on the Louisiana coastline. The 1-D PWP model has been used extensively to study ocean mixing during hurricane conditions (Zedler et al., 2002; Wang et al., 2011; Rudzin et al., 2018; Yang et al., 2019). The PWP model is initialized from profiles of temperature and salinity and forced with observed or idealized wind stress, freshwater surface flux, and heat flux. The bulk and gradient Richardson numbers determine mixed layer and shear stability, respectively. The model uses boundary conditions to solve a non-advective momentum equation for velocity, temperature, and salinity. During the implementation of forcing at each time-step the model will check both bulk ($R_b \geq 0.65$) and gradient ($R_g \geq 0.25$) Richardson number stability criteria. If there is an instability present the water column will be iteratively mixed until the criteria are satisfied. PWP primarily includes processes and parameterizations that represent shear-induced mixing and buoyancy forcing processes, as well as rotational effects due to Coriolis, and is not designed to evaluate 3-D mixing or advective processes. Considering this limitation, we expect our model results to provide insights on the forced stage sensitivity to barrier layer presence and absence analysis of the model simulations on the ahead-of-eye forced stage and sensitivity to barrier layer presence and absence. We do not expect the PWP model to account for all upper ocean mixing and cooling processes during Ida and expect future studies to investigate those processes more broadly.

We limited external PWP model forcing to surface wind stress as in previous studies (Balaguru et al., 2020) to evaluate the isolated impact of salinity stratification on upper ocean shear-driven mixing processes. The surface wind stress was extracted in real-time from the publicly available High Resolution Rapid Refresh (HRRR) model operated by NOAA via their Operational Model Archive and Distribution System. HRRR is a 3km horizontal resolution implementation of the Weather Research and Forecasting model (Skamarock et al., 2019) updated hourly. We evaluated HRRR with the nearest National Data Buoy Center (NDBC) buoy 42040 to the northeast of Ida's track (Figure 1). Other sites were considered, however available data were either located over land, far away from study sites or experienced data loss ahead-of and during the storm event. Evaluation of the HRRR model 10m wind speeds vs 42040 showed that the wind speed magnitudes mean bias for the longest model forcing duration (08/19 to 08/31) was 0.14 m s^{-1} with a correlation coefficient of 0.92. Maximum HRRR winds were 23.63 m s^{-1} at the buoy site, or 1.24 m s^{-1} faster than observed, occurring an hour and forty minutes earlier.

2.3 Enthalpy flux and dynamic potential intensity

For intercomparison of model experiments we estimate both enthalpy flux and dynamic potential intensity. Our enthalpy flux calculations are based on bulk formula as presented in Jaimes et al. (2015) and derived from numerous observational studies in high winds (Powell et al., 2003; Black et al., 2007; Zhang et al., 2008) with wind speed dependent exchange coefficients of momentum and enthalpy. Ocean properties used in bulk formula are extracted from the PWP model experiments with an assumed 98% saturation state. However, atmospheric parameters such as 10m wind speed (U_{10}), air temperature T_a, and atmospheric specific humidity (q_a) are estimated from HRRR model output with an assumed relative humidity of 95%.

For an additional comparison with the PWP model output we calculate the dynamic potential intensity (DPI) (Balaguru et al., 2015; Rudzin et al., 2020) of our pre-storm glider data with and without the barrier layer included to evaluate how the influence of barrier layer presence and absence could potentially impact storm intensity. The DPI is calculated as:

$$DPI = \quad V_{max}^2 = \frac{T_{dy} - T_0}{T_0} \frac{C_K}{C_D} (k_{T_{dy}} - k)$$

Where T_{dy} is the average temperature of the upper ocean, T_0 is the hurricane outflow temperature at 200mb (assumed to be 221 K), $k_{T_{dy}}$ is the enthalpy of air above an ocean with a temperature of T_{dy}, and k is the specific enthalpy of air near the surface ocean. The ratio of enthalpy and drag coefficients is set to 1 for simplicity as in Rudzin et al. (2020).

$$T_{dy} = \frac{1}{L} \int_0^L T(z) dz$$

$$L = h + \left(\frac{2\rho_0 u_*^3 t}{\kappa g \alpha} \right)^{\frac{1}{3}}$$

Where h is the MLD; ρ_0 is a reference density of 1025 kg m^{-3}; $t$is the mixing time period calculated as the radius of maximum winds of the storm divided by the storm's translation speed (t= R_{max}/U_h = 1.15 hours); u_* is the surface friction velocity calculated using the maximum wind stress from HRRR output during time t, $\kappa$is the von Karman constant of 0.4; g is gravitational acceleration; α is the vertical density stratification below the mixed layer calculated as the density gradient from the MLD to 50m below the MLD. L is the forecasted mixing depth based on the initial profile and storm properties based on the Monin-Obukhov mixing length (Balaguru et al., 2015). T_{dy} is the temperature of the upper ocean if the passing storm homogeneously mixes the ocean down to a depth of L.

2.4 Additional datasets

Sea surface temperature (SST) data from the GOES-16 (Schmit et al., 2017) geostationary satellite are used to show storm SST cooling throughout the Gulf of Mexico. Daily composites of hourly GOES-16 images were extracted from 8/25 and 09/03, the last and first clear composite images before and after the storm respectively. Hurricane Ida (2021) best track information was extracted from the International Best Track Archive for Climate Stewardship (IBTrACS) dataset (Knapp et al., 2010; Knapp et al., 2018) including position and maximum wind speeds at 3 hourly intervals, with additional reported data at landfall times.

3 Results

Hurricane Ida impacted Cuba and entered the GoM late on 08/27 and into 08/28 as a category 1 storm (Figure 1). It began to intensify over the central GoM late on 08/28, and rapidly intensified to a category 4 storm over the northern GoM and continental shelf until landfall at 08/29 16:00, gradually weakening on 08/30 as it moved inland (Figure 1). A zoomed in view of Ida's track and intensity in relation to glider NG645's position and pre-storm *in-situ* SST, salinity, and OHC are shown in Figure 2. These *in-situ* data show that the upper ocean was warm, and a freshwater barrier layer was present to the right of the storm track in the week prior to Ida's passage.

SST imagery ahead of the storm (08/25) showed warm pre-storm SSTs above 30°C along the storm track (Figure 3). The first clear composite image was available approximately 4-days after landfall and showed significant cooling (Figures 3) of more than 1°C over more than 230,000 km^2 of the GoM, a maximum cooling of 3.8°C on the shelf near the landfall location and 2.38°C near the glider station keeping location. Ida's rapid intensification despite this cooling implies that a significant portion of the satellite observed SST cooling occurred after the storm's eye-passage. We use *in-situ* glider data to investigate the specific timing of the cooling further.

Cross-sections (Figure 4) and derived upper ocean metrics (Figure 4) demonstrate pre-storm ocean properties during the cross-track storm survey period (08/17 – 08/27) and the ocean response to the right of the storm track during the station keeping period (08/27 – 08/31). During the pre-storm survey period the glider observed an isothermal warm (>30°C) layer extending to ~30 meters depth to the west and ahead of the storm track. As the glider progressed eastward the isothermal layer shoaled to<20 meters. In contrast, the MLD was found near the surface (<5m) because of a shallow layer of low salinity water (~ 32.5 to 34.5 PSU) aside from a brief salty surface salinity on 08/17.

T100 showed warm average upper ocean temperatures to the west peaking at (28.2°C) and cooler temperatures to the east reaching a minimum of 23.4°C where the glider began its station keeping mission (Figure 5C). Ocean heat content (Figure 5D) had a similar pattern as T100, notably with values above the 60 kJ cm^{-2} threshold identified for hurricane intensification by Mainelli et al. (2008) on the western portion of the track. Observed OHC dropped below that threshold on 08/23 as the glider progressed eastward reaching a minimum of 25 kJ cm^{-2} as the glider started its station keeping mission. Aside from a brief dip to 400 J m^{-3} on 08/21 the PEA remained near 500 J m^{-3} throughout the pre-storm survey (Figure 5E). The consistently high PEA indicates that the water column stability was high, and the SST was not likely to cool to the full T100 value, despite the strength of the storm. For context, later in section 4 we detail the difference in PEA with and without a barrier layer as shown in (Figure 6).

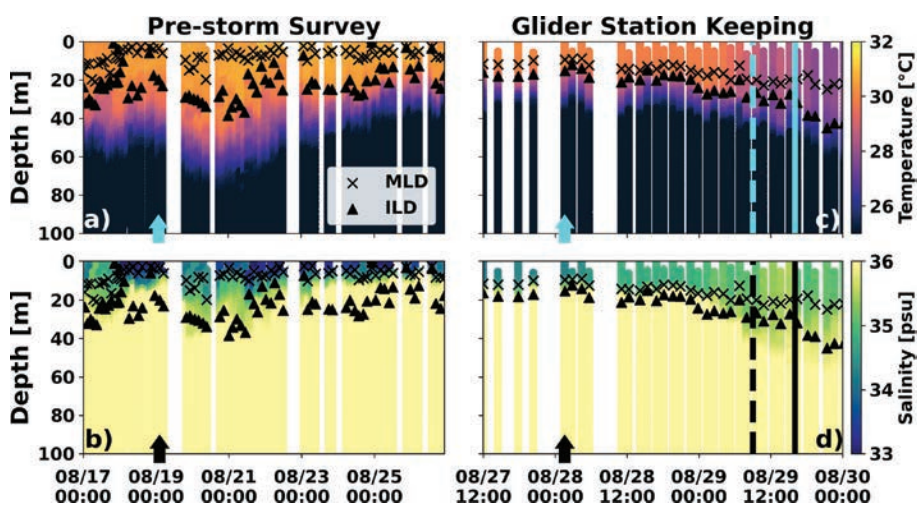

FIGURE 4
Glider NG645 cross-sections of temperature **(A, C)** and salinity **(B, D)** during the pre-storm survey **(A, B)** 8/17 to 8/27 and glider station keeping (c,d) 8/27 to 8/30 0900. MLD and ILD estimates are represented by x's and triangles, respectively in all panels. The arrow in the pre-storm survey **(A, B)** on 8/19 denotes the glider profile used in PWP experiment 1, and the arrow in the glider station keeping **(C, D)** on 8/28 denotes the glider profile used in PWP experiment 2. The vertical lines represent the times that Hurricane Ida passed the glider (dashed line) and made landfall (solid line), respectively.

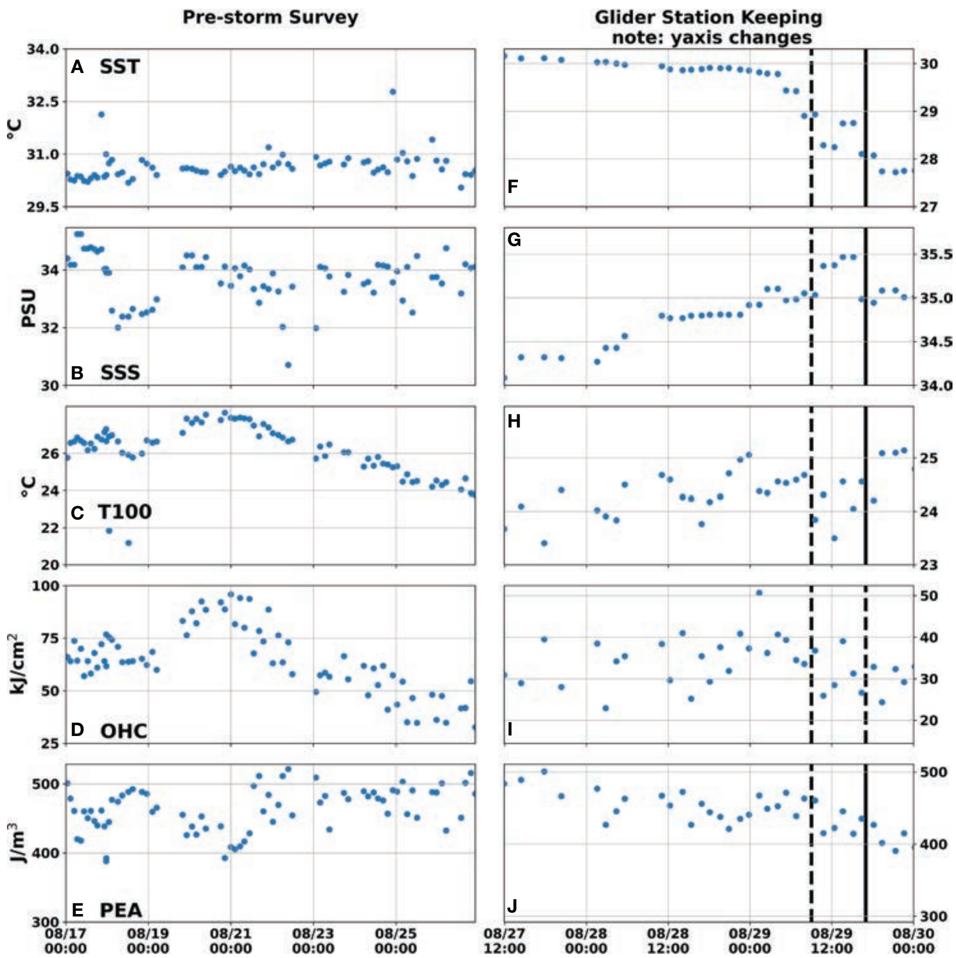

FIGURE 5
Upper ocean metrics derived from NG645 data split into pre-storm survey **(A–E)** 8/17 to 8/27 and glider station keeping **(F–J)** 8/27 to 8/30. SST **(A, F)**, SSS **(B, G)**, T100 **(C, H)**, OHC **(D, I)**, and PEA **(E, J)**. Note the glider station keeping y-axis differs from the pre-storm survey. The vertical lines represent the times when Hurricane Ida passed the glider (dashed line) and made landfall (solid line), respectively.

During the station keeping period the glider showed that the upper ocean cooled, increased in salinity, and both the ILD and MLD deepened throughout and following the storm event (Figures 5F–J). From 8/28 to eye-passage and landfall the SST cooled by 1.1°C and 1.96°C, respectively. This represents less than half of the satellite observed ocean cooling by eye-passage, and 82% by landfall. Sea surface salinity only experienced a small increase of 0.44 PSU for a brief period between eye-passage and landfall (Figure 5G). The MLD and ILD deepened from ~5m to ~20m and ~18m to ~30m. T100 and OHC experienced negligible changes throughout the storm mixing period (Figures 5H, I), while PEA dropped almost 100 J m^{-3} from the station keeping period to landfall and continued to drop to 350 J m^{-3} following landfall (Figure 5J). The minimal changes in T100 and OHC paired with a large drop in PEA suggest ocean mixing processes were first breaking down the upper ocean salinity stratification before accessing deeper cold subsurface waters. We evaluate this with the 1-D PWP model in the following section.

3.1 PWP model simulations

We carry out four 1-D model mixing experiments using the PWP model to evaluate sensitivity of upper ocean temperatures to the presence and absence of the salinity barrier layer. We initialized the PWP model with temperature and salinity profiles extracted from the pre-storm glider data at two locations and times (Figure 6). Specifically, 08/19 ~02:00 where NG645 crossed ahead of Ida's future track, and 08/28 00:00 as NG645 was station keeping to the right of the storm track (Figures 1–3). We selected these two sites to focus on 1) the region of high salinity stratification directly beneath the storms track and 2) the region to the right of the track where the glider was located throughout the storm event.

Twin model experiments for each site included cases with the barrier layer removed at each study site. Initial profiles of temperature and salinity from the glider and calculated ILD and MLDs are presented in Figure 6 at each site. At both sites the initial surface temperatures were >30°C. At the along-track site

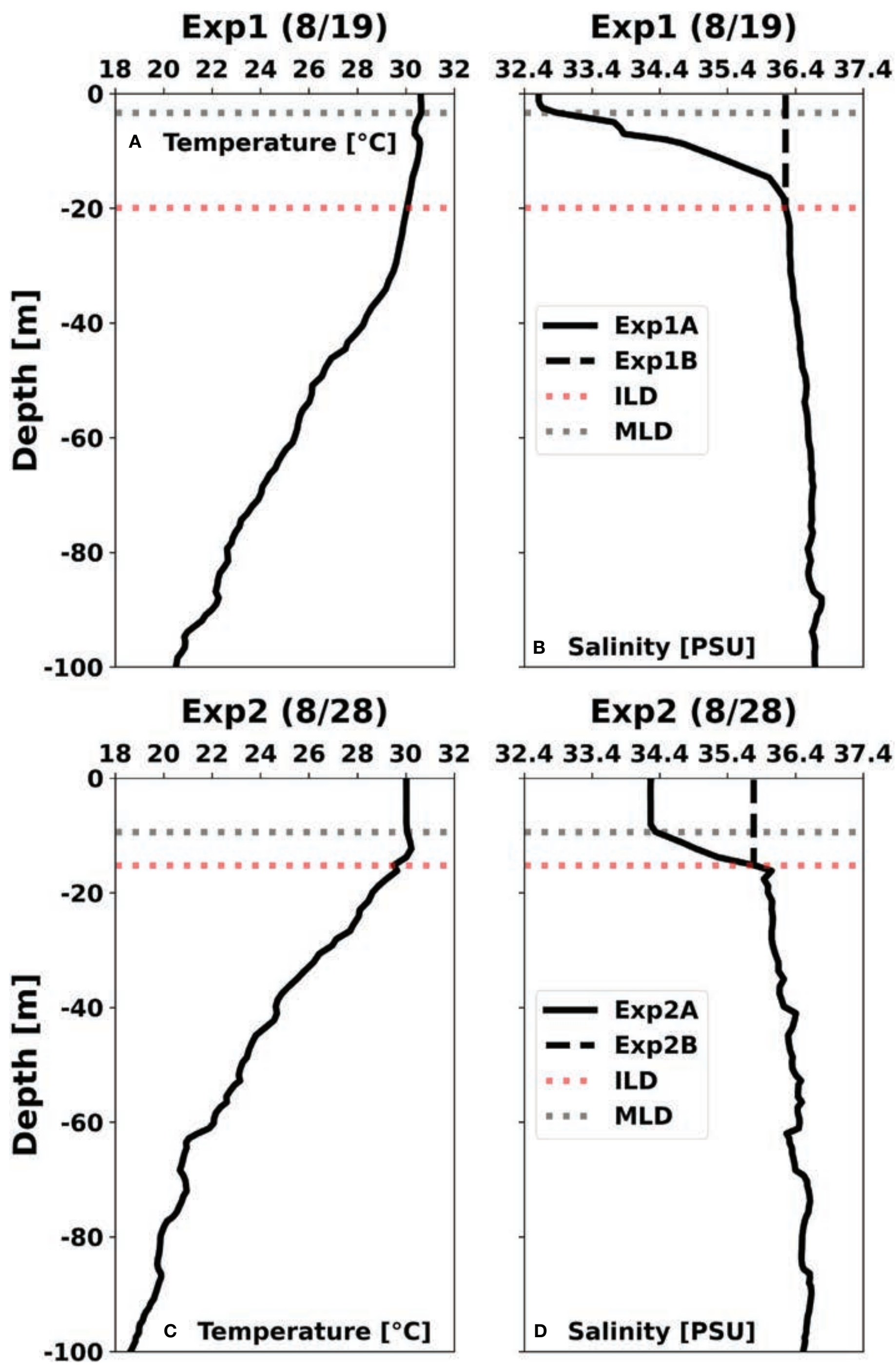

FIGURE 6
Initial profiles of temperature **(A, C)** and salinity **(B, D)** from Glider NG645 on 8/19 and 8/28 used to initalize PWP experiments 1 **(A, B)** and 2 **(B, C)**. Panel a shows the initial temperature profiles from 8/19 for Exp1A and Exp1B. Panel b) shows the initial salinity profiles from 8/19 for Exp1A inclusive of the barrier layer (solid black line) and Exp1B - barrier layer removed (dashed black line). Panel c shows the initial temperature profiles from 8/28 for Exp2A and Exp2B. **(D)** shows the initial salinity profiles from 8/28 for Exp2A inclusive of the barrier layer (solid black line) and Exp2B - barrier layer removed (dashed black line). In all panels, the dashed gray line and dashed red line represent the MLD and ILD, respectively.

(Figures 6A, B) the MLD and ILD were at 3.29m and 19.9m, respectively resulting in a 16.61m BLT. Salinity above the MLD was at 32.5 PSU and increased to 36.3 PSU at the ILD. At the glider station keep location (Figures 6C, D) the initial MLD was deeper at 9.36m and ILD shallower at 15.17m, resulting in a smaller barrier layer of 5.81m. Salinity above the MLD was 34.4 PSU and increased to 35.79 PSU at the ILD. To remove the barrier layer at both sites we extrapolated the salinity from the ILD to the sea surface as in Wang et al. (2011). Experiment 1A (Exp1A) and 1B (Exp1B) were carried out with the initial profiles from the along-track site, while experiment 2A (Exp2A) and 2B (Exp2B) were carried out with initial profiles from NG645's station keeping location. B experiments used extrapolated salinity to artificially remove the barrier layer as shown in Figures 6B, D.

Wind speeds extracted from the HRRR model at each study location are shown in Figure 7. Winds at both locations rapidly increased late on 8/28 and through 8/29 reaching a first peak just ahead of eye-passage at 8/29 08:00. Winds at the glider station-keep location used in Exp2A and Exp2B steadily decreased following this peak, while at the along-track site used in Exp1A and Exp1B winds dropped dramatically as the eye-passed and reached a second, higher, peak of over 30 m s^{-1} from the back side of the storm just before it made landfall. Wind speeds then dramatically weakened as the storm moved inland.

PWP model results for Exp1A and Exp1B are presented in Figures 8, 9. Minimal upper ocean mixing occurred during the first 6 days of the simulation thus we present results starting on 8/25 through when Ida was downgraded to a tropical storm. The upper ocean in Exp1B, with the barrier layer removed, cooled earlier and the ILD and MLD reached deeper depths than Exp1A. In Exp1A SSTs were reduced by 0.19°C at eye-passage and a total of 0.44°C by landfall. ILD and MLD reached 38m and 34m, respectively (Figures 8A, C). In Exp1B SSTs were reduced by 0.4°C at eye-passage and a total of 0.71°C by landfall. The ILD and MLD reached 44m and 41m, respectively (Figures 8B, D). With the barrier layer removed, SST cooled by an additional 0.21°C by eye-passage and 0.27°C by landfall (Figure 9B). Inclusion of the barrier layer resulted in an additional 7% cumulative enthalpy flux to the atmosphere over the 16 hours from 8/29 to landfall (Figure 9D).

For Exp2A and Exp2B presented in Figures 10, 11 we show the period 08/28 00:00 through 08/30 09:00. The upper ocean in Exp2B, with the barrier layer removed, cooled earlier and the ILD and MLD reached deeper depths than Exp2A. In Exp2A SSTs were reduced by 0.44°C at eye-passage and a total of 0.65°C by landfall. ILD and MLD reached 29m and 28m, respectively (Figures 10A, C). In Exp2B SSTs were reduced by 0.73°C at eye-passage and a total of 0.98°C by landfall. ILD and MLD reached 32m and 31m, respectively (Figures 10B, D). Thus, with the barrier layer removed SST cooled by an additional 0.29°C by eye passage and 0.34°C by landfall (Figure 11B). Similar to Exp1, inclusion of the barrier layer resulted in an additional 11% cumulative enthalpy flux over the 16 hours from 8/29 to landfall (Figure 11D).

The Exp2A control run cooled by 0.66°C and 1.31°C less than the glider observed at eye-passage and landfall, respectively. The PWP experiments presented here represent 40% (33%) of the glider observed cooling at eye-passage (landfall). This suggests that PWP captures a significant portion of the cooling and ocean processes ahead of eye-passage but has less utility in the period between eye-passage and landfall. As described previously, we did not expect PWP to capture the full range of 3-D upper ocean mixing processes (advection, Ekman pumping, inertial mixing, waves, and sub-mesoscale stratified upper ocean mixing processes). However, the twin model experiments indicate that for the 1-D shear driven processes represented by PWP the SST cooling during the landfall approach of Hurricane Ida had a large sensitivity to the presence and absence of the barrier layer. This finding agrees with idealized PWP simulations from Rudzin et al. (2019) that showed sensitivity in SST cooling to shear-driven mixing between strong and weak salinity stratification for TC wind forcing.

As an additional comparison we calculate the dynamic potential intensity as described in section 2.3, specifically for the initial conditions extracted from the glider in Exp1A and modified for the removal of the barrier layer in Exp1B at the along-track site. Exp1A initial conditions (Table 1) showed a shallower mixing depth, warmer depth integrated temperature, and higher DPI than Exp1B with the barrier layer removed. The removal of the barrier layer reduced stratification, deepened the initial MLD, resulting in a deeper mixing depth. The enhanced cooling in Exp1B led to a decrease in DPI of 5.01 m s^{-1}, which is approximately the order of the 2022 NHC official intensity error (Cangialosi et al., 2020). These findings along with the PWP model simulations show that there is a demonstrated potential for the freshwater barrier layer to enhance enthalpy flux into the atmosphere by restricting upper ocean cooling, thus contributing to Ida's continued intensification ahead of landfall.

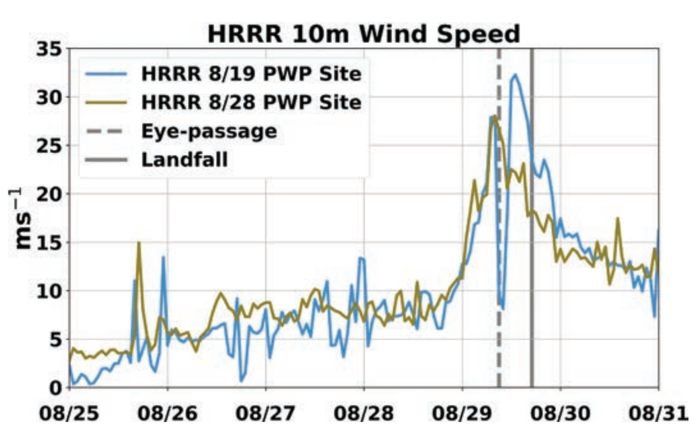

FIGURE 7
10m HRRR windspeeds extracted from the 8/19 Exp1 study-site (blue) and 8/28 Exp2 study-site (brown) used to force PWP simulations. The vertical lines represent the times at which Hurricane Ida's eye-passage (dashed line) and landfall (solid line).

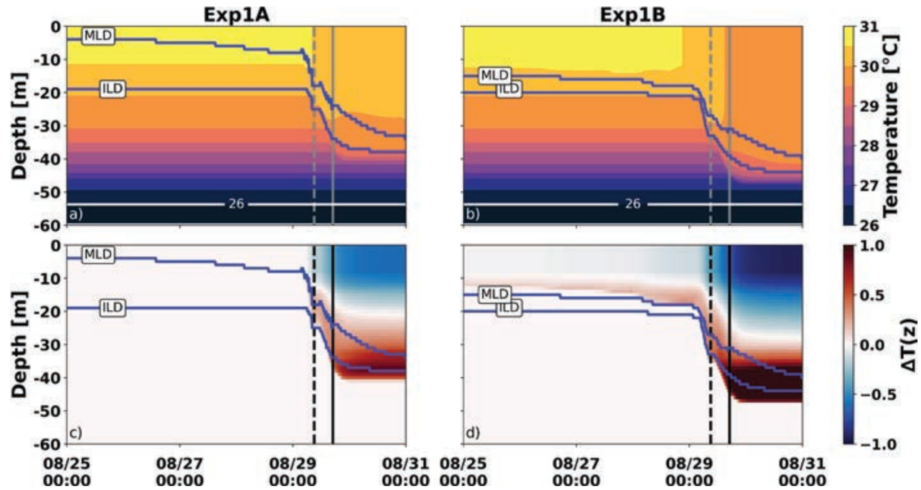

FIGURE 8
PWP model runs initialized using the 8/19 NG645 profile and simulated from 8/19 00:00 to 8/31 00:00. Exp1A **(A, C)** is inclusive of the barrier layer and depicts **(A)** temperature with the 26°C isotherm (white) and **(C)** contoured change in temperature since initialization. The MLD and ILD are labeled and contoured in blue. Panels **(B, D)** are similar but for Exp1B with the barrier layer removed as shown in Figure 6. The vertical lines represent the times at which Hurricane Ida passed the glider (dashed line) and made landfall (solid line). We limit the beginning display period from 8/25 00:00 as limited ocean cooling occurred before that time.

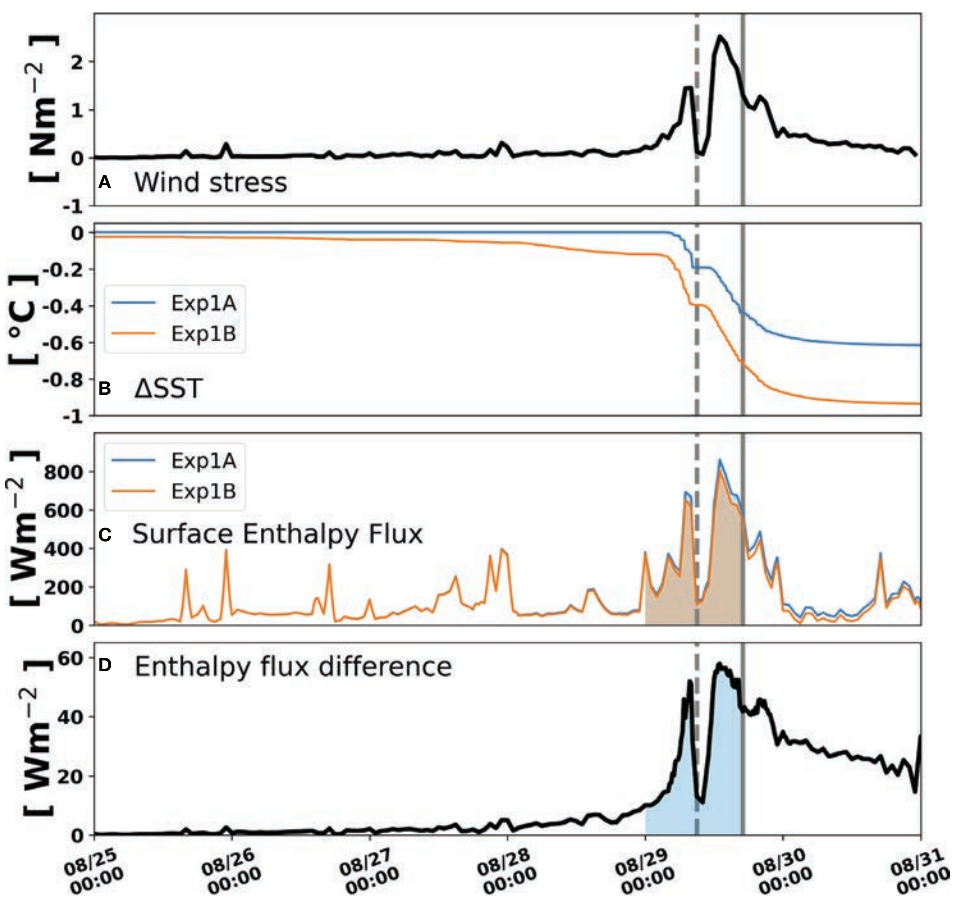

FIGURE 9
Time-series plots from experiment 1 **(A)** wind stress, **(B)** ΔSST from both Exp1A (blue) and Exp1B (orange), **(C)** surface enthalpy flux from both Exp1A (blue) and Exp1B (orange), and **(D)** difference (Exp1A – Exp1B). The shading in c and d represents the period used to calculate the cumulative enthalpy flux. The vertical lines represent the times at which Hurricane Ida passed the glider (dashed line) and made landfall (solid line).

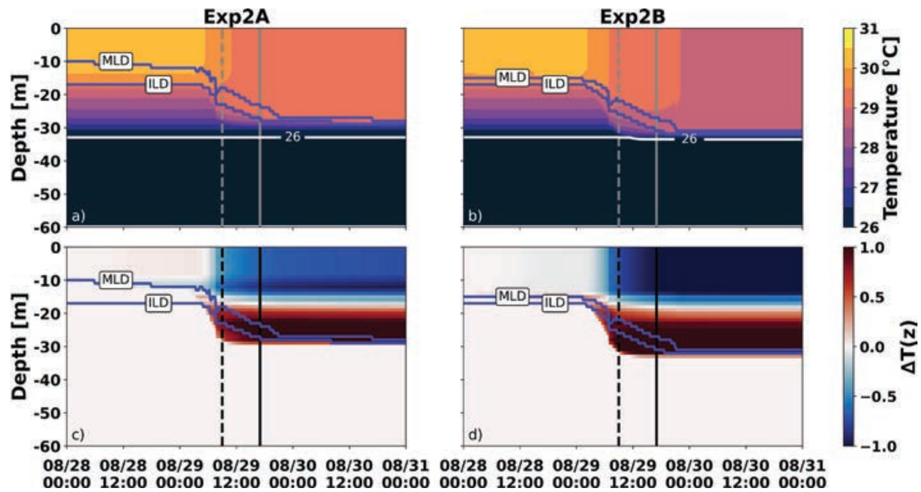

FIGURE 10
As-in Figure 8, but for experiment 2 initialized on 08/28 00:00.

4 Discussion

Observations from Slocum glider NG645 ahead of and beneath Hurricane Ida (2021) in the GoM captured upper ocean cooling ahead of eye-passage and landfall (Figures 4, 5). Despite this cooling, SST at the glider location just prior to landfall remained warm (28.1°C), approximately 3.5°C above T100 (24.6°C) at landfall. This indicates that the standard assumption made in

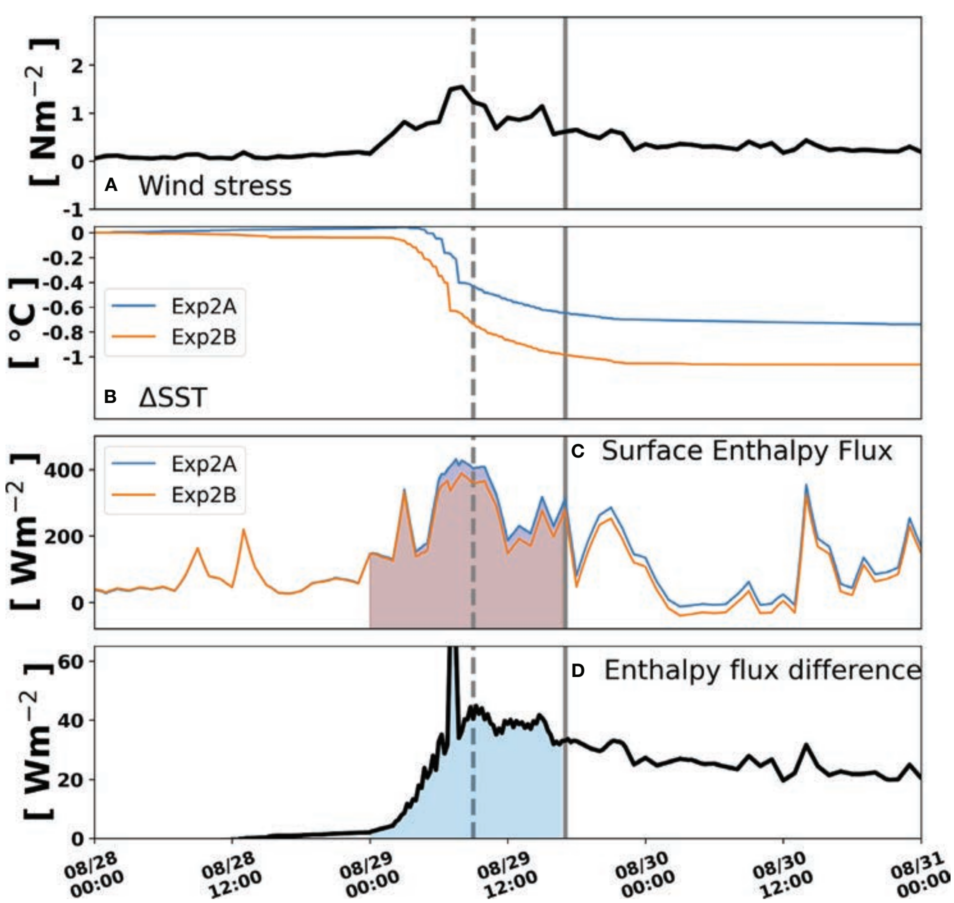

FIGURE 11
As-in Figure 9, but for experiment 2 initialized on 08/28 00:00.

10.3389/fmars.2023.1224609

TABLE 1 A table of dynamic potential intensity parameters showing the difference between Exp1A (Barrier Layer) and Exp1B (No Barrier Layer) initial conditions from the glider location on 08/19.

	L_{pred} [m]	T_{dy} [°C]	DPI [ms^{-1}]
Exp1A (Barrier Layer)	14.51	30.52	84.49
Exp1B (No Barrier Layer)	18.10	30.10	79.48
Difference	3.58	0.42	5.01

Price (2009) that a typical category 3 hurricane will mix to ~100m was not valid for Hurricane Ida (2021) passing over the northern GoM. The freshwater barrier layer located over the deep ocean suggests that the northern GoM could be added to the list of regions where T100 is an unreliable metric such as the Bay of Bengal (McPhaden et al., 2009) or western Tropical Pacific (Price, 2009). Additionally, the glider observed OHC was just above the intensification threshold of 60 kJ cm^{-2} suggested by Mainelli et al. (2008) in its pre-storm survey period (Figure 6) and well below that threshold during the glider station keep period. Despite this relatively low OHC, Ida underwent RI and maintained its status as a Category 4 storm as it passed over the glider sampled region and made landfall. This indicates that OHC in this region was a poor metric for storm intensification, again likely due to salinity stratification as described in Price (2009). In contrast, both in the pre-storm survey and glider station- keep time periods (Figure 5) PEA of the upper 100m suggested the water column was highly stable. For reference, the PEA of the initial profiles used in PWP Exp1A and Exp2A were 460 and 477 J m^{-3}. With the barrier layer removed in Exp1B and Exp2B the initial PEAs were reduced to 327 and 381 J m^{-3}, respectively. This represents a reduction in stability of 29% and 20%, respectively with the largest reduction in the along-track region.

The reduced cooling in PWP experiments at both the along-track and glider locations simulated here due to the barrier layer is consistent with previous studies focused on other regions. In these twin model experiments the salinity barrier layer inhibited SST cooling in Exp1 (and Exp2) by 53% (57%) ahead-of-eye passage, 38% (32%) by landfall. For example, Balaguru et al. (2012) identified a 33% reduction in cooling due to barrier layers in the category 4 hurricane Omar (2008) in the northeastern Caribbean. In the Bay of Bengal Neetu et al. (2012) showed that monsoon generated barrier layers are responsible for a ~40% reduction in cooling by TCs relative to post monsoon seasons. Idealized PWP experiments in Rudzin et al. (2018) were designed to represent a range of ocean features in the eastern Caribbean that showed cooling ranges of 0.4 to 0.8 °C, also consistent with the total cooling presented here. Similarly, an idealized coupled numerical modeling barrier layer sensitivity study (Hlywiak and Nolan, 2019) showed reduced cooling of more than 0.6°C for TCs that were slow moving, strong, and with favorable atmospheric conditions for generation using barrier layer conditions typical of the Amazon-Orinoco River Plume. Balaguru et al. (2020) also carried out extensive PWP model experiments with and without salinity stratification for the Amazon-Orinoco River plume to evaluate the connection between rapid intensification (RI) and salinity barrier layer cooling inhibition. They found for idealized RI cases, salinity barrier layers reduced SST cooling by up to 0.3°C, which is consistent with what we simulated for a rapidly intensifying Hurricane Ida. For non-RI cases in their study, salinity barrier layers were only responsible for inhibiting 0.15°C of cooling, highlighting potential feedbacks between barrier layers and RI. Despite their findings in the Amazon-Orinoco River Plume, they found that barrier layers had limited impact on storm intensity in the GoM. Their study utilized the Navy Global Ocean Forecast System (GOFS) to initialize PWP. The dearth of upper ocean observations to support data assimilation in the northern GoM, and practice of using climatological river inputs in GOFS may have limited their ability to resolve the sharp upper ocean salinity gradients such as those observed by NG645.

One of the few studies (Le Hénaff et al., 2021) of barrier layer and hurricane interactions in the GoM identified a barrier layer ahead of Hurricane Michael (2018). They identified SSS<34 PSU to as far south as 27.5°N, above the 32.6 PSU SSS observed in the pre-storm survey by NG645 (Figure 2) but ~75km further south. However, a study of the intensification of Hurricane Isaac (Jaimes et al., 2016), which followed a similar track to Ida, found no evidence of barrier layers in profiles collected from air-deployed expendables. A recently published study of the ocean conditions ahead of Hurricane Sally (2020) (John et al., 2023) identified similar freshwater salinity barrier layers from the Mississippi River Plume as observed here in Ida, which contributed to continued intensification over the continental shelf. A study investigated the evolution of barrier layers during TCs globally with Argo floats (Steffen and Bourassa, 2018) using a barrier layer potential energy (BLPE) metric with similarities to PEA. They showed Argo floats between 2001 and 2014 with both low BLPE approaching 0 J m^{-2} and high >1200 J m^{-2} near overlapping at our study site. These studies and our findings indicate that barrier layers in the GoM are highly variable and can cover broad areas that hurricanes, such as Isaac (2012), Michael (2018), Sally (2020), and Ida (2021) must pass over before making landfall, and can have an impact on intensity.

The observations from NG645 and the results from the PWP sensitivity study highlight the potential importance of salinity stratification on the deep open ocean region off the continental shelf in the northern GoM, which is clearly influenced by coastal freshwater inputs. In the northern GoM a variety of thermal stratification regimes exist. In the nearshore environment it can be warm throughout the water column or highly thermally stratified. Ahead of Hurricane Michael (2018) subsurface temperatures of 22°C were observed near 10m depth to the northeast of our study-site (Dzwonkowski et al., 2020). This feature was removed during a marine heatwave that dramatically warmed the shelf waters to over 28°C in a few days. Further offshore the presence of LC/LCE waters can lead to warm and salty features that extend throughout the upper 100m and beyond (Elliott, 1982). In contrast, the region between the LC/LCE and continental shelf is typically warm at the sea surface but can have cooler waters beneath the seasonal thermocline in the upper ocean, as evidenced in the glider observations by NG645. In this “gap” region between the LC/LCEs and the continental shelf where the Mississippi River plume can be exported off the continental shelf, our findings suggest that salinity barrier layers can increase stratification and further isolate the subsurface cold water from mixing and cooling the surface. These warm and fresh surface waters would theoretically support storm intensification approaching landfall, or at a minimum reduce the oceans contribution to storm weakening.

5 Conclusion

We have shown that the standard upper ocean metrics OHC and T100 were likely not robust indicators of storm intensity in the deep waters of the northern GoM escarpment ahead of Ida's landfall. An alternative stability metric, PEA, and 1-D upper ocean mixing model experiments indicated that the presence of a freshwater barrier layer likely inhibited additional sea surface cooling and enhanced enthalpy flux under a rapidly intensifying Hurricane Ida (2021). In our experiments the removal of the barrier led to earlier, more rapid, and greater cooling, which resulted in reduced enthalpy flux to the atmosphere, and a greater DPI. This is particularly critical as it highlights an essential ocean feature, a Mississippi River plume freshwater barrier layer, in the "gap" region south of the continental shelf and north of the LC/LCE that landfalling hurricanes must cross before impacting coastal communities. While the limited utility of OHC on continental shelves and T100 in freshwater stratified layers is well-known (McPhaden et al., 2009; Price, 2009; Potter et al., 2019), salinity observations are severely lacking in this region. This study highlights the need and capability of expanded ocean observing assets along the shelf-break of the GoM to identify freshwater barrier layers and improve intensity forecasts of landfalling hurricanes in this vulnerable region.

Data availability statement

The datasets presented in this study can be found in online repositories. The names of the repository/repositories and accession number(s) can be found below: NG645 was operated by the Naval Oceanographic Office and coordinated by the Integrated Ocean Observing System (IOOS) Regional Association Gulf of Mexico Coastal Ocean Observing System through the Commercial Engagement Through Ocean Technology Act of 2018. Data sources included glider NG645 (https://gliders.ioos.us/erddap/tabledap/ng645-20210613T0000.html), Buoy 42040 from the National Data Buoy Center (https://www.ndbc.noaa.gov/station_history.php?station=42040). The PWP model was adapted from https://github.com/earlew/pwp_python_00.

Author contributions

TM, SC, and SG designed the initial experiments and carried out analysis. JE generated figures and carried out data analysis. SC, SG, JR, and ST provided scientific guidance and paper edits. TM prepared the manuscript for publication. All authors contributed to the article and approved the submitted version.

Funding

This work included support by the Integrated Ocean Observing System directed funding via the Mid Atlantic Regional Association Coastal Ocean Observing System (MARACOOS) through NOAA Grant NA21NOS0120096.

Acknowledgments

We thank two reviewers for their thoughtful comments that significantly enhanced this paper. NG645 was operated by the Naval Oceanographic Office and coordinated by the Integrated Ocean Observing System (IOOS) Regional Association Gulf of Mexico Coastal Ocean Observing System through the Commercial Engagement Through Ocean Technology Act of 2018. Data sources included glider NG645 (https://gliders.ioos.us/erddap/tabledap/ng645-20210613T0000.html), Buoy 42040 from the National Data Buoy Center (https://www.ndbc.noaa.gov/station_history.php?station=42040). The PWP model was adapted from https://github.com/earlew/pwp_python_00.

Conflict of interest

The authors declare that the research was conducted in the absence of any commercial or financial relationships that could be construed as a potential conflict of interest.

References

Balaguru, K., Chang, P., Saravanan, R., Leung, L. R., Xu, Z., Li, M., et al. (2012). Ocean barrier layers' effect on tropical cyclone intensification. *Proc. Natl. Acad. Sci.* 109, 14343–14347. doi: 10.1073/PNAS.1201364109.10.1073/PNAS.1201364109

Balaguru, K., Foltz, G. R., Leung, L. R., Asaro, E. D., Emanuel, K. A., Liu, H., et al. (2015). Dynamic Potential Intensity: An improved representation of the ocean's impact on tropical cyclones. *Geophys. Res. Lett.* 42, 6739–6746. doi: 10.1002/2015GL064822

Balaguru, K., Foltz, G. R., Leung, L. R., Hagos, S. M., and Judi, D. R. (2018). On the use of ocean dynamic temperature for hurricane intensity forecasting. *Weather Forecast.* 33, 411–418. doi: 10.1175/WAF-D-17-0143.1

Balaguru, K., Foltz, G. R., Leung, L. R., Kaplan, J., Xu, W., Reul, N., et al. (2020). Pronounced impact of salinity on rapidly intensifying tropical cyclones. *Bull. Am. Meteorol. Soc* 101, E1497–E1511. doi: 10.1175/BAMS-D-19-0303.1

Beven, J. II, Hagan, A., and Berg, R. (2022) *Tropical cyclone report: Hurricane Ida* (National Hurricane Center). Available at: https://www.nhc.noaa.gov/data/tcr/AL092021_Ida.pdf (Accessed January 6, 2023).

Black, P. G., D'Asaro, E. A., Sanford, T. B., Drennan, W. M., Zhang, J. A., French, J. R., et al. (2007). Air–sea exchange in hurricanes: synthesis of observations from the coupled boundary layer air–sea transfer experiment. *Bull. Am. Meteorol. Soc* 88, 357–374. doi: 10.1175/BAMS-88-3-357

Cangialosi, J. P., Blake, E., Demaria, M., Penny, A., Latto, A., Rappaport, E., et al. (2020). Recent progress in tropical cyclone intensity forecasting at the national hurricane center. *Weather Forecast.* 35, 1913–1922. doi: 10.1175/WAF-D-20-0059.1

Cione, J. J., and Uhlhorn, E. W. (2003). Sea surface temperature variability in hurricanes: implications with respect to intensity change. *Mon. Weather Rev.* 131, 1783–1796. doi: 10.1175//2562.1

D'Asaro, E., Sanford, T. B., Niiler, P. P., and Terrill, E. J. (2007). Cold wake of hurricane Frances. *Geophys. Res. Lett.* 34, L15609. doi: 10.1029/2007GL030160

de Boyer Montégut, C., Mignot, J., Lazar, A., and Cravatte, S. (2007). Control of salinity on the mixed layer depth in the world ocean: 1. General description. *J. Geophys. Res. Oceans* 112, 1–12. doi: 10.1029/2006JC003953

Domingues, R., Goni, G., Bringas, F., Lee, S.-K., Kim, H.-S., Halliwell, G., et al. (2015). Upper ocean response to Hurricane Gonzalo, (2014): Salinity effects revealed by targeted and sustained underwater glider observations. *Geophys. Res. Lett.* 42, 7131–7138. doi: 10.1002/2015GL065378

Dzwonkowski, B., Coogan, J., Fournier, S., Lockridge, G., Park, K., and Lee, T. (2020). Compounding impact of severe weather events fuels marine heatwave in the coastal ocean. *Nat. Commun.* 11, 1–10. doi: 10.1038/s41467-020-18339-2

Dzwonkowski, B., Fournier, S., Lockridge, G., Coogan, J., Liu, Z., and Park, K. (2021). Cascading weather events amplify the coastal thermal conditions prior to the shelf transit of hurricane sally, (2020). *J. Geophys. Res. Oceans* 126, e2021JC017957. doi: 10.1029/2021JC017957

Elliott, B. A. (1982). Anticyclonic rings in the gulf of Mexico. *J. Phys. Oceanogr.* 12, 1292–1309. doi: 10.1175/1520-0485(1982)012<1292:ARITGO>2.0.CO;2

Emanuel, K. A. (1986). An air-sea interaction theory for tropical cyclones. Part I: steady-state maintenance. *J. Atmospheric Sci.* 43, 585–605. doi: 10.1175/1520-0469(1986)043<0585:AASITF>2.0.CO;2

Foltz, G. R., and McPhaden, M. J. (2009). Impact of barrier layer thickness on SST in the central tropical north atlantic. *J. Clim.* 22, 285–299. doi: 10.1175/2008JCLI2308.1

Glenn, S. M., Miles, T. N., Seroka, G. N., Xu, Y., Forney, R. K., Yu, F., et al. (2016). Stratified coastal ocean interactions with tropical cyclones. *Nat. Commun.* 7, 1–10. doi: 10.1038/ncomms10887

Gramer, L. J., Zhang, J. A., Alaka, G., Hazelton, A., and Gopalakrishnan, S. (2022). Coastal downwelling intensifies landfalling hurricanes. *Geophys. Res. Lett.* 49, e2021GL096630. doi: 10.1029/2021GL096630

Grodsky, S. A., Reul, N., Lagerloef, G., Reverdin, G., Carton, J. A., Chapron, B., et al. (2012). Haline hurricane wake in the Amazon/Orinoco plume: AQUARIUS/SACD and SMOS observations. *Geophys. Res. Lett.* 39, 1–8. doi: 10.1029/2012GL053335

Hlywiak, J., and Nolan, D. S. (2019). The influence of oceanic barrier layers on tropical cyclone intensity as determined through idealized, coupled numerical simulations. *J. Phys. Oceanogr.* 49, 1723–1745. doi: 10.1175/JPO-D-18-0267.1

Jaimes, B., Shay, L. K., and Brewster, J. K. (2016). Observed air-sea interactions in tropical cyclone Isaac over Loop Current mesoscale eddy features. *Dyn. Atmospheres Oceans* 76, 306–324. doi: 10.1016/j.dynatmoce.2016.03.001

Jaimes, B., Shay, L. K., and Uhlhorn, E. W. (2015). Enthalpy and momentum fluxes during hurricane Earl relative to underlying ocean features. *Mon. Wea. Rev.* 143, 111–131. doi: 10.1175/MWR-D-13-00277.1

John, E. B., Balaguru, K., Leung, L. R., Foltz, G. R., Hetland, R. D., and Hagos, S. M. (2023). Intensification of Hurricane Sally, (2020) over the Mississippi River plume. *Weather Forecast.* 1, 1391–1404.. doi: 10.1175/WAF-D-22-0191.1

Knapp, K. R., Diamond, H. J., Kossin, J. P., Kruk, M. C., and Schreck, C. J. I. (2018) *International best track archive for climate stewardship (IBTrACS) project, version 4* (Accessed January 6, 2023).

Knapp, K. R., Kruk, M. C., Levinson, D. H., Diamond, H. J., and Neumann, C. J. (2010). The international best track archive for climate stewardship (IBTrACS): unifying tropical cyclone data. *Bull. Am. Meteorol. Soc* 91, 363–376. doi: 10.1175/2009BAMS2755.1

Le Hénaff, M., Domingues, R., Halliwell, G., Zhang, J. A., Kim, H. S., Aristizabal, M., et al. (2021). The role of the gulf of Mexico ocean conditions in the intensification of hurricane michael, (2018). *J. Geophys. Res. Oceans* 126, 1–28. doi: 10.1029/2020JC016969

Leipper, D. F., and Volgenau, D. (1972). Hurricane heat potential of the Gulf of Mexico. *J. Phys. Oceanogr.* 2, 218–224. doi: 10.1175/1520-0485(1972)002<0218:HHPOTG>2.0.CO;2

Lim, H. S., Miles, T. N., Glenn, S., Kim, D., Kim, M., Shim, J. S., et al. (2020). Rapid ocean destratification by typhoon soulik over the highly stratified waters of west jeju island, korea. *J. Coast. Res.* 95, 1480–1484. doi: 10.2112/SI95-285.1

Lukas, R., and Lindstrom, E. (1991). The mixed layer of the western equatorial Pacific Ocean. *J. Geophys. Res. Oceans* 96, 3343–3357. doi: 10.1029/90JC01951

Mainelli, M., DeMaria, M., Shay, L. K., and Goni, G. (2008). Application of oceanic heat content estimation to operational forecasting of recent atlantic category 5 hurricanes. *Weather Forecast.* 23, 3–16. doi: 10.1175/2007WAF2006111.1

McPhaden, M. J., Foltz, G. R., Lee, T., Murty, V. S. N., Ravichandran, M., Vecchi, G. A., et al. (2009). Ocean-atmosphere interactions during cyclone nargis. *Eos Trans. Am. Geophys. Union* 90, 53–54. doi: 10.1029/2009EO070001

Miles, T., Seroka, G., and Glenn, S. (2017). Coastal ocean circulation during Hurricane Sandy. *J. Geophys. Res. Oceans* 122, 7095–7114. doi: 10.1002/2017JC013031

Miles, T. N., Zhang, D., Foltz, G. R., Zhang, J. A., Meinig, C., Bringas, F., et al. (2021). Uncrewed ocean gliders and saildrones support hurricane forecasting and research. *Oceanography* 34, 78–81. doi: 10.5670/oceanog.2021.supplement.02-28

Mrvaljevic, R. K., Black, P. G., Centurioni, L. R., Chang, Y.-T., D'Asaro, E., Jayne, S. R., et al. (2013). Observations of the cold wake of Typhoon Fanapi, (2010). *Geophys. Res. Lett.* 40, 316–321. doi: 10.1029/2012GL054282

Neetu, S., Lengaigne, M., Vincent, E. M., Vialard, J., Madec, G., Samson, G., et al. (2012). Influence of upper-ocean stratification on tropical cyclone-induced surface cooling in the Bay of Bengal. *J. Geophys. Res. Oceans* 117, 1–19.. doi: 10.1029/2012JC008433

Pailler, K., Bourlès, B., and Gouriou, Y. (1999). The barrier layer in the western tropical Atlantic Ocean. *Geophys. Res. Lett.* 26, 2069–2072. doi: 10.1029/1999GL900492

Potter, H., DiMarco, S. F., and Knap, A. H. (2019). Tropical cyclone heat potential and the rapid intensification of hurricane harvey in the texas bight. *J. Geophys. Res. Oceans* 124, 2440–2451. doi: 10.1029/2018JC014776

Potter, H., and Rudzin, J. E. (2021). Upper-ocean temperature variability in the gulf of Mexico with implications for hurricane intensity. *J. Phys. Oceanogr.* 51, 3149–3162. doi: 10.1175/JPO-D-21-0057.1

Powell, M. D., Vickery, P. J., and Reinhold, T. (2003). Reduced drag coefficient for high wind speeds in tropical cyclones. *Nature* 422, 279–283. doi: 10.1038/nature01481

Price, J. F. (2009). Metrics of hurricane-ocean interaction: vertically-integrated or vertically-averaged ocean temperature? *Ocean Sci.* 5, 351–368. doi: 10.5194/os-5-351-2009

Price, J. F., Weller, R. A., and Pinkel, R. (1986). Diurnal cycling: Observations and models of the upper ocean response to diurnal heating, cooling, and wind mixing. *J. Geophys. Res.* 91, 8411. doi: 10.1029/JC091iC07p08411

Rudzin, J. E., Chen, S., Sanabia, E. R., and Jayne, S. R. (2020). The air-sea response during hurricane irma's, 2017) rapid intensification over the amazon-orinoco river plume as measured by atmospheric and oceanic observations. *J. Geophys. Res. Atmospheres* 125, e2019JD032368. doi: 10.1029/2019JD032368

Rudzin, J. E., Shay, L. K., Jaimes, B., and Brewster, J. K. (2017). Upper ocean observations in eastern Caribbean Sea reveal barrier layer within a warm core eddy. *J. Geophys. Res. Oceans* 122, 1057–1071. doi: 10.1002/2016JC012339

Rudzin, J. E., Shay, L. K., and Jaimes de la Cruz, B. (2019). The impact of the amazon–orinoco river plume on enthalpy flux and air–sea interaction within caribbean sea tropical cyclones. *Mon. Weather Rev.* 147, 931–950. doi: 10.1175/MWR-D-18-0295.1

Rudzin, J. E., Shay, L. K., and Johns, W. E. (2018). The influence of the barrier layer on SST response during tropical cyclone wind forcing using idealized experiments. *J. Phys. Oceanogr.* 48, 1471–1478. doi: 10.1175/JPO-D-17-0279.1

Sanabia, E. R., and Jayne, S. R. (2020). Ocean observations under two major hurricanes: evolution of the response across the storm wakes. *AGU Adv.* 1, e2019AV000161. doi: 10.1029/2019AV000161

Schmit, T. J., Griffith, P., Gunshor, M. M., Daniels, J. M., Goodman, S. J., and Lebair, W. J. (2017). A closer look at the ABI on the GOES-R series. *Bull. Am. Meteorol. Soc* 98, 681–698. doi: 10.1175/BAMS-D-15-00230.1

Schofield, O., Kohut, J., Aragon, D., Creed, L., Graver, J., Haldeman, C., et al. (2007). Slocum gliders: robust and ready. *J. Field Robot.* 24, 473–485. doi: 10.1002/rob.20200

Sengupta, D., Goddalehundi, B. R., and Anitha, D. S. (2008). Cyclone-induced mixing does not cool SST in the post-monsoon north Bay of Bengal. *Atmospheric Sci. Lett.* 9, 1–6. doi: 10.1002/asl.162

Seroka, G., Miles, T., Xu, Y., Kohut, J., Schofield, O., and Glenn, S. (2016). Hurricane irene sensitivity to stratified coastal ocean cooling. *Mon. Weather Rev.* 144, 3507–3530. doi: 10.1175/MWR-D-15-0452.1

Seroka, G., Miles, T., Xu, Y., Kohut, J., Schofield, O., and Glenn, S. (2017). Rapid shelf-wide cooling response of a stratified coastal ocean to hurricanes. *J. Geophys. Res. Oceans* 122, 4845–4867. doi: 10.1002/2017JC012756

Simpson, J. H., Crisp, D. J., Hearn, C., Swallow, J. C., Currie, R. I., Gill, A. E., et al. (1981). The shelf-sea fronts: implications of their existence and behaviour. *Philos. Trans. R. Soc Lond. Ser. Math. Phys. Sci.* 302, 531–546. doi: 10.1098/rsta.1981.0181

Simpson, J. H., and Hunter, J. R. (1974). Fronts in the irish sea. *Nature* 250, 404–406. doi: 10.1038/250404a0

Skamarock, W. C., Klemp, J. B., Dudhia, J., Gill, D. O., Liu, Z., Berner, J., et al. (2019). *A description of the advanced research WRF model version 4* (Boulder, CO, USA: National Center for Atmospheric Research).

Smith, A. (2020). *U.S. Billion-dollar Weather and Climate Disasters 1980 - present (NCEI Accession 0209268)*. (NOAA National Centers for Environmental Information) (2020). Available at: https://www.ncei.noaa.gov/access/metadata/landing-page/bin/iso?id=gov.noaa.nodc:0209268 (Accessed January 6, 2023).

Sprintall, J., and Tomczak, M. (1992). Evidence of the barrier layer in the surface layer of the tropics. *J. Geophys. Res. Oceans* 97, 7305–7316. doi: 10.1029/92JC00407

Steffen, J., and Bourassa, M. (2018). Barrier layer development local to tropical cyclones based on argo float observations. *J. Phys. Oceanogr.* 48, 1951–1968. doi: 10.1175/JPO-D-17-0262.1

Steffen, J., and Bourassa, M. (2020). Upper-ocean response to precipitation forcing in an ocean model hindcast of hurricane gonzalo. *J. Phys. Oceanogr.* 50, 3219–3234. doi: 10.1175/JPO-D-19-0277.1

Wang, X., Han, G., Qi, Y., and Li, W. (2011). Impact of barrier layer on typhoon-induced sea surface cooling. *Dyn. Atmospheres Oceans* 52, 367–385. doi: 10.1016/j.dynatmoce.2011.05.002

Yang, Y. J., Chang, M.-H., Hsieh, C.-Y., Chang, H.-I., Jan, S., and Wei, C.-L. (2019). The role of enhanced velocity shears in rapid ocean cooling during Super Typhoon Nepartak 2016. *Nat. Commun.* 10, 1627. doi: 10.1038/s41467-019-09574-3

Zedler, S. E., Dickey, T. D., Doney, S. C., Price, J. F., Yu, X., and Mellor, G. L. (2002). Analyses and simulations of the upper ocean's response to Hurricane Felix at the Bermuda Testbed Mooring site: 13–23 August 1995. *J. Geophys. Res. Oceans* 107, 3232. doi: 10.1029/2001JC000969

Zedler, S. E., Niiler, P. P., Stammer, D., Terrill, E., and Morzel, J. (2009). Ocean's response to Hurricane Frances and its implications for drag coefficient parameterization at high wind speeds. *J. Geophys. Res.* 114, C04016. doi: 10.1029/2008JC005205

Zhang, J. A., Black, P. G., French, J. R., and Drennan, W. M. (2008). First direct measurements of enthalpy flux in the hurricane boundary layer: The CBLAST results. *Geophys. Res. Lett.* 35, 3100–3116. doi: 10.1029/2008GL034374

Zhang, F., Li, M., and Miles, T. (2018). Generation of near-inertial currents on the mid-atlantic bight by hurricane arthur, (2014). *J. Geophys. Res. Oceans* 123, 3100–3116. doi: 10.1029/2017JC013584

Zhu, Y.-J., Collins, J. M., Klotzbach, P. J., and Schreck, C. J. (2022). Hurricane ida, (2021): rapid inensification followed by slow inland decay. *Bull. Am. Meteorol. Soc* 103, E2354–E2369. doi: 10.1175/BAMS-D-21-0240.1

ICES Journal of Marine Science, 2023, Vol. 0, Issue 0, 1–14
https://doi.org/10.1093/icesjms/fsad190
Received: 4 April 2023; **revised:** 4 September 2023; **accepted:** 5 November 2023
Original Article

Overlap between the Mid-Atlantic Bight Cold Pool and offshore wind lease areas

Rebecca Horwitz [1,*], Travis N. Miles [1], Daphne Munroe [1,2], Josh Kohut [1]

[1]Department of Marine and Coastal Sciences, Rutgers University Center for Ocean Observing Leadership, 71 Dudley Rd, New Brunswick, NJ 08901, United States
[2]Rutgers the State University of New Jersey, Haskin Shellfish Research Laboratory, 6959 Miller Ave, Port Norris, NJ 08349, United States
*Corresponding author. Department of Marine and Coastal Sciences, Rutgers University Center for Ocean Observing Leadership, 71 Dudley Rd, New Brunswick, NJ 08901, United States. E-mail: bhorwitz@marine.rutgers.edu

Abstract

The Mid-Atlantic Cold Pool is a seasonal mass of cold bottom water that extends throughout the Mid-Atlantic Bight (MAB). Formed from rapid vernal surface warming, the Cold Pool dissipates in the fall due to mixing events such as storms. The Cold Pool supports a myriad of MAB coastal ecosystems and economically valuable commercial and recreational fisheries. Offshore wind energy has been rapidly developing within the MAB in recent years. Studies in Europe demonstrate that offshore wind farms can impact ocean mixing and hence seasonal stratification; there is, however, limited information on how MAB wind development will affect the Cold Pool. Seasonal overlap between the Cold Pool and pre-construction wind lease areas at varying distances from shore in the MAB was evaluated using output from a data-assimilative ocean model. Results highlight overlap periods as well as a thermal gradient that persists after bottom temperatures warm above the threshold typically used to identify the Cold Pool. These results also demonstrate cross-shelf variability in Cold Pool evolution. This work highlights the need for more focused ocean modeling studies and observations of wind farm effects on the MAB coastal environment.

Keywords: stratification; bottom temperature; Cold Pool; offshore wind; Mid-Atlantic Bight

Introduction

The Mid-Atlantic Cold Pool is a seasonal mass of cold bottom water extending throughout the Mid-Atlantic Bight (MAB) from Nantucket, Massachusetts to Cape Hatteras, North Carolina, resulting in one of the largest thermal gradients in the world. The MAB Cold Pool is present primarily between depths of 20–100 m (Bigelow 1933). This stratification and the associated cold bottom temperatures and nutrient-rich environment support a diverse coastal ecosystem, including economically important recreational and commercial fisheries (Miles et al. 2021). Although defined wind lease areas are in flux, as of 2023, within the MAB, over 2 million acres of the continental shelf have been leased for offshore wind energy projects that are under development, including sites that overlap with the seasonal Cold Pool (Miles et al. 2021, Musial et al. 2022, Methratta et al. 2023). Limited information exists about the extent of this overlap as well as the impact of these future wind turbines on the Cold Pool (Miles et al. 2021).

The Cold Pool develops in the winter as cold water from Nantucket Shoals, north of the MAB, is transported southward to well-mixed MAB water (Houghton et al. 1982, Ou and Houghton 1982). In the spring, as surface water temperature increases and storm frequency decreases, a strong thermocline develops that isolates this cold and relatively fresh bottom water known as the Cold Pool (Bigelow 1933, Houghton et al. 1982). Stratification within the MAB is controlled and stabilized by salinity and temperature (Castelao et al. 2010). The strength of the thermocline, driven primarily by temperature, reaches a seasonal peak between July and August (Castelao et al. 2010). As surface temperatures begin to decrease in the late summer and early fall, the thermocline weakens, and fall storms eventually mix warmed stratified surface waters to the bottom, dissipating the Cold Pool (Bigelow 1933, Houghton et al. 1982, Ou and Houghton 1982, Castelao et al. 2010, Lentz 2017, Chen et al. 2018). The seasonal interannual variability of the Cold Pool can be influenced by annual large-scale climate and oceanic processes such as increased upwelling conditions or more frequent storm events (Houghton et al. 1982, Glenn et al. 2004, Li et al. 2014, Chen et al. 2018; Chen and Curchitser 2020).

There is along-shelf variation of the Cold Pool within the MAB that defines three distinct regions: the northern MAB, the central MAB, and the southern MAB (Bigelow 1933, Castelao et al. 2010, Lentz 2017). The geography of the coastline along the Central MAB enhances the coastal upwelling response to summertime southerly winds (Castelao et al. 2010). The proximity to the Hudson River within the central MAB also changes the salinity within the Cold Pool in this region compared to the northern and southern MABs (Castelao et al. 2010). The Central MAB has the coldest bottom water during peak Cold Pool months (Ou and Houghton 1982, Castelao et al. 2010, Lentz 2017).

Seasonal Cold Pool evolution is integral to MAB ecosystem processes. Upwelling along the MAB occurs each summer, transporting Cold Pool waters further inshore and toward the surface near the coast, which can drive phytoplankton blooms (Glenn and Schofield 2003, Glenn et al. 2004, Xu et al. 2011). The presence of Cold Pool water allows species ranges to extend further south than would be anticipated by latitude, supporting many economically and culturally valuable finfish and shellfish fisheries (Gabriel 1992, Lucey and Nye 2010, Murray 2016, Friedland et al. 2022). The Cold Pool can also impact hurricanes along the MAB by enabling ahead-of-eye center cooling through shear-induced mixing of the stratified water column (Glenn et al. 2016).

The USA is anticipated to become one of the largest offshore energy markets by 2030 with an estimated 2.4 million acres under lease and >2100 turbine foundations to be installed (Musial et al. 2022, Shields et al. 2022, Methratta et al. 2023). The MAB region leads the nation in proposed offshore wind energy projects with current regional offshore wind goals totaling >30 gigawatts (GW) of energy within the next decade (Musial et al. 2022, Methratta et al. 2023). European offshore wind energy has been developed extensively and can provide insight into possible interactions between turbines, physical oceanographic processes, and biological systems within the MAB, although there are key differences between the regions (Methratta et al. 2020). While still applicable, results from European studies are more representative of conditions in the MAB during relatively weakly stratified periods and do not represent Cold Pool conditions (Miles et al. 2021). Likewise, many European lease areas use smaller capacity turbines with different spacing, further adding to uncertainty about how relevant prior research is to MAB conditions (Methratta et al. 2020).

Wind turbines can directly impact hydrodynamics within and around wind farms through their underwater infrastructure and indirectly through changes in both the surface and atmospheric wind fields (van Berkel et al. 2020). Structure-induced friction and blocking from flow past cylindrical structures often form Von Kármán vortex streets, increasing the turbulence directly downstream of the turbine. In the context of the Cold Pool, this could lead to less stratified conditions (Miles et al. 2021). It is unclear what the effects will be on a highly stratified system like the MAB Cold Pool if the area of increased turbulence is expanded (Carpenter et al. 2016, van Berkel et al. 2020). Likewise, the extraction of atmospheric kinetic energy by turbines may be amplified by larger clusters of wind turbines, in turn reducing shear-driven forcing at the sea surface, decreasing horizontal velocities, and turbulent mixing within several kilometers of the wind site (Christiansen et al. 2022, Floeter et al. 2022, Golbazi et al. 2022). This could mean that within the MAB, offshore wind projects overlapping with the Cold Pool could strengthen stratification. However, recent MAB-specific modeling has illustrated a surface cooling effect due to the extreme height of the newer turbines proposed within the MAB wind farms (Golbazi et al. 2022), which could reduce stratification. North Sea-focused modeling studies have attributed lower dissolved oxygen concentrations to the potential strengthening of stratification and decrease in depth of the mixed layer due to wind wake generation and upwelling and downwelling dipoles (Daewel et al. 2022). The implications of offshore wind on the hydrodynamic features of the MAB require further study due to the key differences between the two regions such as the broader spatial extent of wind lease areas (WLAs), the weaker tidal strength, and increased storm frequency within the MAB versus Europe, as well as the technological differences in turbine design (Brunner and Lwiza 2020, Miles et al. 2021). In this paper, we evaluate the extent and cross-shelf variability of spatial overlap between pre-construction MAB WLAs and the Cold Pool. We specifically evaluate the overlap between the Cold Pool and the Bureau of Ocean Energy Management lease area call sites listed in Fig. 1. We evaluate the duration, strength, and variability of stratification where the Cold Pool overlaps with these sites within the MAB using output from a data-assimilative regional ocean model known as Doppio (López et al. 2020).

Methods

Data used in this study was simulated by the Doppio model, a Regional Ocean Modeling System (ROMS) application of the MAB and the Gulf of Maine (López et al. 2020, Wilkin et al. 2022). ROMS is a 3D hydrostatic terrain following a primitive equation model used extensively for coastal applications (Haidvogel et al. 2000, Shchepetkin and McWilliams 2005). Doppio is an implementation of ROMS with a uniform 7 km horizontal grid and 40 vertical sigma layers, covering the period of 2007–2021. It includes atmospheric forcing from National Centers for Environmental Prediction (NCEP) products, namely the North American Regional Reanalysis (NARR) (Mesinger et al. 2006) for the period of 2007–2013 and the North American Mesoscale (NAM) (Janjic et al. 2005) forecast model for 2014 and later. Boundary conditions are based on daily mean data taken from the Mercator Ocean system (Dre´villon et al. 2008) provided by Copernicus Marine Environment Monitoring Service (CMEMS) as well as the Oregon State University Tidal Prediction Software (OTPS) (Egbert and Erofeeva 2002) for harmonic tidal forcing of sea level and depth-average velocity along the open boundaries.

Additionally, Doppio uses 4-dimensional variational data assimilation (4D-Var) to obtain the best state estimate of the ocean within the domain. This includes assimilation of satellite sea surface temperature, sea surface height, HF-radar ocean surface currents, and all available *in situ* observations from the MARACOOS and NERACOOS regional associations of the US Integrated Ocean Observing System (IOOS) among other datasets (Wilkin et al. 2022). The output of Doppio used in this study spans from 2007 to 2021 and was generated by the Rutgers Ocean Modeling Group. Data were accessed in July 2023 from the THREDDS catalog of Doppio ROMS 15-year monthly reanalysis, as described in Wilkin and Levin (2022).

Metrics defining the presence and location of the Cold Pool area where the vertical temperature gradient is 0.2°C/m or greater and the bottom temperature is 10°C or less (Houghton et al. 1982, Mountain 2003, de Boyer Montégut et al. 2004, Brown et al. 2012, Li et al. 2015, Lentz 2017, Miles et al. 2021). The density stratification over the MAB region is primarily thermally controlled during the peak Cold Pool months; thus, stratification is determined by calculating the temperature gradient:

$$0.2^{\circ}C/m \leq \delta T/\delta z \,\&\, T \leq 10^{\circ}C \tag{1}$$

All 25 active WLAs within the MAB were analyzed in this study to determine the seasonal and cross-shelf overlap, more specifically with the Cold Pool. Total surface area of the Cold Pool and the MAB WLAs was extracted using ArcGIS and further analyzed (BOEM 2023). The centroid of each of the 25 MAB WLAs was used as the study location for each WLA (Fig. 1). Single points were used because the size of each WLA is small relative to the resolution of Doppio (7 km). Study locations were divided into three MAB segments based on the physical characteristics of each region: north, central,

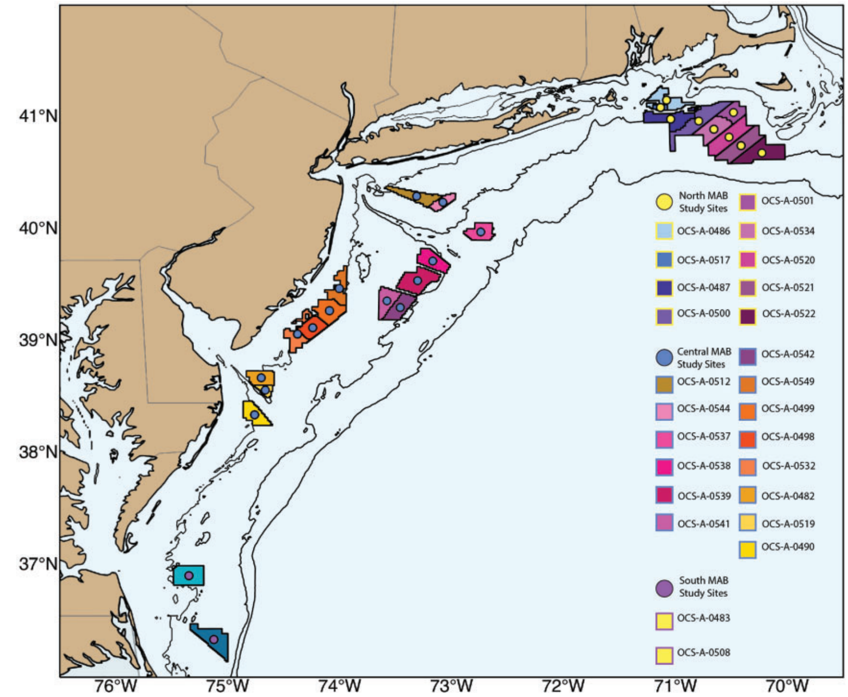

Figure 1. Study locations are depicted with circles and associated wind lease areas (WLAs) are shown as colored blocks, with colors indicating different lease blocks. The 25, 50, and 75 m isobaths are shown in black lines. Northern MAB sites correspond to the yellow circles with the lease blocks outlined in yellow. For northern MAB sites, blue hues represent nearshore sites (<43 m) and purple hues represent offshore sites (<43 m). Central MAB sites correspond to the blue circles with the lease blocks outlined in blue. For central MAB sites, yellow hues represent nearshore sites (<33 m) and pink hues represent offshore sites (<33 m). Southern MAB sites correspond to the purple circles with the lease blocks outlined in purple. The legend is organized from north to south.

and south (Bigelow 1933, Castelao et al. 2010, Lentz 2017). Within the central and northern MAB regions, study sites were further categorized into nearshore and offshore based on the average of the deepest and shallowest depths within each section. For northern MAB WLAs, the defined depth threshold is 43 m, and for central MAB WLAs, the defined depth threshold is 33 m. The southern MAB only has two WLAs, which we evaluate individually; hence, depth categorization was unnecessary. For each of these 25 study locations, the above method was used to determine the 15-year ensemble monthly averages of bottom temperatures and vertical temperature gradients, as well as standard deviations for variability across the 15-year span for each month for both criteria. Thermal gradients for each of the selected study sites were further evaluated by plotting monthly temperature-depth profiles.

Results

The MAB bottom temperatures warm from south to north and inshore to offshore, with the earliest warming along the southern and nearshore MAB regions (Fig. 2). By April, MAB areas south of New Jersey have already reached bottom temperatures above 10°C. Despite a northward bottom temperature warming trend through peak Cold Pool months, the area offshore of the New York Bight, near the Hudson Shelf Valley, remains below 8°C, even when more northern sites reach bottom temperatures close to 12°C (Fig. 2). The setup of the stratification (vertical thermal gradient values above 0.2°C/m) within the MAB is much less uniform (Fig. 3). In contrast to bottom temperature warming, stratification setup initiates in the north; however, the setup is much faster across all depths and latitudes within the MAB (Fig. 3). Reduction of stratification occurs earliest offshore and moves inshore during the later summer months (Fig. 3).

The combined stratification and bottom temperature metrics show that the Cold Pool sets up earliest at the southern edge of the MAB nearshore around North Carolina (Fig. 4). The Cold Pool remains inshore of the 50-m isobath during April and begins to set up in the NY bight at the mouth of the Hudson Shelf Valley and initiation of the Hudson Shelf Valley following stratification setup seen in Fig. 3. By May, the Cold Pool dissipated south of Delaware from warming bottom temperatures but extended northward to Massachusetts and offshore to depths of 100 m (Figs 2 and 4). Following the trend of warming bottom temperatures seen in Fig. 2, the Cold Pool weakens fastest inshore, leaving only a spatial footprint of cold bottom waters along the New York Bight in September (Figs 2 and 4).

For the central MAB WLAs, bottom temperatures within the MAB warm more rapidly nearshore than offshore (Fig. 2). Within the nearshore WLAs, bottom temperatures reach well above 10°C between April and May, while bottom temperatures in the offshore WLAs do not reach 10°C until July (Fig. 2). Nearshore, maximum bottom temperatures exceed 20°C, while the offshore bottom temperatures reach a maximum of 16°C (Fig. 2). A stratified water column (the temperature gradient is above 0.2°C/m) also forms earlier in nearshore WLAs than offshore WLAs, with nearshore values close to 0.6°C/m by April (Fig. 3). However, stratification is sustained for longer in offshore sites, with temperature gradients maintained above 0.2°C/m through September (Fig. 3).

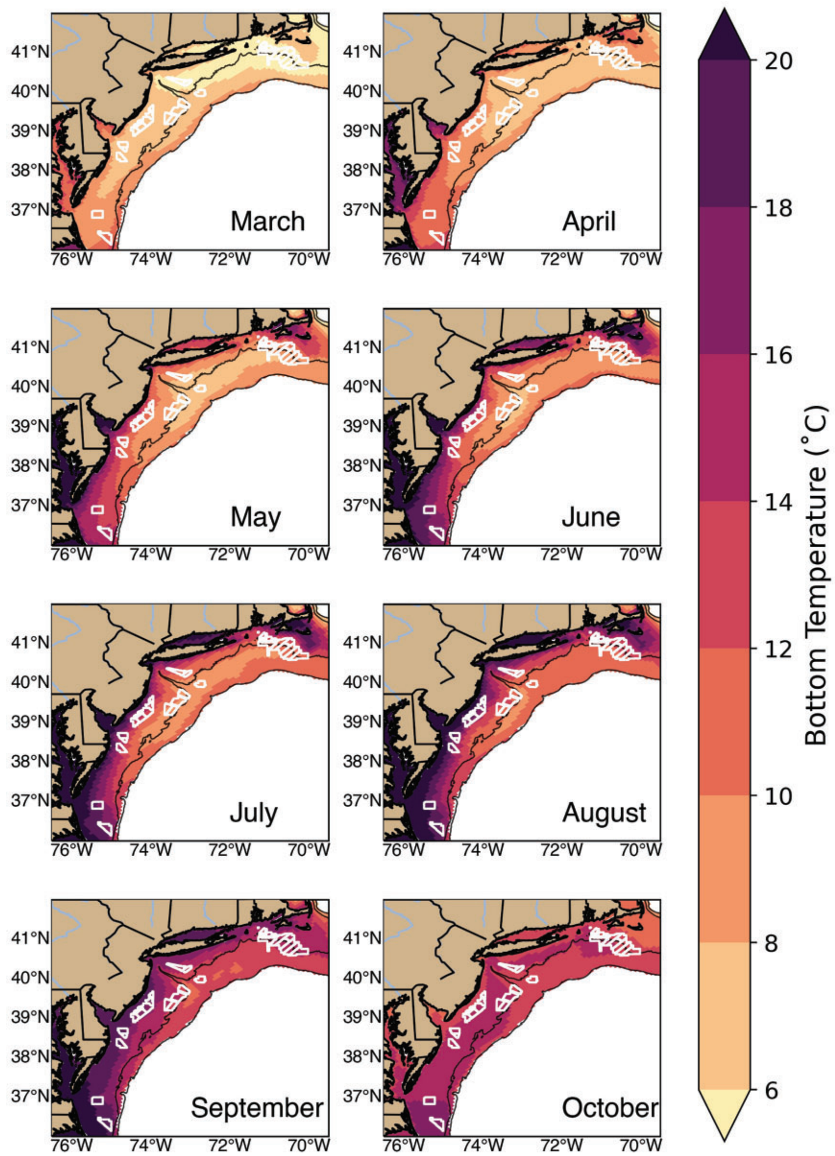

Figure 2. Monthly averaged bottom temperatures based on Doppio simulations spanning 2007 to 2021 within the MAB. Only peak Cold Pool months are included. The Cold Pool bottom temperatures are defined herein as those below the 10°C threshold. WLAs included in this study are outlined in white. The 50 and 100 m isobaths are shown in black.

Throughout peak Cold Pool months, the overlap between MAB WLAs and the Cold Pool varies substantially (Fig. 4). In the month of March, despite the Cold Pool's surface area of 1109 km^2, there is no overlap with the MAB WLAs (Fig. 4). In the month of April, the surface area of the Cold Pool expanded to 19 595 km^2 (Fig. 4). 19% of the MAB WLAs overlapped with the Cold Pool in April, although only 9% of the Cold Pool was covered by MAB WLAs (Fig. 4). In May, the Cold Pool surface area peaked at 56 153 km^2, and the MAB WLAs overlap with the Cold Pool increased to 81%, the highest annual overlap. Despite this large overlap, only 13% of the May Cold Pool was covered by MAB WLAs (Fig. 4). In June, the Cold Pool surface area covered 50 787 km^2, and 62% of the MAB WLAs overlapped (Fig. 4). Only 11% of the June Cold Pool was covered by the MAB WLAs (Fig. 4). In July, the Cold Pool surface area decreased to 36 942 km^2, and 41% of the MAB WLAs overlapped with 10% of the Cold Pool covered by the WLAs (Fig. 4). August is the last month of significant overlap between the Cold Pool and WLAs. The surface area of the August Cold Pool decreased to 19 333 km^2 with only 18% of the Cold Pool covered by WLAs and only 8% of WLAs overlap (Fig. 4). September was the only month that had a larger percentage of WLAs overlap with the Cold Pool (0.3%) than the percentage of the Cold Pool covered by WLAs (0.1%) (Fig. 4).

There are limited latitudinal differences in the duration and strength of the Cold Pool based on both metrics across the nine northern WLAs. Four of the northern MAB sites are nearshore with depths shallower than 43 m. The offshore sites (the remainder of the northern WLAs) are at ∼50 m depth (Fig. 1). All eight northern MAB WLAs had stratification strength reach 0.2°C/m in the month of May while maintaining the bottom temperature below 10°C, signifying the presence of the Cold Pool starting in May (Fig. 5). The four nearshore sites had bottom temperatures warm above 10°C

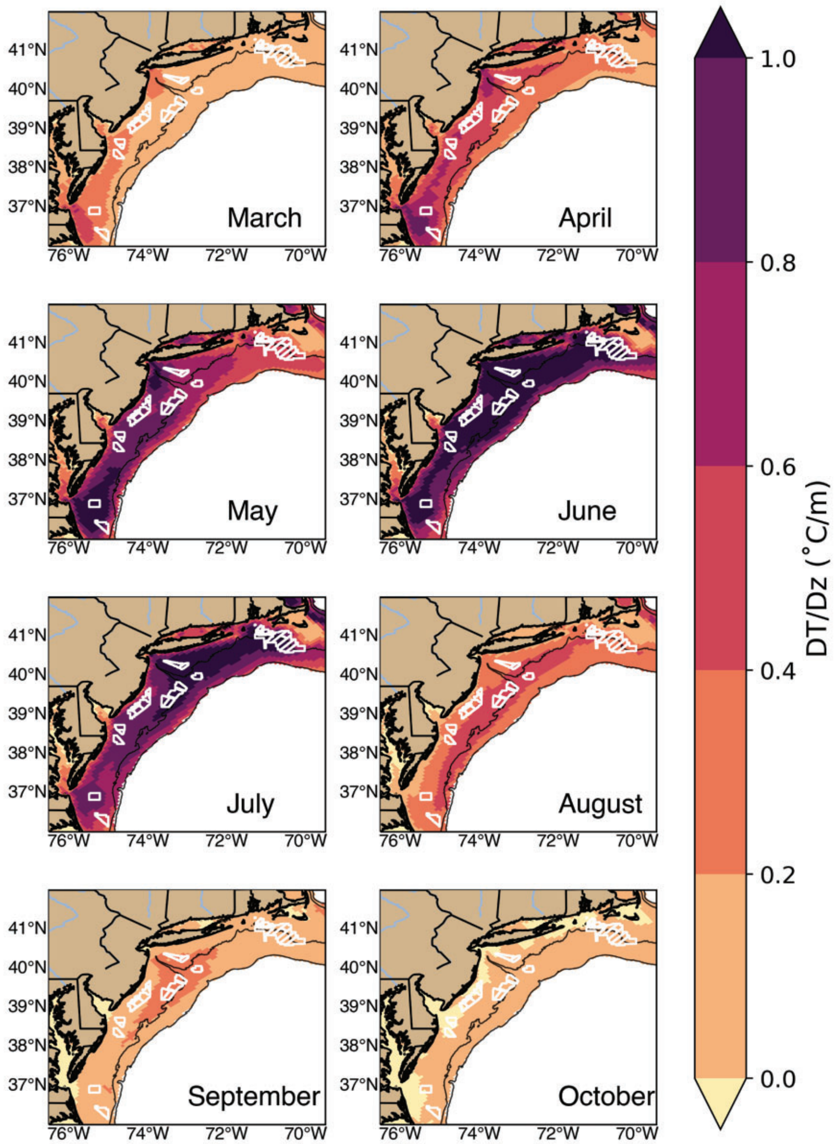

Figure 3. Monthly averaged temperature gradient values (dT/dz [°C/m)] based on Doppio simulations spanning 2007 to 2021 within the MAB. Only peak Cold Pool months are included. Cold Pool stratification is defined herein as dT/dz > 0.2°C/m. WLAs included in this study are outlined in white. The 50 and 100 m isobaths are shown in black.

in the month of June, while the four offshore sites had bottom temperatures warm above the Cold Pool threshold in the month of July (Fig. 5).

Despite the difference in duration of the Cold Pool of one month versus two between the nearshore and offshore sites within the northern MAB, the evolution of the stratification strength and bottom temperatures between the groups was not noticeably different. All eight sites had thermal gradients peak in July at between 1 and 1.5°C/m, despite the faster warming of bottom temperatures within the four nearshore sites (Fig. 5). Even with the rapid warming of the bottom temperature above 10°C, in all eight MAB sites, the stratification strength remained above 0.2°C/m until September (Fig. 5). In all eight northern MAB sites, the minimum bottom temperature occurred well before the stratification strength reached 0.2°C/m in either March or February (Fig. 5). The maximum bottom temperature occurred in October in all eight sites (Fig. 5).

Thermal gradients for each of the northern selected study sites were further evaluated by plotting monthly temperature-depth profiles. In peak Cold Pool months, the vertical temperature gradient is similar between all study sites, despite the differences in depth and distance from shore (Fig. 6). Surface water temperature variability was relatively low across all eight sites with a 2°C difference throughout peak Cold Pool months.

Latitudinal differences can be seen in the duration and strength of the Cold Pool based on both metrics across the 14 central MAB study locations. The six central MAB offshore study locations are below 33 m of water depth, while the eight nearshore sites are <33 m of depth (Fig. 1). All six offshore study locations had bottom water temperatures below 10°C and a thermal gradient >0.2°C/m in the month of May, signifying the presence of the Cold Pool (Fig. 7). The bottom temperature at five of these offshore study points exceeded 10°C in August, meaning the Cold Pool duration there was

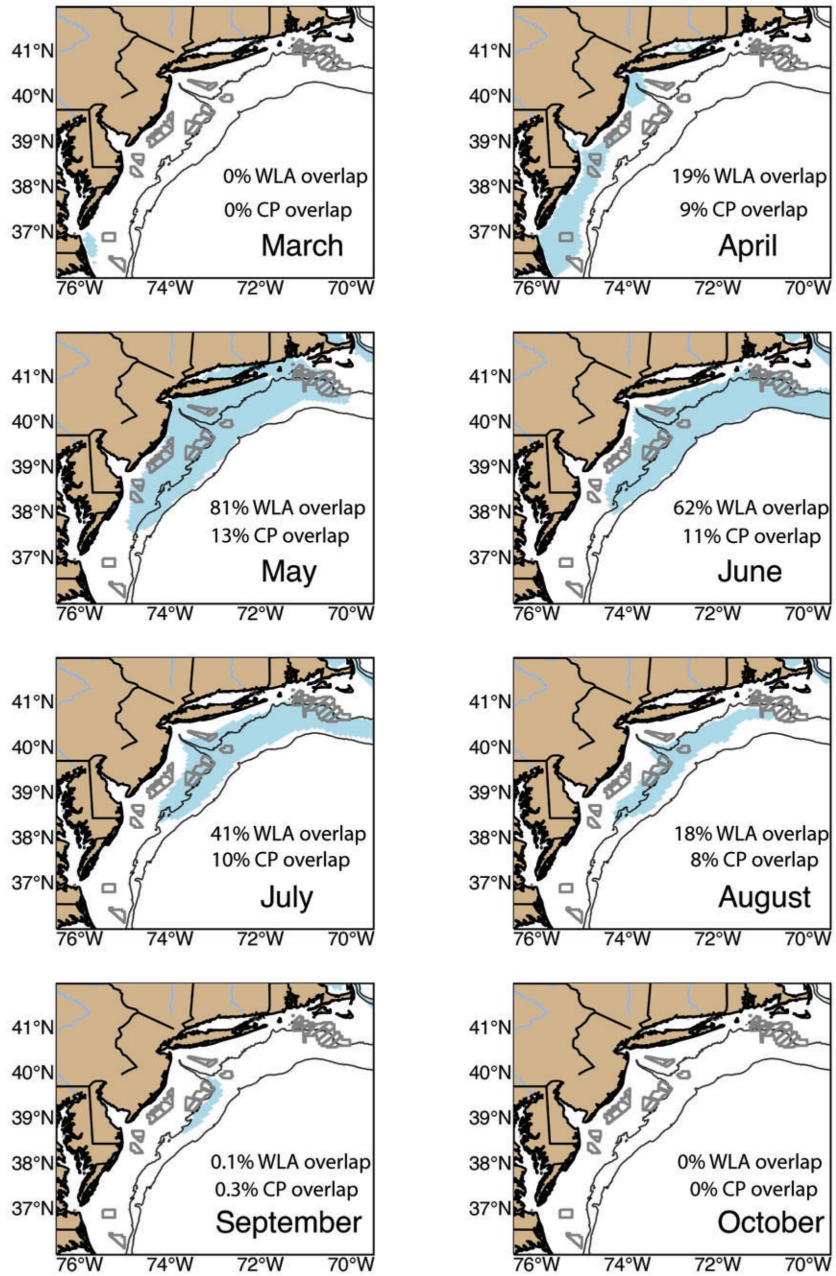

Figure 4. The Cold Pool is present in the areas of the shelf shaded in blue, which represent both bottom temperatures below 10°C and temperature gradients >0.2°C/m. Calculations were made based on Doppio simulations spanning 2007–2021 within the MAB. Only peak Cold Pool months are shown. Wind lease areas included in this study are outlined in gray. The 50- and 100-m isobaths are shown in black. Wind Lease Area Overlap with the Cold Pool (WLA overlap) and Cold Pool Covered by Wind Lease Areas (Cold Pool Overlap) percentages in km^2 are listed for each month in each panel.

approximately three months (Fig. 7). Despite the warming bottom temperatures in all six offshore sites, stratification above 0.2°C/m was maintained for three additional months dissipating in October (Fig. 7). Peak thermal gradient values occurred in July for all six offshore WLAs (Fig. 7). The highest bottom temperatures occurred as stratification broke down around October or November, consistent with downward mixing of warm surface waters due to fall transition storms.

There are notable differences in the Cold Pool evolution between the nearshore and offshore WLAs. In the eight central MAB nearshore, Cold Pool duration was shorter, spanning approximately one month, starting in April with increasing stratification and ending in May when the bottom temperature surpassed 10°C (Fig. 7). Despite the short duration of the Cold Pool, high thermal gradient values (>0.2°C/m) in these eight nearshore sites lasted for six months, dissipating in September (Fig. 7). Like the central MAB offshore WLAs, thermal gradients peaked at the nearshore sites in July. Despite an earlier development of stratification at the nearshore sites, the thermal gradient weakened at approximately the same time as the offshore sites (Fig. 7). Bottom temperatures reached a greater maximum value at the nearshore sites by >3°C (Fig. 7). Peak thermal gradient values were relatively similar between the central MAB nearshore and offshore WLAs.

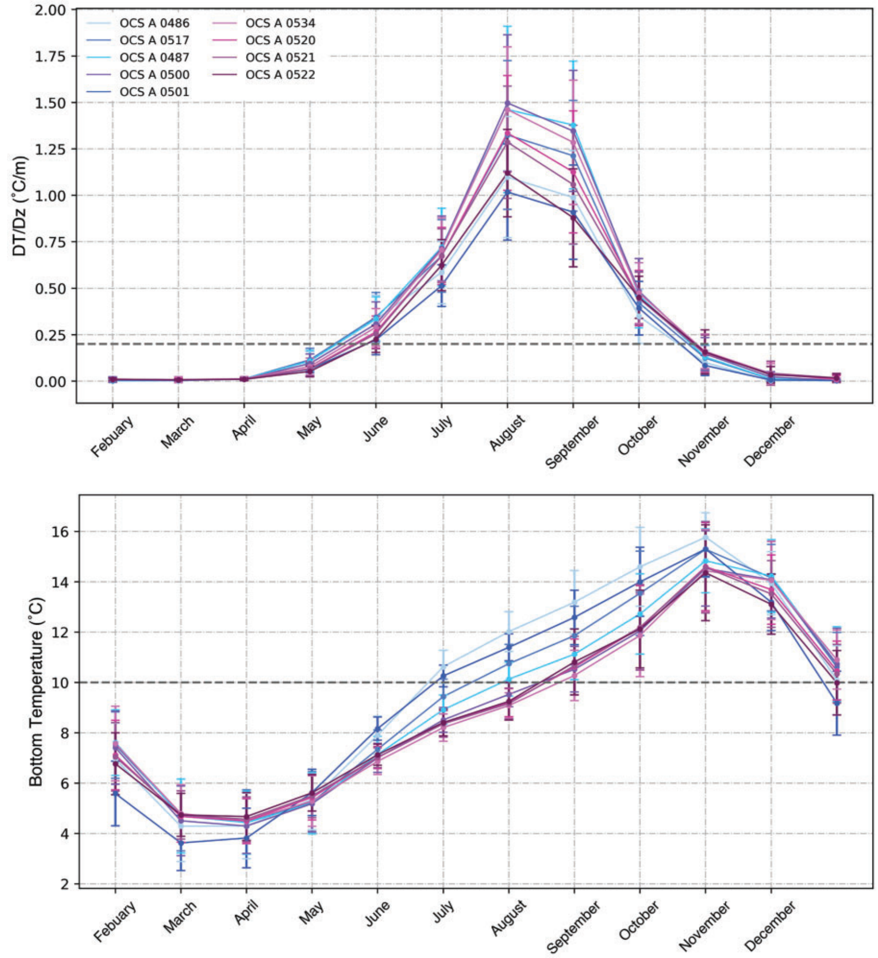

Figure 5. Monthly average bottom temperature (lower panel) and dT/dz values (upper panel) from 2007–2021 for northern MAB study locations based on Doppio simulations. Colors correspond to the specified wind lease area shown in Fig. 1. The Cold Pool exists when bottom temperatures remain below the dashed gray line and dT/dz values are above the above gray dashed line. Error bars show the standard deviation of variability for each month between 2007 and 2022. Blue hues represent nearshore sites (<43 m) and purple hues represent offshore sites (<43 m).

Thermal gradients for each of the selected central MAB study sites were further evaluated by plotting monthly temperature-depth profiles. In peak Cold Pool months, the vertical temperature gradient is similar between all study sites, despite the differences in depth and distance from shore (Fig. 8). Surface temperatures across all six sites differed the most in May and June with 3°C differences among sites. The difference in surface water temperature between sites decreased across Cold Pool months, while the difference in bottom temperatures increased, with a maximum difference in September of around 7°C between nearshore and offshore sites (Fig. 8). During July and August, surface temperatures at the nearshore sites were cooler and bottom temperature warmer than those of the offshore sites. The vertical temperature gradient values at the nearshore and offshore sites were similar, despite differences in depth and bottom temperatures.

Based on bottom temperature and stratification thresholds, the Cold Pool is only present in one of the two southern MAB WLAs, OCS-A-0483. Despite the presence of the Cold Pool according to the thresholds defined, the bottom temperature warms above 10°C within the same month that the stratification reaches 0.2°C/m for OCS-A-0483, meaning the Cold Pool presence is limited to one month (Fig. 9). Even with the warm bottom temperatures for both southern MAB WLAs, the stratification strength does reach 0.2°C/m and remains above the Cold Pool thermal gradient threshold until September for both sites (Fig. 9). Even in the southern MAB site, where the Cold Pool, according to the thresholds given, is not present, the bottom temperature reaches below 10°C. Not, however, simultaneously with the thermal gradient reaching 0.2°C/m. Both sites have peak thermal gradients in the month of June and maximum bottom temperatures warmer than the other two MAB regions. Based on the temperature profiles for the southern MAB WLAs, it is clear that the region does not have the same stratification strength as the northern and central MAB WLAs (Fig. 10).

Discussion

Regional Cold Pool trends offshore of New Jersey in this study are consistent with those of previous studies that discuss the spatial and temporal variability of the Cold Pool (Houghton et al. 1982, Ou and Houghton 1982, Mountain 2003, Castelao et al. 2010, Brown et al. 2012, Lentz 2017, Chen et al. 2018). Our work provides additional

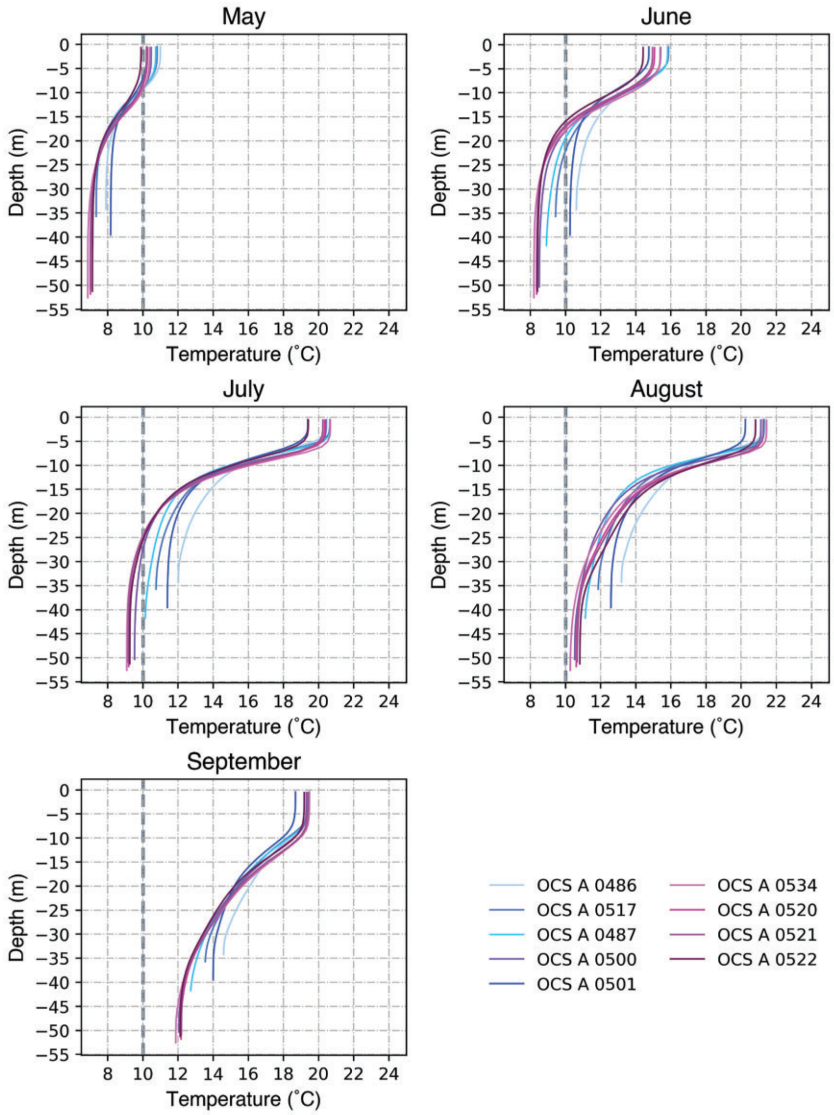

Figure 6. Northern MAB WLAs temperature profiles for Cold Pool months based on monthly averaged Doppio simulations from 2007 to 2021. Cold Pool bottom temperature threshold is depicted with the gray dashed line. The color of each profile corresponds to a study point within the selected wind areas shown in Fig. 1. Blue hues represent nearshore sites (<43 m) and purple hues represent offshore sites (<43 m).

context related to the co-location of this essential ocean feature and WLAs, but we provide some general comparisons with their results. Lentz (2017) utilizes observational data from the National Center for Environmental Information (NCEI) World Ocean Database, generally between 1955 and 2014 (Boyer et al. 2013), while Chen et al. (2018) are based on modeling results from a regional ROMS model that covers 1958–2007. While the DOPPIO model configuration has similarities to Chen et al. (2018), DOPPIO is a data-assimilative ocean model that benefits from both the extensive observations throughout the region and continuous spatial and temporal coverage of a modeling system. Generally, nearshore bottom temperatures warmed more quickly than offshore, which is consistent with previous results (Lentz 2017, Chen et al. 2018). However, we found that the bottom temperatures within the regional MAB were warmer than those reported in previous studies, accompanied by higher temperature gradients (Lentz 2017). Generally, the Cold Pool is shorter in duration at areas of shallower depths (Lentz 2017, Chen et al. 2018). These differences could be a result of the differing time periods between DOPPIO and the observations and models used in Lentz (2017) and Chen et al. (2018), as the Cold Pool has undergone significant warming over the last 40 years (Friedland et al. 2022). Previous studies have defined Cold Pool dissipation as the decrease in stratification strength in early fall from increased mixing by storm events and warming bottom temperatures (Lentz 2017, Chen et al. 2018). While findings in this study support the strengthened thermal gradient extending into the early fall, bottom temperatures at our study locations were consistently above accepted Cold Pool thresholds after May depending on the region. The thermal gradient in the central MAB has been observed to be greater than in other areas of the MAB, which is consistent with previous work (Lentz 2017, Chen et al. 2018). These previous studies indicate the maximum temperature gradients are between 0.5 and 0.8°C/m (Lentz 2017, Chen et al. 2018), while in both offshore and nearshore sites in this study they exceeded 1°C/m.

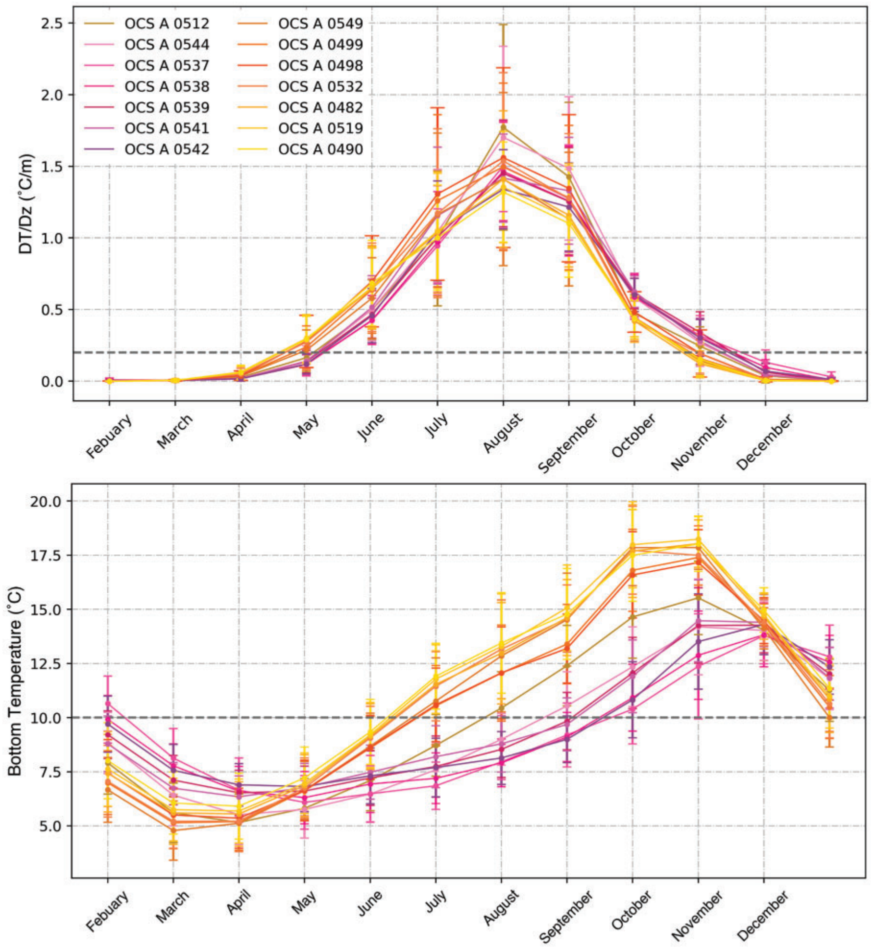

Figure 7. Monthly average bottom temperature (lower panel) and dT/dz values (upper panel) from 2007 to 2021 for central MAB study locations based on Doppio simulations. Colors correspond to the specified wind lease area shown in Fig. 1. Yellow hues represent nearshore sites (<33 m) while pink hues represent offshore sites (<33 m). The Cold Pool exists when bottom temperatures remain below the dashed gray line and dT/dz values are above the above gray dashed line. Error bars show the standard deviation of variability for each month between 2007 and 2022.

Cold Pool breakdown criteria have previously identified as bottom temperatures warming above 10°C and weakening of the thermal gradient below 0.2°C/m (Houghton et al. 1982, Lentz 2017, Chen et al. 2018); however, we found that the vertical thermal gradient remains above 0.2°C/m well beyond the time of bottom temperature warming above 10°C. Even at the nearshore sites where higher maximum vertical thermal gradient values are observed, stratification extends months after the bottom temperature warms. Stratification is the buoyancy force that inhibits mixing by flow past structures such as wind turbines, and it maintains ecologically important habitat (Miles et al. 2021). Atlantic Surf clams, Ocean Quahogs, and Sea Scallops are among the most economically valuable fisheries within the MAB region (Munroe et al. 2016, Powell et al. 2020, Miles et al. 2021, Friedland et al. 2022). These species are thermally sensitive and their distribution is often an indicator of changing bottom temperatures (Powell et al. 2020, Friedland et al. 2022). A 2023 study found that 20% of 177 species of MAB forage fish preferentially used habitat within WLAs (Friedland et al. 2023). Changes in stratification that have the potential to affect primary productivity may heavily impact these ecologically important species (Daewel et al. 2022, Friedland et al. 2023). Other demersal fish, such as the Yellowtail Flounder, use the changing bottom temperatures to trigger important life-stage changes (Sullivan et al. 2005, Sackett et al. 2008). Thermal gradients, changes in bottom temperature, and consequent changes in primary productivity could directly impact these and other commercially and ecologically important species in the region. Climate change has been warming waters within the MAB region in recent years, more specifically bottom temperatures (Wallace et al. 2018, Friedland et al. 2022, Amaya et al. 2023). Despite these warming temperatures, stratification associated with the Cold Pool has maintained values at and above 0.2°C/m. While 10°C is a useful indicator, these warming bottom temperatures may necessitate an updated bottom temperature threshold range. Because of the ecological and environmental importance of the Cold Pool, several metrics, in addition to bottom temperature, should be used to evaluate the Cold Pool.

This study shows a larger spatial and temporal overlap between the Cold Pool and WLAs further offshore versus wind lease areas closer to shore. We observed in this study that the average variation from 2007–2021 in Cold Pool metrics was limited for both bottom temperatures and stratification. Despite limited decadal Cold Pool variation, previous

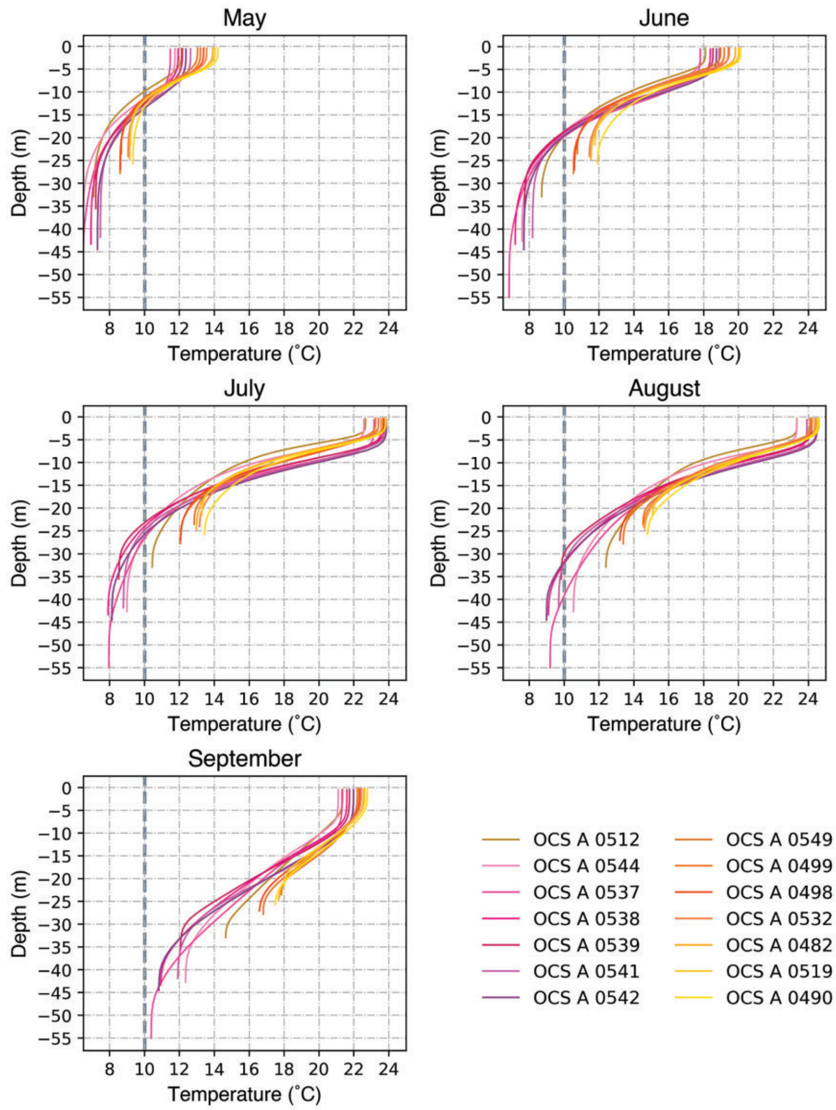

Figure 8. Central MAB WLAs temperature profiles for Cold Pool months based on monthly averaged Doppio simulations from 2007 to 2021. Cold Pool bottom temperature threshold is depicted with the gray dashed line. The color of each profile corresponds to a study point within the selected wind areas shown in Fig. 1. Yellow hues represent nearshore sites (<33 m), while pink hues represent offshore sites (<33 m).

studies have shown that broader ocean processes such as favorable upwelling or downwelling conditions can influence the daily and weekly variability of the Cold Pool (Houghton et al. 1982, Glenn et al. 2004, Li et al. 2014, Chen et al. 2018, Chen and Curchitser 2020). While we observed that there is limited overlap between the Cold Pool and MAB WLAs on a decadal time scale, daily variation in bottom temperatures and stratification can impact this overlap. Future work should evaluate short-term Cold Pool spatial variability to further increase certainty in WLAs overlap with this important regional feature.

Studies focused on European wind farms have shown that wind farms alter the hydrodynamic features of coastal environments (Carpenter et al. 2016, van Berkel et al. 2020, Christiansen et al. 2022, Floeter et al. 2022). These impacts depend heavily on the spatial extent of the wind farms as well as the temporal and spatial variability of stratification and mixing (Carpenter et al. 2016, Christiansen et al. 2022, Daewel et al. 2022). The current WLAs within the German Bight occupy a smaller area of the ocean than those proposed along the MAB. The stratification within the German Bight at depths <50 m is quantified as a 5–10°C difference between surface and bottom water temperatures, and tidal currents in this region can reach near 1.0 m/s (Carpenter et al. 2016, Christiansen et al. 2022). At the peak of thermal stratification in the German Bight during the year 2014, the bottom water temperature along the 40-m isobath only reached 14°C, resulting in a maximum thermal gradient of 0.35°C/m (Carpenter et al. 2016). During the years 2004–2013 along the 35 m isobath within the German Bight, the highest thermal gradient value was 0.37°C/m in July 2009 (Carpenter et al. 2016). The minimum peak thermal gradient value was 0.17°C/m in August 2004 (Carpenter et al. 2016). The maximum MAB thermal gradient value for the nearshore MAB sites, at a depth of ~30 m in the central region was 1.77˚C/m. The maximum stratification within the nearshore MAB sites was close to five times that of the Ger-

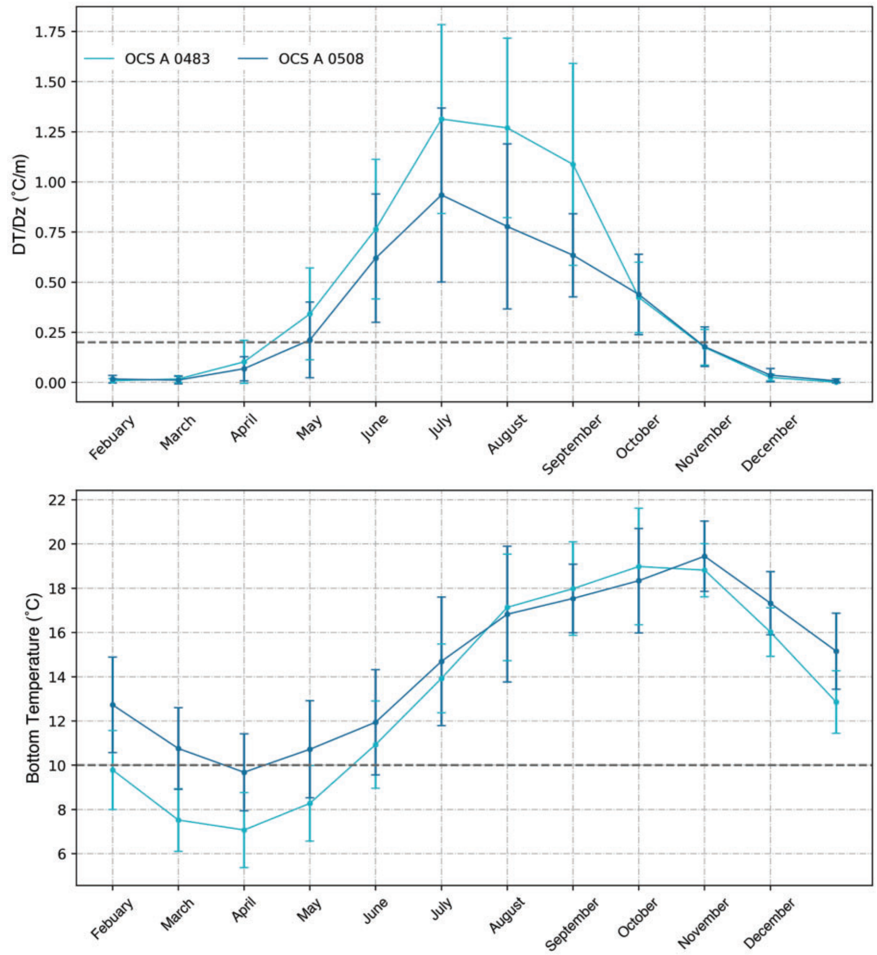

Figure 9. Monthly average bottom temperature (lower panel) and dT/dz values (upper panel) from 2007 to 2021 for southern MAB study locations based on Doppio simulations. Colors correspond to the specified wind lease area shown in Fig. 1. The Cold Pool exists when bottom temperatures remain below the dashed gray line and dT/dz values are above the above gray dashed line. Error bars show the standard deviation of variability for each month between 2007 and 2022.

man Bight. Local tidal forcing within the MAB is much weaker than the German Bight (>0.1 m/s), while storms are more frequent within the MAB (Brunner and Lwiza 2020). The German Bight, consequently, has considerably weaker stratification and stronger currents than the MAB during peak stratification times. Because of the spatial, technological, and environmental differences between the German Bight and the MAB, studies of the hydrodynamic impacts of wind farms in the German Bight cannot be directly extrapolated to the MAB Cold Pool. In November, when storm occurrences become more frequent within the MAB, the weakened stratification might lead to additional impacts from wind farms. The strength of stratification within the MAB and the findings of this study suggest that impacts from turbines on stratification may be less than those found in the German Bight. New studies (Friedland et al. 2023) have indicated that there is significant overlap between MAB forage fish and WLAs; however, the biological responses of the system to changes in habitat from extensive sandy benthic habitats to increased hard structure and intertidal remain unknown. New analyses are currently underway utilizing the methods proposed by Carpenter et al. (2016), but with the MAB stratification conditions. Additionally, more detailed simulations and pre- and post-construction observations should be further explored to fully capture the potential impacts of the turbine structure on the MAB Cold Pool. Our study highlights times and regions of overlap between MAB WLAs and the Cold Pool, which are critical to focus those future studies on.

Conclusion

The MAB Cold Pool is a valuable coastal ocean feature that supports some of the most economically and culturally valuable fisheries in the USA. The Cold Pool influences a variety of oceanographic processes, such as atmospheric and oceanic circulation, coastal primary productivity, and carbon sequestration. Development of offshore wind has been rapidly expanding throughout the MAB. This study found that there is a notable overlap between proposed MAB offshore wind lease areas. In addition, substantial stratification persists past the time at which bottom temperatures warmed above Cold Pool thresholds. Bottom temperatures warm more rapidly in nearshore than offshore, despite stronger thermal gradients in nearshore sites. Although it is evident that MAB WLAs occur

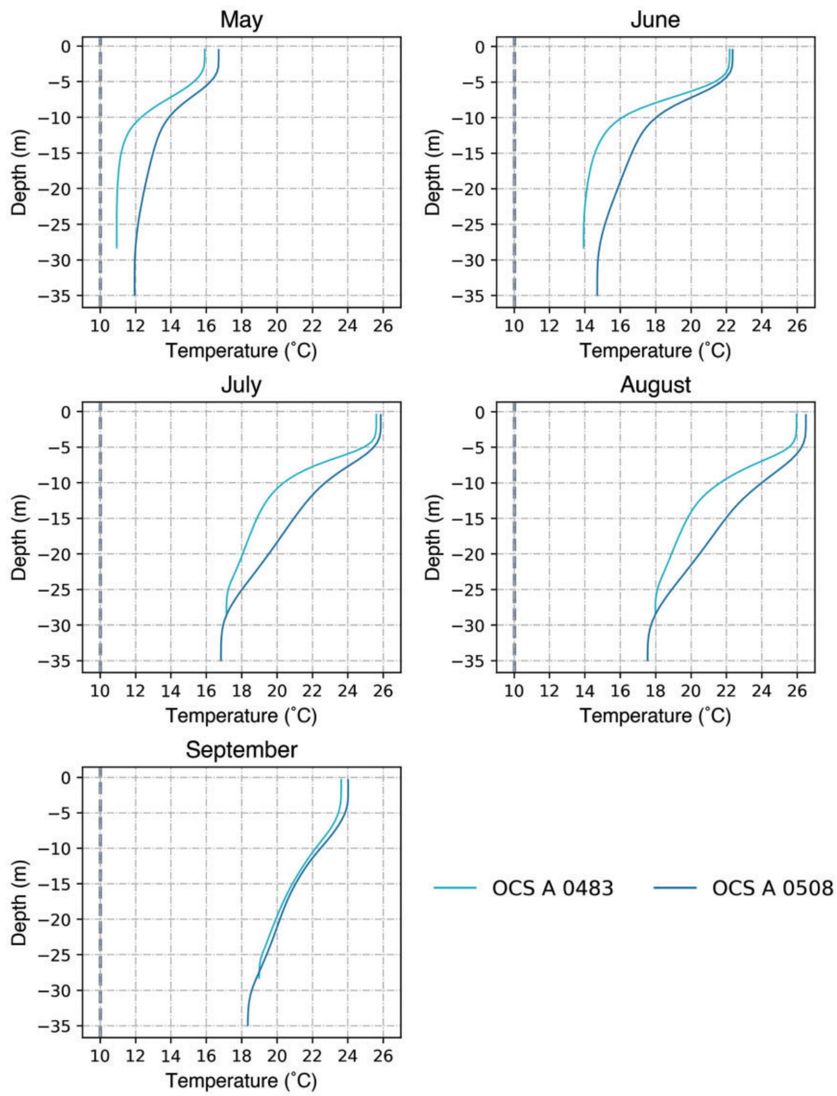

Figure 10. Southern MAB WLAs temperature profiles for Cold Pool months based on monthly averaged Doppio simulations from 2007 to 2021. Cold Pool bottom temperature threshold is depicted with the gray dashed line. The color of each profile corresponds to a study point within the selected wind areas shown in Fig. 1. The x-axis is not consistent with previous like figures (Figs 6 and 8) due to the warmer surface water temperatures within the southern MAB region.

within the Cold Pool, future studies to determine interdecadal trends of Cold Pool evolution and extent are necessary to further evaluate overlap between the Cold Pool and WLAs.

Acknowledgments

We thank the Rutgers University Department of Marine and Coastal Sciences and the Haskin Shellfish Research Lab at Rutgers University for their continued support. We also thank Julia Levin, John Wilkin, and Alex Lo`pez for their help with Doppio and for making their data publicly accessible. Special thanks to Joe Gradone, Jenn Gius, Laura Steeves, and Ailey Sheehan. Rebecca Horwitz was supported by the National Science Foundation Grant No. OCE-1831625, and this research was supported by the National Science Foundation Industry/University Cooperative Research Center SCeMFiS (Science Center for Marine Fisheries) NSF award #1841112. D.M. was partly supported by USDA NIFA Hatch project 1020831/NJ33140.

Conflict of interest: The authors have no competing interests to declare.

Data availability

Open data access for the Doppio model is described at SEANOE (https://www.seanoe.org/data/00785/89673) and was originally published in Wilkin and Levin (2022). Open GIS data access for the most up to date United States' wind lease areas can be found on The Bureau of Ocean Energy Management website (https://www.boem.gov/renewable-energy/mapping-and-data/renewable-energy-gis-data).

Author Contributions

DM and JK acquired funding; RH, TNM, DM, and JK conceived the ideas; RH and TNM developed methodology and contributed to data analysis; RH wrote model output analysis code and conducted overall data collection; RH drafted initial manuscript and further incorporated additional analysis and edits from the review process; all authors contributed to manuscript review and editing.

References

Amaya DJ, Jacox MG, Alexander MA *et al.* Bottom marine heatwaves along the continental shelves of North America. *Nat Commun* 2023;**14**:1038. https://doi.org/10.1038/s41467-023-36567-0.

Bigelow HB. 1933. *Studies of the Waters on the Continental Shelf, Cape Cod to Chesapeake Bay*. Cambridge, MA: Massachusetts Institute of Technology and Woods Hole Oceanographic Institution. https://hdl.handle.net/1912/1144 (last accessed 10 June 2021).

BOEM. Renewable Energy GIS Data. 2023. https://www.boem.gov/renewable-energy/mapping-and-data/renewable-energy-gis-data (last accessed 10 Jul 2023).

Boyer, TP,, Antonov JI,, Baranova, OK,, Garcia, HE,, DR, Johnson,, Mishonov, AV,, O'Brien, TD *et al.* 2013. World Ocean Database 2013. U.S. Department of Commerce, National Oceanic and Atmospheric Administration, National Environmental Satellite, Data, and Information Service, National Oceanographic Data Center, Ocean Climate Laboratory. https://repository.library.noaa.gov/view/noaa/1291 (last accessed 30 August 2023).

Brown W, Boicourt W, Flagg C *et al.* Mapping the Mid-Atlantic Cold Pool evolution and variability with ocean gliders and numerical models. In: *2012 Oceans*, Hampton Roads, VA: IEEE, 2012. http://ieeexplore.ieee.org/document/6404970/ (last accessed 1 March 2022).

Brunner K, Lwiza KMM. Tidal velocities on the Mid-Atlantic Bight continental shelf using high-frequency radar. *J Oceanogr* 2020;**76**:289–306. https://doi.org/10.1007/s10872-020-00545-7.

Carpenter JR, Merckelbach L, Callies U *et al.* Potential impacts of offshore wind farms on North Sea stratification. *PLoS One* 2016;**11**:e0160830. Public Library of Science. https://doi.org/10.1371/journal.pone.0160830.

Castelao R, Glenn S, Schofield O. Temperature, salinity, and density variability in the central Middle Atlantic Bight. *J Geophys Res Oceans* 2010;**115**:2009JC006082. https://doi.org/10.1029/2009JC006082.

Chen Z, Curchitser E, Chant R *et al.* Seasonal variability of the cold pool over the Mid-Atlantic Bight continental shelf. *J Geophys Res Oceans* 2018;**123**:8203–26. https://doi.org/10.1029/2018JC014148.

Chen Z, Curchitser EN. Interannual variability of the Mid-Atlantic Bight Cold Pool. *J Geophys Res Oceans* 2020;**125**. https://onlinelibrary.wiley.com/doi/10.1029/2020JC016445 (last accessed 31 March 2023).

Christiansen N, Daewel U, Djath B *et al.* Emergence of large-scale hydrodynamic structures due to atmospheric offshore wind farm wakes. *Front Mar Sci* 2022;**9**:818501. https://doi.org/10.3389/fmars.2022.818501.

Daewel U, Akhtar N, Christiansen N *et al.* Offshore wind farms are projected to impact primary production and bottom water deoxygenation in the North Sea. *Commun Earth Environ* 2022;**3**:292. https://doi.org/10.1038/s43247-022-00625-0

de Boyer Montégut C, Madec G, Fischer AS *et al.* Mixed layer depth over the global ocean: an examination of profile data and a profile-based climatology. *J Geophys Res Oceans* 2004;**109**. https://onlinelibrary.wiley.com/doi/abs/10.1029/2004JC002378 (last accessed 1 March 2022).

Drévillon M, Bourdallé-Badie R, Derval C *et al.* The GODAE/Mercator-Ocean global ocean forecasting system: results, applications and prospects. *J Oper Oceanogr* 2008;**1**:51–7. https://doi.org/10.1080/1755876X.2008.11020095.

Egbert GD, Erofeeva SY. Efficient inverse modeling of barotropic ocean tides. *J Atmos Oceanic Technol* 2002;**19**:183–204. https://doi.org/10.1175/1520-0426(2002)019%3c0183:EIMOBO%3e2.0.CO;2.

Floeter J, Pohlmann T, Harmer A *et al.* Chasing the offshore wind farm wind-wake-induced upwelling/downwelling dipole. *Front Mar Sci* 2022;**9**:884943. https://doi.org/10.3389/fmars.2022.884943.

Friedland KD, Adams EM, Goetsch C *et al.* Forage fish species prefer habitat within designated offshore wind energy areas in the U.S. Northeast shelf ecosystem. *Mar Coast Fish* 2023;**15**:e10230. https://doi.org/10.1002/mcf2.10230.

Friedland KD, Miles T, Goode AG *et al.* The Middle Atlantic Bight Cold Pool is warming and shrinking: indices from in situ autumn seafloor temperatures. *Fish Oceanogr* 2022;**31**:217–23. https://doi.org/10.1111/fog.12573.

Gabriel WL. Persistence of demersal fish assemblages between Cape Hatteras and Nova Scotia, Northwest Atlantic. *J Northw Atl Fish Sci* 1992;**14**:29–46. https://doi.org/10.2960/J.v14.a2.

Glenn S, Arnone R, Bergmann T *et al.* Biogeochemical impact of summertime coastal upwelling on the New Jersey Shelf. *J Geophys Res Oceans* 2004;**109**. https://onlinelibrary.wiley.com/doi/abs/10.1029/2003JC002265 (last accessed 10 September 2022).

Glenn S, Schofield O. Observing the oceans from the COOL Room: our history, experience and opinions. *Oceanography* 2003;**16**:37–52,. https://doi.org/10.5670/oceanog.2003.07.

Glenn SM, Miles TN, Seroka GN *et al.* Stratified coastal ocean interactions with tropical cyclones. *Nat Commun* 2016;**7**:10887. https://doi.org/10.1038/ncomms10887.

Golbazi M, Archer CL, Alessandrini S. Surface impacts of large offshore wind farms. *Environ Res Lett* 2022;**17**:064021. https://doi.org/10.1088/1748-9326/ac6e49.

Haidvogel DB, Arango HG, Hedstrom K *et al.* Model evaluation experiments in the North Atlantic Basin: simulations in nonlinear terrain-following coordinates. *Dyn Atmos Oceans* 2000;**32**:239–81. https://doi.org/10.1016/S0377-0265(00)00049-X.

Houghton R, Schlitz R, Beardsley R *et al.* The Middle Atlantic Bight cold pool: evolution of the temperature structure during summer 1979. *Journal of Physical Oceanography* 1982;**12**:1019–29. https://doi.org/10.1175/1520-0485(1982)012⟨1019:TMABCP⟩2.0.CO;2.

Janjic Z, Black T, Pyle M *et al.* *High Resolution Applications of the WRF NMM*. Washington, DC. 2005. https://ams.confex.com/ams/WAFNWP34BC/techprogram/paper_93724.htm (last accessed 31 March 2023).

Lentz SJ. Seasonal warming of the Middle Atlantic Bight Cold Pool. *J Geophys Res Oceans* 2017;**122**:941–54. https://doi.org/10.1002/2016JC012201.

Li Y, Fratantoni PS, Chen C *et al.* Spatio-temporal patterns of stratification on the Northwest Atlantic shelf. *Prog Oceanogr* 2015;**134**:123–37. https://doi.org/10.1016/j.pocean.2015.01.003.

Li Y, Ji R, Fratantoni PS *et al.* Wind-induced interannual variability of sea level slope, along-shelf flow, and surface salinity on the Northwest Atlantic shelf. *J Geophys Res Oceans* 2014;**119**:2462–79. https://doi.org/10.1002/2013JC009385.

López AG, Wilkin JL, Levin JC. Doppio—a ROMS (v3.6)-based circulation model for the Mid-Atlantic Bight and Gulf of Maine: configuration and comparison to integrated coastal observing network observations. *Geosci Model Dev* 2020;**13**:3709–29. https://doi.org/10.5194/gmd-13-3709-2020.

Lucey S, Nye J. Shifting species assemblages in the Northeast US Continental Shelf large marine ecosystem. *Mar Ecol Prog Ser* 2010;**415**:23–33. https://doi.org/10.3354/meps08743.

Mesinger F, DiMego G, Kalnay E *et al.* North American Regional Reanalysis. *Bull Am Meteorol Soc* 2006;**87**:343–60. https://doi.org/10.1175/BAMS-87-3-343.

Methratta E, Hawkins A, Hooker B *et al.* Offshore wind development in the Northeast US Shelf large marine ecosystem: ecological, Human, and fishery management dimensions. *Oceanography* 2020;**33**:16–27. https://doi.org/10.5670/oceanog.2020.402.

Methratta ET, Silva A, Lipsky A *et al.* Science priorities for offshore wind and Fisheries research in the northeast U.S. Continental shelf ecosystem: perspectives from scientists at the National Marine Fisheries Service. *Mar Coast Fish* 2023;**15**:e10242. https://doi.org/10.1002/mcf2.10242.

Miles T, Murphy S, Kohut J *et al.* Offshore wind energy and the Mid-Atlantic Cold Pool: a review of potential interactions. *Mar Technol Soc J* 2021;**55**:72–87. https://doi.org/10.4031/MTSJ.55.4.8.

Mountain DG. Variability in the properties of Shelf Water in the Middle Atlantic Bight, 1977–1999. *J Geophys Res* 2003;**108**:3014. https://doi.org/10.1029/2001JC001044.

Munroe DM, Narváez DA, Hennen D *et al.* Fishing and bottom water temperature as drivers of change in maximum shell length in Atlantic surfclams (*Spisula solidissima*). *Estuar Coast Shelf Sci* 2016;**170**:112–22. https://doi.org/10.1016/j.ecss.2016.01.009.

Murray T. Economic activity associated with SCeMFiS supported fishery products (Ocean Quahog & Atlantic Surfclams). 2016. https://scemfis.org/wp-content/uploads/2020/02/Ec_Impact-tjm_rm2.pdf (last accessed 10 September 2022).

Musial W, Spitsen P, Duffy P *et al. Offshore Wind Market Report: 2022 Edition*. U.S Department of Energy. Office of Energy Efficiency and Renewable Energy. Washington, DC. 2022. DOE/GO-102022-5765. https://www.energy.gov/sites/default/files/2022-08/offshore_wind_market_report_2022.pdf (last accessed 10 September 2022).

Ou HW, Houghton R. A model of the summer progression of the cold-pool temperature in the Middle Atlantic Bight. *J Phys Oceanogr* 1982;**12**:1030–6. https://doi.org/10.1175/1520-0485(1982)012%3c1030:AMOTSP%3e2.0.CO;2.

Powell EN, Ewing AM, Kuykendall KM. Ocean quahogs (*Arctica islandica*) and Atlantic surfclams (*Spisula solidissima*) on the Mid-Atlantic Bight continental shelf and Georges Bank: the death assemblage as a recorder of climate change and the reorganization of the continental shelf benthos. *Palaeogeogr Palaeoclimatol Palaeoecol* 2020;**537**:109205. https://doi.org/10.1016/j.palaeo.2019.05.027.

Sackett D, Able K, Grothues T. Habitat dynamics of summer flounder paralichthys dentatus within a shallow USA estuary, based on multiple approaches using acoustic telemetry. *Mar Ecol Progr Ser* 2008;**364**:199–212. https://doi.org/10.3354/meps07391.

Shchepetkin AF, McWilliams JC. The regional oceanic modeling system (ROMS): a split-explicit, free-surface, topography-following-coordinate oceanic model. *Ocean Model* 2005;**9**:347–404. https://doi.org/10.1016/j.ocemod.2004.08.002.

Shields M, Marsh R, Stefek J *et al. The Demand for a Domestic Offshore Wind Energy Supply Chain*. Technical Report, NREL/TP-5000-81602. National Renewable Energy Laboratory (NREL), Denver, CO. 2022. https://www.nrel.gov/docs/fy22osti/81602.pdf (last accessed 10 September 2022).

Sullivan MC, Cowen RK, Steves BP. Evidence for atmosphere-ocean forcing of yellowtail flounder (*Limanda ferruginea*) recruitment in the Middle Atlantic Bight. *Fish Oceanogr* 2005;**14**:386–99. https://doi.org/10.1111/j.1365-2419.2005.00343.x.

van Berkel J, Burchard H, Christensen A *et al.* The effects of offshore wind farms on hydrodynamics and implications for fishes. *Oceanography* 2020;**33**:108–17. https://doi.org/10.5670/oceanog.2020.410.

Wallace E, Looney L, Gong D. Multi-decadal trends and variability in temperature and salinity in the Mid-Atlantic Bight, Georges Bank, and Gulf of Maine. *J Mar Res* 2018;**76**:163–215. https://doi.org/10.1357/002224018826473281.

Wilkin J, Levin J, Moore A *et al.* A data-assimilative model reanalysis of the U.S. Mid Atlantic Bight and Gulf of Maine: configuration and comparison to observations and global ocean models. *Prog Oceanogr* 2022;**209**:102919. https://doi.org/10.1016/j.pocean.2022.102919.

Wilkin J, Levin J. Outputs from a Regional Ocean Modeling System (ROMS) data assimilative reanalysis (version DopAnV3R3-ini2007) of ocean circulation in the Mid-Atlantic Bight and Gulf of Maine for 2007-2021. 2022. SEANOE. https://www.seanoe.org/data/00785/89673/ (last accessed 30 March 2023).

Xu Y, Chant R, Gong D *et al.* Seasonal variability of chlorophyll a in the Mid-Atlantic Bight. *Cont Shelf Res* 2011;**31**:1640–50. https://doi.org/10.1016/j.csr.2011.05.019.

Handling Editor: Steven Degraer

Implementation of Near Real-Time Onboard Processing Software for a Slocum Glider Acoustic Doppler Current Profiler

Julia Engdahl
Center for Ocean Observing Leadership (COOL)
Rutgers University
New Brunswick, USA
engdahl@marine.rutgers.edu

Joseph Gradone
Center for Ocean Observing Leadership (COOL)
Rutgers University
New Brunswick, USA
jgradone@marine.rutgers.edu

Zachary Silva
Teledyne Webb Research
Falmouth, USA
zachary.silva@teledyne.com

David Aragon
Center for Ocean Observing Leadership (COOL)
Rutgers University
New Brunswick, USA
dkaragon@marine.rutgers.edu

Nikitha Shivakumar
College of Computing
Georgia Institute of Technology
Atlanta, USA
nshivakumar6@gatech.edu

Travis Miles
Center for Ocean Observing Leadership (COOL)
Rutgers University
New Brunswick, USA
tnmiles@marine.rutgers.edu

***Abstract*—Advancements in sensor and battery technology over the past two decades have facilitated the integration of complex instruments into autonomous underwater vehicles. The integration of such instruments onto gliders has enabled unprecedented data collection and expanded understanding of ocean processes. Recently, this understanding has been enhanced through the development of a software architecture called "backseat driver" on Slocum gliders, which can increase the efficiency of data collection by increasing the time the glider spends in regions of interest through adaptive mission control. A caveat to this advancement is that sensors that collect large volumes of data cannot efficiently transmit data to shore in real-time, which limits real-time applications (e.g. operational hurricane forecasting, marine mammal detection, water quality monitoring, etc.) and confines shoreside processing to post recovery. This can potentially lead to loss of data in the event of vehicle loss or missions where retrieval is not permissible, resulting in the need to develop a sensor agnostic real-time processing software and hardware architecture. Here, we detail the methodology that will be applied to test a real-time onboard processing algorithm through the use of the backseat driver software on Slocum glider MARACOOS04. An adjunct processor (Raspberry Pi 4) has been integrated into this glider with a data processing algorithm that will parse, process, and compress raw data from an acoustic Doppler current profiler.**

Keywords—Acoustic Doppler Current Profiler, Slocum Glider, Backseat Driver, Real-Time Onboard Processing

I. Introduction

Over the past two decades, advancements in sensor and battery technology have allowed for the integration of a variety of complex sensors into autonomous underwater vehicles (AUV) including but not limited to acoustic doppler current profilers (ADCPs), multi-frequency echo sounders, optical laser diffraction sensors, wave accelerometers, passive acoustics, and turbulence [1]. While integrating these sensors onto platforms such as gliders has led to unprecedented data collection and further understanding of ocean processes, advancement in ocean exploration can be further expanded through the use of a software capability referred to as "backseat driver". This software can increase the glider's working time in regions of high interest through adaptive mission control, which allows the vehicle to change its state (e.g., depth, heading, waypoint, sampling, etc.) based on real-time sensor measurements throughout the duration of the mission [2-3]. Software capabilities like backseat driver are increasingly becoming a necessity as missions become more complex in extreme ocean environments [2,4], and have been implemented on numerous underwater vehicles such as Bluefin SandShark AUV [5], Hydroid REMUS 100 AUV [6], Iver2 AUV [7], Teledyne Gavia AUV [8], Teledyne Webb Research Slocum gliders and many more [2].

The large data volume collected by these sensors during complex missions cannot be transferred to shore efficiently in real-time. As a result, shoreside processing has largely been confined to post recovery, significantly limiting real-time applications. In the event of vehicle loss or missions where retrieval is not immediately permissible, this can lead to an unfortunate loss of data and time. Real-time data processing software is increasingly becoming more important because it can aid in management and scientific applications by increasing data accuracy, preventing data loss, and allowing for adaptive surveys [9]. Recently, some sensors such as the digital acoustic monitoring (DMON) instrument [9], Sequoia Scientific Laser In Situ Scattering and Transmissometry (LISST) sensor [10], and the Fluorescence Induction and Relaxation System (FIRE) [11] have developed self-contained processing algorithms, but they

Funding provided by the Office of Naval Research Project Grant N000142012568.

979-8-218-14218-6 ©2023 MTS

are proprietary to their systems, limited to their internal processing capabilities, and are not easily modifiable [1]. Thus, the development of a sensor agnostic real-time data processing software and hardware architecture is needed for autonomous underwater vehicles.

Although the backseat driver is currently used to autonomously and adaptively modify glider behavior while in mission to efficiently collect data in regions of interest [2], the data processing algorithms are presently only used for adaptive mission control. The resulting data that is telemetered to shore still has to undergo shoreside processing post recovery. We are presently utilizing this software to expand glider real-time data processing capabilities. Here, we detail initial real-time processing experiments focused on ADCP processing via a widely used linear inversion algorithm, first tailored for ship-based surveys [12], then modified for glider platforms to generate depth-binned, absolute ocean velocities [13].

II. Methods

A. Glider

Underwater gliders have been used to monitor and collect data to gain useful information about oceanographic processes [14]. They are considered to be long endurance, low energy, and relatively low cost vehicles [2,14]. Gliders are mobile sensor platforms that are able to collect spatial and temporal data throughout the water column. These vehicles use a change in buoyancy and a set pitch angle to propel itself vertically and horizontally in a sawtooth-like pattern [14-15]. Gliders can be operated in water depths from 5 m to 1000 m and will have a vertical speed of approximately 20 cm/s [14-15]. During glider dives and climbs, the data is sampled every 2 seconds, which results in a robust dataset that can be telemetered to shore via an Iridium satellite phone after decimation [15].

The glider used in this study is a Teledyne Webb Research Generation 3 Slocum glider, MARACOOS04 (MARA04), operated by two STM32 120 MHz processors. This glider is equipped with a standard oceanographic sensor loadout of SeaBird CTD, a 100 m depth-rated buoyancy pump,Wetlabs 3 channel optical sensor, and a 600 kHz Teledyne RD Instruments Pathfinder ADCP. The Pathfinder utilizes a phased array transducer mounted flush to the glider hull with 4-beams in a 30° Janus configuration. Beams 1 and 3 are forward facing and beams 2 and 4 are aft-facing at 22.5° off the glider's center to both starboard and port sides, respectively. The output format of the raw data is configured to be PD0, which is Teledyne RD Instrument's standard binary format. PD0's from an approximately 3-hour long glider segment (time spent underwater between surfacings) result in a file size on the order of thousands of kilobytes which are too large to transfer over an Iridium connection in a timely and cost-effective manner and can only be downloaded post-deployment.

B. Backseat Driver

Prior to the development and implementation of the backseat driver, gliders did not have the capability of adaptive mission control onboard. The pilot sets the initial parameters including but not limited to heading, pitch, target dive depth, and waypoints. These engineering and flight specifications follow the blue (left) pathway shown in Fig. 1A where these parameters are input into the flight computer so that internal calculations can be computed in order to adjust commanded behaviors. The flight computer creates a decimated file (SBD) that is a subset of raw data to be transmitted to shore. Simultaneously, science sensors follow the pink (right) pathway in Fig. 1B where the data collected is then communicated to the science computer to create its decimated file (TBD) that is used to be transmitted onshore. Although the flight and science computers are communicating throughout the duration of the mission, the engineering and flight inputs cannot be dynamically updated. These inputs have to be manually updated by pilots when the glider reaches the surface and establishes communications over iridium.

The development of the backseat driver system by Teledyne Webb Research enhances the glider operation cycle immensely. Gliders equipped with backseat driver follow the same flight and science pathways as Fig. 1A with an additional external processor integrated into the science computer (Fig. 1B). This external processor can receive engineering and science sensor data that enables the system to adaptively update mission parameters. To accomplish the sensor agnostic real-time processing scheme, the external controller is able to receive science sensor data that is both logged to the TBD and data that is logged to a sensor's native data file format. This data is then passed to the external controller, which runs an open-source python processing algorithm (available here: https://github.com/JGradone/Glider_ADCP_Real_Time_Processing) and saves the output to a netCDF file that is able to be efficiently telemetered to shore.

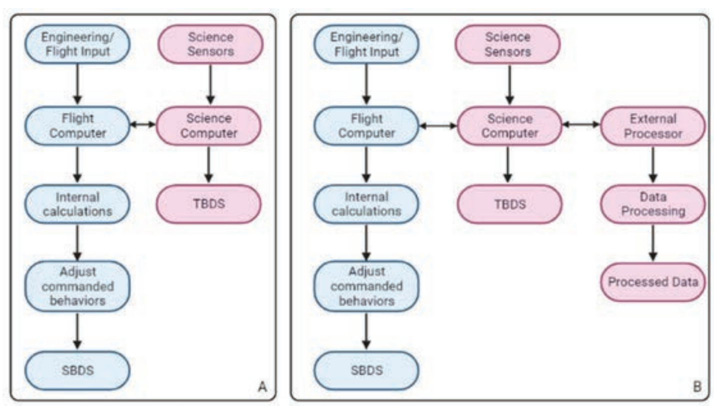

Fig 1. Glider operation cycle (a) without backseat driver and (b) with backseat driver.

a) External Processor Hardware: We are utilizing a Raspberry Pi 4 Model B because it has both sufficient computational power to execute real-time data processing and takes up minimal space within the payload [5]. A Raspberry Pi is a single board computer that is equipped with a 32-bit quad core processor running at 1.8 GHz, standard 40 pin GPIO header, Micro-SD card slot, 2 GB of RAM, 2 USB 3.0 ports, 2 USB 2.0 ports. The Raspberry Pi is being powered through its

5 V USB-C connector by the glider science computer through a USB to serial connector that is equipped with a 12 V to 5 V regulator. This connector utilizes the FTDI chipset and allows communication between the science computer and the Raspberry Pi using RS232 protocol. The Raspberry Pi is running Raspberry Pi OS, a Debian based operating system that has a Linux kernel. Additionally, Python version 3.9.2 is installed which is used to run the external controller script and the linear inversion algorithm. The Raspberry Pi is mounted in the forward section of the glider science payload on the starboard support bar (Fig. 2). The mount pictured, is a UCTRONICS DIN rail mount and is installed with the mounting bracket facing the inside of the payload and the base is fastened to the starboard support bar. Because the mount is made out of 1.2 mm carbon steel, we placed a piece of plastic between the base and the Raspberry Pi so that the pins of the Raspberry Pi do not touch the base of the mount. Additionally, we drilled a large hole into the mounting bracket of the mount so that we can access the power port. The Raspberry Pi is integrated into the science computer using the USB to Serial connector mentioned above. The backseat driver recognizes it through the proglet, but the current version does not include the use of a sensor sample behavior argument to control the power of the Raspberry Pi. This can prove problematic because that means there is a constant power draw throughout the duration of the mission. To address this issue, a new version of backseat driver is under development that will enable sensor sample behavior control over the Raspberry Pi and increase power efficiency for the duration of the mission.

Fig. 2. Raspberry Pi 4 Model B mounted inside glider science payload.

b) External Controller Software: The external controller software is able to communicate with the glider's flight computer through the backseat driver, a software developed by Teledyne Webb Research. This software is able to subscribe state parameters to the backseat driver which enables the subscribed parameter to be processed by an external controller. The external controller can both modify and update the result back to the glider to update desired parameters. In order to facilitate near real-time data transfer, we have developed an enhanced external controller that is a modified version of [1] onboard processing application. When the .PD0 file is read into the script, standard quality control methods are performed to optimize data quality for the final velocity profile derivation [1,16-17]. Data below a correlation threshold of 50%, an echo intensity of 70 dB, and percent good of 80% are discarded. Glider pitch and roll as well as individual beam angles and directions are used to map beam velocity data to depth cells and then transformed to level true depth. Following this transformation, additional QC is performed, where first measurement cells found to be below the seafloor are removed. Velocities relative to the glider exceeding 75 cm/s are also removed [13]. Then, data from the velocity bin closest to the glider are removed to avoid ringing and other contamination and data shallower than 5 m are removed to ensure the glider has achieved a state more typical of glider flight behavior for valid measurements [18]. Lastly, the data goes through a final check to ensure that the inversion can be completed. If the data fails any of the tests included in the final check, the inversion cannot be performed, otherwise the algorithm will continue to the inversion portion. This check includes three steps consisting of a depth range check, missing data check, and if there are two or more non-nan data points. The depth range check looks to see if there is a change in depth. If all depth values are the same, for example 0 m, the error flag is set to 1. The missing data check looks to see if all data is missing, and if it is, the error flag is set to 2. If there are less than two existing data points, then the error flag is set to 3, or if there are two or more existing data points the error flag is set to 4. Two is chosen for the purpose of receiving all possible processed data even if it produces a poor inversion, and may change as testing continues. Once the data has gone through the quality control steps, the data is fed through the linear inversion algorithm that was first developed for ship-based observations [12], modified by [13] to calculate depth-binned absolute ocean velocities on the Spray glider platform, and further modified by [1] for the Slocum glider platform.

III. Testing

To test and optimize the ability of the backseat driver software to initiate real-time processing of the raw data generated from the integrated ADCP. The backseat driver will be implemented via an external controller script, written in Python on the onboard Raspberry Pi computer, which will act as the interface between the backseat driver software and the science computer on the glider. Because it is important to limit the time the glider spends at the surface processing and transmitting data, we are developing precise software triggers to enable the glider to initiate the real-time processing workflow as quickly as possible. The plan is to have the ADCP programmed to sample during dives, climbs, and while hovering (state_to_sample = 7, Fig. 3A). When the glider enters the surface state (m_depth < u_reqd_depth_at_surface), the ADCP closes the .PD0 file and the external controller script is then initiated (Fig. 3B). This enables the processing to begin and, after optimization, finish before the glider is in a state to send data to shore via Iridium. Due to idiosyncrasies of the glider software, we have designed the external controller to start based on the following triggers:

1) ADCP is told to stop samping (c_dvl_on = -1*)*.

2) Glider is physically at the surface (m_depth < u_reqd_depth_at_surface, typically 3 m for shallow gliders and 7 m for deep gliders)

3) Glider's state changes to be at the surface, indicating state_to_sample =7 is no longer fullfilled and the ADCP is no longer sampling (cc_final_behavior_state = 5).

By design, there is overlap in the manner in which these sensors change their state, leading to redundancy in the trigger checks. The external controller script sends the .PD0 from the science computer to the Raspberry Pi and executes the onboard processing linear inversion algorithm, developed by Gradone et al. (2021) (Fig. 3C). This algorithm solves a system of equations for absolute horizontal water velocities using least squares techniques. The resulting velocity profile is exported into a network Common Data Form (netCDF) file that the external controller then sends from the Raspberry Pi to the glider science computer, so that the data can be efficiently transferred onshore in near real-time (Fig. 3C).

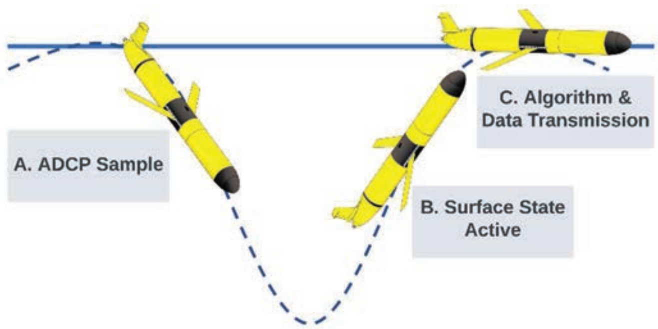

Fig 3. Step by step schematic of near real-time onboard processing.

Additional tests will be conducted to calculate computation time, optimal file size for iridium satellite transmission, and power draw in both simulation mode and the field. Considerations include algorithm constraints, smoothing values, quality control thresholds, and solution vertical resolution among other parameters. We tested the time it took for the Raspberry Pi to execute the linear inversion algorithm on 125 ADCP data files that were a mixture of 30m and 1000m max depth. These files were approximately 4 megabytes each but will be reduced to around 10 kilobytes, making them small enough to transfer over iridium. On average a glider spends 10 to 15 minutes at the surface, processing time would increase surface time by an average of 17.116 seconds, with a minimum of 0.642 seconds and maximum of 28.17 seconds. There will be a myriad of future real-time onboard processing applications once the Raspberry Pi-external controller data processing has been further integrated in the sensor agnostic manner as described here. We achieved our original goals with the resultant short processing time and small processed file sizes in the bench top environment. In the coming weeks we expect to demonstrate this capability in a field environment, including transfer of data to shore via Iridium communications.

Acknowledgment

We thank Rutgers University Center for Ocean Observing Leadership (RUCOOL) glider team for glider preparations. We also thank Eli Hunter and John Kerfoot (RUCOOL) for additional code development. We also acknowledge Teledyne Webb Research staff for technical assistance.

References

[1] Gradone, J. C., Hunter, E. J., Mullison, J., & Miles, T. N.. (2021). Development of Onboard Processing Capabilities for a Slocum Glider Acoustic Doppler Current Profiler. https://doi.org/10.23919/oceans44145.2021.9705895

[2] Wang, Y., Bulger, C., Thanyamanta, W., & Bose, N.. (2021). A Backseat Control Architecture for a Slocum Glider. *Journal of Marine Science and Engineering*, *9*(5), 532. https://doi.org/10.3390/jmse9050532

[3] Ferri, G., Cococcioni, M., & Alvarez, A.. (2015). Mission Planning and Decision Support for Underwater Glider Networks: A Sampling on-Demand Approach. *Sensors*, *16*(1), 28. https://doi.org/10.3390/s16010028

[4] Hwang, J., Bose, N., & Fan, S.. (2019). AUV Adaptive Sampling Methods: A Review. *Applied Sciences*, *9*(15), 3145. https://doi.org/10.3390/app9153145

[5] Naglak, J. E., Page, B. R., & Mahmoudian, N.. (2018). Backseat Control of SandShark AUV using ROS on RaspberryPi. https://doi.org/10.1109/oceans.2018.8604630

[6] Gallimore, E., Stokey, R., & Terrill, E.. (2018). Robot Operating System (ROS) on the REMUS AUV using RECON. https://doi.org/10.1109/auv.2018.8729755

[7] Eickstedt, D. P., & Sideleau, S. R.. (2010). The Backseat Control Architecture for Autonomous Robotic Vehicles: A Case Study with the Iver2 AUV. *Marine Technology Society Journal*, *44*(4), 42–54. https://doi.org/10.4031/mtsj.44.4.1

[8] Keane, J. R., Forrest, A. L., Johannsson, H., & Battle, D.. (2020). Autonomous Underwater Vehicle Homing With a Single Range-Only Beacon. *IEEE Journal of Oceanic Engineering*, *45*(2), 395–403. https://doi.org/10.1109/joe.2018.2877535

[9] Baumgartner, M. F., Fratantoni, D. M., Hurst, T. P., Brown, M. W., Cole, T. V. N., Van Parijs, S. M., & Johnson, M.. (2013). Real-time reporting of baleen whale passive acoustic detections from ocean gliders. *The Journal of the Acoustical Society of America*, *134*(3), 1814–1823. https://doi.org/10.1121/1.4816406

[10] Miles, T. N., Kohut, J., Slade, W., & Gong, D.. (2018). Suspended particle characteristics from a glider integrated LISST sensor. https://doi.org/10.1109/oceans.2018.8604627

[11] Haskins, C., & Schofield, O.. (2015). Glider measurements of phytoplankton physiology in penguin foraging zones along the Western Antarctic Peninsula. https://doi.org/10.23919/oceans.2015.7404376

[12] Visbeck, M.. (2002). Deep Velocity Profiling Using Lowered Acoustic Doppler Current Profilers: Bottom Track and Inverse Solutions*. *Journal of Atmospheric and Oceanic Technology*, *19*(5), 794–807. https://doi.org/10.1175/1520-0426(2002)019<0794:dvpula>2.0.co;2

[13] Todd, R. E., Rudnick, D. L., Sherman, J. T., Owens, W. B., & George, L.. (2017). Absolute Velocity Estimates from Autonomous Underwater Gliders Equipped with Doppler Current Profilers. *Journal of Atmospheric and Oceanic Technology*, *34*(2), 309–333. https://doi.org/10.1175/jtech-d-16-0156.1

[14] Schofield, Kohut, J., Aragon, D., Creed, L., Graver, J., Haldeman, C., Kerfoot, J., Roarty, H., Jones, C., Webb, D., & Glenn, S.. (2007). Slocum Gliders: Robust and ready. *Journal of Field Robotics*, *24*(6), 473–485. https://doi.org/10.1002/rob.20200

[15] Miles, T., Seroka, G., Kohut, J., Schofield, O., & Glenn, S.. (2015). Glider observations and modeling of sediment transport in Hurricane Sandy. *Journal of Geophysical Research: Oceans*, *120*(3), 1771–1791. https://doi.org/10.1002/2014jc010474

[16] Taylor, J. A., & Jonas, A. M. (2008). Maximising data return: Towards a quality control strategy for managing and processing TRDI ADCP data sets from moored instrumentation. IEEE/OES 9th Working Conference

on Current Measurement Technology, 2008, 80– 88. https://doi.org/10.1109/CCM.2008.4480848

[17] Haines, S., Crout, R., Bosch, J., Burnett, W., Fredericks, J., Symonds, D., & Thomas, J. (2011). A summary of quality control tests for waves and in situ currents and their effectiveness. In IEEE/OES 10th Current, Waves and Turbulence Measurements (CWTM) (pp. 100– 106). https://doi.org/10.1109/CWTM.2011.5759534

[18] Gradone, J. C., Wilson, W. D., Glenn, S. M., & Miles, T. N.. (2023). Upper Ocean Transport in the Anegada Passage From Multi-Year Glider Surveys. Journal of Geophysical Research: Oceans, 128(7). https://doi.org/10.1029/2022jc019608

ADVANCING EARTH AND SPACE SCIENCES

JGR Oceans

RESEARCH ARTICLE
10.1029/2022JC019608

Key Points:

- Total transport and transport of South Atlantic Water through the Anegada Passage (AP) may be larger than previously estimated
- The AP is a pathway for both Atlantic Meridional Overturning Circulation return flow and subtropical gyre recirculation
- Gliders are an effective component of the global ocean observing system, needed for measuring subsurface water mass structure and transport

Correspondence to:

J. C. Gradone,
jgradone@marine.rutgers.edu

Citation:

Gradone, J. C., Wilson, W. D., Glenn, S. M., & Miles, T. N. (2023). Upper ocean transport in the Anegada Passage from multi-year glider surveys. *Journal of Geophysical Research: Oceans*, *128*, e2022JC019608. https://doi.org/10.1029/2022JC019608

Received 22 DEC 2022
Accepted 6 JUL 2023

Upper Ocean Transport in the Anegada Passage From Multi-Year Glider Surveys

J. C. Gradone[1], W. D. Wilson[2,3], S. M. Glenn[1], and T. N. Miles[1]

[1]Center for Ocean Observing Leadership, Department of Marine and Coastal Sciences, School of Environmental and Biological Sciences, Rutgers University, New Brunswick, NJ, USA, [2]Center for Marine and Environmental Studies, University of the Virgin Islands, St. Thomas, VI, USA, [3]Ocean and Coastal Observing—Virgin Islands, Inc, St. Thomas, VI, USA

Abstract Caribbean through-flow accounts for two-thirds of the Florida Current and consequently is an important conduit of heat and salt fluxes in the upper limb of the Atlantic Meridional Overturning Circulation (AMOC). Considering there is evidence that up to one-half of the Florida Current originates as South Atlantic Water (SAW), determining the distribution of SAW throughout the Caribbean Island passages is important as this constitutes the major pathway for cross-equatorial AMOC return flow. The Anegada Passage (AP) is a major pathway for subtropical gyre inflow and suggested to be a potential SAW inflow pathway worth revisiting. Here, we present glider-based observations of temperature, salinity and subsurface velocity that represent the first observations of any type in the AP in nearly 20 years. An isopycnal water mass analysis is conducted to quantify the transport of water masses with South Atlantic or North Atlantic origin. Two potentially new aspects of AP transport are revealed. The total AP transport (−4.8 Sv) is shown to be larger than previously estimated, potentially by up to a factor of two. The transport of SAW through the AP (−1.66 Sv) is also shown to be larger than previously estimated, which represents 35% of the total transport reported here and 28% of the SAW entering the Caribbean north of the Windward Island Passages. These results indicate the AP may be an important pathway for cross-equatorial AMOC return flow. These results also provide evidence that gliders with acoustic doppler profilers are a viable method for measuring island passage transport.

Plain Language Summary The Caribbean Sea through-flow is a major transport pathway for heat and salt in the upper limb of the Atlantic Meridional Overturning Circulation (AMOC). The presence of water masses (bodies of water with distinct temperature and salinity properties) that originated in the South Atlantic (SAW) in the Northern Hemisphere is indicative of cross-equatorial AMOC return flow. Ship-based observations in the 1990's identified major pathways for this AMOC return flow but there is still a substantial amount of SAW that is taking an unknown, alternate route northward. This study presents the first observations in nearly 20 years of temperature, salinity, and subsurface velocity in the Anegada Passage (AP). Here, we perform a water mass analysis that suggests the total transport and SAW transport through the AP is larger than previously estimated. This result is significant as the AP may be an important pathway for AMOC return flow. This study also shows that autonomous underwater gliders are a viable method for measuring island passage transport.

1. Introduction

To maintain Earth's radiative balance, both the atmosphere and the ocean drive a net poleward heat flux. However, the net heat flux in the Atlantic Ocean is northward, even in the southern hemisphere. The Atlantic Meridional Overturning Circulation (AMOC) is responsible for this heat flux as warm surface waters are carried northward which is ultimately balanced by cold deep waters returning southward. Increases in anthropogenic atmospheric carbon dioxide (CO_2) leading to a greenhouse warming effect are expected to impact the AMOC in several ways. A reduction in the heat loss from the ocean to the atmosphere and an increase in the input of freshwater at higher latitudes are expected to lower water mass density in the deep-water formation regions (Gregory et al., 2005). Currently, there is evidence for and uncertainty around a slowdown in the AMOC (Caesar et al., 2018; Praetorius, 2018; Thornalley et al., 2018). It is vital to better understand the dynamics of this circulation as variations in the strength of the AMOC have been linked with significant changes in global climate (dos Santos et al., 2010; Schmidt et al., 2004). These AMOC variations have induced changes in global temperature, wind fields, and the hydrologic cycle (Rahmstorf, 2002).

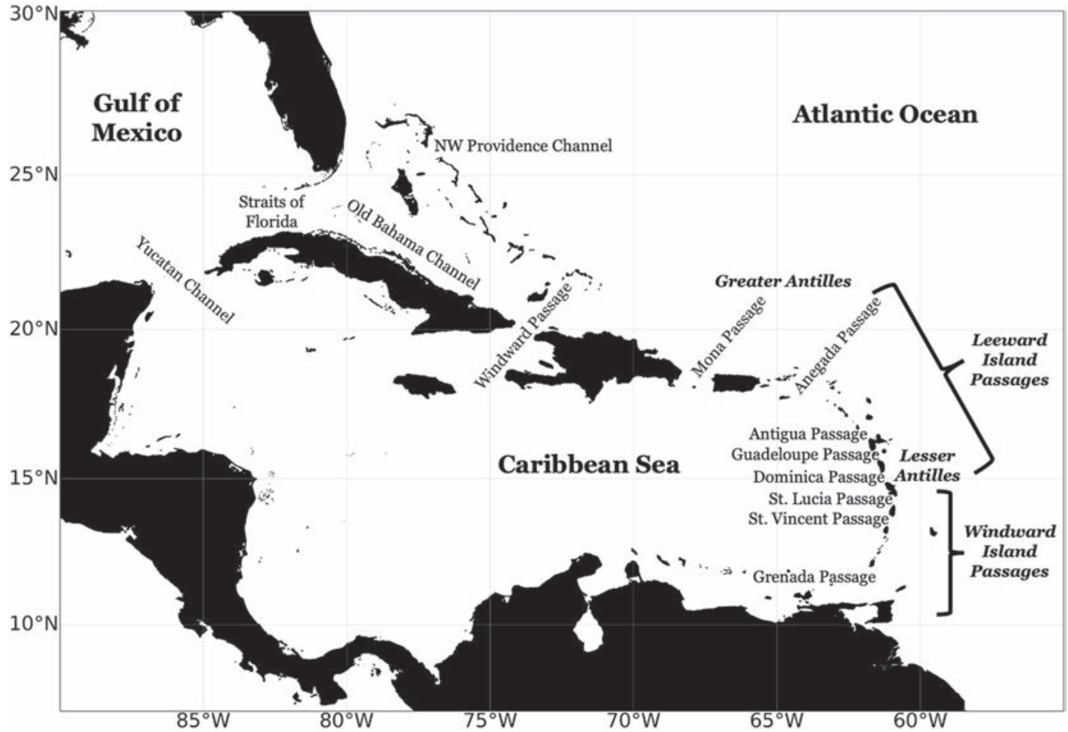

Figure 1. The Caribbean Sea with the major passages between the Atlantic Ocean and Caribbean Sea labeled.

Toward the beginning of the upper-limb of the AMOC's crossing into the North Atlantic lies the complex Caribbean Sea. This semi-enclosed basin is connected to the tropical Atlantic Ocean through a series of passages between the islands of the Greater and Lesser Antilles (Figure 1). The complex bathymetry of the eastern Caribbean passages effectively acts as a sieve for the inflow of Atlantic water due to the average sill depth being approximately 800 m (Johns et al., 2002). The inflow through these passages is highly dynamic. There is variability on synoptic, seasonal, annual, and decadal timescales and forcing from both winds and thermohaline circulation (Johns et al., 1999). Previous studies have found the net inflow to the Caribbean Sea of 28 Sv (1 Sverdrup = 10^6 m^3 s^{-1}) to be nearly equally geographically distributed in thirds: ∼10 Sv through the Greater Antilles passages, ∼8 Sv through the Leeward Island Passages, and ∼10 Sv through the Windward Island Passages (Johns et al., 2002). Throughout the remainder of this analysis, we discuss transport in units of Sverdrups, referring to transport into the Caribbean with a negative sign convention or using the term "inflow." Through a series of modeling experiments Johns et al. (2002) determined that the ∼10 Sv inflow through the Windward Island Passages to the south is almost entirely thermohaline forced as the wind-driven component is essentially zero. The ∼18 Sv inflow through the Greater Antilles and Leeward Islands Passages to the north was found to be driven by the large-scale subtropical gyre circulation. This inflow directly feeds into the dominant surface current, the Caribbean Current, which can account for up to two-thirds of the flow into the Gulf Stream at the Straits of Florida and consequently is an important conduit of mass, heat, salt, and freshwater fluxes in the AMOC (Johns et al., 2002).

While high-latitude sinking and interior mixing processes have a first order control on the magnitude of the AMOC, low-latitude wind-driven processes determine and modify the subsurface density structure of the water masses flowing through the Caribbean Sea, Gulf of Mexico, and eventually the Gulf Stream (Fratantoni et al., 2000). This linkage between upper ocean water mass conditions in the Caribbean and Gulf Stream activity is significant enough to be identifiable in paleoceanographic sediment core records. Planktonic foraminifera assemblages have linked high sea surface temperatures in the Caribbean with diminished Gulf Stream activity (Fischel et al., 2017; Reißig et al., 2019). This connection suggests that the inter-hemispheric atmospheric energy balance ultimately controls the large-scale circulation in this region through its influence on the position of the Intertropical Convergence Zone, which constitutes the main forcing for the North Atlantic Subtropical Gyre (STG) variability (Fischel et al., 2017; Nürnberg et al., 2021; Reißig et al., 2019).

In addition to forcing from STG variability, the modification of the subsurface density structure of the water masses flowing through the Caribbean Sea is also substantially impacted by upstream water mass origin. Historically, 45% (13 Sv) of the Florida Current transport has been considered to be of South Atlantic origin (Schmitz & Richardson, 1991; hereafter SR91), thus there is considerable interest in determining the distribution of South Atlantic Water (SAW) throughout the Caribbean Passages as this constitutes a major pathway for cross-equatorial AMOC return flow (Johns et al., 2002; Kirchner et al., 2009; Tuchen et al., 2022; Wilson & Johns, 1997). However, there are several significant inconsistencies recent publications have raised with the assumptions made by SR91 (Szuts & Meinen, 2017; hereafter SM17):

1. The accepted AMOC value at the time of the SR91's analysis was 13 Sv, whereas recent literature finds a mean value closer to 17 Sv in the Florida Straits at 26°N (Frajka-Williams et al., 2019; Szuts & Meinen, 2017).
2. SR91 consider the transport of all surface waters >24°C to be of South Atlantic origin in their formulation of a 13 Sv AMOC, whereas recent literature has found that surface waters that flow through the Florida Straits do not leave the subtropical gyre and thus potentially do not contribute to the strength of the AMOC (Brambilla & Talley, 2006).
3. SR91 ignore strong mid-depth horizontal gradients in eastern and western Salinity Max Waters and Central Waters in the Florida Current, which suggests these waters are not entirely North Atlantic Water (NAW) as SR91 assume.

In addition to the results from these recent publications, water mass analysis and transport estimates have shown a maximum of 11 ± 2.22 Sv of SAW flows in through the Windward Island Passages and approximately 5.3 ± 0.7 Sv of SAW flows northward from Guadeloupe to the Atlantic across 16°N (Rhein et al., 2005). When these SAW transport estimates are combined, a total SAW inflow of 16.3 Sv is in much better agreement with the accepted AMOC strength of 17 Sv. Therefore, we frame this analysis with an AMOC strength of 17 Sv but continue to reference the pioneering work by SR91 throughout the discussion while acknowledging both the limitations of several of their assumptions as well as the new understandings from more recent literature. With the pathway for a maximum of 11 Sv of SAW constrained to the Windward Island Passages, the route the remaining 6 Sv of SAW take northwards remains largely unresolved. There are uncertainties and consequences for projected changes in the AMOC (Frajka-Williams et al., 2019) and recent evidence that the Caribbean Sea is warming (Antuña-Marrero et al., 2015; Glenn et al., 2015; Jury, 2017), surface waters are freshening (Jury & Gouirand, 2011), and the through-flow is slowing (Jury, 2020). These factors combined with the lack of recent coordinated, sustained ocean observations in this region motivate a reassessment of transport through the Caribbean Passages.

The Anegada Passage (AP), located in the northeast corner of the Caribbean, is the largest and deepest of the Caribbean Passages (sill depth 1915 m, (Fratantoni et al., 1997)). Anegada Passage transport has been shown to be a major pathway for STG inflow in the form of NAW (Johns et al., 2002) and suggested to be an alternate pathway for SAW into the Caribbean (Johns et al., 1999; Wajsowicz, 2002; Wilson & Johns, 1997). Flow through the AP is predominately southwestward into the Caribbean where velocity profiles have shown a subsurface velocity maximum in the center of the passage and weak flow reversals found at times at the surface along both the eastern and western sides of the passage (Johns et al., 1999). There can also be strong eastward components over the western half of the passage and westward components over the eastern half of the passage, leading to strongly convergent flow (Johns et al., 1999).

The eastern Caribbean has been a historically under-sampled region until recently. Ship-based campaigns to collect direct transport observations throughout the Caribbean Passages during the 1990's and early 2000's (Johns et al., 1999, 2002; Kirchner et al., 2009; Rhein et al., 2005; Wilson & Johns, 1997) progressed the state of knowledge immensely. However, ship-based sampling is extremely expensive and limited by weather conditions. The development of autonomous underwater vehicles (gliders) has contributed to filling this data gap in the Caribbean Sea and other regions by providing high quality observations in a novel yet economical manner. Since 2020, gliders equipped with acoustic Doppler profilers (ADP) have been deployed throughout the AP region four separate times covering over ~2,700 km over ~150 days (Figure 2). While ADPs have been integrated onto gliders for over a decade (Miles et al., 2015; Todd et al., 2011, 2017), these field campaigns have served as a unique proof-of-concept that glider deployments can consistently observe passage transport variability at the same, if not better, quality and at comparatively lower cost than traditional ship-based campaigns (Schofield et al., 2007).

The present work builds upon previous Caribbean Passage transport research in several ways. Four glider deployments are utilized to both validate the methodology of using gliders to measure passage transport as well as develop further understandings of the transport dynamics in this region. In 2021, two glider deployments

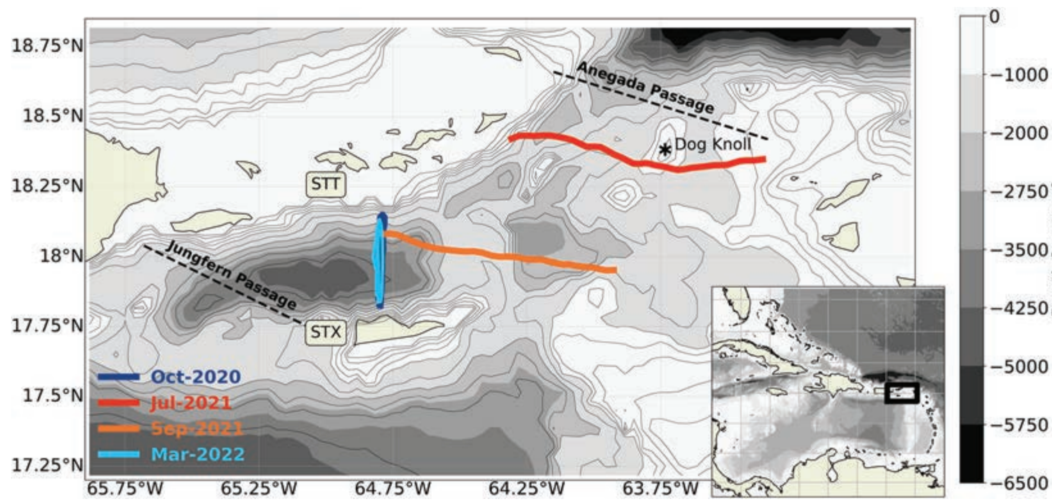

Figure 2. Glider tracks in the Anegada Passage region from 2020 to 2022 glider deployments.

ventured eastward across the AP on a path intentionally similar to historical ship-based transects to allow for a more direct comparison (Johns et al., 1999). In 2020 and 2022, single glider deployments were conducted on a repeating transect line between St. Thomas (STT) and St. Croix (STX) (15 transects in 2020, 6 transects in 2022) to allow for the calculation of a transport time-series from which additional details of the transport dynamics could be gathered. The high resolution, co-located glider observations of temperature, salinity, and subsurface velocity also allow for a detailed isopycnal water mass analysis to quantify the transport of water masses with South Atlantic or North Atlantic origin in the AP transport. To our best knowledge, the results presented in this study are the first published, detailed in-situ analysis of transport below 200 m in the AP region.

2. Observations and Methods

2.1. Transport From Glider-Mounted Acoustic Current Profiler Derived Horizontal Water Velocity

The observations used in this study were collected using Teledyne Webb Research Slocum gliders (Schofield et al., 2007). Gliders are buoyancy-driven, autonomous underwater vehicles that use a combination of changes in their pitch angle and internal volume to move vertically and horizontally in a sawtooth-like pattern. Gliders are modular platforms that can be instrumented with a growing variety of complex sensors. Two deep (1,000 m rated) Slocum gliders, RU29 and RU36, were used in this study. RU29 is a second-generation Slocum glider (G2) equipped with a Sea-Bird Scientific pumped conductivity, temperature, and depth (CTD) sensor and a 1-MHz Nortek AD2CP. RU36 is a third generation Slocum glider (G3) equipped with an RBR *legato*³ inductive cell CTD sensor, a 600-kHz Teledyne RD Instruments (TRDI) Pathfinder ADP, and an Aanderaa Oxygen Optode 4831. The Nortek AD2CP is a four-beam system that was configured to sample 8 pings per second in beam coordinates with a 0.2-m blanking distance in 0.5-m bins. The TRDI Pathfinder is also a four-beam system that was configured to sample one 10-ping ensemble average every second in beam coordinates with a 0.8-m blanking distance in 1-m bins. These configurations were chosen for a variety of reasons. Both instruments were configured to sample as quickly as possible, whereas the other configuration choices were a combination of power consumption capabilities and optimization testing. Data from both current profilers were logged internally and downloaded after the deployment. A summary of glider deployment details and specific configurations is provided in Table 1.

While two different types of current profilers were used in this study, measurements of water velocity relative to the glider were obtained using similar system configurations and processing techniques. The major data processing steps for both current profilers are quality control, correcting the beam velocities to level true-depth, mapping the beam velocities to vertical bins relative to the glider, performing a coordinate transformation to convert from beam to East-North-Up (ENU), and derivation of absolute horizontal water velocities. Raw beam velocity data are quality controlled first through several data screening filters. For the Nortek AD2CP, data below a correlation of 50% or above a high return amplitude of 75 dB are discarded (Todd et al., 2017). For the TRDI Pathfinder, data below a correlation threshold of 50%, an echo intensity of 70 dB, and percent good of 80% are discarded (Haines

Table 1
Glider Deployment Information, Configurations, and Summary of Transport Results

Deployment	October-2020	July-2021	September-2021	March-2022
Duration (days)	24	5.5	4.5	11
Location	St. Thomas-St. Croix	Outer AP	Outer AP	St. Thomas-St. Croix
Number of Transects	15	1	1	6
Current Profiler	Nortek AD2CP	Nortek AD2CP	Nortek AD2CP	TRDI Pathfinder
Absolute Transport from ADP Inversion Method	−2.27 ± 0.66 Sv	−4.43 Sv	−5.24 Sv	−2.47 ± 0.8 Sv
Geostrophic Transport from Thermal Wind	−2.29 ± 0.7 Sv	−4.74 Sv	−4.97 Sv	−3.49 ± 0.35 Sv
SAW Transport	−0.70 Sv	−1.21 Sv	−1.33 Sv	−0.84 Sv

et al., 2011; Taylor & Jonas, 2008). For both current profilers, glider pitch and roll as well as individual beam angles and directions are used to map beam velocity data to depth cells and then transformed to level true depth.

The Nortek AD2CP is mounted in a Janus configuration with beams 1 and 3 oriented forward and aft and slanted 47.5° off vertical and beams 2 and 4 oriented port and starboard and slanted 25° off vertical. A typical dive angle for Slocum gliders is 24–27° so either the forward or aft beams will be nearly horizontal on a climb or a dive for the Nortek system. Because of this configuration, only 3 beams are used in the transformation from beam to ENU velocity (beams 1, 2, and 4 on a dive and beams 2,3 and 4 on a climb). The TRDI Pathfinder is a phased array system also mounted in a Janus configuration where the four beams are angled 30° off vertical but rotated along the central axis of the glider so that beams 1 and 3 are oriented forward and beams 4 and 2 are oriented aft but 22.5° off the central axis of the glider to the port and starboard, respectively. Because of this configuration, all four beams can be used in the transformation from beam to ENU velocity. For both systems, an instrument specific transformation matrix based on the transducer face geometry is used to convert from beam to XYZ velocity (i.e., velocity relative to the glider). Next, another transformation matrix that incorporates the glider magnetic heading is used to convert from XYZ velocity to ENU (i.e., East-North-Up). A final round of quality control is then applied to the ENU velocity. Following Todd et al. (2017), velocities relative to the glider exceeding 75 cm s^{-1} are excluded as the glider's speed through water is ~25 cm s^{-1} and larger relative velocities are not expected over the sampling range of the current profilers (maximum 20 m). Data from the velocity bin closest to the glider are also excluded as this bin can exhibit ringing or other frequent contamination. Lastly, data shallower than 5 m are discarded as the glider typically must travel several body lengths before it achieves a dive angle that is more closely representative of its typical flight behavior as compared to when it is on the surface.

Measurements made by glider-mounted current profilers combine the true water velocity, the velocity of the glider's motion, and noise:

$$U_{\text{adcp}} = U_{\text{ocean}} + U_{\text{glider}} + U_{\text{noise}} \tag{1}$$

There are several methods that can be used to derive absolute horizontal water velocities (U_{ocean}). Fundamentally, they either decompose the different components measured by glider-mounted current profilers or rely on assumptions to ignore them. The inversion method was originally developed for ship-based lowered current profilers (Visbeck, 2002) but has been adapted for use on gliders and used extensively (Ellis et al., 2015; Gradone et al., 2021; Heiderich & Todd, 2020; Ma et al., 2019; Miles et al., 2015; Todd et al., 2011, 2017). This method solves a system of equations for both unknown glider velocities and absolute horizontal water velocities using least squares techniques. An advantage of this method is that constraints (glider estimated depth-average currents, surface drift, bottom-track, etc.) can easily be applied to yield better estimates of the true horizontal water velocities. Additional constraints such as a curvature-minimizing smoothness constraint assist in reducing the noise from missing data (Visbeck, 2002). These constraints can be applied with different weights to determine the degree to which individual constraints should be considered. We follow Todd et al. (2011) by applying weights of 5 and 1 to our glider dead-reckoned depth-average current (DAC) and curvature-minimizing smoothness constraints, respectively. Figure 3 shows example DAC vectors from transects between St. Thomas and St. Croix during the October 2020 deployment. The inversion method is applied with a final solution vertical resolution of 10 m for the Nortek system and 20 m for the RDI system. A coarser vertical resolution was needed for the RDI system to include a larger number of quality data points in each final solution bin. Data from the RDI system

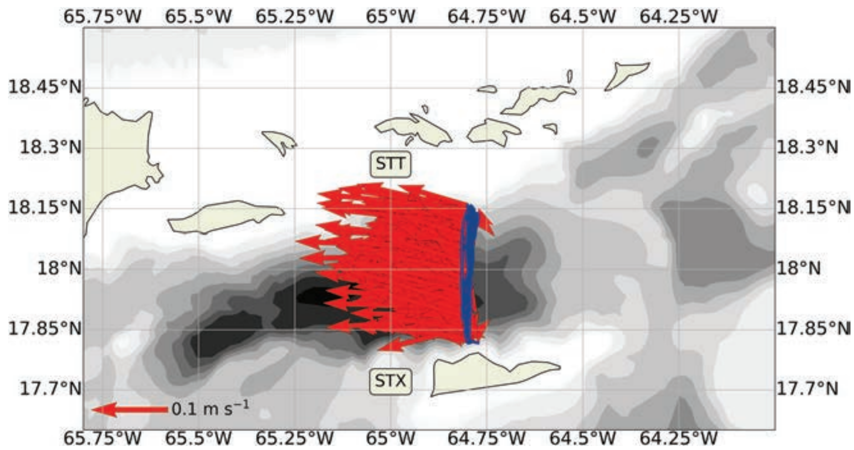

Figure 3. Glider transect track (blue) and segment depth-average current vectors (red) from the October-2020 St. Thomas-St. Croix, Anegada Passage deployment.

experienced degraded data quality with depth likely due to less energy being emitted into the water column and thus a poorer return, especially with decreased scatterers with depth.

The DAC estimate is an integral constraint on the inversion method derivation of absolute horizontal water velocity. DACs can be impacted by a variety of factors such as errors in the internal compass and attitude sensors, accuracy of the hydrodynamic flight model, internal waves, and biofouling (Rudnick et al., 2018). Despite these potential sources of error, DAC root-mean-square accuracy is estimated to be approximately 0.01–0.02 m s^{-1} (Rudnick et al., 2018). This uncertainty is minimal compared to the magnitude of the bulk transport estimates reported here. Furthermore, Todd et al. (2017) apply a quality control step for correcting an instrumental heading bias, which are typically observed in individual velocity profiles as an erroneous heading-dependent shear. Following this correction, substantially smaller heading bias' were found for each deployment presented here to the extent that corrections were not necessary.

For the 2020 and 2022 deployments, horizontal water velocity profiles derived for each glider segment are interpolated onto a regular depth, longitude, and latitude grid representing the mean position of the glider transects between St. Thomas and St. Croix. Glider drift in the E/W direction was minimal so a constant longitude of 64.80° W was chosen. The N/S extent of the transect lines is approximately 30 km. Glider speed over ground for these deployments was consistently ~1 km/hr where a single 1000-m segment (dive and climb) transited ~3 km. Six equally spaced latitude bins (roughly 5 km apart) were chosen so that 2–3 glider segment would be included in the interpolation. This grid interpolation effectively smoothes the absolute velocities. After the velocity profiles are interpolated onto the regular grid, E/W velocity is integrated over the full water column and transect length to produce transport in units of Sverdrups (where 1 Sv = 10^6 m^3/s). Deployment average transport and standard deviation are obtained by calculating transport mean and standard deviation over the total number of transects. E/W transports reported here are effectively cross-passage transport due to the orientation of the transects. There was no attempt to remove tidal variability from the observations. Tides have low spatial variability in this region and are either diurnal or semidiurnal with a relatively small amplitude, typically less than 10-cm (Kjerfve, 1981; Wilson & Johns, 1997). Averaging over the spatial (3-km glider segments, 30-km transects) and temporal (1-hr glider segments, ~36-hr transects) length scales of these observations is assumed to remove tidal variability.

For the 2021 deployments, horizontal water velocity profiles are derived for each glider segment but are not interpolated onto a regular depth, longitude, and latitude grid as there is only one transect per deployment. Because the deployment tracks were designed to travel in a cross-passage direction, the 2021 absolute velocity data are rotated by the orientation of the passage opening (~18°). This rotation transforms the E/W velocity into cross-passage velocity, which enables a more direct comparison with the cross-glider track geostrophic velocities detailed in the following section. This rotation is not needed for the 2020 and 2022 deployments because these tracks were in an approximately N/S direction, so the cross-glider track geostrophic velocities are approximately in a cross-passage direction. Transport is derived for the 2021 deployments by using the start and end locations of each segment to calculate distance in meters and then cross-passage velocity is integrated over the full water column and transect length to produce transport in units of Sverdrups.

10.1029/2022JC019608

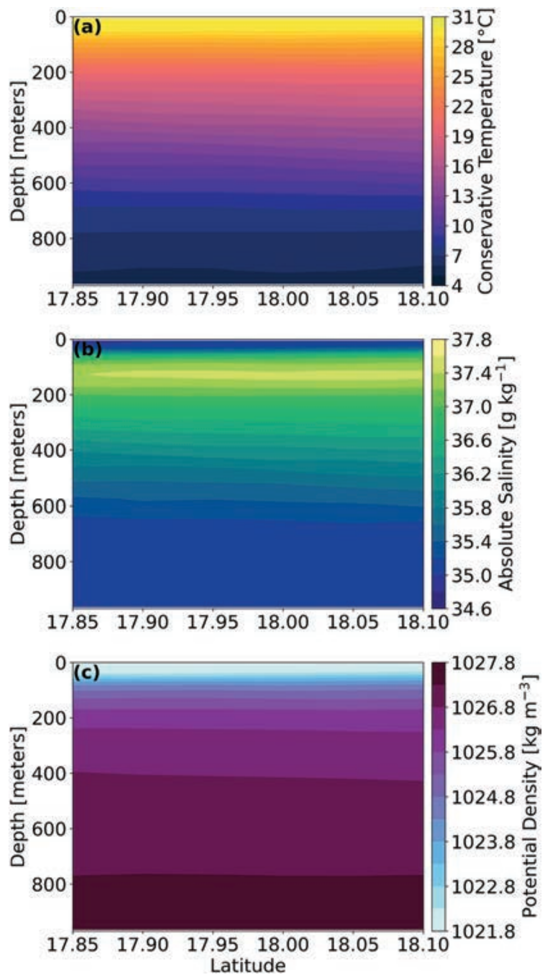

Figure 4. Example conservative temperature (a), absolute salinity (b), and potential density (c) transects in the STT-STX section of the Anegada Passage interpolated onto the regular depth-latitude-longitude grid for thermal wind geostrophic velocity calculation.

2.2. Transport From Geostrophic Velocity

Geostrophic velocity is estimated via the thermal wind relationship following the methodology by Høydalsvik et al. (2013). The CTDs on both gliders were sampled every 2 s throughout full dives and climbs. Potential density (σ_θ, from here on: density) is calculated from conservative temperature (Θ, from here on: temperature) and absolute salinity (S_A, from here on: salinity) measurements using the TEOS-10 standard (Roquet et al., 2015). For the 2020 and 2022 deployments, measurements from dives and climbs were averaged in 2-m vertical bins and interpolated onto the same depth, longitude, and latitude grid used for calculating transport from the current profiler data both to reduce noise and facilitate comparisons. For the 2021 deployments, measurements from dives and climbs were also averaged in 2-m vertical bins but no interpolation onto a regular grid was needed because these deployments were on their own unique tracks. Figure 4 shows an example of temperature, salinity, and density on this grid for the 2020 deployment. Density measurements are then used in the thermal wind relationship to calculate the cross-glider track component of the geostrophic vertical shear:

$$\frac{\partial u}{\partial z} = \frac{g}{\rho_o f}\frac{\partial \rho}{\partial y} \tag{2}$$

where u is the cross-glider track velocity, z is the vertical coordinate, g is the acceleration due to gravity, ρ_o is a reference density (1,027 kg/m^3), f is the Coriolis parameter, ρ is density, and y is the along-track distance. Along-track distance is taken to be the distance between the latitude bin edges for the 2020 and 2022 deployments, roughly 5 km, and true along-track distance for the two 2021 deployments. Relative cross-glider track geostrophic velocity (U_{relative}) is obtained by integrating the previous equation with respect to z:

$$U_{\text{relative}} = \int_{-H}^{0} \frac{g}{\rho_o f}\frac{\Delta \rho}{\Delta y} \tag{3}$$

where H is the maximum dive depth of the glider. Glider dead-reckoned, depth-average currents (U_{DAC}) used to constrain the ADP velocity profiles are also interpolated onto the latitude grid used here. Interpolating the depth-average currents onto this grid effectively results in one representative DAC to be used as a constraint for each latitude point a given transect. For the 2021 deployments, the true DAC is used as a constraint for each glider segment. The depth-average currents are used to reference the relative cross-glider track velocity to absolute geostrophic velocity ($U_{\text{geostrophic}}$) by:

$$U_{\text{geostrophic}}(y,z) = U_{\text{relative}}(y,z) + U_{\text{reference}}(y) \tag{4}$$

The reference velocity is calculated from the DAC as:

$$U_{\text{reference}}(y) = U_{\text{DAC}} - \frac{1}{H}\int_{-H}^{0} U_{\text{relative}}(y,z)\,dz \tag{5}$$

In smaller passages in the southern Caribbean where the flow is expected to have a stronger ageostrophic component, Wilson and Johns (1997) found that smoothing of geostrophic velocity estimates greatly improved comparisons with measured velocities. It was necessary to interpolate the density fields onto the regular grid for the 2020 and 2022 deployments due to the repeating transects, which effectively smoothed these geostrophic velocity estimates. The geostrophic velocity estimates from the 2021 deployments were smoothed using a local least-squares fit by a third degree polynomial in an approximately 30 km rolling filter window similar to Todd et al. (2011). After geostrophic velocity profiles are calculated they are integrated over the full water column and transect length to produce transport in units of Sverdrups. Deployment average transport and standard deviation are calculated in the same manner as was done for the ADP directly measured velocities.

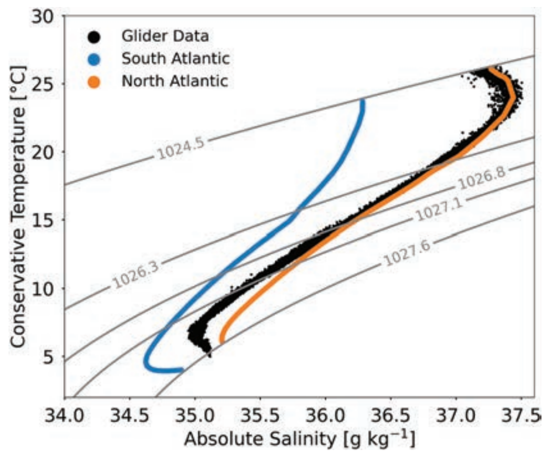

Figure 5. Representative source water mass profiles obtained using mean temperature and salinity profiles from World Ocean Atlas 2018 following Rhein et al. (2005) for the South Atlantic (blue) and North Atlantic (orange). Temperature and salinity data from all four glider deployments shown in black.

2.3. Water Mass Analysis

Water mass analyses using temperature and salinity have been used widely throughout the Atlantic in the past (Poole & Tomczak, 1999; Schmitz & McCartney, 1993; Schmitz & Richardson, 1991) and can applied in a manner to distinguish SAW from NAW in the Caribbean inflow (Garraffo et al., 2003; Johns et al., 2003; Kirchner et al., 2008; Mertens et al., 2009; Rhein et al., 2005). Here, a water mass analysis is conducted following Rhein et al. (2005) by taking an isopycnal mixing approach and expanded through the use of least-squares fitting. Temperature and salinity data are used as constraints in the following system of equations to solve for the mixing fraction of NAW or SAW that is necessary for the observed data to be derived from two distinct source waters.

$$x_{\mathrm{SA}} T_{\mathrm{SA}} + x_{\mathrm{NA}} T_{\mathrm{NA}} - T_{\mathrm{obs}} = R_T \tag{6}$$

$$x_{\mathrm{SA}} S_{\mathrm{SA}} + x_{\mathrm{NA}} S_{\mathrm{NA}} - S_{\mathrm{obs}} = R_S \tag{7}$$

$$x_{\mathrm{SA}} + x_{\mathrm{NA}} - 1 = R_{\mathrm{MC}} \tag{8}$$

Here, (T_{SA}, S_{SA}, T_{NA}, S_{NA}) represent the temperature and salinity definitions for the distinct source water types from the South Atlantic and North Atlantic; (T_{obs}, S_{obs}) represent the observations; (x_{SA}, x_{NA}) represent the fractional relative contributions; and (R_{T}, R_{S}, R_{MC}) represent the residuals which are minimized through a least squares fitting. This method is similar to the optimum multiparameter (OMP) analysis but is limited in the number of source water masses (two) than can be used to still have a determined system of equations. Poole and Tomczak (1999) used OMP analysis to distinguish six source water mass endpoints from three linear T/S relationships in the Atlantic Central Waters (one northern type and two southern types) and constrained this resulting system of equations by including oxygen, silicate, nitrate, and phosphate data along with temperature and salinity. Here, we follow Rhein et al. (2005) and refrain from separating the two South Atlantic source water types which allows for the calculation of fractions of SAW and NAW by T/S data alone. The Python package PYOMPA (version 0.3) is adapted for this analysis (Shrikumar et al., 2021).

The isopycnal mixing analysis is applied from $\sigma_\theta = 24.5$ (~110 m) to $\sigma_\theta = 27.5$ (~1,000 m) which is the glider's maximum operational depth. Representative source water mass profiles are obtained using mean temperature and salinity profiles from World Ocean Atlas 2018 (WOA18; Locarini et al., 2018; Zweng et al., 2018) following the locations of the hydrographic data used by Rhein et al. (2005). The in-situ temperature and salinity profiles from WOA18 are converted to conservative temperature and absolute salinity using the TEOS-10 standard that was applied to the glider data (Roquet et al., 2015). Figure 5 shows these profiles along with all glider temperature and salinity observations below the surface layer analyzed here. The isopycnal water mass analysis is conducted at each depth interval (steps of 2-m vertically) from the respective glider deployments discussed above. At these depth intervals, the T/S properties from the two source water masses along the same isopycnal are used to compute the fraction of each endmember needed to obtain the properties of the observed data. We follow the water mass density ranges and naming conventions of Stramma and Schott (1999) and Rhein et al. (2005) where SW is $\sigma_\theta < 24.5$, salinity maximum water (SMW) is $24.5 \geq \sigma_\theta < 26.3$, upper central water (uCW) is $26.3 \geq \sigma_\theta < 26.8$, lower central water (lCW) is $26.8 \geq \sigma_\theta < 27.1$, and intermediate water is (IW) $27.1 \geq \sigma_\theta < 27.6$. Details regarding differences between the respective North Atlantic and South Atlantic component of each water mass are outlined further in the discussion. The fractional contributions of each source water mass (x_{SA}, x_{NA}) are multiplied by the absolute velocity derived transport at each depth interval to obtain SAW and NAW transport.

The implications of the choices for these source water types have been detailed extensively (Kirchner et al., 2008, 2009; Mertens et al., 2009; Rhein et al., 2005), however we emphasize again that the South Atlantic SMW source water used here is a fresher endmember from the eastern South Atlantic. The more saline SMW from the western South Atlantic is nearly indistinguishable from the North Atlantic SMW. We acknowledge that this choice neglects the contribution of high salinity SAW to the total SAW transport in the SMW layer and estimate potential contributions from this water mass using mass balance assumptions in the discussion (Kirchner et al., 2008; Rhein et al., 2005; Zhang et al., 2003).

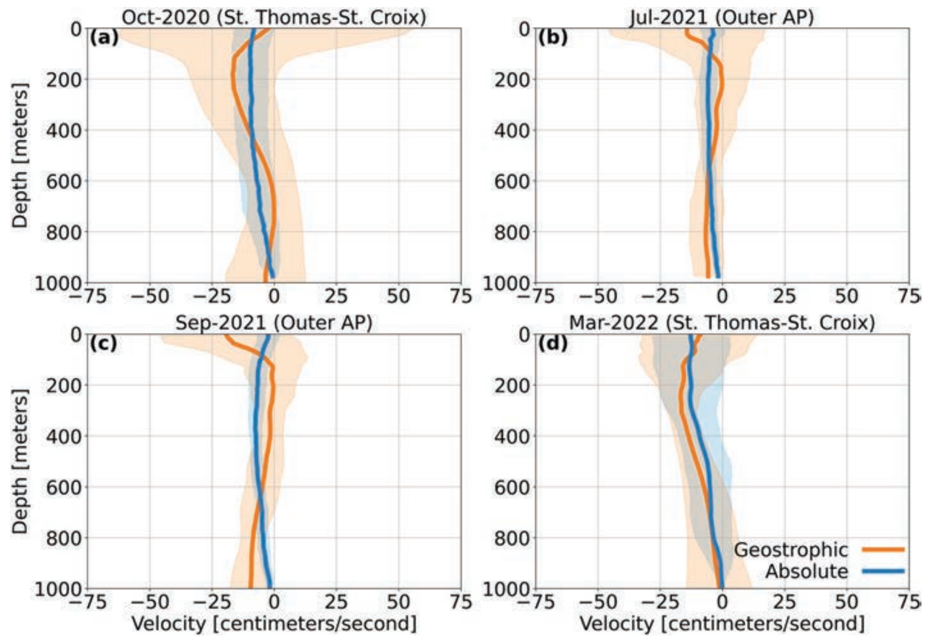

Figure 6. Mean thermal wind derived geostrophic velocity (orange) and acoustic doppler profilers derived absolute velocity (blue) shaded by one standard deviation for all four deployments. Profiles for the 2020 and 2022 deployments represents E(+)/W(−) velocity and cross passage (- into/+ out of passage) velocity for the 2021 deployments.

The isopycnal water mass analysis cannot be applied to the surface layer. Therefore, we follow the assumptions made by SR91, Schott et al. (1998), Hellweger and Gordon (2002), and Rhein et al. (2005) and the subsequent studies that have since adopted the methodology used by Rhein et al. (2005) for this layer. These studies have found that the tropical surface waters warmer than 24°C ranging from the equatorial Atlantic to the Florida Straits are of South Atlantic origin. Thus, here we assign all transport in the $\sigma_\theta < 24.5$ layer as SAW.

3. Results

3.1. Current Structure and Transport

Figure 6 shows mean velocity profiles with a one standard deviation shading for both geostrophic velocity and ADP derived absolute velocity for all four deployments. These mean velocity profiles show the flow is largely barotropic. There is an overall agreement on the mean velocity direction into the Caribbean with larger variability in the geostrophic velocity estimates. Differences between geostrophic and absolute velocity estimates will be discussed further in the following section.

The two 2021 deployments occupied somewhat different transect lengths and orientations, but both generally sampled the entire AP (Figure 2). The first 2021 AP transect, located in the furthest northeast corner of the study area, was occupied from July 4-9, 2021. The ADP derived absolute velocities observed during this glider deployment were also predominately into the Caribbean (Figure 7a). The flow had a slight along passage component, roughly aligned with the shelves on both edges of the transect (Figure 7c). The flow was mainly barotropic, with a slight shearing of the along passage component of the flow occurring near the bathymetric feature Dog Knoll. The average transport was −4.43 Sv into the Caribbean.

The second AP transect, traveling from the area of the St. Thomas-St. Croix transects to approximately 50 km south of Dog Knoll, was occupied from September 14-18, 2021. The ADP derived absolute velocities observed during this glider deployment were predominately into the Caribbean, with a weak reversal in the middle of the transect (Figure 7b). There was more variability in the along passage component of the flow during this deployment, though the magnitude was substantially less than the first deployment (Figure 7d). Again, the flow was mainly barotropic, with a slight shearing of the along passage component of the flow over the entire transect. The average transport was −5.24 Sv into the Caribbean. The mean cross passage velocity for both transects was

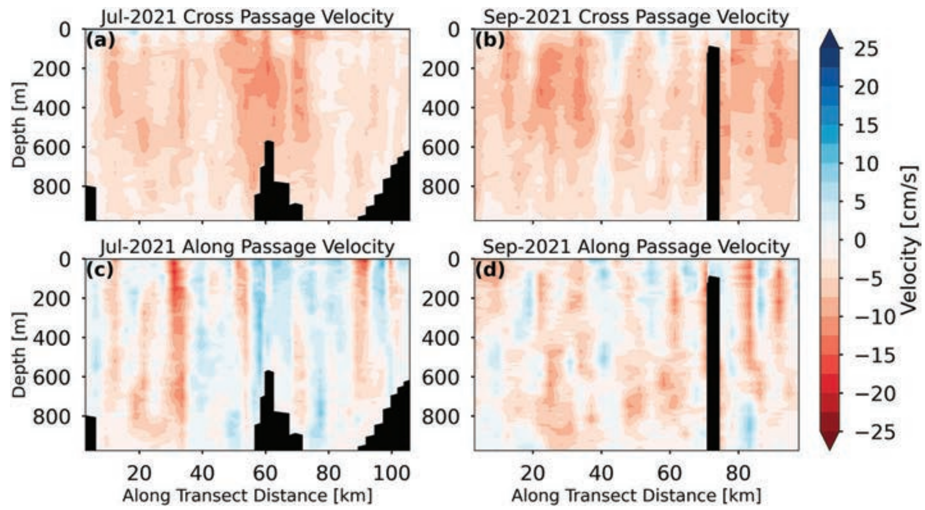

Figure 7. Anegada Passage velocity derived from glider mounted acoustic doppler profilers for the first 2021 deployment (left column) and second 2021 deployment (right column) in the cross passage (- into passage/into Caribbean, + out of passage/into Atlantic) direction (top row) and along passage (- toward bottom of passage/south, + toward top of passage/north) direction (bottom row). Both transects started on the E/NE side of the passage and traveled to the W/SW side of the passage. The duration of the July-2021 deployment was approximately 5.5 days and the duration of the September-2021 deployment was approximately 4.5 days.

approximately -5 cm s^{-1} with a maximum around -20 cm s^{-1} and little to no reversal of the flow. The mean along passage velocity for both transects was approximately zero with a maximum around ± 15 cm s^{-1}. If values for both transects are averaged, the averaged transport observed here is -4.84 Sv into the Caribbean.

Transport time-series' were calculated from the ADP derived absolute velocities collected on the repeat transect lines between St. Thomas and St. Croix during the 2020 and 2022 glider deployments (Figure 8). Mean transport values for the 2020 and 2022 deployments are within each other's error bars, despite more than double the number of transects being occupied in 2020 compared to 2022 (15 vs. 6). Within a deployment and comparing the two deployments, there is very little variability about the mean transport value, suggesting these means are relatively robust. As with the 2021 deployments, the flow here is predominately westward into the Caribbean, with little to no northward component. If values for the 2020 and 2022 deployments are averaged together, the mean transport observed here is -2.33 ± 0.71 Sv into the Caribbean.

Transport values were also derived for each transect from cross-glider track geostrophic water velocities and then averaged for each deployment (Table 1). The mean geostrophic transport for the 2020 deployment is within the error bars of the 2020 deployment absolute velocity transport value. While no standard deviation estimates are available for the 2021 deployments, there is a general agreement on transport into the Caribbean. Furthermore,

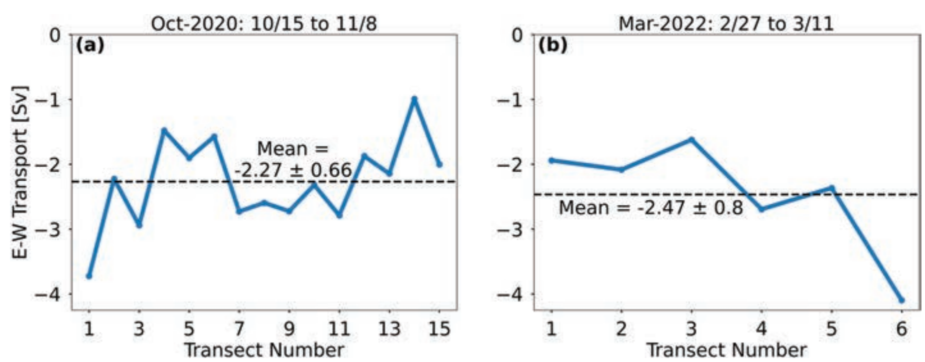

Figure 8. Acoustic doppler profilers derived absolute E(+)/W(−) transport time-series' calculated from the repeat transect lines between St. Thomas and St. Croix for the RU29 October 2020 deployment (a) and RU36 March 2022 deployment (b). Black dashed line represents the deployment mean transport. A single transect consistently took approximately 36 hr.

10.1029/2022JC019608

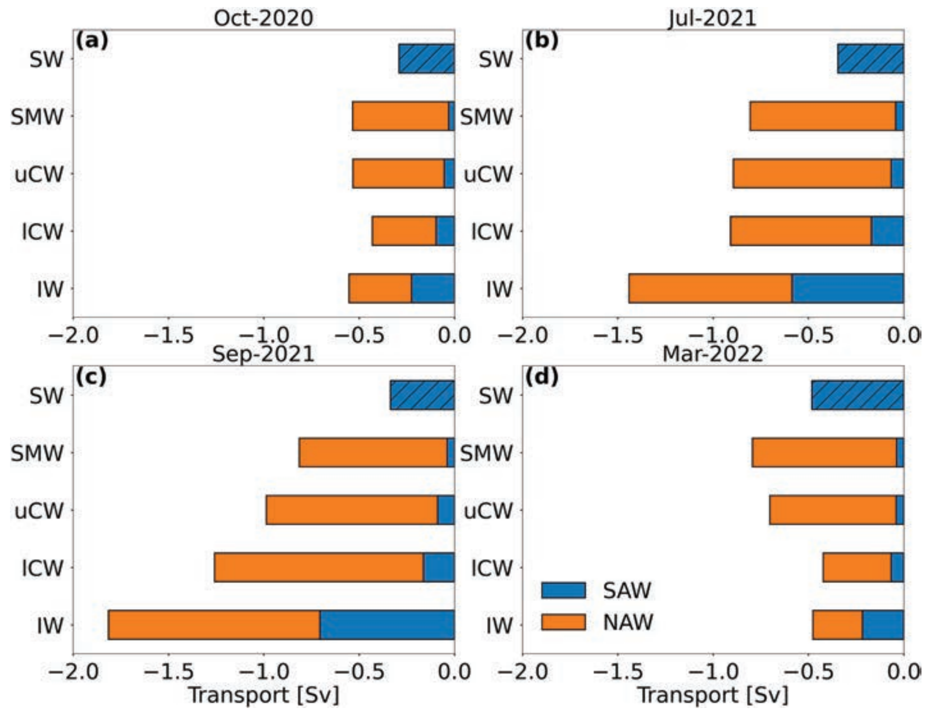

Figure 9. Transport of South Atlantic Water (blue) and North Atlantic Water (orange) in the major water masses from the isopycnal water mass analysis for the four glider deployments. The surface water is hatched blue as it was not included in the water mass analysis. The October-2020 and March-2022 data represent means of the repeat STT-STX transects.

the mean geostrophic transport for the 2022 deployment is outside the error bars of the 2022 absolute velocity transport value, though there is general agreement on transport into the Caribbean here as well.

3.2. Water Mass Analysis and Transport

Following the isopycnal water mass analysis, NAW and SAW transport is calculated per water mass for each deployment (Figure 9). The uncertainties provided below are due to the formulation of a single representative property value (e.g., SAW transport, percentage of SAW in each water mass layer, etc.) for the AP from all four deployments. Including the surface layer, the total SAW transport for each deployment is October-2020: −0.70 Sv, July-2021: −1.21 Sv, September-2021: −1.33 Sv, and March-2022: −0.84 Sv (mean = −1.02 ± 0.26 Sv), which represents 25%–34% of the respective deployment transports (Table 1, mean = 29 ± 3%). The surface layer accounts for the transport of −0.29 to −0.48 Sv of SAW, which represent 8%–20% of the total transport (mean = 11 ± 5%) and 25%–57% of the total SAW transport (mean = 38 ± 13%) for the respective deployment transports.

Excluding the surface layer, the relative percentage of SAW versus NAW gradually increases moving from SMW down to IW. For clarity, only the percentage of SAW is reported here as the percentage of NAW simply reflects the remaining percentage. The SMW is overwhelmingly dominated by NAW, with SAW representing 5 ± 0.4% of the total transport in this layer across all four deployments. The uCW layer is also dominated by NAW. SAW represents 8 ± 1.6% of the total transport in this layer across all four deployments. The percentage of SAW in each respective water mass continues to increase into the lCW layer and below. In the lCW layer, SAW represents 17 ± 3.4% of the total transport in this layer across all four deployments. The IW layer has a much more even split between SAW and NAW. SAW represents 41 ± 2.4% of the total transport in this layer across all four deployments. The relative percentage of SAW or NAW in each water mass is largely consistent across deployments indicated by the low standard deviations. Differences in SAW or NAW transport in these water masses across the deployments can be attributed to the differences in the bulk water mass transport from deployment to deployment.

Characteristic temperature and salinity profiles for this region show dominant features such as freshwater barrier layers and high upper ocean heat content and the approximate ranges of the major water masses (Figure 10). The

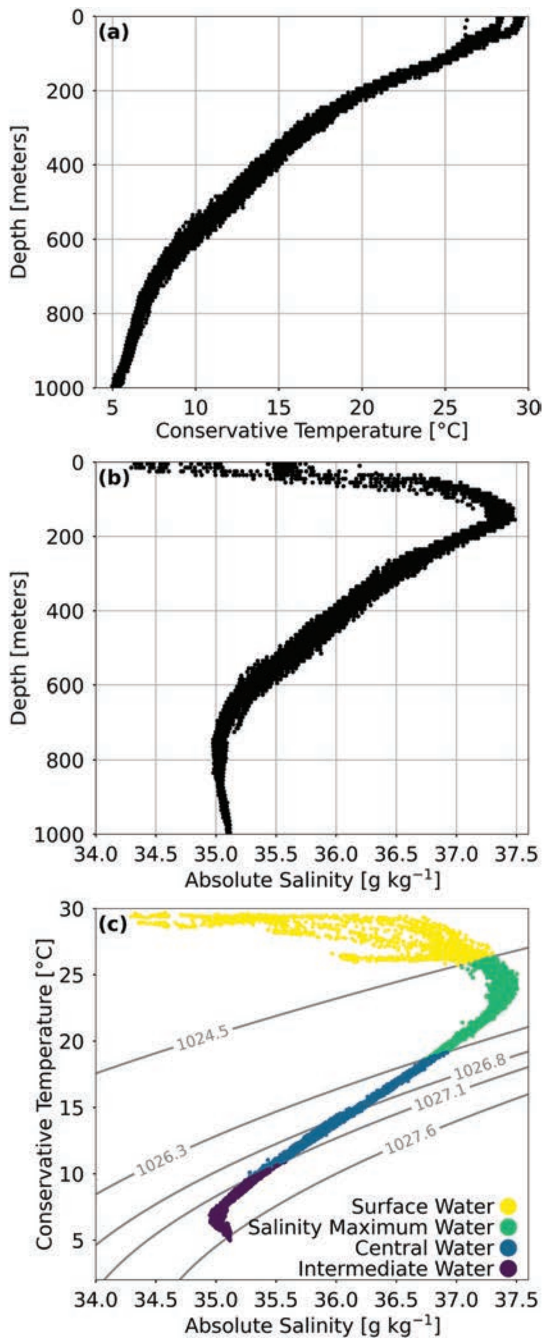

Figure 10. Temperature (a) and salinity (b) profiles in the Anegada Passage region, as well as approximate ranges of the major water masses (c) from all four glider deployments combined.

transport of specific water masses with unique source water types that distinguish their hemisphere of origin within the ranges highlighted in Figure 10 likely play an important role in determining the subsurface density structure of the upper limb of the AMOC. The implications of this balance, the transport of SAW and NAW in these different water masses, are discussed in the following section.

4. Discussion

4.1. Current Structure and Transport

In this study we present glider-based observations of subsurface velocity and integrated transport in the AP that have remarkable similarities with ship-based observations from previous literature. This comparison provides compelling evidence for glider mounted ADPs as a viable alternative to ship-based measurements from ship-mounted ADPs (Johns et al., 1999; Kirchner et al., 2008), lowered-ADPs (Johns et al., 2002), and geostrophic estimates (Metcalf, 1976; Morrison & Nowlin, 1982). While the two 2021 deployments in the AP were single passage crossings, they were intended to be more exploratory in nature, following intentionally similar transects to the two transects in Johns et al. (1999) and consequently provide a particularly valuable comparison point. The magnitude of the subsurface velocity observations from the 2021 deployments agrees well with the magnitude of the observations from the second transect presented in Johns et al. (1999). The 2021 deployments also showed similar structure as subsurface velocity maxima and weak counterflows were common. The magnitude of the subsurface velocity observations from the 2021 deployments were noticeably smaller than the first transect presented in Johns et al. (1999). This difference is likely due to the extremely high velocities in excess of 1.1 m s^{-1} that were highlighted as potentially skewing the observations in Johns et al. (1999).

The observations presented in this study bring to light both potentially new dynamics as well as upper and lower bounds in terms of transport magnitude. Table 1 from Johns et al. (2002) summarized the available transport values and a mean of -2.5 ± 1.4 Sv into the Caribbean was determined for the AP. This value is similar to the -1.8 ± 1.5 Sv mean later reported by Kirchner et al. (2008) but noticeably less than the maximum -8.4 Sv transport observed by Johns et al. (1999) during October 1986. This range in transport estimates and the potential role this flow plays in the pathways and balance of meridional overturning circulation warrant this revisitation of the AP with sustained observations using improved technology. Mean transport values from the St. Thomas-St. Croix transects (-2.27 ± 0.66 Sv and -2.47 ± 0.8 Sv) agree well with the -2.5 ± 1.4 Sv estimate from Johns et al. (2002). However, considering these estimates are more representative of what is historically referred to as the Anegada-Jungfern Passage, or a subset of the greater AP, it is reasonable to expect these values actually represent an underestimation of the total AP transport.

Though these transport estimates may be an underestimate, the repeating St. Thomas-St. Croix transects provide a time-series that sheds light on the variability of this inflow. The means and standard deviations of E/W transport are similar between the October and March deployments. A single transect takes approximately 1.5 days, which suggests the AP transport is stable on weekly time scales. In both the 2020 and 2022 deployments, there is one transect that has a transport value approximately -4 Sv. Though these transport values are greater than one standard deviation from their respective deployment mean transports, they are due to a larger barotropic E/W transport as the N/S component of the glider estimated DAC from these transects are essentially zero. It is also noteworthy that the standard deviation for the glider-based transport estimates (0.66 and 0.8 Sv) are approximately half of the ship-based estimates (1.4 Sv). Part of the reason the standard deviations are likely smaller is because there are 2–3 times more glider-based transport values used for these calculations when compared with the ship-based estimates. The large number of glider observations further highlights gliders with ADPs as a viable, if not potentially more accurate, method for measuring island passage transport.

To place the glider-based transport estimates presented in this study into the context of prior transport estimates in the region, it is important to understand how these observations were collected. First, it is noteworthy that the transport estimates from Johns et al. (1999) were derived from ship mounted ADPs with a range of only 200 m Kirchner et al. (2008) occupied the AP using a ship-mounted ADP with a range of 1400 m. However, this occupation was only for one transect and resulted in a near-zero transport estimate. The -1.8 ± 1.5 Sv mean transport values for the AP was derived by Kirchner et al. (2008) from combining this single, near-zero transport measurement with the five occupations detailed by Johns et al. (2002). Full-depth, lowered-ADPs were only used by Johns et al. (2002), however they only reported transport estimates per deployment and provided no additional details of the flow. The subsurface velocity data presented in this study then represent the first detailed, published observations of AP inflow below the 200-m profiles reported by Johns et al. (1999). This result is noteworthy because transport below 200 m accounts for anywhere from 20% to 50% of this study's 1,000-m transport estimates.

Previous literature has shown there is a common baroclinic velocity structure in Caribbean passage transports, where the upper 200 m contains approximately half of the respective full passage transport (Johns et al., 1999; Wilson & Johns, 1997). With this observation, Johns et al. (1999) applied a factor of 2 to their upper 200-m transport to estimate total passage transport. To better compare our 1000-m transport estimates, we can therefore multiply the 200-m, −2.4 Sv transport value reported by Johns et al. (1999) by a factor of two. This exercise leads to a −4.8 Sv transport estimate that is in much better agreement with the −4.43 and −5.24 Sv transport estimates (mean = −4.84 Sv) for the two 2021 outer AP deployments reported here. A total AP transport of −4.84 Sv for the outer AP also implies that roughly one-half of the transport is split to the north and south of St. Croix as the mean transport north of St. Croix is −2.33 Sv. Therefore, while the two 2021 transport values are only from one occupation, potentially more influenced by tidal and/or spatial impacts, there is reason to believe the actual bulk, mean AP transport is closer to −4.8 Sv. If the St. Thomas-St. Croix deployment transports are taken to be roughly ½ of the total transport and thus multiplied by a factor of 2 (October-2020 = −4.54 Sv, March-2022 = −4.94 Sv), the mean AP transport across all four deployments can be approximated to be -4.8 ± 0.32 Sv. This implies that the AP transport is larger than previously estimated (−2.5 Sv) and, if confirmed through additional transects across the greater AP, would represent close to 20% of the total Caribbean inflow (−28 Sv). The implications of a potentially larger transport and the transport depth structure in relation to different water masses is discussed in further details in the subsequent section.

There is a general agreement in velocity profiles and transport magnitude between the cross-glider track geostrophic velocities and the ADP derived absolute velocities for all four deployments. This is likely due to the flow being largely barotropic and the glider's DAC being used as a constraint for both the geostrophic and absolute velocity estimates. Ageostrophic effects expected in Caribbean passages (friction, curvature, confluence, internal waves, etc.) are less important in the AP as it is the largest passage. Regardless, averaging the repeat transects serves to smooth some of this variability, which is desired when discussing a bulk representation of the flow as we present here. In smaller passages, where these ageostrophic effects have caused disagreement between geostrophic and absolute velocities, averaging repeat transects and smoothing both the absolute velocities and density fields used to calculate geostrophic velocities has led to improvements (Wilson & Johns, 1997).

4.2. Contributions From the Surface Waters to the SAW Transport

In the results presented here for the surface layer, we follow the assumption that the tropical SW is entirely of South Atlantic origin (Hellweger & Gordon, 2002; Kirchner et al., 2008, 2009; Mertens et al., 2009; Rhein et al., 2005; Schmitz & Richardson, 1991; Schott et al., 1998). In their analysis of the sources of the Florida Current, SR91 were the first to consider tropical surface waters warmer than 24°C and waters in the 7–12°C range to be of South Atlantic origin. They used these temperature ranges in their analysis to estimate that ∼45% of the Florida Current transport may originate in the South Atlantic. While a more detailed and accurate water mass analysis using temperature and salinity data is now conducted for the water masses below the surface layer, we adopted the assumption made by SR91 for the surface layer as the isopycnal water mass analysis cannot be applied here. The following interpretation of the results depends only partially on this assumption as the surface layer here accounts for the transport of −0.29 to −0.48 Sv of SAW (mean = −0.36 ± 0.07 Sv), which represents a mean of only 12 ± 5% of the total transport and 38 ± 13% of the total SAW transport reported here. The surface layer contributing 38% of the transport of SAW in the AP is less than the over 50% contribution from the surface layer to the total SAW transport in the passages south of Guadeloupe from Rhein et al. (2005).

4.3. Contributions From the Saline South Atlantic SMW to the SAW Transport

In the SMW layer, the low salinity endmember from the eastern South Atlantic contributes 5 ± 0.4% which is noticeably smaller than the 30%–37% found by Rhein et al. (2005) in the passages south of Guadeloupe. As the isopycnal water mass analysis only permits two source water masses, the saline SMW from the western South Atlantic cannot be distinguished from the North Atlantic SMW and is consequently unaccounted for. Several methods have been applied to estimate contributions from the western South Atlantic SMW source. Zhang et al. (2003) used potential vorticity, salinity, and geostrophic flow maps to determine the transport pathways for waters with densities between $\sigma_\theta = 23.2$ and $\sigma_\theta = 26.0$ between the Subtropical and Tropical Atlantic in both hemispheres. Transports of 2–3 Sv and 4–6 Sv were determined for the saline North Atlantic and saline South Atlantic SMW, respectively. Using this mass balance and converting it to a fraction, Rhein et al. (2005) proposed that the saline western South Atlantic SMW could contribute 47%–54% of the North Atlantic SMW transport. Kirchner et al. (2008) expanded on the approximation made by Rhein et al. (2005) by conducting an isopycnal water mass analysis off the Brazilian coast to 40°W and between 5°S and 7°N. They determined that the fraction of the transport of the low salinity eastern South Atlantic endmember is on the order of 70%–75%, leaving a maximum of 25%–30% from the saline western South Atlantic. Using these estimations, a factor of 25%–54% could reasonably be applied to the NAW component of the SMW transport to account for the saline western South Atlantic source. With these ranges from prior literature, the potential total SAW fraction from both sources, with the 5% observed in this analysis for the fresh endmember, would then sum to 30%–59%. However, using both hydrographic and model data, Kirchner et al. (2009) determined that the low salinity endmember from the eastern South Atlantic dominates the equatorial region and prevents the saline western South Atlantic SMW from spreading northward. Therefore, it is expected that contributions from the saline western South Atlantic SMW in the AP are toward the lower end of this estimate range. Taking the minimum from this range (25%), applying it to the North Atlantic component of the SMW for the respective deployments, and including this additional SAW contribution would increase the total SAW transport for each deployment to October-2020: −0.83 Sv, July-2021: −1.40 Sv, September-2021: −1.52 Sv, and March-2022: −1.03 Sv (mean = −1.20 ± 0.28 Sv).

4.4. Total Transport of SAW Into the Caribbean

If a conceptual box model is applied to the greater Caribbean Sea, there are constraints on the through-flow that reveal unresolved aspects of the AMOC return flow here. Figure 1 may be helpful to geographically guide the reader through this section. The presence of SAW in the northern hemisphere represents AMOC return flow. Through the use of the isopycnal water mass analysis used in this analysis, Rhein et al. (2005) estimated that a maximum of 11 Sv of SAW is flowing into the Windward Island Passages of the southern Caribbean. At 26°N, it is accepted that the strength of the AMOC is 17 Sv (Frajka-Williams et al., 2019). This implies that there are 17 Sv of SAW flowing northward through the Florida Straits at 26°N. With these values as the input and output for this conceptual box model, the pathways for the remaining 6 Sv of SAW entering the Caribbean north of the Windward Island Passages and exiting through the Florida Straits are highlighted as largely unresolved.

If the mean value of −1.20 ± 0.28 Sv from the proposed addition of the saline western South Atlantic SMW is taken as the estimate for the total SAW transport through the AP, this would represent 20% of the 6 Sv of SAW entering the Caribbean north of the Windward Island Passages. However, if the St. Thomas-St. Croix transects are again considered to be representative of ½ of the total AP transport as proposed in Section 4.1, the SAW transports for those deployments would increase the October-2020 deployment to −1.66 Sv and the March-2022 deployment to −2.06 Sv. These values are in much better agreement with the −1.40 Sv for the July-2021 and −1.52 Sv for September-2021. This would bring the mean total SAW transport through the AP up to −1.66 ± 0.25 Sv which would represent 35% of the mean total AP transport reported here (−4.8 Sv) and 28% of the −6 Sv of SAW entering the Caribbean north of the Windward Island Passages.

We show here that the AP is of a larger importance for the inflow of SAW into the Caribbean than previously considered. While transport in the 5–12°C range has historically been attributed largely to the AP due to its deep sill depth (Schmitz, 1995; Schmitz & McCartney, 1993; Wilson & Johns, 1997), Kirchner et al. (2008) is the only reference to consider SAW transport throughout the entire AP through a detailed water mass analysis with co-located transport measurements. This analysis found 0 Sv of SAW transport in observational data and −0.4 Sv of SAW transport in modeled data, both of which are significantly less than the SAW transport values reported here. This difference is likely due to two factors. First, these authors reported a total AP transport of −1.8 ± 1.5 Sv that is lower than the previously accepted value of −2.5 ± 1.5 Sv (Johns et al., 2002) and considerably lower than −4.8 ± 0.32 Sv proposed in this analysis. Second, Kirchner et al. (2008) reported the fraction of SAW in the IW layer to be 21% in their observational data and 38% in their modeled data, both of which are lower than the mean of 41% proposed in this analysis.

4.5. Transport of NAW Into the Caribbean

NAW that recirculates in the North Atlantic subtropical gyre and does not represent any part of the cross-equatorial AMOC return flow still makes up a substantial portion of the transport of the Florida Current and thus must be entering the Caribbean through either the Greater Antilles, Leeward Island, or Windward Island Passages. Following SM17, the water mass with the highest respective transport in the Florida Current is found in what they refer to as intermediate water east (IWE; 14.8 ± 0.2 Sv) water mass class. IWE is comprised of NAW SMW, eighteen-degree water (EDW; Worthington, 1958), and North Atlantic Central Water, all of which have origins in the North Atlantic. This water mass class is considered to be mid-depth waters $24 \geq \sigma_\theta < 27$, above the IW layer and encompassing the SMW, uCW, and lCW layers discussed here. If NAW transport in the SMW, uCW, and lCW layers is summed for each deployment, here considering the entirety of North Atlantic SMW as to formulate an upper limit, the IWE transport in the AP could account for −1.32 Sv for October-2020, −2.33 Sv for July-2021, −2.77 Sv for September-2021, and −1.77 Sv for March-2022 (mean = −2.05 ± 0.55 Sv). A mean of −2.05 Sv would represent 14% of the IWE in the Florida Current. If the St. Thomas-St. Croix transects are again considered to be representative of ½ of the total AP transport as proposed in Section 4.1, the IWE transports for those deployments would increase the October-2020 deployment to −2.64 Sv and the March-2022 deployment to −3.54 Sv. These values are in much better agreement with the −2.33 Sv for the July-2021 and −2.77 Sv for September-2021. This would bring the mean total IWE transport through the AP up to −2.82 ± 0.45 Sv which would represent almost 19% of the IWE in the Florida Current.

4.6. Implications for Water Mass Transport Into the Caribbean

Given the uncertainties and consequences for projected changes in the AMOC (Caesar et al., 2018; Frajka-Williams et al., 2019; Praetorius, 2018; Rahmstorf, 2002; Thornalley et al., 2018) and the fact that the time-series length of our observing systems is just entering the "detection window" for determining statistically significant trends (Lobelle et al., 2020), it is vital to work toward a better understanding of the dynamics of this system. SM17 recently determined that the source of the AMOC flow through the Florida Straits is controlled potentially twice as much by NAW than by SAW. This is further significant as these authors determined decadal changes in salt transport through the Florida Straits may be impacted more by actual salinity changes rather than changes in the transport itself. That is, the Florida Current water mass structure determines the northward transport of salt more than the transport of the Florida Current itself. For example, SM17 found that both NAW and Antarctic Intermediate Water (SAW) have salinified in recent decades which increased the salinity anomaly transport without corresponding changes in the volume transport. Therefore, the transport of SAW and NAW through the Caribbean Island Passages and into the Florida Straits has substantial implications for AMOC heat and salt transport and analyses focused on determining potential upstream changes in the transport of these water masses are needed.

If the −1.66 Sv of SAW transport through the AP are considered with the 11 Sv of SAW transport thought to be flowing in through the Windward Island Passages (Rhein et al., 2005), 12.66 Sv out of the 17 Sv (74%) of cross-equatorial AMOC return flow through the Caribbean are now accounted for. While this leaves the pathways for the approximately 4.34 Sv or 26% of the remaining SAW transport unaccounted for, model analysis from Kirchner et al. (2009) suggests it may enter the Caribbean through either Mona Passage or Windward Passage (between Cuba and Hispaniola, Figure 1). This is further supported by the inconsistencies and potential corrections SM17 raise on the assumptions SR91 make on SAW transport. If we follow SM17 by not including SW transport as part of the AMOC, the 11 Sv of SAW transported through the Windward Island Passages determined by Rhein et al. (2005) would be closer to 5.5 Sv. The 50% of SAW in the SW layer relative to the total transport through the Windward Island Passages is larger than the 38% found here in the AP. If SW transport is excluded from both the 11 Sv Windward Island Passage inflow and 1.66 Sv AP inflow of SAW (5.5 and ~0.63 Sv respectively) the inflow of only 6.53 Sv or 38% of the 17 Sv SAW entering the Caribbean and exiting the Florida Straits can be accounted for. This highlights that there may be more uncertainty and unknowns in the cross-equatorial AMOC return flow pathways than previously considered.

With these results, we have shown that SAW transport in the IW layer is larger in the AP compared to other known passage transports for this layer. IW transport occurs almost entirely below 600 m and thus the deep sill depths of the AP (1,915 m) (Fratantoni et al., 1997) and Windward Passage (1,560 m) (Metcalf, 1976) highlight these passages as likely important IW transport pathways.

SM17 distinguish IWW (Intermediate Water West) as potentially contributing a large percentage of the unaccounted for AMOC transport, however the origin of IWW is noted as difficult to determine based on temperature and salinity alone. It is important to note IWW water mass class used by SM17 consists of the SMW, uCW, and lCW reported here and is distinctly different than IW discussed in this water mass analysis. SM17's IWW has been discussed as originating in the Gulf of Mexico (Schmitz & McCartney, 1993), Caribbean (Schmidt et al., 2004), or the tropical or South Atlantic (Rhein et al., 2005). Measurements of additional parameters such as dissolved oxygen and at least one nutrient parameter, depending on the number of unique source waters, that covaries with respiration/remineralization as a water mass is transported and ages could potentially shed light on water mass origin uncertainty through the use of optimum multiparameter (OMP) water mass analysis (Poole & Tomczak, 1999; Tomczak & Large, 1989). If SW transport is excluded from the SAW transport, a revisitation of all Caribbean passages to measure these additional parameters along with subsurface velocity could help to better constrain this uncertainty. Regardless, the results presented here suggest that a major finding of this analysis is the likely non-negligible transport of SAW at mid-depths in the AP.

5. Conclusion

This study presents glider-based observations of upper ocean temperature, salinity, and subsurface velocity in the AP region of the northeastern Caribbean Sea. The glider observations analyzed in this study represent a proof-of-concept for using gliders as a means for measuring island passage transport. These observations of co-located temperature, salinity, and subsurface velocity also represent the first measurements of this kind in this region in nearly two decades. Four glider deployments were conducted in the AP region, two conducting repeat transects between St. Thomas and St. Croix and two conducting single transects across the wider AP. A detailed isopycnal water mass analysis was conducted to quantify the transport of water masses with South Atlantic or North Atlantic origin in the passage transport. We interpret the transport observations collected during these deployments as showing two potentially new aspects of AP transport. The total transport (-4.8 ± 0.32 Sv) and the transport of SAW (-1.66 ± 0.25 Sv) in the AP may be larger than previously estimated, potentially by up to a factor of two for total transport. An AP SAW transport of -1.66 Sv would represent 35% of the mean total AP transport reported here and 28% of the 6 Sv of SAW entering the Caribbean north of the Windward Island Passages. These results also show gliders with ADPs are a viable method for measuring island passage transport.

Sustained observations of Essential Ocean Variables (EOVs; Lindstrom et al., 2012) improve our ability to understand, predict, and assess components of the climate system. EOVs like sea surface temperature and salinity, subsurface temperature and salinity, temperature and salinity anomaly transport, sea level anomaly, and deep density gradients have been linked to changes in the strength of the AMOC (Frajka-Williams et al., 2019; Szuts & Meinen, 2017). In the Caribbean, EOVs are also impacted by variations in the transport of water masses with differing sources and in the variations of the source waters themselves. In light of the uncertainties surrounding the AMOC, as well as the recent evidence of climate change induced impacts on the Caribbean Sea, sustained and expanded observations of these metrics are needed in this region. Observations of EOVs specifically relevant to the dynamic features of this region (heat content, heat transport, freshwater content, freshwater transport, freshwater barrier layer thickness, depth, and magnitude of salinity maximum, etc.) are especially needed.

This study has added to the growing body of literature supporting the use of gliders as an effective component of the global ocean observing system. In the three decades since Henry Stommel's 1989 vision of the Slocum Mission, the depth and endurance range of gliders have advanced, and a growing number of complex instruments are now being integrated regularly. The maturity glider platforms have now reached make them uniquely well suited to collect the "evolving maps of subsurface variables" needed for sustained climate monitoring developed in the original vision of Stommel (1989).

Data Availability Statement

Glider data used in this analysis can be found at https://gliders.ioos.us/ under the following dataset ID's: ru29-20200908T1623, ru29-20210630T1343, ru29-20210908T1943, and ru36-20220223T1807. The acoustic current profiler data collected during these deployments can be found at https://doi.org/10.5281/zenodo.7468695 (Gradone et al., 2022a). The code used for this analysis can be found at https://doi.org/10.5281/zenodo.7473774 (Gradone et al., 2022b).

Acknowledgments

We are grateful for support from the G. Unger Vetlesen Foundation for the 2020 and 2021 deployments and the Office of Naval Research (N00014-20-1-2568) for the 2022 deployment. We thank Dave Aragon, Nicole Waite, and Chip Haldeman from the RUCOOL glider team and Antonio Farchette from OCOVI for assistance preparing, piloting, deploying, and recovering the gliders used in this analysis. J.C. Gradone acknowledges support from the Department of Defense National Defense Science and Engineering Graduate Fellowship. W.D. Wilson acknowledges support from VI-EPSCoR NSF award OIA# 1946412. This is contribution #268 from the Center for Marine and Environmental Studies, University of the Virgin Islands. We thank Eli Hunter and Sam Coakley for assistance with development of the processing codes used in this analysis, Eleanor Frajka-Williams, Rebecca Jackson, and Johannes Karstensen for insightful discussion that guided the water mass analysis, and the anonymous reviewers whose comments helped greatly.

References

Antuña-Marrero, J. C., Otterå, O. H., Robock, A., Mesquita, S., & d, M. (2015). Modelled and observed sea surface temperature trends for the Caribbean and Antilles. *International Journal of Climatology*, *36*(4), 1873–1886. https://doi.org/10.1002/joc.4466

Brambilla, E., & Talley, L. D. (2006). Surface drifter exchange between the North Atlantic subtropical and subpolar gyres. *Journal of Geophysical Research*, *111*(C7), C07026. https://doi.org/10.1029/2005jc003146

Caesar, L., Rahmstorf, S., Robinson, A., Feulner, G., & Saba, V. (2018). Observed fingerprint of a weakening Atlantic Ocean overturning circulation. *Nature*, *556*(7700), 191–196. https://doi.org/10.1038/s41586-018-0006-5

dos Santos, R. A. L., Prange, M., Castañeda, I. S., Schefuß, E., Mulitza, S., Schulz, M., et al. (2010). Glacial-interglacial variability in Atlantic meridional overturning circulation and thermocline adjustments in the tropical North Atlantic. *Earth and Planetary Science Letters*, *300*(3–4), 407–414. https://doi.org/10.1016/j.epsl.2010.10.030

Ellis, D., Washburn, L., Ohlmann, C., & Gotschalk, C. (2015). Improved methods to calculate depth-resolved velocities from glider-mounted ADCPs. In *2015 IEEE/OES eleveth current waves and turbulence measurement (CWTM)*. IEEE. https://doi.org/10.1109/cwtm.2015.7098120

Fischel, A., Seidenkrantz, M.-S., Nürnberg, D., Kucera, M., & Kuijpers, A. (2017). Upper water mass variability in the Anegada/Jungfern Passage NE Caribbean, during the last 11,100 cal. yr. *The Holocene*, *27*(9), 1291–1307. https://doi.org/10.1177/0959683616687378

Frajka-Williams, E., Ansorge, I. J., Baehr, J., Bryden, H. L., Chidichimo, M. P., Cunningham, S. A., et al. (2019). Atlantic meridional overturning circulation: Observed transport and variability. *Frontiers in Marine Science*, *6*. https://doi.org/10.3389/fmars.2019.00260

Fratantoni, D. M., Johns, W. E., Townsend, T. L., & Hurlburt, H. E. (2000). Low-latitude circulation and mass transport pathways in a model of the tropical Atlantic Ocean. *Journal of Physical Oceanography*, *30*(8), 1944–1966. https://doi.org/10.1175/1520-0485(2000)030<1944:llcamt>2.0.co;2

Fratantoni, D. M., Zantopp, R. J., Johns, W. E., & Miller, J. L. (1997). Updated bathymetry of the Anegada-Jungfern Passage complex and implications for Atlantic inflow to the abyssal Caribbean Sea. *Journal of Marine Research*, *55*(5), 847–860. https://doi.org/10.1357/0022240973224148

Garraffo, Z. D., Johns, W. E., Chassignet, E. P., & Goni, G. J. (2003). North BrazilCurrent rings and transport of southern waters in a high resolutionnumerical simulation of the North Atlantic. In G. J. Goni & P. Malanotte-Rizzoli (Eds.), *Interhemispheric water exchange in the Atlantic Ocean* (Vol. 68, pp. 375–409). Elsevier Oceanographic Series.

Glenn, E., Comarazamy, D., González, J. E., & Smith, T. (2015). Detection of recent regional sea surface temperature warming in the Caribbean and surrounding region. *Geophysical Research Letters*, *42*(16), 6785–6792. https://doi.org/10.1002/2015gl065002

Gradone, J., Wilson, D., Glenn, S., & Miles, T. (2022a). Acoustic current profiler data from multi-year (2020–2022) autonomous underwater glider surveys in the Anegada Passage [Dataset]. Zenodo. https://doi.org/10.5281/zenodo.7468695

Gradone, J., Wilson, D., Glenn, S., & Miles, T. (2022b). JGradone/Anegada-glider-transport: v1.0.0 (v3.0.0) [Software]. Zenodo. https://doi.org/10.5281/zenodo.7789790

Gradone, J. C., Hunter, E. J., Mullison, J., & Miles, T. N. (2021). Development of onboard processing capabilities for a Slocum glider acoustic Doppler current profiler. In *Oceans 2021: San Diego Porto*. IEEE. https://doi.org/10.23919/oceans44145.2021.9705895

Gregory, J. M., Dixon, K. W., Stouffer, R. J., Weaver, A. J., Driesschaert, E., Eby, M., et al. (2005). A model intercomparison of changes in the Atlantic thermohaline circulation in response to increasing atmospheric CO_2 concentration. *Geophysical Research Letters*, *32*(12), L12703. https://doi.org/10.1029/2005gl023209

Haines, S., Crout, R., Bosch, J., Burnett, W., Fredericks, J., Symonds, D., & Thomas, J. (2011). A summary of quality control tests for waves and in situ currents and their effectiveness. In *IEEE/OES 10th Current, Waves and Turbulence Measurements (CWTM)* (pp. 100–106). https://doi.org/10.1109/CWTM.2011.5759534

Heiderich, J., & Todd, R. E. (2020). Along-stream evolution of Gulf Stream volume transport. *Journal of Physical Oceanography*, *50*(8), 2251–2270. https://doi.org/10.1175/jpo-d-19-0303.1

Hellweger, F. L., & Gordon, A. L. (2002). Tracing Amazon river water into the Caribbean Sea. *Journal of Marine Research*, *60*(4), 537–549. https://doi.org/10.1357/002224002762324202

Høydalsvik, F., Mauritzen, C., Orvik, K. A., LaCasce, J. H., Lee, C. M., & Gobat, J. (2013). Transport estimates of the Western branch of the Norwegian Atlantic current from glider surveys. *Deep Sea Research Part I: Oceanographic Research Papers*, *79*, 86–95. https://doi.org/10.1016/j.dsr.2013.05.005

Johns, E., Wilson, W. D., & Molinari, R. L. (1999). Direct observations of velocity and transport in the passages between the intra-Americas Sea and the Atlantic Ocean 1984-1996. *Journal of Geophysical Research*, *104*(C11), 25805–25820. https://doi.org/10.1029/1999jc900235

Johns, W. E., Townsend, T. L., Fratantoni, D. M., & Wilson, W. D. (2002). On the Atlantic inflow to the Caribbean Sea. *Deep Sea Research Part I: Oceanographic Research Papers*, *49*(2), 211–243. https://doi.org/10.1016/s0967-0637(01)00041-3

Johns, W. E., Zantopp, R. J., & Goni, G. J. (2003). Cross-gyre transport by North Brazil current rings. In *Interhemispheric water exchange in the Atlantic Ocean* (Vol. 68, pp. 411–441). Elsevier Oceanography Series. https://doi.org/10.1016/S0422-9894(03)80156-3

Jury, M. R. (2017). Spatial gradients in climatic trends across the southeastern Antilles 1980–2014. *International Journal of Climatology*, *37*(15), 5181–5191. https://doi.org/10.1002/joc.5156

Jury, M. R. (2020). Slowing of Caribbean through-flow. *Deep Sea Research Part II: Topical Studies in Oceanography*, *180*, 104682. https://doi.org/10.1016/j.dsr2.2019.104682

Jury, M. R., & Gouirand, I. (2011). Decadal climate variability in the eastern Caribbean. *Journal of Geophysical Research*, *116*(D21), D00Q03. https://doi.org/10.1029/2010jd015107

Kirchner, K., Rhein, M., Hüttl-Kabus, S., & Böning, C. W. (2009). On the spreading of South Atlantic water into the northern hemisphere. *Journal of Geophysical Research*, *114*(C5), C05019. https://doi.org/10.1029/2008jc005165

Kirchner, K., Rhein, M., Mertens, C., Böning, C. W., & Hüttl, S. (2008). Observed and modeled meridional overturning circulation related flow into the Caribbean. *Journal of Geophysical Research*, *113*(C3), C03028. https://doi.org/10.1029/2007jc004320

Kjerfve, B. (1981). Tides of the Caribbean Sea. *Journal of Geophysical Research*, *86*(C5), 4243–4247. https://doi.org/10.1029/JC086iC05p04243

Lindstrom, E., Gunn, J., Fischer, A., McCurdy, A., & Glover, L. K. (2012). *A framework for ocean observing. By the task team for an integrated framework for sustained ocean observing*. UNESCO. https://doi.org/10.25607/OBP-127

Lobelle, D., Beaulieu, C., Livina, V., Sévellec, F., & Frajka-Williams, E. (2020). Detectability of an AMOC decline in current and projected climate changes. *Geophysical Research Letters*, *47*(20), e2020GL089974. https://doi.org/10.1029/2020gl089974

Locarnini, R. A., Mishonov, A. V., Baranova, O. K., Boyer, T. P., Zweng, M. M., Garcia, H. E., et al. (2018). World Ocean Atlas 2018, volume 1: Temperature. A. Mishonov Technical. In *NOAA Atlas NESDIS 81* (p. 52).

Ma, W., Wang, Y., Wang, S., Zhang, H., Zhang, H., & Gong, Q. (2019). Absolute current estimation and sea-Trial Application of glider-mounted AD2CP. *Journal of Coastal Research*, *35*(6), 1343. https://doi.org/10.2112/jcoastres-d-18-00176.1

Mertens, C., Rhein, M., Walter, M., & Kirchner, K. (2009). Modulation of the inflow into the Caribbean Sea by North Brazil current rings. *Deep Sea Research Part I: Oceanographic Research Papers*, *56*(7), 1057–1076. https://doi.org/10.1016/j.dsr.2009.03.002

Metcalf, W. G. (1976). Caribbean-Atlantic water exchange through the Anegada-Jungfern passage. *Journal of Geophysical Research*, *81*(36), 6401–6409. https://doi.org/10.1029/jc081i036p06401

Miles, T., Seroka, G., Kohut, J., Schofield, O., & Glenn, S. (2015). Glider observations and modeling of sediment transport in Hurricane Sandy. *Journal of Geophysical Research: Oceans*, *120*(3), 1771–1791. https://doi.org/10.1002/2014jc010474

Morrison, J. M., & Nowlin, W. D. (1982). General distribution of water masses within the eastern Caribbean Sea during the winter of 1972 and fall of 1973. *Journal of Geophysical Research*, *87*(C6), 4207. https://doi.org/10.1029/jc087ic06p04207

Nürnberg, D., Riff, T., Bahr, A., Karas, C., Meier, K., & Lippold, J. (2021). Western boundary current in relation to Atlantic Subtropical Gyre dynamics during abrupt glacial climate fluctuations. *Global and Planetary Change*, *201*, 103497. https://doi.org/10.1016/j.gloplacha.2021.103497

Poole, R., & Tomczak, M. (1999). Optimum multiparameter analysis of the water mass structure in the Atlantic Ocean thermocline. *Deep Sea Research Part I: Oceanographic Research Papers*, *46*(11), 1895–1921. https://doi.org/10.1016/s0967-0637(99)00025-4

Praetorius, S. K. (2018). North Atlantic circulation slows down. *Nature*, *556*(7700), 180–181. https://doi.org/10.1038/d41586-018-04086-4

Rahmstorf, S. (2002). Ocean circulation and climate during the past 120,000 years. *Nature*, *419*(6903), 207–214. https://doi.org/10.1038/nature01090

Reißig, S., Nürnberg, D., Bahr, A., Poggemann, D.-W., & Hoffmann, J. (2019). Southward displacement of the North Atlantic subtropical gyre circulation system during North Atlantic cold spells. *Paleoceanography and Paleoclimatology*. https://doi.org/10.1029/2018pa003376

Rhein, M., Kirchner, K., Mertens, C., Steinfeldt, R., Walter, M., & Fleischmann-Wischnath, U. (2005). Transport of South Atlantic water through the passages south of Guadeloupe and across 16N 2000-2004. *Deep Sea Research Part I: Oceanographic Research Papers*, *52*(12), 2234–2249. https://doi.org/10.1016/j.dsr.2005.08.003

Roquet, F., Madec, G., Brodeau, L., & Nycander, J. (2015). Defining a simplified yet realistic equation of state for seawater. *Journal of Physical Oceanography*, *45*(10), 2564–2579. https://doi.org/10.1175/jpo-d-15-0080.1

Rudnick, D. L., Sherman, J. T., & Wu, A. P. (2018). Depth-average velocity from spray underwater gliders. *Journal of Atmospheric and Oceanic Technology*, *35*(8), 1665–1673. https://doi.org/10.1175/jtech-d-17-0200.1

Schmidt, M. W., Spero, H. J., & Lea, D. W. (2004). Links between salinity variation in the Caribbean and North Atlantic thermohaline circulation. *Nature*, *428*(6979), 160–163. https://doi.org/10.1038/nature02346

Schmitz, W. J. (1995). On the interbasin-scale thermohaline circulation. *Reviews of Geophysics*, *33*(2), 151. https://doi.org/10.1029/95rg00879

Schmitz, W. J., & McCartney, M. S. (1993). On the North Atlantic circulation. *Reviews of Geophysics*, *31*(1), 29–49. https://doi.org/10.1029/92rg02583

Schmitz, W. J., & Richardson, P. L. (1991). On the sources of the Florida current. *Deep-Sea Research Part A Oceanographic Research Papers*, *38*, S379–S409. https://doi.org/10.1016/s0198-0149(12)80018-5

Schofield, O., Kohut, J., Aragon, D., Creed, L., Graver, J., Haldeman, C., et al. (2007). Slocum gliders: Robust and ready. *Journal of Field Robotics*, *24*(6), 473–485. https://doi.org/10.1002/rob.20200

Schott, F. A., Fischer, J., & Stramma, L. (1998). Transports and pathways of the upper-layer circulation in the western tropical Atlantic. *Journal of Physical Oceanography*, *28*(10), 1904–1928. https://doi.org/10.1175/1520-0485(1998)028<1904:tapotu>2.0.co;2

Shrikumar, A., Lawrence, R., & Casciotti, K. L. (2021). PYOMPAVersion (0.3). Retrieved 2023, from https://github.com/nitrogenlab/pyompa

Stommel, H. (1989). The Slocum mission. *Oceanography*, *89*(1), 22–25. https://doi.org/10.5670/oceanog.1989.26

Stramma, L., & Schott, F. (1999). The mean flow field of the tropical Atlantic Ocean. *Deep Sea Research Part II: Topical Studies in Oceanography*, *46*(1–2), 279–303. https://doi.org/10.1016/s0967-0645(98)00109-x

Szuts, Z. B., & Meinen, C. S. (2017). Florida current salinity and salinity transport: Mean and decadal changes. *Geophysical Research Letters*, *44*(20), 10495–10503. https://doi.org/10.1002/2017gl074538

Taylor, J. A., & Jonas, A. M. (2008). Maximising data return: Towards a quality control strategy for managing and processing TRDI ADCP data sets from moored instrumentation. *IEEE/OES 9th Working Conference on Current Measurement Technology*, *2008*, 80–88. https://doi.org/10.1109/CCM.2008.4480848

Thornalley, D. J. R., Oppo, D. W., Ortega, P., Robson, J. I., Brierley, C. M., Davis, R., et al. (2018). Anomalously weak Labrador Sea convection and Atlantic overturning during the past 150 years. *Nature*, *556*(7700), 227–230. https://doi.org/10.1038/s41586-018-0007-4

Todd, R. E., Rudnick, D. L., Mazloff, M. R., Davis, R. E., & Cornuelle, B. D. (2011). Poleward flows in the southern California Current System: Glider observations and numerical simulation. *Journal of Geophysical Research*, *116*(C2), C02026. https://doi.org/10.1029/2010jc006536

Todd, R. E., Rudnick, D. L., Sherman, J. T., Owens, W. B., & George, L. (2017). Absolute velocity estimates from autonomous underwater gliders equipped with Doppler current profilers. *Journal of Atmospheric and Oceanic Technology*, *34*(2), 309–333. https://doi.org/10.1175/jtech-d-16-0156.1

Tomczak, M., & Large, D. G. B. (1989). Optimum multiparameter analysis of mixing in the thermocline of the eastern Indian Ocean. *Journal of Geophysical Research*, *94*(C11), 16141. https://doi.org/10.1029/jc094ic11p16141

Tuchen, F. P., Brandt, P., Lübbecke, J. F., & Hummels, R. (2022). Transports and pathways of the tropical AMOC return flow from Argo data and shipboard velocity measurements. *Journal of Geophysical Research: Oceans*, *127*(2), e2021JC018115. https://doi.org/10.1029/2021jc018115

Visbeck, M. (2002). Deep velocity profiling using lowered acoustic Doppler current profilers: Bottom track and inverse solutions. *Journal of Atmospheric and Oceanic Technology*, *19*(5), 794–807. https://doi.org/10.1175/1520-0426(2002)019<0794:dvpula>2.0.co;2

Wajsowicz, R. C. (2002). A modified Sverdrup model of the Atlantic and Caribbean circulation. *Journal of Physical Oceanography*, *32*(3), 973–993. https://doi.org/10.1175/1520-0485(2002)032<0973:amsmot>2.0.co;2

Wilson, W. D., & Johns, W. E. (1997). Velocity structure and transport in the Windward Islands passages. *Deep Sea Research Part I: Oceanographic Research Papers*, *44*(3), 487–520. https://doi.org/10.1016/s0967-0637(96)00113-6

Worthington, L. V. (1958). The 18 water in the Sargasso Sea. *Deep-Sea Research*, *5*(2–4), 297–305. https://doi.org/10.1016/0146-6313(58)90026-1

Zhang, D., Mcphaden, M. J., & Johns, W. E. (2003). Observational evidence for flow between the subtropical and tropical Atlantic: The Atlantic subtropical cells*. *Journal of Physical Oceanography*, *33*(8), 1783–1797. https://doi.org/10.1175/2408.1

Zweng, M. M., Reagan, J. R., Seidov, D., Boyer, T. P., Locarnini, R. A., Garcia, H. E., et al. (2018). World Ocean Atlas 2018, volume 2: Salinity. A. Mishonov Technical. In *NOAA Atlas NESDIS 82* (p. 50).

Workforce Development for the New Blue Economy: Progress and Evolution of a Master's Program in Operational Oceanography at Rutgers University

Alexander López
Department of Marine & Coastal Sciences
Rutgers, the State University of New Jersey
New Brunswick, USA
alopez@marine.rutgers.edu

Josh Kohut
Department of Marine & Coastal Sciences
Rutgers, the State University of New Jersey
New Brunswick, USA
kohut@marine.rutgers.edu

Scott Glenn
Department of Marine & Coastal Sciences
Rutgers, the State University of New Jersey
New Brunswick, USA
glenn@marine.rutgers.edu

Maxim Gorbunov
Department of Marine & Coastal Sciences
Rutgers, the State University of New Jersey
New Brunswick, USA
gorbunov@marine.rutgers.edu

Travis Miles
Department of Marine & Coastal Sciences
Rutgers, the State University of New Jersey
New Brunswick, USA
tnmiles@marine.rutgers.edu

Grace Saba
Department of Marine & Coastal Sciences
Rutgers, the State University of New Jersey
New Brunswick, USA
saba@marine.rutgers.edu

Oscar Schofield
Department of Marine & Coastal Sciences
Rutgers, the State University of New Jersey
New Brunswick, USA
oscar@marine.rutgers.edu

***Abstract*—Rutgers University's accelerated master's degree program in Operational Oceanography (MOO) was established in 2019 to fulfill the workforce gap of the New Blue Economy (NBE), which includes satisfying renewable energy demands as the global population approaches 9 billion by 2050. The MOO program provides students experiential learning opportunities throughout the entire 12-month curriculum, often intersecting with the various technology and data teams that operate a state-of-art ocean observing network and comprise RU COOL (Rutgers University's Center for Ocean Observing Leadership), an internationally oceanographic center of excellence developing new technologies, research, outreach, and educational paradigms for working in the ocean. Students collaborate as a cohort on hands-on activities and assignments involving operational oceanographic equipment, specifically the large fleet of Slocum gliders and expansive network of High-Frequency Radar, both of which are key data pillars for RU COOL. Students work independently on data analysis, learning to analyze, synthesize, and visualize large datasets of real-time oceanographic data and numerical ocean model output on Rutgers University's High-Performance Computing (HPC) cluster, all using the versatile and transferable Python programming language. These were the tenets with which the program was initialized.**

In the past 4 years, the MOO program has evolved considerably. The first 2 years saw the students mostly remote due to the COVID-19 global pandemic, with limited experiential learning opportunities either in the lab or in the field. The program was pivoted to a strong focus on data processing during this time, such that the graduates would still be both competitive and capable upon degree completion. As those restrictions lifted in the third year and the program returned to the original intent, focus was redistributed across both tenets. Internalizing both student feedback and performance after each course and year, as well as industry feedback on desired skills, the program curriculum shifted significantly for the fourth year. Students were tasked to collaboratively run two quarterly glider deployments. This included coordination with our glider staff team for preparation, and real-time marine weather-based decision making for the operation and piloting, as well as extensive subsequent data analysis. This unique learning opportunity came with significant student responsibility, but the cohort collaboration and tapered support from the glider staff team ultimately allowed for great student successes. The endeavor realized the student-led glider transect offshore of New Jersey, originally conceptualized at the creation of the program. This element of the ocean observatory of RU COOL now enables applied, operational experience for subsequent cohorts in the MOO program.

The program's goal has been to capitalize on the unique ocean observing lab resources and capabilities of RU COOL and Rutgers to meet the NBE workforce needs with the accelerated, experiential learning of a new generation of operational oceanography graduate students. Through the continual evolution of the program towards this goal, all MOO graduates have received employment in an oceanography-related career. The program curriculum continues to refine and adapt with each cohort, both to enhance the applied, experiential learning opportunities and to ensure skill proficiency that continually aligns with industry and government workforce needs. And while these global needs exceed the capacity of the MOO program to solely meet, our program may serve as a model for other universities to begin developing their own NBE pipelines.

Keywords—education, ocean observing systems, marine technology

979-8-218-14218-6 ©2023 MTS

I. Introduction

A. Motivation

The New Blue Economy (NBE) presents a paradigm shift in how humanity interacts with the ocean, requiring a skilled workforce to harness its vast potential while ensuring sustainable practices [1]. Graduates of marine science programs hold the key to powering the NBE's multidisciplinary teams, as they are entrusted with the task of unlocking the value hidden within observational data streams. By transforming ocean data into actionable information, these professionals play a critical role in the broader NBE data hierarchy. As the global population continues to concentrate along coastlines, and the effects of climate change, sea level rise, ocean acidification, and extreme weather events intensify, the need for operational oceanographers becomes increasingly urgent. To meet these evolving demands, Rutgers University established in 2019 an innovative master’s degree program in Operational Oceanography (MOO), aimed at providing students with comprehensive training and hands-on experience in the latest ocean observing technologies and methodologies [2][3].

B. Program Overview

The Rutgers University master’s degree in Operational Oceanography is a comprehensive and dynamic program designed to address the increasing demand for skilled professionals in NBE. The NBE represents a paradigm shift in how society interacts with the ocean, requiring a workforce capable of unlocking the vast potential of oceanic resources while ensuring sustainable practices. This cutting-edge program equips marine science graduates with the expertise and hands-on experience needed to excel in operational oceanography, where they play a crucial role in harnessing vast oceanic observational and forecast data streams.

The program's curriculum revolves around four fundamental pillars, carefully tailored to provide students with the necessary knowledge and skills for success in the NBE. First and foremost, students acquire foundational oceanographic knowledge in physical and biological oceanography courses. Delving into the intricacies of ocean dynamics, ecosystem interactions, and environmental changes, this foundational knowledge is essential for interpreting and analyzing data collected through advanced observing systems. Graduates emerge with a thorough understanding of the marine environment, enabling them to contribute effectively to decision-making processes within the NBE.

Secondly, the program places a strong emphasis on observing systems technology expertise through many operational oceanography courses. Hands-on training in hardware units enables students to become familiar with deploying and managing cutting-edge instruments, such as Slocum gliders and High-Frequency Radar. Immersed in authentic, real-world scenarios, students gain practical experience in data acquisition, quality assurance, and real-time data stream management, fostering confidence in handling complex ocean observing systems. This hands-on approach ensures that graduates are well-prepared to tackle the challenges posed by the dynamic marine environment.

To thrive in the era of big data, operational oceanographers must develop data literacy and ocean model proficiency. Through a combination of coursework and hands-on experiences, students acquire the skills to access, manipulate, and analyze large datasets, including real-time data streams from observations and models. Additionally, the program provides comprehensive training in ocean modeling, enabling graduates to work with numerical ocean models like ROMS [4] and WRF [5]. Armed with these essential data literacy and modeling capabilities, graduates can contribute effectively to advanced forecasting and predictive modeling efforts within the NBE.

Finally, the program recognizes the multidisciplinary nature of the NBE and fosters collaborative skills among its students. Team-building exercises and collaborative class projects cultivate students' abilities to work cohesively with diverse groups, mirroring real-world scenarios within the marine industry. The program provides students these operational oceanography challenges, such as operating climate glider surveys and assisting in regional HF radar networks. This emphasis on collaboration ensures that graduates are well-prepared to address complex oceanographic issues within the context of multidisciplinary teams, facilitating their seamless integration into the workforce.

C. Program Goals

The primary goal of the Rutgers master’s degree in Operational Oceanography is to address the critical workforce needs of the NBE. To achieve this, the program maintains close collaboration with industry stakeholders and conducts ongoing workforce assessments. This adaptive approach ensures that the program's curriculum remains responsive and relevant, continually aligning with the demands of the rapidly evolving marine industry. By receiving training that aligns with current and emerging needs, graduates emerge as highly desirable candidates for employment within the NBE, ready to contribute their skills and knowledge to tackle the pressing challenges faced by the marine sector.

Experiential learning is a hallmark of the program, setting it apart as a transformative educational experience. The integration of real-world training within the operational ocean observatory at RUCOOL allows students to gain unparalleled experiences that mirror the challenges and excitement of operational oceanography. Guided by experienced faculty and operational personnel, students actively participate in glider deployments, High-Frequency Radar operations, and software boot camps. These hands-on experiences foster a strong sense of camaraderie within the student cohort and create a supportive learning environment where students can apply their skills in practical settings. This immersion in real-world scenarios develops their adaptability, confidence, and resilience, nurturing a new generation of operational oceanographers who are well-prepared to make immediate contributions to the NBE upon graduation.

The program places a strong emphasis on the integration and synthesis of knowledge, fostering graduates' critical thinking and problem-solving abilities. Graduates develop the capacity to connect data, concepts, and theories into a coherent whole, enabling them to contribute effectively to higher-order functions within the workplace. By understanding the entire marine data life cycle, from data collection and quality assurance to management, interpretation, and knowledge production, students emerge as well-rounded operational oceanographers. Equipped with the ability to make informed decisions and provide valuable insights, graduates are poised to contribute significantly to the sustainable and productive use of ocean resources within the dynamic landscape of the New Blue Economy.

The compact 12-month structure of the program ensures timely graduation and industry readiness, a unique feature known as the "4+1" model. This accelerated pathway efficiently provides marine science undergraduates with the opportunity to earn a master's degree, swiftly transitioning them from their undergraduate studies to advanced training in operational oceanography. The program culminates with a thesis defense during the second summer, where students focus on skill-building for marine industries. This emphasis on practical training and industry-relevant projects ensures that graduates are not only equipped with theoretical knowledge but also possess the hands-on skills demanded by employers in the marine sector. As job-ready professionals, graduates confidently step into the NBE workforce, contributing to innovative solutions and advancements in operational oceanography.

II. Updates

A. Post-COVID-19 Changes

In Summer 2021, Rutgers University returned to in-person classes after the COVID-19 pandemic. This was crucial to the long-term success of the MOO program, as one of the core pillars is the experiential learning opportunities the program provides in an operational oceanography lab, distinguishing it from classical research-focused MS programs. The return to this style allowed for the original intention of the program to be realized, with the students participating in Slocum glider missions, High Frequency Radar services, and various unique research grant opportunities, including prolonged missions at sea. All these experiences allow for the students to interface with colleagues beyond our own operational oceanography lab as well, connecting them with potential future employers. This in-person shift led to an increase in peer collaboration as well, improving the overall teamwork dynamic amongst each cohort. Students learn to interact with one another as peer experts, building camaraderie and support across assignments and experiences.

B. Curriculum Changes

Several curriculum changes have been made since the program's creation in 2019. One of the most fundamental is the program duration. Originally conceptualized and run as a 15-month program, the program was condensed further in 2022 to be strictly 12-months. The difference is predominantly in terms of faculty support for the students, as the program start date of approximately early August remains unchanged. However, in the past, students continued beyond the following August with finalizing their research, as the university deadline was early October for a degree completion date. This allowed for a few months of overlap between separate cohorts of students, as the incoming cohort was getting setup while the exiting cohort was trying to finish their research and defend their theses. This both divided the faculty time and led to the exiting cohort becoming disjointed in the final months. In 2022, we opted to advance the program deadline to the start of August. This shift has had numerous benefits. It allows for better faculty support for the students, as the attention is not split across cohorts. Additionally, it allows for the incoming cohort of students to attend the exiting students' thesis defenses, so they immediately understand their goal for the program in the first week. To compensate for the potential loss of research time, the research component of their degrees was initialized earlier on, in the Fall semester.

Multiple changes have been made to the curriculum as a response to student feedback, as well as industry suggestions. The first of these is an incorporation of a course in Geographic Information Systems (GIS). Only some previous alumni have had experience in their undergraduate or professional careers using GIS. In attending various offshore wind conferences, the industry has voiced proficiency in GIS as a highly desirable skill. The Department of Geography department at Rutgers University offers two courses in GIS, and introductory course and an advanced course. We've since incorporated the introductory course to the MOO curriculum. This will allow the students to learn this valuable skill to make themselves more marketable and to better the NBE workforce.

The second feedback-driven curriculum change is an increase in experiential opportunities for glider piloting. Using the CPU "brain" of a glider, it is possible to simulate a functioning glider as a zero-risk, slow-paced learning environment. This is a remarkable capability, as it allows for scaffolded, authentic assessment opportunities that emulate challenges the students may face as they move to early career. Additionally, the no-risk environment encourages an inclusive space, fostering a classroom culture that focuses on individual growth. This is important in classrooms in general, and especially important to t1he MOO program, which has always strived to facilitate NBE workforce development from varied undergraduate careers.

The third feedback-driven curriculum change is the implementation of situational judgment tests (SJTs) across the program. These psychometric assessments pose authentic challenges faced by the operational workforce, with various responses to each challenge. The students then rank the various responses and justify their decisions in short-answer form. This methodology allows insight into how each student thinks and processes challenges, enabling adaptive instruction. The SJTs are implemented as individual then group assessments, comprising a Team Based Learning (TBL) exercise. TBLs are useful authentic instructional tools that strengthen soft skills such as adaptability, communication, and conflict management, all crucial components to working as part of a team.

All these curriculum changes are subject to review after implementation, to assess their viability and influence, and are continually adapted. The MOO program is meant to meet the needs of the employers, so we are constantly interfacing with the community and soliciting further ideas and changes.

C. Endurance Line Introduction

Originally conceptualized at the creation of the program, this past year saw the first implementation of the MOO Climate

Endurance Line. This transect runs from the Rutgers University Marine Field Station in Tuckerton, NJ out to the Shelfbreak, approximately 140 km, and back, every Fall and Spring. This is segment is run using a Slocum glider and is predominantly operated by the program students, with more support from the RUCOOL operational team in the Fall semester, in line with the program's 12-month experiential scaffolding. The students prepare the glider for the shelf conditions as well as the piloting files. As mentioned previously, the scaffolded glider simulation exercises will better the students' performance with this step, compensating for instructional shortcomings in the original plan. The glider collects water parameters, such as temperature, salinity, and density. This data is collected at two times of year when seasonal dynamics in the shelf waters lead to interesting dynamics, namely the setup and breakdown of shelf stratification. Additionally, the students then have two assessments with data analysis and visualization using the data collected from these transects. This multifaceted exercise serves as two summative TBL assessments, one per program semester, that are used to gauge the students' progression.

D. Thesis Format & Defenses

One of the main shifts this past year was the reformatting of thesis defense expectations. This was done to streamline faculty advising time, bolster cohesion between the students, and aid in the students' successes. The new thesis format consists of faculty-outlined succinct research projects that culminate is a communal thesis defense poster symposium, with a public and committee-only section,. This streamlines faculty time by ensuring each project is both accomplishable in the accelerated time frame of the program, and that each project is finalized by the same deadline. This is important as the deadline is within the first week of the newer cohort of students, so the two cohorts of students only overlap by approximately 1 week, minimizing the advising load on the faculty and program advisor. By having the defenses as a collective symposium, the nature of that deadline builds camaraderie to complete their research by the same date. Students empathize with one another over progress checkpoints and support each other with data analysis and visualization. Lastly, students have a firm deadline established at the start of the program; this enables them while applying for employment, as they know their availability date from the beginning. This helps for career negotiating, life planning, employment relocation.

III. FUTURE WORK

A. Enrollment

A strong component of the MOO program are the small class sizes, allowing for adaptive pacing to ensure comprehension, instructor support, and experiential learning opportunities. From 2019 to 2023, enrollment was 2, 2, 4, 6, and then 8 students. Due to the nature of the program, enrollment will likely be capped at 15 students. As seen in Figure 1, the enrollment has been predominantly white individuals, with slightly more women than men. Figure 2 shows that most of program students are from NJ, specifically Rutgers alumni, indicating both the strong presence and the need for more diverse backgrounds.

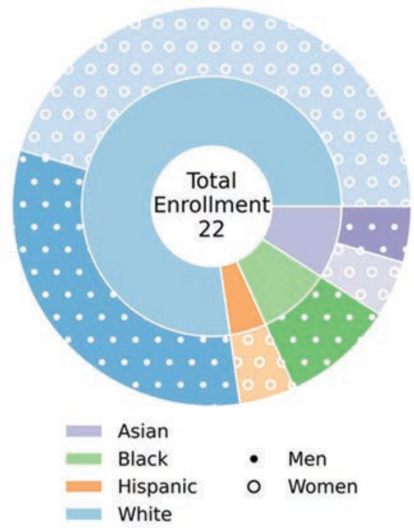

Figure 1. Enrollment demographics for the program.

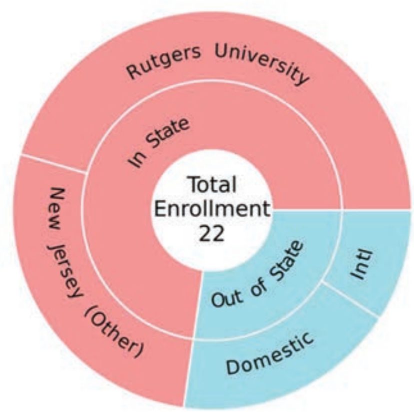

Figure 2. Student residency at time of program enrollment.

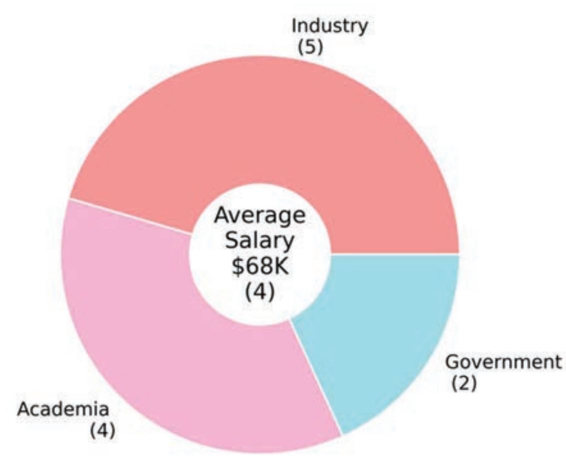

Figure 3. Volunteered career information from graduates.

B. Advisory Board

Another planned addition to the MOO program is the incorporation of an advisory board, comprised of representatives from industry, government, and academia. This board would meet semiannually to discuss the overall program trajectory and ensure that the students are learning the most sought-after skills and information for the NBE workforce. This is meant to be initialized this (2023 – 2024) academic year, and gradually expanded with student enrollment.

C. Career Internships

In line with the Advisory Board, we hope to connect our students with potential employers during the program in a more official capacity, securing internships with these employers. This would provide the students the opportunity to work alongside potential employers and for both sides to determine if each other is a good fit. It could expedite students finding gainful employment in the NBE and raise awareness within the community of the MOO program and the rigorous education the students undergo.

D. Program Certification

The final planned change to note in this program status update is the intention to have the program and its graduates certified. The program curriculum has been developed and maintained alongside individuals from the Marine Technological Society (MTS), with the plan of introducing a suite of micro-credentials, or digital badges, that professionally certify the students' expertise after having completed the program. Consideration has also been made for program certification with Institute of Marine Engineering, Science & Technology (IMarEST), specifically for Marine Technologist (MarTech). Certification from these two organizations, MTS and IMarEST, would further raise awareness within the community about the program while also improving our graduates' competitiveness.

CONCLUSION

In conclusion, the Rutgers master's degree in Operational Oceanography stands at the forefront of workforce development for the New Blue Economy. With its bespoke curriculum, experiential learning opportunities, and emphasis on the integration and synthesis of knowledge, the program produces graduates who are poised to thrive in operational oceanography and contribute significantly to the sustainable and productive use of ocean resources in the ever-changing landscape of the NBE. By inspiring and empowering future generations of operational oceanographers, the program plays a pivotal role in shaping the workforce that will drive advancements in the dynamic and promising era of the New Blue Economy.

REFERENCES

[1] Hotaling, L. (2021), Chapter 20 - Preparing the workforce for the new blue economy, in *Preparing a Workforce for the New Blue Economy*, edited by L. Hotaling and R. W. Spinrad, pp. 387-405, Elsevier, doi:https://doi.org/10.1016/B978-0-12-821431-2.00015-9.

[2] Kohut, J., S. Glenn, J. McDonnell, T. Miles, G. Saba, and O. Schofield (2018), Workforce Development Supporting the Blue Economy: A Master's Program of Integrated Ocean Observing at Rutgers University, paper presented at OCEANS 2018 MTS/IEEE Charleston, 22-25 Oct. 2018.

[3] Beaird, N., S. Glenn, T. Miles, G. Saba, J. Kohut, and O. Schofield (2021), Case study: RUCOOL Operational Oceanography Masters—workforce development case study, in *Preparing a Workforce for the New Blue Economy*, edited by L. Hotaling and R. W. Spinrad, pp. 417-424, Elsevier, doi:https://doi.org/10.1016/B978-0-12-821431-2.02024-2.

[4] Shchepetkin, A. F., and J. C. McWilliams (2005), The regional oceanic modeling system (ROMS): a split-explicit, free-surface, topography-following-coordinate oceanic model, *Ocean Modelling*, *9*(4), 347-404, doi:https://doi.org/10.1016/j.ocemod.2004.08.002.

[5] Powers, J. G., et al. (2017), The Weather Research and Forecasting Model: Overview, System Efforts, and Future Directions, *Bulletin of the American Meteorological Society*, *98*(8), 1717-1737, doi:https://doi.org/10.1175/BAMS-D-15-00308.1.

A Dip in the Pool: Analyzing the stability strength of the Mid-Atlantic Cold Pool

Emily Busch
Department of Marine and Coiastal Sciences
Rutgers University
New Brunswick, USA
eeb104@marine.rutgers.edu

Travis Miles
Center for Ocean Observing and Leadership (COOL)
Rutgers University
New Brunswick, USA
tnmiles@marine.rutgers.edu

Alexander Lopez
Center for Ocean Observing and Leadership (COOL)
Rutgers University
New Brunswick, USA
alopez@marine.rutgers.edu

Rebecca Horwitz
Department of Marine and Coastal Sciences
Rutgers University
New Brunswick, USA
hhorwitzb@gmail.com

***Abstract*— As of March 2023, the U.S. Department of Energy announced the nationwide renewable energy goal of 30 gigawatts (GW) of renewable offshore wind energy by 2030 and setting the standard of 110 GW by 2050. The location of these offshore wind energy areas (WEAs) span along the Mid-Atlantic Bight (MAB) and overlap with the seasonally occurring Cold Pool. The Mid-Atlantic Cold Pool is an economically and environmentally important feature of the northeastern seaboard that supports benthic fauna and commercial fisheries. Monitoring and understanding the stratification strength of the Cold Pool in specified areas along the coast is critical for determining possible future implications caused by offshore wind farm construction. Remote satellite images of existing European wind farms have shown turbulent wakes generated by turbine monopiles in tidal flows, yet the effects of these wakes on Mid-Atlantic stratification are still unclear. In this paper, *in situ* observational data from Slocum gliders provide high-resolution observations of the seasonally occurring thermocline and pycnocline off the southern coast of New Jersey along a commonly sampled transect known as the Rutgers University Glider Endurance Line. Calculations of water column stability using buoyancy frequency are conducted for the summer months of each year between 2016 and 2021 when the Cold Pool is at its peak to evaluate the strength of stratification. Results indicate nearshore regions are more stable than offshore regions based on higher buoyancy frequency values and a higher density gradient.**

Keywords—Cold Pool, stratification, offshore wind, Mid-Atlantic Bight, buoyancy frequency

I. Introduction

Advancements in oceanographic technology in recent decades has allowed for new and improved methods of data collection and observations. Automated underwater vehicles (AUVs) enable oceanographers to collect high-resolution, *in situ* observational data from the water column over time scales from seconds to months [1]. With an abundance of oceanographic data collected off the NJ coast, we have the ability to understand the conditions of the water column in any given time, location, or season. However, despite the increase in instrument deployments in recent years (Fig. 1), the ability to aggregate and analyze raw data has not kept up with the demand for data collection. By creating tools that can widely import, process and analyze data, these products can be used for better understanding of ocean processes and dynamics. With New Jersey's renewable energy goal of 11,000 MW by 2040 on the horizon [2], knowing what the current ocean conditions are off the coast of NJ is essential for assessing the normal amount of mixing and the previous stratification conditions as a basis for future studies on the building of offshore wind farms. In this study, Teledyne Slocum glider AUVs are the primary resource for data collection to determine the baseline state of the water column off the southern coast of NJ. This data is publicly available from the Rutger's ERDDAP data server, which provides quality controlled and assured data from various oceanographic instruments. In this section, a background of the Cold Pool will be discussed as well as the existing research on offshore wind farm impacts on ocean stratification.

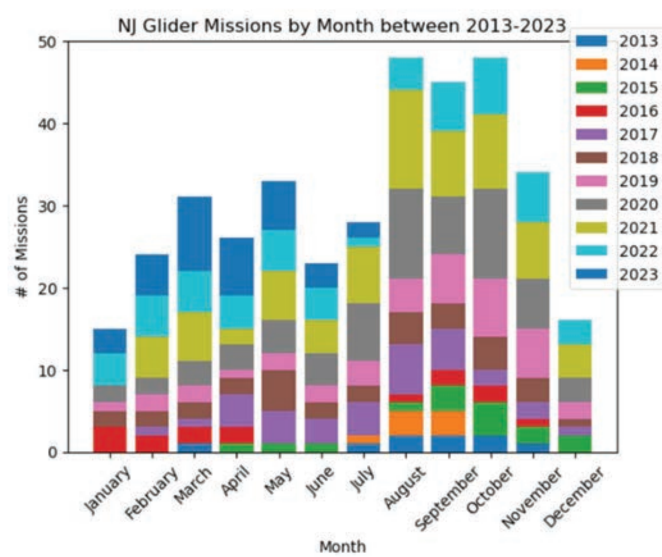

Figure 1: Number of active glider missions by month between January 2013 (bottom dark blue) to July 2023 (top dark blue) off the southern coast of NJ [-74.4 W, 38.0 N, -73.0 W, 39.3 N]. Colors indicate the year in each month. Note the increase in color height in more recent years indicating an increasing number of deployments with each year.

979-8-218-14218-6 ©2023 MTS

At the time this paper is being written, New Jersey is headed towards a renewable energy goal of 11,000 MW of offshore wind energy by 2040 [2]. Preliminary studies of the area are necessary to determine the baseline state of the water column in areas where turbines will be placed as well as gather information for future studies that analyze the impacts of the turbines on the Cold Pool. The Mid-Atlantic Bight undergoes a unique seasonal transformation, from vertically uniform in temperature, salinity, and density during the winter months, to extreme stratification in the spring and summer, becoming one of the strongest top to bottom ocean temperature differences in the world [3]. The Cold Pool experiences an onset-peak-decline life cycle, with stratification setting up in the spring, reaching its peak stability in the summer and then breaking down in the fall. As a primary feature of the MAB, the annual evolution of the Cold Pool is tightly correlated to that of the MAB shelf water [4]. The cycle of Mid-Atlantic stratification begins in the spring, when remnant winter water becomes cut off from the surface as warmer weather and increased solar radiation at the surface increases stratification. Longer days and less storm activity causes stratification to dominate the water column along the New Jersey shelf during the summer months, allowing cold bottom water to persist throughout the summer months. The Cold Pool reaches its maximum spatial extent in the early summer and breaks down in the fall with the seasonal erosion of the thermocline [4].

Existing literature on the effects of offshore wind farms on ocean stratification yield varying results, as the geographical differences between study locations and the difference in wind farm scale make it difficult to predict how turbine structures may influence the MAB. With most offshore wind farm studies based in Europe around existing wind farms, several modeling studies have found there to be an increase in turbulence around monopile structure that may influence the water column. Vanhellemont and Ruddick [5] used Landsat 8 satellite data to analyze offshore wind farm turbid wakes on sediment suspension. They found turbid wakes scaling 30-150 m wide and length scales exceeding 10 km depending on tidal speed and direction. They also noted the possible ecological impacts of the turbid wakes and their effects on primary productivity. Similarly, an unstructured grid modeling study on the impacts of offshore wind turbines on the structure of seasonally stratified seas found monopile induced mixing that extended several kilometers away, enhancing localized mixing in seasonally stratified regions [6].

Conversely, a hydrodynamic modelling study on atmospheric offshore wind farm (OWF) wakes saw a reduction in wind forcing near clusters of wind farms in the German Bight that resulted in a decline in vertical momentum transfer and less turbulent mixing near wind farms [7]. This resulted in stronger stratification during periods of weak stratification, such as the fall breakdown, as well as changes in temperature and salinity distributions that may affect the shallow water mixed layer. Another study conducted on North Sea stratification stated the current capacity of wind turbines occupying the shelf region would not have an effect on large scale stratification, but could have a significant impact on stratification if wind farms occupied an extensive area of the shelf [8]. The contradictory results of several European OWF studies indicate that additional research is needed to understand the relationship between turbine structures and the surrounding water column.

Most existing offshore wind farm research has used modeling to understand the effects of monopile structure on water column stability. While modeling is useful for studying large swath areas of coastal regions, gliders provide high-resolution and spatially-diverse profiles that give insight into the state of the water column [9]. With this in mind, the raw data obtained from gliders is valuable, but also difficult to aggregate and analyze. The lack of tools for aggregating and processing large volumes of AUV data is a challenge that must be addressed with the rising demand for coastal and offshore research. This case study aims to provide tools for processing raw glider data and utilizing the products for research applicable to various topics including offshore wind development, water column stability or stratification, and potential future environmental and ecological impacts. We also aim to determine the existing stratification strength and conditions of a section of the Mid-Atlantic Cold Pool that may provide background information for future research on the impacts of offshore wind farm development on the physical and biological components of our study region.

Due to its large size and seasonal evolution, the Cold Pool is an essential feature of the MAB thermal structure and influences the seasonal dynamics of primary productivity and species migrations. During its seasonal migration down the Mid-Atlantic Bight, the Cold Pool provides feeding and spawning grounds for various benthic fauna and migratory fish species, including Atlantic surf clams, sea scallops, ocean quahog, black sea bass, monkfish, and several species of flounder and skate [4,10]. This region also supports some of the most lucrative shellfisheries in the country, supporting local and commercial fisheries all along the eastern coast and supporting nearly 80% of the fisheries revenue in the Mid-Atlantic [11]. Some of these vital economic species like Atlantic surf clams and sea scallops are ranked high in climate change vulnerability by the National Marine Fisheries Service from changing ocean conditions like increasing temperatures and ocean acidification [11]. Due to their reliance on benthos conditions, these species are also highly vulnerable to offshore wind farm construction. Additionally, the overlap of wind energy areas with areas of highly valued harvest species rank New Jersey the most exposed state to potential economic impact from WEAs [12]. Analyzing existing stratification properties of the Mid-Atlantic Cold Pool will give insight into possible ecological impacts from offshore wind development. Furthermore, the methods of processing raw data in the MAB region may become helpful in future research not only along the eastern seaboard, but also in stratified seas with leased offshore wind farm areas. The results found in this paper will contribute to national ocean observing systems and improve coordination among observing platforms.

II. Methods

The purpose of this case study is to provide a set of tools for aggregating and analyzing multiple glider datasets to evaluate upper ocean stratification across the continental shelf of New Jersey between 2016 and 2021. The focus area of this study was a cross shelf transect in southern New Jersey approximately 39.4°N, 74.2°W to 38.8°N, 73.0°W along the Rutgers

University Glider Endurance Line (Fig. 2). This transect was chosen for its history of frequent glider sampling, its location in regards to leased offshore wind farms, and its swath of nearshore and offshore profiles. The E-Line has been the site of frequent Rutgers glider observations since the early 2000s as the basis of previous NJ shelf studies [13,9]. Its location crosses the Atlantic Shores North (OCS-A 0549) and Atlantic Shores South (OCS-A 0499) commercial wind lease areas [14]. Sampling depths ranged from the surface to 137 m deep, with 3 missions strictly nearshore and 4 cross shore missions. Teledyne Slocum gliders were the primary source of data collection for this case study. Gliders have a wide range of vertical motion spanning from the surface to 1000's of meters deep, allowing a full visualization of the water column and sub-meter scale observations. The data utilized in this study was pulled from the Rutgers ERDDAP Glider TableDap page, a publicly available network of ocean observational data and tools. A specified latitude, longitude, and time constraint were used to narrow the data field down.

Using Jupyter Python notebook, specified glider data was pulled by selecting glider ID's from the ERDDAP Advanced search page. A spatial extent of 39.6°N, 74.5°W to 38.5°N, 72.8°W and a limited time window of July and August when peak stratification occurs [4] were selected for the years 2016-2021. The selected glider missions were further trimmed to only include data within 15 km from the E-Line. This was done by calculating the bearing of the E-Line, then finding the latitude and longitude of 10 points on the map. The 10 points selected were bearings of 0°, 45°, and 90° from the E-Line, creating a decagon around the E-Line. Each dataset was then trimmed to contain profiles within the polygon around the E-Line. This was done by determining if each latitude and longitude point in the dataset was within the bounds of the polygon. Further in-depth methodology for this section may be referenced in the Data Availability section.

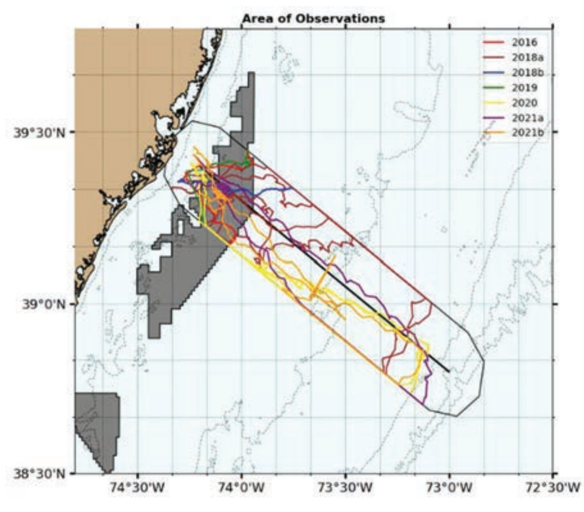

Figure 2: Map of area of observations off the southern coast of New Jersey. The black line represents the E-Line, a frequently sampled transect across the continental shelf. The length of the E-Line is approximately 123 km long, with the 50 m isobath approximately 70 km from the beginning of the E-Line. Each colored track corresponds to an individual glider mission active in July or August between 2016 and 2021. Separate glider missions active in the same year were distinguished with an (a) or (b). The gray areas represent leased offshore wind areas.

Glider missions along the E-Line in the months of July and August between 2016 and 2021, a total of seven individual missions, were included in the case study. Datasets were then separated into nearshore and offshore subcomponents (Fig. 3), with nearshore profiles being defined as profiles inshore of the 50 m isobath and offshore profiles defined as being deeper than the 50 m isobath. This was done by checking the nearest bathymetric value for each latitude and longitude location in the trimmed dataset. The value of the nearest bathymetric point for each row in the dataset was saved to the dataset to then reorganize the data based on the bathymetry value being greater or less than 50 m. Once separated, the maximum density gradient ($\frac{d\rho}{dz}$) and buoyancy frequency (N^2) for each individual or 'unique' profile was calculated. This step was achieved by creating a function that groups or 'bins' the data by a specified depth and averages the data into those specified bin depths. For this study the bin values used were 1m depths from 0 to 150 m. Differences in temperature and density were found with difference in depth across the binned data frame and added back into the dataset. A new subset was then created to find the maximum change in temperature or maximum change in density of each unique profile. The subset with the maximum ($\frac{d\rho}{dz}$) values was then used to calculate N^2 for each unique profile in the subset using Equation (1).

$$Equation\ 1: N^2 = \left(\frac{-g}{\rho} \cdot \frac{d\rho}{dz}\right) \quad (1)$$

Where N^2 is buoyancy frequency, g is gravity, ρ is our reference density value of 1020 kg/m³, and $\frac{d\rho}{dz}$ was the change in density with depth of each profile. The buoyancy frequency measurement determines the strength of stability, defined as the vertical frequency at which a water parcel is vertically displaced [15]. The maximum buoyancy frequency of each unique profile was recorded and added back to the dataset. Boxplots were then created to visualize the distribution of N^2 values for all nearshore and offshore profiles as well as determine the average maximum N^2 for each glider mission.

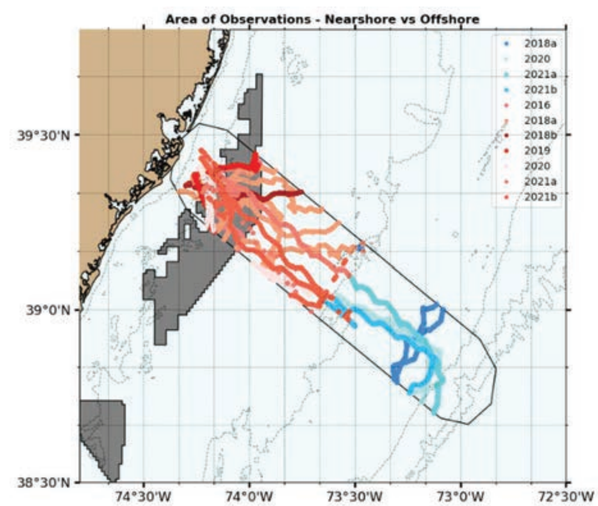

Figure 3: Separation of nearshore (red) and offshore (blue) glider observations separated across the 50 m isobath. Data is limited to within 15 km radii of the historic glider E-Line. Different shades of red and blues correspond to separated glider missions. Gray outlined figures represent wind energy areas.

III. Results

The aim of this case study is to analyze the stratification strength along a transect across the Mid-Atlantic Cold Pool during the summer months July and August between 2016 and 2021. While we focus on this limited 5 year window, future analyses could easily expand and contract the spatial and temporal subset based on study preference. Maximum change in density with depth and the associated maximum buoyancy frequency were calculated for individual profiles of each glider mission to determine the time and location of peak stability. Boxplots were constructed for all profiles across all years separated into nearshore profiles and offshore profiles to visualize and compare the distribution of buoyancy frequencies (Fig. 4, 5, 6). The boxplots show the median N^2 value, the interquartile range (IQR) and the maximum and minimum[1] N^2 value for each year and each region.

The mean buoyancy frequency for nearshore profiles was 0.011 s^{-2} with an IQR between 0.007 s^{-2} and 0.014 s^{-2}. The mean buoyancy frequency values for each year of nearshore profiles were: 0.007 s^{-2} for 2016, 0.012 s^{-2} for 2018a, 0.012 s^{-2} for 2018b, 0.014 s^{-2} for 2019, 0.008 s^{-2} for 2020, 0.010 s^{-2} for 2021a, and 0.010 s^{-2} for 2021b. The interquartile range was largest for 2019, from 0.010 s^{-2} to 0.017 s^{-2} and also had the highest average N^2 value. The mean for offshore profiles was slightly lower at 0.008 s^{-2} with an IQR of 0.006 to 0.010 s^{-2}. Average buoyancy frequencies per year for the offshore regions were 0.007 s^{-2} for 2018a, 0.007 s^{-2} for 2020, 0.009 s^{-2} for 2021a, and 0.009 s^{-2} for 2021b. The widest distribution of N^2 values for the offshore region was in 2021b, with an IQR of 0.007 - 0.011 s^{-2}. The mean buoyancy frequency across the E-Line for all years was 0.010 s^{-2} and the interquartile range of all profiles was 0.007 to 0.013 s^{-2}, with the median buoyancy frequency value being 0.010 s^{-2}. There were outliers for the calculated values stated above, but they were not included in the figures to reduce the scale of the boxplot range.

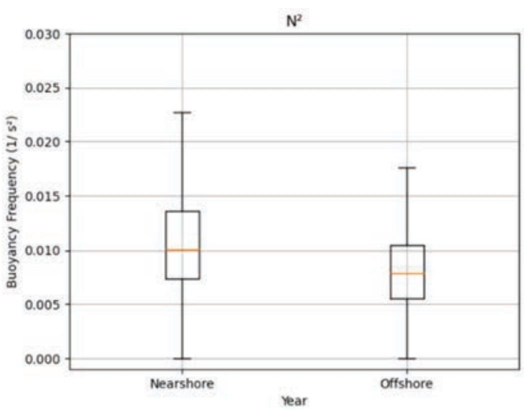

Figure 4: Boxplot of buoyancy frequency (N^2) values for all profiles nearshore (< 50 m isobath) and offshore (> 50 m isobath) across all years. The outliers of each dataset are not shown in these figures.

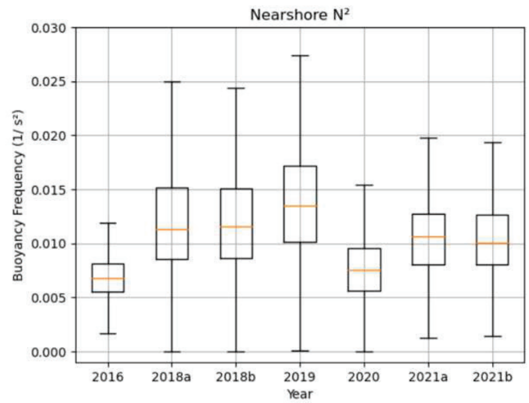

Figure 5: Boxplot of all nearshore profiles (< 50 m isobath) for years 2016 to 2021. Separate glider missions active in the same year were distinguished with an (a) or (b).

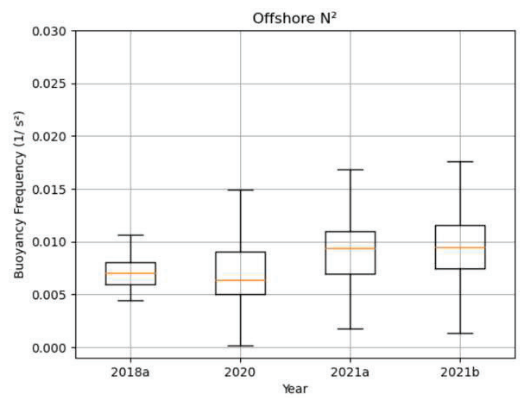

Figure 6: Boxplot of all offshore profiles (> 50 m isobath) for years 2018, 2020, and 2021. There were no profiles over 50m in depth for glider missions RU28 (2016), RU30 (2018b), and RU28 (2019).

IV. Discussion

Using raw glider data available from the public Rutgers ERDDAP data domain, we processed and quantified the mixing parameter buoyancy frequency for multiple years along the Rutgers University Endurance Line. The results indicated the average buoyancy frequency N^2 across the shelf for all years is approximately 0.010 s^{-2}, where nearshore profiles have a similar average N^2 of 0.011 s^{-2} and offshore buoyancy is slightly lower at 0.008 s^{-2}. Plots of buoyancy frequency with depth revealed similar results to past studies along the E-Line that saw a stronger stratification within 80 km nearshore and a more diffused pycnocline offshore [16]. The area of strongest change in N^2 with depth was between 10-20 m for nearshore profiles while offshore profiles had a less distinct change in N^2 (Figure 7b).

Few studies of maximum buoyancy frequency exist within the MAB, however many studies use the vertical temperature gradient to evaluate stratification strength. To compare our results to past studies on Cold Pool stratification, we calculated the maximum change in temperature with depth ($\frac{dT}{dz}$) for each

[1] ¹Due to the presence of outliers in the data the 'minimum' and 'maximum' values illustrated on the boxplots are calculated as Q1-1.5*IQR and Q3+1.5*IQR.

unique profile. We found the temperature gradient to be stronger in the nearshore region than the offshore region. Nearshore profiles had a higher maximum average of 3.16 °C/m and offshore profiles had an average of 2.25 °C/m. Median $\frac{dT}{dz}$ values for the two regions were closer in value than the average values with a nearshore $\frac{dT}{dz}$ median value of 2.92 °C/m and offshore value of 2.12 °C/m. Existing literature on Cold Pool stratification revealed varying maximum thermal gradients from 0.5 - 0.8 °C/m in nearshore profiles to >1.0 °C/m in both nearshore and offshore sites [4, 17].

Our results indicate that nearshore profiles have a higher maximum buoyancy frequency and larger temperature change with depth, which agrees with previous studies that found a stronger thermal gradient in nearshore sites despite a shorter duration of Cold Pool presence [17]. It is possible that river runoff from the Hudson River may contribute to a salinity dominated stratification nearshore during the summer months, whereas offshore is dominated by temperature induced stratification from the Cold Pool and shelf break [9]. The offshore region is also subjected to internal tidal forcings that may result in weaker stratification [18]. A strong density gradient in nearshore sites may be partially attributed to shallow depths where the difference in warm, fresh surface waters and cold, salty bottom waters create a strong top-to-bottom density difference in a relatively short water column (Fig 7a).

Our results may be influenced by the lack of offshore data in our selected time and spatial window. The unequal sample size of nearshore versus offshore profiles may have underestimated the mean buoyancy frequency of offshore regions due to lack of data available in the offshore region from the active glider missions in the area from 2016-2021. Out of the 7 glider missions chosen for this study, 4 of them had profiles deeper than 50 m, whereas all 7 missions had nearshore profiles (< 50 m isobath). This difference in sample size between nearshore and offshore profiles may have biased the calculation of N^2 and $\frac{dT}{dz}$ in the offshore region. Adjusting the nearshore and offshore data pools with additional offshore glider missions in the near future may result in less biased average buoyancy frequency. These findings as well as the notable overlap between the leased offshore wind farms and the Cold Pool indicate there is a need for further research on offshore wind development effects on the Cold Pool.

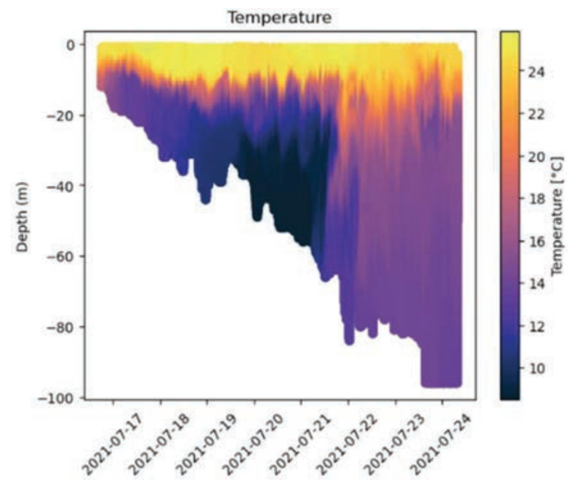

Figure 7a: Cross section of temperature with depth from a segment of RU30 July 2021 mission. Change in color represents the change in temperature with depth with lighter colors corresponding to a greater value. Note the dark (<10 °C) area in the middle of the figure that illustrates the presence of the Cold Pool.

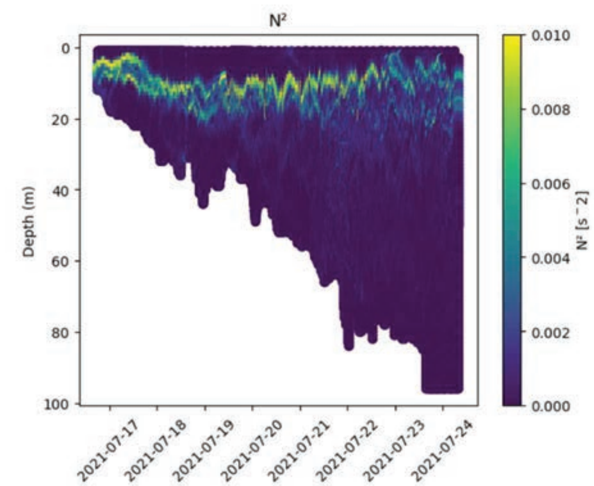

Figure 7b: Cross section of buoyancy frequency with depth from a segment of RU30 July 2021 mission. Change in color represents the change in buoyancy frequency with depth with lighter colors corresponding to a greater value. Note the strong stratification in the nearshore (< 50 m) region whereas in the offshore (> 50 m) regions buoyancy frequency values are spread more evenly with depth.

Analyzing existing stratification conditions in the planned offshore wind energy areas will aid in future research aimed at quantifying the amount of turbulence induced by wind turbines in the Mid-Atlantic region. Understanding the physical effects of monopile structures on stratified seas requires a thorough understanding of the existing state of the water column including the internal wave frequency and its stability. Using *in situ* water column data gives a realistic estimate of buoyancy frequencies in nearshore and offshore regions of the NJ coast, which can be used in models to study possible turbine-induced mixing on the Cold Pool. The methodology used here may assist in preliminary studies that predict the effects of turbine structures in stratified flow. A study conducted in the German Bight observing the stratified flow around wind turbines saw an additional 7-10% of mixing from flow around a monopile structure [19]. The time scale of this enhanced mixing was on a comparable time scale to the rate of stratification formation, indicating this supplementary mixing may have significant effects on a weakly stratified water column. However, a more recent study in the German Bight saw a reduction in wind speed and shear force at the ocean surface, leading to a decrease in momentum transfer between atmosphere and ocean surface that resulted in less turbulent mixing tens of kilometers within offshore wind farms and thus enhanced stratification strength [7]. The multiple influences of atmospheric and oceanic conditions make it difficult to predict the impact of turbines on stratification.

Additionally, regional differences between the North Sea and the MAB limit the correspondence between European studies and the present study. The MAB has both weaker currents (3-15 cm/s versus nearly 1.0 m/s in the German Bight) and a deeper water column than the North Sea [20,8]. The stratification used to analyze turbulent mixing in European OWFs is much weaker than the peak stratification of the Cold Pool during the summer months [8]. Therefore the additional mixing created by flow past turbines will be of greater significance in regions with weak stratification than those with strong stratification such as the Cold Pool. Furthermore, the lack of buoyancy data along the NY/NJ Bight make it difficult to compare the present results to existing studies in which the primary method of determining stratification strength is based on surface to bottom gradient differences [21]. The methods provided in this paper may promote further research on stability of the water column in the MAB especially in regards to monopile installation.

V. CONCLUSIONS

The Mid-Atlantic Cold Pool is an essential feature of the eastern U.S. seaboard that provides habitats and spawning grounds for various economically important benthic species. The strong thermal stratification of the Cold Pool enables cool bottom temperatures to persist throughout the summer months and support local and commercial fisheries. With the development of offshore wind farms overlapping the Cold Pool, little is known about the possible implications of turbine-induced mixing on the stratification of the Cold Pool. By using observational glider data, we quantify the buoyancy frequency of nearshore and offshore regions of Southern NJ to analyze the water column stability of these regions.

Here we provide a new approach to aggregating large volumes of raw glider data and methods of processing the data. The trimmed AUV datasets allow for a precise analysis of the sea state around the E-Line including temperature gradients, density gradients, and buoyancy frequencies of nearshore and offshore profiles. Our results infer coastal waters are more stable than offshore in the Southern NJ area, possibly due to a stronger density gradient and less tidal mixing than offshore. We acknowledge the limitations of our study, including the lack of offshore data that may lower the actual value of offshore buoyancy frequencies. Future research in deeper water (>50m) is needed to improve this estimate of offshore stability. This work will aid in on-going projects and coastal management based on research and monitoring of the MAB in regards to offshore wind construction including the NJ Research and Monitoring Initiative (RMI) as well as current and planned NJDEP projects.

ACKNOWLEDGMENT

We would like to thank Rutgers Department of Marine and Coastal Sciences, the Coastal Ocean Observing and Leadership team, and the Masters of Operational Oceanography students for their endless support.

DATA AVAILABILITY

The data used for this analysis was collected from the Rutgers University ERDDAP Glider Table Dap page (https://gliders.ioos.us/erddap/search/advanced.html?page=1&itemsPerPage=1000&protocol=tabledap) and the Python notebooks described in the Methodology section are available on GitHub (https://github.com/emilybusch1/Separating_nearshore_offshore_glider_profiles).

REFERENCES

[1] Testor, P., et al. (2019). OceanGliders: A Component of the Integrated GOOS. *Frontiers in Marine Science ,6*. https://doi.org/10.3389/fmars.2019.00422

[2] Executive Order no. 307, 3 C.F.R. (2022). https://nj.gov/infobank/eo/056murphy/pdf/EO-307. (accessed 14 July 2023)

[3] Schofield, O. et al., (2008). The Decadal View of the Mid-Atlantic Bight from the COOLroom: Is Our Coastal System Changing? *Oceanography*, 21(4). 108-117.

[4] Lentz, S.J. (2017). Seasonal warming of the Middle Atlantic Bight Cold Pool. *Journal of Geophysical Research Oceans*. 122(2). 941–954, doi: 10.1002/2016JC012201

[5] Vanhellemont, Q., & Ruddick, K. (2014). Turbid wakes associated with offshore wind turbines observed with Landsat 8. *Remote Sensing of Environment*, 145, 105-115. https://doi.org/10.1016/j.rse.2014.01.009

[6] Cazenave, P. W., Torres, R., & Allen, J. I. (2016). Unstructured grid modelling of offshore wind farm impacts on seasonally stratified shelf seas. *Progress in Oceanography*, 145, 25-41. https://doi.org/10.1016/j.pocean.2016.04.004

[7] Christiansen, N., Daewel, U., Djath, B., & Schrum, C. (2022). Emergence of Large-Scale Hydrodynamic Structures Due to Atmospheric Offshore Wind Farm Wakes. *Frontiers in Marine Science*, 9. https://doi.org/10.3389/fmars.2022.818501

[8] Carpenter, J. R., Merckelbach, L., Callies, U., Clark, S., Gaslikova, L., & Baschek, B. (2016). Potential Impacts of Offshore Wind Farms on North Sea Stratification. *PLoS One*, 11(8), e0160830. https://doi.org/10.1371/journal.pone.0160830

[9] Castelao, R. Glenn, S. and Schofield, O. (2010). Temperature, salinity, and density variability in the central Middle Atlantic Bight. *Journal of Geophysical Research*, 115(C10), doi: 10.1029/2009JC006082.

[10] Miles, T. Murphy, S. Kohut, J. Borsetti, S. and D. Munroe (2021). Offshore Wind Energy and the Mid-Atlantic Cold Pool: A Review of Potential Interactions. *Marine Technology Society Journal*, vol. 55, no. 4, pp. 72–87, doi: 10.4031/MTSJ.55.4.8.

[11] National Marine Fisheries Service (2020). Fisheries of the United States, 2020. U.S. Department of Commerce, NOAA Current Fisheries Statistics 2020. https://www.fisheries.noaa.gov/resource/document/fisheries-united-states-2020. (accessed 24 July 2023)

[12] Kirkpatrick, A.J., Benjamin, S., DePiner, G.S., Murphy, T., Steinback, S., &, Demarest, C. (2017). Socio-Economic Impact of Outer BOEM 2017-012 Continental Shelf Wind Energy Development on Fisheries in the U.S. Atlantic. 87-88, https://espis.boem.gov/final% 20reports/5580. (accessed 11 June 2023)

[13] Castelao, R., Schofield, O., Glenn, S., Chant, R., & Kohut, J. (2008a). Cross-shelf transport of freshwater on the New Jersey shelf. *Journal of Geophysical Research*, 113(C7). https://doi.org/10.1029/2007jc004241

[14] Bureau of Ocean Energy Management (2023). Lease and Grant Information. U.S. Department of the Interior.

https://www.boem.gov/renewable-energy/lease-and-grant-information. (accessed 12 July 2023)

[15] Stewart, R. H. (2008) Introduction to Physical Oceanography. Chapter 8. Page 128.

[16] Castelao, R., Glenn, S., Schofield, O., Chant, R., Wilkin, J., & Kohut, J. (2008b). Seasonal evolution of hydrographic fields in the central Middle Atlantic Bight from glider observations. *Geophysical Research Letters*, 35(3). https://doi.org/10.1029/2007gl032335

[17] Horwitz, R., Miles, T., Munroe, D. and Kohut, J. (2021). Investigating the Overlap Between the Mid-Atlantic Bight Cold Pool and Offshore Wind Lease Areas. *Marine Technology Society Journal*. Doi: In Press.

[18] Houghton, R. Schlitz, R. Beardsley, R., Butman, B. and Chamberlin, J. (1982) The Middle Atlantic Bight Cold Pool: Evolution of the Temperature Structure During Summer 1979. *Journal of Physical Oceanography*, 12, pp. 1019-1029, doi: 10.1175/15200485(1982)012<1019:TMABCP>2.0.CO;2.

[19] Schultze, L. K. P., Merckelbach, L. M., Horstmann, J., Raasch, S., & Carpenter, J. R. (2020). Increased Mixing and Turbulence in the Wake of Offshore Wind Farm Foundations. *Journal of Geophysical Research*: Oceans, 125 (8). https://doi.org/10.1029/2019jc015858

[20] Lentz, S.J. (2017). Seasonal warming of the Middle Atlantic Bight Cold Pool. *Journal of Geophysical Research Oceans*. 122(2). 941–954, doi: 10.1002/2016JC012201.

[21] Li, G., et al., (2020). Increasing ocean stratification over the past half-century. *Nature Climate Change.* 10(12): 1116-1123.

Building an Ocean Technician Workforce

Liesl Hotaling
Marine Technology Society
Washington, DC, USA
liesl.hotaling@mtsociety.org

Hans VanSumeren
Marine Technology Society
Washington, DC, USA
hans.vansumeren@mtsociety.org

Josh Kohut
Marine and Coastal Sciences
Rutgers University
New Brunswick, NJ, USA

Nicole Waite
Marine and Coastal Sciences
Rutgers University
New Brunswick, NJ, USA

***Abstract*— There is a global need for skilled workers across multiple sectors within the marine industry (research, renewable energy, fisheries, ports/shipping, infrastructure, national security, tourism, etc.). In order to prepare this workforce, we must collectively take action to establish attractive, innovative, agile and equitable educational opportunities. These opportunities should capitalize on skill sets for a range of workers and encourage engagement pathways for life-long learning through obtaining stackable microcredentials and professional certificates to promote personal growth, keep pace with technological changes, and capitalize upon opportunities within the sector.**

Keywords—ocean technician, workforce development, education, microcredentials, marine technology

I. Introduction

There is a global need for skilled marine industry workers for available positions in various sectors, including research, renewable energy, fisheries, shipping, infrastructure, national security, and tourism [1]. Remarkably, many of these positions do not require advanced degrees in engineering or science but instead necessary skills and proficiencies that align with technical requirements common to the industries they serve.

To foster these vital skills within a condensed timeframe, there is an imperative for innovative and adaptable educational programs. These programs must break away from the conventional, compartmentalized education model and, instead, offer multiple expedited routes to degree and certification attainment. This shift towards a competency-focused credentialing framework will open up opportunities for a more diverse talent pool to meet the expanding workforce requirements.

To address this need, in collaboration with community members, the Marine Technology Society (MTS) is actively establishing the infrastructure necessary to issue a diverse range of stackable microcredentials. These microcredentials will create accessible and flexible pathways to learning and vocational training. The microcredentials address core competencies required for employment in the ocean/marine/blue economy. These flexible learning pathways will be of value to a spectrum of learners including those: entering the workforce; looking to applying skill sets acquired during military service; seeking acknowledgement of skills acquired "on the job"; and in need of employment retraining. The cross training/upskilling provided through the microcredentials framework is intended to form workers capable of generating innovation and new applications and/or refinements of existing technology, and development of new technologies.

II. Development of MTS Microcredentials

A.1. What are microcredentials?

The concept of microcredentials is not new. Microcredentials began their ascent over 20 years ago in computer science as a method for capturing skills and discrete knowledge for recognition by colleagues and employers. The concept took hold in the field with organizations such as Google, Cisco and Microsoft leading the way by recognizing and offering the "stackable" learning opportunities [2]. The concept has grown in several other industries and are currently quickly gaining popularity.

Microcredentials are short, competency-based recognition that are smaller in scale and scope and represent specific knowledge and/or skills acquired and demonstrated. Microcredentials can be "stacked" in various ways – like interlocking blocks, or pathways – to build toward specific certification and/or employment goals.

A.2. Why microcredentials?

Microcredentials are quickly gaining popularity because they represent a personalized approach to education. Learners, within reason, can create their own pathway based on interests and career goals and address gaps in skills. Once a learner demonstrates their competency, a digital badge is issued. Badges are a transferrable symbol used to verify the attainment of specific competencies and can be added to resumes, LinkedIn profiles or other social media platforms as instant recognition of their personal skill set. Therefore, a learner can instantly demonstrate their skills instead of waiting several years for a degree to be issued.

Flexibility is key to the modern college student. Currently, the majority of undergraduate students in the U.S. are employed full-time while attaining their degree, are 25 years or older, and attain their degree while attending college part-time. Less than 20 percent of undergraduates live on a campus [3].

A.3. Why MTS microcredentials?

MTS identified the convergence of the pending and future industry employment needs and the need for flexible learning pathways to engage and broaden the talent pool. These flexible learning pathways will be of value to a spectrum of learners including those: entering the workforce (undergraduate and graduate students); looking to applying skill sets acquired during

National Science Foundation (NSF-OCE 2308556) .

OCEANS 2024 - Halifax | 979-8-3315-4008-1/24/$31.00 ©2024 IEEE | DOI: 10.1109/OCEANS55160.2024.10753811

979-8-3315-4008-1/24/$31.00 ©2024 IEEE

military service; seeking acknowledgement of skills acquired "on the job"; and in need of employment retraining.

MTS also recognized a wide-spread issue of individual schools struggling to have their microcredentials acknowledged by potential employers. With a wide array of definitions, robustness of skill recognition and ability levels represented with individual school issued microcredentials, employers can be at a loss to understand what learning and skills a microcredential represents.

To address this need, MTS applied for and received a grant from the National Science Foundation (NSF-OCE 2308556) to begin the effort of creating microcredentials representing skills needed for the blue economy workforce. In collaboration with community members (academia, industry, military and government), MTS is actively establishing the infrastructure necessary to issue a consensus-based framework of competencies for a diverse range of stackable microcredentials. The framework will be openly available on the MTS website for use by educators and employers. The hope is for employers to use the articulated competencies in job descriptions and educators will partner with MTS to issue microcredentials representing the various competencies.

B. Development Process

The Microcredentials Core Team met over the first three months of the project to discuss the draft framework to house the competencies for the MTS microcredentials. The team settled on the following general structure (Table 1):

Table 1. Trainee/Student Level
Foundational
Learning focus Validated Experience: • 30 – 40 hours (camp cycle) • Fundamentals of the technology • Beginning concepts • Uses/application • Basic knowledge demonstrated
Intermediate
Learning and competency demonstration/practicum Validated Experience: • Months/crosswalk • Technology applications • Intermediate concepts • More complex uses • Intermediate level knowledge demonstrated • PD at work and application
Advanced
Competency mastery through demonstration Validated Experience: • Practical experience leading to success in the course • Capstone Camps ○ Platforms ○ Sensors ○ Data

The National Science Foundation grant is for the development process needed to establish Foundational level microcredentials for the Trainee/Student Level for three marine technologies - Sonar, Glider and ROV – and Intermediate level microcredentials for Sonar and Gliders.

The Microcredentials Development team (technical and education experts) met periodically over the span of four months to generate the draft competencies for the Sonar, Glider and ROV Foundational microcredentials. Once the drafting process was complete, the Microcredentials Core Team recruited people to serve on the Microcredentials Review teams (sonar, glider and ROV). Each team was comprised of representatives from academia, industry, military and government. This action was purposeful to benchmark the competencies required to obtain the Fundamental and Intermediate credentials through the lens of each sector. The intention is to create microcredentials valued in all sectors, and create a malleable talent pool to address employer needs.

The Fundamental competencies for sonar, ROVs and gliders were vetted by the committees during the Spring of 2024.

The development cycle worked well during the first iteration and is planned for use again during the development of the Intermediate microcredentials beginning late Autumn 2024. However, the development cycle will be continually evaluated to look for improvement or streamlining as additional microcredentials are added to the MTS portfolio.

III. Implementation

The developed Foundational competencies were used as the content outline for two MTS Summer Workshops. The first workshop was conducted by partner school Rutgers University, June 10 -14, 2024. Ten learners (Figure 1) attended the workshop and each attendee earned two Foundational microcredentials, Glider Hardware and Glider Software (Piloting). Please see Waite, et al, 2024 OCEANS paper for more details on the workshop.

Figure 1. Workshop participants disassembling a glider.

The second workshop was conducted by partner school Northwestern Michigan College, June 17 – 21, 2024. Thirteen learners attended the workshop and each attendee earned two Foundational microcredentials, Sonar and ROV. Please see Van Sumeren, et al, 2024 OCEANS paper for more details on the workshop.

Figure 2. Workshop participants preparing an ROV for deployment.

Data gathered through program evaluation of the workshops is being analyzed and will inform the guidelines for developing future microcredentials. In addition, a select few workshop participants will be asked for an interview with the Project Evaluator to understand from the student point of view any major gaps in the learning experiences. The evaluation data will be shared with the partners to improve delivery of the material and better understand how to collectively improve the programs and processes.

Both schools, Rutgers University and Northwestern Michigan College, intend to continue the partnership with MTS and issue microcredentials to their registered students throughout the academic year.

IV. PARTNERSHIPS AND EXPANSION

As MTS microcredentials are developed and ready for implementation, MTS will seek partnerships with several institutions to implement the Foundational, Intermediate and Advanced skills training locally. Learners can earn microcredentials at the institutions during discrete workshops, like the MTS summer workshops, or as part of regular college courses. The MTS Microcredentials Core Team will work with the institutions to identify components of existing curricula which address the competencies outlined in the MTS competencies framework. In that scenario, a learner could earn academic credit through their respective colleges, while earning the relevant MTS microcredential badges. If the colleges also offer their own microcredentials, the learner would also earn the "sister" microcredential from the college. The course credit would count toward the eventual degree, however, instantly the student could share their earned microcredentials on their resumes, social media channels, or to employers.

Again, the goal is to create a consensus-based set of competencies led by MTS. Utilizing the openly available framework and partnership model, the "guesswork" will be removed for potential employers. If an applicant provides a transcript and/or resume that contains MTS issued microcredentials, the employer will be able to understand exactly which skills the learner has mastered.

To ensure all partner institutions are providing the agreed upon competencies to their learners, a Partners Review Committee will work with the partners to review curricula and/or instructional materials. Each vetted partner will commit to delivering the core materials to the agreed upon competencies and standards. The application and partner schools will be reviewed periodically to ensure quality control.

V. CONCLUSIONS

The MTS microcredential framework will create accessible and flexible pathways to learning and vocational training and recognize skills and abilities over traditional degrees. The cross training/upskilling provided through the microcredentials framework is intended to form workers capable of generating innovation and new applications and/or refinements of existing technology, and development of new technologies.

The stackable MTS microcredentials, endorsed by accredited partners (government, industry, NGOs, academic) institutions, will directly address the workforce preparation requirements while enhancing education institutions' ability to shift some of their programs towards skills-based credentialing. This approach will better equip learners for the workforce in a shorter time frame. The microcredentials system accommodates various individuals, including those in the early stages of their careers seeking entry into the industry, those looking to enhance their existing knowledge and skillset, individuals aiming to transition into new industries, and those interested in formal recognition for their existing skills.

Recognition of the value of MTS microcredentials across sectors is intended to accelerate job placement and contribute to the development of a globally competitive STEM, and specifically an ocean technician workforce prepared to support the exploration, research and development that lies ahead.

ACKNOWLEDGMENT

The authors would like to thank the many members of the Microcredentials Review teams (sonar, glider and ROV) for their assistance, valuable insight and expectations regarding competencies.

REFERENCES

[1] OECD (2016), The Ocean Economy in 2030. Paris, France: OECD Publishing. https://doi.org/10.1787/9789264251724-en.

[2] Spencer, G. (2019). Microcredentials: Opening the door to an inclusive future of work in the digital age. Microsoft Asia website: https://news.microsoft.com/apac/features/micro-credentials-opening-the-door-to-an-inclusive-future-of-work-in-the-digital-age/.

[3] Le, C., Pisacreta, E. D., Ward, J. D., & Margolis, J. (2019, December 12). Expanding Pathways to College Enrollment and Degree Attainment: Policies and Reforms for a Diverse Population. https://doi.org/10.18665/sr.312296

ICES Journal of Marine Science, 2024, Vol. 0, Issue 0, 1–14
https://doi.org/10.1093/icesjms/fsae036
Received: 13 September 2023; **revised:** 12 February 2024; **accepted:** 29 February 2024
Original Article

Quantifying the role of submesoscale Lagrangian transport features in the concentration of phytoplankton in a coastal system

Jacquelyn M. Veatch [1,*], Josh T. Kohut [1], Matthew J. Oliver [2], Hank Statscewich [3], Erick Fredj [4]

[1]Department of Marine and Coastal Sciences, Rutgers, The State University of New Jersey, 71 Dudley Road, New Brunswick, NJ 08901, United States
[2]College of Earth, Ocean and Environment, University of Delaware, 700 Pilottown Road, Lewes, DE 19958, United States
[3]College of Fisheries and Ocean Sciences, University of Alaska Fairbanks, 2150 Koyukuk Dr, Suite 245 O'Neill Bldg., Fairbanks, AK 99775-7220, United States
[4]Computer Science Department, The Jerusalem College of Technology, 21 Havaad Haleumi St., PO Box 16031 Jerusalem 91160, Israel
*Corresponding author. Department of Marine and Coastal Sciences, Rutgers, The State University of New Jersey, 71 Dudley Road, New Brunswick, NJ 08901 United States. E-mail: jveatch@marine.rutgers.edu

Abstract

Food resources in the ocean are often found in low densities, and need to be concentrated for efficient consumption. This is done in part by oceanographic features transporting and locally concentrating plankton, creating a highly patchy resource. Lagrangian approaches applied to ocean dynamics can identify these transport features, linking Lagrangian transport and spatial ecology. However, little is known about how Lagrangian approaches perform in ageostrophic coastal flows. This study evaluates two Lagrangian Coherent Structure metrics against the distribution of phytoplankton; Finite Time Lyapunov Exponents (FTLE) and Relative Particle Density (RPD). FTLE and RPD are applied to High Frequency Radar (HFR) observed surface currents within a biological hotspot, Palmer Deep Canyon Antarctica. FTLE and RPD identify different transport patterns, with RPD mapping single particle trajectories and FTLE tracking relative motion of paired particles. Simultaneous measurements of circulation and phytoplankton were gathered through the integration of vessel and autonomous glider surveys within the HFR footprint. Results show FTLE better defined phytoplankton patches compared to RPD, with the strongest associations occurring in stratified conditions, suggesting that phytoplankton congregate along FTLE ridges in coastal flows. This quantified relationship between circulation and phytoplankton patches emphasizes the role of transport in the maintenance of coastal food webs.

Keywords: lagrangian transport; coastal oceanography; spatial ecology; food web focusing; lagrangian coherent structures

Introduction

Ocean food resources are patchy, concentrated in some areas and sparse in others. This uneven distribution creates ecosystems with fragmented spatial and temporal distribution of both primary producers and their consumers (Benoit-Bird 2023). Food resources (e.g. plankton) must be concentrated either physically or biologically in order to support larger upper trophic species, maintaining a sustainable food supply (Lasker 1978). The processes that govern the attraction of upper trophic species to areas of concentrated food resources is called food web focusing (Genin 2004). As if visiting marine "grocery stores," mobile grazers and foragers rely on concentrated food sources that have been grown elsewhere and transported and concentrated in higher density patches. Besides transport, biological processes can also drive patchiness including population growth, swarming behavior, or predation. Recent studies have demonstrated the importance of physical advection to both concentrate plankton in the creation of these patches (Hofmann and Murphy 2004, Kohut et al. 2018 Oliver et al. 2019) and to maintain connectivity between neighbouring systems sharing resources (Michael et al. 2006). The role of surface currents in the concentration and transportation of plankton has been widely studied in pelagic, open ocean, mostly geostrophic systems on mesoscale and days-long time-scales (Lehahn et al. 2007, Hernández-Carrasco et al. 2011, 2018, Huhn et al. 2012, Li et al. 2015, Lévy et al. 2018, Liu et al. 2018). However, the role of advective transport in more complex, nonlinear, ageostrophic coastal flows is more difficult to characterize. Flow in productive nearshore ecosystems is complicated by tides, buoyancy, highly variable winds, and complex bathymetry, which all contribute to the advection and concentration of plankton patches. This study investigates how coastal ocean currents create localized marine "grocery stores" by transporting and concentrating phytoplankton into discrete patches.

A variety of Lagrangian Coherent Structure (LCS) metrics are used for their ability to quantify advective transport in fluid flows. Attracting LCS are distinct areas within a flow field that have a strong influence on the attraction of neighboring particle trajectories (Farazmand and Haller 2012, 2013, Haller and Beron-Vera 2012, 2013, Haller 2015) using either a single or a paired particle tracking method. When applied to oceanic systems, attracting LCS metrics have the potential to quantify mechanisms of plankton concentration (Huhn et al. 2012), aid in the rescue of overboard passengers (Serra et al. 2020), and relate ocean features to a variety of biological activity including the migratory patterns of birds (Tew Kai et al. 2009), foraging behavior of apex predators (Cotté et al. 2011, Della Penna et al. 2015, Abrahms et al. 2018) and the distribution and efficiency of fishing vessels (Prants et al. 2014, Watson et al. 2018). This study aims to improve field-wide usage of these metrics by comparing a single particle trajectory metric (Relative Particle Density, RPD) to a more complex paired particle LCS metric (Finite Time Lyapunov Exponent, FTLE). The RPD metric maps regions where particles accumulate, whereas FTLE characterizes how neighbouring particles move relative to each other, diagnosing underlying patterns of trajectories. These two metrics quantify and map unique particle behaviors given the same input ocean circulation. RPD and FTLE were evaluated against alignment with simultaneous observations of phytoplankton patch distribution. Because RPD map accumulation and FTLE identify boundaries between distinct modes of flow, phytoplankton patch centers and edges were distinguished with the hypothesis that RPD will better align with patch centers and FTLE with patch edges. Given these differences in LCS metrics, the following study evaluates the relevance of each to defining phytoplankton patches observed in a complex coastal biological hotspot.

In this manuscript, our approach is to reveal patterns in phytoplankton abundance and advective transport at smaller spatial (O 1 km) and temporal (O 1 h) scales than have been previously examined in ageostrophic coastal flow (Shadden et al. 2009, St-Onge-Drouin et al. 2014). The proper application of LCS metrics allows us to better understand the role of advection in the concentration and transport of plankton patches. The following sections will detail the methodology and results of our comparison between RPD, FTLE, and phytoplankton distribution with a discussion on the implications of using two-dimensional LCS in coastal regions, the differences between single (RPD) and paired (FTLE) particle tracking suggesting when each metric is appropriate, the creation of the interior of phytoplankton patches vs. the border, and how differing levels of stratification affect these relationships.

Materials and methods

Data

The data used in this study are collected from Palmer Deep Canyon, Antarctica in January through March of 2020 as part of a National Science Foundation funded project, SWARM. These data provide coincident dynamic distribution of both plankton patches and underlying physical features over the entire local penguin foraging season. These observations were provided through an integrated polar observatory that included three High Frequency Radars (HFRs), a Slocum glider, and twice-weekly ACROBAT towed surveys between January and March 2020 (Fig. 1). The ACROBAT is small (0.5 m)-winged instrument that profiles the surface ocean (0–50 m), highly resolving light and physical properties. HFRs produce hourly surface current maps at 1 km resolution covering about 1500 km^2, the glider profiled to 1000 m completing one dive (two profiles) every 4 h at the head of Palmer Deep Canyon, and 16 ACROBAT towed surveys (60 km) were completed observing 40 distinct phytoplankton patches (Fig. 1).

Palmer Deep Canyon

Palmer Deep Canyon's relatively short and tightly coupled food web (Saba et al. 2014) makes it a unique ecological laboratory to quantify the impact of concentrating features on phytoplankton. Phytoplankton are a major food sources for Antarctic Krill (*Euphausia superba*), a keystone species for many top predators in the region, including penguins. Penguin colonies surrounding Palmer Deep Canyon have persisted for millennia, according to geologic records (Fraser and Trivelpiece 1996, Emslie et al. 1998, Schofield et al. 2013) despite significant variations in climate conditions. Such endurance of Palmer Deep Canyon's penguin colonies suggests the presence of a strong concentrating mechanism at the base of the food web, able to supply reliable phytoplankton to krill during interannual climate oscillations.

Recent studies in Palmer Deep Canyon have shown the surface residence time scale (~2 days) is much shorter than the phytoplankton doubling timescale (~7–70 days) (Kohut et al. 2018). These findings suggest that increased phytoplankton availability in Palmer Deep Canyon compared to neighboring regions is likely due to transport from other regions rather than stimulated local growth from upwelled, nutrient-rich Upper Circumpolar Deep Water as was previously thought (Kavanaugh et al. 2015). Additionally, recent glider observations have been unable to detect nutrient delivery via upwelling during the growing season (Hudson et al. 2019). Even if nutrient availability was higher in Palmer Deep Canyon compared to neighboring regions, phytoplankton in this system have been shown to be light limited rather than nutrient limited (Carvalho et al. 2019). It is within this transport-driven coastal ecosystem that this study investigates the role of Lagrangian features to define the distribution of phytoplankton patches.

HFR

HFRs use doppler-shifted radio waves backscattered off the ocean surface to observe surface velocity. Signals are transmitted and received by an HFR antenna, and Bragg peaks in the measured Doppler spectra are used to calculate radial components of the surface velocity (Barrick et al. 1977). Measured radial components of the surface ocean velocity are directed toward the HFR antenna with a range resolution of 500 m horizontally and 5° in azimuth. Radial components from the three HFR stations are added together to construct magnitude and direction of surface current velocities using an optimal interpolation algorithm (Kohut et al. 2006) providing hourly maps of surface currents at 1 km spatial resolution (Fig. 2a).

The three-site network included two remote locations on the Wauwermans and Joubin islands operated at a center frequency of 25 MHz and a third site at Palmer Station operated at 13 MHz (Fig. 1). The two remote sites located beyond existing power grids used Remote Power Modules constructed on site. More details on the installation of this 3-site network are provided in Statscewich and Weingartner (2011) and Kohut (2014).

The three HFR sites collected hourly radial maps of ocean surface current component vectors over our study area, covering about 1500 km^2 more than 80% of the time (Fig. 2a). The hourly, two-dimensional surface current maps derived from the radial component vector maps provided by each of the three HFR sites were used to derive our two LCS metrics (Fig. 2b and c). Before the LCS calculations were done, gaps within

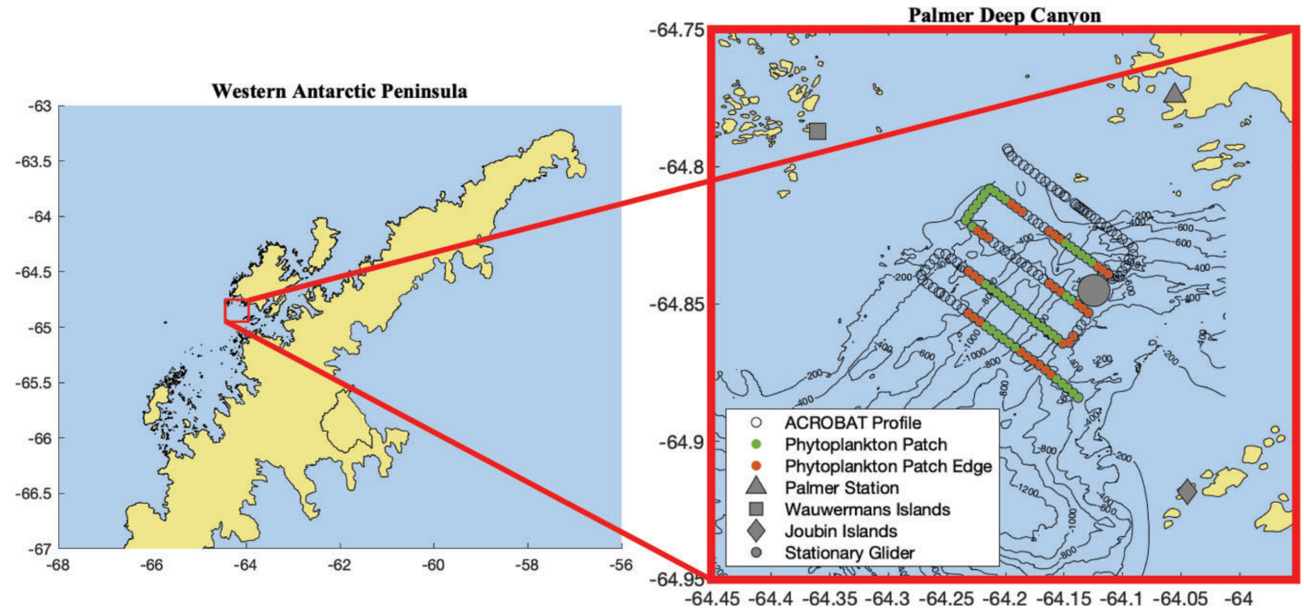

Figure 1 Study area indicating locations of three HFRs (Palmer Station, Wauwermans Islands, and Joubin Islands,) ACROBAT towed survey, and stationary glider around Palmer Deep Canyon, Antarctica. The canyon bathymetry is contoured with 200 m isobars. Plotted is an example of one ACROBAT survey on 12th February 2020, with profiles designation as "phytoplankton patch" and "phytoplankton patch edge." Inset is a map of the Western Antarctic Peninsula, with a box around the study area.

the 80% coverage area of the HFR maps were filled using a rigorous HFR-specific method (Fredj et al. 2016). This follows methodologies in Veatch et al. (2022).

ACROBAT towed surveys

Twice weekly ACROBAT surveys were conducted along transects over Palmer Deep Canyon (Fig. 1) between January and March 2020. The ACROBAT instrument was towed behind a small, (10.2 m) rigid hull boat at ~6 kts (about 3 m s^{-1}) as the instrument undulated continuously between a depth of 1 and 50 m. The ACROBAT was equipped with a fast-sampling (16 Hz) Seabird 43 FastCAT CTD (conductivity, temperature, and pressure), and a Wetlabs Ecopuck optical sensor (chlorophyll-*a* and CDOM fluorescence and optical backscatter at 700 nm). Profiles had a 300-m resolution over the 60-km transect for ~160 vertical profiles per survey. A total of 16 surveys were conducted. ACROBAT data was processed, quality controlled, and profiled using a MATLAB toolbox (Reister 2023) and the methods as described in Martini et al. (2016).

For each profile, the mixed layer depth (MLD) was calculated as the maximum buoyancy frequency in the upper 50 m following methods in Carvalho et al. (2017). For profiles with no clear mixed layer in the upper 50 m, the deepest ACROBAT measurement was designated as the MLD. Phytoplankton abundance was measured as the particle backscatter (m^{-1} sr^{-1}) above the MLD of each profile, integrated using a trapezoidal integration. Particle backscatter was used instead of chlorophyll-*a* fluorescence to negate for effects of nonphotochemical quenching and photo acclimation. Particle backscatter has been shown to correlate linearly with chlorophyll-*a* fluorescence in Palmer Deep Canyon (Carvalho et al. 2016), making particle backscatter a good indicator of chlorophyll biomass. To address the resolution mismatch between the ~300 m separated profiles and the 1-km HFR grid resolution, a sliding filter with a 1-km window was applied to the MLD and particle backscattering data. ACROBAT transects took 4–6 h to complete. It was determined that the ACROBAT did not resample phytoplankton patches that were advected back over the survey from previously sampled waters (Supplementary material S1).

The distribution of phytoplankton patches for each survey were derived from the ACROBAT profiles. To do this, each profile was designated as "phytoplankton patch," "phytoplankton patch edge," or neither. An ACROBAT profile with integrated mixed layer particle backscatter 5% higher than that survey day's median was designated as "phytoplankton patch" following the threshold method from Thomalla et al. (2015). A daily threshold was used for the definition of phytoplankton patches to capture concentrating mechanisms even on days that had lower phytoplankton abundance, which shows a strong seasonal signal. Survey thresholds of particle backscatter ranged from 0.0177 to 0.1184 m^{-1} sr^{-1}. The ACROBAT profiles on either side of the phytoplankton patch, the first and last profile of the phytoplankton patch, and the second and second to last profile of the phytoplankton patch were designated as "phytoplankton patch edges" (Fig. 1), following methodologies in Veatch et al. (2022). Deciphering between patch interior and edge will be used to test for differences in the horizontal advection mechanisms that created the center of accumulation and where the patch ended. Phytoplankton patches that were less than a kilometer and a half long were not used in analysis given that the 1-km resolution of the HFR input data likely did not resolve advective transport that created a phytoplankton patch that small.

Stratification was calculated from the ACROBAT CTD data as the density difference between the surface and 50 m for each ACROBAT profile. "Stratified surveys" were defined as the 8 survey days with the highest average density difference and "mixed surveys" were defined as the surveys with the lowest average density difference (Figure S1).

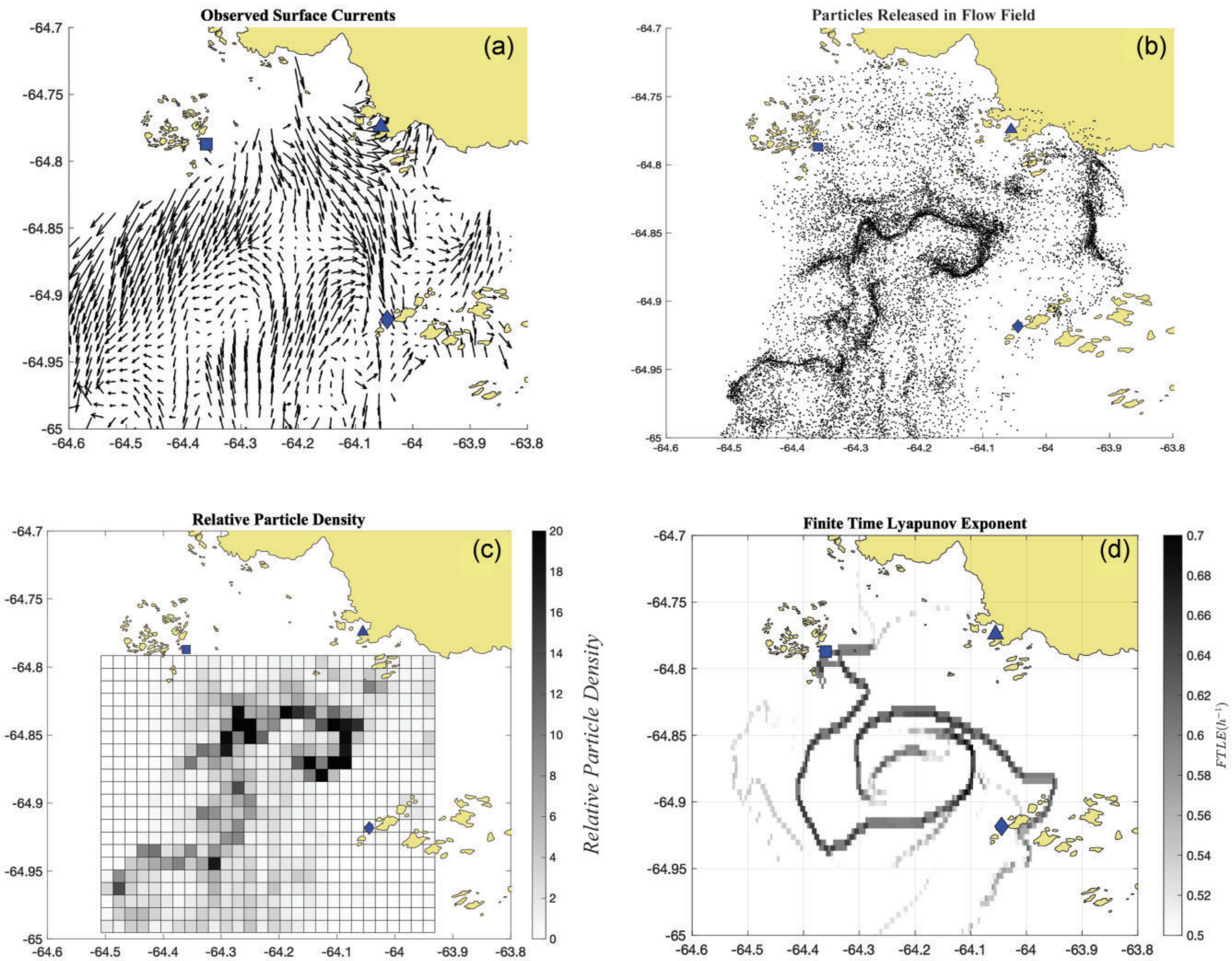

Figure 2 The HFR observed surface current velocity field (a), advected particles released following methods detailed in section, "RPD" (b), RPD, only positive values are shown (c), and FTLE (d) from 9th January 11:00 GMT over the study region. The three HFR stations are indicated with polygons. (© 2022 IEEE. Reprinted, with permission, from Veatch et al. (2022, preprint: not peer reviewed).

Autonomous glider

A Slocum glider was deployed in Palmer Deep Canyon from January to March 2020. Gliders are buoyancy driven autonomous vehicles that dive and climb through the water column in a "sawtooth" pattern. The glider used in this study was piloted to hold station at the head of Palmer Deep Canyon, profiling the same region throughout the season from the surface to 1000 m, just above the seafloor (Fig. 1). The glider sampled at a 0.25-m vertical resolution. Aboard the glider was a sensor suite that measured physical structure of the water column (CTD, Seabird), phytoplankton fluorescence and particle backscatter (Eco Triplet, Wet Labs), and krill biomass (Acoustic Zooplankton Fish Profiler, ASL Environmental Sciences).

Data from the stationary glider was profiled and MLD was calculated as the maximum buoyancy frequency following methods in (Carvalho et al. 2017), the same methodology used to determine MLD from the ACROBAT data. Similar to the ACROBAT, glider profiles were designated as "phytoplankton patches" if the particle backscatter integrated over the mixed layer was 5% higher than the daily median, adapted from Thomalla et al. (2015). These data were used in the calculation of the time-scale of phytoplankton patches detailed in section, "Determining integration time".

LCSs

Several LCS techniques have been applied to ocean systems in the past decade for their ability to quantify areas in ocean currents (or any velocity field) that exert an impact on nearby drifting particles (Haller 2015). Such areas are known as coherent structures. Coherent structures can identify local extrema of repulsion, attraction, and shearing of flow (Haller 2015). Attracting coherent structures will quantify the attraction of passive drifters in a flow field, or plankton in ocean currents (Shadden et al. 2005, Haller 2015).

In this study, LCS metrics from two distinct classes will be used to quantify physical advective features within the HFR observed surface current field: RPD, which have been used in Palmer Depp Canyon in previous studies (Oliver et al. 2019, Veatch et al. 2022) and FTLE, which have been used in a variety of open ocean ecological studies (Haller 2001, Huhn et al. 2012, St-Onge-Drouin et al. 2014, Fahlbusch et al. 2022, Veatch et al. 2022). This paper will suggest appropriate uses for both metrics dependent on available ecological observations, ensuring that the ecological community applies appropriate LCS techniques with an understanding of how these tools differ.

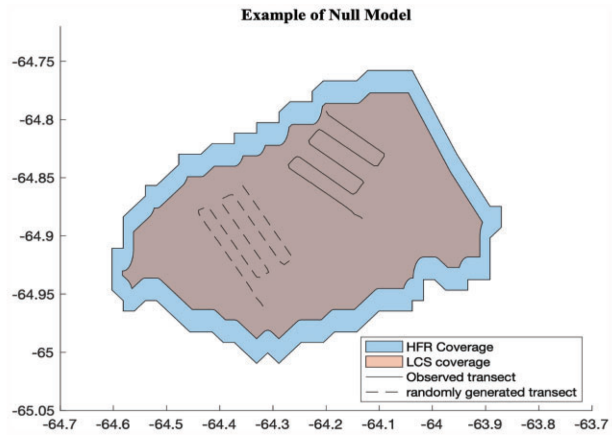

Figure 3 ACROBAT transect (solid line) and one randomly generated transect (dashed line) within the HFR coverage (larger shape) and LCS coverage (smaller shape) of the study region.

RPD

RPD reports the position of drifters at a single timestamp by normalizing the density of drifters within a gridded bin system in the study field. RPD calculations begin with releasing virtual particles over a regular grid and tracking them through a velocity field. RPD is then quantified by summing the number of drifters in each grid box, and normalizing by the median number of drifters in all grid boxes (Fig. 2c). New particles were released in a regular grid across the 80% coverage of the HFR footprint every 3 h. Particles were not counted until they had been advected in the velocity field for 6 h and were no longer counted when they were advected out of the HFR domain, or after they became three days old. The 6-h integration time is explained in section "Determining integration time". Given the average residence time of 2 days (Kohut et al. 2018), the 3-day threshold was chosen to coordinate with the time phytoplankton will spend in the surface layer of the study domain. This methodology follows that used by Oliver et al. (2019) and Veatch et al. (2022). Two dimensional HFR data is used to calculate RPD, relying on the assumption that the integrated surface divergence is zero, and no particles are lost from or added to the surface due to vertical velocities. Therefore, RPD will map the instantaneous concentration of surface associated particles across the entire domain given the evolving surface current fields provided by the HFR.

To negate artifacts in results caused by the edges of the HFR domain where particles entering or leaving the domain may be unaccounted for, the domain of RPD results used was smaller 3 km smaller than the domain of the inputted velocity field (Fig. 3). This is about how far the average particle travels over the integration time (6 h).

FTLE

FTLE use the horizontal separation distance between two particles relative to a fixed point over a defined time interval to quantify the strength of coherent structure (either repelling or attracting) at each point on a gridded velocity field. To calculate repelling FTLEs, a forward trajectory is used, and to calculate attracting FTLEs, a backward trajectory is used. In this study, attracting FTLEs were calculated. FTLE's ability to integrate over trajectories sets this technique apart from instantaneous separation rate (Okubo 1970, Weiss 1991) by introducing particle position "memory." Coherent structures are defined by the FTLE metric as ridges in the flow field where neighboring particles are converged toward, and then diverged along a ridge. The strengths of these ridges are quantified by the integrated attraction/separation rate between two particles (Fig. 2d).

FTLE calculations begin with a velocity field over some selected time. Finite differencing is then used over a defined auxiliary grid to numerically compute the derivative of the flow map. Next, the Cauchy–Green strain tensor field is computed from the derivative of the flow map as well as its eigenvalue field and eigenvector field. Then, the "stretching" of the field is computed as in (1), where $S(x_0)$ is the maximum stretching at point x_0, λ_i is the eigenvector field, and C is the Cauchy–Green strain tensor.

$$S\left(x_0\right) = \left[max_{i=1:N}\lambda_i\left(\mathrm{C}\left(x_0\right)\right)\right]^{1/2}. \tag{1}$$

FTLE is then computed with (2) over a finite time T (Dosio et al. 2005, Haller 2015, Haller et al. 2018).

$$FTLE\left(x_0, t_0, T\right) = \frac{1}{T}\ln(\mathrm{S}(x_0)). \tag{2}$$

These calculations result in a time dependent FTLE field for every timestamp of inputted velocity data. In the case of this study, a map of FTLE was produced every hour for the two-and-a-half-month study period.

This relative motion between two neighboring particles and the inclusion of a rate of change component are the key ways in which the FTLE metric differs from the RPD metric. Like RPD, FTLE will vary over space and time when applied to a discrete set of velocity data. FTLE calculations (1 and 2) result in a material surface that then can be projected at a set resolution back onto the study region. FTLE results were projected at the resolution of the HFR (1 km) so as to not stretch the observations further than the input data should be able to resolve.

FTLE calculations were performed using a MATLAB software toolbox (Halleret al. 2015) that was modified for use on HFR data (Fig. 2d). To negate artifacts in results caused by the edges of the HFR domain where it may seem that particles suddenly stop or are lost, the domain of FTLE results used was smaller than the domain of the inputted velocity field. As with the RPD results, the domain was shrunk by 3 km (Fig. 3).

Determining integration time

In calculating FTLE results, varying integration time will identify transport features of different scales. As if fine tuning a microscope, features of a certain scale will come into focus as the integration time is adjusted. This study is interested in the scale of horizontal advective features that create ephemeral phytoplankton patches, therefore observations of phytoplankton patches and surface currents were used to determine the integration time of LCS calculations. To calculate the biological time-scale, the stationary glider was used (Fig. 1). Glider profiles were determined as observing a phytoplankton patch or not. Consecutive profiles of phytoplankton patches were considered to be from the same phytoplankton patch. The average time of consecutive phytoplankton patch profiles was determined to be the average time a phytoplankton patch remains in the same geographic location, 6.2 h, and therefore is the time-scale of the phytoplankton patches. To calculate the physical time-scale, the HFR observed surface currents were used. The autocorrelation of the HFR observed surface current velocities was calculated at each grid point in the HFR

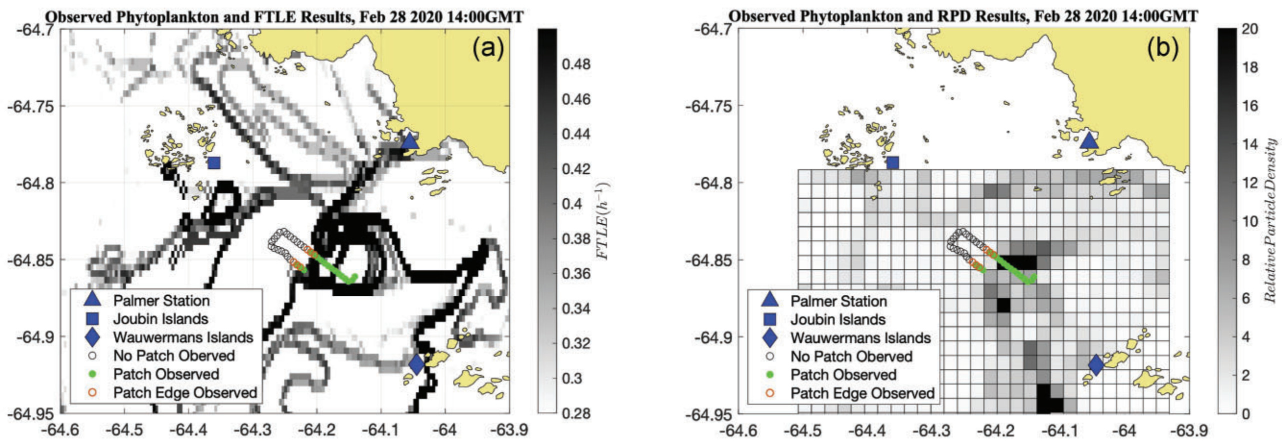

Figure 4 Example of LCS results plotted with 1 h of phytoplankton observations from the ACROBAT towed survey on 28th February at 14:00 GMT, (a) FTLE and (b) RPD.

field and normalized to variance. Autocorrelation was then averaged over each grid point of the same lag time. The time when the HFR observed surface current velocities decorrelated was defined as when the normalized autocorrelation function passed the e-fold scale: 5.5 h. This calculation was repeated with starting times during various stages of the tidal cycle and similar results were found each time. These results are shown in Fig. 3 of Veatch et al. (2022) and follow methods described therein.

The physical and biological timescales of Palmer Deep Canyon reflect the strength of tidal influence in the system. Recent studies have shown the effect of tides on surface ocean particle trajectories (St-Onge-Drouin et al. 2014, Gomez-Navarro et al. 2022) and the response of upper trophic creatures (Adélie penguins) to shifts in tidal regimes in Palmer Deep Canyon (Oliver et al. 2013). Therefore, the tidal cycle influence on particle dispersion, surface currents, and ecology in this system is consistent with these studies.

Based on this analysis, the integration time used for FTLE calculations was 6 h, which approximates the decorrelation time scales of phytoplankton patches and surface current velocities. In the calculation of RPD, particles were not counted in density calculations until 6 hours after their release. Unlike RPD, FTLE's integrate over the particle's trajectory in time, meaning the maps of FTLE results produced at a timestamp incorporate trajectory data from the previous 6 h.

Matching LCS results to phytoplankton patches

To compare the collocation of coherent structures and phytoplankton patches, results were matched in both space and time (Fig. 4). LCS results are space and time dependent, and produce mapped results every hour. The observation time of each phytoplankton patch was rounded to the nearest hour and compared to that hour's corresponding LCS field. Next, each ACROBAT profile was assigned an FTLE and RPD value from the nearest grid point to the ACROBAT profile's GPS location. The ACROBAT profile was always within 500 m of the nearest FTLE and RPD point, which are on 1 km grids. The FTLE and RPD values of all ACROBAT profiles within the same defined phytoplankton patch were averaged into a patch average value. The same was done for each defined patch edge. This resulted in each defined phytoplankton patch having one average patch center FTLE and RPD value and two average patch edge FTLE and RPD values. Phytoplankton patch definitions from the stationary glider were only used to calculate decorrelation scales and were not matched to LCS results to simplify the interpretation of results.

Creating a null model

To evaluate the performance of the LCS overlap with the observed plankton patches, a null model was created to represent a random distribution of patches. Within the bounds of the LCS results (Fig. 3), the ACROBAT transect was randomly rotated and translated along longitude, and randomly translated along latitude. A total of 100 random transects were created from each of the 16 survey days, culminating in 1600 randomly generated transects. The LCS values of each observed phytoplankton patch could then be compared to the LCS values of the 100 randomly generated versions of that patch. If LCS values of the observed patches were significantly greater than the LCS values of the 100 randomly generated versions of those patches, passing a one-sided Wilcoxon rank-sum test, then it was concluded that the observed patches were collocated with a strong LCS. To visualize the difference between observed and randomly generated patch LCS values, the difference was taken between each observed patch LCS value and the average of the corresponding 100 randomly generated patches. This was done for patch centers and patch edges.

Results

Throughout the 16 ACROBAT surveys, 40 distinct phytoplankton patches and 80 phytoplankton patch edges profiles were observed. These data were used to test the collocation of phytoplankton patches in space and time with our two LCS metrics (FTLE and RPD; Fig. 4).

RPD collocated with phytoplankton patches

RPD values had little difference between phytoplankton patches observed by the ACROBAT and randomly generated phytoplankton patches (Fig. 5a). The distributions of observed and randomly generated phytoplankton patch centers failed a one-sided Wilcoxon rank-sum test ($P = .8458$) indicating that the RPD values of the null model (randomly generated patch centers) are not significantly less than the RPD values of the observed phytoplankton patch centers. The distributions of

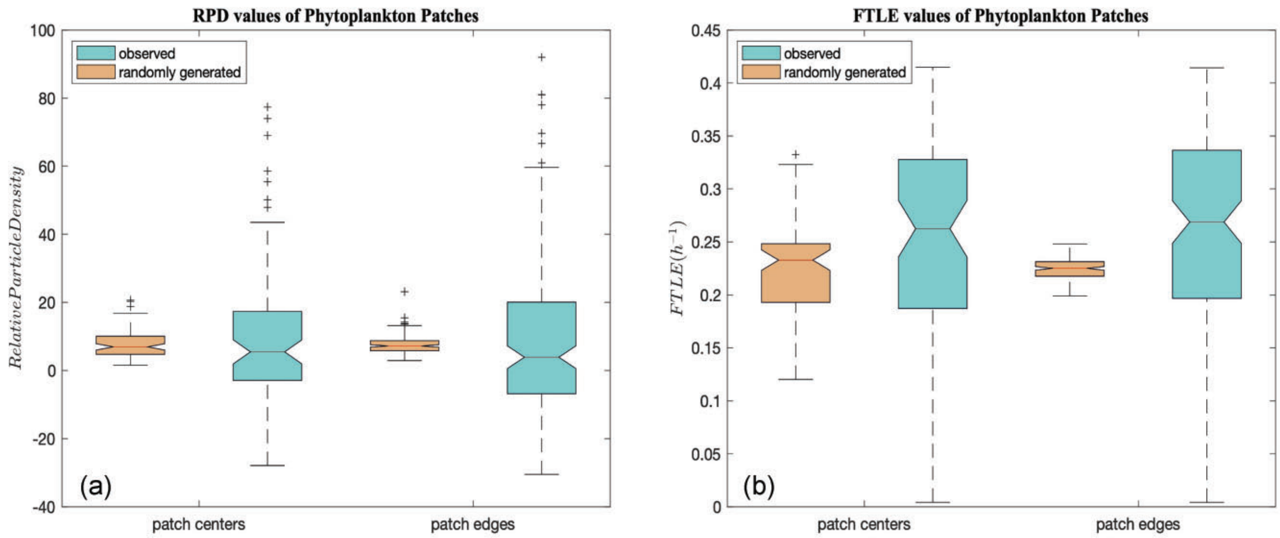

Figure 5 Box and whisker plots of RPD values (a) and FTLE values (b) of phytoplankton patch centers and phytoplankton patch edges of observed (teal) and randomly generated (orange) phytoplankton patches. Boxes represent the interquartile range, whiskers represent the data range, outliers are plotted as +, the median of the data is shown with a horizontal line, and notches represent the confidence interval for the median.

observed and randomly generated phytoplankton patch edges also failed a one-sided Wilcoxon rank-sum test ($P = .9941$) indicating that the RPD values of the null model (randomly generated patch edges) are not significantly less than the RPD values of the observed phytoplankton patch edges.

The distribution of RPD is shifted slightly above zero. Although RPD is a relative amount, this was expected because the edges of the RPD were not used (section "FTLE", Fig. 3), negating the likely low RPD values right at the edge of the HFR domain.

FTLE collocated with phytoplankton patches

The FTLE values of observed phytoplankton patches were higher than the randomly generated null model (Fig. 5b). The distributions of observed and randomly generated phytoplankton patch centers passed a one-sided Wilcoxon rank-sum test ($P = .0034$) indicating that the FTLE values of the null model (randomly generated patch centers) are significantly lower than the FTLE values of the observed phytoplankton patch centers. The distributions of observed and randomly generated phytoplankton patch edges also passed a one-sided Wilcoxon rank-sum test ($P = 4.6017 \times 10^{-6}$) indicating that the FTLE values of the null model (randomly generated patch edges) are significantly lower than the FTLE values of the observed phytoplankton patch edges. In Fig. 6, the distribution of results is mostly positive, indicating that for most patch centers and patch edges the randomly generated "background" FTLE values were less than the observed patch FTLE values. This signal was slightly stronger in patch edges than patch centers for all surveys, although this difference was not significant (one-sided Wilcoxon rank-sum test, $P = .2661$). This pattern holds when the phytoplankton center and edge data are combined and compared to the combined null model values, with the observed data having greater FTLE values with statistical significance (one-sided Wilcoxon rank-sum test, $P = 1.1892 \times 10^{-7}$).

Differences between observed and randomly generated FTLE patch center and patch edge values were separated into "stratified surveys" and "mixed surveys." The difference between observed and randomly generated patch center FTLE values for stratified surveys and mixed surveys are significantly different (one-sided Wilcoxon rank-sum test, $P = .0230$) with higher FTLE values on stratified days. The same pattern holds for patch edges, with the difference between observed and randomly generated patch edges on stratified days having significantly higher FTLE value differences than those on mixed days (one-sided Wilcoxon rank-sum test, $P = .0013$) (Fig. 6).

Case studies of FTLE on stratified and mixed days

To better understand these results, four case study survey days were examined. They were designated as stratified well performing, mixed well performing, mixed poor performing, and stratified poor performing (Fig. 7). Stratified, well performing survey days such as 3rd March had long, thin FTLE structures that persisted for multiple hours (Fig. 7a). The ACROBAT observed phytoplankton patches on these narrow, persistent structures and observed no phytoplankton patches when the survey left these structures. 3rd March also had an average maximum particle backscatter depth of 2.72 m, meaning that most phytoplankton patches were close to the surface within the region where the HFR sampling is most accurate. This is in contrast with the mixed, well-performing survey days such as 28th January which had round, short FTLE structures (Fig. 7b) and an average maximum particle backscatter depth of 17.07 m. On survey days when large amounts of phytoplankton were observed, such as 28th January, there was enough phytoplankton to fill the wider round structures more typical of mixed days and the phytoplankton patches were observed within the FTLE structures. This is shown in Fig. 8(b) where the 28th January survey has many occurrences of high particle backscatter, similar to the 3rd March survey. It was concluded that an abundance of large phytoplankton patches is an important prerequisite to a mixed survey having well-performing FTLE.

Mixed, poor-performing survey days such as 21st February had very few FTLE structures within the survey region (Fig. 7d). Compared to the other three case study days, 21st

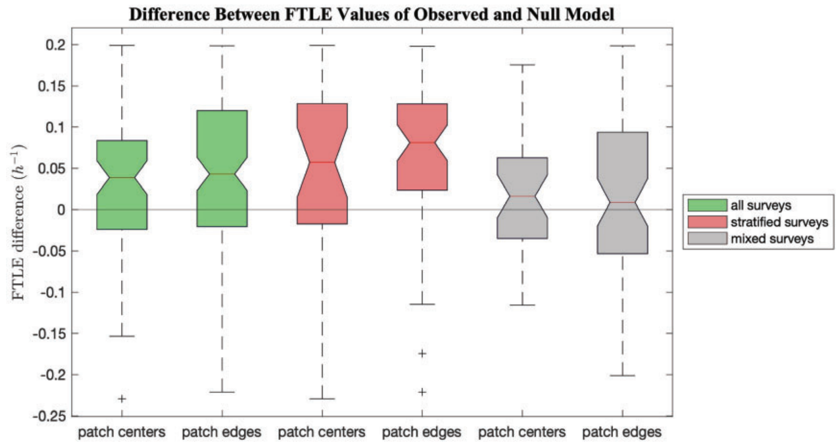

Figure 6 Box and whisker plots of the difference between FTLE values of observed phytoplankton patch centers and edges and randomly generated patch centers and edges of all surveys (left two box and whiskers), stratified surveys (middle two box and whiskers), and mixed surveys (right two box and whiskers). The horizontal line at zero difference separates the well-performing FTLE and patch matches above the line, and poor performing FTLE and patch matches below the line. Boxes represent the interquartile range, whiskers represent the data range, outliers are plotted as +, the median of the data is shown with a horizontal line, and notches represent the confidence interval for the median.

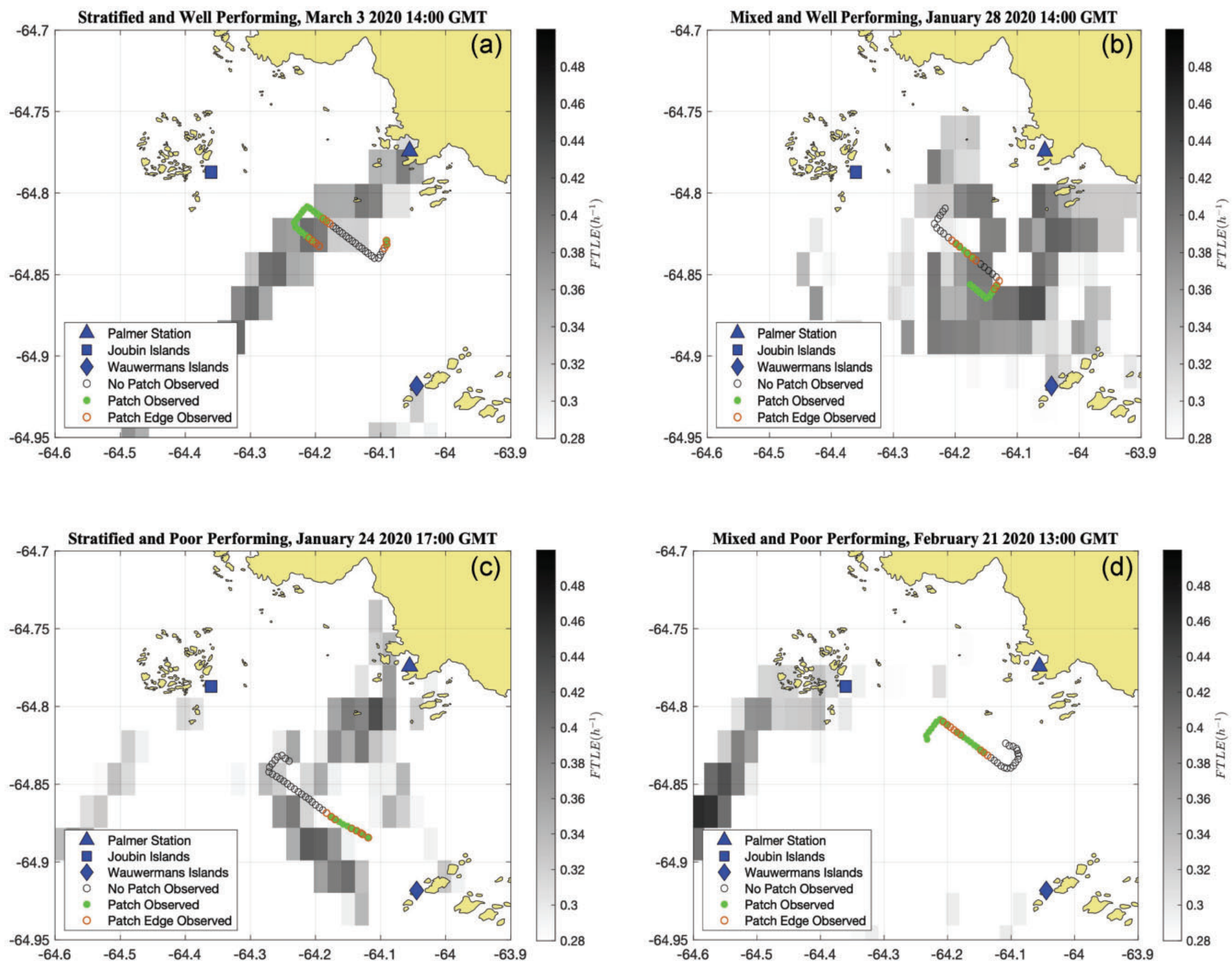

Figure 7 Four case study days of ACROBAT observed patch centers (filled circles) and patch edges scattered over FTLE results. Stratified day with high correlation between high FTLE values and phytoplankton patches (a), mixed day with high correlation between high FTLE values and phytoplankton patches (b), stratified day with low correlation between high FTLE values and phytoplankton patches (c), and mixed day with low correlation between high FTLE and high values and phytoplankton patches (d).

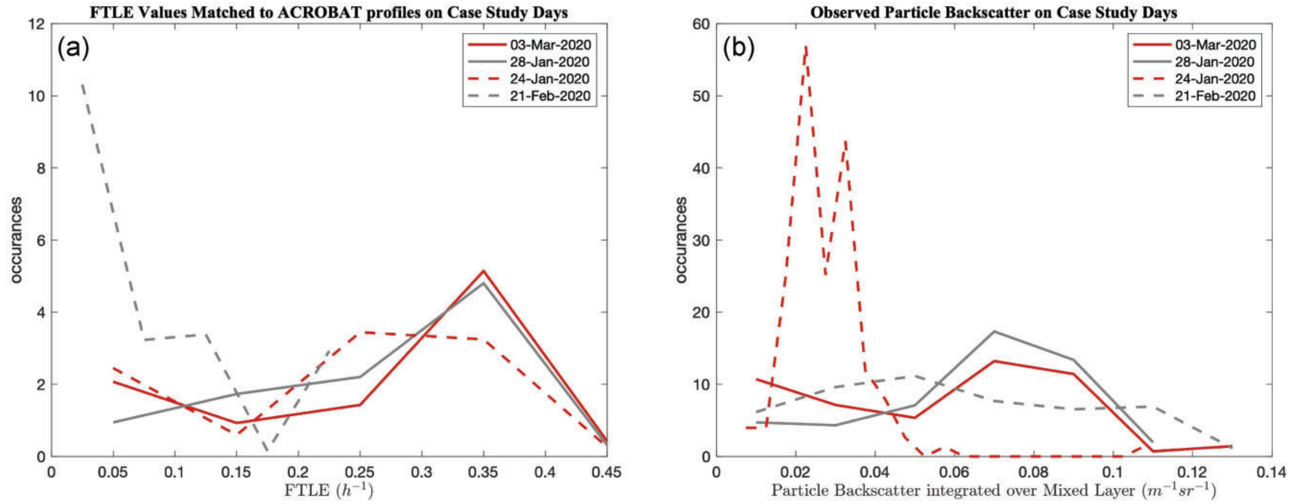

Figure 8 Histogram of (a) FTLE values matched in space and time with each ACROBAT profile observed during the four case study survey days in Fig. 6 and (b) particle backscatter observed by the ACROBAT integrated for each profile to the MLD of the four case study survey days shown in Fig. 7.

February had many observations of low FTLE values (Fig. 8a). It is important to remember that due to the nature of our definition of "phytoplankton patch" normalized to the survey day, there will always be phytoplankton patches defined in a given survey, even if there are no strong FTLE features. It was concluded that the lack of defined FTLE features was the reason this survey day had few phytoplankton patches collocated with FTLE defined attracting features.

Stratified, poor performing survey days such as 24th January were expected to perform well due to well-defined surface layers and shallow phytoplankton patches (Fig. 7c). In the case of the 24th January survey, it is suspected that low abundances of phytoplankton were the cause of the FTLE results' poor performance. In a histogram of integrated mixed layer particle backscatter (the proxy used to define "phytoplankton patches") observed during the ACROBAT surveys of our four case study days, 24th January has a high occurrence of low mixed layer particle backscatter measurements (Fig. 8b). Figure 8(b) suggests that the phytoplankton during the 24th January survey were diffuse across the study region, with many observations of low particle backscatter. Low phytoplankton levels could be because Palmer Deep Canyon had lower abundances of phytoplankton that day, or because our ACROBAT survey transect missed the FTLE features that were concentrating large amounts of phytoplankton. Again, due to the nature of our definition of phytoplankton patch, there were "patches" defined even though phytoplankton observations were overall of low concentration. Many observations of low phytoplankton suggests that the phytoplankton are not well concentrated, but diffuse throughout the study region. On days when there are no attracting features or when the ACROBAT survey does not encounter any attracting features, this is expected. In contrast, the well-performing days have many occurrences of high phytoplankton, suggesting that there is enough phytoplankton biomass to be concentrated into distinct patches.

The poorer performance of FTLE on some survey days could be due to inhomogeneous currents in the surface layer, a lack of large phytoplankton patches on mixed days, a lack of strong attracting physical features, or likely some combination of these three. These four case studies demonstrate that FTLE ridges tend to be narrower and more filament-like on stratified surveys and wider on well-mixed surveys, and that surveys with low amounts of phytoplankton or FTLE do not show phytoplankton patches to align as often with higher FTLE values than surveys that have high amounts.

Discussion

Concentration of sparse food sources into discrete patches is an important mechanism for the maintenance of coastal biological hotspots such as that in Palmer Deep Canyon. Using Palmer Deep Canyon as a natural laboratory, this investigation has determined the importance of physical advection in the distribution of plankton patches at the very base of the food web. LCS metrics, when applied carefully, can be used as tools to elucidate the role of advective transport in complex coastal regions. In this study, FTLE expounds the relationship between HFR observed surface currents and phytoplankton patch location. The difference between single particle tracking methods like RPD and paired particle tracking like FTLE provides a roadmap for when each metric is appropriate to apply to coastal ecosystems.

Two-dimensional assumptions in LCSs

The use of LCS allows for the identification of ocean features that cannot be seen from velocity fields alone. LCS applied to ocean currents have the capacity to quantify underlying patterns in fluid trajectories that potentially concentrate marine resources in the ocean. However, there are limitations to these LCS, which must be thoroughly understood to properly apply metrics and interpret results. LCS must have the same dimensionality as their input. In this study, two-dimensional velocity data from three HFRs were used to calculate LCS, constraining resulting LCS to two dimensions at the ocean surface. Additionally, HFRs observe surface flow while phytoplankton patches can exist at variable depths. Below we explore the implications of two-dimensional LCS in coastal regions and the depth of HFR measurements, demonstrating that these limitations do not impede this study's ability to quantify phytoplankton concentrating features.

Pelagic, open ocean regions that are dictated largely by geostrophic, two-dimensional flow have been the subject of past studies using LCS to identify patterns of phytoplankton transport (Lehahn et al. 2007, Hernández-Carrasco et al. 2011, Huhn et al. 2012, Li et al. 2015, Lévy et al. 2018, Liu et al. 2018). In contrast, coastal regions are complicated by vertical velocities creating a three-dimensional flow field. Vertical velocities in our study region, Palmer Deep Canyon, are small compared to horizontal surface flow, especially given the short residence time of the region. With an average residence time of 2 days (Kohut et al. 2018) and an average vertical velocity magnitude of 2.84×10^{-5} ms^{-1} between January and March (calculated from divergence in HFR), a free drifting particle in Palmer Deep Canyon experiences on average 4.9 m of vertical displacement during its ~2 day residency in the system. This average vertical displacement of 4.9 m is within the average surface MLD of ~20 m. Consequently, it is reasonable to accept the two-dimensional LCS assumptions. Previous work has shown LCS in the open ocean associated with relatively strong vertical velocities at fronts (Mathur et al. 2019, Siegelman et al. 2020). In Palmer Deep Canyon, maximum vertical velocities are around 0.405×10^{-3} ms^{-1}, which is an order of magnitude smaller than maximum vertical velocities found at open ocean LCS by Siegelman et al. (2020) of 1.15×10^{-3} ms^{-1} at fronts. Whereas LCS in the open ocean can last for days, LCS in Palmer Deep Canyon have a lifespan on 5 h on average, which is when the autocorrelation function of FTLE results pass the e-folding scale, on average throughout the study domain and season. Vertical velocities associated with LCS in Palmer Deep Canyon are likely smaller due to the short lifespan of these features.

There could be small vertical velocities not detected by the 1 km resolution of the HFR data, likely more present on survey days designated as "mixed." These vertical velocities although small in spatial scale may be large in magnitude, and are more likely within strong gradients associated with density fronts. Such vertical velocities could have an impact on phytoplankton (Mahadevan 2016). Our dataset cannot resolve these vertical velocities, exposing a limitation of the data rather than of the two-dimensional assumption of the LCS metrics.

HFR measurements observed only the horizontal surface layer of the flow (Stewart and Joy 1974, Paduan and Graber 1997). For the HFR frequencies deployed in Palmer Deep the surface measurement is within the upper 2 m of the water column. When the mixed layer is completely homogeneous, these measurements can be extrapolated to represent the whole mixed layer. Use of HFR to calculate LCS has had some success in previous studies (Shadden et al. 2009, Hernández-Carrasco et al. 2018, Fahlbusch et al. 2022, Veatch et al. 2022) extrapolating HFR data to represent the whole mixed layer. In this study, phytoplankton patches were defined by ACROBAT observed profiles integrated to the observed MLD. The sensitivity of the integration depth to patch definition was evaluated and described in greater detail in Supplementary material S3. This analysis repeated patch definition with a constant integration depth of 5 m, which is closer to the effective depth of the HFR measurements (Stewart and Joy 1974) than most MLDs (average MLD is 20.8 m). However, the same patterns were found with both integration depths (Figures S2 and S3), showing that the depth of integration (constant 5 m or variable mixed layer) did not affect our conclusions.

Further, the physical and biological timescales of Palmer Deep Canyon are ~6 h, within 1 h of each other, which is within the time resolution that we expect the HFR and glider data (Fig. 1) to observe. Matching physical and biological time-scales indicates that both the surface currents and the phytoplankton patches are changing at the same rate, suggesting that the main driver of change in phytoplankton patch location is advection resolved by the HFR observed surface currents. This provides further confidence that LCS can quantify a major mechanism of phytoplankton patch formation in Palmer Deep Canyon.

Phytoplankton patch collocation with FTLE and RPD

LCS values of observed patches in comparison to the null model (the randomly generated patches) suggest that higher values of FTLE results collocate with phytoplankton patches more often than higher values of RPD results (Fig. 5). In assessing this result, it is important to note that the two LCS metrics differ in several ways including single particle (RPD) vs. pair of particles tracking (FTLE), FTLE's ability to incorporate rate of change, and FTLE's flexible integration times.

The fact that FTLE often collocate with phytoplankton patches in Palmer Deep Canyon suggests that phytoplankton are acting as free drifters in the surface layer. So then, why do the particle trajectories of the RPD metric, which is designed to track the accumulation of surface drifters, do such a poor job of collocating with phytoplankton patches? Let us begin with considering cases when simple particle trajectories (RPD) are useful for tracking free drifters. Seeding particles where drifters are observed and running a trajectory backwards in time will track the source of those drifters, or when the source is known, such as in an oil spill, particles released at the observed source will track where those drifters accumulate. However, in this study we seek to identify areas in the HFR observed surface current field that have stronger attracting mechanisms than elsewhere in the field, without any added information about the source or location of drifters (phytoplankton) in the LCS calculations. In this case, LCS calculated from relative positions of pairs of particles characterize these areas of attraction independent of particle initial position, and dependent on the integrated backwards trajectories of those particles. This concludes that simple particle trajectories (RPD) are useful when the source or destination and relative abundance of plankton is known, so particle releases can be catered to location and density. FLTE are useful when the source or destination is unknown and the entire flow field is searched for attracting features. While single particle trajectory methods such as RPD use simpler calculations, these results suggest that ecologists should take the time to use more complex, paired particle tracking such as FTLE when investigating the role of physical advection in the spatial ecology of phytoplankton.

Where RPD only accounts for the location of the drifters at one timestep, FTLE accounts for the velocity of the drifters relative to other drifters, introducing a rate of change consideration into the quantification of attraction (Haller 2015). The rate of change (velocity) used in FTLE calculations incorporates additional information that the location-based calculations in RPD do not. Additionally, FTLE integrate over particle trajectories giving each calculation a "memory" of the inputted integration time (6 h in this case, section "Determining integration time") (Haller 2015). Application of FTLE allows for the scale of the features that are transporting and concentrating plankton in Palmer Deep Canyon to be elucidated (St-Onge-Drouin et al. 2014). The ability to determine this integration time allowed us to calculate FTLEs that identified the scale of feature that we knew to be important in the system from our analysis. Both rate of change and integration considerations could contribute to their better performance, diagnosing the underlying flow responsible for transport rather than following the flow field as the RPD analysis does. Such flexibility in FTLE calculations could make FTLE a powerful tool in coastal systems when working with submesoscale features on subtidal scales and highly variable nonlinear flow. Therefore, the improved performance of FTLE over RPD in aligning with observed phytoplankton patches suggests that processes that overlap with patches are best identified by the attraction of paired particles, not the absolute concentration of a field of released particles.

It should be noted that this study does not account for biological mechanisms of phytoplankton concentration, such as grazing pressure or growth. Because the growth period of phytoplankton is greater than the residence time in Palmer Deep Canyon, growth rate was not considered (Kohut et al. 2018). This study also assumes that phytoplankton are not limiting in Palmer Deep Canyon, meaning grazing pressure would not have a large effect on results.

FTLE performance on patch centers and patch edges during stratified and mixed conditions

For each survey, we mapped both phytoplankton patch centers and edges to investigate if each LCS metric better aligned with specific regions of the patches. It was originally hypothesized that RPD would better align with patch centers while FTLE would better align with patch edges because the FTLE paired particle metric better characterizes boundaries between distinct modes of flow (Haller 2015) while RPD characterize a concentration of drifters (Oliver et al. 2019). The distinction between patch centers and patch edges investigates whether different transport mechanisms determine where the center of attraction (the patch center) vs. the extent or cut-off point of the phytoplankton patch. FTLE performed slightly better on patch edges than patch centers. This could be because the areas where particles diverge along a ridge, categorized by FTLE as strong coherent structures, separate water with different phytoplankton levels. However, in this study the distribution of edge and center FTLE values were not significantly different. If there is a difference between edge and center it is likely that we would need to have a higher sample size to detect it.

FTLE collocated with phytoplankton patches more often on stratified surveys than mixed surveys (Fig. 6). Stratification in the upper water column will change the complexity of the surface flows over our study site. When the upper water column is strongly stratified, the surface layer will flow more independently of the subsurface, with little exchange between the two layers, setting up two-dimensional flow in the surface layer. Mixed conditions are more indicative of the surface and subsurface layers exchanging physical properties through vertical mixing. It was originally hypothesized that LCS would not perform well on a well-mixed water column because vertical velocities would invalidate the two-dimensional assumption of LCS. However, it was found that the vertical velocities in Palmer Deep Canyon were negligible at the studied scales. Additionally, there was little difference between the vertical velocities over the ACROBAT survey on survey days that were determined as mixed and those that were determined as stratified, 3.47×10^{-5} m s^{-1} for mixed days and 3.60×10^{-5} m s^{-1} for stratified days. This suggests that the better alignment of FTLE and phytoplankton patches on stratified surveys was due to (1) homogeneous and inhomogeneous mixed layers or (2) a biological response in the way phytoplankton patches are formed on mixed surveys.

A mixed water column with a deep MLD may be indicative slight differences in ocean velocities between the surface and bottom of the mixed layer. Although these mixed layers pass the definition of a mixed layer (Carvalho et al. 2017), the surface waters where the HFR is observing the flow may be different than a few meters below the surface, still in the mixed layer, where the phytoplankton are experiencing the flow. This would mean that on mixed days the HFR is less representative of the currents that are concentrating the phytoplankton patches.

The four most mixed (smallest difference in density between the surface and 50 m) surveys had an average depth of maximum particle backscatter (the proxy used to define phytoplankton patches) of 11.80 m with a standard deviation of 15.05 m, well below the few meters the HFR can safely observe. The four most stratified surveys had an average depth of maximum particle backscatter of 2.97 m with a standard deviation of 1.98 m. This implies that on mixed days, where the mixed layer may be less uniform, the phytoplankton patches are deeper in the mixed layer and are likely experiencing ocean currents that are not well resolved by the HFR data. Therefore, the poorer match between FTLE and phytoplankton patches on mixed days is likely due to a limitation in observed data rather than a limitation in the dimensionality of the FTLE. However, even on well-mixed survey days, FTLE still often collocated with phytoplankton patches (Fig. 6), just not as often as they did on stratified surveys.

Conclusion

Our analysis indicates that HFR derived FTLE can be used to identify concentrating mechanisms in biological hotspots with complex submesoscale flows, validating their use in coastal systems (Fig. 5). Comparing the single particle tracking metric (RPD) with the paired particle tracking metric (FTLE) provided a mechanistic understanding of how surface currents in Palmer Deep Canyon are transporting and locally concentrating phytoplankton. The paired particle tracking metric (FTLE) more often identified areas of the flow field where phytoplankton were being concentrated into patches. FTLE's ability to incorporate rate of change, flexible integration times, and consideration of relative distance rather than final position allowed this metric to better capture the transport of phytoplankton.

FTLE does a slightly better job at identifying phytoplankton patch edges than centers, characterizing separatrices in ocean currents that separate different ocean flow patterns as well as high phytoplankton from low phytoplankton areas (Fig. 6). However, the difference between patch edges and patch centers was not significant, meaning that phytoplankton patch edges and patch centers both collocate with FTLE-identified coherent structures, and therefore are likely maintained by the same advective mechanisms. It was also concluded that the FTLE metric performs best when the water column is stratified, which is indicative of vertical velocities and heterogeneity in the mixed layer being at a minimum, and phytoplankton patches closer to the surface within the sampling domain of the HFR. This is when the two-dimensional assumption of the FTLE calculations is the most accurate and the phytoplankton patches are closer to the surface enabling the HFR data to best measure the flow that the colocated phytoplankton are experiencing (Fig. 6). FTLE collocate with phytoplankton patches more often when the system has a substantial amount of strong coherent structures (Fig. 8a) and phytoplankton (Fig. 8b), meaning there are physical features present to concentrate the phytoplankton and there are large enough phytoplankton patches to fill the coherent structures.

The novelty of this study's application of LCS lies in the scale at which these metrics are applied, looking for structures that organize plankton dispersion on the order of hours within a few kilometers. This is the scale of the ocean at which the krill and the forage fish are interacting with ocean flows as they swarm, creating the prey availability central place foraging penguins rely on in Palmer Deep Canyon (Oliver et al. 2019). Results solidify the role of physical advection in the concentration of phytoplankton patches in Palmer Deep Canyon on these short time-scales, suggesting this area is sustained by delivery of phytoplankton through advection rather than local growth.

Further investigation of FTLE applied to coastal biological hotspots could inform ecosystem models by predicting bioactivity from ocean currents. Findings will also broaden the use of HFR data to locate areas of food web focusing, furthering our understanding of how coastal biological hotspots are maintained.

Acknowledgements

Many thanks to the Antarctic Support Contractor and their teams aboard the ARSV Laurence M. Gould, at Palmer Station, and headquarters in Denver, CO without whom a study of this scale would not be possible. Thank you to the students, postdoctoral scholars, and field assistants for their valued involvement in the SWARM project, in particular Ashley Hann, Dr Katherine Gallagher, Dr Jerome Pinti, Dr Thilo Klenz, Ethan Handel, and Jordi Maisch. We thank the Palmer Long-Term Ecological Research team and the Commission for the Conservation of Antarctic Marine Living Resources, for their advice and collaboration.

Supplementary material

The following Supplementary material is available at *ICES JMS* online. Supplementary material provides an explanation of methodology used to determine the low reencounter rate of phytoplankton patches on the ACROBAT towed survey mentioned in section "ACROBAT towed surveys". Details on the methodology for determining "stratified" and "unstratified" survey days (Figure S1) are also included. Last is the inclusion of a repeated analysis with a different definition of phytoplankton patch, integrating to a constant 5 m instead of the mixed layer depth (Figures S2 and S3), i.e. mentioned in Section "Two-dimensional assumptions in LCSs".

Conflict of interest: The authors have no conflicts of interest to declare.

Funding

This project is funded through the National Science Foundation, award number: 1745009.

Data availability

Data and code used in this study are publicly available on NSF funded project SWARM's BCO-DMO site and GitHub. High Frequency Radar observed surface currents are available in the gap-filled version used in this study on BCO-DMO (https://www.bco-dmo.org/dataset/917884). Code used to gap-fill these data are available on GitHub (https://github.com/JackieVeatch/SWARM_CODAR). Lagrangian Coherent Structure Results for both FTLE and RPD metrics are available on BCO-DMO (https://www.bco-dmo.org/dataset/917914, https://www.bco-dmo.org/dataset/917926) and the code used to produce these results can be found on GitHub (https://github.com/JackieVeatch/SWARM_LCS). The code was modified from open-source MATLAB library (Haller et al. 2015) for use on HFR data. ACROBAT data used to map phytoplankton can be found on BCO-DMO (https://www.bco-dmo.org/dataset/916046) and the code used to identify phytoplankton patches can be found on GitHub (https://github.com/JackieVeatch/SWARM_ACROBAT). Initial processing of the data was done with an open-source MATLAB library (Reister 2023). Glider data used to calculate the biological time-scale can be found on Erddap (https://slocum-data.marine.rutgers.edu/erddap/tabledap/ru32-20200111T1444-profile-sci-delayed.html) and the code used to calculate the biological and physical time-scales can be found on GitHub (https://github.com/JackieVeatch/SWARM_scales). All other code for analysis can be found on GitHub (https://github.com/JackieVeatch/SWARM_analysis). Any questions can be directed to Jacquelyn Veatch (jveatch@marine.rutgers.edu).

Author contributions

Jacquelyn M. Veatch, Josh T. Kohut, Matthew J. Oliver, Hank Statscewich, and Erick Fredj.

References

Abrahms B, Scales KL, Hazen EL *et al.* Mesoscale activity facilitates energy gain in a top predator. *Proc R Soc B Biol Sci* 2018;**285**:20181101. https://doi.org/10.1098/rspb.2018.1101.

Barrick DE, Evans MW, Weber BL. Ocean surface currents mapped by radar. *Science* 1977;**198**:138–44. https://doi.org/10.1126/science.198.4313.138.

Benoit-Bird KJ. Resource patchiness as a resolution to the food paradox in the sea. *Am Nat* 2023;**203**:1–13.

Carvalho F, Fitzsimmons JN, Couto N *et al.* Testing the Canyon Hypothesis: evaluating light and nutrient controls of phytoplankton growth in penguin foraging hotspots along the West Antarctic Peninsula. *Limnol Oceanogr* 2020;**65**:455–70. https://doi.org/10.1002/lno.11313.

Carvalho F, Kohut J, Oliver MJ *et al.* Defining the ecologically relevant mixed-layer depth for Antarctica's coastal seas. *Geophys Res Lett* 2017;**44**:338–45. https://doi.org/10.1002/2016GL071205.

Carvalho F, Kohut J, Oliver MJ *et al.* Mixing and phytoplankton dynamics in a submarine canyon in the West Antarctic Peninsula. *J Geophys Res Oceans* 2016;**121**:5069–83. https://doi.org/10.1002/2016JC011650.

Cotté C, d'Ovidio F, Chaigneau A *et al.* Scale-dependent interactions of Mediterranean whales with marine dynamics. *Limnol Oceanogr* 2011;**56**:219–32. https://doi.org/10.4319/lo.2011.56.1.0219.

Della Penna A, De Monte S, Kestenare E *et al.* Quasi-planktonic behavior of foraging top marine predators. *Sci Rep* 2015;**5**:18063. https://doi.org/10.1038/srep18063.

Dosio A, Vilà-Guerau de Arellano J, Holtslag AAM *et al.* Relating Eulerian and Lagrangian statistics for the turbulent dispersion in the atmospheric convective boundary layer. *J Atmospheric Sci* 2005;**62**:1175–91. https://doi.org/10.1175/JAS3393.1.

Emslie SD, Fraser W, Smith RC *et al.* Abandoned penguin colonies and environmental change in the Palmer Station area, Anvers Island, Antarctic Peninsula. *Antarct Sci* 1998;**10**:257–68. https://doi.org/10.1017/S0954102098000352.

Fahlbusch JA, Czapanskiy MF, Calambokidis J *et al.* Blue whales increase feeding rates at fine-scale ocean features. *Proc R Soc B Biol Sci* 2022;**289**:20221180. https://doi.org/10.1098/rspb.2022.1180.

Farazmand M, Haller G. Attracting and repelling Lagrangian coherent structures from a single computation. *Chaos Interdisc J Nonlinear Sci* 2013;**23**:023101. https://doi.org/10.1063/1.4800210.

Farazmand M, Haller G. Computing Lagrangian coherent structures from their variational theory. *Chaos Interdisc J Nonlinear Sci* 2012;**22**:013128–12. https://doi.org/10.1063/1.3690153.

Fraser WR, Trivelpiece WZ. *Factors Controlling the Distribution of Seabirds: Winter-Summer Heterogeneity in the Distribution of AdéLie Penguin Populations*. Washington: American Geophysical Union, 1996, 257–72.

Fredj E, Roarty H, Kohut J *et al.* Gap filling of the coastal ocean surface currents from HFR data: application to the Mid-Atlantic Bight HFR Network. *J Atmos Oceanic Technol* 2016;**33**:1097–111. https://doi.org/10.1175/JTECH-D-15-0056.1.

Genin A. Bio-physical coupling in the formation of zooplankton and fish aggregations over abrupt topographies. *J Mar Syst* 2004;**50**:3–20. https://doi.org/10.1016/j.jmarsys.2003.10.008.

Gomez-Navarro L, Van Sebille E, Morales Márquez V *et al.* The effect of model tidal forcing on virtual particle dispersion and accumulation at the ocean surface. *ESS Open Archive* 2023. https://doi.org/10.1002/essoar.10512397.3

Haller G. Distinguished material surfaces and coherent structures in three-dimensional fluid flows. *Phys D* 2001;**149**:248–77. https://doi.org/10.1016/S0167-2789(00)00199-8.

Haller G. Lagrangian coherent structures. *Annu Rev Fluid Mech* 2015;**47**:137–62. https://doi.org/10.1146/annurev-fluid-010313-141322.

Haller G, Beron-Vera FJ. Coherent Lagrangian vortices: the black holes of turbulence. *J Fluid Mech* 2013;**731**. https://doi.org/10.1017/jfm.2013.391.

Haller G, Beron-Vera FJ. Geodesic theory of transport barriers in two-dimensional flows. *Phys D* 2012;**241**:1680–702. https://doi.org/10.1016/j.physd.2012.06.012.

Haller G, Karrasch D, Kogelbauer F. Material barriers to diffusive and stochastic transport. *Proc Natl Acad Sci* 2018;**115**:9074–9. https://doi.org/10.1073/pnas.1720177115.

Haller G, Huhn F, Onu K. LCS tool: a computational platform for Lagrangian coherent structures. *J Comput Sci* 2015;**7**:26–36.

Hernández-Carrasco I, López C, Hernández-García E *et al.* How reliable are finite-size Lyapunov exponents for the assessment of ocean dynamics?. *Ocean Modell* 2011;**36**:208–18. https://doi.org/10.1016/j.ocemod.2010.12.006.

Hernández-Carrasco I, Orfila A, Rossi V *et al.* Effect of small scale transport processes on phytoplankton distribution in coastal seas. *Sci Rep* 2018;**8**:8613–. https://doi.org/10.1038/s41598-018-26857-9.

Hofmann EE, Murphy EJ. Advection, krill, and Antarctic marine ecosystems. *Antarct Sci* 2004;**16**:487–99. https://doi.org/10.1017/S0954102004002275.

Hudson K, Oliver MJ, Bernard K *et al.* Reevaluating the Canyon Hypothesis in a biological hotspot in the Western Antarctic Peninsula. *J Geophys Res Oceans* 2019;**124**:6345–59. https://doi.org/10.1029/2019JC015195.

Huhn F, von Kameke A, Pérez-Muñuzuri V *et al.* The impact of advective transport by the South Indian Ocean Countercurrent on the Madagascar plankton bloom. *Geophys Res Lett* 2012;**39**. https://doi.org/10.1029/2012GL051246.

Kavanaugh MT, Abdala FN, Ducklow H *et al.* Effect of continental shelf canyons on phytoplankton biomass and community composition along the western Antarctic Peninsula. *Mar Ecol Progr Ser* 2015;**524**:11–26. https://doi.org/10.3354/meps11189.

Kohut J. Studying the impacts of local oceanographic processes on Adelie penguin foraging ecology. In: *Marine technology; study data from University of Alaska Update Understanding of Marine Technology*, Vol. **750**. Ecology, environment & conservation (Atlanta). Washington: Marine Technology Society, 2014.

Kohut JT, Roarty HJ, Glenn SM. Characterizing observed environmental variability with HF doppler radar surface current mappers and acoustic doppler current profilers: environmental variability in the coastal ocean. *IEEE J Oceanic Eng* 2006;**31**:876–84. https://doi.org/10.1109/JOE.2006.886095.

Kohut JT, Winsor P, Statscewich H *et al.* Variability in summer surface residence time within a West Antarctic Peninsula biological hotspot. *Philos Trans R Soc Lond Ser A Math Phys Eng Sci* 2018;**376**:20170165.

Lasker R. The relations between oceanographic conditions and larval anchovy food in the California Current: identification of factors contributing to recruitment failure. *Environ Sci* 1978;**173**:212–30.

Lehahn Y, d'Ovidio F, Lévy M *et al.* Stirring of the northeast Atlantic spring bloom: a Lagrangian analysis based on multisatellite data. *J Geophys Res Oceans* 2007;**112**:C08005. https://doi.org/10.1029/2006JC003927.

Lévy M, Franks PJS, Smith KS. The role of submesoscale currents in structuring marine ecosystems. *Nat Commun* 2018;**9**:4758–16. https://doi.org/10.1038/s41467-018-07059-3.

Li W, Tang S, Zhan H. A winter chlorophyll bloom analyzed using Lagrangian diagnoses in the northeastern South China Sea. *Aquat Ecosyst Health Manage* 2015;**18**:462–6.

Liu Y, Wilson C, Green MA *et al.* Gulf stream transport and mixing processes via coherent structure dynamics. *J Geophys Res Oceans* 2018;**123**:3014–37. https://doi.org/10.1002/2017JC013390.

Mahadevan A. The impact of submesoscale physics on primary productivity of plankton. *Ann Rev Mar Sci* 2016;**8**:161–84. https://doi.org/10.1146/annurev-marine-010814-015912.

Martini KI, Stabeno PJ, Ladd C *et al.* Dependence of subsurface chlorophyll on seasonal water masses in the Chukchi Sea. *J Geophys Res Oceans* 2016;**121**:1755–70. https://doi.org/10.1002/2015JC011359.

Mathur M, David MJ, Sharma R *et al.* Thermal fronts and attracting Lagrangian coherent structures in the north Bay of Bengal during December 2015–March 2016. *Deep Sea Res Part II* 2019;**168**:104636. https://doi.org/10.1016/j.dsr2.2019.104636.

Michael ND, Richard KG, Louis WB *et al.* Connectivity in marine protected areas. *Science* 2006;**313**:43–5.

Okubo A. Horizontal dispersion of floatable particles in the vicinity of velocity singularities such as convergences. *Deep Sea Res Oceanogr Abstr* 1970;**17**:445–54. https://doi.org/10.1016/0011-7471(70)90059-8.

Oliver MJ, Irwin A, Moline MA *et al.* Adélie penguin foraging location predicted by tidal regime switching. *PLoS ONE* 2013;**8**:e55163. https://doi.org/10.1371/journal.pone.0055163.

Oliver MJ, Kohut JT, Bernard K *et al.* Central place foragers select ocean surface convergent features despite differing foraging strategies. *Sci Rep* 2019;**9**:157. https://doi.org/10.1038/s41598-018-35901-7.

Paduan JD, Graber HC. Introduction to high-frequency radar: reality and myth. *Oceanography* 1997;**10**:36–9. https://doi.org/10.5670/oceanog.1997.18.

Prants SV, Budyansky MV, Uleysky MY. Identifying Lagrangian fronts with favourable fishery conditions. *Deep Sea Res Part I Oceanogr Res Pap* 2014;**90**:27–35. https://doi.org/10.1016/j.dsr.2014.04.012.

Reister I. isreister/ACROBAT: v1.0.0_UAFOceansACROBAT. v1.0.0UAF_ACROBAT edn. Zenodo, 2023

Saba GK, Fraser WR, Saba VS *et al.* Winter and spring controls on the summer food web of the coastal West Antarctic Peninsula. *Nat Commun* 2014;**5**:4318. https://doi.org/10.1038/ncomms5318.

Schofield O, Ducklow H, Bernard K *et al.* Penguin biogeography along the West Antarctic Peninsula: testing the Canyon Hypothesis with Palmer LTER observations. *Oceanography* 2013;**26**:204–6. https://doi.org/10.5670/oceanog.2013.63.

Serra M, Sathe P, Rypina I *et al.* Search and rescue at sea aided by hidden flow structures. *Nat Commun* 2020;**11**:2525. https://doi.org/10.1038/s41467-020-16281-x.

Shadden SC, Lekien F, Marsden JE. Definition and properties of Lagrangian coherent structures from finite-time Lyapunov exponents in two-dimensional aperiodic flows. *Phys D* 2005;**212**:271–304. https://doi.org/10.1016/j.physd.2005.10.007.

Shadden SC, Lekien F, Paduan JD *et al.* The correlation between surface drifters and coherent structures based on high-frequency radar data in Monterey Bay. *Deep Sea Res Part II Top Stud Oceanogr* 2009;**56**:161–72. https://doi.org/10.1016/j.dsr2.2008.08.008.

Siegelman L, Klein P, Rivière P *et al.* Enhanced upward heat transport at deep submesoscale ocean fronts. *Nat Geosci* 2020;**13**:50–5. https://doi.org/10.1038/s41561-019-0489-1.

St-Onge-Drouin S, Winkler G, Dumais J-F *et al.* Hydrodynamics and spatial separation between two clades of a copepod species complex. *J Mar Syst* 2014;**129**:334–42. https://doi.org/10.1016/j.jmarsys.2013.07.014.

Statscewich H, Weingartner T. *A High-Latitude Modular Autonomous Power, Control, and Communication System for Application to High-Frequency Surface Current Mapping Radars*. New York: IEEE. 2011, 1–3.

Stewart RH, Joy JW. HF radio measurements of surface currents. *Deep Sea Res Oceanogr Abstr* 1974;**21**:1039–49. https://doi.org/10.1016/0011-7471(74)90066-7.

Tew Kai E, Rossi V, Sudre J *et al.* Top marine predators track Lagrangian coherent structures. *Proc Natl Acad Sci* 2009;**106**:8245–50. https://doi.org/10.1073/pnas.0811034106.

Thomalla SJ, Racault M-F, Swart S *et al.* High-resolution view of the spring bloom initiation and net community production in the Subantarctic Southern Ocean using glider data. *ICES J Mar Sci* 2015;**72**:1999–2020. https://doi.org/10.1093/icesjms/fsv105.

Veatch J, Fredj E, Kohut J. High frequency radars as ecological sensors: using Lagrangian coherent structures to quantify prey concentrating features. In: *OCEANS 2022, Hampton Roads*. New York: IEEE, 2022, **2022**, 1–7.

Watson JR, Fuller EC, Castruccio FS *et al.* Fishermen follow fine-scale physical ocean features for finance. *Frontiers in Marine Science* 2018;**5**. https://doi.org/10.3389/fmars.2018.00046.

Weiss J. The dynamics of enstrophy transfer in two-dimensional hydrodynamics. *Phys D* 1991;**48**:273–94. https://doi.org/10.1016/0167-2789(91)90088-Q.

Handling Editor: Rubao Ji

ICES Journal of Marine Science, 2024, Vol. 0, Issue 0, 1–8
https://doi.org/10.1093/icesjms/fsae049
Received: 26 February 2024; **revised:** 26 March 2024; **accepted:** 27 March 2024
Food for Thought

ICES International Council for the Exploration of the Sea
CIEM Conseil International pour l'Exploration de la Mer

Watching the sunrise on our ocean planet in a new era of marine science

Oscar Schofield *

Center of Ocean Observing Leadership, School of Environmental and Biological Sciences, Rutgers University, New Brunswick, NJ 08901, United States

*Corresponding author. Center of Ocean Observing Leadership, School of Environmental and Biological Sciences, Rutgers University, New Brunswick, NJ 08901, United States. E-mail: oscar@marine.rutgers.edu

Food for Thought articles are essays in which the author provides their perspective on a research area, topic, or issue. They are intended to provide contributors with a forum through which to air their own views and experiences, with few of the constraints that govern standard research articles. This Food for Thought article is one in a series solicited from leading figures in the fisheries and aquatic sciences community. The objective is to offer lessons and insights from their careers in an accessible and pedagogical form from which the community, and particularly early career scientists, will benefit. The International Council for the Exploration of the Sea (ICES) and Oxford University Press are pleased to be able to waive the article processing charge for these Food for Thought articles.

Abstract

Over the last 30 years, ocean sciences have been undergoing a technological revolution. Changes include the transition of autonomous platforms from being interesting engineering projects to being critical tools for scientists studying a range of processes at sea. My career has benefitted immensely from these technical innovations, allowing me to be at sea (virtually) 365 days a year and operate ocean networks globally. While these technical innovations have opened many research doors, many aspects of oceanography are unchanged. In my experience, working/talking/scheming with scientists is most effective face-to-face. Despite the growing capabilities of robotic platforms, we will still need to go to sea on ships to conduct critical experiments. As the responsibilities of scientists expand with mandated outreach efforts, I strongly urge young scientists to leverage the expertise of Broader Impact professionals, who are increasingly available to our community, in order to maximize the effectiveness and efficiency of our outreach efforts. Given the increasing observations of change occurring in the ocean, our work is ever-more important while still being fun. I am blessed to have had a career as an oceanographer exploring this planet.

Keywords: ocean observations; marine networks

Reflecting on my science journey is a fun exercise (a BIG surprise given my youthful persona) and has provided me an opportunity to appreciate that I am blessed with having the greatest job in the world. People ask me about what my job is like, and my usual response is that I don't have a job; I have a hobby. What an awesome life! Over the years, my excitement and passion have grown reflecting both an expanding fascination of this amazing, interconnected world and the growing urgency to understand our planet's trajectory given mounting evidence of human impacts on the Earth system. My journey has occurred during a period of fundamental change in how scientists explore the ocean, transition to open data science, and recognition of the importance of translating science knowledge to diverse stakeholders. These changes are altering the definition of what an oceanographer is. I believe that these changes will enable the next generation, armed with novel tools, to meet grand societal challenges. *I must admit to being envious of the new generation of researchers who will be so important in helping society during a critical time. As the sun rises on this new era I am grateful to have been working in the early dawn of the future of oceanography*.

How did I end up as an oceanographer?

I would love to think that my career is a story of committed logical strategic thinking, BUT there has also been much luck that provided me unexpected opportunities, people, and perspectives. Those opportunities started early. I grew up swimming, fishing, diving, and surfing in the Pacific, which dominated any spare time I had. I hope this personal connection to the ocean remains true until I leave this planet. Additionally, my biological father (Max Gumpel) was a driven scientist (Davies and Gumpel 1960) with a full lab in the back of the house and weekends would start with him announcing some projects for us to do. One of my favorites was the weekend we built and installed a Richter scale in the basement. He disappeared when I was young (stories best shared over a beer). My stepfather (Paul Schofield) raised me and even though he was not a scientist, he provided me many career skills. Paul is an amazing storyteller, and early on, he gave me the passion of communicating across diverse communities. My early years hanging out with gifted people in southern California, some going on to become professional surfers, it was clear that my "stork" style of surfing was not going to provide a career path. My love for the ocean expanded to all aspects of the sea (science, history, and art). This led me to my local school (University of California at Santa Barbara), where I was so lucky to join a leading research university with gifted and passionate teachers. At that time, I quickly found myself working with two professors who changed my life. Barbara Prézelin introduced me to the beautiful process of photosynthesis and the physiological ecology of phytoplankton. Raymond (Ray)

Smith introduced me to the strategies and tools for studying processes in a dynamic ocean. Ray's first lecture to me as an undergraduate focused on the importance of understanding spatial and temporal scales in the ocean and that effective sampling would require integrated multiplatform networks. Unknown to me at the time, this concept would become a major focus of my career. Upon graduation, I took a laboratory technician position with ½ of the time focused on mass culturing of algae for a pharmaceutical company in Barbara's laboratory and the other ½ deploying to Antarctica as a krill technician. These experiences convinced me to apply to graduate school working on phytoplankton with Barbara.

Graduate school, remaining with Barbara and Ray, was a joy full of great teachers–friends, and much time at sea studying aquatic bio-optical properties, the impact of the Antarctic ozone hole on plankton, and phytoplankton physiology. When in graduate school I was lucky to be embedded in a culture of open intellectual flexibility that was not averse to students diving into entirely new endeavors. My graduate experience went quickly but much life happened. My first child was born during my Ph.D. After the birth of my daughter, I began to experience physical issues that eventually was diagnosed as Stage 4B Hodgkin's lymphoma. The oncologists put me on a very aggressive chemotherapy and radiation regime but with the support of my wider academic community and family I was able to beat the disease with 8 months of weekly treatments. Seven months after being cleared I deployed to Antarctica to study the impact of the ozone hole on phytoplankton. My cancer experience impacted me as I had gained an appreciation in my early 20's that life is fleeting and for *me* the best remedy was to charge at full speed while able.

During graduate school, I was very lucky to have time interacting with John Kirk. He, while working in the United Kingdom, was one of the first to isolate plant plastids (Kirk 1970, 1971), but then relocated to Australia to start a new career and helped create the field of hydrological optics (Morel 1977, Smith 1978, Kirk 1994, Zaneveld 1995, Morel 2008). His advice to graduate students was to conduct a major shift in research focus about every 5–10 years to keep yourself a hungry novice. I see this reflected in my career with an initial focus on phytoplankton photosynthesis, to the cellular physiology of stress, to autonomous ocean observing networks, to evolution of phytoplankton taxa, to climate-driven changes in ocean systems, and now moving to integrated terrestrial–marine food security strategies. Some of these changes grew organically out of the work being conducted, but often it was the incorporation of new methodologies/technologies that got me invited into large interdisciplinary expeditions. These opportunities early in my career were enabled through the strong advocacy of my graduate student advisors.

As I had been at UC Santa Barbara as an undergraduate and graduate student, my thought when finishing my Ph.D. was that it was time to do something different to expand my horizons and try to differentiate myself from my biological oceanography peers to better compete for a permanent job. Through a friend, I met David Millie at an ASLO Ocean Sciences meeting and our discussion resulted in a postdoctoral position in the Department of Agriculture in New Orleans, as a food flavor quality biologist. The project was to develop methods to discriminate specific taxa of algae using optical approaches and, if possible, provide insight into the physiological state of the algae. This work was motivated by the commercial aquaculture industry, specifically catfish, where a major economic bottleneck for the industry was the production of off-flavor metabolites by cyanobacteria in the farm ponds that made the product unpalatable. I figured the title food flavor quality biologist would catch people's attention, but my Ph.D. advisors were not stoked thinking that I was going to fall out of the oceanography community.

Our first effort focused on identifying specific algal taxa using bio-optical techniques. For those efforts, David and I collaborated frequently with Gary and Barbara Kirkpatrick from Mote Marine Laboratory, where for decades we developed signal processing approaches to discriminate different algal taxa based on their cellular absorption properties (Millie et al. 1997, Kirkpatrick et al. 2000). These efforts resulted in a decades-long partnership with the Kirkpatrick's, focusing not only on the discrimination of harmful algal bloom species but also on the development of new tools to make measurements over sustained periods of time (Kirkpatrick et al. 2003, Schofield et al. 2008). David was an active mentor and within a week of joining his group, he required that I apply to a job at Rutgers University (he said he had a hunch it would be good for me, but I thought I had already pissed him off and he was trying to get rid of me), and I was fortunate to get the job during my first year as a post-doctoral researcher. That said, I applied for many positions in that year (I used to keep a binder of rejection letters for graduate students to see and know that we all go through uncertain periods), but compared to many, I had a relatively short wait. I credit my graduate and postdoctoral advisers, who were always pushing me to be completing manuscripts and finishing projects.

The diverse experiences and collaborations prepared me to thrive when I joined Rutgers in 1995, where I was hired by Frederick Grassle, who was tasked with building a new oceanography program in New Jersey. It was during my job interview that I met Scott Glenn and we started a conversation on ocean dynamics, biophysical coupling, ocean observation, and modeling. That conversation has continued for 30 years. It has been an unparalleled gift to work with a great friend. We come from disparate science backgrounds. He was a physical oceanographer with a background in waves and sediment resuspension processes and I was a biological oceanographer interested in physiological ecology of phytoplankton. Our respective mentoring committees discouraged this partnership often saying it would distract us from our fundamental research, which was important to us achieving tenure. I find this humorous now looking at the numerous current grant calls for transdisciplinary research across disciplines while back then having a physical and biological oceanographer merging groups was considered risky. Both Scott and I are happy that we ignored the well-meaning advice provided at the time.

As a team, we developed the Coastal Ocean Observation Lab (COOL), which grew quickly, hosting many diverse interdisciplinary programs spanning from forecasting coastal upwelling and its biogeochemical consequences to the fate of river plumes and their potential transport of urban contaminants across continental shelves and associated impacts on water quality. Our other focus was on developing tools (instruments and models) to resolve the time and space scales required to address the questions at hand. We hosted the Office Naval Research Hyperspectral Coastal Ocean Dynamics Experiment (HyCODE) off New Jersey, where over 4 years every summer, over 200 researchers, up to 11 ships, and 3 aircraft joined us. Many of the groups that participated in the experiments were not funded by the actual HyCODE project but came through their funding to conduct focused experiments in a well-sampled 3D ocean with a range of forecasting products guiding adaptive sampling of their processes of interest. Some groups arrived unannounced. We had Navy SEALS show up, which was awesome, and my favorite memory was when a science group (who shall go nameless) showed up by accident a year early. Around the 24:7 sampling, a large community of scientists connected as we had rented almost a block of summer rental houses and it became the equivalent of a giant nerd block party with dinner debates ranging from turbulence closure schemes, optical inversion techniques, and who was the best cook in the group. This was much fun, but I was still going through the tenure process, which was stressful. I wish I had more training in management skills/tools and cooking for large groups (I signed up to be our head cook for the group, and quickly found a need to diversify meals outside of my comfort zone).

The success of HyCODE convinced many organizations of the value of these novel data streams. For example, the state of New Jersey has anchored its coastal water quality sampling with COOL gliders for over a decade; hundreds of fishermen throughout the mid-Atlantic use the open-access satellite data on a daily basis; and US Coast Guard Search and Rescue tools now include high-frequency surface current radar data. This was a challenge for us, as COOL was/is funded one project at a time with no sustained funding to maintain the operational data streams that are critically important to numerous external communities. We therefore suggested-forced-coerced the University to transition us into a University Center, which provided a means to garner support to maintain a large portfolio of projects and better utilize resources of the larger University. As we had built the COOL "brand" globally, we also wanted to maintain our existing name recognition and came up with the name Center of Ocean Observing Leadership so that we could keep our acronym. Developing a funding base to maintain a large group is difficult. My advice is to keep an open mind of potential funders and diversifying (federal agencies, foundations, and local stakeholders) the funding pot, which is an effective strategy to survive the shifting priorities of any specific agency. This strategy takes time to develop and working with a cohort collaborators is required to navigate diverse funding streams and to stay sane when funding is tight.

With the autobiographical story out of the way, I want to focus on how much oceanography has been changing. For this, it is important to review where the world was then, and how much it has fundamentally changed to provide context of what I believe are exciting opportunities moving forward.

Where were we in the 1980's and early 1990's?

As I was entering graduate school, it was well known that the ocean was spatially/temporally complex and that the available tools were not up to the task to address many of the critical questions. This was especially true for the coastal ocean characterized by compact turbulent layers and boundaries (land, ocean, and atmosphere). Grand challenges at the time included balancing the planet's carbon budget anchored by understanding the fluxes of carbon and nutrients in the ocean (see Oceanography 2001), uncovering picoplankton communities in the open ocean (Waterbury et al. 1979, Chisholm et al. 1988), and understanding carbon export to the deep sea (Boyd and Trull 2007, Iverson 2023, Siegel et al. 2023). Meanwhile, fundamental ocean features such as marine viruses, one of the most abundant and rapidly evolving forms of life on Earth, were not discovered until the early 1990's (Bergh et al. 1989, Proctor and Fuhrman 1990, Hara et al. 1996). Walter Munk and Carl Wunsch (1982) highlighted that many of the knowledge gaps reflected limitations in our ability to observe the ocean over the relevant time and space scales.

The gaps in ocean-observing capabilities were significant. The ability to transmit and share information remotely was limited. "Live" communication was limited to expensive satellite phones and custom mail messaging services of miniscule bandwidth in the late 1980's and often text messages from land to ships were satellite transmitted and then printed on paper. The "world wide web" was still in its infancy and collaborations relied on "slow" mail. As but one example, I found out where I was going to graduate school via a global community of HAM radio operators while working as a krill technician in Antarctica in 1988. At sea, we relied on fax machines over which we could receive low-resolution maps of satellite imagery. Satellite oceanography had fundamentally transformed oceanography and provided scientists with amazing imagery of warm and cold core rings, major currents, enhanced phytoplankton biomass trailing ocean storms, and ocean weather (Halpern 2000). *In situ* data was collected by ship-based systems for limited windows of space/time or with moorings providing Eulerian time series. Moorings, despite their great value, could never provide a realistic dynamic view of the ocean spatially but drove home the importance of episodic events in structuring marine systems (Dickey et al. 1998, Toole et al. 2000), which was poorly resolved by traditional ship sampling. Autonomous underwater vehicles were still in early development and the few field deployments of robotic platforms were conducted by teams of engineers to learn about feasibility of the technology, not by scientists using the technology to address fundamental questions (Straton 1969, Manley 2003, Wynn et al. 2014). The promise of autonomous sampling was still a dream. A great example of this was the science fiction vision provided by Henry Stommel, who described graduate students at Woods Hole Oceanographic Institute (WHOI) remotely navigating an underwater robot on an ocean circumnavigation (Stommel 1989). Since then, AUVs as well as sea floor cables (Schofield et al. 2002, Favali and Beranzoli 2006), drifters (Lumpkin et al. 2017), profiling floats (Riser et al. 2016, Claustre et al. 2020), animal-borne sensors (Costa et al. 2012, Watanabe and Papastamatiou 2023), and air-borne drones (Johnston 2019) have all matured to become science tools. Ocean modeling, data assimilation, and prediction have rapidly evolved with growing skill, inclusion of increasingly complex chemical–biological processes, and improving temporal and spatial resolution capable of resolving the mesoscale (Peloquin 1992, Smith 1993). These evolving technical capabilities are altering how scientists maintain a sustained presence at sea, which is allowing us to quantify in space and time the importance of episodic events (storms, river plumes, and subsurface jets). As bio-optical and chemical sensors were developed, it revealed the spatial complexity in the subsurface ocean not visible to satellites.

Beyond technical limitations, the dissemination of marine science was different then. It was the era of proprietary data, where all information was formally embargoed by grant specifications for up to 3–5 years. In addition, the timeline to open up the data was rarely enforced. The early years of transitioning to open-access data were an adventure. As part of the COOL group, we started by posting raw real-time satellite data to the web, which resulted in our group being sued by commercial entities that were selling imagery to the general public. These conflicts resulted in clarification of the Federal Open Sky policy, where everyone had the right to share raw tax-payer-sponsored satellite imagery publicly but value-enhanced imagery could be a protected product that could be sold. We as a group decided that we would share data as rapidly as available to facilitate adaptive sampling during large experimental efforts. In the late 90s, our efforts included large community experiments focused on developing ocean forecasting approaches for coastal regions in the mid-Atlantic Bight to coordinate science sampling of the biogeochemical dynamics (Glenn et al. 2004). While managing these field campaigns was a significant time sink, it provided datasets that could serve the wider community simultaneously but did present some frustrations. Despite still being in the tenure stream, some researchers published data that I had worked hard to collect without offering me authorship. My anger was constructively tempered by talking to my colleagues who gently pointed out that I had many more ideas than I had time to publish so don't waste energy and focus on getting my stories out. This did not "right the wrong" but it shifted my frustration into constructive energy. I also saw that the "bad players" were often marginalized over time reflecting their recurring bad behavior. These experiences were rare and more often than not the community were excited to collaborate and work as a team.

The transition to open data has not diminished the importance of peer-reviewed manuscripts but now provides another metric for demonstrating science impact. The fact that the datasets are now published and often required by science journals is a great sign of cultural progress (Pendelton et al. 2019, Fredston and Stewart Londes 2024)! There is still much more progress to be made on this front by increasing open access data (along with the critical metadata) without burdening the scientists that often are not adequately resourced to do so. Many different data systems exist; however, they are often scattered among different disconnected repositories, and so, while publicly available, many data sets are still difficult to find. *Despite the need for more progress, this new era of open data and collaborations, facilitated by the internet, is broadening our oceanographic community. Oceanography is no longer dominated by those lucky few who had access to ship time. Anyone with internet access and desire can now ask fundamental science questions. In my opinion, this will ultimately help democratize oceanography across large and small research-teaching-outreach institutions.*

Finally, it was predicted that science productivity (the rate of getting science manuscripts published) would accelerate if data were delivered in real-time back to the researchers on shore. If data were streaming directly to computers worldwide then the historical lag between data collection and synthesis would be minimized. This idea has been tested by comparing the publication rates from large programs that collected data using either traditional oceanographic approaches vs. those experiments that used real-time data streaming (Schofield and Glenn 2004). The lag between data collection and eventual publication were similar often taking 3 years between data collection and publication. Quality science capable of surviving peer review still requires time for critical thinking and synthesis. Thus, while new technologies do provide us an unprecedented amount of data, science is more than a data report, and our work will still require significant creative and rigorous work to turn data into new science knowledge.

Where are we heading?

The technologies now available to the oceanographic community will enable us to address a wide range of science questions needing information on mesoscale processes with temporal/spatial resolutions that cannot be resolved using traditional approaches (Godø et al. 2014). Future graduate students will conduct studies using autonomous networks of remote sensing and mobile platforms. The platforms will be diverse consisting of airborne, surface, and subsurface vehicles. These systems will provide spatial data over time in which traditional sampling from ships to moorings will be embedded. The networks will allow both ship- and shore-bound scientists to adaptively sample the chemical, physical, and biological properties in a sustained manner over time. Sampling will be aided with model forecasts. This 4-dimensional view will be open access and much of the data will be available and visualized in near real-time (as example see https://www.hubocean.earth/platform). Scientists will know when and where to conduct shipboard experimental manipulations and the observational data will provide context to interpret/extrapolate the experimental results. The open data will allow large communities of scientists to work together despite being distributed across the globe. As the networks grow, they will increasingly rely on machine-to-machine-to-model networks capable of automated optimization of the network in the field to study specific processes of interest (Schofield et al. 2010, Ramp et al. 2009). Like many numerical models, these networks will be nested within each other to provide varying degrees of spatial and temporal resolution. For example, the global ARGO-Global Ocean Biogeochemistry Floats-model arrays will provide basin-scale integrated datasets in which continental-shelf networks will sample more compact space and time scales required to understand these systems. Scientists from around the world will work together using real-time data collected in the ocean and the barriers that prevent groups from working together will continue to be minimized. The exponential growth of machine learning and artificial intelligence will be a new revolution helping synthesize and use diverse, complex, and large data streams. I believe these approaches will complement but not replace analytical modeling built upon fundamental first principles.

Beyond the development of infrastructure enabling science to maintain a sustained presence in the ocean, we are in the midst of an ocean sensor/measurement revolution. A vast array of new tools now allow us to measure the ocean physics, chemistry, and biology with unprecedented detail. This is especially true for the biological sciences, where, e.g. the "omic" revolution provides the first potential synthetic view of overall systems biology that will allow biologists to characterize community diversity, gene expression profiling, transcriptional regulation, protein and lipid identification/modification, metabolism, elemental profiles, morphological, and physical traits. Combinations of these measurements will provide insights into a range of physiological/ecological processes, including particle sinking–flocculation processes, grazing, and animal movements (diel behavior, migrations, and population transport and connectivity). New fluorometers offer the potential to measure photosynthetic activity through measurements of electron transport. These approaches will be important to providing insights into fundamental rate processes (Packard 2018). These new capabilities will benefit from the data/forecasts provided by the ocean observing networks, which will inform when and where data will need to be collected. Discrete ocean sampling will transition from fixed grid sampling to adaptive sampling grids that incorporate the evolving structure of the ocean. As a community, we will need to learn how best to use these new multi-platform approaches. The success of these networks will depend on optimizing measurements to resolve specific processes that will require specific temporal/spatial sampling. Given this, the systems will need to be flexible in their use and open to evolving as the questions change based on our increasing knowledge of the ocean. I am an optimist and believe the combination of sustained high-resolution sampling combined with experimental efforts will provide novel insights into a range of critical transdisciplinary questions facing society.

With these new capabilities, the questions I am increasingly thinking about are broad and, despite my best efforts, will be a focus of our science community well after I retire. A major interest for me is mean state transitions in ocean ecosystems and the adaptive capacity of ecosystems to respond to change. This is critical given a changing climate and a rapidly increasing industrialization/urbanization of the ocean. Additionally, I am thinking about how these changes will influence the overall carrying capacity of the ocean for providing food and energy. This is a question of increasing importance as ocean and inland waters provide >20% of the protein supply for a growing human population. My interest in these questions has grown over the last few decades as I have personally observed the ocean exhibiting significant change. One of my major study sites, for over 30 years, is the West Antarctic Peninsula, which is one of most rapidly warming regions on the planet and I have witnessed declining sea ice and the corresponding changes rippling throughout the food web from the plankton to the penguins. Watching these changes has been eye opening-scary-concerning and has spurred me to think about the potential trajectory of marine food webs in the near future (years to decades). Beyond potential climate-driven changes, the activity of humans on the ocean has been increasing. For example, in my backyard in the mid-Atlantic Bight construction has started on building the world's largest offshore wind network with >3000 turbines to be deployed over the next decade. This development is arguably the deployment of the world's largest artificial reef. How will this construction alter the food web? How will these man-made changes interact with climate-driven changes? All these potential changes increase the importance of marine science to help society navigate potentially dramatic shifts in the ocean.

Over my career, there has been a growing appreciation that there is a critical need to bring science and its processes directly to stakeholders-society. In the past, this was not a scientist's responsibility as it was often assumed our "brilliant" insights would be spontaneously and enthusiastically devoured by the public. This assumption is not grounded in reality. This responsibility has become a formal responsibility for the scientist with many funding agencies now requiring a dedicated focus on outreach. For example, the National Science Foundation in the USA began considering broader impacts in proposal reviews in the 1960s. However, it only became a separate and distinct criterion in 1997. What outreach should be conducted is generally not prescribed and it can span from communicating the process of basic research and the scientific method to the general public, training teachers, or educating local-state-federal regulators. Each of these audiences requires a distinctly different set of communication strategies. Many institutions have dedicated professionals who can help in deciding and connecting with potential stakeholders. Finding these broader impact (BI) professionals to collaborate with is a key to maximizing the effectiveness of the time dedicated to the effort.

I have been uniquely lucky in my career to have collaborated with BI professionals during my entire time at Rutgers. Janice McDonnell has been a partner for broader impacts spanning from student–teacher–scientist training and public engagement efforts. Working with her has been critical for me to learn a totally distinct skill set from my science training and evolve my Broader Impact identity (Risien and Stoeksdieck 2018). Developing a Broader Impact identity is focused on blending science interests to the potential impacts of a specific community of interests. This identity is likely to change over the course of one's career as perspectives/interests evolve. My initial efforts were focused on conducting elementary through high school teacher training and over time expanded to general public outreach associated with feature-length documentary movies (*Atlantic Crossing: A Robot's Daring Mission* and *Antarctic Edge: 70° South*) and national radio (*You're the Expert*, https://podcast.app/youre-the-expert-p8942). What I have learned is that the time commitment and the resources required vary dramatically with the audience. What does not vary is that none of these efforts would have been possible without Janice helping me to navigate the effort and help hone my message. These efforts have generated some of the most rewarding moments of my career. She has been critical to keep me growing as a public outreach communicator, including pushing me out of my comfort zone. My most recent event was a public story reading of a piece I had written in a New York City bar with professional short story tellers. That event was truly humbling. Compared to those experienced and talented speakers, I felt like a novice. I know where my efforts to practice will be focused over the next few years. *Working with BI professionals is critical to maximizing our outreach to stakeholders-society, which is amazing as this growing class of professionals did not exist when I began my career*.

What has not changed?

The importance of curiosity driven science

Ever since Vannevar Bush's groundbreaking report (Science, the Endless Frontier, https://www.nsf.gov/od/lpa/nsf50/vbush1945.htm) advocated for fresh thinking to unleash the intellectual capacity of civil society, basic research has been fundamental to the modern science enterprise. The value of this vision was not only that curiosity-driven science was fundamental to making novel discoveries but also that these advancements would meet the needs of society. To do this well (I am still learning), it is critical to focus on taking the time to develop good science questions. I have found that good questions, whether fundamental research or applied science, can find funding with dogged persistence. Unclear and unfocused questions will often not find a funding home. I warn all new graduate students that the hardest, but most rewarding, part of a thesis is formulating good questions. This is hard work. Make sure that you *take the time* to develop these questions, and continuously bounce them off all your science colleagues. For me, my clarity usually comes at sunrise, when it is quiet, or when I am weeding on the organic farm that my wife and I have. What works is different for each person, so find your creative space and use it! Where to get the good questions funded is another challenge but cast a wide net between local-state-federal-international agencies, foundations, and philanthropies.

Don't forget that science is fun!

Despite the stress of competing for grants and the many commitments associated with a science job, after 35 years, I still find science creative-frustrating-exhilarating-fun-consuming and full of twists and turns associated with each new insight. Too often, with life chaos, it is easy to lose track of the gift of having a career focused on exploration. My curiosity has grown as I am continually learning through field expeditions, laboratory experiments, and the continuous stream of discoveries published in the primary literature. Reading/listening about the science being conducted at this time leaves me stunned by the exciting and audacious work of our community. Given the many demands on our time, what is my advice to keep science fun?

- Increasingly in a virtual world, there are fewer contiguous time windows to focus and just think about the science. Therefore, it is important early on to take control of your calendar and formally block time to think-discuss-do science. In the modern world, everything has deadlines (grants, classes, meetings, and committees) except for the actual science, which does not have a formal deadline, which leads it to be the task too often postponed until tomorrow. Great advice I continually receive from my father-in-law, a successful scientist (Syukuro Manabe), is don't mistake busy work for science thinking. Deep thinking requires time. *Make science deadlines/goals and block the time do it. Treat this time religiously, turn off email and phones, but if needed turn on the music that helps you escape into the work. Close the door or hide in the library but revel in your explorations*.
- Choose a meeting-webinar-lecture series outside your expertise at least once a year. Block out the time to truly attend. When I mean truly attend, keep your computer shut, phone off, with at most a notebook to take notes. As stated in a James Bond movie, "Sometimes the old ways are the best." Stay nimble to learn the questions and languages of different disciplines. Science has transitioned from interdisciplinary to transdisciplinary discussions. This is relatively new. Today I see scientists successfully working with others in engineering, medicine, oceanography, art, public policy, and supply chain economics. What a wonderful evolution and my only response is "amen." This evolution is recent and I believe that the new generation of scientists will need to be trained differently in order to better to conduct transdisciplinary science. What that training is I am still working on. While a broad supporter of these efforts, I often struggle on how to design/conduct this transdisciplinary research, probably a symptom of a small brain. I am still learning the language and communities in completely separate disciplines. *My best advice, given I still learning how to do this, is to go collaborate with creative people who push you into uncomfortable areas you might have never considered*.

Science is important and worth the effort

As our climate changes, humanity is facing many critical issues. Mine and future generations will need to figure out how humanity should respond to changes in the Earth system, how human activity might become sustainable, and how we might develop a science community that reflects humanity's rich diversity. These are not theoretical challenges, but are urgent and require plans, a strategy, and action. Science and technology will be central to meeting these challenges and in an increasingly polarized global political environment decisions will need to be based on science and not ideology. I do not accept the premise that science has become an ideology and believe these verbal attacks are a deliberate strategy to delay and obfuscate what we have learned and delay or prevent societal actions that should flow from fact-based knowledge. Our science is critical to this planet, and in my mind, this is a noble and grand task i.e. worth the energy I invest.

The people in our community are the life gold mine

Above, I identified a handful of people who were critical to my journey. For every person I mention (Barbara, Ray, John, David, Gary, Barbara, Fred, Scott, Janice, Deborah, and Syukuro), there are another dozen who I could/should have highlighted. The take-home message is that our community is blessed with amazing, funny, passionate, and wonderful people. What a blessing that I have an extended "nerd" family. This is a community that provides life-long friends. A great example in my career is my decades-long collaboration with Deborah Steinberg. I met her as an undergraduate freshman in basic biology and we now co-manage large programs together. What a gift to work with your best friends.

While there are occasional bad apples, I have been lucky to not have encountered many. I learned when working on ships that it is critical to make sure everyone feels secure, safe, and valued. I believe it is critically important for science leaders to publicly and formally communicate expectations and be clear that certain behaviors will not tolerated. While issues remain, I have seen improvement. When I was an undergraduate going to sea, my advisor was often the first woman chief scientist in the ship's history, and I witnessed many instances of a toxic male culture. One example was that Barbara often had to insist that the public rooms should not broadcast pornographic movies. This is unfathomable now, but back then, her insistence was met with outrage from the often all-male crew. While we are evolving for the better, much more work is required to ensure at sea and on land, our culture is open, accepting, and supportive.

One piece of advice is to make sure that you work to develop collaborations as much as possible face-to-face. While this web-world allows for global and distributed collaboration, the value of human–human interactions cannot be overemphasized. This was recently highlighted in an article in Nature (Adams 2023) that expounded upon how remote collaboration allows for an expanded pool of knowledge. The cost is that distributed teams often don't integrate fully and thus are less vested in the conceptual debates that can lead to "disruptive" breakthroughs. Given that our community is full of great people, take advantage of this and maximize your time to work with them face-to-face. It leads to great science.

I have had the pleasure of working with Doug Webb for several decades and he has provided me and my students sage advice maybe we should all follow. "*Work hard, have fun and change the world.*"

References

Adams D. 'Disruptive' science: in-person teams make more breakthroughs than remote groups. *Nature* 2023;**624**:20. https://doi.org/10.1038/d41586-023-03618-x.

Bergh Ø, Yngve BØrsheim K, Bratbak G *et al.* High abundances of viruses found in aquatic environments. *Nature* 1989;**340**:467–8. https://doi.org/10.1038/340467a0.

Boyd PW, Trull TW. Understanding the export of biogenic particles in oceanic waters: is there consensus? *Prog Oceanogr* 2007;**72**:276–312. https://doi.org/10.1016/j.pocean.2006.10.007.

Chisholm SW, Olson RJ, Zettler ER *et al.* A novel free-living prochlorophyte abundant in the oceanic euphotic zone. *Nature* 1988;**334**:340–3. https://doi.org/10.1038/334340a0.

Claustre H, Johnson KS, Takeshita Y. Observing the global ocean with biogeochemical-argo. *Annu Rev Mar Sci* 2020;**12**:23–48. https://doi.org/10.1146/annurev-marine-010419-010956.

Costa DP, Breed GA, Robinson PW. New insights into pelagic migrations: implications for ecology and conservation. *Annu Rev Ecol Evol Syst* 2012;**43**:73–96. https://doi.org/10.1146/annurev-ecolsys-102710-145045.

Davies RW, Gumpel M. An infrared mars probe for gathering evidence on extraterrestrial life. In: *National Aeronautics and Space Administration*. The First International Space Science Symposium, external Publication No. 814. California, CA: California Inst of Technology Pasadena Jet Propulsion Lab, 1960.

Dickey T, Frye D, McNeil J *et al.* Upper-ocean temperature response to Hurricane Felix as measured by the Bermuda Testbed Mooring. *Mon Weather Rev* 1998;**126**:1195–201. https://doi.org/10.1175/1520-0493(1998)126%3c1195:UOTRTH%3e2.0.CO;2

Favali P, Beranzoli L. Seafloor observatory science: a review. *Ann Geophy* 2006;**49**:515–67.

Fedston AL, Stewart Lowndes JS. Welcoming more participation in open data science for the oceans. *Annu Rev Mari Sci* 2024; **16**:537–49. https://doi.org/10.1146/annurev-marine-041723-094741.

Glenn SM, Arnone R, Bergmann T *et al.* The biogeochemical impact of summertime coastal upwelling in the mid-Atlantic Bight. *J Geophys Res Oceans* 2004;**109**:C12S02. https://doi.org/10.1029/2003JC002265.

Godø OR, Handegard NO, Browman HI *et al.* Marine ecosystem acoustics (MEA): quantifying processes in the sea at the spatio-temporal scales on which they occur. *ICES J Mar Sci* 2014;**71**:2357–69. https://doi.org/10.1093/icesjms/fsu116.

Halpern D. *Satellites, Oceanography and Society*. Amsterdam: Elsevier Oceanography Series, 2000, 367pp.

Hara S, Koike I, Terauchi K *et al.* Abundance of viruses in deep oceanic waters. *Mar Ecol Progress Ser* 1996;**145**:269–77. https://doi.org/10.3354/meps145269.

Iverson MH. Carbon export in the ocean: a biologist's perspective. *Annu Rev Mar Sci* 2023;**15**:357–81. https://doi.org/10.1146/annurev-marine-032122-035153.

Johnston DW. Unoccupied aircraft systems in marine science and conservation. *Annu Rev Mar Sci* 2019;**11**:439–63. https://doi.org/10.1146/annurev-marine-010318-095323.

Kirk JTO. Biochemical aspects of chloroplast development. *Annu Rev Plant Physiol* 1970;**21**:11–42. https://doi.org/10.1146/annurev.pp.21.060170.000303.

Kirk JTO. Chloroplast structure and biogenesis. *Annu Rev Biochem* 1971;**40**:161–96. https://doi.org/10.1146/annurev.bi.40.070171.001113

Kirk JTO. *Light and Photosynthesis in Aquatic Ecosystems*. Cambridge: Cambridge University Press, 1994, 509pp.

Kirkpatrick G, Millie DF, Moline MA *et al.* Absorption-based discrimination of phytoplankton species in naturally mixed populations. *Limnol Oceanogr* 2000;**45**:467–71. https://doi.org/10.4319/lo.2000.45.2.0467

Kirkpatrick GJ, Orrico C, Moline MA *et al.* Continuous hyperspectral absorption measurements of colored dissolved organic material in aquatic systems. *Appl Opt* 2003;**42**:6564–8. https://doi.org/10.1364/AO.42.006564

Lumpkin R, Özgokmen T, Centurioni L. Advances in the application of surface drifters. *Annu Rev Mar Sci* 2017;**9**:59–81. https://doi.org/10.1146/annurev-marine-010816-060641.

Manley J. Autonomous underwater vehicles for ocean exploration. In: *Oceans*. Celebrating the Past ... Teaming Toward the Future (IEEE Cat. No.03CH37492). New York City, NY: IEEE, 2003. https://doi.org/10.1109/OCEANS.2003.178578.

Millie DF, Schofield O, Kirkpatrick GJ *et al.* Phytoplankton pigments and absorption spectra as potential 'Biomarkers' for harmful algal blooms: a case study of the Florida red-tide dinoflagellate, *Gymnodinium breve*. *Limnol Oceanogr* 1997;**42**:1240–51. https://doi.org/10.4319/lo.1997.42.5_part_2.1240

Morel A. Introduction to optical properties in the sea: theoretical aspects. In: M. Babin, C. S. Roesler, J. J. Cullen (eds), *Real-time Coastal Observing Systems for Marine Ecosystem Dynamics and Harmful Algal Blooms: Theory, Instrumentation and Modeling*. Paris: UNESCO, 2008, 109–52.

Morel A, Prieur L. Analysis of variations in ocean color. *Limnol Oceanogr* 1977;**22**:709–22. https://doi.org/10.4319/lo.1977.22.4.0709

Munk WH, Wunsch CI. Observing the ocean in the 1990s. *Philos Trans Royal Soc Lon A Math Phys Sci* 1982;**307**:439–64. https://doi.org/10.1098/rsta.1982.0120.

Oceanography. *Oceanography 101*. Vol. **14**. Oceanside, CA: Miracosta College, 2001, 121pp.

Packard TT. From Thoreau's woods to the Canary Islands: exploring ocean biogeochemistry through enzymology. *ICES J Mar Sci* 2018;**75**:912–22. https://doi.org/10.1093/icesjms/fsx214.

Peloquin RA. The Navy ocean modeling and prediction program: from research to operations: an overview. *Oceanography* 1992;**5**:4–8. https://doi.org/10.5670/oceanog.1992.25

Pendleton LH, Beyer H, Estradivari G *et al.* Disrupting data sharing for a healthier ocean. *ICES J Mar Sci* 2019;**76**:1415–23. https://doi.org/10.1093/iceasjms/fsz068.

Proctor LM, Fuhrman JA. Viral mortality of marine bacteria and cyanobacteria. *Nature* 1990;**343**:60–2. https://doi.org/10.1038/343060a0.

Ramp SR, Davis RE, Leonard NE *et al.* Preparing to predict: the second autonomous ocean sampling network (AOSN-II) experiment in the Monterey Bay. *Deep Sea Res Part II* 2009;**56**:68–86. https://doi.org/10.1016/j.dsr2.2008.08.013.

Riser SC, Freeland HJ, Roemmich D *et al.* Fifteen years of ocean observations with the global argo array. *Nat Clim Change* 2016;**6**:145–53. https://doi.org/10.1038/nclimate2872.

Risien J, Storksdieck M. Unveiling impact identities: a path for connecting science and society. *Integr Comp Biol* 2018;**58**:58–66. https://doi.org/10.1093/icb/icy011.

Schofield O, Bergmann T, Bissett WP *et al.* Linking regional coastal observatories to provide the foundation for a national ocean observation network. *IEEE J Oceanic Eng* 2002;**27**:146–54. https://doi.org/10.1109/JOE.2002.1002469

Schofield O, Bosch J, Glenn SM *et al.* Bio-optics in integrated ocean observing networks: potential for studying harmful algal blooms. In: M. Babin, C. Roelser, J. J. Cullen (eds), *Real Time Coastal Observing Systems for Ecosystems Dynamics and Harmful Algal Blooms*. Paris: UNESCO, 2008, 85–108.

Schofield O, Glenn S, Orcutt J *et al.* Automated sensor networks to advance ocean science. *Eos Trans Am Geophys Union* 2010;**91**:345–6. https://doi.org/10.1029/2010EO390001.

Schofield O, Glenn SM. On the evolution of coastal ocean observatories. *J Geophys Res Oceans* 2004;**109**:C12S01. https://doi.org/10.1029/2004JC002577.

Siegel DA, Devries T, Cetinic I *et al*. Quantifying the ocean's biological pump and its carbon cycle impacts on global scales. *Annu Rev Mar Sci* 2023;**15**:329–56. https://doi.org/10.1146/annurev-marine-040722-115226.

Smith NR. Ocean modeling in a global ocean observing system. *Rev Geophys* 1993;**31**:281–317. https://doi.org/10.1029/93RG00134.

Smith RC, Baker KS. The bio-optical state of ocean waters and remote sensing. *Limnol Oceanogr* 1978;**23**:247–59. https://doi.org/10.4319/lo.1978.23.2.0247.

Stommel H. The Slocum Mission. *Oceanography* 1989;**2**:22–5. https://doi.org/10.5670/oceanogr.1989.26.

Straton JW. *Our Nation and the Sea: A Plan for National Action Report of the Commission on Marine Science and Engineering and Resources*. Washington, WA: Commission on Marine Science, Engineering, and Resources, 1969. https://doi.org/10.5962/bhl.title.17054.

Toole JM, McCartney MS, Hogg N *et al*. Outposts in the ocean.In: *Oceanus Magazine*. Vol. **42**. Woods Hole, MA: Woods Hole Oceanographic Institution, 2000.

Watanabe YY, Papastamatiou YP. Biologging and biotelemetry: tools for understanding the lives and environments of marine animals. *Annu Rev Animal Biosci* 2023;**11**:247–67. https://doi.org/10.1146/annurev-animal-050322-073657.

Waterbury JB, Watson SW, Guillard RR *et al*. Widespread occurrence of a unicellular, marine, planktonic, cyanobacterium. *Nature* 1979;**277**:293–4. https://doi.org/10.1038/277293a0.

Wynn RB, Huvenne VAI, Le Bas TP *et al*. Autonomous underwater vehicles (AUVs): their past, present and future contributions to the advancement of marine geosciences. *Mar Geol* 2014;**352**:451–68. https://doi.org/10.1016/j.margeo.2014.03.012.

Zaneveld RJ. A theoretical derivation of the dependence of the remotely sensed reflectance of the ocean on the inherent optical properties. *J Geophys Res Oceans* 1995;**100**:13135–42. https://doi.org/10.1029/95JC00453.

Handling Editor: Howard Browman

ADVANCING EARTH AND SPACE SCIENCES

Geophysical Research Letters®

RESEARCH LETTER
10.1029/2024GL109246

Spatial and Seasonal Controls on Eddy Subduction in the Southern Ocean

Michael L. Chen[1] and Oscar Schofield[1]

[1]Department of Marine and Coastal Sciences, Rutgers University, New Brunswick, NJ, USA

Key Points:

- Eddy subduction in the Southern Ocean is observed as subsurface anomalies in spice and oxygen measured by autonomous profiling floats
- Spatial distribution is controlled by weak stratification and strong lateral buoyancy gradients, diagnosed using satellite altimetry
- Bio-optical proxies suggest that eddy subduction is most active in spring/early summer, driven by weak vertical stratification

Supporting Information:

Supporting Information may be found in the online version of this article.

Correspondence to:

O. Schofield,
oscar@marine.rutgers.edu

Citation:

Chen, M. L., & Schofield, O. (2024). Spatial and seasonal controls on eddy subduction in the Southern Ocean. *Geophysical Research Letters*, *51*, e2024GL109246. https://doi.org/10.1029/2024GL109246

Received 1 MAY 2024
Accepted 4 SEP 2024

Abstract Carbon export driven by submesoscale, eddy-associated vertical velocities ("eddy subduction"), and particularly its seasonality, remains understudied, leaving a gap in our understanding of ocean carbon sequestration. Here, we assess mechanisms controlling eddy subduction's spatial and seasonal patterns using 15 years of observations from BGC-Argo floats in the Southern Ocean. We identify signatures of eddy subduction as subsurface anomalies in temperature-salinity and oxygen. The anomalies are spatially concentrated near weakly stratified areas and regions with strong lateral buoyancy gradients diagnosed from satellite altimetry, particularly in the Antarctic Circumpolar Current's standing meanders. We use bio-optical ratios, specifically the chlorophyll *a* to particulate backscatter ratio (Chl/b_{bp}) to find that eddy subduction is most active in the spring and early summer, with freshly exported material associated with seasonally weak vertical stratification and increasing surface biomass. Climate change is increasing ocean stratification globally, which may weaken eddy subduction's carbon export potential.

Plain Language Summary Oceans play an important role in global climate by soaking up and sequestering atmospheric carbon dioxide. Photosynthetic activity at the surface turns carbon dioxide into organic carbon, and if this carbon leaves the surface to the deep ocean, it can be locked away from the atmosphere. One way this occurs is through the physical circulation associated with swirling eddies, which can rapidly transport organic carbon-rich surface waters and "inject" them into deep waters. However, we still don't fully understand the seasonal timing of this process, or what drives its spatial distribution. We investigated this in the Southern Ocean, which is very important to global climate, using data collected by drifting robots. We find that this process is the most active in regions where eddies drive strong surface stirring, and during the spring, when weak stratification allows injections to penetrate deep into the ocean. Because this process is poorly represented in climate models, these findings will improve our understanding of how the ocean absorbs carbon.

1. Introduction

Oceans play a critical role in regulating global climate by sequestering carbon from the atmosphere (Gruber et al., 2009). A key driver of this is the biological pump, a suite of processes that exports carbon from the ocean's surface to the interior, and is estimated to keep 1,300 Pg C sequestered from the atmosphere (Nowicki et al., 2022). The best understood mechanism is the biological gravitational pump, or the sinking of large particles out of the euphotic zone, which is estimated to comprise about 70% of global carbon export (Boyd et al., 2019; Nowicki et al., 2022). However, other mechanisms are increasingly being recognized (Boyd et al., 2019). These include transport by vertically migrating mesopelagic organisms (Bianchi et al., 2013), and physical processes such as carbon detrainment from shoaling mixed layers (the "mixed-layer pump"; Dall'Olmo et al., 2016; Lacour et al., 2019), large-scale water mass subduction (the "subduction pump"; Levy et al., 2013), and submesoscale vertical velocities associated with frontal boundaries and eddies (the "eddy subduction pump", or "ESP"; Omand et al., 2015; Resplandy et al., 2019). If these submesoscale vertical motions coincide with the presence of organic carbon in the surface ocean, carbon export can occur. During phytoplankton blooms, models and observations show that filaments of organic carbon-rich surface waters can be injected to depth along eddy peripheries (Davies et al., 2019; Omand et al., 2015).

Eddy subduction (henceforth, also "subduction") remains particularly understudied due to the challenges of observing submesoscale processes. In recent decades, submesoscale physics has emerged as a key driver of vertical exchange. Advances in numerical modeling have revealed a dynamic eddy field at horizontal scales of O (1–10) m, associated with ageostrophic vertical velocities reaching up to 100 m day^{-1}. These evolve on timescales of O (1) days with a vertical extension of O (100) m, and strongly contribute to vertical tracer variability (Balwada et al., 2018; Capet et al., 2008; Klein & Lapeyre, 2009; Lapeyre & Klein, 2006; Lévy et al., 2012; Mahadevan & Tandon, 2006; Rosso et al., 2014). Mechanisms energizing these vertical submesoscale flows include surface frontogenesis (Held et al., 1995; Lapeyre & Klein, 2006; Rosso et al., 2015) and baroclinic instabilities within the mixed layer ("mixed layer instabilities"), which extract potential energy stored in lateral buoyancy gradients and deep mixed layers (Boccaletti et al., 2007; Callies et al., 2015, 2016; Erickson & Thompson, 2018).

Once subducted, parcels of water retain tracer signatures of their surface origins, including elevated oxygen and surface-like temperature-salinity (Davies et al., 2019; Omand et al., 2015). Recently, Llort et al. (2018) used these signatures to develop an algorithm that detects eddy subduction in BGC-Argo float profiles. This algorithm identified subsurface anomalies in two variables known to reflect recent subduction from the surface: apparent oxygen utilization (AOU) and spice, a temperature-salinity variable least-correlated with density, which helps identify water mass movement along isopycnals. These anomalies were often associated with elevated particulate organic carbon (POC), and were spatially located in energetic regions of the Southern Ocean (SO). Since then, this approach has enabled the identification of eddy subduction in regions such as the SO (Lacour et al., 2023), the North Atlantic (A. R. Johnson & Omand, 2021) and the Kuroshio Extension (Chen et al., 2021), and has generated estimates of eddy subduction's contribution to carbon export. However, these vary widely, ranging from up to 50% of exported POC during spring blooms, to as little as <5% (Davies et al., 2019; Llort et al., 2018; Omand et al., 2015; Resplandy et al., 2019; Stukel & Ducklow, 2017).

A critical knowledge gap is our poor understanding of eddy subduction's seasonality, which determines what kind of particles are exported and their sequestration potential, and is a major uncertainty in global carbon export calculations (Nowicki et al., 2022). Previous observational studies have mixed findings, detecting the most subduction events either during the summer (A. R. Johnson & Omand, 2021; Llort et al., 2018), spring (Chen et al., 2021), or throughout the year (Lacour et al., 2023). A challenge in assessing seasonality in float-based studies is determining the "age" of subduction events. A detected subsurface feature may have been subducted months ago, as AOU and spice anomalies may persist at depth for months (A. R. Johnson & Omand, 2021). To this end, ratios of bio-optical proxies are a promising tool to help "age" subducted material (Lacour et al., 2019), but have yet to be applied to basin-scale studies of eddy subduction.

Here, we use BGC-Argo floats in the SO to provide basin-scale analysis of eddy subduction's spatial distribution and seasonality, and tie them to physical mechanisms. For the first time, we integrate bio-optical ratios in a basin-scale eddy subduction study to more robustly address seasonality, and find a seasonal peak in the austral spring, associated with weak vertical stratification and increasing surface biomass. Integrating satellite altimetry, we find that strong lateral buoyancy gradients and weak stratification shape eddy subduction's spatial distribution. This work demonstrates the utility of bio-optical ratios in observational carbon export studies. Our mechanistic findings are also an important step toward resolving when and where submesoscale carbon export occurs, an urgent need in understanding the ocean's role in carbon cycling and climate change.

2. Data and Methods

2.1. Float Data

BGC-Argo float data are from the Southern Ocean Carbon and Climate Observations and Modeling (SOCCOM) program. Floats conduct 2,000 m vertical profiles every 10 days, and drift at a parking depth of 1,000 m. Vertical sampling frequency varies between two float types: Navis floats sample every 2 m in the upper 1,000 m. APEX floats sample less frequently, with resolution decreasing with depth. Sampling schemes are described in Johnson et al. (2017), as well as processing of bio-optical parameters, including particulate backscatter at 700 nm (b_{bp}), which is used to derive POC, and chlorophyll *a* fluorescence, which is used to derive chlorophyll *a* concentrations (Chl). Quality control procedures for all other variables are described in Maurer et al. (2021). Only data flagged as "good" were used.

Variables such as conservative temperature (CT) and absolute salinity (S_A) were derived using the Thermodynamic Equation of Seawater 2010 (TEOS-10; McDougall & Barker, 2011). Spice was calculated as a function of CT and S_A, following McDougall & Krzysik, 2015. AOU was calculated as (AOU = O_2^{sat}–O_2^{obs}), where O_2^{sat} is the oxygen saturation concentration calculated using the coefficients of Garcia and Gordon (1992, 1993), and

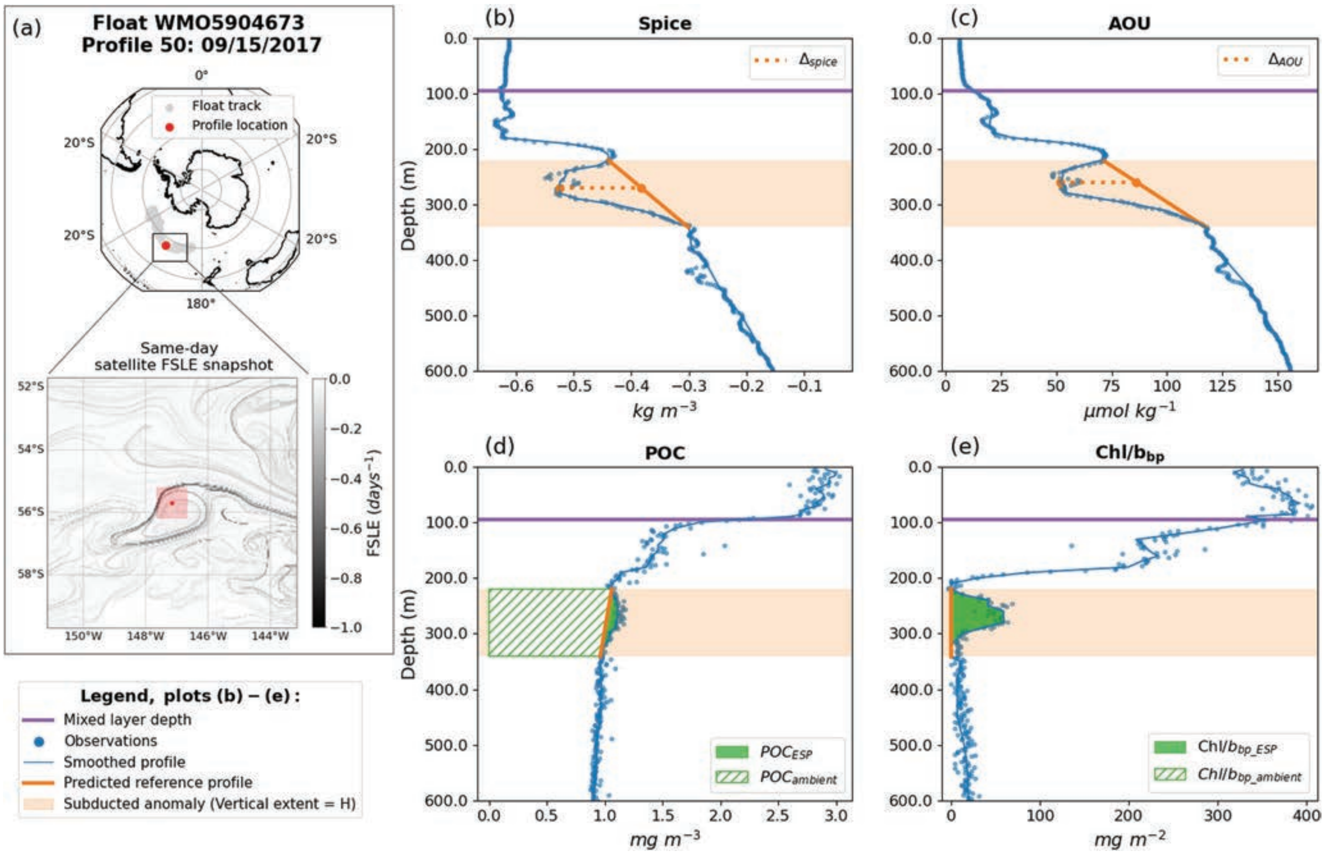

Figure 1. Example of an eddy subduction anomaly detected in a float profile. (a) Map depicting float track and profile location (red circle). Inset shows the same-day surface FSLE field. Red circle = profile location. Shaded red box = the 1° × 1° area used to retrieve the strongest FSLE in the profile's vicinity. The float's vertical profiles are shown in (b)-(d), with the MLD indicated by a purple line. Blue lines depict smoothed profiles. The shaded orange band indicates H, the vertical extent of the subduction anomaly. (b) Spice profile. Dotted orange line shows Δ_{spice} at depth h_{spice}, or the difference between the observed value and the calculated reference value (orange circles). The reference profile is shown by the orange line. (c) AOU profile, with reference profile and Δ_{AOU}, similar to the spice profile. (d) POC profile. Shaded green region: $POC_{ESP,}$ the integrated quantity of subduction-driven POC. Hatched region: $POC_{ambient}$, the subtracted, integrated quantity of ambient POC. (e) Chl/b_{bp} ratio profile. Shaded green area: Chl/b_{bp_ESP}, similar to POC. Hatched region: $Chl/b_{bp\_ambient}$, not visible because values are roughly 0.

O_2^{obs} is the observed dissolved oxygen concentration. Mixed layer depth was defined using a density difference threshold of 0.03 kg m^{-3} from the surface, and buoyancy frequency squared (N^2) was calculated using TEOS-10.

2.2. Eddy Subduction Anomaly Detection

We identified eddy subduction anomalies in float profiles using an algorithm adapted from Chen et al. (2021) and Llort et al. (2018). An example is shown in Figure 1, detected on the periphery of a mesoscale eddy (Figure 1a). We considered profiles between 30°S and 65°S, and discarded profiles with surface salinity >35 psu, following Llort et al. (2018). We also only considered profiles where the median spice value in the mixed layer was lower than that at 600 m, as increasing spice with depth in the upper 1,000 m is characteristic of SO waters (Tailleux, 2021). Navis floats were down-sampled by selecting data at APEX sampling depths, allowing for comparable vertical resolution. Profiles were vertically smoothed with a 3-bin rolling median. The total dataset contained 9,354 profiles with temperature, salinity, and oxygen collected from February 2008 through August 2023, with 8,545 measuring Chl and b_{bp}.

For each smoothed profile, we identified co-occurring peaks in spice and AOU between the MLD and 600 m depth (relative minima found within 30 m of each other, at depths h_{spice} and h_{AOU}; Figures 1b and 1c). We then defined reference profiles to simulate "background", ambient values in the absence of subduction (orange lines, Figures 1b and 1c). An initial guess for the reference profile is defined as the straight line between the maximum values above and below each peak (within 100 m in either direction), following Chen et al., 2021. The top and bottom boundaries of this initial guess are then iteratively adjusted to ensure the boundaries are coherent (see Figure S1 in Supporting Information S1). We then calculated the difference between the observed value and the calculated reference value at h_{spice} and h_{AOU}, yielding Δ_{spice} and Δ_{AOU}, respectively (Figures 1b and 1c). Peaks were classified as eddy subduction pump anomalies ("ESP anomalies") if $\Delta_{spice} < -0.05$ kg/m^3 and $\Delta_{AOU} < -8$ μmol/kg, following Llort et al. (2018). The anomaly depth was defined at h_{AOU}, and the vertical extent of the anomaly (H) was defined as the extent of the reference profile for AOU. We discarded anomalies found within 100 m of the MLD in order to avoid misidentifying detrainment from shoaling mixed layers (Lacour et al., 2019).

We then sought to quantify biogeochemical values (e.g., POC, Chl/b_{bp}, AOU) associated with anomalies, and isolate the portion driven by subduction, versus by ambient processes such as gravitational sinking. Taking POC as an example, we first calculated the total value by integrating the observed profiles over the vertical span of the anomaly (H):

$$\mathrm{POC}_{\mathrm{ESP}_{\mathrm{total}}} = \int_{\mathrm{H_{bottom}}}^{\mathrm{H_{top}}} \mathrm{POC}_{\mathrm{observed}} \tag{1}$$

We estimated the ambient value by integrating through the reference profile (hatched regions in Figures 1d and 1e):

$$\mathrm{POC}_{\mathrm{ESP}_{\mathrm{ambient}}} = \int_{\mathrm{H_{bottom}}}^{\mathrm{H_{top}}} \mathrm{POC}_{\mathrm{reference}} \tag{2}$$

From the ambient and total values, we calculated the subduction-driven value (green shaded regions in Figures 1d and 1e):

$$\mathrm{POC}_{\mathrm{ESP}} = \mathrm{POC}_{\mathrm{ESP}_{\mathrm{total}}} - \mathrm{POC}_{\mathrm{ESP}_{\mathrm{ambient}}} \tag{3}$$

Finally, we normalized these by H to yield the depth-averaged, subduction-driven value in the original units:

$$\mathrm{POC}_{\mathrm{ESP}_{\mathrm{avg}}} = \frac{\mathrm{POC}_{\mathrm{ESP}}}{\mathrm{H}} \tag{4}$$

2.3. Satellite Data

Finite-size Lyapunov Exponents (FSLEs) were downloaded from AVISO+. FSLEs describe stretching and compression by quantifying the exponential rate of separation (λ) of neighboring particles advected in a flow field: $\lambda(d_0, d_f) = \frac{1}{t} log\left(\frac{d_f}{d_0}\right)$, where d_0 and d_f are the initial and final distances between the particles, respectively, and t is the time it takes for the particles to reach d_f (d'Ovidio et al., 2004). The AVISO + product uses daily, altimetry-derived geostrophic velocity fields to advect particles backward-in-time, so FSLEs are negative, with stronger negative values indicating stronger stretching; these FSLE ridges indicate transport barriers and are preferentially located between eddy cores (Siegelman, Klein, Thompson, et al., 2020).

3. Results and Discussion

3.1. Spatial Distribution of Eddy Subduction

The BGC-Argo dataset provides basin-wide spatial coverage of the SO over 15 years. We find eddy subduction anomalies in 4.4% of profiles, defined as coherent, negative mesopelagic anomalies in spice and AOU (Figures 1b and 1c), frequently associated with positive anomalies in bio-optical parameters (67% with positive b_{bp}, 56% with positive Chl a) (Figures 1d and 1e). These anomalies are spatially concentrated around the Polar Front and Antarctic Circumpolar Current (ACC), consistent with Llort et al. (2018) (Figure 2a). Also consistent with Llort et al. (2018) and Dove et al. (2022), their circumpolar distribution is uneven, with most detected in the ACC's standing meander regions: the Eastern Pacific Rise, the Kerguelen, Crozet, and Campbell Plateaus, and the Drake Passage. These regions are known for enhanced eddy kinetic energy (EKE) and vertical exchange (Dove

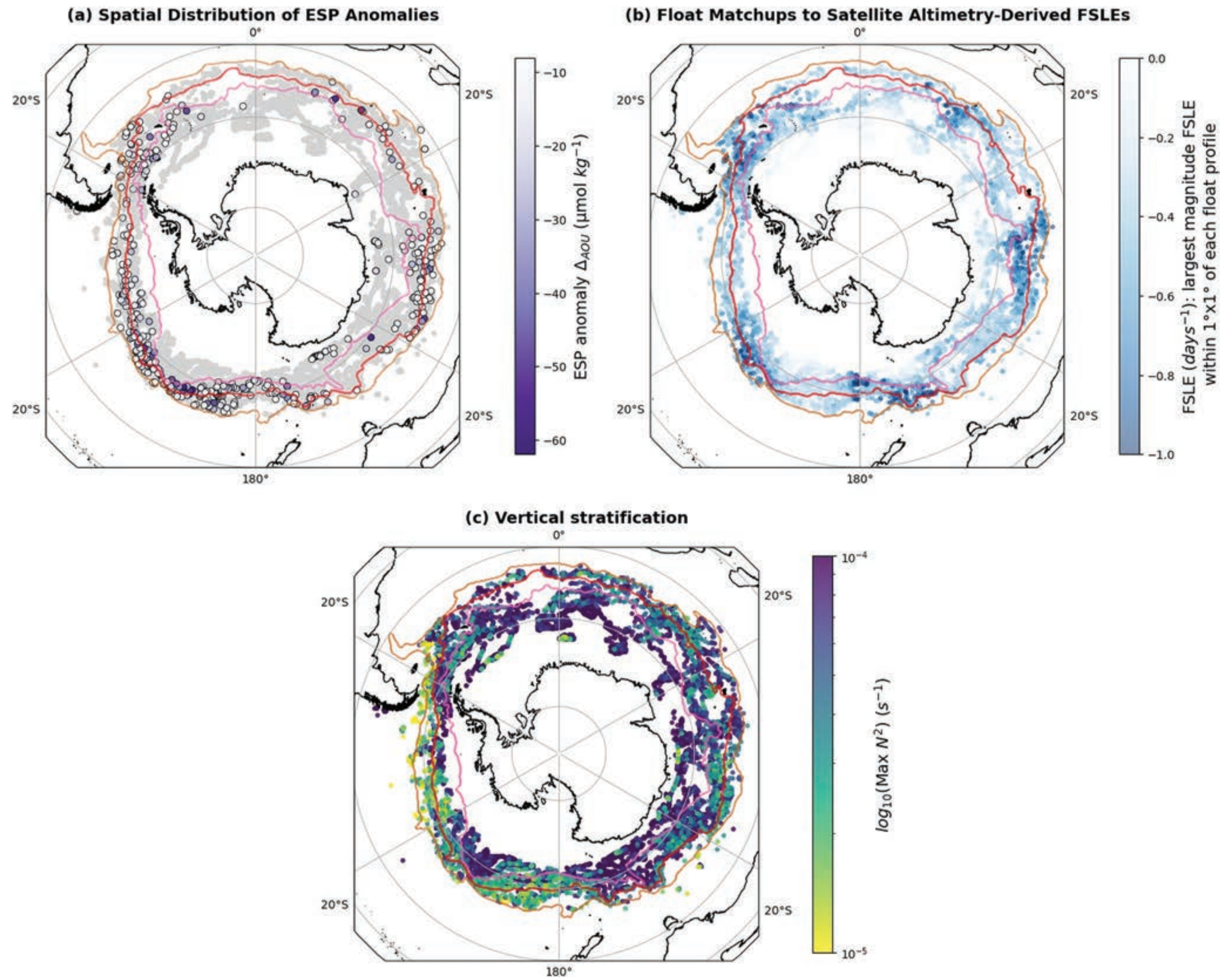

Figure 2. Maps of the float dataset. Colored lines indicate front locations as defined by mean dynamic topography from satellite altimetry (Park & Durand, 2019): orange = Subantarctic Front (SAF); red = Polar Front (PF); pink = Southern ACC Front (SACCF). (a) Locations of eddy subduction anomalies across the SO. Gray circles indicate all profiles considered in the analysis. Purple-scale colored circles indicate detected ESP anomalies, colored by the magnitude of Δ_{AOU}. (b) Spatial distribution of FSLEs. Each point is a satellite matchup to a float profile, showing the strongest FSLE within 1° × 1° of each profile. (c) Spatial distribution of vertical stratification (maximum N^2) in each float profile, and displayed on a log-scale. The colorscale maximum is limited to 10^{-4} (roughly the median of the maximum N^2 distribution; see Figure 4d) to emphasize variation in the lower half of the distribution.

et al., 2022), as the ACC interacts with underwater topography and generates mesoscale eddies that strain surface density fields and energize submesoscale motions (Rosso et al., 2015).

To better assess spatial distribution, we use altimetry-derived FSLEs. FSLEs are elevated within the ACC's standing meanders (Dove et al., 2022), and strong FSLEs are co-located with strong, deep-reaching submesoscale lateral buoyancy gradients and intense vertical velocities (Siegelman, et al., 2020a, 2020b). To assess whether a given float profile was in the vicinity of submesoscale fronts, we matched each profile with its same-day satellite FSLE field and identified the strongest FSLE within the surrounding 1° × 1° area (e.g., within the red square in Figure 1a). These matchups are displayed in Figure 2b and show the ACC's standing meanders as submesoscale hotspots, largely congruent with the distribution of eddy subduction anomalies.

However, groups of anomalies are detected in comparatively quiescent regions in between the standing meanders, such as 60°W–120°W and 150°W–180°W (Figures 2a and 2b). Although stratification shows a less dramatic spatial pattern, many profiles in these regions have comparatively weak stratification (yellow colors in Figure 2c), which may influence eddy subduction's spatial distribution by allowing deeper vertical penetration of

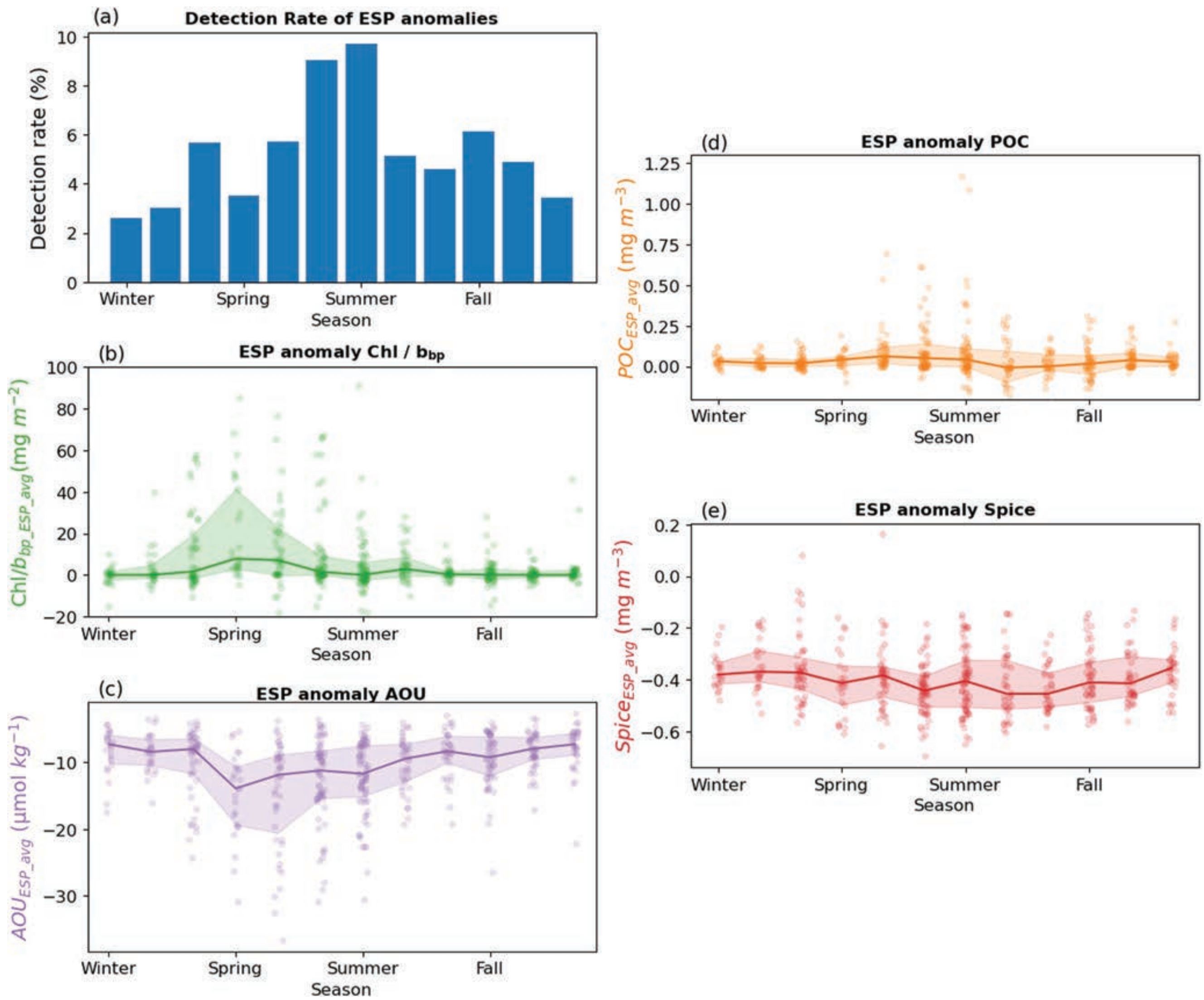

Figure 3. Seasonal patterns across observed ESP anomalies. *X*-axis ticks correspond to [June, Sept, Dec, Mar]. (a) Detection rate of ESP anomalies per month, normalized by the total number of profiles per month. Plots (b)-(e) show seasonality of depth-averaged, subduction-driven properties within ESP anomalies. Line plots depict medians, with shaded regions indicating interquartile ranges. Overlain strip plots show individual data points. (b) $POC_{\_ESP\_avg}$, (c) $Chl/b_{bp\_ESP\_avg}$, (d) $AOU_{\_ESP\_avg}$, (e) $spice_{\_ESP\_avg}$. Axis limits in (b) and (d) display 98% of data points.

submesoscale flows (Callies et al., 2016; Erickson & Thompson, 2018). These mechanistic relationships will be further explored in Section 3.3.

3.2. Seasonality of Eddy Subduction

We detect subduction anomalies more frequently during summer months (Figure 3a). However, our method only identifies subsurface anomalies after subduction occurs, and these anomalies may persist for months at depth afterward (A. R. Johnson & Omand, 2021).

To better assess the timing and "age" of subduction, we integrate bio-optical ratios, particularly Chl/b_{bp} — the ratio of chlorophyll *a* to particulate backscatter. At the surface, this ratio reflects phytoplankton photophysiology, community composition, and particle assemblage (Barbieux et al., 2018; Cetinić et al., 2015; Rembauville et al., 2017). However, beneath the mixed layer, it can be a proxy for the freshness of exported material; after particulate material leaves the mixed layer, Chl/b_{bp} decays by a power law as phytoplankton pigments degrade (Lacour et al., 2019). Calculating a precise age for a given Chl/b_{bp} observation at depth is difficult; however, we argue it is a rough but robust proxy for particle age in the mesopelagic SO. First, values in the surface mixed layer and in the mesopelagic are distinct: over an order of magnitude lower in the mesopelagic (Figure S2 in Supporting Information S1); thus, high mesopelagic values likely indicate recent surface origins. Second, ambient Chl/b_{bp} at depth shows strong seasonality, with a summertime peak that is tightly coupled to seasonal POC maxima at the surface and at depth (Figure S3 in Supporting Information S1), reflecting a pulse of fresh sinking organic matter after surface phytoplankton blooms. By contrast, Chl/b_{bp} at the surface shows weak seasonality (Figure S3 in Supporting Information S1), controlled to first-order in the SO by community composition (Barbieux et al., 2018); thus, seasonality in surface Chl/b_{bp} is unlikely to strongly influence values at depth. Together, these suggest that high Chl/b_{bp} values at depth are largely controlled by how recently material left the surface.

Within subduction anomalies, Chl/$b_{bp\_\mathrm{ESP\_avg}}$ is frequently elevated relative to ambient mesopelagic waters, indicating freshly subducted phytoplankton biomass (Figure 1e). It has a distinct seasonal cycle, with the highest values (the most freshly subducted material), occurring during the spring and early summer (Figure 3b). AOU (as AOU$_{\mathrm{_ESP_avg}}$) shows a similar seasonality, with the most negative values occurring during the spring (Figure 3c), indicating less respiration, or "aging", has occurred. Springtime events are also slightly closer to the mixed layer, consistent with more recent isolation (Figure S4 in Supporting Information S1). By comparison, the seasonal cycle of eddy-subducted POC (POC$_{\mathrm{_ESP_avg}}$) is weak, although the highest POC$_{\mathrm{_ESP_avg}}$ event outliers are detected in the summer (Figure 3d). This suggests that although eddy subduction may be most active in the spring, these events may not necessarily export large amounts of POC. Interestingly, spice$_{\mathrm{_ESP_avg}}$, a purely physical variable, does not show a seasonal cycle (Figure 3e), suggesting that the relative roles of physics versus respiration in dissipating features after subduction need to be untangled through high-resolution sampling.

Most importantly, the seasonal cycles we show are distinct from those of other processes in the mesopelagic and from surface Chl/b_{bp}, lending confidence that they reveal patterns unique to eddy subduction. For example, ambient mesopelagic POC and Chl/b_{bp} are tightly coupled to the summertime peak in surface POC (Figure S3 in Supporting Information S1), and is likely mediated by the gravitational sinking of large particles from surface blooms (Figure S5 in Supporting Information S1). Eddy subduction's springtime peak thus represents a distinct seasonality, and could facilitate export of different pools of carbon present in the spring (i.e., dissolved or inorganic carbon, which we do not discuss here). Future work should investigate this seasonality's implications for carbon sequestration.

3.3. Physical and Biological Mechanisms Controlling Spatial and Seasonal Patterns

Next, we link the previously discussed spatial and seasonal patterns to biological and physical processes required for eddy subduction of POC: POC availability at the ocean's surface, strong lateral buoyancy gradients, deep mixed layers, and weak vertical stratification (Callies et al., 2016; Erickson & Thompson, 2018; Fox-Kemper et al., 2008). We define vertical stratification as the maximum N^2 over the entire profile, as well-defined mixed layers often do not exist in energetic regions (Erickson & Thompson, 2018). However, our results are unaffected if we instead use N^2 at the base of the mixed layer (Figure S6 in Supporting Information S1).

Examining seasonal cycles in these variables, spring/early summer emerges as a period conducive to eddy subduction, with an overlap of deep mixed layers, weak vertical stratification, and increasing surface POC (Figure 4a). This aligns with the seasonality discussed in Section 3.2. Interestingly, altimetry-derived FSLEs do not show a seasonal cycle here (Figure 4b), suggesting that lateral buoyancy gradients in this region may not drive eddy subduction's seasonality.

Statistical distributions of float profiles provide further insights. Profiles with subduction anomalies are shifted towards higher surface POC (Figure 4c), demonstrating that carbon must be available to be exported. Similarly, profiles with subduction anomalies are shifted towards weakly stratified water columns (Figure 4d). Profiles with anomalies in the top quartile of Chl/$b_{bp\_\mathrm{ESP\_avg}}$ values, likely most recently subducted, are even more weakly stratified. Direct comparison of maximum N^2 to Chl/$b_{bp\_\mathrm{ESP\_avg}}$ suggests that weak stratification is a prerequisite for detecting recent eddy subduction (Figure S7 in Supporting Information S1). Interestingly, despite its strong seasonality, mixed layer depth shows little effect–distributions are similar between profiles with and without subduction anomalies (Figure 4e). Conversely, although FSLEs do not show seasonality, profiles with subduction anomalies are strongly shifted towards stronger nearby FSLEs (Figure 4f).

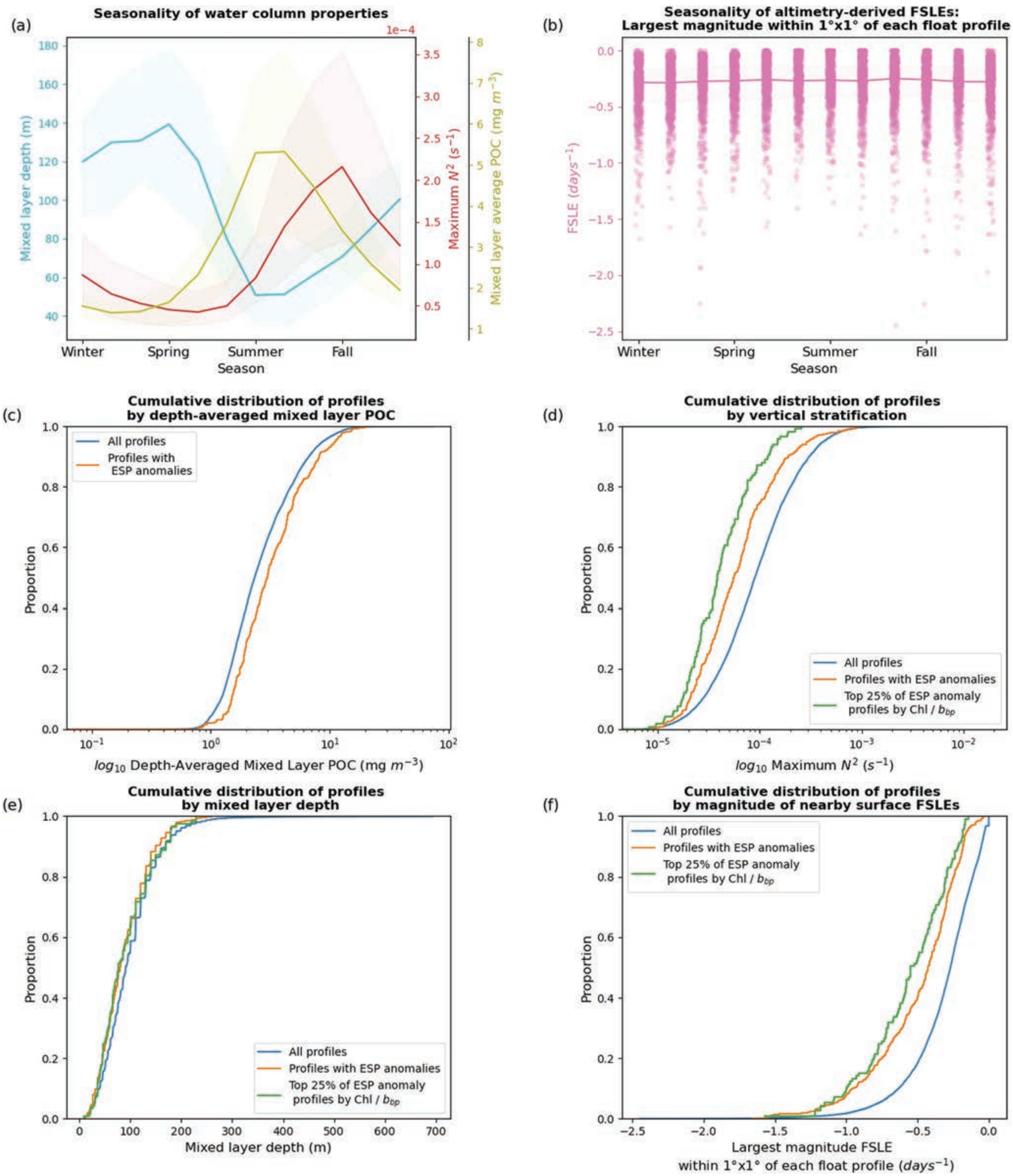

Figure 4. Mechanisms driving eddy subduction. (a) Seasonality of water column properties for all float profiles, showing MLD (blue), maximum N^2 (red), and depth-averaged POC within the surface mixed layer (olive). The line plot depicts medians, with shaded regions indicating interquartile ranges. (b) Seasonality of altimetry-derived FSLE magnitudes. The strip plot shows satellite matchups to each float profile, showing the strongest FSLE within $1° \times 1°$. Line plot as in (a). (c)-(f) Cumulative distribution plots of profiles by various mechanistic variables. Each curve represents the cumulative proportion of observations falling below the corresponding *x*-axis value. Colors indicate all profiles (blue), only profiles with ESP anomalies (orange), and only profiles with ESP anomalies with the highest 25% Chl/$b_{bp\_ESP\_avg}$ values (green) (c) Depth-averaged mixed layer POC (log_{10}) (d) Maximum N^2 (log_{10}). (e) Mixed layer depth. (f) Magnitude of the strongest altimetry-derived FSLE within a $1° \times 1°$ area.

These analyses indicate that in the SO, strong lateral buoyancy gradients and weak vertical stratification exert significant physical controls on eddy subduction. The spatial analyses in Section 3.1 suggest that these drive eddy subduction's concentration in standing meanders and weakly stratified areas. Meanwhile, the seasonal analyses in Sections 3.2 and 3.3 suggest that vertical stratification and seasonal availability of surface POC are dominant drivers of seasonality. Mixed layer depth appears to exert little influence. Consistent with Stommel's Demon theory, weak springtime stratification may act as a seasonal trapdoor in areas prone to submesoscale motions, determining whether they can export material beneath the mixed layer (Stommel, 1979).

4. Conclusions

Our work has broad implications for our understanding of carbon export and submesoscale dynamics, and emphasizes open questions for the community. First, we identify a seasonal cycle in eddy subduction, which has remained unresolved in global carbon export calculations (Nowicki et al., 2022). Future work should assess global variability beyond the SO, and assess the implications of seasonality on what pools of carbon are exported and their sequestration potential. Second, we highlight the utility of bio-optical ratios in studies of carbon export. However, high-resolution sampling is necessary to quantify the evolution and aging of tracers after subduction. Third, we emphasize the power of contextualizing subsurface float observations with Lagrangian surface diagnostics, such as satellite FSLEs. Finally, we identify strong lateral buoyancy gradients, weak vertical stratification, and POC availability as spatiotemporal controls on vertical exchange in the SO. Future investigation should untangle specific physical mechanisms (i.e., frontogenesis vs. instabilities; Archer et al., 2020; Callies et al., 2015; Erickson & Thompson, 2018; Klein & Lapeyre, 2009; Rosso et al., 2015) and use these parameters to model when and where submesoscale carbon export occurs. Finally, climate change is increasing stratification strength across global oceans (Sallée et al., 2021), potentially decreasing eddy subduction's export potential, and underscoring the importance of understanding this process's role in ocean carbon sequestration.

Data Availability Statement

Float data were downloaded from the UCSD SOCCOM and GO-BGC data archive. Our analyses use the delayed-mode, quality controlled, low-resolution snapshot from 2023 to 08-28 (Riser et al., 2023). Altimetry-derived FSLEs were produced by Ssalto/Duacs in collaboration with LOcean and CTOH and distributed by AVISO+, with support from CNES (https://www.aviso.altimetry.fr/en/data/products/value-added-products/fsle-finite-size-lyapunov-exponents.html). Analyses were conducted in Python 3.8.17 using Xarray version 2022.11.0, available under the Apache license at https://docs.xarray.dev/ (The Xarray Development Team, 2022); GSW version 3.6.17, available under the GSW License at https://www.TEOS-10.org (McDougall & Barker, 2011); and Pandas version 1.5.3, available under the BSD 3-Clause "New" or "Revised" License at https://pandas.pydata.org (The Pandas Development, 2023). Figures were plotted using Matplotlib version 3.7.1, available under the Matplotlib license at https://matplotlib.org (The Matplotlib Development Team, 2023); Seaborn version 0.12, available under the BSD 3-Clause "New" or "Revised" License at https://seaborn.pydata.org (The Seaborn Development Team, 2022); and Cartopy version 0.21.1, available under the BSD-3 Clause License at https://scitools.org.uk/cartopy/ (The Cartopy Development Team, 2022). The software associated with this manuscript for data processing and analysis is licensed under MIT and published on GitHub https://github.com/mchen96/southern_ocean_eddy_subduction/, and can be run in a zero-install environment on the cloud at https://mybinder.org/v2/gh/mchen96/southern_ocean_eddy_subduction/main (M. Chen, 2024).

Acknowledgments

The authors are grateful for the comments of anonymous reviewers who greatly improved the manuscript, and for conversations with Joan Llort, Shuangling Chen, Léo Lacour, Laure Resplandy, Kathleen Abbott, Lily Dove, Mara Freilich, and Jackie Veatch. Float data were collected and made freely available by the SOCCOM Project funded by the National Science Foundation, Division of Polar Programs (NSF PLR-1425989 and OPP-1936222), supplemented by NASA, and by the International Argo Program and the NOAA programs that contribute to it. The Argo Program is part of the Global Ocean Observing System. M.L. Chen acknowledges NASA Grant 80NSSC22K1451. O. Schofield acknowledges NASA Grant 80NSSC21K0969.

References

Archer, M., Schaeffer, A., Keating, S., Roughan, M., Holmes, R., & Siegelman, L. (2020). Observations of submesoscale variability and frontal subduction within the mesoscale eddy field of the tasman sea. *Journal of Physical Oceanography*, *50*(5), 1509–1529. https://doi.org/10.1175/JPO-D-19-0131.1

Balwada, D., Smith, K. S., & Abernathey, R. (2018). Submesoscale vertical velocities enhance tracer subduction in an idealized antarctic circumpolar current. *Geophysical Research Letters*, *45*(18), 9790–9802. https://doi.org/10.1029/2018GL079244

Barbieux, M., Uitz, J., Bricaud, A., Organelli, E., Poteau, A., Schmechtig, C., et al. (2018). Assessing the variability in the relationship between the particulate backscattering coefficient and the chlorophyll *a* concentration from a global biogeochemical-argo database. *Journal of Geophysical Research: Oceans*, *123*(2), 1229–1250. https://doi.org/10.1002/2017JC013030

Bianchi, D., Stock, C., Galbraith, E. D., & Sarmiento, J. L. (2013). Diel vertical migration: Ecological controls and impacts on the biological pump in a one-dimensional ocean model. *Global Biogeochemical Cycles*, *27*(2), 478–491. https://doi.org/10.1002/gbc.20031

Boccaletti, G., Ferrari, R., & Fox-Kemper, B. (2007). Mixed layer instabilities and restratification. *Journal of Physical Oceanography*, *37*(9), 2228–2250. https://doi.org/10.1175/JPO3101.1

Boyd, P. W., Claustre, H., Levy, M., Siegel, D. A., & Weber, T. (2019). Multi-faceted particle pumps drive carbon sequestration in the ocean. *Nature*, *568*(7752), 327–335. https://doi.org/10.1038/s41586-019-1098-2
Callies, J., Ferrari, R., Klymak, J. M., & Gula, J. (2015). Seasonality in submesoscale turbulence. *Nature Communications*, *6*(1), 6862. https://doi.org/10.1038/ncomms7862
Callies, J., Flierl, G., Ferrari, R., & Fox-Kemper, B. (2016). The role of mixed-layer instabilities in submesoscale turbulence. *Journal of Fluid Mechanics*, *788*, 5–41. https://doi.org/10.1017/jfm.2015.700
Capet, X., McWilliams, J. C., Molemaker, M. J., & Shchepetkin, A. F. (2008). Mesoscale to submesoscale transition in the California current System. Part I: Flow structure, eddy flux, and observational tests. *Journal of Physical Oceanography*, *38*(1), 29–43. https://doi.org/10.1175/2007JPO3671.1
Cetinić, I., Perry, M. J., D'Asaro, E., Briggs, N., Poulton, N., Sieracki, M. E., & Lee, C. M. (2015). A simple optical index shows spatial and temporal heterogeneity in phytoplankton community composition during the 2008 North Atlantic Bloom Experiment. *Biogeosciences*, *12*(7), 2179–2194. https://doi.org/10.5194/bg-12-2179-2015
Chen, M. (2024). Southern Ocean eddy subduction (version v1.0.3). [software]. https://doi.org/10.5281/zenodo.10999661. *Zenodo*.
Chen, S., Wells, M. L., Huang, R. X., Xue, H., Xi, J., & Chai, F. (2021). Episodic subduction patches in the western North Pacific identified from BGC-Argo float data. *Biogeosciences*, *18*(19), 5539–5554. https://doi.org/10.5194/bg-18-5539-2021
Dall'Olmo, G., Dingle, J., Polimene, L., Brewin, R. J. W., & Claustre, H. (2016). Substantial energy input to the mesopelagic ecosystem from the seasonal mixed-layer pump. *Nature Geoscience*, *9*(11), 820–823. https://doi.org/10.1038/ngeo2818
Davies, A. R., Veron, F., & Oliver, M. J. (2019). Biofloat observations of a phytoplankton bloom and carbon export in the Drake Passage. *Deep Sea Research Part I: Oceanographic Research Papers*, *146*, 91–102. https://doi.org/10.1016/j.dsr.2019.02.004
Dove, L. A., Balwada, D., Thompson, A. F., & Gray, A. R. (2022). Enhanced ventilation in energetic regions of the antarctic circumpolar current. *Geophysical Research Letters*, *49*(13), e2021GL097574. https://doi.org/10.1029/2021GL097574
d'Ovidio, F., Fernández, V., Hernández-García, E., & López, C. (2004). Mixing structures in the Mediterranean Sea from finite-size Lyapunov exponents. *Geophysical Research Letters*, *31*(17), 2004GL020328. https://doi.org/10.1029/2004GL020328
Erickson, Z. K., & Thompson, A. F. (2018). The seasonality of physically driven export at submesoscales in the northeast atlantic ocean. *Global Biogeochemical Cycles*, *32*(8), 1144–1162. https://doi.org/10.1029/2018GB005927
Fox-Kemper, B., Ferrari, R., & Hallberg, R. (2008). Parameterization of mixed layer eddies. Part I: Theory and diagnosis. *Journal of Physical Oceanography*, *38*(6), 1145–1165. https://doi.org/10.1175/2007JPO3792.1
Garcia, H. E., & Gordon, L. I. (1992). Oxygen solubility in seawater: Better fitting equations. *Limnology & Oceanography*, *37*(6), 1307–1312. https://doi.org/10.4319/lo.1992.37.6.1307
Garcia, H. E., & Gordon, L. I. (1993). Erratum: Oxygen solubility in seawater: Better fitting equations. *Limnology & Oceanography*, *38*, 656.
Gruber, N., Gloor, M., Mikaloff Fletcher, S. E., Doney, S. C., Dutkiewicz, S., Follows, M. J., et al. (2009). Oceanic sources, sinks, and transport of atmospheric CO2. *Global Biogeochemical Cycles*, *23*(1). n/a-n/a. https://doi.org/10.1029/2008GB003349
Held, I. M., Pierrehumbert, R. T., Garner, S. T., & Swanson, K. L. (1995). Surface quasi-geostrophic dynamics. *Journal of Fluid Mechanics*, *282*, 1–20. https://doi.org/10.1017/S0022112095000012
Johnson, A. R., & Omand, M. M. (2021). Evolution of a subducted carbon-rich filament on the edge of the North Atlantic gyre. *Journal of Geophysical Research: Oceans*, *126*(2). https://doi.org/10.1029/2020JC016685
Johnson, K. S., Plant, J. N., Coletti, L. J., Jannasch, H. W., Sakamoto, C. M., Riser, S. C., et al. (2017). Biogeochemical sensor performance in the SOCCOM profiling float array. *Journal of Geophysical Research: Oceans*, *122*(8), 6416–6436. https://doi.org/10.1002/2017JC012838
Klein, P., & Lapeyre, G. (2009). The oceanic vertical pump induced by mesoscale and submesoscale turbulence. *Annual Review of Marine Science*, *1*(1), 351–375. https://doi.org/10.1146/annurev.marine.010908.163704
Lacour, L., Briggs, N., Claustre, H., Ardyna, M., & Dall'Olmo, G. (2019). The intraseasonal dynamics of the mixed layer pump in the subpolar North Atlantic ocean: A biogeochemical-argo float approach. *Global Biogeochemical Cycles*, *33*(3), 266–281. https://doi.org/10.1029/2018GB005997
Lacour, L., Llort, J., Briggs, N., Strutton, P. G., & Boyd, P. W. (2023). Seasonality of downward carbon export in the Pacific Southern Ocean revealed by multi-year robotic observations. *Nature Communications*, *14*(1), 1278. https://doi.org/10.1038/s41467-023-36954-7
Lapeyre, G., & Klein, P. (2006). Dynamics of the upper oceanic layers in terms of surface quasigeostrophy theory. *Journal of Physical Oceanography*, *36*(2), 165–176. https://doi.org/10.1175/JPO2840.1
Levy, M., Bopp, L., Karleskind, P., Resplandy, L., Ethe, C., & Pinsard, F. (2013). Physical pathways for carbon transfers between the surface mixed layer and the ocean interior. *Global Biogeochemical Cycles*, *27*(4), 1001–1012. https://doi.org/10.1002/gbc.20092
Lévy, M., Ferrari, R., Franks, P. J. S., Martin, A. P., & Rivière, P. (2012). Bringing physics to life at the submesoscale. *Geophysical Research Letters*, *39*(14), 2012GL052756. https://doi.org/10.1029/2012GL052756
Llort, J., Langlais, C., Matear, R., Moreau, S., Lenton, A., & Strutton, P. G. (2018). Evaluating southern Ocean Carbon eddy-pump from biogeochemical-argo floats. *Journal of Geophysical Research: Oceans*, *123*(2), 971–984. https://doi.org/10.1002/2017JC012861
Mahadevan, A., & Tandon, A. (2006). An analysis of mechanisms for submesoscale vertical motion at ocean fronts. *Ocean Modelling*, *14*(3–4), 241–256. https://doi.org/10.1016/j.ocemod.2006.05.006
Maurer, T. L., Plant, J. N., & Johnson, K. S. (2021). Delayed-mode quality control of oxygen, nitrate, and pH data on SOCCOM biogeochemical profiling floats. *Frontiers in Marine Science*, *8*, 683207. https://doi.org/10.3389/fmars.2021.683207
McDougall, T. J., & Barker, P. M. (2011). Getting started with TEOS-10 and the Gibbs seawater (GSW) oceanographic toolbox. *SCOR/IAPSO WG*, *127*, 1–28.
McDougall, T. J., & Krzysik, O. A. (2015). Spiciness. *Journal of Marine Research*, *73*(5), 141–152. https://doi.org/10.1357/002224015816665589
Nowicki, M., DeVries, T., & Siegel, D. A. (2022). Quantifying the carbon export and sequestration pathways of the oceanocean's biological carbon pump. *Global Biogeochemical Cycles*, *36*(3), e2021GB007083. https://doi.org/10.1029/2021GB007083
Omand, M. M., D'Asaro, E. A., Lee, C. M., Perry, M. J., Briggs, N., Cetinić, I., & Mahadevan, A. (2015). Eddy-driven subduction exports particulate organic carbon from the spring bloom. *Science*, *348*(6231), 222–225. https://doi.org/10.1126/science.1260062
Park, Y.-H., & Durand, I. (2019). Altimetry-drived antarctic circumpolar current fronts. [Dataset]. https://doi.org/10.17882/59800. *SEANOE*.
Rembauville, M., Briggs, N., Ardyna, M., Uitz, J., Catala, P., Penkerc'h, C., et al. (2017). Plankton assemblage estimated with BGC-argo floats in the Southern Ocean: Implications for seasonal Successions and particle export: Plankton assemblage bgc-argo. *Journal of Geophysical Research: Oceans*, *122*(10), 8278–8292. https://doi.org/10.1002/2017JC013067
Resplandy, L., Lévy, M., & McGillicuddy, D. J. (2019). Effects of eddy-driven subduction on ocean biological carbon pump. *Global Biogeochemical Cycles*, *33*(8), 1071–1084. https://doi.org/10.1029/2018GB006125

Riser, S. C., Talley, L. D., Wijffels, S. E., Nicholson, D., Purkey, S., Takeshita, Y., et al. (2023). Southern Ocean carbon and climate observations and modeling (SOCCOM) and Global Ocean biogeochemistry (GO-BGC) biogeochemical-argo float data archive. *UC San Diego Library Digital Collections*. [Dataset]. https://doi.org/10.6075/J0SJ1KT8

Rosso, I., Hogg, A. M. C., Kiss, A. E., & Gayen, B. (2015). Topographic influence on submesoscale dynamics in the Southern Ocean. *Geophysical Research Letters*, *42*(4), 1139–1147. https://doi.org/10.1002/2014GL062720

Rosso, I., Hogg, A. M. C., Strutton, P. G., Kiss, A. E., Matear, R., Klocker, A., & Van Sebille, E. (2014). Vertical transport in the ocean due to sub-mesoscale structures: Impacts in the Kerguelen region. *Ocean Modelling*, *80*, 10–23. https://doi.org/10.1016/j.ocemod.2014.05.001

Sallée, J.-B., Pellichero, V., Akhoudas, C., Pauthenet, E., Vignes, L., Schmidtko, S., et al. (2021). Summertime increases in upper-ocean stratification and mixed-layer depth. *Nature*, *591*(7851), 592–598. https://doi.org/10.1038/s41586-021-03303-x

Siegelman, L., Klein, P., Rivière, P., Thompson, A. F., Torres, H. S., Flexas, M., & Menemenlis, D. (2020). Enhanced upward heat transport at deep submesoscale ocean fronts. *Nature Geoscience*, *13*(1), 50–55. https://doi.org/10.1038/s41561-019-0489-1

Siegelman, L., Klein, P., Thompson, A. F., Torres, H. S., & Menemenlis, D. (2020). Altimetry-based diagnosis of deep-reaching sub-mesoscale ocean fronts. *Fluid*, *5*(3), 145. https://doi.org/10.3390/fluids5030145

Stommel, H. (1979). Determination of water mass properties of water pumped down from the Ekman layer to the geostrophic flow below. *Proceedings of the National Academy of Sciences*, *76*(7), 3051–3055. https://doi.org/10.1073/pnas.76.7.3051

Stukel, M. R., & Ducklow, H. W. (2017). Stirring up the biological pump: Vertical mixing and carbon export in the Southern Ocean: Vertical mixing and carbon export in SO. *Global Biogeochemical Cycles*, *31*(9), 1420–1434. https://doi.org/10.1002/2017GB005652

Tailleux, R. (2021). Spiciness theory revisited, with new views on neutral density, orthogonality, and passiveness. *Ocean Science*, *17*(1), 203–219. https://doi.org/10.5194/os-17-203-2021

The Matplotlib Development Team. (2023). Matplotlib (version v3.7.1). [software]. https://doi.org/10.5281/ZENODO.7697899. *Zenodo*.

The Pandas Development. (2023). Pandas (version v1.5.3). [software]. https://doi.org/10.5281/ZENODO.7549438. *Zenodo*.

The Seaborn Development Team. (2022). Seaborn (version v0.12.2). [software]. https://doi.org/10.5281/ZENODO.7495530. *Zenodo*.

The Xarray Development Team. (2022). Xarray (Version v2022.10.0). [software]. https://doi.org/10.5281/ZENODO.7195919. *Zenodo*.

References From the Supporting Information

Briggs, N., Perry, M. J., Cetinić, I., Lee, C., D'Asaro, E., Gray, A. M., & Rehm, E. (2011). High-resolution observations of aggregate flux during a sub-polar North Atlantic spring bloom. *Deep Sea Research Part I: Oceanographic Research Papers*, *58*(10), 1031–1039. https://doi.org/10.1016/j.dsr.2011.07.007

Predictions of AcousticS with Smart Experimental Networks of GlidERS (PASSENGERS)

Jeffrey W. Book*, Madeline D. Miller†, Nicholas L. Beaird†, Charlie Barron*, Catherine R. Edwards‡, Joseph R. Edwards†, Donglai Gong§, Ashton Lawrence¶ Stephen D. Lynch†, Travis Miles‖, John Osborne*, and Jack Slater§

*Ocean Sciences Division
U.S. Naval Research Laboratory
Stennis Space Center, MS 39529
jeff.book@nrlssc.navy.mil

†Lincoln Laboratory
Massachusetts Institute of Technology
Lexington, MA, 02421
Madeline.Miller@ll.mit.edu

‡Skidaway Institute of Oceanography
University of Georgia
Savannah, GA 31411
catherine.edwards@skio.uga.edu

§Virginia Institute of Marine Science
William & Mary
Gloucester Point, VA 23062
gong@vims.edu

¶Peraton
Peraton Inc.
Stennis Space Center, MS 39529
Ashton.Lawrence.ctr@nrlssc.navy.mil

‖Department of Marine and Coastal Sciences
Rutgers, The State University of New Jersey
New Brunswick, NJ 08901
tnmiles@marine.rutgers.edu

***Abstract*—Predictions of AcousticS with Smart Experimental Networks of GlidERS (PASSENGERS) is a research project on pairing data-assimilative ocean models with adaptive-sampling buoyancy gliders for improved acoustic predictions in strong frontal and eddy-rich environments. The PASSENGERS field campaign consisted of two research cruises near the Atlantis II Seamount in November, 2022 and May/June, 2023. More than 4,500 glider CTD profiles were taken by 7 gliders simultaneously operating in teams and more than 110 days duration of glider hydrophone data were recorded in the vicinity of acoustic source moorings. Tests on using thrusted profiling and hover thrust modes for glider operations in November yielded a maximum through the water glider speed of 0.74 m/s and implementation of these modes in May/June allowed operation of the gliders in the swift Gulf Stream currents over the seamounts. Errors in Naval Coastal Ocean Model facilitated predictions of glider paths ranged from 21-58 km per day in the Gulf Stream, but with daily course corrections the Guidance for Heterogeneous Observation SysTem (GHOST) was able to guide a glider 150 km to pass very close by an acoustic source mooring with similar performance to a human-piloted glider under the same conditions. A PASSENGERS deployed acoustic source generated mid frequency (3-10 kHz) full band LFM up and down sweeps and multi-tone frequency-shift keyed sequences that were recorded by the glider hydrophones. Subsurface acoustic ducts were routinely observed by the gliders operating south of the Gulf Stream and these may have aided reception of the acoustic source transmissions at greater distances.**

***Index Terms*—operational oceanography, ocean observing platforms, forecasting, gliders, acoustics**

I. Introduction

Ocean acoustic propagation is subject to frequency-dependent sensitivity to ocean variability over a wide range of scales: from meter-scale gradients in the vertical to range-dependent horizontal gradients over distances of kilometers to tens of kilometers. Subsurface ocean structure constraints from satellite altimetry are subject to very high uncertainty, and submesoscale features cannot be resolved with their nine days or greater repeat cycles. The world's network of ARGO floats can resolve one-meter vertical scales but have sparse spatial coverage relative to submesoscale ocean structures and profile too infrequently to resolve their quickly evolving dynamics. In regions of strong currents such as the Gulf Stream, mobile ocean sensing platforms are quickly advected $>$ 100 km in less than a day's time. All of the above issues impact ocean forecasting because of the need to assimilate dynamically-representative temperature and salinity profile data on a daily basis. The challenges are compounded for predicting acoustics because acoustic pathways are sensitive to the small-scale temperature and salinity gradients that are particularly difficult to resolve in models.

As part of the Office of Naval Research (ONR) Task Force Ocean (TFO) initiative, the Predictions of AcousticS with Smart Experimental Networks of GlidERS (PASSENGERS) project is conducting research on these challenges in and around the region where the Gulf Stream crosses the Atlantis II Seamount (Fig. 1). A focus of our research is on how teams of buoyancy gliders [1] may be used in novel ways to improve ocean acoustic forecasting. The buoyancy gliders in PASSENGERS serve two purposes in this effort: 1) their temperature and salinity data are used in the ocean forecast model to improve its accuracy, and 2) each glider carries a passive acoustic monitoring system (PAM) that records transmissions coming from deployed acoustic sources for validation of acoustic forecasting. Optimizing glider paths for their sensing capabilities has been studied before, for example in [2], [3], and others, but in PASSENGERS the optimal sampling locations for ocean data assimilation and the optimal paths to collect acoustic data for validation and analysis do

979-8-218-14218-6 ©2023 MTS

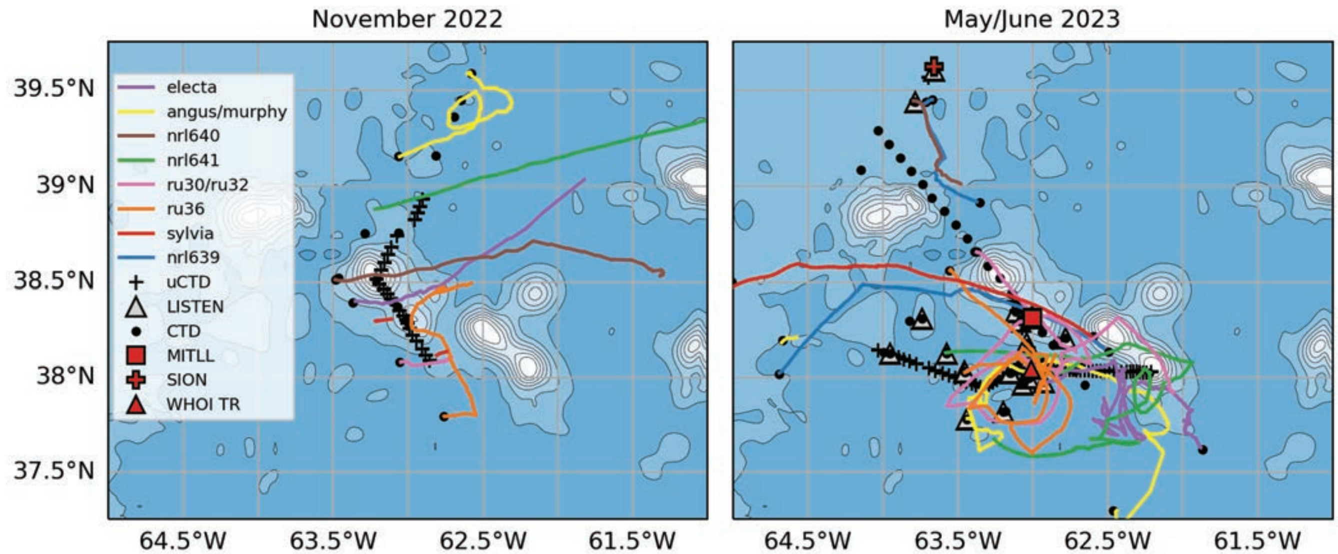

Fig. 1. Maps of measurements made by the PASSENGERS cruises. Bathymetry is shaded in blue with contours drawn in gray to show the seamounts.

not always align. Furthermore, while use of a variational assimilation technique as in [4] is likely to lead to a better solution than objective analysis for a data sparse environment, it also makes the sensor optimization problem more complex. Finally, areas with strong and recurrent small-scale oceanic features tend to also have strong and variable currents, which limit glider path choices and optimization schemes. This is particularly true for the PASSENGERS experiments.

II. Experimental Setting and Measurements

A. PASSENGERS Measurements

The PASSENGERS field research campaign consisted of two research cruises near the Atlantis II Seamount, one pilot cruise in November 2022 and a longer effort in May/June 2023 as part of the New England Seamount Acoustics (NESMA) 2023 field campaign. Atlantis II is a seamount within the far offshore extent of the New England Seamount Chain and close to the normal pathway of the Gulf Stream. The presence of the seamounts and the Gulf Stream fronts make accurate acoustic predictions particularly challenging, which further motivates our research on the effects of small-scale ocean features on acoustic propagation and prediction. Fig. 1 shows the measurements that were taken during the two field campaigns.

During the November 2022 cruise, the glider deployments and ship sampling focused on assessing the capability of gliders to hold station against the strong Gulf Stream currents, while also collecting a baseline ambient acoustic and glider self-noise dataset. The results of the pilot experiment were used for design of the 2023 glider sampling plan and active acoustic transmit schedule. During the November experiment, six gliders were operated in two teams over Atlantis II Seamount, the nearby Caldera seamount structure, and across the Gulf Stream. The gliders were assigned waypoints along two transects originating at Atlantis II Seamount. One transect was aligned southeastward towards the Caldera (NRL640 with 200 m profiles, Electa with 350 m profiles, RU32 with 1000 m profiles, and RU36 with 1000 m profiles), and the other was northwestward towards the open ocean (NRL640 with 200 m profiles, NRL641 with 1000 m profiles, and Murphy with 1000 m profiles).

All gliders were equipped with CTDs, resulting in 1,400 glider CTD profiles. PASSENGERS also collected 16 deep (2000 m) ship CTDs and 58 Underway CTDs to about 900 m depth along the experiment transects in November. All of the gliders were outfitted with calibrated HTI96-min hydrophones and Loggerhead LS1 recorders and they captured ambient and self-noise from gliders in the mid-frequency (3-24 kHz) range throughout the 12-day test.

During May 2023, due to initial technical problems with the PASSENGERS acoustic source (MIT Lincoln Lab, MITLL Fig. 1), PASSENGERS gliders were deployed within hearing range of either the Woods Hole Oceanographic Institution Transceiver (WHOI TR) or the Scripps Institution of Oceanography North (SIO N) moored acoustic sources. WHOI TR had a mooring with low frequency (LF 500-600 Hz) and mid frequency (MF, 2750-4250 Hz) sources at 700 m depth transmitting 2.5-second length, 10-second pulse repetition interval (PRI), linear frequency modulated (LFM) up sweeps for 5 minutes at the top of every hour. SIO N had a source at 1100 m depth transmitting 3 sets of LFM up/down sweeps from 230 Hz to 320 Hz at the top of every hour. Each up or down sweep was 1-minute long, adding up to a total transmission time of 6 minutes.

Two gliders (NRL641 with 1000 m profiles and Electa with 350 m profiles) were deployed near WHOI TR to track the highest predicted sound speed gradients that increased with depth at 300 m. Because temperature stratification at 300 m is usually strong enough to insure that sound speed decreases with depth at that level, an increasing-with-depth sound speed at 300 m is indicative of the presence of a local sound speed minimum above 300 m, forming a subsurface acoustic duct. By tracking these increasing-with-depth subsurface sound speed gradients, we aimed to characterize the subsurface ducts by having gliders profile through them and map their horizontal extents. Sound speed profiles from glider Electa shown in Fig. 2 captured the upper ocean sound speed minimum between 150 and 300 m in the region south of the Gulf Stream. This subsurface acoustic duct feature persisted throughout the study, but varied significantly in strength and vertical structure. The observed sound speed profiles also exhibited strong tidal oscillations as well as near surface effects from the Gulf Stream, both of which could impact acoustic propagation.

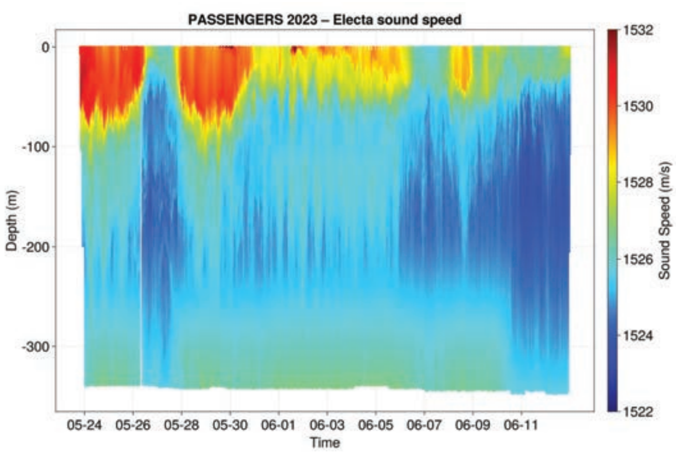

Fig. 2. Time series of the sound speed profiles observed by glider Electa during May/June 2023

Three gliders (RU30 with 1000 m profiles, RU36 with 1000 m profiles, and Angus with 200 m profiles) were deployed to attempt station keeping at fixed distances from WHOI TR. Two other gliders (NRL639 with 200 m profiles and NRL640 with 200 m profiles) were deployed near SIO N and were set to track areas of highest sound speed variability. These two gliders were recovered on June 1st in preparation for a redeployment near the MIT LL acoustic source planned for the second leg of this cruise. However, NRL640 was extremely corroded due to a battery fault and could not be redeployed.

For the June portion of the field work the MITT LL acoustic source was deployed after its repair. The MF (3-10 kHz) source was moored at a nominal 450 m depth and transmitted for 96 hours. The signal schedule was 1-second length, 6-second PRI broadband signals, repeated throughout the duration of the source deployment, to achieve vertical resolution of glider acoustic receptions of about 0.9 m (assuming glider vertical ascent/descent rate of approximately 0.15 m/s). The signals were a mix of full band LFM up and down sweeps and multi-tone frequency-shift keyed sequences (FSKs). NRL639 along with a new glider teammate (Sylvia with 200 m profiles) were deployed upstream in the Gulf Stream on coordinated paths planned to take them nearby the MIT LL source located on the Caldera. In addition, NRL641, RU30, and RU36 gliders were recovered and re-positioned on coordinated paths planned to also take them past the MIT LL source. Gliders Electa and Angus continued to gather data, now relatively far to the southeast of WHOI TR. In total for the May/June 2023 field experiment, 3,186 glider CTD profiles, 60 deep ship CTDs, and 71 Underway CTDs were collected. The hydrophones on the eight gliders recorded more than 110 days duration of sound, primarily in the vicinity of WHOI TR and profiling through subsurface acoustic ducts.

B. PASSENGERS Modeling

PASSENGERS field work was supported by an ocean forecasting system that assimilated both project glider observations and routinely collected observations distributed through the World Meteorological Organization's Global Telecommunication System (e.g., sea surface height anomaly data, sea surface temperature data, ARGO profile data). The numerical core of the forecasting system was the Navy Coastal Ocean Model (NCOM) [5] and data was assimilated via three-dimensional data assimilation in the Navy Coupled Ocean Data Assimilation system (NCODA) [4]. NCOM was configured with 2 km horizontal resolution and 50 vertical levels. The domain extended from 31°N to 43.2°N and from the US East Coast offshore to 54.50°W. Boundary conditions were from the Navy's Global Ocean Forecasting System (GOFS, version 3.1). Because GOFS 3.1 does not have tides, barotropic tides (eight major constituents) were applied at the boundary and sourced from the Oregon State University TPXO Tide Model [6]. GOFS is also the source of initial conditions (Nov. 1, 2022). Atmospheric forcing is from the Navy Global Environmental Model (NAVGEM) [7]. A global model was used due to the relatively large and remote extent of the NCOM domain.

Daily results from the NCOM ocean forecasting model were used in multiple ways during the PASSENGERS experiments. The results were sent to the PASSENGERS and other NESMA scientists at sea to inform adaptive sampling daily plans. NCOM forecasts were also used in the Guidance for Heterogeneous Observation SysTems (GHOST) to generate glider pilot assistance maps by predicting the path of a glider if directed to swim towards a particular waypoint [8]. GHOST can also compare predicted sampling results between different waypoints to allow a glider pilot to select waypoints that are predicted to be optimal for particular sampling goals. GHOST guidance was run daily for many of the PASSENGERS gliders to support their different sampling goals and provide waypoint suggestions for possibly implementation. Glider observations of temperature and salinity profiles were in turn assimilated back into NCOM [4] to improve future glider pathway forecasts.

NCOM results were also used to generate acoustic forecasts using the Bellhop acoustic ray tracing model along the glider transects. Bellhop was set up to model transmission loss for a source frequency of 6 kHz using a range-dependent sound speed section provided by the daily NCOM forecast. Bathymetry was from NOAA Okeanos Explorer (EX1303): New England Seamount Chain Exploration. The transmission loss results from Bellhop were used to determine the acoustic convergence zone or location of highest predicted signal/lowest transmission loss for each transect for the day. These acoustic positions of importance were then used as target goals in GHOST for glider sampling for one glider on each transect in November when possible.

C. Gulf Stream Background Flow

As expected, the Gulf Stream played a prominent role for both the November 2022 and the May/June 2023 experiments as it crossed close by the Atlantis II Seamount. Fig. 3 shows shipboard Acoustic Doppler Current Profiler (ADCP) data gathered by the R/V Atlantic Explorer during a crossing of the Gulf Stream on November 11, 2022 and on May 26-28, 2023. The latter crossing was slower than the former because the ship stopped to take 2000 m CTD casts every 10 km along the track.

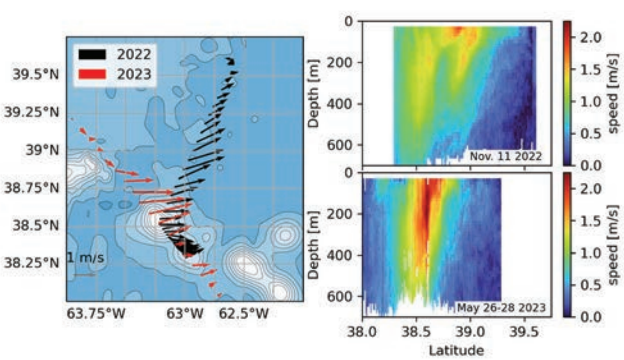

Fig. 3. Left-hand panel shows map of Gulf Stream currents for Nov. 2022 (black) and May 2023 (red) as measured by the shallowest depth bin (27 m) of R/V Atlantic Explorer's shipboard ADCP. The right-hand panels show the measured speed depth structure for Nov. (top) and May (bottom) versus latitude.

There were notable differences in Gulf Stream strength, position, and structure between the two field campaigns. In May 2023, the peak observed speed of the Gulf Stream was 2.22 m/s compared to only 1.86 m/s in November 2022. The core of the Gulf Stream was located directly over the northern flank of the Atlantis II Seamount on May 27. It was located further north on November 11 with a somewhat broader area of strong flow compared to the peaked but narrow core observed in May. Some of the apparent broadening of the flow could be due to different crossing angles, but it is clear that the Gulf Stream was more compact in May than in November. There is also a big difference in the current shear profiles between the two crossing with the May crossing showing very little current shear down to a depth of 600 m. In contrast, the November crossing had areas of high shear in the upper 200 m right under the core and relatively high shear between 200 and 400 m north of the core. Shear was relatively weak directly over the seamount (about 38.5°N) in both cases.

III. Results

Analyses are ongoing for the PASSENGERS data collected in November 2022 and May/June 2023. Here we summarize some of our early results from this field work with a focus on glider operation and measurements.

A. November Glider Speed Tests

Several strategies were tested in November to experiment with glider settings and thruster modes of operation for maintaining station in extreme ocean current conditions for acoustic sampling. Normally such strategies are not tried in the field as typical goals for glider sampling are to maximize duration of sampling and avoid high-battery use settings. However, objectives of acoustic sampling may not require multiple months of observations and it could be more important to maintain position close to a sound source mooring for acoustic monitoring than have an extended mission that is far from the sound source and unable to observe it despite retaining battery reserves.

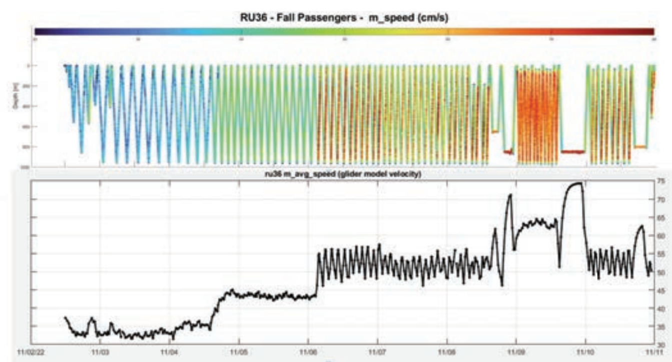

Fig. 4. Top panel shows the time/depth position of the RU36 glider during the PASSENGERS November 2022 field experiment. Bottom panel shows the segment averaged speed (cm/s) through water of the glider versus time. Instantaneous horizontal speed (cm/s) through water is also shown in color on the top panel. Both are calculated onboard the glider using depth rate of change and pitch angle, assuming a nominal 0° angle-of-attack.

Fig. 4 shows the progressively faster speeds through water achieved by RU36 during the November 2022 experiment. From Nov 2 through midday on Nov 4, typical glider settings were used and the speed through water was about 0.35 m/s. RU36 is a generation 3 glider with an expanded capacity buoyancy engine. Therefore, from Nov 4 midday to Nov 6 the buoyancy engine capacity was increased from ± 200 cm^3 of a typical glider to its full expanded capacity of ± 400 cm^3. The resulting speed through water increase was about an additional 9 cm/s to 0.44 m/s. RU36 was equipped with a thruster, which can be used to assist with surfacing through a freshwater plume or to increase the speed of the glider (at the cost of higher energy usage) in either thrusted profiling or hover thrust modes. From Nov 6 to midday on Nov 8, the thruster was turned on during the upcast portion of the glider profile leading to about an additional 8 cm/s speed through water increase to 0.52 m/s. On Nov 9 for about 12 hours, the thruster was used during both the upcast and downcast leading to about an additional 12 cm/s speed through water increase to 0.64 m/s.

On November 9 for 8 hours a hover thrust mode was tried with RU36. This mode sends the glider to depth (in this example to 800 m) and runs the thruster with the glider oriented horizontally (0°) rather than at its typical 26° tilt from horizontal. This use led to a further 10 cm/s increase in speed through water from the case of using the thrusters while profiling. The 0.74 m/s speed through the water was replicated when the Electa glider also was run in a hover thrust mode. This mode has the distinct disadvantage of taking no measurements when used, but has some advantages. In addition to having the highest overall speed through water, it also can take advantage of current shear with depth so that its speed over ground would be, e.g., 0.74 m/s minus the current speed at 800 m depth rather than 0.52 m/s minus the average current speed between 0 and 1000 m as would be the case for using the thruster on the upcast. Running a hover thrust mission continuously is not practical because of its high energy usage and lack of measurements. However, strategies that include hover thrust missions combined with regular profiling should be considered for station keeping in strong currents, especially ones with high levels of vertical current shear.

Theoretical calculations were conducted using the measured ADCP currents from the ship in November and we predicted that using a hover thrust mode for 8 hours per day would have allowed gliders to station keep on the southern boundary area of the Gulf Stream over the Caldera in November 2022. However, in May/June 2023 the Gulf Stream flow over the Caldera was much stronger than in November 2022 and had little shear with depth (Fig. 3). This lack of shear made hover thrusting in May/June less advantageous and therefore the glider thrusters were primarily used during upcast sampling to increase speed during the 2023 experiment. Experimenting with glider thruster modes in November paid off as the strategies practiced then led to better glider performances in May/June (Fig. 1) with no gliders being caught in the Gulf Stream and advected far away.

B. Glider Team Flyby of the MIT LL Acoustic Source

The MIT LL acoustic source was repaired during a port stop in the May/June 2023 PASSENGERS research cruise and the acoustic source mooring (MITLL Fig. 1) was deployed on the Caldera on June 8 at the beginning of the last leg of the cruise. The source was programmed to acoustically broadcast from June 8 to the morning of June 13 (about 4 days) and then programmed to stop transmissions for safety of recovery. Two gliders (NRL639 and Sylvia) were also prepared during the port stop for dedicated acoustic sampling of this source. The Gulf Stream was still flowing close to the Caldera (Fig. 3) as verified by glider RU30 operating just to the south and currents at the Caldera were too strong for glider station keeping even if using the methods of section III-A. Therefore, we planned the deployments of NRL639 and Sylvia for areas of highest predicted sound speed gradients that increased with depth at 300 m and which occurred 160-180 km upstream of the Caldera. If these 200 m gliders lost ground to the Gulf Stream at a rate of 1 m/s, then such a deployment would bring them to the Caldera in about 2 days' time and allow them to sample for 2 days upstream of the acoustic source and for 2 days downstream of the acoustic source before it turned off.

Runs of GHOST predicted that the gliders would both stay south of the acoustic source over their closest 72 hour course approaches, but a northward shift of their deployment positions by 30 km would allow them to make a closer approach. Therefore the gliders were deployed at these northward shifted positions (Fig. 5). Actual deployments were 149 km (NRL639) and 177 km (Sylvia) distant from the source. NCOM predicted southeastward currents between the gliders and the Caldera, so the initial assigned waypoints were to the northeast (blue and green squares in Fig. 5) in order to track a eastward path (dashed lines are the predicted pathways). This turned out to be an over-prediction of the southward component of flow and both NRL639's and Sylvia's true paths (blue and green lines) over the course of the first day were north of the predicted ones.

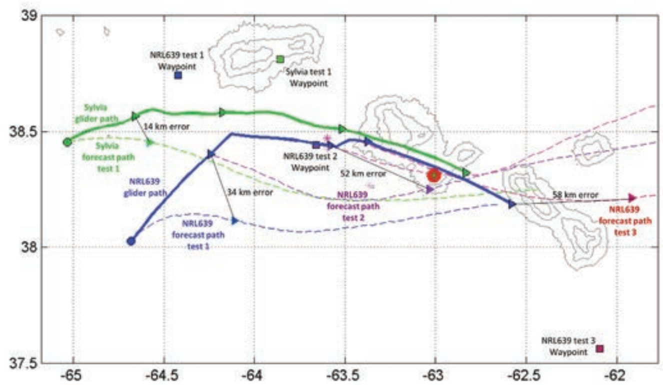

Fig. 5. Map of upstream deployments of Sylvia (solid green line) and NRL639 (solid blue line) for June 9-13, 2023. The red circle is the MITLL acoustic source mooring. Triangles show positions for GHOST glider path forecast initializations and dashed lines show forecast tracks as labeled. GHOST waypoints that were used for tests are shown as squares and labeled. Waypoints used for the glider but not for tests are shown as stars. The pink dashed line is a GHOST forecast path between test 2 and test 3, but was excluded from the test count as waypoints (light purple stars) other than the GHOST one (purple star) were used for that day.

On the second day of the flyby approach with these two gliders it was decided to have Sylvia aim for a waypoint directly on the Caldera. NRL639 continued to use GHOST selected waypoints after vetting by glider pilots. Using the next-day's NCOM forecast and accounting for a new starting position of the glider, the new GHOST recommended waypoint (purple square in Fig. 5) was shifted to be directly east and only slightly north of the day 2 starting point. NRL639's path was predicted to dip southeastward before returning northeastward and passing close by the acoustic source in 28 hours' time (purple dashed lines). This second waypoint was sent to the glider 8 hours later than what GHOST had simulated as can be noticed in NRL639's abrupt turn to the east in its path. NRL639 did not dip southward as predicted and was able to directly fly towards this new waypoint, even passing directly over it. Ghost's new guidance on day 3 kept the waypoint (purple star) near the same location as on day 2. This successfully slowed NRL639 progress much more than predicted (compare the pink dashed line to the distance between the two blue triangles near 63.5°W) and several other waypoints were tried by the piloting team (light purple stars) to try and speed up progress to the acoustic source.

On Day 4 there was a drastic change in GHOST's recommended waypoint as it was shifted far to the southeast (red square in Fig. 5). The path that NRL639 took passed very close to the acoustic source as desired and followed the GHOST predicted path quite closely. However, its progress along this path was much slower than predicted, ending 58 km west (final blue triangle) of its predicted end point (red triangle). Table I summarizes the distance, angle, and speed errors between the predicted pathway and actual pathways of the gliders during these tests. Day 3 guidance for NRL639 is excluded due to the changing waypoints. Timing delays in implementation of the waypoints are not treated separately so a portion of these errors could be attributable to those delays. It is clear that NCOM over-predicted the Gulf Stream flow on June 9-13 for this region with stronger southward and eastward flows than the gliders actually experienced. The average over-predicted speed was 0.48 m/s for these experiments. Despite this, with daily course corrections, GHOST guidance did succeed in the mission of bringing a glider for a very close flyby of the PASSENGERS acoustic source mooring. However, the benefit of flying in the Gulf Stream with GHOST is unclear as Sylvia also succeeded in a close flyby of the source by placing a waypoint at that location.

TABLE I
GLIDER PATH FORECAST ERRORS

experiment	distance error	angle error	duration	avg. current error
Sylvia test 1	14.2 km	150°T	16 hours	0.25 m/s
NRL639 test 1	33.5 km	160°T	22 hours	0.42 m/s
NRL639 test 2	51.7 km	114°T	28 hours	0.51 m/s
NRL639 test 3	57.9 km	87°T	24 hours	0.67 m/s

Glider RU30 was directed to swim towards the MIT LL acoustic source mooring after the mooring was deployed on June 8, but Gulf Stream currents soon swept it far to the east and south (note southeastward extent of pink line in Fig. 1). Therefore, we recovered this glider along with RU36 and NRL641 which were far south of the source mooring, and redeployed them on June 11 (local ADT time) within 55 km of the Caldera (Fig. 6). NRL641 was directed by GHOST to run a straight eastward track in-between the MIT LL and WHOI TR acoustic source moorings. RU36 was directed by pilots to run a southeastward track staying southeast of the topography of Atlantis II and the Caldera. RU30 was directed by pilots to run a parallel southeastward track but passing directly over Atlantis II and the Caldera. All three of these planned tracks were successfully executed even in Gulf Stream currents. Together with Sylvia and NRL639 tracks that had been staged earlier, this formed a five glider team flyby of the MIT LL acoustic source mooring from June 11-13 with appropriate glider spacing for planned future data assimilation studies. On June 13, just before the acoustic source mooring was programmed to stop transmitting, both the R/V Atlantic Explorer and the R/V Armstrong (one of our collaborating partner ships) stopped operations and lowered hydrophones on their CTD profiles to also record the transmissions of the MIT LL source simultaneous to what was being recorded by the 5 glider mobile receiving array that we had formed (Fig. 6).

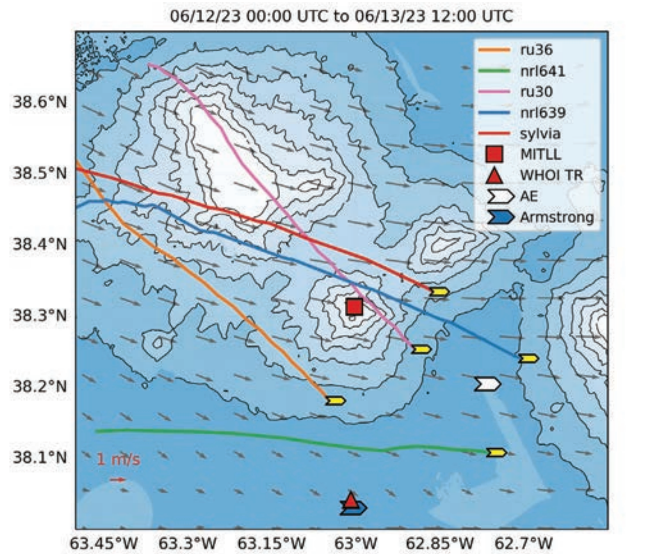

Fig. 6. Map of glider flyby mobile receiving array experiment conducted on June 12-13 (UTC), 2023. Bathymetry is shaded in blue with contours drawn in gray to show the seamounts. Gray arrows are surface current predictions from NCOM. Colored lines show glider tracks with ending positions indicated as yellow symbols. Acoustic source moorings (MITLL and WHOI TR) and research vessel R/V Atlantic Explorer (AE) and R/V Armstrong positions on June 13 are also shown and labeled in the key.

C. Gliders as Mobile Acoustic Receivers

One focus of PASSENGERS was using buoyancy gliders as shallow-water mobile acoustic receivers. Due to the proximity of WHOI TR and MIT LL acoustic sources, gliders that passed between them during favorable acoustic conditions were able to simultaneously capture sound from both. Fig. 7 is a spectrogram from acoustic data recorded on RU30 when it made its first attempted approach towards the MIT LL source on June 9 and the glider was 42 km from the MIT LL source and 46 km from the WHOI TR source. While the MIT LL acoustic source was transmitting throughout this time, the glider was descending and the vertical acoustic refraction was most favorable during the 25-45 s window. RU30 also captured the WHOI TR LF (500-600 Hz) and MF (2.75-4.25 kHz) upchirps starting at the top of the hour, which is around 70 s into this recording section. Overlapping the WHOI TR MF source is broadband glider self-noise from 2.5-4 kHz. The broadband (0-10 kHz) glider self-noise is from the glider's rudder.

Fig. 7 also shows the glider observed sound speed profile recorded at the same time as the acoustic transmissions shown in the spectrogram. The presence of a subsurface acoustic

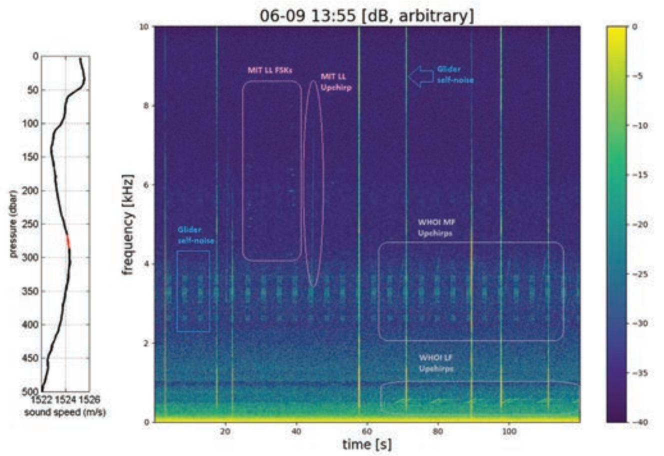

Fig. 7. Left panel shows the sound speed profile in the upper 500 m observed by RU30 glider on 6/9/2023 from 13:35-14:12 UTC. Right panel shows the spectrogram from RU30 glider PAM simultaneously capturing MIT LL and WHOI TR acoustic sources and self-noise. Red highlights on the left panel graph show the depth location (266-286 m) of the glider when the acoustic data was collected as analyzed in the right panel.

duct is clearly indicated by the local sound speed minimum at 136 m depth and the glider was within the duct (above the local sound speed maximum) when the MIT LL and WHOI TR transmissions were heard. Such ducts were routinely observed by all the gliders operating south of the Gulf Stream and in this case may have helped facilitate recording of the acoustic source mooring transmissions.

IV. Summary

PASSENGERS collected a large physical oceanography and acoustic propagation dataset that successfully resolved some of the multiple-scale dynamic processes associated with the Gulf Stream crossing over the Atlantis II and neighboring seamounts. This dataset will facilitate our future work on improving acoustic forecasting for such regions using teams of buoyancy gliders. The November pilot study showed the possibilities for enhancing glider performance with strategic thruster use and the lessons learned allowed us to keep a fleet of 7 gliders of varying capabilities sampling within a 130 km by 110 km box at the edge of the Gulf Stream for the majority of a three week concentrated experiment in May/June (Fig. 1). Results from PASSENGERS illustrate the need for improvements in forecasting the Gulf Stream position and currents for glider path planning and other purposes (Table I). Our future plans include using this PASSENGERS dataset in a multi-scale data assimilation research effort to improve both the physical oceanography and acoustic forecasting capabilities of our real-time modeling systems.

Acknowledgment

This work would not have been possible without many long days from dedicated teams aboard the R/V Atlantic Explorer and on-shore piloting gliders. The offshore team included Leslie Birch, Emily Busch, Angel Diaz, Breana DiRenzi, Anthea Empson, Rhyan Grech, Ian Martens, Jason Noel, Andrew Quaid, Annat Sonion, and Jon Wood. Frank McQuarrie served ashore on one leg and offshore on two others while Karen Dreger did the opposite. Brian Buckingham served offshore during every leg of PASSENGERS. The onshore team also included David Aragon, James Bird, Drew Vincent, and Nicole Waite. Port Captain Rick Verlini was very helpful with all our customs issues and even filled in at the last minute during one leg at sea. Ruth Curry and Jonny Chapman very generously allowed our team use of their glider facilities for ballasting, calibration, and other glider work. Bermuda Institute of Ocean Sciences hosted us during our time preparing for these efforts. The crew of the R/V Atlantic Explorer were exceptional and we would like to especially thank Marine Science Technicians Rory O'Connell, Lydia Sgouros, and Oban Jones, and Captains George Gunther and Patrick Redmond.

References

[1] D. L. Rudnick, R. E. Davis, C. C. Eriksen, D. M. Fratantoni, and M. J. Perry, "Undersea gliders for ocean research," *Marine Technology Society Journal*, vol. 38, no. 2, pp. 73–84, 2004.

[2] N. E. Leonard, D. A. Paley, F. Lekien, R. Sepulchre, D. M. Fratantoni, and R. E. Davis, "Collectivemotion, sensor networks, and ocean sampling," *Proceedings of the IEEE*, vol. 95, no. 1, pp. 48–74, 2007.

[3] N. E. Leonard, D. A. Paley, R. E. Davis, D. M. Fratantoni, F. Lekien, and F. Zhang, "Coordinated control of an underwater glider fleet in an adaptive ocean sampling field experiment in Monterey Bay," *Journal of Field Robotics*, vol. 27, no. 6, p. 718–740, 2010.

[4] J. A. Cummings and O. M. Smedstad, "Variational data assimilation for the global ocean," in *Data Assimilation for Atmospheric, Oceanic and Hydrologic Applications (Vol. II)*, S. Park and L. Xu, Eds. Berlin, Heidelberg: Springer, 2013.

[5] C. N. Barron, "Formulation, implementation and examination of vertical coordinate choices in the Global Navy Coastal Ocean model (NCOM)," *Ocean Modeling*, vol. 11, no. 3-4, pp. 347–375, 2006.

[6] G. D. Egbert and S. Y. Erofeeva, "Efficient inverse modeling of barotropic ocean tides," *Journal of Atmospheric and Oceanic Technology*, vol. 19, no. 2, pp. 183–204, 2002.

[7] T. F. Hogan, "The Navy global environmental model," *Oceanography*, vol. 27, no. 3, pp. 116–125, 2014.

[8] L. F. Smedstad, C. N. Barron, R. N. Bourg, M. W. Brooking, D. A. Bryant, R. J. Carr, K. D. Heaney, E. A. Holmberg, A. C. Mask, and B. L. Mensi, "An expansion of glider observation strategies to systematically transmit and analyze preferred waypoints of underwater gliders," in *Ocean Sensing and Monitoring VII*, W. W. Hou and R. A. Arnone, Eds., vol. 9459, International Society for Optics and Photonics. SPIE, 2015, p. 94590J. [Online]. Available: https://doi.org/10.1117/12.2176560

Risk Assessment of Underwater Glider Turbine Interaction

Julia Engdahl, David Aragon, Kaycee Coleman, Travis Miles, Grace Saba, Josh Kohut
Center for Ocean Observing Leadership (COOL)
Rutgers University
New Brunswick, New Jersey 08901, USA
engdahl@marine.rutgers.edu

Abstract*— The presence of offshore wind infrastructure in the Northeast U.S. ocean is rapidly increasing to achieve the national goal of 30 gigawatts power by 2030. With varying foundation configurations and grid layouts, construction of offshore wind farms will impact several state and federal surveys that provide invaluable insight to stock management and the impacts of climate change on marine species, habitats, and ecosystems. In addition to the risk of active and derelict gear entanglement from vessels engaged in bottom trawling or dredging with offshore wind infrastructure, alternative non-extractive survey methods (e.g., autonomous underwater vehicles such as ocean gliders) share the risk of entanglement and interacting with infrastructure highlighting the need for careful operational planning and risk mitigation strategies. Our study aims to assess the risk of interaction between ocean gliders and offshore wind turbines within the Wind Energy Areas (WEAs) OCS-A 0498, OCS-A 0499, and OCS-A 0512 using a decade of historic glider track data in a simulated environment of turbine pylons. We utilized 142 historical glider deployments from 2013 to 2023, incorporating an interaction algorithm that accounts for varying buffer zones (0, 2, 4, 20, and 30 meters) beyond monopile foundations to model potential interaction scenarios. It was found that about 1 interaction per deployment occurred across our 142 deployments where no avoidance routines were used. The analysis revealed that risk varies across different WEAs and buffer zones. Simulated interactions were more frequent in larger buffer zones and WEAs that had an increased number of deployments, with a noticeable difference in interaction rates between turbine structures and substations. Specifically, simulated interactions with turbines at depth were more prevalent than surface and substation interactions. While surface interactions are less common, they may pose greater risks due to environmental conditions near the surface (e.g., waves, winds, currents, storms, etc.). Additionally, the infrequent substation interactions could pose a greater risk to the glider due to its foundation type (i.e., piled jacket) which has more underwater structure to interact with. The study highlights a trend where increased time spent in WEAs translates to higher interaction frequencies and reduced time between interactions. This study highlights the baseline interaction rates and thus importance of enhanced operational strategies, vehicle vulnerability awareness, and real-time monitoring to mitigate interaction risks in areas of active offshore wind development.

Keywords—Underwater Glider, Turbines, Wind Energy Area, Interaction

I. Introduction

With a national goal of 30 gigawatts of power coming from offshore wind by 2030, the Northeast U.S. ocean is rapidly under development [1]. Offshore wind structures serve different purposes and come in various configurations, including but not limited to monopiles, jackets, and tripods, as well as substations and other support infrastructure. They are designed for use at different depths, encompassing both bottom-fixed and floating foundations. Bottom-fixed foundations and the anchors for floating foundations interact with the soil and water characteristics such as depth, current velocity and direction, waves, and tides in the surrounding area which can elicit erosion of the seabed. To counteract this effect, scour protection, which involves placing an armor layer such as coarse rock material, is installed around the structure [2, 7-9].

The construction of offshore wind farms along the Northeast U.S. coastal shelf will impact several federal and state surveys that are paramount to understanding the effects of climate change on marine species, habitats, and ecosystems [3]. Offshore wind farms can present a risk of gear entanglement with turbine structures and cables for both derelict and active survey gear. The likelihood of entanglement increases for vessels engaged in bottom trawling or dredging when turbines are spaced less than 1 nautical mile apart [4]. Due to safety concerns and gear loss, non-extractive survey methods are being considered as alternative data collection methods to mitigate the impact to these traditional surveys. One platform that could support this non-extractive data collection are autonomous underwater vehicles (AUV) equipped with active acoustic sensor payloads.

AUVs, such as ocean gliders, are considered low-energy, long-endurance, and relatively cost-effective vehicles. These mobile sensor platforms propel themselves vertically and horizontally in a triangle pattern by changing buoyancy, enabling the collection of spatial and temporal data throughout the water column [5]. The modular ability to incorporate sensors for physical, biological, and chemical data collection is integral to filling observational gaps where ships and remote sensing could not succeed. Additionally, this capability aids in the validation and data assimilation of models [5-6]. For these reasons, gliders have become a staple in oceanographic and ecosystem monitoring surveys, from the deep ocean to nearshore coastal environments including the regions identified for offshore wind development.

OCEANS 2024 - Halifax | 979-8-3315-4008-1/24/$31.00 ©2024 IEEE | DOI: 10.1109/OCEANS55160.2024.10754184

Sharing the ocean with large vessels and hardened static structures such as buoys, moorings, or oil platforms has presented interaction risks such as collision, entanglement, and sensor damage that can lead to vehicle loss. This has led to diligent monitoring and piloting to minimize these risks. The offshore wind environment may introduce increased hazard to oceanographic gliders as well as any vehicles with limited amounts of control to avoid interactions. We intend to 1) assess the risk of glider-turbine interaction occurring, 2) estimate the potential impact if the risk were to occur, and 3) suggest mitigation behaviors. We use a decade of historical glider tracks within the New Jersey/New York Bight (NYB) region as well as simulated glider behaviors to explore these topics.

II. Methods

A. Study Area

The Rutgers University Center for Ocean Observing Leadership maintains several operational survey lines off New Jersey. Therefore, this study focused on the near shore Wind Energy Areas (WEAs) off New Jersey (Fig. 1) to evaluate the feasibility of maintaining these historic survey lines. WEAs of focus include OCS-A 0499 (Atlantic Shores Offshore Wind Projects 1 and 2), OCS-A 0498 (Ørsted Ocean Wind 01), and OCS-A 0512 (Empire Wind). This study was limited to the WEAs that overlap with historic glider deployments and have publicly accessible turbine layouts. While Ocean Wind 01 was terminated in October of 2023, we used the proposed turbine design to help inform piloting behavior if development in OCS-A 0498 does occur in the future. Publicly available shapefiles for offshore wind farms designated as WEA borders, proposed and operational turbine locations, and proposed and operational substation locations in the NYB were retrieved from https://marinecadastre-noaa.hub.arcgis.com/ and/or directly from developer.

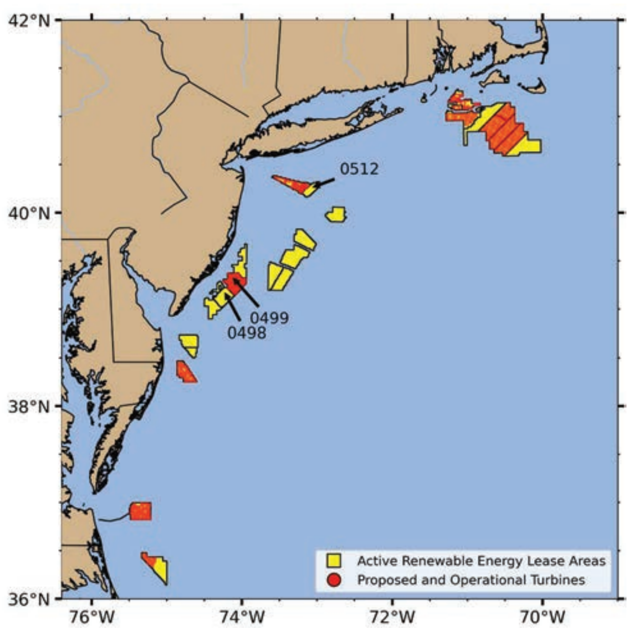

Fig. 1. Map of active renewable energy lease areas (yellow) with proposed and active turbine locations (red) in the Mid-Atlantic region. Arrows pointing areas in the NYB used in this analysis: OCS-A 0512, OCS-A 0499, and OCS-A 0498. Data retrieved from https://marinecadastre-noaa.hub.arcgis.com/.

The terminated Construction and Operations Plan (COP) for OCS-A 0498 spanned 75,525 acres with 98 turbines and 3 substations, featured monopile turbine and piled jacket substation foundation diameters of 11.3 meters and 4.5 meters, respectively, with a grid layout of 1 nautical mile by 0.8 nautical miles. Scour protection was likely rock placement, with a diameter of 55.8 meters [7] and possible 2-meter height [8]. The COP for OCS-A 0499 covers 102,124 acres with 200 turbines and 3 substations, featuring monopile turbine and piled jacket substation foundation diameters of 15 meters and 5 meters, respectively, with a grid layout of 1 nautical mile by 0.6 nautical miles. Scour protection is also likely rock placement, with diameters of 82 meters for monopile foundations and 30 meters for piled jackets – each having a 2-meter height [8]. The COP for OCS-A 0512 spans 79,350 acres and includes 147 turbines and 2 substations, with monopile turbine and piled jacket substation foundation diameters of 11 meters and 2.5 meters, respectively, with a grid layout of 1 nautical mile by 0.65 nautical miles [9]. Scour protection is likely rock placement, with a diameter of 63 meters [9] and possible 2-meter height [8].

On average, this area experiences generally weak southwestward alongshore flow, with current magnitudes typically ranging from 10 to 20 centimeters per second. During strong storms, velocities can exceed 50 centimeters per second. The surface flow in this region is influenced by topography, large-scale circulation, wind, fresh water input, and turbulent dissipation [10-11]. Seasonal variability is governed by the intensity of stratification and the prevailing meteorological conditions that either promote upwelling or downwelling [10]. The largest variability in surface currents was seen in the winter and fall with a standard deviation of 15.4 centimeter per second while summer showed the least variability with a standard deviation of 11.9 centimeter per second [11].

B. Gliders

One decade of historic glider tracks from 2013 to 2023, totaling 142 deployments, in the NYB were retrieved from https://slocum-data.marine.rutgers.edu/erddap/. Most of these deployments have taken place before knowledge of turbine's locations were acquired, and none were designed or piloted to avoid future turbine placement, thus the trajectories are mostly science and operations focused. That means this analysis quantified how many glider-turbine interactions would occur if we carried out without consideration of turbine and substation locations. Each glider track was interpolated to 4 second intervals, based on the assumption of a glider's approximate length of 2 meters and horizontal speed of 0.5 meters per second. This approach maintains high-resolution data (i.e., each point along the track was spaced the length of the glider), preventing any misinterpretation by the algorithm that the track skipped over turbine and substation locations. While the exact position of a glider underwater is not known, the best estimate of position was interpolated position between GPS fixes which take place before submerging and after surfacing. Furthermore, each track was clipped to capture only the part that traversed inside of the of the WEA and thus subject to monopile interactions.

C. Interaction Algorithm

The algorithm to identify interactions is a simple geometry union between the glider's location and circle with a varying radius. Buffer radii of 6, 8, 10, 26, 36 meters were selected as analysis points for an interaction and placed as a buffer around the turbine and substation locations. The initial buffer radius of 6 meters represents the turbine or substation foundation diameter and was chosen based on turbine sizes detailed in each WEA COP [7-9], which detailed foundations ranging from 11 to 15 meters in diameter. The 8- and 10-meter buffer radii account for extensions beyond the foundation such as ladders and anode cages, and potentially derelict debris (nets, line, etc.). The larger 26- and 36-meter buffer radii encompassed entanglement risk due to longer fishing debris and for knowledge on the glider's general proximity to underwater structures. We feel it was helpful to think of the buffer zone beyond turbine in terms of glider size or units. It is assumed a typical glider size is about 2 meters by length (and width) and thus in terms of glider units the interaction buffer zones beyond the foundation are 0, 1, 2, 10, 15 glider units. Furthermore, it is important to differentiate the risk associated with turbines and substations at depth and at surface. Interactions that occur at the surface may impose a higher risk due to intense environments where waves or currents would allow interactions at higher velocities and frequencies (Fig. 2; 1A and 2A). Communications and musings regarding underwater interactions and the velocities involved (10-30 centimeters per second) suggest that the glider should be able to resist damage in a simple interaction, but limited data is available (Fig. 2; 1B). It is unknown what additional interactions with fishing gear or other debris entangled on the foundations might do to a glider aside from entrapment. If a glider were to encounter a piled jacket foundation that could pose a greater risk of the glider getting stuck, causing external sensor appendage damage, or at worse a forced hull breach (Fig. 2; 2B). All these scenarios can potentially lead to vehicle or data loss.

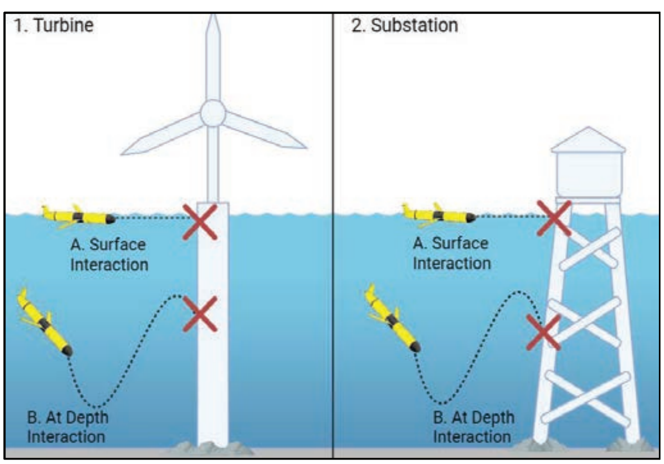

Fig. 2. Schematic of surface (1A) and at depth (1B) interactions with a monopile foundation and surface (2A) and at depth (2B) interactions with a piled jacket foundation.

The algorithm identified glider-turbine interactions defined as all points of intersection, where each glider track overlapped with the range of buffers around each turbine and substation location within the WEA. A glider track was defined as interpolated position between GPS positions. Knowledge of a glider's location underwater is uncertain so any method here results in unknown errors. As a result of the interpolation, consecutive points within the buffer zone separated by a time delta of 4 seconds were categorized as one interaction segment. If the time delta between points in the buffer zone was greater than 4 seconds, a second interaction segment was identified. This approach helped to distinguish multiple encounters with the same turbine, accounting for scenarios where the glider track intersected the turbine buffer zone at different times.

The output is a list of timestamps and locations of the turbines or substations that the track intersects. Each interaction segment was assumed to be a single interaction, and the results were broken down into turbine or substation interactions and if the interaction occurred at depth or at the surface.

Special consideration has been taken for interactions that occur when the glider is drifting at or near the surface. A coastal glider is typically underwater anywhere from 1 to 6 hours per segment with our average segment being about 2 hours. This duration is bookended by GPS positions at the dive and surfacing position and this duration is the amount of time a glider will be dead reckoning navigating underwater. Each underwater duration is also a single data segment or file stored by the glider which helped characterize a surfacing interval without the data burden of depth record. We extrapolated out the start and end times of a surfacing and apply a buffer each end of + 5 minutes to account for variances in surfacing and surfacing departure rates. Applying these surface drift bounds to the interaction output described above allowed for the identification of surface interactions within the buffer zones around turbine and substation locations.

We calculated several metrics for each WEA and buffer zone to analyze glider interactions. Total deployments were defined by each unique glider mission having any part of its track enter a WEA. Total interactions refer to the aggregate of all interaction types—such as at-depth turbines, at-depth substations, surface turbines, and surface substations—that occurred during each deployment within the WEAs. A subset of total interactions included total surface interactions, which specifically accounts for interactions occurring at the surface, and total substation interactions, which focuses on those involving substations. We also computed the average interactions per deployment by dividing the total number of interactions by the number of deployments. Total days in WEA represents the cumulative duration of data collection (or glider presence) within each WEA, calculated by cumulative summing of time spent within the WEA. Finally, days per interaction was derived by dividing the total days in the WEA by the total number of interactions (all types), providing the average time interval between interactions. This metric was also calculated specifically for surface interactions, including both turbines and substations.

III. Results

For all three WEAs, we analyzed buffer zones consisting of 0, 2, 4, 20 and 30 meters (i.e., circle radii of 6, 8, 10, 26, and 36 meters, respectively) (Table 1), which are distances beyond the standard footprint (e.g., 12-meter diameter for a monopile). Out of the 135 tracks in the NYB, lease areas OCS-A 0498, OCS-A 0499, and OCS-A 0512 contained 54, 75, and 8 glider tracks, totaling 123.61, 151.16, and 6.4 days inside the WEA,

TABLE I. SUMMARY METRICS FOR EACH WEA AND EACH BUFFER ZONE. VALUES IN PARENTHESES DENOTE VARIABLES AT THE SURFACE ONLY, THE VALUES OUTSIDE OF THE PARENTHESES ARE INCLUSIVE OF ALL INTERACTION TYPES.

WEA	Buffer Zone (m)	Total Deployments	Total Interactions(surface)	Total Substation Interactions	Average Interactions per Deployment (surface)	Total Days in WEA (surface)	Days per Interaction (surface)
0498	0	54	4 (1)	0	1 (1)	123.61 (37.3)	30.9 (123.61)
0498	2	54	7 (1)	2	1.4 (1)	123.61 (37.3)	17.66 (123.61)
0498	4	54	16 (2)	2	1.33 (1)	123.61 (37.3)	7.73 (61.81)
0498	20	54	37 (11)	2	1.54 (1.2)	123.61 (37.3)	3.34 (11.24)
0498	30	54	50 (11)	4	1.85 (1.1)	123.61 (37.3)	2.47 (11.24)
0499	0	75	14 (5)	0	1 (1)	151.16 (69.1)	10.8 (30.23)
0499	2	75	23 (6)	0	1.10 (1)	151.16 (69.1)	6.57 (25.19)
0499	4	75	26 (8)	0	1.18 (1)	151.16 (69.1)	5.81 (18.9)
0499	20	75	58 (14)	0	1.57 (1)	151.16 (69.1)	2.61 (10.8)
0499	30	75	93 (21)	2	1.94 (1.2)	151.16 (69.1)	1.62 (7.2)
0512	0	8	1 (0)	0	1 (0)	6.4 (2.8)	6.4 (inf)
0512	2	8	3 (0)	0	1 (0)	6.4 (2.8)	2.13 (inf)
0512	4	8	3 (0)	0	1 (0)	6.4 (2.8)	2.13 (inf)
0512	20	8	5 (1)	0	1 (1)	6.4 (2.8)	1.28 (2.8)
0512	30	8	6 (1)	0	1.2 (1)	6.4 (2.8)	1.07 (2.8)

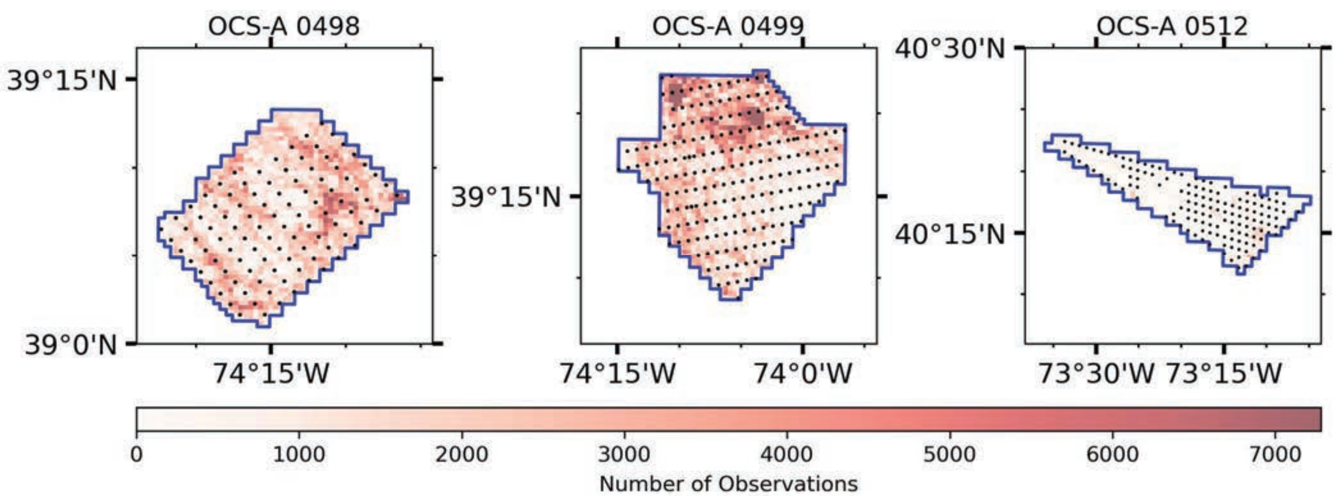

Fig. 3. Utilization of WEAs by historic glider missions using the interpolated tracks. The blue outline represents the area of each WEA, and the black dots represent proposed turbine and substation locations. The colormap represents the number of observations at each grid point.

respectively (Fig. 3). Historic tracks utilized southern WEAs (OCS-A 0498 and 0499) more than OCS-A 0512 due to avoidance of the shipping lanes surrounding the WEA. Both OCS-A 0489 and OCS-A 0499 had tracks available from 2013-2023, while OCS-A 0512 only had tracks available from 2019-2023. The larger number of tracks within OCS-A 0498 and

OCS-A 0499 produced a greater number of total interactions ranging, from a total of 4 to 50 and 14 to 93, respectively, compared to OCS-A 0512 which only had 1 to 6 total interactions as buffer zones increased in size. Across all areas, average interactions per deployment were 1.1 interactions per deployment with approximately 0.6 interactions per deployment at the surface (based on 8-meter radius).

The analysis showed that surface interactions were the minority out of the total interactions, indicating that most interactions occurred at depth, with only 37.3 (OCS-A 0498), 69.1 (OCS-A 0499), and 2.8 (OCS-A 0512) days spent at or near surface. For instance, in OCS-A 0498, out of 50 total interactions in the 30-meter buffer zone, only 11 were surface interactions, demonstrating a lower frequency of surface incidents. Additionally, substation interactions were less frequent than turbine interactions, only occurring in OCS-A 0498 and OCS-A 0499, and zero occurred at the surface. This pattern is consistent across the datasets and demonstrates that while surface and substations interactions do occur, they are relatively infrequent compared to interactions at depth with turbines.

Another metric to define rate of interaction would be days per interaction. A common measure of glider flight time is days deployed or days in mission. Total days was counted only when a glider was inside a WEA. It can be assumed that as days increase, so does hazard or risk [12]. Across all areas, the average days per interaction was about 9 days and 123 days for surface (based on 8 m radius). Days per interaction inversely varied with buffer zone size in all WEAs. Days per interaction, decreased with larger buffer sizes for all WEAs, meaning that the average time between interactions decreased. From buffer zone 0 to 30 meters, days per interaction decreased in OCS-A 0498, OCS-A 0499 and OCS-A 0512 from 30.9 to 2.47 days, 10.8 to 1.62 days, and 6.4 to 2.13 days, respectively. Days per interaction for surface interactions only followed the same trend, but with higher values, as surface interactions are a small subset of total interactions. These trends indicate that, as expected, larger buffer zones lead to more frequent interactions and fewer days between them.

IV. Discussion

Our analysis provides insights into the interaction risk faced by underwater gliders navigating near offshore wind turbines in the NYB region. The results indicate varying levels of interaction between gliders and turbine infrastructure across different WEAs and buffer zones. Buffer zones were determined based on glider length and turbine size. The determination of buffer radii considers the glider's length and the turbine's radius, ensuring that buffer zones reflect realistic interaction distances. The data reveal a clear trend of increased interaction frequency with larger buffer zones and days spent at sea. This can also be assumed in terms of risk for an interaction of a glider in a wind farm: the more time spent in the WEA the higher the chance of interaction. Shown here (Fig. 4) are the layout of turbines in WEA and whether there was a surface or at depth interaction. It is important to note that even if there are very few deployments that enter the WEA, interactions still may occur, as was seen for OCS-A 0512.

Research and monitoring missions are currently underway and being planned within WEAs prior to, during, and after turbine construction. Gliders included, it remains to be seen how underwater vehicles (gliders, propeller-AUV, etc.) and surface vehicles (sailing drones, etc.) will handle these interactions. We generally feel at typical ocean and glider velocities (10-30 centimeters per second, about 0.4 miles per hour) that an underwater interaction should be benign. The larger risk would be for entanglement with sub-structure or derelict marine debris such as fishing gear, ropes, or fouling. We consider a surface interaction to be of higher risk than whilst underwater due to wave action and in our experience of previous glider interactions with fixed sea structures at the surface. This increased surface risk should be considered by other AUVs that operate at or near the surface. Perhaps protection or shielding can be added to current vehicles to ensure science sensor and glider integrity as well as minimized entanglement risk in terms of an interaction.

Given the interaction risk outlined above, we aim to propose strategies for turbine avoidance. Several solutions or approaches are capable in the current software set, others are

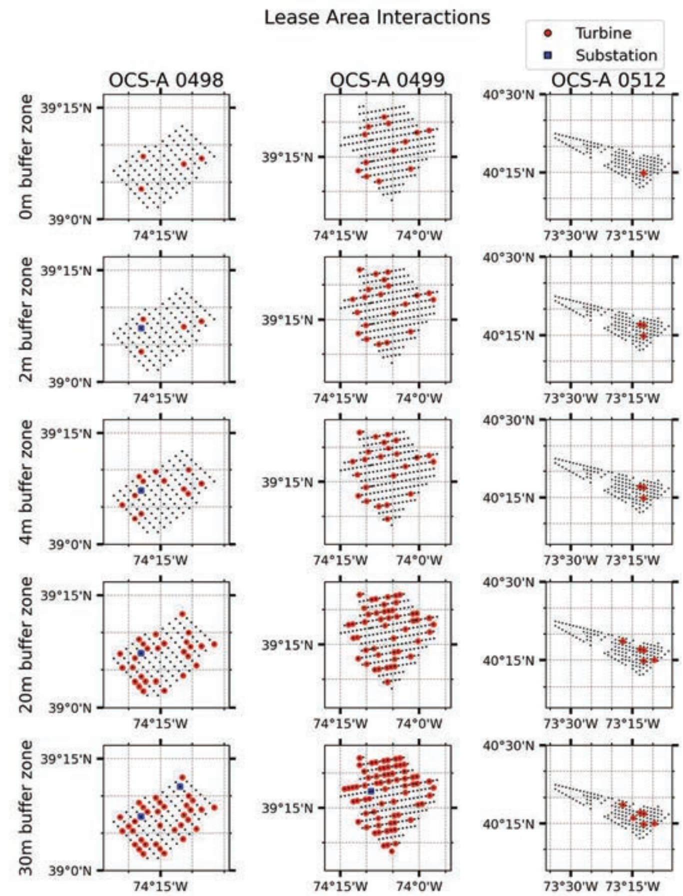

Fig. 4. Interactions with turbines (red) and substations (blue) on proposed turbine and substation location grids (black), which are spatially to scale.

more advanced and would require development. Two approaches that are capable now are: 1) navigate more accurately in between turbines (which would require shorter surfacing intervals and thus more surface hazard) or 2) navigate between turbines with less regard for accuracy in exchange of minimizing surface interaction risk. Additional considerations must be taken for different velocity environments. Areas with small tidal and mean currents may offer safer conditions for navigational accuracy (avoidance), whereas high current and tidal conditions may better be suited for surface avoidance (accepting underwater interaction risk). Variable environmental conditions could impose further risks associated with not only fixed infrastructure, but also mobile infrastructure such as vessel operations which could lead to vessel strikes [13]. Limiting surface time may lower risk of an interaction.

Solutions, including the aforementioned and beyond, will require more accurate dead reckoning capabilities. This often is determined by the ability of the glider to estimate, predict, and implement accurate knowledge of local current fields. Abilities such as tidal predictions or model forecasts could be combined with local knowledge of currents, as determined by the glider, to create a more accurate estimate of currents [14]. Fortunately, the Slocum glider control software has the capability to be piloted locally by an onboard computer utilizing backseat driver control [15]. This will allow rapid development of such current estimating algorithms as well as the initial implementation of such estimates applied over time underwater while the glider is dead reckoning. This will allow solutions that rely on perhaps a pre-programmed turbine field location list to have the glider more accurately determine if it is too close to a known location and to 'turn away' from it – avoiding an interaction.

To help evaluate these two approaches, additional analysis will be conducted to characterize physical forcings using high-frequency radar (HFR) surface currents observations (https://tds.marine.rutgers.edu/thredds/cool/codar/cat_totals.html) in each WEA, in conjunction with field testing mitigation strategies. This will assess the current dead reckoning capability in observed current conditions and help infer which conditions would allow for safe operation in WEAs. Efforts are being made to quantify if active avoidance piloting techniques reduce interaction rates.

Acknowledgment

From Rutgers University, we would like to thank John Kerfoot, Lori Garzio, and Laura Nazzaro for their data management and Joseph Gradone and Nicole Waite for providing glider expertise. We would like to thank Emily Shumchenia for supplying the turbine locations from the marine cadastre. We would like to thank Teledyne Webb Research for discussing glider-turbine interaction risk outcomes with us.

References

[1] The White House. (2021). Executive order on America's supply chains. Washington, D.C. https://www.whitehouse.gov/briefing-room/statements-releases/2021/03/29/fact-sheet-biden-administration-jumpstarts-offshore-wind-energy-projects-to-create-jobs/

[2] Chambel, J., Fazeres-Ferradosa, T., Miranda, F., Bento, A. M., Taveira-Pinto, F., & Lomonaco, P. (2024). A comprehensive review on scour and scour protections for complex bottom-fixed offshore and marine renewable energy foundations. *Ocean Engineering*, 304, 117829.

[3] Hare, J. A., et al. (2022). NOAA Fisheries and BOEM Federal Survey Mitigation Implementation Strategy - Northeast U.S. Region. https://doi.org/10.25923/jqse-x746

[4] Hogan, F., et al. (2023). Fisheries and offshore wind interactions: Synthesis of science. https://doi.org/10.25923/tcjt-3a69

[5] Schofield, O., Kohut, J., Aragon, D., Creed, L., Graver, J., Haldeman, C., Kerfoot, J., Roarty, H., Jones, C., Webb, D., & Glenn, S. (2007). Slocum gliders: Robust and ready. *Journal of Field Robotics*, 24(6), 473–485. https://doi.org/10.1002/rob.20200

[6] Schofield, O., Kohut, J., Glenn, G., Morell, J., Capella, J., Corredor, J., Orcutt, J., Arrott, M., Krueger, I., Meisinger, M., Peach, C., Vernon, F., Chave, A., Chao, Y., Chien, S., Thompson, D., Brown, W., Oliver, M., & Boicourt, W. (2010). A regional Slocum Glider Network in the MidAtlantic Bight leverages broad community engagement. *Marine Technology Society Journal*. https://doi.org/10.4031/MTSJ.44.6.20

[7] Bureau of Ocean Energy Management. (n.d.-a). Ocean Wind 1 construction and operations plan. U.S. Department of the Interior, Bureau of Ocean Energy Management. Retrieved July 18, 2024, from https://www.boem.gov/ocean-wind-1-construction-and-operations-plan.

[8] Bureau of Ocean Energy Management. (n.d.-b). Atlantic Shores Offshore Wind construction and operations plan. U.S. Department of the Interior, Bureau of Ocean Energy Management. Retrieved July 18, 2024, from https://www.boem.gov/renewable-energy/state-activities/atlantic-shores-offshore-wind-construction-and-operations-plan

[9] Bureau of Ocean Energy Management. (n.d.-c). Empire Wind construction and operations plan. U.S. Department of the Interior, Bureau of Ocean Energy Management. Retrieved July 18, 2024, from https://www.boem.gov/renewable-energy/state-activities/empire-wind-construction-and-operations-plan

[10] Kohut, J. T., Glenn, S. M., & Chant, R. J. (2004). Seasonal current variability on the New Jersey inner shelf. *Journal of Geophysical Research: Oceans*, 109, C07S07. https://doi.org/10.1029/2003JC001963

[11] Roarty, H., Glenn, S., Brodie, J., Nazzaro, L., Smith, M., Handel, E., et al. (2020). Annual and seasonal surface circulation over the Mid-Atlantic Bight Continental Shelf derived from a decade of high frequency radar observations. *Journal of Geophysical Research: Oceans*, 125, e2020JC016368. https://doi.org/10.1029/2020JC016368

[12] Rudnick, D. L., Davis, R. E., & Sherman, J. T. (2016). Spray underwater glider operations. *Journal of Atmospheric and Oceanic Technology*, 33(6), 1113–1122. https://doi.org/10.1175/jtech-d-15-0252.1

[13] Merckelbach, L. (2013). On the probability of underwater glider loss due to collision with a ship. *Journal of Marine Science and Technology*, 18, 75. https://doi.org/10.1007/s00773-012-0189-7

[14] Eriksen, C. C., Osse, T. J., Light, R. D., Wen, T., Lehman, T. W., Sabin, P. L., Ballard, J. W., & Chiodi, A. M. (2001). Seaglider: A long-range autonomous underwater vehicle for oceanographic research. *IEEE Journal of Oceanic Engineering*, 26(4), 424–436. https://doi.org/10.1109/48.972073

[15] Wang, Y., Bulger, C., Thanyamanta, W., & Bose, N. (2021). A backseat control architecture for a Slocum Glider. *Journal of Marine Science and Engineering*, 9(5), 532. https://doi.org/10.3390/jmse9050532

Rutgers-MTS Glider Technology Workshop - A Hands-On Experiential Learning Workshop on Slocum Gliders and an Opportunity for Workforce Development and Microcredential Certificates

Nicole Waite A.
Center for Ocean Observing Leadership
Rutgers, the State University of New Jersey
New Brunswick, NJ, USA
waite@marine.rutgers.edu

David Aragon
Center for Ocean Observing Leadership
Rutgers, the State University of New Jersey
New Brunswick, NJ, USA
dkaragon@marine.rutgers.edu

Alexander López
Center for Ocean Observing Leadership
Rutgers, the State University of New Jersey
New Brunswick, NJ, USA
alopez@marine.rutgers.edu

Brian Buckingham
Center for Ocean Observing Leadership
Rutgers, the State University of New Jersey
New Brunswick, NJ, USA
brianbuckingham@marine.rutgers.edu

Jessica Leonard
Center for Ocean Observing Leadership
Rutgers, the State University of New Jersey
New Brunswick, NJ, USA
jnleonard@marine.rutgers.edu

Liesl Hotaling
Marine Technology Society
Washington DC, USA
liesl.hotaling@mtsociety.org

Josh Kohut
Center for Ocean Observing Leadership
Rutgers, the State University of New Jersey
New Brunswick, NJ, USA
kohut@marine.rutgers.edu

OCEANS 2024 - Halifax | 979-8-3315-4008-1/24/$31.00 ©2024 IEEE | DOI: 10.1109/OCEANS55160.2024.10754275

Abstract*— Marine Technology Society is developing a series of Ocean Technician Microcredentials to facilitate both traditional and alternate routes to the Blue Economy workforce. This Microcredential plan consists of skillset tiers for various oceanographic technologies, including autonomous underwater vehicles. Ocean gliders are autonomous underwater vehicles used for an array of science and research applications, such as climate change, tropical storm intensification and model data assimilation, water quality and ocean acidification, and fisheries management. Gliders allow for safe, affordable, and around-the-clock data collection and can be deployed inexpensively, for months at a time in a variety of ocean conditions. Rutgers University Center for Ocean Observing Leadership and the Marine Technology Society host a week-long hands-on workshop on underwater glider technologies each June. Participants are introduced to the Teledyne Webb Slocum glider through experiential learning opportunities including preparing, ballasting, deploying, and piloting the glider. The workshop maximizes the active learning for all participants, while also ensuring comprehension of the essential basics applicable to Slocum gliders and many other AUVs. The goal of the workshop is for participants to gain an introductory knowledge of and justification for underwater glider principles and their associated science applications that can be built upon in future experiences. This workshop's authentic, introductory approach to AUVs, specifically Slocum gliders, fundamentally aligns with MTS's ocean technician microcredential plan at the Foundational tier for a Glider Trainee, meant for core knowledge and experience relevant to the specific technologies. The seamless overlap between MTS's endeavor and RUCOOL's Glider Workshop benefits all participants by providing assessed certification of participant skill and knowledge that will accelerate employment in the New Blue Economy.

***Keywords*— gliders, autonomous observations, ocean observing systems, workforce development, blue economy**

I. Introduction

The National Oceanic and Atmospheric Administration (NOAA) released its Blue Economy Strategic Plan [1] in January 2021 to outline the advancement of America's Blue Economy followed by its New Blue Economy plan in 2022 [2]. The New Blue Economy is a knowledge-based, data-enhanced ocean economy. Skilled workers in multiple areas of the blue economy (e.g. research, infrastructure, fisheries, ports and shipping, national security, renewable energy, tourism, etc.) are needed globally. Engaging, innovative, agile and equitable educational opportunities are needed to prepare this workforce. Training opportunities should encompass a range of workers and experience levels and foster pathways for life-long learning. Stackable microcredentials and professional certificates provide the competency-focused training required and should promote self-development, adapt to technological changes, and maximize opportunities within the New Blue Economy [3].

To address this need, the Marine Technology Society (MTS) is developing a series of stackable microcredentials to create accessible and flexible pathways to learning and vocational training [3]. The microcredentials will address core competencies required for employment in the ocean/marine/blue economy and capture learners entering the workforce from high school; applying skill sets acquired during military service; recognition of skills acquired in a professional capacity; and as a vehicle for employment retraining. Microcredential competency is organized into foundational, intermediate, and advanced levels. The Marine Technology Society is organizing

979-8-3315-4008-1/24/$31.00 ©2024 IEEE

communities around the world to establish a marine technology microcredentialing framework and pilot foundational level content. Here we present activities at Rutgers University to offer students foundational level content and assessment for ocean gliders.

Ocean gliders are increasingly useful and important tools for studying the ocean environment. These autonomous underwater vehicles (AUVs) use buoyancy changes as the primary means of movement through the water column. This unique propulsion method allows several advantages described later. Several types of gliders are available for use by researchers. One type of ocean glider is the Slocum glider AUV, built by Teledyne Webb Research Corporation (North Falmouth, MA). The Slocum glider is an integrated instrument platform designed to operate in the coastal oceans up to 1000 m depth, often with no propeller. It is designed to adjust its volume via a ballast engine, allowing it to dive and climb in a triangle pattern. The result is a low cost, highly adaptable autonomous underwater vehicle with a very low power requirement [4]. While traversing the glide path, the vehicle slowly travels horizontally at about one kilometer per hour, with a fin steering the glider towards continuously adjustable waypoints.

AUVs allow for safe, affordable, and around-the-clock data collection in all conditions. AUVs can be deployed inexpensively for months at a time in a variety of ocean conditions: from coastal shallow waters (10 m) and open ocean environments to the center of a hurricane or ice-adjacent zones of Antarctica. Gliders are equipped with an increasing array of instrumentation to gather ocean conditions, including temperature, salinity, pH, oxygen, zooplankton biomass, marine mammal calls, wave heights, and current speeds. These remote vehicles are well poised for an array of science and research applications, such as climate change, tropical storm intensification and model data assimilation, water quality, ocean acidification, and fisheries management.

II. Rutgers Glider Workshop

A. Workshop Goals

Rutgers University Center for Ocean Observing Leadership (RUCOOL), sponsored by the MTS, hosts a hands-on workshop on underwater glider technologies for one week every June, with a focus on the Teledyne Webb Slocum glider. RUCOOL has hosted 15 glider 'training sessions' over the last 19 years, with six MTS sponsored 'glider workshops', beginning in 2017. The workshop is structured as an informal 'glider camp' with meals provided to allow and encourage interactions between instructors, students, scientists, and RUCOOL technical staff. MTS Workshops, in collaboration with Rutgers University, provides scholarships for students interested in attending this workshop.

The Rutgers-MTS Glider Technology Workshop is designed as an experiential learning opportunity that allows participants to learn about underwater gliders and interact directly with the equipment to gather data. Participants are introduced to the Teledyne Webb Slocum glider including communicating, preparing, ballasting, preparing, deploying, and piloting the AUV. The goal of the workshop is for participants to gain an introductory knowledge of and justification for underwater glider principles and their associated science applications that can be built upon in future experiences. The five-day workshop is structured around maximizing the active learning for all participants, while also ensuring comprehension of the essential basics applicable to Slocum gliders and many other AUVs.

B. Target Audience/Participants

The Rutgers-MTS Glider Technology Workshop is designed to be an introductory workshop for anyone interested in Slocum gliders. No prior work or knowledge with gliders is required. Prior knowledge of density, basic oceanography, and command-line operating systems is helpful though not required. The workshop is largely geared toward undergraduate and graduate students, however, has also had participants in early-career positions from organizations such as the NOAA, US Navy Naval Oceanographic Office, and other research institutions. International participants are also welcome.

C. Workshop Format and Agenda

The workshop is a combination of classroom lectures and demonstrations (Fig. 1a,b), hands-on sessions working with the gliders (Fig. 1c,d), and an 'on the water' day in Raritan Bay, NJ on the R/V Rutgers research vessel to deploy and recover a glider (Fig. 1e,f). Participants spend the week preparing a glider for deployment, deploying and recovering that glider, and analyzing at glider data. The context of the preparation is for operating the glider for a test flight in an estuarine environment. Basic goals are structured for each day so that the students have enough knowledge to operate safely and reference resources properly. Throughout the week, best practices for ocean technology and gliders are introduced and demonstrated. Worksheets are completed by participants at the end of each day to highlight key lessons.

The agenda (Table 1) begins on Monday with an overview of gliders, glider command and control, and an introduction to some scientific research applications of gliders at RUCOOL. Students learn the parts of a glider, basics of how a glider operates, how to communicate with a glider and where to locate information about glider sensors and settings. Beginning on Monday afternoon, students are hands-on in the lab (Fig. 1c) practicing issuing commands and glider communication and opening and closing gliders. The primary goal from day 1 is to be able to interact (communicate) with a glider safely and confidently as well as understand their purpose for ocean monitoring.

Day 2's sessions focus on glider ballasting techniques, glider hygiene, in-water practices, and practical rules for effective weight adjustment (Fig. 1d). Classroom lectures explain the basics of ocean density, density units, and glider ballasting theory (Fig. 1a). Heavy emphasis on density and glider operation round out Tuesday's lessons allowing the participants to fully understand how to ballast a glider reliably.

Final ballasting continues into Wednesday, while also emphasizing the software, hardware, and scientific sensor steps of the checkout procedure. An outdoor compass calibration involving suspending the glider and rotating in as many angles allowed in 3D space begins to show the importance of a properly navigating robot remotely deployed. Classroom sessions on Wednesday cover glider mission structure and defining control

Fig. 1. Glider workshop participants in classroom lectures and demonstrations (a,b), working hands on with the gliders (c,d), and deploying and piloting the gliders during the boat day of the workshop (e,f). Photo credit: b,c,d - Jacqueline Southby; a,e,f - RUCOOL.

TABLE I. AGENDA AND TOPICS TAUGHT IN THE RUTGERS-MTS GLIDER TECHNOLOGY WORKSHOP.

Day	Theme	Topics Covered
Monday	Glider Introduction Command and Control	• Parts of a glider and functions • How to communicate with a glider • General understanding of software behavior • MASTERDATA • How to open and close a glider
Tuesday	Ballasting and Hardware	• Ballasting theory (from grams to cc to kg/m3) • Ballasting rule of thumb • Open/Closing hygiene and practices • Glider checkouts
Wednesday	Ballasting Glider Checkouts Software Introduction	• Glider Checkouts • Compass tests and calibrations • Glider Mission operation • SFMC Operation
Thursday	Glider Deployment and Recovery – Boat Day	• Glider in water command and control • Glider deployment • Deployment analysis • Glider recovery
Friday	Piloting and Data	• Piloting practices and tools • Data QA/QC • Simulation

files which essentially define how a glider operates when deployed. Wednesday concludes with a glider that is prepared and checked-out for deployment. Some aspects of data analysis and collection are introduced at this point in preparation for actual in-water sensor and engineering acquisition.

Thursday relocates from lab to research vessel to highlight ship safety practices, pre-deployment procedures, followed with an actual glider deployment with analysis, and lastly recovering the glider. Participants practice deploying and recovering the glider with a couple of methods for small boat operations (Fig. 1e). Participants also pilot the glider (Fig. 1f), practicing safe in-ocean operations, issuing commands to run missions, and transfer data files to determine glider performance.

The workshop opens on Friday with a debrief of the in water tests as well as the preceding week's knowledge. Switching focus to deployed glider operations (piloting), an overview of piloting best practices, glider diagnostics, available piloting tools, and resources like a flight simulator are introduced (Fig. 1b). Special focus is given to Teledyne's Slocum Fleet Mission Control software and Google Earth with their GIS capabilities and navigational assistance imagery. The workshop concludes with an introduction of glider data publishing and Quality Assurance/Quality Control (QA/QC).

III. MICROCREDENTIALS

The Ocean Technician Microcredential framework being developed by MTS consists of skillset tiers for various oceanographic technologies (Table 2), including AUVs. Microcredentials are designed to be competency-based

TABLE II. EXAMPLES OF GLIDER MICROCREDENTIALS COMPETENCIES FOR A TRAINEE OR STUDENT FOR THE THREE COMPETENCY LEVELS IN THE TRAINEE SERIES: FOUNDATIONAL, INTERMEDIATE, ADVANCED.

Foundational (camp)	Intermediate	Advanced
Knowledge and Justification for:	***Guided Experience with:***	***Supervised Experience with:***
Hardware: opening/closing, o-ring etiquette, battery maintenance	Hardware: replacing/repairing connectors, replacing components, swapping assemblies	Hardware: integrating new instruments, calibrating actuators
Ballasting: density theory, density rule of thumb, ocean densities	Piloting: autoballast, low power operations, abort handling, shoreside handling scripts	Software: mission writing, control file maintenance, telemeter data control
Operations: boat safety, glider deployment protocols boatside	Operations: shore side deployment protocols	Piloting: hover missions, under ice, extreme currents

recognition for mastery in targeted knowledge and skills. Microcredentials are awarded as a digital badge, are modular, and can be stacked to gain more comprehensive certifications. Please see Hotaling et al., 2024 OCEANS paper for more details on the microcredential development [3].

The Foundational Microcredential for a glider trainee focuses on core knowledge and experience relevant to the specific technology. Requirements for this level include 30-40 training hours, technology fundamentals, beginning and introductory concepts, knowledge of uses and applications, and demonstration of basic knowledge of the technology [3]. The glider workshop's authentic, introductory approach to AUVs, specifically Slocum gliders, fundamentally aligns with the foundational microcredential level of the Glider Trainee series.

Participants completed an anonymous survey following the June 2024 Rutgers-MTS Glider Technology Workshop to provide feedback on the workshop structure and glider training received. Completion of the survey did not affect participants' ability to earn microcredentials. Survey results indicate that this glider workshop effectively introduces the Slocum glider, providing participants the foundational knowledge and experience required by the microcredential program and the competency for future work and training with gliders. In their own words, participants described the workshop and their experience as:

> *"I appreciated the time and care that the workshop developers put into building this camp. The camp began at a comfortable level for both inexperienced and experienced participants. The pace and schedule at which the instructions/lessons were given were ideal and holistic, without being over complicated and mundane. The camp developers grouped individuals by experience level to provide more in-depth instruction for the attendees' specific needs, which allowed for more one-on-one examples and discussions. The boat day was appreciated as it*

allowed the students to translate what had been taught and discussed in class into real world applications/scenarios."

"This was an amazing experience and despite me not knowing anything about these machines the speed and detail was fantastic and very insightful."

"They were thorough, professional, not too dry (but not too casual), provided excellent Q&A opportunities with real-world applications towards my specific glider missions.… I think the resources that were provided are going to be INCREDIBLY useful to my personal research and will be the basis for all future deployments and laboratory configurations."

Prior glider experience varied among participants, with 40% having little to no prior experience, 20% having some experience, and 40% having a good amount of experience. Regardless of prior experience, 80-90% of participants felt confident or very confident in their ability to explain the core topics covered in the workshop (Table 3). Additionally, all participants reported feeling prepared (50%) or very prepared (50%) to intern working with gliders. Participants further reported the workshop structure, including hands-on experiential learning, demonstrations, and classroom lectures, as helpful or very helpful to their training and ability to serve as an intern (Table 4).

TABLE III. SURVEY RESULTS FROM PARTICIPANTS IN THE JUNE 2024 RUTGERS-MTS GLIDER TECHNOLOGY WORKSHOP ON THEIR ABILITIES TO EXPLAIN THE CORE TOPICS COVERED.

After completing this workshop, how confident are you in your ability to EXPLAIN the following?						
Learning Objectives	***Mean rating***	***Very***	***Confident***	***Some-what***	***A little***	***Not at all***
How to open and close a glider safely	4.5	60%	30%	10%	0%	0%
How to deploy a glider and recover it safely	4.5	60%	30%	10%	0%	0%
How to communicate and interact with gliders	4.0	20%	60%	20%	0%	0%
How density and ballasting works	3.9	20%	60%	10%	10%	0%

The seamless overlap between MTS's endeavor and RUCOOL's Glider Workshop benefits all participants by providing assessed certification of participant skill and knowledge that will accelerate employment in the Blue Economy. At the completion of the Glider Workshop, participants can apply for a Foundational Tier microcredential in the Glider Trainee series. The first microcredential certificates for this level were issued to participants in June 2024. As Rutgers University is a partner school in the MTS microcredentials program, Rutgers instructors supply MTS with a list of learners who successfully demonstrated the competencies needed to earn microcredentials. MTS directly issues microcredentials to the learners for use on their resumes and social media channels to represent their new skill sets.

TABLE IV. SURVEY RESULTS FROM PARTICIPANTS IN THE JUNE 2024 RUTGERS-MTS GLIDER TECHNOLOGY WORKSHOP ON HOW HELPFUL THE WORKSHOP FORMAT AND ACTIVITIES WERE TO THEM.

How helpful were the following activities in preparing you to intern on a team deploying gliders?						
Instructional strategies	***Mean rating***	***Very***	***Helpful***	***Some-what***	***A little***	***Not at all***
Guided practice in operating the technology	4.9	90%	10%	0%	0%	0%
Working in small teams	4.9	90%	10%	0%	0%	0%
Overview of the technology and its applications (lecture)	4.8	80%	20%	0%	0%	0%
How the technology works and how to operate it (lecture)	4.8	80%	20%	0%	0%	0%
How to operate the technology (demonstration)	4.8	80%	20%	0%	0%	0%
How to interpret data (demonstration)	4.7	70%	30%	0%	0%	0%

ACKNOWLEDGMENT

MTS microcredential development is funded by National Science Foundation grant number NSF OCE-2308556. The authors thank the faculty and staff of RUCOOL and Captain Chip Haldeman that assist in organizing and running the Rutgers-MTS Glider Technology Workshop. We further acknowledge and thank the glider workshop attendees for their participation and providing valuable feedback on the workshop.

REFERENCES

[1] "NOAA blue economy strategic plan 2021-2025." National Oceanic and Atmospheric Administration. June 2022. https://www.noaa.gov/sites/default/files/2022-06/NOAA_FY2226_Strategic_Plan.pdf.

[2] "Building a climate ready Nnation: NOAA FY22-26 strategic plan." National Oceanic and Atmospheric Administration. January 2021. https://aambpublicoceanservice.blob.core.windows.net/oceanservicepro d/economy/Blue-Economy%20Strategic-Plan.pdf.

[3] L. Hotaling, H. VanSumeren, and J. Kohut. Building an Ocean Technician Workforce. OCEANS 2024 MTS/IEEE Halifax, in press.

[4] O. Schofield, J. Kohut, D. Aragon, L. Creed, J. Graver, C. Haldeman, et al. Slocum gliders: robust and ready. J. Field Robotics 24: 473–485. 2007 doi: 10.1002/rob.20200

ARTICLE

Buoyancy Gliders Opening New Research Opportunities in the Southern Ocean

AUTHORS

Oscar Schofield
John Kerfoot
Nicole Waite
Schuyler Nardelli
Rutgers Center for Ocean Observing Leadership (RU COOL), Department of Marine and Coastal Sciences, School of Environmental Sciences, Rutgers University, New Brunswick, NJ

Darren C. McKee
Department of Environmental Sciences, University of Virginia

J. Alexander Brearley
British Antarctic Survey, High Cross, Madingley Road, Cambridge, United Kingdom

Christian Reiss
Southwest Fisheries Science Center La Jolla, CA

Schuyler Nardelli Present address: U.S. Geological Survey, California Water Science Center, 6000 J St, Placer Hall, Sacramento, CA 95819.

ABSTRACT

Polar systems are experiencing major changes that has significant implications for ocean circulation and global biogeochemistry. While these changes are accelerating, access to polar systems is decreasing as ships and logistical capabilities are declining. Autonomous underwater buoyancy gliders have proven to be robust technologies that are capable of filling sampling gaps. Gliders have also provided a more sustained presence in polar seas than ships are able. Along the West Antarctic Peninsula, one of the most rapidly warming regions on this planet, gliders have proven to be a useful tool being used by the international community to link land research stations without requiring major research vessel ship support. The gliders are capable of adaptive sampling of subsurface features not visible from satellites, sustained sampling to characterize seasonal dynamics, and they increasingly play a central role in the management of natural resources. Future challenges to expand their utility include: (A) developing robust navigation under ice, which would allow gliders to provide a sustained bridge between the research stations when ship support is declining, and (B) expanding online resources to provide the international community open access to quality data in near real time. These advances will accelerate the use of gliders to fill critical sampling gaps for these remote ocean environments.
Keywords: gliders, polar, ocean observing, climate

History

Polar oceans are remote, harsh, and unique environments characterized by extreme winds and large ocean-atmosphere heat fluxes, seasonal variability in sea ice extent, infestation by icebergs, and a limited ship presence. Polar marine ecosystems are regions of high seasonal biological productivity supporting unique organisms adapted to extreme conditions, and are driven by local, regional, and remote physical forcing. Over the past 200 years, these ecosystems have provided society with food, fuel, and fiber (Ainley & Pauly, 2013; Chapin III et al., 2005) and play a disproportionately large role, relative to their size, in global biogeochemical cycles (Gruber et al., 2019; Hauck et al., 2015; Moore et al., 2018). For example, the Southern Ocean alone is responsible for 40% of the annual global ocean uptake of anthropogenic CO_2 from the atmosphere (Gruber et al., 2019). These unique systems are regulated by complex interactions between the ice, atmospheric, and oceanic forcing that are difficult to sample using traditional sampling approaches given the limited number of ships in these remote locations.

The limited data collected in polar oceans is problematic as they are among the most rapidly changing on Earth, with changes to temperatures (Meredith et al., 2019; Schmidtko et al., 2014), eddy energy (Hogg et al., 2015), and biological systems (Brown & Arrigo, 2012; Morley et al., 2020; Schofield et al., 2010). These systems are sentinels of climate and ecosystem change, with charismatic species (penguins, polar bears, etc.) serving as public symbols of global change. Therefore, developing a coherent sampling strategy is critical to documenting changes in polar ocean systems and the regional to global consequences of those changes. While satellites have long proven to be an effective tool for documenting surface dynamics of polar systems (Arrigo et al., 2017, 2015; Crawford et al., 2020), these regions are often cloudy (Wang & Key, 2005; Wood, 2012), which often requires data averaging over weeks to months to provide full images. Moorings can provide high-resolution time series of great value (Brearley et al., 2017; Dickson, 2006; Martinson & McKee, 2012; McKee & Martinson, 2020; Mikhalevsky et al., 2015; Yang et al., 2021) and are important in the collection of physical, chemical, and biological data. However, moorings do not provide spatial data, and systems with near-surface measurements can be damaged by the passage of icebergs or the presence of heavy sea ice.

By the late 1990s, underwater autonomous gliders transitioned from a concept first imagined by Stommel (1989) to being a robust tool for conducting oceanographic research (Davis et al., 2002; Schofield et al., 2007), filling data gaps in subject areas ranging from boundary current dynamics to ocean-atmosphere interactions during storms to ecological dynamics in coastal shelves (Rudnick, 2016). In northern high latitudes, gliders have quantified the hydrography and circulation between the Nordic and Atlantic Ocean waters (Beaird et al., 2013; Fraser et al., 2018; Hoydalsvik et al., 2013; Ullgren et al., 2014). Additionally, sustained sampling with repeat surveys helped quantify fluxes through the Davis Strait (Curry et al., 2014) and is being integrated into marine mammal research (Aniceto et al., 2020; Baumgartner et al., 2020). In the Arctic, gliders have also been operated as a central part of a sea ice ocean observing network (Lee & Thomson, 2017; Lee et al., 2019). Using gliders to sustain sampling has been a focus in the Southern Ocean as well (e.g., du Plessis et al., 2019; Nicholson et al., 2022), and this article will highlight the range of applications that gliders have addressed specifically along the West Antarctic Peninsula (WAP) by the international community.

Glider Technology and Capabilities

Gliders are 1- to 2-m-long autonomous underwater vehicles (AUVs) that maneuver vertically through the water column at a forward speed of 20–30 cm/s (Davis et al., 2002). The vertical motion of the platform is regulated by changing the buoyancy of the platform, and wings translate the forward motion providing the ability to sample the full water column ranging from 15- to 1500-m depths. The primary navigation system is an on-board GPS/iridium receiver coupled with an attitude sensor, depth sensor, and altimeter to provide dead-reckoned navigation, with backup positioning and communications provided by an Argos transmitter. Given this, communication is only possible when the vehicle is at surface. The mission duration of a glider is limited by battery life and is largely a function of the number of sensors and the water depth. The largest power drain in the glider involves the operation of the buoyancy pump, and, therefore, the battery life is shortest in shallow seas. Several of the gliders are modular, allowing sensor packages to be customized depending on the specific science mission. The glider duration is variable and largely a function of the number and type of sensors being carried. For gliders that have low sensor payloads Conductivity-Temperature-Depth (CTD) sensor, they have conducted missions for over a year; however, it should be noted that overall battery lifetime is dependent on the water temperature. Customized lithium batteries can extend the duration of the mission. The recent development of rechargeable lithium batteries offers the potential for rapid redeployment of systems not requiring significant ballasting efforts; however, currently, these systems have a shorter battery life.

Spatial/Temporal Coverage Provided By Gliders in the WAP

Gliders have become a critical tool for sampling polar systems. Along the WAP over the last 15 years, gliders have maintained a sustained presence in the field (Figure 1). These platforms have been used to study a variety of processes (see below) when ships are unavailable or when the region of interest is out of the safety limits of small boats launched from shore stations. To date, gliders have conducted over 75 missions over 1000 days at sea and spanning > 20,000 kilometers of the WAP (Figure 2). Given their semi-Lagrangian sampling capabilities, these platforms are filling critical data gaps spanning mesoscale circulation, biological dynamics, and storm-ocean interactions (cf. Rudnick, 2016). Shore-based field stations are maintained by the international community along the WAP with ocean sampling conducted from small vessels (Figure 1). These smaller vessels have limited spatial coverage (measured in tens of kilometers) in large part for safety considerations because weather in the WAP is subject to rapid change and it is not rare for wind intensity to increase by an order of magnitude on time scales of less than an hour. Gliders have provided a unique tool

FIGURE 1

Deployments of gliders along the West Antarctic Peninsula. Yellow lines indicate glider missions from the British Antarctic Survey, red lines indicate the surveys of Rutgers University, and blue lines indicate the missions from the National Oceanic and Atmospheric Administration. The green symbols indicate gliders' locations anchored by land-based stations or ships.

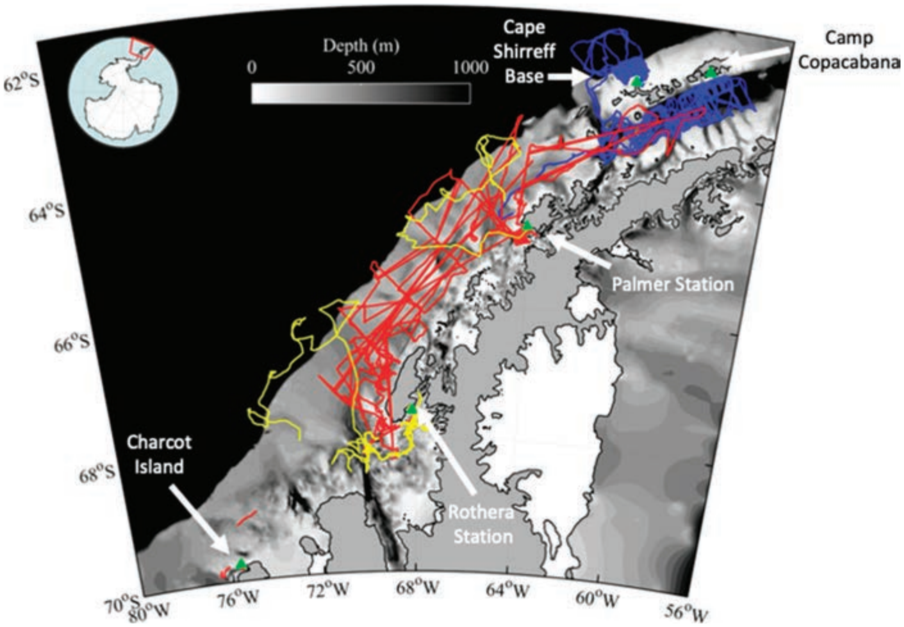

to maintain a sustained spatial presence in the coastal regions surrounding these shore stations.

The Palmer Long Term Ecological Research (LTER) program is focused on how long-term change associated with climate will ripple through the food webs. Figure 2 shows the multi-year presence of gliders deployed from the United States Palmer Station collected as part of the National Science Foundation LTER program. Sampling at Palmer Station is focused on understanding how biophysical interactions influenced by an irregular seafloor topography (especially associated with the Palmer Deep sea floor canyon, Figure 2A) support a biological hotspot with high primary productivity and abundant higher trophic levels (whales, seals, penguins). The sustained sampling in this region (Figure 2B), despite strong local currents (Oliver et al., 2013), is possible given the ability of the glider to remain for long periods in location. The glider presence is allowing for the first time the construction of a summer season climatology of phytoplankton biomass showing an initial summer phytoplankton bloom and then a secondary bloom in the late summer months (Figure 2C).

Further south along the peninsula at the UK Research station of Rothera (Figure 1), small boat-based year-round CTD and biological observations have occurred since 1998 as part of the Rothera time series (RaTS) (Venables et al., 2023). While these measurements take place within a deep coastal embayment (520 m), knowledge initially remained limited around the physical and biological connectivity of the coastal station with the wider WAP shelf, in particular its relationship with the deep Marguerite Trough (up to 1400 m) that provides a pathway between the open Southern Ocean and the inner shelf up to George VI ice shelf. Since 2012, gliders have formed an important part of the RaTS sampling, providing a clearer understanding of this connectivity and its implications for both ocean circulation and near-surface productivity (Venables et al., 2017).

While ship-based sampling is a critical tool for mapping regional biological patterns, efforts chronically under sample of the system, reflecting the relatively low availability of research vessels for these remote locations. One strategy to overcome these limitations is to combine gliders from the numerous field stations spanning the WAP. This offers the unique opportunity for developing an international robotic network. The strategy is based on flying gliders between the shore-based field stations where they can be recovered, rebatteried, and redeployed to then fly back to the original field station. This provides a means to map broad swaths of the WAP continental shelf without significant ship support for sustained periods of time. The potential of this approach was demonstrated when a glider was launched from the United States Palmer Station and flown to and recovered by the United Kingdom Rothera research base (Figure 3). Given that the number of available research vessels is decreasing with the United States moving from a two research vessel operation to a single research operation, this strategy will provide an opportunity to maintain a sustained presence in a remote region.

Adaptive Sampling of Mobile Subsurface Features

The WAP is one of the fastest winter warming locations on the

FIGURE 2

Glider coverage at Palmer Station. (A) Spatial sampling at Anvers Island located over the Palmer Deep sea floor canyon, which is critical for penguin ecology (Schofield et al., 2013). The triangles indicate the long-term time series locations collected using traditional zodiac water sampling. (B) The temporal glider coverage of 12 years at Anvers island. (C) The fluorescence-derived chlorophyll climatology for the region (black line) with the green shading representing the maximum and minimum around the mean.

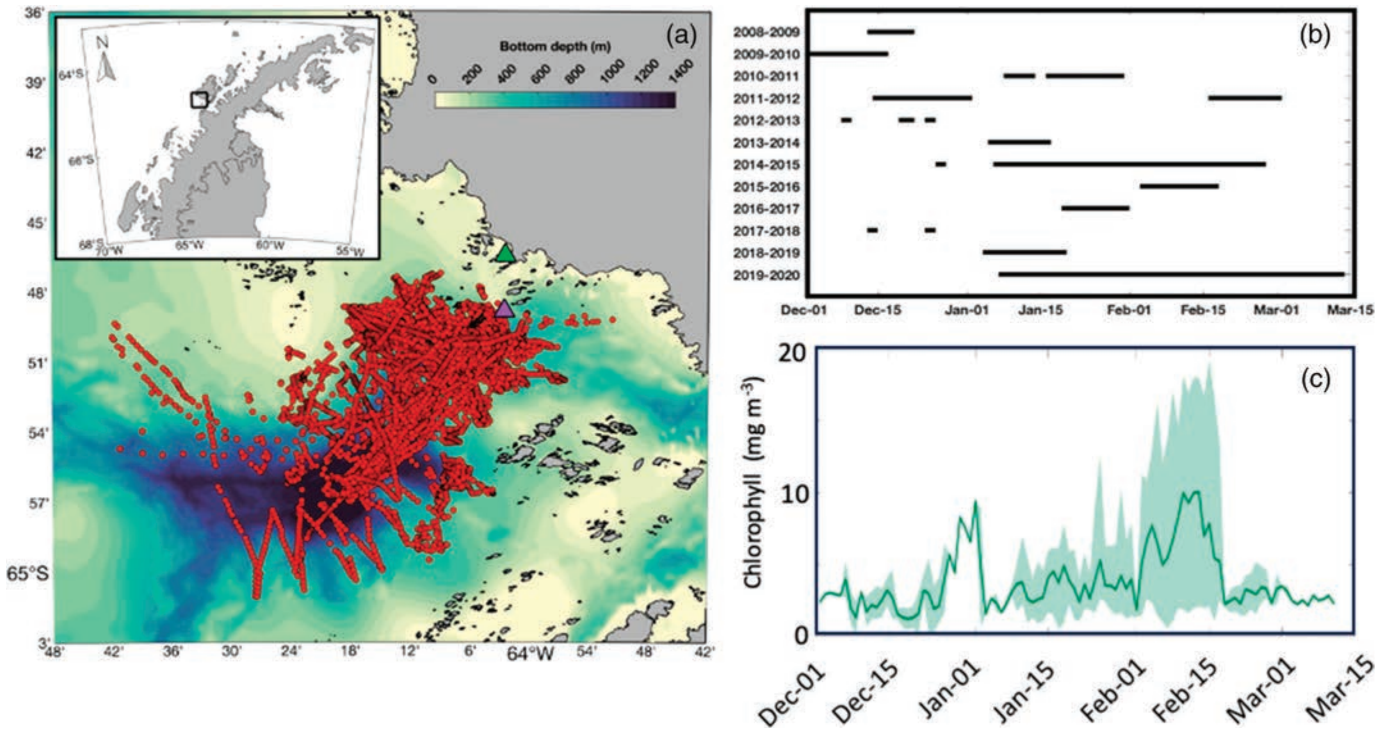

planet with the majority of glaciers in full retreat (Cook et al., 2005) and the annual sea ice exhibiting decadal declines (Stammerjohn et al., 2008). One dramatic example of this was that Rothera had no period of fast ice in the winter of 2022, which is the first time since recording started in the mid-1990s. These changes have been linked to a warming atmosphere and ice melting from below with the heat associated with onshore transport of offshore water (Cook et al., 2016; Couto et al., 2017; McKee et al., 2019; Pritchard et al., 2012; Rignot & Jacobs, 2002). The Upper Circumpolar Deep Water (UCDW) is the largest source of heat to the WAP continental shelf (Hofmann et al., 1996). While upwelling has been suggested as the potential delivery mechanism of UCDW (Dinniman et al., 2011; Martinson et al., 2008), higher resolution data (Martinson & McKee, 2012; Moffat et al., 2009) and models (Graham et al., 2016) suggest the delivery is associated with coherent eddies that move onto shelf and dissipate heat as they move onshore. These subsurface eddies are small with diameters of 10–15 km, cannot be detected by satellite, and move across the shelf, making them difficult to resolve using traditional oceanographic sampling approaches.

Gliders have proven unique tools for studying these dynamic subsurface features. Warm-core, subpycnocline, primarily anticyclonic eddy-like features have been observed and modeled several tens of kilometers from the shelf break, particularly in the vicinity of Marguerite Trough (Brearley et al., 2019; Couto et al., 2017; Graham et al., 2016; McKee et al. 2019; St-Laurent et al., 2013). Glider surveys were designed to sample these dynamic features by first documenting gradients along the axis of advection for any eddies encountered along the way, and then identifying and tracking an eddy in real time through data-adaptive sampling using the warm modified UCDW temperature as a hydrographic fingerprint. This allowed, for the first time, high-spatial and temporal resolution transects directly through some of these eddies and a real-time quantification of the attenuation of their core properties. The transects revealed a composite vertical structure, lateral size, and rotation consistent with theoretical instabilities. To quantify attenuation, a glider occupied a "fence" perpendicular to the

FIGURE 3

Gilder survey of the West Antarctic Peninsula. Panel A shows temperature with the characteristic winter water structure. Panel B shows the optical backscatter with particles largely found in the surface layer. Red circles indicate the land-based field station. The glider was launched from Palmer Station and was remotely piloted to the British Rothera Base in the south.

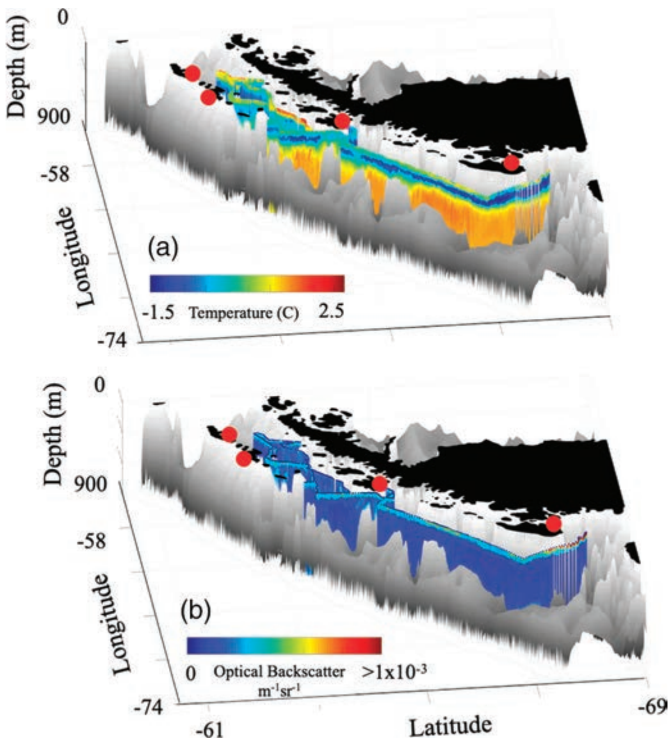

eastern wall of Marguerite Trough (Figure 4) and, when it encountered a feature with the warm signature of the UCDW, the glider sampled the water until the hydrographic feature was no longer detected. The glider was then directed to fly shoreward in the trough to move ahead of the eddy and resample it again. This adaptive sampling strategy was able to look at the heat loss of these eddies for almost 4 days, finding the rate agreed well with that of a simple diffusion model initialized with the eddy's initial structure and governed by diffusivity coefficients parameterized from historical density and velocity data (McKee et al., 2019, Figure 4). The results suggest eddies lose heat both laterally and vertically downward, which preserves the subsurface heat capable of melting marine-terminating glaciers (McKee et al., 2019). Closer to those marine-terminating glaciers, Scott et al. (2021) have used a microstructure instrument on a glider to quantify directly the turbulent diffusivity and vertical heat fluxes out of the CDW layer. While these heat fluxes were low (~1.3 Wm^{-2}), significant enhancement was observed during strong wind events and over a shallow sill linking Ryder Bay (where RaTS is based) with Marguerite Bay.

FIGURE 4

Glider-adaptive sampling of Marguerite Trough. The black line indicates glider trajectory, and dots indicate profile locations, with larger dots indicating presence of modified circumpolar deep water and their color indicating integrated heat content. Color contours indicate vertically integrated heat content from a numerical diffusion model initialized with the eddy's initial condition (box shows domain size), with eddy location at each time step (1–5) determined by grid search algorithm as the location that minimized mismatch between glider sampling of the real and modeled fields. The inferred trajectory (along-isobath) and speed are consistent with regional currents.

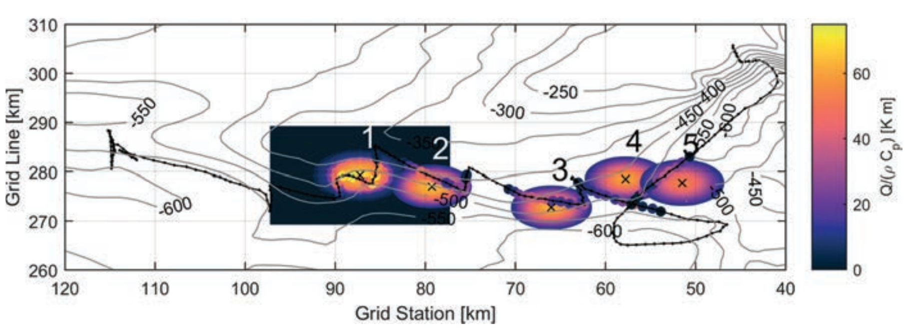

Providing Ecosystem Data to Support Management Requirements

Polar systems are very productive with rich biological resources that have provided great value to society and will continue to do so (Ainley & Pauly, 2013). Managing these resources is difficult given the extreme locations, and many of the key fishing regions are in remote international waters. Management practices are critically important given the historical evidence that humans can overexploit the natural resources. Antarctic krill (*Euphausia superba*) is the principal meso-zooplankton and is critical to Southern Ocean ecology, and it is the target of a large commercial fishery

FIGURE 5

Contour plot of (A) $\log_{10}$ acoustic backscatter coefficient (ABC $m^2\ m^{-2}$), (B) $\log_{10}$ chlorophyll-a fluorescence (mg m^{-3}), and (C) salinity during typical seasonal (mid-December through mid-February) glider deployments off Cape Shirreff Livingston island, Antarctica. Krill aggregations are visible in the upper 100 m of the water column in Panel A, with few large aggregations observed at depth. Glider-based echosounders provide opportunity to examine fine-scale water column relationships between krill, primary production, and the physical environment throughout the water column over deployments spanning multiple months.

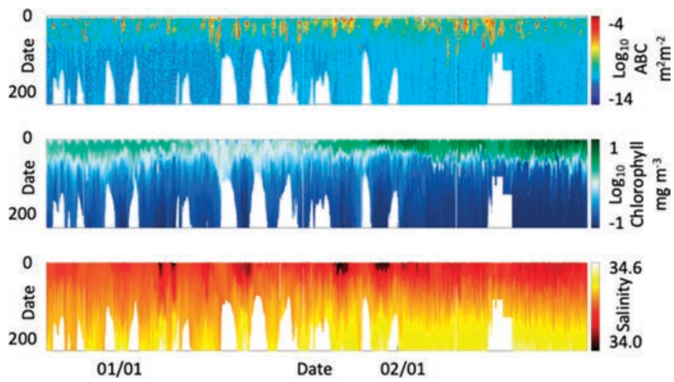

(Nicol & Endo, 1997). This fishery is expanding given the growing demand for krill to supply the increasing demand by fish aquaculture and krill oil/nutraceutical industries (Meyer & Kawaguchi, 2022). This is increasingly important as many regions of krill fishing are exhibiting significant change that includes warming temperatures, declining sea ice, and retreating glaciers (Schofield et al., 2010).

Biological resources in the Southern Ocean, including Antarctic krill, are managed using ecosystem-based approaches, through the Convention for the Conservation of Antarctic Marine Living Resources. For krill, this effort has been historically anchored by ship-based surveys combining net tows with acoustic surveys conducted by research or fishing vessels (Fielding et al., 2014; Hewitt & Demer, 2000; Krafft et al., 2021; Reiss et al., 2008). Globally, the costs for traditional fisheries independent surveys have become prohibitive and there have been efforts to conduct resource surveys autonomously (De Robertis et al., 2021; Reiss et al., 2021). The adaptation of both single frequency (Ainley et al., 2015; Guihen et al., 2014, 2022) and multi-frequency (Chave et al., 2018; Taylor & Lembke, 2017), single-beam or wideband (Benoit-Bird et al., 2018) echosounders onto gliders provides new opportunities to acoustically estimate the biomass of meso-zooplankton, specifically Antarctic krill (Reiss et al., 2021) across time and space scales required to manage resources and to link trophic scales from primary production through secondary production.

Modeling studies have demonstrated that gliders sampling with their sawtooth pattern can effectively recover the time series of biomass density of krill (Kinzey et al., 2022; Figure 5), though some observational evidence exists of avoidance behavior by krill to AUVs, which needs due consideration when designing sampling campaigns (Guihen et al., 2022). Ten years of ship-based acoustic survey data collected in the Antarctic were resampled by flying a virtual glider through the data and then calculating the mean biomass density for each of the ship surveys. A single glider diving to 150 m and acoustically sampling a further 100-m range recovered the temporal pattern of krill biomass density observed in ship-based surveys, and these estimates fell within 1 *SD* of the ship-based estimates nearly 100% of the time. Increasing the number of gliders decreased the variability, while increasing the glider dive depth increased the variability as fewer profiles through the krill swarms in the surface layer are conducted. The results of these simulations provide a roadmap for developing more robust sampling strategies that can be used to provide input in resource assessments.

The use of scientific echosounders to conduct ecosystem or resource surveys requires identification of acoustic targets in order to allocate acoustic energy to targets of interest and to convert acoustic energy to biomass density using appropriate target strength models. Gliders, with the capacity to sample the pelagic ecosystem autonomously for months at a time (Figure 6), are unlikely to always sample with information about the size and composition of planktonic targets. Using multi-frequency or broadband echosounders allows differencing models to be used to discern targets of interest from other acoustic scatters, where the difference in the return strength from different acoustic frequencies are used to provide information about the likely targets (Kang et al., 2002). However, as battery life increases, the addition of optical systems to verify the acoustic targets should become integral to the use of gliders in remote locations, like polar environments where

FIGURE 6

Standard U.S. Antarctic Marine Living Resources Program extended duration, multifrequency (38, 67.5, and 125 kHz), narrowband echosounder-equipped TWR Slocum glider used for estimating krill biomass density around the South Shetland Islands Antarctica during annual resource surveys.

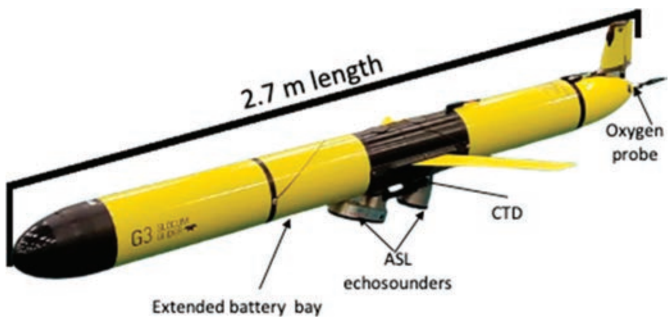

other ecosystem surveys are less likely to be performed.

Challenges and Steps Moving Forward

Under-ice navigation. Many changes in polar systems are associated with critical processes occurring under sea ice and ice sheets. As these ice-covered regions represent ~12% of the world's ocean, it is imperative to sample them for improved understanding of physical circulation, ecosystem structure, vertical mixing, and changes associated with long term anthropogenic change. Unfortunately, these are among the most difficult regions in the ocean to sample. Under-ice navigation has been achieved using fully capable AUVs (see Barker et al., 2020; Norgren et al., 2014) with strategies using acoustics from low-frequency sound sources, or multiple sound sources, and/or a surface vessel directing the robots. These approaches unfortunately are difficult for gliders given their long missions (hundreds of kilometers, multiple month missions), that the platforms undulate and the doppler navigation logs are not gimbled, and that ice complicates the use of surface vehicles.

There are generally two strategies for under-ice navigation by autonomous vehicles. One strategy is based on internal navigation sensors (inertial navigation, doppler velocity log) that estimate the location of the vehicle by tracking the velocity and accelerations. Navigation accuracy over time degrades as long under-ice missions can experience significant navigational drift associated with inertial sensors. Additionally, the types of navigational aids are limited on gliders due to constrained energy budget associated with gliders. The second strategy is based on external signals that often use sonar imaging or acoustic positioning to determine the vehicle position relative to geographic features (Claus & Bachmayer, 2015; Webster et al., 2015). This is a difficult problem given the relatively poor sea floor maps for most polar regions, the relatively low contrast features of ice compared to terrestrial systems, and because features, such as sea ice/icebergs, move (Bandara et al., 2016). Despite these challenges, ice-tethered acoustic navigation beacons have been able to coordinate under-ice missions of Seagliders for up to 12 days (Webster et al., 2015). A high priority and continuing efforts will expand these capabilities. Strategies include the potential use of fixed location beacon "runways" leading to land-based field stations for recovery. This could involve the placement of bottom, or ice, mounted navigation beacons, allowing the glider to track into location. This strategy will benefit from improved onboard processing and adaptive control of the systems (Duguid & Camilli, 2021).

Community cyberinfrastructure. The accelerating use of gliders has fueled the need to develop international open access data systems, allowing the wider community to utilize

FIGURE 7

The glider deployments that are currently available in the NOAA Glider DAC.

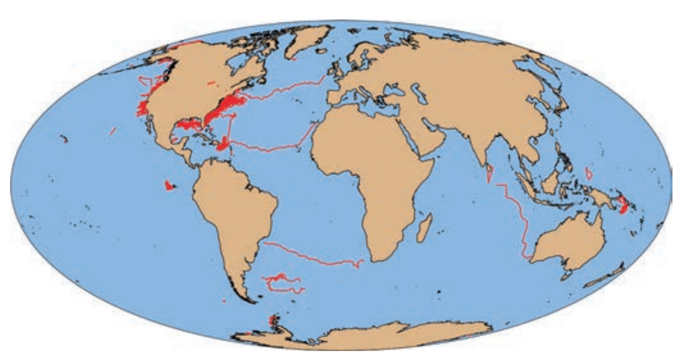

the data. This model of open access has been a hallmark and critical to the global success of the Array fir Real-Time Geostrophic Observatory (ARGO) network. The development of these systems is rapidly evolving. In the United States, the Glider Data Assembly Center (DAC) began development in 2013 and has been maturing over time driven by investments from the Integrated Ocean Observing System. Initial implementation of the DAC focused on physical data for submission to Global Telecommunication System, but in 2017, it began to accept submission of full deployments. Currently data flows to the National Centers of Environmental Information for permanent archiving. The system is also expanding the range of the data types available through the DAC. Use of the Quality Assurance/Quality Control of Real-Time Oceanographic Data protocols is a requirement for inserting data into the DAC. The system is open to anyone willing to provide the correct formats and required metadata. Currently, the DAC has 1,539 total data sets (1,059 real-time and 480 delayed mode data sets) (Figure 7). While the number of data sets is growing, it represents just a subset of the available glider deployments, and future efforts should collate and provide the full data sets as it is possible. A second major data system is the European Gliders for Research Ocean Observation and Management (GROOM). This system is designed to provide a multi-faceted cyberinfrastructure system designed to serve a wider range of autonomous systems and capabilities including system control and optimized links to operational numerical models. It is being developed to provide an integrated system supporting operations-maintenance, data sharing and harmonization, and piloting infrastructure. As systems such as the DAC and GROOM mature, a major challenge will be to ensure wide community adoption to provide a few centralized portals that leverage engineering, methods, and scientific analysis by the distributed community.

In conclusion, gliders are and will increasingly become an indispensable tool for studying polar systems. Given the rapid and accelerating changes in these regions, gliders will be a central tool to filling data and informational gaps. This comes at a critical time as polar systems are exhibiting accelerating change. These changes include hemispheric declines in sea ice (Eayrs et al., 2021) as was evidenced by the 6.4-sigma event in sea ice decline observed in 2023 (Cassella, 2023). The ramifications of these changes on the ocean biogeochemistry and ecology remain an open questions. Gliders will be a critical tool to addressing these important questions. Additionally, the open access data developments will provide a means to engage the wider science community in science discoveries as access to these remote locations is likely to decline in the near term with the declines in the available ship time.

Acknowledgments

These efforts have been supported by a range of programs. The Palmer LTER program (PLR-1440435). Since 2017, the RaTS has been supported by Natural Environment Research Council (NEFRC) award "National Capability – Polar Expertise Supporting UK Research" (NE/R016038/1) and supplemented by Brearley's NERC Independent Research Fellowship (NE/L011166/1). Darren McKee was supported by National Science Foundation Grant PLR-2026045.

References

Ainley, D., & Pauly, D. 2013. Fishing down the food web of the Antarctic continental shelf and slope. Polar Record. 50:92–107. https://doi.org/10.1017/S0032247412000757.

Ainley, D.G., Ballard, G., Jones, R.M., Jongsomjit, D., Pierce, S.D., Smith, W.O., & Veloz, S. 2015. Trophic cascades in the western Ross Sea, Antarctica: revisited. Marine Ecology Progress Series. 534:1–16. https://doi.org/10.3354/meps11394.

Aniceto, A.S., Pedersen, G., Primicerio, R., Biuw, M., Lindstrom, U., & Camus, L. 2020. Arctic marine data collection using oceanic gliders: Providing ecological context to cetacean vocalizations. Frontiers of Marine Science. 7. https://doi.org/10.3389/fmars.2020.585754.

Arrigo, K.R., van Dijken, G.L., Castelao, R.M., Luo, H., Rennermalm, A.K., Tedeco, M., … Yager, P.L. 2017. Melting glaciers stimulate large summer phytoplankton blooms in southwest Greenland waters. Geophysical Research Letters. https://doi.org/10.002/2017GL073583.

Arrigo, K.R., van Dijken, G.L., & Strong, A.L. 2015. Environmental controls of marine productivity hotspots around Antarctica. Journal Geophysical Research Oceans. 120:5545–65. https://doi.org/10.1002/2015JC01088.

Bandara, D., Leong, Z., Nguyen, H., Jayasinghe, S., & Forrest, A. L. 2016. Technologies for under-ice navigation. In: 2016 IEEE/OES Autonomous Underwater Vehicles (AUV). IEEE. pp. 108–14.

Baumgartner, M.F., Bonnelll, J., Corkeron, P., Van Parijs, S., Hotchkin, C., Hodges, B. A., … Bruner, S.M 2020. Slocum glider provide accurate near real-time estimates of baleen whale presence from human-reviewed passive acoustic detection information. Frontiers in Marine Sciences. 7. https://doi.org/10.3389/fmars.2020.00100.

Barker, L.D., Jakuba, M.V., Bowen, A.D., German, C.R., Maksym, T., Mayer, L., … Whitcomb, L.L. 2020. Scientific challenges and present capabilities in underwater vehicle design and navigation for oceanographic exploration under-ice. Remote Sensing.

12(16):2588. https://doi.org/10.3390/rs12162588.

Beaird, N.L., Rhines, P.B., & Eriksen, C.C. 2013. Overflow waters at the Iceland–Faroe Ridge observed in multi-year seaglider surveys. Journal of Physical Oceanography. 43:2334–51. https://doi.org/10.1175/JPO-D-13-029.1.

Benoit-Bird, K.J., Welch, P.T., Waluk, C.M., Barth, J.A., Wangen, I., McGill, P., … McCammon, S. 2018. Equipping an underwater glider with a new echosounder to explore ocean ecosystems. Limnology and Oceanography Methods. 52:123–16. https://doi.org/10.1002/lom3.10278.

Brearley, J.A., Meredith, M.P., Naveira-Garabato, A.C., Venables, H.J., & Inall, M.E. 2017. Controls on turbulent mixing on the West Antarctic Peninsula shelf. Deep Sea Research Part II: Topical Studies in Oceanography. 139:18–30. https://doi.org/10.1016/j.dsr2.2017.02.011.

Brearley, J.A., Moffat, C., Venables, H.J., Meredith, M.P., & Dinniman, M.S. 2019. The role of eddies and topography in the export of shelf waters from the West Antarctic Peninsula Shelf. Journal of Geophysical Research: Oceans. 124:7718–42. https://doi.org/10.1029/2018JC014679.

Brown, Z.W., & Arrigo, K.R. 2012. Contrasting trends in sea ice and primary production in the Bering Sea and Arctic Ocean. ICES Journal of Marine Science. 69:1180–93. https://doi.org/10.1093/icesjms/fss113.

Cassella, C. 2023. 6.4-Sigma event: Antarctic sea ice hits lowest point since official records began. https://www.sciencealert.com/6-4-sigma-event-antarctic-sea-ice-hits-lowest-point-since-official-records-began.

Chapin III, F.S., Berman, M., Callaghan, T.V., Convey, P., Crepin, A.-S., Dannell, H., … Zöckler, C. 2005. Polar Systems. In: Hassan, R., Scholes, R., & Ash, N. (eds.), Ecosystems and Human Well-being: Current State and Trends. Washington, DC: Island Press. pp. 717–43.

Chave, R., Buermans, J., Lemon, D.D., Taylor, J.C., Lembke, C., DeCollibus, C., … Reiss, C. 2018. Adapting multi-frequency echo-sounders for operation on autonomous vehicles. In Proceedings of the OCEANS 2018 MTS/IEEE Charleston, Charleston, SC. https://doi.org/10.1109/OCEANS.2018.8604815

Claus, B., & Bachmeyer, R. 2015. Terrain-aided navigation for an underwater glider. Journal of Field Robotics. 32(7):935–51. https://doi.org/10.1002/rob.21563.

Cook, A.J., Fox, A.J., Vaughan, D.G., & Ferrigno, J.G. 2005. Retreating glaciers fronts on the Antarctic Peninsula over the past half-century. Science. 308:542–4. https://doi.org/10.1126/science.1104235.

Cook, A.J., Holland, P.R., Meredith, M.P., Murray, T., Luckman, A., & Vaughan, D.G. 2016. Ocean forcing of glacier retreat in the western Antarctic Peninsula. Science. 353:283–6.

Couto, N., Martinson, D.G., Kohut, J., & Schofield, O. 2017. Distribution of upper circumpolar deep water on the warming continental shelf of the West Antarctic Peninsula. Journal of Geophysical Research: Oceans. 122:5306–15.

Crawford, A.D., Krumhardt, K.M., Lovenduski, N.S., van Dijken, G.L., & Arrigo, K.R. 2020. Summer high-wind events and phytoplankton productivity in the Arctic ocean. Journal Geophysical Research. 125(9): e2020JC016565. https://doi.org/10.1029/2020JC016565.

Curry, B., Lee, C.M., Petrie, B., Moritz, R.E., & Kok, R. 2014. Multiyear volume, liquid freshwater and sea ice transports through Davis Start, 2004-2010. Journal of Physical Oceanography. 44:1244–66. https://doi.org/10.1175/JPO-D-13-0177.1.

Davis, R., Eriksen, C., & Jones, C. 2002. Autonomous buoyancy-driven underwater gliders. Engineering, Environmental Science. https://www.researchgate.net/publication/245577560_Autonomous_Buoyancy-Driven_Underwater_Gliders.

De Robertis, A., Levine, M., Lauffenburger, N., Honkalehto, T., Ianelli, J., Monnahan, C.C., … McKelvey, D. 2021. Uncrewed surface vehicle (USV) survey of walleye pollock, Gadus chalcogrammus, in response to the cancellation of ship-based surveys. ICES Journal of Marine Science (2021). 78(8):2797–808. https://doi.org/10.1093/icesjms/fsab155.

Dickson, B. 2006. The integrated Arctic Ocean Observing System (iAOOS): An AOSB-CliC observing plan for the international polar year. Oceanologia. 48:5–21.

Dinniman, M.S., Klinck, J.M., & Smith, W.O. 2011. A model study of circumpolar deep water on the West Antarctic Peninsula and Ross Sea continental shelves. Deep Sea Research. https://doi.org/10.1016/j.dsr2.2010.11.013.

Duguid, Z., & Camilli, R. 2021. Improving resource management for untended observation of the marginal ice zone using autonomous underwater gliders. Frontiers of Robotics and AI. 7. https://doi.org/10.3389/frobt.2020.579256.

du Plessis, M., Swart, S., Ansorge, I.J., Mahadevan, A., & Thompson, A.F. 2019. Southern ocean seasonal restratification delayed by submesoscale wind-front interactions. Journal of Physical Oceanography. 49(4):1035–53. https://doi.org/10.1175/JPO-D-18-0136.1.

Eayrs, C., Li, X., Raphael, M.N., & Holland, D.M. 2021. Rapid decline in Antarctic sea ice in recent years hints at future change. Nature Geoscience. 14:460–4. https://doi.org/10.1038/s41561-021-00768-3.

Fielding, S., Watkins, J.L., Trathan, P.N., Enderlein, P., Waluda, C.M., Stowasser, G., … Murphy, E.J. 2014. Interannual variability in Antarctic krill (Euphausia superba) density at South Georgia, Southern Ocean: 1997–2013. ICES Journal of Marine Science. 71(9):2578–88. https://doi.org/10.1093/icesjms/fsu104.

Fraser, N.J., Skogseth, R., Nilsen, F., & Inall, M.E. 2018. Circulation and exchange in a broad Arctic fjord using glider-based observations. Polar Research. 37. https://polarresearch.net/index.php/polar/article/view/2674.

Graham, J.A., Dinniman, M.S., & Klinck, J.M. 2016. Impact of model resolution for on-shelf heat transport along the West Antarctic Peninsula. Journal of Geophysical Research. 121(10):7880–97. https://doi.org/10.1002/2016JC011875.

Gruber, N., Landschützer, P., & Lovenduski, N.S. 2019. The variable Southern Ocean Carbon Sink. Annual Reviews Marine Science. 11:159–86.

Guihen, D., Brearley, A.J., & Fielding, S. 2022. Antarctic krill likely avoid underwater gliders. Deep-Sea Research Part I: Oceanographic Research Papers. 179:10. https://doi.org/10.1016/j.dsr.2021.103680.

Guihen, D., Fielding, S., Murphy, E.J., Heywood, K.J., & Griffiths, G. 2014. An assessment of the use of ocean gliders to undertake acoustic measurements of zooplankton: The distribution and density of Antarctic krill (Euphausia superba) in the Weddell Sea. Limnology and Oceanography Methods. 12:373–89. https://doi.org/10.4319/lom.2014.12.373.

Hauck, J., Völker, C., Wolf-Gladrow, D.A., Laufkötter, C., Vogt, M., Aumont, O., … Totterdell, I. 2015. On the Southern Ocean CO2 uptake and the role of the biological carbon pump in the 21st century. Global Biogeochemical Cycles. 29(9):1451–70. https://doi.org/10.1002/2015GB005140.

Hewitt, R.P., & Demer, D.A. 2000. The use of acoustic sampling to estimate the dispersion and abundance of euphausiids, with an emphasis on Antarctic krill, Euphausia superba. Fisheries Research. 47:215–29.

Hofmann, E.E., Klinck, J.M., Lascara, C.M., & Smith, D.A. 1996. Water mass distribution and circulation west of the Antarctic Peninsula and including Bransfield Strait. In Foundation for Ecological Research West of the Antarctic Peninsula, eds. Ross, R., & Quentin, L. (Vol. 70, pp. 61–80). Antarctic Research Series, American Geophysical Union.

Hogg, A.M.C., Meredith, M.P., Chambers, D.P., Abrahamsen, E.P., Hughes, C.W., & Morrison, A.K. 2015. Recent trends in the Southern Ocean eddy field. Journal of Geophysical Research. 120:257–67. https://doi.org/10.1002/2014JC010470.

Hoydalsvik, F., Mauritzen, C., Orvik, K.A., LaCasce, J.H., Lee, C.M., & Gobat, J. 2013. Transport estimates of the Western Branch of the Norwegian Atlantic Current from glider surveys. Deep-Sea Research. 79:86–9. https://doi.org/10.1016/j.dsr.2013.05.005.

Kang, M., Furusawa, M., & Miyashita, K. 2002. Effective and accurate use of difference in mean volume backscattering strength to identify fish and plankton. ICES Journal of Marine Science. 59(4):794–804. https://doi.org/10.1006/jmsc.202.

Kinzey, D., Cossio, A.M., Reiss, C.S., & Watters, G.M. 2022. Acoustic sampling of Antarctic krill with simulated underwater buoyancy gliders: Does the sawtooth dive pattern work. Frontiers in Marine Science. https://doi.org/10.3389/fmars.2022.1064181.

Krafft, B.A., Macaulay, G.J., Skaret, G., Knutsen, T., Bergstad, O.A., Lowther, A., & Hoem, N. 2021. Standing stock of Antarctic krill (Euphausia superba Dana 1850 (Euphausiacea)) in the Southwest Atlantic sector of the Southern Ocean, 2019. 2021. Journal of Crustacean Biology. 41:1–17. https://doi.org/10.1093/jcbiol/ruab046.

Lee, C.M., Starkweather, S., Eicken, H., Timmermans, M., Wilkinson, J., Sandven, S., … Sørensen, K. 2019. A framework for the development, design and implementation of a sustained Arctic ocean observing system. Frontiers in Marine Science. 6. https://doi.org/10.3389/fmars.2019.00451.

Lee, C.M., & Thomson, J. 2017. An autonomous approach to observing the seasonal ice zone in the Western Arctic. Oceanography. 30(2):56–68.

Martinson, D.G., Stammerjohn, S.E., Iannuzzi, R.A., Smith, R.C., & Vernet, M. 2008. Western Antarctic Peninsula physical oceanography and spatio–temporal variability. Deep Sea Research Part II: Topical Studies in Oceanography. 55:1964–87.

Martinson, D.G., & McKee, D.C. 2012. Transport of warm upper circumpolar deep water onto the western Antarctic Peninsula continental shelf. Ocean Science. 8:433–42. https://doi.org/10.5194/os-8-433-2012.

McKee, D.C., & Martinson, D.G. 2020. Spatially coherent intraseasonal velocity fluctuations on the western Antarctic Peninsula shelf. Journal of Geophysical Research: Oceans. 125:e2019JC015770. https://doi.org/10.1029/2019JC015770.

McKee, D.C., Martinson, D.G., & Schofield, O. 2019. Origin and attenuation of mesoscale structure in circumpolar deep water intrusions to an Antarctic Shelf. Journal of Physical Oceanography. 49:1293–318.

Meredith, M., Sommerkorn, M., Cassotta, S., Derksen, C., Ekaykin, A., Hollowed, A., … Schuur, E.A.G. 2019. Polar regions. In: IPCC special report on the ocean and cryosphere in a changing climate. Pörtner, H.-O., Roberts, D. C., Masson-Delmotte, V., Zhai, P., & Tignor, M., … E. (Eds.). Cambridge, UK: Cambridge University Press. pp. 203–320.

Meyer, B., & Kawaguchi, S. 2022. Antarctic marine life under pressure. Science. 378(6617):230. https://doi.org/10.1126/science.adf3606.

Mikhalevsky, P.N., Sagen, H., Worcester, P.F., Baggeroer, A., Orcutt, J., Moore, S.E., … Yuen, M.Y. 2015. Multipurpose acoustic networks in the integrated Arctic ocean observing system. Arctic. 68:11–27. https://doi.org/10.14430/arctic4469.

Moffat, C., & Meredith, M. 2018. Shelf-ocean exchange and hydrography west of the Antarctic Peninsula: a review. Philosophical Transactions of the Royal Society A: Mathematical, Physical and Engineering Sciences. 376:20170164.

Moffat, C., Owens, B., & Beardsley, R.C. 2009. On the characteristics of Circumpolar Deep Water intrusions to the west Antarctic Peninsula Continental Shelf. Journal of Geophysical Research: Oceans. 114(C5). https://doi.org/10.1029/2008JC004955.

Moore, J.K., Fu, W., Primeau, F., Britten, G.L., Lindsay, K., Long, M., Doney, S.C., … Randerson, J.T. 2018. Sustained climate warming drives declining marine biological productivity. Science. 359:1139–43. https://doi.org/10.1126/science.aao6379.

Morley, S.A., Abele, D., Barnes, D.K.A., Cardenas, C.A., Cotte, C., Gutt, J., … Constable, A.J. 2020. Global drivers on Southern ocean ecosystems: Changing physical environments and anthropogenic pressures in an Earth System. Frontiers of Marine Sciences. https://doi.org/10.3389/fmars.2020.547188.

Nicholson, S.A., Whitt, D.B., Fer, I., du Plessis, M.D., Lebéhot, A.D., Swart, S., … Monteiro, P.M.S. 2022. Storms drive outgassing of CO2 in the subpolar Southern Ocean. Nature. Communications. 13(1). https://doi.org/10.1038/s41467-021-27780-w.

Nicol, S., & Endo, Y. 1997. Krill fisheries of the world. FAO Fisheries Technical Paper. No. 367. Rome, Italy. 100 pp.

Norgren, P., Lubbad, R., & Skjetne, R. 2014. Unmanned underwater vehicles in Arctic operations. 22nd IAHR International Symposium on Ice. Singapore. August 2014. https://www.researchgate.net/publication/330703330.

Oliver, M.A., Irwin, A., Moline, M.A., Fraser, W., Patterson, D., Schofield, O., & Kohut, J. 2013. Adelie penguin foraging location correlated with local tides. PLOS ONE. e55163. https://doi.org/10.1371/journal.pone.0055163.

Pritchard, H., Ligtenberg, S., Fricker, H., Vaughan, H.A., Van Den Broeke, M.R., & Padman, L. 2012. Antarctic ice-sheet loss driven by basal melting of ice shelves. Nature. 484:502–5. https://doi.org/10.1038/nature10968.

Reiss, C.S., Cossio, A.M., Walsh, J., Cutter, G.R., & Waters, G.M. 2021. Glider-based estimates of meso-zooplankton biomass density: A fisheries case study on Antarctic krill (Euphausia superba) around the northern Antarctic Peninsula. Frontiers of Marine Science. 8. https://doi.org/10.3389/fmars.2021.604043.

Reiss, C.S., Cossio, A.M., Loeb, V., & Demer, D.A. 2008. Variations in the biomass of Antarctic krill (Euphausia superba) around the South Shetland Islands, 1996–2006. ICES Journal of Marine Science. 65(4):497–508. https://doi.org/10.1093/icesjms/fsn033.

Rignot, E., & Jacobs, S. 2002. Rapid bottom melting widespread near Antarctic ice sheet grounding lines. Science. 269:2020–3. https://doi.org/10.1126/science.107094.

Rudnick, D.L. 2016. Ocean research enabled by underwater gliders. Annual Reviews Marine Science.. 8:519–41. https://doi.org/10.1146/annurev-marine-122414-033913.

Schmidtko, S., Heywood, K.J., Thompson, A.F., & Aoki, S. 2014. Multidecadal warming of Antarctic waters. Science.. 346:1227–31. https://doi.org/10.1126/science.1256117.

Schofield, O., Ducklow, H., Bernard, K., Doney, S., Fraser-Patterson, D., Gorman, K., … Fraser, W. 2013. Penguin biogeography along the West Antarctic Peninsula: Testing the canyon hypothesis with Palmer LTER observations. Oceanography. 26:78–80. https://doi.org/10.5670/oceanog.2013.63.

Schofield, O., Ducklow, H.W., Martinson, D.G., Meredith, M.P., Moline, M.A., & Fraser, W.R. 2010. How do polar marine ecosystems respond to rapid climate change. Science. 328:1520. https://doi.org/10.1126/science.1185779.

Schofield, O., Kohut, J., Aragon, D., Creed, L., Graver, J., Haldeman, C., & Glenn, S.M. 2007. Slocum gliders: Robust and ready. Journal of Field Robotics. 24(6):473–85. https://doi.org/10:1009/rob.20200.

Scott, R.M., Brearley, J.A., Garabato, N., Alberto, C., Venables, H.J., & Meredith, M.P. 2021. Rates and mechanisms of turbulent mixing in a coastal embayment of the West Antarctic Peninsula. Journal of Geophysical Research: Oceans. 126:26. https://doi.org/10.1029/2020JC016861.

St-Laurent, P., Klinck, J.M., & Dinniman, M.S. 2013. On the role of coastal troughs in the circulation of warm circumpolar deep water on Antarctic shelves. Journal of Geophysical Research. 43(1):51–64. https://doi.org/10.1175/JPO-D-11-0237.1.

Stammerjohn, S.E., Martinson, D.G., Smith, R.C., Yuan, X., & Rind, D. 2008. Trends in Antarctic annual sea ice retreat and advance and their relation to El Niño–Southern Oscillation and Southern Annular Mode variability. Journal of Geophysical Research: Oceans. 113(C3). https://doi.org/10.1029/2007JC004269.

Stommel, H. 1989. The Slocum mission. Oceanography. 2:22–5. https://doi.org//10.5670/oceanog.1989.26.

Taylor, C.T., & Lembke, C. 2017. Echo-sounder for biological surveys using ocean gliders: Extending fishery ecosystem assessments to remote places. Sea Technology. 58:35–8.

Ullgren, J.E., Fer, I., Darelius, E., & Beaird, N. 2014. Interaction of the Faroe Bank Channel overflow with Iceland Basin intermediate waters. Journal of Geophysical Research. 119:228–40. https://doi.org/10.1002/2013JC009437.

Venables, H., Meredith, M.P., Hendry, K.R., ten Hoopen, P., Peat, H., Chapman, A., … Clarke, A. 2023. Sustained, year-round oceanographic measurements from Rothera Research Station, Antarctica, 1997-2017. Scientific Data. 10. https://doi.org/10.1038/s41597-023-02172-5.

Venables, H.J., Meredith, M.P., & Brearley, J.A. 2017. Modification of deep waters in Marguerite Bay, western Antarctic Peninsula, caused by topographic overflows. Deep Sea Research II: Topical Studies in Oceanography. 139:9–17. https://doi.org/10.1016/j.dsr2.2016.09.005.

Wang, X., & Key, J.R. 2005. Arctic surface, cloud, and radiation properties based on the AVHRR polar pathfinder dataset. Part II: Recent trends. Journal of Climate. 18(14):2575–93. https://doi.org/10.1175/JCLI3439.1.

Webster, S.A., Lee, C.M., & Gobat, J.I. 2015. Preliminary results in under-ice acoustic navigation for seagliders in Davis Strait. Ocean. 2014. https://doi.org/10.1109/OCEANS.2014.7003070.

Wood, R. 2012. Stratocumulus clouds. Monthly Weather Review. 140:2373–423. https://doi.org/10.1175/MWR-D-11-00121.1.

Yang, B., Shadwick, E.H., Schultz, C., & Doney, S.C. 2021. Annual mixed layer carbon budget for the West Antarctic Peninsula continental shelf: Insights from year-round mooring measurements. Journal of Geophysical Research: Oceans. 126:e2020JC016920. https://doi.org/10.1029/2020JC016920.

Sensor and Behavior Frameworks for Implimenting Backseat Driver on a Slocum Glider

Sophie Scopazzi
Center for Ocean Observing Leadership (COOL)
Rutgers University
New Brunswick, USA
sophie.scopazzi@marine.rutgers.edu

Travis Miles
Center for Ocean Observing Leadership (COOL)
Rutgers University
New Brunswick, USA
tnmiles@marine.rutgers.edu

Joseph Gradone
Center for Ocean Observing Leadership (COOL)
Rutgers University
New Brunswick, USA
jgradone@marine.rutgers.edu

Dave Aragon
Center for Ocean Observing Leadership (COOL)
Rutgers University
New Brunswick, USA
dkaragon@marine.rutgers.edu

Alex Lopez
Center for Ocean Observing Leadership (COOL)
Rutgers University
New Brunswick, USA
alopez@marine.rutgers.edu

OCEANS 2024 - Halifax | 979-8-3315-4008-1/24/$31.00 ©2024 IEEE | DOI: 10.1109/OCEANS55160.2024.10753744

***Abstract*—The Slocum glider's long-duration and cost-effective data collection capability, coupled with remote operation from shore, makes them ideal platforms for oceanographic research. However, once submerged in standard operation, instrument operation, waypoints, behaviors, and more are fixed until the vehicle surfaces. This lack of underwater adaptive control can lead to limitations in scientific sampling, limiting the glider's ability to meet the mission's scientific goals. In this work, we present a manual for implementing the Slocum Backseat Driver (BSD) architecture on a G3S Slocum glider. It contains examples for configuring an external controller (a Raspberry Pi 4 Model B), managing file transfers, incorporating real-time sensor data for decision-making, and advancing the ocean simulation capability of a glider simulator using a Slocum Fleet Mission Control (SFMC) script. Four simulations were ran, two utilizing the Slocum BSD architecture to autonomously navigate with a heading orthogonal from the Depth-Averaged Current (DAC) value calculated by the glider. The missions utilizing the BSD architecture updated the heading less frequently and did so with a more optimal average heading. Through using the Slocum BSD architecture, we can fully realize the glider's true capability for long-duration and cost-effective persistent oceanographic sampling presence in challenging regions throughout the globe. This research and accompanying manual provide a starting point for glider pilots, technicians, scientists, and others when working through how to use the Slocum glider's BSD architecture.**

Keywords—Slocum Glider, Backseat Driver, External Controller, Slocum Fleet Mission Control, Real-Time Onboard Processing

I. INTRODUCTION

Slocum gliders are well suited to sample the world's oceans. They are highly cost-effective and capable of multi-month missions gathering thousands of vertical casts of oceanographic data [1]. Slocum gliders' capabilities coupled with their remote programmability makes them ideal platforms for oceanographic research. However, like any system purely reliant on onboard power, operators of Slocum gliders must make energy consumption decisions causing tradeoffs between scientific sampling, communication with shore for near-real-time data telemetry, and flight trajectory. The interplay between these variables must be accounted for by glider pilots as they ensure ample data collection for a successful scientific mission. Balancing these trade-offs is further complicated by the limits of Iridium satellite communications.

During an ocean deployment, the standard operating procedure is to have the glider communicate with the shore via the Iridium satellite network. This method is bandwidth limited and connections are lost as the glider is submerged. Therefore, pilots ashore cannot make decisions for an underwater glider in real-time while the glider is submerged: mission parameters about sampling and waypoints are only configurable during surface events. While Slocum gliders have enabled a persistent oceanographic sampling presence in challenging regions ranging from polar oceans [2], beneath tropical cyclones [3], [4], and across ocean basins [5], the lack of adaptive control between vehicle surfacings can limit scientific sampling.

The implementation of a Backseat Driver (BSD) onboard the autonomous underwater vehicle (AUV) can help meet this gap in capability. A system with a BSD can help answer questions ranging from detecting and mapping the extent of oil spills [6], [7], mapping the underwater portion of icebergs [8], following thermoclines [9], coastal upwelling fronts [10], haloclines [11], processing ADCP [12] or side-scan data [13], and optimizing the flight of a glider as it navigates ocean currents, as described in this work. Each of these examples requires optimizing the AUV's flight path intelligently and adaptively, allowing more data collection in scientifically rich areas. To address this desired increase in vehicle capability, the Slocum glider BSD architecture has been in development for over ten years, with significant development efforts in recent years. Its use has been

979-8-3315-4008-1/24/$31.00 ©2024 IEEE

limited by availability of resources and expertise on the subject, resulting in limited end-user implementation.

II. Required Hardware and Software

There are three main components to this work: a G3S Slocum glider or a shoebox glider simulator, an external controller, and the hardware and software connection between the two. A fourth component, a Slocum Fleet Mission Control (SFMC) script was made to verify proper external controller operation.

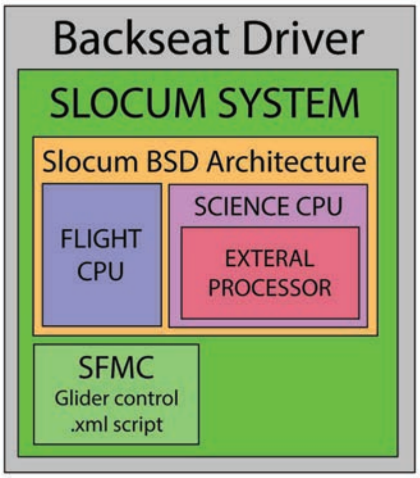

Fig. 1. The layout of the Slocum Backseat Driver architecture and associated system parts within the framework of a Backseat Driver. The SFMC glider control script is external to the glider system, but is within the Slocum system.

A. Slocum G3S Glider Simulator

Termed the "shoebox" due to its oblong rectangular shape, Teledyne Marine makes a dedicated G3S glider simulator. It has a flight computer and science computer with all standard science ports allowing for connection of sensors in the typical manner.

B. External Controller

The external controller must exist within the size and energy consumption constraints that come from being inside a Slocum glider on long-duration missions. Therefore, the external controller should be an energy-efficient small form factor single-board computer. This has led to the adoption of common external controllers such as a BeagleBone Black [14] or a Raspberry Pi 4 Model B [12].

For this work, the external controller selected was a Raspberry Pi 4 Model B due to accessibility of resources and ease of beginner use, making it well suited for educational purposes. Additionally, its Wi-Fi capability is not only useful for the lab setting, allowing remote access through the secure shell protocol (SSH), but its ability to generate its own Wi-Fi connection makes it is also possible to connect to the Raspberry Pi while it is in a glider.

That said, there are many other computers that could be used as an external controller. Selecting the proper external controller comes from the perspective of the science mission. Excess computing power increases power consumption, along with size and/or shape, connection ports, communication protocols, and weight considerations.

C. Simulating a Western Boundary Current with a Slocum Simulator and an SFMC Script

The Slocum BSD architecture program made in this work changes the glider's heading mid-mission based on the vehicles calculated values for ocean current speed and direction; however, in the standard glider simulation the ocean conditions are set once at mission start and remain static throughout. Thus, in order to test this application, we first developed a way to update the glider simulator's water direction and magnitude mid-mission by using a SFMC script.

SFMC is the web application used to manage a Slocum glider in real-time [16]. One of SFMC's capabilities is user-configurable scripts to control the glider, freeing a human pilot from directly issuing commands during every surfacing. A typical script will read the surfacing output from the glider and issue commands for sending and receiving files before commanding the glider to resume the mission and dive. Utilizing this system for our simulation glider, we created a script that reads the glider's longitude from the surface dialog. The script then issues two commands (!put s_water_speed and !put s_water_direction) based on a user defined representation of an ocean current environment. Once the simulated ocean variables are updated, the glider simulator resumes flight using the new values, creating the effect of glider traversing a changing current field (Figure 2).

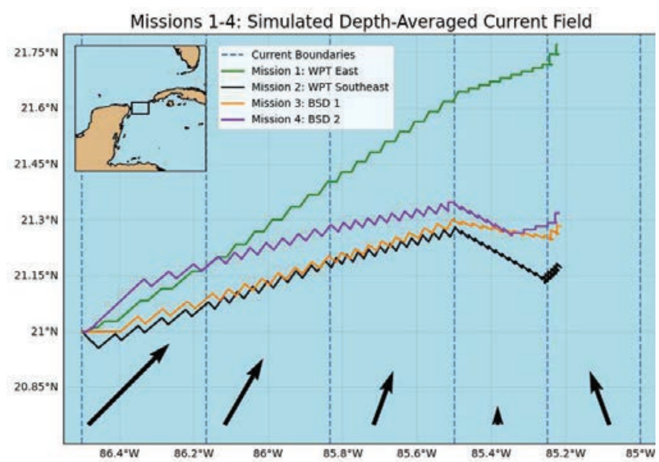

Fig. 2. Blue dashed lines delineate the boundaries between changing currents, with the arrow in each vertical slice of longitude indicating the magnitude and direction of currents within. All gliders started at 21° N, 86.5° W and proceeded east. Four missions were ran in this current field: (1) Green has a waypoint due east of the start location near Africa; (2) Black has a waypoint due southeast of the start location, between South America and Africa; (3) Orange is controlled with the Slocum BSD architecture setting the heading 90° to the right of the DAC; (4) Purple also uses the Slocum BSD architecture to control the heading based upon the DAC, with the addition of calculations to pick the heading that should result in the smallest theoretical northward deflection distance. The sawtooth pattern is due to the time underwater vs time on the surface. The simulated vehicle is subject only to currents (there is no wind forcing).

III. Backseat Driver Concept and Implementation

This paper treats the term BSD as the conceptual context of adding an additional processor onboard a vehicle for improved adaptable capability. Thus, the Slocum BSD architecture is the hardware and software required to implement the BSD concept onboard the Slocum glider (the physical cable connections, communication protocols, and the like). The external controller is the additional computer added to the existing glider control structure.

A Slocum glider has a flight computer and a science computer. The flight computer handles all behavior characteristics and communication protocols with the shore. The science computer handles all scientific sensor and data collection protocols. Although different, the two computers talk with one another via a logic pathway called the clothesline. However, the flight computer typically does not adapt its behaviors based on what the science computer "sees" of the ocean. Like the clothesline between the two glider computers, the science computer and external controller have another physical connection. This is accomplished with a USB to RS232 to Molex connector.

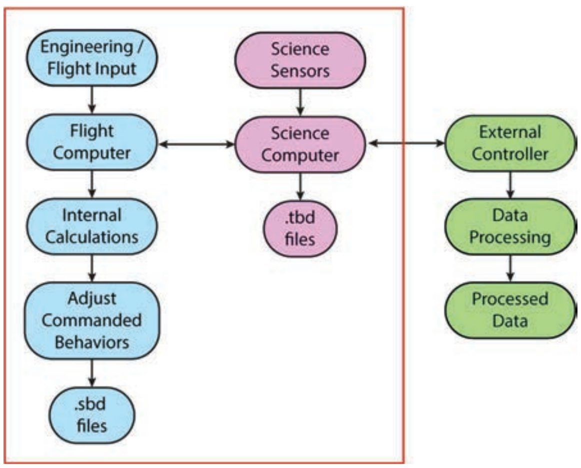

Fig. 3. The external controller is external to the standard Slocum glider's flight and science computer (red box), but still within the physical gider.

Using the connector, we attach the external controller to a science port on the science computer. To the glider, the external controller functions like a typical science sensor where specific commands about when to sample (in this case when to be powered on) are determined by the glider. Standard behavior arguments (b_args) are set once at mission start by the values throughout the glider files and on the surface mid-mission by pilots altering the files via Iridium. The Slocum BSD architecture allows for b_args to be dynamic while under the surface of the ocean by giving the external controller the ability to request and overwrite certain b_arg values stored in glider memory, allowing for in-situ autonomous adaptive control.

The external controller is used and/or controlled in multiple files on the glider. When a mission begins, the glider initializes values from onboard files and stores them in the flight computer's random-access-memory. The external controller then actively overwrites these values as the glider is flying, altering the behavior at that point in time. By allowing the b_args to be dynamic, new glider behaviors can be actualized through the external controller's dynamic controllability and potential increase in computing power, if greater processing is required.

IV. Backseat Driver Manual

To further enhance communities' resources, in this work I have written a manual which provides numerous use-cases of how to use the Slocum BSD architecture: Implementing the Backseat Driver Architecture on a G3S Slocum Glider: A Manual for Operators [15]. The manual is intended as a starting point for anyone to leverage the BSD architecture on a Slocum glider for their own specific use-case.

The manual contains background, practical guidance, and examples for configuring an external controller, integrating real-time glider sensor data, datafile transfer and management, simulating scientific sensors for validating proper external controller behavior, and more. All the glider files and Python code to implement the external controller onboard the glider are in the manual.

V. Simulations

Using the shoebox simulator, the Raspberry Pi 4 Model B as the external controller, and the associated wiring and programming, four simulated missions were run in an SFMC controlled current field roughly approximating the Yucatán Channel's Depth Average Current (DAC). All four began at the same location just offshore the Yucatán Peninsula and represent 22 days and 7 hours of simulation time.

Two missions were run using the goto_list behavior: Mission 1, with a waypoint due east of the start location, and Mission 2, with a waypoint due southeast of the start location. Both waypoints were extremely distant, on the same longitude as the westernmost part of Africa, a common practice to effectively program the glider to fly on a constant heading. Two missions (3 and 4) were run utilizing the Slocum BSD architecture with the set_heading behavior using the external controller to control the glider's heading based upon the glider's calculated DAC. When the glider surfaced and updated its DAC calculation, the external controller would read the new DAC value and update the glider's heading.

Given acceptable time and deflection distance constraints, the missions controlled with the Slocum BSD architecture crossed the fast moving currents in less time and with less northward deflection than when using standard practices for piloting gliders in areas of fast-moving current. Although Mission 2 had the shortest northward deflection distance it took an excessive amount of time. Mission 3 and 4, with headings between Mission 1 and 2, crossed the currents at a more optimal angle, better meeting the time vs distance trade-off (Figure 5A).

Missions 3 and 4 demonstrate the viability of operating an external controller for a total of 8.59 days. While this is not conclusive for weeks-long or multi-month missions, this indicates an external controller is capable of proper operation for the extended periods of time required for a glider mission. That said, the external controller's script run time is not always predictable.

For the duration of Mission 3, the same Python script ran with an execution time ranging from 18.46 seconds to 43.19 seconds. Glider sensor vales are sent to the external controller only when they are updated onboard the glider, causing the external controller to wait to receive all values. This lead to the inconsistent script runtime. Teledyne Marine is addressing this in future versions of the Slocum BSD architecture by working to allow the external controller to actively request a specified glider sensor value.

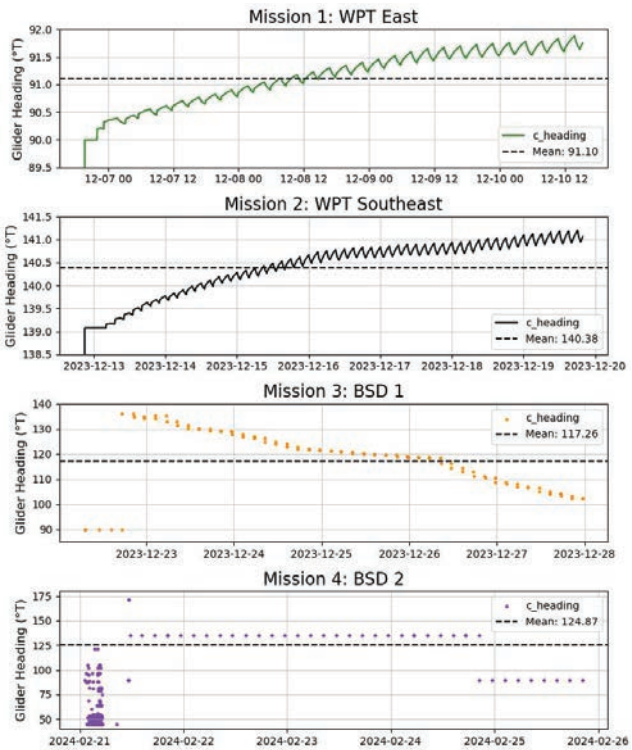

Fig. 4. Mission 1 and 2 are waypoint missions; thus c_heading yaws back and forth as the glider flies towards a distant waypoint. Mission 3 and 4 utilize the BSD architecture updating the set_heading behavior with c_heading only changing when m_water_vel_dir is updated at the surface. At the start of Mission 4 m_water_vel_dir improperly represented s_water_direction causing the external controller to update the heading often and not accurately.

Although setting a distant waypoint could result in the more optimal mean heading of 117°T, doing so would continually update the heading while submerged. In contrast, the two missions utilizing the BSD architecture did not update the heading as often (Figure 4). This is due to the external controller reading the DAC upon surfacing, changing the set_heading behavior's c_heading before diving and resuming the mission. While underwater, the glider's c_heading does not yaw towards a distant waypoint; instead, it remains at the fixed value set by the external controller during the surfacing.

VI. Discussion

The presence of the external controller enables the fine-tuning of the desired cross-current heading to optimize deflection distance versus time, balancing the trade-offs of spending more time for a lower deflection. This also shows the capability for the external controller, via the Python script, to adapt a behavior on a glider as the end-user sees fit.

There are many ways to implement a BSD in a given system; this is but one. However, it is worth remembering that there is no "set" way to utilize the Slocum BSD architecture. Choice of external controller, type of control and glider sensor values are all use-case specific questions that must be decided upon. Also, this work has one main limitation: the glider simulator is not designed to accurately represent a real-life ocean environment, requiring the SFMC script and simulated science sensor work-around. With further development, the SFMC script could integrate latitude for a higher-resolution simulated ocean current and more simulated sensors could be made; however, the simulator's present capabilities place restrictions on lab-based testing, necessitating in-situ ocean missions to properly validate glider characteristics.

The time involved with tests of this nature, simulating glider missions, is long, and there is at present no way to speed up the glider's simulation. Moreover, only one simulation can be run at a time, necessitating thorough testing, debugging, and verification before committing to a multi-day, or longer, test.

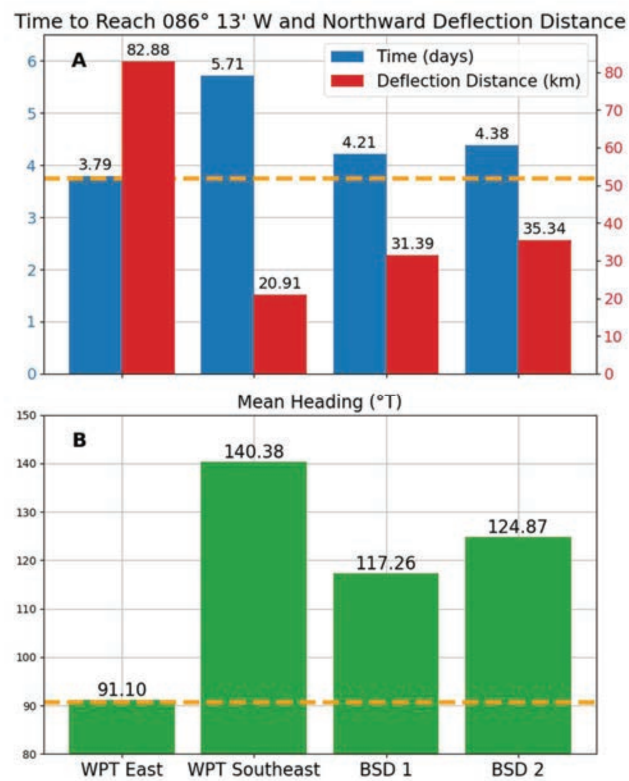

Fig. 5. A: Mission 3 and 4's times and northward deflection distance is more optimal. B: Mission 3 and 4's average heading is between the two waypoint mission heading extremes.

VII. Conclusion

While this work and operational manual created is one step as we continue towards ever greater capability for answering our science questions, there are far more possibilities within the BSD concept than anyone can possibly hope to cover in one work. As the true strength of using a BSD is the creativity in unique vehicle control it can afford, we must continue to leverage and expand upon our existing structures to better capture relevant data. Thus, using the Slocum BSD architecture should be paramount.

To realize this expansion of the Slocum glider's potential, education and outreach is required. Greater collaboration between the engineers creating these systems, scientists desiring data, and the pilots operating the vehicle is necessary.

Translation between the different groups and mindsets to leverage the strengths of each towards the common goal of furthering oceanographic data collection, and ultimately humanities relationship with our planet, is in dire need.

Using the knowledge gained from everyone's backgrounds, we can better implement this incredibly powerful method to enhance the Slocum glider's capabilities for data collection. The Slocum BSD architecture is limited only by our imagination, and our ingenuity.

REFERENCES

[1] O. Schofield *et al.*, "Slocum Gliders: Robust and ready," *J. Field Robot.*, vol. 24, no. 6, pp. 473–485, 2007, doi: 10.1002/rob.20200.

[2] E. P. Abrahamsen, "Sustaining observations in the polar oceans," *Philos. Trans. R. Soc. Math. Phys. Eng. Sci.*, vol. 372, no. 2025, p. 20130337, Sep. 2014, doi: 10.1098/rsta.2013.0337.

[3] T. N. Miles, S. J. Coakley, J. M. Engdahl, J. E. Rudzin, S. Tsei, and S. M. Glenn, "Ocean mixing during Hurricane Ida (2021): the impact of a freshwater barrier layer," *Front. Mar. Sci.*, vol. 10, Aug. 2023, doi: 10.3389/fmars.2023.1224609.

[4] T. N. Miles *et al.*, "Uncrewed Ocean Gliders and Saildrones Support Hurricane Forecasting and Research," *Oceanography*, vol. 34, no. 4, pp. 78–81, 2021.

[5] C. P. Jones, "Slocum glider persistent oceanography," in *2012 IEEE/OES Autonomous Underwater Vehicles (AUV)*, Sep. 2012, pp. 1–6. doi: 10.1109/AUV.2012.6380738.

[6] J. Hwang, N. Bose, H. Nguyen, and G. Williams, "AUV adaptive sampling to delineate subsurface oil plumes," in *2020 IEEE/OES Autonomous Underwater Vehicles Symposium (AUV)*, Sep. 2020, pp. 1–2. doi: 10.1109/AUV50043.2020.9267920.

[7] Y. Wang, N. Bose, W. Thanyamanta, C. Bulger, and S. Shaikh-Upadhye, "Adaptive control for follower gliders mapping underwater oil patches," *J. Hazard. Mater.*, vol. 436, p. 129039, Aug. 2022, doi: 10.1016/j.jhazmat.2022.129039.

[8] M. Zhou, R. Bachmayer, and B. deYoung, "Mapping the underside of an iceberg with a modified underwater glider," *J. Field Robot.*, vol. 36, no. 6, pp. 1102–1117, Sep. 2019, doi: 10.1002/rob.21873.

[9] Y. Zhang, J. G. Bellingham, M. A. Godin, and J. P. Ryan, "Using an Autonomous Underwater Vehicle to Track the Thermocline Based on Peak-Gradient Detection," *IEEE J. Ocean. Eng.*, vol. 37, no. 3, pp. 544–553, Jul. 2012, doi: 10.1109/JOE.2012.2192340.

[10] Y. Zhang, M. A. Godin, J. G. Bellingham, and J. P. Ryan, "Using an Autonomous Underwater Vehicle to Track a Coastal Upwelling Front," *IEEE J. Ocean. Eng.*, vol. 37, no. 3, pp. 338–347, Jul. 2012, doi: 10.1109/JOE.2012.2197272.

[11] Y. Zhang *et al.*, "Autonomous Tracking of Salinity-Intrusion Fronts by a Long-Range Autonomous Underwater Vehicle," *IEEE J. Ocean. Eng.*, vol. 47, no. 4, pp. 950–958, Oct. 2022, doi: 10.1109/JOE.2022.3146584.

[12] J. C. Gradone, E. J. Hunter, J. Mullison, and T. N. Miles, "Development of Onboard Processing Capabilities for a Slocum Glider Acoustic Doppler Current Profiler," in *OCEANS 2021: San Diego – Porto*, Sep. 2021, pp. 1–5. doi: 10.23919/OCEANS44145.2021.9705895.

[13] P. K. Igoe, S. R. Sideleau, and R. Balasubramanian, "Real-time Sensor Data Processing and Reaction in the Context of Autonomous Systems," in *OCEANS 2018 MTS/IEEE Charleston*, Charleston, SC: IEEE, Oct. 2018, pp. 1–5. doi: 10.1109/OCEANS.2018.8604749.

[14] "JMSE | Free Full-Text | A Backseat Control Architecture for a Slocum Glider." Accessed: Oct. 24, 2023. [Online]. Available: https://www.mdpi.com/2077-1312/9/5/532

[15] "sscopazzi/Slocum_Backseat_Driver_Manual: Adding later," GitHub. Accessed: Apr. 15, 2024. [Online]. Available: https://github.com/sscopazzi/Slocum_Backseat_Driver_Manual

[16] "SFMC - About Slocum Fleet Mission Control." Accessed: Apr. 21, 2024. [Online]. Available: https://glider.marine.rutgers.edu/sfmc/about

communications earth & environment

A Nature Portfolio journal

Article

https://doi.org/10.1038/s43247-025-02101-x

Lagrangian coherent structures influence the spatial structure of marine food webs

Check for updates

Jacquelyn M. Veatch[1,2] ✉, Matthew J. Oliver[3], Erick Fredj[4], Hank Statscewich[5], Kim Bernard[6], Ashley M. Hann[6,7], Grant Voirol[3], Heidi L. Fuchs[1], William R. Fraser[8] & Josh T. Kohut[1]

The patchy distribution of prey in marine environments has a large effect on upper trophic level foraging strategies and distributions. While currents can disperse or concentrate low-motility plankton into patches that reflect the dynamic fluid environments they inhabit, it remains unclear whether surface flows affect motile zooplankton. Here, we used an in-situ optical dataset to detect phytoplankton patches, active acoustics to observe krill, and GPS-tagged penguins to observe three levels of the food web. These data allowed us to investigate whether the local food web overlaps with small-scale surface transport patterns as evidence that dynamic flows structure marine food webs. In Palmer Deep Canyon, Antarctica, we deployed High Frequency radars to measure hourly ocean surface currents, which were subsequently applied to estimate attractive Lagrangian Coherent Structures. We found that phytoplankton patches, Antarctic krill (*Euphausia superba*), Adélie penguins (*Pygoscelis adeliae*) and gentoo penguins (*Pygoscelis papua*) were preferentially located in attracting Lagrangian Coherent Structure features. These results provide evidence that Lagrangian Coherent Structures act as hotspots for prey and associated foraging predators, thus spatially focusing the food web. Results highlight the role of small-scale currents in food web focusing and the importance of transport features in maintaining the Palmer Deep Canyon ecosystem.

Distributions of planktonic and nektonic marine organisms are continuously shaped by the dynamic ocean environments in which they reside and are typically patchy in space and time. Phytoplankton and zooplankton are both known to form discrete patches[1,2], with predators that seek out these patches of prey[3], which leads to a form of spatial control on the ecosystem known as food web focusing[4], where small scale fluid flows (hours-days and 1–100 km) structure the relationship between different trophic levels. Here, we are using the term "food web focusing" to describe transient and spatially variable prey patches, as opposed to prey aggregations associated with fixed spatial structures like seamounts[4]. Understanding the mechanisms that control "patchiness" seen in primary producers, primary consumers, and their predators requires integrating environmental observations of physical processes and community structure at relevant temporal and spatial scales[5,6]. These interactions between marine organisms and physical ocean processes are crucial to understanding their distribution within and reliance on the dynamic ocean habitat in which they reside.

Low-motility plankton with low and intermediate Reynolds numbers (Re ~10^{-2}–10^{3})[7], such as phytoplankton and zooplankton, are transported by ocean currents[8]. (Here, Reynolds numbers (Re) refer to how the fluid flows around the animals rather than how the fluid flows on its own). Foraging species with high Reynolds numbers (Re ~10^{6})[7] and greater mobility can employ various foraging strategies to seek out their zooplankton prey, which swim more slowly and are less able to move independently of ocean currents. The transport of low-motility plankton is particularly noticeable in areas with strong currents, often associated with features such as ocean fronts and eddies[9]. In order to understand distributions of phytoplankton, zooplankton, and top predators, we must investigate patterns in ocean transport.

Patterns in ocean transport can be elucidated through particle release experiments within observed ocean velocity fields. By integrating over Lagrangian particle trajectories, attracting structures are quantified within evolving velocity fields using an analysis known as Lagrangian Coherent Structures (LCS)[10]. Several types of LCS exist with different definitions of

[1]Department of Marine and Coastal Sciences, Rutgers, The State University of New Jersey, New Brunswick, NJ, USA. [2]Department of Applied Ocean Physics and Engineering, Woods Hole Oceanographic Institution, Woods Hole, MA, USA. [3]College of Earth, Ocean and Environment, University of Delaware, Lewes, DE, USA. [4]Computer Science Department, The Jerusalem College of Technology, Jerusalem, Israel. [5]College of Fisheries and Ocean Sciences, University of Alaska, Fairbanks, AK, USA. [6]College of Earth, Ocean, and Atmospheric Sciences, Oregon State University, Corvallis, OR, USA. [7]National Oceanic and Atmospheric Administration Uncrewed Systems Operations Center, Silver Spring, MD, USA. [8]Polar Oceans Research Group, Sheridan, MT, USA. ✉e-mail: jveatch@whoi.edu

"attraction" and "repulsion" to quantify the strength of transport features. In this study, we use Finite Time Lyapunov Exponents (FTLE) as a metric to identify attracting LCS, and test if these attracting LCS are acting as a hotspot for low-motility plankton. FTLE were chosen as they provide flexible integration time, allowing for the identification of ocean features at the scale of interest, and have been shown to identify transport features associated with increased phytoplankton patch presence in our study area[11]. LCS can quantify transport patterns in ocean velocities that cannot be seen by studying Eulerian velocity fields alone, allowing for the investigation of the role of transport in food web focusing.

LCS have been shown to overlap with bioactivity on different levels of the marine food web, shaping large phytoplankton blooms[12–15], correlating with the presence of middle trophic levels (fishes)[16], and appearing along the tracks of top predators[17,18]. Much of this previous work has been conducted on larger, geostrophic currents characteristic of open ocean (pelagic) ecosystems. On these scales, satellite-observed ocean color is often used to track the evolution of large phytoplankton patches and Global Positioning System (GPS) tags are used to track movements of large marine animals in relation to LCS calculated from satellite altimetry[12] or long range radars[14]. However, predator and prey patches likely interact at much smaller scales than measured by these systems.

Distributions of zooplankton affect prey availability for many higher trophic level predators[6] including whales[19] and commercially important fishes[20]. Therefore, a major interest in marine spatial ecology has been understanding and quantifying the factors that affect the preyscape of a marine ecosystem. While both phytoplankton and predators have been associated with attractive LCS features, the relationship between zooplankton and LCS are more difficult to obtain as they require in-situ acoustic measurements and/or net tows, and the factors that influence their distribution can be driven by both zooplankton behavior and advection.

Many of the studies linking LCS to top predators assume that, similarly to phytoplankton, zooplankton are also concentrated by attractive LCS features, though these assumptions are typically made without coincident zooplankton measurements. The few studies that have linked zooplankton to LCS were conducted over relatively large scales using data from mesoscale ocean model output[21,22] and long-range (low frequency) radars[23]. These findings suggest links between zooplankton biomass and the presence of LCS at scales of days to weeks and tens of kilometers. Other studies have associated zooplankton distributions with mesoscale eddy kinetic energy[24], tidal cycles phases[25,26], and wind events[25,27] suggesting connections between ocean dynamics and zooplankton swarms. Larger top predators such as whales have also been shown to select for LCS-identified prey concentrating features over larger scales[23]. However, predators likely seek prey patches on much smaller scales[28,29], meaning these coarser-scale associations between LCS and predators could be averages of finer scale processes. Using an Antarctic submarine canyon as our natural laboratory, we resolved the food web at scales of hours to days across spatial scales of hundreds of meters to kilometers and observed transport features experienced by near-shore patches of phytoplankton, zooplankton and associated predators. To our knowledge, the following study is the first, to the best of our knowledge, to include concurrent high-resolution observations of zooplankton, phytoplankton and upper trophic predators in relation to LCS-identified ocean features.

For this study, we focus on the local food web of Palmer Deep Canyon along the Western Antarctic Peninsula (WAP). Here, Antarctic krill (*Euphausia superba*, hereafter referred to as krill) serve as a keystone species and a major food source for marine predators including whales, seals, and penguins[27,30–34]. Local Adélie (*Pygoscelis adeliae*) and gentoo (*Pygoscelis papua*) penguins are both central place foragers, meaning they return to a nest after each foraging trip, with overlapping foraging areas centered over Palmer Deep Canyon (Fig. 1b). Penguin populations in Palmer Deep Canyon have persisted for hundreds of years[35–37], their diets dependent at least in part on the elevated biomass of krill[38] that persists here in relation to neighboring regions[37,39,40], establishing Palmer Deep Canyon as a "biological hotspot". Consequently, Palmer Deep Canyon's ecosystem hinges on the availability of krill as the trophic link between phytoplankton at the base of the food web and higher predators[41]. In this study, we investigate current-driven controls on the distributions of phytoplankton patches and krill

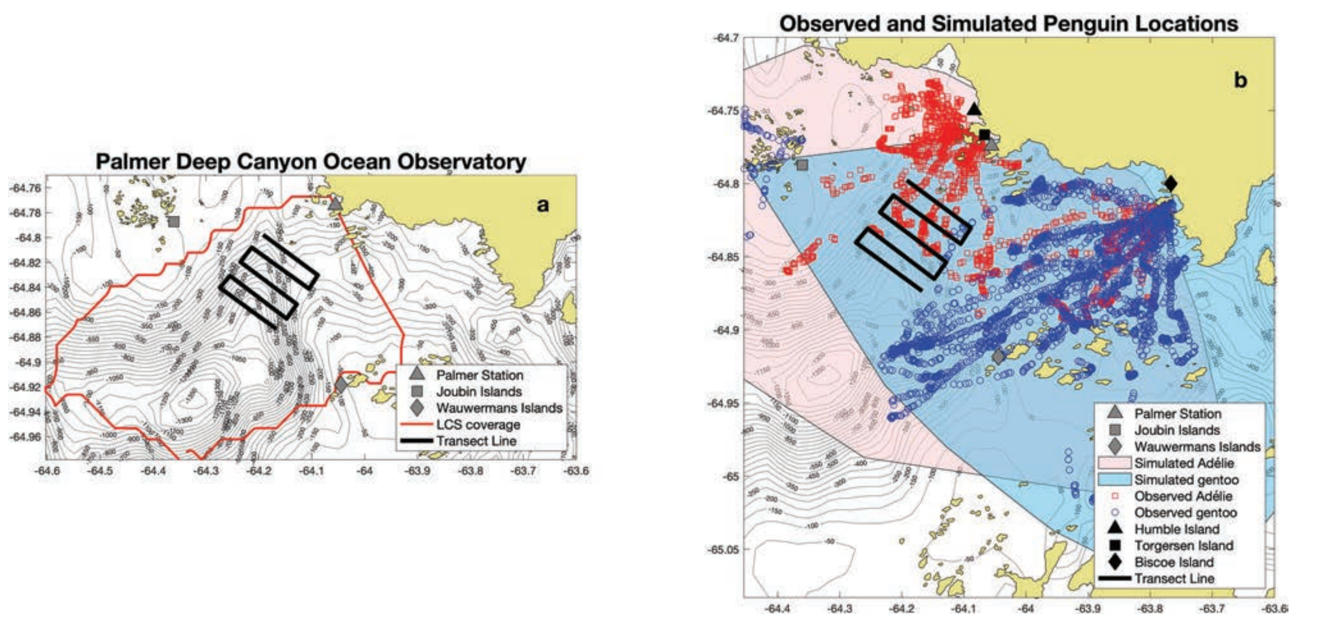

Fig. 1 | Ocean observatory around Palmer Deep Canyon. **a** Palmer Deep Canyon study region with the location of the three High Frequency Radars shown with polygons and the area of LCS results contoured. Within the LCS footprint is the transect line of the active acoustic survey used to detect krill and optical survey used to detect phytoplankton patches. Canyon bathymetry is contoured in 50 m isobaths. **b** Penguin positions observed with GPS tags for Adélie (red squares) and gentoo (blue circles) penguins. Convex hulls of simulated Adélie and gentoo penguins are shown in red and blue respectively, the smallest convex polygon that contains the set of points produced by the simulated penguin tracks. Penguin nests are shown in black polygons. Adélie breeding colonies are located on Humble Island, Torgerson Island, and Biscoe Island, and gentoo breeding colonies on Biscoe Island. Transect line for the surveys that observed krill swarms and phytoplankton patches is shown with a solid black line. Canyon bathymetry is shown in contours of 50 m isobaths. Note that the seemingly strait penguin tracks are likely penguins returning to their nests after satiation.

swarms at the scales of penguin foraging through the use of a multi-platform ocean observing system (Fig. 1a). Integration of multiple observing platforms provides the rare opportunity to analyze the overlapping physical processes and trophic interactions on time and space scales relevant to understanding the physical mechanisms that concentrate high density patches of prey that predators use to efficiently forage.

When integrating both biological and physical observations of an ecosystem, it is important to investigate them at the appropriate space and time scales[42]. Palmer Deep Canyon is a coastal system, characterized by submesoscale ocean currents, strong tidal influences, and short (2–7 days) surface residence times[43]. Similarly, phytoplankton patches have been shown to move through this system quickly (6 h decorrelation)[11], and most penguin foraging trips are between 6 and 24 h[44]. Previous work has established Palmer Deep Canyon as a fast-moving oceanic habitat, characterized by dynamic physical conditions and a similarly variable biological ecosystem. In this study, we determine if the distribution of krill and foraging penguins at these shorter time and space scales show similar association with LCS-identified transport features as previously observed with phytoplankton[11], suggesting small-scale and current-driven controls on food web focusing. The present study maps each level of the food web onto dynamic ocean currents at resolutions that resolve interactions between near-shore creatures and complex coastal flow, providing a unique opportunity to deepen our understanding of potential small-scale physical mechanisms of spatial ecology.

Results

Dynamic feature mapping with Lagrangian Coherent Structures

In this study we used a high-resolution High Frequency Radar (HFR) network to calculate attracting FTLE, projected at the temporal and spatial resolution of inputted HFR data (1 h, 1 km). FTLE is a metric used to characterize the Lagrangian structure in fluid flows. It measures the rate of separation of initially close particles over a finite time interval, providing insights into the stability and chaotic behavior of the flow (see section 5.7 for details). FTLE maps were calculated each hour with a 1 km spatial resolution (Fig. 2 and Supplementary Movie 1), the same spatial and temporal resolution as the HFR velocity field data. Higher values of LCS indicated a higher influence on the attraction of nearby drifting particles. This analysis produced a time resolved 2-dimensional field of attracting features.

Phytoplankton patches occuring in transport features

Phytoplankton patches were observed with an ACROBAT, a towed instrument that undulates between the surface and ~50 m depth (see Section 5.3 for details), outfitted with a Wetlabs Ecopuck optical sensor (chlorophyll-a, CDOM fluorescence, and optical backscatter at 700 nm) and a fast-sampling (16 Hz) Seabird 43 FastCAT CTD (conductivity, temperature, and pressure) following transect lines within the HFR footprint (Fig. 1a). MLD was calculated as the depth of maximum buoyancy frequency for each profile[11,45] using data collected via the towed ACROBAT. Phytoplankton patches were determined following methods in Veatch et al.[11] as profiles with an integrated mixed layer backscatter greater than a threshold, and re-analyzed in this study for direct comparison with krill and penguin foraging observations (Section 5.3, Supplementary Fig. 2).

Previous results found phytoplankton patches were associated with higher FTLE values (indicative of stronger attracting features) than a null model[11]. The distribution of FTLE values associated with phytoplankton patches are shifted towards higher FTLE values, peaking around 0.3 hr^{-1} while the distribution of FTLE values associated with randomized phytoplankton patches (null model) were more symmetrical, peaking around 0.22 hr^{-1} (Fig. 3). Randomized phytoplankton patches were created by generating survey transects in random locations and associating them with LCS (see section 5.6 for details). The distribution of FTLE values associated with observed phytoplankton patches were significantly higher than those of randomized phytoplankton patches (Fig. 3a), according to a one-sided Kolmogorov-Smirnov (KS) test ($p = 0.01187$) which tests whether one sample distribution tends to have greater values than the other. Results were the same when the null model was confined to the area of the observed transect (see section 5.6 for details) passing a one-sided KS test ($p = 2.54e{-}11$).

Krill swarms occuring in transport features

Krill swarms (Fig. 4) were concurrently mapped using active acoustics during small boat surveys within the HFR footprint (Fig. 1a) during daytime surveys. The small boat was equipped with a hull-mounted EK80. Krill were acoustically detected and parameterized following methods previously used in Palmer Deep Canyon[28,46–48]. Mixed layer depth (MLD) was also observed using a CTD aboard a towed ACROBAT instrument (see Sections 3.2, 5.3). Of the 1749 total krill swarms detected, 687 (~39%) were observed above the MLD. A null model representing random distribution of krill aggregations across the survey area was created to compare to observations.

Observed krill swarms as well as randomized krill swarms from a null model were matched in space and time with FTLE. The density distributions of FTLE for krill swarms (above the MLD, below the MLD, and total) are skewed towards higher FTLE with the peak around 0.35 hr^{-1} for krill above the MLD, 0.33 hr^{-1} for krill below the MLD, and 0.35 hr^{-1} for all krill swarms (Fig. 3b). In contrast, the density distributions of FTLE for randomized krill swarms is relatively symmetrical in shape, peaking at a lower value around 0.25 hr^{-1}. A KS test between density distributions of FTLE for observed and randomized krill swarms showed that the distribution of true krill swarms is skewed toward higher FTLE values compared to randomized krill swarms. There was a significant difference between total krill swarms and randomized krill swarms ($p = 9.57e{-}14$). This was also true for krill swarms both above and below the MLD ($p = 0.0028$ and $p = 5.56e{-}12$, respectively) (Fig. 3b). When all krill swarms were compared to null model confined to the area of the observed transect (see section 5.6 for details) results were the same, passing a one-sided KS test ($p = 7.16e{-}39$).

Adélie and gentoo penguins selecting for transport features

Penguin diving locations, tracked using Fastloc GPS archival tags, showed preference for higher values of FTLE. Similar to the krill swarms, density distributions of FTLE associated with observed Adélie penguin diving locations indicated that Adélie penguins tended to forage in regions with higher FTLE compared to the simulated Adélie penguin tracks (KS test, $p = 2.7e{-}5$). Adélie locations with dives less than 10 m deep (KS test, $p = 2.2e{-}15$) and locations with dives greater than 10 m deep (KS test, $p = 0.0017$) both showed higher density distributions of FTLE compared to null models, with 10 m representing the average MLD calculated from the towed ACROBAT instrument. Like Adélie penguins, the density distributions of FTLE associated with observed gentoo penguin diving locations was shifted towards higher FTLE values compared to randomized gentoo penguin foraging locations (KS test, $p < 1.66e{-}15$). Observed gentoo penguin foraging locations were also associated with higher FTLE values compared to randomized foraging locations for dives with maximum depths above and below 10 m ($p < 1.15e{-}13$ and $p < 9.6e{-}12$, respectively). The density distributions of FTLE for Adélie and gentoo penguins are shifted towards higher FTLE (Fig. 3c, d). In contrast, the density distributions of FTLE for simulated Adélie and gentoo penguins are relatively symmetrical in shape. For all three of these comparisons (all dives, dives shallower than 10 m, and divers deeper than 10 m), we systematically removed one penguin from the analysis and recomputed the KS test, as each sampling group was O10 penguins. The resulting distributions showed that no individual penguin was driving the shift of Adélie or gentoo penguins toward higher FTLE values (see the grey shaded area in Fig. 3c, d).

Discussion

In this study, we observed that food web focusing by small-scale currents shapes the spatial ecology of a coastal marine food web at the patch scale of foraging (hours and 100 s of meters to kilometers). Our results show that phytoplankton, krill, and penguins are found in higher attracting FTLE features (LCS), suggesting aggregation of plankton from horizontal ocean

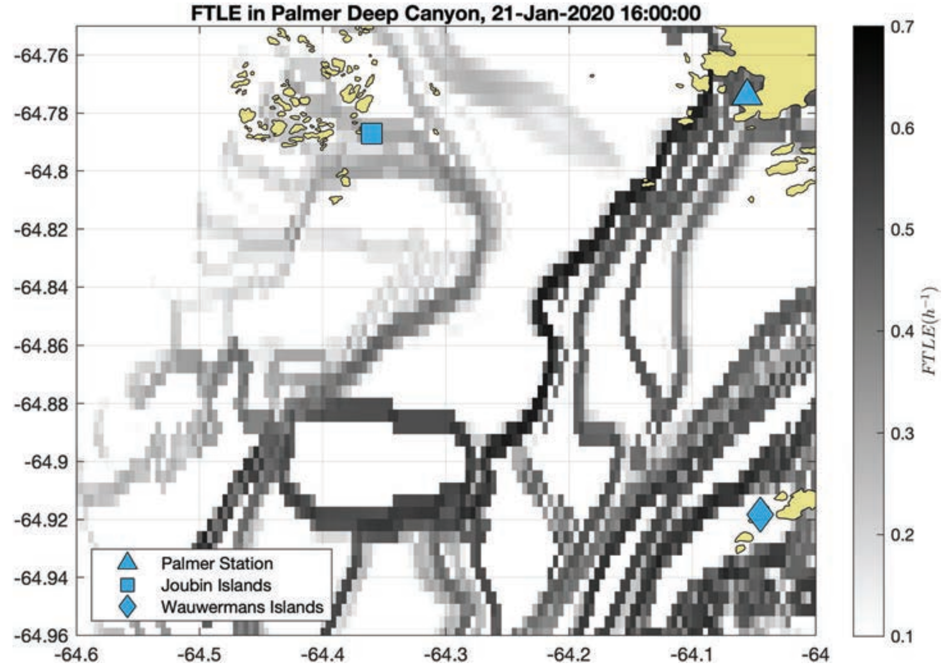

Fig. 2 | Example FTLE results calculated from High Frequency Radar observed surface currents. Locations of three HFR stations are denoted with polygons. FTLE results on January 21st 2020 at 16:00 GMT are shown in greyscale with higher FTLE values corresponding with stronger attracting ocean features.

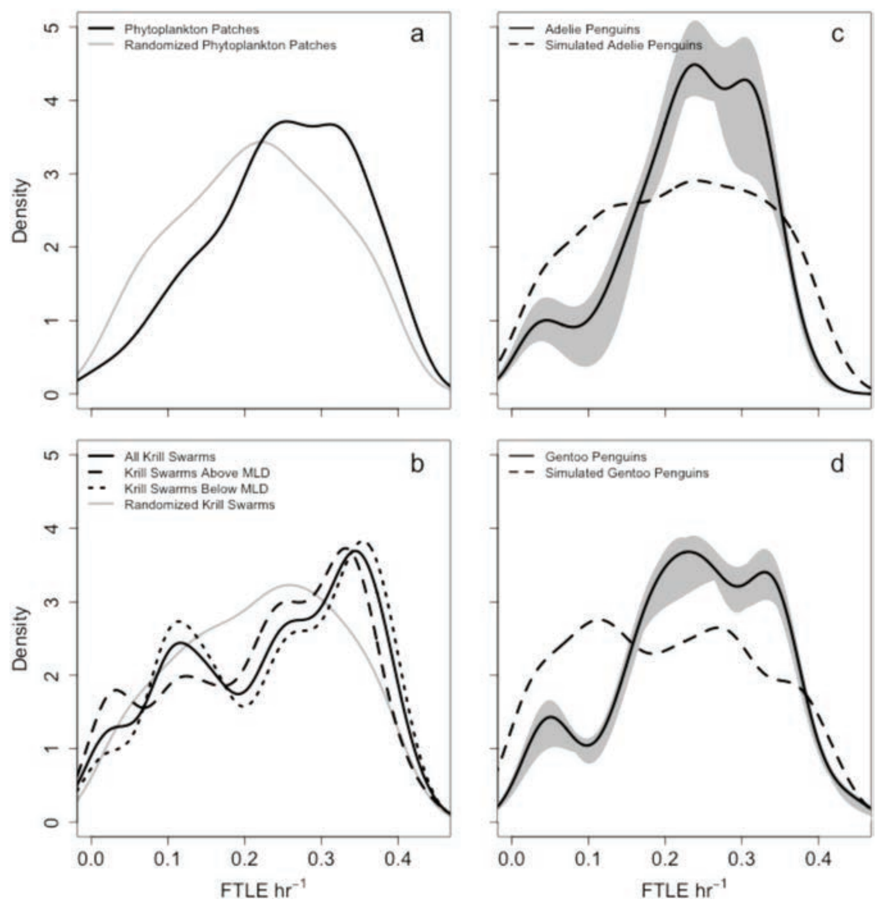

Fig. 3 | Density distributions of FTLE. a Density distributions of FTLE associated with observed phytoplankton patches (black line) and randomized phytoplankton patches (grey line) previously published in Veatch et al.[11]. Phytoplankton patch FTLE value density distribution were skewed toward higher values compared to randomized phytoplankton patches (KS test, $p = 0.01187$). **b** Density distributions of FTLE associated with observed krill swarms (solid line) above (dashed line) and below (dotted line) the mixed layer depth. All three of these distributions are skewed toward higher FTLE values than randomized krill swarms (grey line) (KS test, $p = 9.57e{-}14$, 0.0028, 5.56e−12). **c** Adélie and (**d**) gentoo tagged penguin FTLE values shown in solid line and randomized penguin FTLE values with dashed line. Grey regions represent the distributions of either Adélie or gentoo penguins if individual birds were systematically excluded from the analysis. This was done to determine if an individual bird was driving the results. Both Adélie and gentoo FTLE distributions were skewed toward higher values compared to FTLE values with simulated penguins (KS test, $p = 2.7e{-}5$, $p < 1.66e{-}15$). All curves are kernel density estimates computed with a density function within the statistic package of R[86], with the bandwidth of the kernel smoother set to 0.03. These density curves visualize the frequency of the underlying data.

transport is an important factor in the spatial ecology of Palmer Deep Canyon and providing the first evidence, to the best of our knowledge, of LCS selection at these scales across primary producers, primary consumers, and predators.

Interactions with ocean transport from each trophic level

The three trophic levels tested in this study span a wide range of Reynolds numbers with significant differences in their behavior and in the dependence of their movement on ocean currents. The passive particles used in

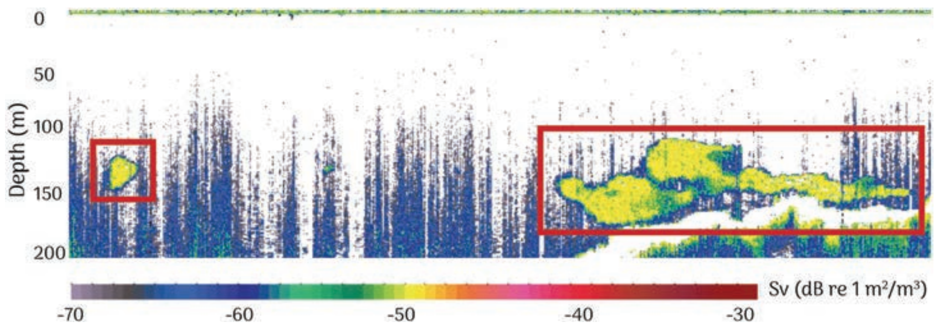

Fig. 4 | Example of acoustic detection of krill swarms. Echogram from survey (see Fig. 1a for survey path) with ACROBAT deployment. Dense yellow regions outlined in red boxes were detected as krill using a threshold of −70 to −30 dB. Raw acoustic data was processed in Echoview software, following methods of Tarling et al.[47,48] to identify krill swarms from all other backscatter.

LCS calculations most closely approximate the non-motile characteristics of phytoplankton at the scales of this study (Re ~10^{-2}, estimated from length scale[7]). The correlation between phytoplankton patches and LCS, their immobility, and their slow growth rates compared to local surface residence time[43] suggests that these patches are formed through horizontal ocean transport.

Unlike the largely passive phytoplankton cells, krill exhibit movement behavior relative to local ocean currents (Re ~10^3) and migrate vertically based on the sun angle[49], which means they can both be transported by ocean currents and swim somewhat independently of them. Our analysis used only passive particles and current velocities at the surface, yet surprisingly, high FTLE values indicated that krill both above and below the MLD were preferentially associated with surface concentrating features. Dynamics below the mixed layer are outside the scope of this study, but we can speculate why krill below the MLD would have higher FTLE values than a null model using surface particles. Krill below the MLD may have recently migrated down from within the mixed layer, and have not yet become decorrelated with surface currents. It is also possible that the velocity field below the MLD may be similar to that in the mixed layer, concentrating sub-surface krill in similar patterns to those reflected in the surface. Similarities between the surface and the sub-surface velocity fields could be driven by this region's barotropic tides[50], creating similar concentrating features in the sub-surface as in the surface velocities used to calculate FTLE. Finally, krill may be attracted to locally concentrated phytoplankton in higher FTLE values, indicating that both advection and behavior explain their affinity for LCS features with high FTLE values. Regardless of the mechanism, these results suggest that the distribution of krill in Palmer Deep is affected by food web focusing driven by small scale currents.

Foraging penguins have very high Reynolds numbers (Re ~10^6), indicating that they may move independently of currents. As a result, their distribution is expected to be most unlike the passive particles used in the LCS calculations. Results from this study show that penguin foraging behavior leads to spatial distribution in which there is more frequent penguin dives around locations with strong concentrating features (high FTLE). This suggests that while penguins may not actively seek out LCS, they are more likely to dive once they reach these features and find concentrated prey. Similar conclusions were drawn by a previous study investigating elephant seals interacting with larger scale currents[51], showing that elephant seals increase their foraging dives when at distinct oceanographic features. Unlike the elephant seals, Adélie and gentoo penguins will return straight to their nests once satiated, which creates the directed return journeys in the penguin tracks (Fig. 1b).

Penguin dives above and below the MLD, associated with stronger FTLE values, suggest that while penguins may use surface cues to initiate dives, they do not limit their foraging to the surface layer. This result is consistent with findings in krill distributions, where krill swarms both above and below the MLD were associated with strong FTLE. Penguins and other marine mammals transit near the ocean surface from where they dive to search and forage for their prey, exhibiting a variety of movement modes[52–54]. Although dive location and frequency can be quantified, little is known about the selective interactions of animals during their foraging trips that produce these patterns[55], including whether animals actively search for prey or use environmental cues associated with prey[56]. Emerging theories suggest that selection for environmental cues is likely[57], but it is unknown if Adélie or gentoo penguins respond to prey or environmental cues. Further research is needed to identify the surface cues Adélie and gentoos use to decide when to dive for prey.

Despite the wide range in the Reynolds numbers of our study species, each species showed selectivity for horizontally concentrating features (LCS) derived from passive particle trajectories. As species size and Reynolds number increases, so does the complexity of their relationship to LCS. Phytoplankton have low Reynolds numbers, and their distributions are likely dominated by ocean transport. Krill have intermediate Reynolds numbers, and their selection for LCS likely reflects a combination of physical concentration by attractive features and behavioral attraction to phytoplankton patches. Lastly, Penguins have high Reynolds numbers and behavior-driven distributions, so their selection for LCS is likely dominated by foraging behavior concentrated at krill patches. Such selectivity across species with varying Reynolds numbers demonstrates the importance of ocean transport to multiple levels of the food web.

Observations of small-scale ocean transport with Lcs

Selection by multiple levels of the food web for LCS quantified by FTLE at a 6-h integration suggests that FTLE capture transport patterns that create small-scale (sub-tidal) food web focusing. FTLE is a paired particle tracking technique, meaning that it uses relative distances between neighboring particles to quantify attraction and repulsion. This allows FTLE to quantify attracting features with little influence of the particle's starting position, unlike the single particle tracking methods[11]. FTLE also assigns scalar quantities to attracting features based on separation rate of neighboring particles (backwards in time, particle accumulation rate), allowing FTLE to account for rate of change of particle position rather than position alone. Additionally, FTLE integrate over particle trajectories, adding "memory" of particle position to the calculation of attracting features. Yet another strength of this method is the integration over time, which pairs well with the high temporal resolution of the HFR velocity data. The incorporation of relative particle motion and integration over particle trajectories makes FTLE a powerful tool for quantifying small-scale transport compared to the use of particle trajectories on their own.

FTLE patterns at these scales are highly variable in space and time, yet ubiquitous throughout the study system (Supplementary Movie 1 and Fig. 1). The null model sensitivity test showed similar results when the null model was constrained to the area closer to the observed transect rather than the entire LCS bounds (Fig. 5). Therefore, FTLE are not concentrated over the observed transect but throughout the study region. It is unknown whether penguins select their colony locations based on proximity to heightened LCS features. This study sets the groundwork for future investigations into whether coastal regions on the WAP near persistent penguin colonies have heighted FTLE activity compared to regions without such colonies.

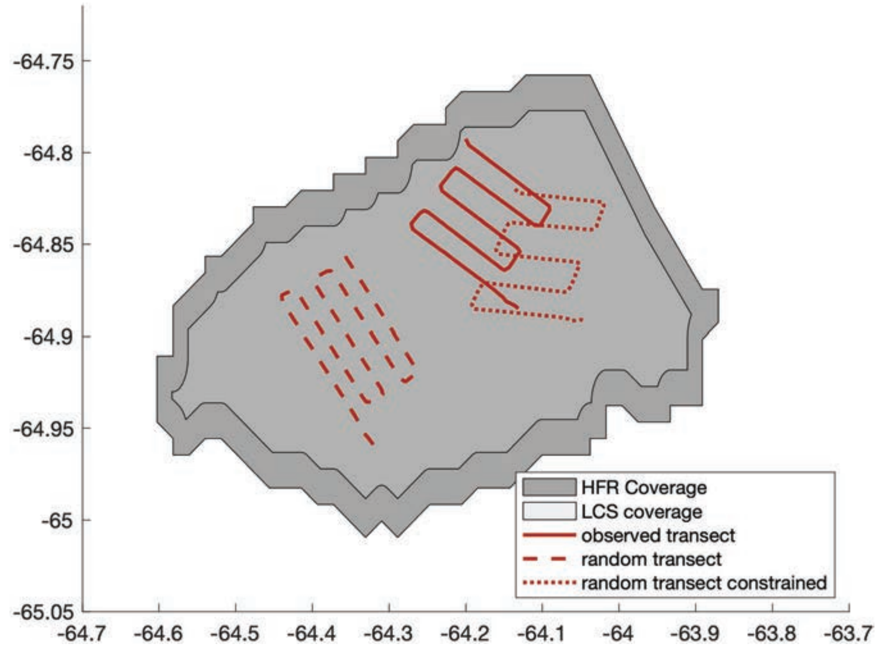

Fig. 5 | Example of null model. The area of LCS coverage is plotted in light grey, shrunk from HFR coverage (dark grey) to exclude edges of data. The transect where phytoplankton patches and krill swarms were observed is plotted with a solid red line, and one of the randomly rotated and translated transects is plotted with a dashed red line. A sensitivity test was conducted on the null model, constraining "randomly generated" transects to the northeast of the solid black line. A randomly rotated and translated transect confined to northeast of the black line is plotted with a dotted red line. Figure modified from Veatch et al.[11] Fig. 3.

In addition to identifying areas of attraction, strong FTLE will appear as horizontal transport barriers, which manifest as horizontal buoyancy gradients (fronts and edges of eddies) in ocean velocity fields. This makes areas of high FTLE oceanographically distinct from areas with low FTLE values. While attractive transport is likely to be a large reason why phytoplankton and zooplankton are associated with high FTLE values, it is unclear if Adélie and gentoo penguins are able to select for areas of high FTLE based on a learned oceanographic cue or if they are able to perceive large krill swarms and those happen to be at areas of high FTLE. Future work is needed to investigate penguin (and other forager) behavior that leads to their association with areas of high FTLE.

Limitations and caveats

There are several biological processes that limit the conclusions that can be made with these observational data. Mapping of prey, which was conducted through small boat surveys twice weekly, provides a snapshot in time of a prey field that is constantly evolving. The timing of observation within the process of food web focusing is unknown. For example, an area where there was an LCS-identified transport feature could have been observed shortly after a predator fed on a krill swarm. Our observations would show that an LCS-identified transport feature was there without presence of food web focusing, when in fact there was. Our observations could have also occurred before the ecosystem was able to respond to the presence of the LCS, perhaps showing high phytoplankton but no krill, or krill swarms but no penguin foraging. Additionally, far fewer predators (penguins) exist than prey (krill), making it more difficult to correlate predators to food web focusing events. With these caveats in mind, the patterns that were observed likely underestimate the food web focusing effect of small-scale transport.

Local and global implications

Results and conclusions from this study increase our understanding of how a coastal biological hotspot is maintained in the context of a larger marine ecosystem. Palmer Deep Canyon was once considered to be a location where phytoplankton production is driven by local upwelling[40]. Recent studies provide evidence against this, showing instead almost no stratified summertime occurrence of nutrient-rich Upper Circumpolar Deepwater in the photic zone[58]. Further, production is light limited rather than nutrient limited[59], suggesting little reliance on locally upwelled nutrient rich waters. Furthermore, a deep, recirculating eddy driven by the bathymetry of Palmer Canyon has the ability to trap krill performing diurnal vertical migration[60]. This feature may provide a seasonal reservoir of krill, which migrate to the surface, and are then aggregated in surface LCS structures. Emerging theories propose that high concentrations of phytoplankton[40] are advected from the shelf break where upwelling of nutrient-rich Upper Circumpolar Deep Water fuels phytoplankton blooms[61,62]. Future work is needed to further investigate larger scale, regional transport that reflects climate scale impacts in the WAP region. Our results further emphasize the importance of ocean transport in this system not just for local phytoplankton abundance but throughout the food web. Oceanographic transport patterns that reliably concentrate prey could be a reason penguins colonies have persisted in this region over ecological time scales[37]. As Palmer Deep Canyon and other ecosystems along the WAP experience rapid warming[63–65], sustained observations are needed to determine if these transport patterns that local food webs rely on will change. Future work must also investigate the fate of the sources of plankton that are being delivered to the system in order to predict Palmer Deep Canyon's resistance to changing climate. A depletion of these sources could be detrimental to Palmer Deep Canyon's ecosystem even if transport patterns are maintained.

Selectivity of LCS calculated with short integrations by intermediate and upper trophic levels illustrates the importance of small-scale transport features in the spatial ecology of coastal systems. This not only supports the emerging theory of trophic focusing by physical ocean processes[4], but demonstrates that these processes occur on the sub-mesoscale. Correlations between LCS and phytoplankton, zooplankton, and top predators stress the importance of incorporating LCS as a covariate in predictions of spatial ecology in marine systems.

Our study provides a link between the preyscape of a coastal ecosystem and ocean transport. This relationship fills the gap in previous studies that link phytoplankton and top predators' distributions to ocean transport without considering the critical mid-trophic level zooplankton. Results also provide a useful tool for the marine ecological community to quantify ocean transport features, namely FTLE. FTLE, although more computationally complex than single particle tracking techniques such as Relative Particle Density[11,66], have been shown to quantify transport features that are selected by each level of the Palmer Deep Canyon food web, justifying their use in dynamic coastal environments. Connections between ocean movement and spatial ecology improve current understanding of how local populations use their ocean habitats, enabling more informed conservation strategies to protect areas of prey accumulation, mitigating anthropogenic impacts on coastal ecosystems.

Methods

An ocean observatory was deployed around Palmer Deep Canyon during January-March 2020, mapping phytoplankton, zooplankton, and penguin foraging behavior onto physical ocean processes. The following section describes the small boat surveys that were conducted along a transect twice weekly to observe phytoplankton and zooplankton as well as the HFR array observations and tagged penguin measurements that overlapped with this transect.

High Frequency radar

Three High Frequency Radars were deployed around Palmer Deep Canyon, using doppler-shifted radio waves backscattered from ocean waves to produce vector maps of surface current velocities each hour. HFRs were deployed on the Joubin Islands, Wauwermans Islands, and at Palmer Station (Fig. 1). Remote sites (Joubin and Wauwermans) were each accompanied by a remote power module, described in refs. 67,68. Radial components from each radar[69] were added together with an optimal interpolation algorithm[70] and gap filled[71] as described in refs. 11,72. The resulting data product is an evolving hourly map of ocean surface currents over a 1 km spatial grid.

Calculating mixed layer depth

On the active acoustic survey transects (Fig. 1a), an ACROBAT (Autonomous Conductivity, temperature, and depth Rapidly Oscillating Biological Assessment Towed) was towed, equipped with a fast-sampling (16 Hz) Seabird FastCAT CTD (conductivity, temperature, and pressure). This instrument undulated between the surface and about 50 m depth, profiling the upper water column about every 300 m in the horizontal. For each profile, MLD was determined as the depth with the maximum buoyancy frequency following methods in Carvalho et al.[45]. MLD measurements were used to calculated mixed layer optical backscatter (Section 5.3) and to determine if krill swarms were above or below the MLD (section 5.4). ACROBAT profiles were matched with observed krill swarms in space and time, assigning a MLD to each krill swarm. If the depth of the krill swarm was shallower than the ACROBAT observed MLD, the swarm was considered to be within the mixed layer.

Optical surveys

Towed ACROBAT surveys were conducted twice weekly collecting optical measurements of the water column along transects shown in Fig. 1a. Methods for identifying phytoplankton patches with ACROBAT optical measurements followed those in Veatch et al.[11], and are explained thoroughly there. In short, the ACROBAT profiled between the surface and about 60 m, completing a profile about every 300 m of horizontal distance traveled. Profiles were determined as “within a phytoplankton patch” or “not in a phytoplankton patch” based on a daily threshold of integrated mixed layer optical backscatter. In this system, optical backscatter is a good proxy for phytoplankton biomass and avoids the problem of non-photochemical quenching that is associated with measuring phytoplankton fluorometrically. Consecutive profiles designated as “within a phytoplankton patch” were assumed to be in the same phytoplankton patch (Supplementary Fig. 2).

Each ACROBAT profile was assigned an FTLE value based on the closest FTLE grid point to the profile in space and time. Phytoplankton patches made up of multiple profiles were assigned an FTLE value based on the average FTLE value assigned to the profiles within that phytoplankton patch.

Acoustic surveys

Active acoustic surveys were conducted twice weekly using a hull-mounted SIMRAD EK80 single-beam, single frequency (120 kHz) echosounder (Kongsberg Maritime) along transects shown in Fig. 1a. The echosounder was configured with a 1 s ping rate, 512 µs pulse duration, and 24 µs sampling duration. Calibrations of the echosounder were performed in the vicinity of Palmer Deep Canyon using a tungsten sphere (diameter = 38.1 mm) during February, 2020. Acoustic data were processed in Myriax Echoview software version 11.1 following methods from Tarling et al.[47] and Tarling et al.[48]. Raw data were processed to consider the echosounder calibration and in situ ocean acoustic conditions via incorporation of onboard CTD data, and to remove background noise and other interferences via the Background Noise Removal[73] and Impulse Noise Removal[74] algorithms in Echoview. Krill were then detected using a target strength threshold of −70 dB to −30 dB[47,48] in Echoview following similar parameterization and protocols to Nardelli et al.[28] and Reiss et al.[75] (Fig. 3).

All acoustically detected krill swarms were manually reviewed before exporting the acoustic data in Nautical Area Scattering Coefficient (NASC) values, a common proxy for organism presence in acoustic measurements. NASC values were calculated per detected swarm and exported along with depth, GPS position (longitude and latitude), swarm height, swarm length, and backscatter (Sv). These methods for acoustic surveys and processing of subsequent acoustic data follow those in Hann et al.[46].

Table 1 | Tagged penguins by colony

Colony	Penguins tagged	Trips recorded
Adélie - Humble Island	12	23
Adélie - Torgersen Island	13	24
Adélie – Biscoe Island	5	13
Gentoo - Biscoe Island	14	32

Number of individual Adélie and gentoo penguins tagged per colony.

Penguin tagging

Adélie penguin colonies were located on Humble Island (64°45'S, 64°05'W), Torgersen Island (64°46'S, 64°04'W), and Biscoe Island, (64°48'S, 63°46'W), with the latter location also including a colony of gentoo penguins (Fig. 1b). Both species were double tagged with GPS tags and time-depth recorders measuring pressure at 0.5 Hz while wet. Penguins were GPS tagged with either a Lotek FastGPS (F5G 234B, 35 g), Sirtrack Fastloc 3 loggers (30 g) or igotU GT-600 (35 g, Mobile Action Technology, Taiwan). IgotU loggers were encased in adhesive-line heat shrink tubing. The time-depth recorders were either a Lotek LAT1810 (10 g) or StarOddi DST CTD (22 g). Tags were adhered to the anterior feathers on the lower dorsal area of the penguin. All protocols were carried out in accordance with the approved guidelines of the Columbia University (Assurance #AAAS2504) Institutional Animal Care and Use Committee for the 2019–2020 season. Tags were generally deployed on individuals for 2–4 days before being removed and reattached to another penguin. We tagged 30 Adélie and 14 gentoo penguins over the course of the austral summers (Table 1).

Drift in the depth data for tags was zero offset corrected using the *calibrateDepth* function in the R package diveMove[76]. Drift was not corrected for 7 deployments, as on 6 of these deployments (all Adélies, 5 Humble Island, 1 Torgersen Island) depth recordings shallower than 1 meter were not taken, and on 1 deployment (1 Adélie, Humble Island) depth recordings shallower than 5 meters were not taken. GPS data were filtered for erroneous locations based on improbable swimming speeds (>2.8 m s^{-1}). GPS location and TDR data were time matched and dives were identified using the *diveStats* function in diveMove[76].

Penguin data collection was conducted by Polar Oceans Research Group (PORG) as part of project SWARM.

Creating null models

Distribution of LCS where phytoplankton patches and krill swarms were observed in our transects were compared to those along simulated “null model” phytoplankton patches and krill swarms. The phytoplankton and krill null models were created by randomly moving the observed distribution of phytoplankton and krill within the LCS field (Fig. 5), maintaining the observed phytoplankton patch and krill swarm size and distribution along the transect. Each of the thirteen surveys were rotated and translated 100 times, creating 100 randomized locations of each observed phytoplankton patch and krill swarm while maintaining the shape of the survey. This ensured that the survey shape did not contribute to differences found between observed and null model phytoplankton patches and krill swarms. These randomized locations make up the phytoplankton and krill null model. Methods for using the survey transect to create the null model were adapted from Veatch et al.[11].

A sensitivity study was conducted on the null model to test if the differences between the null model and observations were due to the area where the survey was conducted having more FTLE than elsewhere in the study area. A new model was created following above methodology but requiring the randomly moved transects to be within a smaller area closer to the observed transect (northeast of the black line in Fig. 5). This constrained null model produced the same results as the original null model (see Results).

Distribution of LCS selected by penguin GPS locations were compared to those along simulated "null model" penguin tracks. Penguin null models were created with simulated Brownian motion of central place foragers (simm.bb in the adehabitatLT R package)[77], having the simulated penguin tracks return to the Adélie and gentoo colonies at the end of each trip (Fig. 1b). Each day that we had overlapping penguin observed data and LCS results from HFR-observed surface currents, ten penguin trips were simulated for each species. These trips were limited to 24 h, and simulated penguin speeds were normally distributed around a mean of 4 km hr^{-1} with a maximum of 8 km h^{-1}. These limitations were set to mimic average foraging trip duration (6–24 h)[44] and swimming speeds[78] of Adélie and gentoo penguins. The Brownian motion used to create these tracks is uncorrelated. Therefore, simulated tracks represent random foragers that do not select for environmental features or remembering previous feeding locations. Simulated penguin locations were used as a null metric for all the available LCS values for non-selecting central place foragers. Methods for the creation of simulated Adélie and gentoo tracks were adapted from Oliver et al.[66].

Calculating Lagrangian Coherent Structures

LCS were calculated from the HFR observed surface currents using the FTLE metric. FTLE were calculated beginning with a velocity field over a selected time interval (in this case, 6 h). Then, from the derivative of the flow map the Cauchy-Green strain tensor field (C) and eigenvector field (λ_i) were computed to be used in Eq. (1):

$$S(x_0) = \left[\max_{i=N^{\lambda_i}}\left(C(x_0)\right)\right]^{1/2} \qquad (1)$$

where $S(x_0)$ is the maximum stretching around point x_0. FTLE is then computed over a finite time (T)[10,79–81]. The resulting FTLE field changes in space and time with inputted HFR observed velocity field. These methods follow those in Veatch et al.[11].

Matching observed presence of null models to LCS

To associate krill and penguin presence with LCS, observations were matched in both space and time. LCS results were calculated each hour and at a 1 km spatial resolution to match the resolution of inputted HFR velocity data. Krill swarms and penguin locations were matched to the nearest hour of LCS map. This means that for the LCS results computed for 13:00 on January 15th, all krill and penguin location observations between 12:30 and 13:30 on January 15th were compared to the LCS results from 13:00. To match krill and penguin presence with LCS in space, a haversine function[82] was used to find the closest LCS result grid point (using the center of the grid point) to the krill or penguin location. The LCS value in that grid point for the LCS results on the nearest hour were associated with the krill or penguin observation. The same was done for null models.

Kolmogorov-Smirnov tests

Two-sample Kolomogorov-Smirnov (KS) tests[83] were used to determine if there are significant differences between the empirical distribution functions of observations and null models. KS tests are conducted using Eq. (2):

$$D = sup_x\left|F_{n,1}(x) - F_{n,2}(x)\right| \qquad (2)$$

where D is the test statistic, $F_{n,1}(x)$ and $F_{n,2}(x)$ are the empirical distribution functions of the two samples. A small p-value from the KS test means that the two samples come from different distributions. One-sided KS tests are especially good at determining if the tails of two cumulative distributions are significantly different from each other.

Reporting summary

Further information on research design is available in the Nature Portfolio Reporting Summary linked to this article.

Data availability

Data and code used in this study are publicly available on NSF funded project SWARM's BCO-DMO site and GitHub. High Frequency Radar observed surface currents are available in the gap-filled version used in this study on BCO-DMO[84]. Lagrangian Coherent Structure Results for FTLE metrics are available on BCO-DMO[85]. EK80 acoustic data used to detect krill swarms are available on BCO-DMO ACROBAT data used to detect phytoplankton patches are available on BCO-DMO[86] Penguin GPS tag data are available University of Delaware's public archive (http://modata.ceoe.udel.edu/public/Antarctica_2020/SWARM_Penguin_CSVs/). Any questions can be directed to Jacquelyn Veatch (jveatch@whoi.edu).

Code availability

Code used to gap-fill High Frequency Radar data are available on GitHub (https://github.com/JackieVeatch/SWARM_CODAR). The code used to produce LCS results can be found on GitHub (https://github.com/JackieVeatch/SWARM_LCS). The code was modified from open-source MATLAB library[80] for use on HFR data. All other code for analysis can be found on GitHub (https://github.com/JackieVeatch/SWARM_analysis, https://github.com/JackieVeatch/SWARM_Krillanalysis, and https://github.com/JackieVeatch/SWARM_PenguinAnalysis). Any questions can be directed to Jacquelyn Veatch (jveatch@whoi.edu).

Received: 9 September 2024; Accepted: 5 February 2025;
Published online: 20 February 2025

References

1. Marquet, P. A. et al. Ecological and evolutionary consequences of patchiness: a marine-terrestrial perspective in *Patch dynamics* 277–304 (Berlin, Heidelberg: Springer Berlin Heidelberg, 1993).
2. Cheriton, O. M. et al. Effects of mesoscale physical processes on thin zooplankton layers at four sites along the west coast of the US. *Estuaries Coasts* **30**, 575–590 (2007).
3. Benoit-Bird, K. J. et al. Prey patch patterns predict habitat use by top marine predators with diverse foraging strategies. *PLoS ONE* **8**, e53348 (2013).
4. Genin, A. Bio-physical coupling in the formation of zooplankton and fish aggregations over abrupt topographies. *J. Mar. Syst.* **50**, 3–20 (2004).
5. Stommel, H. Varieties of oceanographic experience: the ocean can be investigated as a hydrodynamical phenomenon as well as explored geographically. *Science* **139**, 572–576 (1963).
6. Benoit-Bird, K. J. Resource patchiness as a resolution to the food paradox in the sea. *Am. Nat.* https://doi.org/10.1086/727473 (2023).
7. Mann, K. & Lazier, J. *Dynamics of Marine Ecosystems (3rd ed.)* (Wiley, 2013).
8. Power, J. H. Simulations of the effect of advective-diffusive processes on observations of plankton abundance and population rates. *J. Plankton Res.* **18**, 1881–1896 (1996).

9. Keister, J. E., Di Lorenzo, E., Morgan, C., Combes, V. & Peterson, W. Zooplankton species composition is linked to ocean transport in the Northern California current. *Glob. Change Biol.* **17**, 2498–2511 (2011).
10. Haller, G. Lagrangian coherent structures. *Annu. Rev. Fluid Mech.* **47**, 137–162 (2015).
11. Veatch, J. M., Kohut, J. T., Oliver, M. J., Statscewich, H. & Fredj, E. Quantifying the role of submesoscale Lagrangian transport features in the concentration of phytoplankton in a coastal system. *ICES J. Mar. Sci.* **81**, 760–773 (2024).
12. Lehahn, Y., d'Ovidio, F. & Koren, I. A satellite-based lagrangian view on phytoplankton dynamics. *Annu. Rev. Mar. Sci.* **10**, 99–119 (2018).
13. Lehahn, Y., d'Ovidio, F., Lévy, M. & Heifetz, E. Stirring of the northeast Atlantic spring bloom: a Lagrangian analysis based on multisatellite data. *J. Geophys. Res. - Oceans* **112**, C08005–C08005 (2007).
14. Hernández-Carrasco, I., Orfila, A., Rossi, V. & Garçon, V. Effect of small scale transport processes on phytoplankton distribution in coastal seas. *Sci. Rep.* **8**, 8613–8613 (2018).
15. Huhn, F., von Kameke, A., Pérez-Muñuzuri, V., Olascoaga, M. J. & Beron-Vera, F. J. The impact of advective transport by the South Indian Ocean Countercurrent on the Madagascar plankton bloom. *Geophys. Res. Lett.* **39**, n/a (2012).
16. Baudena, A. et al. Fine-scale structures as spots of increased fish concentration in the open ocean. *Sci. Rep.* **11**, 15805 (2021).
17. Emilie Tew, K. et al. Top marine predators track lagrangian coherent structures. *Proc. Natl. Acad. Sci. USA***106**, 8245–8250 (2009).
18. Fahlbusch, J. A. et al. Blue whales increase feeding rates at fine-scale ocean features. *Proc. R. Soc. B, Biol. Sci.* **289**, 20221180 (2022).
19. Goldbogen, J. A. et al. Mechanics, hydrodynamics and energetics of blue whale lunge feeding: efficiency dependence on krill density. *J. Exp. Biol.* **214**, 698–699 (2011).
20. Lomartire, S., Marques, J. C. & Gonçalves, A. M. M. The key role of zooplankton in ecosystem services: a perspective of interaction between zooplankton and fish recruitment. *Ecol. Indic.* **129**, 107867 (2021).
21. Maps, F. et al. Linking acoustics and finite-time L yapunov exponents reveals areas and mechanisms of krill aggregation within the G ulf of S t. L awrence, eastern Canada. *Limnol. Oceanogr.* **60**, 1965–1975 (2015).
22. St-Onge-Drouin, S., Winkler, G., Dumais, J.-F. & Senneville, S. Hydrodynamics and spatial separation between two clades of a copepod species complex. *J. Mar. Syst.* **129**, 334–342 (2014).
23. Fahlbusch, J. A. et al. Submesoscale coupling of krill and whales revealed by aggregative Lagrangian coherent structures. *Proc. R. Soc. B* **291**, 20232461 (2024).
24. Santora, J. A. et al. Krill space: a comparative assessment of mesoscale structuring in polar and temperate marine ecosystems. *ICES J. Mar. Sci.* **69**, 1317–1327 (2012).
25. Bernard, K. S. et al. Factors that affect the nearshore aggregations of Antarctic krill in a biological hotspot. Deep-Sea Res. Part I: Oceanogr. Res. Pap. **126**, 139–147 (2017).
26. Bernard, K. S. & Steinberg, D. K. Krill biomass and aggregation structure in relation to tidal cycle in a penguin foraging region off the Western Antarctic Peninsula. *ICES J. Mar. Sci.* **70**, 834–849 (2013).
27. Warren, J. D., Santora, J. A. & Demer, D. A. Submesoscale distribution of Antarctic krill and its avian and pinniped predators before and after a near gale. *Mar. Biol.* **156**, 479–491 (2009).
28. Nardelli, S. C. et al. Krill availability in adjacent Adélie and gentoo penguin foraging regions near Palmer Station, Antarctica. *Limnol. Oceanogr.* **66**, 2234–2250 (2021).
29. Pickett, E. P. et al. Spatial niche partitioning may promote coexistence of Pygoscelis penguins as climate-induced sympatry occurs. *Ecol. Evol.* **8**, 9764–9778 (2018).
30. Chapman, E. W., Hofmann, E. E., Patterson, D. L. & Fraser, W. R. The effects of variability in Antarctic krill (Euphausia superba) spawning behavior and sex/maturity stage distribution on Adélie penguin (Pygoscelis adeliae) chick growth: a modeling study. *Deep Sea Res. Part II: Topical Stud. Oceanogr.* **57**, 543–558 (2010).
31. Nicol, S. et al. Krill (Euphausia superba) abundance and Adélie penguin (Pygoscelis adeliae) breeding performance in the waters off the Béchervaise Island colony, East Antarctica in 2 years with contrasting ecological conditions. *Deep Sea Res. Part II: Topical Stud. Oceanogr.* **55**, 540–557 (2008).
32. Nowacek, D. P. et al. Super-aggregations of krill and humpback whales in Wilhelmina Bay, Antarctic Peninsula. *PLoS ONE* **6**, e19173 (2011).
33. Santora, J. A. & Reiss, C. S. Geospatial variability of krill and top predators within an Antarctic submarine canyon system. *Mar. Biol.* **158**, 2527–2540 (2011).
34. Santora, J. A., Reiss, C. S., Cossio, A. M. & Veit, R. R. Interannual spatial variability of krill (Euphausia superba) influences seabird foraging behavior near Elephant Island, Antarctica. *Fish. Oceanogr.* **18**, 20–35 (2009).
35. Fraser, W. R. & Trivelpiece, W. Z. Factors Controlling the Distribution of Seabirds: Winter-Summer Heterogeneity in the Distribution of Adélie Penguin Populations 257–272 (American Geophysical Union, Washington, D. C, 1996).
36. Emslie, S. D., Fraser, W., Smith, R. C. & Walker, W. Abandoned penguin colonies and environmental change in the Palmer Station area, Anvers Island, Antarctic Peninsula. *Antarct. Sci.* **10**, 257–268 (1998).
37. Schofield, O. et al. Penguin biogeography along the west Antarctic Peninsula: testing the canyon hypothesis with palmer LTER observations. *Oceanography* **26**, 204–206 (2013).
38. Fraser, W. R. & Trivelpiece, W. Z. Palmer LTER: relationships between variability in sea-ice coverage, krill recruitment, and the foraging ecology of Adélie penguins. *Antarct. J. U. S.* **30**, 271 (1995).
39. Fraser, W. R. & Trivelpiece, W. Z. Factors controlling the distribution of seabirds: Winter-summer heterogeneity in the distribution of Adélie penguin populations. *Found. Ecol. Res. West Antarct. Penins.* **70**, 257–272 (1996).
40. Kavanaugh, M. T. et al. Effect of continental shelf canyons on phytoplankton biomass and community composition along the western Antarctic Peninsula. *Mar. Ecol. Prog. Ser.***524**, 11–26 (2015).
41. Schofield, O. et al. Antarctic pelagic ecosystems on a warming planet. *Trends Ecol. Evol.* **39**, 1141–1153 (2024).
42. Root, T. L. & Schneider, S. H. Ecology and climate: research strategies and implications. *Science* **269**, 334–341 (1995).
43. Kohut, J. T. et al. Variability in summer surface residence time within a West Antarctic Peninsula biological hotspot. *Philos. Trans. R. Soc. Lond. Ser. A: Math., Phys., Eng. Sci.* **376**, 20170165–20170165 (2018).
44. Oliver, M. J. et al. Adélie penguin foraging location predicted by tidal regime switching. *PLoS ONE* **8**, e55163–e55163 (2013).
45. Carvalho, F., Kohut, J., Oliver, M. J. & Schofield, O. Defining the ecologically relevant mixed-layer depth for Antarctica's coastal seas. *Geophys. Res. Lett.* **44**, 338–345 (2017).
46. Hann, A. M., Bernard, K. S., Kohut, J., Oliver, M. J. & Statscewich, H. New insight into Salpa thompsoni distribution via glider-borne acoustics. *Front. Mar. Sci.* **9**, https://doi.org/10.3389/fmars.2022.857560 (2023).
47. Tarling, G. A. et al. Variability and predictability of Antarctic krill swarm structure. *Deep Sea Res. Part I: Oceanogr. Res. Pap.* **56**, 1994–2012 (2009).
48. Tarling, G. A. et al. Varying depth and swarm dimensions of open-ocean Antarctic krill Euphausia superba Dana, 1850 (Euphausiacea) over diel cycles. *J. Crustacean Biol.* **38**, 716–727 (2018).
49. Brierley, A. S. Diel vertical migration. *Curr. Biol.* **24**, R1074–R1076 (2014).
50. Padman, L., Erofeeva, S. Y. & Fricker, H. A. Improving Antarctic tide models by assimilation of ICESat laser altimetry over ice shelves. *Geophys. Res. Lett.* **35**, https://doi.org/10.1029/2008GL035592 (2008).

51. Della Penna, A., De Monte, S., Kestenare, E., Guinet, C. & d'Ovidio, F. Quasi-planktonic behavior of foraging top marine predators. *Sci. Rep.* **5**, 18063 (2015).
52. Berg, H. C. *Random Walks in Biology* (Princeton University Press, 1993).
53. Klafter, J. & Sokolov, I. M. Anomalous diffusion spreads its wings. *Phys. World* **18**, 29 (2005).
54. Okubo, A. & Levin, S. A. *Diffusion and Ecological Problems: Modern Perspectives*. Vol. 14 (Springer, 2001).
55. Nathan, R. et al. A movement ecology paradigm for unifying organismal movement research. *Proc. Natl. Acad. Sci. USA* **105**, 19052–19059 (2008).
56. Fraser, W. R. & Ainley, D. G. Ice edges and seabird occurrence in Antarctica. *BioScience* **36**, 258–263 (1986).
57. Wilson, R. P. et al. Luck in food finding affects individual performance and population trajectories. *Curr. Biol.* **28**, 3871–3877. e3875 (2018).
58. Hudson, K. et al. Reevaluating the canyon hypothesis in a biological hotspot in the Western Antarctic Peninsula. *J. Geophys. Res. Oceans* **124**, 6345–6359 (2019).
59. Carvalho, F. et al. Testing the canyon hypothesis: evaluating light and nutrient controls of phytoplankton growth in penguin foraging hotspots along the West Antarctic Peninsula. *Limnol. Oceanogr.* **65**, 455–470 (2019).
60. Hudson, K. et al. A recirculating eddy promotes subsurface particle retention in an antarctic biological hotspot. *J. Geophys. Res. Oceans* **126**, n/a (2021).
61. Prézelin, B. B., Hofmann, E. E., Moline, M. & Klinck, J. M. Physical forcing of phytoplankton community structure and primary production in continental shelf waters of the Western Antarctic Peninsula. *J. Mar. Res.* **62**, 419–460 (2004).
62. Dinniman, M. S. & Klinck, J. M. A model study of circulation and cross-shelf exchange on the west Antarctic Peninsula continental shelf. *Deep Sea Res. Part II: Topical Stud. Oceanogr.* **51**, 2003–2022 (2004).
63. Gorodetskaya, I. V. et al. Record-high Antarctic Peninsula temperatures and surface melt in February 2022: a compound event with an intense atmospheric river. *NPJ Clim. Atmos. Sci.* **6**, 202–218 (2023).
64. Vaughan, D. G. et al. Recent rapid regional climate warming on the Antarctic Peninsula. *Climatic Change* **60**, 243–274 (2003).
65. Hugh, W. D. et al. West Antarctic Peninsula: an ice-dependent coastal marine ecosystem in transition. *Oceanography***26**, 190–203 (2013).
66. Oliver, M. J. et al. Central place foragers select ocean surface convergent features despite differing foraging strategies. *Sci. Rep.* **9**, 157–157 (2019).
67. Statscewich, H. & Weingartner, T. A high-latitude modular autonomous power, control, and communication system for application to high-frequency surface current mapping radars. *IEEE* **54**, 1–3 (2012)
68. Kohut, J. Marine Technology; Study data from University of Alaska update understanding of marine technology (studying the impacts of local oceanographic processes on Adelie Penguin Foraging Ecology). *Ecol. Environ. Conserv.* **750**, 25–34 (2014).
69. Barrick, D. E., Evans, M. W. & Weber, B. L. Ocean surface currents mapped by radar. *Science***198**, 138–144 (1977).
70. Kohut, J. T., Roarty, H. J. & Glenn, S. M. Characterizing observed environmental variability with hf doppler radar surface current mappers and acoustic doppler current profilers: environmental variability in the coastal ocean. *IEEE J. Ocean. Eng.* **31**, 876–884 (2006).
71. Fredj, E., Roarty, H., Kohut, J., Smith, M. & Glenn, S. Gap filling of the coastal ocean surface currents from HFR data: application to the mid-atlantic bight HFR network. *J. Atmos. Ocean. Technol.* **33**, 1097–1111 (2016).
72. Veatch, J., Fredj, E. & Kohut, J. High Frequency Radars as Ecological Sensors: Using Lagrangian Coherent Structures to Quantify Prey Concentrating Features in *OCEANS 2022, Hampton Roads, Hampton Roads, VA, USA,* pp. 1–7. (2022)
73. De Robertis, A. & Higginbottom, I. A post-processing technique to estimate the signal-to-noise ratio and remove echosounder background noise. *ICES J. Mar. Sci.* **64**, 1282–1291 (2007).
74. Ryan, T. E., Downie, R. A., Kloser, R. J. & Keith, G. Reducing bias due to noise and attenuation in open-ocean echo integration data. *ICES J. Mar. Sci.* **72**, 2482–2493 (2015).
75. Reiss, C. S., Cossio, A. M., Walsh, J., Cutter, G. R. & Watters, G. M. Glider-Based estimates of meso-zooplankton biomass density: a fisheries case study on antarctic krill (Euphausia superba) around the northern antarctic peninsula. *Front. Mar. Sci.* **8**, 604043 (2021).
76. Luque, S.P. Diving Behaviour Analysis in R. *R News* **7**, 8–14 (2007)
77. Calenge, C. The package "adehabitat" for the R software: a tool for the analysis of space and habitat use by animals. *Ecol. Model.* **197**, 516–519 (2006).
78. Ainley, D. *The Adélie Penguin: Bellwether of Climate Change* (Columbia University Press, 2002).
79. Dosio, A., Vilà-Guerau de Arellano, J., Holtslag, A. A. M. & Builtjes, P. J. H. Relating eulerian and lagrangian statistics for the turbulent dispersion in the atmospheric convective boundary layer. *J. Atmos. Sci.* **62**, 1175–1191 (2005).
80. LCS tool: a computational platform for lagrangian coherent structures (<https://github.com/jeixav/LCS-Tool-Article/>).
81. Haller, G. Distinguished material surfaces and coherent structures in three-dimensional fluid flows. *Phys. D.* **149**, 248–277 (2001).
82. Distance calculation using Haversine formula (https://www.matchworkds.com/matlabcentral/fileexchange/27785-distance-calculation-suing-haversine-formula, 2024).
83. Massey, F. J. Jr The Kolmogorov-Smirnov test for goodness of fit. *J. Am. Stat. Assoc.* **46**, 68–78 (1951).
84. Veatch, J., Klinck, J. M., Oliver, M., Statscewich, H., Kohut, J. High Frequency Radar (HFR) observed surface currents at Palmer Deep Canyon in the coastal ocean west of the Antarctic Peninsula in 2020 *BCO-DMO* version 1, https://doi.org/10.26008/1912/bco-dmo.917884.1 (2024).
85. Veatch, J., Klinck, J. M., Oliver, M., Statscewich, H., Kohut, J. Results from Finite Time Lyapunov Exponent calculations using High Frequency Radar observed surface currents around Palmer Deep Canyon from January to March of 2020 *BCO-DMO*version 1, https://doi.org/10.26008/1912/bco-dmo.917914.1 (2024).
86. Bernard, K. S., Hann, A., Veatch, J. Krill swarms detected with active acoustic EK80 onboard small boat surveys in Palmer Deep Canyon, Antarctica during January-March 2020 *BCO-DMO* version 1, https://doi.org/10.26008/1912/bco-dmo.949922.1 (2025).

Acknowledgements

This project was funded through the National Science Foundation, award # OPP 1745009. Many thanks to the Antarctic Support Contractor and their teams aboard the ARSV Laurence M. Gould, at Palmer Station, and headquarters in Denver, CO without whom a study of this scale would not be possible. Thank you to the students and field assistants for their valued involvement in the SWARM project in particular, Dr. Katherine Gallagher, Dr. Jerome Pinti, Dr. Thilo Klenz, Ethan Handel, and Jordi Maisch. We thank the Palmer Long-Term Ecological Research team and the Commission for the Conservation of Antarctic Marine Living Resources for their advice and collaboration, in particular the Seabird team of the Palmer Long-Term Ecological Research who were instrumental in the deployment of penguin tags.

Author contributions

J.V. contributed by writing the original draft of this manuscript, leading the formal analysis, validation and visualization of data, and contributed equally to data curation, developing methodology, and the conceptualization of this manuscript. J.K. contributed by leading the funding acquisition and supervision of this manuscript and contributed equally to the conceptualization, data acquisition, development of methodology, and reviewing and editing of this manuscript. M.O. contributed equally to data acquisition, development of methodology, analysis, and reviewing and editing of this manuscript, led the visualization of penguin tagged data, and contributed supporting supervision. H.S. contributed a leading role to the data acquisition and contributed equally to the conceptualization of this manuscript. E.F. contributed equally to the conceptualization and development of methodology in this manuscript and contributed supporting supervision. K.B. contributed equally to data validation, conceptualization, development of methodology, and reviewing and editing of this manuscript. H.F. contributed equally to conceptualization and reviewing and editing of this manuscript. W.F. contributed to penguin foraging data acquisition, conceptualization, reviewing and editing of this manuscript. A.H. led the validation of the active acoustic data and contributed equally to reviewing and editing of this manuscript. G.V. led the validation of the penguin tagged data and contributed equally to reviewing and editing of this manuscript.

Competing interests
The authors declare no competing interests.

Additional information
Supplementary information The online version contains supplementary material available at https://doi.org/10.1038/s43247-025-02101-x.

Correspondence and requests for materials should be addressed to Jacquelyn M. Veatch.

Peer review information *Communications Earth & Environment* thanks Alberto Baudena and the other, anonymous, reviewer(s) for their contribution to the peer review of this work. Primary Handling Editors: Heike Langenberg, Aliénor Lavergne. A peer review file is available.